

AD-A280 383



The
American
Physical
Society



Proceedings of the 1993 Particle Accelerator Conference

DTIC
ELECTE
JUN 13 1994
S F D

Volume 2 of 5

Pages 748-1640

This document has been approved
for public release and sale; its
distribution is unlimited.

105218

94-17991



Papers from the fifteenth biennial Particle Accelerator Conference, an international forum on accelerator science and technology held May 17-20, 1993, in Washington, D.C., organized by the Continuous Electron Beam Accelerator Facility (CEBAF), jointly sponsored by the Institute of Electrical and Electronics Engineers Nuclear and Plasma Sciences Society and the American Physical Society Division of Physics of Beams, and conducted with support from the U.S. Department of Energy, the National Science Foundation, and the Office of Naval Research.

DTIC QUALITY INSPECTED 1

94 6 10 095

1993 IEEE Particle Accelerator Conference

Abstracting is permitted with credit to the source. Libraries are permitted to photocopy beyond the limits of U.S. Copyright law for private use of patrons those articles in this volume that carry a code at the bottom of the first page, provided the per-copy fee indicated in the code is paid through the Copyright Clearance Center, 27 Congress Street, Salem, MA 01970. For other copying, reprint, or republications permission, write to the IEEE Copyright Manager, IEEE Service Center, 445 Hoes Lane, P.O. Box 1331, Piscataway, NJ 08855-1331. All rights reserved. Printed in the USA. Copyright © 1993 by The Institute of Electrical and Electronics Engineers, Inc.

IEEE Catalog Number: 93CH3279-7

Library of Congress Number: 88-647453

Additional copies of this publication are available from

ISBN Softbound: 0-7803-1203-1

Casebound: 0-7803-1204-x

Microfiche: 0-7803-1205-8

IEEE Service Center

445 Hoes Lane

Piscataway, NJ 08854-4150



The
American
Physical
Society

1993 Particle Accelerator Conference, Washington, D.C., 17-20 May

Conference Chairman
Christoph Leemann, *CEBAF*
Annie Soltys, Executive Assistant
Telephone: (804) 249-7575
E-mail: soltys@cebaf.gov
Fax: (804) 249-5024

18-May-94
Box 2 of 2

Organizing Committee

M. Allen, *SLAC*
W. Barletta, *LLNL*
K. Berkner, *LBL*
D. Berley, *NFS*
J. Bisognano, *CEBAF*
R. Briggs, *SSCL*
Y. Cho, *ANL*
L. Costrell, *NBS*
M. Craddock, *U. of BC*
W. K. Dawson, *TRIUMF*
H. Edwards, *FNAL*
S. Holmes, *FNAL*
S. Krinsky, *BNL*
H. Lustig, *APS*
C. Roberson, *ONR*
S. Schriber, *LANL*
D. Sutter, *DOE*
S. Tazzari, *U. of Rome II & INFN*
M. Tigner, *Cornell*
W. T. Weng, *BNL*

Program Committee

J. Bisognano, Chair, *CEBAF*
Telephone: (804) 249-7521
E-mail: bisognano@cebaf.gov
H. Edwards, Deputy Chair, *FNAL*

Program Treasurer

Julie Leverenz
Telephone: (804) 249-7642
E-mail: leverenz@cebaf.gov

Conference Editor

Steven T. Corneliussen, *CEBAF*
Telephone: (804) 249-7582
E-mail: corneliussen@cebaf.gov

Editorial Assistant

Linda Carlton
Telephone: (804) 249-7690
E-mail: carlton@cebaf.gov
Fax: (804) 249-5024

DEFENSE TECHNICAL INFORMATION CENTER
BUILDING 5, CAMERON STATION
ALEXANDRIA, VA 22304-6145

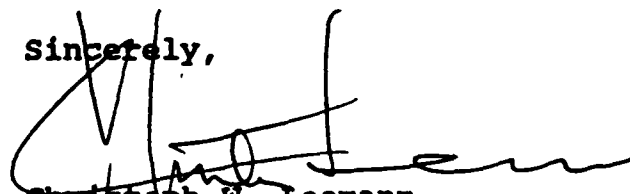
REF.: GRANT NO. N00014-93-1-0623

Dear Sir or Madam:

Enclosed please find two (2) copies of the Proceedings of the 1993 Particle Accelerator Conference (PAC93). The above-referenced \$15,000 grant from the Office of Naval Research helped fund the cost of publishing the Proceedings, enabling us to keep the registration fee to a minimum.

On behalf of the conference organizers and the more than 1300 participants, thank you for supporting PAC93.

Sincerely,



Christoph W. Leemann
Conference Chairman

cc: D. Galicki, IEEE

DTIC QUALITY INSPECTED 1

Five-Volume Contents

Each volume begins with this five-volume table of contents and ends with the five-volume author index. The chairmen's foreword and a list of conference organizers and staff appear as front matter in Volume 1. A list of conference participants precedes the author index in Volume 5.

Accession For		
NTIS	CRA&I	<input checked="" type="checkbox"/>
DTIC	IAS	<input type="checkbox"/>
Unannounced		<input type="checkbox"/>
Justification		
By		
Distribution/		
Availability		
Dist	Avail	
A-1		

Volume 1

Opening Plenary

Chair: J. Bisognano

HERA Operations and Physics — B. H. Wiik, U. Hamburg and DESY..... 1

Single-Particle Beam Dynamics

Chair: W. Weng

Nonlinear Beam Dynamics Experiments at the IUCF Cooler Ring (<i>Invited Paper</i>) — S. Y. Lee, Indiana University	6
The Preservation of Low Emittance Flat Beams (<i>Invited Paper</i>) — T. O. Raubenheimer, SLAC	11
Long-Term Stability Studies for CERN-LHC (<i>Invited Paper</i>) — W. Scandale, CERN	16
Emittance Growth in a Low Energy Proton Beam (<i>Invited Paper</i>) — J. A. Palkovic, SSCL	21
Proton Extraction from the CERN-SPS by a Bent Crystal — S. Weisz and the RD22 Collaboration; CERN	26
Longitudinal Tracking with Phase and Amplitude Modulated RF — D. D. Caussyn, M. Ball, B. Brabson, J. Budnick, J. Collins, V. Derenchuk, G. East, M. Ellison, T. Ellison, D. Friesel, B. Hamilton, H. Huang, W. P. Jones, S. Y. Lee, D. Li, S. Nagaitsev, X. Pei, T. Sloan, Y. Wang, IUCF; A. W. Chao, S. Dutt, M. Syphers, Y. T. Yan, P. L. Zhang, SSCL; M. G. Minty, SLAC; K. Y. Ng, FNAL	29
Measurement of Spin Motions in a Storage Ring Outside the Stable Polarization Direction — N. Akchurin, A. Bravar, J. McPherson, F. Olchowski, Y. Onel, U. Iowa; L. Badano, M. Conte, INFN Genova; A. Penzo, INFN Trieste; J. Hall, U. New Mexico; A. Pisent, INFN Legnaro; M. Pusterla, INFN Padova; T. Rinckel, Indiana U.; R. Rossmanith, CERN; H. Kreiser, U. Hamburg	32
A Clean Way to Measure Nonlinear Momentum Compaction Factor a_1 — J. P. Shan, I. Kourbanis, D. McGinnis, K. Y. Ng, S. Peggs, FNAL	35
Long-Term Tracking with Symplectic Implicit One-Turn Maps — Y. T. Yan, M. Li, M. J. Syphers, SSCL; P. J. Channell, LANL	38
Injection Method Using the Third Order Resonance at TARN II — M. Tomizawa, Y. Arakaki, K. Chida, S. Watanabe, T. Watanabe, T. Katayama, M. Yoshizawa, INS Tokyo; A. Noda, Kyoto U.	41
Effects of Tidal Forces on the Beam Energy in LEP — L. Arnaudon, F. Bordry, W. Coosemans, B. Dehning, K. Henrichsen, A. Hofmann, R. Jacobsen, J. P. Koutchouk, L. Lawson-Chroco, M. Mayoud, J. Miles, R. Olsen, M. Placidi, G. Ramseier, R. Schmidt, J. Wenninger, CERN; A. Blondel, Ec. Polytech. Paris; R. Assmann, MPI Munich; G. E. Fischer, C. Pan, SLAC; R. Olivier, Lausanne U.	44

Poster presentations:

The Appearance of Beam Lines — D. C. Carey, FNAL	47
Multipole Channel Parameters for Equalization of Beam Intensity Distribution — Y. K. Batygin, MEPI	50
Single Beam Effects Due to Errors in Crab Compensation — D. Sagan, Cornell	53
Lattice Design of the LANL Spallation-Source Compressor Ring — B. Blind, A. J. Jason, F. Neri, LANL	56
Optics Simulations of the 5 MeV NPBSE FOX Telescope — M. F. Reusch, D. L. Bruhwiler, Grumman Corp.	59
Longitudinal Kinetic Energy Spread from Focusing in Charged Particle Beams — N. Brown, M. Reiser, D. Kehne, D. X. Wang, J. G. Wang, U. Maryland	62
Numerical and Experimental Studies of Halo Formation Due to Mismatch in a Space-Charge-Dominated Electron Beam — D. Kehne, M. Reiser, U. Maryland; H. Rudd	65
Suppression of the Main LEP Coupling Source — J. Billan, J.-P. Gourber, J.-P. Koutchouk, V. Remondino, CERN	68
Applications of Matrix Optics to Acceptance Studies in Low-Beta Ion Linacs — K. Joh, J. A. Nolen, ANL	71
Analytical Evaluation of the Second Order Momentum Compaction Factor and Comparison with MAD Results — J. P. Shan, S. G. Peggs, S. A. Bogacz, FNAL	74
Chromaticity Compensation Scheme for the Main Injector — S. A. Bogacz, FNAL	77

Proceedings of the 1993 Particle Accelerator Conference

Accelerator Physics Analysis with Interactive Tools — J. A. Holt, L. Michelotti, FNAL	80
The 50 MeV Beam Test Facility at LBL — W. Leemans, G. Behrsing, K.-J. Kim, J. Krupnick, C. Matuk, F. Selph, S. Chattopadhyay, LBL	83
Knowledge Rule Base for the Beam Optics Program TRACE 3-D — G. H. Gillespie, P. K. Van Straagen, B. W. Hill, G. H. Gillespie Assoc.	86
Beam Dynamics Studies of Four-Gap Low-Beta Superconducting Resonators — J. A. Nolen, K. Joh, ANL	89
Third-Order Corrections to the SLC Final Focus — N. J. Walker, R. Helm, J. Irwin, M. Woodley, SLAC	92
Global Tuning Knobs for the SLC Final Focus — N. J. Walker, J. Irwin, M. Woodley, SLAC	95
Sigma Matrix Reconstruction in the SLC Final Focus — P. Raimondi, P. J. Emma, N. Toge, N. J. Walker, V. Ziemann, SLAC	98
Beam Based Alignment of the SLC Final Focus Superconducting Final Triplets — P. Raimondi, P. J. Emma, N. Toge, N. J. Walker, V. Ziemann, SLAC	100
A Design of a Quasi-Isochronous Storage Ring — S. Y. Lee, Indiana U.; K. Y. Ng, FNAL; D. Trbojevic, BNL	102
Optimization Method for Orbit Correction in Accelerators — E. Bozoki, A. Friedman, BNL	105
A Fast Model-Calibration Procedure for Storage Rings — W. J. Corbett, M. J. Lee, V. Ziemann, SLAC	108
Dynamic Accelerator Modeling — H. Nishimura, LBL	111
Procedure for Determining Quadrupole and BPM Offset Values in Storage Rings — W. J. Corbett, V. Ziemann, SLAC	114
Beam Based Alignment of the SLC Final Focus Sextupoles — P. Emma, J. Irwin, N. Phinney, P. Raimondi, N. Toge, N. J. Walker, V. Ziemann, SLAC	116
Analysis of Higher Order Optical Aberrations in the SLC Final Focus Using Lie Algebra Techniques — N. J. Walker, J. Irwin, M. Woodley, SLAC	119
Simulation Support for Commissioning and Operating the SSC Linac — F. W. Guy, J. W. Hurd, C. R. Chang, D. Raparia, C. Y. Yao, SSCL	122
The Provision of IP Crossing Angles for the SSC — Y. Nosochkov, SSCL; D. M. Ritson, SLAC	125
Interactive Simulation of LEB Commissioning Procedure on a Hypercube Parallel Computer — G. Bourianoff, M. Botlo, B. Cole, S. Hunt, N. Malitsky, A. Romero, SSCL	128
Localized Chromaticity Correction of Low-Beta Insertions in Storage Rings — M. Donald, R. Helm, J. Irwin, H. Moshhammer, SLAC; E. Forest, D. Robin, A. Zholents, LBL; M. Sullivan, U. Ca., SLAC	131
Amplitude Function Mismatch — M. J. Syphers, T. Sen, SSCL; D. A. Edwards, DESY/Fermilab	134
SSC Collider Arc Lattice — M. J. Syphers, E. D. Courant, A. A. Garren, S. K. Kauffmann, T. Sen, SSCL	137
Second Order Chromaticity of the Interaction Regions in the Collider — T. Sen, M. J. Syphers, SSCL	140
Chromaticity Correction for the SSC Collider Rings — T. Sen, Y. Nosochkov, F. Pilat, R. Stiening, SSCL; D. M. Ritson, SLAC	143
Effect of Power Supply Ripple on Emittance Growth in the Collider — T. Sen, M. J. Syphers, SSCL	146
The QBA Optics for the 3.2 GeV Synchrotron Light Source ROSY II — D. Einfeld, Res. Ctr. Rossendorf; M. Plesko, Sincrotrone Trieste	149
Dynamic Aperture of the 2.5 GeV Synchrotron Radiation Source LISA — D. Einfeld, Fachhochschule Ostfriesland; D. Husmann, U. Bonn; M. Plesko, Sincrotrone Trieste	152
Four-Cell Third-Order Achromats and Their Application to Multi-Pass Time-of-Flight Spectrometers — W. Wan, M. Berz, MSU-NSCL	155
An Automatic Finder of Field Defects in a Large A.G. Machine — A. Verdier, J. Chappelier, CERN	158
Automatic and Expert Systems for Orbit Analysis — A. Verdier, J. Chappelier, CERN	161
Symplectic Scaling, a DA Based Tool — G. H. Hoffstätter, M. Berz, NSCL-MSU	164
New Features in DIMAD — R. V. Servranckx, TRIUMF	167
A First Order Matched Transition Jump at RHIC — S. Peggs, S. Tepikian, D. Trbojevic, BNL	168
Comparison of Aperture Determinations on RHIC for Single Particles Tracked 10^6 Turns and 100 Particles, Having Randomly Generated Initial Coordinates, Tracked for 1000 Turns — G. F. Dell, BNL	171
Status of the Variable Momentum Compaction Storage Ring Experiment in SPEAR — P. Tran, A. Amiry, C. Pellegrini, UCLA; J. Corbett, M. Cornacchia, M. Lee, H.-D. Nuhn, H. Winick, D. Wu, SLAC; A. Hofmann, CERN; D. Robin, LBL	173
SSC High Energy Booster Resonance Corrector and Dynamic Tune Scanning Simulation — P. Zhang, S. Machida, SSCL	176
Transport Properties of the CEBAF Cavity — Z. Li, Coll. of William & Mary/CEBAF; J. J. Bisognano, B. C. Yunn, CEBAF	179

Each volume begins with this five-volume table of contents and ends with the five-volume author index. The chairmen's foreword and a list of conference organizers and staff appear as front matter in Volume 1. A list of conference participants precedes the author index in Volume 5.

Five-Volume Contents

Global Coupling and Decoupling of the APS Storage Ring — Y. C. Chae, J. Liu, L. C. Teng, ANL	182
Conventional Collimation and Linac Protection — J. Irwin, R. Helm, W. R. Nelson, D. Walz, SLAC	185
Measurement of Beta-Function and Phase Using the Response Matrix — Y. Chung, G. Decker, K. Evans, Jr., ANL ..	188
MATCH 1.0: The Program for Analytical Matching of Insertion — I. P. Yudin, JINR Moscow	191
The Application Package DeCA for Calculating Cyclic Accelerators — P. I. Gladkikh, A. Yu. Zelinsky, M. A. Strelkov, Kharkov Inst.	194
Echo Effect in Accelerators — G. V. Stupakov, S. K. Kauffmann, SSCL	197
Tune Shift Effect Due to the Sextupole Longitudinal Periodic Structure in the Superconducting Dipole Magnets — G. López, S. Chen, SSCL	200
Decoupling Schemes for the SSC Collider — Y. Cai, G. Bourianoff, B. Cole, R. Meinke, J. Peterson, F. Pilat, S. Stampke, M. Syphers, R. Talman, SSCL	203
Matrix Nonlinear Beam Dynamics in Curvilinear Space-Time — A. Dymnikov, U. St. Petersburg; R. Hellborg, U. Lund	206
A Numerical Check of the Thermal Wave-Model for Particle-Beam Dynamics — R. Fedele, G. Miele, U. Napoli; F. Galluccio, INFN Napoli	209
Longitudinal Dynamics for Electrons in the Thermal Wave Model for Charged Particle Beams — R. Fedele, G. Miele, U. Napoli/INFN Napoli; L. Palumbo, U. Roma/INFN-LNF	212
Experimental Measurement of Dynamic Aperture at the Photon Factory Storage Ring — Y. Kobayashi, T. Mitsuhashi, A. Ueda, KEK; T. Yamakawa, Tohoku U.	215
Lattice and Dynamic Aperture of the Duke FEL Storage Ring — Y. Wu, V. N. Litvinenko, J. M. J. Madey, Duke ...	218
Synchrotron Coupling Effects in Alternating Phase Focusing — W. Cheng, R. L. Gluckstern, H. Okamoto, U. Maryland	221
Experimental Determination of a Betatron Difference Resonance — M. Ellison, M. Ball, B. Brabson, J. Budnick, D. D. Caussyn, J. Collins, V. Derenchuk, G. East, T. Ellison, D. Friesel, B. Hamilton, H. Huang, W. P. Jones, S. Y. Lee, D. Li, S. Nagaitsev, T. Sloan, Y. Wang, IUCF; A. W. Chao, S. Dutt, M. Syphers, Y. T. Yan, P. L. Zhang, SSCL; M. Minty, SLAC; K. Y. Ng, FNAL; L. Teng, ANL; X. Pei, BNL	224
Experimental Results of the Betatron Sum Resonance — Y. Wang, M. Ball, B. Brabson, J. Budnick, D. D. Caussyn, J. Collins, V. Derenchuk, G. East, M. Ellison, D. Friesel, B. Hamilton, H. Huang, S. Y. Lee, W. P. Jones, D. Li, S. Nagaitsev, T. Sloan, IUCF; A. W. Chao, S. Dutt, M. Syphers, Y. T. Yan, P. L. Zhang, SSCL; K. Y. Ng, FNAL; M. Minty, SLAC; X. Pei, BNL.....	227
Chromaticity Compensation and Dynamic Aperture Limitation of SIBERIA-2 — V. Korchuganov, E. Levichev, V. Sajaev, BINP	230
RF Voltage Modulation at Discrete Frequencies, for Application to Proton Extraction Using Crystal Channeling — W. E. Gabella, J. Rosenzweig, UCLA; R. Kick, IMSA; S. Peggs, BNL	233
Modification of the Short Straight Sections of the High Energy Booster of the SSC — M. Li, D. Johnson, P. Kocur, R. Schailey, R. Servranckx, R. Talman, Y. Yan, R. York, V. Yarba, SSCL	236
Dynamic Aperture of the Chromatically Corrected Collider Lattice — F. Pilat, Y. Nosochkov, T. Sen, R. Stiening, SSCL	239
An Optimized Formulation for Deprit-Type Lie Transformations of Taylor Maps for Symplectic Systems — J. Shi, U. Houston; Y. T. Yan, SSCL	242
Symmetric Integrable-Polynomial Factorization for Symplectic One-Turn-Map Tracking — J. Shi, U. Houston; Y. T. Yan, SSCL	243
Recent Results from the Dynamic Aperture Experiment at the SPS — W. Fischer, J. Gareyte, M. Giovannozzi, T. Risselada, W. Scandale, F. Schmidt, CERN	246
Higher Order Tune Derivatives Due to Low- β Insertions — A. Verdier, CERN	249
A Quasi-Isochronous Operation Mode for the LNLS UVX Storage Ring — L. Lin, C. E. T. Gonçalves da Silva, Unicamp/LNLS Brazil	252
Tracking Studies and Machine Performance Simulation of the SSC Low Energy Booster — X. Wu, R. York, R. Servranckx, S. Machida, J. F. Knox-Seith, U. Wienands, SSCL	255
Magnetic Correction of RHIC Triplets — J. Wei, R. Gupta, S. Peggs, BNL	258
Beam-Beam Modulational Diffusion in 2 1/2 Dimensions — T. Satogata, S. Peggs, BNL	261
Preparation of an Experiment to Investigate Nonlinear Beam Dynamics at the Storage Ring DELTA — M. Schürmann, U. Dortmund	264
Statistics of the Half-Integer Stopband — S. Dutt, F. Chautard, R. Gerig, S. Kauffman, SSCL	267
Stochastic Dynamics for Accelerators — A. Pauluhn, DESY	270

Proceedings of the 1993 Particle Accelerator Conference

Diffusion Phenomena in Simple Hamiltonian Systems: Some Analytical and Numerical Results — A. Bazzani, S. Rambaldi, G. Turchetti, U. Bologna; M. Giovannozzi, CERN	273
Particle Acceleration in Extremely Strong Electromagnetic Wave Fields — K. O. Thielheim, U. Kiel	276
Laser Powered Beam Conditioner for Free Electron Lasers and Synchrotrons — H. Liu, G. Neil, CEBAF	279
Tracking Studies of Insertion Device Effects on Dynamic Aperture in the APS Storage Ring — Y. Chae, U. Houston; E. A. Crosbie, ANL	282
Particle Diffusion from Resonance Islands in Aladdin at SRC — J. Liu, E. Crosbie, L. Teng, J. Bridges, D. Ciarlette, R. Kustom, D. Voss, F. Mills, M. Borland, ANL; K. Symon, U. Wisc. Madison; W. Trzeciak, SRC Stoughton	285
Alternating-Phase Focusing with Amplitude Modulation — L. Sagalovsky, J. R. Delayen, ANL	288
Full-Turn Symplectic Map from a Generator in a Fourier-Spline Basis — J. S. Berg, R. L. Warnock, R. D. Ruth, SLAC; É. Forest, LBL	291
Synchrotron Resonances Due to Crab Cavities — S. Kurokawa, KEK; D. Pestrikov, KEK/BINP Novosibirsk	294
Third-Order Bending Magnet Optics for Cartesian Coordinates — V. V. Andreev, I. P. Yudin, JINR Moscow	297
Effects of Plane Undulator (Wiggler) Fields on Beam Dynamics at Large Orbit Distortion — S. Efimov, E. Bulyak, Kharkov Inst.	300
Bunching Property of High Current Injector with Subharmonic Prebuncher in Linac — Z. Zhang, Y. Chen, CIAE China	303
Beam Transport Line of CIAE Medical Cyclotron and Its Magnetic Elements Design Studies — T. Zhang, C. Chu, M. Fan, CIAE China	306
Resonant Beam Extraction with Constant Separatrix — K. Hiramoto, M. Tadokoro, J. Hirota, M. Nishi, Hitachi Ltd.	309
The On-Line Control Software for BEPC Beam Transport Lines — X. Zhang, K. Wei, C. Zhang, IHEP China.....	312
About Extraction of 70-GeV Protons by a Bent Crystal from the IHEP Accelerator to the Proza Setup — A. A. Asseev, A. N. Vasil'ev, E. A. Ludmirsky, V. A. Maishev, S. B. Nurusev, Yu. S. Fedotov, IHEP Russia	315
Increase a Bent Crystal Extraction Efficiency by Means of Thin Internal Target — A. A. Asseev, E. A. Myae, S. V. Sokolov, Yu. S. Fedotov, IHEP Russia	318
Influence of Thin Internal Target on the Bent Crystal Extraction Efficiency — A. A. Asseev, S. V. Sokolov, IHEP Russia	320
Extraction of 50 GeV Protons from IHEP Accelerator by Bent Crystal — A. A. Asseev, V. A. Maishev, E. A. Myae, IHEP Russia.....	322
On Using the Thin Target at Extraction of Protons from the Accelerators by Bent Crystal — A. A. Asseev, IHEP Russia	324
A Digital Computer Program for the Simulation of Positive or Negative Particle Beams on a PC — J. E. Boers, Thunderbird Simulations	327
Antiproton Extraction in the Fermilab Antiproton Accumulator — M. Church, S. O'Day, FNAL	330
Beam Optics of LEB-MEB Transfer Line for Superconducting Super Collider — N. Mao, J. A. McGill, K. L. Brown, R. E. Gerig, SSCL	333
Acceleration and Bunching by a Gap — S. Kulinski, INFN-LNF	336
The New Slow Extraction System of the CERN PS — Ch. Steinbach, H. Stucki, M. Thivent, CERN	339
Simulation of Slow Extraction in the Main Injector — C. S. Mishra, F. A. Harfoush, J. Johnstone, FNAL	342
Stability of Beam in the Fermilab Main Injector — C. S. Mishra, F. A. Harfoush, FNAL	345
Correction Schemes to Improve the Dynamical Aperture of the Main Injector — C. S. Mishra, F. A. Harfoush, FNAL	348
Defining the Systematic and Random Multipole Errors for Main Injector Tracking — F. A. Harfoush, B. C. Brown, H. D. Glass, C. S. Mishra, S. Peggs, FNAL	351
Experience with the New Reverse Injection Scheme in the Tevatron — S. Saritepe, G. Goderre, J. Annala, B. Hanna, A. Braun, FNAL	354
Injection and Extraction Performance at the SIS/ESR Facility — H. Eickhoff, K. Blasche, U. Blell, B. Franzke, J. Pinkow, GSI Darmstadt	357
The AGS-Booster Complex for the g-2 Experiment and RHIC Injection — M. Tanaka, Y. Y. Lee, BNL	360
First-Turn Losses in the LAMPF Proton Storage Ring (PSR) — R. Hutson, R. Macek, LANL	363

Each volume begins with this five-volume table of contents and ends with the five-volume author index. The chairmen's foreword and a list of conference organizers and staff appear as front matter in Volume 1. A list of conference participants precedes the author index in Volume 5.

Five-Volume Contents

Stripper-Foil Scan Studies of the First-Turn Beam Loss Mechanism in the LAMPF Proton Storage Ring (PSR) — R. Hutson, D. Fitzgerald, S. Frankle, R. Macek, M. Plum, C. Wilkinson, LANL	366
Measurement of H^0 Excited States Produced by Foil Stripping of 800-MeV H^- Ions — J. Donahue, D. Clark, S. Cohen, D. Fitzgerald, S. Frankle, R. Hutson, R. Macek, E. Mackerrow, O. van Dyck, C. Wilkinson, LANL; H. Bryant, M. Gulley, M. Halka, P. Keating, W. Miller, U. New Mexico	369
Reducing Phase-Dependent Emittance Growth with Local Flattopping — R. E. Laxdal, T. Kuo, G. H. Mackenzie, L. Root, TRIUMF; A. Papash, INR Kiev	372
An Ion-Source Model for First-Order Beam Dynamic Codes — C. L. Fink, B. P. Curry, ANL	375
Lattice Design and Injection Issues for the 2 TeV SSCL High Energy Booster to Collider Injection Lines — F. Wang, R. Schailey, J. McGill, D. Johnson, SSCL; K. L. Brown, SLAC	378
Detailed Studies on the Beam Transfer Line from Linac to Low Energy Booster Synchrotron for the SSC — R. Bhandari, J. McGill, F. Wang, S. Penner, SSCL	381
200 GeV Beam Transfer Lines at the SSC — F. G. Mariani, J. McGill, SSCL; K. Brown, SLAC	384
Effect of Betatron Motion on the Septum Flux in Superslow Extraction at the SSC — B. S. Newberger, U. Texas, Austin; H.-J. Shih, SSCL; J. A. Ellison, U. NM	387
Study of Energy Ramping Process Applied to the LNLS Synchrotron Light Source (Brazil) — L. Jahnel, C. E. T. Gonçalves da Silva, Unicamp/LNLS Brazil	390
Extraction System Design for the SSC Low Energy Booster — X. Wu, R. York, U. Wienands, T. Hunter, S. Sheynin, SSCL	393
Tests and Analysis for SLC Damping Ring Data — J. E. Spencer, SLAC	396
RF Capture Studies for Injection into a Synchrotron — E. S. Lessner, Y. Cho, ANL	399
Results from Beam Diffusion and Collimation Measurements in Preparation for Fermilab Tevatron Crystal Extraction — G. Jackson, FNAL	402
Operational Experience with Third Harmonic RF Cavity for Improved Beam Acceleration Through Transition in the Fermilab Main Ring — C. M. Bhat, J. Dey, J. Griffin, I. Kourbanis, J. MacLachlan, M. Martens, K. Meisner, K. Y. Ng, J. Shan, D. Wildman, FNAL	405
New Method for Control of Longitudinal Emittance During Transition in Proton Synchrotrons — J. E. Griffin, FNAL (Ret.)	408
Remarks on the Differential Luminosity in the Weak Disruption and the Transition Region — H. Heydari, TUB Germany	411
Flat Beam Studies in the SLC Linac — C. Adolphsen, F.-J. Decker, J. T. Seeman, SLAC	414
Method to Evaluate Steering and Alignment Algorithms for Controlling Emittance Growth — C. Adolphsen, T. Raubenheimer, SLAC	417
Experimental Simulation of Ground Motion Effects — M. J. Syphers, A. W. Chao, S. Dutt, Y. T. Yan, P. L. Zhang, SSCL; M. Ball, B. Brabson, J. Budnick, D. D. Caussyn, J. Collins, V. Derenchuk, G. East, M. Ellison, T. Ellison, D. Friesel, B. Hamilton, H. Huang, W. P. Jones, S. Y. Lee, D. Li, S. Nagaitsev, X. Pei, G. Rondeau, T. Sloan, Y. Wang, IUCF; M. G. Minty, SLAC; W. Gabella, K. Y. Ng, FNAL; L. Teng, ANL; S. Tepikian, BNL	420
Bunch Coalescing Studies for the SSC — N. Mahale, Y. T. Yan, J. Ellison, SSCL	423
Compensation of RF-Induced Energy Spread in the CEBAF Injector Chopping System — M. G. Tiefenback, G. A. Krafft, CEBAF	426
The North Arc of the SLC as a Spin Rotator — T. Limberg, P. Emma, SLAC; R. Rossmanith, CEBAF	429
The Evolution of Tensor Polarization — H. Huang, S. Y. Lee, IUCF, L. Ratner, BNL	432
Even Order Snake Resonances — S. Y. Lee, Indiana U.	435
Wiggler as Spin Rotators for RHIC — A. Luccio, BNL; M. Conte, U. Genova	438
Taylor Map and Calculation of Equilibrium Polarization for Proton Storage Rings — V. Balandin, N. Golubeva, INR Moscow	441
Investigation of Spin Resonance Crossing in Proton Circular Accelerators — V. Balandin, N. Golubeva, INR Moscow	444
Electron Beam Depolarization in a Damping Ring — M. Minty, SLAC	447
SPINLIE: New Computer Code for Polarization Calculation — Yu. Eidelman, V. Yakimenko, BINP	450
IHEP Polarized Proton Beam — V. N. Zapolsky, Yu. A. Chesnokov, A. Dyshkant, N. A. Galyaev, V. I. Kotov, V. I. Kryshkin, R. A. Rzaev, R. M. Sulyaev, S. V. Tsarik, V. G. Zarucheisky, IHEP Moscow	454
Measurement of Longitudinal Beam Polarization by Synchrotron Radiation — I. P. Karabekov, Yerevan/CEBAF, R. Rossmanith, CEBAF	457

Volume 1:	1-747
Volume 2:	748-1640
Volume 3:	1641-2545
Volume 4:	2546-3218
Volume 5:	3219-3933

Proceedings of the 1993 Particle Accelerator Conference

The Status of Polarization Studies at HERA — M. Böge, DESY	460
Computer Assisted Accelerator Tuning — J. K. Boyd, LLNL	463
Pulse-to-Pulse Simulation of Orbit Feedback for JLC Final Focus System — N. Yamamoto, K. Hirata, K. Oide, KEK	466
Multi-Dimensional Beam Emittance and β -Functions — J. Buon, LAL Orsay	469
Observation of the Coalescing of Beam into an Asymmetric RF Bucket by Stochastic Cooling — A. M. Halling, X. P. Lu, FNAL	472
Effects of Transverse Coupling on Transverse Beam Size, Simulation and Measurements — A. M. Halling, FNAL ...	474
One of Methods to Extract Truncated Taylor Map for Orbital and Spin Motion in Proton Storage Rings — V. Balandin, INR Moscow	477
Skew Quadrupole Effects in the IBM Compact Synchrotron — C. N. Archie, IBM Semiconductor R&D Ctr.	480
A Simulation Study of Linear Coupling Effects and Their Correction in RHIC — G. Parzen, BNL	483
Eigenfunctions of the Transfer Matrix in the Presence of Linear Coupling — G. Parzen, BNL	486
Emittance and Beam Size Distortion Due to Linear Coupling — G. Parzen, BNL	489
Use of Regularization Method in the Determination of Ring Parameters and Orbit Correction — Y. N. Tang, S. Krinsky, NSLS-BNL	492
Automatic Differentiation of Limit Functions — L. Michelotti, FNAL	495
Corrector Ironing in the SLC Final Focus — V. Ziemann, SLAC	498
General Normal Form Procedure to Correct Tune-Shift and Non-Linear Chromaticity for Large Accelerators like the LHC — M. Giovannozzi, F. Schmidt, CERN	500
Review of Recent Optical Issues in LEP — F. Ruggiero, CERN	503
Emittance and Damping of Electrons in the Neighborhood of Resonance Fixed Points — E. A. Crosbie, ANL	506
Effects of the Third Order Transfer Maps and Solenoid on a High Brightness Beam — Z. Parsa, BNL	509
Simultaneous Cancellation of Beam Emittance and Energy Spread in the CEBAF Nuclear Physics Injector Chopping System — H. Liu, J. Bisognano, CEBAF	512
The Linkage of Zlib to TEAPOT for Auto-Differentiation Map Extraction and Nonlinear Analysis — N. Sun, Y. T. Yan, F. Pilat, G. Bourianoff, SSCL	515
Influence of the Ionization Loss in the Diagnostic Foil on the Phase Motion in the Phasotron — O. N. Borisov, L. M. Onischenko, JINR, Dubna	518

Lepton RF Linacs and Linear Colliders

Chair: Y. Kimura

Recent SLC Developments (Invited Paper) — M. Ross, SLAC	522
CEBAF Commissioning Status (Invited Paper) — A. Hutton, CEBAF	527
Overview of Linear Collider Designs (Invited Paper) — R. H. Siemann, SLAC	532
Progress Report on the TESLA Test Facility — H. T. Edwards and the TESLA Collaboration, DESY/FNAL	537
The CERN Linear Collider — The CLIC Study Group, CERN	540
The Next Linear Collider Test Accelerator — R. D. Ruth, C. Adolphsen, K. Bane, R. F. Boyce, D. L. Burke, R. Callin, G. Caryotakis, R. Cassel, S. L. Clark, H. Deruyter, K. Fant, R. Fuller, S. Heifets, H. Hoag, R. Humphrey, S. Kheifets, R. Koontz, T. Lavine, G. A. Loew, A. Menegat, R. H. Miller, J. M. Paterson, C. Pearson, R. Phillips, J. Rifkin, J. Spencer, S. Tantawi, K. A. Thompson, A. Vlieks, V. Vylet, J. W. Wang, P. B. Wilson, A. Yeremian, B. Youngman, SLAC; N. M. Kroll, UC San Diego; C. Nantista, UCLA	543
High Power CW Linac in PNC — S. Toyama, Y. L. Wang, T. Emoto, M. Nomura, N. Takahashi, H. Oshita, K. Hirano, Y. Himeno, PNC Japan; I. Sato, A. Enomoto, M. Ono, KEK	546

Poster presentations:

A mm-Wave Planar Microcavity Structure for Electron Linear Accelerator System — Y. W. Kang, R. Kustom, F. Mills, G. Mavrogenes, ANL; H. Henke, TU Berlin	549
SCANUR: A Subcritical Reactor with Electron Linacs for Transmutation of Nuclear Wastes — A. Krasnykh, Yu. Popov, V. Rudenko, L. Somov, JINR Dubna; L. Men'schikov, V. Prusakov, S. Subbotin, Kurchatov Inst., Moscow	552
New Irradiation Field Shaping Systems of High Voltage Electron Accelerators for Industry — A. S. Ivanov, V. P. Ovchinnikov, M. P. Svinin, N. G. Tolstun, Efremov Inst.	555
A Versatile 2 MeV, 200 mA Compact X-Band Linac — C. E. Clayton, K. A. Marsh, UCLA	558

Each volume begins with this five-volume table of contents and ends with the five-volume author index. The chairmen's foreword and a list of conference organizers and staff appear as front matter in Volume 1. A list of conference participants precedes the author index in Volume 5.

Emittance Measurements of the 4.5 MeV UCLA RF Photo-Injector — S. C. Hartman, N. Barov, S. Park, C. Pellegrini, J. Rosenzweig, G. Travish, R. Zhang, P. Davis, C. Joshi, G. Hairapetian, UCLA	561
Commissioning of the SIBERIA-2 Preinjector and First Beam Results — V. Korchuganov, G. Kulipanov, E. Levichev, O. Nezhevenko, G. Ostreiko, A. Philipchenko, G. Serdobintsev, E. Shaimerdenov, V. Ushakov, INP Novosibirsk; A. Kadnikov, Yu. Krylov, S. Kuznetsov, V. Ushkov, YL. Yupinov, Kurchatov Inst.....	564
Emittance Measurement and Modeling of the ALS 50 MeV Linac to Booster Line — J. Bengtsson, W. Leemans, T. Byrne, LBL	567
Extended Version of an S-Band RF Gun — S. Park, C. Pellegrini, UCLA	570
Progress Report on the Commissioning of the Lisa 25 MeV SC Linac — F. Tazzioli, M. Castellano, M. Ferrario, S. Kulinski, M. Minestrini, P. Patteri, INFN-LNF; L. Catani, S. Tazzari, INFN Roma	573
The Plane Wave Transformer Linac Development at UCLA — R. Zhang, S. Hartman, C. Pellegrini, UCLA	575
Nanosecond MOSFET Gun Pulser for the CESR High Intensity Linac Injector — C. R. Dunnam, R. E. Meller, Cornell	578
Progress of PLS 2-GeV Linac — W. Namkung, I. Ko, M. Cho, C. Ryu, J. Bak, S. Nam, H. Lee, POSTECH	581
Lattice Design Principles for a Recirculated, High Energy, SRF Electron Accelerator — D. R. Douglas, CEBAF	584
Commissioning and Operation Experience with the CEBAF Recirculation Arc Beam Transport System — Y. Chao, M. Crofford, N. Dobeck, D. Douglas, A. Hofler, C. Hovater, G. A. Krafft, R. Legg, J. Perry, E. Price, S. Suhring, M. Tiefenback, J. van Zeijts, CEBAF	587
Linac Upgrade Plan for the KEK B-Factory — A. Enomoto, S. Anami, T. Kamitani, H. Hanaki, T. Shidara, I. Sato, KEK	590
Performance Characteristics of the Pulsed High Power Klystron Tube for PLS 2-GeV Linac — M. H. Cho, S. H. Nam, J. S. Oh, S. S. Park, H. S. Lee, J. S. Bak, I. S. Ko, W. Namkung, POSTECH	593
Electron Transport of a Linac Coherent Light Source (LCLS) Using the SLAC Linac — K. L. Bane, T. O. Raubenheimer, J. T. Seeman, SLAC	596
Phasing Schemes for the CEBAF Cavities — S. N. Simrock, R. Kazimi, G. A. Krafft, L. Merminga, L. Ninan, S. Witherspoon, CEBAF	599
Initial Data of Linac Preinjector for Spring-8 — S. Suzuki, H. Yoshikawa, T. Hori, K. Yanagida, A. Mizuno, K. Tamezane, K. Mashiko, H. Yokomizo, JAERI	602
Status of the Advanced Photon Source (APS) Linear Accelerator — M. White, W. Berg, R. Fuja, A. Grelick, G. Mavrogenes, A. Nassiri, T. Russell, W. Wesolowski, ANL	605
200 MeV RF Linac for Brookhaven National Laboratory — K. Whitham, H. Anamkath, S. Lyons, J. Manca, R. Miller, P. Treas, T. Zante, Titan Beta; R. Miller, SLAC; R. Heese, J. Keane, BNL	608
Design of the e^+e^- Frascati Linear Accelerator for DaFne — K. Whitham, H. Anamkath, S. Lyons, J. Manca, R. Miller, T. Zante, P. Treas, D. Nett, Titan Beta; R. Miller, SLAC; R. Boni, H. Hsieh, S. Kulinski, F. Sannibale, B. Spataro, M. Vescovi, G. Vignola, INFN-Frascati	611
The Possibility of Introducing Additional Focusing Caused by the Circular Irises in Iris Loaded Accelerator Sections — M. Kurz, P. Hülsmann, H.-W. Glock, H. Klein, Inst. f. Ang. Physik	614
Disruption Effects from the Collision of Quasi-Flat Beams — P. Chen, SLAC	617
Accelerator and RF System Development for NLC — A. E. Vlieks, R. Callin, H. Deruyter, R. Early, K. S. Fant, Z. D. Farkas, W. R. Fowkes, C. Galloway, H. A. Hoag, R. Koontz, G. A. Loew, T. L. Lavine, A. Menegat, R. H. Miller, D. Palmer, C. C. Pearson, R. D. Ruth, S. G. Tantawi, P. B. Wilson, J. W. Wang, C. Yoneda, SLAC; N. Kroll, UCSD; C. Nantista, UCLA	620
Rise Time of the Amplitudes of Time Harmonic Fields in Multicell Cavities — H.-W. Glock, M. Kurz, P. Hülsmann, H. Klein, Inst. f. Ang. Physik	623
CLIC Drive Beam Generation by Induction Linac and FEL Experimental Studies for the CERN Linear Collider — R. Corsini, C. D. Johnson, CERN; J. Gardelle, J. Grenier, CESTA	626
Beam Instabilities Related to Different Focusing Schemes in TESLA — A. Mosnier, CE Saclay	629
Large Aperture Final Focus System for TESLA — O. Napoly, CE Saclay	632
Chicane and Wiggler Based Bunch Compressors for Future Linear Colliders — T. O. Raubenheimer, P. Emma, S. Kheifets, SLAC	635
An "NLC-Style" Short Bunch Length Compressor in the SLAC Linac — J. T. Seeman, R. Holtzapple, SLAC	638
Multibunching Studies for CLIC — I. Wilson, W. Wuensch, CERN	641
Linear Collider Systems and Costs — G. A. Loew, SLAC	644
Application of the Monte Carlo Method to Estimate the Tenth-Value Thickness for X-Rays in Medical Electron Accelerators — J. Ródenas, G. Verdú, U. Politécnica, Valencia	647

Proceedings of the 1993 Particle Accelerator Conference

Burst-Mode Electron Gun Pulser for FEL with the ISIR Linac — K. Tsumori, Sumitomo Elect. Ind.; S. Okuda, T. Yamamoto, S. Suemine, S. Takamuku, Osaka U.	650
Positron Accumulation Ring for the SPring-8 Project — Y. Miyahara, JAERI-RIKEN	653

High-Current Accelerators

Chair: T. Fessenden

Induction Accelerator Development for Heavy Ion Fusion (<i>Invited Paper</i>) — L. L. Reginato, LBL	656
Generation and Focusing of High Energy, 35-kA Electron Beams for Pulsed-Diode Radiographic Machines: Theory and Experiment — R. L. Carlson, M. J. George, LANL; T. P. Hughes, D. R. Welch, MRC	661
Numerical Investigation of High-Current Ion Beam Acceleration and Charge Compensation in Two Accelerating Gaps of Induction Linac — N. G. Belova, Russian Acad.; V. I. Karas', Kharkov Inst.	664
The Light-Ion Pulsed Power Induction Accelerator for the Laboratory Microfusion Facility (LMF) — M. G. Mazarakis, D. L. Smith, L. F. Bennett, T. R. Lockner, R. E. Olson, J. W. Poukey, J. Boyes, Sandia Nat. Lab.	667

Poster presentations:

First Operation of the LELIA Induction Accelerator at CESTA — Ph. Eyharts, Ph. Anthouard, J. Bardy, C. Bonnafond, Ph. Delsart, A. Devin, P. Eyl, P. Grua, J. Labrousche, J. Launspach, P. Le Taillandier, J. de Mascureau, E. Merle, A. Roques, M. Thevenot, D. Villate, CEA-CESTA	670
An Induction Linac and Pulsed Power System at KEK — J. Kishiro, K. Ebihara, S. Hiramatsu, Y. Kimura, T. Ozaki, K. Takayama, D. H. Whittum, K. Saito, KEK	673
Design and Operation of Inductive Acceleration Modules for FEL with Controlled Voltage Ramp — S. Kawasaki, Saitama U.; H. Ishizuka, Fukuoka Inst.; A. Tokuchi, Nichicon Corp.; Y. Yamashita, S. Nakajima, Hitachi; S. Sakamoto, H. Maeda, M. Shiho, JAERI	676
Study on Induction Accelerator for Industrial Applications — Y. S. Cho, K. H. Baik, K. H. Chung, Seoul Nat. U.; B. H. Choi, Korea Atomic Energy Res. Inst.	679
Linear Induction Accelerators for Industrial Applications — M. I. Demsky, Yu. P. Vakhruhin, A. E. Baranovsky, A. A. Volzhev, A. P. Kuprianov, D. E. Trifonov, Efremov Inst.	682
High Power, High Brightness Electron Beam Generation in a Pulse-Line Driven Pseudospark Discharge — W. W. Destler, Z. Segalov, J. Rodgers, K. Ramaswamy, M. Reiser, U. Maryland	685
Experimental Study of Post-Acceleration and Transport of a Pseudospark-Produced Electron Beam — C. J. Liu, M. J. Rhee, U. Maryland	688
Compound-Lens Injector for a 19-MeV, 700-kA Electron Beam — T. W. L. Sanford, J. W. Poukey, J. A. Halbleib, Sandia Nat. Lab.; R. C. Mock, Ktech Corp.	691
Electron Flow in the SABRE Linear Induction Adder in Positive Polarity — J. R. Smith, Titan/Spectra; J. W. Poukey, M. E. Cuneo, D. L. Hanson, S. E. Rosenthal, M. Bernard, Sandia Nat. Lab.	694
Design and Progress of the AIRIX Induction Accelerator — J. de Mascureau, Ph. Anthouard, J. Bardy, C. Bonnafond, Ph. Delsart, A. Devin, Ph. Eyharts, P. Eyl, P. Grua, J. Labrousche, J. Launspach, P. Le Taillandier, E. Merle, A. Roques, B. Sacepe, M. Thevenot, D. Villate, CEA-CESTA	697
Nuclear Fusion of Protons with Ions of Boron — A. G. Ruggiero, BNL	700
Heavy Ion Fusion Injector Program — S. Yu, S. Eylon, W. W. Chupp, A. Faltens, T. Fessenden, E. Henestroza, R. Hipple, D. Judd, C. Peters, L. Reginato, H. Rutkowski, J. Stoker, D. Vanecek, LBL; J. Barnard, G. Caporaso, Y. J. Chen, F. Deadrick, A. Friedman, D. Grote, D. Hewett, LLNL	703
Ion Pulse Propagation Through a Previously Unfilled Electrostatic Aperture Lens Accelerating Column — H. L. Rutkowski, S. Eylon, D. S. Keeney, LBL; Y. J. Chen, D. W. Hewett, J. Barnard, LLNL	706
ILSE-ESQ Injector Scaled Experiment — E. Henestroza, S. Eylon, S. Yu, LBL; D. Grote, LLNL	709
One Dimensional Simulations of Transients in Heavy Ion Injectors — J. J. Barnard, G. J. Caporaso, LLNL; S. S. Yu, S. Eylon, LBL	712
Analysis of Beam Loading in Electrostatic Columns — G. J. Caporaso, J. J. Barnard, LLNL	715
Simulation of Transient Effects in the Heavy Ion Fusion Injectors — Y. Chen, D. W. Hewett, LLNL	718
Electrostatic Quadrupoles for Heavy-Ion Fusion — P. Seidl, A. Faltens, LBL	721
Simulation Studies of Space-Charge-Dominated Beam Transport in Large Aperture Ratio Quadrupoles — W. M. Fawley, L. J. Laslett, C. M. Celata, A. Faltens, LBL; I. Haber, NRL	724

Each volume begins with this five-volume table of contents and ends with the five-volume author index. The chairmen's foreword and a list of conference organizers and staff appear as front matter in Volume 1. A list of conference participants precedes the author index in Volume 5.

Three Dimensional PIC Simulation of Heavy Ion Fusion Beams: Recent Improvements to and Applications of WARP — <i>D. P. Grote, A. Friedman, LLNL; I. Haber, NRL</i>	727
Longitudinal Beam Dynamics for Heavy Ion Fusion — <i>D. A. Callahan, A. B. Langdon, A. Friedman, LLNL; I. Haber, NRL</i>	730
Correction of Longitudinal Errors in Accelerators for Heavy-Ion Fusion — <i>W. M. Sharp, D. A. Callahan, J. J. Barnard, A. B. Langdon, LLNL; T. J. Fessenden, LBL</i>	733
System Modeling for the Longitudinal Beam Dynamics Control Problem in Heavy Ion Induction Accelerators — <i>A. N. Payne, LLNL</i>	736
Development of FET-Switched Induction Accelerator Cells for Heavy-Ion Fusion Recirculators — <i>M. A. Newton, W. R. Cravey, S. A. Hawkins, H. C. Kirbie, C. W. Ollis, LLNL</i>	739
Parametric Studies for Recirculating Induction Accelerators as Drivers for Heavy-Ion Fusion — <i>R. L. Bieri, Schafer Assoc.</i>	742
A Fusion Device of the Continuous Electron Beam Confinement Used by the Accumulating Ring with the Continuous Injection — <i>S. Gao, G. Qian, CIAE China</i>	745

Volume 2

RF Structures <i>Chair: D. Reid</i>	
Operating Experience with High Beta Superconducting RF Cavities (<i>Invited Paper</i>) — <i>H. F. Dylla, L. R. Doolittle, J. F. Benesch, CEBAF</i>	748
Perpendicular Biased Ferrite-Tuned Cavities (<i>Invited Paper</i>) — <i>R. L. Poirier, TRIUMF</i>	753
SRF Cavities for Future Applications (<i>Invited Paper</i>) — <i>D. Proch, DESY</i>	758
Preparation and Testing of a Superconducting Cavity for CESR-B — <i>D. Moffat, P. Barnes, J. Kirchgessner, H. Padamsee, J. Sears, Cornell</i>	763
High Power Operation of Single-Cell 352-MHz Cavity for the Advanced Photon Source (APS) — <i>J. F. Bridges, Y. W. Kang, R. L. Kustom, K. Primdahl, ANL</i>	766

Poster presentations:

Development of Crab Cavity for CESR-B — <i>K. Akai, J. Kirchgessner, D. Moffat, H. Padamsee, J. Sears, M. Tigner, Cornell</i>	769
A New 3-D Electromagnetic Solver for the Design of Arbitrarily Shaped Accelerating Cavities — <i>P. Arcioni, M. Bressan, L. Perregrini, U. Pavia</i>	772
Design Study for the ELFA Linac — <i>W. A. Barletta, LBL; G. Bellomo, INFN/ U. Milan; G. Gemme, R. Parodi, INFN Genova; V. Stagno, V. Variale, INFN Bari</i>	775
The RF Cavity for DAFNE — <i>S. Bartalucci, R. Boni, A. Gallo, L. Palumbo, R. Parodi, M. Serio, B. Spataro, INFN-LNF</i>	778
Mechanical Results of the CEBAF Cavity Series Production — <i>J. Mammoser, J. F. Benesch, CEBAF</i>	781
Fabrication of Complex Mechanical Components — <i>Y. Beroud, SICN</i>	784
Measurements of Higher Order Modes in 3rd Harmonic RF Cavity at Fermilab — <i>C. M. Bhat, FNAL</i>	787
POISSON/SUPERFISH on PC Compatibles — <i>J. H. Billen, L. M. Young, LANL</i>	790
Radio Frequency Measurement and Analysis Codes — <i>J. H. Billen, LANL</i>	793
Progress on RF Superconductivity at Saclay — <i>Groupe d'Etudes des Cavités Supraconductrices, CE Saclay and Institut de Physique Nucléaire, Orsay</i>	796
A New Surface Treatment for Niobium Superconducting Cavities — <i>B. Bonin, C. Henriot, C. Antoine, B. Coadou, F. Koechlin, J. P. Rodriguez, E. Lemaitre, P. Greiner, CE Saclay</i>	798
Using the Panofsky-Wenzel Theorem in the Analysis of Radio-Frequency Deflectors — <i>M. J. Browman, LANL</i>	800
The Effects of Temperature and RF Power Level on the Tuning of the Water-Cooled SSC Low-Energy Booster Cavity — <i>C. Friedrichs, LANL; G. Hulsey, SSCL</i>	803
Superconducting Cavities for the LEP Energy Upgrade — <i>G. Cavallari, C. Benvenuti, P. Bernard, D. Bloess, E. Chiaveri, F. Genesio, E. Haebel, N. Hilleret, J. Tuckmantel, W. Weingarten, CERN</i>	806
TESLA Input Coupler Development — <i>M. Champion, D. Peterson, T. Peterson, C. Reid, M. Ruschman, FNAL</i>	809

Proceedings of the 1993 Particle Accelerator Conference

Computer Simulation and Cold Model Testing of CCL Cavities — C. R. Chang, C. G. Yao, D. A. Swenson, L. W. Funk, SSCL	812
Drive Linac for the Argonne Wakefield Accelerator — E. Chojnacki, R. Konecny, M. Rosing, J. Simpson, ANL	815
Choice of the RF Cavity for the SSC Collider — W. Chou, SSCL	818
High Field Conditioning of Cryogenic RF Cavities — M. Cole, T. Debiak, C. Lom, W. Shephard, J. Sredniawski, Grumman	821
Status of the SSC LEB RF Cavity — P. Coleman, F. Brandeberry, C. Friedrichs, Y. Goren, T. Grimm, G. Hulsey, S. Kwiatkowski, A. Propp, L. Taylor, L. Walling, SSCL; J. Averbukh, M. Karliner, V. Petrov, S. Yakovlev, BINP	824
RF Commissioning of the Superconducting Super Collider Radio Frequency Quadrupole Accelerator — R. I. Cutler, G. Arbique, J. Grippe, S. Marsden, O. Marrufo, R. Rodriguez, SSCL	827
Design of a Tuner and Adjustable RF Coupler for a CW 2856 MHz RF Cavity — M. S. de Jong, F. P. Adams, R. J. Burton, R. M. Hutcheon, T. Tran-Ngoc, AECL, Chalk River; A. Zolfaghari, P. T. Demos, MIT-Bates	829
A 2856 MHz RF Cavity for the MIT-Bates South Hall Ring — M. S. de Jong, F. P. Adams, R. J. Burton, R. M. Hutcheon, T. Tran-Ngoc, AECL, Chalk River; A. Zolfaghari, P. T. Demos, MIT-Bates	832
Cavity RF Mode Analysis Using a Boundary-Integral Method — M. S. de Jong, F. P. Adams, AECL, Chalk River ..	835
Design Considerations for High-Current Superconducting RFQ's — J. R. Delayen, C. L. Bohn, W. L. Kennedy, L. Sagalovsky, ANL	838
Commissioning of the CEBAF Cryomodules — M. Drury, T. Lee, J. Marshall, J. Preble, Q. Saulter, W. Schneider, M. Spata, M. Wiseman, CEBAF	841
Design and Fabrication of High Gradient Accelerating Structure Prototype at 36.5 GHz — V. A. Dvornikov, I. A. Kuzmin, MEPI Russia.....	844
The SSC RFQ-DTL Matching Section Buncher Cavities — T. Enegren, C. M. Combs, Y. Goren, M. D. Hayworth, A. D. Ringwall, D. A. Swenson, SSCL.....	846
Bulk Niobium Low-, Medium- and High- β Superconducting Quarter Wave Resonators for the ALPI Postaccelerator — A. Facco, J. S. Sokolowski, INFN Legnaro; I. Ben-Zvi, BNL; E. Chiaveri, CERN; B. V. Elkonin, Weizmann Inst.	849
A Numerical Method for Determining the Coupling Strengths and Resonant Frequencies of a Nonperiodic Coupled Cavity Chain — M. Foley, T. Jurgens, FNAL	852
Thermal Study of HOM Couplers for Superconducting RF Cavities — M. Fouaidy, T. Junquera, IPN Orsay; S. Chel, A. Mosnier, Saclay	855
Very Wide Range and Short Accelerating Cavity for MIMAS — C. Fougeron, P. Ausset, D. de Menezes, J. Peyromaure, G. Charruau, LNS-CE Saclay	858
Fundamental Mode Detuned Travelling Wave Accelerating Structure — J. Gao, LAL Orsay	862
Demi-Disc Travelling Wave Accelerating Structure — J. Gao, LAL Orsay	865
Analytical Formulae for the Coupling Coefficient β Between a Waveguide and a Travelling Wave Structure — J. Gao, LAL Orsay	868
Automated Bead-Positioning System for Measuring Impedances of RF Cavity Modes — D. A. Goldberg, R. A. Rimmer, LBL	871
Measurements of Higher-Order Mode Damping in the PEP-II Low-Power Test Cavity — R. A. Rimmer, D. A. Goldberg, LBL	874
Nonlinear Effects in Ferrite Tuned Cavities — Y. Goren, N. K. Mahale, L. Walling, T. Enegren, G. Hulsey, SSCL; V. P. Yakovlev, V. M. Petrov, BINP	877
Eddy Current Analysis for the SSC Low Energy Booster Cavity — Y. Goren, L. Walling, F. Brandeberry, N. Spayd, SSCL	880
Voltage Counter-Phasing in the SSC Low Energy Booster — Y. Goren, SSCL; T. F. Wang, LANL	883
An Update on High Peak Power (HPP) RF Processing of 3 GHz Nine-Cell Niobium Accelerator Cavities — P. Barnes, J. Kirchgessner, D. Moffat, H. Padamsee, J. Sears, Cornell; C. Crawford, FNAL; J. Graber, P. Schmüser, DESY	886
Microscopic Investigation of RF Surfaces of 3 GHz Niobium Accelerator Cavities Following RF Processing — P. Barnes, T. Flynn, J. Kirchgessner, J. Knobloch, D. Moffat, H. Muller, H. Padamsee, J. Sears, Cornell; J. Graber, DESY	889
A World Record Accelerating Gradient in a Niobium Superconducting Accelerator Cavity — P. Barnes, J. Kirchgessner, D. Moffat, H. Padamsee, J. Sears, Cornell; J. Graber, DESY	892

Each volume begins with this five-volume table of contents and ends with the five-volume author index. The chairmen's foreword and a list of conference organizers and staff appear as front matter in Volume 1. A list of conference participants precedes the author index in Volume 5.

Characterization of NSLS Accelerating Cavities Using Impedance Measurement Techniques — S. M. Hanna, P. M. Stefan, NSLS-BNL	895
In Search of Trapped Modes in the Single-Cell Cavity Prototype for CESR-B — W. Hartung, Cornell; E. Haebel, CERN	898
Envelope Equations for Transients in Linear Chains of Resonators — H. Henke, M. Filtz, TU Berlin	901
A Broad-Band Side Coupled mm-Wave Accelerating Structure for Electrons — H. Henke, W. Bruns, TU Berlin	904
Accelerator Structure Development for NLC — H. A. Hoag, H. Deruyter, C. Pearson, R. D. Ruth, J. W. Wang, SLAC; J. Schaefer, Texas Inst.	907
HOM Damping with Coaxial Dampers in a Pillbox Cavity Without the Fundamental Mode Frequency Rejection Filter — Y. W. Kang, R. L. Kustom, J. F. Bridges, ANL	910
Reduced Length Design of 9.8 MHz RF Accelerating Cavity for the Positron Accumulator Ring (PAR) of the Advanced Photon Source (APS) — Y. W. Kang, J. F. Bridges, R. L. Kustom, ANL	913
Higher Order Mode Damping System in the UNK RF Cavity — V. Katalev, V. Kudryavtsev, I. Sulygin, IHEP	916
Status and Outlook for High Power Processing of 1.3 GHz TESLA Multicell Cavities — J. Kirchgessner, P. Barnes, J. Graber, D. Metzger, D. Moffat, H. Muller, H. Padamsee, J. Sears, M. Tigner, Cornell; L. Bartelson, M. Champion, C. Crawford, H. Edwards, K. Koepke, M. Kuchnir, H. Pfeffer, FNAL; A. Matheisen, M. Pekeler, P. Schmüser, DESY	918
20 MV/m Accelerating Gradient with Heat Treatment of a Six Cell, 1.5 GHz Cavity for TESLA — J. Kirchgessner, P. Barnes, W. Hartung, D. Moffat, H. Padamsee, D. Rubin, J. Sears, M. Tigner, Cornell; M. Hiller, Babcock & Willcox; D. Saraniti, SLAC; Q. S. Shu, SSCL	921
A New 50 MHz RF Cavity for Aladdin — K. J. Kleman, SRC Madison	924
Performance of a CEBAF Production Cavity After High-Temperature Heat Treatment — P. Kneisel, M. G. Rao, CEBAF	927
Suppression of Higher-Order Modes in an RF Cavity by Resistive Material — T. Koseki, Y. Kamiya, ISSP Tokyo; M. Izawa, KEK	930
A Coaxial-Type Accelerating System with Amorphous Material — V. A. Krasnopolsky, MRTI Russia	933
Applications and Comparisons of Methods of Computing the S Matrix of 2-Ports — R. M. Jones, K. Ko, S. Tantawi, SLAC; N. Kroll, UCSD/SLAC; D. U. L. Yu, DULY Res.	936
Construction of the CEBAF RF Separator — A. Krycuk, J. Fugitt, A. Johnson, R. Kazimi, L. Turlington, CEBAF	939
RF Cavity for the Medium Energy Booster for SSCL — S. Kwiatkowski, J. Curbow, T. Enegren, A. Propp, SSCL; V. P. Yakovlev, V. M. Petrov, Budker Inst.	941
New Achievements in RF Cavity Manufacturing — G. Lippmann, K. Pimiskern, H. Kaiser, Dornier GmbH	944
Analysis of Mechanical Fabrication Experience with CEBAF's Production SRF Cavities — J. Mammoser, P. Kneisel, J. F. Benesch, CEBAF	947
Microphonic Analysis of Cryo-Module Design — A. Marziali, H. A. Schwettman, Stanford U.	950
The Design of a Pill-Box Cavity with Waveguide HOM Suppressors — A. Massarotti, G. D'Auria, A. Fabris, C. Pasotti, C. Rossi, M. Svandrlik, Sinc. Trieste	953
Power Conditioning of the RF Cavities for ELETTRA — A. Massarotti, G. D'Auria, A. Fabris, C. Pasotti, C. Rossi, M. Svandrlik, Sinc. Trieste	956
High Power Test of a SLED System with Dual Side-Wall Coupling Irises for Linear Colliders — H. Matsumoto, H. Baba, A. Miura, S. Yamaguchi, KEK	959
Performance Tests of a Ferrite-Loaded Cavity Under Operation Conditions — S. Papureanu, Ch. Hamm, A. Schnase, H. Meuth, Jülich	962
CLIC Transfer Structure (CTS) Simulations Using "MAFIA" — A. Millich, CERN	965
Magnetron Sputtering Configuration for Coating 1.3 GHz Cavities with a Nb Film — M. Minestrini, M. Ferrario, S. Kulinski, INFN-LNF; S. Tazzari, INFN Roma	968
Accelerator Structure for Low-Energy Electron Beam — A. V. Mishin, MEPI Moscow	971
Higher Order Mode Dampers for the KAON Booster Cavity — A. K. Mitra, TRIUMF	974
Design and Fabrication of a Ferrite-Lined HOM Load for CESR-B — D. Moffat, P. Barnes, J. Kirchgessner, H. Padamsee, J. Sears, M. Tigner, A. Tribendis, V. Veshcherevich, Cornell	977
High-Beta Linac Accelerating Structure — V. G. Andreev, G. I. Batsikh, B. I. Bondarev, B. P. Murin, MRTI	980
Design of a 90° Overmoded Waveguide Bend — C. Nantista, UCLA; N. M. Kroll, UCSD/SLAC; E. M. Nelson, SLAC	983
Numerical Simulation of Coupler Cavities for Linacs — C.-K. Ng, H. Deruyter, K. Ko, SLAC	986

Proceedings of the 1993 Particle Accelerator Conference

TESLA Vertical Test Dewar Cryogenic and Mechanical Design — T. H. Nicol, D. E. Arnold, M.S. Champion, FNAL	989
Update of the TRISTAN Superconducting RF System — S. Noguchi, K. Akai, E. Kako, K. Kubo, T. Shishido, KEK	992
Cryostat for a Beam Test with the CESR-B Cavity — E. Nordberg, P. Barnes, R. Ehrlich, J. Kirchgessner, D. Metzger, D. Moffat, H. Muller, H. Padamsee, J. Sears, K. She, M. Tigner, Cornell; W. Fox, LANL; H. Heinrichs, U. Wuppertal	995
A Statistical Model for Field Emission in Superconducting Cavities — H. Padamsee, K. Green, W. Jost, B. Wright, Cornell	998
Design and Test of Prototype Cavities for the ELFA Linac — G. Bellomo, R. Parodi, G. Gemme, P. Fabbriatore, R. Musenich, B. Zhang, INFN	1001
Frequency Domain Determination of the Waveguide Loaded <i>Q</i> for the SSCL Drift Tube Linac — J. Petillo, W. Krueger, A. Mondelli, SAIC; J. Potter, AccSys Technology	1004
Some Operational Characteristics of CEBAF RF Windows at 2 K — H. L. Phillips, C. Reece, T. Powers, V. Nguyen-Tuong, CEBAF	1007
Photoemission Phenomena on CEBAF RF Windows at Cryogenic Temperatures — T. Powers, P. Kneisel, M. Vaidya, CEBAF	1010
Fabrication of the APS Storage Ring Radio Frequency Accelerating Cavities — K. Primdahl, J. Bridges, F. Depaola, R. Kustom, ANL; D. Snee, FNAL	1013
Performance of Production SRF Cavities for CEBAF — C. Reece, J. Benesch, P. Kneisel, P. Kushnick, J. Mammosser, T. Powers, CEBAF	1016
A New 15 MHz, 4 MV/m RF-Deflector for the Munich Heavy Ion Recoil Spectrometer (MRS)— K. Rudolph, P. Jaenker, U. Munich	1019
Superconducting Multicell Cavity Development Program at Los Alamos — B. Rusnak, G. Spalek, E. Gray, J. N. DiMarco, R. DeHaven, J. Novak, P. Walstrom, J. Zumbro, H. A. Thiessen, J. Langenbrunner, LANL ..	1021
L-Band Superconducting Cavities at KEK for TESLA — K. Saito, S. Noguchi, E. Kako, M. Ono, T. Shishido, T. Tajima, M. Matsuoka, H. Miwa, T. Suzuki, H. Umezawa, KEK	1024
Design of a HOM Damped Cavity for the ATF Damping Ring — S. Sakanaka, K. Kubo, T. Higo, KEK	1027
Measurement of Microwave Properties of X-Band Accelerating Structure Under Pulsed High-Power Operation at Liquid Nitrogen Temperature — A. J. Saversky, I. S. Shchedrin, MEPI Moscow	1030
RF Systems Engineering for the SSC Collider Rings — G. Schaffer, P. D. Coleman, R. E. Mustaine, J. D. Wallace, X. Q. Wang, Y. Zhao, J. D. Rogers, SSCL	1033
Impedance Calculations for a Coaxial Liner — M. Filtz, T. Scholz, TU Berlin.....	1036
Design of a High-Power Test Model of the PEP-II RF Cavity — H. D. Schwarz, R. A. Bell, J. A. Hodgson, J. G. Judkins, K. Ko, N. Kroll, C. K. Ng, R. P. Pendleton, K. Skarpaas, SLAC; G. Lambertson, R. Rimmer, LBL; M. S. deJong, T. Tran-Ngoc, F. P. Adams, M. G. Lipsett, W. Mellors, AECL	1039
Construction of a Superconducting RFQ Structure — K. W. Shepard, W. L. Kennedy, ANL; K. R. Crandall, AccSys Technology	1042
Niobium Coaxial Quarter-Wave Cavities for the New Delhi Booster Linac — K. W. Shepard, ANL; A. Roy, P. N. Potukuchi, Nuc. Science Ctr., New Delhi	1045
Design of High Power Model of Damped Linear Accelerating Structure Using Choke Mode Cavity — T. Shintake, KEK	1048
Suppression of Longitudinal Coupled-Bunch Instability Using Energy Storage Cavity in B-Factory RF System — T. Shintake, KEK	1051
A Two-Gap Booster Synchrotron RF Cavity — W. R. Smythe, D. C. Van Westrum, U. Colorado	1054
HOM (Higher-Order Mode) Test of the Storage Ring Single-Cell Cavity with a 20-MeV <i>e</i> ⁻ Beam for the Advanced Photon Source (APS) — J. Song, Y. W. Kang, R. Kustom, ANL	1057
Performance of a 1500 MHz Niobium Cavity with 2K-LHe Channel Cooling — J. Susta, P. Kneisel, M. Wiseman, CEBAF	1060
Large Scale Production at Ansaldo of 352 MHz Niobium Coated LEP-CERN Cavities: Development Activities and First Results — A. Bixio, P. Gagliardi, M. Marin, S. Moz, W. Sciutto, F. Terzi, G. Zoni, Ansaldo	1063
RF Hardware Development Work for the CLIC Drive Beam — G. Carron, L. Thorndahl, CERN	1066
Accelerating Frequency Shift Minimization — A. V. Tiunov, V. I. Shvedunov, INP Moscow	1069

Each volume begins with this five-volume table of contents and ends with the five-volume author index. The chairmen's foreword and a list of conference organizers and staff appear as front matter in Volume 1. A list of conference participants precedes the author index in Volume 5.

Five-Volume Contents

Calculations and Model Measurements for the Euterpe Cavity — J. A. van der Heide, M. J. A. Rubingh, W. J. G. M. Kleeven, J. I. M. Botman, C. J. Timmermans, H. L. Hagedoorn, Eindhoven U. of Tech.	1072
APPLE Accelerator Prototype Cavity Fabrication and Low Power Tests — A. M. Vetter, T. L. Buller, T. D. Hayward, D. R. Smith, V. S. Starkovich, Boeing D&S	1075
Mechanically Tuned Accelerating Resonators — F. A. Vodopianov, MRTI	1078
Industrial Fabrication of Superconducting Accelerators — D. Dasbach, R. Fleck, D. Kiehlmann, M. Peiniger, H. Vogel, Siemens AG	1080
Broadband Higher-Order Mode (HOM) Damper for SSC LEB Ferrite-Tuned Cavity — L. Walling, G. Hulsey, T. Grimm, SSCL	1083
Design of the Detuned Accelerator Structure — J. W. Wang, E. M. Nelson, SLAC	1086
Construction of an RF Cavity for the LNLS Synchrotron — D. Wisnivesky, IFGW/ Unicamp/LNLS Brazil; M. A. Remy, R. H. A. Farias, LNLS Brazil	1089
Field Emitted Electron Trajectories for the CEBAF Cavity — B. C. Yunn, R. M. Sundelin, CEBAF	1092
Study on TESLA Cavity Shape — D. Zu, J. Chen, Beijing U.	1095

Power Technology and Miscellaneous Subsystems

Chair: D. Reid

Regulation Loops for the Ring Magnet Power Supplies in the SSC Accelerator Complex (<i>Invited Paper</i>) — E. J. Tacconi, C. F. Christiansen, SSCL	1098
High Power CW Klystrode® Amplifier for 267 MHz — M. B. Shrader, D. H. Preist, R. N. Tornoe, Varian	1103
Development of Multimewatt Klystrons for Linear Colliders — G. Caryotakis, R. Callin, K. Eppley, T. Lee, K. Fant, R. Fowkes, H. Hoag, C. Pearson, R. Phillips, S. Tantawi, A. Vlieks, E. Wright, SLAC; E. Lien, Los Altos, CA; G. Miram, Atherton, CA	1106
CEBAF's New RF Separator Structure Test Results — R. Kazimi, J. Fugitt, A. Krycuk, C. K. Sinclair, L. Turlington, CEBAF	1109
Frequency-Domain Analysis of Resonant-Type Ring Magnet Power Supplies — J. M. S. Kim, U. Victoria; K. W. Reiniger, TRIUMF	1112
The Workshop on Microwave-Absorbing Materials for Accelerators — I. E. Campisi, CEBAF.....	1115

Poster presentations:

Analysis and Applications of Quadrature Hybrids as RF Circulators — S. M. Hanna, J. Keane, NSLS-BNL	1118
Flower-Petal Mode Converter for NLC — H. A. Hoag, S. G. Tantawi, H. Deruyter, Z. D. Farkas, K. Ko, N. Kroll, T. L. Lavine, A. Menegat, A. E. Vlieks, SLAC	1121
Development of an S-Band RF Window for Linear Colliders — A. Miura, Grad. U. for Adv. Studies; H. Matsumoto, KEK	1124
High Power Test of RF Window and Coaxial Line in Vacuum — D. Sun, M. Champion, M. Gormley, Q. Kerns, K. Koepke, A. Moretti, FNAL	1127
Mode Selective Directional Coupler for NLC — S. G. Tantawi, SLAC	1130
Window Design with MAFIA — W. Bruns, H. Henke, B. Littmann, R. Lorenz, TU Berlin.....	1133
Dead-Time Tuning of a Pulsed RF Cavity — P. Balleyguier, CEA, Bruyères le Châtel	1136
Frequency Control of RF Booster Cavity in TRIUMF — K. Fong, M. Laverty, TRIUMF	1139
The Phase Servo Tuner Control System of the ALS 500 MHz Cavity — C. C. Lo, B. Taylor, LBL	1142
The Low Level System for the ELETTRA RF Plants — A. Massarotti, G. D'Auria, A. Fabris, C. Pasotti, V. Rizzi, C. Rossi, M. Svandrlik, Sinc. Trieste	1145
A Pulse Sequencer for the KAON Factory Beam Chopper — G. Waters, D. Bishop, M. J. Barnes, G. D. Wait, TRIUMF	1148
A Dual Frequency Resonator — P. Lanz, M. Lipnicky, M. Zach, TRIUMF	1151
The Los Alamos VXI-Based Modular RF Control System — S. P. Jachim, C. Ziomek, E. F. Natter, A. H. Regan, J. Hill, L. Eaton, W. D. Gutscher, M. Curtin, P. Denney, E. Hansberry, T. Brooks, LANL	1154
General Overview of the APS Low-Level RF Control System — J. D. Stepp, J. F. Bridges, ANL	1157
Operation of New RF Drivers for the Bevatron Local Injector — J. Calvert, J. Elkins, D. Howard, M. Hui, N. Kellogg, A. Lindner, R. Richter, LBL	1160
432-MHz RF Source for the JHP Proton Linac — M. Ono, S. Anami, H. Hanaki, Z. Igarashi, M. Kawamura, T. Kubo, C. Kubota, K. Kudo, E. Takasaki, T. Takenaka, KEK	1163

Volume 1: 1-747
Volume 2: 748-1640
Volume 3: 1641-2545
Volume 4: 2546-3218
Volume 5: 3219-3933

Proceedings of the 1993 Particle Accelerator Conference

Test Results of the AGS Booster Low Frequency RF System — R. T. Sanders, P. Cameron, R. Damm, A. Dunbar, M. Goldman, D. Kasha, A. McNerney, M. Meth, A. Ratti, R. Spitz, BNL	1166
Design and Test Results of a 600-kW Tetrode Amplifier for the Superconducting Super Collider — D. E. Rees, D. L. Brittain, LANL ; J. M. Grippe, O. Maruffo, SSCL	1169
Conceptual Design of the 26.7. MHz RF System for RHIC — J. Rose, D. P. Deng, R. McKenzie-Wilson, W. Pirkel, A. Ratti, BNL	1172
Operation of a High-Power CW Klystron with the RFQ1 Facility — J. Y. Sheikh, A. D. Davidson, G. E. McMichael, L. W. Shankland, B. H. Smith, AECL, Chalk River	1175
Design and Results of a 1.3 MW CW Klystron for LEP — E.-G. Schweppe, R. Bachmor, E. Demmel, Philips RHW	1178
Interleaved Wide and Narrow Pulses for the KAON Factory 1 MHz Chopper — G. D. Wait, M. J. Barnes, D. Bishop, G. Waters, TRIUMF	1181
Considerations Regarding the Efficiency of High Power RF Sources for Particle Accelerators — G. Clerc, C. Bearzatto, M. Bres, G. Faillon, Ph. Guidee, Thomson Tubes Elect.	1184
Initial Commissioning of High Power, Long Pulse Klystrons for SSC Injector Linacs — P. Collet, J. C. Terrien, Ph. Guidee, Thomson Tubes Elect.	1187
Simulation of Traveling-Wave Output Structures for High Power rf Tubes — K. R. Eppley, SLAC	1190
Upgrade of an RF Source of the Linac for the B-Factory Project — S. Fukuda, S. Anami, Y. Saito, S. Michizono, K. Nakao, I. Sato, KEK	1193
High-Power RF Pulse Compression with SLED-II at SLAC — C. Nantista, UCLA; Z. D. Farkas, T. L. Lavine, A. Menegat, R. D. Ruth, S. G. Tantawi, A. E. Vlieks, SLAC; N. M. Kroll, UCSD	1196
Rigid-Beam Model of a High-Efficiency Magnicon — D. E. Rees, P. J. Talerico, LANL; S. J. Humphries, Jr., UNM	1199
High Power Operation Results of the X-Band SLED System — S. Tokumoto, H. Mizuno, KEK; O. Azuma, IHI Japan	1202
Automated Testing of a High-Power RF Microwave Tube — A. Young, D. E. Rees, A. Vergamini, LANL	1205
Two-Klystron Binary Pulse Compression at SLAC — Z. D. Farkas, T. L. Lavine, A. Menegat, A. E. Vlieks, J. W. Wang, P. B. Wilson, SLAC	1208
New Compact Mode Converters for SLAC RF Pulse Power Compression System — G. Luo, SRRC Taiwan	1211
Performance of Litton 805 MHz, 12 MW Klystrons — Q. Kerns, M. B. Popovic, C. Kerns, A. Moretti, FNAL	1214
Higher-Order Modes in the APS Storage Ring Waveguides — S.O. Brauer, R. L. Kustom, ANL	1217
The Design and Production of the Higher-Order-Mode Loads for CEBAF — I. E. Campisi, L. K. Summers, B. H. Branson, A. M. Johnson, A. Betto, CEBAF	1220
The High Level RF System for Transition Crossing Without RF Focusing in the Main Ring at Fermilab — J. Dey, C. M. Bhat, A. Crawford, D. Wildman, FNAL	1223
RF System of the CW Race-Track Microtron-Recuperator for FELs — V. Arbuzov, S. Belomestnykh, A. Bushuyev, M. Fomin, N. Gavrilov, E. Gorniker, A. Kondakov, I. Kuptsov, G. Kurkin, V. Petrov, I. Sedlyarov, V. Veshcherevich, BINR, Russia.....	1226
Three Years of Operational Experience with the LEP RF System — S. Hansen, CERN	1229
Measured Performance of the GTA RF Systems — P. M. Denney, S. P. Jachim, LANL	1232
Improved RF System for Aladdin — K. J. Kleman, SRC Madison	1235
The ALS Storage Ring RF System — B. Taylor, C. C. Lo, K. Baptiste, J. Guigli, J. Julian, LBL	1238
The Upgrade Project for the RF System for the Brookhaven AGS — J. M. Brennan, D. J. Ciardullo, T. Hayes, M. Meth, A. J. McNerney, A. Otis, W. Pirkel, R. Sanders, R. Spitz, F. Toldo, A. Zaltsman, BNL	1241
Acceptance Test Performance of the Rocketdyne Radio Frequency Power System — M. Curtin, J. Hall, P. Metty, Rocketdyne; E. Gower, J. Manca, K. Whitham, Titan-Beta Corp.....	1244
The LEP II RF Power Generation System — H. Frischholz, CERN	1247
Overview and Status of RF Systems for the SSC Linac — J. Mynk, J. Grippe, R. I. Cutler, R. Rodriguez, SSCL	1250
Possibilities and Limitations for a Fully Digital RF Signal Synthesis and Control — H. Meuth, A. Schnase, H. Halling, Jülich	1253
RF System Analyses for the SSC Collider Rings — J. D. Rogers, P. D. Coleman, G. Schaffer, J. D. Wallace, X. Q. Wang, Y. Zhao, SSCL	1256
PEP-II Prototype Klystron — W. R. Fowkes, G. Caryotakis, T. G. Lee, C. Pearson, E. L. Wright, SLAC	1259

Each volume begins with this five-volume table of contents and ends with the five-volume author index. The chairmen's foreword and a list of conference organizers and staff appear as front matter in Volume 1. A list of conference participants precedes the author index in Volume 5.

Five-Volume Contents

Low Cost Concepts to Reduce the Voltage Ripple of the DC Power Supply — Y. Cheng, K. Liu, SRRC Taiwan	1262
Magnet Power Supply System for the ALS Storage Ring and Booster — L. T. Jackson, K. Luchini, I. Lutz, LBL	1265
Design and Development of Bipolar Power Supply for APS Storage Ring Correctors — Y. G. Kang, ANL	1268
Circuit Description of Unipolar DC-to-DC Converters for APS Storage Ring Quadrupoles and Sextupoles — D. G. McGhee, ANL	1271
PLL Subsystem for NSLS Booster Ring Power Supplies — J. Murray, Stony Brook; R. Olsen, J. Dabrowski, BNL	1274
Control and Performance of the AGS and AGS Booster Main Magnet Power Supplies — R. K. Reece, R. Casella, B. Culwick, J. Geller, I. Marneris, J. Sandberg, A. Soukas, S. Y. Zhang, BNL	1277
Hierarchical Modelling of Line Commutated Power Systems Used in Particle Accelerators Using Saber — J. A. Reimund, SSCL	1280
Independent Resonant System Tracking Considerations — K. W. Reiniger, TRIUMF	1283
Electrical Characteristics of the SSC Low-Energy Booster Magnet System — A. Young, B. E. Shafer, LANL	1285
Analysis and Design of a High-Current, High-Voltage Accurate Power Supply for the APS Storage Ring — M. Fathizadeh, ANL	1288
Design of the HIMAC Synchrotron Power Supply — M. Kumada, K. Sato, A. Itano, M. Kanazawa, E. Takada, K. Noda, M. Sudou, T. Kohno, H. Ogawa, S. Yamada, Y. Sato, T. Yamada, A. Kitagawa, J. Yoshizawa, T. Murakami, Y. Hirao, NIRS; S. Matsumoto, Dokkyo U.; H. Sato, T. Sueno, T. Kato, K. Endo, KEK; K. Utino, Tsukuba Tech.; Y. Takada, U. Tsukuba; A. Noda, Kyoto U.; T. Tanabe, S. Watanabe, INS; S. Koseki, H. Kubo, Hitachi	1291
A 2-Megawatt Load for Testing High Voltage DC Power Supplies — D. Horan, R. Kustom, M. Ferguson, K. Primdahl, ANL	1294
Energy Storage Inductor for the Low Energy Booster Resonant Power Supply System — C. Jach, SSCL; A. Medvedko, S. Petrov, INP Moscow; V. Vinnik, Y. Fishler, UETM Russia	1297
A High Power Water Cooled Resistor for the High Voltage Power Supply in the TRIUMF RF System — K. Jensen, G. Blaker, R. Kuramoto, TRIUMF	1300
Filament Power Supply Improvement of the TRIUMF RF System — A. K. Mitra, J. J. Lu, TRIUMF	1303
Advances in the Development of the Nested High Voltage Generator — R. J. Adler, R. J. Richter-Sand, North Star Res. Corp.	1306
High-Power Klystron Modulator Using a Pulse-Forming Line and Magnetic Switch — M. Akemoto, S. Takeda, KEK	1309
A Compact Modulator for RF Source Development — J. D. Ivers, G. S. Kerslick, J. A. Nation, L. Schachter, Cornell	1312
High Power Pulse Modulator for PLS Linac — S. H. Nam, M. H. Cho, J. S. Oh, S. S. Park, W. Namkung, POSTECH	1315
Pulse Modulator Developments in Support of Klystron Testing at SLAC — R. F. Koontz, R. Cassel, J. de Lamare, D. Ficklin, S. Gold, K. Harris, SLAC	1318
A Blumlein Type Modulator for 100-MW Class X-Band Klystron — H. Mizuno, KEK; T. Majima, S. Sakamoto, Y. Kobayashi, IHI Japan	1321
Noise Reduction Techniques Used on the High Power Klystron Modulators at Argonne National Laboratory — T. J. Russell, ANL	1324
Novel Gigawatt Power Modulator for RF Sources — I. Yampolsky, G. Kirkman, N. Reinhardt, J. Hur, B. Jiang, Integrated App. Physics Inc.	1327
Optimization of Speed-Up Network Component Values for the 30 Ω Resistively Terminated Prototype Kicker Magnet — M. J. Barnes, G. D. Wait, TRIUMF	1330
Test Results of the 8.35 kA, 15 kV, 10 pps Pulser for the Elettra Kickers — R. Fabris, P. Tosolini, Sinc. Trieste	1333
Preliminary Testing of the LEB to MEB Transfer Kicker Modulator Prototype — G. C. Pappas, D. R. Askew, SSCL	1336
A Novel Technique for Pulsing Magnet Strings with a Single Switch — R. J. Sachschaale, C. Dickey, P. Morcombe, Duke	1339
Linac Pulsed Quad Power Supply — L. Bartelson, FNAL	1342
The AGS New Fast Extracted Beam System Orbit Bump Pulser — J. S. Chang, A. V. Soukas, BNL	1345
Experimental Investigation of High Voltage Nanosecond Generators of Injection System for SIBERIA-2 Storage Ring — A. Kadnikov, Y. Matveev, BINP	1348

Proceedings of the 1993 Particle Accelerator Conference

Design and Preliminary Results for a Fast Bipolar Resonant Discharge Pulser Using SCR Switches for Driving the Injection Bump Magnets at the ALS — G. Stover, L. Reginato, LBL	1351
Design and Preliminary Testing of the LEB Extraction Kicker Magnet at the SSC — D. E. Anderson, L. X. Schneider, SSCL	1354
Development of a High Quality Kicker Magnet System — J. Dinkel, B. Hanna, C. Jensen, D. Qunell, R. Reilly, FNAL	1357
Consequences of Kicker Failure During HEB to Collider Injection and Possible Mitigation — R. Soundranayagam, A. I. Drozhdin, N. V. Mokhov, B. Parker, R. Schailey, F. Wang, SSCL	1360
High Efficiency Beam Deflection by Planar Channeling in Bent Silicon Crystals — K. Elsener, M. Clément, N. Doble, L. Gatignon, P. Grafström, CERN; S. P. Møller, E. Uggerhøj, T. Worm, ISA-Aarhus; M. Hage-Ali, P. Siffert, Strasbourg	1363
Extraction from the Fermilab Tevatron Using Channeling with a Bent Crystal — G. Jackson, FNAL	1366
2 TeV HEB Beam Abort at the SSCL — R. Schailey, J. Bull, T. Clayton, P. Kocur, N. V. Mokhov, SSCL	1369
Electrostatic Septa Design and Performance for Injection and Extraction to and from the MIT-Bates South Hall Ring (SHR) — S. Sobczynski, R. Averill, M. Farkhondeh, W. Sapp, C. Sibley, MIT-Bates	1372
Injection into the Elettra Storage Ring — D. Tommasini, Sinc. Trieste	1375
The Septum Magnets System of Elettra — R. Fabris, F. Daclon, M. Giannini, D. Tommasini, P. Tosolini, Sinc. Trieste	1378
High Voltage Vacuum Insulation in Crossed Magnetic and Electric Fields — W. T. Diamond, AECL	1381
Injection System for the SIBERIA-2 Storage Ring — G. Erg, A. Evstigneev, V. Korchuganov, G. Kulipanov, E. Levichev, Yu. Matveev, A. Philipchenko, L. Schegolev, V. Ushakov, BINP	1384
Fixed Target to Collider Changeover at A0 — K. J. Weber, FNAL	1387
Surface Resistivity Tailoring of Ceramic Accelerator Components — S. Anders, A. Anders, I. Brown, LBL	1390
Compensation of Field Shaking Due to the Magnetic Vibration — Y. Cheng, C. Hwang, SRRC Taiwan	1393
Superconducting Cavity Tuner Performance at CEBAF — J. Marshall, J. Preble, W. Schneider, CEBAF	1396
Test Results and Design Considerations for a 500 MHz, 500 kW Vacuum Window for CESR-B — D. Metzger, P. Barnes, A. Helser, J. Kirchgessner, H. Padamsee, Cornell	1399
An Experimental and Analytical Study of a Buoyancy Driven Cooling System for a Particle Accelerator — B. Campbell, R. Ranganathan, SSCL	1402
Collider Bypass Diode Thermal Simulations and Measurements for the SSCL — C. Rostamzadeh, G. Tool, SSCL ..	1405
Frequency-Feedback Tuning for Single-Cell Cavity Under RF Heating — J. D. Stepp, J. F. Bridges, ANL	1408
A Device of Amplitude and Phase Stabilization for the FEL Injector in the L-Band — Q. Zhang, X. Wang, Y. Sun, S. Bu, M. Zhang, G. Su, CIAE China	1411
A Jet Neutralizer Concept — T. E. Horton, U. Mississippi	1413
Modulator Upgrade of the KEK 2.5-GeV Linac — T. Shidara, H. Honma, S. Anami, I. Sato, KEK	1416
NSLS X-Ray Ring RF System Upgrade — M. G. Thomas, R. Biscardi, W. Broome, S. Buda, R. D'Alsace, S. Hanna, J. Keane, P. Mortazavi, G. Ramirez, J. M. Wang, NSLS-BNL	1419
A Wide Tuning Range Rf Cavity with External Ferrite Biasing — X. Pei, BNL; S. Anderson, D. Jenner, D. McCammon, T. Sloan, IUCF	1421
Longitudinal Rf Matching During AGS-RHIC Beam Transfer — X. Pei, BNL	1424
Photon Sources Chair: J. Galayda	
Commissioning and Performance of the ESRF (Invited Paper) — J. L. Laclare and the Project Team, ESRF	1427
Commissioning and Performance of the Advanced Light Source (Invited Paper) — A. Jackson, LBL	1432
Status of BESSY II, a High-Brilliance Synchrotron Radiation Source in the VUV to XUV Range (Invited Paper) — D. Krämer, BESSY	1436
A Superconducting Short Period Undulator for a Harmonic Generation FEL Experiment — G. Ingold, L. Solomon, I. Ben-Zvi, S. Krinsky, D. Li, D. Lynch, J. Sheehan, M. Woodle, X. Z. Qiu, L. H. Yu, X. Zhang, NSLS-BNL; W. Sampson, M. Gardner, K. Robins, BNL; I. Lehrman, R. Heuer, J. Sheehan, D. Weissenburger, Grumman Corp.	1439
UV-VUV FEL Program at Duke Storage Ring with OK-4 Optical Klystron — V. N. Litvinenko, J. M. J. Madey, Duke; N. A. Vinokurov, BINP-Novosibirsk	1442

Each volume begins with this five-volume table of contents and ends with the five-volume author index. The chairmen's foreword and a list of conference organizers and staff appear as front matter in Volume 1. A list of conference participants precedes the author index in Volume 5.

Five-Volume Contents

A 2-4 nm Linac Coherent Light Source (LCLS) Using the SLAC Linac — H. Winick, K. Bane, R. Boyce, G. Loew, P. Morton, H.-D. Nuhn, J. Paterson, P. Pianetta, T. Raubenheimer, J. Seeman, R. Tachyn, V. Vylet, SLAC; C. Pellegrini, J. Rosenzweig, G. Travish, UCLA; D. Prosnitz, T. Scharlemann, LLNL; K. Halbach, K.-J. Kim, M. Xie, LBL	1445
The Vanderbilt University Compton Scattering X-Ray Experiment — P. A. Tompkins, C. A. Brau, W. W. Dong, J. W. Waters, Vanderbilt U.; F. E. Carroll, D. R. Pickens, R. R. Price, VUMC	1448
Observations of Effects of Ion Accumulation in the Maxwell Model 1.2-400 Synchrotron Light Source — R. P. Johnson (now at CEBAF), D. Y. Wang, Maxwell Labs; H. Bluem, LSU	1451
A Progress Report on the Laboratório Nacional de Luz Síncrotron (Brazil) — A. R. D. Rodrigues, C. E. T. Gonçalves da Silva, D. Wisnivesky, LNLs Brazil	1454
An Overview of the PLS Project — T. Lee, POSTECH	1457
Present Status of SRRC — E. Yen, SRRC	1460
 <i>Poster presentations:</i>	
SOLEIL, a New Synchrotron Radiation Source for LURE — M. P. Level, P. Brunelle, P. Marin, A. Nadji, M. Sommer, H. Zyngier, LURE; J. Faure, J. Payet, A. Tkatchenko, LNS	1465
Conceptual Design of a Compact Electron Storage Ring System Dedicated to Coronary Angiography — Y. Oku, K. Aizawa, S. Nakagawa, Kawasaki Heavy Ind.; M. Ando, K. Hyodo, S. Kamada, PF, KEK; H. Shiwaku, JAERI	1468
Report on DELTA, One Year Before Routine Operation — N. Marquardt, U. Dortmund	1471
Lattice Design for the 1.7-GeV Light Source BESSY II — E. Jaeschke, D. Krämer, B. Kuske, P. Kuske, M. Scheer, E. Weihrer, G. Wüstefeld, BESSY	1474
The Synchrotron Light Source ROSY — D. Einfeld, H. Büttig, S. Dienel, W. Gläser, H. Guratzsch, B. Hartmann, D. Janssen, H. Krug, J. Linnemann, W. Matz, W. Neumann, W. Oehme, D. Pröhl, R. Schlenk, H. Tyrroff, Res. Ctr. Rossendorf; Th. Goetz, M. Picard, U. Bonn; J. B. Murphy, BNL; M. Plesko, D. Tomassini, Sincrotrone Trieste; R. Rossmanith, CEBAF	1477
A Source of Synchrotron Radiation for Research and Technology Applications — E. Bulyak, V. Chechetenko, A. Dovbnya, S. Efimov, A. Gevchuk, P. Gladkikh, I. Karnaukhov, V. Kozin, S. Kononenko, V. Likhachev, V. Lyashchenko, V. Markov, N. Mocheshnikov, V. Moskalenko, A. Mytsykov, Yu. Popkov, A. Shcherbakov, M. Strelkov, A. Tarasenko, Yu. Telegin, V. Trotsenko, A. Zelinsky, Kharkov Inst.; V. Bar'yakhtar, V. Molodkin, V. Nemoshkalenko, A. Shpak, Metallophysics Inst.	1480
Optimum Steering of Photon Beam Lines in SPEAR — W. J. Corbett, B. Fong, M. Lee, V. Ziemann, SLAC	1483
Establishment of a Tolerance Budget for the Advanced Photon Source Storage Ring — H. Bizek, E. Crosbie, E. Lessner, L. Teng, ANL	1485
Study of Transverse Coupled Bunch Instabilities by Using Non-Linear Taylor Maps for the Advanced Light Source (ALS) — M. Meddahi, J. Bengtsson, LBL	1488
Plans to Increase Source Brightness of NSLS X-Ray Ring — J. Safranek, S. Krinsky, NSLS-BNL	1491
A Design Concept for the Inclusion of Superconducting Dipoles Within a Synchrotron Light Source Lattice — M. W. Poole, J. A. Clarke, S. L. Smith, V. P. Suller, L. A. Welbourne, SERC Daresbury; N. A. Mezentssev, BINP Russia	1494
A Conceptual Design and Thermal Analysis of High Heat Load Crotch Absorber — I. C. Sheng, S. Sharma, E. Rotela, J. Howell, ANL	1497
Thermal Analysis of the Beam Missteering in APS Storage Ring — I. C. Sheng, J. Howell, S. Sharma, ANL	1500
Dynamic Response Analysis of the LBL Advanced Light Source Synchrotron Radiation Storage Ring — K. K. Leung, SSCL	1503
The Study of Seismic Vibration of SR Source "Zelenograd" — S. Kuznetsov, Kurchatov Inst.; E. Levichev, BINP	1506
Measurement of the Orbit Parameters at SOR-RING — H. Kudo, K. Shinoue, H. Takaki, T. Koseki, H. Ohkuma, Y. Kamiya, ISSP Tokyo	1509
Challenging Issues During ESRF Storage Ring Commissioning — A. Ropert, ESRF	1512
Upgrading to 500 mA of the Stored Beam Current at SORTEC 1-GeV Source Facility — M. Kodaira, N. Awaji, T. Kishimoto, K. Mukugi, M. Watanabe, SORTEC; T. Iida, H. Tsuchidate, Mitsubishi Corp.	1515
Performance of Upgraded SORTEC 1-GeV 500-mA SR Source Facility — T. Kishimoto, M. Kodaira, N. Awaji, K. Mukugi, M. Araki, SORTEC; Y. Kijima, M. Haraguchi, Mitsubishi Corp.	1518

Volume 1: 1-747
 Volume 2: 748-1640
 Volume 3: 1641-2545
 Volume 4: 2546-3218
 Volume 5: 3219-3933

Proceedings of the 1993 Particle Accelerator Conference

Design of Test Linac for Free Electron Laser — H. Kang, I. Ko, M. Cho, W. Namkung, POSTECH	1521
The Revised ELFA Project — E. Acerbi, F. Alessandria, G. Baccaglioni, G. Bellomo, C. Birattari, R. Bonifacio, I. Boscolo, A. Bosotti, F. Broggi, R. Corsini, L. De Salvo, D. Giove, C. Maroli, P. Pierini, N. Piovela, M. Pullia, G. Rivoltella, L. Rossi, G. Varisco, INFN/ U. Milan; P. Arcioni, M. Bressan, G. Conciauro, INFN Pavia; W. A. Barletta, LBL; G. Gemme, R. Parodi, INFN Genova; V. Stagno, V. Variale, INFN Bari	1524
Design and Construction of a Compact Infra Red Free Electron Laser CIRFEL — J. Krishnaswamy, I. S. Lehrman, J. Sheehan, R. L. Heuer, M. F. Reusch, R. Hartley, Grumman Aerospace Corp.	1527
Coherence and Linewidth Studies of a 4-nm High Power FEL — W. M. Fawley, A. M. Sessler, LBL; E. T. Scharlemann, LLNL	1530
Performance Characteristics, Optimization, and Error Tolerances of a 4 nm FEL Based on the SLAC Linac — K.-J. Kim, M. Xie, LBL; E. T. Scharlemann, LLNL; C. Pellegrini, G. Travish, UCLA	1533
X-Ray Beam Lines and Beam Line Components for the SLAC Linac Coherent Light Source (LCLS) — R. Tatchyn, P. Pianetta, SLAC	1536
Photon Pulse Filtering and Modulation Based on the Extreme Temporal Compression and Correlated Energy Spread of the Electron Bunches in the SLAC Linac Coherent Light Source (LCLS) — R. Tatchyn, SLAC	1539
Infrared (IR) vs. X-Ray Power Generation in the SLAC Linac Coherent Light Source (LCLS) — R. Tatchyn, SLAC	1542
Saturation of a High Gain FEL — R. L. Gluckstern, Maryland; S. Krinsky, BNL; H. Okamoto, Kyoto U.	1545
Numerical Studies of Strong Focusing in Planar Undulators — G. Travish, J. Rosenzweig, UCLA	1548
Generation of High Power 140 GHz Microwaves with an FEL for the MTX Experiment — S. L. Allen, C. J. Lasnier, B. Felker, M. Fenstermacher, S. W. Ferguson, S. Fields, E. B. Hooper, S. Hulse, M. Makowski, J. Moller, W. Meyer, D. Petersen, E. T. Scharlemann, B. Stallard, R. Wood, LLNL	1551
Burst Mode FEL with the ETA-III Induction Linac — C. J. Lasnier, S. L. Allen, B. Felker, M. E. Fenstermacher, S. W. Ferguson, S. D. Hulse, E. B. Hooper, M. C. Jackson, M. A. Makowski, W. H. Meyer, J. M. Moller, D. E. Petersen, S. E. Sampayan, B. W. Stallard, W. F. Fields, LLNL; K. Oasa, JAERI	1554
Design and Experiment of SG-1 FEL — Z. Hui, IEE China	1557
Electron Beam Quality Limitations and Beam Conditioning in Free Electron Lasers — P. Sprangle, G. Joyce, NRL; B. Hafizi, Icarus Res.; P. Serafim, Northeastern U.	1560
An Optical Approach to Emittance Compensation in FELs — G. R. Neil, H. Liu, CEBAF	1563
Ultrahigh-Brightness Microbeams: Considerations for Their Generation and Relevance to FEL — H. Ishizuka, Y. Nakahara, Fukuoka Inst. Tech.; S. Kawasaki, Saitama U.; K. Sakamoto, A. Watanabe, N. Ogiwara, M. Shiho, JAERI	1566
The Groove Guide: A Non-Conventional Interaction Structure for Microwave FEL Experiments — P. Arcioni, M. Bressan, G. Conciauro, U. of Pavia; F. Broggi, P. Pierini, INFN Milano	1569
First Undulators for the Advanced Light Source — E. Hoyer, J. Ake, J. Chin, B. Gath, D. Humphries, B. Kincaid, S. Marks, P. Pipersky, D. Plate, G. Portmann, R. Schlueter, LBL; W. Hassenzahl, LLNL	1572
Insertion Device Magnet Measurements for the Advanced Light Source — S. Marks, C. Cork, E. Hoyer, D. Humphries, B. Kincaid, D. Plate, A. Robb, R. Schlueter, C. Wang, LBL; W. V. Hassenzahl, LLNL	1575
Spectral Quality of ALS U5.0 Undulator and Field Error Effects — C. Wang, S. Marks, B. Kincaid, LBL	1578
Modeling and Measurement of the ALS U5 Undulator End Magnetic Structures — D. Humphries, K. Halbach, E. Hoyer, B. Kincaid, S. Marks, R. Schlueter, LBL	1581
Flux Shunts for Undulators — E. Hoyer, J. Chin, LBL; W. V. Hassenzahl, LLNL	1584
Design, Construction and Testing of Insertion Devices for ELETTRA — R. P. Walker, R. Bracco, A. Codutti, B. Diviacco, D. Mollo, D. Zangrando, Sinc. Trieste; C. Poloni, U. Trieste	1587
Performance Optimization of Pure Permanent Magnet Undulators — B. Diviacco, Sin. Trieste	1590
Magnetic Interaction Effects in ELETTRA Segmented Pure Permanent Magnet Undulators — B. Diviacco, R. P. Walker, Sinc. Trieste	1593
Planar Helical Undulator Sources of Circularly Polarized X-Rays — R. Carr, SSRL	1596
Polarized Wiggler for NSLS X-Ray Ring — A. Friedman, X. Zhang, S. Krinsky, E. B. Blum, NSLS-BNL; K. Halbach, LBL	1599
Magnetic Field Measurements of a Superconducting Undulator for a Harmonic Generation FEL Experiment at the NSLS — L. Solomon, G. Ingold, I. Ben-Zvi, S. Krinsky, L. H. Yu, NSLS-BNL; W. Sampson, K. Robins, BNL	1602

Each volume begins with this five-volume table of contents and ends with the five-volume author index. The chairmen's foreword and a list of conference organizers and staff appear as front matter in Volume 1. A list of conference participants precedes the author index in Volume 5.

Magnetic Performance of the NSLS Prototype Small-Gap Undulator — G. Rakowsky, R. Cover, Rockwell; L. Solomon, NSLS-BNL	1605
Design Considerations for a 60 Meter Pure Permanent Magnet Undulator for the SLAC Linac Coherent Light Source (LCLS) — R. Tatchyn, R. Boyce, K. Halbach, H.-D. Nuhn, J. Seeman, H. Winick, SLAC; C. Pellegrini, UCLA	1608
Adjustment and Measurement of a Hybrid Undulator — B. Wu, Y. Ma, B. Liu, Z. Zhang, CIAE China	1611
Coherent Radiation at Submillimeter and Millimeter Wavelengths — M. Oyamada, R. Kato, T. Nakazato, S. Urasawa, T. Yamakawa, M. Yoshioka, M. Ikezawa, K. Ishi, T. Kanai, Y. Shibata, T. Takahashi, Tohoku U.	1614
Suppression of Coherent Synchrotron Radiation in Conducting Boundaries — R. Kato, T. Nakazato, M. Oyamada, S. Urasawa, T. Yamakawa, M. Yoshioka, M. Ikezawa, K. Ishi, T. Kanai, Y. Shibata, T. Takahashi, Tohoku U.	1617
A Compact Tunable X-Ray Source Based on Parametric X-Ray Generation by Moderate Energy Linacs — X. K. Maruyama, K. Dinova, D. Snyder, Naval Postgraduate School; M. A. Piestrup, Q. Li, Adelphi Tech.; R. B. Fiorito, D. W. Rule, NSWC	1620
Fundamental and Harmonics of Thomson Backscattered X-Rays from an Intense Laser Beam — C. Tang, NRL; B. Hafizi, Icarus Res.; S. K. Ride, UCSD	1623
Generation of Intensive Long-Wavelength Edge Radiation in High-Energy Electron Storage Rings — O. V. Chubar, N. V. Smolyakov, Kurchatov Inst.	1626
The Radiation Emission by a High Energy Electron-Positron Pair and Ultrarelativistic Hydrogen-Like Atom Moving Through Thick Target — A. V. Koshelkin, MEPI	1629
Bremsstrahlung by the Bunch of Ultrarelativistic Charged Particles into a Thick Target — A. V. Koshelkin, MEPI ..	1632
Construction and Commissioning of the SRRC Storage Ring — Y. C. Liu, J. R. Chen, C. C. Kuo, SRRC	1635
Commissioning a Second Superconducting Wiggler in the Daresbury SRS — M. W. Poole, J. A. Clarke, P. D. Quinn, S. L. Smith, V. P. Suller, L. A. Welbourne, Daresbury	1638

Volume 3

Hadron RF Linacs, Cyclotrons, Radioactive Beams

Chair: R. Pollock

An Overview of Radioactive Beam Concepts (<i>Invited Paper</i>) — J. M. D'Auria, TRIUMF	1641
Heavy Ion Beam Accumulation, Cooling, and Experiments at the ESR (<i>Invited Paper</i>) — B. Franzke, K. Beckert, F. Bosch, H. Eickhoff, B. Franczak, A. Gruber, O. Klepper, F. Nolden, P. Raabe, H. Reich, P. Spädike, M. Steck, J. Struckmeier, GSI Darmstadt	1645
The Research Center for Nuclear Physics Ring Cyclotron (<i>Invited Paper</i>) — I. Miura, Osaka U.	1650
The Fermilab 400-MeV Linac Upgrade (<i>Invited Paper</i>) — C. W. Schmidt, FNAL	1655
Use of the Holifield Facility 25-MV Tandem Accelerator in the Oak Ridge Radioactive Ion Beam Project — C. M. Jones, R. C. Juras, M. J. Meigs, D. K. Olsen, ORNL	1660
Realistic Modeling of Radiation Transmission Inspection Systems — K. E. Sale, LLNL	1663
Overview of Accelerators in Medicine — A. J. Lennox, FNAL/Rush U.	1666
Commissioning of the First Drift Tube Linac Module in the Ground Test Accelerator — K. F. Johnson, O. R. Sander, W. H. Atkins, G. O. Bolme, S. Bowling, R. Cole, R. Connolly, P. Denney, J. Erickson, J. D. Gilpatrick, W. B. Ingalls, D. Kersteins, R. Kraus, W. P. Lysenko, D. McMurry, C. T. Mottershead, J. Power, C. Rose, D. P. Rusthoi, D. P. Sandoval, J. D. Schneider, M. Smith, G. Vaughn, E. A. Wadlinger, R. Weiss, V. Yuan, LANL	1669
Acceleration and Isobaric Separation of Radioactive Ion Beams With the Louvain-la-Neuve Isochronous Cyclotrons — M. Loiselet, N. Postiau, G. Ryckewaert, U. Catholique de Louvain; A. Morduev, R. Oganessian, JINR	1672
Linear Accelerator for Plutonium Conversion and Transmutation of NPP Wastes — I. M. Kapchinskiy, I. V. Chuvilo, A. A. Kolomiets, N. V. Lazarev, I. M. Lipkin, V. K. Plotnikov, I. A. Vorobjov, ITEP Moscow	1675

Poster presentations:

Acceleration and Transverse Focusing of Ion Beams in Lineondutron — E. S. Masunov, MEPI	1681
Linac Design Study for an Intense Neutron-Source Driver — M. T. Lynch, A. Browman, R. DeHaven, R. Jameson, A. Jason, G. Neuschaefer, P. Tallerico, A. Regan, LANL	1683

Proceedings of the 1993 Particle Accelerator Conference

Design and Operation of the HIMAC Injector — T. Murakami, H. Ogawa, S. Yamada, Y. Sato, T. Yamada, A. Kitagawa, J. Yoshizawa, S. Fu, T. Kohno, K. Sato, A. Itano, M. Kumada, E. Takada, M. Kanazawa, K. Noda, M. Sudou, Y. Hirao, Nat. Inst. of Radiological Sciences; O. Morishita, K. Sawada, Sumitomo Heavy Ind.	1686
Time-of-Flight Measurements of Absolute Beam Energy in the Fermilab Linac — M. B. Popovic, T. L. Owens, T. K. Kroc, L. J. Allen, C. W. Schmidt, FNAL	1689
Phase Scan Signature Matching for Linac Tuning — T. L. Owens, M. B. Popovic, E. S. McCrory, C. W. Schmidt, L. J. Allen, FNAL	1691
Operational Status of the Uranium Beam Upgrade of the ATLAS Accelerator — R. C. Pardo, L. M. Bollinger, J. A. Nolen, K. W. Shepard, P. Billquist, J. M. Bogaty, B. E. Clifft, R. Harkewicz, F. H. Munson, J. E. Specht, G. P. Zinkann, ANL	1694
One Year Operation of the 7 MeV Proton Linac — T. Shirai, H. Dewa, H. Fujita, M. Ikegami, Y. Iwashita, S. Kakigi, H. Okamoto, K. Noda, M. Inoue, Kyoto U.	1697
The SSC Linear Accelerator — L. W. Funk, SSCL	1700
Finalized Design of the SSC RFQ-DTL Matching Section — M. Haworth, C. Combs, P. Datte, T. Enegren, W. Funk, Y. Goren, F. Guy, J. Hurd, G. Jamieson, D. Martin, A. Ringwall, R. Sethi, D. Swenson, SSCL; D. Barlow, R. Kraus, R. Meyer, LANL	1703
Accelerator Readiness Review Process for the SSC Linac — J. F. Tooker, T. Benke, L. W. Funk, V. Oliphant, SSCL	1706
Commissioning Status of the Continuous Wave Deuterium Demonstrator — P. Den Hartog, J. Dooling, M. Lorello, J. Rathke, Grumman Aerospace; J. Carwardine, D. Godden, G. Pile, Culham Lab.; T. Yule, T. Zinneman, ANL	1709
Design Study for a Superconducting Proton Linac From 20 to 100 MeV — T. P. Wangler, R. Garnett, F. Krawczyk, J. Billen, N. Bultman, K. Christensen, W. Fox, R. Wood, LANL	1712
Design Considerations for High-Current Superconducting Ion Linacs — J. R. Delayen, C. L. Bohn, B. J. Micklich, C. T. Roche, L. Sagalovsky, ANL	1715
Special Design Problems and Solutions for High Powered Continuous Duty Linacs — D. Liska, L. Carlisle, G. McCauley, LANL; S. Ellis, P. Smith, Grumman Aerospace	1718
Status of CIAE Medical Cyclotron — X. Zhang, Z. Li, M. Fan, CIAE China	1721
A 600 MeV Cyclotron for Radioactive Beam Production — D. J. Clark, LBL	1724
Development of a Compact Permanent Magnet Cyclotron for Accelerator Mass Spectrometry — A. T. Young, D. J. Clark, K. Halbach, W. B. Kunkel, K. N. Leung, C. Y. Li, A. Rawlins, R. D. Schlueter, M. E. Stuart, R. P. Wells, LBL; J. X. Yu, Beijing U.; K. J. Bertsche, SSCL	1727
Performance of H ⁺ /D ⁺ Cyclotron Using Internal Source — T. T. Y. Kuo, TRIUMF; G. O. Hendry, Cyclotron Inc.	1730
Operation of the TR30 "Industrial" Cyclotron — K. Erdman, R. Dawson, Ebco Tech./TRIUMF; B. Milton, N. Stevenson, TRIUMF	1733
The First Year with Electron Cooling at CRYRING — K. Abrahamsson, G. Andler, L. Bagge, E. Beebe, P. Carlé, H. Danared, K. Ehrnström, M. Engström, Å. Engström, C. J. Herrlander, J. Hilke, J. Jeansson, A. Källberg, S. Leontein, L. Liljeby, A. Nilsson, A. Paál, A. Pikin, K.-G. Rensfelt, U. Rosengård, J. Starker, M. af Ugglas, Manne Siegbahn Inst. Stockholm	1735
Electron Cooling of Heavy Ions at GSI — M. Steck, K. Beckert, H. Eickhoff, B. Franzke, F. Nolden, P. Spädtké, GSI Darmstadt	1738
The Aarhus Storage Ring for Ions and Electrons ASTRID — S. P. Møller, Aarhus U.	1741
Recent Developments at the Gustaf Werner Cyclotron and CELSIUS — D. Reistad, Svedberg Lab.	1744
Ion Beam Acceleration and New Operation Modes at the TSR Heidelberg — M. Grieser, D. Habs, R.v. Hahn, B. Hochadel, C. M. Kleffner, J. Liebmann, R. Repnow, D. Schwalm, MPI Heidelberg; G. Bisoffi, INFN Legnaro; E. Jaeschke, BESSY; S. Papureanu, IFIN Bucurest.....	1747
A New Design for an EMIS-CYCLOTRON System, for Direct Production of Gaseous PET Radioisotopes — H. Ayvazian, Ion Beam App. Lab.	1750
The Chandigarh Variable Energy Cyclotron and Its Application for Trace Element Analysis Using PIXE Techniques — I. M. Govil, Panjab U.	1753
Proton Linacs for Boron Neutron Capture Therapy — A. J. Lennox, FNAL/Rush U.	1756
Modeling and System Specifications for an Integrated 3-D Proton Treatment Delivery System — J. W. Staples, B. A. Ludewigt, LBL	1759

Each volume begins with this five-volume table of contents and ends with the five-volume author index. The chairmen's foreword and a list of conference organizers and staff appear as front matter in Volume 1. A list of conference participants precedes the author index in Volume 5.

Five-Volume Contents

Shielding and Activation Study for Proton Medical Accelerators — H. B. Knowles, J. L. Orthel, B. W. Hill, G. H. Gillespie Assoc.	1762
Beam Dynamics Studies for Proposed Proton Therapy Facility — D. Raparia, W. Funk, SSCL	1765
Compact Protontherapy Unit Pre-design — D. Tronc, G.E.	1768
High Energy Accelerator Technology in Radiology — J. F. Crawford, B. Larsson, H. Reist, U. Zurich/PSI; L. Goldin, ITEP Moscow; H. Condé, K. Elmgren, E. Grusell, B. Nilsson, O. Pettersson, T. Rönqvist, U. Uppsala	1771
The Neutral Particle Beam Space Experiment (NPBSE) Accelerator Designs — C. C. Paulson, A. M. M. Todd, S. L. Mendelsohn, Grumman	1774
The Continuous Wave Deuterium Demonstrator (CWDD) Design and Status — A. M. M. Todd, Grumman; M. P. S. Nightingale, Culham Lab.; T. J. Yule, ANL	1777
Beam Matching Section in the INS Heavy Ion Linac Complex — K. Niki, S. Arai, Y. Hashimoto, H. Masuda, M. Tomizawa, K. Yoshida, INS Tokyo	1780
A Heavy Ion Linac Complex for Unstable Nuclei — S. Arai, M. Doi, Y. Hashimoto, A. Imanishi, T. Katayama, H. Masuda, K. Niki, Y. Takeda, N. Tokuda, M. Tomizawa, E. Tojyo, K. Yoshida, M. Yoshizawa, INS Tokyo; T. Hattori, Tokyo Inst. of Tech.	1783
Interdigital-H Linac for Unstable Nuclei at INS — M. Tomizawa, S. Arai, M. Doi, T. Katayama, K. Niki, M. Yoshizawa, INS Tokyo; T. Hattori, Tokyo Inst. of Tech.	1786
SPIRAL: A Radioactive Ion Beam Facility at GANIL — A. Joubert, R. Anne, P. Bertrand, MP. Bourgarel, C. Bieth, B. Bru, A. Chabert, M. Duval, R. Leroy, Ch. Ricaud, P. Sortais, GANIL	1789
On Line Isotopic Separator Test Benches at GANIL — R. Anne, B. Bru, A. Joubert, R. Leroy, M. Lewitowicz, P. Sortais, M. G. Saint Laurent, C. Tribouillard, GANIL; J. Obert, J. C. Putaux, IPN Orsay; C. F. Liang, P. Paris, CSNSM Orsay; N. Orr, J. C. Steckmeyer, LPC-ISMRA	1792
The Outlook of MPC-10 Cyclotron Use for the Solution of Applied Problems — S. T. Latushkin, V. V. Leonov, A. A. Ogloblin, L. I. Yudin, V. E. Yarosh, D. I. Yartsev, Kurchatov Inst.	1795
ITEP Heavy Ion Alternating Phase Focusing Linac — V. V. Kushin, N. A. Nesterov, I. O. Parshin, S. V. Plotnikov, ITEP Moscow	1798

Accelerator Control Systems

Chair: D. Gurd

Sharing Control System Software (<i>Invited Paper</i>) — P. Clout, Vista Systems	1801
Control System Architecture: The Standard and Non-Standard Models (<i>Invited Paper</i>) — M. E. Thuot, L. R. Dalesio, LANL	1806
Anatomy of a Control System: A System Designer's View — S. Magyary, LBL	1811
Beam Position Monitor Data Acquisition for the Advanced Photon Source — F. R. Lenkszus, E. Kahana, A. J. Votaw, G. A. Decker, Y. Chung, D. J. Ciarlette, R. J. Laird, ANL	1814
New Tevatron Cryogenic Control System — B. Lublinsky, J. Firebaugh, J. Smolucha, FNAL	1817
Control Software for EUTERPE — P. D. V. van der Stok, F. van den Berk, R. Deckers, Y. van de Vijver, J. I. M. Botman, J. L. Delhez, C. J. Timmermans, Tech. U., Eindhoven	1820

Poster presentations:

Network Management of Real-Time Embedded Processors — C. Kalbfleisch, S. Hunt, K. Low, D. Mathieson, SSCL	1823
High Speed Serial Communications for Control Systems — D. Mathieson, C. Kalbfleisch, S. Hunt, K. Low, SSCL	1826
"BUBBANET": A High Performance Network for the SSC Accelerator Control System — S. Hunt, C. Kalbfleisch, K. Low, D. Mathieson, SSCL	1829
Gateway for Inter-Network Connection in the Pohang Light Source Control System — S. C. Won, S. Kwon, POSTECH	1832
The Star, a Dynamically Configured Dataflow Director for Realtime Control — M. Bickley, J. Kewisch, CEBAF	1835
The SSCL Linac Control System — J. Heefner, C. Cuevas, S. Hunt, D. Murray, J. Sage, SSCL	1838
Proposal to Use Failure Prediction as a Means of Meeting Availability Requirements at the SSC — S. Sarkar, W. Merz, F. Meyer, SSCL	1841
Control, Timing, and Data Acquisition for the Argonne Wakefield Accelerator (AWA) — P. Schoessow, C. Ho, J. Power, E. Chojnacki, ANL	1844

Volume 1: 1-747
 Volume 2: 748-1640
 Volume 3: 1641-2545
 Volume 4: 2546-3218
 Volume 5: 3219-3933

Proceedings of the 1993 Particle Accelerator Conference

The High Level Programmer and User Interface of the NSLS Control System — Y. N. Tang, J. D. Smith, NSLS-BNL; S. Sathe, AGS-BNL	1846
NSLS Control Monitor and Its Upgrade — S. Ramamoorthy, J. D. Smith, NSLS-BNL	1849
NSLS Control System Upgrade Status — J. Smith, S. Ramamoorthy, Y. Tang, J. Flannigan, S. Sathe, J. Keane, S. Krinsky, NSLS-BNL	1852
Digital Signal Array Processor for NSLS Booster Power Supply Upgrade — R. Olsen, J. Dabrowski, BNL; J. Murray, Stony Brook	1855
Control System for NSLS Booster Power Supply Upgrade II — R. Olsen, J. Dabrowski, BNL; J. Murray, Stony Brook	1858
Software Environment and Configuration for the DSP Controlled NSLS Booster Power Supplies — R. Olsen, J. Dabrowski, NSLS-BNL; J. Murray, Stony Brook	1861
Control Units for APS Power Supplies — O. D. Despe, C. Saunders, D. McGhee, ANL	1864
High Resolution ADC Interface to Main Magnet Power Supply at the NSLS — M. Bordoley, NSLS-BNL	1867
Design of the Advanced Light Source Timing System — M. Fahmie, LBL	1869
Ring Diagnostics and Consistency Test of the Model for the AGS Booster — A. Luccio, E. H. Auerbach, BNL	1872
Use of Design Codes for On-Line Beam Diagnostics at the MIT-Bates Accelerator — K. D. Jacobs, B. G. McAllister, J. B. Flanz, MIT Bates	1875
A Graphical User-Interface Control System at SRRC — J. S. Chen, C. J. Wang, S. J. Chen, G. J. Jan, SRRC Taiwan	1878
Machine Protection System Algorithm Compiler and Simulator — G. R. White, G. Sherwin, SLAC	1881
MPS VAX Monitor and Control Software Architecture — S. Allison, N. Spencer, K. Underwood, D. VanOlst, M. Zelazny, SLAC	1884
The Continuous and Seamless Replacement of a Running Control System Succeeded — G.v. Egan-Krieger, R. Müller, J. Rahn, BESSY	1887
Control and Data Acquisition System of Electron Accelerator for Radiation Processing — W. Maciszewski, J. Lukasiewicz, W. Migdal, A. G. Chmielewski, Inst. of Nuc. Tech., Warsaw	1890
Expert System for Magnetic Systems Investigations — S. Lima, R. V. Poliakova, F. F. Nodarse, I. P. Yudin, JINR Moscow	1892
Orbit Correction Implementation at CEBAF — M. Bickley, B. A. Bowling, D. Douglas, A. Hofler, J. Kewisch, G. A. Krafft, CEBAF	1895
Controls Interface Protocols for the SSC Correction and 'DC' Magnet Power Supplies — S. Sarkar, J. Gannon, W. Merz, F. Meyer, SSCL	1898
Parametrization of the AmPS Magnets for the Control System — Y. Wu, G. van Garderen, R. Hart, J. van der Laan, R. Maas, F. Schimmel, NIKHEF-K	1901
Global Voltage Control for the LEP RF System — E. Ciapala, A. Butterworth, E. Peschardt, CERN	1903
Designing RF Control Subsystems Using the VXibus Standard — J. D. Stepp, F. C. Vong, J. F. Bridges, ANL	1906
Automated Measurement of Cavity Frequency and Cavity Tuning at CEBAF — R. Li, S. N. Simrock, B. C. Yunn, CEBAF	1909
A Beam Position Monitor Data Acquisition System for the New Fermilab 400 MeV Line — S. Lackey, J. Firebaugh, C. Johnstone, W. Marsh, J. Smolucha, K. Woodbury, FNAL	1912
A VME Based Quench Protection Monitor for the Tevatron Low Beta Quadrupoles — S. Lackey, C. Briegel, L. Chapman, R. Flora, K. Martin, FNAL; T. Savord, SSCL	1914
Experience with the TRIUMF Main Tank Vacuum Control System — S. Sarkar, D. P. Gurd, SSCL; J. C. Yandon, W. Sievers, P. Bennett, P. Harmer, J. Nelson, TRIUMF	1916
Laser Power Stabilization in the TRIUMF Optically Pumped Polarized H ⁺ Ion Source — S. Sarkar, SSCL	1919
MPS Beam Control Software Architecture — K. Krauter, M. Crane, SLAC	1922
The CEBAF Analog Monitor System — K. Crawford, M. O'Sullivan, J. Perry, S. Simrock, CEBAF	1925
Techniques for Increasing the Reliability of Accelerator Control System Electronics — J. Utterback, FNAL	1928
WindoWorks: A Flexible Program for Computerized Testing of Accelerator Control System Electronic Circuit Boards — J. Utterback, FNAL	1931
Switching the Fermilab Accelerator Control System to a Relational Database — S. Shtirbu, FNAL	1934
The Impact of New Accelerator Control Software on LEP Performance — R. Bailey, A. Belk, P. Collier, M. Lamont, G. de Rijk, M. Tarrant, CERN	1937

Each volume begins with this five-volume table of contents and ends with the five-volume author index. The chairmen's foreword and a list of conference organizers and staff appear as front matter in Volume 1. A list of conference participants precedes the author index in Volume 5.

Five-Volume Contents

A Software System for Modeling and Controlling Accelerator Physics Parameters at the Advanced Light Source — L. Schachinger, V. Paxson, LBL	1940
Machine Physics Application Program for Control, Commissioning and Error Findings for Storage Rings — H. P. Chang, C. H. Chang, C. C. Kuo, M. H. Wang, J. C. Lee, J. Y. Fan, H. J. Tsai, SRRC Taiwan; C. S. Hsue, SRRC/Nat. Tsing Hua U.	1943
CATER: An Online Problem Tracking Facility for SLC — R. C. Sass, H. Shoaee, SLAC	1946
Ramping Control Using a Spreadsheet — D. Y. Wang, R. P. Johnson (now at CEBAF), L. S. B. Ng, W. J. Pearce, Maxwell Labs	1949
Easy and Effective Applications Programs Using DataViews — E. S. McCrory, FNAL	1952
The Graphic Environment for Transport Line Control and Beam Diagnostics — S. Kuznetsov, Kurchatov Inst.	1955
An I/O Subnet for the APS Control System: The BITBUS Universal Gateway — G. J. Nawrocki, N. D. Arnold, M. G. Hoffberg, J. R. Winans, S. J. Benes, ANL	1957
Status and Design of the Advanced Photon Source Control System — W. McDowell, M. Knott, F. Lenkszus, M. Kraimer, N. Arnold, R. Daly, ANL	1960
Controlling the Third Harmonic Cavity During Focus Free Transition Crossing in the Fermilab Main Ring — M. A. Martens, FNAL	1963
AMS: Area Message Service for SLC — M. Crane, R. Mackenzie, D. Millsom, M. Zelazny, SLAC	1966
Adding PCs to SLC Control System — T. Lahey, S. Levitt, R. MacKenzie, N. Spencer, K. Underwood, SLAC	1969
Precise System Stabilization at SLC Using Dither Techniques — M. C. Ross, L. Hendrickson, T. Himel, E. Miller, SLAC	1972
Thermal Stabilization of Low Level RF Distribution Systems at SLAC — D. McCormick, M. Ross, T. Himel, N. Spencer, SLAC	1975
 Lepton Circular Colliders, Synchrotrons, and Microtrons Chair: A. Sessler	
CESR Luminosity Upgrades and Experiments (<i>Invited Paper</i>) — D. Rice, Cornell	1978
LEP Status and Future Plans (<i>Invited Paper</i>) — L. R. Evans, CERN	1983
Challenges on the High Luminosity Frontier of e^+e^- Factories (<i>Invited Paper</i>) — W. A. Barletta, LBL/UCLA	1988
DAFNE, The Frascati F-Factory (<i>Invited Paper</i>) — G. Vignola, INFN-LNF	1993
Commissioning Results of the Amsterdam Pulse Stretcher/Storage Ring AMPS — R. Maas, F. Kroes, J. van der Laan, G. Luijckx, J. Noomen, Y. Wu, NIKHEF	1998
 <i>Poster presentations:</i>	
LEP Operation in 1992 with a 90° Optics — R. Bailey, T. Bohl, F. Bordry, H. Burkhardt, K. Cornelis, P. Collier, B. Desforges, A. Faugier, V. Hatton, M. Jonker, M. Lamont, J. Miles, G. de Rijk, H. Schmickler, CERN	2001
Status of TRISTAN-II Project — S. Kurokawa, KEK	2004
The Long Range Beam-Beam Interaction at CESR: Experiments, Simulations and Phenomenology — A. B. Temnykh, INP Novosibirsk; J. J. Welch, D. H. Rice, Cornell	2007
PEP-II Design Update and R&D Results — W. Barletta, M. S. Zisman, LBL; R. A. Bell, J. M. Dorfan, SLAC	2010
Commissioning and Operation of the LEP Pretzel Scheme — R. Bailey, J. M. Jowett, W. Kalbreier, D. Wang, CERN	2013
Progress of the LEP Energy Upgrade Project — C. Wyss, CERN	2016
Flat Beams in the SLC — C. Adolphsen, T. Barklow, D. Burke, F.-J. Decker, P. Emma, M. Hildreth, T. Himel, P. Krejcik, T. Limberg, M. Minty, N. Phinney, P. Raimondi, T. Raubenheimer, M. Ross, J. Seeman, R. Siemann, W. Spence, N. Walker, M. Woodley, SLAC	2019
The Damping Ring For Novosibirsk F- and B-Factories — V. V. Anashin, S. E. Belomestnykh, A. A. Didenko, N. S. Dikansky, B. I. Grishanov, P. M. Ivanov, V. A. Kiselev, V. I. Kudelainen, N. A. Kuznetsov, V. A. Lebedev, B. L. Militsin, S. I. Mishnev, V. V. Parkhomchuk, A. N. Voroshilov, M. N. Zakhvatkin, BINP, Russia	2022
A Possible Redesign of the SLAC SLC Damping Rings — T. O. Raubenheimer, R. Early, T. Limberg, H. Moshhammer, J. Spencer, SLAC	2025
Update on the Argonne Positron Accumulator Ring — M. Borland, ANL	2028
Measurement on the SRRC 1.3 GeV Electron Booster Synchrotron Operation Parameters and the Ramping Behavior — K. K. Lin, K. T. Hsu, T. S. Ueng, SRRC Taiwan	2031

Volume 1: 1-74
 Volume 2: 748-1040
 Volume 3: 1041-2545
 Volume 4: 2546-3218
 Volume 5: 3219-3933

Proceedings of the 1993 Particle Accelerator Conference

1.3 GeV Electron Synchrotron — J. Modéer, Scanditronix	2034
Performance of the ALS Injection System — C. H. Kim, LBL	2036
Synchrotron of SPring-8 — H. Yonehara, H. Suzuki, T. Aoki, S. Yoneyama, Y. Ueyama, Y. Sasaki, T. Nagafuchi, S. Hayashi, H. Yokomizo, JAERI	2039
Further Study of JINR Tau-Charm Factory Design — E. Perelstein, V. Alexandrov, V. Antropov, O. Arkhipov, P. Beloshitsky, L. Bobylev, V. Kazacha, N. Kazarinov, A. Krasnykh, V. Mironov, D. Kaltchev, L. Onischenko, A. Sissakian, Yu. Smirnov, Ts. Vylov, JINR Dubna; V. Belov, B. Mudiugin, A. Popov, D. Serebrennikov, SRI St. Petersburg; I. Kvashonkin, E. Petrov, I. Umansky, Russian Inst., St. Petersburg ...	2042
A Versatile Lattice for a Tau-Charm Factory That Includes a Monochromatization Scheme (Low Emittance) and a Standard Scheme (High Emittance) — A. Faus-Golfe, U. Valencia; J. Le Duff, LAL Orsay	2045
DAFNE Interaction Region Design — M. Bassetti, M. E. Biagini, C. Biscari, M. A. Preger, G. Raffone, G. Vignola, INFN-LNF	2048
On an Asymmetric Correlated Flavor Factory — D. Cline, A. Boden, W. Gabella, A. Garren, X. Wang, UCLA	2051
Status of the MIT-Bates South Hall Ring Commissioning — J. B. Flanz, K. D. Jacobs, B. McAllister, R. Averill, S. Bradley, A. Carter, K. Dow, M. Farkondeh, E. Ihloff, S. Kowalski, W. Sapp, C. Sibley, D. Tieger, C. Tschalaer, A. Zolfaghari, MIT-Bates	2054
Current Status of the Design of the Kharkov Pulse Stretcher Ring PSR-2000 — S. Efimov, P. Gladkikh, Y. Grigor'ev, I. Guk, I. Karnaukhov, V. Kozin, S. Kononenko, V. Likhachev, V. Markov, N. Mocheshnikov, V. Moskulenko, A. Mytsykov, Yu. Popkov, A. Shcherbakov, M. Strelkov, A. Tarasenko, Yu. Telegin, A. Zelynsky, Kharkov Inst.; M. Nagaenko, Yu. Severgin, ESRI	2057
Moscow State University CW Race-Track Microtron Status — V. I. Shvedunov, A. S. Alimov, A. S. Chepurnov, O. V. Chubarov, I. V. Gribov, B. S. Ishkhanov, I. V. Surma, A. V. Tiunov, INP Moscow	2059
Optical Design of the 75-MeV Eindhoven Racetrack Microtron — G. A. Webers, J. L. Delhez, J. I. M. Botman, H. L. Hagedoorn, Eindhoven U. of Tech.	2062
Example Application for the Hamiltonian Description of an Azimuthally Varying Field Racetrack Microtron — J. L. Delhez, W. J. G. M. Kleeven, H. L. Hagedoorn, J. I. M. Botman, G. A. Webers, Eindhoven U. of Tech.	2065
A 100-MeV Racetrack Microtron — P. Lidbjörk, J. Åström, Scanditronix	2068
Electrostatic Quadrupole Focusing in the AGS g-2 Storage Ring — C. Bennett, R. Larsen, W. Morse, Y. Semertzidis, J. Yelk, BNL; Z. Liu, Boston U.	2070
Design of 8-GeV Rapid-Cycle Booster Synchrotron for the KEK B-Factor — S. Kurokawa, KEK; P. Zenkevich, ITEP Moscow	2073

Instrumentation and Beam Feedback

Chair: R. Shafer

Feedback Control of Coupled-Bunch Instabilities (Invited Paper) — J. D. Fox, N. Eisen, H. Hindi, I. Linscott, G. Oxoby, L. Sapozhnikov, SLAC; M. Serio, INFN Frascati	2076
Electro-Optical Technology Applied to Accelerator Beam Measurement and Control (Invited Paper) — R. J. Pasquinelli, FNAL	2081
RF-Synchronized Imaging for Particle and Photon Beam Characterizations (Invited Paper) — A. H. Lumpkin, ANL....	2086
Diagnostic Instrumentation System for the SRRC 1.3 GeV Synchrotron Radiation Light Source — K. T. Hsu, G. J. Jan, C. H. Kuo, K. H. Hu, SRRC Taiwan.....	2091
Overview and Status of Beam Instrumentation at the SSC — R. C. Webber, SSCL	2094
Performance of Advanced Light Source Particle Beam Diagnostics — J. Hinkson, LBL	2097
Damping in the Fermilab Booster — J. M. Steimel, Jr., D. McGinnis, FNAL	2100
Betatron Function Measurement at LEP Using the BOM 1000 Turns Facility — P. Castro, IFIC, Spain; J. Forer, A. Burns, G. Morpurgo, R. Schmidt, CERN	2103
Adaptive Cascaded Beam-Based Feedback at the SLC — T. Himel, S. Allison, P. Grossberg, L. Hendrickson, R. Sass, H. Shoaee, SLAC	2106
Design of the ALS Transverse Coupled-Bunch Feedback System — W. Barry, J. M. Byrd, J. N. Corlett, J. Hinkson, J. Johnson, G. R. Lambertson, LBL; J. D. Fox, SLAC	2109

Each volume begins with this five-volume table of contents and ends with the five-volume author index. The chairmen's foreword and a list of conference organizers and staff appear as front matter in Volume 1. A list of conference participants precedes the author index in Volume 5.

Poster presentations:

Results of Prototype Particle-Beam Diagnostics Tests for the Advanced Photon Source (APS) — A. H. Lumpkin, Y. Chung, E. Kahana, D. Patterson, W. Sellyey, A. Votaw, X. Wang, ANL	2112
Diagnostics Development for High Current Electron Accelerators at CESTA — J. de Mascureau, C. Bonnafond, A. Devin, E. Merle, G. Ployard, D. Villate, CESTA	2115
Beam Instrumentation for the SSC RFQ — P. Datte, G. Jamieson, R. Aiello, D. Beechy, A. Jones, D. Martin, J. Riordon, R. Webber, F. Wood, SSCL	2118
High Density Data Recording for SSCL Linac — A. L. VanDeusen, Allied Signal; C. Crist, SSCL	2121
Physic Requirements of Commissioning Diagnostics for SSCL Linac — J. W. Hurd, G. M. Arbique, C. E. Crist, F. W. Guy, M. Haworth, G. T. Leifeste, K. Saadatmand, SSCL; M. Krogh, K. McGinnis, D. Stittsworth, A. Vandeusen, S. Wright, Allied Signal	2124
Beam Diagnostic Layout Requirements for SSCL Linac — J. W. Hurd, F. W. Guy, G. Jamieson, D. Raparia, K. Saadatmand, SSCL	2127
SSCL Linac Commissioning Diagnostic Cart — C. E. Crist, L. W. Funk, J. W. Hurd, G. T. Leifeste, SSCL; M. Krogh, K. McGinnis, D. Stittsworth, A. Vandeusen, S. Wright, Allied Signal	2130
A Method for LEBT Automation — J. Sredniawski, L. Solensten, R. Schmidt, J. Porter, Y. Ng, C. Lom, Grumman; W. Newman, AMTEX	2133
Beam Energy Measurement Using the Hall C Beam Line — C. Yan, R. Carlini, D. Neuffer, CEBAF	2136
A Wide Range and High Speed Automatic Gain Control — E. J. Tacconi, C. F. Christiansen, SSCL/ UNLP Argentina	2139
A Beamline Design and Data Acquisition with the 20-MeV, 20-ps Electron Beam for the Higher-Order-Mode Studies of the APS SR-RF Cavities — J. Song, A. Nassiri, R. Daly, ANL	2142
A Bunch Killer for the NSLS X-Ray Electron Storage Ring — R. J. Nawrocky, U. Bergmann, D. P. Siddons, NSLS BNL	2145
The Mechanical Design of a Bunched Beam Stochastic Cooling Tank for the FNAL Tevatron — P. Hurh, G. Jackson, FNAL	2148
Design Study of Laser Compton Scattering with Relativistic Electron to Measure the Electron Beam Energy — I. Hsu, H. Chen, C. Cho, Y. Liu, Nat. Tsing Hua U.	2151
Transverse Beam Impedance Measurement: A New Coaxial Method — M. Cardito, F. Galluccio, R. Losito, M. R. Masullo, V. Vaccaro, INFN Napoli; G. Di Massa, U. Calabria	2154
A Novel Method of Noise Suppression in Beam Transfer Function Measurements — F. Caspers, M. Chanel, U. Oeftiger, CERN	2157
Beam Dispersion Measurements with Wire Scanners in the SLC Final Focus Systems — P. Emma, D. McCormick, M. C. Ross, SLAC	2160
Comprehensive Beam Jitter Study for the Commissioning of the Intermediate Matching Section and Drift Tube Linac at Ground Test Accelerator — D. S. Barr, J. D. Gilpatrick, LANL	2163
A New Method of Ion Beam Diagnostics — A. S. Artiomov, JINR Dubna	2166
Correlation Method of Measurements of Ion Beam Parameters — A. S. Artiomov, JINR Dubna	2169
The Compton Polarimeter at the SLC — G. Shapiro, S. Bethke, O. Chamberlain, R. Fuzesy, M. Kowitt, D. Pripstein, B. Schumm, H. Steiner, M. Zolotorev, LBL; P. Rowson, Columbia; D. Blockus, H. Ogren, M. Settles, Indiana; M. Fero, A. Lath, MIT; D. Calloway, R. Elia, E. Hughes, T. Junk, R. King, T. Maruyama, K. Moffeit, M. Petradza, M. Swartz, M. Woods, SLAC; G. Zapalac, Wisconsin	2172
Measurement of the Spin of a Particle Using Undulator Radiation — A. Luccio, BNL	2175
Quantum Geometrical Phase Signal of NLC Bunch Cross Section Carried by Virtual Photons — J. Shen, IHEP Beijing	2178
Response of Air-Filled Ion Chambers to High-Intensity Radiation Pulses — M. Plum, D. Brown, LANL	2181
The CEBAF Beam Loss Sensors — J. Perry, E. Woodworth, L. Merminga, S. Simrock, R. May, CEBAF; G. Stapleton, SSCL	2184
A Scintillating Fiber Beam Halo Detector for Heavy Ion Beam Diagnostics — M. A. McMahan, A. Assang, S. Herr, F. McCormack, G. Krebs, B. Feinberg, LBL	2187

Proceedings of the 1993 Particle Accelerator Conference

Development and Investigation of the 2π Beam Loss Monitors for Super-High-Energy Accelerators, Part 1: Quad-BLM for "Warm" Machines — S. N. Lapitsky, I. A. Kurochkin, V. S. Seleznev, IHEP Russia	2190
The Design and Performance of a High Sensitivity Loss Monitor System for Use in the Fermilab Antiproton Rings — A. M. Halling, J. R. Zagel, A. Hahn, FNAL	2193
Abort Interlock Diagnostic for Protection of APS Vacuum Chamber — G. Decker, ANL	2196
Experience with Radiation Protection for a Silicon Vertex Detector at a Hadronic Collider — P. F. Derwent, D. Amidei, A. Dunn, T. Song, S. Vejcek, U. Michigan; R. Crouch, R. Ducar, D. Herrup, FNAL; C. Haber, LBL	2199
Design of a New Generation of Collimators for LEP 200 — R. Jung, R. Perret, R. Valbuena, CERN	2202
Synchrotron Radiation Damage Test of Insulating Materials in the TRISTAN MR — H. Mitsui, R. Kumazawa, T. Tanii, T. Chugun, Toshiba Corp.; Y. Ohsawa, T. Ozaki, K. Takayama, KEK	2205
Insulating and Metal-Ceramic Materials for Particle Accelerators — Yu. P. Severgin, M. Z. Filimonov, Efremov Inst.	2208
The Advanced Light Source (ALS) Radiation Safety System — A. L. Ritchie, D. E. Oldfather, A. F. Lindner, LBL ..	2210
Radiation Measurements During Cavities Conditioning on APS RF Test Stand — D. M. Grudzien, R. L. Kustom, H. J. Moe, J. J. Song, ANL	2213
Application of a Simple Analytical Model to Estimate Effectiveness of Radiation Shielding for Neutrons — S. Frankle, D. Fitzgerald, R. Hutson, R. Macek, C. Wilkinson, LANL	2216
Monte Carlo Based Formula for Radiation Shielding Assessment in the Forward Direction — C. Wilkinson, D. Fitzgerald, S. Frankle, R. Hutson, R. Macek, LANL	2219
A High Reliability Oxygen Deficiency Monitoring System — R. Parry, G. Claborn, A. Haas, R. Landis, W. Page, J. Smith, SSCL	2222
Programmable Electronic Safety Systems — R. R. Parry, SSCL	2225
A Pseudo Real Time Tune Meter for the Fermilab Booster — G. Wu, V. Bharadwaj, J. Lackey, D. McGinnis, R. Tomlin, FNAL	2228
Measurement Techniques Using the Tektronix® 3052 DSP System — J. M. Steimel, Jr., D. McGinnis, FNAL	2231
Using Transient Waveform Recorders to Measure and Store Beam Parameters — R. E. Stege, Jr., R. K. Jobe, M. Ross, SLAC	2234
Tune Measurement in the APS Rings — W. Sellyey, E. Kahana, X. Wang, ANL	2237
Integrating Log-Ratio Position Processing for the Los Alamos Proton Storage Ring Extraction Line — T. W. Hardek, A. Band, LANL	2240
Betatron "Ping" Tune Measurement System for the IUCF Cooler Synchrotron/Storage Ring — B. J. Hamilton, M. S. Ball, T. J. P. Ellison, IUCF	2243
Tune Measurement in the NSLS Booster Synchrotron — E. B. Blum, R. Nawrocky, BNL	2246
A Realtime Feedback Microprocessor for the Tevatron — D. A. Herrup, L. Chapman, A. Franck, T. Groves, B. Lublinsky, FNAL	2249
A New Study of the Main Ring Physical Aperture — G. Wu, S. Pruss, D. Capista, FNAL	2252
Electron Beam Stability and Beam Peak to Peak Motion Data for NSLS X-Ray Storage Ring — O. Singh, BNL	2254
Test of Fast-Digital Beamline Feedback Control at the Photon Factory — N. Nakamura, T. Katsura, KEK	2257
Horizontal Movement of the Storage Ring Floor at the Photon Factory — T. Katsura, H. Nakamura, Y. Kamiya, KEK; Y. Fujita, Shimizu Corp.	2260
Closed Orbit Correction Using Singular Value Decomposition of the Response Matrix — Y. Chung, G. Decker, K. Evans, Jr., ANL	2263
Compensation for the Effect of Vacuum Chamber Eddy Current by Digital Signal Processing for Closed Orbit Feedback — Y. Chung, L. Emery, J. Kirchman, ANL	2266
Dynamic Closed Orbit Correction — Y. Cheng, SRRC Taiwan	2269
A Closed-Loop Photon Beam Control Study for the Advanced Light Source — G. Portmann, J. Bengtsson, LBL	2272
Global DC Closed Orbit Correction Experiments on the NSLS X-Ray Ring and SPEAR — Y. Chung, G. Decker, K. Evans, Jr., ANL; J. Safranek, I. So, Y. Tang, BNL; W. J. Corbett, R. Hettel, SSRL	2275
FFT-Oriented Feedback — F.-J. Decker, SLAC	2278
Issues of the Transverse Feedback Systems Design at the SSC — W. Chou, J. Peterson, SSCL	2281
A Digital Feedback System for Orbit Stabilization — A. Friedman, E. Bozoki, O. Singh, J. Smith, BNL	2284
Results from the AGS Booster Transverse Damper — D. Russo, M. Brennan, M. Meth, T. Roser, BNL	2286
Single Board Op-Amp Beam Position Monitors Electronics — M. Ball, T. J. P. Ellison, B. J. Hamilton, IUCF	2289

Each volume begins with this five-volume table of contents and ends with the five-volume author index. The chairmen's foreword and a list of conference organizers and staff appear as front matter in Volume 1. A list of conference participants precedes the author index in Volume 5.

Five-Volume Contents

A Single-Passage Beam-Position Monitor in the TRISTAN AR-to-MR Transport Lines — <i>T. Ieiri, M. Arinaga, KEK</i>	2292
Beam Position Monitoring System Using PIN Diode Switches — <i>K. Shinoe, T. Koseki, Y. Kamiya, ISSP Tokyo; N. Nakamura, T. Katsura, T. Ieiri, KEK</i>	2295
Performance of the CEBAF Arc Beam Position Monitors — <i>A. S. Hofler, B. A. Bowling, C. S. Higgins, P. K. Kloeppel, G. A. Krafft, K. L. Mahoney, CEBAF</i>	2298
The Million Turn Data Acquisition System BOSC — <i>A. Burns, W. Fischer, H. Jakob, I. Milstead, F. Schmidt, L. Vos, CERN</i>	2301
Beam Position Monitor Calibration for the Advanced Photon Source — <i>Y. Chung, G. Decker, E. Kahana, F. Lenkszus, A. Lumpkin, W. Sellyey, ANL</i>	2304
Self Triggered Single Pulse Beam Position Monitor — <i>J. L. Rothman, E. B. Blum, NSLS-BNL</i>	2307
A Prototype BPM Electronics Module for RHIC — <i>W. A. Ryan, T. J. Shea, P. Cerniglia, C. M. Degen, BNL</i>	2310
Dynamic Range Extension of BPM at the NSLS — <i>M. Bordoley, NSLS-BNL</i>	2313
Beam Position Monitoring in the 100-MHz to 500-MHz Frequency Range Using the Log-Ratio Technique — <i>F. D. Wells, R. E. Shafer, J. D. Gilpatrick, LANL</i>	2316
Beam Pinging, Sweeping, Shaking, and Electron/Ion Collecting, at the Proton Storage Ring — <i>T. Hardek, R. Macek, M. Plum, T.-S. Wang, LANL</i>	2319
Test Results of the SSC Log-Ratio Beam Position Monitor Electronics — <i>G. R. Aiello, M. R. Mills, R. E. Gonzalez, SSCL</i>	2322
RF Beam Position Monitors for the TESLA Test Facility — <i>R. Lorenz, TU Berlin</i>	2325
RHIC Beam Position Monitor Assemblies — <i>P. R. Cameron, M. C. Grau, W. A. Ryan, T. J. Shea, R. E. Sikora, BNL</i>	2328
Stripline Beam Position Monitor for the MIT-Bates South Hall Ring — <i>J. B. Flanz, R. Averill, E. Ihloff, K. D. Jacobs, D. Wang, A. Zolfaghari, MIT-Bates</i>	2331
Design and Operation of Button-Probe, Beam-Position Measurements — <i>J. D. Gilpatrick, J. F. Power, R. E. Meyer, C. R. Rose, LANL</i>	2334
Design and Calibration of Pickup-Electrodes for Beam Position Monitoring at SOR-RING — <i>K. Shinoe, Y. Kamiya, ISSP Tokyo; N. Nakamura, T. Katsura, KEK</i>	2337
The Position Monitor Using Stretched Wire Technique — <i>T. Mimashi, S. Kuroda, H. Nakayama, K. Oide, R. Sugahara, N. Yamamoto, KEK</i>	2340
An Over-Moded Stripline Beam Position Monitor — <i>J. G. Noomen, J. Bijleveld, F. Kroes, T. Sluijk, NIKHEF-K</i> ...	2343
Loss of Precision in Resonant Beam Position Monitors Due to Finite <i>Q</i> — <i>J. P. H. Sladen, W. Wuensch, CERN</i>	2346
Simulation of the ALS Longitudinal Multibunch Feedback System — <i>J. Byrd, LBL</i>	2349
Analysis of DSP-Based Longitudinal Feedback System: Trials at SPEAR and ALS — <i>H. Hindi, N. Eisen, J. Fox, I. Linscott, G. Oxoby, L. Sapozhnikov, SLAC; M. Serio, INFN</i>	2352
VXI Based Low Level RF System for Fermilab Linac Upgrade — <i>B. E. Chase, R. J. Pasquinelli, FNAL</i>	2355
Longitudinal Feedback in LEP — <i>J. P. Boiteux, P. Brown, E. Ciapala, H. Frischholz, G. Geschonke, J. C. Juillard, E. Peschardt, CERN</i>	2358
Performance of the Upgraded Stacktail Momentum Cooling System in the Fermilab Antiproton Source — <i>R. J. Pasquinelli, D. McGinnis, FNAL</i>	2361
Energy Vernier System for CEBAF — <i>G. A. Krafft, J. J. Bisognano, M. T. Crofford, J. C. Hovater, L. Merminga, S. N. Simrock, S. D. Witherspoon, CEBAF; K. Kubo, KEK</i>	2364
A Digital Approach for Phase Measurement Applied to Delta- <i>t</i> Tuneup Procedure — <i>G. R. Aiello, SSCL</i>	2367
RF Feedback for Beam Loading Compensation in the SLC Damping Rings — <i>P. Krejcik, P. Corredoura, M. Minty, R. Siemann, R. Tighe, SLAC; F. Pedersen, CERN</i>	2370
Simulation and Analysis of RF Feedback Systems on the SLC Damping Rings — <i>M. Minty, T. Himel, P. Krejcik, R. H. Siemann, R. Tighe, SLAC</i>	2373
Improved Impedance Reduction in the CERN SPS Superconducting Cavities for High Intensity Proton Operation — <i>D. Boussard, G. Lambert, T. P. R. Linnecar, CERN</i>	2376
Damping of Phase Errors at Injection in the LHC — <i>D. Boussard, E. Onillon, CERN</i>	2379
A Digital Beam Phase Loop for the Low Energy Booster — <i>L. K. Mestha, V. Brouk, R. C. Webber, J. Mangino, T. Uher, SSCL</i>	2382
General Time-Varying State-Space Control Model and Its Application for Transient Beam Loading Compensation — <i>L. K. Mestha, C. M. Kwan, SSCL; K. S. Yeung, UTA</i>	2385
A Digital Phase and Amplitude Feedforward Correction System — <i>D. Yu, P. Conway, DULY Res. Inc.</i>	2388

Volume 1	i-747
Volume 2	748-1640
Volume 3	1641-2545
Volume 4	2546-3218
Volume 5	3219-3933

Proceedings of the 1993 Particle Accelerator Conference

Results of Adaptive Feedforward on GTA — C. D. Ziomek, P. M. Denney, A. H. Regan, M. T. Lynch, S. P. Jachim, L. E. Eaton, E. F. Natter, LANL	2391
Fast Bunch-to-Bunch Current Sampling in the Cornell Electron-Positron Collider — C. R. Dunnam, Cornell; K. B. Unser, CERN	2394
A Method for Measuring Dark Current Electron Beams in an RF Linac — X. K. Maruyama, T. Fasanello, H. Rietdyk, Naval Postgraduate School; M. A. Piestrup, Adelphi Tech.; D. W. Rule, R. B. Fiorito, NSWC	2397
High Bandwidth Beam Current Monitor — R. M. Baltrusaitis, C. A. Ekdahl, LANL; R. G. Cooper, E. Peterson, C. E. Warn, EG&G	2400
Rapid Measurements of Two-Dimensional Ion Beam Current Distribution for Pulsed Neutron Source — A. M. Tron, MEPI	2403
Short Bunch Length Detector for Ion Beam with High Bunch Density — A. M. Tron, V. V. Shako, MEPI	2406
Measurement of Bunch Time-Structure in KEK-PF — M. Tobiyama, T. Kasuga, T. Takeo, T. Obina, K. Tamura, Hiroshima U.; T. Katsura, KEK	2409
A Fifth Harmonic RF Bunch Monitor for the ANL-APS Electron Linac — A. Nassiri, A. Grelick, ANL	2412
Characterization of Subnanosecond Heavy-Ion Bunches at the TASSC Superconducting Cyclotron — G. R. Mitchel, N. A. Towne, AECL	2415
Design, Implementation, and Results from a Longitudinal Phase Space Tomography (PST) Monitor in the Fermilab Main Ring — G. Jackson, FNAL	2418
An Electrostatic Sweep Plate Device for Emittance Measurement of Ion Beams to 2 MeV — T. W. Debiak, J. Porter, R. Heuer, I. Birnbaum, Grumman	2420
Length Monitor for 1 mm SLC Bunches — E. Babenko, BINP Novosibirsk; R. K. Jobe, D. McCormick, J. T. Seeman, SLAC	2423
Bunch Shape Monitor for SSCL Linac — J. W. Hurd, G. M. Arbique, C. E. Crist, F. W. Guy, G. T. Leifeste, D. Raparia, K. Saadatmand, D. A. Swenson, SSCL; S. Esin, A. Feschenko, A. Stepanov, A. Mirzozan, INR Moscow	2426
A Field-Based Technique for the Longitudinal Profiling of Ultrarelativistic Electron or Positron Bunches Down to Lengths of ≤ 10 Microns — R. Tatchyn, SLAC	2429
Performance Limits of a Streak Camera in Real Time Three-Dimensional Measurement of Bunch Oscillation in LEP — E. Rossa, CERN; F. Tecker, RWTH Aachen; J.C. Mathae, ARP Strasbourg	2432
Bunch Length Measurements in the SLC Damping Ring — F.-J. Decker, T. Limberg, M. Minty, M. Ross, SLAC ..	2435
Virtual Photon Impulse of Bunch, Beam-pipe Response, Coherent RF Beamstrahlung; and BEPC Bunch Length, BES Jam, Virtual Acceleration — J. Shen, IHEP Beijing	2438
Development on Multistrip Monitor for Nonintercepting Measurement of Beam Geometric Moments — Y. Yin, TRIUMF	2441
Wire Scanner Data Analysis for the SSC Linac Emittance Measurement — C. Y. Yao, J. W. Hurd, J. Sage, SSCL	2444
Real-Time Spot Size Measurement for Pulsed High-Energy Radiographic Machines — S. A. Watson, LANL	2447
High Resolution Beam Monitoring with Optical Transition Radiation at 3 MeV Electron Energy — A. Specka, D. Bernard, R. Guirlet, F. Jacquet, P. Miné, B. Montès, R. Morano, P. Poilleux, LPNHE; F. Amiranoff, LULI; J. Morillo, LSI	2450
Beam Profiling with Optical Transition Radiation — D. W. Rule, R. B. Fiorito, NSWCDD	2453
Beam Emittance from Coherent Cherenkov Radiation in a Solid Dielectric — R. D. Richardson, R. C. Platt, SAIC; C. E. Crist, SNL	2456
A 10 μ m Resolution Secondary Emission Monitor for Fermilab's Targeting Station — P. Hurh, S. O'Day, R. Dombrowski, T. Page, FNAL	2459
Construction of a High Resolution Electron Beam Profile Monitor — J. Norem, J. Dawson, W. Haberichter, W. Novak, L. Reed, X-F. Yang, ANL	2462
Design Study of Beam Profile Monitor of Storage Ring by Using Synchrotron Radiation — I. C. Hs, T. H. Huang, Nat. Tsing Hua U./SRRC	2465
Limitations of a Residual Gas Ionization Beam Profile Monitor for the SSC Collider — R. Meinke, W. Nexsen, E. Tsyganov, A. Zinchenko, SSCL	2468
Full Cycle Beam Diagnostics with an Ionization Profile Monitor — A. Stillman, R. E. Thern, BNL	2471
Electron Beam Diagnostics by Means of Edge Radiation — O. V. Chubar, Kurchatov Inst.; E. S. Masunov, MEPI	2474
CEBAF Beam Viewer Imaging Software — B. A. Bowling, C. McDowell, CEBAF	2477

Each volume begins with this five-volume table of contents and ends with the five-volume author index. The chairmen's foreword and a list of conference organizers and staff appear as front matter in Volume 1. A list of conference participants precedes the author index in Volume 5.

Five-Volume Contents

Prototype Flying-Wire Beam-Profile Monitor — D. B. Barlow, C. M. Fortgang, J. D. Gilpatrick, R. E. Meyer, A. M. Rendon, D. S. Warren, M. D. Wilke, LANL	2480
Emittance Measurement and Data Analysis for the SSC Linac Injector Lab — J. E. Hébert, P. Datte, F. W. Guy, N. C. Okay, K. Saadatmand, J. Sage, D. M. Wetherholt, W. A. Whittenberg, SSCL	2483
Automatic Emittance Measurement at the ATF — X. J. Wang, R. Malone, K. Batchelor, I. Ben-Zvi, BNL	2486
Electron Beam Emittance Monitor for the SSC — E. Tsyganov, R. Meinke, W. Nexsen, S. Kauffmann, A. Zinchenko, A. Taratin, SSCL	2489
Measurement of Vertical Emittance at LEP from Hard X-Rays — H. Akbari, J. Borer, C. Bovet, Ch. Delmere, A. Manarin, E. Rossa, M. Sillanoli, J. Spanggaard, CERN	2492
Performance and Operational Experience of the LEP Synchrotron Light Telescopes — G. Burtin, R. J. Colchester, J. J. Gras, R. Jung, J. M. Vouillot, CERN	2495
High Sensitivity Beam Intensity and Profile Monitors for the SPS Extracted Beams — J. Camas, G. Ferioli, R. Jung, J. Mann, CERN	2498
High Density Harp for SSCL Linac — C. T. Fritsche, M. L. Krogh, AlliedSignal; C. E. Crist, SSCL	2501
High Resolution Measurements of Lepton Beam Transverse Distributions With the LEP Wire Scanners — J. Camas, G. Crockford, G. Ferioli, C. Fischer, J. J. Gras, R. Jung, J. Koopman, J. Mann, CERN	2504
Beam Size Measurements with Noninterceptive Off-Axis Screens — F.-J. Decker, R. Brown, J. T. Seeman, SLAC ...	2507
Resolution Improvement in Beam Profile Measurements with Synchrotron Light — O. V. Chubar, MEPI	2510
The Orsay Spot Size Monitor for the Final Focus Test Beam — J. Buon, B. Delcourt, J. Jeanjean, F. Le Diberder, V. Lepeltier, P. Puzo, LAL Orsay	2513
Beam Monitor Utilizing Transition Radiation — Y. Ogawa, J. Choi, T. Suwada, T. Kamitani, T. Urano, K. Furukawa, S. Ohsawa, A. Enomoto, I. Sato, KEK	2516
Fermilab Main Ring Low Level RF System Modifications for Focus Free Transition Beam Tests — R. G. Scala, K. Meisner, FNAL	2519
RF Synchronous Transfer into Specific Buckets Between Fermilab Main Ring and Tevatron Accelerators — K. Meisner, FNAL	2522
Main Ring Bunch Length Monitor — K. Meisner, G. Jackson, FNAL	2525
A VX1/LabVIEW-based Beamline Tuner — W. Blokland, FNAL	2528
A Frequency-Domain Directivity Enhancement of Beam Position Stripline Detectors — E. L. Barsotti, FNAL	2531
The Control System of ROSY I — T. Goetz, M. Picard, U. Bonn; M. Plesko, Sinc. Trieste	2534
Measuring Emittance Using Beam Position Monitors — S. J. Russell, B. E. Carlsten, LANL	2537
On the Reliability of Measured Results by Non-Destructive Beam Profile Monitor — T. Kawakubo, E. Kadokura, KEK; T. Ishida, Mitsubishi Elect.	2540
Transverse Feedback System with Digital Filter — V. M. Zhabitsky, JINR; I. L. Korenev, L. A. Yudin, MRTI	2543

Volume 4

Advanced Accelerator Concepts

Chair: C. Joshi

R. R. Wilson Prize Lecture: Adventures with Accelerators (<i>Invited Paper</i>) — J. P. Blewett, BNL (ret.)	2546
Demonstration of Plasma Beat Wave Acceleration of Electrons from 2 MeV to 20 MeV (<i>Invited Paper</i>) — C. E. Clayton, K. A. Marsh, M. Everett, A. Lal, C. Joshi, UCLA	2551
Laser Wakefield Accelerator Experiments Using 1 ps 30 TW Nd:glass Laser — K. Nakajima, H. Nakanishi, T. Kawakubo, A. Ogata, KEK; Y. Kitagawa, H. Shiraga, R. Kodama, T. Zhang, K. Suzuki, Y. Kato, Osaka U.; Y. Sakawa, T. Shoji, Nagoya U.; Y. Nishida, N. Yugami, Utsunomiya U.; T. Tajima, U. Texas, Austin	2556
Photonic Band Gap Resonators for High Energy Accelerators (<i>Invited Paper</i>) — S. Schultz, D. R. Smith, UCSD; N. Kroll, UCSD/SLAC	2559
Update on the ATF Inverse Cherenkov Laser Acceleration Experiment — W. D. Kimura, L. C. Steinhauer, G. H. Kim, S. C. Tidwell, STI Optronics; I. Pogorelsky, K. P. Kusche, BNL/STI Optronics	2564
New Directions in RF Sources (<i>Invited Paper</i>) — L. Schächter, Cornell	2567
Criteria for Comparing the Suitability of Microwave Amplifiers for Driving TeV Linear Colliders — V. I. Granatstein, G. S. Nusinovich, U. Maryland	2572

Volume 1: 1-747
 Volume 2: 748-1640
 Volume 3: 1641-2545
 Volume 4: 2546-3218
 Volume 5: 3219-3933

Proceedings of the 1993 Particle Accelerator Conference

High Gradient Acceleration in a 17 GHz Photocathode RF Gun — S. C. Chen, J. Gonichon, L. C-L. Lin, R. J. Temkin, S. Trotz, B. G. Danly, J. S. Wurtele, MIT	2575
An Inverse Free-Electron-Laser Accelerator — A. S. Fisher, J. C. Gallardo, A. van Steenbergen, S. Ulc, M. Woodle, BNL; J. Sandweiss, Yale; J. Fang, Columbia U.	2578
Phase Control in High-Gradient Laser Particle Accelerators — L. C. Steinhauer, W. D. Kimura, STI Optronics	2581

Poster presentations:

Beam Quality in a Cyclotron Autoresonance Accelerator — B. Hafizi, Icarus Res.; P. Sprangle, NRL; J. L. Hirshfield, Omega-P Inc.	2584
Superlattice Crystal Accelerator: Acceleration Beyond GeV/m — S. A. Bogacz, FNAL	2587
Design Study of a Microwave Driver for a Relativistic Klystron Two-Beam Accelerator — T. L. Houck, LLNL	2590
The Standing Wave FEL/TBA: Realistic Cavity Geometry and Energy Extraction — J. Kim, A. M. Sessler, LBL; H. Henke, TU Berlin; W. M. Sharp, LLNL	2593
The Argonne Wakefield Accelerator: Overview and Status — P. Schoessow, E. Chojnacki, W. Gai, C. Ho, R. Konecny, J. Power, M. Rosing, J. Simpson, ANL	2596
A Self-Consistent Theory of Ferromagnetic Waveguide Accelerators Driven by Electron Beams — H. S. Uhm, NSWC	2599
Wakefield Accelerator Driven by a Relativistic Electron Beam in a Ferromagnetic Waveguide — H. S. Uhm, NSWC	2602
Magnetic Field-Decay Accelerator Driven by a Relativistic Electron Beam in a Ferromagnetic Waveguide — H. S. Uhm, NSWC	2605
Three-Dimensional Simulation Analysis of the First Sections of a Standing-Wave Free-Electron Laser Two-Beam Accelerator — C. Wang, A. M. Sessler, LBL	2608
Reacceleration Experiment to Demonstrate the Concept of Efficiency Enhancement in a Relativistic Klystron Two- Beam Accelerator — G. A. Westenskow, T. L. Houck, LLNL	2611
Design Analysis for a 100-MeV Inverse Cherenkov Laser Accelerator — J. R. Fontana, UCSB; W. D. Kimura, L. C. Steinhauer, STI Optronics; I. Pogorelsky, BNL/STI Optronics	2614
An Inverse Free Electron Laser Driven Linear Collider Electron-Positron B-Factory — N. Barov, C. Pellegrini, UCLA; J. Sandweiss, Yale	2617
2.5D Numerical Simulation of Relativistic Electron Bunches (REB) Interaction with Underdense and Overdense Plasmas — O. V. Batishchev, Y. S. Sigov, Keldysh Inst.; V. I. Karas', Y. B. Fainberg, Kharkov Inst.	2620
Propagation of Short Electron Pulses in Underdense Plasmas — N. Barov, J. Rosenzweig, UCLA	2623
Numerical Simulations of Driving Beam Dynamics in the Plasma Wakefield Accelerator — G. Joyce, J. Krall, E. Esarey, NRL	2626
Self-Modulated-Laser Wakefield Accelerator — J. Krall, A. Ting, E. Esarey, P. Sprangle, NRL	2629
A 100 MeV Proof-of-Principle Laser Wakefield Accelerator Experiment — A. Ting, A. Fisher, R. Fischer, J. Grun, J. Krall, E. Esarey, P. Sprangle, NRL; D. Umstadter, G. Mourou, U. Michigan	2632
Recent Work on Short Pulse Laser-Plasma Accelerators — T. Katsouleas, T. C. Chiou, USC; W. B. Mori, C. Decker, UCLA; J. S. Wurtele, G. Shvets, MIT	2635
Plasma Lens Experiments at the Final Focus Test Beam — J. Norem, ANL; D. Cline, W. Gabella, P. Kwok, S. Rajagopalan, J. Rosenzweig, UCLA; B. Barletta, UCLA/LBL; R. Williams, Florida A&M; S. Chattopadhyay, W. Leemans, A. Sessler, LBL; G. Westenskow, LLNL; J. Wurtele, MIT; J. J. Su, NCU Taiwan; K. Nakajima, H. Nakanishi, A. Ogata, D. Whittum, KEK; I. Hsu, NTU Taiwan; D. D. Meyerhofer, U. Rochester; T. Katsouleas, P. Lai, R. Liou, USC; P. Chen, W. Craddock, C. K. Ng, J. Spencer, SLAC; Y. Nishida, Utsunomiya U.	2638
A Plasma Lens and Accelerator Based Upon Magnetically Driven Charge Separation — S. Robertson, U. Colorado	2641
The NRL X-Band Magnicon Amplifier Experiment — S. H. Gold, C. A. Sullivan, W. M. Manheimer, NRL; B. Hafizi, Icarus Res.	2644
Theoretical Investigation of Magnicon Efficiency — B. Hafizi, Icarus Res.; S. H. Gold, W. M. Manheimer, P. Sprangle, NRL	2647
First Test of the X-Band Pulsed Magnicon — O. Nezhevenko, I. Kazarezov, E. Kozyrev, G. Kuznetsov, I. Makarov, A. Nikiforov, B. Persov, G. Serdobintsev, M. Tiunov, V. Yakovlev, I. Zapryagaev, BINP Russia	2650

Each volume begins with this five-volume table of contents and ends with the five-volume author index. The chairmen's foreword and a list of conference organizers and staff appear as front matter in Volume 1. A list of conference participants precedes the author index in Volume 5.

Five-Volume Contents

TM-FEL With a Longitudinal Wiggler and an Annular Beam — L. Schächter, T. J. Davis, J. A. Nation, Cornell	2653
CARM and Harmonic Gyro-Amplifier Experiments at 17 GHz — W. L. Menninger, B. G. Danly, S. Alberti, C. Chen, E. Giguet, J. L. Rullier, R. J. Temkin, MIT	2656
Stability of Gyrotwistrons — P. E. Latham, G. S. Nusinovich, J. Cheng, U. Maryland	2659
Optimum Operation of Gyrotwistrons — P. E. Latham, G. S. Nusinovich, U. Maryland	2661
Large Orbit Gyroklystron Development at Los Alamos — R. M. Stringfield, R. M. Wheat, D. J. Brown, M.V. Fazio, J. Kinross-Wright, B. E. Carlsten, G. Rodenz, R. J. Faehl, R. F. Hoeberling, LANL	2664
Initial Operation of a High Power, K-Band, Harmonic Gyroklystron for Accelerator Applications — J. P. Calame, H. W. Matthews, W. Lawson, B. Hogan, M. K. E. Lee, J. Cheng, V. L. Granatstein, M. Reiser, C. D. Striffler, U. Maryland	2667
Design of a 100 MW, 17 GHz Second Harmonic Gyroklystron Experiment — W. Lawson, P. E. Latham, V. Specht, M. K. E. Lee, Q. Qian, J. P. Calame, B. Hogan, V. L. Granatstein, M. Reiser, C. D. Striffler, U. Maryland	2670
Some Concepts of Relativistic Gyroamplifiers for Particle Acceleration — G. S. Nusinovich, P. E. Latham, V. L. Granatstein, U. Maryland	2673
Experimental Progress Toward a 1 GW, 1 ms Pulse Length, High Current Relativistic Klystron — M. Fazio, B. Carlsten, R. Faehl, W. Haynes, T. Kwan, R. Stringfield, LANL	2675
Relativistic Plasma Klystron Amplifier in Connection with Application to High Gradient Accelerators — H. S. Uhm, NSWC	2678
Sheet-Beam Klystron RF Cavities — D. Yu, DULY Res. Inc.; P. Wilson, SLAC	2681
Beam-Wave Interaction in a Quasi-Periodic Structure — L. Schächter, J. A. Nation, Cornell	2684
Two-Stage, High Power X-Band Amplifier Experiment — E. Kuang, T. J. Davis, J. P. Ivers, G. S. Kerslick, J. A. Nation, L. Schächter, Cornell	2687
Long-Pulse, High-Power, X-Band Relativistic Traveling-Wave Tube Amplifier — T. Kimura, S. Alberti, B. G. Danly, R. J. Temkin, MIT	2690
Tapered Tube, Microsecond Electron Beam Gyrotron Backward-Wave Oscillators — R. M. Gilgenbach, M. T. Walter, P. R. Menge, T. A. Spencer, U. Michigan	2693
Quiet Start and Autotasking for PARMELA — J. Gonichon, S. C. Chen, L. C.-L. Lin, R. J. Temkin, MIT	2696
Waveguide Side-Wall Coupling in RF Guns — L. C.-L. Lin, S. C. Chen, J. Gonichon, S. Trotz, J. S. Wurtele, MIT	2699
A High-Current Micro-Pulse Electron Gun — F. M. Mako, W. Peter, FM Tech. Inc.	2702
Knife-Edge Thin Film Field Emission Cathodes — B. Lee, H. P. Demroff, M. M. Drew, T. S. Elliot, T. K. Mazumdar, P. M. McIntyre, Y. Pang, D. D. Smith, H.-J. Trost, Texas A&M	2705
The Oxidized Porous Silicon Field Emission Array — D. D. Smith, H. P. Demroff, T. S. Elliott, T. B. Kasprovicz, B. Lee, T. K. Mazumdar, P. M. McIntyre, Y. Pang, H.-J. Trost, Texas A&M	2708
Study of Porous Silicon Morphologies for Electron Transport — Y. Pang, H. Demroff, T. S. Elliott, B. Lee, J. Lu, V. B. Madduri, T. K. Mazumdar, P. M. McIntyre, D. D. Smith, H.-J. Trost, Texas A&M	2711
Cold Test Measurements of a BWO Slow-Wave Structure — W. Main, Y. Carmel, K. Ogura, J. Weaver, S. Watanabe, U. Maryland	2714
Collective Accelerator with Variable Energy and Wide Spectrum of Accelerated Ions — R. Meshcherov, G. Batskikh, V. Krasnopol'sky, V. Rybalko, V. Sazhin, MRTI Moscow; A. Vasiliev, MAE Russia	2717
High Gradient Experiments with Nanosecond Pulses — V. Baglin, H. Haseroth, J. Knott, CERN; F. Chautard, SSCL	2720
Development of the Alternate Entry Port for the ATF — Z. Parsa, BNL	2723

Magnets, Cryogenics, and Alignment

Chair: J. Strait

Status of Superconducting Magnet Development (SSC, RHIC, LHC) (Invited Paper) — P. Wanderer, BNL	2726
Electrical Performance Characteristics of the SSC Accelerator System String Test (Invited Paper) — W. Robinson, W. Burgett, T. Dombeck, J. Gannon, P. Kraushaar, A. McInturff, T. Savord, G. Tool, SSCL	2731
Overview of the Final Focus Test Beam Alignment System — V. E. Bressler, R. E. Ruland, D. Plouffe, SLAC	2736
Long Term Experience with Cryoplant Operation for Superconducting Magnets and RF Cavities at CERN — D. Delikaris, J.-P. Dauvergne, P. K. Frandsen, F. Haug, G. Passardi, J.-M. Rieubland, J. Schmid, CERN	2739
Axial Variations in the Magnetic Field of Superconducting Dipoles and Quadrupoles — A. K. Ghosh, K. E. Robins, W. B. Sampson, BNL	2742

Volume 1: 1-74
Volume 2: 748-1640
Volume 3: 1641-2545
Volume 4: 2546-3218
Volume 5: 3219-3933

Proceedings of the 1993 Particle Accelerator Conference

Large Aperture Quadrupoles for RHIC Interaction Regions — R. Gupta, M. Anerella, G. Ganetis, M. Garber, A. Ghosh, A. Greene, A. Jain, S. Kahn, E. Kelly, E. Killian, G. Morgan, A. Morgillo, J. Muratore, A. Prodell, M. Rehak, W. Sampson, R. Shutt, P. Thomson, P. Wanderer, E. Willen, BNL	2745
<i>Poster presentations:</i>	
Design of Superconducting Quadrupole Magnets for CEBAF's Hall A Spectrometer — R. Kreutz, E. Brütsch, K. Dreher, H. Grüneberg, H. Lütkehaus, W. Nick, H. Peschel, B. Rzezonska, F. Sommer, P. Schäfer, Siemens AG	2748
Design of a Superconducting Wiggler for the PLS — B. K. Kang, Y. M. Koo, D. E. Kim, H. S. Seo, Y. U. Sohn, Pohang; P. D. Vobly, N. A. Mezentsev, G. N. Kulipanov, BINP	2751
Calculations of Magnetic Field for the End Design of the RHIC Arc Dipole — S. A. Kahn, R. C. Gupta, A. K. Jain, G. H. Morgan, P. A. Thompson, BNL	2754
Collider Scenario Implications of ASST Operation — A. D. McInturff, W. Burgett, M. Christianson, T. Dombeck, J. Gannon, D. Haenni, P. Kraushaar, M. Levin, M. McAshan, G. Mulholland, D. Murray, W. Robinson, T. Savord, R. Smellie, F. Spinos, G. Tool, J. Weisend II, J. Zatopek, SSCL	2757
Preliminary Analysis of Coil Wedge Dimensional Variation in SSC Prototype Dipole Magnets — D. Pollock, G. Brown, S. Dwyer, R. Gattu, D. Warner, SSCL	2760
SSC String Test Facility for Superconducting Magnets: Testing Capabilities and Program for Collider Magnets — P. Kraushaar, W. Burgett, T. Dombeck, A. McInturff, W. Robinson, V. Saladin, SSCL	2763
"B" Series RHIC Arc Quadrupoles — P. Thompson, M. Anerella, G. Ganetis, M. Garber, A. Ghosh, A. Greene, R. Gupta, A. Jain, S. A. Kahn, G. Morgan, A. Morgillo, J. Muratore, A. Prodell, M. Rehak, W. Sampson, P. Wanderer, E. Willen, BNL	2766
Fermilab-Built SSC Collider Dipoles Using Low Temperature Curing Insulation Systems With and Without Glass Tape — T. S. Jaffery, R. Coombes, A. Devred, J. DiMarco, T. Ogitsu, R. E. Sims, J. C. Tompkins, M. Wake, SSCL; R. Bossert, J. Carson, S. W. Delchamps, I. Gonczy, S. Gourlay, R. Hanft, M. J. Lamm, P. Mazur, D. Orris, J. Strait, FNAL	2769
Design and Tests of UNK Superconducting Correction Magnet Models — E. Rybakov, N. Bogatov, I. Dmitrieva, M. Kosyakin, Yu. Severgin, V. Fedorov, V. Shan'gin, Efremov Inst.; P. Chirkov, S. Kozub, K. Myznikov, V. Sychev, IHEP Moscow; A. Rychagov, V. Sytnikov, A. Taran, All-Union R&D Inst.	2772
Quench and Quench Protection for the SSC Collider Correctors — A. He, SSCL.....	2775
Variation in a_j Saturation in SSC Collider Dipoles — R. C. Gupta, A. K. Jain, BNL	2778
Spool Pieces at the SSCL — T. Clayton, Y. Cai, R. Smellie, S. Stampke, SSCL	2781
Quench Simulations of the 40 mm Aperture SSC-Quadrupole Magnet Connected in Series with 50 mm Aperture SSC-Dipole Magnets — G. López, SSCL	2784
Effective Stress of the SSC 80 K Synchrotron Radiation Liner in a Quenching Dipole Magnet — K. K. Leung, Q. S. Shu, K. Yu, J. Zbasnik, SSCL	2787
Improved Cable Insulation for Superconducting Magnets — M. Anerella, A. K. Ghosh, E. Kelley, J. Schmalzle, E. Willen, BNL; J. Fraivillig, J. Ochsner, D. J. Parish, DuPont	2790
Treatment of the Results of Magnetic Mapping of the SIBERIA-2 Magnets — V. Korchuganov, E. Levichev, A. Philipchenko, BINP	2793
Prototype Quadrupole Magnets for the PLS Storage Ring — Y. M. Koo, D. E. Kim, Y. G. Nah, H. S. Han, B. K. Kang, K. H. Park, J. R. Yoon, H. K. Lee, J. E. Milburn, Pohang	2796
Magnetic Measurement Data of the Injector Synchrotron Dipole Magnets for the 7-GeV Advanced Photon Source — K. Kim, S. H. Kim, L. R. Turner, C. L. Doose, R. Hogrefe, R. Merl, ANL	2799
Magnet Measurement Facility for the 7-GeV Advanced Photon Source — S. H. Kim, K. Kim, C. Doose, R. Hogrefe, R. Merl, ANL	2802
Magnetic Measurements of the Storage Ring Quadrupole Magnets for the 7-GeV Advanced Photon Source — S. H. Kim, K. Kim, C. Doose, R. Hogrefe, R. Merl, ANL	2805
Design and Tests of the Injector Synchrotron Magnets for the 7-GeV Advanced Photon Source (APS) — K. Kim, S. H. Kim, K. M. Thompson, L. R. Turner, ANL	2808
Final Analysis of the ALS Lattice Magnet Data — R. Keller, LBL	2811
Design and Measurement of the Sextupole Magnet for the APS Storage Ring — L. R. Turner, K. M. Thompson, S. H. Kim, K. Kim, ANL	2814
A Pulsed Septum Magnet for the APS — L. R. Turner, D. G. McGhee, F. E. Mills, S. Reeves, ANL	2817

Each volume begins with this five-volume table of contents and ends with the five-volume author index. The chairmen's foreword and a list of conference organizers and staff appear as front matter in Volume 1. A list of conference participants precedes the author index in Volume 5.

Five-Volume Contents

The ELETTRA Storage Ring Magnets — <i>G. Petrucci, D. Tommasini, Sinc. Trieste/CERN</i>	2820
Experience with the Source Evaluation Board Method of Procuring Technical Components for the Fermilab Main Injector — <i>D. J. Harding, J. P. Collins, G. R. Kobliska, N. S. Chester, E. G. Pewitt, W. B. Fowler, FNAL</i> ..	2823
Sextupole Magnets for the Fermilab Main Injector — <i>D. J. Harding, N. Chester, R. Baiod, FNAL</i>	2826
Design and Measurements of Prototype Fermilab Main Injector Dipole Endpacks — <i>D. J. Harding, H. D. Glass, J.-F. Ostiguy, B. C. Brown, F. A. Harfoush, C. S. Mishra, FNAL</i>	2829
Magnetic Measurement of Quadrupole and Sextupole Magnets for the MIT-Bates South Hall Ring (SHR) — <i>D. R. Tieger, J. D. Zumbro, W. W. Sapp, MIT Bates</i>	2832
A Permanent Magnet Dipole Correction Element for the Tevatron — <i>J. E. Goodwin, T. Anderson, A. Franck, N. Gelfand, H. Jostlein, FNAL</i>	2835
Precision Measurement of Transport Components — <i>P. Tenenbaum, J. K. Cobb, D. R. Jensen, D. Sawyer, W. Wagner, H. V. Walz, S. H. Williams, SLAC</i>	2838
Measurement and Adjustment of CIAE Medical Cyclotron Magnet — <i>M. Fan, X. Zhang, T. Zhang, C. Liang, Q. Tao, Z. Zhao, C. Chu, T. Li, Y. Hu, Y. Chen, H. Zhang, H. Jia, C. Jiao, J. Liu, W. Zhang, C. Zhou, J. Jiao, Y. Hou, CIAE China</i>	2841
Magnetic Measurement and Alignment of the ELETTRA Storage Ring Quadrupole, Sextupole and Steerer Magnets — <i>D. Zangrando, R. P. Walker, Sinc. Trieste</i>	2844
Measurement and Correction of the ELETTRA Storage Ring Dipole Magnets — <i>R. P. Walker, D. Zangrando, Sinc. Trieste</i>	2847
Magnet Costs for the Advanced Light Source — <i>J. Tanabe, J. Krupnick, E. Hoyer, A. Paterson, LBL</i>	2850
Automatic Bench for Precise Magnetic Measurements of Linac Multipole Focusing Elements — <i>V. S. Skachkov, M. A. Kozchekin, R. P. Koujbida, V. I. Lulevich, A. V. Selin, O. S. Sergeeva, ITEP Moscow</i>	2853
Measurements of Loma Linda Proton Therapy Gantry Dipoles — <i>H. D. Glass, P. O. Mazur, J. W. Sim, FNAL</i>	2856
Techniques for Measurement of Dipole Endfields with a Rigid Integrating Coil — <i>H. D. Glass, FNAL</i>	2859
Lamination and End Plate Design Studies of SSC Low Energy Booster Magnet Prototypes — <i>N. Li, SSCL</i>	2862
Design and Fabrication of a Multi-Purpose Panofsky Magnet — <i>J. Budnick, T. Hall, D. Li, S. Y. Lee, IUCF</i>	2865
Magnetic Septa Design and Performance for Injection and Extraction to and from the MIT-Bates South Hall Ring (SHR) — <i>R. Averill, K. Dow, H. Enge, J. Flanz, E. Ihloff, M. Farkhondeh, C. Sibley, MIT-Bates</i>	2868
Octupole Magnet Design for the 1/2 Integer Resonant Extraction of Electrons from the MIT-Bates South Hall Ring (SHR) — <i>R. Averill, J. Flanz, E. Ihloff, D. Tieger, MIT-Bates</i>	2871
Ramped Quadrupole Design and Performance for the MIT-Bates South Hall Ring (SHR) — <i>R. Averill, J. Flanz, E. Ihloff, D. Tieger, MIT-Bates</i>	2874
Lambertson Upgrade Program — <i>K. J. Weber, FNAL</i>	2877
Computer Studies of a Combined-Function Bend Magnet for a Proposed Redesign of the SLAC SLC Damping Rings — <i>R. A. Early, T. O. Raubenheimer, SLAC</i>	2880
Comparison of Computer Predictions and Magnetic Field Measurements for an Iron Spectrometer Magnet — <i>G. T. Danby, J. W. Jackson, W. Meng, C. Spataro, BNL</i>	2883
Design and Performance of the Dipole Magnet for the SRRC Storage Ring — <i>C. H. Chang, H. C. Liu, G. J. Hwang, SRRC Taiwan</i>	2886
Specific Features of Magnet Design for the Duke FEL Storage Ring — <i>B. Burnham, N. Hower, V. N. Litvinenko, J. M. J. Madey, Y. Wu, Duke</i>	2889
Dipole Design for the EUTERPE Storage Ring — <i>J. I. M. Botman, C. J. Timmermans, B. Xi, H. Heller, H. L. Hagedoorn, P. Brinkgreve, E. Dekkers, J. Moerel, Eindhoven</i>	2892
Design of a Lambertson Injection Magnet for the RHIC Machine — <i>E. Rodger, N. Tsoupas, J. Claus, H. W. Foelsche, BNL</i>	2895
Combined AC Corrector Magnets — <i>A. J. Otter, P. A. Reeve, TRIUMF; N. Marks, Daresbury</i>	2898
Longitudinal Profile and Effective Length of a Conventional Dipole Magnet — <i>J. Ostiguy, FNAL</i>	2901
Magnetic Flux Shielding for the Muon g-2 Storage Ring Superconducting Inflectors — <i>W. Meng, W. B. Sampson, M. Suenaga, BNL</i>	2904
Three Dimensional Field Analysis for the AGS Combined Function Magnets — <i>W. Meng, M. Tanaka, BNL</i>	2907
Survey and Alignment Data Analysis for the ALS Storage Ring — <i>R. Keller, LBL</i>	2910
A Mechanical System for the Positioning of Accelerator Magnets — <i>R. Viola, R. Martin, SSCL</i>	2913
Preliminary Studies on a Magneto-Optical Procedure for Aligning RHIC Magnets — <i>M. A. Goldman, R. E. Sikora, T. J. Shea, BNL</i>	2916

Volume 1: 1-747
 Volume 2: 748-1640
 Volume 3: 1641-2545
 Volume 4: 2546-3218
 Volume 5: 3219-3933

Proceedings of the 1993 Particle Accelerator Conference

RHIC Survey and Alignment — F. X. Karl, R. R. Anderson, M. A. Goldman, F. M. Hemmer, D. Kazmark, Jr., T. T. Mroczkowski, J. C. Roecklein, BNL	2919
Effect of Magnet Sorting Using a Simple Resonance Cancellation Method on the RMS Orbit Distortion at the APS Injector Synchrotron — F. Lopez, R. Koul, F. E. Mills, ANL	2922
Optimal Magnet Sorting Procedure and Application to the APS Injector Synchrotron — R. K. Koul, F. Lopez, F. E. Mills, ANL	2924
Geodetic Concept for the Storage Ring EUTERPE — S. F. C. L. Wetzels, C. J. Timmermans, G. A. Webers, P. H. J. Schellekens, J. I. M. Botman, H. L. Hagedoorn, Eindhoven U. of Tech.	2927
Alignment of CEBAF Cryomodules — W. J. Schneider, J. J. Bisognano, J. Fischer, D. R. Douglas, K. Macha, J. Mammoser, W. Oren, J. Preble, J. Robb, M. Wiseman, CEBAF	2929
The Hydrostatic Levelling System (HLS) / Servo-Controlled Precision Jacks: A New Generation Altimetric Alignment and Control System — D. Roux, ESRF	2932
Control of Roll in Fiducialization of Quadrupole Magnets for the MIT-Bates South Hall Ring — M. Farkhondeh, K. A. Dow, W. W. Sapp, MIT Bates	2935
Survey and Alignment of the MIT-Bates South Hall Ring — M. Farkhondeh, K. A. Dow, W. W. Sapp, D. R. Tieger, MIT Bates	2938
Magnetic Measurement, Fiducialization and Alignment of Large Dipoles for the MIT-Bates SHR — M. Farkhondeh, K. A. Dow, W. W. Sapp, J. D. Zumbro, MIT Bates	2941
Pulsed Taut-Wire Measurement of the Magnetic Alignment of the ITS Induction Cells — J. G. Melton, M. J. Burns, D. J. Honabarger, LANL	2944
Application of Precision Mechanical Engineering Techniques to the Design of a Moderate Energy Beam Transport for the FAA Explosive Detection System — R. Lujan, K. Christensen, LANL	2947
The Final Focus Test Beam Laser Reference System — V. E. Bressler, R. E. Ruland, SLAC	2950
Thermal Modeling of Cryogenic Accelerator Structures — H. Muller, P. Smith, D. Walend, J. Kirchgessner, Cornell	2953
Cryogenics for the LEP200 Superconducting Cavities at CERN — D. Güsewell, M. Barranco-Luque, S. Claudet, W. K. Erdt, P. Frandsen, Ph. Gayet, J. Schmid, N. Solheim, Ch. Titcomb, G. Winkler, CERN	2956
Measurements of the Ground Motion Vibrations at the SSC — V. V. Parkhomchuk, BINP; V. D. Shiltsev, H. J. Weaver, SSCL	2959
Particle Sources, Beam Formation, and Matching Chair: J. Fraser	
Performance of Photocathode RF Gun Electron Accelerators (Invited Paper) — I. Ben-Zvi, BNL	2962
First Operation of a High Duty Factor Photoinjector — D. Dowell, K. Davis, K. Friddell, E. Tyson, C. Lancaster, L. Milliman, R. Rodenburg, T. Aas, M. Bemes, S. Bethel, P. Johnson, K. Murphy, C. Whelen, J. Adamski, D. Pistoresi, D. Shofstall, Boeing; G. Busch, D. Remelius, LANL	2967
Operation of the High Brightness LINAC for the Advanced Free-Electron Laser Initiative at Los Alamos — R. L. Sheffield, R. H. Austin, K. D. C. Chan, S. M. Gierman, J. M. Kinross-Wright, S. H. Kong, D. C. Nguyen, S. J. Russell, C. A. Timmer, LANL	2970
Performance of the SLC Polarized Electron Source with High Polarization — J. E. Clendenin, R. K. Alley, H. Aoyagi, J. C. Frisch, C. L. Garden, E. W. Hoyt, R. E. Kirby, L. A. Klaisner, A. V. Kulikov, C. Y. Prescott, P. J. Sáez, D. C. Schultz, H. Tang, J. L. Turner, M. Woods, A. D. Yermian, M. S. Zolotarev, SLAC	2973
Quantum Efficiency Measurements of a Copper Photocathode in an RF Electron Gun — P. Davis, G. Hairapetian, C. Clayton, C. Joshi, S. Hartman, S. Park, C. Pellegrini, J. Rosenzweig, UCLA	2976
High-Efficiency Target-Ion Sources for RIB Generation (Invited Paper) — G. D. Alton, ORNL	2979
Performance of SSC Linac Injector (Invited Paper) — K. Saadatmand, G. M. Arbique, F. Guy, M. Haworth, J. Hebert, J. Hurd, J. Lenz, N. Okay, D. Raparia, SSCL	2986
Proposal for a Pulsed Optically Pumped Polarized H ⁻ Ion Source for High Energy Accelerators — A. N. Zelenski, INR Moscow; C. D. P. Levy, P. W. Schmor, W. T. H. van Oers, G. Dutto, TRIUMF; Y. Mori, KEK	2991
Design and Performance of the Inter-RFQ Beam Transport and Matching Section for the SAIC PET Isotope Production Accelerator — W. D. Cornelius, SAIC	2994
Electron Cyclotron Resonance Sources of Multiply Charged Ions: Last Developments at Grenoble — G. Melin, F. Bourg, P. Briand, M. Delaunay, A. Girard, D. Hitz, P. Ludwig, T. K. Nguyen, M. Pontonnier, Grenoble	2997

Each volume begins with this five-volume table of contents and ends with the five-volume author index. The chairmen's foreword and a list of conference organizers and staff appear as front matter in Volume 1. A list of conference participants precedes the author index in Volume 5.

Poster presentations:

Design and Construction of a Full Copper Photocathode RF Gun — X. J. Wang, K. Batchelor, I. Ben-Zvi, D. Lynch, J. Sheehan, M. Woodle, BNL	3000
Streak Camera Measurements of Electron Bunch Length from a Copper Photocathode in an RF Gun — G. Hairapetian, P. Davis, M. Everett, C. Clayton, C. Joshi, S. Hartman, S. Park, C. Pellegrini, UCLA	3003
Possible Efficiency-Enhancement of Metal Photocathode for DISKTRON Electrostatic Accelerator — T. Tanabe, Y. Kawamura, K. Toyoda, RIKEN; D. Li, Changchun Inst., China	3006
Cold Test of Rocketdyne RF Gun — M. Lampel, Rockwell; R. Zhang, UCLA	3009
Design and Construction of a High-Duty-Factor Photocathode Electron Gun — I. S. Lehrman, I. A. Birnbaum, M. Cole, R. L. Heuer, E. Sheedy, Grumman; I. Ben-Zvi, K. Batchelor, J. C. Gallardo, H. G. Kirk, T. Srinivasan-Rao, BNL	3012
An Improved Thermionic Microwave Gun and Emittance-Preserving Transport Line — M. Borland, ANL	3015
Experience with a Radio Frequency Gun on the SSRL Injector Linac — J. N. Weaver, R. D. Genin, P. Golceff, H. Morales, J. Sebek, SLAC	3018
Design of a High Duty Cycle, Asymmetric Emittance RF Photocathode Injector for Linear Collider Applications — J. B. Rosenzweig, E. Colby, UCLA; G. Jackson, T. Nicol, FNAL	3021
Design of a High Brightness RF Photoinjector for the SLAC Linear Coherent Light Source — J. Rosenzweig, UCLA; L. Serafini, INFN Milan	3024
Performance of the SLC Polarized Electron Source and Injector with the SLAC 3 km Linac Configured for Fixed Target Experiments — A. D. Yeremian, R. K. Alley, J. E. Clendenin, J. C. Frisch, C. L. Garden, L. A. Klaisner, A. V. Kulikov, R. H. Miller, C. Y. Prescott, P. J. Saez, D. C. Schultz, H. Tang, J. L. Turner, M. B. Woods, M. Zolotarev, SLAC	3027
An In-Situ Photocathode Loading System for the SLC Polarized Electron Gun — R. E. Kirby, G. J. Collet, K. Skarpaas, SLAC	3030
High Voltage Processing of the SLC Polarized Electron Gun — P. Sáez, J. Clendenin, C. Garden, E. Hoyt, L. Klaisner, C. Prescott, D. Schultz, H. Tang, SLAC	3033
Study of Non-Linear Photoemission Effects in III-V Semiconductors — H. Tang, R. K. Alley, J. E. Clendenin, J. C. Frisch, C. L. Garden, E. W. Hoyt, R. E. Kirby, L. A. Klaisner, A. V. Kulikov, C. Y. Prescott, P. J. Sáez, D. C. Schultz, J. L. Turner, M. Woods, M. S. Zolotarev, SLAC; H. Aoyagi, Nagoya U.	3036
Photocathode Performance Measurements for the SLC Polarized Electron Gun — C. L. Garden, E. W. Hoyt, D. C. Schultz, H. Tang, SLAC	3039
Electron Quantum Yields from a Barium Photocathode Illuminated with Polarized Light — M. E. Conde, S. Chattopadhyay, K.-J. Kim, K.-N. Leung, A. T. Young, LBL; S.-I. Kwon, Kyonggi U.	3042
The 1992 Polarized Light Source — R. Alley, M. Woods, M. Browne, J. Frisch, M. Zolotarev, SLAC	3045
Operation of a Ti:Sapphire Laser for the SLAC Polarized Electron Source — J. Frisch, R. Alley, M. Browne, M. Woods, SLAC	3047
The Argonne Wakefield Accelerator (AWA) Laser System and Its Laser Pulse Shaper — W. Gai, N. Hill, C. Ho, P. Schoessow, J. Simpson, ANL	3050
CANDELA Photo-injector: The Drive Laser — P. Georges, P. Thomas, Inst. d'Opt. Theor. Appl., Orsay; B. Leblond, C. Travier, LAL Orsay	3053
A Flat-Cathode Thermionic Injector for the PHERMEX Radiographic Facility — T. Kauppila, L. Builta, M. Burns, W. Gregory, D. Honabarger, S. Watson, LANL; T. Hughes, Mission Res. Corp.	3055
The ALS Gun Electronics System — C. C. Lo, LBL	3058
Witness Gun for the Argonne Wakefield Accelerator — J. Power, J. Simpson, E. Chojnacki, ANL	3061
Parametric Studies with PARMELA to Improve SLC Performance — T. A. Jones, A. D. Yeremian, R. H. Miller, SLAC	3063
High Current, Low Energy Electron Beams Produced During the High Current Phase of a Pseudospark — T. Hsu, R. Liou, M. A. Gundersen, USC; G. Kirkman, Integrated App. Phys.	3066
Theoretical and Experimental Study of Pseudospark Electron Beam Generation — L. Pitchford, J. P. Boeuf, U. Paul Sabatier; V. Puech, U. de Paris-Sud; R. Liou, M. Gundersen, USC	3069
A Variable Pulse-Length Electron Beam From the Back-Lighted Thyatron — R. Liou, T. Hsu, G. Roth, M. Gundersen, USC; G. Kirkman, Integrated App. Phys.	3072

Proceedings of the 1993 Particle Accelerator Conference

One-Dimensional Simulation Studies of Breakdown and Electron Beam Generation Processes for a Hollow Cathode Pseudospark Discharge — S. Y. Cai, C. D. Striffler, U. Maryland	3075
A High Brightness Electron Beam Produced by a Ferroelectric Cathode — B. Jiang, G. Kirkman, N. Reinhardt, Integrated App. Physics	3078
The UV-FEL at the NSLS: Straight Injection Configuration — X. Zhang, J. C. Gallardo, BNL	3081
Progress on PEP-II Injection R&D — E. Bloom, F. Bulos, T. Fieguth, G. Godfrey, G. Loew, R. Miller, SLAC	3084
New Pre-Injector of the KEK 2.5-GeV Linac and Its Performance — S. Ohsawa, I. Abe, S. Anami, J.-Y. Choi, A. Enomoto, K. Furukawa, H. Hanaki, K. Kakiyama, N. Kamikubota, T. Kamitani, H. Kobayashi, Y. Ogawa, T. Oogoe, I. Sato, T. Suwada, Y. Yamazaki, M. Yokota, KEK; A. Asami, Naruto U.	3087
Hydrodynamic Calculations of 20-TeV Beam Interactions with the SSC Beam Dump — D. C. Wilson, C. A. Wingate, J. C. Goldstein, R. P. Godwin, LANL; N. V. Mokhov, SSCL	3090
First Results Concerning a Crystal Radiator Dedicated to Positron Production by Photons from Channeled Multi-GeV Electrons — R. Chehab, T. Baier, P. Jean, LAL Orsay; X. Artru, M. Chevallier, R. Kirsch, J. C. Poizat, J. Remillieux, IPNL Lyon; A. Jejcic, J. Maillard, J. Silva, LPC Paris; E. Hourany, G. Renou, J. P. Didelez, A. Elayi, L. Rosier, IPN Orsay; V. N. Baier, V. M. Katkov, V. M. Strakhovenko, BINP Novosibirsk; K. Maier, MPI Stuttgart	3093
New Target Results from the FNAL Antiproton Source — S. O'Day, F. Bieniosek, K. Anderson, FNAL	3096
High Current Radioisotope Production with Solid Target System — W. Z. Gelbart, N. R. Stevenson, R. R. Johnson, J. Orzechowski, F. Cifarelli, TRIUMF; F. Nortier, NAC Faure	3099
Isospin Target-Ion Source Shielding — M. M. Barbier, Marcel Barbier Inc.	3102
Beam Raster System at CEBAF — C. Yan, J. Beaufait, P. Brindza, R. Carlini, W. Vulcan, R. Wines, CEBAF	3103
Monitoring Production Target Thickness — M. A. Othoudt, LANL	3106
Beam Loss Handling at the SSC — I. S. Baishev, A. I. Drozhdin, N. V. Mokhov, SSCL	3109
Analytical Study of RFQ Channel by Means of the Equivalent Charges Model — V. M. Pirozhenko, O. V. Plink, MRTI	3112
Design of an 80-MHz RFQ Linac for Heavy Ions — O. Takeda, Y. Tanabe, K. Satoh, S. Kawazu, Toshiba; Y. Oguri, M. Okamura, T. Hattori, Tokyo Inst. of Tech.	3115
Operational Characteristics of a 100-mA, 2-MeV Radio-Frequency Quadrupole — K. F. Johnson, W. B. Cottingham, G. O. Bolme, C. M. Fortgang, W. Ingalls, J. Marquardt, D. P. Rusthoi, O. R. Sander, M. Smith, G. T. Worth, LANL	3118
Analysis of the End Regions of the CERN Lead-Ion 4-Rod RFQ — V. A. Andreev, ITEP Moscow; A. Lombardi, G. Parisi, INFN Legnaro; M. Vretenar, CERN	3121
90°-Apert-Stem RFQ Structure for Wide Range of Frequencies — V. A. Andreev, ITEP Moscow; G. Parisi, INFN Legnaro	3124
The SSCL RFQ System Integration — G. Arbique, A. Calo, C. Cuevas, P. Datte, D. Evans, J. Hurd, E. Marsden, K. Saadatmand, J. Sage, SSCL	3127
SSC Radio-Frequency-Quadrupole Beam: Comparison of Experimental and Simulated Results — F. W. Guy, J. W. Hurd, D. Raparia, K. Saadatmand, W. A. Whittenberg, SSCL	3130
Mechanical Integration of an RF Volume Source and Einzel Lens LEBT to the SSC RFQ — R. A. Valicenti, J. Lenz, N. C. Okay, L. Plesea, K. Saadatmand, SSCL	3133
Segmented Resonantly Coupled Radio-Frequency Quadrupole (RFQ) — L. M. Young, LANL	3136
Experiments with the High Current RFQ Prototype for GSI — A. Kipper, A. Schempp, H. Deitinghoff, J. Madlung, T. Ludwig, K. Volk, O. Engels, A. Firjahn-Andersch, H. Vormann, Inst. f. Angew. Physik	3139
Transport of Ions in RFQ-Accelerators — J. Dehen, W. Barth, A. Schempp, H. Deitinghoff, Inst. f. Angew. Physik	3142
An ESQ Lens System for Low Energy Beam Transport Experiments on the SSC Test Stand — S. K. Guharay, C. K. Allen, M. Reiser, U. Maryland; K. Saadatmand, SSCL	3145
Test of the Transport Properties of a Helical Electrostatic Quadrupole and Quasi-Octupole — L. Xiu, S. Ohnuma, K. Wang, U. Houston; C. R. Meitzler, Y. Xu, Sam Houston State U.	3148
Comparison of Experimental and Simulated Results for the SSC LEBT — J. W. Lenz, J. Hebert, N. Okay, D. Raparia, K. Saadatmand, SSCL	3151
Axial Magnetic Field Lens with Permanent Magnet — Y. Iwashita, Kyoto U.	3154
Design of a Merging Beamlet Pre-Accelerator for an Electrostatic Quadrupole Accelerator (ESQ) — C. F. Chan, M. C. Vella, LBL	3157
Low Energy H ⁻ Injector Design for SSC RFQ — C. F. Chan, K.-N. Leung, LBL	3160

Each volume begins with this five-volume table of contents and ends with the five-volume author index. The chairmen's foreword and a list of conference organizers and staff appear as front matter in Volume 1. A list of conference participants precedes the author index in Volume 5.

Five-Volume Contents

Lithium Lens for Focusing Protons on Target in the Fermilab Antiproton Source — F. M. Bieniosek, K. Anderson, FNAL	3163
Injector Design for High-Current CW Proton Linacs — R. R. Stevens, Jr., J. D. Sherman, J. D. Schneider, LANL ...	3166
A High Power Long Pulse RF-Driven H ⁻ Source — J. W. Kwan, G. D. Ackerman, W. S. Cooper, G. J. deVries, K. N. Leung, R. P. Wells, LBL	3169
Initial Operation of the CW 8X H ⁻ Ion Source Discharge — H. V. Smith, Jr., P. Allison, C. Geisik, D. R. Schmitt, J. D. Schneider, J. E. Stelzer, LANL	3172
Volume H ⁻ Ion Source Development at LAMPF — R. L. York, D. Tupa, D. R. Swenson, R. Damjanovich, LANL	3175
Further Development with Heavy Ion Sources at Brookhaven National Laboratory's Tandem Van de Graaff Facility — M. J. Zarcone, D. B. Steski, K. S. Smith, P. Thieberger, BNL	3178
A Dual-Optically-Pumped Polarized Negative Deuterium Ion Source — Y. Mori, M. Kinsho, KEK	3181
The IUCF High Intensity Polarized Ion Source Project — M. Wedekind, R. Brown, V. Derenchuk, D. Friesel, J. Hicks, P. Schwandt, IUCF	3184
The High Current Ion Source System HOLCROSS — N. R. Lobanov, MEPI Moscow	3187
Positive Hydrogen Ion Beam Production by an RF-Driven Multicusp Source — K. N. Leung, D. A. Bachman, P. R. Herz, D. S. McDonald, L. T. Perkins, LBL; M. Olivo, PSI	3190
Measurements of Emittance and Species Fractions of a Positive Hydrogen Ion Beam Extracted from an RF-Driven Multicusp Source — G. Gammel, T. W. Debiak, S. Melnychuk, J. Sredniawski, Grumman	3193
A New Design of the Sputter Type Metal Ion Source and Its Characteristics of Ion Beam Extraction — W. Kim, B. H. Choi, J. T. Jin, K.-S. Jung, Korea Atomic Energy Res. Inst.; S. H. Do, Pusan Nat. Fishers U.; K. H. Chung, Seoul Nat. U.	3196
K ⁺ Ion Source for the Heavy Ion Induction Linac System Experiment ILSE — S. Eylon, E. Henestroza, W. W. Chupp, S. Yu, LBL	3199
On the Magnetic Compression and Guiding of Electron Beams in E.B.I. S. or E.B.I.T — J. L. Bobin, E. Mercier, UPMC Paris; G. Giardino, LPAN	3202
Choice of Hexapole Parameters for ECR Ion Source — V. P. Kukhtin, E. A. Lamzin, Yu. P. Severgin, S. E. Sytchevsky, Efremov Inst.	3205
Stripping Efficiencies for 277 MeV/amu Gold Beam on Copper Foils — T. Roser, BNL	3207
Management of High Current Transients in the CWDD Injector 200 kV Power System — J. A. Carwardine, G. Pile, AEA Tech. Culham Lab; T. E. Zinneman, ANL	3210
Design and Results of the Radio Frequency Quadrupole RF System at the Superconducting Super Collider Laboratory — J. Grippe, E. Marsden, O. Marrufo, SSCL; A. Regan, D. Rees, C. Ziomek, LANL	3213
Initial Operation and Beam Characteristics of the UCLA S-Band Photo-Injector — C. Pellegrini, N. Barov, P. Davis, G. Hairapetian, S. C. Hartman, C. Joshi, S. Park, J. Rosenzweig, G. Travish, R. Zhang, UCLA	3216

Volume 5

Multiparticle Beam Dynamics

Chair: M. Reiser

Methods of Impedance Calculation (<i>Invited Paper</i>) — R. L. Gluckstern, Maryland	3219
Space-Charge Calculations in Synchrotrons (<i>Invited Paper</i>) — S. Machida, SSCL	3224
Advanced Computers and Simulation (<i>Invited Paper</i>) — R. D. Ryne, LANL	3229
Measured Optimum BNS Damping Configuration of the SLC Linac — J. T. Seeman, F.-J. Decker, R. L. Holtzapple, W. L. Spence, SLAC	3234
Single Beam Phenomena in BEPC — Z. Y. Guo, X. Bai, G. X. Li, J. Qin, Q. Qin, G. Xu, C. Zhang, X. L. Zhang, Z. T. Zhao, IHEP, Academia Sinica	3237
High Intensity Bunch Length Instabilities in the SLC Damping Rings — P. Krejcik, K. Bane, P. Corredoura, F.-J. Decker, J. Judkins, T. Limberg, M. Minty, R. H. Siemann, SLAC; F. Pedersen, CERN	3240
Investigation on Relaxations in Electron Beams — A. Aleksandrov, N. Dikansky, N. Ch. Kot, V. Kudelainen, V. A. Lebedev, P. Logachov, BINP; R. Calabrese, G. Ciullo, V. Guidi, G. Lamanna, P. Lenisa, B. Maciga, L. Tecchio, B. Yang, INFN	3243
Studies of Multipass Beam Breakup and Energy Recovery Using the CEBAF Injector Linac — N. S. Sereno, L. S. Cardman, U. Illinois; G. A. Krafft, C. K. Sinclair, J. J. Bisognano, CEBAF	3246

Volume 1:	1-747
Volume 2:	748-1646
Volume 3:	1647-2545
Volume 4:	2546-3218
Volume 5:	3219-3933

Proceedings of the 1993 Particle Accelerator Conference

Poster presentations:

The Longitudinal and Transverse Beam Dynamics Simulation in the MMF Storage Ring — V. A. Moiseev, INR Moscow	3249
Control of Longitudinal Instabilities in the LEB — T. L. Grimm, P. D. Coleman, SSCL	3252
Simulation of the Transverse Dipole Mode Multibunch Instability for the SSC Collider — S. Chen, G. López, SSCL	3255
HOM RF Cavity Dampers for Suppressing Coupled Bunch Instabilities in the Fermilab Booster — D. Wildman, FNAL; K. Harkay, Purdue	3258
Longitudinal Instabilities in the MEB — J. A. Palkovic, SSCL	3261
A New Formulation of Longitudinal Coherent Instabilities — S. Y. Zhang, W. T. Weng, BNL	3264
Three-Dimensional Simulations for Accelerator Physics Using ARGUS — A. Mondelli, A. Mankofsky, J. Petillo, W. Krueger, C. Kostas, A. Drobot, SAIC; R. Ryne, R. K. Cooper, G. Rodenz, M. J. Browman, LANL	3267
A Higher-Order Moment Simulation Model — K. T. Tsang, C. Kostas, A. Mondelli, SAIC	3270
Collective Effects of the PLS 2 GeV Storage Ring — M. Yoon, J. Choi, T. Lee, Pohang	3273
Nonlinear Evolution of Longitudinal Bunched-Beam Instabilities — A. Gerasimov, FNAL	3276
Multi-Bunch Dynamics in Accelerating Structures Including Interaction with Higher Order Modes — M. Ferrario, F. Tazzioli, INFN-LNF; L. Serafini, INFN Milano	3279
Generation of Space-Charge Waves due to Localized Perturbations — J. G. Wang, D. X. Wang, D. Kehne, M. Reiser, U. Maryland	3282
Three Dimensional Multipole Decomposition of Fields — K. Hahn, LBL	3285
Multi-Bunch Beam-Break-Up Studies for a SWFEL/TBA — J. S. Kim, A. M. Sessler, LBL; D. H. Whittum, KEK; H. Henke, TU Berlin	3288
RF Noise Revisited: The Effect of Coherence — A. Gerasimov, FNAL; S. Y. Lee, Indiana U.	3291
TSD Versus TRL Calibration and Applications to Beam Impedance Measurements — M. Foley, P. Colestock, E. Barsotti, Jr., FNAL	3294
Recent Study of Beam Stability in the PSR — T. Wang, R. Cooper, D. Fitzgerald, S. Frankle, T. Hardek, R. Hutson, R. Macek, C. Ohmori, M. Plum, H. Thiessen, C. Wilkinson, LANL; E. Colton, DOE; D. Neuffer, CEBAF; G. Rees, RAL	3297
Impedance Budget and Beam Stability Analysis of the Fermilab Main Injector — M. A. Martens, K. Y. Ng, FNAL ..	3300
Trapped Ions and Beam Coherent Instability — P. Zhou, P. L. Colestock, S. J. Werkema, FNAL	3303
Comparison of the Coupled-Bunch Mode Theory to Experimental Observations in the Fermilab Booster — K. C. Harkay, Purdue; P. L. Colestock, FNAL	3306
Measurement of Trapped Ion Pockets and Control of Ion Instabilities in the Fermilab Antiproton Accumulator — S. J. Werkema, K. D. Fullett, P. Zhou, FNAL	3309
Study of Possible Energy Upgrade for the ALS and Modeling of the "Real Lattice" for the Diagnosis of Lattice Problems — M. Meddahi, J. Bengtsson, LBL	3312
Study of Coupled-Bunch Collective Effects in the PEP-II B-Factory — J. Byrd, LBL	3315
Study of Coupled-Bunch Collective Effects in the ALS — J. M. Byrd, J. N. Corlett, LBL	3318
Time Domain Solutions for a Coasting Beam with Impedance Feedback — M. Blaskiewicz, BNL	3321
Longitudinal Impedance and Stability Thresholds of the AGS Booster — M. Blaskiewicz, BNL	3324
Calculation of the Bunch Lengthening Threshold — X. T. Yu, J. S. Wurtele, MIT	3327
Computation of Longitudinal Bunched Beam Instability Thresholds — R. Baartman, TRIUMF; M. D'Yachkov, U. British Columbia	3330
Bunch Lengthening Observed Using Real-Time Bunch-Length Monitor in the TRISTAN AR — T. Ieiri, KEK	3333
Transverse Stability in Multibunch Mode for CLIC — G. Guignard, CERN	3336
Simulations of the Longitudinal Instability in the SLC Damping Rings — K. L. F. Bane, SLAC; K. Oide, KEK	3339
Multibunch Beam Break-Up in Detuned Structures — K. A. Thompson, C. Adolphsen, K. L. F. Bane, SLAC	3342
Longitudinal Head-Tail Instability in a Non-Harmonic Potential Well — B. Chen, A. W. Chao, SSCL	3345
Bunch Lengthening Effect and Localized Impedance — B. Chen, A. W. Chao, SSCL	3348
Experimental Reduction of Electron Beam Breakup Instability Using External Coupled Cavities — P. R. Menge, R. M. Gilgenbach, Y. Y. Lau, M. Walter, C. H. Ching, U. Michigan	3351
Beam Breakup in an Annular Beam — Y. Y. Lau, J. W. Luginsland, R. M. Gilgenbach, U. Michigan	3354

Each volume begins with this five-volume table of contents and ends with the five-volume author index. The chairmen's foreword and a list of conference organizers and staff appear as front matter in Volume 1. A list of conference participants precedes the author index in Volume 5.

Five-Volume Contents

RF Focusing Effects and Multi-Bunch Beam Breakup in Superconducting Linear Colliders — <i>J. Rosenzweig, S. Hartman, J. Stevens, UCLA</i>	3357
Required Cavity HOM deQing Calculated from Probability Estimates of Coupled Bunch Instabilities in the APS Ring — <i>L. Emery, ANL</i>	3360
Measurement and Analysis of Transverse Beam Transfer Functions in the Fermilab Main Ring — <i>P. J. Chou, G. Jackson, FNAL</i>	3363
Observation of a Short Bunch Train Longitudinal Instability in the Fermilab Main Ring — <i>X. Lu, G. Jackson, FNAL</i>	3366
Suppression of Longitudinal Coupled-Bunch Instabilities by a Passive Higher Harmonic Cavity — <i>R. A. Bosch, C. S. Hsue, SRRC Taiwan</i>	3369
The Longitudinal Coupling Impedance of a Slot on the SSC Collider Liner — <i>V. Thiagarajan, SSCL</i>	3372
Impedance of a Small-Gap Undulator Vacuum Chamber — <i>K. Bane, SLAC; S. Krinsky, NSLS-BNL</i>	3375
A Formula for the High Frequency Longitudinal Impedance of a Tube With Smoothly Varying Radius — <i>R. L. Warnock, SLAC</i>	3378
A Bench Set-Up for Low-Beta Beam-Current Test Measurements with COSY — <i>Ch. Günther, A. Schnase, H. Meuth, IKP Jülich; F. Caspers, CERN</i>	3381
A Generalized Model for Parametric Coupling of Longitudinal Modes in Synchrotrons — <i>P. L. Colestock, L. Klamp, FNAL</i>	3384
Longitudinal Coupling Impedance of a Cavity — <i>I. Gjaja, R. L. Gluckstern, U. Maryland</i>	3387
Transverse Impedance of an Iris in a Beam Pipe — <i>S. Jiang, R. L. Gluckstern, U. Maryland; H. Okamoto, Kyoto U.</i>	3390
RF Characteristics of the APS Storage Ring Isolation Valve — <i>J. J. Song, R. L. Kustom, ANL</i>	3393
Coupling Impedance of Vacuum Pumping Holes for the APS Storage Ring — <i>J. Zhou, J. J. Song, R. L. Kustom, ANL</i>	3396
Impedance Formalism for an Arbitrary Cumulative Instability — <i>X. T. Yu, J. S. Wurtele, MIT; D. H. Whittum, KEK</i>	3399
Longitudinal Impedance of a Prototype Kicker Magnet System — <i>H. J. Tran, M. J. Barnes, G. D. Wait, Y. Yan, TRIUMF</i>	3402
Beam Coupling Impedance Measurements and Simulations of a Beam Pipe Liner with Pumping Holes or Slots — <i>E. Ruiz, L. Walling, Y. Goren, N. Spayd, SSCL</i>	3405
Measurement and Computation of the Higher Order Modes of the ALS 500 MHz Accelerating Cavities — <i>J. N. Corlett, J. M. Byrd, LBL</i>	3408
Impedance Measurements of Components for the ALS — <i>J. N. Corlett, R. A. Rimmer, LBL</i>	3411
Advances and Applications of ABCI — <i>Y. H. Chin, LBL</i>	3414
On Coupling Impedances of Pumping Holes — <i>S. S. Kurennoy, SSCL</i>	3417
Using a Ceramic Chamber in Kicker Magnets — <i>S. S. Kurennoy, SSCL</i>	3420
An Analytical Treatment of Self Fields in a Relativistic Bunch of Charged Particles in a Circular Orbit — <i>J. L. Delhez, J. M. A. Hofman, J. I. M. Botman, H. L. Hagedoorn, W. J. G. M. Kleeven, G. A. Webers, Eindhoven U. of Tech.</i>	3423
Transverse Wake Fields in the CLIC Transfer Structure — <i>G. Guignard, G. Carron, A. Millich, L. Thorndahl, CERN</i>	3426
The LEP Impedance Model — <i>D. Brandt, K. Cornelis, V. Danilov, A. Hofmann, C. Juillard, E. Perevedentsev, E. Peschardt, E. Rossa, F. Tecker, D. Wang, B. Zotter, CERN; L. Rivkin, PSI</i>	3429
Impedance Calculations for the Improved SLC Damping Rings — <i>K. L. F. Bane, C.-K. Ng, SLAC</i>	3432
Broadband Impedance of Azimuthally Symmetric Devices in RHIC — <i>V. Mane, BNL</i>	3435
Software Development with Two Port Calibration Techniques for RHIC Impedance Measurements — <i>V. Mane, T. Shea, BNL</i>	3438
Resistive Wall Wake Function for Arbitrary Pipe Cross Section — <i>K. Yokoya, KEK</i>	3441
Impedance of a Perforated Liner and Its Impact on the SSC Collider — <i>W. Chou, T. Barts, SSCL</i>	3444
A Generalized Method for Calculating Wake Potentials — <i>O. Napoly, Saclay; Y. H. Chin, LBL; B. Zotter, CERN</i> ...	3447
The Interaction of a Beam With a Beam Line Higher-Order-Mode Absorber — <i>W. Hartung, K. Akai, J. DeFord, T. Hays, J. Kirchgessner, D. Metzger, D. Moffat, H. Padamsee, D. Rubin, M. Tigner, A. Tribendis, V. Veshcherevich, Cornell</i>	3450
Persistent Wakefields Associated with Waveguide Damping of Higher Order Modes — <i>N. M. Kroll, X. Lin, UCSD/SLAC</i>	3453

Volume 1: 1-747
 Volume 2: 748-1640
 Volume 3: 1641-2545
 Volume 4: 2546-3218
 Volume 5: 3219-3933

Proceedings of the 1993 Particle Accelerator Conference

Perturbation Theory of Broadband Impedances — <i>S. Heifets, SLAC</i>	3456
Broadband Impedance of the B Factory — <i>S. Heifets, SLAC</i>	3459
Study of a Detuned Accelerating Section With the Computer Program PROGON — <i>S. A. Heifets, S. A. Kheifets, SLAC</i>	3462
Estimation of Broad Band Impedance of the SPring-8 Storage Ring — <i>T. Nakamura, JAERI</i>	3464
Head-On and Long Range Beam-Beam Tune Shift Spread in the SSC — <i>G. López, SSCL</i>	3467
Beam-Beam Effects with Errors in the Crab Compensation — <i>D. Sagan, Cornell</i>	3470
A Strong-Strong Simulation on the Beam-Beam Effect in a Linac/Ring B-Factory — <i>R. Li, J. J. Bisognano, CEBAF</i>	3473
Some Aspects of the Long Range Beam-Beam Interaction in Storage Rings — <i>A. B. Temnykh, INP; J. J. Welch, Cornell</i>	3476
Experimental Study of Crossing Angle Collision — <i>T. Chen, SLAC; D. Rice, D. Rubin, D. Sagan, M. Tigner, Cornell</i>	3479
Beam-Beam Experiments in the Tevatron — <i>D. Siergie, G. Goderre, FNAL</i>	3482
Beam-Beam Effects for the PEP-II B Factory — <i>M. A. Furman, LBL; J. R. Eden, U. Washington</i>	3485
Equivalent Equations and Incoherent Lifetime Calculated from e^+e^- Beam-Beam Simulation — <i>Y. Orlov, Cornell</i>	3488
Simulation of Beam-Beam Effects in Electron-Positron Rings — <i>K. Hirata, S. Matsumoto, KEK</i>	3491
Longitudinal Beam-Beam Effects in Circular Colliders — <i>M. Hogan, J. Rosenzweig, UCLA</i>	3494
Strong-Weak Beam-Beam Simulation with a Six Dimension Symplectic Code — <i>Y. Funakoshi, H. Koiso, KEK</i>	3497
Synchrotron Beam-Loading Stability with a Higher RF Harmonic — <i>T. F. Wang, LANL</i>	3500
Compensation of Bunch Position Shift Using Sub-RF Cavity in a Damping Ring — <i>K. Kubo, T. Higo, S. Sakanaka, KEK</i>	3503
Analytic Criteria for Stability of Beam-Loaded RF Systems — <i>S. R. Koscielniak, TRIUMF</i>	3506
Beam Loading Effect in SSCL Coupled Cavity Linac — <i>Yu. Senichev, R. Cutler, J. Hurd, D. Raparia, SSCL</i>	3509
The Ion Core Density in Electron Storage Rings with Clearing Electrodes — <i>E. V. Bulyak, Kharkov Inst.</i>	3512
Operation of the CEBAF Linac with High Beam Loading — <i>L. Merminga, J. J. Bisognano, C. Hovater, G. A. Krafft, S. N. Simrock, CEBAF; K. Kubo, KEK</i>	3515
An Idea of Dynamical Cooling of Electron Beam in SR Ring — <i>S. Kato, Osaka U.</i>	3518
The Principle of Ultra-Fast Automatic Cooling for Beams — <i>S. Gao, G. Qian, CIAE</i>	3521
On the Longitudinal Stability of Cooled Coasting Ion Beams — <i>S. Nagaitsev, IUCF</i>	3524
Crystalline Beam Ground State — <i>J. Wei, BNL; X. Li, Rutgers; A. M. Sessler, LBL</i>	3527
Confinement and Stability of a Crystal Beam — <i>A. G. Ruggiero, BNL</i>	3530
Bunched Beam Stochastic Cooling in the Fermilab Tevatron Collider — <i>G. Jackson, E. Buchanan, J. Budlong, E. Harms, P. Hurh, D. McGinnis, R. Pasquinelli, D. Peterson, D. Poll, P. Seifrid, FNAL</i>	3533
Longitudinally Space Charge Dominated Beams in a Synchrotron — <i>T. J. P. Ellison, S. S. Nagaitsev, M. S. Ball, D. D. Caussyn, M. J. Ellison, B. J. Hamilton, IUCF</i>	3536
High Density Plasma Source for Plasma Lens Experiments — <i>K. Nakamura, R. Liou, M. Gundersen, USC</i>	3537
Measurement of Escaping Ions in the Fermilab Antiproton Accumulator — <i>P. Zhou, P. L. Colestock, K. Junck, C. A. Crawford, FNAL</i>	3540
Experimental Demonstration of Plasma Lens Focusing — <i>G. Hairapetian, P. Davis, C. E. Clayton, C. Joshi, S. Hartman, C. Pelligrini, UCLA; T. Katsouleas, USC</i>	3543
Numerical Modelling of Time-Space Behavior of High-Current Relativistic Electron Beam in Plasma Waveguide — <i>V. I. Karas', Kharkov Inst.; N. G. Belova, Russian Acad.</i>	3546
IPROP Simulations of the GAMBLE II Proton Transport Experiment — <i>D. R. Welch, Mission Res. Corp.</i>	3549
Plasma Lens and Plasma Wakefield Acceleration Experiments Using Twin Linacs — <i>A. Ogata, H. Nakanishi, K. Nakajima, T. Kawakubo, D. Whittum, M. Arinaga, KEK; Y. Yoshida, T. Ueda, T. Kobayashi, Nucl. Eng. Res. Lab, Tokyo U.; H. Shibata, S. Tagawa, Res. Ctr. Nucl. Sci. Tech., Tokyo U.; N. Yugami, Y. Nishida, Utsunomiya U.</i>	3552
Plasma Focusing of the Final Test Beam — <i>S. Rajagopalan, UCLA</i>	3555
Emittance Growth in MEB and Its Control — <i>Y. Huang, S. Machida, R. Gerig, SSCL</i>	3558
Longitudinal Diffusion as Inflicted by Arbitrary Band-Width Random-Modulated Currents in Feeders of Detuned Cavities — <i>S. Ivanov, IHEP Moscow</i>	3561
Induced Beam Oscillations from Quadrupole Vibrations in the SLC Linac — <i>J. T. Seeman, R. L. Holtzapple, M. C. Ross, SLAC</i>	3564

Each volume begins with this five-volume table of contents and ends with the five-volume author index. The chairmen's foreword and a list of conference organizers and staff appear as front matter in Volume 1. A list of conference participants precedes the author index in Volume 5.

Five-Volume Contents

Effects of Magnetic Focusing on Longitudinal Emittance and Energy Dispersion of an Intense Short Accelerating Electron Pulse — <i>J.-M. Dolique, J. C. Coacolo, U. Joseph Fourier/CEA</i>	3567
Measurement and Reduction of Transverse Emittance Blow-Up Induced by Space Charge Effects — <i>R. Cappi, R. Garoby, S. Hancock, M. Martini, J. P. Riunaud, CERN</i>	3570
Transverse Emittance Growth in the Fermilab Antiproton Accumulator with High-Current Antiproton Stacks — <i>S. J. Werkema, D. W. Peterson, P. Zhou, FNAL</i>	3573
Transverse Tails and Higher Order Moments — <i>W. L. Spence, F.-J. Decker, M. D. Woodley, SLAC</i>	3576
Simulation of Emittance Dilution in Electron Storage Ring from Compton Backscattering — <i>L. N. Blumberg, E. Blum, BNL</i>	3579
Transverse Effects of Longitudinal Wakefields at High Dispersion — <i>F. Decker, SLAC</i>	3582
Error and Tolerance Studies for the SSC Linac — <i>D. Raparia, C. R. Chang, F. Guy, J. W. Hurd, W. Funk, SSCL; K. R. Crandall, AccSys</i>	3585
Emittance Growth Due to Dipole Ripple and Sextupole — <i>H.-J. Shih, J. A. Ellison, M. J. Syphers, B. S. Newberger, SSCL</i>	3588
Proton-Proton Scattering Contribution to Emittance Growth — <i>T. Garavaglia, SSCL</i>	3591
Source Size Variation and Ion Effects in the SRS at Daresbury — <i>J. A. Clarke, D. M. Dykes, S. F. Hill, E. A. Hughes, M. W. Poole, P. D. Quinn, S. L. Smith, V. P. Suller, L. A. Welbourne, SERC Daresbury</i>	3594
Global Trajectory Correction Algorithms in CLIC and Main Linac Alignment Tolerances — <i>C. Fischer, CERN</i>	3597
Lattice Scaling and Emittance Control in the CLIC Main Linac — <i>G. Guignard, CERN</i>	3600
Decoherence and Recoherence of Beam in Phase Space — <i>J. Shi, S. Ohnuma, U. Houston</i>	3603
Space-Charge-Induced Emittance Growth in an Elliptical Charged Particle Beam with a Parabolic Density Distribution — <i>T. P. Wangler, LANL; P. Lapostolle, A. Lombardi, CERN</i>	3606
Emittance and Luminosity Evolution During Collisions in the SSC Collider — <i>W. Chou, S. Dutt, T. Garavaglia, K. Kauffmann, SSCL</i>	3609
Emittance Growth in Displaced, Space-Charge-Dominated Beams with Energy Spread — <i>J. J. Barnard, J. Miller, LLNL; I. Haber, NRL</i>	3612
An Injection Scheme for the Brookhaven ATF Utilizing Space-Charge Emittance Growth Compensation — <i>J. C. Gallardo, H. G. Kirk, BNL</i>	3615
A Matrix Theory of the Motion of an Ellipsoidal Bunch in a Beam Control System with a Rectilinear Optical Axis and with Space Charge — <i>A. Dymnikov, U. St. Petersburg; R. Hellborg, U. Lund</i>	3618
Space-Charge Dominated Beam Envelope Transport with Rotatable Axes — <i>E. Y. Tsiang</i>	3621
Effect of Space Charge Forces on Particle Tracking and Generation of High-Order Maps — <i>D. L. Bruhwiler, M. F. Reusch, Grumman</i>	3624
Experimental Study of Longitudinal Dynamics of Space-Charge Dominated Parabolic Bunches — <i>D. X. Wang, J. G. Wang, D. Kehne, M. Reiser, U. Maryland; I. Haber, Naval Res. Lab.</i>	3627
Transition Crossing in the Fermilab Main Ring, Past and Present — <i>I. Kourbanis, K. Y. Ng, FNAL</i>	3630
Observation and Correction of Resonance Stopbands in the AGS Booster — <i>C. Gardner, L. Ahrens, J. W. Glenn, Y. Y. Lee, T. Roser, A. Soukas, W. van Asselt, W. T. Weng, BNL; Y. Shoji, KEK</i>	3633
The Stability of Ions in a Storage Ring in the Presence of Small Gap Insertion Devices — <i>E. Bozoki, BNL</i>	3636
Simulation of Space-Charge Dominated Beam Dynamics in an Isochronous AVF Cyclotron — <i>S. R. Koscielniak, TRIUMF; S. R. Adam, PSI Switzerland</i>	3639
Passage Through a Half-Integer Resonance Due to Space Charge for Different Initial Distributions — <i>A. Budzko, INR; Yu. Senichev, SSCL</i>	3642
Estimation of Collective Effects for the EUTERPE Ring — <i>B. Xi, J. I. M. Botman, J. van Laar, C. J. Timmermans, H. L. Hagedoorn, Eindhoven U. of Tech.</i>	3645
A Moment Method Laplace Solver for Low Energy Beam Transport Codes — <i>C. K. Allen, S. K. Guharay, M. Reiser, U. Maryland</i>	3648
Evolution of Hadron Beams Under Intrabeam Scattering — <i>J. Wei, BNL</i>	3651
Simulation Study of Ion Trapping in PLS Storage Ring — <i>J. Jung, I. Ko, POSTECH</i>	3654
Beam Halo Formation From Space-Charge Dominated Beams in Uniform Focusing Channels — <i>J. S. O'Connell, Booz, Allen & Hamilton; T. P. Wangler, R. S. Mills, LANL; K. R. Crandall, AccSys Tech.</i>	3657
Computer Simulation of the Maryland Transport Experiment — <i>I. Haber, Naval Res. Lab.; D. A. Callahan, A. B. Langdon, LLNL; M. Reiser, D. X. Wang, J. G. Wang, U. Maryland</i>	3660
Integrated Numerical Modeling of a Laser Gun Injector — <i>H. Liu, S. Benson, J. Bisognano, P. Liger, G. Neil, D. Neuffer, C. Sinclair, B. Yunn, CEBAF</i>	3663

Volume 1:	1-747
Volume 2:	748-1640
Volume 3:	1641-2545
Volume 4:	2546-3218
Volume 5:	3219-3933

Proceedings of the 1993 Particle Accelerator Conference

Halo Formation in Mismatched, Space-Charge-Dominated Beams — C. L. Bohn, J. R. Delayen, ANL	3666
Collective Effects in the VEPP-3 Storage Ring — S. A. Belomestnykh, A. N. Voroshilov, BINP	3669
Single Bunch Effects in the Daresbury SRS — L. A. Welbourne, J. A. Clarke, D. M. Dykes, S. F. Hill, E. A. Hughes, M. W. Poole, P. D. Quinn, S. L. Smith, V. P. Suller, SERC Daresbury	3672
The Effects of Coulomb Beam Interaction in Multiaperture Linac — A. I. Balabin, G. N. Kropachev, I. O. Parshin, D. G. Skachkov, ITEP Moscow	3675
Longitudinal Instability of an Induction Linac with Acceleration — L. Smith, E. P. Lee, LBL	3678
On Solvable Model with Synchrotron Mode-Coupling — D. V. Pestrikov, BINP/KEK	3681
On Limitations on Low- α Rings Performance Due to —Z-Instabilities — N. S. Dikansky, BINP Russia; D. V. Pestrikov, KEK	3684
On Landau Damping of Collective Beam-Beam Modes — D. V. Pestrikov, BINP/KEK	3687
Synchronous Phase Changes Due to the Gap in the Bunch Train — Z. Greenwald, M. Tigner, Cornell	3690
Simulation and Compensation of Multibunch Energy Variation in NLC — K. A. Thompson, R. D. Ruth, SLAC	3693
The Physical Mechanism of Ultra-Fast Automatic Cooling for Beams in the Six-Dimensional Emittance Space — S. Gao, G. Qian, D. Liang, H. Sun, CIAE China	3696
An Exact Expression for the Momentum Dependence of the Space Charge Tune Shift in a Gaussian Bunch — M. Martini, CERN	3699
Stored Beam Lifetime Evaluation Formulae for Electron Storage Rings — A.V. Makulkin, All-Russ. Res. Inst.	3702
A Simulation Study on Beam Bunching in the KEK 2.5-GeV Linac New Pre-Injector — T. Kamitani, J.-Y. Choi, A. Enomoto, S. Ohsawa, Y. Ogawa, T. Urano, T. Suwada, K. Furukawa, I. Sato, KEK	3705
New Outlooks on Bunched Beam Instabilities in Particle Accelerators: A Proposal for a Simple Method to Release a Potential Self-Consistent High Quality Beam — M. Bergher, LURE	3708
Experimental Study of Collective Effects in BEP Storage Ring with High Stored Current — V. Danilov, I. Koop, A. Lysenko, B. Militsyn, I. Nesterenko, E. Perevedentsev, E. Pozdeev, V. Ptitsin, Yu. Shatunov, I. Vasserman, BINP	3711
Beam Coupling Impedances of Axial Symmetric Structures — W. Bruns, Technische Universität Berlin	3714

Hadron and e-p Colliders and Hadron Synchrotrons

Chair: D. Edwards

Accelerator Physics Issues at the SSC (Invited Paper) — G. F. Dugan, SSCL	3717
Fermilab Collider Upgrade: Recent Results and Plans (Invited Paper) — D. A. Finley, FNAL	3721
Operation of the Brookhaven AGS with the Booster (Invited Paper) — W. T. Weng, BNL	3726
Overview of Future Spallation Neutron Sources (Invited Paper) — G. H. Rees, Rutherford Appleton	3731
The Heavy Ion Synchrotron SIS: A Progress Report — K. Blasche, B. Franczak, B. Langenbeck, G. Moritz, C. Riedel, GSI	3736
Status of the PSR Improvement Program — R. J. Macek, D. H. Fitzgerald, M. Hoehn, R. Ryder, R. York, LANL	3739

Poster presentations:

First Experience with Colliding Electron-Proton Beams in HERA — R. Brinkmann, F. Willeke, DESY	3742
The Development of a Prototype Multi-MeV Electron Cooling System — D. Anderson, M. Ball, D. Caussyn, T. Ellison, B. Hamilton, S. Nagaitsev, P. Schwandt, IUCF; J. Adney, J. Ferry, M. Sundquist, Nat. Electr. Corp.; D. Reistad, Svedberg Lab.; M. Sedlacek, Alfvén Lab.	3745
The Bevalac Long Spill — C. M. Celata, S. Abbott, M. Bennett, M. Bordua, J. Calvert, R. Dwinell, D. Howard, D. Hunt, B. Feinberg, R. Force, R. Frias, J. Halliwell, J. Kalnins, S. Lewis, M. Nyman, L. Shalz, M. Tekawa, LBL; R. Solomons, RAFAEL, Israel	3748
Capture from Pair Production as a Beam Loss Mechanism for Heavy Ions at RHIC — B. Feinberg, A. Belkacem, R. Bossingham, H. Gould, LBL; W. E. Meyerhof, Stanford U.	3751
Acceleration of Deuteron Beam in the KEK Proton Synchrotron — Y. Mori, KEK	3754
Conceptual Design for a One Megawatt Spallation Neutron Source at Argonne — Y. Cho, J. Bailey, B. Brown, F. Brumwell, J. Carpenter, K. Crawford, D. Horan, D. Jerng, R. Kleb, A. Knox, R. Kustom, E. Lessner, D. McGhee, F. Mills, H. Moe, R. Nielsen, C. Potts, A. Rauchas, K. Thompson, ANL	3757
A Los Alamos Design Study for a High-Power Spallation-Neutron-Source Driver — A. J. Jason, R. A. Hardekopf, R. W. Macek, S. O. Schriber, H. A. Thiessen, R. Woods, LANL	3760

Each volume begins with this five-volume table of contents and ends with the five-volume author index. The chairmen's foreword and a list of conference organizers and staff appear as front matter in Volume 1. A list of conference participants precedes the author index in Volume 5.

Five-Volume Contents

On the High Intensity Aspects of AGS Booster Proton Operation — R. K. Reece, L. A. Ahrens, E. J. Bleser, J. M. Brennan, C. Gardner, J. W. Glenn, T. Roser, Y. Shoji, W. vanAsselt, W. T. Weng, BNL	3763
Results from Commissioning the AGS Booster Orbit System — E. Bleser, BNL	3766
The Effect of Global Survey Misalignment on the SSC — T. Garavaglia, N. Mahale, J. Peterson, SSCL	3769
Dealing with Abort Kicker Prefire in the Superconducting Super Collider — A. I. Drozhdin, I. S. Baishev, N. V. Mokhov, B. Parker, R. D. Richardson, J. Zhou, SSCL	3772
Design Status Report on the Collider Utility Straight Insertions — B. Parker, SSCL	3775
Current Design of the SSC Interaction Regions — Y. Nosochkov, A. Garren, T. Sen, R. Stiening, SSCL; E. Courant, BNL; D. M. Ritson, SLAC	3778
The Parameter Spreadsheets and Their Applications — R. Schwitters, A. Chao, W. Chou, J. Peterson, SSCL	3781
Lattice Studies for KAON Factory Accumulator and Booster Rings — A. Iliev, A. V. Budzko, INR-Troitsk; R. V. Servranckx, TRIUMF	3784
Reducing the Coupled-Bunch Oscillation in the Fermilab Booster by Optimizing RF Voltage — J. P. Shan, D. McGinnis, R. Tomlin, FNAL	3787
Beta Measurements and Modeling the Tevatron — N. M. Gelfand, FNAL	3790
The Status of the Fermilab Main Injector Project — D. Bogert, W. Fowler, S. Holmes, P. Martin, T. Pawlak, FNAL	3793
Constructing High Energy Accelerators Under DOE's "New Culture" for Environment and Safety: An Example, the Fermilab 150 GeV Main Injector Proton Synchrotron — W. Fowler, FNAL	3796
Performance and Comparison of the Different Coalescing Schemes Used in the Fermilab Main Ring — I. Kourbanis, G. P. Jackson, X. Lu, FNAL	3799
Operational Experience with Collimators in the Tevatron Collider — S. M. Pruss, FNAL	3802
Reliability of the Fermilab Antiproton Source — E. Harms, Jr., FNAL	3803
Multibunch Operation in the Tevatron Collider — J. A. Holt, D. A. Finley, V. Bharadwaj, FNAL	3806
Operational Experience with the Tevatron Collider Using Separated Orbits — G. Annala, FNAL	3808
Fermilab Antiproton Accumulator in the Main Injector Era — V. Visnjic, FNAL	3811
Study of Betatron Stochastic Cooling in Fermilab Antiproton Debuncher — V. Visnjic, M. Halling, FNAL	3814
Energy and Luminosity Limits of Hadron Supercolliders — W. A. Barletta, LBL/UCLA	3817
Ions Acceleration in the Synchrotrons with Constant RF of Electrical Field — V. P. Belov, Yu. P. Severgin, Efremov Inst.	3820
Ion Storage Ring of the INR Storage-Accelerating Complex — A. V. Dolinsky, A. I. Papash, S. N. Pavlov, A. T. Rudchik, A. E. Val'kov, I. N. Vishnevsky, A. V. Zhmendak, INR Kiev; V. P. Belov, A. A. Kapustin, V. S. Kashihin, A. M. Kokorin, A. A. Makarov, B. G. Mud'jugin, B. V. Rogdestvensky, Yu. P. Severgin, L. A. Schukeilo, M. N. Tarovik, Efremov Inst.	3822
A Compensated Dispersion-Free Long Insertion for an FFAG Synchrotron — P. F. Meads, Jr.	3825

Vacuum Technology

Chair: D. Edwards

Vacuum Technology for Superconducting Colliders (<i>Invited Paper</i>) — A. G. Mathewson, CERN	3828
Dynamic Vacuum in the Beam Tube of the SSCL Collider: Cold Beam Tube and Liner Options — W. C. Turner, SSCL	3833
Distributed Ion Pump Testing for PEP-II, Asymmetric B-Factory Collider — M. Calderon, F. Holdener, W. Barletta, D. Petersen, LLNL; C. Foerster, BNL	3836
High Capacity Getter Pump for UHV Operation — P. Manini, M. Marino, F. Belloni, M. Porro, SAES Getters	3839

Poster presentations:

ELETTRA Vacuum System — M. Bernardini, F. Daclon, F. Giacuzzo, R. Kersevan, J. Miertusova, F. Pradal, Sinc. Trieste	3842
Vacuum Chamber and Crotch Absorber for the SPring-8 Storage Ring Vacuum System — K. Watanabe, S. H. Be, Y. Oikawa, H. A. Sakaue, C. Y. Xu, S. Yokouchi, Y. Wang, JAERI-RIKEN; S. Takahashi, Kobe Steel; M. Tsuchiya, IHI; Y. Yanagi, Hitachi	3845
SYNRAD, a Montecarlo Synchrotron Radiation Ray-Tracing Program — R. Kersevan, SSCL	3848
Vacuum System Design of the MIT-Bates South Hall Ring — E. Ihloff, R. Averill, J. Flanz, K. Jacobs, S. Sobczynski, D. Wang, A. Zolfaghari, MIT-Bates	3851
Design of Vacuum Chambers for Experimental Regions of Colliding Beam Machines — C. Hauviller, CERN	3854

Volume 1: 1-747
 Volume 2: 748-1640
 Volume 3: 1641-2545
 Volume 4: 2546-3218
 Volume 5: 3219-3935

Proceedings of the 1993 Particle Accelerator Conference

Distributed Non-Evaporable Getter Pumps for the Storage Ring of the APS — <i>R. Dortwegt, R. Benaroya, ANL</i>	3857
Test Fabrication of a Copper Beam Duct for the KEK B-Factory — <i>Y. Suetsugu, K. Kanazawa, KEK</i>	3860
FNAL Main Injector Quadrupole Vacuum Chamber — <i>L. Sauer, FNAL</i>	3863
FNAL Main Injector Dipole Installation Equipment — <i>K. Moravec, F. Lange, J. Leibfritz, L. Sauer, FNAL</i>	3864
Solvents and Pumpdown Characteristics of SRF Nb Cavities — <i>M. G. Rao, P. Kneisel, H. F. Dylla, CEBAF</i>	3867
Leak Checker Data Acquisition System — <i>J. Payne, J. Gannon, SSCL</i>	3870
Theoretical and Experimental Study of Sorption Processes on Non-Evaporable Getters St 707 — <i>J. Miertusova, F. Daclon, Sinc. Trieste</i>	3873
Photodesorption Experiments on SSC Collider Beam Tube Configurations — <i>I. Maslennikov, W. Turner, SSCL; V. Anashin, O. Malyshev, V. Osipov, V. Nazmov, V. Pindyurin, A. Salimov, BINP; C. Foerster, C. Lanni, BNL</i>	3876
The Heat Load of an 80 K Liner for the SSC — <i>J. Maddocks, A. Yücel, SSCL</i>	3879
Design of Large Aperture, Low Mass Vacuum Windows — <i>W. J. Leonhardt, M. Mapes, BNL</i>	3882
Observation and Analysis for Motions of Trapped Microparticles in the TRISTAN Accumulation Ring — <i>H. Saeki, Japan SRRI; T. Momose, Miyagi; H. Ishimaru, KEK</i>	3885
Overview of an 80 K Liner Design for Synchrotron Light Interception in SSCL Collider — <i>Q.-S. Shu, W. Chou, D. Clark, W. Clay, Y. Goren, R. Kersevan, V. Kovachev, P. Kraushaar, K. Leung, J. Maddocks, D. Martin, D. Meyer, R. Mihelic, G. Morales, J. Simmons, G. Snitchler, M. Tuli, W. Turner, L. Walling, K. Yu, J. Zbasnik, SSCL</i>	3888
Thermal Model and Associated Novel Approach for Synchrotron Radiation Liner with End Cooling — <i>Q.-S. Shu, K. Yu, W. Clay, J. Maddocks, G. Morales, J. Zbasnik, SSCL</i>	3891
Design of ECR Ion Source Vacuum Systems — <i>J. Pivarc, JINR Dubna</i>	3894
Development of Distributed Ion Pumps for g-2 Beam Vacuum System — <i>H. C. Hseuh, M. Mapes, L. Snyderstrup, BNL</i>	3897
What Joining Method for the New Generation of Accelerators (SSC and LHC) — <i>R. Gillier, Helicoflex; J. Montuclard, M. Lefrancois, Ch. Rouaud, LeCarbone-Lorraine, France</i>	3900
Surface Treatments and Photodesorption of Oxygen Free Copper Used in an Accelerator — <i>T. Kobari, M. Matumoto, S. Ueda, MERL Hitachi; M. Kobayashi, Y. Hori, KEK</i>	3903
The DAFNE Main Ring Vacuum System — <i>V. Chimenti, A. Clozza, H. Hsieh, G. Raffone, C. Vaccarezza, INFN-LNF</i>	3906
Vacuum Tracking — <i>V. Ziemann, SLAC</i>	3909

Closing Plenary *Chair: W. Hess*

Future Accelerators in Japan — <i>N. Toge, KEK</i>	3912
LHC Progress and Status — <i>G. Brianti and the LHC Machine Group, CERN</i>	3917
Status of the SSC — <i>R. J. Briggs, SSCL</i>	3922
Design for Low Beam Loss in Accelerators for Intense Neutron Source Applications — <i>R. A. Jameson, LANL</i>	3926
Is There a Future for High Energy Accelerators? — <i>M. Tigner, Cornell</i>	3931

Each volume begins with this five-volume table of contents and ends with the five-volume author index. The chairmen's foreword and a list of conference organizers and staff appear as front matter in Volume 1. A list of conference participants precedes the author index in Volume 5.

Operating Experience with High Beta Superconducting RF Cavities*

H. F. Dylla, L. R. Doolittle and J. F. Benesch
Continuous Electron Beam Accelerator Facility
12000 Jefferson Avenue, Newport News, VA 23606-1909 USA

Abstract

The number of installed and operational $\beta=1$ superconducting rf cavities has grown significantly over the last two years in accelerator laboratories in Europe, Japan and the U.S. The total installed acceleration capability as of mid-1993 is approximately 1 GeV at nominal gradients. Major installations at CERN, DESY, KEK and CEBAF have provided large increments to the installed base and valuable operational experience. A selection of test data and operational experience gathered to date is reviewed.

I. INTRODUCTION

Superconducting Radio-Frequency (SRF) cavities for speed of light particles ($\beta=1$) are playing an increasing role in high energy and nuclear physics accelerators worldwide. As more cavities are manufactured, tested, and put into service, the breadth and depth of operational experience is growing. Installed acceleration capacity is approximately 1 GeV and a total of about 10^6 cavity-hours of operation has been accumulated. Figure 1 shows the time history of installed SRF acceleration capacity.

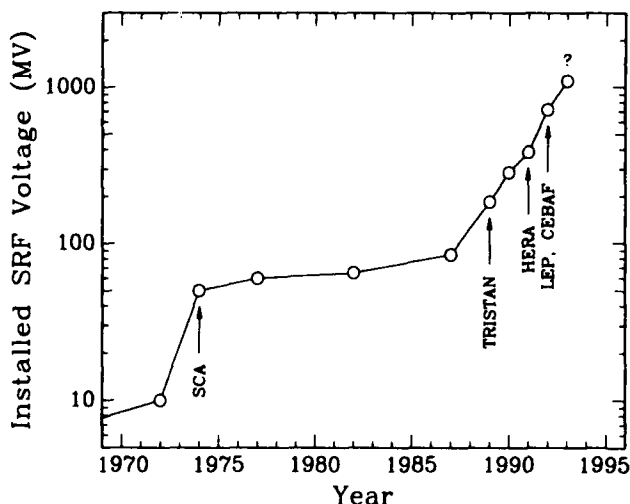


Figure 1. History of installed SRF acceleration capacity

The range of parameters spanned by the cavities in use is substantial. Cavities are constructed either of solid niobium or niobium sputtered onto formed copper. They are operated between 1.8 K and 4.5 K. Frequencies range from 352 MHz to 3000 MHz. Beam currents range up to 70 mA. Gradients in laboratory tests of production cavities range from 5 to 20 MV/m. Once these cavities are installed in cryostat systems, additional constraints due to the system interlocks and the interfaces result in system gradients ranging from 3 to 12 MV/m.

*This work supported by US DOE Contract DE-AC05-84ER401540

Several accelerator SRF projects are complete and operational: Stanford's HEPL, KEK's TRISTAN, Darmstadt's S-Dalinac, DESY's HERA, and CERN's SPS. Accelerator projects using SRF that are under construction and have some operational experience are CEBAF, CERN's LEP, Saclay, and Frascati. Possible future applications include TESLA [13], spallation neutron sources and FEL drivers. See also Table 1.

This paper presents a summary of present performance and experience of the installations worldwide. Topics include operational aspects of the cavities and their peripheral hardware. Particular emphasis is placed on CEBAF's experience with SRF cavities because the authors are closest to it and because the number of units at CEBAF is about 80% of those now installed worldwide.

II. OPERATIONAL EXPERIENCE WITH SRF

A. Tristan (KEK)

This system comprises thirty-two 508 MHz cavities installed in pairs in 16 cryostats and operated at 4.5K.[1] Total active length is 47.2 m. In pre-operational testing, the average gradient was 7 MV/m, while in operation this drops to 3.2–4.7 MV/m. 400,000 cavity-hours of operation with beam have been accumulated. Operational problems at startup included vacuum leaks at beam pipe indium joints, since solved, and coaxial coupler ceramic punch throughs. There have been some difficulties with the piezo-electric devices used to tune the cavity frequency within the cryostat. A few cavities experienced arc trips associated with synchrotron radiation; these were reduced when intercepts were installed.

B. DESY

The HERA electron ring includes sixteen 500 MHz cavities in eight cryostats, totaling 19.2 active meters. The operating temperature is 4.4 K. In pre-operational testing, the average gradient was 6 MV/m, while in operation this drops to 4 MV/m. 160,000 cavity-hours of operation with beam have been accumulated. Operational problems at startup included Q degradation with slow cooldown.[2] This "Q-disease" was determined to be due to hydride formation in the temperature range 70–170 K. A fast cooldown from 170 K to below 70 K eliminates the difficulty, but this can be difficult for some machines due to cryogenic system limitations. [3] Raising the temperature to 200 K for two hours redistributes the hydrogen and Q is often restored. [4] High temperature heat treatment above 800 °C eliminates the problem and in laboratory experiments anodization of the niobium surface considerably reduced the Q-degradation.[3, 5]

C. Darmstadt

S-Dalinac includes ten and one quarter 3000 MHz 20-cell cavities in two cryostats, totaling 10.25 active meters.[6] (Fractional cavities have fewer than the standard number of cells for a given machine.) The operating temperature is 1.8 K. In operation, the average gradient is 5.6 MV/m.

43,000 cavity-hours of operation with beam have been accumulated. Some of the cavities have lower Q than expected. This, coupled with refrigeration limitations, has led the system to be operated at less than design energies. Replacement cavities are due to be installed shortly.

D. Saclay

MACSE includes five 1500 MHz cavities in two and a half cryostats, totaling 2.5 active meters, operating at 1.8 K.[7] (Fractional cryostats have fewer than the usual number of cavities for a given machine.) In operation the average gradient is 12 MV/m. Operational problems at startup included a cold sapphire rf window failure.

Saclay has made great strides in closed loop chemical treatment and cleaning systems for SRF cavities. Results have been excellent, with gradients on test cavities ranging to 28 MV/m.[8]

E. CERN

LEP 200 is the on-going upgrade of the LEP accelerator system with SRF cavities to double the available particle energy. The installation will consist of 192 cavities in 48 cryostats operating at 352 MHz.[9] The operating temperature is 4.5 K. As of May 1993, twelve cavities in three cryostats have been installed and operated with beam. This represents 20.4 m of active length, about 6% of the total planned (326m). In pre-operational testing, the average gradients were 5–6 MV/m, while in operation this drops to 3.5–5.5 MV/m. By contract, the vendors are allowed 20% maximum degradation between vertical test and tunnel horizontal cryostat test results. 30,000 cavity-hours of operation with beam have been accumulated. Startup problems include difficulties with coaxial input power couplers and HOM output couplers.

F. CEBAF

CEBAF now has 113 active meters installed for operation at 2K; upon completion in December 1993 it will comprise 169 active meters. The machine will include 338 cavities operating at 1497 MHz in 42 1/4 cryostats. In pre-operational testing, the average gradients at field emission onset are 7.5–10 MV/m, while in operation in the horizontal cryostat usable gradient is 5–7.5 MV/m. 140,000 cavity-hours of operation with beam have been accumulated.[10] One cryomodule was pushed to an average gradient of 8 MV/m with beam. Operational problems at startup include system performance limited by refrigeration capacity until the 2K cold compressor system functions (expected in late 1993). It appears that consistent system operation above 7.5 MV/m will require rf conditioning of the waveguide transition from room temperature to 2 K and better understanding of the interactions among the hardware interlocks monitoring performance.

III. CURRENT STATE OF THE ART

Significant advances are being made in pushing cavity performance, as reported in several papers at this conference. Proch reviewed this area in these proceedings, [11], so only highlights will be given here. More work is needed: the usable gradient assumed for the contemplated European Electron Machine is 10 MV/m at $Q \geq 4 \times 10^9$. [12] The usable gradient goal for the cavities being fabricated for the TESLA

Test Facility is 15 MV/m at $Q \geq 5 \times 10^9$. TESLA itself will require a usable gradient of 25 MV/m at the same Q.[13]

The best production (5-cell) cavity at CEBAF reached 20 MV/m gradient in the vertical test dewar. No special care was taken in preparing this cavity; it represents the outlier of the distribution. This result is shown in Figure 2. One cavity in the CEBAF production run was specially treated, and achieved 20.5 MV/m. On initial testing (standard processing) this latter cavity reached 16 MV/m without field emission. It was subsequently annealed at 1400°C in an UHV furnace with titanium as a solid state getter, chemically etched and rinsed with water at moderate pressure (10 MPa). [14] Cornell reported at this conference results on a 9 cell cavity at 3 GHz which achieved 30 MV/m.[15] For CEBAF, the surface field is 2.56 times the accelerating field, while the ratio is 2.1:1 for the Cornell cavity.

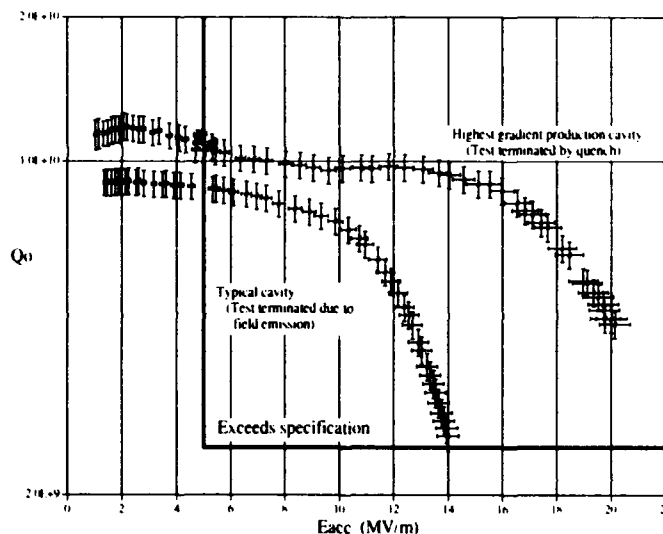


Figure 2. Performance of two CEBAF cavities

IV. CEBAF CAVITY TESTING

At CEBAF, the basic unit of the accelerating structure is a hermetically sealed pair of cavities. The cavities are chemically etched, rinsed with high purity water and alcohol (isopropanol or methanol), assembled in a class 100 clean room with the necessary auxiliary hardware, and evacuated; all within a five hour period. The cavity pairs remain under vacuum thereafter. Each cavity pairs is hung from a dewar lid, connected to variable coaxial couplers, and subjected to a full rf performance test at 2 K in a vertical dewar. This has proved advantageous compared to procedures during which cavities have to be exposed to atmosphere after initial testing, raising the chances of introduction of particulate contamination.

As of May 1, 1993, 250 cavities had been assembled into pairs and tested. CEBAF defines usable gradient as the lower of the gradient with 1 W of field emission dissipation or the quench gradient less 1 MV/m. Using this definition, the average usable gradient achieved was 9.4 MV/m at $Q = 7 \times 10^9$ versus 5 MV/m at 2.4×10^9 specified. In vertical test, gradient was limited by the following mechanisms: 5% quench without any field emission, 35% quench with field emission and 60% field emission sufficient to exceed

available rf power (80 W) or a self-imposed radiation limit. In Figure 2 we show the Q versus E plots of two cavities, a typical unit with field emission loading at moderate gradients and the best production cavity to date, with field emission beginning at 12 MV/m and a thermal-magnetic quench at 20.1 MV/m with 46 W power dissipation, about half in field emission. In Figure 3 we show field emission onset gradients versus time. It is noteworthy that the standard deviation of the field emission onset gradient and usable gradients has not changed since production began: $\sigma=3$ MV/m has remained constant while the average gradients increased by 50%. The source of this performance spread is not understood. A cavity fabrication and performance database is being assembled for further trending and feedback to cavity performance, but no variable examined to date has correlated well with the width of the distribution. This effort will continue after the cavity pair production is complete to provide information to the accelerator community.

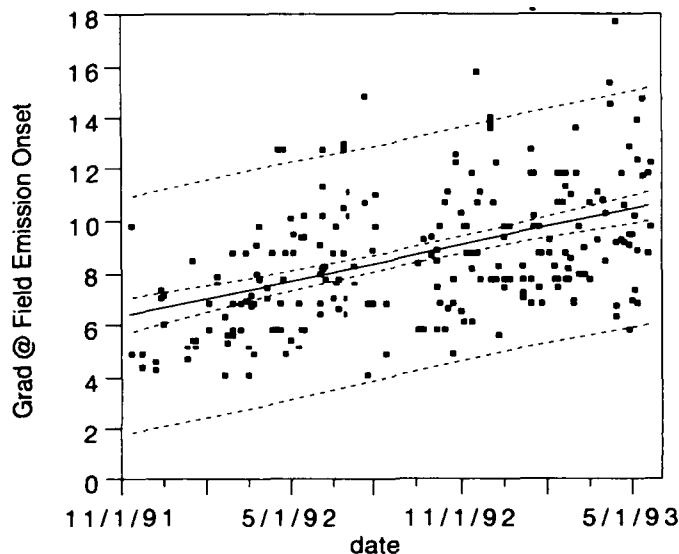


Figure 3. Gradient at field emission onset versus time for CEBAF cavity production

The cavities which did quench without field emission did so with a spread in gradients of 8 to 18 MV/m. This is sufficient data to indicate that the niobium used in the CEBAF cavities, with $RRR=250$ as supplied and $RRR=200$ as welded, does not yet provide the thermal stability needed for $E_{acc} > 15$ MV/m as desired for future accelerators. Even the titanium gettered cavity cited above, with an $RRR>800$, was limited to 20.5 MV/m. More work on the basic materials used in cavities is clearly needed.

V. SRF CAVITY FIELD EMISSION LIMITATION

As mentioned above, only about 5% of the CEBAF cavities show no field emission loading, i.e., have a flat Q profile until quench. There are two types of electron loading in cavities, resonant (multipacting) and non-resonant (field emission). The first is reasonably well understood and can be eliminated by proper cavity shaping.[16] Non-resonant electron loading is due to both intrinsic and extrinsic impurities of the niobium surface. Field emission loading

needs to be limited to minimize radiation damage to coupler ceramics which can result in vacuum leaks and to minimize radiation damage to the niobium itself.

CEBAF has steadily improved its average gradient at field emission onset over time by careful rinsing and attention to clean assembly techniques. The data shows that much improvement is still possible, and many techniques are being investigated in labs around the world. High pressure (10 MPa) water rinsing has shown great promise at CERN [17] and CEBAF [14]. Cornell has also successfully applied high power pulsed processing to eliminate (by explosion) field emission sites.[18] Cornell [19] and Wupertal [20] have shown that heat treatment in a UHV furnace above 1200 °C can also reduce field emission. Of these techniques, the high pressure rinsing is the easiest to implement and therefore the most likely to enter manufacturing service soon.

VI. SRF PERFORMANCE LIMITATIONS IN ACCELERATORS

One has to make a clear distinction between the fundamental capability of the SRF cavity technology and its practical application in an accelerator environment. For the group of people dealing with cavities alone, it is important to stretch the performance of a cavity to its limit. The results of such tests, generally done under well controlled conditions in a vertical configuration without beam, point towards fundamental performance limitations: anomalous losses caused by defects, thermal-magnetic breakdown, or field emission loading. In the accelerator environment, often the prior performance of the cavities cannot be repeated due to external constraints which are not present in the well controlled vertical tests. Among these are power handling problems (rf heating and outgassing) in external waveguides (CEBAF), rf power limitations due to low Q external (CEBAF), insufficient masking of synchrotron radiation (KEK), limitations in cryogenics due to high rf losses (Q -disease, HERA) and non-performing (incomplete) cryo-systems (CEBAF).

At CEBAF, there are several interlocks installed in the cavity cryostats to protect the system. At the present time, since there is little operating experience, these are set very conservatively. Most of these monitor the waveguide between the warm and cold rf windows. There is a phototube which senses the light from arcs in the waveguide. If light is seen for more than 50 μ s, the rf is shut off. There is a thermopile which monitors the IR radiation in the waveguide. If this sensor goes above a set point which corresponds to about 50 °C on a warm polyethylene window, the rf is shut off. The ion pump on this waveguide section is monitored and the rf shut off if the pressure exceeds 10^{-7} torr. Finally, the cavity is administratively limited to 1 W of field emission loading as measured calorimetrically. With all these constraints, the first 12 cryomodules at CEBAF (96 cavities) averaged 7.2 MV/m usable gradient versus a specification of 5 MV/m. Within the allowed dynamic heat load of 45 W, the average gradient is 6.5 MV/m. Cavity performance has continued to improve and these values are expected to increase for the entire machine when installed and commissioned. Further increases are expected as the waveguide is conditioned and the machine is better understood, allowing some interlocks to be relaxed.

Net performance of a cavity necessarily diminishes as more and more requirements and support equipment are considered. This has little to do with actual degradation of the cavity, and more to do with the fact that a chain is only as strong as its weakest link. We note in passing that the design specification for CEBAF cavity operation is 5 MV/m with $Q_0 \geq 2.4 \times 10^9$, and that neither typical cavities nor their supporting hardware has any problems operating at that level. Subsystems and infrastructure start to show their limits when asked to perform at 150% of specifications and higher, although the CEBAF cavities (on average) are capable of operation at about 200% of specifications. In Figure 4 we compare vertical test performance with tunnel commissioning performance for 125 cavities, while in Figure 5 we remove the 47 cavities constrained in the tunnel by interlocks from the comparison.

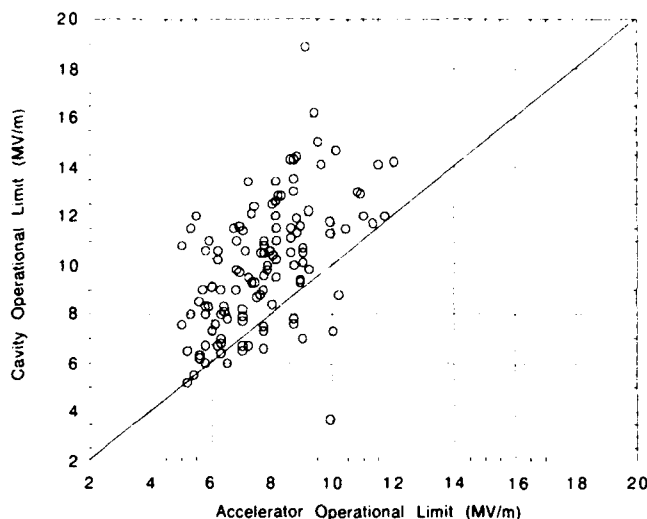


Figure 4. Comparison of vertical test with accelerator limit derived all constraints on tunnel commissioning tests

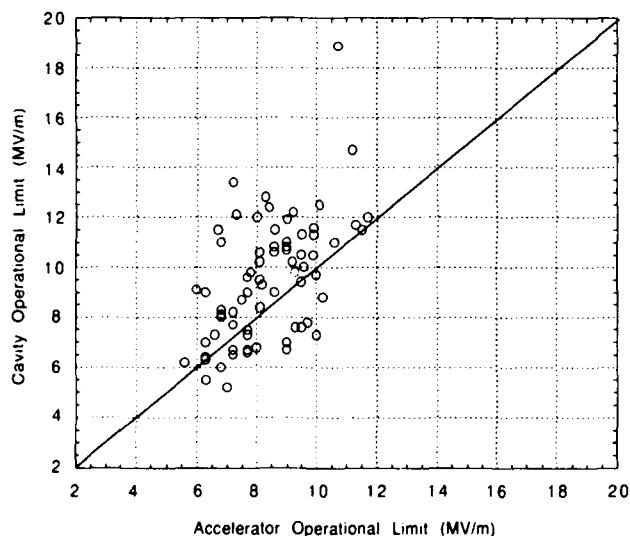


Figure 5 Comparison of vertical test with accelerator limit derived from only those constraints on tunnel operation which are also present in vertical test.

VII. HIGHER ORDER MODE POWER EXTRACTION

Higher order modes (HOMs) must be adequately damped to prevent various forms of beam breakup. Different accelerators have different requirements, and the problems increase with increasing beam current, decreasing rf bucket length, increasing number of passes, and decreasing time between bunches.

High current machines such as storage rings generate large amounts of HOM power. TRISTAN, in fact, has problems with power handling on the HOM output coupler, and has had to replace the couplers. Low current machines like CEBAF, on the other hand, will only dissipate a fraction of a watt of HOM power (0.25 W per 5-cell cavity at a beam current of 1 mA). The heat load involved in couplers to take this power out to room temperature or even a thermal shield at 40–80K would exceed the power in the modes themselves, and therefore CEBAF has HOM loads inside the cryostat at 2 K. Materials requirements for these loads were themselves something of a challenge.[21] They must have temperature independent microwave absorption properties, be vacuum compatible, and have good thermal conductivity.

Operational measurements of the damping of HOMs in CEBAF cavities with beam indicate that the beam breakup (BBU) threshold is about 14 ma, which is 70 times the design current. Future SRF accelerator projects, such as CERN LEP-II, Cornell B-factory, and FEL drivers, will have HOM damping and power handling requirements more severe than those of accelerators in operation today, and research to advance the technology is underway.[21]

VIII. COUPLER CERAMICS

As mentioned above, several laboratories have had trouble with arcing and breakdown of coupler ceramics, leading to reduced power handling limits or vacuum leaks through the ceramics. As a result, many laboratories are contributing to the knowledge base on breakdown properties of ceramics, in particular high purity alumina. There are at least two distinct phenomena related to the interaction of ionizing radiation with the ceramics. Glass (SiO_x) impurities must be minimized because radiation dosage leads to decomposition and formation of vacuoles which increase permeation rates and can eventually link up to form a true leak.[22] Ionizing radiation can also cause surface flashover. The second phenomenon has been seen at CEBAF.[23] These phenomena may be the cause of small ($\sim 10^{-8}$ atm-cc/s) vacuum leaks which are infrequently found in the CEBAF cold rf window ceramic after vertical test.

Multipacting has been identified as a source of rf window failure and antimultipacting coatings, such as TiN, TiO_2 or Cr_2O_3 , are routinely applied to ceramic rf windows.[24] Coatings with controlled resistivity, designed to provide some charge drainage while minimizing rf loss in the coating, are under development. Gold and other impurity dispersions in the antimultipacting coatings cited appear promising.[25] Above all, good surface preparation, cleaning and handling procedures are mandatory.

IX. CAVITY VACUUM INTEGRITY

Cavity vacuum integrity has been a problem for the field because of the sensitivity of the indium sealed niobium flanges to surface preparation. A recent technique developed at CEBAF has increased the sensitivity for measuring the vacuum integrity of cavity assemblies.[26,27] Since the cavity pairs are submerged in liquid helium for roughly a day, an integrated leak test provides great sensitivity. In the CEBAF cavity pairs there are 16 indium joints (4.75m) and 4 copper knife edge seals. The average integrated leak rate for 80 pairs was 5.8×10^{-11} atm-cc/s.

X. SUMMARY

Superconducting rf technology is finally maturing as a reliable and cost effective means of accelerating high quality particle beams. Significant operational experience is being clocked now and will double in the next year. Performance is also improving, with production cavity gradients of 10-20 MV/m in vertical test and 5-12 MV/m when installed in accelerators and subject to additional systems requirements. Significant progress has been made on key technical issues which can limit performance and reliability, including HOM power extraction, cavity assembly vacuum integrity, and power input couplers. Additional work is needed on the last item as power handling requirements increase to the MW level.

XI. ACKNOWLEDGMENTS

The authors wish to acknowledge the assistance of the CEBAF SRF and Operations Departments, especially P. Kneisel, M. Drury, C. Reece, W. Schneider, J. Mammoser, K. Hovater and C. Sinclair. B. Aune of Saclay, W. Weingarten of CERN, D. Proch of DESY, H. Graef of Darmstadt and S. Noguchi of KEK provided information used in the laboratory summaries.

XII. REFERENCES

- [1] S. Mitsunobu, et al., Proc. of the 5th Workshop on RF Superconductivity, p 84, DESY M-92-01 (April 1992); S. Noguchi, private communication.

- [2] G. Enderlein et al., Proc. of the 1991 Particle Accel. Conf, p 2432; and D. Proch, private communication.
- [3] B. Bonin and R.W. Roth, *ibid*, p. 210.
- [4] K. Saito and P. Kneisel, Proc. of the 3rd European Particle Accelerator Conference EPAC 92, p. 1231.
- [5] K. Saito and P. Kneisel, Proc. of the 5th Workshop on RF Superconductivity, p. 665, DESY M-92-01 (April 1992).
- [6] J. Auerhammer, et al., Proc. of the 5th Workshop on RF Superconductivity, p. 110, DESY M-92-01 (April 1992)
- [7] B. Aune, private communication.
- [8] B. Bonin, these proceedings.
- [9] C. Wyss, these proceedings; G. Cavallari, et al., these proceedings.
- [10] A. Hutton, these proceedings.
- [11] D. Proch, these proceedings.
- [12] M. Promé, private communication.
- [13] H. Edwards, these proceedings.
- [14] P. Kneisel and M. Rao, these proceedings.
- [15] J. Graber, et al., these proceedings.
- [16] C. M. Lyneis, Proc. of the Workshop on RF Superconductivity, p. 119, KfK 3019 (November 1980).
- [17] Ph. Bernard, et al., Proc. of the 3rd European Particle Accelerator Conference EPAC 92, p. 1269.
- [18] J. Graber, et al., these proceedings.
- [19] J. Kirchgessner, et al., Proc. of the 5th Workshop on RF Superconductivity, p. 37, DESY M-92-01 (April 1992) and references therein.
- [20] R. W. Roth, et al., Proc. of the 2nd European Particle Accelerator Conference EPAC 90, p.1097 Editions Frontieres.
- [21] I. Campisi, these proceedings.
- [22] D. Howitt, Proc. of the Workshop on Microwave Absorbing Materials for Accelerators, February 1993 (to be published).
- [23] L. Phillips, et al., these proceedings; T. Powers et al., these proceedings.
- [24] A. R. Nyaiesh, et al., J. Vac. Sci & Tech. A3, 1705 (1986).
- [25] L. Phillips, private communication
- [26] M. G. Rao, J. Vac. Sci. & Tech. A11 (to be published in July/August, 1993).
- [27] J. Mammoser and J. F. Benesch, these proceedings.

Table 1 - Machine Parameters

Lab Machine type	HEPL	Darmstadt	CEBAF	Saclay	KEK	DESY	CERN	
	SCA Recycl.	S-Dalinac Recycl.	CEBAF Recycl.	MASCE e linac	TRISTAN e collider	HERA e-p collider	LEP e collider	SPS Acc/Inj
f (MHz)	1300	2997	1497	1497	508	500	352	
Material	Nb	Nb	Nb	Nb	Nb	Nb	Nb,Nb/Cu	
Operating T (K)	2	1.8	2.0	1.8	4.5	4.4	4.5	
length now (m)	6	10.25	73	2.5	48	19.2	20.4	3.4
length planned (m)	6	10.25	168	2.5	48	19.2	326	3.4
(MV/m) pre-op.	-	-	7-10	-	7	6		5.9-6.5
(MV/m) op.	2-3	5.6	5-7.5	12	3.2-4.7	4		3.5-5.5
Q ₀ (10 ⁹)	-	3.0	5.7	10	1.7	1.0-2.0	3.5	4.3
beam current (mA)	0.5	.05	0.2	0.1	14	60	4	0.5

Perpendicular Biased Ferrite-Tuned Cavities

R. L. Poirier

TRIUMF

4004 Wesbrook Mall, Vancouver, BC, Canada V6T 2A3

Abstract

For varying the frequency of accelerating cavities in rapid-cycling rf systems for Synchrotrons, perpendicular biased yttrium garnet ferrites have gained popularity over the conventional parallel biased NiZn ferrites. An important milestone in fast cycling perpendicular biased ferrite tuners was reached at TRIUMF in the spring of 1991. To the best of our knowledge this is the first time that anyone has operated a fast ac perpendicular biased yttrium garnet ferrite tuner over such a large frequency swing at high rf power levels. A similar design is now being developed at SSCL for the Low Energy Booster. This paper will present a brief history of the development of perpendicular biased ferrite tuners, a comparison of the two biasing methods, magnetic field theory of perpendicular biasing, and the problem of eddy currents produced by the ac biasing circuit. A comparison will be made of the requirements and design features of the different tuner designs with special emphasis on the designs in the process of being developed and tested.

I. INTRODUCTION

Parallel biased NiZn ferrite tuners [1][2] have been well established for many years as a means of varying the frequency of accelerating cavities. NiZn ferrites have the disadvantage of very low electric Q's which limit the voltage that can be applied and very high saturation magnetization values which make it impractical to operate in the saturation region for obtaining high magnetic Q's. Also when parallel biasing NiZn ferrites, instabilities caused by dynamic loss effect and high loss effect were observed [3]. On the other hand, yttrium garnet ferrites have very high electric Q's and are available with very low saturation magnetization values, making perpendicular biasing practical for operating in the saturation region for high magnetic Q's. Operating in the saturation region also eliminates the ac dynamic loss effect, which occurs only at low values of bias field. The high loss effect, which is related to the stored rf energy in the ferrite for the case of parallel biasing NiZn ferrite, has not been observed in the case of perpendicular biasing yttrium garnet ferrite. However, the classical non-linear detuning of the resonance curve as a function of power level has been observed [4]. Yttrium garnet ferrites are normally used at microwave frequencies for such devices as isolators, circulators, phase shifters, attenuators and filters. These devices make use of the gyromagnetic resonance phenomena for their properties and never operate much above a bias field which causes a gyromagnetic resonance to occur. The history of perpendicular biased ferrite tuners operating at a bias field far above the gyromagnetic resonance is reviewed. The two biasing methods are based on different physics

phenomena and are compared. Basic magnetic field theory and problems introduced by eddy currents, when perpendicularly biasing ferrites, is presented. A comparison of the different tuner designs is discussed.

II. DEVELOPMENT HISTORY

The idea of operating at a bias field far above the gyromagnetic resonance in order to take advantage of the low value of the dissipative component of the permeability in that region, was first tested at Los Alamos for the Proton Storage Ring [5] at 500 MHz with a 1% tuning range. When the LAMPF II rapid-cycling Synchrotron was proposed, the development of perpendicular biased yttrium garnet ferrite operating above the gyromagnetic resonance was continued at Los Alamos in the 50 MHz to 60 MHz range for a 20% frequency swing and a gap voltage between 130 and 140 kV [6][7]. These tests were with dc magnetic bias only but the principle of operating above the gyromagnetic resonance (lower frequency) was tested at high power. Concurrently TRIUMF was involved in an rf development program on accelerating cavities for a proposed KAON Factory and a collaboration was set up between TRIUMF and Los Alamos to further develop perpendicular biased ferrite tuners. Los Alamos shifted its efforts toward designing an off-axis tuner with a smaller tuning range for the main ring cavity using a radial bias scheme [8]. The radial bias scheme was aborted because of the difficulty in maintaining a uniform magnetic field. The Los Alamos Booster Cavity was shipped to TRIUMF where it was completely rebuilt for ac bias operation and the lower frequency limit extended to 46 MHz [9].

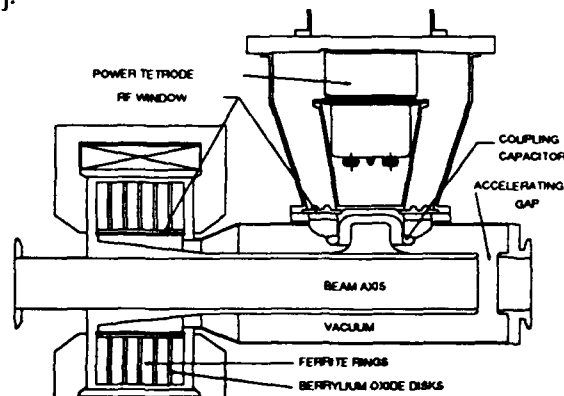


Figure 1. Typical cross section view of the type of ferrite tuned cavity used at Los Alamos, TRIUMF and SSCL with the ferrite tuner on the beam axis

The Los Alamos main ring cavity and RF amplifier was eventually shipped to SSCL for its development program and the collaboration initially set up between Los Alamos and TRIUMF has continued as a TRIUMF/SSCL collaboration.

SSCL has designed a liquid cooled tuner similar to the TRIUMF/LANL design [10] for the Low Energy Booster (LEB) and the Institute for Nuclear Physics in Novosibirsk (INP) has produced an alternative design [11] for the LEB similar to the TRIUMF design except the tuner is an epoxied assembly. A typical cross-section view of the type of ferrite tuned cavity used at Los Alamos, TRIUMF and SSCL is shown in figure 1. The different tuner designs will be discussed later.

The Institute for Nuclear Research (INR) in Moscow has also done extensive design work on perpendicular biased ferrite tuners [12] for their proposed Kaon Factory. Development work on perpendicular biased ferrite tuners was also done at AECL, Chalk River for the PETRA II [13] and HERA [14] RF systems in Hamburg but for much slower and smaller tuning ranges. A tuner using perpendicular biased ferrite was also developed at CERN for the 114 MHz electron accelerating system for the CERN PS [15] but again for a slow and small tuning range. A stripline type fast ferrite tuner with a small tuning range [16] was produced by ANT Bosch Telecom in Germany for BNL but is different from the other designs in that it uses ferrite tiles epoxied to copper cooling plates.

III. COMPARING OF BIASING METHODS [17]

Assuming that the operating rf frequency is sufficiently far below the frequency for gyromagnetic resonance and that the rf field is small compared to the bias field, the effective permeability [18] for parallel biasing is a function of the rate of change of the B-H curve as shown in figure 2 by the slope of the tangent lines at points A and C, while for perpendicular biasing it is a function of the ratio of B/H at any point on the B-H curve (e.g. slope of the lines B and D).

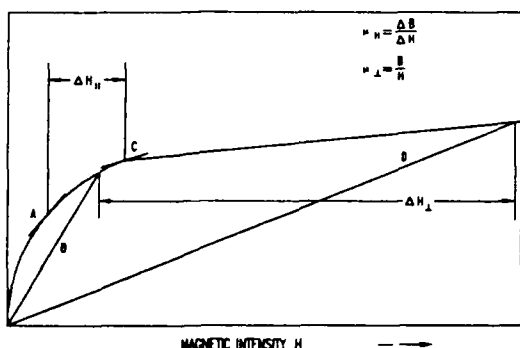


Figure 2 Plot of magnetic induction vs. magnetic intensity

The ΔH shown is for the same tuning range for each case for a particular tuner. For NiZn ferrites which have very high saturation magnetization values (3200 gauss for the NiZn ferrite used at Fermilab), operating in the perpendicular bias mode would require a significantly larger bias range and would make the design of the bias power supply very difficult and expensive. On the other hand yttrium garnet ferrites are available with very low saturation magnetization values (810g for the TRIUMF-KAON ferrites) making the

design of the bias power supply comparable to the one used in parallel biasing NiZn ferrite and making them very attractive for perpendicular biasing.

IV. PERPENDICULAR BIAS THEORY [19][20]

If a dc magnetic field H is applied to a ferrite material and a small rf magnetic field h is applied perpendicular to the dc field, the rotating vector $(H+h)$ of a magnetic field describes a cone and the magnetic moment M precesses around the cone. The condition for gyromagnetic resonance is when the rf is synchronized with the precession and occurs at

$$H = f / 2.8$$

where H is the internal dc magnetic field in oersteds and f is the rf frequency in Megahertz. The permeability of the ferrite is of a tensor nature and has both a dispersive and a dissipative component and can be written as

$$\mu = \mu' - j\mu''$$

Figure 3 is an idealized plot of permeability vs applied magnetic field. The plot of the dissipative component μ'' shows the greatest loss at H_{res} , which is the condition for gyromagnetic resonance. The plot of μ' is the effective μ for the dispersive part of the permeability μ' . The cavity frequency is tuned in the optimum way by varying the dc bias from H_2 to H_1 , thus varying μ' from μ_2 to μ_1 . In the region above resonance the value of μ'' is lowest.

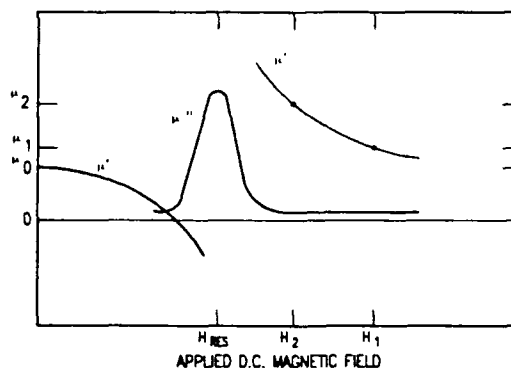


Figure 3. Plot of permeability vs applied magnetic field.

For low frequencies well below the frequency for gyromagnetic resonance [21] and small rf magnetic fields relative to the dc bias field, the expressions for μ' and μ'' to some approximation are:

$$\mu' = 1 + \frac{4\pi Ms}{H} \quad \mu'' = g\Delta H_k \frac{f}{f_0^2} \frac{4\pi Ms}{H}$$

where g is the gyromagnetic resonance ratio, ΔH_k the spinwave linewidth at the gyromagnetic resonant frequency f_0 , f the operating frequency, $4\pi Ms$ the saturation magnetization and H the dc internal bias field. Since the magnetic Q is the ratio of μ'/μ'' , then for a fixed frequency

and a given value of μ' (i.e. the ratio of $4\pi Ms/H$ is constant), it can be seen that a low value of ΔH_k will give a higher magnetic Q. For the same μ' range a lower saturation magnetization will certainly reduce the demands on the bias power supply but care must be taken not to go too low in saturation magnetization because the Curie temperature of magnetic materials decreases with a decrease in saturation magnetization and will limit the maximum operating temperature of the ferrites.

V. AC BIASING CIRCUITS

With ac perpendicular biased ferrite tuners the magnetizing circuit becomes much more complicated [22]. In the parallel bias mode the magnetic path is a circumferential closed loop through the ferrite rings. In the perpendicular bias mode the magnetic path, as shown in figure 4, consists of a toroidal C-shaped return yoke, air gaps, metal walls and the ferrite rings.

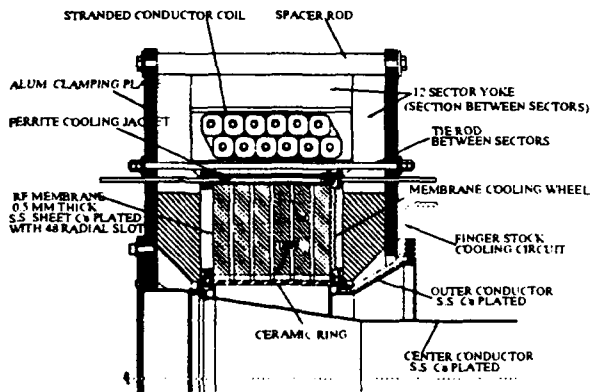


Figure 4. Cross-section view of the TRIUMF ac biased ferrite tuner.

It is desirable that all the components that make up the ferrite tuner be designed so that the induced eddy currents are as small as possible. A complete circular geometry represents a short circuit for the induced emf in the magnetic field so whenever such a geometry can be broken a significant reduction in eddy current losses can be achieved. In order to maintain vacuum integrity the inner circumference of the rf membrane wall forming a short circuit could not be broken. This made the reduction of eddy current losses in the rf membrane end walls very difficult. However, losses due to the eddy currents were minimized by extending 8 of the 48 radial slots in the rf membrane to its outer circumference and introducing 8 insulating breaks in the water cooling jacket in line with the 8 slots in the rf membrane wall. The complicated magnetizing circuit also makes it much more difficult to determine the magnetic parameters. The following formulae have been derived [23] for expressing the magnetic induction, magnetic field strength and ferrite permeability.

$$B_g = \frac{\mu_o NI + B_{sat} L_f}{L_g + L_f} \quad H_f = \frac{\mu_o NI - B_{sat} L_g}{\mu_o (L_f + L_g)}$$

$$\mu_f = \frac{\mu_o NI + B_{sat} L_f}{\mu_o NI - B_{sat} L_g}$$

where B_g is the magnetic induction, H_f the magnetic field strength in the ferrite, μ_f the permeability of the ferrite, μ_o the permeability of free space, NI the applied ampere turns, B_{sat} the saturation magnetic induction of the ferrite material, L_g the magnetic path length in the air gap (including non-magnetic materials) and L_f the magnetic path length in the ferrite. Although these equations look rather simple they are very useful in reaching a conceptual magnetics design for perpendicular biased ferrite tuners.

From an rf control point of view the effect of the eddy currents on the bandwidth response of the tuner assembly and the magnetic field produced by the eddy currents must be considered [24]. The eddy currents induced in the end membranes of the ferrite tuner produces a pole and the extra inductance from the slots in the membrane produces a zero. The magnetic field produced by the eddy currents tends to cancel the field produced from the coil, reducing the effect of the coil current on the resonant frequency. All these effects must be taken into consideration in designing the tuning control loops.

VI. DESIGN COMPARISONS

There are many versions of different designs [25],[26] and [27] which are too numerous to mention in this paper. However table 1 is a comparison of some of the parameters of tuner designs which are being developed or are in operation.

The tuner for PETRA II is very slow and does not have to deal with eddy current losses. However the TRIUMF Booster and the SSCL LEB are fast-cycling machines and require special attention to eddy current losses.

The TRIUMF Booster operates at a repetition rate five times greater than the SSCL LEB tuner making the eddy current problems more severe. It also has an accelerating time five times less than the SSCL LEB which tends to make df/dt and di/dt larger, putting a greater demand on the rf control system and the ferrite bias power supply. However the SSCL LEB tuner operates with a higher RF power density dissipated in the ferrite putting a greater demand on efficient cooling of the ferrite material. Figure 5 is a cross-sectional view of the different types of tuners that have been designed. The PETRA II and HERA type tuners shown in figure 5(c), are water cooled via the tuner walls and BeO disks sandwiched between the ferrite rings. The tuners are inductively coupled to the accelerating cavity and are off the beam axis. The ferrite disks are rather small with an outer diameter of 13 cm and an inner diameter of 7 cm. The TRIUMF tuner is water cooled in a similar manner but the ferrite rings are much larger with an outer diameter of 60 cm and an inner diameter of 30 cm.

Table 1. Comparison of different rf system requirements using perpendicular biased ferrite tuners

	TRIUMF Booster	SSCL LEB	PETRA 11 (AECL)
Min Frequency (MHz)	46.1	47.5	51.63
Max Frequency (MHz)	60.8	59.8	52.03
Peak RF at Gap (kV)	62.5	127.5	100
Accelerating Time (ms)	10	50	7e4
Repetition Rate (Hz)	50	10	0.01
Max RF df/dt (MHz/ms)	3.5	1.03	3e-5
Max Bias di/dt (A/ms)	311	39.2	1e-3
Max df/di (MHz/A)	0.03	0.065	----
Min Bias (AT)	8640	6437	----
Max Bias (AT)	31200	24632	----
Min H internal (AT/m)	19469	25956	40000
Max H internal (AT/m)	119292	136095	100000
Min H _{RF} (A/m)	358	670	----
Max H _{RF} (A/m)	656	3525	----
Ferrite Material	TT-G810	TT-G810	TT-G510
Min $\mu(r)$ of Ferrite	1.48	1.4	1.3
Max $\mu(r)$ of Ferrite	3.94	3.2	2.8
Pk power density (W/cc)	0.50	0.936	----
Avg power density (W/cc)	0.06	0.342	1.7
Cavity Q	2200-3600	2800-3420	----
Cavity R/Q	35	36	----

The INP alternative design for the SSCL LEB cavity is also water cooled in the same way, but only two BeO disks are used which are glued to the ferrite rings as shown in figure 5 (b). The outside surface of the outer ferrite rings and the edges of all of the ferrites at the outer circumference are glued to the tuner rf walls. The size of the ferrite rings are similar to the TRIUMF tuner but only 5 rings are used instead of 6 because of the slightly smaller tuning range. The in-house LEB tuner design is a direct liquid cooled tuner with the ferrite rings totally immersed in the cooling liquid. This requires an additional structure to contain the liquid since the rf tuner walls are slotted to reduce eddy current losses and increase the bandwidth response of the tuner. This design also requires two ceramic windows, one to contain the liquid and the other for the vacuum, as shown in figure 5(a). The tuners for TRIUMF and SSCL are on the beam axis as part of the accelerating cavity and therefore the magnetic fields on the beam axis produced by the ferrite biasing field must be compensated for by mounting two cavities back to back to get first order cancellation of the magnetic field effect on the beam axis.

VII. STATUS OF TUNERS

The PETRA II and HERA tuners are in operation at the DESY laboratory and although they are having rf problems with the cavities, the ferrite tuners themselves are performing very well. The TRIUMF Booster Cavity has operated in a test stand for several one or two hour intervals at a 50 Hz repetition rate to the full design voltage and

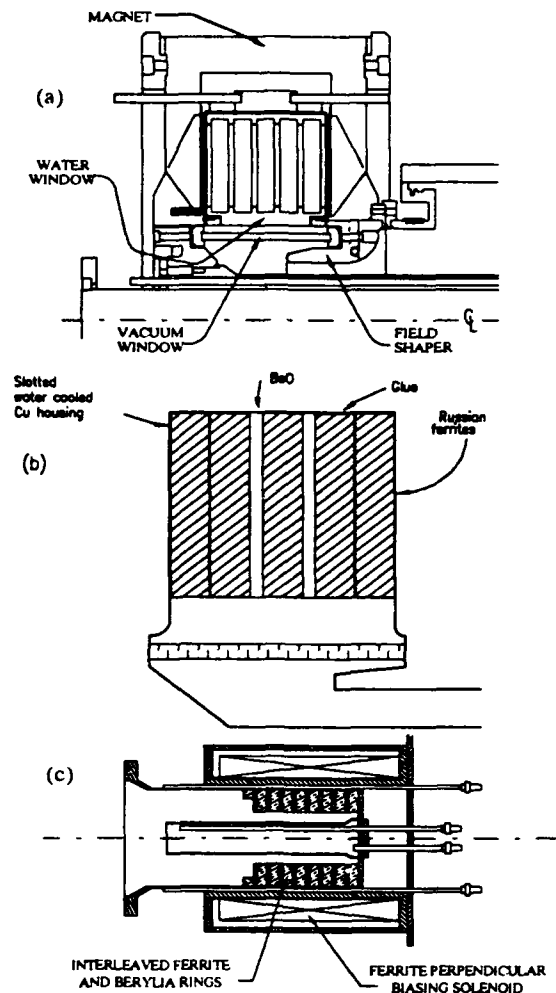


Figure 5. Cross-section view of ferrite tuners. (a) SSCL(LEB) direct water cooled tuner, (b) INP water/BeO cooled alternative for the LEB, (c) PETRA II & HERA type ferrite tuner. The TRIUMF tuner is already shown in figure 4.

frequency swing but with no tuning loops or regulating loops [9]. The ferrite tuner program at TRIUMF is now focussed on developing a control system and proper ferrite bias power supply to implement the above control loops. The INP designed conduction cooled tuner at SSCL was tested under dc bias conditions and maintained 70 kV at 5% duty cycle (100 msec) in 1 Mhz steps over the desired frequency range of 45 to 60 Mhz. However it failed after approximately 12 minutes at 80 kV gap voltage at 28% duty cycle. Their focuss now is on the assembly and test of the liquid cooled tuner [28].

VIII. CONCLUSIONS

The development work in the field of operating yttrium garnet ferrites in the region beyond the gyromagnetic resonance has progressed very well. To the best of the author's knowledge, TRIUMF was the first laboratory to operate a fast ac perpendicular biased yttrium garnet ferrite tuner over such a large frequency swing at high rf power

levels. Hopefully in the future, ac perpendicular biased tuners will become as popular as the now well established parallel NiZn ferrite tuners.

IX. ACKNOWLEDGEMENT

The author wishes to express his appreciation to his colleagues for their dedicated work in this field and for providing information for this paper. Ivan Enchevich, Amiya Mitra, Glenn Blaker and Ken Fong at TRIUMF; Roger Carlini Arch Thiessen, Rod Smythe and Carl Friedrichs who pioneered the work at Los Alamos; Mark DeJong and Ron Hutcheon at CRNL; Jimmy Rogers and Dale Coleman at SSCL; Eric Pivit and Bob Russell at ANT Bosch Telecom; Reinhold Hohbach at CERN; Valentin Paramonov at INR Moscow; Jim Griffin at Fermilab.

X. REFERENCES

- [1] Q. A. Kerns, "Ferrite Measurements for Synchrotron RF Accelerating System Design " IEEE Particle Accelerator Conf, Washington D.C., p185. (1965).
- [2] U. Bigliani et al., " The RF Accelerating System for the CERN PS Booster ", IEEE Particle Accelerator Conference, 1971
- [3] J. E. Griffin and G. Nicholls, " A Review of some Dynamic Loss Properties of NiZn Accelerator RF System Ferrite ", IEEE Trans. Nucl. Sci., NS-26, No. 3, 3965 (1979).
- [4] C. Friedrichs and G. Hulsey, " The Effect of RF Power Level on Resonant Frequency in the SSC LEB Test Tuner ", SSCL TECH NOTE, July 8 1992.
- [5] L. M. Earley et al., " A Resonantly Coupled Ferrite-Tuned Buncher Cavity for the Los Alamos Proton Storage Ring" 1982 IEEE MTT-S International Microwave symposium, pp. 246 June 1982.
- [6] W.R. Smythe et al., "RF Cavities with Transversely Biased Ferrite Tuning", IEEE Particle Accelerator Conference, Vancouver B.C., p 2951. (1985).
- [7] Carl C. Friedrichs et al., "Test Results of the Los Alamos Ferrite tuned RF Cavity", IEEE Particle Accelerator Conference, Washington D.C., p 1896. (1987).
- [8] G. R. Swain et al., " Progress on a Prototype Main Ring RF Cavity ", IEEE Particle Accelerator Conference Chicago, Ill, p177 (1989).
- [9] R.L. Poirier et al., "AC Bias Operation of the Perpendicular Biased Ferrite Tuner Cavity for the TRIUMF KAON Factory Booster Synchrotron", IEEE Particle Accelerator Conf., May 6-9, 1991, p2943.
- [10] D. Coleman, "Status of the LEB Prototype Cavity and Tuners", RF Workshop, SSCL, June 25-26, 1992.
- [11] J. Ferrell et al., " LEB Prototype Cavity/Tuner test Results ", RF Workshop held at TRIUMF, March 4-5th, 1993.
- [12] Ivanov Yu. D., "Particularities of Development of RF System for INR Kaon Project", Proceedings of the All Union Meeting on Particle Accelerators, Dubna, D-9-91-235, Vol. 1, p. 172-176, (in Russian).
- [13] L.W. Funk et al., "The 52 MHz RF System for PETRA II", European Particle Accelerator Conf, vol 2, p1102, Rome, June 7-11, 1988.
- [14] L.W. Funk et al., "52 MHz RF System for HERA", Ibid, p1099.
- [15] B.J.Evans et al., "The 1 MV 114 MHz Electron Accelerating System for the CERN PS", Particle Accelerator Conf., Washington D.C., March 16-19, 1987.
- [16] S. Martin, E. Pivit, S. Lenz " A Stripline Design of a Fast Ferrite Tuner (FFT)", European Particle Accelerator Conference, Nice, June 12-16, 1990, Vol 1, p985.
- [17] R.L. Poirier et al., "Parallel Bias vs Perpendicular Bias of a Ferrite Tuned Cavity for the TRIUMF KAON Factory Booster Ring", European Particle Accelerator Conference, vol 2, p1321, Rome, June 7-11, 1988.
- [18] W.R. Smythe, "Reducing Ferrite Tuner Power Loss by Bias Field Rotation", IEEE Trans. on Nucl. Sci, Vol. NS-30 No. 4 p. 2173, 1983.
- [19] TECH BRIEFS, " A basic Introduction to the Properties and Uses of Microwave Ferrimagnetic Materials", Published by TRANS- TECH INC, 5520 Adamstown Road, Adamstown, MD 21710
- [20] R.D. Carlini et al., " A High Q Perpendicular Biased Ferrite Tuned Cavity", Los Alamos Design Note, LA-9946-MS, UC-28, January 1984.
- [21] V. E. Shapiro and R. L. Poirier, " Magnetic Loss and Instabilities in Ferrite Garnet Tuned RF Cavities for Synchrotrons " TRI-DN-93-K-224, April 1993.
- [22] R.L. Poirier et al., " A Perpendicular AC Biased Ferrite Tuned Cavity for the TRIUMF KAON Booster Synchrotron", European Particle Accelerator Conference, Nice, p. 988, 1990.
- [23] I. E. Enchevich et al., " Magnetic Parameters of the Perpendicular Biased Ferrite Tuned Kaon Booster Cavity " TRI-DN-93-K225, April 1993
- [24] R.L. Poirier et al., " Performance of the AC Perpendicular Biased Ferrite Tuned Cavity for the TRIUMF KAON Factory Booster Synchrotron ", HEACC, Hamburg, Germany, July 20-24, 1992.
- [25] G. Schaffer, " New Design Concepts for Ferrite Tuned Low Energy Booster Cavities ", IEEE Particle Accelerator Conference, Vol.2 748 (1991).
- [26] G.Schaffer, " Improved Ferrite Biasing Scheme for Booster RF Cavities" European Particle Accelerator Conference, Berlin, 24-28 March 1992, p1234
- [27] R. Smythe, " A Ferrite Bonded to Copper Tuner for the LEB Cavity", TRIUMF-SSCL RF Workshop, Vancouver B.C. January 23 1992.
- [28] D. P. Coleman et al., " Status of the SSC LEB RF Cavity ", (these proceedings)

SRF Cavities for Future Applications

D. Proch

Deutsches Elektronen-Synchrotron DESY
Notkestraße 85, 2000 Hamburg 52, FRG

In this paper recent developments and future projects are discussed.

Abstract

Superconducting cavities are under operation or construction for acceleration of electrons and heavy ions at several laboratories. At present gradients around 5 MV/m, beam current up to 10 mA and operating experience exceeding 10,000 h are typical values. The advantage of superconducting RF is the high cw accelerating gradient, the low operating cost to establish RF voltage and the favourable cavity shape for a low loss factor. Ongoing progress in improving Niobium material, simplifying design and fabrication, understanding of performance limitations and investigating cures against field emission promise to increase the operating gradient at reduced investment costs. High beam current applications are investigated to take advantage of the small higher order mode impedance. The most challenging development is the use of superconducting cavities for a TeV Linear Collider (TESLA).

I. INTRODUCTION

For more than ten years superconducting cavities are under use in accelerators. At several laboratories different types of low β cavities operate under routine conditions to boost the energy of heavy ions. They produce cw gradients above the capability of normalconducting resonators and work reliable and cost efficient. This paper deals with cavities designed for $\beta = 1$ applications. A recent review of low β superconducting cavities is given in [1].

Superconducting cavities are used to accelerate electrons in linacs (Darmstadt, Frascati, HEPL, JAERI, Saclay) and in storage rings (CERN, DESY, KEK). A recirculating linac with 160 m of superconducting cavities is under construction at CEBAF [2]. In total about 800 m of superconducting resonators are under operation or construction. Several 10^5 cavity-hours of operating experience demonstrate the mature character of this technology. Details of the experience gained at different laboratories can be found in [3]. Improvements are expected in raising the operating gradient, lowering fabrication costs and in reliability of auxiliary equipment (input- and HOM couplers, windows, etc).

II. RECENT PROGRESS IN CAVITY TECHNOLOGY

A. Niobium material

Superconducting cavities are produced from sheet material by electron beam welding. The mass production of Niobium has a high standard in respect to the purity of the bulk and the cleanliness of the surface. Considerable improvements have been gained in raising the thermal conductivity by further refinement during the melting processes. As measure of the (temperature dependent) thermal conductivity the value of RRR (Residual Resistance Ratio: $R_{300K}/R_{4.2K}$) is often quoted. Nb material with $RRR = 300$ is available in large quantities, an improvement by a factor of ten compared to that ten years ago. A high thermal conductivity stabilizes excessive heat flux, thus increasing the breakdown value of a quench.

A further increase of the thermal conductivity can be reached by Ti solid state gettering. The completed cavity is fired for several hours around 1400 °C together with some Ti material [4]. This purification process is especially valuable to heal mistakes during fabrication (e.g. bad vacuum in the e^- -welder). A maximum value of RRR 1000 at a cavity has been reported recently [5].

B. Cleaning procedures

Field emission is the main effect in limiting the accelerating gradient in superconducting cavities. The low AC-loss of a superconductor makes the cavity sensitive to any additional loss mechanism. Another consequence of field emission is the dark current in linacs. Dust particles (metallic or dielectric) on the surface are the most likely source of field emission although other "irregularities" or intrinsic surface properties cannot be completely excluded. Cleaning of the surface by chemistry (BCP: Buffered Chemical Polish) and thorough rinsing is essential to suppress field emission. An automated chemical cleaning facility has been

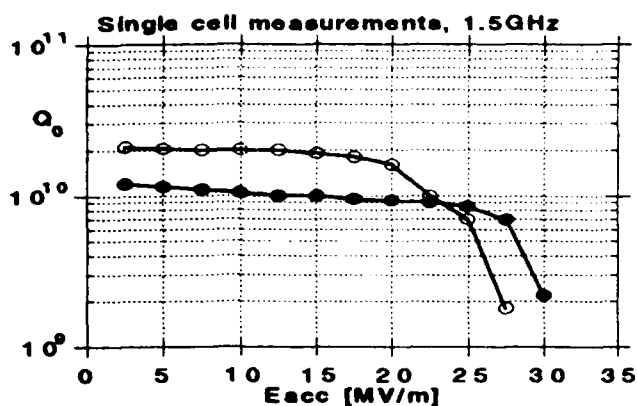


Figure 1: Measured results after application of thorough cleaning technique: (○) single cell (1.5 GHz) treated by automated chemistry [6], (●) single cell (1.5 GHz) treated by high pressure water rinsing [5]

established at Saclay [6]. The cavity undergoes a degreasing, BCP, rinsing and drying process under sealed off conditions. Several single cell cavities have been tested so far. Figure 1 shows a typical result: The cavity stays at a high Q value of 10^{10} and no field emission is seen until 20 MV/m. It has to be demonstrated that these exceptional properties can be gained at multicell cavities, too. A similar equipment is under construction at DESY to process 9 cell 1.3 GHz cavities [7].

Rinsing with high pressure water is another cleaning technique. First encouraging results on 350 MHz sputtered single cell cavities have been reported from CERN [8]. Recently single cell 1.5 GHz cavities have been treated several times at CEBAF [5]. Figure 1 shows a typical result: high gradients without field emission up to $E_{acc} = 25$ MV/m could be measured reproducibly.

C. High power processing (HPP)

In many experiments the onset of field emission is raised to some degree by operating the cavity at high field level (cw or pulsed). The time constant of a superconducting cavity and lack of RF power does not allow to reach higher fields under pulsed conditions in order to do more processing. At Cornell cavities have been HPP treated [10], similar test stands are under construction for 1.3 GHz 5 and 9 cell cavities at Cornell, FNAL, DESY. RF pulsed power (300 kW to 1 MW, 100 μ s to 1 ms) and adjustable input coupler allow to reach high fields before thermal runaway occurs. Figure 2 shows the properties of 9 cell cavities before and after HPP. Further processing was limited by the available RF power. Thermometry and surface studies on these cavities and special demountable single cell resonators (mushroom cavity) [11] have been carried out in parallel. It is concluded that dust particles as possible field emitters are heated during the RF pulse to such an extent that they evaporate in a short time. One attractive feature of HPP is the possibility to apply in situ processing in the linac (to do processing after a dust accident, e.g.).

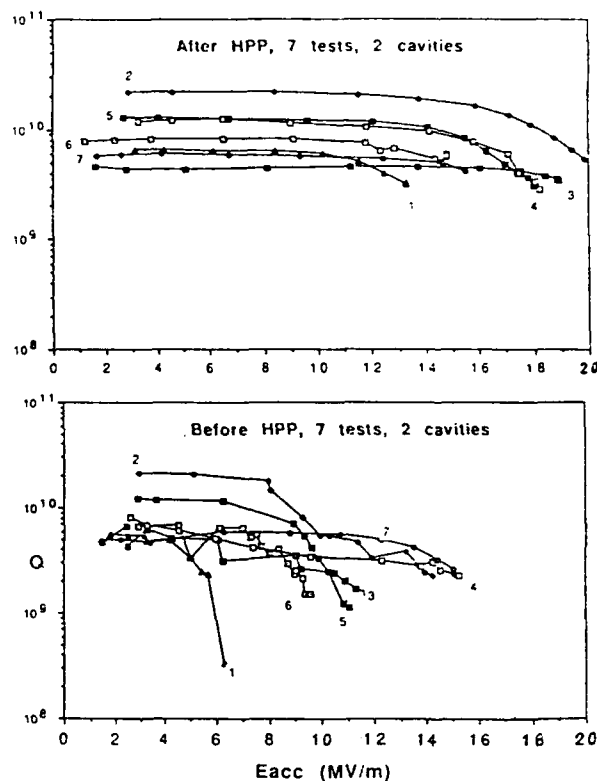


Figure 2: Measured results of 9 cell cavities (3 GHz) before and after HPP [10]

D. Nb sputter technology

At CERN the technology of Nb sputtering for cavities has been developed [12] and was transferred to industry. In total 150 4 cell cavities (350 MHz) are being produced at three companies [13]. The advantages of a sputtered cavity are

- cost saving of Nb material; this is especially true for large cavities at low frequencies,
- reduced surface resistance as compared to bulk Niobium and thus savings in operation costs,
- no need for a magnetic shielding against ambient field,
- stabilization of quench areas by the high thermal conductivity of Cu.

Figure 3 shows performance data of solid Nb and sputtered Nb cavities. It can be seen that sputtered cavities show enhanced Q values. The maximum fields E_{acc} reached are comparable.

E. Field emission

Ongoing experiments at Saclay [15] and Wuppertal [14] investigate the nature of field emission from Nb surfaces by scanning the surface with a needle under high DC voltage. At Saclay dust particles are produced on purpose and their field emission is characterized. An analysis of the large amount of data leads to the following conclusions [15]:

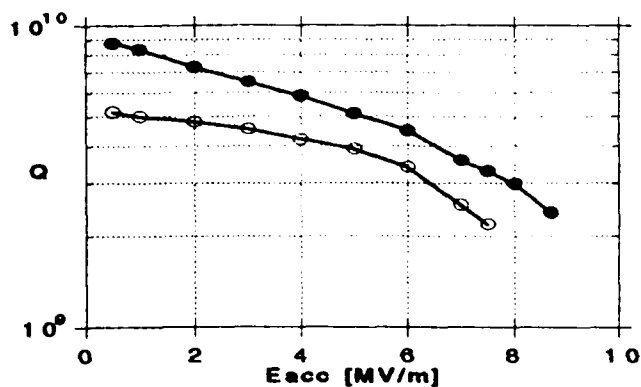


Figure 3: Measured result of 4 cell cavities (350 MHz) at acceptance test [13]: (o) average of 19 cavities made from solid Nb, (•) average of 14 cavities made by sputtered Nb on Cu

- field emitting sites could always be identified with dust particles,
- metallic dust particles emit at lower values of surface field than dielectric dust,
- there is no big influence of the underlying Nb_xO_y layer.

At Wuppertal clean Nb surfaces are investigated. Conclusions are [14]:

- most field emitting sites could not be identified with dust particles,
- very often the field emitting site is near to irregularities of the surface topology (etching pits?, etc.),
- after 1400°C UHV bake out surface fields up to 100 MV/m could be achieved reproducibly without field emission,
- field emitters seem to reappear after heating at 600 – 800°C.

It is not proven, however, that field emission under DC voltage or RF fields is determined by the same processes. RF heating of a loose particle on the surface might initiate a thermal field emission. The benefit of HPP and the obvious evaporation of earlier field emitters indicate that for surface fields in the range of 20 to 50 MV/m dust particles might play a dominant role.

III. NEW DEVELOPMENTS

A. RF power saving

Saving of RF installation and operating cost by use of superconducting cavities is not a new argument. In the past this issue was often underestimated. Doubts about the reliability of superconducting RF accelerating systems prevailed. Operating experience at CERN, DESY and

	U(MV)	$P_{klys.}$ (MW)	P_{ac} (MW)
NC	81.3	3.4	5.66
SC	55.7	0.25	0.42
Cryogenic		(500 W at 4.2 K)	0.15
Tot.	137.0		6.23
NC	137.0	9.65	16.05
SC	-	-	-
Tot.	137.0	9.65	16.05
Energy saving:			- 6.23
saving:			9.82
4000 h \times 9820 KW \times 0.15 DM/KWh = 5.9 MDM			

Table 1: Operating conditions of the RF system in HERA e^- in 1992 (upper part). The part below shows the corresponding expenditures without superconducting RF and gives with the resulting energy savings (NC: Normalconducting, SC: Superconducting)

KEK demonstrates, however, that superconducting cavities work stable and reliable after overcoming difficulties with auxiliary equipment (HOM couplers, cables and connectors, proper synchrotron radiation shielding etc.) which, of course, need adequate attention. It is difficult to give a formula of investment and operating cost saving which covers any case of application. It also varies in case of new or supplementary installation. The operating conditions of the HERA normal- and superconducting RF system is given as example. The upper part of table 1 shows the operational data during the 1992 run. The lower part gives calculated data for the same circumferential voltage but without superconducting cavities.

B. High current applications

There is an increasing demand for superconducting cavities in future accelerators with high beam currents:

- reduced cavity-beam interaction by the intrinsic low value of the HOM loss factor of a typical superconducting cavity shape (no nose cones, large iris hole, low operating frequency),
- high gradient, thus reducing the number of cells needed (benefit for length and HOM impedance),
- saving of RF installation and operating costs.

One example of a high current design is the single cell cavity (500 MHz) developed at Cornell for use in a B-factory (CESR B) [16]. The principle layout is presented in Figure 4. The challenge of this design is the HOM damping scheme and the power rating of the input coupler. The higher order modes are damped by a lossy plating at the outer end of the beam pipe. This broad band damping

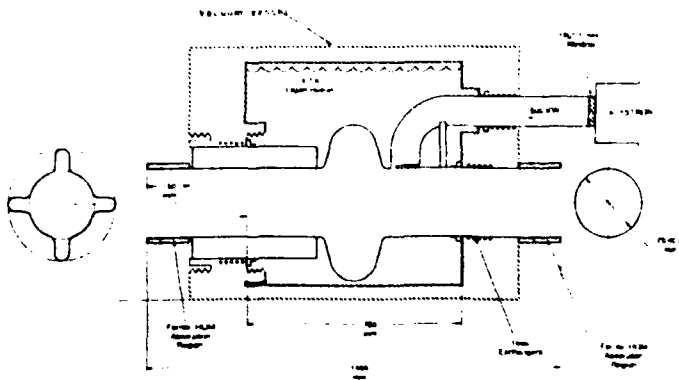


Figure 4: Principle layout of the single cell cavity (500 MHz) for use in a B-factory [17]

scheme is supplemented by a type of rigid waveguide to transfer HOM energy below the cut off frequency of the beam pipe, too. High damping with equivalent Q values of around 100 could be measured with Cu models [17]. The input coupler consists of a rectangular waveguide with a coupling slot towards the cavity. First cold measurements demonstrated $E_{acc} = 10$ MV/m at Q value of 2×10^9 [18].

C. High gradient applications

Superconducting cavities have been proposed for linear colliders since some time [19]. An international collaboration has been formed to work on the design of TESLA [20] (TeV Superconducting Linear Accelerator) and to build a test facility [7]. Superconducting cavities allow storage of RF energy in a very efficient way. As consequence long RF pulses can be established at low frequencies (large cavities). The benefits for a linear collider are:

- low cavity loss factor, thus very relaxed alignment and vibration tolerances,
- long bunch to bunch distance,
- moderate RF peak power demand.

In order to reduce the total costs of TESLA substantial improvements are needed as compared to the state of the art of today:

- the investment costs of about 400 kDM/1 active m (HERA SRF), have to be reduced by a factor of about four,
- the operating gradient has to be raised above 20 MV/m.

In the following paragraphs ongoing and planned R & D effort is described.

1) *Cavity:* The shape of the cavity has to be optimized in respect to

- low value of E_{peak}/E_{acc} to suppress field emission,

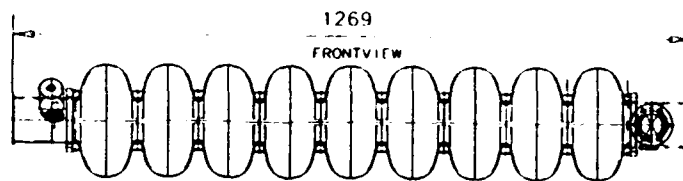


Figure 5: Cross section view of the TESLA 9 cell cavity (1.3 GHz) [7]

- low loss factors $K_{||}, K_{\perp}$ to reduce wake fields,
- high shunt impedance to reduce the refrigerator load,
- high cell to cell coupling to reduce tolerance sensitivity,
- low H_{peak}/E_{acc} values to suppress local heating,
- appropriate shaping to avoid trapped modes (with fields only in the middle cells thus having no damping by end cell couplers).

The elements of the cavity shape (iris \emptyset , curvature of equator and iris boundary) have different or even contradictory consequences to the above mentioned properties. There is no unique cavity design with the exception of a rounded (circular or elliptical) equator region to avoid multipacting. Figure 5 shows the shape of the TESLA cavity. A number of 9 cells per cavity has been chosen. More cells are desirable for economy reasons and might be possible. But sufficient HOM damping and avoiding trapped modes do not recommend an increase of this number without further detailed and time consuming studies. The low value of $E_{peak}/E_{acc} = 2$ is important to succeed in suppression of field emission.

The existence of trapped modes can be explained by a field flatness problem due to heavily detuned end cells (which are compensated for the fundamental mode). One way to overcome this problem is to detune the end cells even more but in an asymmetric way. Detuning one end cell sufficiently more than the other one results in a tilted field profile. As consequence one of the HOM couplers at each end of the cavity damps very effectively. Measurements on three 9 cell Cu cavities with these asymmetric end cells confirmed this idea [21]. It could be demonstrated, too, that the fundamental mode field pattern is undistorted by proper compensation.

At gradients of some 20 MV/m the cavity contour will be deformed and the resonant frequency is shifted by a noticeable value. This is due to the Lorentz force action of the electromagnetic fields to the surface currents. The iris region is bent inwards, the equator region is bent outwards, both result in a lower resonant frequency. Experimental values of 4 Hz per $(\text{MV/m})^2$ have been reported [18].

FEM analysis of the 1.3 GHz TESLA cavity (wall thickness 2.8 mm) predicts about 1000 Hz shift at 25 MV/m [22]. This value has to be compared to the loaded bandwidth of 330 Hz. The proposed stiffening ring at the iris (see Figure 5) reduces the effect to 300 Hz, further reduction requires expensive stiffening schemes at the equator. Modulation of frequency and phase of the RF drive during filling the cavity has been proposed to reduce amplitude and phase variation during the beam pulse to an acceptable value [23].

A naive interpretation of the Brillouin diagram concludes that the slope and thus the group velocity of the π -mode is zero. It was investigated whether the energy withdrawn by one bunch can be restored within the 1 μ s bunch distance in the 9 cell standing wave cavity. The transient behaviour of a coupled resonator model was investigated by applying the Laplace transformation [21]. The result is that the field can be reestablished in each cell but that there are amplitude oscillations at the 10^{-3} level. This can be understood as beating patterns of the non- π mode excitations. The distortion of the energy resolution of the beam by this statistic effect needs more investigation.

2) *Cryostat*: Most savings in the linac costs can be gained by substantial improvements of the cryostat design. The present layout shows warm-cold transitions every few cavities, expensive distribution boxes and separate transfer lines. In the TESLA design a cavity string of 1700 m is cooled by one 10 kW, 1.8 K refrigerator. A 300 mm \emptyset suction line pumps the whole string to 1.8 K and is the mechanical support of the cavities at the same time. One integrated valve box every 144 m supplies LHe to the cavities. The smallest assembly unit is 12 m long, containing 8 cavities and one superconducting quadrupole. Figure 6 shows a cross section of the present layout. Each cavity is surrounded by its own He-tank; couplers and flanges are placed outside the LHe. Slow tuning is done by a motor and gear box at cold temperatures. A coaxial input coupler penetrates the vacuum vessel every 1.3 m. The power rating of the coupler is 200 kW beam power (1.5 ms) and up to 1 MW, 500 μ s for in situ HPP.

ACKNOWLEDGEMENTS

The fruitful discussions and the fast exchange of experience with my colleagues from CEBAF, CERN, Cornell, DESY, Saclay and Wuppertal is gratefully acknowledged.

REFERENCES

- [1] W. Weingarten, *Proc. XVth International Conference on High Energy Accelerators*, page 678
- [2] A. Hutton, this conference
- [3] F. Dylla, this conference

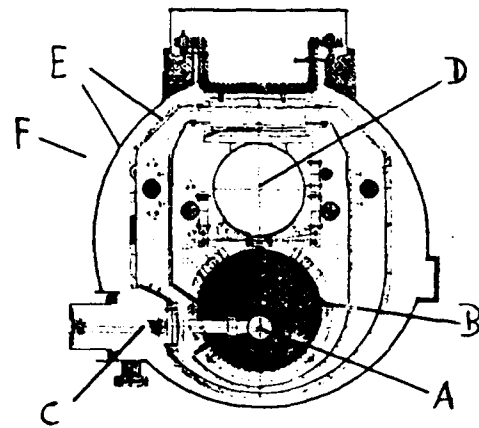


Figure 6: Cross section of the TESLA cryostat: A: cavity, B: LHe vessel, C: input coupler, D: suction line, E: radiation shields, F: vacuum vessel.

- [4] P. Kneisel, *Journal of Less Common Metals*, page 139, 179 (1988)
- [5] P. Kneisel, CEBAF private communication
- [6] B. Bonin, private communication
- [7] TESLA-Report 93-01 (Available from DESY)
- [8] Ph. Bernard et al., *Proc. of the 5th Workshop on RF Superconductivity*, Vol. 1, page 487 (1992)
- [9] H. Padamsee et al., *Proc. of the 1991 PAC*, page 2420
- [10] J.H. Graber, Cornell, *Dissertation*, May 1993
- [11] Q.S. Shu et al., Cornell CLNS-90/1005
- [12] C. Benvenuti, *ibid. ref. 8*, page 189
- [13] G. Cavallari et al., this conference
- [14] E. Mahner et al., *Applied Surface Science* 67 pp. 23 - 28 (1993)
- [15] M. Jimenez et al., DAPNIA/SEA 02/93, Saclay
- [16] CESR-B, "Conceptual Design", CLNS 91-1050
- [17] J. Kirchgessner et al., *Proc. of the 1992 Linac Conference*, Ottawa (1992)
- [18] H. Padamsee, private communication
- [19] M. Tigner, *Nuovo Cimento* 37 (1965) page 1228
- [20] H. Padamsee, editor. *Proc. of the 1st TESLA Workshop*, CLNS Report No. 90-1029 (1990)
- [21] J. Sekutowicz, DESY, private communication
- [22] H. Kaiser, DESY, private communication
- [23] H. Henke, B. Littmann TESLA Report 93-12 (Available from DESY)

Preparation and Testing of a Superconducting Cavity for CESR-B*

D. Moffat, P. Barnes, J. Kirchgessner, H. Padamsee, J. Sears
Laboratory of Nuclear Studies, Cornell University, Ithaca, NY 14853-5001

Abstract

A 500 MHz niobium cavity was delivered to Cornell in January, 1992.[†] The key features of the cavity design are a large, i.e. 24 cm diameter, circular beam tube which allows all but two of the higher-order modes (HOM's) to propagate away from the cavity, a "fluted" beam tube which allows the remaining HOM's to propagate, and a waveguide fundamental input coupler [1]. The cavity was tested vertically in the as-received condition and almost achieved the design criteria. After this initial test the cavity was etched, rinsed and dried, and tested again. Modest helium processing enabled the cavity to exceed the design criteria of $E_{acc} = 10$ MeV/m and $Q_0 = 10^9$. No indication of multipacting was observed in any of the tests. Several warm-up/cool-down cycles have been made. A cool-down procedure which avoids the "Q-virus" problem has been identified.

I. INTRODUCTION

The first Cornell B-factory cavity is shown in Figure 1. The large beam tubes serve as higher order mode (HOM) couplers, allowing the HOM's to propagate to the HOM loads which are outside the cryostat [2]. The CESR-B design calls for each cavity to operate at an accelerating gradient of 10 MeV/m (25 MV/m peak surface field). To provide the necessary acceleration in CESR-B, 400 kW of RF power must flow through a room temperature window [3] and through the coupler. A waveguide, rather than coaxial, coupler was chosen because of the lower power densities and the relative ease of cooling the surfaces subjected to high fields [1].

Several vertical tests have been made to date. Two adjustable coaxial couplers were available for power input for these tests; both could achieve critical coupling. The coupler most often used was the one in the resonant waveguide shorting hat. Two more fixed couplers were used to monitor the cavity fields. Four titanium rods attached to the endplates braced the cavity against collapse while it was evacuated. Several thermometers were affixed to the cavity and X-radiation was monitored directly above the dewar. Our standard cool-down procedure took the cavity from room temperature to 4.2K in a couple of hours. After several tests with this cool-down procedure, several slower cool-downs were tried in an attempt to identify our susceptibility to the "Q-virus". All tests were performed at 4.2K.

* Work supported by the NSF and the US-Japan collaboration

[†] The cavity was fabricated by Dornier GmbH. The RRR of the niobium used was ~240.

0660492-028

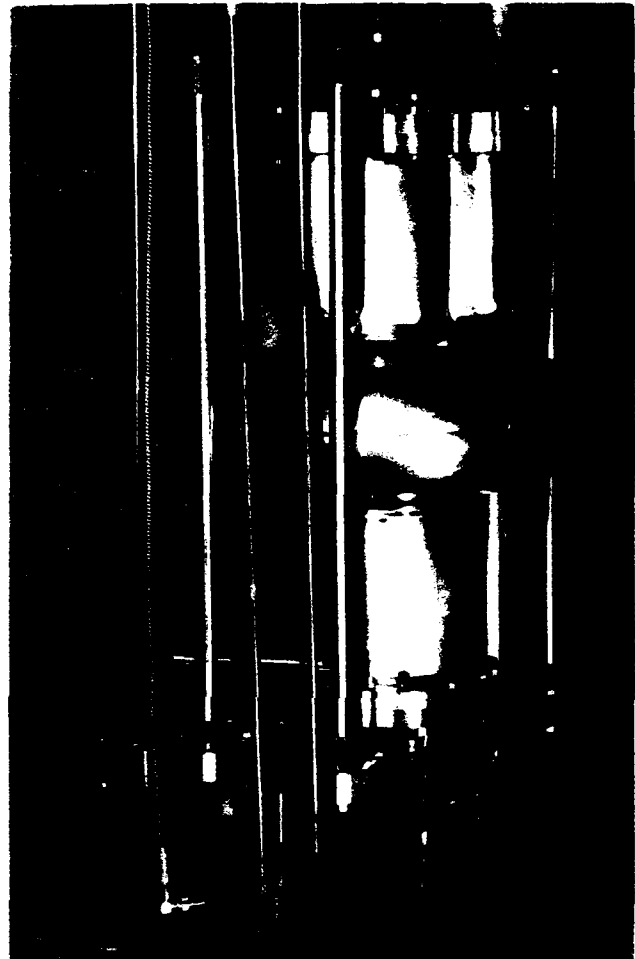


Figure 1. The 500 MHz cavity prepared for vertical testing.

II. TESTING WITH A FAST COOL-DOWN

The cavity received its initial chemical treatments at Dornier. Approximately 90 μm of the cavity surface was removed from the component parts prior to final welding. After welding, an additional 15 μm was removed from the inside surface using 112 BCP at 15-20°C. The cavity was vacuum dried, sealed in a class 100,000 room with ambient air, and shipped to Cornell. Upon receipt at Cornell the cavity was rinsed with methanol sprayed at ~40 psi, dried in a class 100 clean room and sealed for testing.

The results of the first test are shown in Figure 2. No helium processing was used, although a small cold leak developed during testing. It is remarkable that the performance of the cavity was so close to the design goal. Processable breakdown began at 2 MeV/m. This was later found to be

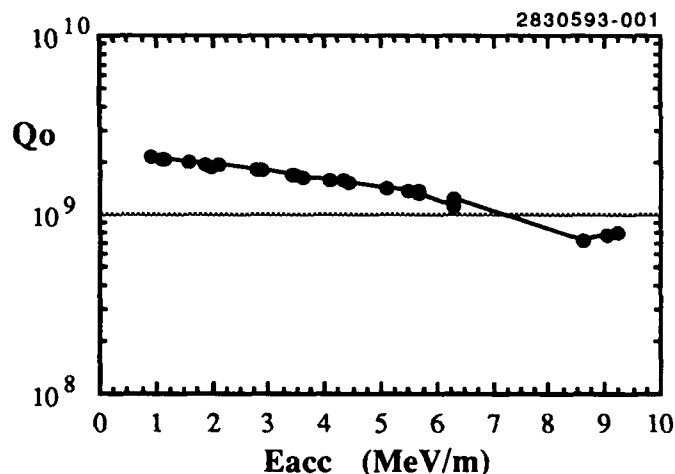


Figure 2. Q_0 vs E_{acc} for the first cavity test. The cavity received only a methanol rinse following shipment.

caused by field emission heating of the coupler tongue. The coupler tongue had been hollowed to admit liquid helium for cooling. When tested vertically, heating of the tongue caused a gas pocket to form. The addition of a snorkel allowed the gas to vent and this problem was eliminated in all subsequent tests.

After the first test it was found that the waveguide indium seal was leaking. This was because the flanges were 0.030"-0.060" (0.76-1.52 mm) thinner than specified and the flange clamps, therefore, could not apply sufficient pressure to compress the indium (shims were used in subsequent tests). The cavity was then disassembled for etching. Before etching, the external Q of the coupler was measured to be 1.75×10^5 . The design value was 2×10^5 .

The cavity was etched with 112 BCP. Four etch cycles of four minutes each were used to remove a total of $\sim 32 \mu\text{m}$. (Only the inside of the cavity is etched with our new etching facility.) Unfortunately, our acid thermometry was not properly calibrated so the temperature of the acid is unknown.

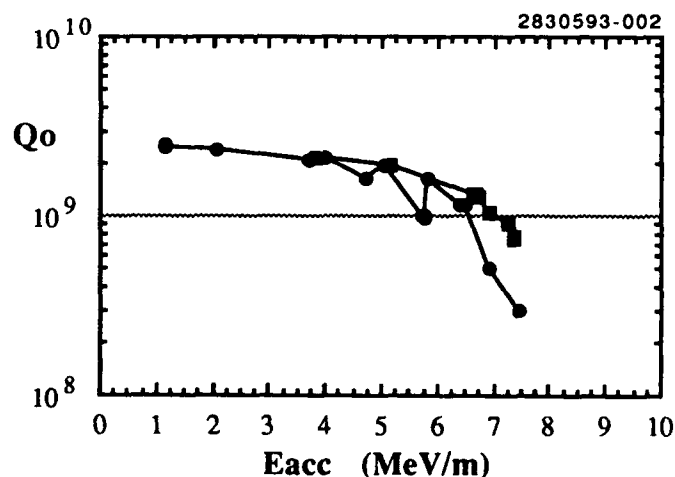


Figure 3. Q_0 vs E_{acc} for the cavity test after etching. RF processing only. The field was increased twice.

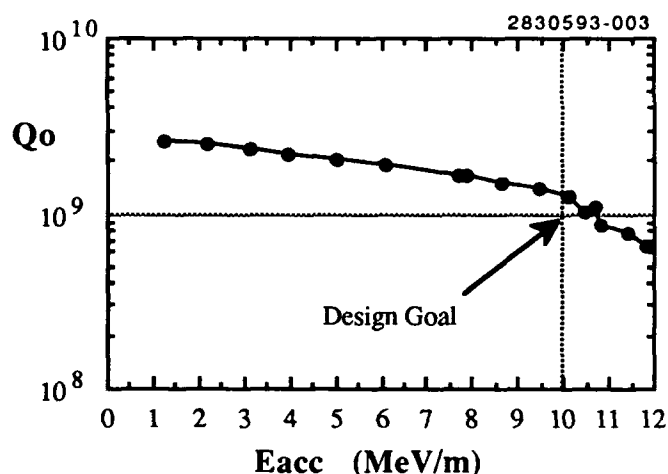


Figure 4. Q_0 vs E_{acc} after modest helium processing.

The cavity performed quite well after this acid treatment. Figure 3 shows the efficacy of RF processing. After two attempts at RF processing, a small amount of helium was admitted to the cavity. Helium processing enabled us to exceed the design criteria, as shown in Figure 4. The effect of radiation pressure on the CW resonance frequency, f , is shown in Figure 5. The input coupling was fixed at high fields at $Q_{ext} \approx 10^9$. As the field was slowly lowered data were taken, portraying a parabolic dependence of f on E_{acc} . The field was increased again and then immediately lowered, yielding the two filled data points in Figure 5. The change in f shown in Figure 5 corresponds to a pressure change of less than 2 torr.

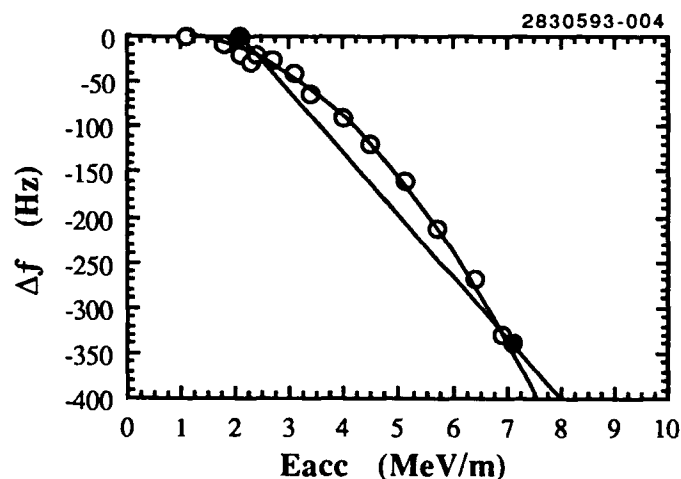


Figure 5. Effect of radiation pressure on the CW resonance frequency. The input coupling was fixed at $Q_{ext} = 10^9$.

III. EFFECT OF COOL-DOWN RATE

In the RF superconductivity literature there have been numerous references to the "Q-virus" (see [4] for the most recent summary of outbreaks and causes). The indication that a cavity is "infected" with this "virus" is that cooling the cavity quickly yields high Q_0 values, while slow cooling

yields Q values an order of magnitude lower. A series of tests was performed in order to understand the extent to which this cavity was affected.

With the cavity installed in its cryostat, an overall cool-down rate of $\sim 10\text{K/hr}$ is anticipated. For deleterious Q effects, the sensitive temperature region during cooling is between 170K and 77K. Cooling at 10K/hr would keep the cavity in this danger zone for 10 hours. A uniform cool-down was approximated by quickly cooling the cavity to a temperature in the danger zone, holding it at that temperature for ~ 10 hours, and then quickly cooling it to 4.2K.

Our first attempt involved holding the cavity at $\sim 130\text{K}$. It was found that the low field Q_0 had degraded to 10^9 .

Because of the uncertainty of the acid temperature during the preceeding etch, it was decided to etch the cavity again, this time paying particular attention to the acid temperature. A total of $\sim 6\text{ }\mu\text{m}$ was removed in two cycles. The acid temperature never exceeded 17°C .

The cooling curves of the next three cool-down tests are shown in Figure 6. Type E thermocouples were attached to the top and bottom flanges of the cavity for temperature measurement. The tests were performed in the following order: slow cool with a 130K hold; fast cool; slow cool with a 160K hold. The cavity was warmed to room temperature between each test. It should be noted that during the fast cool-down the temperature difference between the top and bottom flanges could be as high as 140K.

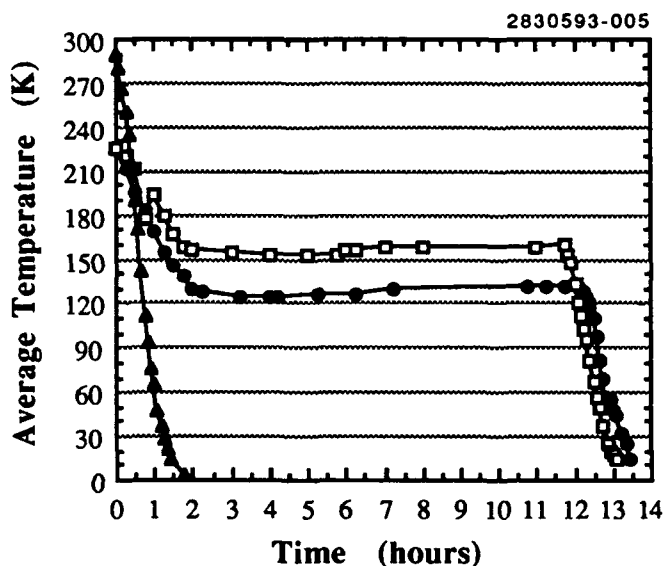


Figure 6. Average temperature of the cavity during the slow cool-down tests.

The Q_0 vs E_{acc} curves are shown in Figure 7. The effect of the "Q-virus" was readily apparent in the test with the 130K hold and, therefore, the test was cut short. Following the fast cool, the Q_0 curve was comparable with that in Figure 3. Helium processing was not tried because the cavity performance was very close to the design goal. Reaching this goal will require only modest helium processing. The

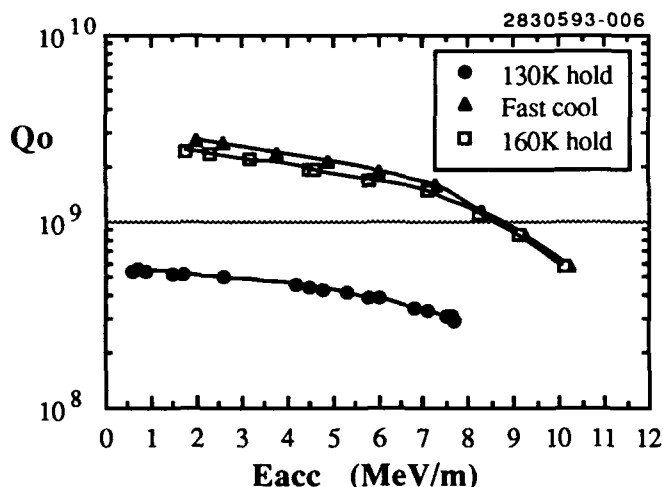


Figure 7. Q_0 vs E_{acc} for the cool-downs shown in Figure 6.

experience at DESY is that 150K is the critical temperature for the "Q-virus" [5]. We left a margin for error and held the cavity at 160K for the last test. As shown in Figure 7, the cavity performance was equivalent to that after a fast cool.

IV. SUMMARY

The Cornell B-factory cavity performed quite well "right out of the box." After brief helium processing the cavity exceeded the design goals of $Q_0 = 10^9$ at $E_{\text{acc}} = 10\text{ MeV/m}$.

Tests of sensitivity to cool-down rate showed that a slow cool-down with a hold at 130K lowered the Q_0 values at all fields by a factor of ~ 6 . Holding at 160K did not adversely affect cavity performance. For the future beam line tests the cryostat will be cooled slowly to 160K and then cooled quickly to 4.2K. Helium processing is not anticipated because of the availability of RF power sufficient to process the cavity.

V. REFERENCES

- [1] H. Padamsee, et al., "Accelerating Cavity Development for the Cornell B-Factor, CESR-B", *Conference Record of the 1991 Particle Accelerator Conference*, Vol. 2, pp. 786-788, San Francisco, CA, May 1991
- [2] D. Moffat, et al., "Design and Fabrication of a Ferrite-lined HOM Load for CESR-B", paper Sa76 in *Proceedings of the 1993 Particle Accelerator Conference*, Washington, DC, May 1993
- [3] D. Metzger, et al., "Test Results and Design Considerations for a 500-MHz, 500-kW Vacuum Window for CESR-B", paper Sb110 in *Proceedings of the 1993 Particle Accelerator Conference*, Washington, DC, May 1993
- [4] B. Bonin and R. R  th, "Q degradation of Niobium cavities due to Hydrogen contamination", *Proceedings of the 5th Workshop on RF Superconductivity*, Vol. 1, pp. 210-244, DESY, Hamburg, Germany, August 1991. Also published in *Particle Accelerators*, Vol. 40, 1992
- [5] A. Matheisen, et al., "Laboratory Activities on s.c. Cavities at DESY", *Proceedings of the 5th Workshop on RF Superconductivity*, Vol. 1, pp. 44-53, DESY, Hamburg, Germany, August 1991.

High Power Operation of a Single-cell 352 MHz Cavity for the Advanced Photon Source (APS) *

J. F. Bridges, Y. W. Kang, R. L. Kustom, K. Prindahl
Advanced Photon Source
Argonne National Laboratory
Argonne, IL 60439 USA

Abstract

The single-cell 352 MHz cavity for the APS 7-GeV positron storage ring has been tested up to one Megavolt gap voltage at 100 kW. Thermal measurements were recorded to ensure adequate cooling. Higher Order Modes were damped using both voltage and current coupled dampers. The dampers have less than 2% the fundamental mode. Stagger tuning of the higher modes has been done by slightly varying the length of each cavity to shift them apart in order to minimize their effect on multi-bunch instabilities.

I. INTRODUCTION

The prototype all-copper cavity for the APS storage ring has been powered to the nominal powers of 32 kW (7 GeV), 50 kW (7.5 GeV) and the engineering design goal of 100 kW. For the measured shunt resistance of 5 Megohms, 100 kW are required for one Mega.

The accelerating cavity shape is basically spherical with a rounded, slightly reentrant beam pipe (see Figure 1). This shape is derived from the program URNEL, and is optimized for highest shunt resistance or maximum voltage per unit power.

The cavity is made from three pieces of solid copper bolted together with an O-ring vacuum seal. To do rf testing, a vacuum of about 10^{-8} Torr without rf power is adequate. With this arrangement, the cavity could be taken apart and the inside shape modified for frequency tuning and/or shunt impedance adjustments. The APS cavities will be e-beam welded at these joints to have a vacuum of 10^{-10} for storing positrons.

The production cavities for the storage ring will be built with a spread in length along the beam axis by 0.3 mm per cavity or ± 3 mm over the twenty cavities. This will spread the higher order modes and thereby reduce cavity-bunch instabilities [1]. The fundamental (accelerating) frequency is not shifted to first order since the increased magnetic field stored in the longer volume is cancelled by the reduction in stored electric energy at accelerating gap. The fundamental mode is re-tuned by the piston tuner to the

correct frequency. This tuner has less effect on the higher order modes.

After the higher order modes (HOM) were measured using low power of about one milliwatt [2], the cavity was evacuated and high power was applied to vacuum condition the surfaces. The cavity was not baked in a vacuum oven during fabrication as is the usual procedure.

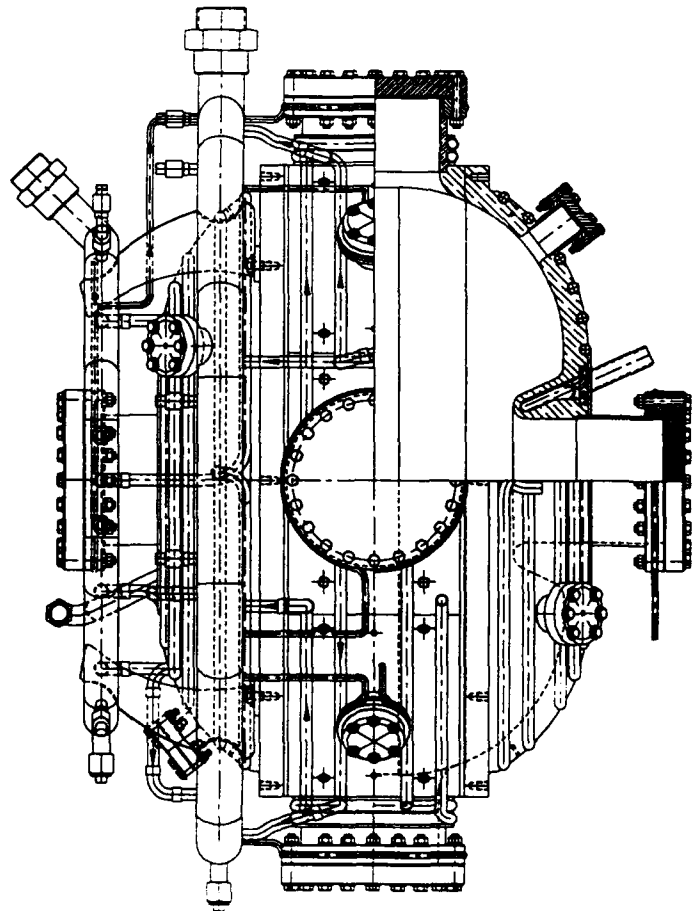


Figure 1. Storage Ring Cavity

*Work supported by the U. S. Department of Energy, Office of Basic Sciences, under the Contract W-31-109-ENG-38.

II. INITIAL HIGH POWER OPERATION

Since the cavity was bought as three machined copper pieces, we chemically cleaned the inside surfaces and stored them in dry nitrogen before assembly. We have no ovens for vacuum baking and so relied only on rf heating of the surfaces for outgassing.

Much outgassing occurred between 3 and 15 kW, but above 20 kW, mostly small glowing copper points and intermittent spark flashes were seen. The vacuum before applying rf power was about 3×10^{-7} T, but after several hours of running even at powers around 10 kW, it dropped into the 10^{-8} range. During rf conditioning, the vacuum was kept at about 5×10^{-7} , with excursions up to 10^{-6} each time the power level was increased. This would fall back to 5×10^{-7} in about a half-hour.

We ran the cavity intermittantly over a three-month period before reaching the 100 kW power goal. We had the usual occasional problems with various equipment comprising the test stand. But we did have an on-going problem during this time with breaking the ceramic vacuum seal located in the waveguide.

III. DRIVE LOOP

We were using a coupling loop developed at CERN and used in the 5-cell cavities at LEP and also at ESRF. So this is a proven design, well tested at both labs. There is a cylindrical ceramic vacuum seal around the waveguide-to-post transition which is connected to a short length of coax, just long enough to reach to the inside wall of the cavity at which a copper bar forms a loop between the center and outer conductors.

During the conditioning, three of the ceramic vacuum windows broke; two at power levels below 20 kW and one at the 100 kW level. The first two we attributed to a combination of outgassing/arcing and mechanical stress from a misaligned waveguide flange which bolts to the loop. The third was used for several weeks (probably 20 to 30 hours total running time) at the 60 kW level and so we concluded no more ceramic problems would be encountered. However, after powering the cavity at 80 kW (see Figure 2 for the computer control diagram of typical operation) for about an hour and at 100 kW for 15 minutes, the ceramic did break.

Similar ceramic failures have occurred elsewhere (see, for example [3]). We were under a time constraint at that time, and knowingly were pushing to reach the design goal of one Megavolt on the accelerating gap. I estimate the total time the cavity was actually powered before it reached stable operation was over 100 hours. As a comparison, the 5-cell LEP cavities for the Booster Synchrotron take about 12 hours of conditioning to reach 20 kW, with only a few hours more to reach 100 kW operation. Presumably this fast rf conditioning is due to the 150 degree C vacuum treatment at the factory.

Figure 2. Control Screen Showing 90.4 kW Power Into Cavity (numbers at left margin)

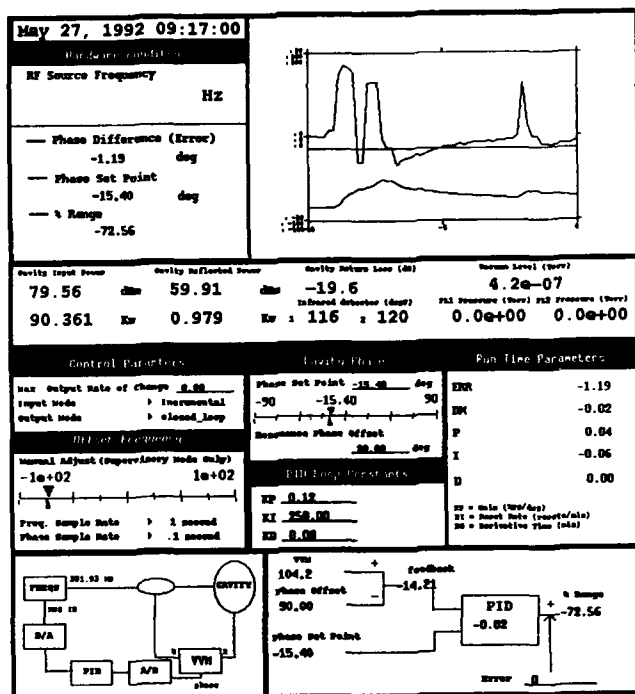
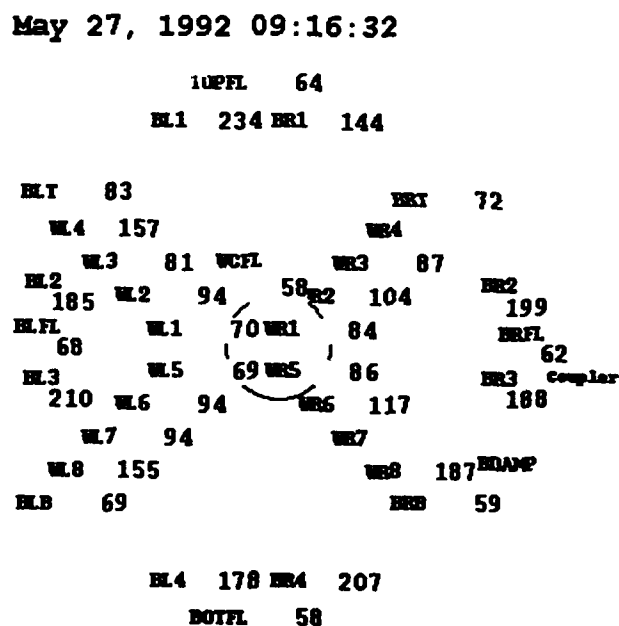


Figure 3. Cavity Temperatures (degrees F)



After consulting with both the designers and users [4] of these loop couplers, we concluded we conditioned the cavity too fast and at vacuum levels higher than appropriate. We then used a fourth loop and powered the cavity keeping the vacuum at 2×10^{-7} , with the vacuum trip level set at 10^{-6} . We also added more uniform air cooling for the ceramic and monitored the ceramic heating using two infra-red temperature meters, one on each side, to convince ourselves that the cooling was uniform. Again, we emphasize that this prototype cavity was not vacuum baked at 150°C and we used only rf power for conditioning the surfaces.

IV. Long-term High Power Operation

We then powered the cavity for about 1000 hours over the next few months, mostly between 80 and 100 kW power levels. As other components were added to or removed from the cavity, the re-conditioning time was typically 4 to 6 hours after vacuum pumping started. For starting with the vacuum intact, a half-hour was typical.

For storage ring operation, there will be four groups of four cavities, each group powered by one one-Megawatt klystron. For typical operation at 7 GeV (beam current of 300 mA) and 9.5 MV per turn, each cavity will operate at just under 600 kV/32 kW; for 7.5 GeV (but beam reduced to 200 mA) and 12 MV per turn, each cavity will run at 750 kV/50 kW. These are the two specified cavity operating points in the APS Design Specification.

If one group is not operational, only 3 MW will be available. In this case, by increasing the gap voltage to 1 MV, the 12 MV per turn and 200 mA beam current can still be maintained.

Figure 4. Beam Current vs. Cavities Available

Harmonic number	1296	
RF frequency	351.929	MHz
Peak voltage per turn	9.500	MV
Cavity parameters:		
Max voltage (estimated)	1.00	MV
Shunt resistance	5.60	MΩ
Max power	89.2	kW
Quality Factor, Q	48.6	10^3
Operating values:		
	7.5 GeV	7.5 GeV
	<u>200 mA</u>	<u>212 mA</u>
Number of cavities	16	12
Voltage per turn	12.0	12.0
Voltage per cavity	750.0	1000.0
Power per cavity	50.2	89.2
Total power	804.0	1070.4
Beam power per cavity	113.7	159.3
Sum	183.9	248.5
Q (loaded)	16.0	15.37
Bandwidth (loaded)	22.1	23.0
Power lost (source to cavity)	17.4	18.0
Source power	2.90	3.00

V. THERMAL STUDIES

Greater than expected temperatures, especially at the large ports of the perimeter, were evident. At 100 kW input, the maximum temperature of the copper was 181°F , at 75 kW, a maximum of 165°F . Thermocouples near the nose cone recorded the lowest temperatures (82°F and 81°F respectively) with a positive gradient radially outward to the high temperatures at the ports. (See Figure 3.) The 75 kW case has been studied analytically, with results indicating a maximum of 28°C ($\approx 82^\circ\text{F}$) above the cooling water temperature, or approximately 38°C ($\approx 100^\circ\text{F}$), can be expected. These high temperatures were attributed to poor brazing of cooling tubes and port heating due to greater resistivity of stainless steel.

We decided that nose cone cooling was sufficient, but port cooling was not sufficient. Production cavities will incorporate greater water cooling surface area, improved brazing techniques, and copper plating of the inside surfaces of the stainless steel port flanges. Supplemental cooling of vacuum flanges was added. The final cooling scheme is shown in Figure 1.

VI. FUTURE PLANS

The first production cavity will be factory tested at Siemens for frequency in June, then will be assembled, baked, and leak-checked with delivery scheduled for mid-July. After full power testing at Argonne, we will decide if we want any modifications and then the full production run of twenty will start in the fall. The last cavities are to be delivered in June, 1994.

References

- [1] L. Emery, "Coupled-Bunch Instabilities in the APS Ring," in *Proceedings of the 1991 Particle Accelerator Conference*, San Francisco, CA, May 1991.
- [2] J. Bridges, J. Cook, R. Kustom, J. Song, "Measurements on Prototype Cavities (352 MHz) for the Advanced Photon Source (APS)," in *Proceedings of the 1991 IEEE Particle Accelerator Conference*, San Francisco, CA, May 1991, pp.693-695.
- [3] Akemoto, "High-Power Input Coupler with a Cylindrical Alumina Window" in *Proc. 1991 IEEE PACSF* May 91.
- [4] Private communication with G. Geschouke of CERN and J. Jacob of ESRF.

Development of Crab Cavity for CESR-B*

K. Akai**, J. Kirchgessner, D. Moffat, H. Padamsee, J. Sears and M. Tigner

Laboratory of Nuclear Studies, Cornell University
Ithaca, NY 14853 U.S.A.

Abstract

In order to realize the crab crossing scheme desired for B-factories, we designed single cell superconducting crab cavities operating in TM110 mode. A coaxial beam pipe was attached to damp dangerous monopole and dipole parasitic modes. We designed two kinds of cell shape depending on the method to cure unwanted polarization of TM110 mode; one is a round cell which will be slightly polarized and the other is an extremely polarized (squashed) cell. We made one-third scale copper/aluminum model cavities to check damping property. Q values of all dangerous monopole and dipole modes are damped to less than the order of 100, as was expected by calculations. We also measured one-third scale niobium model cavity in liquid helium. Design goals of field and Q value to provide necessary kick voltage for CESR-B were achieved successfully. These results show that our design of the crab cavity is promising to realize the crab crossing.

I. INTRODUCTION

In order to attain the luminosity of $3 \times 10^{33} - 10^{34} \text{ cm}^{-2} \text{ s}^{-1}$ required for B-factories, a finite angle crossing scheme is the most desirable method to avoid parasitic collisions and to minimize synchrotron radiation generated near interaction point (IP). Experiences concerning storage rings with a finite angle crossing have shown, however, lower beam-beam limits due to synchrotron-betatron coupling resonances [1,2]. In order to overcome this problem, the crab crossing scheme has been invented by Palmer [3] for linear colliders and by Oide and Yokoya [4] for storage rings. In the crab crossing scheme, bunches are tilted by a time dependent transverse kick in RF deflectors located before the IP in each ring and thereby collide essentially head-on. This tilt is kicked back to the original orientation in another deflector after the IP.

Necessary deflecting voltages for the 8 GeV (HER) and 3.5 GeV (LER) rings of CESR-B are 1.8 MV and 0.8 MV, respectively [5]. Multibunch instabilities should be taken care of also in the crab cavities, as well as in accelerating cavities for B-factories. Q values of dangerous parasitic modes should be sufficiently lowered to typically the order of 100. Since the deflecting mode used for the crabbing is not the lowest frequency mode, special attention is required for damping parasitic modes, as will be described in a later section.

We designed single cell superconducting crab cavities to realize the crab crossing for CESR-B. Since we previously

*Supported by the National Science Foundation with supplementary support from the US-Japan collaboration.

** present address: KEK, 1-1, Oho, Tsukuba, Ibaraki, 305 Japan

reported our design of crab cavity in detail in ref. [6], here we will give a brief summary of the design in section II. Results of measurements of model cavities are described in section III.

II. DESIGN OF THE CRAB CAVITY

Our design is to operate the cavity in TM110 mode since this mode has high transverse shunt impedance, R^*/Q . As for the damping of higher order modes, we adopted the beam pipe coupling scheme. In this scheme, higher order modes propagate in the beam pipe and are absorbed by some absorbing material attached on the beam pipe. However, since the TM110 is not the lowest frequency mode, there are some modes whose frequency is lower than or about the same as this mode. Four unwanted parasitic modes remain trapped in the cavity region with high Q even if a beam pipe with a large radius is attached. Those are TM010 monopole mode, two polarizations of TE111 dipole mode and unwanted polarization of TM110 mode.

In order to solve this problem we attached a coaxial beam pipe at one side of the cavity cell (Figure 1). In a coaxial transmission line there is no cut-off frequency for TEM mode waves, but there is a cut-off frequency for dipole modes. By attaching a coaxial beam pipe to the crab cavity, all monopole modes in the cavity can couple to the coaxial beam pipe as a TEM mode wave and propagate. In addition, all dipole modes in the cavity can couple to the coaxial beam pipe as a dipole mode wave and propagate if the frequency is higher than the cut-off. By designing a cell shape such that $f(\text{TE111}) > f(\text{cut off}) > f(\text{TM110})$, it is possible to make all monopole and dipole modes except the TM110 mode in the cavity to propagate down the coaxial beam pipe. We chose the outer and inner radii so that it has a cut-off frequency of 600 MHz, which makes the attenuation for the crabbing mode 60 dB/m.

One dipole parasitic mode still left trapped in the cavity is the unwanted polarization of TM110 mode. Since this mode has high transverse shunt impedance, it has to be cured. We designed two types of cell shape depending on the method to cure this mode; one is a round cell that will be slightly polarized and the other is an extremely polarized cell ("squashed cell"). In the squashed cell by having a cross section of the cavity cell to be an ellipse or race-track shape with a large eccentricity, we can make the frequency of the unwanted TM110 mode to be above the cut-off of the dipole mode wave in the coaxial beam pipe. Computational studies to optimize the cell shape of the round cell and the squashed cell have been carried out. Finally selected design of the squashed cell is shown in Figure 2.

Asymmetry due to machining inaccuracies or misalignment of the coaxial beam pipe may cause a part of energy of the crabbing mode to couple to the coaxial beam pipe as a TEM mode wave, which propagates down the coaxial beam pipe without attenuation and increases the power dissipation at the absorber. In order to avoid this, a notch filter is attached on the coaxial beam pipe to reject the TEM-coupled crabbing mode back to the cavity.

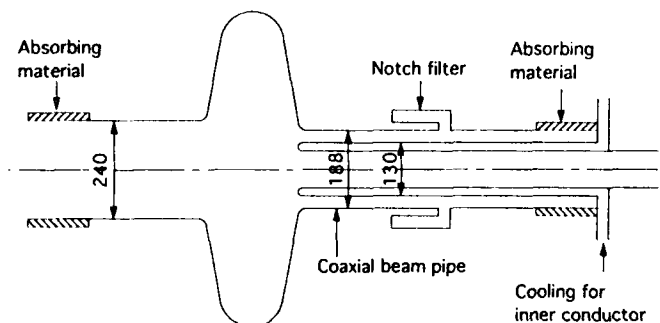


Figure 1. The crab cavity with a coaxial beam pipe.

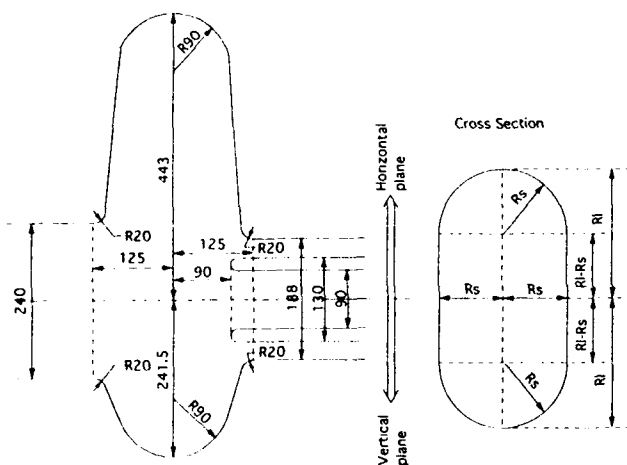


Figure 2. Squashed cell design of the crab cavity.

III. MODEL MEASUREMENTS

A. Damping property

In order to confirm damping property and to study effects of a coaxial beam pipe on the crabbing mode, we made one-third scale (L band) model cavities of round cell of copper and squashed cell of aluminum with a coaxial beam pipe and ferrite absorbers attached.

First of all, we attached the coaxial beam pipe and ferrite absorbers to the round cell cavity, changing the penetration length of the inner conductor of the coaxial beam pipe into the cell. Figure 3 shows the loaded Q of the most dangerous parasitic mode, TM010, as a function of the penetration length. Q value is damped to below 100 when the penetration is 0 mm. With this penetration length calculated surface peak field at the tip of the inner conductor of the coaxial beam pipe

is less than half of the surface peak field on the cell. Thus TM010 is damped to below 100 with a moderate penetration of the inner conductor.

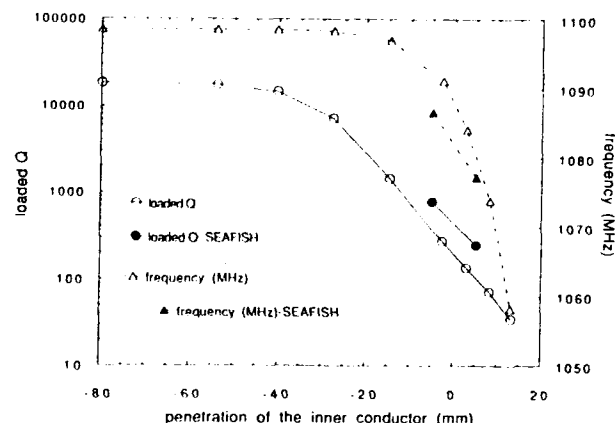


Figure 3. Damping of TM010 mode in the crab cavity with the coaxial beam pipe.

Then we fixed the penetration there and measured all parasitic modes up to 4 GHz. Measurement was done with both of the round cell and the squashed cell. Figure 4 shows frequency spectrum of the squashed cell without the coaxial beam pipe and ferrite absorbers (4a) and with them attached (4b). As was expected with MAFIA calculations, all the dangerous monopole and dipole modes including the unwanted polarization of the crabbing mode are damped to less than the order of 100. One mode observed at 2.6 GHz with high Q is a quadrupole-like TE1-1-1 mode. (For the squashed cell we use rectangular coordinate notation as TE or TM x-y-z rather than cylindrical notation as TE or TM ϕ -z.) Since the beam-cavity coupling of a quadrupole mode is quite small, it is probably not necessary to damp this mode significantly. Using a conventional higher order mode coupler at the same time, this mode can be damped to 10^3 or 10^4 , which is probably safe. Frequency spectrum of the round cell was found to be essentially the same as that of the squashed cell except the unwanted polarization of the crabbing mode.

Next we studied effects of the inner conductor on the crabbing mode. It can be seen in Figure 4b that the crabbing mode has high Q in the presence of the coaxial beam pipe. The effect of misalignment of the inner conductor with respect to the outer conductor on the crabbing mode was measured with the copper model. Loaded Q is almost the same as without the coaxial beam pipe when the inner conductor is aligned with the accuracy of 1 mm. This means that the external Q for the coaxial beam pipe is at least the order of 10^5 with such an alignment because the intrinsic Q is 23000 for this copper cavity. The notch filter assures an additional 50 dB more reduction that makes the external Q more than 10^{10} . Since this is a result of one-third scale model, we can expect the alignment tolerance of about 3 mm for the full scale cavity, which can be achieved easily.

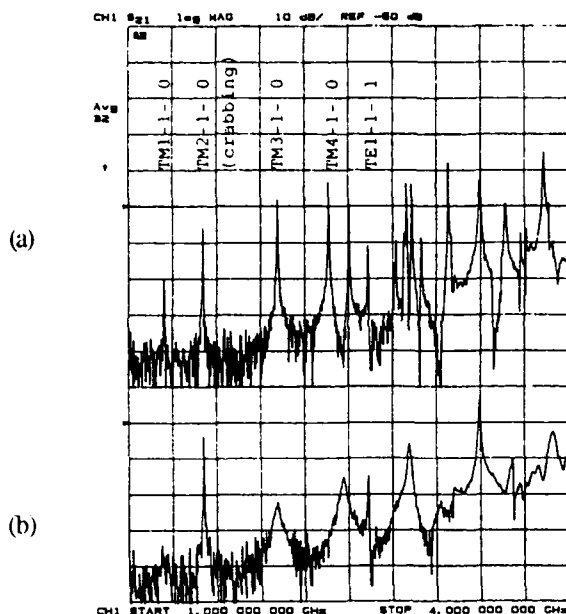


Figure 4. Frequency spectrum from 1 to 4 GHz measured in the squashed crab cavity, (a) without the inner conductor of the coaxial beam pipe and ferrite absorbers and (b) with them attached. Some of the peaks are identified as corresponding resonances in a rectangular cavity.



Figure 5. One-third scale niobium crab cavity with a notch filter and a coaxial beam pipe mounted on a test stand.

B. High Field Performance

Necessary kick voltage for the crabbing is 1.8 MV corresponding to the surface peak field of 20 MV/m. Present technology of superconducting accelerating cavities has shown that the surface peak field of 20 MV/m corresponding to the accelerating gradient of about 10 MV/m can be obtained without serious difficulties. For the crab cavity it is still crucial to check high field performances because our design of the crab cavity has several new features such as the coaxial beam pipe and the notch filter on the beam pipe which are not present in accelerating cavities and might cause some limitation to the field due to multipacting.

We made an one-third scale niobium model of round cell cavity, coaxial beam pipe and notch filter. Figure 5 shows the system mounted on a test stand. It was cooled down to 1.5 K in liquid helium and measured in TM110 mode at 1.5 GHz. At surface peak field of 1 MV/m multipacting was encountered which is considered to occur at the coaxial beam pipe. This was processed away in an hour with RF processing. Figure 6 shows Q value versus peak field curve of this measurement. The maximum surface peak field we reached was 25 MV/m, where field emission occurred. We achieved the design goals of field and Q value to provide necessary kick voltage for CESR-B (1.8 MV/m for HER and 0.8 MV/m for LER).

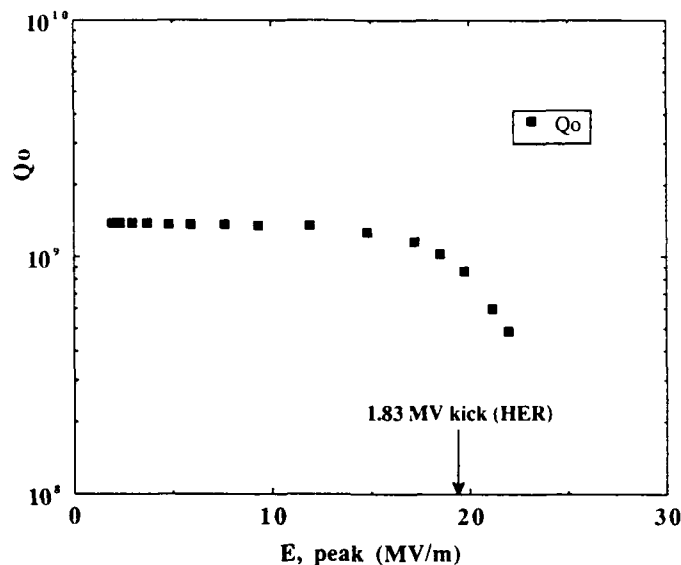


Figure 6. Surface peak field versus Q curve.

IV. REFERENCES

- [1] A. Piwinski, IEEE Trans. on Nucl. Sci., NS-24, p. 1408 (1977).
- [2] A. Piwinski, IEEE Trans. on Nucl. Sci., NS-32, p. 2240 (1985).
- [3] R. B. Palmer, SLAC-PUB-4707 (1988).
- [4] K. Oide and K. Yokoya, Phy. Rev. A40, 315 (1989).
- [5] "CESR-B Conceptual Design for a B Factory Based on CESR", CLNS 91-1050 (1991).
- [6] K. Akai et al., Proc. 15th Int. Conf. on High Energy Accel., p.757 (1992).

A NEW 3-D ELECTROMAGNETIC SOLVER FOR THE DESIGN OF ARBITRARILY SHAPED ACCELERATING CAVITIES *

P. ARCIONI, M. BRESSAN, L. PERREGRINI

Dept. of Electronics, University of Pavia
Via Abbiategrasso 209, 27100 PAVIA, ITALY.

Abstract

We present a new algorithm well suited for the modal analysis of arbitrarily shaped cavities filled with a lossless, isotropic and homogeneous medium. The electric-wall condition is enforced on the field produced by an unknown current sheet, distributed over the cavity wall, and the resulting Electric Field Integral Equation (EFIE) is solved using the method of the moments (MM). Thanks to the special form of the kernel of the EFIE, the algebraic problem can be rearranged to yield the resonating frequencies and the associated currents as eigenvalues and eigenvectors of a standard linear eigenvalue problem. The algorithm yields all resonances up to the maximum frequency of interest by a single evaluation of the MM matrices. For this reason CPU times are reasonably short, even in finding many resonances of quite complicated cavities. The cavity shape is modelled using triangular patches and the code is interfaced with a commercial mechanical CAD.

1. INTRODUCTION

The availability of accurate and efficient computer codes to determine the resonances of arbitrarily shaped cavities is of great importance in the design of interaction structures for particle accelerators. Commercial codes for 3-D structures (MAFIA, ARGUS, etc.) are usually based on Finite Element or Finite Difference methods, which make them very flexible. They need, however, a 3-D mesh and, consequently, a very large number of variables to discretize the problem, thus requiring a large memory allocation and long computing times. When the medium inside the cavity is homogeneous, as in the case of accelerating structures operating in vacuum, it may be advantageous to use a Boundary Integral Method (BIM), that involves quantities defined only on the cavity wall. In this case, indeed, a surface mesh is sufficient, and the order of the matrices involved in the problem reduces dramatically. The conventional approach consists in enforcing the electric-wall condition on the electric field (or on the magnetic field) produced inside the cavity volume V by an unknown current sheet J distributed on its boundary S and radiating in free space at an unknown frequency ω . The resulting Electric Field Integral Equation (EFIE) or Magnetic Field Integral Equation (MFIE) is transformed into a complex matrix problem using the method of the moments: the resonating frequencies ω_r are obtained as those particular values of ω that permit the problem to have a non-trivial solution. This solution yields the modal current distribution J_r , from which the modal fields can be calculated. In both cases the coefficients of the MM matrix depend on the frequency through complex transcendental functions, and each resonance must be found through an iterative procedure that require the repeated evaluation of the MM matrix at closely spaced frequencies [1,2]: this may lead to overlong computing times when many resonances are to be found, a drawback that may overwhelm the intrinsic advantage

of using the BIM.

To overcome this drawback we follow a somewhat different approach, that constitutes the 3-D extension of an algorithm developed for the modal analysis of arbitrarily shaped waveguides [3]. We consider the unknown current J radiating, rather than in free space, inside a spherical volume Ω including V and bounded by an electric wall (see Fig. 1). This is possible because, when J corresponds to one of the J_r , the field outside V is zero, and therefore it does not matter what boundary condition we impose on the exterior field. As shown in [4], the electric field inside Ω due to the current sheet J can be expressed as the sum of two quasi-static contributions plus a high frequency correction:

$$E(r) \approx -\nabla \int_{S'} g(r, r') \frac{\sigma(r')}{\epsilon} dS' - j\eta k \int_{S'} \underline{G}(r, r') \cdot J(r') dS' - j\eta k^3 \sum_{m=1}^M \frac{e_m(r)}{k_m^2 (k_m^2 - k^2)} \int_{S'} e_m(r') \cdot J(r') dS' \quad (1)$$

where $k = \omega \sqrt{\epsilon \mu}$, $\eta = \sqrt{\mu/\epsilon}$, σ is the surface charge density (related to J by the continuity condition) and $g(r, r')$, $\underline{G}(r, r')$, $e_m(r')$ are real frequency independent functions, known in closed form [4]. In particular, $g(r, r')$ is the electrostatic potential Green's function of the spherical cavity and $e_m(r')$, k_m are the (normalized) electric field vector and the corresponding wavenumber of the m -th mode of the spherical resonator. The summation includes all the modes having $k_m \leq k_M$, and it is an accurate approximation of an infinite series, up to a frequency corresponding to about $k_M/2$.

Though more complicated than the equivalent expression for a current radiating in free-space, eq. (1) is much more convenient for the numerical solution of the EFIE, since it is a rational function of k . In fact, thank to this feature the discretization of the EFIE results into a linear matrix eigenvalue problem, as we

are going to show in the following.

2. THE ALGORITHM

The surface S is discretized using triangular patches and the unknown functions $J(r)$ and $\sigma(r)$ are expanded as:

$$J(r) \approx \sum_{i=1}^N a_i f_i(r) \quad ; \quad \sigma(r) \approx -\frac{1}{j\omega} \sum_{i=1}^N a_i \nabla_s \cdot f_i(r) \quad (2)$$

where $\{f_i(r)\}$ are the vector subsectional base functions introduced in [5]. Each $f_i(r)$ has a support Σ_i constituted by the two triangles sharing the i -th edge (see Fig. 2) and is represented by:

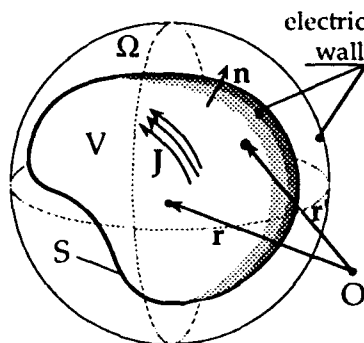


Fig. 1

(*) Work partially supported by C.N.R. under Contract No. 92.02857.CT07.

$$f_i(\mathbf{r}) = \begin{cases} (l_i/2A_i^+) \rho_i^+ & \text{if } \mathbf{r} \text{ belongs to } T_i^+ \\ -(l_i/2A_i^-) \rho_i^- & \text{if } \mathbf{r} \text{ belongs to } T_i^- \\ 0 & \text{elsewhere} \end{cases} \quad (3)$$

where l_i is the length of the i -th edge, A_i^+ and A_i^- denote the area of the two adjacent triangles T_i^+ and T_i^- , and ρ_i^+ and ρ_i^- are vectors emerging from the two vertexes opposite to the i -th edge. The number N of the base function equals the number of the edges. Using these base functions, $\mathbf{J}(\mathbf{r})$ and $\sigma(\mathbf{r})$ are represented by well-behaved functions: in fact, as discussed in [5], the component of the current normal to any edge is continuous, a fact that prevents the need of considering line charges. Moreover, the surface charge density is represented by a zero mean, piece-wise constant function, since we have:

$$\nabla_s \cdot \mathbf{f}_i(\mathbf{r}) = \begin{cases} l_i/A_i^+ & \text{if } \mathbf{r} \text{ belongs to } T_i^+ \\ -l_i/A_i^- & \text{if } \mathbf{r} \text{ belongs to } T_i^- \\ 0 & \text{elsewhere} \end{cases} \quad (4)$$

Introducing eq. (2) into (1), enforcing the boundary condition $\mathbf{n} \times \mathbf{E}(\mathbf{r}) = 0$ ($\mathbf{r} \in S$) and solving the resulting EFIE by the MM by using $\{\mathbf{n} \times \mathbf{f}_i(\mathbf{r})\}$ as test functions, the following set of equations is obtained:

$$\frac{1}{k^2} \sum_{j=1}^N C_{ij} a_j + \sum_{j=1}^N L_{ij} a_j + \sum_{m=1}^M R_{im} b_m = 0 \quad i=1, \dots, N \quad (5)$$

In deriving (5) the set of the M auxiliary variables $\{b_m\}$ have been introduced, which are related to $\{a_i\}$ by the following set of equations:

$$b_m = \frac{k_m^2 k^2}{k_m^2 - k^2} \sum_{j=1}^N R_{jm} a_j \quad m=1, \dots, M \quad (6)$$

The other quantities in (5) are defined as:

$$C_{ij} = \iint_{\Sigma_i} \iint_{\Sigma_j} \nabla_s \cdot \mathbf{f}_i(\mathbf{r}) g(\mathbf{r}, \mathbf{r}') \nabla_s' \cdot \mathbf{f}_j(\mathbf{r}') dS' dS \quad (7a)$$

$$L_{ij} = \iint_{\Sigma_i} \iint_{\Sigma_j} \mathbf{f}_i(\mathbf{r}) \cdot \mathbf{G}(\mathbf{r}, \mathbf{r}') \cdot \mathbf{f}_j(\mathbf{r}') dS' dS \quad (7b)$$

$$R_{im} = \frac{1}{k_m^2} \iint_{\Sigma_i} \mathbf{f}_i(\mathbf{r}) \cdot \mathbf{e}_m(\mathbf{r}) dS \quad (7c)$$

Note that $C_{ij} = C_{ji}$ and $L_{ij} = L_{ji}$ due to the reciprocity properties of g and \mathbf{G} [4].

Introducing the vectors $\mathbf{a} = \{a_i\}$, $\mathbf{b} = \{b_m\}$ and the matrices \mathbf{C} , \mathbf{L} , \mathbf{R} and $\mathbf{D} = \text{diag}\{k_m^{-2}\}$, the two sets of equations (5) and (6) can be grouped as follows:

$$\begin{bmatrix} \mathbf{D} & \tilde{\mathbf{R}} \\ \mathbf{R} & \mathbf{L} \end{bmatrix} \begin{bmatrix} \mathbf{b} \\ \mathbf{a} \end{bmatrix} - \frac{1}{k^2} \begin{bmatrix} \mathbf{I} & \mathbf{O} \\ \mathbf{O} & \mathbf{C} \end{bmatrix} \begin{bmatrix} \mathbf{b} \\ \mathbf{a} \end{bmatrix} = 0 \quad (8)$$

where \sim denotes the transpose and \mathbf{I} and \mathbf{O} are the identity and the zero matrices. Note that all the coefficients of the matrices are independent of the frequency, so that (8) constitutes a generalized linear matrix eigenvalue system in standard form. Moreover, the system matrices are real and symmetric. The largest eigenvalues of (8) yield the first resonating frequencies: they can be found using very efficient library routines.

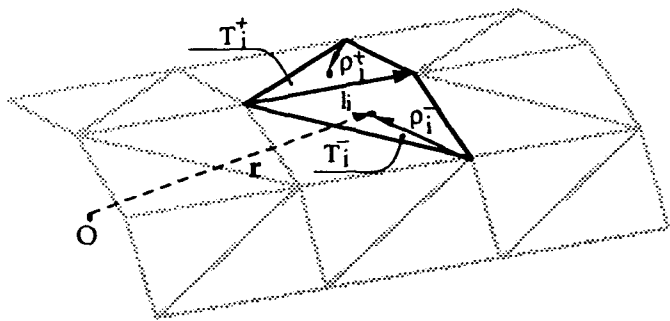


Fig. 2

Compared to the standard EFIE approach [2], a longer time is needed to calculate the MM matrices, due to the more complicated expressions of their coefficients; moreover, besides the desired resonances, this algorithm yields also the resonances of the exterior region $\Omega - V$, i.e. of the fictitious resonator bounded by the spherical surface and the surface S (these spurious solution are easily detected and rejected, since they give rise to a zero field inside the volume V). In spite of these drawbacks, the computer code that implements the new algorithm is very efficient when many resonances are to be calculated. We found that, in the case of typical cavities, the time for computing *all* resonances up to twice the frequency of the fundamental mode is shorter than that needed to find *only one* resonance following the standard EFIE approach (note that, in the conventional approach, typically more than 10 evaluations of the matrices are needed to localize a resonance). Moreover, no problems arise in case of degenerate or nearly degenerate modes.

3. THE COMPUTER CODE

The algorithm has been implemented in a computer code running under VAX-VMS. The program reads the geometry of the cavity from a formatted file: an interface to a commercial mechanical CAD (PATRAN) is available, that eases the definition of the geometry and the generation of a suitable mesh. It is possible to take advantage of symmetries respect to the coordinate planes to reduce the dimension of the problem. Then coefficients (7) are calculated: since functions $g(\mathbf{r}, \mathbf{r}')$ and $\mathbf{G}(\mathbf{r}, \mathbf{r}')$ diverges when $\mathbf{r} \rightarrow \mathbf{r}'$, coefficients c_{ij} and l_{ij} are evaluated analytically in cases where Σ_i and Σ_j overlap (partially or totally). In all other cases a fast gaussian quadrature scheme is used. Problem (8) is solved using the EISPACK routines [6], after a rearrangement, not reported for brevity, useful to reduce memory allocation by taking advantage of the special form of the matrices involved. At present, the selection of the resonances of the outer region must be performed manually, but an automatic procedure for detecting and purging these spurious solution is being implemented. The eigenvalues and the corresponding eigenvectors are stored in a file: a post-processing program can use these data to calculate the normalized modal fields and to evaluate Q-factors and shunt-impedances.

Many calculations have been performed on trirectangular, spherical and cylindrical cavities, and the numerical results have been checked against theoretical ones, in order to validate the program and to investigate the influence of different mesh sizes. Tab. I summarizes the results for a cylindrical cavity (radius=24 cm, height=22 cm) analyzed up to about three times the frequency of its fundamental mode using two different mesh size (see Fig. 3a,b). The symmetry respect to the three coordinate planes were exploited and, to minimize the error arising from the discretization of the surface, the volume of the analyzed structures was kept equal to that of the original cavity in both cases.

Using the finest mesh, consisting of 54 triangles (over which 89 base functions were defined), the accuracy is very good for all modes. Even with the coarse mesh (15 triangles, 27 base functions) the accuracy is reasonable for the first few modes, whereas only a rough estimate of the resonating frequency is obtained for the higher modes, as expected. The same table reports, for each mode, the ratio L_m/λ_r of the mean length of the edges to the free-space resonating wavelength. It is noted that accuracies better than 0.3% are obtained for $L_m < \lambda_r/4$. This result, confirmed by the other tests, suggests a rule of thumb for choosing the mesh size. CPU times (on a VAXStation 4000/60) are about 20 s (coarse mesh) and 240 s (fine mesh) for finding all the modes belonging to each class of symmetry. When dealing with symmetries, some intermediate results, not depending on the particular class of symmetry, can be stored and reused for finding modes with different symmetries. This possibility, not yet implemented, will greatly reduce CPU times for the complete analysis.

A second test example refers to the axisymmetric cavity of Fig. 4. One eighth of the surface is modelled using 136 patches (corresponding to 219 base functions). CPU times were 26 minutes for each symmetry class to find the 34 modes up to 10 GHz. In Tab. II the resonating frequencies of the first 20 modes (classified according to their even or odd symmetry respect to the coordinate planes) are compared with measured values and, when possible, with the results obtained by the program SUPERFISH. Fig. 4 shows the electric field of the dominant mode.

ACKNOWLEDGEMENT - The authors wish to thank Prof. G. Conciauro for the fruitful discussions.

REFERENCES

- 1) F.P. Adams, M.S. de Jong: "A Boundary-Integral-Method Code for Cavity RF Mode Analysis"; Proc. of the 1993 Computational Accelerator Physics Conference, Feb. 22-26, 1993.
- 2) B.E. Spielman, R.F. Harrington: "Waveguide of Arbitrary Cross Section by the Solution of a Non-Linear Eigenvalue Equation", IEEE Trans. on Microwave Theory and Tech., Vol. MTT-20, no. 9, pp. 578-585, Sept. 1972.

Mode	theoretical freq. (MHz)	Coarse Mesh			Fine Mesh		
		computed frequency	Δ (%)	L_m/λ_r	computed frequency	Δ (%)	L_m/λ_r
TM 010	478.42	479.38	0.20	0.20	478.52	0.02	0.10
TM 110	762.29	763.09	0.10	0.31	762.64	0.05	0.16
TE 111	773.98	768.79	-0.67	0.32	774.28	0.03	0.17
TM 011	832.93	827.24	-0.68	0.34	833.28	0.04	0.18
TE 211	913.28	902.24	-1.20	0.38	913.35	0.01	0.20
TM 210	1021.7	1016.7	-0.50	0.42	1022.4	0.07	0.22
TM 111	1022.7	1015.5	-0.70	0.42	1024.3	0.15	0.22
TE 011	1022.7	1005.6	-1.70	0.42	1021.9	-0.08	0.22
TE 311	1078.6	1063.7	-1.40	0.44	1079.3	0.06	0.23
TM 020	1098.2	1100.8	0.23	0.45	1101.6	0.30	0.24
TM 211	1228.3	1201.4	-2.20	0.51	1229.0	0.06	0.26
TE 411	1258.6	1237.4	-1.70	0.52	1258.8	0.01	0.27
TE 121	1260.9	1223.3	-3.00	0.52	1259.2	-0.13	0.27
TM 310	1269.3	1236.0	-2.60	0.52	1270.1	0.06	0.27
TM 021	1292.6	1248.8	-3.40	0.53	1298.1	0.40	0.28
TM 120	1395.7	1359.7	-2.60	0.57	1399.2	0.25	0.30
TE 112	1412.0	1398.9	-0.90	0.58	1417.5	0.39	0.30
TM 311	1440.8	1402.1	-2.70	0.59	1445.8	0.35	0.31
TM 012	1445.1	1416.9	-1.90	0.59	1450.0	0.34	0.31
TE 511	1447.0	1429.9	-1.20	0.60	1450.0	0.20	0.31
TE 212	1492.9	1481.5	-0.76	0.61	1498.0	0.34	0.32
TE 221	1498.3	1472.2	-1.70	0.62	1495.6	-0.18	0.32

TAB. I - Resonating frequencies of the cylindrical cavity of Fig. 3

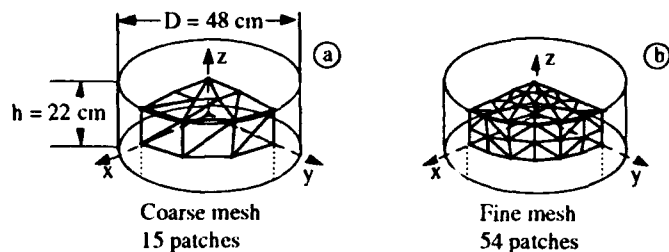


Fig. 3

- 3) M. Bressan, G. Conciauro, C. Zuffada: "Waveguide Modes Via an Integral Equation Leading to a Linear Matrix Eigenvalue Problem"; IEEE Trans. on Microwave Theory and Tech., Vol. MTT-32, n. 11, Nov. 1984, pp. 1495-1504.
- 4) M. Bressan, G. Conciauro: "Singularity extraction from the electric Green's function for a spherical resonator"; IEEE Trans. on Microwave Theory and Tech., vol. MTT-33, n. 5, May 1985, pp. 407-414.
- 5) S. M. Rao, D. R. Wilton, A.W. Glisson: "Electromagnetic Scattering by Surfaces of Arbitrary Shape", IEEE Trans. on Antennas and Propagation, Vol. AP-30, n. 3, May 1982, pp. 409-418.
- 6) B.S. Garbow, J.M. Boyle, J.J. Dougard, C.B. Moler: "Matrix eigensystem routines - EISPACK Guide Extension"; in Lecture Notes in Computer Science, no. 51, G. Goos and J. Hartmanis, Eds., Springer-Verlag, 1977.

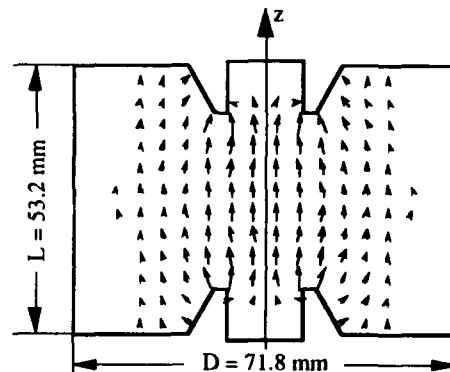


Fig. 4

Symmetry x y z	Calc. res. freq. [GHz]	Superfish	Measured
eeo	2.8642	2.8429	2.8467
eee	3.9191	3.8976	3.8950
oeo	3.9547	--	3.9357
eee	5.0429	--	5.0171
ooo	5.0927	--	5.0544
ooe	6.0471	--	6.0208
oeo	6.1687	--	6.1238
oeo	6.3336	--	6.2938
eeo	6.4608	6.4378	6.4150
ooo	6.5880	--	6.5453
eeo	6.9123	--	6.8627
eeo	7.1340	7.0876	7.0874
eeo	7.2389	--	7.1933
eee	7.5324	7.4741	7.4820
ooe	7.6879	--	7.6327
eee	7.7238	--	7.6645
oeo	7.7759	--	7.7292
ooo	8.1312	--	8.0604
ooo	8.1327	--	8.1016
ooo	8.3276	--	8.2787

TAB. II - Resonating frequencies of the nose-cone cavity of Fig. 4

Design Study For The ELFA Linac

W.A.Barletta¹, G.Bellomo², G. Gemme³, R. Parodi³, V. Stagno⁴, V. Variale⁴

¹ Lawrence Berkeley Laboratory, USA, ² INFN and Univ. of Milan, Italy

³ INFN Genova, Italy ⁴ INFN and Univ. of Bari, Italy

Table I- Beam parameters

Nominal energy	6 MeV
Peak current	> 50 A
Energy spread, rms	< 1%
Norm. rms emittance *	< 50 π mm mrad
micropulse length	> 35 ps
number of micropulses	3
repetition rate	10 Hz

$$* \epsilon_{rms} = \beta \gamma \sigma_x \sigma_x'$$

Abstract

The accelerator for ELFA must provide a 6 MeV electron beam to drive a single pass free electron laser at 100 GHz.

The 1.3 GHz linac will operate at low repetition rate (10 Hz) and short macropulse (2 ns) and should provide peak current over 50 A.

The envisaged accelerator includes a gridded electron gun, a prebuncher and a multicell bunching/accelerating section.

The general characteristics of the accelerator and the expected performances, as evaluated by beam dynamics studies, are presented.

I. Introduction

ELFA (Electron Laser Facility for Acceleration) is a high gain, single pass free electron laser designed to operate in the microwave region (100 GHz) to explore fundamental FEL physics with short bunches.

The project has been revised in 1992 to obtain a reduction in cost, schedule and technical risk while maintaining the physic goals of the original proposal. A detailed review of the project is presented elsewhere at this conference [1].

The minimum beam characteristic satisfying the above requirements are reported in Table I.

The micropulse length of 35 ps, corresponding to three optical wavelength of the 100 GHz radiation, implies the choice of a L-band (1.3 GHz) accelerator in order to minimize the micropulse energy spread.

II. The accelerator

The specifications of table I can be easily met and exceeded by a photocathode RF gun of the type in operation at Los Alamos.

It was felt however that a photocathode RF gun requires a considerable staff effort to be developed and operated. Also, the cost and delivery time can be kept at minimum with a more conventional configuration.

The preference is therefore versus a design that allows the option to buy a commercially available technology and to concentrate the efforts on the experiment.

The design study has been focused on an accelerator with

- a gridded electron gun
- a prebunching cavity at the fundamental frequency
- a bunching/accelerating section

A scheme of the accelerator is shown in fig 1. The main components are described in the following.

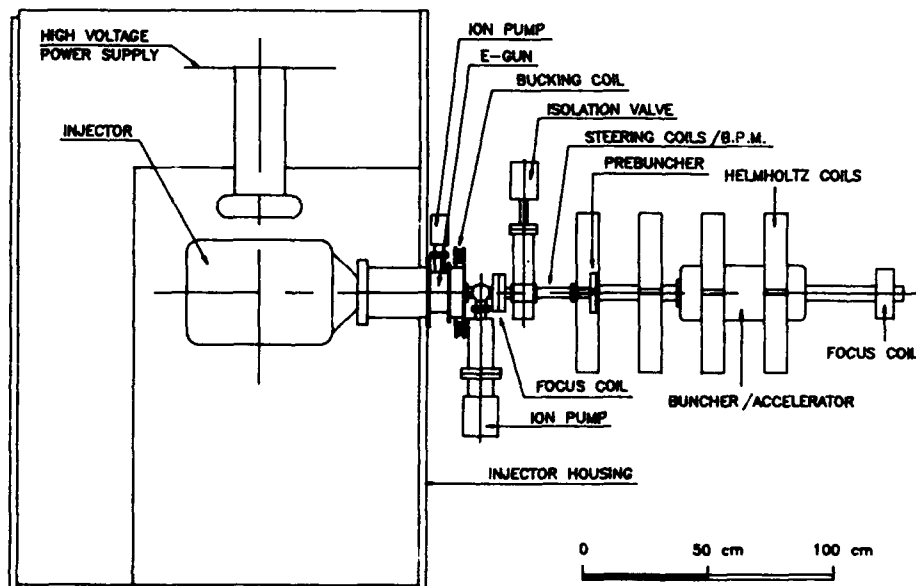


Fig. 1. Schematic view of the accelerator.

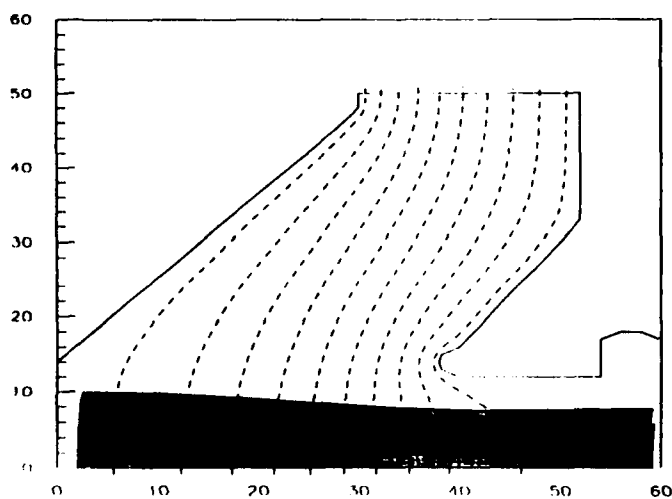


Fig. 2. Electron beam trajectories in the gun. Voltage 120 kV, $I = 11$ A. Units in mm.

Electron gun

The electron source is a standard, high current gun of the type now in use at SLAC. At 120 kV it should provide up to 10 A pulses with a flat-top of 2 ns and subnanosecond rise and fall time.

The gun is a classical Pierce gridded gun with a 3 cm² thermoionic dispenser cathode. The grid is expected to intercept less than 20% of the cathode current.

The geometry and the performances of the gun have been evaluated with the EGUN code[2]. The geometry indicated in fig 2, according to the EGUN simulation, gives 11 A corresponding to a perveance .27 μ P.

The calculated emittance at exit of the gun, including the thermal effects, is $\epsilon_{nrms} = 3 \pi$ mm mrad. A realistic value for the emittance, assumed as nominal value for the beam dynamic evaluation, is $\epsilon_{nrms} = 5 \pi$ mm mrad when considering the grid lens effects.

At the gun exit the beam has an edge radius $r = .8$ cm and is very close to a waist.

Prebuncher

After a drift of 40 cm from the exit of the gun, to allow for pumping and isolation valve, the beam is focused with a thin solenoidal lens to the prebuncher.

The prebuncher will operate at the fundamental frequency of the linac, 1.3 GHz, and should have a peak energy gain up to 40 keV. To minimize the effects of beam loading a low Q value is desired; the peak power should be of the order of few kW.

The prebuncher should compress more than 50% of the beam in 60° RF at the entrance of accelerator located 40 cm downstream.

Bunching/accelerating section

A travelling wave, $2\pi/3$ mode, SLAC type structure has been investigated to bunch and accelerate the beam at 6 MeV.

The section is very short (two wavelengths) and is not graded although the beam at entrance has $\beta = 0.6$.

The structure has a round shape to further increase the shunt impedance and to avoid possible multipactoring problems. A schematic tridimensional view of the structure, including the entrance and exit couplers, is shown in fig. 3.

The required accelerating gradient is 15 MV/m and the corresponding peak surface field is ≈ 30 MV/m. The quality factor is $Q = 22000$ and the group velocity is $v_g \approx 0.5\%$.

This section will operate in the storage energy mode with a single pulse beam loading of $\approx 0.5\%$

An alternative approach for the accelerating section is to use a 4 cells standing wave cavity operating near the π mode. The proposed structure has a shape similar to that used for superconducting cavities with a large bore.

The quality factor of the structure is $Q = 30000$. The peak values of the electric field are 25 MV/m on axis and approximately 50% more on the surface. The corresponding dissipated power is 2.5 MW. The stored energy is 9 J; the corresponding bunch to bunch energy variation should be less than 0.25%.

A detailed description of the design and test of the prototypes for these two structures is given elsewhere in this conference[4].

Both types of structures (as well as other standing wave types) are suitable for the accelerator. The main drawback of the TW structure is the need of a careful design and realisation of the input and exit cell and couplers in order to avoid, especially at the entrance, the dipole field component.

RF system

A klystron, with 5 MW of peak power and 8 μ s pulse, at 10 Hz repetition rate, should be sufficient to power the linac for all the possible structures choices (TW or SW).

Particularly important for the experiment is the pulse to pulse repeatability of the beam characteristics; the amplitude jitter of the klystron should be of the order of 0.1%.

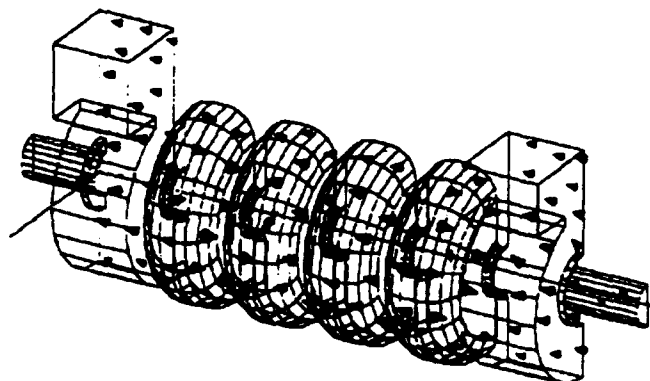


Fig. 3. Tridimensional view of the TW section.

III. Beam dynamics

The beam dynamics has been studied with the code PARMELA[3] which simulated the motion of the electrons in RF cavities (and along beam line) including transversal and longitudinal space charge effects.

The study has been carried out for the following configuration:

- gun at 120 kV, 10 A extracted current, beam radius (edge) 8.5 mm, edge emittance 30π mm mrad ($\epsilon_{rms} = 5 \pi$ mm mrad)
- focusing solenoid (peak field 300 Gauss) placed 15 cm after the exit of the gun
- prebuncher with a peak energy gain 22 KeV
- a 6 cells, $2\pi/3$ mode, travelling wave section with an accelerating gradient of 15 MeV/m
- focusing solenoids providing up to 1.1 Kgauss peak field at the center of the accelerating section

The beam produced by the gun is focused at the prebuncher location and then refocused at the entrance of the accelerating section.

Here the beam emittance has increased to $\epsilon_{rms} = 15 \pi$ mm mrad, due to space charge and to RF coupling effects in the prebuncher, and 75% of the bunch is compressed in 120° RF.

The RF phase of the section is chosen to maximize the bunching process, which is completed in the first cell where the beam reach the energy of .9 MeV, and to minimize the energy spread of the final beam.

The phase plots and the beam profile at the exit of the accelerator are shown in fig. 4. The capture efficiency, 75%, is quite high and this implies long tails in the phase and energy profiles as partially shown in the figure.

Considering the core of the beam, i.e. the beam included in 30° RF around the peak density, as shown the figure, the capture efficiency is 60% (620 particles of the 1000 simulating the bunch) and the corresponding peak current is close to 75 A.

The rms normalized emittance is 30π mm mrad and the full width energy spread of the beam core is 200 keV corresponding to an rms energy spread of 0.8 %.

An optimization of the beam dynamics inside the accelerating section should improve the energy spread and the pulse length (i.e. the peak current) of the beam core.

Comparable values can be obtained with a standing wave section with a proper tailoring of the field in the first cell.

These results are consistent, or even better, with the minimum requirements of the beam also when allowance is given to tuning errors and beam loading effects in the accelerator.

The long tails of the pulse, in energy and phase, should be removed by scraping or by an analysing system along the beam transport and matching line to the wiggler.

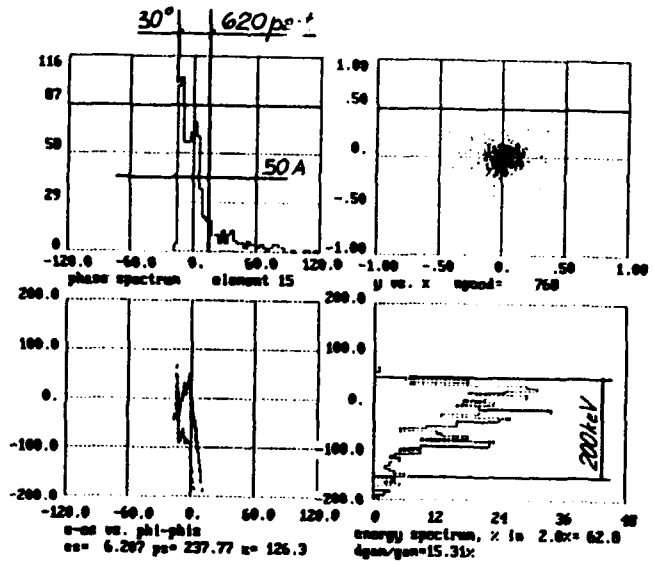


Fig. 4. Phase space plots at the exit of the accelerator. Beam energy 6.2 MeV. Units: cm, mrad, RF°, keV.

IV. Conclusions

The design study has shown that the beam specifications can be met with a conventional accelerator and with different technical solutions (SW or TW).

More detailed investigations will be carried out in order to determine if there are clear advantages, in term of performances, cost, reliability and operation, for some specific configuration.

As already mentioned the accelerator will be ordered as a turn-key machine upon approval and funding of the project.

References

- [1] E. Acerbi et al. - The revised ELFA project - these Proceedings
- [2] W. B. Herrmansfeldt - EGUN - SLAC Report 331 (1988)
- [3] K.R.Crandall and L.Young - PARMELA - unpublished
- [4] G.Bellomo et al. - Design and test of prototype cavities for the ELFA linac - these Proceedings

The RF Cavity for DAΦNE

S. Bartalucci, R. Boni, A. Gallo, L. Palumbo*, R. Parodi†, M. Serio and B. Spataro
I.N.F.N., Laboratori Nazionali di Frascati, C. P. 13, 00044 Frascati, Rome (Italy)

* Dipartimento di Energetica, Università di Roma 'La Sapienza', Via A. Scarpa 14, 00161 Rome (Italy)

† INFN Sezione di Genova, Via Dodecaneso 33 - 16146 Genoa (Italy)

Abstract

The achievement of the highest luminosity in the 510 MeV electron-positron Φ -Factory DAΦNE, in construction at Frascati Laboratories, requires a careful design of the RF accelerating cavity, being the main source of High Order parasitic Modes (HOM) which are responsible for multibunch instabilities. Intense R&D has been carried out to choose the cavity resonator which would better cope with those problems. Theoretical studies and simulations of the longitudinal beam dynamics with various cavity shapes have been performed and several HOM extraction and damping techniques have been studied and tested. This report presents the results of these investigations and the laboratory tests of the proposed accelerating RF cavity for DAΦNE.

I. INTRODUCTION

The very high luminosity of the double ring Φ -Factory DAΦNE, of the order of $10^{32}+10^{33}$ cm⁻².sec⁻¹, will be achieved by filling up to 120 buckets per ring with 47 mA per bunch. One of the main problems arising in the beam dynamics concerns the multibunch instabilities caused by the parasitic resonant fields induced by the beam in the RF accelerating cavity. Due to the high current, the instability rise time can be very fast [1], so it is impossible to stabilize the beam with a feedback system alone. An effort has to be made to reduce the shunt impedance of the cavity HOM's such that the feedback can be effective. This task can be accomplished both by properly shaping the cavity and damping the parasitic modes by extracting the relative energy with suitable RF techniques. The parameters of the DAΦNE RF system for an initial operation at 30 bunches are presented in Table 1. The RF power sources permit to eventually upgrade the operation to 120 bunches.

Table 1. RF Parameters for 30 Bunches

RF Frequency (MHz)	368.25
Harmonic Number	120
Cavities per Ring	1
Cavity Impedance (Ω)	61
Cavity Quality Factor	45000
RF Peak Voltage (kV)	250
Cavity Wall Power (kW)	11.5
Current per Beam (Amps)	1.4
Synchrotron Power Loss (kW)	27
Parasitic Cavity Losses (kW)	< 1
Cavity-Generator Coupling	≈ 3.0
Klystron Power (kW)	150
N° of Klystrons per Ring	1

II. THE DAΦNE RF CAVITY

A considerable reduction of the characteristic impedance of the cavity HOM's can be obtained by opening the beam tubes at the cavity irises in order to let the higher frequency parasitic modes propagate through them. A taper is then used as a gradual transition from the cavity iris to the ring vacuum pipe. A careful analysis of the longitudinal wake potentials was made with the code TBCI, aiming to reduce the cavity contribution to the machine impedance [2]. A design with no beam tubes and two long tapers was compared with a conventional design having tubes and short tapers. The long taper cavity showed a rather low value of loss factor to the HOM's ($k_{pm} = 0.07$ against 0.16 V/pC at an rms bunch duration σ_t of 100 psec) and a slightly larger R/Q at the fundamental mode (FM). Since the total loss factor for a single bunch passage is:

$$k_{pm} = \sum_{n>1} \left(\frac{\omega_n}{2} \cdot \frac{R_n}{Q_n} \cdot e^{-\omega_n^2 \cdot \sigma_t^2} \right)$$

this means that on the average the R/Q's are substantially decreased. This fact was confirmed by a frequency-domain analysis (done by means of the codes OSCAR2D and URMEL), where the presence of some strong HOM's above the beam tube cutoff was observed in the short tapered, but not in the long tapered structure.

Once the basic long-tapered design was adopted, the next step was the optimization of the cell profile. A "nosecone" shaped resonator can concentrate the electric field in the region of the beam, thus increasing the R/Q and also helps to decrease the R/Q of the 0-MM-1 HOM considerably, while the situation of the 1-EM-1 dipole mode is worsened, because of the abrupt discontinuity due to the noses. In a high-Q "bell-shaped" (rounded) structure, on the opposite, the smooth profile is beneficial for dipole modes, but retains a greater value for the 0-MM-1 mode. We have studied and measured both structures, maintaining the same FM shunt resistance. A comparison shows a preference for the 'nosecone' cavity as regards the 0-MM-1 mode and for the 'rounded' cavity as regards the 1-EM-1 mode. The situation of other HOM R/Q's, up to the beam pipe cutoff, is quite similar for the two shapes. Experimental results show that the strong damping of the 0-MM-1 required to be comfortable with a feedback system [3] can be provided in both cases. Thus, there is no reason to choose the 'nosecone' cell as our cavity, while the 'rounded' cell is certainly to be preferred because it is of much easier construction and cooling.

The final shape is shown in Figure 1. In the DAΦNE cavity, only the 0-MM-1 mode has a rather high R/Q value (16 Ω) and for just a few modes R/Q is greater than 1 Ω . Much care was taken to ensure that the higher R/Q HOM's are far away from the most powerful harmonics of the beam spectrum, to avoid resonant enhancement of the parasitic power loss.

The adopted profile makes multipacting unlikely easing the RF conditioning and operation.

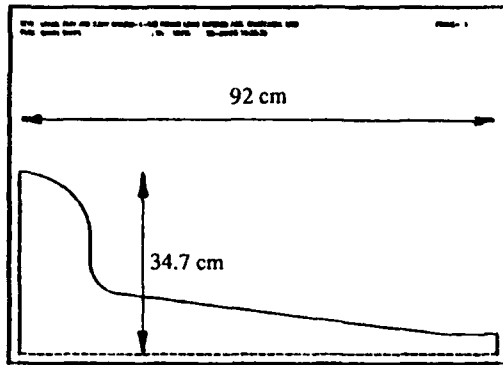


Figure 1. Profile of One Quadrant of the DAΦNE Cavity.

III. EXPERIMENTAL RESULTS

A copper cavity prototype has been fabricated. Due to mechanical imperfections of the model, the FM frequency is slightly lower than the nominal value. We have improved the HOM impedance damping by opening three rectangular slots onto the central body of the cavity model and connecting three 300x40 mm² waveguides (WG) with cut-off at 500 MHz. The WG's are placed 120° apart to avoid perturbing the accelerating field symmetry. The WG's have been positioned in order to couple as much as possible the magnetic field peaks of the highest HOM R/Q's. The guides convey the HOM energy out of the cavity in the TE₁₀ WG mode. Two additional WG's with cut-off at 1350 MHz have been placed, 90° apart, along the tapered pipes. They couple to some higher frequency HOM's which have there intense magnetic field. Figure 2 shows the cavity prototype tested in laboratory and fully equipped with 5 WG's.



Figure 2. The Low Power Cavity Prototype.

The application of the WG's to the test cavity decreases the FM frequency by 2% and the FM quality factor by 16%. Being 25,000 the cavity model Q₀, the WG's external Q is about 180,000. High RF losses ferrite tiles have been applied onto the shorted plane of each WG to dissipate the HOM energy. The ferrites do not require any shaping since their impedance, as shown later on in this article, somewhat matches the 377 Ω vacuum impedance.

Table 2 shows the experimental results obtained by equipping the test cavity with 3+2 WG's and ferrite loads. The damping of the first 8 HOM monopoles is listed together with the FM data. In some cases, the impedance damping is more than 2 orders of magnitude. Such results are very encouraging and let us believe, in accordance with numerical simulations [3], that a feedback system to control the longitudinal beam instabilities is feasible. Table 3 gives the parameters of the highest impedance HOM dipoles and the obtained damping. We plan to perform more precise tests with a high quality electro-formed cavity model.

Table 2. Cavity Model Test Results (Monopoles)

Mode	Freq. [MHz]	Q ₀	R/Q [Ω]	Loaded Q	R _{SH} [k Ω]
0-EM1	357	25000	61	22000	1350
0-MM1	747.5	24000	16	60	0.96
0-EM2	796.8	40000	0.5	270	0.13
0-MM2	1023.6	28000	0.9	-----	-----
0-EM3	1121.1	12000	0.3	600	0.21
0-MM3	1175.9	5000	0.6	140	0.08
0-EM4	1201.5	9000	0.2	110	0.02
0-EM5	1369.0	5000	2.0	300	0.6
0-MM4	1431.7	2000	1.0	150	0.15
0-EM6	1465.0	2000	0.1	200	0.02

Table 3. Test cavity HOM Dipole Damping

Mode	Freq. [MHz]	Q ₀	R/Q' [Ω]	Loaded Q
1-MM1	520.7	30500	5.1	400
	522.3	28500		300
1-EM1	569.6	31500	14.0	130
	569.8	32000		140

IV. STUDY OF THE HOM DAMPERS

The damping of the HOM energy propagating through the test cavity WG's has been achieved by means of Trans-Tech TT2-111R ferrite tiles placed onto the opposite shorted plane of the guides. The ferrites, based on a Ni/Zn compound, present high RF losses in a broad frequency band and do not require special shaping. The most significant RF parameters have been measured in the frequency domain with a reflectometric technique [4]. We report in Figures 3 and 4 the characteristic impedance and the VSWR versus frequency.

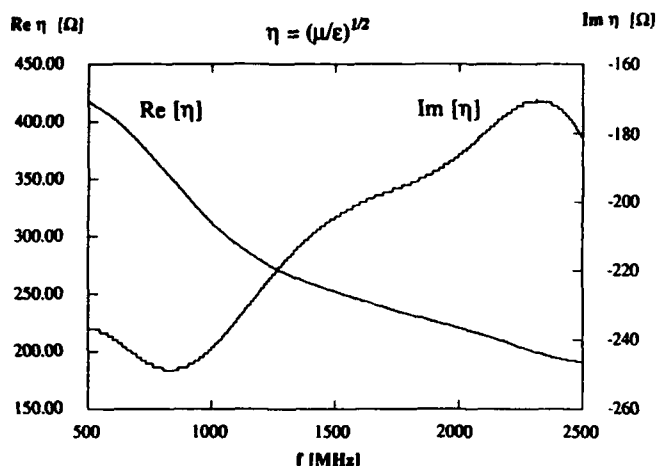


Figure 3. Characteristic Impedance of Ferrite TT2-111R.

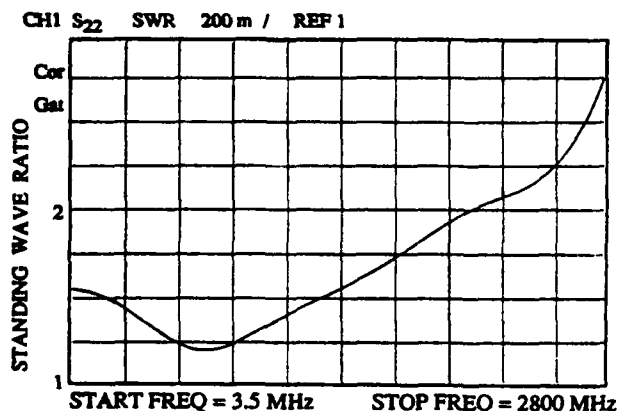


Figure 4. VSWR of Ferrite TT2-111R.

The power transferred from the beam to the cavity HOM's has also been calculated [4] to study the ferrite thermal behavior in ultra high vacuum (UHV) and the needed cooling. With 47 mA per bunch and an asymmetrical machine filling of 27 bunches (instead of 30), required to avoid ion trapping, the HOM power flow is about 150 W per WG. Simulations performed with the code ANSYS [5] assuming a ferrite thermal conductivity of 4.5 W/m/°K and an external temperature of 20 °C, give a maximum temperature of 75 °C for the absorbing material vacuum side. This temperature is well below the 370 °C Curie point. Moderate cooling should then be necessary.

The ferrites have been vacuum tested up to 400°C. They behave compatibly to the UHV since no undesired gas emission has been detected. In the real cavity, the absorbing materials would be applied inside the WG's with a brazing technique that is presently under study.

In alternative to the ferrite load terminations, we are studying a broadband transition from WG to coaxial 1-5/8". A bandwidth of more than 2 octaves (i.e. .5+2.5 GHz) with VSWR ≤ 2.0 seems feasible. This design would allow to dissipate the HOM power on an external 50 Ω load.

V. ACKNOWLEDGMENTS

We are very grateful to the components of the DAΦNE RF Group for their continuous support to this project. We would like to thank the members of other Laboratories [6,7,8,9], also interested in HOM Free Resonator Design, for the contribution of their experience to our work and for the useful discussions.

VI. REFERENCES

- [1] M. Migliorati et al. "Multibunch Instabilities in DAΦNE: Longitudinal and Transverse Coherent Frequency Shift", DAΦNE Note G-18, 1993.
- [2] S. Bartalucci et al., "A low loss cavity for the DAΦNE Main Ring", DAΦNE Note G-6, 1991.
- [3] M. Bassetti et al., "DAΦNE Longitudinal Feedback" Proceedings of the 3rd European Particle Accelerator Conference, Berlin, March 1992, Vol. I, pp. 807-809.
- [4] R. Boni et al., "Study of the Parasitic Mode Absorbers for the Frascati Φ-Factory RF Cavities". Proceedings of the 1th Workshop on Microwave Absorbing Materials for Accelerators, CEBAF, VA, Febr. 1993.
- [5] ANSYS, Swanson Analysis System Inc., PA, USA.
- [6] R. Rimmer, "RF Cavity Development for the PEP-II B Factory", Proceedings of the Workshop on B Factories, KEK BFWS92, Japan, Nov. 1992.
- [7] A. Massarotti et al., "Proposal for a Broadband HOM Suppressor for Radiofrequency Accelerating Cavities", Particle Accelerators 1991, Vol. 35, pp. 167-175.
- [8] T. Tajima et al., "R&D on HOM Absorbers for Superconducting B-Factory at KEK", Proceedings of the 1th Workshop on Microwave Absorbing Materials for Accelerators, CEBAF, VA, Febr. 1993.
- [9] R. M. Hutcheon, "Dielectric and Magnetic Properties Measurements: Data from AECL", Proceedings of the 1th Workshop on Microwave Absorbing Materials for Accelerators, CEBAF, VA, Febr. 1993.

Mechanical Results of the CEBAF Cavity Series Production*

J. Mammoser and J.F. Benesch
Continuous Electron Beam Accelerator Facility
12000 Jefferson Avenue, Newport News, VA 23606 USA

Abstract

Interface dimensions of the full production run of 360 CEBAF cavities manufactured by Siemens are summarized. Analysis indicates that length tolerances of ± 2 mm and fundamental power coupler location tolerances of ± 0.15 mm are achievable on future procurements. Vacuum leaks were a concern early in production but have now been overcome: 2 K helium leak rates integrated over 22 vacuum seals have been measured on 84 cavity pairs and a roughly normal distribution of the \log_{10} (leak rate) is seen, centered about a rate of $10^{-10.2}$ torr-l/s.

I. INTRODUCTION

The Continuous Electron Beam Accelerator Facility (CEBAF) is under construction in Newport News, Virginia, USA. The machine will produce a low emittance electron beam with a current of 200 μ A and energies up to 5+ GeV for fundamental experimental studies in nuclear physics. [1] The accelerator consists of: a conventional source at 0.5 MeV, a single pass injection accelerator with nine pairs of superconducting radio frequency (SRF) cavities providing final energy of 45 MeV, and a main ring in the shape of a racetrack with two linacs. The two linacs each consist of 80 pairs of SRF cavities nominally providing 5 MV each, for a total of 400 MeV/linac and 4 GeV after five passes through each of the two linacs. There are thus 338 SRF cavities in the machine. A total of 360 cavities were purchased from Siemens.

Cavities are measured upon receipt and sorted into pairs according to window height (C), overall length (A) and window flange location (B), with that order of precedence. About one third of the assemblies require custom interface components. About 10% require custom beam tubes to meet the cryostat length interface and another ~20% require custom waveguide interfaces at (C).

II. MECHANICAL TOLERANCES

The outline of the CEBAF cavity, designed at Cornell University (2), is shown in Figure 1.

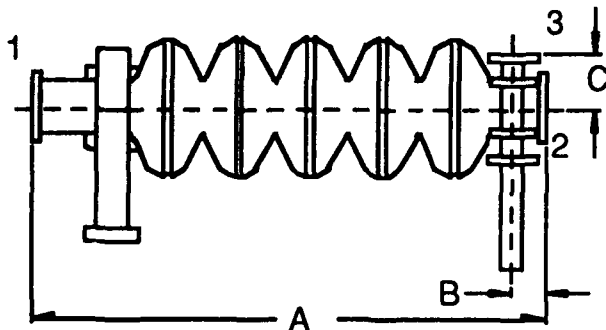


Figure 1. CEBAF cavity

Table 1 - Interface dimensions and tolerances (mm)

Overall length (A)	717.55 \pm 6
Coupler location (B)	46.33 \pm 0.07
Coupler height (C)	76.20 \pm 0.1
Perpendicularity of flanges (1, 2) to beam axis	0.2
Parallelism of coupler flange (3) to beam axis	0.2

Specifications are in Table 1. Means and standard deviations achieved on the three lengths shown, as measured by CEBAF and Siemens, are given in Tables 2 and 3. Table 2 represents the first 36 units (10%) and Table 3 the remaining 324 units. The latter are more representative of full series production, and will be discussed in what follows.

Table 2 - Lengths (mm) - Cavities 1-36

	Mean	σ
Overall length (A)		
CEBAF measurements	720.74	1.73
Siemens	720.44	1.57
Window flange location (B)		
CEBAF	46.33	0.14
Siemens	46.35	0.05
Window height (C)		
CEBAF	NA	NA
Siemens	76.12	0.12

Table 3 - Lengths (mm) - Cavities 37 and higher

	Mean	σ
Overall length (A)		
CEBAF measurements	721.48	0.97
Siemens	721.47	0.98
Window flange location (B)		
CEBAF	46.28	0.07
Siemens	46.32	0.05
Window height (C)		
CEBAF	76.28	0.06
Siemens	76.25	0.07

The agreement between the measurements made of overall length is excellent. Only six cavities (2%) fall outside $\pm 2\sigma$. Since this performance was achieved even though the span allowed was much broader, a length tolerance of ± 2 mm is reasonable for future acquisitions.

Agreement between CEBAF and Siemens measurements on dimensions B and C is not as good. It is believed that this is due to the difference in the way the cavities were supported on the table of each organization's coordinate measuring machine. CEBAF supported the cavity at the first and fifth cells while Siemens supported three of the five cells. Cavities are held by one beam tube and the coupler flange in the

* supported by U.S. DOE contract DE-AC05-84ER40150.

cryostat, so the CEBAF measurement is more representative of use. The cavities sagged. This is shown in Table 4, which gives the angles at points 1, 2 and 3 on Figure 1. Future acquisitions should include explicit descriptions of the measurement setup to be used, including supports.

Table 4 - Interface Angles

	mean	σ
Beam flange angle at HOM (1)	89.93°	0.04°
Beam flange angle at FPC (2)	89.92°	0.04°
Coupler flange angle to beam (3)	0.04°	0.03°

Looser tolerances for dimensions B and C would not require custom machining of interface components if one maintains an inventory of 40 to 50 cavities and sorts. Tolerances of ± 0.15 mm and ± 0.12 mm respectively are deemed achievable for future acquisitions.

The thinness (9 mm) of the flanges of the design did not allow for adequate machining after welding to obtain better length tolerances, better perpendicularity of flanges 1 and 2 and better parallelism of flange 3 to the beam axis. The thinness of the flanges also has been implicated in problems with the integrity of the indium vacuum seals used in the assembly of the cavity pairs (see below). An increase in flange thickness to 15 mm before final machining would stiffen the flange by a factor of three and allow 0.7 mm of material for final machining to form and position. With thicker flanges, the form tolerances in table 1 (parallelism and perpendicularity) could be tightened from 0.2 mm to 0.1 mm, perhaps eliminating the need for custom interface components altogether. The interface parts could also include bellows.

III. INDIUM VACUUM JOINTS

During early production there were a number of leaks in the indium wire seals used as vacuum joints between the cavities and auxiliary components. The vacuum leaks were traced to two causes: (a) inappropriate final surface finishing and (b) deformation of flanges due to flange thickness, bolt hole pattern and bolt torquing procedure. Cause (a) was eliminated by electropolishing stainless steel flanges and lapping of the niobium flanges before chemical etching with a buffered solution of nitric, hydrofluoric and phosphoric acid. Cause (b) was eliminated by modifying the RF window frame to increase stiffness, decreasing the indium wire size from 1.5 mm to 1.0 mm to reduce bolt torque, moving the indium wire seal towards the bolt holes and adopting new assembly and torquing procedures.

There are eighteen indium joints and four Conflat®-style joints in each cavity pair assembly. After two cavities are assembled into a pair with hermetic RF windows, HOM loads and interfaces to the helium vessel, the pair is evacuated and maintained under vacuum thereafter. (3) The pair is mounted on a vertical test stand and placed in a dewar. RF testing is then performed at 2.0 K. If a cavity pair does not meet the final vacuum leak specification at 2 K ($< 2 \times 10^{-8}$ std cc/s) or if there is concern about RF coupler window appearance after the test, then cavity components may be replaced or the cavity pair may be reprocessed. In either case, the pair is retested and only the final results used. The leak rate is tested by an integration method: since the cavity is immersed in LHe for at

least 24 hours and is not pumped during this period, by monitoring the partial pressure of helium in the cavity vacuum as the cavity pair is warmed from 4.2 K to 20 K we can determine the total quantity of helium which leaked into the system while it was immersed. The distribution of the test results is shown in Figure 2.

The data is consistent (Shapiro-Wilk W test, see reference 4) with a normal distribution with mean equal to -10.24 (6×10^{-11} torr-l/s) and standard deviation just under an order of magnitude.

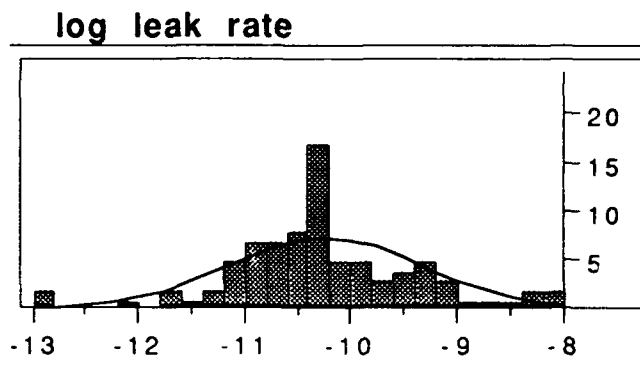


Figure 2. Common log of cold leak rate vs. number of cavities.

We are still having an occasional problem with cold RF window hermeticity. In addition, we have had a few leaks in indium joints due to oxides. Components can be removed and replaced without significant degradation of cavity performance by returning the pair to the clean room, holding it in the vertical orientation, bleeding it up slowly to about 105 kPa with nitrogen through a point of use particle filter, removing external particles with solvent wiping and then carefully replacing the failed component or seal. Nitrogen flow through the pair and out the opening created by the part swap is maintained while the change is made to minimize particle influx. This procedure has been quite successful as is shown in figure 3, a case where the cold RF window was found to leak after vertical test. The two curves show the results of two distinct vertical tests, before and after the window change.

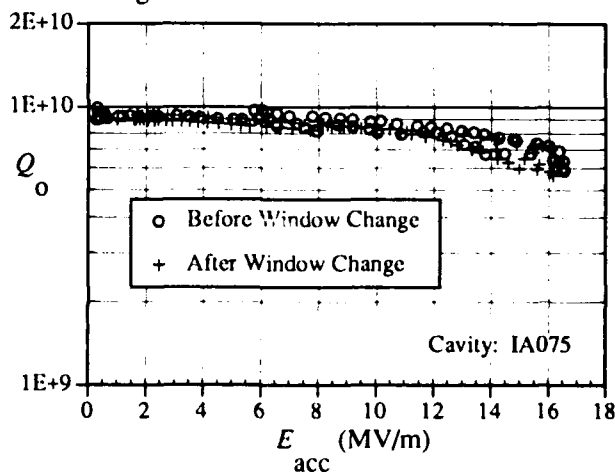


Figure 3. Durability of cavity performance with exchange of cold window

IV. ACKNOWLEDGMENTS

Cavity measurements at CEBAF were made by K. Yopp, H. Ward, A. Forrest and I. Daniels. Figure 1 was provided by K. Yopp and figure 3 by C. Recce.

V. REFERENCES

- [1] H. Grunder, *Proceeding of the 1988 Linear Accelerator Conference*, and CEBAF report 89-001.
- [2] P. Kneisel et al., *Proceedings of 1991 Particle Accelerator Conference*, 91CH3038-7, p. 2384.
- [3] P. Kneisel, *Proceedings of the 1987 Particle Accelerator Conference*, CH2387-9/87, p. 1893.
- [4] S.S Shapiro and M.B. Wilk, *Biometrika* 52, 591 (1965).

FABRICATION OF COMPLEX MECHANICAL COMPONENTS

Yves BEROUD
S.I.C.N.
BP 1, 38113 Veurey-Voroize, FRANCE

Abstract

Precision mechanical components consist of parts which are difficult to fabricate due to their materials of construction and because of the state-of-the-art techniques required to fabricate and assemble them.

This paper presents various materials and fabrication techniques, including combined machining-welding techniques, uranium metallurgy, niobium-steel soldering and micromechanical techniques. It also illustrates each technique with specific examples.

The mechanical components described in the present paper are used primarily in the nuclear industry, as well as in equipment for scientific research.

I. INTRODUCTION

SICN has fabricated nuclear fuel for its parent company COGEMA for over 30 years. Through its fuel fabrication activities, SICN has developed specialized capabilities in machining, welding and non-destructive examination for the fabrication of precision components.

Following a detailed description of the activities and resources of the company, examples of unique fabrication technologies will be provided.

II. SICN ACTIVITIES

SICN has worked with a wide variety of materials and alloys in fabricating precision mechanical components: the entire gamut of stainless steels, aluminium, tungsten, titanium, tantalum, magnesium, zirconium, uranium and inconel as well as graphite and ceramics.

In addition to its expertise in each step of the mechanical component fabrication process- machining, welding, soldering, surface finishing and non-destructive inspection- SICN performs all fabrication activities in accordance with stringent quality assurance requirements.

III. FABRICATION TECHNIQUES

SICN uses a wide variety of fabrication techniques for numerous different applications, from the nuclear industry to space programs, from the defense sector to aeronautics.

A. Machining

The equipment used for precision mechanics is of prime importance and must be constantly updated to reflect the latest developments.

B. Welding

The primary purpose of welding is to fuse two components together. SICN uses several welding techniques, including:

- TIG electric arc welding, with or without filler metal,
- electron beam welding, using both 10 and 15 KW machines, which makes straight, deep welds with high specific energy and,
- laser welding, using the YAG 400 W machine, which makes welds in normal atmospheres with high energy.

When extremely accurate welds are required, SICN redesigns existing welding equipment, by supplying an electron gun, building a vacuum chamber and designing the associated control system to achieve the greatest operating efficiency for the proposed application.

C. Annealing

Annealing is performed at 1500 ° C in large capacity (500 x 600 x 900 mm) highly exhausted vacuum furnaces.

D. Non destructive examination

SICN uses five methods of non-destructive examination:

- x-ray gammagraphy to detect deep defects (NASA agreement),
- dye or fluorescent penetrant test to detect surface defects (NASA agreement),
- ultrasounds to detect deep and surface defects,
- dye penetrant test to detect leaks,
- calibration control: automatic, three-dimensional calibration benches in air-conditioned rooms are used to check component dimensions.

E. Surface finishing

SICN uses the physical vapor deposition (PVD) process on a machine of its own fabrication to deposit a very thin layer (less than 10 microns) of metal, alloy or composites on the surface of a component to increase its resistance to wear, among other purposes.

The plasma jet process is also used to spray metals, refractory metallic oxides, carbides, nitrates and borates onto the component's surface to increase its resistance to friction, to create a thermal barrier.

IV. SPECIFIC PRODUCTS

A. Structural components for fuel elements

SICN, the sole fabricator of gas-cooled reactor (GCR) fuel in Continental Europe, has supplied approximately two million magnesium clad fuel cartridges. A special dry finishing process and a TIG-electron beam welding machine were developed to machine and assemble the magnesium fuel cartridges.

With the start-up of first fast breeder reactors, SICN was called upon to participate in the fabrication of fuel for this reactor series. SICN has supplied precision structural components in stainless steel for Phenix reactor fuel, including the upper and lower nozzles, the upper neutron shielding, and the hexagonal fuel cans.

Fuel mock-ups were made and prior to fabrication, special benches were set up for automatic ultrasonic inspection, TIG welding of fertile fuel pins, and electron beam welding of the lower nozzles of the fuel assembly.

SICN also fabricates standard components for pressurized water reactor (PWR)- fuel elements, including the stainless steel end fittings and the inconel springs. The electron beam welding system and the three-dimensional calibration system were automated to fabricate the end-fittings, which require an average of 1,500 measurements per piece.

B. Liners

The liner is a critical component of complex propulsion systems used for rockets and satellites.

The liner envelopes the pressurized tanks and is an integral part of their structure. With a lifetime of approximately 100 seconds to 10 years, depending on whether it is part of a booster rocket or a satellite, the liner must have a high degree of reliability under all conceivable circumstances.

The production blank is delivered to our facility by the client. The blank, first, undergoes visual examination, then measurements checking. The half spheres of the blank are mechanically prepared on a conventional lathe.

A digitally-controlled lathe with integrated production control is used to machine the outer surface of the half spheres to 1 millimeter. The inside of the blank then undergoes the same operation.

The half spheres are annealed under vacuum using a centering piece for rounding. The final machining of the half spheres is then performed with a digitally-controlled lathe.

The ends and the frame of the liner are machined with a conventional lathe. In the final machining operation, the ends are pierced with a digitally-controlled boring machine.

The liner is approximately 620 millimeters in diameter and 1.2 millimeters thick at the equator, which must be verified by geometric measurement control.

A dye and fluorescent penetrant test, for which SICN obtained NASA certification, is performed on the half spheres. The test is a highly accurate means of detecting metal cracking.

The half spheres are cleaned and their joint edges are chemically scoured before being welded.

A rigorous quality assurance system applies to all fabrication operations. Before equatorial welding can be performed on the half spheres, welds must be performed on test pieces and analyzed for integrity. After the half spheres are welded, weld quality is inspected by x-rays.

Final non-destructive examination of the finished product includes dye and fluorescent-penetrant testing of the weld, weld x-rays as required by contract, and a helium leak test. SICN's x-ray examination procedures have also been certified by NASA.



LINER

C. Components for experimental equipment and scientific research

The Large Electron Positron Collider (LEP) is the large machine of the CERN and will likely remain the largest collider in the world for some time to come.

One of the technologies used in the LEP is radio-frequency. The LEP collider is circular and the loss of energy by synchrotron radiation is compensated by super-conducting radio-frequency accelerating cavities. The energy needed to accelerate the electrons and positrons and to replace the energy lost by synchrotron radiation is transmitted to the circulating beam from these cavities.

C.1 RF Couplers

RF couplers are also called "main couplers". The radio-frequency coupler is the interface between the RF emitter and the super-conducting cavity. The main coupler is made of a niobium-copper double casing stainless steel pipe connected at one end to the vacuum tank and at the other end to the cavity antenna connected to a ceramic window. The length of the antenna introduced inside the cavity is adjustable.

SICN makes the couplers out of stainless steel, copper and niobium, precision machines and welds them by TIG process for the stainless steel materials or by brazing under vacuum for the junction Cu/Cu or Cu/Stainless steel.

C.2 HOM Couplers

The high order mode couplers extract the radio-frequency current lost by the beam inside the non-accelerating areas of the cavities. The HOM coupler is made out of niobium and stainless steel. As extremely difficult area, from a fabrication point of view, is the vacuum brazing of the niobium-stainless steel junction.

C.3. Tuners

SICN also fabricates components associated with super-conducting cavities, called TUNERS.

This component enables the tuning of the cavity of its fundamental resonant frequency. Each anchorage part consists of an assembly of concentric tubes welded together and mounted on a core to allow positioning of the cavity. Between the tubes a path is created for helium flow. The two other main devices belong to the Ni tube :

one heater cable brazed at the outer periphery of the middle of the tube.

two magnetic coils wound on and insulating material.

Both devices enable the tuning of the fundamental frequency through modification of the length of the Ni tube (wave length variation through thermal and magneto-striction effects).

SICN is currently producing 150 RF couplers, 300 HOM couplers and 300 tuners for the LEP project.

D. Instrumented test equipment

SICN has been involved for a number of years in the design and fabrication of instrumented equipment used in research reactor cores to study, for example, the behaviour of new fuel when exposed to radiation.

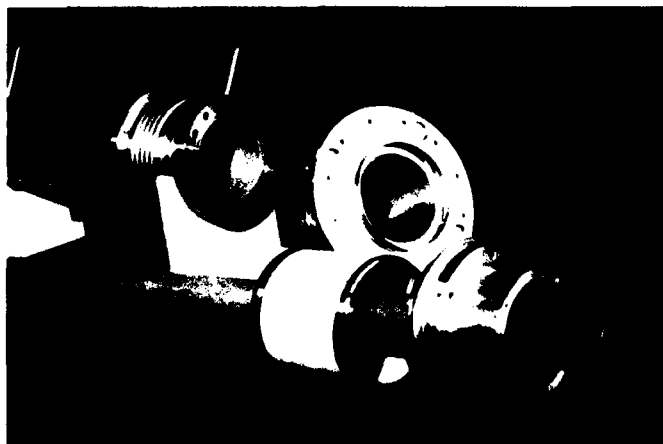
The systems are instrumented poles with numerous temperature, pressure and vibration sensors. Special measures must be taken during their fabrication particularly with respect to the density of the connections, precision machining using micro-mechanical techniques, and precise welding and soldering.

V. CONCLUSION

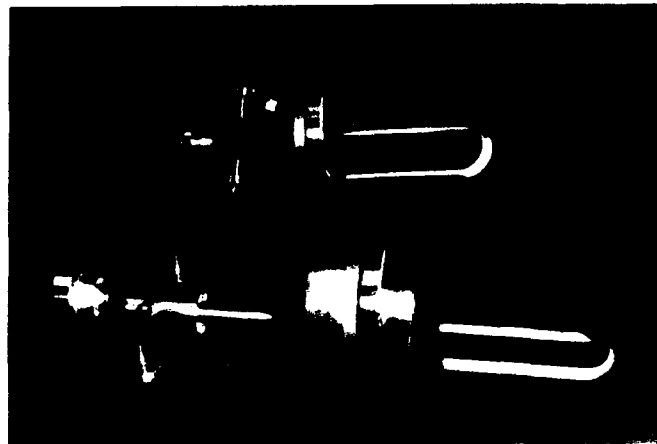
The fabrication of precision mechanical components requires special skills in the metallurgical, metallographic, machining, welding, surface finishing and non-destructive examination fields. The equipment necessary to achieve the required level of precision, of technical excellence and of production throughput is one of the keys to success and it must be constantly updated to take advantage of progress in the field of precision mechanics.

The more complex the component, the more indispensable the skills of machining, assembly and quality control. SICN has created a team where all these skills are present under the same roof.

May 1993



RF COUPLERS



HOM COUPLERS

Measurements of Higher Order Modes in 3rd Harmonic RF Cavity at Fermilab

C. M. Bhat

Fermi National Accelerator Laboratory*
P.O. Box 500, Batavia, IL 60540

Abstract

We have measured the R_s/Q for several higher order modes of the modified CERN 159MHz RF cavity up to 1.5GHz using bead-pull as well as stretched-wire methods. The data have been compared with the predictions of 2D code URMEL. Attempts have been made to investigate coupled-bunch instabilities that can arise from higher order modes of the cavity with the beam-on conditions. No resonances of the third harmonic cavity below 800 MHz were found to give rise to any noticeable beam instability.

I. INTRODUCTION

Recently a focus-free transition crossing rf system has been implemented at Fermilab Main Ring (MR) to reduce the beam loss and emittance growth related to the transition crossing. The details of the principle of this technique, associated hardware and software are described elsewhere¹. One of the main components of this system is a modified CERN RF cavity (sometimes called a third harmonic rf cavity) which has unloaded Q of about 36000 for its fundamental mode (at 159MHz). Predictions made using 2D rf cavity code URMEL² for this cavity structure suggested that there should be many higher order modes with considerably large values below 1.5 GHz. Hence one of our primary concerns was a coupled bunch instability of the beam that would be induced by the third harmonic rf cavity if it is used in the beam along with other MR 53 MHz rf cavities. Before installation of the third harmonic rf cavity in the MR a study of the cavity shunt impedance (R_s) was made. The measurements have been made by two independent methods which are outlined later and carried out under two different conditions viz, with tuner unbiased and biased. After installation of the third harmonic rf cavity in the Main Ring, studies have been performed with the beam.

Here we report our bench measurements of R_s/Q for third harmonic rf cavity higher order modes below 800MHz and a search for coupled bunch MR beam instabilities due to these cavity modes.

*Operated by the Universities Research Association, under contracts with the U.S. Department of Energy

II. MEASUREMENTS OF THE SHUNT IMPEDANCE OF THE CAVITY MODES

In the past, mainly two different methods have been suggested^{3,4} to measure shunt impedance of the resonances of an rf cavity : 1) field perturbation method and 2) wire measurements. The principles of measurement for these two methods have been outlined below. In practice both of these methods have merits and demerits.

A. Bead-Pull Method

The R_s/Q of an rf cavity resonance is related to the shift in its resonance frequency $\frac{\delta f}{f}$ arising from a conducting sphere placed in the magnetic field-free region of the cavity and is given by³,

$$\frac{R_s}{Q} = \frac{1}{2\pi f_0} \left\{ \int_L \sqrt{\frac{\delta f}{f} \frac{4}{3\epsilon_0 \delta v_M}} dz \right\}^2 \quad (1)$$

where f_0 is the resonance frequency of a cavity mode. Q is determined for the unperturbed resonance. L is the length of the cavity. δv_M is the volume of the conducting sphere, ϵ_0 is permittivity of free space. $\frac{\delta f}{f}$ is obtained by measuring the phase shift of the transmitted signal from the cavity due to the perturbing object. If the phase of the unperturbed cavity mode is set to zero then the frequency shift is related to phase shift ϕ by⁵,

$$\frac{\delta f}{f} = \frac{1}{2Q} \tan \delta \phi \quad (2)$$

Thus in an R_s/Q measurement the phase shift ϕ is measured as a function of the position of a conducting metallic bead along the axis of the cavity and used to determine the integrand of Eq. 1.

In our measurements a copper spherical bead of volume 0.113cm^3 was attached to a nylon thread and was pulled along the axis of the third harmonic rf cavity. The motion of the bead was controlled using an automated motor system⁶. The velocity of the bead was about $3.54 \pm 0.30\text{cm/s}$ and synchronized with a network analyzer sweep time. Sitting on a particular resonance of the cavity,

magnitude of the S_{21} phase ϕ was measured with a zero frequency span on a HP8753C 300kHz-3GHz Network Analyzer. The cavity was excited with a very weak signal. The data were digitized to evaluate the integrand in eq. (1). The results of the measurements are tabulated in Table I. One of the limits of the bead-pull measurements is that it can be used only for strong resonances.

B. Stretched-Wire Measurement

In this technique a situation quite similar to beam-on conditions is generated by inserting a thin wire along the axis of the cavity and sending wide band-width high frequency TEM signals through one of the ports. To reduce the reflection due to step transition from 50 Ω transmission line connection to the beam pipe, a matching resistor of an appropriate value is introduced in series with the wire at both ends. Then the impedance of the cavity mode can be obtained⁴ by measuring the amplitude of the scattering parameter $S_{21}=(1+0.01R_s)^{-1}$ which depends on the reflected signal at port 1 and the transmitted signal at port 2 of the stretched-wire insert system. In order to remove the effects arising due to attenuation of the cables and to correct for the path length, measurements have to be done with a reference device. Thus the shunt impedance of a cavity mode is given by⁴,

$$R_s = 2R_o \left(\frac{1}{S_{21dev}} - \frac{1}{S_{21ref}} \right) \quad (3)$$

where $R_o = 50\Omega$. The quantities S_{21dev} and S_{21ref} are measured for the device under test and the reference device. A critical survey of the wire measurements of impedance has been done earlier⁷.

In the case of the third harmonic rf cavity the beam pipe radius with the copper sleeves¹ was 4.0in dia and each sleeves shrink-fitted had a slant starting at about 2in from the nosecones. The acceleration gap was about 4.33in. A stretched-wire system was designed with a 10 mil wire and length of 8.5 in. The wire was supported using two .25in dia G10 rods. The characteristic impedance of the beam pipe with the wire was 359 Ω . Two matching resistors of 300 Ω were used in series with the wire one at each end. A 50 Ω matching for the SMA connector was obtained by using four 220 Ω resistors in parallel and symmetrically placed at both ends of the wire. An aluminium cylinder of 4.0in inner dia and about 14.0in length with one of its end slanted to tight fit to the sleeves-slant was used as a reference device.

Using the network analyzer S_{21} calibration measurements were made with the test device. Then the wire assembly was slid in between the acceleration gap of the cavity without disconnecting the cables. The R_s/Q determined by this method for resonances below 800 MHz are compared with the bead-pull measurements in Table I. The higher order modes of the cavity up to 1.5 GHz are shown in Fig.1.

Table I. A comparison of R_s/Q of third harmonic rf cavity resonances measured* using bead-pull and stretched-wire. The measurements were done for loaded cavity (with a ferrite tuner and power amplifier coupling loop).

Tuner Bias (Amp)	f_o (MHz)	Bead-pull R_s/Q (Ω)	Wire R_s/Q (Ω)	URMEL [†] R_s/Q (Ω)
0.0	159.095	255	457	179
	419.920	30	56	11.5
	561.285	44	8	20
	721.007	4.9	132 §	2.
	776.836	16.2	6.22	7
300	159.040	315	318	
	419.618	29	51	
	561.265	56	8.27	
	721.020	4.5	119 §	
	776.762	7.0	5.47	

* The statistical error in R_s/Q for bead-pull measurements was about 10%.

† URMEL calculations were made for unloaded cavity.

§ The large value of R_s/Q value for this resonance is coming from errors in Q measurements.

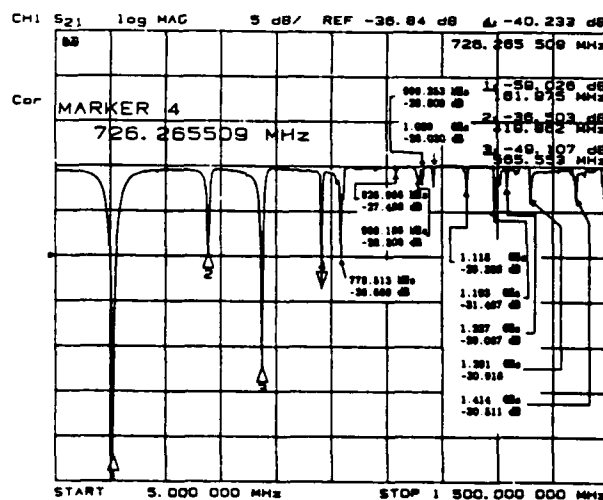


Fig.1. S_{21} stretched wire measurements for third harmonic rf cavity. For high Q resonances a frequency shift by few MHz is seen.

The R_s/Q measured by these two methods are considerably different for tuner unbiased and biased. In the case of wire measurements, the observed cavity Q- values are lowered because of the presence of the conducting wire along

the axis of the cavity. Also a large amount of resonance frequency shift is observed. Hence the present measurements had a large systematic error. A recent⁷ similar wire study on a simple pill-box cavity also found to show similar results; 1-2% frequency shift and measured R_s/Q differed by about 20-30% from the analytical solutions. However, the wire-measurements offers a nice technique to simulate beam on conditions during the bench tests. Our measurements with bead-pull had small errors and were reproducible within about 10%.

III. BEAM-ON STUDIES OF THE THIRD HARMONIC RF CAVITY

Ideally one would like to damp all unwanted modes of a cavity to reduce the coupling of the beam with cavity modes which causes beam instability. Here we have investigated the effects of higher order modes of the third harmonic rf cavity on the MR beam. The measurements were carried out in two steps. First, each of the beam-excited cavity modes up to 1.0 GHz were identified using a spectrum analyzer. Here the beam signals were observed using one of the gap monitors of the third harmonic rf cavity. The pattern of the beam excited resonances were similar to the one shown in Fig.1. Then, sitting on a resonance the growth of amplitude of a mode corresponding to the one detected in the cavity was monitored as a function of acceleration cycle time. The beam signals from a 2GHz resistive wall pickup system were used for this measurement. During this time the spectrum analyzer was triggered on the accelerator clock event at the beginning of the acceleration cycle. This was repeated for each resonance given in Table I for two different beam intensities viz., 0.9×10^{10} ppb and 2.0×10^{10} ppb. We found no modes that show considerable growth indicating none of the third harmonic rf cavity higher order resonances have significant effects on the MR beam during normal operation at these intensities.

IV. ACKNOWLEDGMENTS

Author would like to thank Dr. D. Wildman for useful discussions and B.Fellenz for setting up the wire measurements.

REFERENCES

1. C.M. Bhat et al, "Operational experience with third Harmonic rf cavity for improved beam acceleration through transition in the Fermilab Main Ring", this conference.
2. U. Laustroer et al, URMEL AND URMEL-T USER GUIDE, DESY M-87-03, 1987.
3. L.C.Maier, Jr and J.C. Slater, J. Appl. Physics, **23**, 1, 951 (1952).
4. G. Jackson, " Review of impedance measurements at Fermilab", Proc. of Fermilab III Instabilities Workshop, June 1990, page 245.
5. F. Casper and G. Dome, "Precise perturbation measurements of resonant cavities and higher order mode identification", CERN SPS/85-46 (ARF).
6. K. Harkay, private communication.
7. P.L. Colestock, private communication.

POISSON/SUPERFISH on PC Compatibles*

James H. Billen and Lloyd M. Young
Los Alamos National Laboratory
Los Alamos, NM 87545

Abstract

We have adapted the POISSON/SUPERFISH codes to run on 486 or 386 PCs. The PC version includes features not found in the standard version, including programs for automatically tuning RFQ, DTL, and CCL cavities; a complex version of the rf field solver; memory allocation for temporary data; many line regions for dividing the mesh into fine or coarse sections; full support for multiple-cell DTL cavities; plotting of resonance-search and transit-time data; and on-line documentation. We modified AUTOMESH to generate self-consistent logical and physical coordinates. This new, more robust code greatly reduces the number of crashes in LATTICE caused by ill-formed mesh triangles along boundaries. The codes solve arbitrarily large problems. Each program allows free-format entry of CON array elements, and provides error checking of user entries. Standard release 4 now uses our root finder and convergence criteria.¹

Introduction

In 1985, one of us (Young) adapted the Cray version of these codes to run on IBM-PC-compatible computers. He improved several algorithms that gave trouble in the original version. In 1992, we modified the codes extensively. The goal was to do larger problems, but we also improved the user interface, the field-interpolation algorithm in post processors, and the root finder for resonance searches. We added DOS exit error codes, control programs to tune cavities, post processor support for multiple-cell cavities, and on-line documentation. We use the Lahey FORTRAN compiler F77L-EM/32.² The Lahey debugging tools greatly aided our development work.

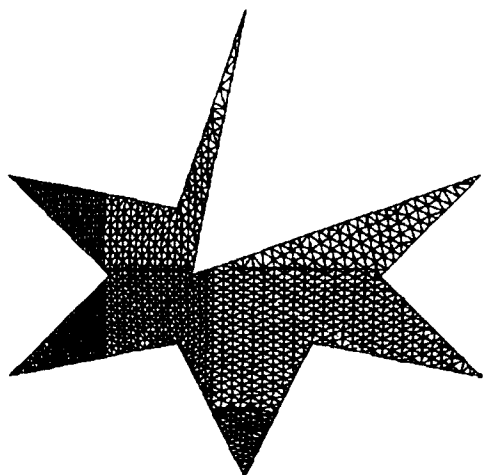


Figure 1. A "star cavity" to test the AUTOMESH code.

The User Interface

AUTOMESH, the first code run on a problem, uses NAMELIST input. We retain the CON array as the method for codes to share information. The PC version allows entry of more variables (including most CON elements) in the NAMELIST file. CON element input is truly free-format and the codes check and warn of possible errors in input values. New CON elements control the field normalization, surface resistance, and accelerated particle mass in SFO. Some CON elements cannot be changed by the operator, and others can change only in appropriate codes. The codes prevent user input of unchangeable CON elements. For example, boundary conditions must not change after program LATTICE. The starting frequency can change in AUTOMESH, LATTICE, or FISH, but not in post processor SFO. Output files list CON values used in their respective programs and show where the user last changed a value.

AUTOMESH

AUTOMESH lists logical coordinates along boundaries for LATTICE. Integer coordinates K,L describe the logical overlay mesh and X,Y are the physical coordinates. Older AUTOMESH routines did little checking for consistency among points, sometimes resulting in triangles for which LATTICE calculates a negative or zero area. We limit choices for K,L for boundary points, line-region intersections with the boundary, and points along the connecting path. For example, all points with identical Y must use the same L, and likewise for X and K. These checks prevent most "negative-triangle" crashes in LATTICE. Figure 1 shows a sample geometry that we use to test AUTOMESH. This "star cavity" has several challenging features. Sharp corners are often hard to mesh. Line regions that intersect near a boundary were usually too much for the old version of AUTOMESH.

A New Root Finder

In SUPERFISH, resonances occur at slope=-1 roots of the $D(k^2)$ function.³ Wave number k corresponds to frequency f ($k=2\pi f/c$). Subroutine FROOT finds a slope=-1 root using polynomial approximations. The original root finder, though used for many years, was not very robust. Occasionally, it did not converge to the nearest mode and sometimes could not find a mode at all. It stored $D(k^2)$ and k^2 at each iteration, but sometimes it swapped a new point with a previous point. It never used new data to update the slope of previous points. Derivatives of $D(k^2)$ were usually wrong because the calculation used adjacent points in unsorted arrays. Because it made little use of these derivatives, SUPERFISH usually converged to a resonance near the initial frequency. Our new

* Work supported by the U. S. Department of Energy.

version of the FROOT subroutine sorts the data by k^2 and recalculates first and second derivatives after every iteration. It analyzes the data to place upper and lower bounds on the location of the desired root. Taking a smaller first step toward resonance gives a more reliable estimate of the local slope and reduces the chances of missing a mode where the function has a narrow local minimum.

After four or more iterations, FROOT selects three points for a parabolic interpolation. Carefully chosen points speed convergence to the root. We use the last chronological point and lower or upper bounds, if available. Other points must be adjacent to or between the bounds. Given a choice, FROOT favors points with slope close to -1 . With only two points, the code examines the two parabolas that go through both points and have slope equal to -1 at $D(k^2)=0$. It picks the k^2 within the current bounds. If parabolic approximations fail to find a new k^2 consistent with the upper and lower bounds, FROOT uses one of several contingencies that give more information about the local shape of the function.

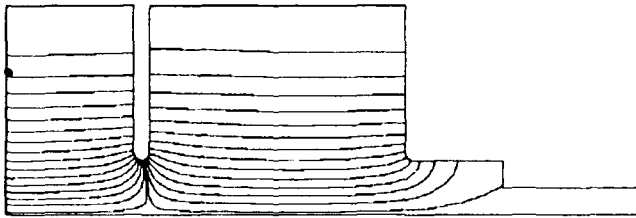


Figure 2. Electric field lines for the lowest π mode of a three-cell cavity. The left edge is a symmetry plane and $r = 0$ is at the bottom of the figure. The dot at left shows the drive-point location.

We tested the new root finder on many cavity shapes, sometimes deliberately placing the drive point in unfavorable locations. Figure 2 shows electric field lines for the 499.58-MHz π mode of a three-cell coupled cavity. Close proximity to the zero mode, 3.7 MHz lower in frequency, was a problem for the old version. The new code always found the nearest mode for 60 starting frequencies between 490 and 505 MHz. FISH makes a plot file of mode-searches and frequency-scan data. Figure 3 shows such a $D(k^2)$ plot over some higher-order modes of this cavity. If the drive is in weak field for a

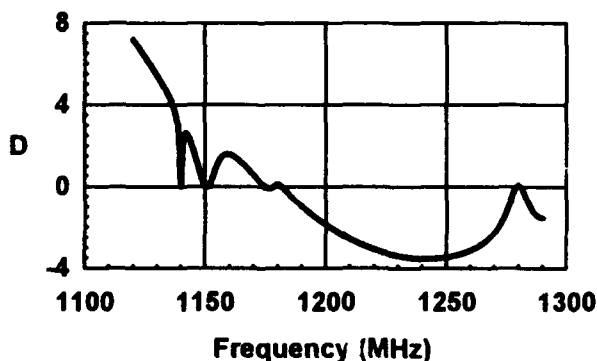


Figure 3. The function $D(k^2)$ plotted versus frequency over the range of 5 higher-order modes.

mode, the function barely crosses zero and challenges the root finder. The new FROOT never failed to find a nearby mode for a wide range of starting frequencies. For example, it found the 1140-MHz mode for 12 starting frequencies from 1139.3 to 1140.4 MHz. The old version found this mode only when the starting frequency was within 40 kHz of resonance.

Convergence Criteria

For convergence to a resonant frequency, SUPERFISH requires that $D(k^2)$ is small enough and has the correct slope:

$$\left| \frac{D(k^2)}{k^2} \right| < \epsilon; \quad \left| \frac{\delta(k^2)}{k^2} \right| < \epsilon; \quad \text{and} \quad -1.02 < \frac{dD}{d(k^2)} < -0.98.$$

The convergence parameter ϵ is typically 0.0001, and $\delta(k^2)$ is the next proposed change in k^2 after an iteration. Standard versions of SUPERFISH through version 3.0 used only the second of these criteria. The code did not actually require a small $D(k^2)$ and it did not check for a negative slope. Newer releases of the standard version use our convergence criteria. Failure to check the slope is not a problem unless the starting frequency is near a positive-slope root. After one iteration, the code does not know the slope. LATTICE initializes the slope to $+1$, forcing a second iteration. If the starting frequency is known to be near resonance, then the operator (or a control program) can set the slope to -1 to allow the code to converge in only one iteration.

Large Problems

Mesh dimensions in the SUPERFISH codes can be as large as the computer resources allow. The original codes were new when memory was scarce, so they shifted and masked bits to store multiple pieces of information in one computer word. The "INDEX" array allotted 5 bits for region numbers and 15 bits for the mesh-point counter. In all, INDEX stored seven items for each point. The PC codes eliminate mask and shift operations. We use a four-byte integer array for the mesh-point counter, two-byte integer arrays for region numbers, and one-byte integer and logical arrays for other data previously coded in the INDEX array. (Standard version 4 now uses a similar strategy.)

FISH and POISSON run faster if the mesh is fine only where it needs to be. AUTOMESH allows many divisions in the mesh, called line regions, for changing the mesh size. Figure 4 shows fields from an example calculation for an entire drift-tube linac tank. The dot above the sixth full drift tube from the left is the location of the drive point. The mesh had about 130,000 points. The mesh resolution near the curved surfaces on drift tubes was about one-fourth of the radius of curvature. For this problem, an iteration took 35 minutes on a 66-MHz 486 computer. Allocating memory for temporary arrays also speeds execution. While solving the tri-diagonal matrix, program FISH stores data for each mesh row, which it later reads back in reverse order. Instead of storing this data on disk, the program can use available memory. For the problem

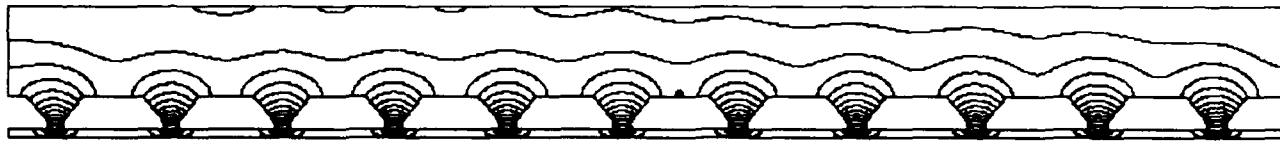


Figure 4. Electric field lines in an 11-cell drift-tube linac. The cavity design includes a ramped field. This calculation used only 130,000 mesh points. Mesh spacing near the drift-tube noses was 25% of the radius of curvature.

shown in Fig. 4, the computer had insufficient memory to hold the temporary data arrays, so the program wrote them to a 120-megabyte disk file.

Post Processors

Post processor codes include SFO, SF7, and VGAPLOT. SFO calculates parameters of interest to the accelerator designer, such as axial field integrals, transit-time factor, power dissipated on metal surfaces, shunt impedance, and frequency shifts from perturbations. SF7 interpolates electric and magnetic fields on lines, arcs, and rectangular grids. VGAPLOT is the SUPERFISH plotting code. Figures 1, 2, and 4 in this paper were drawn by VGAPLOT.

We added new code in SFO for multiple drift-tube linac cells. The code calculates transit-time integrals for all cells and power and frequency shifts for single or multiple stems and post couplers. SFO also now has more field-normalization options. For example, the designer can specify a value for either E_0 or $E_0 T$. The code can calculate rf surface resistance R_s for normal or superconducting materials, or the user can enter a known value of R_s . SFO includes an option to write a plot file of the transit-time integrands.

The field-interpolation algorithm in SFO and SF7 is new. The old version selected points poorly, resulting in large point-to-point fluctuations along lines. The new algorithm first finds the mesh triangle containing physical point x_0, y_0 at which it will calculate fields. The area of this triangle is A_0 . It fits a doubly quadratic polynomial to first and second nearest neighbors of x_0, y_0 . The least-squares fit weights points by their physical proximity to x_0, y_0 . Points within a range $\sqrt{A_0}$ have unity weight. Other mesh points x_i, y_i have weight W_i given by

$$W_i^2 = \frac{A_0}{(x_i - x_0)^2 + (y_i - y_0)^2}.$$

The general fitting polynomial is:

$$H(x, y) = P_1 + P_2(x - x_0) + P_3(y - y_0) + P_4(x - x_0)^2 + P_5(y - y_0)^2 + P_6(x - x_0)(y - y_0).$$

The interpolated magnetic field $H(x_0, y_0) = P_1$. Electric field components E_x and E_y (or E_z and E_r) are proportional to coefficients P_3 and P_2 respectively. The new code imposes boundary conditions by eliminating appropriate terms from the fitting function. For example, on the axis of a cavity with cylindrical symmetry, H and E_r must be zero. For this boundary $P_1 = P_2 = P_4 = 0$. On Dirichlet vertical boundaries and Neumann horizontal boundaries E_z is zero, and on

Dirichlet horizontal boundaries and Neumann vertical boundaries E_r is zero. The code constrains the electric field to be normal to sloping Neumann boundaries.

New Programs

CFISH is a version of FISH that uses complex fields. It is useful for designing rf windows and calculating power losses in dielectric and magnetic materials. Post-processor codes SFO, SF7, and VGAPLOT are compatible with both real and complex versions of the code. VGAPLOT shows the real and imaginary field components in different colors. AUTOFISH is a combined version of programs AUTOMESH, LATTICE, FISH, and SFO. It saves time because it loads only one program and avoids several disk reads and writes.

DTLFISH, MDTFISH, CCLFISH, and RFQFISH are control codes for tuning DTL cells, multiple-drift-tube cavities, CCL cells, and RFQ cavities. An input file may contain starting parameters for many problems. These programs set up the cavity geometry and run the SUPERFISH codes repetitively, varying the cell geometry to tune each problem to within tolerance of a specified frequency. DTLFISH and CCLFISH assume symmetric half cells. DTLFISH adjusts either the tank diameter, drift-tube diameter, gap, or face angle. CCLFISH adjusts the cell diameter, septum thickness, gap, or cone angle; it also tunes buncher cavities and quasi-elliptical cavities. MDTFISH tunes DTL cavities by varying the tank diameter or the average drift-tube gap. Drift tubes have the same diameter and nose radii, but can have different face angles. Output includes the distribution of E_0 . RFQFISH tunes an RFQ cross section by varying cavity volume or the shape of the vane tip.

Acknowledgments

We benefited from discussions with Robert Ryne of the Accelerator Code Group. We thank Richard K. Cooper for helpful suggestions and for several of the test cavities.

References

- 1 Los Alamos Accelerator Code Group, "Reference Manual for the POISSON/SUPERFISH Group of Codes," Los Alamos National Laboratory document LA-UR-87-126.
- 2 Lahey Computer Systems, Inc., 865 Tahoe Blvd., Incline Village, NV 89450.
- 3 K. Halbach and R. F. Holsinger, "SUPERFISH — A Computer Program for Evaluation of RF Cavities with Cylindrical Symmetry," *Particle Accelerators* 7 (1976) 213-222.

Radio Frequency Measurement and Analysis Codes*

James H. Billen
Los Alamos National Laboratory
Los Alamos, NM 87545

Abstract

This paper describes a comprehensive set of computer codes for measuring, analyzing, and displaying field distributions in rf cavities. Development work began in 1984 for 8086-based computers. The codes now run on 486 and 386 PCs and include extensive on-line documentation. BEADPULL and QUADPULL collect frequency shifts as a metal or dielectric bead traverses a resonant cavity at constant speed. QUADPULL measures fields in all four quadrants of radio-frequency quadrupole (RFQ) cavities. Analysis codes apply the Slater perturbation theory¹ to convert frequency shifts to fields. BEADPLOT plots the field distributions and calculates field integrals. DTLPLOT analyzes and plots BEADPULL measurements in drift-tube or coupled-cavity linacs. QUADPLOT does the same for QUADPULL data in RFQs. Supporting programs prepare design data for comparison with the measurements and compute averages of multiple measurements. COUPLING extends the accuracy of an impedance analyzer for Q and VSWR measurements. The code plots reflection coefficients on a Smith chart and analyzes the resonance circle to get β .

Introduction

The measurement and analysis code package includes more than 25 programs for characterizing the fields in rf accelerator cavities. Analysis codes compare measured data to design data from SUPERFISH² or from RFQ design codes. Measurement codes use Hewlett Packard (HP) instruments to record the field distribution in a resonant cavity. The codes communicate with instruments on the General Purpose Interface Bus (GPIB), which is the common name for the communications protocol defined in ANSI/IEEE Standard 488-1978. Our GPIB hardware is from National Instruments Corporation.³ We compile GPIB codes with the Lahey FORTRAN compiler⁴ F77L and link the codes with a National Instruments object module that addresses the GPIB hardware. Analysis codes use Lahey's F77L-EM/32 compiler. Debugging tools from both Lahey and National Instruments proved invaluable for the development work.

Accelerator Cavities

Many accelerators use cavities that operate in a TM_{010} -like mode. The TM_{010} mode in a "pillbox" (a right circular cylinder) has two nonzero components of the electromagnetic field: E_z and H_ϕ . Higher-order pillbox TM_{01x} modes and TM_{010} cavities like the drift-tube linac (DTL) and the coupled-cavity linac (CCL) have nonzero components of E_z ,

E_r , and H_ϕ . The designer most often is interested in E_0 , the average axial electric field. For a cell of length L :

$$E_0 = \frac{1}{L} \int_{-\frac{L}{2}}^{\frac{L}{2}} E_z dz.$$

The RFQ accelerator operates in a TE_{210} -like mode. The TE_{210} mode cannot exist in a pillbox because metallic end walls short out the transverse electric field. The lowest-frequency TE_{21} pillbox mode is the TE_{211} mode. However, a mode resembling TE_{210} exists over most of the RFQ length because the RFQ vanes do not touch the end walls and vane undercuts permit magnetic field lines to wrap around the vane ends into adjacent quadrants. For the RFQ we also seek information about fields near the beam axis. With no vane-tip longitudinal modulations, the only component of the electric field is E_r . This radial field focuses the beam. Vane-tip modulations make a nonzero E_z component that bunches and accelerates the beam.

Perturbation Measurements

Figure 1 is a bead-perturbation measurement showing the relative distribution of axial electric field in a DTL cavity. All figures in this paper are pictures of a computer-code display. A small metallic or dielectric object (the "bead") displaces electromagnetic stored energy, causing an observable frequency shift. This frequency shift is proportional to the original amount of stored energy within the bead volume:

$$\frac{\delta f}{f} = \frac{\delta U}{U},$$

where f is the resonant frequency and U is the cavity's total

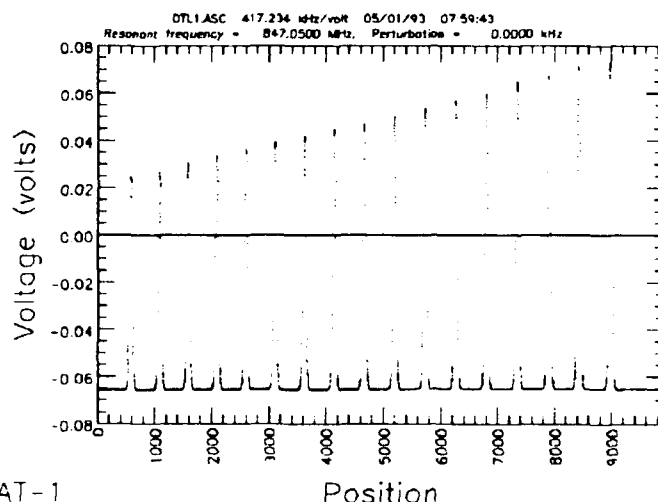


Figure 1. Program BEADPLOT display of a BEADPULL measurement on a 17-cell DTL.

* Work supported by the U. S. Department of Energy.

stored energy. Since U is proportional to the square of the electric or magnetic field, this effect offers a way to measure the fields in the cavity. This Slater perturbation method dates back to the 1940s. For spherical bead shapes:

$$\delta f = f_0 - f = \frac{3f_0}{4U} \int_V (\epsilon E^2 - \frac{1}{2} \mu H^2) dV$$

where the integral is over the volume of the sphere, U is the total cavity stored energy, H is the magnetic field, E is the electric field, and f_0 is the unperturbed frequency. Electric and magnetic terms shift the frequency in opposite directions. A bead in predominantly electric field lowers the cavity frequency and a bead in the magnetic field raises the frequency.

Axial Bead-Perturbation Measurements

For DTLs and CCLs the path of the bead is the axis of the accelerator. The bead is a small metal sphere attached to a thin nylon monofilament line. A system of pulleys keeps the line taut and guides the bead through the cavity at constant speed. Program BEADPULL records at regular intervals the small changes in the cavity's resonant frequency. The data are voltages from a double-balanced mixer measuring the phase shift between the rf drive and a pick-up probe in the cavity. This phase versus frequency has a negative slope. Lower cavity frequency produces a positive phase signal as shown in Fig. 1 for a 17-cell DTL. The baseline signal for no perturbation occurs at -0.065 volts. BEADPULL supports many combinations of instruments and instrument settings. The program controls the rf output level and modulation level of the HP 8660C/D synthesized signal generator. The operator can run the motor manually, or the program can run it through a HP multiprogrammer. The code starts and stops the bead at locations of mechanical or optical switches. BEADPULL has measured DTL cavities whose hardware is inaccessible, for example under vacuum and at cryogenic temperature. The program's main menu is a scrollable table containing setup values and options. The edit keys move a selection bar through the menu.

Bead-Perturbation Measurements in RFQ Cavities

Measurements on or near the RFQ axis are impractical for several reasons. Axial measurements provide no information about the quadrupole and dipole admixture of the field distribution. Also, small spacing between vane tips makes the alignment of the bead path critical. Slight alignment errors produce larger effects than those we are attempting to measure. Finally, fluctuations caused by the vane-tip modulations dominate the measurement. Tolerances on the vane-tip machining guarantee the correct field pattern if the voltage distribution along the vanes is correct. Therefore, we infer the electric-field distribution from a measurement of the magnetic field near the cavity outer wall. One RFQ-tuning goal is a pure quadrupolar field pattern. Differences among quadrants mix dipole-field components with the predominantly quadrupole field, effectively shifting the

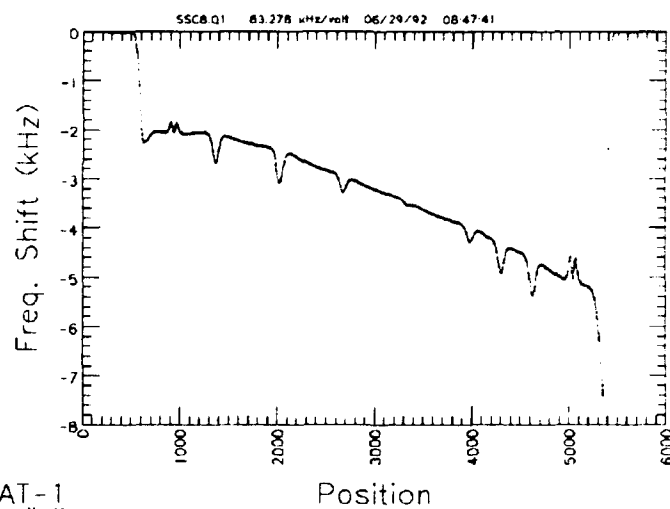


Figure 2. Program BEADPLOT display of a QUADPULL measurement in one quadrant of an RFQ.

quadrupole pattern off axis. Four measurements, one in each RFQ quadrant, quantify the dipole and quadrupole field admixture. Program QUADPULL has all the features of BEADPULL plus the ability to measure all four RFQ quadrants in a continuous loop. It inverts the data for the two quadrants in which the bead travels in reverse. Figure 2 shows frequency-shift data for one quadrant of the SSC RFQ.⁵ Dips in the curve are magnetic field enhancements near slug tuners. The bead passing close to ribbed vacuum ports made the double peaks. These features do not appear in the electric field near the vane tips.

Analysis Codes

The two main analysis codes are DTLPLOT for DTL and CCL data and QUADPLOT for RFQ data. Both codes allow user control of the ordinate scale, and can compare measurements to one another or to design fields. Programs DTLAVG and QUADAVG calculate averages of multiple measurements on the same cavity.

Analysis of DTL and CCL Measurements

DTLPLOT analyzes axial bead-perturbation measurements on DTL or CCL cavities. For each cell the code finds the maximum field E_{peak} , the average field E_0 , and an integral of the frequency shifts proportional to stored energy. Figure 3 illustrates an accurate way to compare a measured field distribution to a desired distribution. It uses data from DTLNORM, which predicts E_{peak} and E_0 from peak shapes calculated by SUPERFISH. DTLNORM integrates the design fields over the bead volume so the predicted fields include a correction for the nonzero size of the perturbing bead. DTLPLOT divides measured peak heights by predictions of E_{peak} for the desired E_0 in each cell. DTLPLOT also can correct for changes in the peak heights caused by the differences in gap length that occur when adjusting the end half drift tubes for tilt-sensitivity measurements.

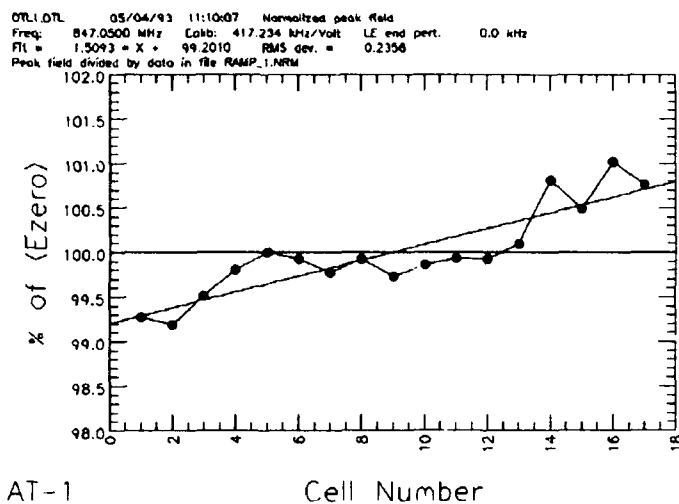


Figure 3. Program DTLPLOT display of E_0 relative to the design distribution.

Analysis of RFQ Measurements

DTLPLOT analysis requires no user input other than configuration data from a file used with all measurements on the same structure. QUADPLOT uses an interactive graphics session to fit a baseline to data outside the cavity and to locate the ends of the rf structure. The code displays the data with several markers that the operator manipulates with the edit keys. After the first setup, the program usually places the markers correctly for subsequent measurements. The code then only needs confirmation to continue. This procedure lines up the four separate measurements for combining the fields to obtain quadrupole and dipole components.

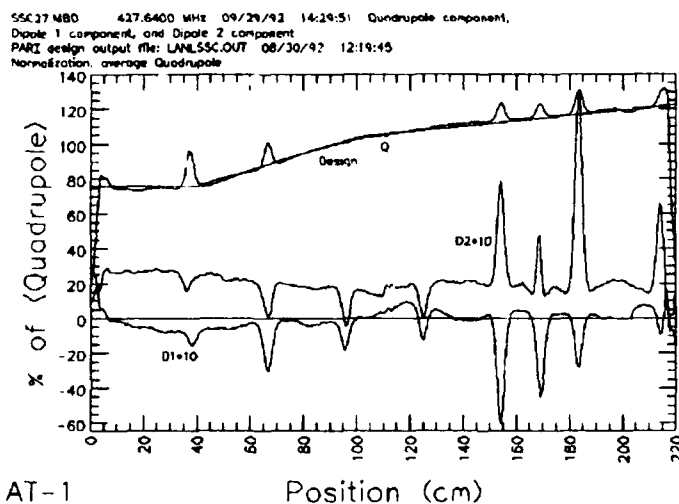


Figure 4. Program QUADPLOT display of the quadrupole and dipole field components.

After the analysis QUADPLOT displays selected data versus longitudinal position in a variety of formats. Figure 4 is a common choice. It shows the measured quadrupole component superimposed on the design field and two orthogonal dipole components (multiplied by 10 to show details). The code also can plot individual quadrant fields,

other linear combinations of dipole field components, a "zero" component used as an error indicator, or the difference between the quadrupole component and a quadrant field. Quadrant fields $F_1(z)$ through $F_4(z)$ are numbered counterclockwise as viewed from the low-energy end of the RFQ. The quadrupole, dipole, and "zero" components are:

$$F_Q = \frac{1}{4}(F_1 + F_2 + F_3 + F_4)$$

$$F_{D1} = \frac{1}{2}(F_1 - F_3)$$

$$F_{D2} = \frac{1}{2}(F_2 - F_4)$$

$$F_Z = \frac{1}{4}(F_1 - F_2 + F_3 - F_4)$$

Fields $F_i(z)$ are positive functions of longitudinal position z . Adjacent quadrants have opposite phase. Lloyd Young's RFQ tuning code⁶ reads QUADPLOT data to compare with a theoretical description of the fields.

Other Programs

Program COUPLING controls the HP 4191A impedance analyzer to measure reflection coefficients versus frequency. From an analysis of the resonance circle in the complex plane, the program extracts the resonant frequency, the voltage standing wave ratio, coupling β , and the unloaded Q . It displays Smith charts of the measured data. PCFIELDS analyzes the magnetic field distribution near post couplers in DTL cavities. LANLHELP displays documentation on the screen. Its companion program DOCUMENT formats and indexes the documentation for hard copy.

Acknowledgments

Many users of these codes have provided helpful suggestions for improvements. I am especially grateful to Don McMurry, Lloyd Young, and Dale Schrage. Don McMurry also wrote software for the HP multiprogrammer used with the PC data-acquisition codes.

References

- 1 J. C. Slater, *Microwave Electronics*, (D. Van Nostrand Company Inc., Princeton, NJ, 1950) pp. 81-83.
- 2 J. H. Billen and L. M. Young, "POISSON/SUPERFISH on PC Compatibles," this conference.
- 3 National Instruments Corporation, 6504 Bridge Point Parkway, Austin, TX 78730.
- 4 Lahey Computer Systems, Inc., 865 Tahoe Blvd., Incline Village, NV 89450.
- 5 D. Schrage et al., "Radio-Frequency Quadrupole Linac for the Superconducting Super Collider," submitted to the 12th International Conference on the Application of Accelerators in Research and Industry, Nov. 2-5, 1992, Denton, TX.
- 6 L. Young, "Tuning and Stabilization of RFQs," Proceedings of the 1990 Linear Accelerator Conference, Los Alamos National Laboratory document LA-12004-C, pp. 530-534.

Progress on RF superconductivity at Saclay

Groupe d'Etudes des Cavités Supraconductrices* DAPNIA-SEA, CE Saclay, F-91191 Gif/Yvette, France
and Institut de Physique Nucléaire** Université de Paris Sud, F-91400 Orsay, France

Abstract

We report substantial progress in R&D on superconducting accelerating cavities at Saclay.

I. INTRODUCTION

The Saclay program of R&D on RF superconductivity has been actively pursued, aiming at applications in the frame of the TESLA and "European Electron Accelerator for Nuclear Physics" projects. The most important issues of this research are the quest for high accelerating gradients and reduced RF dissipation.

II. HIGH GRADIENTS

The gradients available in superconducting cavities are now limited mainly by field emission. This phenomenon has been studied on samples, in both DC and RF regimes, with specific facilities. We have confirmed that the electron emission in cavities is mainly due to micron sized dust particles. Selective contamination experiments showed that metallic particles behave as especially strong emitters. Greater care in cavity cleaning and mounting have in fact resulted in an improvement in cavity performance : accelerating gradients as high as 18 — 20 MV/m can now be reliably achieved in 1.5 GHz single cell cavities (Fig.1).

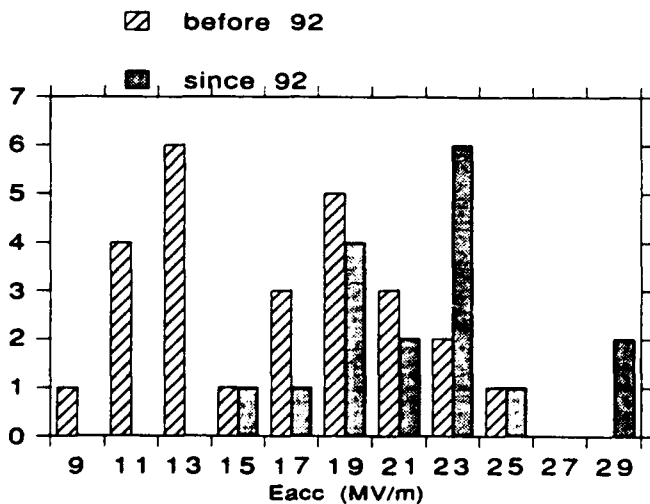


Figure 1 A large number of single cell Nb cavities at 1.5 GHz has now been tested at Saclay by the "Groupe d'Etudes des Cavités Supraconductrices". The corresponding systematics are summarized in Fig.1. It can be seen that the latest tests correspond to results significantly better than the older ones. The improvement is thought to be due to improved cleanliness during cavity treatment and mounting.

One cavity of this type, tested in the same laboratory, has reached an accelerating gradient of 28 MV/m (Fig.2) after a particularly careful surface treatment involving firing and titanification at 1300° C during 16 hours in a vacuum furnace, followed by chemical polishing, rinsing and drying in a recently developed automated facility [1].

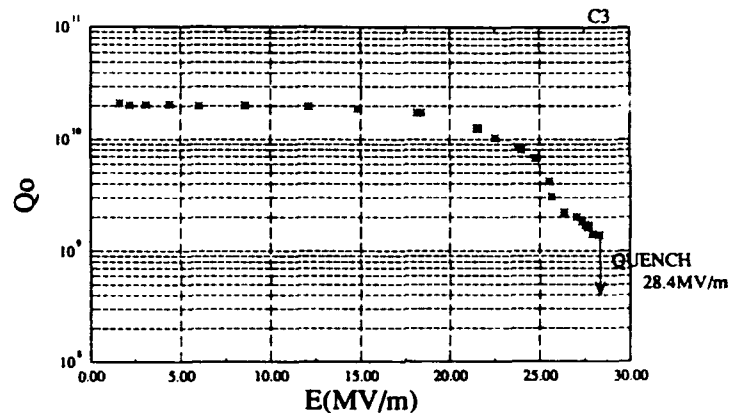


Figure 2 Q value vs accelerating gradient for the "high gradient" cavity

III. LOW DISSIPATION

The residual surface resistance routinely obtained in our Nb cavities is 15 nΩ at 1.5 GHz. The origin of the associated dissipation is now understood as the sum of the contribution due to trapping of the residual magnetic flux during cooldown, plus a new one due to the polycrystalline nature of the niobium used for making the cavities. Both contributions have been studied theoretically and experimentally [2]. This work opens the perspective of improved Q values for superconducting cavities.

A Q value of 5.10¹⁰, corresponding to a residual surface resistance of 4 nΩ, has actually been reached recently with a 1-cell niobium accelerating cavity at 1.5 GHz (Figs 3,4). This is probably the best value ever obtained on an accelerating cavity in the GHz frequency range. The main reasons for this success are improved magnetic shielding and reduced RF losses at the ends of the cutoff tubes. The use of high purity niobium (RRR 320) may also have played a favourable role. We will now try to demonstrate the reproducibility of this result, and its validity in a real accelerator environment.

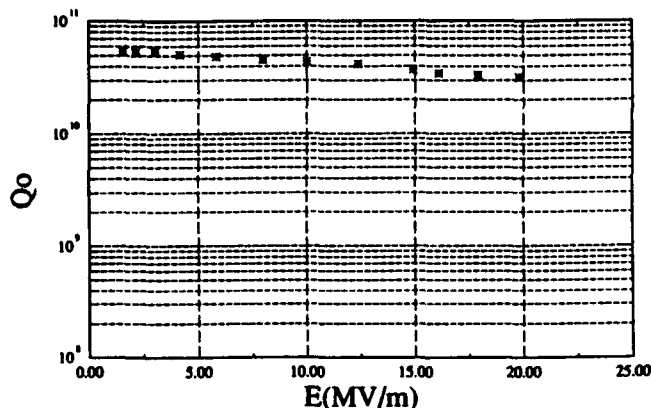


Figure 3 Q value vs accelerating gradient for the "low dissipation" cavity

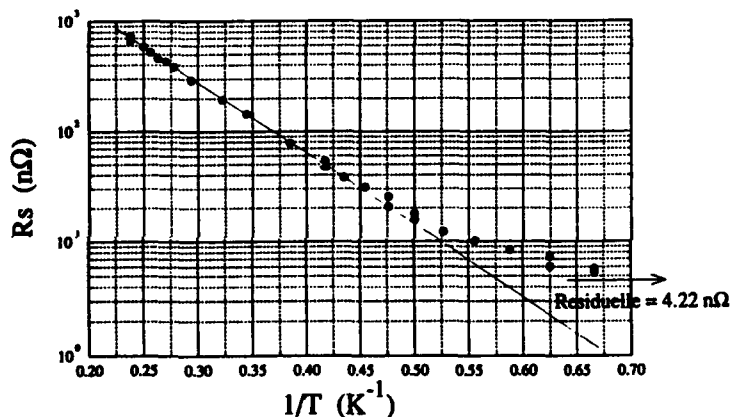


Figure 4 Surface resistance vs inverse temperature for the "low dissipation" cavity

IV. THIN SUPERCONDUCTING FILMS

Efforts have also been continued to develop the thin film coating technology at Saclay [3]. A sample of NbTiN film, deposited on copper substrate by magnetron sputtering, reached a RF field level of 35 mT and exhibited a low residual surface resistance (40 nΩ at 4 GHz), with a very small BCS resistance

and an unusually small dependence of R_s vs RF field. If this result can be reproduced in a full scale accelerating cavity, the "thin film way" will certainly regain some credibility for the construction of superconducting structures.

V. PROGRESS ON THE ACCELERATOR MACSE

A continuous electron beam of 100 μ A was accelerated in the MACSE prototype [4], with excellent stability, emittance and energy resolution ($\Delta E = 7$ keV at $E = 26$ MeV). A distributed RF power scheme (one klystron for 4 cavities) was applied successfully, without energy spread degradation. Pulsed RF processing at moderate power (5 kW) suppressed e^- loading due to field emission in the MACSE cavities. The accelerating gradient was then limited by quench at an average value of 12 MV/m. A gradient as high as 18 MV/m was reached in one cavity. This is the first time that such a gradient is obtained with a superconducting cavity in an electron accelerator.

VI. CONCLUSION

These encouraging results confirm that superconducting cavities are still far from their limits and that the associated technology can make important progress, toward the construction of future large accelerators.

VII. REFERENCES

- [1] C.Z. Antoine et al., Proc. 3rd European Part. Acc. Conf., Berlin (1992) 1319
- [2] C. Vallet et al., Proc. 3rd European Part. Acc. Conf., Berlin (1992) 1295
- [3] P. Bosland et al., Proc. 3rd European Part. Acc. Conf., Berlin (1992) 1316
- [4] J.M. Cavedon et al., Proc. 3rd European Part. Acc. Conf., Berlin (1992) 52

* C. Antoine, B. Aune, M. Boloré, B. Bonin, P. Bosland, Y. Boudigou, J. Bourbonneux, M. Boussoukaya, S. Cantacuzino, J.P. Charrier, S. Chel, B. Coadou, A. Curtoni, B. Daillant, B. Delomez, M. Desmons, J. Gastebois, J. Gobin, J. Gratadour, B. Groux, X. Hanus, C. Henriot, M. Jablonka, M. Jimenez, J.M. Joly, G. Jouve, M. Juillard, E. Klein, F. Koechlin, C. Magne, B. Mahut, J. Martignac, A. Mosnier, R. Noer, J. Novo, B. Phung Ngoc, J.P. Poupeau, J.P. Rodriguez, D. Roudier, H. Safa, J. Tan, C. Vallet, A. Zeitoun.

** M. Caruette, M. Fouaidy, T. Junquera

A new surface treatment for niobium superconducting cavities

B. Bonin, C. Henriot, C. Antoine, B. Coadou, F. Koechlin, J.P. Rodriguez, Groupe d'Etudes des Cavités Supraconductrices
DAPNIA-SEA, CE Saclay, F-91191 Gif/Yvette, France

E. Lemaître, P. Greiner, Laboratoire Moderne de Soudage

DTA-CEREM-DTM-STA-LMS, CE Saclay, F-91191 Gif/Yvette, France

Abstract

A condition necessary for the successful performance of superconducting cavities is the cleanliness of their inner surface. The firing of niobium cavities under vacuum at very high temperature is known to be a particularly effective method for cleaning the surface and for suppressing electron field emission. However, this process is inconvenient and expensive, if it is done in the "usual way", ie in a high vacuum furnace. We propose an alternative technique for cavity firing, using local heating in an electron beam or laser welding facility. This treatment is easy, and can readily be integrated in the usual process of cavity production. Initial tests at Saclay have given very promising results.

I. INTRODUCTION

The cleanliness of the inner surface of superconducting cavities is an indispensable condition for the successful performance of these accelerating structures. The firing of niobium cavities under vacuum at very high temperature is in wide favor in many laboratories for at least two reasons : i) when used in association with solid state gettering (e.g. titanification or yttrification [1]), it permits a purification and a homogenization of the material, with a subsequent improvement of its thermal conductivity, and a better stabilization of the cavity against quenches; ii) this treatment seems to inhibit the activity of the microscopic sites where electron field emission takes place. The field emission threshold which limits the accelerating gradient available in the cavity is then pushed to higher levels.

However, firing is usually done in a high vacuum furnace, which makes the process inconvenient and expensive. There is also a very serious risk of recontamination of the cavity surface during the furnace venting, since the cavity is necessarily open during treatment. The benefits of the bulk purification of the material are then kept, but the protection of the cavity against field emission may be lost after the treatment. Firing of niobium cavities in a high vacuum furnace is thus difficult to integrate in an industrial process of cavity production.

We have explored an alternative technique, which employs local heating in an electron beam welding facility. The interest of the method lies mainly in its simplicity and its rapidity. The local character of the heating may also present some advantages : for instance, the cavity flanges can be spared during the treatment. This alleviates the need for refractory flanges, and opens up the interesting possibility of firing *closed* cavities.

II. EXPERIMENT

All the firing experiments were done in the EB welding machine of LMS, at Saclay. Its TECHMETA electron gun delivers an electron beam of controllable energy, intensity and focusing. The electron beam pencil can be moved and vibrated across the sample surface by means of suitable deflecting electrodes. The vacuum in the vessel is no better than 10^{-3} Pa.

The first firing tests were made on 2mm thick niobium sheet samples. The sample temperature during firing was measured by means of a bichromatic optical pyrometer viewing the sample through a window in the EB welding machine. The accuracy of the measurement was on the order of $\pm 100^\circ$.

In all practical cases, the electron beam dwell time on one given point of the surface was long as compared to the characteristic time of heat diffusion across the niobium sheet. For this reason, we believe that the temperature was identical on both sides of the sheet.

The first tests showed that any chosen temperature between 1000° and 2000° C could be reached and maintained with excellent stability, by a suitable choice of the following parameters : electron energy, beam size, beam intensity and displacement speed.

The fired samples showed a considerable recrystallization: starting from an initial grain size of $50\text{--}70\text{ }\mu\text{m}$, the final grain size was as large as 1 cm for the hottest and longest runs. The initial purity of the Nb samples was $\text{RRR}=200$. No degradation of RRR was observed for the shortest runs (15 sec), but a significant loss of purity ($\text{RRR}=50$) resulted from the long firings (15 min), even at very high temperature. This is attributable to the fact that residual gaseous species present in the vacuum enter readily as interstitials in the niobium lattice at high temperature [2,3]. The important degradation observed can then be ascribed to the poor vacuum in the welding machine.

These considerations led us to protect the niobium before and during firing, by means of a titanium vapor layer deposited on the sample surface by sublimation of a joule—heated titanium filament. Contamination from the residual gases is then confined to the outside titanium layer, and no longer affects the bulk niobium. New RRR measurements after this treatment showed no purity degradation, thus confirming the success of this protection method. In the present experiment, the Ti layer could be deposited only on one side of the Nb sheet sample. In this case, there is probably competition between a pollution of the material from the unprotected side, and a purification from the titanified one. A real purification of the bulk material

could be expected from a more careful titanification, covering both sides of the sample.

As compared to the titanification in general use for the firing of niobium cavities in high vacuum furnaces [1], the above-mentioned method has the advantage that the Ti filament and the niobium sample to be treated are heated separately to (eventually) different temperatures. This gives an appreciable control of the sublimation rate and of the thickness of the Ti layer on the sample surface during firing. This nice feature, which allows the deposition of the titanium layer *before* the firing, should improve the efficiency of the titanification by suppressing the risk of pollution during the passage through the dangerous temperature zone where the niobium is already hot enough for the impurities to enter, and is still unprotected by the titanium sublimation.

In order to assess the validity of the technique for the practical treatment of superconducting cavities, a single cell, 1.5 GHz niobium cavity was heated in the EB machine, with the following particular features :

1) The cavity was mounted on a horizontal mandrel and rotated in front of the fixed electron beam ;

2) The cavity was titanified from outside by sublimation of a joule-heated titanium filament parallel to the cavity axis ;

3) The cavity -already equipped with its antennas- had been sealed under static vacuum before firing. The motivation for this sealing was to protect the cavity against pollution by the (poor) residual vacuum during firing, and against any ulterior contamination by dust particles or by chemical species after firing. The cavity was not reopened after the treatment, and was directly tested in a vertical cryostat, still under the same static vacuum ;

4) All points of the cavity surface were maintained at 1850° C during 1 minute. After the heat treatment, the cavity surface showed the same considerable recrystallization as was observed on sheet samples. No noticeable deformation of the cavity shape could be detected.

This cavity showed excellent RF performance, giving an accelerating gradient of 19 MV/m and a residual Q value above

10^{10} without any electron emission. Although we consider this result very encouraging, it must be noted that this gradient and Q value had previously been obtained with this same cavity after a standard chemical treatment and mounting. Hence, we cannot claim an improvement of the cavity performance due to the heat treatment.

Clearly, the curative virtues of the treatment are still to be demonstrated, but there is some hope that this kind of firing might replace the delicate chemical etching, rinsing and clean-room drying that represent the "state of the art" for superconducting accelerating cavities.

VI. CONCLUSION

We have shown that an electron beam heat treatment of niobium superconducting cavities is an interesting possibility, probably superior to the usual high vacuum furnace heat treatment. Suitable electron beams are already available in industry in EB welding machines, whereas high vacuum furnaces are still laboratory objects. The poor vacuum of our EB welder obliged us to contrive complicated arrangements to avoid the pollution of the niobium by residual gases. However, EB welding facilities with improved vacuum (10^{-5} Pa) are available. In such devices, a high vacuum level during treatment would certainly be easier to achieve than in furnaces, because there are no screens and because the only hot surface is the desired one. The potential cleanliness of this kind of heat treatment is thus excellent. The local heating of the surface opens rich perspectives, which have not yet been explored. Experiments are under way at Saclay to determine the benefits that can be obtained from such a treatment, from the points of view of curing field emission and purifying niobium. The parameters of the treatment (temperature, duration) remain to be determined.

The help of the "Groupe d'Etudes des Cavités Supraconductrices" for testing the cavity is gratefully acknowledged.

VII. REFERENCES

- [1] H. Padamsee et al., IEEE T. Mag 21 1007 (1985)
- [2] M. Hörmann, J. Less Comm. Metals 139 1 (1988)
- [3] K.K. Schulze, J. Metals, May 1981 p.33

Using the Panofsky-Wenzel Theorem in the Analysis of Radio-Frequency Deflectors*

M. Jean Browman
Los Alamos National Laboratory, MS H825
Los Alamos, NM 87545

Abstract

In a 1956 paper Panofsky and Wenzel considered the transverse momentum imparted to a fast particle moving parallel to the axis of a cavity excited in either a TE (no component of the electric field parallel to the axis) or TM mode (no component of the magnetic field parallel to the axis). One conclusion of this paper was that in a TE mode the deflecting impulse of the electric field exactly cancels the impulse of the magnetic field. This result is sometimes misinterpreted as concluding that if the electric field acting on a particle is purely transverse, the deflection impulses from the electric and magnetic fields must cancel one another. This conclusion is false.

Instead

$$\mathbf{p}_\perp = \left(\frac{e}{\omega_0} \right) \int_0^d (-i) \nabla_\perp E_z dz, \quad (1)$$

implicitly derived in the 1956 paper, is a more useful form of the theorem for deflecting cavities. In this equation, \mathbf{p}_\perp is the transverse momentum imparted to the particle, d is the length of the cavity, e is the charge of the particle, ω_0 is the angular frequency of the cavity, and $\nabla_\perp E_z$ is the transverse gradient of the z component of the electric field along the path of the particle. The $-i$ represents a 90° phase advance of the integrand with respect to the electric field. In other words, the integrand has the same phase as the magnetic field.

Eq. (1) is not restricted to TE or TM modes. In particular, it applies to two similar-looking modes in a high-energy deflector that was studied for the Accelerator Transmutation of Waste (ATW) project at Los Alamos National Laboratory.

I. INTRODUCTION

In a 1956 paper, Panofsky and Wenzel showed that no transverse momentum is imparted to particles traveling parallel to the axis of a cavity excited in a TE mode [1]. This result for TE modes is sometimes misinterpreted as concluding that if the electric field acting on a particle is purely transverse, then the deflection impulses from the electric and magnetic fields must cancel one another. In other words, no transverse momentum will be imparted to the particle. We will show why this conclusion is false by rederiving Panofsky and Wenzel's result and showing that

their restricting their work to cavities with pure TE or TM modes is unnecessary.

II. DERIVING THE THEOREM

The transverse momentum \mathbf{p}_\perp , imparted to a particle with velocity \mathbf{v} and charge e and traveling in the z direction through a radio-frequency cavity of length d , is given by

$$\mathbf{p}_\perp = \int_{t(z=0)}^{t(z=d)} \mathbf{F}_\perp dt = (e/v) \int_0^d [\mathbf{E}_\perp + (\mathbf{v} \times \mathbf{B})_\perp] dz, \quad (2)$$

if \mathbf{v} is large enough to allow the particle direction to remain essentially unchanged by the transverse force. Panofsky and Wenzel have shown that we can simplify the above equation by expanding the right hand side of it in terms of the vector potential. To see this recall that in general

$$\mathbf{E} = -\frac{\partial \mathbf{A}}{\partial t} - \nabla V, \quad (3)$$

where \mathbf{A} is the magnetic vector potential, i.e.

$$\mathbf{B} = \nabla \times \mathbf{A}, \quad (4)$$

and where V is the scalar potential. Since V is constant inside a cavity,

$$\mathbf{E} = -\frac{\partial \mathbf{A}}{\partial t} \quad \text{and} \quad (5)$$

$$\mathbf{E}_\perp = -\frac{\partial \mathbf{A}_\perp}{\partial t}. \quad (6)$$

Expressing $(\mathbf{v} \times \mathbf{B})_\perp$ in terms of \mathbf{A} , we get

$$\begin{aligned} (\mathbf{v} \times \mathbf{B})_\perp &= [\mathbf{v} \times (\nabla \times \mathbf{A})]_\perp = [\nabla (\mathbf{v} \cdot \mathbf{A}) - (\mathbf{v} \cdot \nabla) \mathbf{A}]_\perp \\ &= \nabla_\perp (\mathbf{v} \cdot \mathbf{A}) - (\mathbf{v} \cdot \nabla) \mathbf{A}_\perp. \end{aligned} \quad (7)$$

Thus we know that

$$\mathbf{p}_\perp = (e/v) \int_0^d \left[\left(-\frac{\partial \mathbf{A}_\perp}{\partial t} - (\mathbf{v} \cdot \nabla) \mathbf{A}_\perp \right) + \nabla_\perp (\mathbf{v} \cdot \mathbf{A}) \right] dz. \quad (8)$$

Because \mathbf{v} is essentially constant and is in the z direction,

$$(\mathbf{v} \cdot \nabla) \mathbf{A}_\perp = v \frac{\partial \mathbf{A}_\perp}{\partial z} \quad \text{and} \quad (9)$$

$$\nabla_\perp (\mathbf{v} \cdot \mathbf{A}) = v \nabla_\perp A_z, \quad \text{so} \quad (10)$$

$$\mathbf{p}_\perp = (e/v) \int_0^d \left[-\left(\frac{\partial \mathbf{A}_\perp}{\partial t} + v \frac{\partial \mathbf{A}_\perp}{\partial z} \right) + v \nabla_\perp A_z \right] dz \quad (11)$$

*Work supported by the US Department of Energy, Office of High Energy and Nuclear Physics.

$$= e \int_0^d \left[- \left(\frac{1}{v} \frac{\partial \mathbf{A}_\perp}{\partial t} + \frac{\partial \mathbf{A}_\perp}{\partial z} \right) + \nabla_\perp A_z \right] dz. \quad (12)$$

However, it is also true that

$$v = dz/dt, \text{ so} \quad (13)$$

$$dz/v = dt, \text{ and} \quad (14)$$

$$\left(\frac{1}{v} \frac{\partial \mathbf{A}_\perp}{\partial t} + \frac{\partial \mathbf{A}_\perp}{\partial z} \right) dz = \frac{\partial \mathbf{A}_\perp}{\partial t} dt + \frac{\partial \mathbf{A}_\perp}{\partial z} dz = d\mathbf{A}_\perp, \quad (15)$$

because the path of the particle is fixed in the transverse direction. Thus we know that

$$\mathbf{p}_\perp = e \int_{\mathbf{A}_\perp(z=0)}^{\mathbf{A}_\perp(z=d)} - (d\mathbf{A}_\perp) + e \int_0^d \nabla_\perp A_z dz. \quad (16)$$

In order for this relationship to be useful, we need to express \mathbf{A} in terms of \mathbf{E} . If we assume an $e^{-i\omega t}$ time dependence for \mathbf{E} , then

$$\mathbf{A} = -\frac{i}{\omega_0} \mathbf{E} \quad (17)$$

is a valid choice for \mathbf{A} . Notice that $-i = e^{-i\pi/2}$, so \mathbf{A} has a time dependence of $e^{-i(\omega_0 t + \pi/2)}$. Thus \mathbf{A} is shifted 90° in time from \mathbf{E} and has the same phase as the magnetic field, as we would expect.

As Panofsky and Wenzel point out, the first term of Eq. (16) vanishes for any cavity having ends perpendicular to its axis, because $\mathbf{A}_\perp = \mathbf{E}_\perp = 0$ in metal. It can also vanish for a cavity having a beam tube, as long as $\mathbf{E}_\perp = 0$ at $z = 0$ and $z = d$. Thus for these cases we have

$$\mathbf{p}_\perp = e \int_0^d \nabla_\perp A_z dz. \quad (18)$$

Substituting Eq. (17) into Eq. (18), we obtain

$$\mathbf{p}_\perp = \left(\frac{e}{\omega_0} \right) \int_0^d (-i) \nabla_\perp E_z dz. \quad (19)$$

Notice that Eq. (19) is not restricted to TE or TM modes. The change in transverse momentum is indeed zero for a TE mode, because for that mode E_z , and hence $\nabla_\perp E_z$, is identically zero everywhere in the cavity. Notice, however, that for a non-TE mode E_z can be zero everywhere along the path of the particle and still not be identically zero everywhere in the cavity. In such a non-TE mode $\nabla_\perp E_z$ does not have to be zero along the path of the particle, so the particle can be deflected.

III. EXAMPLES

The Panofsky-Wenzel theorem can be useful in gaining insight as to whether a mode in a radio-frequency cavity will deflect the beam. For instance, consider the cavity shown in Fig. 1. (The material around the cavity has been left transparent for clarity.) This 350-MHz, $\beta\lambda/2$ structure

is of the type proposed by Leeman and Yao [2]; it has been modified for a 1-GeV, high-current proton beam and modeled using the three-dimensional MAFIA codes [3]. The cavity is 33.8 cm long and 26 cm in diameter. The rods are 15.57 cm long and 5 cm in diameter; the vertical distance between the rods is 5 cm, and the gap between the ends of the rods is 2.67 cm. The beam pipe is 5 cm in diameter. The beam is moving from left to right (in the $+z$ direction) through the center of the cavity.

The deflecting mode is a TEM-like mode, with the magnetic fields curving around the rods, adding in the beam region. Figure 2 shows plots, taken in a transverse cross section, of the MAFIA-generated electric and magnetic fields for this deflecting mode.

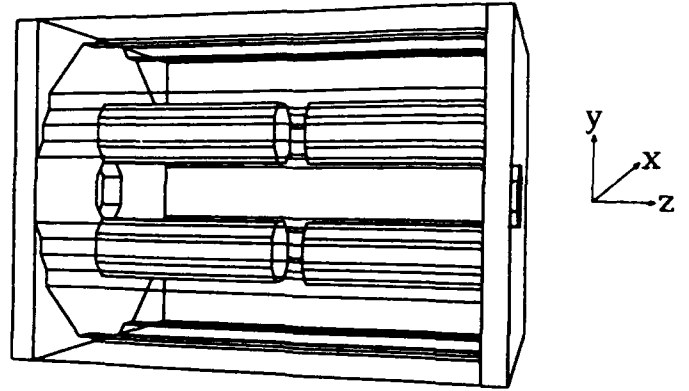


Fig. 1. MAFIA model of deflecting cavity.

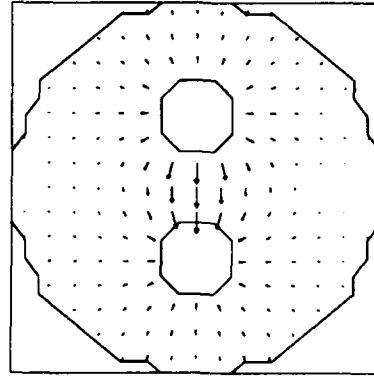


Fig. 2. Electric field of the deflecting mode, taken in an x - y plane.

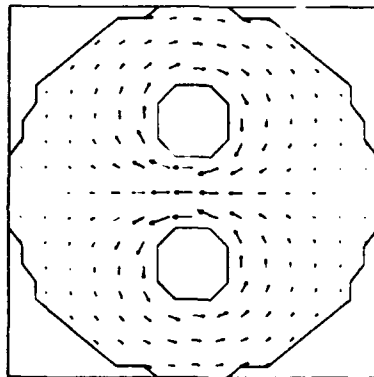


Fig. 3. Magnetic field of the deflecting mode, taken in an x - y plane.

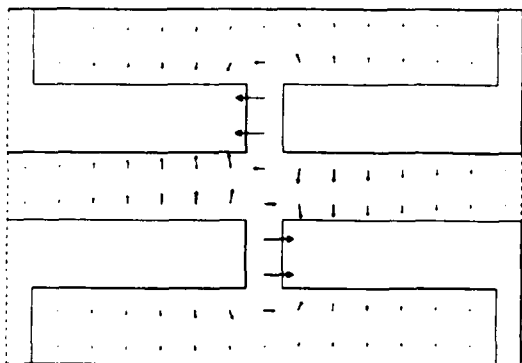


Fig. 4. Electric field of the deflecting mode, taken in a z - y plane.

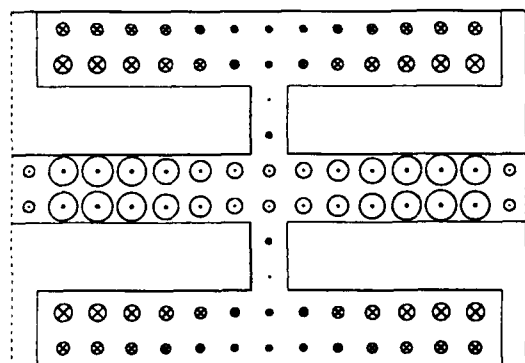


Fig. 5. Magnetic field of the deflecting mode, taken in a z - y plane.

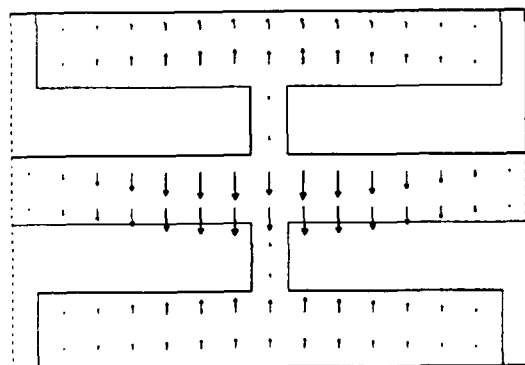


Fig. 6. Electric field of the next-highest mode, taken in a z - y plane.

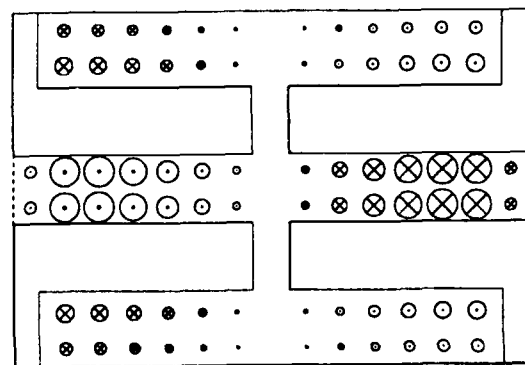


Fig. 7. Magnetic field of the next-highest mode, taken in a z - y plane.

The transverse fields of the next-highest mode are similar to those of the deflecting mode in the region away from the z midplane of the cavity. But as we can see in Figs. 4-7, the z variation is quite different for the two modes. The magnetic field is symmetric about the z midplane for the deflecting mode, but it is antisymmetric for the next-highest mode. The electric fields also have different patterns for the two modes. In particular, the deflecting mode has a large gradient of E_z in the middle of the cavity; the next-highest mode has a much smaller gradient. We can use Eq. (19) to inspect which of the two modes will be the better deflector. In fact, if we calculate the relative deflections using MAFIA, we find that the deflection caused by the deflecting mode is more than twenty times greater than that of the next-highest mode.

IV. CONCLUSIONS

The Panofsky-Wenzel theorem has more general applications than its authors stated in their original paper. The form

$$p_{\perp} = \left(\frac{e}{\omega_0} \right) \int_0^d (-i) \nabla_{\perp} E_z dz$$

does not depend upon the cavity being excited in a TE or a TM mode. It depends only upon the assumptions that (1) the particles are rigid enough that the particle orbit is not substantially affected in its passage through the cavity and (2) the transverse electric field vanishes at each end of the cavity. This form of the theorem is useful in distinguishing between deflecting and nondeflecting modes in a resonant cavity.

V. ACKNOWLEDGMENTS

The author would like to thank Dr. Richard Cooper and Dr. George Spalek for many helpful discussions.

References

- [1] W. K. H. Panofsky and W. A. Wenzel, "Some Considerations Concerning the Transverse Deflection of Charged Particles in Radio-Frequency Fields," *Review of Scientific Instruments*, November 1956, p. 967.
- [2] C. Leeman and C. G. Yao, "A Highly Effective Deflecting Structure," in *Proceedings of the 1990 Linear Accelerator Conference*, Los Alamos National Laboratory Report LA-12004-C, March 1991, pp. 232-234.
- [3] R. Klatt, F. Krawczyk, W.-R. Novender, C. Palm, T. Weiland, B. Steffen, T. Barts, M. J. Browman, R. Cooper, C. T. Mottershead, G. Rodenz, S. G. Wipf, "MAFIA- A Three-Dimensional Electromagnetic CAD System for Magnets, RF Structures, and Transient Wake-field Calculations," *1986 Linear Accelerator Conference Proc.*, Stanford Linear Accelerator Center Report SLAC-303, 276-278 (1986).

The Effects of Temperature and RF Power Level on the Tuning of the Water-Cooled SSC Low-Energy Booster Cavity

C. Friedrichs
Los Alamos National Laboratory

G. Hulsey
Superconducting Super Collider Laboratory

Abstract

The SSC Low-Energy Booster (LEB) cavity must rapidly tune from 47.52 to 59.78 MHz. The cavity tuner will use transversely biased ferrite[1] to control the cavity resonance.

The thermal expansion of a cavity's materials affects its resonance. There are two other known temperature mechanisms that affect resonance in the water-cooled LEB cavity. The saturation magnetization of the ferrite is a function of temperature, and since the ferrite permeability is dependent on the saturation magnetization, the ferrite permeability is also temperature dependent. The ferrite cooling water is present in the tuner rf field, hence the water permittivity, which is very temperature dependent, also affects cavity resonance.

While taking data on the SSC Test Cavity to quantify the effect of temperature on the resonance, we observed that the rf power level also perturbed the resonance. It was readily apparent from the data that the power level affected the resonance much more strongly at low values of control bias than at high values. In fact, when we calculate an apparent modified control-bias H field that produces the observed resonance shift, we noticed an almost perfect, though non-linear, correlation between the ratio of H_{rf} to H_{bias} and the apparent modified bias field, H_{app} .

This paper will present a set of equations to predict the resonance shifts produced by changes in temperature and rf power level. It will also present the techniques, both theoretical and empirical, by which these equations are derived. Finally, some of the methods for dealing with these resonance shifts will be discussed.

I. INTRODUCTION

We will consider three separate effects on the cavity tuning: the effects of temperature on ferrite permeability and on cooling water permittivity, as well as the effects of rf the power level on the ferrite permeability. These are distinctly separate effects and we will treat them separately.

We derived the effect of temperature on ferrite permeability from the fact that the rf permeability of the ferrite is a function of the saturation magnetization of the ferrite, which is in turn a function of temperature. The saturation magnetization vs. temperature is usually available from the ferrite manufacturer.

We could locate no data for the effect of temperature on the water permittivity, so measurements were made at Los Alamos National Laboratory and the Superconducting Super

Collider (SSC) to determine the permittivity and Q of both distilled and de-ionized water in the frequency range of interest.

We do not have a theory to predict the effect of rf power level on cavity tuning. We have empirically derived the predictions so that they fit our measured data. We took the data using the SSC Test Cavity. We used low-duty cycles while taking this data in order to avoid mixing temperature effects with power-level effects. We recorded the frequency and frequency shift vs. rf cavity-gap voltage for gap voltages from 1 kV to 100 kV at various ferrite bias current levels from 105 to 240 amperes. We used the data to calculate H_{rf} and H_{bias} in the ferrite, then used these quantities to produce a consistent empirical formula that matches the measured frequency shift.

II. TEMPERATURE EFFECT ON PERMEABILITY

Saturation magnetization data for Trans Tech G-810 ferrite is shown in Fig. 1.

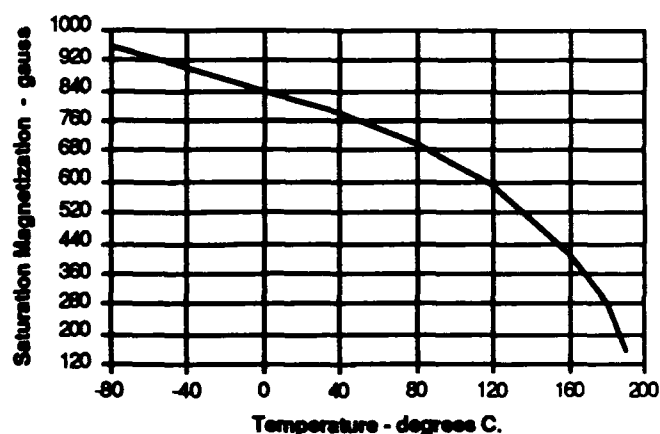


Figure 1. Saturation magnetization vs. temperature

We used curve-fitting techniques to derive a function that matches the curve. We then substituted this function into the equation defining rf permeability. These expressions are given below:

$$B_{sat} = 732.45 \times \log_{10}(215 - T) - 860.17$$

$$\mu = \frac{B_{sat}}{H_{rf}} + 1 = \frac{732.45 \times \log_{10}(215 - T) - 860.17}{H_{rf}}$$

*Work supported and funded by U. S. Department of Energy office at the Superconducting Supercollider Laboratory.

The spacing between the pole pieces of the tuning magnet in the LEB water cooled cavity is 16.9 cm. This spacing contains 12.5 cm. of ferrite. The relation of H to the tuning current is given by the following expression:

$$n \times I = \oint H \cdot dl \approx \sum H \times l = H_{fer} \times l_{fer} + H_{air} \times l_{air} ,$$

where I is the tuner bias current and n is the number of turns in the bias magnet coil. Now

$$H_{fer} = B_{fer} - B_{sat} , \quad H_{air} = B_{air} / \mu_{air}$$

and

$$l_{fer} = 12.5 \text{ cm.}, \quad l_{air} = 4.4 \text{ cm.}$$

Since B is continuous, $B = B_{fer} = B_{air}$. So

$$B = \frac{12.5 \times B_{sat} + nI}{12.5 + 4.4/\mu_{air}} ,$$

and finally

$$\mu_{fer} = \frac{B}{B - B_{sat}} .$$

The cavity resonant frequency as a function of ferrite permeability can be calculated using either Superfish or any of the transmission line codes[2].

III. TEMPERATURE EFFECT ON WATER PERMITTIVITY

Permittivity of de-ionized water as a function of temperature is shown in Fig. 2. This data was obtained from measurements performed at 56 MHz. The permittivity is linearly decreasing with increasing temperature, and can be calculated using the following empirical expression:

$$\epsilon = -0.4168 \times T + 86.519 .$$

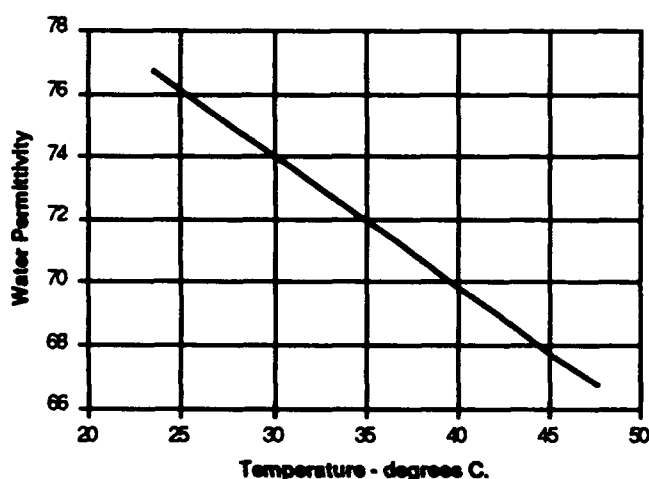


Figure 2. Permittivity vs. temperature

The cavity resonant frequency as a function of water permittivity can be calculated by the same methods mentioned in Section II.

IV. EFFECT OF POWER LEVEL ON TUNING

We first noticed that power level had an appreciable effect on the cavity resonant frequency while we were taking data on the effects of temperature on tuning. Since the tuner and cavity we were testing were substantially different from the LEB tuner design, we felt it was important to be able to make a prediction regarding the strength of this effect in the LEB cavity. After first noticing this effect, we observed that it was much more pronounced at the lower tuning frequencies than the higher ones, or more significantly, it was much more pronounced at lower values of control bias than at higher ones.

We examined the ratio of H_{rf} to H_{bias} and determined that for any value of this ratio, there is a unique factor that apparently modifies H_{bias} . After applying this factor to H_{bias} , a new value of ferrite permeability may be calculated using the expression for μ given in Section II of this paper. The non-linear function for the change factor that matches the measured data is shown in Fig. 3. The peak value of H_{rf} is used.

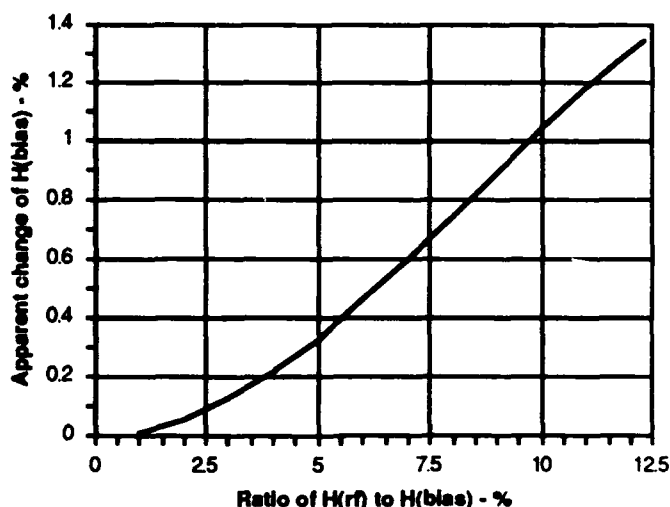


Figure 3. Effect of rf amplitude on apparent H

Once we had quantified this change function, we next sought to realize a simple mathematical model to calculate the apparent control bias H field as a function of H_{bias} and H_{rf} . The following equation expresses our first attempt at this realization (H_{app} is the apparent bias field):

$$H_{app} = \sqrt{H_{rf}^2 + H_{bias}^2} .$$

This expression yields a fairly good correlation with the measured data, but its predicted frequency shift is consistently on the low side.

Rather than accept a slight error on the low side, we elected to modify the expression. H_{app} in the above expression can be readily recognized as the vector sum of H_{rf} and H_{bias} , with the two quantities 90° apart. The simplest way to modify the expression to improve its fit to the data is to increase the angle between the two vectors. The vector addition is illustrated in Fig. 4.

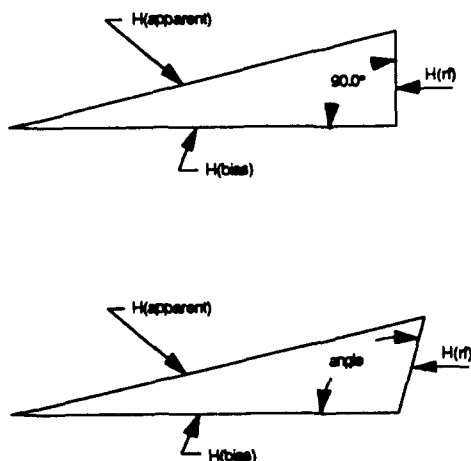


Figure 4. Construction of $H_{apparent}$

The best fit to the data occurs when the angle is increased from 90° to 92.8° . The use of 92.8° results in excellent correlation with the data, and no low side errors appear in the regions where the shift is large.

At first it seems that a frequency shift of less than 2% would not be objectionable in a circuit designed to rapidly tune over a 25% range. The problem is caused by a severe non-linearity that can result from the phenomenon. If the cavity driving frequency is swept from below resonance to above resonance, say from -6 to +6 dB, at an amplitude level sufficiently large to produce significant shift, the cavity impedance will avalanche just after resonance is crossed. This effect occurs because H_{rf} starts decreasing causing the resonance to shift back away from the driving frequency, and a runaway condition occurs. Such an occurrence can be

prevented by the application of sufficient amplitude feedback. A good prediction of the expected shift is, therefore, important to the feedback designers.

A computer simulation of the avalanche effect described above is shown in Fig. 5.

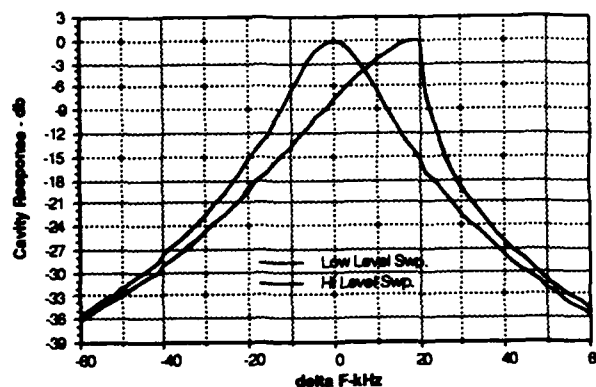


Figure 5. Avalanche effect

V. ACKNOWLEDGMENTS

Many people in both the rf and mechanical engineering departments at SSC made significant contributions to bringing the RF Cavity Test Stand on line. We would particularly like to thank Fred Brandeberry for assistance in the measurements, and Yehuda Goren for his attempts to find a theoretical basis for the frequency shift vs amplitude phenomenon.

VI. REFERENCES

- [1] W.R. Smythe, T.G. Brophy, R.D. Carlini, C.C. Friedrichs, D.L. Grisham, G. Spalek, and L.C. Wilkerson, "RF Cavities with Transversely Biased Ferrite Tuning," *IEEE Trans. Nucl. Sci.* 32 (5), p. 2951. (1985).
- [2] C.C. Friedrichs, "Analytic Evaluation of the LAMPF II Booster Cavity Design," *IEEE Trans. Nucl. Sci.* 32 (5), p. 2843 (1985).

Superconducting Cavities for the LEP energy upgrade

G.Cavallari, C. Benvenuti, P. Bernard, D. Bloess, E. Chiaveri, F. Genesio, E. Haebel, N. Hilleret, J. Tuckmantel, W. Weingarten
CERN - 1211 Geneva 23
Switzerland

Abstract

The technology of sputter coating of Cu cavities with Nb has been developed at CERN. The advantages of this technique have led CERN to order 168 of such cavities in industry. After an initial phase of technology transfer and of prototype development, the series production has been started in fall 92 by the three contractors. The results of the bare cavity tests are reported. Fixed and movable 120kW power couplers (MC) have been designed, manufactured and put into operation. Various models of higher order mode (HOM) couplers have been developed to cope with foreseen increase of the beam intensity. Special care is given to the conditioning of power couplers and of HOM couplers before installation in the machine.

INTRODUCTION

In total 192 superconducting cavities operating at accelerating fields of about 5MV/m are required to reach colliding beam energies suitable for W- W+ pair production physics. In 1988 it was decided to start with 24 cavities of bulk Nb while the technology of sputter coating Nb onto Cu was being developed. In 1990 the results obtained with the NbCu prototypes were positive enough to start the production of 168 sputter coated cavities [1]. The cavity frequency and the geometry were kept as for Nb cavities but a number of changes were introduced in the cryostat [2], the HOM coupler [3] and in the MC design.

THE BULK Nb CAVITIES

All the Nb cavities have been delivered [5] and accepted. The design figures were $Q_0 \geq 3 \cdot 10^9$ at 5MV/m and 4.2 K. The cavities have then been assembled at CERN in four-cavity modules and equipped with MC and HOM couplers. The final tests performed after assembling have shown a systematic degradation of the cavity performances mainly due to non resonant electron loading (field emission) such that the operation at 5MV/m could not be guaranteed. A new rinsing of most of the cavities becomes necessary.

In the mean time movable power couplers have been developed. It has been decided to launch a consolidation process of the bulk Nb cavities in order to install cavities of improved and more reliable performances (cryogenic circuit, capability of higher beam current, matching of RF power to beam intensity). A new planning has been established for the installation of the Nb modules in the 1993-94 winter shutdown.

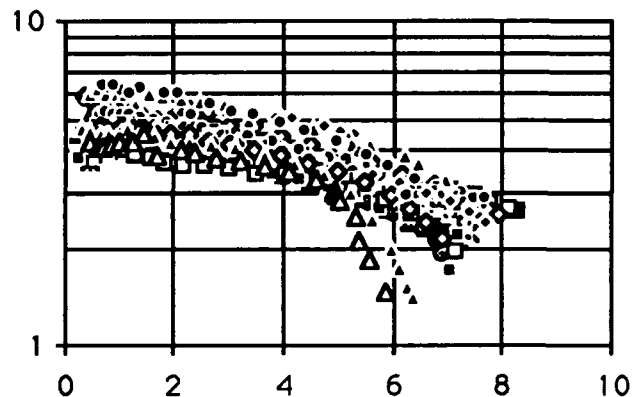


Fig. 1 - Bulk Nb cavities: Q_0 [E9] vs E_{acc} [MV/m]

THE Nb COATED Cu CAVITIES.

Among the advantages of the sputter coated cavities one should mention [1] the higher Q_0 the stability against quenches, the unsensitivity to low ambient magnetic fields [9]. The design figures could be set to $Q_0 \geq 4 \cdot 10^9$ at 6 MV/m and 4.2 K, somewhat higher than the ones for bulk Nb cavities in order to provide a reliable operation at 5 MV/m.

The contract for the 168 cavities has been split to three companies. Almost two years have been necessary in order to install the required facilities [5], transfer the sputter coating technology, train the teams and start the production. At present more than 30 bare cavities have been accepted (Fig. 2) and two 4-cavity modules have been delivered.

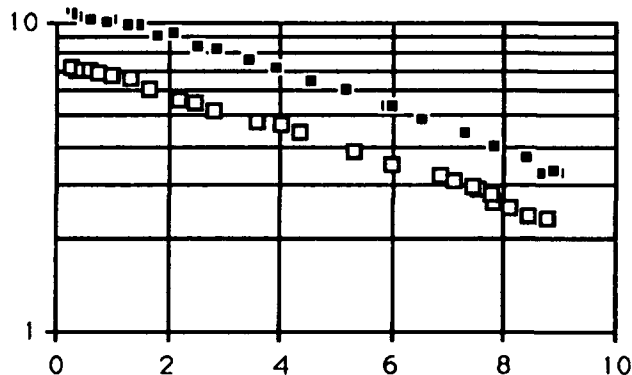


Fig. 2 - NbCu accepted cavities, best and worst : Q_0 vs E_{acc}

The problems encountered so far with the bare cavity test may be grouped in four categories:

- field emission already at low fields, coming from poor final rinsing or handling accidents. If the parameters of the rinsing water (resistivity, particle content, germs and Total Organic Carbon) are carefully controlled, gradients up to 9 MV/m can be obtained after a short time of "RF processing" in nearly all cases, without significant electron loading [6,12]. The gradient is limited by the available RF power. In the exceptional other cases He processing is applied to overcome field emission, otherwise a new rinsing is performed (Fig. 3).

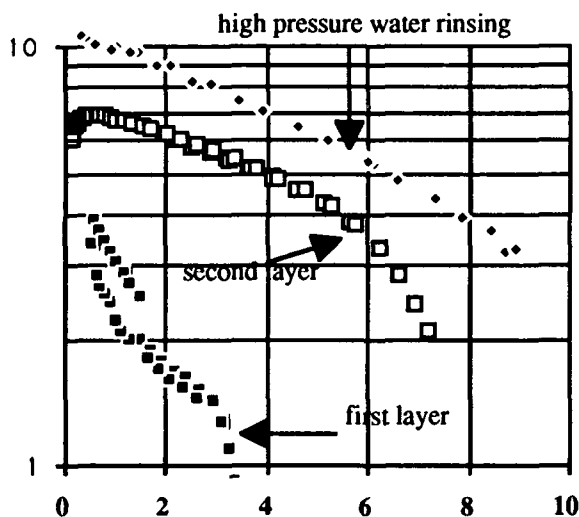


Fig. 3 - Successive coatings: Q_0 vs E_{acc}

- blisters, due to bad adhesion of the Nb film on the Cu substrate. The $Q_0(E_{acc})$ curve suffers from stepwise degradation when rising field, sometimes also from hysteresis (Fig 3). At high fields the blister eventually emits electrons that cannot be processed away by RF and He processing. Removing the blister by e.g. high pressure water rinsing [10] may bring the cavity to working condition. It also shows a poor adhesion of patches of the film. Temperature mapping is routinely applied in order to identify the defect position. The coating is usually removed by chemistry and a new coating is applied after a 20 μ m etching process. It has been noticed that successive coatings led to improved Q_0 values (Fig 3). This problem has been traced to impurities deeply implanted into the Cu sheet during the lamination process. An electropolish etching of 120 μ m instead of 80 μ m reduces drastically the number of blisters.

- poor Q_0 at low fields. After optical inspection the film is removed and a new coating is applied after a 20 μ m chemical polishing.

- good Q_0 at low fields but higher non quadratic losses [6] reduce the Q_0 at 6MV/m below the design figures. The mechanism is not yet fully understood [6,10].

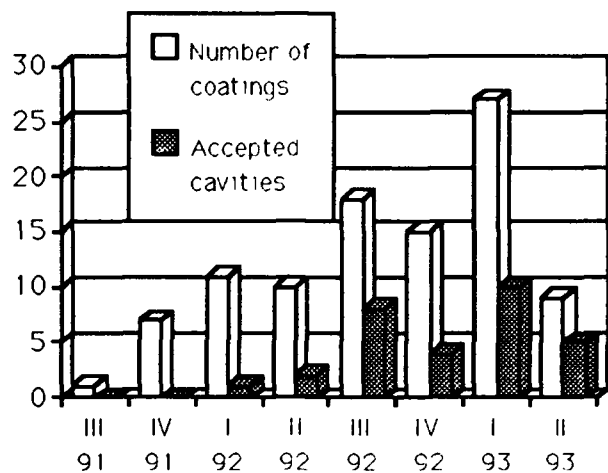


Fig. 3 - Production and acceptance rate of NbCu cavities

THE MOVABLE POWER COUPLER

The optimum coupling of the RF power to the cavity is determined by the beam intensity as well as the maximum accelerating voltage. Therefore, future beam intensity increases would ask for a modification of the coupling factor to avoid excess power consumption. The replacement of a MC on an installed cavity is potentially harmful as it may contaminate the cavity. The present movable coupler design [3] allows to change the coupler's Q_{ext} from $3 \cdot 10^9$ to $3 \cdot 10^5$. A byproduct is the possibility to correct the scatter in cavity coupling and to measure the Q_0 of cavities fully assembled or even already installed in the accelerator. It is precisely in this configuration that the final acceptance tests of the four-cavity modules are performed. The MCs are conditioned on a dedicated setup at room temperature under high vacuum up to 180 kW in travelling wave operation first and in future also in standing wave mode to cover all the SC cavity operating conditions.

THE HIGH ORDER MODE COUPLERS

Various HOM couplers have been developed so far [3], two are best suited : an antenna type (Type 1) for Nb cavities with Q_{ext} of 25000 at the TM011 mode, suitable for four bunch operation and beam intensities up to 8mA, and a hook type (Type 5) for NbCu cavities with Q_{ext} of 6000 at the TM011 mode, suitable up to 8 bunches per beam and beam intensities up to 12 mA.

The cooling of the HOM couplers has been found marginal during cavity conditioning under heavy e- loading although it is largely sufficient for normal operation. Improvements are in progress.

THE CRYOSTAT

The basic concept of the original cryostat layout has been kept [2] as it allows a modular assembling of the cavities in cryomodules, the access to the cavity accessories and to the cabling irrespective of the cavity vacuum. A number of changes has been introduced:

- there are three reinforcing beams instead of one, the structure has been made stiffer such that the modules may be rotated around the longitudinal axis during the transport in the accelerator tunnel.
- a vacuum flange is provided in line with each HOM coupler allowing, in future, counterflow cooled, high power rigid coaxial lines for the HOM coupler, in case the HOM power exceeds 400W per cavity. The actual RF cables, rated to 100 W in vacuum, have been made shorter (80cm).
- the Cu radiation shields have been removed and a total of 80 sheets of superinsulation, in two layers, are installed. The cryogenic static losses are now about 16W per cavity [11] to be compared to 50 W dynamic losses per cavity at 5MV/m.

CONCLUSION

The Nb coated Cu cavity production has encountered some initial difficulties but the success rate on the bare cavity production is above 50% and more than 30 cavities have been accepted. The cooling of the HOM couplers has been found insufficient under heavy e^- loading and new cooling schemes are being designed. Two cryomodules, whose installation is foreseen for September '93, have been delivered by industry and are under acceptance test.

ACKNOWLEDGEMENTS

The continuous support of C.Wyss, the LEP 200 project leader, is here acknowledged.

The three cavity manufactures, Ansaldo (I), CERCA (F) and Siemens (D) have greatly contributed with their competence to the progress of the project. The technicians of our groups have participated with untired enthusiasm to the transfer of knowhow and to the setting up of the test facilities and are now performing a large number of cavity tests.

The supply of large quantities of ^4He by the cryogenics group has been a key issue for the testing of a large number of cavities in a few months.

REFERENCES

- [1] C. Benvenuti et al, *Proc. 4th Workshop on RF Superconductivity, KEK, Tsukuba*, Y. Kojima ed. (1989)
- [2] R. Stierlin, *Proc. 3rd Workshop on RF Superconductivity, Argonne*, K.W. Shepard ed. (1987)
- [3] E. Haebel, *Proc. 5th Workshop on RF superconductivity, DESY Hamburg*, D. Proch ed. (1991)
- [4] C. Arnaud et al., *Proc. 14th High Energy Accel. Conf., Tsukuba 1989*, Y. Kimura ed. (1989)
- [5] G. Cavallari et al., *Proc. 15th Int. Conf. High Energy Accel., Hamburg*, J. Rossbach ed. (1992)
- [6] C. Arnaud et al, *Proc. 3rd European Accel. Conf., Berlin H. Henke ed. (1992)*
- [7] P. Bernard et al, *Proc. 3rd European Accel. Conf., Berlin H. Henke ed. (1992)*
- [8] *Proc. 3rd Workshop LEP Performance, CERN, Geneva*, J. Poole ed. (1993)
- [9] C. Benvenuti et al., *Proc. Part. Acc. Conf. San Francisco*, L. Lizama ed. (1991)
- [10] P. Bernard et al., ref. [3]
- [11] C. Arnaud et al., ref. [1]
- [12] K. Saito et al., *Proc. 4th Workshop on RF Superconductivity, KEK, Tsukuba*, Y. Kojima ed. (1989)

TESLA Input Coupler Development

M. Champion, D. Peterson, T. Peterson, C. Reid, M. Ruschman
Fermi National Accelerator Laboratory*
P. O. Box 500, Batavia, Illinois 60510

Abstract

The TeV Superconducting Linear Accelerator (TESLA) requires a RF input coupler capable of delivering 208 kW of 1.3 GHz power to a 9-cell Niobium cavity. Various electrical, mechanical, and cryogenic constraints present challenges in the design of such a coupler. Two parallel input coupler development programs are in progress at Fermilab and at DESY [1]. The Fermilab TESLA input coupler design and status is reported.

I. INTRODUCTION

The TESLA machine [2] is a next generation electron-positron collider based on two superconducting linear accelerators, each having a length of 10 km. Center of mass energies of greater than 500 GeV are planned, which will require accelerating gradients of 25 MV/m. Nine-cell superconducting Niobium cavities operating in the π -mode at 1.3 GHz will be used for acceleration. Each cryomodule will

* Operated by Universities Research Association, Inc., under contract with the United States Department of Energy.

contain eight cavities with one input coupler and two higher order mode couplers per cavity. The coaxial input coupler (Fig. 1) is mounted to the beam tube adjacent to the end cell of the cavity and is capacitively coupled to the cavity. RF power for two cryomodules (16 cavities) will be provided by a single 4.5 MW klystron.

II. INPUT COUPLER DESIGN

A. Electrical

A critical component of the TESLA machine is the input coupler, which during normal operation must transport 208 kW of 1.3 GHz RF power to a 9-cell Niobium cavity. The pulse length is 1.33 ms with 0.53 ms filling time and 0.8 ms beam-on time. The repetition rate is 10 Hz, hence the average power through the coupler is nominally 2.8 kW. Additionally, it is desirable that the coupler handle power levels up to 1 MW (at reduced pulse lengths and repetition rates) so that *in situ* high peak power processing of field emission sites may be performed. At power levels of 1 MW, field strengths at the inner conductor near the cavity (outer

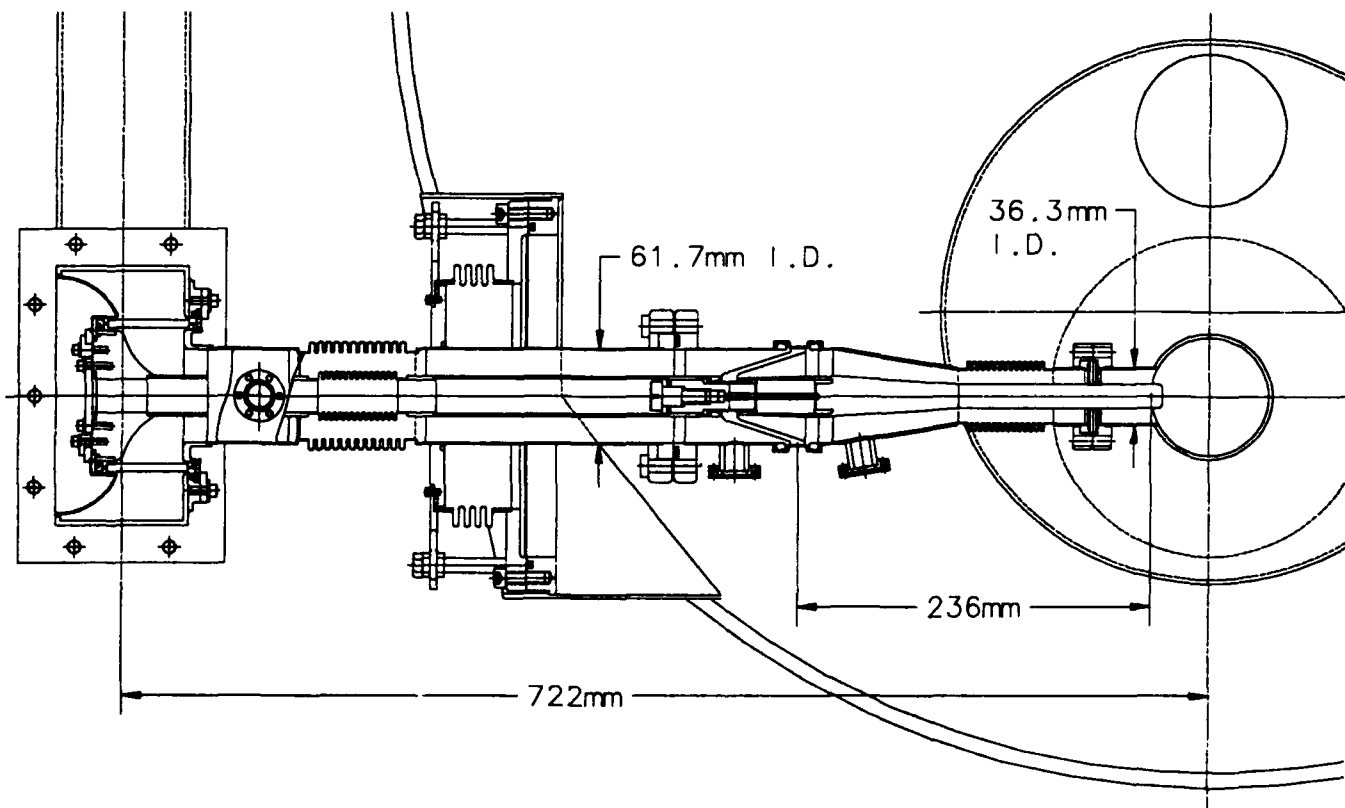


Figure 1. The Fermilab TESLA input coupler.

conductor diameter is 36 mm) will reach 3.04 MV/m for the case of total reflection as the cavity begins to fill with energy. The external Q of the coupler is to be $3e6$, adjustable over the range $1e6$ to $9e6$. The variable coupling is required due to variations in the cavities, couplers, and RF distribution system. The input coupler should be impedance matched for a return loss of better than 20 dB (1 % power reflection).

B. Mechanical

The requirement of variable coupling is met by the use of bellows on the inner and outer conductors of the coaxial input coupler as shown in Fig. 1. The inner and outer conductors move together toward or away from the beam tube by adjusting bolts outside the cryomodule. A range of motion of up to 25 mm is possible, which is adequate for the required range of external Q .

During cool down the eight cavities shrink toward one fixed point at the center of the cryomodule. The input couplers must accommodate this shrinkage, which is 15 mm worst case. Since the waveguide end of the input coupler is fixed, the coupler must be flexible so that the cavity end of the coupler can move with the cavity. This flexibility is achieved via the inner and outer conductor bellows. There is a pivot point outside of the cryomodule about which the coupler can rotate as the cavities shrink. The coupler will be mounted at room temperature so that the center conductor is off center at the beam tube. As the system shrinks during cool down, the center conductor will pivot into a position concentric to the outer conductor. Coupling adjustment will follow the cool down.

In opposition to the requirement for flexibility, there is a need to avoid mechanical vibration of the input coupler, which could lead to difficulties in controlling the amplitude and phase of the RF drive to the cavity. After coupling adjustment is complete, bolts will be tightened to secure the coupler at the cryomodule penetration.

The cold RF window must stay with the cavity once the cavity has been assembled in a clean room. Hence, the portion of the input coupler which extends out of the cryomodule must be removable. This is accomplished with an outer conductor flange joint sealed with a Helicoflex metal seal and an inner conductor joint fastened with a screw.

C. Cryogenic

The input coupler connects room temperature WR650 waveguide to a cavity at 1.8 K, hence minimum heat leak is necessary. This is achieved by using copper plated thin-wall stainless steel coaxial transmission line. Thermal calculations have been performed and indicate a 70 K heat load of 5.8 W and a 4 K heat load of 0.4 W.

D. Vacuum/Cleanliness

Two alumina ceramic RF windows will act as vacuum barriers and ensure the cleanliness of the cavity. A cylindrical

window is utilized in the waveguide to coaxial transition, while a conical window is installed at the 70 K intercept in the 62 cm diameter coaxial line. Ports for pumping and instrumentation of the region between the two windows are included near the waveguide.

III. COMPONENT DEVELOPMENT

A. Conical Ceramic

The conical ceramic window is the first level of protection of the cavity vacuum space. The conical shape was conceived of as a good candidate for a broad band impedance-matched window. The angle formed by the cone with respect to the axis of the coaxial line was chosen to be 18.2 degrees, which is the result of setting the angle of incidence equal to the Brewster angle for the vacuum to ceramic interface. The depth of penetration of the ceramic into both the inner and outer conductors was chosen to reduce the field strengths at the braze joints to approximately 50 % of their nominal values at the surfaces of both conductors. Two possibilities were examined for obtaining a good impedance match. One technique is to taper the ceramic thickness so that it is thinner near the inner conductor. The other method is to taper the inner or outer conductors. The tapered ceramic was rejected in order to simplify the ceramic, and because it is easier to machine metal to a new shape than to modify the ceramic. We chose to taper the inner conductor due to ease of fabrication. The thickness of the ceramic in the conical region is 3.2 mm. The Hewlett-Packard High Frequency Structure Simulator (HFSS) was used to model the ceramic. A return loss of 22 dB was achieved during simulation by iterating on the inner conductor taper.

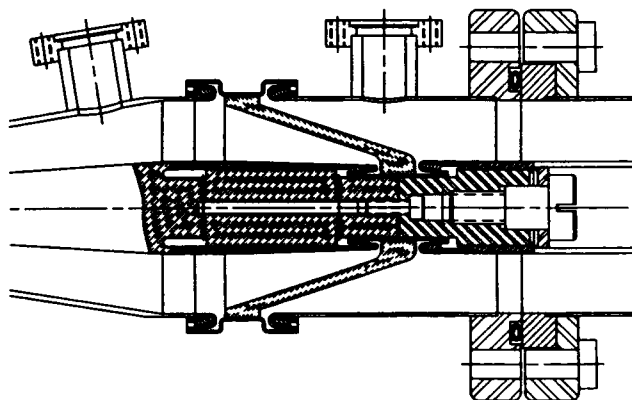


Figure 2. Detail of conical ceramic RF vacuum window.

Implementation of the design is shown in Figure 2. The ceramic is 99.5% Al_2O_3 from WESGO. The OFHC copper inner and outer conductor bands were brazed to the ceramic by Alberox. Initially, the inner conductor band contained a small plug of ceramic to prevent the band from shrinking away from the cone during the brazing cool down period. However, this plug caused cracking of the cone during brazing. The ceramic was coated with Titanium Nitride (TiN) by an evaporative

process at Fermilab. The conical shape requires several evaporations with various filaments in order to achieve a relatively uniform TiN thickness. The thickness goal was 10 nm on the ceramics coated to date. The inner conductors on each side of the ceramic were attached via electron beam welding at Fermilab. The outer conductors were attached via conventional TIG welding in an Helium/Argon atmosphere.

B. Bellows

The bellows used in the prototype input coupler are off-the-shelf units that have adapters resistance welded to each end. The thin wall (0.006") bellows are hydroformed and are rated for a range of travel of 25.4 mm. Copper plating of the outer conductor bellows along with the attached stainless steel tubing is achieved by using a special apparatus consisting of a tubular electrode which is inserted into the outer conductor and is sealed at the opening of the conductor. Plating solution enters the outer conductor through holes drilled in the electrode. The other end of the outer conductor is covered with a plate that has an exit port and attached tubing to carry away the plating solution. Hence, solution is continually circulated through the outer conductor during the plating process, and the exterior of the conductor remains free of plating.

C. Doorknob Transition

The "doorknob" transition is a waveguide to coaxial transition that incorporates a cylindrical knob as the impedance transforming device. This type of transition, when properly designed, has been shown to be capable of transmitting power up to the breakdown level of the coaxial line [3]. The Fermilab doorknob transition (Fig. 3) is complicated by the decision to incorporate a cylindrical ceramic window into the transition. Not only is the transition more difficult mechanically, but also the inclusion of the window tends to reduce the bandwidth of the transition to 1-2 percent. However, this complication makes for a compact and elegant impedance transformer and vacuum barrier.

The ceramic is 99.5 % Al_2O_3 from WESGO. Fermilab fabricated the OFHC copper and 304 SS rings which were brazed to the ceramic by Alberox. The ceramic is to be TiN coated on the vacuum side (inner surface). The waveguide side of the ceramic will be exposed to > 1 Atm dry air.

The addition of a window results in the use of a two-piece doorknob. The outer piece is welded to the waveguide, whereas the inner piece is welded to the ceramic window. The ceramic and inner knob are bolted into the waveguide assembly, so the ceramic may be replaced if necessary. C-seals are used as RF joints in the bolted assembly. The shape and size of the doorknob determines the impedance characteristics of the transition. These parameters have been determined by "cut and try techniques." The HFSS program has been used to model the design and help understand the field characteristics of the transition.

IV. CONCLUSION

A prototype of the coaxial portion has been constructed and tested at 805 MHz at power levels up to 1.7 MW [4]. The design needs to be optimized in terms of impedance match, cost, and assembly procedures. Testing at 1.3 GHz is expected in the coming months.

A low-power prototype of the doorknob transition has been constructed and tested. Impedance matching has been achieved over a 1-2 % bandwidth. A prototype high-power transition is under development and should be ready for testing by July, 1993.

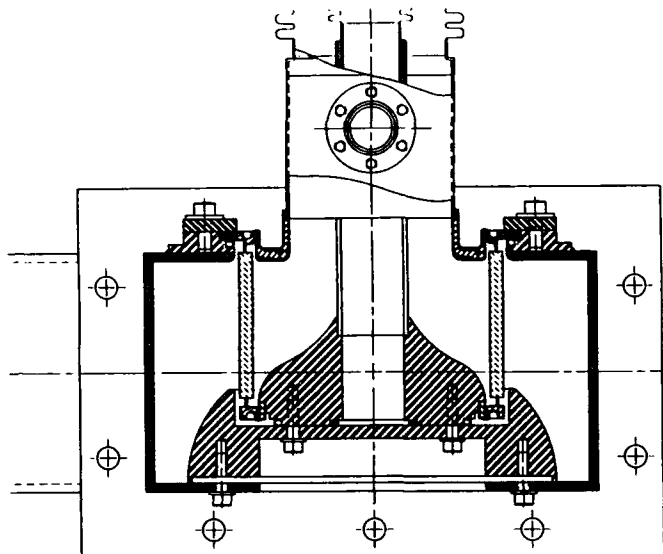


Figure 3. Detail of doorknob transition.

V. REFERENCES

- [1] B. Dwersteg, M. Marx, D. Proch, "Conceptual Design of a RF Input Coupler for TESLA," DESY, 1992.
- [2] *A Proposal to Construct and Test Prototype Superconducting RF Structures for Linear Colliders*, DESY, 1992.
- [3] G. L. Ragan, ed., *Microwave Transmission Circuits*, Boston Technical Publishers, Inc., 1964.
- [4] D. Sun, M. Champion, M. Gormley, Q. Kerns, K. Koepke, A. Moretti, "High Power Test of RF Window and Coaxial Line in Vacuum," Fermilab, these proceedings.

COMPUTER SIMULATION AND COLD MODEL TESTING OF CCL CAVITIES

C. R. Chang, C. G. Yao, D. A. Swenson and L. W. Funk
Superconducting Supercollider Laboratory
2550 Beckleymeade Ave., Dallas, Texas 75237

Abstract

The SSC coupled-cavity-linac (CCL) consists of nine modules with eight tanks in each module. Multicavity magnetically coupled bridge couplers are used to couple the eight tanks within a module into one RF resonant chain. The operating frequency is 1282.851 MHz. In this paper we discuss both computer calculations and cold model measurements to determine the geometry dimension of the RF structure.

I. INTRODUCTION

The SSC CCL cavities are designed in house and fabricated by the Institute of High Energy Physics (IHEP) in China. One of our major tests is to provide the accurate cavity dimensions for machine fabrication. In the past, the cavity dimensions were determined by cold model experiments only, because at that time, no computer code had enough accuracy for such complicated, highly non-axial geometric structures. Our CCL contains 72 accelerating tanks and 63 bridge couplers. Producing cold models for each tank and bridge coupler would be an extremely expensive and time consuming task. We have developed new methods that combine modern codes like MAFIA, SUPERFISH and HFSS and are able to produce cavity dimensions that are correct within a few MHz error. Of course, cold models for the low-, mid- and high- energy end are made and are used to bench mark these codes.

II. DETERMINATION OF ACCELERATING TANK DIMENSIONS

Each CCL tank contains 16 identical accelerating cavities and 15 identical coupling cavities. The structure can be treated as infinitely long if the end cavities are properly tuned. In 3-D MAFIA simulation we include one full accelerating cavity and two half coupling cavities and with proper terminations at symmetric planes z_{min} and z_{max} we can simulate an infinitely long structure. Fig. 1. shows the physical boundary and boundary simulated by MAFIA. We can see "steps" on the boundary because the code uses many "cubics" to produce an approximation for the actual smooth surface. This is a major source of inaccuracy in the solution and can not be completely removed for a finite number of mesh used. We have built

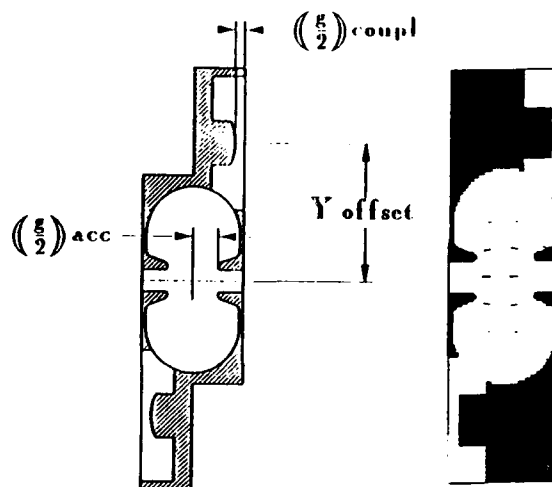


Figure 1: (a) Physical boundary of one accelerating cell and two half coupling cells, (b) boundary simulated by MAFIA

cold models according to the exact dimensions predicted by MAFIA and the measured frequency can be as much as 15 MHz different from the calculated frequency. The agreement on the coupling constant, k , on the other hand, is quite good, as shown in Table 1. The frequency change is very sensitive to the dimension change in the nose region. The geometry of the nose is too complicated to be accurately described by MAFIA. But the slot region is described very well. SUPERFISH with triangular meshes can give very good descriptions of arbitrarily complicated boundaries and the error of calculated frequency is usually smaller than 1 MHz. However, it is a 2-D code and cannot predict the effect of coupling slots, which is not a small effect for 7% coupling. D.A. Swenson proposed a way that combines the SUPERFISH and MAFIA and can eliminate the shortcoming of each code. The procedures are: (1) let MAFIA calculate the coupling constant and the effect of the coupling slots which produce a frequency drop Δf to the accelerating cell; (2) let SUPERFISH determine the nose gap, $(g/2)_{acc}$, of the unslotted cavity to produce a resonant frequency of $f_{operation} + \Delta f$. The cavity with slots should then resonant at $f_{operation} + \Delta f - \Delta f = f_{operation}$. The Δf produced by coupling slots can be calculated by two MAFIA runs: (1) calculate the accelerating cell frequency with coupling slots, f_{slot} , and (2) use the same mesh configuration to calculate accelerating cell frequency without coupling slots, f_0 . Then $\Delta f = f_{slot} - f_0$. Since the mesh configurations are the same for two runs, the error of f_{slot} and f_0 due to the same crude description of

*Operated by the Universities Research Association, Inc. for the U.S. Department of Energy, under contract No. DE-AC35-89ER40486

Y_{off} [cm]	k : Cold Model	k : MAFIA	Difference
11.18	7.904%	7.989%	-0.085%
11.93	4.895%	4.801%	0.094%
12.93	1.507%	1.638%	-0.13%

Table 1: Comparison of coupling constant from cold model and MAFIA

Y_{off} [cm]	Δf_{exp}	Δf_{cal}	Difference
11.18	38.168	38.725	-0.557
11.93	22.505	22.745	-0.240
12.93	6.310	6.295	-0.015

Table 2: Comparison of Δf (Unit: MHz) measured by cold model and calculated by MAFIA and SUPERFISH

the nose should be also the same and therefore the error is subtracted out in Δf . If Δf can be accurately determined, $(g/2)_{acc}$ can be accurately determined. The dimensions of coupling cavities can be calculated in a similar way. To test the validity of this method, we build cold models with different Y_{off} and compare the measured and computed values of k and Δf . Table 1 shows the results of comparison of k and Table 2 shows the comparison of Δf .

The surprisingly good agreements give us confidence with the method and we have generated the rest of tank dimensions entirely on computers. We did make two additional sets of cold models on the med- and high-energy end and the agreements with simulation results are consistently good.

III. DETERMINATION OF BRIDGE COUPLER DIMENSIONS

Fig. 2 shows the geometry of a five-cell bridge coupler with three identical middle cells and two identical end cells. Two end posts as frequency tuners are provided for end cells but not for middle cells. The physics of this type of bridge coupler are described previously^{1,2}. The total length of the bridge coupler grows with the inter tank space which is proportional to $\beta\lambda$. For 63 bridge couplers, the length of the middle cells can only be 7cm, 8cm or 9cm, but the length of the end cells will have 63 different values. Again, the three middle cells can be treated as a part of an infinitely long structure if the two end cells are properly tuned. We thus separately determine the dimensions for middle cells and for end cells.

For middle cells, MAFIA was first used to optimize the geometry of the coupling slots. Because middle cells only have three possible lengths, cold models were built for all three cases. The coupling slots on adjacent disc are rotated by 90° to reduce direct coupling. Half cell termination were used in the experiment. Since this will create images in the end cells that do not have 90° rotations, it does not represent an infinite long structure. However, as the cavity

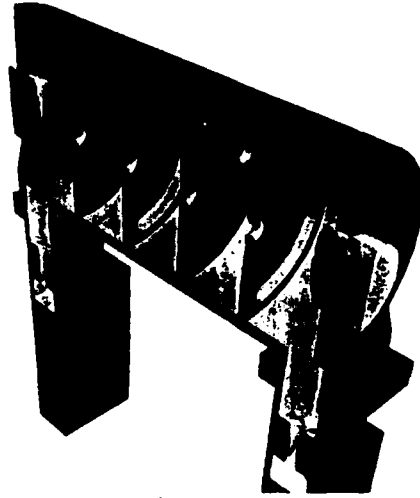


Figure 2: Geometry of Magnetically Coupled Bridge Coupler

chain gets longer, the end cell error effect gets smaller and the structure approaches to an infinitely long structure. With a few measurements, the asymptote can be obtained and it gives the desired frequency value. The radius of these center cavities can then be determined.

Bridge coupler end cells are more complicated. They do not have any well defined symmetric plane and can not be treated as a part of an infinite structure. MAFIA simulation on the bridge end cavities produce quite large errors because some artificial symmetric planes must be assumed to terminate the boundary. The end cell dimensions are completely determined by experiment. Since there are no well defined symmetric planes, no artificial terminations should be used. In the cold model measurement, one must include the entire 5-cell bridge cavity, the two coupling cavities under the bridge, and tank end cells and a few accelerating cavities. All accelerating cavities and bridge center cavities are fabricated at the correct dimensions. Bridge end cavity frequencies are adjustable by end posts. To determine the post length, one should first short out all other cells except the bridge end cell, tank end cell and the coupling cell between them. Adjusting the bridge end cell and tank end cell frequencies by varying the post lengths until the two cavity frequencies are both equal to 1282.851 MHz. At this point, the field level in the coupling cavity is zero. Repeat same procedure for the other bridge end cell. Finally, let all cavities couple together by removing shorting tools and measure the $\pi/2$ mode frequency. The $\pi/2$ frequency should be very close to the desired operation frequency. Adjust the two end posts equally to bring the $\pi/2$ mode frequency to the exact value. The post lengths are now at the correct value. We made three bridge cold models for the low-, med-, and high-energy end. Dimensions for those bridge end cells in between were obtained by interpolation.

IV. DETERMINATION OF COUPLING IRIS BETWEEN WAVE GUIDE AND POWER CELL

RF power is sent from waveguide to a CCL module through a coupling iris at the center bridge coupler power

cell. The dimension of this coupling iris must be determined to provide the correct coupling ($\beta = 1.0$) from the waveguide to one CCL module. Normally this iris is cut last when the entire module is assembled, as is the case for LAMPF and Fermilab. However, for our situation, it is desirable to know the approximate iris size in advance. There are two reasons. (1) In LAMPF and Fermilab each coupling iris only needs to drive two to four tanks, yet it must be cut very large to provide enough coupling. In our CCL, each iris must drive eight tanks, which has at least twice as many cavities. Concern was raised whether one iris can provide enough coupling. (2) Both LAMPF and Fermilab use single cavity bridge couplers. Because of its large volume, the coupling iris will not produce a big perturbation to the bridge cavity. With two end posts as frequency tuners, the power bridges do not need to be specially made so the iris can be cut as the last step. We use multi-cavity bridge couplers and the center cell has much smaller volume so the coupling iris will produce a large frequency drop δf . It is not desirable to add a tuner to the power cell due to the concern of sparking. A better solution is to reduce the power cell diameter in advance to raise the frequency back to the desired value. Thus the knowledge of iris size and the magnitude of δf is desirable.

To estimate the coupling slot dimension without the entire module assembled, we need to do some scaling. Assume coupling cavities are not excited and dissipate no power, then one module contains $N_{acc} = 128$ accelerating cavities and $N_{brig} = 21$ excited bridge cavities. The field level in an excited bridge cavity is approximately equal to half the level in an accelerating cavity so the power dissipation is $P_{brig}/P_{acc} \approx 1/4$, assuming the same Q ($Q_{Cu} \approx 11000$ for module I) value. The total power dissipation of one module is then equal to $N_{acc} + N_{brig}(P_{brig}/P_{acc}) \approx 133$ accelerating cells. In cold modeling we have one bridge coupler and two accelerating cells. From power dissipation point of view it is equivalent to $N_{model} \approx 3$ accelerating cells. Taking into account the fact that the $Q_{Al} \approx 1000$ for aluminium cold models, in order to obtain $\beta_o = 1$ for one CCL module, the equivalent β_{model} we are aiming for in the cold model measurement should be about $\beta_{model} = \beta_o \times (Q_{Al}/Q_{Cu}) \times [N_{acc} + N_{brig}(P_{brig}/P_{acc})]/N_{model} \approx 4$. β should be bigger when power dissipation in coupling cells is taken into account. To obtain the functional relation between β and slot size, a set of "plugs" with different sized rectangular irises are made and β values are measured. Some preliminary results are plotted in Fig. 3. It can be seen that β has a weak dependence on slot width but a very strong dependence on slot length. The β increase with l in a nearly exponential form, for $7\text{cm} \leq l \leq 9\text{cm}$, so we see straight lines in a logarithmic scale. But as l increased to comparable to the height of the wave guide, the curves bend downward because the magnetic flux in the wave guide has a high density near the center but falls off toward the edge. The β value can easily exceed 4, indicating one slot should provide enough coupling to drive one CCL module.

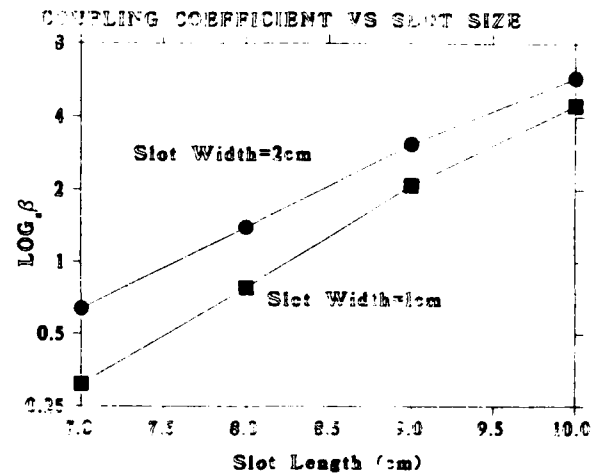


Figure 3: Measured coupling β vs slot length for slot width of 1 cm and 2 cm.



Figure 4: HFSS simulating electric field coupling from wave guide to bridge coupler

We are also doing computer modeling of the problem. The 3-D HFSS code with its powerful S-parameter solver is particularly convenient. Fig. 4 shows how the field is coupled from waveguide through iris into a five-cell bridge coupler. The simulation, however, show β increase with slot length faster than what was observed in the experiment. Further studies are needed to solve this discrepancy.

In summary, we have almost completed the entire CCL cavity dimension table and the only thing not finally determined is the dimension of the power coupling iris. Our preliminary results indicate one iris should provide sufficient coupling but more careful studies are needed to obtain its final dimension. Special thanks to Y. Goren, L. Walling, N. Yao and Y. Tang for their valuable assistance.

V. REFERENCES

- [1] C. G. Yao, *et al*, "A Novel Bridge Coupler for SSC Coupled Cavity Linac", 1992 Linear Accelerator Conference, Ottawa, Canada.
- [2] C. R. Chang, *et al*, "MAFIA Simulation and Cold Model Test of Three Types of Bridge Coupler", *ibid*.

Drive Linac for the Argonne Wakefield Accelerator

E. Chojnacki, R. Konecny, M. Rosing, and J. Simpson
Argonne National Laboratory, Argonne, IL, 60439, USA

I. INTRODUCTION

The drive linac in Phase I of the Argonne Wakefield Accelerator (AWA) will be used to accelerate short duration (10 ps), high charge (100 nC) electron bunches from 2 MV to 20 MV for use in a variety of wakefield acceleration and measurement studies[1]. The high charge is required since this drive bunch will generate the wakefields of interest in various test sections and their amplitudes are proportional to bunch charge. The short bunch duration is required to drive high-frequency wakefields without intra-bunch cancellation effects.

The drive linac design was a balance between having a small wake function to maintain a drive bunch energy spread of $\leq 10\%$ and obtaining an adequate accelerating gradient of ≥ 10 MV/m. This yielded a large aperture, low shunt impedance, high group velocity, L-band, standing-wave linac. Details of the design, fabrication, and testing are presented in the following.

II. LINAC DESIGN

A. Broad Considerations

The first consideration in the drive linac design was standing wave versus traveling wave. In a traveling-wave linac, the iris aperture has to be relatively small (low group velocity) to yield a high shunt impedance to provide an acceptable acceleration gradient given the available rf source power of ~ 20 MW. The small aperture, however, correspondingly causes the structure's wake function to be large, which would yield an unacceptable energy spread in the 100 nC drive bunch. As an example, the SLAC Mark IV constant-impedance linac[2] scaled to 1.3 GHz, powered by a 5 μ s, 20 MW source, and having a length of 15 m would provide an electron energy gain of 65 MeV, but would also produce a 47% energy spread from head to tail of the 100 nC bunch. Refinements such as rf pulse compression and utilizing a constant gradient structure would still result in a woefully large energy spread.

In a standing-wave linac, the iris aperture can be relatively large (high group velocity), yielding a low shunt impedance, but the rf power in the cavity will internally recirculate to a high steady state level, providing a reasonable accelerating gradient. The benefit of the large aperture is a low wake function, which will yield an acceptable energy spread in the 100 nC drive bunch. Indeed, it is this low wake function characteristic of large-aperture standing-wave structures that make them attractive in super-conducting versions for the TESLA linear collider study[3]. Thus, a large-aperture standing-wave cavity was chosen for the drive linac of the

AWA. A brief parameter search of specific standing-wave geometries is presented in section IIB.

In other options, an external feedback rf system (ring resonator) would provide even larger power build up than a standing-wave cavity, but would also require the nearly impossible plumbing of ~ 500 MW of rf power through various waveguide devices. Side-coupled structures were ruled out due to their relatively large wake functions and small acceleration gaps. Enlarging the aperture in a side-coupled structure to obtain an acceptable wake function would destroy the required isolation of adjacent beamline cavities.

B. Parameter Search

In choosing the frequency of operation of the drive linac, the overriding consideration was the longitudinal wakefield strength relative to the acceleration gradient. The amplitude of the fundamental-mode longitudinal wake function for a point source is given by

$$W_z = \frac{E_z}{q} = \frac{\omega r_s}{2 Q (1 - \beta_g)} \quad (1)$$

where all parameters apply to the linac fundamental mode, E_z is the longitudinal electric wakefield, q is the bunch charge, ω is the wake frequency, r_s is the shunt impedance in units of $[\Omega/\text{m}]$, Q is the structure quality factor, β_g is the normalized group velocity, and the units of W_z are, say, $[\text{kV}/\text{m}/\text{nC}]$. The factor $(1 - \beta_g)$ in the denominator of (1) is often ignored in cavities operating at cutoff or in traveling-wave linacs having very low group velocity. Since r_s/Q is proportional to frequency, f , the longitudinal wake function in (1) is proportional to f^2 , but the linac length is proportional to f^{-1} , so the wakefield energy loss per linac cell is proportional to f . Thus, as the linac frequency is lowered, the wakefield energy loss decreases linearly. This is indicative of the iris aperture being proportional to f^{-1} , and a smaller aperture (higher frequency) will "clip off" a larger fraction of the particle's radiation field to be left behind as wakes.

While a low drive linac frequency is desirable from a beam loading point of view, practical considerations regarding waveguide dimensions encourage the frequency to be > 1 GHz. Fortunately, examining a few test cases indicates that an L-band structure can just satisfy the gradient and energy spread goals, ≥ 10 MV/m and $\leq 10\%$, respectively. Table I lists parameters of five standing-wave cavities given a 100 nC drive bunch and 20 MW of rf power. These parameters were obtained from a variety of intermingled calculations utilizing analytic techniques, the URMEI computer code, and the KN7C computer code. Four of the five cases in Table I have $f = 1.3$ GHz and the parameters that vary from case to case are the aperture radius a and iris thickness t , as shown in Fig. 1.

TABLE I. Parameter scan of $\pi/2$ standing-wave linacs powered by 20 MW of rf to accelerate a 100 nC gaussian electron bunch having $\sigma = 5$ ps.

Parameter	Large aperture, thin iris	Small aperture, thin iris	Large aperture, thick iris	Small aperture, thick iris	Large aperture, thin iris
Frequency f (GHz)	1.300	1.300	1.300	1.300	2.856
Aperture radius a (cm)	5.08	2.0	5.08	2.0	2.31
Aperture/wall radius a/b	0.505	0.224	0.472	0.218	0.505
Aperture/wavelength a/λ	0.220	0.087	0.220	0.087	0.100
Iris thickness t (cm)	0.5	0.5	3.50	3.50	0.228
Gap length g (cm)	5.26	5.26	2.26	2.26	2.393
Cavity length L (m)	2.07	2.07	2.07	2.07	0.94
Quality factor Q	17179	17884	10060	9755	12555
Group velocity β_g	0.139	0.014	0.048	0.001	0.139
Shunt impedance r_s (M Ω /m)	21.5	45.4	7.2	6.1	32.0
Wake function W_z (kV/m/nC)	5.9	10.5	3.1	2.6	27.0
HOM beam loading factor	1.6	3.0	3.0	4.5	1.5
Voltage gain V (MV)	18.7	24.7	10.6	9.1	13.7
Voltage spread $\Delta V/V$ (%)	10.2	26.1	17.8	25.8	26.3

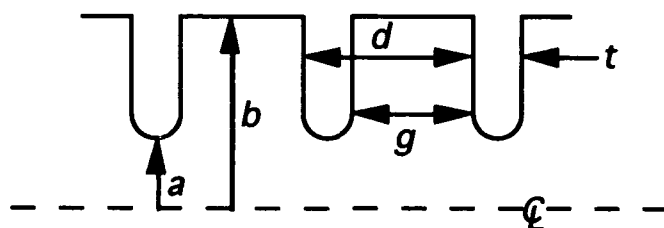


Figure 1. Schematic of standing-wave linac geometry.

It is not surprising that the thinner the iris thickness, t , the greater the bunch energy gain. In general, the iris thickness is made as thin as possible, limited only by mechanical strength and thermal conductivity. The fifth case in the last column of Table I is the same structure as in the first column, but scaled to $f=2.856$ GHz. It is the structure in the first column with the large aperture and thin iris that was chosen for the AWA drive linac.

C. AWA Drive Linac Properties

The AWA drive linac is a $\pi/2$ standing-wave linac with dimensions $a=5.08$ cm, $b=10.05$ cm, $t=0.5$ cm, $d=5.76$ cm, and a hemispherical aperture edge. The program KN7C was used to estimate the contribution of higher order modes to the AWA drive linac axisymmetric longitudinal wakefields. Shown in Fig. 2 is a plot of the longitudinal wake left by a gaussian bunch. The fundamental wake is shown as a dashed line and the "total" wake as a solid line, which includes 42 radial modes up to a frequency of 15 GHz. The drive bunch density profiles, spaced by one rf period, are indicated on the figure as dotted lines, but only the wakefield of the first bunch is shown. From this plot, the higher order mode beam loading factor is estimated to be ~ 1.6 .

Shown in Fig. 3 is a busy plot of the head-to-tail energy distribution that three mono-energetic electron bunches would attain upon passage through 2 meters of the AWA linac. The

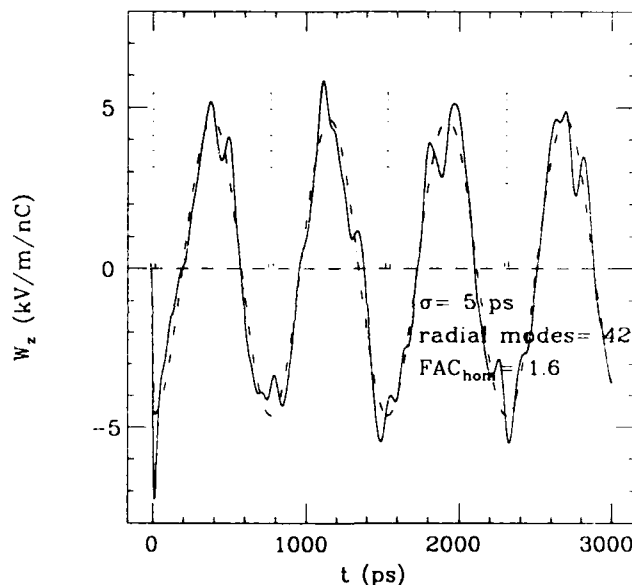


Figure 2. Plot of the longitudinal wake left by a single gaussian bunch having $\sigma = 5$ ps. "Total" wake is the solid line and fundamental wake is the dashed line.

higher order mode beam loading factor is included in the intra-bunch energy spread, but not in the inter-bunch energy spread since the higher order modes may be somewhat out of phase for succeeding bunches. The gaussian bunch density profile is indicated as a dotted line on the first bunch's energy spread.

III. FABRICATION

The AWA drive linac was fabricated from OFE copper, alloy 101, grade 2 or better, with machining of the cell cups performed on a numerical lathe. The relative machining tolerance was ± 0.5 mil, but the absolute tolerance was ± 1.5 mil. Since the linac cavity frequency has to be matched

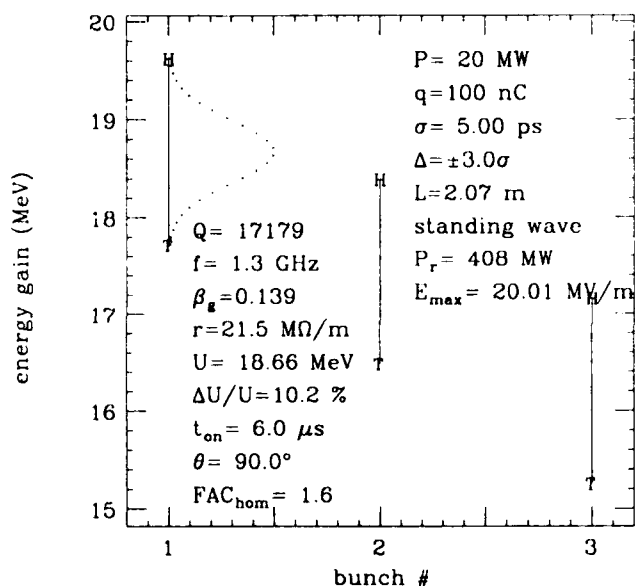


Figure 3. Plot of the head-to-tail energy distribution that three mono-energetic gaussian-profile electron bunches would attain upon passage through 2 meters of the AWA drive linac.

to the 32nd harmonic of the AWA mode-locked laser, the absolute machining tolerance was more critical. Four 1" diameter divots leading to a 1/8" thick cell wall were machined into each cell for final frequency tuning. The rf coupling cell, which included the coupling iris and a socket for half-height L-band waveguide, was machined from a single block of copper. The 2 meter AWA drive linac was split into two 1 m tanks. The final tank assemblies were stacked vertically and brazed in a hydrogen furnace at Pyromet Industrial in San Carlos, CA.

IV. MEASUREMENTS

Prior to brazing, the linac tanks, when clamped together, were slightly under frequency (200 kHz under 1.3 GHz when corrected for temperature and vacuum conditions) and slightly under coupled to the input waveguide ($S_{11} \sim 15$ dB with the target coupling after brazing being $S_{11} \sim 32$ dB). Brazing was expected to improve the quality factor, Q , of the cavities and thus improve the coupling, and the resonant frequency was expected to rise as determined by previous brazing tests. After brazing, the resonant frequency increased only ~ 10 kHz and the coupling actually decreased for an unknown reason. Thus, an iterative process was implemented to improve coupling and raise the resonant frequency by enlarging the coupling iris by filing and pressing the tuning divots to raise the resonant frequency. Plotted in Fig. 4 is a sample of the latest network

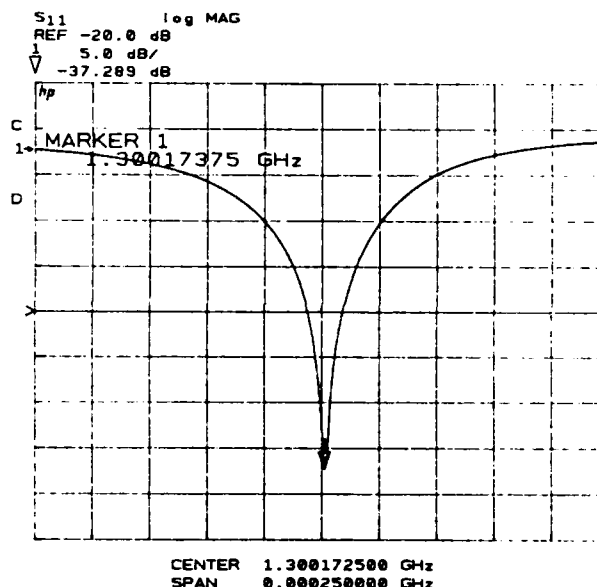


Figure 4. Network analyzer measurement of reflection coefficient S_{11} versus frequency for linac tank A. Measurement performed with a 10 mT vacuum and linac temperature of 75° F.

analyzer measurement of reflection coefficient S_{11} versus frequency for linac tank A. The coupling is satisfactory and the resonant frequency is what is needed to operate under vacuum at $\sim 90^\circ$ F. Slight final frequency tuning has yet to be performed when both tanks are connected to their temperature controlled water chillers.

This work has been supported by the United States Department of Energy, Division of High Energy Physics.

V. REFERENCES

- [1] M. Rosing, *et. al.*, "Argonne Wakefield Accelerator Update '92", *Proc. 1992 Linear Accelerator Conf.* (Ottawa, Ontario, Canada, 1992), p. 79; P. Schoessow, *et. al.*, these proceedings.
- [2] G. Loew, in *The Stanford Two-Mile Accelerator*, edited by R.B. Neal (W.A. Benjamin, Inc., New York, 1968), p. 129.
- [3] J. Rossbach, "An Overview of Linear Collider Plans", *Proc. 1992 Linear Accelerator Conf.* (Ottawa, Ontario, Canada, 1992), p. 25.

Choice of the RF Cavity for the SSC Collider

W. Chou

Superconducting Super Collider Laboratory*

2550 Beckleymeade Ave., Dallas, TX 75237

Abstract

Four types of RF cavities — multiple cell and single cell, superconducting (sc) and normal conducting (nc) — have been compared with respect to the specific needs of the SSC Collider. The single cell cavity is preferable to the multi-cell one because its higher order modes (HOM) are easier to damp. The sc cavity has a number of advantages over the nc one. But its mechanical complexity and operational reliability may present a concern. The impact of different rf frequencies on the beam parameters have also been studied. In the range from 180 MHz to 480 MHz, the parameter variations are generally small.

I. INTRODUCTION

In the SSC Collider, the beam intensity of a single bunch is limited by the detectors. Therefore, in order to achieve the design luminosity $10^{33} \text{ cm}^{-2}\text{s}^{-1}$, one has to use about 17,000 bunches in each ring. The coupled bunch instability is a main concern. The use of a wideband feedback system to damp the instability is difficult because it can lead to emittance dilution, which has been observed in the Tevatron and SPS. An effective way to avoid the instability is to employ passive damping, i.e., to damp the HOM such that all the unstable bunch modes would be Landau damped.

The Collider rf parameters are: $f_{rf} = 360 \text{ MHz}$, $V_{rf} = 20 \text{ MV}$, and $P_{rf} = 2 \text{ MW}$. The frequency must be a multiple of 60 MHz, which is the basic bunch spacing. The voltage is mainly determined by the requirement of the bucket size (in order to avoid the rf noise problem while accommodating a beam with large longitudinal emittance) rather than by the acceleration (which needs 3.9 MV/turn during ramping). The power requirement comes from the beam loading compensation during storage (1.4 MVA, reactive), with adequate safety margin.

The baseline design is to use eight 5-cell cavities of the PEP type and two 1 MW klystrons [1]. However, the calculations show that the HOM of this cavity would cause longitudinal and transverse multibunch instabilities at injection (2 TeV). The e-folding time is in the order of seconds. At top energy (20 TeV), the unstable modes would be Landau damped, but only marginally. Therefore, there was a proposal to change the baseline by adopting the single cell type cavity [2].

*Operated by the Universities Research Association, Inc., for the U.S. Department of Energy under Contract No. DE-AC35-89ER40486.

II. CRITERIA OF CHOICE

A. HOM and coupled bunch instability

For the rf cavity in the Collider, HOM damping is a major design goal. If the HOM are not properly damped, the coupled bunch instability will occur, as experienced in the LEP and HERA. When a wideband feedback system is employed, the noises in the feedback system may blow up the beam emittance. The required transverse emittance (1 mm-mrad, rms, normalized) of the Collider beam is demanding. Any increase in emittance means the decrease in luminosity. The emittance growth rate due to the feedback noise is [3]:

$$\frac{1}{\tau} \equiv \frac{\dot{\epsilon}}{\epsilon} = 0.64 f_0 \left(\frac{x_N}{\sigma_x} \right)^2 \Delta\nu^2 \quad (1)$$

in which f_0 is the revolution frequency, σ_x the rms beam width, and $\Delta\nu$ the betatron tune spread. The pickup resolution of the feedback system, x_N , is proportional to $\Delta f^{1/2}$, where Δf is the bandwidth of the feedback system. A wider bandwidth gives rise to a larger thermal noise. Therefore, it is preferred that the HOM of the cavity can be damped such that the wide-band feedback system will become unnecessary.

B. Transient beam loading

In the train of the Collider bunches, there are seven injection gaps (1.7 μs) and one abort gap (4.2 μs). These gaps will cause phase modulation. In the linear approximation, the modulation amplitude is:

$$\Delta\phi = \left(\frac{I_b R}{V_c} \right) \cdot \left(\frac{\omega_{rf}}{2Q} \right) \Delta t \quad (2)$$

in which R , Q and ω_{rf} are the shunt impedance, quality factor and angular frequency of the cavity, respectively, V_c the cavity voltage, I_b the rf component of the beam current ($I_b = 2I_{dc}$), and Δt the gap size. When the ring is partially filled (for instance, during the injection), this formula is no longer valid and the computation is more involved. The consequences of the phase modulation are: (a) The jiggling of the interaction point in the longitudinal direction. (b) The reduction of the luminosity due to a crossing angle. (c) A larger occupation of the bucket by the oscillating bunch. Therefore, $\Delta\phi$ has to be limited under certain value by feedforward or fast feedback.

C. Detuning and fundamental mode instability

The optimum detuning for reactive compensation is:

$$\frac{\Delta f_{rf}}{f_0} = \frac{I_b \cos \phi_b}{2V_c} \cdot \frac{R}{Q} \cdot h \quad (3)$$

where h is the harmonic number. For a fully detuned nc cavity in the Collider, Δf_{rf} is about -6 kHz. Because f_0 is low (3.441 kHz), the impedance of the fundamental mode will cover several revolution lines. Thus, detuning will strongly drive the following coupled bunch modes unstable: $m = 1$, $n = -1, -2, -3, \dots$. If, on the other hand, not to detune the cavity (at a price of higher power losses) in order to avoid this problem, then the operation and control of the cavity may become difficult. A possible solution is to employ a fast rf feedback, which is widely used at CERN. In this case, the total loop delay is an utmost important parameter and should be made as short as possible when planning the klystron gallery location.

D. Broadband impedance

In addition to the HOM, the rf cavities also have a broadband impedance, which will affect the single bunch instabilities. However, in the Collider impedance budget, the contribution from the rf cavities is small (10% in longitudinal and 0.1% in transverse). Therefore, this should not be a big issue in making the choice of the cavity.

E. RF noise

The phase and amplitude rf noises can cause longitudinal emittance growth, particle loss and reduction of the beam lifetime. Thanks to a large bucket-to-bunch-area ratio in the design (30 at injection and 25 at full energy), this is not a serious problem. Study shows that the emittance doubling time exceeds 50 hours at the specified noise level [4]. One special feature of the Collider is that the synchrotron frequency is so low (4 Hz) that the sideband will always fall into the impedance bandwidth of the cavity no matter it is nc or sc. (This is in contrast to the LEP, in which the synchrotron frequency of the proton beam is several hundreds hertz. Improvement of beam lifetime was observed when sc cavities were used there.)

F. Reliability and availability

Because of the big size of the SSC, the reliability and availability of the rf cavity is a top priority issue. This includes: (a) The failure probability of the cavity; (b) When a cavity is tripped, whether the beam can survive; (c) If the beam has to be dumped, whether an injection is immediately possible. In this regard, it is obvious that using two large klystrons is not a good design. Because the failure of one cavity can lead to the loss of half rf voltage. Using four or eight klystrons is a better scheme. The 500 kW and 250 kW klystron can be available on the market (Varian and Litton) if one needs them. The trip rate of the cavity will be discussed later.

G. Flexibility

It is desirable to use the cavity as a kicker to damp the injection errors and low order coupled bunch instability. For this purpose, the klystron should have enough reserved power and the system should have enough bandwidth (about 500 kHz), which can be achieved by using an rf feedback.

H. Power limitation of the window

The power of each window should not exceed 200 kW by today's technology. Otherwise the manufacture will be difficult and the reliability will be questionable.

I. RF power loss

This is always an important issue in electron machines (e.g., the B-factory). But it is much less so in the SSC, which is a proton machine. The reactive power of the rf cavities is 1.4 MVA, which is a small fraction of the total installed power (about 0.5 GVA). Either detuning or not detuning, sc or nc, this issue does not play a big role.

III. COMPARISONS

A. Multi-cell, nc cavity

This type is cheaper than the single cell cavity. But the problem is that its HOM are not easy to damp because of lack of room for the HOM couplers and because of the cross-talk between neighboring cells. When DORIS installed the PETRA 5-cell cavity, it tried to damp the HOM by inserting couplers through the pickup flanges. The impedance reduction was limited by a factor of 2-3 [5]. A more successful case was the CESR 14-cell cavity, in which the HOM have been damped by a factor of 20-100 [6]. Another concern is the window power that will exceed 200 kW. The two-window-per-cavity design requires a significant amount of R&D work.

B. Multi-cell, sc cavity

This type is excluded because of the following reasons: (a) If two 5-cell sc cavities are used, each window would take 1 MW, which is far beyond the allowable maximum of 200 kW. (b) The HOM couplers can only be installed near the ends of the multi-cell structure in order to avoid multipacting. This makes it difficult to damp those HOM that are confined in the middle part of the cavity.

C. Single cell, nc cavity

This type is ideal for HOM damping, which can be achieved by either installing couplers and/or by staggered tuning. A recent example is the cavity being developed at the Advanced Light Source at ANL. The damping factor is between 10 to 100. The cavity suggested by SLAC/LBL for the B-factory has three waveguide attachments and looks promising. But considerable engineering efforts are needed before it can be put to use. The number of cavities is determined by the power dissipation in the wall (maximum 10 W/cm²). It is possible to achieve 20 MV by using 32 or even 24 cavities.

Parameter	RF Frequency			Variation [†] %	Note
	480 MHz	360 MHz	180 MHz		
Longitudinal emittance, rms (π eV-s)	0.035			-	inj, fixed
RF voltage (MV)	0.233			-	20 TeV, fixed
	6.6			-	inj, fixed
	20			-	20 TeV, fixed
Bunch length, rms (cm)	5.1	5.4	6.5	-6/+20	inj
Energy spread, rms ($\times 10^{-5}$)	5.6	6.0	7.1	-7/+18	20 TeV
	10.4	9.7	8.1	+7/-16	inj
	6.3	5.8	4.9	+9/-16	20 TeV
Synchrotron tune	0.0026	0.0022	0.0016	+18/-27	inj
	0.0014	0.0012	0.0009	+17/-25	20 TeV
Bucket area (eV-s)	2.17	3.34	9.44	-35/+180	inj
	11.9	18.3	51.9	-35/+180	20 TeV
Bucket-to-bunch-area ratio	20	30	86	-35/+180	inj
	16	25	71	-35/+180	20 TeV
Luminosity reduction	0.87	0.85	0.81	+2/-5	20 TeV
Particles per bunch ($\times 10^{10}$)	0.82	0.84	0.91	-2/+8	inj/20 TeV
Synchrotron radiation (kW/beam)	8.9	9.0	9.2	-1/+2	20 TeV
Parasitic heating (kW/beam)	0.89	0.73	0.50	+22/-32	20 TeV
Dynamic aperture (σ)	12.8	12.9	13.3	-1/+3	inj
Longi threshold impedance (Ω)	3.9	3.6	2.8	+3/-22	inj
Trans threshold impedance ($M\Omega/m$)	260	238	185	+9/-22	inj
Longi intrabeam scattering (h)	200	203	205	-1/+1	20 TeV
Trans intrabeam scattering (h)	131	116	83	+13/-28	20 TeV
Space charge tune shift in LEB	0.39	0.40	0.43	-3/+8	inj

[†] The values at 360 MHz are used as the reference.

D. Single cell, sc cavity

This type has a number of advantages: low rf loss, low broadband impedance, low transient beam loading (because of its low R/Q and high V_c) and, most importantly, low HOM (because the total number of sc cavities is smaller than the nc cavities). But the main concern is the complexity of its structure and the associated reliability problem. There are reports about the high average trip rate of the sc cavities at TRISTAN (more than one trip per fill) [7] and CEBAF (one trip per cavity every 16 hours) [8]. The causes have not yet been fully understood. A more careful study is needed to assess the risks if sc cavities are to be used in the SSC.

IV. RF FREQUENCY

When the longitudinal emittance and rf voltage are fixed, many beam parameters have weak dependence on f_{rf} , such as the rms bunch length ($\propto f_{rf}^{-1/4}$), rms energy spread ($\propto f_{rf}^{1/4}$), and synchrotron tune ($\propto f_{rf}^{1/2}$). The bucket size ($\propto f_{rf}^{-3/2}$) has a relatively strong dependence on f_{rf} . The above table lists the beam parameters that correspond to three different rf frequencies. The variations of most parameters are small except the bucket area and bucket-to-bunch-area ratio, of which the changes are noticeable. This ratio determines the tolerable rf noise level. Should this become an issue, one can enlarge the bucket

by increasing the rf voltage ($\propto V_{rf}^{1/2}$). Other factors one needs to consider include:

- Beam transfer from the HEB to the Collider: The HEB rf is 60 MHz. One will have to rotate the beam in the longitudinal phase space before extracting it from the HEB. Higher rf frequency in the Collider makes the injection more difficult.
- Cost: High frequency klystrons are cheaper.
- Market availability: There are 350 MHz and 500 MHz cavities available, which can be modified to 360 MHz and 480 MHz, resp. Also available are the high power klystrons in the range 350-500 MHz.

V. REFERENCES

- [1] *Site Specific Conceptual Design*, SSCL-SR-1056, (July 1990).
- [2] W. Chou and G. Schaffer, "Comments on the Collider rf Cavity in the SSC," SSCL internal technical note PMTN-036C (January 1992).
- [3] W. Chou and J. Peterson, SSCL-623 (1993).
- [4] H.-J. Shih *et al.*, SSCL-520 (1992).
- [5] B. Dwersteg *et al.*, *IEEE Trans. Nucl. Sci.* NS-32, p. 2797 (1985).
- [6] R. Sundelin *et al.*, *IEEE Trans. Nucl. Sci.* NS-28, p. 2844 (1981).
- [7] K. Akai *et al.*, KEK Preprint 91-35 (May 1991).
- [8] R. Sundelin, private communication.

High Field Conditioning of Cryogenic RF Cavities*

M. Cole, T. Debiak, C. Lom, W. Shephard, J. Sredniawski
Grumman Aerospace and Electronics Group
Grumman Corporation, Bethpage NY, 11714 USA

Abstract

Space-based and other related accelerators have conditioning and operation requirements that are not found in most machines. The use of cryogenic copper, relatively poor vacuum, and limited power storage and operating time put unusual demands on the high-field conditioning process and present some concerns. Two CW cryogenic engineering model "sparker" cavities have been fabricated and tested at Grumman to address some of these concerns. Results of these tests have been very positive. The cavities have been tested to fairly high field levels. Tests included initial and repeated conditioning as well as sustained RF operations. The two cavities were an engineering model DTL and an engineering model RFQ. Both cavities operated at 425 MHz. The DTL was conditioned to 46 MV/m at 100% duty factor (CW) at cryogenic temperature. This corresponds to a gap voltage of 433 kV and a real estate accelerating gradient (energy gain/total cavity length) of 6.97 MV/m. We believe this to be record performance for cryo CW operation. During cryo pulsed operation, the same cavity reached 48 MV/m with 200 μ sec pulses at 0.5% DF. The RFQ was conditioned to 30 MV/m CW at cryo, 85 kV gap voltage. During a brief period of cryo pulsed operation, the RFQ operated at 46 MV/m, or 125 kV gap voltage. Reconditioning experiments were performed on both cavities and no problems were encountered. It should be noted that the vacuum levels were not very stringent during these tests and no special cleanliness or handling procedures were followed. The results of these tests indicate that cavities can run CW without difficulty at cryogenic temperatures at normal conservative field levels. Higher field operation may well be possible, and if better vacuums are used and more attention is paid to cleanliness, much higher fields may be attainable.

I. INTRODUCTION

The use of accelerators in space presents special problems that are not encountered with most machines. The use of cryogenic copper for machines that require CW operation is favored since the resistive wall losses can be reduced by cooling with on board liquid hydrogen fuel. Vacuum levels are generally in the range of 10^{-6} to 10^{-7} Torr as opposed to the 10^{-8} Torr or better that one typically encounters in normal machines. The most significant problem may be that the amount of operating time available in space is dictated by the amount of energy stored on the platform. Conditioning requirements must be fairly well known in advance, and cannot be excessive.

A series of experiments was conducted to address these concerns. Two engineering model RF cavities, a drift tube LINAC (EMDTL) and a radio frequency quadrupole (EMRFQ), were fabricated. The designs were representative of cavity designs for real machines. Tests were performed to explore the difficulties of operating cryogenic copper cavities in vacuums of 10^{-5} to 10^{-7} Torr. High field operation of these cavities was explored. Tests were also performed to determine the requirements for reconditioning cavities after periods of inactivity, and to quantify the time required for any such reconditioning.

II. CAVITIES

Figure 1 shows the EMDTL cavity. Table 1 outlines some relevant parameters. The cavity consists of two complete DTL cells. It was manufactured from OFHC copper with an as machined finish. The RF surfaces of the cavity were treated to obtain high Q Enhancement Factor (QEF) [defined as $Q(\text{room temp})/Q(\text{operating temp})$]. The treatment, developed at Grumman, includes a deoxidation dip followed by a brightening and passivating treatment. No additional cleaning or bake out of the surface was performed. After assembly the cavity was stored in a machine shop environment.

The cryostat is a stainless steel vacuum vessel with twenty-five layers of super insulation separating the cavity from the vessel walls. Supercritical neon cryogen (27 K @ 425 psi) cools the cavity. Design operating temperature for both cavities is between 31K and 34K, although during the longest operating periods the cavities reached 41K.

The forward and reflected powers were measured using a

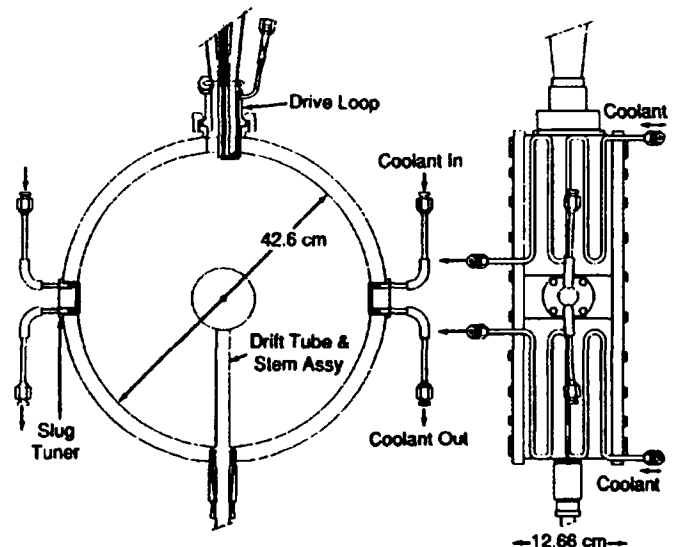


Figure 1. Engineering Model DTL Cavity Showing front cross section and exterior side view

* This work performed under IR&D contract #7256-2709 and 7256-3002

	EMDTL	EMRFQ
Cavity Parameters at Cryo (31 K)		
Frequency (MHz)	424.430	422.201
Q(unloaded)	100518	23581
Design Operating Point (QEF=4)		
Peak Field (MV/m)	28.42	36.54
Power (kW)	17.9	16.7
Peak Voltage (kV)	265.25	77.63
Actual Operating Point		
QEF	5.14	3.46
Peak Field (MV/m)	28.42	36.54
Power (kW)	13.9	19.32
Peak Voltage (kV)	265.25	77.63

Table 1. Summary of important parameters for engineering model cavities

directional coupler at the output of the amplifier. Two pickup loops sampled the cavity field at the outer wall. One of the loops was connected to an RF detector for cavity field measurement. The other was used to provide a signal to a phase-locked-loop frequency tracking system.

The EMRFQ is illustrated in figure 2. Some relevant parameters are outlined in table 1. The cavity is 48 cm in length and was made from tellurium copper. The RF surfaces were machined to a standard finish then treated for high QEF. The EMRFQ then went through several stages of electroforming ending in a finished cavity. After the cavity electroforming was completed no further cleaning was performed and the cavity was stored in a machine shop environment.

III. CONDITIONING EXPERIMENTS

A. First Time Conditioning

Experiments were performed to explore three areas, first time conditioning, operation at high fields, and reconditioning. First time conditioning experiments evaluated different techniques for processing the cavity to operational levels for the first time. The use of room temperature pulsed

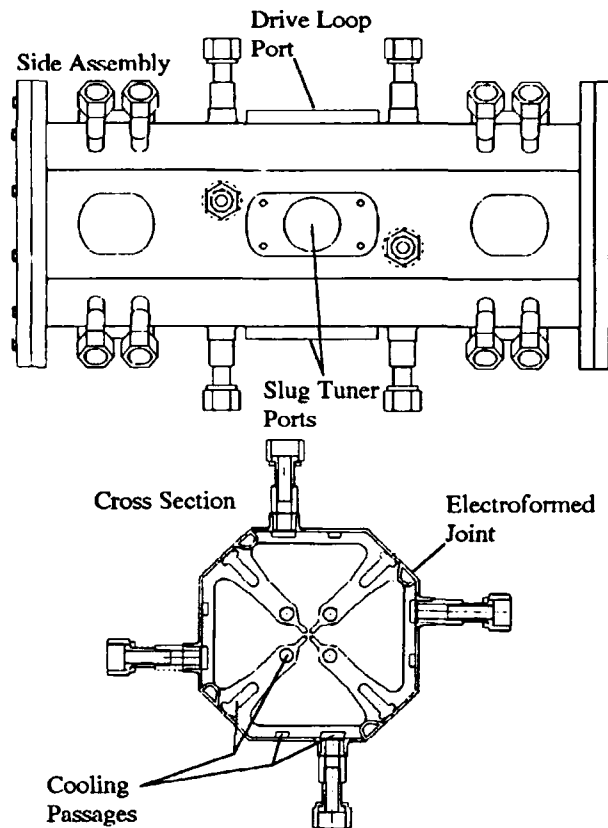


Figure 2. Engineering Model RFQ showing front cross section and exterior profile.

and CW conditioning and cryo pulsed conditioning before cryo CW operation was investigated, as well as the feasibility of going directly to cryo CW operation. High field experiments were performed for both pulsed and CW operation. Reconditioning experiments were performed after inactive periods of 1 and 12 hours at operating temperature. Table 2 is a summary of peak operating conditions. Cavity fields were calculated using the measured net power into the cavity along with the measured Q and the stored energy as calculated by the program Superfish.

The first cavity tested was the EMDTL. The EMDTL

CAVITY	DF	Pulse Width	Peak Field	Real-Estate Accel Gradient	Stand By Time	Recondx Time
EMDTL	CW	6 sec	46 MV/m	6.97 MV/m	NA	NA
EMDTL	CW	51 sec	28 MV/m	4.24 MV/m	NA	NA
EMDTL	0.5 %	200 μ sec	48 MV/m	7.27 MV/m	NA	NA
EMRFQ	CW	5 sec	31 MV/m	NA	NA	NA
EMRFQ	CW	31 sec	28 MV/m	NA	NA	NA
EMRFQ	0.5 %	200 μ sec	45 MV/m	NA	NA	NA
EMDTL	CW	10 sec	28 MV/m	4.24 MV/m	1 hour	instant
EMDTL	CW	7 sec	33 MV/m	5.00 MV/m	12 hour	instant
EMRFQ	CW	5 sec	13 MV/m	NA	First Time	45 sec

Table 2 Summary of peak operating conditions for engineering model experiments

was conditioned both pulsed and CW at room temperature before any operations at cryo. During cryo operations the cavity was conditioned well in excess of design field in pulsed mode, then conditioned CW. This conditioning sequence worked quite well; no difficulties were encountered. The cryogenic portion of conditioning progressed faster than the room temperature portion. This result encouraged us to be more aggressive when the EMDTL was tested for a second time after extended exposure to air. During the second test the EMDTL was conditioned CW at cryo with no room temperature conditioning or cryo pulsed conditioning. No problems were encountered; the cavity conditioned quite readily.

On the basis of our success with the EMDTL, we decided to condition the EMRFQ for the first time at cryogenic temperature CW with no intermediate steps. This approach worked very well. Figure 3 shows 6 of the first 9 CW bursts. All of these were of six second duration with a forward power of 3 kW. During the first six periods the AFC was off. By the third operation period the cavity field was stable although not at the correct frequency. When the AFC was activated during the sixth operating period the cavity field shot way up and significant breakdown was visible. During the eighth operating period the field appears to drop down to a multipacting level, but this is gone in the ninth operating period and the cavity was operating smoothly at 18 MV/m. Due to leaks in the cooling system that developed during the experiment, the vacuum steadily degraded during the EMRFQ test. Near the end of the test the vacuum would climb to the high 10^{-5} Torr range while the RF was on and the cryogen was removing heat. This made conditioning progressively more difficult and limited our ability to reach design operating levels. The bulk of the difficulty in conditioning is generally encountered in the beginning at the

lower field levels and at the end at very high field levels. We believe that with better vacuum, we could have conditioned from 18 MV/m up to the conservative design levels of 36 MV/m fairly easily.

B. High Field Conditioning

The bulk of our high field conditioning was conducted with the EMDTL. Vacuum problems during the EMRFQ test prevented high field CW operations although high field pulsed operations took place. The EMDTL was conditioned to fields well in excess of design levels without great difficulty. No special processing techniques were used to reach these levels. Peak CW levels were limited by the ability of the cavity to hold the fields. Sparking and microdischarge would cause the amplifier to trip out due to high reflected power. The use of a circulator between the amplifier and the cavity may have allowed us to condition the cavity to higher levels without the inconvenience of amplifier trip-outs. Peak pulsed levels were limited by the available power from our amplifier at the time. The ease with which pulsed conditioning was performed leads us to believe that much higher fields could have been reached. As with the EMDTL pulsed conditioning of the EMRFQ was limited by the available power. There is no other reason that higher fields could not be reached.

C. Reconditioning

Numerous reconditioning experiments were conducted with the EMDTL. The cavity was put in standby mode for various lengths of time and then turned on. The goal was to assess the time and energy requirements for operation of cavities in space. We found that no reconditioning was required after periods of up to 12 hours. It should be noted that we were restarting with a burst length of about six seconds at design field of 36 MV/m.

IV. CONCLUSION

These experiments demonstrated the operation of CW RF cavities at cryogenic temperatures in vacuums of 10^{-5} to 10^{-7} Torr. This is consistent with the operation of advanced accelerators in the environment of space. The EMDTL was conditioned to 46 MV/m for a six second CW burst and 36 MV/m for a 51 second CW burst. The EMDTL was conditioned to 48 MV/m pulsed, limited only by available power. It was found that no reconditioning was required to restart the EMDTL after 12 hours at standby. The EMRFQ was conditioned CW for the first time at cryo with no preconditioning at room temperature or pulsed. The EMRFQ was conditioned to 46 MV/m during pulsed operation.

We believe that these experiments have demonstrated the feasibility of this type of operation. While the experiments were not completely rigorous (i.e., we were limited to CW bursts of 30 seconds) they were as complete as time and resources permitted. The experiments showed no major problems or obstacles, and indicated that cryo CW operation may be easier than expected rather than harder

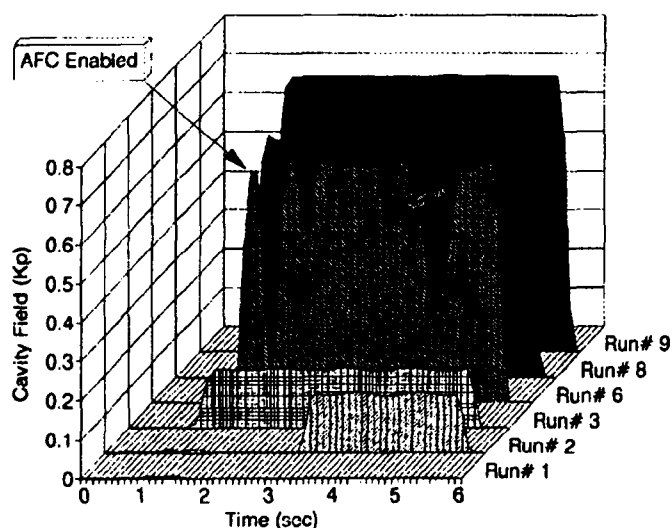


Figure 3. Profiles of six of the first nine RF runs showing rapid progression of conditioning

Status of the SSC LEB RF Cavity

P. Coleman, F. Brandeberry, C. Friedrichs, Y. Goren, T. Grimm, G. Hulsey, S. Kwiatkowski, A. Propp, L. Taylor, and L. Walling
Superconducting Super Collider Laboratory*
2550 Beckleymeade Ave., MS-4010, Dallas, TX 75237

J. Averbukh, M. Karliner, V. Petrov, S. Yakovlev
Budker Institute of Nuclear Physics
Novosibirsk, Russia

Abstract

A tunable, high-accelerating-gradient cavity prototype has been designed and built for use in the rf system for the Low Energy Booster (LEB) at the Superconducting Super Collider (SSC). Testing of the cavity using one tuner cooling variant has been completed. This paper reports on results of low level, high level and tuning tests performed on the cavity. The tuner was damaged during high power testing. Discussion of the fault is included.

I. INTRODUCTION

The LEB will accelerate a 100 mAdc proton beam from 1.2 GeV/c momentum up to 12 GeV/c. The resultant change in proton velocity requires the rf frequency to vary from 47.5 MHz to 59.8 MHz over the 50 ms accelerating ramp. The rf is also required to deliver a peak ring voltage of 765 kV. Lattice space, higher order mode impedance, and cost considerations all push toward achieving this voltage with the minimum number of cavities.

The cavity is a $\lambda/4$ coaxial design with the inductive portion of the cavity being a ferrite loaded tuner. The design goal is to be able to run with as few as 6 cavities (127.5 kV per cavity). This high voltage operation, along with the wide tuning requirement, results in high stored energy and the potential for increased rf losses in the ferrite. Perpendicular magnetic biasing of the ferrite is used to help minimize these losses [1]. Three different ferrite cooling options (beryllium oxide (BeO) disks, water, and dielectric fluid) have been considered. This paper reports in detail on tests done on the BeO conduction cooled tuner.

Figure 1 shows a diagram of the cavity. The tetrode amplifier (150 kW) is capacitively coupled into the cavity. The applied magnetic field, provided by the magnet yoke, biases the ferrite to different permeabilities (μ) and hence tunes the cavity. The conduction cooled tuner was built at the Budker Institute of Nuclear Physics (BINP) and has been tested at SSCL. It uses BeO sandwiched between ferrite rings to help conduct dissipated heat out to the water cooled copper jacket. The ferrite is potted into the tuner housing using thin layers of a flexible glue known as Elastoseal.

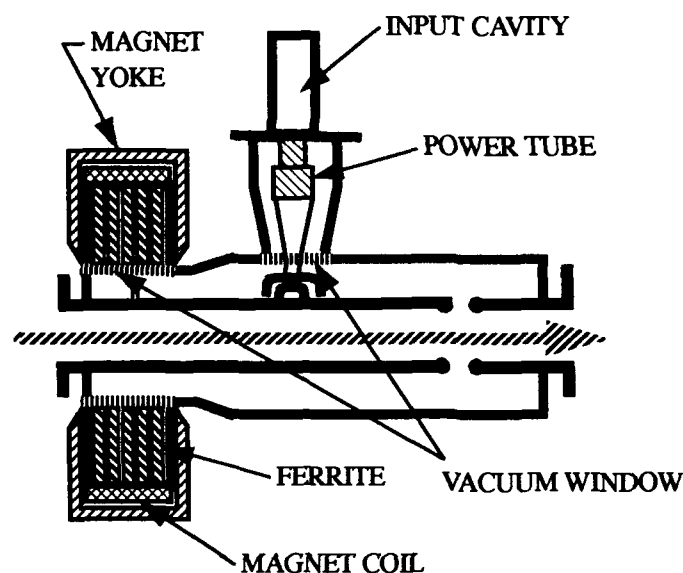


Figure 1. LEB prototype cavity.

II. LOW LEVEL TESTS

A. Tuning range

Figure 2 shows the cavity's resonant frequency as a function of the applied bias current. As the bias field is increased, the ferrite's μ decreases resulting in a higher resonant frequency. The figure shows the cavity is capable of tuning over the required frequency range.

B. Cavity Q

The cavity Q was also monitored at different resonant frequencies (see Figure 3). As the bias field is increased (higher resonant frequency), the ferrite has lower magnetic losses, and the Q rises. However, the calculated Q was approximately two times higher than observed. Calorimetry measurements indicated the unexpected losses were located in the tuner.

C. Temperature effects on tuning

As the ferrite temperature rises, its saturation magnetization M_s falls. This causes a decrease in μ and hence an increase in the cavity's resonant frequency [2]. This effect was characterized by raising the tuner housing temperature by externally heating the tuner's cooling water. The change in resonant frequency was monitored as the tuner, and hence the ferrite's,

* Operated by the Universities Research Association, Inc., for the U.S. Department of Energy under Contract No. DE-AC35-89ER40486

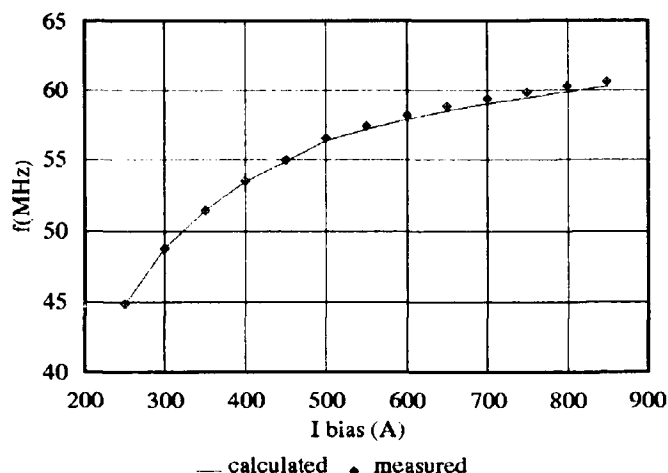


Figure 2. Cavity tuning with bias current.

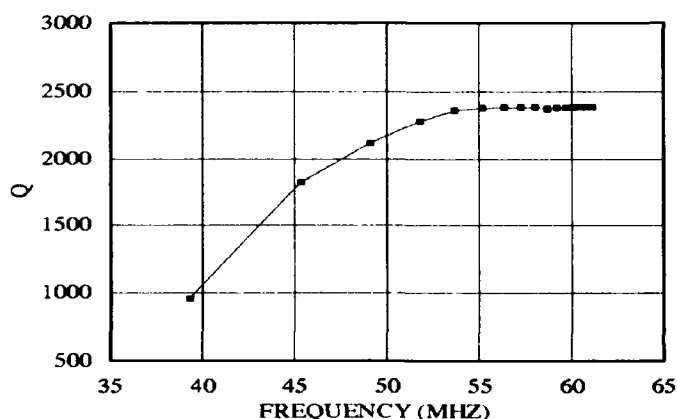


Figure 3. Cavity Q vs. frequency.

temperature changed. An ~ 100 kHz/degC temperature dependence was observed.

III. HIGH POWER TESTS

A variety of tests were performed to thermally characterize the cavity. These were done at relatively low voltages to avoid any electrical stress problems. The average power dissipated in the tuner was measured with calorimetry. This measured power includes not only ferrite losses, but also losses in the cavity walls, BeO and Elastoseal.

A. Power scaling with frequency

The dependence of the dissipated tuner power has been characterized as a function of voltage and frequency. As expected, the power scales as the square of the gap voltage. It was also found that, for a given gap voltage, ~ 1.8 times more power was dissipated at 47 MHz than at 60 MHz. This is a result of a higher percentage of the total cavity energy being stored in the tuner at low frequencies, and the ferrite being more lossy at low bias.

B. Ferrite temperature

The LEB cycles at a 10 Hz rate. For continuous 10 Hz operation, heating of the tuner's ferrite is considered to be a critical consideration. One must be careful not to approach the ferrite's Curie temperature (120°C for this ferrite). Also, a large temperature difference between the ferrite and water cooled wall would lead to thermal stress which might crack the ferrite.

The ferrite temperature was measured under various conditions. The cavity was run at a given voltage and duty factor until it reached thermal equilibrium (~ 30 min). The rf was then turned off, and a thermistor was quickly inserted between the ferrite and vacuum window and touched to the inner radius of the center ferrite.

Figure 4 shows the temperature difference between the ferrite and the water cooled wall normalized by the tuner power (the difference temperature was observed to scale linearly with power dissipated in the tuner). The plot shows that the ferrite temperature depends not only on the dissipated power but also on the frequency. This phenomenon can be explained by the fact that at low frequencies the ferrite is more lossy. Hence, more of the total tuner power is deposited in the ferrite as opposed to the walls, BeO, or Elastoseal.

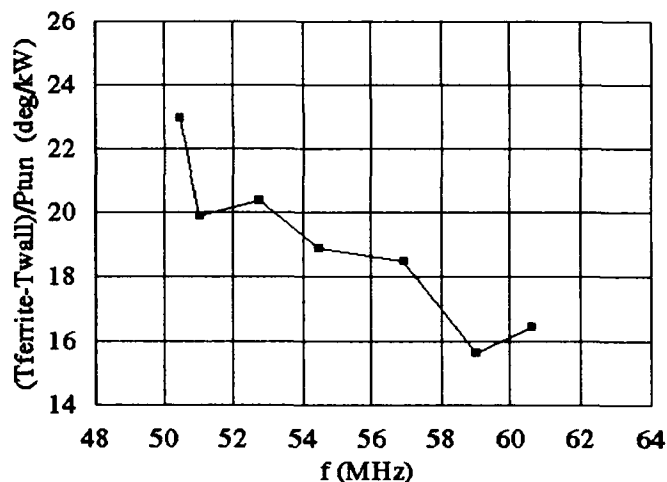


Figure 4. Ferrite temperature scaling.

IV. TUNING PERFORMANCE

The tuner is required to sweep the cavity through the appropriate frequency program over the 50 ms LEB ramp. To help determine the tuner's capabilities in this respect, the frequency response of the tuner has been measured. The amount of shift in the cavity's resonant frequency (df) for a given change in bias current (dI) can be used as a measure of the responsiveness of the tuner. For very slow changes in the bias current (static tuning), a given change in resonant frequency is measured, and df/dI is easily calculated. As the time rate of change in the bias current increases, however, eddy current effects in the magnet yoke and tuner housing will limit the change in resonant frequency.

In order to characterize these effects, the bias power sup-

ply was adjusted to a given dc level with a small amplitude ripple imposed on top of that level. The resultant frequency swing was then measured as a function of ripple amplitude and frequency. Figure 5 shows measurements of df/dI as function of modulating frequency. The response is seen to roll off by 3 dB at ~30 Hz. However the drop in response is relatively slow (-4.5 dB/decade), which indicates that the tuner may have a significant amount of response even at a 1 kHz frequency. Improvements in the power supply will have to be made in order to obtain data at frequencies above 200 Hz.

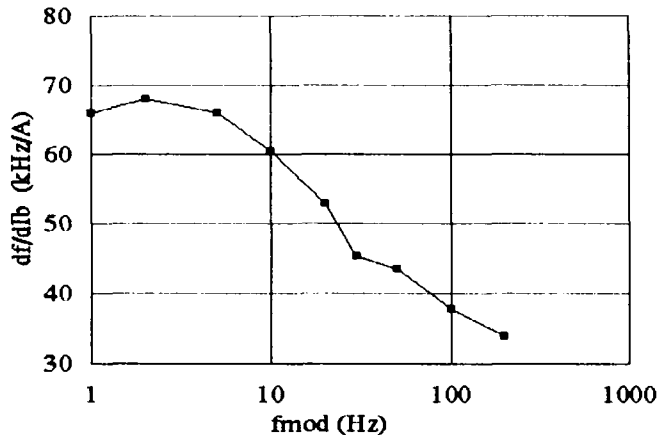


Figure 5. Tuner + cavity frequency response.

V. DISCUSSION OF TUNER DAMAGE

During the course of testing the cavity, it was operated over a wide range of voltages and powers. Figure 6 plots cavity operating points in terms of gap voltages ran at various tuner powers. The cavity was run at > 100 kV, but for only short times and at low duty factors. Most high voltage data was collected at 80 kV and moderate power (1.7 kW).

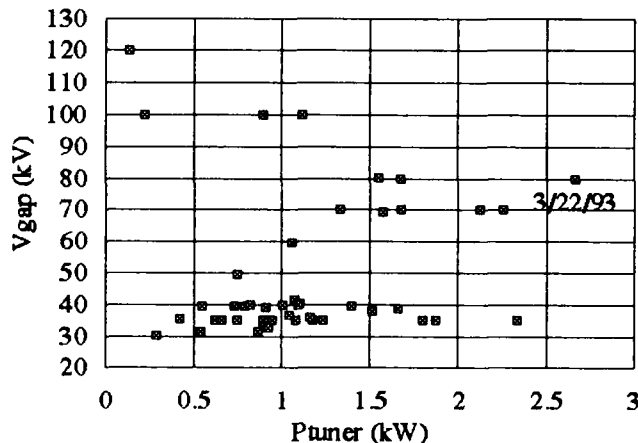


Figure 6. Cavity operating space.

At the time of the failure, the tuner was operating at 80 kV and pushed to higher powers (2.7 kW) than it had achieved before (data point labeled 3/22/93). Therefore, it was being asked to operate at high voltage and high thermal stress simultaneously. The 80 kV gap voltage corresponded to ~30 kV across the tuner at the 58 MHz operating frequency. The ferrite

temperature was estimated to have reached 80° C (30° wall temperature). After ~10 min into the run, the voltage began collapsing ~10 ms into the pulse. Disassembly and inspection of the tuner revealed that the fault was located in a localized area in one of the outer ferrite rings. The deposition of power into this small volume had resulted in very high temperatures that melted some ferrite and caused significant cracking due to the high thermal stresses.

The inspection also revealed an area, away from the damage location, where a small air gap existed between the ferrite and copper wall at the inner radius of the ferrite. It is postulated that such an air gap existed at the location of the damage. At this operating voltage, the fields in such a gap are calculated to be 20 - 25 kV/cm. This could have resulted in the onset of corona and localized heating of ferrite. After some period of time the localized heating thermally induced a crack in the ferrite which then led to intense localized heating and catastrophic failure of the ferrite.

VI. SUMMARY

The prototype cavity has been assembled with a conduction cooled tuner and tested. The tuner fault limited some of the high voltage and power testing, however much valuable information was obtained. The tuning range achieved was more than adequate to cover the LEB requirements. The high frequency tuner response starts to roll off at ~30 Hz, however the roll off appears to be slow and extrapolates to a non negligible response at 1 kHz.

The overall cavity Q was somewhat lower than expected with the extra losses being located in the tuner. The source of these losses is not yet clear, however it is obvious that they limit the high power operation of the tuner.

The cavity was successfully run at 80 kV and at moderate powers. However, the tuner was critically damaged when pushed to higher powers. Explanations of the fault are tied to breakdown of air pockets due to electric field stress and the high thermal stresses present in the tuner.

Testing has now begun on a water cooled version of the tuner.

VII. ACKNOWLEDGMENTS

The support, patience, and technical guidance of J. Ferrell (SSCL) is greatly appreciated. Thanks go to N. Zinevich and D. Sukhanov (BINP) for their help in testing the tuner. Finally, the hard work of the SSCL and BINP technicians is gratefully acknowledged.

VIII. REFERENCES

- [1] W. R. Smythe, "Reducing Ferrite Tuner Power Loss by Bias Field Rotation," *IEEE Trans. Nucl. Sci.*, NS-30, 2173, (Aug. 1983).
- [2] C. Friedrichs, "The Effects of Temperature and RF power Level on the Tuning of the Water Cooled SSC Low-Energy Booster Cavity," these proceedings.

Rf Commissioning of the Superconducting Super Collider Radio Frequency Quadrupole Accelerator*

R. I. Cutler, G. Arbique, J. Grippe, S. Marsden, O. Marrufo, and R. Rodriguez
SSC Laboratory
2550 Beckleymeade Avenue
Dallas, Texas 75237

Abstract

The SSC 2.5-MeV H^- RFQ is powered by a 600-kW, 428-MHz pulsed rf amplifier system [1]. The results of the SSC RFQ rf commissioning, including the measurements of cavity field stability (phase and amplitude) are presented.

INTRODUCTION

The SSC RFQ is required to accelerate a 30 keV H^- beam to 2.5 MeV. The beam design requirement, at the exit of the RFQ, is 25 mA, 7-35 μ s-long macropulse, with a repetition rate of 10 Hz. The RFQ uses a 100 μ s-long rf pulse to establish its accelerating fields. The 100 μ s rf pulse length allows ample time for cavity filling and field stabilization, so that the very stringent rf field control requirements of $\pm 0.5\%$ of amplitude and $\pm 0.5^\circ$ of phase during the beam pulse can be achieved. The RFQ cavity [2] is a 2.2 m long structure with a design peak field strength of 36 MV/m (1.8 Kilpatrick). The rf system for the RFQ consists of a 600-kW, high-power rf amplifier at 427.617 MHz [3], a low-level rf control system (LLRF), and a supervisory control system. This paper describes the initial RFQ cavity conditioning process, and the rf phase and amplitude stability measurements performed with the RFQ cavity at design field levels.

RF CONDITIONING

Rf conditioning is the process of achieving the design field level in an rf cavity. This is usually done by slowly raising rf field levels in the cavity, the rate of rise being limited by the sparking rate and the vacuum levels. As rf fields in a cavity are increased, electrons and ions are accelerated into the cavity walls, devolving more ions and free electrons. This causes a pressure rise, and sometimes a spark or discharge. These sparks are most likely to occur at local high field points, caused by surface irregularities in the cavity. Sparking usually eliminates these points. Eventually, the walls of the rf cavity are cleaned by the ion and electron bombardment, and the rf power levels can be raised to the design value. Each rf cavity has a unique conditioning history, due to microscopic differences in the surfaces of the cavity.

Conditioning of the RFQ cavity was performed at the design frequency of 427.617 MHz. The cavity is maintained on resonance by circulating heated, low-conductivity water (LCW) through channels in the vanes of the RFQ cavity.

The proper resonant cavity temperature was determined by varying the temperature to produce a minimum reflected power as measured with a network analyzer. This temperature was found to be 47.0°C . This was a deviation from the design value of 40.5°C , but was within the temperature tuning range of the RFQ Temperature Control Unit (TCU).

At the start of rf conditioning, a 50 μ s rf pulse was used at 10 Hz. To prevent excessive power during sparking, rf power was controlled open loop - ie. constant input power to the cavity. Base upon Q measurements and SUPERFISH calculations, the expected rf power level to establish the design rf field was 320 kW. Power was initially applied at the 17 kW level, and continuous multipactoring was observed. The power was then raised to the 85 kW level, where intermittent multipactoring and sparking ceased after about 5 minutes. (This power level, as are all power measurements in this paper, has an absolute accuracy of $\pm 5\%$ and a relative accuracy of $\pm 1\%$.)

After the initial clean-up of the cavity, the RFQ ran stably at the 85 kW power level. The cavity reflected power (after the rf fill time) was about 1 kW. The water temperature was varied to ensure that the cavity was at the proper resonance, and 47.0°C produced the minimum reflected power levels. The rf pulse length was then lengthened to 100 μ s, and the rf power was slowly raised over the course of four hours to 340 kW, slightly above the expected nominal field levels. Only slight sparking was observed during this time interval.

The RFQ vacuum level was 7×10^{-5} Pa at the start of commissioning. After the initial clean-up, the pressure level in the cavity dropped to 1×10^{-5} Pa, and did not exceed 3×10^{-5} Pa during the course of conditioning to 340 kW. At this point, the rf power was lowered to 280 kW, and the LLRF closed loop control system, which insures constant field level in the rf cavity, was activated.

An intrinsic Germanium detector was used to measure the bremsstrahlung x-rays produced by free electrons accelerated into the RFQ vanes. These x-rays have an endpoint energy corresponding to the maximum intervane voltage in the RFQ cavity, and thus determine internal cavity voltage levels. (The accuracy of these field level measurements is estimated to be a few percent.) The voltage levels measured verified that the design field level was produced at 330 kW [4].

Rf conditioning was continued for a total of about 8 hours (not continuously) until 430 kW was reached, which is 136% of the design power level (117% of design field levels). When the spark rate at this power level was reduced to one spark/2000 pulses, conditioning was considered complete.

*Operated by the University Research Association, Inc., for the U.S. DOE, under contract No. DE-AC35-89ER40486.

PHASE AND AMPLITUDE STABILITY MEASUREMENTS

Once the RFQ cavity was conditioned, phase and amplitude stability measurements were made at the nominal cavity field level (335 kW) and at plus and minus 10% cavity field levels (400 kW and 260 kW, respectively). The rf system requirements are $\pm 0.5\%$ cavity field amplitude stability and $\pm 0.5^\circ$ cavity phase stability as measured in a 50 μ s window within the total 100 μ s rf pulse. A stability run of four hours duration was made at the design power level of 335 kW at 10 Hz. Phase and amplitude were monitored using the LLRF monitoring system to record the phase and amplitude 55 μ s into each pulse. The amplitude of the total pulse was also monitored using a differential input oscilloscope. The oscilloscope trace was photographed every 15 minutes to check amplitude stability in the 50 μ s window. The phase of the total pulse was also monitored using an oscilloscope. The phase waveform was recorded every 15 minutes. A counter was used to record the number of cavity arcs during the four hour run. The results of these measurements are listed in Table 1.

Table 1

Rf Stability Measurements at RFQ Nominal Field Levels

Cavity power level	335 kW
Frequency	427.617 MHz
Pulse length	100 μ s
Repetition rate	10 Hz
Phase stability:	$\pm 0.2^\circ$
Amplitude stability:	$\pm 0.2\%$
Total number of cavity arcs	109 (18 during last hour of test)
Total number of amplifier crowbars	2 (both within one minute of each other)
Total number of pulses (approx)	144000
Total number of pulses out of tolerance	17 (plus sparks)

These measurements were performed just after the initial cavity conditioning. Since then, the spark rate has dropped considerably, to less than 1 spark/10000 pulses. As can be seen from Table 1, the phase and amplitude control is within specifications for this rf system.

The stability tests were also performed for $\pm 10\%$ RFQ field values ($\pm 20\%$ in power) for two hours and one hour respectively. The results are summarized in tables 2 and 3.

Table 2

Rf Stability Measurements at 110% of RFQ Nominal Field Level

Cavity Power Level	400 kW
Frequency	427.617 MHz
Pulse Length	100 μ s
Repetition Rate	10 Hz
Phase stability:	$\pm 0.1^\circ$
Amplitude stability:	$\pm 0.1\%$
Total number of cavity arcs	278
Total number of Amplifier Crowbars	0
Total number of pulses (approx)	72000

Table 3

Rf Stability Measurements at 90% of RFQ Nominal Field Level

Cavity Power Level	260 kW
Frequency	427.617 MHz
Pulse Length	100 μ s
Repetition Rate	10 Hz
Phase stability:	$\pm 0.1^\circ$
Amplitude stability:	$\pm 0.1\%$
Total number of cavity arcs	109
Total number of Amplifier Crowbars	0
Total number of pulses (approx)	40000

The rf system has again met stability requirements.

SUMMARY

The SSC RFQ was rf conditioned in only 8 hours to 117% of the design field level. The rf system has achieved the design stability values for amplitude and phase control, and the RFQ rf system is operating reliably at the SSC.

REFERENCES

- [1] R. I. Cutler, J. Grippe, O. Marrufo, S. Marsden, J. Mynk, R. Rodriguez, M. Tomek, "SSC Linac RFQ Rf System", *Proceedings of the 1992 Linear Accelerator Conference*, Vol 1, pp 380-382.
- [2] D. L. Schrage, et al., Radio Frequency Quadrupole Accelerator for the Superconducting Super Collider, *Proceedings of the 12th International Conference on the Applications of Accelerators in Research and Industry*, Denton Texas, to be published.
- [3] J. Grippe, S. Marsden, A. Regan, D. Rees, C. Ziomek, "Design and Results of the Radio-Frequency Quadrupole RF System at the Superconducting Super Collider", these proceedings.
- [4] G. Arbique, et al., "The SSC RFQ System Integration", these proceedings.

Design of a Tuner and Adjustable RF Coupler for a CW 2856 MHz RF Cavity*

M.S. de Jong, F.P. Adams, R.J. Burton, R.M. Hutcheon, T. Tran-Ngoc
AECL Research, Chalk River Laboratories
Chalk River, Ontario, Canada K0J 1J0

A. Zolfaghari and P.T. Demos
Massachusetts Institute of Technology, Bates Linear Accelerator Center
Middleton, MA 01949, USA

ABSTRACT

A tuning plunger and an adjustable RF coupler have been designed at AECL's Chalk River Laboratories for a CW 2856 MHz RF cavity for the MIT-Bates South Hall Ring. The tuner provides a frequency range of 1.1 MHz with a frequency resolution of less than 0.5 kHz. The high-power RF drive coupler uses iris coupling and a set of coupling factor (β) adjustment posts to provide fixed β -values from 1 to 10. This paper describes the RF design, mechanical design and performance of these units.

INTRODUCTION

The 2856 MHz RF cavity required by the MIT-Bates South Hall Ring, and described elsewhere,¹ places heavy demands on the cavity's tuning and RF coupling systems. The high average dissipated power, up to 10 kW CW, and a wide range of beam-loading conditions, covering both pulse-stretcher and storage modes of operation, require tuning and coupling systems with a wide range of capability. Reference design requirements for the tuner and RF coupling system are given in Table 1 and Table 2, respectively.

Table 1: SHR Cavity Tuner Specifications

Cavity Frequency	2856.000 MHz
Frequency Range	± 200 kHz
Tuning angle precision	$\pm 0.5^\circ$

TUNER DESIGN

The tuning range specification of 200 kHz covers the expected range of cavity detuning required for beam-loading compensation. However, additional tuning is required to compensate for an approximate 350 kHz frequency shift from thermal expansion of the cavity body at 10 kW dissipated power, and for a frequency shift of up to 200 kHz caused by changes in the RF coupling factor. Consequently, the tuner

Table 2: SHR Cavity RF Coupling Specifications

Design power	> 20 kW
Input line	WR284 waveguide
Input coupling VSWR	< 1.8:1
Coupling factor, β	Adjustable up to 10 in fixed steps

design has over 1000 kHz tuning range about 2856 MHz.

A cross-section of the cavity in the tuner plane is shown in Figure 1. The 12.7 mm diameter tuner plunger is centered in a 15.9 mm diameter hole in the cavity wall. The plunger surface facing the cavity centre is restricted from any position closer to the centre than the cavity wall. This constraint reduces the maximum frequency shift possible, but also reduces the RF dissipation on the plunger. The measured frequency range with this tuner is shown in Figure 2.

The tuning plunger is water cooled using internal coaxial cooling lines, where the water flows down inside the outer wall of the plunger and returns up the centre. Provision has also been made for a small-diameter line to the high-vacuum region inside the tuner. This can be used to provide additional

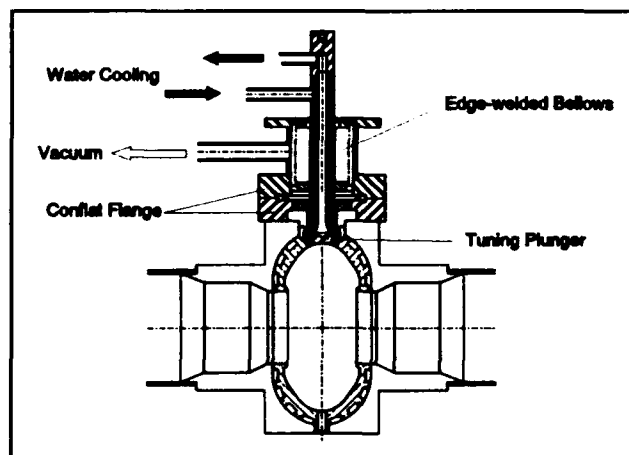


Figure 1: Cross-section of Cavity and Tuner

* This work is performed under US Department of Energy contract number DE-AC02-76ER03069.

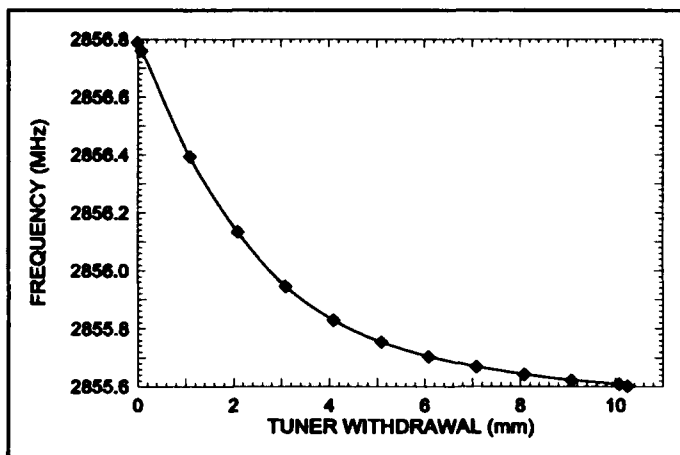


Figure 2: SHR Cavity frequency as a function of tuner withdrawal from a position flush with cavity wall.

pumping in this area if out-gassing is a problem during initial testing. No sliding RF contacts are used between the tuning plunger and the hole walls in the cavity.

At the tuner position nearest the cavity wall, the frequency gradient is almost 400 kHz/mm. When the RF coupling factor, β , is 1 (critical coupling), the frequency shift required to produce a tuning angle change of 0.5° is less than 1.5 kHz or, equivalently, a tuner position shift of less than $3 \mu\text{m}$. A standard, commercial linear actuator, a VP30-10 Stepping Motor Driven Actuator, from Klinger Instruments, operates the bellows. It provides 10 mm of linear travel in $1.0 \mu\text{m}$ steps. This provides a tuning angle precision of better than $\pm 0.2^\circ$ for all β . A shaft encoder monitors the actuator position, with limit switches and origin reference included in the actuator.

RF COUPLER DESIGN

Initially, inductive RF input coupling was considered. Typically, this uses a drive loop at the end of a coaxial line. The coupling factor, β , could be adjusted by rotating the drive loop at the cavity wall. However, the size of drive loop and coaxial line suitable for an S-band cavity would be too small to handle over 20 kW CW RF power. The RF losses in the small line would cause excessive RF dissipation that cannot easily be cooled.

Upon further examination, an RF coupling design based on aperture coupling was considered much more reasonable. Aperture coupling is often used on S-band accelerator structures, but usually with a single, fixed coupling factor. The design strategy was then to find an aperture coupling design with $\beta=10$, and provide a method for reducing the coupling without excessive shifts in the fundamental (TM_{010} -mode) frequency. An adjustable capacitive post, located in the drive waveguide at the first minima in the standing electric field pattern, was selected to adjust the coupling.

A cold model to test this technique was fabricated with two different electric field tapers in the waveguide before the

coupling aperture. The $\lambda/4$ taper produced a coupling factor over 7.0, and the longer, $\lambda/2$ taper produced a coupling factor of 9.5. In both cases, critical coupling, $\beta=1$, could be achieved using a metal post penetrating across the guide approximately $\lambda/4$ away from the iris. An alumina post was also tested. In this case, a substantial range of β was possible, but critical coupling could not be achieved. The maximum change in cavity frequency produced by the post was less than 250 kHz. The improvement in the coupling with the longer taper is caused by the better match between the different waveguide heights produced by the longer taper.

The final RF coupler design is shown in Figure 3. A $3\lambda/4$ taper, made from three separate linear $\lambda/4$ sections approximating an exponential taper, was selected to provide the match between the WR-284 waveguide and the 5 mm high coupling aperture in the cavity. The long taper is essential because of the large reduction in waveguide height required. Calculations of the matching section indicate that the VSWR through the taper is less than 1.2. The 5 mm aperture height is necessary to minimize the perturbation on the cavity cooling channels. This height is sufficiently small to fit between the main outer cooling channels at the mid-section of the cavity. The coupling is only weakly dependent on this height. The aperture also extends 5 mm along the RF propagation direction, again to provide sufficient space for the cooling

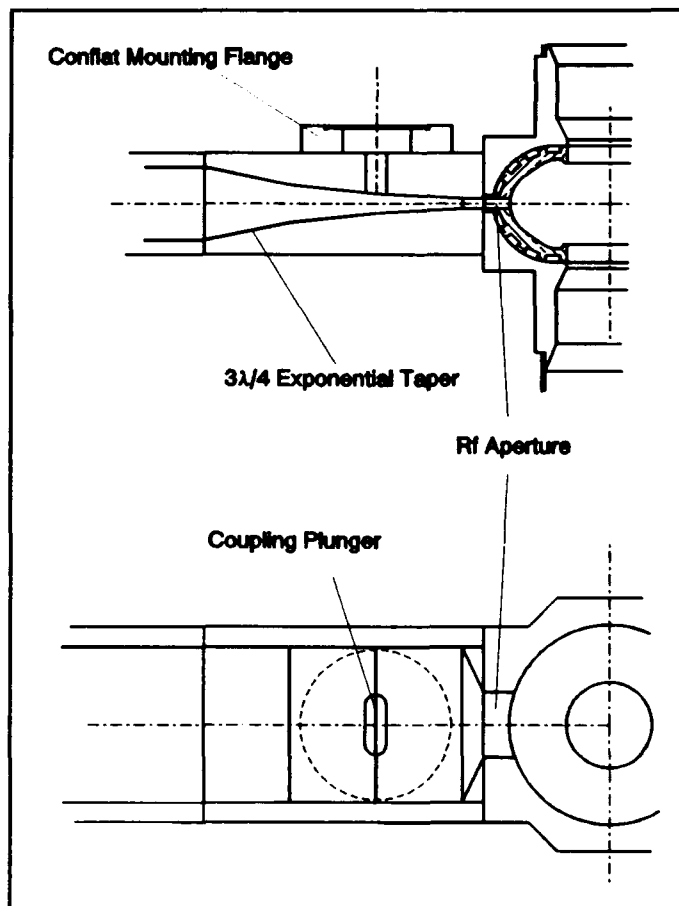


Figure 3: RF Input Waveguide and Aperture-Coupler

channels. Computations have shown that the coupling is not strongly dependent on this thickness, either, provided the thickness is much less than λ .

The post shape and position were selected to provide the full range of coupling required while minimizing the cavity frequency shift produced by changes in the coupling. A set of water-cooled posts was manufactured with varying lengths to cover the full range of β , each brazed to separate 2¼" Conflat flanges. The coupling factor can be changed simply by changing posts. Figure 4 shows the effect of coupling post length on the coupling factor and cavity frequency.

CONCLUSION

A tuner and RF coupler for a high-power, 2856 MHz RF cavity have been designed and fabricated at AECL's Chalk River Laboratories for the MIT-Bates South Hall Ring. The tuner is designed to handle high-power dissipation and provide the frequency precision necessary for accurate control of the cavity detuning angle. The RF coupler provides a range of β from 1 to 10 using a set of fixed capacitive posts, positioned to minimize the cavity frequency perturbation. The entire cavity system, including the tuner and RF coupler, is presently at MIT-Bates awaiting final testing and installation.

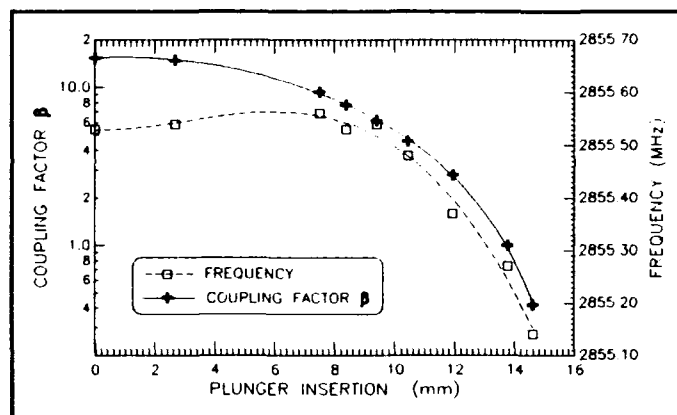


Figure 4: Effect of post length on coupling factor and cavity frequency.

REFERENCES

1. M.S. de Jong, et al., "A 2856 MHz RF Cavity for the MIT-Bates South Hall Ring," in the proceedings of this conference.

A 2856 MHz RF Cavity for the MIT-Bates South Hall Ring*

M.S. de Jong, F.P. Adams, R.J. Burton, R.M. Hutcheon, T. Tran-Ngoc
AECL Research, Chalk River Laboratories
Chalk River, Ontario, Canada K0J 1J0

A. Zolfaghari and P.T. Demos
Massachusetts Institute of Technology, Bates Linear Accelerator Center
Middleton, MA 01949, USA

ABSTRACT

A single-cell 2856 MHz RF cavity for the MIT-Bates Linear Accelerator Laboratory South Hall Ring (SHR) has been designed and built at AECL's Chalk River Laboratories. The SHR is an electron beam storage ring designed to operate with all (1812) RF buckets filled and a circulating current of 80 mA. The RF cavity, designed for CW operation with 10 kW wall dissipation, has a 40 mm diameter beam aperture, on-axis higher-order mode damping and an iris-coupled RF input. This paper describes the cavity RF and mechanical design, the system fabrication and the results of measurements on the completed cavity.

INTRODUCTION

The MIT-Bates Linear Accelerator Center is building an electron storage ring, known as the South Hall Ring (SHR), for medium-energy nuclear physics experiments. The ring will have two modes of operation: a pulse stretcher mode that provides an external CW electron beam from a 1% duty factor injection linac, and an internal target mode that stores the electron beam in the ring, to provide high average current for targets internal to the ring. The SHR has a 190 m circumference, and is designed to store up to 80 mA of

electrons at energies from 300 to 1000 MeV. At the ring RF frequency of 2856 MHz (the same as the linac frequency), the harmonic number is 1812 and every bucket is filled with electrons. The high average current with all buckets full constrains the ring RF system to have very low longitudinal impedance at all frequencies other than 2856 MHz, to avoid multi-bunch instabilities, while providing bucket voltages of up to 129 kV to maintain and control beam bunch shape and energy. A single-cell standing-wave RF cavity has been designed and built to meet these RF requirements with the specifications shown in Table 1.

A series of computations have been performed to analyze and optimize the designed cavity performance. These include an analysis of cavity modes using the RF computer codes, SUPERFISH, SEAFISH, and URMEL, and an analysis of cavity temperature and thermal-mechanical stress at a nominal 10 kW dissipated RF power using the MARC code.

A cross section of the cavity is shown in Figure 1. The main cavity body is fabricated from brazed oxygen-free electrical (OFE) copper segments with embedded water-cooling channels. The cavity uses iris coupling with adjustable β and a mechanical tuning plunger described in more detail elsewhere.¹

Table 1: Specifications for the MIT-Bates SHR RF Cavity

Frequency	2856.000 MHz
Gap voltage	129 kV
On-axis rf electric field	> 2.6 MV/m
Power dissipation	> 10 kW
HOM Impedance	
Longitudinal	< 500 Ω
Transverse	< 100 k Ω
Beam aperture	40.0 mm

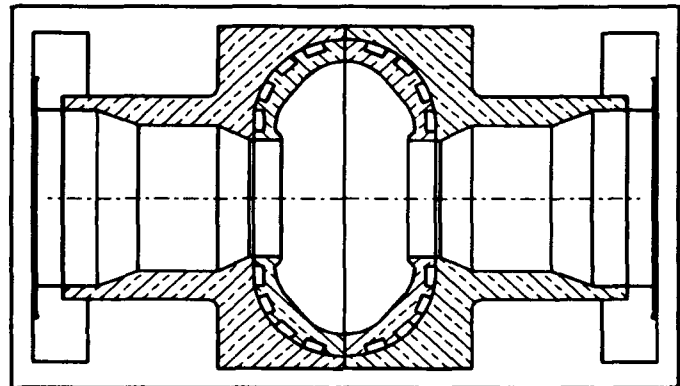


Figure 1 Cross section of MIT-Bates SHR RF cavity showing the copper body with embedded water-cooling channels.

* This work is performed under US Department of Energy contract number DE-AC02-76ER03069.

RF DESIGN

The RF design challenge is to find a cavity profile that maximizes the cavity shunt impedance at 2856 MHz, important for RF operating efficiency, while minimizing the longitudinal and transverse shunt impedance in higher-order modes (HOM), important for beam stability. The high average beam current of the SHR with beam in every RF bucket makes reduction of the effective HOM impedance critical.

The cavity profile design for the SHR has a large 40 mm beam aperture, through which HOM's are coupled out of the cavity and into the 60.3 mm diameter beam-pipe. The profile was adjusted to maximize the separation between the TM_{010} fundamental mode at 2856 MHz and the next lowest azimuthally symmetric (monopole) transverse magnetic (TM) modes. All these TM modes, other than the TM_{010} , and all cavity dipole modes are above the corresponding mode cut-off frequencies in the beam-pipe: 2914 MHz for dipole modes and 3806 MHz for monopole TM modes. This permits damping of HOMs by a thin layer of RF-absorbing ferrite distributed azimuthally inside the beam-pipe, in the region near the cavity. Conceptually, this approach is very similar to that used by Cornell in their design of HOM dampers for super-conducting cavities for a B-factory.²

The results of an analysis of the first few TM monopole modes are given in Table 2. The Q of each mode was determined from SEAFISH computations, and includes both surface RF losses from the finite conductivity of the copper cavity as well as volume RF losses in the HOM damper ferrite. Since only the TM_{010} mode is below the cut-off frequency of the beam-pipe, it is not significantly damped by the ferrite and is the only mode with a high Q. The modes that are anti-symmetric about the cavity mid-plane propagate out of the cavity so well, as indicated by their low Q's, that SEAFISH could not accurately find the resonant frequencies. Thus, the Q's for these modes should be regarded as upper limits.

Table 2: Computed SHR cavity azimuthally symmetric mode characteristics

Frequency (MHz)	Longitudinal Shunt Impedance (k Ω)	Q
2870	953.0	19 480
5204	0.07	50
6000	0.18	81
8100	0.11	43
8167	1.1	209

Table 3: Significant SHR Cavity Dipole Modes Below 10 GHz

Frequency (MHz)	R' (undamped) (k Ω)	R' (damped) (Ω)	Q (damped)
3972.0	237.2	279	23
6029.8	104.7	51	14

Table 3 gives the results of URMEL calculations for all dipole modes up to 10 GHz with the radially independent transverse shunt impedance parameter, R' , greater than 100 k Ω . However, all these modes are above the TE dipole mode cut-off frequency of the beam-pipe, and are strongly damped by losses down the beam-pipe. The effective Q of these modes was computed by a technique described by Mosnier.³ The Q, once these losses are considered, drops below 25. Consequently, no dipole modes below 10 GHz have significant longitudinal shunt impedance.

MECHANICAL DESIGN

Each half of the cavity is machined from two OFE copper segments that are machined with accurately matching surfaces. Four water-cooling channels are machined into this surface on the inner half cavity. The two segments are then brazed together to form the complete cooling channels in each half cavity. This braze is performed before the final machining of the inner cavity profile.

In each half cavity, the two outer channels are connected in series and the two inner channels are connected in series. For a ΔT of 10°C, the total flow required is 0.24 L/s through the cooling channels. With these four parallel cooling circuits, the flow velocities, v , are 3 m/s and 4 m/s in the outer and inner cooling channels, respectively. These flow velocities were chosen to give a fully turbulent flow with the highest possible heat transfer coefficient to the copper cavity body.

Heat fluxes, calculated by SUPERFISH, and the film heat-transfer coefficients for the water cooling, were used to calculate the copper temperature distribution using the MARC finite-element code. The temperature distribution is fairly uniform in the radial direction, with the highest value predicted to be 48°C, based on a water inlet temperature of 15°C. The water-cooling strategy is to regulate the output temperature to a fixed value, using an external water-cooling system. The set-point value for the outlet temperature is 25°C. Thus, with no input power, the cavity body is at 25°C. As the dissipated power increases, the inlet water temperature decreases to maintain the same outlet temperature. For the design temperature difference of 10°C at full power (10 kW), the inlet temperature will be 15°C. This scheme is easy to implement and reduces the average temperature change of the

cavity body, from zero to 10 kW dissipated RF power, to less than 10°C.

The MARC code was used to perform a thermal-stress analysis, including the small additional effects of vacuum and water pressure. The highest von Mises equivalent stress is calculated to be 28 MPa at the cavity nose region near the beam aperture. However, this is well below the yield strength of annealed copper, which is approximately 60 MPa.

The predicted thermally induced cavity deformation produces an increase in the cavity wall radius of about 0.010 mm. This deformation results in an estimated 360 kHz frequency shift of the cavity from zero power at 25°C cavity body temperature to 10 kW dissipated power with 15°C inlet water. At the power levels considered in this analysis, the results scale linearly with power level, so operation at higher dissipated power up to about 15 kW should be possible while remaining well below the yield strength of copper.

LOW-POWER RF MEASUREMENTS

After completion of cavity fabrication and assembly of the cavity tuner and RF drive coupler, the relative distribution of the axial RF electric field was measured using the dielectric-bead frequency-perturbation method (the bead-pull technique). Several distributions were measured to determine the Q-normalized shunt impedance (R/Q) of the cavity at the TM_{010} mode and any TM azimuthally symmetric higher-order modes below 6 GHz. A typical TM_{010} measurement, shown in Figure 2, gives an R/Q of 49 Ω , in good agreement with calculated design value.

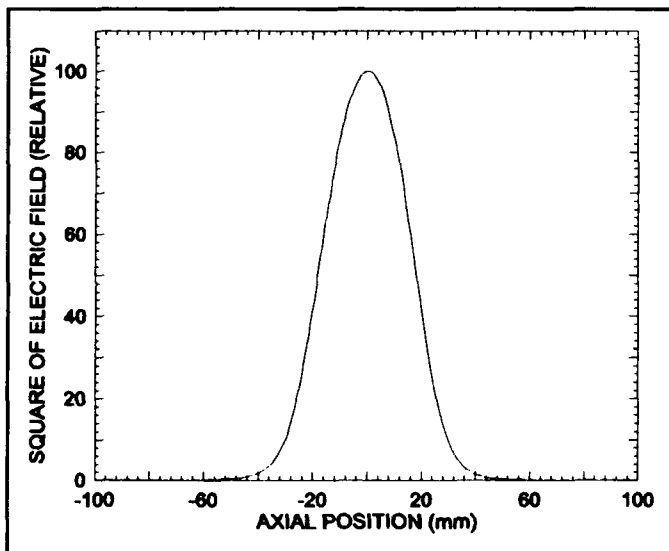


Figure 2: Squared RF electric field distribution from bead-pull on TM_{010} mode.

Measurement of the longitudinal electric field distributions of HOMs was more difficult, since the modes couple strongly to beam-pipe. Any discontinuities in the beam-pipe, such as occur at an open end flange during the measurement, produce

standing wave patterns in the beam-pipe and splitting of the cavity mode. A typical measurement of a TM_{020} -like cavity mode, Figure 3, shows the presence of the standing wave in the beam-pipe sections on either side of the cavity, indicating the large coupling of the mode out of the cavity. The R/Q for this distribution is less than 1 Ω .

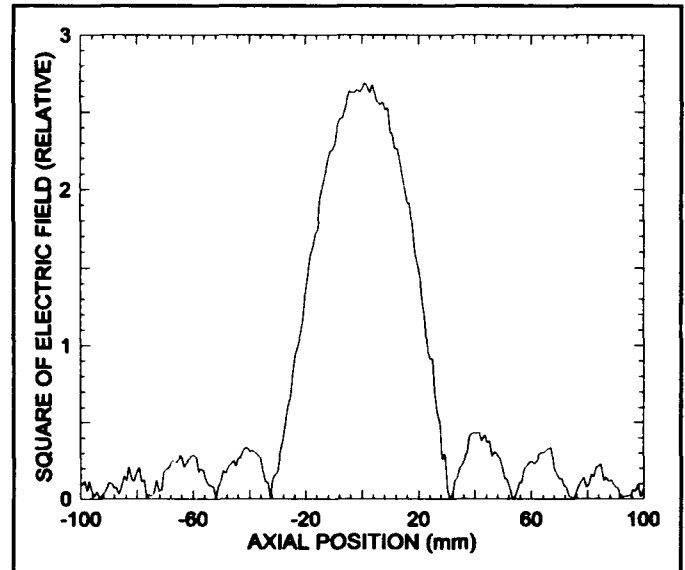


Figure 3: Squared RF electric field from bead-pull on TM_{020} -like mode at 5807 MHz.

Additional measurements of the broad-band shunt impedance to higher frequencies will be made before final cavity installation in the SHR.

CONCLUSION

A high-power CW 2856 MHz cavity has been designed and fabricated at AECL's Chalk River Laboratories for the MIT-Bates SHR. The cavity is characterized by a large 40 mm beam aperture and highly damped HOMs. The cavity is presently at MIT-Bates, awaiting final low-power testing and installation.

REFERENCES

1. M.S. de Jong, et al., "Design of a Tuner and Adjustable RF Coupler for a CW 2856 MHz RF Cavity", in proceedings of this conference.
2. D. Moffat, et al., "Design, Fabrication and Testing of a Ferrite-Lined HOM Load for CESR-B," in proceedings of this conference.
3. A. Mosnier, "Developments of HOM Couplers for Superconducting Cavities", in Proceedings of the 4th Workshop on RF Superconductivity, KEK, Tsukuba, Japan, 1989. KEK Report 89-21.

Cavity RF Mode Analysis Using a Boundary-Integral Method

M.S. de Jong and F.P. Adams
AECL Research, Chalk River Laboratories
Chalk River, Ontario, Canada K0J 1J0

ABSTRACT

A 3-dimensional boundary-integral method has been developed for rf cavity mode analysis. A frequency-dependent, homogeneous linear matrix equation is generated from a variant of the magnetic field integral equation (MFIE) where the domain of integration is a closed surface specifying the rf envelope of the cavity. Frequencies at which the MFIE has non-zero solutions are mode frequencies of the cavity, and the solutions are the corresponding surface magnetic field distributions. The MFIE can then be used to calculate the electric and magnetic field at any other point inside the cavity. Forward iteration is used to find the largest complex eigenvalue of the matrix at a specific frequency. This eigenvalue is 1 when the frequency corresponds to a cavity rf resonance. The matrix equivalent of the MFIE is produced by approximating the cavity surface by a set of perfectly conducting surface elements, and assuming that the surface magnetic field has constant amplitude on each element. The method can handle cavities with complex symmetries, and be easily integrated with finite-element heat-transfer and stress analysis codes.

INTRODUCTION

Computer codes capable of calculating the full 3-dimensional electromagnetic field distributions are now commonly used for designing rf cavities for accelerators. However, most of these codes need large computational resources to compute sufficiently detailed distributions for further mechanical engineering analysis of cavities. Furthermore, the mesh often used by these codes is not compatible with finite-element meshes commonly used in commercial thermal-stress analysis codes used in the mechanical design. Past work at AECL in the mechanical design of high-power rf cavities for a variety of applications showed the desirability of a technique to compute the rf field distribution over the cavity surface on the same surface mesh used in mechanical thermal-stress analysis. This paper presents such a technique that uses a boundary-integral method to compute the surface rf magnetic field distribution in cavities filled with a homogeneous medium. A similar approach using a different boundary-integral relation has been developed at the University of Pavia.¹ In addition to being particularly convenient for coupled rf-mechanical design problems, these techniques usually require considerably less computational effort.

BOUNDARY-INTEGRAL EQUATIONS

Although Maxwell's equations are usually posed as a set of coupled differential equations, many alternative, equivalent sets of integral equations can be derived. One useful integral equation² for harmonically varying fields with angular frequency ω is:

$$H(r') = \frac{1}{4\pi} \int_V (J \times \nabla \phi) dv + \frac{1}{4\pi} \int_S [i\omega \epsilon (n \times E) \phi - (n \times H) \times \nabla \phi - (n \cdot H) \nabla \phi] da \quad (1)$$

where

$$\phi = \frac{e^{ik|r'-r|}}{|r'-r|}, \quad (2)$$

E and H are the electric and magnetic fields, S is any surface enclosing a medium with volume V , dielectric constant ϵ , internal current distribution J and propagation constant k , and n denotes an inward-facing unit vector normal to the surface. If S specifies a cavity with a perfectly conducting surface enclosing a volume with no internal current distribution (i.e., $J = 0$), then (1) simplifies to:

$$H(r') = -\frac{1}{2\pi} \int_S n \times H(r) \times \nabla \phi da \quad (3)$$

for all r', r on the surface. The simplicity of (3) arises since only $n \times H$, the component of H transverse to the surface, is non-zero on a perfect conductor.

This equation is a variation of the magnetic field integral equation³ (MFIE) commonly used for the analysis of antennas of arbitrary shape. Equation (3) is a homogeneous Fredholm integral equation,⁴ which has non-zero solutions for H only at discrete values of ω where the equation is said to be singular. The frequencies where (3) becomes singular are the cavity resonance frequencies, and the corresponding solutions, H , are the resonance field distributions.

NUMERICAL SOLUTION OF THE MFIE

Equation (3) is transformed into a matrix equation using standard techniques in finite-element analysis,⁵ in this case using the collocation technique with pulse basis functions. The surface is approximated by a set of 4-node quadrilateral elements with the tangential rf magnetic field assumed to be constant within each element. The collocation points are the geometric centres of each element. This results in two complex degrees of freedom for each element.

A constant, purely tangential, rf magnetic field is assumed over each surface element. An element basis is defined for each element i , where \mathbf{n}_i^1 and \mathbf{n}_i^2 are orthogonal unit vectors tangential to the element and \mathbf{n}_i is a unit vector normal to the element. Since the four nodes defining a surface element are not constrained to lie in a plane, the unit vector \mathbf{n}_i is defined to be parallel to the cross product of vectors joining opposite corners of the element. The other two unit vectors, \mathbf{n}_i^1 and \mathbf{n}_i^2 , are then defined to be orthogonal to each other and to \mathbf{n}_i . Equation (3) then becomes

$$\begin{aligned} H_j^1 &= \sum_{i=1}^N (A_{i,j}^{11} H_i^1 + A_{i,j}^{21} H_i^2) \\ H_j^2 &= \sum_{i=1}^N (A_{i,j}^{12} H_i^1 + A_{i,j}^{22} H_i^2) \end{aligned} \quad (4)$$

where

$$\mathbf{H} = H^1 \mathbf{n}^1 + H^2 \mathbf{n}^2. \quad (5)$$

The boundary-integral method is used to calculate the terms in the four matrices

$$\begin{aligned} A_{i,j}^{11} &= \mathbf{n}_j^1 \cdot \int_{S_i} \mathbf{n}_i \times \mathbf{n}_i^1 \times \nabla \phi(\mathbf{r} - \mathbf{r}_j) da, \\ A_{i,j}^{12} &= \mathbf{n}_j^1 \cdot \int_{S_i} \mathbf{n}_i \times \mathbf{n}_i^2 \times \nabla \phi(\mathbf{r} - \mathbf{r}_j) da, \\ A_{i,j}^{21} &= \mathbf{n}_j^2 \cdot \int_{S_i} \mathbf{n}_i \times \mathbf{n}_i^1 \times \nabla \phi(\mathbf{r} - \mathbf{r}_j) da, \\ A_{i,j}^{22} &= \mathbf{n}_j^2 \cdot \int_{S_i} \mathbf{n}_i \times \mathbf{n}_i^2 \times \nabla \phi(\mathbf{r} - \mathbf{r}_j) da. \end{aligned} \quad (6)$$

Each surface integration uses 1-point integration for distant elements, and 4-point Gaussian integration for nearby elements. The transition between 1-point and 4-point integration occurs when the distance between collocation points exceeds four times the average dimension of the element. The results are very insensitive to the exact threshold.

Any symmetry that exists in the problem may be incorporated in the surface integration by extending the integral in (6) over all elements that map into element i by symmetry while performing appropriate transformations of the rf magnetic field, \mathbf{H}_i . Possible transformations include rotation, and symmetry or anti-symmetry under reflection.

Matrices A^{11} , A^{21} , A^{12} and A^{22} may be combined into a single $2N$ -by- $2N$ matrix:

$$\mathbf{K} = \begin{bmatrix} \mathbf{A}^{11} & \mathbf{A}^{21} \\ \mathbf{A}^{12} & \mathbf{A}^{22} \end{bmatrix}, \quad (7)$$

and the two N -vectors \mathbf{H}^1 and \mathbf{H}^2 may be combined into a single vector of length $2N$:

The result is an approximation of (3) in the form:

$$\mathbf{H} = \begin{bmatrix} \mathbf{H}^1 \\ \mathbf{H}^2 \end{bmatrix}. \quad (8)$$

$$\mathbf{H} = \mathbf{K}(k) \mathbf{H}, \quad (9)$$

where the equality only holds, for non-zero \mathbf{H} , at values of k corresponding to cavity resonant modes.

These mode frequencies are found by the following method. Equation (9) is generalized to be a standard matrix eigenvalue problem with k -dependent eigenvalues:

$$\lambda(k) \mathbf{H} = \mathbf{K}(k) \mathbf{H}. \quad (10)$$

Since \mathbf{K} is a non-symmetric complex matrix, all λ are generally complex as well. The eigenvalues of (10) are searched while varying k for values meeting the conditions

$$\Re(\lambda(k_m)) \approx 1, \quad \Im(\lambda(k_m)) = 0 \quad (11)$$

when there is a resonant mode with $k = k_m$. The corresponding eigenvector is the rf magnetic field distribution for the mode.

In practice, when searching for the lowest frequency mode, the eigenvalue of (10) that will satisfy (11) is usually the eigenvalue with largest magnitude. In this case, direct iteration⁶ is a convenient technique to find $\lambda(k)$. Frequently, variants of forward iteration can be used to find a significant number of low-frequency modes.

RIGHT-CIRCULAR CYLINDER EXAMPLE

The lowest frequency rf modes of a right-circular cylinder with 100 mm radius and 200 mm height have been found using the boundary-integral method. The symmetry in the problem permits modelling of one octant of the cavity. Only 103 surface quadrilateral elements are used. Unlike most finite-element meshes, a connected mesh is not required for this simple implementation of the boundary-integral method, which permits more flexibility in mesh generation.

Figure 1 shows the distribution of eigenvalues of (10) for a frequency of 1150 MHz. A comparison of several low-order mode frequencies for this cavity computed using this boundary-integral-method mesh, to frequencies calculated from exact analytic expressions,⁷ is shown in Table I. Figures 2 and 3 show the rf surface magnetic field distribution for the two lowest frequency modes.

The boundary-integral calculations were performed on a microcomputer using a 25 MHz Intel 386SL microprocessor with a 387 numeric co-processor. The time to calculate the matrix \mathbf{K} for a specified frequency was 45 seconds; 50 direct iterations, taking 35 seconds, were sufficient to converge on the maximum eigenvalue. Typically, three to four evaluations of \mathbf{K} at different frequencies are required to find each resonant mode. It is not necessary, although often convenient, to find the mode frequencies in increasing order.

SUMMARY

A new approach for analyzing 3-dimensional rf resonant modes using a boundary-integral technique has been presented. The technique was used to compute the several rf mode frequencies and field distributions for a right-circular cylinder. The technique is being applied to several complex rf cavities for particle accelerators.

ACKNOWLEDGEMENTS

The authors thank Jim Diserens for his initial suggestions that led to the development of this technique, and Gordon Pusch for his many helpful comments over the course of this work.

REFERENCES

1. P. Arcioni, et al., "A New 3-D Electromagnetic Solver for the Design of Arbitrarily Shaped Accelerating Cavities", in proceedings of this conference.
2. J.A. Stratton, *Electromagnetic Theory* (McGraw-Hill Book Company, 1941).
3. D.S. Jones, *Methods in Electromagnetic Wave Propagation* (Clarendon Press, 1979).
4. F. Riesz and B. Sz. Nagy, *Functional Analysis* (Frederick Ungar Publishing, 1955).
5. P.P. Silvester and R.L. Ferrari, *Finite Elements for Electrical Engineers* (Cambridge University Press, 1990).
6. J.H. Wilkinson, *The Algebraic Eigenvalue Problem* (Clarendon Press, 1965).
7. S. Ramo, J.R. Whinnery and T. Van Duzer, *Fields and Waves in Communications Electronics* (John Wiley and Sons, 1965).

Table I RF mode frequencies of a cylindrical cavity 100 mm high and 200 mm in diameter

Resonant Mode	Frequency	
	Analytic	Boundary-Integral Method
TM010	1147.43	1152.23
TE111	1737.42	1735.30
TM110	1828.24	1833.90
TM011	1887.72	1889.36
TE211	2090.59	2089.00
TE011	2364.18	2363.10
TM111	2364.18	2368.52
TM210	2450.38	2451.10
TE311	2503.01	2503.46

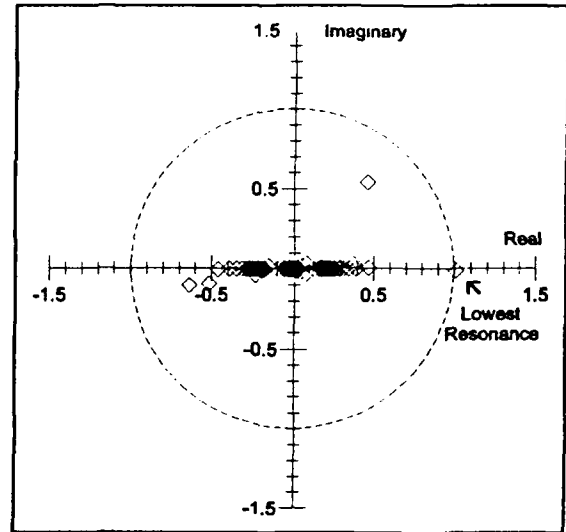


Figure 1. Distribution of eigenvalues for a right-circular cylindrical cavity at 1150 MHz.

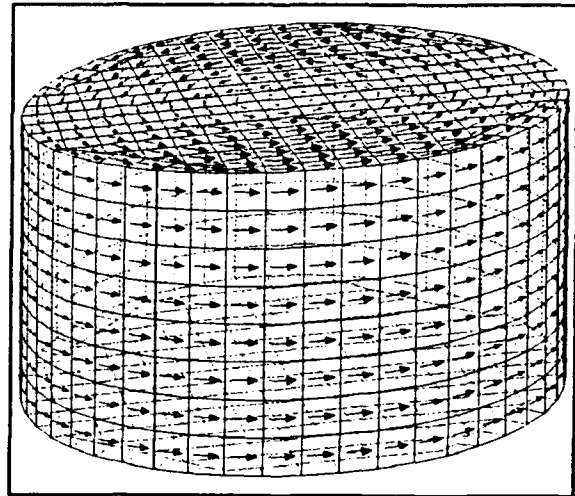


Figure 2. TM_{010} mode surface rf magnetic field distribution calculated using the boundary-integral method.

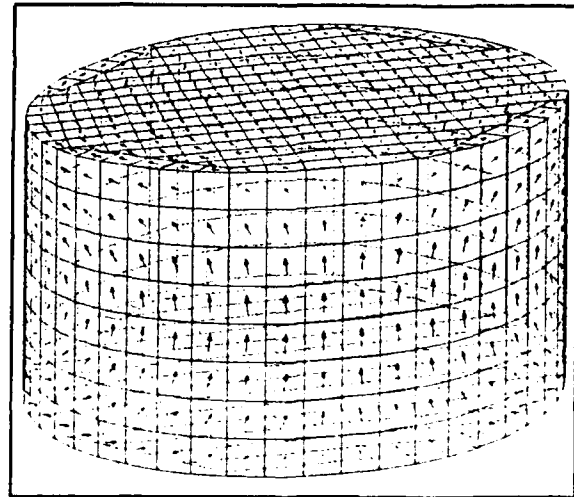


Figure 3. TE_{111} mode surface rf magnetic field distribution calculated using the boundary-integral method.

DESIGN CONSIDERATIONS FOR HIGH-CURRENT SUPERCONDUCTING RFQ'S

J. R. Delayen, C. L. Bohn, W. L. Kennedy, L. Sagalovsky
Engineering Physics Division, Argonne National Laboratory
Argonne, Illinois 60439 USA

Abstract

As part of our ongoing development program of high-current cw accelerators, we are investigating the use of superconducting RFQs to capture, bunch, and accelerate high-current, cw ion beams to energies where they can be further accelerated by more conventional independently-coupled superconducting cavities. This investigation addresses issues related to beam physics, thermal management, electromagnetic design, mechanical design, matching to the ion source, etc.

I. INTRODUCTION

As part of our ongoing program to apply rf superconductivity to high-current superconducting accelerators [1], we are investigating the use of superconducting RFQs to capture, bunch, and accelerate high-current ion beams before injection into superconducting linacs comprised of independently-coupled cavities. This research is motivated by preliminary results which indicated that the superconducting technology may appreciably extend the applications of RFQs [2, 3]. To that end we have been investigating RFQ geometries which seem to be better suited to the superconducting technology [4]. In this paper we address some beam dynamics and design issues associated with the development of high-current superconducting RFQs.

II. BEAM DYNAMICS ISSUES

In the beam current range of 25 mA to 100 mA, thermal management considerations suggest that a tolerable level of beam impingement in a superconducting RFQ (SCRFAQ) is 0.5% or less. Designing a structure with better than 99% transmission presents special challenges. For one, no present beam dynamics code achieves the required accuracy. Another problem is that the design procedures suitable for conventional RFQ's, which use a hard-wired

prescription based on Kilpatrick factor, field enhancement coefficient, and constant capacitance of the RF structure, may be neither optimal nor desirable for SCRFAQ.

As a general guideline, SCRFAQ must have a fairly large aperture equal to at least 5 times the rms beam radius. To accommodate the demand for strong transverse focusing, one should choose a low frequency since the superconducting resonators do not seem to suffer from the frequency-dependent electric-field breakdown.

Longitudinal transmission is affected by the RFQ bunching rate. The trade-off is between the increased particle capture and the overall length of the accelerator. By increasing the energy at the end of the gentle buncher, thereby causing the beam to be bunched at a slower pace as it is accelerated, we can achieve design transmissions above 99%. The overall length of the RFQ would typically rise quadratically with the energy increase.

As a test case we looked at a SCRFAQ design for a 25 mA and a 100 mA rms-matched proton beam accelerated from the initial energy of 100 KeV to the final energy of 3 MeV. We chose a frequency of 200 MHz, peak surface field of 40 MV/m, and a minimum aperture of 5 mm for the beam with initial rms normalized emittance of 0.2 mm-mrad. We varied the energy at the end of the gentle buncher from 0.5 MeV to 1.5 MeV and studied the transmission through the RFQ with PARMTEQ. The energy at the end of the shaper was kept constant, with exception of the last case where it was raised by 25%. The results are shown in Fig. 1. Fig. 1 also shows how the particle loss relates to the overall RFQ length. For the 25 mA beam, for example, raising the design beam transmission from 97.7% to 99.6% to 99.9% would mean respective length increases from 2.7 m to 4.3 m to 6.0 m. Upon closer examination, one sees that the lower transmission in the shorter structures is due to the particles lost longitudinally. Because of simplifications in the way PARMTEQ calculates space-charge forces, these "out-of-the-bucket" particles are not accurately tracked throughout the RFQ. It is not clear if the particles are transported unaccelerated or are deflected into the walls of the accelerator. Clearly, the latter scenario would be detrimental to the successful operation of SCRFAQ.

We can get a rough understanding of what happens to a

*Work supported by the Strategic Defense Initiative Organization and the U. S. Department of Energy.

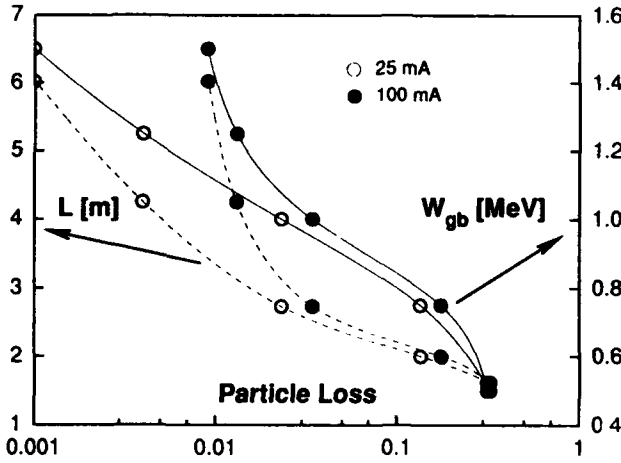


Figure 1: The length L and the energy at the end of gentle buncher W_{gb} as functions of the particle loss. Overall SCRFQ parameters are $f = 175 \text{ MHz}$, $E_s = 40 \text{ MV/m}$, $W_i = 0.1 \text{ MeV}$, $W_f = 3.0 \text{ MeV}$. Parameters at the end of gentle buncher are $a = 0.5 \text{ cm}$, $m = 2.25$, $\phi_s = -30^\circ$.

particle which falls out of the longitudinally stable region by calculating the effect of the trailing bunches on its trajectory. The momentum kick imparted on the particle by a bunch of current I can be approximated by a Rutherford scattering formula:

$$\Delta p_{\perp} = \frac{2qI}{4\pi\epsilon_0\Delta v f r_0}, \quad (1)$$

where q is the particle's charge, f is the RF frequency, r_0 is the initial radial displacement of the particle, and Δv is the relative velocity of the lost particle with respect to the trailing bunch. As the bunch accelerates, its velocity changes but in this rough calculation we assume the velocity to be constant. We take the relative velocity Δv_n to be

$$\Delta v_n = v_n - v_0, \quad (2)$$

where v_n is the velocity with which the n^{th} bunch overcomes the lost particle drifting at constant velocity v_0 .

For a particle initially displaced by r_0 undergoing a betatron oscillation due to the external focusing, we can obtain the oscillation amplitude increase Δr due to the space-charge kick Δp_{\perp} :

$$\Delta r = r_0 \left[\left(1 + \frac{(\Delta p_{\perp})^2}{m^2 \Omega^2 r_0^2} \right)^{1/2} - 1 \right], \quad (3)$$

where m is the particle's mass and Ω is the betatron angular velocity related to the RFQ focusing parameter B and the frequency f as follows,

$$\Omega \approx \frac{B}{\sqrt{8\pi}}. \quad (4)$$

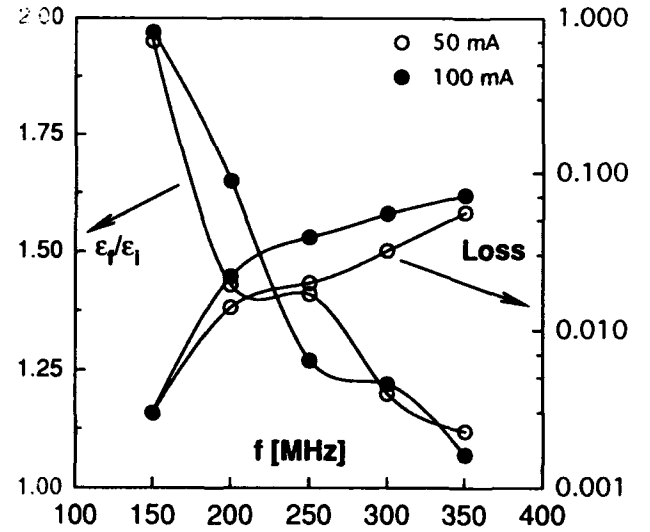


Figure 2: Emittance growth and particle loss versus frequency from PARMTEQ numerical simulation studies of SCRFQ designs for protons at $E_s = 40 \text{ MV/m}$.

For a numerical example, we picked the case mentioned above: a 2.7 m RFQ with the energy at the end of the gentle buncher equal to 1.0 MeV . In this design, all the particle loss occurs about 50 cm upstream the gentle buncher's end; the particle falls out of the bucket when it reaches the energy of 0.32 MeV . The design parameters are as follows,

$$\omega = 1.1 \times 10^7 \text{ sec}^{-1}; \quad f = 2.0 \times 10^8 \text{ Hz};$$

$$\Omega = 1.7 \times 10^8 \text{ sec}^{-1}; \quad r_0 = 0.13 \text{ cm}.$$

Table 1 summarizes the results for the $I = 25 \text{ mA}$ design. Table 2 gives the results for the $I = 100 \text{ mA}$.

Table 1: Effect of four trailing bunches on a drifting out-of-bucket particle for $I = 25 \text{ mA}$.

n	ωt_n	$z_n [\text{cm}]$	$\frac{\Delta v_n}{v_0}$	$\frac{\Delta p_{\perp}}{mv_0}$	$\frac{\Delta r_n}{r_0}$
1	0.375	26.5	1.12	2.46×10^{-3}	3.8×10^{-3}
2	0.554	39.2	1.67	1.66×10^{-3}	1.7×10^{-3}
3	0.701	49.6	2.10	1.30×10^{-3}	1.0×10^{-3}
4	0.951	58.8	2.50	1.10×10^{-3}	7.5×10^{-4}

We see that for the 25 mA beam the radial upward motion of the longitudinally unstable particle is mostly negligible, but for the 100 mA beam the space-charge imparted radial displacement is on the order of 10% of the initial radius.

We have also looked at the frequency choice for the SCRFQ. In general, lower frequency is preferable for better transmission characteristics. However, as a rule [5], lower frequency leads to a larger emittance growth. Fig. 2 shows results of PARMTEQ simulations where the particle loss and emittance growth are given as functions of the frequency for 50 mA and 100 mA proton beam.

Table 2: Effect of four trailing bunches on a drifting out-of-bucket particle for $I = 100$ mA.

n	ωt_n	z_n [cm]	$\frac{\Delta v_n}{v_0}$	$\frac{\Delta p_{\perp}}{mv_0}$	$\frac{\Delta r_n}{r_0}$
1	0.375	26.5	1.12	7.68×10^{-3}	5.9×10^{-2}
2	0.554	39.2	1.67	5.16×10^{-3}	2.7×10^{-2}
3	0.701	49.6	2.10	4.04×10^{-3}	1.7×10^{-2}
4	0.951	58.8	2.50	3.42×10^{-3}	1.2×10^{-2}

III. GEOMETRY

In earlier work [4] we investigated a geometry which is suited to high-current superconducting RFQs. It combined the best features of the 4-vane and 4-rod geometries which are widely used. This geometry is obtained by providing periodic cutouts in a 4-vane geometry which allow magnetic coupling between adjacent quadrants. The resulting structure is simple to manufacture in niobium, is easy to cool, and provides a quadrupole mode which is lower in frequency than, and widely separated from, the dipole mode. We are now extending the analysis of this geometry which was limited to infinite periodic waveguides to include the end effects of a finite RFQ. We have investigated, using MAFIA, the geometry shown in Fig. 3 which consists of 1/8 of an RFQ. The RFQ is terminated by a one-half cell;

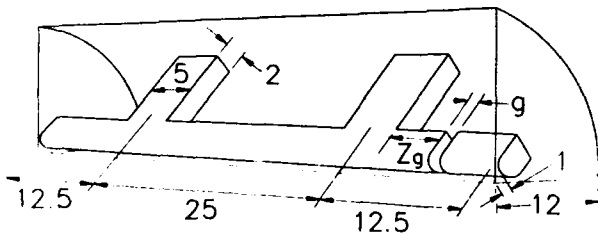
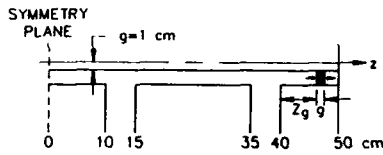


Figure 3: Schematic drawing of 1/8 of the RFQ structure.

the RFQ rods extend a distance Z_g , and are separated by a distance g (assumed to be of the order of 1 cm) from stubs extending from the end plates. Of particular interest is the frequency splitting between the quadrupole and the dipole mode. As shown in Fig. 4, the mode splitting remains almost constant as the length Z_g varies from 0 (no extension on the rods) to 10 cm (no stubs on the end plates). The field flatness, however is affected by the location of the gaps between the rods and the end plate stubs. As shown in Fig. 5, with the end cell dimensions we have assumed, the best field flatness is obtained when the rods

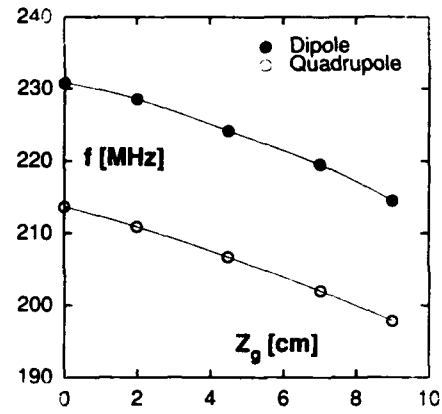


Figure 4: Quadrupole and dipole mode frequencies for structure of Fig. 3 as function of rod extension Z_g .

extend close to the end plates which have short stubs of less than 1 cm.

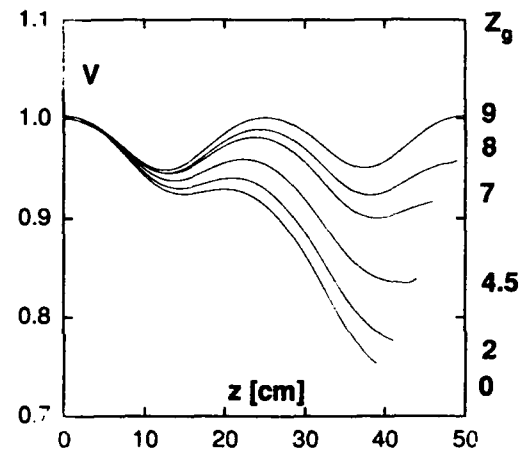


Figure 5: Voltage along the vane (relative units) for various rod extensions Z_g .

REFERENCES

- [1] J.R. Delayen, C.L. Bohn, B.J. Micklich, C.T. Roche, and L. Sagalovsky, "Design Considerations for High-current Superconducting Ion Linacs", these Procs.
- [2] J.R. Delayen, K.W. Shepard, *Appl. Phys. Letters* **57**, 514 (1990).
- [3] A. Schempp, H. Deitinghoff, J.R. Delayen, K.W. Shepard, *Proc. 1990 Linear Accelerator Conference*, Los Alamos Report LA-12004-C, 79 (1991).
- [4] J.R. Delayen, W.L. Kennedy *Proc. 1992 Linear Accelerator Conference* AECL-10728, 692 (1992).
- [5] T.P. Wangler, R.S. Mills, and K.R. Crandall, "Emitance Growth in Intense Beams," *Proc. 1987 Particle Accelerator Conf.*, IEEE 87CH2387-9, 1006 (1987).

Commissioning of the CEBAF Cryomodules*

M. Drury, T. Lee, J. Marshall, J. Preble, Q. Saulter, W. Schneider, M. Spata, M. Wiseman
Continuous Electron Beam Accelerator Facility
12000 Jefferson Ave., Newport News, VA 23606-1909

Abstract

When complete, the Continuous Electron Beam Accelerator Facility will house a 4 GeV recirculating linear accelerator containing 42 1/4 cryomodules arrayed in two antiparallel linacs and an injector. Currently, over half of the cryomodules have been installed. Each cryomodule contains eight superconducting niobium 5-cell rf cavities that operate at 1.497 GHz [1]. A cryomodule must provide an energy gain of 20 MeV to the 200 μ A beam [2]. The resultant dynamic heat load must be less than 45 W. The cavity parameters that are measured during the commissioning process include the external Q 's of the cavity ports, the unloaded Q (Q_0) of the cavity as a function of accelerating gradient, and the maximum operating gradient of the cavity. The sensitivity of the resonant frequency to changes in pressure and gradient is also measured. Finally, the mechanical tuners are cycled and characterized. In all cases, the performance of CEBAF cryomodules has exceeded the design requirements. A portable test stand allows local control of the rf system and provides automated data acquisition. This paper describes the cryomodule commissioning hardware, software, and measurements.

I. INTRODUCTION

Each installed cryomodule must undergo a series of tests to determine whether it meets the requirements for proper operation of the accelerator. The results of these tests provide a set of numbers that describe the rf characteristics of the individual cavities in a cryomodule. These characteristics are important for several reasons. They will become part of the calibration set that will be used by the rf phase and amplitude control system. These results also describe limits for safe operation of the cavities. Furthermore, these results provide useful feedback to the production group. Table 1 lists these parameters with the design requirements.

Table 1.
Cavity parameters

Q_{ext} (fundamental power coupler)	$6.6 \times 10^6 \pm 20\%$
Q_{fb} (field probe)	$1.3 \times 10^{11} \begin{smallmatrix} +62\% \\ -37\% \end{smallmatrix}$
Q_0	$\geq 2.4 \times 10^7$
f_0 (π mode, $T=2$ K)	1.497 GHz
E_{max}	≥ 5.0 MV/m
Pressure Sensitivity	< 60 Hz/torr

These parameters are all measured during the commissioning process. A Q_0 vs. E_{acc} curve is generated, and the effect of the ponderomotive force on the resonant frequency of

the cavity is also measured. Finally the mechanical tuners are cycled several times to insure proper operation.

The cryomodule production group has put together a portable test stand that is controlled by a Macintosh computer. This system is capable of fully interlocked local control of the rf system. With this system, the commissioning of a cryomodule can be completed in about three eight-hour shifts.

II. DESCRIPTION OF THE TEST SYSTEM

A block diagram of the test system is shown in Figure 1. A voltage controlled oscillator (VCO) is used to control the klystron amplifier. The VCO can operate in either a continuous wave (CW) mode or a gated pulsed mode. The pulsed mode is used to measure the emitted power (P_e) from the cavity and to measure the loaded Q (Q_L). A PIN diode is used as a gating device. The VCO uses a phase-lock loop to track the cavity field probe signal. The VCO is connected to a fast shutdown (FSD) node so that rf will be turned off by any fault signal in the interlock chain. These faults include waveguide window arc and temperature faults. The rf will also be turned off by waveguide and beamline vacuum faults, liquid level, and helium pressure faults through the fast shutdown node. Once the klystron drive signal has been tuned and the amplitude has been set, the computer can control the pulsed/CW mode of the VCO.

The VCO routes the gated signal, P_e , to an analog power meter, and to the spectrum analyzer. The analog meter integrates the measurement of the pulsed P_e signal over time. The spectrum analyzer is used in the time domain mode to measure the decay time of the emitted power signal.

Three digital power meter channels are available to measure the incident power (P_i) from the klystron, the transmitted power (P_t) from the cavity field probe, and the reflected power level behind the circulator (P_{refl}). This last signal is part of the interlock chain and is necessary to protect the klystron. A 18 GHz frequency counter is available for fast frequency measurement. All the instruments other than the analog power meter have GPIB capability.

A heater controller is used to power one of the four heaters that are located in the helium vessels. Heater control is required in order to make a calorimetric Q_0 measurement. The heater power level can either be set manually or controlled by the computer.

A self-excited loop is provided that allows the klystron drive to track the resonant frequency of the cavity during tuner cycling operations. The SEL is also connected to the FSD node for interlocked rf operation.

Geiger-Mueller tubes are positioned near each waveguide assembly of each cryomodule and on the beam tube at each end of the cryomodule.

A Macintosh computer is used for control of the test system, data acquisition, and measurement algorithms. The "Labview" software is an object-oriented, icon-based programming language that allows the computer to control ana-

*This work was supported by DOE contract DE-AC05-84ER40150

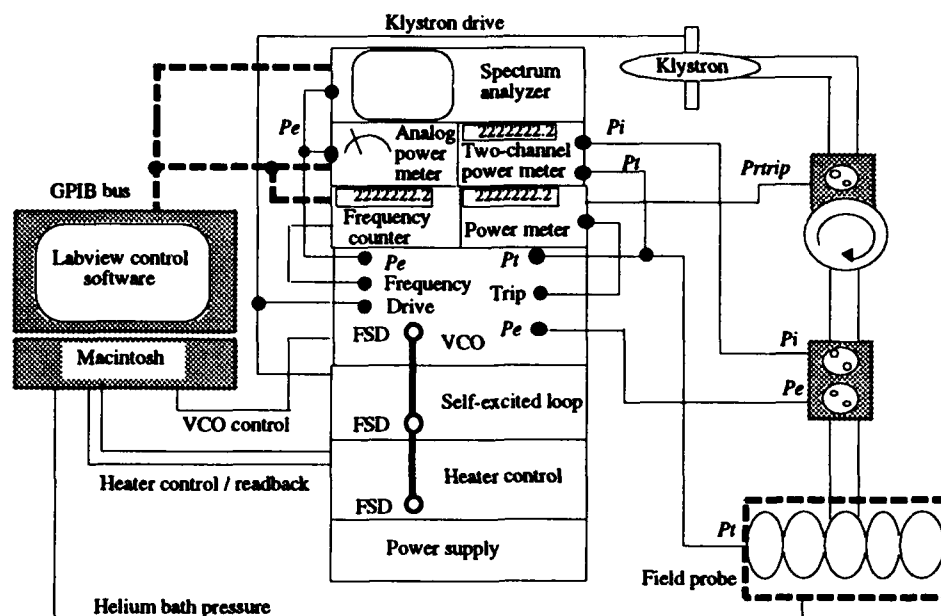


Figure 1. Test stand block diagram

log and digital I/O. This software also allows the computer to function as a GPIB controller. The computer, in its current configuration, can handle 14 analog output channels, 8 differential analog input channels, and 16 digital I/O lines.

III. MEASUREMENT SEQUENCE

Before any high-power operations begin, a series of measurements is made using a network analyzer. These measurements include a bandwidth measurement of Q_L for each cavity:

$$Q_L = \frac{f_o}{\Delta f} \quad (1)$$

The frequency and amplitude of each of the fundamental passband modes are measured for each cavity. Finally, a reflection measurement is made to determine attenuation from the field probe to the external port of the cryomodule for each cavity. This last measurement is combined with other attenuation measurements for cables and couplers to create a matrix of attenuation values. These are entered into the computer, allowing automatic calculation of the absolute power levels at the cavity plane. These measurements may be performed while the cavity temperature is at 4.2 K.

A complete interlock checkout is performed prior to any klystron operations. Simulated fault signals are applied to the various detector circuits while the operator observes the FSD.

When the interlock checkout and low-power measurements have been completed, and the cavity temperature has been lowered to 2.15 K or less, high-power commissioning can begin. The rf phase and amplitude control modules are disconnected from the rf system and replaced by the VCO and power meters.

The VCO drive signal is first tuned until the resonant frequency of the cavity is located. Then, the klystron power

level is raised until the accelerating gradient is at about 4 MV/m. At this time, a measurement of Q_{ex} is made. This is accomplished by using the fact that for a strongly overcoupled cavity ($\beta \gg 1$):

$$Q_L \approx Q_{ex} \ll Q_o, Q_p \quad (2)$$

Q_L can then be measured by the time decay method. While the klystron is in the pulsed mode, the spectrum analyzer is used to examine the emitted power waveform. A measurement is made of the time required for a 20 dB decay in this signal. The following equation is used to calculate Q_L and from that Q_{ex} :

$$Q_L = 4.34 \omega \frac{\Delta t}{20 \text{ dB}} \quad (3)$$

The VCO is switched to the CW mode. The incident and transmitted power levels are then acquired, allowing calculation of the accelerating gradient.

Accelerating gradient calculations begin with the following: [3]

$$\omega U \approx P_i Q_o = P_i Q_{ex} = P_i Q_p \quad (4)$$

The gradient is proportional to the square root of the stored energy in the cavity:

$$E_{ex} = \sqrt{\frac{\gamma_o}{L}} \omega U = \sqrt{\frac{\gamma_o}{L}} P_i Q_o = \sqrt{\frac{\gamma_o}{L}} P_i Q_p = \sqrt{\frac{\gamma_o}{L}} \omega \frac{\bar{P}_i}{PRF} \quad (5)$$

where $\frac{\gamma_o}{L}$ is the shunt impedance per meter, 1920 Ω , and PRF

is the pulse rate frequency, 50 Hz. In terms of the integrated emitted power P_e :

$$E_{\text{acc}} = 8.5 \times 10^4 \sqrt{P_e} \quad (f_e = 1.497 \text{ GHz}, \text{PRF} = 50 \text{ Hz}) \quad (6)$$

In terms of the transmitted power:

$$E_{\text{acc}} = \kappa \sqrt{P_t} \quad (7)$$

From equation (5) it can be seen that:

$$\kappa = \sqrt{\frac{\gamma_0}{L} Q_0} = \sqrt{\frac{\gamma_0 \omega U}{L P_t}} = \sqrt{\frac{\gamma_0 P_e}{L \text{PRF} \cdot P_t}} = 8.5 \times 10^4 \sqrt{\frac{P_e}{P_t}} \quad (8)$$

Q_0 can be determined from κ :

$$Q_0 = \frac{\kappa^2}{1920} \quad (9)$$

In terms of the incident power, the following relation is needed

$$P_i Q_0 = \frac{4\beta}{(1+\beta)} P_i Q_L \quad (10)$$

From equations (5) and (10), it can be seen that

$$E_{\text{acc}} = \sqrt{\frac{\gamma_0}{L} \frac{4\beta}{(1+\beta)} P_i Q_L} = \sqrt{\frac{\gamma_0}{L} 4 P_i Q_L}; (\beta \gg 1) \quad (11)$$

Once the gradient level has been established, Q_0 can be measured. The cryomodule must be isolated from the cryogenic system by closing the supply and return valves. The change in pressure due to the static heat load (ΔP_s) over some constant time (usually one minute) is measured. Then, a known power level (H_r) is applied to one of the internal heaters. The pressure rise due to the heater power (ΔP_h) is measured. Finally, the rf is turned on at the desired field level. While the klystron is in the CW mode, the pressure rise due to the rf (ΔP_{rf}) is measured. The rf heat load can then be calculated from the following equation:

$$P_i = H_r \frac{\Delta P_{\text{rf}} - \Delta P_s}{\Delta P_h - \Delta P_s} \quad (12)$$

From equations (4) and (5) it can be seen that:

$$Q_0 = \frac{E_{\text{acc}}^2}{1920 P_i} \quad (13)$$

The level of the accelerating gradient is raised in 1 MV/m steps and the measurements cycle is repeated. The measurement sequence is complete when E_{max} is reached. Limiting factors for E_{acc} include cavity quench, 1 W of field emission, R/hr of radiation measured at the beamline or waveguide assembly, excessive waveguide arc, window temperature, or

vacuum faults that inhibit sustained operation of the cavity. A Q_0 vs. E_{acc} curve is shown in Figure 2.

Once the phase and amplitude have been adjusted, the entire measurement sequence described above can be performed by the computer with about four keystrokes at each gradient level. About an hour is required to generate a Q_0 vs. E_{acc} curve.

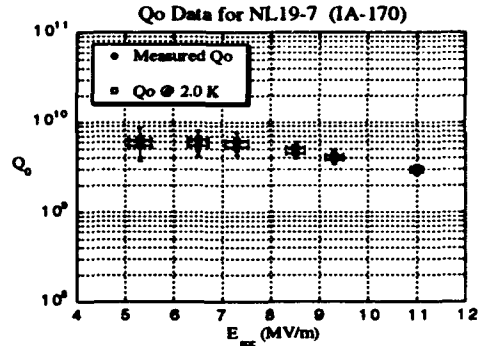


Figure 2. Q_0 vs. E_{acc} curve.

Frequency sensitivity to pressure is measured by setting a constant accelerating gradient. The resonant frequency is then monitored while the helium pressure in the cryomodule is cycled. The effects of the ponderomotive force on the resonant frequency are measured by monitoring changes in the frequency while varying the accelerating gradient. A constant pressure should be maintained during this measurement.

Finally, the tuners are cycled. The SEL is substituted for the VCO as klystron drive. The SEL will track the resonant frequency through the full range of tuner movement. Generally, the tuners are moved through a frequency range of ± 50 kHz around the design frequency, 1497 MHz.

IV. CONCLUSION

The commissioning test system allows fast and flexible testing of cryomodules. The use of a computer to control the test procedures minimizes the time required to test and allows most of the data reduction to be performed automatically. About half of the cryomodules have been installed and tested. Commissioning has shown that all of these cryomodules exceed the design performance requirements.

V. REFERENCES

- [1] P. Kneisel, *et al.*, "Performance of Superconducting Cavities for CEBAF," *Conference Record of the 1991 IEEE Particle Accelerator Conference*, Vol. 4, pp. 2384-86.
- [2] H. A. Gruner, *et al.*, "The Continuous Electron Beam Accelerator Facility," *Proceedings of the 1987 IEEE Particle Accelerator Conference*, Vol. 1, pp. 13-18.
- [3] I. E. Campisi, "The Calibration of the Cavities Field Probe," CEBAF TN-0139, June 1989.

Design and Fabrication of High Gradient Accelerating Structure Prototype at 36.5 GHz*

V. A. Dvornikov and I. A. Kuzmin

Small Accelerator Laboratory Moscow Engineering Physics Institute
Kashirskoe Shosse, 31, Moscow, 115409 Russia

Abstract

Disc loaded waveguide (DLWG) at 36.5 GHz was chosen as prototype of accelerating structure for reaching gradient up to 100 MV/m. The results of calculation and fabrication of DLWG cells are given. The technique of matching DLWG to input and output couplers is described.

I. INTRODUCTION

This paper describes results of design and fabrication of accelerating structure to reach the gradient up to 100 MV/m at 36,5 GHz. We used the results of the investigations, carried out at CLIC [1], to choose DLWG as accelerating structure.

II. DESIGN AND FABRICATION DLWG CELLS

DLWG cell is shown in Fig.1. The calculations were carried out by PRUD-0 [2]. The results of calculations are presented in Table 1.

Table 1
Structure parameters at 36.5 GHz

Parameters	Value
Phase velocity β_{ph}	1
Quality factor Q	4140
Shunt impedance r , $M\Omega/m$	120
Group velocity b_g	0.074
Section length l , mm	164.1
Cells per section N	60
Iris aperture over wavelength α/λ	0.2
Travelling wave mode	$2\pi/3$

The level of tolerances, required on main cell dimensions in order not to exceed the frequency error ± 5 MHz must be ± 0.001 mm. Theoretical estimates show that for copper at 36.5 GHz a surface finish of $R_a \leq 0.04 \mu\text{m}$ is required to obtain 90% of the theoretical Q value. The copper cells were machined to required tolerances and surface finish $R_a \leq 0.160 \mu\text{m}$ on precision diamond tool lathe with using special developed technology. After fabrication the frequency of each cell was measured by resonance method. The five cells of seventy five cells were incorrect. After this, the frequencies of resonance stacks of three, six, nine, twelve cells were measured. The dispersion curve is shown in Fig. 2.

* Work was supported by JINR, Dubna, Russia

III. MATCHING OF COUPLERS TO DLWG STRUCTURE

The problems of matching couplers to DLWG structure with large cell-to-cell coupling are described in [3]. The main difficulty is to get first matched coupler. We choose the coupler of SLAC-type with off-axis iris of coupling and off-axis cutoff frequency hole for vacuum pumping (Fig.3).

The matching was made in several stages.

- 1. The coupler with variable dimension $2b$ was developed.**

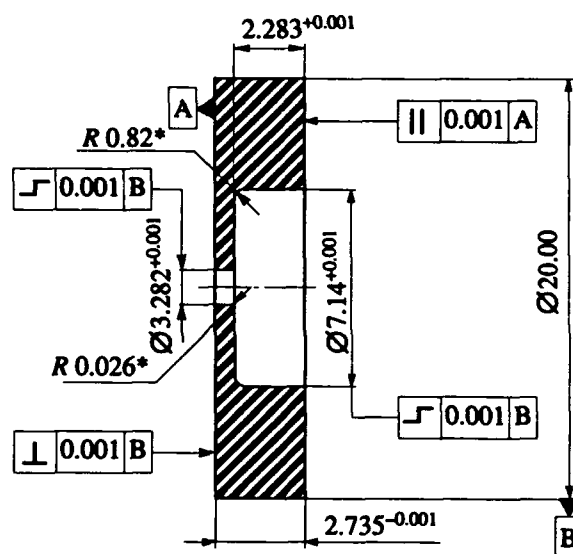


Figure 1. DLWG cell.

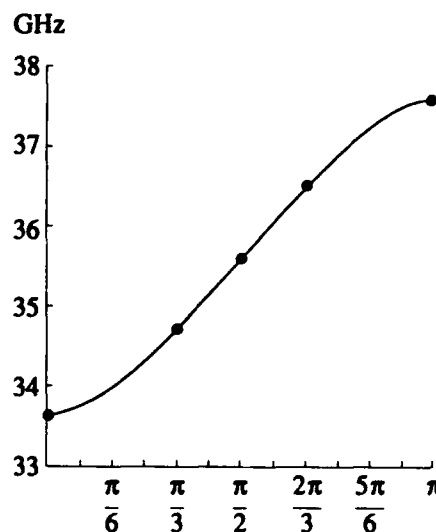


Figure 2. Dispersion curve.

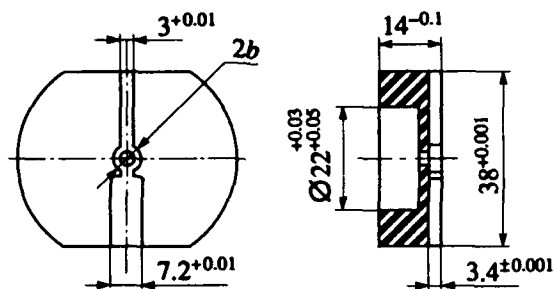


Figure 3. Coupler for DLWG.

2. Two "variable" couplers were matched to twelve cells of DLWG by increasing iris of coupling with rectangular waveguide (7.2×3.4 mm) until VSWR of input coupler ≤ 1.02 .

3. Two working couplers were matched successively as input couplers, when the "variable" matched coupler was connected to output. The procedure of determination VSWR of input coupler was to remove cells (each cell removed changes phase by $2\pi/3$ and 3 impedance points are sufficient to cover 2π) and to measure VSWR [3].

Sixty cells of DLWG were assembled in vacuum tube with two working matched couplers and preliminary vacuum pumping was made.

CONCLUSION

DLWG for operation in the $2\pi/3$ mode at 36.5 GHz was made. VSWR of input coupler at operating frequency was 1.02. Calculations show, that accelerating gradient will be 100 MeV/m at input power about 41 MW.

REFERENCES

- [1] I. Wilson, W. Schnell, and H. Henke, "Design and Fabrication Studies of High Gradient Accelerating Structures for CERN Linear Collider (CLIC)," CERN/LEP - RF/88-50 and CLIC Note 76, October 1988.
- [2] A.G. Daikovskii, I.I. Portugalov, and A.D. Riabov, *Part. Accel.*, 12(1982), p.59.
- [3] I. Wilson, "Status of Structure Studies (CLIC)," The 2-nd International Workshop on Next-Generation Linear Collider.

The SSC RFQ-DTL Matching Section Buncher Cavities

T. Enegren, C.M. Combs, Y. Goren, M. D. Hayworth, A. D. Ringwall and D. A. Swenson
Superconducting Super Collider Laboratory*
2550 Beckleymeade Avenue
Dallas, TX 75237

Abstract

The RFQ-DTL matching section of the SSCL Linear Accelerator matches the 2.5 MeV H^- beam from the RFQ into the acceptance of the 70 MeV Drift Tube Linac (DTL). To provide longitudinal phase space tuning, two rf buncher cavities with a resonant frequency of 427.617 MHz and with a maximum E_0TL of 160 kV are required. To meet the limited space requirements, it was decided to use double gap buncher cavities.

I. INTRODUCTION

The primary goal of the RFQ-DTL matching section is to match 2.5 MeV beam from the RFQ into the acceptance of the DTL, experiencing a minimal growth in beam emittance. The main components consist of two RF buncher cavities and four Variable Field Permanent Magnet Quadrupoles (VFPMQ). It is required that these devices along with beam diagnostics fit into a length of only 534 mm. A drawing of the matching section is shown in Figure 1.

Because of the limited space available it was decided to use two double gap cavities instead of the much larger single gap pillbox type cavity. The cavities are required to have a resonant frequency of 427.617 MHz and provide a maximum E_0TL of 160 kV. However the small size of the double gap did present a challenge in coupling 30 kW of pulse RF power as well providing water cooling, fine tuning and probes for sampling the RF fields.

II. MECHANICAL DESIGN

A drawing of the cavity is shown in Figure 2. The cavity is formed from a section of rectangular slabline transmission line with a washer type structure which forms the double accelerating gap.

*Operated by the Universities Research Association, Inc. for the U. S. Department of Energy under Contract No. DE-AC35-89ER40486.

The submitted manuscript has been authored by a contractor of the U.S. Government under Contract No. DE-AC35-89ER40486. Accordingly, the U.S. Government retains a nonexclusive, royalty-free license to publish or reproduce the published form of this contribution, or allow others to do so, for U.S. Government purposes.

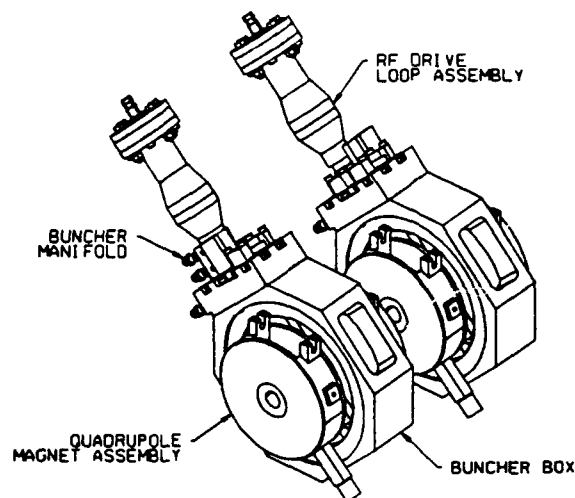


Figure 1: RFQ-DTL matching section.

The cavity is designed such that it can be housed in an octagonal diagnostic chamber. Vacuum is supported by the chamber which eliminates resonant frequency shifts due to pressure deflection on the cavity. The cavities are oriented at 45 degrees with respect to the vertical with the accelerating gaps near the bottom. The maximum power dissipation in the cavity due to RF conductor losses is 30 watt with most of that in the center conductor. Water cooling is provided by water channels that are brazed into the cap and extend the length of the center conductor. This also provides temperature stabilization of the cavity. The cooling water will be derived from the Temperature Control Unit (TCU) of the RFQ. It is expected that the temperature fluctuation will be no greater than 0.4 degrees Celsius. The corresponding frequency change will be 2.9 kHz which is well inside the bandwidth of the cavity (43 kHz). Inductive coupling is used to excite the cavity. Calculations and measurements on a cold model indicate that a loop area of 0.5 cm² is required to achieve matched coupling. It is estimated that only 5 milliwatts of power is dissipated on the loop and water cooling is not required. In the actual design, the loop area will be somewhat greater than required and there will be the capability of rotation so that the desired coupling can be achieved. For phase and amplitude regulation an rf sample is derived from a induc-

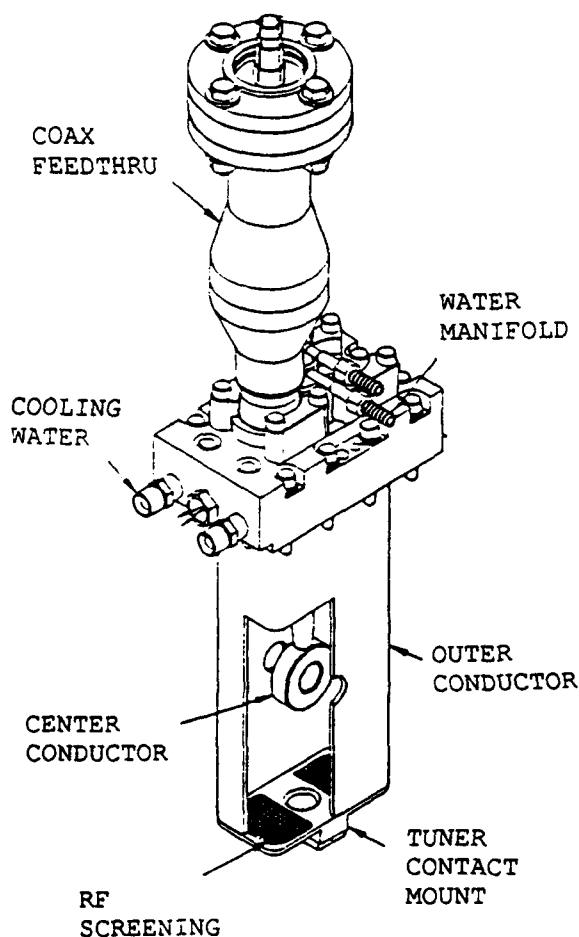


Figure 2: Double gap buncher cavity.

tive loop thru a type N connector assembly located at the top of the cavity. Because of the severe space limitations at the top of the cavity, fine frequency tuning using a rotatable loop was not possible. Instead this is accomplished through installation of a capacitive slug at the bottom of the cavity which couples into the electric field from the accelerating gap. With a travel of 30 mm and with the closest approach to the bottom of the washer being 23 mm a tuning range of 200 kHz can be achieved.

III. MAFIA CALCULATIONS

The 3D code MAFIA was used to set the resonant frequency and calculate the shunt impedance and quality factor of the fundamental mode. These turned out to be 800 $k\Omega$ and 5000 respectively. This quality factor is approximately four times smaller than that calculated for the pill-box type cavity. Hence the double gap buncher will be less sensitive to mechanical disturbances. The transit time factor was calculated to be 0.7. Also calculated were electric field sensitivities as a function of small displacements of the center conductor. These results were used to specify mechanical tolerances.

IV. CERAMIC FEEDTHRU ASSEMBLY

A drawing of this assembly is shown in Figure 3. It is basically a coaxial transmission line that undergoes a transition from o.d. $1\frac{5}{8}$ inch (air) to o.d. $\frac{7}{8}$ inch (vacuum). Providing the barrier between air and vacuum is a ceramic cylinder. The two main considerations in the design of this unit is to minimize the VSWR and minimize the electric fields near the surface of the ceramic. To investigate this problem use was made of the 3D code HFSS to calculate the reflection coefficient and electric field values. It was found that to keep the values of electric fields within acceptable values (1.5 kV/cm) it was necessary to use a relatively large ceramic. This accounts for the bulge in the structure. Also of consideration in the design of this assembly is the distance between the ceramic and the actual coupling loop. During the filling time of the cavity the loop, because its small self reactance (compared to 50 Ω), behaves essentially as a short circuit [1]. This sets up a standing wave on the transmission line with the voltage maximum being located a distance $\lambda/4$ away from the coupling loop (with an effective length assigned to the loop). To minimize the electric stress on the ceramic it is desirable to locate the ceramic as close to the loop as possible or $\lambda/2$ away. Because of space constraints in the actual design this distance could be made no smaller than 0.17 wavelengths. However calculations show that the electric field values are within acceptable values. Using the other option of locating the ceramic at a distance $\lambda/2$ would invite multipactoring problems.

V. SUMMARY

Two double gap buncher cavities are being constructed for the SSCL RFQ-DTL matching section. It is expected

that RF conditioning will take place within the next several months.

VI. REFERENCES

- [1] Vojtech Pacak, SSCL, *private communication*

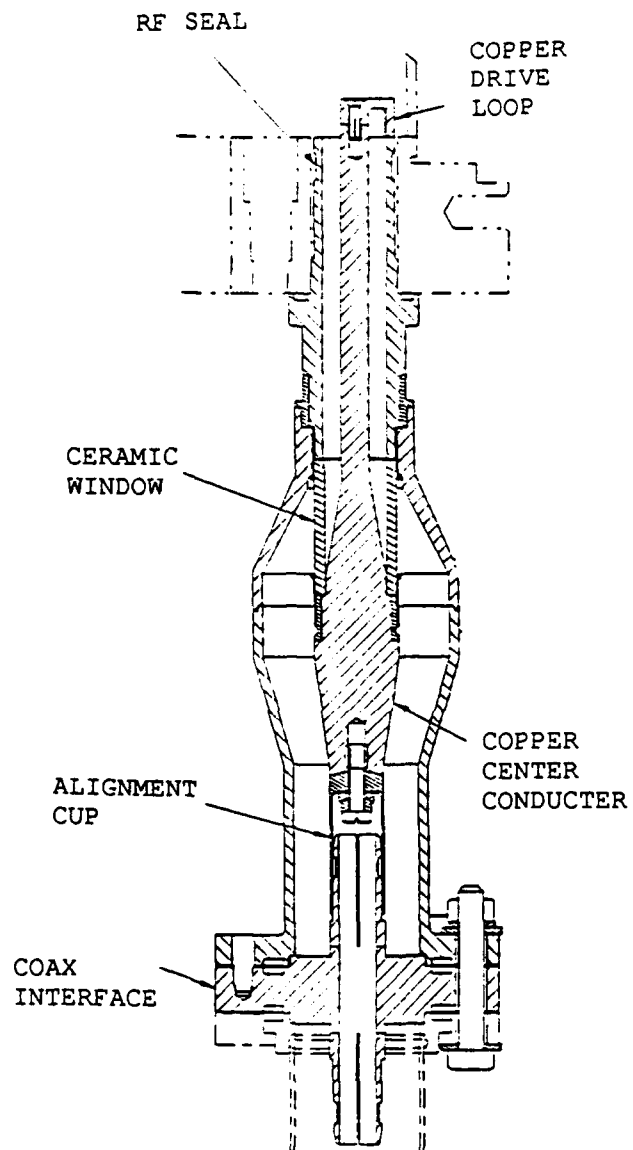


Figure 3: Ceramic feedthru assembly.

Bulk Niobium Low-, Medium- and High- β Superconducting Quarter Wave Resonators for the ALPI Postaccelerator

A. Facco¹, J.S. Sokolowski^{1,2}, I. Ben-Zvi³, E. Chiaveri⁴ and B.V. Elkonin²

¹ INFN-Laboratori Nazionali di Legnaro, 35020 Legnaro (Padova) Italy.

² The Weizmann Institute of Science, Department of Physics, Rehovot 76100, Israel.

³ Brookhaven National Laboratory, Upton, N.Y. 11973, U.S.A.

⁴ CERN, Geneva 23, Meyrin, Switzerland.

Abstract

A family of three solid niobium quarter wave superconducting resonators, cooled by direct contact with liquid helium, having resonant frequencies of 80 MHz, 160 MHz and 240 MHz and optimum velocities $\beta_o = 0.056$, $\beta_o = 0.11$ and $\beta_o = 0.17$ respectively, has been designed, constructed and tested. In addition to the standard chemical surface treatment also thermal treatment at 1200°C using the titanium sublimation technique was applied. The low-beta 80 MHz resonator $Q_o = 2.3 \times 10^8$, and the quality factor was almost constant from low level up to the maximum field achieved of 4.2 MV/m at 5 W. The intermediate beta 160 MHz cavity had $Q_o = 2.2 \times 10^8$, almost constant up to the field of 5 MV/m at 10 W. The high beta 240 MHz resonator, after deionized water high pressure rinsing, reached $Q_o = 3.5 \times 10^8$ and a maximum field of 4.7 MV/m at 6 W. The 80 MHz cavity serves as a prototype for the recently started production of the low-beta section of the ALPI linac.

1 INTRODUCTION

The first all-niobium quarter wave resonator was designed at the Weizmann Institute of Science in 1987. The intention was to build a resonator with much better performance than the lead plated copper resonators in use at that time at the Weizmann Institute. The prototype of this resonator was constructed in cooperation with INFN Laboratori Nazionali di Legnaro and with CERN [1]. The construction flaws prompted us to build another prototype and the tests of this new 160 MHz resonator have proven that our goal was achieved [2]. The successful performance of the 160 MHz resonator has triggered the idea, that also the other resonators, needed to complete the Alpi linac [3], could be constructed of bulk niobium and have a similar conceptual design [4].

The beam dynamics calculations for ALPI have shown that, in order to accelerate ions of all masses coming from the LNL 16 MV tandem, three different sections (with optimum velocities $\beta_o = 0.056$, 0.112 and 0.169 respectively) of two gap resonators would be required; due to the need of a wide phase acceptance for heavy ions the frequency of 80 MHz was chosen for the low beta section.

We matched the velocity of ions along the low, intermediate and high beta sections by using three frequencies, 80, 160 and 240 MHz respectively; that way we could maintain the same resonator shape along the beam line and

the mechanical design of all the resonators stayed almost identical except for their lengths (fig. 1).

2 DESIGN CONSIDERATIONS

A number of basic considerations had to be taken into account when designing the new type of resonators. They had to meet the requirement of short time and relatively low power required for multipactoring conditioning. This condition has been thoroughly investigated [5] and the shape design of the inner conductor of the resonator (see fig. 1) was based upon it.

The resonator is all-niobium in order to allow for high temperature treatment; the outer conductor is cooled directly by liquid helium contained in the double wall structure.

The medium and high beta resonators fit the dimensions of the ALPI cryostat; the low beta cavities require minor modifications in the cryostat design due to their length. The 80 MHz resonator is relatively light and easy to handle in spite of the fact that it is about 1 m long.

The mechanical design of the cavities fits the requirements of relatively easy machining and minimum number of welds. The mechanical parts are identical for all three cavities, except for the lengths of the outer envelope and the inner and outer conductors. The advantages of modularity were obtained without loosing in terms of rf characteristics (see table 1).

Resonator type	low- β	medium- β	high- β
Frequency [MHz]	80	160	240
β_{opt}	0.056	0.112	0.169
Transit time factor	0.9	0.9	0.9
$U/E_a^2 [mJ/(MV/m)^2]$	114	67.3	45
$H_p/E_a [G/(MV/m)]$	100	103	110
E_p/E_a	4.9	5.2	5.4
$R'_{sh} [M\Omega/m]$	20.4	25.1	26.6
$\Gamma [\Omega]$	15.4	29.5	41.9

Table 1: Niobium resonators calculated parameters.

3 PROTOTYPE SURFACE TREATMENT AND TESTS

All three resonators have undergone at least one standard CERN chemical treatment and one thermal treatment at

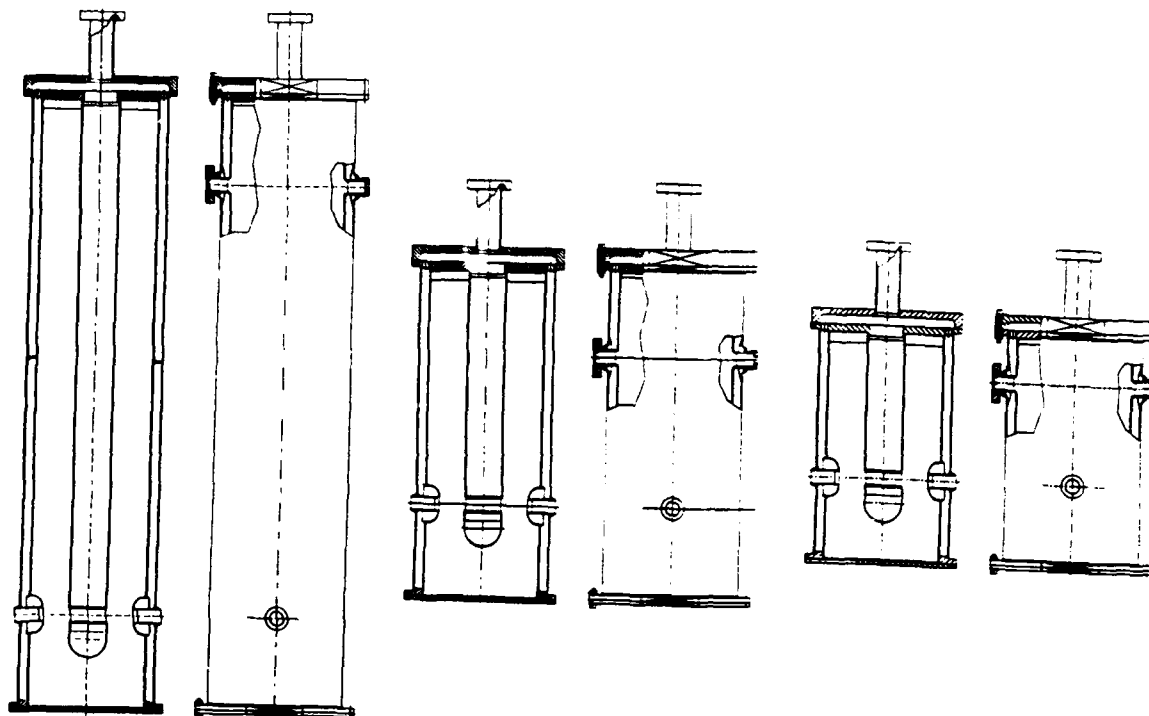


Figure 1: The 80, 160 and 240 MHz niobium resonators.

1200°C and 1×10^{-6} mbar using the titanium sublimation technique.

3.1 The 160 MHz resonator

The chemical treatment was followed by the thermal treatment. No rf test was done after chemical treatment, the measurements after thermal treatment gave the results shown in fig. 2. The maximum field was limited by field emission at 60 W [2]. We have used this resonator on the linac test beam line as a buncher.

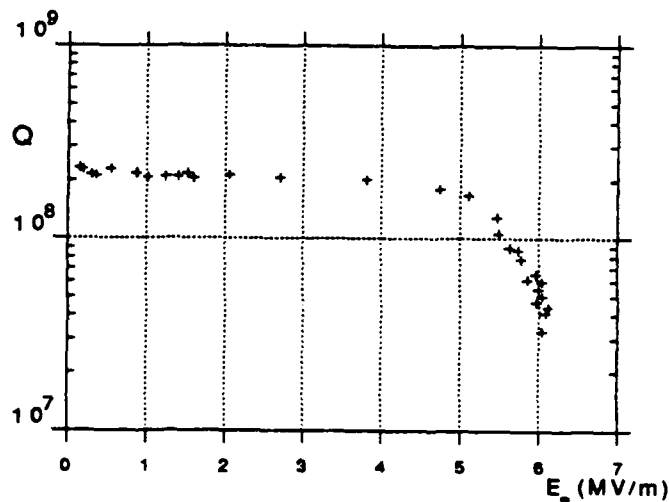


Figure 2: The 160 MHz resonator Q vs. E_a curve

3.2 The 80 MHz resonator

The thermal treatment was followed by chemical treatment. The results of the rf measurements are shown in fig. 3; the maximum field of 4.2 MV/m was reached at 5 W forward power, limited most probably by local thermal breakdown. Power and helium conditioning did not change this limit. The mechanical stability of the resonator at 4.2 K was tested by scanning frequencies from 5 to 1000 Hz applied to the cryostat using a mechanical vibrator. The only resonance frequency detected was 44 Hz with a bandwidth of 2 Hz.

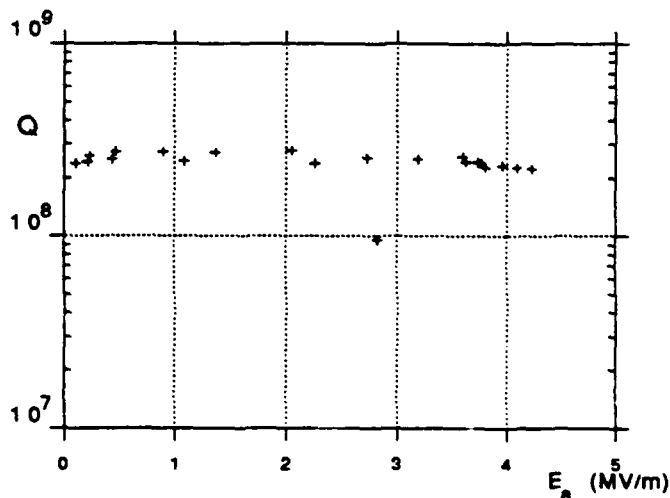


Figure 3: The 80 MHz resonator Q vs. E_a curve

3.3 The 240 MHz resonator

In this resonator we did the thermal treatment first and then the chemical treatment. We tested the resonator and we found a maximum field of 3.2 MV/m at 4 W, again limited by local thermal breakdown as in the 80 MHz cavity. High pressure rinsing with deionized water at 100 bars [6] [7], followed by ethanol rinsing, without nitrogen gas drying of the resonator, was applied. The new rf test showed that the upper limit of field level was shifted up to 4.7 MV/m at 6 W (see fig. 4). This could indicate that the quench was caused by some surface impurity, which has been removed by the high pressure rinse.

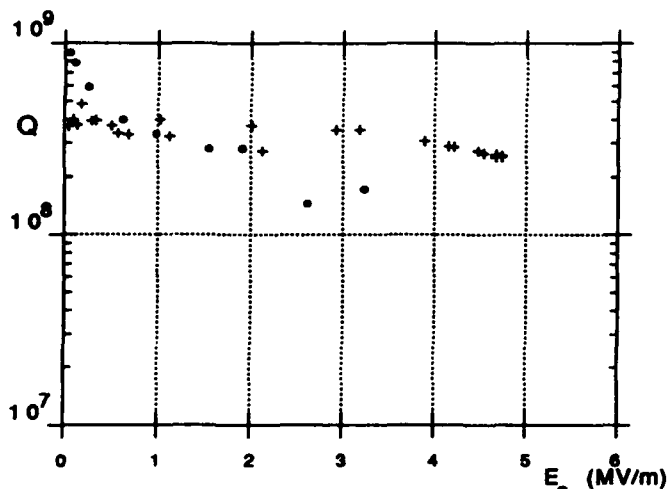


Figure 4: The 240 MHz resonator Q vs. E_a curves: "o" before high pressure rinse; "+" after high pressure rinse.

4 CONCLUSIONS

A set of three resonators, corresponding to the ALPI linac requirements for the low, intermediate and high β sections, was designed, constructed and tested. The resonators are all-niobium made, allowing for high temperature treatment. They have identical shape except for their lengths; the differences in their optimum velocities are due only to their different resonant frequencies. The design similarities simplify considerably the construction procedure and reduce production costs.

A series of experiments aiming at optimising the surface treatment is still continuing; we have had clear evidence that high pressure deionised water rinsing could increase the maximum field attainable after chemical treatment.

The 80 MHz resonator became the prototype for the low β section of the ALPI linac, consisting of 7 cryostats which would be housing 24 accelerating cavities and one buncher; the production of the first 6 resonators of this section has begun recently.

There are still some open questions to be solved in order to have a complete picture of the resonator characteristics and of the operations necessary for optimum performance:

the best sequence of surface treatment operations, the effect of working in clean room conditions, that could not be tested yet on our cavities, and whether a fast tuner would be necessary to cope with the mechanical oscillations.

5 ACKNOWLEDGMENTS

Over the years basically three laboratories and institutes and their staff were involved in the project; The Weizmann Institute of Science, INFN Laboratori Nazionali di Legnaro and CERN. We also collaborated in the first stage of the project with prof. Cramer of the University of Washington in Seattle. We would like to thank the staff of the Weizmann Institute and in particular Y. Wolovelsky and his team at the Design Department, the W.I. mechanical workshops under the leadership of A. Bar-On as well as the Cryogenics Laboratory technicians, they all gave us constant support in design, measurements and in solving many mechanical problems.

Many people at Laboratori Nazionali di Legnaro have contributed to the success of this project; G. Fortuna who always supported and encouraged us in this project, A. Porcellato in rf measurements, V. Palmieri in many fruitful discussions, L. Badan in cryogenics and vacuum systems as well as in thermal treatment, L. Bertasso in construction of the test cryostat, the mechanical workshop led by L. Dona' machined one of the resonators and its staff was always available for help when needed - they all deserve our infinite gratitude.

We are grateful to CERN, where everybody, from H. Lengeler and Ph. Bernard through many people belonging to their or related divisions did their best to help the project. At CERN our first resonator was welded by the EBW group led by B. Thony and again the machine shop gave us a very significant support. Last but not least, let us thank Mr. Insomby for his excellent and difficult work of chemical treatment of the resonators.

6 REFERENCES

- [1] I. Ben-Zvi, B.V. Elkonin, A. Facco and J.S. Sokolowski, "Development of a high performance niobium superconductive quarter wave resonator", Internal report INFN, LNL-INFN(REP)-018/89.
- [2] I. Ben-Zvi, E. Chiaverri, B.V. Elkonin, A. Facco and J.S. Sokolowski, Proceedings of the 2nd European Particle Accelerator Conference, Nice 1990, Vol.2 p. 1103.
- [3] G. Fortuna *et al.*, Nucl. Instr. and Meth. A287 (1990) 253.
- [4] A. Facco and J.S. Sokolowski, Nucl. Instr. and Meth. A328 (1993) 275.
- [5] I. Ben-Zvi and J. Sokolowski, Rev. Sci. Instrum. 57 (1986) 776.
- [6] V. Palmieri, private communication.
- [7] Ph. Bernard, D. Bloess, T. Flynn, C. Hauviller, W. Weingarten, P. Bosland and J. Martignac Proceedings of the 3rd European Particle Accelerator Conference, Berlin 1992, Vol.2 p. 1269.

A Numerical Method for Determining the Coupling Strengths and Resonant Frequencies of a Nonperiodic Coupled Cavity Chain

M. Foley and T. Jurgens
Fermi National Accelerator Laboratory
P.O. Box 500, Batavia, IL 60510 USA

Abstract

Traditionally the coupling strengths and individual cavity resonant frequencies for a chain of coupled oscillators with periodic or biperiodic geometry have been calculated from the dispersion relation. A dispersion relation does not exist for a chain of coupled oscillators with nonperiodic geometry. A numerical procedure for estimating the unknown coupling strengths and resonant frequencies for individual elements of coupled oscillator chains has been developed and tested. This procedure has the novel capability that it is applicable to both periodic and nonperiodic structures.

1 Introduction

A chain of coupled linear accelerator cavities with biperiodic geometry is shown in Figure 1.

RESONATOR R_{2n-2} R_{2n-1} R_{2n} R_{2n+1} R_{2n+2}
NUMBER ω_a ω_c ω_a ω_c ω_a

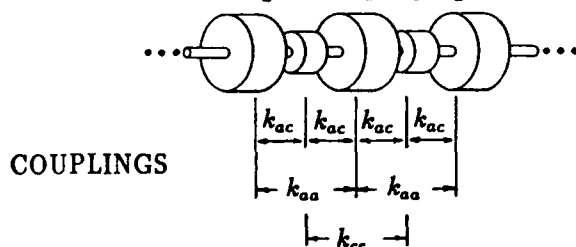


Figure 1: Model for a biperiodic chain of cavities with nearest neighbor and second nearest neighbor coupling

Investigation of the electrical properties of such a chain is accomplished by formulating a mathematical model consisting of a biperiodic chain of coupled oscillators (RLC circuits) with nearest neighbor and second nearest neighbor coupling[1], as shown in Figure 2.

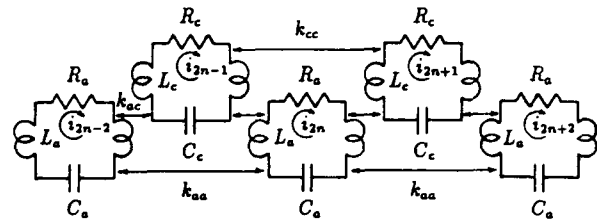


Figure 2: Coupled oscillator model for a biperiodic chain of cavities with nearest neighbor and second nearest neighbor coupling

The coupled equations generated from the model above [1] are of the form (assuming half cell termination):

$$I_{2n} = X_{2n} \left[1 + \frac{\omega_a}{j\omega Q_a} - \left(\frac{\omega_a}{\omega} \right)^2 \right] + \frac{k_{ac}}{2} (X_{2n-1} + X_{2n+1}) + \frac{k_{aa}}{2} (X_{2n-2} + X_{2n+2}) \quad (1)$$

$$I_{2n+1} = X_{2n+1} \left[1 + \frac{\omega_c}{j\omega Q_c} - \left(\frac{\omega_c}{\omega} \right)^2 \right] + \frac{k_{ac}}{2} (X_{2n} + X_{2n+2}) + \frac{k_{cc}}{2} (X_{2n-1} + X_{2n+3}) \quad (2)$$

The quantities I_{2n} , I_{2n+1} are forcing terms, X_{2n} , X_{2n+1} are amplitudes, ω_a is the resonant frequency for individual accelerating cavities in the absence of coupling to their neighbors, ω_c is the resonant frequency for individual coupling cavities in the absence of coupling to their neighbors, Q_a is the quality factor for accelerating cavities, and Q_c is the quality factor for coupling cavities.

There are $2n+1$ solutions to the homogenous equations ($I_{2n} = I_{2n+1} = 0$) for the lossless case (high Q) of the form

$$X_{2n} = A \cos 2n\phi_q \quad (3)$$

$$X_{2n+1} = B \cos(2n+1)\phi_q \quad (4)$$

where $\phi_q = \frac{\pi q}{2N}$, $q = 0, 1, \dots, 2N$, provided that

$$k_{ac}^2 \cos^2 \phi_q = \left[1 - \left(\frac{\omega_a}{\omega_q} \right)^2 + k_{aa} \cos 2\phi_q \right] \cdot \left[1 - \left(\frac{\omega_c}{\omega_q} \right)^2 + k_{cc} \cos 2\phi_q \right] \quad (5)$$

ϕ_q is the phase shift per cavity in mode q , and ω_q , $q = 0, \dots, 2N$ are the frequencies of the normal modes of oscillation of the cavity chain. Equation (5) is the *dispersion relation* for a biperiodic chain of coupled oscillators with nearest and next nearest neighbor coupling.

It is important to note that the dispersion relation is not valid for a chain of nonperiodic coupled oscillators.

2 Application of the Dispersion Relation to a Side-Coupled Cavity Chain

At FNAL the new LINAC side-coupled cavity sections have biperiodic geometry of the form shown in Figure 1. Based on the coupled oscillator model described in Section 1, the phase shift per cavity, ϕ_q , is known for each normal mode frequency. Measurements are made using an HP network analyzer (NWA) of the corresponding normal mode frequencies. These values are used to generate a set of points (ϕ_q, ω_q) in the (ϕ, ω) -plane. The coupling strengths k_{ac} , k_{aa} and k_{cc} and individual cavity resonant frequencies ω_a , ω_c are determined from the dispersion curve by least squares fitting equation (5) to the measured points (ϕ_q, ω_q) using an internal version of the LASL code DISPER[3].

3 Matrix Representation of the Coupled Oscillator Equations

The homogenous form of equations (1,2) for the case with no losses is given in vector-matrix format by

$$\begin{bmatrix} 1 & k_{ac} & k_{aa} & 0 & 0 & 0 & \dots & 0 \\ k_{ac}/2 & 1 & k_{ac}/2 & k_{aa}/2 & 0 & 0 & \dots & 0 \\ k_{ac}/2 & k_{ac}/2 & 1 & k_{ac}/2 & k_{aa}/2 & 0 & \dots & 0 \\ 0 & k_{ac}/2 & k_{ac}/2 & 1 & k_{ac}/2 & k_{aa}/2 & \dots & 0 \\ & & & & & & & \\ 0 & \dots & \dots & \dots & k_{ac}/2 & k_{ac}/2 & 1 & k_{ac}/2 & k_{aa}/2 & 0 \\ 0 & \dots & \dots & \dots & 0 & k_{ac}/2 & k_{ac}/2 & 1 & k_{ac}/2 & k_{aa}/2 \\ 0 & \dots & \dots & \dots & 0 & 0 & k_{ac}/2 & k_{ac}/2 & 1 & k_{ac}/2 \\ 0 & \dots & \dots & \dots & 0 & 0 & 0 & k_{ac} & k_{ac} & 1 \end{bmatrix} \begin{bmatrix} X_0 \\ X_1 \\ X_2 \\ X_3 \\ \dots \\ X_{2N-3} \\ X_{2N-2} \\ X_{2N-1} \\ X_{2N} \end{bmatrix} = \begin{bmatrix} \left(\frac{\omega_a}{\omega}\right)^2 X_0 \\ \left(\frac{\omega_a}{\omega}\right)^2 X_1 \\ \left(\frac{\omega_a}{\omega}\right)^2 X_2 \\ \left(\frac{\omega_a}{\omega}\right)^2 X_3 \\ \dots \\ \left(\frac{\omega_a}{\omega}\right)^2 X_{2N-3} \\ \left(\frac{\omega_a}{\omega}\right)^2 X_{2N-2} \\ \left(\frac{\omega_a}{\omega}\right)^2 X_{2N-1} \\ \left(\frac{\omega_a}{\omega}\right)^2 X_{2N} \end{bmatrix} \quad (6)$$

Equation (6) is equivalent to equations (1,2) with $I_{2n} = I_{2n+1} = 0$ and Q large.

Introducing the scale factor $\left(\frac{\alpha}{\omega_i}\right)^2$, $i = a, c$, equation (6) can be written in vector-matrix form as

$$MX = \lambda X \quad (7)$$

where $\lambda = \left(\frac{\alpha}{\omega}\right)^2$. The eigenvalue problem (7) has $2N+1$ solutions corresponding to the set of discrete eigenvalues λ_q , $q = 0, \dots, 2N$. The corresponding normal mode frequencies are given by

$$\omega_q = \frac{\alpha}{\sqrt{\lambda_q}}$$

where $q = 0, \dots, 2N$.

Consider again the problem of determining the coupling strengths and individual cavity resonant frequencies for a LINAC section. An alternative approach to the application of the dispersion relation is described below.

As before, a HP NWA is used to measure the normal mode frequencies, $(\omega_q)_{\text{measured}}$, $q = 0, \dots, 2N$, for the LINAC section under test. An initial estimate of the coupling strengths and resonant frequencies is made in order to initiate an iterative optimization algorithm. At each step in the execution of the algorithm the eigenvalue problem (7) is solved and corresponding normal mode frequencies ω_q , $q = 0, \dots, 2N$ are calculated. A new step is made by choosing the coupling strengths and resonant frequencies to minimize the sum of the squares of the differences between the ω_q 's and the corresponding measured normal mode frequencies $(\omega_q)_{\text{measured}}$, $q = 0, \dots, 2N$. The optimization algorithm is implemented as a FORTRAN program with calls to two subroutines: (i)

	DISPER	Optimization
$k_{ac}/2$	$2.6575355 \cdot 10^{-2}$	$2.6577377 \cdot 10^{-2}$
$k_{aa}/2$	$-3.8878468 \cdot 10^{-3}$	$-3.8732951 \cdot 10^{-3}$
$k_{cc}/2$	$3.9281018 \cdot 10^{-4}$	$3.9949479 \cdot 10^{-4}$
ω_{end}	806.32192 MHz	806.28166 MHz
ω_a	804.64813 MHz	804.65951 MHz
ω_c	807.88179 MHz	807.88676 MHz

Table 1: Comparison of results from DISPER and Optimization Method for a LINAC side-coupled cavity section

EIGEN2, an eigenvalue solver [2], and (ii) DUNLSF, a least-squares minimization subroutine from the IMSL Mathematics Library. The minimization is carried out until the magnitude of the difference between two successive steps is less than a user specified tolerance.

The accuracy of the coupling strengths and normal mode frequencies determined by this approach, as compared to those determined by the traditional method using DISPER, is directly related to the level of precision obtained measuring the normal mode frequencies, $(\omega_g)_{measured}$.

Consider a typical LINAC side-coupled cavity section as shown in Figure 1. The coupling strengths and individual cavity resonant frequencies for the section were determined from DISPER.

In order to set up a baseline test to determine the accuracy of the proposed procedure, assume the coupling strengths and individual cavity resonant frequencies are unknown. The normal mode frequencies for the section are available from NWA measurements. For the initial estimate $k_{ac}^0/2 = 0.05$, $k_{aa}^0/2 = -0.005$, $k_{cc}^0/2 = 0.0001$, $\omega_a^0 = 805 \text{ MHz}$, $\omega_c^0 = 805 \text{ MHz}$, and $\omega_{end}^0 = 805 \text{ MHz}$, application of the optimisation procedure outlined above yields the results shown in Table 1. Convergence required thirteen iterations. Further tests indicated that varying the initial estimate did not significantly effect either the results or the rate of convergence.

4 Extension of the Optimization Method to Nonperiodic Structures

A prototype LINAC side-coupled cavity module, consisting of two sections joined by bridge side cavities (bsc) and a bridge coupling cavity (bcc), is not a

$k_{a,bcc}/2$	$-1.1082194 \cdot 10^{-2}$
$k_{bcc,bsc}/2$	$3.5754545 \cdot 10^{-2}$
ω_{bsc}	798.79952 MHz
ω_{bcc}	809.58395 MHz

Table 2: Coupling strengths and resonant frequencies for a LINAC side-coupled cavity module

biperiodic structure, and therefore the dispersion relation (5) is not valid. However, the optimization method described in Section 3 is applicable.

A vector-matrix representation of the coupled oscillator equations modeling the prototype LINAC module can be developed analogous to the procedure followed in Section 3. The parameters k_{ac}^i , k_{aa}^i , and k_{cc}^i and ω_a^i , ω_c^i are known for each of the two individual LINAC sections, $i=1,2$. The values of $k_{a,bcc}$, $k_{bcc,bsc}$, ω_{bsc} and ω_{bcc} are unknown, while $k_{bsc,bsc}$ is assumed to equal zero.

The numerical optimization procedure described in Section 3 was applied to determine $k_{a,bcc}$, $k_{bcc,bsc}$, ω_{bsc} and ω_{bcc} for such a nonperiodic structure. Convergence required ten iterations. The results are shown in Table 2.

5 Conclusions

A numerical procedure for estimating unknown coupling strengths and resonant frequencies for individual elements of coupled oscillator chains has been presented. The procedure has the novel capability that it is applicable to both periodic and nonperiodic structures.

References

- [1] E.A. Knapp, B.C. Knapp, and J.M. Potter, "Standing Wave High Energy Linear Accelerator Structures," *The Review of Scientific Instruments*, Vol. 39, No. 7, pp. 979-991, July 1968.
- [2] W.H. Press, B.P. Flannery, S.A. Teukolsky, and W.T. Vetterling, *Numerical Recipes*, Cambridge University Press, pp. 335-380, 1986.
- [3] J. Crisp, "Fitting Frequency Measurements to the Dispersion Relation for a Doubly Periodic Chain of Resonators," FNAL Linac Upgrade Note LU-200, March 1993.

Thermal Study of HOM Couplers for Superconducting RF Cavities

M.Fouaidy, T.Junquera
Institut de Physique Nucléaire (CNRS-IN2P3). 91406 ORSAY France

S.Chel, A.Mosnier
DSM/DAPNIA/SEA CE-Saclay 91191 GIF-SUR-YVETTE France

Abstract

The thermal behaviour of a "fish hook" type HOM coupler [1-2] for Superconducting RF Cavities is analyzed by numerical simulation using a 3D finite element based code for both CW (rings, recirculating linacs) and pulsed (s.c. colliders studies like TESLA) accelerator types. Consequently, a thorough study of the thermal stability of this system is necessary in both transient and steady-state regimes. Numerical simulations, assuming anomalous losses at the end of the HOM inner conductor, were performed. The effects of the HOM coupler geometry and the materials thermal conductivity on the critical heat flux inducing the quench of the system are discussed.

I. INTRODUCTION

The superconducting Higher Order Modes (HOM) couplers used for Superconducting Radiofrequency Cavities (SRF) cooled by Liquid Helium (LHe) are generally limited by thermal breakdown induced by various phenomena for accelerating fields E_{acc} in the range 2-5 MeV/m when no efficient cooling of the inner conductor is provided. These E_{acc} values are much smaller than the values to be reached for future projects (e.g. TESLA [3] : $E_{acc} = 25$ MeV/m). We consider that HOM and beam tubes are located inside the insulation vacuum of the LHe vessel ; this indirect LHe cooling should obviously reduce the thermal quench limit of the HOM couplers. It is then necessary to choose properly the HOM coupler geometry and its construction material in order to increase its capability to withstand anomalous RF losses.

At low temperature, the RF surface resistance, the thermal conductivity (k), the specific heat per unit volume (C_v), the heat transfer coefficient at LHe-metal interfaces are strongly dependent on temperature (T). The resulting heat equation with the pertinent boundary and initial conditions is then nonlinear. Moreover, the system studied is not axisymmetrical, hence a 3D computer code is necessary. We used the CASTEM 2000 code [4] for this purpose : this Finite Element Method (FEM) based code can handle such problems in both transient and steady-state conditions for arbitrarily shaped computational domains with multiple regions (i.e. materials).

II. METHOD AND ANALYSIS

A. The boundary value problem

The temperature field $T(x,y,z,t)$, where x,y,z and t are spatial-coordinates and time respectively, within the

computational domain Ω is governed by the well-known non-linear 3D Heat Diffusion equation with no heat source :

$$\text{div}(k_i(T) \nabla T) = C_{vi} \frac{\partial T}{\partial t}$$

where the subscript "i" refers to thermal properties within the region Ω_i .

For the cases of our concern, the typical boundary conditions are : prescribed heat flux q , heat transfer to the LHe at T_{bath} controlled by the Kapitza conductance H_K ($T_{bath} < T_\lambda = 2.176$ K). For this parameter, we have used the following expression [5] :

$$H_K = 0.017 T_{bath}^{3.62} \left(1 + \frac{3}{2} \left(\frac{\Delta T}{T_{bath}} \right) + \left(\frac{\Delta T}{T_{bath}} \right)^2 + \frac{1}{4} \left(\frac{\Delta T}{T_{bath}} \right)^3 \right)$$

where H_K unit is W/cm²/K, $\Delta T = T - T_{bath}$ and T is the LHe-cooled surface temperature.

Concerning the transient computations, the whole system studied was assumed to be initially at the LHe temperature.

B. Variational problem and approximation

Using the so-called Galerkin Method, the semidiscrete problems corresponding to the above boundary value problem are derived. Briefly, this method consists on subdividing Ω into a set of subvolumes or finite elements, and expanding the solution in terms of FEM using N -components global basis functions. Then, a variational method is applied to these functions leading to N differential (algebraic) equations for time-dependant (steady-state) problems respectively. These equations constitute the semidiscrete variational problem, where the unknown are precisely the nodal values $T_j(t)$ of the temperature field within the Ω -mesh.

C. Resolution Method

In the steady-state case, the above non-linear system is solved by an iterative method using linearisation technique and a relaxation factor for improving the convergence of the process. The steady-state solution is reached when the relative variations of temperature at all the nodes of the Ω -mesh is less than 10^{-3} .

For the transient case, the above equations, discretized in time are solved by a n -step method : the temperature field at a given time is calculated from temperature fields at the n preceeding times (we chose $n=2$).

III. APPLICATION TO THE HOM COUPLER

A. The model and thermal stability criteria

The real system studied (Fig. 1) consists in the beam tube of the cavity, the HOM coupler (diam. : 40 mm and Inner Conductor (IC) diam. : 8 mm), the Nb flange of cryostat tank and the LHe cooled part of the cavity. For numerical simulation, this system was modelled using a slightly modified geometry (Fig. 2) which includes all the parts described previously up to the first iris of the cavity. Notice however that the thermal contact resistances at the sealings (i.e. flanges of the HOM) were neglected, the fish-hook has been replaced by a straight Inner Conductor (IC) which has no influence on the numerical results because the thermal radiations are negligible ($T < 10$ K), and we have also neglected the heat flux coming from the RF coaxial cable (using a simple Nb cover in place of the upper part of the HOM).

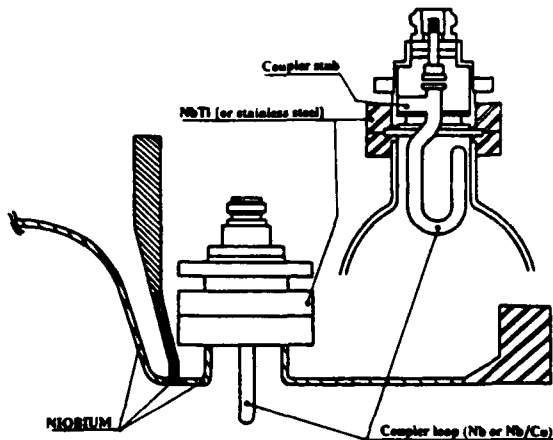


Fig. 1 : Cavity-HOM design.

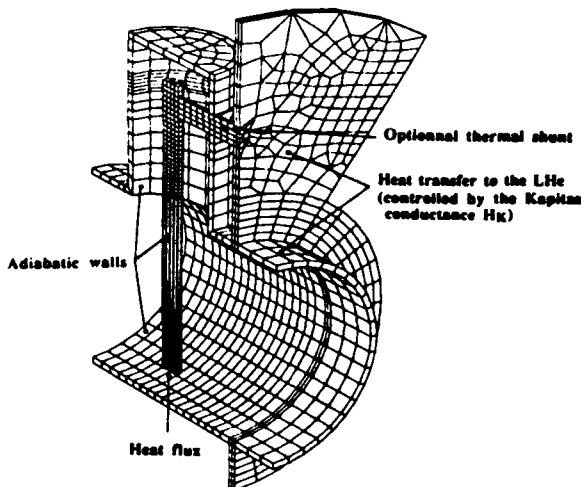


Fig. 2 : Meshed cavity-HOM assembly and applied boundary conditions.

In the defect free case, the total RF losses dissipated on the IC of the HOM remain lower than 0.4 mW (with a peak heat flux density of $40 \mu\text{W}/\text{cm}^2$) for $T_{\text{bath}} = 2.0$ K.

$E_{\text{acc}} = 25$ MeV/m and a residual surface resistance $R_{\text{res}} = 20$ n Ω [6]. These very low RF dissipations can not explain an increase of the hot spot temperature beyond the Nb critical temperature $T_c = 9.2$ K. Consequently, anomalous RF dissipation sources (cavity electron loading, surface defect, multipactor, ...) have to be considered as possible causes of the HOM coupler thermal breakdown. We have then assumed a highly dissipative area, located at the end of the IC, the farthest point from the cold source. With this pessimistic assumption we will obtain the minimum heat flux limit Q_c before the quench.

The thermal stability will be insured if two conditions are fulfilled : the temperature T_{max} at the hot spot must be lower than $T_c = 9.2$ K and the maximum heat flux density transferred to the LHe bath must be below the critical heat flux inducing the Film-Boiling limit.

B. Steady state regime

The steady-state temperature distribution was computed up to the critical heat flux (Q_c) for the following arrangements and the results are summarized in Table 1. :

- # 1. the whole HOM coupler-cavity assembly is machined from bulk Niobium with RRR = 40, 194 or 570,
- # 2. all these parts are in bulk Niobium (RRR = 40, 194 or 570) excepted the IC and the Stub which are made of sputtered Niobium onto a Copper substrate of RRR=300,
- # 3. the same material as in item #1 but with addition of a copper (Cu : RRR=300) thermal shunt between the Coupler and the LHe cryostat flange (see Fig. 2),
- # 4. the same arrangement as in item #2 with addition of the thermal shunt described in item #3.

Nb quality	Arrangement	Critical heat flux Q_c (mW)
RRR 40	# 1	72
RRR 194	# 1	314
RRR 570	# 1	925
RRR 40	# 2	600
RRR 194	# 2	1860
RRR 570	# 2	3418
RRR 40	# 3	79
RRR 194	# 3	347
RRR 570	# 3	1017
RRR 40	# 4	2700*
RRR 194	# 4	3328*
RRR 570	# 4	5430

Table 1 : Critical heat flux inducing the HOM coupler thermal breakdown in the steady-state regime.

* Quench limited by the transition to film boiling on the LHe-cooled Nb flange (heat flux density : $2.4 \text{ W}/\text{cm}^2$).

Analysing the temperature profiles along the IC for the arrangements #1 and #3 with $Q = Q_c$, we note that the non-linear effects increase with the Nb RRR, the temperature difference along the IC is around 3.3 K whatever the RRR may be, there is no sensible effect of the thermal shunt on Q_c which increases (from nearly 70 mW to 1 W) with the Nb RRR (see Table 1). The values of the

thermal impedance of the IC ($R_{th} = \Delta T_{IC}/Q_c$) are 46 K/W, 10.5 K/W and 3.6 K/W for $RRR = 40$, 194 and 570 respectively. So, even in the best arrangement (#3 and Nb $RRR = 570$), the system is limited by the Niobium thermal conductivity.

In order to overcome this limitation, the arrangement #2 was examined, leading to a reduction by a factor 6 of the IC thermal impedance. The adding of a thermal shunt (arrangement #4) improves greatly Q_c (Fig. 3) due to the sufficiently small thermal impedance (0.6 K/W) of the IC, and in this computation, 70% of Q_c is derived through the thermal shunt.

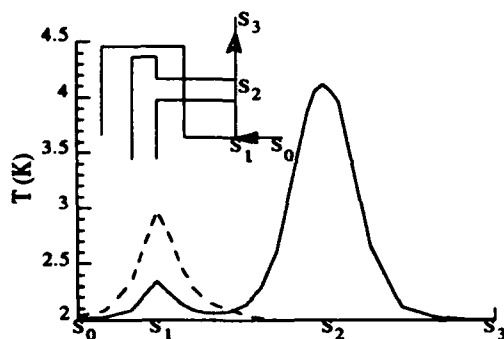


Fig. 3 : Temperature profile along the LHe cooled Nb flange (sketched in the insert).
Full line : with thermal shunt ($Q_c = 5.4$ W)
Dashed line : without thermal shunt ($Q_c = 3.4$ W)

C. Transient regime

This study was limited to the arrangement #1 with $RRR = 194$. The applied heat flux was pulsed close to the TESLA cycle (pulse length $\tau_p = 2$ ms ; $f_{rep} = 10$ Hz). The maximum hot spot temperature during the RF pulse increases up to 8.6K at the end of the first RF pulse for $Q_c = 6$ W, does not recover its initial temperature (i.e. $T_{bath} = 1.8$ K) at the end of the first pulse (4.4K), but reaches its stationary value (9.2K) in nearly 10 pulses (Fig. 4). The higher temperature after an infinity of pulses as function of the heat flux can be evaluated with :

$$T_{max} \approx 3.63 Q^{0.35} + 0.31 Q^{0.49}$$

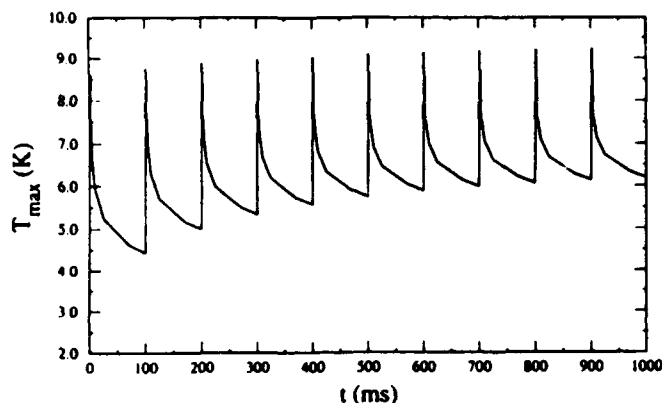


Fig. 4 : Temperature of the hot spot vs time

From the evolution of the temperature along the IC at different times (Fig. 5), the value of $300 \text{ cm}^2/\text{s}$ is obtained for the diffusion coefficient. Consequently, the perturbation during the RF pulse is localized close to the defect point (diffusion length of 1.5 cm in 2 ms) and the corresponding heat flux can not be evacuated in one complete cycle (110 cm in 100 ms, that is to say, the length of the IC).

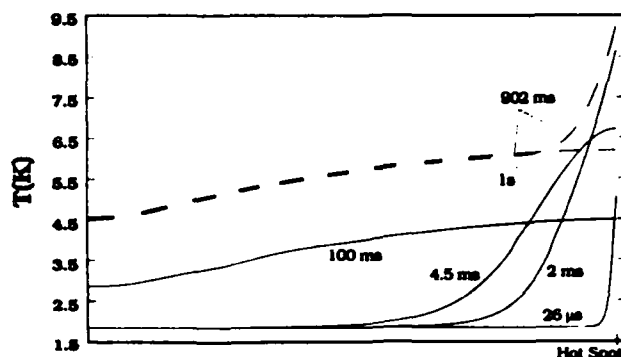


Fig. 5 : Temperature profile along the IC at different times.

Full lines : First pulse
Dashed lines : 10th pulse

IV. CONCLUSION

A HOM coupler heat load capability of over 5 W has been reached in case of a continuous anomalous RF dissipation, by using an IC and a stub made with sputtered Nb onto a Cu substrate, and adding a thermal shunt connected to the LHe flange. In the transient regime, the maximum heat load sustained by the bulk Nb coupler is 6 W. In all the cases and for the corresponding critical heat fluxes, the maximum temperature at the iris of the cavity does not exceed 0.1 K with respect to T_{bath} , so that the thermal stability of the cavity is also insured.

We plane some thermal measurements on a special cavity/HOM assembly, to confirm these calculations and to take into account, if necessary, the effect of the contact resistances at the sealings.

V. REFERENCES

- [1] A. Mosnier, "Developments of HOM couplers for superconducting cavities". 4th Workshop on RF Superconductivity, Tsukuba, 1989.
- [2] Ph. Bernard and al., "Demountable E/H field HOM for the Nb-sputtered 4-cell LEP cavity". 5th Workshop on RF Superconductivity, Hambourg, 1991.
- [3] H. Padamsee, "Review of the superconducting approach to linear colliders". Proc. 3rd Eur. Part. Conf., Berlin, 1992.
- [4] P. Verpeaux and al., "A Modern Approach of a Large Computer Code for Structural Analysis", Structural Mechanics Reactor, n° 10, Los Angeles, 1989.
- [5] K. Mittag, Cryogenics 13 (1973) 94.
- [6] S. Chel, M. Fouaidy, "Thermal behavior of HOM couplers". Internal Report, CE-Saclay/DAPNIA/SEA-93.

VERY WIDE RANGE AND SHORT ACCELERATING CAVITY FOR MIMAS

C. Fougeron. P. Ausset. D. de Menezes. J. Peyromaure. G. Charruau.
LNS - CE-SACLAY 91191 GIF-SUR-YVETTE. F.

Abstract

The frequency ranges of electrical accelerating field for heavy ions synchrotrons have to be often very wide. And their dynamics are limited by the physical characteristics of the magnetic load in the resonant structures.

We built an accelerating system, with only one gap, using amorphous material, able to replace the two actual MIMAS Cavities (the Saturne II booster), in order to make free a part of the ring. The frequency range can be swept at 4 kV. The RF voltage can be increased up to 10 kV, and the frequency to 12 MHz. The geometrical sizes was chosen to minimize the operation troubles during the cavities permutation on the machine.

I. INTRODUCTION

Mimas is the storage booster for the synchrotron Saturne II, on the National Laboratory SATURNE from Saclay (F). It was dedicated to operate protons, deuterons and heavy ions (up to krypton to day) at 12 MeV/amu.

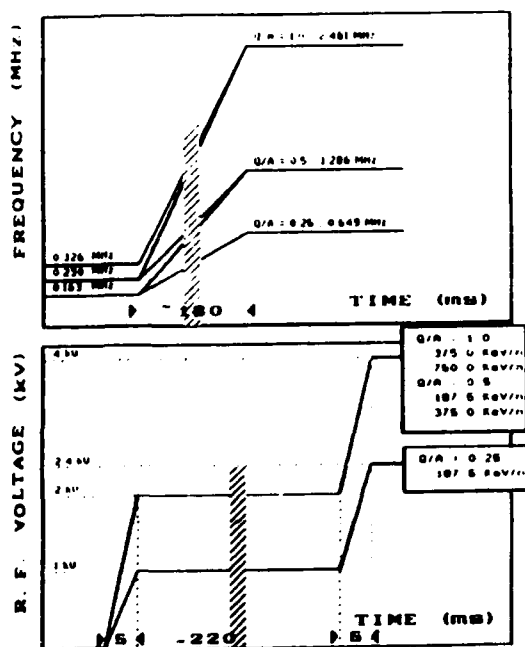


Fig. 1 a, b : frequency law (a) and voltage law (b) of the MIMAS RF system

For that, the accelerating RF system uses two ferrite loaded cavities, at 2 x 2kV peak with a frequency range from 150 kHz to 2,5 MHz. The requirements are illustrated on fig. 1.

Some projects on Saturne and Mimas, mainly to cool the beam inside the booster, needed to make free a part as long as possible of the vacuum pipe.

On the other hand we started a test program on amorphous magnetic materials and arrived at several optimistic conclusions concerning use in accelerating RF structures.

II. MAIN RESULTS OF VAC 6025 TEST

The main differences between ferrites and amorphous, for the RF structure use, have been seen in the permeability, the losses and μQF product, the behaviour with frequency, RF induction, bias field and temperature.

This test was made around the Mimas frequencies, on an VACUUMSCHMELZE material 6025 F.

1° - Permeability : at 150 KHz, μ is 10 time higher than the ferrite SY 7 one. It decreases with the frequency, to the value of the ferrite at 10 MHz, insuring a quasi-self tuning.

2° - The losses : They cannot be given by the traditional $\Delta F/F$ Q factor, because the large permeability variation with frequency. But these losses are greater. The product μQF , where μ is higher and Q lower, is higher than the ferrite one.

3° - Bias current : the magnetic sensitivity of μ is 20 to 40 time higher than ferrites. It means that the current requirements and the turns-number are 20 to 40 time lower (fig. 2).

4° - RF induction : the Q and μ values are quasi independant of the RF induction and we did not see the Q loss effect in the Mimas range, like we saw with Phillips or TdK ferrites (fig. 2).

It is possible to increase the RF voltage by a factor more than 4 (the limit was given by the power dissipation in the small test-cavity).

and changed from a TH 120 - 40 kW Tetrode to a push pull using 2.10 kW TH 541 tetrodes.

5°) - Power Dissipation - temperature : In ferrite, the μ increases by 2 every 30° C. With VAC, the sensivity is very low, not appreciable. But the limit temperature is low, and destructive (90°).

The VAC is metal. The power can be extracted up to more than 1 W/cm³.

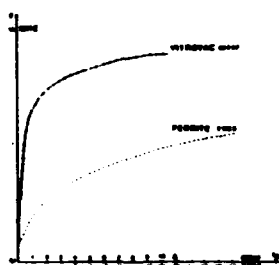
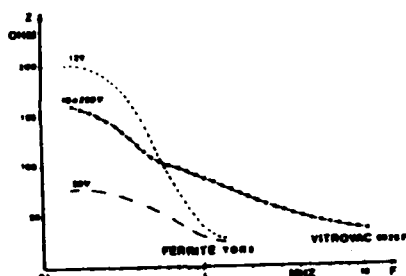


Fig. 2 - Small Test cavity
Impedance for different voltages
Frequency V. bias current

6°) - Cost: the price of the VAC for the same volume is two times this for the ferrite : but one half of the volume is used for the same result. The total price is the same. But the environment is less expensive (power supplies, amplifier, used space, a.s.o...)

III - REAL SIZE LOAD BUILDING

It was possible to think built an alone cavity for MIMAS, to replace the two necessary in operation, and, so, make free 1, 5 meter on the vacuum chamber.

We chose the same size, (l, \varnothing int., \varnothing ext.) for the cavity, the gap and all the components of the magnetic load, but the structure was built in two symmetrical push-pull quasi-resonators (fig. 3). The amplifiers was adapted at this new configuration,

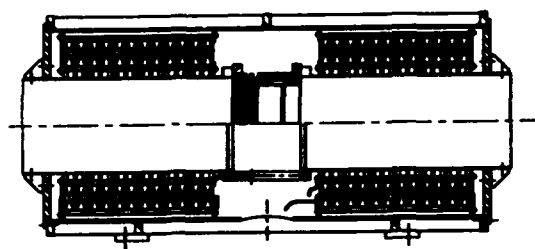


Fig. 3 - Push Pull resonators

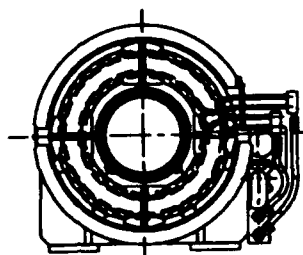
Magnetic load :

- Vitrovac 6025 F
- \varnothing ext. : 510 mm
- \varnothing int. : 355 mm
- e/core : 25 mm
- e ribbon : 25 μ m
- ring number: 2 x 12
- l magnetic : 60 cm
- Bias current $\mu/400$: 4A/4 turns
- cooling : copper rings and water

Cooling system : the amorphous metal is inclosed inside a C form alumina box, insulated by a capton film. A sandwich of two magnetic cores, back to back on the two faces of a new designed copper ring in witch flows the cooling water make an independant module (fig. 4).

Six modules of this type are aligned around the beam pipe for each quasi-resonator.

We tested the cooling up to 2 kW per ring.



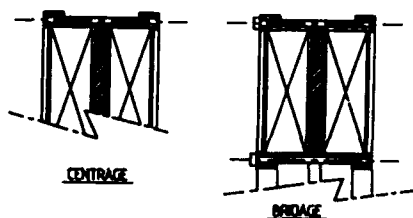


Fig. 4 - Cooling module

IV. TEST OF THE CAVITY

1°) - Impedance - Tuning : we measured the cavity shunt impedance on the total structure, with an Impedance Analyser Hewlett Packard N° 4194 A. The two resonators appear in parallele and the read impedance has to be multiplied by two . The impedance, at the natural tuning 600 KHz is near 500 Ω , and the tune is possible at 10 MHz with 40 Amperes in the 4 bias windings. The impedance decreases at 300 Ω at 2,5 MHz and 230 Ω at 10 MHz (fig. 5).

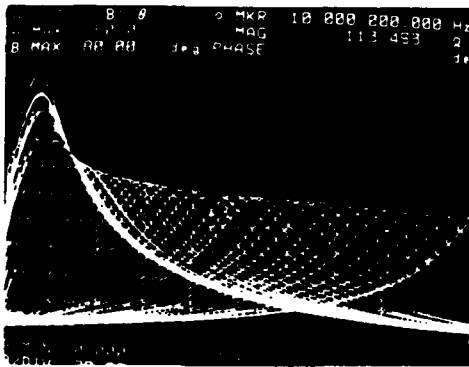


Fig. 5 - Tuning and impedance

2°) - Voltage : the 4 kV peak needed by the Mimas operation was reached on this alone gap, in the used range. Some small parasitic resonances (2 dB losses), due to the coupling loop and bias windings are now in correction.

To obtain this voltage, only an 300 Ω impedance is necessary with the used amplifiers. It can be obtain out of the tune of cavity. Like that, it is not necessary to load the structure with VAC up to

150 KHz tuning. The large ΔF (the low Q) permits to decrease the frequency without excessive impedance losses.

Like that, the frequency dynamic of the load in our configuration, is greater than 20 with 300 Ω impedance, an than 100 with 230 Ω .

3°) Cooling : the Mimas frequency range and voltage program, in operation configuration and at 1 Herz of repetition rate, gave an temperature elevation of 2° C. on the external face of Vitrovac.

V. CONCLUSION

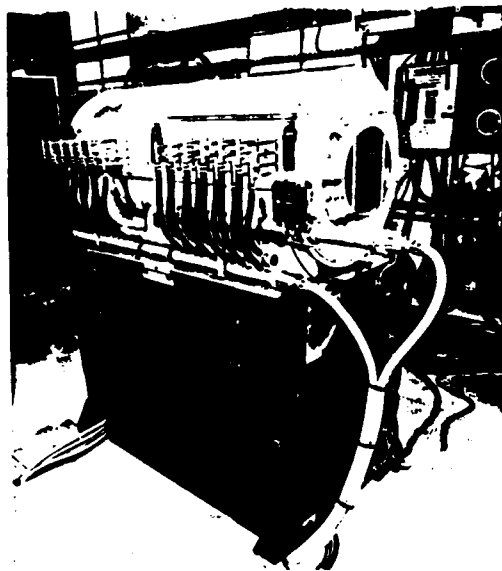
The initial goal is touched : it is possible to replace the two old Mimas cavities by one, and use the free place for other operation. The last work on the model is to put the vacuum chamber inside the cavity internal pipe, and connect the accelerating alumina gap, if the decision to make free the space on Mimas is taken.

This work will be continued by and for new needs.

An european collaboration, between German, Italian and French Laboratories, Universities and Industries is today in study, in order to sum the different "know-how" and capabilities to the same goals.

Two european synchrotron projects will try o use the gain given by this kind of materials, and extend their use at higher frequencies.

This technic can be used today on several existing accelerators.



VI. REFERENCES

- (1) C. Fougeron. P. Guidée. K.C. N'Guyen.
RF System of SATURNE II - IEEE PAC
SAN FRANCISCO 1979 -
- (2) A. Susini.
Low Frequency Ferrite Cavities - Proc.
EPAC - ROME 1988 -
- (3) G. Herzer, H.R. Hilzinger.
Industrial Application of Metallic Glass
Ribbon - Symposium on Amorphous
Metal - BENALMADENA 1987 -
- (4) C. Fougeron. P. Ausset. J. Peyromaure.
Toward the Construction of an Ultra
Short Cavity for an Heavy-Ion
Synchrotron - Proc. EPAC - NICE 1990 -
- (5) C. Fougeron. G. Clerc. M. Langlois.
M. Tardy (Thomson TE)
RF Accelerating Cavity for Cosy.
Low Energy Accelerator Conference -
PADOVA 1992 -
- (6) Istituto Nazionale de Fisica Nucleare
The Adria Project - PADOVA 1992 -
- (7) A. Schnase. H. Halling. H. Meuth
A Digital Synthetiser and Phase
Control System for Acceleration in
Cosy - IEE - PAC - BERLIN 1992 -
- (8) Internal Report -
Compte-rendu de Réunion -
R et D Composants Magnétiques -
LNS - Saclay - 1993 -
- (9) S. Ninomiya
Conceptual Design of Non Resonant
Accelerating System -
KEK Report 1992 -

Fundamental Mode Detuned Travelling Wave Accelerating Structure

J. Gao

Laboratoire de L'Accélérateur Linéaire, IN2P3-CNRS
et Université de Paris-Sud, 91405 Orsay cedex, France

Abstract

In this paper detuning method for the suppression of the long range wakefields in a linear accelerator structure has been investigated theoretically. A novel travelling wave accelerating structure with its accelerating field phase velocity oscillating around the velocity of light along the structure has been proposed in order to suppress the long range longitudinal accelerating mode wakefield. By detuning also the frequencies of the deflecting modes, the longitudinal and transverse long range wakefields can be suppressed at the same time, which is preferable when a train of bunches is to be accelerated.

I INTRODUCTION

In the design of the next generation TeV e^+e^- Linear Colliders (TLC) the wake field induced instability is one of the main concerns. In this paper we concentrate only on the suppression of the long range wakefields which will influence the following beam bunches. In section 2 aiming at suppressing at the same time longitudinal and transverse wakefields, a novel accelerating structure with the phase velocity of the accelerating field oscillating around the velocity of light along the structure has been proposed. In section 3 some discussions are made concerning practical structure designs. The numerical simulation results demonstrate the feasibility of this novel structure.

II THEORY

To start the discussion we consider an uniform structure (so-called constant impedance structure) and one of its passbands. This passband can be the fundamental or any other higher order one. The dispersion relation of this passband is approximated by

$$\omega^2 = \omega_0^2(1 - k \cos \phi) \quad (1)$$

where ϕ is the phase shift between adjacent cavities at angular frequency ω , ω_0 is the midband angular frequency corresponding to $\phi = \pi/2$ and k is the coupling coefficient which can be calculated analytically [1] or numerically if the structure dimension is given. Eq. 1 can be simplified as

$$\omega = \omega_0 - \Delta\omega \cos \phi \quad (2)$$

where $\Delta\omega$ is half the angular frequency bandwidth of this passband.

When a particle with charge Q is going through this structure with $v = c$, the wake potential produced per

period in this passband is [2]

$$W = 2k_w e^{i(\omega_0 - \Delta\omega \cos \phi) \frac{z}{c}} / (1 - \frac{v_g^*}{c} \sin \phi) \quad (3)$$

where W takes the real or imaginary part of the complex number depending on longitudinal or transverse wake potential with k_w being the loss factor or kick factor correspondingly, and v_g^* is the group velocity at the midband. The physical meaning of eq. 3 is that the structure starts right at the beginning to oscillate at the synchronous frequency $\omega(\phi)$. Now we modulate the frequency ω_0 in eq. 3 over N cells without changing the passband width $\Delta\omega$. ω_0 is replaced by

$$\omega_0 + \delta\omega \cos(\frac{2\pi}{N} m) \quad (4)$$

where m is the m th cell with the same start point as N . The average of W over these N cells is

$$\langle W \rangle = \frac{1}{N} \sum_{m=1}^N \frac{2k_w e^{i(\omega_0 + \delta\omega \cos(2\pi m/N) - \Delta\omega \cos \phi) \frac{z}{c}}}{(1 - \frac{v_g^*}{c} \sin \phi)} \quad (5)$$

If N is large and ϕ keeps an almost constant value, eq. 5 can be replaced by an integral as follows:

$$\begin{aligned} \langle W \rangle &= \frac{\int_{-\pi}^{\pi} 2k_w e^{i(\omega_0 + \delta\omega \cos \Phi - \Delta\omega \cos \phi) \frac{z}{c}} d\Phi}{2\pi(1 - \frac{v_g^*}{c} \sin \phi)} \\ &= \frac{1}{(1 - \frac{v_g^*}{c} \sin \phi)} 2k_w e^{i(\omega_0 - \Delta\omega \cos \phi) \frac{z}{c}} J_0(\delta\omega \frac{s}{c}) \end{aligned} \quad (6)$$

The amplitude of the wake potential is modulated by $J_0(\delta\omega s/c)$ and there exist a series of zero amplitude at

$$s_{ni} = u_{0i} c / \delta\omega \quad (i = 1, 2, 3 \dots) \quad (7)$$

where s_{ni} are the locations where a test particle does not suffer wakefield of the n th mode, and u_{0i} is the i th root of the zero order Bessel function. Of course, more complicated modulation is possible as shown in ref. [3].

The discussions made above are quite general since the passband can be anyone of those of a travelling wave structure. To suppress the longitudinal wakefield of the fundamental mode, therefore, the frequency at which the wakefield is produced should be detuned along the accelerating structure as shown in Fig. 1.

We assume

$$\omega_w = \omega_{w0} + \delta\omega \sin(Kz) \quad (8)$$

where ω_w is the wakefield angular frequency, $K = 2\pi/L$ and L is the modulation period along the structure. Since

then

$$|\delta\omega| \leq \left| \frac{2\pi D_0 \Delta\omega \sin\theta_0}{L} \right| \quad (28)$$

Once the half passband width $\Delta\omega$ (related to the designed average group velocity $\langle v_g \rangle$) and θ_0 are determined, the maximum frequency modulation amplitude $\delta\omega$ can be known from eq. 28. It is natural to assume that the distance between two adjacent bunches is

$$d = \frac{u_{01}c}{|\delta\omega|} \quad (29)$$

where the amplitude of the wake potential of the exciting particle is zero. If the rf pulse length is τ_{rf} the maximum number of acceptable bunches in this rf pulse is

$$N_b = \frac{|\delta\omega|\tau_{rf}}{u_{01}} \quad (30)$$

The larger the absolute value of $\delta\omega$ is, the greater the number of the bunches in a given rf pulse can be.

III DISCUSSION

In the following we will give a concrete example of the fundamental mode detuned structure shown in Fig. 2 (S-band). It is seen that there are two stop-bands at $\pi/4$

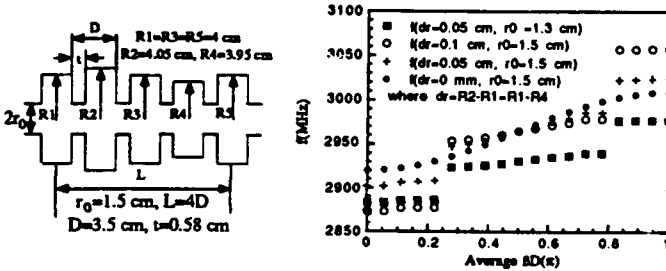


Figure 2: Fundamental mode detuned structure and its dispersion curves

mode and $3\pi/4$ mode, respectively. For a given r_0 the group velocity at $2\pi/3$ mode decreases with increasing cavity outer radius modulation dr . For the case of $r_0 = 1.5\text{cm}$ and $dr = 0.05\text{cm}$, the group velocity v_g/c at $2\pi/3$ mode is about 0.02. The standing wave electric field distribution of 18 cavities at $2\pi/3$ mode is shown in Fig. 3 calculated by using PRIAM [6]. It is obvious that there is

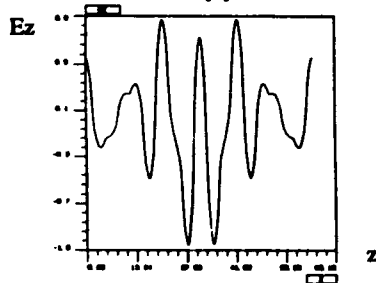


Figure 3: Standing wave pattern of 18 cavities

no attenuation. It is found that the shunt impedance of the synchronous travelling wave is about $30\text{ M}\Omega/\text{m}$ with $Q = 13596$ ($r_0 = 1.5\text{cm}$ and $dr = 0.05\text{cm}$). Since this example uses electric coupling, the iris radius has to be very

large to avoid the attenuation of the travelling wave, and this large iris radius reduces the shunt impedance greatly. In practice, however, one can increase the shunt impedance by using the backward wave structure where the iris radius can be made smaller. The effect of the fundamental mode detuning is checked by using TBCI, and the result is shown in Fig. 4 where the length of the exciting bunch has been

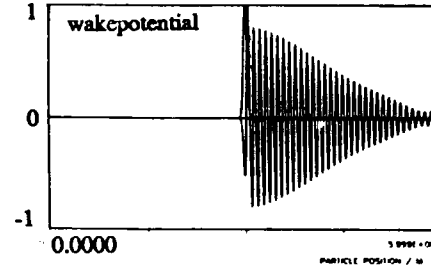


Figure 4: Fundamental wakefield

chosen very long in order to excite only the fundamental mode. The dipole mode wake potentials (longitudinal, radial and azimuthal potentials in the same picture) of this structure are also calculated and shown in Fig. 5. In Fig. 4

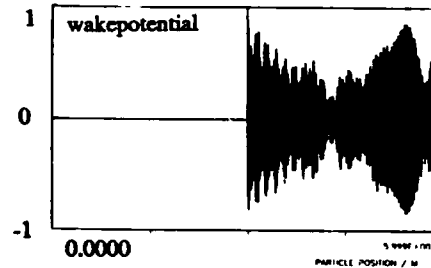


Figure 5: Dipole wakefields

one can see that the first minimum of the wake potential appears at about the 30th wavelength of fundamental accelerating mode after the exciting bunch. The results from PRIAM and TBCI demonstrate the feasibility of this novel accelerating structure.

IV ACKNOWLEDGEMENTS

The author appreciates discussions with J. Le Duff, T. Garvey and G. Bienvu.

V REFERENCES

- [1] J. Gao, Nucl. Instr. and Method, A311 (1992), pp. 437-443.
- [2] B. Epsztin and J.P. Mangin, Proceedings of the Linear Accelerator Conference, 1966, p. 332.
- [3] J. Gao, LAL/RT 91-13. Presented at LC92 Linear collider workshop, Garmitzsch, Germany, July, 1992.
- [4] H. Deruyter, et.al., Proceedings of the 1990 Linear Accelerator Conf., Albuquerque, U.S.A., P. 132, 1990.
- [5] K.L.F. Bane and R. Gluckstern, SLAC-PUB-5783, March 1992.
- [6] G. Le Meur and F. Touz, Proc. of EPAC, June 12-16, 1990, Nice, France, p. 1693.

Demi-Disk Travelling Wave Accelerating Structure *

J. Gao

Laboratoire de L'Accélérateur Linéaire, IN2P3-CNRS
et Université de Paris-Sud, 91405 Orsay cedex, France

Abstract

The dark current in a normal disk-loaded accelerating structure is one of the main obstacles which limit the accelerating gradient going higher. In this paper a demi-disk accelerating structure is proposed in order to reduce the dark current. Its transverse rf focusing forces can reduce the effects of wakefields on the beam's emittance growth which is preferable in future linear colliders. 3D program PRIAM [1] has been used to calculate the field distributions and the dispersion curves of this structure. Estimations of the trajectories of the field emission electrons have been done.

I INTRODUCTION

The next generation TeV e^+e^- linear colliders require that the accelerating structures support high accelerating gradient in order to keep the machine within a reasonable scale. The fact that various beam property control methods, such as BNS damping [2], energy spread compensation [3] and fundamental mode detuning [4], lose acceleration efficiency emphasize also the importance of this requirement. It is found, however, that in a conventional axisymmetric disk-loaded accelerating structure, when the field level reaches certain value, appreciable electrons are emitted from the surface of the accelerating structure and some of them are captured by the travelling wave and accelerated continuously along the axis of the accelerating structure [5][6]. This captured electrons' flow is so-called dark current. The dark current has very wide energy spectrum and therefore produces lot of noises within detectors. On the other hand the dark current excites wakefields and takes precious rf power in the form of beam loading.

In this paper a demi-disk travelling wave accelerating structure is proposed aiming to reduce the dark current. In section 2 we will first look at the dark current in the case of conventional disk-loaded accelerating structures. In section 3 the demi-disk structure is investigated.

II CONVENTIONAL DISK-LOADED ACCELERATING STRUCTURE

In order to get some general ideas of the behaviour of the field emission electron in a conventional axisymmetric structure let's look at the longitudinal and the transverse motions of it.

*Part of this work was first presented at the LC92 linear collider workshop, Garmisch, Germany, July 25 - August 2, 1992.

The longitudinal electric field inside an axisymmetric disk-loaded structure is expressed as:

$$E_z(r, z, t) = E_z(r, z) \sin(\omega t - k_g z + \phi_0) \quad (1)$$

where $\omega = 2\pi f$, $k_g = 2\pi/\lambda_g$ is the fundamental wave number of this travelling wave structure and ϕ_0 is the initial emission phase of the field emission electron when it is emitted at $z = 0$ and $t = 0$. If only linear term is kept, the electric field near the axis can be expressed as:

$$E_z(r, z, t) = E_z(0, z) \sin(\omega t - k_g z + \phi_0) \quad (2)$$

In the following analytical treatment, $E_z(0, z)$ has been chosen to be a constant E_{z0} . From eq. 2 we have

$$\frac{d\gamma}{dz} = \frac{qE_{z0}}{m_0 c^2} \sin(\phi) \quad (3)$$

where

$$\phi = \omega t - k_g z + \phi_0 = k \int_0^z \left(\frac{\gamma}{(\gamma^2 - 1)^{1/2}} - 1 \right) dz + \phi_0 \quad (4)$$

where γ is the ratio between the electron's relativistic energy and the rest energy $m_0 c^2$, $k = 2\pi/\lambda$ and λ is the electromagnetic wavelength in free space. In eq. 4 k_g has been chosen equal to k (the phase velocity of this travelling wave $\beta_p = \omega/kc = 1$ through out this paper). When $\gamma \gg 1$, ϕ will be frozen at its asymptotic value [7]

$$\phi_f = \frac{1}{\alpha \sin(\phi_0 + \delta\phi)} + \phi_0 \quad (5)$$

$$\alpha = \frac{qE_{z0}}{m_0 c^2 k} \quad (6)$$

where $\delta\phi$ can be calculated from an empirical formula which is given as:

$$\delta\phi(\text{degree}) = 19E_{z0}^{-0.9} \quad (7)$$

where E_{z0} is in MV/cm. In fact it is found that $\delta\phi$ can be neglected if $\phi_0 > 60^\circ$. From eq. 3 and eq. 5 one can get the approximate expression of the final energy gain of longitudinally captured electrons with respect to the frozen phase and electron's longitudinal position z :

$$\Gamma_f = 1 + \alpha \sin(\phi_f) k z \quad (8)$$

In the following we will discuss the transverse motion of the field emission electron keeping the simplification of only using linear rf field terms. It is well known that the

transverse rf force acting on a particle with electric charge q travelling at velocity v_z is expressed as:

$$F_r = \frac{qrk}{2}(1 - \beta_p\beta_z)E_{z0}\cos(\omega t - kz + \phi_0) \quad (9)$$

where r is the transverse deviation from the axis and $\beta_z = v_z/c$. Assuming that an electron is emitted at $t = 0$ and $z = 0$ with $\beta_z = 0$ from the cavity wall, one can see from eq. 9 that the electron will be either focused or defocused depending on their initial emission phase ϕ_0 . When the field emission electrons's velocity approach that of light they will no longer feel the transverse rf force and some of them can be continuously accelerated near the axis along the structure as dark current if they are properly focused. Numerical simulation shows that at S-band (3GHz) when $E_{z0} = 30\text{MV/m}$ the field emitted electrons in a 60° phase interval centered around the rf peak ($\phi_0 = 90^\circ$) are captured and accelerated to the end of the accelerating structure [8]. It is obvious that this large capture phase interval should be reduced if one want to increase accelerating gradient without raising the working frequency.

III DEMI-DISK TRAVELLING WAVE ACCELERATING STRUCTURE

A rf properties

The proposed demi-disk accelerating structure is shown in Fig. 1. To compare with the SLAC type $2\pi/3$ mode structure, the same mode has been chosen for this demi-disk structure. The standing wave electric field pattern of $2\pi/3$ mode is shown in Fig. 2. The dispersion curves are shown in Fig. 3 where the radius of the iris has been changed. It is interesting to notice that the group velocity at π mode is not zero, and this is due to the fact that the structure has "quasi" $D/2$ periodicity. Fig. 4 shows the dependences of the group velocity v_g and the shunt impedance R on the iris radius r_0 . What should be pointed out are that the demi-disk structure has very large group velocity when the iris radius is small, and that when the iris radius is larger than some value the rf source might excite another mode which has the same resonant frequency as the desired working mode.

B beam dynamics

The motion of the electron moving inside this structure can be found out from the rf force near the axis just like

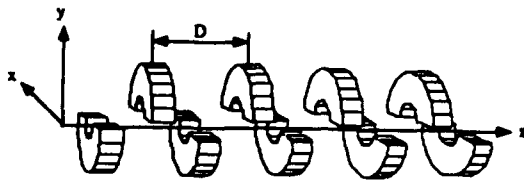


Figure 1: Demi-disk travelling wave structure

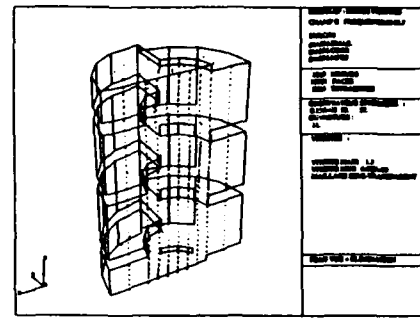


Figure 2: Electric field pattern of $2\pi/3$ mode

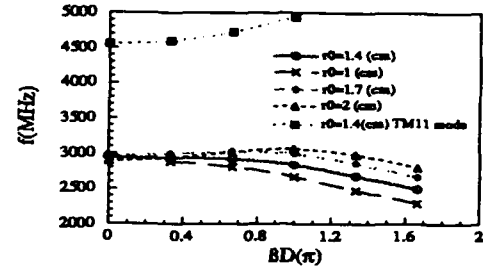


Figure 3: Dispersion curves

what has been done in the previous section. The longitudinal motion can be described by the same formulae derived for an axisymmetric structure. Now, we first look at the transverse motion of the electron in the vertical plane (symmetric plane, $x=0$). According to the numerical results of PRIAM we know that E_z , E_x and H_y can be expressed as:

$$E_z(x, y, z, t)|_{x=0, y=0} = E_{z0}\sin(\omega t - kz + \phi_0) \quad (10)$$

$$E_x(x, y, z, t)|_{y=0} = xK_e\cos(\omega t - kz + \phi_0) \quad (11)$$

$$E_y(x, y, z, t)|_{x=0, y=0} = E_{y0}\cos(\omega t - 2kz + \phi_0) \quad (12)$$

$$H_y(x, y, z, t)|_{y=0} = -xK_h\sin(\omega t - kz + \phi_0) \quad (13)$$

From $\nabla \cdot E = 0$

$$\frac{\partial E_x}{\partial x} + \frac{\partial E_y}{\partial y} + \frac{\partial E_z}{\partial z} = 0 \quad (14)$$

we get

$$\begin{aligned} E_y(x, y, z, t)|_{x=0} &= E_y(0, 0, z, t) - \int_0^y \left(\frac{\partial E_x}{\partial x} + \frac{\partial E_z}{\partial z} \right) dy \\ &= E_{y0}\cos(\omega t - 2kz + \phi_0) - yK_e\cos(\omega t - kz + \phi_0) \\ &\quad + ykE_{z0}\cos(\omega t - kz + \phi_0) \end{aligned} \quad (15)$$

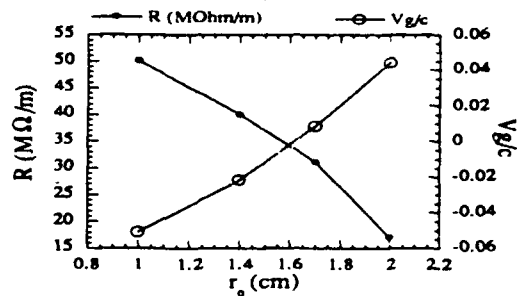


Figure 4: v_g/c and R vs r_0

From $\nabla \times H = \epsilon_0 \frac{\partial E}{\partial t}$, we have

$$\frac{\partial H_z}{\partial y} = \left(\frac{\partial H_y}{\partial x} - \epsilon_0 \frac{\partial E_z}{\partial t} \right) \quad (16)$$

$$\begin{aligned} H_x &= \int_0^y \left(\frac{\partial H_y}{\partial x} - \epsilon_0 \frac{\partial E_z}{\partial t} \right) dy \\ &= -yK_h \sin(\omega t - kz + \phi_0) \\ &\quad - y\epsilon_0 \omega E_{z0} \cos(\omega t - kz + \phi_0) \end{aligned} \quad (17)$$

where the constants E_{y0} , H_{y0} , K_e and K_h can be determined from the numerical results of PRIAM. We know from eq. 15 and eq. 17 that the transverse rf force acting on a particle can be expressed as:

$$\begin{aligned} F_y &= qE_{y0} \cos(\omega t - 2kz + \phi_0) \\ &\quad + qyk(1 - \beta_p \beta_z) E_{z0} \cos(\omega t - kz + \phi_0) \\ &\quad - qyK_e \cos(\omega t - kz + \phi_0) - qy\mu_0 v_z K_h \sin(\omega t - kz + \phi_0) \end{aligned} \quad (18)$$

As for the expression of the rf force in the horizontal plane ($y = 0$), similarly, we have

$$F_x = qxK_e \cos(\omega t - kz + \phi_0) + qx\mu_0 v_z K_h \sin(\omega t - kz + \phi_0) \quad (19)$$

For the accelerated electrons ($\gamma \gg 1$ and $\beta_z \approx 1$), by ignoring the first term in eq. 18 which doesn't synchronize with the electrons and using eq. 5, the transverse rf forces can be rewritten as:

$$F_y = -qyK_e \cos(\phi_f) - qy\mu_0 v_z K_h \sin(\phi_f) \quad (20)$$

$$F_x = qxK_e \cos(\phi_f) + qx\mu_0 v_z K_h \sin(\phi_f) \quad (21)$$

It is obvious that if in one plane it is focusing in another plane it will be defocusing. In order to have focusing for accelerated beam in both transverse planes, rotating the polarization of the demi-disks along the structure is necessary as shown in Fig. 5. The philosophy of this design is to deflect the low energy field emission electrons in each short uniform section as shown in Fig. 1, while keep focusing the accelerated beam in the whole accelerating structure against the transverse wakefields. In this paper attentions will be put to the motions of the field emission electrons in the uniform section only. Based on the linear rf force expressions in eq. 18 and eq. 19, field emission electrons' trajectories have been calculated and shown in Fig. 6 and Fig. 7. From these two figures it can be seen clearly that few electrons can be captured as dark current since in one transverse plane field emission electron is focused in another plane it will be defocused.

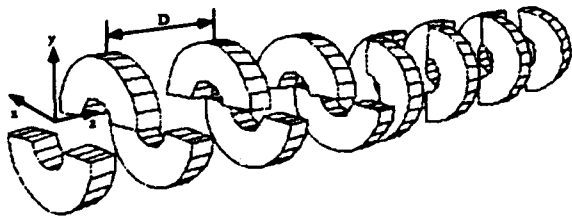


Figure 5: Demi-disk structure with rotating disks

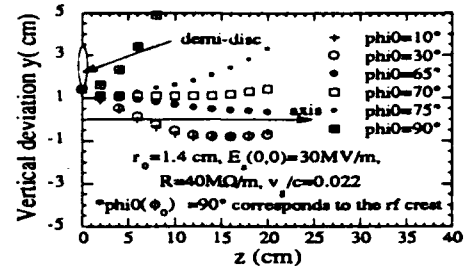


Figure 6: The trajectories of the field emission electrons in the vertical plane with different emission phase ϕ_0

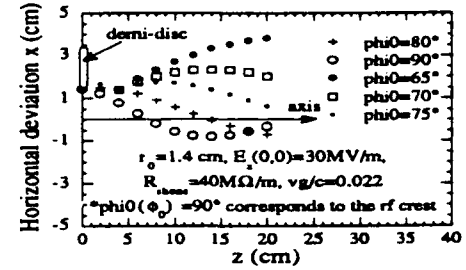


Figure 7: The trajectories of the field emission electrons in the horizontal plane with different emission phase ϕ_0

IV DISCUSSIONS

Even the demi-disk structure discussed above is proposed to reduce the dark current, it might have other applications such as rf wigglers and the positron generation linacs. What should be pointed out is that if it is used as a positron generation linac, the adjacent demi-disks should have 90° polarization difference in order to focus quickly the low energy positrons in both transverse planes.

V ACKNOWLEDGEMENTS

The author appreciates the helps of Y. Thiery, G. Le Meur and F. Touz during using PRIAM. He appreciates also the discussions with G. Bienvenu, P. Brunet, J. Le Duff, T. Garvey and A. Dovbnia.

VI REFERENCES

- [1] G. Le Meur and F. Touz, Proc. of EPAC, June 12-16, 1990, Nice, France, P. 1693.
- [2] V. Balakin, A. Novokhasky and V. Smirnov, Proceedings of the workshop on "Physics of linear colliders", Capri, June 13-17, 1988, p. 167.
- [3] R. D. Ruth, SLAC-PUB-4541, 1988.
- [4] J. Gao, "Fundamental mode detuning travelling wave accelerating structure", presented at LC92 linear collider workshop, Garmitisch, Germany, July 25 - August 2, 1992, in these proceedings.
- [5] G. Bienvenu, Proceedings of EPAC, June 7-11, 1988, Rome, Italy, P. 970.
- [6] G. Bienvenu and P. Brunet, Proceedings of EPAC, June 12-16, 1990, Nice, France, P. 934.
- [7] J. Gao, Proceedings of EPAC, Berlin, March 24-28, 1992, p. 584.
- [8] G. Bienvenu, P. Fernandes and R. Parodi, Nucl. Instr. and Methods, A320(1992) pp. 1-8.

Analytical Formulae for the Coupling Coefficient β between a Waveguide and a Travelling Wave Structure

J. Gao

Laboratoire de L'Accélérateur Linéaire, IN2P3-CNRS
et Université de Paris-Sud, Centre d'Orsay, F-91405 Orsay cedex, France

Abstract

Analytical formulae for the coupling coefficient β of a waveguide-travelling wave structure coupling system have been established and compared with experimental results. The dimension of the coupling aperture on the coupler cavity of a travelling wave structure can be determined easily. The relation between the coupling coefficient β and the other parameters, such as aperture dimension, wavelength, group velocity, wall thickness and coupler dimension, is explicitly revealed. These formulae include that for the case of a waveguide-single cavity coupling system which has been established in ref. [1].

I INTRODUCTION

During the construction of a linear accelerator structure the determination of the dimension of the coupling aperture on the coupler cavity wall is always made by experiments. Recently the three dimensional program MAFIA has been used to design the coupler of a travelling wave structure [2]. Based on Bethe theory [3], however, in this paper analytical formulae which can be used to determine the coupling aperture's dimension are established and compared with experimental result. These formulae apply also to the case of a waveguide coupled to a single standing wave cavity.

II BASIC THEORY

In a linear accelerator the electromagnetic energy is fed from a klystron through a waveguide to the accelerating structure. The coupling is effected by an aperture located on the common wall between the waveguide and one cavity, so-called coupler cavity, of the structure. If the linear dimension of this aperture is small compared with the wavelength, Bethe theory states that the aperture is equivalent to a combination of radiating electric and magnetic dipoles, whose dipole moments are proportional to the normal electric field and the tangential magnetic field of the incident wave, respectively [3]. If the aperture is small, static field solutions for the equivalent dipole moments

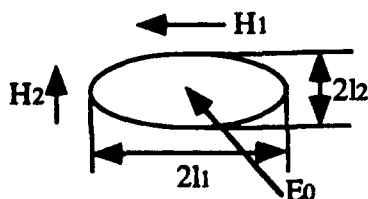


Figure 1: Coupling aperture

of elliptic- and circular-shaped apertures can be found by placing these kind of apertures in static electric and magnetic fields [4].

$$P = -\frac{\pi l_1^3 (1 - e_0^2)}{3E(e_0)} \epsilon E_0 \quad (1)$$

$$M_1 = \frac{\pi l_1^3 e_0^2}{3(K(e_0) - E(e_0))} H_1 \quad (2)$$

$$M_2 = \frac{\pi l_2^3 e_0^2 (1 - e_0^2)}{3(E(e_0) - (1 - e_0^2)K(e_0))} H_2 \quad (3)$$

$$e_0 = (1 - l_2^2/l_1^2)^{1/2} \quad (4)$$

where ϵ is the permittivity of the vacuum. P and M_1 (M_2) are the electric and magnetic dipole moments, respectively. E_0 is the electric field perpendicular to the surface of the ellipse. H_1 and H_2 are the magnetic fields parallel to the major and minor axes of this ellipse. l_1 and l_2 are the lengths of the half-major and half-minor axes, respectively (see Fig. 1). $K(e_0)$ and $E(e_0)$ are complete elliptic integrals of the first and second kinds [5].

$$K(e_0) = \frac{\pi}{2} \left(1 + \left(\frac{1}{2}\right)^2 e_0^2 + \left(\frac{1 \cdot 3}{2 \cdot 4}\right)^2 e_0^4 + \left(\frac{1 \cdot 3 \cdot 5}{2 \cdot 4 \cdot 6}\right)^2 e_0^6 + \left(\frac{1 \cdot 3 \cdot 5 \cdot 7}{2 \cdot 4 \cdot 6 \cdot 8}\right)^2 e_0^8 + \dots \right) \quad (5)$$

$$E(e_0) = \frac{\pi}{2} \left(1 - \left(\frac{1}{2}\right)^2 e_0^2 - \left(\frac{1 \cdot 3}{2 \cdot 4}\right)^2 \frac{e_0^4}{3} - \left(\frac{1 \cdot 3 \cdot 5}{2 \cdot 4 \cdot 6}\right)^2 \frac{e_0^6}{5} - \left(\frac{1 \cdot 3 \cdot 5 \cdot 7}{2 \cdot 4 \cdot 6 \cdot 8}\right)^2 \frac{e_0^8}{7} - \dots \right) \quad (6)$$

For values of e_0 approaching unity,

$$K(e_0) = \ln(4 \frac{l_1}{l_2}) \quad (7)$$

$$E(e_0) = 1 \quad (8)$$

Obviously, for e_0 equal to zero, the aperture becomes circular with

$$P = -\frac{2}{3} l^3 \epsilon E_0 \quad (9)$$

$$M_1 = M_2 = \frac{4}{3} l^3 H_{1,2} \quad (10)$$

where $l = l_1 = l_2$. It should be mentioned that the apertures discussed above have no volumes, only elliptic surfaces, and that all the quantities used in this paper are in MKS units.

III CALCULATION OF THE COUPLING COEFFICIENT β

A waveguide-travelling wave structure coupling system can be equivalent to the case of a waveguide-coupler cavity coupling system where the coupler cavity is coupled to the rest of the travelling wave structure. The coupling coefficient β is defined as

$$\beta = \frac{P_e}{P_0 + P_t} \quad (11)$$

where P_e is the power lost in the matched load of the waveguide, P_0 is the power dissipated inside the coupler cavity and P_t is the power flow from the coupler cavity to the adjacent travelling wave structure. P_t can be also expressed as

$$P_t = \frac{U}{L} v_g \quad (12)$$

where U and L are the stored energy and the length of the coupler cavity, respectively, and v_g is the group velocity of the travelling wave structure. In terms of equivalent circuit, β can also be expressed as

$$\beta = \frac{Y_c}{n^2 G_0} \quad (13)$$

where Y_c is the admittance of the waveguide, G_0 is the equivalent resonant admittance of the cavity and n is the transform ratio of an ideal transformer. Throughout this paper we consider only the lowest propagation mode H_{10} in the waveguide. In terms of Power-Voltage definition,

$$Y_c = \frac{a(1 - (\frac{\lambda}{2a})^2)^{1/2}}{2Z_0 b} \quad (14)$$

$$G_0 = \frac{2(P_0 + P_t)}{V_0^2} \quad (15)$$

where a and b are the width and height of the waveguide, respectively, λ is the wavelength in free space, $Z_0 = 120\pi$ (Ohm) and V_0 is the equivalent voltage across the gap of the cavity. From the definition of an ideal transformer

$$\frac{1}{n} = \frac{V_1}{V_0} \quad (16)$$

where V_1 is the equivalent voltage induced in the waveguide by means of the coupling aperture.

If the coupling aperture is located where there is only magnetic field as shown in Fig. 2, the coupling of energy is

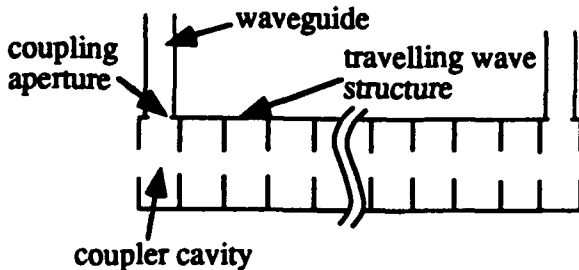


Figure 2: Magnetic coupling

performed by M_1 or M_2 . The H_1 and H_2 in eq. 2 and eq. 3 are the magnetic fields on the wall of the cavity when the aperture is replaced by a metal surface, that is to say H_1 or H_2 can be calculated by a 2-D program such as Superfish if the cavity is cylindrically symmetric. According to the theory stated in ref. [4], if compared with the size of the aperture the cavity wall can be considered as plane rather than bent, the amplitude of the H_{10} mode magnetic field H_0 induced in the waveguide by the equivalent magnetic dipole moment of the aperture is expressed as

$$H_0 = j\omega\mu_0 h_{10}^2 M_{1,2} \quad (17)$$

where

$$h_{10} = \Gamma_{10} \left(\frac{2}{j a b k_0 Z_0 \Gamma_{10}} \right)^{1/2} \sin\left(\frac{\pi x}{a}\right) \quad (18)$$

$$k_0 = \frac{2\pi}{\lambda} \quad (19)$$

$$\Gamma_{10} = j k_0 \left(1 - \left(\frac{\lambda}{2a} \right)^2 \right)^{1/2} = j k_{10} \quad (20)$$

The equivalent voltage V_1 induced in the waveguide could be expressed as

$$V_1 = E_0 b = \frac{Z_0 k_0}{k_{10}} H_0 b \quad (21)$$

where E_0 is the electric field of H_{10} mode. If the coupling aperture is located at the center of the waveguide cross section, that is to say $x = a/2$ in eq. 18, using all the equations in this section eq. 13 can be expressed as

$$\beta_1 = \frac{\pi^2 Z_0 k_0 k_{10} e_0^4 l_1^6}{9 a b (K(e_0) - E(e_0))^2} \frac{H_1^2}{P_0 + P_t} \quad (22)$$

or

$$\beta_2 = \frac{\pi^2 Z_0 k_0 k_{10} e_0^4 (1 - e_0^2)^2 l_1^6}{9 a b (E(e_0) - (1 - e_0^2) K(e_0))^2} \frac{H_2^2}{P_0 + P_t} \quad (23)$$

where β_1 and β_2 correspond to M_1 and M_2 , respectively. It should be noticed that eq. 22 and eq. 23 do not include the effect of the wall thickness of the coupling aperture. Practically, however, it is necessary to take this effect into account. It is natural to imagine that the cavity is connected with the waveguide by a small section of cylindrical or rectangular waveguide with corresponding cutoff wavelength λ_c depending on the shape of coupling aperture. If the thickness of the coupling aperture is d , the electromagnetic power after passing through this aperture will be reduced by a factor $e^{-2\alpha d}$ where

$$\alpha = k_0 \left(\left(\frac{\lambda}{\lambda_c} \right)^2 - 1 \right)^{1/2} \quad (24)$$

where $\lambda \geq \lambda_c$. By joining this factor to the right side of eq. 22 and eq. 23, the final analytical formulae of β are established as

$$\beta_1 = \frac{\pi^2 Z_0 k_0 k_{10} e_0^4 l_1^6 e^{-2\alpha d}}{9 a b (K(e_0) - E(e_0))^2} \frac{H_1^2}{P_0 + \frac{U}{L} v_g} \quad (25)$$

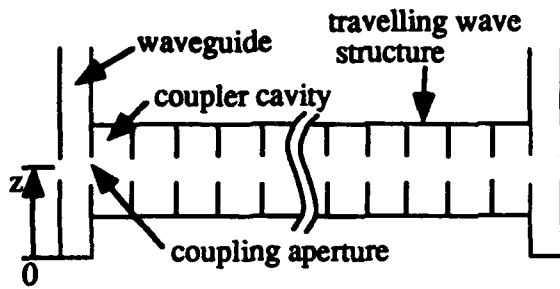


Figure 3: Electric coupling

or

$$\beta_2 = \frac{\pi^2 Z_0 k_0 k_{10} e_0^4 (1 - e_0^2)^2 l_1^6 e^{-2\alpha d}}{9ab(E(e_0) - (1 - e_0^2)K(e_0))^2 P_0 + \frac{U}{L} v_g} \frac{H_2^2}{P_0} \quad (26)$$

where the α in eq. 25 and eq. 26 may not be same. For a cylindrical symmetric coupler cavity the cavity parameters $\frac{H_1^2}{P_0}$, $\frac{H_2^2}{P_0}$, $\frac{H_3^2}{U}$ and $\frac{H_4^2}{U}$, can be calculated by Superfish and for a cylindrically asymmetric cavity three-dimensional program such as MAFIA or PRIAM have to be used. Right now, once the group velocity and the aperture dimension are given one can directly calculate the coupling coefficient β .

If the coupling is effected by electric field as in the case shown in Fig. 3, the coupling coefficient β is found to be

$$\beta = \frac{\pi^2 k_0^3 (1 - e_0^2)^2 l_1^6 e^{-2\alpha d} \sin^2(\lambda_g z)}{9ab Z_0 k_{10} E(e_0)^2} \frac{E_0^2}{P_0 + \frac{U}{L} v_g} \quad (27)$$

where E_0 is the electric field on the surface of the aperture before it is opened, λ_g is the wavelength in the waveguide (H_{10} mode) and z is the distance from the end of the waveguide to the center of the coupling aperture.

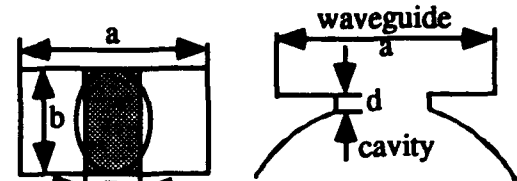
It is obvious that when the group velocity $v_g = 0$ the formulae derived above correspond to the case of waveguide-single cavity coupling system [1].

IV COMPARISON WITH EXPERIMENTAL RESULT

In this section we will compare the analytical result with that of an experiment. We take the output coupler of LIL accelerating structure (which is used as injector for LEP at CERN) as an example. The coupler cavity parameters are listed in Table 1. The rectangular coupling aperture is equivalent to an elliptic one as shown in Fig. 4. The rectangular aperture can be regarded as a section of waveguide of length d working at H_{01} mode with cut-off wavelength $\lambda_c = 2B$, where the wall thickness d is shown in Fig. 4. Fig. 5 shows the comparison between the experimental result and that analytically obtained from eq. 26.

Table 1: Parameters of LIL output coupler cavity

U(J)	L(cm)	c/v_g	P_0 (W)	H_2 (A/m)	d(cm)
0.00107	3.4	147	1375	3420	0.27



$$S_{rect.} = Bb = S_{ellip.} = \pi l_1 l_2, \quad a = 7.2 \text{ cm}, \quad b = 3.4 \text{ cm}$$

Figure 4: Coupling aperture of LIL structure

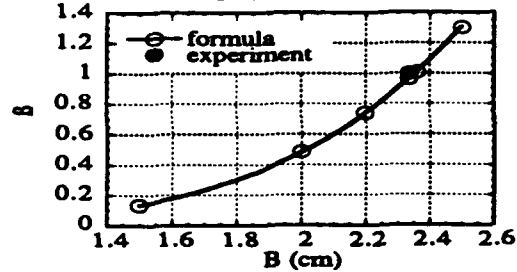


Figure 5: Comparison between analytical and experimental results

V OTHER APPLICATIONS

Another important application of these analytical formulae is to estimate the loaded Q of higher order modes in a damped structure (either a travelling wave structure or a single cavity) when a waveguide is connected to the structure to take out the power of higher order modes [6]

$$Q_L = \frac{Q_0}{1 + \beta} \quad (28)$$

where the dimension of the waveguide should be chosen as that the frequency of the accelerating mode is below the cut-off frequency of H_{10} mode in the waveguide.

VI ACKNOWLEDGEMENTS

I appreciate the help of P. Brunet and G. Bienvenu for providing LIL experimental results. I thank also J. Le Duff for his carefully reading the manuscript and valuable remarks.

VII REFERENCES

- [1] J. Gao, "Analytical formula for the coupling coefficient β of a cavity-waveguide coupling system", Nucl. Instr. and Meth., A309 (1991) p. 5.
- [2] H. Hanaki, "Computer design of coupler cavity for a travelling wave type buncher", EPAC92, Vol. 2, p. 910.
- [3] H. A. Bethe, "Theory of Diffraction by Small Holes", Phys. Rev., Vol. 66, PP. 163-182, 1944.
- [4] R. E. Collin, "Field Theory of Guided Waves", pp. 285-307, McGraw-Hill Book Company, 1960.
- [5] S. M. Selby et al., "Handbook of Mathematical Tables", Chemical Rubber Publishing Company, Ohio, 1962.
- [6] J. Gao, "Absorption of higher order modes in rf cavities via waveguides", submitted to the Workshop on Microwave-Absorbing Materials for Accelerators, Feb. 22-24, 1993, CE-BAF, Virginia, USA.

Automated Bead-Positioning System For Measuring Impedances of R-F Cavity Modes*

D.A. Goldberg and R.A. Rimmer,
Lawrence Berkeley Laboratory
Berkeley, CA 94720

Abstract

We describe a fully automated bead puller system which uses stepping motors to position the bead, and an HP-8510 network analyzer to measure the resulting frequency shifts, both devices being under computer control. Longitudinal motion of the bead is used for measurement of cavity shunt impedance. In addition, azimuthal scans at fixed longitudinal position aid in determining the multipole character of higher-order modes. High sensitivity/accuracy is made possible by measuring phase shifts at the unperturbed resonant frequencies (rather than frequency shifts themselves), thereby permitting averaging factors of > 500 with only modest increases in data acquisition time. Sample measurements will be presented. A comprehensive analysis of the experimental results is presented in an accompanying paper [1].

I. INTRODUCTION

The longitudinal and transverse kicks which a beam of particles experiences, due to either externally imposed or self-generated fields, upon passing through any device in the accelerator can be parametrized in terms of the respective shunt impedances of that device [2]. Those impedances can be represented as integrals along the beam path involving the longitudinal or transverse fields. One of the most com-

mon methods for measuring the fields in a resonant device such as an R-F cavity is to make use of the fact that the introduction of a small perturbing object causes a shift in the resonant frequency which is proportional to the square of the local field [3]. Hence by moving such an object, frequently referred to generically as a "bead," along, say, the axis of the device, and measuring frequency shift as a function of position, one can determine the field values for the integrand of the impedance integral. Furthermore, by measuring the (longitudinal) impedance along a series of transversely displaced paths, we can, through the use of the Panofsky-Wenzel Theorem, determine the transverse shunt impedance as well [2,4].

II. DESCRIPTION OF APPARATUS

Figure 1 shows the bead puller together with a device under test, in this case the model B-Factor cavity described in Ref. 2. The test bead is mounted on a thin Kevlar string which runs longitudinally through the cavity. For most of our measurements, our "bead" consisted of a .040 in. diameter, 1 in. long stainless steel needle, which is almost exclusively sensitive to the longitudinal electric field. However, because analytic expressions for the form factors necessary to convert frequency shift to field strength are only derivable for a limited number of bead shapes (cylinders are

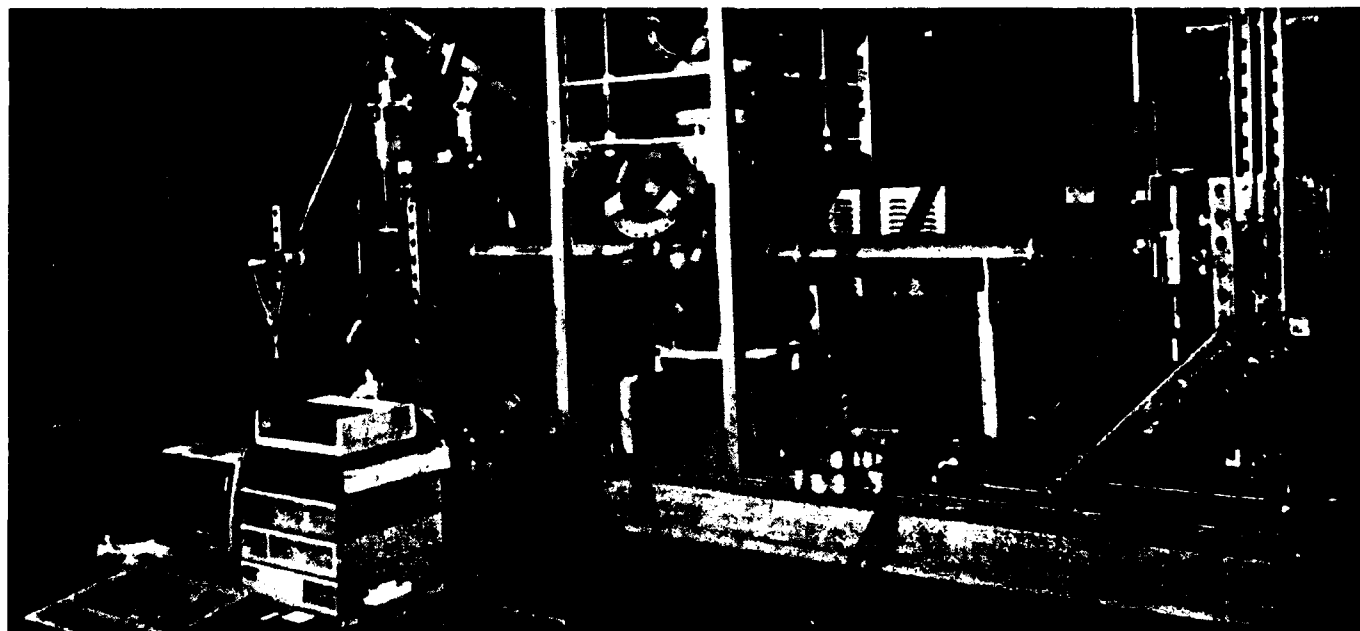


Fig.1 Bead Puller and Model B-Factor Cavity

* Work supported by Director of Office of Energy Research,
U.S.D.O.E., under Contract DE-AC03-76SF00098

not among such shapes; small spheres are), it was necessary to "calibrate" the needle. This was done by first measuring the field in the TM_{010} mode (which is known to be almost perfectly longitudinal on the cavity axis) with a .375" diameter spherical alumina (99.5% purity) bead, remeasuring it with the needle, and normalizing the latter data to the former.

The needle was mounted on a .018" dia. Kevlar string; the bead, on a .023" one. In addition to its high tensile strength (50 lbs. for the former string, 80 lbs for the latter), Kevlar has the added advantage that after it is "run in" by making three or four full-length traverses, it shows negligible further elongation.

Positioning of the bead is accomplished by means of a set of Lintech TWIN RAIL[®] tables which are driven by Compumotor SX 57-102 stepping motors under the control of Model SX programmable controllers. The Lintech tables use an Acme thread lead screw so that in the event of loss of stepping motor power, even the vertically mounted tables retain their position.

Longitudinal (z-)motion is controlled by the long table shown at the far (left hand) end of the cavity; the geometry is shown schematically in Fig. 2. The total table travel is roughly 60 cm, but this can be multiplied with the use of a block and tackle arrangement; the present setup employs a multiplication factor of three, making it possible to measure devices nearly two meters long. Use of an 8 lb. counterweight is sufficient to maintain the vertical position of a bead of mass up to 7 gm. to within 1 mm over its entire distance of travel.

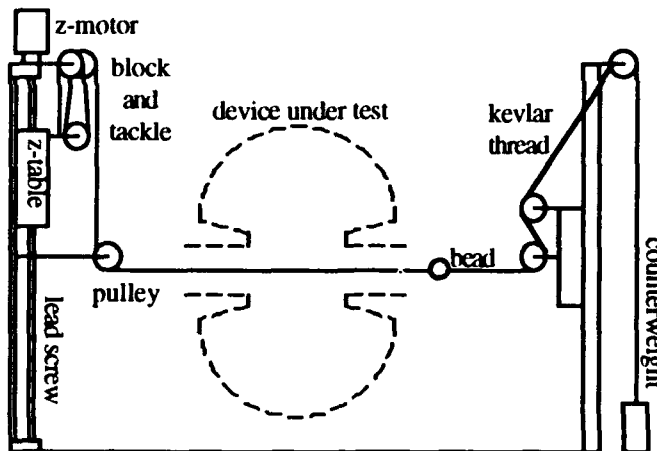


Fig. 2. Schematic Representation of Longitudinal Drive

Transverse bead position is determined by a pair of x,y tables at either end of the apparatus, on one of which the z-drive (table and pulleys) is mounted (see Fig. 1). Both x-table motors are driven by a common controller, as are both y-table motors. The range of travel in both transverse planes is ± 8 cm. Each set of tables is mounted on its own modular frame; in the present experiment, both table frames are mounted on a common bed which also supports the cavity. However, the modular construction also permits transporting the apparatus to measure cavities "in the field" or on their own support stands.

The table motion and controller settings can be directed from a Hewlett-Packard (HP) 216 computer via an RS-232 serial link. (A hand controller can also be used to adjust

table position.) The same computer is also used to control (via the GP-IB) the frequency measurements, as well as to compute the beam impedances from the measurement data.

Measurement of the (shift of the) cavity resonant frequency is done using an HP 8510 network analyzer. In the present setup, we employ two probes, one to excite the cavity, and one to detect the excitation, and determine the resonant frequency from S_{21} . For high-Q modes, one can measure frequency shifts directly. However, for low-Q modes it is much more advantageous to measure the phase shifts at the unperturbed resonant frequency.

A similar measurement technique has been recently reported by the Chalk River group in their measurements of the longitudinal fields of the accelerating modes of RF cavities and RFQ's [5]. Our method differs from theirs in several significant ways. First, instead of measuring "on the fly," we bring the probe to a stop during the measurement, which permits signal averaging at each point,¹ thereby making possible accurate determination of phase shifts as small as even a few tenths of a degree. Secondly, use of the HP 8510 analyzer in the single-frequency (CW) mode makes it possible to use an averaging factor of up to 128 at as little as 1 second per point, or as high as 4096, at less than 2 sec per point, enabling us to do a 100 point scan in less than two minutes.² In addition, the 3-dimensional motion capability permits us to do not only transverse scans (for measuring transverse impedance), but to take angular distributions to facilitate mode identification.

III. RESULTS AND ANALYSIS

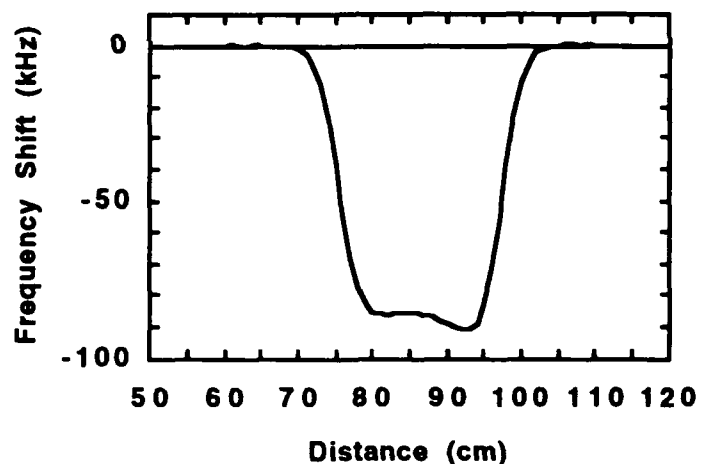


Fig. 3 Frequency shift vs position for fundamental mode of the B-factory model cavity.

Results of the frequency measurements of the fundamental mode are shown in Fig. 3., where we have plotted the

¹Signal averaging is essential for measuring the fields of the strongly damped modes, as well as for accurately determining the small transverse gradients of the longitudinal modes.

²There is also a 2-3 minute measuring "overhead" which includes a recording of the full spectrum at the start and end of each run, as well as a one-half second settling time between the end of the bead movement and the start of the measurement.

frequency shift, proportional to the *square* of the electric field, as a function of longitudinal position. The larger distances correspond to the side of the cavity containing the higher-order mode (HOM) dampers; the longitudinal asymmetry introduced by the dampers is clearly evident.

To compensate for possible short-term temperature drifts, we measure the phase shift at a field-free point at the start and end of the scan, record the times of these measurements as well as the times at which the first and last points of the actual scan are taken, and assume a linear variation; the data in Figs. 3 and 4 reflect this drift correction. Despite being deliberately overcoupled to the input waveguide, the cavity still has a relatively high Q of roughly 1800, so that a relatively modest averaging factor of 256 sufficed. We note that there appears to be a difficulty in reproducing the measured value of RT^2/Q to better than $\pm 1-2\%$ which appears to be unrelated to the signal-to-noise problem which averaging addresses, and presents a problem in measuring the transverse gradients needed to obtain the transverse impedances. The present suspicion is that it is due to short-term temperature fluctuations; the problem is being studied further.

RT^2/Q can be obtained from the dielectric bead data using

$$\frac{RT^2}{Q} = \frac{c^2}{\pi^2} \frac{\epsilon + 2}{\epsilon - 1} \frac{1}{f^2} \left[\int_{path} \sqrt{\Delta f} e^{ikz} dz \right]^2 \quad (1)$$

Eq. 1 has been adapted from Ref. 4; to evaluate the quantity in brackets one breaks the integral into sine and cosine parts, then squares and sums the two parts. As stated above, we then repeated the measurements using the metal needle, set the "epsilon factor" equal to unity (it is 1.353 for the alumina bead), and replaced the c^2/π^2 with an empirical constant. Overall, including the epsilon factor, we find that the needle gives phase shifts roughly 50% greater than those obtained using the bead.

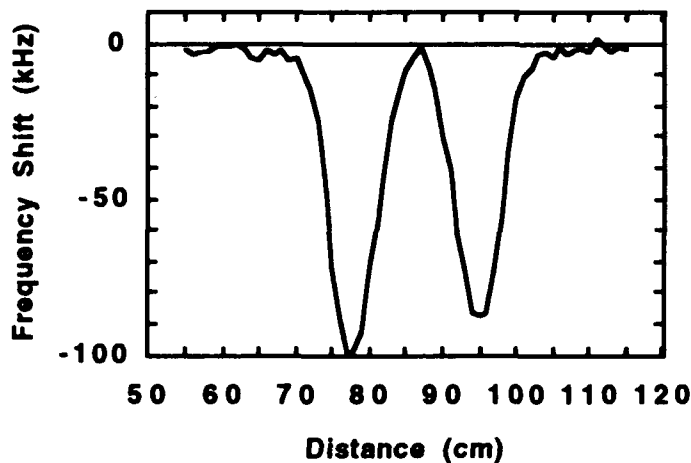


Fig. 4 Frequency shift vs position for TM_{011} mode of the B-factory model cavity.

The advantages of the HP 8510 in CW mode are clearly illustrated in the frequency measurements for the TM_{011} mode, shown in Fig. 4. This is one of the most troublesome HOM's in the undamped cavity, and the dampers' efficacy in reducing its Q -value by over three orders of magnitude to a value of 28 reduces the resulting perturbed phase shifts to a maximum value of 0.4 degrees! Nonetheless, by employing an averaging factor of 4096, we were able to obtain the data in Fig. 4 in less than two minutes.

IV. ACKNOWLEDGEMENTS

We would like to thank Jim Wise and Jim Smithwick for their able assistance in constructing the mechanical apparatus, Jim Hinkson for making available to us his coding for the Compumotor controller, and Greg Goebel of Hewlett-Packard for invaluable assistance in getting the RS-232 control working on the HP 216. This work was performed at the Lambertson Beam Electrodynamics Laboratory under the auspices of the Center for Beam Physics, and was supported by the Director of Office of Energy Research, U.S.D.O.E, under Contract DE-AC03-76SF00098

V. REFERENCES

- [1] R.A. Rimmer and D.A. Goldberg, "Measurements of Higher-Order Mode Damping in the PEP-II Low-Power Test Cavity," these proceedings.
- [2] see, e.g., D.A. Goldberg and G.R. Lambertson, "Dynamic Devices: A Primer on Pickups and Kickers" in *Physics of Particle Accelerators*, A.I.P. Conf. Proc. 249, p. 554 et seq., (1992).
- [3] L.C. Maier, Jr. and J.C. Slater, "Field Strength Measurements in Resonant Cavities," *J. Appl. Phys.* 23 (1952) pp.68-77
- [4] For a detailed description of the conversion of field data to impedance, see W. Barry and G.R. Lambertson, "Perturbation Method for the Measurement of Longitudinal and Transverse Beam Impedance," in *Proc. 1987 IEEE Particle Accelerator Conf.*, Vol. 3, pp. 1602-1604.
- [5] B.H. Smith, R.J. Burton, and R.M. Hutcheon, "High Speed Resonant Frequency Determination Applied to Field Mapping Using Perturbation Techniques," in *1992 Linac Conf. Proc.*, Vol. 2, pp. 468-470.

Measurements of Higher-Order Mode Damping in the PEP-II Low-Power Test Cavity

R. A. Rimmer and D. A. Goldberg*
Lawrence Berkeley Laboratory
1 Cyclotron Road, Berkeley, CA 94720, USA

Abstract

The paper describes the results of measurements of the Higher-Order Mode (HOM) spectrum of the low-power test model of the PEP-II RF cavity and the reduction in the Q's of the modes achieved by the addition of dedicated damping waveguides. All the longitudinal (monopole) and deflecting (dipole) modes below the beam pipe cut-off are identified by comparing their measured frequencies and field distributions with calculations using the URMEL code [1]. Field configurations were determined using a perturbation method with an automated bead positioning system [2]. The loaded Q's agree well with the calculated values reported previously, and the strongest HOMs are damped by more than three orders of magnitude. This is sufficient to reduce the coupled-bunch growth rates to within the capability of a reasonable feedback system. A high-power test cavity will now be built to validate the thermal design at the 150 kW nominal operating level, as described elsewhere at this conference [3].

I. INTRODUCTION

Impedances of higher order modes in the RF cavities can drive coupled-bunch instabilities in high-current storage rings. For the PEP-II B factory [4] we have taken the approach that the HOMs must be damped to a point where a practical broadband feedback system can control the coupled-bunch growth rates. At the same time it is important to maximize the fundamental-mode impedance of the cavities to make most efficient use of RF power and to minimize the number of cavities and RF stations. The R&D effort, shared among LBL, SLAC and LLNL, has produced a normal-conducting cavity design [5,6] which uses a trio of dedicated damping waveguides to reduce the HOM impedances. The target was to reduce the longitudinal impedances to the order of a few k Ω , and the transverse impedances to a few hundred k Ω /m (comparable with the effect of the resistive-wall). The single-bunch parameters are typical of existing machines and not in the regime where microwave instabilities would be expected.

As a result of the ongoing R&D program some of the lattice and RF parameters have changed compared with those given in references 4,5 and 6. All of the changes make the RF design more conservative. Table 1 shows the current PEP-II RF system parameters.

*This work was supported by the Director, Office of Energy Research, Office of High Energy and Nuclear Physics, High Energy Physics Division of the U.S. Department of Energy, under Contracts DE-AC03-76SF00098 and DE-AC03-76SF00515.

Table 1

PEP-II RF system parameters

(including the effect of the 5% gap in the beam)

PARAMETER	HER	LER
RF frequency (MHz)	476	476
Beam current (A)	1.03	2.25
Number of bunches	1658	≥ 1658
Number of cavities	20	10
Shunt Impedance R_s (M Ω) ^a	3.5	3.5
Gap Voltage (MV)	0.93	0.60
Accelerating gradient (MV/m)	4.1	2.7
Wall loss/cavity (kW)	122	51
Coupling factor without beam (β)	7.5	7.5
Unloaded Q of cavity ^b	≥ 30000	≥ 30000

^a $R_s = V^2/2P$

^b with ports, at 40°C

II. LOW-POWER TEST CAVITY

A low-power test cavity (LPTC) has been fabricated, see figure 1, which was designed to show the loading of the HOM Q's and, therefore, the impedance reduction that could be obtained with the waveguide damping scheme.

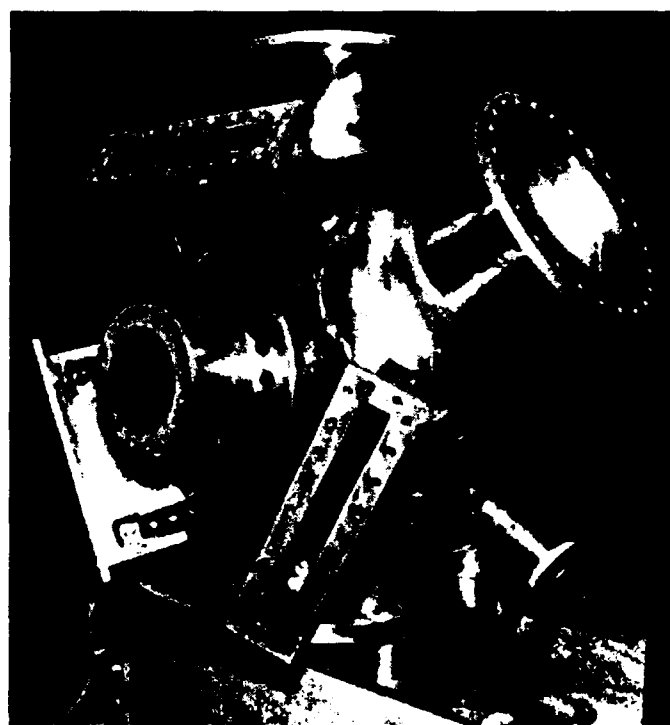


Figure 1. Low-power test cavity. The rectangular ports are for the HOM damping waveguides, the two large circular ports are alternative locations for a loop coupler.

To save cost, the quality of construction, though good, was not intended to show the ultimate Q of the fundamental mode that could be expected in the final cavities. Low-power mock-ups of the waveguide loads were made using ferrite powder in epoxy, cast into long tapered wedges. The load material was placed at the edges of the waveguides at least 36 inches from the cavity, as would be the case in a high-power design, to avoid coupling to the evanescent fundamental mode.

III. MEASUREMENTS

The cavity was excited with small electric-field antennas inserted into the beam pipes and a Hewlett-Packard 8510C network analyzer was used to measure the transmission response (S_{21}) between them. With all the apertures plugged or sealed, approximately flush with the cavity surface, the undamped modes of the cavity were seen as distinct peaks. The resonant frequencies were very close to those predicted by URMEL allowing easy identification of the modes.

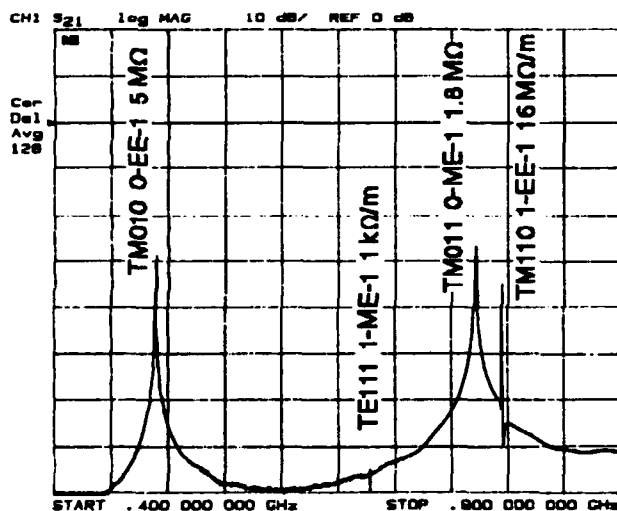


Figure 2. Fundamental mode and first three higher order modes in the LPTC without damping.

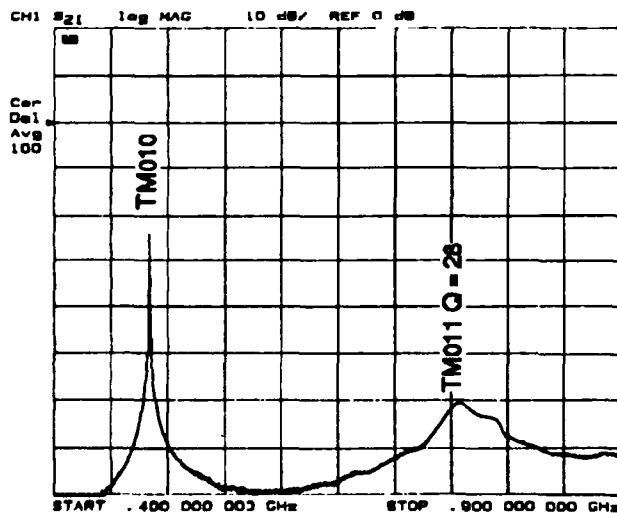


Figure 3. Fundamental mode and first higher order modes in the LPTC with three damping waveguides.

Figure 2 shows the spectrum of modes from below the fundamental (TM_{010}) mode up to 900 MHz without damping. The lowest TE mode (TE_{111} -like), is visible, as are the TM_{011} -like longitudinal mode (the strongest monopole HOM), at about 770 MHz, and the TM_{110} -like deflecting (dipole) mode, at about 795 MHz. Figure 3 shows the same frequency span with the three damping waveguides attached. The fundamental mode is still strong while the HOMs are substantially damped. By changing the azimuthal position of the probes around the edges of the beam-pipes it is possible to enhance or reject the dipole modes relative to the monopole modes, and thereby measure the loaded Q's of overlapping monopole and dipole modes. It is also possible to discriminate between the two orientations of the dipole modes when there is a strong perturbation to the cavity such as the addition of the loop coupler.

Figure 4 shows more of the HOMs, between 900 MHz and 1.4 GHz, without any damping. The monopole and dipole modes are labeled. Figure 5 shows the same span with the

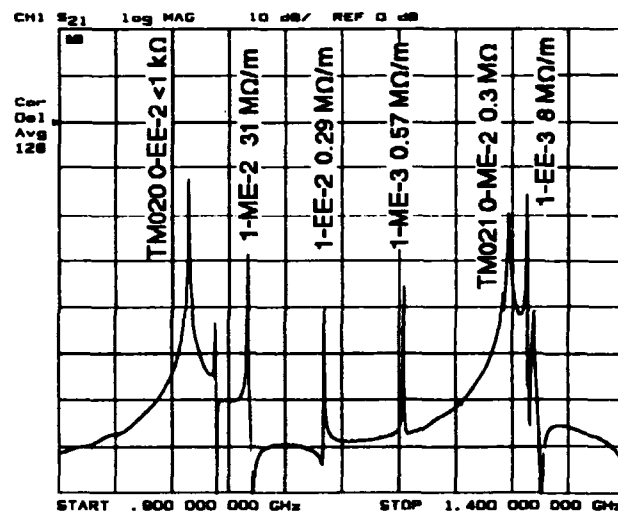


Figure 4. Higher order modes in the LPTC without damping, 0.9-1.4 GHz.

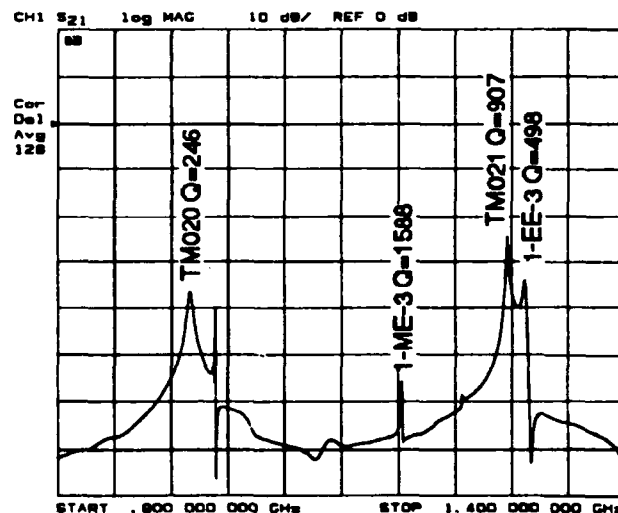


Figure 5. Higher order modes in the LPTC with three damping waveguides, 0.9-1.4 GHz.

three damping waveguides. Still visible are the TM₀₂₀-like monopole mode at about 1016 MHz, the TM₀₂₁-like mode at about 1296 MHz and the dipole mode at 1313 MHz. The residual impedances of these modes are within the capabilities of the feedback system. The results are similar for all the higher frequency HOMs up to the beam-pipe cut off. The residual impedances are shown in table 2 for the longitudinal modes and table 3 for the deflecting modes. A more detailed account of the results is available [7].

Table 2
Calculated and measured properties of longitudinal modes

Mode type	URMEL name	Calc F ₀ (MHz)	R/Q (Ω)	Meas F ₁ (MHz)	Meas Q _L	R/L (kΩ)
TM ₀₁₀	0-EE-1	489.6	108.8	484	*31926	3472
TM ₀₁₁	0-ME-1	769.8	44.97	758	28	1.26
TM ₀₂₀	0-EE-2	1015.4	0.006	1016	246	0.001
	0-EE-3	1291.0	7.68	no	longer	visible
TM ₀₂₁	0-ME-2	1295.6	6.57	1296	907	5.96
	0-EE-4	1585.5	5.06	1588	178	0.90
	0-ME-3	1711.6	4.75	no	longer	visible
	0-EE-5	1821.9	0.06	1821	295	0.018
	0-ME-4	1891.0	1.68	no	longer	visible
	0-EE-6	2103.4	3.52	2109	233	0.82
	0-ME-5	2161.8	0.02	2168	201	0.004
	0-EE-7	2252.2	1.21	2253	500	0.61

*note that model does not test ultimate fundamental-mode Q

Table 3
Calculated and measured properties of transverse modes

Mode type	URMEL name	Calc F ₀ (MHz)	R/Q(kr) ² (Ω)	Meas F ₁ (MHz)	Meas Q _L	R _{LL} * (kΩ/m)
TE ₁₁₁	1-ME-1	679.6	0.002	no	longer	visible
TM ₁₁₀	1-EE-1	795.5	15.263	779	122	1.86
	1-ME-2	1064.8	27.590	no	longer	visible
	1-EE-2	1133.2	0.243	1141	112	0.65
	1-ME-3	1208.2	0.258	1203	1588	10.3
	1-EE-3	1313.2	5.861	1311	498	80.1
	1-ME-4	1429.0	2.873	1435	3955	341
	1-EE-4	1541.0	0.850	1554	59	1.62
	1-EE-5	1586.2	2.045	1588	178	12.1
	1-EE-6	1674.2	5.140	1674	2134	385
	1-ME-5	1704.4	0.096	1704	444	1.52
	1-ME-6	1761.9	0.104	1757	7129	27.3

* R_{LL}=R/Q/(kr²) x Q_L, where r in the beam pipe radius

IV. MACHINE SIMULATIONS

A simulation code has been used to study the growth rates of the longitudinal coupled-bunch instabilities that would be driven in PEP-II by the cavity impedances. The code includes a model of the beam dynamics, all of the residual HOM driving impedances from the cavities and a model of the proposed broad-band feedback system. Running the simulation for the longitudinal modes shows that the beam remains stable and that the large single-bunch transients that occur during injection are quickly damped down.

A transverse simulation program is being developed which

is expected to show similar results for transverse beam motion since the deflecting impedances measured in the test cavity are reduced to the order of the resistive wall impedance.

V. CONTINUING R&D

Studies of the low-power test model are continuing, in particular to evaluate the effects of the loop coupler which may provide additional damping for some of the HOMs. The automated bead-puller is being used to measure the field profiles of the modes and hence the R/Q's, and to study the perturbations introduced by the various ports. The PEP-II R&D effort is now also focusing on building a high-power test model to prove that such a design can be conditioned and powered with up to 150 kW wall dissipation. High-power versions of the HOM loads are also being developed.

VI. CONCLUSIONS

The low-power test model has shown that it is possible to achieve the HOM impedance reduction required for PEP-II with the broad-band waveguide damping scheme. The worst HOMs have been damped by more than three orders of magnitude and the loaded Q's agree well with the calculated values reported previously. The detailed design of a high-power test cavity is well under way.

VII. ACKNOWLEDGMENTS

Although all the measurements were performed in the Lambertson Beam Electrodynamics Laboratory of the Center for Beam Physics at LBL, the design of the cavity has been very much a collaborative effort with the other participants in the PEP-II project. Thanks are due John Byrd at LBL for running the machine simulations.

VIII. REFERENCES

- [1] "Reports at the 1986 Stanford Linac Conference., Stanford, USA, June 2-6 1986," DESY M-86-07, June 86
- [2] D. A. Goldberg, R. A. Rimmer, "Automated Bead-Positioning System for Measuring Impedances of RF Cavity Modes", this conference.
- [3] H. Schwarz et. al., "Design of a High-Power Test Model of the PEP-II RF Cavity", this conference.
- [4] "An Asymmetric B-Factor based on PEP," Conceptual Design Report, LBL PUB-5303, SLAC 372
- [5] R. Rimmer et. al., "An RF Cavity for the B-Factor", Proc. PAC, San Francisco, May 6th-9th, 1991, pp819-21.
- [6] R. Rimmer et. al., "Higher Order Mode Damping Studies on the PEP-II B-Factor RF Cavity", Proc. 1992 Europ. Part. Accel. Conf., Berlin, Germany, March 24-28, 1992, pp 1289-1291.
- [7] R. A. Rimmer, "RF Cavity Development for the PEP-II B Factory", Proc. Int. Workshop on B-Factories, BFW592, KEK, Japan, Nov. 17-20, 1992, (PEP-II ME note 2-93, LBL-33360, ESG-242).

NON LINEAR EFFECTS IN FERRITE TUNED CAVITIES

Y. Goren, N.K. Mahale, L. Walling, T. Enegren, G. Hulsey
Superconducting Super Collider Laboratory†
2550 Beckleymeade Ave., MS-4010, Dallas, TX 75237
V.P. Yakovlev, V.M. Petrov
Budker Institute for Nuclear Physics Russia

Abstract

The phenomenon of dependence of the resonance shape and frequency on the RF power level in perpendicular biased ferrite-tuned cavities has been observed by G. Hulsey and C. Friedrichs in the the SSC test cavity experiment. This paper presents a theoretical as well as numerical analysis of this phenomenon and compares the results with experimental data. The effect of this nonlinearity on the SSC low energy booster prototype cavity is discussed.

I. INTRODUCTION

The tuning of the rf cavities in the SSC Low Energy Booster (LEB) and in the TRIUMF Kaon factory is done using Perpendicular-Biased yttrium-garnet Ferrites (PBF) [1],[2]. In this configuration the rf magnetic field inside the ferrite is perpendicular to the bias magnetic field. The main advantage of the PBF configuration over the more conventional parallel-biased Ni-Zn ferrites is the higher achievable magnetic quality value (Q_m), which in turn allows for higher energy densities and gap voltages. The main limitations to even higher gap voltages are the magnetic losses and nonlinear phenomena. The phenomenon of dependence of the resonance shape and frequency on the rf power level in PBF cavities has been observed by G. Hulsey and C. Friedrichs in the the SSC test cavity experiment [3]. This paper analyzes this nonlinearity and correlates it with the dependence of the permeability on the ratio of rf field to bias magnetic field amplitudes.

The paper is divided into five sections. The first section analyzes the permeability dependence on the rf field amplitude. The analysis is carried out in the quasi-static approximation due to the small ratio, in our experiment, of the rf drive frequency to the biased field gyro-frequency. This nonlinear term in the permeability is used in the second sec-

tion to analyze the dependence of the frequency and resonance shape on the rf power level. Section three compares the analytical and experimental results. The analytical expression fits well with the observed data. Using this comparison we will try to estimate the nonlinear effects expected in the LEB and we conclude with a short summary.

II. PERMEABILITY DEPENDENCE ON RF FIELD AMPLITUDE

Neglecting dissipation effects the equation of motion for the ferrite magnetization is given by

$$d\mathbf{M}/dt = -\gamma \mu_0 \mathbf{M} \times \mathbf{H}_{\text{eff}} \quad (1)$$

where γ is the gyromagnetic ratio, which is about 2.8 MHz/Gauss for most materials. In Eq. (1) μ_0 is the permeability of free space and \mathbf{H}_{eff} is the effective magnetic field at the magnetization location at time t . To make the analysis tractable we solve equation (1) in the Cartesian coordinate system. We define the external bias field H_0 to be in the z direction and the perpendicular rf field, $H_{\text{rf}} \cos(\omega t)$, in the y direction. Neglecting also the difference between the external and the effective magnetic fields, the three components of equation (1) are

$$dM_x/dt = -M_y \omega_0 + M_z \Omega(t) \quad (2a)$$

$$dM_y/dt = M_x \omega_0 \quad (2b)$$

$$dM_z/dt = -M_x \Omega(t) \quad (2c)$$

where ω_0 and Ω are defined by

$$\omega_0 = \gamma \mu_0 H_0 \quad (3)$$

$$\Omega(t) = \Omega_{\text{rf}} \cos(\omega t) = \gamma \mu_0 H_{\text{rf}} \cos(\omega t)$$

†Operated by the University Research Association, Inc., for the U.S. Department of Energy under contract No. DE-AC35-89ER40486

Eqs. (2a)-(2c) are nonlinear equations for the ferrite magnetization vector which preserve its magnitude M_0

$$M_0 = \sqrt{M_x^2 + M_y^2 + M_z^2} \quad (4)$$

The general solution to eqs.(2a)-(2c) is a Fourier sum on all the harmonics of the drive frequency ω . We shall limit the present analysis to the fundamental frequency only. Assume an exponential temporal behavior of the magnetization vector components M_x, M_y in Eqs.(2a) (2b) and making use of Eq. (4) we obtain the following expression for the permeability

$$\mu = \mu_0 + \frac{M_0}{H_0} \cdot \frac{1}{1 - \frac{\omega^2}{\omega_0^2}} - \frac{3}{8} \frac{M_0 H_0^2}{H_0^3} \quad (5)$$

where we neglect terms of the order $\omega^2 \Omega^2 / \omega_0^4$. The permeability in Eq. (5) decreases with increasing rf field amplitude, causing a frequency upshift in ferrite tuned cavities.

III. FREQUENCY AND AMPLITUDE DEPENDENCE ON RF FIELD

To estimate the resonance frequency shift and amplitude distortion as a result of the permeability dependence on the rf field we shall follow Slater's analysis [4]. We assume that the rf fields near resonance can be described by

$$E = V(t) E_r(x) \quad (6)$$

$$H = I(t) H_r(x)$$

where E_r and H_r are the resonance eigenfunctions for the eigenvalue ω_r . Substituting eq. (6) in Maxwell's equations we end with the following equation for the current $I(t)$ in the cavity

$$D = \omega_r I (1 + 3\beta I^2/2) + \omega_r/2Q \dot{I} + \ddot{I} - 3\beta I \dot{I}^2 \quad (7)$$

where D is a drive function, Q is the cavity quality value and β is defined by

$$\beta = \mu_0 M_0 / H_0^3 \int_T d^3x H_r^4 / W_m \quad (8)$$

The above integral is evaluated over the tuner volume and W_m is defined by

$$W_m = \int d^3x \mu_0 (1 + M_0/H_0) H_r^2$$

Assuming a periodic drive function of the form

$$D = \bar{D} \cos(\omega t)$$

in Eq. (7) and following Landau and Lifshitz analysis [5], we find that the resonance frequency

shift is

$$\Delta\omega_r/\omega_r = 3/16 \bar{I}^2 (\omega_r) \quad (9)$$

where \bar{I} is the magnetic field amplitude satisfying the following equation

$$\bar{I}^2 = \frac{\bar{D}^2}{4\omega_r^2 (\omega_r + \Delta\omega_r - \omega)^2 + \omega_r^2 / (16Q^2)} \quad (10)$$

Equation (9) describes a second order dependence of the the frequency shift on the rf amplitude which is directly related to the gap voltage V_{gap} . It also shows an inverse dependence of the shift on the third power of the bias magnetic field. The nonlinear resonance shape is described in Eq. (10).

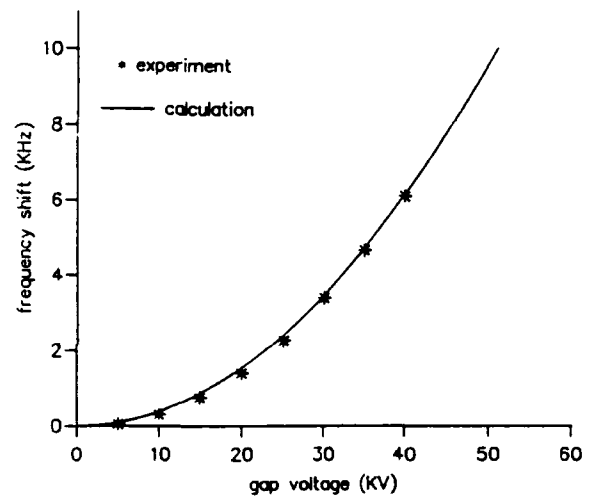


Figure 1. Frequency shift vs. maximum gap voltage $I_b = 105$ A

IV. COMPARISON OF ANALYTICAL AND EXPERIMENTAL RESULTS

Figure (1) plots the frequency shift vs. cavity gap voltage for 105 A bias current. The stars are the experimental points and the continuous curve is a fit of the form

$$\Delta f / f = 7.0 \times 10^{-14} V_{gap}^2 \quad (11)$$

where V_{gap} is in volts. An excellent fit with experimental data is observed. To numerically estimate the coefficient of proportionality between the frequency shift and the gap voltage we used the 3D electromagnetic code HFSS. We end up with the value 1.7×10^{-14} for this particular biasing (about four times lower than the experimental result). The discrepancy can be attributed to the sensitivity of this coefficient on the voltage transformation ratio between tuner to gap. Also a very good fit has been observed in the dependence of the frequency shift

on bias magnetic field using the same correction factor.

Figure (2) presents the gap voltage dependence on frequency for various tetrode current drives using Eq. (10) with the transformation of I to V_{gap} . A resonance shift as well as resonance distortion with increase drive is observed.

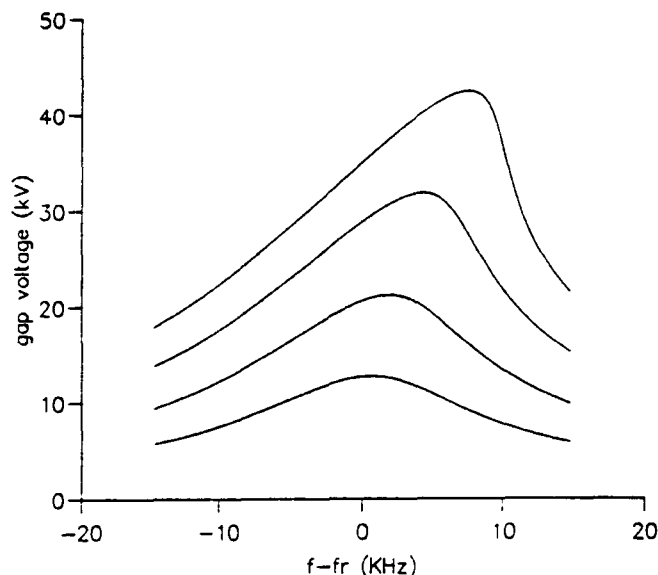


Figure 2. Gap voltage vs. frequency for various drives

Figure (3) presents two oscilloscope traces of the gap voltage vs. frequency. The symmetric case relates to maximum gap voltage of 7 kV and the asymmetric one to 70 kV. The traces can be described very well with Eq. (10) using the frequency shift of Eq. (9).

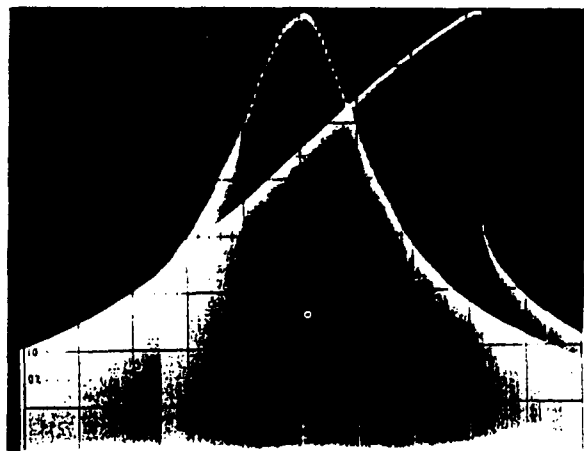


Figure 3. Oscilloscope traces for gap voltages of 7 and 70 kV

Making use of the theory presented in sections II and III together with the experimental correction factor we estimated the frequency shift expected in the LEB. A maximum shift of 23.6 KHz is expected at 50 MHz for about 100 kV gap voltage.

V. SUMMARY

A theoretical analysis of the dependence of the resonance frequency on rf power level in PBF cavities is presented. A good fit with experimental data is obtained. A correction factor of 4.12 is needed to fit the numerical results with experiment. The results of this analysis has been used to predict a maximum frequency shift of 23.6 KHz in the LEB cavity.

VI. REFERENCES

- [1] L.M. Early, G.P. Lawrence, J.P. Potter. *IEEE Trans. Nucl. Sci.* NS-30 3511, (1983)
- [2] W.R. Smith et. al. *IEEE Trans. Nucl. Sci.* NS-32 2951, (1985)
- [3] G.L. Hulsey, V.M. Petrov, V.P. Yakovlev, Tech Note SSCL (Sept. 9 1992).
- [4] J.C. Slater "Microwave Electronics" (D. Van Nostrand 1950)
- [5] L.D. Landau, E.M. Lifshitz "Mechanics" (Pergamon Press 1976).

EDDY CURRENT ANALYSIS FOR THE SSC LOW ENERGY BOOSTER CAVITY

Y. Goren, L. Walling, F. Brandeberry, N. Spayd
Superconducting Super Collider Laboratory†
2550 Beckleymeade Ave., MS-4010, Dallas, TX 75237

Abstract

One of the most important aspects of the SSC Low Energy Booster (LEB) cavity design is control of the eddy currents developed in the tuner during the frequency sweep. The two main difficulties created by the eddy currents are excessive tuner surface heating, and more important, a reduction in the time response of the tuner. We present a detailed analysis of the eddy currents for various tuner designs. The analysis has been done using 2D and 3D time-domain finite element codes (PE2D by Vector-Field and EMAS by MSC). Nonlinear analysis was performed utilizing B-H curves. The codes have been benchmarked analytically and by using measured data for different slotted pillbox structures.

I. INTRODUCTION

The SSCL LEB cavity is designed for a frequency sweep from 47.5 to 59.8 MHz in about 20 msec. The frequency sweep is achieved by varying a biasing magnetic field perpendicular to the r.f. magnetic field. One of the most important aspects of the design is control of the eddy currents in the tuner. The two main difficulties created by the eddy currents are excessive tuner surface heating, and more important, a reduction in the response time of the tuner to a triggered control signal. The eddy currents created on the tuner metallic surface can be reduced in two ways. First, one can slot the surface which increases the path length, or equivalently, increases the material electrical resistivity. The second approach, of using a closed shell tuner with high resistive alloy, is more mechanically suited to the LEB cavity if the ferrites are liquid-cooled. This structure has the electrical disadvantage of reducing the frequency response bandwidth to about 150 Hz for the available resistive alloys. A slotted tuner is mechanically more complex but has a frequency response bandwidth in excess of 2000 Hz.

This paper presents the results of an analytical

treatment of the eddy currents developed in an infinitely long metallic cylindrical shell. We show that, contrary to the widely held belief that the penetration of magnetic field into metals can be described in terms of only the skin depth, in our case the relevant parameter is the square of the skin depth divided by the shell radius. Next we present a numerical analysis of a closed shell tuner made out of Ti-6Al-4V alloy which has a high electrical resistivity as well as very good mechanical strength. This alloy yields a substantial reduction in eddy currents and more than an order of magnitude increase in frequency bandwidth compared with a copper tuner. Finally we show a numerical analysis of a slotted tuner design. It shows that contrary to another widely held belief that eddy current problems can be analyzed by the quasi-stationary approximation, that the rate of penetration of the magnetic field into the tuner through the slots depends on the displacement currents across the slots.

II. EDDY CURRENTS IN A METALLIC SHELL

First we review the results of a long thin metallic shell inside a long solenoid [1],[2]. The geometry of this setup is described in Figure 1.

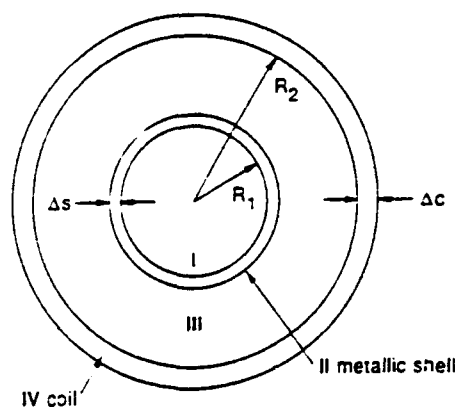


figure 1. Infinitely long metallic shell in solenoidal magnetic field

†Operated by the University Research Association, Inc., for the U.S. Department of Energy under contract No. DE-AC35-89ER40486

The axial magnetic field in region I is given by

$$B_z(t) = \mu \Delta_c \delta_s \exp(-\delta_s t) \int \exp(\delta_s \tau) J(\tau) d\tau \quad (1)$$

and the eddy current in the metallic shell is

$$J_{\text{eddy}} = -J \Delta_c / \Delta_s + \Delta_c / \Delta_s \delta_s \exp(-\delta_s t) \int \exp(\delta_s \tau) J(\tau) d\tau \quad (2)$$

The results in Eqs. (1) and (2) have been obtained assuming a spatially constant current density drive J . The parameter δ_s is defined by

$$\delta_s = 2/(\mu \sigma_0 \Delta_s R_1) \quad (3)$$

where σ_0 is the shell conductivity. The parameter δ_s in Eq. (3) measures the inverse of the magnetic diffusion time through the metallic shell. A tuner design with low eddy currents and fast magnetic time response will be characterized by the inequality $\delta_s T_{\text{ch}} \gg 1$ where T_{ch} is the characteristic time scale of the drive current J . The Ti-6Al-4V alloy, with conductivity of 5.8×10^5 s/m, reduces the eddy-current heating to an acceptable level.

The cavity rf frequency program is achieved by biasing the ferrite. The relationship between the biasing magnetic field to the current drive determines the cavity response to a control signal. It is common to quantify the response in the frequency domain by its 3dB bandwidth. Fourier decomposing Eq. (1) we obtain the following expression for the 3 dB frequency bandwidth:

$$\Delta_f = 1 / (\pi \mu \sigma_0 \Delta_s R_1) \quad (4)$$

For a 5 mm thick titanium alloy shell, this translates into a bandwidth of 292 Hz about two orders of magnitude greater than for a copper shell.

III. NUMERICAL ANALYSIS OF A CLOSED SHELL TUNER

Using the analytical results above as a guide, we simulated the closed shell LEB tuner using 2D and 3D electromagnetic codes which allow materials with a non-linear $B - H$ curve. The maximum eddy current is developed at the top of the tuner close to the external magnetic coil. Fig. 2 describes the magnitude of the eddy current at this point as function of time. The maximum eddy current of 60 amp/cm² is obtained at 17 msec from the beginning of the cycle. Similar results were obtained using Eq. (2).

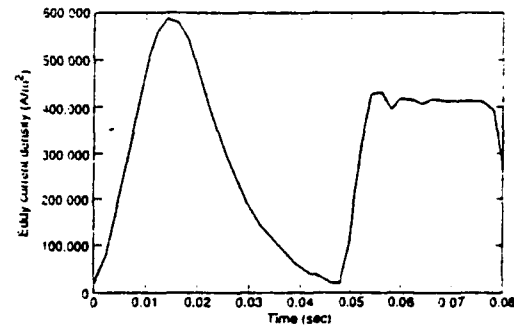


figure 2. Eddy current in Titanium tuner

In comparison, the maximum eddy current for a copper tuner is about 2700 amp/cm [2]. The thermal power, averaged over a cycle, is about 0.18 w/cm³ which can be handled by the tuner internal coolant.

The analysis of the tuner frequency response is done numerically by sending a small ac magnetic signal on top of the dc biased field. We find that the frequency response varied across the tuner cross section with the minimum bandwidth at the bottom of the ferrites. The magnetic field vs. frequency at this location is shown in Fig 3.

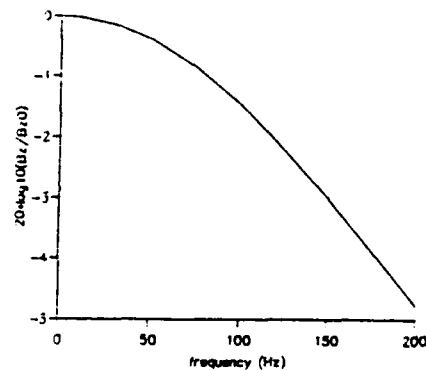


figure 3. Frequency response of Titanium tuner

It can be seen from the figure that the 3 dB bandwidth is about 140 Hz (considerably lower than the 292 Hz expected from an infinitely long metallic shell). The discrepancy corresponds to the relatively slow magnetic penetration through the side walls of the tuner. We confirmed the above results by benchmarking the code using measured data of magnetic field at various locations inside a closed stainless steel can. The narrow frequency response bandwidth led us to abandon the closed shell tuner and design a slotted tuner instead.

IV. NUMERICAL DESIGN OF A SLOTTED SHELL TUNER

The analysis of the closed shell tuner in the last section was performed using the quasi-static approximation which neglects the displacement

current in Maxwell's equations. Using this approximation for the 3D problem of slotted tuner yielded a false solution in which the slots had a very small effect on the rate of magnetic penetration into the tuner. The need for the displacement currents is illustrated in Fig 4.

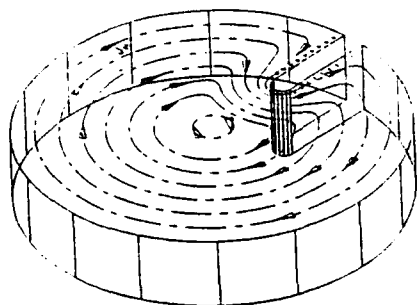


figure 4. Eddy currents around a slot

As the eddy currents approach the slot discontinuity they charge its surface. The charges create electric field which oppose the small internal field in the metal and force the currents to change direction and bypass the slot [3]. We confirmed this assumption by comparing the numerical simulation with measured results for a stainless steel can with various numbers of slots. Encouraged by these benchmark results, we designed a slotted LEB tuner. The tuner is made out of 3-mm-thick stainless steel with 16 5-mm radial slots. The slots are filled with G10 compound (dielectric material) to contain the coolant. The magnetic frequency response of this tuner is shown in Figs 5 and 6. The response function decrease slowly with frequency with a 3 dB bandwidth which exceeds 2000 Hz.

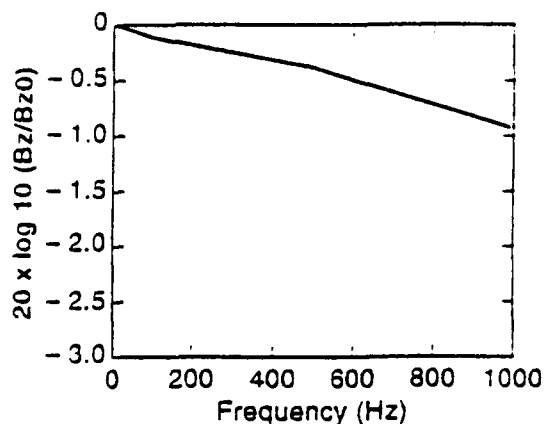


figure 5. Magnitude of magnetic frequency response

A 3-D view of the LEB tuner is shown in Fig. 7

V. SUMMARY

We presented analytical and numerical simula-

tions of two LEB tuner designs. The surface heating due to the eddy currents are controlled in both schemes. The magnetic field frequency response of the closed shell tuner is only marginally acceptable. This lead to the slotted tuner design, which is mechanically more complex, but has the wide bandwidth required for the control system.

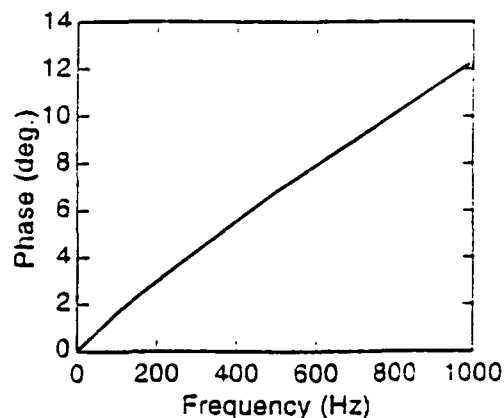


figure 6. Phase of magnetic frequency response

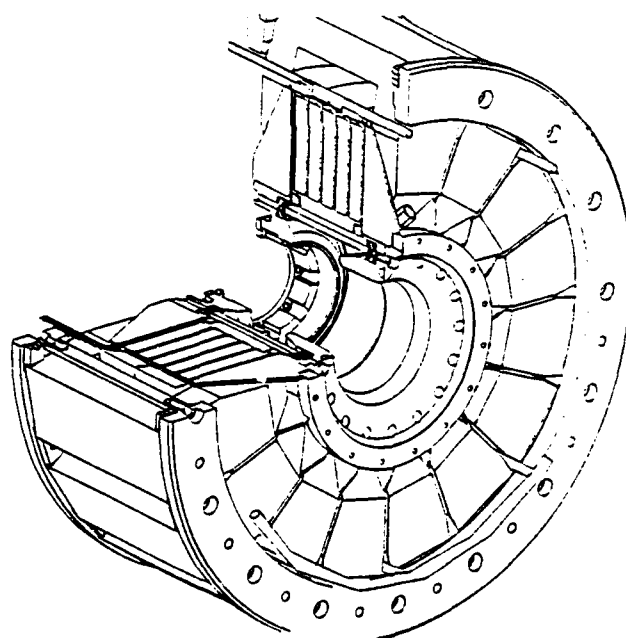


figure 7. LEB tuner design

VI. REFERENCES

- [1] S. Fahy, C. Kittel, S. G. Louie *Am. J. Phys.* **56**, 989 (1988)
- [2] Y. Goren, B. Campbell, SSC Laboratory, SSCL - 505, (1991).
- [3] Y. Goren, L. Walling, Eddy Current Analysis, R.F. Workshop, Dallas (June 1992)

VOLTAGE COUNTER-PHASING IN THE SSC LOW ENERGY BOOSTER

Y. Goren

Superconducting Super Collider Laboratory†
2550 Beckleymeade Ave., MS-4010, Dallas, TX 75237

T.F. Wang

Los Alamos National Laboratory, AT-7 MS-H829
Los Alamos, NM 87545

Abstract

Operating the SSC low energy booster (LEB) in a counterphasing mode is necessary because the low total ring voltage (25 kV) required at injection for adiabatic beam capture would otherwise result in cavity multipacting. Each cavity requires greater than 15 kV gap voltage (there are eight single-gap cavities in the LEB) to be free of multipacting. The analysis of the cavities' behavior in this mode and under time-varying beam loading is presented. It is shown that fast feedback loops with moderate gain are necessary to operate with the available tetrode power. The Robinson instability and the required power and phase histories are discussed.

I. INTRODUCTION

During the adiabatic capturing phase in the SSC LEB the total rf voltage needs to be lowered to 25 kV to achieve the desired capture efficiency [1]. Testings on similar cavity designs developed at Los Alamos and TRIUMF had found multipacting problems when the cavity voltage went below 20 kV. Recently experiments with the LEB prototype cavity indicate that multipacting starts at voltages below 10 kV. Either way with the present design of 8 to 10 cavities it will be impossible to achieve the low total voltage with all cavities in phase. A solution would be to counterphase the cavities, i.e., to operate a set of cavities in an acceleration mode while operating another set in deceleration mode. Certain constraints are imposed on the cavities to follow the total voltage program. These constraints together with the Robinson stability requirement [2] enforce us to operate the cavities above the minimum power condition. We will show that operating the cavities with a moderate rf feedback would reduce the power requirements considerably as well as the rate of phase sweeping. Moreover we will show that there is a critical feedback gain and below this gain no counterphasing is possible with the

available power in our tetrodes.

The paper is divided into three sections. The first section is a short description of the model used in this analysis. The second makes use of the equations described in the first section to estimate the power and phase requirements during the adiabatic capture period. The paper is concluded with a short summary.

II. CAVITIES-BEAM MODEL WITH RF FEEDBACK

We adopt throughout the paper the equivalent circuit model for the cavities-beam system. The model for a single cavity with its rf feedback is shown in fig. (1). The cavity is represented by a parallel RLC circuit with tunable inductor. The beam is modeled as a current generator with a given $I_b(t)$ shape.

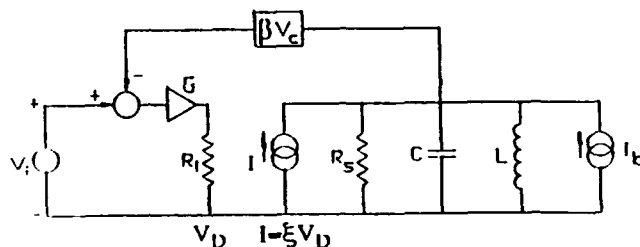


figure 1. circuit model of LEB cavity with rf feedback

Assuming fast rf feedback and using Kirchhoff's law, the cavity voltage V satisfies the following differential equation

$$\frac{d^2 V}{dt^2} + A \frac{dV}{dt} + BV = D \quad (1)$$

where $A = \omega_r / 2Q_L - 2/\omega_r d\omega_r/dt$
 $B = \omega_r^2 - 1/Q_L d\omega_r/dt$
 $D = \omega_r / 2Q_0 (\xi R_s dV_i/dt + R_s dI_b/dt) -$

†Operated by the University Research Association, Inc., for the U.S. Department of Energy under contract No. DE-AC35-89ER40486

$1/Q_0 d\omega_r/dt R_s(\xi V_i + I_b)$
and we define

$$\begin{aligned}\omega_r &= \sqrt{1/LC} \\ Q_0 &= \omega_r / (2CR_s) \\ Q_L &= Q_0 / (1+H) \\ H &= \xi^2 \beta R_s\end{aligned} \quad (2)$$

Assuming a solution of the form

$$V = \bar{V}(t) \exp(-i \int \omega(t) dt) \quad (3)$$

with the same behavior for I_b and V_i , and neglecting lower order terms like $d\omega/dt \ll \omega_r \omega/Q$ and $d^2V/dt^2 \ll \omega dV/dt$, we obtain the following equation for the cavity voltage under beam loading and rf feedback:

$$(2Q_0 Z_L / R_s \omega_r) dV/dt + V = Z_L \xi V_i + Z_L I_b \quad (4)$$

The bar has been omitted from the amplitudes of the voltage, the drive voltage and the beam current. The complex impedance Z_L in Eq. (4) is defined by

$$Z_L = R_s / (1+H) / \{1 - iQ_L(\omega/\omega_r - \omega_r/\omega)\} \quad (5)$$

Eq. (4) is a complex equation which determines the cavity voltage and phase (with respect to the beam) for a given input complex voltage V_i and current I_b . In most of the cases the first term in Eq. (4) can be neglected and we obtain an algebraic equation. In the case of two cavities with a given total voltage and phase, the degrees of freedom exceeds the number of equations and there is no unique solution. In this case the problem can be simplified. We assume the following: a) The cavities are operated with the minimum safe voltage to avoid multipacting, equal detuning phase, and b) symmetric counter-phasing where the angles between the input generator voltages and the beam for the two cavities relates by 180° . The phasor diagram for the symmetric counter-phasing is shown in fig. (2).

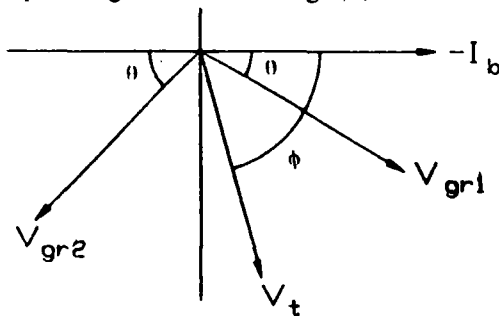


figure 2. phsor diagram for symmetric counter-phasing

Under these assumptions we end up with four equations for the four unknowns: the two input voltages V_{i1} and V_{i2} , the detuning angle ψ , and the

counter-phase angle θ . These equations together with the voltage and current programs will be used in the next section to solve the various rf parameters. The Robinson stability criteria for this model is given by

$$(1 + H)V_t \sin(\phi) / \{R_s I_b \sin(2\psi)\} > 1 \quad (6)$$

(see fig. (2) for the various angles).

III. POWER AND PHASE REQUIREMENTS

The voltage program expected for the LEB is shown in fig. (3) where we plot the voltage for two cavities out of assumed 8 operating ones. The rf current program is shown in fig. (4) where we consider operation in the test beam mode.

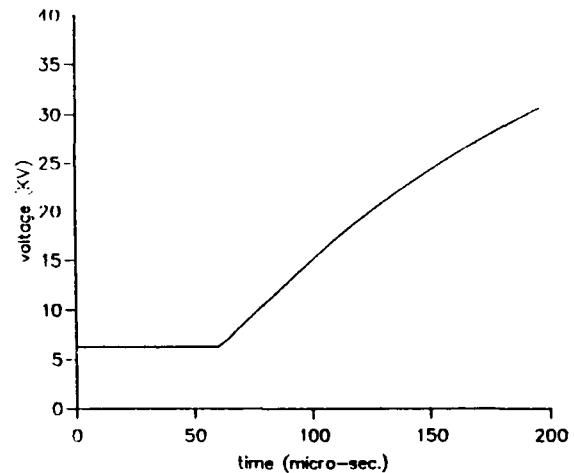


figure 3. the voltage program for two cavities

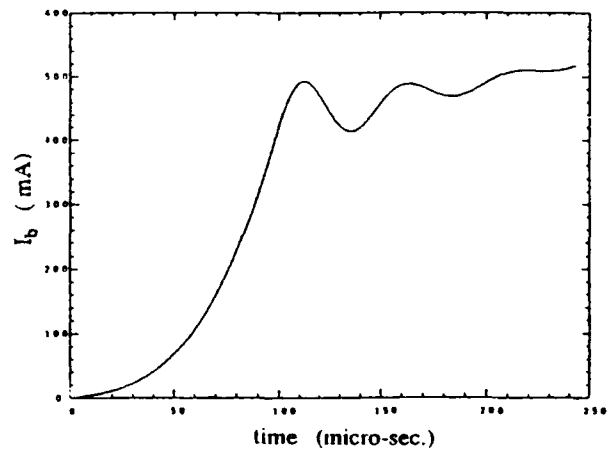


figure 4. the current program

The small synchrotron oscillations in the current 100 μ sec. after injection have been neglected. Using the equations described in section II we draw in fig. (5) the required generator power for the accelerating cavity P_a and the decelerating cavity P_d for Pedersen feedback parameter $H=6.3$ [3]. It can be seen that the maximum power required from

the accelerating cavity generator does not exceed 20 kW and less than 5 kW is required from the decelerating cavity.

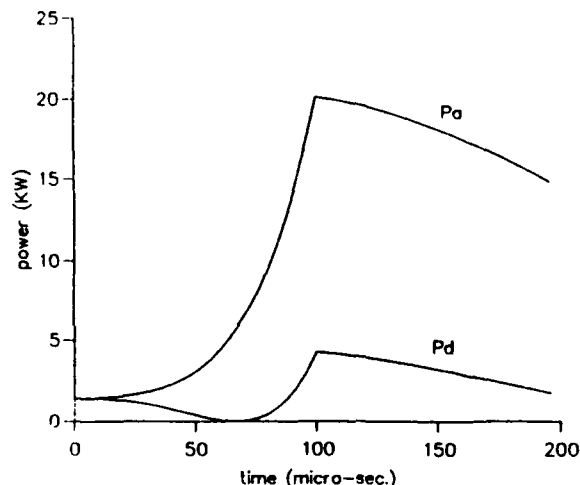


figure 5. generators power ($H=6.3$)

In comparison the required powers for the accelerating and decelerating cavities without rf feedback are 450 kW and 170 kW, respectively, beyond the power delivered by the tetrodes. Fig. (6) describes the required sweep in the counter-phase angle for this feedback level. A maximum rate of 0.3 degrees per micro-second is needed.

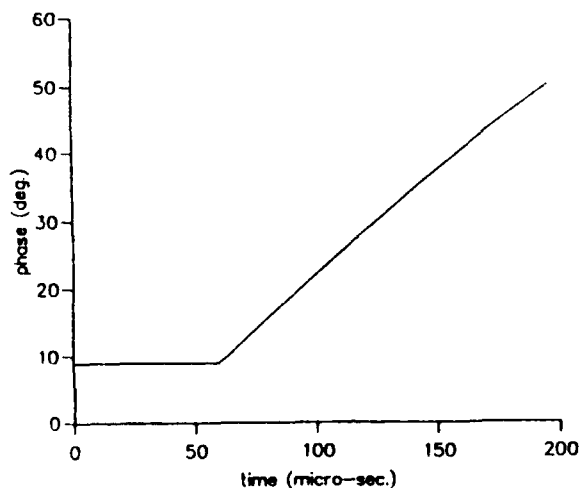


figure 6. counter-phasing angle ($H=6.3$)

In fig. (7) we present the detuning angle vs. time. It can be seen that the rate of detuning is about 0.1 degrees per micro-second. These two sweep rates in the LEB cavities can be achieved without much difficulty. The Robinson stability criteria given in Eq. (6) for $H=6.3$ is presented in fig. (8). It can be seen that through all the adiabatic capturing phase the two cavity system is in a stable state.

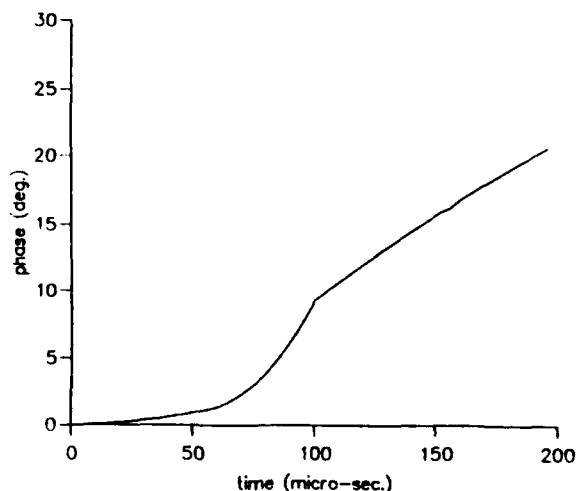


figure 7. detuning angle ($H=6.3$)

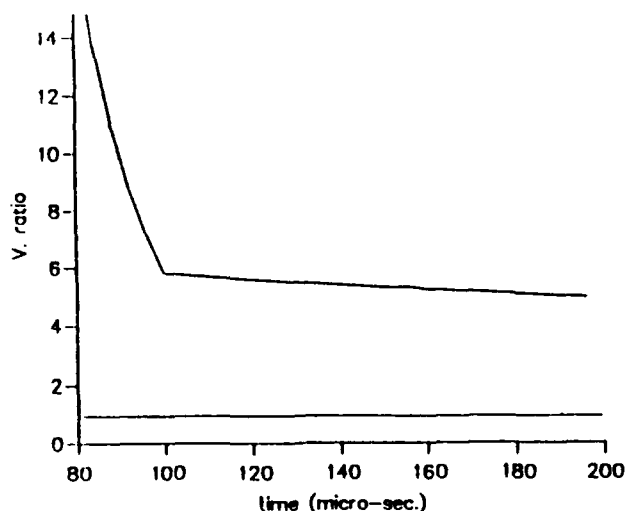


figure 8. Robinson stability

IV. SUMMARY

We have examined the rf counter-phasing during the adiabatic capturing period in the LEB. Our results indicate that counter-phasing with moderate gain of rf feedback is necessary to operate within the available power limits.

V. REFERENCES

- [1] N.K. Mahale (SSC), private communications.
- [2] K.W. Robinson, "Radiofrequency Acceleration II" Report No. CEA-11, Cambridge Electron Accelerator, Cambridge, Mass. (Sept. 1956)
- [3] F. Pedersen, *IEEE Trans. Nuclear Sci.*, Vol. NS-32, p. 2138 (1985)

An Update on High Peak Power (HPP) RF Processing of 3 GHz Nine-cell Niobium Accelerator Cavities*

J. Graber[‡], P. Barnes, C. Crawford[†], J. Kirchgessner, D. Moffat, H. Padamsee, P. Schmüser[‡], and J. Sears
F.R. Newman Laboratory of Nuclear Studies
Cornell University
Ithaca, NY 14853 USA

Abstract

Two 3 GHz, nine-cell niobium accelerator structures have been fabricated and tested multiple times. An unambiguous improvement in cavity performance can be shown due to High Peak Power (HPP) RF processing of the cavities. The average achieved accelerating gradient prior to HPP processing was $E_{acc} = 12$ MV/m, (Standard Deviation = 3 MV/m). The average maximum accelerating gradient following all HPP processing was $E_{acc} = 17$ MV/m, (Standard Deviation = 2 MV/m). Gains in cavity performance can be directly correlated with magnitude of field reached during pulsed HPP processing. Durability of processing gains has been tested by exposing processed cavities to filtered air, at room temperature, and unfiltered air, under both room temperature and cryogenic conditions. Filtered air had no discernable effect on cavity performance. Unfiltered air degraded cavity performance, through increased emission, however much of the cavity performance could be regained through further RF processing.

I. INTRODUCTION

Superconducting Radio-frequency (SRF) cavities are a promising technology for construction of the next generation of electron-positron colliders. In order for SRF to become a viable method for construction of these machines, however, attainable accelerating gradients must be increased from the 5-10 MV/m attained in present SRF accelerators to 25-30 MV/m.⁽¹⁾ Field emission (FE) of electrons from the RF surface has been the primary limitation to SRF cavities for the last five to ten years.

The HPP experiment was designed to explore the benefits of high power pulsed radio-frequency (RF) processing as a means of reducing FE loading in 3 GHz niobium accelerator cavities. RF processing is a method of cavity conditioning, where the cavity is exposed to high RF fields in the absence of a particle beam. The HPP apparatus can deliver up to 200 kW peak power for millisecond pulse lengths during processing.

Early results with HPP (presented previously^{(2),(3)}) showed significant reduction in FE loading in single-cell cavities. It is also important to verify that the HPP technique can successfully reduce FE loading in multi-cell structures as well as it does in single cavities. Two nine-cell cavities were constructed and tested several times each. Between successive tests on a cavity, an acid etch was performed, removing approximately 10 microns from the RF surface. Past studies lead us to believe that retesting following etching is equivalent to testing

a new cavity. A complete description of the HPP experiments can be found in the Ph.D. dissertation associated with this work.⁽⁴⁾

II. OVERVIEW OF NINE-CELL RESULTS

In this paper, we will show that HPP is successful in improvement of low power, continuous wave (CW) behavior of the nine-cell cavities. To support this conclusion, we report on investigation of cavity performance before and after HPP processing, as well as correlation of the improvements with the characteristics of HPP processing.

Figure 1 is a histogram comparison of attainable CW accelerating gradient, before and after HPP processing. HPP processing improved the mean attainable gradient from 12 MV/m to 17 MV/m, an increase of 41%.

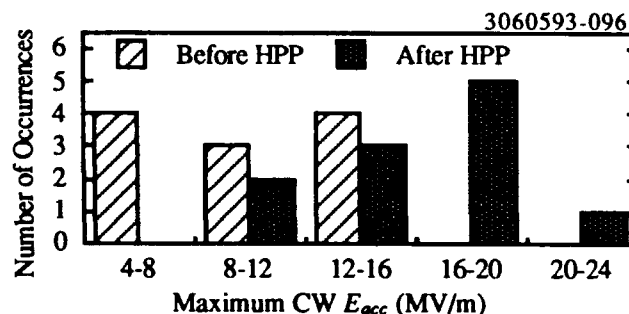


Figure 1. Histogram plot of maximum achieved CW accelerating gradient, before and after HPP processing. Without HPP, $\langle E_{acc} \rangle = 11.9$ MV/m (s.d. = 3.4 MV/m). With HPP, $\langle E_{acc} \rangle = 17.0$ MV/m (s.d. = 2.1 MV/m).

Figure 2 is a histogram comparison of X-ray detection threshold gradient, before and after HPP processing. X-rays are produced when emitted electrons impact elsewhere on the cavity surface. The onset of X-rays is a reproducible method of detecting the onset of FE. HPP processing improved the

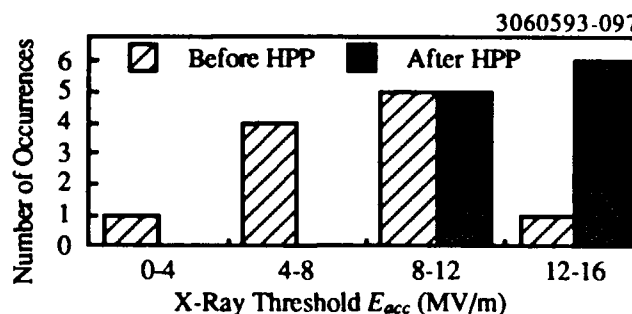


Figure 2. Histogram plot of X-ray threshold accelerating gradient, before and after HPP processing. Without HPP, $\langle E_{acc} \rangle = 7.5$ MV/m (s.d. = 1.3 MV/m). With HPP, $\langle E_{acc} \rangle = 12.4$ MV/m (s.d. = 1.3 MV/m).

Supported by the NSF with supplementary support from the U.S.-Japan collaboration.

[†] Permanent Address: Fermilab, Batavia, IL USA.

[‡] Permanent Address: DESY, 85 Notkestrasse, 2000 Hamburg 52, Germany.

X-ray threshold gradient from 7.5 MV/m to 12.4 MV/m, an increase of 65%.

Figure 3 shows a composite plot of the Q_0 vs E_{acc} plots of the best six experiments with nine-cell cavities. When the FE threshold is exceeded in a cavity, the dissipated power grows exponentially with increasing electric fields, causing the severe drop in Q_0 , as shown in Figure 3.

III. ANALYSIS

Given the success in improving CW behavior of the nine-cell cavities, we would like to characterize the success with relation to the terms of the HPP parameters. A clear correlation can be shown between the electric field reached during HPP processing (E_{HPP}) and the subsequent CW cavity performance. Figure 4 is a plot of maximum attained field as a function of

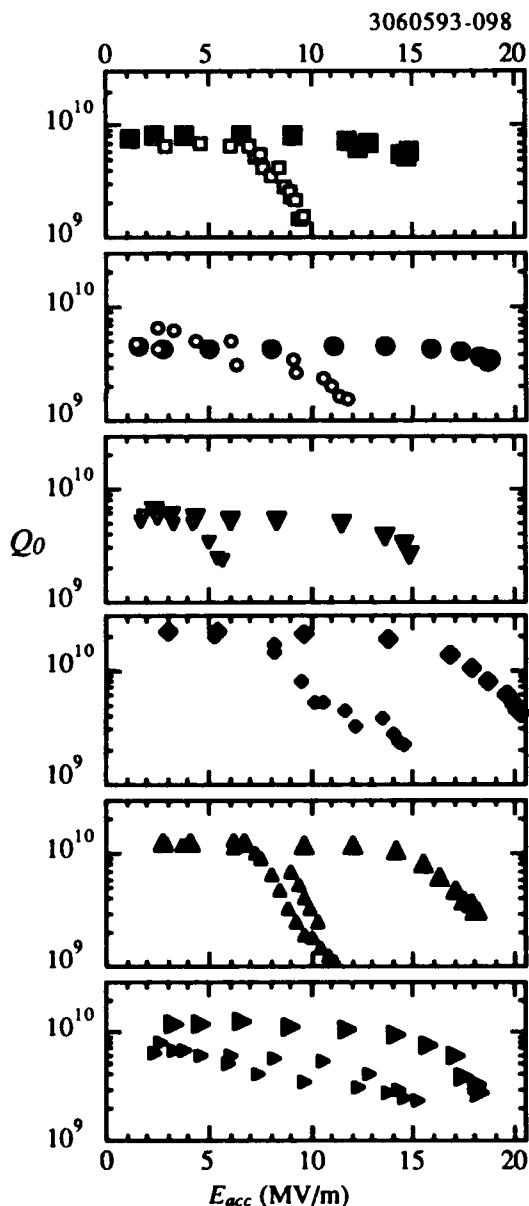


Figure 3. Composite Q_0 vs E_{acc} plots of the six best tests of nine cell cavities. Open symbols show cavity behavior before processing; closed symbols are for after HPP.

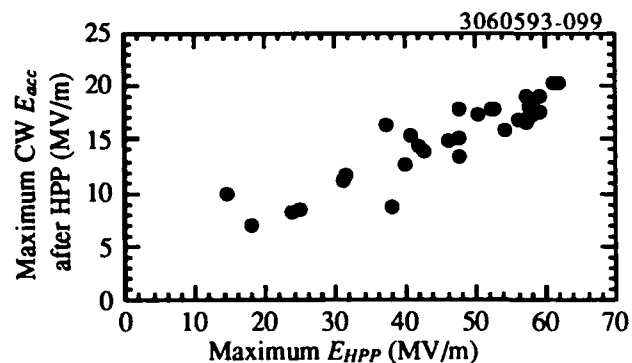


Figure 4. Maximum attained CW E_{acc} plotted as a function of maximum surface electric field during HPP processing.

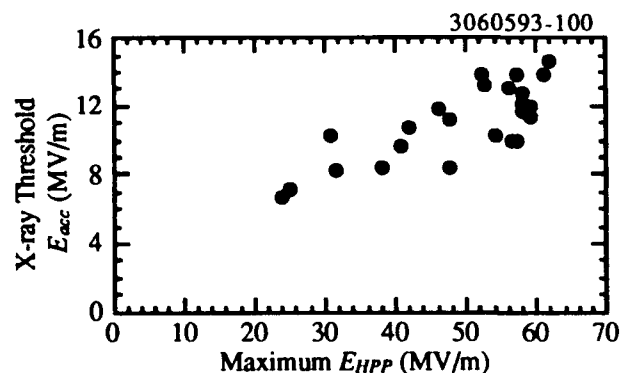


Figure 5. CW FE loading threshold E_{acc} plotted as a function of maximum surface electric field during HPP processing.

E_{HPP} . Figure 5 is a plot of X-ray threshold as a function of E_{HPP} . In these plots we see that increasing E_{HPP} generally leads to reduced FE, and therefore increased attainable accelerating gradients. During HPP, the input power, loaded Q , and pulse length are adjusted to maximize E_{HPP} . We additionally found that in any individual experiment, when E_{HPP} stopped improving, no further reduction of FE was achieved. Q_0 values are estimated to drop as low as 10^6 during HPP.

The current working model for RF processing states that processing occurs when the electric fields are driven sufficiently high so as to induce an emission current which is strong enough to cause melting and/or vaporization of the emission site. This model is supported by the correlation of processing success with E_{HPP} . The microscopic effects of RF processing are more fully investigated in another paper presented at this conference.^[5]

The primary limitation on E_{HPP} has been determined to be thermal breakdown (or quench), where the RF surface of the cavity is locally heated above the critical temperature. It then becomes normal conducting. Methods of characterizing and overcoming the quench limit are further discussed in another paper presented at this conference.^[6]

IV. OTHER RESULTS

A. Durability of Processed Cavities

HPP processing is foreseen as a possible method of cavity preparation for large scale accelerator facilities. In order to show the applicability to this function, it is necessary to learn what care is required for a cavity following processing to

maintain the HPP induced benefits. To this end, we allowed a processed nine cell cavity (low field $Q_0 = 1 \times 10^{10}$, $Q_0 > 10^{10}$ for $E_{acc} = 14$ MV/m, maximum $E_{acc} = 18$ MV/m) and cycled it to room temperature. While at room temperature, the cavity was exposed to filtered air (0.3 micron HEPA filter) for 24 hours, and then re-evacuated. The cavity was then re-cooled to liquid helium temperature, and the FE behavior was measured. Figure 6 shows the Q_0 vs. E_{acc} plots before and after this exposure. No significant change in FE loading is seen.

This is consistent with the findings of RF processing studies performed on low frequency, heavy ion accelerator cavities at Argonne National Laboratory^[7], as well as low power processing of 1.5 GHz cavities at Cornell LNS.^[8]

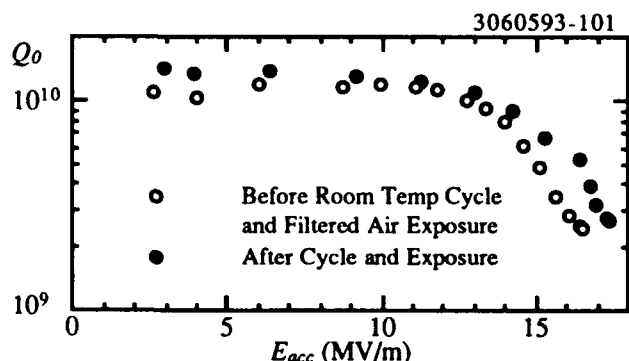


Figure 6. Q_0 vs. E_{acc} plots showing nine-cell cavity behavior before and after a room temperature cycle, with exposure to filtered air. No significant change in FE behavior is measured.

B. Recovery from Vacuum Accidents

Vacuum accidents are an ever present danger in accelerator systems, and the contamination due to such an accident can cause significant degradation of the performance of an accelerator cavity. In this light, we present the results of two exposures of nine cell cavities to unfiltered air, one accidental and one intentional.^[9] It has been established previously that air, especially unfiltered air, is a source of field emitters.^{[8],[10]}

The circumstances of the first accident were: At $T = 4.2$ K, the cavity was exposed to the vacuum pumps which are used to evacuate the experimental dewar in order to reduce the temperature to 1.4 K. Following re-evacuation of the cavity,

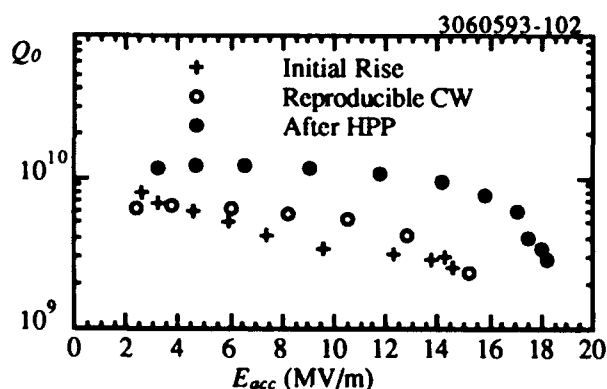


Figure 7. Q_0 vs. E_{acc} plots showing nine-cell cavity behavior before from the first vacuum accident.

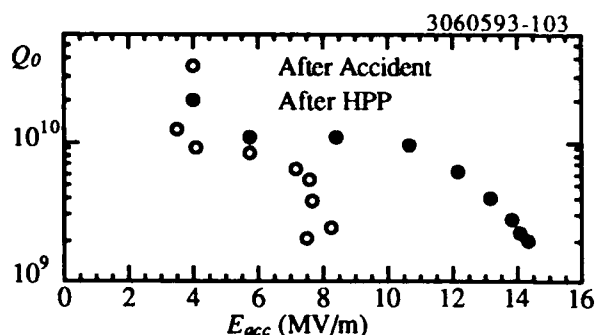


Figure 8. Q_0 vs. E_{acc} plots showing nine-cell cavity behavior before from the first vacuum accident.

the experiment was begun. The Q_0 vs. E_{acc} plots are shown in Figure 7. The initial rise of power was characterized by very heavy FE, some of which was processable with low power. The second curve in Figure 7 is the reproducible Q_0 vs. E_{acc} , following all possible low power processing. The cavity was then HPP processed with power as high as 90 kW, and fields as high as $E_{peak} = 58$ MV/m. The HPP processing was not only successful in reducing the FE loading, but it also seemingly improved the low field Q_0 value, possibly through RF removal of resistive contaminants on the cavity surface.

The second event to be reported was an intentional test of a vacuum accident. Following the above described test, the cavity was cycled to room temperature, re-cooled, and re-tested. Then, while the cavity was at liquid helium temperature, the cavity interior was exposed to unfiltered atmosphere. The cavity was then remeasured, showing heavy field emission, as well as a low field Q_0 degradation. Following a room temperature cycle, the cavity was HPP processed, with peak power up to 105 kW, and fields up to $E_{peak} = 42$ MV/m. Again, partial recovery was made via HPP processing. All Q_0 vs. E_{acc} curves for this experiment are shown in Figure 8.

Based on these results, we conclude that if cavities are damaged by vacuum accidents, the performance may be regained through HPP RF processing, and sometimes with low power.

V. REFERENCES

1. *Proc. of the 1st TESLA Workshop*, Cornell University, Ithaca, NY, CLNS 90-1029 (1990).
2. J. Graber, et al., *Proc. of the 5th Workshop on RF Superconductivity*, D.Proch ed., DESY, Hamburg, Germany, DESY M-92-01, 576 (1992).
3. J. Graber, et al., *Proc. of the 1991 Particle Accelerator Conference*, IEEE Cat. No. 91CH3038-7, 2411 (1991).
4. J. Graber, Ph.D. Dissertation, Cornell University (1993).
5. J. Graber, et al., this conference, poster Sa43.
6. J. Graber, et al., this conference, poster Sa44.
7. K. Shepard, Argonne Nat. Lab., priv. comm.
8. Q. S. Shu, et al., *IEEE Trans. Mag.*, MAG-25, 1868 (1985).
9. P. Schmueser, et al., SRF 921117-10 (1992).
10. Ph. Niedermann, Ph.D. Thesis No. 2197, U. of Geneva (1986).

Microscopic Investigation of RF Surfaces of 3 GHz Niobium Accelerator Cavities Following RF Processing*

J. Graber†, P. Barnes, T. Flynn, J. Kirchgessner, J. Knobloch, D. Moffat, H. Muller, H. Padamsee, and J. Sears
F.R. Newman Laboratory of Nuclear Studies
Cornell University
Ithaca, NY 14853 USA

Abstract

RF processing of Superconducting accelerating cavities is achieved through a change in the electron field emission (FE) characteristics of the RF surface. We have examined the RF surfaces of several single-cell 3 GHz cavities, following RF processing, in a Scanning Electron Microscope (SEM). The RF processing sessions included both High Peak Power ($P \leq 50$ kW) pulsed processing, and low power (≤ 20 W) continuous wave processing. The experimental apparatus also included a thermometer array on the cavity outer wall, allowing temperature maps to characterize the emission before and after RF processing gains. Multiple sites have been located in cavities which showed improvements in cavity behavior due to RF processing. Several SEM-located sites can be correlated with changes in thermometer signals, indicating a direct relationship between the surface site and emission reduction due to RF processing. Information gained from the SEM investigations and thermometry are used to enhance the theoretical model of RF processing.

I. INTRODUCTION

The HPP experimental program was initiated in order to investigate high power RF processing as a method of reducing and understanding field emission in superconducting accelerator cavities. Results of this program have been presented at previous and present Particle Accelerator Conferences.^{[1],[2]} An extensive description of the entire HPP program can be found in the recently completed Ph.D. dissertation associated with this work.^[3]

We report here on the effort to characterize the microscopic effects of RF processing. Surface investigation studies of the cavities in the HPP program was initiated with the goal of finding physical evidence of processing on the RF surface. We were encouraged by the findings of the Mushroom cavity project^[4] at Cornell, in which a specially designed, nonaccelerating cavity was examined in a Scanning Electron Microscope (SEM) following RF cold tests. Multiple phenomena were encountered in the high electric field regions of the cavity, indicating a strong link to field emission activity.

In order to better establish the link between surface features and RF processing, the experimental apparatus included an array of 100 thermometers placed in ten boards of ten resistors, spaced at 36 degree intervals around the azimuth of the cavity. Thermometers such as these have been a common diagnostic tool in SRF work for the last ten years.

SEM investigation of the cavities involves dissection of

the single cell cavities in order to facilitate investigation of the RF surface, and is the final step performed on a test cavity.

II. PHYSICAL EVIDENCE OF RF PROCESSING

Ultimately it is desirable to gather microscopic information on field emission sites. DC field emission studies^[5] have shown that these are micron or submicron features, for example, superficial particles. Even with guidance from thermometry, where the resolution is of the order of a few square millimeters, location of such minuscule features after dissection of a cavity presents a significant challenge. Fortunately, as this study shows, if the emission site processes, or undergoes significant change during cavity operation, then the additional features associated with the processing event make it substantially easier to locate the site.

Several sites were found which have both a significant thermometry signal, a change in signal after processing, and an associated surface feature. One example stands out above the rest, as the clearest processing event, therefore we will expand upon this site here. This site was found in a cavity (designated 1-5) which was RF tested specifically with the goal of limiting the run to one or two processing events. More examples of SEM located processing sites, as well as other phenomena can be found in references [3] and [6].

Figure 1 shows the Q_0 vs. E_{peak} plots from the three CW power rises of this experiment. The initial CW power rise was limited by heavy FE at $E_{peak} = 32$ MV/m. HPP processing was then performed with $P_{RF} = 2$ kW, $t_{RF} = 630$ μ sec. Peak fields during processing reached 49 MV/m. The second CW measurement was limited at 34 MV/m, again by heavy FE. The second HPP session was performed with $P_{RF} = 3.5$ kW, $t_{RF} = 630$ μ sec. Peak fields during processing reached 54 MV/m. In the final CW session, E_{peak} reached 36 MV/m, again limited by FE.

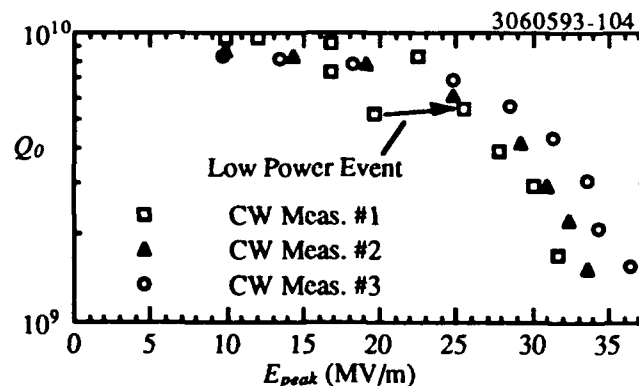


Figure 1. Q_0 vs. E_{peak} curves from low power measurements on single-cell cavity 1-5.

* Supported by the NSF with supplementary support from the U.S.-Japan Collaboration.

† Permanent Address: DESY, 85 Notkestrasse, 2000 Hamburg 52, Germany.

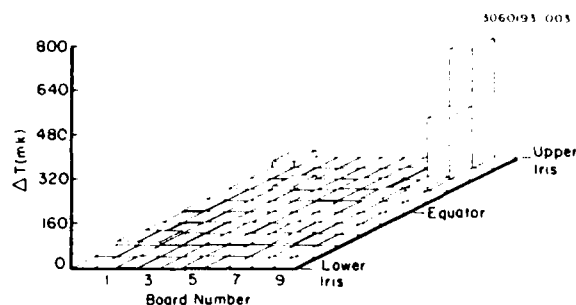


Figure 2. Temperature map measured at $E_{peak} = 31$ MV/m in the first CW power rise.

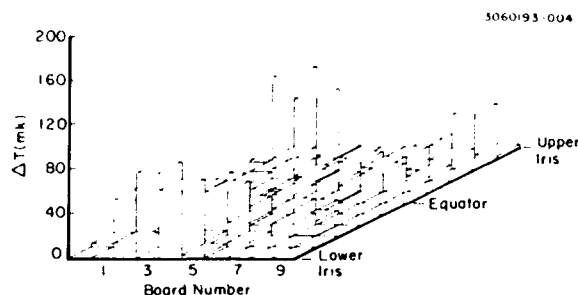


Figure 3. Temperature map measured at $E_{peak} = 36$ MV/m in the final CW power rise, following HPP processing.

Figure 2 is a temperature map of the cavity taken during the first CW measurements, at $E_{peak} = 32$ MV/m. The temperature map shows that the cavity was clearly dominated by a single emission site, located near the upper iris of the cavity board number 8. Figure 1 shows that, in addition to HPP processing, a processing event took place in the initial CW rise of the cavity, marked by the arrow. Inspection of the temperature maps reveal that this event was accompanied by a reduction in the heating at the dominant site shown in Figure 2.

Figure 3 is a temperature map taken during the final CW measurement, at $E_{peak} = 36$ MV/m. Note the reduced scale of the plot. While emission is still present, the site at the upper iris of board 8 is no longer dominating the cavity behavior. The change in heating is attributed to a change in FE characteristics through RF processing.

Given the measured change in heating, we then model the emission heating characteristics, before and after RF processing. In order to model the emission heating, we use a simulation^[7] which assumes that the emission current is consistent with the enhanced Fowler-Nordheim (F-N) theory of emission:

$$I_{FN} = \frac{CA}{\phi} (\beta E)^2 \exp\left(-\frac{B\phi^{3/2}}{\beta E}\right) \quad (1)$$

where I_{FN} is the FE current, E is the local surface electric field, ϕ is the work function of the metal, C and B are constants and β and A are the F-N field enhancement factor and emitter area, respectively. The present best model of the enhancement allows for both geometrical and material mechanisms of field enhancement. Furthermore, while no definite physical significance can be attributed to β or A , they are still useful quantities for characterizing the nature of emitters.

We therefore wish to extract values of β and A in order to better understand RF processing and its effect on emission

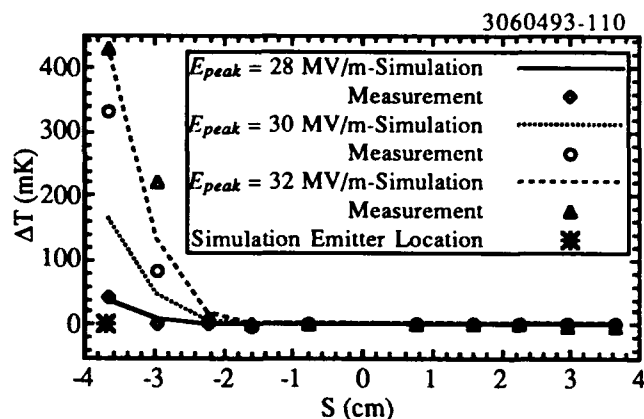


Figure 4. Comparison of measured and simulated temperature along board 8, in the first CW power rise.

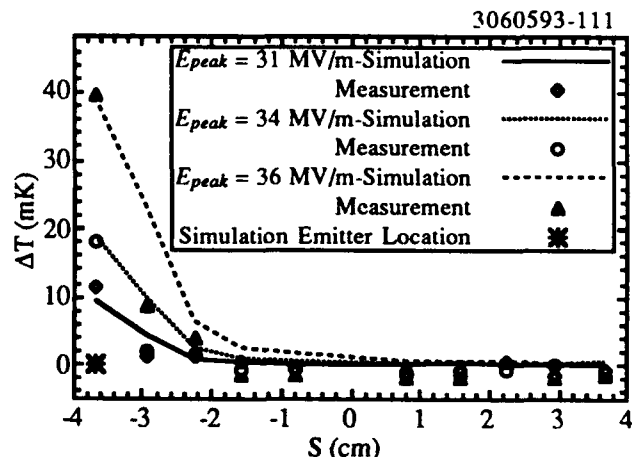


Figure 5. Comparison of measured and simulated temperature along board 8, in the final CW power rise.

sites. The method of extracting these values is to vary β and A in the simulation to best match the simulated with measured temperature signals on the cavity over several different electric field values. The field distribution of the fundamental mode of a cavity is such that emitted electrons follow trajectories with no azimuthal change, therefore all heating due to an emission site will be along a single board. S is the distance from the cavity equator along the cavity surface.

Figures 4 and 5 show the measured and simulated temperature signals along board 8 for the initial and final CW measurements on cavity 1-5, respectively. Simulation of the initial CW rise assumes the emission source at $S = -3.7$, $\beta = 200$, and $A = 3.2 \times 10^{-9} \text{ cm}^2$. The simulation of the final CW power rise assumes $S = -3.7$, $\beta = 300$, and $A = 1 \times 10^{-13} \text{ cm}^2$.

Given this agreement between measured and simulated thermometry, the cavity was dissected and put into the SEM, for examination in the region indicated as the processed emission site. The examination was successful, as one "starburst" feature was detected. Photographs of this starburst are shown in Figures 6 and 7. No other surface phenomena were detected in a position to explain the change in emission characteristics.

As with most starbursts, the feature is dominated by a darkened (as viewed in the SEM) burst region, with diameter approximately 200 microns. At the center of this starburst are

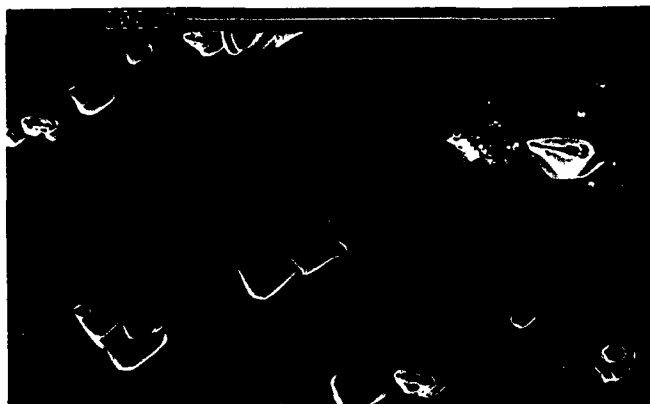


Figure 6. SEM photograph of the starburst region found in cavity S3C1-5. The starburst and craters are located in a position to explain the processing event.



Figure 7. SEM photograph of the central region of Figure 6. Contaminant materials include Ca, Ti, C, and O.

several small (10 microns) crater regions, which appear to have become molten. The craters are shown in Figure 7.

The working model for RF processing, and the creation of a starburst is that as fields are increased, the emission current increases until the resistive losses become so high that the emitter melts/vaporizes. The event appears to be explosive in nature, as evidenced by the splash appearance of many crater regions. A more complete description of this model can be found in references [3] and [6].

Examination of X-ray information in the SEM indicate that contaminant materials at this site include Calcium, Carbon, Oxygen, and Titanium. The crystalline appearing features are called "etch pits," and are a pitting phenomena which occur frequently in cavities which are acid etched following high temperature baking. These pits appear throughout the cavity, and therefore are not thought to be significant to cavity behavior.

In all, we have examined 6 cavities following HPP processing. The general rule we have found is that the higher the fields that the cavity is exposed to, the more starbursts are found. This is consistent with the model presented above, as higher fields are capable of processing more sites.

This phenomena is demonstrated more conclusively, by examining the radial distribution of starbursts in the cavities. Figure 8 shows such a distribution, superimposed with the relative electric field as a function of radius and aligned with a

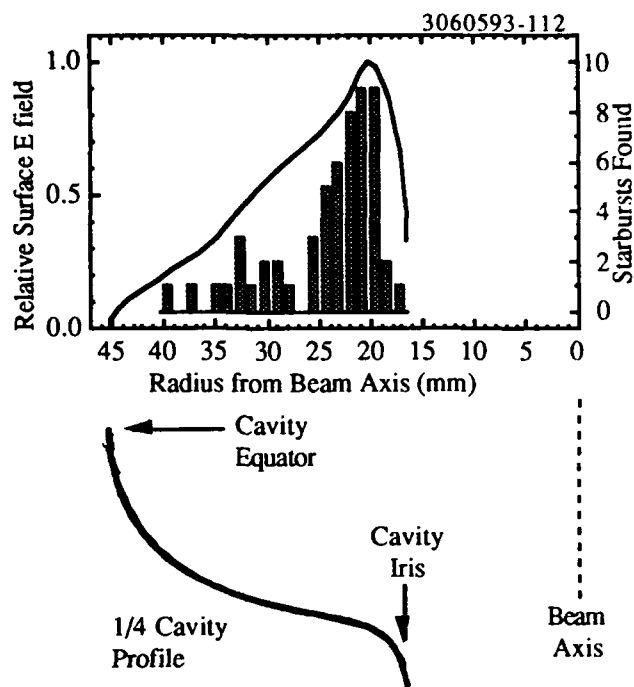


Figure 8. Radial distribution of "Starburst" phenomena found in all examined single-cell cavities, plotted along with relative surface electric field.

TABLE 1: CONTAMINANT ELEMENTS FOUND IN STARBURSTS IN HPP CAVITIES

Element	Starbursts	Element	Starbursts
Indium	19	Calcium	1
Iron	11	Silicon	1
Copper	4	Oxygen	1
Chromium	2	Carbon	1
Titanium	2		

quarter cavity profile. The starbursts are well concentrated in the high field region of the cavity, again supporting the model presented above.

Finally, in Table 1, we present a listing of the various contaminant materials detected in starburst in single-cell cavities.

III. ACKNOWLEDGMENTS

The authors thank Karen Sauer, Will Dickinson, and Adam Leibovich for their assistance on the thermometry portions of the HPP set-up.

IV. REFERENCES

- 1 J. Graber, et al., *Proc. of the 1991 Particle Accelerator Conference*, IEEE Cat. No. 91CH3038-7, 2411 (1991).
- 2 J. Graber, et al., this conference, posters Sa42 and Sa44.
- 3 J. Graber, Ph.D. Dissertation, Cornell University (1993).
- 4 D. Moffat, Cornell Report CLNS 90/991 (1990).
- 5 Ph. Niedermann, Ph.D. Thesis No. 2197, U. of Geneva (1986).
- 6 D. Moffat, et al., *Proc. of the 5th Workshop on RF Superconductivity*, D.Proch ed., DESY, Hamburg, Germany, DESY M-92-01, 245 (1992).
- 7 Cornell Report CLNS/D 910121/24, W. Hartung ed. (1989).

A World Record Accelerating Gradient in a Niobium Superconducting Accelerator Cavity*

J. Graber[‡], P. Barnes, J. Kirchgessner, D. Moffat, H. Padamsee, and J. Sears

F.R. Newman Laboratory of Nuclear Studies

Cornell University

Ithaca, NY 14853 USA

Abstract

A two-cell, 3 GHz, niobium superconducting accelerator cavity has sustained a continuous wave (CW) accelerating gradient of 34.6 MV/m, with corresponding peak surface electric field of 100 MV/m, record performances in each category for a superconducting accelerator cavity. Field emission (FE) loading of the cavity initially limited the cavity to $E_{acc} = 21$ MV/m ($E_{peak} = 60$ MV/m). The record field was achieved by reducing the FE loading through High Peak Power (HPP) RF processing of the cavity. Analysis of previous results of the HPP experimental program indicated that maximum fields under both pulsed and CW conditions were limited by thermal breakdown, which is related to the surface magnetic field in the cavity. The two-cell cavity shape was chosen to bypass the thermal breakdown limitations by reducing the ratio of peak surface magnetic field to peak surface electric field, from a value of $H_{peak}/E_{peak} = 23$ Oe/(MV/m) in the previous cavity, to 14 Oe/(MV/m) in the two-cell cavity. A simple thermal model accurately simulates the pulsed breakdown.

I. INTRODUCTION

A. SRF Cavities

Niobium Superconducting Radio-frequency (SRF) cavities are a promising technology for construction of the next generation of electron-positron colliders. In order for SRF to become a viable method for construction of these machines, however, attainable accelerating gradients must be increased from the 5-10 MV/m attained in present SRF accelerators to 25-30 MV/m.^[1] The gradients reached in this work show that it is possible to achieve the desired performance for TeV colliders, using HPP to overcome field emission (FE), the major limitation to high gradients.

The HPP experiment was designed to explore the benefits of high power pulsed radio-frequency (RF) processing as a means of reducing FE loading in 3 GHz niobium accelerator cavities. RF processing is a method of cavity conditioning, where the cavity is exposed to high RF fields in the absence of a particle beam. The HPP apparatus can deliver up to 200 kW peak power for millisecond pulse lengths during processing. An in depth description of all results of the HPP experiments can be found in the Ph.D. dissertation associated with this work.^[2]

B. Thermal Limitations of Previous HPP Work

The HPP experiments have shown that high power processing is a successful method of reducing FE loading in SRF cavities.^[3] The initial studies were performed with single-cell

and nine-cell cavities, using a geometry termed the S3C geometry. Results of the tests on nine-cell cavities are being presented in another paper to be presented at this conference.^[4] Success in FE reduction via processing has been directly linked to the magnitude of the electric field attained during processing (E_{HPP}). Furthermore, the attainable E_{HPP} has been shown to be limited by thermal breakdown, the phenomena where the RF surface is locally heated above the critical temperature, initiating the growth of a normal conducting region. Thermal breakdown limited single-cell cavities to $E_{peak} = 55$ MV/m ($H_{peak} = 1265$ Oe) CW and $E_{peak} = 72$ MV/m ($H_{peak} = 1650$ Oe) during HPP. Nine-cell cavities reached $E_{peak} = 42$ MV/m ($H_{peak} = 840$ Oe) CW and $E_{peak} = 62$ MV/m ($H_{peak} = 1250$ Oe) during HPP.

Thermal breakdown is driven by the surface currents which are required to support the magnetic fields at the RF surface. We therefore chose to investigate a cavity with a lower ratio of H_{peak}/E_{peak} . This ratio is determined by the cavity geometry, and can be obtained by numerical solution of Maxwell's Equations. Several programs exist for this purpose, e.g. SUPERFISH^[5]. The S3C cavities used for the single-cell and nine-cell experiments have H_{peak}/E_{peak} ratios of 23 Oe/(MV/m) and 20 Oe/(MV/m), respectively.

II. TWO-CELL W3C2-1

A. Cavity Fabrication and Preparation

After some investigation of potential cavity shapes, we chose a two-cell cavity using the geometry of the SRF group at the University of Wuppertal. A larger rounding of the equator region reduces the magnetic to electric field ratio of this cavity, designated W3C2-1, to $H_{peak}/E_{peak} = 14.2$ Oe/(MV/m). Interatom GmbH graciously agreed to press the half cells for this cavity (gratis). Final trimming, yttrification (for purification, and thus higher thermal conductivity), and electron beam welding were performed at Cornell.

The initial attempts at testing this cavity were limited by anomalously low thermal breakdown, initially due to insufficient surface chemistry then later due to the "Q virus." The final preparation prior to the successful test was a 2 hour bake at 900° C to eliminate the hydrogen contamination which has been identified as the cause of the Q virus.

B. Cold RF Measurement

Based on the reduced H_{peak}/E_{peak} ratio and the observed magnetic field break-down levels ($H_{bd} = 1250$ -1300 Oe) from the S3C cavities, we predicted that the cavity would reach 90-95 MV/m prior to thermal breakdown limitation. The cavity performance exceeded this prediction. The results of the best experiment with cavity W3C2-1 are shown in Figure 1. This cavity experiment extended over two cool downs, with a room temperature cycle, but no vacuum break between.

* Supported by the NSF with supplementary support from the U.S.-Japan Collaboration.

‡ Permanent Address: DESY, 85 Notkestrasse, 2000 Hamburg 52, Germany.

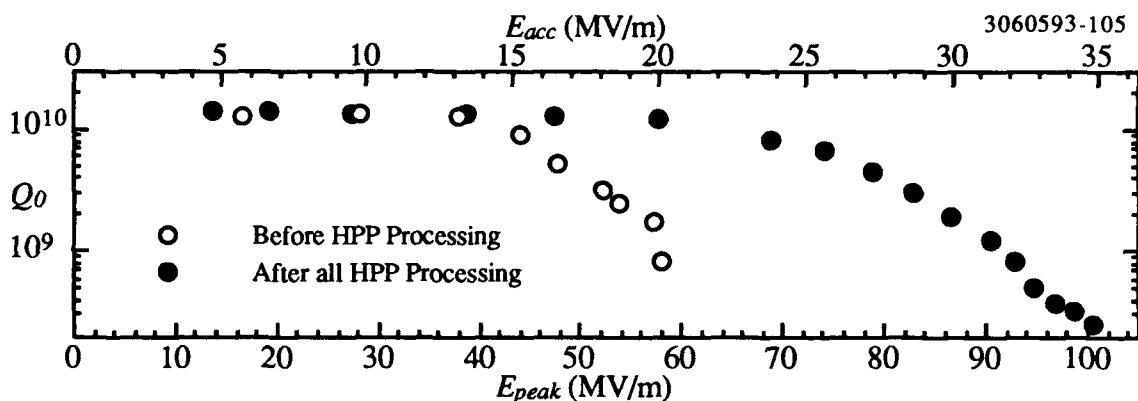


Figure 1. Q_0 vs. E_{peak} (E_{acc}) plots for the best experiment with cavity W3C2-1.

On initial rise of power, the cavity performance was measurable at $E_{peak} = 25$ MV/m, though low power processing with $P_{inc} = 10$ W increased the threshold to $E_{peak} = 35$ MV/m. The second plot in Figure 1 is the best CW measurement from the second day of testing the cavity. This CW measurement followed processing with incident power up to 130 kW, and fields as high as $E_{HPP} = 103$ MV/m, a room temperature cycling, and processing with power up to 100 kW, and fields as high as $E_{HPP} = 113$ MV/m. During HPP, analysis indicates that Q_0 values dropped to 10^6 . As can be seen, the improvement is remarkable. The maximum attained CW field was $E_{peak} = 100.6$ MV/m, limited by thermal breakdown ($H_{peak} = 1430$ Oe). This peak electric field is 20 MV/m higher than any accelerating cavity has ever been operated CW. The corresponding accelerating gradient at $E_{peak} = 100.6$ MV/m was $E_{acc} = 34.8$ MV/m. The Q_0 of the cavity remained above 5×10^9 for peak fields as high as 75 MV/m ($E_{acc} = 26$ MV/m). The experiment was repeated, reaching $E_{peak} = 85$ MV/m (with nearly identical field emission behavior), where it was limited by a superfluid helium leak.

C. Comparison with Previous HPP Results

We can now compare the results of all tests of two-cell cavity W3C2-1 with the results of tests of the S3C shape cav-

lar to that of pre-HPP single cell cavities. FE related Q_0 drop ities. Figure 2 plots maximum attainable CW electric field as a function of the maximum processing field preceding the CW measurement. The results of the two cell cavity are in good agreement with an extrapolation of the single-cell and nine-cell results. Furthermore, this clearly supports the correlation between processing field and success in processing.

Figure 3 is a similar plot, showing the X-ray detection threshold electric field as a function of maximum E_{HPP} . X-rays are produced when emitted electrons impact elsewhere in the cavity, and X-ray detection is a reproducible method of characterizing the onset of field emission in a cavity.

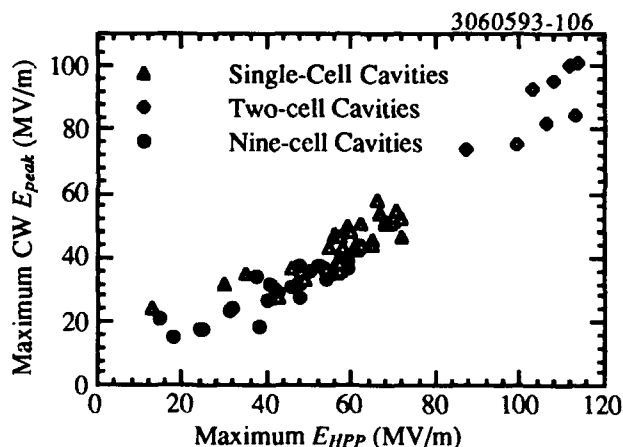


Figure 2. Maximum attainable CW peak electric field as a function of peak field attained during HPP processing. Note that the two-cell cavity behavior is in good agreement with an extrapolation of nine-cell and single-cell behavior.

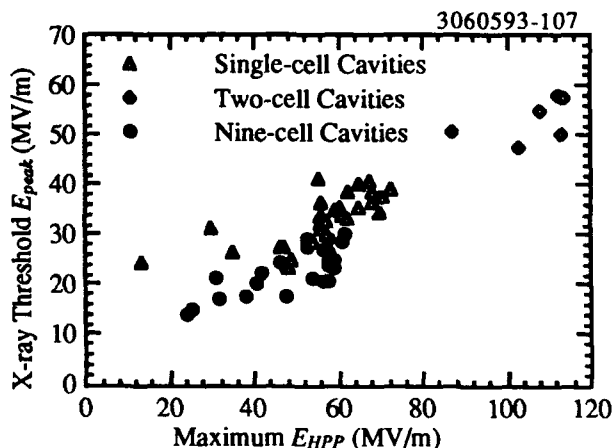


Figure 3. X-ray threshold peak electric field as a function of peak field attained during HPP processing.

III. MODELING OF THERMAL LIMITATIONS

A. The Model

With the predominance of thermal breakdown as a limitation to attainable fields during processing (and therefore success in processing), it is instructive to model the thermal processes in the cavity. Previous work on modeling (e.g. program HEAT^[6]) has been done on the simplified system of a niobium disk, with magnetic fields (power input through dissipation) at one circular face, and a helium bath (cooling) at the opposite face. Steady state solutions of this problem provided reasonable predictions for thermal breakdown field levels

in typical cavities. More recently, this model was expanded, in program **Transient_HEAT**,^[7] to include transient effects. With **Transient_HEAT**, we were able to gain an initial understanding of the time evolution of a normal conducting region on a superconducting surface. With this understanding, the following model was developed.

We allow for four different loss mechanisms: superconducting wall losses, FE losses, input coupler losses, and normal conducting wall losses. FE losses are estimated by extrapolating the low field behavior to HPP conditions.

We assume the cavity has a single breakdown initiation region, which activates at a fixed magnetic field (H_{BD}). When H_{BD} is surpassed, a circular normal conducting region begins to grow on the RF surface of the cavity, with expansion velocity v_{nc} , which was obtained by determining the growth rate of the normal conducting region as a function of magnetic field with **Transient_HEAT**. The results of **Transient_HEAT** indicate that v_{nc} varies quadratically with increasing magnetic field, with a typical growth rate being 500 m/s for $RRR = 400$, $H_{BD} = 1200$ G, $H_{surface} = 1400$ G.

During application of high pulsed power, it is possible to exceed the CW thermal breakdown field while the NC region grows in size. The amount of overshoot is a function of many parameters, including incident power, CW breakdown field, loaded Q, FE loading.

A more complete description of this model can be found in the previously mentioned dissertation.^[2]

B. Model Predictions and Analysis

The result of simulation is an explanation of the relationship between CW thermal breakdown field and the attainable peak field during HPP. Given the experimental conditions of RF processing, this model predicts the "overshoot" of CW breakdown field. Figure 4 is a comparison of measured and predicted E_{HPP} , as only the input coupling (designated by Q_{ext}) changes; pulse length and input power remain constant. The CW thermal breakdown field and the predicted peak field without taking breakdown into account are also shown for reference.

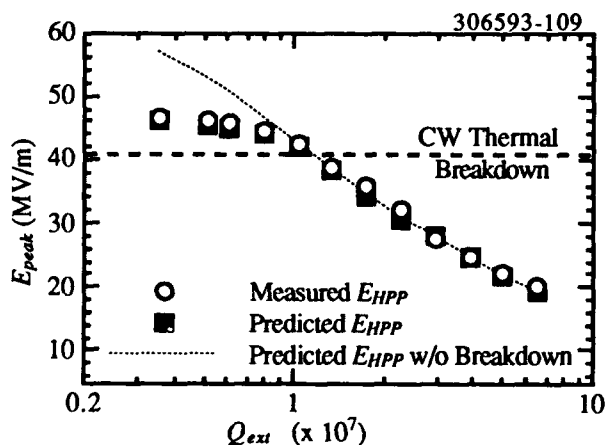


Figure 4. Comparison of Measured and Predicted E_{HPP} during HPP on a nine-cell cavity.

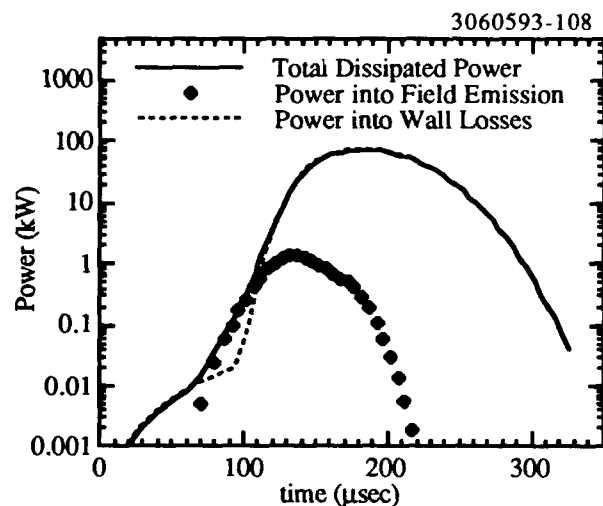


Figure 5. Power dissipation as a function of time during pulsed operation of a nine-cell cavity in quench conditions. Note that FE losses account for only 1% of total dissipation.

With this model, we are also able to analyze where the power being dissipating during HPP processing. HPP was performed with 50 kW (maximum) on single-cell cavities, 130 kW on the two-cell cavity, and 200 kW on nine-cell cavities. Based on this analysis, however, we find that if thermal breakdown is occurring during the HPP, a very small part of the dissipated power is going into field emission. Figure 5 shows an example of the time evolution of the power dissipation in a nine-cell cavity with 200 kW peak power incident upon it. While the power dissipation reached as high as 100 kW, we find that only slightly more than 1 kW was coupled into FE. Similarly, we find that in all single-cell, two-cell, and nine-cell tests, if thermal breakdown is occurring, then FE losses account for no more than 5% of the total losses. In order to optimize future HPP processing, thermal breakdown must be avoided if possible. Possible methods include higher purity material, lower RF frequencies, or lower H_{peak}/E_{peak} ratios. The last method was successfully implemented in cavity W3C2-1, allowing the record performance reported here.

IV. ACKNOWLEDGMENTS

We wish to thank G. Mueller at Wuppertal, and M. Peiniger and D. Dasbach at Interatom for their assistance in fabrication of the W3C2-1 cavity.

V. REFERENCES

- [1] *Proc. of the 1st TESLA Workshop*, Cornell University, Ithaca, NY, CLNS 90-1029 (1990).
- [2] J. Graber, Ph.D. Dissertation, Cornell University (1993).
- [3] J. Graber, et al., *Proc. of the 5th Workshop on RF Superconductivity*, D.Proch ed., DESY, Hamburg, Germany, DESY M-92-01, 576 (1992).
- [4] J. Graber, et al., this conference, poster Sa42.
- [5] K. Halbach and R.F. Holsinger, *Part. Acc.* 7, 213 (1976).
- [6] H. Padamsee, *CERN/EF/RF 82-5* (1982).
- [7] X. Cao, *ibid.* ref. 3, 727 (1992).

CHARACTERIZATION OF NSLS ACCELERATING CAVITIES USING IMPEDANCE MEASUREMENT TECHNIQUES

S.M. Hanna and P.M. Stefan
National Synchrotron Light Source
Brookhaven National Laboratory
Upton, NY 11973

Abstract

Impedance measurements, using a central wire to simulate the electron beam, were performed on a 52 MHz accelerating cavity at the National Synchrotron Light Source (NSLS). To damp higher-order modes (HOM) in this cavity, damping antennas have been installed. We implemented the impedance measurement technique to characterize the cavity modes up to 1 GHz and confirm the effectiveness of the damping antennas. Scattering parameters were measured using a network analyzer (HP 8510B) and values for R and Q were extracted using a new analytical technique. Our results showed good agreement with URMEL simulations and with other independent Q measurements. This technique offers a more time-effective technique for obtaining R/Q, compared with the bead-pull method.

I. HOM MEASUREMENTS ON THE NSLS 52 MHZ CAVITY

As part of an upgrade for the X-ray Storage Ring at the NSLS, a fourth 52 MHz cavity was recently installed. To damp higher-order modes (HOM) in this cavity, five damping antennas have been installed, as shown in Fig 1. To characterize the cavity modes and the effectiveness of this damping technique, we implemented the impedance measurement technique [1-3], where a wire is introduced at the center of the component under test (the cavity). An rf current is fed into this coaxial configuration and the resulting surface current distribution on the inner surface of the structure simulates the current distribution produced by a beam of charges. The existence of any discontinuity in the structure perturbs the current.

A central wire of radius $r_1 = 1.6$ mm was fitted through the center of the cavity. Two spacers of 30 cm length and a radius $r_2 = 36.4$ mm were connected to the cavity flanges, as shown in Fig. 2.a. The characteristic impedance of the spacers and the beam pipe in the cavity was $Z_2 = 187.5 \Omega$. Each spacer was inserted between a cavity flange and a coaxial cable ($Z_1 = 50 \Omega$), which was connected to a port of the network analyzer. A frequency range from 45 MHz to 1 GHz was examined to locate higher-order modes. Any mode which produced a change in $S_{21} \geq 5$ dB was included in the

subsequent high-resolution measurements. Seventeen modes were identified with the damping antennas in place, and thirty with the antennas removed. Following these measurements, the gap in the cavity was shorted by inserting an expanding sheet-metal sleeve, and all forty-seven high-resolution scans repeated.

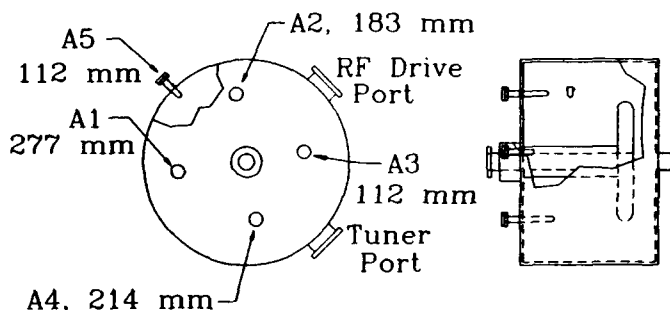


Fig. 1 HOM damping antennas in the 52 MHz cavity.

II. EXTRACTION OF CAVITY IMPEDANCES FROM SCATTERING PARAMETERS MEASUREMENTS

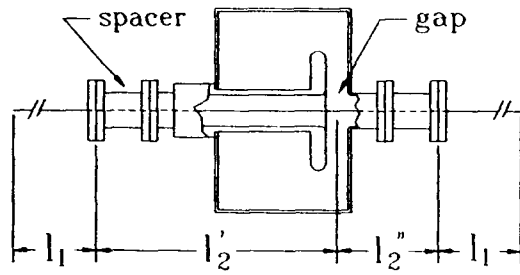
Characterizing different modes of the 52 MHz cavity involved evaluating the shunt resistance R_{sh} , and the quality factor Q, for each mode, before and after damping. This required calculating the impedance $Z(\omega)$ for each mode from the measured transmission response $S_{21}(\omega)$ for the system shown in Fig 2.a, and modeled in Fig 2.b.

The system was modeled as cascaded networks, each of which is described by an S-matrix. It is more convenient to describe each section of the system by a transfer matrix relating incident and reflected waves at one port to the incident and reflected waves at the other port [4]:

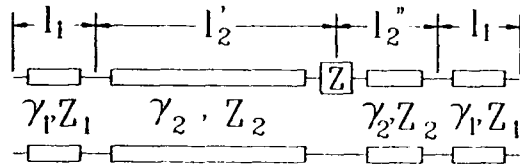
$$\begin{pmatrix} a_1 \\ b_1 \end{pmatrix} = \begin{pmatrix} T_{11} & T_{12} \\ T_{21} & T_{22} \end{pmatrix} \begin{pmatrix} b_2 \\ a_2 \end{pmatrix} \quad (1)$$

This form of network description is mathematically convenient for obtaining the overall T-matrix of the cascaded system. Since the network analyzer measurements are in terms of S-parameters, one needs to convert from the T-matrix to the S-matrix, using Eq. 2.

*Work performed under the auspices of the U.S. Department of Energy, under contract DE-AC02-6CH00016.



(a) System Configuration



(b) Network Model

Fig. 2 Configuration for impedance measurement and the corresponding network model

$$\begin{pmatrix} S_{11} & S_{12} \\ S_{21} & S_{22} \end{pmatrix} = \begin{pmatrix} \frac{T_{21}}{T_{11}} & T_{22} - \frac{T_{21} T_{12}}{T_{11}} \\ \frac{1}{T_{11}} & -\frac{T_{12}}{T_{11}} \end{pmatrix} \quad (2)$$

Based on the network model shown in Fig 2.b, the T-parameters representation for the system can be written as:

$$\begin{aligned} T &= \begin{pmatrix} e^{\gamma_1 l_1} & 0 \\ 0 & e^{-\gamma_1 l_1} \end{pmatrix} \begin{pmatrix} \frac{1}{1-\Gamma} & \frac{\Gamma}{1-\Gamma} \\ \frac{\Gamma}{1-\Gamma} & \frac{1}{1-\Gamma} \end{pmatrix} \begin{pmatrix} e^{\gamma_2 l_2'} & 0 \\ 0 & e^{-\gamma_2 l_2'} \end{pmatrix} \\ &\cdot \begin{pmatrix} \frac{Z + 2Z_2}{2Z_2} & -\frac{Z}{2Z_2} \\ \frac{Z}{2Z_2} & \frac{2Z_2 - Z}{2Z_2} \end{pmatrix} \\ &\cdot \begin{pmatrix} e^{\gamma_2 l_2''} & 0 \\ 0 & e^{-\gamma_2 l_2''} \end{pmatrix} \begin{pmatrix} \frac{1}{1+\Gamma} & -\frac{\Gamma}{1+\Gamma} \\ -\frac{\Gamma}{1+\Gamma} & \frac{1}{1+\Gamma} \end{pmatrix} \begin{pmatrix} e^{\gamma_1 l_1} & 0 \\ 0 & e^{-\gamma_1 l_1} \end{pmatrix} \quad (3) \end{aligned}$$

where,

$\gamma \equiv$ Propagation constant in each transmission line section.

$\Gamma \equiv$ Reflection coefficient,

$$\Gamma = \frac{Z_2 - Z_1}{Z_2 + Z_1} \quad (4)$$

Conversion to S-parameters, gives

$$\begin{aligned} S_{21} &= (1 - \Gamma^2) / \left[\left(\frac{Z + 2Z_2}{2Z_2} \right) e^{2\gamma_1 l_1 + \gamma_2 l_2' + \gamma_2 l_2''} \right. \\ &\quad + \left(\frac{Z}{2Z_2} \right) \Gamma e^{2\gamma_1 l_1 + \gamma_2 l_2' - \gamma_2 l_2''} \\ &\quad + \left(\frac{Z}{2Z_2} \right) \Gamma e^{2\gamma_1 l_1 - \gamma_2 l_2' + \gamma_2 l_2''} \\ &\quad \left. - \left(\frac{2Z_2 - Z}{2Z_2} \right) \Gamma^2 e^{2\gamma_1 l_1 - (\gamma_2 l_2' + \gamma_2 l_2'')} \right] \quad (5) \end{aligned}$$

Solving for the cavity impedance gives

$$Z = \frac{\left[\frac{2Z_2}{S_{21}} (1 - \Gamma^2) e^{-2\gamma_1 l_1} - 2 Z_2 e^{\gamma_2 l_2} (1 - \Gamma^2 e^{-2\gamma_2 l_2}) \right]}{[e^{\gamma_2 l_2} (1 + \Gamma^2 e^{-2\gamma_2 l_2}) + \Gamma e^{\gamma_2 \Delta l_2} (1 + e^{-2\gamma_2 \Delta l_2})]} \quad (6)$$

where,

$$l_2 = l_2' + l_2'', \quad \Delta l_2 = l_2' - l_2''$$

A program was written to obtain the impedance $Z(\omega)$ (magnitude and phase) for each of the cavity modes from the measured S-parameter data. A normalization step was included to account for phase shift and attenuation in the network analyzer. The program then calculates $Z(\omega)$ according to Eq.(6) using corrected $S_{21}(\omega)$ values (in phase and magnitude). The resulting $\phi_z(\omega)$ and $|Z(\omega)|$ for each cavity mode serve as inputs to a search program to find shunt the resistance R_{sh} , the resonant frequency f , and the 3dB-bandwidth. As a sample of the results obtained, the extracted $Z(\omega)$ for the cavity HOM at $f = 275.1$ MHz, with and without damping antennas installed, is shown in Fig 3.

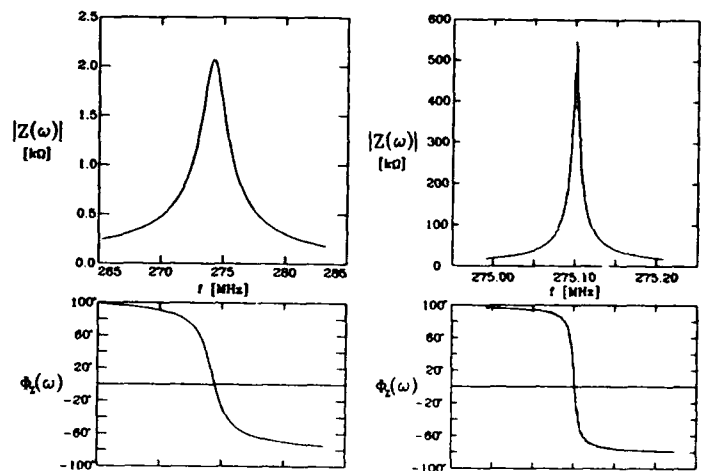


Fig. 3 Mode ($f=275.1$ MHz) impedance with and without damping antennas installed.

TABLE 1 - RESULTS AND COMPARISONS

f(MHz)	COMPARISON WITH COMPUTER SIMULATION		COMPARISON WITH PROBE Q-MEASUREMENT			
			UNDAMPED		DAMPED	
	R/Q (Ω)		Q		Qd	
	THIS WORK	URMEL	THIS WORK	PROBES	THIS WORK	PROBES
53.2	66.053	64.102	10,471	16,100	7598	13800
275.1	14.156	14.848	36,122	33,050	145.0	160
338.1	0.413	0.209	26,663	26,500	---	30
397.8	5.492	5.240	27,367	26,800	---	30
511.2	6.302	18.034	23,342	26,450	---	200
586.1	20.555	15.129	29,447	---	333.7	---
663.6	0.323	0.213	37,092	37,500	1697	1900
713.8	0.260	0.347	44,822	44,000	---	180
756.8	0.066	0.045	35,746	37,100	3355	3600
792.3	2.556	3.882	14,806	10,750	1737	1900
878.2	29.799	13.869	22,260	22,680	817.7	420
954.7	0.007	0.211	30,329	48,900	2729	200
975.4	1.519	1.635	6,471	6,080	1493	340

III. RESULTS AND COMPAISON WITH CAVITY SIMULATIONS AND WITH PROBE Q-MEASUREMENTS

A partial summary of our results, together with various comparisons, is presented in Table 1. An important quantity to characterize a cavity mode is its geometrical impedance R/Q. We compared our measured values of R/Q to values obtained from URMEL computer simulations. Examining the field patterns for different cavity modes using URMEL simulations reveals some explanation for the variation in agreement between measured and calculated values of R/Q. We noticed that when the fields associated with a certain mode are more concentrated in the volume close to the gap, the agreement is generally not as good, compared to other modes. Based on this observation, we argue intuitively that the perturbation introduced by the wire in the measurement has more effect on the field in such modes.

Our measured values for the Q were compared with other independent Q measurements, where transmitting and receiving probes were placed on axis [5]. These results are also listed in Table 1.

IV. CONCLUSION

The impedance measurement technique was applied to the characterization of higher-order modes in a 52 MHz

accelerating cavity at the NSLS. The results of the measurements are in good agreement with computer simulations for this cavity and in reasonable agreement with other independent measurement methods. We have developed and implemented a technique to extract the impedances of different modes from the measured S-parameters. Our analytical technique is a convenient alternative to the two approaches commonly used, namely, tapered transitions or a full calibration, which are normally needed in this type of measurement.

References

- [1] F. Caspers, *Frontiers of Particle Beams: Intensity Limitation*, Springer-Verlag, pp. 80-109, 1992.
- [2] L.S. Walling et al., "Transmission-Line Impedance Measurements for an Advanced Hadron Facility" *Nucl. Instru. and Meth. in Phys. Res.*, A281, pp. 433-437, 1989.
- [3] S.M. Hanna and P. Stefan, "Application of Impedance Measurement Techniques to Accelerating Cavity Mode Characterization", submitted to *Nucl. Instru. and Meth. in Phys. Res.*
- [4] R.E. Collin, *Field Theory of Guided Waves*, New York, McGraw Hill, Ch.3, pp.79-83, 1960.
- [5] R. Biscardi and W. Broome, Private communication.

In Search of Trapped Modes in the Single-Cell Cavity Prototype for CESR-B*

W. Hartung

Laboratory of Nuclear Studies, Cornell University, Ithaca, New York 14853

E. Haeberli

CERN, AT Division, CH-1211 Geneva 23, Switzerland

"Success has made a failure of our HOM."

S. O'Connor

I. INTRODUCTION

Plans for CESR-B, the proposed upgrade of the CESR e^+e^- storage ring to a B-factory, call for single-cell superconducting cavities with heavily damped higher-order modes (HOMs); $Q \leq 100$ is required for the dangerous modes in order to avoid multi-bunch instabilities [1]. The cavity is designed to enable all HOMs to propagate into the beam pipe, where they are damped by a layer of microwave-absorbing ferrite. Other "single-mode cavity" designs have been shown to have trapped modes, i.e. HOMs with low fields in the beam tube even though they are above cutoff [2, 3]. Trapped modes in the CESR-B cavity would be poorly damped by the ferrite loads and might have excessively high Q 's.

Several different approaches have been taken in assessing the effectiveness of the CESR-B cavity design: (i) the Q 's of monopole and dipole modes have been measured in a full-size copper cavity with ferrite loads [4, 5]; (ii) the Q 's of monopole modes have been predicted using SEAFISH to model the cavity and loads [5]; (iii) the current-voltage method has been used to search for trapped monopole modes. The results of (iii) are discussed in this paper. An explanation of the current-voltage method and some recent improvements to it are also given. A more detailed treatment is given in a separate report [6].

II. THE CURRENT-VOLTAGE METHOD

The current-voltage method was developed to calculate damping using programs like SUPERFISH [7] or URMEL [8] that do not model power absorption. The method predicts the Q of a cavity mode which can propagate energy into the beam tube or some other transmission line. The transmission line is assumed to be terminated with a matched load (the method can in principle handle a line terminated by an arbitrary impedance).

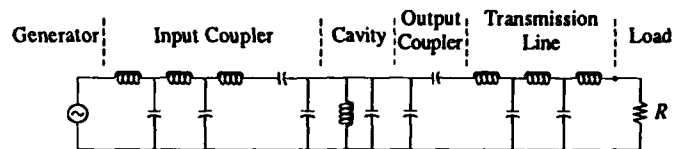
Consider a resonant cavity driven by a generator and damped by a load. A possible circuit model for this situation is shown in Figure 1a. A Thévenin equivalent circuit for the cavity, generator, couplers, and transmission lines is shown in Figure 1b. The power P dissipated in the load resistor R is

$$P = \frac{1}{2} R \frac{|V_{th}|^2}{|Z_{th} + R|^2}.$$

*Work supported by the National Science Foundation, with supplementary support from U. S.-Japan collaboration.

(a)

3180593-007



(b)

3180593-008

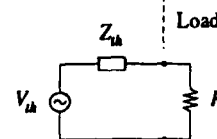


Figure 1. (a) A circuit model for a lossless resonant cavity excited by an ideal generator and damped by a resistive load at the end of a lossless transmission line; (b) the circuit model with the cavity, couplers, transmission line, and generator replaced by their Thévenin equivalent circuit.

P cannot be calculated directly. If we replace R by an open circuit and a short circuit in turn, however, we can express P in terms of V_{open} and I_{short} . In the usual case, in which R is real and Z_{th} is imaginary (meaning that the rest of the circuit has no resistive elements), the result is

$$P = \frac{1}{2} R \frac{|V_{open}|^2}{\left| \frac{V_{open}}{I_{short}} \right|^2 + R^2}.$$

If the load is matched, then R is equal to the characteristic impedance of the propagation mode. V_{open} is determined from the transverse \vec{E} field with an open boundary condition ($\vec{H}_\parallel = 0$) and I_{short} is determined from the transverse \vec{H} field with a short boundary condition ($\vec{E}_\parallel = 0$).

The voltage and current must be defined so that the power flow in a forward-travelling wave is $\frac{1}{2} V I^*$ (where I^* is the complex conjugate of I) and the characteristic impedance of the line is V/I . Suitable definitions of V and I can be chosen for any waveguide or TEM transmission line (V and I are uniquely defined only in a TEM line). For the TM_{01} mode in a circular waveguide, satisfactory definitions are

$$V \equiv \sqrt{\pi a} E_r(r=a, \phi); \quad I \equiv \sqrt{\pi a} H_\phi(r=a, \phi),$$

where a is radius of the guide.

The procedure for using the method is then as follows: (i) Calculate the resonant modes of the cavity with the beam pipe terminated in an open and a short using a program like URMEL. (ii) Calculate V_{open} and I_{short} and

deduce

$$Q_V \equiv 2\omega UR \frac{1}{|V_{open}|^2}; \quad Q_I \equiv 2\omega U \frac{1}{R |I_{short}|^2}, \quad (1)$$

where ω and U are the calculated resonant angular frequency and stored energy, respectively. (iii) Identify the mode pairs that correspond to the same cavity mode with the opposite boundary condition in the beam tube. The coupling to the beam tube for that cavity mode is then

$$Q_{ext} = Q_V + Q_I. \quad (2)$$

Q_{ext} should be independent of the beam tube length ℓ .

It should be noted that (i) a single mode of propagation is assumed, (ii) the frequency shift due to the open or short in the beam tube is neglected, and (iii) the energy stored in the transmission line is not subtracted. Because of (ii) and (iii), the method is most appropriate in the case of weak coupling to the beam tube.

III. AN ORTHOGONALISED CURRENT-VOLTAGE METHOD

There is one disadvantage to the current-voltage method as outlined above: the calculated Q_{ext} is influenced by the fields of other non-propagating or propagating modes. One must therefore choose ℓ large enough to eliminate contribution from evanescent fields. This also means that the method cannot be used if there is more than one mode of propagation. There is a remedy for these drawbacks, however: if the modes of propagation are orthogonal, the contribution to the calculated Q_{ext} from the other modes of propagation can be eliminated using orthogonality.

If the modes of propagation are orthogonal, then for each mode j of propagation, one can define transverse "unit fields" \vec{E}_j and \vec{H}_j which are proportional to the transverse fields in a forward-going wave; these unit fields must satisfy

$$\int_A \vec{E}_j \times \vec{H}_j^* da = \delta_{jj'}, \quad (3)$$

where the integral is over the cross-section A of the transmission line. Equation (3) is a necessary and sufficient orthogonality condition. The current I_j and voltage V_j for the j th mode of propagation are obtained from the unit fields and the \vec{E} and \vec{H} fields calculated by URMEL or SUPERFISH as follows:

$$V_j = \int_A \vec{E} \times \vec{H}_j^* da; \quad I_j = \int_A \vec{E}_j^* \times \vec{H} da.$$

The Q_{ext} for the j th mode of propagation is obtained from V_j and I_j using (1) and (2).

For the TM_{0n} mode in a circular waveguide, a suitable choice of unit fields gives the following expressions for the orthogonalised V and I :

$$V = \frac{1}{\sqrt{\pi}aJ_1(x_{0n})} \int_0^{2\pi} \int_0^a E_r(r, \phi) J_1\left(\frac{x_{0n}}{a}r\right) r dr d\phi$$

$$I = \frac{1}{\sqrt{\pi}aJ_1(x_{0n})} \int_0^{2\pi} \int_0^a H_\phi(r, \phi) J_1\left(\frac{x_{0n}}{a}r\right) r dr d\phi,$$

where $J_m(x)$ is the ordinary Bessel function of the first kind of order m and x_{0n} is the n th zero of $J_0(x)$.

IV. COUPLING PREDICTIONS FOR THE CESR-B CAVITY

Q_{ext} calculations for TM monopole modes in the CESR-B cavity shape with a matched beam pipe were done with URMEL. Several different beam tube lengths were examined for "even" monopole modes (TM_{0-EE} and TM_{0-EM} in URMEL lingo); only one beam tube length was used for the "odd" monopoles (TM_{0-ME} and TM_{0-MM}). An even TM_{012} -like mode near 1.5 GHz was sought, as the TM_{012} has acquired a bad reputation in another single-cell cavity shape [2].

The calculated resonant frequencies of the first few even TM monopoles are shown in Figure 2. There is a pair of modes at about 1.6 GHz which remain close in frequency for all ℓ ; they also have lower fields in the beam tube than neighbouring modes. The calculated values of Q_V and Q_I for these two modes are shown in Figure 3a, along with the Q_{ext} obtained with the hypothesis that they represent a single cavity mode. There is significant deviation for small ℓ , but the Q_{ext} converges to about 120 for large ℓ . Q_V , Q_I , and Q_{ext} values obtained using the orthogonalised

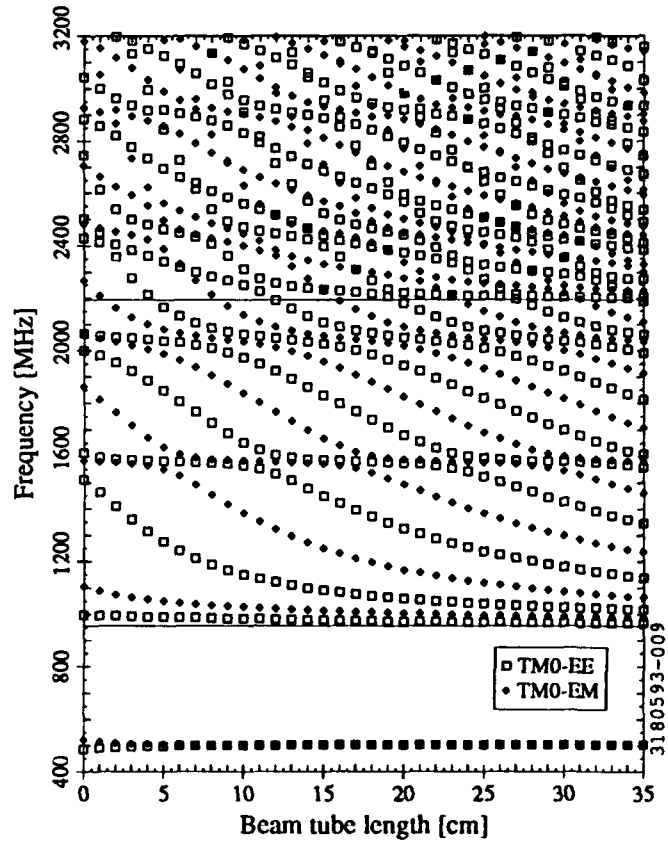


Figure 2. Dependence of the calculated resonant frequencies of even modes on ℓ . The first two cutoff frequencies for TM_0 propagation are indicated by solid lines. The two modes at 500 MHz are the cavity fundamental.

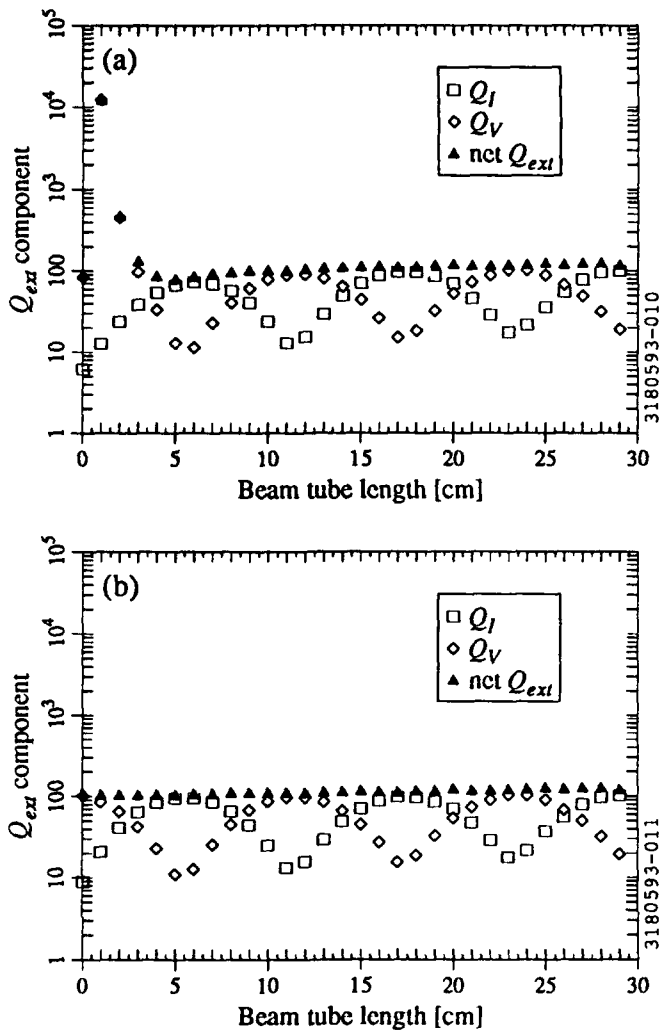


Figure 3. Dependence of the calculated Q_V , Q_I , and Q_{ext} of the 1.6 GHz modes on beam tube length (a) without and (b) with orthogonalisation. For (b), the values are based on TM_{01} propagation.

method are shown in Figure 3b. The Q_{ext} predicted with the orthogonalised method is almost constant even down to $\ell = 0$.

The other modes were not paired up, so their Q_{ext} cannot be predicted exactly, but it can be estimated from Q_V and Q_I . Values of Q_V and Q_I calculated using the orthogonalised method with $\ell = 20$ cm are listed in Table 1. From (2), we expect $Q_{ext} \leq 124$ for all of the modes listed.

Methods for calculating the shunt impedance Z_s of these modes are still under study. The evidence suggests that $Z_s/Q \sim 0.1 \Omega$ for the 1.6 GHz mode. The Z_s/Q of modes with lower Q 's may not be calculable with URMEL, because their resonant frequencies and field patterns are significantly affected by the boundary condition in the beam tube.

Table 1. Q_I and Q_V predicted with the orthogonalised method for $\ell = 20$ cm. Modes above TM_{01} cutoff and below TM_{02} cutoff are listed.

TM0-EE Modes		TM0-EM Modes	
Frequency [MHz]	Q_I	Frequency [MHz]	Q_V
973.9	26	1005.8	22
1059.7	11	1170.3	7
1326.8	6	1494.9	8
1574.6	70	1589.0	54
1681.5	9	1824.8	11
1944.3	15	2018.2	35
2049.2	61	2090.5	25
2182.0	16		
TM0-ME Modes		TM0-MM Modes	
Frequency [MHz]	Q_I	Frequency [MHz]	Q_V
972.3	27	1008.4	18
1066.9	11	1165.8	8
1289.7	8	1407.8	10
1527.8	9	1677.0	8
1833.4	11	1925.0	24
1995.3	16	2135.8	10

V. CONCLUDING REMARKS

A trapped monopole mode was found in the CESR-B cavity. Since its Q is predicted to be 120, we expect that it will not engender beam instabilities. The Q 's predicted by the current-voltage method are of the same order as the Q 's measured on the copper model and predicted by SEAFISH, which suggests that the ferrite layer is close to a matched load.

VI. REFERENCES

- [1] H. Padamsee *et al.*, *Conference Record of the 1991 IEEE Particle Accelerator Conference*, p. 786-788.
- [2] E. Haezel *et al.*, CERN/EF/RF 84-1 (1984).
- [3] S. Fornaca *et al.*, *Proceedings of the 1987 IEEE Particle Accelerator Conference*, p. 1818-1820.
- [4] V. Veshcherevich *et al.*, *Proceedings of B Factories: The State of the Art in Accelerators, Detectors, and Physics*, SLAC-400/CONF-9204126, p. 177-180.
- [5] D. Moffat *et al.*, "Design, Fabrication and Testing of a Ferrite-lined HOM Load for CESR-B," these proceedings.
- [6] W. Hartung, NS/RF-92-1701, National Superconductor, 160000 Lincoln Avenue, Brentwood, Colorado 80523 (1992).
- [7] K. Halbach & R. F. Holsinger, *Particle Accelerators* 7, 213 (1976).
- [8] T. Weiland, *Nucl. Instrum. Methods* 216, 329 (1983).

Envelope Equations for Transients in Linear Chains of Resonators

H. Henke and M. Filtz

Technische Universität, EN-2, Einsteinufer 17, D-1000 Berlin 10, Germany

Abstract

Transient signals in strings of resonators consist of regimes with different time constants: high frequency oscillations, beat signals and exponentials. If one is interested only in the signals envelope one can transform the system of second order differential equations into a system of first order differential equations. The latter carries fast varying terms, which are averaged out, and slowly varying terms. The resulting equations are well behaving and can be integrated numerically. Results are shown for the filling process under beam loading of the superconducting nine-cell TESLA cavity.

I Introduction

Transients in strings of resonators are usually calculated by means of a Laplace transform in matrix notation or by a discrete Laplace transform (see for instance [1]). Both approaches become quite awkward if the string is not homogeneous and/or has branches. Also, one is often not interested in the full time response but only the signals envelope. Then, it may be convenient to take advantage of the fact that the system consists of three regimes with normally very different time constants: First, the high frequency oscillations with the time constant T_{RF} of one period. Second, beating signals with time constants T_{RF}/k where k is the coupling between resonators. Third, signals which are related to the filling time Q/ω_{RF} .

In the following it is shown how to transform the system of second order differential equations (DE) describing the individual resonators into a system of first order DE's of twice the size. The system is written in a way that the fast varying terms can be averaged out and only slowly varying terms remain. The left over system of DE's is integrated numerically yielding the signal envelopes.

The method is applied to the filling process of the superconducting TESLA cavity consisting of nine resonators. Due to the high Q of the cavity the filling time is of the order of one ms whereas the RF period is less than one ns . The coupling between cells is in the percent region. Thus, the time constants are well separated and the proposed method is ideally suited.

II Filling of a Single Resonator

Let us assume a single resonator which is driven by a generator via some coupling device, Fig. 1

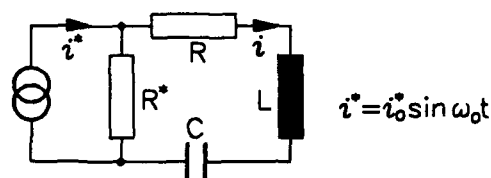


Figure 1: Single resonator driven by a generator with transformed current i^* and internal impedance R^* .

i^* and R^* are the generators current and impedance transformed by the coupling device. The loop equation of the circuit can be written as

$$\ddot{q} + \frac{\omega_0}{Q_L} \dot{q} + \omega_0^2 q = f_0 \sin \omega_0 t \quad (1)$$

$$q = \int i dt, \quad \omega_0 = \frac{1}{\sqrt{LC}}, \quad Q_L = \frac{\omega_0 L}{R+R^*}, \quad f_0 = \frac{R^*}{L} i_0^*.$$

For q we try an ansatz called variation of constants

$$q(t) = a(t) \cos \omega_0 t + b(t) \sin \omega_0 t \quad (2)$$

(1), (2) are two equations for three unknown functions q , a , b . Hence, we can impose a third condition which we choose as

$$\dot{a} \cos \omega_0 t + \dot{b} \sin \omega_0 t = 0. \quad (3)$$

Differentiation of (2) while considering (3) and substituting into (1) gives

$$(\dot{b} + \frac{\omega_0 b}{Q_L}) \cos \omega_0 t - (\dot{a} + \frac{\omega_0 a}{Q_L}) \sin \omega_0 t = \frac{f_0}{\omega_0} \sin \omega_0 t. \quad (4)$$

Now, multiplying (4) with $\sin \omega_0 t$ and (3) with $\cos \omega_0 t$ we can eliminate b through subtraction. In a similar way we eliminate a and obtain a system of first order DE's

$$\begin{aligned} \dot{a} + \frac{\omega_0}{2Q_L} a + \frac{f_0}{2\omega_0} &= \\ &= \frac{\omega_0}{2Q_L} (a \cos 2\omega_0 t + b \sin 2\omega_0 t) + \frac{f_0}{2\omega_0} \cos 2\omega_0 t \end{aligned}$$

$$\begin{aligned} \dot{b} + \frac{\omega_0}{2Q_L} b &= \\ = \frac{\omega_0}{2Q_L} (a \sin 2\omega_0 t - b \cos 2\omega_0 t) + \frac{f_0}{2\omega_0} \sin 2\omega_0 t. \end{aligned} \quad (5)$$

So far, equ. (5) is still exact. We only have transformed the second order DE (1) for q into two first order DE's for a and b . Not much seems to be gained. But (5) is well suited to determine approximately a and b if they are slowly varying, i.e. if they do not change much over one period $T_0 = 2\pi/\omega_0$. Then, we can average the eqs. (5) over T_0 and the right sides become zero. The solutions of the remaining left sides are straight forward.

III Transients in a Chain of Coupled Resonators

Next we consider a chain of N coupled resonators, Fig. (2).

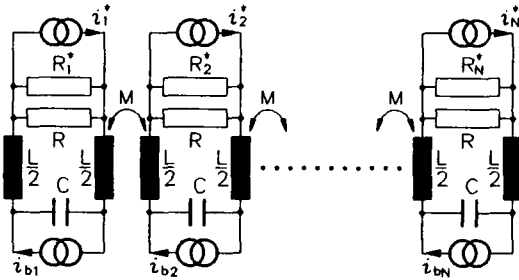


Figure 2: Chain of N coupled resonators driven by generator currents i_n^* and beam currents i_{bn} .

Each resonator is coupled to a generator with transformed current i_n^* and impedance R_n^* . The beam currents i_{bn} are assumed to be δ -function like, so they can be taken into account as a jump in q_n at any instant t . Then the second order DE's for each loop can be written in a matrix notation

$$\ddot{\mathbf{q}} + \frac{\omega_0}{Q_0}(\mathbf{I} + \beta)\dot{\mathbf{q}} + \omega_0^2\mathbf{q} - k\mathbf{K}\mathbf{q} = \mathbf{f} \quad (6)$$

with

$$\mathbf{q} = \begin{bmatrix} q_1 \\ q_2 \\ \vdots \end{bmatrix}, \quad \beta = \begin{bmatrix} \beta_1 & 0 & \cdots \\ 0 & \beta_2 & \\ \vdots & & \ddots \end{bmatrix}$$

$$\beta_n = R_n^*/R, \quad \omega_0^2 = 1/LC, \quad Q_0 = \omega_0 L/R, \quad k = L/M$$

$$\mathbf{K} = \begin{bmatrix} 0 & 1 & 0 & 0 & \cdots \\ 1 & 0 & 1 & 0 & \\ 0 & 1 & 0 & 1 & \\ \vdots & & & & \ddots \end{bmatrix}, \quad \mathbf{f} = \begin{bmatrix} f_1 \sin \omega_{01} t \\ f_2 \sin \omega_{02} t \\ \vdots \end{bmatrix}$$

In order to solve the system (6) we try an ansatz

$$\mathbf{q} = \mathbf{Q}[\mathbf{Ca} + \mathbf{Sb}], \quad \dot{\mathbf{q}} = \mathbf{Q}[\mathbf{C}\dot{\mathbf{a}} + \mathbf{S}\dot{\mathbf{b}} - \omega\mathbf{Sa} + \omega\mathbf{Cb}] \quad (7)$$

where

$$\mathbf{a} = \begin{bmatrix} a_1(t) \\ a_2(t) \\ \vdots \end{bmatrix}, \quad \mathbf{b} = \begin{bmatrix} b_1(t) \\ b_2(t) \\ \vdots \end{bmatrix}, \quad \mathbf{Q} = \begin{bmatrix} q_1^{(1)} & q_1^{(2)} & \cdots \\ q_2^{(1)} & q_2^{(2)} & \\ \vdots & & \ddots \end{bmatrix}$$

and ω , \mathbf{C} , \mathbf{S} are diagonal matrices with elements ω_i , $\cos \omega_i t$, $\sin \omega_i t$, respectively. $a_i(t)$, $b_i(t)$ are the slowly varying amplitudes in each cell and ω_i , $q^{(i)}$ are the eigenfrequencies and eigenvectors of the steady-state, loss-free, homogenous system respectively. The latter can easily be derived with standard matrix algebra as for instance treated in [2]. For a so-called flat-tuned π -mode structure they are given as

$$\omega_i/\omega_0 = (1 - 2k \cos i\phi)^{-1/2}, \quad \phi = \pi/N$$

$$q_n^{(i)} = \sin[(n - \frac{1}{2})i\phi] / \sqrt{\sum_n \sin^2[(n - \frac{1}{2})i\phi]}. \quad (8)$$

Similar to the case of a single resonator, we impose the condition

$$\mathbf{C}\dot{\mathbf{a}} + \mathbf{S}\dot{\mathbf{b}} = 0 \quad (9)$$

in order to reduce the degree of freedom for the functions in (7). After differentiating (7) once more and making use of (9) we substitute (7) and $\dot{\mathbf{q}}$ into (6) and find

$$\mathbf{A}(\mathbf{C}\dot{\mathbf{b}} - \mathbf{S}\dot{\mathbf{a}}) + \frac{\omega_0}{Q_0}(\mathbf{I} + \beta)\mathbf{Q}\omega(\mathbf{C}\mathbf{b} - \mathbf{S}\mathbf{a}) + \mathbf{M}(\mathbf{C}\mathbf{a} + \mathbf{S}\mathbf{b}) = \mathbf{f} \quad (10)$$

with $\mathbf{A} = (\mathbf{I} - k\mathbf{K})\mathbf{Q}\omega$, $\mathbf{M} = \omega_0^2\mathbf{Q} - \mathbf{A}\omega = 0$.

\mathbf{M} is the system matrix of the steady-state, loss-free, homogenous case and thus vanishes.

Because of the unitarian character of \mathbf{Q} , $\mathbf{Q}^{-1} = \mathbf{Q}^t$, we can invert \mathbf{A} and obtain for (10)

$$\mathbf{C}\dot{\mathbf{b}} - \mathbf{S}\dot{\mathbf{a}} + \frac{\omega}{\omega_0 Q_0}(\omega + \mathbf{P}\omega)(\mathbf{C}\mathbf{b} - \mathbf{S}\mathbf{a}) = \frac{1}{\omega_0^2}\omega\mathbf{Q}^t\mathbf{f} \quad (11)$$

with $\mathbf{P} = \mathbf{Q}^t\beta\mathbf{Q}$. Successive elimination of $\dot{\mathbf{a}}$ and $\dot{\mathbf{b}}$ from (9) and (11) yields

$$\begin{aligned} \dot{\mathbf{a}} + \frac{1}{\omega_0 Q_0} [\omega^2(\mathbf{S}^2\mathbf{a} - \mathbf{S}\mathbf{C}\mathbf{b}) + \omega\mathbf{S}\mathbf{P}(\mathbf{S}\omega\mathbf{a} - \mathbf{C}\omega\mathbf{b})] &= \\ = -\frac{1}{\omega_0^2}\omega\mathbf{S}\mathbf{Q}^t\mathbf{f} \\ \dot{\mathbf{b}} + \frac{1}{\omega_0 Q_0} [\omega^2(\mathbf{C}^2\mathbf{b} - \mathbf{C}\mathbf{S}\mathbf{a}) + \omega\mathbf{C}\mathbf{P}(\mathbf{C}\omega\mathbf{b} - \mathbf{S}\omega\mathbf{a})] &= \\ = \frac{1}{\omega_0^2}\omega\mathbf{C}\mathbf{Q}^t\mathbf{f} \end{aligned} \quad (12)$$

In (12) we find again products of sine- and cosine-functions which we decompose into slowly and fast varying terms, e.g.

$$\sin(\omega_i t) \cos(\omega_j t) = [\sin(\omega_i - \omega_j)t + \sin(\omega_i + \omega_j)t]/2.$$

Now, we average the system over a time span approximately equal to the period of the fast varying signals and obtain, finally, the system of first order DE's for the slowly varying signals

$$\begin{aligned} \dot{\mathbf{a}} + \frac{1}{2\omega_0 Q_0} [\omega(\mathbf{I} + \mathbf{P}_c)\omega\mathbf{a} - \omega\mathbf{P}_s\omega\mathbf{b}] &= -\frac{1}{2\omega_0^2}\omega\mathbf{R}_c \\ \dot{\mathbf{b}} + \frac{1}{2\omega_0 Q_0} [\omega(\mathbf{I} + \mathbf{P}_c)\omega\mathbf{b} + \omega\mathbf{P}_s\omega\mathbf{a}] &= -\frac{1}{2\omega_0^2}\omega\mathbf{R}_s \end{aligned} \quad (13)$$

where

$$\mathbf{P}_c = \begin{bmatrix} p_{11} & p_{12} \cos(\omega_1 - \omega_2)t & p_{13} \cos(\omega_1 - \omega_3)t & \cdots \\ p_{21} \cos(\omega_2 - \omega_1)t & p_{22} & p_{23} \cos(\omega_2 - \omega_3)t & \\ \vdots & & & \ddots \end{bmatrix}$$

$$\mathbf{R}_c = \begin{bmatrix} q_1^{(1)} f_1 \cos(\omega_1 - \omega_{01})t + q_2^{(1)} f_2 \cos(\omega_1 - \omega_{02})t + \dots \\ q_1^{(2)} f_1 \cos(\omega_2 - \omega_{01})t + q_2^{(2)} f_2 \cos(\omega_2 - \omega_{02})t + \dots \\ \vdots \end{bmatrix}$$

\mathbf{P}_s , \mathbf{R}_s are equal to \mathbf{P}_c , \mathbf{R}_c with the cosine replaced by sine. The system (13) yields non-oscillating solutions and is very stable. It can easily be integrated over 10^5 periods $T = 2\pi/(\omega_i - \omega_j)$, for instance with a fifth order Runge-Kutta method. The initial conditions are normally given in \mathbf{q} and $\dot{\mathbf{q}}$ and define $\mathbf{a}(0)$ and $\mathbf{b}(0)$ by (7) and (9).

The beam currents can be taken into account by jumps in q_i and continuity in \dot{q}_i , i.e. by $\delta q(t_j)$. Then, from (7), (9) follows

$$\delta \mathbf{a}(t_j) = \mathbf{C}(t_j) \mathbf{Q}^T \delta \mathbf{q}(t_j), \quad \delta \mathbf{b}(t_j) = \mathbf{S}(t_j) \mathbf{Q}^T \delta \mathbf{q}(t_j). \quad (14)$$

Having solved for \mathbf{a} , \mathbf{b} we are still left to find reasonable envelopes from (7). Since, typically, the resonator chain is driven by a single generator with frequency ω_{0n} and the particles to be accelerate have to stay in phase with $\omega_{0n}t$ it is best to develop all frequencies around ω_{0n} , e.g.

$$\cos \omega_i t = \cos \delta \omega_i t \cdot \cos \omega_{0n} t - \sin \delta \omega_i t \cdot \sin \omega_{0n} t.$$

then, (7) can be written as

$$\begin{aligned} \mathbf{q} &= \mathbf{Q}[(\delta \mathbf{C} \mathbf{a} + \delta \mathbf{S} \mathbf{b}) \cos \omega_{0n} t + (\delta \mathbf{C} \mathbf{b} - \delta \mathbf{S} \mathbf{a}) \sin \omega_{0n} t] = \\ &= \mathbf{Q}[\mathbf{a}^* \cos \omega_{0n} t + \mathbf{b}^* \sin \omega_{0n} t] \end{aligned} \quad (15)$$

where $\delta \mathbf{C}$, $\delta \mathbf{S}$ are diagonal matrices of $\cos \delta \omega_i t$ and $\sin \delta \omega_i t$ respectively. $(\mathbf{Q} \mathbf{a}^*)_i$ is now the envelope signal in cell i which is relevant for particles in phase with $\cos \omega_{0n} t$. $(\mathbf{Q} \mathbf{b}^*)_i$ is a signal which decays and which rings with $\sin \omega_{0n} t$, i.e. it is out of phase with the particles.

IV Filling of the TESLA Cavity

As an example we choose the filling process of the superconducting cavity for the TESLA linear collider study. The cavity is a nine-cell, flat-tuned, π -mode structure. It is driven by a generator in the first cell. We assume that the beam induced voltage is half of the voltage generated by the driver. Then, the cavity voltage stays constant after the time $t_0 = \tau \ln 2$ when the beam is switched on. τ is the filling time

$$\tau = \frac{2Q_0}{\omega_\pi (1 + \beta_1) q_1^{(9)^2}} = 0.832 \text{ ms}$$

The parameters used are

$$\begin{aligned} f_\pi &= f_{09} = 1.3 \text{ GHz}, \quad Q_0 = 3 \cdot 10^9, \quad R/Q_0 = 112.3 \Omega/\text{cell} \\ \beta_1 &= 9 \cdot 882 = 7938 \text{ generator coupling constant} \\ L &= 115.4 \text{ mm cell length} \\ k &= 0.0185 \text{ cell-to-cell coupling} \\ T_b &= 1 \mu\text{s bunch distance}, \quad N_b = 800 \text{ \# bunches} \\ N_e &= 5 \cdot 10^{10} \text{ \# } e^-/\text{bunch} \end{aligned} \quad (16)$$

Fig. 3a shows the exponential increase of the cavity voltage and its flat top under beam loading. The curve is an overlay of the voltage envelopes in the first and the ninth cell. A zoom of the curve for very short times, Fig. 3b, and for the first and last bunches of the beam, Fig. 4, resolve the different signals in the cells. Evaluating the time delay between the filling of the 1st and 9th cell, see Fig 3b, clearly proves that the wavefront in an empty cavity travels with the average group velocity in the pass-band, i.e. with essentially the group velocity at the $\pi/2$ -mode. The same is true for the refilling of the cavity when a bunch has taken out a certain amount of the energy. From Fig. 4 it can be seen that field levels are different in every cell and that the differences are larger at the beginning of the beam. But averaging over all cells only results in a maximum voltage variation of about 0.5% for the bunches. Finally, a study of the voltage sensitivity ΔV at the end of the beam against changes in the bunch charge ΔN_e gives $\Delta V/V \approx 0.4 \Delta N_e/N_e$.

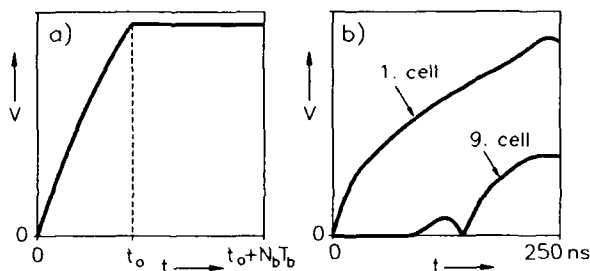


Figure 3: Filling process of the TESLA cavity with beam for $t > t_0$. a) Voltage envelopes in the 1st and 9th cell, b) zoom for small times.

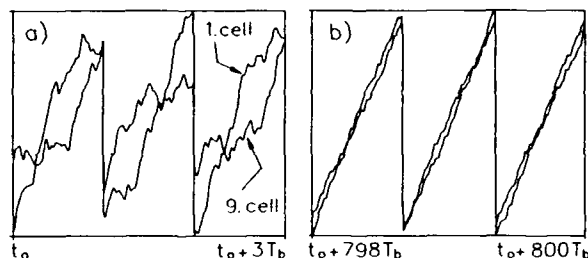


Figure 4: Blown-up curve of Fig. 3 for the a) first and b) last bunches of the beam.

References

- [1] M. F. Gardner and J. L. Barnes, Transients in linear systems. Wiley, New York 1942.
- [2] M. C. Pease, Methods of matrix algebra. Academic Press 1965.

A Broad-Band Side Coupled mm-Wave Accelerating Structure for Electrons.

H. Henke and W. Bruns

Technische Universität Berlin, EN-2, Einsteinufer 17, D-1000 Berlin 10, Germany

Abstract

Modern micrometer etching techniques could be well suited for the fabrication of accelerating structures in the mm-wave region. But keeping fabrication tolerances within a few thousandths or tuning the structures is not at all obvious. Therefore we propose side coupled structures with a confluent π -mode which are expected to have large bandwidth, high group velocity and to be insensitive against errors. The proposed structures are planar, side coupled muffin tins. Three different geometries are investigated with coupling cells arranged symmetrically or alternately on both sides. Dimensions and basic RF parameters are given.

I. Introduction

Recently a double sided muffin tin has been proposed for electron acceleration in the mm-wave region [1]. The structure is planar and thus ideally suited for modern fabrication techniques like lithography and etching. On the other side it is not obvious to keep fabrication tolerances within a few thousandths or to tune such a structure. Also, due to the high losses per unit length one might get intolerably high temperature gradients. Therefore, one would like to operate the structure in a mode which has a high group velocity and which is the least sensitive to errors.

The $\pi/2$ -mode fulfills most of the above mentioned requirements. But it has a low shunt impedance because of the close spacing of the irises. Better are, normally, double-periodic structures with confluence in the π -mode. They have high shunt impedance and high group velocity and are very insensitive to errors, especially if the dispersion relation is antisymmetric around the π -mode.

In the paper we investigate three different side coupled cavity arrangements, see fig. 1, with coupling cavities arranged symmetrically or alternately on both sides. All three geometries are planar and require no more complicated or more costly fabrication than the single periodic structure [1].

II. Choice of Geometry and Mode of Operation

The operating frequency is 120 GHz. This corresponds

to a wavelength of $\lambda = 2,5\text{mm}$ with typical cavity dimensions in the submillimeter range.

Looking at the mode of operation we have the option to use standing waves or travelling waves in π -mode, since the geometries are made confluent at π -mode, yielding a non vanishing group velocity and good mode separation.

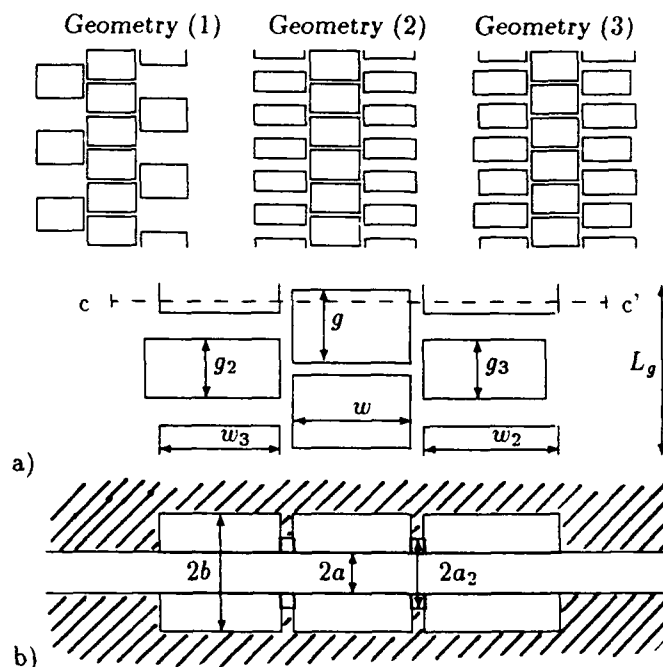


Figure 1: The double-sided muffin-tin structures
a) Top-view b) transverse cut of structure (3) (c-c')

Geometry: Three different confluent structures have been found. The structures have a geometric period length of $L_g = \lambda = 2,5\text{mm}$, and an electric period length $L_e = L_g/2$.

Structure 1 consists of two accelerating cavities and two coupling cavities per period L_g .

Structure 2 consists of two accelerating cavities and four coupling cavities per period.

Structure 3 consists of two accelerating cavities and four coupling cavities per period, with two different sizes of the coupling cavities.

The period length is given by $L_g = 2\pi/\beta = 2,5\text{mm}$. The other dimensions are chosen to obtain confluence. For 120

GHz the dimensions were found to be (all in mm):

	(1)	(2)	(3)		(1)	(2)	(3)
$a =$	0,3	0,3	0,3	$w_2 =$	1,65	1,78	1,95
$b =$	$w/2$	$w/2$	$w/2$	$w_3 =$	—	1,78	1,75
$w =$	1,70	1,68	1,7	$g_2 =$	1,20	0,95	0,85
$g =$	1,05	1,05	1,05	$g_3 =$	—	0,95	0,85

The 'iris'-thickness t follows from the total length and the gapwidth g to $t = 0,2\text{mm}$. This is also the thickness of the walls between the accelerating and the coupling cells. To obtain a higher magnetic coupling the walls between the accelerating and coupling cavities have been cut to a depth $a_2 = 0,5\text{mm}$.

III. The basic RF Parameters

The RF parameters of the structures in Fig. 1 have been calculated with MAFIA [2]. The resulting parameters are ($\kappa = 56 \times 10^6/(\Omega\text{m})$) (Standing Wave):

Geometry	(1)	(2)	(3)
Q_0	2822	2593	2723
$r_0[\text{M}\Omega/\text{m}]$	260	246	266
$r_0/Q_0[\text{k}\Omega/\text{m}]$	92	95	98

The dispersion relations are given in Fig. 2. Note that the periodicity length is L_g , the phaseshift goes from 0 to 2π .

From the dispersion relations we get

	(1)	(2)	(3)
v_g/c_0	0,055	0,058	0,04
Bandwidth[GHz]	9,2	8,9	3,3
$\alpha[\text{m}^{-1}] = \frac{\omega_r}{2v_g Q_0}$	8,10	8,36	11,54

The following parameters depend on the number of cells per wafer. We have chosen $N = 56$ accelerator cells per wafer, giving a wavelenght of $l = N\lambda/2 = 7\text{cm}$.

	(1)	(2)	(3)
$\tau = \alpha l$	0,57	0,59	0,81
$T_f[\text{ns}] = \frac{l}{v_g} = 2 \frac{Q_0 \tau}{\omega_r}$	4,3	4,1	5,9

The mode separation Δf is well above the theoretical need of f_r/Q_0 . We could even have more cells on a wafer, if it wouldn't be limited by the available size:

	(1)	(2)	(3)
$\Delta f[\text{MHz}] = \frac{1}{2\pi L_g} v_g \frac{\pi}{N}$	118	124	86
$120\text{GHz}/Q_0[\text{MHz}]$	43	46	44

The dispersion diagrams need a little explanation:

In the case of geometry 1, the lower branch corresponds to fields in the accelerating cavities.

In the case of geometry 2, the lower branch also has the field in the accelerating cavities, the middle and upper branch have their fields in the side cavities. The middle branch has an odd field with respect to the transverse co-ordinate (dipol mode), the upper branch has an even field.

The case of geometry 3 is more difficult to describe: The field is in the accelerating cavities at the lowest 0 mode and

one of the confluent 2π -modes. The field is in the greater coupling cavities (w_2) at the middle 0 mode and the lowest 2π -mode. The field is in the smaller coupling cavities (w_3) at the highest 0 mode and one of the highest 2π -mode. The accelerator mode jumps over the mode in the greater side cavities.

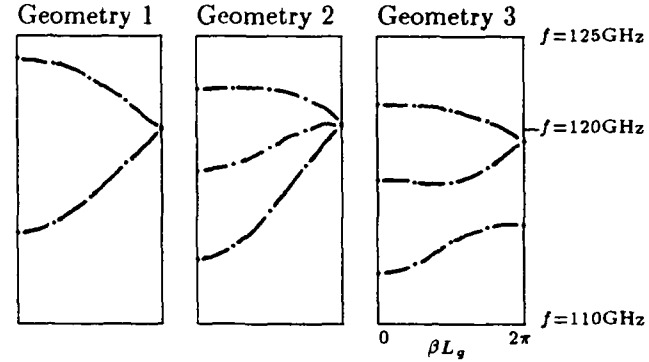
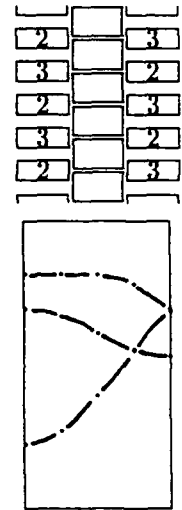


Figure 2: Dispersion relations of the structures (1)-(3)



Numbering the cavities of geometry 2 with all left coupling cavities named 2 and all right cavities named 3 leads to a dispersion relation as in fig. 2. Since geometry 2 has $w_2 = w_3$, we could renumber the cavities to a alternating structure. This leads to a dispersion diagram where the middle branch is swapped, as shown right. The dispersion diagram of geometry 3 can now be understood as the one of geometry 2 with the middle branch pulled down.

IV. Conclusions

Three different side coupled muffin tin structures have been investigated. All three geometries could be made confluent in the π -mode with only a slight reduction of the shunt impedance as compared to the single periodic structure [1].

Problems were the inevitable coupling between the coupling cells in the case of geometries (2), (3). It influences the interplay between modes in such a way that the dispersion relation could not be made very well antisymmetric around the π -mode. The geometry (1) has a quite antisymmetric dispersion relation but on the cost of deforming the fields in the main cells.

The bandwidth is typically twice as high as for the single periodic structure. Further work should evaluate and compare the sensitivity against errors of the different geometries.

V. Acknowledgement

We would like to thank the APS project at Argonne National Laboratory, especially R.L. Kustom and the RF group for supporting this work.

References

- [1] H. Henke, Y. W. Kang and R. L. Kustom, "A mm-wave RF structure for relativistic electron acceleration", Argonne National Laboratory, internal report ANL/APS/MWM-1, 1993
- [2] R. Klatt, F. Krawczyk, W. R. Novender, C. Palm, B. Steffen, T. Weiland, T. Barts, M. F. Browman, R. Cooper, C. T. Mottershead, G. Rodenz and S. G. Wipf, Proc. of the 1986 Linear Acc. Conf., Stanford internal report-303, Sept. 1986.

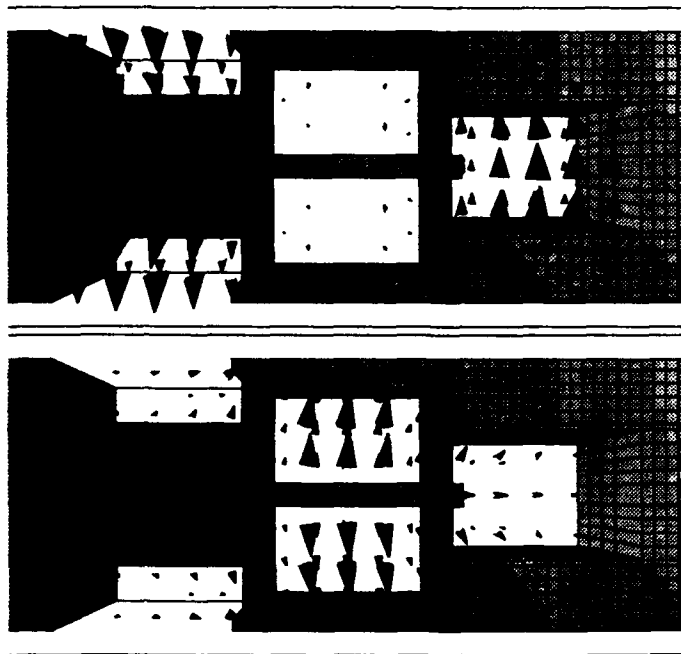


Figure 3: Confluent 2π -modes in structure (1)

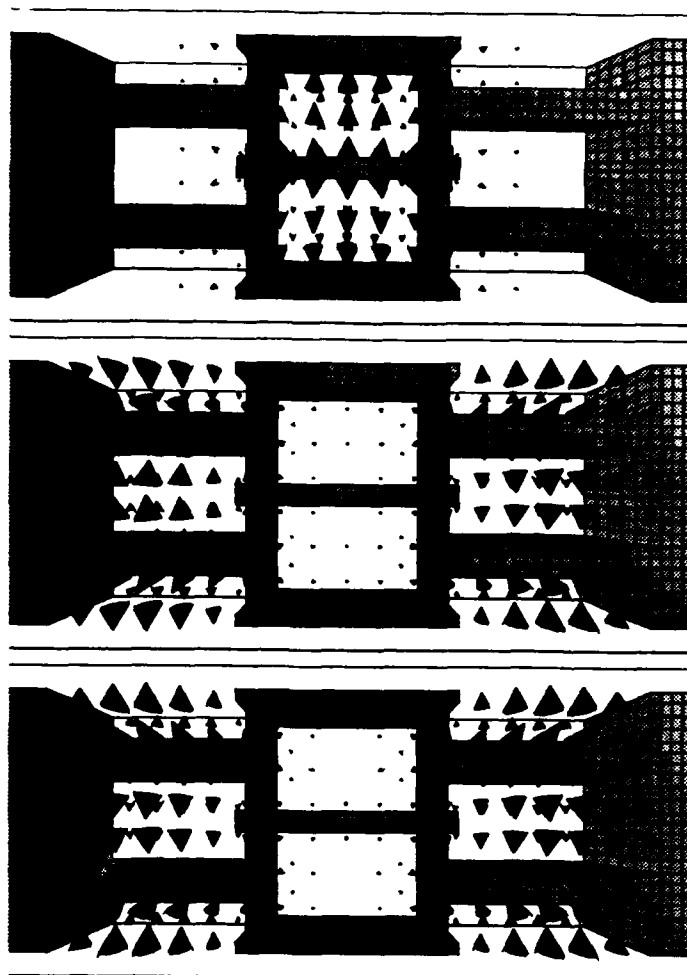


Figure 4: Confluent 2π -modes in structure (2)

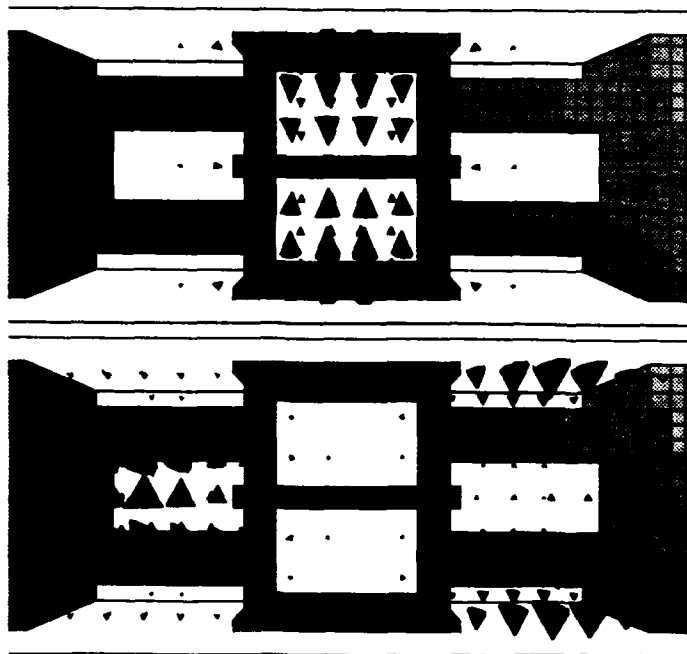


Figure 5: Confluent 2π -modes in structure (3)

ACCELERATOR STRUCTURE DEVELOPMENT FOR NLC*

H. A. Hoag, H. Deruyter, C. Pearson, R. D. Ruth, and J. W. Wang
Stanford Linear Accelerator Center, Stanford University, Stanford, CA 94305
and
J. Schaefer
Texas Instruments Inc., Dallas, Texas

Abstract

In the program of work directed towards the development of an X-Band Next Linear Collider accelerator structure, two different test accelerator sections have been completed, and a third is being fabricated. The first is a simple 30-cell constant-impedance section in which no special attention was given to surface finish, pumping, and alignment. The second is an 86-cell section in which the cells were precision diamond-turned by Texas Instruments Inc. The structure has internal water-cooling and vacuum pumping manifolds. Some design details are given for the third section, which is a 206-cell structure with cavities dimensioned to give a Gaussian distribution of dipole mode frequencies. It has conventional-machining surface finishes and external water and pumping manifolds. Component design, fabrication, and assembly brazing are described for the first two experimental sections.

I. INTRODUCTION

All three structures described are designed to operate in the $2\pi/3$ mode at four times the SLAC frequency, or 11.424 GHz. The first is of the simplest construction, with constant-impedance cavities and rudimentary water-cooling, intended primarily as a first test at SLAC of high rf fields in an X-Band traveling-wave structure, following on from earlier work on cavities and a standing-wave section [1]. It was also the test vehicle for our newly-developed symmetrical double-input coupler [2], and it provided the first accelerator 'load' for the X-Band high-power klystrons under development [3]. Results of the first tests in the Accelerator Structures Test Area (ASTA) [4] have been reported elsewhere [5].

The second structure is also constant-impedance. However, it represents our first attempt at improving accuracy of construction, smoothness of surface finish, and vacuum pumping along the beam path. It is also intended to be primarily a vehicle for high-field breakdown and dark current tests, although it will later be used to accelerate an electron beam.

The third will be the first prototype of the quasi constant-gradient structure with Gaussian dipole mode detuning which is being developed for the Next Linear Collider Test Accelerator (NLCTA). It will be 1.8 m long, and will also be tested in ASTA, as will similar sections which will follow it. However it is also planned to install this section in the SLC for wake-field measurements in the Accelerator Structure Setup (ASSET) experiment.

II. 30 CELL STRUCTURE

The small, 30-cell accelerator structure comprises simple nesting cups, as shown with the two halves of the symmetrical

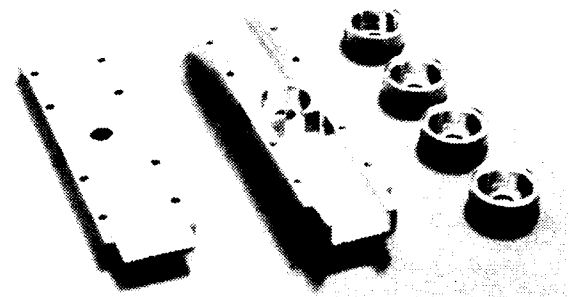


Figure 1. Input coupler and four cells of 30-cell structure.

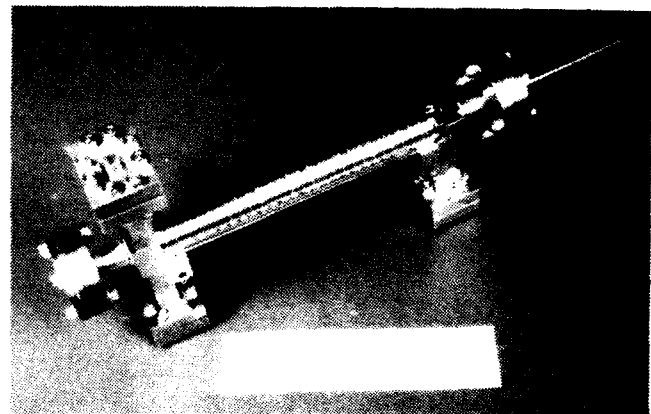


Figure 2. Completed 30-cell accelerator.

double-input coupler in Figure 1. The complete section, brazed with 35/65 Au/Cu shims, is shown in Figure 2.

III. THE 75 cm STRUCTURE

This structure is designed to achieve 100 MV/m when driven by 220 MW pulses generated using the SLED II system [6]. There are 84 cells plus two coupler cavities. The latter have symmetrical double coupling irises, very similar to those shown in Figure 2. The cell design is illustrated in Figure 3. Water cooling tubes and parallel vacuum pumping manifolds are integrated into each cell. Two additional holes provide thin wall segments on two opposite sides of each cavity. Stainless steel tuning studs are brazed on the outsides of these segments, allowing the cavities to be tuned either up or down in frequency by pushing or pulling on the studs. Pumping slots connecting the accelerator cavity to the manifolds can be seen. It was originally intended to use these slots in every cell, but concerns arose about the cumulative effects of leakage of rf power from every cavity into the pumping manifolds. Vacuum calculations showed that a tenfold increase in conductance

* Work supported by Department of Energy contracts DE-AC03-76SF00515 (SLAC).

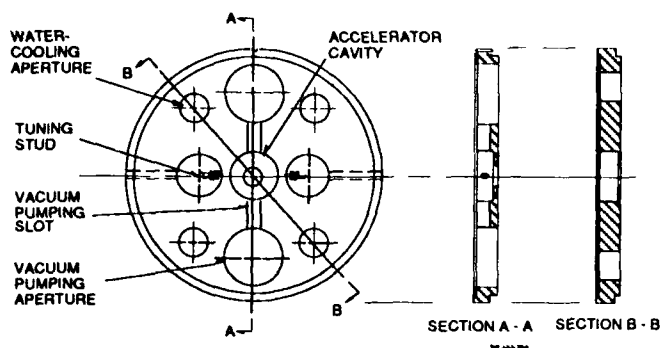


Figure 3. Features of 75 c structure cell.

between the middle of the accelerator section and pumps at each end could be achieved by using only four pumping cells approximately evenly spaced along the section, so this approach was followed. Theoretical work has shown [7] that cell-to-cell misalignment in structures that rely upon dipole mode detuning to achieve wake-field suppression needs to be kept about $5\text{ }\mu\text{m}$. We also know that the tuning rate for the $2\pi/3$ mode as a function of cavity diameter is about $0.6\text{ MHz}/\mu\text{m}$. As a first step towards the alignment goal, and also to improve the cavity dimensional tolerances and possibly reduce dark current, we decided to have the cells made by single-point diamond turning (SPDT). The work was done by Texas Instruments Inc., Dallas, Texas. SPDT utilizes a single crystal, gem quality, diamond tool along with ultra-precision machine tool refinements to produce optical quality surface finishes on nonferrous metals. Diamond has excellent wear characteristics, and can be micro-polished chip-free at a magnification of 800X. The machine in which the tool is used employs air bearing spindles and slideways along with a 10 nm resolution laser interferometer tool positioning system.

The OFE copper blanks were first machined with $75\text{ }\mu\text{m}$ of excess material on the surfaces to be finished by SPDT. The first SPDT operation was to flycut the back surface flat to $1\text{ }\mu\text{m}$ to mate with the lathe vacuum chuck, which was faced to the same flatness to establish a Z-axis zero reference. This reference was used in the multiple-pass CNC program for cutting both sides of the cell. The part was then positioned in the vacuum chuck and indicated to the spindle to less than $2.5\text{ }\mu\text{m}$. Multiple tooling was used to reduce the wear rate on the finishing diamond tool. The latter was designed with a $.38\text{ mm}$ radius and 120° sweep in order to be able to machine flat surfaces and inside and outside diameters in the same setup. The $.38\text{ mm}$ tool radius allowed the $.50\text{ mm}$ internal fillet radius called for to be profiled rather than plunged, eliminating tool chatter and surface degradation. The cavity diameter was held to $\pm 2.5\text{ }\mu\text{m}$ and measured on the machine with an LVDT probe. Centering of the cavity diameter with respect to the outer surface was held to $5\text{ }\mu\text{m}$. To avoid additional set-ups and associated tolerance accumulations, the two surfaces were machined in the same operation, necessitating a reversal of spindle rotation in the middle of the CNC program. The part was then reversed in the vacuum chuck and indicated on the outside diameter to less than $.6\text{ }\mu\text{m}$. This ensured that the two sides of the iris radius blended smoothly. After dimensional

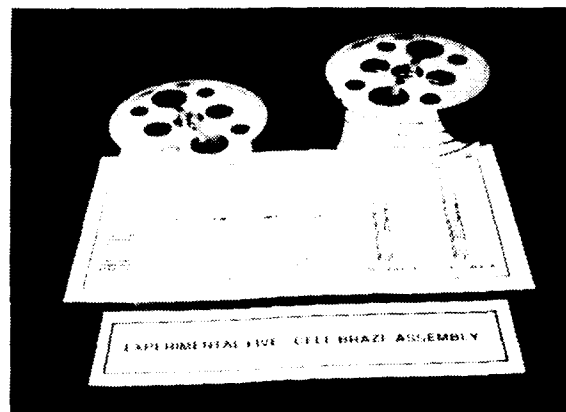


Figure 4. Test braze five-cell assembly.

verification, the parts were vapor degreased, wrapped in lens tissue, sealed in air-tight dessicant bubble bags, boxed and shipped to SLAC.

The first five cells test-brazed at SLAC are shown in Figure 4. Brazing shims of 35/65 Au/Cu alloy $50\text{ }\mu\text{m}$ thick were used. It was a great disappointment to find that the assembly had multiple vacuum leaks. Theories advanced for the failure included contamination on the surfaces of the copper cells and the brazing shim, inadequate flatness of all surfaces, inadequate hydrogen ventilation of the brazing surfaces to reduce oxides and carry away the products of reduction, and surfaces too smooth to permit the braze to 'wet' and flow. Many tests were run under a variety of conditions. Sections were taken, etched, polished and examined. The belief that inadequate hydrogen ventilation was the problem led to a radical change of design for the first 1.8 m section to follow. However, it turned out that the problem lay in the brazing cycle: the time allowed for the temperature of all parts to 'equalize' below the true brazing temperature was too long. This allowed excessive diffusion of copper into the brazing alloy, making it copper-rich and raising its melting point so that, when the assembly was taken up to the expected brazing temperature, the shim did not melt uniformly. The combination of a slightly higher furnace temperature, and a shorter time for 'equalization' cured the problem. However, these troubles did underline the fact that the use of shims with multiple air/water/vacuum internal interfaces was very undesirable. The probability of a failure in a stack of 200 cells so joined would not be negligible. The design had looked attractive in the first place because it afforded a clean outer surface comprised of a stack of precisely machined cells, the surfaces of which could be used for precision alignment.

Continuing nervousness about vacuum leaks in the final assembly led us to use thicker brazing shim ($75\text{ }\mu\text{m}$) than was probably necessary. Tests had shown that the residual braze region would add $52\text{ }\mu\text{m}$ per cell to the period of the structure, so the machined length of each cell was reduced by this amount. The design of the input and output couplers was done using MAFIA and confirming and fine-tuning the dimensions by means of accurately machined and brazed copper models.

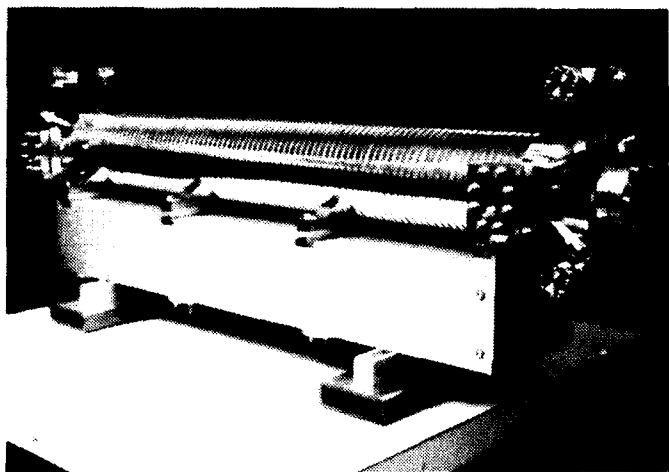


Figure 5. Completed 75 cm accelerator.

The detuning caused by the slots in the pumping cavities was also computed and confirmed by low-power measurements on aluminum model cells.

The final assembly of the structure was done in stages. First, subassembly brazes of three stacks of cells were made. Two stacks had 25 cells, and one 26 cells. After brazing, it was easy to check them and confirm that they were leak-tight. They were also checked for straightness on a coordinate measuring machine (CMM). Secondly, the two couplers were brazed with beam tubes, end pumping manifolds, and the first (and last) two cells which were of special design. Finally, the subassemblies were stacked together vertically, with the output coupler at the bottom, and with pumping cells inserted between each subassembly. The completed accelerator section, leak-checked, mounted on its strongback, and awaiting low-power testing, is shown in Figure 5.

IV. THE 1.8 m STRUCTURE

A first model of the structures intended to be used in the NLCTA is being built. It has 204 cavities plus two coupler cavities, and is approximately 1.8-m long. The filling time is 100 ns, and it is designed for final operation at 100 MV/m gradient, requiring an input power of 346 MW. However, the first goal is to run it successfully at 50 MV/m. The cavity diameter, iris diameter and iris thickness are different for each cavity. Details of the theory leading to this design are given in [6] and [7]. As mentioned earlier, brazing problems with the 75 cm section led to a more conventional and conservative design for this structure. External water tubes and pumping manifolds are employed, and the diameter of the cells containing the cavities

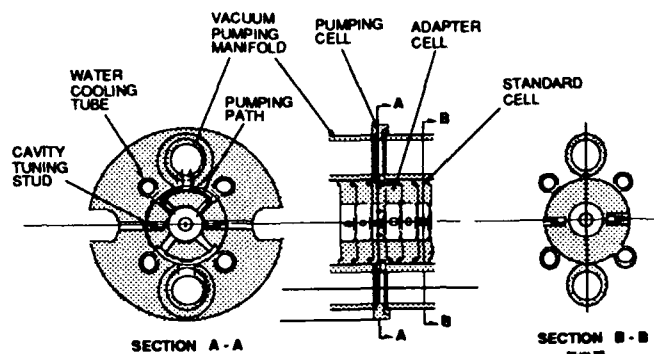


Figure 6. Design features of the 1.8 m structure.

is reduced to 50 mm. General design features are illustrated in Figure 6.

In order to expedite the fabrication of this first section, it was decided to use conventional machining techniques. Tolerances and concentricities are about $10\text{ }\mu\text{m}$ and the surface finish is about $0.4\text{ }\mu\text{m}$. So far, 190 of the cells have been made. Brazing shims and nesting cells are still employed, so the structure periodicity and cell-to-cell alignment will not meet our goals. However, it is expected that much will be learned from the first exercise in putting such a long X-Band structure together. A special furnace is being constructed to accommodate the accelerator length.

V. REFERENCES

- [1] G. A. Loew and J. W. Wang, "Progress Report on High-Gradient rf Studies in Copper Accelerator Structures," XIVth Int. Symp. on Discharges and Electrical Insulation in Vacuum, September 16-20, 1990.
- [2] H. Deruyter et al., "Symmetrical Double Input Coupler Development," 1992 Linear Accel. Conf. Proc., Vol. 1, pp. 407-409.
- [3] G. Caryotakis et al., "Development of Multimegawatt Klystrons for Linear Colliders: A Progress Report," these proceedings.
- [4] A. E. Vlieks et al., "Accelerator and rf System Development for NLC," these proceedings.
- [5] J. W. Wang et al., "High-Gradient Studies on 11.4 GHz Copper Accelerator Structures," 1992 Linear Accel. Conf. Proc., Vol. 2, pp. 716-718.
- [6] J. W. Wang et al., "Design of the Detuned Accelerator Structure," these proceedings.
- [7] K. Thompson et al., "Multibunch Beam Breakup in Detuned Structures," these proceedings.

HOM Damping with Coaxial Dampers in a Pillbox Cavity without the Fundamental Mode Frequency Rejection Filter *

Y. W. Kang, R. L. Kustom, and J. F. Bridges
Accelerator Systems Division
Argonne National Laboratory
9700 S. Cass Ave., Argonne, IL 60439

Abstract

Coaxial dampers with E-probe and H-loop couplers are used to damp higher-order mode (HOM) in an 840-MHz cylindrical prototype cavity. The dampers are positioned to have minimum coupling at the fundamental frequency, f_0 , without using any blocking circuit. The E-probe dampers are used at the equatorial plane of the cavity. The H-loop dampers are used in the end wall of the cavity. The fundamental mode decoupling can be done by positioning the loop plane in the direction of the H-field of the mode. For both dampers, the fundamental mode coupling can be better than -50 dB. The damper load resistance is varied to find the optimum loading. Measurement is made for three cases with 1) three E-probe dampers, 2) three H-loop dampers, and 3) three E-probe and three H-loop dampers.

I. INTRODUCTION

There has been much work on development of HOM dampers in accelerating RF cavities. The most important tasks in designing a HOM damping system are broadbanding and suppression of fundamental mode power coupling. Coaxial dampers are used in both superconducting and normal conducting cavities for particle accelerators [1-5]. Aperture-coupled hollow waveguide type dampers have been recently investigated [6, 7]. These hollow waveguide dampers are used in multiples (usually three to damp the degenerate modes). The fundamental frequency rejection is achieved by the cutoff characteristic of the waveguide. However, degradation of the Q-factor at f_0 is appreciable in this approach.

In coaxial HOM damper designs, the f_0 decoupling is a difficult task. However, the coaxial dampers can be used anywhere in the cavity if a proper f_0 rejection method is used. The coaxial dampers can have the following advantages:

- The fundamental frequency power loss can be minimized with a proper f_0 rejection scheme.
- Dampers are compact, lightweight, and inexpensive.
- Cooling is easy and does not disturb the cavity heat distribution.

E-probe dampers can be used in the cavity equatorial plane without any f_0 rejection filter, since the radial component of the TM_{01} electric field is zero in the midplane.

*Work supported by U.S. Department of Energy, Office of Basic Energy Sciences under Contract No. W-31-109-ENG-38.

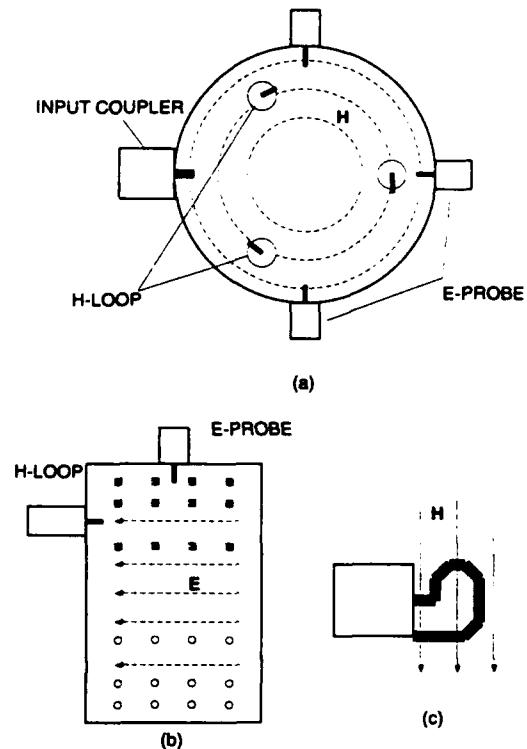


Figure 1

a) E-probe and H-loop coaxial dampers in a cylindrical pillbox cavity. b) Probes and the loops are positioned for least coupling to the TM_{01} accelerating mode. c) The loop plane is parallel to the H-field.

If H-loop dampers are used in the equatorial plane of the cavity, the loop plane must be positioned perpendicular to the fundamental mode H-field to couple to the higher order TM modes. Then, a fundamental frequency rejection filter must be used. H-loop dampers use a half-wavelength short stub in parallel [1] or a quarter wavelength short stub in series [2]. These short stub fundamental frequency rejection circuits also block the signal frequencies at around the even and odd multiples of f_0 , respectively, and also increase the fundamental mode power loss due to the increased current path.

Figure 1 shows the coaxial dampers used with a cylindrical pillbox cavity without a f_0 rejection circuit. A pillbox cavity with $f_0=840$ MHz is used in the measurement. The HOM frequencies are found using the URMEL-T code.

The E-probes are used in the cavity equatorial plane. The H-loops are used in the cavity side-wall. The loop plane is parallel to the TM_{01} mode H-field. Three dampers

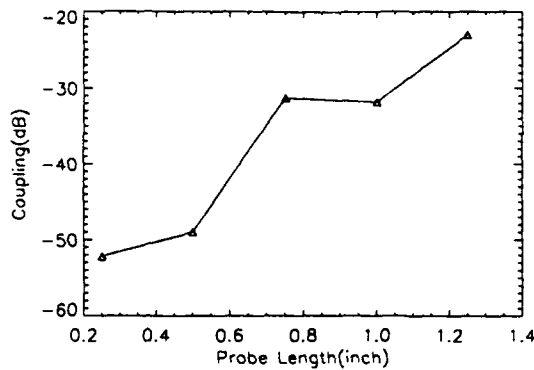


Figure 2

Isolation between power input loop and an E-probe damper at f_o . $R_L = 50\Omega$

are used to increase the coupling to the degenerate modes.

The size of the loop or the probe as well as the location in the cavity determine the coupling to specific HOM fields and thus the damping ratio. The fundamental mode coupling to the dampers is also dependent on the position and size. The coupling between the input coupler and a damper at f_o with respect to the size of the probe or the loop is measured and shown in the next sections.

II. E-PROBE DAMPERS

The fundamental mode coupling as a function of the probe length is shown in Figure 2. A probe diameter of $d = 0.25$ " is used. The probe in this position should not couple to the fundamental TM_{01} mode field. But, due to imperfect probe alignment and mutual coupling between the two coupling devices, a small amount of coupling exists.

Three E-probe dampers are used in the cavity equatorial plane with an angular separation of 90° . The load resistance is varied to see how the damping ratios change. A probe with diameter $d = 0.25$ " and length $\ell = 0.50$ " is used. Measurement of the damping ratio of thirteen HOMs is shown in Table 1. These modes are the cylindrical equivalent of the higher-order TM modes of the storage ring single cell cavity to be used in the APS and can cause beam instability [8, 9]. Measurements are taken in dB scale which is related as $10 \log |S_{21}|^2$. The Q-factor for a mode is proportional to $|S_{21}|$. TM0 denotes the monopole modes and TM1 denotes the dipole modes. ME and EE denote the boundary conditions with magnetic and electric conductors in the cavity equatorial plane, respectively. The results show that the modes with E-field at the cavity mid-plane (ME boundary condition) are damped effectively and the modes with no E-field in the midplane (EE boundary) are not.

III. H-LOOP DAMPERS

The power input loop to the damper coupling was measured and is shown in Figure 3. The plane of the H-loop

Table 1
HOM damping with E-probe dampers. $R_L = 30, 50, 100\Omega$

Mode type	$f(\text{MHz})$	Damping (dB)		
		30Ω	50Ω	100Ω
TM0-EE-1	840.412	0	0	0
TM0-ME-1	1293.773	20.0	28.5	25.0
TM1-EE-1	1340.911	0	0	0
TM1-ME-2	1663.036	21.5	28.0	21.0
TM0-EE-2	1928.998	4.5	0.5	3.5
TM0-EE-3	2141.433	2.5	0.2	3.0
TM0-ME-2	2165.287	18.5	4.0	14.0
TM1-EE-3	2379.244	4.5		
TM1-ME-4	2643.410	15.5	>30	18.0
TM1-EE-5	2708.200	0		3.0
TM0-EE-4	2758.015	2.7	4.5	1.5
TM0-ME-3	3067.968	6.5	>20	1.5
TM1-EE-6	3147.284	9.5	5.0	
TM0-EE-6	3611.091	>30	>30	>30

is turned carefully to the minimum coupling position. The coupling increases drastically as the loop area increases over $\sim 0.15 \text{ inch}^2$. This indicates that the input loop and the damper loop couple directly, not through TM_{01} mode. The coupling can be $< -50 \text{ dB}$ which is less than 1 W of power dissipation for a 100 kW cavity input power.

Three H-loop-coupled coaxial dampers are used in an uniformly spaced circular array at $r=0.6r_o$ as shown in Figure 1(a). Each damper has a loop area of 0.04 inch^2 . The load resistance is varied as in the E-probe damper measurement. Table 2 shows the measured damping ratios. Most ME boundary modes and EE boundary modes are damped effectively with the exception of some EE boundary monopole modes.

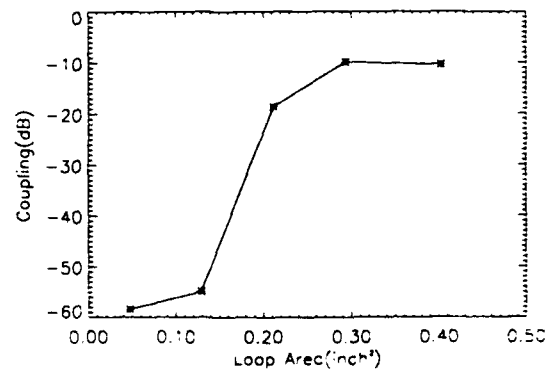


Figure 3

Isolation between power input loop and an H-loop damper at f_o . $R_L = 50\Omega$

Table 2
HOM damping with H-loops. $R_L = 30, 50, 100\Omega$

Mode type	$f(\text{MHz})$	Damping (dB)		
		30 Ω	50 Ω	100 Ω
TM0-EE-1	840.412	0	0	0
TM0-ME-1	1293.773	0	0	0
TM1-EE-1	1340.911	4.0	7.0	7.0
TM1-ME-2	1663.036	12.0	21.0	14.0
TM0-EE-2	1928.998	19.0	19.5	17.5
TM0-EE-3	2141.433	1.5	3.5	5.3
TM0-ME-2	2165.287	28.0	24.5	30.5
TM1-EE-3	2379.244	20.0	17.5	23.5
TM1-ME-4	2643.410	20.0	>30	>30
TM1-EE-5	2708.200	10.0	13.5	10.0
TM0-EE-4	2758.015	16.5	22.5	17.4
TM0-ME-3	3067.968	6.0	4.5	3.0
TM1-EE-6	3147.284	4.5	11.0	7.0
TM0-EE-6	3611.091	11.5	22.0	14.5

IV. COMBINED E- AND H-DAMPERS

Three E-probe dampers and three H-loop dampers were used together in a measurement. The measured damping ratios are shown in Table 3. The result shows that most modes (both ME and EE boundary) are damped effectively. 50 Ω loads are used in E-probe dampers while 50 Ω and 100 Ω are used for two separate measurements in H-loop dampers. The results from the two cases are about the same except for the TM1-EE-5 mode.

V. CONCLUSION

The above measurements show that the HOM can be damped with E-probe and H-loop dampers with negligible fundamental frequency power loss. They can therefore be compact in size, inexpensive, and easy to maintain. The E-dampers in the equatorial plane and the H-dampers in the endwall can achieve very weak coupling at the fundamental frequency without using decoupling circuits. The mode selectiveness of the two damper designs are nearly complimentary to each other.

Since each damper port input impedance is a function of frequency, a fixed resistance loading cannot damp each mode completely but can be the optimum for all modes. Although the sizes of the E-probe and the H-loop are not optimized, the damping is enough for use in actual APS storage ring cavities.

The next activity is to apply this design in the actual 352 MHz APS single cell cavity and find the optimum probe and loop sizes.

Table 3
HOM damping with E- and H-dampers. $R_L = 50\Omega$

Mode type	$f(\text{MHz})$	Damping (dB)	
		50,50	50,100
TM0-EE-1	840.412	0	0
TM0-ME-1	1293.773	26.0	22.5
TM1-EE-1	1340.911	18.0	18.5
TM1-ME-2	1663.036	28.0	28.0
TM0-EE-2	1928.998	24.0	23.0
TM0-EE-3	2141.433	4.5	5.0
TM0-ME-2	2165.287	28.5	29.0
TM1-EE-3	2379.244	19.0	20.0
TM1-ME-4	2643.410	25.0	23.5
TM1-EE-5	2708.200	13.5	10.0
TM0-EE-4	2758.015	23.0	22.5
TM0-ME-3	3067.968	6.0	7.0
TM1-EE-6	3147.284	7.5	10.0
TM0-EE-6	3611.091	>30	>30

VI. REFERENCES

- [1] Y. Yamazaki, K. Takata, and S. Tokumoto, "Damping test of the higher-order modes of the re-entrant accelerating cavity," *IEEE Trans. on Nuclear Science*, Vol. NS-28, No. 3, June 1981.
- [2] B. Dwersteg, E. Seesselberg, and A. Zolfaghari, "Higher order mode couplers for normal conducting DORIS 5-cell cavities," *IEEE Trans. on Nuclear Science*, Vol. NS-32, No. 5, Oct. 1985.
- [3] P. E. Faugeras, et al, "The new rf system for lepton acceleration in the CERN SPS," *IEEE Trans. on Nuclear Science*, Vol. NS-34, No. 5, Sep. 1987.
- [4] E. Haebel, and J. Sekutowicz, "Higher order mode coupler studies at DESY," DESY M-86-06.
- [5] A. Mosnier, "Developments of HOM couplers for superconducting cavities," 4th Workshop on RF Superconductivity, August, 1989.
- [6] G. Conciauro, and P. Arcioni, "A new HOM-free accelerating resonator," 1990 EPAC Symposium Digest, pp. 149-151.
- [7] R. Rimmer, D. Goldberg, G. Lambertson, F. Voelker, K. Ko, N. Knoll, R. Pendleton, H. Schwarz, F. Adams, M. De Jong, "Higher Order Mode Damping Studies on the PEP-II B-Factor RF Cavity," *Proc. 1992 EPAC*, May 1992.
- [8] J. F. Bridges, et al., "Measurement of prototype cavities for the Advanced Photon Source." *Proc. 1991 PAC*, pp. 693-695, May 1991.
- [9] L. Emery, "Coupled-bunch instabilities in the APS ring," *Proc. 1991 PAC*, pp. 1713-1715, May 1991.

Reduced Length Design of 9.8 MHz RF Accelerating Cavity for the Positron Accumulator Ring (PAR) of the Advanced Photon Source (APS) *

Y. W. Kang, J. F. Bridges, and R. L. Kustom
Accelerator Systems Division
Argonne National Laboratory
9700 S. Cass Ave., Argonne, IL 60439

Abstract

A 9.8-MHz RF accelerating cavity is developed for the first harmonic system in the APS PAR [1] and an aluminum unit is tested. The design goal is 40 kV at the accelerating gap, Q-factor of $\sim 7,000$ for the accelerating mode, 1.2-m diameter, 1.6-m length with good mechanical strength and stability. The design employs no dielectric or ferrite loading for tuning. The cavity is a plunger-loaded reentrant coaxial structure; the end of the inner conductor facing the wall has a piston-shaped loading structure which consists of a circular disk and a cylinder. The RF characteristic of the cavity was investigated using the URMEL-T and MAFIA programs. Compared with a coaxial structure with lumped element capacitive loading, this design gives improved RF characteristics.

I. INTRODUCTION

Designing low-frequency tuned RF accelerating cavities for high power operation with a cavity length ℓ much less than a quarter wavelength is impossible without extra capacitive loading. One way to shorten cavity length is to use folded coaxial structures as shown in Figure 1. However, if the maximum radius of the cavity is specified, the characteristic impedance of the coaxial transmission line becomes lower as the number of folds increases. The reactance at the open end of a short-circuited coaxial line is $Z_{in} = jZ_o \tan(\beta\ell)$. The characteristic impedance of the coaxial transmission line

$$Z_o = 60 \ln \frac{r_2}{r_1}, \quad (1)$$

where r_2 and r_1 are the radii of the outer and inner conductors, respectively. With lower characteristic impedance of the transmission line, Z_o , Z_{in} does not increase appreciably until the total line length ℓ approaches $\lambda/4$.

By analogy of an equivalent $L - C$ resonant circuit, greater capacitance is needed near the accelerating gap and greater inductance is needed near the short-circuited end to reduce the cavity length. Eq. (1) suggests that using the outermost conductor for the low Z_o coaxial section and the innermost conductor for the high Z_o coaxial section is more efficient in getting a shorter cavity length for a specified cavity radius. A design of this cavity is shown in Figure 1. In Figure 2, a capacitive loaded, foreshortened $\lambda/4$ coaxial cavity is shown. In the following section, these

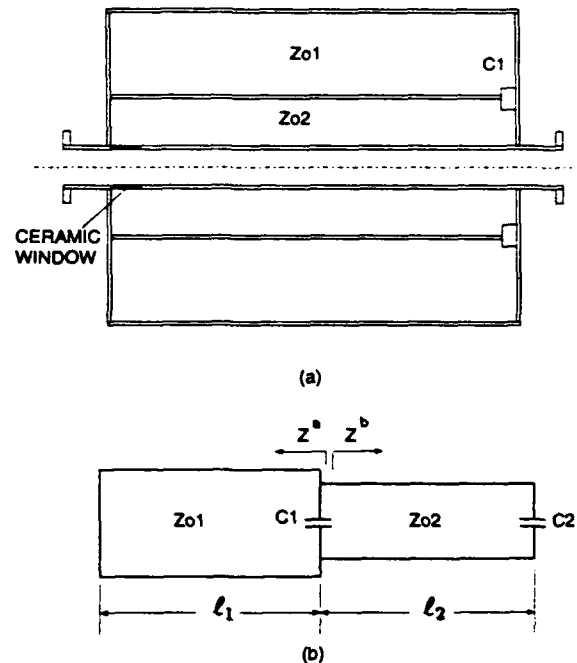


Figure 1
Folded coaxial cavity and equivalent circuit

two reduced length coaxial cavities are discussed and compared with equivalent transmission line circuit analysis. This design is found to be good for determining the cavity dimensions for a given fundamental mode frequency and voltage distribution. The URMEL-T and MAFIA codes were used in computer simulation of the cavities to find the frequencies, modal field patterns, and shunt impedances. The conductivity of copper was used in the simulation.

II. CAVITY DESIGNS

A. Folded Coaxial Cavity

The folded coaxial cavity with lumped element capacitive loading is shown in Figure 1. Using the equivalent circuit, the loading capacitance C_1 is solved as

$$C_1 = \frac{Z^{b*} - Z_{o1} \tan 3\ell_1}{\omega Z_{o1} Z^{b*} \tan 3\ell_1}, \quad (2)$$

where Z^b is the impedance looking into coaxial line with Z_{o2} as shown in Figure 1 and * denotes the complex con-

*Work supported by U.S. Department of Energy, Office of Basic Energy Sciences under Contract No. W-31-109-ENG-38.

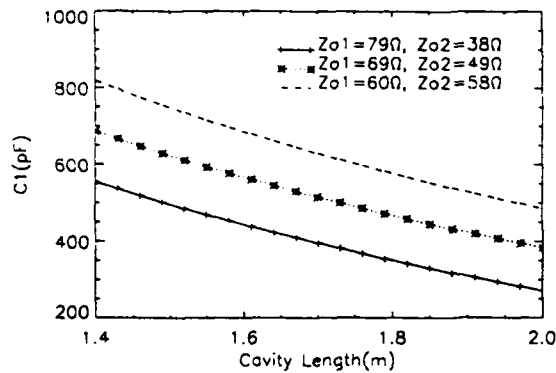


Figure 2

Loading capacitance in a folded coaxial cavity.
 $f = 9.8 \text{ MHz}$, $r = 0.6 \text{ m}$.

Table 1

Computed modes for the 9.8-MHz folded coaxial cavity
 TM0-monopole modes, TM1-dipole modes, EE-end plates
 are electric wall. Voltage integrated at $R_o = 0.0 \text{ m}$
 off-axis for monopole modes and at $R_o = 0.076 \text{ m}$ off-axis
 for dipole modes.

MODE	FREQ (MHz)	Q	R_s (MΩ)
TM0-EE- 1	9.82	12689	0.635
TM0-EE- 2	49.88	9372	1.010
TM1-EE- 1	76.04	10040	0.000
TM0-EE- 3	97.24	34276	0.007
TM0-EE- 4	140.46	15537	0.599
TM1-EE- 2	157.28	58638	
TM0-EE- 5	192.41	47295	0.005
TM1-EE- 3	228.76	61723	

jugate.

The loading capacitance C_1 with respect to the cavity length and the characteristic impedances Z_{o1} and Z_{o2} are shown in Figure 2 for the case of the 9.8-MHz cavity. The cavity has a length $\ell = 1.6 \text{ m}$, a radius $r_2 = 0.6 \text{ m}$, and a 13.0-cm accelerating gap length. These results show that lower Z_{o2} and higher Z_{o1} are required to lower the resonant frequency of the cavity for a fixed cavity length. The voltage across C_1 is $> 90\%$ of the gap voltage across C_2 [2]. The lower Z_{o2} requires smaller distance between the inner and the outer conductors, which is incompatible with high voltage operation. In order to increase the distance between the conductors, greater loading capacitance is required. The URMEL-T code was used with the constraints $\ell = 1.6 \text{ m}$, $r_2 = 0.6 \text{ m}$, 0.13 m of accelerating gap length, and 10.0 cm of conductor separation in the inner coaxial structure and permittivity of the annular dielectric ring was varied to simulate the $\sim 500 \text{ pF}$ of extra capacitive loading. Table 1 shows the properties of the monopole

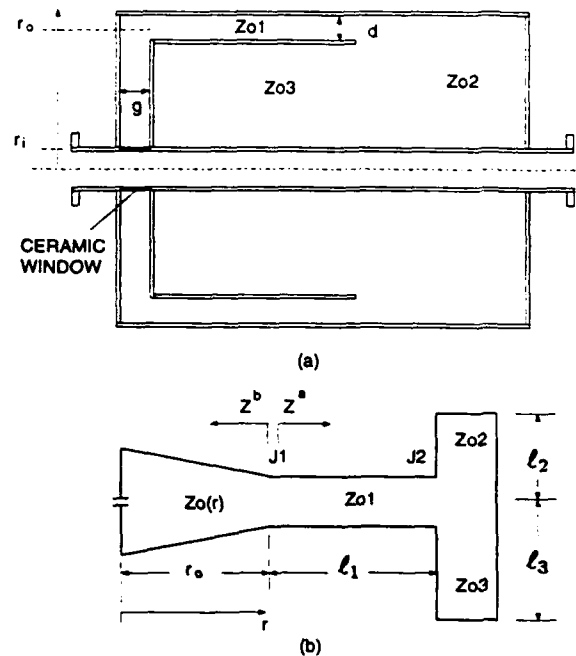


Figure 3

Loaded gap cavity and equivalent circuit

and the dipole modes of the folded coaxial cavity obtained from the computer simulations.

The inner coaxial structure must have a minimum of 10 cm of separation between conductors for high voltage operation [1, 2]. The capacitive loading may be realized by using one or more circular disks at the junction of the coaxial transmission line sections. A circular parallel plate capacitor with 50-cm radius will have a capacitance of about 500 pF if the spacing between the plates is 1.5 cm. However, this small spacing is not desirable for high-voltage application.

B. Loaded Gap Cavity

A coaxial cavity and its equivalent circuit are shown in Figures 3(a) and 3(b), respectively. This design uses a parallel plate radial transmission line across the accelerating gap for the low Z_o structure. This configuration is useful in lowering the resonant frequency for a fixed cavity size. since the coaxial line section near the short-circuit with Z_{o3} utilizes the beam pipe as the smaller radius of the center conductor, and the section closer to the gap with Z_{o1} utilizes the cavity outer wall as the outer conductor.

The input impedance seen in the direction of the short-circuited coaxial transmission line is Z^a , and at J_2 the two transmission line sections 1 and 2 are connected in series.

At a desired resonant frequency, $Z^a = Z^b$ and the length of the high impedance transmission line section ℓ_2

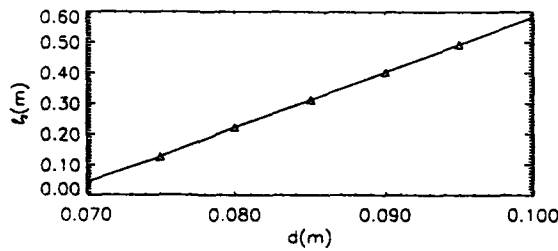


Figure 4

Transmission line length ℓ_2 vs. conductor spacing d of coaxial section with Z_{o1} for 9.8 MHz. $\ell_1=1.1$ m, $r=0.6$ m, $g=0.13$ m.

Table 2

Computed modes for the 9.8-MHz loaded gap cavity TM0-monopole modes, TM1-dipole modes, EE-end plates are electric wall. Voltage integrated at $R_o=0.0$ m off axis for monopole modes and at $R_o=0.076$ m off axis for dipole modes.

MODE	FREQ (MHz)	Q	R_s (M Ω)
TM0-EE- 1	9.82	10581	0.762
TM1-EE- 1	95.27	16225	0.004
TM0-EE- 2	97.07	22692	0.148
TM0-EE- 3	112.59	17871	0.332
TM1-EE- 2	158.80	20027	0.014
TM0-EE- 4	188.90	22431	0.690
TM1-EE- 3	193.48	68873	0.002
TM0-EE- 5	204.95	43563	0.012

Table 3

Measured frequencies and Q-factors of the 9.8-MHz loaded gap prototype cavity.

MODE	f (MHz)	Measured	
		f (MHz)	Q
TM0-EE- 1	9.82	9.85	5171
TM1-EE- 1	95.27	94.85	4806
TM0-EE- 2	97.07	99.22	3026
TM0-EE- 3	112.59	114.87	1625
TM1-EE- 2	158.80	156.18	5315
TM0-EE- 4	188.90	180.00	4745
TM1-EE- 3	193.48	195.06	4744
TM0-EE- 5	204.95	249.26	2297

is found to be

$$\ell_2 = \frac{1}{\beta} \tan^{-1} \left(\frac{N_1 - N_2}{D} \right), \quad (3)$$

where

$$N_1 = Z^{b*} (Z_{o1} - Z_{o3} \tan \beta \ell_1 \tan \beta \ell_3)$$

$$N_2 = j Z_{o1} (Z_1 \tan \beta \ell_1 + Z_3 \tan \beta \ell_3)$$

$$D = Z_{o2} (j Z_{o1} + Z^{b*} \tan \beta \ell_1).$$

and Z^{b*} is the input impedance of the radial transmission line at $r = r_o$ [2, 3].

In a computer simulation for 9.8 MHz, a 0.6-m outer radius and a 1.6-m total length were used. The accelerating gap length g and the conductor spacing d were chosen to be 13 cm and 9 cm, respectively. This gap length is sufficient for accelerating voltage. Figure 4 shows the length ℓ_2 versus the spacing d of the low impedance coaxial line with Z_{o3} .

The monopole and dipole modes found from the computer simulation are listed in Table 2.

III. PROTOTYPE MEASUREMENT

One loaded gap cavity has been built and tested. The cavity is made of aluminum with a copper center conductor. The shunt impedance and the Q-factor are 160 k Ω and 4900, respectively, at the fundamental mode frequency of 9.8 MHz. Table 3 shows the measured frequencies and Q-factors. The measured frequencies agreed well with the simulation. The fact that the computed shunt impedance and Q-factor are greater than the measurement may be due to unwelded conductors. For the required accelerating voltage of 40 kV, the input power is ~ 5 kW.

IV. CONCLUSION

The loaded gap cavity is easier to implement and requires much less critical capacitance than the folded cavity. Comparing simulation results of the folded and the loaded gap structures for the fundamental mode, the loaded gap design has higher R/Q by $\sim 40\%$ and lower Q by $\sim 15\%$ than the folded structure. Comparing the simulation results for the above two cavities, it can be seen that the higher-order mode frequencies differ significantly and the monopole and dipole modes are ordered differently. The prototype loaded gap cavity has acceptable RF characteristics and required mechanical strength.

V. REFERENCES

- [1] M. Borland, "Update on the Argonne Positron Accumulator Ring," these proceedings.
- [2] Y. W. Kang, R. L. Kustom, and J. F. Bridges, "Reduced length design of 9.8 MHz APS/PAR cavity," APS Light Source Note LS-211, May 1992.
- [3] Ramo, Whinery, and Van Duzer, Fields and Waves in Communication Electronics, John Wiley and Sons, New York, 1965.

Higher Order Mode Damping System in the UNK RF Cavity.

V.Katalev, V.Kudryavtsev, I.Sulygin
IHEP,Protvino

I. INTRODUCTION

The accelerating structure of the UNK consists of two cavities, working at 200 MHz and fed by an RF power generator via a 3dB hybrid [1]. The UNK bunched proton beam will have an extremely high intensity ($6 \cdot 10^{14}$ ppp) and therefore the problem of acceleration stability is a paramount one. One of the causes of instability is known to be higher order modes (HOM) excited by the beam itself in the accelerating structure. In order to eliminate the beam instability the HOM coupling impedances must be reduced to a certain threshold level. A threshold value of the coupling impedance for the first ring of the UNK is $Z_c/n = 6 - 16 \Omega$ [2] (the first ring contains 16 accelerating cavities). Here n is the HOM frequency - revolution frequency ratio. In this report the damping system reducing the cavity HOM impedances to the threshold level is described.

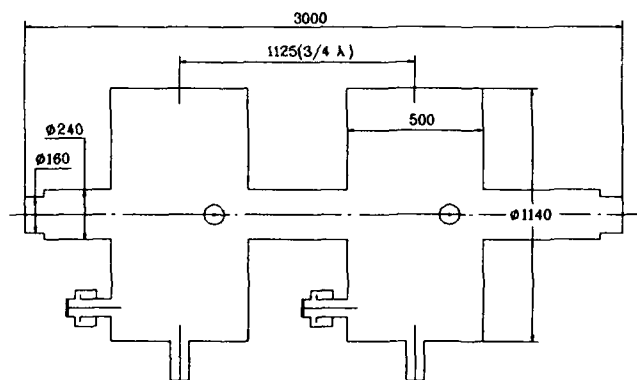


Figure 1: RF unit geometry

For the accelerating system of the UNK the cylinder-shaped single-cell cavity was chosen as the simplest in production and analysis of HOM, e.g. identification, computations (see fig.1). The beam-tube diameter of the cavities is fairly large, 240 mm. As a result, the number of the HOM localized in the cavity are limited and there is the possibility to suppress a HOM propagated in the beam-tube by special ferrite absorbers. The parameters of an azimuthal-homogeneous E modes were calculated with the help of the standard code PRUD-0 [3] in the frequency range to 1500 MHz that is cutoff frequency for 160 mm OD vacuum chamber. For each mode the following parameters were computed: frequency, shunt impedance R_s ,

Q-factor, transit-time factor T (max. value), the longitudinal coupling impedance:

$$Z_c = R_s \cdot T^2$$

The analysis of the computations shows that in this frequency range the accelerating structure has about 15 modes whose coupling impedance exceeds the threshold values. Some modes require a high degree of damping, e.g. E_{011} by 120 times, E_{021} by 70 times, and E_{022} by 30 times, etc. Accordingly, a high coupling between the absorbers and the HOM fields and a high cutoff of the fundamental mode are needed.

II. DESIGN OF MODE DAMPERS

Each cavity has three suppressors, one placed on the plate and two others on the shell(see fig.1) . Each suppressor has a coupling probe.

On the plane wall a "rejection" damper is placed (see fig.2a) [4]. It is coupled with all E modes, but it is needed primarily to suppress HOM which do not have field variations over the cavity length (E_{ono} modes).

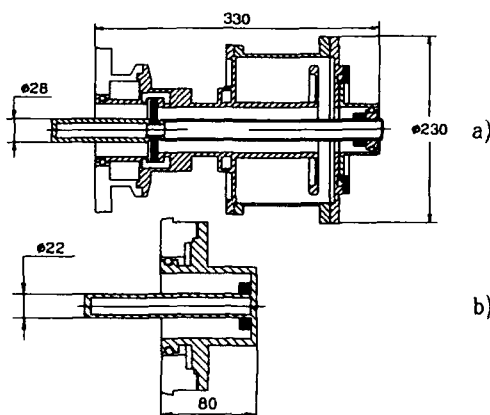


Figure 2: Rejection(a) and radial(b) dampers

To cut off the current of the fundamental frequency, the coaxial cavity loaded on the capacity is used. The fundamental frequency attenuation is about 60 dB whereas in the bandwidth for HOM it does not exceed 2 dB.

The RF loss in this damper on the fundamental frequency is about 500 W, that is less than 2% of the total loss in the accelerating cavity. About 50% of it dissipates

in the coupling probe, 30% - in the coaxial cavity and the remaining in the coaxial line and ceramic window.

The coupling probe and central conductor of the line are cooled by water. The gap voltage of the coaxial cavity is about 6 kV under an accelerating voltage 0.8 MV.

Two other suppressors coupled with the radial field component of HOM are placed on the cylindrical shell of the cavity. One of them is placed in the middle and another one at a quarter of the cavity length from the plate. This arrangement allows one to achieve the maximum coupling with the HOM having a different number of fields variations over the length. In order to dump the dipole (φ -dependence) modes, these suppressors are shifted by 90° in the azimuth. The coupling between "radial" dampers and the fundamental mode field is almost absent. Therefore these dampers contain only coaxial line terminating with a matched load (see fig.2b). The RF loss depends on the eddy currents of the fundamental frequency in the coupling probe and is about 200 W. The probe is cooled by water.

The absorbing load in each damper is a ferrite ring. VSWR of such loads does not exceed 2 in the 300-1500 MHz frequency range.

In the damped structure almost the whole power at HOM frequency dissipates in the damper loads. Because of a great difference between the frequencies of HOM and RF harmonics of the beam currents ($f_k = 200 \cdot k, k = 1, 2, \dots$) this loss is not greater than several Watts.

III. MEASUREMENTS

In a frequency range of 300-1500 MHz the azimuthal-homogeneous E-modes with the E-field longitudinal component on the axis were investigated.

Higher-order mode resonances were computed by the PRUD-0 [3] code and then identified using a perturbation method. These experiments include a comparison of the computed and measured distributions of HOM E - field longitudinal components and R_s/Q values accordingly. The measured R_s/Q values coincide with computed ones to an accuracy of 10-15%. Then the influence of all three dampers on the HOM was determined. The damping de-

gree of each mode was estimated by comparing their Q-factors with and without dampers. In this experiment we assumed R_s/Q to be constant and the coupling impedance to be defined by the formula

$$Z_c = \left(\frac{R_s}{Q}\right) \cdot Q T^2$$

The results of the damping are shown by the diagram in fig.3, where the frequency dependence of the threshold impedance for one cavity [2] is shown by the dashed line. It is seen that all HOM in this frequency range are damped to the degree required.

The possibility of damping HOM by means of the absorber placed in the beam-tube is investigated too. Ferrite rings were placed in the beam-tube at a rather long distance from the cavity so that the fundamental mode has no additional loss. This experiment showed that this method provides the required reduction impedances of the majority of HOM modes in a frequency range of 960-1500 MHz.

IV. CONCLUSIONS.

The performed measurements showed the possibility of using 3 dampers on each accelerating cavity for reducing the HOM coupling impedances to a threshold level of 300-1500 MHz. If required, the damping degree can be increased by optimizing the shape and dimensions of the coupling probe. HOM the frequency range 960-1500 MHz are damped effectively by the ferrite absorber placed in the beam-tube.

V. REFERENCES

- [1] Katalev V.V. et al. The 200 MHz Accelerating Structure for the UNK. EPAC, 1992, Vol.2, p.1197.
- [2] Balbekov V.I., Ivanov S.V. Atomnaya Energiya, 1986, V.60, N1, p.45-51.
- [3] Abramov A.G et al. PRUD0 Program Package for Computing Accelerating Structures, Preprint IHEP 83-3.
- [4] Shembel B.K. et al. Authors Certificate 984077, 1981, USSR.

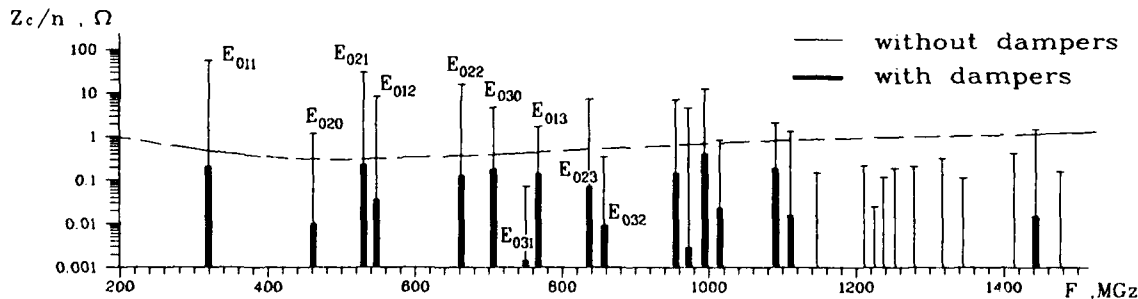


Figure 3: HOM coupling impedances

Status and Outlook for High Power Processing of 1.3 GHz TESLA Multicell Cavities,*

J. KIRCHGEISSNER, P. BARNES, L. BARTELSON†, M. CHAMPION†, C. CRAWFORD†, H. EDWARDS†, J. GRABER, K. KOEPKE†, M. KUCHNIR†, A. MATHEISEN††, D. METZGER, D. MOFFAT, H. MULLER, H. PADAMSEE, M. PEKELER††, H. PFEFFER†, P. SCHMÜSER††, J. SEARS, and M. TIGNER
Laboratory of Nuclear Studies, Cornell University, Ithaca, NY 14853 USA

SUMMARY

In order to increase the usable accelerating gradient in Superconducting TESLA cavities, the field emission threshold barrier must be raised. As has been previously demonstrated on S-Band cavities, a way to accomplish this is with the use of high peak power RF processing. A transmitter with a peak power of 2 Mwatt and 300 μ sec pulse length has been assembled and has been used to process TESLA cavities. Several five cell TESLA cavities at 1.3 GHz have been manufactured for this purpose. This transmitter and the cavities will be described and the results of the tests will be presented.

INTRODUCTION

High pulsed power processing (HPP) has been proved to be an effective method to overcome field emission in SC cavities. Many experiments done with 1-cell, 2-cell and 9-cell cavities at 3 GHz are discussed in other papers at this conference. The salient results of these experiments are:

1) Accelerating fields between 15-20 MV/m were reached with two 9-cell cavities (3 GHz) in 7 consecutive tests. For each test the surface of the cavity was prepared anew. In each case, heavy field emission was successfully processed with HPP to reach the final field levels. The low power Q was undamaged from HPP, so damage is not a concern.

2) The effectiveness of the processing depends clearly on the highest surface electric field reached during the pulsed processing stage. The highest pulsed surface field reached was 72 MV/m for a 1-cell, and 60 MV/m for a 9-cell. Power levels up to 50 kwatts were used for 1-cells and up to 200 kwatts for 9-cells.

3) In 9-cell cavities, field emission was completely eliminated for field levels up to $E_{cw} = 0.5 E_{pulsed}$. If field emission is tolerated till the Q falls to about 5×10^9 , then higher fields can be reached, typically: $E_{cw} = 0.60 E_{pulsed}$.

4) Processing takes place by an explosive mechanism. Dissection of processed cavities shows 1 - 10 μ m size molten craters with traces of the original contaminants responsible for the field emission.

5) The processing is effective against new field emission when additional contaminants are introduced, such as by vacuum accidents.

6) During processing the Q falls to between 10^7 and 10^6 .

7) It is possible, during pulsed operation, to exceed the field at which cw thermal breakdown is encountered; but then there is a strong competition for the applied high power between field emission losses for processing and the growth of

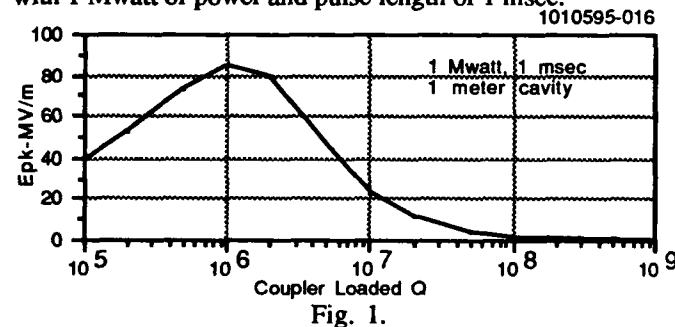
the normal conducting region(s). The method is, therefore, ultimately limited by breakdown, initiated by the maximum surface magnetic field. A low H_{pk}/E_{acc} ratio and a high RRR are, therefore, advised.

8) In a special 2-cell cavity with reduced magnetic surface field, it was possible to reach a surface electric field of 113 MV/m pulsed, and 100 MV/m cw, corresponding to a world record accelerating field of 34.6 MV/m.

EQUIPMENT FOR HPP AT 1.3 GHz TESLA CAVITIES

Needed Power

For TESLA, the RF frequency chosen is 1.3 GHz, and the structure is a 9-cell with length 1.038 meters and $E_{pk}/E_{acc} = 2.1$. It is desired to eventually reach 25 MV/m accelerating, or $E_{pk} = 53$ MV/m at a Q of 5×10^9 . To determine the peak power we need to apply, we are guided by the results from our 3 GHz HPP experiments. If we can expect, $E_{cw} = 0.6 E_{pulsed}$ after HPP, with some field emission still present, we need to be prepared to reach more than 90 MV/m surface field pulsed. We must also be prepared for the Q_0 to fall to 2×10^6 during HPP. The pulse length over which the field can be built up during the pulse is a very important parameter in assessing the power. Fig. 1 shows that the needed peak surface field can be reached with 1 Mwatt of power and pulse length of 1 msec.



Klystron and Modulator

While preparations are proceeding for installation of SRF infrastructure and a TESLA TEST FACILITY at DESY, a

*Supported by the National Science Foundation, with supplementary support under the U. S. -Japan Agreement.

†FNAL

†† DESY, Hamburg, Germany

program has been launched at Cornell to test HPP at 1.3 GHz as soon as possible. The Boeing Defense and Space Group kindly agreed to lend us a klystron (Thompson TH2104) and PFN modulator. The system is intrinsically capable of 10 MWatts peak at 200 μ sec with 185 Kvols, or 5 Mwatts at 300 μ sec. With commercial constant charge, constant current regulated pulsed capacitor charging supplies, we were successful in providing 110 KV to the klystron to obtain uniform 200 μ sec long pulses of 2 MWatt peak power. The klystron and modulator system as installed at Cornell are shown in Fig. 2.

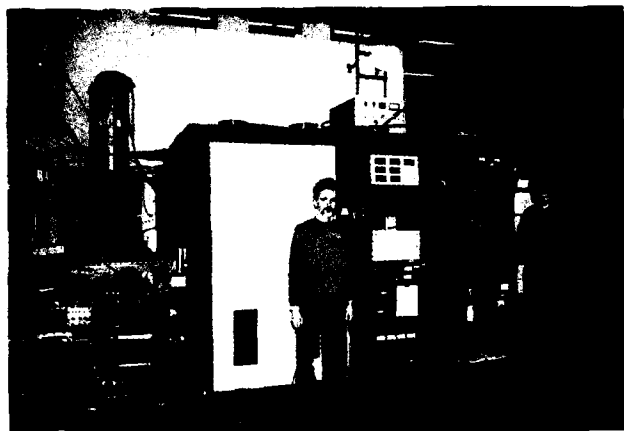


Fig. 2.

Niobium cavities

We decided to fabricate and test 5-cell structures instead of the final 9-cell structures for two important reasons: a) The available klystron/modulator operates at a maximum pulse length of 300 μ secs, b) The existing SRF facilities at Cornell (chemical treatment, shielded cold test area, furnace, clean rooms, etc) are not of the appropriate size to handle a 1 meter long cavity. Fig. 3 shows the expected peak field that can be reached with 1 Mwatt of power and a 5-cell cavity at the available pulse length.

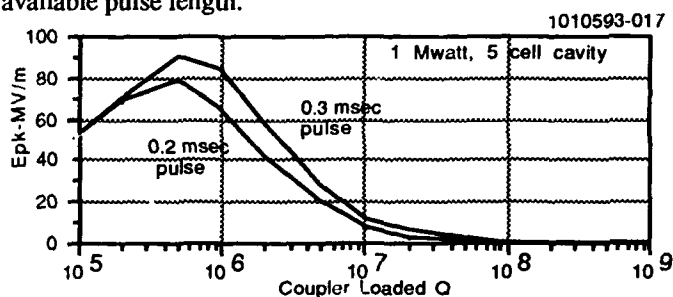


Fig. 3

Two 5-cell Nb cavities of the TESLA shape were built at Cornell. The accelerating mode properties of the cavity are listed in Table 1

Frequency	1308 MHz
R/Q	1088 Ω /m
E_p/E_{acc}	2.1
H_p/E_{acc}	42 Oe/MV/m

Table 1.

The cells are polarized as shown in Fig. 4 so that eventually a single HOM coupler can damp both polarizations of dipole higher order modes. The measured splitting for the dominant dipole modes was 13 MHz (TE_{111}) and 50 MHz (TM_{110}) modes. Fig. 5 shows a complete structure installed in the chemical treatment facility. One 2-cell and two 1-cell Nb cavities were also built. The RRR of the Nb used to fabricate these cavities was between 250 and 300. Copper cavities were also built to test the dies and fixtures.

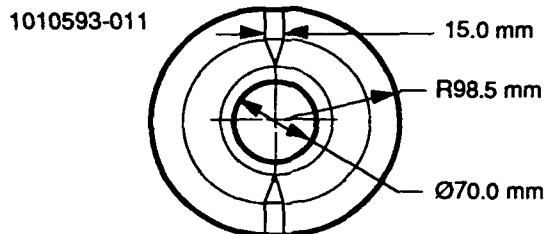


Fig. 4



Fig. 5

1.3 GHz HPP Test Set Up

A high power cold test set up shown in Fig. 6 was built. The high power enters the cryostat top plate (not shown) through a WR650 reduced height waveguide. A room temperature teflon window above the top plate allows a vacuum in the waveguide. Near the bottom of the cryostat is a waveguide to coax doorknob transition, with an integrated cylindrical ceramic window to isolate the high vacuum, cavity region. The window was coated with TiN to reduce the secondary emission coefficient. After fabrication, the VSWR of the input coupler was less than 1.6 between 1280 and 1320 MHz. The penetration of the antenna into the cavity is adjustable by a copper plated hydroformed bellow in the outer conductor. Q_{ex1} can be changed from 10^5 to 10^{10} with 4" of travel. The slotted region of the outer conductor just above the doorknob is connected to the cavity vacuum pumping line. To check the microwave performance of the coupler, the BCS Q at 4.2 K of a 1.3 GHz Nb cavity was measured and verified for different positions of the antenna.

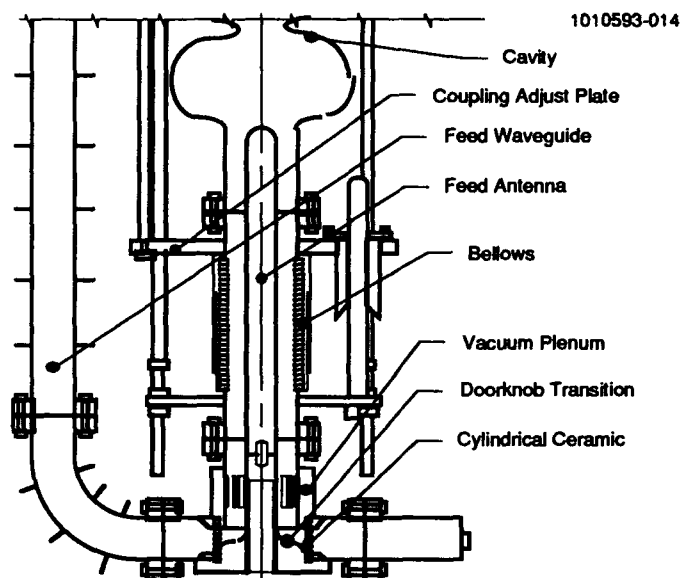


Fig. 6

COLD TEST RESULTS

One problem is that the top of a 5-cell cavity stands at about 70% of the useable liquid helium reservoir height. Even with several batch fill and pump down iterations, it was difficult to keep the cavity completely under liquid at 2 K. A good solution to this problem was to pump down a 500 litre storage dewar to 2.2 K and then transfer 2.2 K liquid across into the test cryostat. By this method the running time at 2 K could be extended by many hours. While this solution was still being developed, it was decided to test the HPP method with the 2-cell cavity.

Fig. 7 shows three Q vs E curves for the test of the 2-cell cavity

- The initial cw test with low power
- after conditioning with cw low power only
- after HPP up to 320 kwatts, 200 msec, maximum field 67 MV/m.

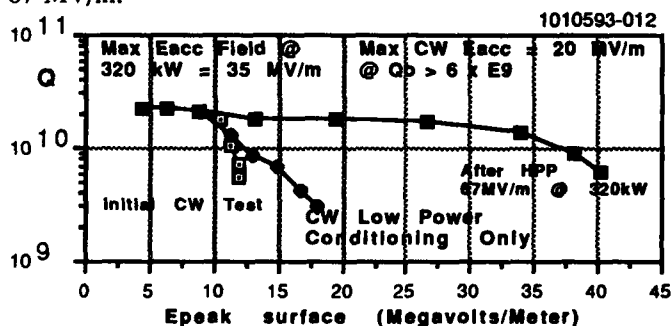


Fig. 7

During pulsed power application, the maximum peak surface electric field reached was 67 MV/m.

The 2-cell result confirms many of the aspects of HPP that were proved in the 3 GHz program. Field emission was successfully processed away without damaging the low power Q. The maximum field reached during the pulsed stage shows, as expected, that the Q fell to about 2×10^6 . The predicted E_{pk}

was 70 MV/m for a 2-cell cavity, on applying 320 kwatts (200 μ sec) and assuming that the Q_0 during processing fell to 2×10^6 . The maximum predicted field is very close to the experimental result (67 MV/m). The field level E_{cw} at which the Q from field emission drops to 6×10^9 is $0.6 E_{pulsed}$.

After the helium level problem was brought under control, a 5-cell cavity was tested. Unfortunately, due to reasons not yet understood, the preparation was not as clean as we desired. Both the low power Q and the field emission threshold were significantly lower than our usual results. Fig. 8 shows three Q vs. E curves. Although the initial field emission was heavy at 4 MV/m accelerating, with HPP we were still able to process and reach about 10 MV/m accelerating. The maximum power applied was 300 kwatts, at which power the E_{pk} reached during the pulsed stage was 40 MV/m. Again this implies that the Q fell to about 2×10^6 during HPP. We were not able to couple more than 300 kwatts because we encountered severe breakdown in the coupler.

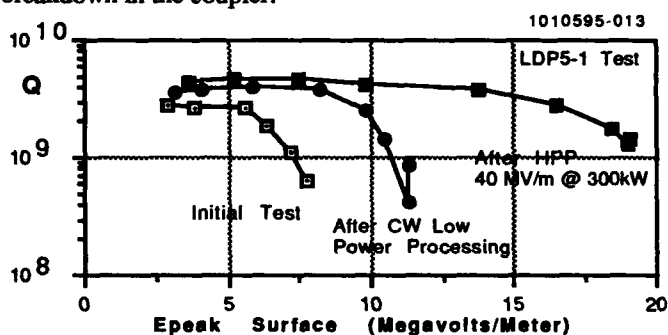


Fig. 8

Two types of coupler conditioning events were seen in the 1.3 GHz HPP coupler. Between 10 and 300 kwatts the first type, called the staircase, was usually accompanied by severe vacuum degradation in the waveguide region. After some conditioning, it was possible to process this type of event, with improvement in vacuum and the return of the transmitted rf power signal to the expected exponential decay. The staircase event would restart on raising the power. Above 300 kwatt, a second type of coupler event was encountered. Nearly all the power was absorbed or reflected, so that very little power could be coupled to the cavity. Studies are in progress to determine the location of the coupler troubles. So far, the teflon window is exonerated, so the problem is originating from the cold end, i.e. the window/doorknob/coax/bellows area.

CONCLUSIONS

All the equipment necessary to test HPP at 1.3 GHz has been completed, installed and tested: 2 Mwatt klystron, 200 μ sec pulse length modulator, high power test stand, and several multi-cell niobium cavities. The first test of HPP at 1.3 GHz shows that the technique works against field emission as expected, $E_{acc} = 20$ MV/m was reached. The processing power levels needed are as predicted from 3 GHz experiments. Understanding the limitations of the coupler is the next step to overcome the present 300 kwatt limit.

20 MV/m Accelerating Gradient with Heat Treatment of a Six Cell, 1.5 GHz Cavity for TESLA,*

J. KIRCHGESSNER, P. BARNES, W. HARTUNG, M. HILLER†, D. MOFFAT, H. PADAMSEE,
D. RUBIN, D. SARANITI††, J. SEARS, Q. S. SHU†††, and M. TIGNER
Laboratory of Nuclear Studies, Cornell University, Ithaca, NY 14853 USA

SUMMARY

In order to use superconducting RF accelerating structures in the construction of a high energy linear collider, the structures must be designed to meet specific goals. These include low peak surface electric fields, good higher order mode power extraction from the ends, maximum accelerating gradient and, above all, low cost per unit accelerating voltage. Such a structure has been designed, manufactured and tested. Preliminary results have been reported.^[1] The cavity was then mechanically braced with Niobium braces and then heat treated. The final test gave 20 MV/m accelerating field. Details of some difficulties encountered will also be presented at this time.

INTRODUCTION

At this time in the development of superconducting RF accelerating cavities, the accelerating gradient is limited by two phenomena, electron field emission and thermal breakdown. The first of these makes it imperative to choose a cell shape that minimizes E_{pk}/E_{acc} and the second phenomena to minimize H_{pk}/E_{acc} (the ratio of the peak surface fields to the accelerating gradient). As field emission is the dominant gradient limitation, there is considerable premium in lowering E_{pk}/E_{acc} . The cell to cell coupling (K) is also effected by the shape. This is true of the coupling of the HOM's as well as the fundamental TM_{010} mode. Because of this, the number of coupled cells comprising an accelerating unit is limited. A larger number of cells/module helps reduce the structure cost by reducing the number of couplers as well as by improving the filling factor for the machine. Another consequence of the cell to cell coupling in the TM_{010} mode is the relative ease of tuning the structure to achieve uniform accelerating gradient along the length of the unit.

DESIGN OF THE STRUCTURE

In order to test our ability to produce an accelerating structure which best meets the requirements of a linear collider, a series of calculations were made in which we tried to design the shape of the structure which had the following properties:

- Low E_{pk}/E_{acc} .
- Tolerable cell to cell coupling (K) in the TM_{010} mode.
- More than 5 cells/unit.
- Low cost.
- Tolerable Q_{ext} in all HOM's with couplers on the beam pipe.

Although it is straightforward to reduce E_{pk}/E_{acc} by reducing the beam pipe radius BT, this is undesirable because

the transverse wakefields increase as BT^{-3} which makes it more difficult to control multibunch instabilities and meet alignment and vibration tolerances for the linac.

The cavity shape that was manufactured and tested is shown in Figure 1.

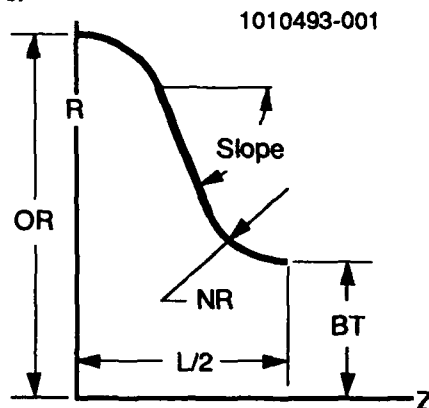


Figure 1.

The five independent variables describing the shape were as follows:

- OR, the outside radius.
- BT, the beam tube radius.
- $L/2$, the half length of the cell.
- NR, the nose radius, and
- Slope, the slope of the straight wall segment.

The OR which primarily determines the fundamental mode frequency is adjusted in all cases to obtain the desired frequency. The $L/2$ value is determined by the frequency as the particles to be accelerated must be kept in phase with the RF oscillations. Namely $L/2$ must be equal to $1/4$ wavelength.

In order to minimize the number of couplers required on the cavity module, the cells were polarized in a manner such that both polarizations of the dipole modes could be damped with one coupler.^[2]

CONSTRUCTION

The cavity chosen to best meet the stated requirements was manufactured of 1.5 mm Niobium sheet and was 6 cells long. The number of 6 cells was limited by the available furnace and by the available testing facilities. The cell parameters are shown in Table 1.

* Supported by the National Science Foundation, with supplementary support under the U. S. -Japan Agreement.

† Babcock & Wilcox, Lynchburg, VA

†† Now at Stanford University, Palo Alto, CA

††† Now at SSC Laboratory

Frequency	1500 MHz
OR(Equator Radius)(average)	9.48 (9.43 ends) cm
NR(Nose Radius)	1.09 cm
BT(Beam Tube Radius)	3.56 cm
Slope	70 degrees
L/2(1/2 cell length)	4.93 cm
Coupling K	1.8%
E_{pk}/E_{acc}	2.1
R/Q	89 ohms /cell
H_{pk}/E_{acc}	57 gauss/MV/meter
Length of Polarizing Segment	1.27 cm
% Freq. Split of TM ₁₁₀ mode	2.9% (2.03 GHz)
% Freq. Split of TE ₁₁₁ mode	0.22% (2.02 GHz)

Table 1

TESTS OF CAVITY

This six cell niobium cavity (LTP6-1) was initially tested twice. In both tests the structure reached fields of $E_{acc}=18$ MV/meter with considerable field emission, but final thermal breakdown. These tests were reported in Reference 1 and the curves from these tests are shown in Figure 2.

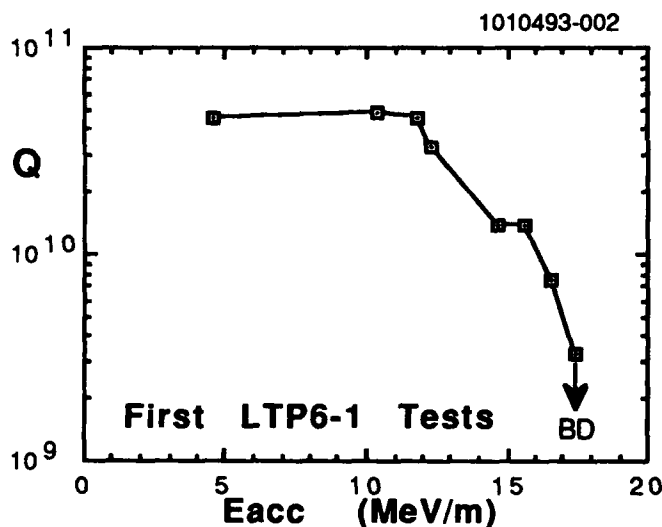


Figure 2

In order to reduce field emission we wished to vacuum fire the structure. Because the cell walls were only 1/16" thick, three longitudinal braces were welded to the equator of each of the cells to prevent distortion during firing and collapse during later tests.

In the process of welding on these braces, a gun arc in the EBW (electron beam welder) melted a 1/2" diameter hole in one of the cells. A very careful repair was made and when the cavity was remeasured at room temperature it was found to still retain adequate tune of all cells to give a level field profile.

The cavity was retested at this stage and the results were not very good. There was thermal breakdown at an E_{acc} level of 8-10 MV/meter. This data is shown in Figure 3.

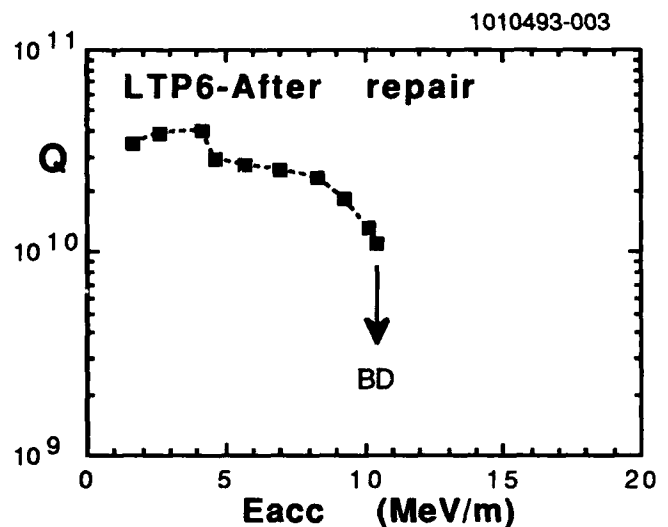


Figure 3

After a heavy etch to hopefully remove the apparent new defect, the cavity was fired for four hours at 1500 deg. C in a standard titanium lined niobium box.^[3] After firing, the structure was rinsed, but the titanium was not chemically removed from the outside of the structure. In this test, the E_{acc} value achieved was 15.3 MV/meter. The results of this test is shown in Figure 4.

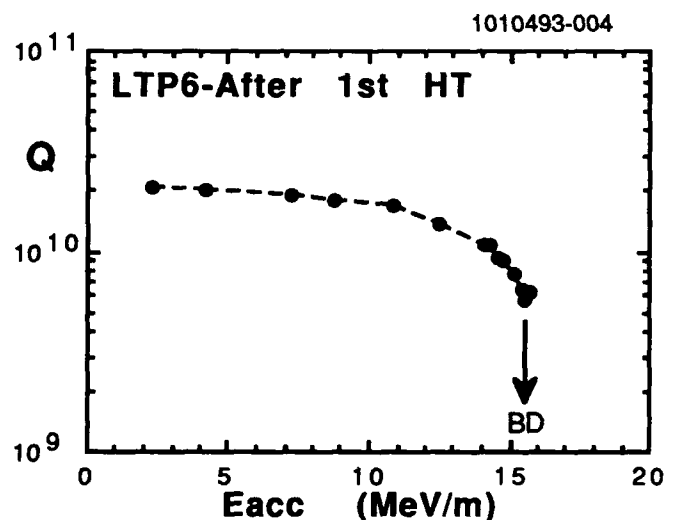


Figure 4

After this test the field flatness was measured to see if the firing had detuned the cavity. The E_{max}/E_{min} cell ratio was measured to be 1.9. This value of cell to cell field variation is excessive. During the firing the braced cavity was suspended from the top beam tube. This caused the top end half cell to be deformed by the force applied to it while the niobium was in the hot, softened condition. It was found that by tuning only

the top half cell, that had taken all the cavity weight, the cell fields could be completely leveled.

After this first heat treating, the field level in the cavity was still not quite as high as the field achieved in the first tests. In an attempt to push to higher fields, the cavity was again chemically etched and fired for 4 more hours at 1500 C. After firing, the cavity was tuned in the clean room. This was followed by a Methanol rinse followed by ultrasonic cleaning with Methanol, then a final Methanol rinse.

After mounting, the cavity was again tested and the results are shown in Figure 5.

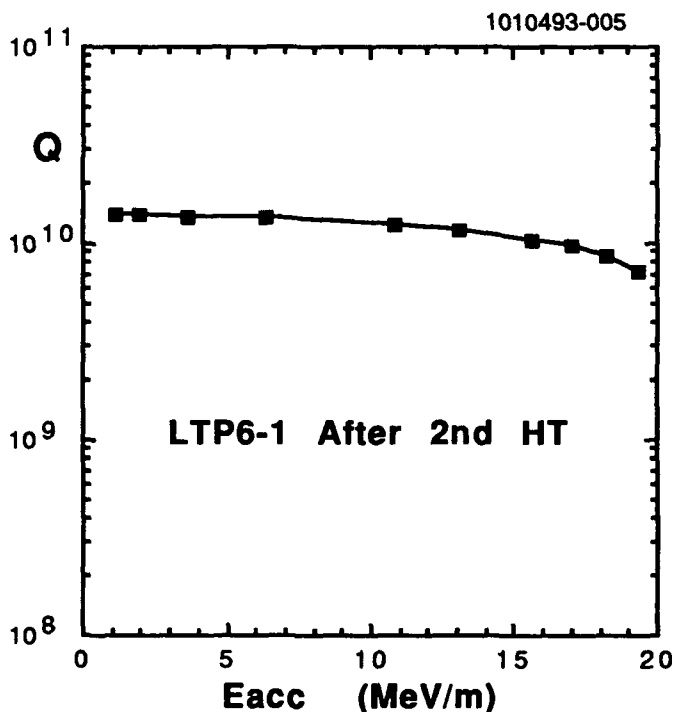


Figure 5

As can be seen, the field level of $E_{acc} = 19.5$ MV/m at a very good Q value was finally realized.

CONCLUSIONS

Several important lessons were learned in the course of the experiments on this cavity structure. They could be listed as follows:

- The ratio of H_{pk}/E_{acc} must be watched when the cell shape is designed. Since the time when this cavity shape was developed a new shape has been developed for TESLA which does not suffer from this high value of H_{pk}/E_{acc} .
- Sometimes a very good result is achieved on the first test.
- Bracing of the cells is very effective in stabilizing the parts that are braced.
- Furnace treatment with Titanium is effective in increasing RRR and, therefore, raising the thermal breakdown limits.
- Very extensive repairs may be made on the cells with no long term bad effects.
- Chemical cleaning of the structure seems to completely restart history in terms of the surface field emission behavior.
- Polarized cells seem to exhibit no different behavior in the TM₀₁₀ mode by virtue of being polarized.
- Careful records were kept of the costs of the manufacture and treatment of this structure. The total was less than \$6000.
- Bead pull measurements can be made on a cavity in a clean room, under clean conditions without introducing excessive field emitters that are difficult to remove.

The experiments with this structure were important steps in the process of achieving high field, low cost superconducting linear collider cavities.

REFERENCES

- [1] J. Kirchgessner et. al., Proc. 1991PAC, San Francisco, p 2426
- [2] J. Kirchgessner et. al., Proc. 1989 PAC, Chicago, p 479
- [3] Q. S. Shu et. al., Proc. 1989 PAC, Chicago, p 491

A New 50 MHz RF Cavity for Aladdin*

Kevin J. Kleman

Synchrotron Radiation Center, University of Wisconsin – Madison
3731 Schneider Drive, Stoughton WI 53589 USA

Abstract

The 50.58 MHz RF system for the Aladdin synchrotron light source at the University of Wisconsin – Madison has been upgraded with the installation of a new aluminum RF cavity. The new cavity is a foreshortened quarter wave type designed to eliminate multipactoring under high field conditions by incorporating a toroidal shape for the short circuit end[1]. Rigidity and ease of construction are enhanced by machining critical components from solid aluminum instead of using welded assemblies. A novel diaphragm tuner was incorporated to avoid the introduction of tuner modes. Drive power is coupled through a loop in air using a ceramic thimble for vacuum isolation. Coating of surfaces in the gap region with titanium made penetration of the first order multipactor region very easy and has eliminated all higher order multipactoring in the accelerating gap.

I. INTRODUCTION

The original Aladdin RF cavity was an aluminum quarter wave coaxial resonator. The cavity was installed in one of the long straight sections provided in Aladdin to allow the installation of insertion devices. Aladdin is now developed to the point where it is desirable to free the RF straight section for the installation of an insertion device as all three of the remaining sections are already committed. The old cavity also had high field multipacting problems when operating above 100 kV. For these reasons a new cavity was built which would fit into a smaller space and be capable of operating at higher fields without difficulty.

II. CAVITY DESIGN

A. General

The new cavity (Fig. 1) was designed with the URMEL code. The cavity parameters are listed in Table 1. The shunt impedance and Q are approximately the same as the old cavity. A large tuning range is required because Aladdin is operated with low RF voltage at injection[2]. Substantial reactive compensation is required under high beam loading conditions. The RF input coupling loop is in air and is isolated from the cavity vacuum by an alumina thimble that protrudes into the cavity. The thimble was given a light coating of titanium to prevent multipactoring.

The cavity was constructed from 6061-T6 aluminum. It is built in three sections using aluminum wire seals that function both as vacuum seal and RF contact. Wire seals are also used in transitions to the stainless steel vacuum chamber of the ring and to seal the titanium thimble flange. The short circuit end of the cavity is constructed with a toroidal cross section to suppress multipacting at high fields. Areas such as the loading disc, stem core and toroidal end section that required extensive cooling were machined from solid aluminum with integral cooling passages. The machined

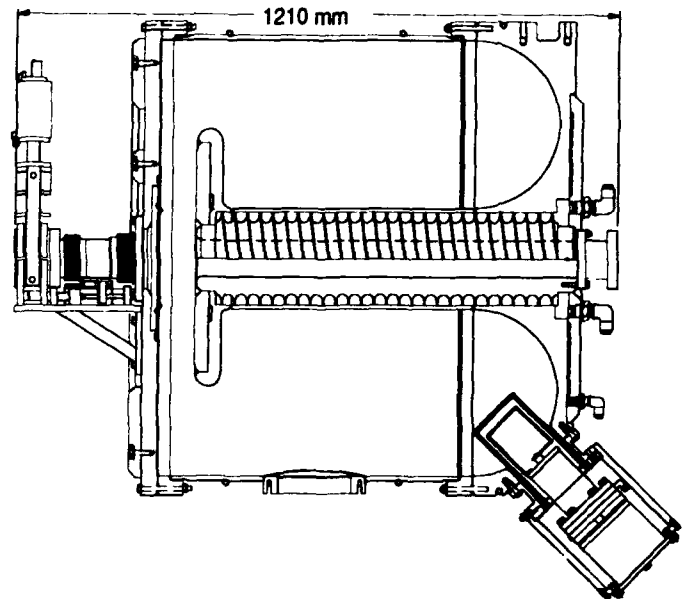


Figure 1. 50 MHz Aluminum Cavity

pieces give the cavity excellent rigidity. Assembly of the cavity was also facilitated because of the smaller number of welds required. The high precision of the machined pieces also made the remaining welds easier to perform.

Frequency	50.582 MHz
Shunt Impedance	800k Ω
Q(unloaded)	13000
Tuning Range	250 kHz
Max. Gradient	120 kV
Max. Cavity Loss	9 kW

Table 1. Cavity Parameters

B. Thermal Design

The small size of the cavity results in high power densities, especially in the stem and inner portion of the toroidal end section. In addition, the large capacitive loading required to resonate such a short cavity makes the resonant frequency very sensitive to dimensional changes in the inner stem. For these reasons the design of the cooling passages for the stem was approached with a great deal of care. Finite element models of the cavity temperature distribution were used to determine the location of cooling passages and their flow rates. Simulated heat loads were applied using data from URMEL power distribution plots. The effects of various cooling configurations were modeled and used to calculate temperatures in the cavity. Several iterations were used to optimize the cooling configuration.

The use of a double helix heat exchanger for the stem gives maximum water contact to the inner skin of the stem and allows a single water path to cool the stem and end

* Work supported by the NSF under contract DMR-92-12658

loading disc. The helix core is machined from bar stock with a hole bored in the center forming the beam aperture.

A spiral heat exchanger cools the rear of the cavity. A cooling passage is machined into a plate that is welded into a recess in the cavity end section. The inner portion of the toroidal section is cooled by the stem core. This is the most difficult area to access and also has a high thermal load. Having the end section machined from a solid plate makes cooling this area much easier.

Heat loads are much more reasonable on the outer shell and outer portion of the end section. A single cooling tube set into a groove in the outer diameter of the end section is sufficient to cool it. The outer shell is cooled with two hoops of tubing clamped into shallow grooves in the shell. Convection over the large shell surface provides additional cooling. The heat load on the gap end plate is so low that no additional cooling is required.

The end result of this effort is a rigid, well-cooled cavity that shows very little sensitivity to vibration or water flow noise. Detuning of the cavity due to RF heating is less than 25 kHz at maximum power.

C. Diaphragm Tuner

It was desired to tune the cavity by a method that did not introduce additional HOM's or use sliding contacts. A large tuning range was also required. A segmented capacitive diaphragm covering part of the accelerating gap was designed. It is constructed from 250 μm beryllium copper and incorporated into the gap end plate (Fig. 2). The diaphragm was plated with 50 μm copper to increase its electrical and thermal conductivity. Less than 10 W is dissipated in the diaphragm at maximum power so it is cooled by conduction to the aluminum end plate. The diaphragm segments are held in place by retaining rings on their inner and outer diameters. The inner ring is attached to a section of tubing that acts as the actuating link as well as providing the beam aperture.

Axial displacement of the diaphragm is permitted by incorporating an S-shaped section near the center of each segment. The tuner is driven by axially moving the beam pipe attached to its inner diameter. A pair of bellows isolates this motion from the cavity and the rest of the ring. The bellows next to the cavity is automatically shielded from RF by the beam pipe that passes through it.



Figure 2. Diaphragm tuner installed in cavity end plate

D. Anti-multipacting Coating

Low field multipacting is a serious problem in aluminum cavities. Initial conditioning of a bare cavity of this type is nearly impossible due to the large areas that need to be conditioned. To suppress multipacting, the accelerating gap and coupler port were coated with a layer of titanium that was applied by sublimation. Titanium wire held in a rotating fixture was used for the gap and a commercial sublimator was used for the loop port. Processing consisted of sublimation at a moderate rate for about 15 minutes at $\sim 10^{-5}$ torr followed by backfilling with N_2 . The composition of the final coating is probably more oxide than nitride but this does not seem to affect its performance.

This procedure gave excellent results. Without the coating breaking through the first multipacting level at about 500 V took over a day with pulsed drive. With the coating breakthrough can be achieved in about one hour using low power CW drive. Without the coating higher order levels were observed in the 5–10 kV range and the conditioning did not seem to be permanent. With the coating no high order levels were observable provided the coating thickness was adequate. No degradation in the coating effectiveness has been observed over time. Re-conditioning after vacuum cycling appears to behave similarly to initial conditioning. No high field discharges that did not condition away were evident below 150 kV.

E. Vacuum

The vacuum system of the new cavity consists of a 220 l/s ion pump mounted on the bottom of the cavity. The pump port is equipped with a grid that carries the RF current in the cavity wall. This also prevents coupling of the pump modes to the cavity. A titanium sublimation pump is attached to the bottom of the ion pump to assist in pump down. An RGA head is attached to the roughing port to provide in situ leak checking and vacuum analysis capabilities.

Aluminum cavities require more care in vacuum preparation than copper cavities. The porous coating formed on an aluminum surface can adsorb large quantities of water. This makes it necessary to perform a thorough bakeout in order to obtain the lowest possible pressure. The cavity was baked for one month at 150°C. After baking the pressure was 4×10^{-10} torr. Operation at full power results in a pressure in the low 10^{-9} range.

III. HOM DAMPING

Higher order modes are a concern in Aladdin due to its low injection energy. Radiation damping is so weak that it is practically impossible to eliminate coupled bunch instabilities at injection. The method used to attack this problem in the new cavity was to concentrate damping efforts on modes that have the potential of causing the most trouble for injection, in order to minimize injection difficulties. The injection bunch length of 5 ns means that modes below about 500 MHz are the most important ones to damp. The cavity design helps in this because it has no modes below 235 MHz. However, the use of a low frequency cavity means that high frequency modes (≈ 1 GHz) which are potentially troublesome at the operating energy are very numerous and difficult to attack without knowledge of how the system performs with beam.

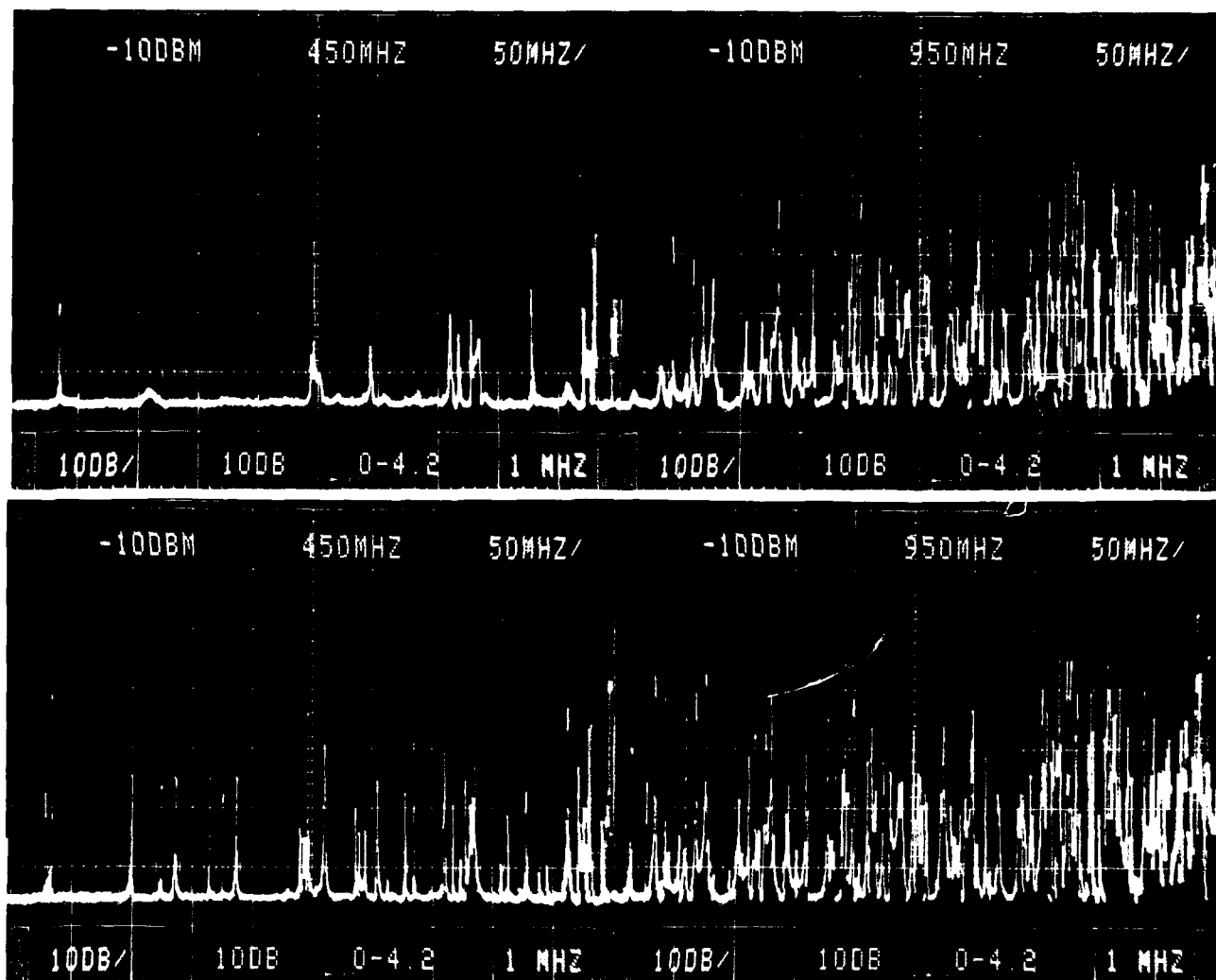


Figure 3. Cavity HOM spectrum with and without damping loads installed

HOM damping is accomplished using four damping antennas inserted radially through the outer shell of the cavity. Axially oriented antennas were precluded by the design of the end section. Two antennas damp modes in the 500 MHz region with two additional antennas cut for 235 MHz and 375 MHz. The position of the antennas was determined using URMEL field plots. Coupling of the fundamental mode to the antennas is reduced by terminating them in tuned coaxial stubs which also allow some adjustment of the damping at particular frequencies.

The antennas are constructed from commercial UHV copper tube feedthroughs with machined copper tips. The tips are attached by hydrogen brazing with AgCu eutectic. The antennas are cooled with water from a tube that runs down their central bore. The tuning stubs allow easy separation of the water and RF paths.

Figure 3 shows the HOM spectra of the cavity with and without damping in the frequency range from 200 to 1200 MHz. The damping is very effective up to about 700 MHz. The tuning of the antenna stubs was adjusted to optimize the damping over the low end of the frequency range shown.

IV. PERFORMANCE

The cavity was installed in January 1993 and has performed well. Injection performance is much better due to the elimination of a severe coupled bunch instability caused by low frequency HOM's in the old cavity that made stacking at high currents difficult. Operation at 800 MeV has revealed a coupled bunch mode that appears to be caused by a mode in the cavity at about 1 GHz. Future experiments are planned using microwave absorbing materials in the coaxial feedline to the cavity to damp some of the high frequency modes via the RF input coupling loop. Tests have shown that damping can be achieved in this way without dissipating a large amount of power at the fundamental frequency. The absorber might possibly be able to serve another function as a damping element for the RF power amplifier, suppressing unwanted resonances in the anode circuit when the cavity is off resonance.

V. REFERENCES

- [1] R. Boni et al., *IEEE Trans. Nucl. Sci.* NS-32, No. 5, 2815 (1985).
- [2] K. Kleman, these proceedings.

Performance of a CEBAF Production Cavity after High-Temperature Heat Treatment*

P. Kneisel and M. G. Rao

Continuous Electron Beam Accelerator Facility
12000 Jefferson Avenue, Newport News, Virginia 23606

Abstract

CEBAF's production cavities are tested in a vertical configuration after appropriate chemical surface treatment prior to installation into the accelerator. The performance of these cavities is excellent, often exceeding the specifications of $E_{acc}=5$ MV/m at 2 K by factors of 2 to 3. In such cases the cavities are often limited by thermal-magnetic breakdown. A cavity that exhibited a limiting gradient of $E_{acc}\leq 16.4$ MV/m has been heat-treated at 1400°C for 6 hours in the presence of titanium as a solid state gettering material to improve the thermal stability of the niobium. After the heat treatment a gradient of $E_{acc}=20.5$ MV/m corresponding to a peak surface electric field of $E_{peak}=52$ MV/m has been measured. In addition to the cavity results, data on thermal conductivity and tensile properties of samples which have undergone the same treatments as the cavity are reported.

I. INTRODUCTION

Superconducting niobium cavities for accelerator application are presently limited in their high-gradient performance by either field emission loading or thermal-magnetic breakdown.

CEBAF's 5-cell production cavities—even though they perform excellent and exceed the design gradient of $E_{acc}\geq 5$ MV/m on the average by a factor of ≈ 2 —are in 20% of the cases limited by quenches, more often by strong field emission loading [1].

It is generally accepted that field emission loading is caused by artificial contamination of the sensitive cavity surfaces due to handling and assembly procedures or by intrinsic emitters embedded in the surface. In several cases it has been shown that the severity of the field emission can successfully be reduced by improved cavity handling and cleaning techniques like e. g. "closed chemistry" [2], high-pressure rinsing with ultra-pure water [3], high-temperature heat treatment or high-peak-power processing [4]. Nevertheless, cavities made from presently commercially available high-purity niobium of RRR ≈ 250 to 300 become thermally unstable if a significant amount of rf heating is generated at microscopic defects. Such defects as foreign material inclusions, weld imperfections, chemical residue from surface treatments, surface irregularities or dust and debris on the surface limit quench fields to ≤ 90 mT corresponding in a typical accelerating cavity to ≤ 20 MV/m. Improvement of the thermal conductivity of the wall material, which can be achieved by high-temperature heat treatment in an ultrahigh vacuum in the presence of a solid state gettering

material like titanium [5], will significantly improve the thermal stability of such cavities, and gradients can possibly be shifted towards higher values [6].

In the following sections we report about experiments on a 5-cell CEBAF production cavity, which had been post-purified after initial testing.

II. EXPERIMENTAL

A. Cavity Processing

For the investigations reported here, production cavity IA080 manufactured from high-purity niobium with RRR ≥ 250 was used. For the baseline test the cavity received the standard removal of a surface layer of ≈ 60 μm by buffered chemical polishing followed by an ultrapure water rinsing combined with ultrasonic agitation over a period of 1 hour with several water changes in between. Assembly of the external cavity parts like rf window, gate valve at one beam-pipe end, blank-off plates and rf coupling ports took place in the class 100 production clean room after a threefold rinsing of the cavity with reagent-grade methanol.

In preparation for the heat treatment in the KfK-furnace,* the cavity was again slightly chemically polished (≈ 5 μm of material removal) and then enclosed in a Ti/Nb foil assembly with a titanium foil arrangement on the inside of the cavity as indicated in Figure 1. Stiffening bars of niobium on the cells were used to avoid cell deformations, and spacer pieces of niobium at the beam-pipe ends were used as a precaution to avoid direct contact between the inside titanium foil and the cavity surface. This assembly was heat-treated at 1400°C for 6 hours in an ultrahigh vacuum; after 4 hours at this temperature, the vacuum had improved to 3×10^{-9} torr.

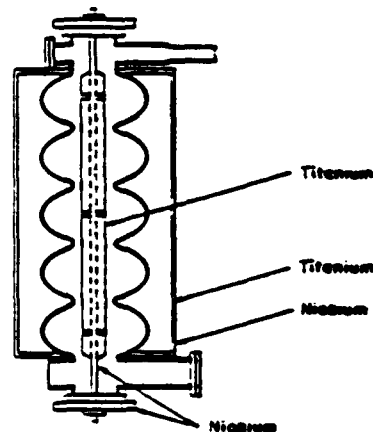


Figure 1. Experimental setup for post-purification of the 5-cell niobium cavity with titanium.

*This work was supported by DOE contract DE-AC05-84ER40150

*Kernforschungszentrum Karlsruhe, Germany

Unfortunately, the cavity tilted at the high temperature because of improper support in the furnace, and portions of the inner titanium foil got in contact with the two lowest irises of the cavity. This caused some problems as discussed in the next section and made it necessary to heavily chemically treat the cavity.

B. Cavity Testing

Before fast cooldown within ≈ 1 hour the cavity was evacuated to a pressure of $< 6 \times 10^{-7}$ torr after the assembly; the external static magnetic field in the vicinity of the cavity was shielded to better than 10 mGauss by an active compensation coil and a μ -metal layer.

During the experiments the temperature dependence of the surface resistance was measured between 4.2 K and 2 K and data for the dependence of the Q -value on the cavity fields were taken.

III. RESULTS AND DISCUSSION

A. Measurements on Samples

Niobium samples for tensile testing and for thermal conductivity measurements were placed inside the cavity during the heat treatment. For the thermal conductivity two different thicknesses for the test samples were chosen, simulating the material thickness of a cavity cell (3.2 mm) and of a weld (1.6 mm). Figure 2 shows the thermal conductivity of both samples: at 4.2 K the values are 294 W/mK for the thin sample and 214 W/mK for the thicker sample. These values represent an improvement of a factor of 3 to 4 over the starting material.

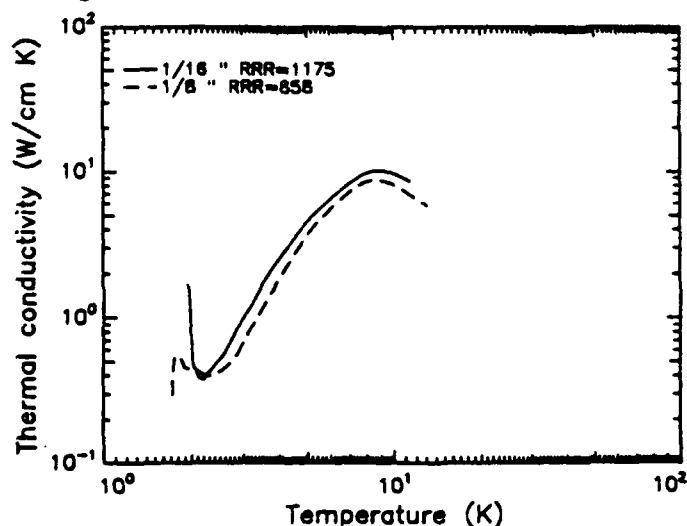


Figure 2. Thermal conductivity of post-purified niobium.

Table 1 summarizes the results of the tensile measurements carried out with a cross-head speed of ≈ 0.13 mm/min. The sample at 293 K showed a ductile fracture, whereas at 4.2 K a brittle fracture occurred. Nevertheless, the heat treated sample showed a dramatic increase in the elongation to 21.8% in comparison to the non-heat-treated material, which fractured at $< 2\%$ [7].

Table 1
Tensile Properties of Post-Purified Niobium at 293 K and 4.2 K.

[YS = yield strength, TS = tensile strength]

T [K]	As received			Heat treated		
	YS [ksi]	TS [ksi]	Δ/l	YS [ksi]	TS [ksi]	Δ/l
293	14.5	23	42%	5.9	14	48%
4.2	130	131	< 1	—*	102.8	21.8%

*Serrations started before reaching 0.2 offset yield

B. Q-Value and Gradient Measurements

In the baseline test of the non-heat-treated cavity a Q -value of $Q_0 = 1.7 \times 10^{10}$ was measured at 2 K. From the temperature dependence of the Q -value a residual resistance of 6 n Ω was calculated; field emission loading started in this test at $E_{acc} = 9$ MV/m after some processing at lower field levels had taken place. A maximum gradient of $E_{acc} = 15$ MV/m was measured limited by a Q -degradation at a dissipated power level of ≈ 60 W. In the $4\pi/5$ -mode magnetic breakdown was observed at a stored energy in the end-cell, which would be equivalent to 16.4 MV/m in the π -mode.

As mentioned earlier, during the heat treatment of the cavity the inside titanium foil got attached to the two irises closest to the higher-order-mode coupling waveguides due to deformation of the cavity. Therefore—after the cavity had mechanically been straightened out and the frequency, field profile and Q_{ext} of the fundamental power coupler had been readjusted—the suspicious areas of the defective surface were mechanically ground. Subsequently, 50 μ m of material were chemically removed from the surface prior to the first test after the heat treatment. The result of this experiment was quite disappointing: The Q -value at 2 K was only $\approx 4 \times 10^9$ and the cavity quenched at $E_{acc} = 6.5$ MV/m. In the next two tests additional mechanical grinding was done and niobium was chemically removed in steps of 25 μ m. Each time some improvement in the cavity performance was observed. Because of an uncontrolled exposure of the cavity surface to air after initial evacuation, rather strong field emission loading was observed in test #3a starting at $E_{acc} = 7.5$ MV/m. The cavity was taken apart and only rinsed with a high-pressure jet of ultrapure water, resulting in an improvement of the obtainable gradient to $E_{acc} = 14$ MV/m. No radiation was observed even at this gradient; the degradation of the Q -value seemed to be caused by heating of some areas on the surface, presumably some spots of titanium or NbTi as a result of the contact between cavity surface and Ti foil. The effectiveness of the high-pressure rinsing had been demonstrated prior to this experiment on several tests with a single-cell cavity, which consistently resulted in peak surface fields of $E_{peak} > 50$ MV/m without any signs of field emission loading [8].

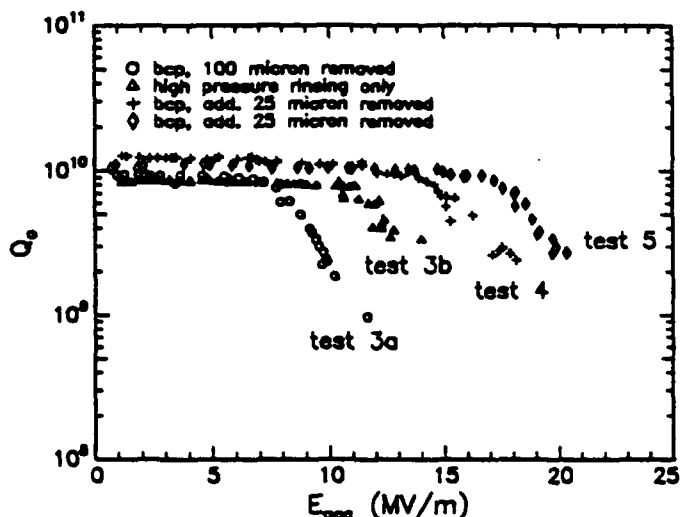


Figure 3. Summary of test results on heat-treated cavity after subsequent chemical surface treatments (bcp=buffered chemical polishing).

In two subsequent tests additional material (25 μm each time) was removed followed by 1 hour of high-pressure rinsing at 8.3 MPa. These tests are labeled as #4 and #5 in Figure 4. Each time the gradient improved and no or very little field emission loading occurred. The decrease of the Q -value beyond 16 MV/m in test #5 is proportional to the square of the cavity field and hints again to some heating, probably occurring at remaining spots of Ti contamination. Even at the maximum gradient of $E_{\text{acc}}=20.5$ MV/m, corresponding to a peak surface field of $E_{\text{peak}} = 52$ MV/m, the highest field ever achieved in this type of cavity, only very little X-radiation was observed. At this field level the cavity could tolerate ≥ 100 W without thermal instability. In the $4\pi/5$ -mode the end cells of the cavity could tolerate a stored energy equivalent to 28 MV/m in the π -mode.

B. Additional Measurements

Prior to the post-purification, the pressure sensitivity of the cavity between 760 torr and 23 torr was measured to be 68.8 Hz/torr. In the first test after the heat treatment, this value had increased to 77.4 Hz/torr. This change can be attributed to the thinning of the wall material due to the additional chemical treatment after the post-purification.

The response of the cavity frequency to the static radiation pressure was measured in the range $5 \text{ MV/m} \leq E_{\text{acc}} < 20 \text{ MV/m}$ and resulted in a value of $\Delta f/E^2=3.1 \text{ Hz}/[\text{MV/m}]^2$.

IV. CONCLUSIONS

Post-purification of the presently commercially available high-purity niobium with a solid state getter material like titanium can improve the thermal stability of accelerator cavities significantly. This might be necessary for future high-gradient applications, even though very good cavity

performances have been achieved with non-heat-treated material. But the quench fields in these cases vary over a wide range of values as experienced at CEBAF [1]. Chemical treatment after post-purification in combination with high-pressure pure water rinsing seems to be a very useful method to reduce field emission loading up to peak surface fields of $E_{\text{peak}}=50$ MV/m. In optimized cavity geometries with a ratio of $E_{\text{peak}}/E_{\text{acc}}=2$, such fields correspond to gradients of $E_{\text{acc}}=25$ MV/m, which are needed for future linear collider projects.

V. ACKNOWLEDGEMENTS

We would like to thank all our colleagues who contributed to this investigation. Our special thanks go to B. Lewis, L. Turlington, J. Pauley, D. Carless, R. Afanador, E. Hanson, J. Brock, J. Susta and K. Yopp. We are indebted to the Kernforschungszentrum Karlsruhe for its generosity in making the furnace available and in particular to H. Baumgärtner for carrying out the heat treatment.

VI. REFERENCES

- [1] C. Reece, P. Kneisel, J. Mammoser, "Performance of Production SRF Cavities for CEBAF," these proceedings.
- [2] B. Bonin, "A New Surface Treatment for Niobium Superconducting Cavities," these proceedings.
- [3] Ph. Bernard, *et al.*, "Superconducting Niobium Sputter-Coated Copper Cavities at 1500 MHz," *Proc. 1992 European Part. Acc. Conf.*, pp. 1269—1271
- [4] J. Graber, "Overview of Results of the HPP Experiments," Report SRF 930128, Lab. Nucl. Studies, Cornell University, NY (1993).
- [5] P. Kneisel, "The Use of the Titanium Solid State Gettering Process for the Improvement of the Performance of Superconducting RF Cavities," *Journ. Less-Comm. Metals*, 139, 179 (1988).
- [6] H. Padamsee, "Calculations for Breakdown Induced by "Large Defects" in Superconducting Niobium Cavities," *IEEE Trans. Mag.*, MAG-19, 1322 (1983).
- [7] P. Kneisel, *et al.*, "Superconducting Cavities from High Thermal Conductivity Niobium for CEBAF," *Proc. of the Conf. on Electron Beam Melting and Refining*, (1990), pp. 177—188.
- [8] P. Kneisel, B. Lewis, L. Turlington, "A High Pressure Ultra Pure Water Rinsing System for Niobium Cavities," CEBAF Tech. Note TN #93-029.

Suppression of Higher-Order Modes in an RF Cavity by Resistive Material

Tadashi Koseki, Masaaki Izawa* and Yukihide Kamiya

The Institute for Solid State Physics, The University of Tokyo, Tanashi, Tokyo 188 Japan

*Photon Factory, National Laboratory for High Energy Physics, Tsukuba, Ibaraki 305 Japan

Abstract

A new 500-MHz cavity which has a simple damped structure for the 1.5-GeV VUV ring will be presented in this paper. The feature of the cavity design is that higher-order modes(HOMs) propagate out from the cavity through the beam-duct with a large diameter and are absorbed in resistive parts in the duct. A low power measurement on a prototype model of the cavity has been carried out and the Q-values of HOMs are confirmed to drastically reduce. Thus the coupled-bunch instabilities due to HOMs are expected to be sufficiently suppressed.

Introduction

A high-brilliant synchrotron radiation source for soft x-ray and VUV experiments is being designed at ISSP of the University of Tokyo in collaboration with the Photon Factory at KEK. The storage ring with an energy of 1.5 GeV has a circumference of 240 m and twelve long straight sections for extensive use of insertion devices. It is aimed at obtaining a low emittance of several nm-rad and a maximum beam current of 400 mA. The main parameters of the storage ring are summarized in Table 1.

Table 1: Main parameters of the ring.

Energy [GeV]	1.5
Circumference [m]	236.4
Superperiod	12
Length of straight section [m]	7.0
Maximum beam current [mA]	400
Natural emittance [m-rad]	6.4×10^{-9}
Energy spread	5.8×10^{-4}
Momentum compaction	1.5×10^{-3}
Energy loss/turn [keV]	90.2
RF frequency [GHz]	497.12
Harmonic number	392
Number of RF cavities	4
Momentum acceptance($\Delta p/p$) [%]	± 3.0
RF voltage [MV]	1.4
Bunch length [mm]	3.5

Because of its relatively low beam energy and proposed high beam current, very low impedances of higher-order modes are required for the accelerating cavity to

suppress the coupled-bunch instabilities. Furthermore, a simple cavity structure is preferable for reliable operation. We have designed an RF cavity and carried out its low-power test with the prototype model. The specific features of the present cavity are that a beam-duct with large diameter is attached to the cavity and that a part of the beam-duct is made of the resistive material. Since the frequency of accelerating mode is sufficiently below the cutoff frequency of the beam-duct, the accelerating field is fully trapped in the cavity. On the other hand, the HOMs, which can propagate out of the cavity through the beam-duct, are damped by the resistive part.

Design Consideration

Four cavities made of copper will be installed in a long straight section of the VUV ring. They are required to generate an RF voltage of 1.4 MV in total. To maintain the dissipation power for each cavity below 40kW, it is desirable that the cavity should have the shunt impedance of more than 6 M Ω . The cavity shape was optimized using the computer codes of SUPERFISH and URMEL. In this calculation, the power loss of HOMs on the wall was estimated by taking into account the conductivity of resistive material.

The schematic of a quadrant of the designed cavity is shown in Fig. 1. In this design, the conductivity of the

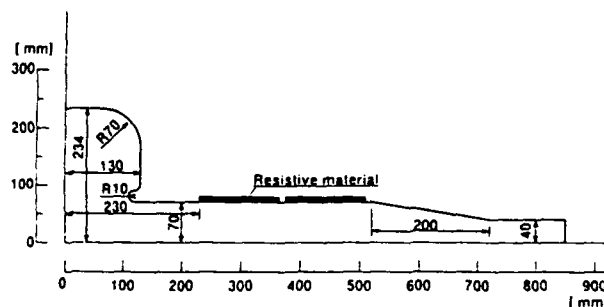


Figure 1: Schematic view of the cavity.

resistive material was assumed to be 100 (Ωm)⁻¹. The small nose cones are introduced to the cavity not only to increase shunt impedance of accelerating mode but also to prevent the accelerating power from being absorbed in the region of resistive material. We obtained the shunt impedance R_s of 7.75 M Ω and Q-value of 44000 for the accelerating mode.

Figures 2 and 3 show the longitudinal and transverse coupling impedances of the HOMs in this cavity, respectively. The critical impedances in these figures denote the impedances, above which a coupled-bunch instability may occur at the beam current of 400 mA. Most of HOMs, whose frequencies are higher than the cutoff frequency of the large beam-duct, are absorbed by the resistive material and their impedances become smaller than the critical impedance. For some survived HOMs, having high Q-values, the coupled-bunch instabilities will be suppressed by a detuning of resonance frequencies of the cavity[1].

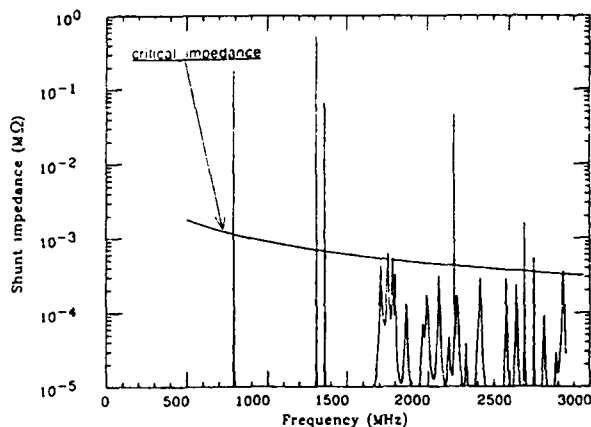


Figure 2: Longitudinal HOMs in the cavity.

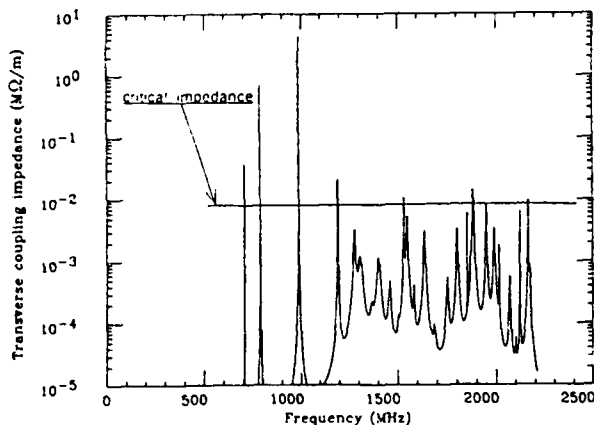


Figure 3: Transverse HOMs in the cavity.

Low power measurements

A prototype cavity of the same size as in Fig. 1 was made and its low power test was carried out. The prototype was made of aluminum and two types of beam-duct were prepared for the test. One is made of aluminum and the other of sintered SiC. The RF characteristics of both fundamental and HOMs were measured using a network analyzer (HP8510C).

Figure 4 shows the field distribution of the fundamental mode in the case of Al-duct. It was measured with the method of the perturbation technique[2],[3] using metallic sphere of 10 mm diameter. R_s/Q , calculated from the field distribution, was 168 Ω and the calculated value by SUPERFISH was 177 Ω . We measured the field distributions of all longitudinal HOMs, whose frequencies are below the cutoff of the $\phi 80$ mm duct,

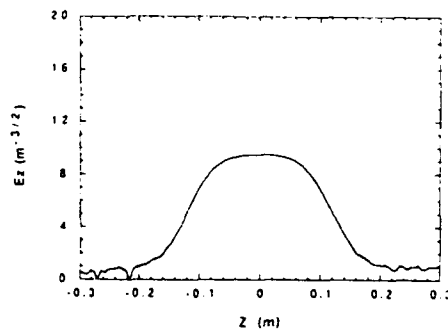


Figure 4: Field distribution of the fundamental mode.

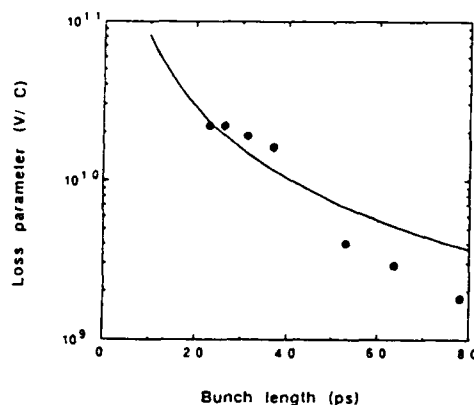


Figure 5: Loss parameter of the SiC-duct.

and some of transverse HOMs. The measured field distributions well agree with those calculated by URMEL.

The resistive duct is 135 mm long and is made of sintered SiC (TPSS, TOSHIBA CERAMICS). From Q-measurement of the SiC-duct, the conductivity of the SiC was estimated to be $250 \sim 500 (\Omega \text{m})^{-1}$ in the frequency region of 1.5 GHz to 4.5 GHz. As shown in Fig. 1, two SiC-ducts were installed each side of the cavity. The Q-values for Al- and SiC-duct are summarized in Table 2, where the measured and calculated Q-values are denoted as Q_m and Q_c , respectively. Assuming the conductivity of Al alloy as $2.0 \times 10^7 (\Omega \text{m})^{-1}$ and that of SiC as $333 (\Omega \text{m})^{-1}$, most of measured Q-values are consistent with calculated ones in both cases of the Al-duct and the SiC-duct. As seen in this table, strong reduction of Q-values were observed for the SiC-duct. The conductivity of the sintered SiC is slightly larger than the required value in the design stage described in the previous section. Therefore some of the HOMs are not damped sufficiently. However if we use a little high-resistive SiC, we will be able to damp these HOMs enough to suppress the coupled-bunch instabilities in the VUV ring.

We measured the loss parameters of the SiC-duct by using the network analyzer in a similar method described in ref[4]. The results are shown in Fig. 5. The solid curve is the loss parameter k_r calculated by[5];

$$k_r(\sigma) = \frac{1}{\pi} \int_0^\infty \text{Re}\{Z(\omega)\} e^{-\omega^2 \sigma_b^2} d\omega, \quad (1)$$

where σ_b is the bunch length. $Z(\omega)$ is the impedance of

Table 2: Summary of Q-values for Al- and SiC-duct.

Freq.(MHz)	Al-duct		SiC-duct	
	Q _m	Q _c	Q _m	Q _c
<u>Longitudinal mode</u>				
496.466	24000	25000	24000	25000
790.908	22000	22000	21000	22000
1153.14	32000	35000	31000	34000
1308.64	32000	33000	33000	33000
1362.33	24000	27000	23000	25000
1660.16	1000	24000	100	110
1662.73	18000	23000	-	120
1710.64	24000	27000	290	300
1729.52	22000	24000	200	200
1754.68	23000	25000	350	310
1786.33	29000	31000	690	570
1801.78	40000	42000	690	590
1852.60	24000	27000	290	270
1869.72	24000	28000	320	280
1968.67	-	30000	320	270
1995.71	24000	26000	300	240
2067.31	33000	33000	350	390
2127.39	28000	28000	320	290
2160.14	23000	28000	350	360
2177.43	-	26000	-	1100
2232.61	29000	29000	510	450
2292.61	-	27000	340	310
2320.40	26000	29000	510	460
2402.41	-	33000	460	540
2449.07	-	28000	420	340
2478.96	38000	43000	630	710
2541.39	28000	34000	770	370
2581.88	-	30000	450	400
2590.37	35000	35000	4500	3900
<u>Transverse mode</u>				
702.931	24000	30000	22000	27000
786.049	26000	33000	24000	28000
985.814	18000	25000	12000	14000
1189.47	-	31000	-	1500
1216.21	39000	49000	-	2900
1276.75	19000	21000	200	210
1287.27	15000	18000	-	90
1305.93	16000	20000	130	120
1363.72	18000	20000	210	170
1399.48	17000	21000	180	150
1456.52	-	23000	270	220
1502.09	30000	38000	510	490
1529.57	30000	33000	1300	690
1547.88	-	24000	480	370
1581.14	31000	35000	640	470
1635.88	-	28000	410	340
1685.28	23000	27000	290	320
1749.80	-	29000	390	340
1798.85	-	27000	540	410
1850.12	-	75000	33000	25000
1869.33	-	33000	550	450
1880.97	21000	27000	560	580
1945.87	-	35000	960	760
1986.94	-	30000	600	470

the duct written as[6] ;

$$Z(\omega) = (1 + i) \frac{L}{2\pi b \sigma \delta} \quad (2)$$

Here δ is the skin depth, σ the conductivity of the duct. L and b are radius of the duct and its length. The constant conductivity of $333 (\Omega\text{m})^{-1}$ was used in this calculation. The measured loss parameters well agree with this simple calculation.

The wall heating due to ohmic loss in the SiC-duct become serious for a short bunch such as in the VUV ring. At the bunch length of 11.7 ps (3.5 mm), which is the design value of the VUV ring, the loss parameter calculated by Eq.(1) is 0.12 V/pC per one SiC-duct. Here, the conductivity of the SiC-duct is assumed to be $100 (\Omega\text{m})^{-1}$. In addition, since there are HOM losses due to cavity shape, the problem of the wall heating become more serious. In our rough estimation of the HOM losses, cooling system for the SiC-duct is necessary.

Near-future plan

Another type of SiC-duct with the conductivity of about $5 (\Omega\text{m})^{-1}$ will be tested and a comparison between these two type of SiC will be made in detail. Then the shape of the cavity, especially the position and length of the SiC section will be optimized furthermore. We also intend to investigate the effects of tuner and coupler on the RF characteristics by using the prototype cavity. The vacuum test of the SiC-duct is also now in progress.

Acknowledgements

We would like to thank Prof. T. Ishii, director of the Synchrotron radiation laboratory of ISSP, and Prof. H. Kobayakawa, director of the light-source division of the Photon Factory, for their continuous support. We also thank Dr. T. Toyomasu for useful discussions.

References

- [1] H.Kobayakawa, et al., "Suppression of beam instabilities induced by accelerating cavity", Rev. Sci. Instrum., Vol.60, No.7, pp. 1732-1735, July 1989
- [2] J.Jacob, "Measurement of the higher order mode impedances of the LEP cavity", ESRF-RF/88-02, January 1988.
- [3] Y.Yamazaki et al., "Measurement of the longitudinal and transverse coupling impedances of the higher-order modes of the re-entrant accelerating cavity", KEK 80-8, August 1980.
- [4] M.Izawa et al., "Impedance measurements at the Photon Factory storage ring", Rev. Sci. Instrum., Vol.63, No.1, pp. 363-366, January 1992.
- [5] P.B.Wilson, "Fitting the SPEAR II impedance function using measured energy loss data", PEP-233, February 1977.
- [6] For example, see F.Sacherer, "Transverse instabilities of relativistic particle beams in accelerators and storage ring, Part II- Bunched beams", CERN 77-13, pp. 198-218, 1977.

V.A. Krasnopolsky
MRTI, Russia, 113519

Abstract

In order to accelerate low-energy protons and heavy-ions, a wide accelerating frequency range is necessary. Such applications of accelerating structures with amorphous cores loaded cavity have been studied by several laboratories. In this article a method of computation the impedance of a coaxial cavity loaded with amorphous toroidal cores is described. In this computation is shown, what a dominant role is played by the skin-effect in a core with a foliated structure. As a result of an analysis of electric and magnetic fields distribution, the cavity impedance is computed. The impedance depends on capacity and magnetic permeability, having real and imaginary parts. These parts depend on frequency, the sheet thickness, conductivity, and on permeability of the material at zero frequency. It is important that this impedance may be stabilized in some frequency range. Applications of accelerating systems of this type are discussed in different cases..

1. INTRODUCTION

A very high magnetic permeability of amorphous metals permits to use it in various accelerating systems [1],[2]. In these systems a coaxial cavity loaded with amorphous toroidal cores having a foliated structure is used. In case of homogenous material with zero conductivity having constant magnetic and electric permeability in a coaxial-type cavity, electric and magnetic fields in most part of cavity have only E_r and H_φ components on T mode. But in case of amorphous toroidal cores with a foliated structure and non-zero conductivity the longitudinal components electric field E_z and current J_z are presented too. As a result electromagnetic fields are non-uniform in each layer of metal. This skin-effect is small usually in low frequency transformers, but it can play a dominant role at radio-frequency range. As a result of the analysis of electric and magnetic fields in layers of the metal and in isolation between layers the input cavity impedance will be calculated over wide frequency range.

II. ANALYSIS OF THE FIELDS AND GENERAL RESULTS

The coaxial cavity with the foliated structure is shown in Figure 1. The time harmonic azimuthal symmetric mode must satisfy the Maxwell equations which can be solved in local layers of metal or isolation.

$$E_z = (\alpha_s / \beta_s) Z_0 e^{j(\omega t - Kz)} \quad (1)$$

$$E_r = (jK / \beta_s) Z_1 e^{j(\omega t - Kz)} \quad (2)$$

$$H_\varphi = Z_1 e^{j(\omega t - Kz)} \quad (3)$$

$$H_\varphi / r = I / 2\pi a \quad (4)$$

where

$$Z_0 = A_s J_0(\alpha_s r) + B_s N_0(\alpha_s r)$$

$$Z_1 = A_s J_1(\alpha_s r) + B_s N_1(\alpha_s r)$$

$$\alpha_s^2 = \omega^2 \epsilon_s \mu_s - j \mu_s \sigma_s \omega - K^2$$

$$\beta_s = \sigma_s + j \epsilon_s \omega; \quad s = 1, 2, \dots$$

$\mu_s, \epsilon_s, \sigma_s$ - are magnetic permeability at zero frequency, dielectric permeability and conductivity in layer; $J_{0,1}, N_{0,1}$ - are the Bessel functions; A_s, B_s - are constants for the layer; I - is the current in the inner tube.

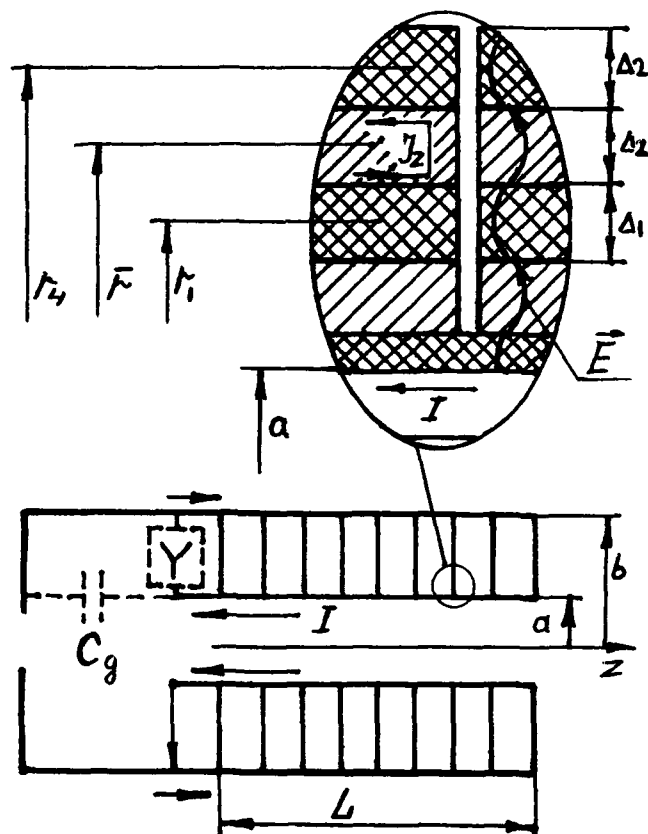


Figure 1. Coaxial-type cavity with foliated toroidal cores.

In Figure 1 we can see three layers (dielectric-metal-dielectric) at one radial period of core. We assume that in case of foliated structure the longitudinal component electric field is equal to zero just on the local surfaces.

$$E_z(r) = E_z(r) = E_z(r_4) = 0 \quad (5)$$

We assume the continuity the tangential components electric and magnetic fields on boundaries between metal and isolation as well. In such case the longitudinal current J_z passing in opposite directions in two zones of metal, and force lines of electric field have "snake-type" shape. This current passes from zone $r < r$ to $r < r$ along end face of the layer, and the gaps between cores do not disturb picture of the field. Using equations (1), (3), (5) and continuity the fields, we can write the linear equations system which contains six constants A_s, B_s . Using this system we can write the dispersion equation in the following general form:

$$D = |Z_{m,n}| = 0 \quad (6)$$

$$m, n = 1, 2, 3, \dots, 6$$

where

D - is a determinant of the linear system, $Z_{m,n}$ - are the Bessel functions with coefficient, or zero. During further investigations we assume fulfilment of the following conditions:

$$\omega \epsilon_2 \ll \delta_2; 1 \ll \alpha_2 r \quad - \text{in the metal;}$$

$$\alpha, \Delta_1 \ll 1; \mu_1 = \mu_0; \delta_1 = 0 \quad - \text{in the dielectric;}$$

$$\Delta_{1,2}/r \ll 1; \Delta_{1,2} K \ll 1 \quad - \text{in cores as a whole.}$$

Using asymptotic form of the Bessel functions in zone of metal and expansion in series in zone of dielectric [3] we can present equation (6) in the following form:

$$G_4 \alpha^4 + G_2 \alpha^2 + G_0 = 0 \quad (7)$$

where

$$G_4 = j(\Delta_1^2/4)(\delta_2/\epsilon_1 \omega) \sinh 2P/2P$$

$$G_2 = (\Delta_1/\Delta_2) \cos 2P$$

$$G_0 = \omega^2 \epsilon_1 \mu_2 \sinh 2P/P$$

$$P = (\Delta_2/2)(-j\mu_2 \delta_2 \omega)^{1/2} \quad (8)$$

Dispersion equation (7) can be solved relative to α , and to

wave vector K

$$K^2 = \omega^2 \epsilon_1 [\mu_0 + (\Delta_2/\Delta_1) \mu_2 \tanh P/P] \quad (9)$$

Of equations (1), (3), (5), (7) we receive the following consequence as well.

$$r_1 H_\varphi(r_1) = r_4 H_\varphi(r_4) \quad (10)$$

As a result of relation (10) in dielectric dependence analogous to T mode in case with the homogenous material is obtained. But in metal drop of the magnetic field is observed. This drop depends on P (8) because of the skin-effect. Using these result and addition condition (4) we can compute intensity of vortex U between inner and outer tubes. Summation of two waves having wave vector $\pm K$ gives the cavity input impedance Z and vector admittance Y .

$$I U^{-1} = I \left[\int_a^b E_r dr \right]^{-1} = Z^{-1} = Y \quad (11)$$

where

$$Y = -j \frac{2\pi L}{\ell_n(b/a)} \sqrt{\frac{\tilde{\epsilon}}{\tilde{\mu}}} \coth(KL) \quad (12)$$

$$\tilde{\epsilon} = \epsilon_1 (\Delta_1 + \Delta_2) / \Delta_1 \quad (13)$$

$$\tilde{\mu} = \frac{\Delta_1 \mu_0}{\Delta_1 + \Delta_2} + \frac{\Delta_2 \mu_0}{\Delta_1 + \Delta_2} \frac{\tanh P}{P} \quad (14)$$

$$\tanh P/P = \eta [1 - i \tanh \delta]$$

$$\eta = (3h\bar{P} + 3i\sinh\bar{P}) [\bar{P}(ch\bar{P} + \cos\bar{P})]^{-1}$$

$$\tanh \delta = (3h\bar{P} - 3i\sinh\bar{P}) (3h\bar{P} + 3i\sinh\bar{P})^{-1}$$

$$\bar{P} = \Delta_2 (\mu_2 \delta_2 \omega/2)^{1/2}$$

In these formulas $K = \omega(\tilde{\epsilon}\tilde{\mu})^{1/2}$ is the complex wave vector (9); $\tilde{\epsilon}$ - is the resulting dielectric permeability; $\tilde{\mu}$ - is the resulting magnetic permeability in the foliated core. Formula (14) generalizes result [4] in case of foliated core.

III. THE SPECIAL CASES

On of the typical conditions:

$$\Delta_2 \approx 10^{-5} \text{ m}; \quad \omega = 2\pi \cdot 10^6 \text{ s}^{-1};$$

$$\delta_2 \approx 10^6 \text{ ohm}^{-1} \text{ m}^{-1}; \quad \mu_2 = \mu_0 \cdot 10^4$$

parameter $\bar{P} \approx 2$ and as a result $tg \delta \approx 1$. In this case the general formulas (12), (14) will be as follows:

$$\tilde{Y} = |\tilde{Y}| e^{-j\pi/4} \quad (15)$$

$$Z^{-1} = Y = \frac{2\pi}{\ell n(b/a)} \sqrt{\frac{\tilde{\epsilon}}{|\tilde{Y}|}} [\Psi_1 + j\Psi_2] \quad (16)$$

where

$$|\tilde{Y}| = (\Delta_1 + \Delta_2)^{-1} \sqrt{\frac{2\mu_2}{\pi \epsilon_2 f}} \quad (17)$$

$$\Psi_1 = A \cos(\pi/8) + B \sin(\pi/8)$$

$$\Psi_2 = A \sin(\pi/8) - B \cos(\pi/8)$$

$$A = \sinh \theta_s / [\cosh \theta_s - \cos \theta_c]$$

$$B = \sin \theta_c / [\cosh \theta_s - \cos \theta_c]$$

$$\theta_s = 2\Phi \sin(\pi/8); \theta_c = 2\Phi \cos(\pi/8)$$

$$\Phi = |K|L = 2\pi f (\tilde{\epsilon}/|\tilde{Y}|)^{1/2} L$$

The result (17) gives attenuation - frequency characteristic $|\tilde{Y}|$ at high frequency. Both parts computation result of the vector admittance is shown in Figure 2.

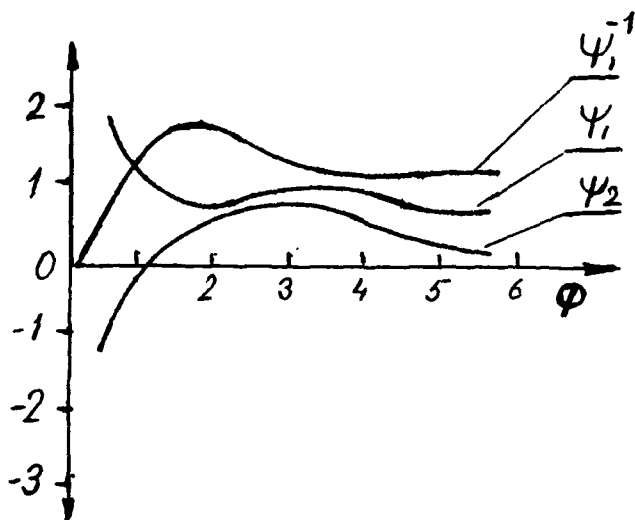


Figure 2. Characteristics of the vector admittance and shunt impedance $R_s \sim \Psi_1^{-1}$

In zone $\Phi < 1$ ("short cavity") the impedance and vector admittance will be as follows:

$$Z^{-1} = Y = \frac{\Delta_1 + \Delta_2}{2L \ell n(b/a)} \sqrt{\frac{\pi \epsilon_2}{\mu_2 f}} (1-j)$$

In zone $3 < \Phi$ ("long cavity") the impedance and vector admittance are low-dependent on L or f as a result of an attenuation over the length L . In this zone impedance matching with generator over wide frequency range is more simple, but the losses may be high.

Resonance takes place only in one point $\Phi \approx \pi/2$. In this zone the losses are low, but impedance matching may be more complicated. The operating zone and cavity length may be selected with taking into account the accelerating gap capacity C_g

$$\bar{Z}^{-1} = \bar{Y} = Y + j2\pi f C_g,$$

dissipative power P_d

$$P_d = (U^2 R_s)/2 = \frac{U^2 \pi}{\ell n(b/a)} \sqrt{\frac{\tilde{\epsilon}}{|\tilde{Y}|}} \Psi_1,$$

and output generator impedance.

IV. ACKNOWLEDGEMENT

I would like to thank I.M.Bolotin, A.I.Glazov and V.A.Skuratov for the discussions of the problem, and G.I.Klenov for the support investigations in this direction.

IV. REFERENCES

- [1] C.Fougeron, P.Ausset, J.Peyromaure, "Towards the Construction of an Ultra Short Cavity for Heavy Ions Synchrotron." Proceedings of the 2-nd EPAC, Vol. 1. PP. 961-963 (1990)
- [2] S.Ninomiya, "Conceptual Design of a Non-Resonant Accelerating System for Low-Energy Proton and Heavy-Ion Accelerators." KEK Report 92-2. April 1992, A.
- [3] Handbook of Mathematical Functions. Edited by M.Abramowitz and I.Stegun. 1964. Translation into Russian 1979.
- [4] R.Bozort, "Ferromagnetism." Foreign Literature, 1956.

APPLICATIONS AND COMPARISONS OF METHODS OF COMPUTING THE S MATRIX OF 2-PORTS†

Roger M. Jones*, Norman M. Kroll*[^], Kwok Ko*, Sami Tantawi*, and David U. L. Yu#

*Stanford Linear Accelerator Center, Stanford University, Stanford, CA 94309

[^]University of California, San Diego, La Jolla, CA 94093

#DULY Research Inc. Rancho Palos Verdes, CA 90732

Abstract

We report on the application of four different methods of computing the S Matrix for 2-port microwave circuits. The four methods are modal expansions with field matching across boundaries, time domain integration of Maxwell's equations as implemented in MAFIA, HFSS (high frequency structure simulator), and the KKY frequency domain method. Among the applications to be described are steps in rectangular waveguides and irises in waveguides.

I. INTRODUCTION

The Kroll-Kim-Yu (KKY) [1] method of determining the S matrix of 2-port microwave circuits is an elementary algebraic procedure which can be used in conjunction with any computer program which determines the resonant frequency and electromagnetic fields of closed cavities. As such it may be thought of as supplementary to computer codes which accomplish the same objective, but which may not be available to a particular user. It may also be used to provide mutual validation of alternate procedures. While the basic theory of the method is given in [1], no actual examples were presented. The purpose of this paper is to remedy this deficiency, and thereby to demonstrate the practicality of the method. As an example of the symmetric case we discuss reflecting iris design in circular waveguide for application to SLED II [2]. As an example of the unsymmetric case we chose a transversely symmetric H-plane step in rectangular waveguide (i.e. a discontinuous increase of waveguide width). As will be discussed below, this simple geometry allow us to compare the KKY results with those obtained from highly accurate mode matching calculations. Comparison with other lattice based computer codes will also be given.

II. THE KKY METHOD

A. Description Of The Method

Following [1], we consider a lossless 2-port and parameterize its S-matrix as follows:

$$S_{11} = -\cos(\theta) \exp[j(\phi + d\phi)] \quad (1)$$

$$S_{12} = S_{21} = -j \sin(\theta) \exp(j\phi) \quad (2)$$

$$S_{22} = -\cos(\theta) \exp[j(\phi - d\phi)] \quad (3)$$

Unique values for the parameters θ , ϕ , and $d\phi$ as functions of frequency are defined by restricting their ranges as follows: $-\pi/2 < \theta \leq \pi/2$, $-\pi/2 < d\phi \leq \pi/2$, and $-\pi < \phi \leq \pi$. From the definition of the S matrix:

$$b_i = S_{ij} a_j \quad (4)$$

where a_i and b_i are incoming and outgoing wave amplitudes respectively.

Now let us suppose that we have available the field configuration and frequency of some mode of the 2-port transformed into a closed cavity by shorting the waveguides associated with the ports at distance L_i from the reference planes. We consider here only the case in which one has single mode propagation in each waveguide. Then we have:

$$\begin{aligned} b_1 / a_1 &= -\exp(2j\psi_1) \\ a_2 / a_1 &= r \exp[j(\psi_1 - \psi_2)] \end{aligned} \quad (5)$$

where ψ_i is $k_i L_i$ and r is the ratio of the incoming wave amplitudes evaluated at the shorts. The wave amplitude ratio r is readily computed from appropriately chosen field amplitudes as will become clear from the examples. Substituting Eqs. (3) and Eqs. (1) into Eqs. (2) provides us with two equations for the three unknown S matrix parameters. Through algebraic and trigonometric manipulation we obtain explicit expressions for θ and ϕ in terms of the known quantities ψ_i and r and the unknown $d\phi$:

$$\tan(\theta) = 2 \sin(d\psi) / (r - 1/r) \quad (6)$$

where $d\psi = \psi_1 - \psi_2 - d\phi$, and $\bar{\phi}$ is defined in [1].

B. The Symmetric Case

A symmetric structure with symmetrically selected reference planes has $S_{11} = S_{22}$, and hence $d\phi = 0$. Thus for such circuits (provided we have chosen $L_1 \neq L_2$) these formulas determine the complete S matrix for each frequency which appears in the mode spectrum of a computer run.

We have applied the method to the design of a number of circular iris's in circular TE_{01} waveguide. For application to SLED II, design to a specified value of reflection coefficient was required. The iris thickness was specified for mechanical reasons to be .080 inches, the waveguide diameter was 1.75 inches, and the problem was to

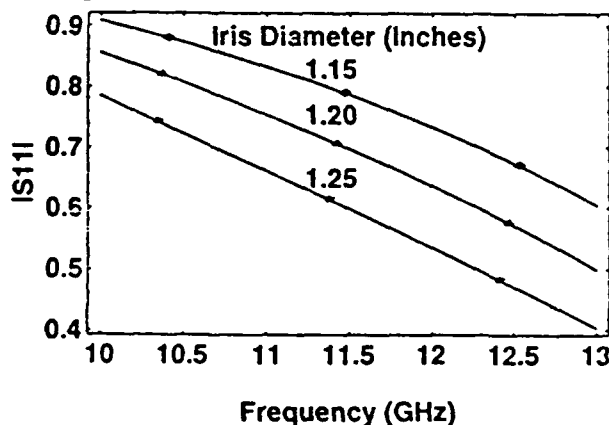
†Supported by Department of Energy, DE-AC03-76SF00515*, DE-FG03-92ER40759*, and SBIR grant DE-FG03-91ER81116*

determine the correct iris diameter. Three URMEL runs were carried out, one for each of three choices of iris diameter, and each with the waveguides shorted at 2.15 inches and 1.80 inches respectively from the center of the iris.

The quantity r for this configuration is given by the negative of the ratio of the maximum magnetic fields at each end. The sign is to some extent a convention, but with this choice, S_{11} is unity when the iris diameter coincides with the waveguide diameter. This configuration yields eight modes in the frequency range lying between the cutoff frequencies of the TE_{01} and TE_{20} modes, and S matrix parameters could have been determined for all of them. This was actually carried out, however, only for the three frequencies closest to the design frequency, 11.424 GHz, of SLED II. The parameters at the design frequency were obtained by interpolation from these data at each of the three diameters, and the diameter required to provide the specified reflection coefficient was again found by three point interpolation from these numerical values. Experimental values were obtained in the course of the SLED-II measurements reported in [2] and are in excellent agreement with the theoretical values.

Since the completion of the above, the mode matching program to be discussed below has been extended to allow very accurate evaluation of the S matrix for these iris's. The curves obtained with the mode matching method are shown in figure 1 (the points are obtained with the KKY method).

Figure 1: Reflection Coefficient of Circular Iris



C. Application To An Asymmetric Case

We have seen in the previous section that from a mode at a specific frequency with a specific choice of shorting lengths we get two equations for determining the three S matrix parameters. To obtain additional equations it is merely necessary to find a different pair of shorting lengths which produces an independent solution at the same frequency. There is, in fact, a continuum of (L_1, L_2) pairs which satisfy this condition, but one such is actually more than enough. That is, from a second set with, say L'_1, L'_2 , and an associated r' , we have four equations for the three parameters. We can obviously write down a set of expressions analogous to Eqs. (6) and the associated equation

for $\bar{\phi}$ in [1] in terms of the primed quantities and temporarily designate the associated S matrix parameters as primed quantities. Then setting $d\phi = d\phi'$ and setting $\tan(\theta)$ equal to $\tan(\theta')$ in the unprimed and primed versions of Eq. (5), we obtain:

$$\tan(d\phi) = \frac{[(r'-1/r')\sin(D\psi) - (r-1/r)\sin(D\psi')]}{[(r'-1/r')\cos(D\psi) - (r-1/r)\cos(D\psi')]} \quad (7)$$

where $D\psi = \psi_1 - \psi_2$. We may then obtain ϕ and ϕ' from Eq. (6) and its primed counterpart using $d\phi$ as obtained from Eq. (11). They should, of course, be equal to one another and the extent to which this will be found to be the case depends upon the accuracy of the computer programs which produce the input data and the accuracy with which the frequencies of the primed and unprimed cases have been matched.

As a test of the practicality of the KKY method in the asymmetric case we considered a rectangular waveguide in which the width increased from 0.4 inches to 0.6 inches. With L_1 and L_2 measured from the junction equal to 1.1 inches and 1.3 inches respectively, a MAFIA computation produced eight modes in the frequency range between the TE_{10} and TE_{20} cutoffs. (Because the junction is transversely symmetric there is no coupling between the TE_{10} and TE_{20} modes.) MAFIA runs with equal lengths of 1.2, 1.25, and 1.3 inches produced corresponding sets of eight modes whose frequencies bracketed each of the modes of the unequal length set. The $L_1 = L_2$ values needed to match each of the eight frequencies of the unequal length run were determined by interpolation from the three equal length runs. The associated r values were determined by interpolation from the r values from the three computed lengths. To determine the r values we used $r = -K(H_2/H_1)$ where the H_i are the maximum magnetic fields at the ends of the waveguides and K is given by: $K = [(f^2 - f_{c1}^2)/(f^2 - f_{c2}^2)]^{1/4}$, where f and f_c are the mode frequency and waveguide cutoff frequencies respectively. Thus four MAFIA runs yielded the data to compute the S matrix parameters at eight frequencies, providing thereby a comprehensive description of the behavior of the S matrix over a broad range of frequencies. A subset of results obtained will be shown in connection with those obtained by other methods in the next section. The ϕ values to be shown were obtained from the unequal length set. The discrepancies between them and those obtained from the interpolated equal length set were very small, a result which provides us with a consistency check.

III. COMPARISON WITH OTHER METHODS

The S matrix of both the circular iris and the H-plane step can be very reliably and accurately computed by the mode matching technique. In order to ascertain the veracity of the KKY method we conducted a detailed

written utilizing the mode matching method, MAFIA in the time domain and HFSS.

The mode matching method entails a decomposition of the tangential electromagnetic field in region 1 into the form:

$$E_1 = \sum_{n=1}^{\infty} (a_n^+ \exp[-jk_n^+ z] + b_n^+ \exp[jk_n^+ z]) \sqrt{Z_1^+} e_n^+ \quad (8)$$

$$H_1 = \sum_{n=1}^{\infty} (a_n^+ \exp[-jk_n^+ z] - b_n^+ \exp[jk_n^+ z]) \sqrt{Y_1^+} h_n^+ \quad (9)$$

where e and h are the characteristic mode functions of the structure, k_n^+ is the wavenumber of mode n and, $Y_1^+ = 1/Z_1^+$ is the characteristic admittance of mode n . A similar expansion of fields is made in region 2. The electromagnetic fields on both sides of the waveguide junction ($z = 0$) are equated to each other and this results, in principle, in an infinite set of coupled equation for the mode coefficients a_1^+ , a_2^+ , b_1^+ and b_2^+ , which in practice, are truncated to N in region 1 and M in region 2. The solution to these equations for a WN (wide to narrow) transition enables the normalized generalized scattering matrix to be obtained in the compact form:

$$S_{11} = Y^{1/2} (Y + Y_1)^{-1} (Y - Y_1) Y^{1/2} \quad (10)$$

$$S_{12} = Y^{1/2} [2a(\hat{Y} + Y_1)^{-1}] \hat{Y}^{-1/2} \quad (11)$$

$$S_{21} = \hat{Y}^{1/2} [2a^{-1}(Y + Y_1)^{-1}] Y^{-1/2} \quad (12)$$

$$S_{22} = \hat{Y}^{1/2} (\hat{Y} + Y_1)^{-1} (\hat{Y} - Y_1) \hat{Y}^{-1/2} \quad (13)$$

where a is the matrix of scalar products of mode functions integrated over the cross-sectional area of the aperture region, Y and \hat{Y} are diagonal matrices with elements Y_1^+ and Y_2^+ respectively, and the admittance of the smaller waveguide viewed from the larger and vice-versa, respectively, are given by:

$$Y_1 = (a^{-1})' \hat{Y} a^{-1}, \text{ and } Y_2 = a' Y a \quad (14)$$

The above relation reveals the interesting result that the impedance of the smaller guide, viewed from the larger waveguide, is given exactly (i.e. no matrix inversions are required), in terms of a summation of the product of matrix elements. Moreover, the above results for the scattering matrix are applicable to both an H-plane step and to a transition in the radius of circular waveguide. Furthermore, for a WNW (wide to narrow to wide) transition, as is apposite to the SLED-II iris, the overall S matrix may be obtained by using the inherent symmetry properties of the system [3], or by cascading [4] the WN matrix with a matrix corresponding to a shift in phase along the length of waveguide and, with a matrix corresponding to a NW transition; the latter matrix is, of course, readily obtained from the WN matrix. In our computations we have utilized both methods to provide a check as to the efficacy of the calculations.

A representative sample of S matrix parameters as a function of frequency (GHz) for an H-plane step in rectangular waveguide is shown in table 1. for four different methods, namely, MM (mode matching) using both the cascaded approach and the symmetrical approach (the difference between the two methods is in the eighth decimal place), KKY, MAFIA applied in the time domain, and HFSS.

Table 1: S Parameters For An H-Plane Step

f	θ	ϕ	d ϕ	Method
15.1590	-1.00935	-1.35441	1.14863	MM
	-1.00987	-1.35374	1.13839	KKY (ω)
	-1.00858	-1.35159	1.13868	MAFIA (t)
	-1.00910	-1.34078	1.12459	HFSS
16.0159	-1.22911	-1.40363	1.03246	MM
	-1.22843	-1.40268	1.02089	KKY (ω)
	-1.22847	-1.40105	1.02126	MAFIA (t)
	-1.22632	-1.38731	.983884	HFSS
17.7145	-1.37354	-1.44954	.854241	MM
	-1.37297	-1.44981	.841649	KKY (ω)
	-1.37283	-1.44762	.840349	MAFIA (t)
	-1.37179	-1.45437	.811546	HFSS
19.3840	-1.43435	-1.47581	.694889	MM
	-1.43368	-1.47632	.678899	KKY (ω)
	-1.43364	-1.47447	.678542	MAFIA (t)
	-1.43185	-1.48811	.630695	HFSS

The agreement between MM, KKY, and MAFIA in the time domain, for ϕ and θ is encouraging. This indicates that the absolute value of either the reflection coefficient or the transmission coefficients and indeed, the phase of the transmission coefficients, may be quite reliably obtained by either method. However, the values for d ϕ only agree in the first and second decimal place, indicating that the phase of the reflection coefficients of the S matrix is somewhat less reliable.

V. REFERENCES

- [1] N. Kroll, et al, 1992, *Computer determination of the scattering matrix properties of N-port cavities*, 1992 Linear accelerator conference proceedings, AECL-10728, 217, (1992)
- [2] C. Nantista, et al, 1993, *High power RF pulse compression with the SLED-II system at SLAC*, SLAC-PUB 6145 (sb 33, 1993 Particle accelerator conference).
- [3] R. E. Collin, 1991, *Field Theory of Guided Waves*, (McGraw-Hill Book Company, N.Y.)
- [4] R. Mittra and S. W. Lee, 1971, *Analytical techniques in the theory of guided waves* (Macmillan Company, N.Y.)

Construction of the CEBAF RF Separator*

A. Krycuk, J. Fugitt, A. Johnson, R. Kazimi, L. Turlington
Continuous Electron Beam Accelerator Facility
12000 Jefferson Avenue, Newport News, VA 23606-1909 USA

Abstract

The CEBAF accelerator is designed in a multipass racetrack configuration, with two 1497 MHz linear accelerator sections joined by independent magnetic transport arcs. Room temperature subharmonic rf separator cavities will be used on each independent arc to extract a portion of the recirculating beam, and one additional cavity will be used to divide the final full-energy beam between CEBAF's three experimental end stations. A single-cell prototype cavity has already been built and tested at low power levels. The next stage of the design process is the construction of a cavity capable of operation at full power, i.e. at a gradient sufficient to provide the required 100 μ rad bend to a 6 GeV beam. The paper will discuss both the electrical and mechanical design of the cavity, construction techniques employed, and preliminary test results.

I. INTRODUCTION

The CEBAF accelerator is designed in a multipass racetrack configuration, with two 1497 MHz linear accelerator sections joined by independent magnetic transport arcs. A room temperature subharmonic rf separator cavity will be placed on each independent arc to extract a portion of the beam, and one additional cavity will be used to divide the final full-energy beam between the three experimental end stations.

II. CAVITY DESIGN

The rf separators used at CEBAF are quarter-wavelength cavities with four opposed rods placed parallel to the beam axis (Figure 1)[1]. This creates a field pattern close to that of a TEM dipole mode, resonant at 499 MHz, the third subharmonic of the fundamental accelerator frequency. The rods serve to compress the field into the center of the cavity, increasing the transverse shunt impedance R_{\perp} to on the order of 250 $M\Omega$. The Q_0 of the cavity is measured to be 5000, from which the power required to deflect the different beams the required 100 μ rad can be derived according to

$$P = \frac{(E \times 100 \mu\text{rad} / \sin 60^\circ)^2}{(236 M\Omega / \text{m})(.30 \text{ m})}$$

The above result is for a single-cell structure. Multiple-cell geometry will be used on the higher-energy passes of the accelerator, as is summarized in Table 1.

* Supported by U.S. DOE contract DE-AC05-84ER40150

Table 1

Separator Requirements for CEBAF Accelerator

Beam Pass	Energy (GeV)	No. of Cavities	Power Req'd (W)
1	1.2	1	270
2	2.4	1	1000
3	3.6	2	1200
4	4.8	2	2200
5	6.0	3	2250

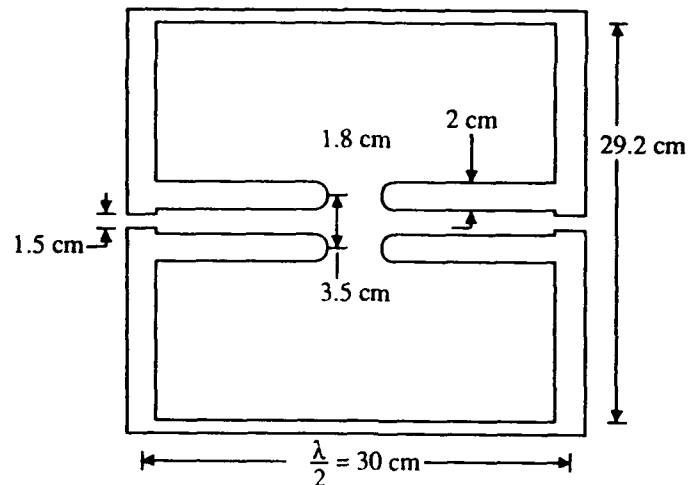


Figure 1. Single Cell Cavity Geometry

III. CAVITY FABRICATION

In order to standardize parts while maintaining the flexibility necessary to support the multiple cell geometry needed for beam separation, it was decided to fabricate the cavity in modular elements. Thus the spool piece, end flanges and center flanges (of multiple cell structures) are discrete elements.

The spool piece, which is the cylindrical body of the cavity, is made from stainless pipe, with a 14 inch knife-edge flange welded on either end. Additional ports on the circumference of the spool are provided for pumpdown and tuner control. The entire assembly, with the exception of the knife edges, is acid copper plated to lessen surface resistivity.

Due to the field concentration caused by the rods, most of the surface current flows from the base of one rod to the next. The control of resistance in this area is critical to maintaining the Q of the cavity. As machining such a complex geometry is feasible, but prohibitively expensive, it was decided to use a gold-copper braze alloy to join the individual OFE rods to an OFE copper insert. This maintains good conductivity while providing reliable seal of the water passages which cool the

rods. At the same time that the rods are brazed to the insert, a stainless steel ring is brazed around the insert.

This sst ring serves as an intermediate between the copper insert and the remainder of the end flange, which is machined from a 14" knife-edge blank. The insert assembly is subsequently electron beam welded to the flange with a full penetration weld. It was felt a copper-steel weld would not provide a reliable water to vacuum seal, while at the same time it is not recommended practice to subject a knife edge seal to braze temperatures. Beam tube, rf input, and cavity field probe flanges are also present on the end flange.

The center flange assembly contains a double-sided rod insert, as it carries rod assemblies for two quarter-wave cells. Two symmetric magnetic coupling irises are present to admit rf to the attached cell(s). RF power is coupled into the cell structure using a coupling loop originally designed as the output coupler on a 5 kW klystron. The loop is cooled by conduction to the outside.

In order to maintain the cavity at the correct resonant frequency, a capacitive tuner was included. The tuner consists of a copper flap, grounded to the wall of the cavity on one end, that can be bent by means of an externally adjusted linear motion feedthrough to close proximity of the rods. A tuning range of 5 MHz is obtained. No dynamic tuning capability was included in the tuner design, as the frequency shift with respect to temperature of the cavity is 2 kHz/deg C. The cooling of the separators limits the temperature increase in any part of the cavity to 1–2 deg C in the rods, while maintaining the remainder of the cavity at 95 deg C. Therefore, it can be seen that any temperature-induced frequency changes are well within the cavity bandwidth.

IV. SYSTEM CONSIDERATIONS

The rf separators are used in two configurations. The four that are placed on the lower energy recirculating arcs deflect the beam in the horizontal direction. The phasing of the rf in these cavities (see Figure 2) and the downstream magnet configuration are such as to allow a portion of the beam to be steered to only one of the experimental halls, while the remainder is recirculated back into the linacs. The remaining separator on the high-energy leg is phased to divide the beam in three for the end stations.

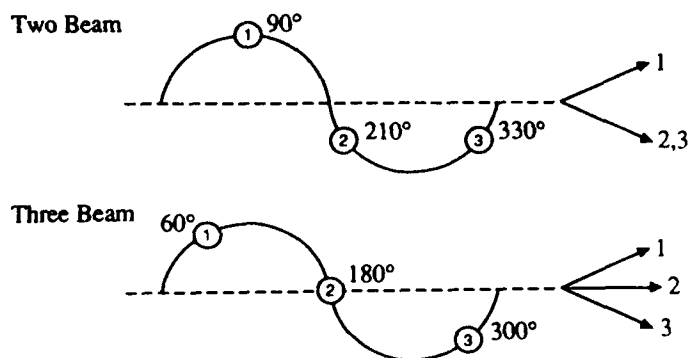


Figure 2. Two and Three Beam Separation

As can be seen from Table 1, the cavities require on the order of kilowatts to achieve separation. Fortunately, the frequency used for the separators is close to the UHF amateur and television bands (420–450 MHz), so amplifiers of the gain and output required for driving the cavities can be obtained commercially with only a slight shift in bandwidth. Currently, only one amplifier has been obtained. Manufactured by Henry Radio, it is capable of producing 1.5 kW at 499 MHz with a gain of 40 dB.

Phase and amplitude stability of the rf in the separator cavities is achieved by using the same modules as the rest of the CEBAF rf control system [2], modified to operate at 499 MHz. The rf system for the separators is locked to the accelerator frequency through the frequency reference system [3].

The major concern in operation of the separators is phase slippage of the cavities with respect to the injector. The experimental halls require differing currents, with Hall B being limited to nanoamperes, while the other two are set to receive microamperes of beam. The injector, through use of a subharmonic chopper and current-limiting apertures, defines the beam current for each bunch. Should the phase of the separators change with respect to the injector, it could result in the beam being sent to the wrong hall. To prevent this, a direct measurement of the injector-separator phase is being implemented. A sample of the field in the chopper cavity is compared to one from the high-energy cavity; if the phase difference between the two has changed, the beam is shut off.

V. CONCLUSION

A separator cavity capable of operating at full gradient has been constructed and is awaiting high-power rf test. All five of the separators will be installed by June 1994. Beam will be provided to the first cavity by March 1994.

VI. REFERENCES

- [1] C. Leemann and G. Yao, "A Highly Effective Deflecting Structure," 1990 Linear Accelerator Conference, May 1990.
- [2] S. Simrock, "RF Control System for CEBAF," 1991 Particle Accelerator Conference, May 1991.
- [3] A. Krycuk, J. Fugitt, and S. Simrock, "Construction of the CEBAF Frequency Distribution System," presented at this conference.

RF Cavity for the Medium Energy Booster for SSCL

S. Kwiatkowski, J. Curbow, T. Enegren, A. Propp

Superconducting Super Collider Laboratory*

2550 Beckleymeade Avenue, MS-4010, Dallas, TX 75237

V.P. Yakovlev, V.M. Petrov

Budker Institute for Nuclear Physics, Russia

Abstract

The RF cavity for the Medium Energy Booster (MEB) is required to accept beam from the low energy booster (LEB) at a momentum of 12 GeV/c (possibly 10 GeV/c) and accelerate it to 200 GeV/c. Each cavity must provide a maximum gap voltage of 250 kV, and must be tunable from 59.7 MHz to 59.96 MHz with a maximum sweep rate of 450 kHz/s. This requires a ferrite-tuned cavity with a high quality factor. A quarter-wave cavity was designed which meets these requirements while minimizing beam-loading problems (minimizes R/Q). This paper describes the design of this cavity, results from measurements of a corresponding cold model, and several proposed Higher Order Mode (HOM) damping system designs.

I. INTRODUCTION

During each accelerating cycle the RF system of the MEB must overcome heavy static and dynamic beam loading effects. These effects are most pronounced in the high current mode of operation of the MEB, when the dc component of the beam current reaches 500 mA. Difficulty in achieving acceptable beam-dynamic phase, and amplitude stability of the gap voltage at this current required careful design of the RF system. The calculations and the simulations show that it will be necessary to cancel bunch-to-bunch beam loading. Both feedforward and fast-feedback systems will be required to accomplish this. The growth rate of the couple bunch mode instabilities for the existing lattice and the accelerating scenario depends on the frequencies, R/Q values, and shunt impedances of the HOM spectrum. Low R/Q values of the HOM is been achieved by shaping the inner and outer conductors of the cavity in the accelerating gap region. Shunt impedances of the parasitic resonances will be lowered by applying HOM dampers (two types of HOM dampers are being considered for use and

will be discussed in Section 4). The power amplifier using a 4CW150000 EIMAC tetrode will be mounted on the top of the cavity and capacitively coupled via a 14 pF capacity. The cavity will be tuned with an off-axis, conductively-coupled tuner. The tuner will employ perpendicular biasing of annular, yttrium-iron garnet rings for its tuning.

II. MECHANICAL DESIGN

As shown in Figure 1 the cavity is a simple, quarter-wave structure. Except for the stainless steel beam pipe it will be made from oxygen free copper.

The maximum power density in the inner conductor of the cavity will reach 8 W/cm^2 , so the cooling system of this unit has been carefully designed. The cross-section of the inner conductor is shown in Figure 2. The copper cooling tubes will be brazed in place between the inner conductor and the supporting tube. The outer conductor of the cavity will be cooled by 3/8 inch copper cooling tubing soldered to its outer skin.

Power dissipated in the power tube section is only few hundred watts and should therefore require no additional cooling. The vacuum window in this already-fabricated section is made from Rexolite 2200 ($Q_e = 2000 @ 10 \text{ MHz}$).

A prototype of the cavity is being built for us by INP (Novosibirsk, Russia), and will be delivered to SSC by the end of August 1993. The nearly-complete tuner design is similar to that of the LEB cavity except the tuner is off axis rather than on axis. The magnet core is mechanically isolated from the tuner housing and is independently attached to the supporting frame of the cavity. Two ferrite rings with an inner diameter of 10 cm and an outer diameter of 16 cm are epoxied to the copper walls of the tuner shell. A one cm thick Rexolite 2200 spacer holds the ferrite rings apart. The vacuum window is made out of 99.8% pure Alumina. The power dissipated in the tuner will be about 8.5 kW.

*Operated by Universities Research Association Inc., for the U.S. Department of Energy under Contract No. DE-AC35-89ER40486

The submitted manuscript has been authored by a contractor of the U.S. Government under Contract No. DE-AC35-89ER40486. Accordingly, the U.S. Government retains a nonexclusive, royalty-free license to publish or reproduce the published form of this contribution, or allow others to do so, for U.S. Government purposes.

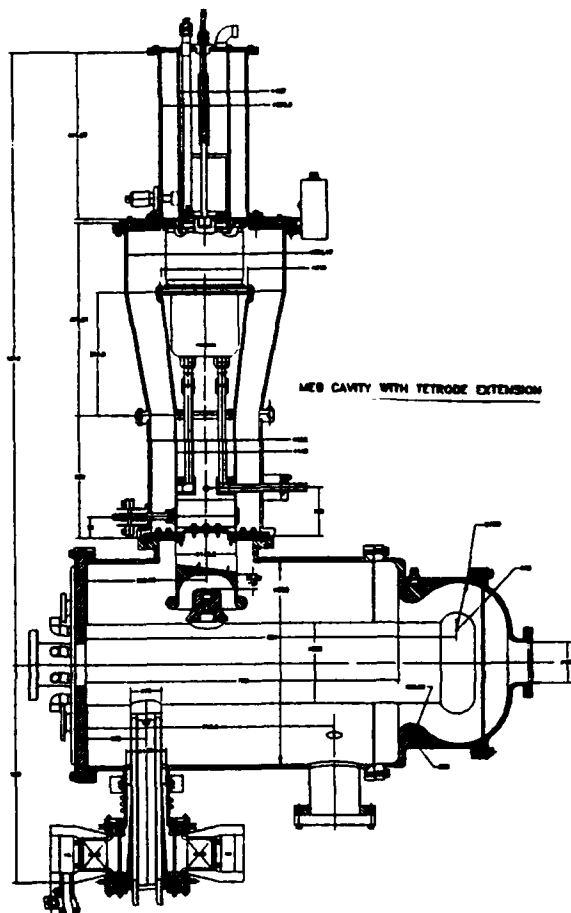


Figure 1. MEB RF cavity.

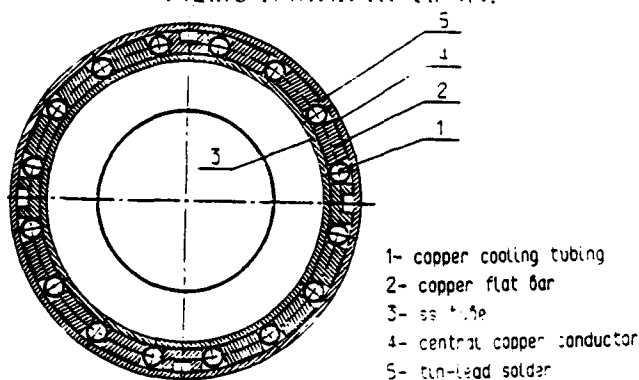


Figure 2. Cross section of the inner conductor.

III. ELECTRICAL DESIGN

A. Cavity

The maximum gap voltage in the MEB cavity in the presence of the high power feedforward system is limited to 250 kV by the power dissipated on the anode of the power tube (4CW150000 tetrode). The final dimensions of the cavity were determined based on calculations (Superfish and MAFIA), and the cold model measurements. The maximum electric field in the accelerating gap region will be 67 kV/cm, the shunt impedance at the fundamental frequency will be 650 k Ω and R/Q 51 Ω . Total power

dissipation in the cavity including the tuner and tube sections was estimated using Mafia to be 48 kW. The actual value will likely be 10-15% larger due to imperfect surface finishes and the resistance of the RF joints.

B. Power tube section

The power amplifier configuration for the MEB cavity will be similar to that used in the LEB. For a large-gain, fast-feedback system this configuration is optimum. If we use a long transmission line system to feed power to the cavity, stability could be effected by transmission line resonances. Sudden changes of the dc component of the tube current creates oscillations of the anode network at its natural resonant frequencies (feedforward system creates this problem). The most important of these is the lowest one, the frequency of which is determined mainly by the rf choke inductance, output capacity of the power tube, and the coupling capacity. The amplitude of this effect is determined by the characteristic impedance of the parasitic resonance and the tube current. By decreasing the self inductance of the rf choke we can decrease the amplitude of this phenomenon. SABER simulations show the optimum value of the RF choke inductance to be about 150 nH (choke placed in the voltage node). The gap-to-anode voltage transformation ratio was chosen to be 14 (coupling capacity \sim 14 pF).

C. Tuner

The total power dissipated in the tuner at 250 kV continuous wave (CW) will be about 8.5 kW. The tuner has been carefully designed in order to avoid the multipactoring problems and to minimize electrical stresses. The Poisson software was used to determine the main parameters of the tuner magnet. The main parameters of the tuner are given in Tab.

TABLE 1.

MEB Tuner Parameters

MAGNETIC PERMEABILITY AT 59.96 MHz		1.4
MAGNETIC PERMEABILITY AT 59.7 MHz		3.0
TUNER REACTANCE AT 59.96 MHz	[OHM]	32.4
TUNER REACTANCE AT 59.7 MHz	[OHM]	38.1
POWER LOSSES IN COPPER 59.96 MHz	[kW]	8.2
LOSSES IN THE FERRITE 59.96 MHz	[kW]	0.3
VACUUM WINDOW VOLTAGE 59.96 MHz	[kV]	13.2
MAX. E-FIELD ON WINDOW 59.96 MHz	[kV/cm]	2.3
VOLUME OF FERRITE	[dm ³]	3.0
NUMBERS OF AMPERE-TURNS		12000
MAXIMUM CURRENT	[A]	300
COIL RESISTANCE	[mOHM]	27
DC POWER	[kW]	2.4

VI. HOM DAMPERS

A simple, aluminum, cold model of the MEB cavity has been built with three main purposes:

- Determination final dimensions MEB cavity.
- Determination of the HOM frequencies and their R/Q values
- Testing different types of HOM dampers.

The cold model is shown in Figure 3. The measured and calculated (MAFIA-3D code) longitudinal modes are given in Table 2. Simple non-inductive resistors connected at the voltage node in the tube section of the cavity provide a very effective HOM damping tool. Two 50 W carbon resistors have been used in our cold model (see Figure 3). All longitudinal modes except those with the frequencies near multiples of 500 MHz were damped to less than 300 Ω . For high power operation it will be necessary to isolate the d.c. voltage and the fundamental frequency using blocking capacitor and a band stop filter.

Also being considered is a variation of the coupled line damper that has been investigated at TRIUMF[2]. For the MEB cavity the damper is located at the rear of the cavity as is shown in Figure 4. Inductive tuning provided by the short-circuited transmission line is used to minimize the voltage developed on the damping resistor at the fundamental frequency.

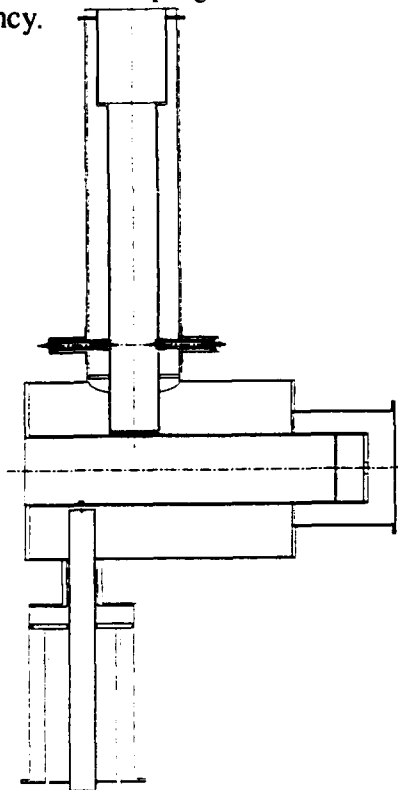


Figure 3. Cold model of the MEB cavity

Table 2.
Measured and calculated longitudinal modes of the MEB cavity.

MODE NR.	MAFIA RESULTS				COLD MODEL MEASUREMENTS			
	F [MHz]	Rsh [kOHM]	Qo []	R/Q [OHM]	F [MHz]	Rsh [kOHM]	Qo []	R/Q [OHM]
1	60.0	650	12750	51	60.0	285	5600	51
2	93.0	14	9600	1.4	91.8	3.1	1100	2.8
3	168.0	53	12800	4.2	163.8	8.8	2000	4.4
4	183.4	12	11400	1	179.6	1	1000	1
5	230.0	47	15800	3	246.8	3.5	1060	3.3
6	292.2	74	22400	3.3	298.5	2.3	880	2.6
7	357.3	47	25600	1.9	369.3	4.2	2500	1.7
8	392.6	135	21500	6.3	395.8	3	630	4.8
9	459.3	95	23400	4.1	420.0	1.6	400	4
10	471.4	16	14100	1.2	470.0	1.2	480	2.5
11	491.5	164	22650	7.2	509.6	14.6	1350	10.8
12	561.8	7	11700	0.6	544.6	0.6	230	2.6
13	597.8	53	33300	1.6	569.0	0.7	780	0.9
14	611.4	9	16000	0.6	611.0	0.8	800	1

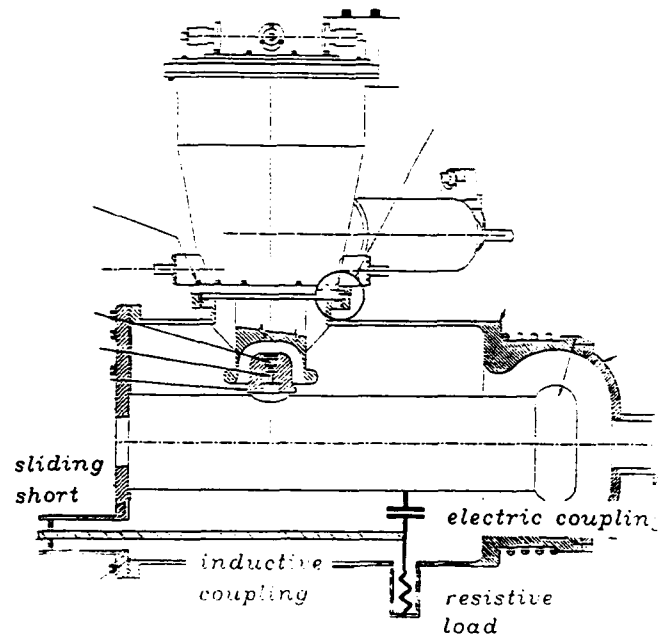


Figure 4 Coupled Line HOM Damper.

V. CONCLUSIONS

The mechanical and electrical designs for the MEB cavity have been discussed. The main body of the cavity is currently being fabricated and the tuner should be completed in December, 1993

VI. REFERENCES

- [1] S.Kwiatkowski, "MEB cavity and power amplifier" KAON/SSCL Workshop, March 4-5, 1993
- [2] T.A. Enegren, "Coupled Transmission Line Higher Mode Damper." TRIUMF design note TRI-DN-89-K105, June, 1990

New Achievements in RF Cavity Manufacturing

G. Lippmann, K. Pimiskern, and H. Kaiser

Dornier GmbH, P.O. Box 1420, D-7990 Friedrichshafen, Germany

Abstract

Dornier has been engaged in development, manufacturing and testing of Cu-, Cu/Nb- and Nb-cavities for many years. Recently, several different types of RF cavities were manufactured:

A prototype superconducting (s.c.) **B-Factory** accelerating cavity (1-cell, 500 MHz) was delivered to Cornell University, Lab. of Nuclear Studies.

A second lot of 6 s.c. cavities (20-cell, 3000 MHz) was fabricated on contract from Technical University of Darmstadt for the **S-DALINAC** facility.

Finally, the first copper RF structures (9-cell, 1300 MHz) for **TESLA** were finished and delivered to DESY, two s.c. niobium structures of the same design are in production.

Highlights from the manufacturing processes of these cavities are described and first performance results will be reported.

I. INTRODUCTION

Development, design and manufacture of RF accelerating structures has a tradition at Dornier for more than ten years. Single and multicell structures made from copper, superconducting (s.c.) niobium or from niobium sputtered on copper have been manufactured in a variety of configurations and sizes, from the 95mm ϕ 3 GHz structures up to the 350 MHz cells of the LEP size with 735 mm diameter. The production of 8 complete cryomodules - each housing two s.c. 4-cell 500 MHz cavities - for HERA at DESY was one of Dornier's outstanding achievements in the past years. These modules are now in full operation on the beam at HERA and contribute to the 30 GeV electron beam energy. Several publications exist on the manufacturing and the performance of these cavities [1], [2], [3].

II. NEW CAVITIES PRODUCED AT DORNIER

A. B-Factory cavity for Cornell University, Laboratory of Nuclear Studies

On contract from Cornell University, LNS, two prototype cavities were manufactured for the planned B-factory; one RF model, made from 3 mm OFHC copper sheet metal, and one made from 3 mm niob material with an RRR of 200 (fig. 1). The design strictly followed the layout derived by Cornell which is described e.g. in [4]. Both cavities were

complete with waveguide couplers which consist of a mechanically rather complicated, tongue-shaped coupling iris. A special feature of this cavity type is the so-called "fluted" beam tube which is to take care of the propagation of the TM_{110} and TE_{111} modes; both tubes (the Cu and the Nb one) were provided by Cornell and integrated into the cavity at Dornier. First measurement results of the copper model as well as of the niobium structure are reported in [5] and [6].

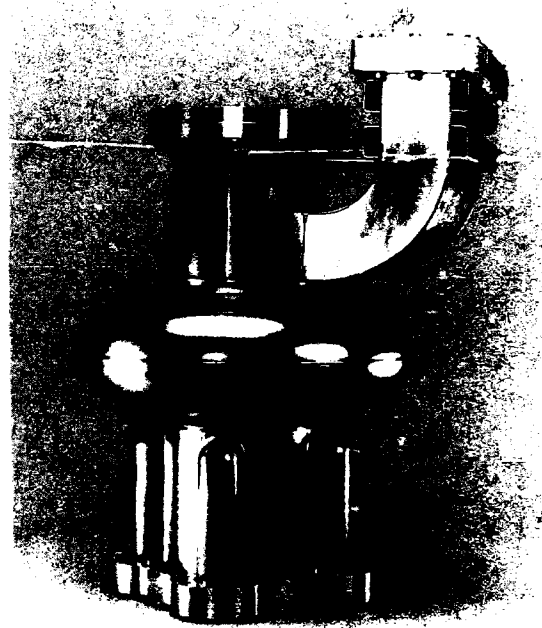


Figure 1. Superconducting Prototype B-factory cavity.

While the manufacture of the cavities followed standard procedures - the cells were made by spinning -, special care had to be taken for the chemical treatment of the Nb prototype in order to avoid the "Q-virus" [7], a degradation of the Q-factor due to a niobium-hydride phase change at the inner surface of a cavity. A buffered chemical polish (BCP) was used consisting of HF (48 %), HNO_3 (65 %) and H_3PO_4 (85 %) in a ratio 1:1:2; in total 100 μm were removed in several steps (30 + 30 + 30 + 10 μm); special caution was obeyed to control the temperature of the acid bath at 21 °C and, especially, to drain the used acid as fast as possible from the cavity vessel and to start rinsing with ultrapure water (conductivity < 0.055 $\mu S/cm$) immediately after. First performance tests made at Cornell indicate that this process may have been a successful remedy for curing the Q disease (s. fig. 2).

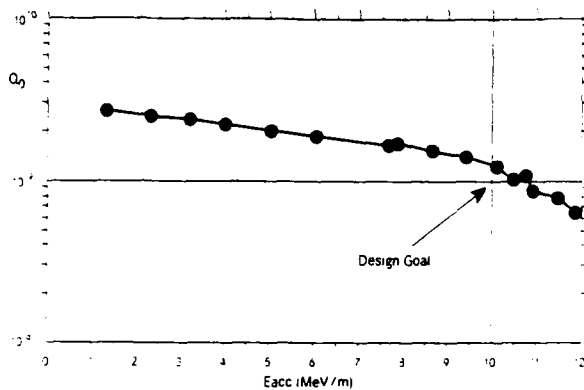


Figure 2. Q vs. E_{acc} for B-factory cavity at 4.2 K (courtesy of Cornell/LNS).

B. S-DALINAC Cavities

Further to the six s.c. 20-cell cavities delivered earlier for the upgrading of the electron accelerator at Darmstadt University, another set of six 3 GHz structures was manufactured recently, together with a two- and a five-cell structure of the same design which are to be used in the injector section of the accelerator (fig. 3). The material was essentially the same as used before (2mm sheet, RRR 280 for the cells, RRR 100 for the cut off tubes), the manufacturing steps were already described before [1]. After deep drawing of the half cells, the individual cells were welded and chemically tuned; this is done by carefully etching the inner surface until the desired design frequency of $2991.0 \pm .2$ MHz (at 300 K) is reached. Any deviation of $1.5 \mu\text{m}$ results in a frequency shift of about 100 kHz. The tedious matching of the 120 cells for the six structures was performed by Darmstadt University as well as the tuning of the completed cavities to a field flatness of $\pm 1\%$ (fig. 4).

After the final chemistry, the cavities were baked out (750 C, UHV) at University of Wuppertal before they were installed in the accelerator. Thus, a maximum accelerating gradient of 10.1 MV/m and an average value of 5.6 MV/m was achieved.

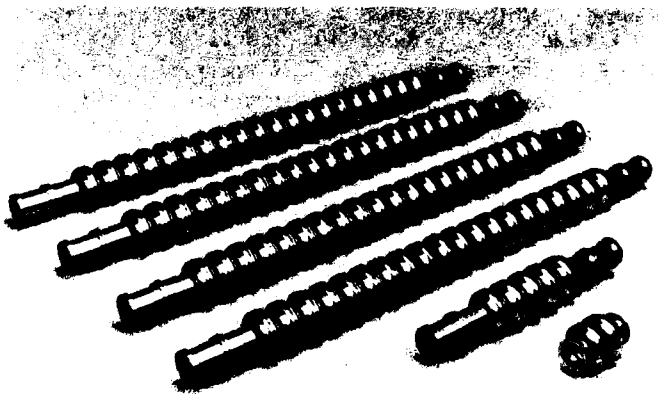


Figure 3. 3 GHz cavities for S-DALINAC.

C. TESLA cavities

The optimization of the shape of the cavities for the 1.3 GHz TESLA-Collider has been subject to intensive study [8]. It was analyzed [9] that the mechanical loads imposed during resonator fabrication and pressure tests and those loads exerted by the Lorentz forces during operation at gradients above 20 MV/m must not lead to inelastic cell deformation. Otherwise, the induced frequency shift due to wall deformation of the cavity cells would be considerably larger than the bandwidth of the resonator.

These requirements implied that a sufficient wall thickness of at least 2.5 mm has to be kept also after deep drawing of the cells and that the calculated geometry of the cells must be met by ± 0.2 mm. Finally, the alignment tolerance of the iris diameters of the 9 cell structure has to be below ± 0.3 mm.

On contract from DESY, Hamburg, we manufactured five copper RF models of the 9 cell 1.3 GHz TESLA cavities (fig. 5). The half cells were formed by deep drawing from 2.5 mm OFHC copper sheet material. By special jigs and tools for shaping the half cells, by chemical preparation of the welding edges and by experimental verification of the welding shrinkage the required accuracy could be achieved for the cell shape (fig. 6) as well as for the iris alignment. The high level of reproducibility of the manufacturing process is underlined by the fact that a field unflatness of $< \pm 5\%$ was reached for all five cavities without tuning (fig. 7).

For testing purposes, the cut-off tubes were made removably, also three different diameters for the input couplers were machined into these tubes for testing. These parameters are being optimized by the involved laboratories.

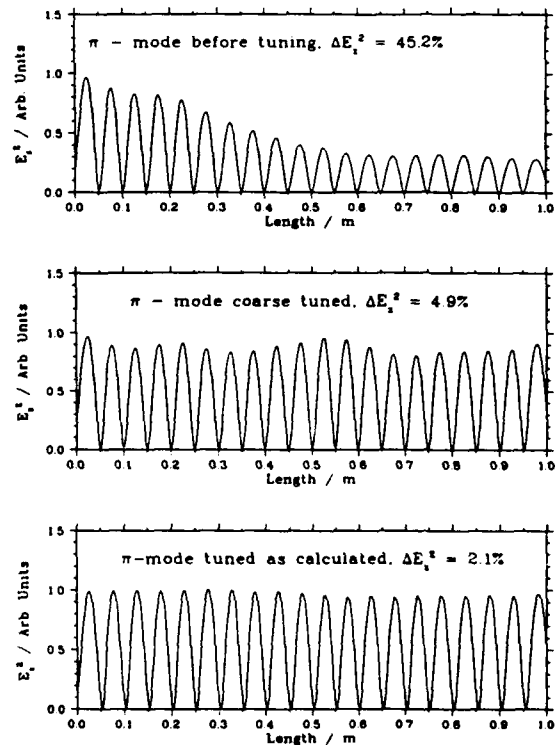


Figure 4. Field flatness of S-Dalinac cavities (courtesy of TH Darmstadt).

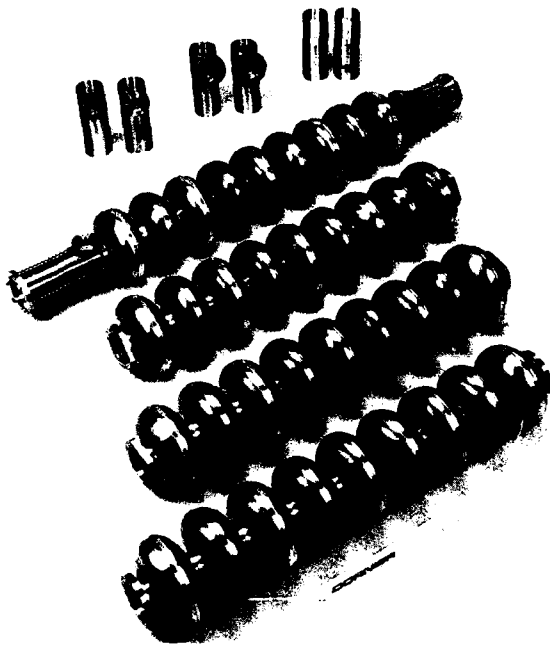


Figure 5. RF models of 1.3 GHz TESLA cavities.

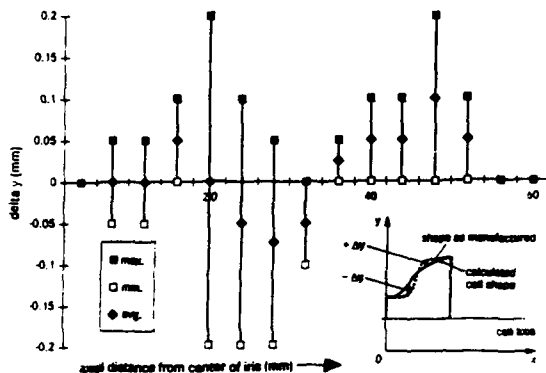


Figure 6. Deviation of cell geometry, as deep drawn, from calculated shape (avg. for 10 copper half-cells).

The experience gained during the manufacture of the Cu models will be transferred to the fabrication of the first two full size 9-cell Nb cavities for TESLA which are presently under production. The main design change as compared to the Cu models will be stiffening rings between the steep slope of the cells near the irises in order to increase the mechanical stiffness of the structure especially with respect to the expected Lorentz forces during beam operation.

IV. REFERENCES

- [1] G. Arnolds-Mayer, K. Jäger, R. Mayer, "Industrial production of 8 s.c. accelerator modules for HERA and 6 s.c. accelerating cavities for DALINAC," *Proc. of the 2nd EPAC, Nice 1990*, pp. 1070-1072.
- [2] B. Dwersteg et al., "Status of the Superconducting Cavity Program for HERA," *Proc. of the 1991 IEEE Particle Accelerator Conference, San Francisco*, pp. 2429-2431.
- [3] D. Proch et al., "Superconducting Cavities for HERA," *Proc. 15th Intern. Conf. on High Energy Accelerators, Hamburg 1992*, pp. 688-690.
- [4] H. Padamsee et al., "Accelerating Cavity Development for the Cornell B-Factor, CESR-B," *ibid. [2]*, pp. 786-788.

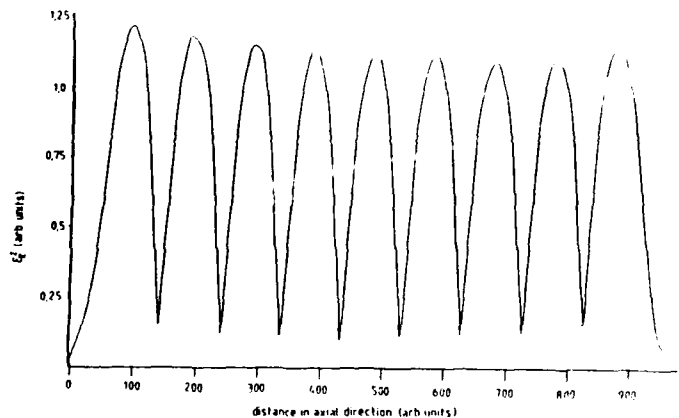


Figure 7. Field flatness of TESLA RF models (courtesy of DESY Hamburg).

III. CONCLUSION

From the experience gained in the described cavity projects we trust that we derived the necessary know-how in order to meet the challenging tasks of future large scale cavity production which has to meet demands for high accuracy as well as low cost. It seems essential to us that already in an early stage of cavity design industry will be involved in order to find a reasonable compromise between the scientists' demand (which mostly is at the edge of what is physically achievable) and the requirements of the manufacturer in order to arrive at a cost-effective product.

IV. ACKNOWLEDGEMENT

We are indebted to the involved laboratories - Cornell University/LNS, TH Darmstadt/Inst. für Kernphysik and DESY/MHF group - for providing their measuring data and for valuable comments to this paper.

- [5] V. Veshcherevich et al., "Higher order modes damping in CESR-B Cavity," *Proceedings of B-Factor Workshop, SLAC 1992*, pp. 177-180.
- [6] J. Kirchgessner et al., "The application of heavily damped superconducting cavities to the acceleration of high current electron beams," *Proc. of the LINAC Conference, Ottawa 1992*, pp. 453-455.
- [7] K. Saito, P. Kneisl, "Q Degradations in Superconducting Niobium Cavities," *ibid. [2]*, pp. 2387-2399.
- [8] E. Haezel, A. Mosnier and J. Sekutowicz, "Cavity Shape Optimization for a Superconducting Linear Collider," *ibid. [3]*, pp. 957-959.
- [9] A. Matheisen, H.B. Peters and A. Mosnier, "Mechanical Properties of the 1.3 GHz TESLA Cavity," *ibid. [3]*, pp. 960-962.

Analysis of Mechanical Fabrication Experience with CEBAF's Production SRF Cavities*

J. Mammoser, P. Kneisel and J. F. Benesch
Continuous Electron Beam Accelerator Facility
12000 Jefferson Avenue, Newport News, Virginia 23606 USA

Abstract

CEBAF has received a total of 360 five-cell niobium cavities, the largest group of industrially fabricated superconducting cavities so far. An extensive data base exists on the fabrication, surface treatment, assembly and cavity performance parameters. Analysis of the mechanical features of the cavities includes the following: the spread in fabrication tolerances of the cells derived from field profiles of the "as fabricated" cavities and the "as fabricated" external Q -values of the fundamental power coupler compared to dimensional deviations. A comparison is made of the pressure sensitivity of cavities made of materials from different manufacturers between 760 torr (4.2 K) and 23 torr (2 K).

I. INTRODUCTION

The Continuous Electron Beam Accelerator Facility presently under construction in Newport News, VA is scheduled to produce a low emittance 200 μ A electron beam of 4 GeV for experimental studies in nuclear physics by mid-1994. This beam is accelerated by a string of 338, 5-cell, 1500 MHz niobium cavities arranged in two anti-parallel linear accelerators and operating above design gradients of 5 MV/m and Q_0 values of 2.4×10^9 at 2 K. This system will represent the largest assembly of superconducting accelerator cavities in the US, and a large data base already exists on the performance of these cavities. Industry has manufactured 360 cavities in accordance with CEBAF's specifications [1] and the superconducting properties of these cavities exceed the design values of field and Q_0 value by a factor of about 2 to 3 [2]. Most of these cavities have been inspected and evaluated on the basis of compliance with mechanical specifications; about 60% have been tested, and data are available on frequency variations during chemical processing and pressure sensitivity between 760 torr and 23 torr. In the following sections the current experiences with the above-mentioned features of the cavities are discussed.

II. MECHANICAL FABRICATION

A. Cavity Tolerances

The CEBAF/Cornell 5-cell cavity has been specified in CEBAF's "Statement of Work" based on earlier experiences gained at Cornell University [3]. Besides very detailed prescriptions for material inspections, material handling and chemical treatment and requirements for electron beam welding, this document also specifies the frequency of the "as-

manufactured" cavity as $f=(1494.7 \pm 2)$ MHz, which in turn determines the tolerance on the overall length to ± 6.5 mm. Since the cavity cells are deep drawn from 3.2 mm thick niobium sheet, these tolerances represent a certain challenge to the industrial partner because of spring back, non-uniformity of the starting material and possible variations in weld shrinkage during the electron beam welding of the cavity subsystems. The manufacturer was asked to provide frequency and field profile measurements before and after final tuning and machining of the cavities. From these data the frequency errors of each individual cell of each cavity can be obtained by making use of a lumped circuit analysis of coupled resonators ("tuning program") [4].

This work supported by the U.S. Department of Energy under

Figure 1 shows the frequency spread of the "as-manufactured" cavities. The cells were manufactured so that the mean frequency is approximately 1495.4 MHz, which is greater than the desired frequency. The cavities were tuned by the manufacturer, all in the same direction. Typical stored energy distribution of as-manufactured cavities is shown by frequency errors in Table 1. In most of the cases the stored energy was concentrated in the center cells which allowed the manufacturer to restrict tuning to these cells to obtain equal stored energy in all cells ($\pm 2.5\%$).

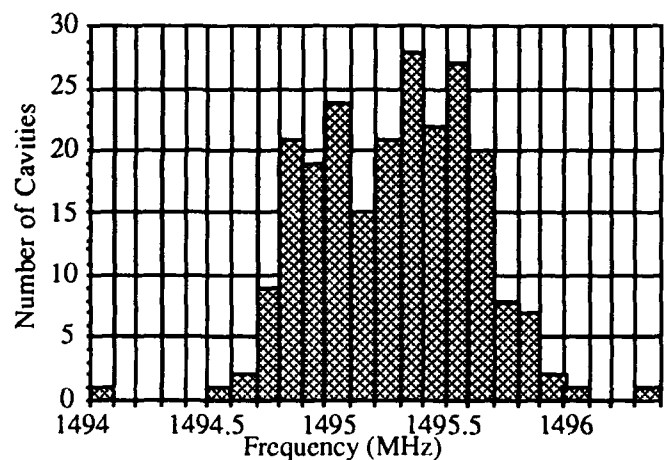


Figure 1. As-received cavity frequencies.

Table 1
Frequency Errors in kHz of Each Cell as Manufactured

	Cell#1	Cell#2	Cell#3	Cell#4	Cell#5
Mean	-610	1101	1464	1100	-331
Std dev	455	628	577	637	486
Min	-1760	-1440	-726	-1318	-1375
Max	1906	4439	4279	4439	1227

*This work was supported by DOE Contract DE-AC05-84ER40150.

The spread of the cell-to-cell coupling coefficient k as derived from the frequencies of the fundamental passband modes according to

$$k = \frac{f(\pi)^2 - f(\pi/5)^2}{f(\pi)^2 + (f(\pi/5)^2 \cos(\pi/5))}$$

is shown in Figure 2. It can be seen that the cell-to-cell coupling varies, depending on the amount of tuning which had to be done in the π -mode for each individual cell. This variation in k causes a desirable spread in the frequencies of the higher-order modes, increasing the instability threshold of the accelerator [5].

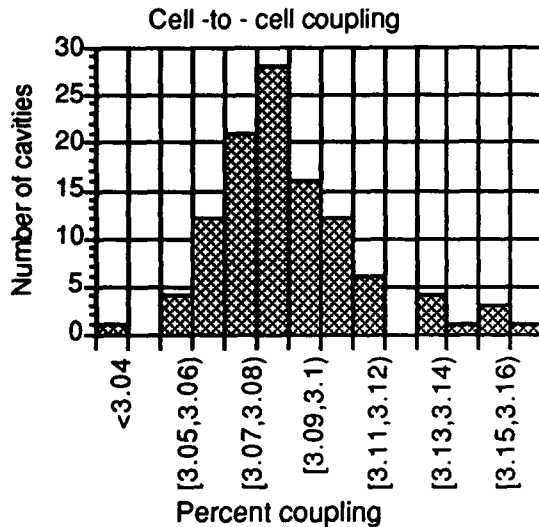


Figure 2. Variations in cell-to-cell coupling.

B. Fundamental Power Coupler (FPC)

The coupling of the rf power into the CEBAF/Cornell cavity is provided by a waveguide system shorted at one end. The coupling strength has been selected at $Q_{ext} = 6.6 \times 10^6 \pm 20\%$. This strength of the coupling is 0.8 times the value required for critical coupling at full beam. This value of coupling permits adequate control bandwidth, requires somewhat less klystron power at less than full current than would critical coupling at full beam, and permits operation at higher gradients with the available rf power than would critical coupling at full beam. The coupling of the rf to the cavity fields is established by the linkage of a standing wave in the input coupler waveguide and the cavity fields. Figure 3 shows the standing wave pattern as measured by a perturbation measurement for two different cases of Q_{ext} : a less strong coupling is achieved by shifting the standing wave in the region of the iris opening of the end cell, which can be accomplished by varying the distance of the waveguide short to beam axis.

Similarly, the coupling strength can be decreased by squeezing the input waveguide or increased by opening up the waveguide at the point of the highest stored energy [6]. This method is used for final adjustment of the Q_{ext} value. As a practical matter the value of Q_{ext} is very sensitive to mechanical dimensions of the waveguide arrangement, as is

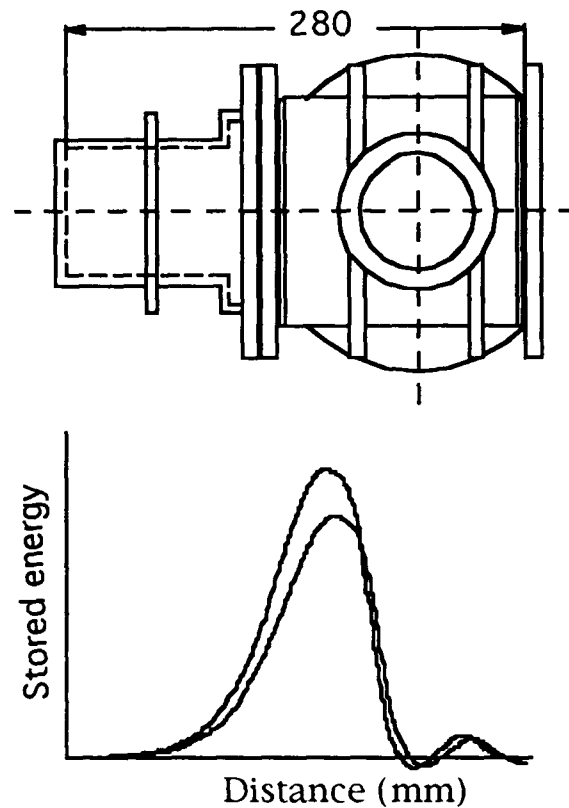


Figure 3. Standing wave measured in FPC with bead pull on FPC axis for two different Q_{ext} values (upper trace $Q_{ext}=8.6E6$, lower trace $Q_{ext}=6E6$).

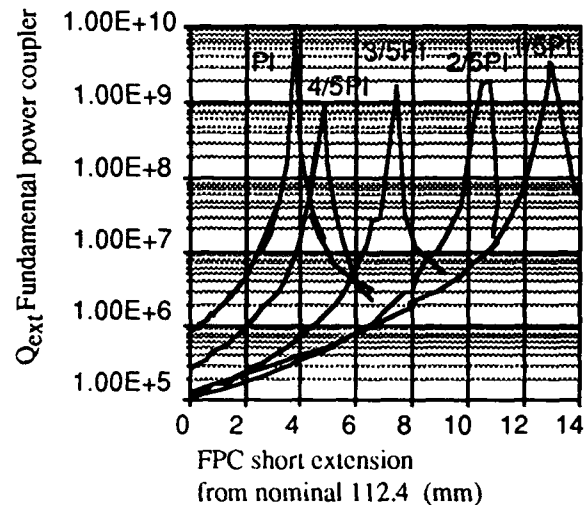


Figure 4. Q_{ext} as a function of short distance to beam axis.

shown in Figure 4. Here the Q_{ext} values for all 5 passband modes are plotted as a function of the short distance to the beam axis.

According to these measurements, a fixed dimension of 114.6 mm will provide the desired design value for Q_{ext} . Any

deviation from this number is caused by fabrication tolerances such as weld shrinkage, warpage, deflections of the waveguide or machining tolerances. The Q_{ext} values of 329 "as-fabricated" cavities have an average of $7.55E6$. Fortunately, in most cases the desired value can be achieved easily by slight mechanical deformations of the waveguide as mentioned above.

III. FREQUENCY SHIFTS

A. Chemical Treatment of the Cavities

When delivered by the manufacturer the cavities have received only a very slight material removal for cleaning purposes after the final welding and machining steps. The major chemical treatments are done at CEBAF. It has been established [3] that at least a layer of $50\ \mu\text{m}$ ("surface damage layer") has to be removed from the surface to achieve or exceed CEBAF's design values for Q_0 value and accelerating gradient. Assuming uniform material removal from the surface by immersing the whole cavity into an acid bath of equal parts of hydrofluoric (48%), nitric (69%) and phosphoric (86%) acids and using a calculated value of $\Delta f / \Delta d = 5.7\ \text{kHz}/\mu\text{m}$ as attained from "Superfish" [7], a frequency decrease of $350\ \text{kHz}$ has to occur for $50\ \mu\text{m}$ of removal. This corresponds to $\approx 5\ \text{min.}$ of chemical polishing at 23°C . In our surface treatment procedure, pre-chemistry is done in two steps of $2.5\ \text{min.}$ each with intermediate rinsing of the cavity to avoid overheating the acid bath. Subsequently the cavity frequency is measured and if necessary readjusted as well as the field profile. The final chemical treatment of $1\ \text{min.}$, corresponding to a frequency change of $\approx 70\ \text{kHz}$, is then very predictable and the cold cavity frequency falls within the range of the cold cavity tuner of $\pm 200\ \text{kHz}$.

B. Pressure Sensitivity between 760 torr and 23 torr

The cells of CEBAF's 360 cavities are made from high-purity niobium of 3 different suppliers: 3% were manufactured from W. C. Heraeus niobium, 20% of the material was supplied by Teledyne and the remainder was manufactured by Fansteel Corp. The room temperature yield strength of this high purity-material was specified to exceed $74\ \text{MPa}$. This value varied from manufacturer to manufacturer and from batch to batch. Measurements on samples of the different materials at $300\ \text{K}$ and $4.2\ \text{K}$ [7] also showed significant differences in the yield strength and possible changes in Young's Modulus. Analysis of 45 cavities showed variations in the pressure sensitivity from $80\ \text{Hz/Torr}$ to $137\ \text{Hz/Torr}$, over each material and from each shipment of material.

IV. CONCLUSIONS

Analysis of the "as-fabricated" cavity data suggests that the frequency tolerance of $\pm 2\ \text{MHz}$ as specified by CEBAF was easily attainable by the manufacturer. The cavity frequency was intentionally kept above the desired $1494.7\ \text{MHz}$ for tuning purposes and the spread was kept within $\pm 1\ \text{MHz}$.

Frequency errors in each cell, however, did vary up to

several MHz. This variation is probably due to non-uniform spring back in the forming process, machining tolerances and variations in weld shrinkage during electron beam welding. These variations cause different field distributions and require different tuning of each cell resulting in a spread in the-cell-to-cell coupling.

The design of the fundamental power coupler (FPC) is such that Q_{ext} of the coupler is sensitive to fabrication tolerances, but the Q of $6.6E6 \pm 20\%$ can be easily attained with inelastic deformation of the FPC waveguide.

Chemical surface treatment of cavities at CEBAF has rather good reproducibility as long as a stringent control of the bath temperature is maintained. With a cold tuner range of $\pm 200\ \text{kHz}$ there was no problem obtaining assembled cavities within that range, even though variations in the material properties have resulted in 50% differences of the sensitivity of the cavities to the helium bath pressure.

Sheet metal technology as applied in the fabrication of the CEBAF cavities without any annealing steps after the mechanical forming operations requires tolerances on the order of $\pm 2\ \text{mm}$ [9]. Tighter tolerances would probably cause an increase in manufacturing costs.

V. ACKNOWLEDGMENTS

Many thanks go out to the CEBAF SRF Staff whose efforts have made this paper possible, and a special thanks to K. Yopp who provided CAD support.

VI. REFERENCES

- [1] M. Dzenus, *et al.*, "Production of Superconducting Niobium Cavities for CEBAF," *Conference Record of the 1991 Particle Accelerator Conference*, p. 2390.
- [2] C. Reece, P. Kneisel, J. Mammoser, "Performance of Production Cavities for CEBAF," these proceedings.
- [3] P. Kneisel, *et al.*, "Performance of Superconducting Storage Ring Cavities," *IEEE Trans. Magn.* MAG 21, 1000 (1985).
- [4] R. M. Sundelin, private communications.
- [5] R. M. Sundelin, "Frequency Spreads Caused by Manufacturing Tolerances," SRF Tech. Note-830102 LNS Cornell University.
- [6] C. Reece, "Fundamental Power Coupler E-Field Profile Measurements," SRF 831201 LNS Cornell University.
- [7] K. Halbach, R. F. Holsinger, "Superfish: A Computer Program For Evaluation of R.F. Cavities With Cylindrical Symmetry," *Particle Accelerator* 1976, Vol. 7, pp 213—222.
- [8] P. Kneisel, *et al.*, "Superconducting Cavities From High Thermal Conducting Niobium For CEBAF," *Proceedings of The Conference Electron Beam Melting and Refining*, pp. 177 (1990).
- [9] J. Benesch, J. Mammoser, "Mechanical Results of The CEBAF Cavity Series Production," these proceedings.

MICROPHONIC ANALYSIS OF CRYO-MODULE DESIGN¹

A. Marziani and H.A.Schwettman
W.W.Hansen Experimental Physics Laboratory
Stanford University
Stanford, CA 94305-4085

Abstract

Mechanical resonances in superconducting accelerator structures and cryo-module components can lead to coupling between mechanical noise and electron beam parameters. We have studied the mechanical resonance spectrum of a 500 MHz 2-cell structure and cryo-module that was designed and built by Siemens for TRW, Inc., and have measured the effect of these vibrational modes on the RF eigenfrequency of the structure. We identify the most dangerous resonances of this system and discuss related design issues.

I. Introduction

Mechanical vibrations in superconducting accelerator structures can lead to unwanted modulation of the structure RF eigenfrequency and the electron beam energy, position, and direction. Though eigenfrequency modulation produces well-documented problems for RF control systems, modes also exist which modulate electron beam parameters without modulating the RF eigenfrequency[1].

The frequency and character of mechanical modes which affect the operation of an accelerator are determined by the mechanical design of both the accelerating structure and the cryo-module. The microphonic behavior of a specific design is determined by how it addresses the issues of mechanical isolation, damping of unwanted motion, frequency of resonant modes, and by the mechanical constraints imposed on the accelerator structure.

We have performed vibrational measurements on a 500 MHz 2-cell cryo-module designed and built by Siemens for TRW, Inc.. The accelerometers used for the present tests have been improved over those used in our previous measurements[2] to provide a flat (± 1 dB) response from 8 Hz to 500 Hz. Mechanical vibrations are induced by a small speaker in contact with the outer vessel of the cryo-module. In this paper we analyze the observed mechanical modes of this cryo-module and assess their effect on the structure eigenfrequency. We identify design elements which have contributed to the creation of dangerous mechanical modes and discuss related design issues.

II. Mechanical modes of the accelerator structure

The mechanical mode spectrum of the freely-suspended accelerator structure was measured before installation in the cryo-module. The lowest longitudinal mode was found at 94 Hz and the lowest transverse mode at approximately 40 Hz. When the structure is mounted in the cryo-module, its length is, to good approximation, constrained and thus the structure modes resemble those of a 'clamped' beam, retaining the same frequencies as in the 'free' case. The lowest longitudinal mode (L1) of the installed structure was found at 100 Hz while the lowest frequency transverse modes (T1) were found at 40.6 Hz in the vertical and at 50.0 Hz in the horizontal direction.

In the lowest longitudinal mode (L1), the structure length remains fixed while the iris between the two cells oscillates longitudinally. This motion has no effect on the eigenfrequency of the structure but causes electron beam energy modulation[1]. The relative energy modulation expected when driving this mode at resonance with a 0.5 N force is calculated to be 2×10^{-5} . In the lowest transverse mode (T1), the maximum motion occurs at the iris while nodes occur near the position where the structure is attached to the cryo-module. Previous work[2] indicates that, due to symmetry, this sort of bending motion should not produce any modulation of the eigenfrequency at the mechanical oscillation frequency. The large eigenfrequency shift observed at the 40.6 Hz mode is due to asymmetries of the motion, caused by asymmetries of the structure and by mixing of the mode with other cryo-module modes.

III. Mechanical modes of the cryo-module

A schematic diagram of the cryo-module indicating regions of mechanical flexibility (for frequencies below 150 Hz) is shown in Figure 1. At these frequencies, it can be assumed that vessel side-walls are relatively stiff, while flexing mostly takes place in the vessel end-walls, the cell walls of the accelerator structure, and the short section of beam tube connecting the helium vessel and the outer vessel. To allow RF tuning by changes in the structure length, one end of the helium vessel is connected to the beam tube by a bellows and is therefore represented as being unconstrained at that connection. Thin steel rods connecting the helium vessel to the outer vessel provide some restoring force for both vertical and horizontal transverse motions.

¹Work supported in part by the Office of Naval Research, Contract No. N00014-91-J-4152.

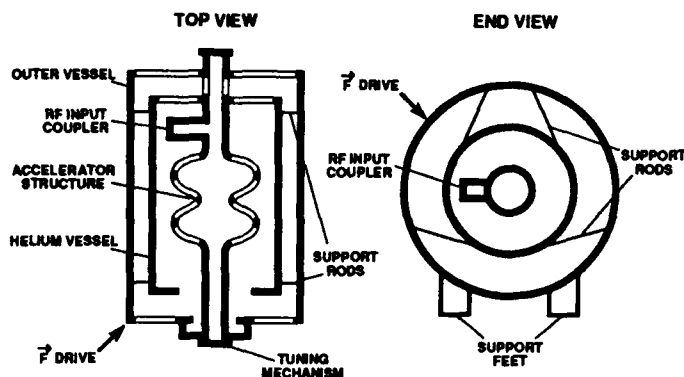


Figure 1. Schematic of cryo-module. The empty lines represent module components which are flexible at low frequencies.

Mechanical modes are classified as either longitudinal, transverse (horizontal and vertical), or torsional, and have been segregated as being principally related to the support system, to the helium vessel or outer vessel, or to the accelerator structure. Table 1 lists the principal modes below 150 Hz. Table 2 lists the amplitude of RF eigenfrequency modulation and the amplitude of structure motion for the most interesting modes when driven by a 0.5 N frequency-swept force applied to the outer vessel at the location shown in Figure 1. These amplitudes are up to 100 times larger when the force is applied at resonance. Mechanical Q values range from 60 to 100 with the exception of the horizontal support modes for which the Q value is 150 to 200.

Table I: Mechanical modes of a 500 MHz cryo-module.

Mode Type	Frequency in Hz			
	Longitudinal	Horizontal	Vertical	Torsional
Support	13 (split)	8.5 (0) 11.6 (π)	30.2 (0) 36.6 (π)	23.7
Helium Vessel	36.6 40.6	39.1	40.6	72 79
Structure	99.9(L1)	50 (T1) 72,79(T2)	40.6 (T1) 51.8 (T2)	
Outer Vessel	138			

Table II: Effects of Selected Modes.

Mode Type	Freq.(Hz)	RF Δ f(Hz)	Δ x cell(nm)
Horizontal Support	8.5	12	7000 (hor.)
Longitudinal Support	13.5	17	800 (lon.)
Longitudinal He Vessel + Vertical Support	36.6	7.5	6 (lon.) 95 (ver.)
Longitudinal He Vessel + Vertical He Vessel+ Vertical T1 Structure	40.6	8.5	69 (lon.) 154 (ver.)
Horizontal T1 Structure	50	< 1	102 (hor.)
Horizontal T2 Structure + Torsional He Vessel	72 79	< 1	11 (hor.) 32 (hor.)
Longitudinal L1 Structure	99.9	< 1	3.6 (lon.)
Longitudinal Outer Vessel	137.8	12	9.2 (lon.)

Support structure modes: As listed in Table 1, the lowest frequency modes of the cryo-module result from motion associated with the supports (Fig. 1). In all these modes, the helium vessel, outer vessel and structure move as one large mass against restoring forces provided by the supports. Bending takes place in the outer vessel wall where the supports are attached. The transverse modes of this set are split into 0 and π modes. The 0 modes consist of transverse center-of-mass motion of the entire module during which the ends move in phase. The π modes consist of transverse rotation about the center of mass, during which the module ends move in opposite directions. Frequency splitting of the longitudinal mode was observed but could not be attributed to any cryo-module element. Despite the relatively small amount of structure deformation expected in these modes, large eigenfrequency modulation occurs as a result of the enormous amplitudes of motion associated with these low frequencies (see Table 2).

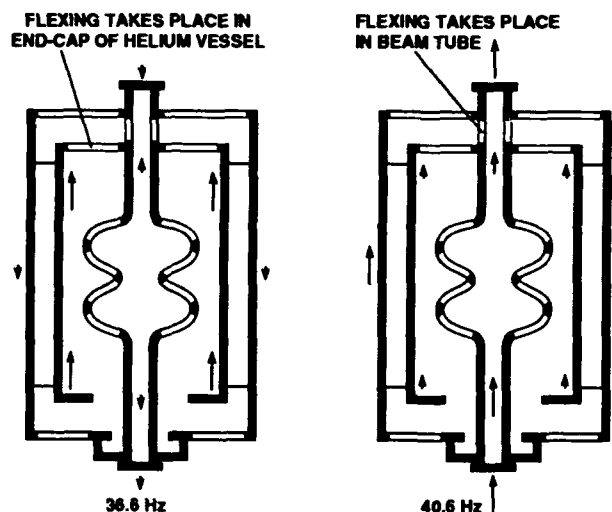


Figure 2. Longitudinal mechanical modes associated with the helium vessel. Only longitudinal motion is shown.

Helium Vessel and Outer Vessel modes: Figure 2 shows the two longitudinal modes associated with motion of the helium vessel relative to the outer vessel. The arrows indicate relative magnitude and direction of motion. The 36.6 Hz mode consists of the mass of the helium vessel moving against the outer vessel mass. Flexing takes place primarily in the end-wall of the helium vessel, with some flexing also occurring in the beam tube connecting the helium vessel to the outer vessel. In the 40.6 Hz mode, the helium vessel and outer vessel move longitudinally in the same direction but with different amplitudes. Vertical motion also takes place and will be discussed later. Flexing in this mode occurs primarily in the beam tube with some flexing occurring in the helium vessel end-wall. For both these modes, the outer vessel end-walls are rigid. Both modes produce substantial change in the length of the accelerator structure, thus causing a marked shift in eigenfrequency (see Table 2).

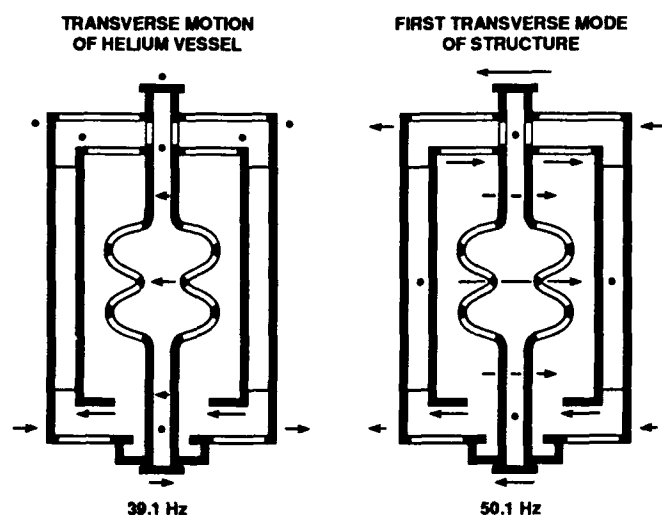


Figure 3. Selected transverse modes of cryo-module. Only transverse motion is shown.

Transverse motion of the helium vessel with respect to the outer vessel occurs at 39.1 Hz and 40.6 Hz. As seen in Figure 3, this motion consists of the helium vessel pivoting on its fixed end and moving transversely in opposition to the outer vessel. Restoring forces are provided by both the beam tube and by the 1/4" steel rods connecting the two vessels. These modes also cause substantial structure deformation as a result of torques applied to the beam tube at the pivot point of the motion. Torsional motion of the helium vessel in opposition to the outer vessel occurs at 72 Hz and 79 Hz. This mode couples weakly to a horizontal transverse structure mode and consequently is split into two modes.

At 138 Hz, the outer vessel cylinder moves longitudinally in opposition to the helium vessel which is attached through a beam tube to one of the end-walls. In the resulting motion, the end-walls flex and move out-of-phase with each other, producing large eigenfrequency modulation even for small amplitudes of motion.

Mixing of modes: Problems associated with some modes are made worse by frequency coincidence with other modes. The 36.6 Hz mode is both a longitudinal helium vessel mode and a vertical support mode and strongly couples vertical support motion, which causes little deformation of the structure, to a mode which causes substantial deformation. An even worse case occurs at 40.6 Hz where longitudinal and vertical helium vessel modes couple to a vertical transverse mode of the accelerator structure. The resulting mode produces large amplitude transverse motion in the structure and large eigenfrequency modulation. Weak coupling may cause frequency splitting of modes as seen at 72 Hz / 79 Hz.

IV. Cryo-module design issues

To reduce microphonics, one should attempt to isolate the accelerator structure from external noise sources, avoid low frequency resonances in the structure and cryo-module, raise the frequency of unavoidable resonances, and apply damping when practical. Also, coupling between mechanical vibrations and electron beam parameters must be reduced. Our studies indicate that avoiding asymmetries in the structure and cryo-module, and avoiding mixing of mechanical modes helps achieve this. Our measurements also show that in the design of load-bearing supports of the system, such as the support feet and rods of Figure 1, care must be taken to avoid low frequency oscillation of the large masses supported.

An important issue in cryo-module design is support of the accelerator structure. This issue is often complicated by the desire to perform RF tuning through structure length variation. The approach taken in the system studied here is to use the cryo-module vessels to both support the structure and constrain its length. This provides direct coupling between cryo-module motion and structure length, and is the cause of many of the dangerous vibrational modes we encountered. If the structure length is to be constrained by a mechanical element, this element should not be coupled to the cryo-module and should be designed such that its lowest modes of vibration are at high frequency. Very dangerous modes will result if resonances of the structure coincide with resonances in its length constraining components.

V. Conclusion

We have documented mechanical modes and identified elements of the Siemens cryo-module design which lead to microphonic sensitivity. Design issues have been discussed which, if appropriately addressed, may reduce microphonic effects in future designs.

VI. References

- [1] H.A.Schwettman, "Microphonics and RF Stabilization in Electron Linac Structures", Proceedings of the Fifth Workshop on RF Superconductivity, Hamburg, Germany, 1991.
- [2] A.Marziali, H.A.Schwettman, "Microphonic Measurements on Superconducting Linac Structures", Proceedings of the 1992 Linear Accelerator Conference, Ottawa, Canada, 1992.

The Design of a Pill-Box Cavity with Waveguide HOM Suppressors

A. Massarotti

Sincrotrone Trieste and Dipart. di Fisica, Universita' di Trieste

G. D'Auria, A. Fabris, C. Pasotti, C. Rossi, M. Svandrlik

Sincrotrone Trieste, Padriciano 99

34012 Trieste, Italy

Abstract

High suppression of the higher order mode (HOM) spectrum of an accelerating radio frequency cavity can be obtained with two waveguide suppressor coupled through a large aperture to the cavity. An intensive experimental work led us to choose a pill-box shape for the central body of the resonator. Along with a heavy damping of the whole HOM spectrum, the electromagnetic characteristics measured on a 'cold' prototype show that the accelerating performance of the fundamental resonator mode remains satisfactory. After having thoroughly tested the cold prototype, the design of a power resonator has been started. The more interesting aspects of this design, concerning mainly mechanical, thermal and vacuum topics are described here. The choice of the microwave absorbing material is discussed as well.

1. INTRODUCTION

The HOM of the radio frequency cavities of the Elettra Synchrotron Light Source Storage Ring could drive multibunch instabilities, due to the high current and to the many short length bunches [1], [2].

From the very early beginning of the project, the use of dedicated waveguides to suppress almost the whole HOM spectrum has been investigated in order to prevent the rise of these instabilities [3], [4], [5], [6].

Large apertures in the cavity walls should guarantee the highest possible coupling to most HOM. The electromagnetic power of the HOM is then fed through waveguides to absorbing loads, while the accelerating mode frequency lies quite below the cut-off frequency of the guides. To improve the transmission of the power to the load the section of the waveguide has been chosen square; in this way also the TE₁₁ mode of the waveguide can propagate at relatively low frequencies.

The challenging tasks of this design are to provide large apertures on the cavity walls without affecting too much the fundamental mode parameters, like quality factor and R/Q, and to overcome the mechanical, thermal and vacuum topics presented by the connection of large waveguides to the resonator. Along with this, the microwave absorbing material for the load and the shape of the termination have to be chosen.

On the other hand, the behaviour of such a resonator during the conditioning procedure and the power operation is still unknown. Therefore, after an intense experimental activity on a cold resonators, with satisfactory results, which are shown in

the following, we are presently concerned with the design of a power prototype.

2. THE COLD PROTOTYPE

Dedicated waveguides to damp the HOM spectrum have been tested in our laboratory on several cavities of different shape, pill-box, pill-box with nose cones, smooth shape (bell shape). It has been found that for our design the optimal shape is the pill-box without nose-cones.

The geometry of this shape presents wide plane surfaces. On these surfaces it is quite simple to open large square section apertures and the connection to a square section waveguide doesn't present particular mechanical problems.

At the same time in the pill-box cavity the frequencies of the first dipole and monopole modes can be distributed, with a proper choice of the internal profile of the resonator, in a way that minimizes the dimension of the waveguide section.

Hence the pill-box shape has been chosen. Its profile has been optimised with OSCAR2D and URMEL-T simulations. The fundamental mode parameters for the final profile are listed in Table 1 [7].

Table 1
Pill-box cavity fundamental mode parameters
(Electrical definition of shunt impedance)

f_r (MHz)	Q	R/Q (Ω)	R_{sh} (M Ω)	$R_{sh}T^2$ (M Ω)
509	36800	150	5.5	3.4

The first dipole mode (TM₁₁₀) frequency lies for this cavity around 794 MHz, while the first monopole mode (TM₀₁₁) frequency is about 980 MHz. Thus, a waveguide with a 250x250 mm square section, that is TE₁₀ cut-off frequency at 600 MHz and TE₁₁ cut-off frequency at 850 MHz matches the requirements for this cavity. The reactive attenuation at 500 MHz is roughly 60 dB/m, which should be sufficient to limit within an acceptable range the spread of the accelerating mode field into the waveguide.

Two holes are placed on the side walls of the cavity. They are 180x180 mm large; their position is asymmetrical with respect to the waveguides symmetry plane, in order to avoid coincidence of the zero's of the cavity fields with the symmetry planes of the waveguides. There is an azimuthal angle of 90° between the two apertures, so both polarizations of the dipole modes should be damped.

The waveguides are 1500 mm long, plus 250 mm of the connection piece to the cavity; they are terminated with a

pyramid of commercial absorber, ECCOSORB VHP-45®. The pyramidal load has a 250x250 mm large base and is 1140 mm long. It is a low power absorber, not cooled, which has been useful for the low power tests.

A sketch of the cavity is presented in figure 1. The connection between cavity and waveguide is pointed out.

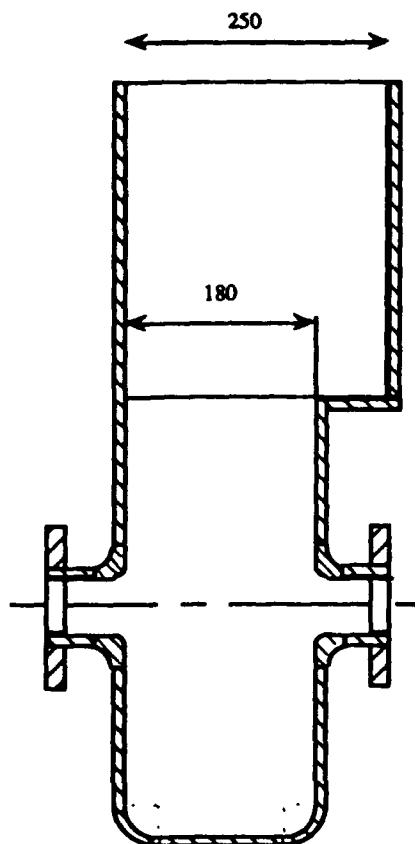


Fig. 1 Lateral view of the cavity-waveguide connection

The electromagnetic parameters of the accelerating mode, as measured on the damped cavity, are shown in Table 2. It should be noted that, for this low power prototype, no particular care has been taken in brazing; furthermore the connection pieces between the cavity and the waveguides are just screwed. Thus the information on the Q-factor is not very significant; we expect an improvement in the power prototype.

Table 2
Pill-box cavity fundamental mode parameters
with waveguide suppressors

f_r (MHz)	Q	R/Q (Ω)	R_{sh} (M Ω)
500	25000	120	2.8

Even if we consider a pessimistic value of 2.5 M Ω for the shunt impedance, six cavities installed on the Elettra storage ring will be able to provide the required energy to the beam, at 1.5 GeV as well as at 2.0 GeV, with the present 60 KW RF plants. Actually we expect a nicely higher value for the Q

factor, that is a shunt impedance value between 3.5 and 4.0 M Ω .

Once it was verified that the damped cavities could be adequate for the light source, the performance of the suppressor has been measured. The results are summarized in Table 3.

Table 3
HOM suppression results

mode	Without damping		With damping	
	f_r (MHz)	Q	f_r (MHz)	Q
D1	790	31100	/	/
D2	971	25000	980	20
M2	1047	28300	1039	70
M3	1173	46900	1138	20
D3	1184	20600	1175	25
D4	1404	41300	1388	50
D5	1431	23100	1428	50
M4	1515	33300	1530	40
D6	1668	14400	1631	55
D7	1699	8200	1680	50
M5	1822	50300	/	/
M6	1902	16600	1916	190
M7	2079	29600	2026	50
M8	2190	20800	2176	80

The results in Table 3 concern monopole and dipole modes, that is the modes that can cause the growth of instabilities. The resonances above the cut-off frequencies of the beam tubes are not taken in consideration. The dipole modes are classified with D#, the monopole modes with M#. This kind of classification is used rather than that with the original pill-box modes, since the identification of some field patterns in the damped resonator is quite uncertain.

The first monopole mode, D1 or TM₁₁₀, is completely damped. The other two resonances below 1.0 GHz present now a Q value lower than 70. Furthermore all the Q's are reduced to better than 1% of the undamped value.

The M2 resonance, that is the TM₀₁₁ or common mode, is one of the most dangerous one. The Q value is now reduced to 70, but some experimental work on the load shape has shown that an improvement can be achieved by optimizing the termination. This is true also for other resonances.

The cold prototype has thus been completely characterized. The indication for the construction of a power prototype is very positive, so this will be the next step in our design.

3. CONSIDERATIONS ON THE POWER PROTOTYPE DESIGN

A. Cavity Design

A preliminary sketch of the pill-box cavity can be seen in figure 2. In this sketch the two apertures in the cavity walls

are shown, together with the connection pieces to the waveguides.

In order to avoid any effect on the electron beam caused by the asymmetric geometry of the cavity, it has been decided to install two cells on the ring, close each other, with the second having the waveguides rotated by a 180° angle. The cells should be de-coupled and should take few space on the ring. So the beam tubes of the cavity will have exactly the same section of the vacuum chamber, as it is shown in figure 2. The higher cut-off frequency of the vacuum chamber section could limit the HOM power transmission through the chamber, but this should be acceptable since the low power measurements showed a good behaviour of the HOM dampers also in the higher frequency band.

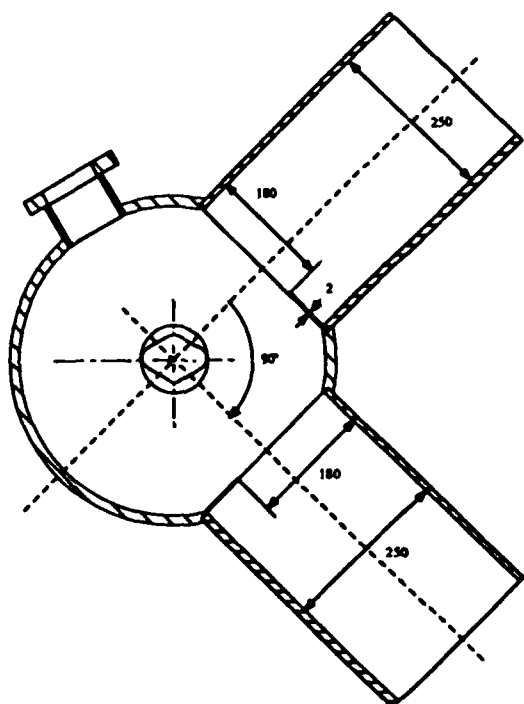


Fig. 2 Sketch of the power prototype.

The cooling system of the cavity will be designed taking into account particularly those areas surrounding the apertures on the walls where the power dissipation is expected to be critical, especially between the two waveguides. An intensive simulation activity is under development, with the support of commercial f.e.m. packages.

B. Suppressor Design

Along with the design of the power resonator, we are concerned with the study of the suppressor, that is the waveguide and the absorbing load.

Since the waveguide volume is big, it would be advisable to have the most part of the waveguides in air, by insulating the vacuum of the cavity with a ceramic window in order to

limit the pumping requirements. At the same time this would allow a relatively easier design of the absorbing load.

The ceramic window should be inserted into the waveguide sufficiently far away from the cavity in order to avoid heating due to the fundamental mode field. Depending on the material characteristics and on the shape of the ceramic window there could be a negative effect on the HOM damping capability of the suppressor. Therefore we performed measurements on a prototype in which a glass window, 5 mm thick, was inserted in the waveguide. It was found that the smallest shape for a still acceptable damping effect is equal to a circular window with a diameter of 200 mm; the Q-values measured in this configuration are similar to those in Table 3. Since the window for the power prototype will be an alumina window, we are investigating how the damping changes with different permittivity and different thickness.

An alternative to the ceramic window is to have the waveguides under vacuum. This design would be more advisable from the suppressing point of view, since there is no mismatching along the waveguide, but it would present more technical difficulties. A powerful pumping system should be dimensioned to keep under high vacuum the waveguides.

Furthermore the load should be designed for operation under ultra high vacuum. Thus the microwave absorbing material should have a low outgassing rate, should be a good thermal conductor and, finally, should adapt a wide frequency band. Microwave absorbing materials with these characteristics have been already produced, but their reliability should be tested [8].

So, even if we develop the research activity also in this direction, we will first study the feasibility of a prototype with an alumina window placed into the waveguide.

4. REFERENCES

- [1] "ELETTRA Conceptual Design Report", Sincrotrone Trieste, Trieste, Italy, April 1989, ch. II pp. 7, 92, 97.
- [2] E. Karantzoulis and A. Wrulich, "Multibunch Instabilities Investigation for the ELETTRA Cavities", in Proceedings of the 2nd EUROPEAN PART. ACC. CONF., Nice, France, June 1990, pp. 1618-1620.
- [3] A. Massarotti and M. Svandrik, "Proposal for A Broadband Higher-Order-Modes Suppressor for Radiofrequency Accelerating Cavities", Particle Accelerators, vol. 35, pp. 167-175, 1991.
- [4] A. Massarotti et al., "500 MHz Cavities for the Trieste Synchrotron Light Source Elettra", in Proceedings of the 2nd EUROPEAN PART. ACC. CONF., Nice, France, June 1990, pp. 919-921.
- [5] A. Massarotti et al., "Status Report on the ELETTRA RF System", in Proceedings of the 1991 PARTICLE ACC. CONF., S.Francisco, CA, USA, May 1991.
- [6] A. Massarotti et al., "Further Developments of the Broad-Band H.O.M. Suppressor at Trieste", in Proceedings of the 3rd EUROPEAN PART. ACC. CONF., Berlin, FRG, March 1992, vol. 2, pp. 1185-1187.
- [7] M. Svandrik et al., "A Pill-box Resonator with very Strong Suppression of the H.O.M. Spectrum", ST/M-92/14, Sincrotrone Trieste, Trieste, Italy, July 1992.
- [8] L.K. Summers, B. Branson, A.M. Johnson, I. E. Campisi, "CEBAF HOM Loads", presented at the Workshop on Microwave-Absorbing Materials for Accelerators, CEBAF, Newport News, VA, USA, February 1993.

Power Conditioning of the RF Cavities for ELETTRA

A. Massarotti

Sincrotrone Trieste and Dipart. di Fisica, Universita' di Trieste

G. D'Auria, A. Fabris, C. Pasotti, C. Rossi, M. Svandrik

Sincrotrone Trieste, Padriciano 99

34012 Trieste, Italy

Abstract

The cavities for the Synchrotron Light Source Elettra have been conditioned at full power. The OFHC copper cavities have a smooth shape, working at 499.654 MHz. The conditioning has been performed in the laboratory with a prototype power plant. The RF power provided by the klystron amplifier is fed to the cavity by means of a coupling loop. The cavities have been conditioned starting from pulsed operation; the power and the duration of the pulse have then been raised till the requested CW gap voltage was reached. The whole conditioning procedure, starting from the bakeout of the cavities, and the test results are described here.

1. INTRODUCTION

Four cavities working at 499.654 MHz will be installed in the ELETTRA storage ring. The required gap voltage for each cavity at beam energy equal to 1.5 GeV is 607 kV, thus leading to a wasted power into the cavity of about 26.5 kW [1].

The cavities have been built in OFHC copper and are water cooled by means of cooling pipes brazed on the cavity walls (fig. 1).

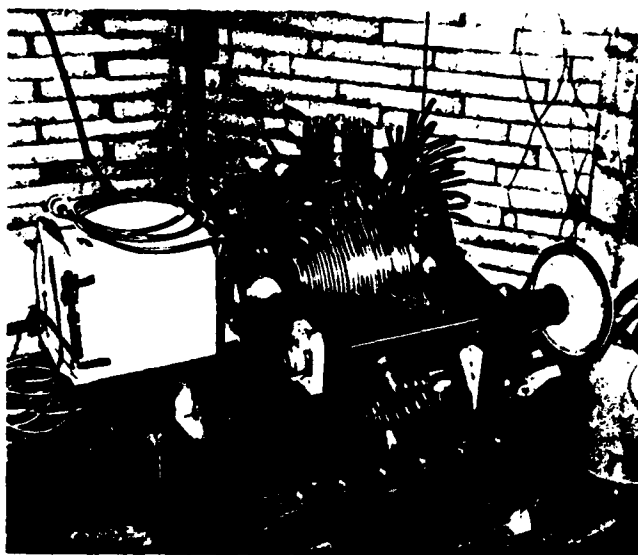


Fig. 1 The cavity with cooling pipes brazed on the outer surface, the tuning cage and one vacuum pump

Before starting with the installation of the cavities in the storage ring, each cavity has been conditioned at full power by using the RF 60 kW power plant mounted in the laboratory.

The RF power is fed to the cavity via a coupling loop. The feedthrough is copper made and water cooled.

To start the conditioning of each cavity, a fast rise time, low repetition rate and short RF pulse has been used. At the beginning the cavity has been fed with a low RF power level. The power level and/or the pulse duration have been increased once stable RF operation and safe vacuum condition of cavity were reached. The conditioning procedure has been stopped at 35 kW CW RF power corresponding to a gap voltage of 700 kV.

A duration test of several hours has been performed at this input power level to ensure the reliability of the conditioning procedure.

2. RF UNIT ASSEMBLY AND BAKEOUT

The 500 MHz cavity is a smooth shape one [2]. The RF power is fed into the cavity via a coaxial copper power coupler. An alumina ceramic window brazed to the inner and outer conductors of the coaxial line provides the vacuum insulation.

The last step of the mechanical construction of the cavity as well as of the vacuum feedthrough was the brazing in the high temperature vacuum oven. Afterwards the cavity and the vacuum feedthrough have undergone a further surface ultra high vacuum cleaning procedure.

Then the RF unit has been assembled in the laboratory. The coupling coefficient between the feedthrough and the cavity has been adjusted to 1.0.

The vacuum system for the first conditioning procedure consists of a turbo molecular pump of 180 l/s and two ion pumps of 120 l/s each. The vacuum pressure is monitored with a Pirani gauge for the lower vacuum range and a Penning cold cathode gauge head for the high and ultra high vacuum range.

The RF units were baked out for 48 hours. The cavity body and the feedthrough were heated up to 150 °C with hot water circulating in the cooling pipes. The stainless steel parts like the flanges were heated up to 180 °C with electrical heaters. The ion and turbo pumps were baked out at 200 °C and 100 °C respectively.

After five hours of cool down a pressure level of $2.2 \cdot 10^{-10}$ mbar has been achieved in the cavity.

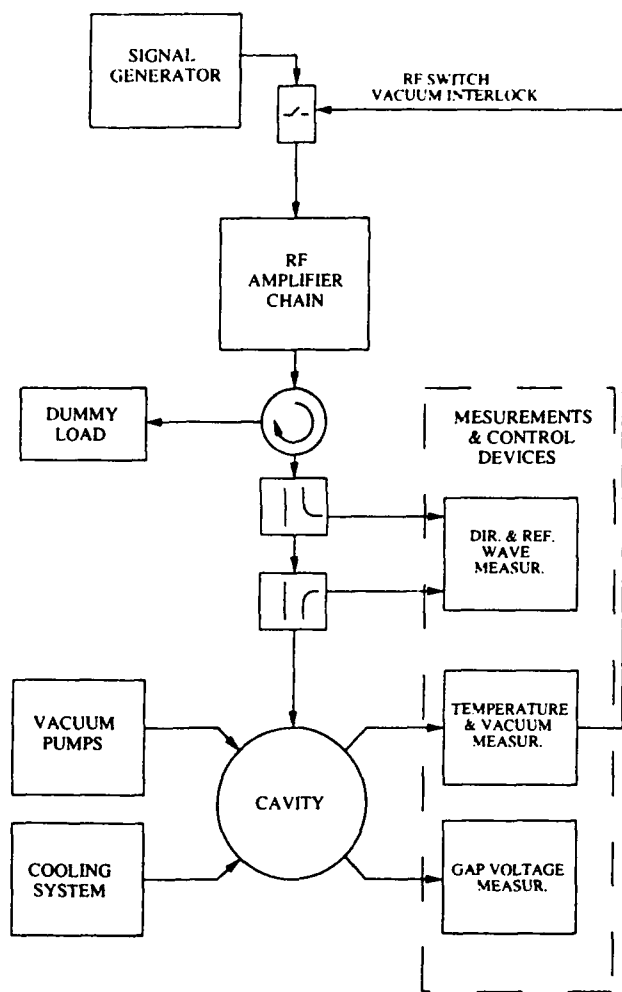


Fig. 2 Layout of the RF plant for the conditioning

3. RF UNIT CONDITIONING

The RF plant of the laboratory is a prototype of the RF storage ring plants [3]. It is made up of a 60 kW amplifier, a 500 MHz power circulator with a dummy load on the third port and a 6 1/8" coaxial line to feed the RF unit. A sketch of the whole plant is shown in fig. 2.

The vacuum equipment for the conditioning is the same installed for the bakeout.

The cavity and the power coupler are water cooled. The water flow is about 13 m³/h for the cavity and 0.5 m³/h for the vacuum feedthrough. A temperature mapping of the RF unit has been provided during the test.

The cavity tuning is performed changing its axial length by means of a tuning cage which is driven by a dc motor. The tuning range is ± 100 kHz; within these limits the mechanical stress of the cavity remains below the elastic limit [2].

The RF power is interlocked with the vacuum level of the RF unit. The vacuum gauge controller switches the RF off when the threshold of $1.0 \cdot 10^{-7}$ mbar is exceeded.

The RF conditioning has started with a short RF pulse at a period of 100 Hz. The starting length of the pulse was 80

μ s. The peak power has been increased up to the final value of 35 kW. Once the peak power was reached, the duty cycle has been slowly increased from 0.8% to 100%.

During the whole power raising procedure the pressure level has been kept in the $10^{-8} + 10^{-9}$ mbar range.

The cavity gap voltage was monitored on an oscilloscope as well as the direct and reflected wave, to detect any possible discharge in the resonator.

The typical duration of the conditioning procedure is between 40 and 50 hours. The peak and average cavity input power plot versus the conditioning time for one of our RF unit is shown in fig. 3. It should be noted that the conditioning procedure is not continuous; it is shared during more days. The turning off of the procedure is indicated with zero power points. It can be seen that in the first 15 hours the peak power has been increased with the minimum pulse length. In the following hours the pulse has been lengthened till the CW operation has been reached.

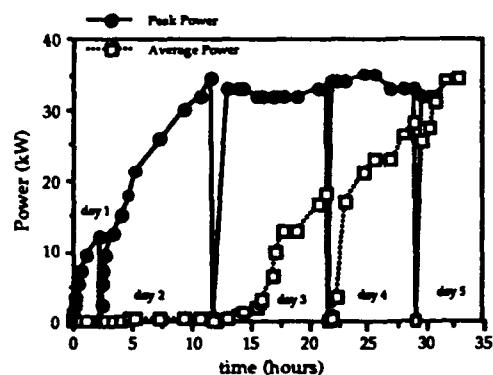


Fig. 3 Peak and average power versus conditioning time

The pressure versus time plot for the same RF unit can be found in fig. 4. The "plow" points indicates the cavity pressure level before a power increase. The "phigh" values have been recorded after one minute of each power increase. These plots refer to an RF unit in which the pressure as always been lower than 1.10^{-8} mbar, while other RF units have shown a worse pressure curve (see fig. 5).

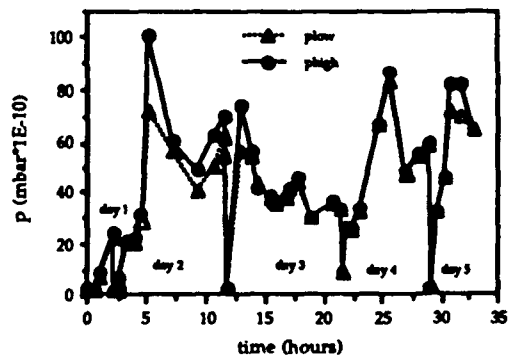


Fig. 4 Pressure versus conditioning time. Best results

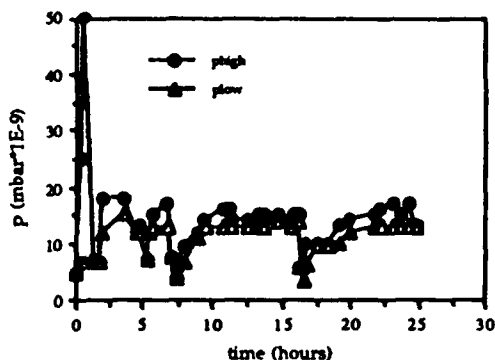


Fig. 5 Pressure versus conditioning time. Worse results

After achieving CW full power level, each unit has been operated at this level for several hours. During the duration test no significant trouble rose, thus we concluded that the unit was successfully conditioned.

The final pressure level at the end of the test improved to the $5.0 \cdot 10^{-9}$ mbar range with 35 kW CW fed to the RF unit.

In these conditions a maximum x-ray dose rate of 130 $\mu\text{S/h}$ has been measured nearby the cavity.

Neither multipacting or discharge phenomena have occurred during the whole conditioning. Thus no metalization on the ceramic windows should have taken place. Actually the temperature gradients of the vacuum feedthrough remain constant also after several operating hours at full power.

Is is interesting to note that, during the conditioning, if the cavity is excited at its resonant frequency, the pressure level slightly increases. This happens also for frequencies below the resonance, while detuning the cavity at higher frequencies the vacuum pressure reaches the minimum values. Thus, to avoid any risk of ceramic window contamination we operate the cavity at slightly higher frequency than the resonant one [4]. This occurrence disappears at the end of the conditioning, operating the cavity in the continuous wave mode at a power level just below the maximum value achieved in the pulse mode operation.

4. CONCLUSION

The RF cavities for ELETTRA have been successfully conditioned to the required peak power.

The conditioning procedure has avoided any multipacting or discharge phenomena in order to prevent any sputtering of the ceramic window surface.

The RF units are therefore ready for installation on the storage ring. In the meantime they have been stored in nitrogen atmosphere to avoid any possible and further contamination of the surfaces.

Thus we expect to repeat quickly and without trouble the conditioning procedure once the cavities will be installed in the storage ring.

5. REFERENCES

- [1] A. Massarotti et al., "Status Report on the ELETTRA RF System", in Proceedings of the 1991 PARTICLE ACC. CONF., S.Francisco, USA, May 1991.
- [2] A. Massarotti et al., "RF Power System for the Trieste Synchrotron Light Source ELETTRA", in Proceedings of the 2nd EUROPEAN PART. ACC. CONF., Nice, France, June 1990, pp. 913-915.
- [3] A. Massarotti et al., "500 MHz Cavities for the Trieste Synchrotron Light Source Elettra", in Proceedings of the 2nd EUROPEAN PART. ACC. CONF., Nice, France, June 1990, pp. 919-921.
- [4] E. Weihrer et al., "High Power Test of the RF Window for the SRRS Storage Ring", SRRS/RF/IM/92-01, Hsinchu, RoC, April 1992.

High Power Test of a SLED System with Dual Side-Wall Coupling Irises for Linear Colliders

Hiroshi Matsumoto, Hiroshi Baba, Atsushi Miura and Seiya Yamaguchi
KEK, National Laboratory for High Energy Physics
Oho 1-1, Tsukuba-shi, Ibaraki-ken 305, Japan

Abstract

A new SLED cavity has been developed for the 1.54 GeV injector linac of the KEK Accelerator Test Facility (ATF). A significant reduction of electric fields near the irises has been achieved by adopting dual side-wall coupling irises. The new SLED cavities were successfully operated at an output rf-power of 380 MW after the total operation time of 500 hours without any serious breakdown problems.

I. INTRODUCTION

The Japan Linear Collider (JLC) [1] aims to deliver electron-positron collisions at a center-of-mass energy of 300–500 GeV with a luminosity of $\sim 5 \times 10^{33} \text{ cm}^{-2}\text{s}^{-1}$. The KEK Accelerator Test Facility (ATF) [2] is presently under construction as a test facility for the JLC. The ATF consists of a 1.54 GeV S-band injector linac and a 1.54 GeV test damping ring.

To meet the energy goal 1.54 GeV of the injector linac with a given site constraint the accelerating gradient has to reach 33 MV/m. The mission of SLED cavities is to deliver the required 400 MW output power with an 85 MW input from the klystron. The regular unit of the linac consists of two 3 m-long accelerating structures, an 85 MW klystron with a SLED and a klystron modulator. High power (85 MW) klystron with 4.5 μs pulse width have been developed by TOSHIBA corporation and available since 1989 [3].

The original SLED [4] scheme has been used extensively and reliably at SLAC for the SLC over the past several years. At the SLC the klystron output power is 65 MW with a pulse width 3.5 μs . The achieved peak power, after the pulse compression, is 300 MW. The maximum power from SLED in practice could be limited by the rf breakdown around the irises due to the high surface electric field [5]. At the ATF the input rf-power will be 85 MW, well above the SLC SLED case. An excessive surface field within the cavity leads to potentially serious breakdown problems and radiation safety hazards. Thus a care must be taken to reduce the surface field around the irises. We have found that adopting two port side-wall coupling irises is a good solution for this problem.

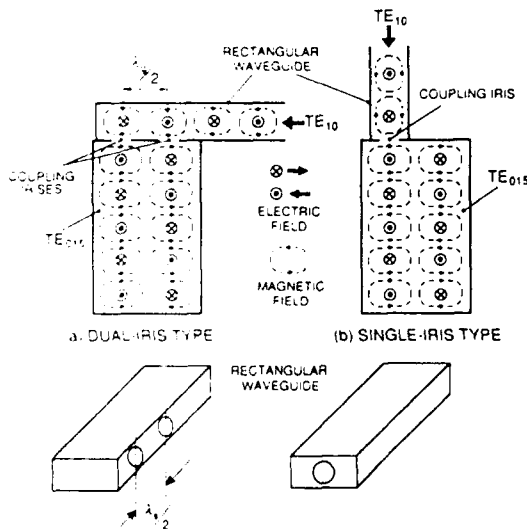


Figure 1. A schematic diagram of a SLED system for rf-power compression.

II. DESIGN AND FABRICATION OF THE SLED

Figure 1 shows a schematic diagram of the dual-iris (new) and single-iris (original) SLED systems. Important design principles of the dual-iris SLED system are: (1) implement two irises for the rf-coupling, (2) the coupling is made on the side wall of the wave guide so as to reduce the surface electric field, and (3) adopt a sturdy mechanical structure for operational stability.

A. Main Parameters of SLED

Parameters of the present SLED cavity such as Q_0 and β have been chosen so as to achieve a maximum energy gain of the accelerating structures for the ATF with an input rf-power of 85 MW and pulse width of 4.5 μs [3, 6]. They are summarized in Table 1.

Table 1
Main parameters of the dual-iris SLED system.

Operation frequency	2856	MHz
Cavity size : length (L)	33.59	cm
: Diameter ($2a$)	20.51	cm
Groove size : Width (w_g)	1.0	cm
: Depth (d_g)	0.9	cm
Iris size : Diameter (D)	2.98	cm
: Thickness (t_w)	1.2	cm
Quality factor (Q)	$\sim 10^5$	
Coupling coefficient (β)	4.8	
SLED filling time, $T_c = 2Q_0 / w(1+\beta)$	1.92	μs
Klystron pulse width (t)	4.5	μs
SLED output pulse width	1.0	μs
Mode separation between TE_{015} and TM_{115}	20	MHz
Structure : Length	3	m
: Attenuation parameter (τ)	0.57	
Filling time	0.83	μs

B. Coupling Irises

The surface electric field E that appears around the coupling iris is qualitatively written as

$$E \approx \frac{\sqrt{P}}{D} \quad (1)$$

where P is the power transmitted through the iris and D is the iris diameter. Here we evaluate the benefits of a dual-iris structure compared to a single-iris scheme. We use suffixes 1 and 2 to denote the parameters in a single-iris and dual-iris cases. We assume that the allowed surface field strength E is limited by breakdown conditions. Therefore, the maximum E should be limited at the same value, independent of the iris scheme choice. Thus we set $E_1 = E_2 = E$. It follows that

$$\frac{\sqrt{P_1}}{D_1} = \frac{\sqrt{P_2}}{D_2} \quad (2)$$

Hence,

$$\frac{2P_1}{P_2} = \frac{2D_1^2}{D_2^2} \quad (3)$$

The coupling coefficients per iris for both type cavities are

$$\beta_1 = 2\beta_2 \quad (4)$$

Here the β is known to be proportional to D^2 in an ideally simplified case. If the power loss in the cavity and the wave guide can be neglected, the β is also proportional to the coupling magnetic field [7, p. 143-149]. Thus we get

$$D_1^* = 2D_2^* \quad (5)$$

We apply the relation (5) in the equation (3) to obtain:

$$\frac{2P_2}{P_1} = \frac{2D_2^2}{(2^{1/2}D_1)^2} = 1.59. \quad (6)$$

This means that the excitation of the dual-iris SLED cavity can be 1.59 times that of the original single-iris cavity. This gain can be further increased by building irises on the side wall of the wave guides, rather than having them on the end wall, as shown in Figure. 1. This is because the electric field strength on the side wall of the wave guide near the iris is smaller than the maximum transverse electric field in the wave guide which appears when the rf-power propagates. In the case of the S-band rectangular wave-guide (72.1 mm × 34.0 mm), their ratio λ_c/λ_g is 0.924, where λ_c and λ_g are the cutoff- and guide-wavelength. Therefore, the equation (5) can be modified as

$$D_1^* = (0.924)^2 \times 2D_2^* = 1.71D_2^* \quad (7)$$

By using the equation (7), instead of (5), in (3) we obtain

$$\frac{2P_2}{P_1} = \frac{2D_2^2}{(1.71^{1/2}D_2)^2} = 1.67. \quad (8)$$

By adopting dual side-wall irises, the transmitted power into the SLED cavity can be increased by a factor 1.67, while maintaining the same iris surface field.

In the discussion above the wall thickness at the irises and the power loss on the copper surface have been neglected. Because of their effects in a real SLED cavity a small correction needs to be applied to the expected ratio $2P_1/2P_2$ in equation (8).

C. Design of the S-band SLED Cavity

To determine optimum cavity dimensions such as the radius (a) and length (L), we have taken a procedure as follows:

- (1) Calculate various modes and obtain the optimum $Q(\delta/L)$ as function of $2a/L$, where δ is the skin depth. The a and L are searched for in a reasonable range for fabrication.
- (2) Evaluate the mechanical stability for the preferred $2a/L$
- (3) Examine the distribution of neighboring modes and the electromagnetic fields.

At SLAC the TE₀₁₅ mode has been chosen from considerations on cost, mechanical stability and mode separation [8]. The SLAC decision has a proven performance record. We have taken the same choice. The degeneracy of TM₁₁₅ and TE₀₁₅ modes can be removed by introducing a circular groove on the end plate of the cavity. The URMEL code [9] was used to calculate the resonant frequencies of the two modes as functions of the groove width (w_g) and depth (d_g). The resonant frequency of the TM₁₁₅ mode is always decreased by introducing a groove. Considering the high Q value of the TE₀₁₅ mode, the dimension of the groove was chosen to be $w_g = 10$ mm and $d_g = 9$ mm, which gives a mode separation of 20 MHz.

D. Three Dimensional Calculations with MAFIA

Having confirmed the principle of a dual-iris scheme with a cold model, we have carried out three dimensional (3D) field calculations using the MAFIA code [10]. The goal was to find the geometry that minimizes the electric fields at the irises. Figure 3 shows the electromagnetic fields for both SLED schemes. It can be seen that the two irises in the dual-iris SLED scheme [11] are excited at opposite phases. This means that the TM₁₁₅ mode is hard to be excited at this frequency. By adding the effect of the groove discussed in the pervious section to this fact, the dual-iris SLED cavity is completely free from the TM₁₁₅ mode at this frequency.

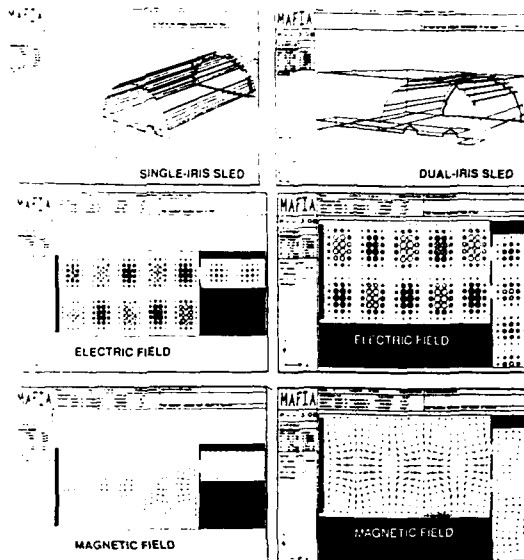


Figure 3. Electromagnetic fields in the SLED cavities calculated by MAFIA code.

The relationship between the coupling coefficient β and the iris diameter D has been calculated in two steps. In the first step the external Q value of the coupling iris (Q_{ext}) was determined by using the "Tuning Method" developed by J.C. Slater [7, p. 87]. In the second step the β was calculated from the relationship $\beta = Q_0/Q_{ext}$. Figure 4 shows the measured and calculated relationship between β and D of our dual-iris SLED cavities for the varying iris thickness obtained by using a cold model. The results are plotted for several different iris thickness t_w .

The agreement between the calculations and measurements is quite good. The combination of the Tuning Method and 3D calculations with MAFIA turns out very useful in design work of SLED cavities. In the dual-iris scheme SLED cavity it has been shown that β is proportional to $D^{0.4}$ and $\exp(-0.224t_w)$. It is seen that the iris surface field can be reduced by increasing D and t_w .

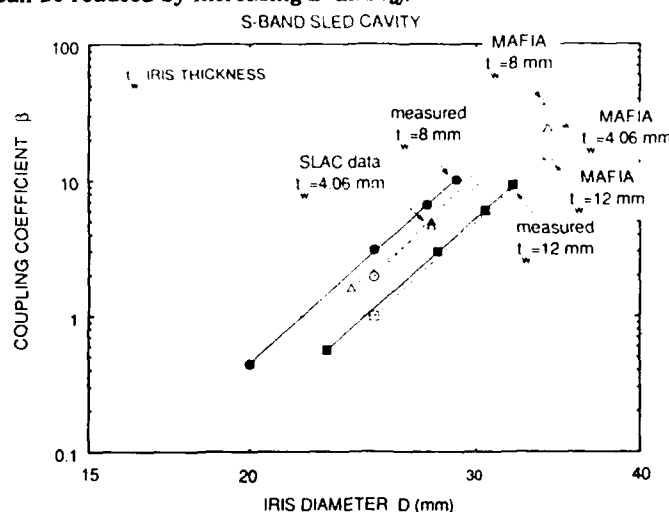


Figure 4. Calculated and measured β values as a function of iris diameter and thickness.

E. Mechanical Structure and Fabrication of the Cavities

Figure 5 shows a photograph of the present dual-iris S-band SLED system. A part of the end wall of the cavity was

machined to form a thin area so that the position of the end wall can be moved with a differential screw which is attached on an external jig. This allows a frequency tuning of ± 1 MHz.

A copper cooling water pipe was welded to the cylinder wall and the grooves were formed on the outside of the end walls as a cooling water channel. The positions of water pipes were chosen to match the wall current pattern of the TE₀₁₅ mode for efficient cooling.

The two cavities were held within four thick plates (3 cm) of stainless steel. These plates were connected with each other by four pipes of stainless steel which were also used as headers of the cooling water system. Since this support structure is an integral part of the cooling system, the temperature difference between the cavity and the support is minimized. Because of this rigid and stable support system, these SLED cavities can be used even in a free posture.

The cavity material is class 2 OFHC which has been delivered by Hitachi Densen Corp. The machining of the cavity surface was made with an accuracy of ± 5 μ m and the surface roughness < 0.2 μ m. The Q_0 has been measured to be the order of 10^5 .

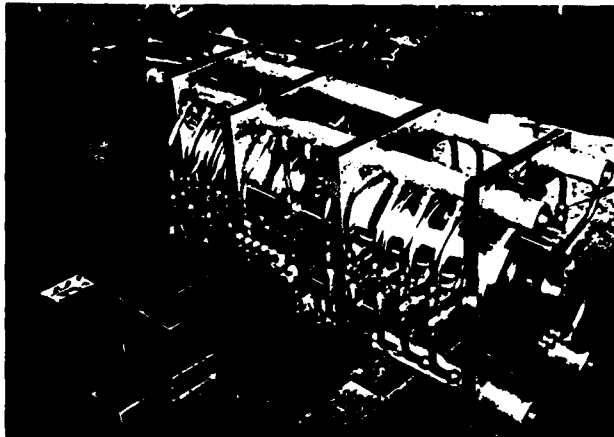


Figure 5. A photograph of the present dual-iris SLED system.

III. EXPERIMENTAL SETUP AND PROCEDURE

The final goal of the present experiment is to demonstrate the peak power of ~ 400 MW with the pulse compression for the KEK ATF. Experimental set up consists of an 85 MW klystron system, the SLED cavities, high power wave-guides, rf-loads and a vacuum pump system. To absorb the high peak power (~ 400 MW) from the SLED cavities, four dummy loads are used. They have been developed at SLAC for use with 100 MW power with 1 μ s pulse length at 30 pps repetition rate. The phase reversal response time of the circuit is less than 40 ns [13, 14]. The base vacuum pressure of 6×10^{-9} Torr was achieved by using three ion pumps.

The rf processing was carried out while monitoring the vacuum pressure and the rf power levels from various spots in the system. The characteristic time constants in this procedure are determined empirically, and are incorporated in the computer control program.

IV. EXPERIMENTAL RESULTS

The rf processing of the wave guide and the rf loads were first carried out by detuning the SLED cavities by up to 75 MW with a full-length 4.5 μ s pulse. Then the cavities were tuned to the operation frequency and the rf processing was applied again until the input power is increased to 80 MW. This was done without using phase reversing. At this stage the peak output power from the SLED cavities was 2.2 times the input power.

After the pre-processing, SLED operations with rf phase switching were started, first at a low rf power level. The

resonant frequency of the cavities was measured during the rf processing from time to time. It was confirmed that the mechanical structure of the SLED cavity was very stable, and a re-tuning of the cavities was not necessary after the initial low rf power turning. During the rf processing the vacuum pressure was maintained below 5×10^{-8} Torr and the reflecting rf-power less than 1 MW.

After the total operation time of 500 hours, the input power was increased up to 80 MW with 4.5 μ s pulse width. The peak output power 380 MW was achieved as shown in Figure 6. The maximum X-ray intensity measured on the irises was 4.8 mR/h during the whole process of the operation.

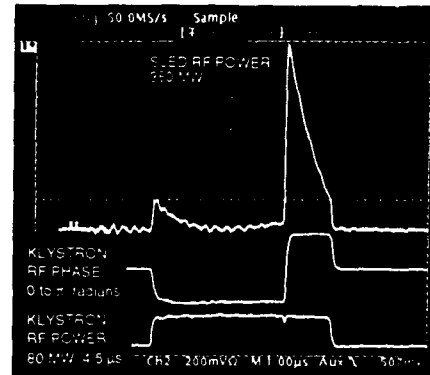


Figure 6. A photograph of the wave forms of input (lower) and output (upper) rf-power of SLED system and phase of the input rf signal (middle).

V. ACKNOWLEDGMENTS

The authors wish to thank Professors Y. Kimura and K. Takata of KEK for their continuous encouragement. The present work has been carried out as part of the construction program of the KEK ATF, collaboration by: S. Takeda, M. Akemoto, H. Hayano, T. Naito, Y. Otake, J. Urakawa, and others too numerous to list at KEK, and T. Matsui and S. Morita of ATC Corp. Their help is greatly appreciated. The authors are grateful for critical reading of the manuscript by N. Toge, M. Yoshioka and T. Shintake. A special mention has to be made that the present work could not have been carried out without many discussions with and information from Professor G. A. Loew, Mrs. Z. D. Farkas, R. Forks, H. Deruyter and their colleagues at SLAC. Their generosity in sharing their expert knowledge is greatly acknowledged.

VI. REFERENCES

- [1] JLC group, KEK report 92-16, A/H/M, National Laboratory for High Energy Physics, Japan, December 1992.
- [2] S. Takeda, Proc. of the Second Workshop on Japan Linear Collider (JLC), KEK, 1990, p. 6-17.
- [3] H. Yonezawa, S. Miyake, K. Gonpei, K. Ohya and T. Okamoto, Proc. 14th Int. Conf. on High Energy Accelerators, Tsukuba, JAPAN, 1989, p. [1177/219-224.
- [4] P. B. Wilson, SLAC-TN-73-15, 1973.
- [5] G. A. Loew, Private discussion for the present status of SLAC SLED system, SLAC, 1990.
- [6] Z. D. Farkas, H. A. Hogg, G. A. Loew and P.B. Wilson, Proc. 9th Int. Conf. on High Energy Accelerators, SLAC, 1974, p. 576.
- [7] J. C. Slater, "Microwave Electronics", Van Nostrand Company Inc., p. 87, p. 143-149.
- [8] Z. D. Farkas, H. A. Hogg, G. A. Loew and P.B. Wilson, SLAC-PUB-1561, March 1975.
- [9] T. Weiland, Nucl. Inst. Meth. 216 (1983), p. 329 - 348.
- [10] M. Bartsch, M. Dehler, M. Dohlus, P. Hahne, R. Klatt, F. Krawczyk, Z. Min, T. Pröpper, P. Schütt, T. Weiland, S. Wipf, M. Marx, F. Ebeling and B. Steffen, Proc. 1990 Linac Conference, Albuquerque, 1990, p. 372-377.
- [11] A. Fiebig, R. Hohbach, P. Marchand and J. O. Pearce, CERN/PS 87-45 (RF), March 1987.
- [12] Heinz D. Schwarz, SLAC-PUB-3600, March 1985.
- [13] S. Araki and Y. Otake, Proc. of the 16th Linear Accelerator Meeting in Japan. September 3-5, 1991, p. 97-99.

Performance Tests of a Ferrite-Loaded Cavity under Operation Conditions

S. Papureanu, Ch. Hamm, A. Schnase, and H. Meuth
Forschungszentrum Jülich, P.O. Box 1913, D-54245 Jülich

Abstract:

The ferrite loaded, tunable reentrant-coaxial symmetric ($2 \times \lambda/4$) accelerator cavity for the cooler synchrotron COSY is of the SATURNE type. For $h=1$, frequencies range from 450 kHz at injection to a maximum of 1.6 MHz, with a maximum rf power level of 50 kW. We have determined the cavity circuit properties both at low signal levels with standard rf test equipment, and at operation conditions, depending on frequency and power level. Moreover, the acceleration system was tested for its suitability to pass through gamma transition. For this end, a sudden phase jump of 180° was imposed at the input of the amplifier chain by means of the digital frequency synthesizer developed for COSY. At higher frequencies, a loss of Q was observed, partly aiding the transition crossing speed. Finally, a simple replacement circuit, incorporating the measured quantities, is used to model the cavity.

1. INTRODUCTION

Synchrotrons with non-relativistic injection energy require a large tuning range, to adjust to the continuously varying revolution frequency during acceleration. Tuning is achieved by biasing a ferrite material inside the cavity by means of a polarisation current. High-permeability ferrites are required to reduce wavelengths at low frequencies to a few meters. Thus, ferrite-loaded cavities are used with virtually every proton or heavy-ion synchrotron accelerator.

There exist a number of basic configurations of such cavities, the most predominant types being a single-sided $\lambda/2$ structure, as used in MIMAS/LNS or LEAR/CERN, and a double-sided symmetric (push-pull) configuration, as used in SATURNEII/LNS or PSBooster/CERN. For biasing, both the common figure-eight windings around the ferrite toroids inside the cavity, and an external quadrupole magnet is used. The latter method was proposed and developed, in cooperation with MPI Heidelberg, by one of us (S.P.) for TSR, to eliminate any possibility of rf-to-biasing crosscoupling [1].

Cavities are regularly coaxial reentrant, to provide the geometry for a beam tube on axis, and a suitable electric accelerating field in axial direction. Cavity characteristics are somewhat complex, depending on the nonlinear thermal and magnetic properties, the latter being also strongly frequency dependent. Measurements on such cavities, therefore, sensitively depend on the actual measurement and operation conditions.

In the following, we restrict ourselves to measurements made on the acceleration station for COSY [2], which is of the coaxial reentrant symmetric type, with a push-pull RF-power amplifier, consisting essentially of TTE TH120 power tubes, capable of dissipating 45 kW each, integrated directly into the acceleration station [3]: The power amplifier is coupled to the cavity capacitively and

inductively (Fig. 1).

The station operates in the $h=1$ acceleration mode, with frequencies ranging from 450 kHz to 1.6 MHz. Acceleration voltage amplitudes up to 5 kV are possible.

COSY very likely will have to pass transition in order to reach its topmost energy design values, this also poses demands on the performance of the acceleration system. The entire station was, with the exception of all low-level rf signal synthesis components [4], manufactured by a consortium of Thomson Tubes Electroniques, and the Laboratoire National Saturne. Since its installation in 1992, the system was continually adapted to the needs of COSY, as they emerged during commissioning.

2. ELECTRIC CHARACTERISTICS

To define the acceleration station's electrical performance characteristics, we must first consider a suitable lumped-element circuit schematic.

2.1 Circuit Schematic

Main features of the circuit are the cavity itself, defined by an inductor and capacitor on each side, coupled via the gap capacitance, and the polarisation windings, which are fed by a slowly varying ("DC") current, as mandated by the tuning requirement (Fig. 1). The amplifier may, on each side, be simplified to a voltage source with a following load resistor, the rf tube's internal resistance, to act somewhat like a current source.

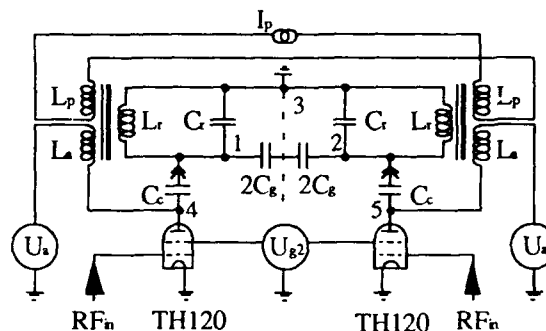


Fig. 1: Simplified circuit schematic of the COSY acceleration station

It was the goal of our measurements to either directly determine or derive from these measurements, the value of each of these circuit elements.

2.2 LCR bridge and vector impedance measurements

For both measurements a standard set up was used. However, care has to be taken to avoid errors induced by supplementary grounding loops.

The LCR-bridge and vector impedance meter both have to be supplied over a decoupling transformer

Also, due to the hysteresis of the ferrites, one has to establish specified magnetic conditions. In this case all measurements were taken by starting from the upper saturation point on the hysteresis loop.

Cavity inductance for low frequencies ($f = 1$ kHz) was measured directly via the LCR-Bridge connected across points 1 and 2 (Fig 1) by setting the polarisation current to the predetermined value required for saturation and then decreasing this current in small steps, taking down the inductance at each step.

To determine if the inductance of this cavity is also dependent on frequency, the impedance over polarisation current was measured across points 1 and 2 of Fig. 1 with a vector impedance meter for frequencies between 0.5 and 1.5 MHz, the operating range of our cavity. With a known value of C the Inductance can be derived from frequency and the absolute value and phase angle of the complex impedance as given by the vector impedance meter. The results of these measurements are given in Fig. 2.

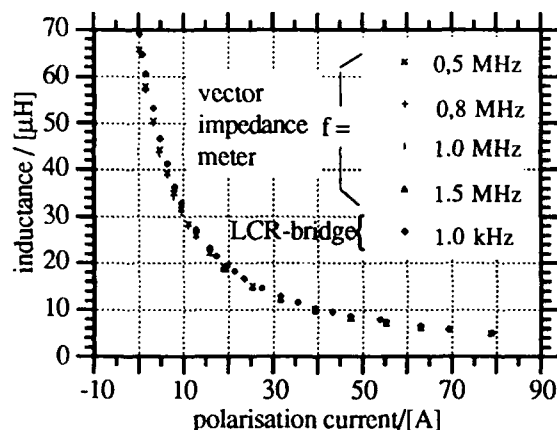


Fig. 2: Inductance over polarisation current

2.4 High-Power Measurements

Cavity Q i.e. power dissipation and the response of the cavity to a phase jump of 180° were measured over a variety of frequencies between 540 kHz and 1.5 MHz and RF-voltages between 1 and 5 kV_p. The measurement set up is depicted in Fig. 3.

One evident method of determining Q is switching off the power generator and observing the decay of gap voltage. Here, an alternative method is used, employing the response of the resonator to a phase jump as is necessary when crossing transition energy. This method has the advantage of determining Q at operating conditions, and also, we get the variation of the gap voltage after the phase switch. For these measurements, the phase and amplitude control were switched off, since they would falsify the measured Q value.

The phase of the NCO's signal is switched 180° at the zero crossing t_0 of the gap voltage. The oscillogram of the resulting gap voltage is digitally recorded by a digitizing oscilloscope of the type HP DSA 602A.

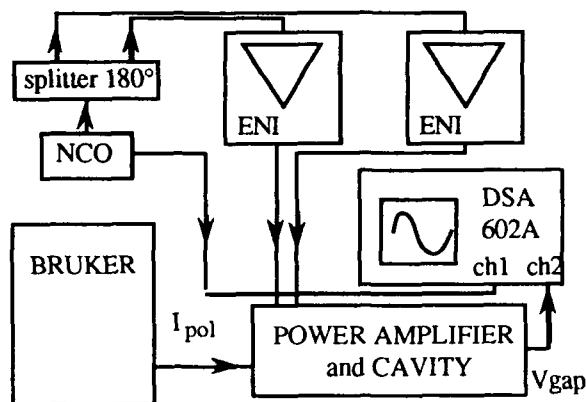


Fig. 3: Set up for testing phase jump of 180°

For low frequencies and moderate RF-amplitudes (Fig. 4) the gap voltage over time after the phase switch is given by the solution of the standard differential equation for forced oscillations:

$$V(t) = V_0 \cdot \exp\left(-\frac{\omega}{2Q} t\right) \cdot \sin(\omega_r t + \varphi_0) + \hat{V} \sin(\omega t + \pi)$$

$$\text{with } \omega_r = \omega \sqrt{1 - (2Q)^{-2}} \quad (1)$$

V_0 and φ_0 being determined by initial conditions. For a phase jump of 180° at zero crossing one obtains for the damped oscillation:

$$V(t) = 2 \cdot \hat{V} \cdot \sin(\omega t) \cdot \exp\left(-\frac{\omega}{2Q} t\right) \quad (2)$$

Above some critical value $\approx 6 \text{ kV} \cdot \text{MHz}$ of $f \cdot V_{RF}$ (Fig. 5) there is sudden breakdown of cavity Q , resulting in a serious overshoot (Fig. 6) of the gap voltage. The behavior of the cavity can no longer be described by (1). The amplitude over time of the transient solution is some function $f(t)$, as Q now strongly depends on frequency and RF-amplitude. At 1.5 MHz and an amplitude of 5 kV, approximately the RF-parameters when crossing the transition energy at COSY, the amplitude stabilizes to the initial value only after about 2 ms (not depicted here). By switching on the control loop, settling time can be considerably reduced

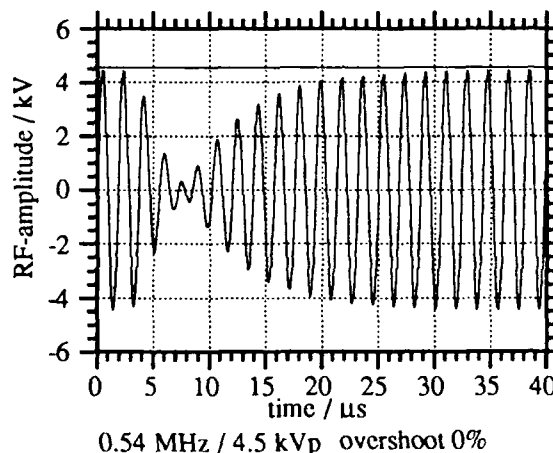


Fig. 4: Gap voltage over time after phase switch

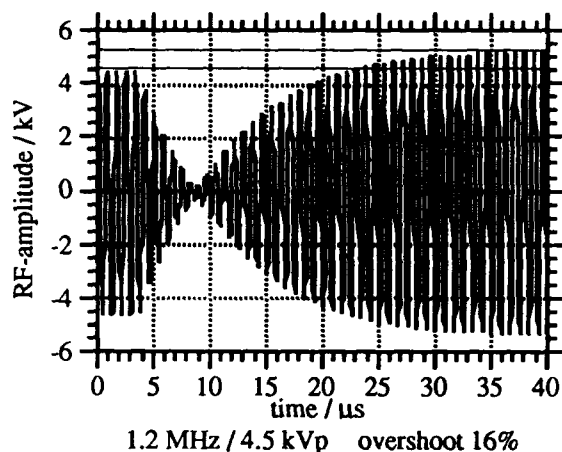


Fig. 5: Gap voltage over time after phase switch

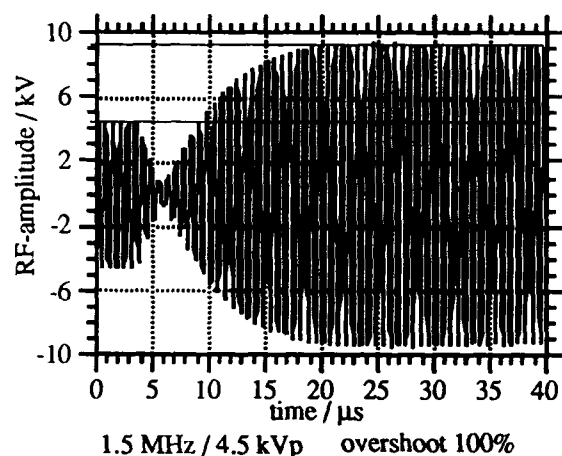


Fig. 6: Gap voltage over time after phase switch

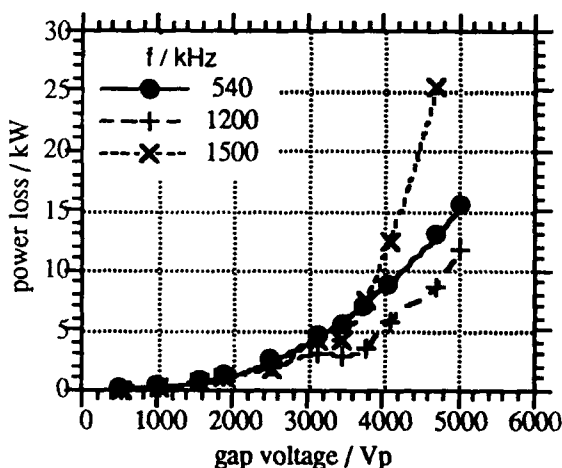


Fig. 7: Power dissipation over gap voltage

From the measurements mentioned above, parameters were derived for a SPICE model of the resonator, which is capable of simulating some aspects of the non linear response characteristics shown here

3. THERMAL CHARACTERISTICS

Under normal operating conditions the power dissipated in the resonator's ferrites is considerable (in excess of 10 kW), i.e. they have to be efficiently cooled. Each ferrite is intercalated between two copper cooling discs. There are four groups of six cooling disks with a serial water flow connection for each side of the cavity. The water temperature at the output from each of the 48 cooling discs is depicted in Fig. 8 for $f = 1.6$ MHz at $V_{gap} = 3.7$ kVp, cw mode and a water input temperature of 21.9°C.

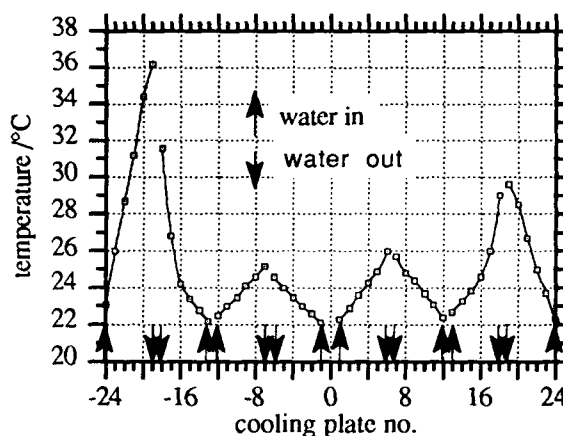


Fig. 8: Cavity cooling water temperature repartition

We can observe an asymmetry in the dissipated power between the left and the right side of the resonator which is probably due to the difference in the RF-characteristics of the ferrites. An increase of V_{gap} of only 5% produces the Q-loss effect in our ferrites resulting in a continuous rise of the cooling water temperature. In order to obtain higher cw gap voltages, we improved cooling at the shorted end of the cavity. The results for power dissipation derived from these measurements are in rough agreement with those derived from the measurements of Q mentioned in this paper. We will report on the improvements obtained hereby and on further measurements elsewhere.

4. REFERENCES:

- [1] M. Grieser et. al., *Recent Developments at the Heidelberg Heavy Ion Cooler Storage Ring TSR*, EPAC 92, p. 152
- [2] R. Maier, U. Pfister, *The COSY-Jülich Project March 1992 Status*, EPAC 92, p. 149
- [3] C. Fougeron, Ph. Guidée, and K.C. N. Guyen, *RF System for SATURNE II*, PAC, San Francisco 1979.
- [4] A. Schnase, et al., EPAC 92; H. Meuth, A. Schnase, and H. Halling, this conference.
- [5] Ch. Hamm, *Ein SPICE Modell der COSY h=1 Beschleunigerstation*, Diploma Thesis 1993 Univ. Bonn

CLIC Transfer Structure (CTS) Simulations Using "MAFIA".

A. Millich

CERN
1211 Geneva 23, Switzerland

struct

In the two-beam accelerator scheme of CLIC the Transfer Structure serves the purpose of extracting 30 GHz power from the drive beam. The purpose of the 3D simulations of the 30 GHz CTS using the MAFIA set of codes has been to assist designers in the choice of the final dimensions by appreciating the sensitivity of the RF characteristics to the mechanical parameters. The results of the frequency domain analysis have allowed plotting of the dispersion curves of the waveguides and appreciation the relative importance of higher modes. The time domain investigations have produced results on the shape and magnitude of the beam-induced longitudinal and transverse wake fields and of the loss factors.

1. INTRODUCTION

The CLIC Transfer Structure serves the purpose of extracting 30 GHz power from the drive beam in the two-beam accelerator scheme of CLIC [1]. Initial design of the CTS was based on model work using the wire method of beam simulation [2]. This provided the designers with approximate CTS dimensions and wake field magnitudes.

A complementary method, described here, makes use of simulations of the 30 GHz structure by computer codes. The CTS geometry not being axes-symmetric, a three dimensional simulation using the code MAFIA [3] was performed on a JN-IPX workstation. In spite of the restrictions on the number of mesh points imposed by the limited memory space (2 Mbytes of main memory) the results obtained confirmed and completed the ones obtained by model measurements.

2. CTS GEOMETRY AND FUNCTION

The CTS essentially consists of a smooth cylindrical beam chamber of 12 mm diameter, which is coupled by means of diametrically opposite slots to two periodically loaded rectangular (8 x 4 mm) waveguides (Fig. 1). The periodicity of the waveguide 'teeth' is such that the phase velocity of the $2\pi/3$ mode at 30 GHz is equal to the speed of light in vacuum.

The ultra relativistic drive beam creates in the waveguides a field that propagates in phase with the exciting bunch, so that constructive transfer of energy to the waveguide mode is possible all along the structure. The drive beam is made up of a train of bunches spaced by one wavelength of the 30 GHz mode, which is 10 mm, so that each bunch contributes to the coherent excitation of the mode, the energy of which increases until the last bunch has left the structure. At that moment the waveguides are filled with energy which propagates at the group velocity of about one third the speed of light and which is transferred to the main linac disc-loaded structure.

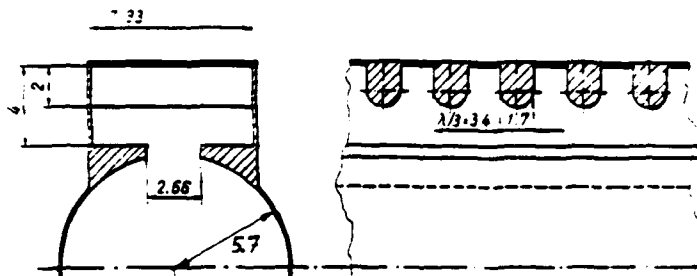


Fig. 1 CLIC Transfer Structure Geometry (upper half)
Courtesy of L. Thorndahl and G. Carron.

The length of the CTS is such that the duration of the energy discharge pulse fills the gap between two successive bunch trains spaced 2.84 nsec or one 352 MHz period. Taking into account the bunch train transit time and its time span, one CTS is about 0.50 m long and presents 144 rounded teeth in the waveguides. Four bunch trains are therefore necessary to provide a pulse of duration longer than 11.1 nsec, which is the main linac disc-loaded waveguide filling time. The energy stored in the CTS waveguides by one train of bunches must supply a power level of 80 MW during 2.84 nsec.

3. MESH GENERATION AND FREQUENCY DOMAIN ANALYSIS

By means of the MAFIA module M310 the CTS geometry was simulated as shown in Fig. 2.

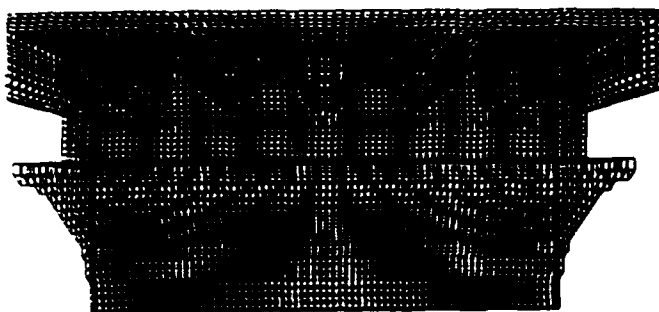


Fig. 2 Mesh of a six cells section of CTS (only one quarter shown).

Thanks to symmetry, only one fourth of the structure needs to be retained in the simulation. The memory space available in the workstation being limited, only six cells were used in the frequency domain computations with 64000 mesh points, whereas 12 cells with 128000 mesh points were used in the time domain computation of wake fields. The average resolution in the three dimensions is 0.3 mm. The beam trajectory is the z axis which coincides with the axis of the cylindrical chamber.

By means of modules R310 and E310 the resonant modes of the CTS were computed. The solutions found varying the boundary conditions of the z end planes present a phase shift per cell from 0 to π in steps of $\pi/6$. They are shown in Table 1, while the dispersion characteristic is plotted in Fig. 3.

Table 1. Normal modes found by MAFIA for the first CTS pass band.

Mode number	Frequency (GHz)	Phase shift/Cell
1	19.729	0
2	20.759	$\pi/6$
3	23.430	$\pi/3$
4	26.858	$\pi/2$
5	30.000	$2\pi/3$
6	32.027	$5\pi/6$
7	32.690	π

The dimensions of the CTS were chosen such that the intersection of the line representing a phase velocity equal to the speed of light with the dispersion curve occurs at the frequency of the $2\pi/3$ mode, which is 30.00 GHz. The group velocity of the $2\pi/3$ mode is 32% of the speed of light.

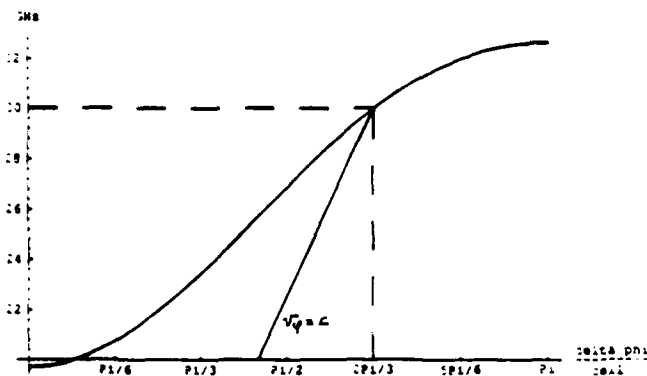


Fig. 3 Dispersion characteristic of the CTS

By means of the post processor P310, the Q of the structure was computed together with the shunt impedance per unit length R' and the $r'=R'/Q$ parameter. Table 2 gives the numerical values including those of the longitudinal loss factor per unit length and per structure for the $2\pi/3$ mode.

Table 2. CTS RF parameters

Synchronous mode frequency	=	30.00	GHZ
Q factor	=	3808	
Shunt impedance R' (true ohms)	=	12.6	K Ω/m
$r' = R'/Q$	=	3.30	Ω/m
Loss factor k'	=	0.156	V/pCm

4. WAKE FIELDS COMPUTATION IN TIME DOMAIN

4.1 Longitudinal wake fields

For this analysis the 12 cells geometry was used in module T3310. The boundary conditions were chosen as perfect magnetic conductors for the $x = 0$ and $y = 0$ symmetry planes, while for the z end planes the waveguide condition was imposed. For the computation of the longitudinal wake field, a bunch of $\sigma_z = 1$ mm and charge normalised to 1 pC was placed in the centre of the beam chamber. The longitudinal wake is shown in Fig. 4. It is a damped sinusoid with zero crossings distant exactly one 30 GHz wavelength or 10 mm.

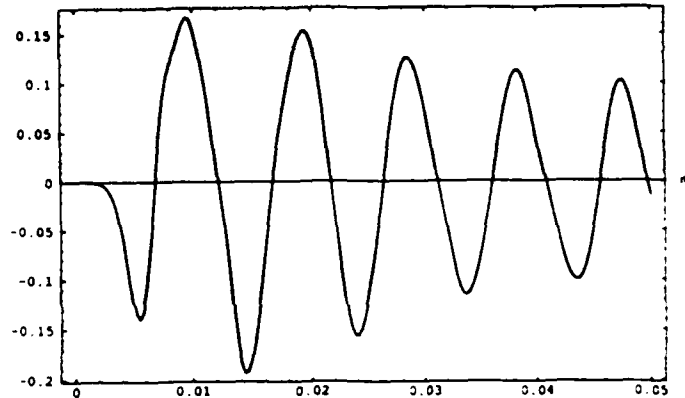


Fig. 4 Longitudinal wake field of a bunch of $\sigma_z = 1$ mm charge 1pC traversing one CTS structure. Vertical scale V/pC, horizontal scale: m)

The peak field seen by the second bunch in the train is found to be $1.5 \cdot 10^{-2}$ V/pC for the 12 cells length, or 0.375 V/pCm. A bunch of 160 nC generates a peak wake field of 60 KV/m at the second bunch position. The last bunch in the train, say the 11th, experiences ten times this peak field plus its own wake, that is about 630 KV/m, so that on average the bunch train sees a decelerating voltage of 330 KV/m with a loss of 0.58 J/m, which is the energy that gets transferred to the waveguide modes.

4.2 Transverse wake fields

The knowledge of the amplitude and shape of these wake fields is of paramount importance for the studies of the transverse drive beam stability by means of tracking programs. [4]

Setting the $y = 0$ symmetry plane as perfectly conducting, only the deflecting modes are excited by the bunch placed one mm off centre in the y direction. The bunch exciting the wake experiences its own deflecting action which reaches a maximum at its tail. Since the transverse wake is offset by $\pi/2$ with respect to the longitudinal one, the subsequent bunches arrive at the nodes of the wake field and therefore no cumulative deflecting effect occurs for particles near the bunch centre. The peak transverse wake field is found to be $2.9 \cdot 10^{-3}$ V/pC for 1 mm beam displacement and 12 cells length, which corresponds to 32 V/pCm for one CTS structure. Fig 5 shows the computed transverse wake field.

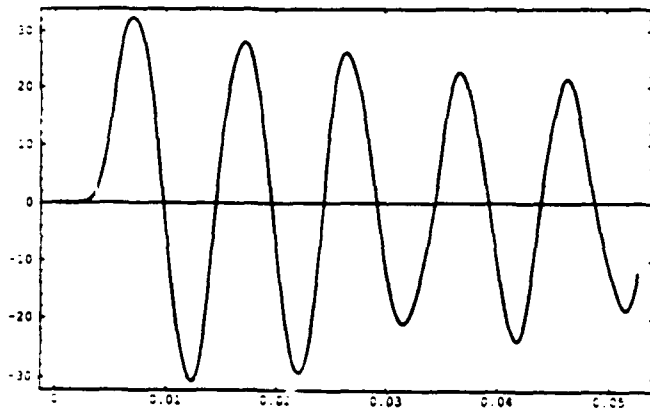


Fig. 5 Transverse wake field of a bunch with $\sigma_z = 1$ mm, charge 1 pC, traversing one CTS structure. (Vertical scale V/pCm, horizontal scale: m)

5. HIGHER ORDER MODES

The present version of the MAFIA program does not allow to explore the resonant modes of a structure in a user defined frequency interval but it finds all the modes starting with the lowest one. This feature sets a limitation on the number of higher bands one can explore given a fixed amount of computer memory available. Using the six cells geometry of the rectangular waveguide without the cylindrical beam chamber, it was possible to find some forty modes in the frequency band from 18 GHz to 72 GHz. Fig 6 shows the resulting dispersion diagram. The intersections of the straight line representing a phase velocity equal to the speed of light with the dispersion curves indicates the synchronous modes that may be harmful to the beam. The relative importance of the shunt impedance of these modes with respect to the fundamental one, the synchronous $2\pi/3$ at 30 GHz, has been computed and the results have shown that only the TE₃₀ mode has an appreciable effect, of the order of 5%.

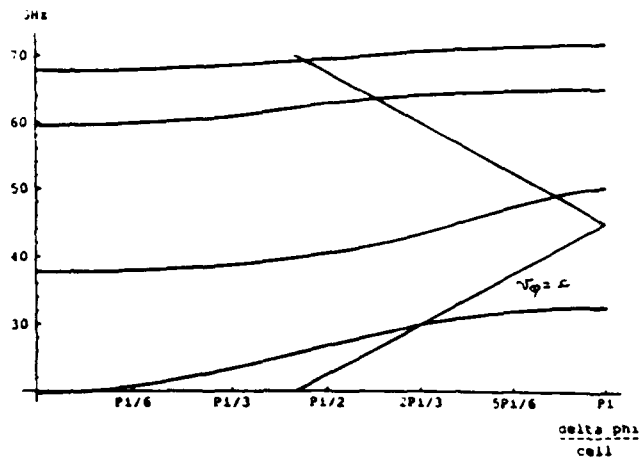


Fig. 6 Pass bands of the periodically loaded CTS waveguide in the range 18 GHz to 72 GHz

6. MECHANICAL TOLERANCES

MAFIA has proved to be a very helpful tool in the determination of the sensitivity of the CTS RF properties to the mechanical parameters of the structure [5]. To this end small variations have been applied to the four main parameters of the waveguides, namely their width and height as well as to the teeth height and length in the z direction, and the resulting variation in the $2\pi/3$ mode frequency computed by means of the E310 module.

Table 3. Sensitivity of the $2\pi/3$ mode frequency to the mechanical parameters: Wh, Ww, Th, Tl, respectively height and width of the waveguide and height and length of teeth.

Wh	= 4.0 mm	$\Delta f / \Delta Wh$	= 0.44 MHz/ μ m
Ww	= 8.0 mm	$\Delta f / \Delta Ww$	= 1.67 MHz/ μ m
Th	= 2.0 mm	$\Delta f / \Delta Th$	= 4.30 MHz/ μ m
Tl	= 1.666 mm	$\Delta f / \Delta Tl$	= 2.45 MHz/ μ m

REFERENCES

1. W. Schnell, The CLIC Study of an Electron-Positron Collider, Contribution to LC92 ECFA Workshop on e^+e^- Linear Colliders, Garmish Partenkirchen, August 1992. CERN SL/92-51 and CLIC Note 184.
2. L. Thorndahl, G. Carron, Impedance and Loss Factor Measurements on a CLIC Transfer Structure (CTS), Proceedings of the Third European Particle Accelerator Conference, EPAC 92, Berlin, 24-28 March 1992, pp 913,915.
3. MAFIA User Handbook, The MAFIA Collaboration.
4. G. Guignard, Beam Dynamics Investigations for the CLIC Drive Beam, CERN SL/92-22(AP) and CLIC Note 157.
5. L. Thorndahl, G. Carron, RF Hardware Development Work for the CLIC Drive Beam. These Proceedings.

Magnetron Sputtering Configuration for Coating 1.3 GHz Cavities with a Nb Film

M. Minestrini, M. Ferrario, S. Kulinski*
S. Tazzari#

* INFN, LNF, P.O. Box 13, 00044 Frascati, Italy

INFN Sezione di Tor Vergata, Via E. Carnevale, 00178 Roma, Italy

Abstract

In the framework of the ARES project and as possible application for TESLA project, we are assembling, in the 2nd University of Rome, a system to study the deposition of Nb film on TESLA type copper cavity. Magnetron sputtering to coat accelerating cavities with superconducting film was developed at CERN for 500 MHz cavities, 3 times larger than TESLA cavities; while it's relatively easy to scale the technique up to larger cavities (as for instance to the 350 MHz LEP cavities) there are some difficulties to scale it down, particularly as concerns the coils located on the inside of the cathode used at CERN to stabilize the discharge, unless small permanent magnets are used that do not allow full control over all discharge parameters. A possible solution is to put the coils outside the cavity in a magnetic bottle configuration. A brief review on sputtering of cavities, the simulation of electrons trajectories in a magnetic bottle and the sputtering test setup are described.

I. INTRODUCTION

Sputtering is a well known and useful technique for coating RF copper cavities with superconducting thin film. In the sputtering process [1] one ejects source material from the cathode in vapor phase by bombarding the surface of the cathode with ions of sufficient energy (at least 30 eV), in our case Argon ions accelerated by an electric field; the ejected atoms condense on the wall in front of the cathode forming the thin film.

There are different sputtering configurations of which the simplest is the diode one. In this configuration the cathode is negatively polarized with respect to grounded copper substrate electrically connected to the anode. Some of the problems of this configuration are film contamination due to impurities coming from the pumping system, unavoidable at high working pressures and from the chamber wall degassing due to discharge heating, and mechanical complications in case of sputtering inside a cavity (first CERN approach [2], [3]).

Low pressure is therefore mandatory but to obtain reasonable sputtering rates at low pressure the ionization degree of sputtering gas has to be increased by increasing the ionization efficiency of electrons in the discharge. To accomplish this the electrons active path must be restrained to the vicinity of the cathode, for instance superposing a perpendicular magnetic field on the electric one so as to prevent electrons from losing their energy through collisions at the anode rather than through ionization.

This is the present sputtering system configuration used at CERN to coat 350 MHz copper cavities with Nb films [4]. The magnetic field necessary to confine electrons is produced by a coil placed inside the cathode; the coil is moved in steps along the cavity axis to achieve a uniform coating.

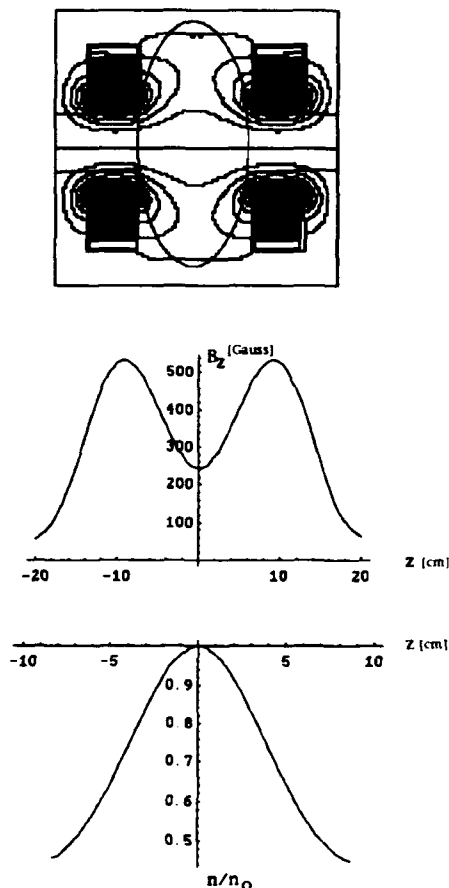


Figure 1. a) Magnetic mirror field lines
b) Longitudinal magnetic field intensity on cathode surface
c) Normalized longitudinal plasma density

The RF frequency selected for TESLA being 1.3 GHz, the cavities are 3 times smaller than those on which the CERN technique has been optimized. The CERN technique cannot therefore be scaled down straightforwardly, unless small permanent magnets (typically Samarium-Cobalt alloy) are used that fit comfortably inside the cathode. The latter however produce a fixed magnetic field configuration that limits the range of the discharge parameters variation. An alternative way of confining the discharge is to use a magnetic mirror field

configuration. The latter is well known from plasma physics and refers to the fact that charged particles spiraling around a static magnetic field line will be reflected by a region of stronger field due to the adiabatic constant of the motion $\mu = mv_{\perp}^2 / 2B$. A magnetic mirror can be obtained, as it is in our design (Fig.1a) by means of two coils placed on the outside of the cavity cut-off pipes. The field shape is obtained by suitable soft iron poles.

The field has a minimum (~ 200 Gauss) at the center of the cavity and a mirror ratio (that is a measure of the trapping efficiency) $B_{\max}/B_{\min} = 2$ (Fig.1b).

Doing so we expect to trap electrons and ions very close to the center of the cathode. In such a configuration in fact charges are subjected to an axial restoring force $F_z = -\mu(dU(z)/dz)$, where $U(z) = \mu B(z)$ is a potential well proportional to the magnetic field strength. Charges are confined if the condition $(v_{\perp}/v) \geq \sqrt{(B_{\min}/B_{\max})}$ holds. The charge density longitudinal distribution is given by

$$n(z)/n_{\min} = e^{-\frac{U(z)-U_{\min}}{KT}}$$

and is shown in Fig.1c for the worst case $(v_{\perp}/v) = 1/\sqrt{2}$.

II. ESTIMATE OF PLASMA PARAMETERS

Usual external discharge parameter ranges are: pressure of the working gas $(10^{-4}+10^{-2})$ mbar corresponding to $n=2.65(10^{12}+10^{14})\text{cm}^{-3}$, potential difference between electrodes $V \approx (500+1000)$ Volt, magnetic field $B \approx (200+1000)$ Gauss. To estimate the ionization fraction n_i/n , we neglect for the moment secondary electrons created by impinging ions and therefore assume that the cathode current is due to ions only.

The current is then given by $I = qn_i v_i S_c$ where q is the ion charge, n_i the ion density, v_i the ion velocity and S_c the active surface of the cathode.

The ion density is thus:

$$n_i = \frac{I}{qv_i S_c} = 9.5 \times 10^{10} \text{ I} \times \text{cm}^{-3} = 9.5 \times 10^{10} \text{ cm}^{-3}$$

with $S_c \approx 15\text{cm}^2$,

$v_i = 2.18 \times \sqrt{u} 10^5 \text{ cm/s} = 4.366 \times 10^6 \text{ cm/s}$ and $u = 400 \text{ V}$.

The degree of ionization is

$$d_i = \frac{n_i}{n} \approx \frac{10^{11}}{2.65 \times 10^{13}} \approx 3.8 \times 10^{-3}$$

with $P=10^{-3}$ mbar $\Rightarrow n=2.65 \times 10^{13} \text{ cm}^{-3}$.

Because the main part of the plasma is neutral, $n_e \approx n_i \approx 10^{11} \text{ cm}^{-3}$. Assuming that the temperature (energy) of electrons is close to the ionization potential of Ar $V_i \approx 15.8\text{eV}$, the Debye length for the plasma becomes

$$\lambda_D = \sqrt{\frac{KT_e \epsilon_0}{ne^2}} = 7.43 \times 10^2 T^{1/2} n_e^{-1/2}$$

where λ_D in cm if T_e in volts and n_e in cm^{-3} .

For $T_e \approx 10 \text{ eV}$ and $n_e \approx 10^{11} \Rightarrow \lambda_D \approx 0.743 \times 10^{-2} \text{ cm}$.

The electrons Larmor radius is $r_{Le} = 3.37 \sqrt{u} / B$ cm, for u in volts and B in Gauss: taking $u = KT_e \approx 10\text{eV}$ and $B=200$ Gauss one obtains $r_{Le} \approx 5.3 \times 10^{-2} \text{ cm}$.

Finally, because the main potential drop in the plasma, in our case corresponding to the cathode drop, occurs over approximately one Debye length, one can assume that in this thin sheet no collisions occur; all ions created in the plasma and arriving to the cathode can thus be assumed to have at least an energy corresponding to the cathode voltage drop, i.e. about $0.75+0.80$ of the total potential difference. On the other hand the secondary electrons, created at the cathode surface by impinging ions, also gain the same energy but, having Larmor radius much larger than Debye length, can enter the main plasma and thus become the primary source of ionization. Furthermore since the radial motion of electrons in the magnetic field is periodic, most of the electrons return to the cathode, unless they have experienced a collision with an atom or an ion.

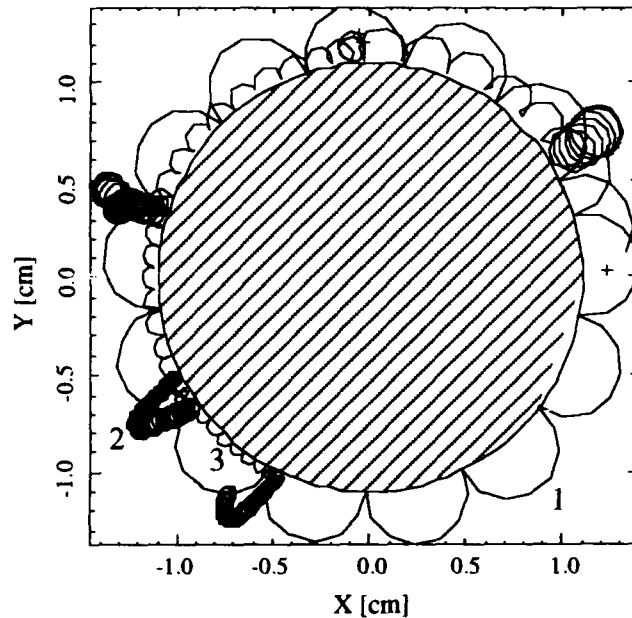


Figure 2. A simulated transverse electron trajectory with random collision (+)

Unless a collision occurs, the electron path in the transverse plane (X,Y) (Fig. 2) is always linked to the same magnetic field equipotential surface: an electron originating from the cathode experiences an intense electric field and starts to move in a cyclodial orbit around the cathode because of the drift effect $\mathbf{E} \times \mathbf{B}$ takes place (orbit 1). Usually collisions will occur in the main plasma body where the electric field is weak so that the orbit will be almost circular with a radius r_L depending on the perpendicular energy (orbit 2). At the same time electron with longitudinal component of the velocity, moves towards the stronger magnetic field end regions; its orbit is shifted closer to the cathode and if it moves back into the cathode drop region it restarts on a cyclodial path (orbit 3). In the longitudinal direction (Z) (Fig 3) the electron is reflected by the mirror (orbit 4) because $(v_{\perp}/v) > 1/\sqrt{2}$. Collisions will be another source of energy gain for low energy electrons created in the plasma and of radial and axial drift. We have estimated that on average electrons can have more than 100

collisions before arriving to the anode and can gain an energy of the order of 10 eV.

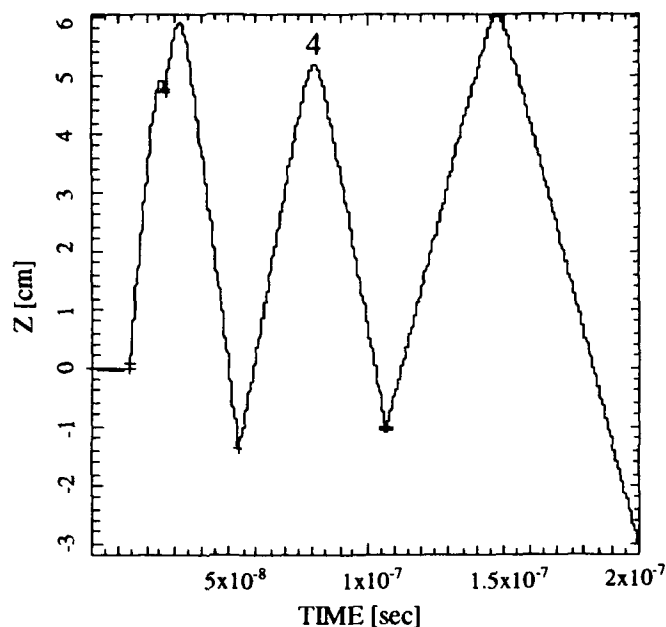


Figure 3. Longitudinal electron displacement with random collision (+)

III. SPUTTERING SYSTEM

The sputtering system that we are assembling is schematically shown in Fig.4.

It can accommodate different stainless steel TESLA type cavities on the inner walls of which, along the whole cavity profile, copper and sapphire samples can be fastened that allow studying the characteristics of the film over a wide portion of the surface. We plan to characterize the Nb film through RRR (Residual Resistivity Ratio) and T_c measurements, Auger, SEM (Scanning Electron Microscope) and X rays analysis. Plasma characteristics will be studied using Langmuir probes.

The system is evacuated by an ultraclean pumping group consisting of a 4 m³/h diaphragm pump for the primary vacuum and two cascaded turbo molecular pumps (pumping speed respectively 180 l/sec and 520 l/sec) one of which on magnetic bearings. A very good compression ratio for hydrogen, good ultimate pressure ($\sim 10^{-10}$ mbar) and total absence of hydrocarbons is obtained.

The system is equipped with a residual gas analyzer (RGA) to study the ultimate pressure gas composition, and to monitor the percentage of gas produced during sputtering, notably hydrogen, that damages the film structure if it exceeds a certain threshold. To use the RGA while sputtering, in a relatively high operating pressure ($\sim 10^{-3}$ mbar), we need differential pumping; the RGA therefore communicates with the cavity through a 0.6 mm diaphragm and it is equipped with another pumping system that produces a 3 order of magnitude pressure drop through the diaphragm.

The cathode consists of a vacuum tight stainless steel tube (17 mm inner diameter) surrounded by a niobium liner (20/24 mm inner/outer diameters). The liner is an high purity Nb tube (RRR value better than 100) without welds. The stainless steel tube is also equipped with an inner support to hold and center 7 SamCo permanent magnets (small cylinders 8 mm diameter 16 mm long) cooled by a liquid freon circuit sized to handle about 2 KW of power. Preliminary tests to optimize discharge parameters will be carried out both with permanent magnets and with the magnetic bottle field configuration.

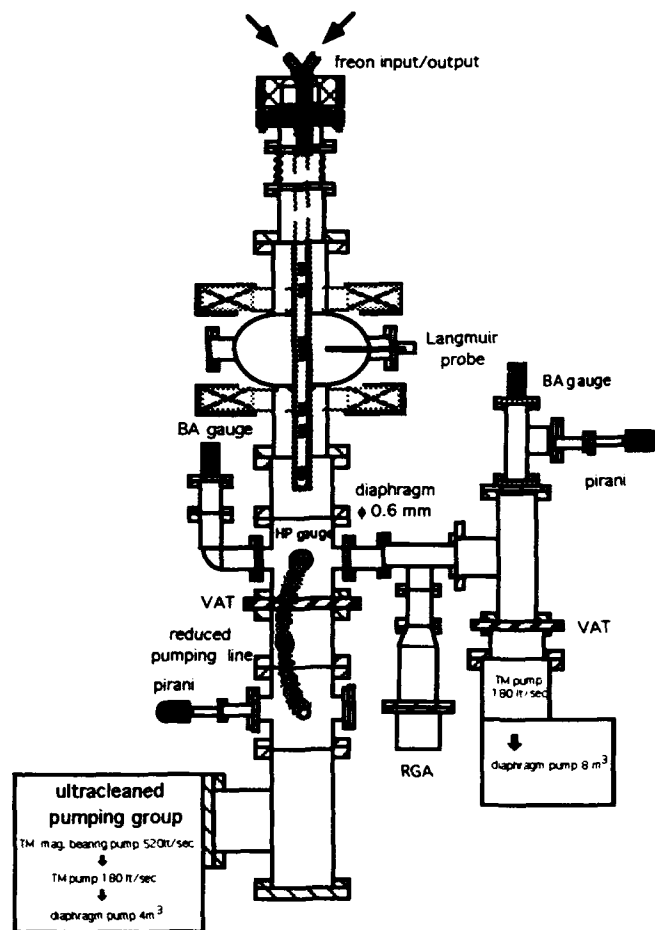


Figure 4. Sputtering system scheme

IV. REFERENCES

- [1] J.A.Thornton, A.S.Penfold, Thin film processes, J.L.Vossen Academic Press, New York (1978).
- [2] C.Benvenuti, N.Circelli, M.Hauer, IEEE Trans. Magn. MAG-21 153 (1985).
- [3] C.Benvenuti, N.Circelli, M.Hauer, Appl. Phys. Lett. 45, 5 (1984).
- [4] C.Benvenuti, D.Bloess, E.Chiaveri, N.Hilleret, M.Minestrini, W.Weingarten, Proc. 3rd workshop on RF superconductivity, Argonne Sept 1987.

ACCELERATOR STRUCTURE FOR LOW-ENERGY ELECTRON BEAM

A.V. Mishin
Moscow Engineering Physics Institute
Moscow, Russia

Abstract

A special high quality bunching cell for low-energy electron beam pre-acceleration is described. This cell was tested in an X-band standing wave accelerator. 25-keV electrons were injected into this bunching cell, connected to a linac structure, and more than 50% of them accelerated to the nominal energy.

I. INTRODUCTION

The problem of low-energy electron injection into an accelerator structure is of interest from a practical point of view, particularly for industrial and medical portable linacs [1], [2], and [3]. But this problem is difficult to solve easily. It is well known that commonly used accelerator structures such as disc loaded wave guide (DLWG), and on-axis coupled or side-coupled resonant structures are not effective in the normalized particle velocity interval under 0.4 - 0.5 because of high attenuation parameters and accordingly low quality factor and shunt impedance values.

On one hand, this undesirable range can be avoided by using the high injection voltage - not less than 50 kV and sometimes up to 185 kV, as in the Tokyo University accelerator [4]. This is not desirable.

On the other hand, if the acceleration field is high enough we can "cut out" a short phase range of injected particles without care about the capture rate. This is also not desirable. In addition, the above methods are much more complicated at X- and Q-band.

The offered standing wave structure [5], [6] has a higher quality factor and shunt impedance in low energy ranges and allows bunching and preaccelerating of more than 50% of injected particles without an external focusing field. This structure can be easily integrated with others.

II. GENERAL REMARKS

As indicated above, the lower the particle velocity the less efficient the structure when using the main field space harmonic for acceleration.

Next we consider higher number space harmonics for

acceleration [7]. The phase speed we can write as

$$v_p = 2\pi f D / (\theta + 2\pi m) \quad (1)$$

f - frequency;
D - structure cell length;
 θ - phase shift per cell;
m - Fourier series harmonic number.

For example, using $m = \pm 1$ harmonics

$$v_{p0} = 3v_{p-1} \quad (2)$$

and

$$v_{p0} = 5v_{p+1}$$

we can make the cell three or five times longer and reduce the attenuation parameter. Table 1 presents the DLWG travelling wave shunt impedance values in MOhm/m for three different space harmonics and variable iris hole radius in synchronized particle velocities interval.

Table 1 Space Harmonics Shunt Impedance, MOhm/m

particle velocity	0.2 x c			0.4 x c		
	a/ λ	0.1	0.12	0.14	0.1	0.12
m = +1	0.3	0.11	0.02	1.7	1.6	0.96
m = -1	0.8	0.24	0.06	10.2	6.7	4.1
m = 0	0.9	0.05	0.02	11.8	7.5	4.7

There are a number of advantages and disadvantages in using different space harmonics, but the essential result is that their efficiency is comparatively low in this velocity interval.

Actually, we can consider the process of acceleration using different space harmonics numbers as having different transit time effects. Using the relationship between accelerating gap transit time (tt) and microwave field oscillation period (T) we

obtain

$$tt = 1.5 \times T, m = -1 \quad (3)$$

In the second case, when $m = -1$, a particle sequentially sees the accelerating, the decelerating and then the accelerating field during the gap transition time, so the integral effect is positive. But the deceleration field seen by a particle is in the gap middle area and has a maximum efficiency.

The main idea of the offered structure is to place a drift tube in the middle of the gap, where a particle normally sees the decelerating field, as it is done in the Alvarez structure. This keeps the field phase locked on the opposite sides of the drift tube as shown in Fig. 1.

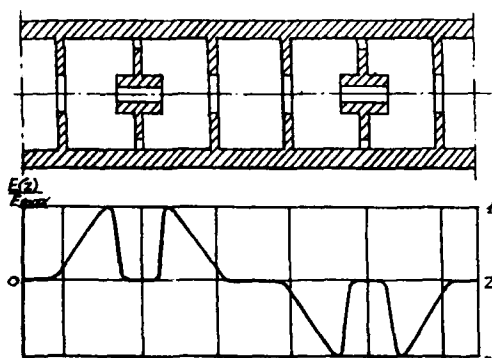


Fig. 1 Cross-section of the Structure

The dependence of the offered structure shunt impedance on the synchro-particle normalized velocity compared to those of the usual structures is shown in Fig. 2.

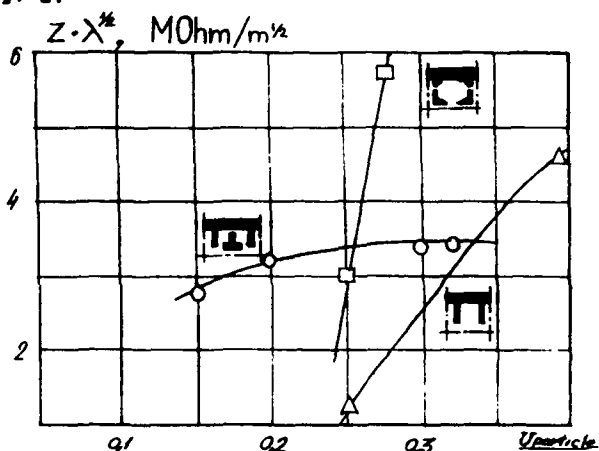


Fig. 2 Shunt Impedance versus Particle Velocity

At very low values close to β_{min} as considered in this case the Q -cell structure impedance is close to that of the DLWG with the same iris thickness and is even smaller than shown in Fig. 2. The zero shunt impedance is referred to the case when the length between neighbor irises becomes zero because of the iris thickness t so that $D = t$.

$$\beta_{min} = 2\pi/\theta \times t/\lambda_0, \quad (4)$$

λ_0 - free space wavelength.

The smaller the wavelength (for example in X- and Q-band), the higher β_{min} .

Using Fourier analysis and considering the center of the drift tube as a starting coordinate we determine that the number of the acceleration field harmonic is $m = 5$ for the field shown in Fig. 1.

III. EXPERIMENTAL VERIFICATION

The single dual-cell resonator for the offered structure is shown in Fig. 3. Two types of investigated parameters are shown in Table 2.

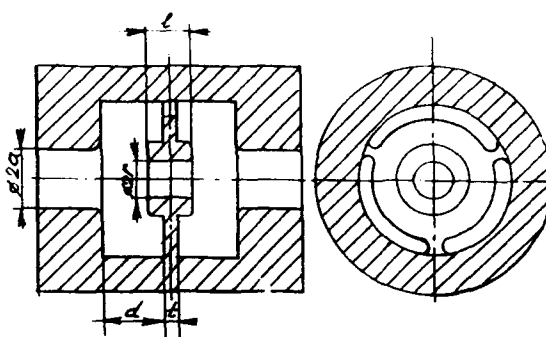


Fig. 3 Experimental Resonator Formed by a Pair of Cells

Table 2
Parameters of X-Band Resonators

N^0	d	$2r$	$2a$	Q_0	$E_{max}/(PQ)^{1/2}$
	mm	mm	mm	--	kV/MW ^{1/2} /m
1	12.56	5.00	7.68	4000	1336
2	8.08	5.00	7.68	4000	1336

For both types the parameter $(2d+t)/l$ that is responsible for the quality and field values is about 3. The two pair of cells were joined together over the coupling cell and formed a segment of a structure shown in Fig. 1. The unloaded Q -value became 5800 and the field parameter - about $1158 \text{ kV/MW}^{1/2}/\text{m}$.

The frequency field distribution along the central axis obtained by perturbation technique is presented in Fig. 4. Particle dynamics modelling using this field distribution indicated that with 40 kW dissipated in this resonator, the fields accelerate about 56% of the injected particles to the energy 150 - 180 keV without any external focusing field.

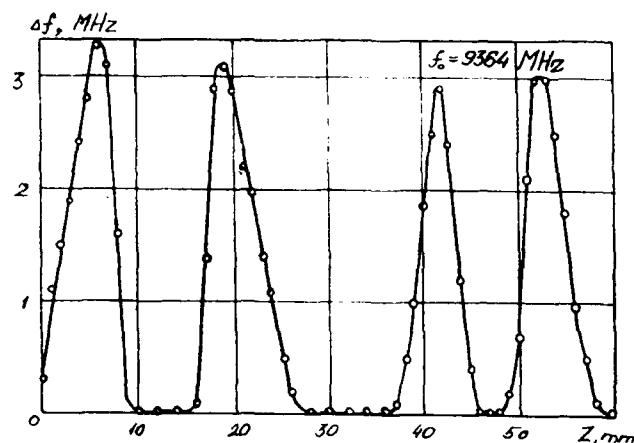


Fig. 4 Experimental Frequency Deviation Distribution Along the Axis Obtained by Perturbation Technique

The pair of cells N⁰1 was used as the first cell of the experimental X-band structure shown in Fig. 5. The total length of the structure is 11.6 cm and the loaded quality factor is 2000. The accelerator is shown in Fig. 6 under high power test. The structure used no external focusing coils.

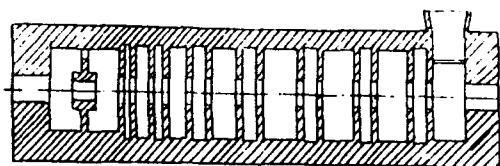


Fig. 5 X-Band Standing Wave Biperiodic Structure with Bunching Cell.

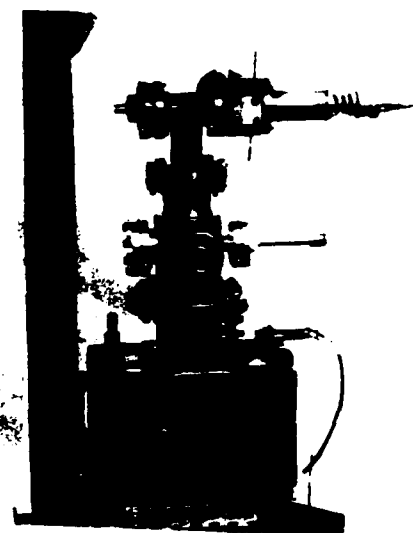


Fig. 6 Experimental Accelerator Device with Vacuum Pump

Initial energy.....25 keV
Final loaded energy.....0.7 MeV
Pulse current.....30 mA
Accelerated beam spot diameter.....~ 1 mm

IV. CONCLUSIONS

This structure was useful for field modelling and gentle beam forming at the bunching stage. It was recommended for use in the portable linac project [8].

V. ACKNOWLEDGEMENTS

This work has been carried out in the Small Accelerator Laboratory of MEFHI. I appreciate all help and support of the laboratory staff members.

VI. REFERENCES

- [1] I.S. Shchedrin, "X-Band Linear Accelerators," Proceedings of All-Union Charged Particles Linacs Seminar, in Kcharkov, 1985, (in Russian).
- [2] Russell G. Schonberg, "Field Uses of a Portable 4/6 MeV Electron Linear Accelerator," Nucl. Instr. and Methods in Phisic Research, B24/25, p. 797-800, 1987.
- [3] A.V. Mishin, E.A. Ermilov, V.P. Komarov, A.P. Shaltirev, "Portable X-Band Linac Project for Industrial Applications," Abstracts of XIII Linear Accelerator Conference, in Dubna, 1992, (in Russian).
- [4] Fukumoto S., Mizumachi Y., "An X-Band Electron Linear Accelerator", Oyojutury, V.36, N⁰1, p. 19-30, (1967).
- [5] A.V. Mishin, V.P. Komarov, Charged Particle Accelerator Structure, invention, a.s.N⁰1577678 08.03.90.
- [6] A.V. Mishin, "Portable X-Band Linear Accelerator," Ph.D. thesis, Moscow, MEFHI, 1992, (in Russian).
- [7] B.V. Bahtev, "Portable Broad Energy-Tuning Linac Design and Experimental Study," Ph.D. thesis, Moscow, MEFHI, 1977, (in Russian).
- [8] E.A. Ermilov, V.P. Komarov, A.V. Mishin, A.P. Shaltirev, "Portable X-Band Linac for Industrial and Medical Applications," Abstracts for XII International Conference on the Application, Research & Industry, University of North Texas, 2-5 November, 1992.

The linac parameters are as follows:

Microwave pulse power.....500 kW

Higher Order Mode Dampers for the KAON Booster Cavity

Amiya Kumar Mitra
TRIUMF

4004 Wesbrook Mall, Vancouver, BC, Canada V6T 2A3.

Abstract

A prototype higher order mode (HOM) damper cavity has been designed and tested on a ferrite tuned booster cavity proposed for the KAON factory at TRIUMF. The damper cavity has been designed to keep the overall length minimum and has been optimized by using SUPERFISH code. Low level signal measurements of unloaded and loaded Q of the booster cavity without and with the damper cavity respectively have been reported and it has been demonstrated that nearly all modes up to 1 GHz which couple to the accelerating gap are damped by the mode damper. In order to reduce the coupling at the booster fundamental frequencies by this type of damper, a new concept of damping higher order modes in the KAON booster cavity by employing a high-pass filter is presented. Conceptual design, prototype realization of such a filter in coaxial form and measurements of damping are outlined. Preliminary measurements show that the higher order modes up to 900 MHz are damped significantly with very little power absorption at the fundamental frequencies.

I. INTRODUCTION

The ferrite tuned booster cavity for the proposed KAON project at TRIUMF operates from 46 MHz to 61 MHz [1]. Higher order modes (HOM) are inherently present in these structures and if not suppressed adequately can cause beam instabilities. The cavity HOMs must be damped substantially to reduce their shunt impedances to acceptably low values. Since the cavity operates over a broad range of frequencies, externally applied tuned dampers may be difficult to implement. For a broad bandwidth it is more effective to install the dampers inside the cavity. A reentrant cavity damper [2], [3] and [4] and a coaxial high-pass filter as a damper [5] are discussed in this paper.

II. DESIGN OF HOM DAMPERS

The design goal of HOM dampers is to attenuate all the higher order modes up to 1 GHz without affecting the shunt impedance of the cavity at the operating frequency.

A. Reentrant Cavity Damper

A reentrant $\lambda/4$ cavity with heavily loaded tip capacitance, as shown in figure 1, is appended at the gap of the booster cavity. Four 50 ohms terminating resistors are connected to the annular ring of the damper cavity and are placed

symmetrically around the perimeter. As long as the damper cavity provides a high shunt impedance for the higher order modes, the damping is in effect since most of the currents produced by the HOMs will flow through the gap capacitance to the terminating resistors. The damper becomes ineffective at the frequency for which it produces a voltage null at the terminating resistor. This frequency is the series resonant frequency, most commonly known as $\lambda/2$ mode and should be as high as possible. The dimensions of the damper cavity were optimized by using SUPERFISH. The $\lambda/4$ resonant frequency mode (high shunt impedance of the reentrant cavity) was chosen to be 185 MHz and the series resonant frequency to be 1570 MHz. This leads to a broad bandwidth of the damper cavity. Decreasing the $\lambda/4$ frequency below 185 MHz would increase damping of the first HOM of the booster fundamental frequencies but would couple more power at the fundamental frequencies.

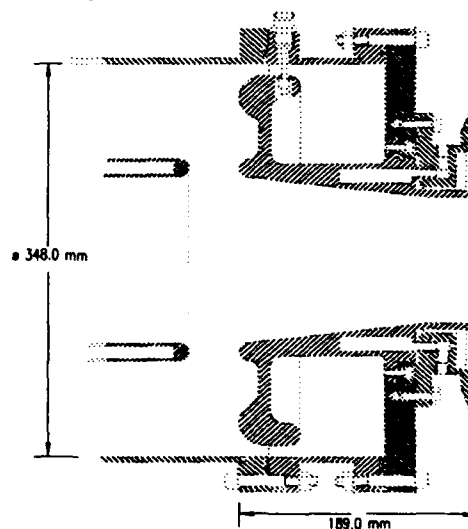


Figure 1. Reentrant damper cavity.

When the damper cavity was connected to the booster, the coupling of the two cavities lowered the $\lambda/4$ frequency to 161.97 MHz compared to the computed value of 169.726 MHz.

B. High pass filter Damper

A new concept of HOM damper in the form of a coaxial high pass filter is connected at the gap of the cavity. If the cut-off frequency of the filter is chosen to provide no attenuation into the terminating load for the currents produced by the HOMs and provide adequate attenuation for the currents at the

fundamental frequencies, then such a filter would be ideally appropriate as a HOM damper.

A five element 0.1 dB ripple Chebyshev high-pass filter would provide more than 40 dB attenuation at the highest fundamental booster frequency of 61 MHz if the high-pass cutoff frequency of the filter is chosen to be 150 MHz. Since the design aim is to damp all the HOMs up to 1 GHz, the passband must be at least 1 GHz. This leads to the following filter specifications.

High-pass cutoff frequency 150 MHz.
Maximum passband frequency 1 GHz.
Minimum attenuation at 61 MHz 40 dB.
Maximum passband ripple 1 dB.
Source impedance less than 1 ohm.
Load impedance 50 ohms.

The high-pass Chebyshev filter which satisfies the above requirements is shown in figure 2 with the corresponding element values.

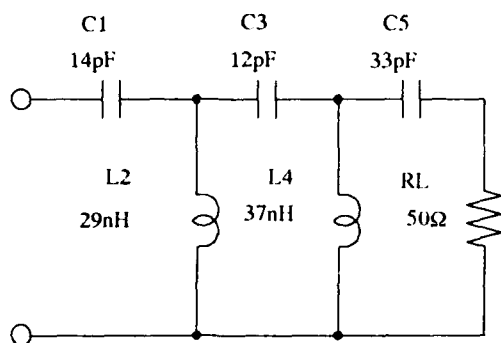


Figure 2. Schematic of the high-pass filter.

The challenge here is to realize these values in a coaxial structure rather than lumped elements. The capacitance's C3 and C5 can be formed out of coaxial rings or discs and the inductors L2 and L4 are provided by hollow rods connected from the short-circuit plate to the respective capacitors. Four terminating resistors are connected to C5 via low inductive connections. The capacitance C1 of 14 pF is the capacitance of the open end of the cavity to the first ring or the disc of the filter. Figure 3 and figure 4 show conceptual model of the ring and disc type coaxial high pass filters. Although prototype of both the filter structures have been made, the disc type is found to be more suitable for the particular application and fabrication tolerances can be relaxed.

III. MEASUREMENTS OF THE DAMPERS

All the measurements are done with a Network Analyser at a signal level of 20 dBm with two loosely coupled capacitor probes in the cavity. The reentrant damper cavity was tested

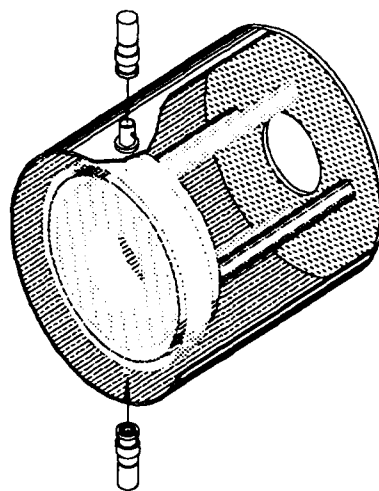


Figure 3. Isometric view of the ring type filter.

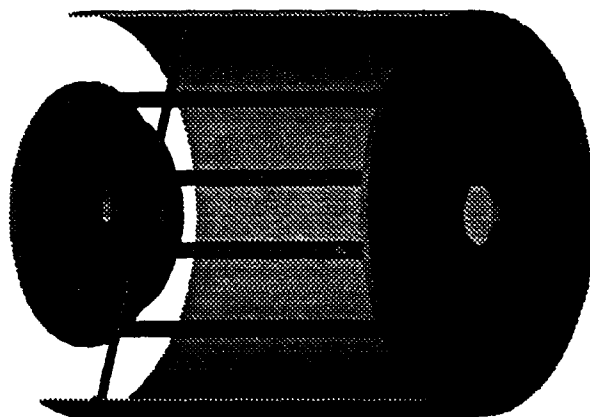


Figure 4. Isometric view of the disc type filter.

on the booster cavity whereas the high-pass filter damper was tested on a 6 inch quarter wave transmission line cavity. The 50 Ω resistors are connected or disconnected for loaded and unloaded Q measurements.

A. Reentrant Cavity

Different combinations of termination are tried and Qs are measured for all the resonances in the 10 to 1000 MHz spectrum with a dc bias current of 964 Amps on the ferrite of the booster cavity. Measured unloaded and loaded Q for some of the frequencies are listed in Table 1. It should be noted that with four 50 Ω resistors most of the HOMs are absorbed adequately however the Q at the fundamental frequency is lowered by 22 %. Loss of Q is more pronounced at higher booster frequency (40 % at 57.33 MHz).

Table 1
Unloaded and Loaded Q Measurements

Frequency	Designation	Unloaded	One Load	Four Loads
f/MHz		Q_0	Q_1	Q_1
52.075	Fundamental	2782	2680	2173
148.097	3 rd harm.	1720	≈ 35	≈ 10
157.715	Damper $\lambda/4$	1000	≈ 10	≈ 10
229.279	5 th harm.	2170	332	100
268.519		500	500	100
304.103	TE01 damper	300	300	≈ 20
346.103	7 th harm.	1200	1100	208
502.391		118	100	≈ 50
765.772		272	260	≈ 50
867.255		500	480	≈ 50

B. High pass filter damper

The characteristic of the high-pass filter was measured before it was mounted to the 6 inch cavity. With four 50 Ω resistors, the cut-off frequency was measured to be 150 MHz with a passband ripple of ± 1.5 dB and an attenuation of 50 dB at 50 MHz. A peak was observed at 187.9 MHz which was 3 dB above the passband ripple. This is due to the fact the element values of the constructed filter was different from the values of Figure 3. Figure 5 shows the undamped and damped response of the cavity and the filter from 1 to 1000 MHz. Quality factor for all the HOMs up to 500 MHz was reduced by a factor of 100 or more and for the HOMs lying between 500 MHz and 1 GHz, Q was reduced by at least a factor of 10. The shunt impedance for all the HOMs was below 1 k ohms. Only 1 % of Q at the fundamental frequency is lost due to the filter. The filter has also been tested for broad band operation by varying the cavity frequency without altering any filter parameters. The results show desired broad band characteristic of the filter.

IV. CONCLUSIONS

The reentrant cavity damps all the HOMs effectively however the power loss (loss of Q) at the fundamental frequency is very high. On the other hand the high-pass filter damper may lower the Q at the highest booster operating frequency to a maximum value of 5%. This new type of higher order mode damper employing a high pass filter in a coaxial structure is unique and couples very little power at the operating frequency. The final version of the filter is now being fabricated to operate at a gap voltage of 60 kV for the ferrite tuned booster cavity. This filter can also be used for a cavity operating at a single frequency. The practical limit of such a coaxial filter is about 1 GHz.

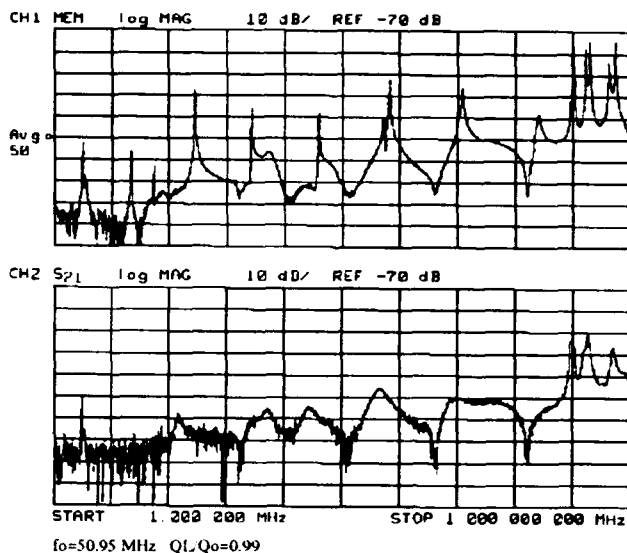


Figure 5. Undamped and damped response of the high-pass filter damper and the cavity.

V. ACKNOWLEDGMENTS

The author wishes to thank Roger Poirier for many stimulating discussions on the dampers and Peter Harmer for fabrication of the damper cavities.

VI. REFERENCES

- [1] R. L. Poirier, T. A. Enegren and I. Enchevich, "AC bias operation of the perpendicular biased ferrite tuned cavity for the TRIUMF KAON factory booster synchrotron," Conference Record of the 1991 IEEE Particle Accelerator Conference, Vol. 5, pp. 2943-2945.
- [2] W. R. Smythe, T. A. Enegren and R. L. Poirier, "A versatile rf cavity mode damper," Proceedings of the 2nd European Particle Accelerator Conference, Vol. 1, pp. 976-978 (1990).
- [3] W. R. Smythe, C. Fredrichs and L. S. Walling, "Proton synchrotron rf cavity mode damper tests," Conference Record of the 1991 IEEE Particle Accelerator Conference, Vol. 1, pp. 643-645.
- [4] A. K. Mitra, "A prototype HOM damper cavity for KAON booster," TRIUMF KAON factory project definition study, Design Note TRI-DN-92-K219.
- [5] A. K. Mitra, "Realizing a new concept of HOM damper using a high-pass filter," TRIUMF KAON factory project definition study, Design Note TRI-DN-92-K218.

Design and Fabrication of a Ferrite-lined HOM Load for CESR-B*

D. Moffat, P. Barnes, J. Kirchgessner, H. Padamsee, J. Sears, M. Tigner,
A. Tribendis[‡], V. Veshcherevich[‡]

Laboratory of Nuclear Studies, Cornell University, Ithaca, NY 14853-5001

Abstract

The beam tubes on the CESR-B cavity have been designed so that all of the higher order modes (HOM's) will propagate out of the cavity. To damp these modes to Q values of ~ 100 , we have proposed the use of HOM loads that are an integral part of the beam tube, though located outside the cryostat. The absorbing medium is ferrite tiles which are bonded to the inside of a 304 series stainless steel water-cooled jacket.¹ The bonding agent is an alloy which melts at $\sim 220^\circ\text{C}$. This alloy provides good thermal, as well as electrical, conductivity. Calculations indicate that these loads will provide the necessary damping and measurements using full-size models have verified this. It is anticipated that each HOM load for CESR-B will have to absorb 10-20 kW of beam induced power. High power tests of a scale model of the CESR-B load have been performed. The full-size load awaits final construction to be followed by testing.

I. INTRODUCTION

CESR-B is the culmination of a proposed series of upgrades to the Cornell Electron Storage Ring. Each cavity in this asymmetric collider will have an HOM load located just outside the cryostat on either end of the cavity. The large beam tubes of the cavity function as the HOM couplers (for more on the cavity design see [1]). In the low energy ring of CESR-B each load must absorb 14-24 kW ($13\text{-}23\text{ W/cm}^2$) of HOM power. The Q's of the HOM's with high R/Q's must be less than ~ 100 .

Each HOM load is a composite structure consisting of RF absorbing tiles bonded to a water cooled 304 SS shell. The end view of a load is shown in Figure 1. The back surface of the tiles is ground to a radius $0.005''$ (0.13 mm) smaller than the inner radius of the shell; the inside surface of the tiles is planar. The tiles are $0.125''$ thick at the thickest point, $\sim 0.063''$ (1.6 mm) at the thinnest. A helical winding forces the cooling water to flow around the jacket.

A lossy ferrite will be used as the RF absorbing material. The chosen ferrite must: 1) suitably damp the HOM's; 2) be amenable to bonding to a metallic substrate; 3) not break during fabrication or under RF load; 4) be UHV compatible; 5) be dust free; 6) have some DC conductivity to prevent the buildup of charge due to stray particles. Items 4, 5 and 6 are

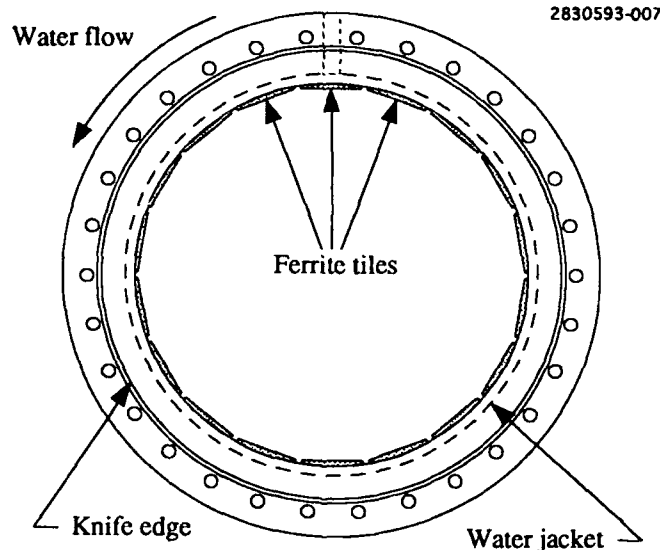


Figure 1. End view of the HOM load. The tiles are radiused on the outside surface only.

required because the loads are on the beamline. We have identified three potential materials, described in Table I.

Table I
Potential RF Absorbing Ferrites for Use in CESR-B

Ferrite	DC Resistivity ($\Omega\text{-cm}$)	Tensile Strength (ksi)
Ferrite-50 ²	10-100	$\sim 4.3^\dagger$
TT2-111R ²	4 - 100,000	59 ± 5
CMD-10 ³	1000	13 ± 4

[†] The presence of microcracks throughout sintered Ferrite-50 pieces makes this number very unreliable.

II. HOM DAMPING CAPABILITY

The effectiveness of HOM damping by the loads may be either measured or calculated. Because the properties of the ferrites are frequency dependent, damping measurements must be made on full-scale models in order to be relevant. The damped Q's of the monopole modes may be calculated using SEAFISH [2]. Lossy materials are accommodated in SEAFISH

* Work supported by the NSF and the US-Japan collaboration

[‡] Visiting scientist from the Institute of Nuclear Physics, Lavrentev Avenue 11, Novosibirsk, Russia 630090

¹ This process was developed by Reasearch & PVD Materials Inc., Ridgefield, NJ 201-943-1650

² Product of Trans-Tech Inc., Adamstown, MD 301-695-9400

³ Product of Ceramic Magnetics Inc., Fairfield, NJ 201-227-4222

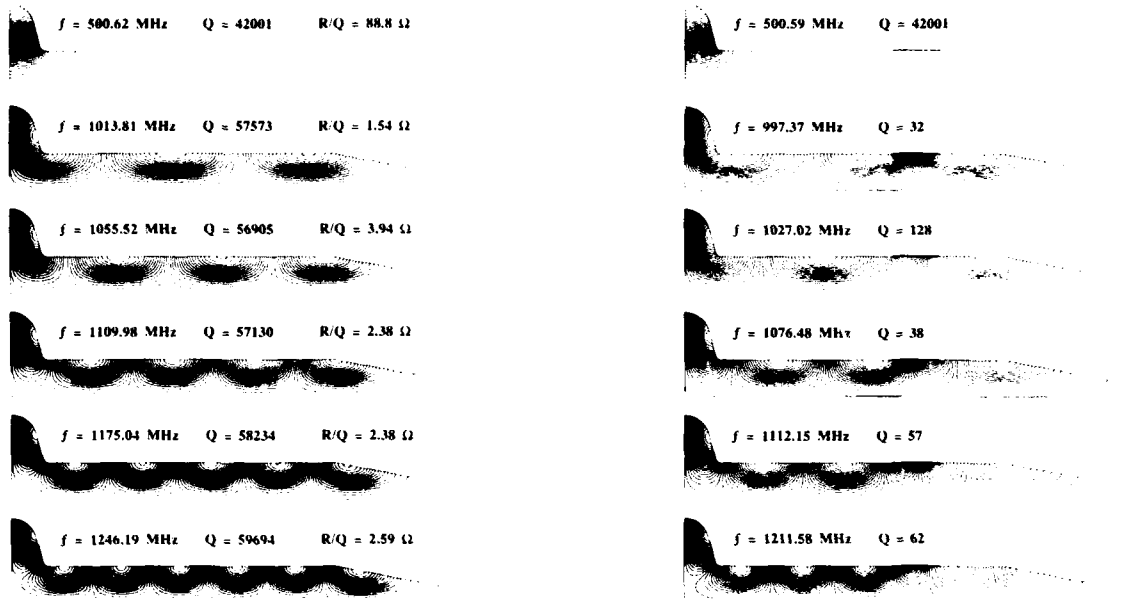


Figure 2. Calculated field patterns of the undamped and damped monopole HOM's. These modes have the highest R/Q's. The RF absorbing material was TT2-111R. The undamped modes were calculated using SUPERFISH, the damped modes using SEAFISH.

through the use of a complex ϵ and μ . It is, therefore, necessary to know ϵ and μ as a function of frequency for each ferrite. These parameters have been measured for several ferrites and are reported in another work [3]. Examples of the field patterns of undamped and damped modes are shown in Figure 2.

A comparison of measurements using a full-scale copper cavity and SEAFISH calculations is given in Figure 3. TT2-111R was the RF absorber in both cases. The measured Q's for the undamped higher order modes are lower than the calculated values because of joint losses. The agreement for the damped Q's is quite good. The results of damping on the dipole and quadrupole modes is given in another work [4].

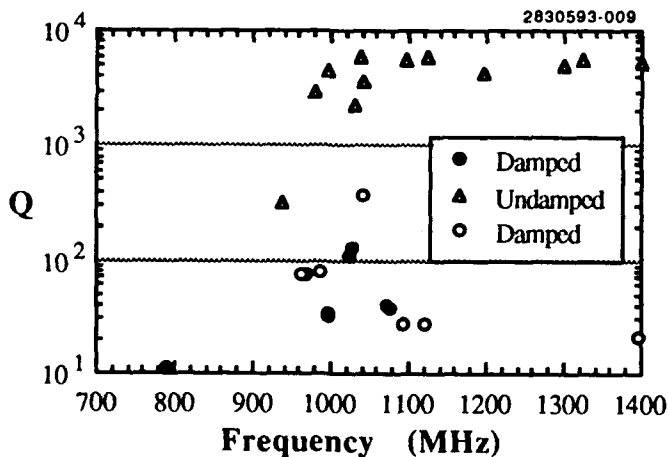


Figure 3. A comparison of measured (open symbols) and calculated (filled symbols) Q's for the monopole HOM's. The RF absorber was TT2-111R.

III. BONDING

Copper-silver based brazing alloys have limited usefulness for this application. The vacuum brazing ensures that the ferrite will be well-outgassed, but it may cause severe oxygen loss in the ferrite [5]. A through-transmission ultrasonic image of a piece of TT2-111R brazed to 410 SS is shown in Figure 4. Any break in the ultrasound path appears as a dark region in the image. A subsequent SEM examination of this sample in cross-section showed that some regions of the ferrite were not wet by the braze alloy. In other regions the wetting was good, but the ferrite cracked a grain away from the joint. It is presumed that this cracking was caused by the stresses produced when the composite was cooled to room temperature after brazing.



Figure 4. Through transmission ultrasonic image of TT2-111R brazed to 410 SS. The bright areas indicate a good bond. The sample dimensions are $\sim 0.5'' \times 1.0''$ ($\sim 13 \times 25$ mm).

Tiles of Ferrite-50, TT2-111R and MN67 (another ferrite from Ceramic Magnetics) have been successfully bonded to 304 SS using a low temperature soldering process.¹ An ultrasonic image of TT2-111R soldered to 304 SS is shown in Figure 5. In this process, the ferrite is metallized and then "tinned" with the solder without the use of flux. The stainless steel substrate is plated with ~ 0.0005 " ($\sim 13 \mu\text{m}$) of electroless nickel. To prevent oxidation problems and to further avoid the use of flux, tin is plated to a thickness of ~ 0.0001 " ($\sim 2.5 \mu\text{m}$) on top of the nickel. The pieces are then clamped together and heated to $\sim 250^\circ\text{C}$. The low temperature required by this process has an advantage in that it does not affect the electromagnetic properties of the ferrite. It also makes the fixturing required for fabrication relatively simple. The disadvantage is that it limits the temperature one may use for vacuum outgassing.

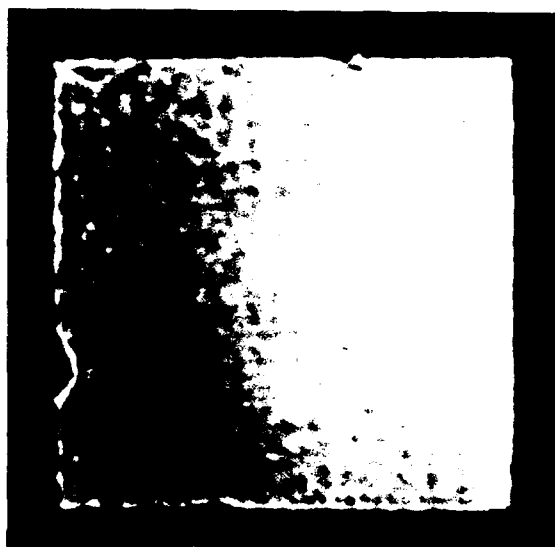


Figure 5. Through-transmission ultrasonic image of TT2-111R soldered to 304 SS. The contrast was increased in this image to visualize the mottled intensity caused by thickness variations in the solder joint. The sample dimensions are ~ 1 " x 1 " (~ 25 x 25 mm).

IV. POWER HANDLING CAPABILITY

A scale model of the load was tested under high RF power. The load consisted of eight 0.6 " x 2.0 " (~ 15 x 51 mm) tiles of TT2-111R ferrite soldered to a water cooled 304 SS jacket. This load was used as the outer conductor of a 1.625 " rigid coaxial line. RF power up to 800 watts was supplied by a 2450 MHz magnetron.

With this apparatus a power density of $\sim 10 \text{ W/cm}^2$ on the ferrite surface could be achieved. The ferrite tiles suffered no ill effects, i.e. they did not crack or fall off. The power absorption was roughly linear, implying that ϵ and μ are not field dependent, at least up to these fields.

Cooling water at an input temperature of 30°C will flow through the full-size load at a rate of ~ 10 gpm. Under these

conditions, the ferrite temperature is expected to rise to $\sim 80^\circ\text{C}$ when the absorbed HOM power is ~ 20 kW.

V. UHV COMPATIBILITY

We have opted to pre-bake the tiles at a high temperature before bonding them to the load shell in order to drive off the major vacuum contaminants. This is done after all of the grinding and cleaning operations. The bake cycle that has been recommended [6] for TT2-111R is as follows: ramp at 100°C/hr to 900°C ; hold for two hours; ramp to room temperature at 100°C/hr . The firing must be done in air in order to prevent dissociation of the ferrite. We have followed this procedure and have found no significant change in the ϵ and μ of a sample. Following this firing, the tiles will be handled in a clean, dry manner when soldered to the load shell. The fully assembled load will receive a low temperature vacuum bake if necessary.

It should be noted that the TT2-111R ferrite has been used in the ACOL Ring at CERN with good results [7]. Several square meters have been operating in a vacuum of 10^{-11} torr. The tiles were baked at 250°C .

VI. SUMMARY

This approach to HOM damping appears to supply the damping required for stable operation of superconducting cavities in CESR-B. We have identified at least one complete fabrication path. Crucial to the success of load fabrication was the development of the low temperature soldering process. RF testing has been successfully completed up to a power density of $\sim 10 \text{ W/cm}^2$, approximately half that expected in CESR-B. A full scale load is being completed and will be tested this summer.

V. REFERENCES

- [1] H. Padamsee, et al., "Accelerating Cavity Development for the Cornell B-Factor, CESR-B", *Conference Record of the 1991 Particle Accelerator Conference*, Vol. 2, pp. 786-788, San Francisco, CA, May 1991
- [2] SEAFISH is a complex version of SUPERFISH. SEAFISH was written by Mark de Jong, AECL Research, Chalk River Laboratories, Chalk River, Ontario, Canada K0J 1J0. SUPERFISH was written by R.F. Holsinger and is maintained by AT-6 Division, M.S. H829, Los Alamos National Laboratory, Los Alamos, NM 87545.
- [3] W. Hartung, D. Moffat, T. Hays, *Measurements of the Electromagnetic Properties of Some Microwave-Absorbing Materials*, Internal Report SRF-930113/01, Laboratory of Nuclear Studies, Cornell University.
- [4] V. Veshcherevich, et al., *Higher Order Modes Damping in CESR-B Cavity*, Internal Report SRF-920701-04, Laboratory of Nuclear Studies, Cornell University.
- [5] Mark deJong, AECL Research, Chalk River, private communication.
- [6] Lou Domingues, Trans-Tech, private communication.
- [7] Fritz Caspers, CERN, private communication.

HIGH-BETA LINAC ACCELERATING STRUCTURE

V.G.Andreev, G.I.Batsikh, B.I.Bondarev,
B.P.Murin

Moscow Radiotechnical Institute of Russian Academy of Sciences
Russia, 113519, Moscow, Varshavskoe shosse, 132

Introduction

At the present time the two sets of thetypical parameters of the proton high-current high-energy linac are considered. The first one with the beam energy of 1.5 GeV and average current of 0.3 A serves for the transmutation of long-living radioactive wastes of atomic power engineering (ATW Program). The second one with the energy of 800 MeV and average current of 10 mA belongs to the conversion program ABC of war plutonium utilization. There are sets of parameters (for example one of Los-Alamos projects: 800 MeV, 140 mA), which occupy intermediate position within the aforementioned limits.

The basic problem for all parameter configurations is the selection of accelerating structure for high-energy linac part because this choice influence on linac manufacture, exploitation and reliability.

The D&W accelerating structure invented in MRTI was used in 100-600 MeV energy range for Moscow Meson Facility (MMF). This structure is also preferable for the above designs.

1. Comparison Between High-Beta Accelerating Structure

The main part of the burner-reactor linac used in the USA, Russia and Japan projects is based on resonators divided into sections with magnetic quadruple lenses (doublets or single) between them. Each resonator is fed from a separate generators.

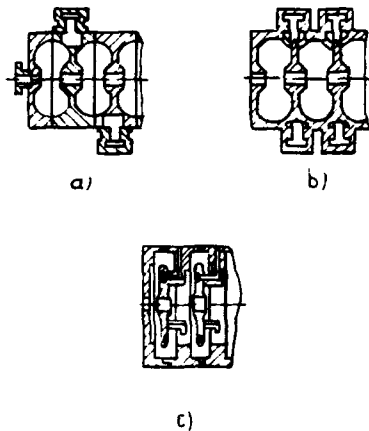


Fig. 1
a) SCS b) RCS c) D&WS

In Fig. 1 the three types of accelerating structures are shown: with side-coupling cells (SCS), with ring coupling cells (RCS), disk and washer structure (D&WS). All the structures operate at a $\pi/2$ wave, so that in neighboring accelerating cells RF fields have opposite signs.

These three structures have approximately the same value of shunt impedance. The disk and washer structure's effective shunt impedance as a function of beta is shown in Fig 2.

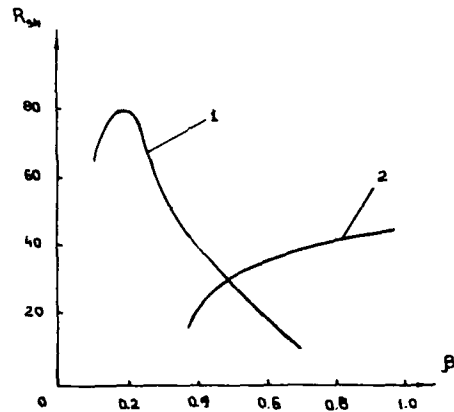


Fig. 2
Shunt impedance of Alvarez (1) and D&W (2) structures
as a function of beta

The coupling coefficient between the neighboring cells is an important characteristic of the accelerating structure. As it increases, sensitivity of the resonators accelerating field distribution to various perturbations (geometrical errors included) decreases. The combination of the two characteristics (shunt impedance and coupling coefficient) shows that the disk and washer structure is the most suitable for the main linac part. As it is clear from the Table 1, it has a number of advantages over other structures belonging to the same energy range [1,2].

The design of D&WS resonator is shown at Fig 3.

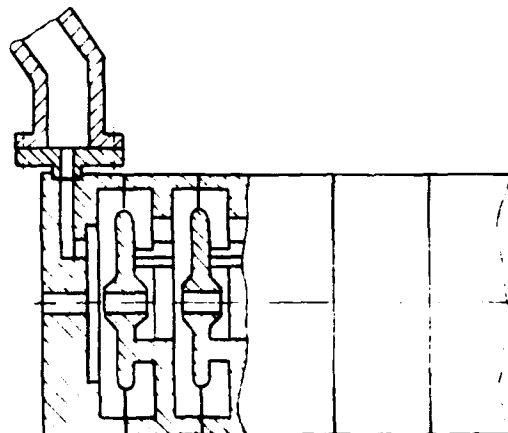


Fig. 3.

Table 1

Comparable Performances

Side Coupled Structure

D&W Structure

I. Coupling Coefficient

$$K_c = 5\%$$

1. Highly sensitive to errors caused by manufacturing and inaccurate tuning.
2. Individual tuning of each cell ($\Delta f = \pm 30$ kHz)

$$K_c = 30-50\%$$

The same sensitivity is less by 40-100 times.
The cavity may be tuned as a whole unit without tuning of separate cells.
($\Delta f = \pm 800$ kHz)

II. Efficiency of RF Power Use for Providing a given rate of acceleration

Approximately equivalent

III. Proximity of Parasitic modes

Parasitic modes in structure band are not available

Parasitic modes of the Moscow Meson Factory are spaced by $\pm(15-20)$ MHz out of operation frequency

IV. Bridging Devices

Mechanical rigid coupling with acceleration section: accuracy of manufacturing is about 0.01 mm.

Mechanical uncoupled with acceleration sections: accuracy of manufacturing is 2-3 mm.

V. Vacuum conductance

Insufficient:
Vacuum collector is required.

High:
Vacuum collector isn't necessary

VI. Design and technology of manufacturing

It is complicated with regard to design and technology

Design and technology are simple.

RCS has the same features

Besides many advantages, D&W structures in its initial variant had a defect which first seemed to be substantial and prevented its propagation. The fact is that the operational oscillations mode was surrounded with a number of parasitic modes having the azimuthal field variation. The frequency of which with the growth of b shifted, finding itself in close neighborhood or even coinciding with the operational frequency. Such neighborhood is extremely undesirable. In this case the operational mode frequency depends on the coupling with inoperational modes, the RF power losses in the structure grow, the operation of various automatic control systems is impeded, the beam stability is endangered and so on.

Shifting of inoperational oscillations frequency from the operational one was affected in a way, which did not cause field (frequency) perturbation of the operational mode, using combined slits (Fig. 4), cut in washers [3].

Frequency spectra around the operational mode without slits (a) and with them (b) are shown in Fig. 5.

Disk and washer resonators, consisting of four sections coupled with bridges, are used in the Moscow Meson Facility (MMF) linac. They ensure stable acceleration of the beam.

The resonators in the main part of the burner-reactor linac will consist of large number of sections coupled with bridges. For example in MRTI project the resonator consists of eight sections. Bridges are manufactured of pieces of standard waveguide with the rectangular cross-section (220x104 mm)

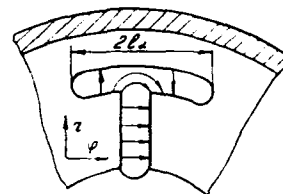
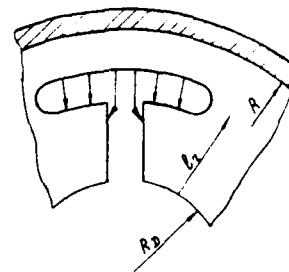


Fig. 4
Excitation of combined slit electromagnetic oscillations with the help of operation wave (top) and parasitic wave (bottom)

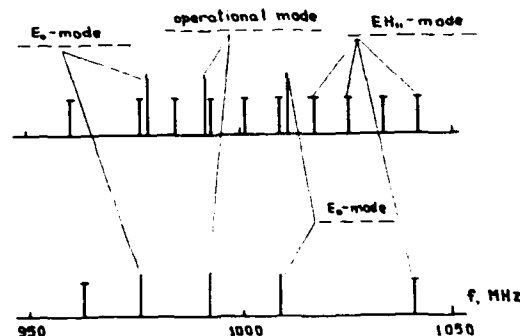


Fig. 5
Resonator electromagnetic oscillation spectrum of D&W before and after application combined slits into disk

The dispersion characteristic of a resonator (Fig. 6), consisting of eight accelerating sections and seven bridges has fifteen oscillation modes, of which the two nearest to the operational one are spaced at 1 MHz from it, at a distance 8 times as large as the passband of a resonator with the lowest quality factor. It is quite enough to ensure the stable linac operation.

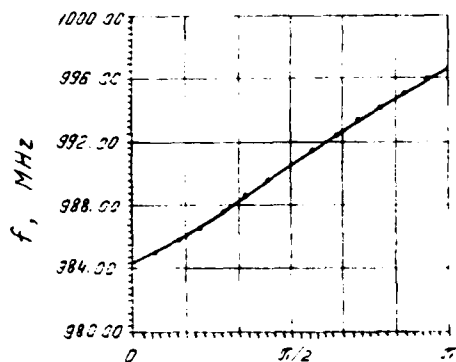


Fig. 6
Dispersion characteristic of resonator

The overall number of accelerating sections in the linac with the output energy of 1.5 GeV and acceleration rate 1 MeV/m is equal to 610, the number of resonators - 77, bridges - 540. The RF power of about 490-500 MW must be fed into resonators, of which 40-50 MW will be lost in resonators walls and 450 MW will be transferred to the beam.

For focusing in the main linac part are used 612 quadrupole lenses of permanent magnets placed between resonators and their accelerating sections. Side by side with the FODO focusing structure which is taken as basis, FDO structure is considered too. Choice of the optimum structure will be made later.

Each resonator of the main linac part is fed from one regotron having seven energy outputs with the overall output power of 5 MW [3.5]. The typical linac module is shown in Fig. 3 [2.3]. The module is designed to operate with energy gain of 15 MeV and cw current of 300 mA.

2. The Outlook for the Modification of the Main ATW Linac Part

Further modification of the main linac part (the increase of the focusing channel acceptance, facilitation of radiation pureness problem) may be ensured with the aid of superconducting solenoids and resonators not divided into sections.

The latest MRTI design is based on the proposals of 1972-1974 years, presented in [6.7], which show that focusing by a strong longitudinal magnetic field allows to increase the acceptance of the focusing channel with the same aperture and to reduce its sensitivity to random errors.

The channel acceptance V is:

$$V = \frac{\nu_{\min} \cdot R^2}{L_f} \cdot \beta \gamma$$

where R is the channel aperture radius, ν_{\min} - minimum within the limits of a focusing period unitless transverse oscillations frequency, L_f - focusing period length, β - relative particles velocity, γ - relativistic factor.

With the strong longitudinal field focusing ν is equal to 1.0-1.4, while with the quadrupole focusing this value does not exceed 0.6. Therefore the acceptance with the longitudinal magnetic field focusing is 1.5-2 times as large as that with the quadrupole focusing at the same channel aperture.

In the main part of the burner reactor linac with quadrupole lenses focusing the average ν_{\min} is equal to 0.6. The transverse magnetic field focusing with the same channel

aperture ensures $\nu_{\min} = 1$. The increase of ν_{\min} by factor of 1.7 at the fixed beam emittance results in the reduction of its radius by 30%. The possibility of such a considerable decrease of the aperture radius allows either to improve radiation pureness of the main linac part or to decrease by 20% the RF power losses. With the focusing period length of 200 cm at the energy of 100 MeV and 350 cm at the energy above 600 MeV the magnetic field intensity will amount to 4-6 T. Solenoids producing such fields may be constructed only with the use of superconductivity.

The beam of particles in a channel with solenoids is less susceptible to random errors influence [5]. There are two variants of positioning superconducting solenoids:

1. Solenoids are placed between accelerating sections in the place of quadrupole doublets. The aperture of a "warm" solenoid is small and its construction is relatively simple.

2. Solenoids are ring-shaped with big "warm" aperture inside which is placed the accelerating structure. Though such a structure is unwieldy, this variant is attractive, since the accelerating focusing channel acquires a number of useful qualities:

a) Absence of coupling bridges between accelerating sections increases the coupling coefficient for DaW structure up to 50%. The nearest to the operational mode couple of side modes is shifted away from it by about ± 2 MHz (instead of 1 MHz in an 8-sectioned resonator).

b) Overall reduction of RF power losses in the accelerating structure amounts to 10% as compared with an 8-sectioned resonator having the same aperture radius.

c) Owing to the absence of spaces between accelerating sections, the main linac part length gets shorter by about 25%.

d) The focusing periods length may be chosen irrespective of the length of accelerating sections, which allows to prevent the beam radius growth caused by abrupt changes of focusing period length in those places where the accelerating field frequency or focusing channel structure are changed.

References

1. Accelerating Complex for Mean Energy Physics (Meson Facility). Proc. of Radiotechnical Institute, No.16, Moscow, 1974.
2. V.G.Andreev, G.I.Batsikh, B.I.Bondarev, A.P.Fedotov, B.P.Murin, A.A.Vasiliev. High-P Linac Design.
3. B.P.Murin. The Prospect for High-Power Ion Linear Accelerator Construction for Energy Function. Moscow Radiotechnical Institute. Preprint No.9210, 1992.
4. V.G.Andreev, V.M.Belugin et al. Parasitic Modes Removal out of Operating Mode Neighborhood in the DaW Accelerating Structure - IEEE Trans. on Nucl. Sci., v NS-30, No.4, 1983, p.3575-3577.
5. A.P.Durkin, B.P.Murin, O.Yu.Shlygin, I.V.Shumakov. Super-Power RF Regotron-Type Generator for Linear Accelerators with High Mean Current. - Proc. of the 1990 Linear Accelerator Conf., Albuquerque, New Mexico, 1990, p.584-586.
6. B.P.Murin, B.I.Bondarev et al. Random Perturbations of Proton Transverse Motion in Linac with Superconducting Solenoid Focusing. - Proc. of Radiotechnical Institute USSR AS, 1974, No.16, p.336-341.

Design of a 90° Overmoded Waveguide Bend*

C. Nantista^o, N. M. Kroll[†] and E. M. Nelson
Stanford Linear Accelerator Center
Stanford University, Stanford, CA 94309 USA

Abstract

A design for a 90° bend for the TE₀₁ mode in overmoded circular waveguide is presented. A pair of septa, symmetrically placed perpendicular to the plane of the bend, are adiabatically introduced into the waveguide before the bend and removed after it. Introduction of the curvature excites five propagating modes in the curved section. The finite element field solver YAP is used to calculate the propagation constants of these modes in the bend, and the guide diameter, septum depth, septum thickness, and bend radius are set so that the phase advances of all five modes through the bend are equal modulo 2 π . To a good approximation these modes are expected to recombine to form a pure mode at the end of the bend.

I. INTRODUCTION

Some designs for the Next Linear Collider[1] (NLC) transmit power from the source (a klystron or the output of a pulse compressor) to the accelerator structure in the TE₀₁ mode of overmoded circular waveguide in order to have small transmission loss. The waveguide run from the source to the accelerator includes some 90° bends. Ideally these bends would be loss-less.

Two algorithms and some results are presented for the design of one type of overmoded waveguide bend. A curved section of waveguide connects two straight sections as shown in Figure 1a. The curvature in the bend is constant so the waveguide follows a 90° arc with radius of curvature ρ_c between the two straight sections. The cross-section of the waveguide is uniform throughout the curved section, but the cross-section is not simply a circle. The cross-section and radius of curvature ρ_c will be chosen so that the incoming wave propagates through the curved section with negligible mode conversion. This is the principal form of loss considered here. Reflection and wall losses are only considered heuristically. The straight sections are adiabatic tapers from and to circular waveguide.

II. TELEGRAPHIST'S EQUATION

Curvature in overmoded waveguide causes coupling between the straight guide modes. Such coupling is afforded by the generalized telegraphist's equations[2], which have been applied to curved circular guide[3]. In terms of the forward and backward wave amplitudes, a_n^\pm , these are

$$\frac{da_m^\pm}{dz} = \mp i \sum_n (C_{mn}^\pm a_n^+ + C_{mn}^\mp a_n^-), \quad (1)$$

* Work supported by U.S. Department of Energy contract DE-AC03-76SF00515 and grants DE-FG03-92ER40759 and DE-FG03-92ER40695.

^o Visitor from Department of Physics, UCLA, Los Angeles, CA 90024.

[†] Also from Department of Physics, UCSD, La Jolla, CA 92093.

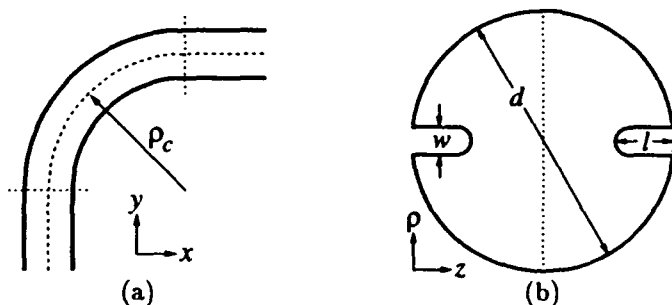


Figure 1. Outer geometry (a) and cross-section (b) of the bend. The cross-section's dashed line is a symmetry plane.

where $C_{mm} = \beta_m$ are the propagation constants and the other C_{mn} involve inner products of the transverse fields.

The power transfer between two modes in a curved section is limited by the difference in their propagation constants. The TE₀₁-TM₁₁ degeneracy presents a problem, so the degeneracy is split by introducing partial septa perpendicular to the bend plane as shown in Figure 1b. The modes can no longer be found analytically, but the β_m can be computed using SUPERFISH[4].

If $\rho_c \gg d/2$ then the coupling is weak and the TE₀₁-like mode amplitude varies little along the bend. A small amount of power will beat in and out of the n th coupled mode in an arc length $l_b \simeq 2\pi/|\beta_n - \beta_o|$, where o indicates the TE₀₁-like mode. The interaction with each mode cancels when the relative phase advance is a multiple of 2 π . By adjusting the cross-section and ρ_c , the β 's are manipulated so that the three propagating modes coupled to first order all beat out at the end of the 90° bend.

This is the approach first taken. However, a compact bend which cannot rely on the above assumption is desired. As the coupling coefficients become comparable to the mode spacings, the beat lengths are altered, and modes coupled to second order may be important. The coupling coefficients C_{mn} are required to verify parasitic mode suppression at the end of the bend. Since the C_{mn} are not easily obtained from the field solver, a different approach was taken.

III. MODES IN CURVED GUIDE

A curved guide can be treated as a portion of a cylindrically symmetric structure. For the 90° bend the structure starts at $\phi = 0$ and ends at $\phi = \pi/2$. The fields in the waveguide can be decomposed into modes with azimuthal dependence $e^{im\phi}$. In the axisymmetric waveguide paradigm the waves propagate along ϕ with propagation constant m . Compare this with the phase $e^{i\beta z}$ for waves propagating along z with propagation constant β in straight waveguides. The curved guide does not close on

itself so there is no requirement that m be an integer.

The finite element field solver YAP[5] is capable of computing the frequencies of the modes of axisymmetric structures for any real m . Non-integral m is allowed. YAP was used to compute dispersion diagrams for curved guide with various cross-sections. One such dispersion diagram is shown in Figure 2. A dispersion diagram for curved guide looks similar to dispersion diagrams for straight guide. However, the simple dispersion formula $\omega^2/c^2 = k_c^2 + \beta^2$ for a straight waveguide containing no media does not apply to curved guide. This can be seen best in figure 2, where the dispersion curves are not parallel lines. A power series of the form

$$\frac{\omega^2}{c^2} = k_c^2 + \alpha_1 \left(\frac{m}{\rho_c}\right)^2 + \alpha_2 \left(\frac{m}{\rho_c}\right)^4 + \dots \quad (2)$$

approximates the dispersion curves well. The cutoff k_c^2 and the coefficients α_i depend on ρ_c and on the cross-section Ω of the guide. When ρ_c is large then $\alpha_1 \cong 1$ and the cutoffs k_c^2 are approximately the same between straight and curved guide with the same cross-section. In the large ρ_c limit the two approaches described in this paper are equivalent.

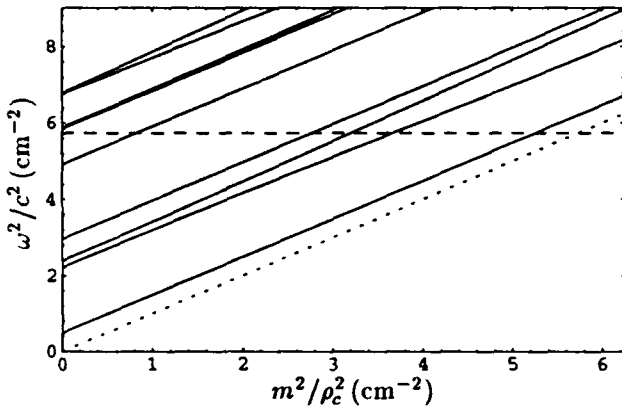


Figure 2. Dispersion diagram of the curved guide for the first design listed in Table 1. The dashed line is the drive frequency 11.424 GHz. The dotted line corresponds to the speed of light along the center of the guide.

IV. SCATTERING AT THE INTERFACE

There is potentially some reflection at the interface between the straight waveguide and the curved waveguide. A generalized scattering matrix S_i for the propagating modes in the straight and curved guides can be constructed.

As an example, the scattering matrix for the straight-to-curved interface in an overmoded rectangular H-plane waveguide bend was computed using a mode-matching method. Only TE_{n0} modes were considered so the fields are uniform vertically. In the straight guide propagating along y the modes are $E_z \propto \sin(2\pi nx/w)$ where $0 \leq x \leq w$ is the horizontal domain of the waveguide. In the curved guide the modes involve Bessel functions. They are $E_z \propto AJ_m(k\rho) + BY_m(k\rho)$ where $\rho_c - w/2 \leq \rho \leq \rho_c + w/2$

and $k = \omega/c$ is the drive frequency. Note that m is real for propagating modes and imaginary for evanescent modes.

The boundary conditions $E_z = 0$ at $\rho = \rho_c \pm w/2$ yield a characteristic equation for the propagation constants m . Solutions were obtained by numerically integrating Bessel's equations and using a shooting method to match the boundary conditions. This yielded numerical values for m^2 for both propagating ($m^2 > 0$) and evanescent ($m^2 < 0$) modes. The field E_z for each mode was obtained similarly.

The normalized generalized scattering matrix S_i was computed for an example with $w/\lambda = 1.36$ and $\rho_c/\lambda = 3.87$, where λ is the free space wavelength. There are two propagating modes in the guides. Using 14 modes for the field expansion on each side of the interface, the computed scattering matrix for the interface is

$$S_i = \begin{bmatrix} 4 \cdot 10^{-3} \angle -8^\circ & 8 \cdot 10^{-4} \angle -2^\circ & 0.982 & 0.190 \\ 8 \cdot 10^{-4} \angle -2^\circ & 8 \cdot 10^{-4} \angle -12^\circ & -0.190 & 0.982 \\ 0.982 & -0.190 & 3 \cdot 10^{-4} \angle -4^\circ & 8 \cdot 10^{-4} \angle -4^\circ \\ 0.190 & 0.982 & 8 \cdot 10^{-4} \angle -4^\circ & 6 \cdot 10^{-4} \angle -8^\circ \end{bmatrix} \quad (3)$$

where $[a_{s1}, a_{s2}, a_{c1}, a_{c2}]^T$ is the incoming wave vector. The wave amplitudes a_{sn} and a_{cn} are for the modes in the straight and curved guides, respectively.

Notice that the reflection amplitude is less than 10^{-3} . If one assumes the reflections are similar for bends with different cross-sections but similar curvature, then reflection at the straight-to-curved interface can be neglected. The reflected power will be negligible as long as resonances are avoided. The principal concern, then, is mode conversion.

V. AROUND THE BEND

The scattering matrix S_b for a bend over angle ϕ_b can be easily computed given S_i for the straight-to-curved interface and the propagation constants m_1 and m_2 for the two propagating modes in the curved guide. The example above has $m_1 = 22.85$ and $m_2 = 16.18$. The next mode is evanescent with $m_3 = i11.38$. The transmission coefficient for the (straight guide) fundamental mode for various bend angles ϕ_b was computed. At $\phi_b = 2\pi/(m_1 - m_2) = 0.941$ the transmission is nearly perfect. At this bend angle the two propagating waves in the curved guide arrive at the output end of the bend with the same relative phases they had at the input end of the bend. The propagating field at the output is the same as at the input except for an overall phase, so waves are faithfully transmitted through the bend with no mode conversion.

The evanescent waves at the interfaces have decayed sufficiently in the curved guide so that they can be neglected in the transmission calculations for $\phi_b = 0.941$.

This example leads to the principal design criterion for this type of overmoded waveguide bend: the phases $e^{im\phi_b}$ must be identical for all modes propagating in the curved guide. In addition, evanescent modes should be sufficiently above cutoff so that they decay well over the length of the bend, and thus can be neglected.

Table 1
90° Overmoded Waveguide Bends

d (cm)	l (cm)	w (cm)	ρ_c (cm)	m_1	m_2	m_3	m_4	m_5	f_{c6} (GHz)
4.372	0.986	0.465	31.786	72.873	60.873	56.873	52.873	28.874	11.536
4.275	0.971	0.611	36.655	83.867	67.867	63.867	59.867	23.868	11.819
4.358	1.054	0.593	38.754	89.034	73.034	69.034	65.034	25.033	11.579
3.940	0.765	0.476	23.891	53.870	41.870	37.870	33.870	9.871	12.726
4.157	0.904	0.622	33.894	77.212	61.212	57.212	53.212	17.213	12.163

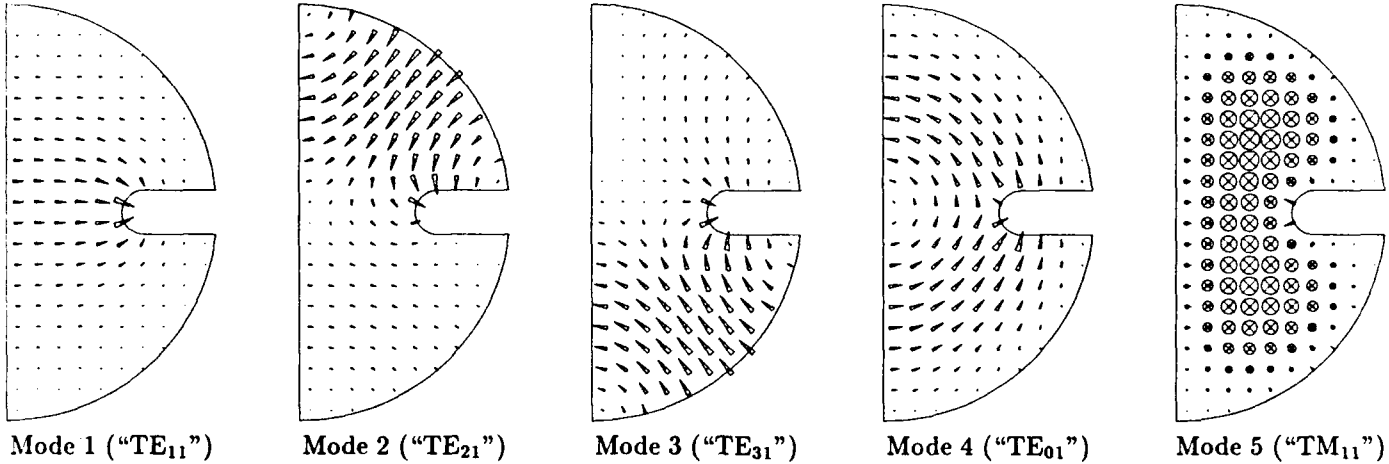


Figure 3. Electric field patterns for the five propagating modes of the first design in Table 1.

VI. 90° BEND DESIGN

Designs for a 90° bend with a cross-section as shown in Figure 1b were computed. The phases $e^{m_i\pi/2}$ for the five lowest propagating modes excited by the incoming wave can be fixed relative to each other by adjusting the four parameters: d , ρ_c , l and w . Propagating modes not excited by the incoming wave (due to symmetry) are neglected. Dispersion diagrams were computed using YAP and the bend parameters were adjusted so that the phases were the same. This corresponds to the propagation constants m_i differing from one another by multiples of 4. The cutoff ($m = 0$) frequency of higher order modes were computed in order to discard designs with more than five propagating modes at 11.424 GHz. Table 1 lists the parameters for five solutions. It also lists the propagation constants for the five lowest modes and the cutoff frequency f_{c6} for the sixth lowest mode.

The cross-section in Figure 1 and the dispersion diagrams in Figure 2 correspond to the first design in Table 1. The field patterns for the propagating modes are shown in Figure 3. At cutoff the field patterns for the modes in curved guide are similar to the corresponding modes in straight guide, but for large m the second and third modes are mixed. This is evident in the field plots and in the dispersion diagram, where it appears that the second and third curves are repelling each other. These modes arise, with the introduction of the septa, from the TE_{21} and TE_{31} modes of circular guide. The incoming wave is similar to the fourth mode, which is a TE_{01} -like mode.

The cutoff frequency for the sixth mode of the first design appears close to cutoff. The estimated propagation constant using the straight guide formula is $m_6 \cong i0.7$

and the decay amplitude over the length of the waveguide is $e^{im_6\pi/2} = 5 \times 10^{-8}$.

VII. FURTHER WORK

Further designs can be found, perhaps with smaller radii of curvature and shorter septa so that the bend will have smaller wall losses and be easier to manufacture.

A variation of the YAP field solver will compute the evanescent modes in curved guide. With these modes a mode-matching algorithm can be employed to calculate the scattering matrix S_i for the straight-to-curved guide interface, and then verify that reflections are negligible and that the design criterion is appropriate.

Calculation of the wall losses through the bend and mode-conversion losses (due to manufacturing errors) also requires knowledge of S_i in order to obtain the mode amplitudes in the bend as well as the evanescent fields near the interface.

VIII. REFERENCES

- [1] R. D. Ruth, "The Development of the Next Linear Collider at SLAC," SLAC-PUB-5729 (1992).
- [2] S. A. Schelkunoff, "Generalized Telegraphist's Equations for Waveguides," *Bell System Technical Journal*, 31, pp. 784-801, July, 1952.
- [3] S. P. Morgan, "Theory of Curved Circular Waveguide Containing an Inhomogeneous Dielectric," *B.S.T.J.*, 37, pp. 1209-1251, Sept., 1957.
- [4] K. Halbach and R. F. Holsinger, *Particle Accelerators* 7, 213 (1976).
- [5] E. M. Nelson, "A Finite Element Field Solver for Dipole Modes," SLAC-PUB-5881, 1992 *Linear Accelerator Conference Proceedings*, pp. 814-816.

Numerical Simulation of Coupler Cavities for Linacs*

C.-K. Ng, H. Deruttyer and K. Ko
Stanford Linear Accelerator Center
Stanford University, Stanford, CA 94309

Abstract

We present the numerical procedures involved in the evaluation of the performance of coupler cavities for linacs. The MAFIA code is used to simulate an X-Band accelerator section in the time domain. The input/output coupler cavities for the structure are of the symmetrical double-input design. We calculate the transmission properties of the coupler and compare the results with measurements. We compare the performance of the symmetrical double-input design with that of the conventional single-input type by evaluating the field amplitude and phase asymmetries. We also evaluate the peak field gradient in the coupler.

I. INTRODUCTION

At SLAC, we have an active program on the Next Linear Collider (NLC) R & D, and couplers are an important part of the accelerator structure work in this program. Indeed, the efficient delivery of power from RF sources such as klystrons to disk-loaded accelerator structures in linear colliders depends crucially on the coupler cavity. There are several requirements to be satisfied by such a cavity. First, it is to be well matched to the feeding waveguides (see Fig. 1) in order to couple the maximum amount of power into the structure to achieve the highest possible accelerating gradient. Second, it must be tuned to the synchronous frequency for the proper phase advance in the structure. Third, it must have minimal deleterious effect on the beam. Fourth, the couplers should ideally have surface fields no higher than the interior. These considerations, coupled with the fact that the geometry is intrinsically three-dimensional, make the design of the coupler cavity a nontrivial problem.

Previously, coupler cavities for disk-loaded accelerator structures have been designed following a set of procedures based on the Kyhl method^[1]. It involves a sequence of experiments to determine the matching and tuning. Several iterations on actual prototypes may be needed before an optimal configuration can be obtained. The effort can be time-consuming and requires substantial empirical expertise. In this paper, we study an alternative approach by numerical simulation. We build a computer model that approximates closely the coupler cavity. Since changes in dimensions can be easily implemented on the computer, this approach offers a distinct advantage over cold tests in optimizing a design. Furthermore, valuable field information such as asymmetries and peak gradients, for example, is readily obtainable numerically, which otherwise would be difficult to measure experimentally. These advantages provide the motivation for our effort to develop an accurate and reliable computational procedure for matching and tuning this particular RF component.

II. THE NUMERICAL MODEL

* Work supported by Department of Energy contract DE-AC03-76SF00515.

We model the symmetrical double-input coupler in the 30-cavity structure which was used in high power tests. Instead of all 30 cells, we simulate only a short section which is sufficient for matching the coupler and it is computationally more practical. Fig. 1 shows the mesh geometry we have constructed using MAFIA. It consists of two identical coupler cavities and two regular accelerator cavities. The coupler cavities are fed by WR90 rectangular waveguides through irises. Because the feeds are symmetrical, we only need to model one-quarter of the structure. The magnetic boundaries imposed at the two symmetry planes are consistent with the waveguide fields as well as the fields of the accelerating mode in the structure. The SLAC NLC operating frequency is chosen to be at X-band around 11.424 GHz. Accordingly, the dimensions of the regular cells in our model have been designed for that frequency at the $2\pi/3$ phase advance per cell. The dimensions of the couplers are different in order to fulfill the matching and tuning requirements described earlier.

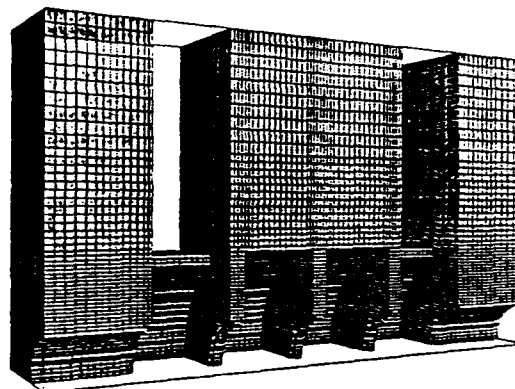


Fig. 1 MAFIA geometry for a 4-cell traveling wave section.

Given a coupler geometry, we perform a MAFIA simulation in the time domain. Power is fed continuously at the input waveguide port in the TE_{10} mode at a particular frequency, starting with a smooth initial rise and reaching 1 watt at flat-top. The input power couples to the accelerating mode via the irises, propagates through the section and exits by way of the output coupler. The simulation extends over many filling times of the section until a traveling wave at steady-state is reached. At the end of the run, the reflection coefficient S_{11} at the input waveguide port and the transmission coefficient S_{21} at the output waveguide port are evaluated. In addition, the electric field on axis and in designated regions of interest is recorded for subsequent post-processing.

III. MATCHING AND TUNING OF COUPLER CAVITY

The cross-section of the coupler cavity is shown in Fig. 2(a). There are three dimensions to be determined: the coupler diameter, the iris aperture and its thickness. Assuming that the iris thickness is held fixed, the design program is then to choose the two remaining dimensions in such a way that the matching and tuning are optimal.

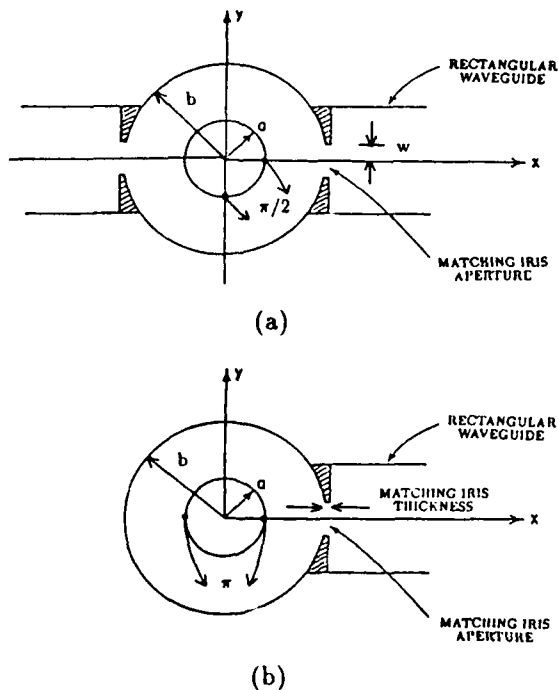


Fig. 2 Schematics of (a) symmetrical double-input coupler; (b) single-input coupler.

These conditions are assessed as follows. As far as matching is concerned, we look for the minimum VSWR for the section. In the simulation, this corresponds to the smallest reflection coefficient S_{11} at the input waveguide port. Fig. 3 shows the time history of S_{11} for a typical case when the coupler is matched. We see that the steady-state can be reached after several filling times and the amount of reflection is quite acceptable (VSWR = 1.023 in this case).

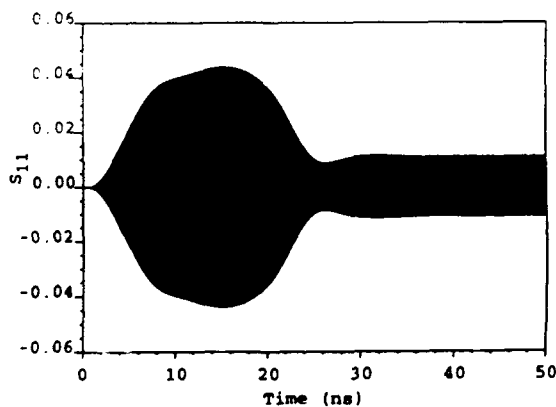


Fig. 3 The reflection coefficient as a function of time for a matched coupler

To evaluate tuning, we examine the amplitude and phase variations of the electric field on axis. One can write

$$E_T(z) = |E_T(z)|e^{-i\theta_T(z)}, \quad (1)$$

where the time variation has been left out. In the MAFIA run at steady-state, the electric field on axis along the structure is stored over several cycles which can be Fourier-analyzed to obtain E_T and θ_T . They are plotted in Figs. 4(a) and (b) for the same matched case mentioned above. The dashed lines mark the boundaries between cells. In both plots we see that the field is periodic in the

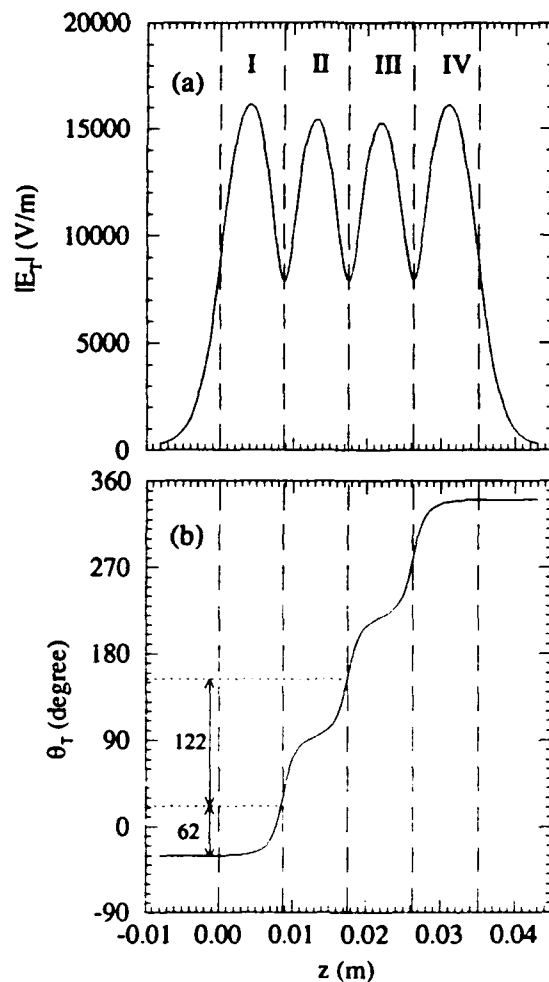


Fig. 4 Amplitude and phase variations for a matched coupler. Regions I, II & III, and IV are the input coupler cavity, the two structure cells and the output coupler cavity, respectively.

regular cells. We also notice that it is symmetric about the center of the structure which should be the case when the couplers are nearly matched. In this case the fields look identical whether power is fed in at the input or output end. The phase advance in the two regular cells is 122° , close to the expected value of 120° at the driving frequency of 11.42 GHz. In the coupler cavities, the phase variation is zero across roughly half the cavity and totals to 62° for the whole cell. This suggests that the field in the half of the coupler cavity near the cut-off beam pipe is essentially a standing wave while the traveling wave in the other half advances by half the phase shift as compared to the regular cell. These results confirm earlier data from dielectric bead perturbation measurements^[3]. As pointed out in that paper, the field amplitude and phase variations can provide a means by which the tuning of the coupler can be accurately determined. Numerically such a procedure is much easier to implement than in actual cold tests. A detailed account of the numerical procedure can be found in Ref. 4.

IV. COMPARISON WITH EXPERIMENTS

In designing the symmetrical double-input coupler for the 30-cavity section, we performed a systematic numeri-

cal search for the optimal dimensions, using the matching and tuning conditions described above. We varied the cavity diameter and iris aperture, then calculated the VSWR and phase shifts in each iteration. With the coupler dimensions that we found for optimal matching and tuning, one can vary the frequency to explore the bandwidth. Fig. 5 shows a comparison of VSWR versus frequency between the MAFIA simulations and experiments^[5]. Near the desired operating frequency of 11.424 GHz, the agreement is very good and the dimensions of the actual coupler are very close to those used in the MAFIA model. This is encouraging because it means that we can reasonably model the geometry for design purposes without expending an unrealistic amount of computational resources.

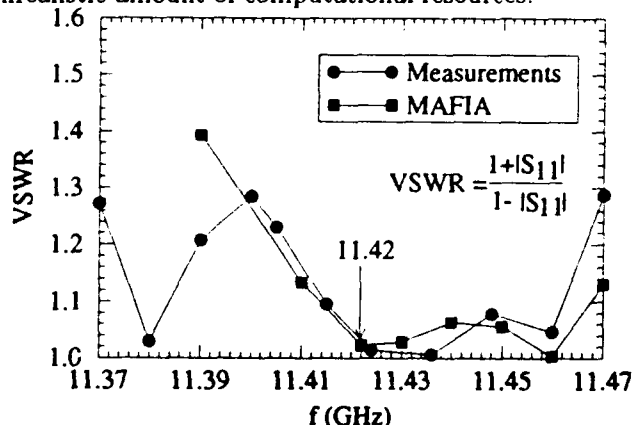


Fig. 5 VSWR versus frequency from MAFIA and measurements.

V. FIELD ASYMMETRIES IN COUPLERS

Conventional couplers are of the single-input type (see Fig. 2(b)) where power is fed in from a single waveguide. This configuration inherently introduces field asymmetries across the beam aperture in the form of a dipole component. The amplitude asymmetry leads to a shear force which spreads the bunch while the phase asymmetry results in a deflecting force on the bunch^[6]. As discussed in Ref. 6, the amplitude asymmetry can be corrected by offsetting the cavity with respect to the beam axis. The effect of phase asymmetry on the beam can be reduced by tilting the coupler cavity or by feeding successive sections from opposite sides.

In the symmetrical double-input coupler, assuming that the fields in both feeds are equal in amplitude and have the same phase, the dipole component is eliminated by virtue of symmetry. The remaining asymmetries are then due to the quadrupole component which can be measured by comparing fields at points 90° around the beam aperture (see Figs. 2(a) and (b)). In Table 1, we list the asymmetries for the single-input coupler before and after offset, and for the double-input coupler. The data for the single-input coupler are taken from Ref. 6 while those for the double-input are obtained from the MAFIA simulation of the matched case. We conclude from the results that the field asymmetry should be negligible near the beam axis in the double-input coupler. This makes it a superior design over previous single-input types. Presently, the input couplers for the 75 cm and 1.8 m structures being planned at SLAC have incorporated this double-input feature.

Asymmetry	Single-input before offset	Single-input after offset	Double-input
$\frac{\Delta E}{E} _{\pi}$	10%	0.1%	0
$\Delta\phi _{\pi}$	1.5°	1.5°	0
$\frac{\Delta E}{E} _{\frac{\pi}{2}}$			6%
$\Delta\phi _{\frac{\pi}{2}}$			0.1°

Table 1. Amplitude and phase asymmetries for single-input and double-input couplers. The designations " $\frac{\pi}{2}$ " and " π " correspond to asymmetries shown in Fig. 2(a) and (b) at $r = a$.

VI. PEAK FIELD GRADIENTS

One of the problems of common concern in accelerator structures is RF breakdown, which occurs when the peak electric field gradients reached in these structures exceed a certain critical value. At SLAC, an X-band 30-cavity accelerator section has been RF processed up to a stable accelerating field of about 100 MV/m, for a peak input power of 100 MW. While it is difficult to determine the locations of peak gradients experimentally, these can readily be obtained from our simulations. The maximum peak gradient was found to be 240 MV/m and occurs near the top part of the disk next to the first structure cell. Our result is in reasonable agreement with the measurement of the 30-cavity structure^[7], where damage was seen near the top part of the coupler disk. Furthermore, the maximum peak gradient in the structure cell is found to be very close to that in the coupler from our simulation.

V. CONCLUSION

A numerical procedure for matching and tuning couplers has been developed, and good agreement has been found between simulations and experiments. The advantage of the double-input over single-input geometry has been shown in terms of lower field amplitude and phase asymmetries, and the location of the peak gradient in the coupler cavity has been identified. The present paper demonstrates that numerical simulations can provide very useful shortcut to cut-and-try prototyping in the design and analysis of linac coupler cavities.

ACKNOWLEDGEMENTS

We are grateful to G. Loew and R. Miller for valuable suggestions. We also acknowledge H. Hoag, J. W. Wang, J. Haimson, N. Kroll, E. Nelson and W. Herrmannsfeldt for their interest in the problem.

REFERENCES

- [1] R. L. Kyhl, Impedance matching of disk loaded accelerator structures, unpublished.
- [2] The MAFIA Collaboration, F. Ebeling et. al., MAFIA User Guide, 1992.
- [3] J. Haimson, Nucl. Instru. Meth., **39**, 13 (1966).
- [4] C.-K. Ng and K. Ko, Numerical simulations of input and output couplers for linear accelerator structures, SLAC-PUB-6086 (1993).
- [5] H. Deruyter et. al., Proceedings of Linac 92 Conference, p407-9, Ottawa, Canada, August, 1992.
- [6] G. A. Loew and R. B. Neal, Accelerator structures, in Linear Accelerators, p39-133, ed. P. M. Lapostolle and A. L. Septier, 1970.
- [7] J. W. Wang et. al., High-gradient studies on 11.4 GHz copper accelerator structures, SLAC-PUB-5900 (1992).

TESLA Vertical Test Dewar Cryogenic and Mechanical Design

Thomas H. Nicol, Donald E. Arnold, and Mark S. Champion
Fermi National Accelerator Laboratory*
P.O. Box 500, Batavia, IL 60510 USA

Abstract

Collaborators on the design of a Tevatron Superconducting Linear Accelerator (TESLA) are working toward construction of a test cell consisting of four full length cryostats, 12 meters long, each containing eight, 9-cell superconducting RF cavities. In order to ensure that each cavity meets its performance requirements, 'as received' structures will be tested in a vertical dewar prior to installation in the cryostat vessels. In addition, the dewar system will accommodate cavities installed in their helium containment vessels for testing if performance problems occur during later stages of fabrication. The vertical dewar system permits testing of the RF performance and high power processing of the cavity structures at their operating temperature of 1.8 K. The design of the cryogenic system, vacuum system, RF input, test instrumentation, and tuning system will be described in detail.

I. INTRODUCTION

The design center for the TESLA collaboration is the Deutsches Elektronen Synchrotron (DESY) in Hamburg, Germany. The initial focus of this collaboration is the construction of a test facility consisting of four 12-meter long cryostats containing eight 9-cell RF cavities. Each cavity is approximately one meter long and is contained in its own helium containment vessel. Prior to assembly, each cavity must be tested to ensure that its performance meets the design criteria.¹ In addition, one would like to be able to test cavities after they have been welded into their helium shells to verify that performance has not been degraded during assembly processing.

The initial testing on all cavities received from manufacturing is done in a vertical dewar. This dewar provides the capability of testing 'as received' cavities at 1.8K under full RF power. It also allows high power processing of cavities to enhance performance which may be degraded due to surface contamination. As such the dewar consists of a complete cryogenic system as well as an RF insert for powering the cavity. The cryogenic system consists of an inner helium vessel, an LN₂ shield, and an outer insulating vacuum vessel. The RF insert consists of the cavity itself, the input

waveguide, a waveguide to coaxial transition, an RF tuning system, and supporting instrumentation.

II. CRYOGENIC SYSTEM

During the initial design phase of the TESLA cryogenic system a distribution box was envisioned which attached to a conventional helium liquefaction plant at DESY. The purpose of the distribution box was two-fold. First it was to contain heat exchangers to subcool liquid prior to distribution to the remainder of the system, including the vertical dewar. Second it was to provide valving for independent control of all downstream devices. To simplify the design of this distribution system, the heat exchangers and J-T valves for subcooling 4.5K helium to 1.8K were moved to the individual downstream devices. As such the design of the vertical test dewar involves more than a helium vessel, LN₂ shield, and insulating vacuum vessel. Figure 1 illustrates the cryogenic system in the vertical dewar. Helium at 4.5K is supplied through a warmup and cooldown valve to the bottom of the inner vessel for initial filling. After the vessel is full, this valve is closed and flow passes through the tube side of a heat exchanger which provides counterflow exchange with gas being pumped from the liquid volume. The subcooled inlet flow, initially at 4.5K, enters the inner helium vessel and is controlled by a J-T valve. The gas flow on the shell side of the heat exchanger is pumped by cold vacuum compressors and is controlled by a 60 mm isolation valve. The design flow in all the piping circuits is 5 grams/sec helium. The heat exchanger and all of the valves are located in the annular space between the inner helium vessel and the LN₂ shield.

III. VACUUM SYSTEM

RF power to the cavity under test is supplied through a full-height WR650 waveguide. At the cavity connection a transition is made to a coaxial connector into the cavity itself. To minimize the potential for damage to the cavity in the event of a failure in the waveguide system, a ceramic window is installed at the waveguide to coaxial transition. This necessitates the use of two separate vacuum systems; one for the waveguide capable of achieving 10^{-7} torr or better and one for the cavity system capable of 10^{-8} torr or better. At this writing, it was unclear what type of pumping

* Operated by Universities Research Association under contract with the U.S. Department of Energy.

systems would be employed in these applications. Similar dewar systems in use rely primarily on ion pumps. There is some risk with ion pumps, however, of titanium contamination in the cavity. In fact, such contamination has been observed and is a concern for these systems. The waveguide and cavity vacuum systems for this vertical dewar will likely be pumped by means of high speed turbo-pumps. They provide the pumping capacity required and eliminate the potential contamination problems. Once operating vacuums are achieved the pumping systems will be taken off-line, precluding the potential concern about vibration induced cavity resonances.

III. RF INSERT

The previous sections outlined the requirements of the cryogenic and vacuum systems for the vertical

dewar. These are only services for operation of the actual device under test, i.e. the RF cavity. The actual cavity is only a small part of the components suspended in the dewar, the sum total of which is referred to as the RF insert. This insert is suspended from the inner vessel closure plate and consists of the cavity, RF waveguide, waveguide to coaxial transition ('doorknob'), and RF tuning system. Figure 2 illustrates a cross section of the dewar with the RF insert installed.

The waveguide is a full-height WR650 assembly fabricated from stainless steel to minimize heat load into the 1.8K bath and copper plated for good RF conductance. A room temperature window and a cold cylindrical ceramic window isolate the waveguide vacuum from atmosphere at the warm end and from the cavity vacuum at the cold end.

The doorknob transition converts the rectangular waveguide to a coaxial coupler. The outer conductor of

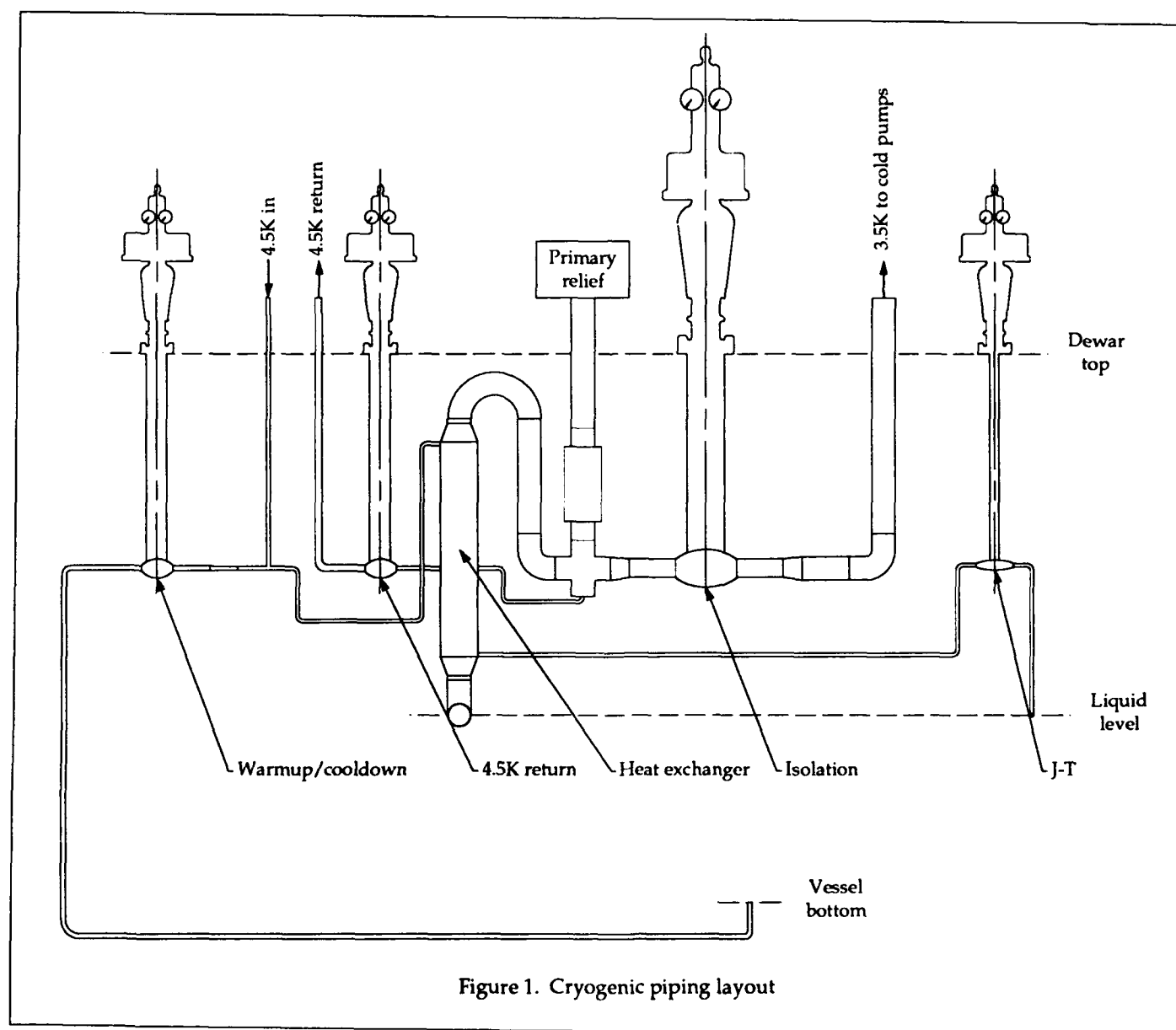


Figure 1. Cryogenic piping layout

the coax is a copper plated stainless steel bellows which allows the cavity to be raised and lowered with respect to the center coaxial conductor. This provides the tuning capability needed to match the RF performance of the coupler to each individual cavity. Movement of the cavity is provided by means of a linear drive system mounted to the top plate of the RF insert. The drive

system provides 100 mm total vertical adjustment of the cavity position relative to the center conductor of the coaxial assembly.

IV. INSTRUMENTATION

Instrumentation will be provided to measure the thermal and RF performance of the dewar and RF systems. Although complete requirements have not been defined as of this writing, the following illustrates a partial list of the instrumentation requirements.

- Helium level probe
- Thermometers for cavity temperature mapping and quench detection
- RF measuring probes for the cavity and high order mode couplers
- Electron detectors for the high order mode couplers
- Accelerometers
- Pressure transducers for the LHe volume
- Light monitors for the cold ceramic window
- Bake-out heaters
- X-ray monitor and spectrometer
- Cavity, waveguide, and insulating vacuum gauges

V. SUMMARY

Fermilab is responsible for fabrication of the complete vertical dewar system, i.e. the inner LHe vessel, LN₂ shield, outer vacuum vessel, and RF insert. Due to both ASME and German pressure vessel code requirements on the inner vessel, it is being fabricated by a commercial manufacturer. Fermilab will install and test all the piping, valves, access ports, partial instrumentation, and other mechanical equipment. The present schedule requires that the first vessel be shipped to DESY for installation in the TESLA test facility late in the summer of 1993. Current plans provide for fabrication of a second, identical dewar in fiscal year 1994.

VI. REFERENCES

- [1] *A Proposal to Construct and Test Prototype Superconducting RF Structures for Linear Colliders*, (DESY, April 1992).

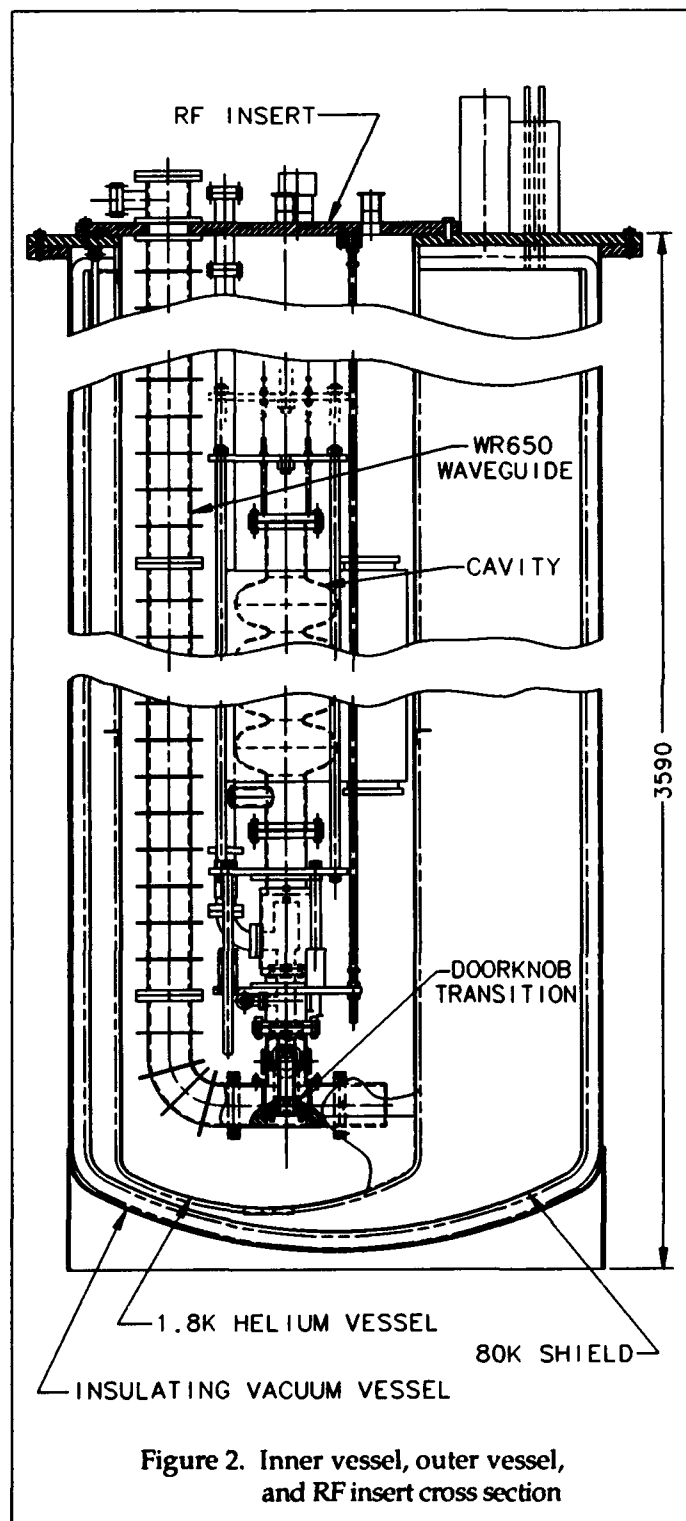


Figure 2. Inner vessel, outer vessel, and RF insert cross section

Update of the TRISTAN Superconducting RF System

S. Noguchi, K. Akai, E. Kako, K. Kubo and T. Shishido

KEK, National Laboratory for High Energy Physics
1-1 Oho, Tsukuba-shi, Ibaraki-ken, 305, Japan

Abstract

The TRISTAN superconducting RF system has been operated since 1988. The remaining operational problem is the trip of the cavity caused by synchrotron radiation. In order to reduce the trip rate, we made realignment of Q-magnets in the straight section and put a movable radiation mask near the end of the arc section. The effect of these improvement, operating status and long term performance are reported.

I. INTRODUCTION

The TRISTAN superconducting RF system continues to provide 40% of the total ring accelerating voltage. The history of the operating condition is summarized in Table 1. Once in 1992, the number of operating cavities was decreased to 23, because of many troubles such as vacuum leak at beam pipe indium joints and water leak at outer water jackets of input coupler ceramic windows [1]. Three water leaked pairs of cavities were electro-polished again, and four leaked pairs were simply reassembled. In the last winter shutdown, the last cavity pair, one of which was never operated since its installation, was replaced by a repaired pair. But unfortunately, one of HOM coupler connectors was found to be sputtered probably by excessive fundamental power due to HOM coupler quench during horizontal test. After exchange of the connector, the cryostat was installed again and full 32 cavities came into operation from April, for the first time since the commissioning in 1988.

Also in the last summer shutdown, the following 3 counterplans were performed in order to reduce trip rate.

- 1) Correction of Q-magnet alignment near the collision point.
- 2) Installation of a movable radiation mask at the place 7 m arc side from the outermost cavity (10D#4).
- 3) Improvement of the orbit control scheme during acceleration and replacement of beam position monitors around the sc cavities.

The effect of these on the trip is discussed later.

II. CAVITY PERFORMANCE IN THE RING

After the last report [2], the cavity performance was measured three times. Figure 1 shows the distribution of the maximum accelerating gradient, where "First 16" means that cavities were installed in 1988 and never electro-polished afterwards. One of the worst cavities (11B#4) was degraded after reassembling. "Last 16" are those installed in 1989, and "Spare & Repair" are those installed in 1991 (4 cavities) and those reelectro-polished after 1991 because of contamination or degradation. As a whole, the cavities are keeping the initial gradient, but a few cavities show degradation during operation (Fig. 1 b). The limitation of these cavities (11D#3,#4) is coupler arc [2]. Since the gradient recovers after warm up and the input couplers can handle enough power if the cavities are detuned, we think the limiting mechanism is multipacting around the coupling port due to gas adsorption from the arc side and by so many trips (discharge).

Table 1: Summary of the operation of SC Cavities in TRISTAN-MR

Period		Number of cav. (at 4K)(operated)		Total Vc (MV)	Eacc(ave.) (MV/m)	Energy (GeV)	Current (mA)	Physics Run (days)
1988	Nov-Dec	16	16	105-109	4.4-4.6	30.0	10	18
1989	Jan-Mar	16	14	82-88	4.0-4.2	30.4	9	49
	May-Jun	14	14	87	4.2	30.4	10	17
	Jun-Jul	16	16	105	4.4	30.7	10	37
	Oct-Dec	30	28-29	190-200	4.6-4.7	32.0	12	25
1990	Feb-Mar	32	31	160	3.5	29.0	12	37
	Apr-May	32	30-31	160	3.5-3.6	29.0	12	25
	May-Jun	32	28-30	150-160	3.6	29.0	13	39
	Jul	30	25	130	3.5	29.0	13	31
	Jan-Jul	32	29-30	140-145	3.3	29.0	9	36
1991	Oct-Dec	30	26	140	3.6	29.0	13	35
	Feb-Mar	26	23	125	3.6	29.0	12	31
1992	Apr-Jun	28	23-25	135-140	3.8	29.0	13	77
	Oct-Dec	32	25-31	150-170	3.3-4.1	28.8-29.9	13	66
1993	Feb-Apr	30-32	28-32	145	3.2	29.0	13	48
Total accumulated time of cavities		at 4.4 K :		23300 hours				

Figure 2 shows the result of Q measurement by liquid He consumption. The worst data point at 5 MV/m is that of the degraded cavity, 11B#4.

III. TRIP

A. General Feature

There have been many types of trips and reports. Here we summarize the present our understanding. In some cases, the trips were caused by troubles of input couplers [3], but in the other most cases, they are not related to hardware performance, they happen from the beginning of a running period. The general features of these trips are summarized as follows.

- 1) They are concentrated on some location, both are sides (10D and 11D) and around 10B. Once the cavities at 10B#1,#2 and 11D#3,#4 were exchanged to other cavities, but the trip rate was not reduced. Figure 3 shows the distribution of the trips in the last two running period.
- 2) The trip rate changes day by day, which is more remarkable for the trips at Flat Top [2]. Figure 4 shows the recent Fill by Fill trip rate of 11D#4 and 10D#2,#4 at Flat Top. Very high trip rates of 10D#4 and 11D#4 in Fig. 3 a) were due to heavier bunching of the trips.
- 3) Trips during acceleration are sometimes concentrated around some energy corresponding to each cavity [3].
- 4) Trips during acceleration are liable to happen with higher beam current [2]. But on the other hand, trips at Flat Top do not strongly depend on the beam current, they happen also with lower current at the end of fills.
- 5) Most of trips seem to be discharge in the cavity or around the coupling ports of input couplers and monitor couplers.

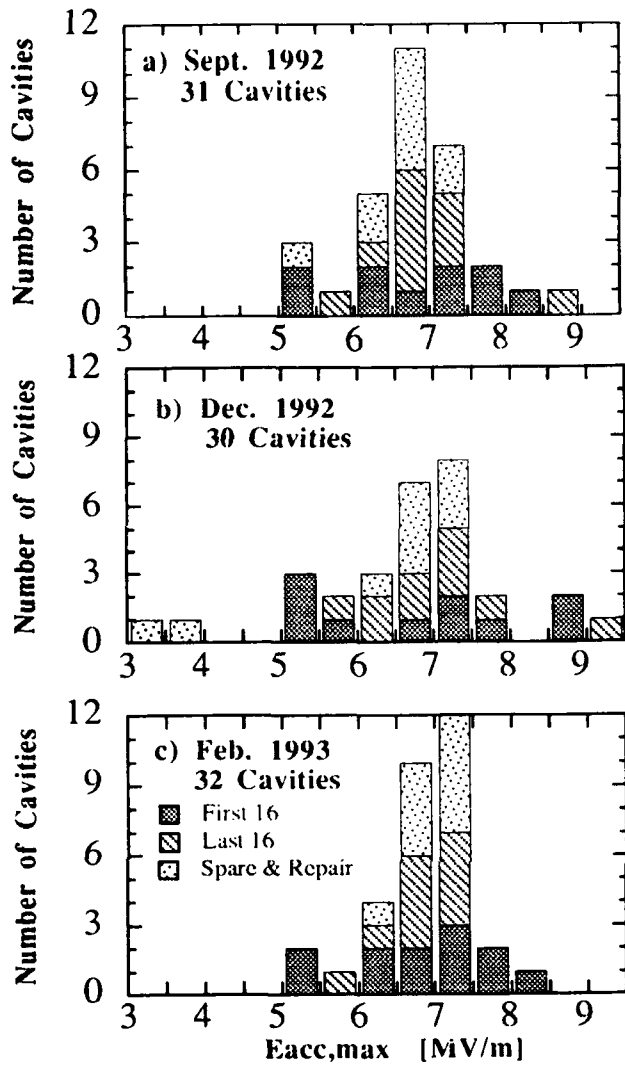


Fig. 1 Distribution of the maximum accelerating gradients.

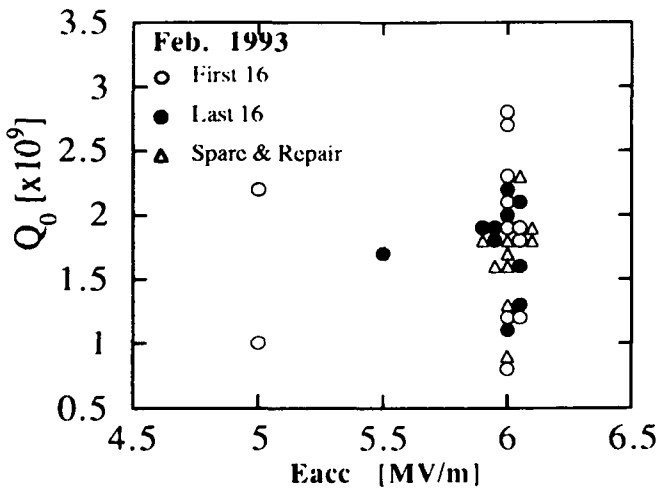


Fig. 2 Distribution of the unloaded Q values.

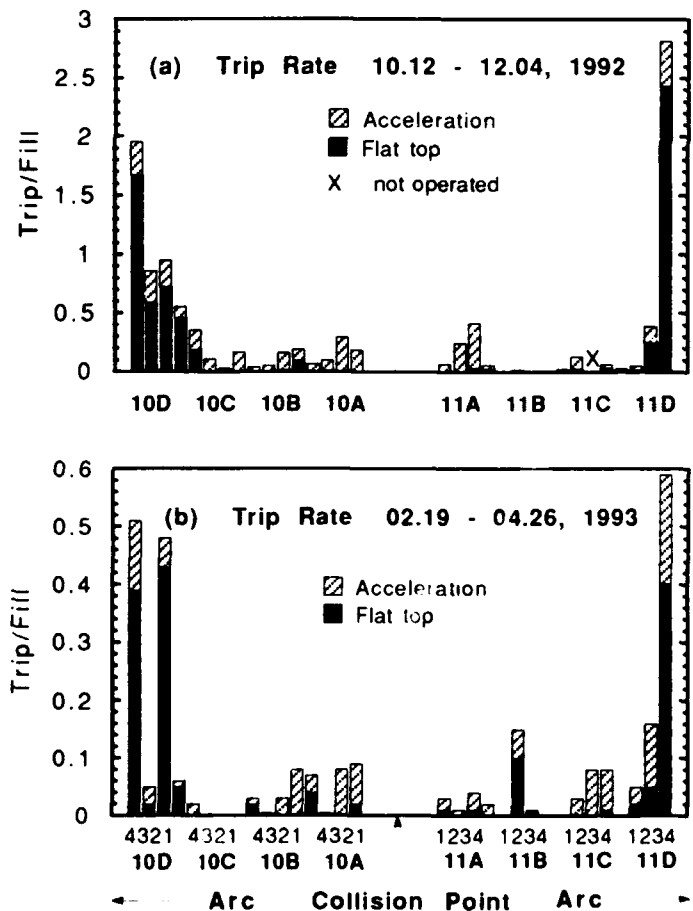


Fig. 3 Distribution of the trips.

Number of Trips / Fill

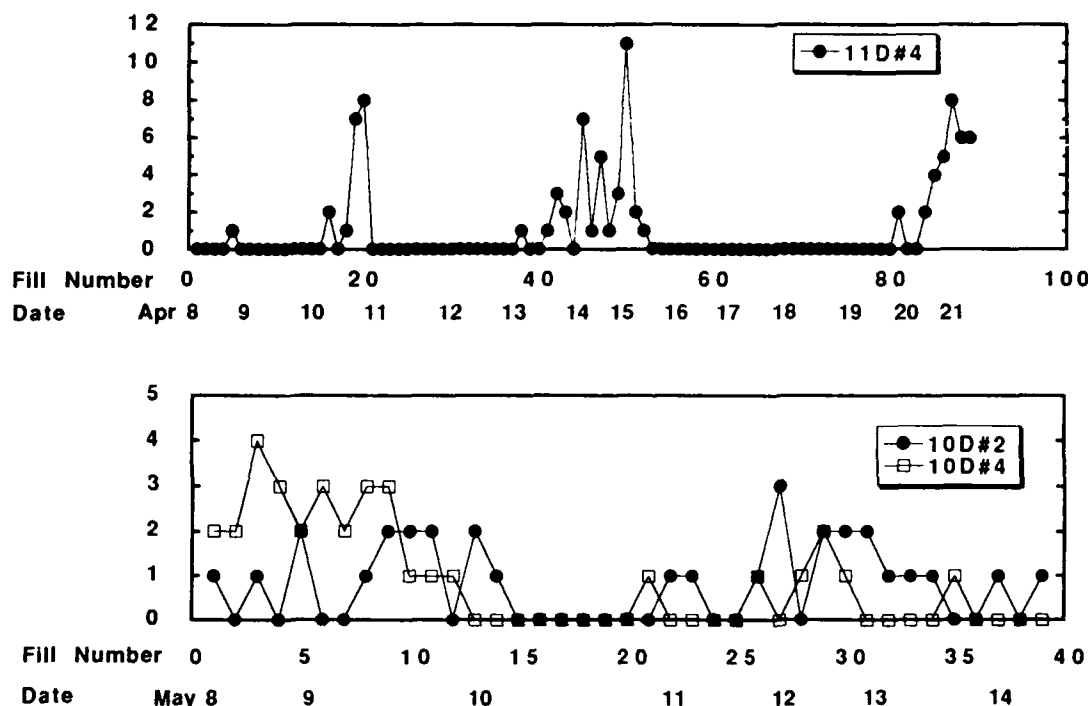


Fig. 4 Fill by Fill trip rate at Flat Top.

B. Counterplans

We have supposed that the main trigger is the synchrotron radiation. In 1990, we moved fixed radiation masks of both outermost cryostats into the ring center by 1 mm. The effect was very drastic for the trip of 11D#3 during acceleration but was not seen for the other trips [3]. The mask of the cryostat containing 10D#3,#4 was moved by another 1 mm in the summer of 1991, and then the trip of 10D#3 during acceleration became quiet. So the trips of these cavities during acceleration are supposed to be due to the synchrotron radiation from bending magnets.

The trips of the cavities from 10A#3 to 10B#2 were prominent in 1991 and the first half of 1992 [1,2]. Since they became prominent after installation of the superconducting quadrupole magnets, we doubted the alignment of the magnets. In the summer of 1992, the correction of horizontal alignment for the superconducting and the neighboring normal conducting Q-magnets, which are located at the same side as 10A, was done by 1 mm and 1.6 mm respectively to the direction of the outer side of the ring. The effect is striking, the trips around 10A and 10B have become quiet as is seen in Fig. 3. This means that COD of mm order at superconducting Q-magnets can produce enough radiation to cause the trips.

The remaining frequent trips are those of 10D#2,#4 and 11D#4 at the Flat Top. They are all arc side cavities in cryostats and are completely hidden by the masks from the

radiation coming from arc side. But, we thought that the scattered radiation at the masks might be a trigger and installed a new movable mask which can hide the fixed masks of three arc side cryostats. This movable mask came into operation in the last December, but we can not find the effect on the trip rate. This might be reasonable, since the trip rate of these cavities depends strongly on the time, but it is hard to imagine that the situation of the radiation changes strongly with the time. Now, we doubt the fluctuating synchrotron radiation from Q-magnets around the collision point and schedule the beam test in the next week.

IV. REFERENCES

- [1] T. Shishido et al., "Operating Status of the TRISTAN Superconducting RF System", *Proc. of the 3rd Euro. Part. Acc. Conf.*, Berlin, Germany, Mar. 1992, pp. 57-59.
- [2] K. Kubo et al., "Four Years of Operation of the TRISTAN Superconducting RF System", *Proc. of the 15th Int. Conf. on High Energy Accelerators*, Hamburg, Germany, July 1992, pp. 691-693.
- [3] K. Akai et al., "Operational Experience with the TRISTAN Superconducting RF System", *Proc. of the 1991 Part. Acc. Conf.*, San Francisco, U.S.A., May 1991, pp. 2405-2407.

Cryostat for a Beam Test with the CESR-B Cavity,*

E. Nordberg, P. Barnes, R. Ehrlich, W. Fox#, H. Heinrichs+ J. Kirchgessner,
D. Metzger, D. Moffat, H. Muller, H. Padamsee, J. Sears, K. She, M. Tigner
Cornell University, Ithaca, New York 14853

I. INTRODUCTION

Superconducting cavities have been chosen as the best approach to meet the rf requirements of the proposed Cornell B-Factory. These requirements involve high beam power, low Q for higher order modes, short beamline space and low cost. The next procedure in the development program of these cavities, following the successful tests of the prototype cavity in a vertical dewar, is to place it in a horizontal cryostat in the Cornell Electron Storage Ring and test under operational conditions with circulating beams. A later step in the upgrade of CESR before the switchover to a B-Factory will be to place four such cavities in the ring as the accelerating cavities for circulating beams of 2 x 500 mA. The B-Factory will require twelve cavities in the high energy ring (1A) and four in the low energy ring (2A), see Table 1.

Table 1
SUPERCONDUCTING RF FOR CESR-B

	High Energy Ring	Common Energy Ring	Low Energy Ring
Luminosity ($\text{cm}^{-2} \text{s}^{-1}$)		10^{33}	
Energy (GeV)	8.0		3.5
Beam Current (A)	0.9		2.0
Number of Cavities	12		4
Total Required			
Voltage (MV)	35		12
Synch. Rad. Power (MW)	4.5		1.5
Volts per Cavity (MV)	2.9		3.0
Load H O M Power (kW)	4-5		14-24
Cavity Beam Power (kW)	380		400
Cavity Dissipation at 4K (W)	100		
Q-Value		10^9	
Frequency (MHz)		500	
Tuner range (+/-kHz)		400	

Initial design concepts for the prototype cryostat were developed in drawings by the authors. These concepts included layouts of the beamline and waveguide components, bellows for accomodating thermal contractions and misalignments, helium and vacuum vessels and other needed features. On the basis of these drawings and other specifications we circulated a request for proposal and Meyer Tool and Mfg., Oak Lawn, Ill. were the successful bidder. Meyer Tool have completed engineering calculations, created fabrication drawings and are in the process of constructing the cryostat. Figure 1 shows their assembly drawing of the cryostat and cavity. Since this is a prototype and we expect to disassemble it several times, a design with O-rings and indium seals is chosen. We expect design modifications for the final production cryostats, one of which may be to use grindable welds in the helium vessel. Another modification will involve the rf waveguide, which, in the prototype test location, need not clear the low ceiling of the CESR tunnel.

In the order for the prototype niobium cavity from Dornier GmbH., Friedrichshafen, Germany, we also purchased a copper version with identical mechanical dimensions in order to make rf and mechanical tests.[1] We plan to augment this cavity with the thermal transitions constructed at Cornell and complete the initial assembly at Meyer Tool with this subassembly. Complete vacuum, pressure, LN2 temperature and other mechanical tests will be performed with this unit. Low power rf tests will be performed with this unit after it is shipped to Cornell. The reassembly with the niobium cavity will be done at Cornell in clean room conditions. This system will be tested at low power first, then moved to a test location with full rf power available and finally moved again to CESR for beam tests.

II. THERMAL TRANSITION PIECES

Within the vacuum envelope of the cryostat are thermal transition pieces on the two beampipes and the waveguide designed to keep radiation and conduction to the liquid helium bath to a low level.[2] The beamline transition pieces are of the same cross section as the ends of the niobium cavity, round on one end and fluted on the other end. They

*Supported by the National Science Foundation, with supplementary support under the U. S. - Japan Agreement.

#LANL

+University of Wuppertal, Germany

are made of 1 mm thick stainless steel plated on the inside with 1.3 microns of copper and are 24 cm long with LN2 intercepts 8 cm from the room temperature ends. They do not incorporate gaseous helium heat exchangers at the 4K ends.

The thermal transition for the waveguide does incorporate a gaseous helium heat exchanger to help carry away the heat generated in the walls by the high incoming rf power. The passages in this heat exchanger are formed by expanding double wall stainless steel sheets on each of the four sides. This unit is 25 cm long and is plated on the inside with 1.3 microns of copper. The next portion of the waveguide, the 90 degree elbow, is held at LN2 temperature, thus greatly cutting the thermal radiation load within the waveguide to the cavity. In addition the specular reflection of radiation from the room temperature portion of the waveguide to the cavity is reduced by shaping the internal surface of the elbow such that the 300K radiation cannot reach the helium bath via a single reflection. This elbow is heavily plated with 6 microns of copper since it is

at a uniform temperature. The final portion of the waveguide within the cryostat is the vertical section 25 cm long, going from LN2 to room temperature. The rf vacuum window is in a section of waveguide just above the cryostat.[3]

The calculated radiation and conduction heat loads of the thermal transition pieces are included in Table 2. The range of values for radiation depends on the assumption of the ratio of specular to diffuse reflection on the internal copper plated surfaces.[2]

III.EXTERNAL BEAM LINE COMPONENTS

In both directions along the beam line outside the cryostat are the components consisting of the higher order mode loads, sliding joints, gate valves, and round section, water cooled pipes of diameter 24 cm and length 24 cm. They are designed to absorb the calculated HOM power of 24 kW each in the worst case.[4] Outside these loads will be sliding joints, also of the full 24 cm diameter as required in the B-Factory. These fittings consist of silver plated rf

0570593-001

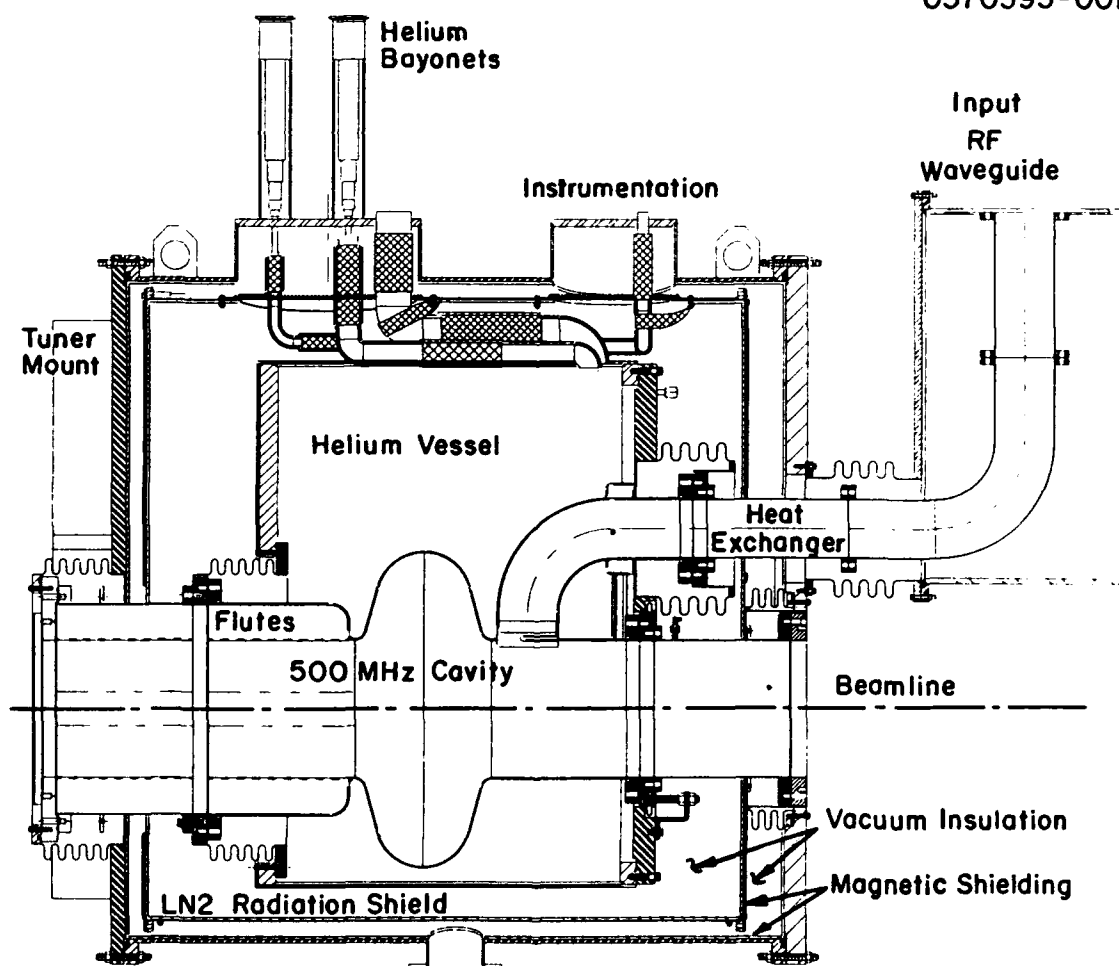


Figure 1. Assembly Drawing (Elevation) of the Cryostat for the CESR-B Cavity

finger stock sliding on copper plated stainless steel which is surrounded by a bellows vacuum seal. Their axial range is 25 mm and they allow angular adjustment but no radial offset. Next in line are specially designed rf shielded gate valves. These have been designed and constructed in cooperation with MDC Vacuum Products, Hayward, California as rf shielded versions of their 24 cm diameter gate valves. Outside these valves are tapered sections taking the beam pipes from the cavity diameter down to the existing beampipe sizes, which happen to be about 7 cm by 12 cm in the section of CESR selected for the test. These tapered sections are needed to minimize HOM power generation from the circulating beams. They have rf shielded pumping ports to which 270 l/s noble diode, ion pumps are attached. Two additional 60 l/s pumps are located on the waveguide for pumping the cavity during operations when the gate valves are closed.

Table 2
CALCULATED HEAT LOSSES (Watts)

	To Liquid Helium Radiation	Helium Conduction	To LN2
Round Pipe	3.3 to 5.1	3.8	38
Fluted Pipe	3.4 to 5.3	6.5	65
Waveguide	0.1 to 0.2	2.0	55
LHe Vessel	0.1		
Supports		0.3	3
Bayonets		4.8	
Ports		0.4	4
LN2 shield			25
Totals	8.8	17.8	190
R.F. Dissipation	100		
Grand Total	127		

IV. TUNER

The required range of tuning of the cavity during operation in CESR is 400 KHz in order to detune the cavity sufficiently to prevent unwanted excitation of the cavity by the coasting CESR beam. The bandwidth of the cavity at the planned Q_{ext} of 2×10^5 will be 2.5 kHz with a resolution of the order of 1 Hz. The cavity will be tuned by mechanically stretching the

cavity along the beam line relative to the cryostat. The tuning coefficient of the cell is measured to be 390 kHz/mm with a required force due to the cavity alone of 7100 N/mm. Added to this force is the hydrostatic force of 22000 N of the cryostat. The tuner has been designed for ± 1 mm at 45,000 N. The drive train will consist of a stepping motor, a 100:1 harmonic drive speed reducer, and a ball screw. This is followed by a 10:1 lever arm terminating in a dual parallel flex hinge arrangement patterned after the proposed LANL PILAC cavity tuner.[5] Such a mechanism has been built and tested. The advantage of such a flexible linkage system is that there are no bearings with the inherent alignment and backlash problems.

V. INSTRUMENTATION AND CONTROL

Within the cryostat are rf probes located on the thermal transition pieces and waveguide near the cavity. The cavity itself does not have any penetrations for instrumentation. Temperature monitors, a liquid helium level gauge and heaters are the only other internal instrumentation. All other devices are external, such as, helium vessel pressure relief and gauge, helium liquid input and gaseous output flow control valves, the LN2 control valve, the tuner and various other rf monitors. A hard-wired interlock system will shut down the power from the rf klystron in case of rf, vacuum or beam related mishaps.

VI. REFERENCES

- [1] H. Padamsee, et al., "Accelerating Cavity Development for the Cornell B-Factory, CESR-B", IEEE Part. Acc. Conf. Proceedings, 1991, p.786.
- [2] H. Muller, et al. "Thermal Modeling of Cryogenic Accelerator Structures", these proceedings.
- [3] J. Kirchgessner, et al., "Prototype 500 MHz Planar RF Input Window for a B-Factory Accelerating Cavity", IEEE Part. Acc. Conf. Proceedings, 1991, p.678.
- [4] D. Moffat, et al. "Design, Fabrication and Testing of a Ferrite-Lined, HOM Load for CESR-B", these proceedings.
- [5] D. J. Liska, et al., "Design Features of a Seven-Cell, High-Gradient Superconducting Cavity", 1992 Linear Accelerator Conference Proceedings, p.163.

A Statistical Model for Field Emission in Superconducting Cavities*

H. PADAMSEE, K. GREEN, W. JOST, B. WRIGHT

Laboratory of Nuclear Studies, Cornell University, Ithaca, NY 14853 USA

THE MODEL

SUMMARY

A statistical model is used to account for several features of performance of an ensemble of superconducting cavities. The input parameters are: the number of emitters/area, a distribution function for emitter β values, a distribution function for emissive areas, and a processing threshold. The power deposited by emitters is calculated from the field emission current and electron impact energy. The model can successfully account for the fraction of tests that reach the maximum field E_{pk} in an ensemble of cavities, for eg, 1-cells @ 3 GHz or 5-cells @ 1.5 GHz. The model is used to predict the level of power needed to successfully process cavities of various surface areas with high pulsed power processing (HPP).

INTRODUCTION

Field emission is the most important gradient limiting mechanism operative in SRF cavities. Over the last 5 years, a large amount of data has accumulated on the performance of cavities limited by field emission. At the same time, there have been significant advances in understanding of the nature of field emission, the Fowler Nordheim (FN) properties of field emitters, their density of occurrence and their microscopic nature. Significant advances have also been forthcoming in understanding the nature of processing. Field emission currents increase with increasing field to initiate a microdischarge. This is an explosive event that leaves behind molten craters, surrounded by starburst shape patterns[1]. We present here a statistical model that encompasses a large body of known data on emitter properties to simulate a variety of features about the known behavior of SRF cavities limited by field emission.

*Supported by the National Science Foundation, with supplementary support under the U. S. -Japan Agreement.

The surface of a SC cavity is divided up into a large number of segments (typically 20 per cell). Each segment i is sprinkled with a random number of emitters n_i , proportional to the surface area of the segment. The maximum emitter density, n_i/area_i is the one free parameter of the model. As is well known from DC and RF studies of field emission, the FN properties (β and emissive area S) can fall within a range of values; typically β is between 40 - 600, and $\log S$ (m^2) is between -8 and -16. We also chose β and S randomly, but the distributions for β and S values were chosen to mimic observed distributions from DC field emission studies[2]. Accordingly, (see Fig.1)

$$N(\beta) \sim \exp(-.01\beta)$$

$N(\log S)$ is a gaussian with half width of 2

After choosing an emitter set, we calculated at a given operating field, the trajectories of the emanating electrons and determined the power deposited on the wall of the cavity by the impacting electrons according to established techniques[3]. We then compare the total power for all emitters to the available CW rf power. For example, 10 watts for a 1-cell 3 GHz cavity, or 100 watts for a 5-cell 1.5 GHz cavity. If the simulated total power is less than the available rf power, the test is declared a "success". As a final feature, if the power deposited by a single emitter exceeds 100 watts, that emitter is declared to be processed and extinguished. The cut-off value corresponds reasonably with the recent discovery that when the total field emission current drawn from an emitter exceeds 10 mA, there is a significant processing factor[4].

RESULTS

By choosing 0.3 emitters/ cm^2 for the single free parameter, we show in Fig. 1 the simulated performance for several sets of cavities: 1-cell @ 3 GHz, 1-cell @ 1.5 GHz and 5-cell @ 1.5 GHz. We calculate the fraction of cavities that "successfully" reach a field value, given by E_{pk} . The simulated results are compared to the data from 100 tests at Los Alamos on 1-cells @ 3 GHz[5], 25 tests at Cornell on 1-cells at 1.5 GHz[6], and 100 tests at CEBAF on 5-cells at 1.5 GHz[7]. All data used are from cavities prepared by nominally the same standard chemical treatment. No advanced treatment data are used (eg. heat treatment or high pressure rinsing or high pulsed rf power processing).

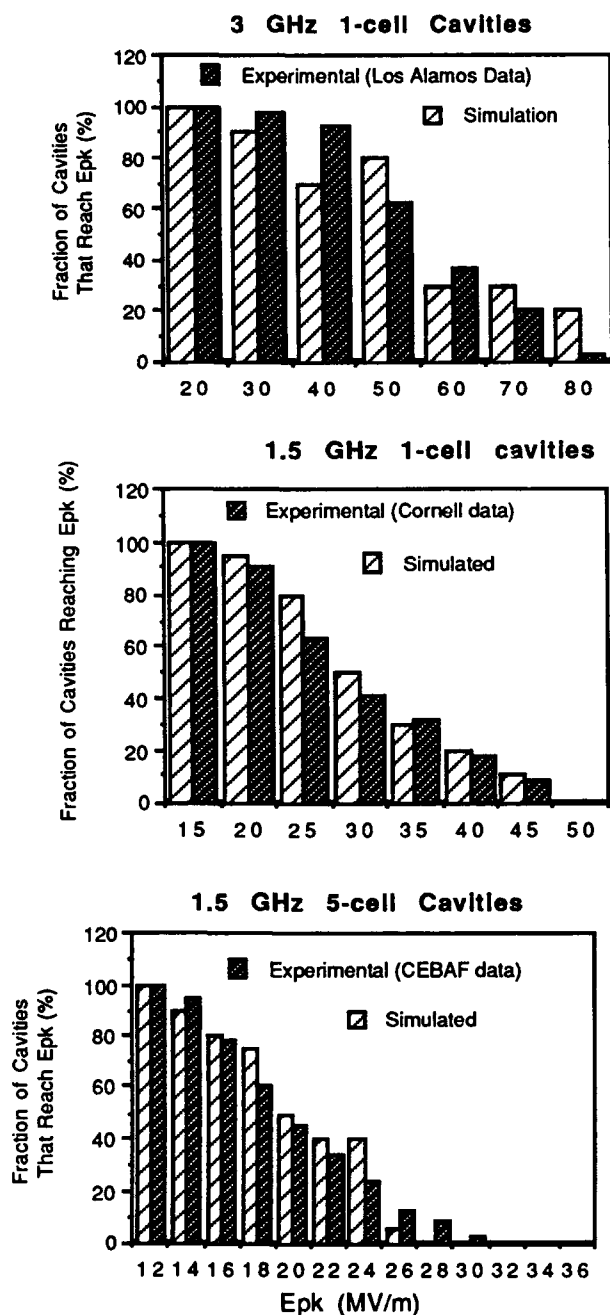


Fig. 1: Comparison between model and experiments

We see remarkable agreement between simulations and data over the 3 sets of data. The most important feature is that, as the area of cavities increases, the successful fraction of cavities at a desired field level decreases. Note that the 5-cell 1.5 GHz cavities have 20 times the surface area of the 1-cell 3GHz cavities.

Fig. 2 compares the measured and simulated β distributions from 1-cell, 1.5 GHz Cornell cavity data. Measured β values were obtained from thermometry data[6].

Fig. 3 shows the location of processed emitter sites for a 1-cell 3 GHz cavity operated at 80 MV/m surface field.

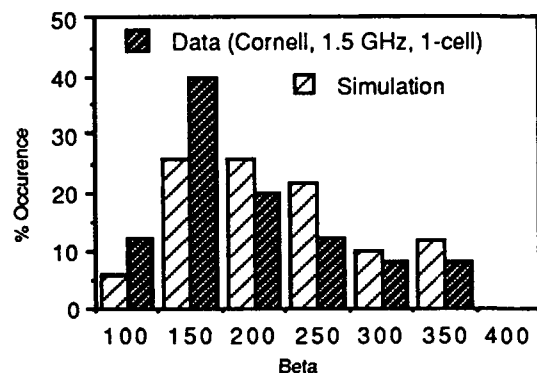


Fig. 2: Comparison between model and experiment

The distribution of processed emitter location corresponds well to the surface electric field, and compares favorably with the observed distribution of processed emitter sites (starbursts/molten craters) reported in [8].

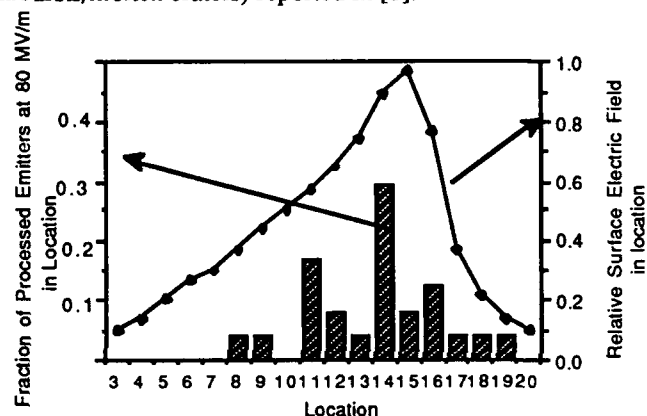


Fig. 3: Model predictions for location of processed emitters

The agreements obtained so far encourage us to examine the predictions of the statistical model for effectiveness of HPP (high pulsed rf power processing). We determine the behavior of a cavity at $E_{pk} = 40$ MV/m, after it is processed at fields of 50, 60, 70 and 80 MV/m each. Table shows a list of emitters encountered in a 1-cell 3 GHz cavity at $E_{pk} = 40$ MV/m. Because of the power into field emission the Q would drop to 5×10^8 . After processing at 50 MV/m and returning to 40 MV/m, some of the emitters are predicted to process. The remaining emitters and their deposited power are listed under the column headed 50 MV/m. The Q would rise to 3×10^9 . Note that the power and Q are re-calculated at the operating field of 40 MV/m. Similarly the result of processing at 60, 70 and 80 MV/m are listed under the appropriate columns. Again the predicted deposited power and Q are re-calculated at 40 MV/m.

The statistical model confirms that, for CW operation at $E_{pk} = 40$ MV/m and with no field emission, it is necessary to carry out HPP at 80 MV/m. i.e [8]

$$E_{cw} = 0.5 E_{pulsed}$$

Table 1: Single Cell 3GHz Monte Carlo HPP

Process at E (MV/m)	40		50		60	70	80
Watts at 40 MV/m for Run No. 1	5.8	25.9	5.8	0	5.8	5.8	0
2	8.5	0.6	0	8.5	0.6	0	0
3	23.3	1.6	0	1.6	1.6	0	0
4	0		0	0	0	0	0
5	78		0	0	0	0	0
6	1.7	3.6	5.3	1.7	0	0	0
7	3.9	0.3	0	1.3	0	0	0
8	1.5		1.5		1.5	0	0
9	18		0		0	0	0
10	7.5	0.6	0.6	0.6	0.6	0.6	0
Average power for one run (watt)	18.1		2.7		1.01	0.64	0
Q0 at 40 MV/m	5.5×10^8		3.1×10^9		10^{10}	2×10^{10}	$> 10^{11}$

We carried out a similar evaluation for HPP on 1.5 GHz, 10-cell cavities, close to TESLA type cavities. We found that the relationship between Ecw and Epulsed is preserved. At Eacc = 12 MV/m, we first found that the Q would be lowered to 8×10^8 because of field emission. Only 5 emitters/cavity would be successfully processed. If HPP were carried out to establish a surface Eacc = 40 MV/m, then 110 emitters would be processed, and there would be no remaining field emission visible at Eacc = 20 MV/m. At Eacc = 25 MV/m, the Q would be lowered to 5×10^{10} . Hence the statistical model predicts that if TESLA cavities could be prepared with standard chemistry as the cavities today, it will be possible to reach the TESLA goal, provided HPP conditions could establish Eacc = 40 MV/m or Epk = 80 MV/m, if only for a short period, even μ secs[1]. Another work has shown[9] that a klystron and coupler that could provide pulsed power of 1 Mwatt for a pulse length of 1 msec would be sufficient to establish the desired field, even if the Q would fall to 2×10^6 during HPP.

CONCLUSIONS

A simple statistical model using known data about emitters can explain the behavior of SRF cavities when they are limited by field emission. The model can be used to predict the requirements for HPP.

REFERENCES

- [1] D. Moffat, et al. Part. Accel. 40:85 (1992)
- [2] Ph. Niedermann, PhD thesis. Univ. of Geneva. 2197 (1986)
- [3] H. Piel, Proc. of the 1st Workshop on RF Superconductivity, ed. M Kuntze. Karlsruhe: KFK. KFK-3019:145 (1980), p. 85
- [4] J. Graber, PhD Thesis, Cornell University (1993).
- [5] B. Rusnak et al, 1992 Linear Accel. Conf. Proc., p.728 (1992)
- [6] H. Padamsee, et al. Proc. of the 4th Workshop on RF Superconductivity, KEK Rep. 89-21:445 (1990), p. 207.
- [7] W. Schneider, CEBAF, private communication.
- [8] J. Graber et al, this conference.
- [9] J. Kirchgessner et al, this conference.

Design And Test of Prototype Cavities For The ELFA Linac

G. Bellomo

Istituto Nazionale di Fisica Nucleare - Sezione di Milano
via Fratelli Cervi 201, Segrate (MI), I 20090 ITALY

R. Parodi, G. Gemme, P. Fabbriatore, R. Musenich, B. Zhang
Istituto Nazionale di Fisica Nucleare - Sezione di Genova
via Dodecaneso 33, Genova, I 16146 ITALY

Abstract

The design study of two possible configurations for the ELFA linac are presented. The first one is a multicell SLAC-type structure scaled down to 1300 MHz, the operating frequency of ELFA. The second one is a multicell standing wave structure similar to the one foreseen for the Tesla project. The effect of the input and output couplers on the beam dynamics in the Travelling Wave is carefully studied by computing the fields of the whole structure (including the couplers) by using the HFSS electromagnetic solver developed by Hewlett-Packard. Last the computed dispersion relation for the model structure is compared with the measured one of a prototype structure.

I. INTRODUCTION

ELFA (Electron Laser Facility for Acceleration) is a high-gain free electron laser designed to operate in the microwave region (radiation wavelength ≈ 3 mm) with goals that are both fundamental and technological in nature [1]. Among the basic features of the ELFA experiment there is an RF linac to provide electron beams with characteristics sufficient to drive a free electron laser amplifier at 30-100 GHz in the high gain regime in the presence of strong space charge forces. The accelerator should deliver a 50 A peak current electron beam at 6 MeV, with low emittance. The principal performance parameters required for the ELFA accelerator are reported in [2].

The choice of an operating frequency of 1.3 GHz for the RF structure allows to fit the need of a train of several micropulses with small energy spread.

II. LINAC DESIGN STUDY

Two possible configurations for the ELFA linac are considered. The first one is a SLAC-type 6 cavity section, operating at 1.3 GHz in a travelling wave $2\pi/3$ mode to maximize the shunt impedance; the second one is a standing wave section of 4 cavities operating in the π mode. For the latter approach we have been studying a structure similar to the one foreseen for the TeV Superconducting Linear Accelerator (TESLA).

A. Standing wave structure.

A four cell structure was chosen to have two complete accelerating periods in the π mode at 1300 MHz. The results of the 2D calculations are summarized in Table 1.

Table 1.
Characteristics of the SW accelerating structure.

Structure length, L	65 cm
Frequency, f	1301.4 MHz
Stored energy, U	9 J
Energy gain, V	6 MeV
Transit time factor, T	0.69
Power loss, P	2.5 MW
Peak surface electric field	33.5 MV/m
Peak axial electric field	24.9 MV/m
Shunt impedance, V^2/P	14.1 $M\Omega$
Quality factor, Q	$3 \cdot 10^4$

The structure shape and the axial electric field are shown in figures 1 and 2.

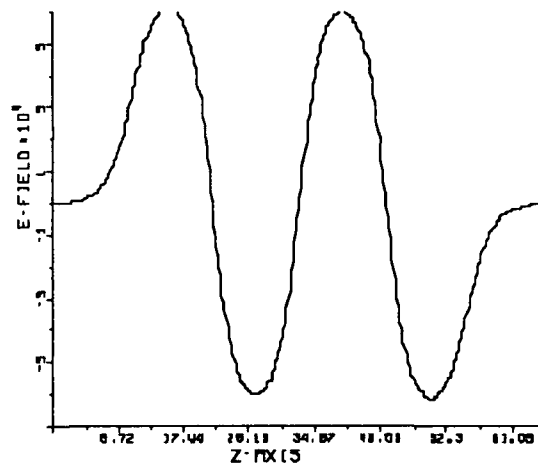


Figure 1. SW axial field.



Figure 2. SW accelerating structure.

B. Travelling wave structure.

The results of the 2D calculation for one period of the TW structure are presented in Table 2. The same normalization condition was chosen as for the SW case.

The cavity shape and axial electric field are shown in fig. 3 and 4.

A 3D calculation of the TW structure, scaled to 3000 MHz, including the input and output power couplers was also performed. Due to the very short length of the structure the presence of the power couplers can severely modify the field distribution. In particular an accurate calculation of the fields in the first cell of the structure (that is in the low β section) is needed to fulfil the tight requirements on beam quality. To compensate for the presence of the power couplers the first and last cells of the structure were greatly modified.

The results of the 3D simulations are summarized in Tables 3a and 3b.

The cavity shape for the 3D simulation was identical to

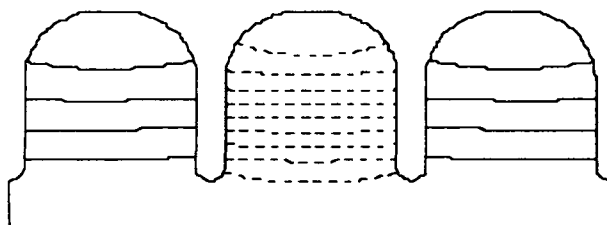


Figure 3. TW accelerating structure (one period).

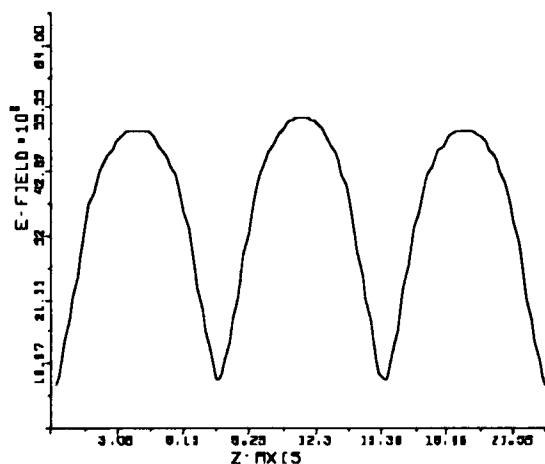


Figure 4. TW axial field (one period).

the one used for the 2D calculation, and was chosen to match the design of the NEPAL cavity at 3 GHz [3]. The first and last cells in the structure were modified to compensate for the presence of the input and output power couplers and beam tubes [4]. An outline of the full 3D structure is shown in figure 5, while the calculated axial electric field is shown in figure 6.

For the 3D calculation the High Frequency Structure

Table 2.

Characteristics of the TW accelerating structure (one period).

Structure length, L	23 cm
Frequency, f	1300 MHz
Stored energy, U	2.2 J
Energy gain, V	3 MeV
Transit time factor, T	0.79
Power loss, P	0.78 MW
Peak surface electric field	25 MV/m
Peak axial electric field	15 MV/m
Shunt impedance, V^2/P	11.5 $M\Omega$
Quality factor, Q	2.3 10^4
Group velocity, v_g	0.6 %

Simulator (HFSS) code from Hewlett-Packard was used.

Table 3a.

Results of the 3D simulations of the TW accelerating structure at 3000 MHz.

Structure length, L	28 cm
Frequency, f	3000 MHz
Stored energy, U	2.2 J
Energy gain, V	6 MeV
Transit time factor, T	0.7
Power loss, P	2.8 MW
Peak surface electric field	100 MV/m
Peak axial electric field	80 MV/m
Shunt impedance, V^2/P	12.5 $M\Omega$
Quality factor, Q	1.5 10^4
Group velocity, v_g	0.45 %

Table 3b.

Results of the 3D simulations of the TW accelerating structure scaled at 1300 MHz.

Structure length, L	65 cm
Frequency, f	1300 MHz
Stored energy, U	5 J
Energy gain, V	6 MeV
Transit time factor, T	0.7
Power loss, P	1.8 MW
Peak surface electric field	43.5 MV/m
Peak axial electric field	34.8 MV/m
Shunt impedance, V^2/P	19.6 $M\Omega$
Quality factor, Q	2.2 10^4
Group velocity, v_g	0.45 %

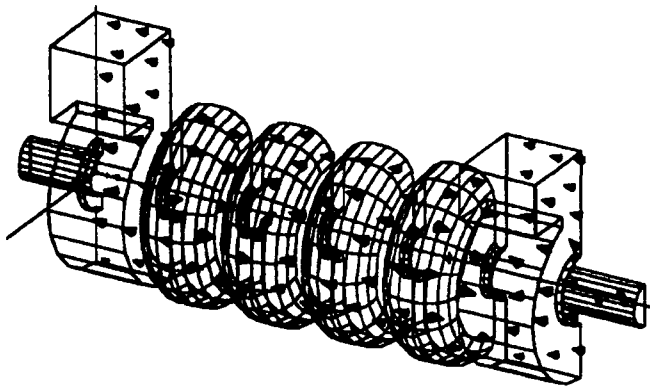


Figure 5. 3D TW accelerating structure.

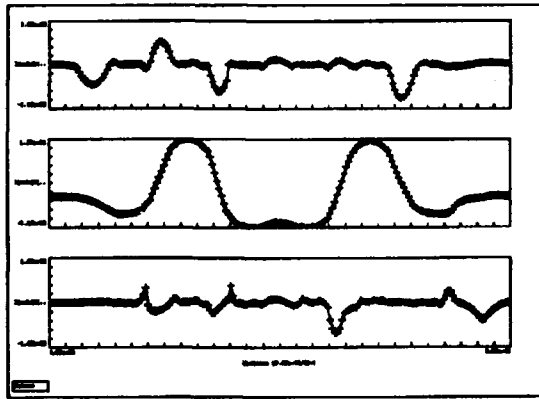


Figure 6. 3D TW structure axial field.

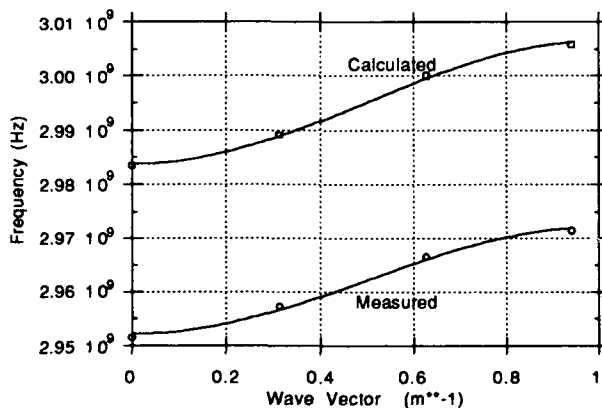


Figure 7. TW structure dispersion relation.

To verify the results of the calculation a model (scale 1:1) of the six-cell periodic structure was built. The dispersion relation of the model was measured by an HP 8510C Network Analyzer. A comparison between the measured and calculated dispersion relation is shown in figure 7.

III. CONCLUSIONS

From the calculations performed and the measurements done on the model, we can conclude that both the TW and the SW structure are suitable to fulfil the requirements on beam quality for ELFA operation using well established technologies.

Nevertheless much care must be taken in the design and realization of the TW structure, particularly with respect to the first and last cells and the power couplers, to compensate for the presence of transverse field components that can alter beam characteristics at the structure output. Furthermore much more power is needed to operate the TW structure with respect to the SW one with the same energy gain.

Due to its shortness the main drawback of the SW structure, i.e. the sensitivity to tolerances in cell realization, is much less important than it is the case for long accelerating sections [5]. In addition the presence of a single power coupler that can be positioned in a high β section reduces the problem of transverse field components compensation.

IV. ACKNOWLEDGEMENTS

We gratefully acknowledge Dr. G. Bienvenu of LAL-SERA Orsay, for giving us the drawings of the NEPAL power couplers, and for the fruitful discussions on TW accelerating structure design and realization problems.

V. REFERENCES

- [1] E. Acerbi et al., "The Revised ELFA Project", these proceedings.
- [2] W. Barletta et al., "Design Study for the ELFA Linac", these proceedings.
- [3] G. Bienvenu and P. Brunet, "Operational Limits of High Accelerator Gradients", *Proceedings of the Second European Particle Accelerator Conference, Nice, (1990), Vol. 1, p. 938.*
- [4] G. Bienvenu, private communication.
- [5] C. De Martiniis et al., "Design and Test of a Prototype Cavity for the ELFA Injector", *Proceedings of the Third European Particle Accelerator Conference, Berlin, (1992), Vol. 2, pp.1286-1288.*

Frequency Domain Determination of the Waveguide Loaded Q for the SSCL Drift Tube Linac*

J. Petillo, W. Krueger, A. Mondelli
Science Applications International Corporation
1710 Goodridge Drive, McLean, VA 22102

J. Potter
AccSys Technology, Incorporated
1177 Quarry Lane, Pleasanton, CA 94566

I. INTRODUCTION

An important problem in the design of RF linacs is the coupling between the waveguide that feeds RF power into the accelerator and the cavity through which the beam is being accelerated. The designer needs to know the coupling coefficient, the frequency shift, and the external Q due to the waveguide. In addition, the details of the field geometry in the vicinity of the aperture are important in the design.

In this paper, the simulation code ARGUS has been employed in a collaboration between SAIC and AccSys Technology, Inc. to model the external Q of the drift tube linac (DTL) tanks in the injector of the Superconducting Super Collider (SSC). (The drift tube linear accelerators are designed and built by AccSys Technology.) As the coupling aperture (iris) size and shape is changed, the coupling factor changes. This paper presents results of numerical simulations produced to aid in determining the optimum iris size for power coupling to the tank. A comparison of the simulation results will be made with results from experimental data.

II. DTL MODEL

The intrinsic Q of the DTL cavity is about 40,000. Figure 1 presents a cross section of the device, showing the waveguide feed, the coupling iris, and the cavity. Dimensions of the structure are the following: tank radius, $R_t = 21$ cm; tank wall thickness, $T_w = 1$ cm; waveguide height and width, $H_w = 9$ in by $W_w = 18$ in. It was desired to study iris widths of $W_i = 12, 15$, or 18 cm, with iris lengths ranging from $W_i < L_i < 30$ cm. Due to time constraints, only the $W_i = 12$ cm set of irises were fully modeled. It should be noted that the coupling iris is oval, in general, when projected onto a plane transverse to the waveguide axis. The smallest iris for any of the widths listed above is represented by a circle in the projected plane.

The requirements for the model were that the tank diameter be the same as the DTL so that the coupling iris would have the actual curvature, and that the frequency

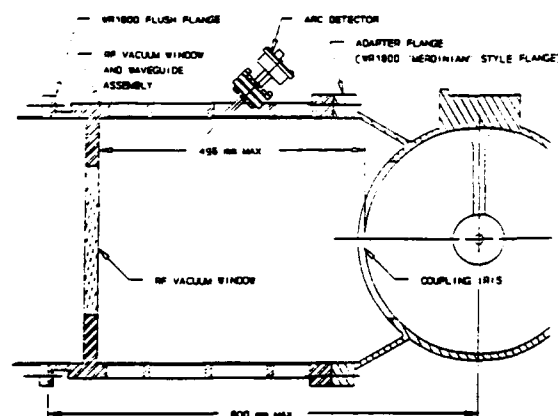


Figure 1: Waveguide to DTL tank coupling geometry.

be the same as the DTL. It was chosen to load the cavity with a dielectric rod along the axis to achieve the desired frequency. The dielectric has a radius of 4 cm and a relative dielectric constant of $\epsilon_R = 4.98$. This results in a cavity frequency of $f_c = 427.717$ MHz. Scaling the SUPERFISH data for the dielectric loaded cylinder to the same wall current as the DTL yields a required cylinder length of 10.525 m for the model to have the same stored energy as the DTL operating at the design field.

Due to the expected high Q of the device (17,500-70,000) and the high detail of the structure in the vicinity of the coupling iris (requiring high resolution gridding), time domain calculations are too costly. However, there are several methods available for determining the external Q of a waveguide loaded cavity device using a resonant frequency and eigenmode solver. We used two of these methods; one by Goren and Yu[1], and another by Kroll and Yu[2]. Although both methods provide good results, each has its inherent advantages and disadvantages for our particular use. The ARGUS code provided the frequency domain solver.

In our study, although both of the methods are used and compared, only the Goren and Yu (GY) method is used for all the iris sizes studied. A comparison of the simulation results will be made with results from experimental data.

*This work has been supported under a DOE/SSCL contract.

III. METHODS

The two methods, the Kroll-Yu (KY) method and the Goren-Yu (GY) method, are similar in that they both employ a frequency domain solver to find the modes of a shorted waveguide loaded cavity. In particular, for each iris shape, several runs are made where the distance to the waveguide short is varied from run to run. However, the two methods differ by using the resulting simulation data in completely different ways to arrive at the external Q .

In the Kroll-Yu (KY) method, four runs are required for a good result[2] in our case. In this method, a resonance curve of phase shift along the waveguide vs. mode frequency shift is mapped out as shown in the example of Fig. 2. The simulation data (denoted by the four solid black circles in the plot) is fitted to a resonance curve. The slope of that curve multiplied by one-half the resonant frequency (apart from a small correction[2]) results in the Q_{ext} . An important point for the KY method is to

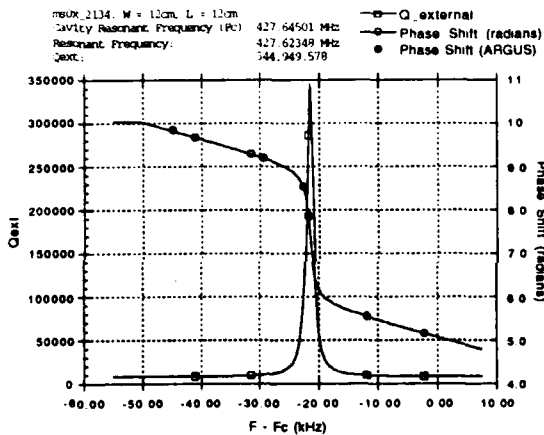


Figure 2: Phase shift vs. frequency example for a 12 cm by 12 cm iris aperture with a truncated DTL tank length.

choose lengths for the waveguide that sufficiently sample the slope inside the resonance curve, since the Q results from the maximum derivative of the curve. The difficulty here is that some of the shorting planes must be placed in extremely close proximity to the actual null in the transverse fields along the waveguide for this to occur. It may take several runs to find the proximity of this null. It should be noted that, by chance, if the short could be placed exactly at the null, then the actual solution to the problem would be known.

Another difficulty in using the KY method is that sampling several points inside this resonance requires judicious choices for gridding techniques as the shorted waveguide length is changed from run to run. The changes in frequency from run to run occur in the sixth and seventh decimal point, requiring about eight significant digits for sufficient accuracy. It should be noted that, although the

numerical procedure cannot get the continuous-space answer to the frequency to eight significant digits, it can get the result on the numerical grid to that accuracy. This point is crucial to the use of both of the methods used in this paper. It means that the changes to the grid from one waveguide length to another have to be done carefully. Basically, the grid along the axis of the waveguide has to be uniform in the vicinity of the short, and the lengths modeled have to be such that they lay on multiples of that uniform cell size. This seemed to allow the solver to behave sufficiently to give the necessary eight significant digits for the mode of interest. Given this restriction, in addition to the loaded Q , the KY method provides an accurate resonance frequency so that frequency shifts are attained.

In the Goren-Yu (GY) method, only two runs are required. This method is based on determining the power flow through the waveguide from an analysis of the details of the standing-wave fields inside the waveguide. Each run provides a relationship between the outgoing electric field versus the reflection coefficient due to the coupling iris. Thus, two runs can be sufficient to solve the problem. With the resultant outgoing power, a shunt resistance can be calculated, giving a waveguide loaded Q .

This method works extremely well, and does not require locating the short circuit so close to the actual zero in the transverse fields along the waveguide. However, this method still requires the same cautious gridding in the vicinity of the short circuits. In addition, for sufficient accuracy, the method demands a particularly accurate location of the peak in the field along the waveguide axis, as well as the field's null position.

IV. SIMULATION RESULTS

Although the full range of iris widths and lengths mentioned previously were considered, this paper only presents the case of the iris width of $W_i = 12$ cm with heights of $H_i = 12, 18, 24$, and 30 cm. Figure 3 shows views of the waveguide/iris/cavity geometry as represented by the ARGUS code.

Since the two methods can use data from the same frequency domain calculation, (although each uses the data differently) a direct comparison between the two methods could be done. This comparison was made on the 12 cm by 12 cm iris only. On the basis of predicting a waveguide loaded Q , the comparison yielded extraordinarily good agreement. The two methods predicted values for the Q within 1% of one another. (Please note that the results shown in Fig. 2 are for a truncated DTL tank and does not represent the nontruncated results presented below.)

Only the GY method was used on the full family of four iris shapes. Figure 4 shows the results of these four runs for the 12 cm wide iris. The solid black dots represent the results from the GY method. For the KY method, only one value for Q was attained (corresponding to the leftmost one on the plot), along with the frequency shift noted by the solid black square on the plot. For the GY method,

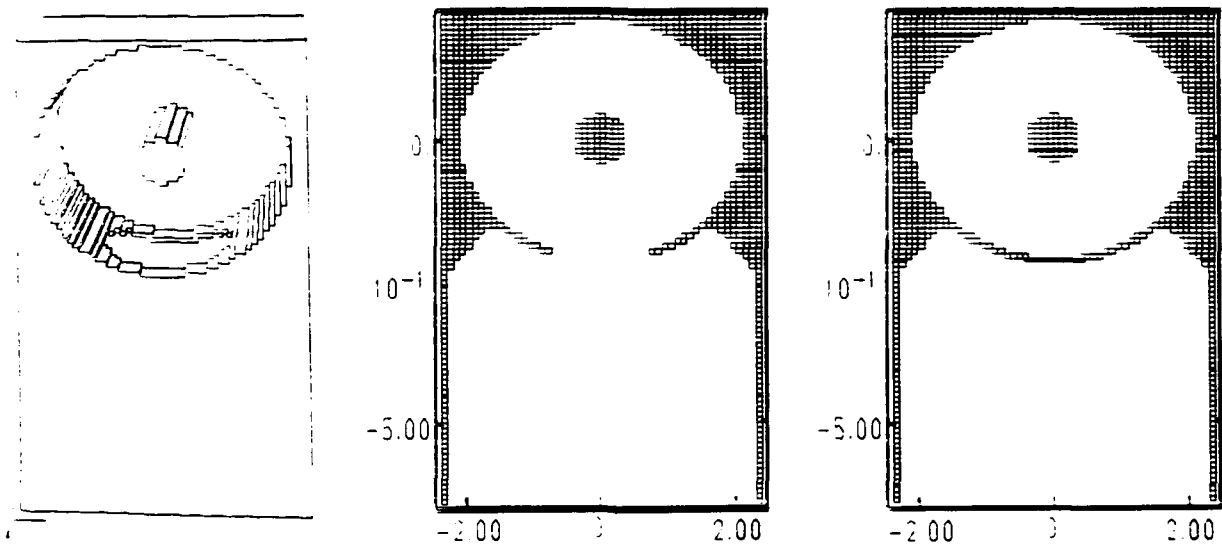


Figure 3: Waveguide to DTL tank coupling iris geometry as represented by ARGUS.

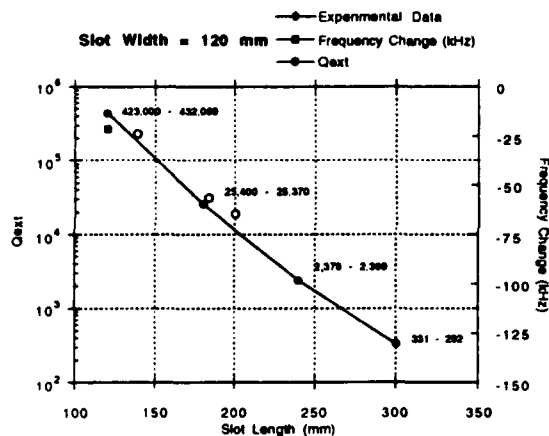


Figure 4: External Q and frequency shift vs. iris length for the 12 cm wide iris aperture.

several values of Q were determined for each case, since more than two runs were made for each case. This was done to determine the robustness of the method. On the plot, the numbers adjacent to the solid black dots represent the range of values of Q from the GY method. For the leftmost value, the KY method gave a result within 1% of the values in the band. As can be seen from the plot, these ranges of values were within a 2% range for the leftmost three points, where the rightmost point's range spanned slightly more than 10%. On the plot in Fig. 4, the experimental results (shown by the hollow circles) show excellent agreement with the numerically predicted values.

V. CONCLUSION

The need to determine the waveguide loaded Q for vari-

ous iris shapes by numerical procedures is very important for many reasons. It is ultimately desired to produce a highly efficient system by exploring many different designs. An experimental determination in our case by trying many iris sizes and shapes is somewhat unfeasible; however, using computer simulations to study a myriad of irises is more realistic. In our collaboration, we were able to verify results of experimental measurements combined with theoretical methods with the simulation model's results.

With respect to the two frequency domain methods used, the Kroll-Yu method and the Goren-Yu method, it was shown that the two methods give excellent agreement with one another. The KY method has the disadvantage that it required shorting the waveguide in close proximity of the true null for best results. Also, it required four runs for a result; however, that result gave, in addition to the Q , a resonant frequency indicating the frequency shift. The GY method, on the other hand, although not directly giving the resonant frequency of the resultant structure, only required two runs for a result for the Q , and did not necessarily dictate choosing the shorting planes so close to the true null. In all cases, the agreement between the simulation models and experimental results was quite good.

VI. REFERENCES

- [1] Y. Goren and D. U. L. Yu. "Computer Aided Design of Three-Dimensional Waveguide Loaded Cavities," SLAC/AP-73, Feb. 1989.
- [2] N. M. Kroll and D. U. L. Yu. "Computer Determination of the External Q and Resonant Frequency of Waveguide Loaded Cavities." *Particle Accelerators*, 34(231), 1990.

Some Operational Characteristics of CEBAF RF Windows at 2K*

L. Phillips, C. Reece, T. Powers, and V. Nguyen-Tuong
Continuous Electron Beam Accelerator Facility
12000 Jefferson Avenue, Newport News, 23606 USA

Abstract

A CEBAF superconducting rf cavity was instrumented to examine RF window behavior at 2K. Of special interest was window performance at levels of cavity power dissipation considerably above normal operating conditions. A variety of transient electronic activity was observed to occur at or near the rf window, including the emission of light, a precipitous increase in reflected power, and interesting cooperative effects between the window and cavity. Typically, the initiation of this activity at the window is correlated with the presence of a high x-ray and energetic electron flux at the window produced by the cavity. Electronic activity at the window can occasionally trigger the sudden disappearance of all stored energy in the cavity, herein referred to as an "electronic quench". Variable delays of up to 40 μ sec have been observed between the onset of window activity and the decay of the cavity field, which can occur in less than 200 nsec and is always accompanied by an intense pulse of x-rays. When the cavity is off resonance with negligible stored energy, rf fields at the window can be increased even further without the appearance of these effects.

I. INTRODUCTION

It is common experience at most laboratories that superconducting cavities, even after very careful cleaning, can show substantial degradation in performance after installation in horizontal cryostats [1]. It is believed that this is due in part to particulates introduced into the cavity from the mounting of couplers and other components during assembly. To avoid this degradation in the CEBAF design, an rf window is attached along with other components directly to the cavity in the clean room immediately after processing. This procedure serves to seal pairs of cavities as hermetic units which are then evacuated in the clean room and remain under vacuum during assembly into the horizontal cryostat [2].

The success of this procedure can be seen in production test results in which the performance of cavities installed in the tunnel shows little degradation when compared to performance measured immediately after processing [3]. This direct attachment to the cavity in the cleanroom, however, places additional requirements on the window design, namely, that it operate at 2K, 8 cm from the beam line. These unique conditions have produced unusual operating behaviour which is the subject of this paper.

The CEBAF cold rf window consists of a thin, high-purity aluminum oxide ceramic mounted in a niobium waveguide flange. It is sealed to the cavity fundamental

power coupler port, separating the cavity vacuum from a guard vacuum maintained by a 300K polyethylene window outside of the cryostat. In this location, the 2K window is exposed to the outgassing load from the guard vacuum and an intense x-ray flux from the cavity when field emission is present.

In the presence of very high levels of field emission in the cavity, the window produces occasional flashes of light. Operationally an arc detector (photomultiplier) watching the window and waveguide space shuts off the rf source when a sustained flash of light occurs. Because an excessively high rate of such trips could disrupt operations, a series of investigations have begun to examine the phenomena in detail.

II. EXPERIMENTAL ARRANGEMENT

To study this behavior, a standard CEBAF cavity was tested in a vertical cryostat configuration shown in Figure 1.

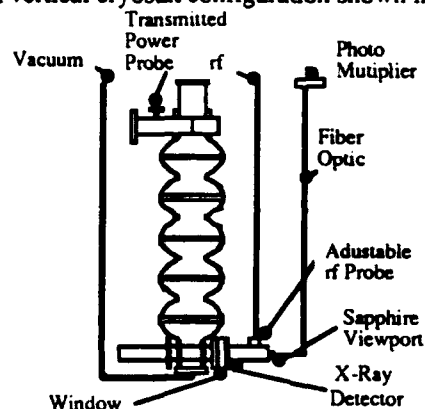


Figure 1.

In this arrangement, the waveguide normally used to carry rf power to the window was replaced by a coax-to-waveguide transition consisting of an adjustable coaxial rf probe coupled to a shorted niobium waveguide, which was in turn bolted to the window.

A fiber optics cable carried light from the window as viewed through a sapphire viewport to a photomultiplier tube outside of the cryostat. A radiation-sensitive diode was placed next to the window to monitor x-rays produced by field-emitted electrons striking the cavity surface.

Reflected and transmitted power, photomultiplier output, and radiation detector output signals were monitored and recorded simultaneously in a 100 μ sec time interval triggered either by a change in reflected power or photomultiplier signal or both. For all measurements the input rf coupling probe was critically coupled before an event.

III. RESULTS

A variety of events were seen involving the four parameters recorded. The simplest and least frequently

*This work supported by DOE contract DE-AC05-84ER40150.

observed event involved light and reflected power transients and is shown as Figure 2.

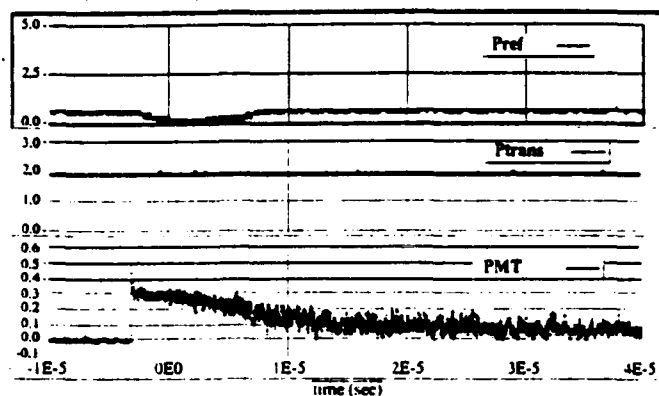


Figure 2.

The transients are coincident. An event of this type is consistent with a plasma being created in the waveguide on the outside of the cold window. The discharge, once initiated, can effectively reflect rf power, produce light, and be fed by an abundant supply of frozen gas on the cold waveguide walls. This process can, but need not, involve the window and has no immediate effect on the cavity. This is evident from the lack of change in the transmitted power signal in the 100 μ sec time window. Since the external Q of the fundamental power coupler port is 6.6×10^6 , the minimum time constant for any change of stored energy in the cavity produced only by events in the fundamental power coupler waveguide or window is nearly a millisecond.

For most events, however, a new and extremely interesting phenomenon was observed in which the stored energy decayed from 10^3 to 10^4 times faster than expected. Figure 3 is typical.

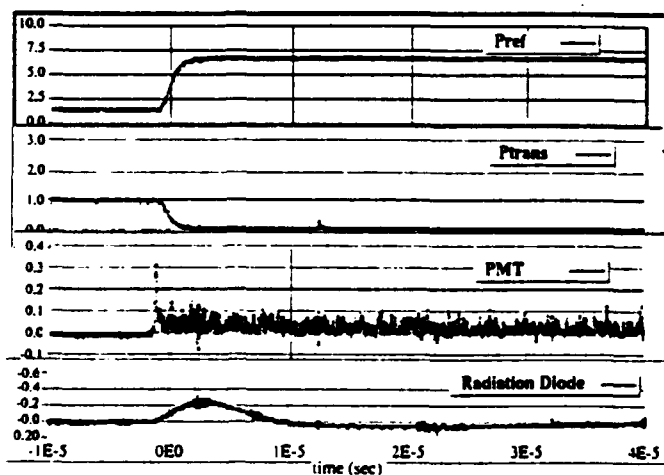


Figure 3.

Here, the transmitted power decays in a few microseconds, indicating a quenching process inside the cavity triggered by activity initiated at the window, but with the window not participating in the energy dissipation. An intense radiation pulse, centered exactly on this fast energy decay indicates a sudden proliferation of electrons appearing in the cavity field as the energy-absorbing mechanism, or "electronic quench". Here all signal transients occur at the same time.

This simultaneity, however, is often absent. In some fraction of the events another new phenomenon was observed, yet even stranger. A variable time delay, sometimes as much as 200 times longer than the cavity "electronic quench" time, appears between the light pulse and the transmitted power decay. The reflected power transient remains coincident with the light pulse, and the x-ray pulse remains centered on the transmitted power decay or the collapse of the cavity field. An example is shown in Figure 4, in which the delay is about 35 μ sec.

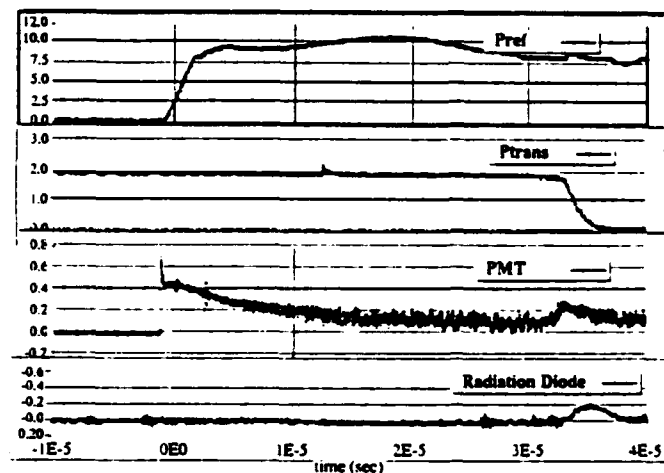


Figure 4.

A variety of delay times have been observed between 0 and 40 μ sec. It has been observed that the delay time tended to process toward zero with continued arcing.

The mechanism for this time delay is not understood. One possible explanation is that a discharge at the window would trigger the arc detector and at the same time liberate a cloud of frozen gas from the window. This gas propagates into the cavity field. After some level of ionization and the production of enough secondary electrons, an electron avalanche precipitously absorbs the cavity energy. It is known that in some events a plasma or conducting medium exists briefly in the fundamental power coupler at the beam pipe just after the trigger. This can be discerned from the shape of the reflected power signal in Figure 5.

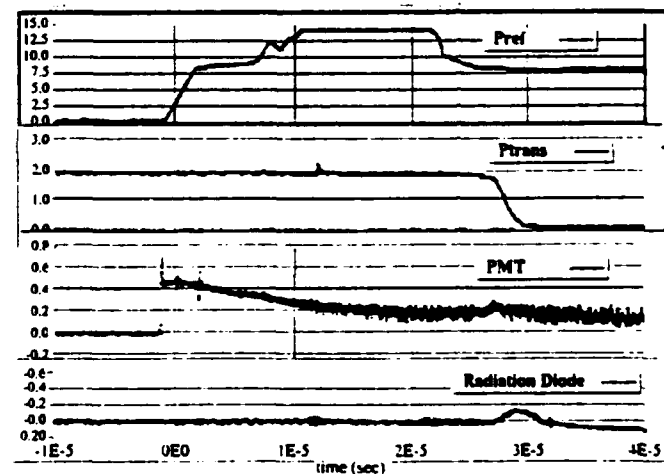


Figure 5.

By the end of the trace the signal has saturated at a value indicating complete reflection of the incident rf power from the discharge in the waveguide. At 20 μ sec, however, the reflected power signal is even greater, indicating some portion of the reflected power signal is momentarily augmented by rf power emitted from the cavity. This may be attributed to a sufficient quantity of charge in the coupler region at the beam pipe to lower the external Q , briefly allowing an increased power flow from the cavity to the waveguide.

Some of these measurement have been repeated with similar phenomena observed on production test cavities and, more extensively, on a special single-cell cavity which has been instrumented to examine the spectral content of light emitted [4].

Another interesting event is shown in Figure 6.

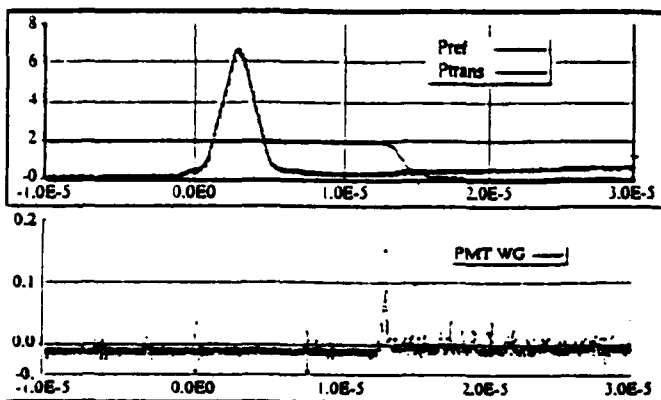


Figure 6.

Here there is no light pulse at all. A small phantom pulse in the light signal (PMTWG) coincident with an electronic quench at 13 μ sec arises from the fact that the fiber optic and photomultiplier assembly are not immune to x-rays. The event was triggered on a reflected power transient shown here on a very reduced vertical scale to illustrate the size of the rf pulse emitted from the cavity. Without light at the photomultiplier, it would seem that this event occurs completely on the cavity side of the window.

One of the most important observations established by this series of tests is the fact that all of the phenomena mentioned above do not occur unless field emission is present. Furthermore, when field emission is present, the arc event rate, which can be as high as 10 per hour, increases with increasing rf power dissipation in field emission.

In fact, window field alone cannot induce this activity. To demonstrate this, the rf system was tuned to the coupler waveguide mode (the waveguide resonator formed by the shorted end of the waveguide coupler and the detuned short of the cavity which includes the window) at 1427 MHz. Under these conditions, the cavity is empty and no field emission is produced. This was done in the middle of a testing period in which arcing events were regularly observed. About 75 W was coupled into this resonance, producing electric fields at the window more than seven times higher than before. No arcing was observed until the rf system was returned to the accelerating mode (1497 MHz).

In one testing period in which arcing occurred with field and rf power held constant, the arc event rate was seen to condition, suggesting the removal of gas from the waveguide walls or window by repeated discharges.

The addition of gas, however, does not necessarily increase the arc rate. In one experiment with arcing present, the test was interrupted to add 7.8 Torr-liters of air into the guard vacuum on the coupler side of the cold window. The test was resumed and except for some initial low field multipacting, which was conditioned away in 10 minutes, there was no significant change from the preceding test.

IV. DISCUSSION

We assume that the window is charging in the presence of field emission. Flashes of light which trigger the arc detector are produced when a discharge occurs.

There are several thoughts on the process by which field emission might induce a surface charge on the ceramic window. It has been suggested that secondary electrons produced near the coupler by field emission current could follow trajectories terminating on the window surface [5]. Another means of surface charging arises from photoelectron emission induced by x-rays arising from field emission in the cavity passing through the window.

Window charging has been demonstrated by electrically insulating the entire window from the cavity and waveguide coupler by inserting thin sheets of VESPEL between flanges. Current flow from the window was monitored during operation. In the absence of field emission, the window current was less than one pA and independent of field. In the presence of field emission, the current rose to as much as 20 nA.

Both charging mechanisms described are consistent with the observed increase in arc rate with increased power dissipation in field emission. Tests are in progress which will isolate these mechanisms.

V. ACKNOWLEDGEMENT

The authors wish to acknowledge N. Luo and P. Kushnick for their valuable support of this work.

VI. REFERENCES

- [1] Y. Kojima, *et al.*, in "Superconducting Activities at KEK," in *Proceedings of the 4th Workshop on RF Superconductivity*, August 1989, Vol. 1, pp. 85—95.
- [2] P. Kneisel, "Test of Superconducting Accelerator Structures in a Closed Vacuum System," in *Proceedings of the 1987 IEEE Particle Accelerator Conference*, Washington, DC) Vol. 3, pp. 1893—95
- [3] H. F. Dylla, "Operating Experience with SRF Cavities," in the proceedings of this conference.
- [4] T. Powers, P. Kneisel, and M. Vaidya, "Photoemission Phenomena on CEBAF RF-Windows at Cryogenic Temperatures," in the proceedings of this conference.
- [5] B. Yunn and R. Sundelin "Field-Emitted Electron Trajectories for the CEBAF Cavity," in the proceedings of this conference.

Photoemission Phenomena on CEBAF RF Windows at Cryogenic Temperatures*

T. Powers, P. Kneisel and M. Vaidya
Continuous Electron Beam Accelerator Facility
12000 Jefferson Avenue, Newport News, Virginia 23606 USA

Abstract

This paper reports on the photoemission observed during the tests on a single-cell 1500 MHz niobium cavity with a polycrystalline alumina rf interface window operated at 2 K. The light emission from the window at 2 K was detected using a multi-channel fiber optics/PMT system and recorded with a 100 Ms/sec acquisition system. The spectral composition of two types of discharges has been measured. The results indicate that both broadband and narrow-band emissions are present, depending on the discharge type.

I. INTRODUCTION

The CEBAF accelerator system uses 338 superconducting niobium cavity assemblies at 2 K to provide a continuous electron beam of 200 μ A and 4 GeV after 5 recirculations through 2 anti-parallel linear accelerators. Each cavity is equipped with a ceramic rf window located in the input coupler waveguide 7.6 cm away from the beam axis. This window hermetically seals the sensitive superconducting surfaces against the waveguide guard vacuum in line with the 5 kW klystrons. The CEBAF rf windows are presently made from a high-purity (99.9%) polycrystalline aluminum oxide (Al_2O_3) sheet of dimensions 13.3 cm \times 2.5 cm \times 0.4 cm thick, which is brazed to a thin niobium foil frame that is in turn electron beam welded to a solid niobium frame for connection to the waveguide system in a bolted flange joint. This window design satisfies the requirements for operation at the machine's design values of an accelerating gradient of $E_{\text{acc}} = 5$ MV/m and a Q value of $Q \geq 2.4 \times 10^9$. At higher gradients, however, several unwanted features such as surface flashover at the ceramic window or possible arc-induced vacuum leaks have been observed, especially in the presence of heavy field emission loading in the cavity [1].

Arcing phenomena at ceramic rf windows, especially when operating at room temperature with high peak power levels, have been previously observed: Y. Saito [2] reported characteristics of alumina windows operated in an S-band resonant ring configuration. Best power handling capabilities were obtained on alumina with high resistivity and a dense microstructure; the window failures were caused by multipacting electrons impinging on the ceramic surfaces with a secondary electron emission coefficient > 1 . As a pre-breakdown phenomenon, broadband optical emission centered at 300 nm and 700 nm with a narrow emission line located at 694 has been observed and is interpreted as cathodoluminescence due to electron bombardment. More recently, spectroscopic observations of surface flashover on alumina under pulsed excitation revealed that the light spectrum contained not only lines due to gas desorption during the arcing but also aluminum oxide bands [3]. This

observation suggests that not only desorbed gases but also bulk material excitations from the specimen may contribute to the initiation of the surface flashover plasma.

II. EXPERIMENTAL TEST SETUP

For the experiments reported in this paper, an end cell of a 5-cell cavity with a fundamental power coupler waveguide (FPC) was modified into a single-cell cavity (see figure 1) by the addition of a beam pipe. Cut-off tubes with flanges were electron beam welded to the FPC and the coax-to-waveguide adapter (tophat), permitting one to view the ceramic rf window from both sides through sapphire or quartz windows. Additionally, the interior of the cavity was monitored via a view port attached at the lower beam pipe. The entire cavity assembly was immersed in liquid He at 2 K.

The light produced in the cavity, beam pipe or FPC was transmitted from each of the view ports to the external environment at room temperature using a non-coherent bundle of 37 commercial grade 1 mm diameter acrylic fibers. The transmission characteristics of a 10 m section of fiber were measured at room temperature, 4.2 K and 2.0 K. The ratio of input to output optical signal was between 10% and 30% from 350 nm to 720 nm with no measurable change when 5 m of the fiber was cooled. Outside of the cryostat the light signal from each fiber bundle was split into 10 individual channels by means of an optical splitter which insured a uniform light input was provided to each of ten S-20 characteristic photomultiplier tubes. Using narrow band (10 nm FWHM) optical filters, which were placed between the individual fibers and nine of the calibrated photomultiplier tubes, it was possible to measure the temporal characteristics of the spectrum of the arcing phenomena.

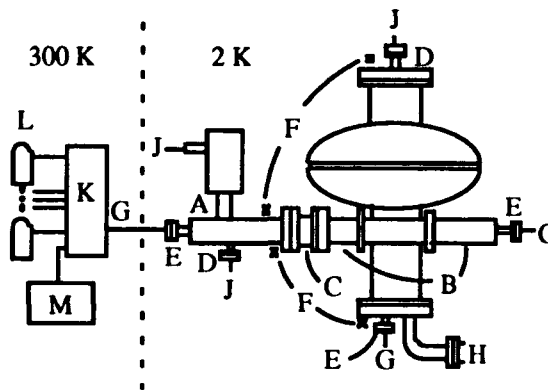


Figure 1. Diagram of a single-cell cavity showing (A) top hat with variable coupler, (B) fundamental power coupler, (C) ceramic window, (D) field probe locations, (E) optical windows, (F) x-ray detectors, (G) fiber optic bundles, (H) cavity pump-out port, (J) rf cables, (K) optical splitter, (L) photomultiplier/filter assembly and (M) monochromator.

*This work supported by DOE Contract DE-AC05-84ER40150

During the experiments the cavity was typically operated at a peak surface field of 22 to 25 MV/m with field emission loading producing > 100 Rad/hr at the cavity. Field levels in the cavity and the window-waveguide space were measured by means of pickup probes located at the beam pipe and tophat, respectively. Silicon photodiodes (Hamamatsu A1221-01) were used as X-radiation detectors [4]. They were placed on the cavity window frame and at the beam pipes. The transfer function of the 20 kHz BW signal conditioning amplifier was $15 \text{ V}/\mu\text{A}$. It has been empirically determined that the output voltage of this amplifier detector combination is on the order of 10 Rad/hr-mV [1].

Data acquisition was provided by four 100 Ms/s digital oscilloscopes with a total of 12 channels. Typical sample rates were 20 Ms/s with a record length of 1000 points. The PMT signal, which was not optically filtered, was used by a detection circuit that provided a latched trigger signal when the PMT current was above a level, typically $20 \mu\text{A}$, for more than $2 \mu\text{s}$. This trigger signal simultaneously triggered all acquisition channels. The data were transferred via IEEE-488 protocol to a Macintosh computer for storage, and the arc detection circuitry was reset automatically using the LabVIEW® software package.

III. RESULTS AND DISCUSSION

A. Types of arcing phenomena

Two types of light-emitting events will be discussed in this paper. In both types of events the energy stored in the cavity disappears several orders of magnitude faster than the 80 ms decay time of a cavity with a Q_L of 10^9 . In one type of event which has recently been identified [1, 5], the stored energy, as measured by the transmitted power signal, is fully dissipated in less than $5 \mu\text{s}$. Decay times as short as 150 ns have been measured. This is accompanied by a large, short duration X-ray pulse of approximately 500 kRad/hr for less than $5 \mu\text{s}$ and a short intense light pulse which is detected at the beam pipe and on both the cavity and waveguide side of the ceramic window. Typical rf and photomultiplier signals for this type of event are shown in figure 2. This class of phenomena, which we call "electronic quenches," are interpreted as the effects produced by the sudden injection or liberation of a large number of electrons into the cavity. The electrons and their secondaries quickly absorb the rf energy stored in the cavity and produce an intense bremsstrahlung pulse as they strike the cavity wall, beam pipe, or endplate. This "beam" loading of the cavity is consistent with the effects seen at DESY when a superconducting cavity is heavily beam loaded [6].

In the second type of event, the cavity stored energy is dissipated in several hundred microseconds (typically $500 \mu\text{s}$). Figure 3 is an example of this type of event. The field level in the tophat is extinguished in a few hundred nanoseconds, but it starts to build up again as the stored energy is drained from the cavity. When the cavity energy reaches a minimal level the field in the tophat collapses and the discharge is extinguished. This type of event is interpreted as a discharge occurring in the window/tophat region which is sustained by the stored energy in the cavity. The light emission during this type of discharge has three different temporal phases. During the first $50 \mu\text{s}$ a relatively large light pulse, which has the

same temporal and spectral characteristics as that of an electronic quench, is observed. For the next $350 \mu\text{s}$ an emission, which has distinctly different spectral characteristics from an electronic quench, is observed. This is followed by a long tail, which has similarities to the long decay tail of the electronic quench.

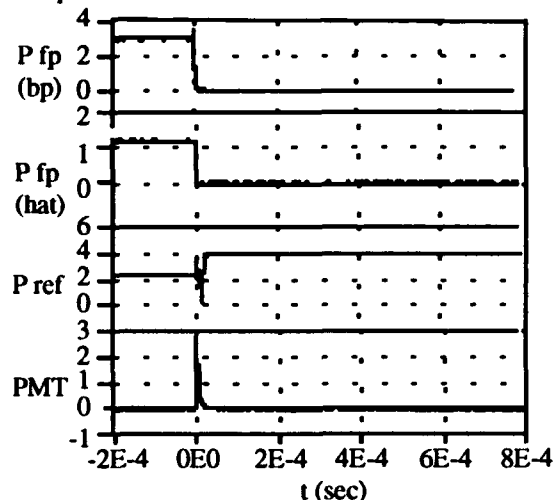


Figure 2. Beam pipe rf probe, tophat rf probe, reflected power and PMT signals for an electronic quench (vertical units are arbitrary).

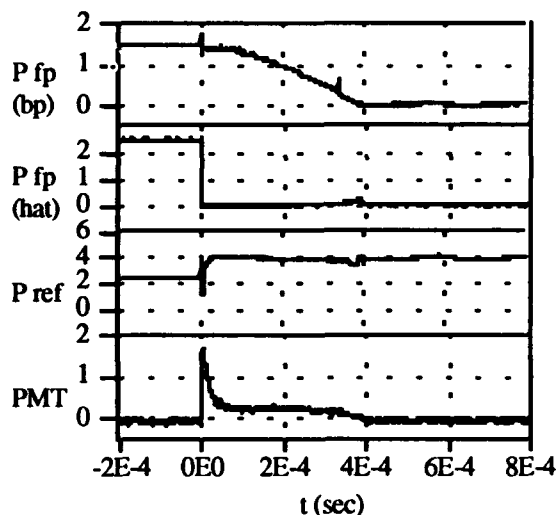


Figure 3. Beam pipe rf probe, tophat rf probe, reflected power and PMT signals for a window/tophat discharge (vertical units are arbitrary).

B. Spectral characteristics

The optical emission data were extracted from the raw data as follows. The average value of the photomultiplier tube current for different temporal regions of the discharges was calculated. These values were scaled by the tube and filter attenuation factors. The ratio between the channel in question and the output of the unfiltered photomultiplier tube for the same section of the waveform was calculated. Several data points were calculated for each filter value and temporal region of the different discharge types and averaged. Typically, the spread in the data was 20 percent of the value shown in the graphs. In total 200 discharge events were used to generate the results reported in this paper.

As shown in figure 4a, for the first 50 μ s of both types of events the spectral responses are almost identical. Preliminary studies with a monochromator indicate that the large emission peak occurs at 394.2 ± 1 nm. We suspect that this line is a solid state line associated with the ceramic material. However, this is yet to be confirmed. The next spectral type was measured during the period of time between 50 μ s and 400 μ s on a window/tophat discharge (see figure 4b). This temporal region of the discharge is characterized by several

different peaks covering the entire spectrum measurable with the current optical fibers. Analysis of this data will be performed when better diagnostics become available. The final two spectral data plots, which are combined in figure 4c, represent the data taken during the long (tens of milliseconds) decay tails. Although they are different they both contain a strong line between 685 nm and 695 nm. Other researchers [2, 7] have reported on a line at 694 nm, identifying it as a chromium impurity level in alumina. In our experimental setup this line could originate in the ceramic window or at the sapphire view ports.

IV. CONCLUSIONS

The experimental investigations reported here are preliminary tests to understand the arcing phenomena encountered when ceramic rf window materials are operated at cryogenic temperatures. It is obvious that this phenomenon is very complex, involving both solid state processes in the ceramic material and probably desorption processes at the cryogenic surfaces under the influence of ionizing and optical radiation. Existing data from dc-pulsed and rf experiments indicate that the microstructure and impurity content of the material as well as the surface conditions influence the flashover characteristics. It is believed that temporal spectral data of the surface flashover phenomena will help to untangle the complex nature of this phenomenon, which can become a serious impediment to the operation of an accelerator with cavities run well into field emission. Future work involves the use of a spectrometer and a gateable detector array to further resolve the temporal and spectral information to try to identify the initiating mechanisms associated with the discharge process.

V. REFERENCES

- [1] T. Powers, *et al.*, "RF Window Arcing Studies Update, A Comparison of Results from Cryomodule 17 and Vertical Cavity Testing," CEBAF TN93-030.
- [2] Y. Saito, *et al.*, "Breakdown of Alumina RF Windows," *IEEE Trans. on Electrical Insulation*, **24** (6), 1029—1032 (1989).
- [3] T. Sudarshan, *et al.*, "Spectroscopic Observations of Surface Flashover Across an Insulator in Vacuum Under Pulse Excitation," to be published.
- [4] B. Fischer, "Untersuchungen an Supraleitenden 9-zelligen Prototyp Resonatoren für TESLA," Report University of Wuppertal, Fachbereich Physik, July 1992, Wuppertal, Germany.
- [5] L. Phillips, *et al.*, "Some Operational Characteristics of CEBAF RF Windows at 2 K," in proceedings of this conference.
- [6] Y. Sekutowicz, private communication.
- [7] K. Lee, *et al.*, "Luminescence of the F Center in Sapphire," *Phys. Rev.*, **19** (6), 3217—3221 (March 1979).

VI. ACKNOWLEDGMENTS

We would like to thank Bret Lewis, Pete Kushnick, Carl Zorn and the cryogenic support team for their effort in the work described in this paper.

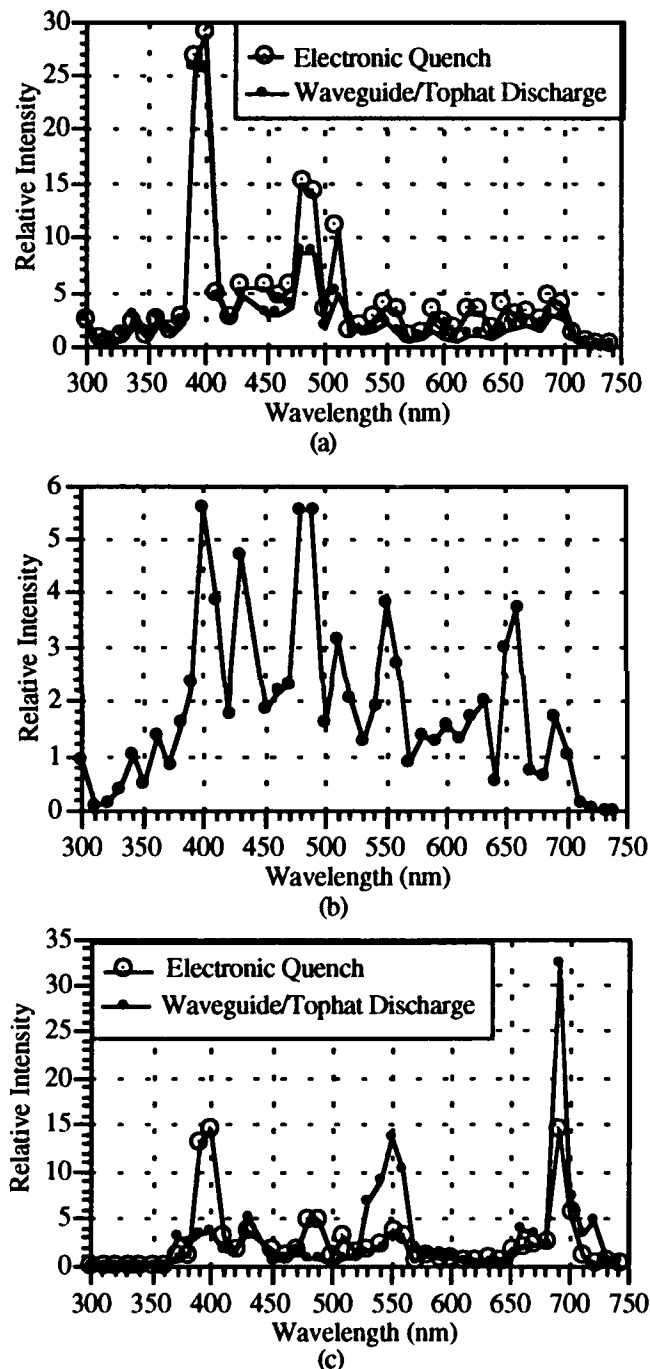


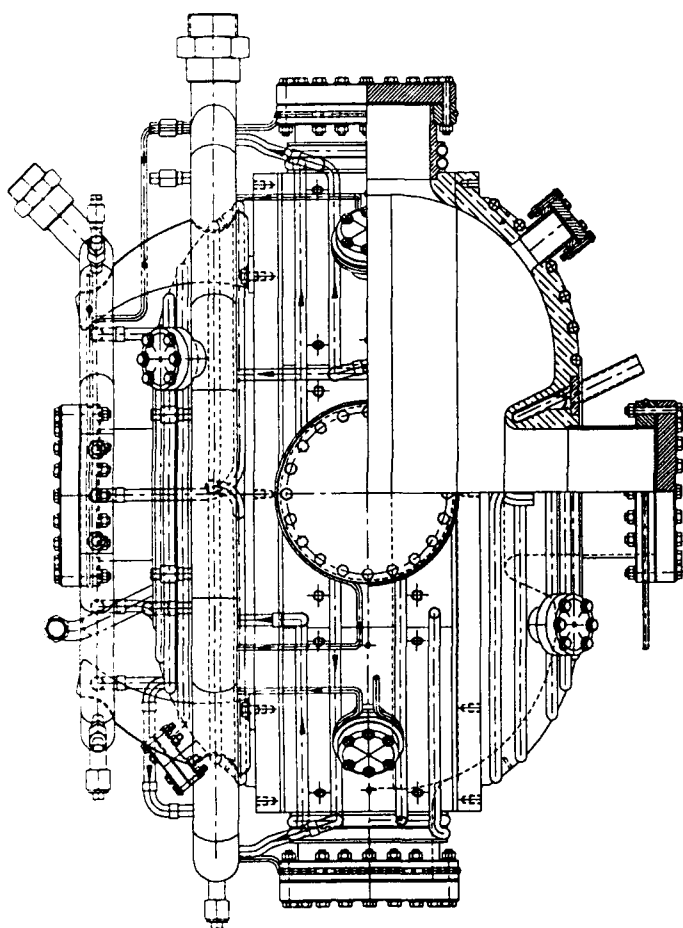
Figure 4. Spectral characteristics of different temporal regions of the two different discharge types. (a) First 50 μ s of both the electronic quench and waveguide/tophat discharge. (b) Second temporal region for a waveguide/tophat discharge 50 μ s < t < 400 μ s. (c) Last 400 to 600 μ s of both an electronic quench and a waveguide/tophat discharge.

Fabrication of the APS Storage Ring Radio Frequency Accelerating Cavities

K. Primdahl, J. Bridges, F. DePaola, R. Kustom, D. Snee¹
Argonne National Laboratory, 9700 S. Cass Avenue, Argonne, IL 60439

Abstract

Specification, heat treatment, strength, and fatigue life of the Advanced Photon Source (APS) Storage Ring 352-MHz radio frequency (RF) accelerating cavity copper is discussed. Heat transfer studies, including finite element analysis, and configuration of water cooling is described. Requirements for and techniques of machining are considered. Braze and electron beam joint designs are compared. Vacuum considerations during fabrication are discussed.



APS Storage Ring RF Accelerating Cavity
(water manifolds removed on one side)

I. INTRODUCTION

The 7-GeV Advanced Photon Source positron storage ring will require sixteen separate 352-MHz RF accelerating cavities. Cavities will be installed, four each, in straight sections used elsewhere for insertion devices. Specifically, the RF cavities will

* Work supported by U.S. Department of Energy, Office of Basic Sciences, under Contract W-31-109-ENG-38.

¹ Fermi National Accelerator Laboratory.

occupy the first such straight section after injection, along with the last three just before injection. Power is supplied via waveguide from an adjacent building, with a coupling loop incorporating a cylindrical ceramic window. A single tuning plunger will be provided. Cavity beamline aperture of 140 mm (5.512 in) was chosen to limit cavity area subject to synchrotron radiation.

Cooling will be provided by a closed loop system, exchanging heat with the APS chilled water system. Water skirts will be located in the adjacent klystron building, yet as close to the cavities as is reasonable. Vibration will be minimized by mounting the pumps on cushioned concrete bases. A 400 liter/sec ion pump with a lumped-non-evaporative-getter will be installed on a drop line adjacent to each cavity. The vacuum tube-cross to the drop line allows for independent alignment of each cavity, and is designed for low impedance to the positron beam.

II. MATERIALS

Room temperature RF cavities have been successfully fabricated of solid Oxygen Free High Conductivity (OFHC) type coppers, copper-electroplated steel, copper-clad steel, and aluminum. Important considerations include: electrical conductivity, thermal conductivity, mechanical characteristics, vacuum outgassing rate, coefficient of secondary electron emission, formability/machinability, weldability/brazeability, and cost. For the APS, Oxygen Free Electronic (OFE) copper, UNS C10100, Class 2 is specified. In specifying copper, "grade" refers to chemical content, while "class" refers to metallurgical characteristics; primarily grain size and inclusions. ASTM B170 and F68 provide the standards for grades and classes of copper suitable for RF cavities. OFE copper is at least 99.99% copper, with less than 5 ppm of oxygen. Low oxygen content is important to electrical conductivity and brazeability (hydrogen atmosphere of a braze retort will combine with oxygen to cause pitting of the surface where oxygen is present in copper). Whereas oxygen is displaced by adding phosphorus in cheaper grades of copper, no such additives are allowed for high purity copper; hence, care must be taken not to introduce oxygen during each refining/processing step. In addition, we required a vacuum degas during the casting process, an operation that removes hydrogen and is normally important only for production of Class 1 copper. The essential difference between Class 1 and 2 is hydrogen interstitials vs. void interstitials along grain boundaries.

As rough shapes for APS cavities exceed cake width ("cake" refers to a rectangular cross-section, while "billet" refers to a circular cross-section), it is necessary to forge the cast copper in order to generate a size/shape that allows APS cavities to be fabricated of three pieces: two cup-shaped ends, and one ring-shaped center. Moreover, we require that the three shapes be cross-grain forged in order to break up the grain boundaries. For high purity copper subjected to furnace brazing temperatures, grain growth can be significant; in fact, a single grain boundary through the thickness of a cavity wall is possible [1]. After cross-

The submitted manuscript has been authored by a contractor of the U. S. Government under contract No. W-31-109-ENG-38. Accordingly, the U. S. Government retains a nonexclusive, royalty-free license to publish or reproduce the published form of this contribution, or allow others to do so, for U. S. Government purposes.

grain forging to width and thickness (no forming), our copper shapes were rough machined, allowing the supplier to immediately recycle a great deal of "hogged out" copper.

III. THERMAL ANALYSIS & COOLING

Important considerations for thermal performance include: thermal gradient/stress/distortion within the copper, outside to inside copper surface temperature difference, water to outside surface temperature difference, temperature rise of cooling water, total water flow rate, water velocity, and number/size/location of cooling tubes. As is typical for accelerator systems, water-to-vacuum joints are prohibited at the APS.

A two-dimensional, axisymmetric URMEL model generated the distribution of heat load on the cavity surface. Results were used as input to an ANSYS[†] thermal/stress analysis. Using hand-calculated convection coefficients for water flowing in copper tubes at several flow rates, and varying the numbers of tubes, several ANSYS[®] models were generated for comparison. Distortion of the cavity due to thermal stresses may affect the resonant frequency, a characteristic which can be used to tune the cavity, provided copper fatigue does not become critical. Enhanced heat transfer with increasing water velocity must be balanced against possible erosion corrosion where the protective layer of copper oxide on the inside wall of copper tubes is stripped away, leaving the soft copper subject to erosion by flowing water (especially at the outer edge of a formed elbow, where the wall has already been thinned by forming). The final design is optimum in that: temperature differences are within the range of a conventional water cooling system, water velocity can be held to a range where erosion corrosion of the copper tubes is not a concern, thermal gradient/distortion within the copper is not severe, and fabrication/attachment of cooling tubes is straightforward.

In the final design, a nose-cone cooling channel is milled into each end piece from the outside (sealed with a brazed cover), and twenty 12.7-mm-diameter (0.5-in) copper tubes are brazed into milled channels (slightly deeper than half the tube diameter). Measurements taken on a prototype cavity with 19.0-mm (0.75-in) tubes, where thermal contact was suspect, showed that tubes with only half their diameter embedded in the bulk copper are capable of approximately 93% of the heat transfer of fully embedded tubes as predicted by Dittus-Boelter [2]. Finally, we selected copper tube extruded with rifling on its inside surface to increase turbulence and surface area. Total flow of 4736 cm³/sec (75 gpm) will be supplied in an all parallel arrangement, divided into three circuits. Orifice plates and thermocouples will be used to balance flows for uniform temperature rise. Average velocity will be 111 cm/sec (3.7 ft/sec), whereas the velocity above which erosion corrosion becomes a concern is reported to be 227-364 cm/sec (7.5-12 ft/sec). For the worst-case of 75-kW heat load, a 3.7 K water temperature rise will result.

Our ANSYS[®] thermal analysis showed maximum copper temperature to be 17°C above the water temperature. Mean-

while, the prototype cavity was found to have higher temperatures around the ports, especially within stainless steel where electrical and thermal conductivity are lower than for copper. We subsequently reduced the amount of stainless steel exposed to RF, then copper plated (pure copper) the stainless steel surfaces wherever possible (including vacuum surfaces of blank-off flanges). Furthermore, we have provided flange cooling.

Similarly, our ANSYS[®] stress analysis shows a peak stress intensity of 27.6 MPa (4000 psi) with non-peak stress intensity up to about half that value, in the same range as is reported for 0.2% yield strength of fully annealed copper [1]. With such a low yield strength, cycling into the plastic range seemed unavoidable; accordingly, a fatigue analysis was performed. Applying the strain-life approach showed fully annealed copper to be very accommodating: using conservative boundary conditions, a fatigue life of over 10²⁴ cycles was esumated [3].

IV. MACHINING

Although we had first planned to hydrogen-retort-anneal the rough machined copper as a proof test against oxygen content, our fabricator preferred to machine the outside features of the cavities before annealing the copper (believed to be in approximately the "half-hard" state after forging). Nevertheless, inside features are machined from fully annealed copper, after brazing of the cooling tubes and cavity ports. Nearly all machining operations of the inside surface are turning operations, where tight tolerances and required surface finish are most easily achieved. Care has been taken not to introduce sulfurized (discolors copper) or chlorinated (future corrosion problems as chlorine migrates throughout a vacuum system) cutting fluids. Specifically, we allow only waterbased cutting fluids, diluted with deionized water. All tooling is prohibited from touching any vacuum surface, and aluminum prohibited from contacting any braze surface (said to interfere with wetting during brazing). End and center pieces are machined incrementally; being removed for inspection (while tooling remains in place), to allow for checking of residual stresses and machine errors, by coordinate measuring machine. Machining parameters are adjusted to accommodate small deviations.

A small amount of excess material, in the form of a circumferential step, is left during inside machining of the center section; hence, part of the inside diameter remains undersize. A set of two ends and one center are test assembled, then resonant frequency is measured. Resonant frequency is to be within ±50 kHz at 27°C. Predicting the effect of ambient temperature, electropolishing, and electron beam welding (0.5-0.6 mm shrinkage per weld), an amount by which step material must be machined away is calculated. This final machining is performed (center piece only), then resonant frequency checked again.

In order to vary higher-order modes among the sixteen cavities and thereby reduce cavity-bunch instabilities, each cavity varies in length (distance between the nose-cones) by 0.30 mm (0.012 in). This is achieved by machining each center section to a different length. We expect the effect on resonant frequency to be small and, in any event, negated by the resonant frequency testing and final machining described above.

[†] ANSYS is a registered trademark of Swanson Analysis Systems, Inc., Houston, PA.

V. BRAZING/ELECTRON BEAM WELDING

Brazing is possible in a hydrogen retort or vacuum oven. A hydrogen retort offers a reducing atmosphere; however, the dew point must be controlled according to the types of oxides present. Temperature vs. dew point data is available in the literature: copper oxide is relatively easy to reduce, chromium oxide (stainless steel) less so [4]. In fact, for the lower temperature filler metals, chromium oxide will not reduce—in these situations stainless steel is usually nickel plated before brazing. Alternatively, this characteristic can be used to an advantage where fixturing is concerned (prevents adhesion of fixture to parts). Oven temperature is ramped to just below the filler melt temperature, then held while all parts come into thermal equilibrium. Temperature is then raised to just above the melt temperature for a short time. Afterwards, oven and parts are cooled with inert gas before exposure to atmosphere.

Several brazing schemes were considered where one to four brazing steps would be required. Brazing in sequence can be done with different filler metals having decreasing melt temperatures. The advantage of several steps is the ability to leak check after each braze and the ease of sending a subassembly back into the furnace for a rebraze. Nearly all braze joints are tube-in-to-bore, where we show 0.025-0.076 mm (0.001-0.003 in) clearance, inside to outside diameter.

The part-line is 645 mm (25.4 in) in diameter at the inside edge; hence we considered it the most challenging joint. Although we originally planned to braze this joint, we later concluded that an electron beam weld, performed at the cavity fabricator's facility using a cryo-pumped weld chamber, is superior. The electron beam weld is from the outside; hence, a small (1.5 mm) step is machined on the part-line surfaces to serve as an electron beam stop. Trial welds were necessary to determine welding parameters so that the melt zone extends to the stop, but not through to the cavity (where surface irregularities and spatter would result). It should be noted that the small part-line "crack" closes during weld cooling/shrinking resulting in a smooth surface for RF currents, but prohibiting the future use of any cleaning solutions. As electron beam welding is the final fabrication step, we expect that rigorous cleaning will never again be required.

VI. ELECTROPOLISHING

In order to enhance vacuum performance, APS cavities will be electropolished after resonant frequency testing and final machining, but before electron beam welding. In one sense, electropolishing can be thought of as an aggressive cleaning procedure—it removes surface oxides, hydroxides, etc. A metal typically has a residual level of contaminant throughout the bulk, and a higher level at the surface. Though the residual levels cannot be "cleaned away," the surface level can be reduced significantly, allowing outgassing to more quickly decay to residual level. Electropolished surfaces are denser and smoother (less effective surface area); hence, can recover faster from venting to atmosphere. Similarly, smoother surfaces have lower field emission. We expect less arcing, faster conditioning, and less sputtering/migration of copper as a result of electropolishing [5].

Though electropolishing of our first end and center section subassemblies has not yet been performed, a copper/copper-plated-stainless-steel port subassembly has been successfully electropolished, insuring that electropolishing of copper-plated stainless steel can be performed without complication.

VII. ACKNOWLEDGMENTS

We express our appreciation to D. Dasbach, E. Klein, and H. Vogel, Siemens AG, Köln, Germany for their technical assistance and timely communication. Also, to T. Smith, D. Voss, E. Wallace, APS, for their extraordinary efforts in preparation and testing our prototype cavity and to L. Morrison for his perseverance with drawings and revisions. Finally, to D. Meyer, J. Maj, and C. Verdico, APS, for their assistance with thermal testing and braze development.

VIII. REFERENCES

- [1] Fritz, Jim, FNAL, Personal communication with author.
- [2] Incropera, Frank, and David DeWitt, *Fundamentals of Heat and Mass Transfer 2nd Ed.*, New York: John Wiley & Sons, 1985.
- [3] Bannantine, Julie, Jess Comer, and James Handrock, *Fundamentals of Metal Fatigue Analysis*, Englewood Cliffs, New Jersey: Prentice Hall, 1990.
- [4] Schwartz, Mel, *Brazing*, Materials Park, Ohio: ASM International, 1987.
- [5] Noonan, John, Personal communication with author.

Performance of Production SRF Cavities for CEBAF

C. Reece, J. Benesch, P. Kneisel, P. Kushnick, J. Mammosser, and T. Powers
Continuous Electron Beam Accelerator Facility
12000 Jefferson Avenue, Newport News, VA 23606-1909 USA

Abstract

Construction of the Continuous Electron Beam Accelerator Facility recirculating linac represents the largest scale application of superconducting rf (SRF) technology to date. Over 250 of the eventual 338 SRF 1497 MHz cavities have been assembled into hermetic pairs and completed rf testing at 2.0 K. Among these, 52% demonstrated usable gradients greater than 10 MV/m.

Although the rf performance characteristics well exceed the CEBAF baseline requirements of $Q_0 = 2.4 \times 10^9$ at 5 MV/m, the usual limiting phenomena are encountered: field emission, quenching, Q -switching, and occasional multipacting. An analysis of the occurrence conditions and severity of these phenomena during production cavity testing is presented. The frequency with which performance is limited by quenching suggests that additional material advances may be required for applications which require the reliable achievement of accelerating gradients of more than 15 MV/m. The distributions of frequency and Q for a higher-order mode are also presented.

I. INTRODUCTION

The Continuous Electron Beam Accelerator Facility in Newport News, Virginia, USA is presently constructing a recirculating linac designed to produce a low-emittance electron beam with a current of 200 μ A and energies upwards of 4 GeV for fundamental experimental studies in nuclear physics. Currents in excess of 260 μ A have been achieved from the 45 MeV injector. Low-current precommissioning activities have produced a 245 MeV beam with the desired emittance characteristics.[1] The performance of the SRF accelerating cavities exceeds design requirements.

As of 1 May 1993, 127 cavity pair assemblies have completed testing and 28 1/4 cryomodules have been installed in the tunnel. Construction and installation will continue through December 1993. Nuclear physics experiments are to begin in 1994.

II. CEBAF SRF CAVITIES

In 1989 CEBAF placed a contract with Siemens for the manufacture of 360 5-cell niobium cavities according to a design developed at Cornell University. These cavities have been fabricated in accordance with CEBAF's "Statement of Work" using high-purity niobium of RRR ≥ 250 for the cavity cells and reactor grade niobium for beam pipes, waveguide couplers and flanges. The order has been completed recently as scheduled. Experiences with mechanical features of these cavities are described in papers [2] and [3] contributed to this conference.

The cavities are tuned for a flat field profile by the vendor, but received no surface treatment except for a preliminary cleaning.[4] The chemical processing takes place at CEBAF with a material removal of $\geq 50 \mu$ m, ultrapure water rinsing

This work is supported by US DOE Contract DE-AC05-84ER401540.

assisted by ultrasonic agitation, and final solvent rinsing with ultrapure methanol or isopropanol. Two cavities are assembled into a hermetically sealed pair, the basic building block of the CEBAF acceleration system, in a class 100 cleanroom. Ceramic rf windows, higher-order-mode loads [5], high-vacuum gate valves, and rf probes are attached to the cavity openings with indium seals. The pair is evacuated in the cleanroom and is maintained under vacuum thereafter.[6] After assembly, each pair is mounted on a vertical test stand and placed in a dewar in the CEBAF Vertical Test Area (VTA). The cavities are cooled quickly through the 100 K range to avoid Q degradation, and rf testing is performed at 2.0 K. The ambient magnetic field at the cavity is reduced to ≤ 10 mG by an active coil and layers of magnetic shielding. The cavity vacuum is $\leq 10^{-6}$ torr prior to cooldown.

A new He desorption leak detection technique with a sensitivity of 10^{-15} std cm³/sec has been developed to verify seal integrity at cryogenic temperatures.[7]

III. RESULTS AND DISCUSSION

A. Cavity Performance in Pair Tests

Typically 45 minutes per cavity is required to characterize the Q_0 and E_{acc} performance and calibrate the transmission pickup probe. In addition, measurements are made of Q s of higher-order modes (HOMs) and a resonance in the fundamental power coupler. The latter is done to assess rf dissipation in the cold ceramic window. Test results for three cavities are presented in Figure 1.

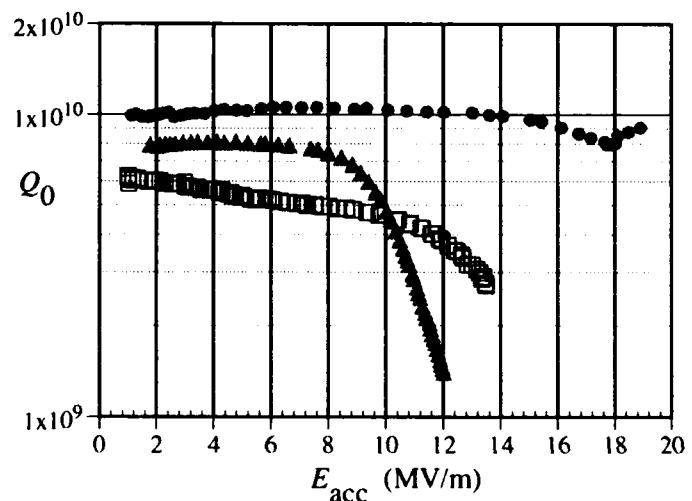


Figure 1. Typical cavity performance in vertical testing.

In the majority of cases the Q value at 2 K is $\approx 10^{10}$, corresponding to a residual resistance of ≈ 15 n Ω . Lower Q values have been observed when the ambient magnetic field at the cavity during cooldown had increased due to current

fluctuations in the coil or when insufficient amounts of material had been removed during chemical processing.

From the perspective of cavity performance alone, the "usable" accelerating gradient of a cavity has been defined as that field which is the minimum of:

$$E_{acc}[Q_0 = 2.4 \times 10^9], E_{acc}[Q_{FE} = 10^{10}], \text{ and } E_{acc}[\text{quench}] - 1 \text{ MV/m.}$$

Figure 2 presents the distribution of usable gradients of cavities which completed testing in the VTA through 1 May 1993.

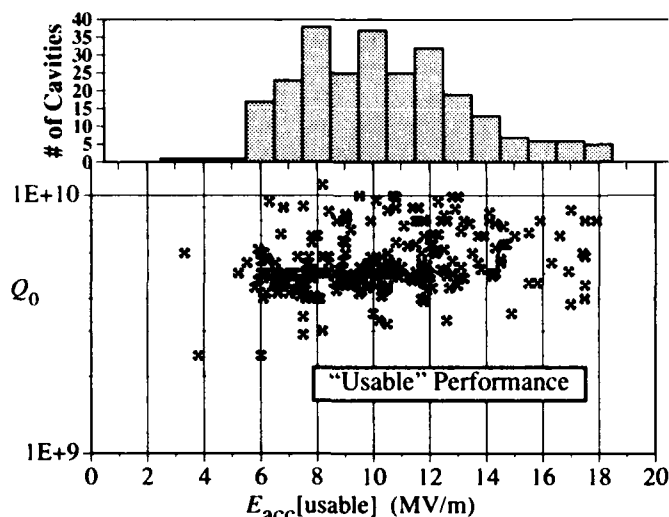


Figure 2. Cavity Q factor at maximum "usable" gradient.

These performance results were reached in initial testing of the cavities in all but 2% of the cases; a statistic is important for large-scale applications of SRF technology such as the proposed TESLA machine.

Several minutes of cw rf processing with up to 100 W critically coupled to the cavity produces 10–30% gain in performance in approximately 50% of the cavities. This rf processing normally takes place as a continuous process, until a "jump" in field level occurs. "Electronic" quenches ($\tau \leq 150$ ns) have been observed in that instance.

There have been cases where rather strong barriers were encountered below 1 MV/m. Such barriers are very unlikely to be multipacting barriers in the cavity because they would represent a very high order of multipacting. Possibly these low-field barriers are caused by some electronic processes in the variable coupler or the rf window, but this has still to be confirmed. Sometimes it has been beneficial to apply high rf power to the other members of the fundamental passband in order to process a barrier.

The incorporation into the test stands of hermetically sealed rf cable assemblies with welded dewar feedthroughs eliminated a problem with low-pressure gas discharges at standard rf connectors inside the dewar.[8]

Field emission (FE) loading is the most common performance limiting mechanism, although 104 cavities have exceeded gradients of 9 MV/m without significant FE loading. See Figure 3. The degradation of the Q value due to FE has been analyzed on the basis of the modified Fowler-Nordheim theory, and the fit parameter "field enhancement factor", β , has been extracted.[9] After processing per above, this value is observed to peak at around 200 as shown in Figure 4.

Minor Q -switches have been observed in about 2% of the

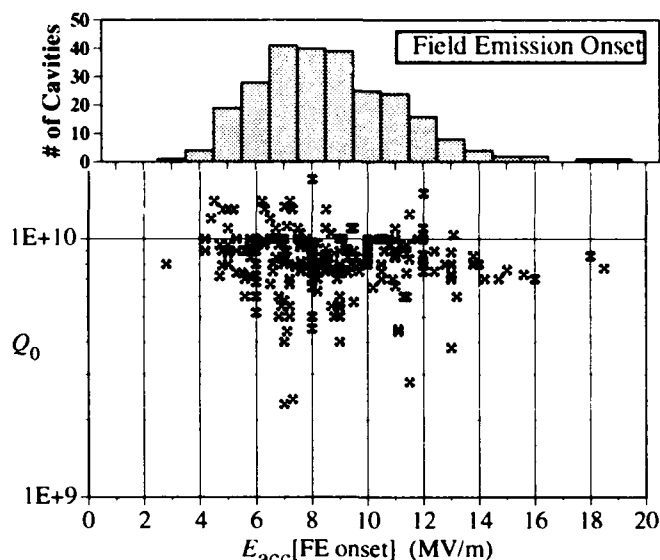


Figure 3. Q and gradient at onset of field emission loading.

cavities. Typically, a hysteretic step in Q from 9×10^9 to 6×10^9 was seen at a gradient of 3 to 7 MV/m. The Q -switches usually persist after cavity reprocessing.

It has been found that the lower of the two cavities in a vertical pair test tends to exhibit greater FE loading than the upper unless the initial cooldown conditions are controlled so that the assembly is cooled as uniformly and as quickly as possible. The enhanced field emission is attributed to locally concentrated adsorbed gas from the residual components of the cavity vacuum.

Thermal-magnetic quench has been exhibited by about half of the cavities in the last 100 qualified pairs. Among these, the average $E_{acc}[\text{quench}]$ is 13.0 MV/m. The Q value and gradient just below quench are presented in Figure 5. In the best case the cavity tolerated a dissipated power of 55 W just prior to quench.

It should be noted that this paper addresses only the performance of CEBAF cavities during vertical testing. Detailed performance testing of cavities installed in CEBAF cryomodules is more complicated. In most cases, operational gradients are constrained by hardware protection interlocks monitoring the waveguide section between the warm and cold rf windows.[10]

B. Performance Durability

On occasion, the ceramic rf windows show leaks of less than 10^{-7} torr l/sec after cryogenic testing of the cavities. The mechanisms for these failures are not yet understood, but

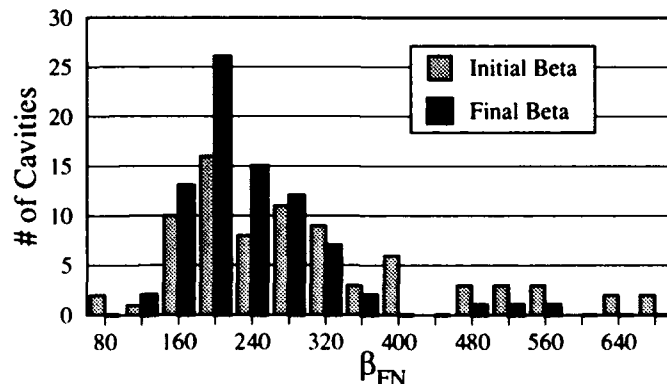


Figure 4. Field enhancement factors for FE limited cavities.

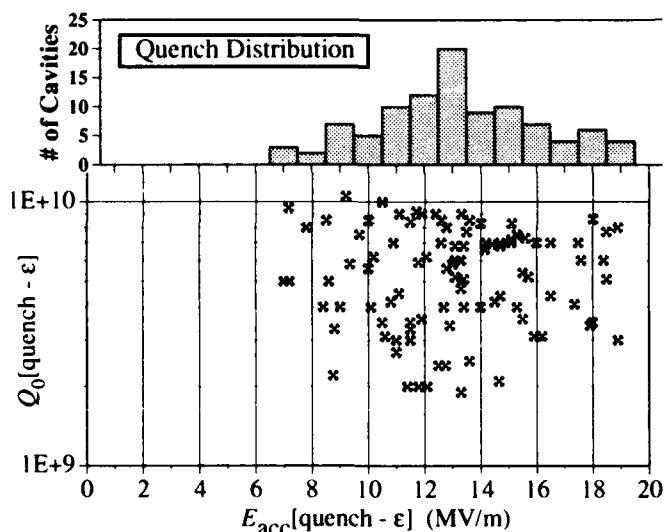


Figure 5. Cavity Q and gradient just below quench.

several investigations are underway at CEBAF.[11],[12] In such instances, the rf windows have been exchanged in the cleanroom after careful venting of the cavity pair with filtered N_2 gas. The pair was reevacuated and retested with no degradation of rf performance even on the best performing cavities with $E_{acc} \geq 16$ MV/m.

Less successful were attempts at exchanging the assemblies which interface to the helium vessel of the horizontal cryostat. In all cases where the assemblies at both ends were replaced, the cavities performed worse after the exchange than before. We attribute this to our inability to maintain a positive flow of nitrogen during the more complex exchange operation thus allowing some particulate contamination of the cavity surface.

On several occasions cavity pairs which had proceeded on through subsequent assembly into horizontal cryostats were removed and retested vertically to assess the durability of the cavity rf performance through these handling procedures. The rf performance did not degrade in those cases where the cavities received exposure only to filtered N_2 or cleanroom air.

C. HOM Measurements

Included in the vertical pair testing is the measurement of the frequency and loaded Q values of two members of the TE_{111} passband. This is used to verify the effectiveness of the HOM loads and to determine the distribution of frequencies produced by the manufacturing tolerances and cavity tuning. Figure 6 presents the results for the mode with a nominal frequency of 1980 MHz, showing quite adequate damping of this mode.

IV. CONCLUSIONS

CEBAF has completed the assembly and testing of 250 out of 338 SRF cavities. Thanks to an excellent industrial partner and stringent QA procedures, the performance of the cavities consistently exceeds CEBAF design specifications of $Q_0 = 2.4 \times 10^9$ and $E_{acc} = 5$ MV/m. In the cases where the achievable gradients were limited by thermal-magnetic breakdown, a rather large spread between 7 to 18 MV/m was observed. This suggests that the presently available high purity niobium of $RRR \geq 250$ does not yet provide sufficient thermal stability to reliably support the gradients of $E_{acc} \geq 20$ MV/m needed for future linear collider applications.

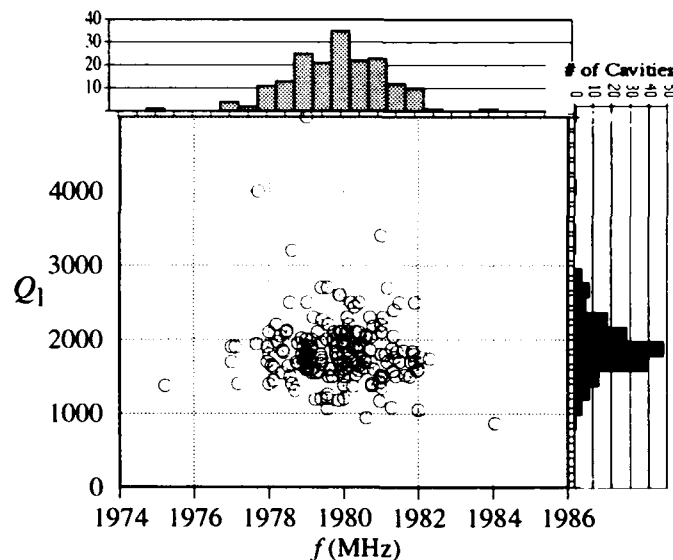


Figure 6. Distribution of frequency and loaded Q for a HOM.

V. ACKNOWLEDGEMENTS

We would like to thank all colleagues who contributed to this work, especially the members of the chemroom, assembly, and VTA teams.

VI. REFERENCES

- [1] A. Hutton, "CEBAF Commissioning Status," these proceedings.
- [2] J. Mammoser *et al.*, "Analysis of Mechanical Fabrication Experience with CEBAF's Production SRF Cavities," these proceedings.
- [3] J. Mammoser and J. F. Benesch, "Mechanical Results of the CEBAF Cavity Series Production," these proceedings.
- [4] M. Dzenus *et al.*, "Production of Superconducting Niobium Cavities for CEBAF," *Conference Record of the 1991 IEEE Particle Accelerator Conference*, Vol. 4, pp. 2390-92.
- [5] I. E. Campisi *et al.*, "HOM Damping and Absorption at 2K," *Proceedings of the 3rd European Particle Accelerator Conference*, Vol. 2, pp. 1237-1240.
- [6] P. Kneisel, "Test of Superconducting Accelerator Structures in a Closed Vacuum System," *Proceedings of the 1987 IEEE Particle Accelerator Conference*, Vol. 3, pp. 1893-95.
- [7] M. G. Rao, "He Desorption Leak Detection Method," to be published in the proceedings of the 1992 National Vacuum Symposium (*J. Vac. Sci. Technol.*).
- [8] Cable assemblies were custom fabricated by Kaman Instrumentation, Colorado Springs, CO.
- [9] R. J. Noer, "Electron Field Emission from Broad Area Electrodes," *Applied Physics A*, Vol. 28 (1982) pp.1-24.
- [10] H. F. Dylla, "Operating Experience with SRF Cavities," these proceedings.
- [11] H. L. Phillips *et al.*, "Some Operational Characteristics of CEBAF RF Windows at 2 K," these proceedings.
- [12] T. Powers *et al.*, "Photoemission Phenomena on CEBAF RF Windows at Cryogenic Temperatures," these proceedings.

A new 15 MHz-4 MV/m RF-Deflector for the Munich Heavy Ion Recoil Spectrometer (MRS)

K. Rudolph and P. Jaenker
Sektion Physik, University of Munich
Am Coulombwall 1, 8046 Garching, W-Germany

abstract

A new 15 MHz resonant deflection system has been developed. It reaches 4 MV/m with an input power of 20 kW. It opens new possibilities to study strongly inverse reactions with the Munich Recoil Spectrometer.

1. INTRODUCTION

A new rf system has been designed and constructed for the Munich Heavy Ion Recoil Separator ¹, ². This system generates a strong electrical field between two deflector plates. It has an operation frequency of 15 MHz and reaches an electrical field strength of 4 MV/m. This limit is only given by the available generator power of 20 kW. Since insulator materials have been avoided, the maximum field strength is not restricted by electric breakdown in insulators.

A sophisticated regulation system provides field amplitude stabilisation and resonance tuning. An electronically regulated mechanic damping system prevents the excitement of mechanic oscillation caused by electromagnetic-mechanic feedback (ponderomotive oscillations³). Also external mechanic disturbances as caused by floor vibration are compensated.

2. DESIGN OF THE DEFLECTION SYSTEM

2.1 Choice of the deflector type

At frequencies as low as 15 MHz the construction of a discrete resonance circuit is an adequate choice. Quarterwave resonators have more or less the same power consumption but are very inconvenient due to their length ($\lambda/4 = 5$ m). Therefore the deflection unit consists of a pair of deflector plates through which the heavy ion beam passes and a discrete coil completing the resonance circuit.

2.2 Mechanical construction

The whole deflection system is mounted on the top flange of a vacuum box making assembly and maintenance very easy. The resonance circuit is a self supporting structure made out of copper tubes (diam. 28 mm) with 10 mm thick stainless steel deflection plates brazed to the ends of the copper tubes. The structure is stiff enough to dispense with positioning insulators. Hence, the performance of the

structure is not limited by electrical breakdown in insulator material.

The coil was constructed with straight pieces of tubes and commercially available 90 degree tube fittings. This way the coil resulted with a rounded square profile. The parts were brazed together using silver solder. This manufacturing method allows the inductance of the coil to be tuned to the desired value by changing the coil length or by adding or subtracting windings. After final tuning the brazed construction was electro-plated with copper achieving a shiny surface with an excellent RF-conductivity. This construction method is very versatile and can generally be recommended for building high power coils.

To carry away the dissipated power we installed an inner flexible stainless steel hose. For both halves of the coil, cooling water enters at ground potential into the coil centre, flows through the flexible tube to the coil end where the deflection plates are attached, and returns in the outer tube to the middle of the coil. RF power is inductively fed to the resonant circuit by a coupling loop diving into the middle of the coil. The vacuum flange carrying the loop can be rotated for impedance matching.

The relevant mechanical dimensions of the deflection system are summarised in table 1.

Table 1
Mechanical characteristics of the deflection system

coil diameter	200 mm
tube diameter	28 mm
no. of windings	8
winding distance	35 mm
coupling loop diameter	50 mm
deflection plate length	250 mm
deflection plate width	120 mm
defl. plate separation	70 mm
vacuum box dimensions	1000*800*400 mm ³

Power dissipated in the coupling loop is carried away by flowing compressed air through the hollow loop tubing. Macor ceramics are used for vacuum sealing and insulating the inner conductor.

The magnetic flux induces eddy currents in the coil housing. To keep power losses in the walls of the stainless steel vacuum vessel as low as possible we surrounded the deflection system by a screening shield made of a coaxially welded copper sheet.

2.3 RF characteristics

The tube diameter of 28 mm selected for mechanical rigidity is also near the optimum value for maximum shunt impedance of the resonator at the given vacuum chamber dimensions. Thus the values given in table 2 could be measured. Maximum reachable RF-voltage was only limited by the available power.

Table 2

RF performance of the resonator	
resonance frequency	15 MHz
shunt impedance	2 MOhm
quality number Q	3000
RF-voltage	270 kV at
RF-power	20 kW

2.4 The power source

An air-cooled tetrode push-pull class C amplifier supplies up to 20 kW c.w. to the resonator by a 8/13-Flexwell coax cable.. The power flow from the source to the load and the reflected wave is observed with a standing wave meter. Amplitude and phase of the deflection field are measured with a small pickup-loop.

3. TUNING AND AMPLITUDE CONTROL

Due to the high electrical quality of the circuit a precise resonance tuning is necessary. The deflector circuit is easily put out of tune by small mechanic deformations as:

- field strength dependence: the deflector plates are attracted by the radiation pressure
- thermal expansion caused by the dissipated power

We use adjustable capacitors to tune the resonance frequency of the deflector circuit: Two electrically grounded spherical bodies are excentrically mounted near both ends of the coil. Their capacity can be changed by turning them towards or away from the coil.

3.1 Slow tuning

A regulation circuit drives one of these capacitors by a gear-motor and tunes automatically the deflector circuit measuring the relative phase between pickup signal and power source with an rf mixer unit.

3.2 Fast damping system

In spite of all efforts to get the resonator as stiff as possible, the avoidance of any stabilising insulators leads to a somewhat shaky construction that tends to mechanical oscillations. This fact not only leads to an extreme susceptibility to external vibrations but especially to heavy ponderomotive oscillations. We suppress these oscillations with a fast tuning loop that keeps the resonator always on top of resonance regardless of the actual mechanical state. To be able to control the mechanic oscillation the cut-off-frequency of the tuning system must be higher than the frequency of the mechanic mode of the coil (3 Hz). Therefore we gyrate the second variable capacitor with a galvanometer motor originally constructed to drive the pen of an electrocardiograph recorder. The movement is transmitted into vacuum by a low friction rotational feedthrough with ferrofluidic vacuum isolation. The arrangement acts like a gyrating pendulum with a resonance frequency mainly determined by the momentum of inertia of the capacitor body that must be kept as low as possible. A light-weighted hollow ball (diameter 10 cm) was manufactured of copper by a galvano-plastic method. A weight of 39 g and a cut-off frequency of 7.5 Hz was obtained.

To drive the fast tuner the same signal as for the slow tuning is used as the input. The driving amplifier for the galvanometer coil uses current feedback in order to avoid additional phase shifts due to the inductance of the coil.

3.3 amplitude stabilisation loop

A feedback loop between pickup loop and power source regulates the amplitude of the electrical field to the desired value within 0.5 %.

References

- ¹ K.Rudolph et al.Nucl. Instr. and Meth. 204 (1983) 407
- ² S.J. Skorka et al. Il Nuovo Cimento 81A (1984) 331
- ³ V. E. Shapiro Soviet Physics JETP 28 (1969) 301

Superconducting Multicell Cavity Development Program at Los Alamos*

B. Rusnak, G. Spalek, E. Gray, J. N. DiMarco, R. DeHaven, J. Novak,
P. Walstrom, J. Zumbro, H. A. Thiessen, and J. Langenbrunner**
Los Alamos National Laboratory
Los Alamos, NM 87544 USA

Abstract

The Superconducting rf (SCRF) Cavity Development Program at Los Alamos has designed, fabricated, and tested single-cell niobium cavities at 3-GHz and 805-MHz. This work is being done in preparation for procuring and testing a multicell niobium cavity. The multicell cavity is designed to accelerate protons at $\beta = 0.9$; initial tests will be without beam. Programmatic changes have required us to modify our plans to install a 6800-liter helium cryostat and a 12.8-g/s helium pump. We will use an installed cryostat to test the multicell cavity. Also, the cavity will be modified from a seven-cell to a four-cell structure to match the dimensions of the installed cryostat. Previous reports concentrated on 3-GHz results. In this paper, some of the latest results of the 805-MHz cavity tests are presented. Modifications to allow high pulsed power (HPP) testing on 805-MHz single- and four-cell cavities are proceeding. Glow discharge cleaning of an 805-MHz niobium cavity resulted in a decrease in cavity performance. The cavity was restored to previous performance levels with buffered chemical polishing (bcp). Initial results with high-pressure water cleaning show the process is useful in restoring cavity performance.

I. INTRODUCTION

The primary goal of our SCRF program is development of the technical data base for the design, fabrication, handling, and testing of superconducting (SC) cavities that will apply to eventual fabrication of SCRF proton accelerators.

Information from the cavity development program was used to design and initiate fabrication of a multicell cavity. The cavity is to be fabricated by industry to our specifications. Programmatic considerations have resulted in the cavity having four $\beta = 0.9$ cells. This cavity will be tested at LANL and used to address technical feasibility questions regarding the use of superconducting structures in high-current proton accelerators.

Work reported at the 1991 PAC conference¹ concentrated on 3-GHz cavities. We have expanded the work to 805-MHz cavities; initial results² for the average of the peak surface electric fields were 29 MV/m and 23.5 MV/m at 2 K and 4 K, respectively. We now achieve 35 MV/m (Q of 5×10^9) and 30 MV/m (Q of 5×10^8) at 2 K and 4 K, respectively.

*Work supported by the Los Alamos National Laboratory Institutional Supporting Research, under the auspices of the United States Department of Energy.

**University of Minnesota.

Our investigation of cleaning techniques has concentrated on systems that could also be used on the four-cell cavity. High-pressure pure-water spray is a viable technique for removing particulates from the surface of the niobium. We have tested an 805-MHz single-cell cavity that was initially cleaned in the standard way by a bcp. The cavity was "dirtied" by exposure to room air. Performance of the cavity was restored after high-pressure cleaning. This equipment is being modified to clean the four-cell cavity.

II. MULTICELL CAVITY

A cavity structure consisting of seven niobium cavities, supporting structure, and tuning system has been described in a previous publication³. This structure consisted of seven $\beta = 0.9759$ cells. For programmatic reasons, the cell shape was changed to $\beta = 0.9$ to match 1200-MeV protons. Also, the number of cells in the cavity was reduced from seven to four. A four-cell cavity conforms to defined power handling constraints of windows/couplers in conceptual designs of some high power proton accelerators. The smaller structure also fits into a cryostat that is presently installed in the SC laboratory. The new cavity also includes high order mode (HOM) couplers mounted on the beam tubes, at each end of the cavity. Window and variable coupler tests have started in preparation for 100-kW pulsed rf power conditioning tests, initially with single 805-MHz cells.

III. SINGLE-CELL RESULTS

A. Summary of cavity testing results

Previous reports² concentrated on the results from 3-GHz single-cell cavities. The emphases of the SC lab work has moved to performance tests of 805-MHz cells. These cells are prepared with the same procedure as the 3-GHz cells. Primary surface treatment is a nitric acid bath followed by removal of approximately 70 nm of niobium using a 1,1,1 bcp. Two 805-MHz single-cell cavities are available for these tests. A total of 28 individual cavity tests are displayed in figure 1; figure 2 displays the results from eight cavity tests. All cavities are removed from the cryostat and reprocessed before running another test. Reprocessing typically starts with bcp and proceeds through a "standard"^{1,2} treatment procedure. However, there are some cavities that were only wiped clean and rinsed with pure water and/or menthol. The statistics are insufficient to resolve differences in the processing techniques.

The measured Q's as a function of the peak surface electric fields are shown in figure 1 and figure 2 for operation

at 2 K and 4.2 K, respectively. Some of the tests require an initial conditioning of the cell by gradually increasing rf power

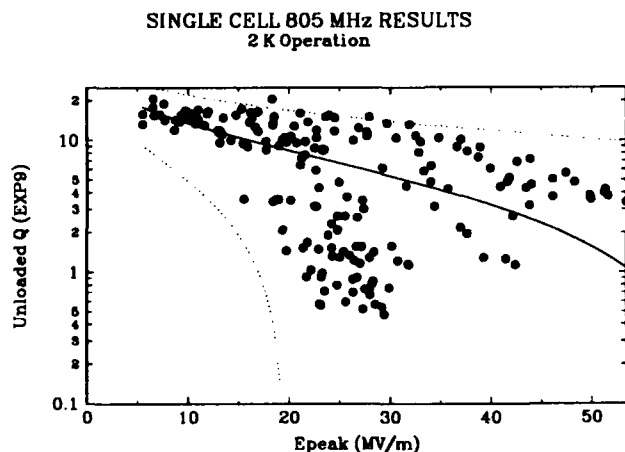


Figure 1. Q vs. Peak surface electric field at 2 K. Dotted lines indicate 95% confidence level.

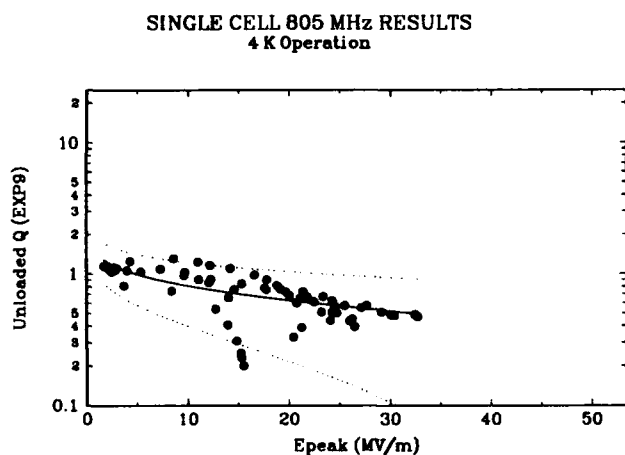


Figure 2. Q vs. Peak surface electric field at 4 K. Dotted lines indicate 95% confidence level.

until the cell "cleans up." The data shown in figures 1 and 2 are obtained after the conditioning process.

B. High Pressure Water Jet

A high-pressure pure water (HPPW) jet was used to recondition 805-MHz cavities. The cavities for these tests were previously used to obtain the data in figures 1 and 2. The HPPW cleaning was performed on a cavity that was exposed to room air, at room temperature. The pressure at the jet head was 800 psi; the pump is capable of 2000 psi. Cavitation at the pump inlet forced us to adjust the pressure to the lower value. Duration of the HPPW cleaning was 10 minutes for these tests. A single nozzle with three holes

ejected the water in a horizontal direction. The nozzle head moved vertically inside the cavity, driven by a motorized drive screw at the rate of 5 cm/minute.

At this time, three cavity tests have been done. The results are shown in figure 3. After exposure to room air, the

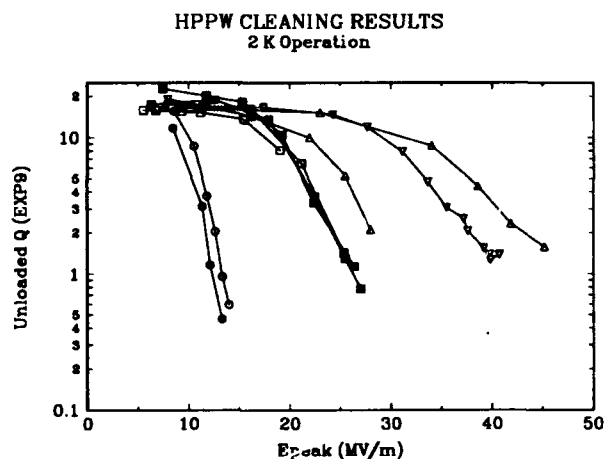


Figure 3. Q vs peak surface field at 2 K. a) Cavity performance after exposure to room air (circle), b) Cavity performance after first HPPW cleaning (box), c) Cavity performance after second HPPW cleaning (triangle).

cavity performance was degraded due to heavy electron loading. After cleaning with HPPW, the performance improved, attaining some of the highest values for all cavity tests.

C. Glow Discharge Cleaning

An 805-MHz cavity was cleaned using glow discharge cleaning in Argon. A niobium rod of 1.3-cm diam. was inserted axially to serve as the cathode. A niobium disk (7.6 cm dia., 0.9 cm thick) was mounted at the end of the rod and positioned in the center of the elliptical cavity. Currents of approximately 300 ma at voltages of 600 volts were maintained for 8 hours. Visual inspection of the vacuum-seal end plates on the cavity demonstrated that niobium had been sputtered from the cavity surface. The initial results, after glow discharge cleaning, show that the performance was reduced by a factor of approximately four (11 MV/m, at a Q of 0.5×10^9). The cavity was removed from the test system and vacuum baked at 200 C for 180 hours. After the bake, the partial pressure of the argon was reduced by a factor of 6. A subsequent test showed that the performance was still adversely affected (10 MV/m, at a Q of 0.5×10^9). After a 30-second dip in 1.1,1 bcp the performance improved (18 MV/m at a Q of 0.5×10^9). Our calculations indicate that a dip of this duration will only remove approximately 4 mm of niobium. These results are in accord with the idea that the sputtered niobium was the cause of the degraded performance of this cavity.

D. Superconducting Magnet to study cavities performance in a DC field

Compared to copper cavities, SC cavities can achieve substantially greater accelerating gradients with negligible thermal loss in the cavities. A parameter related to the accelerating gradient that must also be considered in accelerator facility design is the real-estate gradient (total potential change/total length of accelerator). Depending on the facility parameters maximizing the real-estate gradient can be of major importance. One possible way of doing this with SC structures is through the use of focusing elements that operate at cryogenic temperatures. Such focusing elements can eliminate transition to room temperature, and minimize the spacing between cavities. While this has the advantage of an increased real-estate gradient, there are several potential problems:

- how does the proximity of the DC fringe fields from the focusing elements to the iris of the SC cavities affect the performance of the cavity?
- how difficult is it to recover from a cavity quench?

To study these problems, we have constructed a small (5.7 cm long by 4.9 cm inside diameter) solenoid with superconducting wire⁴. This solenoid is about the size of a focusing solenoid for an accelerating structure made from the 3-GHz cavities. This solenoid has been tested to a current of 100 Amperes where the central, on-axis, field was measured to be 2 Tesla. With a 4-Tesla central field, we expect to generate fields at the cavity iris that approach the critical field in niobium. Experimentally for the initial test, we plan to cool

a cavity and measure the cavity performance with the solenoid off. Then measurements of the cavity performance, at discrete values of the solenoid field, will be performed. These measurements are similar to measurements of Ref. 5 performed with a 50-MHz structure. Other studies will be performed to determine methods for recovery after a cavity quench in the presence of the DC magnetic field.

IV. REFERENCES

- [1] B. Rusnak et al., "Superconducting Cavity Development at Los Alamos National Laboratory," Conference Record of the 1991 IEEE Particle Accelerator Conference, Vol. 2, pp. 1046-1047.
- [2] B. Rusnak et al., "Evaluation of Surface Contamination and Cleaning Techniques on Superconducting RF Cavities," 1992 Linear Accelerator Conference Proceedings, Vol. 2, pp. 728-730.
- [3] D. J. Liska et al., "Design Features of a Seven-Cell Cavity High-Gradient Superconducting Cavity," 1992 Linear Accelerator Conference Proceedings, Vol. 1, pp. 163-165.
- [4] Wire used has 54 filaments of NbSn with a copper-to-superconductor ratio of 1.35 to 1, and is 0.035-in diameter (without insulation). Insulation of formvar was added to bring the wire diameter to 0.037 inches.
- [5] R. Benaroya and K. W. Shepard, Rev. Sci. Instruments **59**, 2100 (1988).

L-band Superconducting Cavities at KEK for TESLA

K. Saito, S. Noguchi, E. Kako, M. Ono, T. Shishido, T. Tajima, M. Matsuoka*, H. Miwa**,
T. Suzuki**and H. Umezawa***

KEK, National Laboratory for High Energy Physics

Oho, Tsukuba-shi, Ibaraki-ken, 305, Japan

*; MHI, Mitsubishi Heavy Industries, Ltd.

Wadasaki, Hyougo-ku, Kobe-shi, Hyogo-ken, 652, Japan

**; Nomura Plating Co., Ltd.

Satsuki-cho, Kanuma-shi, Tochigi-ken, 322, Japan

***; Tokyo Denki Co., Ltd.

Higashisuna, Koto-ku, Tokyo-to, 136, Japan

Abstract

An attractive future application of superconducting cavities is a TeV energy superconducting linear collider (TESLA). Large merits of TESLA comparing to normal conducting linear collider are to loose alignment tolerance and less wake field due to the lower frequency (1.3GHz). The final focus also is easy by the large electron/positron population in bunches. TESLA demands up-grading field gradients of over 25 MV/m. KEK has started R&D on 1.3GHz niobium superconducting cavities since 1990. So far seven single cell cavities and two 9-cell cavities have been fabricated and tested. Parallel to them, input coupler design and niobium material study are being conducted. This paper reports the present status of KEK's efforts for TESLA.

I. INTRODUCTION

After the HEACC '92 three single cell cavities and one 9-cell cavity fabricated with MHI were tested. As presented in the HEACC'92 [1] the acceleration field in our single cell cavities is limited to 15-20 MV/m very reproducibly and we are making efforts to understand the limitation mechanism. We suspect three issues; 1) multipacting at equatorial section, 2) arcs from around input coupler or pick-up probe, 3) defects of electron beam welding at equatorial section. A diagnostic system was built up in order to observe heating sites and electron trajectories at the quench. Our cavity test activity was stopped for four months up to this May due to move from the TRISTAN assembly hall to a new sc experimental building. In this while we made a study of clean surface with laser dust analyzer. High temperature annealing (1400°C) became usable for single cell cavities in our existing UHV furnace. Niobium samples were annealed in this furnace and the RRR values were improved to 400.

Our TESLA activity is joined to the JLC (Japan Linear Collider) program from this fiscal year. Our one target will be to test beam quality and reliability of sc operation in the ATF (Accelerator Test Facility at KEK) which is under construction and to be completed in 1995.

II. TEST RESULTS AFTER HEACC '92

Our cavity test results after the HEACC '92 are summarized in Table 1 and the Q_0 -Eacc curves are presented in Fig.1. The 9-cell cavity as a TESLA prototype was tested twice and the field gradient was limited to 10-12 MV/m by

field emission. With single cell cavities except one field gradients were limited to the low field of 8-12 MV/m by field emission. Reason for these field emissions is contamination during high pressure water rinsing [HPR]. Water pressure of the HPR system has reduced from 85 to 65 kg/cm² in the long term operation. Foreign material fragments (50 μ m) were detected on a tested niobium sample in a surface analysis with EPMA. In addition the field gradient of 20 MV/m without field emission was achieved in C2 as before [1] when HPR was not conducted after the chemical procedure. These facts mean that high pressurized water removed nozzle material and contaminated cavity surface.

M1-(II) and M2-(III) have abnormally large residual surface resistance. One third in 151 n Ω of M1-(II) can be explained by the Q_0 -dropping in 4.2K measurement conducted previous to 2K one, in which field emission made an additional residual surface resistance same as the case of C2-(IV) discussed later. Probably the remained surface resistance and one of M2-(III) were due to Q_0 -disease by hydrogen [2]. As M1 (RRR=100) had many porosities on the equatorial EBW seam, it was rewelded from inside and annealed at 1400°C for 4 hours at CEBAF. Then it was sent back to KEK, electropolished (EP) 80 μ m and tested. The cavity would be picked up again much hydrogen during the heavy EP. Since this cavity was pre-cooled down with liquid nitrogen and held around 100K for one night as usual, it would have the Q_0 -disease. On the other hand a CEBAF's high RRR cavity with RRR>250 which was

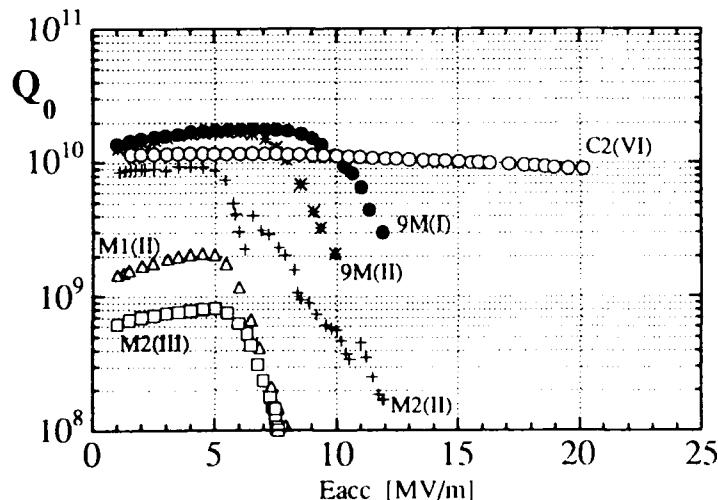


Fig. 1 Q_0 -Eacc curves with the cavities measured after the HEACC '92.

Table 1. Summary of cavity treatments and test results.

Cavity	Surface Treatment	Annealing	Rres (nΩ)	Eacc,max (MV/m)	Q ₀ (Eacc,max)
9M - (I)	E.P (80μm+10μm), HPR	760°C, 5 hours	13	9.9	2.1×10 ⁹
- (II)	E.P (20μm), HPR	no	11	12.0	3.1×10 ⁹
M1 - (II)	E.P (80μm), HPR	1400°C, 4 hours	151	8.1	9.0×10 ⁷
M2 - (II)	Tumbling (100μm), E.P (100μm+30μm), HPR	765°C, 7 hours	29	12.0	1.7×10 ⁸
- (III)	C.P (100μm+5μm)	760°C, 6 hours	321	7.6	1.5×10 ⁸
C2 - (VI)	C.P (35μm)	no, (1400°C)	22	20.2	9.0×10 ⁹

[9M is the 9-cell cavity ; M1, M2 and C2 cavities are the 1-cell cavities.]

annealed at 1400°C for 4 hours dose not show the Qo-disease any more even after heavily electropolished (120μm) [3]. A discrepancy in these facts might be in a difference of the material. M2-(III) was chemically polished (CP) by an unusual chemical procedure in which we cooled the cavity outer surface at 20°C with water during the CP and that resulted in a long CP time (40 minutes for 100 μm removal), then annealed at 760°C for 6 hours and chemically polished by 5 μm, then tested with usual cooldown procedure. Probably the cavity picked up more hydrogen during the unusual CP and our annealing process was poor to degas the hydrogen.

III. PROGRESS IN EQUIPMENTS

We have prepared some tools to understand and improve our field limitation. Several results from them are described here.

A. Diagnostic System

A temperature mapping system was built up to observe what happen in our cavity quench. The same data acquisition system in the reference [4] was used but thermometers are different. An Allen-Bradley's 51 Ω carbon resistor is surrounded with Stycast and stuck an aluminum nail (2mmφ) on the behind to thread a spring and to be supported by G-10 base plate. This sensor is forced on the cavity outer wall by the spring action. GE-varnish is coated to get a good thermal contact between the sensor and the cavity wall. Thermal sensitivity of the sensor is 5 mK. Apart 10 degree each, 19 sensors are distributed on one meridian at about one centimeter interval. Totally 684 sensors are fixed on the cavity wall.

This system was used first in the test C2-(VI) and temperature rise in the quench at 20 MV/m was observed (see Fig. 2). No temperature rise was detected before the quench (Eacc=20.5 MV/m) within present sensitivity as seen in Fig. A. However, after the quenching one local heating site appeared on the lower iris and the second spot came out on the same iris by the successive RF-processing (Fig.2 B,C). These heating sites were localized on the iris. The temperature rising can be fitted by the F-N plot and Qo-dropping also is explicable by field emission, however, any clear field emission trajectories are not observed in the temperature mappings. Maybe our thermosensor's sensitivity has to be improved more. Probably field emitted electrons from some

seed makes the heating spot but we do not yet understand what mechanism makes such a seed which limits the field gradient at 20 MV/m.

Another interesting phenomenon was observed in the measurement of M2-(III) (see Fig.3). During RF-processing at the maximum field of the field emission region, Qo-value degraded 1×10⁸ to 2×10⁷ and Eacc dropped 7 to 2 MV/m suddenly (we refer it as intermediate state). This state was stable but if RF-power was reduced and the dissipated power loss became small, it changed to the previous field emission state. This phenomenon is very reproducible. Fig. 3 shows the heating maps in the intermediate state. It is estimated that a large area(at least 650 mm², 29mmφ) of inner wall is normal conducting state. The site of this macro local heating was not fixed and changed three times from the equatorial section to the lower straight section of the cavity. The stationary field emitted electron's bombardments may be a trigger of this phenomena.

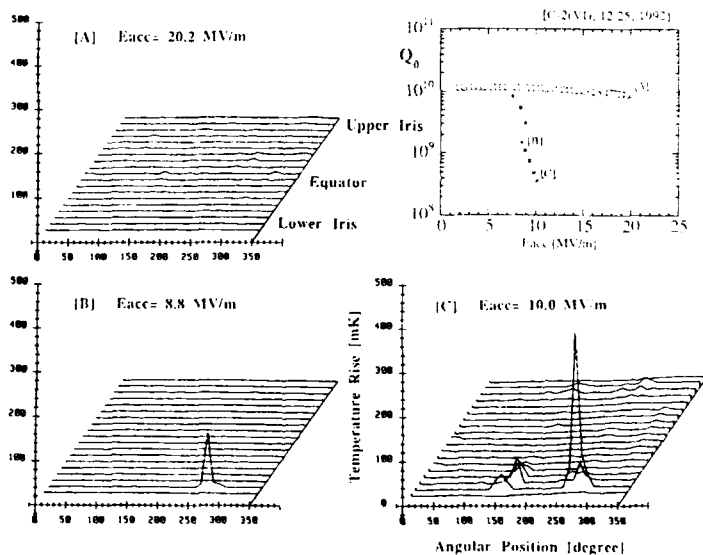


Fig. 2 Heating sites after the 20MV/m quench.

C2 had quenched finally at 20.5MV/m same as before [1]. Qo degraded by the successive RF processing after the quench. The indexes of A,B,C in the heat mappings are corresponding with ones in the Qo-Eacc curve.

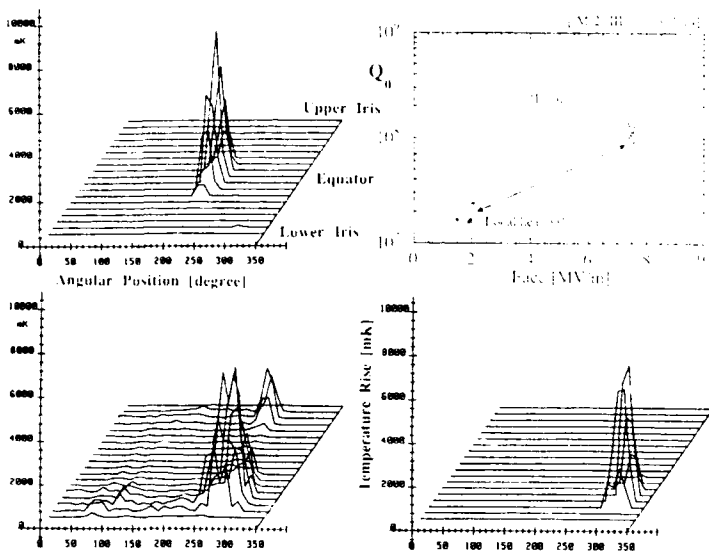


Fig. 3 Temperature rise in the intermediate state.

B. High Temperature UHV Annealing

It is well known that high temperature UHV annealing is a very effective tool on high field gradient of sc cavities [5]. We can expect three effects in this treatment, 1) upgrading thermal conductivity in niobium material, 2) reduction of inhomogeneity which weakens magnetic property in the superconducting state, 3) a perfect solution of Qo-disease by hydrogen. We have used a 700-760°C UHV annealing for hydrogen out gassing and a higher temperature annealing furnace became usable recently. We made a sample test using this furnace. Samples with initial RRR value of 54, 117, 159, 213 and 246 were annealed at 1350°C for 6 hours combined with titanium gettering and improved to 273, 308, 351, 383 and 394 with the RRR value, respectively. After this testing, a single cell cavity (M2) was annealed at 1400°C for 6 hours with this furnace.

C. Dust Analysis

Residual micro dust particles on a cavity inner surface have a large influence on field emission. Field emission is the today's most serious problem not in high field sc cavities but also high field copper cavities as JLC. We have just started a study on the ultra-clean surface. We analyzed dust particles in the TRISTAN sc cavity's surface treatment procedure using a laser scattering dust analyzer in cooperation from an semiconductor industry. We simulated the rinsing procedure using silicon wafers (90mm ϕ). This is the same way in the reference [6]. Fig.4 shows the residual dust particle's

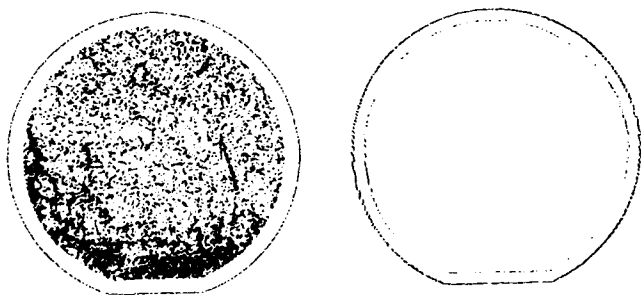


Fig. 4 Dust analysis with our chemical process.

The left is a result of the silicon wafer rinsed with our full rinsing procedure. The right is one rinsed with a megasonic agitator (950KHz).

distribution and the number on the silicon wafer which was finally rinsed with ultra-pure water in a hot bath [7]. The dusts of 0.2-3 μ m were analyzed. Micro particles (>1 μ m) over one thousand are remaining on the wafer. It shows our dust particle control is poor even ultra-pure water is used. Tools which transfer an energy and remove actively dust particles on the surface have to be developed. One method is HPR. Our HPR system had a contamination problem as mentioned above but CEBAF confirmed recently that it is a very powerful tool against field emission with niobium bulk cavities [3]. A maximum surface electric field over 50MV/m ($E_{acc} > 28$ MV/m) was achieved without any field emission. We are considering a megasonic agitation rinsing as another method to remove submicron particles. Fig. 4 (right) shows a result rinsed with such an agitator (950 KHz). No particle larger than 0.6 μ m is detected and totally only 8 particles of 0.19-0.6 μ m are seen.

IV. DEVELOPMENT OF INPUT COUPLER

We are considering wave guide input couplers for TESLA cavities from the TRISTAN operational experience. As the first test we have measured the Qext of such a coupler using a cooper single cell cavity. Enough coupling to 1×10^5 was confirmed if the distance between the iris of the cavity and the edge of the coupler was less than about 55 mm. We have a plan to make a single cell niobium cavity with a wave guide coupler. In this fabrication forming method of the coupler and its influence on the fundamental field distribution and so on will be studied.

V. ACKNOWLEDGMENTS

The authors would like to Prof.s. Kimura, Takata and Kurokawa for their continuing supports and encouragements for our study. We would also like to thank Dr.K.Hosoyama and Mr.Y.Kojima for cooperation in liquid helium supplying to our cavity cold tests. We are deeply indebted to Mr.K.Kurosawa in Sony Technology Center in Atugi for his help for our dust analysis.

VI. REFERENCES

- [1] E.Kako et. al., "Development of High Gradient L-band Superconducting Cavities" *Proc. of the HEACC'92 Conference*, P.966.
- [2] K.Saito and P.Kneisel, "Q-Degradation in High Purity Niobium Cavities-Dependence on Temperature and RRR-Value" *Proc. of the 3rd EPAC conference*, 1992
- [3] P.Kneisel; private communication.
- [4] T.Tajima et. al., "Temperature Mapping System Developed at KEK for Field Emission Studies on Superconducting Cavities", *ibid. ref.[1]*, P.751
- [5] H.Padamsee et. al., "New Results on RF and DC Field Emission", *Proc. of the 4th Workshop on RF Superconductivity*, 1989 at KEK, P.207.
- [6] C.Z.Antoine et.al., "Dust Contamination during Chemical Treatment of RF Cavities:Symptoms and Cures" *Proc. of the 5th Workshop on RF Superconductivity*, 1991 at DESY, P.456.
- [7] K.Saito et.al., "R&D of Superconducting Cavities at KEK", *ibid. ref.[5]*, P.635.

Design of a HOM Damped Cavity for the ATF Damping Ring

S. Sakanaka, K. Kubo and T. Higo
National Laboratory for High Energy Physics (KEK)
1-1 Oho, Tsukuba-shi, Ibaraki-ken, 305 Japan

Abstract

A HOM (Higher-Order-Mode) damped cavity for the ATF Damping Ring was designed at KEK. Damping both by waveguides and by big beam holes was adopted. Numerical calculations on external-Q's of low-frequency HOMs showed good damping characteristics. Low-power measurements are under way with a cold-model cavity.

I. INTRODUCTION

A 1.54 GeV Damping Ring (DR) [1] is being constructed at KEK as an accelerator subsystem of ATF (Accelerator Test Facility). This facility is purposed to investigate the feasibility of providing highly-brilliant electron beams of multi-bunches which is required for future linear collider project. The ATF DR will be operated with beam currents up to 600 mA with multibunches.

A frequency of 714 MHz, a subharmonic of the injector linac frequency, was chosen for rf acceleration, considering beam dynamic issues related to wake fields of the fundamental mode [2]. The need for short bunches ($\sigma_z < 5$ mm) requires a gap voltage of 1 MV, which will be provided by four single-cell copper cavities. Because the ATF DR adopts very narrow beam pipes ($\phi 26$ mm in arc sections), there exist many HOMs in the rf cavities up to the cutoff frequencies (8.83 and 6.76 GHz for TM01- and TE11- modes, respectively). Therefore, the requirement to store a large beam current free from coupled-bunch instabilities forces one to design the cavities whose longitudinal and transverse coupling impedances arising from HOMs are sufficiently reduced.

The requirements for the HOMs are derived from tracking simulations [2], and are summarized below:

$$(R_{sh}/Q) \cdot Qf < 10-30 \text{ [k}\Omega\text{GHz/ring]} \text{ for monopole modes,}$$

$$(R_T/Q) \cdot Q < 2-3 \text{ [M}\Omega\text{m/ring]} \text{ for dipole modes}^*,$$

* assumed that a bunch-to-bunch tune spread of 10^{-3} (peak-to-peak) will be introduced in each bunch-train.

where R_{sh} is the shunt impedance ($=V^2/P$), f the resonant frequency and R_T the transverse impedance. For TM011-like mode, which has particularly large R_{sh}/Q , a severer condition of $Q < (15-20)$ may be required.

II. CAVITY DESIGN

Among several schemes for HOM damping, we adopted a waveguide damping scheme similar to that proposed for PEP-II [3]. A cylindrical cavity, with round corners ($R=30$ mm) and nose cones, was chosen for the basic shape (see Figs. 1 and 2). For damping HOMs, four waveguides ($170\text{mm} \times 20\text{mm}$, $R=5$ mm at corners; cutoff freq. is 885 MHz) are attached at the corners, where magnetic fields of most HOMs are large. Two of the waveguides are attached to one ($z > 0$) side of the cavity, parallel to horizontal (x) axis, while the other two to the other

($z < 0$) side, parallel to vertical (y) axis. In this configuration, each of degenerated dipole modes, together with monopole modes, will be damped, while holding 180° rotational symmetry of the shape. The cooling for this shape may be easier than that for PEP-II because of more spaces between the waveguide-slots, though the rotational symmetry is lower.

Even with the damping by waveguides, it is difficult to damp all HOMs up to the beam-pipe cutoff because too many modes exist. Thus, an additional beam-hole damping scheme [4,5] was introduced, in which the power from high-frequency HOMs propagates out of the cavity via big beam-holes ($\phi 100$ mm) and is dissipated in microwave absorbers attached on big beam-pipes beside the cavity. The beam-hole radius was chosen so that several HOMs which do not couple to the waveguides well are extracted, while holding the fundamental

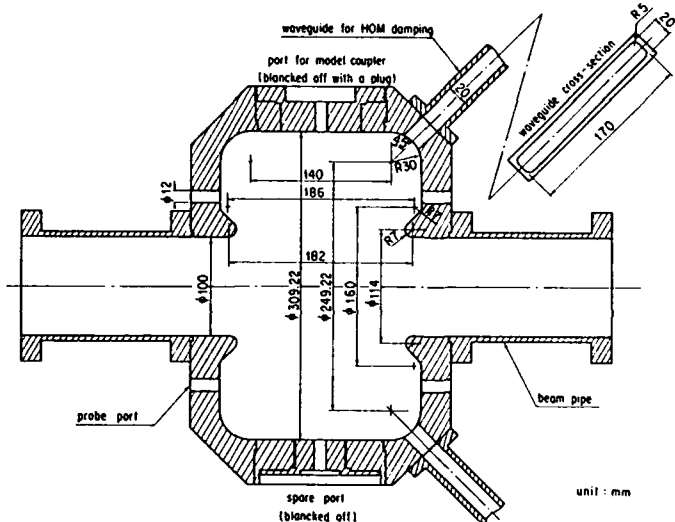


Fig. 1. Cross-section of a low-power test cavity.



Fig. 2. Low-power test cavity under measurement.

Table 1. RF related parameters of the ATF DR.

rf frequency	f_{rf}	714 MHz
Shunt impedance per cavity	R_{sh}	3.6 M Ω
Unloaded-Q	Q_0	22,100
Dissipated power per cavity	P_c	17.4 kW
Total gap voltage per ring	V_c	1 MV
Radiation loss per turn	U_0	0.190 MeV
Maximum beam current	$(I_0)_{max}$	600 mA
Transmission power per coupler	P_{gl}	45.9 kW
Coupling coefficient of coupler	β	2.6

shunt impedance acceptable. Principal parameters of the cavity were calculated with such codes as SUPERFISH and MAFIA, and are shown in Table 1. The Q_0 -value in the table includes the degradation of ~23% (calculated) arising from attaching the waveguides and further of ~20% (assumed) from other causes.

III. CALCULATIONS OF HOM DAMPING

External-Q's of low-frequency HOMs were calculated with the method developed by Slater, Gluckstern, Kageyama, Kroll, Yu et al. [6-10]. The resonant frequencies of the lossless cavity-waveguide coupled structure were calculated with MAFIA 3D code, with waveguides shorted at different lengths. Figure 3 shows the cavity shape used for the calculations. Only 1/8 of the cavity was modeled to save the number of mesh-points, though the actual cavity is not symmetrical at $z=0$ plane. Then, the phase $\phi (=2\pi L/\lambda_g - n\pi)$ were plotted against the frequencies, where L is the distance of a short from the cavity center, λ_g the guide wavelength and n the branch number. Near resonances, ϕ can be represented by the following relations [10]:

$$\phi(\omega) = \sum_i \arctan\left(\frac{v_i}{\omega - u_i}\right) - \chi(\omega),$$

$$\chi(\omega) \approx \chi_0 + \omega \cdot \chi',$$

where $u_i + jv_i$ represents the complex resonant frequency of i -th mode and $u_i/2v_i$ gives the external-Q (Q_{ex}).

Figure 4 shows an example of the phase-frequency plot obtained from six MAFIA runs for a MME-boundary condition (i.e. Magnetic-, Magnetic- and Electric- short conditions on $x=0$, $y=0$ and $z=0$ planes, resp.). As the range 1.45-2.05 GHz contains four overlapped-resonances, the data in this range were fit with ten parameters (u_i , v_i , $i=1-4$, and χ_0 , χ'). The resonant frequencies and Q_{ex} 's obtained are summarized in Table 2. By inspecting field plots of the above resonances, it was found that these could be the mixed modes of the original (no waveguides) modes. It is worth noticing that this "mode mixing" phenomenon sometimes limits the performance of the waveguide damping. Let us show an example in our early design of the cavity. The frequency separation between TM012- and TM210- like modes was only 13 MHz without waveguides. When the waveguides were attached, these modes mixed and split into two modes, one has a very large Q_{ex} ($=1600$) while the other a small ($Q_{ex}=17$), both having an R_{sh}/Q of a few ohms. This was caused by a large perturbation introduced by the waveguides. In our present design, this problem has been removed by making the frequency separation large via modifying the cavity shape.

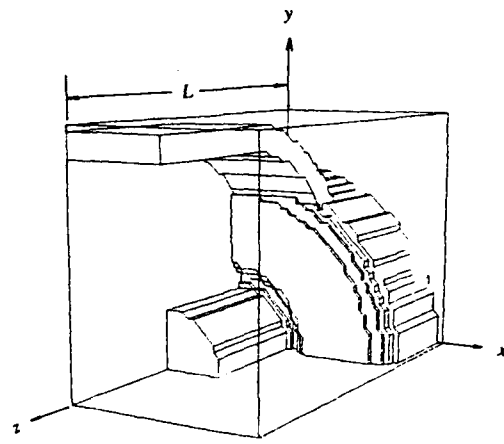


Fig. 3. Cavity shape used for the MAFIA calculations.

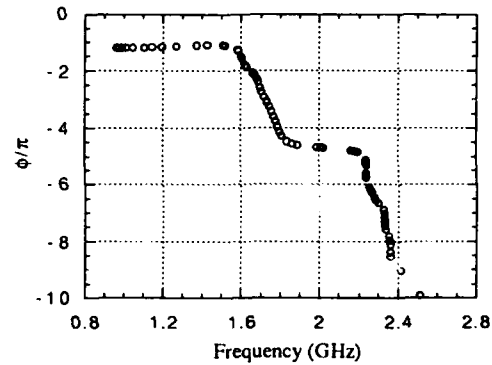


Fig. 4. Phase-frequency plot for MME-boundary condition.

Table 2 also shows the results for other boundary conditions. For harmful HOMs below the beam-hole cutoff, the calculated Q_{ex} 's seem to be acceptable for the requirement. These results are to be checked by calculations with a 1/4 model, correctly taking the cavity symmetry into account.

IV. MEASUREMENT WITH A TEST CAVITY

A low-power test cavity (Figs. 1 and 2) was made by assembling three pieces machined from aluminum alloy (A5052) blocks. The cavity has four ports for test-couplers and tuners (blacked-off with plugs at present) and seven probe ports, together with damping waveguides and beam pipes.

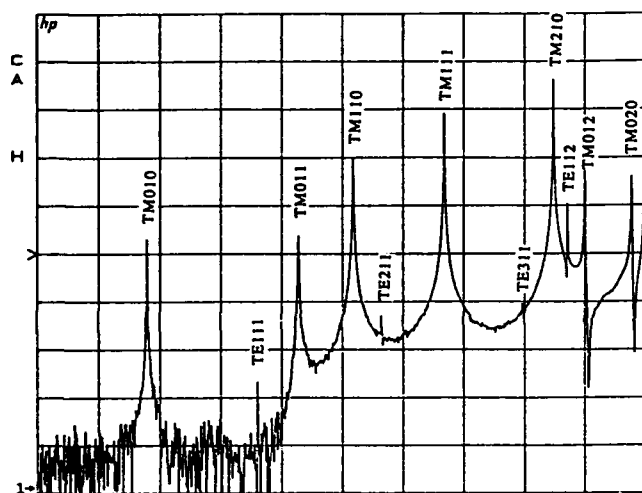
Firstly, we observed undamped resonance-spectrum by shorting waveguide-slots. Figure 5(a) shows the transmission parameter S_{21} between two antennas put at both end-plates, measured with an HP8510B Network Analyzer. Then, the damping waveguides with 80-cm-long terminating loads were attached to the cavity. As shown in Fig. 5(b), most resonances in the measured range were heavily damped to $Q_L < 100$, except for the fundamental (TM010) mode and for the mode appeared at 0.89 GHz. TM011-like mode is not discernible, and the loaded-Q's (Q_L) for TM110- and TM111- like modes are ~25 and ~20, respectively. The peak at 0.89 GHz ($Q_L \sim 20$) is, possibly, a damped TE101-like resonance in the waveguide coupled to some cavity modes (TE111 or TM011), which arises from the poor termination of the loads slightly

Table 2. Result of the calculations on HOM damping by 164mm×20mm rectangular waveguides ($f_c=914$ MHz). A 1/8 part of the cavity was modeled. Note that the waveguide dimensions are slightly different from those of the final design.

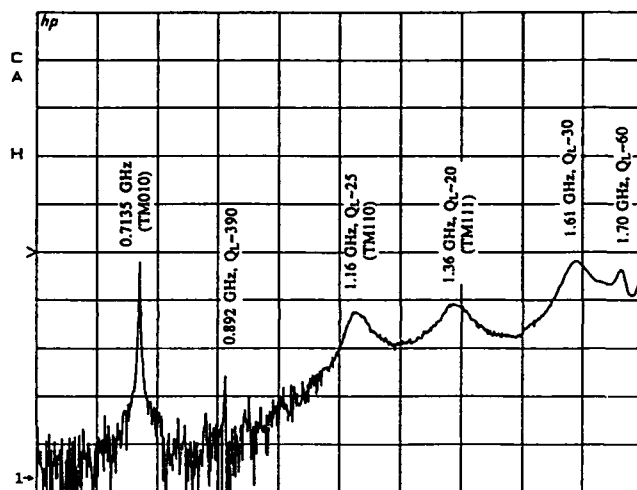
Boundary condition	No waveguides (MAFIA)				With four waveguides (MAFIA/Kroll-Yu)			
	Mode	f (MHz)	Q _o	R _{sh} /Q or R _T /Q	(Mode)	f (MHz)	Q _{ex} *	R _{sh} /Q or R _T /Q**
MME	MME-1 (TM010)	724.7	34,500	168.6 Ω	(TM010)	709.3	below cutoff	168.0 Ω
	MME-2 (TM210)	1591	59,400		(mixed mode)	1605	40	~ 0.2
	MME-3 (TM012)	1682	35,700	10.7	(mixed mode)	1693	48	~ 8.3
	MME-4 (TM020)	1747	63,000	0.21	(mixed mode)	1754	29	~ 0.5
	MME-5 (TE2xx)	1803	44,100		(mixed mode)	1791	37	~ 0.5
MMM	MMM-1(TM011)	1044	28,000	62.5	(~TM011)	1075	7.1	~ 37
	MMM-2 (TE211)	1217	39,400		(~TE211)	1215	21	~ 0.1
	MMM-3(TM211)	1787	43,700		(TE411+TM211)	1800	~870	~ 0.02
	MMM-4 (TE411)	1804	39,800		(TM211+TE411)	1808	18	~ 0.7
	MMM-5(TM021)	1959	38,500	6.6	(~TM021)	1952	27	~ 5
MEE	MEE-1 (TM110)	1152	45,400	263 Ω/m	(~TM110)	1160	24	~ 190 Ω/m
	MEE-2 (TE112)	1600	45,900	17	(~TE112)	1605	100	~ 20
MEM	MEM-1 (TE111)	953.6	38,700	2.0	(TE111)	896.6	below cutoff	9.6
	MEM-2 (TM111)	1349	33,900	726	(~TM111)	1363	24	~ 490
	MEM-3 (TE311)	1502	40,300		(TE311+TM111)	1500	115	~ 50

* For dipole modes, two times the calculated results are shown by taking the proper symmetry of the cavity into account.

** Note that non-zero R_{sh}/Q or R_T/Q can be introduced to (originally) higher-multipole ($m>1$) modes due to the mode mixing. R_{sh}/Q or R_T/Q , which are evaluated at the detuned waveguide length for each resonance, are shown in this column as a measure of the mode mixing. But in some cases, they may be different from those of individual resonances due to mode-overlapping.



(a) Without waveguides.



(b) With waveguides and terminating loads.

Fig. 5. Resonance spectrum of the test cavity. Abscissa: frequency, 0.5-1.75 GHz. Ordinate: transmission parameter S_{21} , 10 dB/division, reference value (center line) -60 dB.

above the guide cutoff. As this mode may be contaminated by TM011-like mode, further efforts are needed to measure its R_{sh}/Q .

Work is continuing to check the performance of the designed cavity both experimentally and computationally. Especially, study on the beam-hole damping of high-frequency modes should be performed. As the next step, cooling design has to be made towards the high-power test cavity. Developments on input couplers, tuners and in-vacuum waveguide loads are also needed.

Acknowledgments

The authors wish to thank Y. Yamazaki for valuable advices, M. Izawa, S. Tokumoto and members of ATF group for useful discussions.

V. REFERENCES

- [1] J. Urakawa et al., *Proc. of XVth International Conference on High Energy Accelerators*, Hamburg, 1992, Vol. I, p. 124.
- [2] K. Kubo, KEK Proceedings 92-6, pp. 155-165 (edited by J. Urakawa and M. Yoshioka).
- [3] R. Rimmer et al., *Conference record of the 1991 IEEE Particle Accelerator Conference*, Vol. 2, pp. 819-821.
- [4] T. Weiland, DESY 83-073.
- [5] H. Padamsee et al., *Conference record of the 1991 IEEE Particle Accelerator Conference*, Vol. 2, pp. 786-788.
- [6] J.C. Slater, *Microwave Electronics*, D. Van Nostrand, 1950.
- [7] R.L. Gluckstern and R. Li, *1988 Linear Accelerator Conference Proceedings*, 1988, pp. 356-358.
- [8] T. Kageyama, KEK Report 89-4 (1989).
- [9] N.M. Kroll and D.U.L. Yu, *Part. Accel.* 34 (1990) p. 231.
- [10] N.M. Kroll and R. Rimmer, *Conference record of the 1991 IEEE Particle Accelerator Conference*, Vol. 2, pp. 801-803.

MEASUREMENT OF MICROWAVE PROPERTIES OF X-BAND ACCELERATING STRUCTURE UNDER PULSED HIGH-POWER OPERATION AT LIQUID NITROGEN TEMPERATURE

*A.I.Saversky and I.S.Shchedrin
Moscow Engineering Physics Institute
31 Kashirskoe Road, Moscow, 115409 RUSSIA*

Abstract

After required chemical treatments a disk-loading structure was operated at liquid nitrogen temperature with X-band magnetron as an RF source. The peak RF pulse power was variable from 150 to 300 kW and the average power was altered by changing the pulse repetition rate between 1400 and 2800 pps. Measurements on this structure both at low and at high power indicated the Q factor of 6800 at room temperature, which increased to 17000 at liquid nitrogen temperature — an enhancement factor greater than 2,5 in good agreement with theory.

INTRODUCTION

There are several applied applications of linear accelerators where the space available for the accelerating structure and the RF source is limited, or where there is a limitation on the RF power available. The efficiency of guide structure made of conventional materials can be increased by reducing its operating temperature and increasing its operating frequency.

The advantages of superconducting materials application in particle accelerators have been limited by the cost of constructing and operating the refrigerating systems necessary to maintain the low temperature required. In addition, at temperatures very close to the critical temperature T_c , the surface resistance of superconductors would strongly depend on temperature T , which results in variation of the linac characteristics due to the fluctuations or drifts of the cryogenic refrigerator temperature. On the contrary, the surface resistance of all normal metals is nearly independent of temperature in the anomalous skin-effect domain.

In the past, the microwave surface resistivity of copper and aluminium was carefully measured both at room and liquid nitrogen, hydrogen and helium temperatures [1,2]. Using appropriate surface treatment technology, the theoretical value of surface resistance was experimentally obtained at low power and cryogenic temperatures in microwave structures of complicated shape. However, the Q-factor of S-band accelerating structures at liquid nitrogen temperature decreases with peak RF power [3].

In order to evaluate the advantages and problems associated with a system operating at liquid nitrogen temperature, an investigation was undertaken with the following objectives: first, to establish the feasibility of operating an accelerator structure at 77 K, and, second, to determine what advantages might be realized with respect to size or power input requirements. We report here experimental results which show the increasing of Q-factor by cooling X-band accelerator cavity working at 9,35 GHz from $T = 293$ K to $T = 77$ K, these result being compared to the theoretical value.

RF SURFACE RESISTANCE OF COPPER AT LOW TEMPERATURE

For RF currents, the surface resistance decreases first as $\delta^{-1/2}$ (δ — conductivity of metal) by lowering the temperature until a certain limit and at relatively low frequencies. But at very low temperatures and very high frequencies, RF field amplitude changes rapidly in space along an electron mean free path l , and during the time t between two successive collisions. For both reasons Ohm's law can no longer be applied.

The surface resistance of normal metals in anomalous skin effect domain can be obtained by using the Dingle's expressions. This formula can be used at all temperatures and microwave frequencies, considering both specular and diffuse electron reflection at the metal surface, but neglecting relaxation. At frequencies less than 35 GHz, the influence of relaxation effect on R_s may be neglected [1].

The temperature dependence of copper enhancement factor $K_R(T) = R(293 \text{ K})/R_s(T)$ can be seen on figure 1. The frequency dependence of K_R can be seen on figure 2. The curves were obtained by computation of Dingle formulas [4] (for specular and diffuse electron reflection) at 9,35 GHz (fig.1) and at 77 K (fig.2). The experimental points of K_R (fig.2) for different kinds of cavity

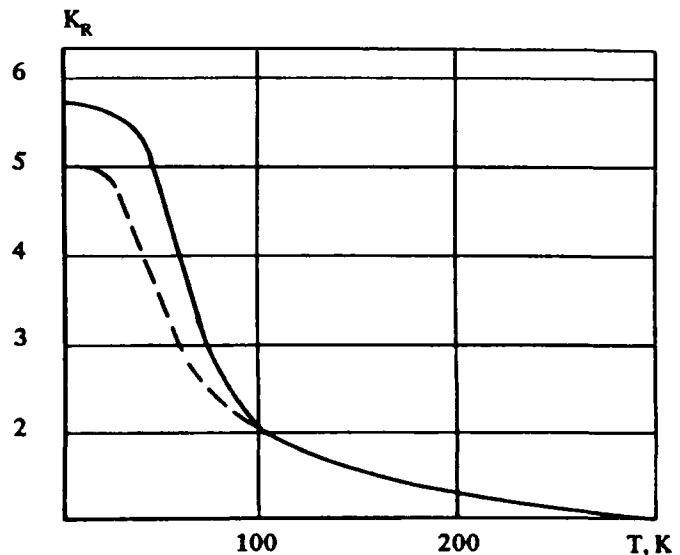


Fig. 1. Temperature dependence of enhancement factor K_R for OFHC copper at 9.35 GHz.

———— specular reflection
- - - - - diffuse reflection

surface treatments shows, that for the enhancement factor value at low temperatures in good agreement with theory to be obtained chemical (or electrochemical) polishing and finally annealing in hydrogen atmosphere must be used. The best results were achieved by using copper single crystals [1] or OFHC copper with 1% of yttrium [5]. According to this results the enhancement factor of 2,8 can be obtained at nitrogen temperature and X-band frequencies.

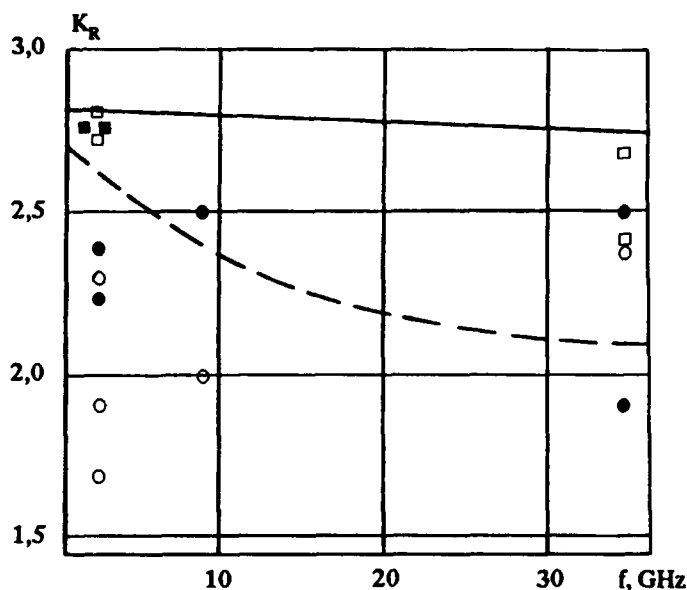


Fig. 2. Frequency dependence of enhancement factor K_R for OFHC copper at 77 K.

1) computed

— specular reflection
- - - diffuse reflection

2) experimental

○ — before chemical treatment
● — after chemical treatment
■ — after electrochemical treatment
□ — after annealing in hydrogen

Q-FACTOR MEASUREMENT METHOD, EXPERIMENTAL SET UP AND RESULTS

For high-power tests a 12-cell disk-loading cavity was constructed. The length was chosen $L = 4\lambda_g$ at 9,35 GHz. This cavity was operated in standing wave of $2\pi/3$ mode. It was fitted with standard $28,5 \times 12,6$ mm² rectangular waveguide input, which includes a section made out of thin walled stainless steel to minimize the thermal losses. Despite the relatively poor conductivity of stainless steel, the insertion losses are less than 0,5 dB in this section. A cavity was made out of oxygen-free high-conductivity copper with a purity of 99.99%. A chemical polishing in a $1/3 \text{ H}_3\text{PO}_4 \cdot 1/3 \text{ HNO}_3 \cdot 1/3 \text{ CH}_3\text{COOH}$ during a few minutes at a room temperature is sufficient for obtaining mirror like surfaces.

The cavity was cooled down in a cryostat filled up with liquid nitrogen, the working temperature being 77 K. The cavity with its supporting waveguide was pumped down to a low pressure (less than 10^{-6} Pa) to avoid gas condensation on the walls during the cooling process.

At low power the unloaded quality factor Q_0 was obtained by an impedance measurement method both at room and nitrogen temperatures. It is known, that the external quality factor Q_1 depends only on the coupling; it remains constant if the coupling is not modified. At low temperatures and high power unloaded quality factor $Q_0(T)$ can be obtained by measuring the input VSWR [3]. In practice, it is, however rather difficult to measure this value with error required when there are reflections in supporting waveguid.

Unloaded quality factor at low temperature can be obtained from the relation:

$$Q_0(T) = \frac{Q_0(T_0)}{1 - Q_0(T_0) [Q_1^{-1}(T_0) - Q_1^{-1}(T)]}$$

where $Q_0(T_0)$, $Q_1(T_0)$ are unloaded and loaded quality factor respectively at temperature T_0 ($T_0 = 293$ K for this case); $Q_0(T)$, $Q_1(T)$ — the same parameters at nitrogen temperature. At high power $Q_1(T)$ can be obtained by a decrement measurement method.

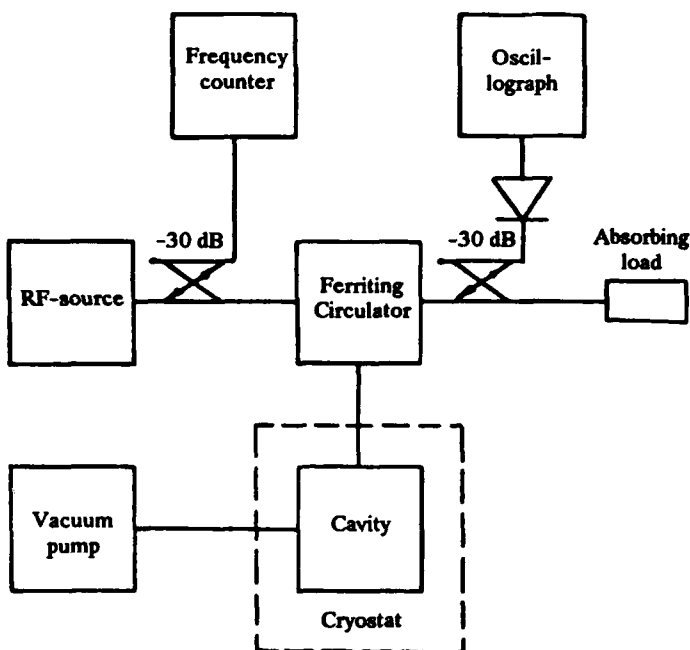


Fig. 3. Electron set up for high power operation.

Table 1.

Calculated and experimental resonator parameters

Parameters	T = 293 K	T = 77 K
Calculated Parameters		
Stored Energy per Cavity for 1 MV/m, J	$4,2 \cdot 10^5$	$4,2 \cdot 10^5$
Power Loss per Cavity for 1 MV/m, W	316	113
Unloaded Q-Factor	7850	22000
Shunt Impedance, MOh/m	57	160
E_p / E_0	1,52	1,52
Experimental Results		
Resonant Frequency, MHz	9379,8	9348,0
Unloaded Q-Factor	6800	17000
Coupling Factor	0,62	1,53
Enhancement Factor	—	2,5

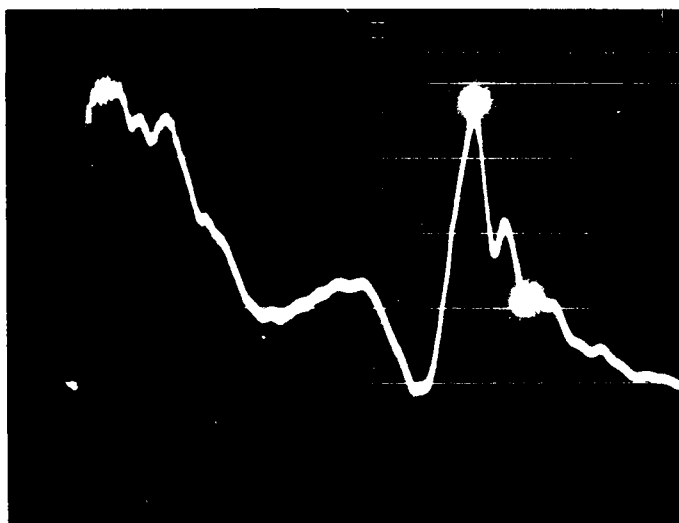


Fig. 4. Oscillogram of RF pulse reflected from the cavity at $T = 293$ K. Scale — 100 ns/cm.

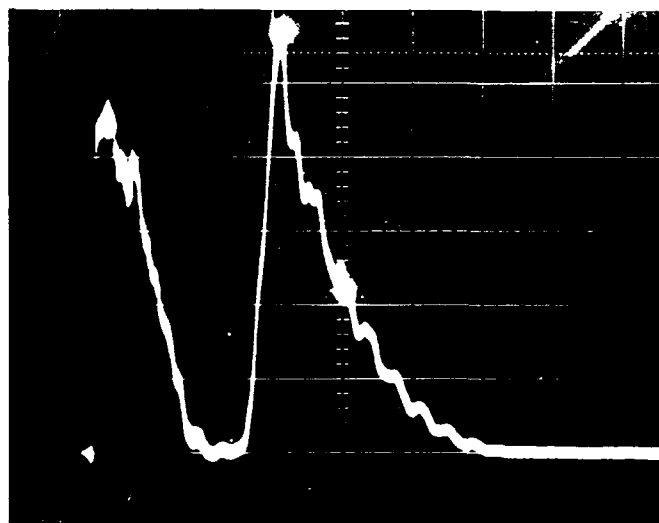


Fig. 5. Oscillogram of RF pulse reflected from the cavity at $T = 77$ K. Scale — 200 ns/cm.

The electron set-up for high power operation is shown in figure 3. The peak RF pulse power from the X-band magnetron was variable from 150 to 300 kW by changing the anode voltage. The average power was altered by varying the pulse repetition rate between 1400 and 2800 pps. The RF pulse width was equal to 0,5 μ s. The tests were carried out on $\pi/2$ and $2\pi/3$ mode. The frequency was measured by electronic frequency counter.

Calculated and experimental results are shown in table 1. In figure 4 and figure 5 the oscillograms of rf pulse reflected from the cavity at resonant frequency are shown at $T = 293$ K (fig.4) and $T = 77$ K (fig.5). At low and at high power as well the same value of unloaded quality factor was obtained. The accelerating field for 300 kW at $T = 77$ K is equal about 50 MV/m.

CONCLUSION

The anomalous skin effect should be taken into account for computation the surface resistance of an X-band cavity at nitrogen temperature.

Using appropriate surface treatment techniques to the cavity fabricated out of OFHC copper, the theoretical value of Q-factor can be obtained at cryogenic temperature.

The enhancement factor of X-band accelerator cavity (after

chemical polishing) at nitrogen temperature was equal 2,5 both at low and at high power.

No decreasing of the Q-factor at $T = 77$ K was observed at high power. The maximum accelerating field was approximately equal 50 MV/m.

REFERENCES

- [1] Benard J., Minyaw N.H., Viet N.T. Reduction of RF losses at 35 GHz in high purity copper resonant cavities by coling to cryogenic temperature. - *Revue de Phys. Appl.* V.13, 1978, 10, 483.
- [2] Biqvard F., Septies R. Amelioration de la conductivite superficielle du cuivre et de l'aluminium en hyperfrequences, par abaissement de temperature. - *Nuclear Instruments and Methods*, 1966, 44, 18.
- [3] McEuen A.H., Lui P., Tanabe E., Vaguine V. High-power operation of acceleration structure at liquid nitrogen temperature. - *IEEE Trans. on NS*, Vol NS-32, N 5, 2972.
- [4] Dingle R.B. The anomalous skin effect and the reflectivity of metal. - *Physics*, 1953, XIX, 4, p. 311.
- [5] Private communication with V. A. Kutovoy of Kharkov Inst., 1991, Kharkov, Ukraine.

RF Systems Engineering for the SSC Collider Rings

G. Schaffer, P. D. Coleman, R. E. Mustaine, J. D. Wallace, X. Q. Wang, Y. Zhao, J. D. Rogers
Superconducting Supercollider Laboratory*
2550 Beckleymeade Ave., Dallas, TX 75237 USA

Abstract

Acceleration and storage of 70-mA proton beams in the 2 x 20 TeV Supercollider rings can be performed both with normalconducting as well as superconducting 360-MHz rf systems. A normalconducting accelerating structure would use 32 or 24 single-cell cavities per ring, operating with a mean gradient of 2 - 2.6 MV/m to generate the required peak voltage of 20 MV in the beam holding mode. Superconducting cavities would allow operation with mean gradients up to about 5 MV/m, and tolerate higher transient beam loading due to nearly tenfold larger stored energy in the accelerating structure. A superconducting structure could consist of five pairs of single-cell resonators per ring, each pair being fed by a 250-kW cw klystron amplifier. The use of 500-kW or 250-kW klystron amplifiers, six or eight per ring, would seem appropriate for feeding normalconducting structures. Provisions for feedforward and feedback (rf amplitude and phase) are included in the low-level rf system. Furthermore, active damping of undesired modes and corrections of bunch phase deviations are planned by means of auxiliary (broadband) rf systems.

I. INTRODUCTION

The SSC collider rings have to raise the energy of the injected beams from 2 to 20 TeV, maintain the tight bunching during collisions, and compensate for synchrotron radiation losses (of the order of 0.12 MeV/turn). The bunch spacing is chosen to be 5 m, leading to a bunch frequency of 60 MHz. For the collider rings, 360 MHz has been chosen as the most convenient rf frequency [1,2,3].

The beam acceleration in the rings takes nearly 25 minutes, requiring about 3.6 MeV energy gain per turn. The rf power transmitted to each of the 70 mA beams will be about 267 kW, the peak rf voltage at injection is 6.6 MV, bucket area approximately 3.3 eV-s. The particles circulate with a frequency of 3.44 kHz on the 87120 m long machine circumference.

In the storage mode the rf peak voltage has to be raised to 20 MV, corresponding to a bucket area of about 18.3 eV-s. The rms bunch length is kept to 6 cm. Each of the 70-mA beams requires about 1.4 MVA reactive rf power, and 8.8 kW real power for covering the synchrotron radiation losses.

Instead of using 5-cell cavities as proposed in the baseline design, single-cell cavities will be used for beam acceleration. The reason for this change is easier damping of undesired resonant modes as outlined in references [2] and [3].

In the following, we describe some details of technical solutions which are based on either using normalconducting or superconducting cavities. Both options appear feasible and have their specific merits. Using superconducting cavities is more complex but attractive for handling transient beam loading [3,4,5]. Preliminary results of cost studies indicate lower costs for a system based on superconducting cavities [6].

II. REDUNDANCY IN THE RF POWER SYSTEM

The baseline design suggests the use of two 1.1-MW klystron amplifiers per ring to cover the rf power required for eight 5-cell cavities (i.e., 40 cells) in each ring. This amount of rf power would also be sufficient for 32 normalconducting single cells per ring, and there is no concern about the reliability and lifetime of 1.1-MW klystrons as they are used in great numbers at CERN for LEP I (their average life is reported to be 17000 hrs so far [7]). However, any failure in a cavity group of a nature which would enforce an interrupt would inevitably lead to a loss of the stored beam. It would therefore seem to be an advantage for the collider operation if the number of rf power units would at least be doubled. In this case the use of klystrons similar to the PEP design [8] could be considered.

A further reduction of the number of single cells per ring to 24 would lead to a 6 x 500-kW layout of the rf power part whereby each klystron amplifier feeds 4 cavities. We show a corresponding diagram in Fig.1. The system may include one or two spare amplifier units which can be switched into any other channel via a series of 13 waveguide switches.

III. KLYSTRON GALLERY LOCATION AND LAYOUT

The preferred location of the klystron gallery is on ground level. This facilitates swift access for maintenance work, and reduces overall cost for rf buildings and cooling plants. The rf equipment would occupy a ground floor for the klystrons, HV rectifiers, and local controls, and a basement for waveguides (WR 2300), circulators, power splitters, dummy loads, and cooling water distribution.

A possible layout of the ground floor is shown in Fig. 2. An annex may be added to this floor and used for any cavity testing and improvement work while the collider is operating. The standby klystron(s) could be used for this purpose.

The distance between ground level and beam paths is approximately 58 m. Straight waveguide runs in 2-m shafts from the basement to the beam tunnel sidewall, followed by rainbow-shaped shielded entrance arcs to an enlarged portion of the beam tunnel would transport the rf power down to the power splitters and cavities in the tunnel as shown in Fig.3.

The lengths of the waveguide runs add to the group delay which limits the maximum loop gain in the case of fast feedback. The analysis shows that the total group delay is still acceptable [9].

IV. KLYSTRONS

High-power CW klystron amplifiers for frequencies near 360 MHz have been produced by commercial manufacturers and by SLAC. The power levels range from 125 kW (SPEAR II, 1975) to 500 kW (PEP, 1980-) [8], to 1.1 MW (LEP I, 1989-) and 1.3 MW (LEP II, to be operational end of 1994).

*This work supported by U. S. Department of Energy under contract No. DE-AC35-89-ER40486.

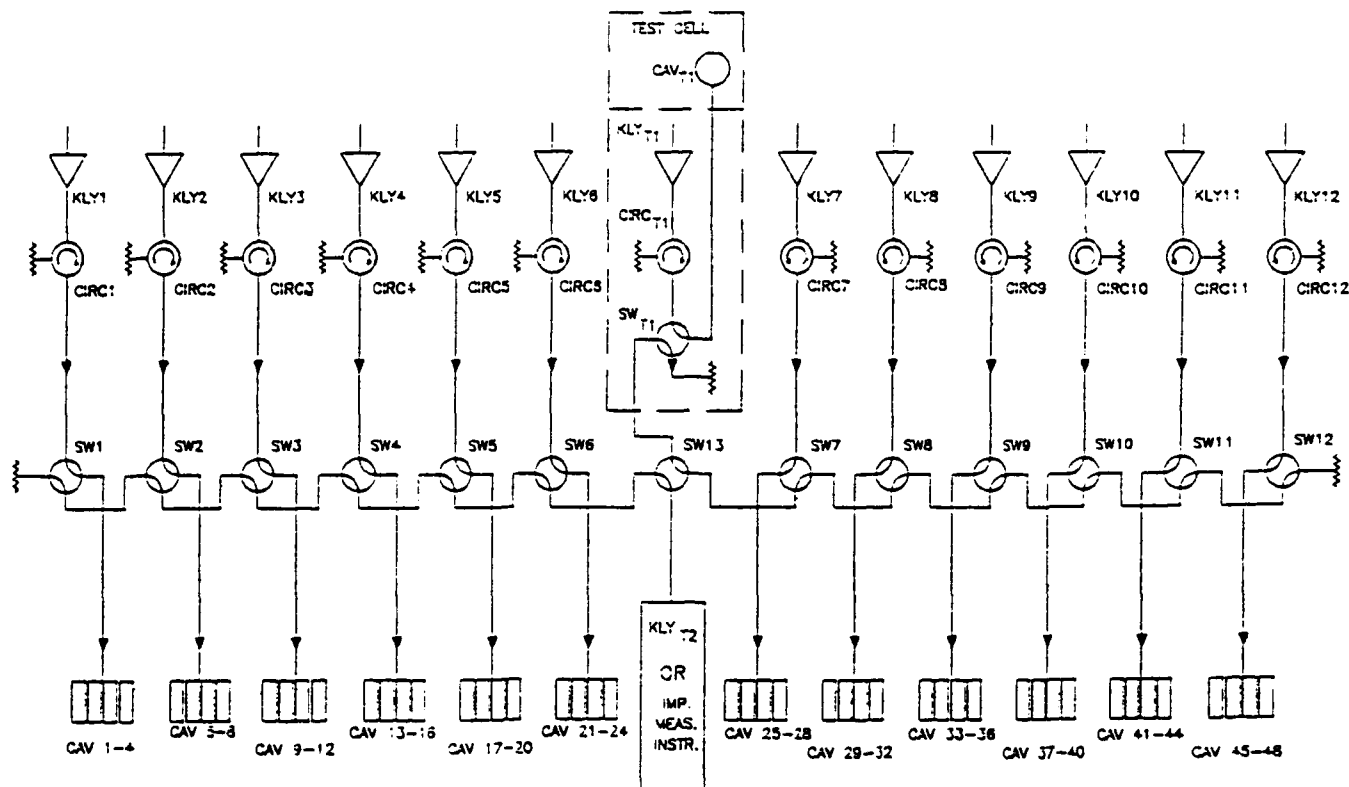


Fig. 1. RF switching system for 2 x 6 klystrons (500kW) with 1 or 2 spares.

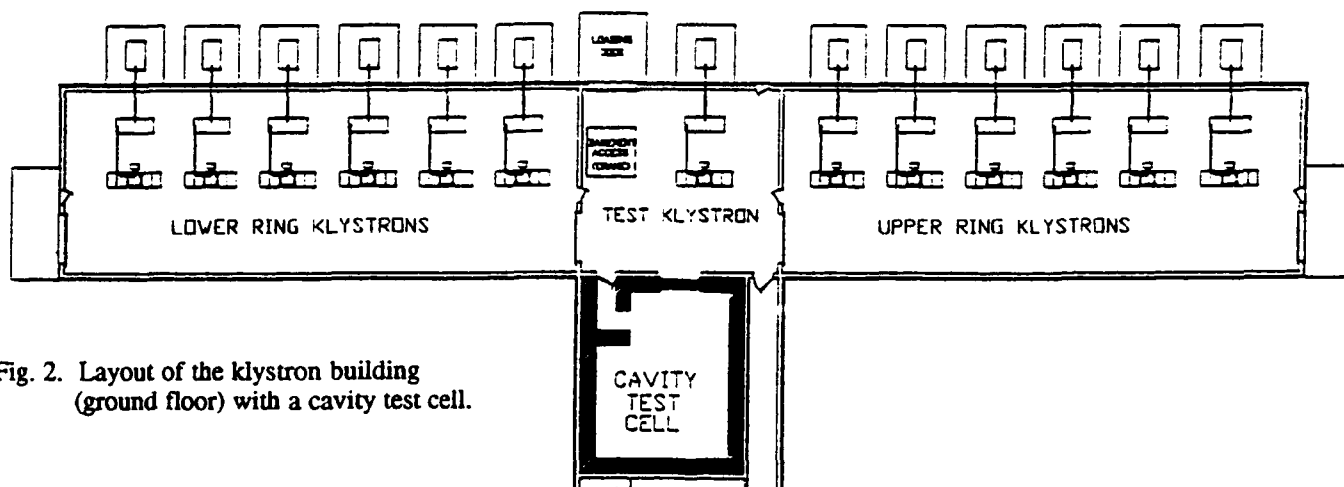


Fig. 2. Layout of the klystron building (ground floor) with a cavity test cell.

Typical klystron beam voltages are 35 kV (for 125 kW), 50 kV (for 250 kW), and 65 kV (for 500 kW). These values permit the use of air-insulated guns. Oil insulation of other HV components inside the klystron building can also be avoided.

Klystron output windows require protection against excessive reflected power. Ferrite circulators will be used (see Fig. 1).

Klystron damages due to sudden beam- or body current rise will be prevented either by crowbar discharge circuits or by application of high-power pulse-step modulators [10].

V. NORMALCONDUCTING SINGLE CELL CAVITIES

A system using 24 single-cell cavities and six klystrons per ring (as shown in Fig. 1) would require the installation of a total of twelve magic T's, twenty four 3-db hybrids, and 36

balancing absorbers in a larger beam tunnel section for proper power splitting. Part of the installation is sketched in Fig. 3.

A modular cavity-to-cavity distance of 1.5 wavelengths has been chosen. This distance permits the insertion of ion pumps between adjacent cavities. The 3-db hybrids supply counter-phase signals to their cavities. Each subsequent cavity pair is excited by inversely oriented coupling loops to maintain the mode pattern. Installation length is 30 m per ring.

To supply 833 kV effective acceleration voltage per cavity requires an electric field of 2.6 MV/m if an ANL-APS type cavity [11] is chosen. At this (gap) gradient, the power loss per cell is 62 kW. Total losses for 2 x 24 cells are 3 MW.

In the case of 2 x 32 cells (and 2 x eight 250-kW klystrons) the loss per cell would be 35 kW, and the total 2.2 MW.

Highly efficient watercooling of the cavities is crucial.

VI. POWER COUPLERS AND HOM DAMPERS

Adjustable loop (or antenna-) couplers with waveguide-to-coax transitions and cylindrical alumina vacuum windows will be used for feeding power into normal- (or super-)conducting cavities. Power handling limit is estimated to be 200 kW [5].

At least two HOM couplers per cavity will be added, similar in design to the types used for CERN-LEP [12].

VII. SUPERCONDUCTING SINGLE CELL CAVITIES

The application of superconducting cavities has been discussed in various notes, reports and committees, see for instance ref. [2, 3, 5, 9]. Transient beam loading of the collider rf cavities during filling, acceleration and storage of beams is the main reason to consider cavities capable of operating at much higher voltages than regular copper cavities. Based on a mean fieldstrength of 5 MV/m, single-cell superconducting cavities would operate at about 2 MV effective acceleration voltage. A total of 2 x 5 pairs of cavities would be used for the SSC. They would occupy 2 x 17 m tunnel space. It is envisaged to put at least 2 cavities into one 4.5-K cryomodule, and to leave sufficient room between modules to install vacuum pumps. The (preferably separate) cryoplant has to cool about 700 W.

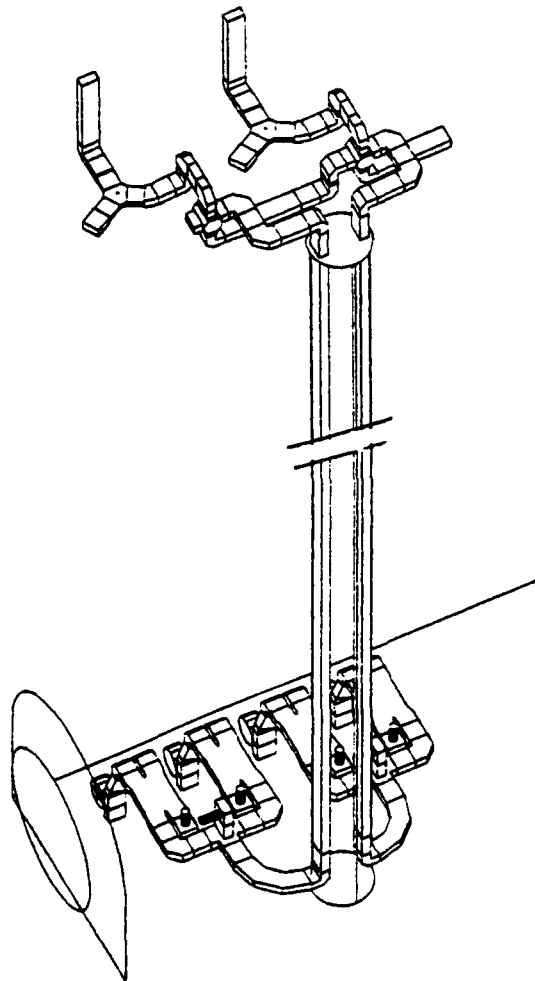


Fig. 3. Waveguide connection from two klystron outputs to two groups of normalconducting cavities in the beam tunnel. The length of the vertical shaft is approximately 55 m.

The cavity geometry will be similar to the LHC cavity under development at CERN [4]. The low R/Q value which is about 40 ohms versus 150 ohms for copper cavities, in combination with a 2.4-fold increase in cavity voltage, reduces the speed of phase excursions due to transient reactive beam loading by a factor 9. Higher loop gain is applicable for fast controls [4,9]. Furthermore, the cavity can supply reactive power to the beam in half-detuned operation. With a practical margin for linear klystron characteristics, the nominal klystron output power for a pair of cavities should be about 250 kW.

Critical issues for superconducting cavities are the "relative delicacy of the superconductive state, sensitivity to contamination, assembly complexity, complexity of cooling system, thermal isolation, vibration sensitivity. These properties have made themselves felt but are being overcome" (statement by M. Tigner in ref.[11]).

VIII. SUMMARY

At this point in time, two valid solutions are competing in how to achieve the best performance of the rf system for the SSC collider rings. More engineering work is required to complete the layout studies and to decide on the final choice.

IX. ACKNOWLEDGEMENTS

The authors have been benefited from close collaboration with colleagues at CERN, DESY, INR Novosibirsk, KEK, CERN, Cornell Univ., FNAL, LANL, SLAC, and from discussions with commercial manufacturers. We also wish to thank numerous colleagues in PMO and ASD divisions for comments, especially R. Meinke for his support.

X. REFERENCES

- [1] SSC Laboratory, "Site Specific Conceptual Design," ch. 4.2.6, June 1990.
- [2] W. Chou, G. Schaffer, "Comments on the collider rf cavity in the SSC," ADOD-036C, Jan. 1992.
- [3] X. Wang, et al., "A comparison of conceptual rf system designs for the SSC collider," SSCL-613, Dec. 1992.
- [4] D. Boussard, "RF power requirements for a high-intensity proton collider," *US Part. Acc. Conf.*, San Francisco, May 1991.
- [5] G. Schaffer, "Application of superconducting cavities to the collider rings of the SSC," *3rd Eur. Part. Acc. Conf.*, Berlin, March 1992.
- [6] G. Schaffer, "RF cost figures for the SSC-collider rings," Internal report, April 1992.
- [7] S. Hansen (CERN), private communication, Feb. 1993.
- [8] G.T. Konrad, "High-efficiency, cw, high-power klystrons for storage ring applications", SLAC-PUB-1541, 1975.
- [9] J. D. Rogers, et al., "RF systems analyses for the SSC collider rings," this conference.
- [10] W. Schminke, comments on high-power pulse-step modulators, private communication, 1992, (see also article in BBC Rev. 72, 1985).
- [11] Argonne National Laboratory, *Proc. of the Meeting on RF Systems for Synchrotron Light Sources*, Sept. 1992.
- [12] E. Haebe, "Coupler developments at CERN," *3rd Workshop on RF Superconductivity*, ANL, Oct. 1987.

Impedance Calculations for a Coaxial Liner

M. Filtz and T. Scholz

Technische Universität, EN-2, Einsteinufer 17, D-1000 Berlin 10, Germany

Abstract

Cold beam pipes like in SSC or LHC require shielding tubes with pumping holes called liner. As a first approximation instead of holes a tube with an arbitrary number of rotationally symmetric interruptions is analyzed using the mode-matching-technique. Results are presented for the longitudinal coupling impedance.

I Introduction

For cold beam pipes like in SSC or LHC coaxial waveguides are required where the inner conductor shields the outer surface from synchrotron radiation. The pumping holes in the inner conductor represent a coupling impedance of the beam to these discontinuities. For small holes this impedance can be obtained according to the Bethe theory of diffraction [1]. To avoid limitations w.r.t. the size and number of holes as well as the thickness of the inner conductor we use the mode matching technique to get an accurate solution.

To fit the surfaces of the structure to coordinate surfaces $\varrho, \varphi, z = \text{const.}$ we have to restrict ourself to holes with rectangular cross section (Fig.1a). But as a first approxi-

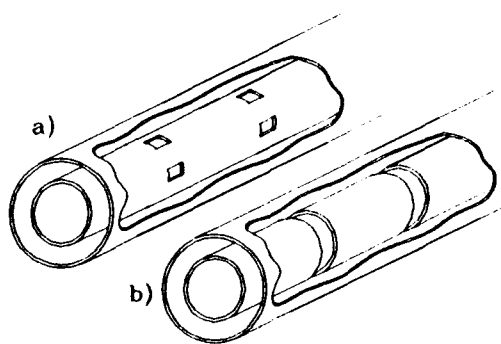


Figure 1: sketch of a liner

mation we will treat the simplified arrangement as shown in Fig.1b. Later the analysis described below will be extended to the really three dimensional problem of holes with rectangular cross section.

II Scattering matrix and excitation vector for one single cell

Let us assume a charged particle Q moving with the velocity of light parallel to the axis with an offset r . The m -th azimuthal spectral components of the electromagnetic field in the frequency domain are well known if the surrounding vacuum chamber is smooth. To take the discontinuities into account we first separate the whole structure into cells (Fig.2). Due to the symmetry of one segment we split the

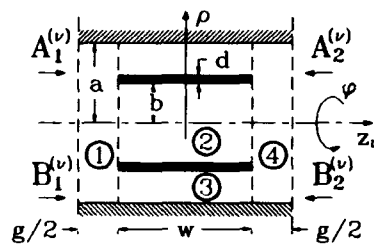


Figure 2: one segment of the rotational symmetric liner

exciting field E_s in two standing waves with a phase shift of 90° w.r.t. time and position

$$\frac{E_s'}{E_s''} \sim \frac{1}{2} e^{-j(k_0 l/2 + \Phi_\nu)} \{ e^{-jk_0 z_\nu} \pm e^{jk_0 z_\nu} \} \quad (1)$$

where $k_0 = \omega/c_0$ and $\Phi_{\nu+1} = \Phi_\nu + k_0 l$.

In- and outgoing TE and TM waves exist at the considered two ports of one segment. The amplitudes of them we call $A_{1,2}$ and $B_{1,2}$ respectively. Now we introduce the wave amplitudes A', A'', B', B'' referring to the excitation (1). Then we have

$$\frac{A'}{A''} = \frac{A_1 \pm A_2}{2}; \quad \frac{B'}{B''} = \frac{B_1 \pm B_2}{2} \quad (2)$$

On the other hand we can write the relation between A and B in matrix form

$$\begin{pmatrix} B_1 \\ B_2 \end{pmatrix} = \begin{pmatrix} S_{11} & S_{12} \\ S_{12} & S_{11} \end{pmatrix} \begin{pmatrix} A_1 \\ A_2 \end{pmatrix} + \begin{pmatrix} W_1 \\ W_2 \end{pmatrix} \quad (3)$$

$$\begin{pmatrix} B' \\ B'' \end{pmatrix} = \begin{pmatrix} S' & 0 \\ 0 & S'' \end{pmatrix} \begin{pmatrix} A' \\ A'' \end{pmatrix} + \begin{pmatrix} W' \\ W'' \end{pmatrix}$$

After calculation of the reflection matrices S' , S'' and the excitation vectors W' , W'' as described below the matrices S_{11} , S_{12} and vectors W_1 , W_2 become

$$\begin{matrix} S_{11} \\ S_{12} \end{matrix} = \frac{S' \pm S''}{2}; \quad \begin{matrix} W_1 \\ W_2 \end{matrix} = W' \pm W'' \quad (4)$$

Now we make the following ansatz in subspace 1 of Fig.2 for the beam induced transverse electromagnetic field with even symmetry using a compact matrix notation

$$\begin{aligned} \vec{E}_{i,1}^{(\nu)'} &= \frac{Z_0 Q}{2\pi a} \vec{F}^T(\frac{\xi}{a}, \varphi) \{ Z^+(z_\nu) A_1^{(\nu)'} + Z^-(z_\nu) B_1^{(\nu)'} \} \\ \vec{e}_z \times \vec{H}_{i,1}^{(\nu)'} &= \frac{Q}{2\pi a} \vec{F}^T(\frac{\xi}{a}, \varphi) Y_1 \{ Z^-(z_\nu) B_1^{(\nu)'} - Z^+(z_\nu) A_1^{(\nu)'} \} \\ Z^\pm &= \exp(\mp j K_1 [z_\nu + l/2]) \end{aligned} \quad (5)$$

where $Z_0 = \sqrt{\frac{\mu_0}{\epsilon_0}}$. In (5) we have defined

- the vectorial column matrix

$$\vec{F}(\xi, \varphi) = \vec{e}_\rho F_\rho(\xi, \varphi) + \vec{e}_\varphi F_\varphi(\xi, \varphi) \quad (6)$$

with elements

$$\begin{aligned} F_{\rho,i}^{TE} &= \cos(m\varphi) \frac{m}{\rho} J_m(j'_{mi}\xi) \\ F_{\rho,i}^{TM} &= \cos(m\varphi) j_{mi} J'_m(j_{mi}\xi) \\ -F_{\varphi,i}^{TE} &= \sin(m\varphi) j'_{mi} J'_m(j'_{mi}\xi) \\ -F_{\varphi,i}^{TM} &= \sin(m\varphi) \frac{m}{\rho} J_m(j_{mi}\xi) \end{aligned}$$

- the diagonal matrices K_1 and Y_1 with the modal wave numbers and wave admittances respectively

$$\begin{aligned} K_{1,i}^{TE} &= \sqrt{k_0^2 - j'^2_{mi}/a^2} \quad ; \quad Y_{1,i}^{TE} = K_{1,i}^{TE}/k_0 \\ K_{1,i}^{TM} &= \sqrt{k_0^2 - j_{mi}^2/a^2} \quad ; \quad Y_{1,i}^{TM} = k_0/K_{1,i}^{TM} \end{aligned}$$

J_m are the Besselfunctions, J'_m their derivatives and j_{mi}, j'_{mi} their zeros. The superscript (T) describes the transpose of a matrix. In a similar way we can make an ansatz for subspace 2 and 3. Note that in subspace 3 a TEM-field must be taken into account. After matching the field in the planes $z_\nu = \pm w/2$ we get the matrices S' , S'' , and vectors W' , W'' . All appearing coupling integrals can be solved analytically. For example the coupling matrix for the transition from subspace 2 to subspace 1 reads

$$M_{21} = \frac{1}{ab} \int_0^b \int_0^{2\pi} \vec{F}(\frac{\xi}{b}, \varphi) \cdot \vec{F}^T(\frac{\xi}{a}, \varphi) \rho d\varphi d\rho \quad (7)$$

III Field of the entire structure

Let us now consider an infinitely long shielding tube with N interruptions. This can be simulated by combining $N-2$ cells, as shown in Fig.2, and two cells at the end of our tube

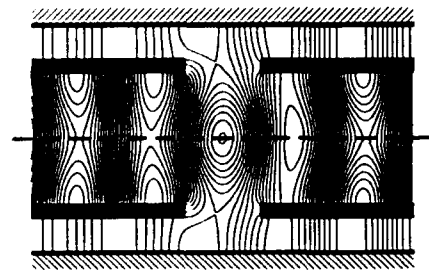


Figure 3: lines of force for two segments, $k_0 a = 1.76$

with $w \rightarrow \infty$. Then, the relation between incoming and outgoing waves at port 1 of segment $\nu + 1$ is given by

$$B_1^{(\nu+1)} = R^{(\nu+1)} A_1^{(\nu+1)} + V^{(\nu+1)} \quad (8)$$

where R and V include the influence of the entire structure to the right of segment $\nu + 1$. Taking into the account the ν 'th segment results in the recurrence formula

$$\begin{aligned} R^{(\nu)} &= S_{11}^{(\nu)} + S_{12}^{(\nu)} Q^{-1} R^{(\nu+1)} S_{12}^{(\nu)} \\ V^{(\nu)} &= W_1^{(\nu)} + S_{12}^{(\nu)} Q^{-1} (R^{(\nu+1)} W_2^{(\nu)} + V^{(\nu+1)}) \\ Q &= 1 - R^{(\nu+1)} S_{11}^{(\nu)} \end{aligned} \quad (9)$$

Iterating through the whole structure we get finally at the interface between segment 1 and 2 the equations

$$\begin{aligned} \{1 - R^{(1)} R^{(2)}\} B_2^{(2)} &= R^{(1)} V^{(2)} + V^{(1)} \\ A_2^{(1)} &= R^{(2)} B_2^{(1)} + V^{(2)} \end{aligned} \quad (10)$$

The wave amplitudes at all other interfaces can now be determined by a forward recurrence using (3).

As an example Fig.3 shows the lines of force for $N=2$.

IV The coupling impedance

Here, we will restrict ourself to the evaluation of the longitudinal coupling impedance for $m = 0$. Using the abbreviation

$$\mathcal{F}_{1,2}^{(\nu)}(z) = -jk_0(a, b)^2 \sum_i \frac{1}{j_{0i}^2} \left[E_{x1,2}^{(\nu)} \right]_i + \frac{Z_0 Q}{2\pi} \ln \frac{a}{b} - U_{TEM}^{(\nu)} \quad (11)$$

we get

$$\begin{aligned} Z &= -\frac{1}{Q} \sum_{\nu=1}^{N-1} \left\{ \mathcal{F}_2^{(\nu)}([\nu-1]l - \frac{\xi}{2}) - \mathcal{F}_1^{(\nu+1)}([\nu-1]l - \frac{\xi}{2}) \right. \\ &\quad \left. + \mathcal{F}_1^{(\nu+1)}([\nu-1]l + \frac{\xi}{2}) - \mathcal{F}_2^{(\nu+1)}([\nu-1]l + \frac{\xi}{2}) \right\} \end{aligned} \quad (12)$$

It can easily be shewn that U_{TEM} in (10) is essentially given by the voltage between the inner and outer conductor, i.e.

$$U_{TEM}^{(\nu)} = e^{jk_0 z} \int_{b+a}^a E_{e3}^{(\nu)} d\rho \quad (13)$$

where only the TEM field contributes. $[E_{z1,2}^{(\nu)}]_i$ describes the i 'th mode of the longitudinal electric field in subspace 1 and 2 respectively.

Fig.4 - Fig.7 show impedances for some configurations. Note that the value in Fig.4 for $\omega \rightarrow 0$ is given by

$$\Re[Z(\omega \rightarrow 0)] = \frac{Z_0}{\pi} \ln \frac{a^2}{b^2 + d^2}$$

The frequency independent behaviour of the real part of the impedance in Fig.4a for $d = 0$ agrees with the results in [2].

V Conclusion and outlook

In the present paper we have proposed an analytical method to calculate the impedance of annular interruptions in the inner conductor of a coaxial waveguide. The written computer code is an extension of existing codes. The advantage of the method used here is that we can change transverse dimensions from cell to cell. So in principle we are also able to analyse the so called detuned iris loaded waveguide while choosing $b + d = a$. In this case and if a, b are constant for all cells, we obtain exactly the same results as presented in [3].

The generalization to holes with rectangular cross section will be presented next.

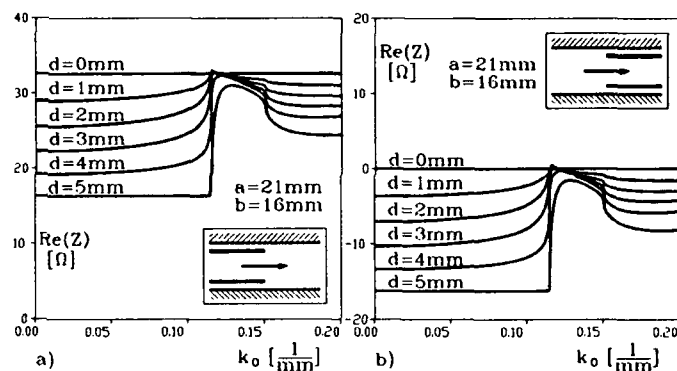


Figure 4: real part of the impedance of a single discontinuity a) for a charge leaving the inner conductor, b) entering the inner conductor

References

- [1] R.L.Gluckstern, "Coupling Impedance of Many Holes in a Liner within a Beam Pipe", SSC, internal paper, January 8, 1992, Waxahachie, Tx
- [2] L.Palumbo, "Analytical Calculation of the Impedance of a Discontinuity", Particle Accelerators, Vol.25, 1990, S.201-216
- [3] H.Henke, "Impedances of a Set of Cylindrical Resonators with Beam Pipes", Particle Accelerators, Vol.25, 1990, S.183-199

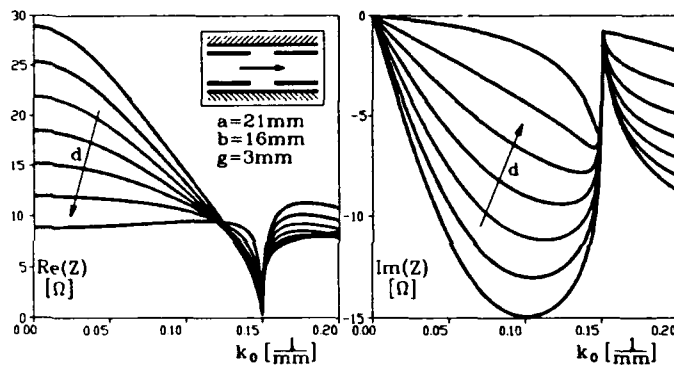


Figure 5: impedance of an annular interruption in the inner conductor with $d=0.5, 1.0, 1.5, 2.0, 2.5, 3.0, 3.5$ mm

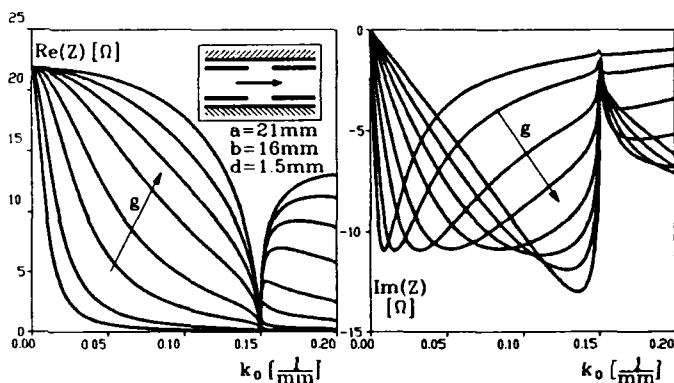


Figure 6: as Figure 5, but with varying gap in the inner conductor $g=0.1, 0.5, 1.0, 1.5, 2.0, 3.0, 4.0, 5.0$ mm

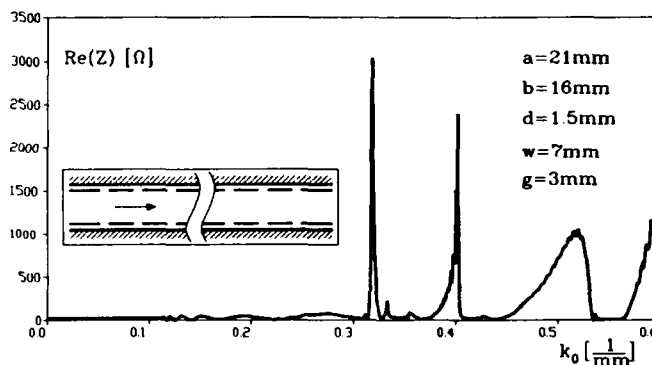


Figure 7: real part of the impedance for 20 annular interruptions

Design of a High-Power Test Model of the PEP-II RF Cavity *

H.D. Schwarz, R.A. Bell, J.A. Hodgson, J.G. Judkins, K. Ko, N. Kroll[^], C.K. Ng, R.P. Pendleton, K. Skarpaas,
Stanford Linear Accelerator Center, Stanford, Ca 94309, USA

G. Lambertson, R. Rimmer,
Lawrence Berkeley Laboratory, Berkeley, Ca 94720, USA

M.S. deJong, T. Tran-Ngoc, F.P. Adams, M.G. Lipsett, W. Mellors,
AECL Research, Chalk River Laboratories, Chalk River, Ontario K0J1J0, Canada

Abstract

The design of a normal-conducting high-power test cavity (HPTC) for PEP-II is described. The cavity includes HOM loading waveguides and provisions for testing two alternate input coupling schemes. 3-D electromagnetic field simulations provided input information for the surface power deposition. Finite element codes were utilized for thermal and stress analyses of the cavity to arrive at a suitable mechanical design capable of handling the high power dissipation. The mechanical design approach with emphasis on the cooling channel layout and mechanical stress reduction is described.

I. INTRODUCTION

The PEP-II B-factory design at SLAC will use normal-conducting copper cavities at 476 MHz for acceleration of the beam. In order to minimize the possibility of multi-bunch oscillations the total number of cavities is kept to a minimum and higher order mode (HOM) impedances are reduced by specific loading schemes [1]. The minimized number of cavities requires higher than usual gap voltages of almost 1 MV per cavity and correspondingly higher power dissipation of up to 150 kW in the cavity walls. The Higher Order Mode impedance is reduced by lowering the Q of HOMs by up to three orders of magnitude with the use of special loading waveguides terminated into broad band HOM loads.

The major design choices for the cavity are described based on electromagnetic field simulations and thermal and stress calculations. A conceptual design [2] has been established which could dissipate the required 150 kW without excessive stress.

A preliminary design for broad band HOM loads is presented. There are two choices for coupling networks, coaxial loop and iris coupling. Both are planned to be evaluated with the prototype cavity. The coupling networks need to handle the power dissipated in the cavity plus power delivered to the beam totaling 500 kW. The coupling factor through a coupling iris was calculated using the MAFIA code.

II. CAVITY DESIGN CONCEPT

A reentrant cavity shape with three HOM loading ports and ports for coupling and tuning has been developed and extensively analyzed using the 3D electromagnetic codes MAFIA and ARGUS. To generate the surface heating distribution the magnetic field of the fundamental mode was translated from the finite-difference mesh of the electrical

codes onto the 3D finite-element mesh used by the thermal-mechanical codes, and scaled to give a total dissipated power of 150 kW. The power density, F (W/m^2), is derived by directly calculating the tangential magnetic field, H_{tan} at the surface, and converting to surface heating via the relation:

$$F = \frac{1}{2} R_s H_{tan}^2$$
$$R_s = \left[\frac{\omega \mu}{2\sigma} \right]^{1/2} = 0.0057 \Omega \quad \text{OFE Cu @ 476 MHz}$$

where R_s is the surface resistance at 27°C. Power flow densities of 33 W/cm² at the base of the nose cones and up to 90 W/cm² in small areas at the intersection of the HOM loading waveguides with the cavity body were calculated. In order to cool the cavity for this relatively high power flow, a closely spaced cooling channel layout has been selected covering as much of the outside of the cavity as possible. An outline drawing of the cavity with its ports is shown in Figure 1. This preliminary cavity design was then used as the basis for finite element code simulations to evaluate thermal and stress behavior of the cavity under full power.

III. THERMAL AND STRESS CALCULATIONS

First a 2D analysis was made to model the basic layout of the cooling channels. The analysis assumed a water velocity of 5 m/s resulting in a heat transfer coefficient of 21.2 kW/m²°C. The inlet water temperature was set at 35°C which, with a specified 10°C temperature rise of the water, results in an average water temperature in the cooling channels of 40°C. The resultant average temperature of the inside surface of the cavity was 52°C. This would cause a reduction in Q of 6.3% due to the increase in copper resistivity with temperature. The peak temperature occurred at the flat part of the nose cone and was only 60°C, and the maximum calculated Von Mises stress was 16 MPa, well below the yield point of OFE copper. The frequency shift caused by the deformation of the cavity from the combined affects of water pressure, vacuum and thermal loading, was calculated to be -130 kHz.

Next a 3D model was made. The results for this baseline 3D case were an average temperature of about 60°C, peak temperature of 97°C at the intersection of the HOM waveguide with the cavity and a peak Von Mises stress of 71 MPa in the same region. It is noteworthy that the peak stress occurs in a very localized region and is compressive. A number of variations on the baseline case were analyzed in an effort to better understand how to optimize the cavity design. The variations included adding stiffening supports at various locations along the waveguides and other regions of the cavity, specifying the cooling water routing, etc. In one of these variations the water velocity was reduced to 3.7 m/s

*Work supported by the Department of Energy, contracts DE-AC03-76SF00515 and DE-AC03-76SF00098, Grant DE-FG03-92ER40759, and AECL Research, Canada.

[^]Also Dept. of Physics, UCSD, La Jolla, Ca 92093

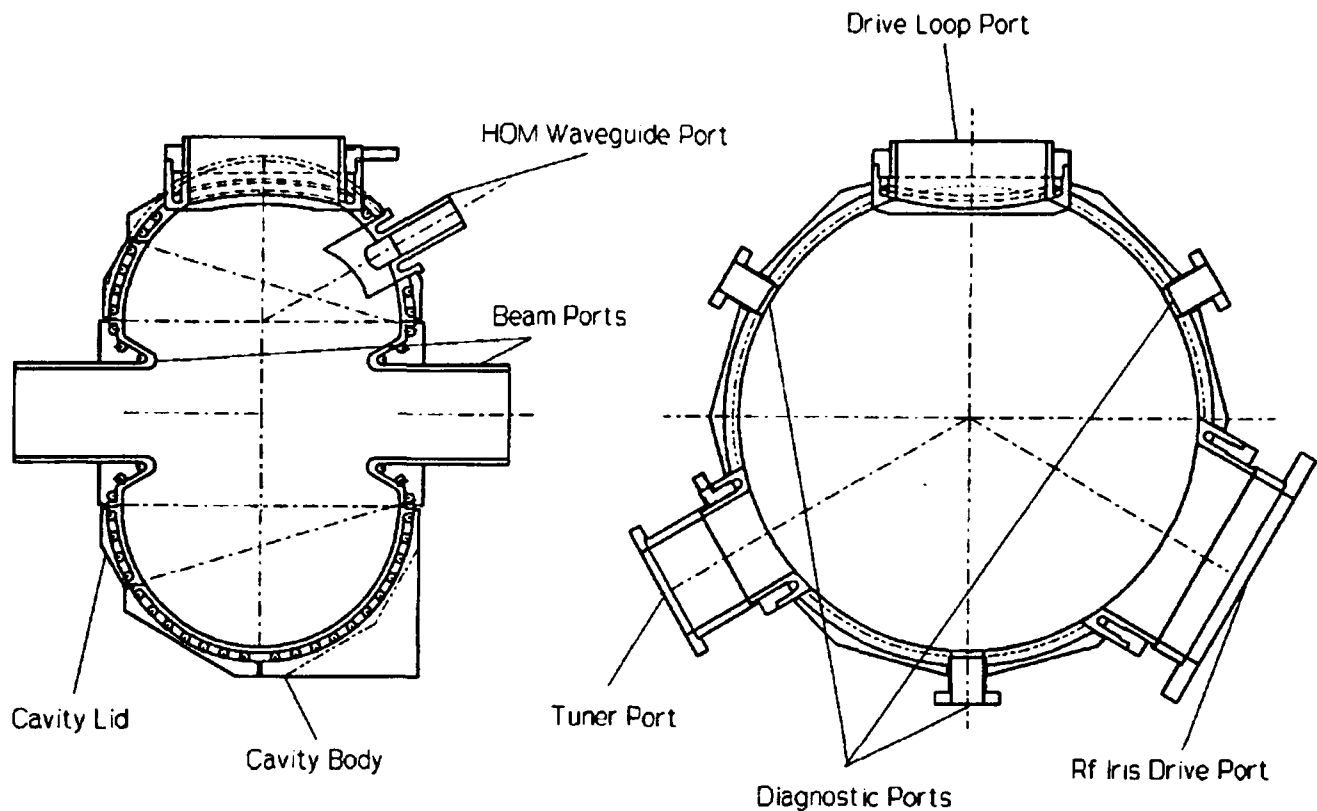


Figure 1. Port Location and Cooling Channel Layout for the PEP-II High Power Test Cavity

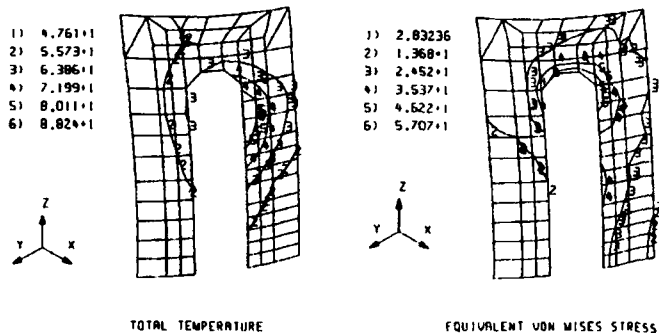


Figure 2. Temperature (°C) and stress (MPa) of HOM waveguide cavity opening.

which led to a peak temperature at the end of the iris of 101°C. Using this *peak* temperature as an overall *average* temperature the reduction in Q would be 14.5%; this is an upper bound on the reduction in Q. Combined with the calculation at an average temperature of 52°C, a reasonable estimate for the reduction in Q due to the increase in copper resistivity is 10%. An analysis incorporating all of the beneficial changes resulted in a reduction of the peak stress to 57 MPa, Figure 2. The knowledge gained from these variations is being incorporated into the detailed design of the high power test cavity.

The maximum stress in the HOM waveguide intersection with the cavity is predicted to be close to the yield point of fully annealed OFE copper of 70 MPa. If the stress in the HPTC were to exceed the yield point in this isolated region, the region would undergo a small inelastic deformation in the

initial conditioning period, and from then on would deform elastically. Because the region is small this should not be a problem for either the RF or the mechanical characteristics of the cavity.

IV. MECHANICAL DESIGN

The cavity will be assembled as two bowls, one constituting about 80% of the cavity body, the other 20%. The cooling channels will be cut into the outside of the copper bowls and then covered either by brazed lids or electroformed copper. Port holes will then be machined into the cavity body. All ports and two reentrant nose pieces will be fabricated separately, with integrated cooling channels, and then brazed into the cavity bowls. This step will be followed by a final machining of the cavity interior together with a frequency tuning by trimming the length of the nose cones. A last brazing cycle will join the cavity bowls together. The exact fabrication procedure is being finalized with the objective of simplifying the assembly. Once the design is finished another thermal-mechanical analysis will be performed using the exact cooling channel layout to confirm that the design meets the specifications.

V. HOM LOADS

The RF cavities for the PEP-II B-factory are designed with waveguides as high pass filters to couple out the HOM power while perturbing the fundamental mode relatively lightly. In practice this requires a wide band low reflection load at the end of the waveguides. A load that has high reflections may decrease the effectiveness of the HOM

damping scheme and may result in higher Q_s for the cavity HOMs. The design requires that the load must work in vacuum, have a VSWR less than 2.0:1 over the frequency range 700 MHz to 2500 MHz for all propagating waveguide modes, and be capable of dissipating 10 kW.

Using the time domain module of MAFIA various geometries for the HOM load have been investigated and one has been found that can be the basis for a workable design. The load consists of a shaped alumina piece sandwiched between two tapered sheets of a lossy ceramic jointly developed at CEBAF and CERADYNE [3] (aluminum nitride filled with 7% glassy carbon), Figure 3. The alumina section draws the field in from the waveguide and in this way couples the fields into the lossy ceramic more efficiently. Preliminary thermal calculations indicate the load will be able to dissipate the design goal of 10 kW. Continued work will be directed at reducing the overall length of the design, investigating the bonding techniques required to build a load with these materials, and building a prototype.

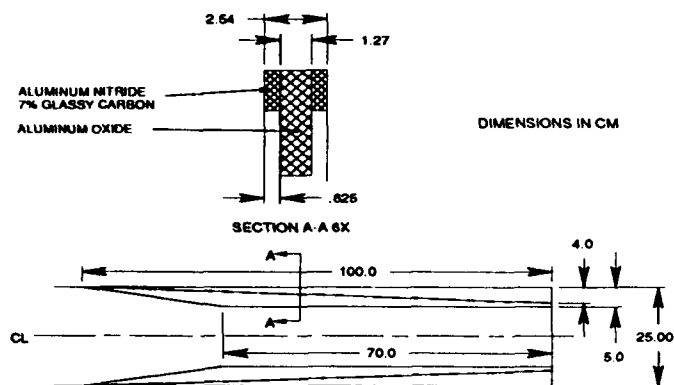


Figure 3. HOM Load Design

VI. COUPLING NETWORKS

Two variations of input coupling networks for 500 kW power transmission are presently being designed and will be tested in the high power test cavity. One will use a coupling loop in a 6.4-inch coaxial line combined with a coaxial window. The coupling factor can be set between zero and 10 by rotating the loop. The coupling of the loop coupler has been measured using an existing PEP coupling loop in a cold test cavity.

The second coupling method will utilize iris coupling and a waveguide window, Figure 4. The coupling of a 2 x 8 inch iris 4 inches deep has been analyzed by calculating Q_{ext} via the Kroll-Lin and Kroll-Yu methods, using data from MAFIA simulations [4],[5], and deriving $\beta = Q_0/Q_{ext}$. The length of the waveguide in the simulation is set to $1/2$ wavelength so that two resonant modes close in frequency appear in the output of one MAFIA run. These two modes are the 0 and π mode of the waveguide-cavity coupled resonator system and occur at what Ref. 5 terms the avoided crossing region. The Kroll-Lin method is particularly well suited to the evaluation of large Q_{ext} . The Kroll-Yu method was only used as a rough check. The coupling factor can be varied by inserting exchangeable waveguide quarter-wavelength transformers in-between the coupling iris and the waveguide. Time domain simulations in MAFIA are being used to calculate wall current densities at vacuum joints in the waveguide. A commercial product HELICOFLEX [6] has been selected for a vacuum seal and

will be tested to verify its current carrying capability at 500 kW CW power level.

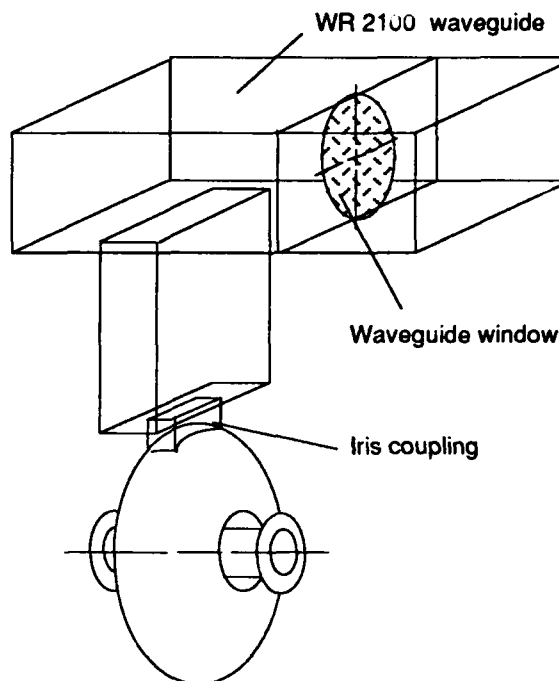


Figure 4. Iris Coupling Network

VII. CONCLUSION

A PEP-II cavity design has been developed using electromagnetic and thermal-mechanical codes to check its design feasibility. The model predicts that the design at the required gap voltage and power can be built and stay within allowable stress limits. A preliminary cooling channel layout has been analyzed on which a final layout will be based. The MAFIA code has been used to calculate the coupling for an iris coupling network. The details of the high power test cavity design are being finalized and a cavity will be built and tested to 150 kW wall power dissipation within the next year.

VIII. REFERENCES

- [1] R. Rimmer et. al., "An RF Cavity for the B-Factor", *Proc. PAC*, San Francisco, May 6th-9th, 1991, pp. 819-821.
- [2] M. S. de Jong et al, "Mechanical Design Development of a 476 MHz RF Cavity for the PEP-II Asymmetric B-Factor", AECL-10782, Feb. 1993.
- [3] I. Campisi, K. Finger, L. Summers, M. Johnson, "Higher Order Mode Damping and Microwave Absorption at 2 °K", *Proc. Third EPAC*, Berlin, March 24-28, 1992
- [4] N. Kroll, X. Lin, "Computer Determination of the Properties of Waveguide Loaded Cavities", *Proc. Linear Acc. Conf.*, Albuquerque, NM, Sept 10-14, 1990, Los Alamos Report LA-12004-C, pp. 238-240 (1991). Also SLAC-Pub 5296, July 1990.
- [5] N. Kroll, D. Yu "Computer Determination of the External Q and Resonant Frequency of Waveguide Loaded Cavities", *Particle Accelerators*, 1990, Vol.34, pp. 231-250.
- [6] HELICOFLEX, Columbia, South Carolina.

Construction of a Superconducting RFQ Structure

K. W. Shepard and W. L. Kennedy
Argonne National Laboratory
9700 South Cass Avenue, Argonne, IL 60439 USA

K. R. Crandall
AccSys Technology Incorporated
1177-A Quarry Lane, Pleasanton, CA 94566

Abstract

This paper reports the design and construction status of a niobium superconducting RFQ operating at 194 MHz. The structure is of the rod and post type, novel in that each of four rods is supported by two posts oriented radially with respect to the beam axis. Although the geometry has four-fold rotation symmetry, the dipole-quadrupole mode splitting is large, giving good mechanical tolerances. The simplicity of the geometry enables designing for good mechanical stability while minimizing tooling costs for fabrication with niobium. Design details of a prototype niobium resonator, results of measurements on room temperature models, and construction status are discussed.

I. INTRODUCTION

Although cw electric fields exceeding 100 MV/m have been achieved in a superconducting niobium RFQ structure, the structure tested had vanes only 6.5 cm long, and was not suitable for accelerating beam [1]. The RFQ design presented here is intended as a next development step [2,3] for the niobium short-vane RFQ with the following objectives:

1. See if high accelerating fields can be obtained in a superconducting RFQ structure of useful length (50 cm).
2. Permit testing with beam at the ATLAS heavy-ion facility.
3. Exhibit sufficient mechanical stability for cost-effective operation in low-beam-current applications.

The potential for testing with an ATLAS heavy-ion beam provides considerable flexibility [6]. The velocity profile, and the vane modulation, can be specified without knowing precisely what electric field gradients can be achieved, since the charge-to-mass ratio Q/A of a test beam can be varied over a substantial range, from 1/10 to 1/2. A test area is available in which a bunched beam of velocity as low as .02 c can be made available. To permit such testing, the entrance velocity of the structure is chosen to be 0.02 c, and the operating frequency to be the 16th harmonic of the ATLAS bunching frequency, or 194 MHz.

II. RESONATOR DESIGN

A. General Characteristics

Figure 1 shows the resonator geometry. Although the

structure has four-fold rotational symmetry the dipole-quadrupole mode separation is large, yielding good mechanical tolerances. The mode separation results from the large electric-field coupling between the longitudinal rods or vanes, the inductive coupling between the radial posts being relatively weak in this geometry.

The four-fold symmetric rod and post geometry has several advantages for construction of a superconducting niobium RFQ:

1. The large mechanical tolerances are compatible with the need to heavily chemically polish the niobium surface, with resulting uncertainties of tens of microns in the final position of the interior cavity surfaces.
2. The cost of tooling and fabricating in niobium are minimized by the simplicity of the structure, which can be formed by joining eight simple "T" sections.
3. Since peak surface field, rather than shunt impedance, is the primary design constraint for superconducting niobium structures, the rod and post structure can assume massive proportions, providing excellent mechanical stability.

B. Mechanical Features

The resonant cavity, fabricated of niobium, is jacketed in a stainless steel housing which forms a liquid helium container through which pass beam ports and rf coupling ports which access the resonator interior. This design permits operation with a common beam and cryogenic vacuum system (characteristic of the ATLAS accelerator) while avoiding the use of copper-niobium composite material. The rod and post structures will be formed of 1/8 inch niobium sheet, and the resonator cylindrical wall of 3/16 inch material.

C. Vane Modulation

The vane modulation is chosen so that if surface fields as high as were obtained in the earlier short vane tests can be attained in the larger structure, a $^{238}\text{U}^{24+}$ beam will be matched. If the structure proves limited to lower surface fields, it will still match beams of higher Q/A , so that a beam test at ATLAS would be possible for a range of possible accelerating gradients.

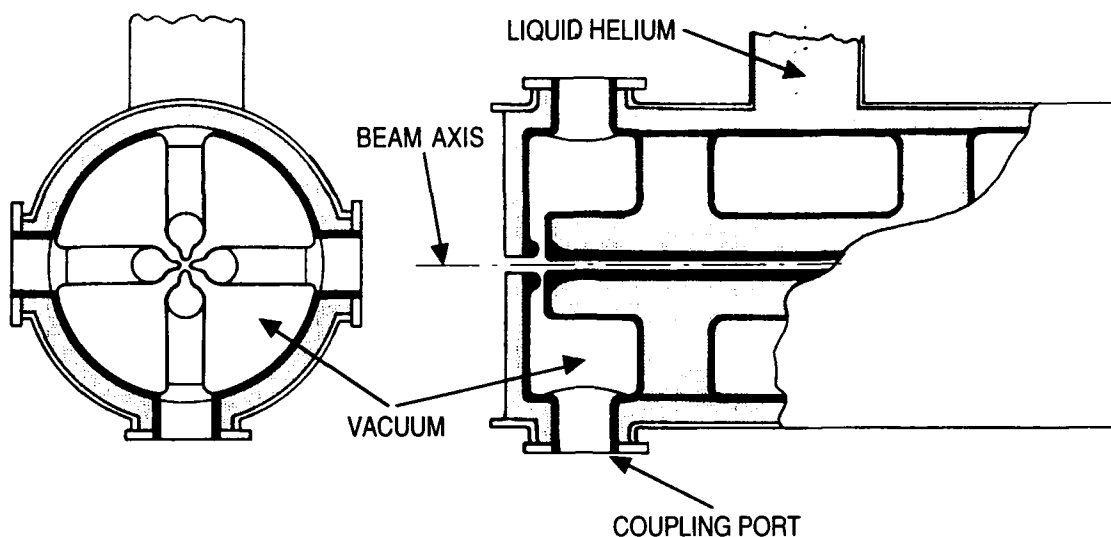


Figure 1 - End-section and cut-away view of the four-fold symmetric superconducting RFQ. The operating frequency is 194 MHz, and the active length 46.6 cm. The resonant cavity will be formed of niobium, then housed in a stainless steel outer jacket which serves as a liquid helium container. For details, see the text.

For the vane design, we assume the upper limit of possible performance for a superconducting structure to be a peak surface electric field of 120 MV/m. To match possible test beams from the ATLAS accelerator, we also assume the following parameters:

Frequency	194 MHz
Entrance velocity	$\beta_0 = 0.02$
Transverse Emittance	$\epsilon_x = 10 \pi \text{ mm-mrad}$
Longitudinal Emittance	$\epsilon_z = 40 \pi \text{ KeV-nsec}$

The design chosen calls for the vanes to be formed of niobium plate with a constant (transverse) thickness of 7.65 mm. The vane modulation is chosen to yield as high an accelerating gradient as is consistent with good longitudinal and transverse focussing, and the requirement to maintain a low peak surface electric field. Principle parameters of the resulting design are:

Modulation factor	2.53
Minimum Aperture (radius)	2.85 mm
Synchronous Phase	-30°
Number of cells	21
Overall Length	46.6 cm
Peak surface electric field	120 MV/m
Mean Accelerating Gradient	8.64 MV/m
Inter-Vane Voltage	465 KV

It should be noted that the above electric field gradients represent the upper limit of possible performance for the structure which could still be tested with beam at ATLAS. Achievement of even one-half the above gradients would provide exceptional performance for a cw RFQ.

III. WARM MODEL MEASUREMENTS

A. Electrodynamic Properties

Electromagnetic properties were modeled first numerically, using the MAFIA code, then by measurement with a room-temperature model of the structure with unmodulated vanes set at the average beam aperture (5.03 mm radius).

Table 1
Numerical and Measured Electromagnetic Properties

Parameter	MAFIA	Warm Model
Quadrupole Mode	199.5 MHz	198.6 MHz
Dipole Modes	215.6 MHz	214.9 MHz 214.2 MHz
B_{peak}	702 Gauss	680 Gauss
E_{peak}	120 MV/m	
RF Energy*	6.1 Joule	10.1 Joule

* Normalized to an inter-vane voltage of 465 KV

The peak magnetic field is substantially reduced from that reported [3] for an earlier model, primarily because the cross-sectional area of the support posts was more than doubled for the present model. Since superconducting ion-accelerating structures currently in use in the ATLAS linac

frequently operate at $B_{\text{peak}} > 700$ gauss [7], in the absence of surface defects, performance limits for the device are expected to be electric-field-induced electron emission rather than magnetic-field-induced losses in the superconductor.

MAFIA results indicate that variation of the rf voltage along any vane is less than 3% [3].

B. Mechanical Properties

Because of the wide quadrupole-dipole mode-splitting, mechanical tolerances are excellent. For the present model, on initial assembly, during which mechanical tolerances of typically .005 inch were maintained, and with no subsequent tuning, the voltages on the four vanes were balanced to better than 10% of mean.

A high-degree of mechanical stability is desirable for low-beam-current applications because of the difficulty of stabilizing the rf phase of high-Q superconducting resonators in the presence of microphonic-induced-excitation of mechanical vibrational modes of the cavities. Measurements of the vibrational properties of the present model have not yet been made. We note however, that measurements on an earlier model showed adequate mechanical stability [3]. Since the support posts for the present model have nearly twice the cross-section and are substantially shorter than for the earlier model, the resonator mechanical stability should be appreciably increased.

III. CONSTRUCTION STATUS AND FUTURE PLANS

The design of the prototype niobium structure is complete. Procurement of niobium and fabrication of tooling are currently underway. RF tests of a prototype unit are expected within the next year.

Primary questions for prototype tests are:

1. Can the high electric surface fields (> 100 MV/m) obtained in a short niobium RFQ be repeated in a structure of useful length?

2. Is the structure sufficiently mechanically stable to permit phase control?

3. Do multipacting phenomena in such a structure present operational problems?

IV. ACKNOWLEDGEMENTS

The authors wish to acknowledge the contributions of J. Givens and J. M. Potter of AccSys Technology in the construction and testing of the room temperature model resonators. We would also like to thank Gerry McMichael of the Chalk River Laboratories for a helpful discussion of the vane design, and N. Freed at Argonne for assisting with model measurements.

This work was performed under the auspices of the U. S. Department of Energy, through the SBIR program, contract no. DEFG0391ER81098.

V. REFERENCES

1. J. R. Delayen and K. W. Shepard, *Appl. Phys. Lett.* **57**, 514 (1990).
2. A. Schempp, et al., *Proceedings of the 1990 Linear Accelerator Conference*, Albuquerque, New Mexico, September 10-14, 1990, p. 79, (1990).
3. K. W. Shepard, et al., *Proceedings of the 1992 Linear Accelerator Conference*, Ottawa, Canada, August 24-28, 1992, p. 441 (1992).
4. J. M. Bogaty, et al., *Proceedings of the 1989 IEEE Particle Accelerator Conference*, Chicago, Illinois, March 20-23, 1989, p. 1978 (1989).
5. N. Added et al., *Proceedings of the 1992 Linear Accelerator Conference*, Ottawa, Canada, August 24-28, 1992, p. 181 (1992).
6. R. Pardo, et al., *Proceedings of the 1992 Linear Accelerator Conference*, Ottawa, Canada, August 24-28, 1992, p. 70 (1992).
7. K. W. Shepard, *IEEE Trans. Nucl. Sci.* **NS-32**, p. 3574, (1985).

Niobium Coaxial Quarter-wave Cavities for the New Delhi Booster Linac^{*}

K. W. Shepard
Argonne National Laboratory
9700 South Cass Avenue, Argonne, IL 60439 USA

A. Roy and P. N. Potukuchi
Nuclear Science Centre
JNU New Campus, P.O. Box 10502, New Delhi-110067 INDIA

Abstract

This paper reports the design and construction status of a prototype superconducting niobium accelerating structure consisting of a pair of quarter-wave coaxial-line cavities which are strongly coupled with a superconducting loop. Quarter-wave resonators are two-gap accelerating structures and are relatively short, so that a large number of independently-phased cavities is required for a linac. Strongly coupling several cavities can reduce the number of independently-phased elements, but at the cost of reducing the range of useful velocity acceptance for each element. Coupling two cavities splits the accelerating rf eigenmode into two resonant modes each of which covers a portion of the full velocity acceptance range of the original, single cavity mode. Using both of these resonant modes makes feasible the use of coupled cavity pairs for a linac with little loss in velocity acceptance. Design details for the niobium cavity pair and the results of preliminary tests of multipacting behavior are discussed.

I. INTRODUCTION

The superconducting accelerating structure discussed here is to be employed in a heavy-ion booster linac for the 16UD pelletron electrostatic accelerator at the Nuclear Science Center in New Delhi, India.

Several recent heavy-ion booster linac projects employ superconducting quarter-wave coaxial-line (QWCL) resonant cavities [1 - 7]. The QWCL geometry is characterized by excellent mechanical stability and broad velocity acceptance. Also, QWCL resonators made with superconducting niobium have achieved very high accelerating gradients [5].

A disadvantage of the QWCL geometry, however, is that the single-drift-tube, two gap structure is short, and a relatively large number of independently controlled resonators is required to form a useful linac.

The present project is aimed at developing a high-performance structure based on the QWCL geometry, with

the design focussed on reducing construction costs and maximizing operational simplicity and stability.

In what follows, we first discuss the design of a two-gap resonant cavity, usable as a stand-alone structure, then some characteristics of a coupled pair of such cavities. Finally, we discuss the multipacting behavior observed in a superconducting niobium simulation of the drift-tube region of the proposed resonant geometry.

II. RESONANT CAVITY DESIGN

A. General Approach

The design begins with a 100 MHz, two-gap resonant cavity optimized for particle velocity $\beta = v/c = .08$. Such a structure has a large enough range of velocity acceptance that a single resonator geometry will suffice for the entire booster linac, as presently envisioned [7].

Two cavities as described above are being constructed as prototypes, and will be tested, first individually, and then as a coupled pair in order both to test the superconducting coupler and also to ascertain the feasibility of operating the cavities in strongly-coupled pairs, and thus combine the advantages of two-gap and many-gap cavities.

B. Quarter-wave Coaxial-line Cavity

The cavity is formed entirely of niobium, rather than bonded niobium-copper composite as is used in the ATLAS linac and several other accelerators. This choice was taken both because of the cost of forming and welding the composite material, and also because the cost is increased by the relatively large number of two-gap cavities required.

Figure 1 shows a coupled pair of cavities. For the moment, we consider a half of the coupled pair, which constitutes a single QWCL resonant cavity. We note several features:

1. The high-voltage end of the coaxial line consists of a relatively large diameter section which capacitively loads the quarter-wave line and shortens the cavity nearly 20 cm. This is done both to reduce the size of the resonant cavity, and to improve mechanical stability, which decreases rapidly with

^{*}This work is being performed at Argonne, and is funded through the Nuclear Science Center, New Delhi by the University Grants Commission of the Government of India

increasing length of the coaxial line. By using a cylindrically symmetric drift tube, large capacitive loading can be obtained while keeping the peak surface electric field low.

2. The niobium cavity is closely jacketed in a vessel of stainless steel, which contains the liquid helium required to cool the superconducting structure. This design permits an array of cavities to operate in a cryostat with the beam-line and cryogenic vacuums being one common system. Such an arrangement is almost universally used in superconducting heavy-ion linacs, because it facilitates the large number of connections to room temperature required to operate an array of independently-phased resonant cavities. A small amount of niobium-stainless bonded composite material is used to provide welding transitions where beam ports and coupling ports penetrate the stainless steel jacket.

3. A pneumatic tuner is incorporated into the bottom end face of the resonant cavity and will consist of a three-section niobium bellows. The end face will move about 3 mm with 1 atm of internal pressure, and provide a tuning range of approximately 100 KHz, substantially more than required for

single cavity operation, but necessary for operating the cavities in coupled pairs.

C. Electrodynamic Parameters

The QWCL resonant geometry has been modeled numerically and measurements have been performed on a copper model to determine the mechanical properties of the design, which proved entirely satisfactory [7].

Some parameters for a single QWCL resonator (1/2 of a pair) at a nominal accelerating gradient of 1 MV/m are:

Resonant Frequency	95 MHz
Synchronous Velocity	0.081 c
Drift Tube Voltage	86 KV
Energy content	0.116 J
Peak Magnetic Field	108 G
Peak Electric Field	3.9 MV/m
Geometric factor QR_s	18

D. Coupled Cavity Pair

Coupling a pair of QWCL cavities creates a structure in which the two lowest-frequency rf eigenmodes consist of the fundamental rf eigenmode in each of the independent cavities, the two of which can be either in phase (the anti-symmetric mode of the coupled structure) or π radians out of phase (the symmetric mode). As is discussed in reference [7], if each half of the pair can be independently tuned, both modes can be used for beam acceleration, providing a wide range of velocity acceptance.

III. MULTIPACTING TEST

The design chosen could be at risk for severe low-level multipacting for two reasons. The cylindrical drift-tube termination of the QWCL has a high degree of symmetry which might enable multipacting over large areas. Also the drift-tube characteristics, with 3.33 cm gap at 97 MHz, imply an electron transit time that could lead to two-point multipacting at gap voltages in the range 200 - 600 volt, a range in which secondary electron reflection coefficients are generally large. To gain an early indication of multipacting behavior, an existing niobium QWCL resonator was modified by terminating the high-voltage end with a 8.75 inch long, 5.375 inch OD niobium cylinder (coaxial with the 8.0 inch ID of the outer resonator wall). This modification provided a 3.33 cm gap over a substantial area and changed the resonant frequency to 97 MHz.

The modified resonator was electropolished, assembled, cooled to 4.2 K, and the severity of multipacting was observed by logging the time required to RF condition through the multipacting barriers. During the conditioning process, typically 1 watt of RF power was coupled into the

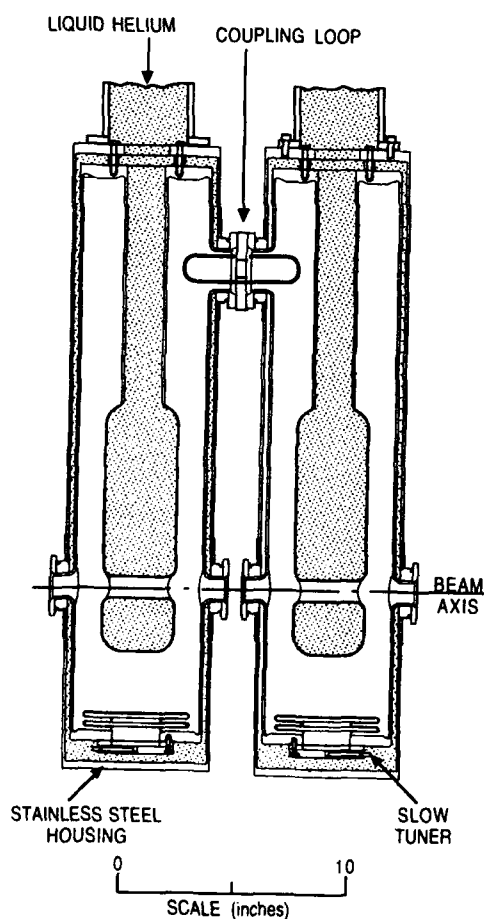


Figure 1. Coupled pair of 100 MHz quarter-wave coaxial-line resonant cavities. The shaded region shows the volume occupied by liquid helium.

multipacting resonator. In figure 2 the conditioning process is shown both after the initial cooldown (Curve 1), and again after warming the resonant cavity to room temperature for several days and cooling again without exposure to air (Curve 2). After conditioning no further multipacting was observed as long as the cavity was maintained below 77 K.

Under similar conditions, the split-ring and interdigital superconducting cavities employed in the ATLAS accelerator typically require one to five hours of rf conditioning to eliminate multipacting. Although multipacting in the present geometry seems appreciably more severe, as manifested by the increased conditioning time, the conditioning process seems entirely effective, and no operational problems are foreseen at this time.

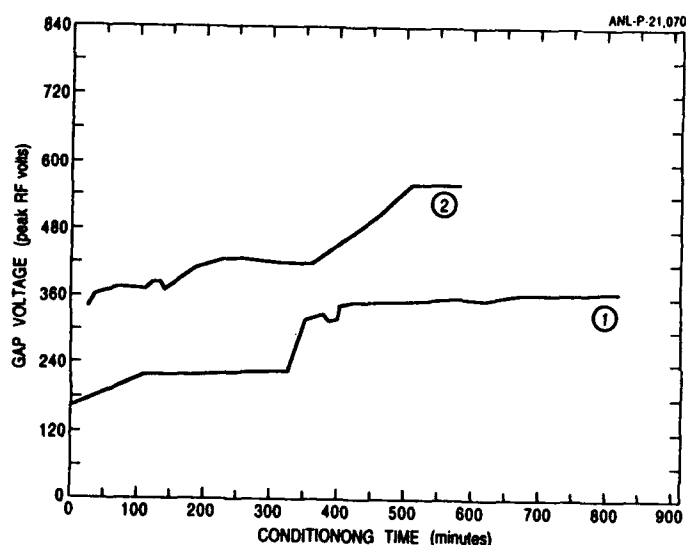


Figure 2 - Multipacting conditioning behavior of a niobium multipacting test cavity at 4.2 K. Multipacting level as a function of conditioning time is shown for (1) the initial cooldown and (2) after warming to room temperature for several days without exposure to air. During conditioning, typically 1 watt was coupled into the cavity.

IV. CURRENT STATUS

Construction of a prototype cavity pair is well advanced. Most of the tooling has been made, and machining and welding of the resonator elements is currently in progress. Completion of the first QWCR and initial cold tests are expected within FY 1993.

V. ACKNOWLEDGEMENTS

The authors would like to thank G. K. Mehta for his support and Lowell Bollinger for several helpful discussions.

VI. REFERENCES

1. I. Ben-Zvi and J.M.Brennan, Nucl.Instr.and Meth.212, p73-79, (1983).
2. K. W. Shepard, S. Takeuchi, and G. P. Zinkann, IEEE Trans. Magn. MAG-21, p. 146 (1985).
3. D.W.Storm et al., Proc. of the 2nd Workshop on RF Superconductivity, Geneva, p. 173, (1984).
4. D. W. Storm et al., Nucl.Instr. and Meth. A287, p. 247 (1990).
5. S.Takeuchi, Proc. of the 5th Workshop on RF Superconductivity, DESY, p. 76 (1991).
6. A.Facco et al., Proc. of the 5th Workshop on RF Superconductivity, DESY, p. 58 (1991),
7. K. W. Shepard and A. Roy, Proc. of the 1992 Linear Accelerator Conference, August 24-28, 1992, Ottawa, Canada, p. 441, (1992).
8. J. M. Bogaty, et al., Proc. of the 1989 IEEE Particle Accelerator Conference, May 20-23, 1989, Chicago, Illinois, p. 1978 (1989).
9. in ATLAS - a Proposal for a Heavy-ion Accelerator, Physics Division, Argonne National Laboratory (1978).

Design of High Power Model of Damped Linear Accelerating Structure using Choke Mode Cavity

Tsumoru Shintake

KEK: National Laboratory for High Energy Physics

1-1 Oho, Tsukuba-shi, Ibaraki-ken, 305 JAPAN

Abstract

A high power model of a damped linear accelerating structure using the choke mode cavity has been designed.

1. INTRODUCTION

In the course of design study of the e+e- linear collider[1], a new type HOM damped cavity: the choke mode cavity was proposed by the author[2]. Using a cold model of this cavity at S-band, it was demonstrated that most of all the higher order modes were fully damped, while small effect on the dominant accelerating mode. In the frequency spectrum measurement, since the damped Q was very low, no any peak was observed around the most dangerous TM110 mode. By means of the time domain simulation using TBCI-code, the damped-Q of TM110 mode was estimated to be less than 10. [3]

Since this cavity is a simple structure, and it has perfect cylindrical symmetry around the axis, it is quite suitable for mass production of large number of cells for traveling wave accelerators requested for e+e- linear colliders. Since, wall dissipation power density is uniform around the axis, and there is no heat concentration at any point, this structure is also suitable for high-power CW accelerating cavity in storage rings, especially for B-factories[4,5].

In order to study practical problems of this cavity, we started design study of S-band high power model. In this paper, current status of this design study is reported.

2. ACCELERATING MODE

Schematic drawing of the high power model is shown in Fig. 1. Since the structure has many slots for HOM damping, it will be installed in a vacuum vessel. It consists of 14 cells: 12 regular cells of the choke mode cavity, input and output coupler cells.

A. Accelerating Mode : Phase Advance per Cell

In order to get enough space for the choke structure, we use the $3\pi/4$ mode, rather than $2\pi/3$ mode. Cross-sectional dimension is shown in Fig. 2. The disk-to-disk spacing: D in $3\pi/4$ mode is 39.364 at 2856 MHz. This is 4.4 mm longer than the $2\pi/3$ mode. The Brillouin diagram of this mode is shown in Fig. 3 comparing with the $2\pi/3$ mode. The group velocity is $0.01c$ for both modes. Since the $3\pi/4$ mode is near to π -mode, the rise time of pulse microwave propagating along this structure becomes slower than in $2\pi/3$ mode. The estimated rise time from the band width ($\tau = 1/(\pi(f - f_{rf}))$) is 64 nsec

for this mode and 41 nsec for $3\pi/4$. This is sufficient value for practical application of S-band linear accelerator. The shunt impedance of $3\pi/4$ mode is almost same as the $2\pi/3$ mode.

B. Degradation of Q-factor due to the Choke HOM Damping Structure

The damping slot, radial transmission line and the choke structure dissipate microwave power due to wall loss. This is 25% of the wall dissipation power per cell of conventional disk-loaded structure. Therefore, the shunt impedance of this structure becomes 25% lower due to attaching this choke HOM damper. Design parameter are listed in Table-1. Since the stored energy in the damping structure is 10% of the total, R/Q parameter becomes 10% lower. The Q-factor becomes 85% of conventional disk-loaded structure.

Since the choke is a kind of a notch filter, the power stop-band is limited. If the operating frequency moves from the design center frequency, or the choke resonance is different from the rf frequency due to dimension errors, some fraction of the accelerating microwave power can leak-out from the cavity. Figure 4 shows degradation of Q-factor due to this power leakage as a function of relative frequency detuning. Qleak denotes the power leakage effect. If we accept a degradation of a few % of Q-value, that is 98 % of Q_0 , the tolerance on the choke center frequency becomes ± 0.16 %. Therefore, the dimension tolerance for the choke depth is approximately $\pm 40 \mu\text{m}$ for 25 mm choke depth. This is easy value to realize by machining on a turning lathe.

The frequency bandwidth required for the traveling wave structure ($v_g=0.01$) is around ± 0.5 %. Since the Q-factor is higher than 10000 within this bandwidth, the pulse response will not be disturbed.

C. Dimension Tolerance & Tuning

Sensitivity of the resonance frequency on dimension errors and their tolerances for 100 kHz frequency error are listed in Table 2. Tolerances on 2a, 2b and D dimensions are same as that in the conventional disk-loaded structure. The tolerances on choke dimensions are not so tight. Since 2b dimension tolerance is tight, conventionally it is tuned by pushing the body from outside after braising.

However, we can not access to 2b dimension after the braising. Therefore, firstly we will measure the center frequency ($\pi/2$ -mode) using two detuned dummy-cavity and slightly machine the 2b dimension for coarse tuning, and

D dimension (spacer length) for fine tuning. Since the tolerance on D dimension is not tight, it will not be necessary additional tuning after the braising process.

3. HIGHER ORDER MODES

Since the choke is a quarter-wavelength line, it has higher order resonances at $3f_0$, $5f_0$.. If we use a simple straight choke, the 3rd resonance can trap some higher order modes in the accelerating cavity. In the previous measurement[2], a peak of trapped TM021 mode was observed at 8.5 GHz. In order to eliminate this peak, we reduced the choke length and widened the bottom as shown in Fig. 2. With this modification, the 3rd resonance becomes 9.5 GHz, while the dominant frequency does not move. Since the gap width of the radial line is 13 mm at the choke, and 24 mm at outer region, the 3rd resonance field can propagate along the radial line by higher order mode as shown in Fig. 5(b). Therefore the 3rd resonance does not trap cavity modes. Fig. 5(c) is parasitic resonance of the choke at 10.7 GHz. Because of the same reason as 3rd mode, this mode does not disturb the HOM damping.

Fig. 6 shows the calculated wake potential of single cell of this cavity. The estimated damped Q-value from the decay time was approximately 14 for TM110 mode. Since only the TM010 dominant accelerating mode is trapped inside this cavity, the longitudinal wake potential shows coherent oscillation at 2856 MHz.

4. CONCLUSIONS

We will fabricate this high power model in this year, and examine the high power test.

In the second model, we will implement the microwave absorber made of SiC for the HOM damping.

ACKNOWLEDGEMENTS

The author would like to thank Tatsuya Kageyama, Kazunori Akai and Yoshishige Yamazaki for stimulating discussions. The author would like to thank Hiroshi Matsumoto and Hitoshi Baba for useful suggestions on fabrication process.

- [1] JLC Group, "JLC-I", KEK Report 92-16, December 1992 A/H/M
- [2] T. Shintake, "The Choke Mode Cavity", Jpn. J. Appl. Phys. Vol. 31 (1992) pp. L1567-L1570, Part 2, No. 11A Nov. 1992
- [3] T. Shintake, "HOM Free Linear Accelerating Structure using Choke Mode Cavity", Proc. 17th Linear Accelerator Meeting in Japan, Sendai, Japan (1992); KEK Preprint 92-66, July 1992 A
- [4] B-factory Accelerator Task Force, "Accelerator Design of the KEK B-factory", KEK Report 90-24.
- [5] "An Asymmetric B Factory based on PEP", conceptual design report, Feb. 1991, LEL PUB-5303

Table-1

Operating Frequency	f_0	2856 MHz
Wavelength	λ_0	104.969 mm
Phase Shift per Cell		$3\pi/4$
Cell Unit Length	D	39.364 mm
Structure Length	L	511.7 mm
Cell Number	N	14 cells
(2 couplers + 12 regular cells)		

Impedance	Cl: constant impedance	
Aperture	2a	24.0 mm
Cell Diameter	2b	82.94 mm
Disk Thickness	t	8.0 mm
Q-factor	Q_0	12000
Group velocity	V_g/c	0.0096
Shunt Impedance	r	42 MΩ/m
Attenuation Parameter	τ	0.13
Filling Time	T_F	171 nsec

Accelerating gradient at 100 MW rf input.

at input	Ea1	45.7 MV/m
at output	Ea2	40.1 MV/m

Table-2 Dimension Tolerance

Dimensions	Target	Sensitivity	Tolerance
(mm)	(mm)	(kHz/μm)	(μm)
2a	24.00	4.0	± 25
2b	82.94	- 36	± 3
D	39.36	- 5	± 20
t	8.00	10	± 10
Lchoke	(26.25)	- 4.4	± 23
Rchoke	(66.1)	- 11	± 10

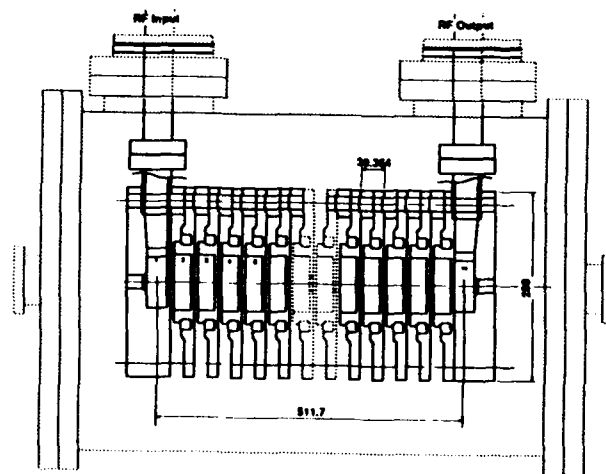


Fig. 1 S-band High Power Model

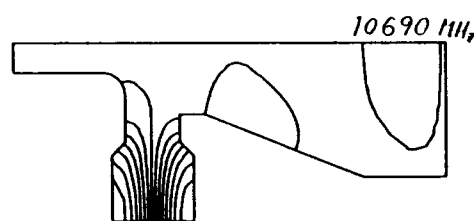
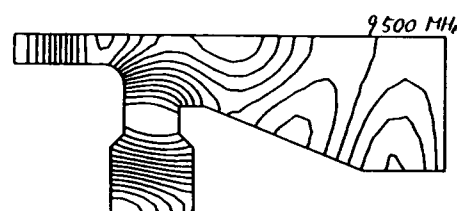
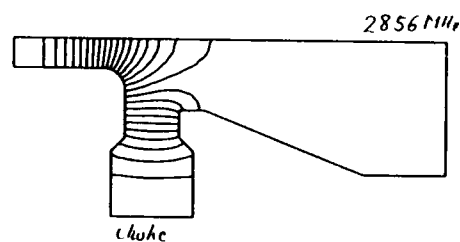
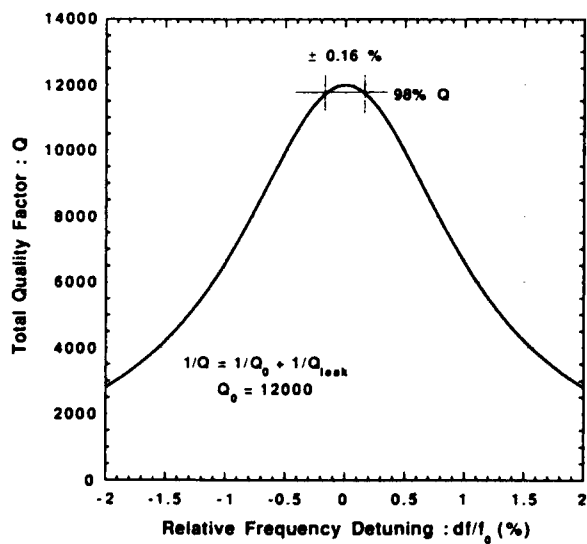
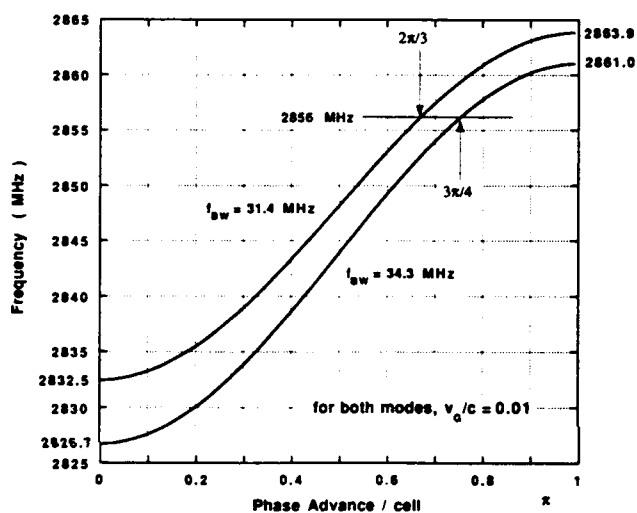
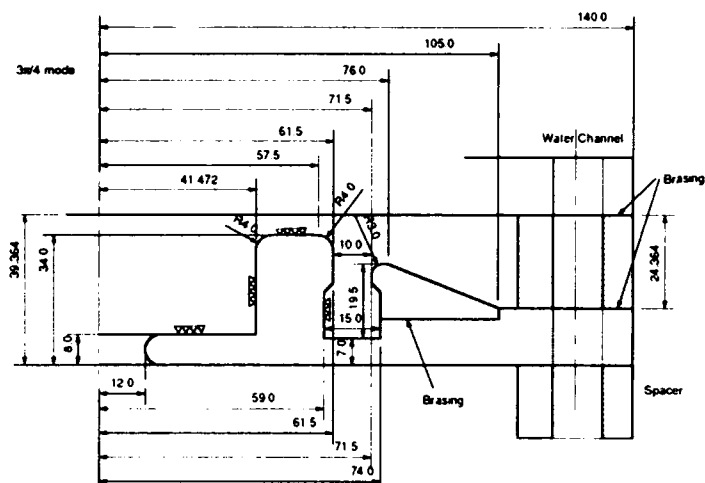
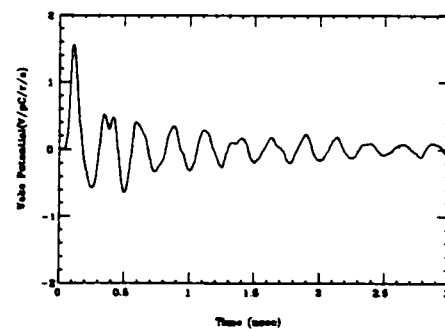
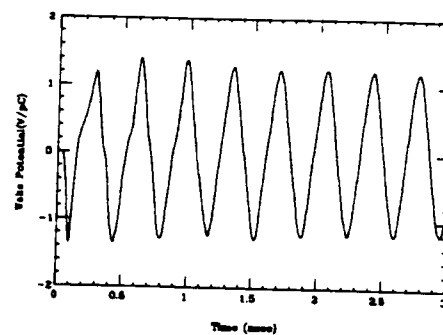


Fig. 5 Choke Resonances



(b) Transverse

Fig. 6 Wake potential calculated by TBCI code.

Suppression of Longitudinal Coupled-Bunch Instability using Energy Storage Cavity in B-factory RF System

Tsumoru Shintake

KEK: National Laboratory for High Energy Physics
1-1 Oho, Tsukuba-shi, Ibaraki-ken, 305 JAPAN

Abstract

The longitudinal coupled bunch instability due to the fundamental accelerating mode can be suppressed by attaching an energy storage cavity to a normal conducting accelerating cavity. Since the stored EM-energy in this system is very large, a small frequency detuning is sufficient to compensate reactive part of the beam loading voltage induced by extreme high beam current in B-factory storage rings. In KEK B-factory case, it is possible to use a normal conducting single cell accelerating cavity connected to an energy storage cavity of 1.2 m diameter by 1.9 m length. The stored energy in this system is 8.3 Joule, and the loaded Q is 7.2×10^4 . The effective impedance for the coupled bunch mode ($m=-1$) is reduced to as low as 18 k Ω /ring. Since the growth time of the instability is 22 msec, which is comparable to the radiation damping time, this type of instability will not occur.

I. INTRODUCTION

In B-factory storage rings [1,2], since extreme high beam current must be accumulated, the coupled-bunch instabilities become very serious problem. Instabilities are excited not only by the higher order modes (HOM) in RF-cavity, but also by the fundamental accelerating mode itself. To cure HOM problem, various type of damped cavity have been proposed. However, according to the longitudinal coupled-bunch instability due to the fundamental mode, no any realistic solution has been found out, except to use a super-conducting RF cavity with relatively higher accelerating field.

Recently, the author [3] proposed a possible solution to this problem, which uses an energy storage cavity connected to a normal conducting accelerating cavity. Due to large EM energy stored in the storage cavity, this system becomes quite stable against the longitudinal phase oscillation of the high current multi-bunch beam circulating in the storage ring. In this paper, concept of the storage cavity scheme is explained briefly, then discussions are given on problems to realize this system in practical machine, such as KEK B-factory.

II. THE STORAGE CAVITY SCHEME

An accelerating RF cavity is usually operated at off the resonance in order to compensate the reactive part of the beam loading voltage induced by the beam. In high beam current storage rings, this detuning frequency becomes quite large, and in a large storage ring it exceeds the revolution frequency of the beam. In this case, the coupled bunch synchrotron oscillation of $m \neq 0$ mode is

excited by the large impedance of the accelerating mode itself at the instability resonance. To eliminate this type of instability, it is essential to reduce the detuning frequency of the cavity, and also to reduce the impedance tail at the instability resonance.

We here briefly review the cavity detuning. When a beam is accelerated by the cavity voltage it induces a beam loading current in the rf cavity as its reaction. In electron or positron storage rings, in order to insure stability against phase oscillation the beam is accelerated at off the crest of the accelerating voltage. Therefore, the beam current I_b is out of phase ϕ with the beam accelerating voltage, where ϕ is called the synchronous phase. The real part of the beam loading power, $\text{Re}(1/2V_c I_b^*) = 1/2V_c I_b \cos\phi$, is the time average of the net energy transfer utilized for beam acceleration. On the other hand, the imaginary part, $1/2V_c I_b \sin\phi$, is the reactive beam loading power, which can not be utilized for beam acceleration, and reflects back to the rf generator. Finally, it reduces the system power efficiency. In order to reduce this reflection power and to minimize the required generator power, the rf-cavity resonance is generally detuned from the generator frequency, and the imaginary part is compensated by bypassing through the resonator. The compensating condition is

$$j\omega CV_c + \frac{V_c}{j\omega L} = I_b \sin\phi. \quad (1)$$

Thus the detuning frequency required for compensation is

$$\frac{\Delta\omega}{\omega_0} = \frac{I_b \sin\phi}{2\omega_0 CV_c} = \frac{\text{Im}(\frac{1}{2}V_c I_b^*)}{2\omega_0 W_0}, \quad (2)$$

where W_0 is the energy stored in the cavity. This equation implies that the required frequency detuning is equal to the reactive energy flow per one cycle to the stored energy inside the cavity. Therefore, in order to minimize the frequency detuning we need to increase the stored energy.

For this purpose, here we introduce an energy storage cavity connected to a conventional single cell accelerating cavity as shown in Fig. 1. If the coupling between two cavities is sufficient, the electrical performances of total system become;

$$(R/Q)_{\text{tot}} = \frac{W_A}{W_{\text{tot}}} (R/Q)_A, \quad (3)$$

$$\Delta f_{\text{tot}} = \Delta f_A \cdot \frac{W_A}{W_{\text{tot}}} \quad (4)$$

$$Q_{\text{tot}} = \omega_0 \frac{W_{\text{tot}}}{P_{\text{tot}}} \quad (5)$$

$$R_{\text{tot}} = \frac{R_A}{1 + P_S/P_A} \quad (6)$$

where the subscripts A, S and tot. represent the accelerating cavity, the storage cavity and the total system, respectively. Since we use a large volume storage cavity, it is easy to store a large amount of EM energy. Therefore as known by eqs. (3) and (4) the R/Q parameter of this system becomes much smaller than that in the case of only the accelerating cavity is used, and the detuning frequency for the beam loading compensation becomes very small. If we use a low loss mode in the storage cavity, the total wall dissipation power does not increase so much, and this system shows quite high Q factors as indicated by eq. (5). Both small frequency detuning and a high Q-factor are very important to reduce and cancel out the impedance tails at the instability resonances. Therefore the present scheme can be one of the best solution to cure the multi-bunch longitudinal instability due to the fundamental accelerating mode. Since the shunt impedance of this system: eq. (6), is not degraded so much, we can operate this system with reasonable RF input power.

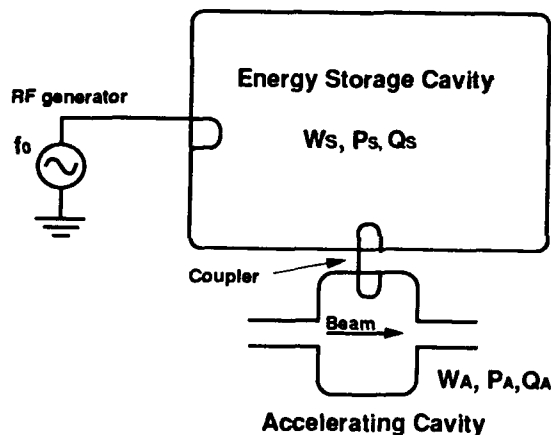


Fig.1 An accelerating cavity connected to an energy storage cavity.

III. APPLICATION TO THE KEK B-FACTORY

In the KEK B-factory, we need to store a beam current of 2.6 amperes in the low-energy ring, and 1.1 amperes in the high energy ring in order to achieve the maximum design luminosity of $1 \times 10^{34} \text{cm}^{-2} \text{sec}^{-1}$. Since the coupled bunch instability problem is more severe in the low-energy ring than the high-energy ring, we discuss here only the low-energy ring case. The principal machine parameters are listed in Table 1. We assumed the maximum capable wall-dissipation power per one-cell of the accelerating cavity to be 60 kW. Then the cavity voltage becomes 0.6 MV per cell and 22.2 MV per ring.

We use low loss mode of TE₀₁₅ in the storage cavity. Such mode has been successfully used as a high-power storage cavity in an rf-pulse compressor system of SLED at S-band frequency. The cavity dimensions at 508 MHz become a length of 1.9 m and a diameter of 1.2 m. The

unloaded Q-value is 2.6×10^5 . We connect this storage cavity to a conventional accelerating cavity as shown in Fig. 2. We assumed a single cell pillbox type accelerating cavity, which has a HOM damping structure of "Choke Mode Cavity"[4]. The shunt impedance of this cavity without connecting to the storage cavity is $6.3 \text{ M}\Omega/\text{cell}$, which includes a degradation of -25% due to the wall dissipation power in the choke HOM damping structure.

The field intensity ratio: HS/HA between the storage cavity and the accelerating cavity is a free parameter. If we increase the field intensity in the storage cavity, we can store larger energy, but the wall dissipation power in the storage cavity becomes large. On the other hand, if we choose the field intensity in the storage cavity to be low, the total stored energy becomes small, as a results the detuning frequency becomes large again and the instability will occur. Here we choose the field intensity ratio at 0.5. Electrical performance of this system is summarized in Table 2. The total stored energy is 8.3 Joule, which is twelve time larger than that in the case of using only the accelerating cavity. As a consequence, the detuning frequency is only -15 kHz at the maximum beam current of 2.6 amperes, which is much smaller than the beam revolution frequency of 99.3 kHz. The system has a very high loaded-Q of 7.2×10^4 , this is comparable parameter with that in a super conducting cavity system. Because of this high Q-factor and the small frequency detuning, the impedance tail becomes very small and the impedance cancellation works well between the damping and anti-damping mode, finally the effective impedance for the coupled-bunch mode of $m=-1$ becomes $18 \text{ k}\Omega/\text{ring}$. Since the growth time of the instability is 22 msec, and this is comparable to the radiation damping time, this type of instability will not occur.

IV. DISCUSSION AND CONCLUSIONS

A. Cure of parasitic coupled resonator modes.

Since the proposed system is a kind of coupled resonator, it is inherent to have multiple resonances according to the number of cavities. Two-cavity-coupled system shows two different modes (zero and π) according to the phase difference between the two cavities. If we use the π -mode for beam acceleration, another zero-mode will appear near to the accelerating frequency, and may cause the same instability. To cure this parasitic mode is therefore a key issue in using this type of coupled cavity system.

Recently, Y. Yamazaki and T. Kageyama[5] proposed a scheme of a three-cavity system to solve this problem. They introduced a coupler cavity between the accelerating and the storage cavity. The $\pi/2$ mode is used for beam acceleration. The parasitic impedance of zero and π -modes are effectively damped by a coupler installed in the coupling cavity, while minimal effect on the accelerating cavity. At the same time, since the impedance distributions of zero and π mode are almost symmetry around the accelerating $\pi/2$ mode, the impedance cancellation will work well between two parasitic modes. As a consequence, the residual impedance due to the parasitic mode can be made lower than the instability thresholds of $R_+ - R_- < 290 \Omega/\text{cavity}$.

B. Cure of the higher order modes in the accelerating cavity.

The choke mode cavity[4] will be one of the most suitable structure to effectively damp all of the higher order modes in the accelerating cavity. It is possible to achieve damped Q-value of less than 10 for the most dangerous mode of TM110 by optimizing the choke structure[6]. Since the choke mode cavity has perfect cylindrical symmetry, the heat density of wall power dissipation is very uniform and there is no heat concentration at any point. Therefore, we may apply higher acceleration voltage per cell, and reduce the total number of cavity around the ring. This is an important factor to reduce the instability impedance for both of the higher order modes and the fundamental mode. The total TM011 mode impedance is 50 k Ω /m/ring.

ACKNOWLEDGEMENTS

The author would like to thank Yoshishige Yamazaki, Tatsuya Kageyama and Kazunori Akai for stimulating discussions.

REFERENCES

- [1] B-factory Accelerator Task Force, "Accelerator Design of the KEK B-factory", KEK Report 90-24.
- [2] "An Asymmetric B Factory based on PEP", conceptual design report, Feb. 1991, LBL PUB-5303, SLAC-372, CALT-68-1715, UCRL-ID-106426, UC-IIRPA-91-01
- [3] T. Shintake, "Proposal of Accelerating RF-Cavity coupled with an Energy Storage Cavity for Heavy Loading Accelerators", to be published, KEK Preprint 92-191, January 1993 A
- [4] T. Shintake, "The Choke Mode Cavity", Jpn. J. Appl. Phys. Vol. 31 (1992) pp. L 1567 - L 1570, Part 2, No. 11A, 1 November 1992
- [5] Y. Yamazaki and T. Kageyama, "A Three-Cavity System which Suppresses the Coupled-bunch Instability Associated with the Accelerating Mode", to be published, KEK Preprint 93-15, May 1993, A
- [6] T. Shintake, "HOM-Free Linear Accelerator Structure using Choke Mode Cavity", Proc. 17th Linear Accelerator Meeting in Japan, Sendai, Japan (1992); KEK Preprint 92-66, July 1992 A

TABLE 1:
Principal Machine Parameter of KEK B-factory
(low energy ring)

Beam Energy	E	3.5	GeV
Beam Current	I_0	2.6	A
Revolution Frequency	f_{rev}	99.3	kHz
RF frequency	f_0	508.6	MHz
Total Cavity Voltage		22	MV
Energy Loss per Turn		0.95	MV
Synchronous Phase	ϕ	87.5	deg.
Synchrotron Frequency	f_s	6.9	kHz
Cavity Voltage	V_c	0.6	MV/cell
Number of Cells		37	

TABLE 2 : Performance of
the Storage Cavity Coupled System

Stored Energy / unit			
in accelerating cavity	W_A	0.68	Joul
in storage cavity	W_S	7.6	Joul
in total system.	W_{tot}	8.3	Joul
Wall Dissipation Power / unit			
in accelerating cavity	P_A	57	kW
in storage cavity	P_S	93	kW
Beam acceleration power	P_b	67	kW
Input RF-power / unit	P_{in}	217	kW
Shunt Impedance	R_{tot}	2.4	M Ω /cell
	$(R/Q)_{tot}$	13.6	Ω / cell
Unloaded-Q	Q_{tot}	1.76×10^5	
Optimum Coupling	β_0	1.45	
Loaded-Q	Q_L	7.2×10^4	
Detuning Frequency	Δf	- 15	kHz
Effective Impedance			
	for the coupled-bunch mode($m = -1$)		
	$R^+ - R^-$	18.0	k Ω / ring
Growth Time of the Instability		22	msec

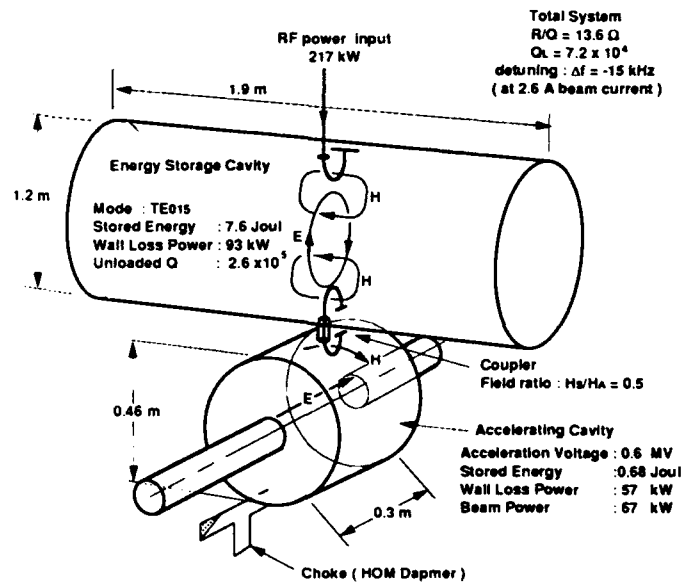


Fig. 2 Proposed accelerating rf cavity
for KEK B-factory.

A Two-Gap Booster Synchrotron RF Cavity[†]

W. R. Smythe and D. C. Van Westrum
University of Colorado
Boulder, CO 80309-0446

Abstract

Booster synchrotrons, such as the SSC Low Energy Booster, typically require a megavolt rf system which must tune about 25%. The cavity proposed here is longitudinally symmetric with the gaps separated by 140° in proton phase. The two perpendicularly biased ferrite tuners are directly connected to the center conductor and are located on either side of the cavity. The power tube is capacitively coupled to the midpoint of the drift tube. The cavity is designed to provide an energy gain of 1.88×90 keV. The tuner features ferrite toroids which are bonded with epoxy to water cooled copper surfaces. The cavity walls are slotted so that a significant fraction of the ferrite can be tuned by high frequency components of the bias field.

I. INTRODUCTION

Since the first proposed application of transversely biased ferrite tuners to synchrotron rf cavities [1],

[†]Supported in part by the Superconducting Super Collider Laboratory, operated by Universities Research Association under contract with the U.S. DOE.

there has been a continuing search for an optimum configuration. Most of the cavity configurations considered have been comprised of a single accelerating gap and a tuner which surrounds the beam line. Such tuners often have magnetic bias fields which result in a kilogauss size magnetic field in the beam line. An alternative configuration is proposed here, which is equivalent to two such cavities merged into a single cavity with two gaps, and which is distorted so that the tuners are not on the beam line. The cavity parameters have been chosen to match the requirements of the Low Energy Booster Synchrotron of the Superconducting Super Collider.

II. CAVITY DESCRIPTION

The basic cavity geometry is illustrated in Figure 1. The gap spacing is 1.94 m, which corresponds to 140° in proton phase for the 5.00 m bunch spacing which is common to all of the SSC synchrotrons. The drift tube structure is supported in vacuum by the rf tuner windows, which are shown in Figure 2. The tuners are located outside of the accelerator vacuum and can be removed and replaced without breaking vacuum. There is good access to the drift tube through the center of

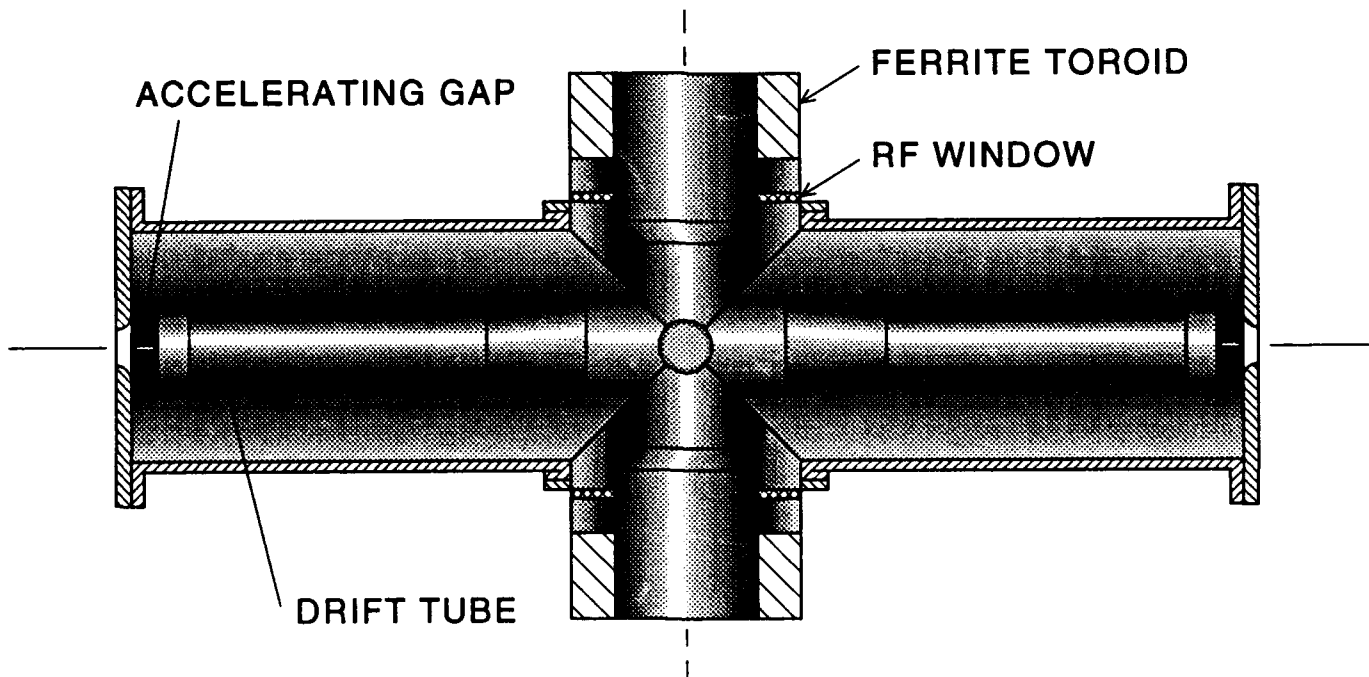


Figure 1. A partial horizontal cross section view of the cavity. The cavity consists of a long drift tube inside of a cylindrical tank with accelerating gaps at each end. The drift tube is supported by two coaxial ferrite tuners, as a cannon is supported by its trunnions. Not shown in this view is the power tube which sits vertically above the center of the drift tube and is capacitively coupled to it.

the tuners for water cooling, alignment devices, probes, or even mechanical support. The power tube is mounted directly above the center of the cavity and is coupled to it by a cup-shaped, vacuum insulated capacitor. In addition, higher order mode dampers, previously described [2], would be added at each gap.

III. TUNER DESIGN

Each tuner consists of a ferrite filled short circuited coaxial line. As can be seen from Fig. 3, it is very

important that the bias field be quite uniform at the low frequency tuning limit, since the tuner dissipation rises very steeply with decreasing bias field. A laminated steel return yoke and coil configuration which achieves reasonable uniformity is illustrated in Fig. 4. The ferrite is bonded by epoxy to the water cooled copper surface which carries rf current around it, to cool the ferrite. The copper surface has longitudinal and radial slots extending around the ferrite. These slots inhibit eddy

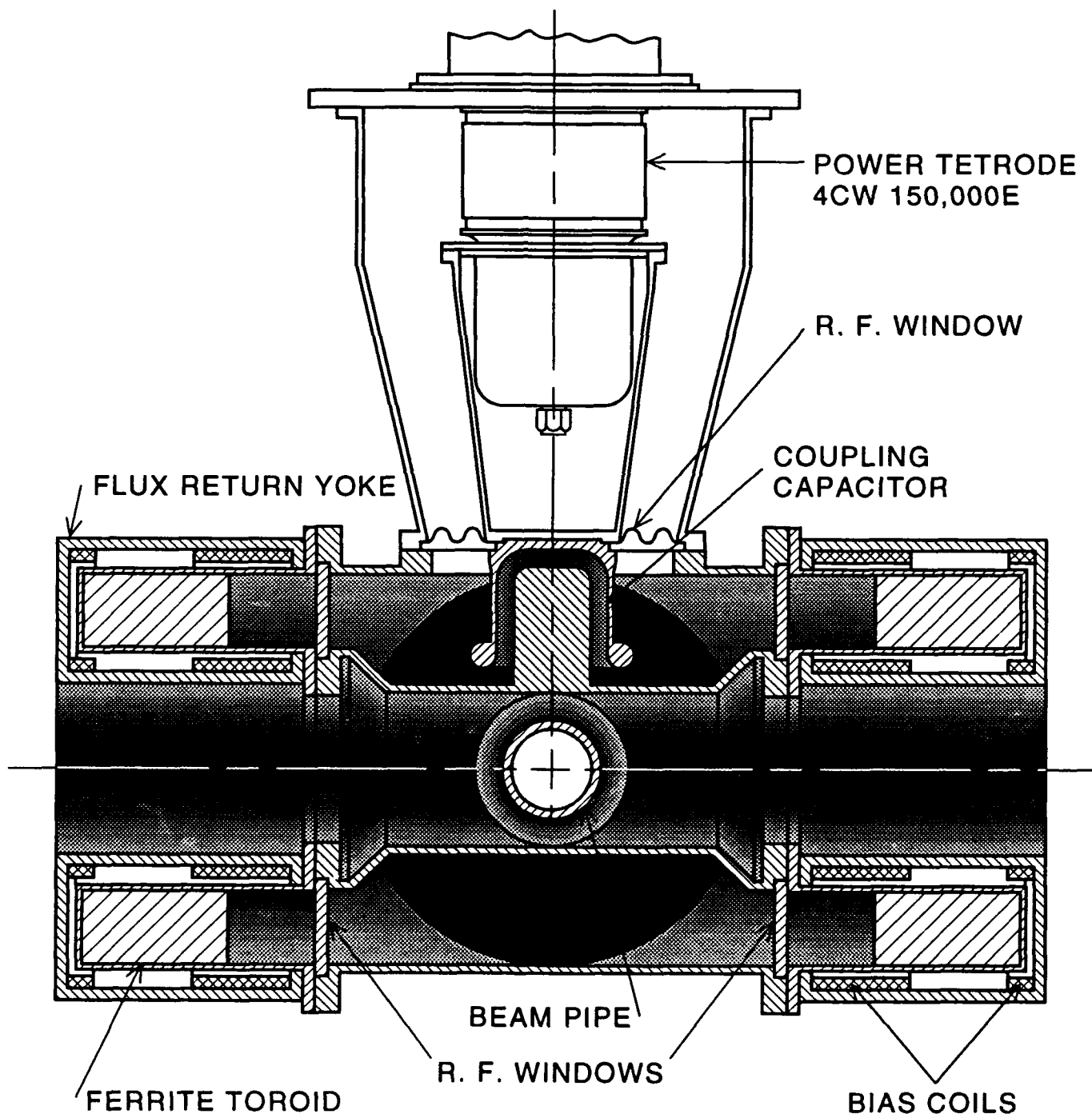


Figure 2. A vertical cross section through the center of the cavity, the power tube and the tuners, looking along the beam pipe. Each tuner can be removed and replaced without breaking the vacuum integrity.

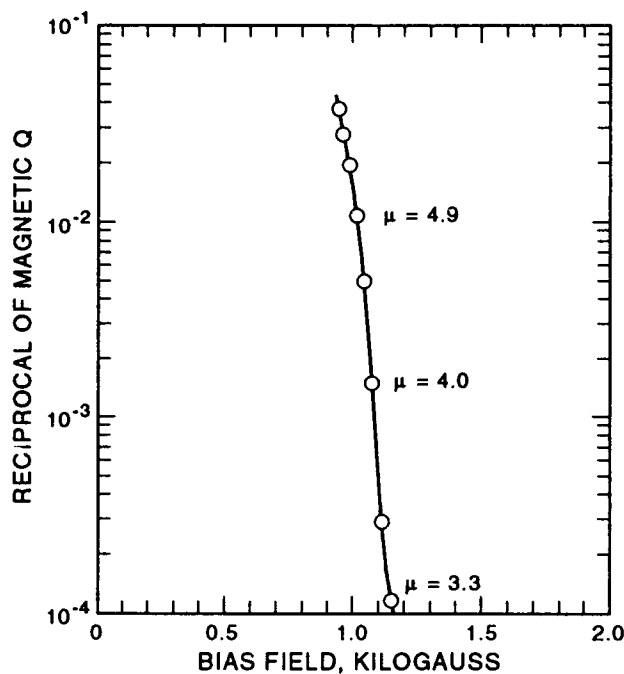


Figure 3. A plot of the reciprocal of the measured magnetic Q of Trans-Tech G-810 ferrite as a function of the dc magnetic bias field, for the case of perpendicular bias. The measurement method has been previously described [1]. The power dissipation in the ferrite is inversely proportional to the magnetic Q, so this plot makes clear the importance of achieving good bias field uniformity, when approaching the low bias field limit.

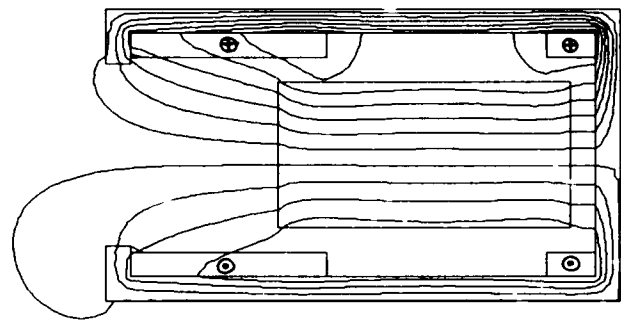
currents and permit high frequency components of the bias field to penetrate a large fraction of the ferrite volume, enhancing tuner frequency response.

IV. ANALYTICAL METHODS

The primary method used to analyze this cavity has employed a transmission line model to calculate voltage distribution, currents, electric and magnetic energy density, power loss, etc. Approximations for gap capacitance, and conical shapes were verified by use of the computer program SUPERFISH. The approximation used for the four way coaxial intersection was validated by use of the three dimensional computer program MAFIA. The advantage of the transmission line method of analysis is the speed with which a variety of configurations can be explored.

V. SUMMARY AND DISCUSSION

The calculated parameters of the cavity are listed in Table 1. It is seen that the cavity achieves the desired tuning range with reasonable power dissipation in the ferrite. This cavity employs about half as much ferrite per gap as do comparable single gap cavities [1], due to its lower stored energy. The lower stored energy results in a somewhat higher R/Q per gap. A major mechanical simplification results from having a configuration in which the beam does not pass through the tuner. Tuner maintenance and replacement can be achieved while the cavity remains under vacuum.



TUNER AXIS

Figure 4. Magnetic bias field plot at the low frequency limit, calculated with POISSON. Each inner coil current is equal and opposite to the corresponding outer coil current, resulting in zero net ampere turns about the tuner axis, and greatly reducing magnetic fields external to the tuner.

Table 1. Calculated Performance Characteristics of the Proposed Two-gap Cavity Design.

Frequency	47.4 MHz	59.9 MHz
Ferrite μ	3.4	1.4
Gap voltage, each gap	82 kV	99 kV
Tuner/window voltage	39 kV	23 kV
Copper loss	7.2 kw	10.8 kw
Q	3400	7400
R/Q (Two Gaps)	92 Ω	136 Ω
Ferrite	Trans-Tech G-810	
Ferrite bias H	26,500 A/m	158,800 A/m
Ferrite magnetic Q	4,000	10,000
Ferrite electric Q	5,000	5,000
Ave. ferrite pwr. dens.	1.3 w/cm ³	0.27 w/cm ³
Ferrite volume	24,100 cm ³	
Cavity length	2.0 m	
Gap to gap beam phase	140°	
Energy gain	1.88 V _{gap}	

VI. ACKNOWLEDGEMENT

We wish to express our appreciation to Linda Walling of the SSC Laboratory who kindly used the three-dimensional program MAFIA to provide runs for verification of the transmission line approximation to the "four-way junction" at the center of the cavity.

VII. REFERENCES

- [1] W.R.Smythe, T.G.Brophy, R.D.Carlini, C.C.Friedrichs, D.L.Grisham, G.Spalek, and L.C.Wilkerson, "RF Cavities with Transversely Biased Ferrite Tuning," *IEEE Trans. Nucl. Sci.* NS-32, No. 5, 2951 (1985).
- [2] W.R.Smythe, C.C.Friedrichs, and L.S.Walling, "Proton Synchrotron RF Cavity Mode Damper Tests," *Conference Record of the 1991 IEEE Particle Accelerator Conference*, 643 (1991).

HOM (Higher-Order Mode) Test of the Storage Ring Single-Cell Cavity with a 20-MeV e⁻ Beam for the Advanced Photon Source (APS)*

J. SONG, Y. W. KANG, and R. KUSTOM
Argonne National Laboratory, Advanced Photon Source
9700 S. Cass Ave. Argonne, IL 60439, USA

ABSTRACT

To test the effectiveness of damping techniques of the APS storage ring single-cell cavity, a beamline has been designed and assembled to use the ANL Chemistry Division linac beam (20-MeV, FWHM of 20 ps). A single-cell cavity will be excited by the electron beam to investigate the effect on higher-order modes (HOMs) with and without coaxial dampers (H-loop damper, E-probe damper), and wideband aperture dampers. In order for the beam to propagate on- and off-center of the cavity, the beamline consists of two sections-- a beam collimating section and a cavity measurement section-- separated by two double Aluminum foil windows. RF cavity measurements were made with coupling loops and E-probes. The results are compared with both the TBCI calculations and 'cold' measurements with the bead-perturbation method. The data acquisition system and beam diagnostics will be described in a separate paper [1].

I. INTRODUCTION

HOMs of the prototype APS-SR 1-cell cavity were already analyzed as shown in Table 1. The left column is a summary of the URMEL calculations [2], showing the mode type, frequency, and R/Q. Ten modes were calculated to have impedance that will cause coupled-bunch instabilities near the 300 mA of positron beam current that is the

design goal of the APS. These modes were also measured with the standard bead-perturbation method [3]. All the frequencies of the modes are very close to those predicted by URMEL simulation, though they are not exactly the same, since one cannot simulate a real structure with a 2-D computer code such as URMEL.

HOMs can be observed and identified with field probes by sending a beam on-axis and off-axis of the cavity. Various types of HOM dampers are also tested with this measurement. The primary reason for building this test facility is to measure those HOMs near and above the cutoff frequency of the beampipe. These modes cannot be easily calculated well because of strong geometric effects. Bench measurements cannot be easily related to beam-induced effects. With the beam-cavity measurement, one can evaluate impedance measurement techniques such as the bead-perturbation method and the wire method with the synthetic pulse [4].

The 20-MeV electron beam will be good for testing because of the similarities of its pulse shape and charge to those of the APS storage ring bunch. Comparisons of the linac beam and the APS storage ring bunch parameters are given in Table 2.

Table 2 Main Beam Parameters
for the APS-SR System and the Chemistry Linac.

	7-GeV APS Storage Ring			20-MeV Linac
Mode	single	Nominal	Maximum	1 - 60 Hz
# of bunch	1	20	60	
average current	5 mA	100	300	>1.5 μ A
peak current	700 A			> 625 A
bunch length (FWHM)	27.5 ps	50	72.5	25 - 40 ps
Total # of particle	1.2×10^{11}	2.3×10^{12}	6.9×10^{12}	$>1.5 \times 10^{11}$
total charge	18.5 nC			1 - 20 nC
natural emittance	8.2 x 10 ⁻³ mm-mrad			10 mm-mrad

Table 1 Mode Comparison

URMEL Calculation			Measurements perturbation	Measurements (20 MeV Beam)
# mode	f	R/Q	All 4 tuners in flush	No tuners/input coupler
	(MHz)		f	f
0 E-1	353.6	114.3	352.6	351.3
0 M-1	536.7	40.7	536.4	537.3
1 E-1	588.7	200	588.3	587
1 M-2	761.1	483	758.6	759
0 E-3	922.5	5.8	920.1	919
0 M-2	939	5.5	936.4	940
1 E-3	962	113	958	950.5
1 M-4	1017.4	63.4	1015	1018
1 E-5	1145.1	29.3	1141	1146
0 M-3	1210.8	5.2	1208	1205
0 E-6	1509.1	4.1	1507	1509

*Work supported by U.S. Department of Energy, Office of Basic Sciences, under Contract W-31-109-ENG-38.

II. BEAMLINE SYSTEM

The Argonne Chemistry linac is an 'L' band (1.3 GHz) traveling wave accelerating structure. An electron beam (1-60 Hz repetition rate, 1 - 20 nC total charge, and 25 - 40 ps bunch length) can be obtained.

A beam position monitor or beam stripline (BPM) and an integrating current transformer used in the first section

The submitted manuscript has been authored by a contractor of the U. S. Government under contract No. W-31-109-ENG-38. Accordingly, the U. S. Government retains a nonexclusive, royalty-free license to publish or reproduce the published form of this contribution, or allow others to do so, for U. S. Government purposes.

are used in the first section for beam diagnostics. The BPM serves as a triggering signal for the rest of the beam diagnostic system. The second section of the beamline includes the RF cavity, two fluorescent screens (FS), an integrating current transformer, and a beam dump. One FS is located upstream of the cavity and the other downstream of the cavity. A detailed description of the beam parameter measurement can be found in reference [1].

The second section is movable with respect to the first section by ± 2 cm in the X and Y directions and 10 cm along the beamline to have a beam off-center of the cavity. The beamline pressure is about 1×10^{-4} Torr.

III. CAVITY MEASUREMENT SYSTEM WITH HOM DAMPERS

HOMs are measured with two H-loops and two E-probes that are connected to the cavity. One H-loop (H_1) is oriented to couple to the TM-like mode and the other H-loop (H_2) is oriented to couple to the TE-like mode. These are connected onto the ports of the equatorial plane which are 90 degrees apart (i.e., orthogonal to each other). The coupling with these H-loops is easily changed without breaking the vacuum.

The E-probes are made of 1/4" Cu coaxial transmission line and connected through SS Quick-Disconnects (or a Wilson Seal) to give the probe coupling flexibility. One E-probe (E_1) is near the beam port, and the other (E_2) is near, but not on, the equatorial plane. The output of these H-loops and E-probes are connected to the HP microwave multi-throw switches and HP switch driver. These probes are well calibrated with the calibration cavity ($f_0 = 1.6$ GHz) and the HP 8510 network analyzer.

The EPICS (Experimental Physics and Industrial Control System) software is used for control and data collection (mainly beam parameter measurements). The operator interface (OPI) is a SUN workstation running the UNIX operating system. The SUN workstation communicates with a VME-based Input/Output Controller (IOC) through an Ethernet LAN. By controlling the HP switch driver, one can switch from one probe to another easily and quickly.

H-loop and E-probe dampers have been tested as shown in Fig. 1. An alumina ceramic disk window is used in the coaxial line near the vacuum flange to isolate the ferrite load from the cavity vacuum. The center conductor is water-cooled. The E-probe damper was tested successfully in the cavity up to 100 kW CW input power [5]. The H-loop damper also has a $\lambda/2$ notch filter to avoid coupling to the fundamental mode of the cavity. The dampers are connected to ports on the equatorial plane. Tests were made with only one E-probe damper with about 1 inch into the cavity, two E-probe dampers orthogonal to each other, and one H-loop damper alone.

IV. RESULTS AND DISCUSSION

Data was taken with an HP spectrum analyzer up to 2.9 GHz and saved onto a 128 K ram card for future analysis. Typical data taken from the E_1 probe without any HOM damper is shown in Fig. 2. Most HOMs are found, even though the resolution of the frequency response is not accurate in this broadband frequency span.

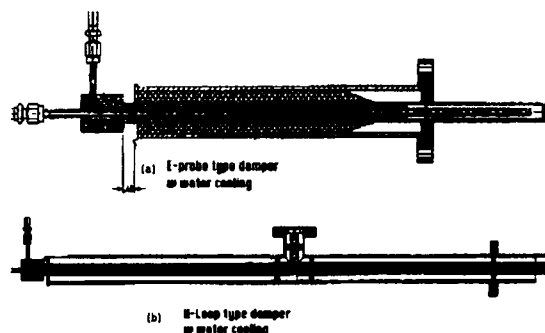


Fig. 1 HOM dampers:
(a) E-probe Damper, (b) H-loop Damper.

The results are summarized in the third column of Table 1. The amplitudes of most of the signals are large enough so that a 30-dB attenuation is regarded over the frequency span. Notice that there are more than eight HOMs above 1.3 GHz which is the cutoff frequency of the beampipe near the cavity. Their signal amplitudes are above -50 dBm and their Q-values are comparable to those of the fundamental mode. These are the modes that will be most extensively studied.

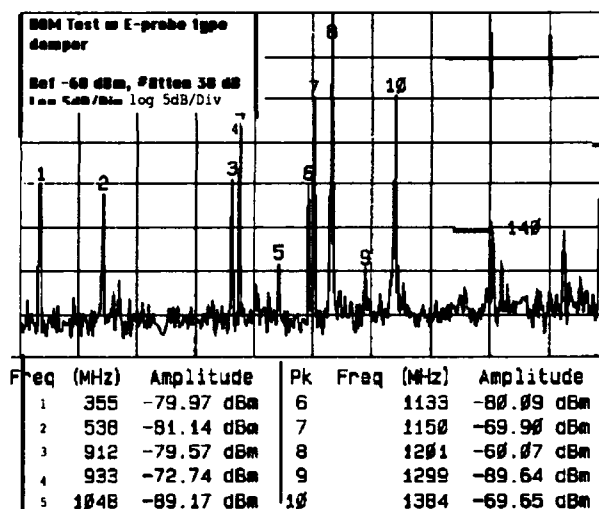


Fig. 2 HOMs in the Cavity w/o any Damper.

Signals from H-loops appeared to be very selective and sensitive to the couplings as expected. The H_1 probe picks up mainly TM₀ modes, but H_2 couples only strongly at 1210 and 1386 MHz.

To measure the damping ratio, a frequency response from the E_2 probe is obtained for each HOM. One is without damper and the other is with only one E-probe damper. Typical data are measured around 759 MHz and are plotted in Fig. 3. The effect of the E-probe damper can be easily seen in this figure. As one can see, there are two peaks adjacent to each other. This is due to the nature of the dipole mode. This is an E₁₁₁-like mode. They are damped out by 12.4 and 9.8 dBm at 759.275 and 759.913 MHz, respectively. One HOM at 761.212 MHz is not affected by the E-probe damper.

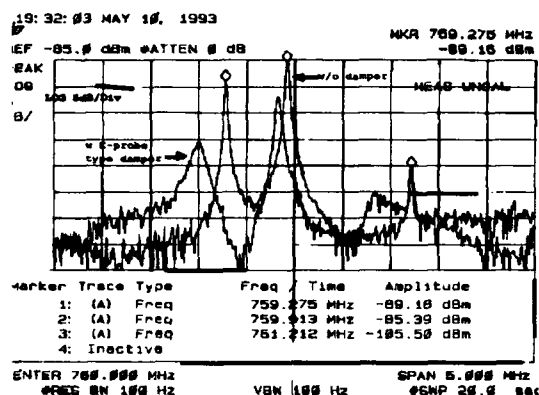


Fig. 3 HOM at 759 MHz (Dipole), with & without one E-probe Damper.

Figure 4 shows the HOMs for the Monopole mode at 940 MHz. The damping ratio is more than 20 dBm.

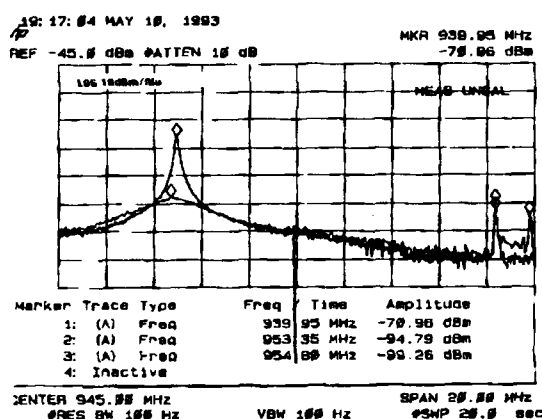


Fig. 4 HOM at 940 MHz (Monopole), with & without one E-probe Damper.

Table 3. HOM Damping Ratio.

		Measurements		Measurements	
		perturbation		(20 MeV Beam)	
# mode	Thres- hold Current	2 E-probe dampers damping ratio	H-Loop damper damping ratio	Vacuum 1x10 ⁻⁴ No tuners No input coupler	E-probe damper damping ratio
0 E-1	mA	No effects		351.3 f	1 dB
0 M-1	80	23		537.3	7.4
1 E-1	81	9		587	?
1 M-2	43	30	30	759	12.4
0 E-3	130			919	no
0 M-2	340	27		940	22.6
1 E-3	180			950.5	N/A
1 M-4	320	13		1018	10
1 E-5	80		5?	1146	no
0 M-3	80			1205	no
0 E-6	80		20	1509	not found

The damping ratios for most of the HOMs are summarized in Table 3. For comparison, the results from the per-

turbation measurement are also tabulated in columns 3 and 4 for two E-probe and one H-loop dampers, respectively. Also shown are the calculated threshold currents for coupled bunch instabilities in the second column. There is no effect on the fundamental mode to within 30 Hz resolution of BW measurements of the HP spectrum analyzer. In most cases, the damping ratio measured with the beam is followed by the bead-perturbation method. To accurately test the dipole mode, at least two identical dampers are needed.

V. CONCLUSION AND FURTHER WORK

The results of the HOM test with the beam-cavity measurements agree very well overall with the previous measurements, especially for the monopole modes, but more study on the dipole mode is needed.

HOMs near and above the cutoff frequency will be investigated and tested with various HOM dampers, including a broadband aperture-coupling damper. Figure 5 shows HOMs between 2.5 and 2.7 GHz.

The transverse impedance due to the HOMs will be measured, having the beam off-center of the cavity.

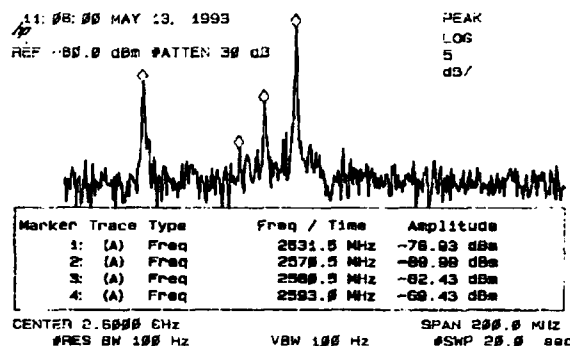


Fig. 5 HOMs above Cutoff Frequency

VI. ACKNOWLEDGMENTS

The authors would like to thank Don Ficht, Eric Landahl, Ed Wallace, and Portia Young for their technical support.

VIII. REFERENCES

- [1] J. Song, et al., "A Beamline Design and Data Acquisition with the 20-MeV, 20-ps Electron Beam for the Higher-Order Mode Studies of the APS SR-RF Cavities" these proceedings.
- [2] L. Emery, "Coupled-Bunch Instabilities in the APS Storage Ring", Conference Record, 1991 IEEE Particle Accelerator Conference, pp 1713-1715, 1991.
- [3] J. Bridges, et al., "Measurements on Prototype Cavities (352 MHz) for the Advanced Photon Source (APS)," Conference Record, 1991 IEEE Particle Accelerator Conference, pp 690-692, 1991.
- [4] J. Song, "Experimental Study of Coupling Impedance," APS LS-Note-201, ANL, Oct. 11, 1991.
- [5] J. Bridges, et al., "High Power Operation of Single-cell 352-MHz Cavity of the Advanced Photon Source (APS)," these proceedings.

Performance of a 1500 MHz Niobium Cavity with 2K-LHe Channel Cooling*

J. Susta, P. Kneisel, and M. Wiseman
Continuous Electron Beam Accelerator Facility
12000 Jefferson Avenue, Newport News, Virginia 23606 USA

Abstract

$\beta=1$ superconducting accelerator structures are traditionally operated immersed in a liquid helium bath. Nevertheless, several attempts have been made in the past to make use of the numerous operational and cost advantages of a pipe-cooling configuration: reduction in liquid helium inventory, minimized cooldown/warmup times, and elimination of the LHe-vessel, which reduces the sensitivity to microphonics and provides easier access to all cavity components.

This paper reports on tests performed with a 1500 MHz niobium cavity with 2K-LHe cooling channels covering only a fraction of the cavity surface. The cooling channels are made of niobium to preserve the capability for high temperature-treatments.

In the initial test the cavity was immersed in a helium bath; subsequently the cooling was only provided by superfluid helium in the cooling channels.

The experimental results are compared to thermal model calculations. In addition, the computer model is used to investigate the variations in cavity performance as a function of the cooling channel geometry and thermal conductivity properties of the niobium.

I. INTRODUCTION

The geometries of superconducting low- β structures such as helices [1], split rings [2], or quarter-wave resonators [3] allow the use of the structures themselves as a helium container for forced helium flow at 4.2 K. External parts, like couplers or the outer tanks, are cooled by conduction using composite materials like niobium explosion bonded to high thermal conductivity copper.

Superconducting $\beta=1$ accelerating cavities are traditionally cooled by immersion in a LHe bath. Early attempts were made to change this arrangement by building double-walled cavities [4,5] which still provided direct LHe cooling to the whole surface. Encouraged by the results of computer simulation calculations of the thermal effects on cavities made of niobium-copper composite material [6], further attempts to reduce the direct LHe contact cooling on 1000 MHz and 500 MHz cavities were made in the early 80's [7,8]. In these cavities cooling pipes for LHe at 4.2 K were attached to the outer cavity surface. In the first tests the outside niobium surface had been coated with high thermal conductivity silver; later a niobium-copper clad composite was used to take advantage of the high thermal conductivity of copper combined with the superior features for attachment of cooling channels by either brazing or electron beam welding. Even though these experiments were successful and demonstrated the feasibility of the pipe cooling concept at 4.2 K, they were not further pursued because of schedule pressure

and budget constraints.

1500 MHz cavities have to be cooled down to superfluid helium temperatures in order to sufficiently lower the superconducting surface resistance of the material to achieve Q -values of $>5 \times 10^9$. At 2.0 K the thermal conductivity of niobium decreases to 20% of the value at 4.2 K. This imposes a stronger limitation on the spacing between the cooling channels especially if no copper layer is used.

Some of the advantages of a channel-cooled configuration are:

- Lower sensitivity to microphonics
- Capability of supporting higher pressures in the cryogenic system
- Easily recoverable low helium inventory
- Faster cooldown and warmup times
- Easier accessibility of components and diagnostics cables
- Reduction in the number of feedthrus for rf, tuners, and diagnostics
- Easier assembly and disassembly of cryostat

In the following sections we report on measurements carried out with a channel-cooled cavity, and compare the results with model calculations.

II. EXPERIMENTAL

A. Cavity

A single-cell 1500 MHz cavity with the CEBAF cell shape was modified to add cooling channels as shown in Figure 1.

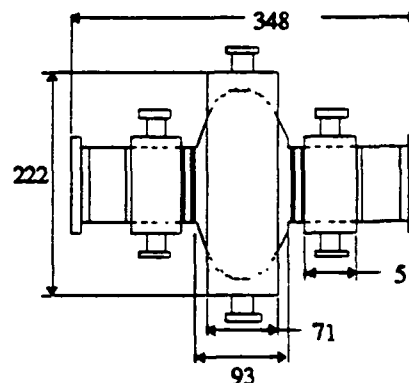


Figure 1. Channel cooled cavity (dim. in mm).

The cell of the cavity was manufactured with high purity niobium with RRR > 220 supplied by Tokyo Denki. The cell was postpurified at 1400°C for 4 hours in the presence of titanium as a solid getter material [9]. As indicated by measurement on samples, the thermal conductivity had improved by at least a factor of two after this treatment.

* This work was supported by DOE Contract DE-AC05-84ER40150.

B. Test sequence

A standard chemical surface treatment was applied to the cavity. It was subsequently attached to the cryogenic testing station and pumped to a vacuum of $< 5 \times 10^{-7}$ torr. The first measurement of the Q -value as a function of rf field was done with the cavity fully immersed in LHe. In the second measurement, the cavity was cooled only by the LHe inside the cooling channels. Between these tests the cavity remained under vacuum, and no changes in the test arrangement except for the cooling were made. The test arrangement is shown schematically in Figure 2.

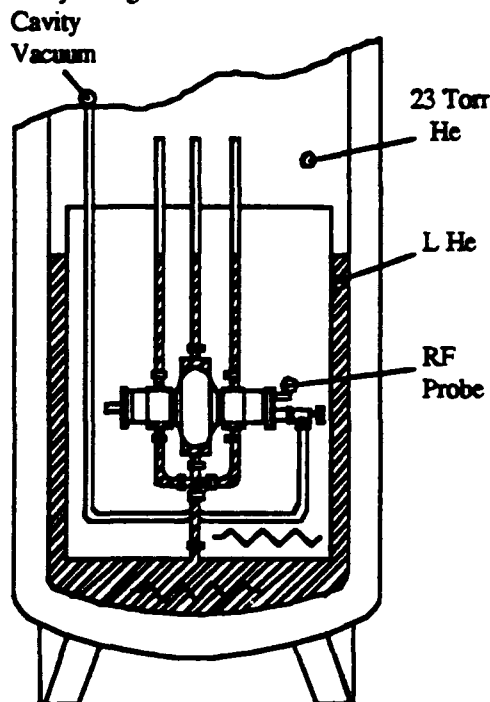


Figure 2. Test arrangement.

C. Measured results

Experimental results are shown in figures 3 and 4. The fully immersed cavity reached a peak surface field of $E_{\text{peak}} = 55$ MV/m at 2.0 K, and 57 MV/m at 1.8 K. When the cavity was cooled only through the cooling channels, it performed as well as the immersed cavity up to a peak surface field $E_{\text{peak}} = 27$ MV/m at 2.0 K, and $E_{\text{peak}} = 35$ MV/m at 1.35 K. Pulsed-rf operation increases significantly the attainable fields as shown in Figure 4.

D. Computer modeling

Several alternative geometries can be explored with the aid of computer modeling. A program developed for pipe-cooled Nb-Cu cavities [10] was modified and adapted to the channel-cooled niobium cavity.

The results obtained by varying several parameters are shown in Table 1.

The experimental model parameters are taken to calculate the base case. It is defined by a He-bath temperature = 2.0 K, wall thickness = 3.2 mm, cooling channel length = 100 mm, and a niobium thermal conductivity of 40 W/m/K at 2 K. This case shows a three percent reduction in Q_0 at a peak field $E_{\text{peak}} = 18$ MV/m and agrees very well with the experimental

results, (Figure 5). For all other cases presented in Table 1, one property was changed from the base case. A reduced bath

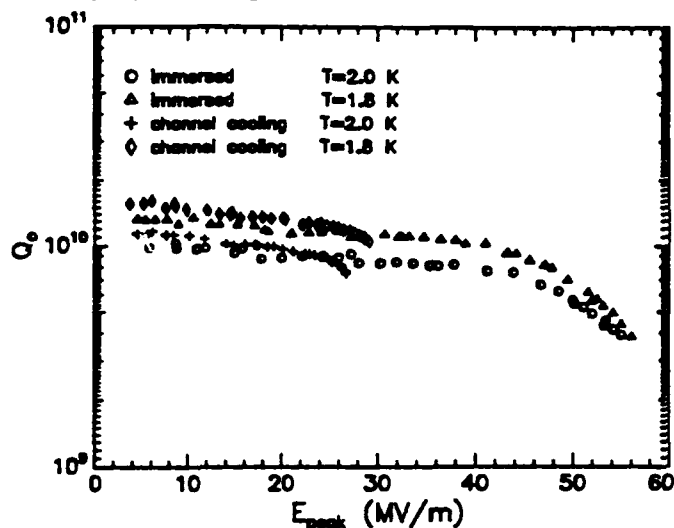


Figure 3. Q_0 as a function of peak surface field E_{peak} for the tested cavity at 2.0 K and 1.8 K.

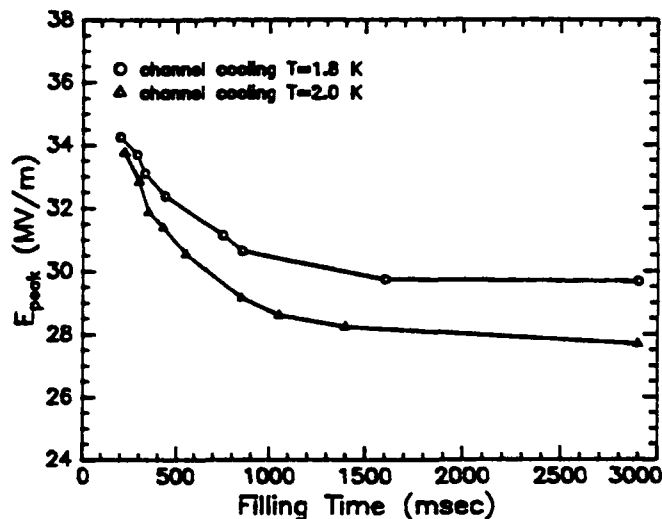


Figure 4. RF-peak surface field vs. rf-pulse length (50% duty cycle).

temperature of 1.8 K gives the predicted improvement in Q_0 . The most critical factor is shown to be the size of the cooling channel. Other factors investigated showed little deviation from the base case up to the maximum calculated field.

The defect was modeled as a 400 mm² ring located 12 mm from the central cooling channel. The defect element contributed 0.5 W to the power dissipated at an E_{peak} of 9 MV/m.

III. CONCLUSION

The test results confirm the computer calculations. They indicate that a channel-cooled cavity made from high thermal conductivity niobium can perform nearly as well as a fully immersed cavity up to cw peak surface fields of 27 MV/m,

TABLE 1. Computer model results

		EXPER. CASE	Case 2	Case 3	Case 4	Case 5	Case 6	EXP. MODEL W DEFECT
	FULLY IMMERSED AT 2K	k=40 Tb=2 Cl=100 th=3.18	k=70 Tb=2 Cl=100 th=3.18	k=40 Tb=2 Cl=100 th=4.18	k=40 Tb=2 Cl=100 th=2.18	k=40.5 Tb=1.8 Cl=100 th=3.18	k=40 Tb=2 Cl=76 th=3.18	k=40 Tb=2 Cl=100 th=3.18
E_p $Q_0 \times 10^9$ P	9 10.091 0.2815	9 10.027 0.2833	9 10.032 0.2832	9 10.032 0.2832	9 10.020 0.2835	9 15.027 0.1891	9 9.971 0.2849	9 3.527 0.7952
E_p $Q_0 \times 10^9$ P	18 10.091 1.126	18 9.831 1.156	18 9.856 1.153	18 9.851 1.154	18 9.797 1.160	18 14.820 0.767	18 9.580 1.186	18 3.51 3.391
E_p $Q_0 \times 10^9$ P	36 10.091 4.504	27 9.486 2.695	36 9.101 4.995	29 9.456 3.076	22 9.660 1.694	25 14.546 1.531	20 9.461 1.453	25 2.631 8.464

Tb=helium bath temperature (Kelvin)

Cl=channel length (mm)

E_p = E_{peak} (MV/m)

k=thermal conductivity at Tb (W/m/K)

th=wall thickness (mm)

P=dissipated power (watts)

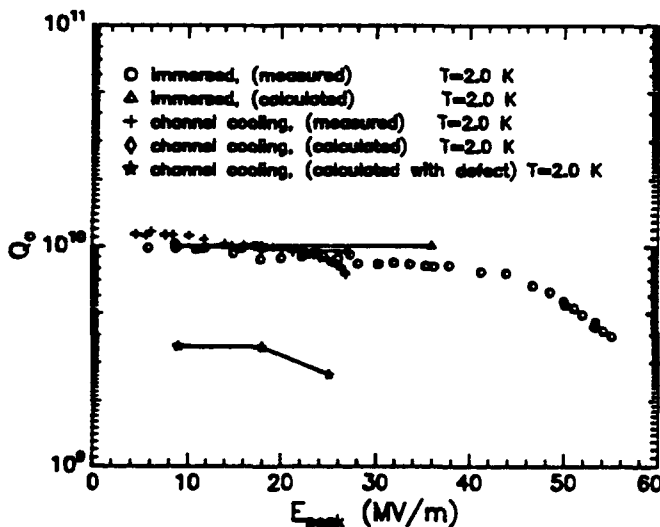


Figure 5. Calculated results at 2.0K (base case).

with a Q_0 -value of 10×10^9 at 1.8 K, as measured in our experiments. This would correspond to an accelerating gradient of 10–11 MV/m in a 5-cell CEBAF cavity. Pulsed RF operating modes would allow significantly higher fields.

The channel configuration can be further optimized to support higher helium pressures and also to increase the cell mechanical stability. The cost savings in the cryogenic system, as well as in the cryostat fabrication and assembly, could offset the higher material and fabrication costs of the cavities.

IV. ACKNOWLEDGEMENTS

We would like to thank all our colleagues who contributed to this investigation, and Kathy Yopp for the illustrations. Our special thanks go to John Brawley, Jody Brock, Brett Lewis, and Larry Turlington for the fabrication and implementation of the test assemblies, and to the operators of CEBAF's vertical test apparatus for their support

during the cryogenic tests.

Many thanks to the DESY rf group and H. P. Vogel (now with Siemens AG) for providing the computer program for the pipe cooling calculations.

V. REFERENCES

- [1] A. Brandelik *et al.*, "Accelerating Tests on the First Section of the Karlsruhe Superconducting Electron Accelerator," *KFK-Ex. 3/72-9*, Kernforschungszentrum Karlsruhe (1972) and Part. Acc. 4 (1972) III.
- [2] K. W. Shepard, G. P. Zinkham, "A Superconducting Accelerating Structure for Particle Velocities from 0.12 to 0.23 c," *IEEE Trans. Nucl. Sci.* NS-22, of (3), 1156 (1977).
- [3] K. W. Shepard, "Status of RF-Superconductivity at Argonne," *Proc. of the 4th Workshop on RF-Superconductivity*, KEK (1989), Vol 1, 140.
- [4] J. Kirchgessner *et al.*, "Superconducting Cavities for Synchrotron Use," *IEEE Trans. Nucl. Sci.*, NS-22, (3), 1141 (1975).
- [5] K. Mittag, "Superconducting Accelerating Cavities for Medium Energy Protons," *IEEE Trans. Nucl. Sci.* NS-24, (3), 1156 (1977).
- [6] H. Padamsee, "Superconducting Cavities Made from Niobium-Copper Composite Material," CERN/EF/RF 83-1.
- [7] J. Susta, "Development in Fabrication Methods," *2nd Workshop on RF-Superconductivity*, CERN (1984), Part 2, 597.
- [8] B. Dwersteg, W.-D. Moeller, D. Proch, U. Klein, A. Palussek, H. Vogel, "Experiment on the First Prototypes of Pipe Cooled 500 MHz Cavities from Explosion Bonded Copper," EPAC (1988).
- [9] P. Kneisel, "The Use of the Titanium Solid Gettering Process for the Improvement of the Performance of Superconducting RF Cavities," *Journ. Less Comm. Metals*, 139, 179–88 (1988).
- [10] H. Vogel, "Temperature Distribution in Superconducting Pipe Cooled Cavities," DESY M-87-04.

Large scale production at Ansaldo of 352 MHz niobium coated LEP-CERN cavities: development activities and first results.

A. Bixio, P. Gagliardi, M. Marin, S. Moz, W. Sciutto, F. Terzi, G. Zoni
ANSALDO GIE - Magnet & Special Product Div.
v. N. Lorenzi 8, 16152 Genoa, ITALY

Abstract

The program of energy upgrading of LEP needs about 200 superconducting RF cavities of 352 MHz frequency.

Since 1984 CERN has developed a method to produce niobium coated cavities by sputtering procedure.

During last years, an intensive collaboration between Ansaldo and CERN, has carried out the necessary transfer of technology from laboratory to industry.

In this paper we present the activities developed for a series production of 13 cryomodules, with special attention to the first rf results.

The excellent performances obtained with the first cavities gave a confirm of the feasibility of the production of high quality superconducting cavities at Ansaldo.

I. INTRODUCTION

For several years CERN developed the necessary technologies to produce superconducting cavities required by the LEP energy upgrading project [1].

That development work started, at CERN, with the construction of bulk niobium cavities. However at high accelerating field, the RF performance of a superconducting cavity is mainly limited by strong dissipation of the stored power because of low thermal conductivity of niobium at liquid helium temperature.

In a superconducting material, the penetration depth of the electromagnetic field is a few nanometers. This characteristic induced CERN laboratories to develop a new technology [2] to produce 4-cell cavities with the internal surfaces coated by a very thin (1 micron) niobium film: this solution reduces considerably the RF losses at cryogenic temperature.

During last years the necessary technology for a large scale production of Nb/Cu cavities has been transferred from CERN to Ansaldo [3].

At the end of 1990, Ansaldo drew up a supply contract about 52 superconducting cavities equipped with cryogenic and RF components, and assembled in 13 cryomodules for LEP 200 project. (Fig. 1)

Now Ansaldo is equipped with high-tech manufacturing plants to carry out the industrial production of 352 MHz superconducting niobium copper coated cavities by magnetron sputtering [4].

II. MANUFACTURING PROCEDURE

The production of superconducting RF cavities, needs high technology plants (Table 1) to ensure excellent quality of each manufacturing procedure.

Half cells are made by spinning or by deep drawing from OFHC copper sheets and chemical treated by electropolishing. The 4-cell assembling is performed by electron beam machine to weld all the components from the inside. So the whole cavity is tuned at the resonant frequency and the field profile adjusted to reach the necessary field flatness within a $\pm 5\%$ of maximum deviation of the field of each cell, from the average value.

The chemical polishing is performed by a circulating bath to produce a deoxidized, high polished surface which guarantees a good film adhesion: then the cavity is rinsed with demineralized water and alcohol and finally dried.

Niobium coating of internal copper surfaces is made by magnetron sputtering. After coating, cavity is rinsed again with ultrapure (18 MOhm cm) water jet by a moving tube and dried. All these operations about rinsing and drying are executed under high cleanness conditions in cl.100 clean-room to avoid any kind of contamination

Then cavity is sent to CERN for RF test at 4.2 K: if RF performance is acceptable (Target values: $Q_0 = 8.0 \cdot 10^9$ at $E_{acc} = 0.1$ MV/m and $Q_0 = 4.0 \cdot 10^9$ at $E_{acc} = 6$ MV/m) the cavity is ready for the assembly of He-tank, tuners and cryostat; otherwise, in case of poor RF performance because of bad

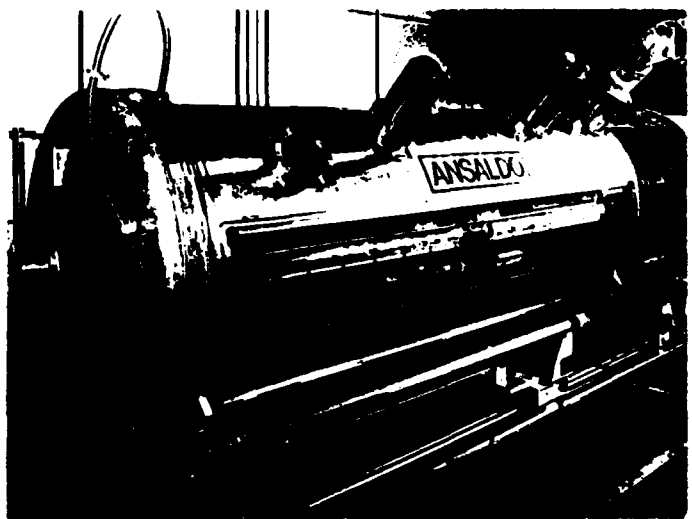


Fig. 1 - Assembly of a 4-cavities module

Table 1

352 MHz Nb/Cu LEP cavities production - Installations in ANSALDO

CLEAN-AREAS

- cl.100 clean-room for Nb cathode mounting, cavity rinsing and drying
- cl.100/1000 clean-rooms 30 m. long for module assembling
- Laser particle counter monitoring system

CHEMICAL PLANTS

- Electropolishing plant for components treatment
- Chemical polishing plant for 4-cell treatment: both plants operate under computer control
- Chemical degreasing equipment for stainless steel UHV components
- Water demineralizing 2-level system and ultrapure (18 MOhm cm) water plant for final cavity rinsing

BRAZING AND WELDING INSTALLATIONS

- Electron beam welding machine:
 - two guns of 6 KW and 70 KW output power with 90 ° magnetic deflector
 - stainless steel vacuum chamber 32 m³ of volume, at present one of the larger EB welding equipment in Italy
- Vacuum electric furnace for copper tube-stainless steel flange brazing
 - 280 litres volume; ultimate vacuum of 10⁻⁶ Torr at 1320 °C

SPUTTERING PLANT

- UHV turbomolecular pumping system
- Diagnostic system with quadrupole mass spectrometer for residual gas analysis
- Cathode power supply 800 V /50A
- Data acquisition system for continuous monitoring of sputtering parameters

DIAGNOSTIC DEVICE

- Chromatography system for chemical solutions analysis (Anions, Cathions, Alcohols analysis)

film adhesion or film contamination, cavity is stripped, chemically treated and Nb coated again.

Finally each cavity with cryostat is assembled in a 4-cavities module in a cl.100 clean room and mylar alluminized superinsulation blankets for thermal insulation are installed.

Then cavity is carried in a cl.100 clean room to perform the final rinsing with ultrapure water and ethanol, and dried under dust free air laminar flow.

B. Niobium sputtering***A. Chemical treatments***

All copper components, half cells and cut-off tubes, are degreased and prepared, before welding, with electropolishing treatment.

First a thorough decreasing is carried out with alkaline detergent at T = 60 °C with ultrasonic agitation. Then the electropolishing eliminates the layers damaged by the copper sheet lamination or any other manufacturing process.

This treatment removes about 100-120 microns from the inner surface of a half cell, using a mixture of phosphoric acid and n-butanol at room temperature with a current density of about 5.5 A/dm².

After assembling the cavity is treated with a circulating bath (sulfamic acid, n-butanol, hydrogen peroxide and ammonium citrate) at T = 72 +/- 2 °C, for about 45 min., to produce a removal of 25-30 microns.

Niobium coating of cavity internal surface is performed by magnetron sputtering with a glow argon discharge.

The large volume of a 352 MHz 4-cell cavity and the peculiarity of its geometrical shape, has necessarily induced to carry out a sputtering system with cylindrical configuration: a niobium cathode coaxial to cavity is used and an internal set of magnets ("magnetron") gives the necessary rate of argon ionization to obtain the uniformity of the film both on the equator and on the iris regions.

This configuration, together with the intrinsic instability of the argon discharge, involved many efforts to define the sputtering parameters (Ar pressure, cathode voltage and magnets current).

In particular we had to perform a fine adjustment of the electronic control unit between cathode and magnetron power supplies to minimize the oscillations of the discharge at such a low argon pressure of 6.0 10⁻⁴ Torr.

The niobium RRR values as well as the RF performance of the cavity at liquid helium temperature, are strongly affected by any kind of contamination which may occur before, during and after the coating process.

Residual components of the chemical bath may remain trapped inside surface microdefects and they could cause poor adhesion of the niobium film.

So before coating, cavity (under vacuum) is submitted to a baking process of about 24 hour at 200°C: that also drastically reduces the probability of film contamination by surface degassing during the film growing.

Another sort of contamination could come from the niobium cathode: some high power sputtering process are useful for a good niobium conditioning before starting with the coating of a copper cavity for series production.

The sputtering plant is also equipped with a diagnostic system for residual gas analysis: a quadrupole mass spectrometer is used and the rates of argon and nitrogen are continuously monitored during the process.

At last, great attention has to be paid during the final water rinsing to eliminate the large amount of electrons which may be trapped on the niobium film.

III. FIRST RESULTS OF RF TEST

We send each cavity to CERN laboratories for RF test at 4.2 K temperature: that consists in a high power RF test to evaluate the Q_0 -value vs. accelerating field E_{acc} and, eventually, in a temperature mapping of the cavity to identify the causes of field and Q_0 limitation.

A conditioning process of the cavity (He processing) is also performed to eliminate the electron loading effect.

The RF performances of the first cavity prototypes, were badly influenced by a sort of soft global contamination of the film perhaps caused by low conditioning of niobium cathode, stainless steel vacuum components or copper cavity surface.

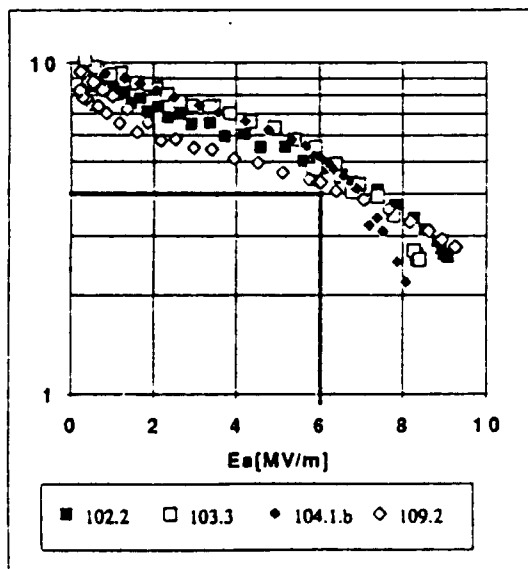


Fig. 2 - Q_0 vs. accelerating field E_{acc} (courtesy CERN)

After these first results, a continuous increasing of the Q_0 -value was obtained and high quality niobium coated cavities were produced ($Q_0 = 5.4 \cdot 10^9$ at 6 MV/m). (Fig. 2)

We also noted that, in some cases, a second standard water rinsing of the cavity after niobium coating, may increase the Q_0 -value especially at high accelerating field.

IV. CONCLUSION

Series production of superconducting niobium copper coated cavities for LEP is a very important result for European industries. Many efforts have been carried out in Ansaldo to develop and get ready the necessary technologies about chemical treatments, electron beam welding and thin film deposition.

At present Ansaldo is delivering to CERN the first accelerating module fully equipped with tuning system, RF couplers, diagnostic devices and the assembly of the second one is being done.

Ansaldo plants have showed their reliability in large scale production of high performance cavities according to the specifications required by the LEP 200 project.

V. RESEARCH AND DEVELOPMENT WORKS

Ansaldo is also engaged in cavity production for INFN-LNF. The design of two accelerator modules has been completed and the production of two 4-cell bulk Nb and Nb/Cu coated prototypes started. On the basis of the experience we carried out during LEP cavities production, we are developing, in collaboration with INFN-LNF/TOV (Frascati and Roma -Tor Vergata) and INFN-LASA (Milano), a method to produce a 500 MHz niobium coated 4-cell prototype.

VI. REFERENCES

- [1] C. Benvenuti, "Superconducting coatings for RF accelerating cavities: past, present and future", *Proc. of 5th Workshop on RF superconductivity*, DESY, Hamburg, 1991
- [2] C. Benvenuti et al., "Superconducting niobium sputter-coated copper cavities modules for LEP energy upgrade", *Proc. of 1991 Particle Acc. Conference*, San Francisco, USA, 1991
- [3] C. Arnaud et al., "CERN's technology for superconducting cavities in European industry", *Proc. of 3rd European Particle Acc. Conference*, Berlin, 1992
- [4] A. Bixio et al., "Manufacture at Ansaldo of 352 MHz superconducting cavities for LEP", *Proc. of 3rd European Particle Acc. Conference*, Berlin, 1992

RF Hardware Development Work for the CLIC Drive Beam.

G. Carron & L.Thorndahl

CERN, 1211 Geneva 23, Switzerland

ABSTRACT

It is foreseen that the transfer structures (CTS) of the drive linac will produce 40 MW, 11.4 ns, 30 GHz RF power pulses for acceleration purposes in the CLIC main linac. Extensive model work, using the beam simulating wire method, has been undertaken in order to study the properties of the CTS with oversize models working at 8.6 GHz. At present a real size Cu 30 GHz CTS is under construction for beam tests in the CLIC Test Facility. A second Cu structure is in preparation for power testing with an MIT 33 GHz FEL power source. Further work is the development of power phase shifters and, inspired by the SLAC SLED-II studies [1], investigation into the use of longer RF pulses (than 11.4 ns) from the CTS (by a factor 3-4) combined with pulse compression. With longer RF pulses the drive beam bunchlet generation should become easier since the total drive beam charge of 7.04 μC would be distributed over more bunchlets.

DESCRIPTION OF A PERIODICALLY LOADED CLIC TRANSFER STRUCTURE (CTS)

In the CLIC design the drive linac uses four trains spaced by 2.84 ns of 43 bunchlets (1 cm bunchlet spacing, 40 nC each) to produce via the transfer structures 30 GHz power pulses of 40 MW for the main linac [2]. With the 2.84 ns train spacing all 4 trains can be preaccelerated at 352 MHz.

The structure shown in Fig. 1 consists of a smooth round beam chamber containing two coupling slits into two periodically loaded (with "teeth") rectangular waveguides. The TEM wave accompanying the bunchlets has radial electrical fields and azimuthal magnetic ones at the slits causing constructive excitation of a hybrid forward mode in the waveguides (useful power) and non constructive excitation of the backward mode (not useful, terminated). The forward output is intended for acceleration in a module of the main linac. The condition for constructive interference between the beam and the hybrid mode is that the it has a phase velocity equal to c at the operating frequency; this is obtained by loading the waveguide with the periodic "teeth" structure.

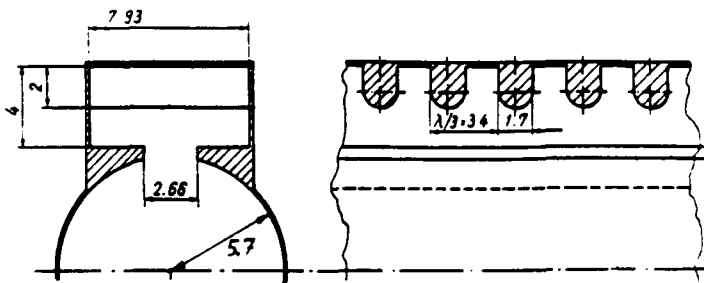


Fig. 1: Upper half of the vertically symmetric CTS showing the round beam chamber and the upper periodically loaded ("teeth") waveguide with $\lambda/3$ cells. Units: millimeters.

A further requirement is that the structure should work as a "pulse stretcher" by extracting from each train of 43 bunchlets (lasting 1.4 ns) a 40 MW RF pulse lasting 2.84 ns is met by using a forward wave in the waveguide as shown in Fig. 2 where a single bunchlet is followed as it crosses the structure.

There is constructive superposition in the waveguide of 43 successive RF wave packages (from the 43 bunchlets) spaced in time by one RF period (33.3 ps) to create a rising flank (1.4 ns), a flat top (1.4 ns) and a falling flank (1.4 ns) for the output pulse. Four successive bunchlet trains (43 bunchlets each) create a global pulse approximately 11.4 ns long (flat top) to fill a module of the CLIC main linac.

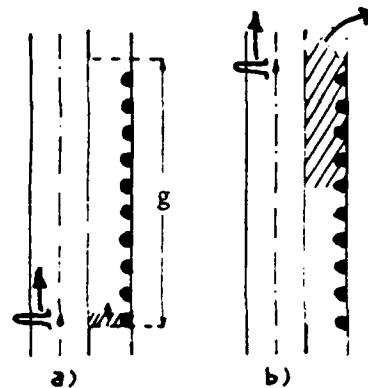


Fig. 2:

- a) Arrival of a bunchlet at the structure. The waveguide extremity is immediately energised (no output power yet).
 - b) The bunchlet exits the structure g/c later leaving the waveguide energised over the length $g(1 - \beta_{gr})$.
- Total RF pulse duration: $g(1/\beta_{gr} - 1)/c$
 β_{gr} : normalised group velocity in the waveguide.

SCALE MODEL MEASUREMENTS

The TEM fields of the bunchlets have been simulated by a $Z_0 = 300 \Omega$ transmission line situated at the centre of the beam chamber. At each extremity of the oversize model (scale factor=3.5, 8.6 GHz instead of 30 GHz) conical matching transitions from 300 to 50 Ω have been installed adjacent to damping sections against TEM, TE and TM modes of the chamber. There is adiabatic matching of the hybrid mode to the terminated TE₁₀ output waveguide by gradual "teeth size" reduction at the extremities (see figs. 3 and 4).

The longitudinal beam coupling impedance $Z_L(\omega)$ of the model is obtained from a calibrated (the coupling slits are closed for calibration) measurement of the transmission

$S_{21}(\omega)$ along the wire in the frequency range 0-40 GHz (This includes the three first harmonics of the scaled bunchlet frequency 8.6 GHz):

$$Z_L(\omega) = 2 Z_0 (1 - S_{21}(\omega)) / S_{21}(\omega)$$

Multiplying the beam current spectrum $i(\omega)$ with $Z_L(\omega)$ and applying an inverse Fourier transform, we obtain the beam wake. In a similar way $i(\omega) S'_{21}(\omega)$ and inverse Fourier transformation yields the output power pulse (S'_{21} : transmission from wire input to structure waveguide output port).

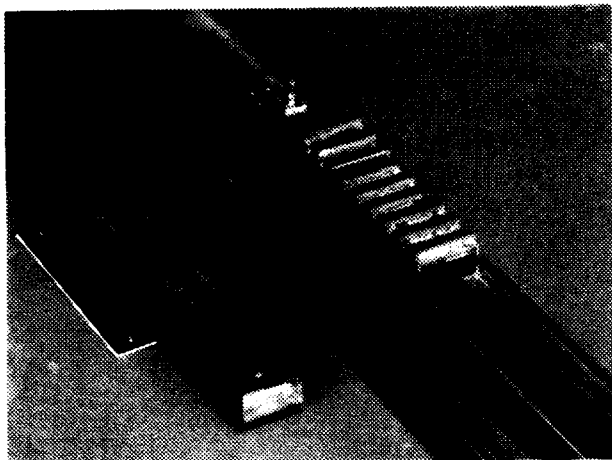


Fig. 3: Scaled CTS wire model for 8.6 GHz. The periodic waveguide has been cut into 2 pieces; the piece to the left is upside down to visualise the coupling slit and the periodic loading. The wire is too thin to be seen.

Both wake and output pulse obtained are in good agreement with recent results from MAFIA calculations [3]. Furthermore the MAFIA and the wire method indicate that HOMs cause insignificant loss factors compared with the fundamental. RF leakage through the coupling slits may be the mechanism that prevents HOM confinement in the waveguide.

30 GHz COPPER CTS PROTOTYPE

Recently a real-size prototype design was undertaken to investigate manufacturing possibilities as well as precision and RF breakdown problems. The design should be suited for mass production, since the 2 drive linacs of the project would require about 12 000 units distributed over 6 Km of active length. The design proposed, see figs. 5 and 6, consists of 2 side pieces forming the central beam chamber and the coupling slits held together by 2 comb like precision spacers. The necessary tolerances ($\sim 5\mu$) were evaluated with MAFIA [3] and it turned out that mainly the teeth parameters mattered for the beam/wave synchronism; the most important being the distance between teeth. One prototype for 33 GHz power testing at an MIT 40 MW FEL power source as well as two 30 GHz structures are under construction by industry.

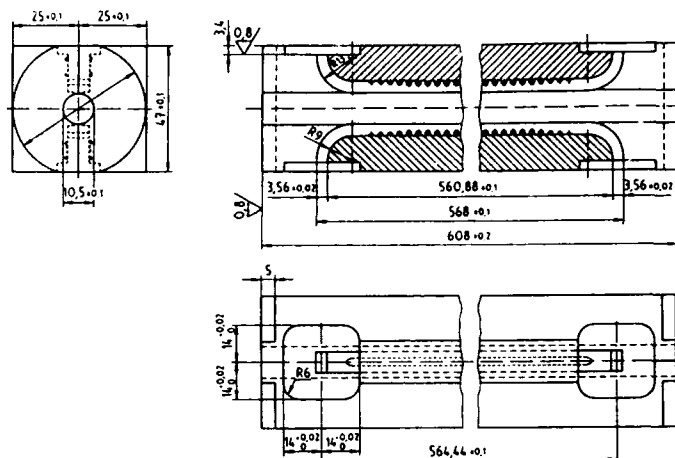


Fig. 4: Vertical cross sections through the Cu CTS prototype showing the central beam chamber and the periodic waveguides and a top view with flanges for WR28 waveguide.

One of the 30 GHz structures is intended for studies with beam in the CLIC TEST FACILITY. The delivery of the first unbrazed unit is imminent and the beam/wave synchronism will be checked with the wire method. The feasibility of an electrolytic method for "teeth tuning", if necessary prior to brazing, is being considered.

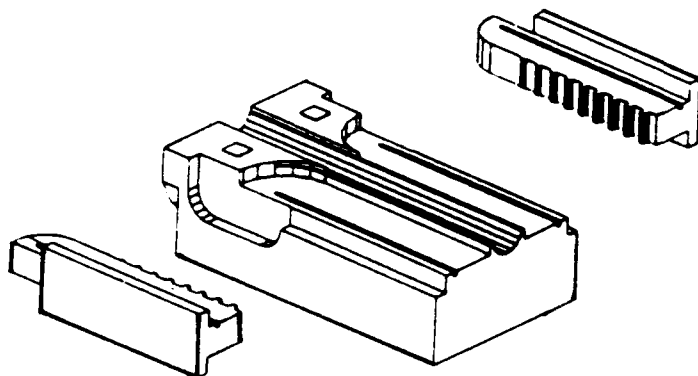


Fig. 5: One end of the 30 GHz CTS prototype made from 2 sidepieces (only one is shown in a horizontal position) and the 2 precision spacers forming the waveguide ceiling with periodic loading (courtesy KM -Kabelmetall AG).

30 GHz POWER PULSE COMPRESSOR

The purpose of the pulse compressor is to ease the drive bunchlet production by distributing the total drive beam charge of $7.04 \mu\text{C}$ over, say, 12-16 trains of 43 bunchlets rather than 4 trains as in the original CLIC design. An experimental compressor for 11.5 GHz using SLAC SLED-II

components was built and measured at low level to gain general experience and to check that sufficient bandwidth is available for the CLIC drive pulse (360 oscillations instead of 860-1720 at SLAC). Transmission measurements $S_{21}(\omega)$ and inverse Fourier transformation of $S_{21}(\omega) * I(\omega)$ show that the compressed pulse, even in the case of only 240 oscillations, suffers little from the limited device bandwidth. (see fig. 6, $I(\omega)$): Fourier transform of compressor input pulse). Furthermore the compressed output pulse contained 78% of the input pulse energy. One of the device inventors, A.Fiebig, had previously estimated that efficiency to be 82%.

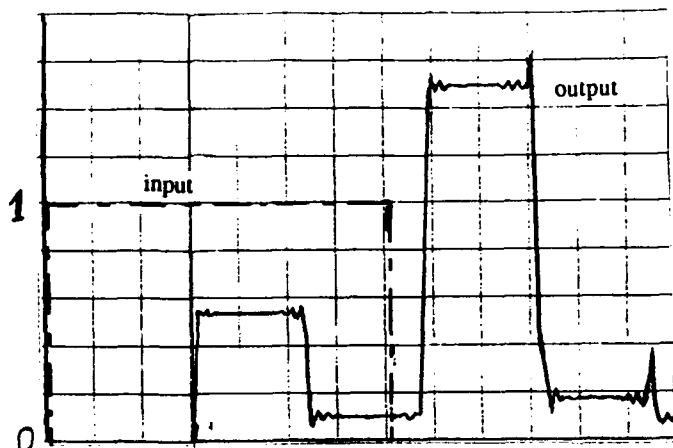


Fig. 6: Relative amplitudes of compressor input and output pulses (time compression factor = 3). Horizontal: 120 osc./div

Since twice as many compressors ($\approx 24\,000$, one per output channel) would be required as transfer structures it is important to simplify their construction. Fig. 7 gives a sketch of a concept for mass production based on 10 machined Cu pieces assembled by brazing (this design has neither been measured nor built). To the left is the input mode converter from the rectangular TE_{10} waveguide to the circular (low loss) TE_{01} mode through 4 slits (flower petals) followed by a hybrid 3 dB coupler (coupling slit between the 2 TE_{01} waveguides).

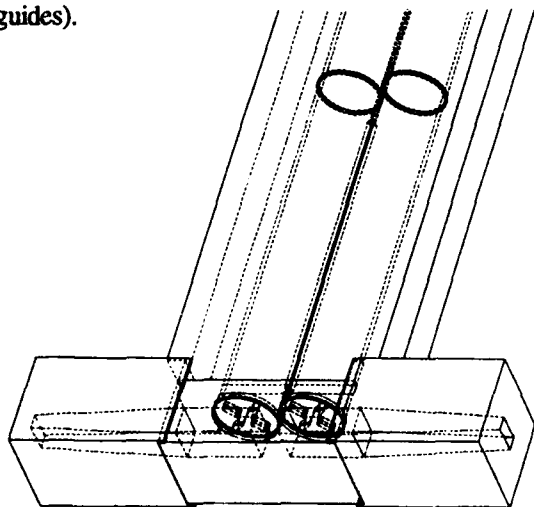


Fig. 7: Sketch of a 30 GHz pulse compressor concept for mass production. Only the lower part of the resonator is visible.

A reflecting iris is situated between the coupler and a round shorted TE_{01} resonator with an el. length of half the output pulse length. The right half of the device is symmetrical to the left one and contains a second mode converter with a rectangular output flange.. Since the mode converter is considered the component with the highest field strengths (in the flower petals) a version for 33 GHz is under construction for power testing at the MIT FEL power source.

POWER PHASE SHIFTER

RF quadrupoles in the main linac will be powered by CTS units in the drive linac. In order to adjust the focusing/defocusing strength one method could be to arrange quadrupoles in pairs with phases ϕ and $-\phi$ such that for $\phi=90$ deg. the strength is zero and maximum for 0 deg. This requires power phase shifters for 30 GHz as shown in fig. 8. The component is based on a TE_{10} waveguide (WR28) with variable width. The ceiling and the floor of the guide contain in the middle (where there are no transverse currents) a rounded slit of variable width (slotted line). The waveguide halves are brazed to a thin-walled vacuum tube and the slit width is changed by squeezing. Slit width and rounding radius have been chosen to keep local field increases below 50% and the shifter range is ± 90 deg.. A 33 GHz prototype is in preparation for power tests.

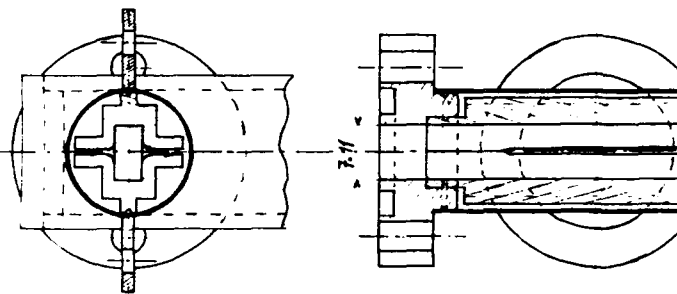


Fig. 8: Cross sections of power phase shifter.

ACKNOWLEDGEMENTS

The authors to are indebted to A.Fiebig and S.Luetgert for discussions as well as to P.Wilson (SLAC) for helpful information and advice. The flower petal mode converter is a SLAC design. The hybrid 3 dB coupler was optimised by C. Nantista also at SLAC.

REFERENCES

- [1] P. B. Wilson et al., 1992 HEACC proceedings, p. 824-827.
- [2] G.Carron and L. Thorndahl, "Impedance and loss factor measurements on a CLIC transfer structure", paper presented at the 1992 European Particle Accelerator Conference, Berlin, 24-28 March 1992, in CERN-SL/92-15 (DI).
- [3] A. Millich, Clic Transfer Structure Simulations using MAFIA. These proceedings.

Accelerating Frequency Shift Minimization.

A.V.Tiunov, V.I.Shvedunov

INSTITUTE OF NUCLEAR PHYSICS, MOSCOW STATE UNIVERSITY
119899 MOSCOW, RUSSIA

Abstract

A method of thermocompensation of the resonant frequency shift for accelerator structures is proposed. Using the bimetallic construction allowed us to design the accelerator structure without the resonant frequency shift under rf power. The results of computer simulation of thermal conditions for the on-axis coupled structure are presented.

I. INTRODUCTION

Room temperature continuous wave (cw) accelerator structures have been applied in developing cw racetrack microtrons (RTM) with output energies of hundreds of MeV and industrial accelerators with output beam energies up to 10 MeV and beam powers of hundreds of kilowatts as well as accelerating cavities for storage rings. Considerable progress in the development of accelerator structures for RTMs has been achieved at Mainz University (Germany) /1/ and NIST (USA) /2/, in the design of high power industrial accelerators on the basis of cw accelerator structures - at AECL (Canada) /3/.

The main problem in operating room temperature cw accelerator structures is the high levels of rf power dissipated per structure unit length (from 10 to more than 100 kW/m). Due to heating and deformations of these structures: a) there is a frequency shift in the accelerating and coupling cells, b) there are changes in a stopband frequency gap and c) distortions of accelerating field distributions take place.

A cw RTM of 175 MeV output energy and average beam current of 100 mA is presently under construction at the Institute of Nuclear Physics of Moscow University /4/. In this paper accelerator structure characteristics and the results of a numerical simulation for thermal stresses, which allows a suggestion for an accelerator structure version that is free of frequency shifts during the structure start-up are discussed.

II. ON-AXIS COUPLED ACCELERATOR STRUCTURE CALCULATIONS.

The electrodynamic characteristics were calculated and optimized using the computer code *PRUD-0* /5/, and for the thermal stresses analysis the program *HAST* /6/

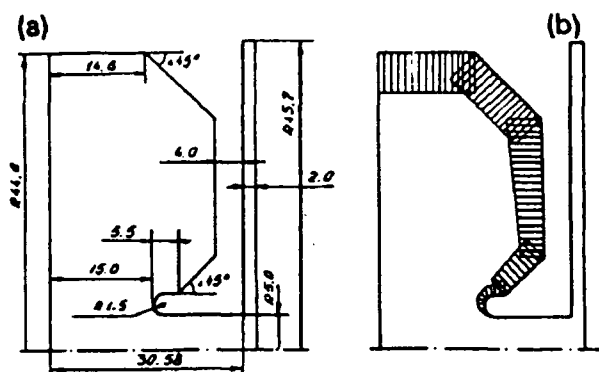


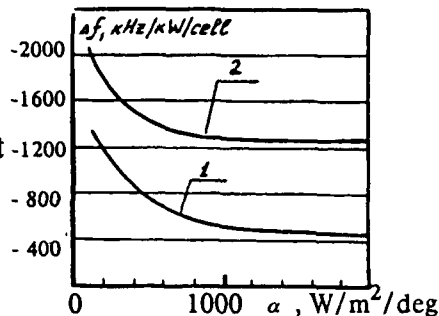
Fig. 1. a) - Parameters of the OCS,
b) - distribution of rf losses among
structure element.

was applied. A common finite element mesh generator simplified the processing of the data.

Fig. 1 shows a cross-section of accelerating and coupling half-cells profiles and the basic dimensions of a $\beta=1$ cell for a rf frequency of 2450 MHz. For the $\beta<1$ accelerating sections, the cells differ only by their length and gaps between the noses. The absence of elements with spherical surfaces reduces the structure's effective shunt impedance, ZT^2 , by several percent, yet, it also simplifies the cells fabrication and tuning and allows the coupling slots to be a greater distance from the structure axis in a magnetic field of higher magnitude. Thus the same coupling constant, as for the cavities with spherical surfaces, can be obtained with a smaller azimuthal angle of coupling slots, i.e. with a smaller reduction in shunt impedance. The calculated values of the quality factor and the effective shunt impedance are $Q_0 = 17500$, $ZT^2 = 92 \text{ MW/m}$, respectively. This calculation doesn't take the influence of the coupling slots into account.

The density distribution of the rf losses over the surface of an accelerating cell is shown in fig. 1b. An analysis of the thermal stresses was carried out for a structure with peripheral cooling. Fig. 2 shows α -dependences of accelerating and coupling cells frequency shifts for $\beta=1$. 1 kW of rf power was dissipated in a single accelerating cell. In order to ensure the correct description of boundary conditions, the calculations of thermal deformations were carried out for a significantly long structure, and deformations of the central cell were used to estimate the cells frequency shifts. The accelerating cell frequency shift

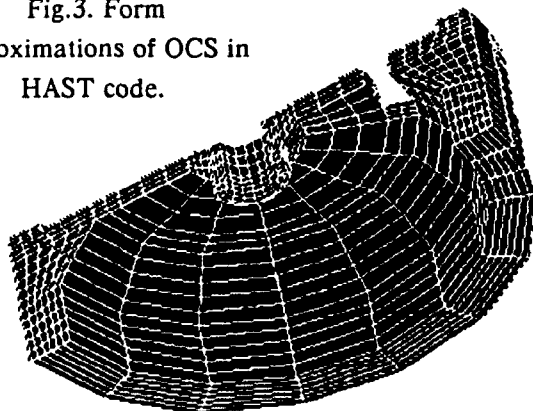
Fig. 2.
Accelerating
(1) and
coupling (2)
cells
frequency shift
versus a heat
transfer
coefficient.



for $\beta=1$, $\alpha > 10000 \text{ W/m}^2/\text{C}$ is $\Delta f_a = -455 \text{ kHz/kW/cell}$. The frequency shift of the coupling cell is $\Delta f_c = -1300 \text{ kHz/kW/cell}$. So a stopband frequency gap of 845 kHz per 1 kW of dissipated rf power appears in the structure tuned at a low rf power level.

Understanding the time dependence of frequency shifts is important for the development of the start-up procedure. According to calculation the time necessary to reach thermal equilibrium is about 20 - 25 seconds. In order to estimate the coupling slot influence, 3-D calculations of temperature distributions were made using the code *HAST*. 3-D approximation of form of OCS using *HAST* is shown in fig. 3. The azimuthal temperature variation, which is affected by the presence of coupling slot, doesn't exceed 1.03°C , thus when accounting for, the coupling slot can not essentially change the results of 2-D calculations.

Fig.3. Form
approximations of OCS in
HAST code.



III. ACCELERATING FREQUENCY SHIFT MINIMIZATION.

Accelerating frequency shifts during start-up considerably complicate the operation of the accelerating sections under cw conditions. That is why a design of an accelerator structure with minimal frequency shifts is of great interest. Frequency shifts can be reduced by designing more extensive cooling circuits. It was shown /6/

that web cooling in addition to circumferential cooling reduces the accelerating frequency shift by a factor of 2.5. However, the problem can not be completely solved by more elaborate cooling circuits. Though it is possible to reduce temperature gradients and to increase construction rigidity by increasing the web thickness, it would result in extreme changes of the effective shunt impedance /7/.

The accelerating frequency reduction is caused by increasing the cells volume and displacing the construction elements relative to the initial positions. However, the displacement of some construction elements, in particular, an increase of the gap between the accelerating cells noses increases the accelerating cells frequencies. Thus, by changing the picture of deformations it is possible to completely compensate frequency shifts during start-up. Two methods of the frequency shift compensation calculated using the program *HAST* are discussed: a) by realizing more extensive cooling circuits and b) by changing the picture of deformations using bimetallic constructions made on the base of copper and molybdenum. Fig. 4 illustrates different variants of molybdenum insertions and an additional cooling channel location near the axis. In all the design possibilities, circumferential cooling is assumed. The results of calculations for these variants are listed in table 1: frequency shifts and effective shunt impedance reduction are all normalized to 1 kW per cell of the dissipated rf power; ; maximum levels of the dissipated rf power and maximum energy gains per unit length are limited by elastic limit deformations. The calculations were carried out for a single half-cell, this limitation reduced frequency shifts by 50 - 100 kHz. In the most interesting

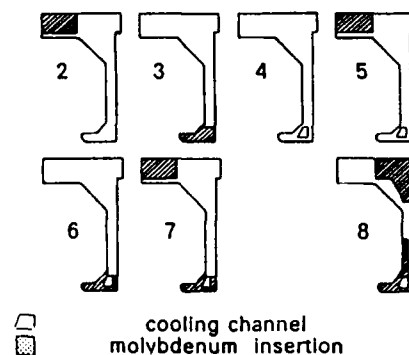


Fig. 4. Different variants of molybdenum insertions and of additional cooling channel.

cases, the results were specified by calculations made for a greater number of cells. These cases are marked by an asterisk in table 1.

From the analysis of the results given in the table 1 the following conclusions can be drawn. The minimum frequency shift without additional cooling takes place in variant 3. Compared to the initial variant, 1, the frequency shift is reduced by a factor of 4, that the energy gain limited by copper elastic limit deformations is 1.65 MeV/m. An

energy gain of 2.8 MeV/m was obtained with additional nose cooling without molybdenum insertions with the frequency shift reduced by a factor of 3 comparing to variant 1. A high energy gain and a positive frequency shift calculated for a single half-cell, were obtained in variant 7. However, the specification of boundary conditions for an increased number of cells, gives a frequency shift of -40 kHz/kW/cell. Finally, a positive frequency shift of +90 kHz/kW/cell was obtained in variant 8, calculated for several cells, which can compensate a frequency shift caused by water heating. A positive frequency shift was obtained as a result of increasing the gap between the accelerating cells noses by 22 mm, normalized to 1 kW of the rf power. A comparison of deformations for this variant with variant 1 is given in fig. 5. The large value of deformations limits the energy gain to 1.54 MeV/m. As the energy gain increases for a fixed beam power, the accelerator efficiency is reduced. This variant of the structure can be used for racetrack microtrons with typical energy gains of 1 MeV/m and for industrial linacs with beam powers up to 100 kW and energies up to 5 MeV. The absence of frequency shifts during start-up makes it possible to design multi-section accelerators with a simple rf power system. It should be noted that the discussed results were obtained for the on-axis coupled structure. The positive frequency shift was obtained to a considerable extent by reducing the coupling cells resonant frequencies. For variant 8, the coupling cell frequency shift is -7 MHz/kW/cell. This shift, however, can be compensated by preliminary coupling cells tuning at higher frequencies.

- [3] J.Mckeown et al. Proc. 1981 Linear Accelerator Conf. Santa Fe, 332
- [4] A.S.Alimov et al. Nucl. Instr. and Meth. A-326 (1993) 243
- [5] A.G.Abramov et al. Preprint IHEP 83-3, Serpuchov (1983), in Russian.
- [6] A.G.Abramov et al. Preprint IHEP 84-64, Serpuchov (1984), in Russian.
- [7] J.P.Labrie and H.Euteneuer. Nucl. Instr. and Meth. A-247 (1986) 281
- [8] M.K.Brussel et al. Report of Nuclear Physics Laboratory University of Illinois (December 1984) IV-52.

TABLE 1 The results of calculations for different accelerator structures

variant No	P_{\max} [kW/m]	$\Delta f / \Delta P$ [kHz/kW]	$\Delta ZT^2 / ZT^2$ [%]	ΔW [MeV/m]
1	45.5	$\begin{matrix} -345 \\ -455 \end{matrix}_b$	4.2	1.68
2	39.4	-282	4.2	1.62
3	41.5	-86	4.3	1.65
4	130.8	-114	2.4	2.8
5	121.8	-69	2.4	2.72
6	139.	-46	2.5	2.85
7	128.2	$\begin{matrix} +8.5 \\ -40 \end{matrix}_b$	2.6	2.75
8	35.9	+90.3	5.2	1.54

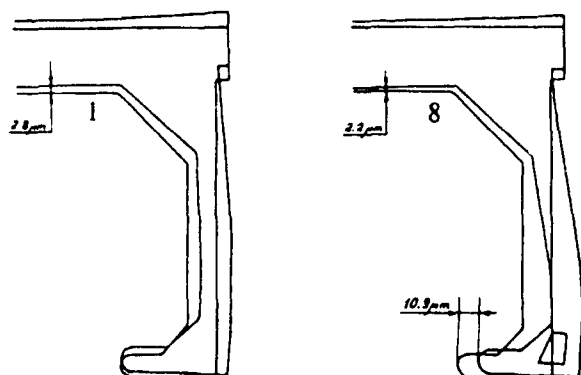


Fig. 5. Comparison of deformations for variant 8 and variant 1.

REFERENCES

- [1] H.Euteneuer and H.Scholer, Proc. 1986 Linear Accelerator Conf., SLAC-Report 303 (1986) 508.
- [2] L.D.Hansborough et al. SLAC-Report 303(1986) 128.

Calculations and Model Measurements for the Euterpe Cavity

J.A. van der Heide, M.J.A. Rubingh, W.J.G.M. Kleeven, J.I.M. Botman, C.J. Timmermans and H.L. Hagedoorn,
Eindhoven University of Technology, P.O. Box 513, 5600 MB Eindhoven, Netherlands.

Abstract and Introduction

The 400 MeV storage ring Euterpe[1] is under construction. A quarter wave cavity (45 MHz, 50 kV) will accelerate the electrons. Due to space limitations the cavity length should not exceed 0.5 m. Therefore three special geometries are considered which have an 'electrical length' several times the physical length of the cavity. The first employs radial transmission line folding, the second longitudinal folding and the third capacitive loading of the transmission line. Transmission line theory is used to predict the cavity properties. Good agreement is found with SUPERFISH calculations. The capacitive loading option is superior considering its simplicity of construction and high shunt impedance. An LC equivalent circuit is used to model the impedance matching w.r.t. the rf generator. Results are in good agreement with measurements on a scale 1:1 cold model.

I. RADIAL FOLDING

The phase velocity of a voltage wave on a transmission line is $v = 1/\sqrt{LC}$, where L and C are the inductance and capacitance per unit length respectively. To lower the effective wavelength one may increase L or C . Fig. 1a shows a cavity derived from a coaxial line but with C increased substantially by the presence of disks connected to the inner and outer conductors. One cavity cell can be represented by a series inductance ΔL and a shunt capacitance ΔC . The inductance $\Delta L = L_1 + L_2 + L_3$ is simply the contribution of three sections of coaxial transmission line as indicated in Fig. 2a. The capacitance ΔC can be approximated by seven contributions. Two of these are usual coaxial line contributions. The third is the capacitance between two disks. The remaining four are due to the fringing fields at the corners of a disk. Formulas as collected by van Genderen et.al.[2] were used to approximate these fringing capacitances. The total cavity is modelled by a series circuit of N separate cells as depicted in Fig. 2b. There are N possible modes of which the ground mode is the desired accelerating mode. Its frequency is given by $f \approx 1/(4N\sqrt{\Delta L \Delta C})$. Losses are taken into account by the resistance $\Delta\Omega$ which is calculated analytically by integrating the wall material specific resistance over the surface, assuming a constant current in one cell. The shunt impedance and the quality factor can then be expressed as

$$R_{sh} = \frac{V_{gap}^2}{P_{dis}} = \frac{4}{N\Delta\Omega} \frac{\Delta L}{\Delta C}, \quad Q = \frac{\pi}{2N\Delta\Omega} \sqrt{\frac{\Delta L}{\Delta C}}. \quad (1)$$

As an example we designed a 10 cell structure at 75 MHz, with an overall length of 0.25 m and an outer diameter of

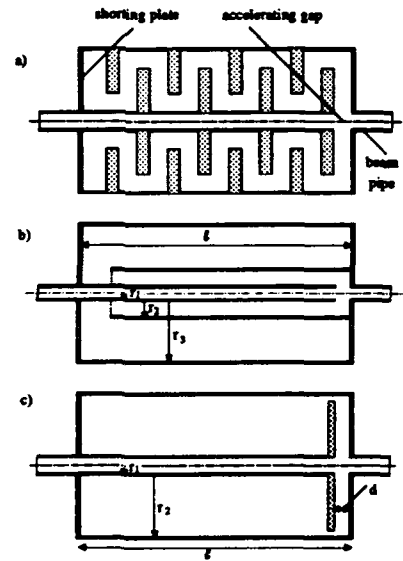


Figure 1: Three types of $\lambda/4$ transmission line cavities a) employing radial folding, b) employing longitudinal folding, c) employing capacitive loading.

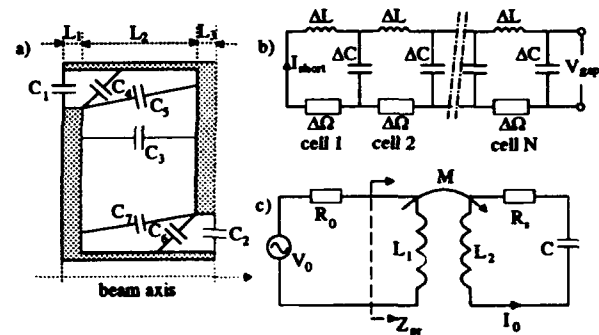


Figure 2: a) The capacitances and inductances in one cell of a cavity employing radial folding b) equivalent circuit used to model a cavity with radial folding c) equivalent circuit used to model impedance matching.

0.25 m. The analytical predictions ($f = 76.4$ MHz, $R_{sh} = 61.2$ k Ω , $Q = 1810$) compare very well with SUPERFISH results ($f = 75.6$ MHz, $R_{sh} = 61.9$ k Ω , $Q = 1880$).

II. LONGITUDINAL FOLDING

A considerable improvement in shunt impedance is obtained with the cavity depicted in Fig. 1b. This cavity consists of two coaxial layers connected by a return section. Therefore its physical length will approximately be half the electrical length. Further shortening is possible by adding more coaxial layers. The voltages and currents in two different points on a transmission line are related

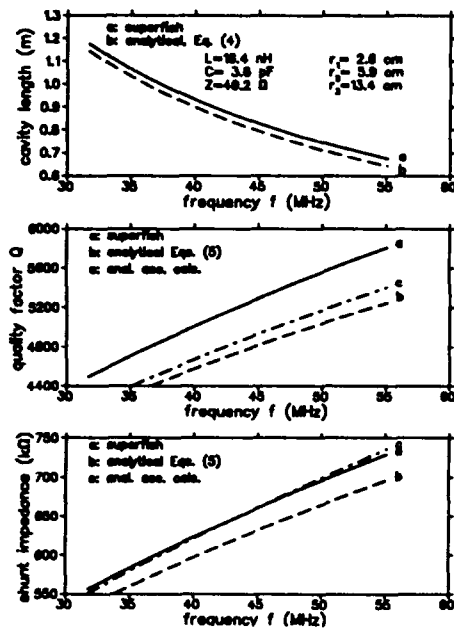


Figure 3: Comparison between analytical and SUPERFISH results for a cavity employing longitudinal transmission line folding.

by the matrix equation

$$\begin{pmatrix} V \\ I \end{pmatrix}_2 = \begin{pmatrix} \cos kx & -jZ \sin kx \\ -\frac{j}{Z} \sin kx & \cos kx \end{pmatrix} \begin{pmatrix} V \\ I \end{pmatrix}_1, \quad (2)$$

where x is the distance between the points, Z is the line impedance and $k = \omega/c$ is the propagation constant. The return section can be modelled by a series inductance L and a shunt capacitance C which are determined similarly as in the previous section. The voltages and currents at the section input and output are related by

$$\begin{pmatrix} V \\ I \end{pmatrix}_{out} = \begin{pmatrix} 1 & -j\omega L \\ -j\omega C & 1 - \omega^2 LC \end{pmatrix} \begin{pmatrix} V \\ I \end{pmatrix}_{in}. \quad (3)$$

With Eqs. (2,3) we can transfer the vector (V, I) from the shorting plate to the accelerating gap. The resonance condition is obtained by putting the right/under element of the overall transfer matrix equal to zero. As a special case we consider a cavity consisting of two layers with equal impedances $Z_1 = Z_2 = Z$. In the approximation that $\omega L/Z \ll 1$ and $\omega CZ \ll 1$ we obtain for the cavity length

$$l = \frac{\pi c}{4\omega} \left[1 - \frac{1}{\pi} \left(\frac{\omega L}{Z} + \omega CZ \right) \right]. \quad (4)$$

The shunt impedance R_{sh} and quality factor Q are calculated similarly as in the previous section. For simplicity we ignore the influence of the return section on the current profile in the second layer. Then we find

$$R_{sh} = \frac{(\delta \mu_0 / \pi \rho \epsilon_0) \ln^2(r_3/r_2)}{2 \ln \frac{r_2}{r_1} + \left(\frac{1}{r_2} + \frac{1}{r_3}\right) \left(\frac{1}{2} + \frac{1}{\pi}\right) l + \left(\frac{1}{r_1} + \frac{1}{r_2}\right) \left(\frac{1}{2} - \frac{1}{\pi}\right) l}$$

$$Q = \frac{kl R_{sh}}{2/Z}, \quad (5)$$

where δ is the skindepth and ρ is the specific resistance of the wall material. As an example we compare in Fig. 3 the analytical results with SUPERFISH results. The cavity accelerating gap was 3 cm and the return section gap 5 cm. The capacitance $C=3.6$ pF was calculated with the numerical program RELAX3D. As can be seen, there is good agreement between both results. A further improvement of the analytical results is obtained if the influence of the return section on the current profile in the inner coaxial layer is taken into account (curves c).

III. CAPACITIVE LOADING

The construction of the previous cavity becomes rather complicated because more than two coaxial layers are needed to reduce its length to 0.5 m. A simpler construction is achieved with the cavity depicted in Fig. 1c. This can be seen as a coaxial transmission line terminated with a capacitance. The current and voltage profiles on the coaxial line are determined by the matrix equation Eq. (2). The capacitive loading is taken into account with a matrix as in Eq. (3) but with L put to zero. The resonance condition now becomes

$$\tan kl = \frac{1}{\omega CZ}, \quad (6)$$

where $Z = \sqrt{\mu_0/\epsilon_0} \ln(r_2/r_1)/2\pi$ is the line impedance, l is the length of the coaxial line, r_1 and r_2 are the inner and outer radii of the coaxial line and C is the loading capacitance. In good approximation this capacitance is $C = \pi \epsilon_0 r_2^2/d$, where d is the accelerating gap. For this case the analytical shunt impedance and Q -value are

$$R_{sh} = \frac{4\pi\delta}{\rho \ln \frac{r_2}{r_1} + \left(\frac{1}{r_1} + \frac{1}{r_2}\right) \left(\frac{1}{2} + \frac{\sin 2kl}{4k}\right)},$$

$$Q = \frac{2kl + \sin 2kl}{8 \sin^2 kl} \frac{R_{sh}}{Z}. \quad (7)$$

In Fig. 4 the analytical results are compared with SUPERFISH results for a cavity with $r_1=2.5$ cm, $r_2=15$ cm and $d=1$ cm. Once more there is quite good agreement. For the proposed cavity, a shunt impedance of 580 kΩ and a Q -value of 6600 can be achieved with a cavity length of 45 cm and at a frequency of 45 MHz. For a gap voltage of 50 kV, the required rf power would be 4.3 kW.

IV. IMPEDANCE MATCHING

Assuming inductive coupling, the complete rf system can be modelled with the equivalent circuit given in Fig. 2c. The rf source is represented as an ideal rf voltage supply V_0 in series with the characteristic impedance R_0 of the transmission line feeding power to the cavity. The inductive coupling is represented by the mutual inductance $M = k\sqrt{L_1 L}$ where k is the coupling constant and L_1 is the inductance of the coupling loop. The secondary circuit represents the cavity. Its angular resonance frequency and Q -value are given by $\omega_0 = 1/\sqrt{LC}$,

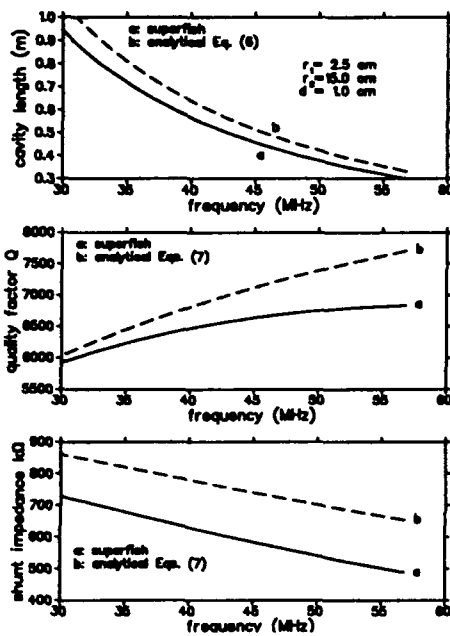


Figure 4: Comparison between analytical and SUPERFISH results for a cavity employing capacitive loading of the transmission line.

$Q = (1/R_s)\sqrt{L/C}$. Further, we choose the current I_0 to represent the shorting plate current. Then the shunt impedance is $R_{sh} = 2Z_t^2/R_s$, where $Z_t = V_{gap}/I_0$ is the 'transfer impedance' from the shorting plate to the accelerating gap. The impedance of the cavity as seen from the transmission line is

$$Z_{pr} = j\omega L_1 + \frac{\omega^2 M^2}{R_s(1 + 2jQ\delta)}, \quad (8)$$

with $\delta = (\omega - \omega_0)/\omega_0$. In the complex plane this impedance is a circle with radius $\omega^2 M^2/2R_s$. The voltage reflection coefficient Γ as measured on the transmission line feeding the rf power is given by $\Gamma = (Z_{pr} - R_0)/(Z_{pr} + R_0)$. The requirements for zero reflection can be written as

$$\delta = \frac{\omega L_1}{2QR_0}, \quad M = \frac{\sqrt{R_0 R_s}}{\omega} \left(1 + \left(\frac{\omega L_1}{R_0}\right)^2\right)^{1/2}. \quad (9)$$

The first condition can simply be satisfied if the cavity is detunable. The second condition can be satisfied for example if the loop is rotatable such that the induction M can be varied from zero to a maximum value. This maximum must be larger than the r.h.s. of the second of Eqs. (9). In order to verify the above theoretical predictions, a cold copper model was built of a 2-layer coaxial cavity employing longitudinal transmission line folding. The physical length of this cavity was $l=86.3$ cm and its inner, middle and outer radii $r_1=2.5$ cm, $r_2=5.4$ cm and $r_3=12.2$ cm. In table 1 we compare the analytical and SUPERFISH predictions of the resonance frequency f_0 , quality factor Q and shunt impedance R_{sh} with the measured results. Two different loops were used to couple the rf signal into the cavity. Fig. 5 shows the primary impedance Z_{pr} as measured with a vector impedance meter (Hewlett Packard

method	f_0 (MHz)	Q (-)	R_{sh} (kΩ)
analytical	43.9	4625	556
superfish	44.0	4745	573
measured	43.8	4217	579

Table 1: Calculated and measured properties of a cold cavity model

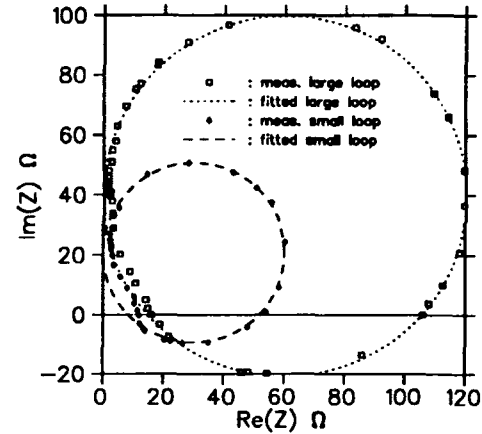


Figure 5: Cold model cavity impedance as measured on the input transmission line.

4815A). The smaller circle in Fig. 5 corresponds with the smallest of the two loops (area 11 cm² compared to 15 cm² for the larger loop), which also was made of a thicker wire in order to lower its inductance. For both loops, perfect matching to $R_0 = 50 \Omega$ is possible but the larger loop needs a rotation over approximately 35 degrees.

The measured shunt impedance in table 1 was deduced from the radius ρ_c of one of the circles in Fig. 5. This radius is related to R_{sh} by

$$\rho_c = \frac{\omega^2 M^2}{4Z_t^2} R_{sh}. \quad (10)$$

with $Z_t \approx 48 \Omega$ for the model cavity. If the area A of the loop is not too large then the mutual induction M can be approximated as

$$M = \frac{\mu_0 A}{2\pi r} \frac{I_c}{I_0}, \quad (11)$$

where r is the radial position of the loop and I_c is the circuit current at the coupling position. For the measurement in Fig. 5 the coupling loop was located close to the shorting plate so that $I_c \approx I_0$. From Eqs. (10) and (11) the shunt impedance is easily estimated.

V. REFERENCES

- [1] J.I.M. Botman et.al., Nuclear Instruments and Methods B49(1990)89-93
- [2] W. van Genderen et.al., Nuclear Instruments and Methods A258(1987)161-169

APLE ACCELERATOR PROTOTYPE CAVITY FABRICATION AND LOW POWER TESTS*

A. M. Vetter, T. L. Buller, T. D. Hayward,
D. R. Smith, and V. S. Starkovich
Boeing Defense & Space Group
P.O. Box 3999, M/S 2T-50
Seattle, WA 98124-2499

Abstract

The first 5-cell, 433-MHz accelerator cavity [1] for the APLE free electron laser experiment at Boeing has been assembled and tuned. Low power RF measurements indicate that the critical electrical parameters (Q_0 , f , and β) for the accelerator and TM_{110} -like modes are consistent with expectations based on measurements made on an 800-MHz model cavity. The cavity is being readied for its initial vacuum bakeout, during which the constituents of the residual gas will be monitored. First application of high power RF is scheduled for late summer of 1993.

I. INTRODUCTION

A 5-cell, 433-MHz accelerator cavity [1] has been developed for high average power FEL application. The cavity electrical design is derived from the familiar storage ring cavity exemplified in PEP [2] and PETRA. The cavity is a slot-coupled, π -mode standing wave structure, center fed through a waveguide coupler. Design and operational parameters are summarized in Table 1. The general layout of the cavity is shown in Fig. 1.

Table 1
APLE 5-Cell Accelerator Cavity Parameters

Accelerator Mode Frequency	433.33 MHz
Relative BW $(f_0 - f_\pi)/f_\pi$.02
Q_0	27000.
R/Q	337. Ω /cell
Shunt Impedance (V^2/P_c)	45. $M\Omega$
Accelerating Voltage	1.1 MV
Average Beam Current	.23 A
External Coupling Coeff	3.
Duty Factor	.25
Thermal Dissipation	165. kW
TM_{110} Band Q_L	< 10000.
Operational Pressure	5×10^{-8} Torr

II. MECHANICAL DESIGN

A. Basic Fabrication Concept

We have elected to fabricate the cavities using bright copper plated aluminum 6061 parts with O-ring sealed joints. Using this approach rather than brazing together OFHC copper parts, we expect to: reduce the weight of the structure by half, affording easier handling and support; enhance structure ruggedness; allow repair in case of damage dur-

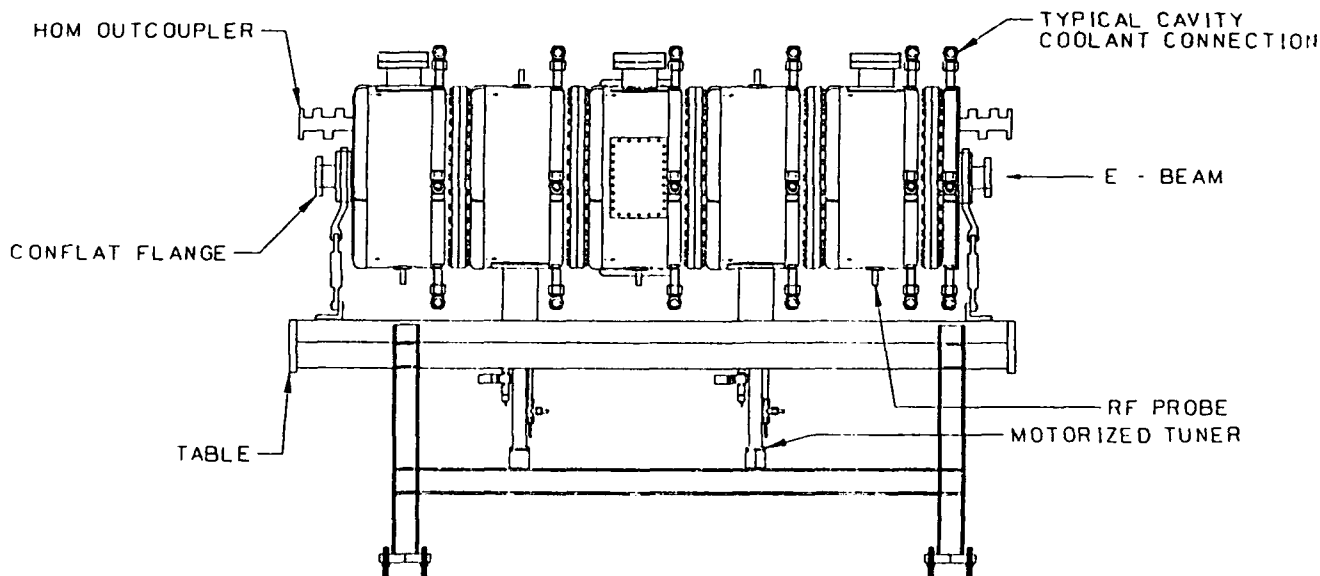


Figure 1. APLE 5-cell cavity layout.

*Work supported by USASDC/BMD contract
DASG60-90-C-0106.

ing fabrication or operation; and avoid difficulties associated with brazing a very large copper structure.

The required processes are now well understood (a 95% yield rate is obtained in brazing and ~80% yield is obtained in plating), and the convenience of working with a lighter, stronger structure is appreciated daily.

B. Cell Design

In order to avoid having the equatorial joint between the two halves of a cell pass through the holes cut for tuners and external couplers, the joint has been moved longitudinally until the clamping bolt heads come up against the water manifold feeding the radial holes in the web. A mechanical unit cell is shown in Fig. 2. The external coupling aperture and tuner ports are shifted slightly relative to the center of the accelerating gap. An electrical cell therefore consists of one side of the web and associated shell of one mechanical unit, and the shallow side and web of the adjacent unit. The last cell is completed with an end cap which has a nose cone on one side only.

Both vacuum and RF seals are required at circumferential joints between cell parts. The RF joint is formed by a 6.5-mm section silver plated C-seal [3], vented to avoid virtual leaks. Behind the C-seal, a 7-mm section Viton O-ring seal forms the vacuum joint. These seals are clamped by 36 3/8-18 studs equally spaced around the circumference.

C. Cooling

The high average power application of the cavity dictates that cooling channels must be embedded in the nose cones. These are fed by holes drilled from the outer cooling manifold radially through the web to the nose cone channels. These web channels lead the water around the ends of the coupling slots, which are also sites of high thermal flux. Water returning from the nose cones is circulated through half of the (typically) 32 holes run-

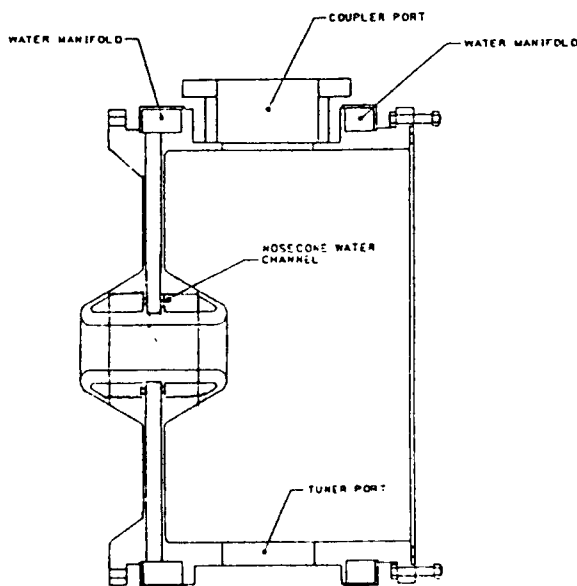


Figure 2. APLE cavity mechanical unit cell.

ning the length of the shell of the cell, collected in a manifold, and returned through the other longitudinal holes to a collection manifold over the web.

D. Accessories

Each cell is provided with a tuner and RF sample probe. Tuners in the end cells and center cell are not movable after initial adjustment for field flattening; tuners in the next-to-end cells are equipped with stepper motors. Tuner plungers are water cooled, and movable tuners have graphite RF dampers to spoil resonances behind the plungers, as in PEP and earlier Boeing cavities [4].

Each end cell is provided with a high order mode (HOM) outcoupler mounted in the end wall. The loop of this probe is oriented in the tangential plane, so that a minimum of 433-MHz power is coupled out. Following the loop is a high pass filter which prevents residual 433-MHz power from reaching the 10-W termination load.

The cavity is pumped through the waveguide coupler, which is fitted with a 10-c.m. cryopump. Provision is made for an optional titanium sublimation pump. The pumps are mounted on an H-plane miter bend, which isolates the RF window from direct line of sight of the coupling aperture.

After assembly and initial pump down, the evacuated cavity will be baked at 180° C for 24 hrs. We anticipate the base pressure will be 5×10^{-8} Torr after the bake.

III. FABRICATION

A. Brazing and Heat Treating

The cells, which ultimately differ slightly in inner diameter depending on their position within the cavity, were formed from identical 6061 aluminum forgings. The embedded nose cone cooling channels were machined in the forgings in an initial machine process during which the coolant holes were drilled in the web, the coolant manifold cut around the circumference, and the interior contours roughed out.

The exposed cooling channels in the nose cones were covered by annular rings which were vacuum brazed onto the forging. This braze step was initially conceived as a dip braze, but it was recognized that vacuum brazing would avoid problems with removing flux trapped in the cooling channels in the web. Initial attempts at vacuum brazing resulted in porous joints which leaked and often cracked during the subsequent heat treating. This was corrected by increasing the thickness of braze alloy, adding more getter to the vacuum chamber, and improving the clamping fixture.

Following the braze, the aluminum is very soft. T4 temper is recovered by reheating the part, followed by a glycol immersion quench and artificial aging. (A water spray quench was tried, but did not cool the part fast enough to recover temper.) The improved temper proved to be of value in subsequent machine operations during which the interior contour of the cell was taken to net dimensions, coupling slots were cut in the webs, longitudinal cooling and bolt holes drilled

in the outer shell, and many minor features added. Beam pipe and HOM outcoupler flanges, water manifold covers, and the waveguide coupler box end were welded onto appropriate cells before turning the final inside contour.

The only remaining machine work at this juncture was the cutting of the O-ring grooves and mating surfaces on the major circumferential joints. This was deferred until after plating operations, which require much handling of the parts, in order to avoid damage to these critical sealing surfaces.

B. Plating

To prepare the 6061 aluminum parts for plating, the exterior surfaces were coated with plastisol and the surfaces to be plated chemically cleaned. The zincate bright copper plating process began with a zincate strike followed in turn by .5-mil electroless nickel plating, a cyanide copper strike, and finally 2.5 mil of bright copper plating.

For plating uniformity, special lead anodes were made to conform to the shape of the part. These anodes were enclosed in rayon fabric bags to prevent particles which form on the anode from falling onto the plating.

Several trials were required to determine the required thickness of the electroless nickel plating, which is consumed in the subsequent cyanide copper strike during which the pH must be carefully controlled. Considerable care is required at each step of the plating process.

After plating, assuming there were no obvious defects, the parts were baked for one hour at 100 Celsius. If no significant blisters or delaminations appeared, the parts were then baked for 24 hours at 200 Celsius. Any blisters greater than .1 inch across, or more than ten blisters of any size, or any blister on a nose cone resulted in rejection of the part, which must then be replated. Acceptable blisters were vented and pressed flat against the underlying aluminum. We also found occasional occurrences of millimeter sized pits, which are acceptable if not located on the noses.

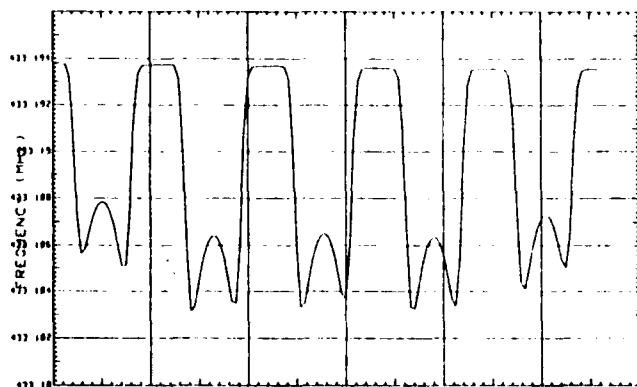


Figure 3. Field profile data. Downward deflection of trace is proportional to square of local field strength.

C. Final Assembly

Accepted plated parts were stripped of plastisol, and the O-ring grooves and mating surfaces turned. Interiors were scrubbed with ScotchBrite and wiped with acetone and isopropanol until clean. A final wipe with absolute ethanol preceded the stacking of the cells in vertical orientation. After the 180 clamping bolts were tightened, the cavity was tipped horizontal and placed on a transport cart for installation of accessories, leak checking, and various electrical measurements.

IV. LOW POWER ELECTRICAL MEASUREMENTS

The Q_0 of the assembled cavity has been measured at 26,600, with an external coupling coefficient of 2.94. This is the Q expected for a brazed copper cavity with this geometry, so the RF quality of the plating and C-seal joints is evidently quite satisfactory.

The field profile (Fig. 3) shows the end cells about 5% below the mean field strength, and interior cells about 3% above. Sample probes are adjusted to deliver approximately 400 mW into 50 Ω with 1 MV/cell accelerating voltage.

TM_{110} band Q_L varies from 2000 to 9000, depending on the particular structure mode, with the HOM outcoupler adjusted for minimum accelerator mode loading. Relative to the main power coupler input, the outcoupler insertion loss exceeds 80 dB at 433 MHz.

Electrical measurements have consistently been predicted on the basis of previous measurements made on an 800-MHz aluminum model cavity, except that the end cell frequencies are unexpectedly high by a few hundred kHz. End cell diameters have been corrected on the follow-on three-cell cavities.

V. ACKNOWLEDGEMENTS

The authors extend special thanks to many people at the following companies: Lenape Forge, Inc. of West Chester, PA; Thompson Industries, Ltd. of Hawthorne, CA; Harbor Island Machine, Lukas Machine, Inc., and Industrial Plating of Seattle, WA; and AccSys Technology of Pleasanton, CA. Due to the efforts of these principal vendors, total flow time from ordering the forgings to completion of low power measurements on the first 5-cell cavity has been 14 months, with completion of the second 5-cell and two 3-cell cavities expected within five months.

VI. REFERENCES

- [1] T. L. Buller, et al., "Design of the APLE Accelerator Cavity," Proc. 1992 Linear Accelerator Conf., Vol. 2, p. 689.
- [2] M. A. Allen, et al., "RF System for the PEP Storage Ring," IEEE Trans. Nucl. Sci. NS-24, No. 3, 1780 (1977).
- [3] B. Rusnak, et al., "Evaluation of RF Seals for Resonant Cavity Applications," Proc. 1990 Linear Accelerator Conf., p. 129.
- [4] A. M. Vetter, et al., "High Power Tests of 433 MHz Single-Cell Accelerator Cavities and Associated Feed System," Proc. 1989 Particle Accelerator Conf., p. 183.

MECHANICALLY TUNED ACCELERATING RESONATORS

F.A. Vodopianov

Russia Academy of Sciences. Moscow Radiotechnical Institute

As an extension of the proposal [1] two types of mechanical variators of the accelerating gap capacity are considered. In the first of them the stationary plates placed on the end outer surface of the inner tube and the moving - inside of ring rotor of a reactive reductor type motor are placed. The rotor is installed in vacuum with the possibility to roll over inner surface of the outer tube with the stator on its outer surface. In the second variator the moving plates swing along the resonator axis direction in front of the inner tube and by means of the outer electromagnetic driver. The characteristics of the capacity variators in a HOM relationship are compared.

The some order current increase of the modern synchrotron in a comparison with the first such type accelerators current was achieved by means of the using boosters with a higher injecting energy and by means of increasing frequency following the accelerating cycles. The consequence of this means is an accelerating field frequency diapason narrowing, increasing of the accelerating voltage and a needed of accelerating stations power. The natural step to loss power decreasing is a discovery of the high quality factor resonators. One of such resonators with a wide range frequency tuning is the resonator with the UNF perpendicular magnetisation ferrite. Other method of the power loss decreasing is based on the using unloaded by ferrite mechanically tuned resonators [1]. The way to this suggestion open mentioned narrow frequency band of an accelerating voltage.

The mechanical change of resonator frequency can be achieved by two methods: by means of a resonator dimension changing and by means of a variator parameters changing. The first method found some practical realisation when only a small frequency variation was needed. The frequency variator connection is possible as in case of inside resonator placing [1] and in a case of outside placing by means of a connecting loop or rod type antenna. In [1] the inner resonator variator is described for the Triumph booster parameters having frequency band $45 + 60$ MGc and length 0,8 m. At the frequency 60 MGc in case $D_0/D_1=2,71$ the resonator selfcapacity is 25 pF. For decreasing frequency to 45 MGc the increasing capacity to ~ 60 pF is needed. This can be activated by means of rotating condenser (Fig. 1) or by means of vibrating one (Fig. 2) in both cases the resonator is coaxial type.

Roating plates 3 of condenser (Fig. 1) are fixed in ring ferrum withoutwinding rotor of a synchronous motor of a reactive reductor tupe. The rotor is inserted with a

possibility of rolling on the bearing around inner side of outer tube. The plate 3'of large capacity serves for the sparking exluding. The stator with its winding is installed on an outer surface of the external tube.

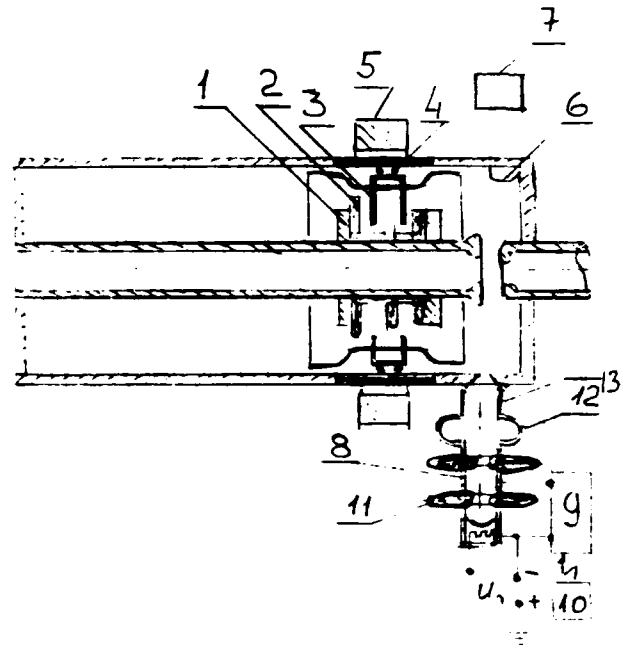


Fig. 1 Rotating condenser tuned resonator

1 - unmoved plates, 2 - isolators, 3 - rotating plates, 4 - rotor, 5 - stator, 6 - coupling loop, 7 - outer trimming device, 8 - electronic tube, 9 - HF modulator, 10 - HF source, 11 - accelerating tube, 12 - HF resonator, 13 - drift channel

The reactance 7, for examhle a small inductance with a ferrite core inserted by means of a loop 6, serves for an achievement of the rapid accurate tuning in the limits of $of/f \sim \pm 1\%$ [1]. In this boundary can be included all the faults of the production and the installation of all resonators.

Universally adopted HF feeding of the resonator by an inserted into it power electron tube leads to a symmetry distortion and to arising of the conditions of HOM oscillations. It seems to be expedient to suggest a new variant of HF feeding by means of electron beam gun with the bunched electron beam. Shown on Fig. 1 HF modulator 9, driven by an optical cable from grounded source 10, modulates an electron beam energy which transformed in density modulation of a beam during it transition through

the accelerating tube 11, passive HF resonator 12 and drift channel 13.

remark that in such cases the resonator can have a cylindrical form with much smaller length. The evaluations show possibility of gain with described resonators in the cost and and HF power approximately to one order while in the driving power by several orders.

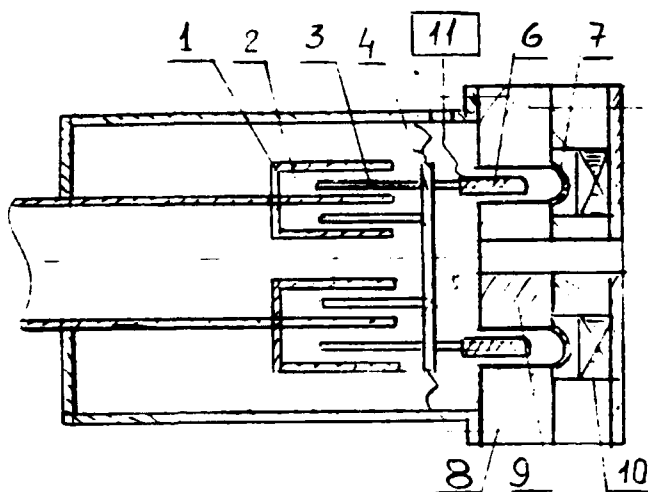


Fig. 2 Vibrating condenser tuned resonator

- 1 - unmoved plates, 2 - isolators, 3 - vibrating plates,
- 4 - elastic HF shorting ring, 5 - driving ring,
- 6 - single winding coil, 7 - vacuum joint, 8 - stell
- core, 9 - inner core, 10 - magnetisation coil,
- 11 - frequency discriminator signal amplifier

Shown in Fig. 2 variant has a stationary ring 2-3 plates stator 1, isolating rings 2, vibrating plates 3 fastened by means of a ring 4 on a forming HF volume elastic membrane 5. The ring vibrates together with the onewind coil of a like dynamic loudspeaker drive with a ferrum cores 8, 9 and a magnetization coil 10. The ring 6 is fed by current of the control ampltier 11. For a ficsation of the rings 6,4 axial position can be provided by installation 3 longitudinal setting small diameter plugs, sliding in the pits of the core 9 and on the resonator inner tube. Such system with the elastic membrane 5 is similar to logometer. The plates positioning is achieved by properly applied current to ring 6 from the initial frequency signal meter and ampltier.

This variant of condenser is more simple than the revolving plates condenser (Fig. 1). In addition there are less probability of parasitic HOM oscillations exitation, but the strong dynamic kicks lead to much shorter servise life. The absence of such kick in the Dubna phasotron frequency rotating variator has achieved its reliable work during approximately 25 years.

The innerresonator installation of the tuning condencers is reasonable in the casses of wide frequency bands. In a narrow frequency band case the involving by means of a loop or a rod of the outer reactances allows to solves the problem completely. It is very important to

REFERENCES

- [1] F.A. Vodopianov. Mechanically tuned accelerating resonators. - Particle Accelerators Conference. - Dubna, 1992.

Industrial Fabrication of Superconducting Accelerators

D. Dasbach, R. Fleck, D. Kiehlmann, M. Peiniger, H. Vogel
Siemens AG, KWU, Accelerator and Magnet Technology
51425 Bergisch Gladbach 1, Germany

Abstract

During the last two years major progress has been achieved in the industrial production of superconducting accelerators. A technology program with CERN has been completed in order to transfer the technology to sputter niobium onto copper cavities. Several cavities have surpassed design values and series production for LEP 200 is in progress. Secondly a complete linac consisting of 2 single cell and 2 five cell accelerator modules has been designed and fabricated based on inhouse experience. All 4 modules have surpassed the design values (5 MV/m, $Q > 2 \times 10^9$, cryogenic losses ≈ 3 Watt) during tests at Siemens. All 4 modules are in the meanwhile delivered to JAERI. Details and recent results of the projects are presented.

I. INTRODUCTION

Production of superconducting accelerators in the past has been conducted by the laboratories itself. The work has only been partly contracted to Industry (cavities, other components). Siemens has shown that the complete scope starting from design, followed by manufacturing, assembly, test and delivery with guaranteed performance is available from Industry.

The following gives two examples for this new development.

Fig. 1: One completely assembled superconducting accelerator module for LEP Energy upgrade

II. NB COATED CAVITIES FOR LEP UPGRADE

Scope of the project

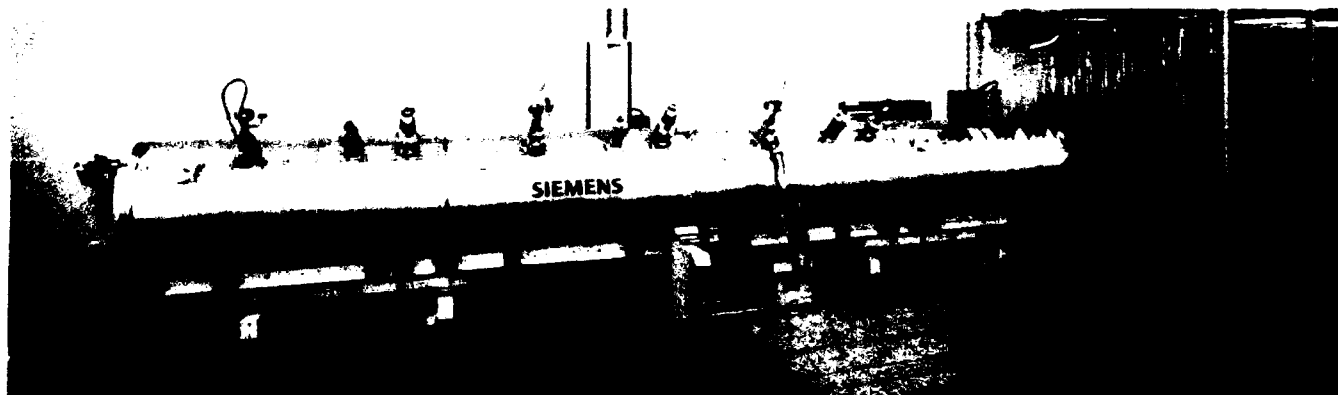
The scope of this project covers fabrication of the copper cavities, chemical preparation and coating, cold rf-test at CERN, fabrication of all other components (He-tanks, tuners, vacuum tanks, cryogenic domes) and finally assembly of the complete module.

Technology transfer

With a very intense technology transfer phase the project started with the installation of a new chemical treatment plant, the sputter equipment as well as clean rooms (class 100) for magnetron assembly and final assembly of the modules and was continued by establishing all the necessary procedures in close collaboration with CERN. The development of the coating procedure is described in [1], [2], [3].

Test results

After coating at Siemens all the cavities are tested in a vertical cryostat at CERN. Up to now 12 Siemens-cavities have surpassed the design values of Q_0 (at 6 MV/m) $> 4 \times 10^9$. The summary of all accepted cavities up to now is shown in figure 2. Investigations on the copper base material resulted in a change of the chemical preparation procedure. After increasing the thickness of the layer removed by electropolishing (from 60 μm to 120 μm) all test results significantly have improved (cmp. figure 2).



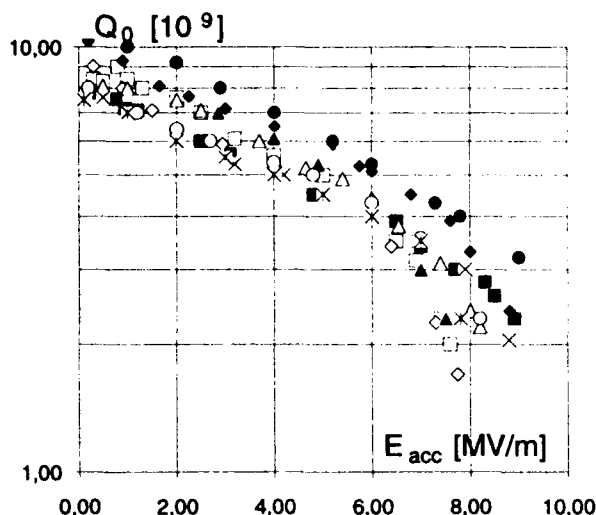


Fig. 2: Results of the 12 accepted cavities (vertical test)

The 4 cavities which have passed the acceptance test first were assembled to a module (figure 1) and send to CERN for cold test in December 1992. Unfortunately a leak in one of the beamtubes supplied by CERN and assembled to the module lead to an uncontrolled air-filling and a deterioration of the cavity performances. A repair cycle which includes disassembly, clean water rinsing (High pressure or normal pressure) and re-assembly at Siemens is in progress. One of the 4 Cavities has already been rinsed and passed the specification.

III. 4 TURNKEY ACCELERATOR MODULES FOR JAERI FEL EXPERIMENT

In 1/91 the contract for the delivery of 4 superconducting 500 MHz accelerator modules was concluded. The contract covered design and layout, manufacture and cold rf test of the two single cell modules and the two five cell modules.

Design and Layout

The purpose of the accelerator modules for the FEL-experiment and the special mode of operation (pulsed rf-mode 1 - 3 % duty cycle) required a different approach to the cryogenic design.

As the rf-losses are only 0.5 to 1.5 Watt (five cell cavity) the accelerator module is dominated by the standby losses. The design thus aimed to minimise the cryogenic losses below 4.5 Watt per module. By choosing a duplex heat shield cooled with closed loop refrigerators (20 K/80 K) the standby losses could be minimised to about 3 Watt at 4.2 K. The table below summarizes the achieved results.

For the He-tank a closed loop recondensor could be used (10 Watt) thus avoiding a central refrigerator with LHe-transfer line.

Development

Following a former contract were Siemens produced an accelerator module with a variable power coupler (400 MHz single cell module) [4] an improved power coupler with variable coupling factor for 500 MHz cavities was developed and manufactured for the modules.

It could be demonstrated that the coupler allows adjustment of the external Q for about 3 decades $3.0 \times 10^5 < Q_L < 2 \times 10^9$ with the antenna length (fig. 3).

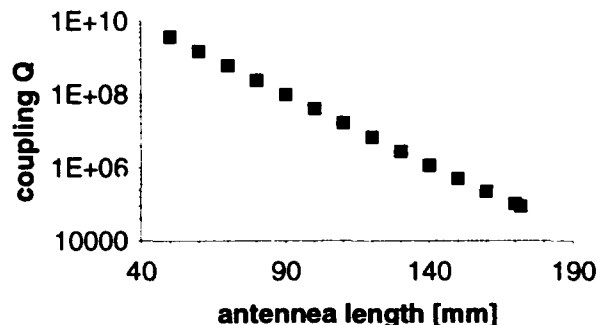


Fig. 3: External Q vs coupling antenna length for a superconducting 500 MHz single cell module

Manufacture

Manufacturing of the modules comprised the fabrication of all components (cavities, He-tanks, vacuum tanks, tuners, couplers), chemical preparation and assembly in clean condition. A cross-section of the five-cell module is shown in figure 5.

RF-Test

The cold rf tests have been performed as acceptance tests before shipping the modules to JAERI with the following results:

Module	Type	Q (at 5 MV/m)	Eacc max (at $Q = 1 \times 10^9$)	Cryostat standby losses (4.2 K)
1	1 cell	2.5×10^9	7.3 MV/m	3.6 W
2	1 cell	2.1×10^9	6.8 MV/m	3.0 W
3	5 cell	2.2×10^9	6.4 MV/m	3.5 W
4	5 cell	2.0×10^9	6.4 MV/m	3.5 W

The maximum fields have been obtained after only a few minutes of Helium-processing and are limited by electron field emission loading in all cases.

After installation of the 4 modules on site by JAERI and connecting the beamlines, rf-feeds etc. the modules were tested again and after few minutes of rf-processing the performance as shown at Siemens could be achieved again or slightly surpassed.

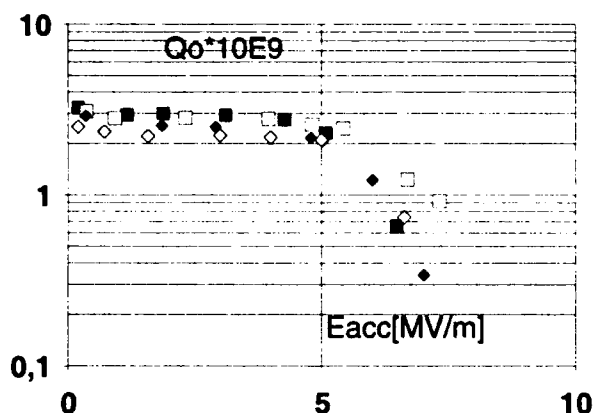


Fig. 4: Performance of the 4 JAERI accelerator modules during acceptance test before shipment

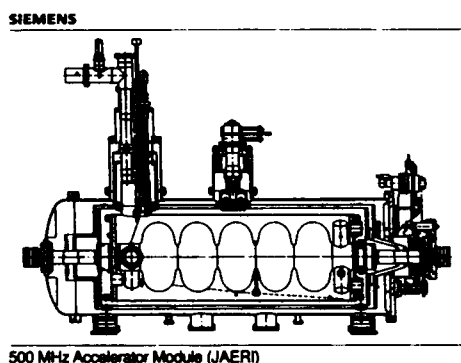


Fig. 5: Cross section of the five cell accelerator module

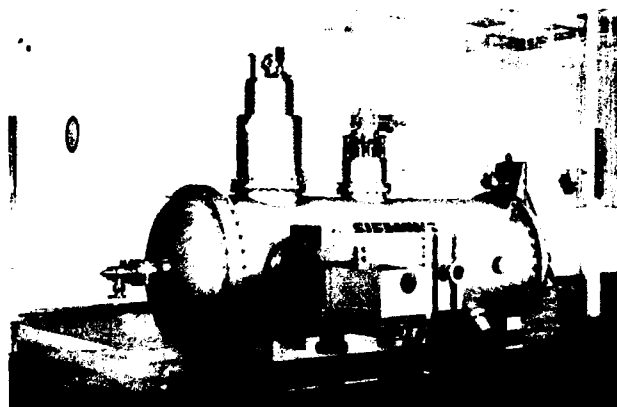
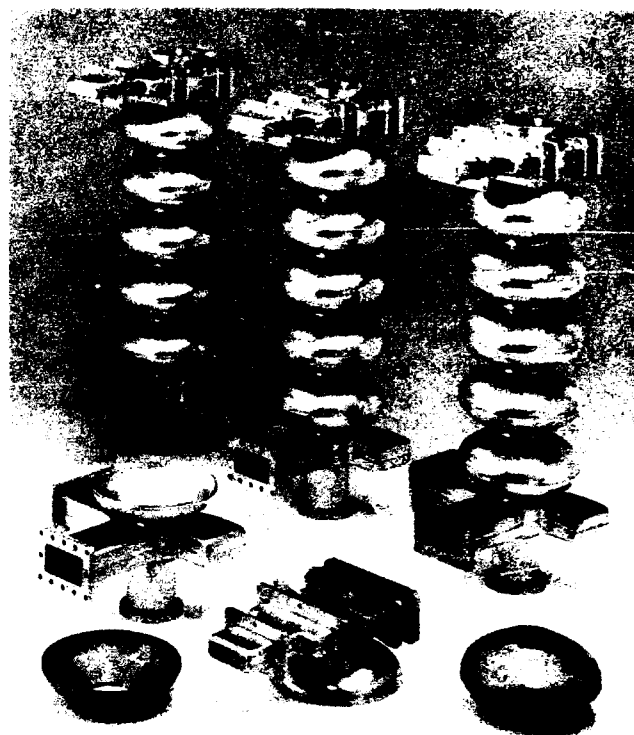


Fig. 6: The five cell module completely assembled before shipment to JAERI

IV. 360 Cavities for CEBAF

In March 1993 the delivery of 360 cavities for CEBAF has been completed as scheduled. All cavities are delivered tuned to correct field profile frequency and Q_{ext} .

They receive their final chemical preparation at CEBAF, two cavities are assembled to "pairs" and tested in vertical cryostats prior to assembly into the cryomodule (beam-line cryostat).



Over 250 cavities have been assembled and tested at 2.0 K. The guaranteed performance is $Q_0 = 2.4 \cdot 10^9$ at 5 MV/m. More than 50 % of the vertically tested cavities demonstrate usable gradients greater than 10 MV/m. Details of the test and statistics on the results are given in [5].

V. SUMMARY

Superconducting cavities have been chosen as the accelerators for several projects. It could be shown that industry is well equipped and able not only to produce bare Nb-cavities (CEBAF) but also complete accelerator modules (LEP, CERN) as well as completely designed, manufactured and tested turnkey Modules (JAERI-FEL) ready for operation.

VI. REFERENCES

- [1] C. Benvenuti "Superconducting Coatings for Accelerating Cavities: Past, Present, Future", CERN/MT-DI/91-6
- [2] G. Cavallari et. al "Superconducting Cavities for LEP Energy upgrade", CERN/AT-RF (Int)92-4, December 1992
- [3] C. Benvenuti et. al., "Superconducting Niobium sputter coated copper cavity modules for the LEP upgrade", CERN/AT-Rf-91-6, May 1991
- [4] O'Donnell et. al., "A superconducting radio-frequency cavity for manipulating the phase space of pion beams at LAMPF"
- [5] Reece et al. "Performance of Production SRF Cavities for CEBAF", these proceedings

BROADBAND HIGHER-ORDER MODE (HOM) DAMPER FOR SSC LEB FERRITE-TUNED CAVITY*†

L. Walling, G. Hulsey, and T. Grimm
Superconducting Supercollider Laboratory
MS-4010, 2550 Beckleymeade Ave. Dallas, TX 75237

Abstract

This paper reports results of using High-Frequency Structure Simulator (HFSS) to design a Smythe-type broadband longitudinal HOM damper for the SSCL low energy booster (LEB) ferrite-tuned cavity. The damper is designed to have a shunt impedance varying from less than 1 kohm between 100-200 MHz to about 3 kohm at 1 GHz. Above 1 GHz, the ferrite should effectively damp all HOM.

broadband damper. A Smythe-type³ broadband damper has been designed using two-element high-pass filters between the damping cavity and four discrete water-cooled loads. A cross-section of the gap end of the cavity with HOM damper is shown in Fig. 2. The filter/loads are distributed around the circumference of the damping cavity in such a pattern as to damp transverse as well as longitudinal modes (Fig. 3).

I. INTRODUCTION

The LEB cavity¹ is a ferrite-tuned $\lambda/4$ coaxial cavity that tunes from 47.5 to 59.8 MHz in about 20 ms and requires 127 kV on the gap at the peak voltage in the cycle. R. Baartman of TRIUMF did a coupled bunch mode beam instability analysis² for the LEB. According to his analysis, the allowable longitudinal shunt impedance of the cavity HOM's as a function of frequency is shown in Fig. 1. Also shown is the calculated achieved shunt impedance.

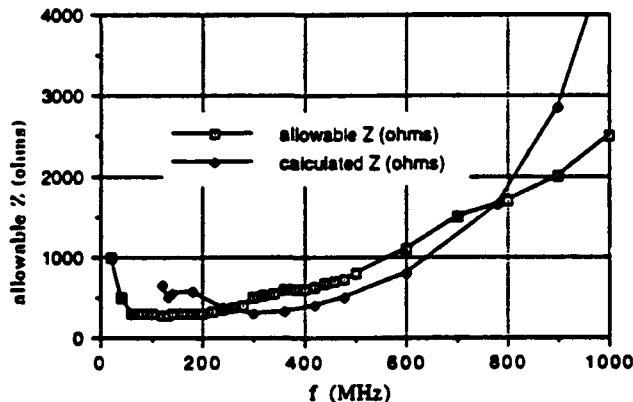


Fig. 1. Narrow Band Impedance in the SSC LEB.

For fixed-frequency machines, HOM dampers can be designed to address individual modes. Since the LEB has a large frequency swing, it is more convenient to build a

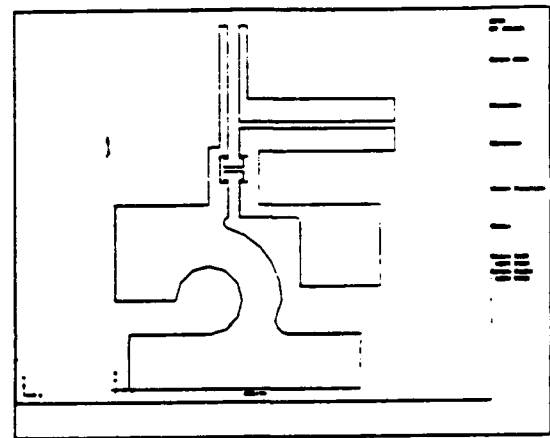


Fig. 2. Cross-section of Final LEB HOM Damper.

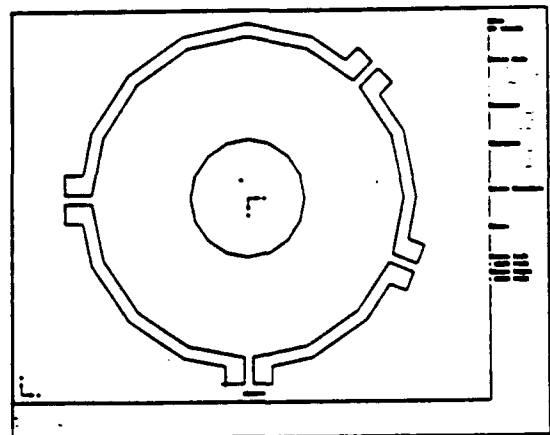


Fig. 3. Axial Arrangement of Filters and Loads on HOM Damper.

* To be submitted at the "1993 IEEE Particle Accelerator Conference" May 17-20, 1993.

† Operated by the Universities Research Association, Inc., for the U.S. Department of Energy under Contract No. DE-AC35-89ER40486.

II. DESIGN TECHNIQUE

Smythe showed that his damper could be modeled as a circuit element that is in shunt with the gap of the cavity. The circuit representing the cavity and damper is shown in Fig. 4. Then r_{sh} , the shunting resistance of the damper, is

$$r_{sh} = 1/\text{Re}\{1/z_d\} \quad (1)$$

The damper impedance, z_d , can be approximated by solving the circuit,

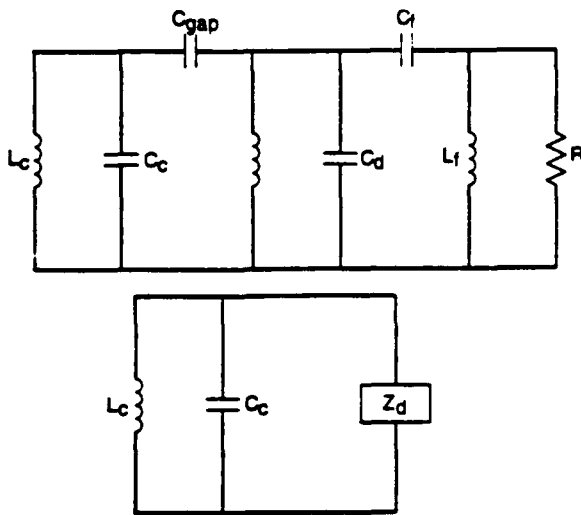


Fig. 4. Circuit for LEB HOM Damper with High-Pass Filters between Smythe Cavity and Loads.

where L_c and C_c are the cavity inductance and capacitance, L_d and C_d represent the damper cavity and L_f and C_f the filter parameters.

Originally, we intended to design a simple Smythe damper. However the $3\lambda/4$ mode occurs at a frequency much lower than three times the fundamental due to the heavy capacitive loading of the cavity. This is aggravated by the large coupling to the damping cavity which is required to damp the low-frequency modes so strongly. After determining the amount of coupling that would be required, we determined that it would be impossible to find a design that would yield the required damping over the band while leaving the accelerating mode with a large enough shunt impedance so as not to overdrive the power amplifier (and burn up the 5 kW damping resistors). This could be determined easily using the lumped circuit model. Therefore we decided to try adding a high-pass filter between the damper and the load. The lumped circuit model for the damper plus filter could be used to estimate the required coupling capacitance to the damping cavity and roughly estimate the circuit parameters. Because the required coupling capacitance turned out to be very large (about 12 pF), the current paths from the gap to the point at which the filter/load is shunted across the Smythe capacitor became long, which reduces the damping of the HOMs. This results in a

damping cavity that is not well-represented by any type of circuit approach.

HFSS, with its s-parameter format and finite-element mapping of the rounded surfaces, was the ideal tool for such a design. The main problem was to find an approach that would be fast and efficient, since modelling the entire damper including filter results in a large problem that takes hours to run. Therefore the design was done in three stages which combined the use of numerical results from HFSS and lumped element analysis in the first two stages to speed up the design process.

Step 1. Pseudo-2d HFSS analysis (Fig. 5). We modeled an angular wedge of 2 slices of about 5-10 degrees each (we have found that one thin slice of elements does not yield an accurate solution.) The load is represented by a thin disk of resistive material which represents the four loads in parallel. This is a one-port problem with the port located at a cross section of the cavity just far enough away from the gap such that the fields are approximately transverse. The reflection coefficient is calculated by HFSS and written out to a file. This file was read using a small FORTRAN code which transformed S11 from the port to the gap, then calculated r_{sh} . This was useful to develop a cavity that had approximately the desired r_{sh} over the band, although the fundamental mode shunt impedance was too low.

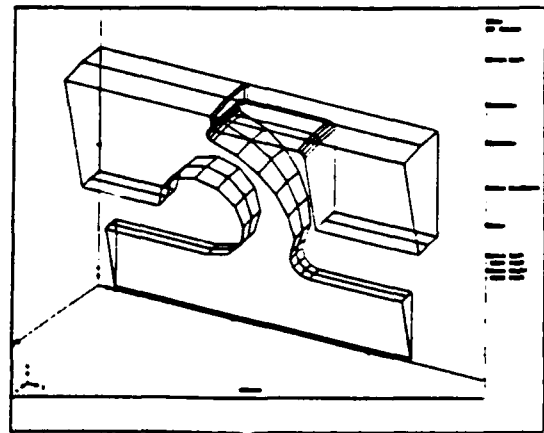


Fig. 5. HFSS Model Using a Disk of Resistive Material to Represent the Loads.

Step 2. Next, another HFSS model (Fig. 6) was built which modeled 1/8 of the axial geometry and which included a port at the position the filter/load would be placed. The full 2-port solution was obtained over the frequency range, the s-parameters stored in a file, then read into a FORTRAN code which cascaded the high-pass filter/load parameters onto port 2, then calculated r_{sh} from S11 with the new termination. The damper cavity dimensions were modeled in HFSS, then the filter quickly optimized for that geometry using the

FORTTRAN code. By systematically varying the cavity dimensions and cycling through this process, the entire circuit was quickly optimized.

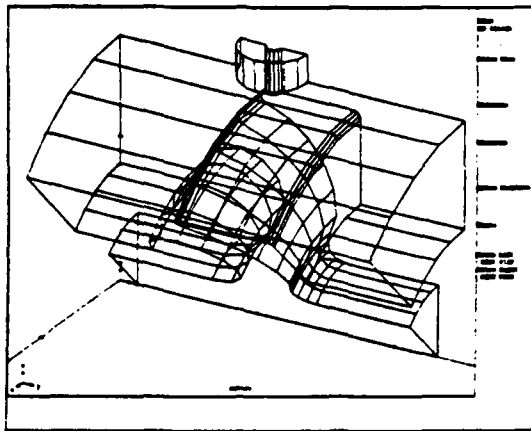


Fig. 6. HFSS Model Using 1/8 Axial Symmetry and Load Represented by Coaxial Port.

Step 3. The actual filter was added to the HFSS model (Fig. 7) to do the final checking of the design for damping, field maximums and heating. The shunt impedances of the HOMs as calculated by this HFSS model are shown in Fig. 1.

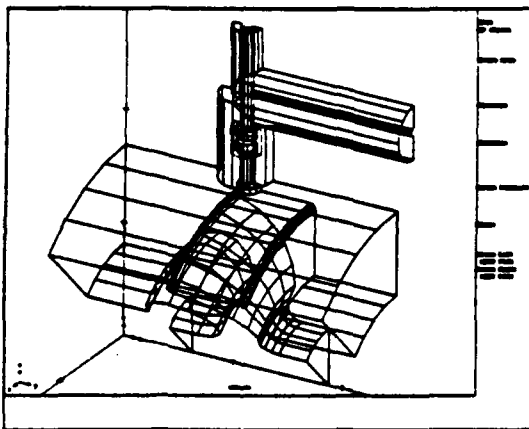


Fig. 7. HFSS Model of Entire HOM Damper.

In parallel to this effort, a hardware model of the filter using high-voltage ceramic capacitors and 5 kW water-cooled loads was built and tested at both low and high-power.

III. TRANSVERSE MODE DAMPING

We then tested the possibility of damping transverse modes by arranging the loads axially as shown in Fig. 3. A simplified model of the entire cavity with a simple Smythe damper was built using HFSS. The loads were arranged as suggested by Grimm and the cavity was excited by an off-center wire placed about 1 cm to the right and to the top of the cavity axis, looking down the axis from the gap to the tuner. This method of excitation would excite all longitudinal and transverse modes of the cavity. All materials in the cavity were artificially specified with a loss tangent that would ensure that as the cavity was swept from 300 MHz to 1 GHz at 20 MHz intervals that any resonances would be identified. Then when resonances were found, they were identified as to longitudinal or transverse by looking at the fields near resonance. Finally, the loss tangents were reduced to zero and the frequencies were swept around the resonances. A rough analysis determined that the impedances of all transverse modes were below 100 k Ω /m. A similar analysis has not been done with the actual damper with filters, however we expect even better results because the damper has much greater coupling to the cavity than the one simulated with asymmetric loads.

IV. CONCLUSIONS

HFSS has proven to be an ideal tool for designing HOM dampers because of its s-parameter format, matched port, lossy material capabilities, and finite-element modeling technique which allows close approximation of rounded surfaces. It is very easy to model problems and make changes in models. Measurements of the cavity with damper will be performed in early spring of 1993 to verify the design.

REFERENCES

1. C.C. Friedrichs, L. Walling, B.M. Campbell, Design of an Accelerating Cavity for the Superconducting Supercollider Low-Energy Booster, IEEE PAC, 1020 (1991).
2. R. Baartman, Allowed Narrow-Band Impedance in the SSC LEB, TRIUMF Design Note (1992).
3. W.R. Smythe, Proton Synchrotron RF Cavity Mode Damper Tests, IEEE PAC, 643 (1991).

Design of the Detuned Accelerator Structure*

J. W. Wang and E. M. Nelson
Stanford Linear Accelerator Center
Stanford University, Stanford, CA 94309 USA

Abstract

This is a summary of the design procedure for the detuned accelerator structure for SLAC's Next Linear Collider (NLC) program[1]. The 11.424 GHz accelerating mode of each cavity must be synchronous with the beam. The distribution of the disk thicknesses and lowest synchronous dipole mode frequencies of the cavities in the structure is Gaussian in order to reduce the effect of wake fields[2]. The finite element field solver YAP calculated the accelerating mode frequency and the lowest synchronous dipole mode frequency for various cavity diameters, aperture diameters and disk thicknesses. Polynomial 3-parameter fits are used to calculate the dimensions for a 1.8 m detuned structure. The program SUPERFISH was used to calculate the shunt impedances, quality factors and group velocities. The RF parameters of the section like filling time, attenuation factor, accelerating gradient and maximum surface field along the section are evaluated. Error estimates will be discussed and comparisons with conventional constant gradient and constant impedance structures will be presented.

I. ACCELERATING MODE

The accelerator structure is a disk loaded waveguide driven at 11.424 GHz. The phase advance per cell is chosen to be $\phi = 2\pi/3$. In order for the accelerating mode to maintain synchronism with the beam the phase velocity must be $v_\phi = c$, thus the cell length is $l = 0.8748$ cm.

Synchronism with the beam is a constraint on the dimensions of a cell. The dimensions are the disk aperture $2a$, the cell diameter $2b$ and the disk thickness t . The inner edge of the disks are round with full radius, not flat. The RF parameters of a cell can be computed by treating the cell as part of a periodic structure. Let $f_o(2a, 2b, t)$ be the accelerating mode frequency at $\phi = 2\pi/3$. Then the synchronism constraint is

$$f_o(2a, 2b, t) = 11.424 \text{ GHz}. \quad (1)$$

This can be considered an implicit formula for $2b(2a, t)$ for the cells of the accelerator structure. That is, given the parameters $2a$ and t of a cell, solve (1) for $2b$.

The finite element field solver YAP[3] was used to compute the accelerating mode frequency f_o for various cell dimensions covering the range $0.7493 \text{ cm} \leq 2a \leq 1.1684 \text{ cm}$ and $0.1016 \text{ cm} \leq t \leq 0.2540 \text{ cm}$. The range of cell diameters was $2.0828 \text{ cm} \leq 2b \leq 2.3622 \text{ cm}$. For a given set of dimensions ($2a$, $2b$ and t) meshes for one cell of a periodic structure were constructed using triangular elements. The

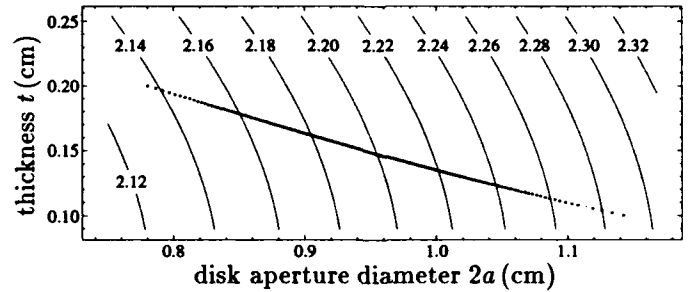


Figure 1. The cell diameter $2b$ (in cm) which yields synchronism with the beam ($v_\phi = c$). The dots are the 206 cells of the detuned accelerator structure. The rightmost dot is the first (input) cell and the leftmost dot is the last (output) cell.

number of elements and the topology of the meshes are independent of the cell parameters, so the mesh depends smoothly on the cell dimensions. Then discretization error can be considered a systematic error when comparing two cells with slightly different dimensions.

The accelerating mode frequency f_o was calculated by YAP using four successively refined meshes composed of quadratic elements. The estimated relative accuracy of the frequency calculation for the finest mesh is $\sim 10^{-6}$. Further accuracy was obtained by extrapolating the four calculations to zero element size (an infinitely refined mesh). Conservative error estimates for the extrapolated f_o range from 5 KHz for large t cases to 30 KHz for small t cases.

The calculations were fit to the polynomial

$$f_o(2a, 2b, t) = \sum_{i=-1}^1 \sum_{j=0}^2 \sum_{k=0}^4 \tilde{f}_{ijk}(2b)^i (2a)^j t^k. \quad (2)$$

Only 165 calculations with $|f_o - 11.424 \text{ GHz}| < 150 \text{ MHz}$ were included in the least squares fit for the 45 parameters. The polynomial approximates the calculations with residual errors $< 80 \text{ KHz}$. The polynomial can be used to solve (1) for the cell diameter $2b$ with an error $\sim 1 \mu\text{m}$. This error is comparable to the skin depth in copper at the operating frequency and about an order of magnitude smaller than available machining tolerances. A contour plot of $2b(2a, t)$ is shown in Figure 1.

II. DIPOLE MODE

In order to reduce the effect of wakefields it is useful to detune or spread out the frequencies of the undesired modes. A Gaussian distribution of the modes leads to very good cancellation of the wakefield effects. The wakefield decoheres in a time comparable to the reciprocal of the width of the frequency distribution of the modes.

*Work supported by U.S. DOE contract DE-AC03-76SF00515.

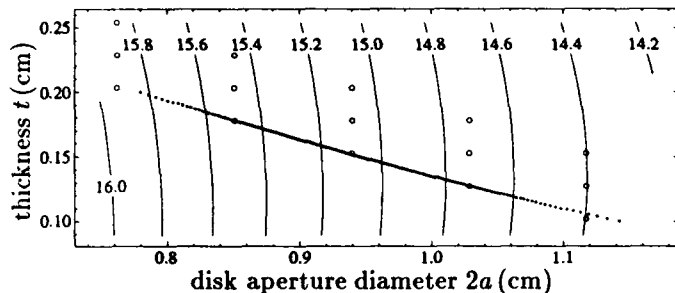


Figure 2. The lowest synchronous dipole mode frequency f_1 (in GHz). The cell diameter $2b$ is determined from the synchronism condition. The open circles are the dimensions at which f_1 was computed. The dots are the 206 cells of the detuned accelerator structure.

The largest wakefield by far comes from the lowest dipole mode. Higher dipole modes have less effect and can be effectively detuned by varying the disk thickness t along the structure such that the distribution of thicknesses is nearly Gaussian[4]. The disk thickness t has little effect on the lowest dipole mode, so the aperture diameter $2a$ is varied along the structure such that the distribution of lowest synchronous dipole mode frequencies f_1 is nearly Gaussian. While the synchronous dipole mode frequencies of the cells are not the same as the dipole mode frequencies of the structure, the distributions of the frequencies are similar according to equivalent circuit models of the structure[5].

A Gaussian distribution with rms width $2\sigma = 0.7$ GHz provides decoherence of the wakefield effects by the time the following bunch arrives (1.4 ns). To obtain good cancellation of wakefield effects over the whole bunch train (perhaps 90 bunches) it is necessary to have a good distribution of modes. Beam dynamics simulations[6] for the NLC indicate the tolerance for systematic relative frequency errors is approximately 10^{-4} , hence accurate calculations of f_1 are important for the design of detuned accelerator structures.

The lowest synchronous dipole mode frequency f_1 was calculated using YAP[7]. The cell diameter $2b$ was fixed using the beam synchronism constraint (1), so two parameters remain for the dipole mode calculations: $2a$ and t . Frequencies at two phase advances ϕ close to the synchronous phase and 0.02 radians apart were computed for 15 cells. Calculations on three successively refined meshes were extrapolated to zero mesh size, with conservative error estimates ranging from 120 KHz for large t cases to 400 KHz for small t cases. Then the lowest synchronous dipole mode frequency and phase advance were obtained using linear interpolation. The frequencies were fit to a polynomial quadratic in $2a$ and t . The estimated error of the fit is 600 KHz. The fit is shown in Figure 2 and is expected to be good only near the region encompassed by the 15 calculated points.

The Gaussian distributions for t and f_1 for 206 cells were truncated at $\pm 2\sigma$. The range of the disk thickness t was chosen to be 0.1 cm to 0.2 cm. This is sufficient to spec-

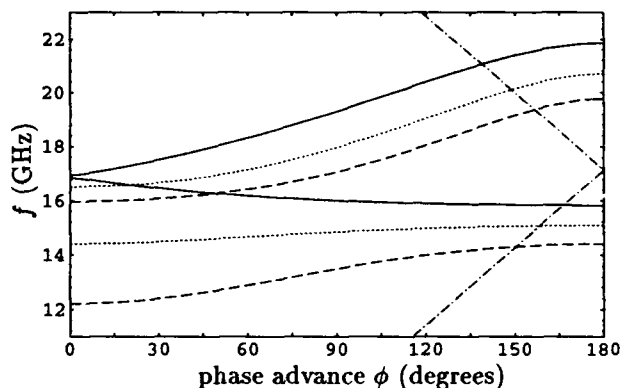


Figure 3. Dispersion diagram for the two lowest dipole modes of three different cells of the structure. The dashed line is the first (input) cell, the dotted line is the middle cell and the solid line is the last (output) cell. The dot-dash line is the velocity of light line.

ify t for all cells. The relative range of f_1 was chosen to be 10.1%. With this information only one free parameter for the whole structure remains. In practice the parameter was the aperture diameter $2a$ of the first cell, but the average lowest synchronous dipole mode frequency is also a viable free parameter. In either case the free parameter determines f_1 for each cell. Given f_1 and t for a cell the aperture diameter $2a$ was found using the quadratic polynomial approximation to the lowest synchronous dipole mode frequency. Then the cell diameter $2b$ was obtained from $2a$, t and the synchronism constraint (1).

III. STRUCTURE RF PARAMETERS

RF parameters like the shunt impedance, quality factor Q , group velocity v_g and peak surface field to accelerating gradient ratio $E_{s,max}/E_{acc}$ were computed for the accelerating mode by SUPERFISH[8] for a few of the cells. While the code calculates RF parameters for periodic structures, the calculations are still valid locally for the detuned structure since the cell dimensions vary slowly. A polynomial fit was used to obtain the RF parameters for the remaining cells. The filling time of the structure was computed from

$$T_f = \int_0^{1.8\pi} \frac{dz}{v_g(z)}. \quad (3)$$

The free parameter (e.g., the aperture diameter $2a$ of the first cell) of the structure was varied to achieve $T_f = 100$ nsec. The corresponding cell dimensions are plotted in Figures 1 and 2.

Dispersion curves for the two lowest dipole modes of three cells (first, middle and last) of the structure were computed using YAP and are shown in Figure 3.

The accelerating gradient along the length of the structure was computed[9] by first finding the attenuation $\tau(z)$ along the structure,

$$\tau(z) = \int_0^z \frac{\omega dz}{2Q(z)v_g(z)} \quad (4)$$

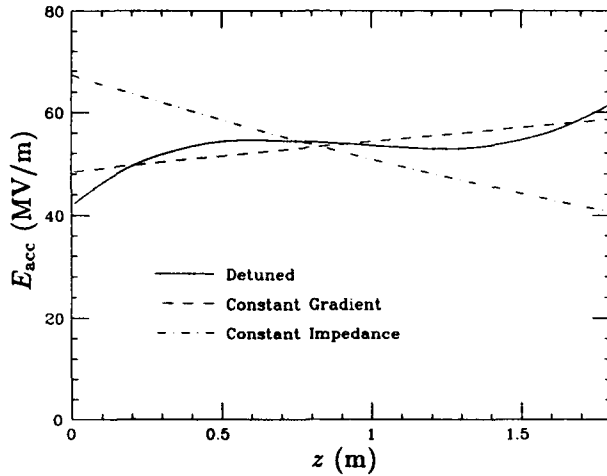


Figure 4. Accelerating gradient along the length of the structure for 100 MW input power and various structure types.

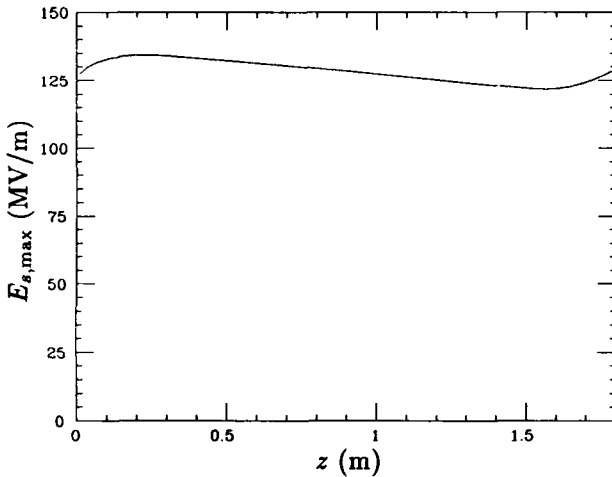


Figure 5. Peak surface gradient along the length of the detuned accelerator structure for 100 MW input power.

where $\omega = 2\pi f_0$ is the angular frequency. Then the power flow $P(z)$ in the structure is

$$P(z) = P_{in} e^{-2\tau(z)} \quad (5)$$

and the accelerating gradient is

$$E_{acc}(z) = \sqrt{\tau(z) \frac{dP}{dz}(z)} \quad (6)$$

where $\tau(z)$ is the shunt impedance per unit length. The gradient is shown in Figure 4 along with gradients for a conventional constant gradient structure and a constant impedance structure. All three structures in Figure 4 have the same attenuation constant τ .

It is noteworthy that the peak surface field $E_{s,max}$ on the disk edges varies little along the structure as shown in Figure 5. The first cell has a thin disk and large aperture, so $E_{s,max}/E_{acc}$ is high ($\cong 3$) but E_{acc} is small due to the low shunt impedance and high group velocity. For the last cell the situation is just the opposite. Other RF parameters are listed in Table 1.

Table 1
Structure RF Parameters

Section length	1.8 m
Phase advance per cell	$2\pi/3$ radians
Iris aperture:	
radius	5.72–3.91 mm
normalized radius	0.218 λ –0.149 λ
Group velocity	0.12c–0.03c
Filling time	100 ns
Unloaded time constant	207–186 ns
Attenuation constant	0.517 nepers
Shunt impedance	67.5–88.0 M Ω /m
Elastance	853–946 V/pC/m
For 50 MV/m average gradient:	
Peak input power/(1.8 m)	48.1 MW/m
Peak power per feed	86.5 MW
Average power dissipation for 250 ns pulses, 180 pps	1.4 kW/m

IV. REFERENCES

- [1] R. D. Ruth, "The Development of the Next Linear Collider at SLAC," SLAC-PUB-5729 (1992).
- [2] H. Deruyter, et. al., "Damped and Detuned Accelerator Structures," SLAC-PUB-5322, 1990 *Linear Accelerator Conference Proceedings*.
- [3] E. Nelson, "A 2d Field Solver for Periodic Structures with Special Corner Elements," SLAC-PUB-5532, *Conference Record of the 1991 IEEE Particle Accelerator Conference*, pp. 722-724.
- [4] K. Bane, private communication.
- [5] K. Bane and R. Gluckstern, "The Transverse Wake-field of a Detuned X Band Accelerator Structure," SLAC-PUB-5783, submitted to *Particle Accelerators*.
- [6] K. A. Thompson, C. Adolphsen and K. L. F. Bane, "Multibunch Beam Break-up in Detuned Structures," SLAC-PUB-6153 (1993), these proceedings.
- [7] E. M. Nelson, "A Finite Element Field Solver for Dipole Modes," SLAC-PUB-5881, 1992 *Linear Accelerator Conference Proceedings*, pp. 814-816.
- [8] K. Halbach and R. F. Holsinger, *Particle Accelerators* 7, 213 (1976).
- [9] J. W. Wang and B. W. Littmann, "Design Study on Quasi-Constant Gradient Accelerator Structure," SLAC/AP-92, Sep. 1991.

CONSTRUCTION of an RF CAVITY for the LNLS SYNCHROTRON

D.Wisnivesky°, M.A.Remy and R.H.A.Farias

Laboratório Nacional de Luz Síncrotron - LNLS/CNPq

Cx Postal 6192, 13085 Campinas S.P. Brazil

° IFGW/ UNICAMP

Abstract

A construction program for an RF cavity for the LNLS storage ring is under development. The cavity main frequency is 476 MHz, and should operate with 60 kW CW. The cavity design is based on the development made for the proposed PEP II B factory^[1]. Special wave guide dampers are used in order to reduce HOM instabilities. In order to get the precise mechanical dimensions of the 476 MHz cavity, a scaled prototype (approximately 1200 MHz) was built based on the results of numerical simulation. Low power tests were used to fully characterize the HOM spectrum. Using the measured values, couple-bunch instabilities are studied.

I. INTRODUCTION

The synchrotron light source under construction at the LNLS requires an RF system operating with a CW RF power of 56 kW at the input coupler of the cavity. Construction of the RF transmitter, coaxial and wave line system and cavity control system has been completed. A 3 cell RF cavity resonating at 499 MHz is available at the LNLS. Different tests performed with this cavity however indicated that it would be desirable to develop a new one that should include several improvements. The new cavity's main characteristics should be:

- Fundamental frequency: 476 MHz (linac sub-harmonic).
- 60 kW CW.
- Single cell.
- Standard conflat vacuum seals.
- 500 kV gap voltage.
- Coupling factor: 1.4
- Tuning range: ± 150 kHz.

II. CAVITY DESIGN

The cavity geometry is similar to that proposed for the PEP II B factory^[1]. It is a reentrant type cavity with 3 ports located around the equatorial plane to accommodate for a mechanical tuner, a 45 dB RF monitor and an RF input aperture coupler. Three wave guides, symmetrically located around the axis, are used to damp the HOM. The wave guide is dimensioned so that the fundamental frequency is about 200 MHz below cut off. Figure 1 gives a general view of the cavity.

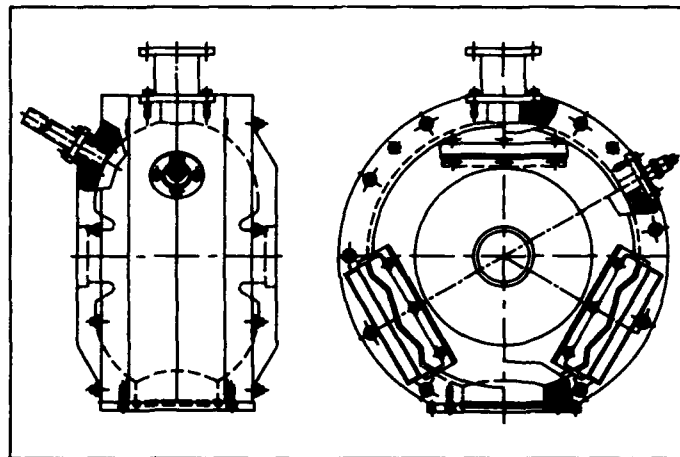


FIG 1

Schematic design of the RF cavity.

Considering the cavity's narrow range of tuning, the final shape, after assembling all ports and couplers, should give a fundamental resonant frequency within $2 \cdot 10^{-4}$ of the desired value. Thus it was decided to construct a small model with a fundamental frequency at 1200 MHz, 2.5 times smaller. Dimensional measurements were performed on the constructed model. Also measurement of the resonant frequency, coupling factor and other parameters was done with the model. Finally the exact scaling geometrical factor for the real-size prototype was determined. A prototype, made of aluminum is shown in Figure 2. The picture shows the 3 damping wave guides with adjustable broad band loads inside, a step motor driven-plunger, an RF monitor and the wave guide coupler that communicates with the cavity through a ceramic disk located some distance away from the cavity's standing wave fields. The fundamental frequency was measured to be 476 MHz at room temperature and normal pressure. The plunger's tuning range is 350 kHz, enough to compensate for the frequency shift due to vacuum, cavity operating temperature and beam loading.



FIG 2

III. HOM CONFIGURATION

HOM were calculated using URMEL-T code^[2]. In multibunch instabilities study, monopole and dipole modes are the most interesting. In order to identify these modes a computer simulation of the aluminum cavity was performed using URMEL-T code. Table 1 gives the result of the calculation up to the beam pipes cut off frequency.

TM MONOPOLE MODES			
Mode	Freq.(MHz)	Q	R/Q (M Ω)
0-EE-1	484.2	37600	110.8
0-ME-1	763.6	32600	47.5
0-EE-2	1003.9	33700	0.9E-5
0-EE-3	1275.3	73000	7.69
0-ME-2	1282.9	33200	7.02
0-EE-4	1564.5	34500	6.68
0-ME-3	1693.5	69000	3.30
0-EE-5	1798.5	87000	.85E-1
0-ME-4	1869.2	36700	3.32
0-EE-6	2075.3	52000	0.74
0-ME-5	2136.7	67000	0.12
0-EE-7	2224.6	47000	1.27
0-EE-8	2331.4	71000	2.37

DIPOLE MODES			
Mode	Freq.(MHz)	Q	R/Q M Ω /m
1-ME-1	670.9	38500	.28E-3
1-EE-1	785.7	48600	15.2
1-ME-2	1055.1	40600	27.1
1-EE-2	1121.5	40900	0.25
1-ME-3	1190.4	73000	0.32
1-EE-3	1301.9	42000	5.64
1-ME-4	1421.1	32200	2.74
1-EE-4	1521.9	82000	1.05
1-EE-5	1575.0	68400	1.42
1-EE-6	1667.6	31000	6.17
1-ME-5	1701.5	59900	.21E-1
1-ME-6	1745.4	82500	.73E-1
1-ME-7	1913.6	38800	.97E-1
1-ME-8	1947.3	56000	1.49
1-ME-9	2001.7	71600	2.00
1-EE-7	2048.4	78900	.25E-2
1-EE-8	2057.5	101100	.68E-1
1-EE-9	2152.2	56400	.31E-1
1-EE10	2223.7	36600	.17E-1
1-ME10	2296.1	93900	.31E-2
1-EE11	2371.9	88700	0.39
1-EE12	2388.3	86600	1.00

TABLE 1

IV. HOM MEASUREMENTS

Different measurements of the HOM spectrum were performed using several antennas at different locations in order to correctly identify the resonances. The cavity modes were first measured with all ports closed and Q_0 was determined. This allowed a comparison to be made with the theoretical values. Next, the ceramic window, all 3 damping wave guides and the tuner were mounted and mode parameters were measured for different plunger positions. The results are condensed in table 2. Six columns of the table show the measured frequency and Q value for 3 different positions of the plunger: maximum, middle and minimum course with the 3 loaded wave guides, the wave guide coupler and 2 pipes simulating the vacuum chamber. It can be noticed that for the fundamental mode there is a 20% decrease in the value of Q when the wave guide couplers are added. The Q expected for a copper cavity properly machined and brased should go up to about 30000. The reduction in Q is much stronger for all HOM, showing the strong damping effect produced by the wave guides. A study of multibunch stability was performed using ZAP^[3] for the parameters given in table 2 and a beam energy and current of 1.15 GeV, 200 mA. The results are shown in the last column of table 2, which gives the ratio of the growth time of instability for the mode relative to the synchrotron damping time for the longitudinal modes and betatron damping time for the transverse dipole modes.

TM MONOPOLE MODES

Mode	Close ^r cavity		Cavity with dampers Plunger position						relat. growth
	Freq.	Q ₀	out Freq.	Q	middle Freq.	Q	in Freq.	Q	
0-EE-1	481.7	20000			476.1	15500			
0-ME-1	760.8	18100	--	--	--	--	--	--	--
0-EE-2	--	--	--	--	--	--	--	--	--
0-EE-3	1270.9	31900	--	--	--	--	--	--	--
0-ME-2	1281.6	5800	1280.5	450	1279.9	500	1277.5	680	0.37
0-EE-4	1558.4	14100	1566.0	200	--	--	--	--	0.51
0-ME-3	1691.0	11200	1685	200	1684.8	200	1683.8	250	0.97
0-EE-5	1798.3	37400	1797.2	200	1798	150	1798.4	500	37.8
0-ME-4	1863.9	4200	1867.3	300	1867.3	350	1867	450	0.58
0-EE-6	2067.9	10000	2077.9	200	2077.9	200	--	--	3.91
0-ME-5	2130.7	2300	--	--	--	--	--	--	--
0-EE-7	2219.8	10100	2224.5	400	--	--	--	--	1.02
0-EE-8	2327.4	17900	2334	100	2332.7	800	2333.1	650	2.12

DIPOLE MODES

Mode	Closed cavity		Cavity with dampers Plunger position						relat. growth
	Freq.	Q ₀	out Freq.	Q	middle Freq.	Q	in Freq.	Q	
1-ME-1	668.1	24700	646.5	50	646.5	100	646.7	100	1.23
1-EE-1	784.8	24900	788.5	120	788.1	150	788.4	150	1.18
1-ME-2	1118.9	27600	--	--	--	--	--	--	--
1-ME-3	1189.2	44000	1189.2	1564	1188.9	1300	1188.3	550	1.22
1-EE-3	1289.2	19000	--	--	1291.8	580	--	--	--
1-ME-4	1417.7	7900	1418.5	950	1418.4	750	1418.7	800	1.19
1-EE-4	1518.4	25300	--	--	--	--	--	--	--
1-EE-5	1567.1	12800	1560.5	300	--	--	--	--	--
1-EE-6	1663.1	9200	1653	1460	1651.2	500	1652.3	1400	0.75
1-ME-5	1704.4	2800	1698.9	250	1700.9	300	1699.7	260	1.22
1-ME-6	1737.5	26000	1738.5	350	1738.0	360	1738.0	350	1.22
1-ME-7	1905.6	4010	--	--	--	--	--	--	--
1-ME-8	1940.6	3800	1944	290	1943.8	280	1944.1	240	1.17
1-ME-9	1998.1	1500	--	--	--	--	--	--	--
1-EE-7	2042.3	14500	--	--	--	--	--	--	--
1-EE-8	2054.7	4030	2056.9	780	2056.7	1000	2056.7	780	1.22
1-EE-9	2150.0	1020	--	--	--	--	--	--	--
1-EE10	2214.4	2170	2219.5	350	2219.7	340	--	--	1.22
1-ME10	2298.2	17700	--	--	--	--	--	--	--
1-EE11	2368.9	26030	2371.4	650	2371.8	980	--	--	1.18
1-EE12	2381.9	66000	2379.6	540	2379.9	560	2380.0	260	1.15

TABLE 2

V. CONCLUSIONS

A 476 MHz aluminum prototype RF cavity was built using computer simulation and a 1200 MHz model. The cavity has 3 wave guides which couple the high order modes to broad band load termination. Measurements of the Q values of the HOM for the cavity, with and without the wave guides, were performed. The results show that there is a strong damping effect due to the loading. Multibunch instabilities calculations were done using the LNLS storage ring parameters and the cavity HOM impedances. All transverse modes, except one, are stable for beam currents up to 200 mA.

ACKNOWLEDGMENT

We would like to thank H. Kuniyoshi for his help in the design of the cavity and C. Pardini for his help in performing the measurements. We are also grateful to H.D. Schwarz for the information given on the work done for the PEP II RF system.

REFERENCES

- [1] "An Asymmetric B-Factor based on PEP" Conceptual Design Report, LBL PUB-5302, SLAC 372.
- [2] U. Laustroer, U. van Rienen and T. Weiland, "URMEL and URMEL-T User Guide", DESY M-17 03 (1987).
- [3] M.S. Zisman et al., "ZAP User's Manual", LBL-21270 (1986).

Field Emitted Electron Trajectories for the CEBAF Cavity*

Byung C. Yunn and Ronald M. Sundelin
Continuous Electron Beam Accelerator Facility
12000 Jefferson Avenue, Newport News, VA 23606, USA

Abstract

Electromagnetic fields of the superconducting 5-cell CEBAF cavity with its fundamental power coupler are solved numerically with URMEL and MAFIA codes. Trajectories of field emitted electrons following the Fowler-Nordheim relation are studied with a numerical program which accepts the URMEL/MAFIA fields. Emission sites and gradients are determined for those electrons which can reach the cold ceramic window either directly or by an energetic back-scattering. The peak and average impact energy and current are found. The generation of dark current by field emitted electrons has also been studied, and its relevance to CEBAF operation is briefly discussed.

I. INTRODUCTION

There are two principal reasons for interest in studying trajectories of field emitted electrons and of energetic back-scattered electrons. One would like to know what emission sites and gradients can result in electrons reaching the cold ceramic window. There have been several instances of breakdown of this window at CEBAF when rf powered. A speculation that field emitted electrons might be the cause of this damage has provided an initial motivation to this study. It is also interesting to find out under what conditions field emitted electrons could be accelerated the full length of the accelerator and constitute a halo to the beam. Some of the experiments planned at CEBAF require only a few nA beam currents. Depending on the circumstances, dark currents could become a detrimental noise source to such experiments, if not eliminated before reaching the experimental halls.

II. TRACKING ELECTRON TRAJECTORIES

As an analytical treatment of trajectories of field emitted electrons from the cavity surface is almost impossible, we decided to study them numerically. The trajectory of an electron under the influence of external electromagnetic fields is followed numerically providing information on the position and the momentum of the electron at any given instant. When an electron collides with the cavity surface made of niobium, a large fraction of incident energy may be carried away by a back-scattered electron. At the same time, secondary emission from the surface is responsible for low energy electrons with energies typically less than 50 eV. Those electrons are also followed until all particles generated are processed. The computer code we developed for this purpose is based on the Mulpac program^[1], although most subroutines have to be rewritten to adapt to

the change of input files now prepared with the electromagnetic field codes, URMEL and MAFIA instead of LALA. Particle pushing is also simplified adopting the Runge-Kutta method of order four. The Adams fourth-order predictor-corrector algorithm was used in the Mulpac code. We find it more expedient to improve on accuracy, if necessary, by reducing the size of a fixed time step rather than dynamically adjusting the step size constantly by correcting the prediction of the Adams-Bashforth four step method with the Adams-Moulton three step algorithm. Mulpac's back-scattering and secondary emission routines, however, remain unchanged. Presently, boundary checking routines for a portion of a structure, which require M3 generated mesh data, are to be tailor-made for each specific problem.

III. CALCULATION OF FIELDS

Electromagnetic fields excited in the CEBAF cavity powered from a klystron are calculated with the computer codes URMEL and MAFIA^[2]. The properties of resonant modes of the 5-cell CEBAF cavity without the fundamental power coupler (FPC) were estimated with URMEL in detail^[3], with a good agreement to measured data^[4]. For the operating π mode, some URMEL results are: frequency is 1492.85 MHz, R/Q is 964.77 Ω/m , the ratio of peak surface electric field to the gradient is 2.24 found near the irises.

The FPC is located at the beam tube 3.17 cm away from an end-cell. It consists of two rectangular waveguides of different widths, 13.44 cm and 7.90 cm respectively, but of the same height of 2.54 cm. External Q of the cavity is adjusted by varying the location of the transition from narrow-width to wide-width waveguide. The input coupling goes through a minimum as the waveguide transition is moved. The FPC breaks the cylindrical symmetry of the structure requiring a 3-D code to investigate this cavity-waveguide coupled system. A further complication is that the resonant mode of interest is above the TE_{10} cutoff frequency, which is at 1115.19 MHz. The proper position of a waveguide short, necessary in any frequency domain code, is determined to be at a location 20.70 cm from the cavity centerline, which is a quarter-wavelength away from the detuned short. A consistency check on the numerically computed fields is based on the following observation. The ratio of the peak electric energy density in the FPC to the peak electric stored energy density in the center of the cavity cell is measured to be nearly independent of both the coupling strength and of the passband mode. For the π mode at a nominal Q_{ext} of 6.6×10^6 , the reported value of this ratio is 0.0282. As it turns out to

*Supported by D.O.E. contract #DE-AC05-84ER40150.

be impractical to solve the whole 5-cell cavity-FPC structure, we divide the problem into two: a 5-cell cavity with the axial symmetry and one end-cell plus the FPC coupled system. An input to the trajectory program is then constructed with the MAFIA fields for the FPC including the section of beam pipe attached to the end cell, and the URMEL fields for the 5-cell cavity.

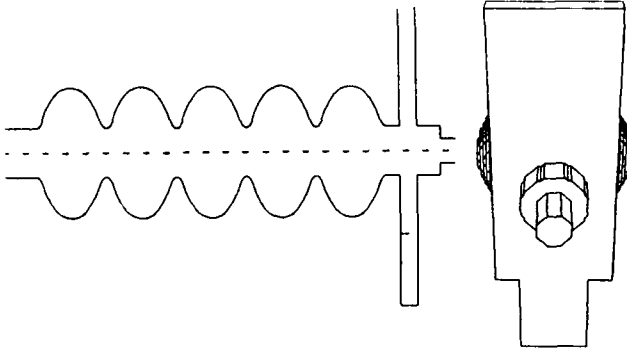


Figure 1. Cross-sectional view of 5-cell CEBAF cavity with the FPC and the front view of the FPC.

It is to be mentioned that higher order mode couplers also break the axial symmetry of the 5-cell cavity, further contaminating the fundamental mode with higher order modes. However, these effects are much weaker, and we neglect their presence for the study reported in this paper.

IV. RESULTS

The theory of field emission mechanism formulated by Fowler-Nordheim^[5] describes the quantum mechanical tunneling of electrons through the modified potential barrier at the surface of a metal in a high external electric field. The field electron emission current density J in A/m² is given by

$$J = \frac{1.54 \times 10^6 (\beta E_{\text{surf}})^2}{\phi} \exp\left(-\frac{6.83 \times 10^3 \phi^{1.5}}{\beta E_{\text{surf}}}\right)$$

where E_{surf} is the surface electric field in MV/m, β is the surface field enhancement factor, and ϕ is the work function of the metal surface in eV. We note that $\phi = 4$ eV for niobium. For the present study, we assume a well processed cavity with $\beta=100$ and scan the cavity surface for field emission at accelerating gradients of 3, 5, and 10 MV/m. The emission from a given site is normalized to a total dissipated power of 1 W for primary electrons, which determines the emitting area A_E in m². In other words, $A_E \int J(\theta) E_{\text{kin}}(\theta) d\theta = 2\pi$ W, where $J(\theta)$ is the current density determined with the instantaneous field at rf phase θ , $E_{\text{kin}}(\theta)$ is the impacting energy of the electron emitted at that phase, and the integration runs from 0 to π or π to 2π depending on the location of the site in the cavity. Average impact energy is determined by $\int J(\theta) E_{\text{kin}}(\theta) d\theta / \int J(\theta) d\theta$, and peak energy can be read directly from the output. It turns out that there are two classes of emission sites. One class of emission sites is completely self-contained and can be neglected for the purpose

of this study. Also, the nature of π mode is evident in the emerging pattern of trajectories in the remaining sites. Finally, we also note that we have looked at the trajectories of primary and energetically back-scattered secondary electrons only. Our assertion that a given site can not produce electrons landing at a certain location should be understood with such restriction in mind.

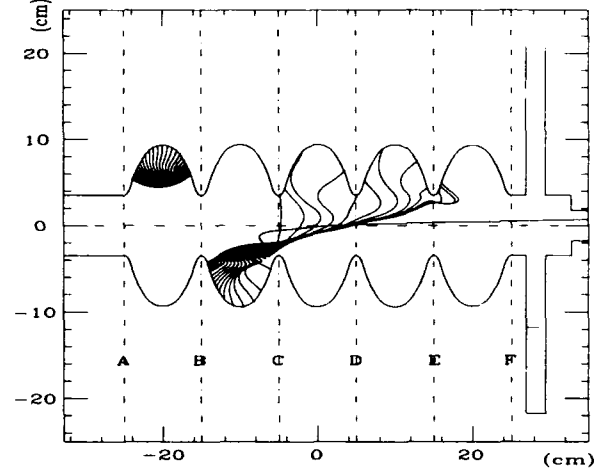


Figure 2. For the gradient range of 3 to 10 MV/m, electrons emitted from the vicinity of A, B, C, D, E, and F only can move to other parts of the cavity, and could in some cases become a dark current. Sample trajectories shown are for 10 MV/m gradient.

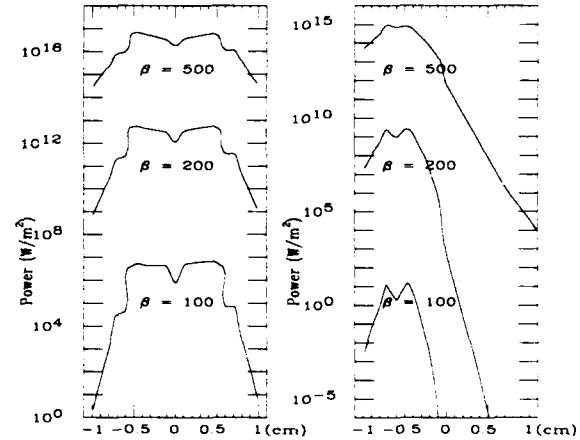


Figure 3. Total dissipated power depends strongly on β ; left figure for emission sites near C, and right for sites near F.

A. Electrons Which Can Hit the Cold Window

We find that there are very few emission sites from which electrons can strike the window directly. There are several sites on the short beam pipe section between the end cell and FPC which actually can emit electrons which reach the ceramic window, but the surface field there is below the level we require for an emission site to be of any significance ($E_{\text{surf}} = 3, 5, \text{ and } 10$ MV/m for $E_{\text{acc}} = 3, 5, \text{ and } 10$ MV/m, respectively). In the case of 10 MV/m gradient, we find five emission sites, which may possibly be direct hit sites, and electrons from there can travel beyond 5 cm from the beam axis into the FPC. We note that

the window is located at 7.9 cm from the beam axis. For lower gradients of 3 and 5 MV/m, only two sites are found in each case. Emission characteristics of those sites are summarized below in Table 1.

Table 1. Possible direct hit sites

Site (cm)	E_{kin} (keV)	J (A/m ²)	$\Delta\theta$ (°)	A_E (m ²)	E_{surf} (MV/m)
10 MV/m					
C-0.5969	672	1.12	0.1	2.18×10^{-5}	19.6
D-0.5969	92	2.13	0.5	1.3×10^{-5}	20.0
D+0.8034	94	1.19×10^{-15}	2.5	1.03×10^{-3}	8.98
D+0.8825	118	5.19×10^{-18}	2.0	1.17×10^{-2}	8.27
E-0.4696	157	0.69	0.25	4.01×10^{-5}	19.3
E+0.7243	92	8.94×10^{-13}	10.0	3.51×10^{-4}	10.0
5 MV/m					
E-0.1174	33	7.60×10^{-14}	0.1	1.74×10^6	9.62
F-0.3522	32	2.82×10^{-24}	4.0	4.59×10^{17}	6.63
3 MV/m					
E-0.3522	25	0	0.1	∞	6.09
F-0.4696	16	0	0.5	∞	4.23

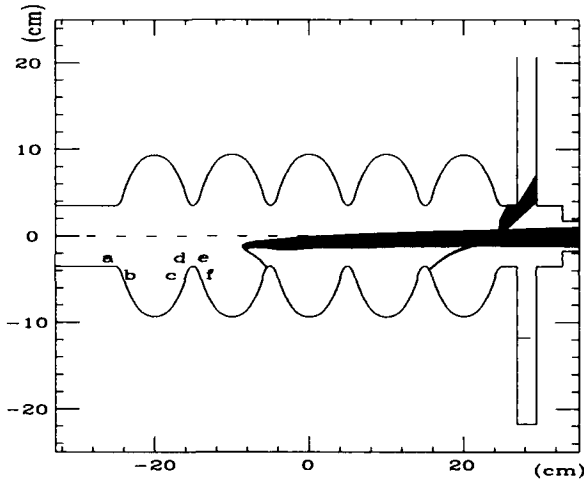


Figure 4. Two field emission sites which contribute to the electron loading of the ceramic window, and to the generation of dark currents, respectively, are shown.

For back-scattered electrons, the impact energy and current of secondary electrons are calculated in a Monte Carlo approach. We notice that each emitting area around noses can further be divided into four subregions (two subregions near A and F). Electrons from two of those subregions (e.g., d and f in Fig. 4) move in general direction toward the FPC side, while field electrons emitted from the remaining two subregions (c and e in Fig. 4) propagate to the opposite end of the cavity. For a given β we also find that the emission from the site d (and from the equivalent site of other cells) is the dominant source of impact power on the window due to the fact that the primary electrons from such a site are produced at the rf phase near 90° at the maximum acceleration. Interesting parameters of back-scattered electrons crossing the window are listed in Table 2 for a few selected emission sites. We note that Table 2 is constructed from trajectories with the cavity

gradient of 10 MV/m.

Table 2. Back-scattered electrons

Site (cm)	E_{kin}^{peak} (MeV)	E_{kin}^{avg} (MeV)	I^{peak} (μA)	I^{avg} (μA)	A_E (m ²)
A+0.5969	4.07	2.55	4.78×10^{-6}	3.25×10^{-6}	0.521
B-0.4696	3.78	2.37	6.50×10^{-5}	1.26×10^{-5}	1.71×10^{-6}
C-0.4696	1.97	1.14	4.17×10^{-3}	1.75×10^{-3}	1.93×10^{-7}
D-0.4696	1.47	0.805	2.43×10^{-3}	2.43×10^{-3}	1.55×10^{-7}
E-0.4696	0.759	0.406	0.443	0.243	4.01×10^{-5}
F-0.4696	0.323	0.168	1.06×10^{-2}	1.03×10^{-2}	6.79×10^{-2}

B. Dark Currents

We find that almost every emission site near A, B, C, D, E, and F is a potential source of dark currents with electrons transported out of the cavity when emitted at a proper phase. All possible emission sites have been identified. However, in this report we concentrate on the emission site # 175, to be identified with the site C-0.4696 in Table 2, for the case of 10 MV/m gradient (a factor of 2 above design gradient). This site turned out to be one of the strongest sources of field emission for the CEBAF cavity. Electron trajectories from this site moving parallel to the beam axis are shown in Fig. 4. We find that electrons emitted at phases between 105 and 111° can form a bunch with bunch length = 12.6 ps, energy = 3.32 MeV, energy spread (rms) = 52.7 keV, bunch charge = 0.03 fC, and angular spread (half width) = 14.5 mrad. Half beam width of 1 cm at the narrow beam pipe is required for trajectories which form the bunch. Transverse phase space at this point has a slope of 1.5 mrad/mm and an angular offset of 14.5 mrad. Average current is estimated to be 45.6 nA when $A_E = 1.93 \times 10^{-7}$ m² is used. This indeed can cause a significant background problem to Hall B experiments, if transmitted. However, it is expected that forward moving field emitted currents from the linacs will be intercepted at the spreaders (and backward currents at the recombiners, respectively) because of low energy acceptance of less than one percent level of such beam transport modules. On the other hand, dark currents from injector cryomodules need to be stopped at the injector chicane. The effectiveness of transport elements in blocking dark current transmission merits further study.

V. REFERENCES

- [1] I. Ben-Zvi, J. F. Crawford, and J. P. Turneare, *IEEE Trans. Nucl. Sci.* NS-18, 166 (1971).
- [2] R. Klatt et al., *Proc. 1986 Linear Accelerator Conf.*, 276 (1986).
- [3] B. C. Yunn, "URMEL/URMELT Study of the CEBAF/CORNELL Cavity," unpublished.
- [4] J. C. Amato, "Summary of HOM measurements to date," Cornell Univ. LNS report, SRF-831002 (1983).
- [5] R. H. Fowler and L. Nordheim, *Proc. R. Soc. London* A119, 173 (1928).

Study on TESLA Cavity Shape*

Donglin Zu, Jia-erh Chen

Technic Physics Department, Peking University

Beijing 100871, P. R. of China

Abstract

A new 9-cell cavity shape is designed for TeV Superconducting Linear Accelerators (TESLA). The ratio of the maximal Surface electric field to the accelerating gradient, E_{pk}/E_{acc} , was lowered down to 2.024 in the center cell while the cell to cell coupling is 1.95% for the 1.3GHz accelerating mode. The properties of the higher order modes were investigated with a "dissipated band model".

Introduction

At this time in the development of superconducting RF accelerating cavities, the accelerating gradient is limited by two phenomena, electron field emission and thermal breakdown. The first of these makes it imperative to choose a cell shape that minimizes E_{pk}/E_{acc} and the second phenomena to minimize H_{pk}/E_{acc} . As field emission is the dominant gradient limitation, there is considerable premium in lowering E_{pk}/E_{acc} . The cell to cell coupling (k) is also effected by the shape.

The concept of multicell cavity

As everyone know, for the standing-wave modes, the multi-cell cavities behave like weakly coupled oscillators. When going from a single-cell cavity to a multicell cavity with n cells, one single-cell mode splits into n different multi-cell modes, each of which has a slightly different frequency in a "passband" and a different phase shift Φ between different cells. The q th mode eigen frequency ω_q and its longitudinal electric field $E_n(q, t)$ in the n th cell can be expressed as following formula respectively:

$$\omega_q = \omega_0 \times (1 + k(1 - \cos \alpha_q))^{1/2} \quad (1)$$

$$E_n(q, t) = E_0 \sin\left(\frac{2n-1}{2} \alpha_q\right) \cos \omega_q t \quad (2)$$

Where k is the cell to cell coupling. The E_0 is the maximum of longitudinal electric field. The α_q is the phase shift.

$$\alpha_q = q \cdot \frac{\pi}{n} \quad (q = 1, 2, \dots, n) \quad (3)$$

The cell to cell coupling k could be indicated as following:

$$k = \frac{f_\pi^2 - f_{\pi/n}^2}{2f_{\pi/n}^2 - (1 - \cos \frac{\pi}{n})f_\pi^2} \quad (4)$$

The f_π is the π mode frequency, in which adjacent cells oscillate with the opposite phase. Apparently, π mode is just the accelerating mode. The $f_{\pi/n}$ is called "in phase" mode frequency. As n goes to infinity, the $\alpha_1 = \pi/n$ mode becomes a

$\alpha_1 = 0$ mode. Sometime one also likes to use term $\Delta f/f$ indicating the size of dispersion. It is defined as following:

$$\frac{\Delta f}{f} = \frac{2(f_\pi - f_{\pi/n})}{f_\pi + f_{\pi/n}} \quad (5)$$

Searching for a new cell shape

The goal of searching for a cell Shape is following:

1. $E_{pk}/E_{acc} \rightarrow 2$, cell number $\rightarrow 9$;
2. cell to cell coupling k in the TM010 mode $\geq 1.8\%$;
3. Tolerable Q_{ext} in all HOMs with couplers on the beam pipe.

Five independent variables describes a "CSC" (circle — straight — circle) type cell shape:

OR: cell outer radius;

IR: beam tube radius;

R1: curvature radius at iris;

L: length of half cell;

TD: degrees inclination of wall.

The L is determined by the frequency as the particles to be accelerated must be kept in phase with the RF oscillation. The TD is held in 79° in consideration of stability mechanically. This leaves three parameters to explore. Because each of the three parameters affects the fundamental mode frequency, our strategy is adjusting the IR as well as R1 for a certain OR value to obtain the right frequency 1.3 GHz.

According to our knowledge, the LEP 4-cell shape has the minimum in OR, R1 and IR and Cornell 10-cell TESLA1 shape has the maximum if they all are scaled to 1.3GHz. We try to choose a shape between the two set of extreme parameters. We found that it was important to keep the resonant frequency nearly equal to 1.3GHz in order to get the true E_{pk}/E_{acc} . We also found that the IR nearly is proportional to the OR when R1 and TD keep invariant while TM010 frequency is kept at 1.3GHz, as show in figure 1.

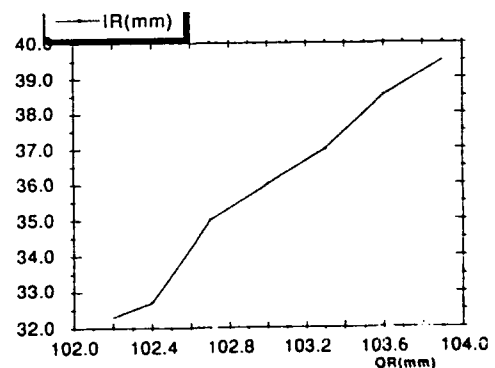


Fig. 1. Relationship between IR and OR when keeping 1.3 GHz resonant frequency of fundamental mode @1.3GHz and R1=10mm, TD=79 degree

* supported by the National Science Foundation on China

In URMEL^[1], the term NPMAX is the maximum of number of mesh points. D. Proch and our experience tell us E_{pk}/E_{acc} is strongly a function of NPMAX as well as mesh density ratio D/d , as show in Figure 2 and Figure 3.

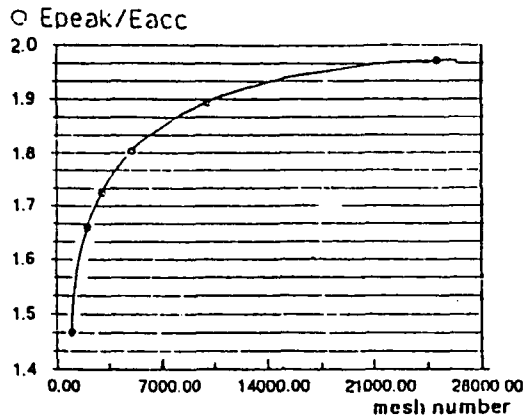


Fig. 2 The E_{pk}/E_{acc} of a single cell sc cavity as a function of mesh number.

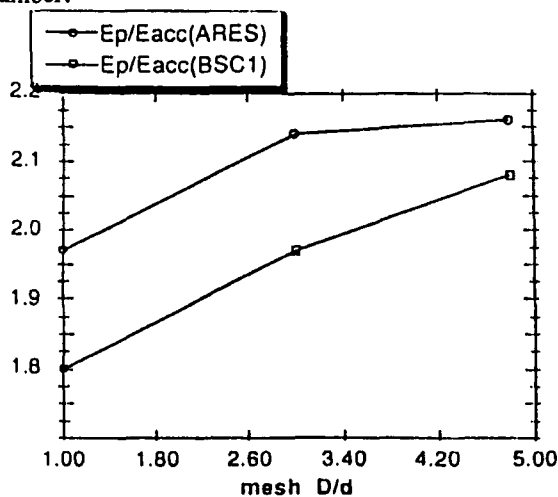


Fig. 3. The E_{pk}/E_{acc} of two single cell SC cavity as a function of mesh density ratio D/d .

The true E_{pk}/E_{acc} must be calculated with 25000 Mesh points. It seems difficult to get a shape with $E_{pk}/E_{acc}=2.0$ and $k \geq 1.8\%$ for a "CSC" type cell.

We try a "CSE" (circle-straight-ellipse) type cell. The A_2 and B_2 are the semi-axis length of ellipse at iris at y and x directions respectively. The others are the same as that of "CSC" type. Eventually we found a shape with $E_{pk}/E_{acc}=2.024$ and $k=1.95\%$ for a 9-cell structure. Figure 4 shows the cell shape named BT shape.

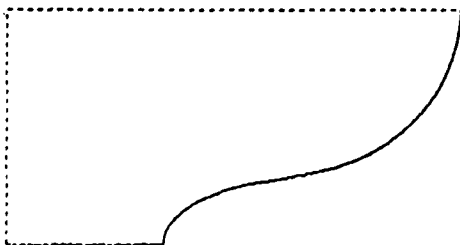


Fig. 4. BT cell shape

properties of accelerating mode of BT cell Shape

We have re-calculated the cell shape of Cornell TESLA^[2], KEK TESLA1 and LEP 4-cell with single in cell. The table 1 compares the properties of the fundamental mode of BT cell shape with that of the others. The data of Saclay and DESY TESLA shape (in designing) come from D. Proch. All of them are scaled to 1.3GHz.

Computer tuning of BT cavity

We tune the 9-cell BT cavity by changing the end half cell length with URMEL, 25000 mesh points. Fig. 5 shows the half cavity input and the tuning curves. The field flatness ($\Delta E_z/\bar{E}_z$) is nearly 0.028. The tuning sensitivity is 2880 Hz per micrometer.

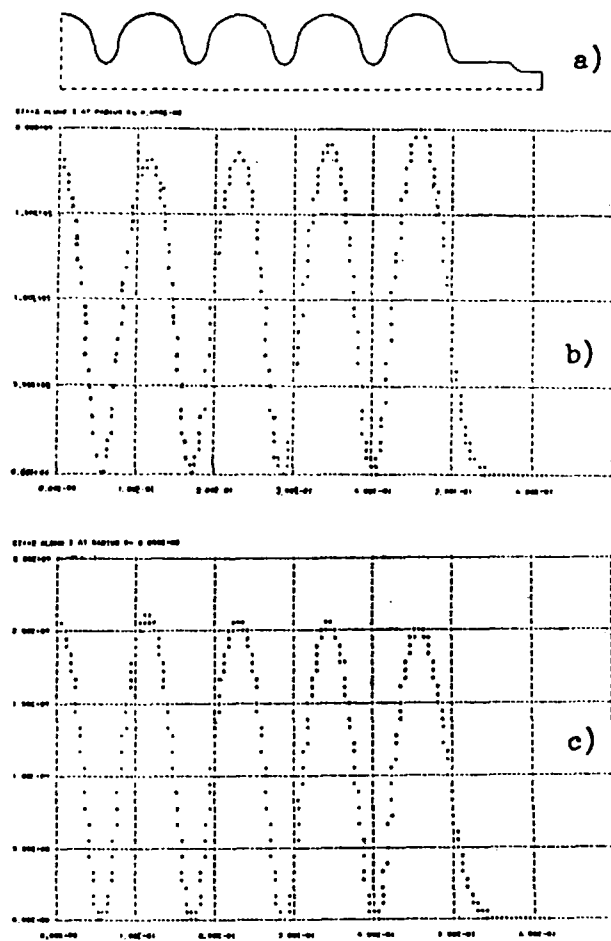


Fig. 5. (a) Input shape of 9-cell BT structure for URMEL. (b) tuning curve when $L=5.27\text{cm}$, (c) tuning curve when $L=5.28\text{cm}$.

TM monopole HOMs of BT cell shape

We calculated the half-cell E field pattern of the BT shape and LEP 4-cell shape. The spreads of the higher order monopole modes of the two structures scaled to 1.3GHz are showed in Figure 6. The BT shape likes as LEP shape, has no mode passband overlap of the longitudinal mode and therefore

no true multicell trapped modes results from the mode mixing.

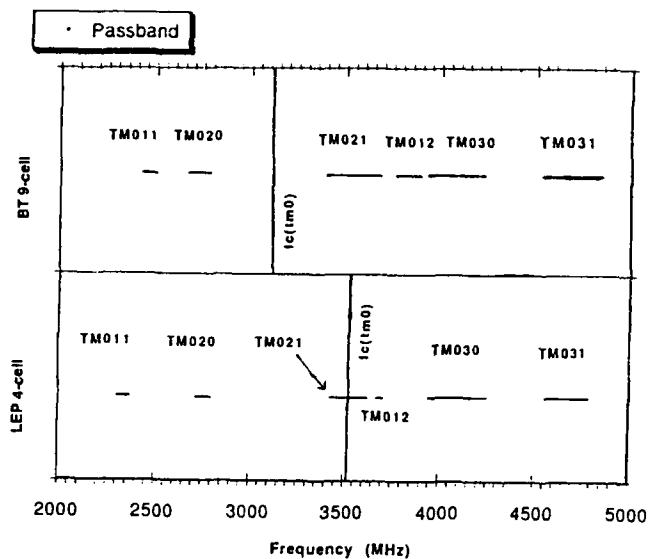


Fig.6. The spreads of the six higher order longitudinal modes for the BT cell shape and the LEP cell shape.

Conclusion

Fig. 7 Shows the geometry and dimensions of the 9-cell BT structure ($A2=32$, $B2=16$).

Although the dispersion diagrams, R/Q and Q_{ext} of the first 80 monopole modes of the structure and the first 50 monopole modes of LEP 4-cell structure were examined with URMEL-T using 'dissipated band model'^[3] developed by W. Hartung for comparison purpose. They still need to be examined with I-V method^[4]. However it seems to be a promising TESLA shape candidate.

Acknowledgement

Thanks are due to H. Padamsee and W. Hartung for their guidance and giving SHAPE, SUMURM programs and D. Proch for his parameter list and helpful discussions.

Table 1; Comparison of various TESLA Shape (LEP is non TESLA)

	LEP	Cornell	KEK1	KEK2	Beijing	Saclay	DESY
Numbers of cells	4	10	9	9	9	9	9
Requator (mm)	102.2	109.0	104.15	103.3	103.6	102.2	103.3
Riris (mm)	32.67	40.9	40.0	38.0	35.8	32.31	35.0
NP MAX in URMEL	20000	20000	20000	25000	25000	25000	25000
Hpk/Eacc (Oe/(MV/m))	39.33	54.30	49.86	43.10	42.91	39.70	41.70
cell to cell coupling $k(\%)$	2.0	1.8	1.22	2.66	1.95	1:42	1.85
$R/Q (\Omega)$ per cell	121.48	90.96	112.12	108.00	110.87	124.33	115.22
Epk/Eacc	2.359	2.054	2.039	2.220	2.024	2.000	2.070
type of structure	CSC	CSC	SCSCS		CSE	CSC	CSC
Trapped monopole modes under 3 times of fund. frequency	no				no		

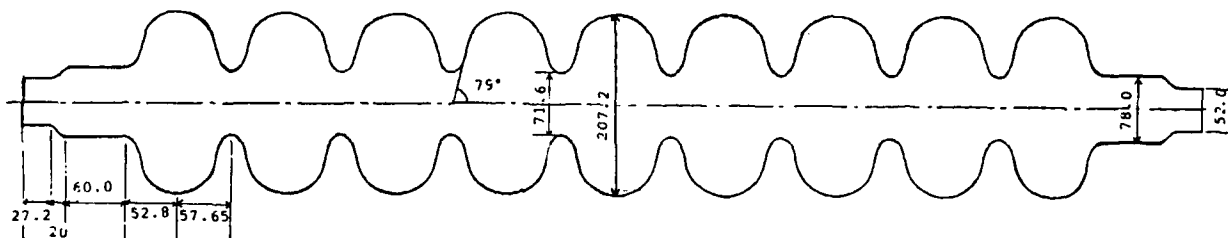


Fig.7. Geometry and dimensions of 9-cell BT superconducting accelerating structure.

References

- [1] T. Weiland, Nuclear Instruments and Methods, 216, 329 (1983)
- [2] H. Padamsee et al, "A New Shape Candidate for a Multicell Superconducting Cavity for TESLA" CLNS 90-985
- [3] W. Hartung "Optimum number of cells for an accelerating structure" SRF-890621/4, Cornell University.
- [4] A. Mosnier, "The trapped modes in a multicell SC cavity", proceeding of the 1st TESLA workshop, 1990

Regulation Loops for the Ring Magnet Power Supplies in the SSC Accelerator Complex

Eugenio J. Tacconi[†] and Carlos F. Christiansen^{*}
Superconducting Super Collider Laboratory*
2550 Beckleymeade Avenue, MS 4004
Dallas, Texas 75237

Abstract

The SSC complex consists of five cascaded accelerators; the linear accelerator (linac) and four synchrotrons: the low energy booster (LEB), the medium energy booster (MEB), the high energy booster (HEB) and the collider. Twelve or twenty-four pulse phase-controlled SCR power supplies are used for energizing the ring magnets. Each power supply has a voltage loop designed to regulate the voltage applied to the magnets. The voltage regulation loops for these synchrotrons and the current regulation for LEB are analyzed in this work. The digital voltage regulator is fiber-optic isolated from the power converter. It has a closed-loop bandwidth of 150 Hz with band rejections for 60 Hz and 120 Hz perturbations. The LEB has a very precise current regulation system composed by a feedforward compensator, a fast feedback regulator and a slow synchronous regulator. The current regulation design is corroborated by computer simulations.

I. INTRODUCTION

The SSC basic design goal is to collide beams of oppositely-directed protons at 20-TeV energy. A cascade of accelerators provides protons at successively higher energy into the following accelerator. Protons are brought to 0.6 GeV in a linear accelerator. Following that are three booster synchrotrons: LEB which accelerates to 11 GeV in a 0.54 km circumference ring of magnets; MEB, which accelerates to 200 GeV in a 3.96 km ring; and HEB, which accelerates to 2 TeV in a 10.9 km ring. The collider itself consists of two vertically separated rings, each a 20 TeV proton accelerator 87 km in circumference. The LEB and MEB are synchrotrons using room temperature magnets; while the HEB and collider use superconducting magnets cooled to liquid helium temperature.

The magnet current has to be regulated with a tolerance of a few parts in 10^6 (ppm) in all synchrotrons' magnets. This high current accuracy is obtained by using a fast voltage regulation loop and a slow current regulation system. The dynamic behavior is improved by using feedforward compensation, while adaptive techniques are needed to achieve long term stability. Both, voltage and current regulation systems, are described in the following sections.

^{*} Operated by the Universities Research Association, Inc., for the U.S. Department of Energy under Contract No. DE-AC35-89ER40486.

[†] On leave from Leici, UNLP, Conicet, Argentina

II. VOLTAGE REGULATION

Twelve or twenty-four pulse power supplies are inserted into the ring for energizing the ring magnets. The number and ratings of the power supplies are as follows:

LEB, three twenty-four pulse power supplies, 2000V, 4000A
MEB, ten twenty-four pulse power supplies, 2000V, 5200A
HEB, four twenty-four pulse power supplies, 1000V, 7000A
COLLIDER, forty twelve pulse power supplies, twenty 200V, 7000A and twenty 40V, 7000A.

Each power supply has its own voltage loop and output passive filter. The voltage loop is designed to have a high frequency response and its main function is to regulate the voltage applied to the magnets. It must follow a predetermined voltage reference related to the current reference, rejecting line voltage changes, offset errors and other voltage perturbations. Due to bandwidth limitations, the voltage loop only rejects voltage perturbations up to 120 Hz while the output filter rejects the ripple at 360 Hz and other higher frequency perturbations [1].

The design of the digital voltage regulator is similar in all ring magnet power supplies. The block diagram of the voltage loop is shown in figure 1.

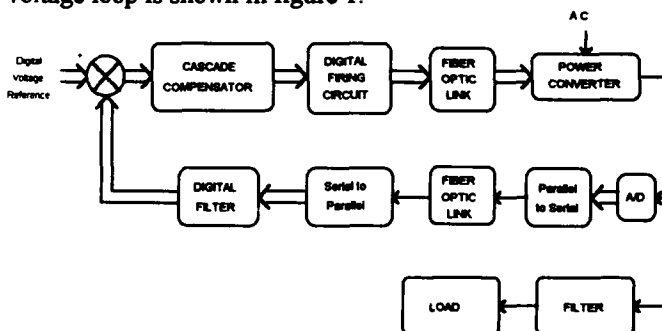


Figure 1, Block Diagram of the Digital Voltage Loop

A distributed grounding system is used in the magnet string. The power supplies voltage to ground changes from one synchrotron to another and is also depending on the synchrotron operating condition. The worst case is in LEB where an electrical isolation of 7.5 kV is required. In order to obtain this high voltage isolation, optical links are used in the voltage regulation for firing the power converter thyristors and to monitor the output voltage (Figure 1). A 12 bit A/D converter digitizes the power converter output voltage at a frequency rate higher than 50 kHz. The 12 bits digitized voltage is serial transmitted across the fiber-optic link. The

optical receiver is followed by a digital filter which calculates the voltage mean value at a frequency rate of 1440 Hz.

The error between voltage reference and voltage feedback goes through a digital cascade compensator that also operates with the 1440 Hz clock. The compensator has an integral action with very high dc gain and two passband filters at 60 Hz and 120 Hz respectively. The compensator also includes a linearizer to compensate the non-linear transfer function of the power converter.

The digital firing circuit is basically an open loop system with a single 60 Hz PLL. It presents a high frequency bandwidth, having a time resolution better than 0.1° .

The voltage loop feature includes a bandwidth of 150 Hz with more than 20 dB rejection to 60Hz and 120Hz perturbations. The ripple at 720/1440 Hz and other higher frequency perturbations are rejected by the output passive filter.

A prototype of the digital voltage regulator has been developed and tested, with good results, in a twelve pulse phase-controlled SCR power supply.

III. CURRENT REGULATION

The period of the magnet current waveforms ranges from 0.1 second for LEB up to about 24 hours for collider. A current regulation tolerance of a few parts in 10^6 is required in all synchrotron magnets and in some cases (MEB - Collider) a precise tracking between bending magnets and quadrupoles or between sectors is also required. In order to satisfy these requirements, different regulation schemes, including feedforward, feedback and adaptive techniques are used. In fast cycling synchrotrons (LEB, MEB) the emphasis is made in obtaining a good dynamic behavior, while in the slower superconducting magnets (HEB, Collider) the main current regulation problems are related to long term stability and noise and ripple reduction. Among the different ring magnet current regulation loops, only the current regulation design for LEB 10 Hz biased sinewave operation mode is described in this paper.

The LEB magnet system consists of 48 dipoles and 90 quadrupoles connected in series circuit. The power system has to operate in either of two modes: 10 Hz biased sine wave and linear ramp. For 10 Hz biased sinewave operation, dipoles and quadrupoles magnets resonate with 12 distributed capacitors [2]-[4]. The capacitors are bypassed by a 40 mHy choke to provide a path for the d-c component of the magnet current. For the linear operation mode, the twelve resonant banks are short-circuited. Three 24-pulse SCR phase-controlled power supplies are inserted into the ring to produce both current waveforms.

The maximum and minimum current flowing through the magnets has to be regulated, in both modes, within 50 ppm of the actual current. A typical required magnet current waveform for the 10 Hz biased sinewave mode is shown in figure 2. For satisfying this requirement, a current

regulation system with a high open-loop gain at dc and 10 Hz is necessary.

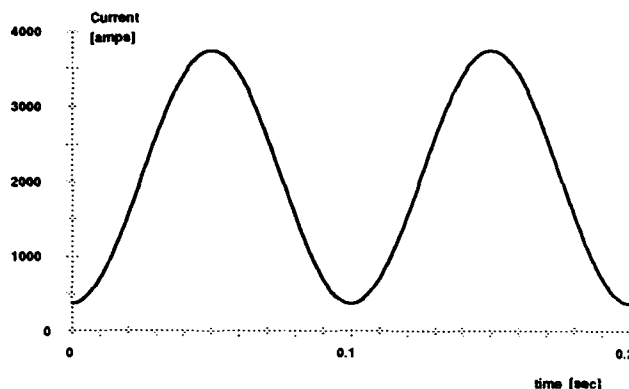


Figure 2. Magnet Current Waveform
10 Hz Biased Sinewave mode

A high open-loop gain at 10 Hz with adequate closed-loop stability can not be simultaneously fulfilled by using a conventional regulator. The regulation problem has been solved by combining feed-forward compensation and conventional feedback regulation with frequency conversion techniques.

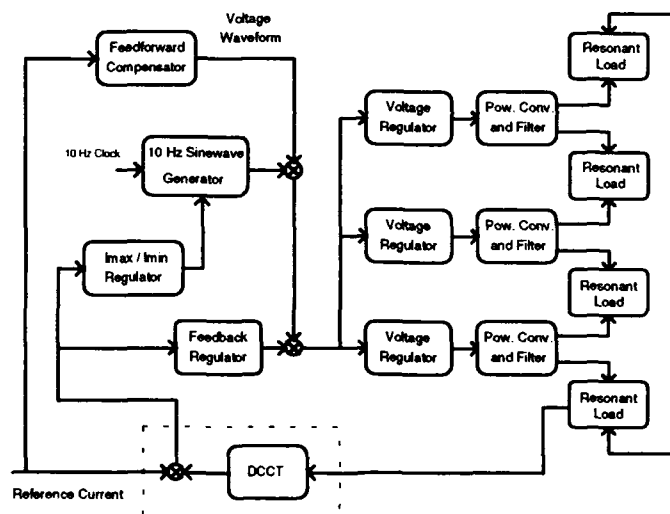


Fig. 3. Block diagram of the current loop
10 Hz. Biased Sinewave mode

The schematic diagram of the current loop is shown in figure 3. The central computer provides the maximum and minimum current values while the 10Hz biased sinewave current reference, synchronized with the utilities, is locally generated.

The magnet current is measured with a very precise Zero-Flux DC Current Transducer (DCCT). An analog differential amplifier with a gain of 30 amplifies the difference between the current reference and the magnet

current. A 18 bit D/A converts the digital reference current while a 16 bit A/D digitizes the differential amplifier output. D/A, A/D converters and the differential amplifier are built inside the DCCT in a temperature regulated chamber with a precision of 0.01°. The same current measuring system is used for both LEB operation modes; while at least two high precision DCCTs were required in a former current regulation design [5].

The digital current regulator is fully digital operating at a frequency rate of 1440 Hz. It is composed by a feedforward compensator, a feedback regulator and a synchronous I_{\max}/I_{\min} regulator. The voltage reference is generated by adding the outputs of the three regulation blocks. The three ring magnet power supplies are driven by the same voltage reference.

Feedforward Compensator

The feedforward compensator provides the necessary voltage for having a current flowing through the magnets that equals the reference current. This voltage waveform is also a biased sine wave calculated considering the load in perfect resonance. A feedforward system is an open-loop compensation unable to correct current perturbations. It has to be usually complemented with a feedback system.

Feedback Regulator

For designing the feedback loop, the load characteristic has to be fully understood. The voltage loop has a bandwidth of 150 Hz and the output passive filter is basically a second order, critically damped, low-pass filter with a resonant frequency of about 130 Hz. The admittance of the resonant load is represented in frequency domain in figure 4.

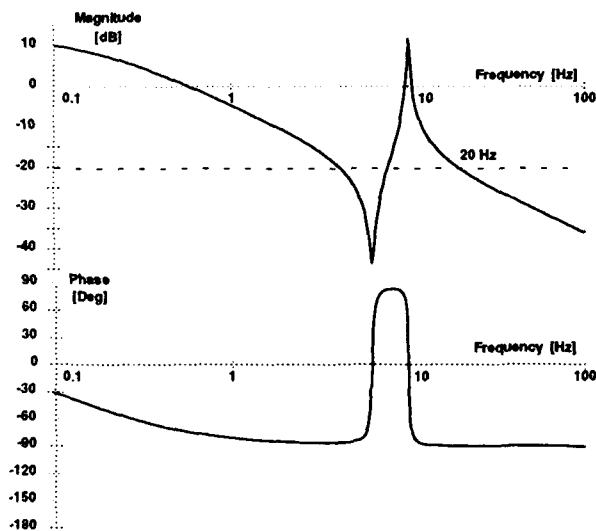


Figure 4. Magnitude and phase frequency response of the load admittance

The feedback regulator has been designed with a proportional cascade compensator with a total gain of 20 dB. This additional gain is indicated in dotted line in figure 4. The feedback loop is stable, having a closed-loop bandwidth of 20 Hz. Considering that the phase introduced at 20 Hz by the voltage loop and passive filter is less than 30°, a 60° phase margin is obtained. The feedback loop has a gain of 30 dB at dc and 10 Hz. This gain is not enough to satisfy the regulation requirements. The gain at low frequencies can be increased using integral action but the gain at 10 Hz cannot be substantially increased, using standard techniques, without reducing the phase stability margin.

Synchronous Regulator

The basic idea of the synchronous regulator is to take advantage of the periodicity of the reference current. The current error is measured during one signal period and the correction is synchronously and gradually applied during the following periods. In this way, an equivalent high gain at 10 Hz can be obtained while limiting the closed-loop bandwidth of the synchronous regulator to less than 1 Hz.

The high gain in the low frequency band is easily obtained by integrating the mean value of the error signal (dc). The integrator gain has been calculated for having a correction bandwidth of 0.6 Hz.

Frequency conversion techniques are used for obtaining high gain at 10 Hz. The residual 10 Hz sine wave on the error signal is detected in amplitude (ac component only) and integrated. The output of this integrating amplifier modulates the amplitude of a synchronized sine wave.

The first step to design the a-c amplitude regulation loop is to obtain a mathematical model of the system including detection and modulation processes. The block diagram of figure 5 will be used for this purpose.

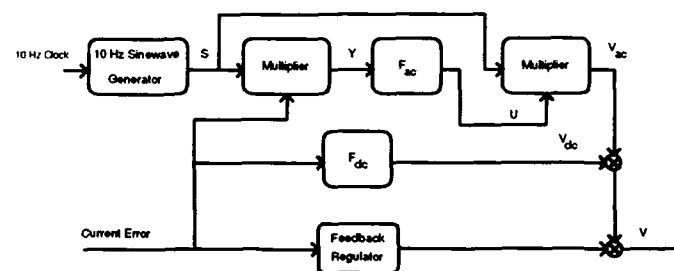


Fig. 5. Block diagram representing the detection and modulation process

In the above figure, the signal demodulation has been implemented with a synchronous or a linear phase detector [6]. In fact, as the carrier frequency is available, this efficient method for amplitude or phase detection can be readily implemented. The ac and dc components of the error signal are filtered with the integrating amplifiers F_{ac} and F_{dc} respectively.

$$F_{ac} = \frac{K_{ac}}{s} \quad F_{dc} = \frac{K_{dc}}{s} \quad (1)$$

The amplitude modulation and detection are nonlinear processes that can be handled by the Laplace transform using s-plane convolution [7]. The same structure employing a multiplier excited by the 10 Hz sine wave is used in figure 5 for implementing both, modulation and detection processes.

Denoting the Laplace transform of $e_{ac}(t)$ and $u(t)$ by $E_{ac}(s)$ and $U(s)$, the transform of both products can be expressed by the following s-plane convolutions.

$$U(s) = \frac{1}{2\pi j} \int S(\lambda) \cdot E_{ac}(s - \lambda) \cdot d\lambda \quad (2)$$

$$V_{ac}(s) = \frac{1}{2\pi j} \int S(\lambda) \cdot U(s - \lambda) \cdot d\lambda \quad (3)$$

Both convolution integrals are readily evaluated by taking residues at poles of $S(\lambda)$. Neglecting high frequency components, the transfer function of the ac synchronous regulator can be approximated by

$$\frac{V_{ac}(s)}{E(s)} \cong \frac{K_{ac}}{2} \cdot \frac{s}{s^2 + \omega_o^2} \quad (4)$$

Thus, the transfer function of the equivalent feedback regulator can be expressed by

$$\frac{V(s)}{E(s)} = K_p + \frac{K_{dc}}{s} + \frac{K_{ac}}{2} \cdot \frac{s}{s^2 + \omega_o^2} \quad (5)$$

where K_p represents the proportional gain of the feedback regulator.

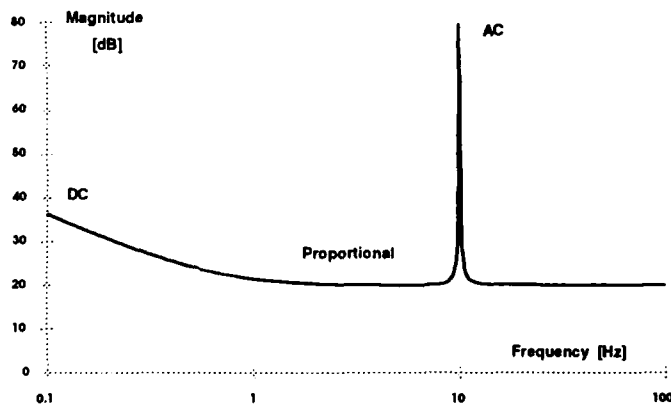


Figure 6. Magnitude frequency response of the equivalent feedback regulator

The frequency response of the equivalent feedback regulator is represented in figure 6 using the following constant values: $K_p=10$, $K_{dc}=40$, $K_{ac}=160$. The effect of the proportional feedback regulator as well as the ac and dc components of the synchronous regulator can be easily identify in figure 6. Using equation (5), the transfer function of the total open-loop feedback regulation can be calculated. Its frequency response is represented in figure 7.

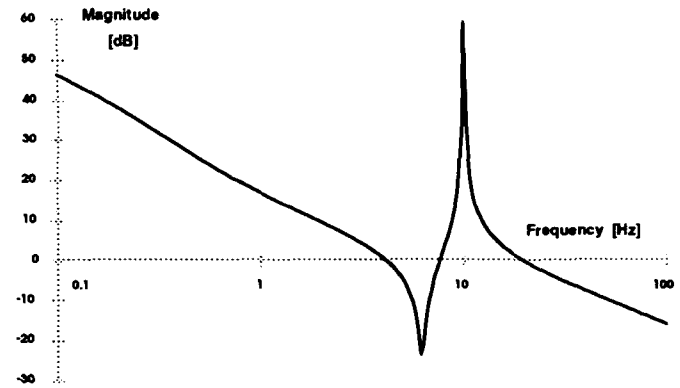


Figure 7. Magnitude frequency response of the total open-loop feedback regulation

Comparing figures 4 and 7, the improvement of the synchronous regulator is apparent. The 20 Hz closed-loop bandwidth, controlled by the proportional constant K_p , has not been modified. The system is stable, the phase margin has been reduced in only 6° (equation (5)) and the equivalent open-loop gain at dc and 10 Hz has been dramatically increased. The constant values K_{dc} and K_{ac} have been chosen for having a correction bandwidth of 0.6 Hz for both, dc and 10 Hz components.

IV. SIMULATION RESULTS

The linear phase detector of figure 5 has been replaced, in figure 3 and in the computer simulations, by a timing circuit and two sample and hold. The timing circuit generates sample pulses synchronized with the maximum and minimum of the magnet current. Two sample-and-hold circuits measure the current error at the maximum and minimum points. Thus, this measuring system works in a similar way as a synchronous detector but has a different d-c gain. In fact, if the error signal is a non-biased sinusoid with amplitude \hat{I} and the same frequency and phase of the carrier signal $s(t)$, the difference between maximum and minimum sample-and-hold outputs will yield a d-c component of amplitude $2\hat{I}$. Under similar conditions, the output of a linear phase detector would be $\hat{I}/2$. The addition of the maximum and minimum sample-and-hold outputs is proportional to the error signal bias and is used to drive the dc regulator. The dynamic behavior of the feedforward compensation and the

feedback regulation is shown in the simulation results of figures 8 and 9.

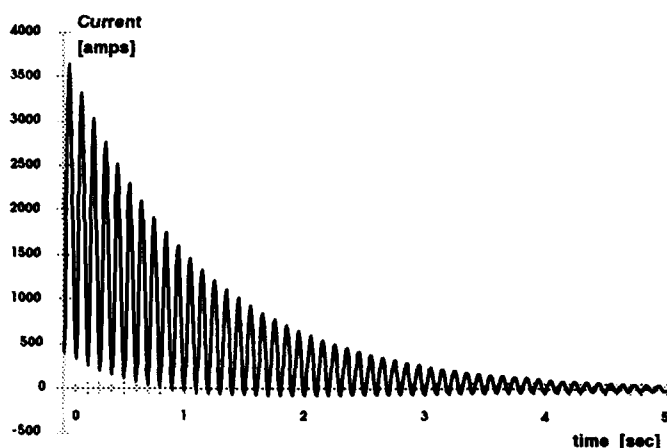


Figure 8. Difference between reference and magnet current by using feedforward compensator

The time domain response of the feedforward compensator is shown in figure 8. At the time origin, the feedforward compensator is connected while the feedback and the synchronous regulator remain disconnected. The reference current waveform is as shown in figure 2. The figure shows that if a good model of the plant is available, due to the action of the feedforward compensator, the current error goes to zero in a few seconds.

Due to changes in the load, specially in the resonant capacitors, a good model of the load is not always available. In the following simulation the feedforward compensator output has a 10% error in the dc value as well as in the sinewave amplitude. The feedback regulator has a fast response (20 Hz bandwidth) and reduces the residual dc and ac current errors by a factor of 30.

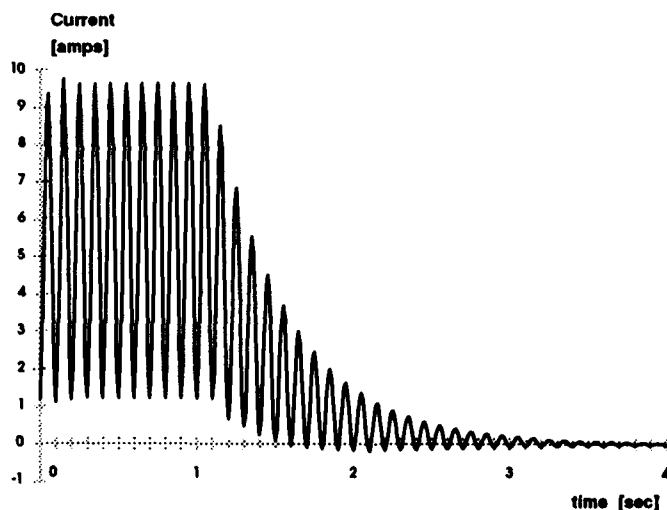


Figure 9. Difference between reference and magnet current by using feedback synchronous regulator

In the first part of figure 9, a 10% error feedforward compensator and the feedback regulator are in steady-state. At a time of 1 sec, the ac/dc synchronous regulator is connected. The figure shows that the residual current error goes to zero with a constant time, for both ac/dc components, of about 0.25 sec, corresponding to a bandwidth of 0.6 Hz.

V. CONCLUSIONS

The analysis and design of the digital voltage regulation for all ring magnet power supply as well as the current regulation system for biased sinewave current mode of LEB have been presented.

Conventional feedforward and feedback techniques are not enough to maintain the magnet current within the required tolerance. A synchronous feedback regulator based on the periodicity of the current waveform has been used to improve the current regulation performance. The current regulation design has been corroborated by computer simulations. The prototype of the described digital current regulator is still under development.

VI. REFERENCES

- [1] E. Tacconi. "LEB Ring Magnet Power Supply System, Voltage and Current Regulation Design", *SSC Laboratory SSCL-N-785*, January (1992).
- [2] J. R. Sanford and D. M. Matthews, "Site-Specific Conceptual Design of the Superconducting Super Collider", *SSC Laboratory, SSCL-SR-1056*, July (1990).
- [3] C. Jach, "Switchable 10Hz/1Hz LEB Magnet Power Supply System", *Conference Record of the 1991 IEEE Particle Accelerator Conference*, Vol. 2, pp. 816-818.
- [4] C. Jach, R. Winje, E. Tacconi, R. Harold and K. Smedley. "Low Energy Booster Main Magnet Power Supply System", *Proceedings of the 1992 Third European Particle Accelerator Conference*, Vol. 2, pp. 1438-1440.
- [5] E. Tacconi, C. Jach and R. Winje. "10 Hz resonant LEB magnet power supply system, current regulation design", *Conference Record of 1992 IEEE Nuclear Science Symposium and Medical Imaging Conference*, Vol. 2, pp. 1018-1022.
- [6] P. Horowitz and W. Hill, "The art of Electronics", Cambridge University Press, (1989).
- [7] W. R. LePage, "Complex Variables and the Laplace Transform for Engineers", New York, Dover Publications, (1980).

HIGH POWER CW KLYSTRODE® AMPLIFIER FOR 267 MHz

M. B. SHRADER, D. H. PREIST AND R. N. TORNOE
VARIAN POWER GRID TUBE PRODUCTS
301 INDUSTRIAL WAY
SAN CARLOS CA 94070

ABSTRACT

A 250 KW CW 267 MHz Klystrode has been designed and built as part of a major program in conjunction with the Chalk River National Labs (CRNL), Chalk River, Ontario, Canada. The high CW power design has evolved from previous work for UHF television and the SDI program. A major step was taken on this program to simplify and reduce the complexity of the RF input circuit. CW power in excess of 250 KW and efficiencies in excess of 70% were readily obtained with power gain in excess of 21 dB. Three tubes and associated circuitry were tested and delivered as part of the effort.

INTRODUCTION

Klystrode® technology has continued to expand both in UHF TV service and in the high power accelerator field. The basic Klystrode operating principles are now well understood and accepted in the U.S., and their application is expanding overseas. The operating principles have been described in numerous publications by the authors and others. REF [1]-[9]. The Klystrode depends upon density modulation of an electron beam at the cathode by a control grid and acceleration of the bunched beam into an output cavity. These simple basics have survived for over a decade and continue to make possible unique compact highly efficient UHF RF power sources at many different power levels and frequencies.

CRNL PROGRAM

In September of 1989 Varian Power Grid Tube Products entered into an agreement with Atomic Energy of Canada Ltd. (AECL) to design, develop and produce three 267 MHz, 250KW CW Klystrodes. The Klystrodes were to be delivered to CRNL and used to drive a test accelerator. This program, which was partially supported by the U.S. SDI Organization, represented the first effort at obtaining high CW power (>50KW CW) from a Klystrode. The program was also the first to have as an objective the study of the suitability of CW Klystrodes as accelerator drivers without the use of isolators between the source and accelerator cavity.

Previous to this program the highest power Klystrode developed was a 500KW peak 50KW average power 425 MHz Klystrode sponsored by SDI and Los Alamos National Labs (LANL) under Contract No. 9-XSD-7840D-1 REF [9]. This tube, which met or exceeded the contract goals, served as the basis for the design and the procurement specification for the new 250KW CW 267 MHz Klystrode.

OBJECTIVES OF THE PROGRAM

Power Output - CW:	250KW
Operating Frequency:	267 MHz
Efficiency:	70%
Beam Voltage:	65 KV
Beam Current:	5.5A
Power Gain:	20 dB Min.
Tuning Range:	±2 MHz
Bandwidth 3 dB:	±1 MHz

TUBE DEVELOPMENT

The development plan involved scaling the existing 425 MHz LANL/SDI Klystrode REF [9] downward in frequency and upwards by a factor of 5 in average power handling capability. The plan called for using the identical electron gun from the 425 MHz tube, scaling the input and output cavities to the proper frequency and designing a new and much larger collector to handle the CW power.

Fig. 1 is a photo of the complete tube, gun, output cavity and collector: dramatic evidence of the compactness of the 250 KW Klystrode when compared to a 3-story high klystron which would be required for the same power and frequency.



FIG 1
250 KW Klystrode

INPUT CIRCUIT PROGRAM

Testing of the complete amplifier system began in the summer of 1991. The output circuit of the 250KW Klystrode is a simple single tuned cavity similar to those used on high power klystrons. The input circuit was scaled in frequency from the 425 MHz SDI tube and from the EIMAC UHF TV Klystrode manufactured by Varian. The input circuit relied on a folded coaxial cavity which was designed to present the proper phase and amplitude RF voltages between the grid and cathode, to furnish the RF drive, and the proper phase and amplitude voltage between grid and accelerating anode to permit stable operation. Depending on these phase and amplitude relationships, the input circuit could either be regenerative or degenerative with stability depending on how the coaxial lines were tuned.

In TV service and in the 425 MHz Klystrode, this basic design has worked well giving good power gain and long term stability. On the CRNL program at 267 MHz the input circuit turned out to be a different story. It was soon discovered that a Ferrite isolator between the driver Klystrode and final amplifier was required to secure any degree of stability.

A fresh look at the input circuit was started as a parallel program in January of 1992 while testing of the HPA continued with the original circuit. A strip line mockup of a totally different approach was tested using a Klystrode gun tester which was built during the 425 MHz SDI program. The circuit involved a simple tuned circuit between grid and cathode and a novel means for handling the RF circuit between grid and accelerating anode. The details of this breakthrough in Klystrode circuit technology will be the subject of another paper.

Fig. 2 shows the new input circuit (square box) assembled on the high power Klystrode with lead shielding, magnetic coil and tube stand. Overall height of the complete amplifier is 72".

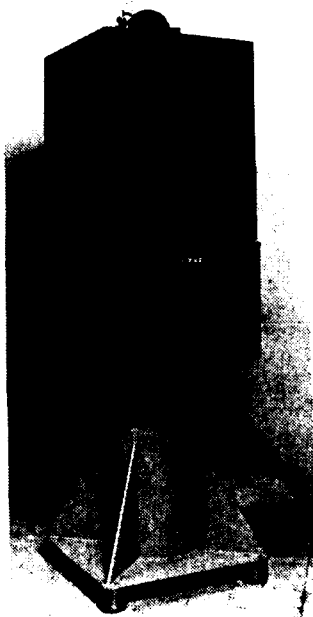


FIG 2
New Input Circuit
Assembled on Klystrode

TEST RESULTS

The test procedure followed a pattern of starting with low duty pulsing, and as the tube aged in and the proper loading and tuning were accomplished, the pulse length and repetition rate were increased until CW conditions were reached. Pulsing the low level drive stages and frequency sweeping made it relatively easy to monitor and adjust all of the tube and circuit parameters with little risk to the High Power Amplifier (HPA). Since one of the prime objectives of this program was to operate the HPA into an accelerator cavity without the use of an isolator, an output cavity sampling loop was installed internal to the tube. The purpose of the loop was to monitor the output cavity gap voltage, and through suitable control circuitry adjust the drive to the system to compensate for varying loads presented to the HPA. The data for the loop is presented; its effectiveness has yet to be determined when the HPA is coupled to the accelerator cavity.

Fig. 3 shows how the probe voltage varies with power output. Power output and beam current versus drive are also shown. Good linearity with no discontinuities or instability has been repeatedly demonstrated.

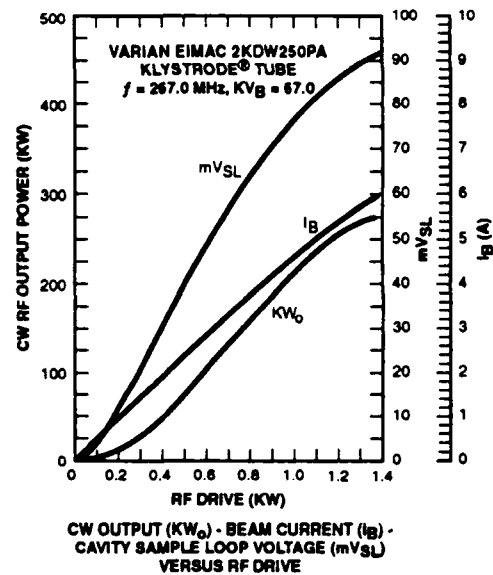


FIG 3

Figs. 4 shows overall bandwidth of the HPA. The ± 1 MHz 3 dB requirement was exceeded. Fig. 5 is a plot of output phase change versus RF output. An 80% change in power output gives only a 25° phase change. Fig. 6 shows phase change versus a VSWR and phase angle of the load for VSWR of 1.5.

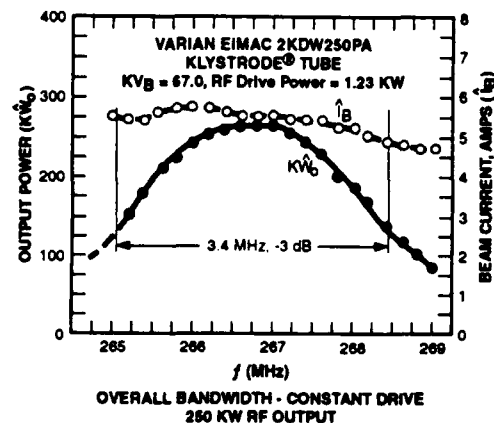


FIG 4

CW powers in excess of 280 KW were measured and efficiencies of 72-74% were readily obtainable. Power gain in all cases was greater than 21 dB. CW testing also included operating the amplifier into a 1:5 VSWR load with the phase of the load adjusted to present the highest and lowest impedance to the amplifier. Under these conditions 235 KW and 260 KW CW were obtained. The test was repeated with VSWR of 3:1 and 70 to 62 KW CW measured.

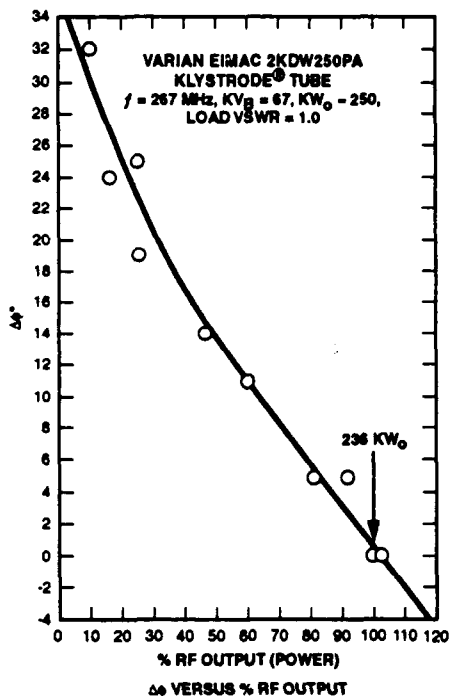


FIG 5

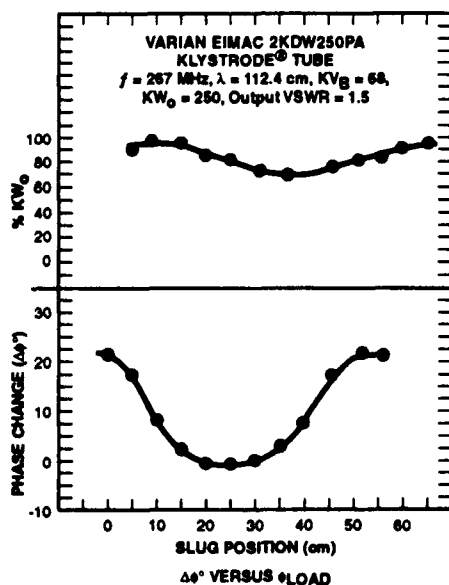


FIG 6

Normal operating beam voltage for 250 KW CW is 65-67 KV. The cavity and tube were high voltage processed to 100 KV and tested at 85 KV. This was accomplished with air insulation thus eliminating the need for oil or SF₆. A 24-hour burn-in run was successfully completed at the 250 KW CW level.

CONCLUSION

Klystron technology has come a long way in the past decade, and the successful completion of this project has demonstrated that there is no technical reason why Klystrons cannot generate high CW powers with excellent efficiency and reliability. The 250 KW CW Klystron developed on this project points the way for the next logical step of 1 MW CW. The frequency of operation at this power level could be from 100 MHz to 800 MHz depending upon the need. The 70-74% efficiencies obtained give an attractive base for further increases in efficiencies by coupling Klystron technology with multiple output cavities and/or multiple-stage depressed collectors. 80% efficiency and 1 MW CW would certainly be an appropriate target for the next step.

REFERENCES

- [1] D. H. Preist and M. B. Shrader, "The Klystron®--An unusual transmitting tube with potential for UHF-TV," Proc. IEEE, vol. 70, no. 11, Nov. 1982.
- [2] ---, "Klystron® TV amplifier performance at UHF," Rep., EIMAC-San Carlos, CA., 1984.
- [3] ---, "Recent developments in Klystron® technology," Varian/EIMAC Rep., presented at the 14th Int. TV Symp., Montreux, Switzerland, also in Symp. Rec. (Broadcast Sessions), 1985.
- [4] G. M. Badger, "The Klystron®, a new high-efficiency UHF-TV power amplifier," Varian/EIMAC in NAB Proc., 1985.
- [5] M. B. Shrader and D. H. Preist, "Compact high efficiency, light weight 200-800 MHz high power RF source," presented at the Particle Accelerator Conf., May 1985.
- [6] M. Shrader, D. Preist and B. Gaiser, "Pre-bunched beam devices--Efficient sources of UHF and microwave power," reprinted from IED Meet., Washington, DC, Dec. 1985.
- [7] N. Ostroff and A. Whiteside, "Using Klystron® technology to create a new generation of high efficiency UHF-TV transmitters," in Proc. NAB Show 1986.
- [8] M. P. Chase and D. H. Preist, "A new 15KW air cooled Klystron®," Varian/EIMAC Rep., presented at the 15th Int. TV Symp., Montreux, Switzerland, also in Symp. Rec. (Broadcast Sessions), 1987.
- [9] D. H. Preist, M. B. Shrader, "A high-power Klystron® with potential for space application," IEEE Transactions on Electron Devices, vol. 38, no. 10, Oct. 1991.
- [10] D. H. Preist U.S. Patent No. 4,527,091, Density Modulated Electron Beam Tube with Enhanced Gain, July 2, 1985.

April 1993

DEVELOPMENT OF MULTIMEGAWATT KLYSTRONS FOR LINEAR COLLIDERS

G. Caryotakis, R. Callin, K. Eppley, T. Lee, K. Fant, R. Fowkes,
H. Hoag, C. Pearson, R. Phillips, S. Tantawi, A. Vlieks, E. Wright
Stanford Linear Accelerator Center, Stanford, CA 94309 USA
E. Lien, Los Altos, CA
G. Miram, Atherton, CA.

Abstract

A number of experimental klystrons have been constructed and evaluated at SLAC, KEK and INP, aiming toward output power objectives of 100 and 120 MW at 11.4 GHz (SLAC and KEK respectively) or 150 MW at 14 GHz (INP), with pulse lengths on the order of 1 μ s. Since rf breakdown is considered to be the principal mechanism limiting power for such tubes, most of the effort has been concentrated on the design of output circuits that reduce rf gradients by distributing fields over a longer region of interaction. Another klystron component receiving emphasis has been the output window, where the approach for future tubes may be to use a circular TE₀₁-mode, half-wave window.

Best results to date in this continuing international effort are: 50 MW with 1 μ s pulses, using a traveling-wave output circuit (SLAC and INP), and 85 MW with 200 ns. pulses (SLAC), using two conventional reentrant, but uncoupled, output cavities. At KEK a klystron with a single, but not reentrant, cavity has produced 80 MW in 50 ns pulses. Finally, Haimson has demonstrated 100 MW at 50 ns with a traveling-wave output. This paper addresses primarily the work performed at SLAC during the last two years.

I. THE PROBLEM

A future electron-positron collider, if it operates at X-Band, will require approximately 2000 klystrons at the 100 MW level, for a center-of-mass energy of 0.5 TeV. For 1 or 1.5 TeV, which are top energies that physicists would like to build into the design of such a machine, the number of tubes becomes so large that economics would force consideration of sources with powers of more than 100 MW per unit. Such sources may have to be different from conventional klystrons. Research on other devices is in progress at various institutions.

The conventional klystron (with some form of extended interaction output) appears to offer the most direct, and probably the most economical approach to the 100 MW level for several reasons: The peak power has already been demonstrated, the necessary manufacturing processes are standard, and the klystron is a high gain, stable, sturdy tube, capable of high average powers. There are two remaining problems: Producing 100 MW at the required pulse length, which in current SLAC collider designs is 1.5 μ s; and finding an alternative focusing system for an electromagnet, since its DC power con-

sumption is prohibitively expensive, given the number of tubes in the machine.

The magnetic focusing issue is not serious. Superconductivity provides a solution, and beyond that, there is reason to hope that periodic permanent magnet focusing (PPM) can be made to work for these tubes.

The principal problem is the pulse length in combination with high peak power. In a well-designed klystron with good beam optics and little beam interception, the vulnerable areas will be the windows and the output circuit. Windows have in fact accounted for most of the experimental klystron failures at SLAC. The weakness is in the metallized and brazed joint between the ceramic window and its copper sleeve. There is a solution, however, described later. The major remaining hurdle is in the output circuit which must develop high gradients in order to extract energy from the bunched beam and may cause breakdown in vacuum.

To avoid very high gradients, interaction between circuit and beam must take place over an extended space, rather than the usual short gap in a reentrant klystron cavity. Such extended interaction circuits, however, whether of the standing or traveling wave variety, are large compared to wavelength and capable of supporting unwanted modes or resonances. Some of these may be trapped if they do not couple well to the output waveguide. When excited they can develop very high fields and cause oscillations or, if they are of the dipole variety, steer the beam into the drift tube. These effects may not manifest themselves unless the beam pulse is long enough, due to high Q's and long filling times, in some cases appearing 200 ns or more after the onset of the pulse.

The work at SLAC has been focused on the study of various output circuit alternatives, the objective being to minimize rf gradients while maintaining good interaction efficiency. In parallel with this effort, various types of output windows have been evaluated in a resonant ring.

II. EXPERIMENTAL KLYSTRONS

Results on the first three experimental klystrons built at SLAC were reported at this conference two years ago. Subsequently, the basic klystron was redesigned, with new optics and provisions for re-using a tube, by switching output circuits. Five tubes were built with this configuration. The gun for these tubes has a microperveance of 1.8 and an area convergence of 100. It is not intended for extended service and has both high cathode current loading and high gradients. Beam parameters for the XC series of tubes are listed in Table I.

*Supported by Department of Energy contract
DE-AC03-76SF00515.

Table I: Beam parameters for XC series of SLAC klystron

Voltage (kV)	440
Microperveance	1.8
Tunnel Diameter (cm)	0.953
Filling Factor (nominal)	0.65
Solenoid Field (kG)	5.7

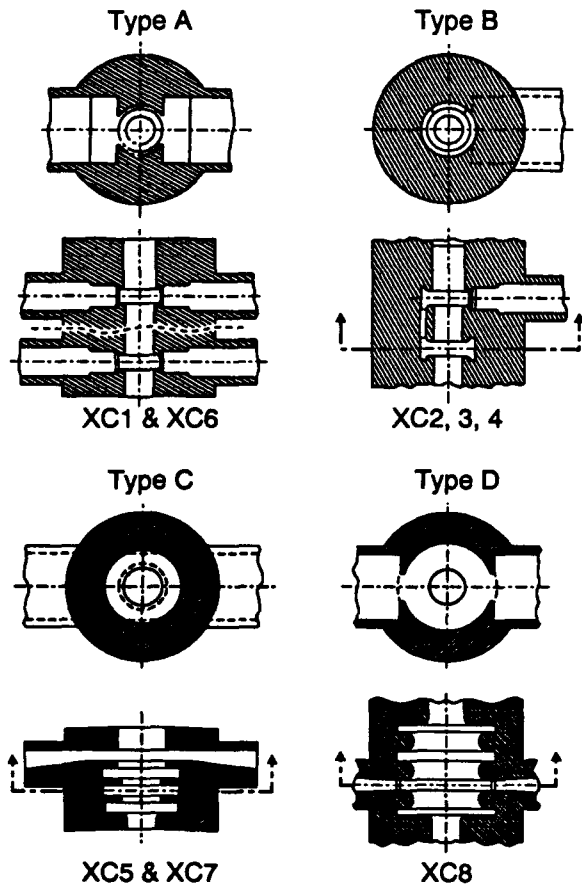


Figure 1. Five types of output circuits tested by SLAC in XC series.

The klystrons built in this program to date have been designated XC1 through XC8. All tubes in the XC series were equipped with two output waveguides and two output windows, except for the XC6 klystron which used four waveguides and windows.

III. OUTPUT CIRCUITS

Five types of output circuits have been tested and are shown in Fig. 1. Representative results for each type of circuit are shown in Fig. 2.

The basic strategy in the development of output circuits is to reduce rf gradients immediately next to the beam, while preserving a high degree of overall coupling between beam and

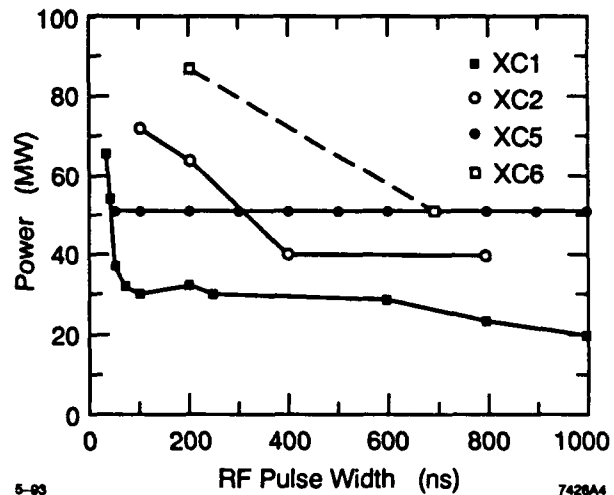


Figure 2. Effect of pulse width on achievable peak power.

circuit. The approach has been to apply standard klystron or traveling-wave tube design formulae, and analyze candidate circuits for R/Q, coupling coefficient and surface gradients using SUPERFISH and MAFIA. Subsequently, large-signal interaction between beam and circuit is investigated with either one-dimensional disk models or two-dimensional particle-in-cell codes. In the early stages of the program, the latter were not available except for the simpler varieties of standing-wave circuits, but now it is possible to simulate both standing and traveling-wave circuits with either CONDOR or MAGIC.

A single reentrant cavity (Fig. 1, Type A) in XC1 produced less than 20 MW without pulse breakup at a full microsecond. The tube failed because of a broken window, but a post-mortem showed severe erosion of the output cavity drift tube tips. The cavity interaction gap was 0.5 cm long and 0.95 cm in diameter. The calculated gradient at the gap (for 100 MW output) was 1 MV/cm. Clearly, that was excessive.

More recently in the program the XC6 klystron used two uncoupled Type A cavities with much better results. The spacing and tuning of the cavities was adjusted by CONDOR simulation to divide the output power equally between the two cavities. Actual tests showed good agreement with theory in both power distribution and predicted efficiency as seen in Fig. 3. This klystron failed because of gun arcing before testing was completed. It also produced 50 MW at a pulse length of 700 ns and could conceivably have been processed to the same or longer pulse length at 86 MW. Power from the four waveguides was measured independently. A complete test of the tube would have included combining the power from the two cavities in two Magic-Ts, but the gun failure prevented further tests. XC6 will be rebuilt.

Output circuits of the B type (2π transit angle between two inductively coupled cavities) were used in three klystrons. Two of these are still in use as power sources. A third, XC4, was built with no windows and integral loads in order to test the power limits of the circuit without window failures. The circuit

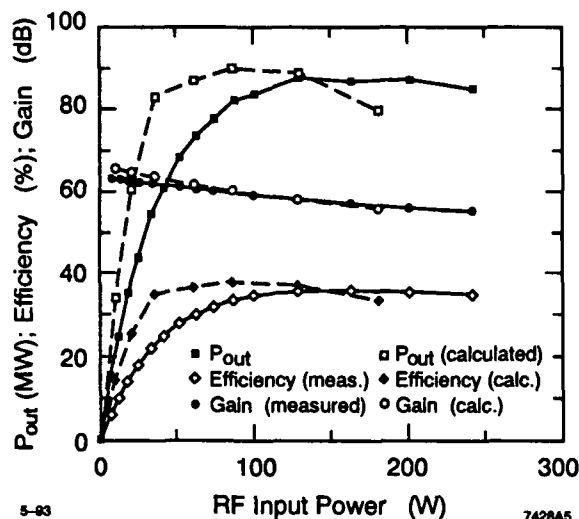


Figure 3. Comparison of computed and measured performance of XC6—two uncoupled output cavities (200 ns pulses, 60 pps).

failed at approximately the 40 MW, 1 μ s level and was found to be badly damaged in the iris coupling the two cavities.

The XC5 klystron employed a Type C traveling-wave output. This disc-loaded circular waveguide circuit operated in the $2/3\pi$ mode, but at the time of its design only one-dimensional simulations were possible. These predicted good efficiency but provided no detail on either matching conditions or surface gradients. This klystron produced 52 MW at 1 μ s (29% efficiency) with excellent stability and no pulse breakup. It was lost because of an open cathode heater. The tube was rebuilt with a modified output, using four, rather than three cells prior to the waveguide coupler. This circuit was not as successful; although its efficiency was comparable, it could not be operated at the longer pulse lengths, conceivably because of a trapped mode.

Standing-wave disk-loaded waveguide circuits, operate in the π -mode with thick disks and large iris openings (Type D). The result is a very low R/Q and low surface fields in the vicinity of the beam. Because of the low R/Q, the optimum loaded Q is relatively high (about 100) which, together with the large separation between the 0 and π modes due to the large irises, results in little mode mixing. Calculated surface fields at 100 MW are on the order of 350 KV/cm at the entrance and exit of the circuit and 850 KV/cm at the middle iris tip.

IV. WINDOW DEVELOPMENT

In the early stages of the program the windows used were thin circular ceramic wafers, approximately 0.8 mm thick, coated with titanium nitride. These windows had the virtue that they were very wide-band and largely free of ghost modes, thus reducing the risk of trapping modes in the output circuit, or the window itself. They were found to be very fragile, both in resonant ring tests and in the tubes themselves. They were replaced with 0.43 wavelength windows (TE11 mode, 3.7 mm thick). All klystrons tested in the latter stages of the program

employed these windows. They are not reliable with longer pulses and have failed in resonant ring tests as well. In one such test the onset of failure was recorded with a TV camera, making it obvious that the eventual discharge which fractured the window originated at a hot spot on the periphery, at the maximum field point.

The SLAC design for the RF feeds in the linear collider calls for 7.5-cm TE01 waveguides connecting klystrons to pulse compressors and to the accelerator. A very compact and very efficient WR-90-to-circular waveguide transition has been developed for this purpose. It is planned for use in future klystrons, together with a half-wave TE01 window. We expect a single window of this type to operate well at full peak power and pulse length.

V. KLYSTRON DEVELOPMENT IN JAPAN AND RUSSIA

The klystron development program at KEK (and Toshiba) parallels the work at SLAC. The approach differs in that the micropervance used is 1.2 instead of 1.8, but future work at SLAC will also be performed at lower pervance. The output circuit used is a single TM01 cavity, with no reentrancy, but with a longer transit angle than the reentrant cavities in SLAC klystrons. The calculated gradient for this cavity at the 120 MW output level is 720 KV/cm. This klystron is reported to have produced 80 MW with 50 ns pulses, at an efficiency of 30%.

There are no recent results reported from the Russian klystron effort at Novosibirsk and Protvino. The Russian frequency is 14 GHz, and the previously published performance of their very advanced klystron (grid-modulated, PPM focused, traveling-wave output) was 55 MW at 700 ns.

VI. FUTURE PROGRAM AT SLAC

The XC8 klystron will be the last of the experimental klystrons at SLAC aiming at the 100 MW level with a micropervance 1.8 beam. The next klystrons will be 50 MW, 1.5 μ s sources for the NLCTA (Next Linear Collider Test Accelerator), which requires four klystrons. They will operate at the same voltage (440 KV) as the XC series, but at a micropervance of 1.2, so the transition to the new design will not involve too many new parts. The first tube in the series will use a 3-cell π -mode standing wave circuit (Type D) and a TE01 window. An improved, CONDOR validated, traveling-wave backup design exists. The first tube, XL1, should be tested in August. Shortly after that it is expected that a PPM version of the XL1 will be built and tested.

A new modulator is being constructed at SLAC for the purpose of eventually continuing the 100 MW program at a micropervance of 1.2 and 550 KV. This phase should begin when the tubes required by the NLCTA are delivered.

CEBAF's New RF Separator Structure Test Results*

Reza Kasimi, J. Fugitt, A. Krycuk, C. K. Sinclair, L. Turlington

Continuous Electron Beam Accelerator Facility
12000 Jefferson Avenue, Newport News, VA 23606 USA

Abstract

Prototypes of the rf separator for CEBAF have been made and successfully beam tested. The structure is a new design which has a high transverse shunt impedance together with a small transverse dimension compared to more conventional rf deflecting structures. Five rf separators will be used at CEBAF to allow beam from any one of the five recirculation passes to be delivered to any of the three experimental halls. We have already described the basic design of the structure and theoretical calculations. We have also reported some results from rf measurements and beam tests. In this paper we present more beam test results, our final design parameters, and test results of coupling two $1/2$ wavelength cavities together.

I. INTRODUCTION

The CEBAF rf separator is a new design [1]. In our previous paper we have discussed the purpose of rf separators at CEBAF, the basic design of the structure, and characteristics and advantages of the new structure [2]. The following sections present a summary of our previous test results and an update of our progress.

II. TEST CAVITY RF TEST

A test cavity with the dimensions listed in Table 1 was constructed [2]. Since one can not incorporate all the geometrical details into MAFIA to arrive at the exact resonant frequency, the rods were intentionally made slightly longer than needed. This resulted in a lower resonant frequency, about 489 MHz. Then, through several iterations the rods were cut shorter and the resonant frequency was raised to about 1 MHz above the 499 MHz target. The final tuning was done with capacitive tuners which come in at the center of the cavity and are capable of driving the frequency down as much as 20 MHz with little degradation of the Q .

Table 1
RF Separator Test Cavity Parameters

Frequency	499 MHz
Cavity length	30 cm
Cavity diameter (d_{out})	33 cm
Gap between facing rods	2 cm
Rod separation (center to center)	4 cm
Rod diameter (d)	2 cm
R_{\perp}/Q (MAFIA)	47 k Ω /m

Figure 1 shows the frequency spectrum of the cavity (before tuning) from 320 to 580 MHz. The second mode

at 501 MHz is our desired mode [2]. The unloaded Q factor for this mode was measured to be 5400.

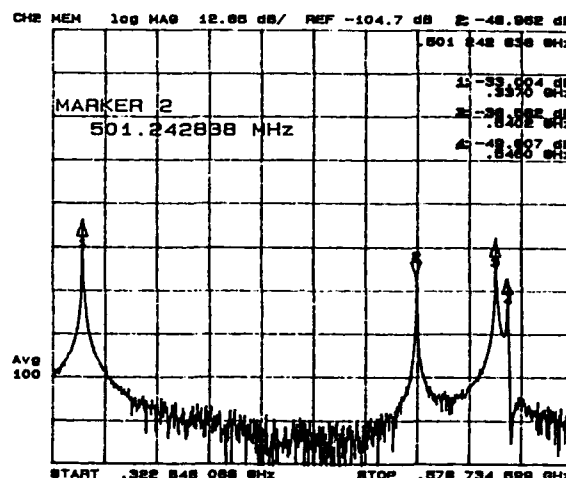


Fig. 1 Cavity modes from 320 MHz to 580 MHz.

III. BEAM TEST RESULTS

For our test, we used the electron beam from the CEBAF injector at 45 MeV. Consequently, only 9.5 W of rf power can produce a separation angle of 0.5 mrad, or 0.5 cm separation at 10 m away. This is a large enough separation to easily measure on a view screen. At approximately 9 m downstream from the separator cavity, the beam can be observed on a view screen and measured by a harp (a wire scanner). As soon as the rf was turned on to the cavity, the one beam spot on the screen was split into three spots (Fig. 2). Changing the rf phase changed the relative positions of the three spots.



Fig. 2 The separated beam on the view screen. Two and three beam creation.

Since the beam is split in the y direction, the beam was focused in y and defocused in x to give a sharper signal in the y direction. Figure 3 shows the harp traces of the beam for the two different rf phases. The first signal on the harp trace is the x scan and the others to the right of it

*Supported by D.O.E. contract #DE-AC05-84ER40150

are the y scan. Using the amount of the beam separation vs. rf power, the measured R_{\perp}/Q was determined to be 43.8 ± 2.4 k Ω /m, which compares well with 47 k Ω /m from MAFIA. ($R_{\perp} = \frac{V_{\perp}^2}{P}$; V_{\perp} is the integrated deflection voltage.) We measured the field uniformity by moving the beam within the cavity aperture and observing the change in the amount of the deflection; however, we did not see a significant change. We also measured the emittance for zero and maximum deflection. We observed, within 10% measurement error, no change of the emittance due to the separator. This is consistent with the very short measured bunch length in the CEBAF injector.

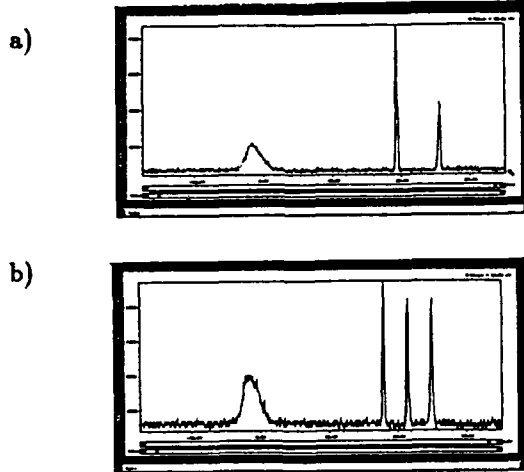


Fig. 3 Harp scan of the beam for a) two and b) three beam creation.

VI. FINAL DESIGN PARAMETERS

The parameters for the CEBAF RF Separators are listed in Table 2.

Table 2
CEBAF RF Separator Parameters

Frequency	499 MHz
Cavity length	30 cm
Cavity diameter (d_{out})	33 cm
Gap between facing rods	1.8 cm
Rod separation (center to center)	3.5 cm
Rod diameter (d)	2 cm
R_{\perp}/Q (MAFIA)	75 k Ω /m
Max surface E -field	<0.5 Kilpatrick

The R_{\perp}/Q value is about a factor of 50% larger in Table 2 than in Table 1. This is due to the change of distances between the rods. With R_{\perp}/Q given by MAFIA, and $Q \approx 5000$, then $R_{\perp} \approx 375$ M Ω /m. The required rf power for a separation angle of 0.1 mrad at 4 GeV is then:

$$P = \frac{V_{\perp}^2}{R_{\perp} \ell} = \frac{(4 \text{ GeV} \times 0.1 \text{ mrad} / \sin 60^\circ)^2}{(375 \text{ M}\Omega/\text{m}) (0.60 \text{ m})} = 1.0 \text{ kW}$$

The maximum surface E -field listed in Table 2 is an over estimation of the maximum E -field on the tip of the rods. In our calculation, we considered the highest electric field on two conducting spheres separated by the distance equal

to the minimum separation between the rods. The radius of the spheres is equal to the minimum radius on the rods, and the voltage on the spheres is the maximum voltage between the tips of the rods.

VI. COUPLING TWO $\lambda/2$ CELLS

Two $\lambda/2$ structures can be coupled to each other to obtain a 60 cm long two-cell structure. The longer structure will require half as much rf power for the same deflection. The coupling is done magnetically through two rectangular shape ($2'' \times 5''$) openings in the wall between the cells. This coupling creates symmetric (zero mode) and anti-symmetric (π mode) fields in the structure. The size of the opening is chosen to produce about 2 MHz separation between the modes. We arrived at this frequency separation by iteratively increasing the size of the openings. The desired mode is the π mode in which the deflection from the first and second cells adds. Because of magnetic coupling the π mode has a lower frequency than the zero mode. To confirm which resonant frequency is the zero and which is the π mode experimentally, a cold model was used. The phase of the magnetic field was measured in one of the cells at both frequencies. Then without changing the orientation of the loop, the loop was moved to the other cell and the phase of the magnetic field was measured again at the same frequencies (Fig. 4). At the lower frequency mode, the phase was changed by 180 degrees between the two measurements; however, at the higher frequency mode, the two measurements had the same results. Therefore, the lower mode was the desired π mode.

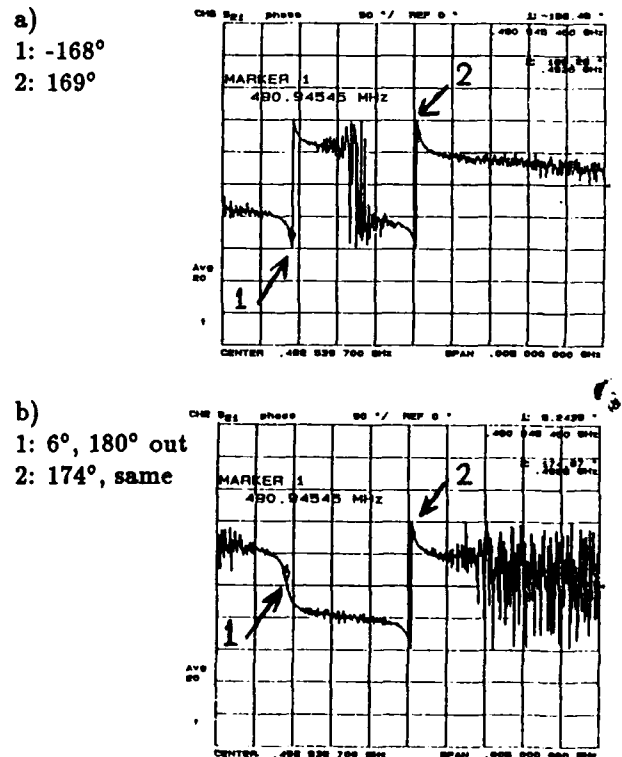


Fig. 4 Phase of the S_{11} . a) RF_{in} and RF_{out} loops in the same cell b) RF_{out} in a different cell.

Two tuners are used in the structure, one in each cell. Two tuners are required to tune the structure to the right frequency and to ensure equal field amplitudes in both cells. The equality of the field amplitudes was studied by a bead-pulling experiment and, also, by comparing the magnitude of S_{11} (reflected wave amplitude) for the zero and π modes. We found equal field amplitudes, when the two reflected wave amplitudes were equal. In this situation, frequency separation between the two modes is the least. In addition to cold models, a full-size two-cell (one λ) structure was constructed to study the structure properties [3]. Figure 5 shows the π and zero modes. We are planning to perform full rf power tests of this structure soon.

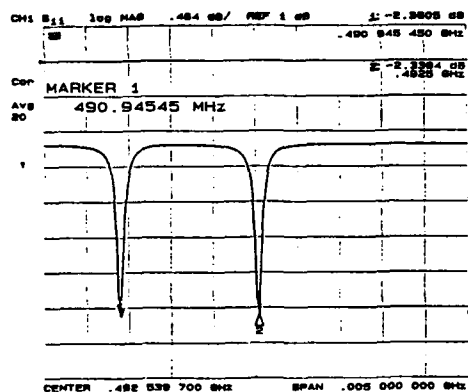


Fig. 5 π and zero modes for two-cell (one λ) structure.

VI. CONCLUSION

A proof of principle experiment has been conducted with successful results [2]. We have verified the high transverse shunt impedance properties of the cavity and we have also seen no degradation of the beam characteristics of the deflected beam. We have established that this new design is well suited to the CEBAF rf separator requirements.

VII. REFERENCES

- [1] C. Leemann and G. Yao, "A Highly Effective Deflecting Structure," 1990 Linear Accelerator Conference, Albuquerque, New Mexico.
- [2] R. Kazimi, *et al.*, "Test of a new rf separator for CEBAF," 1992 Linear Accelerator Conference, pp. 244-246.
- [3] A. Krycuk, *et al.*, "Construction of the CEBAF rf separator," These proceedings.

Frequency-Domain Analysis of Resonant-Type Ring Magnet Power Supplies

J. M. S. Kim
Dept. of Elec. and Comp. Engg.
University of Victoria
Victoria, B.C. CANADA

K. W. Reiniger
TRIUMF
4004 Wesbrook Mall
Vancouver, B.C. CANADA

Abstract

For fast-cycling synchrotrons, resonant-type ring magnet power supplies are commonly used to provide a dc-biased ac excitation for the ring magnets. Up to the present, this power supply system has been analyzed using simplified analytical approximation, namely assuming the resonant frequency of the ring magnet network is fixed and equal to the accelerator frequency. This paper presents a frequency-domain analysis technique for a more accurate analysis of resonant-type ring magnet power supplies. This approach identifies that, with the variation of the resonant frequency, the operating conditions of the power supply change quite dramatically because of the high Q value of the resonant network. The analytical results are verified, using both experimental results and simulation results.

I. INTRODUCTION

For fast-cycling synchrotrons such as TRIUMF KAON Factory Booster Ring, resonant-type magnet power supplies are commonly used. The operating conditions of this power supply configuration have been analyzed by Fox[1], with simplifying assumptions. Assuming the resonant frequency of the ring magnet network is fixed and equal to the accelerator frequency, all the voltage and current waveforms can be described by a set of ideal analytical expressions. To the best of our knowledge, these operating conditions have never been related to the parameters of the resonant network and their variation, including the variation of the resonant frequency.

On the other hand, Reiniger[2] has reported his experimental findings on the effects of resonant frequency drift on the operating conditions of the ring magnet power supply. With the variation of the resonant frequency, the operating conditions of the power supply change quite dramatically because of the high Q value of the resonant network.

This paper presents the frequency-domain analysis of resonant-type ring magnet power supplies, using frequency spectrum of energy make-up currents and ac transfer characteristics of the resonant network. With this approach, effects of resonant frequency variation can be identified and a more accurate analysis of the magnet power supply is possible. Reiniger's experimental results are confirmed using analytical results and simulation results.

II. MODELLING OF RESONANT-TYPE MAGNET POWER SUPPLY

The resonant-type magnet power supply is illustrated in Fig. 1. The resonant network provides a sinusoidally-varying magnet current, while the energy make-up network maintains a constant ac excitation of the ring magnets by injecting make-up energy into the resonant network via a pulse-forming network.

The fundamental frequency of the pulse currents, ω_a , is determined by the repetition rate of the SCR firing and is set by the acceleration frequency. This frequency is also the fundamental frequency of the magnet current, but is not necessarily same as the resonant frequency, ω_o , of the resonant network.

The waveshape and the ringing frequency of the pulse currents are determined by circuit parameters of the pulse-forming network, including the filter capacitor, C_f , and the pulse inductor, L_p . Since the pulse currents are formed using the resonance of these circuit parameters and the SCR is naturally commutated, the pulse waveform is well defined and its frequency components can be identified.

Thus, the pulse-forming network can be modelled by a dependent current source between the input filter and the resonant network. The waveform and frequency spectrum of the source current are determined by design parameters of the pulse-forming network, and its magnitude depends on the desired level of magnet current.

At steady state, operating conditions of the power supply are determined by ac transfer characteristics of the resonant network. The resonant network amplifies the fundamental component of input pulse currents and attenuates harmonic components to produce a sinusoidal magnet

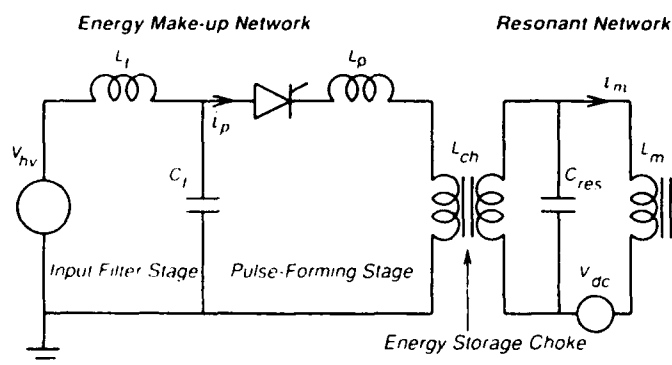


Figure 1: Resonant-Type Magnet Power Supply

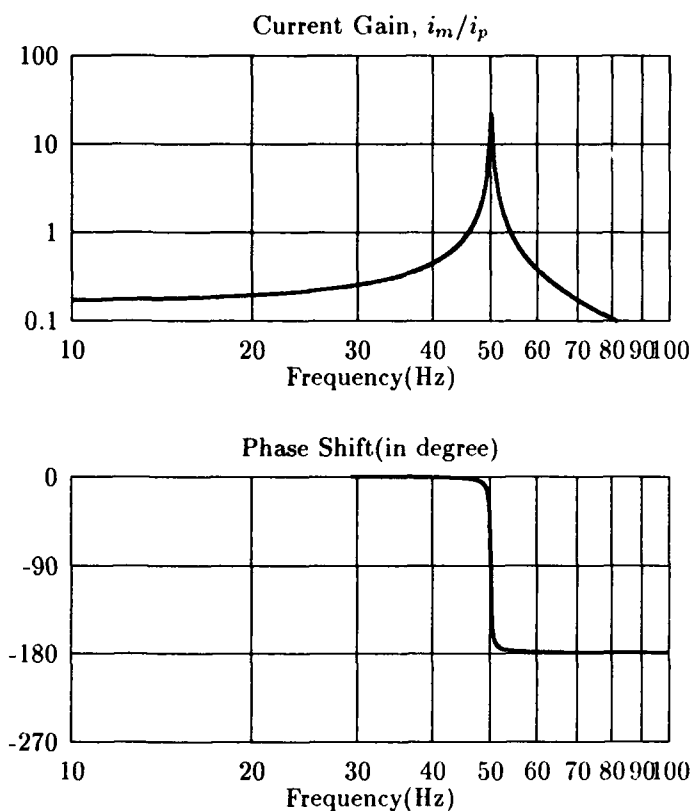


Figure 2: Bode Plot of Current Gain, i_m/i_p

current. This ac transfer characteristics is a typical second-order response with high Q factor.

Fig. 2 shows the Bode plot of the current transfer, i_m/i_p , where i_m is the magnet current and the i_p is the pulse current. As an example, circuit parameters of the dipole magnet power supply for the KAON Factory Booster Synchrotron is used in the analysis and simulations. The parameters are specified in the Accelerator Design Report[3].

As illustrated in Fig. 2, if the resonant frequency varies due to secondary effects such as temperature, the gain and phase shift change quite dramatically due to the high Q factor of the resonant network, and the magnitude and phase angle of the pulse currents must change significantly in order to maintain a constant ac excitation of the ring magnets.

III. FREQUENCY-DOMAIN ANALYSIS

To analyse a resonant-type ring magnet power supply in frequency domain, the following steps are used:

1. For a given design of the pulse-forming network, the pulse ringing frequency, ω_p , and the frequency spectrum of pulse currents are determined.
2. Then, the fundamental component of the pulse current is adjusted to generate a desired level of the magnet current, using the ac transfer characteristics of the resonant network with a given resonant frequency.

3. The required fundamental component and the frequency spectrum of pulse currents determine the peak pulse current as well as its dc component.
4. To see the effect of resonant frequency variation, repeat the previous two steps for a set of resonant frequencies.

The peak pulse current variation is shown in Fig. 3(a) as a function of resonant frequency. As the resonant frequency drifts away from the accelerator frequency, the current gain decreases and increased pulse currents are required for a constant ac excitation of ring magnets. Due to the high value of Q factor, however, the change in the current gain can be quite dramatic as shown and as predicted in the ac transfer characteristics of Fig. 2.

The voltage requirement of the energy make-up network can be obtained by considering that, during the pulse period, the average voltage of the filter capacitor, must be equal to the average voltage of the resonant capacitor voltage, assuming no losses in the pulse forming network.

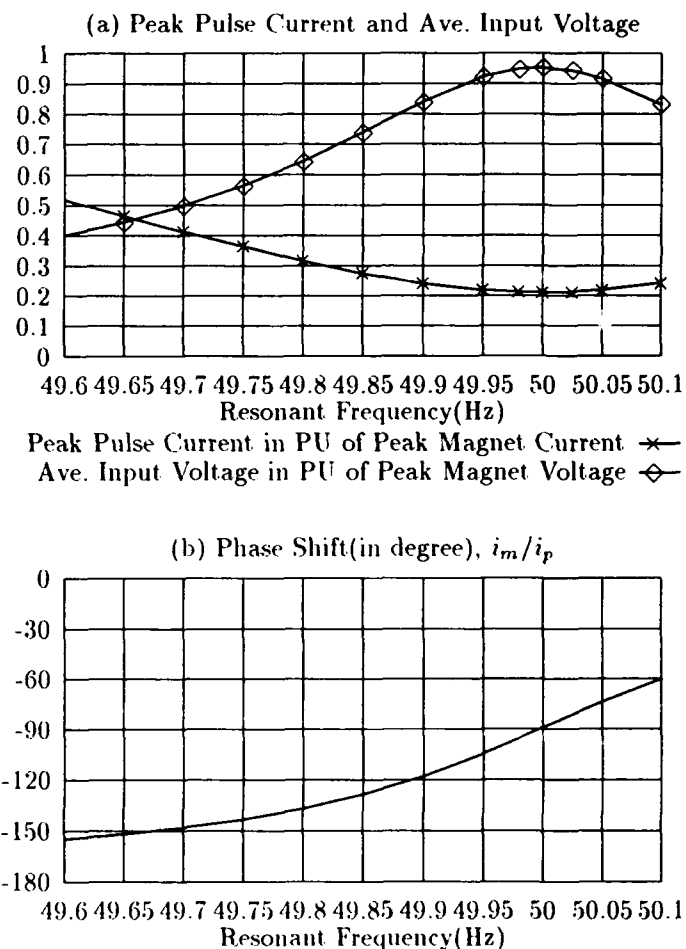


Figure 3: Effects of Resonant Frequency Variation

However, the Bode plot of Fig. 2 indicates that the position of the pulse period in relation to the magnet current shifts as the resonant frequency changes. As ω_o approaches ω_a , the phase shift get closer to 90° and the pulse current coincides with the zero crossing of the magnet current and the peak of the magnet voltage. The average input voltage to the pulse-forming network during the pulse period is also shown in Fig. 3(b) as a function of resonant frequency. The variation in the phase shift is shown in Fig. 3(b).

The results of frequency-domain analysis illustrated in Fig. 3 identify that the current and voltage requirements of the pulse-forming network change significantly with the variation of the resonant frequency. Nonetheless, the variation in current and voltage requirements does not mean the variation in the make-up energy to be pumped into the resonant network.

As long as the ac excitation of ring magnets is kept at a constant magnitude, the ac loss in the resonant network remains nearly constant and so does the energy to be pumped into the network via the pulse-forming network. With the variation of resonant frequency, the average input voltage and current change in such a way that the input power to the resonant network remains constant. This result has been verified by the SPICE simulation of the power supply system[4].

IV. EXPERIMENTAL RESULTS

The experimental results for the effects of resonant frequency variation have been reported in [2], using the dipole test set-up for KAON Factory Booster Ring. The analytical results presented in this paper confirms the experimental findings, as shown in Fig. 4. Fig. 4(a) illustrates the resonant-network gain predicted by the analysis agrees with the experimental results.

In Fig. 4(b), the make-up power to the resonant network is estimated using the frequency-domain analysis and compared to the experimental results. Some discrepancy can be identified at the high magnet current. This is due to the loss in the energy make-up unit of the experimental set-up. In the analysis, the ideal energy make-up is assumed and no power loss is accounted for.

V. CONCLUSIONS

The frequency-domain analysis of resonant-type ring magnet power supplies is introduced in this paper. It is shown that the analysis based on frequency spectrum of pulse currents and ac transfer characteristics of the resonant network provides more informations than the approximated analytical solutions. The analysis can not only determine the operating conditions for different design parameters of the pulse-forming network, but it can also relate them to parameters and conditions of the resonant network. The analysis identifies significant effects of resonant frequency variation on the current and voltage requirements of the pulse-forming network, which have not been possible with the approximated analytical solutions.

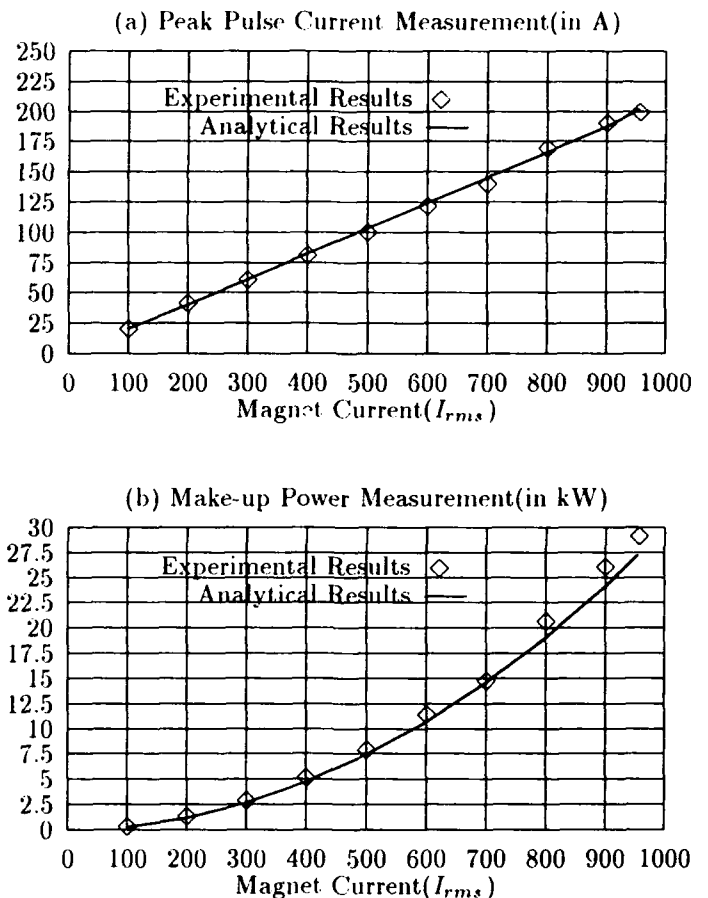


Figure 4: Experimental Results

The degree of resonant frequency drift will be minimized by switching trimming capacitors, but the frequency-domain analysis can be used to quantify the maximum drift of resonant frequency that can be allowed.

VI. REFERENCES

1. J. A. Fox, "Resonant Magnet Network and Power Supply for the 4 GeV Electron Synchrotron NINA", Proc. IEE, Vol. 112, No. 6, June 1965, pp 1107 - 1126
2. K. W. Reiniger, "Power Supply System for the TRIUMF KAON Factory", Conf. Record of 1991 IEEE Particle Accelerator Conference,
3. Accelerator Design Report, KAON Factory Study, TRIUMF, 1990
4. J. M. S. Kim, "SPICE Simulation of Resonant-Type Booster Ring Magnet Power Supply", TRIUMF KAON Factory PDS Design Note TRI-DN-91-K178

The Workshop on Microwave-Absorbing Materials for Accelerators.*

Isidoro E. Campisi
Continuous Electron Beam Accelerator Facility
12000 Jefferson Avenue, Newport News, VA 23606-1909 USA

Abstract

A workshop on the physics and applications of microwave-absorbing materials in accelerators and related systems was held at CEBAF February 22-24, 1993. The gathering brought together about 150 scientists and representatives of industries from all over the world. The main topics of discussion were the properties of "absorbing" materials and how the stringent conditions in an accelerator environment restrict the choice of usable materials.

I. INTRODUCTION

The use of materials for microwave absorption is a topic of interest to various scientific communities. Among those interested in special materials are accelerator builders, microwave tube experts, fusion device builders and materials scientists from various areas of technology.

In the past, most of the design of accelerator components that dealt with microwave absorption relied on known and tested materials first used in other areas of technology and which were not specifically developed for accelerator applications. Microwave losses in a number of traditional materials (silicon carbide or ferrites, for instance) have been utilized in accelerator-related systems without a thorough analysis of the physics of loss processes and without simultaneously considering other essential properties of the lossy materials, such as structural properties, thermal conductivity, radiation resistance, temperature dependence of the microwave absorption, vacuum compatibility, broad frequency bandwidth as well as manufacturing and reproducibility issues.

The incomplete analysis of the field of microwave absorbers could lead to difficulties in the construction and operation of future machines, because many new accelerator projects are being designed and built with key performance parameters strictly dependent on the availability of good microwave absorbers (for instance, higher-order-mode control in various types of accelerators, such as linear colliders and high-current circular machines). Thus it seemed that a useful activity would be a workshop which would gather experts from various fields of science and technology who could interact with each other and address issues in materials science and new technologies related to materials for microwave power control which can have a great impact on the construction of new machines.

In accelerator laboratories, the dissipation of microwaves is often considered a necessary evil (for example, in lowering the overall efficiency of high-power microwave systems and dissipating as heat the precious high peak power of pulsed klystrons), and it has not received adequate attention because of its negative connotation. Low losses, high accelerating fields and high efficiencies are of primary importance in accelerator physics, and the development of new microwave-ab-

sorbing materials for accelerators and similar systems has not been given a high priority.

The author's experience with the consequences of the incomplete knowledge in this area turned into a special project of fast development of a new material, and into a determined effort to prevent other researchers' future misuses of materials in this context. The workshop on Microwave-Absorbing Materials for Accelerators (MAMA) is an attempt to provide better understanding of the problems related to these special materials and to increase cooperation and communications among scientists and engineers with widely different backgrounds.

In this paper an attempt is made to give a general flavor of the problems and subjects treated during the workshop. Due to the large number of contributions, this single paper cannot do justice to all the authors and participants, but should serve as a stimulus for those interested in pursuing the interest further and in working with other experts on the subject. The author apologizes for the necessary inadequacy of the report.

II. GENERAL PROPERTIES OF ABSORBERS

Among the particle accelerators that are being planned or designed and which require specialized absorbers, the most important are electron (or positron) accelerators, because of the critical importance of controlling beam instabilities due to higher-order-mode power generation.

The presence of absorbers is necessary because the charge bunches traveling along the non-uniform cross section of the accelerating microwave cavities interact with the metal structures, depositing a fraction of the energy into cavity modes other than the fundamental (usually the TM_{010} mode). In most cases, these higher-order modes (HOMs) are damped by the ohmic losses at the cavity surfaces, but when either normal conducting cavities have small dimensions or the cavities are superconducting (thus, with very long decay times of the energy stored in HOMs) the modes can feed back onto the beam and affect its trajectory, leading to uncontrolled beam instabilities [1], especially in extreme cases of high currents or particularly sensitive system geometries.

These instabilities must be avoided by extracting the HOM power and disposing of it in a suitable way. In some cases this power is extracted to room temperature before being dissipated. It is, however, desirable to convert the power into heat before crossing physical boundaries. Transporting microwaves across transitions makes the absorption less controllable and the engineering of the absorbers much more problematic.

A general approach to the problem of absorbing microwaves in accelerator systems can be visualized in figures 1 and 2. Figure 1 shows how feedthroughs carrying RF across vacuum boundaries make the design difficult and the operation of accelerators hazardous (brazed joints that must deal simultaneously with high RF power, broad bandwidth, vacuum and/or coolant interfaces).

* Supported by US DOE Contract # DE-AC05-84ER40150

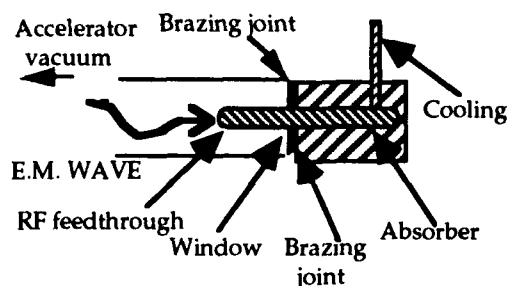


Figure 1 The geometry of extraction of microwave power from accelerators stems from unreliable absorbing materials used in the past, which require isolation from the accelerator vacuum and feedthroughs to carry the RF across boundaries.

Generally, new load designs might be possible, and compact absorbers could be made to work under vacuum or controlled atmosphere and without water cooling systems which make the system narrow banded, complicated by the cooling system. Although these loads have been in the past used extensively and with a good track record [2], they are potentially prone to vacuum accidents. Compact loads of high thermal conductivity materials with dielectric properties independent of temperature could in principle run without cooling (dry loads) and only with minor protection against thermal runaway up to several hundred degrees centigrade [3].

BRAZE JOINT CERAMIC-METAL (SUPPORT AND THERMAL CONTACT ONLY)

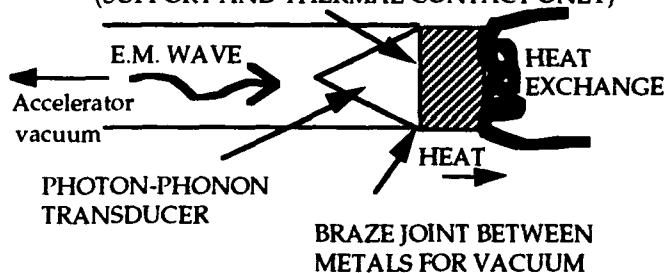


Figure 2 A better geometry for absorption involves the use of vacuum-compatible lossy materials placed inside the accelerator vacuum.

Similar problems of high-power loads compatible with ultrahigh vacuum and having to work under varying high-power loading conditions are experienced in Tokamak fusion devices, in which the plasma is heated by microwave power and termination must be placed inside the toroidal structure [4]. Due to the varying load as the plasma heats up, materials with temperature independent absorption and with very high thermal conductivity would be desirable for this application. One special requirement for these materials is the resistance to radiation, a property which is also of great importance in any accelerator installation [5].

III. MICROWAVE-ABSORBING MATERIALS AND THEIR PHYSICAL PROPERTIES

Because a thorough understanding of the phenomena involved in microwave absorption is important in choosing the proper material for a specific application, several talks were given at the MAMA workshop on the physics of absorption. Newnham, Jacobs, Rodrigue, Booske, Galstjan and Katz [6] described several loss phenomena. In general, losses can be thought of as photon-phonon scattering processes. Whereas

photon-phonon scattering mediated by polarization effects in crystals, or by ionic transport within crystals or at the grain boundaries of crystallites, or by materials with semiconducting properties, yields temperature-dependent losses, one loss mechanism which has a weak temperature dependence is the ohmic effect at radio frequencies in metals, where the electron population in the conduction band is never zero and the anomalous skin effect prevents major loss variations at low temperatures.

Other loss mechanisms can be ascribed to magnetic field effects, such as magnetization losses in ferrites [7], which however are affected by the external bias fields. The materials can have remnant magnetic field and the losses are nonlinear. The linearity of the ohmic losses in the conducting grains of an artificial dielectric lead to materials which are insensitive to large external magnetic fields, and can tolerate large amounts of dissipated power. Ferrites cannot be easily operated at high power levels, due to the poor thermal conductivity (typically few $W/(m \cdot K)$), the large dissipation per unit volume and the fact that they could heat up above the Curie point and give varying absorption properties. Ferrites have been used successfully in many microwave absorption applications and a large amount of work exists on the subject, which makes their use very reliable. Recent work in various accelerator laboratories has advanced the understanding of such materials for these applications [8].

IV. RAW MATERIALS, CERAMICS AND MANUFACTURING PROCESSES

Ceramic materials are among the best suited for an accelerator's vacuum systems. Several of their properties are very well understood and under control [9], but in most cases ceramics have not been used in the past for their electrical properties. A notable exception is silicon carbide in various forms, the properties of which were reviewed extensively at the workshop [10]. The manufacturing problems of artificial dielectrics were addressed by Mikiel [11], with particular emphasis on the properties of various mixtures which can give reproducible results.

The standard and advanced processes involved in the sintering of ceramics were discussed by Spriggs [12], and Guiton [13] presented data on the remarkable improvement in thermal conductivity of ceramics (AlN in particular) when processed in various ways. Special powder manufacturing results by plasma spray were discussed [14] with the possibility of controlling the purity and grain size of several metals, ceramics and alloys. Properties of carbon powders were presented by Pierson [15], as carbon in its many forms may present itself as one of the best materials for microwave absorption in specific and very constraining applications such as in accelerators.

One important issue in the design and construction of absorbers for special applications such as accelerators is the problem of making consistent and reliable brazing between the absorbers and the surrounding metals of the vacuum chamber. Extensive work is needed in this area, and Greenhut covered many of the issues [16]. The necessity of vacuum compatibility of these materials was outlined by Dylla [17], with arguments which favor ceramic materials over other types of absorbers. The special ceramic compounds used for ferrite absorption and the manufacturing methods associated with them were described by Blankenship [18].

One of the most complicated and unresolved issues in the manufacturing of lossy materials is the reproducibility of results and of material properties. A variety of materials parameters and their interconnections play a role in the production of materials for microwave absorption [19]. Whereas most manufacturers produce ceramics for their structural properties, nowadays electrical and thermal properties are becoming important and the producers of powders and finished products are not fully aware of the need of some consumers. This workshop provided an opportunity for users and manufacturers to get together and let each other know their needs and capabilities. The work of Ho [20] is of great importance to the whole community because it shows how materials with nominally the same composition can have vastly different properties from the electrical point of view. This problem must be traced and controlled all the way from the powder fabrication processes and producers to those who make final use of these materials so that a concerted improvement can be achieved. An important aspect of this process of improvement is given by the accuracy and precision of the measurement of electrical properties of these materials. Weil [21] and Hutcheon [22] addressed some of these issues. The design of complete absorbers will benefit in the future by the existence of computer codes that can both simulate special materials and at the same time include lossy dielectrics in the computations [23]. These tools will eventually provide great flexibility in the use and design of absorbers in accelerators.

V. CONCLUSIONS

In several laboratories around the world materials have been used for damping of higher-order modes in accelerators or for absorption of microwaves in general. Often the lack of availability of materials for absorption within the accelerator or microwave tube vacuum has limited the performance of the systems designed around them. The availability of increasingly better ferrites and artificial dielectric materials will certainly provide new ideas and solutions to accelerators builders who will benefit from the existence of improved microwave absorbers.

A very close collaboration between those who build accelerators and materials scientists in national laboratories, industries and academic environments all over the world is not only desirable but necessary. The development of tight manufacturing and measurement techniques and of procedures must be achieved in this area in order to obtain a wider and more reliable use of these special materials.

Due to the diverse requirements that such materials must satisfy, all the problems related to them must be addressed simultaneously. The use of materials which only satisfy the electrical requirements cannot lead to more complicated application problems. The approach of finding ideal materials for each application requires close collaboration among scientists with varied and diverse knowledge and skills. The MAMA workshop has attained this goal and will provide again in the future an arena for these diverse disciplines.

ACKNOWLEDGMENTS

The author would like to thank Dennis Barnes, President of SURA; C.W. Leemann, R. Talman, W.T. Doyle, J.D. Buckley, S. Albin, D.E. Clark, A. Krycuk, S. Simrock, L.R. Doolittle, E. Haebel, R.M. Sundelin, W. Hartung, and D.

Manos for invaluable contributions to the MAMA Workshop; and Roger Lewis of DoE, for the enlightening talk on technology transfer during the Workshop's banquet.

REFERENCES

All references below (unless otherwise indicated) are included in the *Proceedings of the First Workshop on Microwave-Absorbing Materials for Accelerators (MAMAs)*, (I. E. Campisi and L. R. Doolittle, Eds.) CEBAF, Newport News, Virginia, February 22—24, 1993. (In print.)

- [1] J. J. Bisognano "The need for MAMAs in accelerators and tube technology"; R. Rimmer "Extraction and absorption of higher-order modes in room temperature accelerators"; H. Padamsee "HOM control in superconducting cavities"; J. Calame "Applications of microwave absorbing materials in microwave tubes".
- [2] L. Nielsen "Engineering issues in microwave loads design".
- [3] I. E. Campisi, et al. "CEBAF HOM loads".
- [4] H. K. Park "Design criteria and materials for ultra-high broad band microwave absorbers for scattering experiments in tokamak plasmas".
- [5] D. G. Howitt "Radiation-induced transformations in materials in electron accelerator environments".
- [6] R. E. Newnham "Fundamental interaction mechanisms between microwaves and matter"; I. S. Jacobs "Metal-dielectric composites (artificial dielectrics)"; J. H. Booske "Effects of high-power microwave fields on ionic transport in ceramics and ionic crystalline solids"; E. A. Galstjan "The effective electrodynamic parameters of a medium impregnated by two-layer spherules"; J. D. Katz "Microwave processing of ceramics".
- [7] G. P. Rodrigue "Theory of electromagnetic properties of ferrites".
- [8] W. H. Hartung "Measurements of the microwave properties of some absorbing materials".
- [9] S. A. Wise "Ceramics: structural, thermal, and vacuum properties".
- [10] R. F. Davis "Polytypism, process routes, and microstructures and the effect of these parameters on the electrical properties of silicon carbide"; G. Fischman "Thermo-mechanical properties of silicon carbide".
- [11] B. Mikijelj and I. E. Campisi "Development of an artificial dielectric ceramic for use at CEBAF".
- [12] R. M. Spriggs "Ceramic sintering".
- [13] T. A. Guiton "Improving the thermal conductivity of ceramics".
- [14] R. Cheney "Plasma manufacturing of fine metal and ceramic powders".
- [15] H. O. Pierson "Carbon powders: properties, processing and applications".
- [16] V. A. Greenhut "Fundamentals, techniques and recent developments in ceramic-metal joining and metallization".
- [17] H. F. Dylla "Vacuum properties of materials".
- [18] A. C. Blankenship "Commercial ferrite manufacturing".
- [19] I. E. Campisi, *Proc. Am. Cer. Soc. Meet.*, 1993 (in print).
- [20] W. W. Ho, M.R.S. Symp. vol. 124, 137—148 (1988).
- [21] C. M. Weil "Dielectric and magnetic properties measurements: NIST Metrology Program".
- [22] R. Hutcheon "Dielectric and magnetic properties measurements: data from AECL".
- [23] D. Shenton "Computational codes for load design".

ANALYSIS AND APPLICATIONS OF QUADRATURE HYBRIDS AS RF CIRCULATORS*

S.M. Hanna and J. Keane
National Synchrotron Light Source
Brookhaven National Laboratory
Upton, NY 11973

Abstract

The operation of a quadrature hybrid as a power combiner is analyzed. The analytical results are compared with data measured experimentally using a 211 MHz cavity. Graphical solutions of the measured cases are in good agreement with analytical predictions. The use of the 90°-hybrid as an RF circulator is also analyzed. The active operation of the harmonic cavity in the NSLS VUV-ring is used to demonstrate this application. This fourth-harmonic cavity is used to change the shape of the bucket potential to lengthen a stored bunch. Thus, a longer stored-beam lifetime can be achieved without compromising the high brightness of the VUV photon beam. If operated actively, the harmonic cavity would present a mismatched load to an RF generator. Thus, a need exists for a circulator. Similarities in operation between the 90°-hybrid and a circulator are discussed.

I. ANALYTICAL MODEL FOR THE HYBRID AS A POWER COMBINER

The quadrature hybrid [1], is a four-port network with 90° phase shift between two of the ports and no phase shift between the other two ports. Referring to Fig. 1, one can write its S-matrix as:

$$\begin{pmatrix} V_1^- \\ V_2^- \\ V_3^- \\ V_4^- \end{pmatrix} = \frac{1}{\sqrt{2}} \begin{pmatrix} 0 & 1 & -j & 0 \\ 1 & 0 & 0 & -j \\ -j & 0 & 0 & 1 \\ 0 & -j & 1 & 0 \end{pmatrix} \begin{pmatrix} V_1^+ \\ V_2^+ \\ V_3^+ \\ V_4^+ \end{pmatrix} \quad (1)$$

In this section we summarize the results of our analysis for a 90°-hybrid [2]. As shown in Fig. 1, the hybrid analysed is used to combine the power from two transmitters feeding ports 1 and 4. A cavity is being connected to port 2, and a waster load is connected at port 3.

Assumptions:

- The cavity represents an impedance mismatch of Γ_c .
- The transmitters T_A and T_B have the same impedance mismatch represented as Γ_s .
- The two transmitters are providing two identical voltages except for a 90° phase shift,

$$V_{T_A} = V_s \angle 0^\circ ; V_{T_B} = V_s \angle 90^\circ$$

*Work performed under the auspices of the U.S. Department of Energy, under contract DE-AC02-76CH00016.

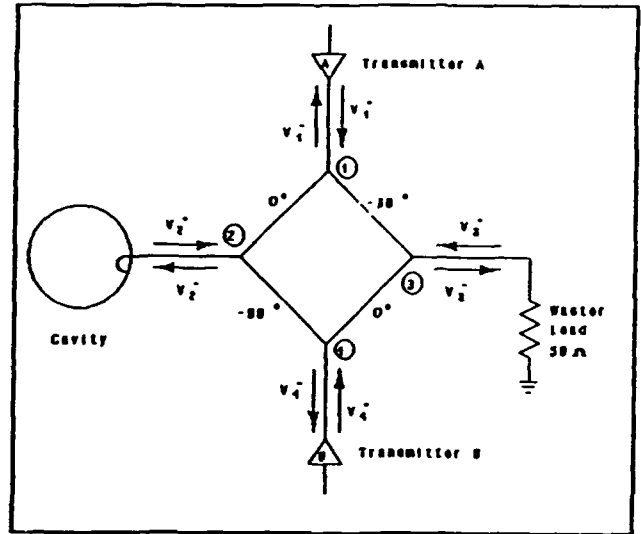


Figure 1. Configuration for the case analyzed.

- A load ($Z_L = Z_o$ of the hybrid) is connected at port 4.

Approach:

Here we use the linearity of the system and apply the superposition principle. T_A is activated while T_B is OFF (case 1). Then, T_B is activated while T_A is OFF (case 2), as follows:

Case 1: Since the active port in this case is port 1, one needs to solve first for the ratio V_1^-/V_1^+ as seen by the transmitter T_A , when T_B is OFF. This is done by using Eq. 1 to solve for V_1^+ , as follows:

$$\begin{pmatrix} V_1^- \\ V_2^- \\ V_3^- \\ V_4^- \end{pmatrix} = \frac{1}{\sqrt{2}} \begin{pmatrix} 0 & 1 & -j & 0 \\ 1 & 0 & 0 & -j \\ -j & 0 & 0 & 1 \\ 0 & -j & 1 & 0 \end{pmatrix} \begin{pmatrix} V_1^+ \\ \Gamma_c V_2^+ \\ 0 \\ \Gamma_s V_4^+ \end{pmatrix} \quad (2)$$

Solving for V_1^+ , one can get ,

$$V_1^+ = \left(\frac{2 + \Gamma_s \Gamma_c}{2} \right) \left(\frac{1 - \Gamma_s}{2} \right) V_s \angle 0 \quad (3)$$

Now, we can solve for the reflected voltages. This is done by solving Eq. (4).

$$\begin{pmatrix} V_1^- \\ V_2^- \\ V_3^- \\ V_4^- \end{pmatrix} = \frac{1}{\sqrt{2}} \begin{pmatrix} 0 & 1 & -j & 0 \\ 1 & 0 & 0 & -j \\ -j & 0 & 0 & 1 \\ 0 & -j & 1 & 0 \end{pmatrix} \begin{pmatrix} \left(\frac{2+\Gamma_g\Gamma_c}{2} \right) \left(\frac{1-\Gamma_g}{2} \right) V_g \angle 0 \\ \Gamma_c V_2^- \\ 0 \\ \Gamma_g V_4^- \end{pmatrix} \quad (4)$$

giving,

Reflected voltages

Incident voltage

$$V_1^- = \frac{\Gamma_c}{2} \frac{(1-\Gamma_g)}{2} V_g \angle 0 \quad V_1^+ = \left(\frac{2+\Gamma_g\Gamma_c}{2} \right) \left(\frac{1-\Gamma_g}{2} \right) V_g \angle 0$$

$$V_2^- = \frac{1}{\sqrt{2}} \frac{1-\Gamma_g}{2} V_g \angle 0 \quad V_2^+ = \frac{\Gamma_c}{\sqrt{2}} \frac{(1-\Gamma_g)}{2} V_g \angle 0 \quad (5)$$

$$V_3^- = \frac{j}{\sqrt{2}} (1+\Gamma_g\Gamma_c) \frac{(1-\Gamma_g)}{2} V_g \angle 0 \quad V_3^+ = 0$$

$$V_4^- = -j \frac{\Gamma_c}{2} \left(\frac{1-\Gamma_g}{2} \right) V_g \angle 0 \quad V_4^+ = -j \frac{\Gamma_g\Gamma_c}{2} \left(\frac{1-\Gamma_g}{2} \right) V_g \angle 0$$

Case 2: Following the same steps as in Case 1, we solve for V_4^+ , giving

$$V_4^+ = \left(\frac{2-\Gamma_g\Gamma_c}{2} \right) \left(\frac{1-\Gamma_g}{2} \right) V_g \angle 90$$

Similar to Case 1, we can solve for the incident and reflected voltages at the four ports for this case.

Total Incident and Reflected Voltage:

By applying the superposition principle, we can get the total voltages at the four ports when both transmitters are ON [2]. The resulting voltages are:

$$\begin{aligned} \text{Transmitter A: } V_1^+ &= (1+\Gamma_g\Gamma_c)V_1^- ; V_1^- = \Gamma_c V_1^+ \\ \text{Cavity: } V_2^+ &= \sqrt{2} \Gamma_c V_1^+ ; V_2^- = \sqrt{2} V_1^- \\ \text{Load: } V_3^+ &= 0 ; V_3^- = \sqrt{2} \Gamma_g \Gamma_c V_1^+ \\ \text{Transmitter B: } V_4^+ &= j(1-\Gamma_g\Gamma_c)V_1^+ ; V_4^- = j\Gamma_c V_1^+ \end{aligned}$$

where

$$V_1^- = \frac{(1-\Gamma_g)}{2} V_g \angle 0$$

II. ANALYSIS OF MEASURED DATA

To verify the above analytical results, measurements were carried out using the configuration shown in Fig. 1. The forward and reflected powers were measured using directional couplers connected to a power meter. The measurement was done using a 211 MHz cavity. The power was measured at three different cavity phase settings (0° , -45° , and 45°). The results of the measurements are shown in Table 1 where the voltages are in volts.

Table I

Cav. Phase	V_1^+	V_1^-	V_2^-	V_2^+	V_3^-	V_4^+	V_4^-
0°	524 (0°)	63 (60°)	765	100	18.7	548 (95°)	55 (-55°)
-45°	990 (-20°)	530 (-150°)	1142	830	774	900 (100°)	485 (115°)
45°	1166 (20°)	485 (-55°)	1116	791	656	354 (40°)	524 (-150°)

To fully determine the reflection coefficients of the cavity (Γ_c) and the transmitters (Γ_g), we use a combination of analytical computation and graphical solutions where we use phasor diagrams and loci for different phasors. To illustrate that we will consider the phasor diagram in Fig. 2 which represents a sample case (cavity at 45°).

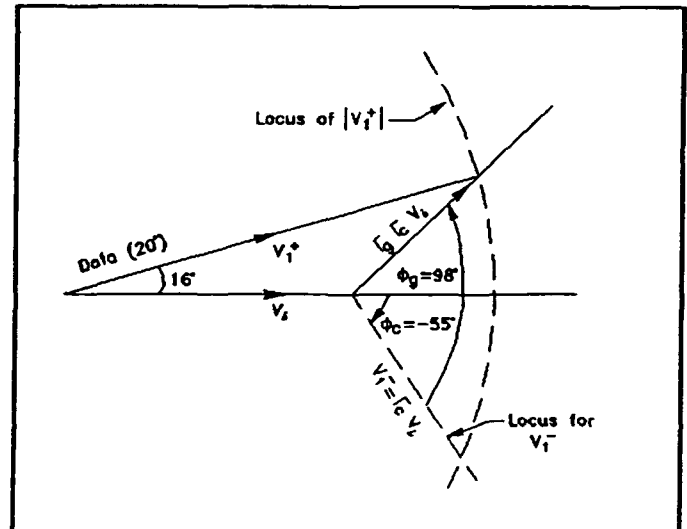


Figure 2. Phasor diagram for graphical solution

If we consider the phasor V_1 as the reference, we can find ϕ_g (phase angle for Γ_g) and ϕ_c (phase angle for Γ_c) as shown in Fig 2. Using the data in Table 1, the graphical solution gives

$$\Gamma_c = 0.7 \angle -55^\circ \quad \text{and} \quad \Gamma_g = 0.83 \angle 98^\circ$$

Data measured were generally consistent with predictions from the analytical model represented in Eq. (6), except for a systematic phase difference of 10° .

III. THE 90°-HYBRID AS A CIRCULATOR FOR THE VUV RING HARMONIC CAVITY

A fourth-harmonic cavity is being used in the VUV-storage ring at the NSLS to change the shape of the bucket potential. The harmonic cavity would present a mismatched load to a generator if operated actively. The need exists for a circulator to steer any power reflected from the harmonic cavity to a waster load. In this section, we demonstrate the use of the 90°-hybrid as circulator. We use the parameters for the harmonic cavity given below as a numerical example [3].

Main Cavity	Harmonic Cavity
$V_{MC} = 80 \text{ KV}$	$V_{HC} = 20 \text{ KV}$
$\Psi_s = 79^\circ$	$\Psi_H = -92.8^\circ$
(Rsh = 1 MΩ)	(Rsh = 300 kΩ)

To achieve this goal, we will analyze one of three approaches that we considered [4] for the active operation of the VUV harmonic cavity. In the tuner-compensation approach, the cavity is phased such that the beam current is in quadrature with the cavity gap-voltage. The tuner is operated to compensate for the beam-induced reactive power. The generator current is in-phase with the gap voltage. Lowest generator power requires matched coupling loop to the cavity. Since other practical considerations may require deviations from this ideal case; we have analyzed a general case where coupling can be made different from matched. Referring to Fig 3, we can define the coupling coefficient as

$$\beta = \frac{R_{sh}}{n^2(50)} \quad (7)$$

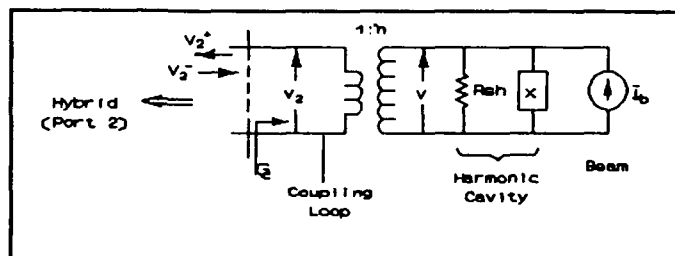


Figure 3. Cavity-port equivalent circuit.

For the conditions discussed above, and analyzed in detail in [4], we can obtain the powers at the four ports as,

Cavity Power: The power dissipated in the cavity is

$$P_w = \frac{1}{2} \frac{V^2}{50 n^2 \beta} = \frac{1}{2} \frac{V^2}{R_{sh}} \quad (8)$$

Load Power The power dissipated in the waster load is

$$P_l = P_w \left[\frac{(\beta - 1)^2}{4\beta} \right] \Gamma_g^2 \quad (9)$$

Transmitter A

$$P_A = P_w \frac{[(\beta + 1) + \Gamma_g (\beta - 1)]^2 - (\beta - 1)^2}{4\beta}$$

Transmitter B

$$P_B = P_w \frac{[(\beta + 1) - \Gamma_g (\beta - 1)]^2 - (\beta - 1)^2}{4\beta}$$

Combined Generator Power

The combined power from transmitter A and transmitter B is

$$P_g = P_A + P_B = P_w \frac{[(\beta + 1)^2 - (\beta - 1)^2 (1 - \Gamma_g^2)]}{4\beta} \quad (10)$$

From the above equations the power balance gives,

$$P_g - P_l = P_w \quad (11)$$

From this analysis it can be shown that, under certain conditions (for example the case where the generators can be considered as ideal current sources, $\Gamma_g = 1$), the hybrid's operation is identical to that of a ferrite circulator [4].

IV. CONCLUSION

In this report we have analyzed in detail the performance of a 90°-hybrid. The analysis is based on 4-port scattering matrices. Analytical results were compared with experimental measurements. Graphical solutions based on the measured data gave good agreement with our analytical results. The use of the 90°-hybrid as a circulator was demonstrated using the harmonic cavity in the NSLS VUV-ring as an example.

Acknowledgement

We thank M. Thomas and S. Buda for their effort in the measurement of experimental data analyzed in this work.

References

- [1] D.M. Pozar, "Microwave Engineering," Adison-Wesley Publishing Co., NY, p. 411, 1990.
- [2] S.M. Hanna and J. Keane, "Analysis of Quadrature-Hybrids for Accelerator Applications", submitted to Nuc. Inst. & Meth. in Phys. Research.
- [3] S. Krinsky, et al., "Storage Ring Development at the National Synchrotron Light Source," BNL 46615, 1991.
- [4] S.M. Hanna and J. Keane, "Active Operation of the Harmonic Cavity for Bunch Lengthening at the VUV-Storage Ring", NSLS Tech. Note #480, 1993.

FLOWER-PETAL MODE CONVERTER FOR NLC*

H. A. Hoag, S. G. Tantawi, R. Callin, H. Deruyter, Z. D. Farkas, K. Ko,
N. Kroll, T. L. Lavine, A. Menegat, and A. E. Vlieks

Stanford Linear Accelerator Center, Stanford University, Stanford, CA 94305

Abstract

It is important to minimize power loss in the waveguide system connecting klystron, pulse-compressor, and accelerator in an X-Band NLC. However, existing designs of klystron output cavity circuits and accelerator input couplers utilize rectangular waveguide which has relatively high transmission loss. It is therefore necessary to convert to and from the low-loss mode in circular waveguide at each end of the system. A description is given of development work on high-power, high-vacuum 'flower-petal' transducers, which convert the TE_{10} mode in rectangular guide to the TE_{01} mode in circular guide. A three-port modification of the flower petal device, which can be used as either a power combiner at the klystron or a power divider at the accelerator is also described.

I. INTRODUCTION

Various types of transducers have been developed for converting the TE_{10} mode in rectangular waveguide to the low-loss TE_{01} mode in circular waveguide. Many employ adiabatic tapering from the cross-section of one waveguide to the other, as exemplified by the design originally proposed by Marié [1]. These designs require elaborate machining or electroforming, and the finished transducers are quite long, which leads to significant insertion loss, and possibly trapped weak resonances due to mismatches. They are most suited to communications systems, where broad bandwidth is required.

The rf systems used to drive linear accelerators can be relatively narrow-band. In these applications the so-called 'flower-petal' transducer [2] can be used. It is compact and, as will be seen, can be designed to have low loss and high mode purity. The essential features of the transducer are shown in Figure 1. The input rectangular waveguide is bifurcated through matched transformer steps into two rectangular guides having the same cross-section as the input guide. The two guides are coupled to a circular waveguide by an arrangement of four slots (the flower-petal) in their side walls. After the coupling slots, the two rectangular guides are terminated in short circuits. Although the transducer is required to couple into 1.75-inch circular guide, the diameter of the section of guide coupled directly to the slots is 1.6 inches. The reason for this is to guarantee that the TE_{41} mode generated by the slots is sufficiently evanescent over the intended bandwidth. A non-linear taper is provided to match this section to the required 1.75-inch circular guide.

In recent years, 3-D computer modeling has proved to be both feasible and practical for the design and analysis of complex microwave structures. In the case of the flower-petal transducer, the 3-D electromagnetic codes HFSS and MAFIA have been used successfully to simulate its behavior.

*Work supported by Department of Energy contract DE-AC03-76SF00515.

‡Also at UCSD and supported by DE-FG03-92ER40759.

Low-power measurements have been made to optimize the bifurcation transformer and the dimensions of the flower-petal slots, and to quantify the power in unwanted modes generated in the circular waveguide.

Several models of the finished transducer have been made for high-power and high-vacuum operation. Two have been tested back-to-back in an X-Band resonant ring up to a power level of 150 MW.

II. PRINCIPLE OF OPERATION

We present here symmetry-based arguments which provide some insight into why the design works as well as it does. Referring to Figure 1, it can be seen that the symmetry (both in terms of the structure and the excitation) is such that it is sufficient to consider only the positive y side of the x-z plane and modes consistent with a metal boundary condition being imposed there. This implies that, at most, five of the ten propagating modes in the circular guide can be excited. These are TE_{01} , TE_{11} , TM_{11} , TE_{21} and TE_{31} . The TE_{01} and TE_{21} modes satisfy a symmetry relation with respect to radial planes at 45° to the axes, corresponding to a metal boundary for the TE_{01} and a magnetic boundary for the TE_{21} . If an individual petal slot is approximated to the form of a thick elliptical iris, then by using formulas appropriate to that geometry, it is found that the ratio of the induced magnetic dipole moments associated with the two symmetries is approximately 0.012 in the sense which discriminates against the TE_{21} mode. Since the ratio of the powers in the two modes is the square of this quantity, there is a strong discrimination against driving the TE_{21} mode, which improves with increasing iris thickness.

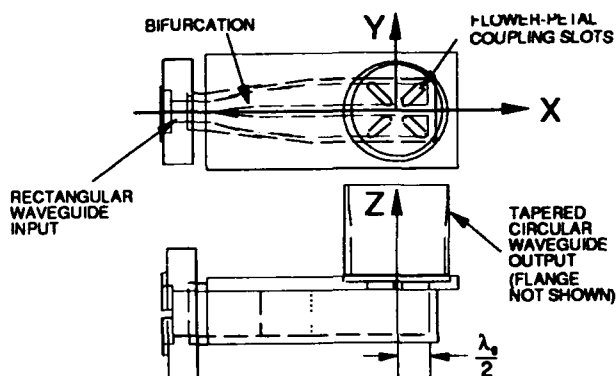


Figure 1. Schematic diagram of the mode transducer.

It is a good approximation to assume that the shorting plane in the rectangular section is one half a guide wavelength from the origin, and that this has the effect of requiring the fields in the circular guide to satisfy a metal boundary condition on the y-z plane. To the extent that this is the case, the TE_{11} , TM_{11} and TE_{31} modes are not excited. The failure of

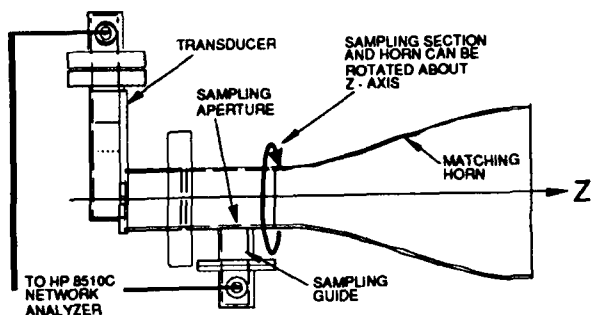


Figure 2. Schematic diagram of mode analyzer.

this condition to hold exactly is likely to manifest itself as an inequality in the excitation of the slots nearest the shorts, as compared to the other pair, with perhaps also a small departure from the precise phase equality which the assumed symmetry would imply. A similar situation has been considered in connection with the four-spoke mode transducer [3], and the formulas derived there are likely to hold approximately here. Let d represent the fractional amplitude deficiency of the more weakly excited pair, and ϕ the phase difference. Then, according to [3], the fractional power lost to non- TE_{01} modes is

$$[d^2 + 4(1 - d)(\sin\phi/2)^2] / [4(1 - d + 0.5d^2)] ,$$

from which one can estimate the deviations which will produce significant power loss to unwanted modes. The details of the slot design, apart from discrimination against the TE_{21} mode, determine what fraction of the incident power will be reflected. The slot width which minimized the reflection was determined experimentally and, as is described later, a tuning post was added to obtain the best match.

III. EXPERIMENTAL DEVELOPMENT

Numerical modeling of the flower-petal transducer has been described in [4]. Here we discuss the experimental development. The all-important measurements of mode purity in the circular guide were made with a rotating H_z probe coupled to a network analyzer and a computer, as shown schematically in Figure 2. The circular waveguide output of the transducer is coupled to another circular guide section of the same diameter which is free to rotate about the common z -axis. This rotating section is connected in turn to a nonlinearly tapered horn which acts as a well-matched load for many modes. A small circular-hole in the wall of the rotating section couples to a rectangular waveguide with its large dimension parallel to the axis of the circular guide. The coupling is small enough to avoid significant perturbation of the fields in the circular guide, and large enough to provide signals within the dynamic range of the network analyzer. About -45 dB is optimum. Mode conversion due to the hole is negligible for most modes. The H_z is sampled at sixteen equi-spaced points around the periphery. At each point the phase and magnitude of the complex transmission coefficient as a function of frequency over a selected band, between the input of the transducer and the output of the sampling guide, is dumped from the network analyzer via a GPIB link onto a PC disk.

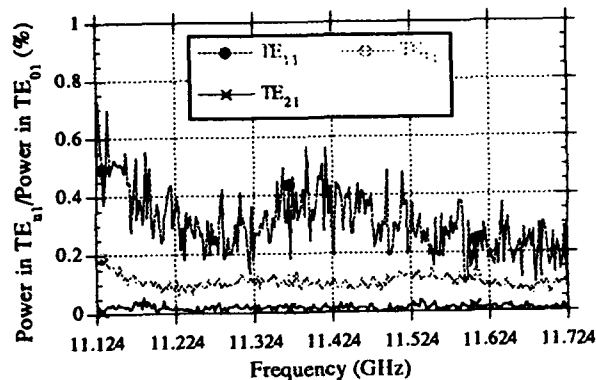


Figure 3. Mode analyzer measurements of fractional power in unwanted TE mode propagating in 1.5-inch circular guide

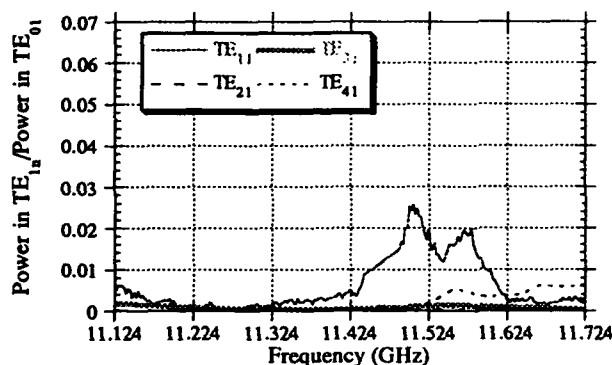


Figure 4. TE mode contamination with taper.

From these data, azimuthal space harmonics of H_z can be calculated and, in turn, the power contained in a TE mode which has m azimuthal repeats can be deduced [4]. The mode analyzer is insensitive to TM modes. Figure 3 shows the results obtained with the mode analyzer in 1.5-inch guide, while Figure 4 shows the results after the taper to 1.75 inches. The rise in TE_{11} power above 11.424 GHz is probably spurious. The mode analyzer cannot distinguish between TE_{11} and TE_{12} , and a comparison of Figures 3 and 4 suggests that the striking difference is associated with the passage of TE_{12} through cut-off. If one assumes that the excess excitation is TE_{12} , the actual power loss associated with it is reduced by a factor $\lambda_{g11}/\lambda_{g12}$.

As mentioned earlier, it is necessary to add an inductive post in the input rectangular waveguide, close to the beginning of the bifurcation section, in order to obtain a well-matched input. The resultant input VSWR is shown in Figure 5.

In order to measure the conversion efficiency from the rectangular guide to the desired circular guide mode, two flower-petal transducers were joined at the circular flanges and S-parameter measurements were made between the rectangular waveguide flanges. After correcting for flange losses at the rectangular junctions, the observed transmission loss was $1.0 \pm 0.7\%$, and the reflection loss was 0.25% . Variations in these measurements as the transducers were rotated with respect to each other at the circular flange junction were below

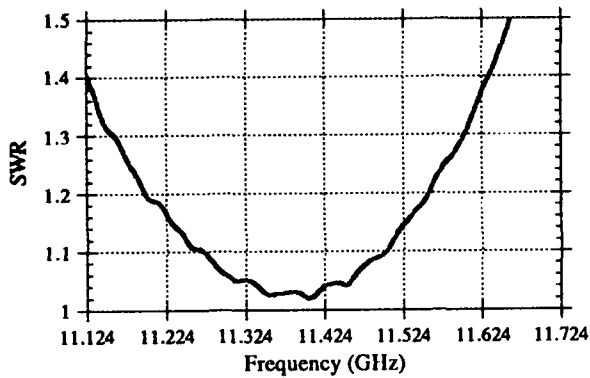


Figure 5. Transducer input VSWR

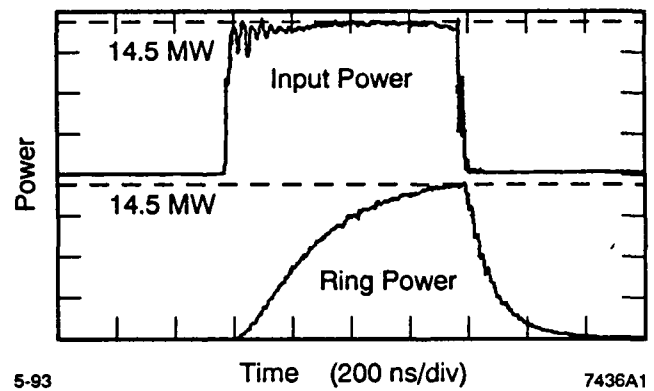


Figure 7. High power performance of transducer.

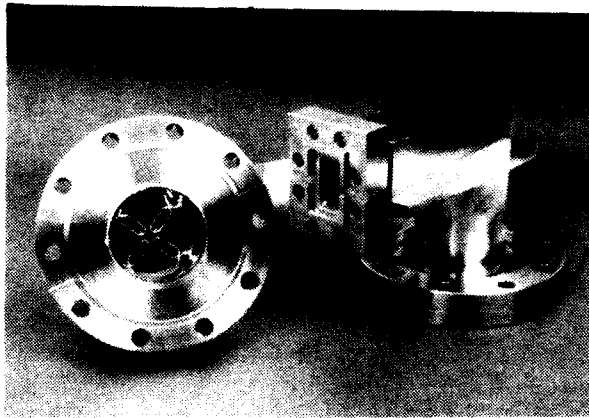


Figure 6. Completed flower-petal transducer

the level of measurement sensitivity, thus providing additional evidence that conversion to azimuthally varying modes is small, and our only evidence that conversion to the TM_{11} mode is small. We take these results to indicate that the loss attributable to a single transducer is less than 0.7%.

IV. HIGH POWER TESTING

A completed flower-petal transducer, suitable for high-power operation under high-vacuum is shown in Figure 6. Two of these units have been operated back-to-back in an X-Band resonant ring up to 150 MW, with a pulse width of 800 ns. The pulse waveforms for the klystron and the resonant ring are shown in Figure 7. The power level reached was limited by the klystron and its window, and not by the transducers under test.

V. TRANSDUCER/COMBINER/DIVIDER

A three-port version of the transducer, in which the flower-petal couples to two rectangular waveguides which are not

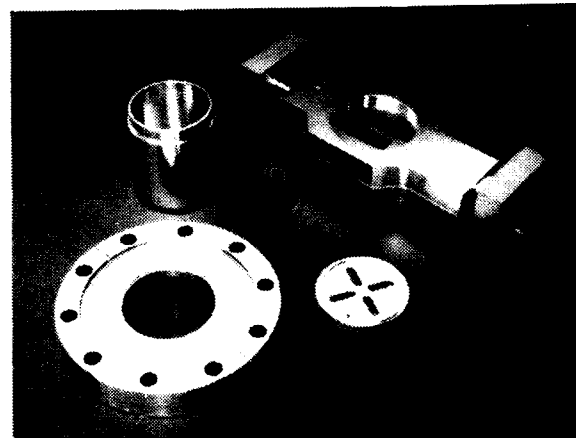


Figure 8. Transducer/combiner/divider.

joined by a bifurcation section, but are taken to two separate ports symmetrically placed on each side of the flower-petal has been built, and is shown in Figure 8. It is expected that this device will be used in the NLC Test Accelerator, both as a power combiner and as a power divider. Preliminary tests will begin shortly.

VI. REFERENCES

- [1] S. S. Saad et al., "Analysis and design of a circular TE_{01} mode transducer," *Microwaves, Optics and Acoustics*, Vol. 1, No. 2, January 1977.
- [2] Formerly manufactured for several high-frequency bands by Alpha Industries Inc. This device was brought to our attention by George Spalek.
- [3] N. Kroll and K. Ko, "The Four-Spoke Mode Transducer/Power Combiner," in preparation.
- [4] S. Tantawi, K. Ko and N. Kroll, "Numerical Design and Analysis of a Compact TE_{10} to TE_{01} Mode Transducer," *Computational Accelerator Physics Conf.*, Pleasanton, CA, February 1993.

Development of an S-band RF Window for Linear Colliders

A. Miura and H. Matsumoto*

The Graduate University for Advanced Studies

1-1 Oho, Tsukuba, Ibaraki 305, Japan

**KEK, National Laboratory for High Energy Physics*

1-1 Oho, Tsukuba, Ibaraki 305, Japan

Abstract

We report on our research and development of an S-band (2856 MHz) alumina RF window for a high power transmission which exceeds 100 MW. We have studied the mechanism of RF breakdowns of alumina disks experimentally with a test facility based on a resonant ring. At a higher power transmission (>50MW), impurities within alumina due to sintering binder materials and internal voids were shown to be mostly responsible. An experiment at a resonant ring has shown that the new RF window by using high-purity (99.9%) and low porosity (0.5%) alumina disks can successfully withstand a maximum peak transmission-power of 310 MW with a pulse width 2.5 μ s at 10 Hz repetition rate, and a maximum average transmission-power of 300 MW with pulse width 2.5 μ s at 50 Hz.

I. INTRODUCTION

At the KEK Accelerator Test Facility (ATF) for the Japan Linear Collider (JLC), an S-band linac with the energy of 1.54 GeV will be used as an injector for a damping ring. Each accelerating unit consists of two 3 m long accelerating structures with accelerating gradient of 22 MV/m, an 85 MW klystron (TOSHIBA) with a SLED, and a klystron modulator. An RF window with a power capability up to 100 MW must be used between the klystron and SLED cavities for an ease of klystron maintenance work. However, window failures often occur in the power range of a few tens of MW. An improved reliability of RF windows is highly desirable [1].

Until now many studies of window failure were mainly made on local heat build-up due to multipactoring [2], and a variety of surface coating materials, such as TiN, were tested as a cure [3]. More recently it was calculated that multipactor phenomena occurred when the RF power transmission is below 50 MW at the S-band frequency [4]. We have come to suspect that in the power regime of up to 50MW high power breakdowns of alumina disks may be due to phenomena taking place inside alumina rather than at its surface. We considered that the root cause of the problem could be voids within alumina or structural defects due to binder materials used during the sintering process. In order to reduce the porosity (volume fractions of voids) in alumina we have applied a Hot Isostatic Pressing (HIP) treatment [5]. This allows an unambiguous study of effects of binding materials used during the sintering process. We have studied behaviors of alumina disks with a varying amount of binders in an RF environment with the resonant ring. We

have experimentally examined time profiles of breakdown phenomena.

II. PREPARATION OF HIGH PURITY, LOW-POROSITY ALUMINA WINDOWS

Typical disks for RF windows have been made of 99.5 % purity alumina. The sintering binders, such as MgO, account for a major part of impurities. It has recently become possible to manufacture fine alumina particles with diameters of less than 0.5 μ m. This and concerning the progress of a sintering technique allow us to make alumina disks with an ultra-high purity of 99.9%. In addition, it has been learned recently that the RF loss due to the binders depends strongly on the choice of binder materials [6]. For example, it is very sensitive to the presence of MgO. We have fabricated alumina disks with a varying purity with and without MgO, and have measured their RF loss. If the alumina disk does not contain MgO at all, a very low dielectric loss ($\tan \delta = 2.0 \times 10^{-5}$, $f = 1000$ MHz) is achieved.

By using high-purity ultra fine alumina powder as the raw material and using a sintering process without MgO as the binder, high purity and low RF loss alumina disks can be fabricated. Then by treating them with a HIP method, remaining voids are further removed to porosity of 0.5 % level. We have fabricated several of these new alumina disks for our RF power testing.

III. HIGH POWER TESTS

We have conducted high power tests of alumina disks as RF windows with a varying fraction of sintering binders with a resonant ring. In order to study the high power behaviors and properties of high purity alumina material itself, in our test several noteworthy points are 1) we have significantly reduced the alumina porosity with the HIP treatment. 2) None of the alumina samples has TiN coating.

A. Alumina Samples

We have tested six alumina disks. Table 3 summarizes their parameters. The samples #1 and #2 are based on 99.5 % purity grade alumina. While sample #1 had no visible imperfections, the sample #2 had a concentration of impurities which looked like a dark cloud. The sample #3, #4, #5 and #6 are made of 99.9 % alumina. Especially the sample #4 does not contain any MgO binder. The test with sample #5 is made to study the reproducibility of the result with

sample #3. The sample #6 was made intended 10 pin-holes whose diameter is 0.5mm in order to investigate behavior of multipactoring around the pin holes.

Table 1 parameters of tested alumina disks

	#1	#2	#3	#4	#5	#6
Purity (%)	99.5	99.5	99.9	99.9	99.9	99.9
Impurity concentrated	no	yes	no	no	no	no
MgO (Binder)	yes	yes	yes	no	yes	yes
Intended pin hole	no	no	no	no	no	yes

All alumina disks performed HIP treatment and no coating

B. Experimental Apparatus

The diagram of the resonant ring is shown in Figure 1. The vacuum pressure monitored with cold cathode gauges (CCGs) and B-A gauges (BAGs). Photo multiplier tubes installed on a downstream view window are used to measure the time profile of light emissions from the alumina disk. The X-rays from the RF window are measured with scintillation counters in the upstream and downstream neighborhood of the RF window. On the outer wall of the RF window Alumel-Chromel thermocouple detectors were installed to monitor the temperature rise of the alumina disk.

A schematic diagram of the window structure is shown in Figure 2. The vacuum on both sides of the alumina disk is separated by the Helicoflex. Since it allows to replace the alumina disk easily without disturbing the window frame.

The RF pulse width is always maintained at 2.5 μ s. In the first step the repetition rate of is set to 10 Hz, and the power transmission is gradually increased. When the peak transmission power reaches 200 - 310 MW and the alumina disk survives, the same procedure is repeated at the pulse repetition rate of 25 Hz and 50 Hz.

More detail of experimental apparatus was shown in reference [5].

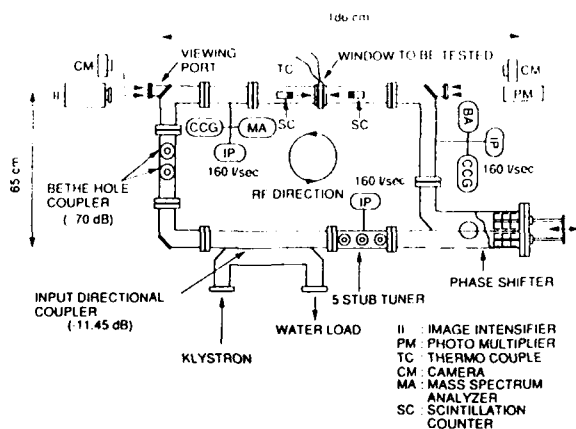


Figure 1. The diagram of the resonant ring

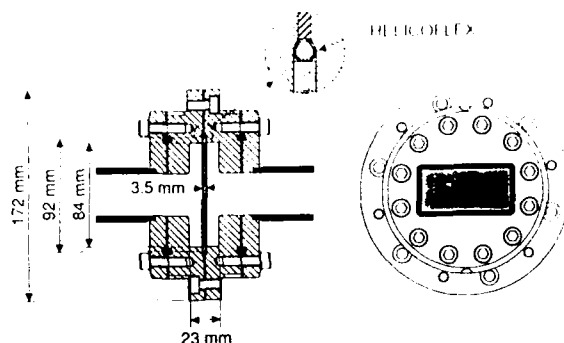


Figure 2. A schematic diagram of the rf window

C. Experimental Results and Discussions

Figure 3 summarizes the results of the experiment, showing the observed temperature rise at the window frame as function of the average power for each sample.

Sample #1: During the first 10 Hz operation, a localized light emission from a same single spot continuously increased. With a transmission power 200 MW a large discharge took place, and the disk was destroyed. An inspection with an electron microscope indicated numerous melted pin-holes and cracks at the point where the light emission was seen. Sample #1 showed the highest temperature rise among the samples tested. Our interpretation is that a highly localized multipactor started on a defective spot on the surface, and resultant electron collisions on the surface has become the heat source to cause the disk failure.

Sample #2: No localized discharge was seen during the test. It did not experience a steep temperature rise as the sample #1. After running with 204 MW at 10 Hz, the repetition rate was raised to 25 Hz. At 25 Hz, when the power reached 113 MW, the alumina disk was cracked and destroyed. No traces of melting were seen on the surface. We interpret this failure as caused by a heating due to the localized sintering binder.

Sample #3: After running up to 200 MW at 10 Hz, the test was continued up to 280 MW at 25 Hz, then up to 200 MW at 50 Hz. The test was terminated at that moment. The alumina disk has seen no damage. Figure 4 shows the time profile of the light emission from sample #3. The signal trace is superimposed with the RF power profile. At the rising and falling edge of the RF pulse, when the power transmission reaches near 10 MW, light emissions for a few hundred nano-seconds are clearly seen. We understand that although the canonical operation power was well above the multipactor regime, during the pulse transient time the disk momentarily experiences the power level where multipactor is prominent. Therefore, for real-life RF window disks, TiN coating is still required.

Sample #4: After running at 203 MW at 10 Hz, the power was raised to 230 MW at 25 Hz, then 280MW at 50 Hz. No failure occurred. Sample #4 showed a very stable performance after aging with the lowest temperature rise even at the maximum

power of 280 MW at 50 Hz. No traces of melting or cracks were found on alumina surface.

Sample #5: After running at 310 MW at 10 Hz, the transmission power was raised to 280 MW at 25 Hz, then 300 MW at 50 Hz. No failure occurred. Figure 3 shows that the temperature rise with sample #5 is very similar to that of sample #3. No melting spots or cracks were found on the disk after 500 hours of operation.

Sample #6: after running at 200 MW at 10 Hz. No failure such as a crack occurred. During rf operation local discharge was continuously occurred around pin-holes. Temperature rise of this sample was very high compare with that of sample #3 and #5 which were made from a same alumina quality as sample #6. It clearly this heat source was electron bombardment due to local discharge at the pin-holes. At this moment this test has continued.

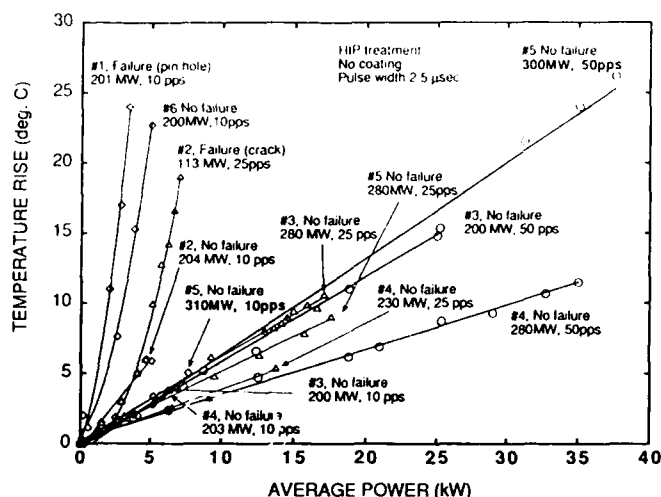


Figure 3. Temperature rise at the window frame as function of the average power for each sample

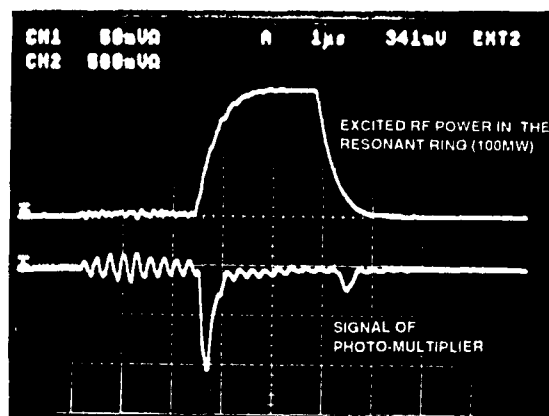


Figure 4. The time profile of the light emission from sample #3

IV. CONCLUSION

For the power level higher than the multipactor region, imperfections inside the alumina disk are the dominant

source of breakdowns. As a cure, we have developed a technique based on a combination of i) high-purity alumina disk, ii) avoidance of MgO sintering binder, and iii) the HIP treatment. This significantly improves reduces the dielectric RF losses and the porosity. The high power performance of alumina disks fabricated this way is significantly superior to that of disks made in a traditional way. It was found that multipactor occurs during the RF pulse transient time at the high power region. Therefore, coating with TiN is still necessary to maintain the best possible overall characteristics of alumina disks for RF windows.

V. ACKNOWLEDGMENTS

The authors wish to thank Professors Y. Kimura and K. Takata at KEK for their continuous encouragement. The discussions with Drs. T. Shintake and S. Yamaguchi at KEK inspired us to initiate the present study on the breakdown mechanism of alumina disks. The present work has been carried out as part of a research and development program for the JLC-I with the following participants: Drs. S. Takeda, J. Urakawa, H. Hayano, Messrs. Y. Otake, T. Naito, S. Araki and many other people at KEK. The authors are grateful for their help. The authors thank Messrs. R. S. Callin and W. R. Fowkes at SLAC, Drs. Y. Saito and S. Michizono at KEK and Dr. H. Baba at Nihon Koshuha Co. Ltd. They generously contributed advise and information on the breakdown phenomena of RF windows and on high power experiments. The authors wish to thank the NKK Corporation for the HIP work, Nihon Ceratic Co. Ltd. for fabrication of high-purity fine alumina disks and Kobe Steel Co. Ltd. for production of high-purity low rf-loss alumina disks. The help by Messrs. S. Morita and T. Matsui of ATC Co. for resonant ring tests are also appreciated. A part of the resonant ring experiment was carried out under a collaboration with Drs. M. Nagl, B. Dweresteg and M. Summerfeld from DESY. Finally, thanks are due to Drs. N. Toge and M. Yoshioka at KEK for fruitful discussions and critical reading of the manuscript.

VI. REFERENCES

- [1] A. Miyamoto, "The third workshop JLC", *KEK proceedings* 92-134, December 1992 A/H/D
- [2] R. Hayes, "Research on Microwave Window Multipactor and it's Inhibition", Final Report, # AD 256259, Eitel-McCullough Inc., 1964
- [3] S. Michizono et al., Proc. of the 16th Int. Symp. on Discharge and Electrical Insulation. in Vacuum, 1992
- [4] A. Miura and H. Matsumoto, "Development of S-band High-Power Pillbox-type RF Window", *Proc. of Int. Linear Accelerator Conf.*, 1992
- [5] A. Miura and H. Matsumoto, "Development of S-band High-Power Pillbox-type RF Window", *Proc. of Int. Conf. for High Energy Accelerators*, 1992
- [6] W. D. Kingery et al., "Introduction to Ceramics", John Wiley & Sons Ink, 1982

High Power Test of RF Window and Coaxial Line in Vacuum

D. Sun, M. Champion, M. Gormley, Q. Kerns, K. Koepke, A. Moretti
Fermi National Accelerator Laboratory*
P.O. Box 500, Batavia, IL 60510

Abstract

Primary rf input couplers for the superconducting accelerating cavities of the TESLA electron linear accelerator test to be performed at DESY, Hamburg, Germany are under development at both DESY and Fermilab. The input couplers consist of a WR650 waveguide to coaxial line transition with an integral ceramic window, a coaxial connection to the superconducting accelerating cavity with a second ceramic window located at the liquid nitrogen heat intercept location, and bellows on both sides of the cold window to allow for cavity motion during cooldown, coupling adjustments and easier assembly. To permit in situ high peak power processing of the TESLA superconducting accelerating cavities, the input couplers are designed to transmit nominally 1 ms long, 1 MW peak, 1.3 GHz rf pulses from the WR650 waveguide at room temperature to the cavities at 1.8 K. The coaxial part of the Fermilab TESLA input coupler design has been tested up to 1.7 MW using the prototype 805 MHz rf source located at the A0 service building of the Tevatron. The rf source, the testing system and the test results are described.

I. INTRODUCTION

TESLA [1] is a proposed 500 GeV center of mass energy e^+e^- linear collider utilizing superconducting rf accelerating cavities. An international effort under the direction of DESY is collaborating to assemble a TESLA test facility at DESY including an electron source, 40 m of superconducting accelerating cavities, cryostats, accelerating rf, beam diagnostics, and the infrastructure necessary to produce and test the superconducting cavities.

A TESLA accelerating module consists of a cryostat nominally 10 m long and contains 8 niobium accelerating cavities. Each accelerating cavity is nominally 1 m long and contains 9 contiguous niobium accelerating cells that are tuned to 1.3 GHz. Each 9 cell cavity is excited in the pi mode with a single input coupler.

Input couplers are under development at DESY [2] and Fermilab [3]. The Fermilab input coupler design is shown in Figure 1. The function of the input coupler is to transmit the rf energy from the klystron power distribution system, WR650 waveguide at room temperature, to the cavities at 1.8 K. The cylindrical ceramic window within the WR650 "doorknob" transition

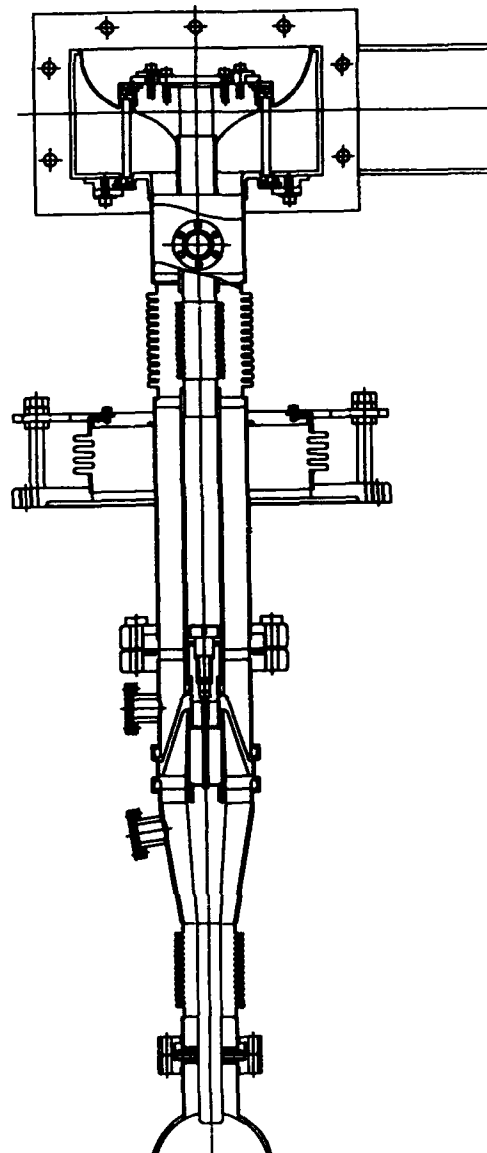


Figure 1. TESLA input coupler tested at A0.

isolates the pressurized waveguide from the required high vacuum of the cold coaxial section. The conical ceramic window maintains the ultraclean environment required by the superconducting cavities during their assembly and testing. During normal operation, this window acts as backup to the warm window and prevents contamination of the entire accelerator in the event of a warm ceramic window failure.

*Operated by Universities Research Association under contract to the U.S. Department of Energy.

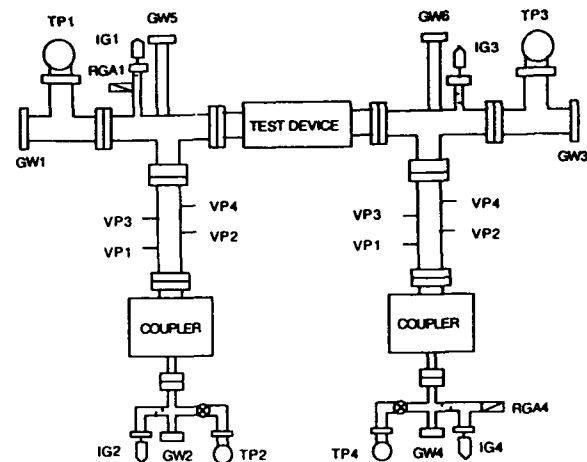
Normal operating conditions for the coupler during beam acceleration are a peak power of 200 kW, a nominal 2 ms pulse length and a pulse repetition rate of 10 Hz. An estimated 1 MW peak power with reduced pulse length and repetition rate to keep the average coupler power unchanged, is necessary if in situ high peak power conditioning of the cavities is planned. At this peak power level, the performance of the coupler, and in particular, the behavior of the ceramic windows and bellows, can no longer be reliably predicted, and at the very least, careful initial rf conditioning of the coupler is expected to be necessary before it functions reliably.

As an rf system at 1.3 GHz and at a peak power level above 1 MW is currently not available to us, we have used the operating spare klystron of the Fermilab linac upgrade [4] to test the coaxial part of the Fermilab TESLA input coupler. This source is located in the A0 service building of the Tevatron where it was previously used to rf condition the Fermilab Linac Upgrade accelerating cavities. The rf source produces 120 μ s long, 12 MW peak power rf pulses at a frequency of 805 MHz. Except for multipactoring, the difference in operating frequency does not significantly affect the behavior of the coaxial part of the input coupler as it was designed to have a constant 50 ohm impedance throughout, and the conical ceramic window is "thin". The complete coupler, including the "doorknob" transition with its narrow band width, will be tested at a later date with a 1.3 GHz rf system under assembly at Fermilab.

II. GEOMETRY AND INSTRUMENTATION

The goals of the rf tests at A0 were to subject TESLA input coupler components to peak power levels at least equal to their 1 MW design level, to find the rf breakdown thresholds by raising, if necessary, the peak rf power above 1 MW, and to determine the locations and mechanisms of the rf breakdown. These goals necessitated a somewhat more elaborate test geometry than normally used to condition rf components.

The test equipment that has been added to the A0 rf system is depicted in Figure 2. The rf power enters and leaves the test equipment through the two WR975 to 3 1/8 inch coax couplers shown at the bottom of the figure. Not shown are the forward and backward directional couplers in the waveguide upstream of the test insertion to measure the rf power, and the waveguide ceramic windows contiguous to the WR975 couplers to allow high vacuum in the test device. Two standard 3 1/8 inch rigid coax sections, each 12 inches long, and two rigid 3 1/8 inch coaxial elbows complete the rf circuit. The test geometry is physically symmetric relative to the test device. The coaxial part of the TESLA input coupler tested has an outer coaxial diameter between 4 cm to 6 cm. Therefore,



A0 TEST SETUP

TP: TURBO PUMP
IG: ION GAUGE
RGA: RESIDUAL GAS ANALYZER
GW: GLASS WINDOW
VP: VOLTAGE PROBE

Figure 2. Test geometry used to test the input coupler.

conical transitions were used to match the inner and outer coax conductors to the 3 1/8 inch rigid coax on either side of the test device. The rf insertion is approximately matched and most of the power is absorbed by an rf load located downstream of the test circuit.

Four turbo pumps were used to evacuate the test volume. Four ion gauges and a residual gas analyzer were used to monitor the vacuum during pumpdown and during the rf testing. Six glass windows, two in line with the test device (GW1 and GW3) and their associated photomultipliers were used to monitor the light output within the test volume. Two additional windows, one glass with a photomultiplier and one KBr window for an infrared monitor, were mounted on either side and close to the cold TESLA window to monitor this critical area. Finally, 8 rf voltage taps spaced 1/8 wavelength apart, 4 upstream and 4 downstream of the test device, were available to locate a breakdown region in the event that the breakdown reflected a measurable amount of rf power.

The controls of the A0 rf system contain 8 triggerable data recording channels that were intended to record transient signals during klystron modulator performance checks or fault diagnosis. Each data channel consists of a digitizer connected to a 120 μ s circular buffer with a 1 μ s time resolution. These channels were available for transient analysis. In addition, a single data

point per channel was recorded 4 times per minute and stored in a Sun Work Station to maintain a slow time record of the test over many days.

III. PROCEDURE

During the test, the rf pulse length and pulse repetition rate were maintained at 120 μ s and 15 Hz, the maximum available from the A0 rf system. The average vacuum at the start of the test was $2.8 \cdot 10^{-7}$ torr. The peak rf power was increased in steps; the amplitude increase per step was determined by the vacuum pressure which was arbitrarily maintained below $2.0 \cdot 10^{-6}$ torr. The vacuum pressure was allowed to recover at constant rf power until it reached a pressure of $4.0 \cdot 10^{-7}$ torr at which point the rf power was again increased. The power threshold at which the vacuum first responded to the rf was 3.6 kW.

The photomultipliers were calibrated by measuring their outputs when located at the same position. Their outputs indicate relative light intensities as a function of rf power, time, and location. The photomultiplier outputs were continuously observed during the coupler conditioning but were not used to determine the rate at which the rf power was increased.

The temperature of the conical ceramic window was monitored with an infrared detector looking directly at the ceramic, and with two thermocouples located on the outer coax conductor near the location where the ceramic was attached with a braze joint. These thermometers were monitored to prevent damage to the ceramic due to thermal stress, and to record the heating rate of the ceramic as a function of rf power through the ceramic window.

IV. RESULTS

Testing has been in progress for one week. The coupler was conditioned to a 1.4 MW peak power level within three days. This time could have been reduced to two days with an automatic conditioning system as the system was operated at a constant reduced power level (20kW and 100 kW) while unattended overnight. Since this initial conditioning, the coupler has operated without interruption for 40 hours at a peak power level of 230 kW, for 16 hours at 1 MW, and 1 hour at 1.7 MW.

During conditioning, the klystron shut off twice due to a klystron window spark and/or high reflected rf power. The first trip occurred at 1.3 MW. The cause of this trip has not been established. The second trip occurred at 1.44 MW and was caused by a spark downstream of the conical window, perhaps in the 4 cm region of the coupler or in the 3 1/8 inch transition. This spark was isolated through high light output at GW3 and GW4, the photomultipliers mounted downstream of the conical window, by low light output from the photomultiplier mounted by the conical

window, and by the high vacuum pressure downstream of the conical window. Since then, several more sparks have occurred, apparently in the downstream region, all at or above a peak power level of 1.4 MW.

Steady light related to the rf power has been observed by the photomultiplier located at GW1, that looks at the upstream part of the coupler as far as the conical window, by the photomultiplier located immediately downstream of the conical window, and by the photomultiplier located on the downstream waveguide transition (GW4). The light at GW4 can be conditioned away, reappearing only if the rf is turned to a lower level for an extended time and then returned to its higher original level. The light on either side of the conical window occurs at specific power levels, increasing and decreasing as the power is continuously raised, and up to now has not been completely conditioned away.

V. CONCLUSIONS

The conical part of the tested TESLA input coupler appears to satisfy the normal peak power operating condition of 200 kW. After conditioning, no light is seen below a peak power of 230 kW. Effort continues to understand and eliminate the light still present. A possibility is to locate the conical window at a voltage minimum to reduce the voltage at the window during mismatched operation.

Operation at a peak power level of 1 MW for in situ high peak power conditioning of the cavities is still not certain. Some light during conditioning is acceptable as the conditioning time is short. However, the location of the observed sparks needs to be determined and the cause corrected.

VI. REFERENCES

- [1] *A Proposal to Construct and Test Prototype Superconducting R. F. Structures for Linear Colliders*, DESY, April 1992
- [2] B. Dwersteg, M. Marx, D. Proch, "Conceptional Design of a RF Input Coupler for TESLA", DESY 1992
- [3] M. Champion, D. Peterson, T. Peterson, C. Reid, "Tesla Input Coupler Development", these proceedings
- [4] H. Pfeffer, et al, "Solid State 24 MW Modulator for Fermilab's 400 MeV Linac", Twentieth Power Modulator Conference, Myrtle Beach, South Carolina, June 1992

Mode Selective Directional Coupler for NLC*

S. G. Tantawi

Stanford Linear Accelerator Center, Stanford University, Stanford CA 94309

Abstract

The design method for a high power, X-band, 50 dB, circular to rectangular directional coupler is presented. The circular guide is over moded and is intended to operate in TE₀₁ mode. The rectangular guide operates at the fundamental TE₁₀ mode. A small percentage of higher order modes in the circular guide can cause considerable errors in the measurements because the magnitude of the axial magnetic field of these modes is higher than that of the operating mode, especially near their cutoff. We used a Hamming window pattern for the coupling slots to achieve mode selectivity. Comparison of theory and experiment will be presented.

I. INTRODUCTION

Over-moded waveguides are often used to minimize the losses in waveguide transport systems. One key component in these systems is directional couplers. These are used either to couple power from one guide to another or to monitor the power in one guide. In either case the coupler should introduce very little mode conversion into the original guide and couples only to the design mode of operation. This paper is concerned with the design of a mode-selective directional coupler for the Next Linear Collider (NLC) RF system[1]. This system uses a circular waveguide with a 1.75" diameter. The operating frequency is 11.424 GHz. These waveguides are expected to transport RF power up to 200 MW. A directional coupler with a coupling level around -50 dB is required to monitor the power level in these guides. The guide operates in the low loss TE₀₁ mode. This mode has a small magnetic field near the wall unlike other modes that can be supported by the guide. Hence, unless the coupler is highly mode selective, a small percentage of mode impurity causes errors in the measurements.

The methodology normally used in designing mode selective directional couplers for high power over-moded guides discriminates against other modes by properly choosing the distance between coupling slots [2]. As the number of modes inside the original guide is increased, the number of holes and the length of the coupler are increased. This makes the coupler hard to manufacture and very sensitive to the accuracy of slot positions and size. When this problem was studied for communication systems, it was possible to make the wavelength of the dominant mode in the side arm equal to that of the main guide. In this case, it was realized that natural mode discrimination occurs independent of slot positions [3]. However, there is no theory developed for designing couplers in a manner independent of slot position.

In this paper we present a rigorous approach for designing mode-selective directional couplers using the analogy between the coupling between guides with slots and digital filters. The theory is presented in section II. An example of a coupler design and comparison between theory and experiment is presented in section III.

II THEORY

Figure 1 shows a schematic diagram of the problem. The circular guide is over-moded, but the rectangular guide that forms the side arm is assumed to be able to support only one propagating mode. The rectangular guide is coupled to the circular guide by the side wall (the narrow side of the rectangular guide). This means that the rectangular guide couples only with H_z (the magnetic field in the Z direction); hence the side arm will couple to no TM modes in circular guide. The coupling between a TE mode with wavelength λ_n , and an axial magnetic field H_z^n to TE₁₀ mode in the rectangular guide with wavelength λ_s can be written as a phasor addition of the contribution of each slot in the coupler; i.e.,

$$H_{\pm}^{n,s} = \sum_{i=1}^N |H_z^n| C_i e^{-2\pi j z_i (\frac{1}{\lambda_n} \mp \frac{1}{\lambda_s})}, \quad (1)$$

where $H_{\pm}^{n,s}$ is a phasor representing the Z magnetic field in the coupler side arm. The plus sign is for coupling in the forward direction, and the negative sign is for coupling in the reverse direction. The symbol z_i refers to the coupling slot position in the Z direction relative to some arbitrary reference. Equation (1) can be viewed as a *discrete convolution* of a signal represented by the field inside the main coupler guide as a function of z_i , i.e.,

$$s(i) = |H_z^n| e^{-2\pi j z_i \frac{1}{\lambda_n}}, \quad (2)$$

with a filter represented by the coupling in the side arm as a function of z_i , i.e.,

$$h(i) = C_i e^{-2\pi j z_i (\pm \frac{1}{\lambda_s})}. \quad (3)$$

The output signal is then given by

$$y(l) = \sum_{i=1}^N s(i) h(l-i). \quad (4)$$

Equation (4) is equivalent to eq.(1) at $l=0$. The input signal $s(i)$ can be viewed as a summation of different harmonics each having a frequency $2\pi/\lambda_n$. The filter $h(i)$ can then be designed using standard methods for Finite Impulse Response (FIR) digital filters [4]. If $N \rightarrow \infty$ and C_i is a constant, it can be seen immediately that the frequency response of the filter is $\delta(2\pi/\lambda - 2\pi/\lambda_s)$ where $\delta(\cdot)$ is the Dirac delta function. This means that by choosing the wavelength in the side arm equal to the wavelength of the desired mode in the main guide and having long enough coupling length, the side arm will couple only to

* Work supported by the department of Energy, contract DE-AC03-76SF00515

that mode. However, we do not require the coupling response to be as narrow as a delta function. It is sufficient to have a band-pass FIR filter with band width equal to $2|2\pi/\lambda_f - 2\pi/\lambda_p|$ where λ_f is the wavelength of the operating mode in the main guide and λ_p is the wavelength of the mode closest in wavelength to the propagating mode. The filter should have side lobes (or ripples) as low as the desired rejection value for the unwanted modes.

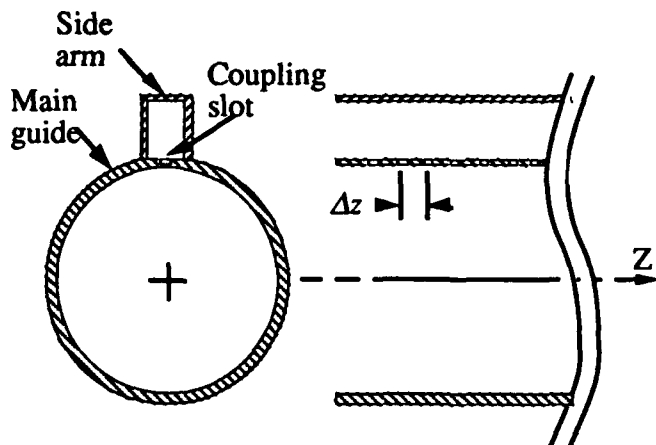


Figure 1 Schematic diagram of the basic coupler geometry

One standard and widely used FIR filter is the so called Hamming window [4]. A Hamming window with its main lobe centered at $2\pi/\lambda_s$ is given by equation (3) while substituting for the coefficients C_i as follows:

$$C_i = 0.54 + 0.46 \cos\left(\frac{2\pi}{N}\left(i - 1 - \frac{N-1}{2}\right)\right), \quad 1 \leq i \leq N \quad (5)$$

Using a discrete Fourier transform one can obtain the impulse response of that filter. This is shown in Fig. 2 as a function of the normalized frequency $\theta = 2\pi \Delta z / \lambda$, where Δz is the separation between slots. The peak side lobe amplitude is -41 dB. The main lobe width is $8\pi/N$. This determines the required coupler length (L):

$$N\Delta z \equiv L > 2 \left| \frac{\lambda_f \lambda_p}{\lambda_f - \lambda_p} \right| \quad (6)$$

The sampling distance Δz must obey the Nyquist sampling criteria, i.e.,

$$\Delta z < \lambda_{\min} / 2, \quad (7)$$

where λ_{\min} is the smallest possible wavelength in the main guide. If the slots are small and circular, the relation that governs the H_z coupling between the two guides is well known; see for example [5]. The equations that relate the propagating power to H_z , the relations relating the slot dimensions to its coupling coefficient, and equations (5) through (7) are the main design equations. The resulting mode selective directional coupler is insensitive to large dimensional tolerances between the slots.

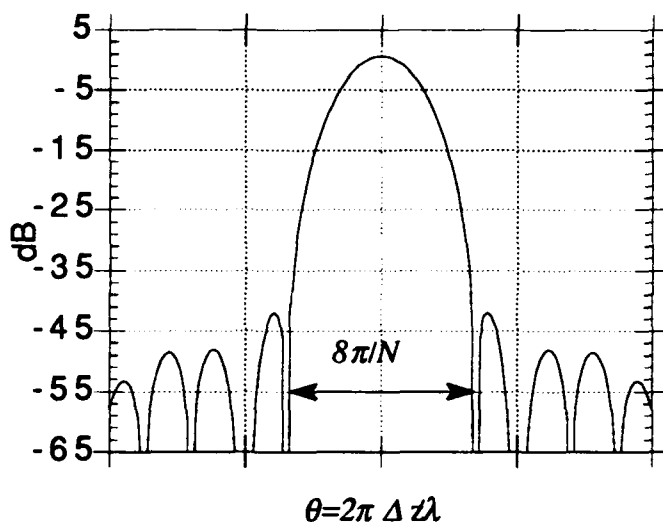


Figure 2. Hamming window impulse response

The filter impulse response, shown in Fig 2, shows a dip between each side lobe and the next. These dips will exist whether this type of filter is used or not. At the wavelengths at which a dip occurs, the distance between the slots is such that no coupling occurs. The distance between the slots can be adjusted so that the wavelength of each unwanted mode lie in exactly one of these dips. This is the normal methodology in designing couplers. However, as the number of modes gets larger, the coupler length and number of slots also becomes large. In this case it becomes very difficult to fabricate the coupler because of the tight tolerances imposed on the distances between the slots

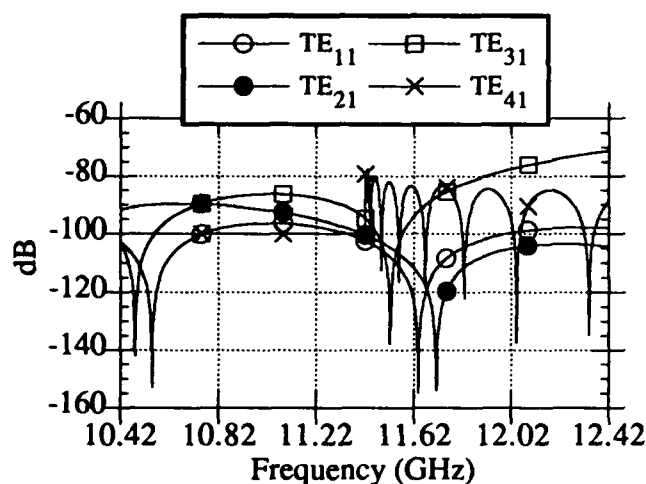
It worth noting that the filter function being used for coupling will be just as effective in eliminating any mode contamination and mismatch in the main guide due to the coupling slots. Each slot will produce an amount of mode conversion and reflection that will add up according to Equation(1). Hence, they will cancel each other according to the filter function except for the operating mode in the forward direction.

III A 50 dB COUPLER for NLCTA

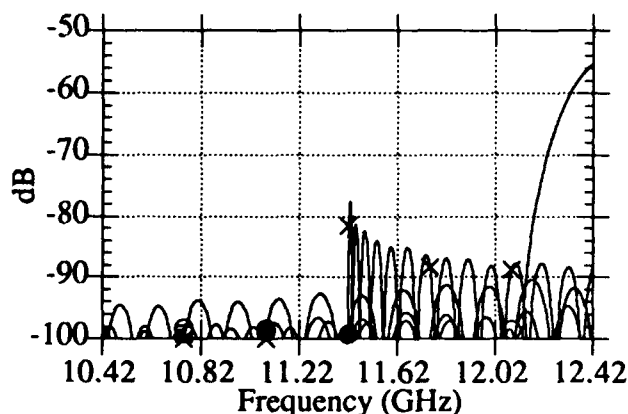
We used the design method described above to design a mode selective directional coupler for the NLCTA RF system described briefly in the introduction. The coupler has 50 holes separated from each other by $\Delta z = 0.574$ ". This separation agrees with eq. (7) and at the same time equals to $\lambda_f/2$ at 11.424 GHz. Thus the directivity is enhanced at this particular frequency. The coupling wall thickness is 0.03". The diameters of the holes are tailored to simulate the hamming window. The large dimension of the rectangular guide that forms the coupler side arm is 0.717". This makes the wavelength of the dominant mode in the side arm (TE_{10}) equals to that of the operating mode in the main guide (TE_{01}). To taper up from this dimension to the standard WR90

X-band waveguide, a taper was included in the bend that separate the side arm from the main guide. This bend was designed with the help of the finite element code HFSS. To keep the coupler under vacuum, the side arm was terminated by a standard SLAC vacuum window[6].

Figure 3 shows the theoretical coupling to all parasitic TE modes. Near 11.42 GHz TE_{41} has a higher coupling value relative to the other modes because it is very close to cutoff. This makes it has a very large axial magnetic field. The coupling from that mode is attenuated by more than 41 dB because of the Hamming window. If the coupler did not have a way of discriminating against that mode, a considerable error in the measurements could occur due to a small impurity in the original mode. Since the Hamming window impulse response is periodic, the coupler will start to couple well with backward TE_{11} after 12.1 GHz.



(a)



(b)

Figure 3. Theoretical coupling to parasitic TE modes: (a) Forward coupling (b) Backward coupling

The coupler response was measured using an HP8510 network analyzer system. We used a near perfect Marie' mode transducer to excite the TE_{01} mode in the circular coupler. A PC was used to control the network analyzer system and to calibrate it correctly for measurements with mixed type transducers (one for

TE_{10} in rectangular guide and another for TE_{01} in circular guide). The main guide was terminated with a slowly tapered horn to simulate a matched load.

Figure 4 compares experiment and theory for both forward and reverse coupling. The forward coupling agrees very well with theory. The reverse coupling shows a good directivity of about 30 dB. However it does not agree very well with the predicted 40 dB directivity. This can be attributed to the fact that the load which terminate the coupler has a reflection coefficient that is greater than -40 dB.

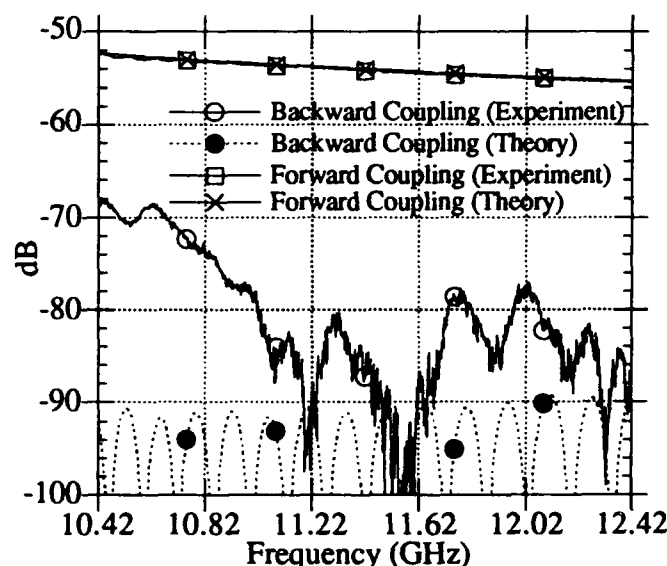


Figure 4. Comparison between theoretical and experimental coupling for the operating mode (TE_{01})

IV. ACKNOWLEDGMENT

The author is grateful for the many useful discussions with Dr. A. E. Vlieks. The author wishes to thank C. Pearson, S. Bebe for their help in the mechanical design and fabrication of the coupler, and R. Callin for his help with vacuum windows.

V REFERENCES

- [1] A. E. Vlieks, et al., "Accelerator and RF System Development for NLC," Published in these proceedings; SLAC-PUB-6148.
- [2] W. X. Wang et al, "Design of a Mode Selective Directional Coupler," International Journal of Electronics, vol. 65, pp. 705, 1988.
- [3] S. E. Miller, Bell System Technical Journal, vol. 33, pp. 661, 1954
- [4] Fred J. Taylor, "Digital Filter Design Handbook," Marcel Dekker, Inc., New York, 1983, chapter 5.
- [5] F. Sporleder and H. G. Unger, "Waveguide Tapers Transitions and Couplers," Peter Peregrinus, 1979, pp. 36-55.
- [6] W. R. Fowks et al, "High Power RF Window and Waveguide Component Development and Testing above 100MW at X-Band" SLAC Pub-5877.

Window Design with MAFIA

W. Bruns, H. Henke, B. Littmann and R. Lorenz

Technische Universität Berlin, EN-2, Einsteinufer 17, D-1000 Berlin 10, Germany

Abstract

A window design scheme using the MAFIA code is presented. Two sample windows in UHF and Ku-band are designed. The UHF window is dimensioned for high power CW operation (narrow band). It consists of a single ceramic, with the possibility to direct a blower. The Ku-band window is designed for pulsed operation. It consists of two single windows. Sensitivity calculations are carried out using a mode matching code which calculates S-parameters of axis-symmetric geometries. An arbitrary number of cross section changes and different material fillings (dielectrics) is allowed.

1 Introduction

The window is a bottleneck in the RF supply system. Operation disruption has been reported at SRS [1]. Main failure mechanisms are heating (losses in the dielectric or in the anti-multipactor coating) and multipactoring mechanical damages [2]. With ever higher accelerating gradients and therefore higher power requirements the window design will demand increased attention.

2 UHF-band Window

MAFIA [3] versions 3.10 and higher have the capability to compute S-parameters of arbitrary waveguide components. Simulation is done in time domain, with an incident wave at one port. The stationary S-parameters are obtained after some 25-50 time steps. Typically 20,000-60,000 mesh-points were used, which sums up to 30-60 minutes user time on a RS6000/320 for each simulation.

The window was designed to be installed in a waveguide WR1800 (dimensions 18" x 9", frequency $f_{RF} = 476$ MHz). The MAFIA mesh is shown in Fig.1. Note that only a quarter of the structure was modelled to exploit all symmetries. Design performance is displayed in Table 1.

A single window design was preferred to multiple windows (say three or five) distributed over the waveguide cross-section. The general feeling was that costs would rise and chances to fail would be higher. Here the design steps taken are listed:

1. Choice of window size and material. The first step was to select a ceramic (material and size). Alumina (Al_2O_3)

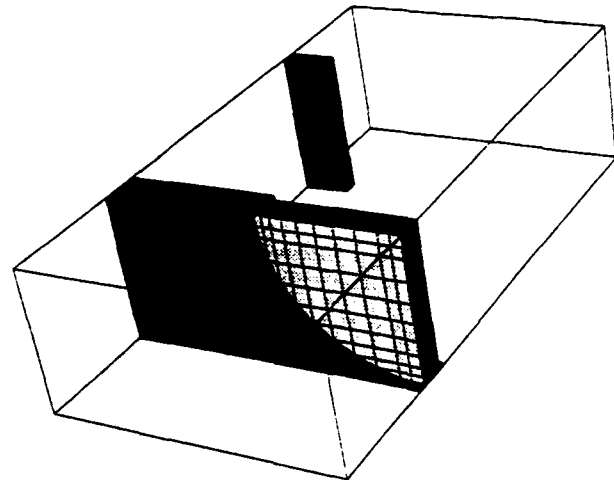


Figure 1: MAFIA mesh of the window.

was preferred to beryllia (BeO) on grounds of lower cost and easier handling (non-toxic, copper brazeable). A dielectric constant $\epsilon_r = 9.5$ was assumed. The waveguide height restricts the possible window aperture. Leaving room for a small copper sleeve, the aperture was set $d_{ap} = 8''6/8$. The window thickness is determined in the next step.

2. Window simulations. The window reflection was computed with MAFIA. Some 5-10 simulations were required to determine the dependence of reflection with the window

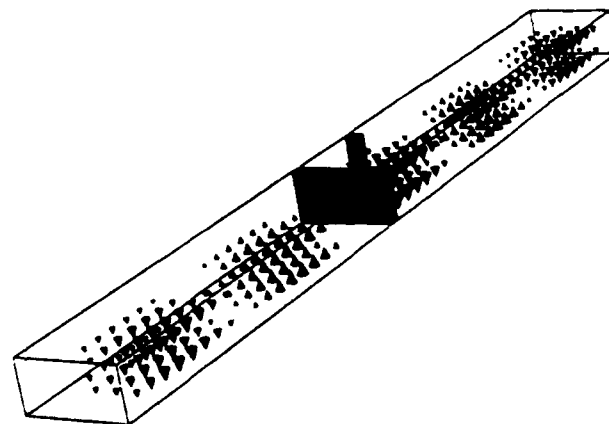


Figure 2: MAFIA mesh of the trapped mode calculation.

Parameter	Value
Operation frequency	476 MHz
Reflection	0.008 (- 42 dB)
Bandwidth $ S_{11} \leq 0.1$	0.033
VSWR between window and inductive element	1.11

Table 1: Performance data.

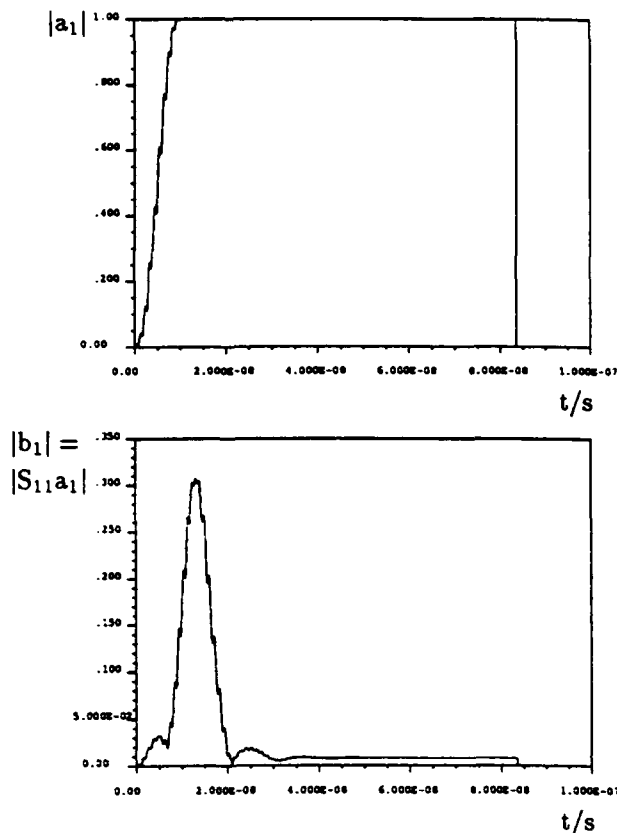


Figure 3: Envelopes of the input pulse and S_{11} .

thickness and find zero reflection ($|S_{11}| = 0$ @ $d_{th} = 2.38$ cm). Next the thickness was rounded to some available size, thereby introducing some reflection ($S_{11} = 0.101 \cdot e^{-j1.9^\circ}$ @ $d_{th} = 0''7/8$).

3. Matching element. Matching was performed with an inductive element. Again MAFIA was used to model the element. This step required less CPU-time since the mesh was coarse. Three simulations were needed, as the reflection depends almost linearly on the aperture of the element. The element with the same absolute value of reflection as the window was selected.

4. Matching element position. With MathCad the exact element position was computed (cancellation of reflected waves).

The matching introduces standing waves:

$$VSWR = |S_{21}^{ind}| \cdot \left(\sum_{n=1}^{\infty} |S_{11}^{win}|^n \cdot |S_{11}^{ind}|^{n-1} + \sum_{n=1}^{\infty} |S_{11}^{win}|^n \cdot |S_{11}^{ind}|^n \right) = 1.11$$

5. Final MAFIA runs. The reflection of the complete window design (window and inductive element) was checked. Fig.3 shows the resulting envelopes of the input pulse and $|S_{11}|$. The geometry is shown in Table 2.

Geometry	Size, material
Waveguide	WR1800 (18" x 9")
Window material	Al_2O_3 , $\epsilon_r = 9.5$
Window diameter	8"3/4
Window thickness	0"7/8
Inductive element width	1"1/2
Inductive element thickness	0"1/2
Distance between window and inductive element	8"11/64

Table 2: Window geometry and ceramic material.

Variable u	$ \Delta S_{11} $	$(\Delta S_{11} /\Delta u)$
Dielectric constant ϵ_r	0.028	0.3
Window diameter	0.048	0.45 1/cm
Window thickness	0.017	0.8 1/cm
Inductive element width	0.0017	0.04 1/cm
Inductive element thickness	0.00015	0.02 1/cm
Distance between window and inductive element	0.0018	0.009 1/cm
Frequency	0.06	12.0 1/GHz

Table 3: Window sensitivity with a variation of parameters of about 1%.

Sensitivity calculations were carried out with a variation of parameters of about 1%. Results are shown in Table 3. Obviously the sensitivity of the window size and material is highest, whereas tolerances of the inductive element are relaxed by about one order of magnitude.

Finally, the design was examined for trapped modes. Long waveguide sections were shortened (see Fig.2). No trapped modes were discovered within the frequency range of interest (one was discovered at $f = 913$ MHz).

3 Ku-band Window

The Ku-band window has been designed for a circular waveguide at 18 GHz. It consists of two thin windows spaced 4.8 mm apart in an outer pipe of 6.09 mm diameter. A cooling agent can thus flow through the space between the windows to reduce the possible thermal failure. Thin irises have been added for more flatness and to increase the bandwidth. The geometry is shown in Fig.4 and some parameters are given in Table 4.

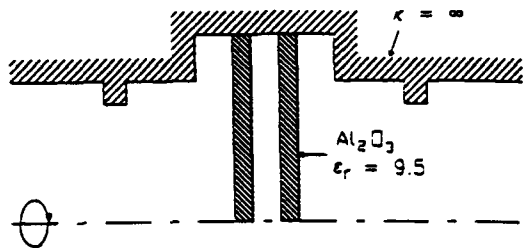


Figure 4: Geometry of the Ku-band window, Al_2O_3 .

Parameter	Value
Operation frequency	18 GHz
Reflection	0.01
Bandwidth $ S_{11} \leq 0.025$	0.04
Waveguide	C190
Window material	Al_2O_3 , $\epsilon_r = 9.5$
Window radius	6.09 mm
Window thickness	2.89 mm
Distance between windows	4.8 mm
Iris radius	5.4 mm
Distance between a window and one iris	14.2 mm

Table 4: Parameters of the Ku-band window.

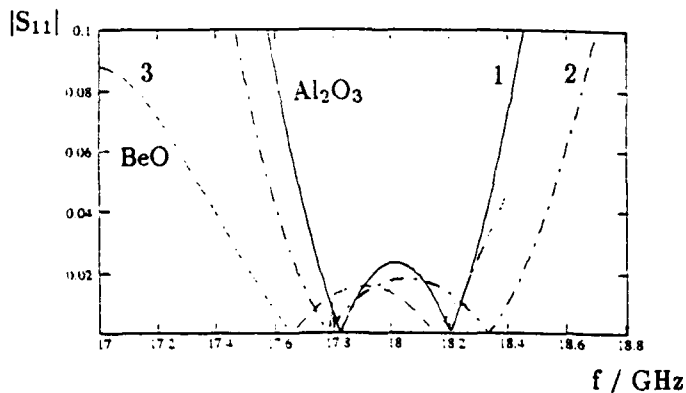


Figure 5: Frequency dependency of $|S_{11}|$.

A mode matching code which calculates the S-parameters of axis-symmetric geometries with an arbitrary

number of cross section changes and various material fillings have been used to check the results and to calculate some tolerances. The structure has a bandwidth of $B \approx 3\%$ with $|S_{11}| \leq 2.5\%$ (curve 1, Fig.5). With additional irises the curve became flatter and the bandwidth increased up to $B \approx 4\%$ (curve 2, Fig.5). The parameter with the highest sensitivity is the window thickness which determines the center frequency. Other parameters were uncritical with respect to the bandwidth within 1% mechanical tolerances.

Finally, we checked the design for trapped modes. In fact, this provisional design shows two trapped modes at $\Delta f = \pm 520$ MHz away from the operation frequency. But we have good hopes to shift them further away by changing the thickness of the ceramics.

The parameters for a single BeO-window have been calculated, too. We achieved $|S_{11}| = 0.1$ with a bandwidth of $B \approx 12\%$, however the design is very sensitive to the window thickness. BeO is toxic and has brazing difficulties, but on the other hand it has a thermal conductivities close to copper [4]. For this structure trapped modes appeared at $\Delta f = \pm 370$ MHz.

The frequency behavior of $|S_{11}|$ for both windows was calculated with a mode matching code and is shown in Fig.5.

4 Acknowledgement

One of us (B. L.) likes to thank R. A. Rimmer for valuable discussions.

References

- [1] A. Jackson, *RF Window Failures In The SRS Up To 30 November 1983*, SRS/APN/83/54, 1983
- [2] R. A. Rimmer, *High Power Microwave Window Failures*, Thesis, 1988
- [3] T. Weilandt et al., DESY Report M-86-07, 1986
- [4] A. E. Vlieks et al., *Breakdown Phenomena in High Power Klystrons*, SLAC-PUB-4546, 1988

DEAD-TIME TUNING OF A PULSED RF CAVITY

P. Balleyguier

Commissariat à l'Energie Atomique

Service de Physique et Techniques Nucléaires

B.P. 12, 91680 Bruyères-le-Châtel, FRANCE

Abstract

A scheme for tuning a high-power pulsed RF cavity using a low-power source during dead-time is given. This principle has been used for the injector cavity of the free-electron laser ELSA. Its advantages, with respect to the classical way which consists of measuring the high power signal phase, are discussed.

1. Introduction

Like any high Q resonator, the injector cavity of ELSA [1-2] (see characteristics in table 1.) has to be precisely tuned. In a way to keep it tuned in spite of thermal shifts, its resonance frequency can be adjusted by a movable plunger.

The fast phase variation nearby the resonance frequency can be used for automatic tuning: the phase difference between transmitted and incident RF signals gives an error signal which can command the plunger after filtering.

On a first period of time, we used the classical scheme (fig.1) in which the RF signal used for cavity tuning is issued from the power signal itself. Tests showed that this tuning system did work but was not convenient for our pulsed machine.

Table 1: Some RF characteristics of ELSA injector cavity.

Frequency	: 144.444 MHz
Internal Q	: 30000
Maximum pulsed RF power	: 2 MW
Reflected power threshold	: 100 kW
Pulse duration (flat part)	: 200 μ s
Pulse duration (total)	: 500 μ s
Repetition rate	: 0.4 to 50 Hz

2. Drawbacks of the classical tuning system

The power chain is ended by a 2 MW tetrode which is protected against reflected power by switching off the RF source if necessary. Thus, if the cavity is initially detuned, no adequate error signal (issued from phase comparison) is available, and the cavity cannot be tuned. The only way to fix the problem is then to start with a low RF power level, in a way that the security switch keeps the "on" position in spite of reflected power. Then, the tuning loop can be closed, and after waiting for the end of its transient response, one can gradually increase the RF power.

Moreover, because the phase comparator dynamic range is rather narrow, variable attenuators have to be adjusted in case of RF level increasing. But since their phase shift depends on attenuation, it is difficult to keep the phase loop locked while the RF power is increasing.

In our pulsed machine, the error signal is only available during the pulse, and a sample-and-hold circuit followed by a low-pass filter has to be provided for the error signal treatment. The frequency response of the low-pass filter has to be compatible with the lowest repetition rate of the machine. As this rate can be lowered to 0.4 Hz in our case, the transient response of the tuning loop should be very long.

Furthermore, when the cavity is detuned, RF power causes strong outgassing which damages the photocathode in the injector.

3. Dead-time tuning system

Since the cavity is inactive during most of the time (from an RF point of view), this dead-time can be used for tuning it (see fig.2). The basic idea of phase comparison between incident and transmitted signals remains, but these signals are now independent from the pulsed RF power. The principle of the dead-time tuning system is to inject a low-power CW RF signal in the cavity, to pick-up a transmitted signal and to measure its phase after amplification. The only problem is that this system has to keep working and remain stable when high-power pulses occur.

First, a CW RF signal issued from a 10 W amplifier is injected in the cavity with a low coupling antenna (-40 dB) to avoid high-peak power on the injection line. A circulator is provided to protect the amplifier from the pulsed RF power (200 W). First tests showed that cavity leakages could destroy the circulator. For that reason, the device is now supplied with an EMP protector.

Note that the CW signal level is about 1 mW in the cavity; this is 93 dB lower than the pulsed power which is assumed to be 2 MW.

The transmitted signal is picked up with another low coupling antenna (-40 dB also) and its level is amplified to 0 dBm with a low-noise amplifier to match the phase comparator standard input level. A passive limiter has been provided to protect this amplifier against high-power pulses.

Since both the limiter and coupling antenna are total reflection terminations from a high power point of view, dangerous standing waves could appear between them during high-power pulses. In a way to damp these eventual standing waves, a 10 dB attenuator was provided, and the actual output antenna coupling was increased to -30 dB. Note that this attenuator has then to support a pulsed RF power of 2 kW.

Finally, the error signal issued from the phase comparator, is blanked during high-power pulses.

4. Conclusion

Experiments showed that this dead-time tuning system works perfectly and supports high-power pulses. With such a system, the injector cavity of ELSA is always tuned and ready to receive high-power pulses of any level and repetition rate. A similar system has been developed for tuning the ELSA 433 MHz accelerating cavities [3].

5. References

- [1] S.Joly et al., "Progress report on the ELSA FEL and first lasing", 14 th International Conference on Free-Electron Laser, Kobe, 1992.
- [2] P.Balleyguier and R.Dei-Cas "RF pulse shape control using a recurrent algorithm for a FEL RF gun cavity", Linac Conference, Albuquerque, 1990. LA-12004-C, p.499.
- [3] P.Balleyguier et al., "Experimental study of a 433 MHz 3 cell cavity for FEL application", European Particle Accelerator Conference, Nice, 1990. Editions Frontières, p.910.

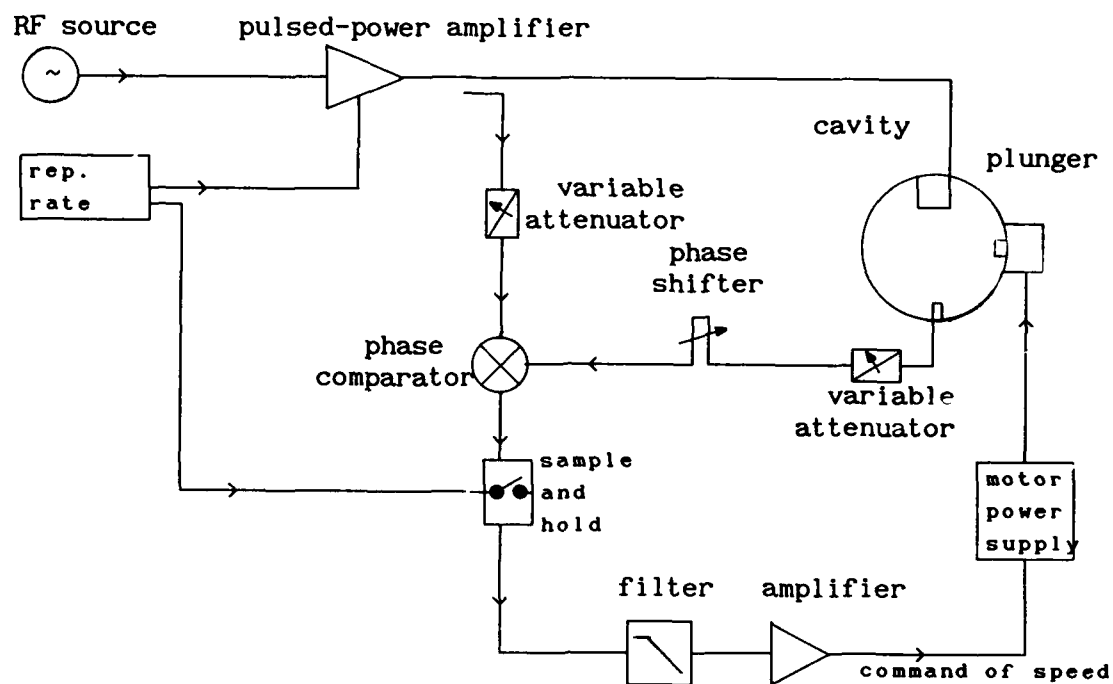


Fig.1: Classical tuning system.

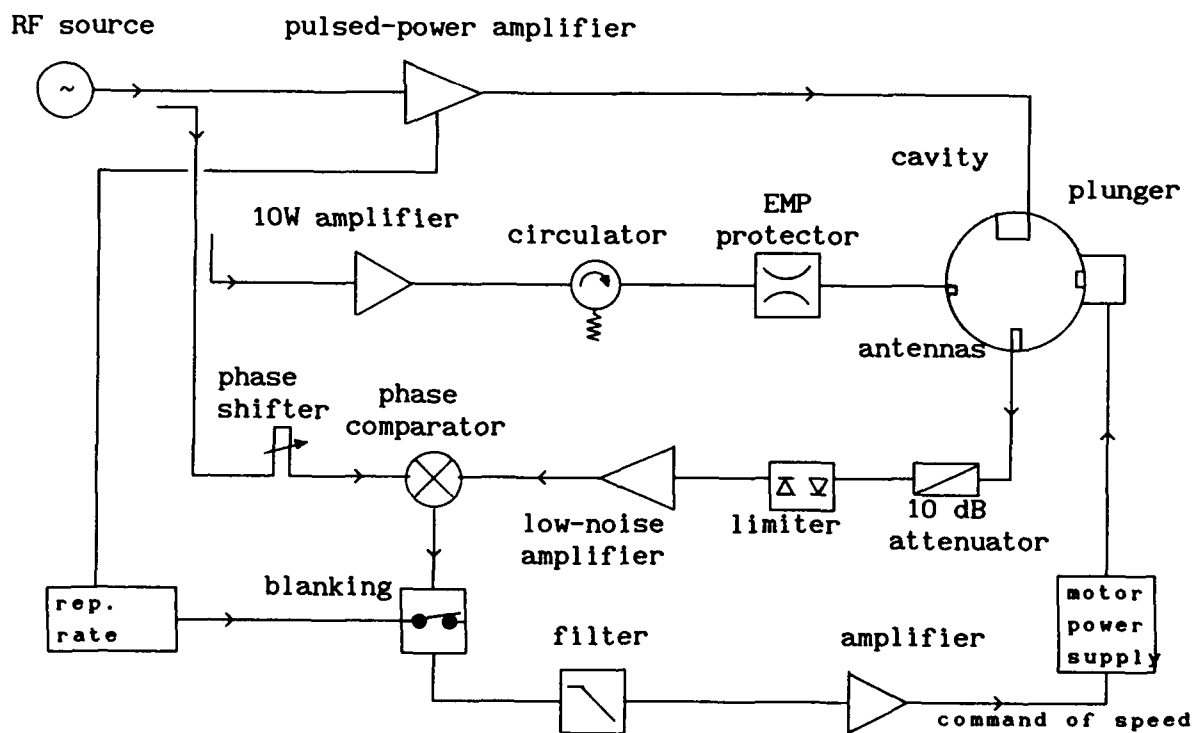


Fig.2: Dead-time tuning system.

Frequency Control of RF Booster Cavity in TRIUMF

K. FONG and M. LAVERTY

TRIUMF, 4004 Wesbrook Mall, Vancouver, B.C., Canada, V6T 2A3

Abstract

A booster cavity is used in the TRIUMF cyclotron to increase the energy gain per turn for beam orbits corresponding to energies greater than 370 MeV. It operates at 92.24 MHz, the 4th harmonic of the cyclotron main rf, and at a nominal voltage of 150 kV. Excitation is provided by a 90 kW rf system that is phase locked to the main rf. When the main rf is interrupted due to sparking or other causes, a controller built into the low level frequency source of the booster rf system disables the phase-locked loop, and reconfigures the source as a temperature stabilized oscillator operating at the last locked frequency. When the cyclotron rf is restored it usually will be at a different frequency. The oscillator tunes automatically to this new frequency. The acquisition time is extended by the controller to match the response time of the mechanical tuner in the cavity.

I. INTRODUCTION

The TRIUMF rf booster is an auxiliary accelerating cavity operating at the 4th harmonic of the cyclotron rf. It provides 150 kV at its accelerating gaps for additional acceleration of the beam at energies above 370 MeV [1], [2]. By altering the phasing between the fundamental and the 4th harmonic one can also produce longitudinal splitting of beam bunches [3]. There are several requirements that the frequency source for the rf booster must satisfy. First, for proper acceleration of the beam the 92.24 MHz booster rf must be phase-locked to the 23.06 MHz cyclotron rf at the dee. This is necessary since the cyclotron rf is not phase regulated, and its phase varies as the resonator detunes due to mechanical vibrations. Second, when using the cyclotron rf as the reference, it is liable to shut off due to a variety of reasons. When this occurs it is desirable to maintain rf power in the booster for thermal stability reasons. Third, when the reference returns after a length of time, it will usually be at a different frequency. The source cannot jump instantly to this new frequency since the booster cavity is not tuned to this new operating point. The transition must be gradual enough for the mechanical tuning system to follow. Fourth, the frequency source should be capable of being decoupled from the reference and performing limited frequency sweep. This is necessary during power up sequencing for cavity conditioning. The above requirements are met with a multiply by 4 phase-locked loop that is able to work with the non-cooperative cyclotron rf as the reference. A digital sample and hold circuit driving the voltage controlled oscillator in the PLL enables the oscillator to free run at the

same frequency when the reference is absent, for intervals from minutes to hours. An embedded microcontroller controlling the S/H circuit is used to extend the acquisition time of the phase-locked loop when the cyclotron's rf is restored at a different frequency. The input to the VCO is only permitted to vary slowly under software control. Furthermore, this control also allows one to sweep the output to find the most favorable frequency during power-up sequencing.

II. SCHEMATIC DESCRIPTION

A functional block diagram of the frequency source is given in Figure 1. Its main components consist of a multiply by 4 analog phase-locked loop with an input frequency of 23.06 MHz, and a pair of Analog-to-digital/Digital-to-analog converters controlled by a microcontroller. During normal

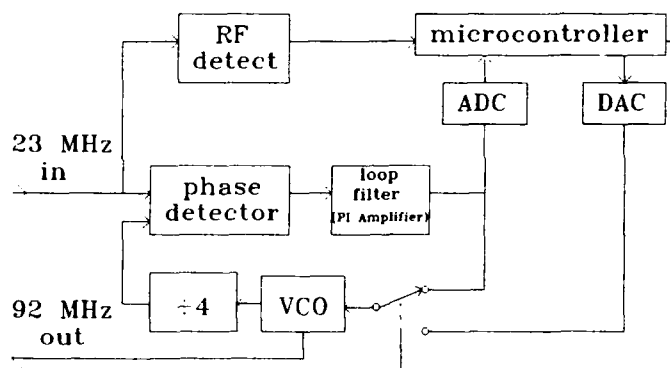


Figure 1. Over-simplified Functional Block Diagram of the booster frequency source.

operation, when the input reference is present, the PLL operates as a second order loop. A frequency/phase detector compares the phases between the reference input from the cyclotron rf and a divided by 4 output of a VCO with a centre frequency of 92.24 MHz. The phase difference is filtered to remove the 23 MHz component. It is connected by an analog switch to the loop filter, a proportional-integral amplifier, whose output is used to vary the frequency of the VCO. This results in a second order feedback loop, with one integration provided by the loop filter and the other provided by the VCO. The microcontroller assumes a supervisory mode and instructs the ADC to repetitively sample the voltage at the loop filter output. This value is stored in the memory of the microcontroller. When the reference is off, the microcontroller breaks the feedback path and reconfigures the source to operate in an open loop mode. It recalls the stored value of the last sampled voltage, converts it into analog

voltage via the DAC and drives the VCO to the last sampled frequency. The switching between the loop filter output and the DAC output is designed to prevent voltage spikes from appearing at the VCO input. Due to its very high low frequency gain, the PI amplifier once taken out of the feedback path will have integrator wind-up, and cannot be switched in again without causing a voltage spike. For this reason the PI amplifier is always in some sort of feedback path. During open loop operation, the PI amplifier is incorporated in a minor loop as shown in Figure 2. The output of the DAC does not drive the VCO directly, but instead is compared with the output of the PI amplifier and the error is feedback to the input of the PI amplifier. This completes a voltage feedback loop that regulates the output of PI amplifier to be the same as the output of the DAC. The output of the PI amplifier is at all times connected to the VCO. When the reference is restored, the microcontroller measures the frequency differences between the input and the VCO output/4, and instructs the DAC to slowly ramp the VCO towards the 4th harmonic of the input. This slow ramping is necessary since, if the difference in frequency is large when compared to the resonator bandwidth, simply

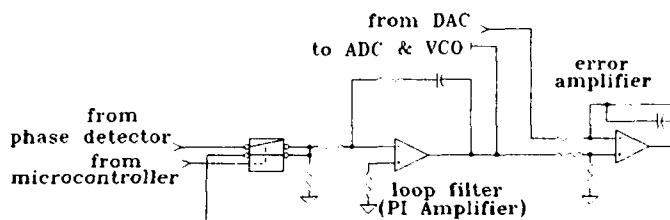


Figure 2. Detailed schematic of minor loop between the loop filter and the phase detector for glitchless closing of PLL.

enabling the PLL will cause a fast frequency shift and the mechanical tuning motors would not be able to catch up. This would result in excessive forward and reverse power demands from the power amplifier and can cause catastrophic failure of the power amplifier. When the microcontroller detects that the difference in frequency is less than the 3 dB bandwidth of the cavity, the switches are re-engaged to enable normal closed loop operation. The DAC is also stepped during the initial power up sequencing. By sweeping the frequency this way one is able to choose the optimum frequency for cavity conditioning.

III. BANDWIDTH

Measurements show that the phase detector gain K_ϕ is 0.16V/rad and the VCO gain K_o is 8.3×10^5 rad/sV. The closed loop gain of a $\times 4$ PLL with a PI loop filter having proportional gain A_p and a zero at frequency ω_b is given by [4]

$$H(s) = \frac{2\zeta\omega_n s + \omega_n^2}{s^2 + 2\zeta\omega_n s + \omega_n^2},$$

where $\omega_n = 1/2\sqrt{K_f K_\phi \omega_b A_p} = 1.82 \times 10^2 \sqrt{\omega_b A_p}$ is the closed loop bandwidth, and $\zeta = \omega_n / 2\omega_b = 9.1 \times 10^1 \sqrt{A_p / \omega_b}$

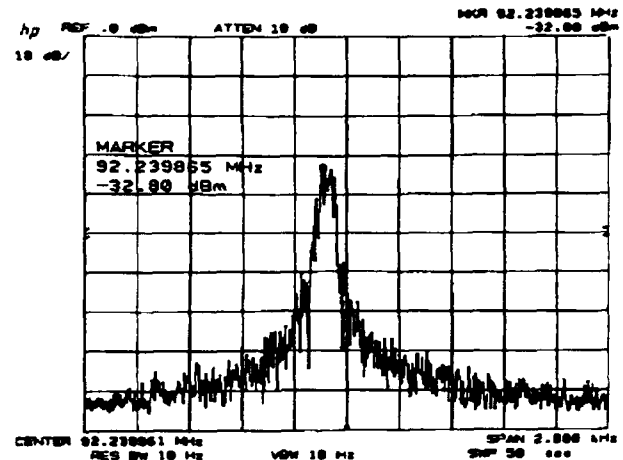


Figure 3(a). Spectrum of VCO output in unlocked condition

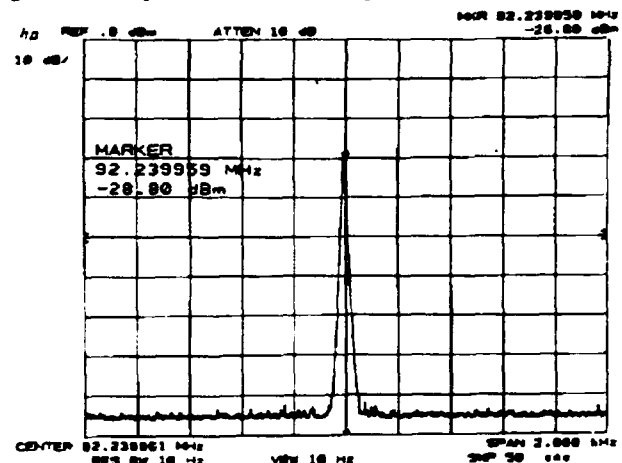


Figure 3(b). Spectrum of VCO output in locked condition

is the damping factor. The design starts with a target bandwidth of 500 Hz and a damping factor of 2. Using standard component values one gets a bandwidth of 425 Hz and a damping factor of 1.7. The open loop gain at 5 Hz is 10,000. Since the phase variation of the reference is predominantly due to mechanical vibrations of the resonator structure that centers at 5 Hz, this open loop gain is more than sufficient to track the phase variation occurring in the reference.

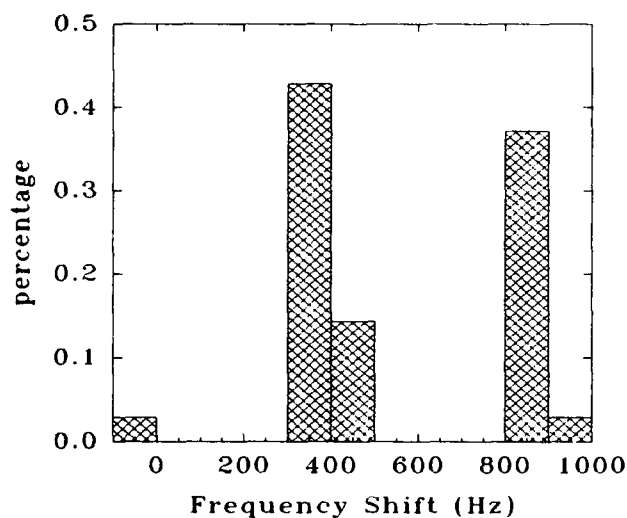


Figure 4. Amount of frequency shift when the frequency source switches from phase locked mode to free running mode.

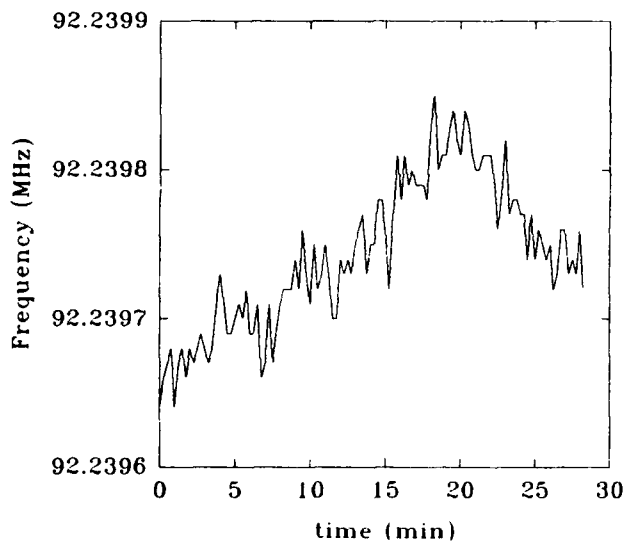


Figure 5. Frequency variation of the VCO in free running condition.

Since the acquisition process is controlled by the microcontroller, with the DAC driving the VCO, the capture range of the frequency source is determined by the voltage swing capability of the DAC. With an 8-bit DAC, the frequency step in turn is $1/256$ of the capture range. This leads us to a compromise of a 400 Hz step size, resulting in a 100 kHz capture range. This gives sufficient range to lock on to the main cyclotron rf during warm-up and normal operating conditions.

IV. SPECTRAL OUTPUT

Comparison of the output spectra of the source under locked and unlocked condition is shown in Figure 3. The actual output power is +13 dBm but is attenuated at the input of the spectrum analyzer. Figure 3(a) shows the output when the PLL is disabled. Frequency stability and phase noises are not particularly good. This is to be expected from a free running VCO. The output spectrum improved significantly when the PLL is enabled and locked as shown in Figure 3(b). In this case spurious noises are at least 55 dB below carrier. Fig. 4 shows the statistical distribution of the frequency shift at the output of the PLL when the input reference is switched off. Due to digital quantization there are 3 distinct peaks of shift, each separated by about 400 Hz, which is in agreement with the selected step size. One can also see that the maximum shift is less than 1 kHz, well below the bandwidth of the cavity. The "long" term frequency stability under free running condition is shown in Figure 5. The maximum frequency excursion is only 200 Hz over a time interval of 30 minutes. This stability is obtained by using temperature compensating capacitors in the VCO LC tank circuit.

V. CONCLUSION

The performance of the frequency source of the booster has to satisfy several requirements: it must be able to track the phase and frequency variation of the reference input, which may be absent for a long period of time, while acquisition time must be slow enough for the mechanical tuning system to follow. These would be conflicting requirements in an ordinary PLL, but are avoided by using an embedded microcontroller to control the operation of the loop. This controller determines the acquisition timing, as well as the opening and closing of the analog PLL. Safe and reliable operation of the source has been demonstrated with this system.

VI. REFERENCES

- [1] R.E. Laxdal, K. Fong, G.H. Mackenzie, V. Pacak, J.B. Pearson, L. Root, M. Zach, "Initial Operating Experience with the Auxiliary Accelerating Cavity for the TRIUMF Cyclotron," IEEE Particle Accelerator Conference Proceedings, San Francisco, May 1991, pp. 810-812.
- [2] K. Fong and M. Laverty, "RF Control for TRIUMF Booster Cavity," Proceedings of the Third European Particle Accelerator Conference, Berlin, March 1992, pp. 1176-1178.
- [3] R.E. Laxdal and W. Joho, "Longitudinal Splitting of Bunches in a Cyclotron by Superposition of Different RF Harmonics," Proceedings of the Third European Particle Accelerator Conference, Berlin, March 1992, pp. 590-592.
- [4] R.E. Best, "Phase-Locked Loops," McGraw-Hill, 1984.

The Phase Servo Tuner Control System of The ALS 500MHz Cavity*

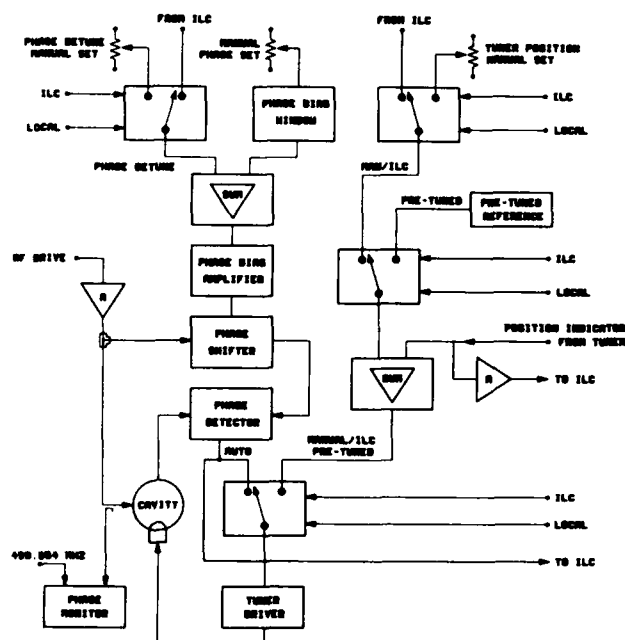
C.C. Lo and Brian Taylor
Lawrence Berkeley Laboratory, University of California
1 Cyclotron Road, Berkeley, CA 94720 USA

Abstract

Three 500 MHz cavities are used in the Booster and Storage Ring of the Advanced Light Source (ALS). Due to different varying parameters, a control system is required to keep the cavities in tune during operation. The tuning of the 500 MHz cavity is achieved by detecting the phase error between the drive signal and the cavity probe signal. The error signal is amplified and used to drive a stepping motor which in turn moves a metallic cylinder in or out of the cavity to achieve tuning.

I. INTRODUCTION

There is one cavity[1] in the Booster and two in the Storage Ring. The tuning of each of these cavities is controlled by a Phase Servo Tuner Control Module. The tuner, a metallic cylinder, is driven by a five phase stepping motor, which in turn is driven by a driver. The driver accepts a bipolar input signal derived from a phase detector in the Phase Servo Tuner Control Module. The amplitude and the polarity of the signal determines the speed and the direction of rotation of the motor. The resolution of the stepping motor is 0.5 degree of rotation per step.

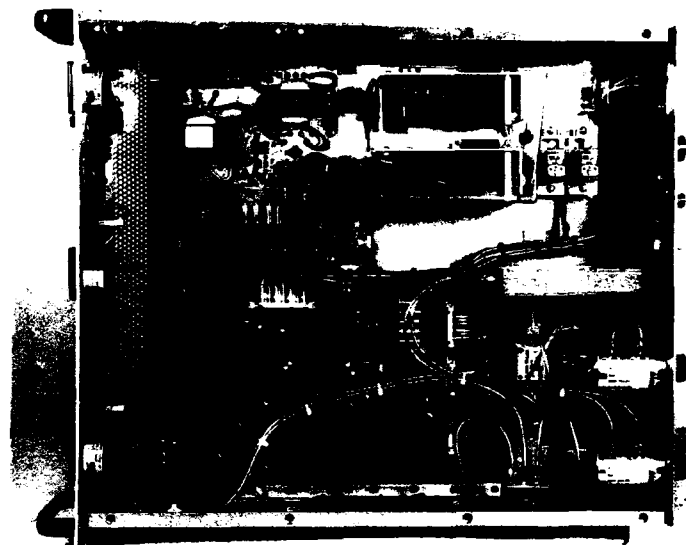


XBL 934-536

Figure 1. Block diagram of the control module.

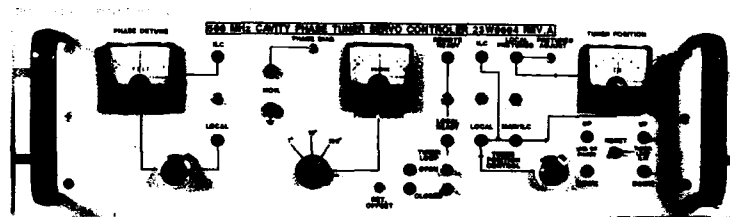
*Supported under the U.S. DOE Contract No. DE-AC03-76SF00098.

Figure 1 shows the block diagram of the control module. Most controls have been implemented with the capability of operating under local controls or remotely via the Intelligent Local Controller (ILC)[2] and the computer in the main control room. With the exception of some discrete RF components all electronic circuits are built on a printed circuit board with a ground plane. Figure 2 is a photograph of the component layout of the module which is a standard 19" rack mount unit. Figure 3 is a photograph of the front panel of the module which shows practically all of the functions the system is capable of performing.



CBB 9210-8838

Figure 2. Component layout of the Module.



CBB 9210-8852

Figure 3. Front view of the module.

II. TUNER POSITION CONTROLS

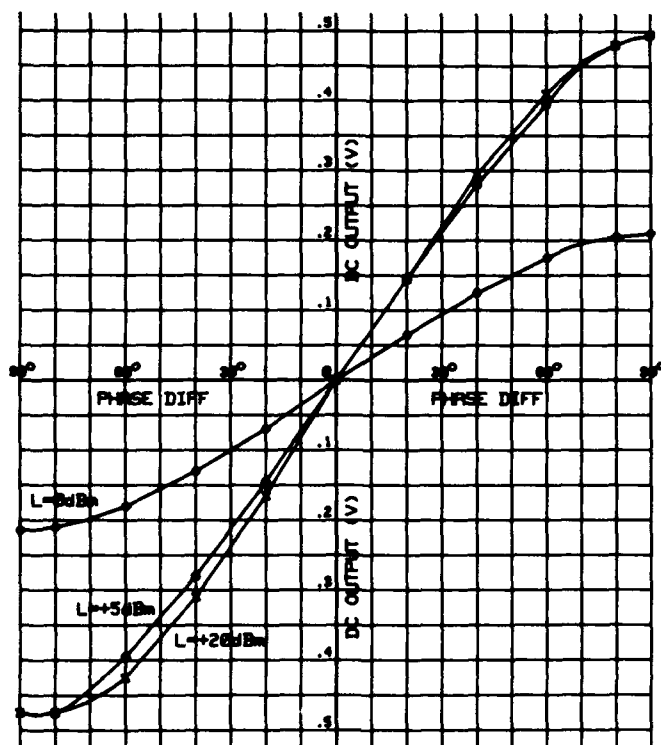
The tuner position can be set either locally or remotely by the ILC. The total travel of the tuner is approximately 10 cm. A pot attached to the tuner provides the feedback signal for the control module. The two electronic limit switches of the tuner

down the drive to the motor below 20% and above 80% of the travel. Should one of these switches be activated a drive signal for the other direction is able to put the tuner back in the normal operating range. The two mechanical limit switches in the tuner provide additional insurance to protect the tuner from ramming the end points of the travel. If for any reason one of these mechanical switches is activated the tuner can be restored to the operating range by two push button switches together with a logic circuit.

A pretuned position setting has also been implemented to bring the tuner back to the tuned position at any time by activating the pretuned switch. This is particularly useful in cases where the tuner is at some arbitrary position during an interrupted operation.

III. TUNING THE CAVITY

A reference signal and a RF sample signal from the cavity are required to produce a tuner correction signal with a phase detector. A double balanced mixer is used as the phase detector. In the reference signal path, a mechanical and an electronic phase shifter together with an attenuator are put in series for phase and amplitude offset and adjustment purposes. The RF signal for the signal port is derived from the cavity monitor. Again, proper attenuators are used to bring the signal level down to a range of +3dBm to +20dBm with the nominal level center around +13dBm at the signal input ports of the phase detector. A transfer function of the phase error and the DC output voltage from the phase detector is given in figure 4.



XBL 934-534

Figure 4. Transfer function of the phase detector.

The signal input port of the phase detector is used as the reference signal port and the local oscillator input port is used as the RF signal port. The reference signal level for this measurement was +5 dBm. The resolution of the phase detector is approximately 7 mV per degree. With the proper amplification of this error signal matching the resolution of the servo driver of the tuner, tuning resolution of approximately 0.1 degree is achieved. The tuning error of the tuning system at the nominal operating power level is of the same order as the tuning resolution. Therefore, the over all worst case phase error should still be better than 0.25 degree. The tuner servo motor tuning rate is 114KHz per second, therefore an 11.4KHz detuning would require 0.1 second to get the cavity back in tune. The dynamic operating range without adjusting any attenuation in both signal paths is approximately 23 dB, whereas the phase detection range is +/- 90 degrees. Both parameters have been shown to be quite adequate in day to day operation.

IV. PHASE DETUNING OF CAVITY

An electronic phase shifter is used to adjust the phase of the reference signal in the case of closed loop operation either to fine tune the phase detector or to detune the cavity by offsetting the tuner to resonate the cavity at a lower frequency by approximately 10 KHz. The detuning is used mainly to counteract instability due to beam loading. Figure 5 shows the typical detuned phase angle and detuned frequency as functions of the detune bias voltage of the servo control modules. The detuned phase angle transfer function was measured by observing the phase angle between the waveguide signal and the cavity signal while changing the detune bias.

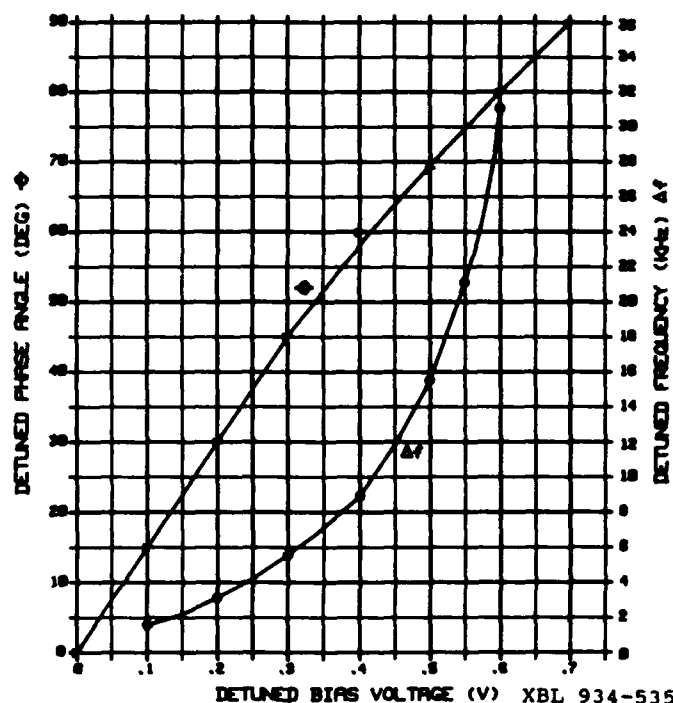


Figure 5. Transfer functions of the detuned phase angle and detuned frequency.

The detuned frequency is calculated by the following expression:

$$\Delta f = \frac{a}{Q} \times f_0$$

where Δf = detuned frequency
a = a constant obtained from the
Universal resonance curve[3]
Q = Q of the cavity
f₀ = resonant frequency

The two cavities in the storage ring have been operating with a detune bias voltage of approximately 0.4V. The Q of the cavity is approximately 45,000.

The best operating range of the phase shifter is used by selecting the proper bias voltage range. The local phase bias is set at the mid range of the phase shifter to provide enough room on both sides for the phase detune to work properly. However, under normal operation, the phase angle only needs to be detuned to the lower frequency side. Because the phase shifters used in the servo control modules have different transfer functions, variations in detune voltages from different modules should be expected.

V. CONCLUSION

One Phase Servo Tuner Controller Module has been operating in the cavity test stand for over two years, one in the Booster Ring for over a year, and two have been in operation in the Storage Ring for a couple of months. All four units have been performing well. Network analyzers with Polar displays have been used to monitor the operation of the storage ring cavities. At the time of the writing of this report, the capability of computer tuning of the cavities has not been implemented. Operating experience will tell whether this procedure will be necessary.

VI. ACKNOWLEDGMENTS

This work was funded by the director, Office of Energy Research, Office of Basic Energy Sciences, Material Science Division of the U.S. Department of Energy under Contract No. DE-AC03-76SF00098 with Lawrence Berkeley Laboratory. Reference to a company or a product name does not imply approval or recommendation of the product by the University of California or the U.S. Department of Energy to the exclusion of others that may be suitable.

VI. REFERENCES

- [1] C.C. Lo and Brian Taylor, "Computer-Aided Studies of the ALS 500 MHz Storage Ring Cavity", Proceedings of 1989 IEEE PAC, Vol. 1, pp. 121-123, LBL-25976.
- [2] S. Magyary, et al, "Advanced Light Source Control System", Proceedings of 1989 IEEE PAC, Vol. 1, pp.74-78, LBL 28412.
- [3] F.E. Terman, Electronic and Radio Engineering, McGraw Hill Book Company, Inc. 1955.

The Low Level System for the ELETTRA RF Plants

A. Massarotti

Sincrotrone Trieste and Dipart. di Fisica, Universita' di Trieste
G. D'Auria, A. Fabris, C. Pasotti, V. Rizzi, C. Rossi, M. Svandrik
Sincrotrone Trieste, Padriciano 99
34012 Trieste, Italy

Abstract

The four RF plants of the ELETTRA storage ring are driven by the reference RF signal derived from the machine master oscillator. Each RF plant will operate with three active loops controlling the tuning of the cavity and the phase and amplitude of the gap voltage. The complete feedback loops are described here and the results of bench tests are given.

1. INTRODUCTION

A mechanical tuning loop, a fast phase loop and an amplitude loop will ensure the required stability condition for the ELETTRA cavities operation. In the following sketch a general layout of the logical allocation of the control loops is given

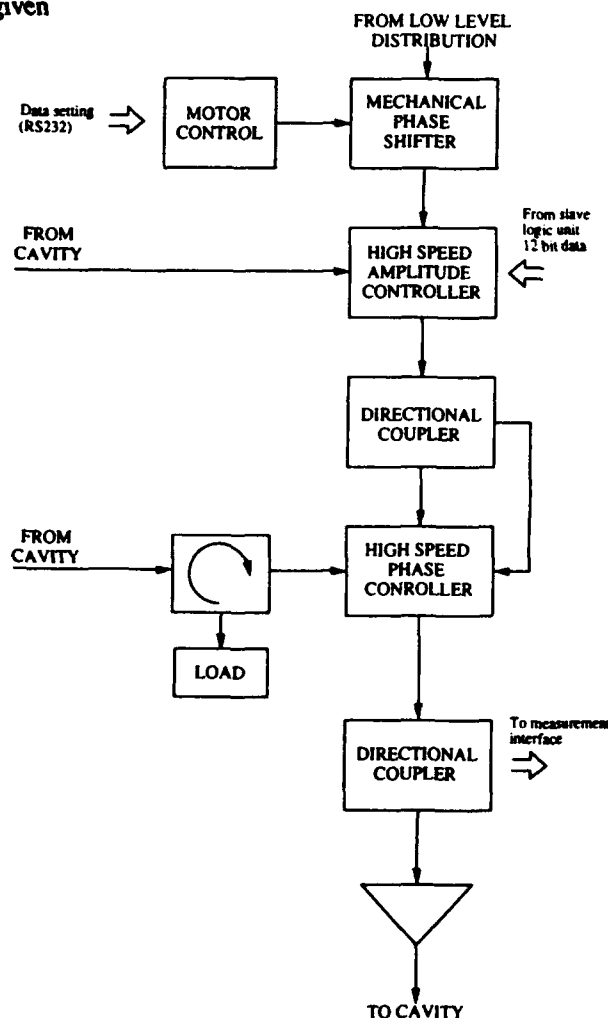


Fig. 1 Block diagram of the RF plant control loops

The complete set of these control loops has been built and each one has been deeply tested. The final tests of the fast phase feedback loop and the detailed study of cross talk interaction among the different loops will be performed in the very next months.

We give here a list of typical response times and regulation accuracies.

2. MECHANICAL TUNING LOOP

The structural description of the loop is shown in fig. 2 and its operational behavior has been described [1].

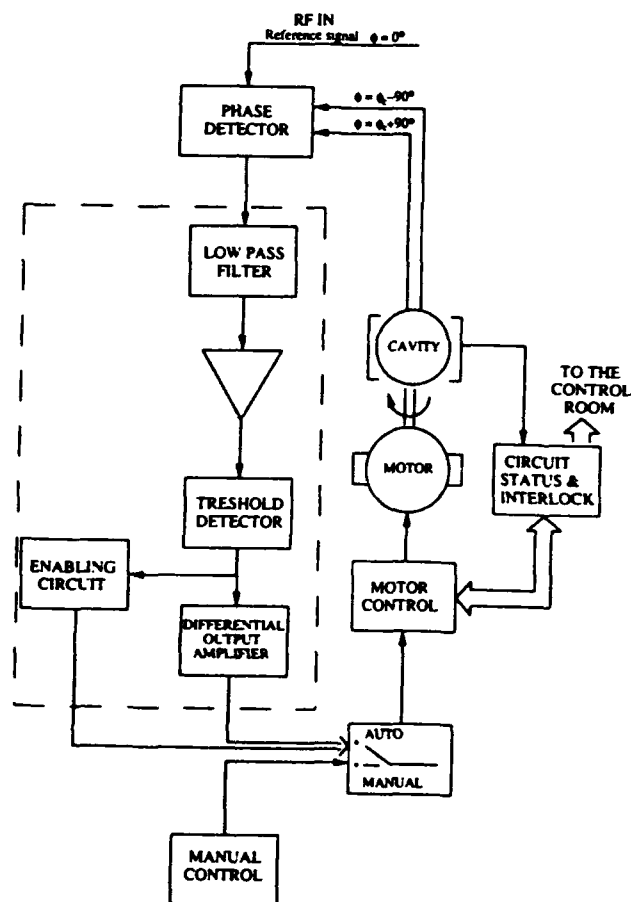


Fig. 2 Block diagram of the mechanical tuning loop

The cavity tuning, which is obtained changing the axial length of the cavity [2], can be controlled both manually and

automatically. The working conditions of the loop are remotely transferred to the control room.

The velocity of the loop has been raised to a correction speed of 500 Hz/sec with respect to the previous design (200 Hz/sec), in order to ensure a proper tuning control during the RF plant start up procedure and to avoid interaction with the temperature control loop.

3. FAST PHASE LOOP

A block diagram of the fast phase loop is shown in fig. 3.

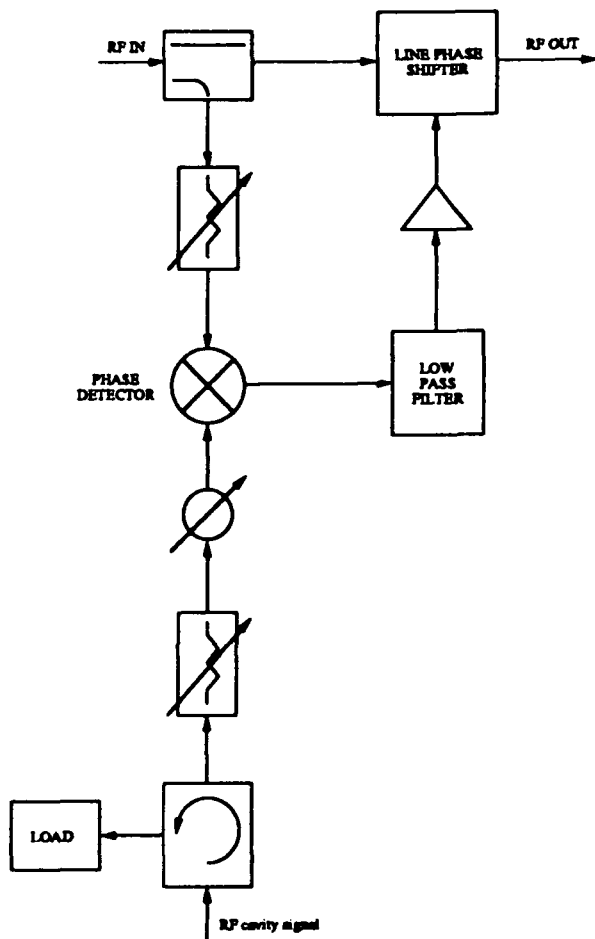


Fig. 3 Block diagram of the fast phase loop

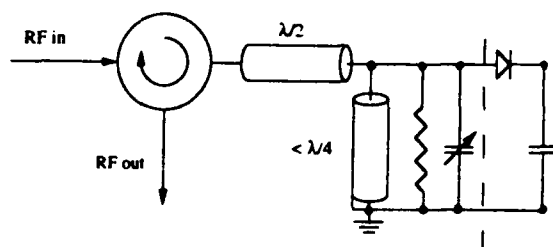


Fig. 4 Schematic drawing of line type phase shifter

After some unsatisfactory tests on available commercial phase shifter it has been decided to develop a line type phase shifter. According to this, a phase shifter based on a quarter

wavelength resonant coaxial line properly connected to a circulator has been selected (see fig. 4).

This configuration has shown a satisfactory constant RF attenuation in the range of operation, which is ± 20 degree, as it can be seen from the table 1. Moreover the phase variation speed has been improved and the amplitude modulation of the radiofrequency signal has been prevented .

Table 1
Phase shifter characteristics

Dephasing (degrees)	Attenuation (dB)
21.3	- 1.40
15.5	- 1.44
8.9	- 1.48
4.5	- 1.51
0	- 1.53
- 3.1	- 1.54
- 7.5	- 1.57
- 12.1	- 1.59
- 16.8	- 1.61
- 22.1	- 1.63

The preliminary bench measurements have reported an open loop gain of about 30 dB with a phase margin of more than 50 degrees.

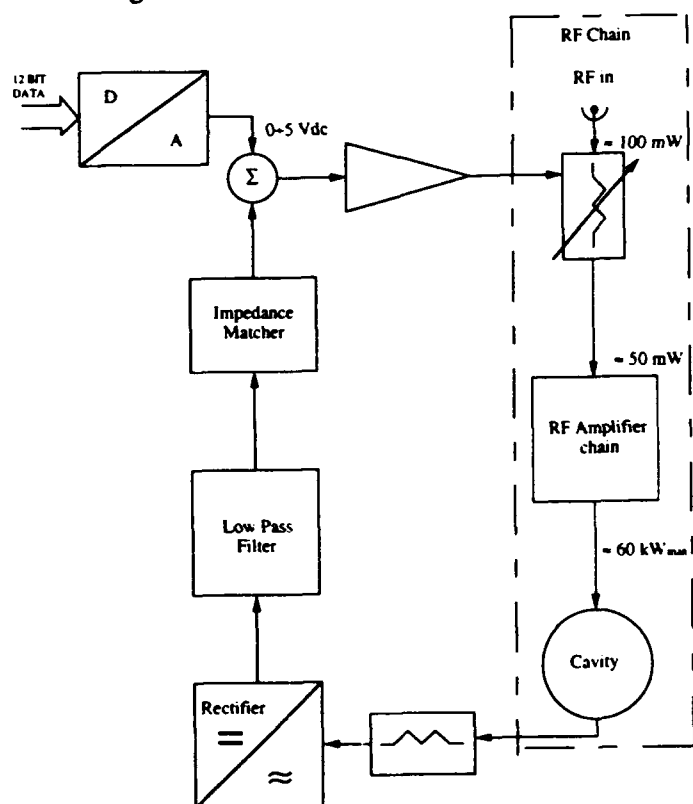


Fig.5 Block diagram of the amplitude loop

4. AMPLITUDE LOOP

In fig. 5 a definitive sketch of the cavity voltage amplitude loop is shown.

The rectified signal from the cavity should be connected through a long distance cable to the regulating chain. To overcome this problem, an impedance matching circuit driving a 100 Ω low attenuation cable has been used. The signal error between the cavity voltage and the reference analog input drives a commercial variable attenuator to set the RF attenuation to the proper value by means of an amplifier with voltage gain of 50.

The variable attenuator provides the fine regulation of the signal amplitude. This device has been tested. The attenuation resolution of this device at 20 dBm of RF input power is 0.05 dB in the range of 30 dB. Its phase variation in the full range of attenuation is better than ± 1.5 degree.

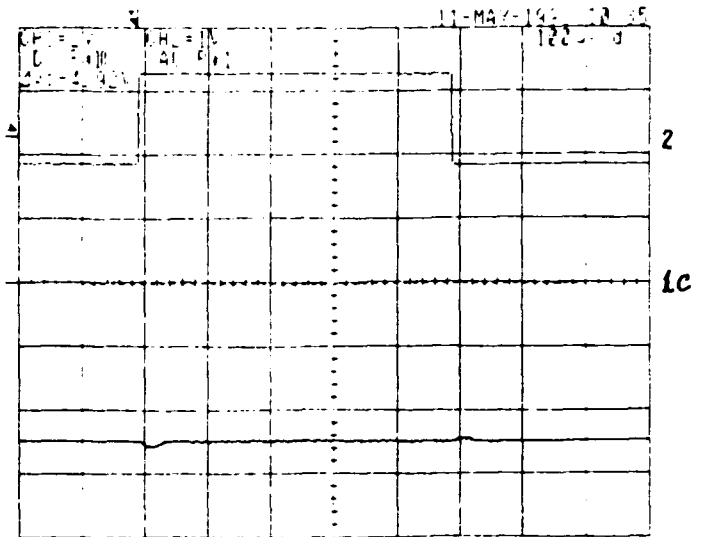
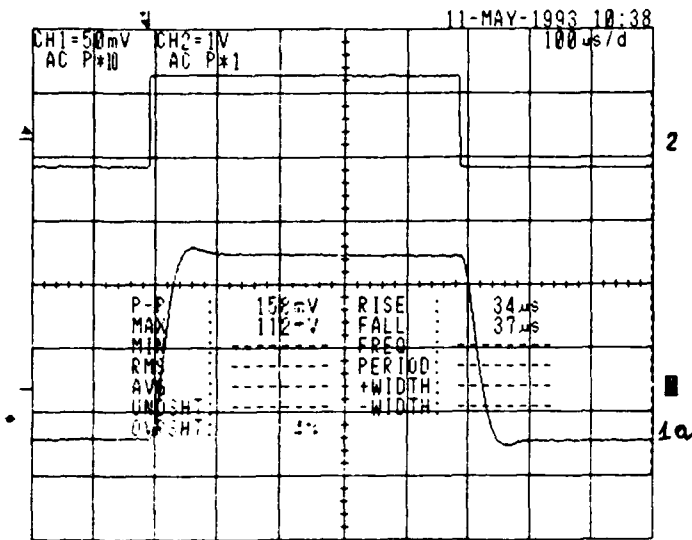


Fig. 6 Waveform 2: modulating signal
 waveform 1a: feedback signal- imp. matcher input
 waveform 1b: error signal - RF rectifier output
 waveform 1c: DC level of the modulated signal
 RF rectifier output

In the scope plots (fig. 6) the response of the feedback loop to 20 % amplitude modulated signal by a square wave modulation is shown. Similar results can be obtained in the presence of a phase modulation.

As can be seen the typical response time is about 50 μ sec with a precision of the regulated value better than 0.6 %.

5. CONCLUSION

The reliable and efficient operation of the different loops, which we consider satisfactory, cannot be separated from the complete RF plant characteristics, in order to have an efficient control of the whole RF cavity parameters. For this reason the definitive parameter configuration of the ELETTRA RF low level system will be set after the tests on the whole system will be performed.

6. REFERENCES

- [1] A. Massarotti et al., "Status Report on the ELETTRA R.F. System", in Proceedings of the 4th EUROPEAN PART. ACC. CONF., Berlin, Germany, March 1992.
- [2] A. Massarotti et al., "500 MHz Cavities for the Trieste Synchrotron Light Source Elettra", in Proceedings of the 2nd EUROPEAN PART. ACC. CONF., Nice, France, June 1990, pp. 919-921.

A Pulse Sequencer for the KAON Factory Beam Chopper

G. Waters, D. Bishop, M.J. Barnes, G.D. Wait

TRIUMF, 4004 Wesbrook Mall, Vancouver, B.C., Canada V6T 2A3

Abstract

The beam chopper consists of a low-loss transmission line center fed from a tetrode. The transmission line is terminated with a short-circuit at one end and an open-circuit deflector plate at the other end. The complex reflections from the open-circuited and short-circuited ends allow a single tetrode to generate a deflector pulse with good rise and fall times. The shape of the pulse at the deflector plate is extremely sensitive to the frequency of the grid driver pulse. A variation of 1ns in timing significantly alters the deflector pulse. To provide the required pulse pattern, a FET based grid pulser and sequencer has been built. This sequencer is able to produce alternating narrow and wide 900 volt grid pulses with rise and fall times of 20ns. Under computer supervision it is able to generate and control pulse patterns with a stability of ± 125 ps. The pulse pattern is synchronized to an RF synthesizer to simulate operation with the 23 MHz TRIUMF cyclotron RF system.

I. INTRODUCTION

Kicker magnets will be required for ring-to-ring transfers in the KAON factory synchrotron at TRIUMF. The cyclotron will be used as an injector for the synchrotron. To prevent beam spill at the transfer points, gaps must be introduced into the injected beam of sufficient duration to allow the kicker magnets

to switch on and off. These gaps are produced using an electric kicker [1] operating at up to 15kV. This beam chopper is required to remove 2 and 3 beam bursts alternatively at approximately 1 μ s intervals.

Within the cyclotron the pulse period is 43.5ns. Each pulse has a width of 2.4ns with approximately 2.4ns of jitter. This results in an effective time between beam bursts of about 39ns. Therefore to remove two and three beam bursts the chopper pulses must be 48ns and 92ns alternatively with a rise and fall time of less than 39ns. In the final design the repetition rate will be 1.022 MHz.

In the prototype, which operates at 1.9MHz, the electrical pulses that produce this field are stored in a low-loss transmission line. One end of the transmission line is terminated with the open-circuit deflector plates while the other is terminated with a short-circuit (see fig 1). The one way propagation delay from the open-circuit to short-circuit, is about 1 μ s. A type CY1170J 75kW tetrode [4] whose cathode is at a high negative voltage (-15kV) is utilized to center feed the transmission line. A separate paper at this conference [2] reports on the status of this device. The complex reflections from the open-circuited and short-circuited ends allow a single tetrode to function both as a charger and as a clipper depending upon the polarity of the reflected pulses. This is illustrated in the lattice diagram (figure 2). A narrow charger pulse, after two reflections, appears at the tetrode with a positive amplitude. By triggering the tube at the trailing edge of this pulse it can be effectively clipped. A second (wide) charger pulse is launched shortly after and is clipped in a similar manner by clip pulse number two (fig 3). When, after five reflections,

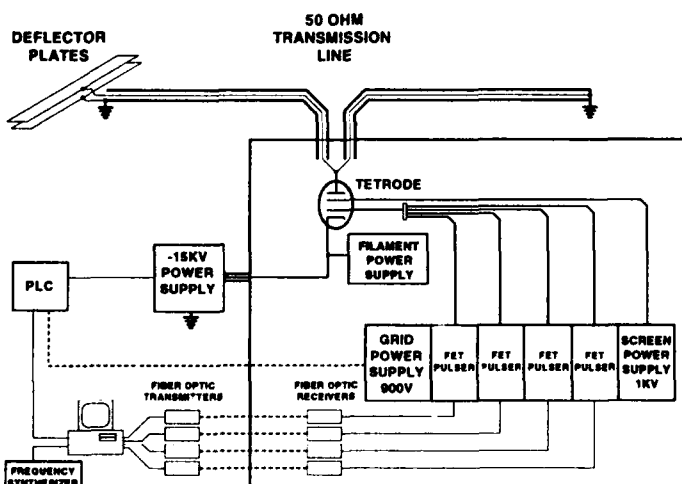


Figure 1 Beam Chopper

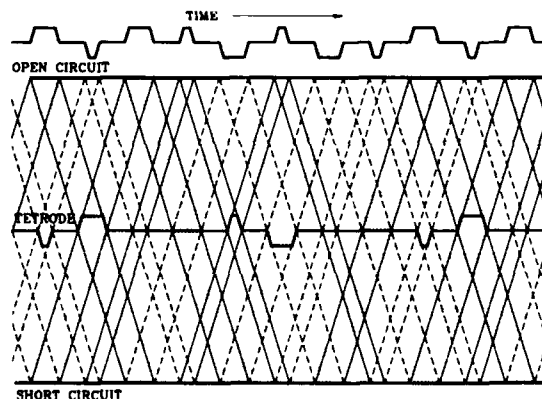


Figure 2 Lattice Diagram

the narrow (or wide) pulses add as a single negative pulse the tetrode is triggered to restore the leading edge.

The quality of the pulse within the center fed transmission line is extremely sensitive to the timing of the grid pulse. A variation of 1ns in the one way cable delay can typically cause a 10-15ns variation in the rise or fall time of the stored pulse. To meet these stringent requirements we built a precision 23MHz grid pulser driven from a synthesizer to simulate the TRIUMF cyclotron main RF.

To drive the tetrode grid, reprogrammable PALs and programmable delay line were used to produce pulse sequences of arbitrary duty cycle and repetition rate. The sequencer output was connected to a FET based grid pulser (fig 1) using fibre optics to give the required high voltage isolation and good noise immunity.

II. HARDWARE

A. Sequencer

The chopper specifications require that alternating narrow (48ns) and wide (92ns) pulses appear at the deflector plates with a repeating pattern corresponding to 45 beam burst [2]. The interval between the narrow and wide pulses must correspond to 20 beam bursts (fig 3). Two programmable logic array devices (PAL16V8) were employed as a counter and state machine to generate the correct sequence of timing and strobe pulses. Clock pulses for the counter are derived from the cyclotron 23Mhz main RF system. Precision programmable delay lines (AD9501) are used to generate pulses of variable pulse width [7]. Each delay line has associated with it two 8-bit latches for pulse

width selection (fig 4). An additional delay line provides fine adjustment of the clip pulse timing. Alternating narrow and wide pulses are selected by switching between the two sets of latches (charger widths groups 1 and 2 in fig 4) using strobe pulses generated by the state machine. There are two charger and two clipper channels (A and B). The timing and width of each channel may be independently adjusted to facilitate pulse shape adjustments and to minimize over-swing on the trailing edge of the stored pulse. The pulses are multiplexed and transmitted by four 100Mb/s optical fibre links to the FET pulser units.

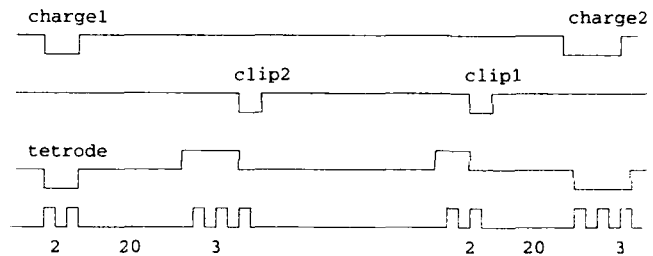


Fig 3 Sequencer output

B. FET Pulser

This device is built around a DEI 150FPS 1kV mosfet driver [3]. It is capable of driving high voltage FETs at frequencies up to 25MHz with pulse widths of 25ns or more with rise times of 3-5 ns. Each channel has two DEI pulser units connected in parallel for a total of eight. The FETs operate

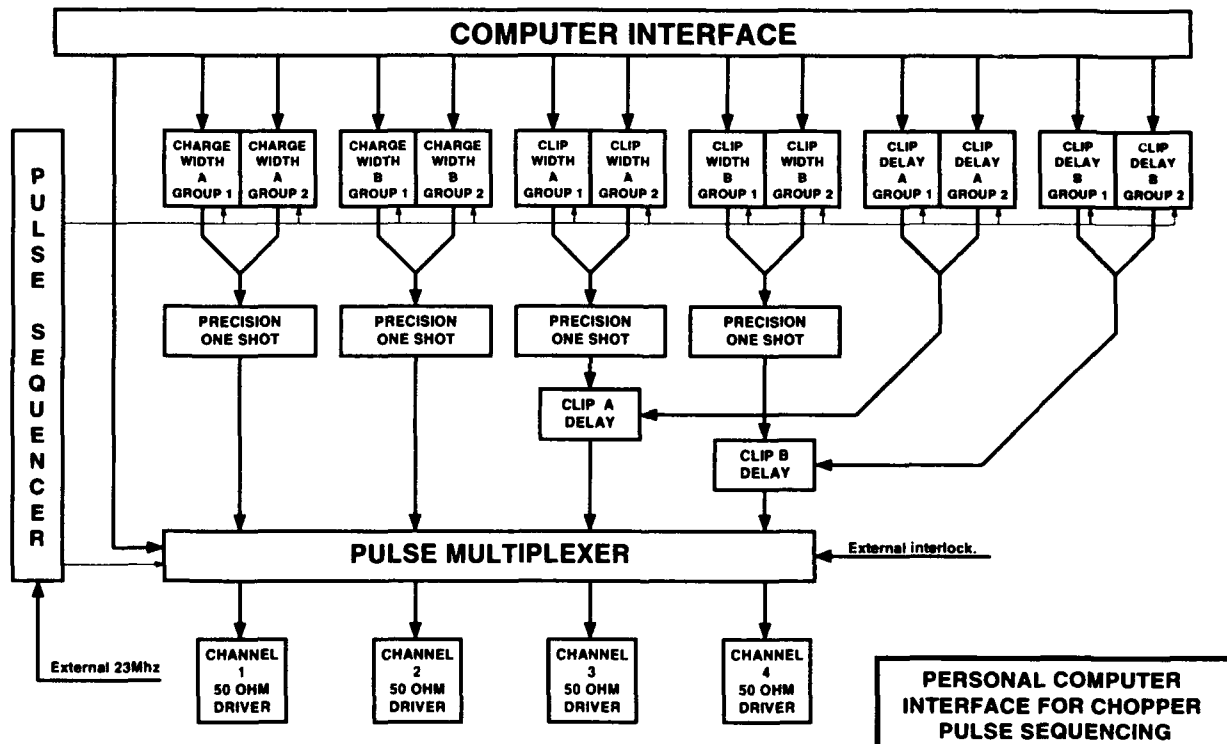


Figure 4 Block Diagram of the Grid Pulse Sequencer

with a common but variable source voltage to a maximum of -600 volts. In addition the drain voltage of each of the units can be variable or fixed at ground. Each of the four channels is connected to a summing point close to the grid with one of four 75 ohm coaxial cables. The pulse multiplexer (see fig 4) and the eight FET pulser units allow us to produce a versatile composite grid pulse at the control grid of the tetrode.

An integral part of the chopper test stand is a PC-AT. This is used for a variety of applications including programming the PLC used in the safety interlock system [5]. We therefore integrated the pulser controls by designing the pulser module as a PC card. The PC interface allows the pulse widths and timing to be placed under software control. Also included is a register to monitor the state of an external interlock.

III SOFTWARE

The software is written in the C language and compiled with the Borland C compiler and executes under DOS. Upon startup the pulse widths default to a minimum with all four pulser channels off. A simple user interface (see fig 5) allows the operator to control all pulse width and delay settings. Function keys initiate major system changes and the saving and restoring of settings. The program monitors the state of an external interlock and uses it to disable the pulser if the high voltage power supply is off while the filament is on. This is necessary to protect the screen grid. The status of the pulser and external interlock is displayed on the computer screen.

Narrow pulse settings		Channel A1	Channel B1	Channel C1	Channel D1
Charger width 1	255	Chrg1 ENB	Char2 ENB	Chrg1 ENB	Chrg1 ENB
Charger width 2	0	Clip1 ENB	Clip1 ENB	Clip2 ENB	Clip2 ENB
Clipper width 1	0	ON	ON	ON	ON
Clipper width 2	39				
Clipper delay 1	255				
Clipper delay 2	255				

Wide pulse settings		Channel A1	Channel B1	Channel C1	Channel D1
Clipper width 1	49	Chrg1 ENB	Char2 ENB	Chrg1 ENB	Chrg1 DIS
Clipper width 2	2	Clip1 ENB	Clip1 ENB	Clip2 ENB	Char2 DIS
Clipper width 3	3	ON	ON	ON	ON
Clipper width 4	44				
Clipper delay 1	36				
Clipper delay 2	76				

Loading setup file setting.def		SYNTH OK INTLK OK
Last setup before exit.		
Mon Apr 26 14:24:23 1993		
Done		

<F1> OFF <F2> SEQU ON <F3> SAVE <F4> LOAD F6=DOS <F1> EXIT

Fig 5 Pulser Control Screen

IV FUTURE DEVELOPMENT

A. Pulser

The current mode of operation is open loop thus we have no control over long term drift. A timing shift relative to a master trigger is not a major concern since in a sense the chopper is the master trigger for KAON. However, as already described, drift in the clipper timing can have a major effect on the shape of the chopper pulse. This can manifest itself as a change in the DC level of the inter-pulse region. We plan to add a gated ADC to detect this level and use the signal to adjust the settings. In the final design we may need to double the number of parallel FET

pulsers and the number of clip delays in order to improve the control of the inter-pulse ripple.

B. Computer

Although adequate in a development environment a PC does not represent a good choice for an operational system. We are currently developing an intelligent controller for applications in embedded systems. The controller is a single-board module in a Euro-card format based on a Motorola MC68332 microcontroller. An onboard Ethernet interface will allow software downloading and remote device control. Also included are 8 A-D channels, 8 D-A channels, 48 bits of digital I/O and 2 serial ports. The controller is designed to function as a VME slave device. Enough EPROM capacity will be included to hold large standalone application software including the VxWorks kernel [7]. We plan to redesign the pulser module as an expansion board to this controller.

V REFERENCES

- [1] M.J. Barnes, D.C. Fianders, C.B. Figley, V. Rodel, G.D. Wait. "A 1 MHz Beam Chopper for the KAON factory", Proceedings of European Particle Accelerator Conference, 1990
- [2] G.D. Wait, M. Barnes, D. Bishop, G. Waters "Interleaved Wide and Narrow Pulses for the KAON Factory Beam Chopper" Proceedings of this Conference.
- [3] Direct Energy, Inc, 2301 Research Blvd., Ste. 101, Fort Collins, Colorado 80526.
- [4] English Electric Valve Co. Ltd., Chelmsford, Essex, UK.
- [5] G. Waters, D. Bishop, M.J. Barnes, G.D. Wait. "Controls and Interlocks for a Prototype 1MHz Beam Chopper", Proceedings of 1991 IEEE Particle Accelerator Conference, San Francisco, California.
- [6] Wind River Systems, 1010 Atlantic Ave, Alameda, California 94501.
- [7] Analogue Devices, One Technology Way, P.O. Box 9106, Norwood, MA 02062-9106.

A Dual Frequency Resonator

P. Lanz, M. Lipnicky, M. Zach
TRIUMF, 4004 Wesbrook Mall, Vancouver, B.C. V6T 2A3

Abstract

A dual frequency resonator system operating at 74/37 MHz and using nested coaxial conductors for the dee stems in a proton/deuteron isotope production cyclotron is described. The design alternatives are discussed, basic computations presented, and compared with results from model measurements.

I. INTRODUCTION

Cyclotrons for production of isotopes used in medical and pharmaceutical applications typically deliver proton beams at low to medium energies. In recent years a need for deuteron beams at corresponding energies and lower beam intensities was expressed. The 2/1 mass ratio allows acceleration of both particles in one dee system by selecting the appropriate harmonic number. All available options require changes either to the magnetic field or to the rf frequency when switching between modes.

For reasons of economy, small size, and ease of operation, isotope producing cyclotrons are built as fully automated compact units. A cyclotron with these features (TR30/15), built by Ebco Technologies Ltd. of Vancouver with the design and technical assistance from TRIUMF, is at this time undergoing final acceptance tests at INER* in Taiwan. The dees of this cyclotron are operated at 74 MHz/50 kV for H⁻, and at 37 MHz/25 kV for D⁻ acceleration. A description of the design options and considerations leading to the chosen concept is in (Ref. [1]). This paper deals with one of the options, namely the 'folded line configuration', in more detail.

II. FOLDED LINE CONCEPTS

In most cyclotrons the rf resonator system must be located within a very limited space not to adversely affect the stringent requirements on the magnetic field. This limitation is even more severe with compact cyclotrons where the overall dimensions are minimized as possible. Resonators operating at low frequencies become long, and the mechanism for switching between frequencies further increases the length. For low operating costs the power dissipated in the rf system must be minimized, and since the skin losses per unit area are highest in the stems and shorting planes, the characteristic impedance of these line sections should be maximized. This requirement is usually in conflict with the permitted tolerances on the magnetic field.

The stems of the resonator can be either perpendicular to the cyclotron beam plane or attached to the outer

diameter of the dees and extend radially. A layout using the former arrangement is shown schematically in Fig. 1. where the position of the shorting plungers for switching between the high/low frequency modes is indicated in the left/right halves of the symmetrical system.

The operation at the high frequency is shown in Fig. 2. together with the the rf field distribution obtained by SUPERFISH. The moveable shorting plane is also used for frequency adjustments in a broad range of frequencies.

At the low frequency the overall length of the stems that resonate with the capacity of the same dees is substantially shortened by folding the outer conductor by 180°, and using both surfaces of the intermediate cylinder as rf field boundaries. In Fig. 2. is the schematic arrangement and the field distribution.

A second possible solution is shown in Fig. 3. where the operation at the higher frequency is confined to the inner volume between the cylinders. The switching and tuning arrangement is analogous to the one in Fig. 2.

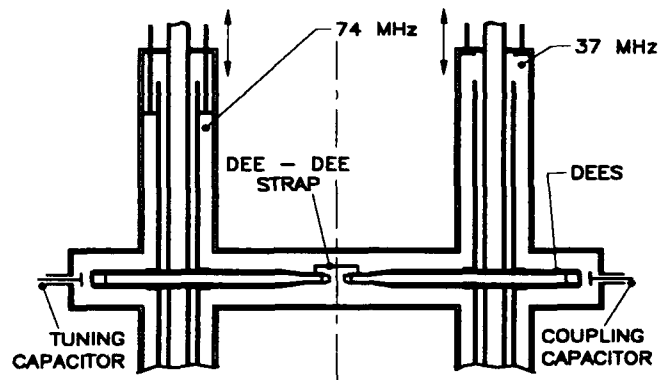


Fig. 1. Resonator layout.

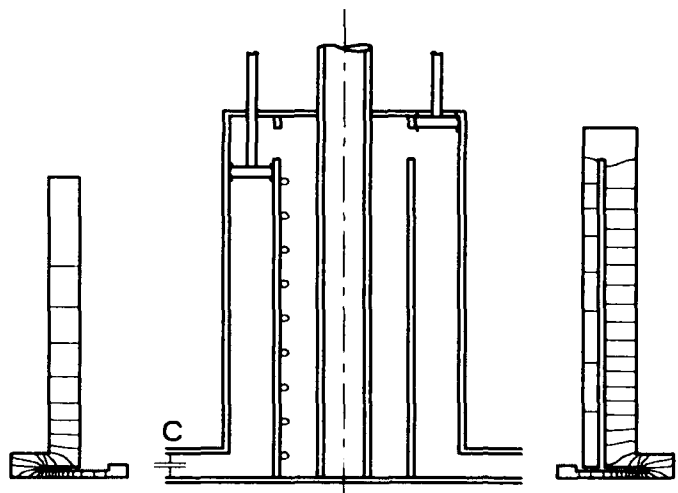


Fig. 2. High/low frequency modes.

*Institute of Nuclear Energy Research, Taiwan, Republic of China.

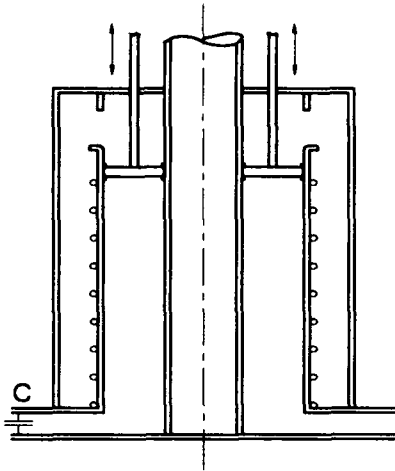


Fig. 3. Alternative concept.

The choice of the best concept for given boundary conditions depends mainly on the space available for the resonator system, the amplitude of rf voltage at both frequencies, and which mode of operation will be prevailing in production runs. The designer will then optimize the cavity dimensions within the available space. The power loss in the system is strongly affected by the characteristic impedance of the coaxial sections which in turn depends on the radial dimensions. A comparison below illustrates the effects of individual parameters for the two configurations, and it could serve as a guide when selecting a real system.

III. BASIC THEORY

For a shorted transmission line of characteristic impedance Z and length l , which is used to resonate the equivalent dee capacity C (capacitively loaded $\lambda/4$ resonator) the following equations apply (high frequency approximation, dielectric losses $\rightarrow 0$):

$$C = \frac{1}{\omega Z \tan \beta l} \quad (1)$$

$Z = 60 \ln(D/d)$, and β is the phase factor.

When two transmission lines are used in series with characteristic impedances Z_1 and Z_2 of corresponding lengths l_1 and l_2 (Fig. 4), resonance occurs when

$$\frac{1}{\omega C} = \frac{Z_1 \tan \beta l_1 + Z_2 \tan \beta l_2}{1 - \frac{Z_1 Z_2}{Z_1^2} \tan \beta l_1 \tan \beta l_2} \quad (2)$$

For the folded transmission line $l_1 \sim l_2$, and neglecting the wall thickness of the intermediate conductor we have

$$\frac{1}{\omega C} = \frac{Z_1 + Z_2}{1 - \frac{Z_1 Z_2}{Z_1^2} \tan^2 \beta l} \quad (3)$$

Expressing the length l from Eq. 3.

$$l = \frac{1}{\beta} \arctg \left(\frac{Z_1 + Z_2}{Z_2 - Z_1} \omega C Z_2 \right) \quad (4)$$

The rf power dissipated in the folded transmission line is

$$P = \frac{R_1 I_0^2}{8\beta} \left(2\beta l + \sin 2\beta l \right)_0^l + \frac{R_2 I_s^2}{8\beta} \left(2\beta l + \sin 2\beta l \right)_l^{2l} \quad (5)$$

where R_1 and R_2 are the distributed line resistances.

The above equations were tested by measurements on physical models and by SUPERFISH. There the accuracy is mostly affected by modelling the simplified dee which for the code has to be represented in axial symmetry as opposed to a true 3-D case.

IV. MODEL MEASUREMENTS

The measurements were taken on a simple 1:1 wooden, copper-clad model, as in Fig 2.

With conductor radii of 10/5.1/3 cm the line impedances were $Z_s = 40 \Omega$, $Z_1 = 32 \Omega$. Measured values are in Table 1.

Table 1. Data measured on model.

Measured:	A	B
Frequency f [MHz]	73.7	36.8
Stem length l_r [cm]	39.0	2×70.5
Voltage [†] V_c [kV]	23.2	38.0

[†]All quantities are normalized to dee voltage equal to 50 kV at 74 MHz and 25 kV at 37 MHz.

From the above results the relevant system parameters are computed at both frequencies, and the results summarized in Table 2.

Table 2. Results computed from measurements.

		Current at short [A]	Power [§] [kW]
74 MHz	analytically	1564	4.60
	SUPERFISH	1480	4.30
37 MHz	analytically	747	3.40
	SUPERFISH	754	3.45

[§]Shorting plate not included.

The analytic treatment of the problem yields sufficiently accurate results for the design of a folded stem accelerating system.

V. COMPARISON OF CONCEPTS

Assume a dual frequency acceleration system with a limit of 200 mm on the outer conductor (I.D.), dee capacity 74 pF, operating at 36.8 and 73.7 MHz.

[†]Note: The values obtained from Eq. 5 represent one quarter of the power for the whole accelerating system. They do not include the power loss in the dee region and in the shorting planes, nor do they include any losses due to imperfect contacts between rf parts. The real rf loss is $\approx 20\%$ higher than calculated. The rf power delivered to the beam must also be added as ohmic load.

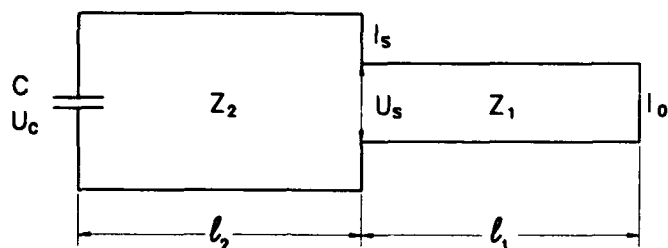


Fig. 4. Folded line equivalent circuit.

At the low frequency the two concepts under comparison are in Figs. 2 and 3. The equivalent circuits are the same as in Fig. 4.

The two configurations are schematically shown in the corresponding sketches, and the results obtained analytically for both operating frequencies are summarized in Table 3.

Table 3. Comparison of concepts (Figs. 2 and 3).

Parameter	Configuration	
	Fig. 2.	Fig. 3.
Frequency $f=73.7$ MHz; dee voltage=50 kV		
Line impedance Z_0 [Ω]	55	40
Current amplitude I_0 [A]	1278	1616
Power loss calc. P_c [kW]	3.9	3.7
Expected P_e [kW]	5	4.5
Frequency $f=36.8$ MHz; dee voltage=25 kV		
Line impedances [Ω]	$Z_1=17.3$ $Z_0=55$ $Z_1=30$ $Z_0=40$	
Current amplitudes [A]	$I_s=637$ $I_0=778$ $I_s=640$ $I_0=747$	
Power loss calc. [kW]	$P_c=2.1$	$P_c=3.3$
Expected [kW]	$P_e=3.0$	$P_e=4.0$

Note: For the complete system the power loss is multiplied by four.

The results show that both configurations represent viable design options. The difference in the capital cost of both variants will be of little importance, and the param-

eters most affecting the choice would be the outer dimensions, and power consumption. In comparison to a system with straight stems (Ref. [1]) in both configurations the overall length is $\approx 25\%$ less, and the respective power losses are about equal at the high frequency, and 20 or 50% higher in the low frequency mode.

VI. RESONATORS WITH MULTIPLE FOLDS

It is obvious that the idea of using nested cylindrical conductors can be extended to include multiple folds. For the same diameter of the outermost conductor the resonator is then further shortened at the expense of higher power losses. An example of such resonator with two moveable shorts is in Fig. 5, again showing the rf field distribution obtained by SUPERFISH. Practical applications of these resonators are promising, and they will be explored in the future.

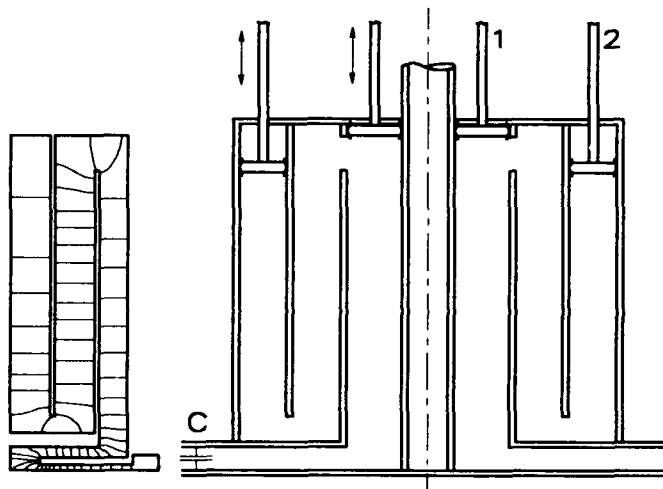


Fig. 5. Line with two folds.

VII. REFERENCE

- [1] M. Eiche, K.L. Erdman, P. Lanz, M. Lipnicki, and M. Zach, *Dual frequency resonator system for a compact cyclotron*, Proc. XIII Intern. Conf. on Cyclotrons and Their Applications, (World Scientific, Singapore, 1992) p. 515.

The Los Alamos VXI-Based Modular RF Control System*

S. P. Jachim, C. Ziomek, E. F. Natter, A. H. Regan, J. Hill, L. Eaton,
W. D. Gutscher, M. Curtin, P. Denney, E. Hansberry, T. Brooks

MS-H827, Los Alamos National Laboratory, Los Alamos, NM 87545

Abstract

This paper describes the design and implementation of the Los Alamos modular RF control system, which provides high-performance feedback and/or feedforward control of RF accelerator cavities. This is a flexible, modular control system that has been realized in the industry-standard VXI card-modular format. A wide spectrum of system functionality can be accommodated simply by incorporating only those modules and features required for a particular application. The fundamental principles of the design approach are discussed. Details of the VXI implementation are given, including the system architecture and interfaces, performance capabilities, and available features.

Introduction

The AT-5 group at Los Alamos National Laboratory (LANL) is developing the RF system for the Ground Test Accelerator (GTA), including the RF control system, which is the topic of this paper. The GTA Program is a development vehicle for Neutral Particle Beam (NPB) physics and technology.

Because GTA operates at several different harmonically-related frequencies using various power amplifier technologies, a decision was made early on to pursue a modular RF control-system architecture. This architecture is designed to be independent of RF frequency, power level, and type of accelerating structure. This approach has proven successful on GTA and has allowed the same hardware to be used in a wide variety of other accelerator applications worldwide.

The first LANL VME Extensions for Instrumentation (VXI) module was designed and built in 1989, and the fourth complete control system began operating for GTA in 1992. Additionally, four other systems have been installed and are operating at various other institutions. In all, more than 200 C-size VXI modules have been built to date.

System Requirements

The primary purpose of an RF control system is to tightly regulate the RF field in an accelerator cavity [1]. This regulation must be maintained in the presence of variations in the accelerator system parameters, such as cavity resonant frequency, beam current, and power-amplifier performance. The design objective for field regulation tolerance in the GTA RF control system is $\pm 0.5\%$ in amplitude and $\pm 0.5^\circ$ in phase. This applies for beam loading conditions up to 80%.

*Work supported and funded by the US Department of Defense, Army Space and Strategic Defense Command, under the auspices of the US Department of Energy.

To achieve this level of regulation and to ensure efficient RF power transfer to the cavity, the resonant frequency of the accelerator cavity must be maintained within prescribed limits. A regulation tolerance of $\pm 2^\circ$ was chosen as an objective for the cavity reflection coefficient phase on GTA.

System Architecture

Figure 1 illustrates the essential aspects of the LANL RF control-system architecture as applied to a particular accelerating cavity [2,3]. A sample of the cavity field is downconverted to a 20 MHz IF signal and synchronously detected against the RF reference signal. The in-phase (I) and quadrature-phase (Q) components of this detected signal are compared to their respective commanded values, or setpoints.

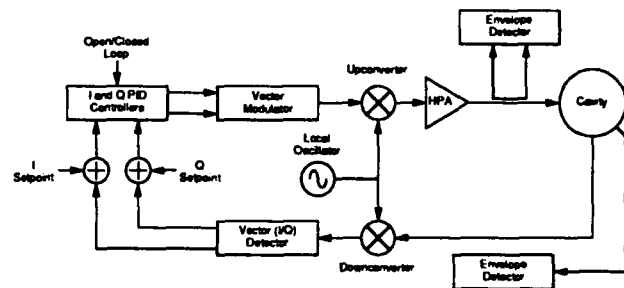


Figure 1. LANL RF control system architecture.

The difference between the detected components and their setpoints produces an error vector. Proportional, integral, and differential (PID) closed-loop control actions are then derived from this error vector, producing a control vector. An open-loop control vector can optionally be generated at the beginning of the acceleration cycle to fill the cavity in a programmed manner.

A vector modulator translates the control vector to a 20 MHz IF carrier, which is subsequently upconverted back to the original RF frequency. This RF control vector is applied to a high-power amplifier (HPA) whose output is an RF cavity drive vector, thus closing the feedback loop.

The RF control system is partitioned into several functional VXI modules as shown in Figure 2. The modules with solid outlines constitute the basic RF control system. The modules with dashed outlines are optional system components and can be incorporated as desired to enhance the performance of the basic control system. The Beam Feedforward Module estimates the beam loading disturbance and applies appropriate feedforward signals to minimize field perturbations. The Control Predistorter Module provides dynamic decoupling of the I and Q control rails, which are cross-coupled by the cavity. The Adaptive Feedforward Module measures, integrates, and corrects repetitive loop disturbances in a pulsed RF system. Details of these optional modules can be found elsewhere [2-6].

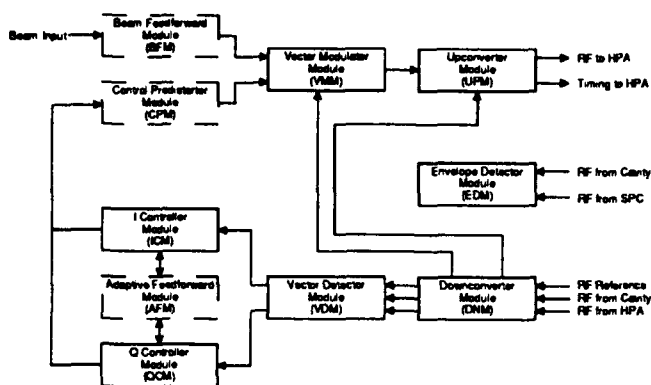


Figure 2. VXI modular implementation.

Feedback control is also employed to regulate the resonant frequency of the cavity [7,8]. As shown in Figure 3, this is achieved by detecting the forward- and reverse-traveling waves in the cavity drive line, computing the complex reflection coefficient of the cavity, and taking corrective feedback action by applying a control signal to a mechanical cavity tuner. Accuracy is assured by calibration and vector error correction [9]. All computations for this process are performed in software, and the feedback loop is closed through a virtual network connection to the tuner actuator.

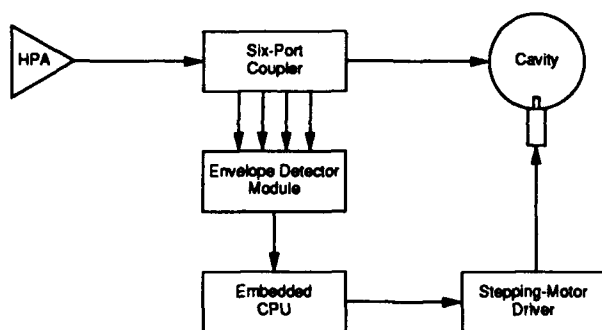


Figure 3. Resonance control system.

Several ancillary functions are assigned to the RF control system as well. Measurements of various RF signal amplitudes in the system, such as the cavity field amplitude and drive, are supported with Envelope Detector Modules. These modules sample and quantize each of eight RF input signals once per RF pulse.

The RF system associated with each cavity is sequenced and timed by the RF control system. This function is performed in the Upconverter Module, which sends two independent optical timing signals to the HPA.

The RF system, like the rest of the accelerator, is required to operate remotely under complete automation. Thus, supervisory computer control, data acquisition, and remote signal monitoring are implemented in the GTA RF control system. All relevant RF control system parameters are writable and readable through the GTA database, and all control functions are integrated and operated through Experimental Physics and Industrial Control System (EPICS) control screens [10].

Hardware Realization

The VXI standard [11], which emerged in the 1988-89 time frame, was developed by a consortium of leading instrument manufacturers. This standard builds on, and is compatible with, the ubiquitous and powerful VME standard, producing a robust card-modular medium capable of supporting high-performance analog, digital, and microwave instruments. The design of the RF control system commenced in this time period, and VXI was chosen as the packaging medium. VXI held the promise of not only supporting the needs of the RF control hardware, but also of fitting seamlessly into the GTA computer control system, it being of a VME-based distributed architecture.

The promise of VXI has held true in practice. Most of the RF control modules have been, of necessity, designed in-house. In all cases, adherence to the VXI standard has been maintained. Several commercial VME cards, such as a 68020-based processor and an Ethernet™ interface card, had already been integrated into the computer control system. These VME modules were directly embedded in the VXI RF control system and integrated together without significant difficulty.

Figure 4 shows a conceptual layout of a typical LANL VXI module. Details of the register-based VXI interface can be found elsewhere [12]. All timing and signal conversion functions are distributed down to the module level. A 10 MHz clock and a synchronizing trigger are broadcast to all modules on the VXI backplane. Counters on each module's interface circuit count down from preloaded register values and provide on-board timing signals. As needed, A/D and D/A converters are provided on each module. Signal sampling is triggered by the on-board timing signals, which are under software control. This approach greatly simplifies system integration and configuration management. Because the number of connectors and cables in the system has been minimized, reliability is improved.

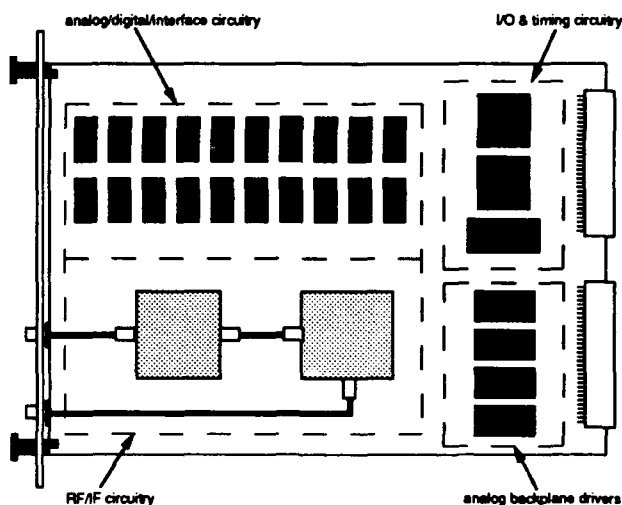


Figure 4. Conceptual VXI module layout.

Analog, digital, and mixed-signal circuits are judiciously combined on the LANL VXI printed circuit (PC) boards. The structure of these PC boards ranges from 2 to 10 layers, depending on the complexity of the application. Sensitive RF

and microwave circuits are housed in traditional-style metal enclosures and mounted on their respective VXI motherboards. Figure 5 shows a typical design, in this case an 8-channel RF Envelope Detector Module. Pulsed RF signals are applied to the front-panel connectors, and digitized samples are readable in the module's VXI registers.

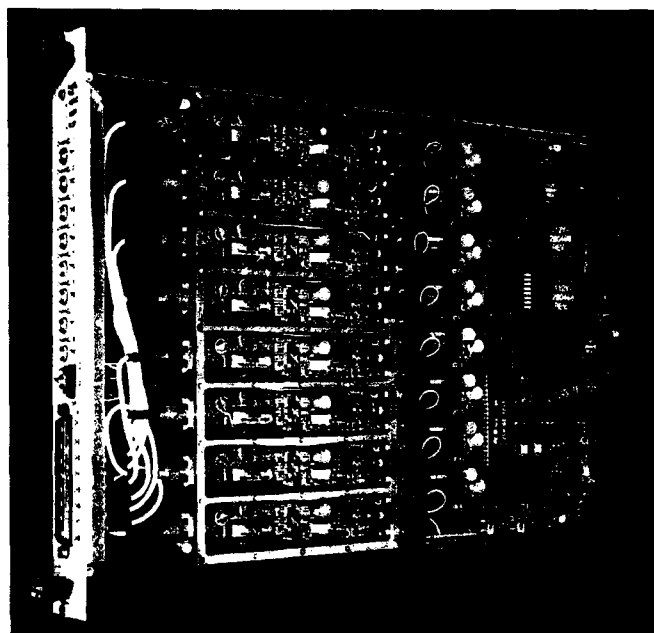


Figure 5. LANL 8-channel envelope detector module.

Remote monitoring of analog signals is provided, if needed, by an insertable monitor multiplexer daughter board. This circuitry selectively accesses, under software control, any two of eight designated analog signals on its associated motherboard. Each module in a crate, again under software control, places its selected signals on the VXI backplane. These signals are sensed by another module, which in turn transmits them to a remotely located receiver. Through this multiplexing technique, a large number of real-time analog signals is efficiently accessed remotely for tune-up, monitoring, and troubleshooting of the RF control system.

The measured performance of the LANL RF control system meets or exceeds all performance requirements [13]. After the integration and shakedown periods typical of all new designs, remote operation of the control system has been highly reliable.

Other Applications

The success of the generic, modular design approach described in the introduction is proven by its successful application to machines other than GTA. LANL control systems have been applied to the FEL accelerators at both the Boeing and the University of Twente FELs with good results. In the latter case, the operating environment is an embedded Macintosh™ controller running LabVIEW™, illustrating the general utility of the VXI format. The SSC Laboratory has applied a LANL control system to their RFQ, and is evaluating applications to other machines. The APS linac at Argonne National Laboratory is incorporating the front-end

LANL modules, with upgraded signal acquisition speeds, for machine control and diagnostics.

Summary

The LANL VXI RF control system has been successfully applied not only to its original target, GTA, but also to various other machines. This validates the original design goals of a high-performance, modular, generic control system.

References

- [1] B. R. Cheo and S. P. Jachim, "Dynamic Interactions Between RF Sources and LINAC Cavities with Beam Loading," *IEEE Trans. Electron Devices*, vol. ED-38, pp. 2264-2274, Oct. 1991.
- [2] S. P. Jachim, "Some New Methods of RF Control," *Proc. LINAC Conf.*, pp. 573-577, 1990.
- [3] C. D. Ziomek, S. P. Jachim and E. F. Natter, "Design of a Multivariable RF Control System Using Gain-Shaping in the Frequency Domain," *Proc. IEEE Particle Accelerator Conf.*, 1991, pp. 1329-1331.
- [4] L. Eaton, S. Jachim and E. Natter, "An Adaptive Control Technique for Accelerators Using Digital Signal Processing Technology," *Record of the Europhysics Conference on Control Systems for Experimental Physics*, 1987.
- [5] C. D. Ziomek, "Adaptive Feedforward in the LANL RF Control System," *Proc. LINAC Conf.*, 1992.
- [6] C. Ziomek, et. al., "Results of Adaptive Feedforward on GTA," *Proc. IEEE Particle Accelerator Conf.*, 1993.
- [7] S. P. Jachim, et. al., "High-Power Measurement and Tuning of Accelerator Cavities Using a Six-Port Reflectometer," Los Alamos National Laboratory Document LA-CP-89-304, 1989.
- [8] C. M. Fortgang, et. al., "Heavy Beam Loading Measurements of an RF Accelerating Cavity Under Amplitude and Phase Control," *Review of Scientific Instruments*, vol. 61, Nov. 1990, pp. 3405-3411.
- [9] S. P. Jachim and W. D. Gutscher, "A Statistical Method for Calibrating the Six-Port Reflectometer Using Nonideal Standards," *IEEE Trans. Microwave Theory Tech.*, vol. MTT-37, pp. 1825-1828, Nov. 1989.
- [10] L. R. Dalesio, "EPICS Architecture," *Proc. International Conf. Accelerator and Large Experimental Physics Control Systems*, pp. 278-281, Dec. 1992.
- [11] VXIbus Consortium, inc., *VMEbus Extensions for Instrumentation System Specifications*, rev. 1.4, May 22, 1992.
- [12] C. D. Ziomek, "Interfacing RF Control Electronics to the VXIbus for the Ground Test Accelerator," Los Alamos National Laboratory Document LA-CP-90-217, 1990.
- [13] P. Denney and S. P. Jachim, "Measured Performance of the GTA RF Systems," *Proc. IEEE Particle Accelerator Conf.*, 1993.

General Overview of the APS Low-Level RF Control System*

Jeffrey D. Stepp, James F. Bridges
Argonne National Laboratory
9700 S. Cass Ave., Argonne, IL 60439 USA

The submitted manuscript has been authored by a contractor of the U. S. Government under contract No. W-31-109-ENG-38. Accordingly, the U. S. Government retains a nonexclusive, royalty-free license to publish or reproduce the published form of this contribution, or allow others to do so, for U. S. Government purposes.

Abstract

This paper describes the proposed low-level rf system of the positron accumulator ring (PAR), the injector synchrotron, and the storage ring of the 7-GeV Advanced Photon Source. Four rf systems are described since the PAR consists of a fundamental frequency system at 9.8 MHz and a harmonic system at 117 MHz. A block diagram of an accelerating unit is shown and descriptions of various control loops are made (including amplitude control, phase control, and cavity tuning control). Also, a brief overview of the computer interface is given.

I. POSITRON ACCUMULATOR RING (PAR)

There are two rf systems in the PAR. One operates at 9.8 MHz to collect the linac pulses, and a second operates at 118 MHz for the last 100 ms of the 2-Hz injection cycle to bunch the beam until extraction. Each system consists of one cavity, one rf amplifier, and associated control circuitry. The control system also synchronizes operation with the linac during injection and with the synchrotron during extraction.

TABLE I. FUNDAMENTAL PARAMETER LIST

Frequency	9.77584 MHz
Harmonic Number	1
Peak Voltage	40 kV
Power	4.7 kW
Cavity Type	Cap-loaded Coaxial
Number of Cavities	1
Cavity Tuning	Electronic
Control Loop Bandwidth	10 kHz
Transit Time (2Q/w)	248 μ s
Phase Detector Resolution	1.0 degrees

9.8-MHz System

The slow thermal tuning of the 9.8-MHz cavity will be accomplished by a coarse tuner. A fast tuner will be accomplished by ferrite.

Since beam loading is incremental, with 24 linac bunches injected over a 400-ms period, a modest feedback control system keeps the cavity voltage constant and the power amplifier load impedance real. (Control parameters are listed in Table I.) Programming of the power amplifier input voltages and fine tuning of the cavity are included to offset the transient from each injected bunch.

* Work supported by the U.S. Department of Energy, Office of Basic Sciences, under Contract No. W-31-109-ENG-38.

TABLE II. TWELFTH HARMONIC PARAMETER LIST

Frequency	117.3101 MHz
Harmonic Number	12
Peak Voltage	30 kV
Power	1.82 kW
Cavity Type	$\lambda/2$ coaxial
Number of Cavities	1
Cavity Tuning	Electronic and Mechanical
Control Loop Bandwidth	10 kHz
Transit Time (2Q/w)	68 μ s
Phase Detector Resolution	1.0 degrees

117-MHz System

The cavity is electronically adjusted during operation of the 9.8-MHz cavity so as not to interact with the beam, since only the fundamental cavity is used during accumulation.

A 2-kW amplifier is located outside the shield wall, and the cavity is powered via coaxial cable. Resistive loading is included by using a stainless steel cavity. The rf power is then equal to the beam power giving a maximum detuning of 45 degrees. If rf feedback is needed, this amplifier could be mounted on the cavity to minimize phase delay at 117 MHz. [1]

When the cavity is switched from a passive (imitating a beam pipe) to an active state, beam loading is rapid. A fast tuning and voltage control system, including feed-forward techniques, is used, and large induced voltages are avoided with programmed tuning. The amount of circulating beam controls the program signals to the power amplifier and to the tuning device, so that as the cavity is turned on for the last 50 ms of the PAR cycle, the accelerating voltage has the correct phase with respect to the 9.8-MHz bucket and the power amplifier sees a real load. Using a programmed correction signal improves the operation of the cavity; thus, for a given tolerance of cavity parameters, the feedback loop dynamic range and gain can be smaller. The correction signal is derived from the bunch signal from the master clock.

The rf amplifier produces a 30-kV accelerating voltage. Since only 222 Watts is needed to power a copper cavity, resistive loading is provided via the stainless steel cavity which lowers the shunt impedance and reduces the phase shift between beam current and generator current. This makes the programming and feedback systems less sensitive to variations in beam loading and increases the stability of the feedback system. Parameters for operation are listed in Table II.

The frequency source for the PAR system is a frequency division of the 351.9-MHz storage ring frequency source. The signal is first divided by 3 to generate a 117-MHz source which is phase-shifted to allow placement into one of three buckets at -120° , 0° , or $+120^\circ$. This signal is then further divided by 12 to produce the 9.8-MHz signal. Using this method, all three fre-

quency sources are phase coherent with the storage ring frequency source.

II. BOOSTER SYNCHROTRON

The low-level system generates the rf signal to drive a klystron amplifier. The synchrotron signal generator is phase-locked to the storage ring master oscillator. The storage ring rf signal is transmitted to the synchrotron signal generator over phase-stabilized cable.

The low-level system also includes the analog phase and amplitude regulation systems that maintain the cavity rf voltages. Figure 1 shows this schematically for one of the systems of the storage ring, and Table III lists specific parameters.

TABLE III. BOOSTER PARAMETER LIST

Frequency	351.930 MHz
Harmonic Number	432
Revolution Frequency	814.3 kHz
Repetition Time	0.5 s
Acceleration Time	0.25 s
Cycle Rate	2 Hz
Peak Voltage for 7 GeV	9.5 MV
Injection Voltage	100 kV
Peak Power	700 kW
Cavity Type	5-cell
Number of Cavities	4
Cavity Tuning	Dual Piston/Motor
Amplifier	Klystron
Synchrotron Frequency	21.1 kHz
Phase Detector Resolution	0.1 degrees
Dynamic Range	40 dB Volts

A single 1-MW klystron drives four five-cell cavities. The cavities are separated into two groups of two each, on opposite sides of the ring. The second and fourth cells are fitted with ports for the tuners which provide amplitude and phase balance. The tuner slugs are fitted to worm gears and stepper motors which provide 1 μ m of step resolution. A feedback system monitors the phase difference in the cavity and adjusts the tuners in tandem to keep the cavity at the resonant frequency with $\pm 0.1^\circ$ under rf heating. Also, the field amplitudes in each of the two cells are detected and the tuners are adjusted differentially to balance the voltage to within ± 1 dB.

The klystron output is monitored and a feedback system is used to eliminate the power supply ripple and phase variations due to cathode voltage variations. The rf drive signal is modulated in amplitude and phase.

Each cell of the cavity has a field monitor. The tuner-port cells derive the field-balance signal. The end cell fields are added in phase to derive the average cavity phase and control both tuners in parallel. The resultant signal is compared to the driving signal with a phase meter. For slow tuning, the digital phase information goes to the control computer to offset the tuners for rf heating by varying the water temperature. For fast tuning a copper tuner piston is activated by a stepping motor controlled by a servo amplifier system. The feedback loop that drives the tuning piston works on only the reactive element of the

cavity input impedance. Since the beam loading is so small, no de-tuning is foreseen to accommodate the "Robinson Stability" criteria. [2] The computer then controls the offset of the two tuners of each cavity to keep it properly tuned.

Waveguide Phase Shifter

A mechanical waveguide phase shifter is located in the feed-line to the more distant pair of 5-cell cavities. This phase shifter adjusts the rf phase to be the same in both the nearer and farther pairs of 5-cell cavities regardless of temperature variations within the building.

The storage ring rf signal is transmitted to the synchrotron over phase-stabilized coaxial cable from the rf source cabinet. This ensures phase continuity with the storage ring.

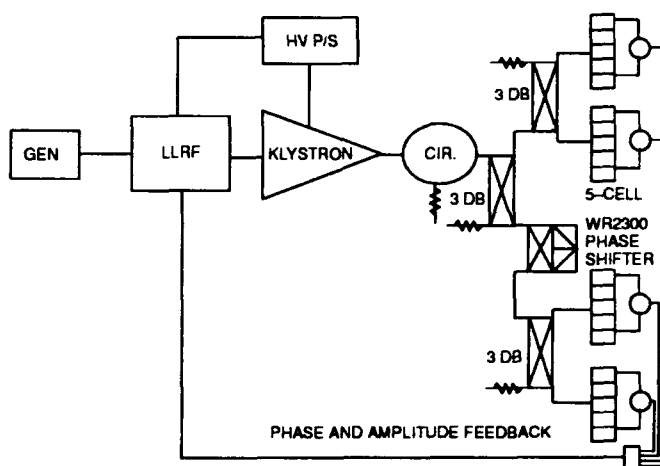


Figure 1. Synchrotron Block Diagram

III. STORAGE RING

The low-level rf system controls the amplitude and phase of the rf signal which drives the klystron amplifier. It also includes the tuning regulation that maintains each cavity's resonance point. See Table IV for specifications.

TABLE IV. STORAGE RING PARAMETER LIST

Frequency	351.93 MHz
Revolution Frequency	271.5 kHz
Harmonic Number	1296
Filling Time, Multibunch	0.9 min
Filling Time, Single	2.7 s
Cavity Type	Single-cell
Number of Cavities	16 in 4 groups
Cavity Tuning	Piston/Motor
Amplifier	1 MW Klystron
Number of Amplifiers	4
Cavity Peak Voltage	600 kV
Synchrotron Frequency	1.96 kHz
Phase Detector Resolution	0.1 degrees
Control Loop Bandwidth	1 kHz

The low-level rf system consists of five different control loops. An rf drive control loop is used to set the gap voltage across the storage ring cavities. A klystron operating loop is used

to set the operating level of the klystron in the linear or saturation region. A cavity tuning loop is used to keep the cavity input impedance real during beam loading and rf heating. The loop moves a tuner piston through a stepper motor which changes the inductance of the cavity. A klystron phase control loop keeps the output phase constant due to changes in voltage and power levels. A cavity phase control loop keeps the sum of the phases of all the cavities constant for proper synchronous phase operation.

The input to each klystron amplifier driver has a computer-controlled rf amplitude modulator and a computer-controlled relative phase shifter. An amplitude comparator compares the sum of the voltages from all cavities to a reference, and adjusts the rf modulator to maintain the required voltage. The phase of the voltage developed in the cavities is compared with the reference, and the phase of the drive to the klystrons is adjusted to maintain the cavity voltage phase to $<1.0^\circ$.

The klystron power is controlled by a control loop through the modulating anode system, while the klystron operating point is maintained in the linear gain region. In this way the klystron efficiency remains optimum. [3]

The cavity tuner port has an 11.5-cm diameter and a 6.0-cm travel. This results in a frequency tuning range of 1.0 MHz to compensate for beam loading, temperature effects, etc. The copper plunger is activated by a stepping motor controlled by a servo amplifier system. The feedback loop that drives the tuning piston works on only the reactive element of the cavity input impedance.

Beam Compensation

Compensation for the reactive component of the beam loading is done prior to injection by detuning to comply with the requirement of the Robinson instability criterion. For the APS storage ring cavity this amounts to a negative 16 kHz of detuning from the no-beam resonance condition to the fully loaded condition. After beam filling is completed the cavities are tuned closer to resonance, and the Robinson instability is counteracted with dynamic feedback via the low-level feedback system.

V. COMPUTER INTERFACE

The rf system is under active computer control and is continuously monitored by computer. Each cavity has a field monitor. The monitors are added in phase, and the resultant signal is compared to the driving signal with a digital phase meter. The digital phase information goes to the control computer which adds the required offset to satisfy the requirements of the Robinson stability criteria. The computer then controls both tuners of each cavity to keep it properly tuned.

The computer interface, in real time, reads the phase of the voltage developed in each storage ring cavity relative to the input phase, the phase error of the klystron output power relative to the input drive phase, and the gap voltage developed across the cavity. This phase is compared to the phase of the power into the cavity. The computer drives the tuner stepper motor to maintain the required relationship to satisfy the requirements of the Robinson stability criteria.

Each control loop has local operation and diagnostics as well as a computer bus interface for remote operation and diagnostics.

The computer interface additionally monitors the operating environment of the klystron, circulator, and cavity. This includes water flow, air flow, temperature, and cavity vacuum, and warns of "out of tolerance" operating conditions and shuts off components if necessary.

The computer interface will also regulate the klystron beam voltage and current (through the modulating anode control element) to keep enough power in the klystron beam for efficient conversion to rf power for different amounts of stored beam.

VI. RF SOURCE

The frequency and phase of the storage ring rf system affect the beam position and energy. The main frequency source, a 10-MHz temperature-controlled oscillator, is stable to several parts in 10^{11} with phase continuity. A stability of 10^7 is needed for storage ring operation (see Table V). The low-level rf system utilizes a direct digital synthesizer to control a phase-locked, voltage-controlled oscillator as the source for the storage ring. The output of this common frequency source is fed via phase-stable cables to each of the klystron amplifiers in the system as well as to the synchrotron, PAR, and clock distribution for the kicker magnets.

TABLE V. RF SOURCE PARAMETERS

Operating Frequency	10.0 MHz
Output Frequencies	9.77 MHz
	117.3 MHz
	351.9 MHz
Long-Term Stability	10^{-11} /day
Short-Term Stability	10^{-9} /s
Phase Noise @ 1 kHz Offset	-100 dBc/Hz
Distance to Stations	300 ft.
Phase Stability	0.1 degrees
Minimum RF Output Power	+20 dBm

Two types of rf distribution subsystems are a star configuration [4] and a serial configuration [5]. Both provide phase stable rf signals to the multiple cavities located an appreciable distance from the rf source. The star configuration will be used to feed rf to the storage ring and synchrotron.

V. REFERENCES

- [1] D. Boussard, "Control of Cavities with High Beam Loading," IEEE, NS-32, No. 5, October 1985.
- [2] K. W. Robinson, "Stability of Beam in Radio Frequency System," CEAL-1010, p. 8, February 17, 1964.
- [3] J. Bridges, J. Stepp, "RF System Design for the Storage Ring of the Advanced Photon Source (APS)," these proceedings.
- [4] A. H. Regan, P. M. Denny, "RF Reference Generation for the Ground Test Accelerator," Proceedings of the 1991 Particle Accelerator Conference, pp. 2946-2948, 1991.
- [5] R. K. Jobe, H. D. Schwarz, "RF Phase Distribution Systems at the SLC," Proceedings of the 1989 Particle Accelerator Conference, pp. 1987-1989, 1989.

Operation of New RF Drivers for the Bevatron Local Injector *

J. Calvert, J. Elkins, D. Howard, M. Hui, N. Kellogg, A. Lindner, R. Richter
University of California, Berkeley, CA 94720

Abstract

A new 200 Mhz power amplifier system has been used operationally on the Bevatron Local Injector 20 MEV LINAC with two different power tetrodes: an EIMAC 4CW100,000E and a Thomson-Houston TH-535. The same basic anode and grid structures were used with both tubes. The system has provided increased power output over the 4616 tetrode previously used. Maximum operational gradients were achieved with both tubes. System testing, tube interchangeability, and high power operating data will be presented.

I. INTRODUCTION

After satisfactory high power testing of the prototype version of the amplifier with the EIMAC 4CW100K tube, described in Reference [1], mechanical design of the final version of the cavity and the output paddle was completed. The final version of the amplifier was installed as the driver to the TH-516 final amplifier for Tank 2 of the Bevatron Local Injector LINAC in place of the existing 4616 tetrode. Operational tests of the amplifier cart with the EIMAC tube installed proved very successful, reaching a higher gradient than had ever been achieved in this tank. Concurrently, neutralization tests were begun on the TH-535 in the prototype cavity. After neutralization of the TH-535 was completed, it was installed in the amplifier cart for high power testing; as expected, its power output was lower than that of the EIMAC tube, but it also proved capable of exceeding all required operational gradients.

II. FINAL CAVITY CONSTRUCTION

The prototype had been constructed with a copper-lined plywood box as the anode cavity. The final version of the cavity (shown in figure 1) was made with half-inch aluminum plates for the top and bottom, supported by brass pipes in the four corners. The sides were made of sheet aluminum panels set into a frame of aluminum extrusions of the type used to build standard electronic equipment cabinets. The bottom plate was machined to accommodate the Thomson tube socket directly (shown in figure 2.) and the EIMAC socket with an adapter ring. A high voltage interface assembly, constructed of large diameter, heavy walled aluminum

* This work was supported by the U.S. Department of Energy, under contract No. DE-AC03-76SF00098

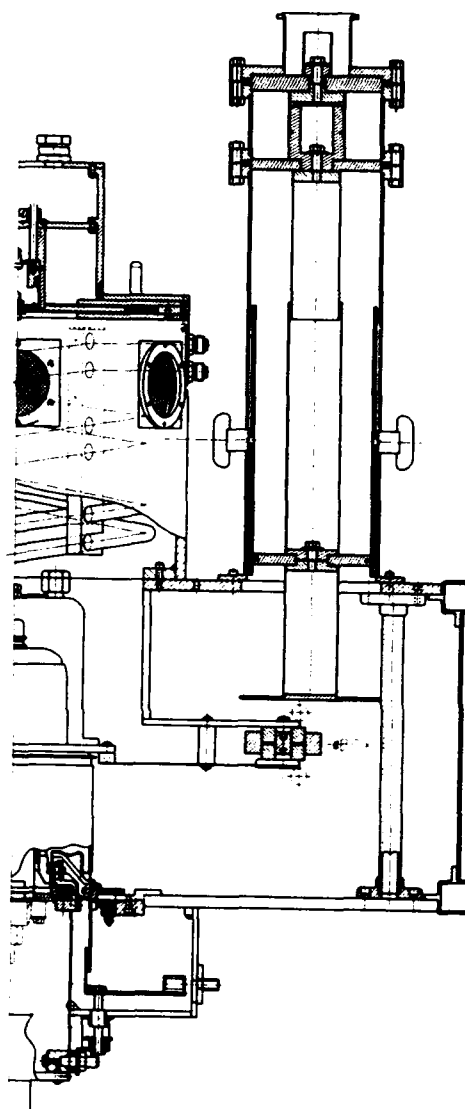


Figure 1. Scale drawing of the final cavity with the EIMAC 4CW25K tube installed.

tubing, was bolted to the top plate of the anode enclosure from the inside, and the entire structure was designed so that no access is possible without opening interlocks in the anode high voltage chain.

The radial line for the anode resonator is end loaded with eighteen capacitors which also provide mechanical support for the line. The dielectric for these capacitors was machined

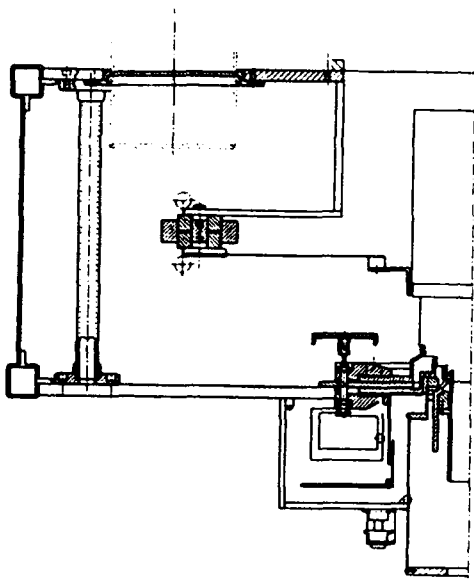


Figure 2. Scale drawing of the final cavity with the Thomson TH-535 tube installed.

at LBL from Teflon rod in an annular re-entrant shape which was chosen to provide mechanical strength and a long leakage path for the anode voltage present on the lower plate of the line, as well as the necessary capacity. The capacitor "plates" are machined aluminum rings. These locally manufactured capacitors were also lower in cost than commercially available ones.

Energy was coupled out of the prototype cavity with a loop which was not readily adjustable to vary the amplifier loading. In the final version, this arrangement was changed to a circular capacitive coupling paddle which is easily adjusted.

The output flange is designed to be fitted with either a standard 6-1/8 inch EIA flange or a pressure tested 6-1/8 to 3-1/8 inch adapter. This adapter will allow for greater than four atmospheres of air pressure in the 3-1/8 inch line. In the tests described below, a 3-1/8 inch line pressurized to 20 psi was used.

III. AMPLIFIER CART COOLING

Both tubes require water cooling for their anodes and air cooling for their bases. In addition, the various power supplies located in the double rack enclosure described in Reference [1] require air cooling. The air cooling requirements were met by providing two air sources: a high pressure centrifugal blower and a low pressure axial fan.

The high pressure centrifugal blower feeds air through a manifold to the base in the case of the TH-535 and to the grid cavity in the case of the 4CW100K. The manifold also supplies air to the 4CW25K stage tube base and grid cavity. When the 4CW100K is installed, an additional centrifugal

blower is mounted on the tube socket to blow air directly on the filament connections. Both of these blowers are interlocked to the filament power supply.

Air for general cooling of the electronics cabinet is taken in by the ten-inch axial fan. This air is passed from the cabinet into the anode cavity through screened ports in the four corners of the cavity baseplate. It then passes through the anode radial line and is exhausted through ports in the high voltage interface assembly. This path prevents ionized air from standing in the anode cavity and causing arc-over problems.

Low conductivity water is circulated through the 4CW100K anode through fittings on the high voltage interface assembly; the anode voltage is isolated from ground with coils of insulating tubing. The anode of the 4CW25K stage is cooled in similar fashion. Tests on the prototype showed that some heat from the filaments was transferred to the supporting structure despite the air cooling of the tube bases, therefore supplementary parallel water cooling loops were provided for the bases in the final version.

IV. TH-535 NEUTRALIZATION

It had been planned to neutralize the TH-535 with a screen grid to control grid resonator in the manner described in Reference [1] for the 4CW25K stage. However, succeeding tests proved that a resonator much larger than the space available was required. We then opted for the more conventional method of using a shielded rotating inductive coupling loop in the grid cavity connected to a capacitive pickup disc in the anode cavity. As tested in the prototype, this neutralizing circuit provided more than 45 DB of isolation.

V. HIGH POWER OPERATION

The amplifier cart was installed adjacent to the TH-516 final amplifier stand for Tank 2 in order to minimize the required length of pressurized output line. It was first tested with the 4CW100K tube, then with the TH-535. Operating results are presented in Table 1.

When drive was first applied, arcing occurred between the radial line corona ring and the output paddle. This problem was corrected by installing a shallow Teflon cup on the paddle. Initial tuning with the 4CW100K installed in the amplifier cart showed that it was closely coupled with the final stage: the TH-516 grid tuning had considerable effect on the anode tuning of the cart. The TH-516 grid tuning was held constant when the TH-535 was installed and it was matched using the cart anode tuning slugs. The tuning range of the slugs proved sufficient to resonate both tubes at the operating frequency of 198.965 Mhz, although with the TH-535 they were almost at the extreme "all in" end of their range.

The power output for the 4CW100K tube given in Table 1 is not the maximum achievable. The screen voltage

Table 1.

Tank Level	4CW100K		TH-535	
	8.2 V = 2.69 Megawatts			
	Pulse Pk (T=100us)	Pulse End (T=1ms)	Pulse Pk (T=100us)	Pulse End (T=1ms)
E_g (V)	-660	-660	-216	-232
I_g (A)	1	0.8	1.06	0.84
E_{sg} (V)	750	750	1350	1350
I_{sg} (A)	2	1.2	2.2	1.8
E_b (V)	20.4	19.2	21	20
I_b (A)	29.4	24.6	30 ₁	25.2
P_{out} (KW)	428.3	342.9	438.8	342.9
P_{ref} (KW) ₂	7.1±1	5.9±0.7	11.2±1.3	8.3±0.9
Gain (DB)	11.4	10.7	13.3	13.3
Eff (%)	58	52	70	68
Driver (EIMAC 4CW25K):				
E_b (KV)	10	10	9	8
I_b (A)	4.3	4	3.4	3
P_{out} (KW) ₃	24.8	20.8	20.5	16.1
Tank Level 8.4 V = 2.82 Megawatts				
E_g (V)	-660	-660	-216	-236
I_g (A)	1	0.8	1.06	1
E_{sg} (V)	1250	1250	1350	1350
I_{sg} (A)	2.4	1.8	2.2	2
E_b (KV)	20.2	18.5	21	20
I_b (A)	36.6	30.6	30 ₁	28.2
P_{out} (KW)	541	372	438.8	372
P_{ref} (KW)	13.8±1.6	8.9±1.1	11.2±1.3	8.9±1.1
Gain (DB)	11.7	11.4	13.3	13.1
Eff (%)	73	66	70	66
Driver (EIMAC 4CW25K):				
E_b (KV)	10	10	9	9
I_b (A)	4.6	4	3.4	3
P_{out} (KW) ₃	36.5	27.1	20.5	18.1

(1) Manufacturer's limit of 25 A plate current was exceeded with their permission for test purposes only.

(2) The reflected power measurement accuracy is determined by the directional coupler directivity, which was measured at approximately 25 DB.

(3) The 25K stage output power was estimated by using the same efficiency as the 100K stage because we did not use a directional coupler between the stages.

(Frequency= 198.965 Mhz, Pulse Width= 1 ms, Pulse Repetition Rate= 2 pps)

was deliberately kept low, limiting the power output in order to avoid excessive x-ray production from the tank and reduce the risk of output line sparking. Power output of the TH-535 was limited by the manufacturer's specified maximum plate current.

VI. CONCLUSION

The simplified operation of the LINAC RF system anticipated in Reference [1] was achieved when the new amplifier cart was installed and operating. Fixed bias was used in the cart for all three tube stages. After the cart had been initially tested in the operating system and proved capable of producing the necessary drive power, the pulsed bias system described in Reference [2] for the TH-516 final amplifier was also replaced with a simple DC bias supply.

The cart was used with the LINAC for ten months (including approximately one month with the TH-535 tube installed), until the end of operations at the BEVALAC. During this time, it proved to be extremely reliable and maintainable.

VII. ACKNOWLEDGMENTS

The authors wish to thank Marshal Loring and Reid Brandon from Varian for their technical support; all those from Thomson, and John Mulroe from SMA representing Thomson, for providing the TH-535, the socket, and their technical support; Robert Kerns of the BEVALAC Electronics Installation Shop and his staff for the many hours of work they spent building and modifying equipment for this project; and the BEVALAC electronics maintenance and plant maintenance crews for their willingness to provide support for a new and unknown piece of equipment.

VII. REFERENCES

- [1] D. Howard et al., "RF Drivers for the BEVALAC Injector Final Stage RF Amplifiers," Conference Record of the IEEE Particle Accelerator Conference, Vol. 2, pp. 745-747
- [2] D. Howard et al., "BEVALAC Injector Final Stage RF Amplifier Upgrades" Conference Record of the IEEE Particle Accelerator Conference, Vol. 2, pp. 742-744

432-MHz RF Source For The JHP Proton Linac

M. ONO, S. ANAMI, H. HANAKI, Z. IGARASHI, M. KAWAMURA, T. KUBO,
C. KUBOTA, K. KUDO, E. TAKASAKI and T. TAKENAKA
National Laboratory for High Energy Physics(KEK)
1-1 Oho, Tsukuba-shi, Ibaraki-ken, 305, Japan

Abstract

A high duty UHF(432-MHz) RF source for the intense proton linac of the Japanese Hadron Project (JHP) has been constructed at KEK. A test-linac consisting of a RFQ and a drift-tube (DTL) structures is under construction. The UHF RF power generated by 2-MW peak power klystron will be fed into these structures with 650 μ sec pulse-duration and 50 Hz repetition-rate through an waveguide system with a Y-junction circulator. A dc high voltage (max.-95 kV) is applied to a cathode of the klystron and a beam current is modulated up to 40 A by a pulsed high voltage(max. 80 kV) applied to a modulating anode. The klystron power supply can operate two such klystrons simultaneously with two individual anode modulators. The first operation of this RF power source and the preliminary test of an RF signal processing such as PLL and ALC will be reported.

I. INTRODUCTION

The proton linac of the JHP[1] has been designed to have three types of accelerating structures such as an RFQ, a DTL and a coupled-cell structure. The test-linac consisting of the former two linacs and a proton-source (H^+) is under construction to prove a feasibility of the intense proton beam linac required for the JHP. The UHF(432-MHz) RF sources for the RFQ and the DTL will be generated by the two high-power, high-duty klystrons with 650 μ sec pulse-duration and 50 Hz repetition-rate. The klystron power supply can feed electric-power to two klystrons with a same cathode voltage but with two individual modulating anode controls. The first operation of the klystron generating 2-MW peak power with 600 μ sec pulse-duration and the basic test of the ALC (automatic level control) within the pulse duration has been done. The high power feed to the cavities with the needed RF processing such as ALC and PLL (phase lock loop) will soon start.

II. RF SYSTEM

A. Klystron

The RF power required from the test-linac is ~ 1 MW/klystron with $\sim 3\%$ duty (650 μ sec \times 50 Hz). Within the pulse duration the RF processing such as ALC and PLL are expected. Not only such feedback processing, some kind of feed-forward processing is also expected to compensate the heavy beam loading for every pulse duration. The klystron can't be operated at a saturation to cope with such requirements. The installed klystron (TH2134, THOMSON-CSF) can produce a 2-MW peak power at the saturation with the required duty, and it will be operated in a linear region with a reduced power to realize the needed RF processing. Such a capability of generating an excessive power may also ensure a stable operation of these high-power and high-duty system. The nominal cathode- and anode-voltages are -93 kV and 80 kV respectively to generate 2-MW power with a 40A beam current.

B. Power Supply

The scheme of the klystron power supply is shown in Figure 1. The power supply is able to operate two klystrons simultaneously. It generate maximum -110 kV cathode voltage with $46 A \times 2$ beam current at 650 μ sec pulse-duration and 50 Hz repetition rate. Thyristor switches control and stabilize the cathode voltage. With allowing 5% sag at the above condition, 10.8 μ F filter condenser is chosen. A crowbar switch consisting of 6-series ignitrons (Richardson Elect., NL-35391) is installed for klystron protection. If the crowbar is triggered the thyristor switch will reduce a flow-in electric power within ~ 5 msec and then VCB is switched off at ~ 20 msec. A series-resistor is installed in the tank just before of the klystron cathode to suppress a flash-over current. The crowbar is also set aside the tank to minimize a cable length. In order to check the crowbar switch, the cathode-voltage-shortening-tests were carried out using a thin copper wire ($\phi 0.35$) shortened at the klystron socket. Due to the adopted 27.5 Ω series-resistor and the fast crowbar work (less than 6 μ sec) an estimated deposit energy at the wire is much less than 10 Joule at -91 kV cathode voltage. The estimation is carried out by using a measured shortening current and an estimated wire resistance.

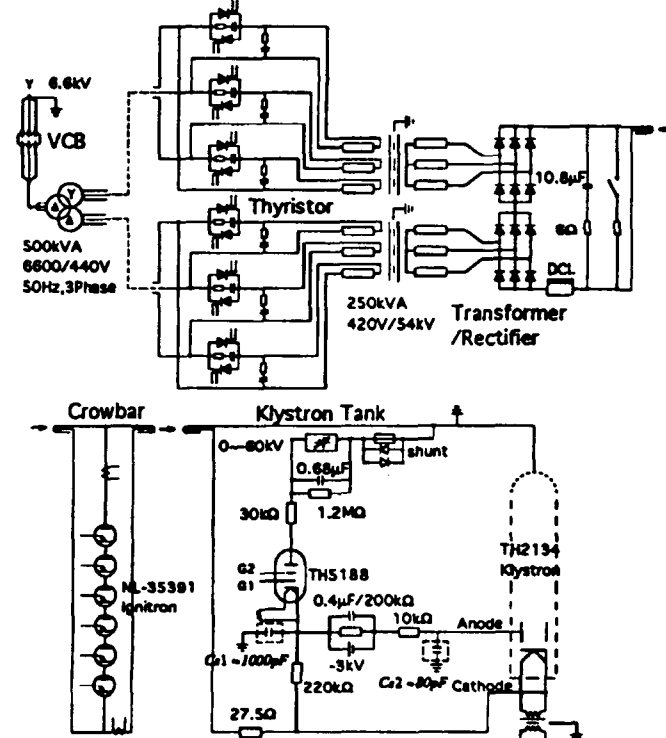


Figure 1. Klystron Power Supply.

C. Anode Modulation

The klystron beam current is modulated by the anode voltage produced by the switching tube (TH5188, THOMSON

-CSF) with the resistor-chain divider. At the switch-on of this tube, the observed current which flow across the tube, was several hundreds mA consisting of ~160 mA anode-current of the klystron and ~360 mA current through the 220 k Ω , in the 2-MW output operation. The grid-pulse of the switching tube is easily controlled by a low level signal through light guide cable. The control units of G1 and G2 of the switching tube are all set in a box, and this box is connected to the cathode voltage's potential. The stray capacitor that is estimated from the box configuration in the tank is relatively large. Even though this large capacitor is responsible to a large rise- and fall-time of the anode voltage, we adopted this scheme because of its rather simple and reliable method. A clamp voltage (0 to -60 kV) is prepared between the ground and the resistor-chain to control anode voltage in the range defined as follow,

$$V_{\text{Anode}} = -(V_{\text{Cathode}} - V_{\text{Clamp}}) \times R_2 / (R_1 + R_2) + V_{\text{Bias}},$$

where R_1 and R_2 are resistors shown as 30 k Ω and 220 k Ω in Figure 1, and V_{Bias} (-3 kV) is a bias voltage to secure the cut-off state of the klystron at the inter-pulse. Comments are in order. If the average current which flow across the resistor-chain exceeds the clamp-power-supply-current expressed as $V_{\text{Clamp}}/1.2 \text{ M}\Omega$, the clamp voltage becomes uncontrollable because each current is opposite direction. Then the anode voltage becomes discrepant from the equation at deeper modulation and higher duty operation. The relatively large anode current also modify the equation. The R_2 should be replaced by $R_2' = R_2 / R_{\text{eff}}$, where R_{eff} is an effective anode resistance. The anode voltage shows also a sag within the pulse-duration, because a charge-up of the capacitor of 0.68 μF shown in Figure 1 is starting at the switch-on of the tube. In Figure 2 the typical pulse shapes are shown at an operating condition of 2-MW output. The relatively small sag of the cathode voltage (2-3%) is seen, because only one klystron was connected to the power supply. The anode voltage measured to the ground level shows an almost flat shape partially due to the anti-sag of the anode voltage. The rise- and fall-times of anode voltage are explained by the stray capacitor C_{S1} shown in Figure 1.

D. Low Level Control

A drive power controls the amplitude and the phase of the klystron output in the linear region. A circuit shown in Figure 3 is prepared to process the RF signal. Among the several signals shown in the figure, the "Compensation" signal can be used as a feedforward signal to compensate the beam loading.

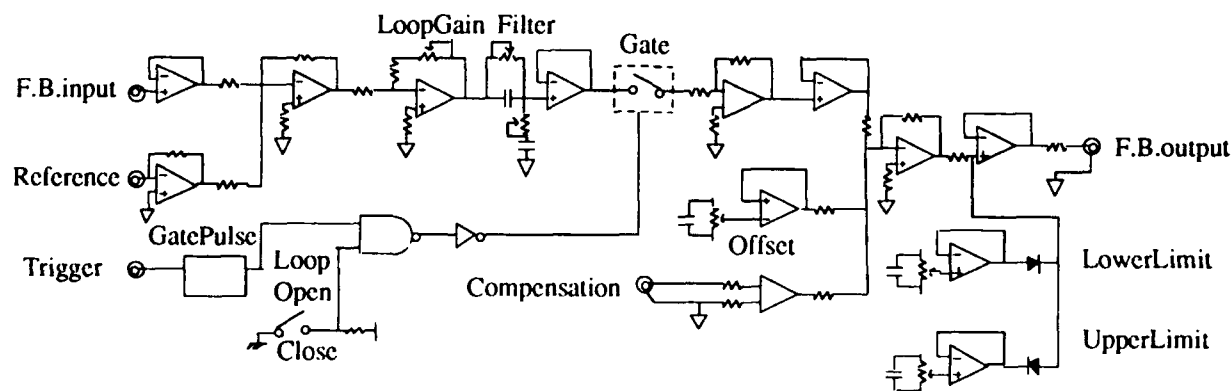
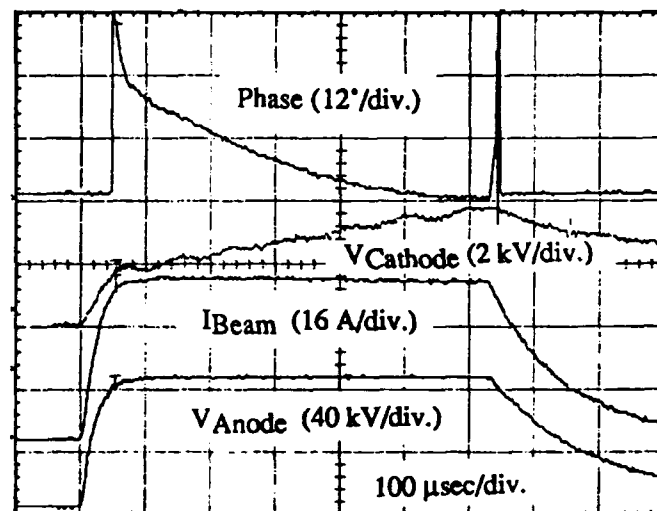


Figure 3. Block Diagram of Feedback Circuit.

We take into account the filling times of the RFQ (5.2 μsec) and the DTL (14.7 μsec) in the design of the circuit parameters. The preliminary test of the ALC has been done to stabilize the klystron output at ~1MW level. Due to the sag of V_{Cathode} the amplitude and the phase aren't stable. In the present parameters, the loop gain can't be large enough because of the oscillation at the leading part of the pulse. The obtaining stability defined as a power change per 1 kV V_{Cathode} change is 19.5 kW/kV at loop-on, while 73.7 kW/kV at loop-off. For the PLL, basically same module will be used but the control signal of the phase shift should be bipolar to control \pm phase shift. The final optimization of the parameters should be done with including the cavities.



The data are taken at 600 μsec pulse-duration, 10 Hz repetition-rate and 93 kV cathode voltage. The clamp voltage is 0 kV.

Figure 2. Typical Pulse Shapes.

III HIGH POWER TEST

A. Experimental Set up

Only one klystron was ready to operate at the test. The power generated at the klystron was directed to a dummy load by WR-1800 waveguide. The dummy load is a coaxial type with a resistive thin film coated on a ceramic pipe as an inner conductor. The input port is the WX-203D flange and the resistor is cooled by a water-flow at the inside-and-outside of the

pipe. A space between the water-proof pipe and outer conductor is filled with SF₆ gas to prevent the arcing. The load is designed to absorb the RF power of 2-MW output with 65 kW average power (650 μ sec \times 50 Hz duty). Two loads were used in parallel at the test, because one load had been damaged by the arcing at 1.6 MW output and 600 μ sec \times 50 Hz duty operation with no SF₆ gas filling. The power measured with a directional coupler was checked by a calorimetric measurement at the dummy load with a $\pm 5\%$ accuracy. The measurements were done at the duty of 600 μ sec pulse-duration \times 10 Hz repetition-rate. The klystron showed relatively stable operation during the test, even though 2 ~ 3 times crowbar trips had been encountered at an acceptance test.

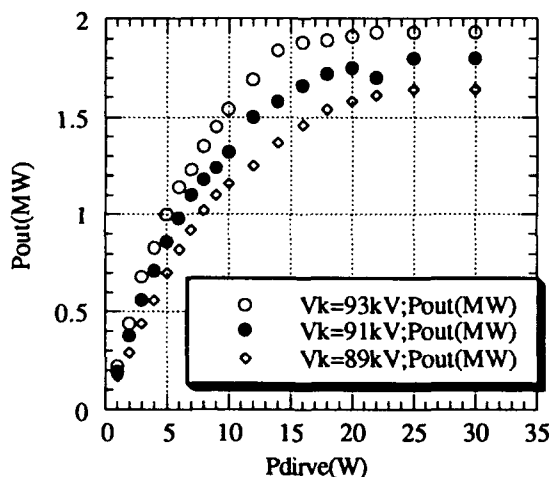


Figure 4. Output Power vs. Drive Power.

B. Performances of the Klystron and Discussion

In Figure 4, the output power is shown as a function of the drive-power at three cathode voltages. The observed efficiency at saturation point (drive power = 30 W) is 52% for 2-MW output at -93 kV cathode voltage. An observed gun-perveance of the klystron is $1.8 \times 10^{-6} \text{ A/V}^{3/2}$. The phase shift

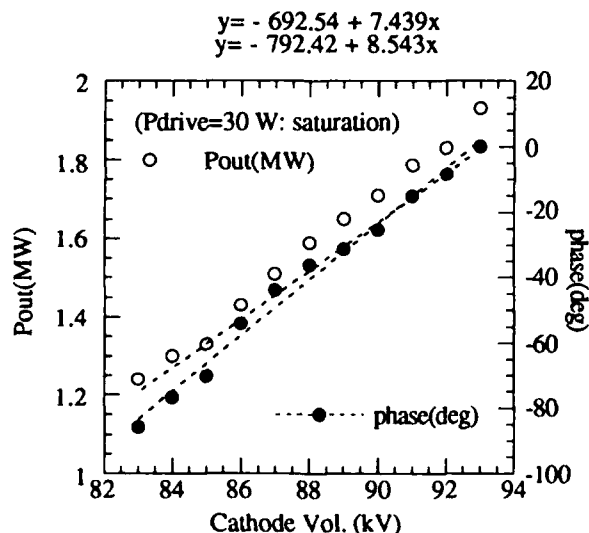
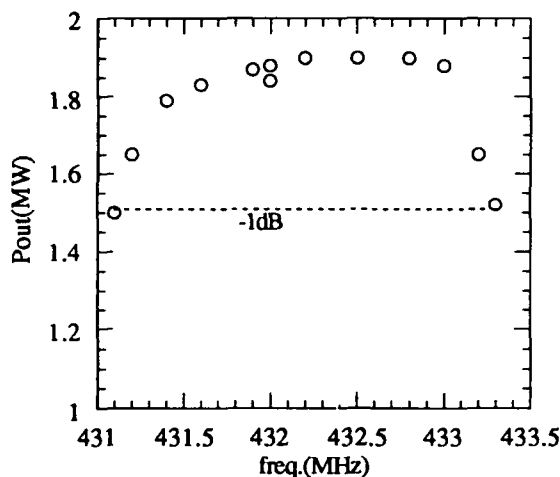


Figure 5. Output Power and Phase Shift.



Measured at saturation point (Drive power= 30 W).

Figure 6. Band Width at -1 dB.

measured at saturation are shown in Figure 5 as a function of the cathode voltage. The phase shift per 1 kV cathode voltage change is $\sim 8^\circ/\text{kV}$ as shown in the fitting of Figure 5. Because the klystron could be operated without drive power even at the rated cathode- and anode-voltages for generating 2-MW output, the clamp voltage was set to zero at the test; the test was carried out at a deepest modulation. This fact shows the possibility to omit the clamp power supply from the system. At the phase shift measurement, the anode voltage is also changed as a function of cathode voltage as described in II-D. Therefore, the measured phase shifts include the effect of the anode voltage changes. The phase shift during the pulse duration exhibited in Figure 2 are consisted with the sag of cathode voltage and the rate of phase shift change; $\sim 18^\circ$ corresponding to $\sim 2 \text{ kV}$ droop. A band-width for -1 dB decrease of output power is shown in Figure 6. More than 2-MHz range is wide enough band width for the RF processing.

IV. SUMMARY

The first operation of the UHF RF source for the JHP test-linac has been so far accomplished. It may be proved that the constructed system is feasible to supply the well-controlled RF power to the linac. There are still many jobs which should be completed until the start of the linac beam test, such as the stable two klystrons' operation of the system at the nominal output power with nominal duty, the stable RF processing without sacrificing the high loop-gain, etc. The components of the high power transmission system, such as a Y-junction circulator and the dummy load should be tested at high-power and high-duty. The fabrication of the 2 MW circulator has been already finished. The same test of the cavity itself is a most crucial one.

V. REFERENCES

- [1] Y. Yamazaki and M. Kihara, Proc. 1990 Linear Accel. Conf., 543 (1990), Albuquerque, New Mexico.

Test Results of the AGS Booster Low Frequency RF System*

R.T. Sanders, P. Cameron, R. Damm, A. Dunbar, M. Goldman, D. Kasha, A. McNerney, M. Meth, A. Ratti, R. Spitz

AGS Department, Brookhaven National Laboratory
Upton, NY 11973 USA

Abstract

The Band II RF system was originally built to support the Booster operations during the acceleration of heavy ions. Designed to sweep from 0.6 to 2.5 MHz, it was build and successfully tested over a much broader range reaching 4 MHz. Voltages up to more than 20 kV were reached over the design frequency range. The system consists of two stations, each of which is made of one single gap cavity directly driven by a grounded cathode push pull power amplifier. The low Q high permeability ferrites needed in the coaxial cavity in order to reach the lower end of the band make tuning extremely easy. Both systems were thoroughly tested both at single frequencies and on a sweep and are now installed in the ring, ready for operations. Static measurements showed no high-loss effects. The Band II system has been fully described in a previous paper [1]; presented here are the results of the "bench" tests that lead to important performance improvements.

I. SYSTEM DESCRIPTION

The Booster RF systems are built with the twofold purpose of accelerating both protons at a 7.5 Hz repetition rate and ions as heavy as gold. The fast cycle and high intensity of protons (5×10^{12} protons per bunch), requires a high total gap voltage and a low gap impedance. Gold ions impose the requirements of a large frequency swing, since the relative velocity β goes from 0.047 to 0.68. These dissimilar needs are fulfilled by two different types of RF systems. The first system, termed Band III [2,3], covers the voltage requirements of proton acceleration, 90 kV provided on four gaps (two per station), and a frequency sweep of 2.4 to 4.2 MHz. The second system, Band II, provides 35 kV on two gaps (one per station), and a frequency sweep of 0.6 to 2.5 MHz to accommodate the low β ions.

A. The Band II Cavity

Each of the band II stations consists of a single gap ferrite loaded quarterwave coaxial resonator. In order to achieve the low frequency resonance in reasonable dimensions, the cavity uses 66 TDK SY7 ferrite rings [4], with a remnant permeability of 1100. Tuning bias is applied via two figure of eight windings connected in series to obtain the maximum biasing field and thus the maximum frequency range. The low frequency end was reached without the need for additional external gap capacitance.

B. The power amplifier

The cavity is driven by an adjacent push pull power amplifier capable of an output power in excess of 200 kW. It employs two EIMAC Y567B power tetrodes, remotely driven by two solid state class A drivers each capable of 500 W of RF power. Input cross coupling is ensured via an input trans-

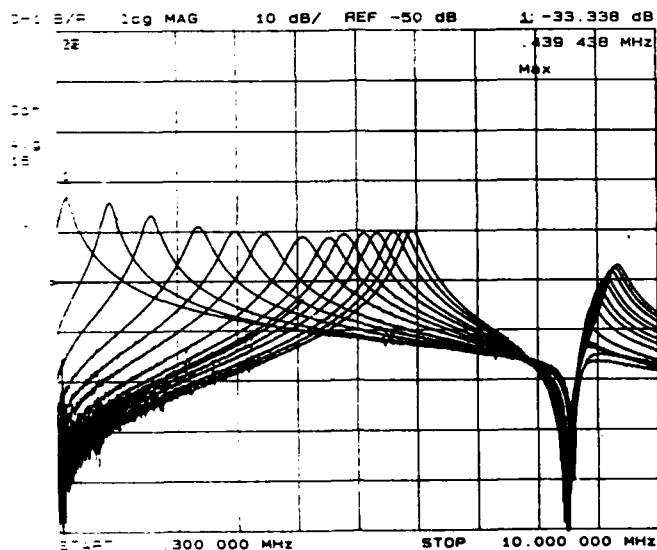


Figure 1. Cavity resonant frequency for increasing bias current at low power - single turn bias (I ranges from 0 to 520 A in 40 A increments)

* Work supported by the U.S. Department of Energy

former, which also provides resistive matching to the 150 ohms input low pass filter. The cavity biasing figure of eight windings also guarantee the load cross coupling and help improving the push-push mode rejection.

II. BENCH TEST

The system has been fully tested with very satisfactory results. The full design voltage of 17 kV was comfortably achieved, and the required frequency range greatly exceeded: sweeps from 0.6 to 4.0 MHz were performed using the available 200A of current power supply, which was the only limit that prevented a larger frequency swing. Both static and dynamic measurements were performed by calorimetry to study the ferrite losses. Table 1 shows the measured static losses of the system in the design operating frequencies; the maximum measured power was 123 kW at the high frequency end, whereas the dynamic losses are very moderate and do not contribute for more than an additional 10% to the total power dissipation. With an input drive of 212 volts to obtain 10kV on each side of the gap, the final stage gain is about 33.5 dB. Dynamic tests showed no need for neutralization of the internal feedback capacitance in the power tubes.

Table 1: Static measurements results (calorimetry)

Freq [MHz]	Power @ 10kV [kW]	Power @ 20kV [kW]	Vdrive @ 10kV [V]	Vdrive @ 20kV [V]	I tuning [A]
0.6	15.6	56	75	145	10
1.0	17.8	70.2	83	155	30
1.5	19.8	94.2	94	177	50
1.9	22.3	114	98	205	70
2.3	28.3	118	110	221	90
2.7	31.3	123	120	212	110

Sweeps were also performed at a much faster rate than originally requested [5]: the system was swept from 0.6 to 2.5 MHz in 45 ms, which corresponds to a rate of 42 MHz/sec. No measurements are available though on the power dissipation during this fast sweeps. The quality factor Q ranges from 1.5 to 3; no sign of the well known high loss (Q -loss) effect has been found during the tests. The large bandwidth corresponding to such a low Q makes tuning particularly easy. Fig. 2 shows the response of the phase detector during a full frequency sweep and indicates an error of much less than 10 degrees throughout the whole cycle.

The inductance of a single turn bias winding was measured to be ranging from 470 μ H to 18 μ H for a 200 Ampere bias current. When the two bias windings were connected in series the inductance scaled according to the square law. The bandwidth of the tuning system, is approximately 20 kHz.

III. BEAM EXPERIENCE

After the first cavity was installed in the Booster ring, its impedance has been measured by circulating a beam focussed with the Band III system and reading the voltage induced in the properly tuned Band II cavity. This does not take into account the amplifier damping (not available at that time). The cavity shunt impedance as measured with the beam is on average 2.0 k Ω , and is in reasonable agreement with the one calculated via calorimetry (1.7 k Ω).

IV. COMMENTS

The encouraging results of the bench tests on the system, originally build to cover the initial portion of the acceleration of heavy ions, open the possibility of using it in other applications. For example it can be used to perform the entire heavy ion cycle, since its operating range has reached the higher frequencies required to accelerate the ions to the top energy. Also it can be used as a second harmonic system during the injection of protons, by extending the frequency range to reach 5 MHz. This would only require modifications on the power amplifier input low pass filter and a larger bias current supply.

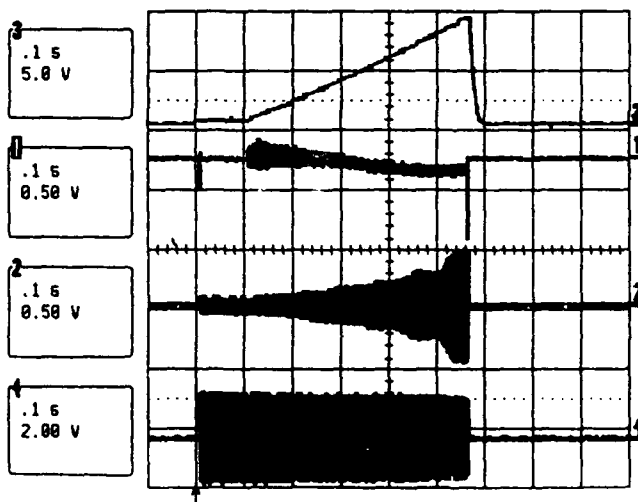


Figure 2. Full 0.6 to 4 MHz sweep at 17kV: 1. phase detector (10deg/V), 2. Low level drive, 3. Frequency program, 4. Cavity voltage (3550:1)

VII. REFERENCES

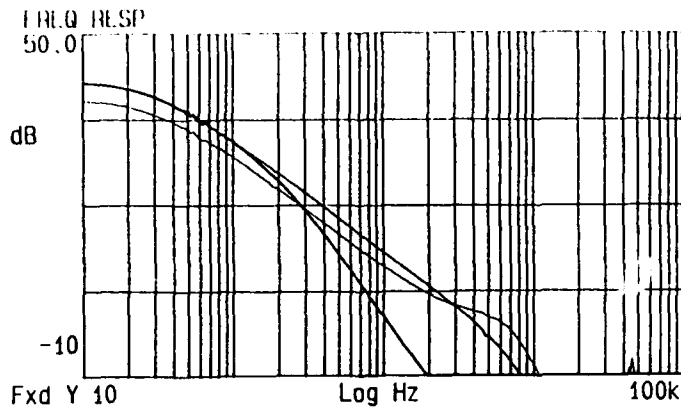


Figure 3. Dynamic response of the tuning system phase loop (at biasing currents of 10, 50 and 110 A)

V. CONCLUSIONS

The low frequency RF system for the AGS Booster has been build. Its broad band characteristics make it a very attractive feature that can actively contribute both in the heavy ions and in the proton operations. Further improvements are possible to tailor its characteristics to the most urgent needs that can arise during operations.

Installation is now completed for both Band II stations; they will be commissioned during the next scheduled heavy ions run this summer.

VI. ACKNOWLEDGMENTS

The work presented here benefits from contributions from the whole AGS community. In particular, P. Benjamin, C. Gardner, K. Rogers and S. Valentino provided an excellent technical support. The help of M. Błaskiewicz during the beam experiments was very important. The crucial support from J. M. Brennan and N. Lalouidakis is also acknowledged.

- [1] R.T. Sanders, et al., "The AGS Booster low frequency RF system", Proc. of the 1991 IEEE Particle Accelerator Conference, Vol 2, pp.739-741, S. Francisco, CA, May 1991
- [2] R.T. Sanders, et al., "The AGS Booster high frequency RF system", Proc. 1987 European Particle Accelerator Conference, Rome, June 1987
- [3] R.T. Sanders, et al., "The AGS Booster high frequency RF system", Proc. of the 1991 IEEE Particle Accelerator Conference, Vol 2, pp.681-683, S. Francisco, CA, May 1991
- [4] M.A. Goldman, et al., "Studies of ferrite materials for the Booster synchrotron", Proc. of the 1989 IEEE Particle Accelerator Conference, Vol. 1, pp. 165-167, Chicago, IL, March 1989
- [5] Booster Design Manual, Rev. 1, Oct 1988
- [6] D. P. Deng, J.M.Brennan, private communication.

Design and Test Results of a 600-kW Tetrode Amplifier for the Superconducting Super Collider*

Daniel E. Rees and Donna L. Brittain
Los Alamos National Laboratory
P.O. Box 1663, Los Alamos, NM 87545

James M. Grippe and Orlando Marrufo
Superconducting Super Collider Laboratory
2550 Beckleymeade Ave., Dallas, TX 75237

Abstract

This paper describes the design and testing of a pulsed 600-kW tetrode amplifier that will be used to drive a radio-frequency quadrupole (RFQ) for the Superconducting Super Collider (SSC). Three stages of amplification provide a nominal gain of 77 dB and peak output power of 600 kW. The amplifier is operated at a pulse width of 100 μ s and a repetition frequency of 10 Hz. This paper presents the RF design and calculated operating conditions for the amplifier. Details of the electrical design are presented, along with test results.

I. INTRODUCTION

The purpose of the radio-frequency quadrupole (RFQ) amplifier is to provide an adequate amount of power at the proper operating frequency to enable the RFQ to increase the velocity of the input beam from .00864 times the speed of light to .0729 times the speed of light. The energy in the beam increases from 35 keV to 2.5 MeV. To perform this function the amplifier must provide a minimum of 225 kW at a frequency of 427.617 MHz at each of two input ports of the RFQ. In addition, enough overdrive must be available to ensure a fast fill time. To adequately meet the requirements, the amplifier must meet the performance requirements specified in Table 1.

Table 1
600-kW Amplifier Electrical Requirements

Operating Frequency	427.617 MHz
Bandwidth	300 kHz (minimum)
Power Output	600 kW (peak)
Gain	77 dB (nominal)
Pulse Length	100 μ s
Pulse Repetition Rate	1 to 10 Hz
Pulse Droop	1% (maximum)
Input VSWR	1.5:1 (maximum)
Linear Range	15% to 85% of peak power rating
Amplitude Stability	<0.5 dB within any one hour

*This work supported by the U.S. Department of Energy.

Phase Stability	<10 deg. within any one hour
Spurious Signals	>60 dB below carrier
Prime Power	208 VAC, 3 phase

A similar amplifier with slightly different performance characteristics—300-kW, 425-MHz, 2% duty factor—was developed for the Ground Test Accelerator (GTA). This GTA amplifier was modified to meet the Superconducting Super Collider (SSC) requirements.

The SSC amplifier is located in the source area of the LINAC Building. Cooling water, whose temperature cannot exceed 95°C, is provided for cooling the output cavity. Building temperature is well regulated. Therefore, no special provisions are necessary for air cooling, other than fans and blowers.

Input RF is obtained from the low-level RF control system, which is designed to maintain cavity field amplitude and phase to a preset level in the presence of beam-induced field perturbations. A high-power circulator isolates the load from the amplifier. The load on the amplifier can be manually switched between the accelerating cavity or a test load via a coaxial switch.

II. OPERATING CONDITIONS AND AMPLIFIER CONFIGURATION

The SSC amplifier is a three-amplifier chain, consisting of an 800-W solid-state driver, an intermediate triode amplifier, and a final tetrode amplifier.

The solid-state amplifier requires a maximum input of 13 dBm and can provide up to 800 W of power for 2-ms pulses at a maximum repetition rate of 10 Hz. The amplifier has a 4% bandwidth, and its output is protected by an internal circulator. It is configured to accept an optical trigger, which is used in conjunction with a PIN diode switch to act as an RF gate.

The intermediate amplifier uses an EIMAC 8938 triode. It is configured to be cathode-modulated with a grounded grid. A high-power hexfet is driven into saturation to modulate the cathode. The triode is operated at its rated dc voltage of 4 kV by means of a 5-kV power supply that charges a small capacitor bank to provide the pulsed current.

Approximately 50 ohms of series resistance is inserted between the capacitor and triode to dissipate the energy in case of an internal tube arc.

The final amplifier is a Burle 4616 tetrode. It requires approximately 500 W of filament power. The operating conditions for the cathode, as well as pertinent maximum operating conditions, are shown in Table 2. The final amplifier requires three high-voltage power supplies. The 25-kV plate voltage is supplied by a 30-kV supply with an average current capability of 80 mA. This supply has a crowbar and small capacitor bank sized to meet the 1% pulse droop requirement. A 3-kV screen supply and 1-kV grid supply are also required. The screen supply feeds a small capacitor bank to supply the pulsed screen current. The screen supply does not use a crowbar triggered simultaneously with the plate supply crowbar. Rather, series resistance is used to limit the current and dissipate the energy that could result from a tube arc.

To provide the required linear range of operation, the solid-state amplifier is operated class AB, the intermediate triode amplifier is operated class A, and the final tetrode amplifier is operate class B. The intermediate triode amplifier takes advantage of the cathode modulator to operate class A during the RF pulse without suffering the corresponding anode dissipation during the interval when the RF pulse is not present.

Table 2
4616 Operating Conditions

Operating Parameter	Value	Max. Value at 100 μ s
DC Plate Voltage	25,000 V	25,000 V
DC Screen Voltage	1,800 V	
DC Grid Voltage	-300 V	
DC Plate Current	38.2 A	80 A
DC Screen Current	2.25 A	15 A
DC Grid Current	1.4 A	15 A
DC Cathode Current	42 A	
Fund. Peak Plate Current	64 A	
2nd Harmonic Peak Plate Current	35 A	
3rd Harmonic Peak Plate Current	8 A	
Fund. Peak Cathode Current	71 A	
Peak Plate Swing	20,000 V	
Output Power	638.7 kW	
RF Plate Load	313 Ω	
Peak Grid Swing	400.0 V	
Drive Power	540 W	
RF Grid Input Resistance	148 Ω	
Peak Plate Dissipation	302 kW	
Peak Screen Dissipation	4050 W	
Peak Grid Dissipation	156 W	

III. TEST RESULTS

Test results for the 600-kW amplifier are shown in Figures 1 and 2. Figure 1 shows the frequency response of the amplifier at the upper end of the linear range. Figure 2 shows the linear performance of the amplifier. The test conditions are summarized in Table 3. Table 4 summarizes the test results.

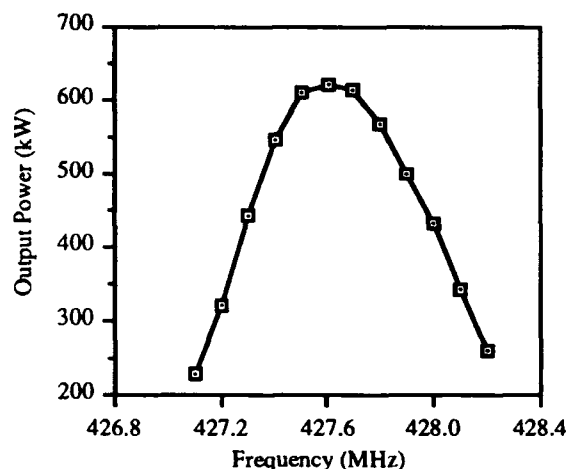


Figure 1. Frequency Response

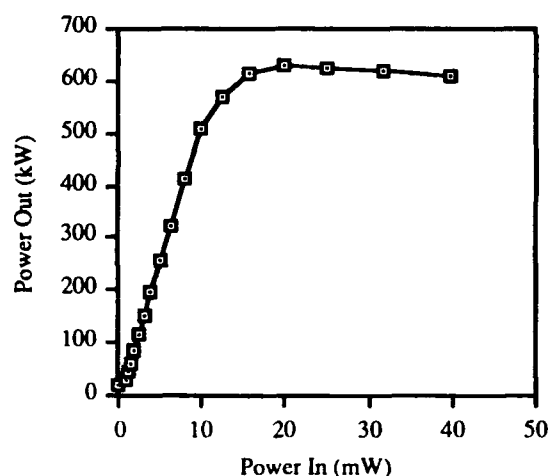


Figure 2. Linear Dynamic Range

Table 3
Test Operating Conditions

Parameter	Value
4616 Grid Voltage	-380 V
4616 Anode Voltage	26,000 V
4616 Screen Voltage	2200 V
4616 Filament Current	510 A

Table 4
Test Results

Parameter	Value
Maximum Power Output	625 kW
Linear Range	200 kW to 500 kW
Gain	77.4 dB (nominal)
3-dB Bandwidth	900 kHz
1-dB Bandwidth	550 kHz
Efficiency	63%

Note: The dc anode voltage used for testing is slightly above the ratings. This was necessary because the high-voltage dc power supply had a series resistance that would drop approximately 1 kV during the RF pulse. We did not suffer any degradation in operational testing as a result of the 26-kV anode voltage, however.

IV. CONCLUSION

We have successfully modified the GTA 300-kW amplifier to operate as a 600-kW amplifier for SSC. The amplifier met or exceeded all performance requirements and is currently in service at SSC.

Conceptual Design of the 26.7 MHz RF System for RHIC*

J. Rose, D.P. Deng, R. McKenzie-Wilson, W. Pirkel, A. Ratti
Relativistic Heavy Ion Collider
Brookhaven National Laboratory
Upton, N.Y. 11973

Abstract

The 26.7 MHz (harmonic # $h=342$) RF system will be used to capture the injected bunched beam from the AGS and accelerate it to a kinetic energy of up to 250 GeV for protons; 100 GeV/u for gold ions. All ions except protons cross transition, and are finally transferred to a storage RF system working at 196 MHz. Each RHIC ring will be provided with two single-ended capacitively loaded quarter-wave cavities; each of these can be dynamically tuned by 100 kHz to compensate for the change in speed of the beam, and can deliver at least 200 kV voltage. A 100 kW tetrode amplifier with local RF feedback is directly coupled to the cavity to minimize phase delay. Prototypes of cavity and amplifier have been built and first test results are presented.

I. INTRODUCTION

The Relativistic Heavy Ion Collider at Brookhaven consists of two counter-rotating beams of ions ranging from protons to gold colliding at up to six interaction regions. The machine consists of superconducting magnets with room temperature RF systems located in warm sections of the ring. Major machine parameters are given in Table I.

The accelerating RF system must capture the injected beam from the AGS, accelerate to top energy and transfer (rebucket) to the 196 MHz storage system. Table II shows the relevant bunch parameters at injection and top energies.

Table I Machine Parameters

Circumference	3833.852 m
Rotation Freq	78.196 kHz
γ_{tr}	22.8
B- ρ inj/top	96.7/839T-m
Average Radius	610 m
Horizontal Tune	28.19
Vertical Tune	29.18

* Work performed under the auspices of the Department of Energy

Table II Bunch Parameters

	Protons Inj./Top	Au Inj./Top
Energy (γ)	31.2/268.2	12.6/108.4
Full Bunch Length (ns)	6.5/4.0	13.5/7.5
Synch. Freq (Hz)	45/25	90/27
Z, A/Z	1/1	79/197
$\Delta P/p$ (10^{-4})	10/1.7	8.3/3.4
Bunch Area (eV-s/u)	0.30/0.33	0.2/0.4
# bunches/ring	57(114)	57 (114)
# ions/bunch	10^{11}	10^9
Norm. Emittance (π mm-mrad, 95%)	20/20	10/15

II. SYSTEM DESCRIPTION

The 26 MHz system consists of a capacitively loaded quarter wave cavity with a close-coupled tetrode amplifier. The cavity is two meters long and 0.84 meters in diameter with the amplifier situated directly underneath. A prototype system has been constructed and is shown in Figure 1. This prototype will be used to study methods of tuning, HOM suppression, feedback design and susceptibility to multipacting. The prototype cavity is of copper plated steel construction. Provisions for vacuum pumping and water cooling have been made to allow full power testing. It is designed to allow amplifier coupling at either end of the cavity, it is currently configured with coupling to the capacitor electrode at the high voltage end. Numerous ports have been included for field probes, HOM damping tests and access for titanium nitride coating in the development program.

The codes SUPERFISH and URMEL were used to calculate the Higher Order Modes (HOM) of the structure.¹ This data was then used to calculate the growth rates of longitudinal coupled bunch instabilities using the Sacherer formalism.² The HOM frequencies, shunt impedances, Q's, and the coupled bunch mode growth rates are given in Table III. Analysis of transverse coupled bunch modes is in progress.

The first two HOM's are associated with coupled bunch modes with particularly fast growth rates of 6.7 s^{-1} and 3.9 s^{-1} respectively. Because of the low frequencies involved classical mode damper designs (waveguides above cutoff, quarter wave notch filters) are excessively large. The transverse waveguide dimension can be greatly reduced by capacitive loading, but in general the length cannot. In order to transmit the 67 MHz mode a cutoff frequency of about 50 MHz is required. The fundamental would then be attenuated in the guide below cutoff as

$$V = V_0 e^{j\beta z}$$

where z is in meters and β is the propagation constant in rad/s and is defined as

$$\beta = \sqrt{\frac{\omega^2}{c^2} - \frac{\pi^2}{a^2}}$$

with a being the waveguide width. Below cutoff β is imaginary and the above exponential becomes negative and real. It would then require over 2 meters of waveguide length just to reduce the fundamental voltage by a factor of 10. Likewise a quarter wave notch filter would require a length of 2.8 m, 1.4m even if folded back in half. Therefore there was an incentive to develop a lumped element mode damper. The approach being developed is a lumped L-C notch consisting of a parallel arrangement of a high voltage vacuum capacitor and a short coil in series with the load resistor. Work is continuing on this and alternate dampers.

The tuning range required is set by the velocity change of gold between injection and top energy. The frequency shift required is given by

$$f_{rf} = \frac{hc}{C} \sqrt{1 - \frac{1}{\gamma^2}}$$

Where c is the speed of light, C is the RHIC circumference and h is the harmonic number. The frequency spread is then limited at the low end by gold at injection ($\gamma=12.6$) and by protons at top energy ($\gamma=268.2$) resulting in $f=26.6537$ to $f=27.7435$ respectively.

Tuning for compensation of beam loading falls within these limits since gold is below transition and the tuning is positive while protons are above transition and the tuning is negative. The maximum tuning rate is for gold at the beginning of the acceleration cycle and is 23 kHz/sec.

Two tuner approaches have been studied in detail. The first used three discrete ferrite loaded transmission lines connected in parallel to the cavity via a large disk integral with the inner conductor to minimize the series inductance of the tuner connection.³ The ferrite is a low loss perpendicular biased garnet, Transtech G-810. The design predicted a 180 kHz frequency shift, in excess of the required 100 kHz to allow some flexibility in operation. The second approach is

to change the gap capacitance via a mechanically actuated motion of the ground electrode. The preliminary design calls for a stepper motor driven lead screw to change the gap by 1 cm to provide 100 kHz of tuning. If implemented the mechanical tuner would eliminate the need for the large low inductance tuner disk which currently dominates the cavity design.

The ferrite tuner design concept was tested on the prototype cavity by using dummy tuners constructed of 3/4 coaxial line with a sliding short capable of providing the same input impedance as the ferrite tuners. The resulting frequency range was 220 kHz, slightly in excess of the predictions. A choice will be made on the tuner approach based on cost, reliability and risk.

The voltage requirement is set by the requirement for a bunch rotation to rebucket the bunched beam into the 196 MHz system. This requires the accelerating system to adiabatically reduce voltage from 300 kV to 45 kV to increase the bunch length and then quickly step back up to 300 kV to rotate the bunch. After a quarter of a synchrotron period when the bunch length is at a minimum the 196 MHz system voltage is raised to capture the bunch. Each system is being designed to provide 200 kV, for a total of 400 kV per ring to allow flexibility and future upgrade capability.

Table III 26 MHz Cavity Longitudinal HOM's and coupled bunch mode growth rates

Freq. (MHz)	R_{sh} (M Ω)	Q (10^3)	Growth rate sec ⁻¹ /mode# (Gold)	Growth rate sec ⁻¹ /mode# (Proton)
26.8	0.93	12	n/a	n/a
64.8	0.038	15	2.8/34	6.7/31
119.3	0.048	27	0.1/46	3.9/44
205.7	0.009	36	<<0.1	0.24/10
287.9	0.111	23	<<0.1	0.15/34
349.4	0.164	18	<<0.1	0.19/23
360.6	0.018	26	<<0.1	<<0.1
427.0	0.080	45	<<0.1	<<0.1
479.6	0.014	47	<<0.1	<<0.1

The amplifier is housed in a wheeled cabinet beneath the cavity to allow easy installation and removal. It utilizes an EIMAC 4CW150000 in a grounded cathode configuration. The tube is used in class AB₁, with a quiescent current of 3A and an anode voltage of up to 20kV. A neutralization loop provides > 60 db of isolation between anode and grid. A 4:1 input transformer is used to drive the grid more efficiently in a 200 Ω impedance. A simplified schematic is shown in Figure 2. The machine cycle mandates beam gymnastics for ions at transition crossing, and for protons and ions alike at beam

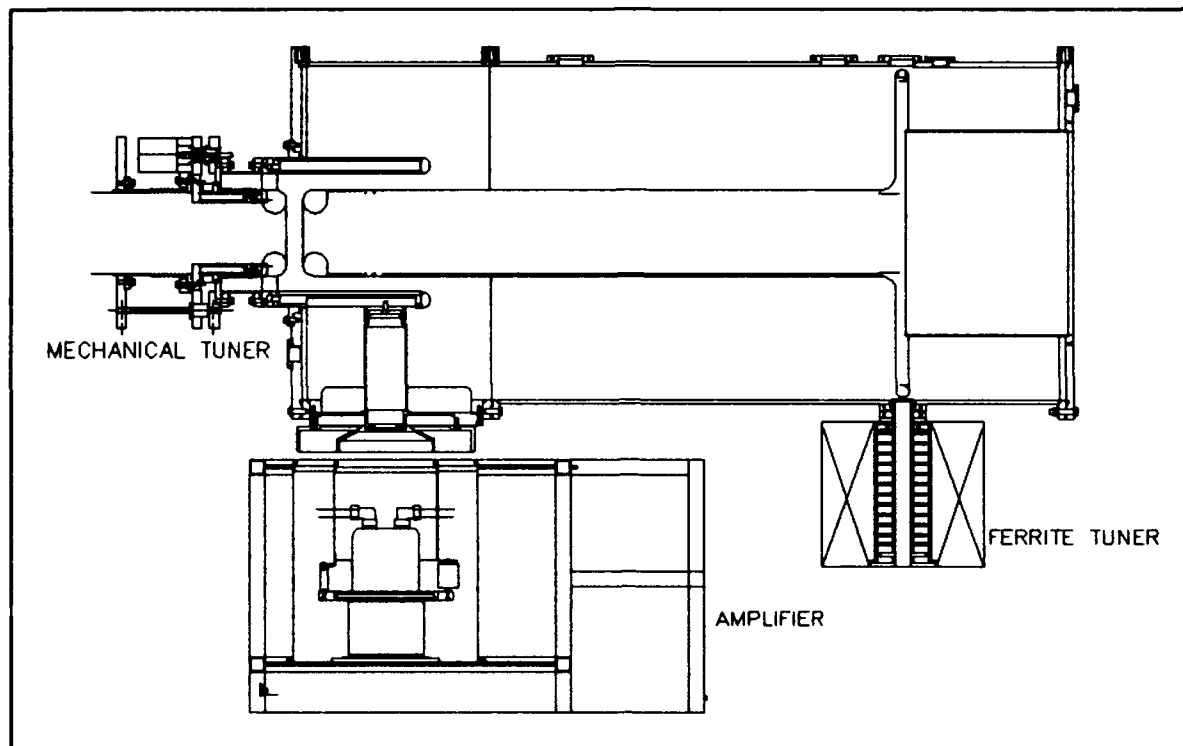


Figure 1 Prototype Cavity and Amplifier with Conceptual Tuners.

rebucketing. Feedback performance to meet these requirements has been studied using PSPICE and a direct integration method.⁴ Assumptions include a delay of $6 \times 18.73 = 112.7$ nsec, which covers a 500 W ENI drive amplifier (33 nsec) plus 2*10m of foam coaxial cable (2×36.7 nsec). Results conclude that RF feedback can be implemented with a loop gain of a least 100 which meets the requirements of the beam gymnastics.

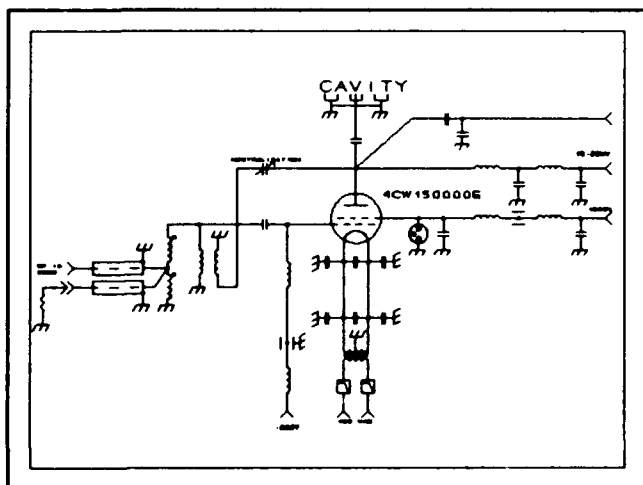


Figure 2 Simplified Power Amplifier Schematic

III. CONCLUSIONS

A conceptual design of the accelerating system for RHIC has been completed and a prototype system fabricated. An experimental program has begun to explore in detail system performance with high power. The cavity-amplifier

system has been tested to 70 Kv in air and is being readied for vacuum pumpdown. Testing of tuners and HOM dampers has begun. Future work includes cavity conditioning under vacuum, diagnosis and possible cures of multipacting, and the development of the RF driver amplifier and implementation of local feedback.

ACKNOWLEDGEMENTS

The authors wish to thank M. Blaskiewicz for performing the coupled bunch instability analysis. Special thanks go to S. Ellerd and J. Greco for their excellent technical support.

REFERENCES

- 1) J. Rose, Note RHIC RF-6
- 2) M. Blaskiewicz, Private communication
- 3) J. Rose, Note RHIC RD-42
- 4) W. Pirkel, Note RHIC RF-8

OPERATION OF A HIGH-POWER CW KLYSTRODE WITH THE RFQ1 FACILITY*

J.Y. Sheikh, A.D. Davidson, G.E. McMichael, L.W. Shankland and B.H. Smith
AECL Research, Chalk River Laboratories
Chalk River, Ontario, Canada K0J 1J0

Abstract

A high-power klystron rf system for the RFQ1 facility at the Chalk River Laboratories (CRL) has been manufactured by Continental Electronics Corporation (CEC), Dallas using klystron amplifier tubes developed by Varian, San Carlos. The system consists of two units, each capable of 250 kW in pulsed or cw mode. The two units can be operated independently to drive two separate accelerator structures, or together in a master/slave combination to drive one structure. This system is the first high-power klystron to power a cw accelerator, and is a significant step in high-power klystron development, increasing the average power per tube by a factor of 5 (to 250 kW). Commissioning, initial operation of one unit of this system with the RFQ1 facility, and data obtained to date, is described.

I. INTRODUCTION

The RFQ1 facility [1] was the major component of a program at CRL to develop 100% duty factor accelerators for applications requiring high-current beams of protons or other light ions. The accelerator was first built for an energy of 600 keV (RFQ1-600), and later was rebuilt with new vanes to double the output energy to 1.25 MeV (RFQ1-1250). The rf system used for RFQ1-600 and the initial runs of RFQ1-1250 was a gridded-tube system based on an RCA 2054 triode. This system lacked flexibility and was becoming unmaintainable. Late in 1989, an order was placed with Varian to develop and supply a new system that would include two 250 kW cw klystrons [2,3]. In 1992 February, AECL decided to terminate the cw ion linac development program, effective 1993 March 31. An arrangement was put in place to transfer the RFQ1 hardware to the Los Alamos National Laboratory (LANL), where it would be used to assist their program. Consequently, there was only time to install and commission one 250 kW module at CRL; the second module was delivered directly from CEC to LANL.

II. FINAL OPERATION WITH TRIODE

The output windows of klystrons require protection from the effects of sustained high reflected power from a mismatched load. Varian's original design used a signal from a cavity-gap sensor (installed at a suitable spot in the output cavity) to decrease the rf drive via the output levelling loop if too high

a reflected power level occurred. To provide further protection and facilitate conditioning of resonant structures, a 250 kW coaxial circulator was purchased. It was initially used on the RFQ with the triode system to obtain experience with a circulator.

Initial operation with the circulator up to 175 kW appeared no different from operation without it. However, attempts to increase the power level beyond 175 kW resulted in arcing in the RFQ, which shut down (tripped) the rf system. After each trip, the subsequent power level attainable decreased until the power could not be raised above 20 kW. Because the RFQ had been easily conditioned to over 200 kW cw without the circulator, it was apparent that adding the circulator either introduced a new problem or nullified some mechanism that had prevented damaging arcs. Further analysis indicated that, without the circulator, high reflected power from the RFQ at an arc caused the triode gain to decrease, thereby lowering the output power, allowing an arc to extinguish. With the circulator isolating the RFQ from the amplifier, the output power was unchanged. This level sustained the arc and sputtered a lot of copper onto the drive-loop ceramic window. A test arrangement using a storage scope, an analogue scope and a pulse generator was developed to sense high reflected power and remove the rf drive for a few microseconds, to allow the arc to extinguish. This arrangement allowed the RFQ to be reconditioned, and demonstrated the need for an arc suppression circuit for operation with the klystron amplifier. An rf blanking module incorporating a similar control algorithm was subsequently developed for LANL, and was used during cw beam and rf experiments with the klystron system (described in section V).

III. DESCRIPTION OF RF SYSTEM

A block diagram of a 250 kW module is shown in Fig. 1. Through three stages of amplification, the signal generator input of 10 mW is amplified to 250 kW with an overall gain of ~74 dB. The output of the solid-state amplifier, A2, is connected to the driver klystron amplifier through a circulator and a directional coupler.

The EIMAC 2KDX15LA driver klystron is a UHF TV tube rated for 15 kW peak power; however, in the modified circuit assembly, it supplies up to 4 kW cw. It is connected to the EIMAC 2KDX16LA final klystron through directional couplers and a circulator. The final klystron is connected to the load via a 15 cm coaxial transmission line that incorporates directional couplers and a variable coupler, E4.

*This work was partially supported by Los Alamos National Laboratory under contract No. 9-X5D-7824D-1.

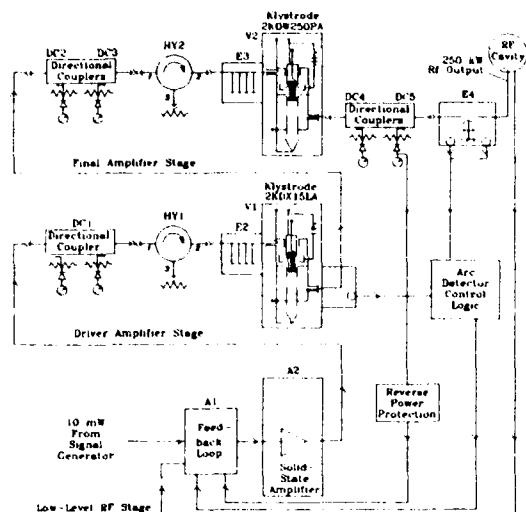


Fig. 1. RF block diagram of the system

The variable load coupler uses two Teflon slugs, which slide on the centre conductor of transmission line. It matches the load at the tuned frequency by reflecting a voltage of adjustable phase back into the output cavity of the klystron. Optical detectors mounted on the line generate signals to activate a blanking circuit that reduces the gain by 40-60 dB. A coaxial transition (15 to 23 cm) follows the variable coupler. The connection to the circulator and the RFQ1 is via 23 cm transmission line.

The feedback loop, A1, is a dual control loop. It has an outer loop that senses the output power level and adjusts the input to the solid-state amplifier, to keep the output power constant

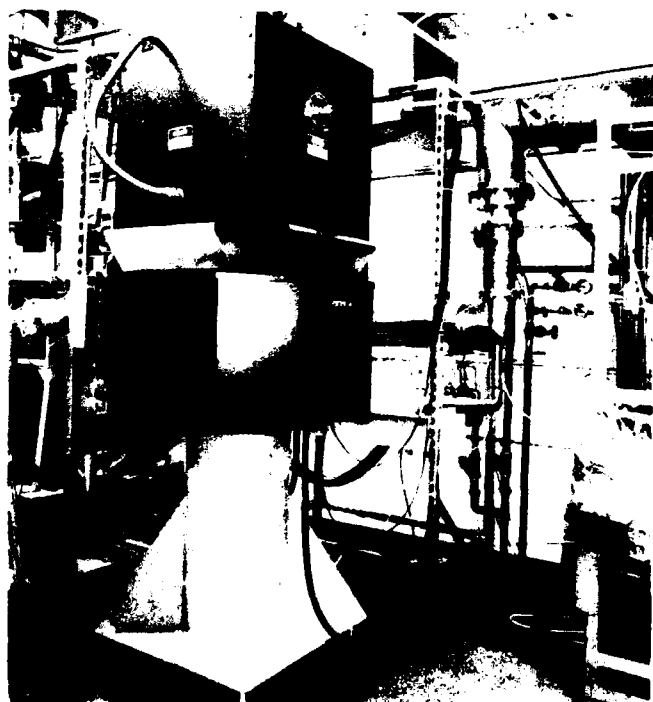


Fig. 2 Final klystron amplifier

within $\pm 1\%$. The bandwidth of this loop is > 500 kHz, sufficient to remove amplitude modulation due to ripple on the high-voltage power supply. The faster inner loop protects the final and driver tubes by limiting the drive power if the operator (open-loop mode) or the outer loop (closed-loop mode) requests a drive power that would make the reflected power, output-window voltage, or driver-amplifier power exceed safe operating levels. The output-window power sensor signal has proved to be reliable and has replaced the cavity gap sensor originally used in the design.

For operation into a resistive load, a forward-power-signal from a directional coupler can be used for the feedback signal for the outer loop. The loop parameters are optimized for a loaded Q range of 2000 to 20 000. A capacitor to simulate the cavity Q is placed on the rf feedback controller circuit board, to provide loop stability when controlling power to a resistive (low Q) load. The outer of the two feedback loops has been designed to allow operation of two 250 kW amplifiers in a "master/slave" configuration for a combined output of 500 kW.

IV. INSTALLATION & SYSTEM PERFORMANCE

Both of the 250 kW rf systems were acceptance tested at CEC. The first completed system was shipped to CRL. Installation began on 1993 January 04 and was completed, with first rf power out of the final amplifier, by 1993 February 02. An overview photograph of the installed amplifier is shown in Fig. 2. The system was tuned to 267 MHz and initially operated into a 300 kW resistive load. The signal from the output-window sensor was found to be somewhat larger during operation at CRL than it had been at both Varian and CEC. The upper limit of 500 mW allowed for this signal was reached at an output power of only 237 kW, whereas previously the observed signal was less than 400 mW at an output power of 300 kW. The time allowed for tests of the amplifier was too short to allow a detailed investigation of this

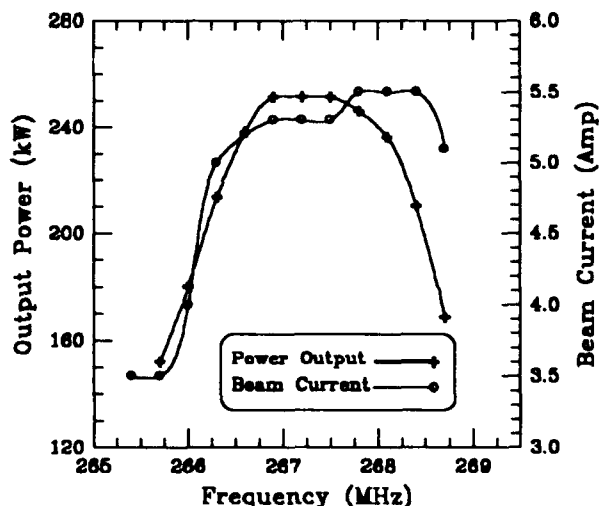


Fig. 3 System bandwidth with system tuned at 267 MHz

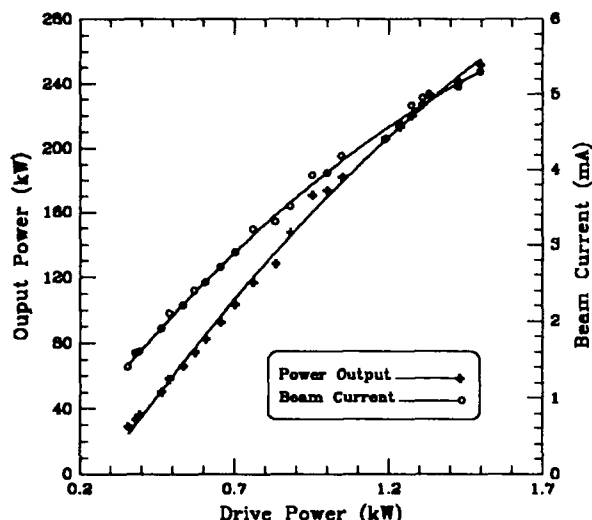


Fig. 4 System linearity at 267 MHz

discrepancy, and since the power obtainable was sufficient to meet the needs of the beam experiments with RFQ1, the problem was not resolved. Tuning errors that were initially suspected now appear unlikely, leaving instrumentation differences as the most probable explanation. Varian now believes that the 500 mW limit is conservative, and has reviewed increasing this limit if similar readings are obtained following recommissioning of the system at LANL. The bandwidth and linearity of the rf system observed during the acceptance tests are shown in Figs. 3 and 4.

V. OPERATION WITH RFQ

Prior to first operation with the klystrone system, the RFQ had been left unpowered but under vacuum for over four months. Some reconditioning was required, but with the pulsing capability of the new system it was much easier to break through multipactor and to condition for high, cw power. Beam acceleration was attempted immediately after the RFQ would accept the design 150 kW cw power. Within three days, a cw proton beam of > 50 mA was accelerated from 50 keV to 1.25 MeV without incident. As expected, transmission and emittance were similar to that observed previously with the triode amplifier [4]. During the very limited time available for experiments before the 1993 March 31 shut down, minor incompatibilities between the level controller and the rf-blanking module prevented closed-loop RFQ-field control during beam acceleration. These incompatibilities were identified and necessary modifications checked out at the module level prior to shut down; none appear to present serious long-term concerns.

VI. CONCLUSIONS

The beam operation was similar to that with the triode system. Closed-loop beam operation was not achieved, but no "show-stoppers" are expected. The pulse capability of the rf system significantly eased and shortened RFQ conditioning. Coarse tuning adjustments to change the amplifier frequency are easy; however, considerable fine tuning is required to achieve best efficiency ($>70\%$) and final-amplifier gain (>22 dB). The high, output-window, sensor-power problem is not yet resolved, but should not limit operation at LANL. Cavity-gap sensor readings were inconsistent; output-window probe readings proved much more useful as input to the protection circuit.

The successful tank and beam operation has demonstrated that a klystrone is a suitable rf amplifier for accelerator cavities, and thus deserves serious consideration as the power source for the next generation of high-power cw or pulsed accelerators in the 0.2 to 1 GHz frequency range.

VII. ACKNOWLEDGEMENTS

Many people from CRL, CEC, LANL and Varian worked extremely hard to install, commission and test this system in the very limited time available between system delivery and program termination. The authors would like to particularly acknowledge the contributions of W.L. Michel and J.F. Mouris in providing the software, beam diagnostics and beam production; G. Bolme (LANL), who helped with the control and operation; and G. Thompson and R. Summers (CEC) and R. Tornoe (Varian), who directed the installation and testing. In addition, the authors acknowledge technical help provided by B. Chidley, C. Brown, P. Talerico and D. Reid during the system specification stage, design review meetings and throughout the course of the development of the rf system.

VIII. REFERENCES

- [1] G.M. Arbique, B.G. Chidley, W.L. Michel, G.E. McMichael and J.Y. Sheikh, "Beam Transmission and Emittance Measurements on the RFQ1 Accelerator", Proc. 1991 Particle Accel. Conf., IEEE 91CH3038-7, p. 845.
- [2] J.Y. Sheikh and J.C. Brown, "Specification for High-Power Amplifier Systems", unpublished report RC-189, available from Scientific Document Distribution Office, Chalk River Laboratories, Chalk River, Ontario, KOJ 1JO.
- [3] M.B. Shrader, D.H. Priest and R.B. Tornoe, "High Power CW Klystrone Amplifier for 267 MHz", these proceedings.
- [4] G.M. Arbique, B.G. Chidley, G.E. McMichael and J.Y. Sheikh, "Beam Parameter Measurements on the CW RFQ1-1250 Accelerator", Proc. 1992 Lin. Accel. Conf., AECL Report #10728, 1992 November. p.55.

Design and Results of a 1.3 MW CW Klystron for LEP

E.-G. Schweppe, R. Bachmor, E. Demmel
Philips HFPT Hamburg
Stresemannallee 101, 2000 Hamburg 54, Germany

Abstract

The development of a high power CW klystron prototype delivering 1.3 MW at 352 MHz is presented. The design was carried out using CAE / CAD tools. Particular attention was given to design optimizations with regard to the modulating anode electron gun, the focusing system and the RF region for a wide range of operating conditions typical for accelerator applications. Two new technological features were introduced, PHILIPS low temperature cathode for long life stable operation and a multipactor suppression coating on the RF output window. Test and operational results is included in the presentation.

I. INTRODUCTION

For the increase of the LEP energy from 55 GeV to 100 GeV additional RF units with superconducting cavities and 1.3 MW cw klystrons will be installed in the LEP machine by 1994. The design of the new klystron must be made such that it can replace the presently installed 1 MW cw klystron. This restricted the development mainly in the overall length. Testing one of our 1 MW klystrons YK 1350 in 1.3 MW operation we found a small decrease in efficiency and stability but all components withstand the 30% increase in power without failure. Main objective of the 1.3 MW klystron development was therefore the improvement of stability and efficiency.

II. GUN DESIGN

The new 1.3 MW klystron is designed to operate at three different operation points as:

- I. 1.3 MW 100 kV 20 A $\eta \geq 65\%$
- II. 1.0 MW 88 kV 18 A $\eta \geq 63\%$
- III. 0.7 MW 77 kV 15 A $\eta \geq 60\%$

The difficulty in the design of a high power klystron gun with a modulating anode is to find a compromise between full power and medium/cutoff operation. The first CAE design with EGUN [1] was a confined flow beam without ripple at full beam power (100 kV / 20 A, see Figure 1A). But when calculating the beam shape at lower levels of modulating anode voltage as shown in Figure 1B the beam ripple increased more and more until it hits the drift tube at a beam current of 2 A. Changing the shape and magnitude of the focusing magnetfield we could get a final design shown in Figure 1C/D which fulfills cutoff operation

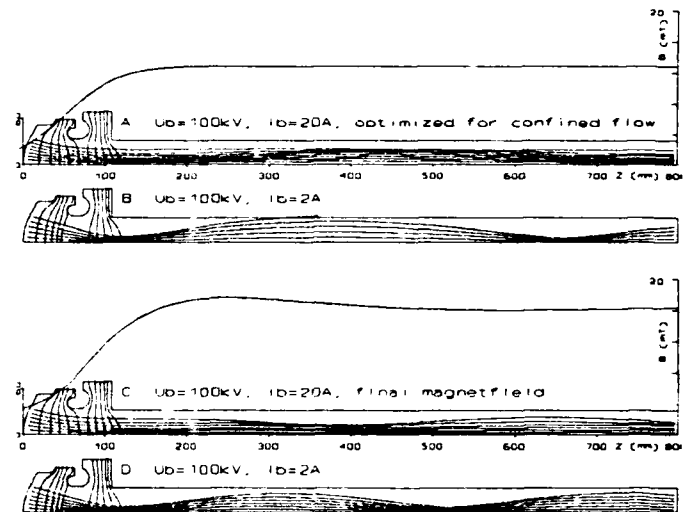


Figure 1. Static gun design

as well as full power operation with an acceptable beam ripple. A next step was to replace the "B" - type cathode by the PHILIPS low temperature cathode which accomplishes the strong demands of long life stable emission, low evaporation rate, high current density and low working temperature in modern electronic tubes. The PHILIPS low temperature cathode [2] is a "M"-type cathode and consists of a porous tungsten pellet matrix which is impregnated with BaO, CaO and Al₂O₃ in a molar ratio of 5:3:2. The

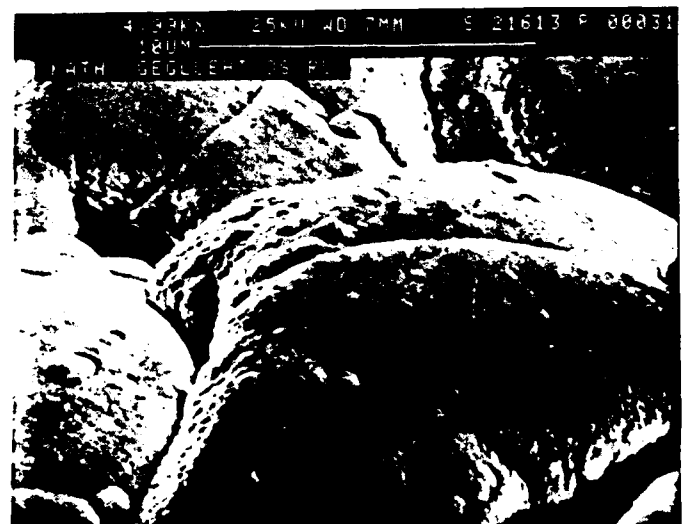


Figure 2. SEM picture of OsRu coated "M"-type cathode

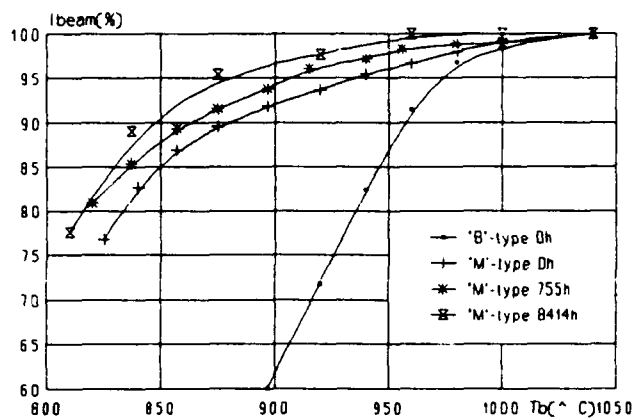


Figure 3. Underheating and lifetime plot of cathodes

emission surface is coated with a film of osmium-ruthenium with a thickness of $0.5\mu\text{m}$ - $1\mu\text{m}$. The work function is 0.2eV lower than that of the uncoated cathode. Therefore "M"-type cathodes can be operated at a temperature about 80°C - 100°C lower than an uncoated cathode. A comparison of underheating behavior between "M"-type and "B"-type cathodes is shown in Figure 3 together with a life time report.

III. RF - DESIGN

Computer simulations with the particle in cell code FCI [3] starting from the 1 MW cw YK 1350 RF design with 6 cavities (5 fundamental, 1 harmonic) showed that an increase in efficiency could only be obtained by increasing the spacing of adjacent cavities. In order to keep the overall length of the klystron unaffected we dropped one of the two penultimate buncher cavities. During the optimization process we varied spacing and frequency of each cavity as well as loaded Q of output cavity taking into account efficiency, gain and stability at the desired dc operational points. At the end of the optimization phase we could obtain the calculated values listed in Table 1.

Table 1
Calculated results of 1.3 MW klystron YK 1353

Ub/kV	Ib/A	Po/kW	$\eta/\%$	G/dB
100	20.0	1394	69.7	39.4
88	17.5	1070	69.5	39.9
77	13.8	662	62.3	38.6
77	21.5	1010	61.0	41.6

Klystrons with high efficiency tend to instabilities when operating into a mismatched load. Depending on phase

angle one can observe an increase in modulating anode current and sideband oscillations near RF carrier on output signal. These instabilities have their origin in electrons, which are reflected and accelerated in reverse direction by the high output gap voltage. Reaching the gain cavity they build an internal loop which may cause oscillations. Figure

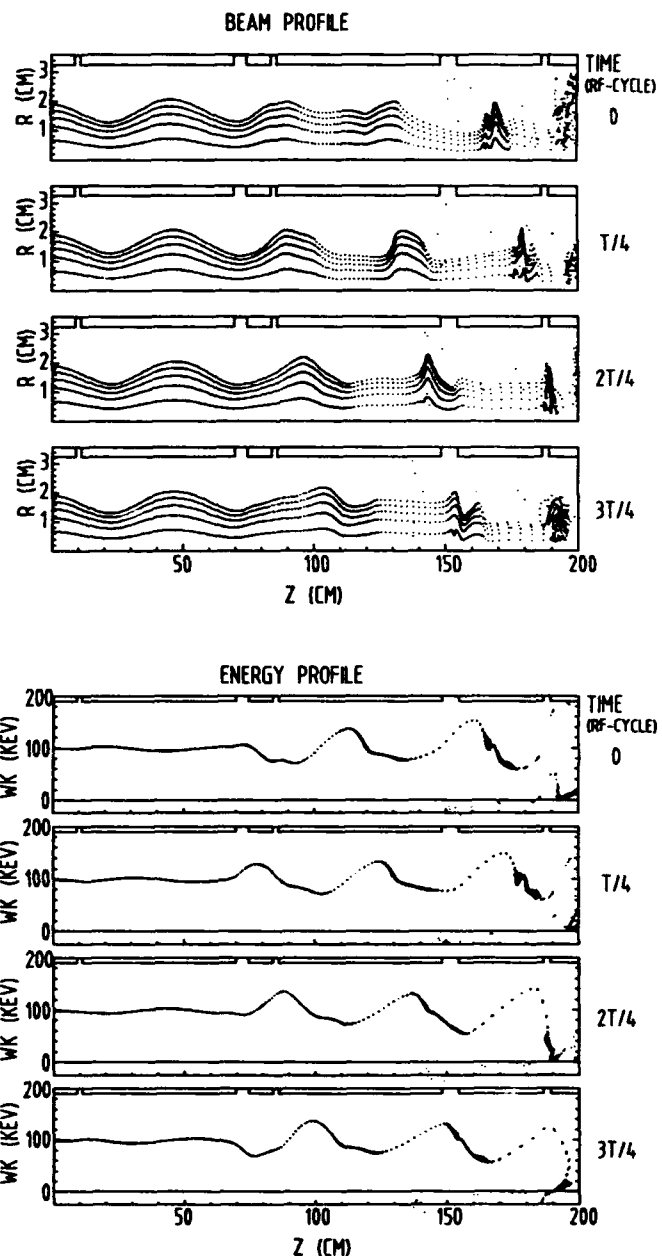


Figure 4. Beam and energy profile of YK1353 under mismatch condition.

4 shows a FCI simulation of a load mismatch operation (VSWR=1.5) at a phase angle which cause high gap voltage. Besides the BEAM PROFILE where the location

of the electrons is calculated in dependence of time, the ENERGY PROFILE is a good indicator for backstreaming electrons shown here with negative energies. Further simulations demonstrated that detuning the penultimate cavity by a few percent to higher frequencies reduced instable operation and did not affect efficiency.

IV. OUTPUT WINDOW

The output window is a forced air cooled Al_2O_3 ceramic koaxial window as it was used in the 1 MW tube. To suppress multipactoring it is additionally coated with a thin film of TiN. This is done by plasma supported CVD. During RF processing and testing the coated prototype window no multipactor occured even in low and medium RF power range, while the older uncoated windows very often showed multipactoring.

V. TEST RESULTS

The klystron was tested under different operational conditions as shown in Table 2. A comparison to the calculated results in Table 1 demonstrates excellent agreements.

Table2
Test results of YK 1353

PHILIPS YK 1353	
1.3 MW cw Klystron 352 MHz	
Operating data	
- 1.3 MW at 100 kV / 19.3 A	$\eta = 67.5 \%$
- 1.0 MW at 88 kV / 17.1 A	$\eta = 66.5 \%$
- 1.0 MW at 77 kV / 22.4 A	$\eta = 62.0 \%$
- 0.7 MW at 77 kV / 15.2 A	$\eta = 60.3 \%$
Typical data at 1.3 MW operation:	
Beam voltage	: 100.0 kV
Beam current	: 19.3 A
Anode Voltage	: 53.0 kV
Drive power	: 70.0 W
Gain	: 41.0 dB
Collector dissipation	: 1.0 MW
Body dissipation	: 16.0 kW

Remarkable is the operation point 1MW at 77kV/22.4A with an efficiency greater than 60% and a beam perveance of $1.05 \mu\text{P}$. An overload test at 1.35 MW for 1 hour showed no electrical or thermal instabilities. A load mismatch test was also made with a movable teflon plate of $\text{VSWR} = 1.2$ inserted in the waveguide between klystron and matched water load. At 1 MW operation or below no

intabilities like sidebandoscillations occured. At 1.3 MW output power sidebands appeared 45 dB or less below carrier at transformed reflection phase angles around 0 degrees.

REFERENCES

- [1] "EGUN: An Electron Optics and Gun Design Program." W.B. Herrmannsfeldt, SLAC-PUB-0331 (October 1988)
- [2] "Osmium dispenser cathodes", P.Zalm and A.J.A van Stratum, Philips Tech. Rev., vol.27, no. 3/4, pp. 69-75, 1966.
- [3] "High-Power Klystron Simulations using FCI-Field Charge Interaction Code." T. Shintake, KEK Report 90-3 (May 1990)

Interleaved Wide and Narrow Pulses for the KAON Factory 1 MHz Chopper

G. D. Wait, M. J. Barnes, D. Bishop, G. Waters
TRIUMF, 4004 Wesbrook Mall, Vancouver, B.C., Canada V6T 2A3

Abstract

A beam chopper is required in the transfer line between the 1 GeV/c TRIUMF cyclotron and the Accumulator ring of the proposed 30 GeV/c KAON Factory synchrotron. The beam chopper must generate pulses with a magnitude of at least 9.5 kV with rise and fall times of less than 38 ns (corresponds to kick rise/fall time of less than 39 ns) at a repetition rate of 10^6 pulses per second at a 100% duty cycle. The pulse pattern must be synchronized to the 23 MHz RF system for the TRIUMF cyclotron. Two different pulse widths are required to deflect a total of 5 beam bursts out of every 45 beam bursts that are extracted from the cyclotron. The inter-leaved pulses will have flat-top durations of more than 48 ns and 92 ns. Results of measurements on a prototype chopper are presented where pulses of two different widths are synchronized to an RF synthesizer and stored in a low loss delay cable. Rise and fall times of 20 ns to 40 ns have been achieved with 12 kV to 15 kV wide and narrow pulses at 1.9×10^6 pulses per second continuous operation.

I. INTRODUCTION

The TRIUMF cyclotron will be used as an injector for the KAON Factory synchrotron. The beam chopper will create holes of 108 ns duration in the 100 μ A, 1 GeV/c H^- beam in the accumulator ring to allow enough time for the magnetic field to be established in the kicker magnets [3,4] in each of the 5 rings. The H^- burst period within the cyclotron is 43.5 ns and the burst width is 2.4 ns with a jitter of approximately 2.4 ns. Hence the effective gap between beam bursts within the cyclotron is about 39 ns. If the H^- beam were extracted with the same pattern, as is the case for H^+ extraction, then the chopper "kick" would require a rise and fall duration of less than 39 ns and a flat top duration of more than 48 ns and 92 ns on alternate pulses, as shown in Figure 1, so that 2 and 3 beam bursts would be removed alternately at approximately 1 μ s intervals. However the H^- extraction scheme that has been

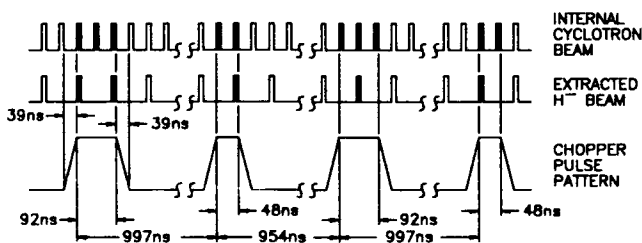


Figure 1: Beam Chopper pulse pattern synchronized with internal cyclotron beam and extracted beam

developed for the KAON Factory performs in such a manner that every second burst is extracted [7]. Thus the period of the extracted H^- beam is 87 ns. In Figure 1 the cyclotron internal burst pattern and the extracted burst pattern are shown in relation to the chopper timing. The beam chopper pattern as shown in Figure 1 will deflect a total of 5 beam bursts with 4 deflector pulses over a period of exactly 4 accumulator periods of about 1 μ s each. Ten beam bursts are un-deflected between each chopper pulse and these beam bursts are inter-leaved in such a manner that there are 40 consecutive beam bursts in the accumulator ring and 5 consecutive missing beam bursts.

The angle of deflection Θ , from an electric field is

$$\Theta[\text{rads}] = \arctan \left[\frac{V \times \ell}{d \times p \times \beta} \right] \quad [10^9 \text{V/GeV/c}] \quad (1)$$

where $\beta \times c$ is the particle velocity and p is the beam momentum. The required deflection of 1 mrad can be achieved with a set of plates 5 cm (d) apart in which the product of voltage, V and plate length, ℓ is 37.7 kV-m. Thus 9.5 kV pulses are required for 4 m long deflector plates. The deflected H^- beam bursts will impinge on a stripper foil and emerge as H^+ and be further separated from the un-deflected H^- beam by a dipole magnet and directed to a 10 μ A beam dump.

II. CHOPPER DESIGN CONCEPT

The 1 MHz chopper design concept has been described extensively (see [5,8,9] and references cited therein). The cathode of an EEV [6] CY1170J 75 kW tetrode is connected to a negative high voltage power supply. The anode

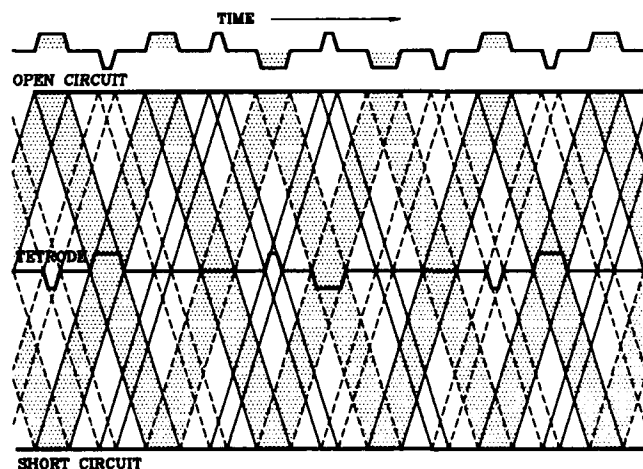


Figure 2: Lattice diagram of inter-leaved chopper pulses.

of the tetrode is connected to two 50 Ω storage cable cables of approximately equal length. One cable is short circuited at the far end. The far end of the other cable is connected to the center of a set of deflector plates which are configured as a 100 Ω strip-line and are center-fed to match the impedance of the 50 Ω storage cable. The deflector plates are open circuit. The propagation delay in the two cables can differ by ± 3 ns without any measurable degradation in performance. Thus as the cables temperature changes, the system can be synchronized precisely to the cyclotron by simply changing the position of the short circuit stub. However the sum of the delays of the two cables must be accurate to within about 1 ns.

Figure 2 shows the lattice diagram of the double width pulse pattern at the tetrode and at the open circuit end of the pulse storage cable. Alternate wide and narrow pulses are shown in Figure 2 at the deflector plates. Since the deflected beam will strike a stripper foil in either direction the polarity of the deflector voltage is not important.

In Figure 2 the path of negative pulses is indicated by dashed lines and the path of positive pulses is indicated by solid lines. The pulses reflected from the short circuit are reversed in polarity and those reflected from the open circuit maintain the same polarity. There are actually two narrow pulses and two wide pulses on the cable travelling in opposite directions. Alternate reflections from the remote ends of the cables cause a voltage null at the anode when the pulses are of opposite polarity. When the two narrow (or wide) pulses add together as a single negative pulse at the anode of the tetrode, then the tetrode is pulsed on to restore the leading edges (charge). When the two narrow (or wide) pulses add together as a single positive pulse, the tetrode is pulsed on to restore the trailing edges (clip). The magnitude of the stored pulses are doubled at the deflector plates. Storage cables which have a total delay of 2 μ s are required so that four pulses (2 wide and 2 narrow) can be stored to give a repetition rate of 10^6 pulses per second at the deflector plates. Note that the repetition rate at the tetrode is 1/2 of the repetition rate at the deflector plates since the pulses arrive at the tetrode in pairs.

III. MEASUREMENTS

The prototype tests which were reported in Hamburg [5] were carried out at 2.2×10^6 pulses/s, with one width of pulse. The prototype was upgraded with a new pulse sequencer [2] and with an increased length of the storage cable. The base of the tetrode was re-configured and the screen power supply and the grid driver circuit were re-designed to reduce the inter-pulse ripple [1]. The wide and narrow pulses were controlled independently using the new timing control system which can be synchronized to the 23 MHz cyclotron pulse pattern. The length of the storage cable was \approx double that used for the previous results [5] so that both wide and narrow pulses could be stored simultaneously. This keeps the repetition rate at $\approx 2 \times 10^6$ pulses/s and maintains the power dissipation at a reasonable level. The two cables were connected to the tetrode as described in reference [5] as a lumped element 50 Ω

transmission line with a delay of 5 ns. The total one way delay of the storage cables, including the 4 m long deflector plates and the tetrode connection, was 1079.8 ns when the short circuit position was adjusted so that the delays on either side of the tetrode were equal. This corresponds to a fundamental resonant frequency of 926.1 kHz.

The pulse sequencer [2] counts the number of RF cycles and generates timing signals that are used to synchronize the charge and clip timing for two different widths of pulses. The synthesizer was set to a frequency that is 45 times the required chopper frequency. The synthesizer frequency was 41.79 MHz rather than 23 MHz (cyclotron frequency) due to the available length of the storage cable. The high voltage power supply voltage was set to -15 kV and the grid drive timing was tuned independently for the narrow pulse and then for the wide pulse at 928.7×10^3 pulses/s (41.79/45). The voltage pulses shown in Figure 3 were measured at one end of the 4 m long deflector plates. The top two traces in Figure 3 show the narrow and wide pulses obtained independently on the deflector plates. The first negative and the first positive pulse in the narrow (wide) pattern is actually one pulse delayed by twice the total cable length. See Figure 2. The second negative and second positive pulse in the narrow (wide) pattern is the other pulse. These two pulses differ in magnitude by about 2 kV. Part of this is due to a baseline 2.5 kV peak to peak, 232 kHz oscillation which is due to excitation of the $\lambda/4$ resonance of the total delay of the cables. However there is still an asymmetry in pulse amplitudes of about 1 kV which is present and is under investigation.

The bottom trace in Figure 3 shows the wide and narrow pulses inter-leaved. The repetition rate for two widths of pulses was 1.8574×10^6 pulses/s. This is almost twice the required design repetition rate. The magnitude of the inter-leaved pulses is about 1 kV less than that of the independent pulses. The peak magnitudes of the various pulses in the 8 pulse pattern varied from 12 kV to about 15 kV so that the useful pulse voltage is only 12 kV. The kick angle

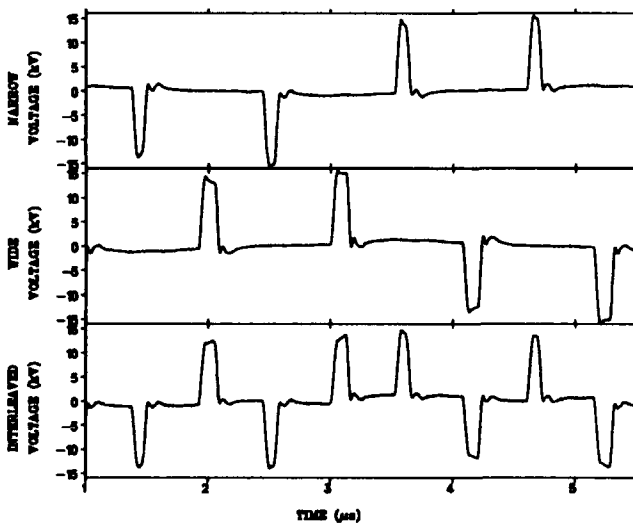


Figure 3: Measured wide, narrow and inter-leaved pulse patterns.

of the smallest pulse would be about 1.25 mrad with 4 m long deflector plates. The inter-pulse ripple which includes a 232 kHz component is about 3.0 kV peak to peak which is $\pm 13\%$ of the pulse magnitude for the 12 kV pulses. The variation in the kick strength from pulse to pulse is not important since the deflected beam is directed to a beam dump. The average current in the 75 kW tetrode was 3 A when both pulses were present giving a total dissipation of 45 kW.

Table 1.

Measured rise and fall times (including jitter) to ± 12 kV for the wide and narrow pulses independently and inter-leaved.

Pulse Edge	Measured Pulse Timing (ns)	
	Independent Phase + Δt 15-90%	Inter-leaved Phase + Δt 15-90%
2 nd neg Narrow		
Lead	20.0	30.8
Trail	21.5	28.8
1 st pos Narrow		
Lead	23.9	28.6
Trail	25.9	26.0
2 nd pos Narrow		
Lead	24.2	35.5
Trail	23.2	30.9
1 st neg Narrow		
Lead	29.1	36.0
Trail	28.9	29.8
2 nd neg Wide		
Lead	21.0	28.2
Trail	17.5	19.9
1 st pos Wide		
Lead	25.0	32.0
Trail	20.8	22.6
2 nd pos Wide		
Lead	25.0	33.4
Trail	22.0	23.5
1 st neg Wide		
Lead	31.1	40.1
Trail	25.5	28.3

Table 1 shows a summary of the measured leading and trailing edge durations (Δt , 15% to 90% of ± 12 kV) which includes timing jitter of the 8 voltage pulses for independent and inter-leaved pulses shown in Figure 3. The timing jitter was measured relative to the period of the grid drive and varied from 0 to 8 ns depending on the pulse edge being measured. The rise and fall times were all measured from 15% to 90% since the inter-pulse ripple shifted the baseline of one of the inter-leaved pulses to about 14% of 12 kV. The 10% to 90% rise and fall times were measured for all but one pulse and were found to differ from those shown in Table 1. by only 1 or 2 ns. The rise/fall times + jitter for the independent pulses are as much as 11 ns less than that measured for the inter-leaved pulses. This was

due to the limitations on the grid pulser circuit which can not quite handle the higher repetition rates.

IV. CONCLUSION

The requirements for the prototype chopper are operation at 1.025×10^6 pulses/s continuously at 9.5 kV with kick rise and fall times (including phase jitter) of less than 39 ns. The measured results show that the prototype chopper can achieve operation at 1.9×10^6 pulses/s continuously at 12 kV or more with kick rise and fall times (including phase shifts) of less than 39 ns, with one exception. However the measurements show that at about 1×10^6 pulses/s the rise and fall times are all much less than 39 ns. The power dissipation in the CY1170J tetrode, with 12 kV stored pulses at 1.9×10^6 pulses/s is approximately 45 kW which is well within the 75 kW rated dissipation of the tetrode. This dissipation will be approximately halved at 1×10^6 pulses/s. The inter-pulse ripple is about $\pm 13\%$ and further study is required to reduce this to less than 10%. In future tests, the asymmetry in the pulse heights will be investigated and the long term stability of the system will be tested.

V. REFERENCES

- [1] G. D. Wait and M. J. Barnes, "Pulse Width Control at 2×10^6 Pulses/sec and 15 kV for the KAON Factory Beam Chopper" to be published in the Proceedings of the ninth Pulse Power Conference, June 1993. Albuquerque
- [2] G. Waters, D. Bishop, M. J. Barnes, G. D. Wait, "A Pulse Sequencer for the KAON Factory Beam Chopper" Proceedings of this Conference.
- [3] M. J. Barnes, G. D. Wait, "Optimization of Speed-Up Network Component Values for the 30 Ω Resistively Terminated Prototype Kicker Magnet" Proceedings of this Conference.
- [4] M. J. Barnes, G. D. Wait, "Kickers for the Kaon Factory" Proceedings of XVth International Conference of High Energy Accelerators (HEACC'92), Hamburg, July 1992.
- [5] G. D. Wait, M. J. Barnes, "Results for the 75 kW Prototype 1 MHz Chopper at 100 % Duty Cycle" Proceedings of XVth International Conference of High Energy Accelerators (HEACC'92), Hamburg, July 1992.
- [6] English Electric Valve Co. Ltd., Chelmsford, Essex, UK.
- [7] R. E. Laxdal, private communication.
- [8] G. D. Wait, M. J. Barnes, C. B. Figley, "Results for the 150 kW Prototype 1 MHz Chopper at 100 % Duty Cycle" Proceedings of Power Modulator Symposium, Myrtle Beach, S. Carolina, June 1992.
- [9] G. D. Wait, M. J. Barnes, "An Alternative Design Concept for a 1 MHz Beam Chopper for the KAON Factory" Proceedings of Power Modulator Symposium, Myrtle Beach, S. Carolina, June 1992.

CONSIDERATIONS REGARDING THE EFFICIENCY OF HIGH POWER RF SOURCES FOR PARTICLE ACCELERATORS

G. CLERC, C. BEARZATTO, M. BRES, G. FAILLON and Ph. GUIDEE

THOMSON TUBES ELECTRONIQUES

Bât. CHAVEZ - B.P.121

78148 Vélizy cedex /FRANCE

1- INTRODUCTION

Recent advances in accelerator technology are now making possible the operation of high duty factor or CW facilities. Emphasis is therefore frequently put on accelerators designed not only on purely technical factors, but also on cost criteria. From this point of view, the efficiency of high power RF sources feeding the electromagnetic power to the accelerating structures becomes an important issue in the design of a modern accelerator.

It is thus important to consider the efficiency of high power RF sources in a very objective manner and to examine advantages and drawbacks for each possible RF generator. The objective of this paper is to give a broad survey of this issue and to clarify this performance and its consequences.

2 - GRIDDED TUBES

Like all RF sources, triodes and tetrodes used in accelerators convert dc power provided by the HV anode power supply into RF power. The efficiency depends largely on the class of operation and also the quality of the amplified RF signal. The theoretical efficiency of a gridded tube is given by :

$$\rho = \frac{\theta - \sin\theta \cos\theta}{\sin\theta - \theta \cos\theta} \times \frac{1}{2} \times \frac{V_p}{V_{po}}$$

where θ is the passing angle of the anode current, V_p is the peak RF voltage and V_{po} the dc anode voltage.

When a sinusoidal signal is applied between the cathode and the grid, three classes of operation are defined :

A- class : variation of the anode current is sinusoidal; the maximum theoretical efficiency exceeds 50%. At low level the efficiency drops to zero; all the power is dissipated on the anode.

B- class : the anode current flows for only a half period; the maximum theoretical efficiency reaches 79% and is only slightly degraded with a diminution of the output power.

C- class : the anode current flows less than half a period; with a 60° passing angle, the maximum theoretical efficiency is 89,5%.

Beyond these usual classes of operation, it is possible to increase the efficiency by working in D- class with a square wave obtained by adding the 3rd harmonic to the fundamental signal.

Because of the relatively low gain of the tetrodes and non negligible consumption of ancillary power supplies, there is a significant difference between the conversion efficiency discussed above and the overall efficiency, which takes into account dc power, RF drive power and heater power applied to the tube. Also operational efficiencies are less than maximum values because of the residual anode to cathode voltage which must be of the same order of magnitude as the

screen to cathode voltage.

The loss in efficiency is around 5%. This effect is minimized by operating with a high load impedance as seen by the tube, i.e. with very high voltage and a low anode current.

Class-A operation does not generate harmonics; other classes of operation generate harmonics, whatever the quality of the tube linearity.

Finally the gain changes inversely to efficiency and increases from C-class. In scientific applications, it is frequent to operate in B-class to take advantage of a good efficiency while keeping a large enough gain. Table I shows the results obtained with TH 526 tetrode operated at TORE-SUPRA for Ion Cyclotron Resonance Heating (ICRH) experiments.

PARAMETER	80	120	200	UNIT
RF FREQUENCY	24	18	24.2	KV
ANODE VOLTAGE	1750	1750	1600	V
SCREEN GRID VOLTAGE	-350	-350	290	V
CONTROL GRID BIAS VOLTAGE	115	120	126	A
ANODE DIRECT CURRENT	5	5	2.7	A
SCREEN GRID DIRECT CURRENT	4	4	2.5	A
CONTROL GRID DIRECT CURRENT	760	660	680	KW
ANODE DISSIPATION	2	1.5	2	MW
PEAK OUTPUT POWER	70	60	50	KW
PEAK DRIVE POWER	> 30	> 30	2.10 ⁴	S
PULSE DURATION	72%	69%	66%	
EFFICIENCY				

TABLE I - EXAMPLES OF OPERATION FOR TH 526 TETRODE

3 - KLYSTRONS

In a conventional klystron, the efficiency η is usually defined as the ratio of the RF output power P_o to the beam power (cathode voltage x cathode current), without taking into account the heater consumption and the focusing power (if any). Due to the high gain of the klystron - at least 35 to 45 dB - the RF drive power has no incidence on the efficiency. This efficiency η is called interaction efficiency, and corresponds to the conversion in the output circuit of the kinetic energy of the bunched electron beam into RF energy. The main factor affecting efficiency is the perveance :

$$K = I_{beam} \times V_{beam}^{-3/2}$$

directly related to beam space charge forces. Fig.1 shows how efficiency increases with perveance and there is no doubt that 80% efficiencies could be obtained.

The physical explanation of this relationship is the following :

- As also perveance increases, the electron density in the bunches also increases, and repulsive forces between electrons make this bunching less and less sharp and efficient. Since the bunching is deteriorated, a increasing number of electrons comes out of the optimum phase for interaction with the electromagnetic fields in the cavities,

especially in the output cavity. Some of them are completely out of phase and pick up energy from the RF instead of providing it.

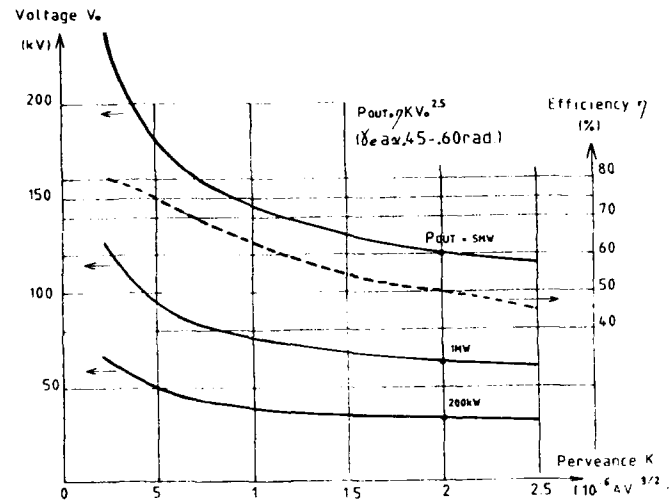


FIG. 1 : RELATIONSHIPS BETWEEN EFFICIENCY, CATHODE VOLTAGE AND PERVEANCE (KLYSTRONS)

- Another reason is related to the beam dynamics. As soon as the beam enters the first drift tube, the electrons encounter electrostatic repulsion from other ones already traveling in the tube. This ΔV depression becomes significant as the perveance increases and is deeper on the axis than on the edge.

Because the beam velocity and therefore the output power are related to $V_{beam} - \Delta V$, and not to V_{beam} , efficiency decreases as the perveance increases.

Beam diameter variations, laminarity and radial density variations play also an important role and explain why the magnetic focusing field must be carefully adjusted along the beam path from the cathode to the collector. The diameters of the drift tubes and beam are also important design parameters, because of their incidence on the space charge forces and the coupling between the beam and cavities.

The design of the interaction structure of a klystron must provide bunches as sharp as possible at the entrance of the output cavity. This is why many codes (1 and 2 1/2 codes, Z and time stepping, PIC...) have been developed to improve the design of the RF structure and subsequently the efficiency. As a consequence of the use of such codes, some high efficiency klystrons include a second harmonic cavity in the RF structure, but the effectiveness of such a device is not commonly accepted.

4 -EFFECT OF VSWR ON KLYSTRON EFFICIENCY

The interaction efficiency we are talking about is the optimum efficiency obtained when the RF power is delivered to a matched load (VSWR = 1 : 1) Around saturation , a klystron can be considered as a generator of current and maximum efficiency is obtained when the internal impedance is equal to the load impedance. When the load is

mismatched, the efficiency decreases according to the RIEKE diagram. Further more, over a large phase range of the mismatched load, the impedance seen by the bunched beam is such that the RF voltage induced across the output cavity gap is too large, greater than the accelerating beam voltage ($V_0 - \Delta V$). Therefore some electrons are reflected towards the cathode, causing beam interception and dangerous breakdowns. As a consequence, a high efficiency klystron does not accept a load with large variations of VSWR and phase. This point is often minimized or omitted, and a difficult trade-off is always necessary between efficiency and the range of possible load variations. This fact is particularly important in RF heating of plasmas, which are very unstable loads.

5 - DEPRESSED COLLECTORS

Depressed collectors are often seen as a solution to increase efficiency. Their design includes several electrodes whose voltages are gradually distributed between the ground and cathode potentials. Electrons coming from the output cavity - with a velocity dispersion $\Delta v/v$ related to the magnitude of their interaction in this cavity - are slowed down in the collector and ideally arrive on the electrodes with a small velocity. For a given design, the collector efficiency depends on the velocity dispersion.

Depressed collectors are really attractive if some conditions are met :

1) The interaction efficiency is low; the advantage of depressed collectors is high because of the increasing margin between the interaction efficiency and the overall efficiency. It is the case for traveling wave tubes, especially under operating conditions where energy is expensive, as in space (table II).

P/N	FREQUENCY	RF POWER	BEAM VOLTAGE	INTERACTION EFFICIENCY	OVERALL EFFICIENCY		
					2 STAGES	3 STAGES	4 STAGES
TH 3626	Ku-Band	20 W	3,9 kV	18 %	45 %	50 %	-
TH 3754	Ku-Band	110-130 W	5,6 kV	25 %	-	59 %	62 %
TH 3781	Ku-Band	55 W	4,7 kV	24 %	-	57 %	60 %

TABLE II - EFFICIENCY OF TWTs FOR SPACE APPLICATIONS WITH DEPRESSED COLLECTORS

2) The tube is not used at saturation, i.e. for telecommunications and some TV systems.

3) Voltages and powers are moderate, so depressed collectors do not involve too much technological complexity or too many operational difficulties for the product.

The interest of depressed collectors is limited to certain well defined cases, and they do not appear to be valid at high power levels.

6 - INDUCTIVE OUTPUT TUBE

This tube combines features of two types of tubes :

- gridded tubes for the grid excitation
- klystrons for the gun optics and the internal use of resonant cavities.

When a klystron works in A-class and therefore has theoretical efficiencies limitations, an IOT may be biased in B-class or C-class. Efficiency is as high as 60% were

reported at nominal power levels of some tens of kW in UHF-range (TV broadcasting). These efficiencies do not drop below 35 to 40% at low RF levels (fig.2).

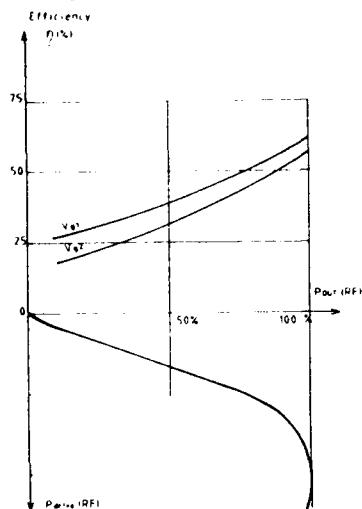


FIG. 2 : TYPICAL EFFICIENCY OF AN IOT (10 TO 100 % RF POWER / 2 GRID BIAS VOLTAGES)

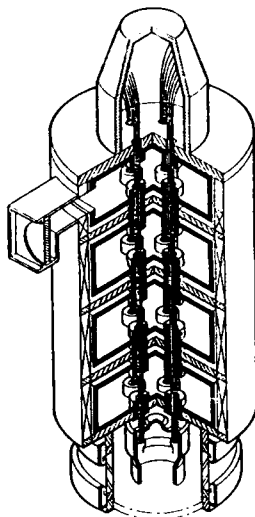


FIG. 3 : INTERNAL VIEW OF A MBK STRUCTURE

Apart from this advantage, and other ones such as small size and low weight, this device suffers some drawbacks :

- Beam voltage is significantly higher than the corresponding klystron voltage.
- The gridded gun is complicated and has to handle higher electric fields between electrodes; so risks of breakdown and failures are increased.
- With a value around 18 to 20 dB, the gain is within 2 to 3 orders of magnitude below the gain of a klystron; so the driver becomes an item which cannot be neglected in terms of size and power systems.
- Because of high beam voltage, X-ray shielding is a more important issue than for klystrons.
- The design of the tube induces a limitation at high frequency; a klystron does not have so stringent limits.

In conclusion the IOT seems to have a field of operation limited to UHF frequencies at a power level of a few tens of kW CW or average, where an interesting efficiency may be obtained.

Finally, the most common way to obtain high efficiencies remains to design the microwave source with a low perveance. To get the same amount of power, it is necessary to increase the beam voltage (fig.1). High efficiency devices, such as magnicons, gyrocons or IOTs, are always tubes characterized by low beam perveance, operating with beam voltages significantly higher than klystron voltage; as a consequence of the use of high voltages, power supplies, modulators and HV links become bulky, quite expensive and less reliable.

7 - MULTIBEAM KLYSTRON (MBK)

The MBK concept originates from the search for a trade-off between the following features :

- As high an efficiency as possible.
- As low beam voltages as possible.
- Use of proven technology and intrinsic advantages - gain, frequency range,... - of the klystron.

Basically the MBK is a microwave tube in which several electron beams in parallel propagate across a common RF interaction structure (cavities) in a single vacuum envelope. For a given output power, this arrangement gives a high current and low voltage tube. Since the length of the RF structure is approximately proportional to the square root of the voltage, a significant reduction of size can also be obtained.

Because the perveance of each individual beam can be small, the interaction efficiency is high (fig.1). Table III shows comparative data of klystron and MBK; 39 kV is enough to obtain 1 MW of output power with the 0.78 μ perv perveance of each beam.

	KLYSTRON	MBK	MBK	MBK
FREQUENCY	352 MHz	425 MHz	850 MHz	1700 MHz
OUTPUT POWER (CW)	1300 kW	1000 kW	1000 kW	850 kW
CATHODE VOLTAGE	100 kV	39 kV	38,5 kV	40 kV
NUMBER OF BEAMS x CURRENT	1 x 20A	7 x 5,7A	7 x 6,5A	6 x 6,4A
EFFICIENCY	65%	65%	58%	56%
GAIN/DRIVE POWER	42 dB/ 80 W	45 dB/ 30 W	45 dB/ 30 W	42 dB/ 50 W
GUN LENGTH	75 cm/OIL	35 cm/AIR	35 cm/AIR	35 cm/AIR
OVERALL LENGTH	4,75 m	2,9 m	2,20 m	1,85 m
OVERALL DIAMETER (WITH MAGNET)	90 cm	58 cm	36 cm	34 cm
OVERALL WEIGHT (WITH MAGNET)	2150 Kg	650 kg	580 kg	450 kg
WATT/GRAMM RATIO	0,60 W/g	1,54 W/g	1,72 W/g	1,78 W/g

TABLE III - COMPARATIVE DATA OF HIGH POWER KLYSTRON AND MBK (TENTATIVE)

TTE has carried out R&D on MBKs and manufactured a development model to verify the theory and prove the feasibility of such a concept. Experimental results are consistent with computations and show that this device could be suitable for high power, high efficiency RF sources to be used in scientific applications. Indeed it simplifies technology equipment with lower voltages and a higher power to weight ratio. Further developmental work will investigate the domain of operation of such a device.

8 - CONCLUSION

Efficiency is a key feature of modern RF sources because of its technical and economical implications. High power RF sources include many high efficiency electron tubes, but they generally require high voltages, with all the drawbacks involved. MBK are not yet a well explored solution to combine high efficiency and high voltage. However, they could provide a cost effective and reliable answer to RF transmitters and modulators for scientific applications.

INITIAL COMMISSIONING OF HIGH POWER, LONG PULSE KLYSTRONS FOR SSC INJECTOR LINACS

P. COLLET, J.C. TERRIEN, Ph. GUIDEE.
THOMSON TUBES ELECTRONIQUES
Bâtiment CHAVEZ - B.P. 21
78148 Vélizy Cedex - FRANCE

1 - INTRODUCTION

H⁺ ions are injected into the SSC boosters and main ring at a energy of 600 MeV by means of a three stage injector. It is composed of a RF quadropole, a drift tube Linac, both operated in UHF-band, and a coupled cavity Linac operated in L-band at the third harmonic of the two first stages. These Linacs are powered by two types of klystron, and their procurement contracts were awarded to THOMSON TUBES ELECTRONIQUES in October 1991. A design review held in January 1992 finalized the proposed design and fixed the final details concerning the operation and specifications of the tubes optimized for SSC requirements. Since November 1992, the commissioning of both type of klystrons has been underway and several tubes of each type have so far been accepted in accordance with the tight contractual schedule. It is expected that all deliveries will be completed by the end of 1993.

2 - MAIN FEATURES OF KLYSTRONS FOR SSC INJECTOR LINACS

RF operation of SSC injector Linacs is characterized by two main features [1] :

- The use of one Radio Frequency quadropole (RFQ) at 427.6 MHz and two successive Linacs operated at the same frequency for the drift tube Linac (DTL), at the third harmonic frequency for the coupled cavity Linac (CCL) coupled cavity Linac (CCL).
- The operation in long RF pulses, which reach a 100 μ s duration.

At the end of the DTL section, the beam energy is 70 MeV and the peak RF power supplied to the RFQ is estimated at 600 kW. DTL operation requires 3 MW peak power per klystron, which are designed and tested up to 4 MW to give a large margin for operation reliability. These values are consistent with performances obtained with other types of klystrons previously developed by TTE (Table I).

To accelerate H⁺ ions from 70 to 600 MeV in the CCL accelerating sections, the unit peak power requirements per klystron are more demanding. Each L-band klystron will have to provide 15 MW peak power in operation, and its contractual performance in acceptance test is 20 MW peak for the same reason as above. A special klystron design was necessary to provide sound tube operation at the required pulse duration.

	UNITS	SSC SPECIFICATION	TH 2134 Typical	TH 2118 Typical
OPERATING FREQUENCY	MHz	427.617	432	433.33
BANDWIDTH (-1 dB)	MHz	1	1	0.75
OPERATING DUTY CYCLE	%	0.1	5	3.3
RF PULSE WIDTH	μ s	100	1000	222
VIDEO PULSE WIDTH	μ s	110	1100	225
REPETITION RATE	Hz	10	50	150
PEAK OUTPUT POWER	MW	4	2	6
GAIN	dB	50	46	50
EFFICIENCY	%	> 40	55	55
BEAM VOLTAGE	kV	130	95	180
BEAM CURRENT	A	80	80	75

TABLE I : COMPARATIVE SPECIFICATIONS OF SSC KLYSTRON
FOR DRIFT TUBE LINAC AND TWO EXISTING TTE KLYSTRONS.

3 - TH 2140 KLYSTRON FOR RFQ AND DTL SECTIONS

3.1. GENERAL DESIGN

Based on the design already used and successfully proven with other high power klystrons produced by TTE, the TH 2140 klystron is cathode-modulated and has a built-in focusing magnet and a single window directly mounted on the output waveguide (Fig.1). It completes the already extensive family of UHF high power, long pulse klystrons produced by TTE for accelerator applications (Table II).

P/N	RF FREQUENCY (MHz)	RF OUTPUT POWER PEAK (MW)	AVERAGE (kW)	EFFICIENCY*	GAIN (min.) (dB)	RF PULSE LENGTH (max)	PEAK BEAM* VOLTAGE CURRENT (kV) (A)
TH 2142*	352	2.5	100	60%	42	250 μ s	120 35
TH 2140	428	4	4	50%	48	100 μ s	129 70
TH 2134*	432	2	100	55%	46	1 ms	95 40
TH 2118	433	6	200	58%	50	220 μ s	185 65
TH 2120	433	4	500	55%	48	10 ms	120 60
TH 2131	805	12	25	50%	50	115 μ s	210 115
TH 2138*	850	1.25	75	52%	48	2 ms	87 28

* Modulation by anode

* typical values

TABLE II : MAIN CHARACTERISTICS OF HIGH POWER, LONG PULSE, LOW FREQUENCY TTE KLYSTRONS

Because of the very low duty cycle and resulting very low average power, it was possible to accept a slight reduction of the gain and efficiency. Such a trade-off allows a four-cavity design instead of the usual five, and significantly saves on length, weight and cost.

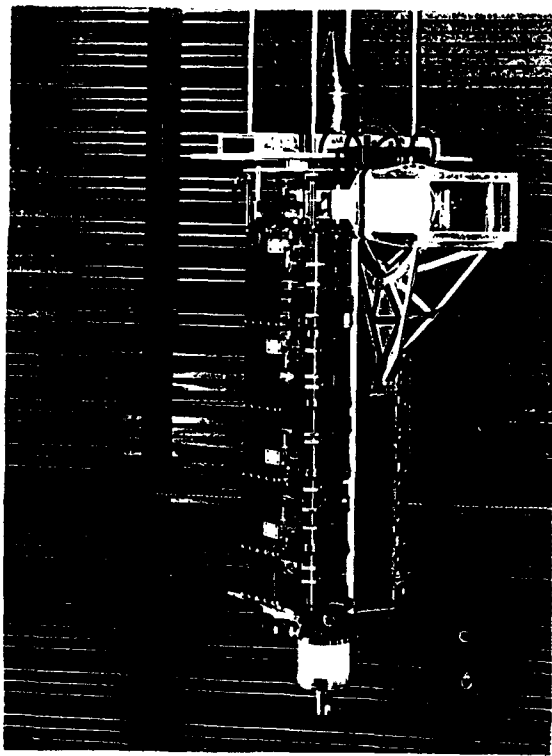


FIG. 1 : TH 2140 KLYSTRON

3.2. EXPERIMENTAL RESULTS.

As previously mentioned, the TH 2140 klystron provides RF power to the RFQ and DTL sections and so is operated at two different modes. Table III summarizes the results obtained in these two operating conditions, as compared with SSC specifications for the 4 MW nominal mode.

PARAMETER	UNITS	SSC SPECIFICATIONS (FOR MODE I/DTL)	TH 2140 TYPICAL RESULTS MODE I DTL	TH 2140 TYPICAL RESULTS MODE II RFQ
RF FREQUENCY	MHz	427.617	427.617	427.617
BANDWIDTH (-1dB)	MHz	1 (min)	1	1
DUTY CYCLE		0.1 %	0.1%	0.1%
RF PULSE WIDTH	μ s	100 (min)	100	100
REPETITION RATE	Hz	10	10	10
PEAK OUTPUT POWER	MW	4	4.1	0.63
GAIN	dB	40 (min)	48.5	42.5
EFFICIENCY		40% (min)	54%	31%
BEAM VOLTAGE	kV	130 (max)	125	73
BEAM CURRENT	A	80 (max)	61	28
FOCUSING MAGNET POWER	kW	3.9	1.9	

TABLE III : COMPARISON BETWEEN SSC SPECIFICATIONS AND TH2140 TYPICAL EXPERIMENTAL RESULTS

Phase and amplitude stability of the RF source are very important features for accelerator designers, as well as gain curve smoothness. Special care was taken during tube tests to detect any anomaly concerning these data. Figure 2 shows typical gain curves for modes I and II and Table IV compiles the stability measurements in mode I, as witnessed with the SSC.

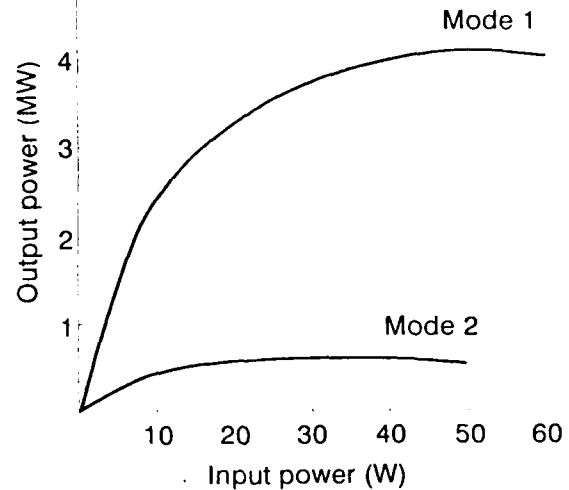


FIG. 2 : GAIN CHARACTERISTICS FOR TH 2140 KLYSTRON

PARAMETERS	UNITS	SSC SPECIFICATION (maximum limits)	TH 2140 EXPERIMENTAL RESULTS
RF PHASE VARIATION VS-BEAM VOLTAGE -FILAMENT VOLTAGE -RF DRIVE POWER	ϕ/V ϕ/V ϕ/dB	0.05 0.01 10	0.0023 not detected 3.9
RF AMPLITUDE VARIATION VS-BEAM VOLTAGE -FILAMENT VOLTAGE	dB/% dB/%	0.2 0.1	0.1 not detected
2nd HARMONIC 3rd HARMONIC SPURIOUS	dB dB dB	-30 -30 -40	-40 -50 < -60

TABLE IV - STABILITY CHARACTERISTICS OF TH 2140 KLYSTRON

4 - TH 2143 KLYSTRON FOR CCL SECTIONS

4.1. GENERAL DESIGN

Stimulated by the requests issued for RF-Linac driven free electron lasers, the state of the art in high power, long pulse klystrons reached 20 MW peak power for 20 microseconds or 10 MW peak for 250 microseconds in L-band a few years ago. Table V summarizes the main data for some L-band long pulse klystrons manufactured by TTE.

PART NUMBER	RF FREQUENCY (MHz)	RF POWER (MW)	EFFICIENCY*	GAIN (min dB)	PULSE LENGTH μ s	PEAK BEAM* VOLTAGE	MOD ANODE CURRENT
TH 2104 A	1296	5	45%	47	600	126	89
TH 2115	1300	2.5	48%	43	1000	94	5"
TH 2113	1300	4	56%	54	10 ms	120	60
TH 2095 B	1300	7.5	45%	42	100	142	11"
TH 2104	1300	15	43%	46	100	200	180
		10	43%	44	200	168	138
TH 2104 L	1300	10	45%	4"	250	165	135
TX 2022C	1300	20	40%	50	20	235	215

* typical values

TABLE V - MAIN CHARACTERISTICS OF HIGH POWER LONG PULSE L-BAND TTE KLYSTRON

After an initial request for 50 μ s pulse length, the SSC final demand called for 20 MW peak for 100 μ s. This could not be met with the standard designs implemented on existing tubes. TTE had however anticipated this evolution towards higher peak powers and longer pulses expressed by

accelerator designers, and an internally funded R&D program was initiated in 1990 to develop a new generation of high power, long pulse klystrons for both L-band and S-band applications [2].

The first application klystron to benefit from this effort is the TH 2143 (fig.3), which reuses the basic technology of other

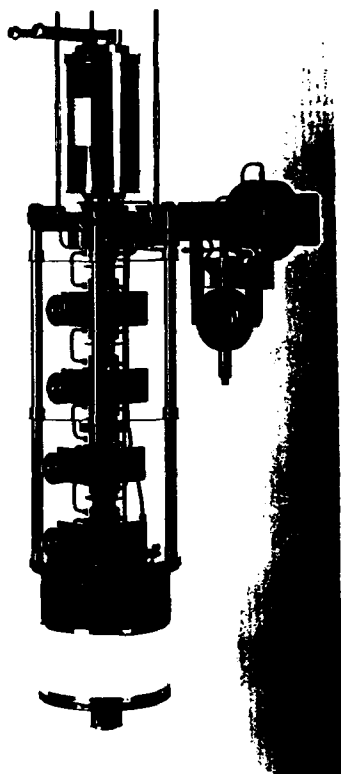


FIG. 3 : TH 2143 KLYSTRON

L-band klystrons, except for the gun. This has been redesigned to decrease inter-electrode electric fields and electrode temperatures. The resulting modifications allows the TH 2143 to withstand 230 kV HV pulses as long as 120 μ s.

4.2 EXPERIMENTAL RESULTS

TH 2143 klystron also has two operating modes at 20 MW and 2 MW peak. Table VI gives the results obtained in both modes, as compared with SSC specified values for the nominal operating mode. Figure 4 shows typical gain curves for both modes.

Also stability in operation has been carefully checked and measured during acceptance tests; results obtained are below the specified values.

PARAMETER	UNIT	SSC SPECIFICATION (FOR MODE I)	TH2143 TYPICAL RESULTS	
			MODE I	MODE II
RF FREQUENCY	MHz	1282.85	1282.85	1282.85
BANDWIDTH (-40dB)	MHz	5	5	0.1%
DUTY CYCLE		0.1%	0.1%	0.1%
RF PULSE WIDTH	μ s	100	100	100
VIDEO PULSE WIDTH	μ s	100	100	100
REPETITION RATE	Hz	10	10	10
PEAK OUTPUT POWER	MW	2	2	2
GAIN	dB	40.2	40.2	40.2
EFFICIENCY		27.7%	27.7%	27.7%
BEAM VOLTAGE	kV	230	230	230
BEAM CURRENT	A	72	72	72
FOCUSING MAGNET POWER	kW	17	17	17

TABLE VI : COMPARISON BETWEEN SSC SPECIFICATIONS AND TH 2143 TYPICAL EXPERIMENTAL RESULTS

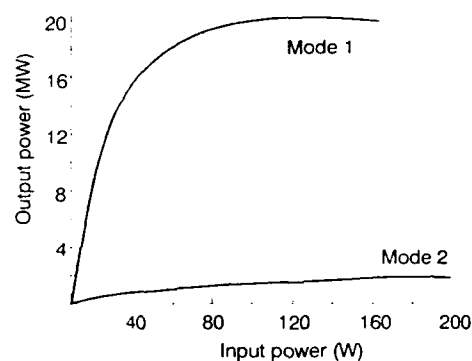


FIG. 4 : GAIN CHARACTERISTICS FOR TH 2143 KLYSTRON

5 - CONCLUSION

Two types of klystrons have been designed by THOMSON TUBES ELECTRONIQUES and are in production to equip the SSC injector Linacs. The commissioning of first tubes occurred in fall 1992 and the production is now under way in agreement with a tight delivery schedule. Design, manufacturing and test stages were carried out in a very cooperative manner between SSC and TTE to meet SSC requirements. With the successful development of the TH 2143, able to reach 20 MW peak in pulses of 100 μ s in L-band, extensive possibilities are now open to klystrons; a future S-band klystron with similar features is now under development, and will be an appropriate solution for long pulse S-band linear accelerators.

REFERENCES

- [1] L. Warren Funk, "The SSC Linac", 1992 Linear Accelerator Conference Proceedings, EACL-10728, OTTAWA, ONTARIO, CANADA.
- [2] J.C. Terrien, G. Faillon and Ph. Guidée, "RF Sources for recent linear accelerator projects", 1992 linear Accelerator Conference Proceedings, AECL-10728, OTTAWA, ONTARIO, CANADA.

Simulation of Traveling-Wave Output Structures For High Power rf Tubes*

Kenneth R. Eppley
Stanford Linear Accelerator Center
PO Box 4349, Stanford, California, 94309

Abstract

Travelling wave output structures can in principle provide higher efficiency and lower surface gradients than a single output cavity. We discuss simulations of TW structures designed for X-band klystrons to be used in the SLAC NLC. The PIC Code CONDOR [1] calculated efficiency over 50 percent for one such circuit. When the circuit was built in the SLAC XC7 klystron, the match was so poor that it had to be modified. When tested, the tube produced less than half the efficiency calculated. We subsequently found significant differences between the field distribution calculated by CONDOR versus that from the 3-D code MAFIA [2]. We have now developed a procedure which gives much better agreement between the 2-D and 3-D models. We use a $\pi/2$ disk-loaded structure, with the waveguide coupling to an output cavity through an iris, rather than directly to the drift tube as in the XC7. The disk radii are tapered to produce an approximately constant gradient. The output coupling is adjusted to match to a uniform structure replicating the cell before the waveguide. The simulations predict 75 MW, 49 percent efficiency, with peak surface fields of 73 MV/m. from a 440 kV, 350 amp beam at 11.424 GHz.

I. INTRODUCTION

The NLC design at SLAC requires a klystron producing at least 50 MW peak power at 11.424 GHz with a pulse length of at least 800 ns. A single gap output cavity would break down under these conditions. An extended output circuit should provide lower gradients and potentially higher efficiency. We have studied several disk-loaded travelling-wave output circuits at SLAC. Our main design tools have been the 1-D TWT code HARMON and the 2-D PIC code CONDOR. In CONDOR, we model the buncher cavities with the port approximation [3]. In the output section we model the actual geometry of the disks. The coupling to the waveguide is imposed as a port boundary condition on the outer wall of the last cell. This behaves like a radial transmission line whose impedance we can adjust. We can also adjust the coupling by adding a reactive phase to the impedance, or alternately tune the output cell by adjusting its dimensions.

There are two main difficulties we have encountered. For narrow band circuits, a very fine mesh may be required to accurately model the geometry. In addition, the non-axisymmetric nature of the coupling to the external waveguide is not always correctly modelled as a radial trans-

mission line. We discuss how these problems affected our early modelling attempts and the progress we have made in overcoming them.

II. SLAC XC7 OUTPUT CIRCUIT

The output circuit that was used in the SLAC XC7 klystron originated with Phillips based on results from the 1-D HARMON code. The circuit had four cells plus a waveguide which intersected the drift tube directly, rather than through an iris to an output cavity. The intention was to operate in a $2\pi/3$ mode. The operating conditions were 440 kV, microperveance 1.9. The cell radii were modified by the author based on the results of CONDOR simulations. A buncher section designed by Lien gave I_1/I_0 of 1.5, much higher than previous bunchers used in the X-band klystrons. The 2-D simulations predicted efficiencies over 50 percent, with peak power of about 120 MW and peak surface fields under 100 MV/m. When the circuit was modelled with the 3-D code MAFIA, the match was poor, with a VSWR of 8:1. The fourth cell radius was then reduced to produce a better match. The circuit was mounted on a rebuilt version of the XC5 klystron. The tube produced about 50 MW, similar to the XC5 at short pulses, but performed more poorly than XC5 at long pulses. The rebuilt tube did not have the improved buncher used in the design. We believe that the discrepancy between the CONDOR simulations and the experiment was due to incorrect modelling of the 3-D effects of the waveguide. The analysis was complicated by the narrow bandwidth of the structure. This caused the simulations to be very sensitive to the mesh size. To deal with this problem we borrowed a method used in the MAGIC code. We partially fill the outer radius of the cell so that the average radius is much closer to the desired value.

We subsequently resimulated XC7, using the fourth cell radius as built rather than as initially designed, and using the actual buncher section. The code predicted 46 MW, agreeing fairly well with the experiment. Since XC5 and XC7 produced almost identical power for short pulses with very different circuits, the simulation agreement does not prove that the fields in the model were in good agreement with the tube. A MAFIA cold test of the circuit was compared to a CONDOR cold test, both driven by an antenna on axis upstream of the input cell. A frequency scan showed four resonant peaks, which would not be present for a true travelling wave structure. Thus the circuit was operating in a hybrid mode, partially standing wave and partially travelling wave. The actual operating point was about 100 MHz above the $3\pi/4$ mode, about 200 MHz below the π mode.

* Work supported by the Department of Energy, contract DE-AC03-76SF00515.

With no external waveguide, both MAFIA and CONDOR agreed well to URMEL calculations of the resonant frequencies. With the coupling, the two central resonances merged in a broad peak in the 2-D model, but not in the 3-D model or in the lab. Comparing both 2-D and 3-D models at the frequencies where each put the $3\pi/4$ mode, we found a substantial discrepancy between the field amplitudes and phases. Retuning the output cell in the 2-D model (by adding tuning stubs) it was possible to recover the four peak resonant pattern, and, by careful adjustment, it was possible to get agreement with MAFIA for all the phase shifts to within .1 radian. The phases also tracked well when the codes were compared 100 MHz above the $3\pi/4$ mode. However, the amplitudes still showed substantial differences. Although the number of nodes in the field patterns were the same, the location of the peaks was shifted. From our findings below, we believe the discrepancy is due to the strongly non-axisymmetric nature of the waveguide when coupled to the drift tube without an output cavity.

III. CONSTANT GRADIENT $\pi/2$ STRUCTURE

We learned of a different approach that had been developed by Symons and Begum at Litton while designing a klystron for the DOD (through TRW). They used a four cell, disk-loaded structure, but with a $\pi/2$ phase shift and with varying disk radii to maintain an approximately constant gradient for all cells. This structure also had a very broad bandwidth. This was not essential for SLAC, but makes the design simpler by making the results less sensitive to small changes in the dimensions. This circuit used a cavity with a coupling iris in the fourth cell rather than a waveguide only. The coupling was adjusted for the best match when looking into a long uniform structure replicating the cell before the waveguide (making both disks the radius of the downstream side). The tapered disk radii were predicted to compensate for the beam so as to give a good match with the beam present. A linear variation of beam energy with position was assumed. Symons' design assumed the beam energy became zero at the end of the circuit, but we assumed 50 percent. Symon also assumed constant rf current, but we assumed a linear decline to 30 percent. The disk radii were chosen to produce approximately uniform fields strengths for each cell, based on URMEL and SUPERFISH calculations. The cavity radii were adjusted to have $\pi/2$ phase shifts at the operating frequency. There are some ambiguities in this process, as the phase shifts vary with radius, and the analysis of a periodic structure based on a single cell gives quite different results depending on which of the unequal disk radii is used. Fortunately the design is fairly robust.

The matching was done using a uniform structure, as described above. We modelled a five cell structure with input and output couplers and three inner cells identical to the cell before the waveguide. We did this with both CONDOR and MAFIA to see if we could obtain the same field distributions. In MAFIA, the radius of the coupler

cell and the aperture of the iris were varied to obtain the best match. For CONDOR, the radius and the impedance of the port was varied. In both cases the input and output cells were always adjusted to be identical. When we got the best agreement between CONDOR and MAFIA, the radius of the output cell in CONDOR was much closer to the value of the other cells than in MAFIA. Because CONDOR does not allow a variable mesh, the matching needs to be checked and possibly readjusted whenever the mesh size is changed. Alternately one can make small adjustments to the geometry of the structure to make it more closely approximate the results one would obtain with a very fine mesh. The mesh used was relatively coarse, with only six points modelling the rounded end of the disk. We obtained very good agreement between the 2-D and 3-D field distribution, with amplitudes agreeing to about 10 percent (normalized to the power level) and phases agreeing to better than .1 radian.

The first match we thought we found with MAFIA proved to be spurious. The reflection coefficient was very small but the fields in the cells were unequal. When an extra cavity was added, the reflection coefficient became larger. This is worth mentioning because the 2-D model continued to track the 3-D model closely when the extra cell was added. We obtained a true match with further variation of the cell parameters, and again were able to get good agreement between the 2-D and 3-D field patterns. Now the cell amplitudes were all nearly equal, and the reflection coefficient remained small when another cell was added.

We then studied the cold properties of the tapered circuit, using the matching conditions on the last cell determined above. We took care to keep the same mesh size so that the modelling of the last disk and cell would be unchanged. The tapered circuit was initially designed by Phillips using URMEL and SUPERFISH. The author made some small modifications to make the match better and the voltages more uniform.

Generally we have done cold test calculations with a single antenna, usually on axis or across one of the cavity gaps. We discovered that a volume phased array of antennas can give a much better approximation to the behavior of a beam. The array extends over a cylinder with radius equal to the beam, with constant radial current density. The phases change with phase velocity equal to the beam velocity. A further refinement is to taper this velocity, assuming a linear variation in beam energy through the circuit. The current can also be tapered linearly if desired. This new driver is a better design tool for the tapered circuits than a single antenna, making it more apparent whether the gradients are constant and whether the phase shifts are correct.

We also used a current array with the exact current and phase distribution (with no radial variation) produced by the simulation with beam. The result agreed very closely to the full beam simulation. This calculation is

much faster than the particle simulation. It is also useful in checking the results with a finer mesh, and may be used for 3-D simulations with MAFIA, which otherwise would be very costly.

The preliminary CONDOR results from the tapered circuit are highly encouraging. With almost no experimentation, the design produced 49 percent efficiency (75 MW). The peak surface field was 73 MV/m. The beam was 350 amps at 440 keV, perveance 1.2, with $I_1/I_0 = 1.5$. The rf current was produced with an imposed velocity and density modulation. Wright has designed a buncher which is predicted to produce $I_1/I_0=1.6$.

Table 1.
Field Pattern in the Output Structure (Hot)

Cell	E_z on axis (MV/m)	Phase Shift (radians)	Peak Surface Field (MV/m)
1	14.7	—	38.1
2	14.6	-1.66	60.4
3	14.6	-1.85	60.6
4	20.5	-1.04	72.8

IV. FUTURE WORK

We will redo the simulation with a buncher-modulated beam. We will perform a parameter study to further optimize the performance. We will model the tapered structure on MAFIA to assure that the field pattern is being represented correctly by CONDOR.

V. CONCLUSIONS

It is possible to represent a disk-loaded output structure reasonably well with a 2-D model, if one couples the waveguide to a cylindrical cell through an iris, uses a broad band circuit, and uses 3-D modelling to verify the field patterns. We have designed a circuit using a $\pi/2$ mode tapered to give a constant gradient which simulations predict will give high efficiency with moderate gradients.

IV. REFERENCES

- [1] B. Aiminetti, S. Brandon, K. Dyer, J. Moura, and D. Nielsen, Jr., *CONDOR User's Manual*, Livermore Computing Systems Document (Lawrence Livermore National Laboratory, Livermore, CA., April, 1988).
- [2] T. Weiland et al., "MAFIA, Das universelle Software-System fur elektromagnetisches CAD," the MAFIA Collaboration, Darmstadt, Germany, 1991.
- [3] K. Eppley, "Algorithms for the Self-Consistent Simulation of High Power Klystrons," SLAC PUB 4622, Stanford Linear Accelerator Center, May 1988.
- [4] R. Begum, private communication, February, 1993.

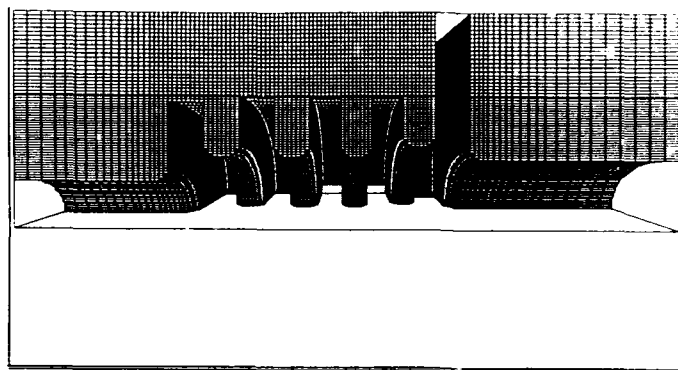


Figure 1. MAFIA simulation of XC7 output structure.

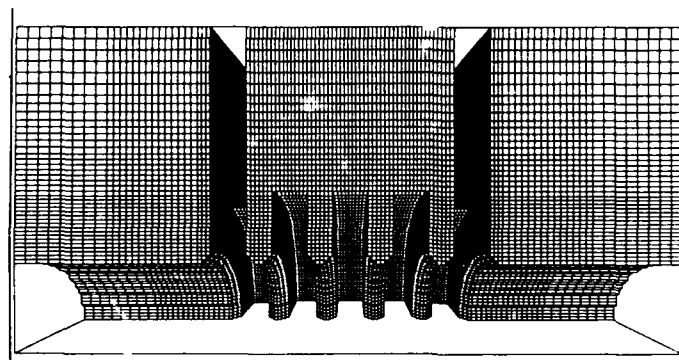


Figure 2. MAFIA simulation of 5 cell coupler used to match the $\pi/2$ structure into the waveguide

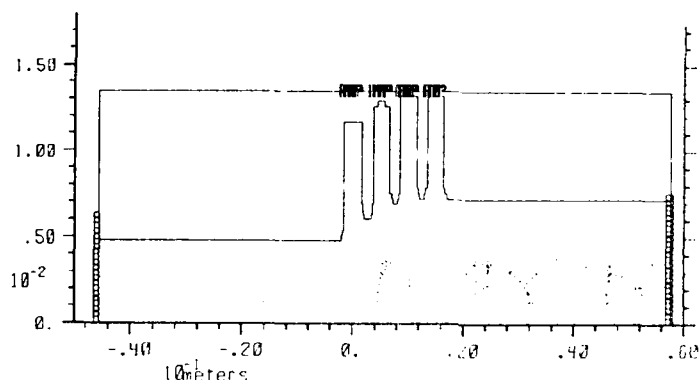


Figure 3. CONDOR simulation of $\pi/2$ structure (not to scale). Electron position space distribution is shown. Horizontal scale is Z, vertical is R.

Upgrade of an RF Source of the Linac for the B-Factory Project

S.Fukuda, S.Anami, Y.Saito, S.Michizono, K.Nakao and I.Sato

National Laboratory for High Energy Physics (KEK)
Oho-1, Tsukuba, Ibaraki, 305 Japan

ABSTRACT

The B-Factory project is a future plan at KEK requiring an energy upgrade of the KEK linac from 2.5 GeV to 8.0 GeV. This paper describes an upgrade plan and recent progress concerning the rf source. A test to increase the rf power using the existing 30-MW klystron is being carried out and an output power of 51.5 MW has been obtained by increasing the beam voltage up to 310 kV while optimizing the focusing magnetic field. Tests using a 60-MW klystron are also planned. The choice between upgrading of the present klystron and the use of a 60-MW klystron depends on the pulse-compression system to be adopted. The most efficient way regarding costs is being surveyed in order to use the existing components, such as the focusing magnet and the pulse transformer with only slight changes.

I. INTRODUCTION

An energy upgrade of the linac for the KEK B-Factory project has recently been proposed. The B-Factory rings will be nominally operated at 8.0 GeV(e^-)x3.5 GeV(e^+). It requires an energy upgrade of the linac from 2.5 GeV to 8.0 GeV for the direct injection of the beams to the rings. The energy upgrade of the linac is planned along with a power increase of the klystron and a suitable pulse compression.

There are two candidates as the pulse-compression system; a traveling-wave resonant ring in the accelerating structure (TWRR) and a SLED system [1]. We have already developed and tested both systems, which are being installed in the linac to evaluate their performance [2].

Specifications of a high-power klystron depend on the type of the pulse-compression system. Table 1 shows the parameters of rf sources for a TWRR case and two SLED cases with different pulse widths[3]. The parameters in Table 1 are introduced with the assumption that one-pulse output energy from a modulator is twice as large as in the present system. Since the beam energy in this Table is calculated based on the present 40 klystron units, it is necessary to add several units for 8.0-GeV acceleration. The required klystrons are 60-MW klystrons for the TWRR case and 46-MW klystrons for the SLED case if a pulse width is chosen to be 4 μ sec.

II. THE REINFORCEMENT OF A MODULATOR

Two pulse modulators are to be reinforced based on the plan given in Table 1. They are installed in the klystron test hall and the klystron gallery to test klystrons. The main parts which were replaced in the modulator are IVR's, charging choke transformers, PFN's and thyatrons. Particularly the PFN connected with two 20-section PFN units in parallel is adopted in order to produce a pulse of a 4 μ sec width. The

modulator in the klystron gallery has been operated to study the total performance of an rf system including SLED cavities[4].

Table 1. Possible Plans for B-Factory RF Source

	Unit	Present	TWRR	SLED-3	SLED-4
<u>Modulator</u>					
pulse energy	J	84x3.5	84x3.5x2	<=	<=
peak power	MW	84	155	131	101
width	μ s	3.5	3.8	4.5	5.5
voltage	kV	22.5	<=	<=	<=
PFN impedance	Ω	6	3.3	3.9	4.7
<u>Pulse transformer</u>					
step-up ratio		12	15.7	14.6	13.5
V-t	MV- μ s	0.95	1.3	1.5	1.7
<u>Klystron</u>					
beam voltage	kV	270	352	329	304
beam current	A	295	439	397	352
beam power	MW	84	155	131	107
rf width	μ s	<2.0	2.3	3.0	4.0
rf peak max.	MW	(36)	67	56	46
rf peak av.	MW	26	60	51	41
<u>Beam Energy</u>					
mult. factor		1	1.34	1.88	2.0
e energy/40 units	GeV	>2.5	5.6	7.3	7.0

III. HIGH POWER KLYSTRON

The currently available S-band klystrons and their characteristics are listed in Table 2. A Toshiba E3712 klystron and a SLAC 5045 klystron have been excluded since their large size does not fit our existing system

A 60-MW klystron required in the TWRR case is being developed by two Japanese tube companies independently; both have succeeded in producing 60 MW as stated in Table 2 and shown in Figure 1. The single output window is adopted in both tubes. These tubes will be tested in our facility in June with the collaboration of the companies. Their focusing electromagnet and pulse transformer with a step-up ratio of 1:15.5 for 350 kV operation were designed and manufactured.

The upgrading of the existing 30-MW klystrons is being developed at KEK. We have been using 48 30-MW klystrons for the 2.5-GeV acceleration of e^-/e^+ beams ($V_0=265$ kV, $P_0=33$ MW rating). Several tubes are the low-gradient type with a large curvature of the gun electrode and anode in order to reduce failures due to the arcing in the cathode region (PV3030A2) [5]. A simulation analysis of the PV3030A2 with the FCI code [6] suggested the possibility that it can produce more than 60 MW of an output power at a 350 kV beam voltage with reasonable efficiency. From this simulation

Table 2. Various Candidate Tubes for the KEK B-Factory Project

Vendor	Type	Voltage (kV)	Current (A)	Rep. (pps)	Pulse Width (μ s)	Output Power (MW)	Efficiency (%)	Average Power (kW)	Total Length (m)	Running Data	Comment
Toshiba	E3712	400	482	(54)	6.7	80	43	18	1.9	JLCx2 Pohang	Double windows
SLAC	5045	350	414	180	3.5	67	46	42	1.7	SLACx240 KEK-Test	Double windows
Toshiba	E3726	347	380	50	2.0	62	47	6.2	1.7	Toshiba Prototype	Single window
MELCO	PV 3060	347	440	20	2.0	62.4	41	2.5	1.5	MELCO Prototype	Single window
MELCO	PV- 3030A2	265	300	50	3.5	33	42	5.8	1.3	KEKx49	Low Gradient Single window
KEK- Test	PV- 3030A2	310	370	50	4.0	51.5	44	10.2	1.3	KEK- Test	Under developing Large High Vol. Seal

the characteristics of the tube were found to strongly depend on the focusing magnetic field near to the output cavity region [7]. A tentative test of the 30-MW klystron up to a beam voltage of 300 kV was carried out with a low duty rate to prevent the tube from failures due to a high voltage ceramic seal and an output window. At that level a peak power of 47.3 MW with a reasonable efficiency of 44% was obtained. The focusing magnetic field was varied in order to keep the beam loss in the drift tube small by measuring the water temperature rise at the output cavity region. After obtained this test result, we replaced a high-voltage ceramic-seal with a larger one in order to increase the insulating length.

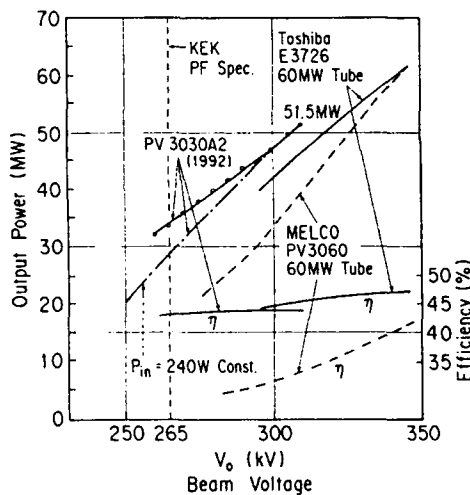


Fig.1 The output characteristics of the PV3030A2 klystron and the 60-MW tubes.

A second test was performed using this improved klystron up to a beam voltage of 310 kV. At this level a peak output power of 51.5 MW with an efficiency of 44% was obtained under the condition of a repetition rate of 30 pps, a beam pulse width of 5.5 μ sec and an rf pulse width of 4 μ sec. The limit was set by the modulator of the test stand. These test results are shown in Figure 1. Figure 2 shows the output power characteristics with the variation of the focusing magnetic field. Figure 3 shows the output waveforms of the beam pulse and the rf. In this test the temperature of the

output window of the klystron was measured; 22 °C of the temperature rise was observed at $P_0=46$ MW, 4 μ sec, 40 pps conditions. The temperature rise changes linearly to the average output power. It was found out that the window worked normally up to that rating. This window material is a high-density pure alumina of 99.7% (HA997) and has a very low $\tan\delta$ value. Recently, the failures of the klystron output window that uses another material have been observed, therefore the reliability of the tube window seems to be a key point regarding klystron performance. The evaluation of the window performance will be continued by operating it in the klystron gallery, where the evaluation of a SLED system is performed at the same time.

The application of a higher beam voltage than 310 kV is being planned in order to study the maximum capability of this tube in June using a newly-developed modulator and pulse-transformer. In the future a slight modification of the gun of the tube might be necessary since the average pulse current density of the cathode reaches 8A/cm².

IV. FOCUSING MAGNET AND PULSE TRANSFORMER

There are 41 permanent magnets and 7 electromagnets which are currently in use as focusing magnets of the klystrons [8]. The test results previously mentioned show that the maximum of the focusing magnetic field is about 1150 G. This exceeds the available maximum field of the permanent magnets presently used. The existing electromagnets are possible to be used. We can expect the low manufacturing costs for these magnets, since their sizes are small comparing with the focusing magnets for 60-MW klystrons. Figure 4 gives a size comparison with other focusing magnets to mate the tubes listed in Table 2.

It is necessary to reinforce the existing pulse transformer of which step-up ratio is 1 : 12. These pulse transformers are operated without a core reset bias. Therefore, the size of the cores has been chosen to be larger compared with the other pulse transformers that are operated at 270 kV [8]. We are changing the windings of the primary and secondary slightly to obtain a step-up ratio of 1 :13.5. We reuse the same cores,

so that the size of the primary winding frame must be made smaller in order to increase the insulating space between the

shape at 300 kV. (time scale 1 μ sec/div.) pulse transformer is about one third of the price of a newly manufactured one.

V. FUTURE WORK

A survey of the possible upgrade plans for the rf source of the B-Factory project will be continued this year. The final specifications of the rf systems will then be determined. Running data to evaluate the reliability will be accumulated by installing them in the klystron gallery and being used for routine operation.

The evaluation of 60-MW klystrons and the higher voltage operation of a PV3030A2 tube will be carried out in the near future. A window study and the necessary modification of the PV3030A2 will also be continued.

REFERENCES

- [1] I.Sato et al., "Injector for B-Factory" (in Japanese), Proc. of 17th Linac Meeting in Japan, pp.127-129, Sendai, Japan, 1992.
- [2] A.Enomoto et al., "Linac Upgrade Plan for the KEK B-Factory", presented in this conference.
- [3] S.Anami et al., "Upgrade of the PF Linac RF Source for the KEK B-Factory" (in Japanese), Proc. of 17th Linac Meeting in Japan, pp.177-179, Sendai, Japan, 1992.
- [4] T.Shidara et al., "Modulator Upgrade of the KEK 2.5 GeV Linac", presented in this conference.
- [5] K.Nakao et al., "Improvement of S-band Klystron and its Power Test" (in Japanese), Proc. of the 15th Linac Meeting in Japan, pp.239-241, Sapporo, Japan, 1990.
- [6] T.Shintake, "High Power Klystron Simulations Using FCI-Field Charge Interaction Code", KEK Report 90- 3, May, 1990.
- [7] S.Fukuda et al., "Simulation and Test of the KEK PV3030A2 S-band High Power Klystron" (in Japanese), Proc. of the 17th Linac Meeting in Japan, pp.162-164, Sendai, Japan, 1992.
- [8] S.Fukuda, "Status of the PF Klystron and Modulator", Proc. of 3rd Joint Symp. on Synchr. Rad. Source, pp.369-380, Pohan, Korea, 1992.

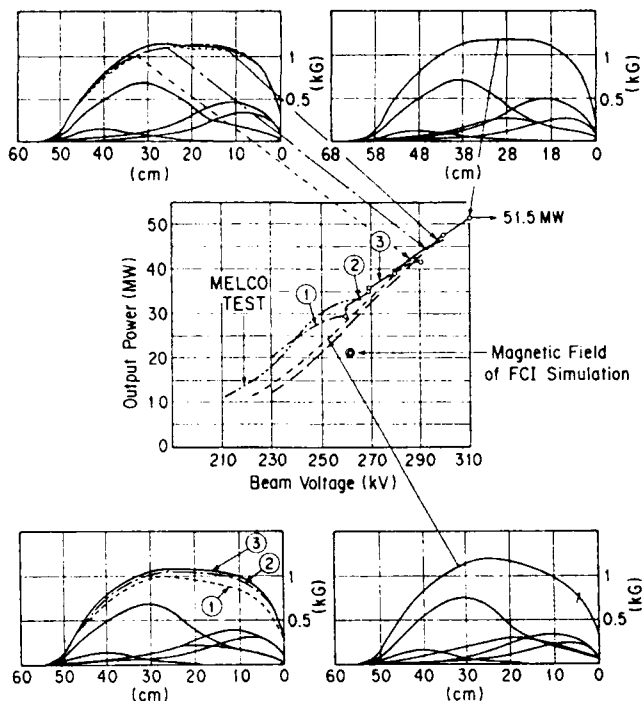


Fig.2 The output power of the PV3030A2 with the variation of the focusing magnetic field.

primary winding and the secondary winding. The overall size of the pulse transformer is not changed, therefore the pulse-transformer oil tank can also be reused by adding a height-extension flange. A capability of more than 330 kV voltage operation is expected due to these modifications. Operation of this pulse transformer with a suitable core reset bias has already been performed successfully. The cost to modify this

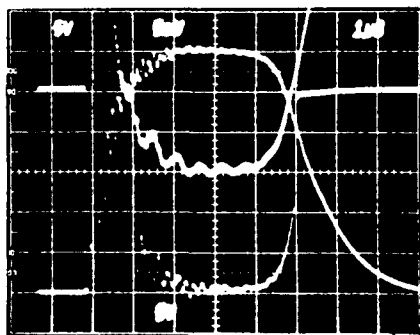


Fig.3 Beam current pulse(top trace), beam voltage pulse(middle), and rf pulse(bottom)

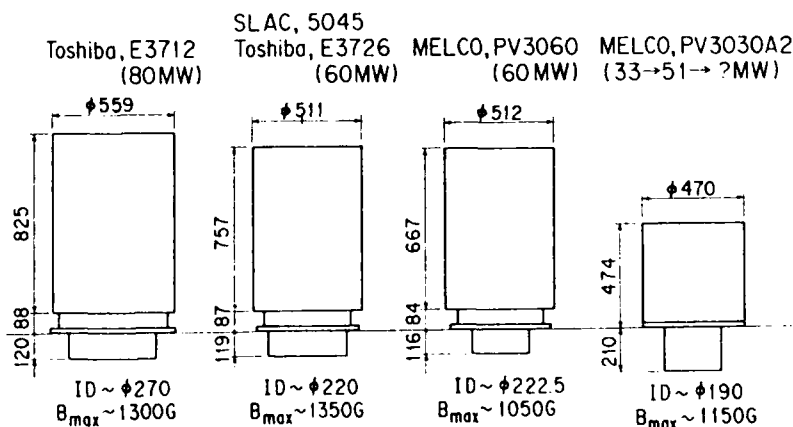


Fig.4 Various sizes of the focusing magnets.

HIGH-POWER RF PULSE COMPRESSION WITH SLED-II AT SLAC*

C. Nantista,[†] Z. D. Farkas, N. M. Kroll,[‡] T. L. Lavine, A. Menegat,
R. D. Ruth, S. G. Tantawi, A. E. Vlieks, and P. B. Wilson
Stanford Linear Accelerator Center, Stanford University, Stanford, CA 94309

Abstract

Increasing the peak rf power available from X-band microwave tubes by means of rf pulse compression is envisioned as a way of achieving the few-hundred-megawatt power levels needed to drive a next-generation linear collider with 50–100 MW klystrons. SLED-II is a method of pulse compression similar in principal to the SLED method currently in use on the SLC and the LEP injector linac. It utilizes low-loss resonant delay lines in place of the storage cavities of the latter. This produces the added benefit of a flat-topped output pulse. At SLAC, we have designed and constructed a prototype SLED-II pulse-compression system which operates in the circular TE₀₁ mode. It includes a circular-guide 3-dB coupler and other novel components. Low-power and initial high-power tests have been made, yielding a peak power multiplication of 4.8 at an efficiency of 40%. The system will be used in providing power for structure tests in the ASTA (Accelerator Structures Test Area) bunker [1]. An upgraded second prototype will have improved efficiency and will serve as a model for the pulse compression system of the NLCTA (Next Linear Collider Test Accelerator).

I. INTRODUCTION

Originally conceived by Fiebig and Schieblich [2] in 1988 and independently developed by Farkas, Wilson and Ruth [3] at SLAC, SLED-II is an extension of the SLED [4] pulse compression technique. SLED uses high-Q resonant cavities to store energy during most of the duration of the incoming pulse. One compressed-pulse-time from the end, the phase of the input is reversed. The field reflected from the coupling interface then adds constructively with the field emitted from the charged cavity, and the stored energy is extracted. The cavities are implemented in pairs and fed through a 3-dB coupler so that the outgoing power is directed away from the source. A distinctive feature of the SLED output is the exponential spike of the compressed pulse, characterized by the time constant of the cavities.

In SLED-II, the resonant cavities are replaced by long resonant delay lines. These can be lengths of low-loss waveguide, shorted at one end and iris-coupled to adjacent ports of a 3-dB coupler at the other. The length

of the delay lines is determined by the desired width of the compressed pulse and must be an integer number of guide half-wavelengths. As the wave emitted from the lines changes amplitude at discrete time intervals, given by the round-trip travel time, a flat output pulse can be produced. This makes SLED-II useful for the acceleration of long trains of bunches. It also increases intrinsic efficiency and reduces the peak-to-average field ratio in the compressed pulse.

II. THEORY

Let s be the iris reflection coefficient. Let t_d be the delay time given by $2L/v_g$, where L is the delay line length and v_g the group velocity in the line. Define an integer compression ratio C_r as the ratio of the input pulse length to t_d . Finally, let 2τ represent the round-trip field attenuation parameter. Then, during the time interval beginning at $t = nt_d$, the emitted field for constant input E_i can be expressed as

$$E_e(n) = \frac{(1 - s^2) e^{-2\tau}}{1 - se^{-2\tau}} (1 - s^n e^{-n2\tau}) E_i.$$

Superposition with the iris reflection yields the output

$$E_{out}(n) = E_e(n) - sE_i, \quad n = 0, 1, \dots, C_r - 2.$$

At time $t = (C_r - 1)t_d$, the phase of the input pulse is shifted by π , so that the waves add and we get a compressed output pulse of duration t_d with amplitude

$$E_p = E_{out}(C_r - 1) = E_e(C_r - 1) + sE_i \\ = \left\{ \frac{(1 - s^2) e^{-2\tau}}{1 - se^{-2\tau}} [1 - (se^{-2\tau})^{C_r - 1}] + s \right\} E_i. \quad (1)$$

For a given C_r and τ , s can be chosen to maximize E_p . The power gain and compression efficiency are

$$G = (E_p/E_i)^2, \quad \text{and} \quad \eta_{pc} = G/C_r. \quad (2)$$

The theoretical limit on G is nine. Realizable systems with finite compression ratios will have somewhat lower capabilities. There is an inherent inefficiency of this method due to power emerging before and after the compressed pulse. A table of the optimized iris reflection, ideal gain, and intrinsic efficiency η_i for several compression ratios is given in Table A. The effect of component losses can be considered as the efficiency η_c of round-trip reflected transmission through the coupler and an efficiency η_L due to the delay line loss. The latter is plotted versus round trip power transmission in the delay lines for different compression ratios in Figure 1. The efficiency of

* Work supported by the U.S. Department of Energy under contract DE-AC03-76SF00515 and grants DE-FG03-92ER40759 and DE-FG03-92ER40695.

[†] Visitor from Department of Physics, UCLA, Los Angeles, CA 90024.

[‡] Also Department of Physics, UCSD, La Jolla, CA 92093.

pulse compression can then be thought of as

$$\eta_{pc} = \eta_i \eta_c \eta_L. \quad (3)$$

Table A

C_r	s_{opt}	G_{ideal}	η_i
2	.500	1.56	.781
3	.548	2.66	.887
4	.607	3.44	.860
6	.685	4.48	.746
8	.733	5.15	.644
10	.767	5.62	.562
12	.792	5.98	.499

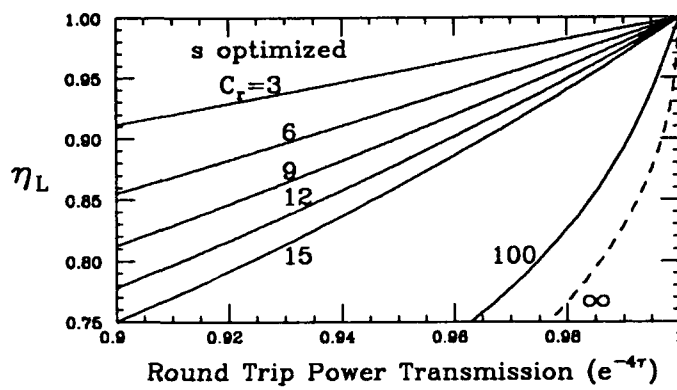


Figure 1. Compression efficiency of delay lines with optimized s .

III. COMPONENTS

The schematic layout of our SLED-II system is shown in Figure 2. The frequency of operation is 11.424 GHz. Overmoded waveguide is used to keep transmission loss down and to achieve low-loss high-power delay lines. The TE_{01} mode in circular guide was chosen for its unpolarized nature as well as for the fact that its attenuation constant drops faster with increasing guide radius than that of any other low mode, quickly becoming the smallest.

As the klystron output and load or structure input utilize rectangular (WR-90) waveguide in the fundamental TE_{10} mode, efficient mode transducers between this and our circular mode are a necessary part of the system. Rather than standard Marić transducers, we use a compact design based on an old KU-band device and developed at SLAC. This component is described in detail in reference [5].

The TE_{01} 3-dB coupler was also designed and built at SLAC.[6] It is basically a copper block, about a meter in length, with two closely spaced 1.75"-diameter bores

connected by a longitudinal coupling slot. The slot is introduced and removed adiabatically to preserve mode purity. The proximity of the coupler guides necessitates circular waveguide offsets to further separate the axes and allow connection to other components. These were designed using generalized telegraphist's equations to minimize mode conversion. This prototype coupler requires its own vacuum manifold because it was machined in halves and bolted together.

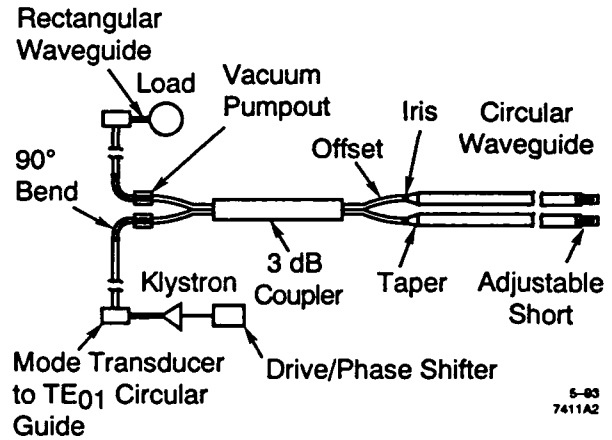


Figure 2. Schematic of high-power SLED-II system.

The irises were designed by the KKY method as described in reference [7]. They are inserted before the tapers where excited higher order TE_{0n} modes are cut off. A reflection coefficient of about 0.8 was chosen in anticipation of running with a compression ratio of 12 for structure tests. The irises were machined from stainless steel flanges and copper plated for improved conductivity.

The delay lines are each composed of about 33' of OFHC copper circular waveguide. Non-linear tapers between the 1.75" diameter used in the rest of the system and the 2.81" diameter (for reduced wall loss) of the delay lines were provided by General Atomics, San Diego, CA. The same company provided the corrugated 90° bends used in the power transfer lines. Vacuum feedthroughs at the ends of the delay lines allow us to electronically tune aluminum shorting plungers. This is done via MDC stepping motors controlled with a PC. Finally, the system is evacuated via pump-out vacuum manifolds inside which the waveguide is interrupted by 6" stacks of 15 carefully aligned copper rings with support rods recessed from the inner diameter. The gaps do not disturb the TE_{01} mode, as it involves no longitudinal currents.

IV. EXPERIMENTAL RESULTS

Non-vacuum tests were made first, with power levels of a few hundred milliwatts. The shorts were placed on the offsets to measure the transmission loss from the input port to the final output port of the 3-dB coupler.

The round-trip loss of the coupler with offsets was determined to be approximately $7.5\% \pm 1\%$ ($\eta_c \approx 0.92$). The iris reflection coefficients were calculated from power measurements to be 0.805 ± 0.005 . The loss per round trip in either delay line was determined from the steady state backwards wave to be about $4.6\% \pm 0.3\%$, and the delay time confirmed to be 75ns. The delay line waveguide, taken from an old experiment, has imperfections, resulting in less-than-ideal performance.

The SLED-II system was then assembled with the mode transducers on the pump-outs and a PSK (phase shift keyer) in our drive system. The shorts were adjusted differentially to minimize reflected power and together to maximize compressed power. The power gain was measured for different compression ratios as plotted in Figure 3. (Note: s not optimized for each C_r .) The measurements are consistent with the measured component losses, as shown by the solid curve. An output waveform recorded for $C_r = 12$ is shown in Figure 4.

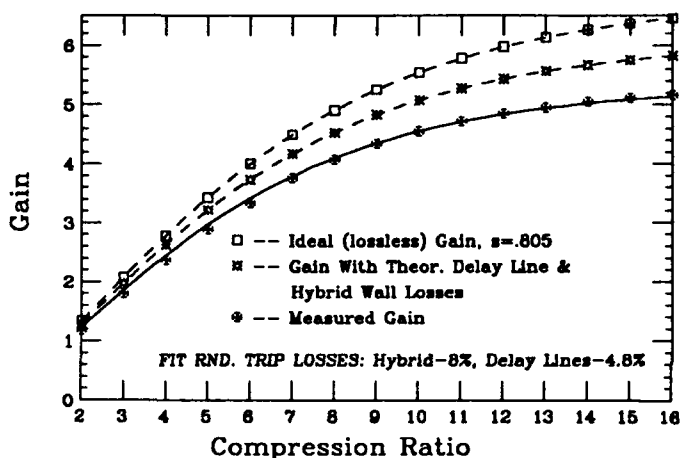


Figure 3. Measured performance of SLED-II versus ideal. The solid line fit is expected for the indicated component losses.

The input was then connected to an X-band klystron via a run composed mostly of 1.75" circular guide as indicated in Figure 2., and the output was connected to a high-power water load. The system was pumped down to the 10^{-8} Torr range and successfully run with power levels reaching 16 MW. This power level was limited by the time we had for rf processing, due to competing programs. We expect to run at considerably higher power in the near future.

V. FUTURE MODIFICATIONS

In the coming months, we plan to overhaul our SLED-II system, incorporating improved components. The 2.81" diameter waveguide of the delay lines will be replaced by 4.75" guide, whose attenuation constant is a factor of five less. With careful joint connection, this should significantly reduce their loss, despite our doubling

their length to test a longer fill-time structure. New shorting plungers will contact the wall in places to maintain better perpendicularity with the guide axis. The 3-dB coupler will be replaced either by a more compact, better machined, vacuum-brazed model, or by a rectangular waveguide coupler attached to four of our successful mode transducers. The 90° bends may also be replaced by rectangular guide and mode transducers. Finally, new pumpout sections will be engineered and possibly be included in the delay lines. It is hoped that this second prototype will have adequate efficiency to meet the goals of a SLED-II system for the NLCTA [8].

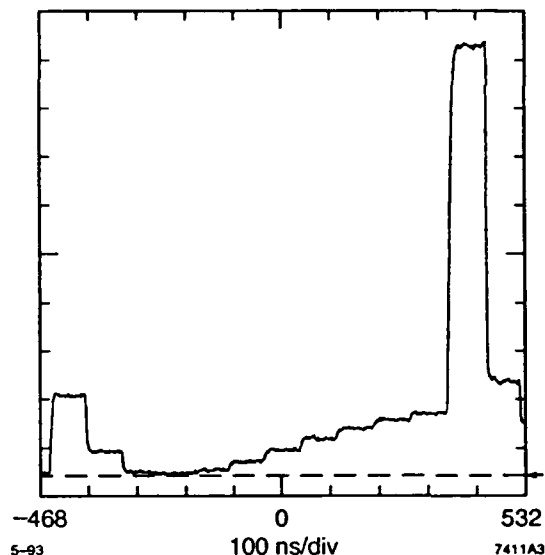


Figure 4. Output waveform for $C_r = 12$.

VI. REFERENCES

- [1] A. E. Vlieks, et al., "Accelerator and RF System Development for NLC," these proceedings; SLAC-PUB-6148.
- [2] A. Fiebig and C. Schlieblich, "A Radiofrequency Pulse Compressor for Square Output Pulses," European Particle Accel. Conf., Rome, Italy, June 1988.
- [3] P. B. Wilson, et al., "SLED II: A New Method of RF Pulse Compression," Linear Accel. Conf., Albuquerque, NM, September 1990; SLAC-PUB-5330.
- [4] Z. D. Farkas, et al., "SLED: A Method of Doubling SLAC's Energy," presented at 9th International Conf. on High Energy Accel., Stanford, CA, May 1974; SLAC-PUB-1453.
- [5] H. A. Hoag et al., "Flower-Petal Mode Converter for NLC," these proceedings; SLAC-PUB-6182.
- [6] N. M. Kroll, et al., "A High Power SLED-II Pulse Compression System," 3rd European Particle Accel. Conf., Berlin, Germany, March 1992; SLAC-PUB-5782.
- [7] R. Jones, et al., "Applications and Comparisons of Methods for Computing the S Matrix of 2-Ports," these proceedings; SLAC-PUB-6142.
- [8] R. D. Ruth, "The Next Linear Collider Test Accelerator," these proceedings.

Rigid-Beam Model of a High-Efficiency Magnicon

Daniel E. Rees and Paul J. Tallerico
Los Alamos National Laboratory
P.O. Box 1663, Los Alamos, NM 87545

Stanley J. Humphries, Jr.
University of New Mexico
Albuquerque, NM 87131

Abstract

The magnicon is a new type of high-efficiency deflection-modulated amplifier developed at the Institute of Nuclear Physics in Novosibirsk, Russia. The prototype pulsed magnicon achieved an output power of 2.4 MW and an efficiency of 73% at 915 MHz. This paper presents the results of a rigid-beam model for a 700-MHz, 2.5-MW 82%-efficient magnicon. The rigid-beam model allows for characterization of the beam dynamics by tracking only a single electron. The magnicon design presented consists of a drive cavity; passive cavities; a pi-mode, coupled-deflection cavity; and an output cavity. It represents an optimized design. The model is fully self-consistent, and this paper will present the details of the model and calculated performance of a 2.5-MW magnicon.

I. INTRODUCTION

The magnicon is a descendant of the gyrocon [1], a deflection-modulated amplifier. Like the gyrocon, the magnicon consists of an electron gun, a deflection cavity, possible passive intermediate cavities, and an output cavity. In both devices, the deflection cavities are TM_{110} mode. The magnicon improves on the gyrocon in two ways: it uses a confining magnetic field to improve gain and improve the electron dynamics, and it substitutes a cusp field for a deflection field in the beam transport to the output cavity. The use of the magnetized beam in the magnicon makes the beam's deflection more circular and even reduces the beam loading in the cavities, as predicted by Nezhevenko [2]. With a low-emittance input beam, and using high voltages to minimize beam spread, the magnicon appears to operate at frequencies as high as 11 GHz, but the device is certainly easier to build for operation at frequencies under 1 GHz. Magnicons operating at high voltages and at many GHz are being developed both in the U.S. [3] and in Russia, primarily as the RF source for the Next Linear Collider. However, the experimental evidence to date [4] indicates that the electron dynamics in the magnicon are complicated, and it has been difficult to verify the predictions of magnicon computer models.

For the past two years, we have been developing a computer model [5] of the magnicon. This model is fully three-dimensional, relativistic, and self-consistent, although space-charge forces are neglected. The goal of the model is to show that high-efficiency magnicons operating at frequencies below 1 GHz are better than competing RF amplifiers for high-power, CW accelerator applications. A

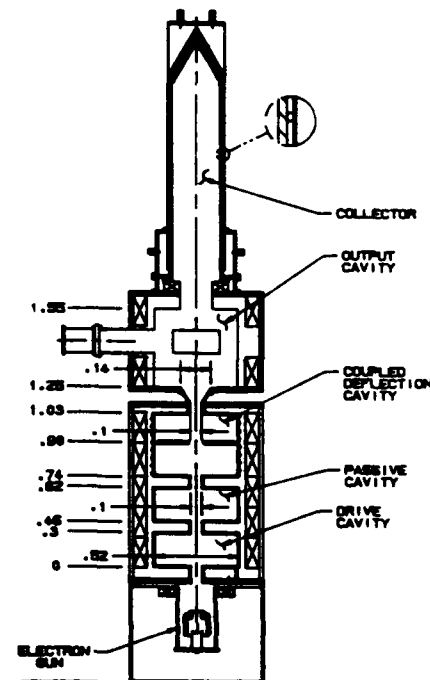


Figure 1. Magnicon architecture.

second goal of the model is to confirm that a multi-megawatt magnicon may operate at a reasonable voltage (below 180 kV) and still maintain its operating advantages over competing generators. The computer model is much smaller than the fully three-dimensional codes that account for space-charge, such as ISIS [6], but the intent is to include all the essential physics and develop a design code for the magnicon that can run on smaller computers. A novel method of assuring self consistency and energy balance is also presented.

II. ENERGY-BALANCE APPROACH TO SELF-CONSISTENT SOLUTIONS

The energy-balance approach to calculating the self-consistent solution for cavity amplitude and phase follows these steps:

1. Select an initial value for cavity field amplitude.
2. Determine the phase that extracts the most power from the beam. This phase is the self-consistent cavity phase.
3. Calculate the power dissipated in the cavity walls for the current value of cavity field amplitude.
4. If the power dissipated in the cavity walls is equal to the power provided by the beam, then the cavity field

amplitude is the self-consistent solution for the cavity amplitude. With the self-consistent phase from Step 2, the self-consistent cavity field has been determined.

5. If the conditions of energy balance are not satisfied, then the cavity field amplitude estimate is updated and the process repeats, starting at Step 2.

A unique aspect of the nature of the beam/field interaction in the magnicon is used to simplify implementation of the energy balance approach to self-consistent cavity field determination. In the beam-driven magnicon cavities, under the rigid beam assumption of zero radius in the steady state, each electron sees exactly the same RF fields. This results from the fact that both the entrance vector of the beam and the cavity fields are rotating at the RF frequency. Thus, each subsequent particle that enters the cavity has an entrance vector that has shifted. But the RF fields have shifted by the same amount. Therefore, the energy given up by each electron in the beam during the transit of the cavity is constant. Because each electron sees exactly the same RF fields while in the cavity, a single electron trajectory can be used to calculate the self-consistent fields rather than an entire electron beam, whose longitudinal length exceeds the cavity length. In addition, because the energy extracted from each electron as it passes through the cavity is a constant in time and is proportional to the energy given up by the beam in the cavity at any moment in time, the time-averaged value of power provided by the beam is also a constant and proportional to the energy provided by a single electron as it crosses the cavity. Thus, simply equating the energy lost by a single electron as it crosses the cavity to the time-averaged power dissipated in the walls provides the basis for the self-consistent solution.

The initial estimate at cavity field amplitude should be as close as possible to the self-consistent amplitude in order to minimize the time required for the algorithm to converge on the self-consistent solution.

The phase that extracts the most energy from the beam is determined from a component of the conservation of energy equation. From [7], the real power supplied by the beam is given by

$$P_s = - \iiint_{\text{Volume}} \mathbf{E} \cdot \mathbf{J} dV, \quad (1)$$

where \mathbf{E} is the instantaneous electric field and \mathbf{J} is the instantaneous current density. For the rigid-beam model, \mathbf{J} is represented, according to [8], by

$$\mathbf{J} = I_s \delta(x - x_s) \delta(y - y_s) \quad (2)$$

Substituting Eq. (2) into Eq. (1) results in

$$P_s = - \frac{1}{2} \int \mathbf{E}(x, y, z, t) I_s \delta(x - x_s) \delta(y - y_s) dx dy dz \quad (3)$$

This equation is evaluated numerically as particles are advanced through the beam-driven cavity. As an example, for any given cavity-field amplitude and phase, the electron is advanced through the cavity by a constant time step. The

instantaneous electric field value at the center of a time step is multiplied by the change in z , Δz , and the beam current. The variation in Δz for the constant time step weights the numerical integral. For example, as longitudinal velocity is transferred into the transverse direction, Δz decreases, lessening the contribution to the numerical integral. This is equivalent to a numerical integration with a constant step in Δz , with the beam current weighted by the ratio of present longitudinal velocity to initial longitudinal velocity. The numerical integration can be represented by

$$P_s = - \frac{1}{2} \sum_k I_s \mathbf{E}_k \Delta z_k, \quad (4)$$

where k represents the cavity transit time divided by the constant time step.

The supplied power calculated in Eq. (4) is compared to the power dissipated in the cavity walls given by [9] as

$$P_d = R_s \left(\frac{E_s}{\eta} \right)^2 \pi J_0^2(\chi_{11}) [a^2 + ah]. \quad (5)$$

III. RIGID-BEAM MODEL RESULTS

The magnicon architecture modeled is shown in Figure 1, which also includes the dimensions of the magnicon geometry. For our modeling, we used a beam voltage of 170 kV, a beam current of 18 A, a frequency of 700 MHz, and a deflection-system focusing field resulting in a deflection-system cyclotron frequency 1.4 times the RF frequency. The parameters for the model were derived from [10]. With the rigid-beam assumption, this model results in a magnicon that produces over 2.8-MW of RF power at an efficiency in excess of 90%. (Of course, the efficiency with a finite beam size would be lower and will be the focus of future work..)

Figures 2, 3, 4, 5, and 6 illustrate the results of the magnicon modeling. Figure 2 shows the radial displacement as a function of longitudinal distance along the magnicon. Figure 3 and 4 show the radial velocity as a function of longitudinal distance. Figure 6 is a view looking at the particle trajectories along the axis of the magnicon, and Figure 5 shows the variation in gamma and v_z as a function of longitudinal position.

IV. CONCLUSION

We have developed a self-consistent approach to calculating magnicon passive- and output-cavity fields. This approach has been used to determine high-efficiency magnicon geometries using a rigid-beam approximation. Geometries that provide a conversion efficiency in excess of 80% have been obtained. The next step in the analysis is to extend the approach to a model with finite beam size and evaluate the performance sensitivity of these geometries to finite beam width.

References

- [1] G.I. Budker, E.V. Karliner, et al, "The Gyrocon—An Efficient, Relativistic, High-Power VHF Generator, Particle Accelerator," *Particle Accelerators* 10, pp.41-60 (1979).

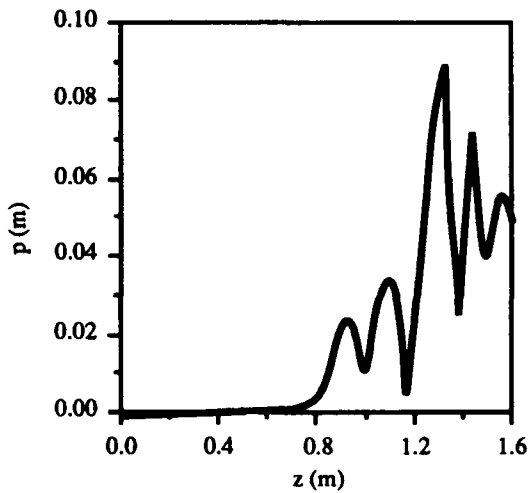


Figure 2. Radial displacement of single particle.

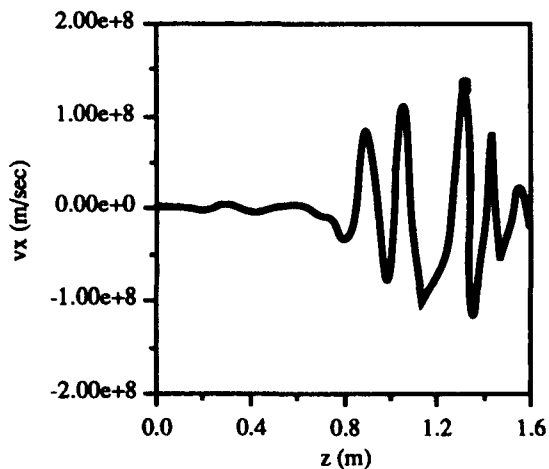


Figure 3. X-directed component of radial velocity.

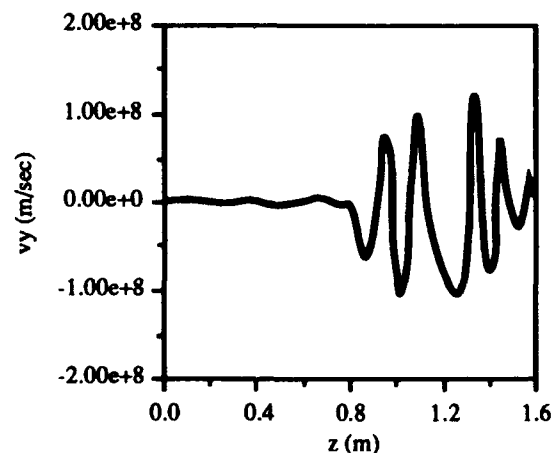


Figure 4. Y-directed component of radial velocity.

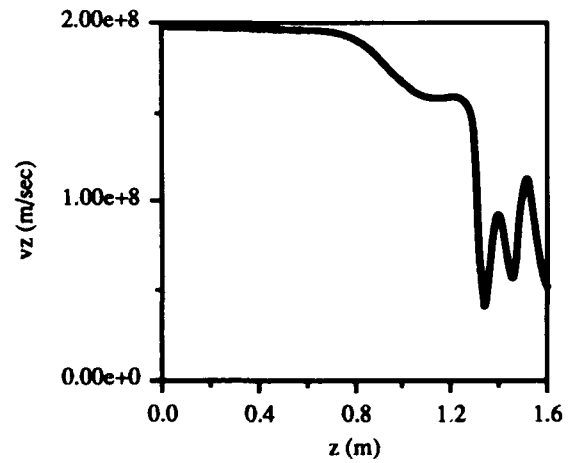


Figure 5. Variation of v_z .

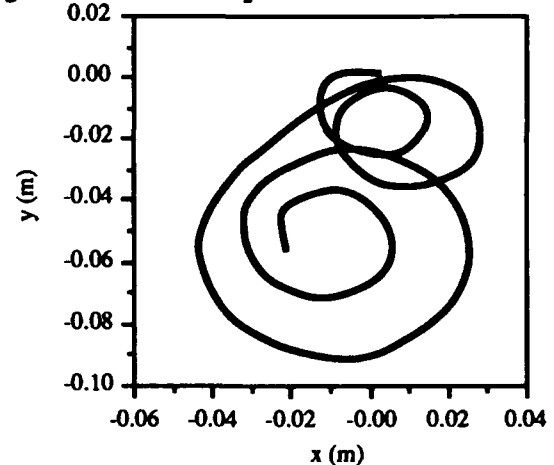


Figure 6. Top view of particle trajectories.

- [2] E.V. Karlner, O. Nezhevenko, et al., "The Magnicon: An Advanced Version of the Gyrocon," *Nucl. Instr. & Methods A* **269**, 459-474 (1988).
- [3] W.M. Manheimer, "Theory and Conceptual Design of a High-Power, Highly Efficient Magnicon at 10 and 20 GHz," *IEEE Trans. Plasma Sci.* **18** (3), (1990).
- [4] B. Hafizi et al, "Analysis of the Deflection System for a Magnicon-Field-Immersed Magnicon Amplifier," *IEEE Trans. Plasma Sci.* **20** (3), p. 232 (1992).
- [5] D. Rees and P. Tallerico, "Fields and Trajectories in the Magnicon," in *IEEE Proc. of the 1992 Particle Accelerator Conference* (San Francisco, Calif., 1992), pp. 640-642.
- [6] G. Gisler, M.E. Jones, and C. M. Snell, "ISIS: A New Code for PIC Plasma Simulation," *Bull. Am. Phys.Soc.* **29**, p. 1208 (1984).
- [7] R.E. Collin, *Foundations for Microwave Engineering*, McGraw-Hill, New York, 1966.
- [8] Stanley Humphries, Jr., "Numerical Studies of the Scantron Microwave Amplifier," accepted for publication in *IEEE Trans. Plasma Sci.*
- [9] D. Rees, "Analysis of High-Efficiency Magnicon Amplifier," Ph.D. thesis, University of New Mexico, 1993.
- [10] Private conversation with O. Nezhevenko, Feb. 1992.

High Power Operation Results of the X-Band SLED System

Shuichi Tokumoto, Hajime Mizuno
KEK, National Laboratory for High Energy Physics
1-1 Oho, Tsukuba-shi, Ibaraki-ken, 305 Japan

Osamu Azuma
Ishikawajima-Harima Heavy Industries Co., Ltd.
Toyosu 3-1-15, Koutou-ku, Tokyo, 135 Japan

Abstract

This report describes the results of high power operations of the X-band (11.424 GHz) SLED system. After 32 hours of 5 pps processing, the peak output reached to 59 MW with the RF input pulse of 15 MW with 470 ns duration. Up to this power level the processing had been carried out smoothly, and no serious discharge was observed. Later this system was utilized as an RF pulse compression method for the high power test of an accelerating structure.

I. INTRODUCTION

Supplying RF pulses with high peak power of over 100 MW with 100 ns duration, it will be possible to produce very high accelerating gradient of 100 MV/m in the X-band (11.424 GHz) main linac of JLC. For realizing this plan, a lot of R&D works on microwave tubes with high output power of 100-150 MW have been carried out at KEK [1]. Recently, high output power of 80 MW with 50 ns duration was provided by the newest klystron. Side by side with these efforts, development of some RF components for high power use has been also carried out. It becomes necessary to test critical components by using high RF power of around 100 MW. The RF pulse compression is very useful as well as traveling wave resonator to generate such a high power for testing a critical component [2]. Using these it is possible to boost a relatively low power pulse with relatively long pulse length to a shorter pulse with higher peak power. The principle of operation of the RF pulse compression is reported elsewhere [3,4,5]. As a first step, the SLED system was chosen for high power test bench where the RF windows, the waveguide system including power monitor and matched load would be examined with very high peak power enhanced an output of klystron.

The SLED system was originally developed in S-band to increase the beam energy of the SLAC linac [3].

The advantage of the SLED are:

- 1) the assembly comprising a 3-dB hybrid and a couple of pillbox cavities were simple and compact made, so as expected to sustain high electric stress.
- 2) it is easy to reinstall itself in any high power RF circuit.

At the high power test-bench, in the first place, an output power of 0.5-15 MW from 30 MW class klystron (XB-50K) was supplied into the SLED assembly so as to examine its performance under high electric stress.

Maximum amplitude and decay time are depend on the Q-value and the coupling coefficient β of the cavity. The peak voltage is obtained at time t_1 , that is the charging time before the phase was reversed, and the theoretically calculated value for the case $t_1=400$ ns with using measured value by low level RF $\beta=4.5$, $Q_0=52000$, is 2.28 times as high as the klystron output voltage (5.2 times as high in the power). As already reported [6], the experiment with low level RF has been successfully carried out and the obtained result showed good agreement with the one calculated theoretically. Here, we report on fabrication and high power test result of the X-band SLED system.

II. COMPONENTS

A. The TE-015 cavities

Room temperature cavities made of copper (O.F.H.C.) were used as pillbox cavities for the assembly. The TE015 mode was chosen as the S-band SLED system of the SLAC. The Q-value of the each cavity were measured as 52000 and 52300, respectively. To lower the resonant frequency of the TM115 mode, a groove was circularly cut in one end-plate, also following the model of the SLAC. This groove, which was width of 1.5 mm and depth of 1.5 mm, shifted the center frequency of the TM115 mode nearly 45 MHz with no influence on the TE015 mode. A coupling aperture was drilled through the other end-plate. That was a hole, 8.2 mm in diameter with 1.5 mm thick, and finished in a round shape to avoid the breakdown. The measured coupling coefficient β of the each cavity were 4.55 and 4.57, respectively.

B. The 3-dB coupler

As the 3-dB hybrid of the assembly, the Riblet short-slot coupler made with wire-cutting method was employed. Through this coupler an output of the klystron is guided to a couple of cavities, and waves from the each cavity are combined so as to add and transmitted to the load as well known. The value of coupling depends on the width and the length of the coupling region. For 3-dB coupling, they were designed 36.0 mm and 26.6 mm, respectively. A couple of posts made of copper, called as capacitive dome, were attached for fine tuning at the center of top and bottom walls of coupling region. Measured characteristics of the coupler are listed in Table 1.

Table 1
Measured characteristics of the 3-dB coupler

COUPLING (MAIN LINE)	-3.16 DB
(SUB LINE)	-3.14 DB
PHASE DIFFERENCE	96.1 DEG
ISOLATION	-25.0 DB
INPUT VSWR	1.09
OUTPUT VSWR	1.15

This type of 3-dB coupler has relatively simple structure enough to sustain high electric stress, but actual fabrication of the model for high power use is not so easy. In this time, the microwave transmission line including the coupling region was made by cutting away the shape accurately by wire from a copper block (300 l x 70 w x 10.15 h) as shown in Fig.1, and then a couple of copper plates were brazed in a hydrogen furnace on each side of that block. Finally, four connecting flanges were attached on each port.

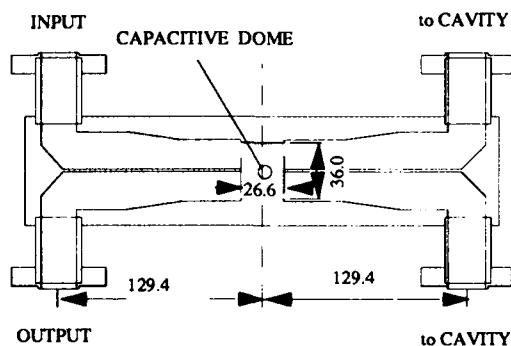


Figure 1. A cross section view of the 3-dB hybrid.

The wire-cut surface was finished within 6 microns enough to avoid serious breakdown under high electric field. A sample of measured roughness after wire-cutting on the test piece is illustrated in Fig.2.

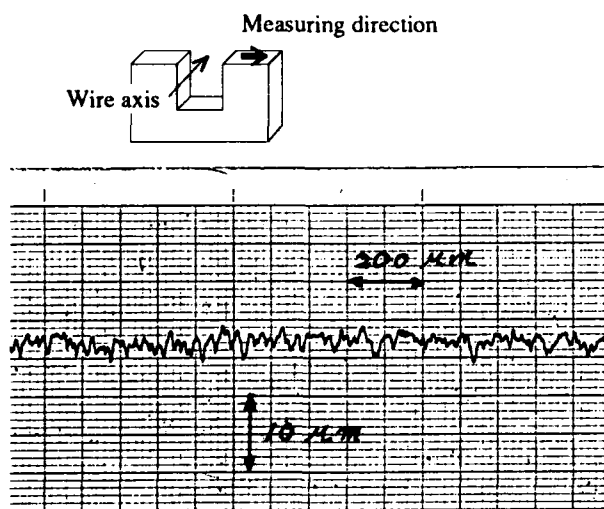


Figure 2. Measured roughness of surface after wire-cutting.

III. TEST RESULTS

An experiment with low level RF has been successfully carried out as already reported. Peak RF power enhanced by the SLED reached almost five times as high as input RF power of which pulse width was 500 ns with the phase reversed in the rear of 100 ns. That was nearly 90% of the calculated value, so it was found that the assembly was well fabricated for practical use at the test-bench. The phase control system of the klystron input pulse was also successfully made for use. The measured time for reversing phase of input pulse was less than 3 ns. The design and fabrication of this circuit are described in detail in reference [7].

In the first aging run, high RF output of 0.5-15 MW with repetition rate 5 pps of the 30 MW class klystron (XB-50K) was supplied to the SLED system. This klystron had been operated for long time and was expected to generate relatively long pulse with high RF power. The pulse width of the klystron output was adjusted 470 ns with keeping flatness of the pulse including reversal phase time of 70 ns in the rear. Some interlock systems were prepared for protect the assembly from serious damage caused by discharge around the coupling iris of the cavities or inside of the 3-dB coupler. When reflected pulse with high peak power or abrupt out-gassing were detected, they worked so as to stop the operation. The output power of the klystron was raised step by step with careful observation on the RF ceramic window set at an output port of the klystron and on the vacuum pressure in the RF transmission line including the SLED assembly. In thirty-two hours operation, an output of the SLED was reached to 59 MW smoothly which was 4 times as high as klystron output of 15 MW. The peak power obtained in high power operation was, however, slightly lower than that expected from the test result with low level RF. This was influenced by following phenomena that the time of reversing the phase of the klystron output was longer (more than 10 ns) and reflected wave from SLED was added to the output of the klystron. Observed output signals are shown in Fig.3 and Fig.4.

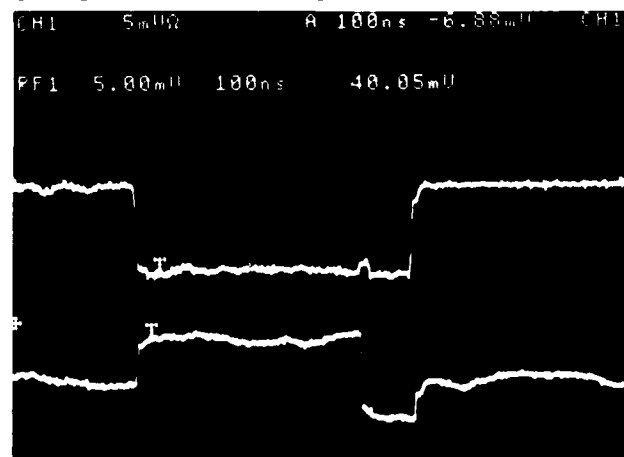


Figure 3. Observed output signals of the 1 kW preamplifier. Top: Output of the 1 kW preamplifier. Bottom: Observed phase signal of the pulse.

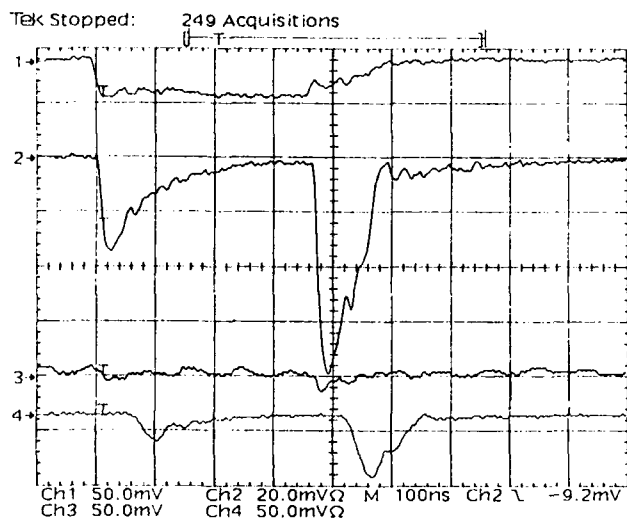


Figure 4. Observed signals at high gradient experiment.
 1: Output power of 10 MW of the klystron.
 2: Output power of 37 MW of the SLED.
 3: Reflected power from the test structure.
 4: Transmitted power through the test structure.

To the output power level of almost 60 MW, the aging run had been carried out smoothly as shown in Fig.5.

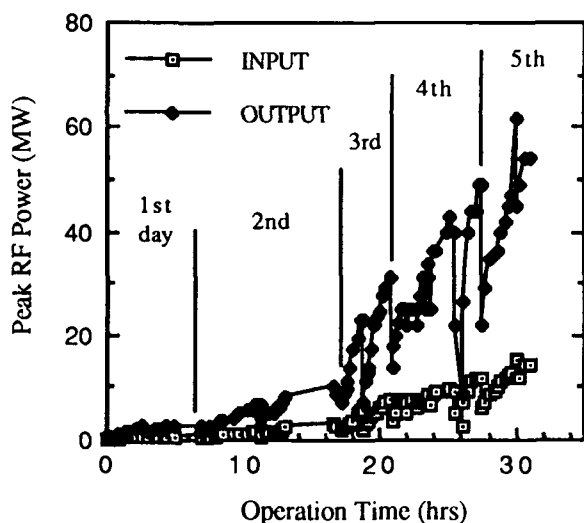


Figure 5. An aging result of the X-band SLED

The SLED system was pumped by ion pumps in the high power RF test-bench. Without RF input, the vacuum pressure reached down to 10^{-6} Pa range in three days and stay under this range. In the high power aging run, due to RF discharge, the vacuum pressure frequently rose up to 3×10^{-5} Pa which was previously set as the threshold value to stop the klystron output. With proceeding the conditioning of the SLED, the vacuum pressure at the same RF input decreased.

After this aging process, the SLED assembly was installed in the high gradient test system for accelerating structures. The same klystron was used as an RF source. The accelerating

structure had been operated with high RF power of less than 15 MW in the previous aging run. Finally, an output pulse of the SLED system was successfully introduced into the structure without serious breakdown up to 50 MW peak power. At that time, the power enhancement by the SLED looked lower as well as the rear part of the klystron output pulse during 70 ns, when the phase of input pulse was reversed. These might be caused by the reflected RF power from the structure and the noise around power measuring system. Further investigation is necessary for these problems.

IV. CONCLUSION

Construction of the X-band SLED for high power use was successfully completed. The result of the SLED operation with low level RF gave good agreement with the value which had been obtained by theoretical calculation in the case of $\beta=4.5$, $Q_0=52000$, $t_1=400$ ns and $t_2=500$ ns. That shows the cavities and the 3-dB coupler has been well fabricated for practical use.

In high power aging process of 32 hours, peak output of 59 MW became available without any serious problems. The results of high gradient experiment show that the SLED is useful for high power experiment of critical RF components.

Acknowledgement

The authors wish to acknowledge Mr. Odagiri for operating the high-power RF system, including high-power klystron. The authors are grateful to Dr. Higo, Dr. Yamamoto, and Dr. Taniuchi at KEK, Dr. I. Willson at CERN for valuable discussions and their supports in this high gradient experiment.

V. REFERENCES

- [1] H.Mizuno, J.Odagiri, T.Higo, H. Yonezawa and N.Yamaguchi, "X-band Klystrons for Japan Linear Collider", Proc. 1992 Linear Accelerator Conference, AECL-10728, p.127, (1992)
- [2] Z.D.Farkas, T.L.Lavine, A.Menegat, R.H.Miller, C.Nantista, G.Spalek and P.B.Willson, "Radio Frequency Pulse Compression Experiments at SLAC", SLAC-PUB-5409, (1991)
- [3] Z.D.Farkas, H.A.Hogg, G.A.Loew and P.B.Willson, "SLED: A Method of Doubling SLAC's Energy", SLAC-PUB-1453, (1974)
- [4] P.B.Willson, Z.D.Farkas, and R. D. Ruth, "SLED II: A New Method of RF Pulse Compression", Proc. 1990 Linear Accelerator Conference, SLAC-PUB-5330, (1990)
- [5] Z.D.Farkas, "Binary Peak Power Multiplier and its Application to Linear Accelerator Design", IEEE Trans. MTT-34, p. 1036, (1986)
- [6] S.Tokumoto, H. Mizuno and O. Azuma, "X-band (11.424 GHz) SLED System", Proc. 1992 Linear Accelerator Conference, AECL-10728, p.133, (1992)
- [7] S.Araki and Y.Otake, "Development of low-power RF components for JLC (II)", Proc.16th Linear Acc. Meeting in Japan, p. 97, (1991)

Automated Testing of a High-Power RF Microwave Tube*

Andrew Young, Daniel E. Rees, and Anthony Vergamini

Los Alamos National Laboratory

P.O. Box 1663, Los Alamos, NM 87545

Abstract

This paper describes an automated procedure for testing the high-power klystron amplifiers used in the Ground Test Accelerator (GTA). To verify klystron performance, we have developed an automated test system using data-acquisition and control programs based on LabVIEW™, a program that can communicate with both an Allen-Bradley PLC5/15 controller over RS232 interface and with other devices that use the GPIB interface.

Three automated tests were developed and performed on the high-power klystron: swept-frequency, power-transfer, and VSWR. This paper describes the tests performed, presents test data on the GTA klystrons, provides block diagrams of the automated test facility, and characterizes all the capabilities for the automated test system. This test facility is being used by the GTA program to fully characterize the klystron amplifiers before they are commissioned.

I. INTRODUCTION

Shown in Figure 1 are the equipment racks of the high-power test stand, which uses the LabVIEW data-acquisition system because of its flexibility in programming and its ability to communicate with a wide variety of other controllers or instruments. LabVIEW is a virtual-instrument (VI) engineer workbench. LabVIEW itself provides some VIs and others can be created by a programmer using C language. LabVIEW communicates through a serial-port to RS232 devices such as Allen-Bradley programmable controller and through a general-purpose interface bus (GPIB) to devices such as power meters. LabVIEW also has analog ports that can send a 0 to 10-V signal to an external device, such as a switch. The high-power test stand uses LabVIEW to monitor and record the status of safety interlocks and input/output parameters.

Currently, we perform three tests on the high-power amplifiers: swept frequency, power transfer, and voltage standing-wave ratio (VSWR). Each of these tests is carried out by a LabVIEW VI, which uses many other VIs that are integrated into the program when an operator initiates the main VI. The program then records data and fault conditions. Using these VIs, we have fully automated the test stand.

*Work supported and funded by the U.S. Department of Defense, Army Strategic Defense Command, under the auspices of the U.S. Department of Energy.

Figure 1 shows three test-stand equipment racks that can operate two high-power RF amplifiers. The rack on the left contains the Allen-Bradley Programmable Logic Controller (PLC) input/output cards and the display monitor, which is situated at the top of the rack. Just below the PLC is the AC distribution chassis, which contains the circuitry for the filaments and the focus coils. The next chassis contains the water-flow monitors for the high-power RF load. The next three chassis contain the solid-state RF driver amplifiers and the measuring circuitry. The middle rack contains the Vacion pumps, high-voltage power supply interlock circuitry, acoustic arc-detector circuitry, and a stack of solenoid supplies. The rack on the right contains all the instrumentation for the three tests. At the top of the rack are the stepper-motor controllers for the VSWR test. Three power meters permit the measurement of forward and reflected input power, forward and reflected output power, and forward and reflected power at the load. The microprocessor used in the test stand is a dedicated Macintosh IIfx.



Figure 1. Equipment racks for the high-power test stand.

II. HIGH-POWER AMPLIFIER TESTS

All the data files generated by the three test have a generic format. The data file contains the test name, the time and date, the klystron tube's serial number, a number that indicates the cathode current setting, and a suffix that indicates the test type (-px=power transfer, -fs=swept frequency, and -vswr=Reike diagram). Along with the title information, the data file contains information on the cathode voltage (VC), modulated anode voltage (VM), cathode current

(IC), and modulated anode current (IM), the filament voltage (FV) and current (FI), focus coil voltage (FCV) and current (FCI), operating frequency (F), pulse width (PW), and pulse repetition frequency (PRF). A typical header for this data is shown in Table 1 along with the units of measurement.

VC	VM	IC	IM	FV	FI	FCV	FCI	F	PW	PRF
kV	kV	A	mA	V	A	V	A	MHz	ms	Hz

Table 1. Typical data file header.

In addition, by using Cricket Graph as a post-processor tool, we were able to generate graphs at the conclusion of each test. This allowed us to quickly determine if the test was completed without a fault.

Power-transfer test

The power-transfer test allows us to calculate the efficiency, the gain, and the saturated power of the amplifier at different operating conditions. The operating conditions selected involved a fixed cathode voltage and three different cathode currents. The cathode voltage, filament voltage, filament current, solenoid focus coil voltage, and solenoid focus coil current were all set to the manufacturer's test specifications. By doing this, we could verify their test.

The LabVIEW power transfer VI is shown in Figure 2. The "font panel" allows us to input the klystron station number, a filename for data storage, input parameters for the signal generator, and the input parameters for the pulse generator. Once the test is completed we can view and verify the data on the graph that is generated at the end of the test.

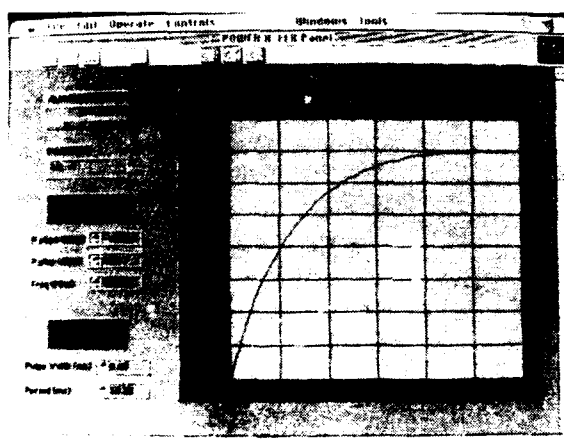


Figure 2. Power transfer virtual instrument.

The operating parameters for the klystron amplifier are shown in Table 2.

VC	VM	IC	IM	FV	FI	FCV	FCI	F	PW	PRF
kV	kV	A	mA	V	A	V	A	MHz	ms	Hz
85.2	32.4	28.1	8	15.7	20.8	75.4	22.3	850	0.67	30

Table 2. Operating parameters for the klystron amplifier.

The test data follows the header shown in Table 3. The first column represents the input forward power (PIF), the second column is the output forward power (POF), the third column is the forward power going into the load (PLF). The remaining columns are the reflected power at each of these locations. All values are given in watts.

PIF (W)	POF (W)	PLF (W)	PIR (W)	POR (W)	PLR (W)
0	0	0	0	0	0
0.12	84 670	82 000	0.04	918	426
0.13	94 940	92 300	0.04	951	431
0.15	105 810	102 400	0.05	1034	438
0.16	118 560	114 900	0.05	1101	478
0.18	131 370	127 600	0.06	1158	460
0.21	146 660	141 600	0.06	1229	452
0.23	162 750	158 300	0.07	1329	480

Table 3. Power transfer data for the klystron amplifier

Based on the results of this test, the graph shown in Figure 3 was generated. It is important to note that the power output of the klystron matches the power going into the load. Thus, the load impedance matches the output impedance of the klystron.

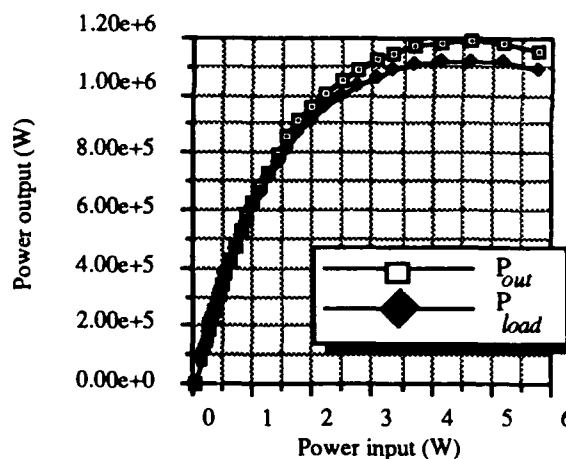


Figure 3. Power transfer of the klystron with cathode current of 28 A.

Swept-frequency test

This test is used to determine the frequency response of the amplifier at different drive levels. The header for the data file is basically the same as shown in Table 3. The only thing that changes is the organization of the raw data. The frequency is given in the first column, while the next five columns contain the forward and reflected output power. However, here each column includes a separate subcolumn for each tested drive level. The subcolumns for the klystron's forward power output (POF) are shown in Table 4.

Forward power input (PIF)					
F (MHz)	PI1 (W)	PI2 (W)	PI3 (W)	PI4 (W)	PI5 (W)
850	0.999	2.018	3.015	4.06	5.04
Forward power output (POF)					
845	39 870	80 450	120480	162250	199320
845.2	44 960	90 420	134610	182310	223390
845.4	50 800	102 350	152460	205930	252410
845.6	57 760	116 670	17278	232920	284150
845.8	65 960	133 000	197330	263160	320840
846	75 360	151 720	223740	298440	359700
846.2	85 290	173 240	255640	338440	407300

Table 3. Swept-frequency data for the klystron amplifier.

It is important to note that the swept-frequency program is linked to the power transfer program. The power transfer program determines the saturated drive and output power, and the swept-frequency program uses this information to determine the five different drive levels. This was done to prevent overdriving the amplifier. Thus, the swept-frequency program is programmed to do five frequency curves at five different drive level, one being at the saturated power level as illustrated below.

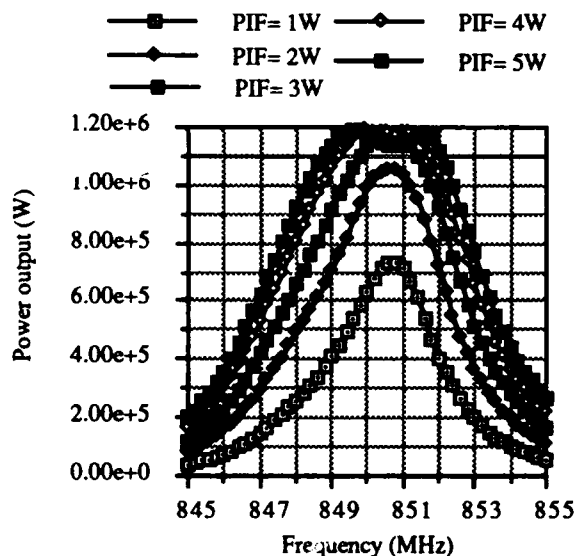


Figure 4. Frequency sweep of the klystron with cathode current at 28 A.

VSWR test

The VSWR test is conducted using a mismatch (tuner) section, which is located between the output power coupler and the coupler located before the load. Each tuner is evenly spaced apart at approximately 30°. Each test LabVIEW calculated the VSWR by measuring the reflected and the forward power and then adjusting the position of the tuner using a stepping motor.

The VSWR test data file contains six sets of power transfer data. One power transfer test is performed for each tuner. A sample of a data file is shown in Table 5.

PIF (W)	POF (W)	PLF (W)	PIR (W)	POR (W)	PLR (W)
VSWR #1					
0	0	0	0	0	0
0.444	447 300	416 600	0.13	8200	843
0.498	510 000	471 200	0.148	9210	949
0.559	562 700	519 400	0.155	10 140	1021
0.628	612 400	564 700	0.171	11 000	1107
0.703	650 600	607 800	0.182	11 760	1145
0.794	712 900	653 200	0.198	12 630	1208
0.886	766 900	704 700	0.224	13 580	1293

Table 5. Sample of the data file for the VSWR test.

The graph shown in Figure 5 shows a Rieke diagram for the klystron amplifier. (VSWR #1 stands for tuner #1 on the mismatch section).

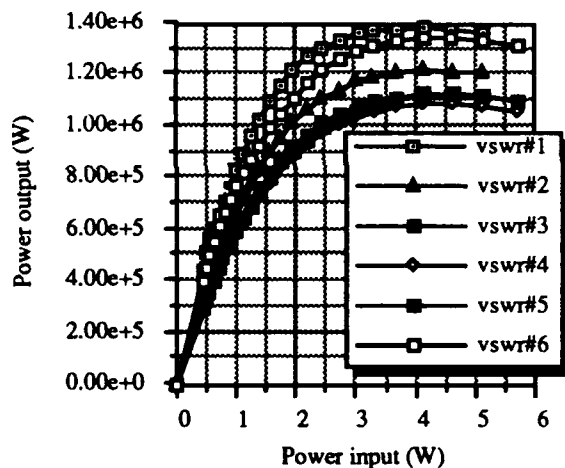


Figure 5. Rieke diagram of the klystron with the cathode current at 28 A.

III. CONCLUSION

With the automated high-power amplifier test stand, full characterization of a high-power amplifier at several operating conditions can be completed in one day. The test stand has allowed the 12 GTA klystrons to be accurately tested in a timely manner. The data from the test stand has also allowed our group to refine our models of the amplifiers.

Two-Klystron Binary Pulse Compression at SLAC*

Z. D. Farkas, T. L. Lavine, A. Menegat, A. E. Vlieks, J. W. Wang and P. B. Wilson
Stanford Linear Accelerator Center, Stanford University, Stanford, CA 94309 USA

Abstract

The Binary Pulse Compression system installed at SLAC was tested using two klystrons, one with 10 MW and the other with 34 MW output. By compressing 560-ns klystron pulses into 70 ns, the measured BPC output was 175 MW, limited by the available power from the two klystrons. This output was used to provide 100-MW input to a 30-cell X-band structure in which a 100-MV/m gradient was obtained. This system, using the higher klystron outputs expected in the future has the potential to deliver the 350 MW needed to obtain 100 MV/m gradients in the 1.8-m NLC prototype structure. This note describes the timing, triggering, and phase coding used in the two-klystron experiment, and the expected and measured network response to three- or two-stage modulation.

INTRODUCTION

The Binary Pulse Compression (BPC) system [1] consists of a BPC network and its appropriately modulated drive. A BPC network consists of one or more stages. Each stage consists of a hybrid whose two isolated ports are used as inputs and the remaining two ports as outputs with one output port followed by a delay line. The delays decrease in a binary fashion, with the last delay equal to the output pulse width.

Because more klystrons became available, the one-klystron BPC [2] was converted into the standard two-klystron, BPC system. The system consists of a three-stage BPC network, followed by a combiner, with its klystron drive and its load, and is shown in Fig. 1.

If, and only if, the two input powers are equal, does a switchable π phase-shift (PSK) direct all of the input powers into one or into the other output port of each hybrid. But, as we shall now show, the deviation from this ideal is small even for large input power ratios. Using superposition and energy conservation one can show that the two output powers of a hybrid in terms of its two input powers are

$$P_{oa} = \frac{P_{ia}}{2} + \frac{P_{ib}}{2} + \sqrt{P_{ia}P_{ib}}\cos\phi \quad (1)$$

$$P_{ob} = \frac{P_{ia}}{2} + \frac{P_{ib}}{2} - \sqrt{P_{ia}P_{ib}}\cos\phi \quad (2)$$

Here, ϕ is the phase difference between the input fields. We adjust the phase shifters so that $\phi = 0.0^\circ$. Then

$$P_{oa} = \left[\sqrt{\frac{P_{ia}}{2}} + \sqrt{\frac{P_{ib}}{2}} \right]^2, \quad P_{ob} = \left[\sqrt{\frac{P_{ia}}{2}} - \sqrt{\frac{P_{ib}}{2}} \right]^2 \quad (3)$$

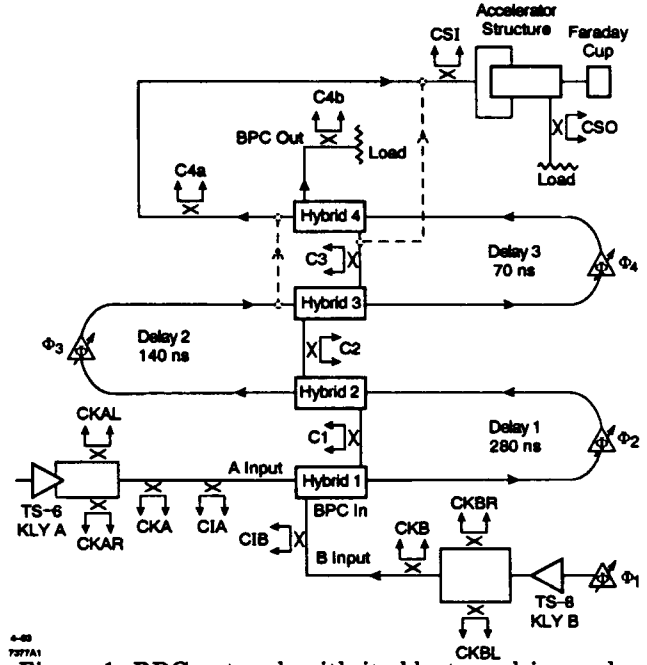


Figure 1. BPC network with its klystron drive and accelerator structure load.

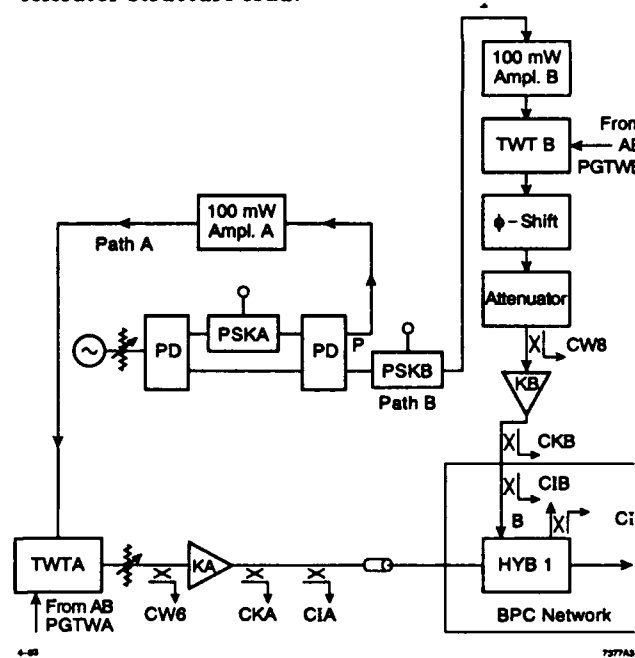


Figure 2. Two-klystron BPC drive system.

Let $x = P_{ib}/P_{ia}$ and $P_s = P_{ia} + P_{ib}$, then

$$P_{oa}/P_s = \frac{[1 + \sqrt{x}]^2}{2(1 + x)}, \quad P_{ob}/P_s = \frac{[1 - \sqrt{x}]^2}{2(1 + x)} \quad (4)$$

If we switch to $\phi = 180^\circ$, then the roles of outputs A and B are reversed. An input power ratio of 3:4, reduces the output by 0.5% and a ratio of 1:4 reduces the output by 10%.

* Work supported by Department of Energy contract DE-AC03-76SF00515.

TIMING

The Two-klystron BPC drive system is shown in Fig. 2. The output pulses from the two klystrons and the modulation transitions must arrive simultaneously at the two inputs to hybrid 1, which are also the inputs to the BPC network. Thus the time delay of the two paths of the RF leaving the PSK modulator, path A and path B, shown in Fig. 2, must be equal. The modulation of PSK A traverses both paths, and, therefore, it was used to adjust the delay of the two paths to make them equal to each

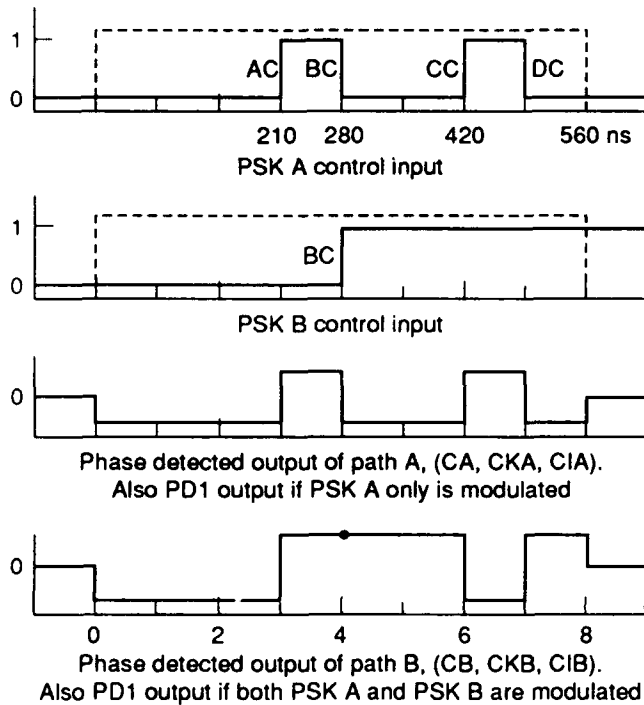


Figure 3. Three-stage BPC modulation (horizontal unit = 70 ns).

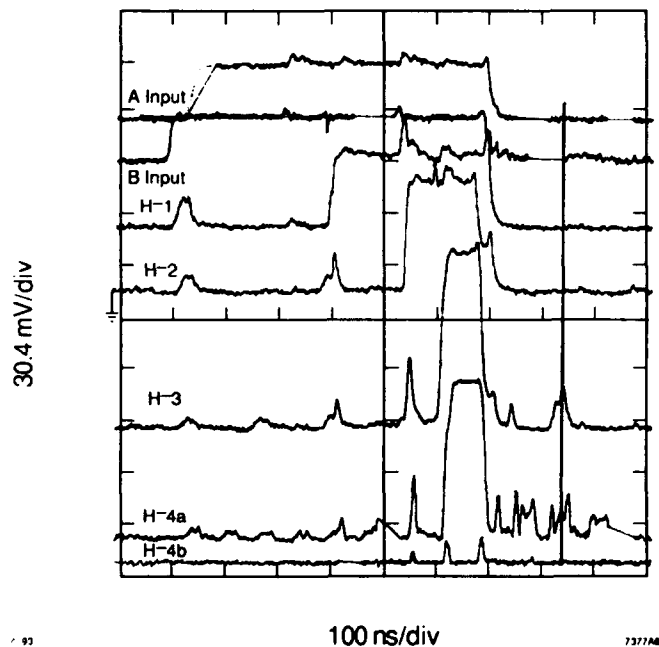


Figure 4. Three-stage BPC outputs.

other. It was accomplished as follows. A phase transition was applied to PSK A and the detected pulse was monitored at the output C1 of hybrid 1. With klystron B turned on, the position of the phase transition, as indicated by its "marker" on the scope, was noted. Then klystron B was turned off and klystron A was turned on. Again the position of the "marker" was noted. The delay of this marker from its previous position was the delay, in the form of WR90 waveguide, added to path A. If both klystrons are on then both markers will appear and will coincide when Path A and path B time delays are equal.

THREE-STAGE BPC.

The coding for a three-stage BPC and the resulting phase detected waveforms are shown in Fig. 3. We have a three-stage BPC followed by a combiner. The time delay of the last delay line, and hence the duration of the output pulse, is 70 ns. The experimentally obtained outputs are shown in Fig. 4. The amplitude and phase of the combiner output pulse are shown in Fig. 5. The power was increased over several weeks, as the various components underwent RF processing, until the three-stage BPC plus combiner provided ≈ 175 MW, 50 μ s flat-top output pulse. This output was fed into the 30 cavity accelerator where it was used to study dark current in the section at up to 100 MV/m accelerating gradients. This is reported on at this conference [3].

The peak power of the 600 ns klystron output pulses was 34 MW for klystron B and 10 MW for klystron A. Thus the BPC plus combiner power gain was $175/44=4$, rather than the ideal gain of 8. It is not difficult to account for the 3dB loss. The turn-around and phase-shifter loss is $0.4 \times 3 = 1.2$ dB, the hybrid loss is $0.3 \times 4 = 1.2$ dB, the total delay line loss including the loss of several WR90 stainless-steel flanges (the loss can be eliminated by copper plating them) is 0.6 dB.

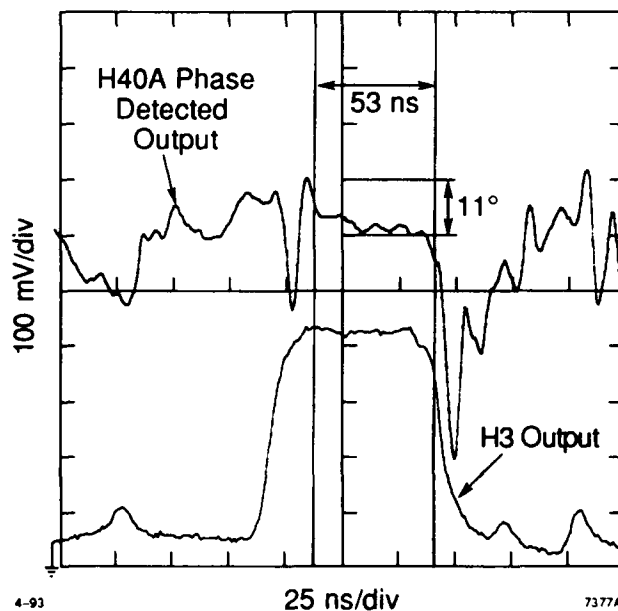


Figure 5. Amplitude and phase of the combiner output pulse.

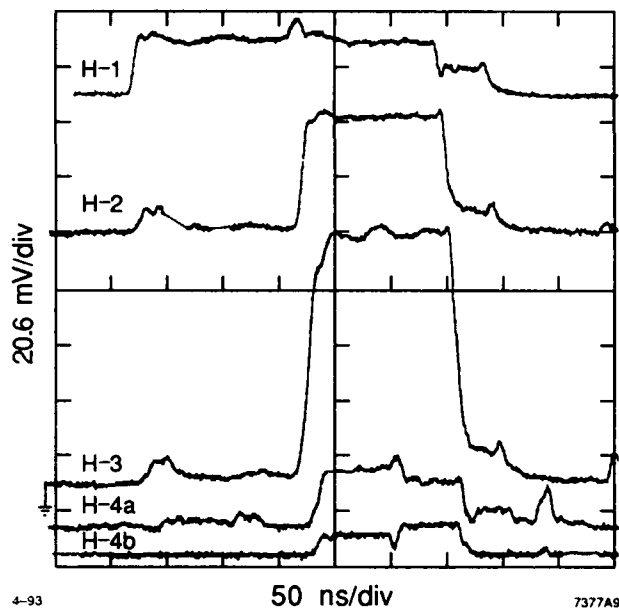


Figure 6. Two-stage BPC outputs.

TWO-STAGE MODULATION.

The three-stage BPC network presents a match to the klystrons no matter what the setting of the phase shifters or the input modulation (see Fig. 1). With two-stage modulation turned on, adjust ϕ_1 to minimize H1OB during $t=0$ to $t=4$. Then adjust ϕ_2 to minimize H2OB during $t=4$ to $t=6$. During $t=6$ to $t=8$, both inputs to H3 are 4 units high and 2 units wide. Adjust ϕ_3 to combine the powers at H3OB. This output is 2 units (140 ns) wide and 8 units high pulse. Hybrid 4 divides the its input power at H4IB into two equal 4-unit high at H4OA and at H4OB. We still have a two-stage BPC, each klystron output is quadrupled and its pulse width reduced by a factor of 4. But the combiner is neutralized by a divider. The experimentally obtained outputs are shown in Fig. 6. With some minor mechanical modification we can send the combined two-stage BPC outputs directly into the bunker to the accelerator section input, as indicated in Fig. 1.

POWERS FOR SLAC EXPERIMENTAL SECTIONS

Table 1 lists the requirements needed to attain accelerating gradients of $G_r = 100$ MV/m in the SLAC experimental accelerator sections. The third and fourth lines list the required pulse widths and peak powers into the SLAC experimental accelerator sections. The bottom line lists the power/klystron needed to achieve this. A 0.5 dB attenuation from Klystron output to BPC input was assumed. Assuming that our present klystrons can deliver a 34 MW- 600 ns pulses, a gradient of 100 MV/m in the 75 cm section is attainable. With the three-stage BPC, 70 ns output pulse, the required power/klystron to attain 100 MV/m in the 180 cm section is 55 MW, but the section will be only half full. With 34 MW, and a three-stage BPC the gradient attainable in the 180 cm section

Table I. Peak powers for 100 MV/m gradient in the SLAC experimental accelerator sections

Structure Length	30 cm	75 cm	180 cm	180 cm
Structure Fill Time	50 ns	50 ns	100	100 ns
Input Pulse Width	70 ns	70 ns	70 ns	140 ns
Structure Input Power	100 MW	220 MW	350 MW	350 MW
Atten. BPC Output to Struc. Input	1.76 dB	0.5 dB	0.5 dB	0.5 dB
Combiner Output	150 MW	224 MW	389 MW	389 MW
Power Gain	4	4	4	3 (2 stage)
Sum of BPC Input Powers	37.5 MW	61 MW	97.2	129 MW
Sum of Kly. Output Powers	42 MW	68 MW	109 MW	144 MW
Power/Klystron	21 MW	34 MW	55 MW	72 MW

$G_r = \sqrt{34/55} \times 100 = 79$ MV/m. With the two-stage BPC, 140 ns pulse, $G_r = \sqrt{34/72} \times 100 = 69$ MV/m.

COMPARISM WITH SLED-II

For the SLAC three-stage BPC, the measured combined power divided by the power per klystron was 8. It probably can be increased to 10 with minor modifications. A klystron output pulse width of 600 ns means an 8:1 compression factor for a 70 ns structure input pulse, and 5:1 for a 140 ns structure input pulse. The ideal SLED-II power gain is about half the actual BPC gain. Hence, for the same klystron power and pulse width, the gradients attainable with SLED-II are about $1/\sqrt{2}$ that of the BPC. Of course, one can combine the outputs of two klystrons and reach the same gradient as with the BPC. But this would require the installation of another high power hybrid. With the BPC, the combiner is already in place.

The delay line time delays are $T_d = (P_g + 1)T_p$ for the BPC and $T_d = T_p$ for SLED-II. For $P_g = 2$, the BPC requires half the SLED-II delay line length per klystron, and its efficiency is 100% rather than the 78% for SLED-II. The required line that transmits power to the second accelerator section can be made part of the delay line. Practical efficiencies greater than 90% are achievable. The length of the delay line per klystron for a two-stage BPC, is 1.5 times that of SLED-II.

REFERENCES

1. Z. D. Farkas, "Binary Peak Power Multiplier and its Application to Linear Accelerator Design", IEEE TRAN. MTT-34, p. 1036, October 1986.
2. Z. D. Farkas, et. al. "Radio Frequency Pulse Compression Experiments at SLAC", SLAC-PUB-5409, January 1991.
3. J. W. Wang, et. al. "High-Power Experiments in X-band Accelerator Structures" PAC'93, May 1993.

New Compact Mode Converters for SLAC RF Pulse Power Compression System*

Gwo-Huei Luo

Synchrotron Radiation Research Center
1 R & D Road VI, Hsinchu, 30077, Taiwan, R. O. C.

Abstract

A RF pulse power compression scheme has been developed at SLAC (Stanford Linear Accelerator Center) where they adopt a method of a long delay line, in an overmoded circular waveguide, to rephase the transmission mode. A low loss mode, TE_{01} in a circular waveguide is required. However, the output mode of a megawatts klystron is a TE_{10} mode in rectangular waveguide. A transition and mode conversion system needs to be developed. Conventional mode conversion sequence of TE_{10} in rectangular waveguide, to TE_{01} mode, in circular waveguide, is using Marie' Transition which requires very long transition length and very complicated structure. We have developed several mode converters with very compact length and high efficiency. The proposed conversion sequence is TE_{10} - TE_{11} - TE_{01} . In this sequence, our main interests are in developing the TE_{11} and TE_{01} uptaper, and TE_{11} - TE_{01} serpentine mode converter at 11.4 GHz.

I. INTRODUCTION

High-power microwave tubes producing output power from several kilowatts up to many megawatts often generate modes which are not suitable for long distance transmission, plasma heating and radar applications. To obtain a more desirable mode, a sequence of mode converters is often used with various high-power microwave sources such as gyrotrons, and klystrons.

In order to produce high-gradient linear accelerators (Linac) for next generation linear collider, it is required several hundreds of megawatts of peak power per unit length. Binary Pulse Compression (BPC) is a promising technique to deliver, at least, a five-fold peak power output compared to the input peak power [1]. This technique increases peak power at the expense of reducing the pulse width which was still long enough to fill the accelerator section.

The delay line, which was used at the BPC system, has the freedom to operate the propagation mode, such as TE_{01} mode, in an overmoded circular waveguide. The TE_{01} mode was operated at considerably above cutoff frequency, for example, 11.4 GHz with 3.57 cm of waveguide radius. We can have negligible ohmic loss even with a small diameter pipe. With the consideration of available pulse klystron and Linac, an X-band microwave frequency, 11.4 GHz, has been chosen as operating frequency at current stage.

The proposed transmission and conversion sequence was shown in Fig.1 [2]. In the following sections, we will use these conversion sequence and waveguide radius to design our mode converters and tapers at 11.4 GHz.

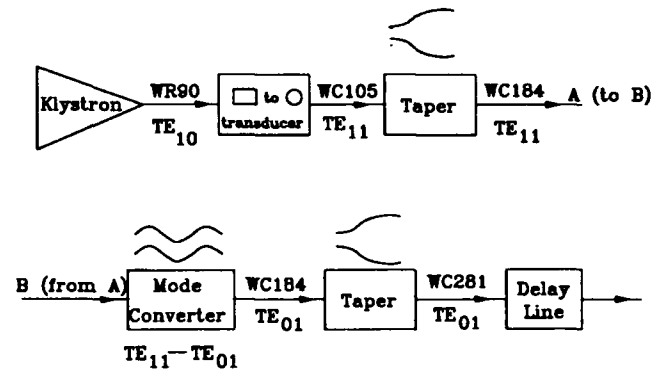


Figure 1. The proposed transmission modes, waveguide size, and conversion sequence for binary pulse compression system at 11.4 GHz operating frequency.

II. VARYING-RADIUS MODE CONVERTERS

A. Coupled Mode Equations

For varying-radius mode converters, the coupled mode equations for the TE_{0n} modes can be written in the form of [3]

$$\frac{dA_n}{dz} = \beta_n(z)A_n(z) + \sum_{j \neq n} C_{nj}(z)A_j(z)$$

where $\beta_n(z)$ is the propagation constant of mode n at location z . $|A_n|^2$ is the power that transported in positive z direction by mode n . C_{nj} , as function of z , is the coupling coefficient between mode n and mode j .

For quasi-periodic varying radius mode converters following Kovalev [4], we used a radial variation of the form

$$a(z) = a_0 + \epsilon_1[1 - \cos(H(z))]$$

where a_0 is the input waveguide radius, ϵ_1 is the perturbation amplitude of waveguide taper. $H(z)$ is a harmonic function of the beat wavelength between the transmission mode and the strongest coupled nearby-mode. A multi-dimension

*This work was supported by the U.S. DOE, and NSC of R.O.C.

optimization scheme has been used to optimize the tapers such that we will get the best conversion efficiency with very compact structure. The backward traveling modes, calculated by shooting method to match the two points boundary condition, have been shown to be negligible in all the cases considered here.

B. The Designs of TE_{01} and TE_{11} Uptaper

A TE_{01} uptaper has been designed from the waveguide radius of 2.34 to 3.57 cm. For the varying-radius mode converter, TE_{0n} modes will couple with TE_{01} mode. The taper length is 15 cm with 99.9% of transmission efficiency and 0.05% of ohmic loss. The waveguide profile can be expressed as following

$$a(z) = .0234 + .00615(1 - \cos(20.94z - .1\sin(20.94z))).$$

As shown in Fig. 2, a TE_{11} uptaper with input diameter of 2.67 cm and output diameter of 4.67 cm has been designed. The coupled TE_{1n} and TM_{1m} modes families were considered for the case of TE_{11} uptaper. The overall length of the taper is 13.1 cm with 99.8% of transmission efficiency and 0.13% of ohmic loss. The profile of the mode transducer can be written as

$$a(z) = .0133 + .00503[1 - \cos(23.98z - .06\sin(23.98z))].$$

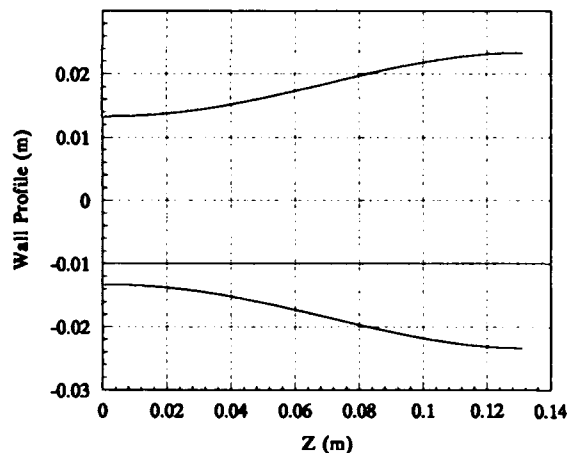


Figure 2. The waveguide profile of an optimized 11.4 GHz TE_{11} uptaper with input and output diameter of 2.67 and 4.67 cm respectively.

IV. TE_{11} - TE_{01} SERPENTINE MODE CONVERTER

A similar coupled mode equations can be found by using Morgan's [5] method for a constant-radius serpentine-type mode converter. The coupled mode equations can be written as

$$\frac{dA_n}{dz} = \beta_n A_n + \sum_{j \neq n} C_{nj} A_j$$

where A_n is the amplitude of mode n , β_n is the propagation constant of mode n at waveguide radius a_0 . C_{nj} is the coupling coefficient between mode n and mode j , which is independent on z .

The coupling coefficients for the modes that we are interested in can be derived by applying perturbation theory and solving the Maxwell's equations for the waveguide surface deformation.

We only consider the first and second order coupling. The third order coupling is too small to be included as we try to optimize the conversion efficiency. A very strong coupling between TE_{11} and TE_{21} , and TE_{01} and TE_{12} has been found during solving the coupled mode equations.

From conventional design philosophy, it would be possible to design a mode converter using a large number of perturbation periods to suppressed spurious modes. However, it is not a practical solution while we consider the ohmic loss, frequency response, and the available space to accommodate the mode converter. A quasi-periodic structure has been used to optimize the structure of the serpentine mode converter.

It is very difficulty to find a high efficiency mode converter with perturbation period less than 3-periods. The coupling diagram is shown in Fig. 3. The mode contents of the TE_{11} - TE_{01} serpentine mode converter along the waveguide axis is shown in Fig. 4. The detail waveguide profile can be expressed as following:

For the first section,

$$a(z) = .0234 + .391 \cdot 10^{-2} \{1 - \cos[62.33z + .829\sin(62.33z) + .028\sin(124.7z)]\} \text{ where } 0 \leq z \leq .1008 \text{ m.}$$

For the second section,

$$a(z) = .0234 + .665 \cdot 10^{-2} \{1 - \cos[42.89z - .101\sin(42.89z) + .350\sin(85.78z)]\} \text{ where } 0 \leq z \leq .1465 \text{ m.}$$

For the third section,

$$a(z) = .0234 + .405 \cdot 10^{-2} \{1 - \cos[55.65z + .114\sin(55.65z) + .179\sin(111.3z)]\} \text{ where } 0 \leq z \leq .1129 \text{ m.}$$

The waveguide profile of the optimized mode converter was shown in Fig. 5. The conversion efficiency is 98.9% with .19% of ohmic loss. The output mode purity is 99.1% with overall length of 36.02 cm.

V. CONCLUSION

A series of compact mode converters have been designed which can be used as a substitution of current Marie' Launcher and the tapers at current BPC system. The mode purity of the designed serpentine-type mode converters and tapers were above 99%. A similar computer codes has been used to design a single-period TM_{01} - TE_{11} serpentine mode converter at 8.6 GHz [6]. The measurement results of

previous designed mode converter, TM_{01} - TE_{11} , were in excellent agreement with the computer simulation.

VI. ACKNOWLEDGEMENT

The valuable discussion with Z.D. Farkas, A. Menegat and Dr. P.B. Wilson about the BPC system at SLAC is gratefully appreciated. The help from Prof. R.J. Vernon at University of Wisconsin-Madison is also gratefully acknowledged.

VII. REFERENCES

- [1] Z.D. Farkas, "Binary Peak Power Multiplier and its Application to Linear Accelerator Design," IEEE Trans. MTT-34, No. 10, pp. 1036-1043.
- [2] P.B. Wilson, Private communication
- [3] H.G. Unger, "Circular Waveguide Taper of Improved Design," Bell System Tech. J., Vol. 37, pp. 899-912, 1958.
- [4] N.F. Kovalev, I.M. Orlova and M.L. Peletin, "Wave Transformation in a multimode Waveguide with Corrugated Walls, " Radio Phys. Quant. Electron, pp.449-450, 1969.
- [5] S.P. Morgan, "Theory of Curved circular Waveguide Containing an Inhomogeneous Dielectric," Bell System Tech. J., Vol. 36, pp. 1209-1251, 1957.
- [6] G.H. Luo, et al, "Design of a Single-Period 8.6 GHz TM_{01} - TE_{11} Serpentine Mode Converter and TM_{01} and TE_{11} Bends in a Moderately Overmoded Circular Waveguide," 15th Int. Conf. on Infrared and Millimeter Waves, pp. 434-436, 1990.

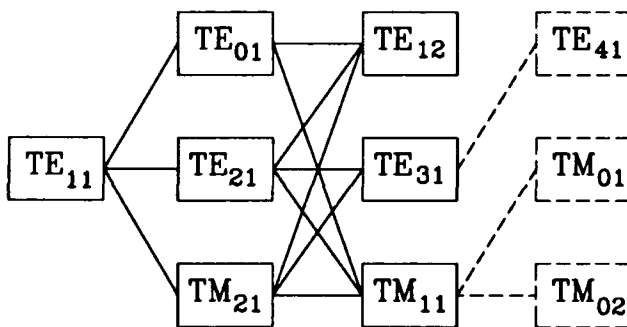


Figure 3. Coupling diagram of a TE_{11} - TE_{01} single plane serpentine mode converter at 11.4 GHz with a diameter of 4.67 cm.

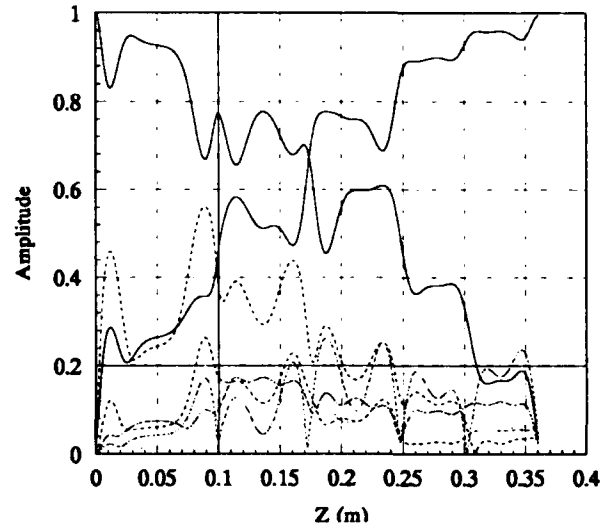


Figure 4. The mode contents along an optimized 11.4 GHz TE_{11} - TE_{01} serpentine mode converter with 4.68 cm of diameter. The TE_{01} output mode purity is 99.1%.

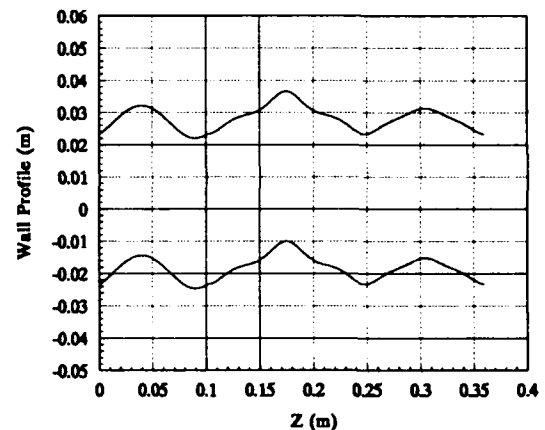


Figure 5. The waveguide profile of an optimized 11.4 GHz TE_{11} - TE_{01} serpentine mode converter with waveguide radius of 2.34 cm.

PERFORMANCE OF LITTON 805MHz, 12MW KLYSTRONS

Q. Kerns, M.B. Popovic, C. Kerns and A. Moretti
Fermi National Accelerator Laboratory*
Batavia, IL 60510, USA

ABSTRACT

The Fermilab Linac Upgrade[1] will increase the energy of the H⁻ linac from 201 to 401.5 MeV. This will be achieved by replacing the last four 201.24 MHz drift-tube linac cavities with seven 805 MHz side-coupled cavity modules. Each accelerator module will be powered with a 12 MW klystron-based power supply. The purpose of this report is to present a body of representative data for the klystron tubes at various conditions and to detail the procedures used.

TESTS

Below is the list and description of the tests[2] performed on three klystron tubes. Each tube was received with an acceptance test datasheet. All tube parameters were

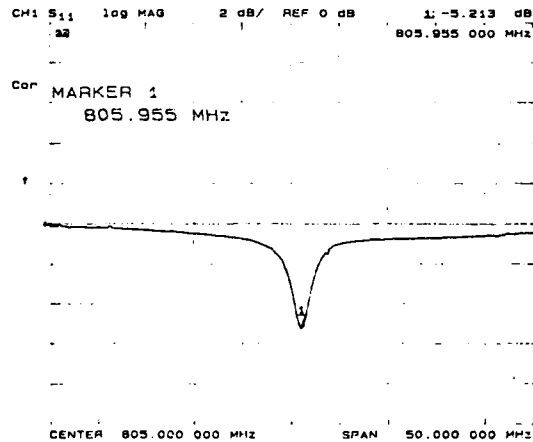


Figure 1.

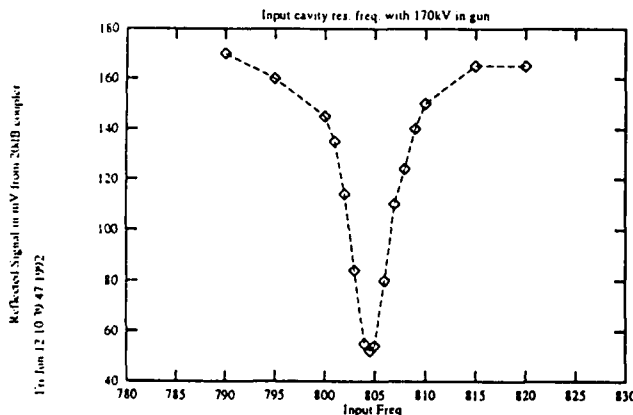


Figure 2.

in the range suggested by Litton. Connected to the output of each klystron was a Varian water-load (model L975FA1).

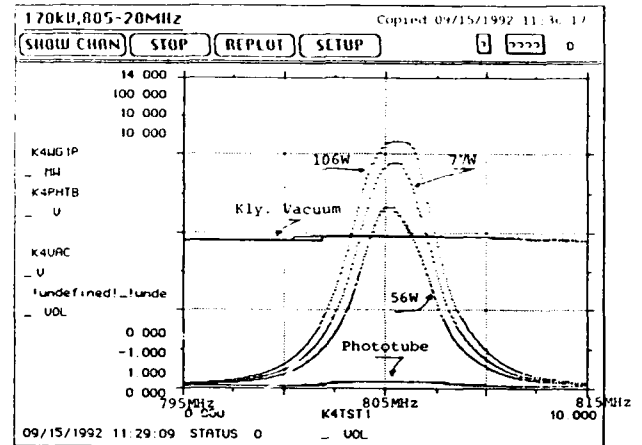


Figure 3.

Figures 1 and 2 present measurements of input cavity match with and without beam current. The input cavity on one of the tubes (serial#0002) is ~10MHz above the nominal frequency of 805MHz for no apparent reason.

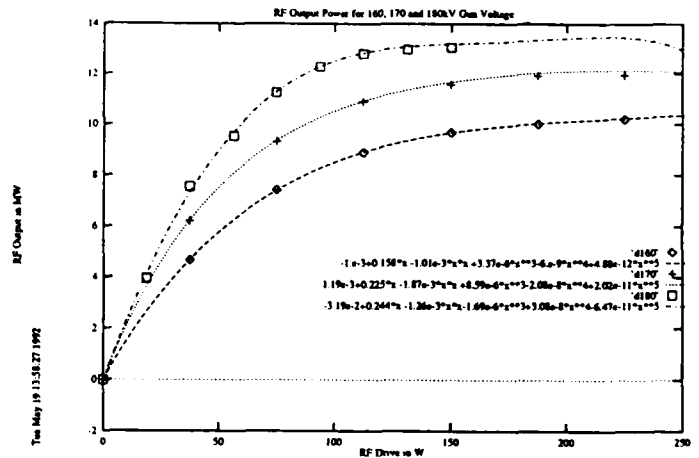


Figure 4.

Figure 3 shows klystron power bandwidth. The output power

* Fermilab is operated by the Universities Research Association under contract to the US Department of Energy.

is plotted as function of rf frequency, from 795MHz to 815MHz, for three different levels of rf drive power.

Above, see Figure 4, are displayed plots of klystron power output vs. drive power at gun voltages of 160kV, 170kV and 180kV.

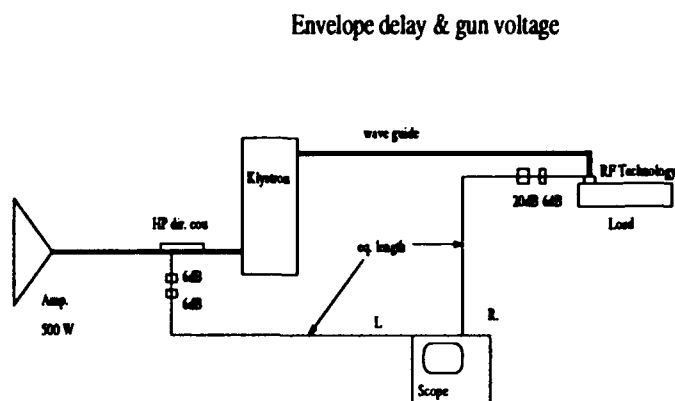


Figure 5.

The envelope delay vs. gun voltage was measured using the setup shown schematically in figure 5. Table 1 summarizes results of measurements for tube number 0002.

Table 1.

Gun V	Gun I	Power	Delay
kV	A	MW	nsec
140	100.7	5.9	94.0
150	111.3	7.6	92.0
160	122.2	9.7	94.0
163	125.6	6.0	88.0
170	133.4	11.1	92.0
180	145.0	12.9	94.0

All data were taken at 805.9632 MHz and we found mean delay to be 92.33 nsec.

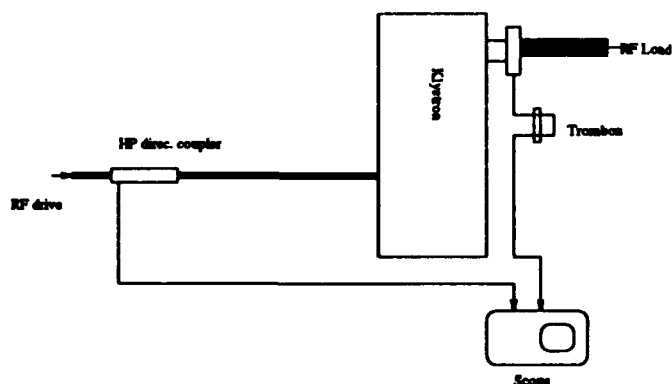


Figure 6.

RF phase shift as function of gun voltage was measured using the setup illustrated in figure 6. Table 2 summarizes results of measurements for the tube serial #0002.

Table 2.

Sat. Pwr.	Gun V	Gun I	Tromb.	Phase	Ampl.	Calc. Eff
MW	kV	A		Matched		
	150		1/2"	Yes	Yes	
9.8	160	132.1	2 10/16"	Yes	No	50%
11.9	170	134.2	4 1/2"	Yes	No	52%
13.4	180	145.9	6 1/4"	Yes	No	51%
14.22	185	151.8	7 1/4"	Yes	No	50.6%

Figure 7 shows RF phase as function of gun voltage for tube serial #0002.

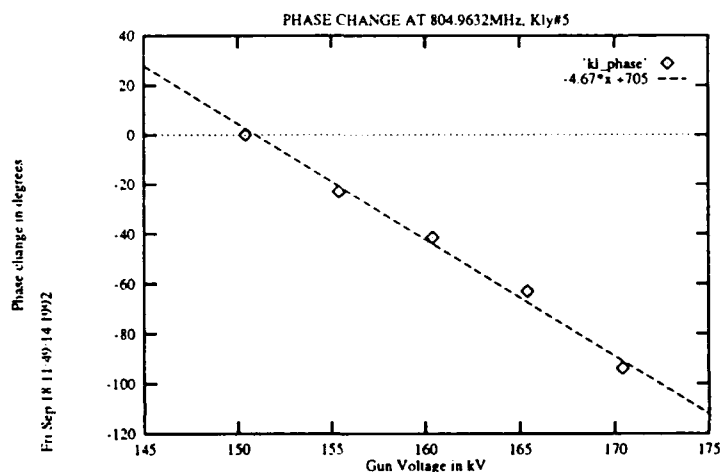


Figure 7.

Klystron gun current and klystron filament voltage are plotted as function of time for different settings of klystron filament voltage in figure 8 (Miram plot).

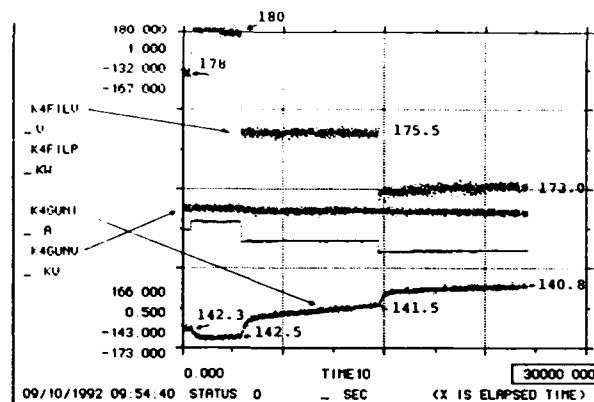


Figure 8.

Results of perveance measurements are summarized in Table 3.

Table 3.

<i>Gun V</i>	<i>Gun I</i>	<i>Perveance</i>
kV	A	in 10^{-6}
150.7	112.3	1.92
160.4	123.0	1.91
165.5	128.6	1.91
170.4	134.4	1.91
175.5	140.0	1.90
180.3	146.0	1.91

The following discrepancies in klystron performance specifications are noted:

1. The input cavity in one tube is tuned ~10MHz higher than the nominal 805MHz for no apparent reason.
2. The solenoid currents had to be adjusted to FNAL values to avoid spurious oscillations which would occur with Litton settings when running less than saturated power output.
3. The power output pass-band is displaced to the high side of 805MHz, possibly due to input cavity mistuning. The Litton rating of a 3MHz 0.5dB pass-band appears optimistic.
4. The output window shows a mild glow, above 10MW, possibly due to multipactoring in the output waveguide.

In conclusion the tubes which were tested delivered 13MW at 50% efficiency at a gun voltage of 180kV, and with 150 watts of drive power and are considered successful tubes.

CONCLUSIONS

Three tubes have been tested and are installed on rf stations one, two and three. The tubes are now fully operational. To date, over 3.9×10^7 high voltage pulses have been applied to tube 0005, 8.8×10^7 high voltage pulses have been applied to tube 0004 and 0.6×10^7 high voltage pulses have been applied to tube 0002.

REFERENCES

- [1] C. W. Schmidt, "The Fermilab 400-MeV Linac Upgrade", this conference.
- [2] A. S. Gilmour, "Microwave Tubes", Artech House, 1986.

Higher-Order Modes* in the APS Storage Ring Waveguides

S.O.Brauer, R.L.Kustom
Advanced Photon Source
Argonne National Laboratory
9700 S. Cass Ave, Argonne, IL 60439, USA

Abstract

Twelve higher-order modes (HOMs) in the single-cell accelerating cavities for the Advanced Photon Source (APS) storage ring were calculated to have complex impedances that will cause coupled-bunched instabilities near or below the 300mA positron current which is the design goal. Some of these modes couple, through the coupling loop, from the storage ring cavity into the waveguide. This study investigates the transmission of these modes from the cavity into the waveguide. The standing wave ratio (VSWR) of a WR2300 hybrid waveguide component has been measured at each HOM frequency, and its effect on the transmitted modes in the waveguide is studied.

I. INTRODUCTION

When a particle bunch from a stored beam travels through an RF cavity, the electrical charge and current of the bunch produce electric and magnetic fields at the walls of the cavity [1]. Induced charges and currents are generated in the walls of the cavity by the fields and these charges and currents induce wakefields that can interfere with the bunch and can cause deflections or changes in energy of the particles in the bunch. After the passage of the beam bunch, electromagnetic energy is deposited in resonant HOMs which are determined by the geometry of the RF cavity. These HOMs of RF cavities are the largest contributors to coupled-bunch instabilities.

In the APS, the stored beam will have approximately 60 bunches, 5mA per bunch, for a total beam current of 300 mA. In a multibunch operation of a storage ring, the stability limit is reached at a threshold current value which is inversely proportional to the shunt impedance R_s of the driving HOM [2]. The threshold current value for instabilities is determined by the synchrotron radiation damping rate and the growth rate of the instabilities. During the synchrotron acceleration process the amplitude of small phase oscillations and radial oscillations of the bunch are reduced as energy increases; this is defined as synchrotron radiation damping [3]. The radiation damping rate is a constant while the instability growth is proportional to the stored current. The current at which the instability growth is

equal to the damping rate is the stability threshold. Since the maximum beam current is 300mA, the threshold current for a HOM with a value less than 300mA may cause coupled-bunch instabilities. Twelve HOMs with current thresholds less than or close to 300mA are listed in Table 1 [4].

Table 1

Longitudinal Modes (Monopoles)		Transverse Modes (Dipoles)	
freq HOM (MHz)	I _{thresh} (mA)	freq HOM (MHz)	I _{thresh} (mA)
536.7	80	588.7	80
922.5	130	761.1	43
939.0	340	962.0	190
1173.2	340	1017.4	435
1210.8	130	1145.1	410
1509.1	130	1219.2	315

To avoid the development of beam instabilities due to the existence of these HOMs in the RF cavity, damping of the modes will be required. E-probe and H-loop dampers will be used for damping some HOMs in the cavity. The possibility of the HOMs present in the RF cavity coupling into the loop coupler and traveling through the coupler into the waveguide, may allow damping of some of the HOMs by the insertion of dampers into the waveguide adjacent to each cavity. In order to investigate the feasibility of using waveguide dampers, the HOMs which couple into the waveguide must be determined.

II. BEAD PULL MEASUREMENTS

Several of the HOMs listed in Table 1 were not considered because the I_{thresh} was substantially higher than the 300mA limit. Additionally, three of the modes were successfully damped in the 352-MHz cavity [5]. Table 2 lists the remaining HOMs to be studied, their corresponding frequencies and modes in an equivalent (348 MHz) pillbox cavity (radius = 0.33m, length = 0.375 m), and the per unit difference between the two. The difference is small enough that the pillbox can be used for a good model.

*Work supported by U.S. Department of Energy, Office of Basic Energy Sciences under Contract No. W-31-109-ENG-38.

The submitted manuscript has been authored by a contractor of the U. S. Government under contract No. W-31-109-ENG-38. Accordingly, the U. S. Government retains a nonexclusive, royalty-free license to publish or reproduce the published form of this contribution, or allow others to do so, for U. S. Government purposes.

Table 2

Mode	f pillbox	f cavity	f _{cav} /f _{pillbox}	Δ
TM110	554.0	588.7	1.0626	0.0626
TM012	872.0	922.5	1.0579	0.0579
TM112	973.0	962.0	0.9887	0.0113
TM120	1014.0	1145.0	1.1293	0.1293
TM013	1249.0	1210.8	0.9684	0.0305
TM122	1292.0	1219.2	0.9437	0.0563

Verification of the HOM field configuration in the pillbox for each one of the frequencies under consideration was done by performing a bead-pull measurement. According to perturbation theory, the resonant frequency of a mode in a cavity is shifted when an object is placed inside the cavity, by [6]:

$$\frac{\delta\omega}{\omega} = \frac{\iiint_{V_1} (E_1 D_0 - E_0 D_1) - (H_1 B_0 - H_0 B_1) dv}{\iiint_{V_0} (E_0 D_0 - H_0 B_0) dv} \quad (1)$$

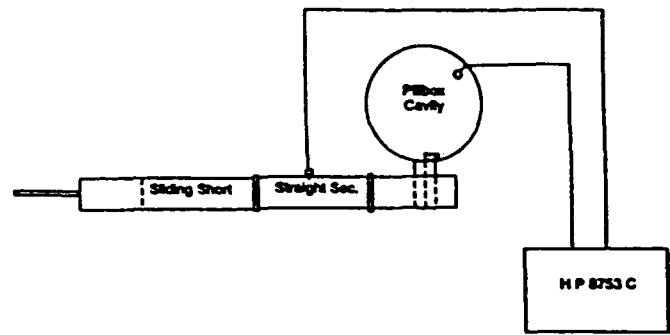
The bead-pull measurement setup consisted of the pillbox, a small conducting needle epoxied to a silk string, an apparatus to suspend the string through the beam axis of the conducting cavity, a stepper motor to step the needle through the cavity, a Hewlett Packard 8753 C Network Analyzer to take measurements of the phase shift of the resonant frequency due to the needle, and for automated control of the 8753 C, an IBM PC. From the results of the bead-pull measurements and their comparison to a previous bead-pull done on the prototype single-cell RF cavity [7], Table 2 was confirmed.

III. MEASUREMENTS IN WAVEGUIDE

To obtain the measurements needed for the determination of the mode configuration of the HOMs at the frequencies of interest, the pillbox, analyzer, and waveguide components were arranged as shown in Figure 1. The loop coupler used to couple the RF power from the waveguide into the cavity was inserted into the pillbox and the transition between the coaxial loop coupler and the waveguide was attached to the coaxial end of the coupler. A straight section of half-height WR2300 waveguide, 1.2 meter (λ_p), was added to the transition and it was terminated with a sliding waveguide short. In the center of the straight section, perpendicular to the flanges, small E-probe antennas were inserted. They were evenly spaced along one broad-wall and one side-wall for measurement of any E-field that would be perpendicular to the wall of the guide.

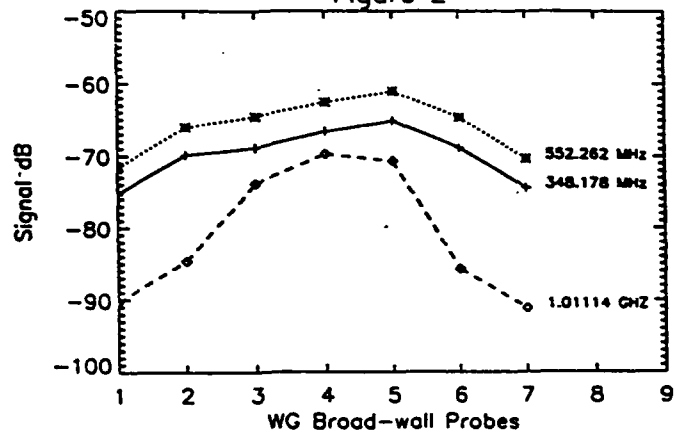
Because some shift in frequency was expected due to the insertion of the coupling loop into the cavity, bead-pull measurements were taken at each frequency to verify that the correct mode was being excited in the cavity. Measurements were taken from the E-probe antennas at each corresponding frequency. The sliding short was used to optimize each resonant frequency in the guide which provided the best possible signal from the probes.

Figure 1



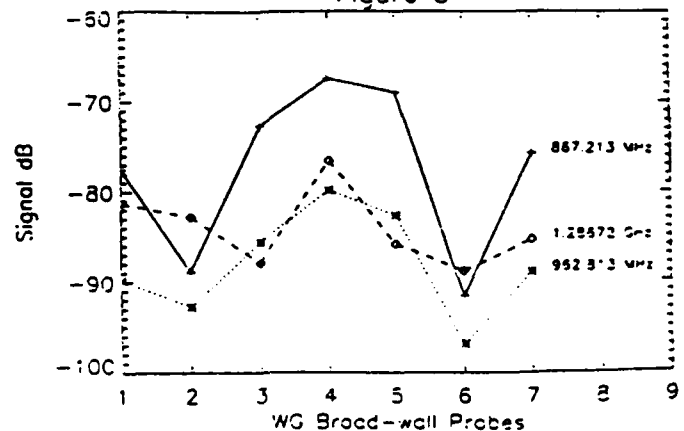
All of the modes listed in Table 2 were found in the waveguide. Figures 2, 3, 4, and 5 show graphs of the signal versus position of the seven probes that were placed in the broad-wall of the waveguide. As shown in Figures 4 and 5, only one of the modes found in the waveguide had E-field components perpendicular to the broad-wall and side-wall. The loop coupler was located on the radial wall of the pillbox. As a result, the variation of the E and H fields along the length of the cavity with respect to the loop was the main contribution to the determination of the configuration of the mode in the waveguide.

Figure 2

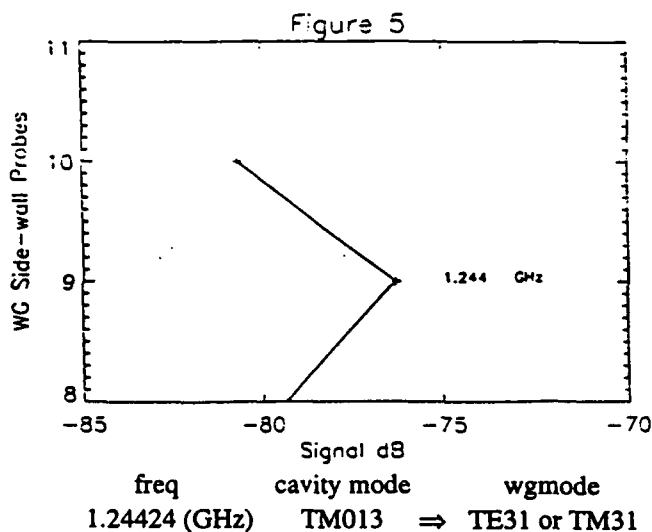
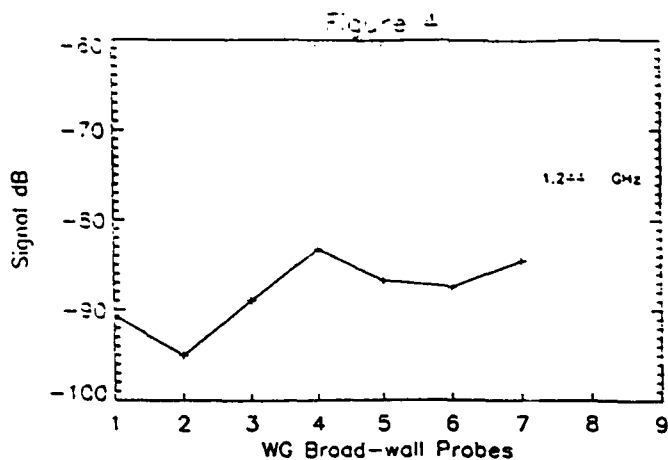


freq	cavity mode	wg mode
348.178 (MHz)	TM010	⇒ TE10
522.626 (MHz)	TM110	⇒ TE10
1011.14 (MHz)	TM120	⇒ TE10

Figure 3



freq	cavity mode	wgmode
867.213 (MHz)	TM012	⇒ TE30
962.813 (MHz)	TM112	⇒ TE30
1.28677 (GHz)	TM122	⇒ TE30



IV. HYBRID MEASUREMENTS AND EFFECTS

Those modes which couple into the waveguide and are not damped by loads on the hybrids become resonant and will require waveguide dampers. The previous measurements were taken with the waveguide terminated in a short resulting in total reflection. This will not be the case in the storage ring RF system. Rectangular waveguide components generally are not broadband devices and the impedance of the component varies substantially at frequencies other than the designed fundamental frequency. In order to determine which HOM frequency will couple to loads and be damped and which will become resonant in the waveguide, a measurement of the VSWR of the component at each HOM frequency was made. The first component that was measured was the WR2300 3dB Hybrid. Results are listed in Table 3.

Table 3

freq HOM (MHz)	VSWR	freq HOM (GHz)	VSWR
552.24	17.228:1	1.0143	3.970:1
867.11	57.367:1	1.2442	30.004:1
961.5	1.322:1	1.2867	4.850:1

V. CONCLUSION

The above measurements show that the HOMs listed in Table 2 are coupled into the waveguide. The measurements of the standing wave ratio (VSWR) of the WR2300 hybrid indicate that three of the six modes under consideration will not be damped by the coaxial loads in the hybrids and will require additional waveguide dampers.

VI. REFERENCES

- [1] M. Sands and J. Rees, "A Bench Measurement of the Energy Loss of a Stored Beam to Cavity," PEP-95, Stanford, CA, August 8, 1974.
- [2] J. Jacob, "Measurement of the Higher Order Mode Impedances of the LEP Cavities," ESRF-RF/88-02, Grenoble, pp.2-12, January 1988.
- [3] H. Bruck, *Circular Particle Accelerators*, Presses Universitaires de France, pp. 233-236, 1966.
- [4] L. Emery, "Coupled-Bunch Instabilities in the APS Ring," *Proceedings of the 1991 Particle Accelerator Conference*, San Francisco, CA, pp.1713-1715, 1991.
- [5] J. F. Bridges, J. M. Cook, R. L. Kustom, J. Song, "Measurements on Prototype Cavities (352 MHz) for the Advanced Photon Source (APS)," in *Proceedings of the 1991 Particle Accelerator Conference*, pp. 693-695, 1991.
- [6] R. A. Rimmer, "High Power Microwave Window Failures," Thesis for the Degree of Doctor of Philosophy Appendix A, October 1988.
- [7] T. Smith, Argonne National Laboratory, private communication.

The Design and Production of the Higher-Order-Mode Loads for CEBAF*

Isidoro E. Campisi, Lynda K. Summers, Ben H. Branson, A. Michelle Johnson and Aldo Betto
Continuous Electron Beam Accelerator Facility
12000 Jefferson Avenue, Newport News, VA 23606-1909

Abstract

At CEBAF, 676 Higher-Order-Mode (HOM) loads are being installed, within the beam vacuum at 2 K, to damp HOM's that affect the stability of the recirculating electron beam. In this paper, the requirements imposed on the loads and the microwave absorbing material comprising them are discussed together with an analysis of their performance and effect on some relevant modes.

I. INTRODUCTION

The Continuous Electro. Beam Accelerator Facility (CEBAF) will provide by design an electron beam of 200 μ A with an energy as high as 4 GeV. This performance is achieved by recirculating the electrons up to five times in two antiparallel linear accelerators which make use of niobium superconducting cavities resonating at 1497 MHz and kept at 2 K. When cold, the vacuum in the cavities is better than 10^{-10} torr. Any component that is placed within the accelerator must satisfy a number of environmental constraints designed to prevent surface contamination of the superconducting cavities or excessive heat dissipation on the part of the fundamental mode which must have an unloaded Q of at least $2.4 \cdot 10^9$ at 5 MV/m. Under normal operating conditions only tens of milliwatts of HOM power per cavity are expected making it thermodynamically advantageous to keep the loads at 2 K.

The electrical properties of the HOM loads must be such that they provide return losses of about 10 dB, in the special size HOM rectangular waveguide ($1.500'' \times 3.110''$), from 1.9 GHz (the waveguide cutoff) up to 10 GHz and beyond, in all the possible waveguide modes and at any frequency in that range [1]. This requirement translates into damping some of the modes from Q 's potentially in the 10^9 – 10^{10} down to the 10^2 – 10^3 level.

The HOM loads developed for CEBAF provide the proper attenuation by using a compact yet broadbanded design [2]. This design incorporates an absorbing material developed specifically for this application which shows dielectric properties independent of temperature [3] and high thermal conductivity [4]. This makes it an ideal material for several accelerator applications [5].

II. LOAD DESIGN

A. Geometry

The cutoff frequency of the HOM waveguides is 1.9 GHz for the TE_{10} mode. Above 3795 MHz, additional modes (TE_{20} , TE_{01} , TE_{11} , TM_{11} , etc.) propagate in the guide, contributing to the extraction of the HOM power. Since the best matching of a dielectric absorber to the electromagnetic waves occurs at locations where the electric field is lowest, the design of the

load is such that its leading edge is as close as possible to the corner where the electric field is zero for all TE waveguide modes which dominate the HOM power extraction at the lower and most critical frequencies (Figure 1). With this geometry a very compact loads design is achieved (Figure 2) which can be assembled in a few economical manufacturing steps.

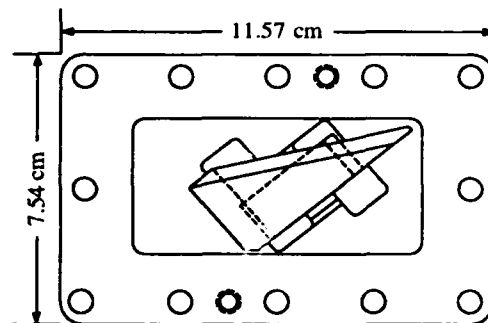


Figure 1. CEBAF's HOM load assembly. The geometry is designed to effectively match to several waveguide modes and over a broad frequency range.

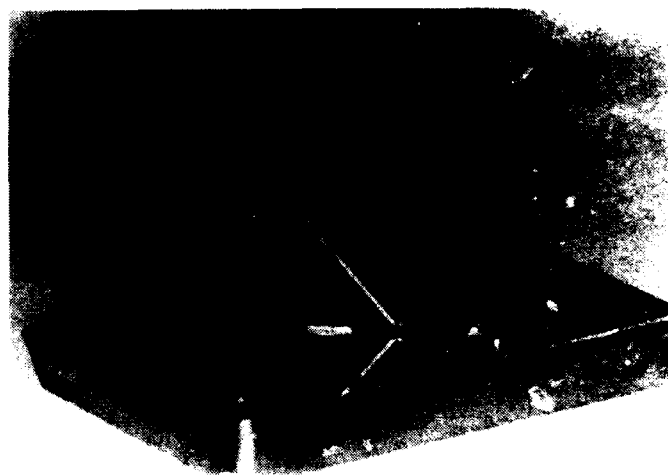


Figure 2. The CEBAF HOM load assembly, with the stainless steel flanges and the braided lossy ceramic parts. The load is only 7 cm long, thanks to the high dielectric constant of the absorber material.

B. The Material

A totally new ceramic material had to be developed to provide temperature-independent absorption down to 2 K. The ceramic composite is based on the artificial dielectric model [6][7]. It consists of a mixture of aluminum nitride (a matrix which provides good strength and high thermal conductivity, ≥ 60 – 80 W/[m·K] [4]) with glassy carbon spheres of 3–12 μ m diameter which dissipate most of the microwave power

* Supported by US DOE Contract # DE-AC05-84ER40150

(Figure 3). Glassy carbon is an amorphous form of carbon produced by pyrolysis of phenolic resins [8]. The material is hot pressed [9] to achieve full density vacuum compatibility.

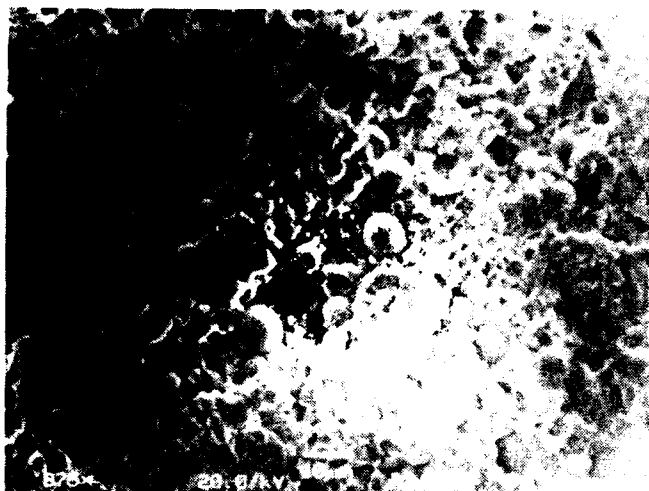


Figure 3. SEM image of the ceramic artificial dielectric used in the construction of CEBAF's loads. Note the glassy carbon spheres embedded in the aluminum nitride ceramic.

The relative dielectric constant needed to meet CEBAF's requirements was determined to be in the range 20–30, with a loss tangent greater than 0.1, over the frequency range of 1 to 6 GHz [10]. The dielectric constant and the loss tangent of the AlN-glassy carbon composite as a function of frequency were measured at room temperature using a Hewlett-Packard dielectric probe HP85070A in conjunction with a HP8753C network analyzer (Figure 4)[11]. Dielectric and magnetic properties to 20 GHz were measured by Hartung [12]. His data show that the losses have no magnetic component and that the dielectric loss tangent increases monotonically to higher frequencies.

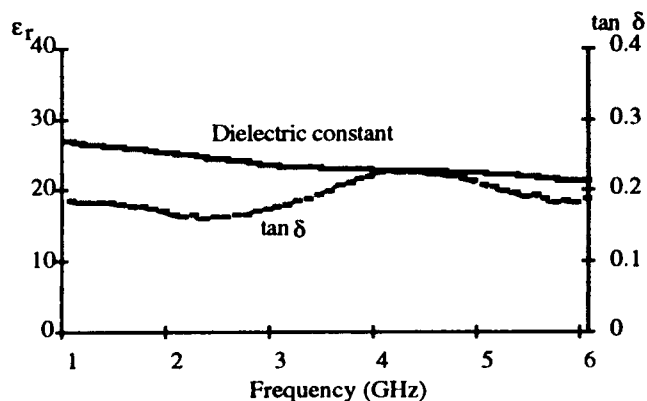


Figure 4. Dielectric constant and loss tangent of AlN loaded with glassy carbon. AlN alone has a dielectric constant of about 8 and a loss tangent $< 10^{-4}$ at room temperature.

Measurements of the loads' return losses at any temperature between 1.5 and 300 K show that the dielectric properties of the material are independent of temperature in that range (Figure 5). This independence was corroborated by direct measurement of HOM's Q 's at low temperature.

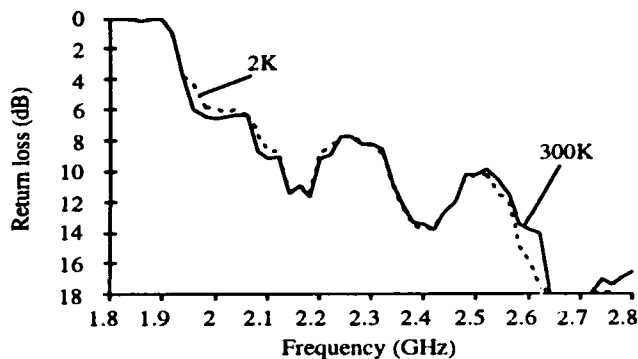


Figure 5. Return loss of AlN glassy carbon measured at 2 K and at room temperature.

III. PRODUCTION

A. Production Components and Assembly

Most of the fabrication steps for the production of the HOM loads were developed at CEBAF and several assembly procedures were performed in the laboratory to guarantee uniform quality and control of production parameters.

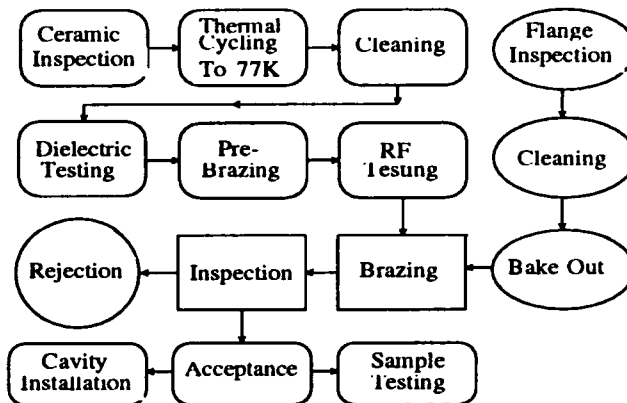


Figure 6. Flow chart of the production process. At any step before the final braze, parts can be rejected and/or reworked without major loss of added value. A fraction of the accepted loads undergoes more severe tests.

The ceramics are manufactured by industry [9] as hot-pressed tiles which are tested prior to cutting and approved for compliance with the above dielectric properties' ranges. The ground parts are again tested with the dielectric probe to ensure repeatable microwave performance. Approved ceramic parts are brazed together in high vacuum with Ticusil® (Wesgo), and the load's return losses measured before final brazing to the support flange. The temperature ramp rate to and from the melting point of the alloy (830 °C) is controlled to avoid thermal stresses to ceramic material.

The 316L stainless steel flange with 16 μ m electropolished surface finish provides a backing for the indium seal. A copper support is brazed to the stainless steel flange. The copper part prevents excessive stresses at the ceramic-to-metal braze. In other applications, this copper support can also be thermally grounded either to the helium bath or to other heat sinks to remove larger amounts of dissipated power.

Flange inspections ensure that the surface finish requirement of 16 μin , or better, is consistently met at the indium sealing surface area. The flange surface is also visually inspected for stains, scratches, machining marks, pits, and other imperfections which could lead to unreliable vacuum seals and/or possible surface contamination of the cavities. Any surface irregularity within the sealing surface is cause for flange rejection. Special care is also taken to measure the dimensions of the copper insert in the flange. Tight dimensional tolerances are required to make the ceramic-copper braze structurally strong and insensitive to the thermal cycling.

As Figure 2 shows, the load consists of two ceramic parts. Every ceramic piece is inspected for dimensional tolerances as well as for the presence of any visible flaws such as chips, laminations, cracks, or inclusions. Ceramic parts are then thermally shocked three times by submersion into liquid nitrogen to test the structural integrity of the material.

Return loss measurements are performed on the brazed ceramics at room temperature using a single test flange. The final braze of the ceramics to the flange is performed after the return loss measurement to eliminate the possibility of damaging a cleaned flange during RF testing.

A comprehensive final inspection is performed on each load prior to cavity installation. Under current production procedures, the load acceptance rate is greater than 95%. Five percent of the accepted loads undergoes subsequent testing of RF, vacuum, and mechanical properties at cryogenic temperature. These test loads are not installed in the accelerator, because some of the tests can potentially damage the indium seal surface or the ceramic-to-metal joint integrity. Lifetime thermal cycling tests have indicated that the loads can withstand and exceed the equivalent of 20 years of operation thermal cycling in the accelerator environment.

B. Uniformity and Production Experience

In excess of 1200 AlN-glassy carbon ceramic parts have been processed and have undergone extensive testing and inspections and have been utilized in the construction of more than 600 HOM loads. Although occasional deviations from specifications have been observed, the production has proceeded with consistent results.

Variations in dielectric constant of the ceramic composite over the production have ranged, depending on the glassy carbon lot, over $\pm 5\%$ within a given lot and by as much as $\pm 10\%$ from lot to lot. The latter variation seems to be also associated with minute density differences of the ceramics. Lot-to-lot variations can be compensated for by adjustments in the concentration of the glassy carbon (by as little as 0.1% by weight). This control on the dielectric constant is a primary advantage of artificial dielectric composites and makes it possible to consistently maintain this parameter over large production quantities.

Most of the ceramic material manufactured by Ceradyne meets and exceeds the UHV standards needed for installation in the superconducting cavities. One batch of ceramics manufactured from a specific glassy carbon lot yielded parts with slightly lower density (less than 1% lower) but with notably higher baseline pressure (Figure 7). By standard thermogravimetric analysis of the glassy carbon powders prior to hot pressing it is however possible to select lots which predictably provide parts with full density and extremely low outgassing rates (less than 10^{-11} torr liter/(s \cdot cm 2)).

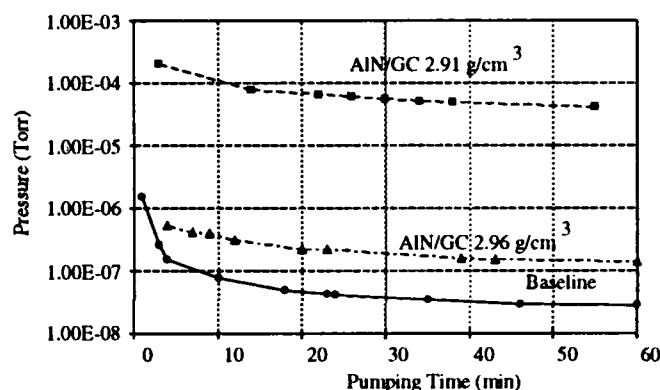


Figure 7. Comparison of vacuum pump-down times for two lots of ceramic parts. Different densities correspond to different lots of glassy carbon powders.

IV. CONCLUSIONS

The HOM loads developed at CEBAF provide damping of higher-order modes at any temperature between 1.5 K and room temperature and are compatible with the accelerator ultra-high vacuum. The reproducibility of their properties leads to dependable and well-controlled production. The special characteristics of the ceramic composite developed for the CEBAF HOM loads make it an ideal material in other applications where vacuum-compatible, temperature-independent, high thermal conductivity materials are needed.

V. ACKNOWLEDGMENTS

The authors would like to thank G. Pauley and K. Finger of CEBAF for their valuable contributions to the development and production of the HOM loads.

VI. REFERENCES

- [1] J. J. Bisognano, CEBAF TN-0147, July 1989.
- [2] I. E. Campisi, U.S. Patent No. 07/522,131.
- [3] R. Hutcheon and M. De Jong, 1993, private communication.
- [4] T. Guiton, 1993, private communication.
- [5] I. E. Campisi, et al. *Proceedings of the First Workshop on Microwave-Absorbing Materials for Accelerators (MAMAs)*, (I. E. Campisi and L. R. Doolittle, Eds.) CEBAF, Newport News, Virginia, February 22-24, 1993.
- [6] I. S. Jacobs, "Advanced Artificial Dielectric Materials for Millimeter Wavelength Applications", *Report 90-SRD-001, GE CRD*, Schenectady, 1990, and references therein.
- [7] B. Mikijelj and I. E. Campisi, *op cit.*, ref. [5].
- [8] Manufactured by SIGRI Inc., Germany.
- [9] Manufactured by Ceradyne Inc., Costa Mesa, California.
- [10] J. J. Bisognano and I. E. Campisi, CEBAF TN91-065, 1991.
- [11] I. E. Campisi, L. K. Summers, K. E. Finger, and A. M. Johnson, "Microwave absorption by lossy ceramic materials", in *Microwave Processing of Materials III, Proc. MRS Symp. Vol. 269*, 157-162 (1992).
- [12] W. Hartung, D. Moffat, and T. Hays, "Measurements of the electromagnetic properties of some microwave-absorbing materials", *op cit.*, ref [5]

The High Level RF System for Transition Crossing without RF Focusing in the Main Ring at Fermilab*

J. Dey, C. M. Bhat, A. Crawford, and D. Wildman
Fermi National Accelerator Laboratory
P.O. Box 500 MS-306, Batavia, IL 60510 USA

Abstract

A new method for crossing transition at the Fermilab Main Ring has been developed. Near transition a third harmonic component is added to the fundamental RF voltage producing a flattened RF waveform. To generate this waveform required the development of a third harmonic system consisting of a 159 MHz cavity, a perpendicularly biased tuner, and a 10 kW power amplifier. The cavity is a modified CERN SPS 200 MHz cavity whose frequency was lowered to 159 MHz by inserting two sleeves at the cavity gap. This cavity is electrically tuned over a 60 kHz range by using an orthogonally biased Iron-Yttrium-Garnet ferrite tuner. The power amplifier is a grid driven tetrode that has a $3/4 \lambda$ anode resonator and produces a RF cavity gap voltage of greater than 300 kV. The power amplifier drives the cavity by way of a coupling loop. An overview of this high level RF system and the resulting waveform will be given.

I. THE RF CAVITY

The RF cavity design called for a single cavity capable of developing a peak gap voltage of 270 kV over a ± 30 kHz tuning range centered at 159.08 MHz [1]. The cavity would operate for up to 20 ms around the transition time with a repetition rate of less than 0.5 Hz. A tunable, high Q cavity was considered to be desirable in order to reduce the 159 MHz final amplifier power requirements. One of the CERN SPS 200 MHz RF cavities for LEP operation [2] was generously sold to Fermilab for conversion to 159 MHz operation. The bare 200 MHz SPS cavity without its coupling loop and HOM suppressor has a Q of 50,000 and a shunt impedance of 8.5 M Ω . To modify the CERN SPS cavity for the transition crossing experiment the resonant frequency had to be lowered from 200 MHz to 159 MHz, a perpendicularly biased ferrite tuner needed to be attached, and a new input coupling loop had to be installed. A mechanical tuning slug to set the final adjustment of the center frequency and a removable

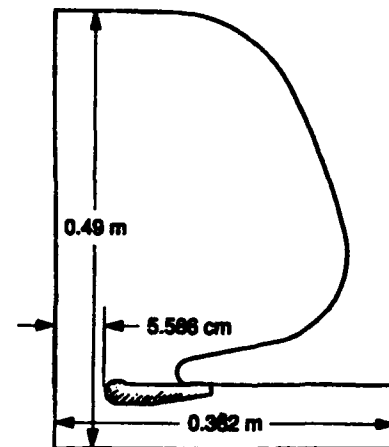


Figure 1. Modified RF Cavity profile with copper extension in nose cone.

cavity gap shorting bar were also added to the CERN cavity.

To lower the cavity resonant frequency to 159 MHz, two different methods of increasing the gap capacitance were considered. One idea was to suspend a large annular metallic ring in the center of the cavity between the nose cones. This method would require inserting the ring in sections through the 6" dia. access ports and assembling it inside the cavity. The tuning ring would require a rigid support structure and a means of external cooling. A simpler approach, shown in Figure 1, was taken of making two new OFHC copper nose cone extensions that could be shrink fitted into the existing nose cones. The existing water cooled nose cones would provide both a rigid support and a means of cooling the new extensions. The installation of the extensions was a two step process. First two aluminum inserts with a slightly smaller diameter than the final copper extensions were machined and inserted into the nose cones through one of the access ports. The positions of the aluminum inserts were then adjusted to maximize the cavity Q at the new cavity center frequency of 159 MHz. Once the aluminum inserts were in their correct positions, retaining stops were placed behind the inserts in the beam tube section of the cavity. The aluminum inserts were then removed. The actual OFHC copper extension sleeves were then cooled to liquid nitrogen temperatures and inserted through the access port into the nose cones until they touched the

*Operated by Universities Research Association, Inc. under contract with the U.S. Department of Energy.

retaining stops. With the copper extensions in place, the gap spacing was reduced from 27 cm to 11 cm. The final 100 kHz adjustment of the cavity's resonant frequency was made with a 6" dia. X 3" long cylindrical aluminum tuning slug which was mounted in one of the access ports. The position of the slug could be adjusted under vacuum by a rare earth magnet coupled linear motion feedthrough. After retuning, the cavity's Q was 36,000.

The cavity gap voltage was calibrated using a small B-field loop pick-up embedded in the cavity wall and an HP85024A 3 GHz active probe with a x10 probe tip placed directly across the copper nose cones. The gap monitor pick-up was adjusted to give a gap to monitor voltage ratio of 30,000.

The cavity is installed in the FØ straight section of the Main Ring in place of one of the normal h=1113 accelerating cavities. The 159 Mhz power amplifier and anode resonator are located in the FØ service building directly above the cavity in the Main Ring tunnel. Power is transmitted to the cavity through a 1-5/8" 50 Ω transmission line to a coaxial feedthrough with a 6" OD X 2" ID X .75" thick alumina ceramic disk window. This coaxial structure is terminated in a coupling loop whose impedance is nominally matched to the 50 Ω output impedance of the power amplifier anode resonator. It is not necessary to water cool the coupling loop due to the low duty cycle for this experiment.

II. PERPENDICULARLY BIASED TUNER

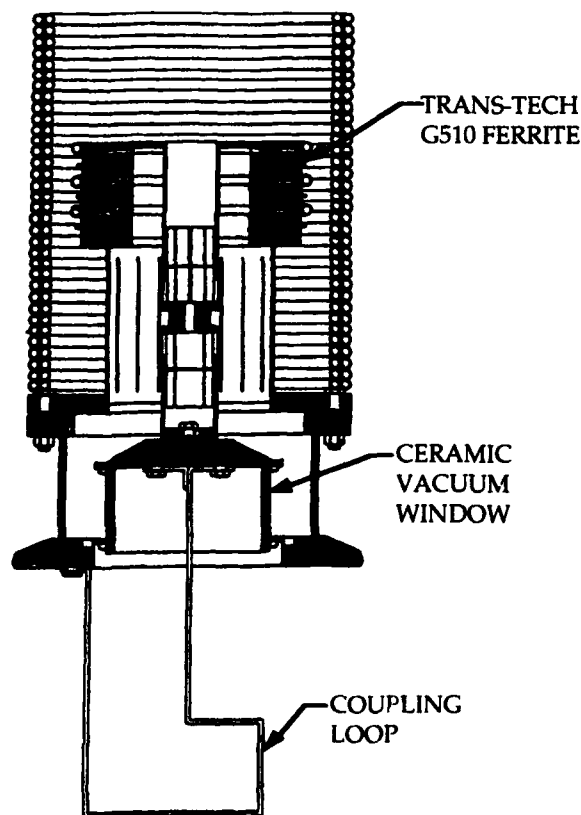


Figure 2. Perpendicularly biased ferrite tuner.

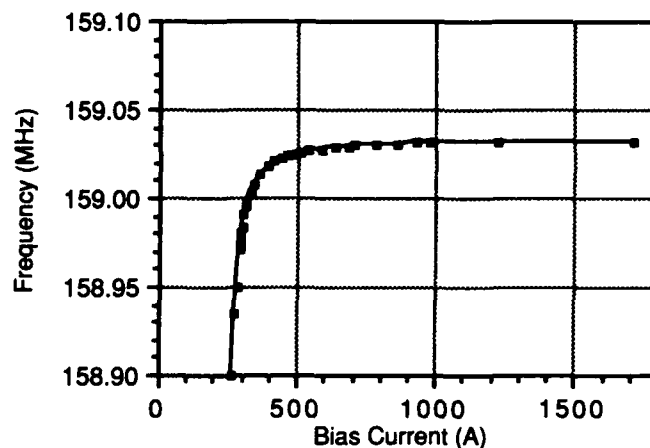


Figure 3. Tuner Frequency vs. Bias Current.

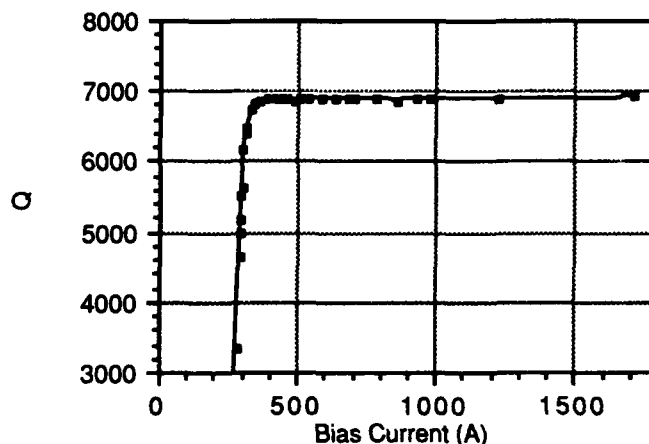


Figure 4. Tuner Q vs. Bias Current.

In order to tune the cavity over its 60 kHz tuning range an orthogonally biased ferrite tuner shown in Figure 2 was built. The tuner uses three 5" OD X 2.75" ID X 0.5" thick Trans-Tech G510 aluminum-doped, Iron-Yttrium-Garnet ferrite toroids. These high frequency, low loss ferrites are separated by water cooled, radially slotted OFHC copper plates which are welded together to form the outer conductor of the tuner structure. The OFHC copper coupling loop has an area of 54 cm² and is attached to the tuner center conductor through a 3.5" dia. cylindrical alumina ceramic vacuum window. This design allows the ferrite loaded section of the tuner to be removed from the cavity while the cavity remains under vacuum. The biasing magnetic field is generated by a solenoid formed from a double layer of 32 turns of 0.25" OD X 0.049" wall, water cooled, copper tubing wound on a 6.5" diameter. The current to the solenoid is supplied by a 0 - 2500 A pulsed dc supply. The output current of the supply is controlled by a feed-forward program which is a function of time in the acceleration cycle and a feedback circuit which compares the phase of the cavity gap monitor signal to the phase of the low level RF drive signal. These two circuits allow the

cavity phase to be controlled to within \pm five degrees of its required value throughout the tuning cycle.

The measured frequency tuning range and tuner Q as a function of the solenoid bias current are shown in Figures 3 and 4. The frequency tuning data shown in Figure 3 was taken before the final adjustment of the mechanical tuning slug in the cavity which accounts for the lower center frequency value. Assuming a maximum allowable ferrite power dissipation of 0.5 W cm^{-3} , the total Q is only allowed to change from 5000 to 7000 during the tuning cycle. This restriction on the tuner Q limits the cavity tuning range at high power to 62 kHz.

III. POWER AMPLIFIER AND ANODE RESONATOR

The power amplifier final tube is an Eimac 4CW25000B water cooled tetrode. It is operated class C in the grounded cathode, grid-driven configuration. The tube is mounted in a modified Eimac SK-360 air cooled socket with 11 - 1000 pf screen bypass capacitors. The dc plate voltage is supplied by a 9 kV, 18 A dc anode supply. The output power level is adjusted from 0 - 10 kW by varying the RF drive level to the tuned grid input circuit.

The anode resonator circuit consists of a fore-shortened $3/4 \lambda$, 50 Ω coaxial aluminum transmission line shorted at one end. The lower quarter wave section of the resonator has an adjustable output tap point and is separated from the rest of the resonator by a 2000 pf dc blocking capacitor. The tap point is nominally set for a 50 Ω output impedance. The anode dc voltage lead and the water cooling tubes for the 4CW25000B anode are attached to the center conductor of the resonator at an RF voltage minimum. The resonator is designed so that the peak RF voltage developed in the resonator is approximately twice the RF plate voltage swing on the power tube. A 3" dia. aluminum tuning slug, mounted through the side wall of the resonator, is used to adjust its center frequency. The unloaded Q of the final tube and anode resonator circuit is 2000.

IV. THE RF WAVEFORM

To produce a non-focusing RF waveform, the amplitude of the third harmonic should be kept at 13% of the fundamental 53 MHz component which itself is increasing from 1.85 to 2.08 MV during the transition crossing time [3]. The amplitude of the third harmonic grid drive low level signal is controlled by a time dependent amplitude program and an amplitude feedback error signal. This error signal is derived by comparing the amplitude of the diode detected RF signals from the Main Ring RF fanback 53 MHz sum

and the third harmonic gap voltage monitor. The error signal is then used to adjust the 159 MHz grid drive amplitude to maintain the constant 13% ratio. Figure 5 shows the result of summing the 159 MHz and 53 MHz fanback signals to produce the required non-focusing waveform.

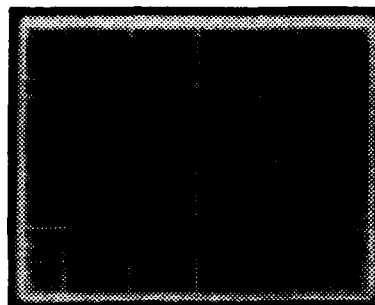


Figure 5. Oscilloscope trace (2 ns/div.) of non-focusing RF waveform.

V. REFERENCES

- [1] Synchrotron Phase Transition Crossing Using an RF Harmonic, J. Griffin, Fermilab TM 1734 (1991).
- [2] The New RF System for Lepton Acceleration in the CERN SPS, P. E. Faugeras, H. Beger, H. P. Kindermann, V. Rödel, G. Rogner, and A. Warman, Proc. 1987 IEEE PAC, Washington D.C., 1719 (1987).
- [3] Operational Experience with Third Harmonic RF for Improved Beam Acceleration Through Transition in The Fermilab Main Ring, C. Bhat, J. Dey, J. Griffin, I. Kourbanis, J. Maclachlan, M. Martens, K. Meisner, K. Y. Ng, and D. Wildman, these proceedings.

RF System of the CW Race-Track Microtron-Recuperator for FELs

V. Arbuzov, S. Belomestnykh, A. Bushuyev, M. Fomin, N. Gavrilov, E. Gorniker,
A. Kondakov, I. Kuptsov, G. Kurkin, V. Petrov, I. Sedlyarov, V. Veshcherevich
Budker Institute of Nuclear Physics
630090 Novosibirsk, Russia

Abstract

Geometry, engineering design and characteristics of an RF cavity and a tetrode power amplifier are described. They are parts of an RF system at the frequency of 181 MHz. The cavity has a copper clad stainless steel body and has a Q of 42,500 and a shunt impedance of 9.0 MOhm. Two cavities have been successfully tested up to an accelerating voltage of 1.2 MV what is 30% over the design value. One of them is mounted into the Duke's storage ring at Duke University. More than 20 RF cavities will be built and installed in a race track microtron-recuperator for FEL program at Novosibirsk. The RF power amplifier has a modular design. Several single tetrode modules can be easily combined in a high power unit. Two modules were used during cavity tests. A CW RF power of 300 kW was obtained from this unit. This type of tetrode modules will be used in different e^-e^+ colliders and storage rings.

INTRODUCTION

A 60 MeV, 1 A CW race-track microtron-recuperator is to be built at Novosibirsk for a free electron laser project [1]. An RF system is one of the key parts of this machine. Due to beam-cavity interaction during the acceleration cycle a part of electromagnetic energy, stored in RF cavities, is transformed to kinetic energy of the electron beam. During the recuperation cycle the kinetic beam energy is transformed to electromagnetic energy of the cavities. Therefore the average beam loading of RF cavities is small despite a high value of beam current.

The accelerator RF system will operate at 181 MHz. The main reason of this choice is the availability of RF high power tubes in Russia. More than 20 single cell RF cavities will be built and installed in the machine.

GENERAL DESCRIPTION

Fig. 1 shows a general scheme of the RF system. RF cavities of buncher, injector, and compensator are driven by separate 20 kW or 200 kW power amplifiers. All cavities of the main accelerator are divided in 4 groups, each of them is driven by a 600 kW unit.

RF cavities, fed from one RF power source, are located at a distance of one wave length from each other. Coaxial lines of equal length connect cavities to a rectangular waveguide which is used as a power distribution unit. Waveguide dimensions are chosen so that the waveguide

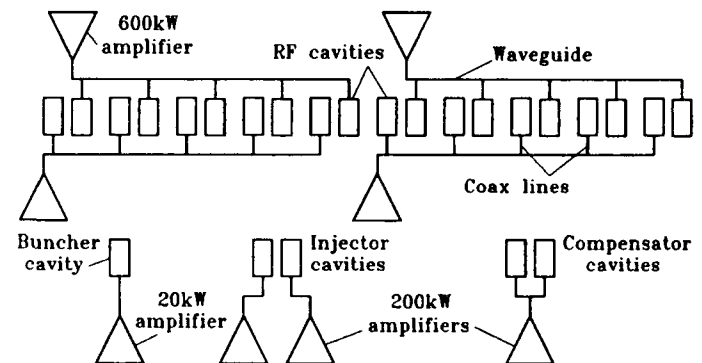


Figure 1: Scheme of RF system for microtron-recuperator.

wave length is equal to two free-space wave lengths. Therefore the coax-to-waveguide transitions are spaced by each half of the guide wave length.

A design of the coax-to-waveguide transition and a length of coaxial line to a cavity are chosen so that the matrix of transmission from the waveguide to a cavity has a form: $\begin{pmatrix} 0 & i/G \\ iG & 0 \end{pmatrix}$, where $G = I_c/V_w$ is a transconductance (I_c is a current, driving a cavity, and V_w is a waveguide voltage). Power distribution along the cavity chain is proportional to distribution of cavity shunt impedances. Right phases of cavity fields are ensured by proper rotation angles of coupling loops in the cavities. With this scheme the RF current, driving a cavity, does not depend on cavity tune. Emergency operation conditions are excluded due to this feature. Similar scheme is used in RF system of the VEPP-4 collider [2].

RF CAVITIES

Geometry of an RF cavity is shown in Fig. 2. The side walls have conical shape. It is good for mechanical rigidity and cavity electrical characteristics. The fundamental cavity mode is of E_{010} -like type. It has longitudinal electric field with angular symmetry. Cavity characteristics are summarized in Table 1.

Cavities have copper clad stainless steel walls. They have low RF losses due to low RF resistance of copper. A high thermal conductivity and a large thickness (8 mm) of copper exclude very high temperature rise at cavity surface. Stainless steel (7 mm thick) provides mechanical strength and prohibits corrosion. All cavity parts are joined to each other using TIG welding.

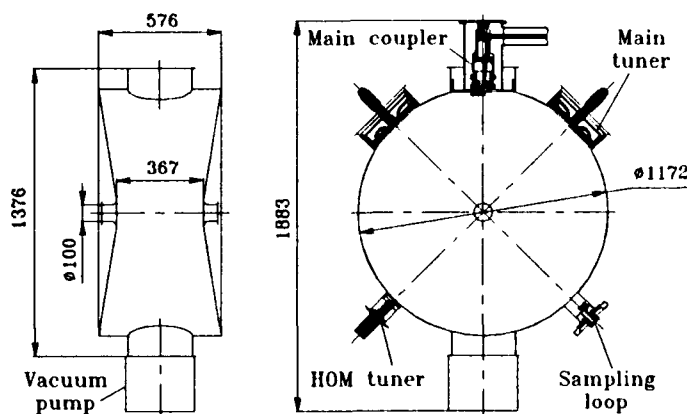


Figure 2: Sketch of the RF cavity.

Table 1: Parameters of the cavity

Accelerating voltage -	40-1000	kV
Q value -	42,500	
R/Q value -	212	Ohm
Shunt impedance -	9.0	MOhm
Resonance frequency -	181.3	MHz
Tuning range of cavity frequency -	360	kHz
Tuning rate -	5	kHz/s
Power loss at $V = 1000$ kV -	110	kW

Different units are assembled to cavity flanges. One of them is a main coupler. It has a coaxial design. A cylindrical ceramic RF window is incorporated in it. Coax input line has a wave impedance of 75 Ohm, the diameters of its outer and inner conductors are 160 mm and 45 mm respectively. Another unit is a sampling loop. It provides electrical signals which amplitude and phase are proportional to amplitude and phase of the cavity voltage. They are used in the RF control system.

Two main tuners are used basically for tuning the fundamental mode. Two additional HOM tuners are provided for making corrections of frequencies of higher order modes of the cavity. (At some unfavorable circumstances the higher order modes may cause beam instabilities).

A very high vacuum in the cavity ($10^{-7} - 10^{-8}$ Pa) is obtained by means of a pumping unit PVIG-630 which is a combination of a sputter ion pump and a gettering pump. But such a high vacuum can be achieved only after baking out the cavity up to a temperature of 300–400°C after its assembling. This is possible to do using tape heaters and thermal insulation, mounted on the outer cavity walls.

Walls of the cavity and its units are cooled by demineralized water. Special water channels are provided in SS parts of the cavity walls for this purpose. Any contact of

water with copper walls is excluded. A water distribution system is mounted under the cavity, inside of its support frame.

All cavities are assembled in pairs. Each pair is mounted on a single support frame which height is adjustable. Each cavity can be aligned individually in a horizontal plane.

RF cavities produce X-rays during their operation due to field emission from the cavity surface in the areas of high electric field. The X-ray rate goes up very steeply with cavity voltage. At $V = 1000$ kV the X-ray rate at a distance of 1 m from the cavity is as high as 4-6 R/h.

Pilot RF cavities have been successfully tested up to an accelerating voltage of 1200 kV. This voltage level was achieved after many hours of RF processing to suppress multipacting. Coaxial RF windows have been tested up to an RF power level of 170 kW.

One of the cavities has been delivered to FEL Laboratory of Duke University. It has been installed into Duke's 1 GeV storage ring which will be used for FEL experiments. The geometry of this cavity was slightly modified to accommodate its frequency to the one of Duke's requirements (178.4 MHz).

RF POWER AMPLIFIERS

A modular principle of design was applied to RF power amplifiers. It gives a possibility to build power amplifiers for different applications from few standard units. A GU-101A CW tetrode [3] with the limiting value of anode dissipation of 250 kW is used in the output stage. But for better reliability the RF power, which this module can provide, does not exceed 150 kW. Several single tetrode modules can be easily combined in a higher power unit.

A 20 kW tetrode unit is used as an intermediate amplifier stage. It can be used for driving a 150 kW stage. A 150 kW module can be used for driving a multitube high power unit.

A frequency doubler is used in the pre-amplifier unit. Therefore it is driven at a frequency of 90 MHz (an input power is 5 W). This way of frequency isolation provides a better stability of the RF control system.

The output tetrode stage has an original design. It provides simplicity of combining the power of several tubes and convenience of tuning the stage.

As an example Fig. 3 shows a schematic view of a 2-tube 300 kW output stage. Tetrode assemblies are connected to a line which is a part of the anode resonator. Its size is chosen in such a way that the transfer matrix between points "a" and "b" has a form: $\begin{pmatrix} -1 & 0 \\ 0 & -1 \end{pmatrix}$ at the operation frequency. A contactless design of the frequency tuner and the output coupler provides a high reliability and the absence of parasitic modulation. Water and air cooling is used in power amplifier units.

A coaxial line can be used for transmitting the RF power from power amplifier to RF cavities if the distance

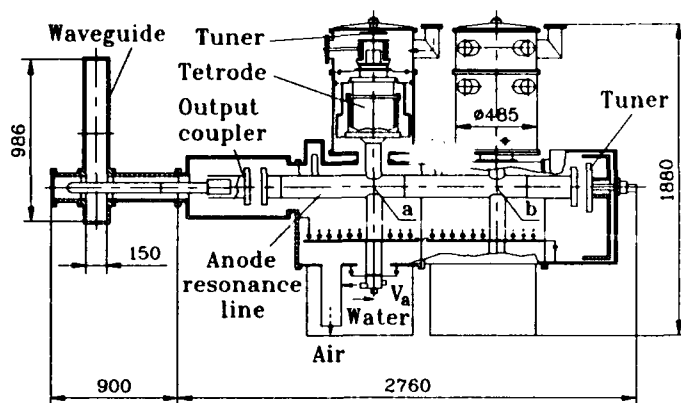


Figure 3: Design of a 2-tube RF power stage.

is not too long and the RF power is relatively low. In other cases a rectangular air-filled waveguide is used with coax-to-waveguide transitions at both ends of the waveguide.

A 8 kV dc power supply is provided for output tetrodes and a 6 kV dc power supply is provided for intermediate tetrode stages. The high voltage power supplies are equipped with fast protecting system for the protection of RF power tubes against occasional breakdowns. The time of activating this protection system does not exceed 100 μ s.

This type of tetrode modules will be applied to different e^-e^+ colliders and storage rings. E. g. a 2-tube module is used in present RF system of VEPP-4 collider. Similar modules will be used in RF system of Siberia-2 storage ring. 4-tube modules are being prepared for upgraded RF system of VEPP-4.

A 2-tube unit was tested. A CW RF power of 240 kW was obtained with a water cooled resistor as a load. The load limited the power in this case. With four RF cavities as a load of power amplifier, a CW power of 300 kW was obtained.

REFERENCES

- [1] N. G. Gavrilov et al., "Project of CW race-track microtron- recuperator for free-electron lasers," *IEEE J. Quantum Electron.*, **27**, No. 12, 2626 (1991).
- [2] V. S. Arbuzov et al., "Multicavity RF System of the VEPP-4 Storage Ring for an Energy of 5.5 GeV," *Proc. of the 8th All-Union Particle Accelerator Conf.*, Vol. 1, pp. 143-145. Dubna, 1985 (in Russian).
- [3] Svetlana Corp., 194156 St. Petersburg, Russia.

Three years of Operational Experience with the LEP RF system

Sigmund Hansen
CERN, 1211 Geneva 23, Switzerland

Abstract

The LEP copper RF system is characterised by the use of storage cavities coupled to the accelerating cavities; the number of such assemblies installed in the accelerator and the total RF power available. The physical distance between the various elements that makes up the total RF system is also specific to LEP.

The RF system has now been running for more than three years under operational conditions in LEP. We report here on the global operational experience during this period and on the performance of the various elements making up the LEP RF system.

INTRODUCTION

The beams circulated in LEP in July 1989 less than two months after the installation of the last accelerating cavity, and colliding beams for physics started two months later. A full description of the copper RF system can be found in [1], but as a reminder, there were initially 128 copper cavity assemblies installed powered by 16 1MW CW klystrons at 352 MHz. The 128 cavities are divided into 8 Units of 16 cavities each powered by two klystrons. 22 racks of low power and controls electronics have been installed in each Unit. Each of these Units can be run completely independent of each other. There are 230 protective equipment interlocks per unit, where any activated will switch off that Unit but not affect any of the other Units.

In each Unit there are 1342 control points that can be addressed over the control system either locally or remotely.

The cavities are installed around two diametrically opposite collision points [2 and 6] spaced about 13.5 kilometres apart around the circumference of the LEP tunnel. The central control room (PCR) is situated at a physical distance of about 6 KM from pt 2 and 13 KM from pt 6.

Superconducting cavities for the LEP upgrade to higher energies are integrated into the RF system as they are being installed. At present the installed sc cavities are still in a commissioning stage and are not used routinely for operation although some cavities have been used for physics operation for about 700 hours. The part of the RF system involving these cavities is not included in this review.

OPERATIONAL ASPECTS

For a nominal output power of 1 MW from each klystron, the copper system with 128 cavities can deliver a maximum of about 375 MV circumferential volts taking into account the losses in the waveguide system which amounts to about 6% of the total power. The total available voltage was reduced in 1992 when 8 cavities were removed to make room for electrostatic separators for eight bunch Pretzel operation.

The way LEP is normally run for physics will allow one RF Unit to drop out without losing the circulating beams.

Some rapid adjustments to the remaining units to compensate for the lost circumferential volts are normally required.[2] The drop out of one RF Unit is referred to as an "RF trip".

By constant improvements to the equipment reliability, the number of RF trips have considerably decreased since the initial commissioning. Statistics from the operations group show a decrease in lost coasts caused by RF from nine in 1991 to five in 1992. A coast lost due to RF failure requires more than one RF Unit to drop out simultaneously or some abnormality that affects several units.(RF phase jumps, water failure, etc.)

Until 1992 LEP operated with a 60° phase advance lattice and a constant synchrotron tune during the ramp from injection energy of 20 GeV to the collision energy with a Qs of 0.085. For a collision energy around the Z⁰ peak (45.6 GeV), this required the RF system to deliver a maximum of 250 MV circumferential voltage, corresponding to about 450 KW RF output from each klystron with all units operational.

In 1992 LEP was run with a lattice of 90° phase advance with a corresponding change in the momentum compaction factor by two compared to the 60 degree lattice, and therefore doubled the required RF voltage for the same Qs and collision energy. With the presently available RF volts it was no longer possible to keep the Qs constant at 0.085 during the ramp all the way up 45 GeV. So for physics during 1992 LEP run with a lower Qs at the collision energy than in the previous years.

The synchrotron frequencies of the two beams are monitored continuously in the control room. These signals are transmitted from one of the RF Units in the tunnel to the control room via the optical transmission system. The global voltage control system will eventually allow the RF voltage to be adjusted directly as a function of the synchrotron frequency.

Each of the accelerating cavities is coupled to a low loss spherical storage cavity (fig1). This concept increases the shunt impedance of the accelerating cavities from 26 MΩ/m to 40 MΩ/m and in this way requires less drive power to produce a given accelerating voltage than for a single accelerating cavity. The modulated waveform in the cavities (fig1) set up by the coupled system has been chosen to be two times the bunch frequency for four bunch operation or the bunch frequency for eight bunch operation per beam. For more than eight bunches per beam, one would have to run the RF system with a single frequency and with a correspondingly lower shunt impedance.

The modulated waveform can be shifted in phase with respect to the bunch position at each RF Unit. This possibility was used to run LEP with slightly different synchrotron frequencies for the electrons and the positrons, allowing longitudinal feedback to be applied via the RF cavities to the electrons and positrons independently. In 1992 a dedicated longitudinal feedback system working at 1 GHz was installed and made operational [3].

Energy calibration of the LEP beams by the LEP experiments to a precision of a few MeV imposed a very precise knowledge and stability in time of the RF phase with respect to the beams. Dedicated recording equipment have been installed for this purpose.

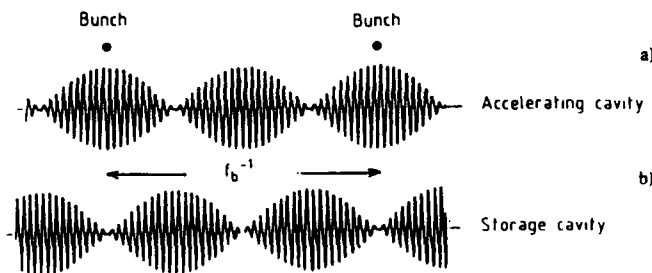
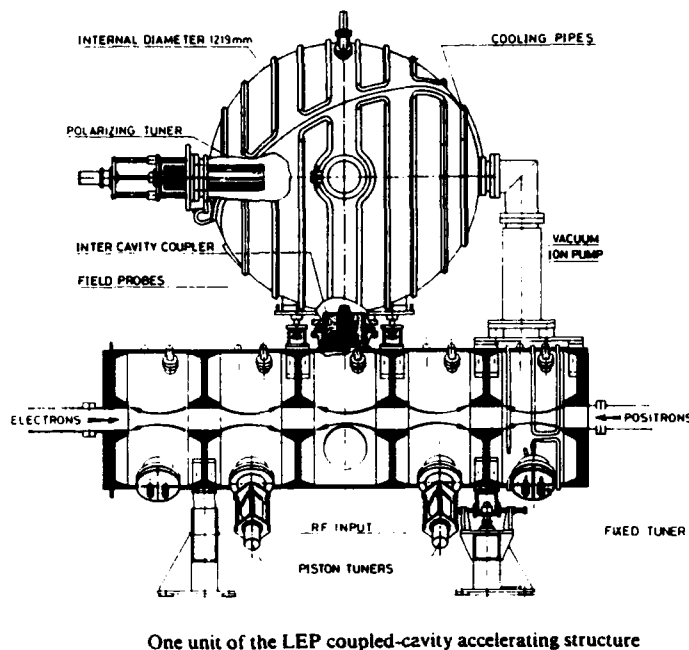


Fig. 1

EQUIPMENT BEHAVIOUR

A. The Cavities

Prior to installation in LEP, the assemblies of accelerating/storage cavities have all been baked to 150 °C for 24 hours and RF conditioned up to 140 KW, well above the nominal value of 125 KW. The cavities have not been rebaked after installation.

At present the cavities have about 18 000 operating hours (including conditioning before installation) at various power input levels ranging from a few kilowatts (injection level) to close to one hundred kilowatts (collision level).

Out of the 128 input power couplers, we have changed six which had developed a vacuum leak in the ceramic window. Five of these couplers were all in the same straight section at adjacent cavities and happened after a shut down. We strongly suspect that mechanical stresses set up by distortions to the

waveguide system (someone run into the system with a transport vehicle ?) is the main cause for these leaks.

There are 768 ceramic cups in total installed on the cavities. These cups house loops used for monitoring and the tuning control system. After some initial problems with vacuum leaks these ceramic cups have behaved reliably.

The 384 active piston tuners together with their drive electronics have performed very satisfactorily. So has the rather complex tuning system for the two cavity assembly.[4] Regular maintenance of the drive mechanism for the piston tuners (cleaning and greasing) as well as frequent changes of air filters for cooling fans has reduced trips due to reflections from the cavities and other interlocks related to the cavities.

B. Klystrons and Circulators

The 1 MW CW klystrons working at 352 MHz developed specially for LEP by two European firms [5] have performed extremely well.

Out of the 16 initially installed klystrons, 11 have by the end of 1992 operated for more than 17000 hours in LEP. The five others have been replaced for various reasons during the first 5000 hours of operation, all under guarantee from the manufacturer.

Klystron instabilities that might appear at high output power have not been a problem during these three years of operation. It should be noted however that the required output power from a single klystron rarely exceeds 700 KW for normal LEP operation for physics. Reflected power back into the klystron from the circulator is kept to a minimum and constant by the use of a regulation system that compensates impedance variation in the circulator as a function of the output temperature of the cooling water.

Electrically the 1 MW CW circulators have performed well. However, a weakness in the mechanical design of the water cooling circuit leading to water leaks, provoked some problems early on in LEP operation. This weakness in the design has since been corrected for by the manufacturer.

C. High Voltage Equipment

The maximum operating voltage for the 1 MW klystron is 90 KV. For normal LEP operation, the klystrons are operated either at 77 KV or 88 KV depending on the required output power. The 100 KV high voltage power supply is located on the surface, whilst the high voltage interface equipment sits in the klystron gallery next to the machine tunnel. Neither the power supply nor the several hundred meter long HT cable have ever created any serious problems.

The high voltage interface equipment consists basically of a smoothing capacitor, a modulator connected to the modulation anode of the klystron, series resistors, insulating transformers and a fast acting crowbar device. The various elements are located in separate oil tanks and connected with cables fitted with connectors for easy dismantling.

Initially we considered to use a spark-gap as the crowbar element, based on excellent experience with such a device in the ISR. We did, however, pursue a development in collaboration with EEV to see if a multigap thyatron could be used. Finally we decided to use a five gap thyatron rated for 90 KV. This choice was based on several factors, the main one being its compactness and easy triggering. In the initial design, a rather complex triggering circuit based on semiconductors

was used to insure multi-triggering of the thyatron. This way of triggering the thyatron gave rise to a lot of spurious firing of the crowbar and have since been changed to a straight-forward current transformer. This direct firing of the crowbar has proven to be efficient and reliable, and spurious triggering of the thyatron has by now become very rare.

D. Low power and controls

Two optical fibre links are used for the transmission from the LEP control room (PCR) of RF phase and frequency reference to the RF stations at pt.2 and pt.6 of LEP [6]. These links have a total length of 5.4 km and 7.9 km respectively and uses a total of eight monomode fibres per cable without repeaters. A rather complex transmission system including optical feedback forms part of these links. A maximum phase variation of 800 electrical degrees at 176 MHz has been measured due to length variation of the fibres caused by temperature fluctuations. The feedback system reduces these variation to less than a few degrees.

Spurious phase jumps (glitches) have been responsible from time to time of beam losses. These kind of faults are rather difficult to localise, especially in a huge system like the one in LEP. These phase jumps have in most cases been attributed to the regeneration electronics located in the klystron galleries rather than the optical transmission system. To detect and localise such glitches additional analogue diagnostic equipment have been installed.

Apart from these occasional problems with phase jumps, the low power electronics has turned out to work very reliably. The same approach and design is used for low power high frequency electronics that is being installed for the LEP upgrading with 192 superconducting cavities.

The modular approach [7] for the digital control of the LEP RF system, together with an interactive local control facility has turned out to be vital for the commissioning, testing and operation of the RF system. It also allows for additional units with superconducting cavities to be integrated gradually into the controls system with minimum disturbance to the operation of the accelerator. Over the years a number of improvements have been incorporated into the digital controls

system without modifying the basic concept. Direct Ethernet access to the Data Manager of the individual units together with more powerful processors and corresponding software improvements in the Data Managers have been the most important changes. These changes allow for a permanent logging and storage locally of all important RF parameters and also remotely via the general LEP controls system.

Due to the distances involved, the possibility for direct access to the RF Units from anywhere on the controls network has turned out to be of paramount importance for surveillance and remote fault diagnostics by the equipment specialists.

CONCLUSIONS

To keep a huge high power rf plant like the one in LEP operational around the clock is not an easy task. The importance of reliable equipment is obvious, but a certain built in redundancy is almost as important. This redundancy in the LEP RF system is not only found in the design of the equipment, but also in the modular way the total plant is built up. The fact that the beams in LEP will survive if one RF unit drops out, has made coasts in LEP lasting for 12 hours almost a routine, and more generally beams lost due to RF failure has become less and less frequent.

REFERENCES

- [1] G.Geshonke, S.Hansen, Status and Performance of the LEP RF System, *Proceedings 14 Int. Conf. on High Energy Accelerators*.
- [2] E.Ciapala, Global Voltage Control of the LEP RF System, *this conference*.
- [3] E.Peschardt, Longitudinal Feedback in LEP, *this conference*
- [4] P.Brown, Status of the LEP Accelerating Structure, *Proceedings PAC 1989*
- [5] H.Frischholz, The LEP Main Ring High Power RF System, *Proceedings PAC 1989*
- [6] E.Peschardt, J. Sladen, Phase Compensated Fibre-Optic Links for the LEP RF Reference Distribution, *Proceedings PAC 1989*.
- [7] S.Hansen et.al., Digital Control of the LEP RF System, *Proceedings PAC 1989*

Measured Performance of the GTA RF Systems*

Peter M. Denney[†] and Stephen P. Jachim

MS-H827, Los Alamos National Laboratory, Los Alamos, NM 87544

Abstract

This paper describes the performance of the RF systems on the Ground Test Accelerator (GTA). The RF system architecture is briefly described. Among the RF performance results presented are RF field flatness and stability, amplitude and phase control resolution, and control system bandwidth and stability. The rejection by the RF systems of beam-induced disturbances, such as transients and noise, are analyzed. The observed responses are also compared to computer-based simulations of the RF systems for validation.

I. INTRODUCTION

In recent months, an experiment was performed on GTA that resulted in the successful commissioning of the 3.2-MeV accelerator [1]. The 3.2-MeV stage included four RF accelerating cavities along the beam line: a radio frequency quadrupole (RFQ), two intermediate matching sections (IMSA and IMSB), and a drift tube LINAC (DTL1). The measured performance of the RF control systems with and without beam disturbances is presented.

II. RF SYSTEM DESCRIPTION

Much has been written in the literature regarding the design of the RF control system for GTA [2-5]. For ease of understanding the measurements, however, a brief explanation of important concepts is in order.

Figure 1 shows a block diagram of the essential RF system operating in closed-loop control. Additional modules can be incorporated for improved performance [6-10]. However, that is beyond the scope of this paper.

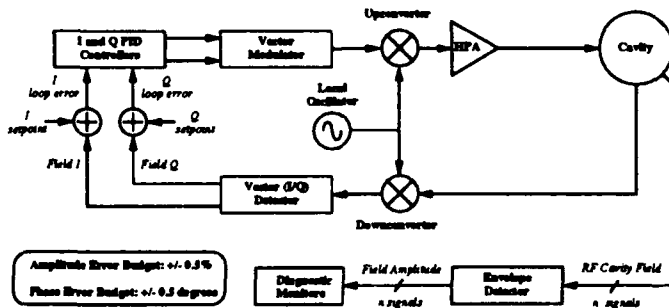


Figure 1. Block Diagram of the RF Control System

The implementation used to achieve the $\pm 0.5\%$ and $\pm 0.5^\circ$ error specification relies on the control of the in-phase (I)

*Work supported and funded by the US Department of Defense, Army Strategic Defense Command, under the auspices of the US Department of Energy.

[†] Industrial Partner: Grumman Corporation

and quadrature (Q) components of the cavity field. These orthogonal components, Field I and Field Q, are baseband signals that are controlled independently via the I Controller and Q Controller, respectively. Regulating the Field I and Field Q vectors implies that the RF cavity field vector is regulated to the same degree. This assumes, however, that the transfer function of the sense loop (cable between the cavity and Downconverter, the Downconverter, and the Vector Detector) remains constant. Since long-term phase stability has not been implemented as yet [6], all the measurements presented in this paper will address short-term stability. The Field Amplitude and Field Phase stability can be derived using the following simple equations.

$$\text{Field_Amplitude} = \sqrt{\text{Field_I}^2 + \text{Field_Q}^2} \quad (1)$$

$$\text{Field_Phase} = \text{TAN}^{-1}(\text{Field_Q}/\text{Field_I}) \quad (2)$$

As an independent verification of the Field Amplitude stability, cavity field signals from various pick-up loops were also measured by Envelope Detectors.

III. TEST RESULTS

A. Waveform Digitization Measurements

In order to analyze various control parameters, including noise rejection, a waveform digitizer was employed. The digitizer possessed four synchronous data channels that allowed beam data and RF control system data to be measured simultaneously. The sampling rate was 5 MSamples/s and its effective resolution was 9 bits (due to digitizer noise). This provided measurement capability of $\pm 0.4\%$ resolution of a full-scale signal. Because the Field I and Field Q measurements needed to be resolved to within $\pm 0.1\%$ for noise analysis, this was clearly a limiting factor. Fortunately, however, the I Loop Error and Q Loop Error signals were magnified by a factor of 10 before being sent to the digitizer, so the Field I and Field Q signals could be derived to $\pm 0.04\%$ using the following equations.

$$\text{Field_I} = \text{I_Setpoint} - \text{I_Loop_Error} \quad (3)$$

$$\text{Field_Q} = \text{Q_Setpoint} - \text{Q_Loop_Error} \quad (4)$$

Figure 2 shows synchronously taken data of the RFQ beam input current, the RFQ Field Amplitude and RFQ Field Phase Error. The RF-related data was derived from the Vector Detector signals. Table 1 summarizes the Field Amplitude and Field Phase characteristics for both the RFQ and DTL1 RF systems.

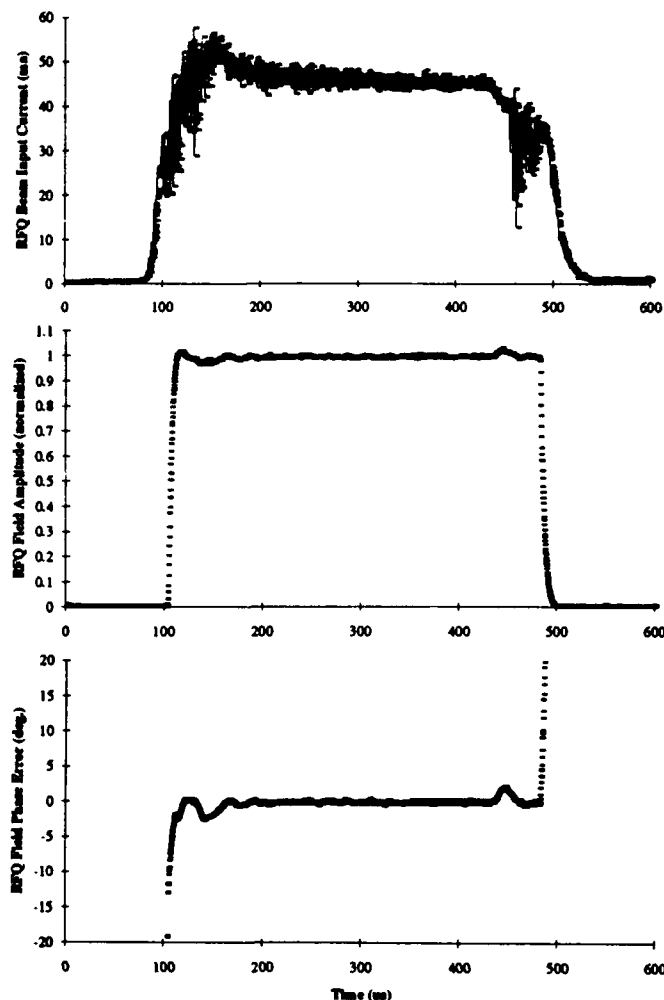


Figure 2. Synchronous Waveforms of the RFQ Beam Input Current, Field Amplitude and Field Phase.

Table 1. Characteristics of RFQ and DTL1 RF systems

Measurement	RFQ	DTL1
Cavity Fill Time (μ s)	6	5.2
Cavity Fill Overshoot (%)	2	6
Beam Induced Amplitude Overshoot (%)	4	2
Beam Induced Phase Overshoot (deg)	3	1

Figure 3 expands the waveforms of Figure 2 from 200-400 μ s. Clearly, the field signals contain noise at frequencies of 50 kHz - 100 kHz. The beam signal clearly contains high-frequency noise. Figure 4 shows Field Amplitude and Field Phase Error waveforms without the beam. The noise is reduced considerably. However, the same frequency components are present. Open-loop tests did not reveal any noise at these frequencies, but the sensitivity of the measurement was only $\pm 1\%$. Further testing using higher resolution digitizers is required to quantify correlations. Table 2 shows relative disturbance rejection of the RFQ and DTL1 closed-loop systems. A constant voltage signal was applied at the output of the I Controller while the Field I was measured. The data was normalized to the 10-kHz value and shows higher sensitivity to noise at 25 kHz - 100 kHz.

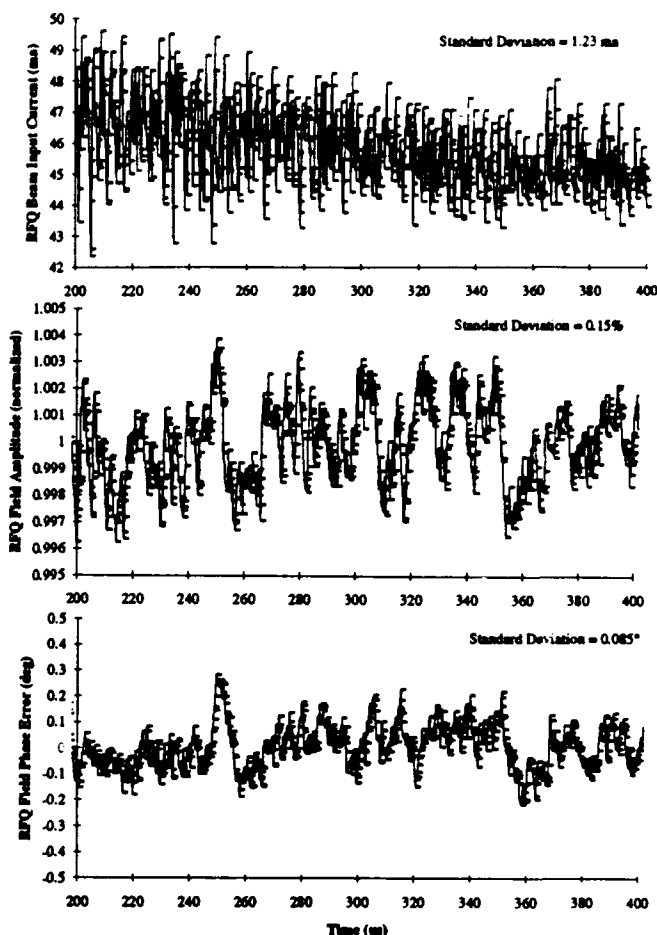


Figure 3. Data from figure 2 expanded from 200-400 μ s

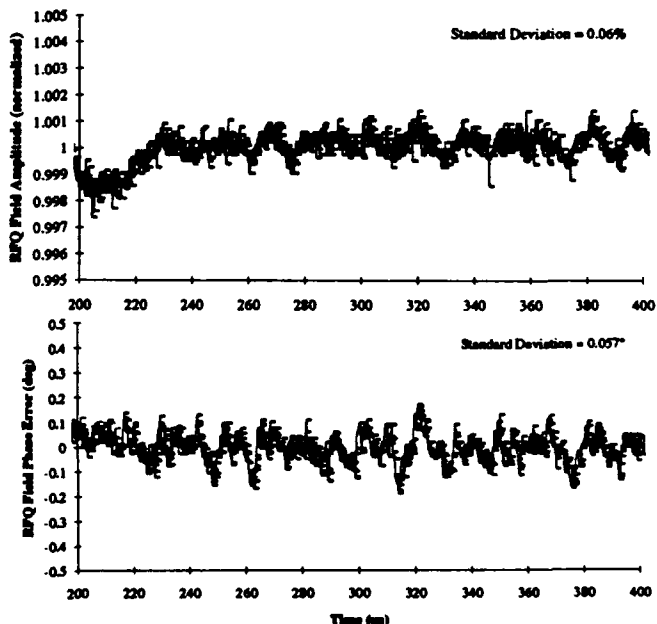


Figure 4. RFQ Field Amplitude and Field Phase without beam

Table 2. Relative Disturbance Rejection of RFQ & DTL1

RF System	10 KHz	25 KHz	50 KHz	75 KHz	100 KHz	250 KHz
RFQ	0 dB	-7.4 dB	-13 dB	-11.7 dB	-8.5 dB	7.7 dB
DTL1	0 dB	-6 dB	-10.5 dB	-11.3 dB	-8.9 dB	-3.2 dB

IV. SUMMARY

B. Single Sample per Pulse Measurements

Equipped with 12-bit A/D converters, the Vector Detector and Envelope Detector synchronously sampled the Field I, Field Q, and various Field Amplitude signals at a single point during the RF pulse. A single snapshot consisted of 15 consecutive pulses. By incrementing the timing along the RF pulse, the field flatness was measured. Figure 5 shows the flatness of the DTL1 Field Amplitude without beam as measured from the Envelope Detector.

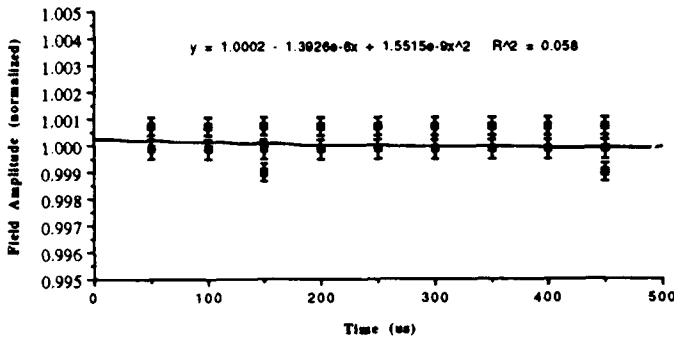


Figure 5. DTL1 Field Amplitude Flatness without beam

The statistics are summarized in Table 3 for all four RF systems. Please note that the amplitude values are normalized, and the mean values are relative to the setpoints. Because the Envelope Detector readings were normalized to the mean value, its mean is equal to unity. Also, STD represents standard deviation. Table 4 gives the statistics with beam.

Table 3. Statistics of all 4 RF systems without beam

STATISTIC	RFQ	IMSA	IMSB	DTL1
I/Q Detector				
Amplitude Mean	0.9988	0.9993	1.0023	0.9971
Amplitude STD (%)	0.041	0.081	0.12	0.074
Ampl. min,[max]	0.9980,[0.9990]	0.9972,[1.0028]	1.0014,[1.0063]	0.9964,[0.9979]
Phase Mean (deg)	0	0.04	-0.1	-0.04
Phase STD (deg)	0.068	0.064	0.161	0.051
Pha min,[max](deg)	-0.24,[0.24]	-0.06,[0.17]	-0.74,[0.20]	-0.13,[0.13]
Env. Detector				
Amplitude STD (%)	0.038	0.088	0.085	0.034
Ampl. min,[max]	0.9986,[1.0009]	0.9990,[1.0028]	0.9989,[1.0029]	0.9990,[1.0007]

Table 4. Statistics of all 4 RF systems with beam

STATISTIC	RFQ	IMSA	IMSB	DTL1
I/Q Detector				
Amplitude Mean	0.9987	0.998	1.003	0.9953
Amplitude STD (%)	0.11	0.11	0.11	0.075
Ampl. min,[max]	0.9968,[1.0003]	0.9970,[0.9999]	1.0004,[1.0052]	0.9935,[0.9970]
Phase Mean (deg)	-0.03	0.06	-0.11	-0.12
Phase STD (deg)	0.089	0.11	0.124	0.055
Pha min,[max](deg)	-0.24,[0.17]	-0.17,[0.23]	-0.42,[0.02]	-0.23,[0.00]
Env. Detector				
Amplitude STD (%)	0.089	0.032	0.065	0.054
Ampl. min,[max]	0.9981,[1.0013]	0.9970,[1.0010]	0.9989,[1.0011]	0.9992,[1.0008]

To summarize, all RF control systems exceed the performance specifications with and without the beam present in the cavities. As expected, the amplitude and phase errors are greater with beam present. However, further testing and analysis is required to quantify any cross correlations. The increase in forward RF power while the beam is present may also contribute to the noise. Comparisons between measured results and computer simulations will be the topic of future investigation.

Good agreement of the standard deviations was noticed between the RFQ waveform digitization measurements and the single sample per pulse tests. Also, there is excellent agreement of the standard deviations between Vector Detector and Envelope Detector Field Amplitude. This, in essence, verifies the accuracy of the measurements.

V. ACKNOWLEDGMENTS

The authors would like to thank the following individuals for their assistance and patience along the way: B. Atkins, D. Barr, S. Bowling, R. Cole, C. Geisik, D. Gilpatrick, B. Graybill, M. Jenkins, K. Johnson, D. Kerstiens, J. Power, A. Regan, O. Sander, B. Weiss, A. Young, and C. Ziomek.

VI. REFERENCES

- [1] K. F. Johnson et al., "Commissioning of the First Drift Tube LINAC Module in the Ground Test Accelerator," *Proc. IEEE Particle Accelerator Conf.*, 1993.
- [2] S. P. Jachim, "Some New Methods of RF Control," *Proc. LINAC Conf.*, pp. 573-577, 1990.
- [3] S. P. Jachim et al., "The Los Alamos VXI-Based Modular RF Control System," *Proc. IEEE Particle Accelerator Conf.*, 1993.
- [4] S. P. Jachim and E. F. Natter, "Beam Loading and Cavity Compensation for the Ground Test Accelerator," *Proc. IEEE Particle Accelerator Conf.*, pp. 1870-1873, 1989.
- [5] A. H. Regan and P. M. Denney, "RF Reference Generation for the Ground Test Accelerator," *Proc. IEEE Particle Accelerator Conf.*, 1991.
- [6] S. P. Jachim et al., "A Phase-Stable Transport System," *Proc. Neutral Particle Beam Tech. Symp.*, 1990.
- [7] C. D. Ziomek, S. P. Jachim, and E. F. Natter, "Design of a Multivariable RF Control System Using Gain-Shaping in the Frequency Domain," *Proc. IEEE Particle Accelerator Conf.*, 1991, pp. 1329-1331.
- [8] C. D. Ziomek, "Adaptive Feedforward in the LANL RF Control System," *Proc. LINAC Conf.*, 1992.
- [9] L. Eaton, S. Jachim, and E. Natter, "An Adaptive Control Technique for Accelerators Using Digital Signal Processing Technology," *Records of the Europhysics Conference on Control Systems for Experimental Physics*, 1987.
- [10] C. D. Ziomek et al., "Results of Adaptive Feedforward on GTA," *Proc. IEEE Particle Accelerator Conf.*, 1993.

Improved RF System for Aladdin*

Kevin J. Kleman

Synchrotron Radiation Center, University of Wisconsin – Madison
3731 Schneider Drive, Stoughton WI 53589 USA

Abstract

A new 50.58 MHz RF system has been installed in the Aladdin synchrotron light source at the University of Wisconsin – Madison. A more compact aluminum RF cavity was constructed to make the original RF straight section available for a future insertion device. The original grounded cathode 4CW100000E power amplifier was also modified to improve its stability and control system. The new system delivers enough power to run the cavity at maximum gradient while supporting large beam currents. New low level RF electronics were constructed, including low level RF feedback. Feedback allows the use of a smaller RF bucket at injection to improve beam capture and eliminates operational difficulties with the Robinson instability. Operational results with the new system are presented.

I. INTRODUCTION

The original Aladdin RF system consisted of an aluminum quarter wave coaxial resonator and a grounded cathode 4CW100000E power amplifier[1]. Stability problems with the PA prompted the acquisition of a surplus Collins 20 kW amplifier that had previously seen service on SPEAR. The ring has been running with the Collins unit since commissioning. The original cavity was installed in a long straight section that is now desired for future use by an insertion device. The need for higher gradients during 1 GeV operation also prompted the construction of a new cavity. The only place available for a new cavity was a short section at the beginning of a quadrant of bending magnet cells. A much smaller aluminum cavity[2] was designed which had approximately the same Q and shunt impedance as the original cavity. This gave an opportunity to address the problems of the original power amplifier. The 4CW100000E amplifier was modified to correct its problems. New low level electronics were built and the system tested with the new cavity insuring that it performed properly before installation.

II. POWER AMPLIFIER

A. Modifications

Improvements made to the power amplifier (Fig. 1) consisted of the addition of a 50 ohm grid damping resistor and simplification of the neutralization circuit. The neutralization cable is now connected to the grid end of the input circuit in parallel with the RF drive.

The amplifier is operated at rather low bias levels for a tube of this type. This is because the tube's full output capability is not needed and a low anode load impedance is desirable for stability. A section of 3 1/8 inch rigid coax one half wavelength long connects the PA to the cavity. Impedance matching at the amplifier is through a tap on the coaxial anode resonator. A coaxial rotatable joint at the cavity end allows the adjustment of the cavity coupling coefficient.

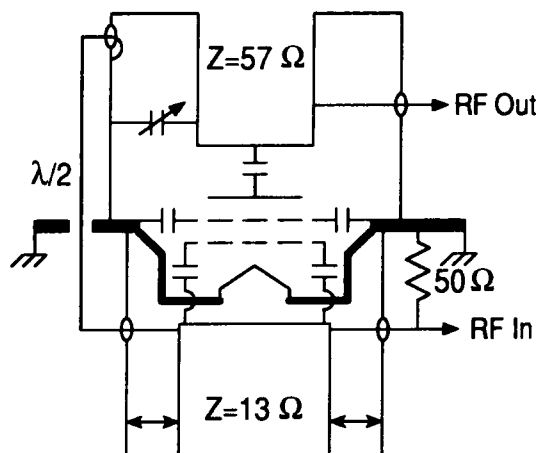


Figure 1. 4CW100000E Amplifier Circuit

Anode Voltage	9 kV
Screen Voltage	1.1 kV
Grid Voltage	-215 V
Load Impedance	550Ω
Power Gain	23 dB
Anode Bias Current	2.8 A
Power Output	35 kW

Table 1. Power Amplifier Operating Parameters

B. Instability Cures

Operation of the power amplifier into a high Q cavity load presents some problems. The interaction of the anode resonator tap with the feedline and coupling loop results in a pair of resonances in the plate circuit about 5 MHz above and below the operating frequency. These unloaded resonances present a very high impedance to the tube anode. In addition the bandwidth of the neutralization circuit is limited due to the $\lambda/2$ phase inversion line. The combination of these effects causes a stability problem that is not evident unless operating with a narrowband resonant load.

The solution to the problem is to provide damping for the off frequency resonances without dissipating too much power at the operating frequency. To accomplish this both the power amplifier and cavity are overcoupled by a factor of three. The resulting standing wave on the $\lambda/2$ connecting feedline has a voltage minimum at the center when the cavity is resonant and a voltage maximum when off resonance. The addition of shunt resistive loading at the center of the line produces the required damping while dissipating only a small percentage of the RF power. Figure 2 is the output from a SPICE simulation showing the effect of a 250Ω damping resistance at the center of the feedline on the anode load impedance as a function of frequency. The damping reduces the impedance of the undesirable resonances to approximately the level seen by the anode at cavity resonance.

*Work supported by the NSF under contract DMR-92-12658

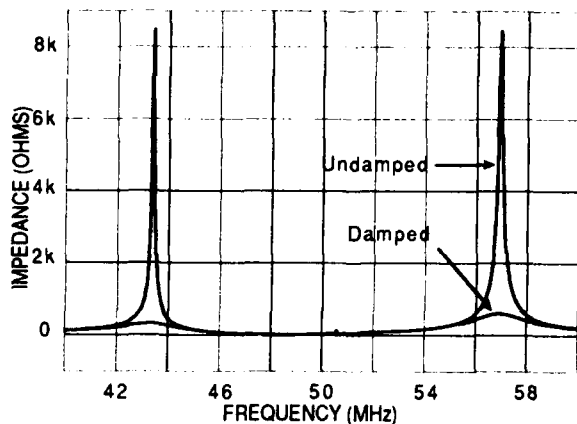


Figure 2. SPICE output showing off resonance behavior

IV. LOW LEVEL RF CIRCUITRY

A. Circuitry

The low level RF stages (Fig. 3) are conventional in design. A modular approach was adopted to allow easy servicing and modification. Amplitude and phase control are performed by a double balanced mixer acting as a current controlled attenuator and a phase shifter using a quadrature hybrid loaded with varactor tuned series LC circuits. The amplitude control loop uses a compensated schottky diode detector to measure the cavity field. A phase loop locks the phase of the beam signal generated by a pickup to the master oscillator phase. Both of these loops have modest bandwidths (<500 Hz) because the RF feedback already reduces any low frequency noise in the system. An ENI 5100L amplifier is presently used to drive the power amplifier. If high current operation at 1 GeV is desired this amplifier will be inadequate and a 300 W MOSFET amplifier module will be constructed to replace it.

V. RF FEEDBACK

The injection scheme of Aladdin imposes some unusual requirements on the RF system. An unbunched beam is injected from a 100 MeV microtron at a rate that is much faster than the radiation damping time. This makes injection and stacking more critical than usual. The energy loss per turn is only 4 eV at injection so most of the beam will be captured if it can be held within the machine aperture. To capture effi-

ciently it is necessary to keep the RF voltage low so as to limit the amplitude of the energy oscillation. However, the voltage must be kept high enough to stabilize the beam against phase instability as the beam loading is inversely proportional to V/R_s . An effective feedback mechanism is the solution to meeting these conflicting requirements.

There are several approaches to solving the beam loading problem[3]. Wideband amplitude and phase control loops are not suitable for this purpose due to the very large beam loading factor. Feedforward compensation is a possibility but the sensitive amplitude and phase adjustments are a discouragement. Baseband feedback processing using in-phase and quadrature components[4] would be practical but complicated. Clearly in our case the simplest and most effective solution is the use of direct proportional RF feedback to lower the effective shunt impedance of the cavity as seen by the beam thereby reducing beam loading.

An RF feedback loop is implemented at low level with a summer and amplifier module that can be switched into the signal path at the output of the low level RF stages. A pair of SPDT PIN diode switches allows the feedback to be turned on and off under remote control. The signal from a cavity pickup is adjusted in amplitude to match the drive signal amplitude without feedback and is summed out of phase with the drive signal. The difference signal is amplified and fed to the driver amplifier. The loop gain is 20 dB increasing the effective cavity bandwidth to about 50 kHz and lowering the effective shunt impedance to below 100 k Ω .

During commissioning it was found that the Robinson instability was affecting the beam even with the feedback operating. This problem was more severe at high energy. Inspection revealed a phase error in the feedback loop that resulted in the system being tuned to the unstable side of resonance. Although it is not immediately obvious, a phase error in the feedback signal will result in a shift in resonant frequency of the system when the feedback is turned on. This effect is clearly shown in Figure 4. The phase of the RF feedback was advanced 10 degrees from the out of phase condition. This shifted the system resonance to about 10 kHz below the RF frequency, providing Robinson damping and eliminating the problem. This shows that the use of classical Robinson damping must still be considered when using RF feedback, especially with modest loop gains such as employed here.

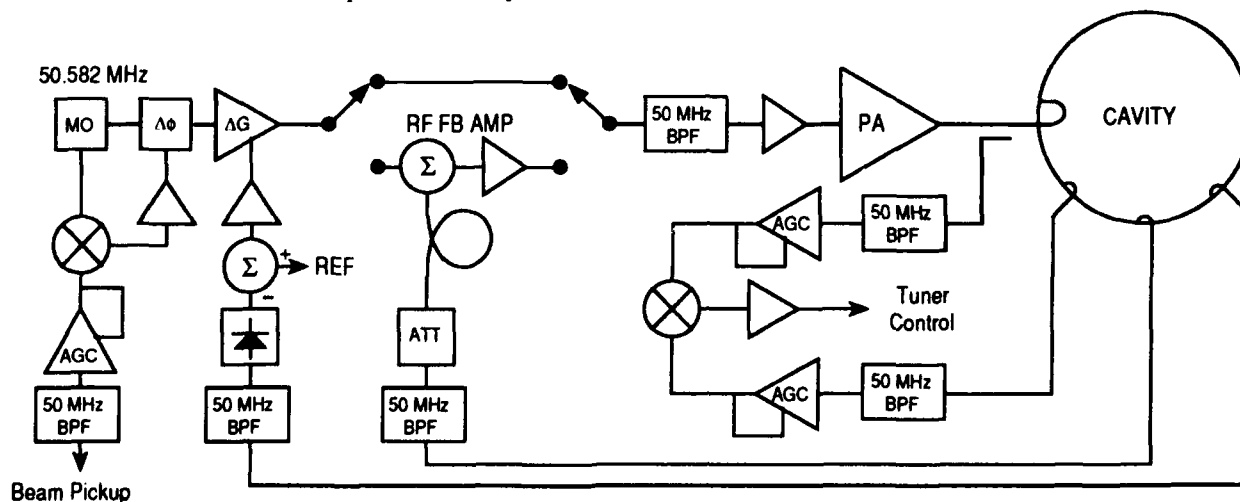


Figure 3. Aladdin RF System Block Diagram

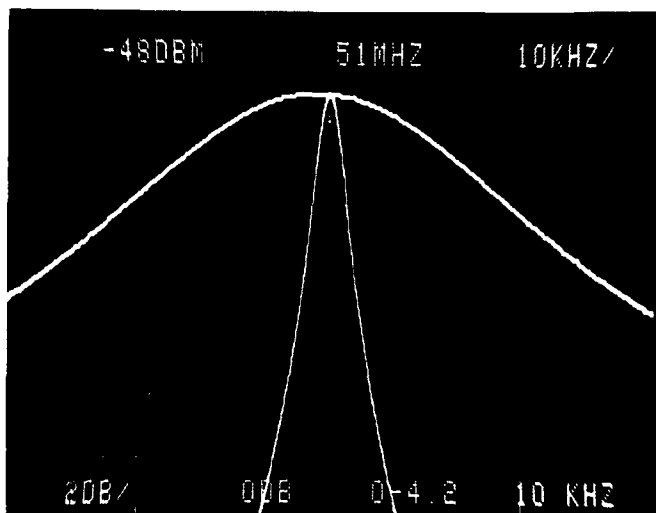


Figure 4. Effect of RF feedback on system frequency response

The reactive impedance required to obtain Robinson damping is better obtained by misphasing the RF feedback instead of detuning the cavity. The effect of cavity detuning is reduced by the feedback loop gain. The result is that the power amplifier is required to drive a very reactive load, which contradicts one of the original reasons for using RF feedback. Slightly misphasing the feedback also shifts the resonance of the system, altering the impedance seen by the beam. This provides Robinson damping without introducing a large reactive component in the load impedance, allowing efficient operation of the power amplifier.

V. PERFORMANCE

The performance of the new system has been quite satisfactory. Injection is much improved due to the elimination of a HOM problem in the old cavity that caused periodic debunching of the beam at high current, severely impairing stacking above 150 mA. The lower number of low frequency HOM's in the new cavity design and the damping of modes that are present has resulted in a reduction of the equilibrium bunch length at injection by about 30 percent. Tests using RF

feedback at injection have verified that the dependence of the Robinson instability on cavity tuning has been eliminated. With feedback it is also possible to lower the cavity voltage by 50% from the level required without feedback without causing instability. This is enough to improve beam capture and stacking significantly. The result of this is that typical stored beam currents are increased by about 15 percent over the no feedback case. The low current stacking rate is nearly doubled.

Operation at 800 MeV is reasonably good. There are several coupled bunch modes that appear to be generated by high frequency HOM's in the cavity but they do not impair machine operation. Initial tests using RF feedback revealed additional instabilities. The bunch modulation resulting from these instabilities interfered with beam position measurements. This problem was traced to HOM transmission through the RF feedback loop. An additional bandpass filter inserted before the driver amplifier eliminated the problem.

Since the high energy coupled bunch problems appear to be caused by one or two modes at about 1 GHz, There is a particularly simple damping method that will be investigated as soon as machine time is available. Preliminary experiments have shown that a section partially loaded with microwave absorber inserted into the feedline will damp the offending HOM's by means of the cavity coupling loop. The frequency dependent loss of the material will possibly allow the use of enough material to significantly damp the 1 GHz HOM's while simultaneously providing the much smaller attenuation required to damp the feedline resonances at 50 MHz. The feedline damping network could then be replaced by the absorber section resulting in a much simpler arrangement.

VI. REFERENCES

- [1] E. M. Rowe, *IEEE Trans. Nucl. Sci.* NS-28, No. 3, 2780 (1981).
- [2] K. J. Kleman, these proceedings.
- [3] D. Boussard, *IEEE Trans. Nucl. Sci.* NS-32, No. 5, 1852 (1985).
- [4] S. P. Jachim, E. F. Netter, *Proc. of the 1989 IEEE Particle Accelerator Conf.*, Vol. 3, 1870.

The ALS Storage Ring RF System*

B. Taylor, C.C. Lo, K. Baptiste, J. Guigli, and J. Julian
Lawrence Berkeley Laboratory, University of California
1 Cyclotron Road, Berkeley, CA 94720 USA

Abstract

The ALS Storage Ring RF System is characterized by the use of the following features:

1. High power loading of two single cell cavities.
2. The use of a tubular ceramic input window employing aperture coupling.
3. The use of waveguide filters and matchers designed for HOM absorption.
4. A comprehensive HOM monitoring system.
5. The use of waveguide water-wedge loads for the magic tee and circulator loads.

The results of cavity measurements and high power tests are reported together with the performance of the system during the commissioning and operation phases of the ALS project. Plans for future window development are discussed.

I. INTRODUCTION

The ALS Storage Ring RF system employs two single cell cavities fed via a magic "T" from a circulator protected high power 500 MHz klystron. The system is capable of delivering 150 kW cw at each cavity input window. Some unusual features of the system are the use of tubular ceramic cavity coupling windows and the use of water wedge waveguide loads for the circulator and magic tee[1].

II. RF CAVITIES DESIGN AND CONSTRUCTION

The RF cavities are a further adaptation, progression and development of the aperture coupled toroidal cavities used at the "SRS" Daresbury Laboratory machine. Firstly, the cooling system of the cavity was redesigned by the manufacturer to dissipate 70 kW employing a turbulent flow of ~130 gpm (US) and a Δt of 2°C. Extra cooling was also added to the waveguide connecting flange and the tuner neck area. Secondly, the disc ceramic input window of the SRS design was replaced by a ceramic cylinder which extends the full 18" of the WR1800 waveguide greater dimension. The cavity will, however, still accommodate disc windows. Thirdly, a hybrid SRS/LEP tuner was designed using a LEP drive system but retaining the SRS-style non-contacting tuner and tuner well arrangement. Fourthly, the manufacturer[2], who also made the SRS cavities, chose an inside out arrangement as compared to the SRS construction method. The inner shell of the ALS cavity is machined and welded whereas the complex outer shell and water passages are electroformed. The general arrangement of the bare cavity is shown in Figure 1. The higher order mode damping port is at the right of the picture.

*This work was supported by the Director, Office of Energy Research, Office of Basic Energy Sciences, Materials Sciences Division of the U.S. Department of Energy under Contract No. DE-AC03-76SF00098.

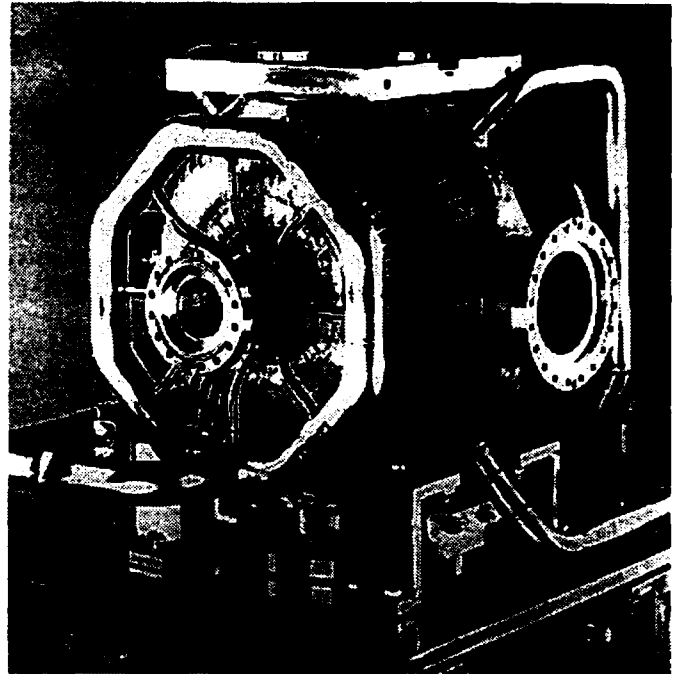


Figure 1. Single Cell Cavity [2]

III. CAVITIES MEASUREMENT AND PERFORMANCE

Table 1
Shows the Measured Performance of Each Cavity

Unloaded Q	= 40,000
Shunt Impedance	= 10 M Ω (2ZT ² L)
Design Peak Effective Volts VPT	= 750 kV
Mechanical Tuner Range	= -0.6 MHz to +3 MHz
Coupling Factor β	= 1 to 3 with tubular window
Max Power Dissipation Test	= 70 kW cw Δt 2°C inlet to outlet
Normal Controlled Water Temperature	= 40°C \pm 0.5°C
Highest Outer Envelope Spot Temperature	= 50°C (70 kW input water at 40°C)
Ceramic Window Temperature Rise	= ~0.2°C/kW (at mid point of tube)

Cavities were tested under vacuum to 70 kW cw in the LBL cavity test facility. Some instances of sparking due to dc charging of the ceramic were encountered at ~50 kW. This effect was either traced to inadequate window antimultipactor coating, or the problem conditioned out with prolonged

running. This exercise proved the excellence of the window arc detectors designed by C.C. Lo. A conditioning period of about 20-30 hrs was normally adequate for the cavities.

At the time of writing, two cavities have operated in the ALS storage ring with a total input of ~110 kW producing a 400mA (250 Bunch) stored beam at 1.5 GeV, lifetime being vacuum limited at this stage.

IV. WAVEGUIDE SYSTEM AND HOM ABSORBERS

The basic waveguide HOM filters and HOM monitoring devices follow the proposals made in the authors' original ALS RF paper[1] of 1989. The actual layout of the waveguide system is shown in Figure 3.

The magic tee dual H plane and E plane HOM filters and tee wedge water load are accommodated on the shield tunnel roof, feeding downwards to the cavities.

The waveguide 300 kW circulator and load are also on the tunnel roof. This layout has proved very compact and has released valuable real estate at ground level for experimenters' use. The waveguide wedge loads although large have worked well providing an excellent match and acting as power absorbers over a wide range of frequencies. Quiet in operation the loads share one 3/4 HP pump for water circulation

Numeric data on the power absorbed by the HOM filters and "transparent" matchers, when the cavities are beam excited, has not yet been collected. The fact, however, that a 400mA 250 bunch beam of 1.5 GeV can be rapidly and smoothly accumulated is significant. Plentiful evidence of

HOM excitation is visible on all of the 30 pick up antennae available in the HOM damping systems. When running a 40mA mean, 4 bunch beam, HOM power interference was experienced by ion gages and IR temperature monitors mounted on the cavity. No gross beam effects however, were noticed. An examination of the ALS cavity HOM characteristics is presented in a companion paper[3].

V. FUTURE DEVELOPMENTS

The presence of a ceramic disc window in the coupling port of a cavity lowers the cut off frequency of that port. As a result, for the same size coupling port, a higher coupling factor β may be obtained with a disc window than with a tubular window. The relative figures for an ALS cavity are, $\beta_{\text{max disc}} \sim 5.0$, $\beta_{\text{max tubular}} \sim 3.0$. Experiments have been conducted showing that the coupling factor of a tubular window may be increased by providing ridges on the coupling aperture in the manner of a ridged waveguide. Such a shaped aperture may also be effective in increasing the coupling out of lower frequency HOM components, both from the input coupling port and other ports.

A problem sometimes encountered with ceramic windows of all kinds is the phenomenon of dc charging of the ceramic, the attendant dc sparking leading to RF arcing. The ALS tubular window has been designed with a central access/inspection port in the top cap. The effect of a biased collector electrode coaxial with the window ceramic will be explored in order to diagnose or possibly suppress the charging action.

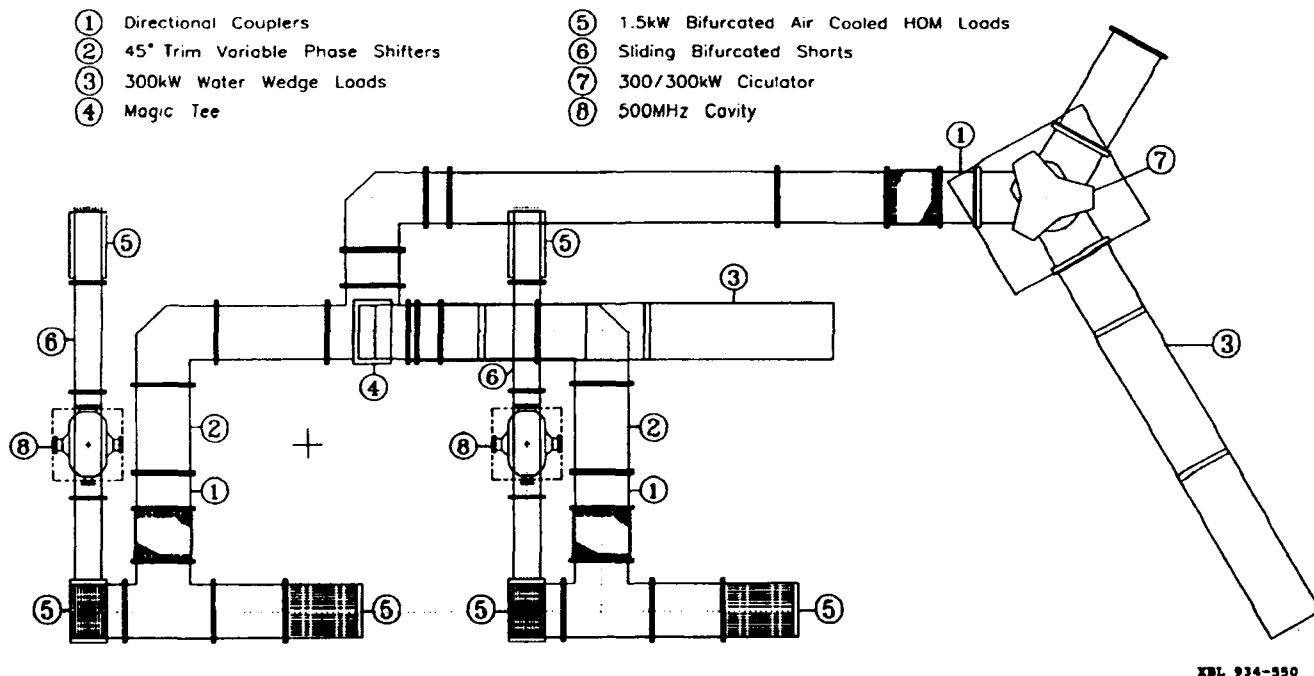


Figure 2. Storage Ring Roof Waveguide Layout

VI. ACKNOWLEDGMENTS

Thanks are due to many people and organizations who provided advice and encouragement during the design and construct of this project. The authors would, however, in particular like to thank the scientific and engineering staff of the SRS Daresbury Laboratory who provided both technical and material assistance.

VII. REFERENCES

- [1] B. Taylor, K. Baptiste, H. Lancaster, and C.C. Lo, Advanced Light Source Storage Ring RF System, Proceedings of 1989 IEEE PAC, Vol. 1, pp. 124-125, LBL-25978.
- [2] Normal Conducting RF Cavities for Accelerators Pamphlet, Accelerator and Magnet Technology Interatom/Siemens.
- [3] Measurements of the Higher Order Modes of the ALS 500 MHZ Accelerating Cavities, J. Corlett, J. Byrd, LBL, IEEE PAC93.

The Upgrade Project for the RF System for the Brookhaven AGS*

J.M. Brennan, D.J. Ciardullo, T. Hayes, M. Meth, A.J. McNerney, A. Otis,

W. Pirkel, R. Sanders, R. Spitz, F. Toldo, and A. Zaltsman

AGS Department, Brookhaven National Laboratory

Associated Universities, Inc.

Upton, New York 11973

I. INTRODUCTION

The AGS operates a varied program of proton, heavy ion, and polarized proton acceleration for fixed-target experiments and will soon serve as the injector of these beams into the Relativistic Heavy Ion Collider, RHIC[1]. The new Booster synchrotron[2] extends the range of intensities and masses that can be accelerated. The 1.5 GeV injection energy increases the space charge limit by a factor of four to more than 6×10^{13} protons per pulse. To accommodate the increased beam current the rf system will be upgraded to provide more power and lower impedance to the beam. The flexibility of the rf system will also be enhanced by virtue of a new rf beam control system[3] and installation of individual tuning servos for the ten rf cavities.

The fundamental necessity for upgrading the rf system is to deliver more power to the accelerating beam. At 6×10^{13} ppp the power demand will peak at 740 kW. The present ten power amplifiers can produce 40 kW each. Moreover, stability of the beam and the rf system in this heavily beam-loaded regime demand that the effective impedance of the cavities be reduced. The intrinsic impedance of the cavities (given mostly by losses in the ferrites) is about 16 k Ω which implies a generator current at 20 kV (midrange) of 1.25 A. At full intensity with short bunches the beam current will reach 7.2 A, giving a beam loading parameter[4] of $Y=5.8$. An impedance reduction of at least a factor of three is called for in order to avoid multi-loop instabilities[5]. An additional requirement also applies. Since the AGS is batch-filled by four injections from the Booster it must operate with a partially filled ring and transient beam loading effects are important[6]. Transient beam loading is a broadband phenomenon and therefore determined not by the impedance of the cavity but by its R/Q.

Three key ingredients of the upgrade project address these requirements; 1. new power amplifiers provide the necessary power, and are closely coupled to the cavities, 2. wideband rf feedback reduces the effective impedance by a factor of 10, 3. the capacitors loading the acceleration gaps

*Work performed under the auspices of the U.S. Department of Energy

1) Permanent address, CERN

(four per cavity) are increased from 275 pF to 600 pF. Including 130 pF of intrinsic capacitance the stored energy is increased and the R/Q decreased by a factor of 1.8. This is the practical limit of additional loading capacitance because of Q-loss phenomena in the ferrites at high bias fields.

II. POWER AMPLIFIER

The Upgrade Power Amplifier uses the Thomson-CSF TH573 300kW power tetrode in a single-ended grounded cathode configuration. The choice of tube was based on many factors of which the current and power handling capabilities required at phase transition were the most important. Other factors in the choice included conservative rating for long life and a low plate resistance.

At phase transition the load is reactive and the operating line for the tube is elliptical. Because of this, plate dissipation at phase transition will be typically 200kW with a peak plate current of 125 amperes. During the acceleration cycle, at maximum beam intensity, the average plate current will range from 24 to 33 amperes. At maximum acceleration the anticipated plate dissipation will be 100kW and the peak plate current will be nominally 80 amperes. Combined power output, cavity losses plus beam loading, will be as high as 200kW. The power tube is biased so that it operates in an AB1 mode. The operating parameters are as follows:

Plate voltage.....12kVdc
Screen voltage1500 Vdc
Grid bias.....-370 Vdc
Quiescent cathode current.....5.0 amperes
RF plate voltage(maximum).....10kV peak

The cavity impedance is lowered by the low dynamic plate resistance (unusual for a tetrode, about 500 Ω at full drive) which is coupled to the gap by a 1:1 balun.

The required drive for full output is less than 300 Volts peak rf, thus the control grid never is driven into the positive region. The power amplifier is packaged in an all aluminum enclosure and located at the cavity for close coupling. All controls and associated power equipment and circuitry are located outside the tunnel.

III. RF FEEDBACK

The proximity of the power amplifier to the cavity allows the implementation of wideband rf feedback. Although the feedback does not change the demands made on the power amplifier, it does change profoundly the beam loading interaction. In essence, the voltage induced by the beam (within the bandwidth of the feedback) and therefore the effective beam loading parameter are reduced by the open-loop feedback gain. The gain, however, is limited by time delay around the loop which reduces the phase margin. Low phase margin causes the closed-loop impedance to increase with respect the open-loop value away from the cavity resonance. This effect can reduce the threshold for multi-bunch instabilities[7]. This system achieves 20 dB gain with a time delay of 80 ns and less than 3 dB of impedance increase. Figure 1 shows a block diagram of the system. $G_1(s)$ represents the cavity, G_2 the power amplifier, H is a broadband voltage divider measuring the gap voltage, and $G_3(s)$ is the feedback amplifier. The magnitudes of the gains at resonance are indicated.

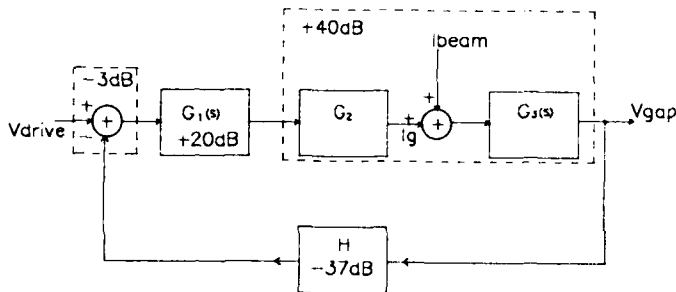


Figure 1. Block diagram of rf feedback servo system.

The feedback amplifier, $G_1(s)$, is also a closed-loop system. It must drive the power tube control grid (950 pF) to 300 Volts peak with a minimum of phase shift. A tunable inductance in parallel with the grid makes the grid impedance real. The inductor is tuned via an open-loop program based on a measurement of the rf drive frequency, which may vary from 1.7 to 4.5 MHz. The Q of this tuned circuit should not be high because then the accuracy of the tuning program would have to be high. The Q is set to <5 by a 200 Ω power attenuator connected to the grid. This attenuator (-20dB) serves as the feedback element for the local loop. Using a 200 Ω load proved superior to transformer matching a 50 Ω load because the transformer led to spurious resonances at high frequency. The inductor is an autotransformer of eight turns wound on two 125 mm o.d. toroids of 4M2 ferrite with 54 x 31 mm cross section. The open loop gain to the 200 Ω load is 46 dB, achieved with two stages of four EIMAC 4CX350 tetrodes in parallel. Radiation hardness precluded solid state devices. Figure 2 shows the feedback amplifier circuit.

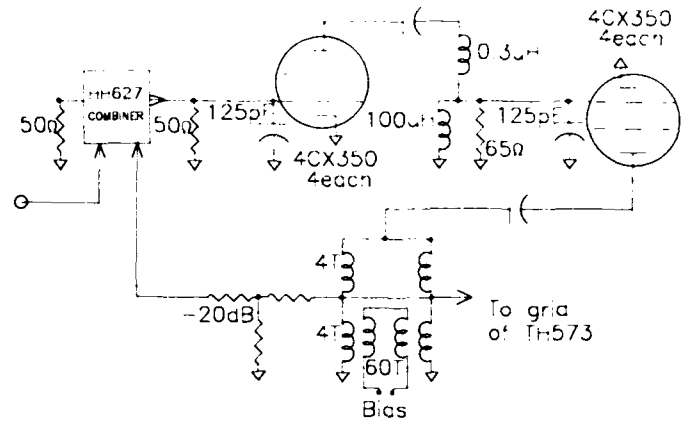


Figure 2. Feedback amplifier and tuned transformer

The interstage network is optimized for minimum open loop group delay since the local feedback has wide bandwidth. Commercial hybrid transformers, ANZAC HH627, are used for the summing junction to close the feedback loop with 23 dB loop gain. Figure 3 shows the open and closed loop frequency response and group delay of the feedback amplifier. At the resonance frequency of the transformer the closed loop group delay is 50 ns.

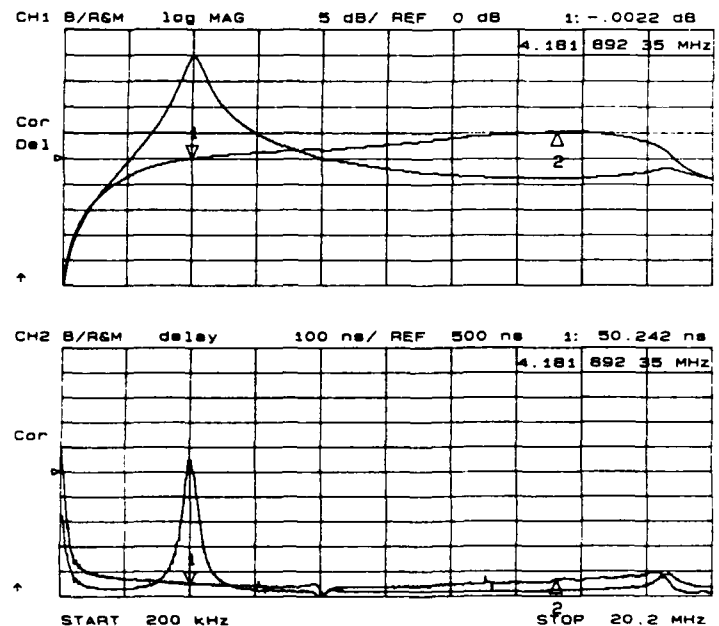


Figure 3. Feedback amp., freq. response and group delay

The loop around the cavity is closed by sensing the voltage at one of the gaps with a capacitor voltage divider of -37 dB and summing with the cavity drive signal via another sum and difference hybrid (developed and produced in-house for this application). The gain from the grid of the power tube to the acceleration gap is 40 dB so that the loop gain around

the cavity is 20 dB and 200 W of drive power is required for 10kV per gap, ie: 400 kV per turn. Figure 4 is a measurement of the open and closed loop frequency response of the cavity loop.

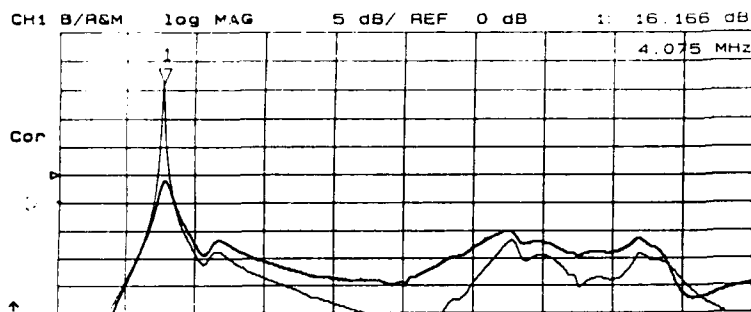


Figure 4. The open and closed response of the cavity loop. The frequency axis is linear, 1 to 21 MHz.

IV. HIGHER MODES IN THE CAVITY

Although the feedback system is intended to have gain only within ± 0.5 MHz of the cavity resonance, higher order responses of the cavity were seen to cause four spurious peaks in the loop gain between 12 and 25 MHz, all potentially unstable. See Figure 5. The responses are caused by spurious inductances of the cavity assembly. The cavity comprises four cells of ferrite loaded push-pull resonators connected in parallel by three pair of heavy copper bus bars, which also carry the ferrite bias current (1200 A). The gaps of the resonators are loaded with 600 pF capacitors. Since the combined length of the bus bars is 2.5 m, they and the capacitors form standing wave resonances in this band. The coupling line between the power amplifier and the cavity is of comparable length, forming a system of four coupled modes.

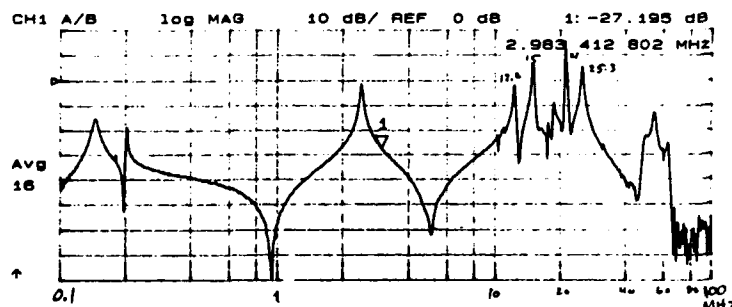


Figure 5. Higher order modes due to cavity bus bars.

It was possible to effectively damp the higher order modes by modifications to the bus bar arrangement. Fortunately the cavities were built with four leadout connections per gap, an inside and outside lead both upstream and downstream. By adding bus bars to the inside, as well as the outside leads, the inductances were cut in half. Furthermore, the 600 pF of loading capacitance was installed symmetrically inside and outside the gaps, increasing the frequencies of the bus bar modes. The then higher frequency

modes could be damped by installing 40 Ω , 25 mm diameter by 600 mm power resistors in parallel with the bus bars. The mode due to the line between the power tube and the cavity remained. The effect of this mode on the rf feedback was greatly reduced by taking the feedback from the gap itself, as apposed to the anode of the power tube.

V. BEAM TEST

A prototype of the power amplifier and the rf feedback was tested in the AGS ring. A single, low longitudinal emittance, bunch was accelerated to 1.2 GeV in the Booster and injected into the AGS ring with the rf on. The bunch executed quadrupled oscillations in the miss-matched bucket and attained a minimum length of 28 ns. This bunch served as an impulse stimulus to the test cavity. The response of the cavity was observed with the feedback on and off and is shown in Figure 6. One can see that the free oscillation is damped within two rf cycles with feedback on. The FFT of these responses are also shown in the figure. Since the Fourier transform of the impulse response is the impedance of a system, these plots show the impedance reduction due to the rf feedback, a factor of 12.

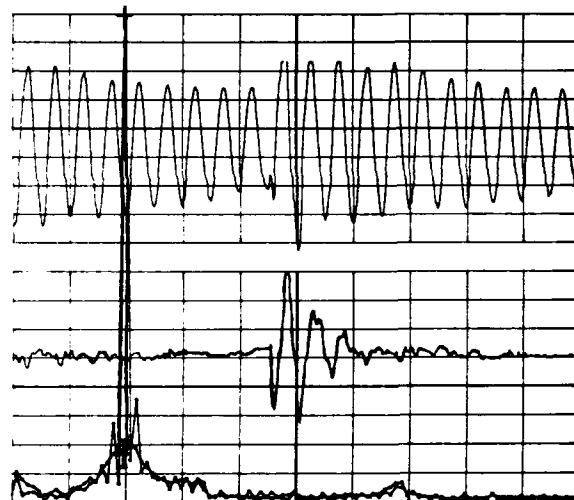


Figure 6. Cavity response to an "impulse". Top, feedback off. Middle, feedback on. Bottom, FFTs of above, linear axes, abscissa is zero to 20 MHz.

REFERENCES

- [1] Foelsche, et al. Adv. Accel. Phys. & Tech. Vol.12, 1993
- [2] W.T. Weng, these proceedings.
- [3] J.M. Brennan, XVth Intl. Conf. H.E. Accel., Hamburg, Germany, July 1992, pp. 275-277.
- [4] F.Pedersen, IEEE Trans. Nuc. Sci., NS-22, 1975, p1906.
- [5] D.Boussard, Proc. CERN School on RF Engineering, Oxford, England, April 1991.
- [6] M. Meth et al, 1989 IEEE PAC Conf. Proc., p.168.
- [7] R.Garoby, Proc. US-CERN School on Particle Accel, Hilton Head Island, USA November 1990, p531.

Acceptance Test Performance of the Rocketdyne Radio Frequency Power System

M. Curtin, J. Hall, P. Metty
Rocketdyne Division of Rockwell International
6633 Canoga Ave., Canoga Park, CA 91303

and

E. Gower, J. Manca, K. Whitham
Titan-Beta Corporation
6780 Sierra Court, Dublin, CA 94568

Abstract

We present initial results of performance testing of the RF power system built for the Rocketdyne Free Electron Laser program. The RF power system consists of a SLAC 5045 klystron powered by a modulator unit built by the Beta Division of the Titan Corporation. The system is capable of providing 65 MW, 3.5 μ sec macropulses at 180 pps and employs innovative feedback and feed-forward control techniques in order to achieve amplitude flatness and phase stability. Preliminary rf amplitude, pulse flatness and phase stability measurements indicate phase stability better than $\pm 1^\circ$ and pulse flatness better than $\pm 0.25\%$ are achievable at the 65 MW operating point.

I. INTRODUCTION

The Rocketdyne Free Electron Laser group is currently under contract to demonstrate a high-current, high-brightness electron beam injector based on a photocathode-driven, rf microwave gun with magnetic compression. The rf power system supplies the electron-beam injector [1] with highly regulated rf power at the 5-10 MW level. The remaining 55 MW of available rf power will feed four linac sections allowing electron beam energy to be increased from 5 MeV to 80 MeV. The high-brightness, 80 MeV electron beam will enable FEL operation in the visible portion of the spectrum using previously fabricated undulators [2].

II. SYSTEM DESIGN

A. 5045 Klystron Tube

The klystron unit was purchased by Rocketdyne and supplied to Titan-Beta Corporation for integration into the rf power system. The klystron unit consisted of the klystron tube, solenoid focusing magnet, 15:1 oil-immersed transformer and high-voltage cable. The SLAC 5045

klystron is characterized by typical operating parameters as listed in table 1.

Table 1.
Nominal operating parameters of a 5045 klystron

<u>PARAMETER</u>	<u>UNITS</u>	<u>VALUE</u>
operating frequency	MHz	2856
beam voltage	kV	350
beam current	amps.	420
pulse repetition frequency	pps	180
peak rf output power	MW	65
average rf output power	kW	45

Operating experience accumulated at SLAC with the 5045 klystron suggests an average tube life of 40,000 hours.

B. Modulator

The modulator was designed to power the 5045 klystron over a large operating range by providing variable PFN charging and variable pulse repetition frequency. The required PFN voltage needed to achieve a 350 kV pulse at the klystron is given by:

$$V_{PFN} = \frac{2V_{beam}}{15} = \frac{700[kV]}{15} \approx 47[kV] \quad (1)$$

The design goals for the rf power system were to design and fabricate a robust, highly regulated system capable of operating at variable peak power levels between 20 MW and 65 MW and variable pulse repetition frequencies between 1 pps and 180 pps. The most challenging specifications were placed on rf pulse flatness and phase stability.

Table 2.

RF pulse specifications for the RF power system

RF PARAMETER	UNITS	VALUE
pulse width	μsec	3.7
peak power	MW	20 - 65
pulse repetition frequency	pps	1 - 180
phase stability	degrees	$\pm 1^\circ$
pulse flatness	%	± 0.25
pulse jitter	nsec	± 10
long term ampl. stability	%/hr	± 0.5
short term ampl. stability	%/5 min.	± 0.2

C. Control System

An innovative control system was designed to achieve the desired performance goals which would incorporate differing levels of feedback and feed-forward control on both phase and amplitude parameters associated with the rf drive and high voltage pulse supplied to the klystron. It was felt that controlling the flatness of the high voltage pulse to the klystron at the $\pm 0.1\%$ level would insure rf pulse flatness at the $\pm 0.25\%$ level. If this approach was not sufficient to meet rf pulse specifications then modulation of the rf drive amplitude and phase would be added to obtain the required rf specifications. The rf power system design incorporated a number of feedback and feed-forward control loops, as depicted in figure 1., to achieve the desired regulation and stability.

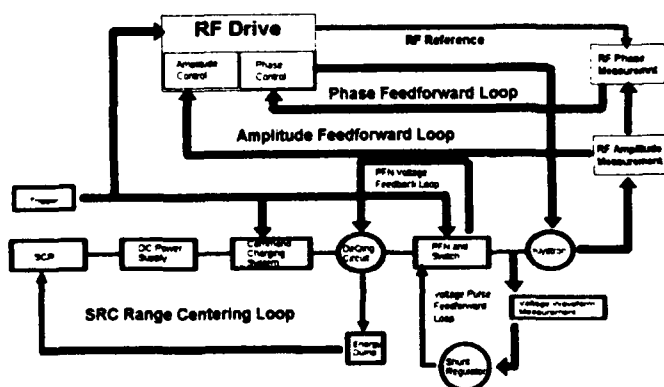


Figure 1. Block diagram illustrating the feedback and feed-forward control loops built into the control system.

The need for control of the rf power system from a remote area was required and accomplished by incorporating an IEEE 488 bus which linked the rf power system interface module with a Macintosh II computer running LABVIEW software. The rf power system could run in either local mode or remote mode set by a switch on the control panel.

The software was written to provide a relatively simple user interface for control of the rf power system.

D. Interlock System

Another important feature of the rf power system was the interlock-chain design built to prevent component damage due to unsafe operating conditions. The interlock system was built with first-fault detection capability to assist operators in rapidly debugging system problems.

III. EXPERIMENTAL TEST SETUP

The rf pulse characteristics were measured by outcoupling a small fraction of forward-going rf power from a test port located just downstream of the klystron. The rf power was attenuated to levels compatible with a HP detector which was used to measure rf amplitude and pulse flatness. A portion of the forward-going power was diverted to the phase measuring system where it was mixed with the rf reference to provide a phase error profile across the pulse. A Tektronix 540 oscilloscope was used to display and analyze the captured data as illustrated in figure 2. The measurement of small error signals in the presence of large current loops associated with the rf power system required judicious placement of highly shielded cables in order to keep the signal to noise within acceptable levels.

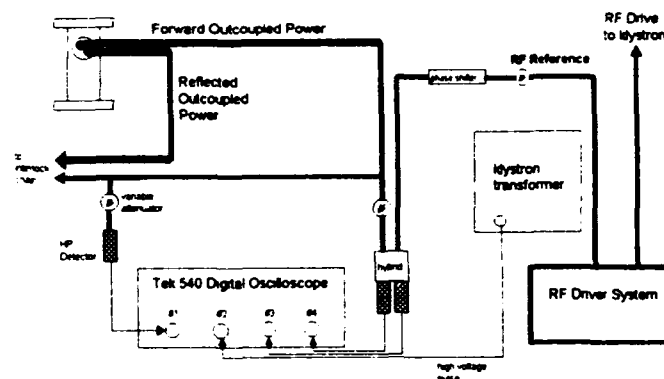


Figure 2. Block diagram of the test setup used to measure rf pulse parameters.

A. Measurement System Calibration

Calibration of the detectors, attenuators, outcouplers and phase measurement system were crucial in verifying compliance with contractual specifications. Calibration of the total rf output power using a power-balance technique was attempted but did not provide adequate calibration accuracy at low average power operation necessitated by the damaged klystron window. A peak power meter was used to measure the magnitude of

outcoupled rf power and calibrated against the supplied rf output power curves as a function of beam voltage and current. The phase measurement system was calibrated against controlled variation of the phase shifter. Manufacturer specifications were used for detector, attenuator and cable characterization.

IV. PERFORMANCE DATA

The acceptance test matrix originally included measurements of rf output parameters, as listed in table 2., at three peak power levels (20,45,65) MW and two pulse repetition frequencies (10,180) pps. In addition, a 6 hour "heat-run" at the system's maximum average power level was required to measure system robustness. Unfortunately, a vacuum mishap resulted in a klystron window failure which would not permit high-average power rf operation. The rf amplitude flatness was measured at the 65 MW and 10 pps operating point. The rf pulse flatness at 65 MW peak output power was achieved by employing two arbitrary waveform generators used to control both phase and amplitude modulation of the rf drive signal. Achieving the required flatness and phase stability necessitated an interactive process of looking at the captured scope trace and adjusting each arbitrary waveform generator in such a manner as to modify the pulses so that they conformed to the required specifications. The resultant oscilloscope trace as depicted in figure 3. indicates that $\pm 0.22\%$ was achieved for pulse flatness at the 65 MW and 10 pps operating point.

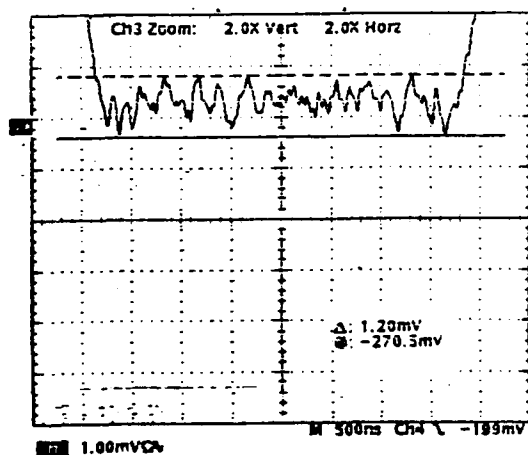


Figure 3. Oscilloscope trace depicting rf pulse flatness at the 65 MW and 10 pps operating point.

The phase variation across the pulse was measured at $\pm 1^\circ$ as depicted in figure 4.

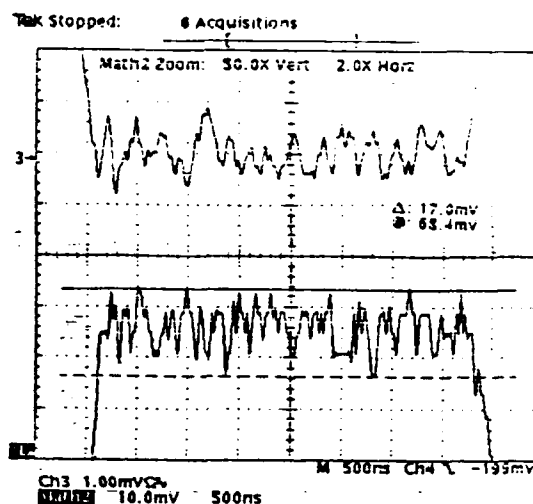


Figure 4. Oscilloscope trace depicting a) rf pulse flatness (top trace) and b) rf pulse phase stability (bottom trace) at the 65 MW and 10 pps operating point.

The heat run was performed with reduced pulse width using the klystron in diode mode and lasted just short of the required 6 hour test.

V. REFERENCES

- [1] M. Lampel et.al., these proceedings.
- [2] R. A. Cover et. al., SPIE Proceedings Vol. 1868, Los Angeles, CA (January 1993)

The LEP II RF Power Generation System

H. Frischholz

CERN, 1211 Geneva 23, Switzerland

Abstract

By means of the LEP II RF System the maximum circumferential accelerating voltage will be increased from 350 MV at present to about 2000 MV, required for the W^\pm pair production at centre-of-mass energies around 180 GeV. The accelerating voltage will be provided by the existing copper RF cavity system (LEP Phase I) and 192 superconducting RF cavities to be installed in LEP by 1995. These sc cavities will be powered by 12 high power klystrons via junction circulators and a WR 2300 waveguide power distribution system. Compared to the existing LEP I installation the output power of the LEP II klystrons has been increased from 1000 to 1300 KW cw by making use of the full capacity of the HV power converters, rated at 100 KV and 40 A. Simultaneously, the power-handling capability of the junction circulators, when operated into a sliding short, could also be enhanced by the same amount. A description of the LEP II RF power generation system is given and, in particular, the improved performance of the high power klystrons, circulators, thyatron crowbars and hard tube modulators is discussed.

INTRODUCTION

For the W^\pm pair production in LEP a circumferential acceleration voltage of about 2000 MV is required. This will be achieved by means of the LEP II RF system; i.e. in addition to the existing LEP I RF system [1] 12 more RF units will be installed in LEP by 1995. Each of these RF units consists of one high power klystron with its HV interface, a junction circulator, a WR 2300 waveguide power distribution system with four Magic Tee splitting stages, four cryostat-modules, each of which houses four superconducting RF cavities, and the associated controls and interlock electronics.

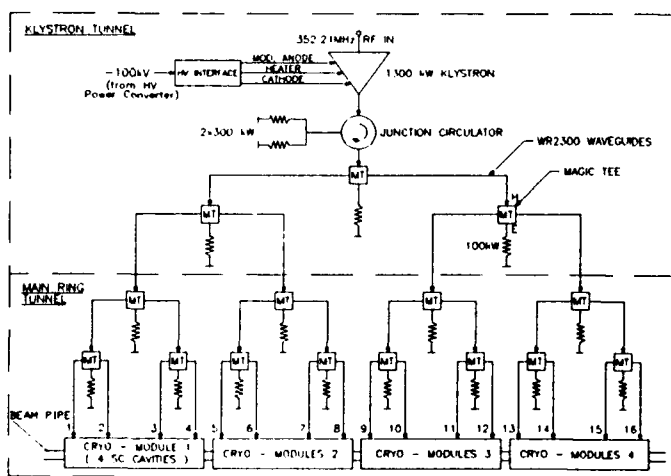


Fig. 1 - RF Power Distribution of a LEP II RF Unit

As can be seen from Fig. 1 the general layout of the LEP II RF units is very similar to that of LEP I. The main difference are the substitution of the copper cavities by superconducting ones and the need of only one klystron per RF unit.

At a specified sc cavity voltage gradient of 5 MV/m a total accelerating voltage of 136 MV will be produced by one RF unit. At beam intensities of about 5 mA/beam the required RF power will be then 1300 KW.

By operating the klystrons at 100 KV and 20 A, the full capacity of the HV power converters, the rated klystron output power could be increased from 1000 to 1300 KW. Simultaneously the RF power handling capability of the circulators could also be increased to 1300 KW, even when the output signal is fully reflected at any RF phase angle.

The HV interface [2], consisting of a thyatron crowbar, a hard tube modulator and a 2 μ F smoothing capacitor, had to be adapted to the enhanced HV operating voltage. The main modification with respect to the original layout is the replacement of the 5-gap EEV-CX 1194B thyatron by the 8-gap model CX 2098B of the same firm and the controls and interlock electronics associated to it.

GENERAL

For compatibility and cost reasons the general layout of the LEP II RF units is very similar to that of a LEP I unit. Beside the substitution of the copper cavities by superconducting ones [3], the use of only one high power klystron with HV interface and one high power junction circulator, each with improved performance, only minor changes were required. In order to avoid cavity tuning errors, which can be caused by cross coupling of the fundamental RF signal between adjacent cavities [4], the isolation via the feeder lines had to be increased. Improved intercavity isolation is achieved by supplying the 100 KW coaxial water loads, required for the E-port termination of the 12 Magic Tees of the two last power splitting stages (see Fig. 1), with saltwater. The substitution of demineralised water by doped water with a NaCl content of 1‰ decreases the reflection of the loads from -17 to -28 dB and improves thus the fundamental signal isolation between adjacent cavities via the feeder lines from -19 dB to -26 dB.

Another modification concerns the terminating load of the junction circulator. In case of beam loss the incident RF power is partly or fully reflected by the sc cavities, i.e. up to 1300 KW of RF power will be diverted by the junction circulator into the terminating load at its port #3. Minor cavity tuning errors also result in high reflected power levels. For these reasons the port #3 of the circulator is terminated via a specially developed waveguide-to-double coax transition with two 300 KW coaxial loads. These loads, although limited to a continuous absorption of 2 x 300 KW, are capable to absorb up to 1300 KW for about 1 minute.

By April 1993 the klystrons, circulators, HV interfaces and waveguide components had been installed in four LEP II

RF units, but only in one unit two cryo-modules (8 sc cavities) are in place. One of the four units is equipped with two klystrons and circulators, i.e. 8 sc cavities will be powered by one klystron, in order to gain experience for a possible upgrade to two klystrons per 16 cavities (one klystron per 8 cavities, but one HV power converter for two klystrons) which might become necessary when the accumulated beam intensities in LEP would exceed 5 mA/beam. The HV power converters, which are of the same type as those for the LEP I RF system, have a rated capacity of 100 KV and 40 A [5] and could thus cope with the max. HV power requirement of two klystrons.

KLYSTRONS

In 1990 a programme was launched with industry to increase the maximum klystron output power by making use of the rated capacity of the HV power converters. The programme resulted in a new series of high power klystrons with technical specifications, the main parameters of which are listed in table I. The main feature of the klystron operation at 100 KV and 20 A is the maximum output power achieved, namely 1300 KW; corresponding to a DC-to-RF conversion efficiency of 65% (see Fig. 2). This is to be compared with the LEP I klystron operation at 88 KV and about 18 A where a maximum output power of 1000 KW is achieved.

Due to the generation of relatively high accelerating voltages at low RF power the output of each klystron must be reduced drastically during beam accumulation at 20 GeV. Therefore, the specification calls for a minimum klystron beam current of 2.5 A at an operating voltage of 100 KV. The output power, which is exclusively controlled by the klystron's beam, is then below 1 KW. The focusing current settings must be such that they can remain unchanged when the beam current is varied between 2.5 and 20 A.

* KLYSTRON TESTS *

Date: Monday 18 04 93 Time: 15 37 08

POWER SUPPLY		KLYSTRON		LOAD	
VOLTAGE	99.9 KV	RF IN	352.21 MHz	WATER FLOW	64.28 CU M/HR
CURRENT	20.0 Amps	RF PWD	57.80 W	TEMP IN	18.5 deg C
		RF GAIN	43.55 dB	TEMP OUT	35.9 deg C
DC POWER	1998. KW	I Fil	20.3 Amps	LOAD POWER	1305. KW
Ptot	1992. KW	I ma	1.6 mA	(av)	1309. KW
Ptot=Pload+Pcoll+Pbody		I gip	0.0 uA	RF RFL	1.870 KW
Uma	54.9 KV	I Foc1	9.38 Amps	SWR	1.078
Uma/Ucat	0.54	U Foc1	210.8 Volts		
		I Foc2	9.07 Amps		
		U Foc2	207.0 Volts		
		WINDOW AIR IN	38.1 Deg C		
		WINDOW AIR OUT	48.4 Deg C		
		WATER TEMP IN	24.3 Deg C		
BEAM PER	0.633 up	BODY POWER	15.5 KW (Body 4.01 KW/Cav 11.5 KW)		
GUN PER	1.554 up	COLL. POWER	672.0 KW (Water Flow 800. l/mn)		
		(av)	679.8 KW		
THW. EFF. (Pload/Ptot)	65.49 %	(av)	65.29 %		
ELEC. EFF. ((Pload-Prefl)/Pdc)	65.47 %	(av)	65.27 %		
Note (av) is the average of the last 10 readings.					
(*) Load Power = 1.005 (waveguide losses)					
CAVITY WATER FLOW	1500 l/h				
BODY WATER FLOW	800 l/h				

Fig. 2 : Computer Printout of a Klystron Acceptance Test (Sample)

Rated Output Power	1300 KW cw
Operating Frequency (fo)	352.21 MHz
-1 db Output Bandwidth	fo ± 500 KHz
DC-to-RF Conversion Efficiency	65%
RF-Input-to-Output Gain	≥ 40 db
Max. Load VSWR	1.2
DC Operating Voltage	100 KV
DC Beam Current	20 A
Gun Perveance	1.5 μAV ^{-1.5}
Body Dissipation	≤ 30 KW
Focusing Coil Current	≤ 12 A
Modulation Anode Current	≤ 5 mA
Collector Dissipation Ability	≥ 800 KW

Table I : Main Electrical Klystron Parameters at Rated Output Power

CIRCULATORS

Contrary to the LEP copper cavities, at which the RF reflection depends very little on the beam intensity, the incident RF power is fully reflected by the strongly over-coupled sc cavities at the absence of beam. Therefore, the LEP II circulators are specified for 100% reflection, i.e. $P_{\text{forw}} = P_{\text{refl}} = 1300 \text{ KW cw}$. Prior to the installation in LEP each circulator is power tested at full reflection and any phase angle by terminating the output port with a sliding short and port #3 with a 1500 KW waveguide load ($VSWR \leq 1.05$). When at all RF phase angles of the reflected signal no arcs occur, and the input reflection (S_{11}), isolation (S_{12}) and insertion loss (S_{21}) fulfil the specifications (Table II) the circulator is provisionally accepted. Since the insertion loss depends on the phase angle of the reflected signal the external magnetic field has to be adjusted accordingly by means of an electro-magnet [1] in order to obtain the specified values for isolation and input reflection. Prior to the high power test the specified values for the isolation (S_{12}) of -20 and -10 dB within the bandwidth of $fo \pm 10 \text{ MHz}$ and $fo \pm 16 \text{ MHz}$ respectively are verified at signal generator power level. The high power behaviour is then simulated by the circulation of warm water in the ferrite cooling channels which increases the ferrite temperature to values as under high power operation conditions.

Rated RF Power at Input Port	1300 KW cw
Max. Reflected RF Power at Output Port (at any RF phase angle with respect to incident signal)	1300 KW cw
Operating Frequency (fo)	352.21 MHz
Output-to-Input-Port Isolation (S_{12})	
a) at $fo \pm 10 \text{ MHz}$	≤ - 20 db
b) at $fo \pm 16 \text{ MHz}$	≤ - 10 db
Input Reflection (S_{11})	≤ - 20 db
Insertion Loss (S_{21}) (at $P_{\text{refl}} \ll P_{\text{forw}}$)	≤ 0.1 db

Table II : Main Y-Junction Circulator Parameters

Circulators with clockwise and counterclockwise RF power flow are required in the LEP II RF system. (6 of each). For reasons of compatibility the circulators must be made such that they can be used for both rotation modes by simply turning them by 180° around their horizontal plane.

HV INTERFACE

The HV interface of a LEP II RF unit [6] comprises a commutator switch, a smoothing capacitor, a thyatron crowbar, a hard tube modulator, protection resistors and insulation transformers (see Fig. 3). Since the above mentioned components are immersed in oil they must be housed in a fire-proof bunker which is located in the klystron gallery. The high power klystron to be supplied with cathode, filament and modulation anode voltage is installed at a distance of about 20 m from this HV bunker whereas the distance to the HV power converter at the surface is about 500 m.

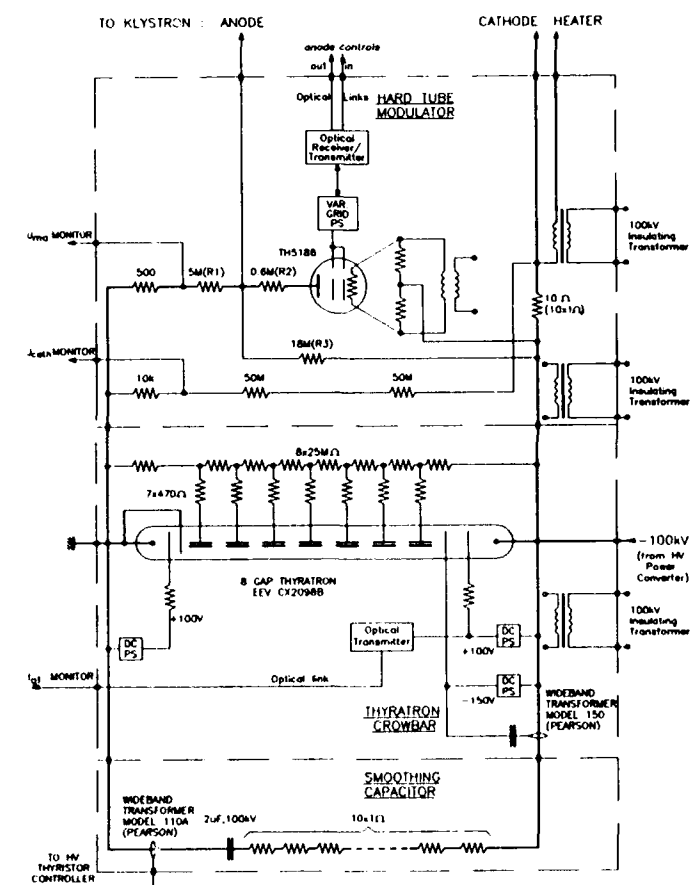


Fig. 3 : HV Interface of LEP II RF Unit

The higher klystron operating voltage does not necessitate the replacement of the 2 μ F smoothing capacitor including its current limiting ceramic resistor since its rated voltage is 100 KV and a max. discharge current of 10000 A, which occurs in the event of crowbar operation, is acceptable. A wideband current transformer is inserted in the low voltage line of the capacitor. Its output is connected to the thyristor control unit of the HV power converter. At a discharge current of about 500 A the thyristor will turn off the HV within 10 ms.

However, the 5-gap, double ended thyatron CX 1194B in the crowbar tank had been replaced by the 8-gap model CX 2098B of the same firm. By lowering the voltage per gap to 12.5 KV the reliability of the HV interface is expected to further improve. The electronic trigger circuit had been simplified to a commercially available wideband current transformer the output of which is connected to grid 2 of the thyatron via a ceramic capacitor. The wideband transformer with its incorporated integrator insures thyatron firing at discharge currents ≥ 500 A. when the grid 2 biasing voltage is set to -150 V.

The cathode/grid 1 area is kept ionised by the +100 V grid 1 biasing power supply. A current of about 25 mA is drawn, when the cathode is correctly heated, by which the readiness of the thyatron to act as a rapid protection device is indicated. This current is monitored and incorporated in the interlock system via an optical link (see Fig. 3).

The output power of the klystron is controlled by the modulator via the modulation anode voltage. The modulator comprises mainly HV power resistors and the HV tetrode TH 5186, which is suited for 100 KV operation. Its two grids have been short-circuited and the tube acts thus as a triode, requiring only one grid biasing supply. The function of the tube is that of a variable high voltage resistor. By the resistors R_1 , R_2 and R_3 the minimum and maximum modulation anode voltage and thus the klystron output power (< 1 KW and 1300 KW) are determined. The tube represents then either an infinite or a very small resistor value compared to those of the above mentioned HV resistors. By means of a variable grid supply which is controlled via an optical link the internal impedance of the tube can be varied between these two extremes.

An additional feature of the new resistive divider is the attractive possibility to achieve a maximum klystron output power of 1000 KW when operated at 77 KV only. This is to be compared with 700 KW previously achievable. At the 77 KV operating point the RF system has demonstrated proven reliability during the last years of LEP operation.

ACKNOWLEDGEMENTS

The author would like to thank P. Bricchi, J.P. Boiteux, B. Lambert, S. Livesley, G. Pecheur and G. Rochepeau for their valuable contribution to the development of the LEP II high power system and also E. Rugo, A. Simonini and W. Sunier for their contribution to the realisation, testing and building of much of the electronics and mechanical components. Thanks are also due to many other members of the SL-RFL Group.

REFERENCES

- [1] H. Frischholz, *Proc. 1989 IEEE Particle Accel. Conf.*, Chicago, p. 1131-1133.
- [2] H. O'Hanlon, G. Pecheur, *Proc. 1987 IEEE Particle Accel. Conf.*, Washington, p. 1619-1621.
- [3] G. Cavallari et al, *Proc. XVth International conf. on high energy Accel.*, HEACC '92, Hamburg, p. 694-695.
- [4] G. Geschonke, private communications.
- [5] P. Proudlock, H.W. Isch, *Proc. 2nd EPAC 1990*, Nice.
- [6] H. Frischholz, G. Pecheur, "HV Interface for the LEP II RF System", to be published.

Overview and Status of RF Systems for the SSC LINAC

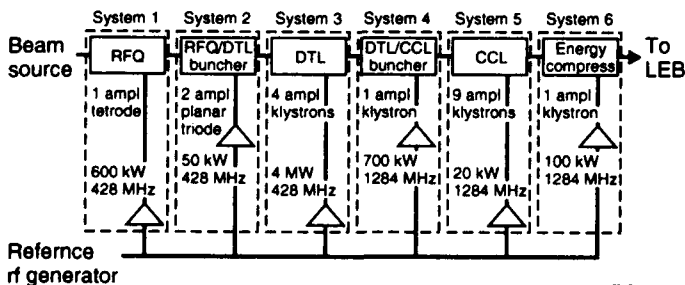
J. Mynk, J. Grippe, R. I. Cutler, and R. Rodriguez
Superconducting Super Collider Laboratory*
2550 Beckleymeade Ave., Dallas, TX 75237

Abstract

The Superconducting Super Collider (SSC) Linear Accelerator (Linac) produces a 600-MeV, 35- μ s, H⁻ beam at a 10-Hz repetition rate. The beam is accelerated by a series of RF cavities. These consist of a Radio Frequency Quadrupole (RFQ), two bunchers, and four Drift Tube Linac (DTL) tanks at 427.617 MHz, and two bunchers, nine side-coupled Linac modules, and an energy compressor at 1282.851 MHz. The RFQ amplifier and the low-frequency buncher cavity amplifiers use gridded tubes, while the other cavities use klystron amplifier systems. The RF control system consists of a reference line and cavity feedback and feedforward loops for each amplifier. The RF amplifier system for each of these accelerator cavities is described, and the current status of each system is presented.

I. INTRODUCTION

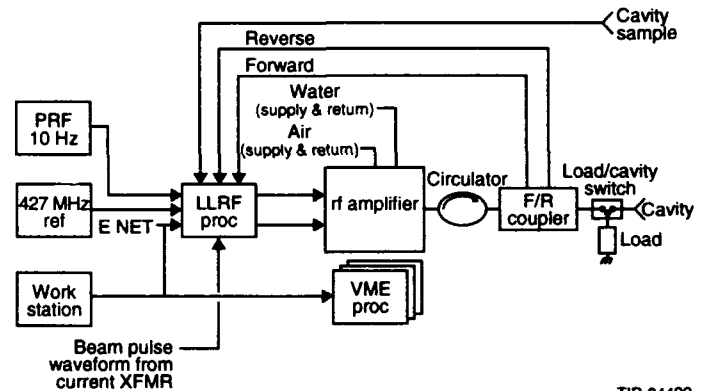
The operation of the SSC Injector Linac [1] requires a series of 18 power amplifiers that can be defined in six groupings, or RF systems, as shown in Figure 1. The operating frequency is tripled at the output of the 70-MeV Drift Tube Linac (DTL), from 427.617 to 1282.851 MHz. This wide spread in operating frequencies, and the wide range of peak amplifier power requirements (50 kW to 20 MW), leads to the selection of a diversity of technologies in the implementation of these amplifiers. A 400-W solid-state pre-amplifier and two UHF grid-tubes, and a high- μ triode driving a super-power beam power tetraode, are used to provide a 600-kW power source for the 2.5-MeV RFQ Linac. The RFQ RF Amplifier, and each of the other amplifiers, has its own independent Low-Level RF (LLRF) processor, (Figure 2). There are two double-gap buncher cavities in the RFQ/DTL input matching section. Each buncher is driven by a 50-kW power source, consisting of a 250-watt solid-state linear pre-amplifier using RF power MOSFETs; a one-tube, 5-kW planar triode intermediate power amplifier stage; and a two-tube, 50-kW planar triode final power amplifier stage. The four Alvarez tanks in the DTL are driven by four high-gain, 4-MW klystrons. Nine 20-MW, 1282.851-MHz klystron amplifiers are used to power the Coupled-Cavity Linac (CCL), accelerating beams of H⁻ ions from 70 MeV to 600 MeV.



TIP-04428

Figure 1. Block diagram showing the six LINAC RF systems.

Each amplifier is controlled and monitored by two single-card processors (Figure 2). A VME-based processor controls and monitors all amplifier power supply/modulator functions, and a VXI-based processor controls all RF functions. The primary purpose of the LLRF is to control the cavity fields in amplitude and phase to 0.5% and 0.5°. The LLRF and its stable RF reference source have been previously described [2-4].



TIP-04429

Figure 2. Typical LINAC RF system.

II. RFQ AMPLIFIER

The purpose of the RFQ amplifier [2-6] is to provide power to enable the RFQ to increase the energy in the beam from 35 keV to 2.5 MeV. The amplifier must provide a minimum of 225 kW at 427.617 MHz, at each of two input ports of the RFQ. The amplifier will operate inside a closed loop system that, when combined with the low-level RF circuitry, will maintain the RF output to 0.5% and the RF phase to 0.5°. The amplifier must meet the requirements of Table 1.

Table 1
RFQ RF Amplifier Specification Requirements

Operating Frequency	427.617 MHz
Bandwidth	300 kHz
Power Output	600 kW peak
Gain	77 dB nominal
Pulse Length	100 microseconds
Pulse Repetition Rate	0-10 H
Pulse Droop	1% maximum
Linear Range	15% to 85% of peak power rating

The RFQ amplifier was built in a joint venture with the Los Alamos National Laboratory. It consists of a 400-W solid-state amplifier, a triode-cavity intermediate amplifier, and a 600-kW maximum power output amplifier using a Burle 4616 tetrode tube. Its design and test results are discussed in Reference [6].

The amplifier and associated control processors were integrated into an RF system (Figure 2) in late 1992. The RF system was finally integrated with the RFQ Linac [3] in Feb.-Mar. 1993. The SSC RFQ LINAC achieved its first 2.5-MeV beam operation on April 9, 1993.

The submitted manuscript has been authored by a contractor of the U.S. Government under Contract No. DE-AC35-89ER40486. Accordingly, the U.S. Government retains a nonexclusive, royalty-free license to publish or reproduce the published form of this contribution, or allow others to do so, for U.S. Government purposes.

*Operated by Universities Research Association, Inc., for the U.S. Department of Energy under Contract No. DE-AC35-89ER40486.

III. RFQ/DTL MATCHING SECTION AMPLIFIER

Two buncher cavities are used for matching from the RFQ into the DTL. Since this operation is critical to the preservation of beam transverse emittance [1], an independently controlled RF amplifier is used to power each buncher cavity. The open-loop operational requirements for each amplifier are listed in Table 2.

Table 2
RFQ/DTL MS Amplifier Specification Requirements

Operating Frequency	427.617 MHz
Bandwidth	10 MHz minimum
Power Output	50 kW peak
Pulse Length	100 μ s
Pulse Repetition Rate	0-10 Hz
Linear Range	<0.5 dB from 10 kW to 42 kW

In October 1992, AccSys Technology, Inc., was contracted to design and manufacture two amplifiers for the matching section. Their design uses three stages of amplification. The first stage is a 250-W amplifier using MOSFET technology and is operated class AB1. The second stage is a 5-kW power amplifier using an EIMAC YU-176 planar triode, running class AB2. The final stage has a pair of YU-176 triodes in a cluster-cavity arrangement, also running class AB2. The amplifier has an embedded control unit for local test and fault location. However, when it is installed in a LINAC RF system (Figure 2), control and monitoring of the amplifier are assumed by the VME/VXI processors.

The amplifiers are in the final phase of assembly and test. Delivery to the SSC Laboratory is scheduled for early June 1993.

IV. DTL RF AMPLIFIER

Four DTL RF amplifiers [2] supply power to four Alvarez accelerator tanks in the DTL [1]. The DTL amplifier klystrons, power supply/modulators, and waveguide components are being obtained from industry after competitive bids. The DTL klystrons, designated TH2140, were purchased from Thomson Tubes Electronics. Four tubes have completed acceptance testing. The TH2140 has an integrally wound focusing magnet that is comprised of three coils; gun, body, and collector solenoids. The collector, the body, and the upper focusing coil are liquid cooled. The tube assembly weighs 3300 lbs. The RF output is constructed in WR 1800 waveguide. Key characteristics of the TH2140 are listed in Table 3. An important feature of the design is a long-life cathode [7].

The DTL klystron modulator (Table 4) was purchased from the Balboa Division of Maxwell Laboratories, Inc., after an intensive technical and cost competition. It is a line-type modulator with a 20-section pulse forming network (PFN). The PFN is a 30.5- Ω , 20-section Rayleigh-type network with tunable inductors to achieve the 0.5% voltage ripple requirement and to compensate for pulse transformer droop. The PFN is charged on-command by two Maxwell CCDS-835 power supplies operating in parallel. The CCDS-835 40-kHz series resonant switching power supply. It has a constant current charge rate of 8 kJ/s and can regulate the network voltage to better than 0.1%. This design approach minimizes the number of high-voltage components in the power supply and eliminates the requirement for high-voltage charging switch tubes and their associated circuits.

Modulator parameters will be monitored through a remote control interface by a VME-based processor. The remote control interface will collect all the interlock/fault/ monitoring information from the individual modulator assemblies and route them to the appropriate VME module in the processor crate. Protection from computer and/or operator error will be provided by hardware circuits.

The DTL modulators have passed all critical design reviews, and fabrication and assembly are proceeding on schedule for acceptance test and delivery in late July 1993.

The output waveguide assemblies consist of arc detectors, forward and reverse power detectors, a Y-junction circulator/isolator, waveguide switch and full power dummy load, and various bends and straight WR1800 waveguides. The high-power circulator/isolator is being built for the SSC by Ferrite Components, Inc. The first unit has completed factory tests, demonstrating isolation greater than 25 dB and insertion loss less than 0.1 dB. All of the DTL waveguide components have been purchased for delivery in June-July 1993.

Table 3
DTL Klystron (TH2140) Characteristics

Frequency	427.6 MHz
Output Power Peak	4.0 MW
Output Power Average	5.0 kW
Pulse Width (Max)	110 μ s
Duty Factor	0.125
Beam Perveance	1.4×10^{-6}
Efficiency	50%
Gain	48 dB
Drive Power	60 W
Bandwidth (-1 dB)	1.0 MHz
Cathode Voltage	125 kV
Cathode Current	64 A
VSWR (Max)	1.30:1
Heater Voltage	25 V
Heater Current	25 A
Cathode Loading	1.0 A/cm ²
Theoretical Life	100 000 h

Table 4
DTL Klystron Modulator Characteristics

Type	PFN/Thyratron
Thyratron Tube	ITT F-307
Peak Pulse Power	8 MW
Klystron Peak Beam Voltage	125 kV
Klystron Peak Beam Current	64 A
HV Pulse Flat-Top Width (100%)	90 μ s
HV Pulse Top Ripple	<0.5% (p-p)
HV Pulse Droop	<1.0%
Klystron Voltage Rise Time	<10.0 μ s
Klystron Voltage Fall Time	<20.0 μ s
Pulse Repetition Rate	1 to 10 Hz
Klystron Duty Cycle	0.00105 max
Recharge Time	95 ms
Klystron Peak Beam Voltage Time Jitter	10 ns
Klystron Peak Beam Voltage	
Pulse-to-Pulse Amplitude Variations	0.2%
Approximate size (LxWxH)	11 x 6 x 9 ft
Weight	26 180 lb

V. CCL RF AMPLIFIER

A 20-MW, 1282.8-MHz klystron amplifier [2] will be used to power each of nine Coupled-Cavity LINAC (CCL) structures [1]. The system design architecture (Figure 2) of the CCL RF amplifiers is practically identical to that of the DTL amplifiers. The VME/VXI control processors run the same software for both amplifiers. This commonality is, of course, an important economical factor in the construction of the SSC LINAC.

The CCL Klystron tube, designated the TH2143, is the product of an upgrade design program [7] conducted by Thomson Tubes Electronics. Improvements in the gun voltage standoff and the

RF output structure enable these klystrons to provide 20 MW of peak power (Table 5) at pulse widths of 100 μ s. Three tubes completed qualification and acceptance testing by early April 1993.

The CCL klystron modulator (Table 6) and the DTL klystron modulator (Table 4) are similar in every way except that the CCL supplies four times the pulse energy at nearly twice the pulse voltage of the DTL modulator. The CCL uses five of the Maxwell CCDS-835 high-voltage power supplies operating in parallel.

A tenth CCL klystron amplifier is used to power the two CCL input matching section buncher cavities. This amplifier operates a TH2143 klystron at a reduced beam voltage of 125 kV, supplying a saturated peak output power of 2 MW. The output of the klystron is split in a variable waveguide power divider and routed to the two buncher cavities. One output goes directly to the first buncher cavity, and the other divider output is routed through a variable waveguide phase shifter to the second buncher. Three tubes have been tested at the reduced beam voltage and have demonstrated linearity of control in the desired region of 1.2-MW power output. The flexibility of the CCL modulator and its command charge power supply allows this reduced pulse operation without modification to the modulator.

Table 5
CCL Klystron (TH2143) Characteristics

Frequency	1282.8 MHz
Output Power Peak	20 MW
Output Power Average	22 kW
Pulse Width (Max)	110 μ s
Duty Factor	0.11%
Beam Perveance	2.3×10^{-6}
Efficiency	>40%
Gain	50 dB
Drive Power	200 W
Bandwidth (-1 dB)	8 MHz
Cathode Voltage	230 kV
Cathode Current	238 A
VSWR (Max)	1.30:1
Heater Voltage	28 V
Heater Current	28 A
Cathode Loading	4 A/cm ²
Theoretical Life	50 000 h

Table 6
CCL Klystron Modulator Characteristics

Type	PFN/Thyratron
Thyratron Tube	ITT F-331
Peak Pulse Power	46 MW
Klystron Peak Beam Voltage	230 kV
Klystron Peak Beam Current	200 A
HV Pulse Flat-Top Width (100%)	60 μ s
HV Pulse Top Ripple	<0.5% (p-p)
HV Pulse Droop	<1.0%
Klystron Voltage Rise Time	<10.0 μ s
Klystron Voltage Fall Time	<20.0 μ s
Pulse Repetition Rate	1 to 10 Hz
Klystron Duty Cycle	0.00075 max
Recharge Time	95 ms
Klystron Peak Beam Voltage Time Jitter	10 ns
Klystron Peak Beam Voltage	
Pulse-to-Pulse Amplitude Variations	0.2%
Approximate Size (L \times W \times H)	12 \times 6 \times 10 ft
Weight	29 200 lb

VI. SUMMARY STATUS

The design and production status of the LINAC RF amplifiers is summarized in Table 7. The RFQ and the DTL/RFQ matching section amplifiers will be used in the SSC Central Facility at Waxahachie, Texas, to complete the initial beam commissioning of the accelerator structures up to the 25-MeV input to the first DTL accelerator. Then the systems will be disassembled and transported to the LINAC building on the SSC injector site.

The Transport Line Energy Compressor Amplifier requires a 100-kW power output at 1282.8 MHz. This amplifier will be required on-site and operating in the first quarter of 1995 for the final stages of the 600-MeV beam commissioning.

Table 7
Status of LINAC RF Amplifiers

UNIT	STATUS
RFQ Amplifier	Completed; in service.
RFQ/DTL MS Amplifier	Fabrication completed; delivery in early June.
DTL Klystron	Four Units delivered; two spares in fabrication.
DTL Modulator	Design complete; in serial fabrication.
DTL Waveguide Assemblies	Procurement cycle complete; delivery in June-July 1993
CCL Klystron	Three units delivered; seven units and two spares in serial fabrication.
CCL Modulator	Design complete; in serial fabrication.
CCL Waveguide Assemblies	In the procurement cycle.
Energy Compressor Klystron	In the procurement cycle.
Energy Compressor Modulator	In the procurement cycle.

VII. REFERENCES

- [1] W. Funk, "The SSC Linac," *Conference Proceedings of the 1992 Linear Accelerator Conference*, Vol. 1, pp. 8-12.
- [2] J. Grippe et al., "The Superconducting Super Collider Linac RF Systems," *Conference Record of the 1992 Twentieth Power Modulator Symposium*, pp. 53-56.
- [3] R. Cutler et al., "RF Commissioning of the Superconducting Super Collider Radio Frequency Quadrupole Accelerator," this conference.
- [4] R. Cutler et al., "SSC Linac RFQ System," *Conference Proceedings of the 1992 Linear Accelerator Conference*, Vol. 1, pp. 380-382.
- [5] J. Grippe et al., "Design and Results of the Radio Frequency Quadrupole RF System at the Superconducting Super Collider Laboratory," this conference.
- [6] D. Rees et al., "Design and Test Results of a 600 kW Tetrode Amplifier for the Superconducting Super Collider," this conference.
- [7] J. Terrien et al., "RF Sources for Recent Linear Accelerator Projects," *Conference Proceedings of the 1992 Linear Accelerator Conference*, Vol. 1, pp. 130-132.

Possibilities and Limitations for a Fully-Digital RF Signal Synthesis and Control

H. Meuth, A. Schnase, and H. Halling

Forschungszentrum Jülich GmbH

Postfach 1913, D-52425 Jülich

Abstract

Since the advent of VLSI circuits capable of data rates in excess of 30 MWords/s, real time digital rf synthesis has become an interesting and viable avenue to be used with accelerators. This technique builds up rf signals from a real-time sequence of digital words with minimum use of analog components. With digital rf, hitherto not achieved agility, precision, and reproducibility for frequency and phase are now possible. This permits optimum acceleration ramp functions, subject to any desired constraints in longitudinal phase space, as given phase or voltage or acceptance, or yet another bucket quantity. Since phase fidelity is crucial with accelerator applications, a high degree of over-sampling is mandatory, posing the only actual limitation to these new techniques. However, with clock rates of more than 1 GHz, today's component technology limits the rf carrier to some ten to about 100 MHz, depending on which signal-to-noise ratio is acceptable. This range can further be extended by means of analog up-conversion. A number of digital rf techniques have been developed at the COoler SYnchrotron COSY, e.g. for rf acceleration and ultraslow extraction, and were made available also for the acceleration with TSR, Heidelberg. Further possible applications are being explored.

1. INTRODUCTION

Acceleration systems in synchrotrons commonly consist of (current-biased) ferrite loaded cavities, controlled by a phase-locked loop (PLL) type tuning control, a high power amplifier, a low-level variable-frequency oscillator, and a beam-phase to gap-voltage phase feedback, again of PLL type.[1] The associated frequency signals, and also the control loop signals are commonly generated and manipulated by analog methods, mainly by mixer circuits, and by voltage controlled oscillators (VCO), to accommodate the large frequency swings of up to a factor of ten. To overcome the inherent drawbacks of VCOs, like their lack of absolute accuracy and stability limitations, specifically, their hystereses in output frequency, digital synthesis methods are now being used more and more, since very large system integration (VLSI) in circuits for this end have emerged on the market. While many of these synthesis methods had been thought of, and, at some instances, used since several years in hybrid circuits, only today's availability of the compact VLSI components make direct digital synthesis (DDS) practical for the large number of variable frequency signal generation tasks common in synchrotrons. However, unlike DDS with audio applications, where digital signal processors can be used, DDS in the rf range must employ dedicated function circuits. To preserve phase fidelity,

moderate to high over-sampling is necessary, which essentially curtails the maximum carrier frequencies and/or signal-to-noise ratios, the latter being directly related to the digital value resolution (number of Bits).

2. DEDICATED-FUNCTION COMPONENTS

The major DDS building blocks are numerically controlled oscillators (NCO), multipliers (used for mixers or in filters), and converters from the analog signal world to the digital realm (ADC) and back (DAC). Characteristic performance values of such devices, which are commercially available at this time, are shown in Fig. 1.

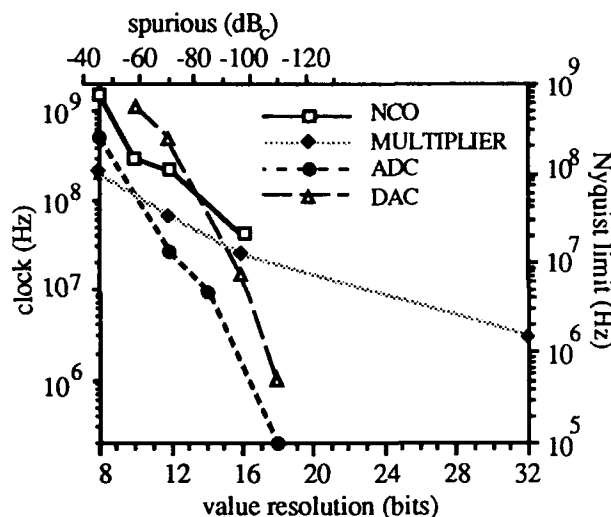


Fig. 1: Performance of present day digital rf VLSI circuits

2.1. Numerically controlled oscillators

According to Fig.1, NCOs can generate frequencies, that typically are on the order of particle revolution frequencies (or their lower harmonics) in synchrotrons. Hybrid and up-conversion schemes with additional analog local oscillator frequency signals extend the range even more, or allow to further reduce spurious content. NCO techniques are thus well suited for generating frequency signals in synchrotrons, including frequency generation for beam diagnostics. [2]

Inside an NCO, a clock continuously advances by the increment $\Delta\Phi$ a polar phase vector on the unit circle, passing on the corresponding projections as $\sin(\omega t)$ and/or $\cos(\omega t)$ computed via a cordic algorithm, or looked up from a table (LUT). Thus, the (synthesized carrier) frequency $f = \omega/2\pi$ follows from this increment $\Delta\Phi$, given in N-Bit resolution, and the clock frequency, f_c , as

$$f = \frac{\Delta\Phi f_c}{2\pi (2)^N} \quad (1)$$

Equation (1) suggests two possibilities for varying the frequency f : Either one varies the phase increment, or one varies the clock frequency. The constant clock frequency is the usual approach. Choosing the clock frequency to be an exact harmonic will greatly reduce the LUT, and thus the NCO. It will improve signal to noise ratio to better than the "theoretical" 6.02dB/N. This shifts the task to the variable (programmable) clock, for which we used, for our applications, again the NCO principle. In any event, NCOs commonly outperform conventional rf generators in typical characteristics, as accuracy, stability, tuning range/bandwidth, resolution, tuning speed, and signal modulation capability. The reason for this is, that the NCO frequency is derived from a high clock frequency, whether fixed or varying. Phase noise stems essentially from the clock oscillator, and is, moreover, reduced due to the frequency down-division by the amount $20\log_{10}f/f_c$ [dB]. Switching speeds are characterized by electronic on-chip delays, and not by a quality factor, as in analog oscillators. NCOs, together with the attached output DAC, are limited by their real-time "computing" and conversion speed, resulting, for practical applications, in carrier synthesis of up to 500 MHz at signal-to-noise ratios (or spurious levels) of 42 dBc, or better for lower clock (i.e. carrier) frequencies. On the other hand, frequency resolution of a fraction of a Hertz is no exception. Hybrid and up-conversion schemes with additional analog local oscillator frequency signals extend the range even more, or allow to further reduce spurious content. NCO techniques are thus well suited for generating frequency signals in proton or heavy ion synchrotrons, including frequency generation for beam diagnostics.[2]

2.1. Modulation and demodulation schemes

As in the analog realm, digital rf signals can be amplitude, frequency and phase modulated. This is done either by direct modulation of the input values for frequency and phase, or by separate multiplication via a VLSI multiplier.[3] Amplitude modulation, if not critical, may be done by suitable gain control in the analog output stage. For correlated digital modulation of frequency, phase and amplitude, again a multiplier must be used, or two suitably phase-modulated NCOs with subsequent signal summing.[4] Again by means of digital multiplication, amplitude, frequency and phase demodulation is possible in quadrature, permitting, e.g., a full 4π phase demodulation within only a few rf cycles.[3]

3. RAMP-FUNCTION SYNTHESIS [5]

One attractive possibility with a completely digital synthesis is the direct digital generation and input of RF acceleration ramping functions, without to resort to the analog realm. These ramping functions for frequency, rf voltage amplitude and (beam-to-rf) phase may be precisely computed beforehand, to take into account beam-dynamic evolution or constraints, as for instance, adiabatic cooling during the acceleration pro-

cess. This suggests the continuous optimization of the longitudinal phase space available for the beam particles during the acceleration process. The direct digital synthesis of rf signals with high value precision has, thus, to face the issue of generating a rapid digital ramp input on a corresponding level of value precision, and, as a consequence, of temporal resolution.

3.1. Frequency Law

Due to the velocity variation during acceleration in proton and heavy-ion synchrotrons, the rf frequency must be tuned along according to the temporal law for the particle momentum $p(t)$, or synonymously, for the magnetic dipole fields.

$$f_{rf}(t) = f_{rev}(t) = \frac{f_\infty}{\sqrt{1 + \left(\frac{E_0}{cp(t)}\right)^2}} \quad (2)$$

The revolution frequency for particles at speed of light is denoted by f_∞ , their momentum by $p(t)$, and their rest energy by E_0 . Especially the resolution needs for the frequency may be high, easily on the order of 24 to 32 Bit, while phase and amplitude may pose less demanding requirements. Note, that with a required frequency resolution Δf based on physics considerations, the associated requirement for digital value resolution, N Bits, follows the rule $N + 1 = \log_2 f_c - \log_2 \Delta f$. With a resolution of $N=20$ or more Bits, a timing discretisation of some hundred nano-seconds may become necessary, in order to retain the intended resolution at all times, as can be shown generally (Fig. 2).[5] For a dipole field variation of 1 T/s, for protons and a frequency resolution of 10^{-6} , the time step is about 1 μ s. Today's fast memory banks, that can provide one 32-Bit data point in less than 100 nano-seconds for several seconds guarantee a precise ramp input. Real-time ramp value computation, based on rapid linear or quadratic inter- or extrapolation in between a sparser grid of ramp points relaxes the time step resolution for these ramp points somewhat, Fig. 2, but poses problems due to the slope quantization of the then needed digital accumulation procedure.[5]

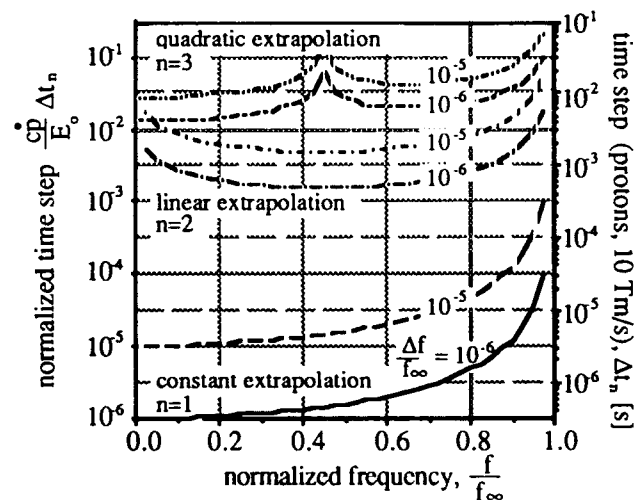


Fig. 2: Frequency and time step resolution

3.2. Phase and amplitude law

The ramp functions for phase $\phi_s(t)$ and amplitude $U_o(t)$ are more involved, but may be computed generally for arbitrary rf.[5] They depend on the wanted particle energy increment per turn, $\Delta(t) = U_o(t)\sin\phi_s(t)$, and also possible constraints in longitudinal phase space. One relevant constraint, especially early into the acceleration, is the momentum acceptance $\delta(t)$ of the bucket, that at no time should exceed the transverse acceptance of the ring. Only two of these temporal dependencies may freely be assumed; all others follow then directly from this choice.

4. BOARD-LEVEL DEVELOPMENTS [3,6]

For various tasks, as frequency signal generation, real-time filtering, ramp function generation, modulation and demodulation, real-time precision phase measurement and phase correction (0.1°/2MHz/5μs), programmable time varying clock signal generation (>100 MHz, 150 ps jitter), and the associated interfacing to accommodate these circuits within the VME/VXI standard, we have developed a number of DDS boards. All these boards may be combined in various configurations, to achieve a wide variety of synthesis, measurement, control and feedback functions. Table I shows some of the boards' key features. Our systems, in various functions, have proved indispensable during acceptance and commissioning of the COSY rf acceleration station, and of the entire COSY ring. In addition, one system was made available for, and by now, was successfully used with acceleration experiments in TSR, Heidelberg. Similar plans exist for CRYRING, Stockholm.

function	f_c [MHz]	N.of Bits		used for
NCO1	25	16	I+Q	frequ. synthesis
NCO2	90	12	I or Q	frequ. synthesis
NCO3	var.	16	I or Q	frequ. synthesis
DAC1	>100	12		signal synthesis
DAC2	>10	16		control loops
ADC	>25	12		measurement/control
Multiplier	>25	16x16		mixer, phase shifter
A-demod	>25	16x16		instant. ampl. demod.
Adder1	50	16+16		simple arithmetics
Adder2	90	12+12		amplitude modulation
Var.Clock	1-1.6x10 ³	8		phase control system
FIR-Filter1	>25	16	2 ⁴ taps	phase control system
FIR-Filter2	>25	16	2 ¹¹ taps	phase measurement
(r,θ)↔(x,y)	>25	16		coord. transform.
Converter	1	20		ramp funct. synthesis

Table I: Some DDS boards developed by COSY-RF

5. FURTHER DDS APPLICATIONS

Other, more exotic applications are also studied, as the phase-correlated second and third-harmonic synthesis required for higher-harmonic drives to modify bucket properties, especially, when passing transition or for other beam pulse shape gymnastics.[7,8] With several NCOs, the phase-rigid (or

phase-corrected) and exactly frequency-tracking synthesis of higher harmonics is no problem. Another interesting method may be employed, when operating a truly wide-band rf high power structure, as does the new accelerator CRYRING.[9] Instead of standard harmonic signal generation via a look-up table containing trigonometric information, an arbitrary-value look-up table permits the time-varying synthesis of saw-tooth type signals, by which phase space may be maximized.

Finally, we have also embarked on the development of the digital signal synthesis for an ultraslow extraction system, where a beam coherent harmonic is to be superimposed with exactly tailored phase and/or amplitude noise, so as to modify the momentum distribution of the particle beam.[10,4] One appealing aspect of this is, that the digital synthesis of noise should permit a direct comparison with standard longitudinal particle simulations.

6. CONCLUSIONS

High-precision, fully digital rf frequency synthesis, phase control, and measurements for carriers up to tens of Megahertz have become feasible with the advent of modern VLSI circuits of high clock-rate capability. Moreover, some features impossible with conventional methods may now be tackled with these digital rf techniques. Due to their board modularisation, systems can be configured flexibly, and should be suitable for other accelerator applications as well. The limitations in clock speed and/or value resolution (i.e. S/N) pose the only true limit for higher frequency applications, although these limits are continually being pushed ahead with the availability of faster and faster circuits.

7. REFERENCES

- [1] D. Boussard, CERN Accel. School '90.
- [2] D. Peterson and J. Marriner, PAC 1991, San Francisco; T. Hayes and A. Zaltsman, *ibid*.
- [3] A. Schnase, H. Rongen, and H. Meuth, EPAC 1992, Berlin; A. Schnase, Ann. Rep. 1992, IKP, Forschungsz. Jülich, p. 201; A. Schnase, and H. Meuth, Ann. Rep. 1992, IKP, Forschungsz. Jülich, p. 205.
- [4] G. Heinrichs, F.-J. Etzkorn, H. Halling, H. Meuth, H. Rongen and S. Papureanu, Intl. Conf. on Accelerators and Large Experimental Phys. Control Systems, 1993.
- [5] H. Meuth, *RF Accel. Ramp. Functions for Digital Ramp Control*, COSY-RF-Rep., Forschungsz. Jülich 1992.
- [6] A. Schnase, Doctoral Thesis, RWTH, Aachen, and IKP, Forschungszentrum Jülich, 1993.
- [7] C. Hamm, H. Meuth, and A. Schnase, Ann. Rep. 1991, IKP, Forschungsz. Jülich.
- [8] J.M. Baillod, L. Magnani, G. Nassibian, F. Pedersen, W. Weissflog, CERN/PS/BR 83-17; J.A. MacLachlan and J.E. Griffin, IEEE PAC, San Francisco, 1991.
- [9] K. Abrahamsson, G. Andler, and C.B. Bigham, NIM in Physics Research B31 (1988), p. 475.
- [10] H. Meuth, G. Heinrichs, H. Halling, and S. Papureanu, *rf-expo* East Conference, Tampa, 1992.

RF System Analyses for the SSC Collider Rings

J. D. Rogers, P. D. Coleman, G. Schaffer, J. D. Wallace, X. Q. Wang, Y. Zhao
Superconducting Super Collider Laboratory*
2550 Beckleymeade Ave., Dallas, TX 75237

Abstract

The Collider RF system is required to accelerate and store a 70 mA DC proton beam from 2 TeV to 20 TeV. Various approaches have been studied as possible ways to accomplish this task. These include systems based on five-cell normal conducting cavities, single-cell normal conducting cavities, and single-cell superconducting cavities. This paper outlines the physics requirements that the system must meet and presents comparisons of the expected performance of various systems. Transient beam loading, injection error, power requirements, coupled bunch mode instabilities, etc. are considered.

I. INTRODUCTION

The SSC (Superconducting Super Collider) consists of two rings, both having a circumference of 87,120 m. Each ring has its own RF system, which accelerates and stores a 70 mA proton beam from 2 TeV to 20 TeV. The beam injected from the HEB (High Energy Booster) is grouped into 8 batches. The total number of bunches is about 16000 per ring, and there are gaps between batches.

The main requirements for the RF system are two fold. The first is to raise the proton energy. This specifies the main data as follows: frequency 360 MHz, peak RF voltage 20 MV, accelerating voltage per turn 3.6MV, and 0.12 MV to compensate the synchrotron radiation loss at 20 TeV. The second is to ensure the beam quality by removing instabilities and suppressing emittance growth.

The unique characteristics of the Collider are a small revolution frequency (3.44 kHz), large number of bunches and relatively high beam intensity. Our main concern pertinent to the beam quality are coupled bunch instabilities, transient beam loading and injection error. These will be discussed later.

To accomplish the above task, there are three approaches being considered based on different cavities. These are five-cell normal conducting cavities, single cell normal conducting cavities and superconducting cavities [1,2,3]. Table 1 shows their parameters.

This paper is intended to analyze the problem and make a comparison of different approaches with their

advantages and disadvantages. Table 2 summarizes the performance of each system. The following sections explain the table entries.

II. TRANSIENT BEAM LOADING

Since an abort gap exists and there are spaces between the batches, and also the ring is only partially filled during the injection period, the beam passing through a cavity is nonuniform. This will cause a modulation of the cavity voltage in both amplitude and phase, known as transient beam loading effect.

The phase modulation is harmful because it may cause the bunches to no longer be exactly equidistant along the ring. The amplitude modulation of the cavity voltage V is less important.

For the simple case when the beam current is constant except at a gap of Δt , which is much less than the cavity filling time, the approximate maximum phase excursion is: [4]

$$\Delta\phi_{max} = \frac{1}{2} \left(\frac{R}{Q} \right) \frac{\omega_{rf}}{V} \bar{I}_B \Delta t$$

where \bar{I}_B is average current at fundamental RF frequency. When the gap is comparable with, or larger than the cavity filling time, it can be shown that the phase excursion $\Delta\phi_{max}$ can be estimated by the following formula:

$$\Delta\phi_{max} = \tan^{-1} \left\{ \frac{I_B}{V} \left(\frac{R}{Q} \right) Q_L (1 - e^{-\sigma\Delta t}) \right\}$$

where $\sigma = \omega/2Q_L$ and I_B is the beam current change in question. The worst case occurs during injection when the ring is only partly filled. During storage the maximum excursion occurs at the abort gap, for which $\Delta t = 4.2 \mu s$. The data are shown in Table 2 for different scenarios. The superconducting cavity has lower R/Q and higher V compared to the normal copper cavity, implying more stored energy, so it will cause less phase excursion.

Table 1. Cavity parameters

Scenario	NC-5	NC-1	SC
Number of Cavities	8	24	10
Number of Cells per Cavity	5	1	1
R/Q per Cavity	625	140	43
Q_{Loaded}	10^4	10^4	6×10^5

*Operated by the University Research Association Inc., for the U.S. Department of Energy under contract No. DE-AC35-89ER40486

The submitted manuscript has been authored by a contractor of the U.S. Government under Contract No. DE-AC35-89ER40486. Accordingly, the U.S. Government retains a nonexclusive, royalty-free license to publish or reproduce the published form of this contribution, or allow others to do so, for U.S. Government purposes.

In order to minimize the phase error, it is necessary to compensate the transient beam loading by modifying the generator current so that extra current is introduced to the cavity with equal amplitude of the transient beam current but opposite phase. To realize this compensation, one can make use of either fast feedback or feedforward [5]. The schematic of these loops are shown in Fig. 1. Feedforward can in principle compensate completely for the beam loading, but in practice, experimental realities limit its effectiveness to ~90% compensation of the transient.[6] Feed-forward may be implemented with a one turn delay which helps reduce the effective impedance presented to the beam at the revolution harmonics.

The effectiveness of fast feedback can be quantified by the ratio of generator induced voltage to beam induced voltage (V_{gen}/V_{beam}). The larger this ratio, the more effective the feedback in reducing the transients. The minimum beam induced voltage achieved using fast feedback is given by[7]

$$V_{beam} \cong I_B N \cdot \frac{R}{Q} \cdot (4f_r \tau)$$

where N is the number of cavities, and τ is the loop delay.

Transient loading is most critical at injection when the RF voltage is its lowest (6.6 MV). For a klystron gallery located on the surface, the expected loop delay is 1.4 μ s. With this delay, it is found that feedback would result in V_{gen}/V_{beam} varying from 5 for a normal conducting multicell system, to 55 for the single cell superconducting approach.[7] The data are shown in Table 2.

In addition to the transient effect discussed above, another consequence of beam loading is its effect on the RF control loops (tuning, phase and amplitude).[8] Usually, with low beam they are stable. When the beam current is comparable with the generator current, the loops may become strongly affected by the beam and coupled to each other. This is a concern for the superconducting cavity, since the generator current is mainly used to compensate for beam loading.

For an adequate stability margin, the beam current should not be larger than the generator current. A ratio V_{gen}/V_{beam} larger than 5 is desirable. From Table 2, all the approaches meet this requirement.

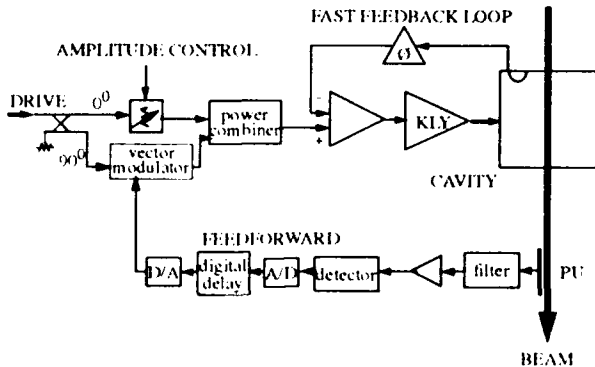


Fig.1 Schematic of feedback and feedforward

III. INJECTION ERROR

A newly injected batch will cause transient beam loading as noted above, and the injected batch may deviate from the desired position. This injection error may be longitudinal or transverse, or both. The transverse error will result in betatron oscillation and has to be damped by a transverse damper. The longitudinal error will result in synchrotron oscillation. Unlike electron machines, a proton ring has little natural synchrotron damping, thus a dedicated damping loop is necessary to avoid undesired emittance growth. This can be done by a slow feedback loop making use of the main klystron amplifier as a power source. The same scheme is applied to damp the low order coupled bunch instability. We address this later.

IV. RF POWER REQUIREMENT

Since the specified accelerating rate is 3.57 MeV per turn, and the synchrotron radiation loss is only 0.123 MeV per turn, a peak cavity voltage of 20 MV is adequate to meet the bunching requirements. Only 6.6 MV is needed during the injection period for a matched beam transfer.

The generator power P_g must establish the above voltages, and compensate for the beam loading. In the general case, where the cavity is detuned with an angle ϕ_z , P_g can be expressed as follows:[3]

$$P_g = \frac{V^2 (1 + \beta)^2}{2R_s 4\beta} \left\{ \left[-\tan \phi_z + \frac{I_B R_s}{V (1 + \beta)} \cos \phi_B \right]^2 + \left[1 + \frac{I_B R_s}{V (1 + \beta)} \sin \phi_B \right]^2 \right\}$$

where R_s is the unloaded shunt impedance and β is the cavity coupling coefficient. For a superconducting cavity, where both R_s and β tend to become very large, but the load impedance $R_L = R_s / \beta$ remains finite, the above expression is still applicable. One can optimize the coupling (β or R_L) to minimize the power requirement. For the normal conducting cavity, where the beam current is much smaller than the generator current, the major portion of the power is required for establishing the cavity voltage. For a superconducting cavity, power is mainly needed for compensating the beam loading. Table 2 gives the minimum power requirements.

V. COUPLED BUNCH INSTABILITY

Coupled bunch instabilities (CBIs) are seen as a serious potential problem for Collider operation. Due to the large ring circumference, the beam's current spectrum has lines every 3.4 kHz. This very dense spectrum will interact with impedances in the ring, resulting in CBI growth. The most dominant sources of impedance will be the accelerating cavities' fundamental and higher order modes (HOM).

The cavity's fundamental mode (i.e. the accelerating mode) can drive low order CBIs. Due to the small

revolution frequency, the cavity bandwidth will typically overlap several revolution sidebands. If the cavity is detuned, it will present different impedances to upper and lower sidebands, hence resulting in CBI growth. This problem is helped, although not completely eliminated, when using the higher Q superconducting cavities.

Low order CBIs that fall within the accelerating system's bandwidth can be addressed using the system's klystrons and cavities. The fast RF feedback discussed earlier is also helpful in suppressing low order CBIs. The feedback loop reduces the fundamental mode impedance seen by the beam by a factor of G (the open loop gain) and hence reduces growth.

Two approaches will be used to address the CBIs driven by HOMs. These cavity modes will be passively damped (and probably staggered tuned) in order to minimize their contribution to the CBI growth. The remaining growth will then be addressed using an active damper system. Such a system would require a broadband amplifier (30 MHz) driving a wide band kicker structure. The estimated growth times and required active damping voltages for the different scenarios are shown in Table 2.

VI. SUMMARY

Various Collider RF system problems and their potential solutions have been discussed. For proper system operation transient beam loading must be compensated. Fast feedback, feed-forward, or both may be used for this purpose. CBIs and injection errors are also important and can be addressed with fast feedback, passive damping and active damping.

Table 2. Performance comparison

Scenario	NC 5-cell	NC 1-cell	SC 1-cell
Number of Cavity	8	24	10
Phase Excursion During Injection ¹	46°	35°	22°
Phase Excursion During Storage ²	7.6°	5.1°	0.8°
V_{gen}/V_{beam} ³	5	8	55
RF Power Required (MW)	1.65	2.0	0.43
CBI (HOM) Growth Time(sec)	7	19	34
Active Damping Voltage (kV)	7.5	3	1

1. Estimated maximum, due to transient beam loading at injection without feed-back.

2. With an abort gap of 4.2 μ s without feed-back.

3. With feedback applied.

Three different cavity approaches have been investigated. As for the normal conducting systems; the single cell system requires more power, however, it has better CBI performance and less transient beam loading problems. Superconducting single cells are predicted to be better than the other two approaches in power requirements, transient beam loading, and in minimizing CBI growth. However, complexity of the superconducting system is of some concern. Technical layouts of the RF systems are discussed in reference [9].

VII. ACKNOWLEDGEMENTS

We would like to thank D. Boussard (CERN), P. Morton (SLAC), and Tai-Sen Wang (LANL), who have contributed a great deal to our analyses.

VIII. REFERENCES

- [1] J. D. Jackson, ed., "Conceptual Design of the Superconducting Super Collider (CDR)," SSC Report SSC-SR-2020 March 1986.
- [2] W. Chou, G. Schaffer, "Comments on the Collider RF cavity in the SSC," Internal memo in SSCL, 1992
- [3] X. Wang, P. Coleman, G. Schaffer, "A comparison of conceptual RF designs for the SSC collider," SSCL-613, Dec. 1992.
- [4] D. Boussard, "RF power requirement for a high intensity proton collider," (part 1 & 2), CERN SL/91-16, (RFS), April 1991
- [5] A. Gamp, "Servo control of RF cavities under beam-loading," DESY HERA-91-09, May, 1991.
- [6] J. Griffin, "Compensation for beam loading in the 400-GeV Fermilab main accelerator," *IEEE Trans. on Nuc. Sci.*, Vol. NS-22, No. 3, June 1975, p. 1910
- [7] D. Coleman, SSCL Internal presentation, Jan. 1993.
- [8] F. Pederson, "Beam loading effects in the CERN PS Booster," *IEEE Trans. Nucl. Sci.*, Vol. NS-22, No. 3, June 1975.
- [9] G. Schaffer et.al. "RF systems engineering for the SSC collider rings," this conference

PEP-II Prototype Klystron

W. R. Fowkes, G. Caryotakis, T. G. Lee, C. Pearson, and E. L. Wright
Stanford Linear Accelerator Center
Stanford University, Stanford CA 94306

Abstract

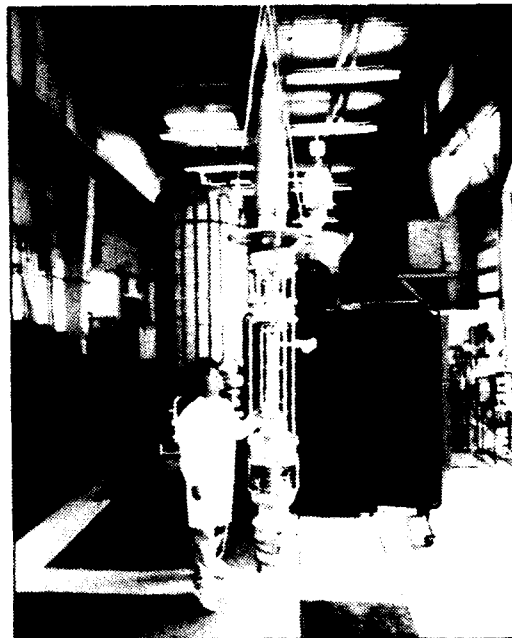
A 540-kW continuous-wave (cw) klystron operating at 476 MHz was developed for use as a power source for testing PEP-II rf accelerating cavities and rf windows. It also serves as a prototype for a 1.2 MW cw klystron presently being developed as a potential rf source for asymmetric colliding ring use. The design incorporates the concepts and many of the parts used in the original 353 MHz PEP klystron developed sixteen years ago. The superior computer simulation codes available today result in improved performance with the cavity frequencies, drift lengths, and output circuit optimized for the higher frequency. The design and operating results of this tube are described with particular emphasis on the factors which affect efficiency and stability.

I. INTRODUCTION

The initial goal was to develop a 500-kW cw klystron to operate at 476 MHz for use as a power source for testing rf cavities destined for the PEP-II Asymmetric Storage Ring. This tube is also considered as a prototype for a 1.2-MW klystron currently being developed as a potential rf source for PEP-II. It became apparent that the 500-kW cw PEP klystron operating at 353-MHz developed at SLAC sixteen years ago, might be used as a basis for scaling. Some quick calculations showed that the same gun, beam tunnel diameter, and collector could be used in a klystron operating at 476 MHz and at the same power level of 500 kW. The cavity designs, drift tube lengths, and output circuit would have to be changed to operate at the new frequency. Many of the design concepts and some of the existing parts from the original PEP klystron could also be used on the 476-MHz tube. It was determined that the development effort could be completed in approximately one year because of this similarity between the two klystrons. Approximately 175 new part and assembly drawings were required.

II. COMPUTER CODE PREDICTIONS

Both the one-dimensional JPNDISK and two-dimensional CONDOR were used to compare the original 353-MHz PEP design with its measured results. While the two codes gave different results and the absolute values in efficiency cannot be relied upon completely, the relative values are meaningful. Both codes predicted an optimized 476-MHz design efficiency about 8 percent higher than the 353-MHz tube. It was also apparent that the efficiency of the 353-MHz PEP tube could have been higher using the now



improved simulation codes, but this would have been at the expense of additional tube length.

III. DESIGN

The design parameters for the klystron are given below.

DESIGN PARAMETERS

Operating Frequency (MHz)	476
Output Power (kW cw)	540
Beam Voltage (kV)	65
Beam Current (Amperes)	12.4
Beam μ perveance (μ amp/volt ^{3/2})	0.75
Efficiency	0.67
Saturation Gain (dB min.)	42
RF Drive Power (watts)	≤ 30
Number of Cavities (Incl. 2nd Harm.)	5
Normalized Drift Tube Radius, γa	0.67
Normalized Beam Radius, γb	0.43
Reduced Plasma Wavelength, λ_q (meters)	4.05
Output Waveguide	WR 2100
Focusing Magnetic Field (gauss)	190 ($2.4 \times B_{Br}$)
RF Interaction Length (meters)	1.67

The cathode is the dispenser type and the gun optics are identical to that of the PEP I klystron which had an oxide cathode operating at 353.2 MHz. The average loading is 98 mA/cm². The beam-tunnel diameter on both tubes is 7 cm. The cavity geometries were changed to accommodate the 35 percent higher operating frequency, but most could be

* Work supported by Department of Energy contract DE-AC03-76SF00515.

machined from the same stainless steel spinings used on PEP I. The cavity diameters were unchanged from PEP I; the resonant frequencies were determined by cavity length and gap spacing. Cavity three, operating at the second harmonic, was an exception and had to be completely redesigned. All five cavities are tunable, and cavities one through four have diagnostic loops. The drift tube lengths were all changed for optimum performance at 476 MHz as determined by computer codes.

INTERACTION SPACE PARAMETERS

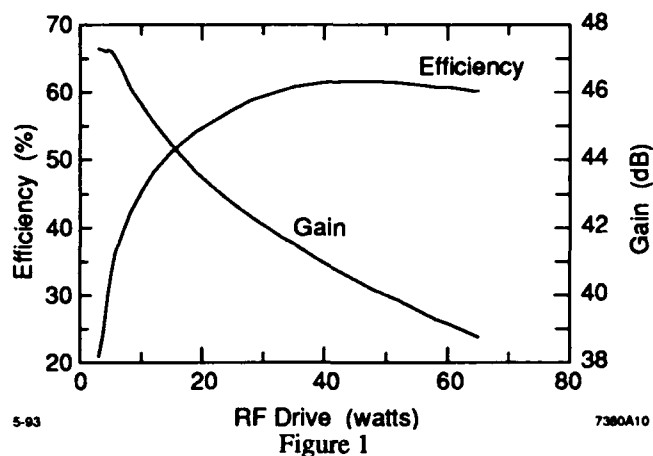
Cavity No.	Frequency (MHz)	R/Q (ohms)	Transit Angle (radians)	Drift Lengths (360°xL/λ _q)
1	476.3	108	1000	0.95
2	477.5	103	∞	1.14
3	948.0	68	∞	0.80 (@2xf ₀)
4	483.8	106	∞	1.00
5	476.4	102	70	1.00

The output coupling loop design that was used on PEP I did not provide enough coupling for the design external Q of 70. The diameter of the output coax center conductor that forms the loop in the output cavity had to be tapered down from 3.34 cm to 1.91 cm in diameter. The coax-to-waveguide transition (56 Ω to reduced height WR 2100) that houses the cylindrical alumina ceramic window was not altered. The position of the abrupt step to full-height waveguide remained the same, but the inductive matching post was moved to provide a perfect match the waveguide to the 56-ohm, 8.5-cm diameter coax exiting the output cavity. The changes resulted in improved bandwidth compared with the original PEP I output window assembly.

The final external Q achieved on the cold test model of the output cavity after five machining iterations was 70, the design value. The measured external Q, however, on the brazed version destined for the tube turned out to be 57. Unfortunately, no quick way of adjusting the coupling exists. It was decided to assemble the tube and optimize the external Q artificially in the waveguide output as described later.

IV. OPERATING RESULTS

The klystron began testing in spring 1992. The design power output of 500 kW was achieved at 66 kV instead of the design value of 65 kV. The efficiency was slightly lower than expected due in part to a lower than optimum external Q for the output cavity as described above. The initial measured efficiency was about 60 percent but was increased to 61.6 percent by artificially raising the external Q of the output cavity with an external matching element and some minor tuning of three of the cavities. No instabilities, such as multipactor, spurious frequencies, or sideband frequencies due to returning electrons were observed. The beam is well



behaved, and the usual tradeoff between focusing for maximum power output and minimum body interception was not present. The first two cavities and the entire output circuit were coated with titanium nitride as a precaution against multipactor.

A saturation gain of 40 dB was achieved instead of the design value of 42 dB, and the optimum focus magnetic field was 234 Gauss instead of the design value of 190 Gauss. Plots of efficiency and gain are plotted as a function of rf drive in Figure 1.

V. CHANGING THE EXTERNAL Q OF THE OUTPUT CAVITY

The effective external Q was changed by placing a capacitive post in a section of waveguide with a longitudinal slot along its centerline on one broadwall so that the gap impedance could be changed by controlling the height and position of the post. The initial assumption was that the gap impedance should be increased by approximately the ratio

$$\sigma = \frac{Q_{\text{ext-desired}}}{Q_{\text{ext-actual}}} = \frac{70}{57} = 1.23 ,$$

and the magnitude of the normalized capacitive susceptance to accomplish this is given by

$$\left| \frac{B}{Y_0} \right| = \frac{\sigma - 1}{\sqrt{\sigma}} = 0.206 .$$

The location of the capacitive post with respect to the output-cavity detuned short is given by

$$\ell = \frac{\lambda_g}{4} + \frac{\lambda_g}{2\pi} \tan^{-1} \left[\frac{1}{2} \left[\sqrt{\left| \frac{B}{Y_0} \right|^2 + 4} - \left| \frac{B}{Y_0} \right| \right] \right]$$

towards the load. This produces a normalized admittance at the detuned short position of

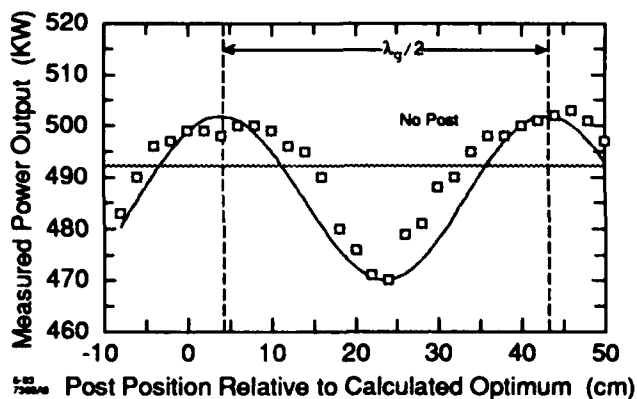


Figure 2

$$\frac{Y}{Y_0} = 0.814 + j0.$$

Capacitive post spacers were constructed to produce capacitive susceptances slightly larger and smaller than the calculated value, but the calculated value was found to be optimum for improving efficiency. The effect on efficiency of the z position in the slotted waveguide is shown in Figure 2.

VI. FUTURE PLANS

A 1.2 MW klystron operating at the same frequency is jointly being developed by SLAC and Varian Associates. This new tube must have a combination of wide bandwidth and short group delay needed for powering high-current accelerator systems requiring fast rf feedback stabilization. The bandwidth and group delay of the 500 kW klystron described in this paper are not adequate. The first tube will be built and tested at SLAC but the design will be a joint effort by both organizations. Testing of this tube is expected to start in the summer of 1994.

VII. ACKNOWLEDGMENT

The authors would like to acknowledge the members of the klystron manufacturing and testing groups who put their energy, dedication and skill together to bring this project together within a year of its inception. Particular thanks go to Harry Greenhill and Charley Griffin who made many valuable contributions to the tube design and testing facility.

current. This arrangement allows the maximum feedback voltage but minimum size of the toroidal core.

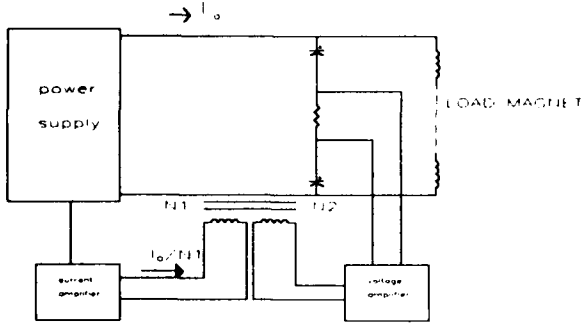


Figure 2: The active filter.

The cross section A of the toroidal core is decided by the following formula:

$$A = \sum_i \frac{\sqrt{2} V_{rms}^i}{2\pi f_i B_{max}}, \quad \dots(1)$$

where V_{rms}^i is the maximum rms voltage ripple of the f_i component to be removed and B_{max} is the saturation flux density of the core. The output voltage ripple of 60Hz (main component) is about $0.3V_{rms}$. We need a cross section of 10 cm^2 for the toroidal core with one Tesla saturation flux density. Since the transformer can be treated as open at the load side, the feedback amplifier needs the output voltage swing

$$V_{cc} = \frac{1}{2} N V_p, \quad \dots(2)$$

and the maximum output current is

$$I = \frac{l V_{cc}}{2\pi f_{min} \mu AN}, \quad \dots(3)$$

where N is the winding number and l is the circumference of the core.

In our application, we set $N=20$, $V_{cc}=15\text{V}$ and $I=0.3\text{A}$. The strip wound core is made of the material VITROPERM from the German company VAC with the strip thickness of $20\mu\text{m}$. The response is flat to 300kHz.

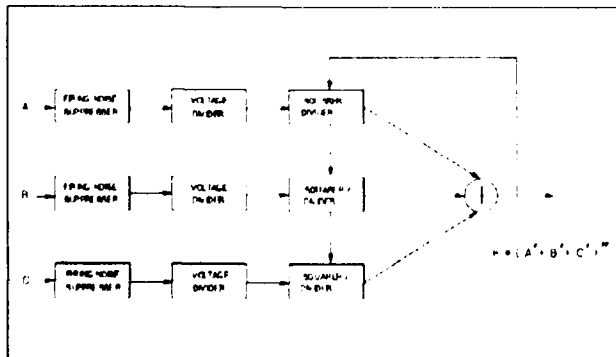


Figure 3: The AC level detector.

IV. AC level detector

The maximum rating of the active filter mentioned in the last section is limited by the cross section of the core and the amplifier. We have to restrict the voltage ripple passed to the active filter. Therefore, a fast AC detector is developed to pick up the signal of the line change, the imbalance and the higher harmonics (figure 3).

The detector consists of three rms to DC converter. The detector output is

$$V_{out} = k(A^2 + B^2 + C^2)^{1/2} = \sqrt{\frac{3}{2}} k V_{AC}$$

$$A = V_{AC} \sin(\omega t)$$

$$B = V_{AC} \sin\left(\omega t + \frac{2}{3}\pi\right)$$

$$C = V_{AC} \sin\left(\omega t + \frac{4}{3}\pi\right) \quad \dots(4)$$

where A,B,C are the three phase line voltage and k is a scaling constant. The accuracy of the detector is better than 0.1% with a carefully calibration. Comparing with the 12 pulses peak detector in our original design, it contains unwanted 720Hz ripple to be filtered. We compare these two detectors on the line with the integration over one line cycle to eliminate the harmonics of 60Hz. The RMS detector has the same behavior but is faster. Figure 4 shows the step response of the power supply with and without the feedforward.

All power supplies for the transport line and storage ring locate in the core area of the storage ring. They share the common 1.5 MW step-down transformer. Hence, only one AC level detector is sufficient to distribute the AC information to those power supplies. To avoid the grounding loop, the signal is transmitted by a voltage to frequency converter and received by isolated frequency to voltage converter.

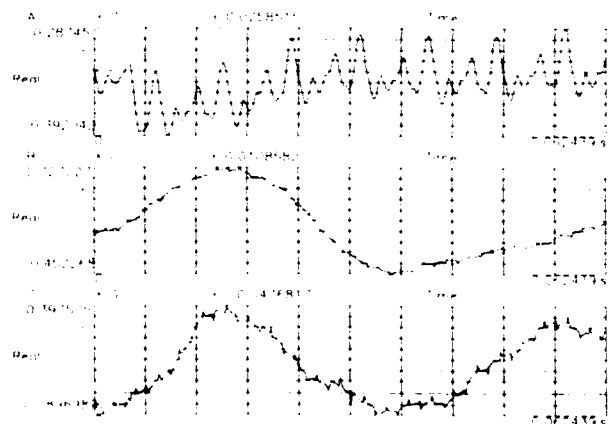


Figure 4: The step response. (a) FFW signal (FS: 7V). (b) Current without FFW (FS: 250A=1KV). (c) Current with FFW (FS: 250A=1KV).

V. AC Current Feedback

The detector of the three phase AC level mentioned in the last section can be also applied on the AC input current. For a constant current source, we have following power relation

$$I_{DC}^2 \cdot R + P_{loss} = (\overline{V_{AC}} + \Delta V_{AC}) \cdot (\overline{I_{AC}} + \Delta I_{AC}), \quad \dots(5)$$

where P_{loss} is the power loss of the power supply. If we neglect the high order term, the AC input current is proportional to the AC voltage

$$\Delta I_{AC} = -\Delta V_{AC} \cdot \frac{\overline{I_{AC}}}{\overline{V_{AC}}}. \quad \dots(6)$$

This information of the AC current contains not only the AC line input but also the characters of the step-down transformer and the SCR's. The harmonics of output current at 60Hz and 120Hz are reduced by the factor of ten.

VI. Conclusion

The DC power supply of the SCR control type without the passbank current regulation is sensitive to the line change. The sub-harmonics of the line is the most harmful part of the ripple. If we compare the passbank current regulation. There are economical ways to reduce the voltage ripple. We developed the DCCT like active filter, which is compact and easy to mount. The information of the three phase AC line (voltage and current) is helpful to reject the line variation. We use the feedforward of the AC voltage to suppress the transient excitation. On the other hand, we reduce the harmonics with the feedback of the AC current. Hence, the size of the active filter can be very small.

One AC level detector (voltage) is sufficient to serve many power supplies in the group. In this case, it is also economic to use DSP type of the AC level detector, which can calculate the higher harmonic and compensate the phase shift due to the firing angle respectively for each power supply.

VI. References

- [1] SRRRC Design Handbook, Synchrotron Radiation Research Center, Taiwan, 1990.
- [2] SRRRC Status Report, (SRRRC, April 1993).

Magnet Power Supply System for the ALS Storage Ring and Booster*

L. Terry Jackson, Ken Luchini, and Ivan Lutz
Lawrence Berkeley Laboratory, University of California
1 Cyclotron Road, Berkeley, CA 94720 USA

Abstract

The Magnet Power Supply System is described by specification, design, hardware, and operating experience. A unique system for the one Hz, 1.5 GeV Booster, where the wideband QF and QD power supplies track the dipole current to within 0.1% at injection will be detailed. AC distribution system considerations related to inverting the stored energy of the booster magnet back into power grid will be discussed. The rationale for linear correctors and individual quad supplies (225 total units) will be placed within the context of the storage-ring requirements.

I. LINAC TO BOOSTER MAGNET P.S.

The power supplies for this transport line are EMI Power Supplies for the dipole magnets, Kepco power supplies for the quadrupole magnets and Techron power amplifiers for the vertical/horizontal corrector magnets. The attempt in this transport line system was to use commercially available equipment in totality. The EMI Power Supplies were bought with amplifiers added so that the input and output interface was zero to 10 V in both cases to allow interfacing with the Intelligent Local Controllers (ILC) used throughout the ALS system. The Kepco supplies were modified at LBL by adding components to the interface plug located on the back of the Kepco to make a high-gain close-loop current control system. The utilization of the interface plug-in allowed use of the two amplifiers internally mounted in the Kepco to again provide input and output reference and feedback signals at 0 to 10 V. The Techron Supplies could not be internally modified to allow input and output interfacing at 0 to 10 V. An attempt was made to do this internally by changing the gain of the amplifiers but internal wiring practices cause oscillations to occur when the gains were raised on these amplifiers so the decision was made to fabricate an interface chassis, each to interface to four of the Techrons on the LTB line. There is a divider to lower the input reference from 10 volts to the 0.6 volts maximum required by the Techron and then an amplifier to take the 0.6 V max. outputs current monitor signal up to the 10 V required by the ILCs. The basic level of operation of this whole system was $\pm 0.1\%$ of the maximum current, and with the components as described the system has proven to work satisfactorily.

II. BOOSTER POWER SUPPLY SYSTEM

As was described in the 1989 paper[1] on the plans for this system, the booster power-supply system operates at 1 Hz and therefore it was not necessary to use a resonant system (using a White circuit for instance) as has been done on systems that operate at higher frequencies (typically 10 Hz and above). The supply for the ALS Booster Dipole string of magnets runs as an open loop 12 pulse supply with a 0 or 10 V control signal

and goes into full rectification for ramping up the current, and then into almost full inversion for completion of the cycle and returning the current to zero. This approach was chosen for minimum cost knowing that the current would vary from pulse to pulse as the line voltage varies, and this it does.

The quadrupole (QF and QD families of magnets) supplies are closed-loop high-performance systems that track the dipole current and make it possible to have the large 1 MVA dipole-supply running without any closed loop operation. This approach has worked very satisfactorily both for tracking and perturbations of the dipole current. The equipment from the manufacturer, with some modifications, has proven eminently satisfactory for our operation. The crucial requirement on the ramp operation is that the quadrupole supplies are tracking the dipole current at injection, which is approximately 1/30 of the maximum energy (and 10 msec from start of ramp), so they must have wide bandwidth to be able to catch up and have the performance necessary at the time of injection. The sextupole and corrector supplies are small units and they also track the dipole current as their reference.

The dipole reference current signal (0 to 10 V) is distributed to the quadrupole, sextupole, and corrector circuits through an interface circuit that allows correction to be made to the basic booster current signal as a function of energy level for each power supply. There are two parts to this interface. One is the digital-multiplier circuit which allows each circuit to have its own level of reference as a percentage of the 0 to 10 V peak signal from the dipole transducer. The other element of the circuit is a summer which is controlled from a look-up table in the ILC which gets timing information from energy markers generated by the timing system (approximately 5 msec repetition rate at injection). The small correction (0.1%) necessary on the basic dipole signal is particularly important at injection and extraction energies. Hysteresis effects are the main sources of error between the dipole signal and the required quadrupole signal at injection. Saturation effects require small correction at extraction energy levels. All the corrections for the supplies are done by the operators in the control room through the ILC system. The concept and execution of this approach have worked out well and the booster operation is today basically push-button operation using all the stored information on settings.

A. Dipole Power Supply

The supply is pulse rated for 1175 V, 800 A peak operation with a triangular wave duty cycle at a 1 second repetition rate. Initially the twelve pulse rectifier would not operate without SCR failure during inversion. It was determined that the dv/dt transients during inversion were severe enough to fire SCRs at the wrong time resulting in these failures. A more substantial snubber circuit corrected this problem and then satisfactory operation resulted.

By having the power supply come on to full output voltage at the beginning of the rectification period the ripple at injection is minimized. The inversion level is set at approximately three quarters of the full inversion to allow

*This work was supported by the Director, Office of Energy Research, Office of Basic Energy Sciences, Materials Sciences Division, of the U.S.DOE, under Contract No. DE-AC03-76SF00098.

substantial phase margin during inversion. "Light" filtering with a damped LC circuit ($f_0 = 100$ Hz) is used to allow a fast step response at the start of rectification.

B. Booster Quadrupole P.S.

The quadrupole power supply is complicated by the high performance required to track the dipole current and the size of the supply required. To get the required dynamic performance to follow the ramp dipole current signal at injection and beyond, a current loop is closed through a series transistor bank composed of 24 Gentron MOSFETS rated 32A/400V each (EFM049-M46). A second loop is closed on the transistor-bank voltage through the 270 V, 460 A SCR controlled power supply. A further complication of this multi-loop system is that the reference voltage to the loop monitoring the transistor voltage is varied as a function of magnet current (through a look-up table in the ILC). This was necessary so that at the beginning of each cycle the transistor voltage is at a high value that then allows the initial step required to the magnet for $L di/dt$ startup at the beginning of each cycle. Then the transistor voltage reference decreases as the current rises so that starting from an initial voltage of 100 V across the transistors, the voltage drops to 25 V by the end of rectification. So there are three loops in this system and the operation of all three had to be carefully tailored to meet the performance requirements.

An additional clamp circuit had to be added to the supply on the transistor voltage because of transients on that voltage at the top-of-ramp transition. This clamp limits the peak dissipation in the transistor bank and eliminated the early problem that was encountered of random failures among the 24 parallel transistors. The concept and initial design of the clamp circuit was provided by Henry Lancaster whose assistance is gratefully acknowledged.

The bandwidth of the small signal transistor loop is set at 10 kHz. At this bandwidth there is a substantial difficulty with noise pick-up in the system and careful attention had to be paid to lead dress and shielding throughout the system. As the bandwidth was increased, in the check-out process, improvements were made as required and now the system is highly satisfactory and trouble free over the last year of operation. The same mode of operation for the sextupoles and correctors is employed, utilizing Techron amplifiers with satisfactory results.

C. Line Voltage Effects

With a rectifying-inverting system of this magnitude there must be concern for the effect of pulsing on other equipment operating from the 12 kV/480 V transformer that is supplying the dipole quadrupole power supplies. This includes the other pulsing supplies and low-level electronic equipment associated with the booster including the beam position monitor (BPM) which operates on low beam signal levels. The BPM system is designed with sufficient buffering that the pulsing of the booster dipole has not presented any problems. The booster pulsing system is fed from a 12 kV/480 V transformer on the pad at a 2 MVA level. This transformer is in turn fed from a 20 MVA transformer at the Grizzly Peak substation which was also used to provide power to Bevatron (a pulsed load which now has been shut down).

III. BOOSTER TO STORAGE RING (BTS) P.S.

The supplies needed for the booster to storage ring transport line are similar to those used in the LTB line except that the dipole supplies are large enough that it was decided to specify these supplies, and (as can be seen in table 1) the price per kilowatt turned out to be very competitive with commercially available supplies.

IV. STORAGE RING P.S. SYSTEM

In the storage ring there are four large supplies and 220 small supplies. The large supplies are the gradient, QFA quadrupole, and SF and SD sextupole supplies. These supplies all drive families of magnets that are distributed around the storage ring in 12 sectors. The gradient power supply has the tightest specification at ± 50 PPM maximum allowable variation in current. These are all DC steady state supplies that normally run at currents necessary for 1 1/2 GeV operation with the capabilities of ramping slowly up to their rated currents necessary for 1.9 GeV operation. The other quadrupoles in the storage ring lattice are called QF and QD quadrupoles and each of the magnets have separate power supplies. These 48 quadrupole supplies are part of a family of supplies that were specified and purchased in total from Inverpower. There are five different types of supplies within this family. The two quadrupole supplies already mentioned, vertical and horizontal corrector supplies that drive separate windings on a single iron frame magnet, and supplies for the vertical/horizontal corrector windings mounted on the sextupole magnets. As can be seen from table 1, there is also a skew quad supply in this family of five different types of power supplies. These supplies range in power level from 7 kW to 900 W and all the correctors are bipolar supplies. All of these supplies are linear supplies with series pass banks of parallel FET transistors as the controlling elements. Experience in building these supplies shows that linear supplies were cost competitive with switching supplies of in the same size. The advantage of using the linears compared to switchers for approximately the same cost is the elimination of possible second-order beam effects associated with switching noise.

The gradient power supply is manufactured by PEI and is a 12 pulse steady-state rated supply. The required performance can be satisfactorily achieved with careful attention to low drift front-end design, a wide-band voltage-loop, and a quality firing circuit designed by the manufacturer. The 12 pulse generation was specified to be achieved in this supply by using two identical octagon-primary rectifier transformers each feeding 6 pulse bridge rectifiers. This was specified because the booster twelve pulse dipole supply with delta/delta and delta/bye transformers did not provide the 12 pulse ripple that was desired but rather a combination of 6 and 12 pulse ripple. The 2 sextupole power supplies are also manufactured by PEI and although they have a lower performance requirement use the same hardware components except the water-cooled front-end package required by the gradient supply.

The QFA power supply is manufactured by Inverpower and utilizes the same hardware as their BTS power supplies with a higher performance front end. These supplies all came into operation within a minimum of difficulty and have so far proven to be quite reliable. The only reliability problem has been with the phase information transformers produced by PEI

of which three have failed at this point. The failure is felt to be because of the very small wire that is utilized (#35 AWG) on the 480 V primaries.

A. Small Power Supplies

Because of the number of these small supplies (220) that needed to be produced, an integrated approach to all of them with the same package of mechanical and electrical features was desirable. This concept was achieved through common specifications and has been carried out in an exemplary fashion by Inverpower in their design and construction. The only variation in the mechanical package is that the smaller supplies are in a 10 inch high chassis rather than the 12 inch chassis needed for the large supplies. The low powered units are fed from single phase 120 V power while the vertical corrector and quadrupole supplies are fed from three phase 208 V power. All the chassis utilize quick-disconnect water fittings and water-cooled heat sinks for the FET pass transistors.

The supplies all have the same operational layout whether large or small. Immediately behind the front panel is a printed circuit board which extends across the whole chassis. This board contains all controls, interlocks, and analog circuitry necessary for the operation of any of the power supplies. Some of the components are not used on some of the smaller supplies. Immediately in back of the master control board is the water-cooled shunt which is manufactured by Vishay-Mann in England and has a 1 V max. output signal level for all

units. Above the water-cooled shunt is the water-cooled heat sink for the FETs which also has thermal interlocks connected to it. The number of transistors varies greatly between the various applications. The horizontal bipolar steering supplies utilize only one FET on either side whereas the quadrupole QF supply has eight in parallel in the unipolar application. Inverpower used two different models of MOSFET, both manufactured by International Rectifier, the 150A/100V IRFK6H150, and the 150A/200V IRFK6H250 (the bipolar supplies are quasi-complementary). In behind the water-cooled heat sink is the power transformer and in the rear is the contactor and water-flow switch.

These power supplies have proven to be reliable in operation. The biggest operational problems have been related to the water cooling circuits with flow switches failing and flow restrictors plugging. The operation of this supply family has been very satisfactory and the performance of these supplies with a 1 kHz unity gain-bandwidth and low-thermal drift has been very adequate for all of the operations so far and anticipated.

V. REFERENCES

- [1] L.T. Jackson and I. C. Lutz, "Magnet Power Supplies for the Advanced Light Source", Proceedings of 1989 IEEE PAC, Vol. 3, pp. 1910-1912, LBL-26012.

TABLE I — MAGNET POWER SUPPLIES

Loc.	Type	No.	E (V)	I (A)	P(w)	P(kw)	Mfr	\$/Cost	\$/kw	+/- %
LTB	Dipl.	4	12	220		2.6	EMI-TCR	3100	1200	0.05
	Quad	6	15	15	225		Kepco ATE	1600	7100	0.1
	Sext	1	36	15	540		Kepco ATE	1800	3300	0.1
	V Cor.	7	+/- 40	6	240		Techron 7521	860	3600	0.1
	H Cor.	7	+/- 40	6	240		Techron 7521	860	3600	0.1
Bstr.	Dipl.	1	1175	800		940	PEI	57,000	61	N.A.
	Quad.	2	245	460		113	Alpha Sci.	40,600	360	0.03
	Sext.	8	+/- 40	6	240		Techron 7521	860	3600	0.1
	V Cor.	16	+/- 40	6	240		Techron 7521	860	3600	0.1
	H.Cor.	16	+/- 40	6	240		Techron 7521	860	3600	0.1
BTS	Dipl.	4	33	820		27	Inverpower	12,599	453	0.1
	Quad.	11	40	130		5.2	Inverpower	5580	1073	0.05
	V Cor.	9	+/- 40	6	240		Techron 7521	1186	5000	0.1
	H.Cor.	9	+/- 40	6	240		Techron 7521	1186	5000	0.1
SR	Gradt	1	535	1000		535	PEI	79,400	148	0.005
	QFA	1	400	550		220	Inverpower	53,000	241	0.01
	Sxt F	1	215	400		86	PEI	33,700	392	0.1
	Sxt D	1	215	400		86	PEI	33,700	392	0.1
	QF	24	54	130		7	Inverpower	6480	926	0.01
	QD	24	40	130		5.2	Inverpower	5580	1073	0.01
	H Cor.	48	+/- 12	40	480		Inverpower	2160	4500	0.01
	V Cor.	48	+/- 13	120		1.6	Inverpower	4050	2531	0.01
	H CorS	48	+/- 45	20	900		Inverpower	3150	3500	0.01
	V CorS	24	+/- 45	20	900		Inverpower	3150	3500	0.01
	Sk. Qd	4	+/- 45	20	900		Inverpower	3150	3500	0.01

Design and Development of a Bipolar Power Supply for APS Storage Ring Correctors*

Y. G. Kang

Argonne National Laboratory, 9700 S. Cass Avenue, Argonne, IL 60439

Abstract

The Advanced Photon Source (APS) requires a number of correction magnets [1]. Basically, two different types of bipolar power supplies (BPS) will be used for all the correction magnets. One requires dc correction only, and the other requires dc and ac correction. For the storage ring horizontal/vertical (H/V) correctors, the BPS should be able to supply dc and ac current. This paper describes the design aspects and considerations for a bipolar power supply for the APS storage ring H/V correctors.

I. INTRODUCTION

Basically, two different types of bipolar power supplies are used for all the APS correction magnets. One requires dc correction only, and the other requires dc and ac correction. For the storage ring H/V correctors, the magnet current consists of a dc component and an ac component. Normally a power amplifier would be used for the BPS. Since the power amplifier type BPS uses the linear-mode power conversion which results in poor efficiency and large size, commercial BPSs are available for lower power levels. Therefore, it is desirable to design such a BPS using the switch-mode power conversion. However, due to the low pass filter effect of the vacuum chamber [2] used in the storage ring, the amplitude of the ac component is substantially large, which makes designing a bipolar power supply using the switched-mode conversion techniques difficult. This paper deals with the design and development of a BPS using switch-mode power conversion for the APS storage ring H/V correctors. A 150A BPS has been designed, prototyped, and tested, and about 650 units are being manufactured.

II. SPECIFICATIONS

The specifications for the BPS are given as follows:

- a. Input dc bus voltage: 70V +10%/-15%
- b. Maximum output current: 150A bipolar = $I_{dc} + I_{ac}$
 - * Maximum ac component: 75A(peak) @ 25Hz
 - * Correction frequency: 0 ~ 25Hz
 - * DC offset current: -150A ~ +150A
- c. Horizontal corrector:
 - Inductance: 6mH @ dc, 3.25mH @ 25Hz
 - Resistance: 72mΩ @ dc, 137mΩ @ 25Hz
- d. Vertical corrector:
 - Inductance: 7.6mH @ dc, 6.1mH @ 25Hz
 - Resistance: 118mΩ @ dc, 237mΩ @ 25Hz
- e. Maximum output power: 5kW

*Work supported by the U.S. Department of Energy, Office of Basic Energy Sciences under Contract No. W-31-109-ENG-38.

The submitted manuscript has been authored by a contractor of the U.S. Government under contract No. W-31-109-ENG-38. Accordingly, the U.S. Government retains a nonexclusive, royalty-free license to publish or reproduce the published form of this contribution, or allow others to do so, for U.S. Government purposes.

- f. Ripple current: 0.14 A (peak-to-peak)
- g. Stability: ± 300 ppm of $I_{o,max}$
- h. Reproducibility: ± 600 ppm of $I_{o,max}$
- i. Tracking error: ± 500 ppm of $I_{o,max}$
- j. Reference resolution: 16-bit

III. SYSTEM DESCRIPTION

Figure 1 shows the simplified block diagram of a bipolar power supply. It consists of a power modulator (main power section), four Euro-cards for the regulator, digital-to-analog and analog-to-digital converters (DAC/ADC), converter and magnet monitoring & interlocks, and a control power supply board. This BPS is water-cooled. The power supply control unit (PSCU) contains the intelligence that interfaces directly to each power supply hardware for control, monitoring, and communicating to the host computer. One PSCU can control as many as eight BPSs.

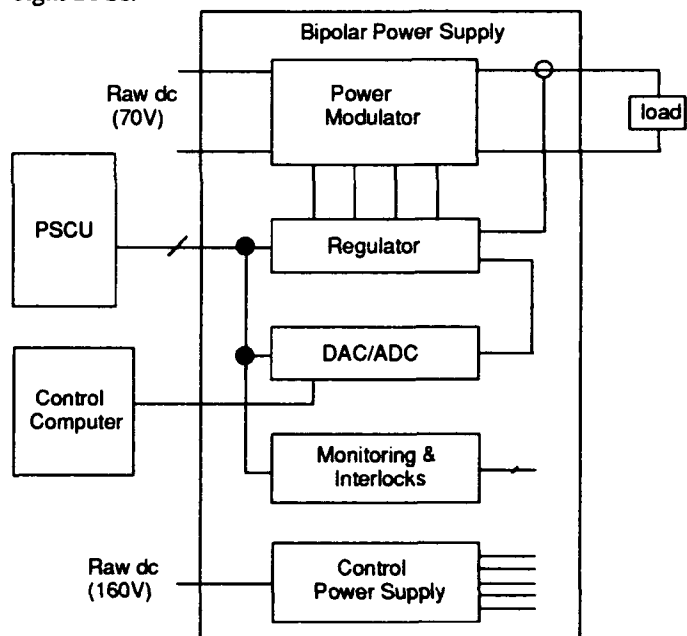


Figure 1: Simplified block diagram of the BPS.

Figure 2 shows the simplified circuit of the main power section. The topology is a full-bridge converter, and the switching frequency is 20 kHz synchronized with the main clock. The regulation is achieved by controlling the pulse width. Insulated gate bipolar transistors (IGBTs) are considered for the switching devices due to their high current and voltage handling capability and easier drive requirement. Two water-cooled IGBT modules, Powerex IGBT type CM300DY-12H (dual package), are used for the switches. L_m and R_m represent the inductance and resistance of a correction magnet. For positive magnet current, switches Q1 and Q4 are closed. Only the upper switch, Q1, is controlled according to the pulse width modula-

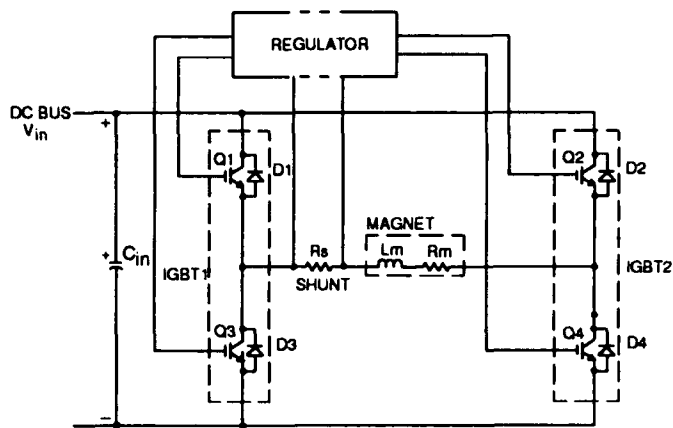


Figure 2. Simplified circuit of the main power section. tion (PWM) signal, while the bottom switch, Q4, remains closed. When Q1 is opened, the magnet current decays through the still-closed switch Q4 and diode D3. However, double gating, which controls both Q1 and Q4 simultaneously, is required for the negative di/dt. For negative current, switches Q2 and Q3 and diode D4 are used in a similar fashion. In order to regulate the magnet current, the magnet current information is fed back to an error amplifier input via a current measuring device and is compared with the reference voltage provided by a digital-to-analog converter (DAC). A 2mΩ water-cooled shunt resistor is used for the current measuring device. The unregulated dc input bus voltage, V_{in} , is provided by a separate three-phase ac/dc rectifier. The input dc bus, V_{in} , is determined by the following expression:

$$V_{in} = I_{pk} [(\omega L_m)^2 + R_m^2]^{1/2} \sin(\omega t + \phi) + I_{dc} R_m$$

where

$$I_{pk} = \text{peak value of the ac current,}$$

$$\omega = 2\pi f \quad (f = 0 \sim 25 \text{ Hz}).$$

IV. CONTROL

Figure 3 shows the simplified block diagram of a control scheme of correction magnet power supplies for the storage ring. The PSCU communicates to each power supply using op-

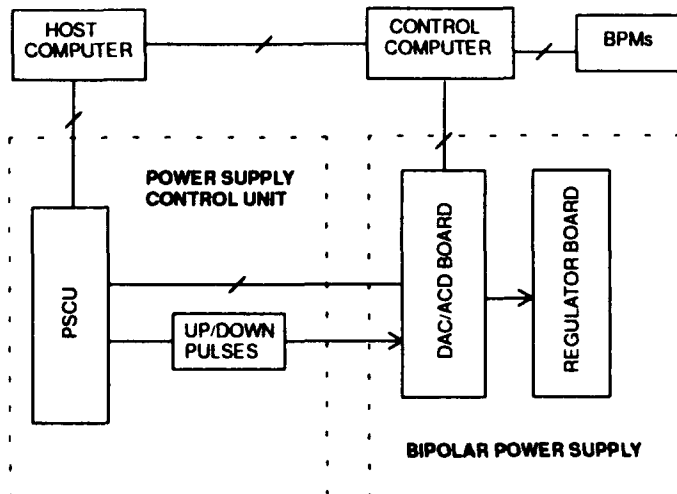


Figure 3. Simplified block diagram of a control scheme.

tically coupled digital signals and differential shielded twisted pairs for analog signal transmission [3].

A 16-bit DAC is used for the reference signal generation. The host computer provides a current value to the PSCU and sends out a pulse train to the DAC to set the converter's output current. This current is the average (bias) correction current, and the current setting is done with an open loop. The control computer will sense the beam position using a number of beam position monitors (BPMs) and manipulate the information to compensate for the attenuation and phase delay due to the eddy current effect of the vacuum chamber. It then takes control from the host computer externally without passing through the PSCU and modulates the correction magnet's current by directly sending a pulse train in every 250μs to the DAC board for the dynamic correction, which is done with a closed feedback loop.

V. REGULATOR

Figure 4 shows the simplified regulator circuit used to generate gating signals. The reference signal, V_r , from a DAC is 0 to +10V for the positive magnet current and 0 to -10V for the negative current. A polarity signal, which determines a set of switches to be controlled, is derived from the error voltage signal by using a comparator. A logic high signal, which selects switches Q1 and Q4, is obtained for a positive value. Similarly, a logic low signal, which selects switches Q2 and Q3, is obtained for a negative value. The feedback signal, V_f , is provided from a current measuring device. The voltage developed across a 2mΩ shunt resistor is amplified by an isolation amplifier to produce +10V (-10V) for maximum positive (negative) current. The output of the error amplifier, V_e , is compared with a 10V ramp signal, V_s , at a comparator generating a pulse train. This PWM signal is combined with the polarity signal using an AND gate to determine which switch, Q1 or Q2, is to be controlled. The maximum duty cycle could be 100%, including dc offset current and ac current.

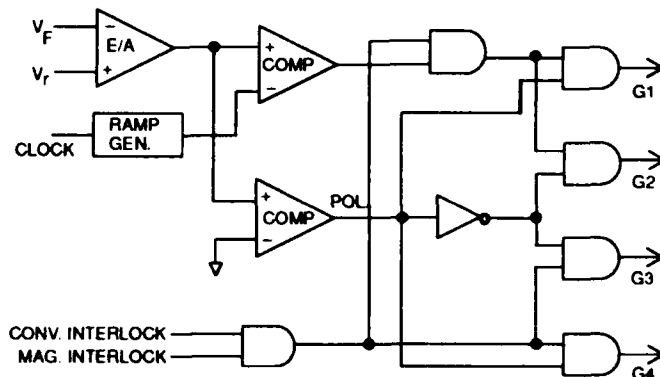


Figure 4. The simplified regulator circuit.

VI. DAC/ADC

The reference signal for the regulator card is provided by a 16-bit DAC, and the magnet current information (feedback voltage) is converted to digital information by a 20-bit ADC to be used for monitoring. The DAC's input values are set by an input counter, which has three optically coupled input signals: one to reset it to zero for soft start, a second to increment it one

bit at a time, and a third to decrement it one bit at a time. These input values are from the PSCU which also serially clocks out the 16 most significant bits from the DAC. For dynamic correction, the DAC is loaded directly by the control computer in a serial to parallel manner.

VII. MONITORING & INTERLOCKS

There are two Euro-cards provided in the BPS chassis for monitoring and interlocks, one for the converter (BPS) and the other for the magnet. The converter interlock card can monitor and interlock five temperatures for two IGBT modules, an input capacitor, return water, and control power supply heat sink using PN junctions as temperature sensors over the range of 0 to 100 °C and three voltage signals for the magnet current, input bus, and control-power-supply failure. The magnet interlock card monitors and interlocks four temperatures for the magnet and its return water.

Each of the signals is compared to a fixed reference and the output of the comparator is used to set a flip/flop that latches the interlock until reset by a local or external reset pulse. All of these analog signals are buffered and output to the PSCU for monitoring. The analog signals for each interlock card are ORed, and the ORed output signals are sent out to the regulator card. The ORed output signals from the converter and magnet interlock cards are combined by an AND gate to generate a shut down signal. This causes the IGBT gate signals at the output of the regulator to be clamped, in case any of the failure signals activates.

VIII. CONTROL POWER SUPPLY

The control power supply card generates nine output voltages for the control circuitry as well as the IGBT driver circuitry. The topology used is a flyback converter with a feedback winding, which is used for line regulation and bias supply for the PWM IC, and the switching frequency is 80kHz. Nine linear regulators are used for the load regulation. The input is fed from an output of the ac/dc unregulated rectifier, which also provides the dc bus for the main power section.

IX. TEST RESULTS

A 150A BPS was prototyped and tested successfully. Figure 5 shows a measured magnet current waveform with its command signal, which is 25Hz sinusoidal at 75A(peak). Also, Figure 6 shows a measured magnet current waveform with its command signal, which is 25Hz sinusoidal at 75A(peak) plus +75A dc current. Note that the magnet currents follow their command signals.

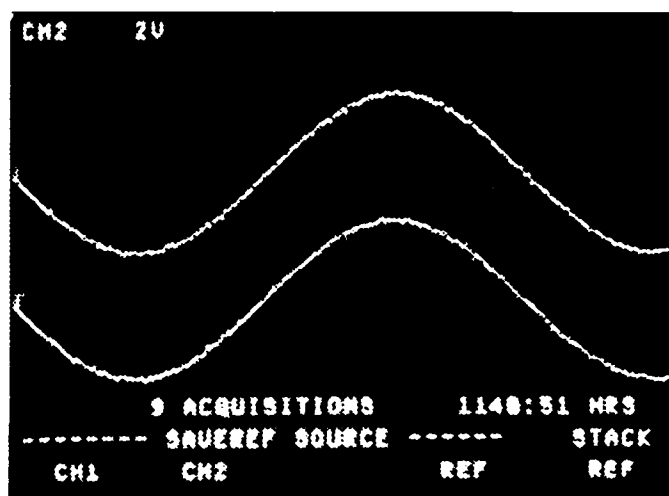


Figure 5: Measured magnet current with its command signal.
Top: Magnet current Bottom: Command signal.
($I_{ac}=75A_{pk}$, $I_{dc}=0A$, $f=25Hz$)

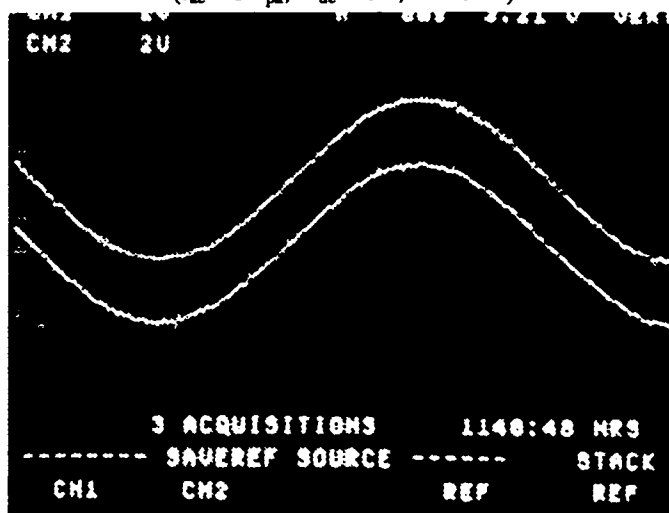


Figure 6: Measured magnet current with its command signal.
Top: Magnet current Bottom: Command signal.
($I_{ac}=75A_{pk}$, $I_{dc}=+75A$, $f=25Hz$)

REFERENCES

- [1] Y. G. Kang, "Correction Magnet Power Supplies for APS Machine," 1991 IEEE Particle Accelerator Conference Proceedings, pp. 911-913, 1991.
- [2] W. Praeg, "Frequency Response of Storage Ring Magnets, Eddy Current Shielding of Vacuum Chamber," ANL Light-Source Note LS-45, December 1985.
- [3] O. D. Despe, C. Saunders, and D. G. McGhee, "Control Units for APS Power Supplies," these proceedings.

Circuit Description of Unipolar DC-to-DC Converters for APS Storage Ring Quadrupoles and Sextupoles

D. G. McGhee
Argonne National Laboratory
9700 S. Cass Avenue
Argonne, IL 60439-4814

ABSTRACT

This paper describes the control, interlock, and power circuits for 680 unipolar switch mode DC-to-DC converters used to regulate the Advanced Photon Source's (APS's) storage ring quadrupole and sextupole magnet currents. Quadrupole current stability is $\pm 6 \times 10^{-5}$ and the sextupole current stability is $\pm 3 \times 10^{-4}$. The stability is obtained with pulse width modulation, operating at a switching frequency of 20kHz with full current switching. The converters are housed in 200 cabinets located on top of the storage ring tunnel. Raw DC power is distributed from 80 AC-to-DC power supplies, four at each of 20 locations around the storage ring. Voltages, currents, and temperatures are computer monitored and logged for the converters and magnets. All converters and magnets are water cooled with the flow and pressure monitored at the inlet and outlet of groups. Water is interlocked with the raw power supplies and not the individual converters.

I. INTRODUCTION

All 680 unipolar switch mode DC-to-DC converters have the same circuit design and components with the exception of the current measuring device, the reference digital-to-analog converter (DAC), and the input capacitance. The quadrupole converters can operate at a DC output current of 0 to 460A and the sextupole converters from 0 to 200A. The output bus has a series damped low pass filter. There is also a 50 Ω resistor across the magnet bus to parallel damp the cable used to connect a converter to the magnet. All converters are water cooled.

A total of up to four unipolar (quadrupole/sextupole) converters along with up to four bipolar correction magnet converters are housed in a 5ft x 3ft x 7ft cabinet. Each cabinet also houses a microprocessor and interface cards to monitor and control the converters and magnets. A cabinet with converter chassis is shown in Fig. 1. This cabinet is used to power one magnet girder in the APS storage ring. There are 40 sectors with five magnet girders each (five converter cabinets) and one insertion device (ID) girder per sector. Each pair of sectors has four raw (not regulated) power supplies feeding the converters in the two sectors. The raw power supplies for two sectors also provide raw control power for the converter cabinets, ground protection, crowbar/shorting circuit for the DC-bus feeding the converter, and water flow interlock.

One of the 400 quadrupole DC-to-DC converters is shown in Fig. 2

* Work supported by the U. S. Department of Energy,
Office of Basic Energy Sciences, under Contract
No. W-31-109-ENG-38.



Fig. 1 One of the 200 storage ring converter cabinets.

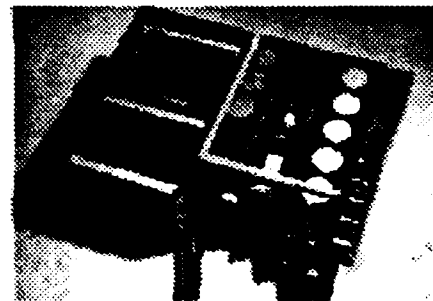


Fig. 2 One of the 400 quadrupole DC-to-DC converters.

II. POWER CIRCUIT

The unipolar converter's power circuit is a buck converter operating into an inductive load, one of the storage ring quadrupole or sextupole magnets. This circuit is shown in Fig. 3. The charging voltage from the raw power supply was chosen to be ≥ 2 times the voltage drop of the magnet at 110% of full design current with a -10% low AC line. Two DC voltages are being used to supply all unipolar DC-to-DC converters.

Circuit Equations

The switching time for one cycle is $T_s = 50\mu s$ and the switching frequency is

The submitted manuscript has been authored by a contractor of the U. S. Government under contract No. W-31-109-ENG-38. Accordingly, the U. S. Government retains a nonexclusive, royalty-free license to publish or reproduce the published form of this contribution, or allow others to do so, for U. S. Government purposes.

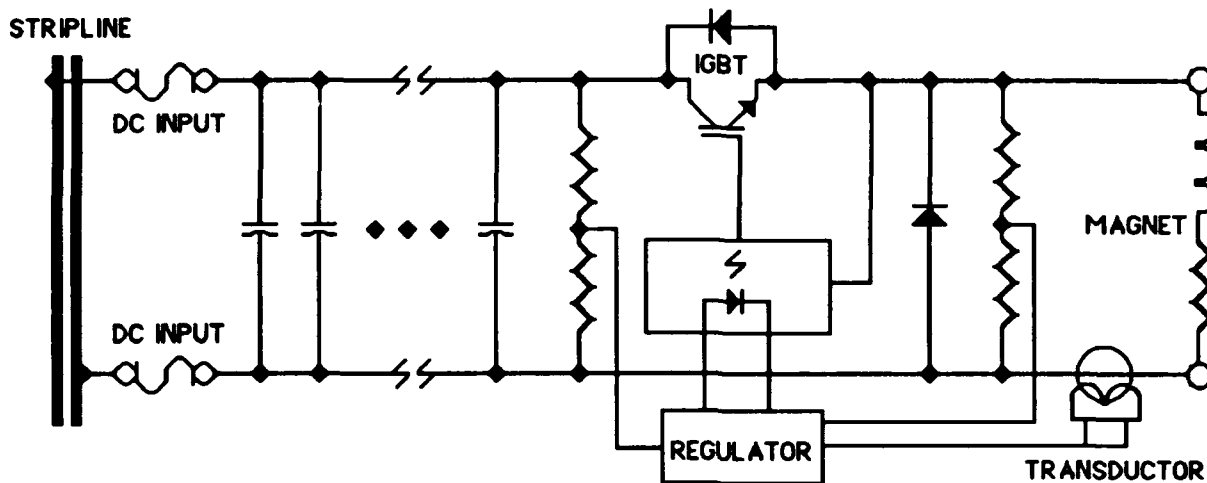


Fig. 3 A single line diagram of the DC-to-DC converter

$$F_s = \frac{1}{T_s} = 20 \text{ kHz} \quad (1)$$

In this circuit the switching frequency is maintained constant at 20kHz and the switching element, insulated gate bipolar transistor's (IGBT) on time (t_1) is modulated to regulate the magnet current. The IGBT's duty cycle is

$$D = \frac{t_1}{T_s} \quad (2)$$

The raw DC power supply voltage is given as V , the magnet inductance as L , and the circuit resistance as R . The normalized inductor time constant is

$$\tau_L = \frac{L}{R \times T_s} \quad (3)$$

Minimum magnet current is

$$I_{L(\min)} = \frac{V \times D}{R} \left[1 - \left(\frac{1-D}{2\tau_L} \right) \right] \quad (4)$$

maximum magnet current is

$$I_{L(\max)} = \frac{V \times D}{R} \left[1 + \left(\frac{1-D}{2\tau_L} \right) \right] \quad (5)$$

and the peak-to-peak magnet current ripple is

$$\Delta i_L = I_{L(\max)} - I_{L(\min)} \quad (6)$$

III. CONTROL

Control is divided into two parts. The first part is a hardwired clamp of the DAC that comes from the raw power supply. It is applied when the main contactor in the raw power supply is open and is removed a fixed time after it closes. The second part, performed by a computer using bit bus or RS232 communications, raises and lowers the reference DAC and resets the DC-to-DC converter and magnet interlocks. This reset (system normal) is required before the raw power supply interlocks can be made up and the main contactor closed; it is also hardwired.

Major components of the DC-to-DC converter's control circuits are:

1. An analog reference. Developed by an 18-bit DAC, it uses only the 16 most significant bits. This DAC is counted up or down 1 least significant bit at a time.
2. A direct current current transformer (DDCT) is used for the quadrupoles and a folded Zaran water-cooled shunt is used for the sextupoles. The DDCT has a bandwidth of 50 kHz, a ratio error of 50 ppm that changes 1 ppm/°K and/or 1 ppm/month. Its linearity error is < 20 ppm and offset error is < 10 ppm. The Zaran shunt has a temperature coefficient of resistance of $\pm 3 \text{ ppm/°K}$.
3. A high-gain, slow-current error amplifier. This amplifier with a $0.3 \mu\text{V/°C}$ max offset voltage drift, together with the current transducer, allows the regulator to operate in the storage ring environment without temperature compensation (an oven).
4. A real-time, applied-voltage ramp circuit. Since the current's rate of change is slow compared to the 20kHz switching frequency, the ramp generator (integrator) is reset by the voltage across the freewheeling diode during the non-conducting period of the IGBT.
5. A very high gain comparator.
6. An IGBT gate driver circuit.
7. Switchmode control power supplies operating at $\sim 100 \text{ kHz}$. Since the total control power needed is $\ll 150 \text{ W}$ (the upper limit for flyback configuration), and

Magnet (D)	$I_{L(\max)}$	$I_{L(\min)}$	Δi	$\pm \frac{\Delta i}{I_{(\text{Rated})}}$
0.8M Quad(0.33)	460.1250	460.0996	0.025340	2.754E-05
0.6M Quad(0.39)	460.4848	460.4614	0.023452	2.549E-05
0.5M Quad(0.34)	460.4159	460.3894	0.026449	2.875E-05
Sextupole (0.49)	200.8274	200.8135	0.013921	1.513E-05

Table 1. Magnet ripple current operating at rated current.

the varied voltage outputs require transformer isolation, a switchmode flyback topology was selected.

VI. INTERLOCKS and MONITORING

There are three groups of interlocks: the raw DC power supply, the DC-to-DC converter, and the magnet interlocks. They are all hardwired. The dc-to-dc converter has eight binary interlocks and two magnet interlocks. The magnet's binary interlocks are two chains of temperature switches per magnet. The ten binary interlocks per DC-to-DC converter/magnet are ANDed into a single hardwired system normal and connected to the raw power supply. Anyone can shut off the raw power supply by opening the main contactor and clamping the DC-to-DC converter's reference DAC. When the raw power supply's main contactor is open, the output bus has a shorting (crowbar) switch across it. The raw power supply also has common interlocks for the DC-to-DC converters and magnets. These consist of magnet and power supply waterflow and ground circuit overcurrent.

Monitoring is accomplished by power supply control units (PSCUs). Each DC-to-DC converter is monitored by a PSCU combining ten binary interlocks to eight, selecting four of the five analog temperature signals and the precision analog-to-digital converter (ADC), and logging the data. Also, the PSCU used to monitor and control the raw power supplies in two sectors monitors water flow and pressure for both magnets and power supplies.

V. TEST SET UP AND RESULTS

Four unipolar DC-to-DC converters were installed in a converter cabinet with the outputs connected to magnets or dummy loads. A local computer connected to the PSCU controlled and logged the following 8-hour test run during preparation for large scale testing of converters. The test results of one of the quadrupole converter's output current transducer during this 8-hour run is shown in Fig. 4.

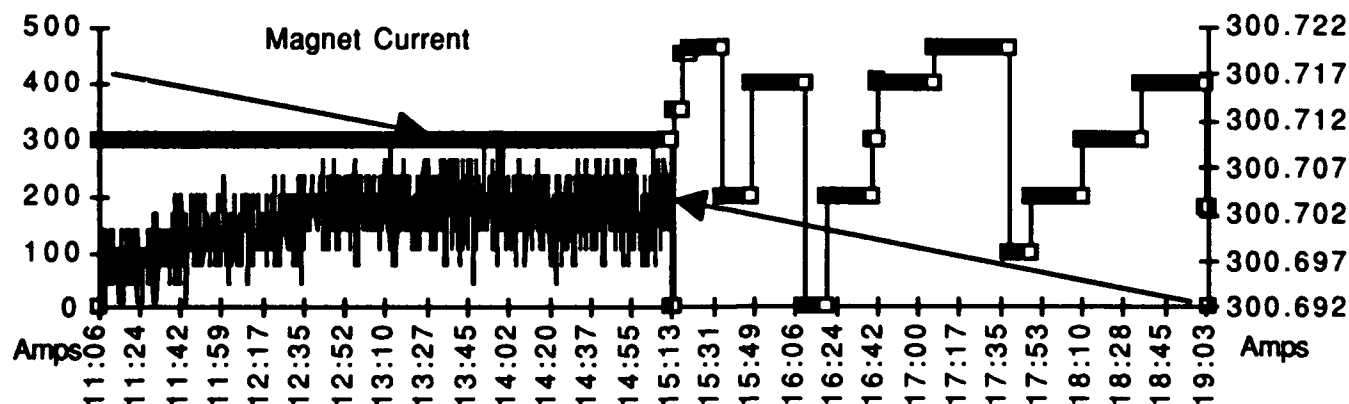


Fig. 4 The internal and external transducer signal for the full-current part of an 8 hour test run.

All of the APS storage ring power supplies will be test run in a temperature-controlled room with the temperature varying between 20°C and 50°C, even though the ambient temperature in the permanent location will be 24°C ± 1.5°C. A test run of the temperature-controlled room is shown in Fig. 5.

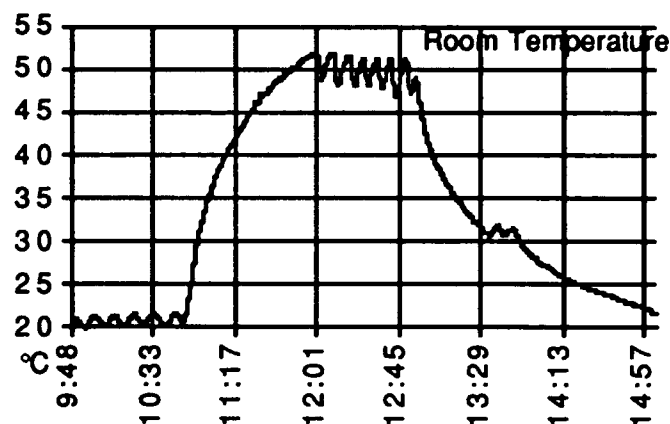


Fig. 5 Room temperature during a 5-hour test run.

The testing plan is to cycle each DC-to-DC converter to maximum and back to minimum to verify proper operation. All converters are set to maximum design value and the temperature is raised to 50°C. It will be held at 50°C for one hour, then lowered back to 20°C and held there for one hour. The temperature is then cycled back to 50°C and held. The output currents of the DC-to-DC converters are randomly varied until we have run a minimum of eight hours. The unit data will be checked and, if acceptable, the converters will be installed. Failed converters will be repaired and retested.

V. REFERENCES

1. D. McGhee, "Status of Magnet Power Supply Development for the APS Storage Ring," 1989 IEEE Particle Accelerator Conference Proceedings, March 1989.
2. Rudolf P. Severns, and Gordon E. Bloom, "Modern DC-to-DC Switchmode Power Converter Circuits," Van Nostrand Reinhold Company, 1985.

PLL Subsystem for NSLS Booster Ring Power Supplies*

J. Murray

Electrical Engineering Department, SUNY at Stony Brook,
Stony Brook, NY 11794-2350, USA

R. Olsen, J. Dabrowski

National Synchrotron Light Source, Brookhaven National Lab
Upton, NY 11973, USA

Abstract

A high-performance digital phase-lock loop subsystem has been designed as part of the upgrade to the magnet power supplies in the booster ring at the National Synchrotron Light Source. The PLL subsystem uses a dedicated floating-point digital signal processor to implement the required filters and the startup, fault-handling, and running logic. The subsystem consists of two loops; the first loop tracks long-term changes in the line frequency, while the second tracks more rapid variations. To achieve the required performance, the order of the loop transfer functions was taken to be five, in contrast to the second- or third-order loops usually used. The use of such high-order loops required design techniques different from those normally used for PLL filter design. The hardware and software elements of the subsystem are described, and the design methodology used for the filters is presented. Performance is described and compared to theoretical predictions.

I. INTRODUCTION

Output voltage control of high-current power supplies is usually based on the firing of thyristors at the appropriate phase-angle of the rectified A.C. line voltage. For this reason, accurate control requires a phase-reference which is accurately synchronized to the line over its range of frequency variation (± 0.1 Hz); this is typically provided by a phase-locked loop (PLL) driven by the A.C. line. As the accuracy requirements of power supplies become more stringent, the performance demands on the PLL increase correspondingly.

To address this need, a high-accuracy digital PLL has been designed as part of the upgrade to the NSLS booster magnet power supplies. The design is based on the digital PLL previously used in this application [1]; in addition, to achieve the required performance, it was decided to use a relatively inexpensive floating-point digital signal-processing (DSP) chip, the Texas Instruments TMS320C31, to implement the required filters.

Since the design of DSP-based filters for PLL use is substantially different from that of analog filters, and the use of a signal-processing chip promotes a different design approach, the main emphasis in the following will be on the design of these filters.

*Work performed under the auspices of the U.S. Department of Energy under contract DE-AC02-76CH00016

II. PLL HARDWARE

A. Overall System

A block diagram of the overall PLL subsystem is shown in figure 1. The core of the system is the block labeled "Fast Loop"; in normal operation, this provides the required phase-reference signal. The slow loop's function is to provide a relatively constant reference for short-time variations in the line and the fast loop; this is used mainly for diagnostic and measurement purposes. A secondary purpose is to provide a reference to which the fast loop can switch when the line fails.

It was decided, rather than attempting to provide multiple samples per cycle of the line phase, which would be sensitive to the purity of the line voltage, to use only a measurement of the length of each cycle. Since this is sensitive to noise in the zero-crossing region, the prefilter is used to provide a clean 60 Hz squarewave as input to the loops.

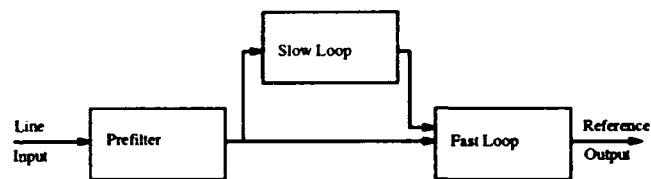


Figure 1: PLL Subsystem Block Diagram

B. Fast Loop

The fast loop follows the usual PLL configuration; a block diagram is shown in figure 2. The digital VCO is essentially an overflow adder driven by a 23.592960 MHz crystal-controlled clock, and configured so that the output frequency is linearly proportional to the 20-bit input value, with an output frequency of 5.898240 MHz at midrange input, and a maximum frequency deviation of ± 737.28 kHz at inputs of 1 and $2^{20} - 1$. The frequency divider divides by 98,304 to give a center output frequency of 60 Hz, and a deviation of ± 7.5 Hz. The phase comparator consists of a 20-bit counter clocked at 10 MHz; this gives a resolution of .002 degrees.

C. Slow Loop

The slow loop is similar to the fast loop except for the following: 1) the VCO is a voltage-controlled crystal oscillator, with the control voltage set by the output of a

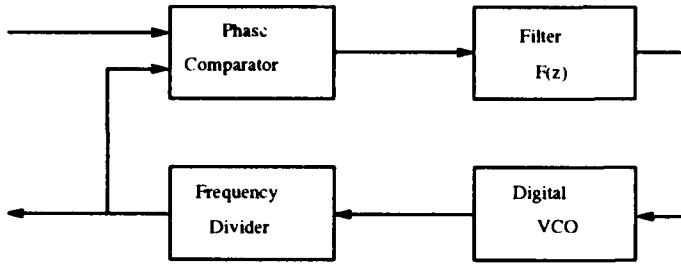


Figure 2: Fast Loop Block Diagram

16-bit D/A converter; 2) since this gives a very low frequency range, the frequency divider is also made variable to increase the range. This arrangement was chosen to achieve extremely fine resolution for VCO, since the time-constant for the slow loop is of the order of hours.

III. PLL FILTER DESIGN

A. Loop Requirements

The main requirements were for acceptable acquisition time (not more than a few seconds), asymptotic tracking error of better than .02 degree across the frequency range 59.9-60.1 Hz, and good rejection of noise, harmonic distortion (120 Hz up), and disturbances induced by the power supply ramping itself (25 Hz down).

Since a DSP chip is being used, low order is *not* a requirement. This makes the "coprime fractional representation" approach to feedback design [2] very attractive; the version used here is taken from [3].

B. Fast Loop

Since the phase difference is sampled at the end of each cycle, and gives the average phase difference over that cycle, the transfer function of the VCO and frequency divider, as seen by the filter, can be modeled as

$$P(z) = \frac{Kz^{-1}}{1 - z^{-1}}$$

where K is a hardware-dependent gain. The phase-comparator is simply a difference operator followed by a gain K_d .

The problem then becomes: find a filter $F(z)$ which stabilizes this loop, asymptotically tracks a ramp input, and rejects noise and disturbances. Tracking of a ramp input is required since a step change in frequency is a ramp in phase, and asymptotically zero phase error is desired over the frequency range.

Following the method in [3], $P(z)$ is first expressed as a quotient n_p/d_p ; in this case $n_p = Kz^{-1}$ and $d_p = 1 - z^{-1}$ are natural choices. The pair of functions $u_p = 1/K$ and $v_p = 1$ is then chosen as a solution for the equation (2.15 in [3])

$$u_p n_p + v_p d_p = 1$$

Next, since the Z-transform of a ramp is $z^{-1}/(1 - z^{-1})^2$, the functions in equation 3.2 in [3] can

be taken to be $n_t = z^{-1}$, $d_t = (1 - z^{-1})^2$, $u_t = 2 - z^{-1}$, and $v_t = 1$.

In a similar way, the functions u_{pt} and v_{pt} in equation 3.14 in [3] can be taken to be $(2 - z^{-1})/K$ and 1, respectively, and the functions in equation 3.28 in [3] can be taken to be $n_a = 1$, $d_a = 1 - z^{-1}$, $u_a = 1$, and $v_a = 0$.

It then follows from the theory presented in [3] that, for *all* stable functions $e(z)$, the filter

$$F(z) = \frac{1}{K_d} \frac{-e(z)d_a d_p + d_p v_p u_{pt} + u_p}{e(z)d_a n_p - n_p v_p u_{pt} + v_p}$$

$$= \frac{1}{K K_d} \frac{-K e(z)(1 - z^{-1})^2 + 3 - 3z^{-1} + z^{-2}}{K e(z)z^{-1}(1 - z^{-1}) + (1 - z^{-1})^2} \quad (1)$$

will give a stable closed-loop system which will track a ramp input, and that *all* such filters are of this form. Further, the gain from the input to the sampled output is given by

$$H(z) = -e(z)d_a d_p n_p + d_p v_p u_{pt} n_p + u_p n_p \quad (2)$$

$$= 1 - (1 - z^{-1})^2(1 - z^{-1} + K e(z)z^{-1}) \quad (3)$$

which is linear (more accurately, affine) in $K e(z)$. The arbitrary stable function $K e(z)$ can therefore be taken as a free parameter to optimize the other requirements. In this case, $e(z)$ was taken to be a general second-order stable transfer function, and the coefficients were chosen to give a low-pass characteristic with good rejection at 2 Hz, which is the ramp frequency of the final system [4]. The filter transfer function for this weighting factor was found by substituting this $K e(z)$ in equation 1; the result was

$$F(z) = 0.92262464 \frac{3 - 3z^{-1} + z^{-2}}{1 - z^{-1}} \times \frac{1.022612 - z^{-1}}{1 + .29733659z^{-1}} \times \frac{1 + z^{-1}}{1 - .31896065z^{-1} + .072725713z^{-2}}$$

which was implemented in cascade form.

C. Slow Loop

The procedure for the slow loop was identical except for the loop constants and the weighting factor; the latter was chosen so that the 3-dB point of the PLL frequency response was about 6×10^{-5} Hz, corresponding to about 4.6 hours response time.

D. Prefilter

The problem with the prefilter was to design a bandpass filter with approximately *constant* phase across a small region in the middle of the band. This was achieved by first satisfying the condition at 0 Hz in the analog domain, using a frequency transformation to transform to a bandpass filter, and a bilinear transform to transform to the Z-domain. More specifically, since phase and amplitude matching was required at DC, and a second-order

rolloff at was desired at high frequency, the transfer function of the prototype filter had to take the value 1 to the second order at zero (assuming unity gain), and had to have a second-order zero at infinity. This led to the form

$$H_a(s) = \frac{a_1 s + a_0}{s^3 + a_2 s^2 + a_1 s + a_0}$$

and the values a_0, a_1 , and a_2 were determined by iteration. After the lowpass-to-bandpass and bilinear transformations, the following sixth-order filter was obtained (in cascade form):

$$H(z) = \frac{6.9980052 - 13.976087z^{-1} + 6.9880187z^{-2}}{1 - 1.9965836z^{-1} + 0.9980031z^{-2}} \times \frac{5 \times 10^{-6}(1 - z^{-1})^2}{1 - 1.988673z^{-1} + 0.99008866z^{-2}} \times \frac{(1 + z^{-1})^2}{1 - 1.9886052z^{-1} + 0.99001764z^{-2}}$$

IV. PERFORMANCE

A. Predicted Performance

The calculated amplitude response for the fast loop is plotted in figure 3; its 3-dB frequency is .6 Hz. By design, the filter is stable, and has zero asymptotic tracking error for a ramp input.

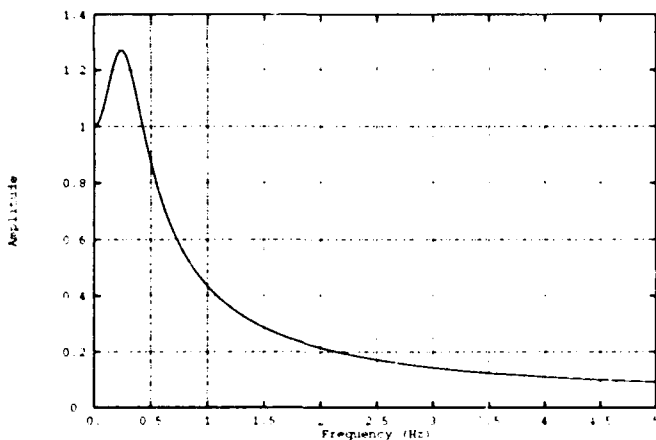


Figure 3: Fast Loop Amplitude Response

The calculated amplitude response for the prefilter had a bandpass characteristic with 3-dB points at 53 and 67 Hz, and had an attenuation of > 27 dB below 30 Hz and above 120 Hz.

Finally, the prefilter phase response for the range 59.9 - 60.1 Hz is shown in figure 4; the maximum phase deviation over the band of interest is less than ± 0.1 degrees.

B. Measured Performance

The prefilter and the remainder of the PLL system were implemented separately

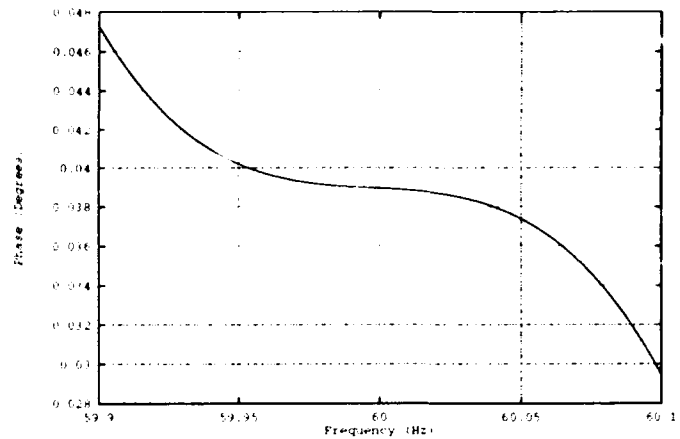


Figure 4: Prefilter Phase Response

The prefilter was implemented on the Texas Instruments TMS320C30 EVM board, and was tested with a function generator as input. Within the limits of measurement error, it functioned as predicted.

The remainder of the PLL system was implemented on a VME-bus system, controlled by a VME-based TMS320C30 board; the algorithm included all initialization, status, error condition handling, and the loop filters. The measured steady-state ramp tracking error was 0 across the frequency band (within the resolution of the phase detector) when the input was taken from a bench function generator.

Because of the long time-constant, precise measurements of the slow loop were not possible; however, it functioned as expected, and had an extremely long response time. The lock-in performance of the fast loop is so good that the slow loop will be necessary only for measurement and diagnostics.

VI. REFERENCES

- [1] R. Olsen, "A High-Performance Digital Triggering System for Phase-controlled Rectifiers," Proceedings 1993 IEEE Particle Accelerator Conference, March 21-23, Santa Fe NM, p.2867
- [2] D.C. Youla, J.J. Bongiorno, and H.A. Jabr, "Modern Wiener-Hopf Design of Optimal Controllers: Part I," *IEEE Trans. Autom. Contr.*, Vol. **AC-21**, 1976, pp. 3-15.
- [3] R. Sacks, J. Murray, O. Chua, C. Karmokolias, and A. Iyer, "Feedback System Design: The Single-Variate Case -- Part I," *Circuits, Systems, and Signal Processing* Vol. 1, No. 2, 1982, pp. 137-169.
- [4] R. Olsen, J. Dabrowski, and J. Murray, "Control System for NSLS Booster Power Supply Upgrade II," these proceedings.

CONTROL AND PERFORMANCE OF THE AGS AND AGS BOOSTER MAIN MAGNET POWER SUPPLIES*

R.K. Reece, R. Casella, B. Culwick, J. Geller, I. Marneris, J. Sandberg, A. Soukas, S.Y. Zhang
AGS Department, Brookhaven National Laboratory
Upton, NY 11973

SUMMARY

Techniques for precision control of the main magnet power supplies for the AGS and AGS Booster synchrotron will be discussed. Both synchrotrons are designed to operate in a Pulse-to-Pulse Modulation (PPM) environment with a Supercycle Generator defining and distributing global timing events for the AGS Facility. Details of modelling, real-time feedback and feedforward systems, generation and distribution of real time field data, operational parameters and an overview of performance for both machines are included.

FACILITY OVERVIEW

The AGS Booster synchrotron is an intermediate accelerator between the 200 MeV Linac and the AGS and operates in two modes. This machine is $\frac{1}{4}$ the radius of the AGS and its primary function is that of the source of protons for the AGS. The alternate mode is to accelerate partially stripped heavy ions to be fully stripped after extraction toward the AGS. The high vacuum nature of the Booster (10^{-11} Torr) permits very efficient injection and acceleration of these partially stripped ions to an energy sufficient to allow them to be fully stripped in the transfer line between the Booster and the AGS.

POWER SUPPLIES

The AGS Booster Main Magnet Power Supply (BMMPS) has been well documented in earlier publications [1,2]. In this description, the performance of the system will be limited to that necessary for a proton physics program. For this mode, the BMMPS operates in a rapid cycling mode (5-7.5 Hz) with a current range of 410A to 2500A and back in the repetition period. The power supply consists of six independent rectifier modules that operate in series. Depending upon the nature of the B(t) cycle defined, any one to all six of these modules can be used to power the series connected ring dipole and quadrupole magnets.

Although there are two special case modules for high current operation (6000A), the fast cycle operational limits of the power supply are 1000V per module at 3000A. When not

in use for any portion of a given magnet cycle, a specific power module is automatically bypassed by triggered SCR switches.

This power supply system is connected directly to the local utility line without buffering. Of concern therefore, are the induced harmonics on the utility power grid due to the cycling of this supply. In order to be protected from damage to their system due to these "disallowed" harmonics, a circuit breaker has been installed on the 69 kV line feeding the Booster. The utility can disconnect the BMMPS from the line if the power content of any of these restricted harmonics exceeds the allowed limit as determined by the pulsed power monitoring relay, which performs repetitive Fourier transform calculations. An FFT analysis of the power waveforms is done prior to operating with a specific set of magnet functions.

The AGS Main Magnet Power Supply (AMMPS) is buffered from the utility through a motor generator set (Siemens) that has been in operation for many years. During a recent upgrade, the rectifier system, triggering circuits, feedback loops and the monitoring and controls systems have been replaced. A large number of the relay control functions are accomplished by PLCs. The new rectifiers are comprised of eight total modules, four for flattop (F) and four for pulsing (P). The F and P modules are operated in parallel as opposed to the Booster series connection. The triggering and control loops are identical to the Booster. The cycles are programmed, as in the Booster, by a set of vector function generators.

In further discussion, techniques described are applicable to both power supplies.

CORRECTION LOOPS AND AUTO-CALIBRATION SYSTEM

There are a number of correction loops that are utilized to provide the necessary tracking of the field with respect to the reference functions, and to preserve the regulation of cycles. The loops are of two types, real-time feedback and real-time feedforward. Also, field triggers derived from a Gauss Clock (GC) and a self-correction field loop provide enhanced operation. Each module (Booster = 6; AGS = 8) has a voltage feedback loop for voltage regulation and short term magnet current reproducibility due to disturbances from the AC input lines. To compensate for medium to long term current drift two systems are used; one being a real-time

*Work performed under the auspices of the U.S. Dept. of Energy.

current feedback loop and the other a long term feedforward correction. The analog current loop can only play a minor role due to the long time constant in the magnet loads. The long term correction system improves the absolute output current calibration of the power supply by averaging the current error over several cycles. The present mode takes a running/updating average during the dwell portion of the cycle and holds the average current over this interval to an absolute value of about ± 0.2 Amperes.

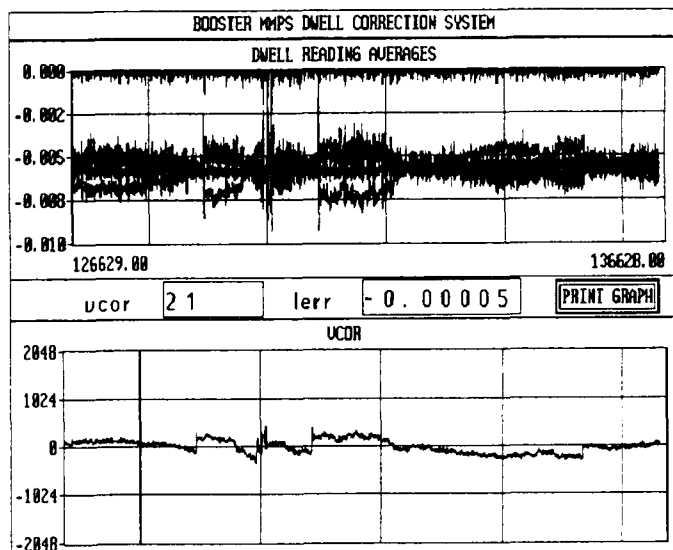


Figure 1.

The Gauss Clocks for the Booster and AGS consist of long pickup coils in a reference magnet for each machine connected to a temperature stabilized bipolar voltage-to-frequency converter; providing both Up and Down Gauss Clock counts to the Gauss Line Generator for global distribution during a magnet cycle.

Although the Gauss Clock marks the incremental (0.1G/count) field as the magnet cycle changes, it must be referenced to an absolute measurement of field to assure major events (injection, extraction) reproducibly occur at the same field from cycle to cycle and day to day. The method developed for the Booster and AGS is to sample a Hall probe installed in the reference magnets over one 60 Hz line cycle during a period in each magnet cycle when the field is changing little. The calibrate system maintains its own accumulator of Gauss Clock Up/Down counts. During each measurement, a closed loop is enabled which slews the accumulator up or down to match the reference Hall voltage. This updated GC signal is then used to reset (via a high speed (50MHz) interface) the Gauss Line Generator to the measured value immediately following this interval for each magnet cycle.

With both the long term and field auto-calibration systems in operation, all field triggers throughout the cycle have a long term reproducibility of about ± 0.5 Gauss.

TIMING

Timing for AGS Complex of accelerators is distributed for real time processes as well as B(t) timing from each machine for general use. These field markers are distributed for general use, primarily within an accelerator, to define critical events in a cycle such as injection, rf capture, extraction start and in the AGS, transition.

Fundamental to the timing, is the use of a Supercycle which operates on a line synchronized 60 Hz clock and defines the repetitive nature of the magnet functions [3]. Major machine events are globally distributed and include the primary markers, Time = 0 (TO), events to start clocking each magnet function. Several different magnet cycles can be stored and executed in sequence by defining different "Users" within the Supercycle. Up to four separate Users can operate in sequence, each with its own unique main magnet cycle.

HIGH LEVEL CONTROL

Control of guide field at the AGS facility has historically been from the engineering view where the electrical properties of the system were defined and the cycle was fixed. The new AGS distributed control system based on a workstation with remote computer environment (Apollo/HP) has allowed the user to shift control perspective to that of detailed definition of the B(t) function as required to best control beam parameters. To achieve this higher level mode, software was developed to allow the user to request a given B(t) function and then convert this request into a form the hardware could respond to using an electrical model of the power supply system as a whole. The B(t) function is derived by defining zones with specific field properties that are joined by using interpolation options within the program.

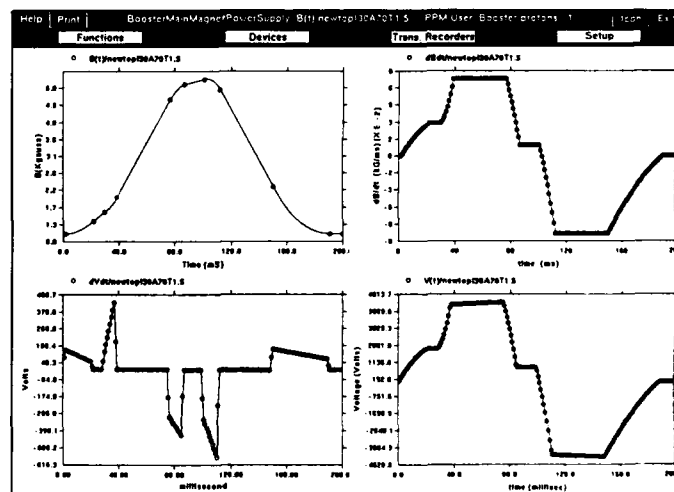


Figure 2 - MMPS program view of several B(t) related functions allows the User to verify they are as required for the cycle.

The local control hardware is driven by a family of vector functions for the system. Vector functions provide a great deal of flexibility in defining a magnet cycle. A series of linear vectors, up to 256, are fitted to the requested cycle and loaded to the hardware; a reference current function and the corresponding set of voltage functions. In the Booster, there are six voltage functions corresponding to each of the individual modules, even when the required voltage is zero. The AGS has one current and four voltage functions that are generated. Of importance to an accurate model for the system is the voltage drop across a power supply module that is bypassed for any part of a cycle. Given that at low currents or on flattops, this bypass voltage represents a significant fraction of the total voltage driving the magnet, this was first calculated, then empirically refined to image the integrated power supply - magnet system.

The conversion of a requested $B(t)$ function into a family of electrical signals begins with a derivation of the corresponding current function from the measured B to I transfer function of the main ring magnets/power supply system. The calculation of the total voltage functions depends upon refined models of the basic R/L circuits. A time delay is included to accommodate the sampling delay of the basic rectifier circuits. A typical set of conversion parameters used in the program is shown in Figure 3.

Formula $V = L \cdot di/dt + R \cdot I$
 where $L \Rightarrow$ Inductance; $R \Rightarrow$ Resistance;
 and if $V < 0.0$, V is scaled by NegScale

Parameter AdjustTimeV is used to compensate power supply delay.

Bypass modelling $V = A + B \cdot I + C \cdot I^2$
 where A , B and C are coefficients

L in Henry:

R in Ohm:

AdjustTime in millisec:

A in Volts:

B in Ohm:

C in microOhm/Amp:

NegScale (%):

Figure 3 - MMPS program electrical model coefficients for a given magnet cycle.

The total voltage is divided into components according to the individual module maximum ratings. Once this function family is generated from the requested $B(t)$, the electrical constants and function/vector fitting parameters, they can be archived for immediate use and loaded to the hardware, or saved for later recall.

SET-UP OF CONSTANTS

Although this view of a system model is sufficient for simple and/or single magnet cycles, it is not adequate when

two dissimilar cycles operate within a Supercycle. The system resistance is not truly linear at high currents and the inductance also varies at these higher currents. Methods for determining these parameters experimentally have been developed. Alternately, tables of values as a function of operating current can be used.

Knowledge of the magnet cycle is most critical during the injection process given that the injected beam of fixed rigidity must be well controlled. Also, since these magnet cycles are contiguous, they must be smooth and continuous from one to the other. The DC or dwell value is this constant amplitude which is usually 10% - 15% less than the injection field. The resistance term (R) for the cycle is determined by setting the magnet to a constant dwell value from the program $B(t)$ and measuring the resultant current and field from the Hall probe in the reference magnet. The value of R is then adjusted within the program until the current and field match that requested.

Once the resistance is fixed, the best approximation for the inductance (L) is obtained by pulsing the magnet system with a moderate current (2500A) from a defined $B(t)$ function and adjusting the L term until the measured peak current is equal to the requested peak current. With the accounting for the individual bypass voltages throughout a magnet cycle, this should provide in principle, a sufficient power supply - magnet model. However, due to the simple modeling of the R , L and bypass voltage terms and the finite gain of the voltage feedback loops, it was found that once this process was completed for a given magnet cycle, the integral of the total voltage during the cycle from all sources was not zero and therefore the magnet field was different at the end of the cycle than from the beginning. This led to an offset injection field for the following cycle.

The offset is corrected within the high level program by introducing independent calibration constants for the positive and negative phases of the power supply voltage output. The negative calibration is empirically adjusted to give a zero net current change over a magnet cycle.

Given this present definition of main magnet cycle control, previously cumbersome changes to a magnet cycle that may be small in nature but lead to improved control of beam properties are now routinely available.

REFERENCES

- [1] A. Soukas, et al., Operational Status of the AGS Booster Main Ring Power Supply, XVth International Conf. on High Energy Accelerators, Hamburg, Germany, 1992.
- [2] A Soukas, et al., The AGS Booster Main Ring Power Supply System, Particle Accelerators, 1990, 29, pp. 121-126.
- [3] D. Barton, private communication.

Hierarchical Modelling of Line Commutated Power Systems Used in Particle Accelerators Using Saber*

James A. Reimund
Superconducting Super Collider Laboratory
2550 Beckleymeade Avenue, Dallas TX 75237

Abstract

This paper discusses the use of hierarchical simulation models using the program SaberTM [1] for the prediction of magnet ripple currents generated by the power supply/output filter combination. Modeling of an entire power system connected to output filters and particle accelerator ring magnets will be presented. Special emphasis is made on the modeling of power source imbalances caused by transformer impedance imbalances and utility variances. The affect that these imbalances have on the harmonic content of ripple current is also investigated.

I. Introduction

In order to design power equipment for ring magnet systems it is necessary to know how subsystems interact with each other. This can get quite complicated when dealing with rings of hundreds of magnets, pulsed power supply systems and power supply output filters. In order to design a power supply output filter one must first know the ring load characteristics and the harmonic content under various load conditions of the power supply. Imbalances due to rectifier transformer winding error and ac utilities can also affect the harmonic content of the power supply output. In order to understand the interactions of these three systems hierarchical models were developed that addressed these systems and their imbalances.

II. The Accelerator Ring Model

The model of the accelerator ring is made up of hierarchal blocks that represent the magnets comprising the main ring. Within these block representations reside the circuit that models the magnets. A swept frequency ac analysis was then performed yielding the common mode and differential mode admittance responses of the ring or for an element within the ring. These responses were saved and then multiplied by the frequency spectrum derived from the power supply/output filter combination to yield a simulated current ripple (see figure 1).

III. The Power Supply Model

This model is the most complex of the three. In this model reside the various imbalances due to ac utilities and transformer winding errors as well as the models for the SCRs being used in the bridges, the snubber circuits, the gate firing

circuit, and a simplified load. To accomplish this without creating a very large and complicated schematic, three levels of hierarchy were used. For a 24 pulse system the top level schematic consists of four, six pulse bridge power supplies connected in series to form a complete 24 pulse power supply connected to its load. Below each six pulse supply there is a model of a three phase transformer secondary including impedances, gate firing circuit and three phase bridge. Below this level are the elements that make up the transformer secondary and the schematic representations of the SCR models connected to snubber circuits. The final level of hierarchy contains the device model for the SCRs.

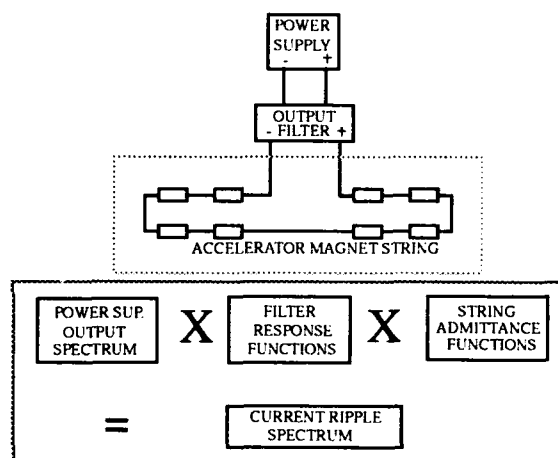


Figure 1.
Block Diagram for Obtaining Current Ripple

With the power supply model complete, common and differential mode simulations at the currents and voltages of interest were run. This resulted in a detailed Fourier voltage spectrum of the power supply output (see figures 2&3). Applying this spectrum to the load admittances yielded an expected ripple current spectrum. The frequency response of the output filter was then tailored to provide the desired ripple currents within the ring magnets.

IV. The Filter Model

The filter type used is a Praeg topology modified to incorporate L-C series traps (see figure 4). This model does not contain other levels of hierarchy. With the basic filter response requirements known, the filter design and simulation can be performed separately from the power supply and load. Once this design is complete the filter response can be verified by incorporating it with the power supply output spectrum and the ring magnet load response.

*Supported By U.S. DOE Contract #DE-AC35-89ER404846

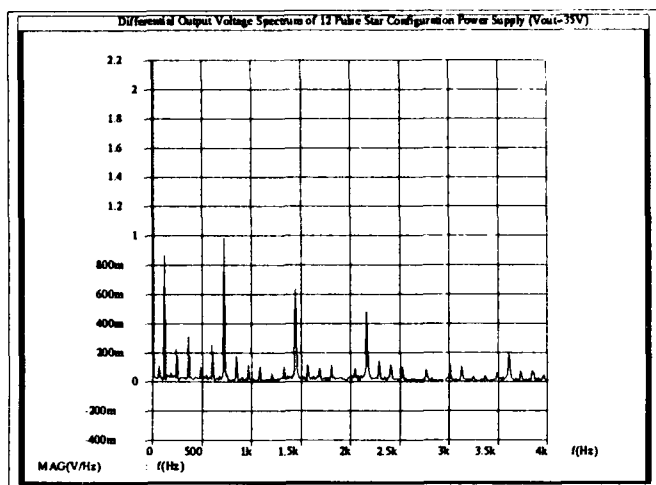


Figure 2.
12 Pulse Differential Power Supply Output Voltage Spectrum

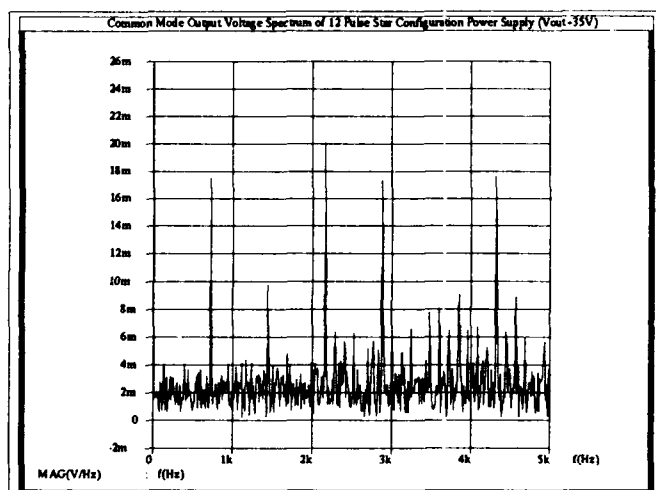


Figure 3.
12 Pulse Common Mode Power Supply
Output Voltage Spectrum

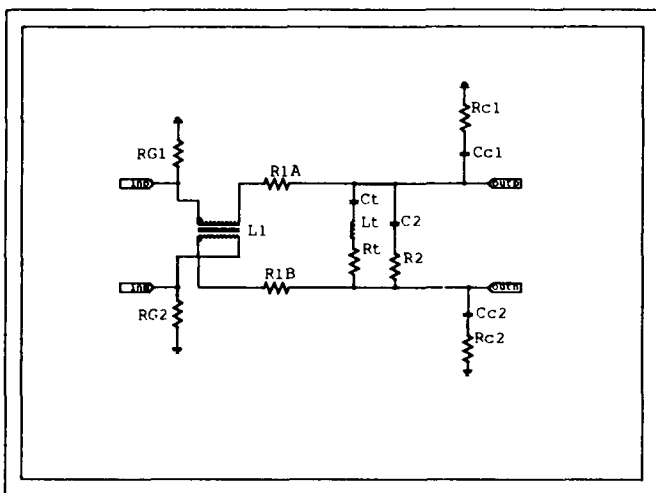


Figure 4.
Modified Praeg Filter Topology

V. Simulated Magnet Current Ripple

The results of the previous simulations were used to obtain a simulation of the ripple current spectrum existing in the ring magnet load. Within Saber, the waveform of the power supply output voltage spectrum is multiplied by the filter transfer function and the ring magnet load admittance. The resulting spectrum is that of the ripple current within the load. This ripple current depends on the admittance transfer function taken. It is also possible to reconstruct an approximate real time waveform of the ripple current. Current or voltage sources containing the correct amplitude and frequency of the ripple harmonics can be summed together. The resultant waveform is a simulated current ripple waveform (see figure 5).

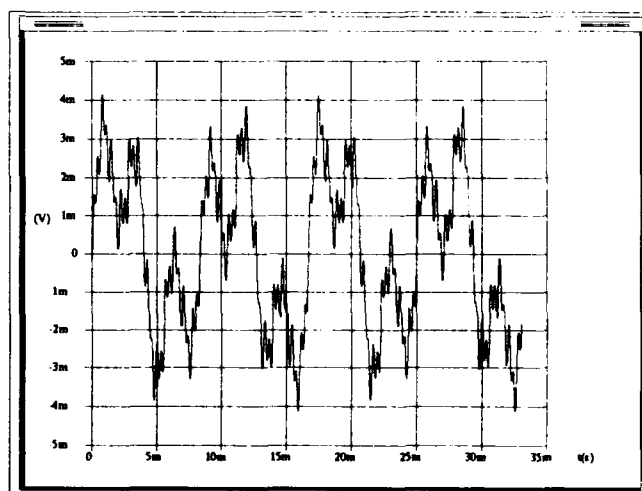


Figure 5.
Simulated Magnet Current Ripple
From 24 Pulse Power Supply

Arriving at current ripple can also be achieved by a different method. Instead of combining output spectra and load frequency responses, each of these models can be connected together to form an entire ring magnet power system. The ripple current is then measured within the ring magnet load at the desired location. Obtaining current ripple in this way, however, is about four to five times slower than the method previously described. The ripple waveforms obtained using both methods were very similar.

VI. Power Source Imbalances

There were two sources of power supply harmonics that were investigated. The first and most obvious source is due the number of pulses per line cycle produced by the power supply. The second is caused by imbalances in such things as transformer windings and ac utilities. The primary harmonics are well known and can be easily accounted for but the harmonics caused by utility power and transformer variances is not as apparent. These imbalances cause voltage and phase asymmetries that produce low frequency harmonics (i.e. sub-harmonics of the primary switching frequency). These harmonics may not

be nearly as high in amplitude as the primary switching harmonics but because of their low frequency they are harder to filter out. This can be a problem if these low frequency harmonics occur at critical frequencies of interest. For a multi-kiloamp filter, the capacitance and inductance values can become quite high which adds to the expense of production and the size of the overall filter. Figures 6 and 7 show the output voltage spectrum of a balanced and imbalanced six pulse system respectively. The imbalances consisted of a 1% voltage and a 2% transformer impedance imbalance.

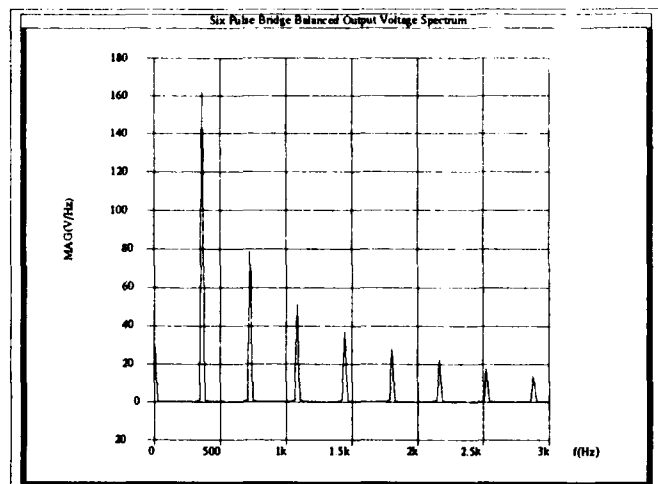


Figure 6.
Six Pulse Balanced Output Voltage Spectrum
(firing angle=85 deg., I=1500A)

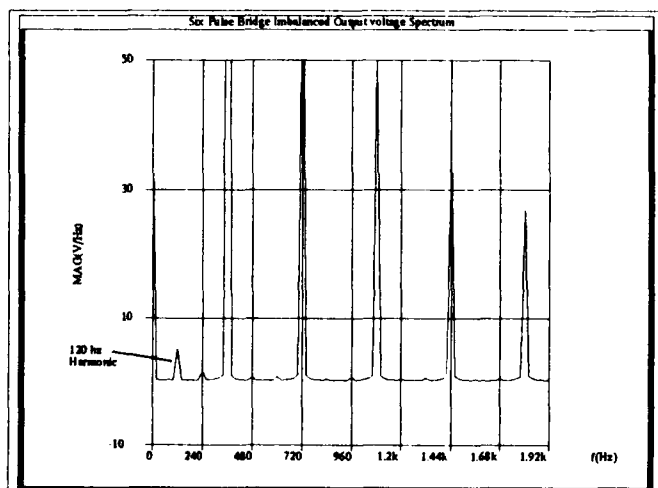


Figure 7.
Six Pulse Imbalanced Output Voltage Spectrum
(firing angle=85 deg., I=1500A)

With these imbalances in the transformer secondary new harmonics are observed in figure 7. The harmonic at 120 hz is particularly large with smaller harmonics occurring at 60 hz intervals. For a system with more pulses per cycle and with series connected bridges the effects and harmonic production will be different depending on the asymmetries of the system. In the case presented three fold asymmetries are introduced in both the phase voltages and the line to neutral impedances. This is the cause of the predominant 120 hz harmonic. For a power supply with four of these bridges in series (i.e. a 24 pulse system) the possibility of two, three and four fold asymmetries exist.

Affects of current overlap can also be observed using this model. Overlap is not the result of any imbalance but can still cause a shift in harmonics that could prove troublesome.

VII. Conclusion

With Saber it is possible to model an entire ring magnet power supply system, either in its entirety or in separate parts whose responses are then combined. This allows the simulation and measurement of such parameters as common and differential mode magnet ripple current due to converter type, filter design, and transformer/ac utility imbalances. It is also possible to use the ripple spectrum created to reconstruct an approximate real time current waveform for examination of peak to peak ripple.

VIII. REFERENCES

- [1] SaberTM is a registered trademark of Analogy Inc.

Independent Resonant System Tracking Considerations

K.W. Reiniger,
TRIUMF, 4004 Wesbrook Mall, Vancouver, B.C. V6T 2A3

Abstract

The TRIUMF KAON Factory Booster and Driver rings are to be excited using a resonant topology, with independent dipole and Qf and Qd quadrupole resonant systems. Dipoles and quadrupoles for the same ring must track and the booster and driver rings must be phase locked. This paper presents some of the considerations which need to be taken into account for this system to be feasible.

I. INTRODUCTION

In the TRIUMF KAON Factory booster and driver rings the dipole and quadrupole magnets are separately excited, each having their own resonant circuits. This separated function mode of operation allows for flexibility in tuning of these elements by having independent amplitude control without having to resort to trim quadrupoles which would occupy additional space on the rings which is already at a premium.

This additional flexibility however complicates the powering of these magnets since one has at least three independent resonant systems per ring whose magnetic fields must track, in terms of frequency and phase.

II. SYSTEM DESCRIPTION

The three resonant networks are comprised of magnet inductance, dc bypass choke inductance and capacitors. The inductance and capacitance determines the nominal natural resonant frequency of the network. The natural resonant frequency varies as a function of excitation and am-

bient conditions. The overall circuits are of a distributed resonant cell configuration which serves to minimize the peak voltage to ground.

Since the repetition rate of the acceleration cycle is fixed, the resonant networks are excited at a fixed frequency in a driven mode, as opposed to free running. For reasons of electrical efficiency, the resonant cells are tuned to be very close to the driven frequency. The tuned response of course will vary as a result of component value drifts but this is dynamically compensated to some extent by the use of switchable trim capacitors for each system.

Figure 1 shows a typical resonant circuit configuration for the booster dipoles. Central to this circuit is found the pulse forming network which is used to establish and control the ac resonant response used to drive the magnets. The two quadrupole networks have a similar configuration, differing only in the number of resonant cells which are required.

The pulse forming network provides the energy to control the peak to peak resonant response by providing for the energy loss of the system once per oscillatory cycle. This occurs through the primary windings of the dc bypass chokes. Timing of these pulses also defines the operating frequency of the respective tuned resonant systems. A more detailed description of the energy makeup system is presented in reference [4].

Given the fixed driven response and the variations in the natural frequency tune, there exists a variable phase shift between the energy makeup waveform, which determines system timing, and the resulting magnet current. The only time these two are in phase is when the driven frequency corresponds exactly to the natural resonant frequency.

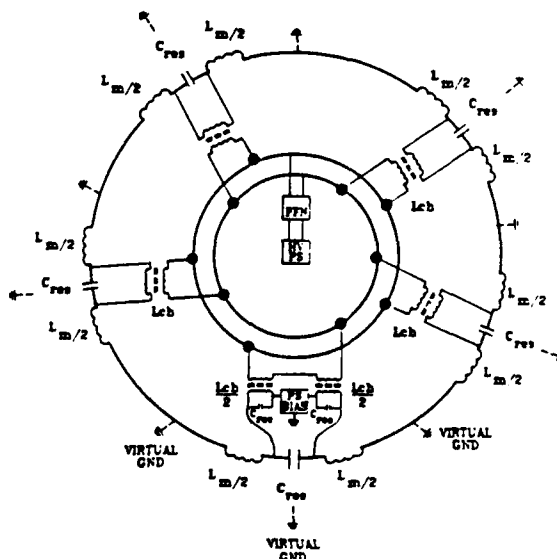


Fig. 1. Typical resonant network.

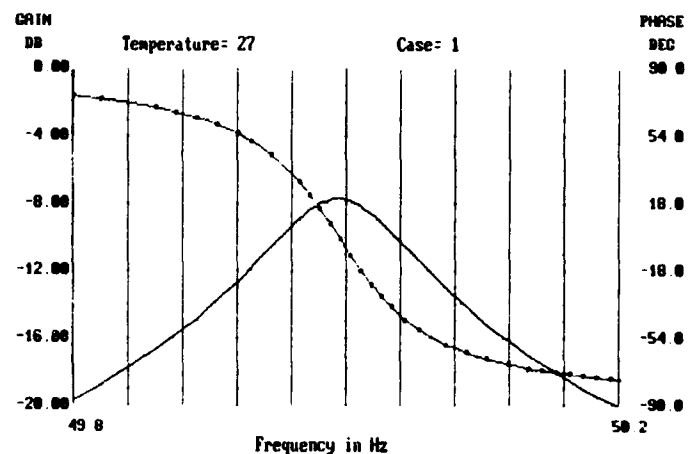


Fig. 2. Typical resonant network gain phase plot.

Figure 2 shows a typical gain phase relationship of a single network which is representative of all three. Since one is running very close to resonance one is in a region of maximum phase transition as a function of frequency and large phase transitions are possible due to small natural resonant frequency variations [2,3].

Whether energy makeup is done with a sinusoidal forcing function or with a pulse forming network, the phase angle difference of excitation and response results in a varying time delay of the oscillatory response with respect to the master clock. Since none of the three networks stays tuned to the same natural resonant frequency, the three responses exhibit different phase angles. As all three circuits exhibit a Q of about 100 these individual phase shift variations are pronounced.

The natural resonant frequency of the three distributed magnet systems can not be perfectly matched, but will be trimmed as close as possible.

Variations of the natural resonant frequency are due to thermal variances which effect the value of capacitance and the magnet gap. The capacitors for example have a thermal coefficient of about -0.04% per degree centigrade.

The second factor which must be taken into account is the dependence of the natural resonant frequency on excitation level [1].

The dipole circuit which has the highest stored energy serves as the master reference for the two quadrupole circuits. The problem now is that of synchronizing the quadrupole circuits. If one were to use the same pulse train timing for all three circuits, there would appear phase differences of the two quadrupole currents with respect to each other as well as to the dipole current.

III. SYSTEM TIMING

The solution is to tune the quadrupole resonant frequency to have energy makeup pulses which are sufficiently time delayed with respect to those of the dipole circuit. One then uses the dipole timing as a reference, and provides the quadrupole circuit ac makeup pulses with the same repetition rate as for the dipoles but with an adjustable time delay with respect to the dipole pulses to achieve phase lock of the fundamental quadrupole currents to the fundamental dipole current.

The time delay and natural resonant frequency tuning would have to be optimized to provide sufficient dynamic range and to minimize the generation of harmonic disturbances due to the time displacement of the energy makeup pulses [3].

Driving the quadrupoles further off resonance implies a less efficient powering of the quadrupole circuits, though this is necessary to have sufficient dynamic range for the system to be feasible.

To achieve good tracking by phase locking the fundamental current components of course requires that the magnetic properties of the dipoles and the quadrupoles are carefully matched in terms of saturation characteristics

etc. Since the natural response of the resonant circuits exhibit an exponential decay between energy makeup pulses, the dipole and quadrupole circuits must have an equivalent Q to match the asymmetry of the current waveforms in each circuit to achieve reasonable tracking of their magnetic fields.

The required timing correspondence between booster and driver will be handled in a similar manner where the booster dipole again will be used as the master timing reference for the driver dipoles and the corresponding quadrupoles will be slaved to the driver dipoles.

IV. CONCLUSIONS

Tracking of independent resonant networks is feasible based on experimental work done at TRIUMF for purposes of magnet measurements of the booster dipole prototype. An appropriate phase sensing network needs to be developed which functions in the presence of the tunable dc bias. As well a detailed analysis of the phase control loop which copes with the severe phase transitions encountered in the three systems needs to be done.

Though I have not had the opportunity of setting up independent networks the experience gained in running the existing resonant configuration at full power leads me to believe that the methodology contemplated will be successful.

I would like to thank Dr. Jonathan Kim of the University of Victoria and Neil Marks from Daresbury Laboratory for their invaluable assistance on this project.

V. REFERENCES

- [1] K.W. Reiniger, "Power Supply System for the TRIUMF KAON Factory", Conference Record IEEE, Particle Accelerator Conference 91CH3038-7 pp.920-922 (1991).
- [2] J.M.S. Kim, "SPICE Simulation of Resonant Booster Ring Magnet Power Supply", KAON Design note TRI-DN-K178 (Aug 1991).
- [3] N. Marks, "Disturbance Generated in the Booster Magnet Networks by the Energy Makeup Pulses", TRI-DN-92-210 (1992).
- [4] J.M.S. Kim, K.W. Reiniger, "Frequency-Domain Analysis of Resonant-Type Ring Magnet Power Supplies", (these proceedings).

Electrical Characteristics of the SSC Low-Energy Booster Magnet System*

A. Young and B. E. Shafer

Los Alamos National Laboratory

Abstract

The purpose of this paper is to review the electrical design of the magnet system for the Superconducting Super Collider (SSC) Low-Energy Booster (LEB). The primary operating mode of the LEB is as a 10-Hz rapid-cycling proton synchrotron. In this mode, capacitor banks are used to make the entire magnet circuit resonant at 10 Hz. This resonant system thus eliminates the requirement of having to provide (and recover) a large amount of reactive power. The primary focus of this paper is to analyze the electrical properties of the magnet system. In addition to the 10-Hz mode, the magnet system is capable of operating as a 1-Hz ramped proton synchrotron, with flat "front porches" and "flattops" for injection and extraction. This mode is initiated through bypassing the choke-capacitor system and exciting the magnet system with a SCR power supply using predetermined waveforms. Both these operating modes (10 Hz and 1 Hz) are analyzed using SPICE (Version 3E).

I. INTRODUCTION

Because the energy gain during the acceleration cycle of the Superconducting Super Collider (SSC) Low-Energy Booster (LEB) is from 600 MeV to 12 GeV, the magnet current must swing through a factor of 10, from 400 A to 4000 A. Because capacitors cannot conduct dc current, the capacitors are placed in parallel with inductors (chokes) so that the magnet system can operate with a biased-sine-wave excitation. The primary focus of this paper is to analyze the electrical properties of this magnet power system.

The major components of the magnet power system include the 2-m dipole magnets, the quadrupole magnets, the chokes, the capacitors, and the power supplies. These can all be represented by electrical circuit models that have the same electrical behavior (both dc and ac) as the actual components. The electrical-equivalent circuit for the dipole is shown in Fig. 1.

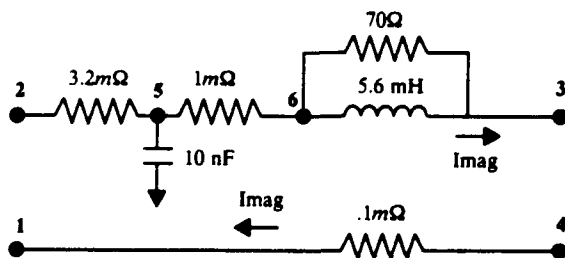


Figure 1. Equivalent circuit for a pair of 2-m LEB dipoles.

II. SYSTEM LAYOUT AND COMPONENT VALUES

The overall electrical layout of the magnet system is shown in Fig. 2. The magnet system is divided into 12 approximately equal cells and separated by 12 choke-capacitor cells. The ring is powered by three power supplies and filters. The magnet bus turn-around point (not shown) is in magnet cell No. 12. The magnet bus wraps around on itself so as not to create a single-turn 180-m-diameter current loop. This strategy not only minimizes system inductance but also minimizes stray 10-Hz fields. (Also not shown is the resonance control loop, which attaches to the choke secondary windings.)

Ring magnet power is derived from three series-connected dc power supplies (2200 A) and three series-connected 10-Hz ac supplies (1800 A peak). The entire system is made resonant by tuning the capacitors. The resultant current excitation is a biased sine wave whose magnitude varies from a minimum of 400 A to a maximum of 4000 A.

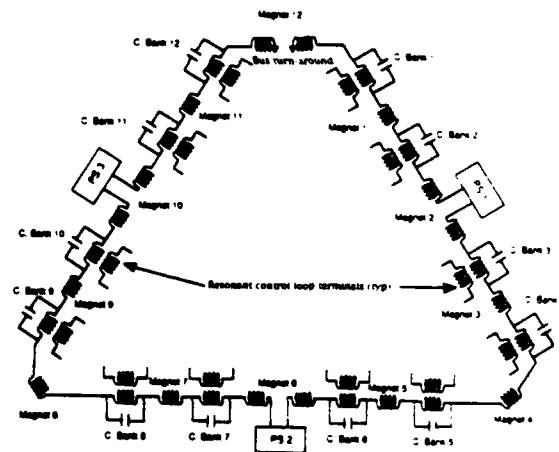


Figure 2. The overall LEB ring magnet system electrical layout.

The major electrical properties of the LEB magnet system include its total inductance (about 296 mH) and dc resistance (about 690 mΩ with the chokes). Thus, the peak stored energy in the LEB is about 2.7 MJ (2.4 MJ in the magnets and 0.3 MJ in the chokes at $I_{MAG} = 4000$ A). The general characteristics of the LEB magnet system can be seen in Table I.

* Work supported and funded by the U.S. Department of Energy office at the Superconducting Super Collider Laboratory.

General Characteristics	
Ring Circumference	570 meters
Injection energy	600 MeV
Extraction energy	12 GeV
Operating modes	10-Hz resonant, 1-Hz ramp cycle
Magnet injection current	400 A
Magnet extraction current	4000 A
Total ring inductance (magnets only)	296 mH
Total ring resistance (without chokes)	332 mΩ
Total ring resistance (with chokes)	692 mΩ
Dipole magnets	
Quantity	96
length	2 m
Peak field	1.3 T (approx.)
Maximum field ripple	± 100 ppm (est.)
Inductance	2.8 mH
dc resistance	2.1 mΩ
Capacitance to ground	5 nF (est.)
Quadrupole magnets	
Quantity	90
Inductance	0.3 mH
Maximum field ripple	±100 ppm (est.)
dc resistance	1.3 mΩ
Capacitance to ground	5 nF (est.)
Capacitors	
Quantity	12
Capacitance	16.61 mF
Max. Voltage	2900 V
Max. Power dissipated (ea.)	5 kW
Chokes	
Quantity	12
Inductance	40 mH
Max. ac current	1109 A
Max. dc current	2200 A
Capacitance to ground	50 nF (est.)

Table I. General characteristics of the LEB ring and magnet system.

Because the driving current of the ring is known [$2200 + 1800 \sin(\omega t)$ amps], it is possible to estimate the maximum choke current and the maximum capacitor voltage at 10 Hz. For the baseline design, it was decided that the inductance (L) of each choke should be 40-mH [1], which minimizes the estimated cost for 12 choke-capacitor circuits. The final choice for capacitance (C) was 16.61 mF. Thus, a resonant frequency equal to 6.17 Hz. The projected cost for the L and C components was based on an estimated fixed cost per Joule of energy storage capability in the chokes and capacitors.

The dc and ac electrical properties of the ring components were estimated using equivalent-circuit component values. The magnets and the chokes were modeled using a series resistance to represent the dc coil resistance and a resistance in parallel with the inductance to represent the eddy-current ac and hysteresis losses. The capacitors are expected to have ac losses not exceeding 5 kW each. Because the excitation current is known, it is possible to estimate both the dc and ac power requirements. The overall estimate is 3351 kW of dc power, plus an additional 1476 kW for the ac power component.

III. ANALYSIS OF THE OPERATING MODES

Analysis of the 10-Hz resonant Mode

Eight issues relating to the operation of LEB in the 10-Hz resonant mode were analyzed. These were magnet current in the frequency domain, magnet current in the time domain, the characteristics of the choke-capacitor circuit, unequal capacitance among the choke-capacitor cells, resonance control, transients caused by switching capacitors, power supply ripple, and effects of eddy currents in magnets.

All these topics cannot be thoroughly covered in this paper. However, a selected few will be discussed. (A complete discussion of the analysis is provided in a report submitted to the SSC Laboratory [2]).

Three simulations that examined the amplitude and phase (in relation to the excitation voltage) of magnet current in the frequency domain were used to determine the driving-point transconductance of the magnet system. One simulation spanned frequencies from 1 Hz to 100 Hz. The results of this simulation are illustrated in Fig. 3. The other simulations more closely examined the small-signal transconductance between 5 Hz and 10 Hz.

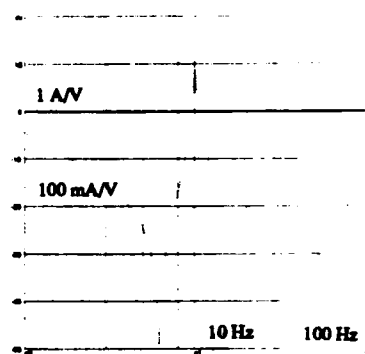


Figure 3. Simulated small-signal transconductance magnitude of the LEB.

Because the capacitors have a temperature coefficient and they will be housed in an unheated enclosure, the capacitance is expected to vary diurnally. To maintain resonance at 10 Hz, each capacitor bank includes discrete levels of switch-selectable capacitance that can be switched in or out remotely. There are three issues related to whether or not the ac and dc power can be present when the capacitors are switched into or out of the circuit. First, are there differential-mode current or

voltage surges that can damage components when the power supplies are operating? Second, will there be current transients in the magnet system that can cause the beam to be lost? Third, are there common-mode surges that can lead to excessive voltage-to-ground transients?

To simulate the effects of switching a capacitor into the magnet string, the method of superposition was used. Here, an initial dc voltage of approximately 3000 V was placed on the 400- μ F capacitor. When the switch is closed, the 400- μ F capacitor discharges into the 16.6-mF capacitor through the snubbing circuit. Figure 4 shows the transient voltage across the capacitor bank as a function of time. The peak half-cycle voltage is 140 V and the frequency is 1 kHz while the other resonant frequency is 6.17Hz.

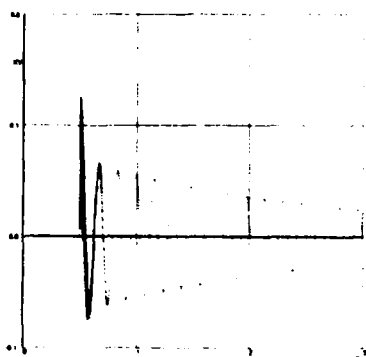


Figure 4. Transient voltage across capacitor bank as a function of time (3 second duration).

Analysis of the 1-Hz resonant Mode

In the 1-Hz operating mode, the choke-capacitor banks are removed from the magnet circuit and the three dc power supplies are ramped using a waveform generator to provide the correct voltage profile. Removal of the choke-capacitor banks is preferred to shorting them out because of the large expected shunt capacitance to ground in the choke-capacitor circuit that adversely impacts the rejection of power supply ripple voltage (especially common-mode).

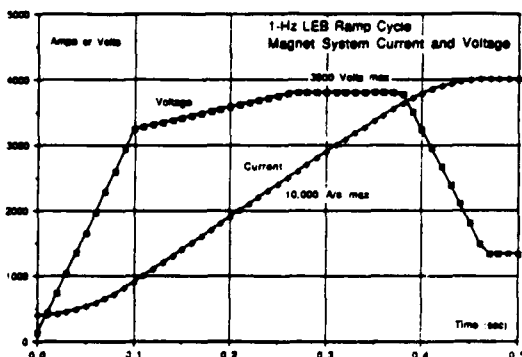


Figure 5. Sample ramp voltage and current profile.

The power-supply voltage and current waveform for 1-Hz ramping is limited by four constraints: maximum current ramp rate, maximum voltage ramp rate, injection and extraction parabolas, and maximum ring voltage. Figure 5 illustrates a sample ramp voltage and current profile that

achieves a 470 ms acceleration cycle from 400 A to 4000 A with the current ramp rate equal to 10,000 A/s, voltage ramp rate equal to 32,000 V/s, injection and extraction parabolas equal to 100 kA/s², and ring voltage equal to 3800 V.

This ramp waveform is adequate to achieve a 1-s cycle time. Other ramp programs can be used to produce faster acceleration cycles. This ramp cycle is based on a ring resistance of 332 m Ω and inductance of 296 mH and requires only two 2000-V power supplies.

The dc voltage and 1440-Hz ripple voltage on a single power supply at injection will be 133 Vdc and 110 Vac peak, respectively, assuming the full-scale power supply output voltage is 1333 V (33% of 4000 V). The expected differential-mode driving-point transconductance for a single power supply with the choke-capacitor banks removed is about 1.3 mA per volt at 1440 Hz. Thus, the expected ripple current at 1440 Hz is 140 mA peak (360 ppm at 400 A). So some filtering is required. Eddy currents in magnets, beam tubes, etc., will provide some filtering of the magnetic-field ripple.

III. CONCLUSIONS

There are no critical issues in the design or operation of the magnet power supply system for the LEB. However, there are some issues that do need further consideration.

- The stray capacitance—specifically coil-to-ground (magnetic components) and shunt capacitance to case (capacitors)—should be estimated better. This stray capacitance leads to higher common-mode ripple and displacement currents in the magnets.
- The resonant frequency needs to be controlled to about 0.05 Hz (0.5%). The resonance control loop is inadequate for controlling the 10-Hz resonance. A power-factor monitor at the 10-Hz power supplies appears to be a better monitor for the resonant frequency.
- Because the LEB is a separated-function-synchrotron, the eddy-current time constants of the dipoles and quadrupoles should be matched in order to minimize tune shifts during acceleration. The source of the tune shift is a retardation of the magnetic fields due to eddy currents. The matching is best done by adding external bypass resistors across dipoles or quadrupoles. The magnets should be designed to allow for the attachment of external bypass resistors in order to control the magnetic field retardation.

IV. REFERENCES

- [1] C. Jach, et. al., "Energy Storage Inductor for the Low-Energy Booster Resonant Power System," To be published in 1993 Proc. Particle Accelerator Conference.
- [2] R.E. Shafer and A. Young, "Electrical Characteristics of the SSC Low-Energy Booster Magnet System," Los Alamos National Laboratory document number LA-UR-92-3298-01.

Analysis and Design of a High-Current, High-Voltage Accurate Power Supply for the APS Storage Ring*

M. Fathizadeh
Argonne National Laboratory
9700 South Cass Avenue, Argonne, IL 60439

Abstract

There are 81 dipole magnets contained in the storage ring at the Advanced Photon Source (APS). These magnets are connected in series and are energized by only one 12-phase power supply. The eighty-first magnet is located in a temperature-controlled room with an NMR probe to monitor the magnetic field in the magnet and provide a reference signal for correction of the field drift due to aging of the components. The current in the magnets will be held at 497 A. The required current stability of the power supply is ± 30 ppm, the current reproducibility is ± 50 ppm, and the current ripple is ± 400 ppm. The voltage required to maintain such a current in the magnets is about 1700 V. Different schemes for regulating current in the magnets are studied. Pspice software is used to simulate the behavior and the design of such a power supply under different conditions. The pros and cons of each scheme will be given and the proper power and regulating scheme will be selected.

I. INTRODUCTION

The storage ring of the Advance Photon Source (APS) at Argonne National Laboratory (ANL) contains 81 dipole magnets. These magnets are connected in series and fed by a 12-phase accurate and stable power supply. In order to provide a stable reference for the power supply, a 17-bit digital-to-analog converter (DAC) is programmed by the control computer. The 81st magnet is placed in a temperature-controlled room with an NMR probe to monitor the magnetic field in the magnet and provide the correction signal due to the aging of the components. The correction signal is sent to the DAC to modify the reference signal. The power supply is equipped with a passive L-C-R filter to reduce the ripple content of the output current. To regulate the current in the magnet, a high precision, low drift, zero flux current transducer is used. The transducer senses the magnet current and provides the controlling signals through the regulator. Several control loops are used to regulate the current in the magnet load. Fast correction for the line transient is provided by a relatively fast response voltage loop controlled by a high gain slow response current loop. Different design topologies are studied and will be given in the following.

II. POWER SUPPLY SPECIFICATION

The power supply must deliver 497 A continuously to a chain of 81 dipole magnets. The output voltage at full load operation is 1662 V [1].

*Work supported by U.S. Department of Energy, Office of Basic Energy Sciences under Contract No. W-31-109-ENG-38.

REGULATION ($\Delta I/I_{max}$)

Stability	$\pm 30 \times 10^{-6}$
Reproducibility	$\pm 50 \times 10^{-6}$
Current Ripple	$\pm 400 \times 10^{-6}$
Tracking Error	$\pm 100 \times 10^{-6}$

III. DESIGN AND TOPOLOGY

In order to provide current to the magnets, several types of power supplies are used. Phase-controlled thyristor rectifiers and switched-mode power supplies (SMPS) are the most common types used to energize the magnets. In phase-controlled power supplies a low pass filter is used to somewhat filter the ripple current. The accuracy and the response of the output current depends on the number of silicon-controlled rectifiers (SCRs) used in the power bridge and the low-pass filter frequency response. Due to the imperfection and imbalance in the power transformers, the output current may contain ripple content with the line frequency. Several techniques have been suggested in the past [2] and currently being employed to regulate the output current. To compensate for the load disturbance and ripple in the output current, active filters such as transistor banks or coupled reactors are used. The use of transistor banks means an inherent reduction in the output voltage and, consequently, lower efficiency. Use of coupled reactors can reduce the output current ripple, but reduces the tracking speed of the power supply.

The SMPSs, however, are highly efficient, quick to respond, and introduce high frequency ripple in the output current that can be filtered more easily than the low frequency ripples in the phase-controlled cases. On the other hand, the switched-mode power supplies can cause a high electromagnetic interference (EMI) due to their high di/dt and dv/dt [3]. In some cases, EMI filtering may be required to avoid perturbations to other equipment next to the power supply or the power line [4].

Another technique uses the phase-controlled and switched-mode power supplies in series combination. Usually the phase-controlled section delivers 90% to 95% of the output power and the SMPS delivers the rest. The 5% to 10% of the output which is delivered by the SMPS is required for the regulation. Phase-controlled power supplies have limited bandwidth depending on the number of the SCRs used in the power bridges. For instance, in a 12-pulse phase-controlled power supply the bandwidth is limited to 720 Hz while the switched-mode power supply can have very large bandwidth up to 500 kHz. The utilization of the SMPS allows fast and precise correction of the output current.

IV. DESIGN AND RESULTS

A. Filter Design

A filter with a cut-off frequency of 720 Hz was designed to eliminate the fundamental and higher harmonics of the current in the power supply. The transfer function of the filter is given in the following [2]:

$$\frac{e_o}{e_i} = \frac{sT_2 + 1}{s^3 T_2 L_1 C_1 + s^2 (T_1 T_2 + L_1 C_1 + L_1 C_2) + s(T_1 + T_2 + T_3) + 1} \quad (1)$$

where $T_1 = R_1 C_1$, $T_2 = R_2 C_2$, $T_3 = R_1 C_2$, $L_1 = 650 \mu\text{H}$, $C_1 = 16200 \mu\text{F}$, $C_2 = 37800 \mu\text{F}$, and $R_2 = 0.265 \Omega$.

However, due to imbalances in the power transformers, the 60-Hz component passes through the filter and is noticeable in the output current if it is not filtered. The use of a pass transistor between the filter and the output can act as an active filter. The base current for such a transistor is proportional to the output current. Care must be taken to ensure a limited amount of voltage across the pass transistor. The pass transistor can fail due to high power dissipate or high voltage across it. Usually four or more control loops are used to ensure the safe and reliable operation of the pass transistor. One relatively slow but high gain current loop, a high gain output voltage loop, high gain voltage loop for AC line compensation, and a voltage loop to maintain certain voltage drop across the pass transistor are needed. Other loops may be used in conjunction with the above control loops. A feed forward loop is usually used for AC line voltage compensation. The limitation of this technique appears when a relatively high output voltage is required because the pass transistor must support the output voltage in the short circuit situation. This configuration is shown in Figure 1.

In order to test the above technique, a power supply with the following characteristics was prototyped.

Max. Output Voltage	80	V
Max. Output Current	1100	A
Stability	$\pm 30 \times 10^{-6}$	
Reproducibility	$\pm 50 \times 10^{-6}$	
Current Ripple	$\pm 30 \times 10^{-6}$	

A 12-phase power supply with pass transistors was designed. A set of twelve parallel Powerex water-cooled transistors (D7ST) was used for the pass transistor bank. These transistors are designed for switching applications; the voltage rating of these transistors is specified only for that purpose. In the linear application the voltage rating of the transistors must be drastically de-rated. In our case, the 400 V transistor was de-rated to 30 V application. Under a higher voltage application the transistor may fail. The failure under such a condition is a short circuit. In order to reduce the power drop across the transistor bank, an adaptive control loop was designed to maintain a minimum power drop across the transistor bank under different load conditions. The voltage drop across the transistor bank decreases as the load current increases, thus result in a constant

power drop for all load conditions. A certain minimum voltage across the transistor bank is always needed for the current regulation. In the prototype power supply the voltage drop across the bank varied from 25 V to 7 V and load currents from 10 A to 1100 A. For AC line voltage compensation a feed forward loop was used. Measurements were taken at full load conditions, and the ripple of 15 ppm and stability of 45 ppm was measured.

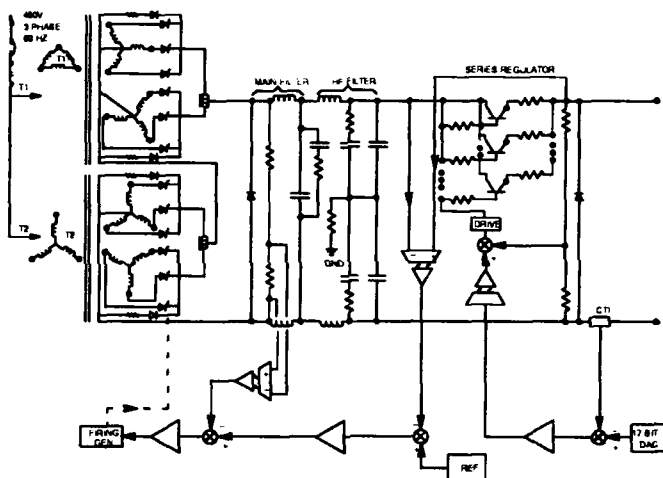


Figure 1 Block diagram for storage ring dipole power supply using phase-controlled and pass transistor.

A second alternative to the above design is the use of switched-mode power supply in conjunction with the phase-controlled power supply. The phase-controlled part delivers the main power and the switched-mode part performs the regulation and the fine tuning of the output current. The switched-mode power supplies have a relatively larger bandwidth than the phase-controlled ones, thus the correction of the current is fast and a low ripple current can be obtained easily. For this scheme, usually about 10% of the output voltage must be delivered by the SMPS and the other 90% is delivered via the phase-controlled power supply. The switched-mode power supply must carry the output current which is a drawback of this scheme. The instantaneous output voltage of the total power supply is used to determine the transistor switching, while the output voltage of the SMPS is used to determine the firing angle of the thyristors. Since the output voltage of the SMPS is compared against a fixed voltage reference, the SMPS always maintains a certain portion of the output voltage. This configuration is shown in Figure 2. The switching transistor in the SMPS must be protected against the di/dt and dv/dt due to the output filter and the magnetic load. The SMPS in Figure 2 is fed from bridge rectifier with a typical R-L-C filter. The filter characteristic may cause oscillation in conjunction with the SMPS and its load. The filter is usually designed to be near critically damped to improve the overall efficiency. The R-L-C filter can give rise to low frequency oscillations at its output when it is subject to periodic load changes, e.g. when supplying power to an SMPS. In order to avoid such a problem, the inductance in the R-L-C filter must be reduced and the R and C increased [5].

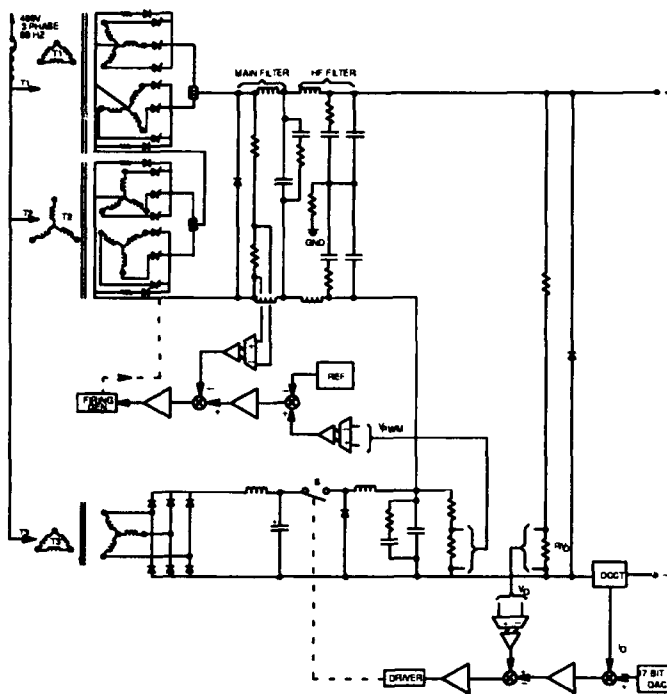


Figure 2 Block diagram for storage ring power supply using phase-controlled and switched-mode power supply

V. CONCLUSION

Different configurations for the power supply of the storage ring dipole magnets were studied. In order to eliminate the output current ripple, an active filter was needed. Use of a pass transistor as the active filter was investigated and it was concluded that complicated control circuitries are needed to make such a scheme work. It was also concluded that under high output voltage, the pass transistor may fail. A prototype was built to investigate the operation of such a configuration, and the results indicate almost one order magnitude better performance than the required regulation.

The use of SMPS in conjunction with phase-controlled power supply was also investigated and the required control loops were shown. The SMPS may cause oscillation when the input filter inductance is relatively high. The switching transistor must be protected against di/dt and dv/dt due to the output filter and load inductances.

VI. REFERENCES

- [1] Advanced Photon Source Design Handbook Vol. II, Dec. 1989.
- [2] W. F. Praeg, "A high-current low pass filter for magnet power supplies," *IEEE Trans. Industrial Electronics and Control Instrumentation*, Vol. IECI-17, No.1, pp. 16-22, Feb. 1970.
- [3] N. Mohan, T. M. Underland, and W. P. Robinson, Power Electronics Converters. Application and Design, (New York: John Wiley & Sons, Inc. 1987).

- [4] J. A. Pomilo, D. Wisnivesky, and A. C. Lira, "A Novel Topology for the Bending Magnets Power Supply at LCLS," *IEEE Trans. on Nuclear Science*, Vol. 39, No. 5, pp. 1506-1511, Oct. 1992.
- [5] M. Fathizadeh, O. D. Despe, D. G. McGhee, "Analysis and Correction of Noise on Electronic Circuits in an Accelerator Environment," *Nuclear Science Symposium and Medical Imaging Conference*, Orlando, Florida, 1992.

Design of the HIMAC Synchrotron Power Supply

M. Kumada, K. Sato, A. Itano, M. Kanazawa, E. Takada, K. Noda, M. Sudou, T. Kohno, H. Ogawa,
S. Yamada, Y. Sato, T. Yamada, A. Kitagawa, J. Yoshizawa, T. Murakami, Y. Hirao,
National Institute of Radiological Sciences,
4-9-1, Anagawa, Inage-ku, Chiba, 263, Japan

S. Matsumoto, Dokkyo University, Medical School,
H. Sato, T. Sueno, T. Kato, K. Endo, National Laboratory for High Energy Physics,
K. Utino, Tsukuba Tech. College,
Y. Takada, University of Tsukuba,
A. Noda, Kyoto University,
T. Tanabe, S. Watanabe, Institute for Nuclear Study,
S. Koseki, and H. Kubo, Hitachi Ltd.

Abstract

The design for lattice magnet power supplies of the HIMAC synchrotron is described. Characteristic feature includes separate neutral line, a configuration of separate coil of a magnet, an accurate description of load magnet and dynamic load analysis.

I. INTRODUCTION

HIMAC, the world first medical heavy ion accelerator complex dedicated to cancer treatment[1], is in the final construction stage. An initial beam test of the injector linac has been successful[2]. An alignment of machine components of the synchrotrons has started and preliminary tests of the synchrotrons without beam are expected to begin in this coming summer. The main accelerator comprises two separate synchrotrons where the slow extraction is based on the 3rd order resonance. Being medically dedicated, extraction energy, ion species, and intensity must be variable in a wide range, while a stable beam spill is required. Thus, tolerance for current stability, current ripples, and current spikes for lattice magnets is extremely tight in wide range of magnet current. In order to achieve high performances, we have carefully designed for power supplies from the point of view of the best combination of the power supply and the load magnets. Some parameters are given in Table 1.

We describe in this paper the design rationale of the system and an example of the analysis of the power supply and the magnets where an importance of the equivalent circuit of 6-terminal, a separation of common and normal mode and a separation of magnet coil is particularly emphasized.

II. DESIGN RATIONALE

In usual system configuration of a thyristor power supply and lattice magnets, a common mode component of coil current ripples and spikes are spatially distributed over whole load magnets and deteriorates the circulating beam as a closed orbit distortion and a tune shift which suggests an insufficient suppression of the common mode components in contrast to that of the normal mode. In order to suppress both modes simultaneously we separate magnet coils into upper and lower coils, we prepare the third neutral line, and we equip the common mode static filter for the power supply in addition to the normal mode static filter. As the lattice magnets are connected and excited in series by the power supplies, the parasitic resonance results like in a distributed circuit. In

order to overcome this problem, bridging resistors are connected to each magnet coils: the resistor performs the damping of the resonance and bypasses the higher frequency components of the coil currents. From this viewpoint our thyristor power supply of 24 pulses is advantageous that that of conventional one. Lower frequency components as 50 Hz and 100Hz are suppressed by a technique of repetitive digital control developed at KEK. In order to achieve repetitive control of higher performance, we made much effort to increase an accuracy of the load parameter. To this end, a fractional polynomial fitting and an idea of effective inductance are developed. We adopted the VME and fast PDOS real time operating system to facilitate the control.

To get reproducible data for the repetitive control the sampling timing of a voltage and a current is synchronized to event clock signals which is phase-locked to a primary 50 Hz ac line voltage and an event generator, dual pattern memory for switching the spill pattern are developed.

The effect of the resonance is weakened by crossing-over cabling of the upper coil to lower coil from magnets to magnets. We carefully choose a standard cabling to reduce the lower frequency components of the spatially distributed coil currents.

Table 1 Main parameters of the power supplies and load.

Power supplies		
stability goal(ppm)		20
repetition(Hz)		0.3- 1.5 at 600 MeV/u
rise / flat top duration(s)(600MeV)		0.7/0.5 at 0.5 Hz
rate of field change (T/s)		1.4
Filter parameters	dipole	quadrupole
L _{static} (mH)	2.5	0.5
C1(mF)	0.4	2
C2(mF)	2	10
R(Ω)	2.2	0.44
L _{dynamic} (mH)	n.a.	0.5
Load	dipole	quadrupole
output power(MW)	5.13	0.538
voltage(kV)	2.27	0.32
current(kA)	2.26	1.35
total inductance(mH)	633.1	110.8
resistance(m Ω)	200.2	116.8

A. Configuration of power supplies and load magnets

The unique feature of the system of the power supply and load magnets is shown in Fig. 1. Three lines from the power supply, which are a positive, a negative and a neutral output, respectively, are connected to the load magnets. These three lines are connected to the upper coil, lower coil, and magnet yoke. The third line that performs as the neutral line of the power supply is introduced, for the first time, to separate the normal mode and the common mode more clearly. The neutral point of an upper half and a lower half of symmetric thyristor banks of the power supply are connected to the third line. In addition, low level electronics refers to this line.

In this viewpoint, the magnet coils comprise self inductance, mutual inductance, series resistance, capacitance between upper coil and lower coil, and capacitance to the magnet yoke. Consequently, circuit of six terminals is formed. It can be shown that the circuit is decoupled to a circuit of four terminals by the use of sum of upper coil current and lower coil current (normal mode), and by difference (common mode).

It should be emphasized that a conventional configuration of the power supply and its load should also be treated as 6 terminal-circuit. An advantage of introducing this neutral line is to clarify and visualize a circuit of an unpredictable leakage capacitance among an excitation cable, coil and a ground line of which location is also quite unpredictable. In our new scheme this ghost ground line is replaced by the physical neutral line.

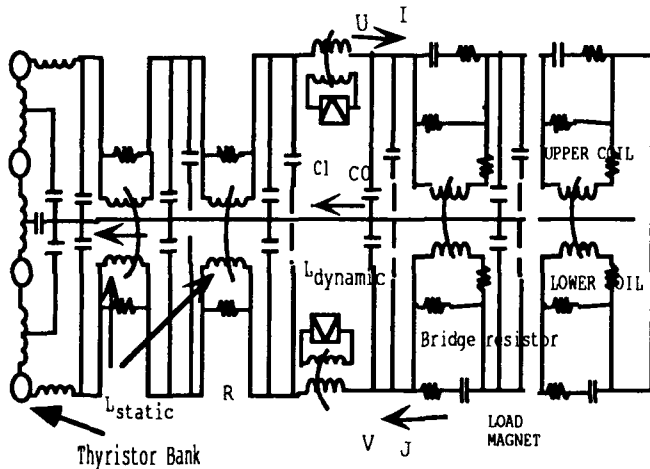


Fig.1 Equivalent circuit of the power supply system

B. Analysis

Frequency characteristic of voltage difference, $U-V$, current difference $I-J$, voltage sum $U+V$, current sum $I+J$ of the unit magnet with leakage capacitance are able to be calculated by multiplying transfer matrix. Neglecting the resistance that bridges the coil inductance in order to damp the resonance and to by-pass the coil current, we get the six-terminal transfer matrix for each magnet:

$$\begin{pmatrix} 1 & -(pL + R) & 0 & 0 \\ -pC0 & 1 + pC0(pL + R) & 0 & 0 \\ 0 & 0 & 1 & -(pL + R) \\ 0 & 0 & -pC & 1 + pC(pL + R) \end{pmatrix}$$

with $C = C0 + 2C1$, $p = j\omega$. As is seen, the difference and the sum components are decoupled. Multiplying the matrix of a number of magnets and terminating the end coils depending upon the short or open connection, we can calculate the electrical characteristics of the system. Numerical computing of the resonant frequency shows a dispersive nature as shown in Fig. 2. Although above expression is for the simple case, it can be shown that any complicated circuit could be decoupled by decomposing into simpler circuit. Fig. 2 shows resonance characteristic of the current sum of quadrupole load where angular frequency ω_0 is normalized by the resonant frequency ω_0 , which is given by the load inductance and leakage capacitance. In this case, the number of resonance is 10 for 12 units of quadrupole magnets. Note the appearance of lower frequency, lower than that of the resonance frequency of the unit cell of the magnet. Beyond $\omega / \omega_0 = 2$, which corresponds the cutoff frequency, the resonance is suppressed.

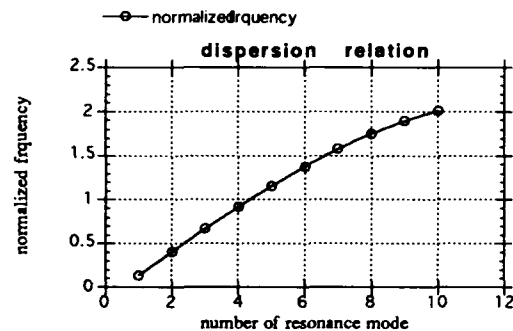


Fig.2 Dispersion relation of the sum current of quadrupoles

Analytic expression of the difference of the upper coil and lower coil current is obtained as

$$\frac{I_m - J_m}{U_i - V_i} = Z_0 \left(\sinh m\zeta - \frac{Z_0 \sinh m\zeta + Z \cosh m\zeta}{Z_0 \sinh N\zeta + Z \cosh N\zeta} \sinh N\zeta \right)$$

with $\tanh N\zeta = -\frac{Z_0}{Z}$, where $2Z$ is an impedance of a unit magnet treated as an element of the ladder circuit and Z_0 is usual characteristic impedance. This expression suggests the effectiveness of the bridging damping resistor.

In Fig. 3, a typical example of the spatial distribution of the resonance is shown. As shown, the mode is characterized by $(2n-1)/4$ wave length where the fundamental mode, $\omega/\omega_0 = 0.127$, is a quarter wave length. This mode must be carefully avoided. This pattern is universal regardless of various parameters.

C. Shuffling of magnets by cabling

Due to a property of a ladder circuit of the load magnet and cable, a resonated current has a cosine shaped spatial distribution along the magnet. The inhomogeneity caused by the effect of the particular resonance is minimized by a proper pattern of combinations of reversing the direction of the

magnetic field among unit magnets, by cable shuffling.

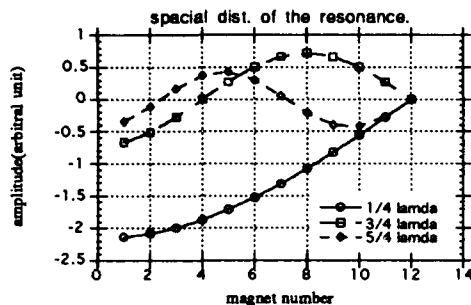


Fig.3 Typical example of the spacial distribution

For the case of dipole magnets, we have studied closed orbit displacement of third and fourth order components of every possible amplitude of the resonant frequency. The result tells no transposable (standard cabling) is the best for the fundamental mode for our operational tune. At design stage, it is difficult to predict the mode of the most dominant resonance. And the choice of shuffling may subject to change depending upon the actual mode of resonance.

D. Electrical characteristics by a fractional polynomial fitting

To express a magnetic field strength B by the excitation current I or voltage V or vice versa, instead of polynomial expansion, a fractional polynomial equation is proposed:

$$B(I) = \frac{a_0}{1 + b_1 I + b_2 I^2} + a_1 \left(1 - \frac{c_0}{1 + c_1 I + c_2 I^2 + c_3 I^3 + c_4 I^4} \right) I$$

where a_0 is proportional to H_c , a_1 ampere turn and $1/c_0$ permeability of an iron core. This equation is a natural extension of Ampere's law and is able to express three distinct regions of an excitation level: low field where remanent field dominates, medium field of high permeability, high field where saturation effects dominate. In an actual digital repetitive feedback algorithm, more sophisticated expression is used corresponding to a hysteresis effect.

E. Effective Inductance

Time derivative of magnetic flux is an induced voltage. In the case of time dependent field strength, an effective inductance L_{eff} that is viewed from the power supply, should be defined by a usual inductance L_0 and its time derivative.

$$L_{eff} = L_0 + I \frac{dL_0}{dt} = S \frac{dB}{dI}$$

where S is an effective area of the flux density.

An excitation dependence of the inductance is calculated from a test data of a power supply with following equation;

$$L_{eff} = \frac{V - IR}{\frac{dI}{dt}}$$

where a resistance is appropriately calculated at flat-base and flat-top periods. As shown in Fig. 4., the effective inductance depending on the excitation current shows a strong saturation effect due to the effect of the derivative of the field strength with respect to the current by an order of magnitude compared to the saturation of the field strength itself. For this reason, fitting equation in the proceeded section is used and its derivative is taken. Accurate calibration of the absolute inductance is now required. This is done by an analog integrator system developed for the magnetic field measurement. With this method the inductance and the resistance of the load is precisely determined, where decoupling of the resistance and the inductance is possible with two different timing conditions.

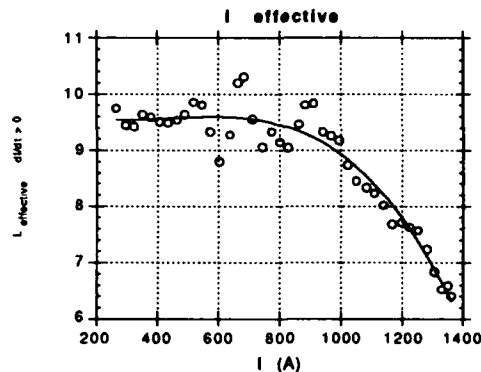


Fig.4 Excitation dependence of Quadrupole Inductance

III. DISCUSSION

Performance of the power supply was checked at the factory with dummy load. Ripple current calculated (division by the nominal inductance) from ripple voltage is at a level of design goal although it must be checked with actual current. This is because even a small amount of a spurious ripple generated by the transient spike could enhance the ripple current under resonance condition. In the preceding argument, a description about the SVC (Static Var Compensator) which will help to improve ac power line is omitted because of the limited space. With a help of the SVC, actual neutral line with full load magnet, moreover with a full set of damping resistor, the better performance of the power supply is expected in an operation scheduled this summer.

IV. ACKNOWLEDGEMENTS

We gratefully acknowledge the support of all the other member of the division of accelerator physics and engineering, research center of heavy charged particle therapy, NIRS.

V. REFERENCES

- [1] Y. Hirao et al., NIRS-M-89, HIMAC-001 (1992).
- [2] T. Murakami et al., this conference.
- [3] M. Kumada et al., 8th Symp. Accel. Sci & Tech., 1991, RIKEN

A 2-Megawatt Load for Testing High Voltage DC Power Supplies*

D. Horan, R. Kustom, M. Ferguson, K. Primdahl
Argonne National Laboratory, 9700 South Cass Avenue, Argonne, IL 60439

Abstract

A high power water-cooled resistive load, capable of dissipating 2 Megawatts at 95 kilovolts is being designed and built. The load utilizes wirewound resistor elements suspended inside insulating tubing contained within a pressure vessel which is supplied a continuous flow of deionized water for coolant. A sub-system of the load is composed of non-inductive resistor elements in an oil tank. Power tests conducted on various resistor types indicate that dissipation levels as high as 22 times the rated dissipation in air can be achieved when the resistors are placed in a turbulent water flow of at least 15 gallons per minute. Using this data, the load was designed using 100 resistor elements in a series arrangement. A single-wall 316 stainless steel pressure vessel with flanged torispherical heads is built to contain the resistor assembly and deionized water. The resistors are suspended within G-11 tubing which span the cylindrical length of the vessel. These tubes are supported by G-10 baffles which also increase convection from the tubes by promoting turbulence within the surrounding water.

I. INTRODUCTION

A resistive load capable of dissipating 2 megawatts at 95 kilovolts DC is required by Argonne National Laboratory to test klystron power supplies used in the Advanced Photon Source. The overall design of the test load is intended to simulate the load seen by the power supply during normal klystron operation. In this way, power supply maintenance and testing can be performed without risk of damage to the klystrons.

The operating parameters of the load are dictated by the TH2089A klystron power supply requirements. A resistive load is required for each power supply sub-system, as given in Table I.

The beam power dissipation of 1900 kilowatts is the most difficult design specification to meet, due to the high voltage and power dissipation levels. The mod-anode and filament loads, although relatively low in power dissipation, have specific design requirements due to the high voltages involved. The focus magnet load is considered optional at this time, as its design requirements are much simplified due to the fact that the operating voltages are much lower.

A block diagram of the entire load system is shown in Figure 1. The beam load consists of wirewound resistor elements enclosed in a stainless steel pressure vessel which is supplied a continuous flow of deionized water for cooling. Due to its size, the pressure vessel is located in a fixed location inside the RF/Extraction building at the Advanced Photon Source, in close proximity to all five klystron power supplies.

The mod-anode and filament loads are contained in an oil tank which can be moved to each individual power supply location within reach of the power supply output cables. Mating connectors on the oil tank allow easy connection of the load to the power supply. The pressure vessel is connected to the power supply through the oil tank by a 350-foot coaxial high-voltage cable. All operator controls and instrumentation are mounted on the oil tank assembly.

A safety interlock system is utilized to insure personnel safety and prevent equipment damage in the event of a malfunction in the load. The pressure vessel is interlocked to prevent overloads due to over-temperature, over-pressure, or insufficient deionized water flow. An internal arc detector is utilized to detect arcing of internal components. The oil tank is interlocked to prevent over-temperature operation and access to high voltages. All of these interlock circuits are connected in a normally-closed series arrangement and are used to shut down and/or prevent turn-on of the power supply under test should a malfunction occur in the test load system.

Table 1
TH2089A Power Requirements [1, 2]

Parameter	Voltage/Current	Power Level	Equivalent Resistive Load	Duty
Beam power	10 to 95 kV DC @ 20 amps max.	1900 kW max.	4750 ohms	cont.
Mod-anode	5 to 85 kV DC @ 10 mA max.	850 watts	8.5 megohm	cont.
Filament	25 vac @ 25 amps	625 watts	1 ohm	cont./int.
Focus Magnet Coils	300 V DC @ 24 amps	7200 watts	25 ohms (x2)	cont./int.

* Work supported by U.S. Department of Energy, Office of Basic Energy Sciences, under Contract W-31-109-ENG-38.

The submitted manuscript has been authored by a contractor of the U. S. Government under contract No. W-31-109-ENG-38. Accordingly, the U. S. Government retains a nonexclusive, royalty-free license to publish or reproduce the published form of this contribution, or allow others to do so, for U. S. Government purposes.

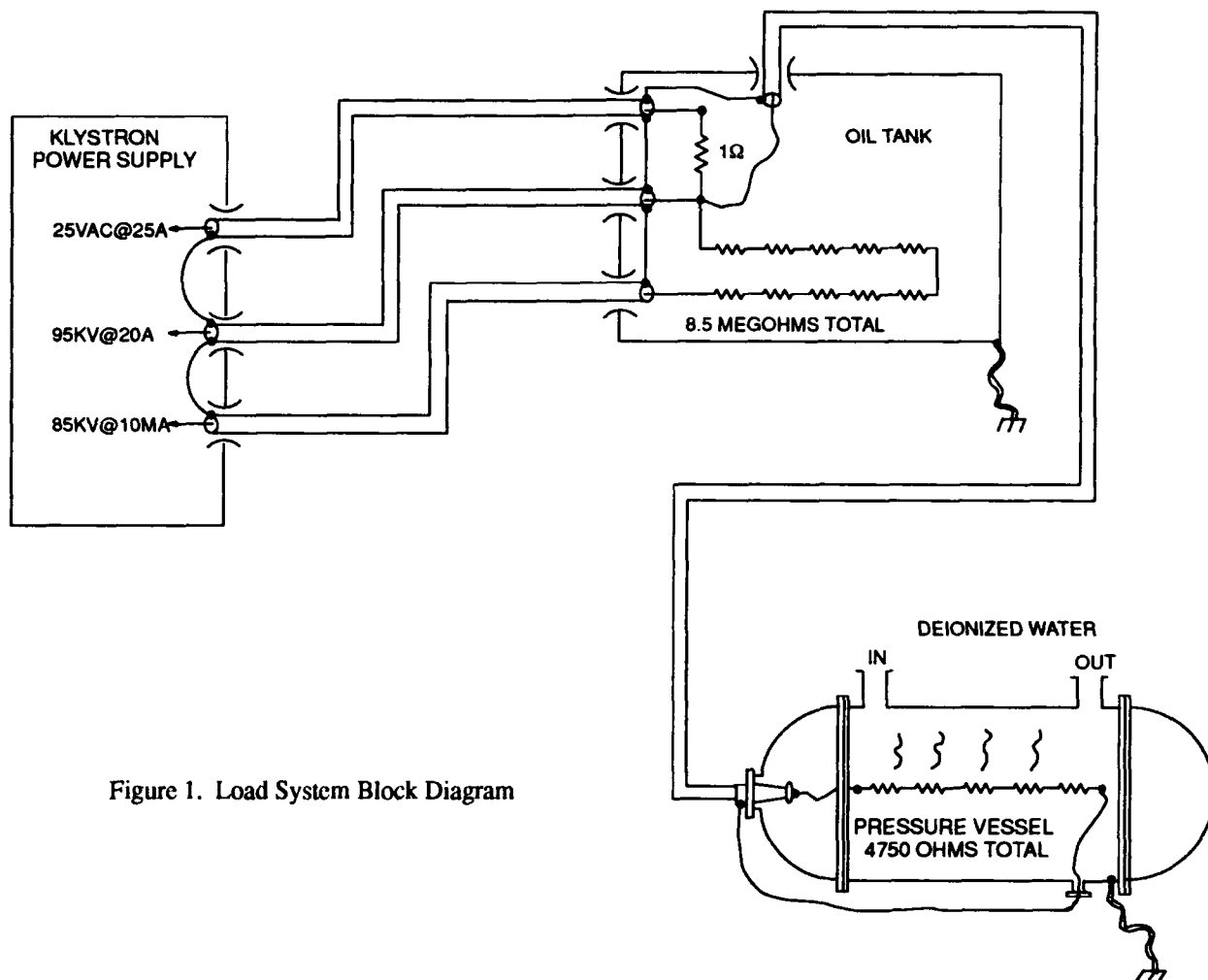


Figure 1. Load System Block Diagram

II. DESIGN OVERVIEW

The pressure vessel contains the resistor network for the beam power supply load. The selection of a resistor best suited for this application was made after extensive power testing of sample units. Compatibility with the deionized water system was also a determining factor in resistor selection, which limited metals in contact with the water to copper and stainless steel.

A test chamber was built to determine the power dissipation capacity of resistor designs when cooled by a turbulent deionized water flow (see Figure 2). The chamber consists of a 5-inch ID clear Plexiglass pipe, 36 inches long, connected to a supply/return system of deionized water. The resistor under test is suspended inside the tube, in the water stream, and supplied electric power through watertight feedthrough bushings. Inlet and outlet water temperatures were monitored to verify power input to the test system.

Electric power was supplied to the test resistor from a 0–560 volt AC/60 Hz source (variable autotransformer) capable of 40 kilowatts maximum power output. Design and cost constraints restricted the choice of resistor types to molded composition (tubular) and wirewound designs, with both types capable of dissipating approximately one kilowatt in free air.

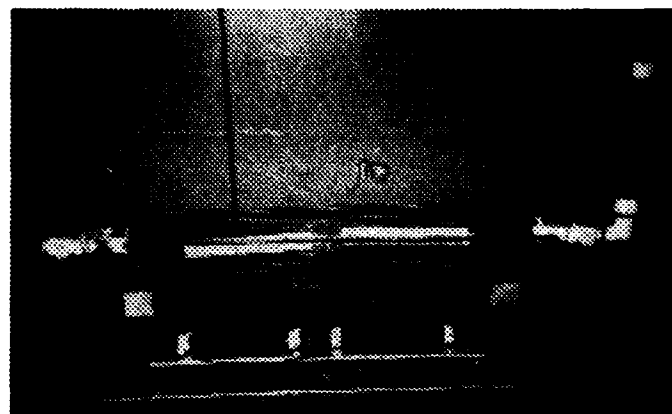


Figure 2. Test Chamber

Power dissipation tests were carried out using a resistor of each variety. The results of the tests are given in Table 2.

The composition resistor failed at a power input level of 18.92 kilowatts and a water flow of 15 gallons per minute. Water temperature data was not accurate because the resistor failed before temperature data could be taken. Observation of the resistor during the test revealed steam production on the interior surfaces of the resistor, beginning at 11 kilowatts input. At 18

kilowatts input, steam production was intense, resulting in hot spots being created on the resistor due to cavitation of the cooling water on the resistor surface. After approximately 45 seconds of operation at 18.9 kilowatts, the resistor failed due to a crack in the resistor body.

Tests of the wirewound resistor indicated that it was capable of dissipating at least 22 kilowatts of power with no distress, at water flow rates between 7.5 and 15 gallons per minute. No active steam production was noted, and an inspection of the resistor after the tests revealed no physical damage.

Results of the power tests revealed that the wirewound resistor design was capable of dissipating at least 22 times its rated dissipation in air when cooled by a turbulent deionized water flow of at least 7.5 gallons per minute. Using this data, the beam load was designed using 100 series-connected resistors of equal resistance value, with each dissipating 20 kilowatts at full power input, and a combined dissipation of 2000 kilowatts. The water flow through the pressure vessel should be maintained between 250 and 500 gallons per minute, resulting in acceptable cooling water temperature rise.

The oil tank contains the mod-anode and filament power supply load resistors, and has a volume of approximately 25 cubic feet. It will contain all of the resistors and approximately 175 gallons of dielectric insulating oil. Due to the relatively low combined power dissipation level of the two loads (1475 watts) and the intermittent nature of their operation, natural convection cooling of the oil tank will be utilized.

III. ELECTRICAL DETAILS

The beam load consists of 100 wirewound resistors connected in series. Each resistor has a cold resistance value of 43.2 ohms, and a free-air dissipation rating of 1000 watts. The resulting total load resistance, assuming a 12% increase in resistance at full power input due to the positive temperature coefficient of the resistor material, will be approximately 4750 ohms.

The mod-anode load consists of ten non-inductive resistors connected in series. Each resistor has a resistance value of 850k-ohms and a free-air dissipation rating of 300 watts. The resulting total resistance is 8.5 megohms. The filament load is a one-ohm wirewound resistor with a free-air dissipation rating of 1000 watts. Both types are suitable for use in oil.

IV. MECHANICAL DETAILS

The pressure vessel, fabricated from 304 stainless steel, will be stamped and manufactured in accordance with section

VIII of the ASME Boiler and Pressure Vessel Code. Two support pads will be used to distribute the total weight load of 35,000 pounds. Torispherical flanged heads and Viton o-rings will be used to seal the vessel and welding will be performed in accordance with ASME Code, Section IX. The maximum external pressure for the vessel will be 30 psi.

The operating pressure for the vessel will be 85 psig, with a MAWP of 110 psig. The relieving pressure (set pressure + overpressure + atmospheric pressure) will be 135 psia. Two ASME-stamped relief valves will be used to relieve pressure on the vessel. A hydrostatic relief valve, with a set-pressure of 103 psig, will have a rated capacity of 75 gpm. The steam relief valve, with a set-pressure of 110 psig, will have a rated capacity of 18,100 pounds/hour.

Based on a deionized water inlet temperature of 90 degrees F and 25 degrees F temperature rise through the vessel, the operating temperature will be 115 degrees F. The maximum temperature for the vessel is 350 degrees F, and is based on the saturation temperature of steam at 135 psia.

V. SUMMARY

We have outlined in detail the specifications and design of a high-power resistive load to be used in testing klystron power supplies at Argonne National Laboratory. The load simulates the loading conditions of the TH2089A klystron. This allows testing and maintenance of the klystron power supplies without risk of damage to the klystron tubes. Utilization aspects of the load were presented along with design details related to personnel safety and equipment protection.

VI. ACKNOWLEDGEMENTS

We thank J. F. Bridges and H. Frischholz for discussions which produced vital input to this project, and to C. Verdico, E. Wallace, and D. Meyer for their efforts in building prototype materials and the test stand.

VII. REFERENCES

- [1] Thomson TH2089A Klystron Amplifier Operating Manual, UTH 2089, November, 1986.
- [2] Technical Specification for Amplifier Tube Power Supply System, Document No. 3104010202-00001, Argonne National Laboratory.

Table 2
Resistor Dissipation Test Data

Type	Flow	Water Temp, °C		Voltage AC, RMS	Current Amps	Power E•I	Power Water ΔT
		In	Out				
Wire 13-ohm	15 gpm	24.05	29.38	552	39.8	21.97 kW	21 kW
	7.5 gpm	24.33	34.27	552	39.8	21.97 kW	20 kW
Comp. 10-ohm	15 gpm	29.33	30.66	435	43.5	18.93 kW	—

Energy Storage Inductor for the Low Energy Booster Resonant Power Supply System

C. Jach, SSCL, USA; A. Medvedko, S. Petrov, BINP Russia;
V. Vinnik, Y. Fishler, UETM Russia

Abstract

The Energy Storage Inductor (ESI) is an important part of the Low Energy Booster (LEB) Resonant Power Supply System. The ESI is a 40 mH, 3400 A, two-legged, picture frame, ONAN-cooled, linear inductor. The ESI is currently under construction at the UETM plant in Ekaterinburg (Russia) as a part of an inter-laboratory collaborative agreement between BINP (Russia) and SSCL (USA). This paper gives an overview of the ESI requirements and describes the design approach and testing methods.

Introduction

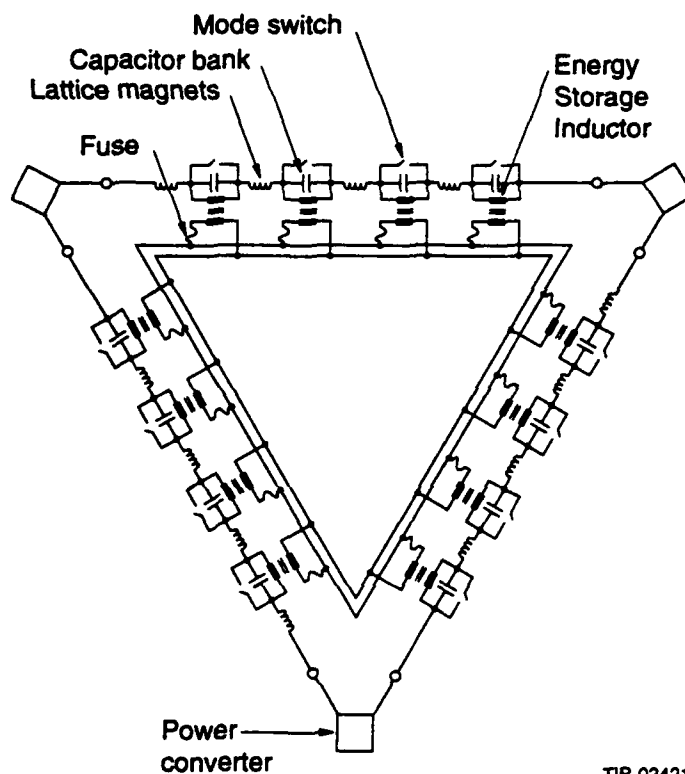
The LEB is a conventional magnet booster that accelerates the proton beam from the Linac (momentum 1.2 GeV/c) to an extraction momentum of 12 GeV/c for beam injection into the Medium Energy Booster of the Superconducting Super Collider. The LEB main magnet system contains 96 dipole and 108 quadrupole (F+D) magnets supplied in series from a Power Supply (PS) system (see Figure 1). The main operating cycle of the booster requires a magnetic field variation from 0.12 T to 1.3 T (in dipole magnets) with 10 Hz frequency. The operating cycle PS system must produce a DC current of 2.2 kA, and AC current very close to sine form with the same frequency and a 10 Hz sinewave AC current with an amplitude of 1.8 kA.

The LEB PS system [1] will contain power supplies connected in series with 12 resonant cells, each having a 10 Hz resonance frequency (Figure 1). Each cell consists of several dipole and quadrupole magnets, and a capacitor shunted by the ESI to provide a path for the DC current. Dividing the resonant system into 12 resonant cells permits a notable decrease in the system voltage to ground. The ESIs are equipped with auxiliary windings connected in parallel with each other. This equalizes the resonant cell parameters and, therefore, the voltage-to-ground distribution. An off-resonance condition in any resonant cell can be detected by monitoring current in the auxiliary windings.

ESI in the Resonant Cell

The principal parameters of the PS system determine the essential ESI characteristics. ESI current is determined from the expression:

$$I(t) = 2200 + 1200 \sin(2\pi \cdot 10t), \text{ (Amp)} \quad (1)$$



TIP-02421

Figure 1. LEB Magnet Power Supply Network

The more significant ESI performance characteristics are presented in Table 1. Very rigid mechanical vibration requirements also were specified.

ESI Design

The ESI consists of a core and coils inside an oil-filled tank (see Figure 2). Radiators on the tank provide a passive system of oil cooling. After comparing different designs [2,3], we found that only an ESI with a closed magnetic circuit containing distributed nonmagnetic gaps and with coils placed around the core of the magnetic circuit can satisfy these difficult requirements.

The ESI core is made of Type 3408 anisotropic, 0.3 mm-thickness, transformer steel according to Russian GOST 21427.1-83. The steel characteristics are presented in Figures 3A and 3B. The total length of nonmagnetic gaps is 475 mm; an average cross-section of the core is about 0.3 square meter.

Table I. ESI Characteristics

Characteristic	Dim	Coil #1	Coil #2
Current, peak	A	100	3400
Current, average	A	-	2200
Current, rms	A	70	2400
Fault current surge, peak	A	800	4000
Voltage across terminals, RMS	V	2300	2350
Voltage to ground, RMS	V	1200	1300
Coil #2 inductances spread at 3400 A current for all ESIs	mH	-	40-41
Inductance nonlinearity (*)	-	<0.01	
Turns ratio coil #1/coil #2		1:1	
Coupling coefficient	-	>0.95	
Hottest spot coil temperature rise above ambient	Cels. deg.	<60	<60

(*) The inductance nonlinearity is:

$$N=[L_{3400A}-L_{1700A}]/L_{3400A} \quad (2)$$

The stored energy distribution through the ESI active part is as follows:

- In non-magnetic gaps, approx. 84%,
- In the magnetic core, less than 1%
- Elsewhere, approx. 15%

This distribution of the stored energy depends upon the physical design, as well as upon the characteristics of the steel used. The steel has high relative magnetic permeability (up to 70,000) in rolling direction, and high value of saturation induction [B(sat) approximately equal to 2 Tesla]. With a 3400 A current in the main coils, the average B field in the core is 1.6 T. Since the relative magnetic permeability for this field is 40,000, the core is not saturated.

The energy distribution and the required value of coupling coefficient between the coils (>0.95) also influences the coil design. The high current coil (#2) was developed as two pairs of concentric windings on each core leg. The low current coil (#1) is divided into two windings, with one placed on each core leg in the space between concentric windings of the high current coil. The windings are epoxy-impregnated. The weight of the coils is approx. 6,000 kg. The total ESI weight (with oil) is approx. 55,000 kg.

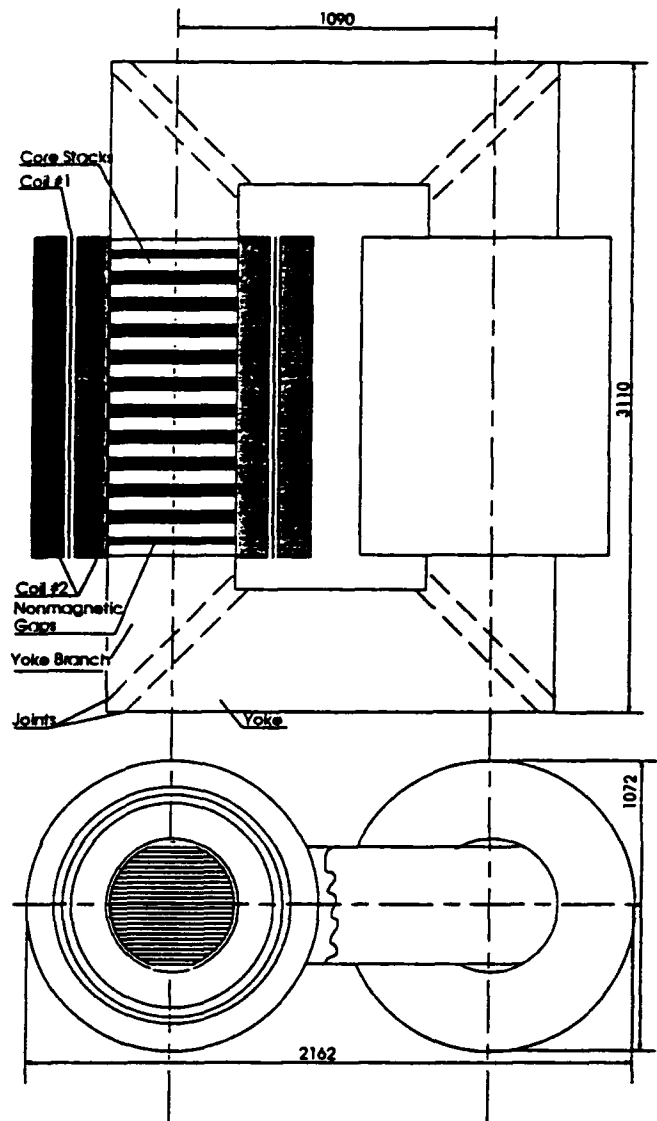


Figure 2. ESI Construction

ESI Inductance Nonlinearity

The inductance was calculated with the help of the "MAG-3D" program developed by scientists from BINP [4] for three-dimensional DC magnetic field calculations. The simulations showed the most saturated areas to be the joints between the top and bottom yoke and columns. Of the calculated -0.4% nonlinearity, -0.35% was attributed to the joints. The static inductance and its nonlinearity are measured indirectly. It is useful here to recall the definitions of static and dynamic inductances, as:

$$L_{st} = \frac{\Psi}{I} = \frac{1}{I} [aI + bI^3 + cI^5 + dI^7 + eI^9] \quad (3)$$

$$L_{dyn} = \frac{d\Psi}{dI} = a + 3bI^2 + 5cI^4 + 7dI^6 + 9eI^8 \quad (4)$$

where: L_{st} , L_{dyn} are static and dynamic inductances
 Ψ is magnetic flux
 I is dc current in the ESI
 a , b , c , d , and e , are polynomial coefficients.

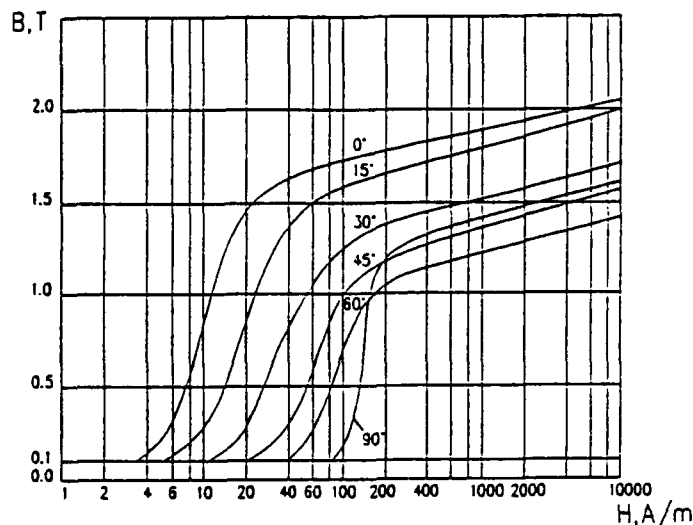


Figure 3A. B/H Curves for 3408-Type Steel in Measuring Under Different Angles in Steel Rolling Direction

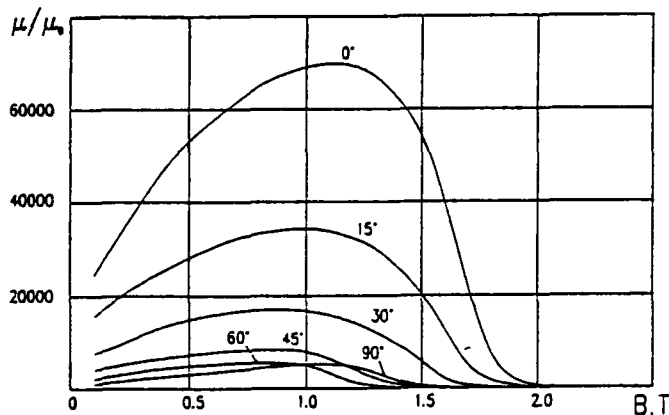


Figure 3B. Induction Dependence of Relative Magnetic Permeability for 3408-Type Steel in Measuring Under Different Angles in Steel Rolling Direction

Dynamic inductance measurements are performed at several DC current levels with superimposed small AC excitation. The computer program calculates polynomial coefficients of dynamic inductance using a curve-fitting routine and calculates values of

static inductance and its nonlinearity for DC currents ranging from 1700 A to 3400 A.

Mechanical Vibration

The level of ESI vibroactivity is dependent on the active part vibration, and is produced by electromagnetic forces and magnetostriction forces associated with the presence of magnetic fields excited by the AC and DC currents of the ESI coils. Mathematical models of ESI vibroactivity were developed. The ESI active part model consisted of 28 finite elements, ESI tank with radiators of 305 elements. Oil was considered as additional mass, and the foundation as the tank base attachment. The calculations show that the maximum amplitude of the oscillations will be 70 micrometers for the active part, and 25 micrometers for the tank.

Test Results

The ESI prototype was manufactured at the UETM plant (Ekaterinburg, Russia) and was tested in February, 1993. This unit satisfied all specified requirements. Results of some of the tests are:

- Static inductance - 40.667 mH
- Static inductance nonlinearity - 0.0092
- Coupling coefficient - 0.97
- Vibration Level - 40 micrometers at the nominal current excitation

Manufacturing Plan

All ESIs will be manufactured during 1993 and delivered to the SSCL site no later than January 1994.

References

1. C. Jach, "Switchable 10Hz/1Hz LEB Magnet Power Supply System," SSCL-407, May, 1991.
2. D. Pavlik, "Engineering Design Considerations for the Energy Storage Inductor used in the LEB Power Supply," Westinghouse Electric Corporation Science and Technology Center, Pittsburgh, PD.15235, Rev: 920306.
3. European Synchrotron Radiation Facility, "ESRF Foundation Phase Report," Grenoble Cedex, February, 1987.
4. M. Tiunov, B. Fomel, "Three-Dimensional Magnetic Field Calculation Program," Preprint-INP-83-150, BINP, Novosibirsk, Russia, 1983 (in Russian).

A High Power Water Cooled Resistor For the High Voltage Power Supply in the TRIUMF RF System

K. Jensen, G. Blaker, R. Kuramoto
TRIUMF, Vancouver, B.C., Canada V6T 2A3

Abstract

The Triumf RF system high voltage power supply requires 0.5 ohm current limiting resistors to protect amplifier components during transients and crowbar operations. The crowbar typically causes a 16,000 amp transient pulse, followed by a 4,000 amp current for 55 ms until the circuit breaker opens. The resulting stresses produced catastrophic failure of the original design within 100 crowbar cycles. A new resistor design has been developed to improve heat transfer characteristics and reduce current densities. Design changes were evaluated during extensive testing of a full scale model. The test results are reported with the resulting design described in detail.

I. INTRODUCTION

Continental Electronics supplied the high voltage power supply for the main cyclotron RF system with four water-cooled resistors in its circuit. The resistors are used as current limiting devices, and serve to protect other power supply components and the power amplifiers from current transients. This circuit is shown in Figure 1. R10 limits the current that charges the capacitor banks after the initial charging period when energizing the power supply. R58 and R59 act as current limiting devices for the amplifiers, as well as limiting the crowbar current through the ignitron tube. R60 does not see any crowbar current, and simply limits current to the amplifiers.

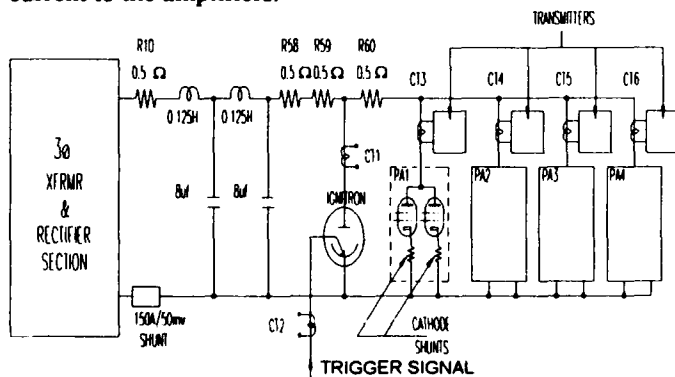


Figure 1. Simplified Schematic of Power Supply

The resistors were supplied as Nichrome wire wound on an epoxy glass G10 core. Bifilar winding was used to reduce the inductance of the 200 in. long wire used. The wound core measures 22.75 in. long and is housed inside a 3.0 in. dia. pipe. Water was supplied to the resistors via 1 inch flexible plastic hoses at 17 USG PM and 55 psig, with the water connections in series.

The power supply operates at a nominal 20 kV. and draws 65 amps. In this state each resistor must dissipate 2.1 kW continuously. During a crowbar event the power dissipation spikes to 128 MW per resistor, then settles back to 8 MW for 55 ms. before ramping down. Figure 2 shows an oscilloscope trace of the peak output current during a crowbar. Figure 3 shows the output current for the duration of the 55 ms until the circuit breaker opens. This type of operation puts extreme stress on the power supply components and has resulted in numerous failures. Crowbars occur on an average of ten per month with resistor failure recorded in as little as two crowbars.

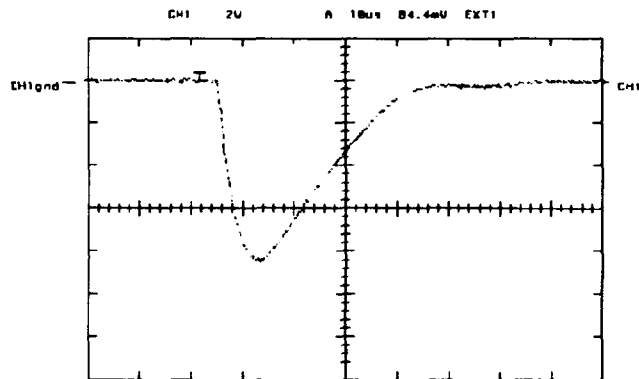


Figure 2. Peak current during a crowbar.
Calibration is -0.00052 V/A

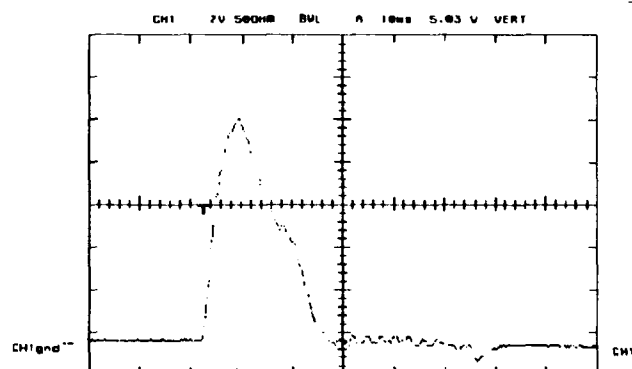


Figure 3. Power supply current for duration of crowbar.
Calibration is 0.005 V/A

There are no cases of resistor failure not associated with a crowbar event. However, the crowbar current limiting resistors were not the only ones to fail. The resistor limiting current to the capacitor banks, R10, often failed in dramatic fashion.

II. HISTORY

There were two distinctly different forms of resistor failure exhibited, passive failure where the winding simply melted to produce an open circuit, and catastrophic failure where the resistor exploded. The passive failure could be attributed to overloading of the resistive wire or insufficient cooling. There is no evidence to indicate if the effect developed gradually or rapidly.

The catastrophic failure was clearly a case of instantaneous pressure surge. The one inch thick PVC flange would often shatter while the flexible line 4 inches away would remain intact. The pressure relief valve located 12 inches away and set to 125 psi. never tripped yet the force to break the PVC flange required an internal pressure of 2000 psi. Thus the event that would cause the resistor housing to explode must have been a dynamic blast, possibly caused by instantaneous boiling of cooling water into superheated steam. The effects of this blast were absorbed within a very localized area. This would account for explosive failure of stronger materials while adjacent, weaker materials did not even yield.

In the 12 month period before the new design was implemented there were seven resistor failures recorded. This accounted for approximately 22 hours of lost beam time which was 13% of the RF total for the year.

III. HEAT GENERATION

Investigation of the failures included a reconstruction of a shattered housing to determine the location of the center of the explosion. This confirmed our suspicions that the source of the problem was the termination point where the core winding was connected to the terminal plate. The joint consists of two sections of Nichrome wire, approximately .080" dia., wrapped under the head of a bolt which compresses the wire against a copper conductor. The conductor is attached to the terminal plate by a small copper angle. The terminal plate consists of a 0.250" thick copper plate with cutouts for coolant flow.

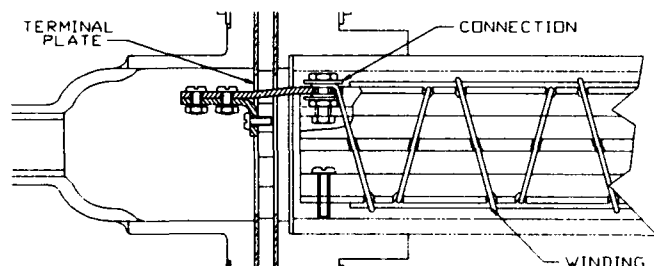


Figure 4. Original Resistor Design

The connection problems are related to current density. With peak currents reaching 16,000 amp. the contact area proved to be insufficient. The maximum contact area with a single wrap of wire under the head of a 1/4-20 NC bolt is

estimated to be .100 to .150 square inches. The corresponding peak current distribution is 160,000 amps per square inch, assuming maximum contact has been achieved.

The exact effect these conditions produce is difficult if not impossible to predict. However, what is clear to see is the wire melted at the connections and the core scorched where the wire has been burned away when a resistor fails. A new connection method was required. Previous efforts to form a fused connection with various soldering techniques had met with failure. This combined with concerns about altering the wire's characteristics with the application of heat and a desire to keep assembly and repair as simple as possible produced a design requirement that the connection maintain a clamped configuration.

Several different connection techniques were evaluated with consideration given to area of contact, ease of manufacture and assembly. The new design is referred to as the connection pod. It resembles a one inch diameter copper bullet with two inches of each wire inlaid at the center. This provides four to five times more surface area for electrical contact and a more predictable path of current flow. In the old design there was a potential for one wire to carry the current of both, resulting in overload and failure.

IV. HEAT TRANSFER

In the heat generation analysis we found the nut and bolt connection to be the main problem source. The method provided inconsistent electrical contact area at the bolt, but its major drawback was the poor coolant flow around the joint. Figure 5 shows how the flow is divided into six passages by the core fins. Entrance to these passages is impeded by the stems of the copper terminal plate.

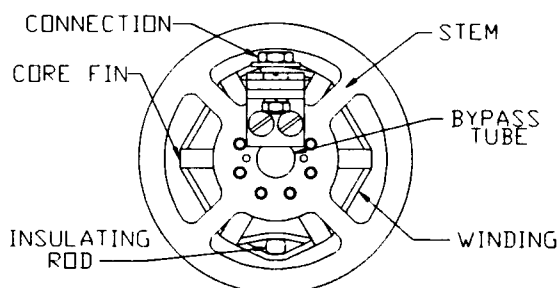


Figure 5. Coolant Passages in old design

The critical passage contains the wire connections which produce the highest temperatures. It also is one of two passages where the bifilar windings cross. This not only concentrates the heat sources but the windings are separated with an insulating rod which further restricts coolant flow.

Another complication comes in the form of stand offs which center the core within the housing. Two of these are located in the critical passage. Thus we have a design with the major sources of heat combined in a passage with all of the restrictions to flow.

One last complication comes from the fact that the center of the winding core was designed to provide a bypass tube to allow some of the coolant to miss the resistor windings. This was done because the resistor's coolant flows in series and the designers presumably were trying to ensure a good supply of fresh coolant reached the downstream resistors. This bypass may work too well at providing a low resistance route for the water. It is estimated that a mere eight percent of the coolant actually passes through the critical passage. That translates into less than 1.5 USG PM. flow of a fluid corrupted by cavitation and stagnant sections. The best flow occurs in the passages that only have to cool the windings, not the connections. These three passages receive 16 USG PM.

Connector designs were evaluated for restriction to flow, generation of turbulence, cavitation and even distribution of coolant in an effort to maximize heat transfer capability. Since there is a connection at both ends of the resistor the design must flow well in both directions. The result was a series of design changes including;

- Removing the connection from within the resistor body.
- Blocking the central bypass tube.
- Reducing winding support fins from 1/4" to 1/8" thick.
- Eliminating the winding separator rods.
- Eliminating the core stand offs.
- Reducing the number of stems on the copper terminal plate from six to two.
- Aligning the remaining stems with the core fins.
- Reducing the winding diameter to increase the clearance from resistor wall.

The final design is shown in figures 6 and 7.

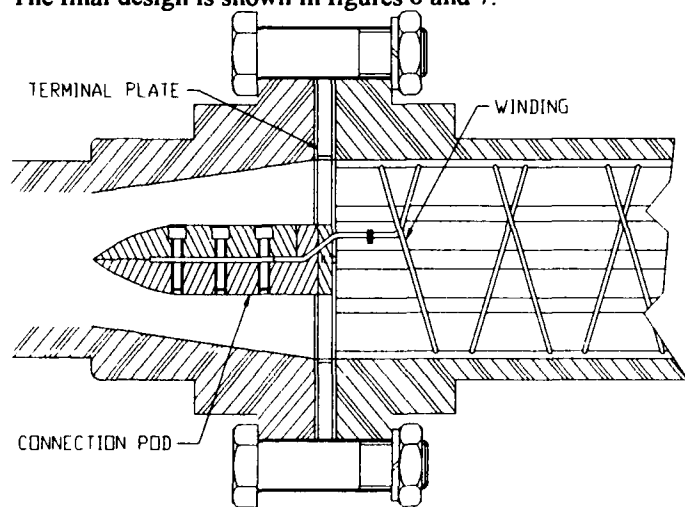


Figure 6. New Resistor Design

The final bullet shape of the connecting pod was found to produce the least disturbance in the coolant flow, resulting in an even flow with no stagnant sections. It provides a substantial thermal mass to absorb surges and distribute the heat flux, thereby reducing surface temperatures. The resulting large surface area greatly improves heat transfer to the coolant, further reducing temperatures.

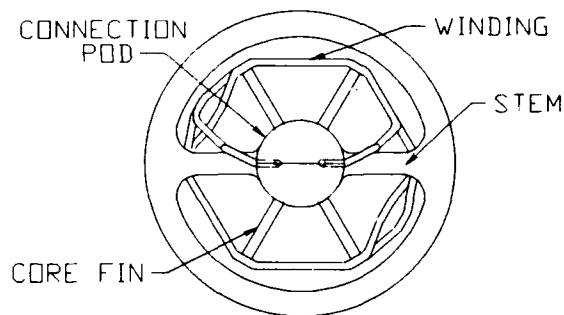


Figure 7. Coolant Passages in new design

The pod is split at the centerline and clamped with three fasteners. This provides simple removal and reassembly without solder. The top pod half encloses half of the wire while the remainder is laid in the bottom pod. A great deal of care is required to fit the wires into the pod halves. We were able to limit the pod center gap to a maximum of .0015 inch on assembly. Several techniques to eliminate the gap were tested including using a displaceable soft metal filler such as Indium. We found that the small improvement they offered did not justify the additional complication. The carefully fitted wire and pod connector suits the design requirements of good contact and ease of reassembly.

With these changes we eliminated the resistor as the limiting factor in the heat transfer equation. The resistors will now flow all of the water that the system can supply. The one inch supply line was upgraded to two inches which, when limited to 10 ft/sec to avoid cavitation, offers a supply potential of 98 USG PM. The flow to the resistors is regulated to 90 USG PM. at 65 psi.

The new resistor is capable of absorbing large power surges by distributing the effects over a large volume and removing the resulting heat with high efficiency and capacity. Under steady state conditions the cooling system keeps the resistor at the water supply temperature. When a crowbar occurs local temperatures will rise but they will be kept below destructive levels and quickly returned to the supply temperature. The oversized cooling capacity will also eliminate the possibility of gradual overheating and resultant deterioration of the nichrome wire during steady state operation. We have also virtually eliminated air pockets, bubbles and cavitation in the resistors to remove the explosive potential.

In the seven months since the new resistors were installed there have been approximately 90 crowbars with no resistor failures or related RF down time.

V. ACKNOWLEDGMENT

The authors wish to recognize Josef Holec and Gus Mannes, whose assistance during testing and input during the design evaluation process was invaluable.

Filament Power Supply Improvement of the TRIUMF RF System

Amiya Kumar Mitra and Joseph J. Lu

TRIUMF

4004 Wesbrook Mall, Vancouver, BC, Canada V6T 2A3.

Abstract

The TRIUMF rf system, operating at a fixed frequency of 23.06 MHz, employs four push-pull power amplifiers using eight EIMAC 4CW250,000 tetrodes. The filament power supplies for the above tetrodes uses simplified 3 phase SCR control circuits to slowly ramp up the output voltage. Failure of SCR's during ramping and also during power bumps has been a source of rf downtime. A new SCR control scheme has been developed and tested which relies on the fact that the secondary output voltage from a 3 phase transformer will be 57.7 % of it's rated output voltage if only two phases of the primary are connected. In this scheme, one phase is connected directly and the second phase is connected through two SCR's of which the conduction angle is controlled by a slow ramp. The third phase is initially blocked by two SCR's which are turned on fully after a fixed delay thereby limiting the surge current of the filament during start up. A greatly simplified firing circuit and smaller number of components has improved the reliability and the performance of such a power supply. Also, an alternate scheme of a power supply with series resistors in the primary of the transformer is described.

I. INTRODUCTION

The TRIUMF rf system [1] and [2] operates at a fixed frequency of 23.06 MHz with a power capability of 1.8 MW. Four push-pull power amplifiers employing eight EIMAC 4CW250,000 tetrodes generate the required power. Since the cold resistance of the filament is much smaller than the nominal resistance (11.5 V/ 900 Amps), slow ramping of the output voltage of the filament power supply is needed to limit the surge current to its rated value. The original power supply uses three phase transformer, full wave rectifier, choke and filter capacitor to produce the required rated dc voltage and current. It employs one SCR and one diode back to back in each phase in the primary of the transformer. It means only half of the cycle is controlled. Small unbalances among the trigger signals in three phases may trip off the AC circuit breaker or even damage the SCR's during the ramp up period. Many hours of beam time was lost due to the malfunction of these power supplies. Also, repairing of these power supplies was time consuming due to the fact that various voltages and time constants in the firing circuit of the SCR's had to be set precisely to obtain balanced triggering for all the SCR's. Various options for the filament power supplies were considered and a new SCR control circuit has

been designed. This circuit only controls the conduction angle of one phase. The second phase is always connected and the third phase is turned on after a fixed delay, with SCR's acting as a switch. An alternate scheme using a power supply with series resistors in the primary of the transformer was used as a quick interim solution.

II. POWER SUPPLY REQUIREMENTS

The filament power supply for the EIMAC 4CW250,000 must fulfill the following requirements:

Rated maximum output voltage : 11.5 V dc.

Rated maximum output current : 900 Amps.

Maximum surge current must be limited to 1800 Amps.

The maximum in-rush current of the 440 V ac circuit breaker should not exceed 15 Amps.

III. SINGLE PHASE CONTROLLER

The single phase controller uses two SCR's, SCR1 and SCR2, back to back of which the conduction angle is controlled by a ramp voltage such that in about 20 seconds 57 % of the rated filament output voltage is gradually established. This is due to the fact that when only two phases of a three phase transformer are energized 0.577 of the nominal output voltage is obtained. The filament is heated under this voltage for about 20 seconds, its resistance rises

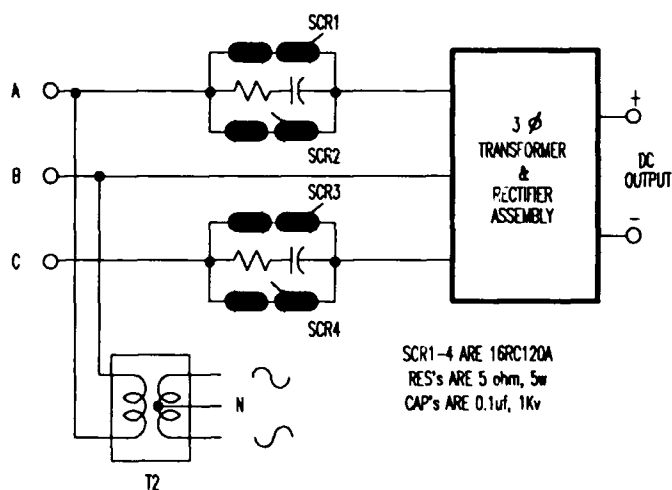


Figure 1. Basic scheme of the single phase SCR controller.

to nearly 80 % of it's rated value. The third phase is then fully turned on by switching on SCR3 and SCR4 to achieve the full rated output voltage and the surge current is limited to 1.25 times the nominal filament current of 670 Amps.

Figure 1 shows the basic scheme of the single phase SCR controlled circuit . T2 is a 480 to 30 Volt transformer which provides 1): the phase reference for the control circuit, and 2): the ac source for the controller's dc supplies.

Circuit Description

Figure 2 is the block diagram of the system which consists mainly of a dc supply for the controller, a ramp generator, a 20 kHz oscillator, firing angle control circuit, three trigger drivers and a counter to provide 20 or 40 seconds delay. The system is constructed on two circuit boards. The ramping board consists of the dc supply, the ramp generator and the 20 kHz oscillator and the firing board consists of the rest of the building blocks.

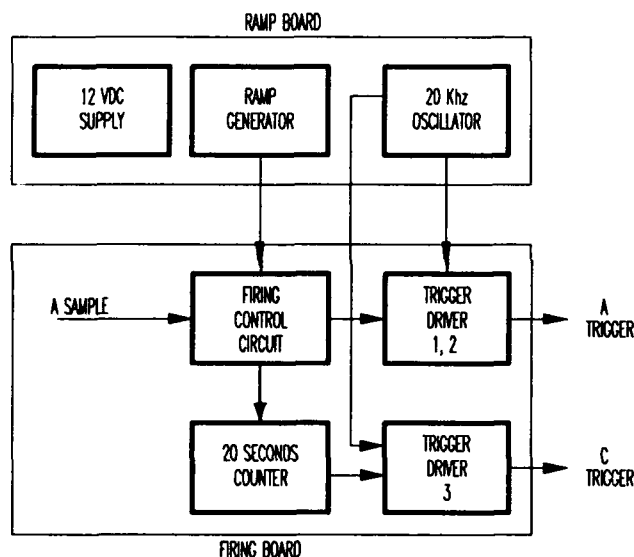


Figure 2. Block diagram of single phase controller.

The ramping board circuit is shown in figure 3. The 20 kHz signal is produced by the 555 timer IC3, it's output is amplified by the emitter follower Q1 to provide adequate drive power for the trigger. C7 is a power up reset capacitor to prevent unwanted SCR triggering when the power is turned on but the control is not yet established . The ramp voltage of -10 to +11 V is generated by charging up C10 slowly with negative pulses produced by IC4 and Q2 and is available at the emitter follower output of Q4. The ramp slope can be adjusted by varying the value of resistor PT1. Diode D7 is to prevent the capacitor C10 from discharging when Q2 is off. D9 discharges C10 when control power is off. This ensures that the ramping voltage will start from -10 Volts every time the power supply is turned on.

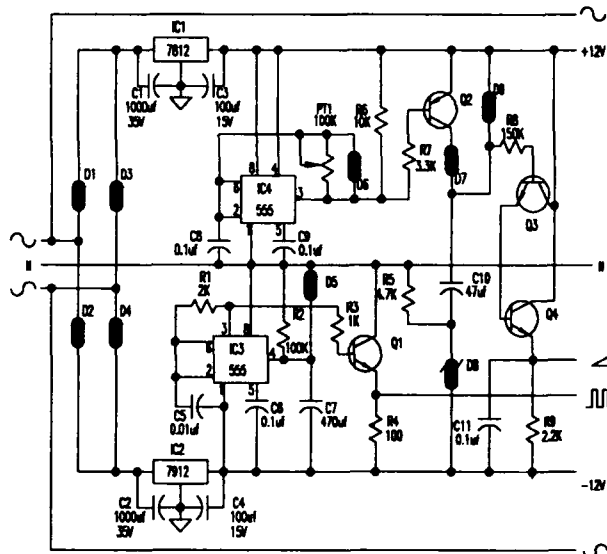


Figure 3. Schematic of ramping board.

The firing circuit, shown in figure 4, provides trigger signal for all the four SCR's. The output of the integrator IC1, which is 90 degrees leading from the sample input of phase A, is compared with the ramp voltage. For the positive half cycle of the input phase, when the output of IC1 is lower than the ramp voltage, the output of IC3 will go high enabling Q1 to amplify the 20 kHz signal. This signal is rectified by D9 as the trigger signal for SCR1. Therefore, as the reference voltage ramps from -10 volts to 11 volts, the conduction angle of SCR1 gradually increases from zero to full conduction. For the negative half cycles of the same phase, IC2, IC4 and Q2 generate the trigger signal for SCR2. Since the third phase is fully blocked during this period, a little unbalance in trigger signal will not cause large current in one phase to trip off the AC circuit breaker or to damage the SCR's,

The 20 second time delay for firing SCR3 and SCR4 is obtained from the 12 bit counter IC6. The counter is constantly reset till the output at IC4 goes to a steady high. After 20 seconds of counting, Q_M of IC6 goes high, disabling the clock so that Q_M remains high. Q4 is then enabled and amplifies the 20 KHz signal to provide the firing voltage for SCR3 and SCR4.

IV. SERIES RESISTOR CIRCUIT

This type of filament power supply evolved as a standby emergency solution when the old 3 phase 3 SCR controlled power supplies failed. This configuration is shown in figure 5 where three 16 ohm resistors are provided by cooking range elements, and are connected in series with the primary of the transformer to limit the initial surge current as the 480 Volts ac source is turned on.

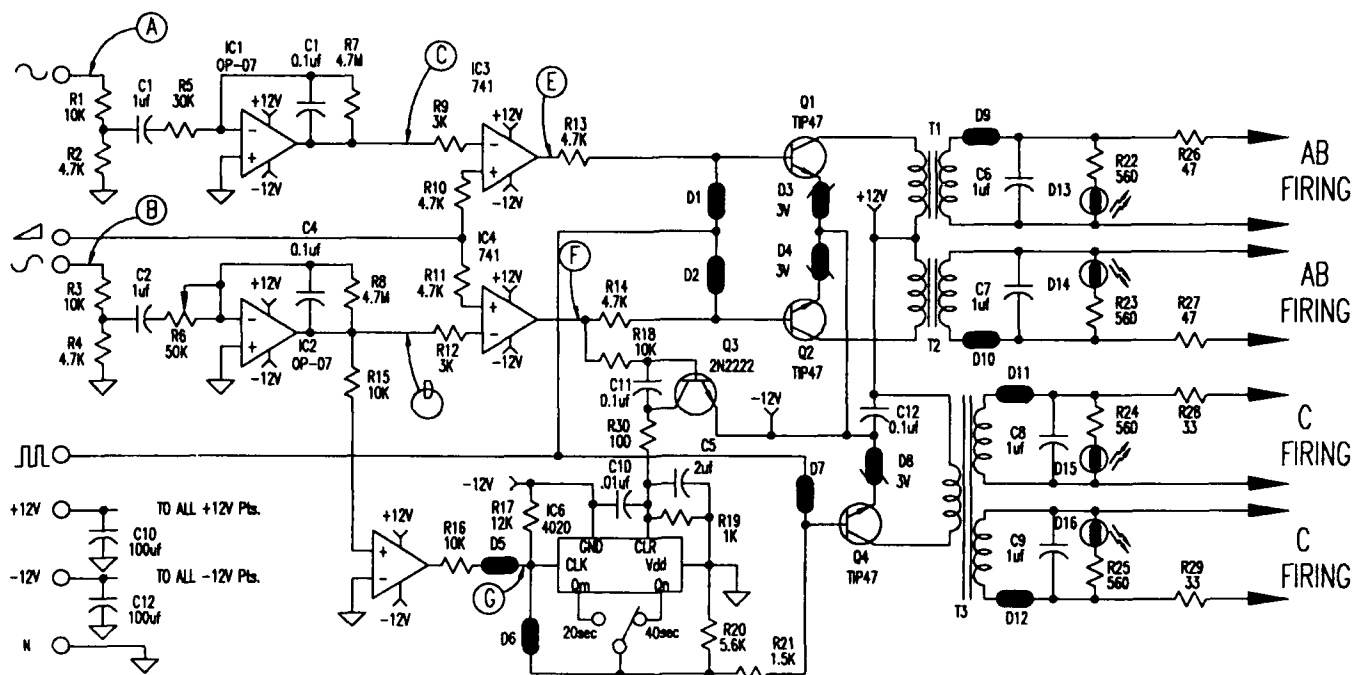


Figure 4. Schematic of firing board.

A time delay relay provides a delay of 20 seconds to allow the filament to reach about 80 % of its resistance and the series resistors are then bypassed. In case of power bump or loss of mains, the time delay relay restarts. The resistors are mounted in a box outside the filament power supply housing and provision is made such that after the filament has reached it's rated voltage and current, the resistor box can be disconnected from the power supply and used for another supply.

IV. CONCLUSIONS

The newly developed single phase controller has worked for a period of six months without any failure. At present all the eight filament power supplies are being modified with this new type of soft start circuit.

V. ACKNOWLEDGMENTS

The authors wish to thank Roger Poirier for encouraging the development of such power supplies. Thanks are also to Glen Blaker, Marek Lipnicki, Richard Shanks, Bruce Whiteside, Joseph Hlek and Gus Mannes for their help in assembly, testing and troubleshooting the power supplies..

VI. REFERENCES

- [1] K.L. Erdman et al, "TRIUMF amplifier and resonator system," Proceedings of the 6th International Conference, AIPCP 9, 451(1972).
- [2] R.H.M Grummer, R.L. Poirier and M.Zach, " TRIUMF rf system - initial operating problems and their solutions," Proceedings of the 7th Conference on Cyclotrons and their applications, pp. 167-170(1975).

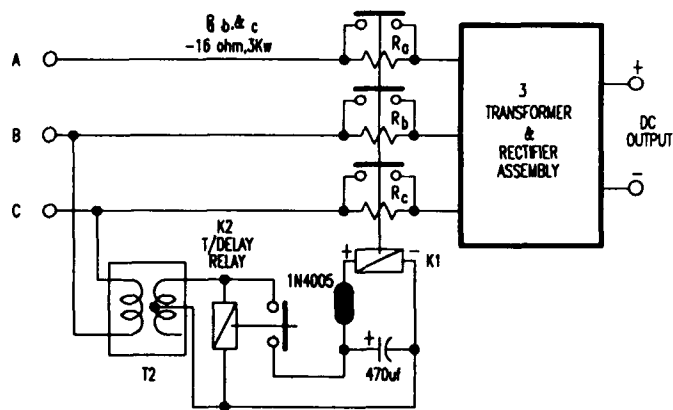


Figure 5. Schematic of series resistor circuit.

Advances in the Development of the Nested High Voltage Generator

R.J. Adler and R.J. Richter-Sand

North Star Research Corporation,
9931 Lomas, NE, Albuquerque, NM, 87108

I. Introduction

The Nested High Voltage Generator (NHVG) is a high voltage accelerator/power supply topology which can potentially satisfy a variety of requirements for a compact, reliable inexpensive DC accelerator in the 0.25 - 10 MeV range. Applications for this technology include the generation of high voltage, high current pulsed electron beams for microwave generation, the sterilization of medical products, the curing of polymers, and the sterilization of medical waste. This technology has recently been demonstrated in an accelerator which has operated at 500 kV with an electron beam in a 36 inch long, 17 inch diameter device.

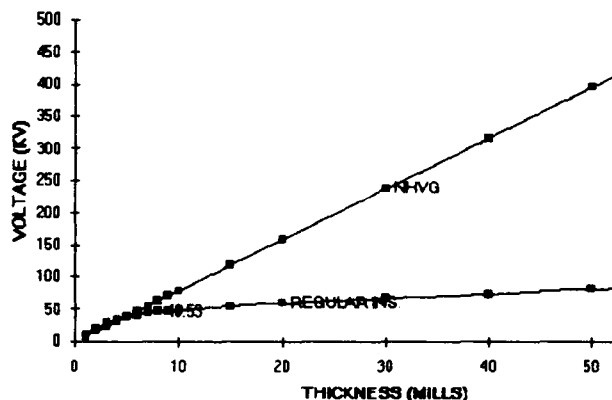


Figure 1. Maximum voltage as a function of insulation thickness from the Handbook for Electrical Engineers.

In this paper, we briefly describe the technology, and the operation of 3 machines built since the initial discussion of the technology in the 1991 Particle Accelerator Conference Proceedings¹. The operation of a machine at up to 500 kV and 83 % efficiency has been demonstrated, and is particularly noteworthy.

II. Description of Nested High Voltage

There are two critical generic questions in the design of a high voltage, high power accelerator--how do you insulate the voltage ? and how do you get the power required into the high voltage system? Traditional DC systems include the Insulated Core Transformer (ICT), the Van de Graaf or Pelletron, the Cockroft Walton, and the Dynamitron. These systems all use gas (typically SF₆) insulation and they have varying power supply systems including electrostatic charge motion (Pelletrons/Van de Gaafs), capacitive coupling (Dynamitron), conventional transformer cores (Insulated core transformer), and voltage multipliers (Cockroft-Walton).

The primary motivation for the development of the NHVG was the requirement to significantly reduce the size of a DC accelerator, and the primary means of reducing the size was to use solid insulation in order to decrease the diameter of the machine. The fundamental problem of solid insulation is that as the voltage increases, the allowable electric field for insulation drops. This is illustrated by the standard data shown in Figure 1^{2,3,4}. The straight line of Figure 1 shows the insulation trend if the voltage across a single insulator is rigidly subdivided.

The NHV concept is that the only way that the voltage can only be subdivided uniformly without voltage concentration in a fault mode is to split the high voltage structure into nested Faraday Cages in which each one has it's own power source. The power is supplied to the Faraday cages by allowing azimuthal electric fields (axial magnetic fields) into the individual cages. In this embodiment, the NHVG is a distributed air core switching transformer with each coil/power supply coupled to it's own insulation.

An intrinsic advantage of the NHVG relative to other DC generators is the way that the segmented voltage system affects the behavior of the system components in case of a fault mode as shown in Figure 3. Because each vacuum interface (hatched element in the figure) is associated with it's own capacitance, and there is no other total system capacitance, the voltage in a fault does not exceed the ambient voltage. In DC accelerators, spark gaps are placed along the

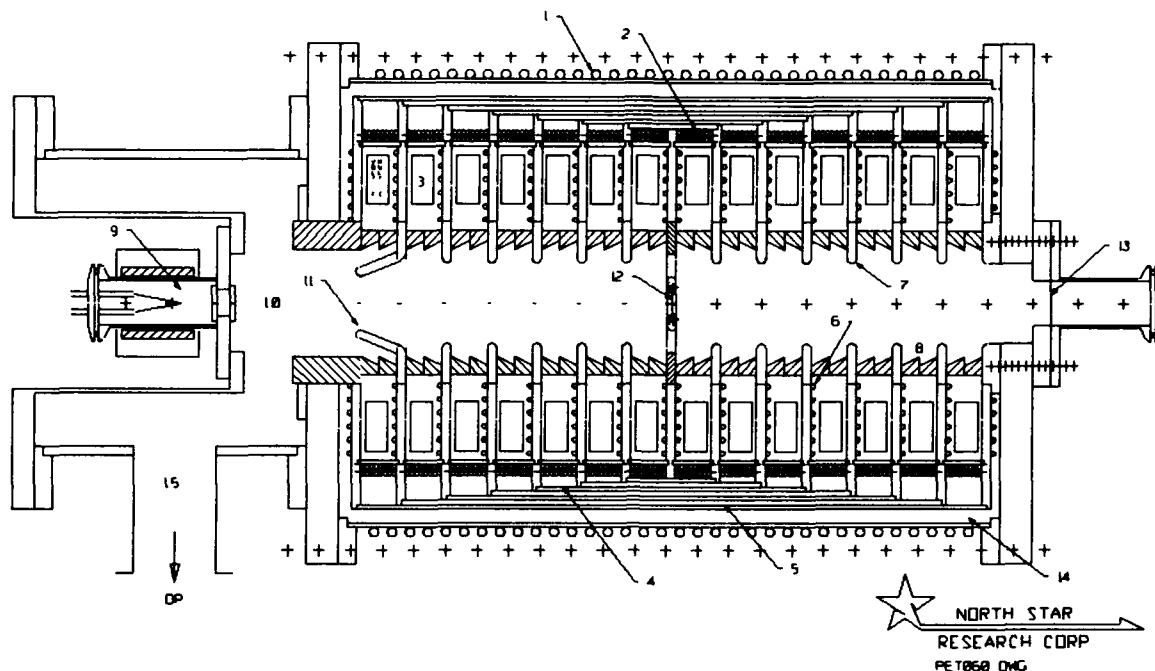


Figure 2. Detailed schematic of the PET NHVG negative ions. 1)Primary winding 2)Secondary winding 3)Voltage multiplier 4)Conducting shell 4)Insulator 6)Conductor 7)Grading ring 8)Vacuum insulators 9)Ion Source 12)Stripping foil.

column to prevent voltage transients from building up, but even with spark gaps, components are subjected to 3 time the ambient voltage because the pulsed hold-off voltage of the spark gap is typically 3 times the DC hold-off voltage.

The most common machine fault modes involve flashover along the insulators, and we have designed the accelerator with resistance between the nested conductors and the associated vacuum electrode. This means that almost all of the stored energy is dissipated in resistors in the case of a fault.

A typical cross-section of an NHVG is shown in Figure 2. Insulation is provided in the radial direction by multiple layers of high dielectric strength film, and in the axial direction by a combination of plastic film or sheet, and dielectric fluid (oil). All films are impregnated with thin layers of this fluid. The potentials of each stage are defined by axial, cylindrical, conducting metal sheets which form the outer and inner boundary of each stage. These sheets are terminated on the ends by spiral conductors which are used to connect the grading rings on the insulator stack to the cylindrical metal sheets. No electrical connections are made between stages except by the conducting sheets.

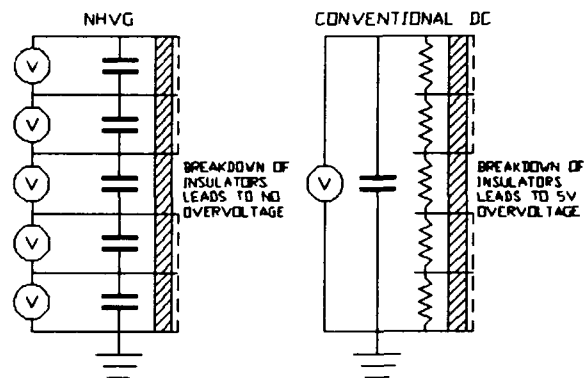


Figure 3.

Nested High Voltage and DC accelerators in a fault mode. The NHVG fault mode voltage does not exceed the operating voltage. The DC accelerators is subject to extreme over-voltage.

III. Existing Accelerators

Work on this concept has been supported by a number of agencies. In the work of reference 1, an 11 inch diameter, 30 inch long device with 1 cm. of total radial insulation was operated at 150 kV. Since the writing of that article, that device has been operated at up to 300 kV. Three other devices have also been operated.

500 kV Tandem Accelerator

A 500 kV tandem accelerator has been built and tested at full voltage (albeit with an electron rather than ion beam load). That device was designed for Positron Emission Tomography applications and has been operated successfully to test the sterilization of medical products under contract to a major medical manufacturer.

The efficiency of the 500 kV NHVG has been tested at low powers and is found to be as high as 83 % in operation at 60 kV. This level of efficiency is expected to scale to much higher powers. The distributed air core transformer can be very efficient. Both solid state and tube based power supplies have been used in testing this device.

A unique feature of the NHVG is the ease with which power can be supplied to the terminal of the device by providing primary/secondary combinations tuned to different frequencies. We demonstrated this on the 500 kV NHVG in electron beam mode.

200 kV Accelerator for Well Logging

A 200 kV device with a 4 inch diameter has been successfully tested at NSRC. This device accelerated electron

beams up to 200 kV using a Cockcroft-Walton type power system. We believe, based on the test data from this device, that MeV level accelerators can be built with diameters of 4 inches. This work was supported by the National Science Foundation.

300 kV Pulsed Beam Accelerator

A 300 kV device has been built to test operation of the NHVG in DC operation with grid controlled pulsed beam extraction. In operation with a ceramic accelerating column and a dispenser cathode, beams with currents of up to 80 amperes were accelerated for 200 ns. pulses at repetition rates of up to 200 Hz. This type of power system is capable of operation at repetition rates up to 10 kHz. depending on the details of grid dissipation and the prime power system.

Systems of this type have been designed to operate at 1 kA and 200 Hz. with 200 ns. pulses for applications to linear colliders, and at 100 amperes and 5 kHz. with application to high power microwave generation. Work in this area has been funded by the Department of Energy and the US Army Research Laboratory.

IV. Conclusions

The NHVG has been demonstrated to be both versatile and useful. To date, with 4 accelerators tested, we have experienced no problems with dielectric breakdown. The NHVG principle will allow a new class of inexpensive DC accelerators to be used in a variety of industrial and research applications.

References

1. R.J. Adler, and R.J. Richter-Sand, Proceedings of the 1991 Particle Accelerator Conference, IEEE, 1991. See also R.J. Adler, US Patent 5,124,658.
2. J.P. Shannon, S.F. Philip, J.G. Trump, "Insulation of high voltages across solid insulators in vacuum," Proc. First International Symposium on Insulation of High Voltages in vacuum, M.I.T., Cambridge, MA, October 1964.
3. R.V. Latham, High Voltage Vacuum Insulation: The Physical Basis, Academic Press, 1981.
4. Fink and Carrol, "Standard Handbook for Electrical Engineers", 10th Edition, McGraw-Hill, New York Section 4-301.

High-Power Klystron Modulator Using a Pulse-Forming Line and Magnetic Switch

Mitsuo Akemoto and Seishi Takeda
KEK, National Laboratory for High Energy Physics
Oho 1-1, Tsukuba, Ibaraki 305, Japan

Abstract

A new type of klystron modulator has been developed for the Japan Linear Collider. It consists of a pulse-forming line (PFL), a pulse transformer and a magnetic switch. In order to realize a compact modulator, a triplate strip transmission line using deionized water as a dielectric was adapted for the PFL. A preliminary test has shown that an output pulse with a peak voltage of 600 kV, a pulse length (flat-top) of 460 ns and a rise time of 153 ns can be generated for a dummy load with an impedance of 500 Ω .

I. INTRODUCTION

In the rf system of the Japan Linear Collider (JLC), X-band klystrons with a peak rf power of 100 MW-class and a pulse width of 400 ns, and their modulators are necessary to obtain the designed accelerating gradient of 100 MV/m [1]. Since the pulse width for the X-band is particularly short, short rise and fall times are required for the modulator in order to obtain high efficiency. Moreover, a high-reliability modulator of compact size is necessary, since JLC is a large-scale accelerator system with ~ 3,600 klystrons. For X-band klystrons of the JLC [2], a conventional modulator using a thyatron and a pulse-forming network (PFN) has been developed [3]. However, it is difficult for this PFN-type modulator to realize these requirements. Especially, the lifetime of the thyatron is a serious problem for stable operation of JLC. The modulator using all-solid-state components provides the nearly endless lifetime. An all-solid-state modulator prototype has been designed, and a discharge unit has been constructed. In this paper, the design, specifications and results of performance tests of the discharge unit are described.

II. DESIGN

A. Specification

Table 1 gives the specifications of the X-band klystron modulator. The output impedance of the modulator depends on the micro-perveance of the klystron. Although the impedance of the prototype X-band klystron is on the range of 1~2.5 k Ω , the impedance of the modulator was designed to be 500 Ω , considering the following points: (1) The modulator system of that a single modulator provides power to more than two klystrons is one of the suitable methods to reduce both the cost

and size. (2) A low output impedance is preferable for short rise and fall times.

Table 1
Specifications of the X-band klystron modulator

Output pulse voltage	600 kV
Output pulse current	1200 A
Output impedance	500 $\Omega \pm 16\%$
Pulse rise time	150 ns
Pulse length(flat-top)	400 ns
Pulse height deviation from flatness	< $\pm 1.0\%$
Pulse repetition rate	50 pps

A simplified diagram of the whole modulator system is shown in Figure 1. This system consists of a 10 kV dc power supply controlled by SCRs, a capacitor bank, a two-stage saturable reactor, a water-filled PFL and a pulse transformer. A pulse triggered by the GTO switch is transferred from C1 to the PFL by increasing the voltage through the 1:8 pulse transformer. The pulse is finally transferred from the PFL to a klystron load through the 1:15 pulse transformer.

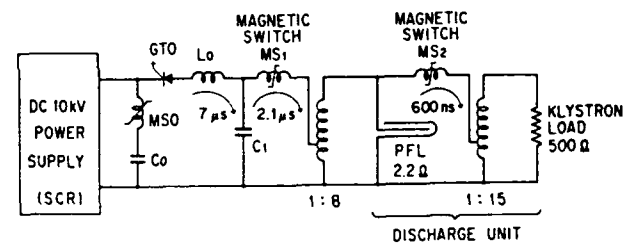


Figure 1. Simplified diagram of the all-solid-state klystron modulator.

B. Pulse-Forming Line

A triplate strip transmission line, which is a simple structure and can be made easily, was adapted for the PFL, and deionized water was used as a dielectric. Figure 2 shows the cross section of the PFL. The impedance Z of this PFL is given by

$$Z = \frac{377}{2\sqrt{\epsilon_r}} \frac{d}{w}$$

where ϵ_r is the dielectric constant, d is the spacing between lines and w is the width. The spacing d was determined to be 12 mm by assuming that the limitation of the electric field strength is 12 kV/mm in deionized water. The width w was

determined to be 140 mm by giving $d=12$ mm, $\epsilon_r=76.8$ (at 30°C) and $Z=1.848 \Omega$. The line length L of the PFL was determined by

$$L = \frac{\tau \cdot c}{2\sqrt{\epsilon_r}}$$

where τ is the pulse length of the PFL and c is the speed of light in vacuum. The line length L was determined to be 12 m by giving $\tau=700$ ns and $c=3.0 \times 10^8$ m/s.

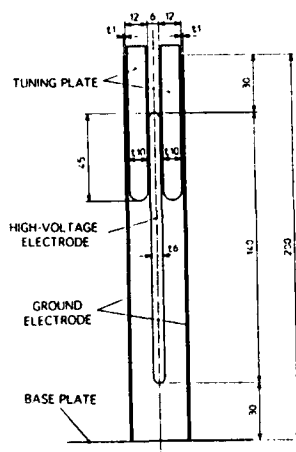


Figure 2. Cross section of the PFL.

The structure of the PFL has one high-voltage electrode between two ground electrodes as shown in Figure 2. These electrodes are made of stainless steel. In order to realize a compact PFL, the line is bent eleven times. Moreover, plastic plates are inserted between the high-voltage and ground electrodes in each of straight lines. This mechanism enables us to adjust the impedance of the PFL as well as the flat-top of the output waveform. Two ground electrodes are mounted on a stainless steel base plate. This assembly is housed in 1260 mm wide x 660 mm deep x 390 mm high water box made of stainless steel. The parameters of the PFL are summarized in Table 2.

Table 2
Parameters of the PFL

Line length	12 m
Characteristic impedance	$2.2 \Omega \pm 16\%$
Pulse length	700 ns
Width of the high-voltage electrode	140 mm
Width of the ground electrode	200 mm
Thickness of the high-voltage electrode	6 mm
Gap between the high-voltage and the ground electrodes	12 mm

C. Magnetic Switch

The magnetic switch was designed by setting the allowable range for the switch volt-seconds production and the saturated inductance. From the charging voltage waveform of the PFL,

the volt-seconds production for the switch must be 0.084 v-s. To achieve the required output rise time, the saturated inductance of the switch should be less than 120 nH. The core size of the switch was calculated by the following equation:

$$v-s = N \cdot \Delta B \cdot A$$

$$L_{\text{sat}} = \frac{\mu_{\text{sat}} \cdot N^2 \cdot h}{2\pi} \ln\left(\frac{r_o}{r_i}\right)$$

where

- $v-s$ = volt-seconds production for the switch
- N = number of turns around the core
- A = cross-sectional area of the magnetic core
- ΔB = total magnetic flux density swing of the magnetic core
- L_{sat} = saturated switch inductance
- μ_{sat} = permeability of free space multiplied by the relative permeability of the core when saturated
- h = axial length of the core in magnetic switch
- r_o = outer radius of magnetic core
- r_i = inner radius of magnetic core.

For the core material of the magnetic switch, a Fe amorphous AC 10 (TDK Ltd Co.), which has a high magnetic flux density swing of 2.1 T was chosen to reduce the size of the magnetic switch. The relative unsaturated and saturated permeabilities of the core are 2.0 and 2000, respectively. The core comprises 8 smaller subcores. Each subcore is wound from a 22 μm thick, 48 mm wide amorphous ribbon and a 4 μm thick, 52 mm wide PET film with a heat-transfer coefficient of 200 W/m²K. The saturated switch inductance was estimated to be 110 nH. The parameters of the magnetic switch are summarized in Table 3.

Table 3
Parameters of the magnetic switch

Number of turns	1
Outer radius of the magnetic core	230 mm
Inner radius of the magnetic core	130 mm
Axial height of the core in the magnetic switch (eight cores used with $h=48$ mm)	384 mm

D. Pulse Transformer

To generate a square-wave pulse, we must design a pulse transformer with a low stray capacitance and leakage inductance. The core comprises 3 subcores, which is the same core used in the magnetic switch. The primary and secondary windings of the pulse transformer comprise one turn and fifteen turns, respectively. The leakage inductance and stray

capacitance that were referred to regarding the high-voltage side were estimated to be 17.5 μH and 134 pF, respectively.

III. PERFORMANCE TEST

A preliminary test of the discharge unit was performed in order to confirm the performance of this modulator. Figure 3 shows the test circuit. The impedance of the dummy load was set at 500 Ω .

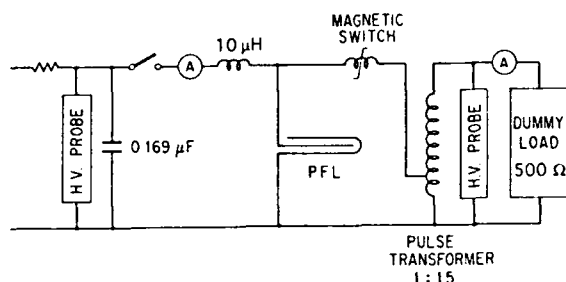


Figure 3. Test circuit.

A. Output Pulse Waveform

After the primary capacitor was charged to 82 kV, a gap switch for an initial switch was triggered to charge the PFL. The input and output voltage waveforms were measured by low inductance high-voltage dividers, and the current was measured by a Rogowski coil. Figure 4 shows the output pulse waveforms.

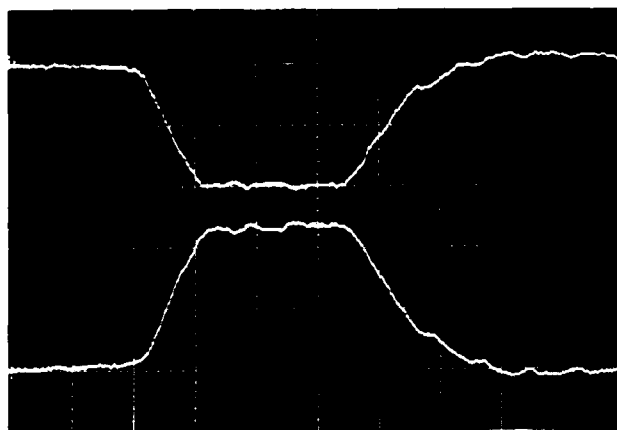


Figure 4. Output pulse waveforms at the dummy load.

H: 200 ns/div

Upper trace: Output pulse voltage (300kV/div)

Lower trace: Output pulse current (520A/div)

A pulse with a peak voltage of 600 kV and a width of 730 ns was successfully generated. Although a rise time (10-90%) of 153 ns and a flat-top of 460 ns satisfy the requirement, a flatness of $\pm 3.7\%$ is fairly larger than the expected value $\pm 1\%$.

B. Power Efficiency and Loss Analysis

The power efficiency of the modulator is very important for the application of a large-scale modulator system. The power efficiency of the modulator in this experiment was estimated from the input power at the primary capacitor and output power at the dummy load. The result was 82%.

The power losses of the modulator were mainly due to magnetic core losses, as well as resistive and Joule losses of the PFL. These losses under this condition could be calculated, and are summarized in Table 4. The calculated power efficiency was 82% from an initial stored energy of $1/2CV^2 = 563$ Joules; there was good agreement between the calculation and the experiment.

Table 4
Energy losses of the modulator

Components	J/pulse	%
Magnetic Switch	30	29
PFL resistive losses	42	41
joules losses	19	18
Pulse Transformer	12	12
Total energy losses	103	100

IV. SUMMARY

A compact klystron modulator using a PFL, a pulse transformer and a magnetic switch has been developed for the JLC. From performance tests, this modulator should enable us to generate an output pulse with a peak voltage of 600 kV, a pulse length (flat-top) of 460 ns and a rise time of 153 ns for a dummy load with an impedance of 500 Ω . The improvements of the pulse transformer are now under way to obtain a good flatness.

V. ACKNOWLEDGMENTS

The authors would like to express their thanks to Profs. Y. Kimura and K. Takata for their encouragement concerning this work. They also wish to thank Messrs. A. Tokuchi, H. Yoshimoto and N. Ninomiya of Nichicon Co. for the fabrication and test of the modulator.

VI. REFERENCES

- [1] K. Takata, "The Japan Linear Collider," Proc. of the 1990 Linear Accelerator Conference, Albuquerque, 13-17(1990).
- [2] H. Mizuno et al., "X-band Klystrons for Japan Linear Collider," Proc. of the 1992 Linear Accelerator Conference, Ottawa, 127-129(1992).
- [3] M. Akemoto et al., "X-band Klystron Modulator for Accelerator Test Facility," Proc. of the 1991 IEEE Particle Accelerator Conference, San Francisco, 1040-1041(1991).

A Compact Modulator for RF Source Development *

J. D. Ivers, G. S. Kerslick, J. A. Nation and L. Schächter
Laboratory of Plasma Studies and School of Electrical Engineering
Cornell University, Ithaca, NY 14853 USA

Abstract

A compact, low repetition rate, pulse modulator is being developed for use as a driver in high power microwave experiments. A single stage of the modulator consists of a $16\ \Omega$ pulse forming network in a Blumlein configuration driving a 3:1 coaxial ferrite loaded pulse transformer. The output of the transformer is a 100 kV , 150 ns (FWHM) pulse, with a 70 ns flat top ($\pm 1.0\%$), into a matched load. A second device, driven with a different pulse line, gives a 130 ns flat top pulse. To obtain the flat top requires tuning with a reactive circuit in the transformer primary. We plan to stack transformer modules in series to obtain a 500 kV , 1 kA modulator. A second stage is currently being built and various stacking techniques are being investigated.

I. INTRODUCTION

A compact, pulse modulator is being developed for use in high power laboratory microwave experiments. The goal of the program is to produce a 500 kV , $\sim 100\text{ ns}$ pulse operating at $\approx 1\text{ Hz}$ capable of driving a matched $500\ \Omega$ load with an efficiency of greater than 50%. A number of designs are being considered for such a modulator [1]. Early work has focused on modulators to be composed of a number of 3:1 coaxial transformer modules driven by Blumlein pulse forming networks. The transformer uses a ferrite loaded coaxial cable geometry, which provides good coupling, and has an adequate voltage standoff to meet the modulator requirements.

The transformer is designed to drive an electron beam in a vacuum diode immersed in an axial magnetic field. We propose to use a ferroelectric cathode as the electron source and experiments are currently in progress to test the emission characteristics of the cathode in high voltage diodes. First results on the emission are reported in the text.

II. BLUMLEIN CHARACTERISTICS

The primary pulse for the modulator is provided by an artificial Blumlein. The Blumlein and a single stage

transformer module are shown schematically in fig. 1.

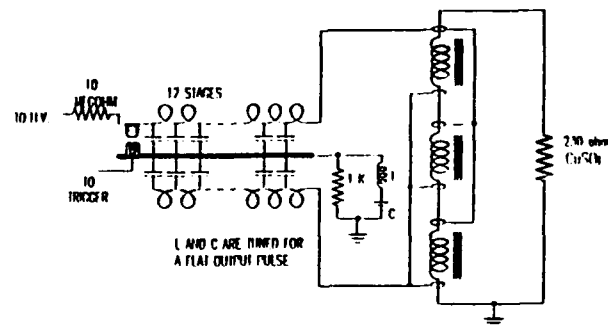


Fig 1. Coaxial pulse transformer module.

Two pulse lines have been used in the present work. The first has a maximum energy storage of 12 J and uses $24, 40\text{ kV}$, 570 pF capacitors. The inductance per stage is 40 nH and the line impedance nominally $16\ \Omega$. The full width, half maximum pulse duration is 150 ns and the line delivers, when properly tuned a 75 ns flat top pulse into a matched load. The line is mounted inside two cylindrical pipes with the inductor on the axis. This arrangement reduces the effect of the stray capacitance from the inductor to ground. The second line has twelve stages and a stage capacitance and inductance of 3.6 nF and 350 nH respectively. The line impedance is $18\ \Omega$ with the 250 ns FWHM pulse duration giving a 130 ns flat top pulse into a matched load. The maximum energy stored in the Blumlein is 54 J with a capacitor charge of 50 kV . In both cases the center conductor is grounded, the opposite arrangement to that usually employed in Blumlein transmission lines.

III. TRANSFORMER DESIGN

The pulse forming network drives a 3:1 ferrite loaded coaxial cable transformer as shown in Fig 1. The transformer consists of a three turn primary with each turn connected in parallel and a three turn series connected secondary. Each turn is $\sim 1.5\text{ m}$ in length and is made of RG-8 cable. The performance of the coaxial cable transformer is strongly affected by the cable capacitance, approximately 150 pF for each turn. In the three to one step up transformer the voltage across the cable is equal to the load voltage for the second turn and twice the load (charging) voltage for the third turn. The energy required to charge the cables comes from the Blumlein, and the current flow required for the charging makes a significant change in the output voltage. This effect is strongest in

* Work supported by USDOE and AFOSR.

the case when the transformer is energized by the 12 J Blumlein. The charging current is maximum during the rise and fall times of the output pulse and hence its effects are noted by a second harmonic contribution to the output voltage. To help overcome this effect, and to obtain a flat output voltage pulse, the Blumlein is charged with the center conductor tied to ground through a resistor. In this configuration all three sections of the transformer are initially charged to the Blumlein voltage. On pulsing the transformer the charge stored in the transformer capacitance is redistributed as required by the potential distribution along the length of the transformer. The path for the current flow is through the $1k\Omega$ ground resistor in the Blumlein. The circuit may be tuned to obtain a flat output pulse by adding a series resonant circuit in parallel with the ground resistor as shown in figure 1. The resonant frequency of the circuit is chosen to match the ringing frequency of the charging cable, and for the 12 J Blumlein is about $14MHz$. The second harmonic contribution to the output voltage in the second and 54 J Blumlein is significantly smaller for the same transformer and has not required the tuning used and described above.

Although the stray capacitance effects in the transformer affect the pulse shape strongly, the dominant effect on the transformer performance is set by the ratio of the leakage inductance in the transformer compared to the mutual inductance. To achieve a satisfactory performance requires that the mutual inductance be increased by a ferrite core loading of the cables. This is achieved by adding 114 ferrite rings (id.=1.27 cm, od.=2.54 cm, 1.27 cm thick) onto each length of the coaxial cable. The total Volt-second product of each stage is then increased to about $4.10^{-3} Vs$. This provides a large enough flux swing to allow for a 100ns pulse at the 40kV rated voltage of the 12 J Blumlein. The cores have an initial permeability of about 850, a flux swing of 4300 Gauss, and a maximum permeability of 2500. The core resistivity is about $1.10^8 \Omega - cm$ allowing for good high frequency operation.

Single transformer modules have been tested on various impedance loads and for excitation with both pulse lines. With the transformer driven by the smaller Blumlein the output pulse into a 500Ω load is shown in fig. 2. The 100 kV, 150 ns (FWHM) pulse has a 70 ns flat top. The LC tuning has reduced the output voltage ripple to less than 1%. In this figure six shots have been overlaid, illustrating excellent shot-to-shot performance of the module, especially in view of the fact that the switch, a spark gap, was not triggered but allowed to self break. In this example the Blumlein was initially charged to 33kV. Note that although the transformer gain was 3:1 the load was mismatched and the efficiency was correspondingly

lower than the design figure.

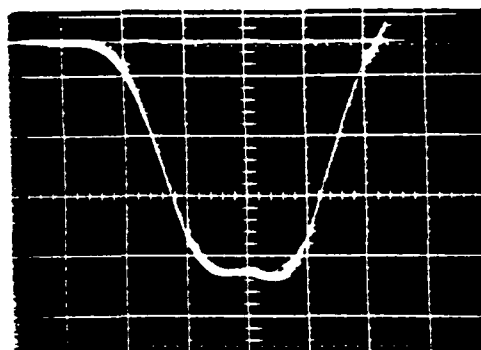


Fig 2. Output pulse from single module of the 12 J system. 23 kV/div, 50ns /div.

When excited by the larger Blumlein the pulse rise time and flat top durations are both increased. The flat top duration now extends to 130ns as shown in the overlay of six switch self break discharges. The output pulse into a 500Ω load is shown in fig. 3. In this case the Blumlein was charged to 12kV and the 50 kV, 250 ns (FWHM) output pulse has a 130 ns flat top. The output voltage is about four times the dc charging voltage on the Blumlein, commensurate with the mismatched load. Operation of the system with a 230Ω load gives the expected three to one step up ratio. For the 12 kV charging voltage the operation into the 500Ω load yields an efficiency of 42%.

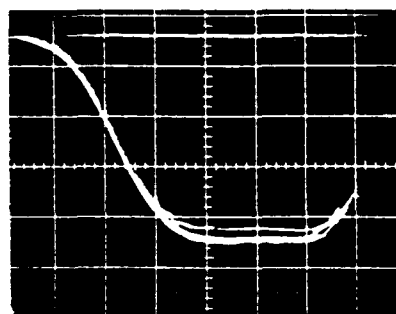


Fig 3. Output pulse from single module of the 54 J system. 12 kV/div, 50ns /div.

IV. ELECTRON BEAM GENERATION

A third transformer system, which uses a four to one step up transformer and gives a 70kV output pulse (limited by the volt-second product of the ferrite cores), has been used to test the electron emission from a ferroelectric cathode. This work, which is currently in progress, is being used to obtain data on the suitability of ferroelectric materials as sources for high current ($\sim 1 kA$) electron beams. In this configuration the ferroelectric cathode is pulsed by a second artificial Blumlein, which is inductively coupled to the ferroelectric through a one to one isolation transformer. Electron emission occurs when the ferroelectric sample (LTZ-2M in these experiments) is pulsed to about 1kV, with a field gradient of about $10kV/cm$ [2].

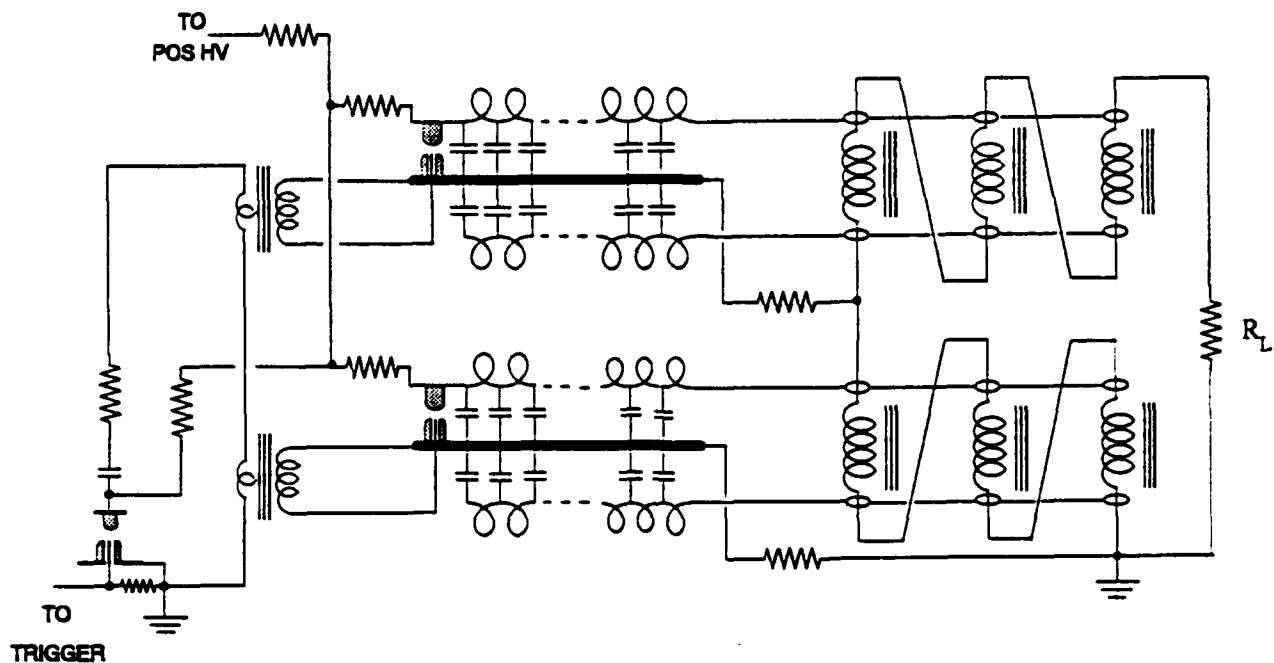


Fig. 4 Schematic of a two Blumlein stacked pulse modulator.

The 70 kV main transformer pulse is applied, in the present configuration, across a planar vacuum diode gap which is typically 3 – 4 cm. The electron current through the gap is monitored as a function of the applied voltage. The effect of the time delay between the pulse applied to the ferroelectric (V_{fe}) and the diode gap pulse (V_d) is also measured. Initial results show the following: (i) Diode current pulses up to 200 A, 250 ns have been measured. (ii) If V_d is applied before V_{fe} no significant diode current (I_d) is measured. ($I_d < 10$ A). (iii) If the ferroelectric is replaced with a simple carbon cathode the measured diode current is below the 4 A level set by noise limitations.

These initial results have been limited by the significant shot-to-shot variations in this experiment, and we shall be seeking to improve the performance of this ferroelectric diode in the future. It should be noted that the measured diode current corresponds to an emission current density of 200 A/cm² and is about 40 times greater than the emission expected on the basis of the Child-Langmuir law. The diode voltage is limited in the current arrangement to 70 kV, with a 130 ns flat top output pulse. We are also working on the construction of a transformer with a larger volt-sec product to allow operation of the module up to its design value of 150 kV.

V. TRANSFORMER MODULE STACKING

In order to achieve the required output parameters of ~ 500 kV and 1 kA requires that two or three transformer modules be stacked in series. We accomplished this experimentally some time ago [3] with each transmission line being set as an element in a Marx generator. We plan to attempt stacking initially with the arrangement shown in fig. 4. In this case the energy required to float the successive Blumleins comes from the lines themselves. The separate sections will be switched inductively as shown in the figure. This arrangement is currently in satisfactory use for the triggering of the ferroelectric cathode as described above. The transformer modules will be fabricated on RG-218 cable to allow for the greater voltage hold off required in the second stage (or third, if needed).

To complete our design program we have in progress work on stacking of multiple transformer stages and also on extending the flat top width of the voltage output pulses.

VI. REFERENCES

- [1] Pulse Generators, Ed. G. Glasoe and J. Lebacqz, MIT Radiation Series, M^cGraw Hill 1948.
- [2] J. D. Ivers, L. Schächter, J. A. Nation, G S. Kerslick, and R. Advani, *J. Appl. Phys.*, **73**, 2667, (1993).
- [3] J. D. Ivers, and J.A. Nation, *Rev. Sci. Instrum.*, **54**, 1509, (1983).

HIGH POWER PULSE MODULATOR FOR PLS LINAC*

S.H. Nam, M.H. Cho, J.S. Oh, S.S. Park, and W. Namkung
Pohang Accelerator Laboratory, POSTECH
P. O. Box 125, Pohang 790-600, Korea

Abstract

Complete design, assembly, and testing of 200 MW modulators are in progress at Pohang Accelerator Laboratory (PAL) for the full energy injection linac system of the Pohang Light Source (PLS). A 150-MW pre-prototype modulator (350 kV, 3.5 μ s flat-top width, and 840 Ω load) has been assembled and tested up to 175 MW. Design, construction, and test of a 200-MW prototype modulator (400 kV, 4.4 μ s flat-top width, 800 Ω load) has also been completed. Eleven units of main 200-MW modulators are under construction, and their assembly is expected to be completed in 1993. This paper presents the design and the current status of performance results of 150-MW and 200-MW modulators.

I. INTRODUCTION

The specification of the full energy injection linac system of the PLS requires total eleven units of 200-MW modulator and 80-MW klystron [1]. A 150-MW pre-prototype and a 200-MW prototype modulators are already constructed. Preliminary results of the 150-MW modulator is presented elsewhere [2]. Currently the 150-MW modulator is installed in PLS test laboratory. The 200-MW prototype modulator is installed in linac gallery and tested up to 145-MW beam power with a 80-MW Toshiba klystron. Eleven main 200-MW modulator units is under parallel construction in PAL and is expected to be completed this year.

II. MODULATOR PERFORMANCE AND CONFIGURATION

A plot of beam voltage versus E-3712 klystron RF output power is shown in Fig. 1. The 150-MW pre-prototype modulator is used to take the data shown in the figure. A Toshiba E-3712 klystron with an 1:17 turns ratio pulse transformer is used as a load. A SLAC RF water load is installed to absorb the RF output power of the klystron during the test. As shown in the figure, maximum 175-MW beam power (i.e., 375 kV beam voltage) is applied to the klystron load. A peak power capability of a thyatron (ITT F-241) in the 150-MW modulator is 125-MW. Therefore, the tested peak beam power is much higher than the ITT's specification. The 150-MW modulator will be continuously used for the purpose of conditioning high power klystrons. Specifications of the 200-MW modulator are listed in Table 1. It shows required parameters of current PLS linac, designed parameters for future upgrade, and tested parameters. The 200-MW modulator test is done using a water dummy load (250 kV max. at 10 Hz) as well as a E-3712 klystron load. Modulator test with a E-3712 klystron which is connected to the linac waveguide and accelerating column is also successfully done.

*Work supported by Pohang Iron & Steel Co. and Ministry of Science and Technology, Korea.

Table 1: 200-MW modulator specification

Description	Required	Designed	Tested
Peak power (MW)	200	200	145
Ave. power (kW)	97	289	33
Peak output volt. (kV)	400	400	357
Rep. Rate (PRR) (Hz)	10 to 60	180 max.	30
ESW (μ s)	---	7.5	7.5
Flat-top width* (μ s)	4.4	4.4	3.0
Charging time (ms)	---	5.76 max.	5.76

* less than ± 0.5 %.

Electron beam energy of 200-MeV is actually extracted by using the 200-MW modulator and 80-MW klystron unit along with a 60-MeV preinjector section. The 145-MW tested power in Table 1 is limited by the progress of solid RF load power conditioning. Full required parameter test of the 200-MW modulator at 14 Hz will be performed with a solid dummy load that is currently in fabrication, and the result will be reported in the near future.

Table 2: Specification of major parts in 200-MW modulator

SCR	700A rms, 400A ave., 1.600V	
3 ϕ transformer	440V rms, 19kV rms, 12A rms, 98% eff.	
Rectifier diode	48 (1600V, 25A ave.) in series per arm.	
Filter choke	5 H min. at 15A DC	
Filter capacitor	3 (4.7 μ F, 30 kV) in parallel, total 14.1 μ F	
Charging inductor	Primary	2.4 H, 11A DC
	Secondary	1:25 ratio, 55A DC, 2 kV
Charging diode	80 (1600V, 95A DC) in series	
Despiking circuit	L	min. 14 mH at 11A DC
	R	2 k Ω
EOLC	Diode	same as charging diode
	Resistor	4 (10 Ω , 70 W) in parallel
	Thyrite	32 (275V DC, 10 W) in parallel
PFN	C	total 28 (50 nF, 50 kV)
	L	total 28 (4.5 μ H max.)
Thyatron	ITT F-303	
Triaxial Cable	Double	
Pulse Transformer	1:17 ratio, >96% efficiency	

Fig. 2 shows a simplified circuit diagram of the 200-MW modulator. In Table 2, major component specifications of the 200-MW modulator are shown. The 200-MW modulator circuit can be divided by four major sections: charging, discharging, a pulse transformer assembly, and a klystron load. The primary power is adjusted by a phase-control system with six SCRs. To gain a

fine DC output voltage regulation, active feedbacks of primary AC voltage and current as well as high voltage (HV) DC are supplied to the SCR gate trigger unit (GTU) as shown in the Fig. 2. Portion of charge in the filter capacitor is resonantly transferred to a pulse forming network (PFN) through a charging inductor and a charging diode. A De-Q'ing circuit is installed at the secondary of the charging inductor to regulate a PFN charging voltage. Final goal of a pulse-to-pulse beam voltage regulation in the 200-MW modulator is less than 0.5%. Details of the HV DC and beam voltage regulation results will be presented in [3]. Two parallel, fourteen section, type-E Guillemin networks are used in the PFN. The total PFN impedance is about 2.8 Ω . While PFN capacitors have a fixed value, PFN inductors are variable. The inductance variation enables us to tune a flat-top quality of an output beam voltage pulse. An end of line clipper (EOLC) circuit is employed to remove excessive negative voltage swing on PFN capacitor and a thyatron. The thyatron used in the 200-MW PLS modulator is ITT F-303. Specifications of the ITT F-303 thyatron are listed in Table 3.

Table 3: 200-MW thyatron (ITT F-303) specification

Description	ITT spec.	PLS spec.	
		60 Hz	180 Hz
Peak power (MW)	200	202	
Ave. power (kW)	200	91	273
Peak anode V (kV), epy	50	47	
Peak anode I (kA), ib	15	8.6	
dib/dt (kA/ μ s)	50	10.75	
Ave. anode I (A DC)	8 in air 12 in oil	3.87	11.61
epy x ib x PRR	300×10^9	24.3×10^9	72.8×10^9
epy x dib/dt x PRR	---	30×10^{15}	91×10^{15}

As shown in the table, the thyatron does not have a capability of handling the full designed specification of the 200-MW modulator. However, it can of course handle the full required parameters in current PLS linac. Forced air cooling is used for the thyatron. Two triaxial cables in parallel are used to make electrical connections between the PFN and a pulse transformer. By using the double configuration, stress on the cable [4] is reduced. Components in the pulse transformer tank are immersed in high voltage insulating mineral oil. The klystron load is placed on top of the transformer tank. The klystron impedance seen at the primary of the pulse transformer is 2.8 Ω . PFN impedance is adjusted so that there is a positive mismatch (~5 %) between PFN and load. The method of positive mismatching has many advantages over negative mismatch and not significantly affect thyatron recovery time [2,5]. In Fig. 3, an arrangement of major components in the 200-MW modulator cabinet is shown. As shown, the modulator has a control cabinet, a main cabinet, and a circular tank with a klystron load. The control rack encloses all low voltage monitor, control, and interlock compartments. The main cabinet is separated in two parts; charging and discharging cabinets. The charging cabinet covers from 480V AC primary power line inlet to de-spiking circuit. The discharging cabinet encloses PFN and thyatron related

circuits. Low voltage controllers related to the thyatron and klystron is mounted on the discharging cabinet. A center metal plate separates the charging and discharging cabinet in order to reduce noise coupling between the two compartments. There are two BNC boxes and four filter boxes in the modulator. Double shielded 50 Ω coaxial cables and ferrite cores are used to treat signals through the BNC boxes in order to reduce noise level during discharging. All multi-conductor signal wires coming in and out of the main modulator cabinet goes through filter boxes in which EMI filters are installed. Completely enclosed metal wire ducts are also installed on the roof of the 200-MW modulator main cabinet. Signal wires connecting to the modulator circuit escape from the main cabinet as early as possible and go through the duct to their destination. This effectively reduce the chance of high frequency noise coupling. In this configuration, the whole 200-MW modulator cabinet including the tank assembly is considered as one completely enclosed faraday cage. A single point ground is effectively used for the whole modulator circuit. Points where grounds are connected to form loops are isolated by means of filters and transformers.

VI. REFERENCE

- [1]. W. Namkung et al, "Progress of 2 GeV Linac," these proceedings
- [2]. S.H. Nam, J.S. Oh, M.H. Cho, and W. Namkung, "Prototype Pulse Modulator for High Power Klystron in PLS Linac," *IEEE Conf. Records of the 20th Power Modulator Symp.*, Myrtle Beach, SC, 1992, pp. 96-99.
- [3]. J.S. Oh, S.H. Nam, S.S. Park, M.H. Cho, and W. Namkung, "200 MW Modulator for 80 MW Klystron in PLS Electron Linac," to be appeared in the *Ninth IEEE Pulsed Power Conf.*, Albuquerque, NM, 1993.
- [4]. A.R. Donaldson, C.W. Allen, J.R. Ashton, "SLAC Modulator Operation and Reliability in the SLC Era," *Records of Klystron-Modulator Technical Meeting*, CERN, Oct. 1991.
- [5]. R.B. Neal, ed., *The Stanford Two-Mile Accelerator*, (Q.A. Benjamin, New York, 1968).

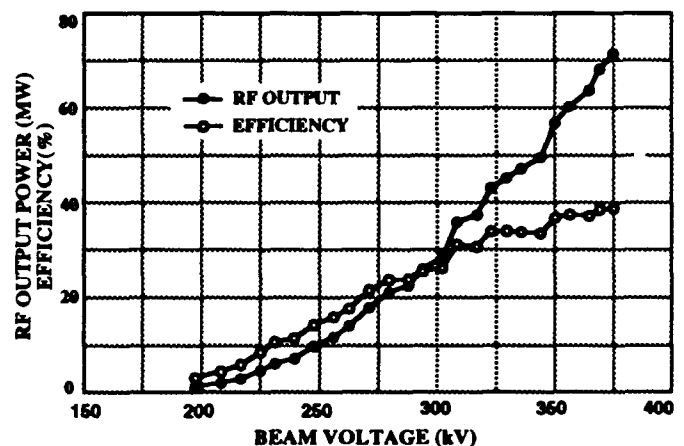


Fig. 1: Plot of beam voltage versus E-3712 klystron RF output power. 150-MW modulator is used to measure the data. (ISOL = 16.5 A, RF drive power = 250W, PRR = 50Hz, Heater power = 440W)

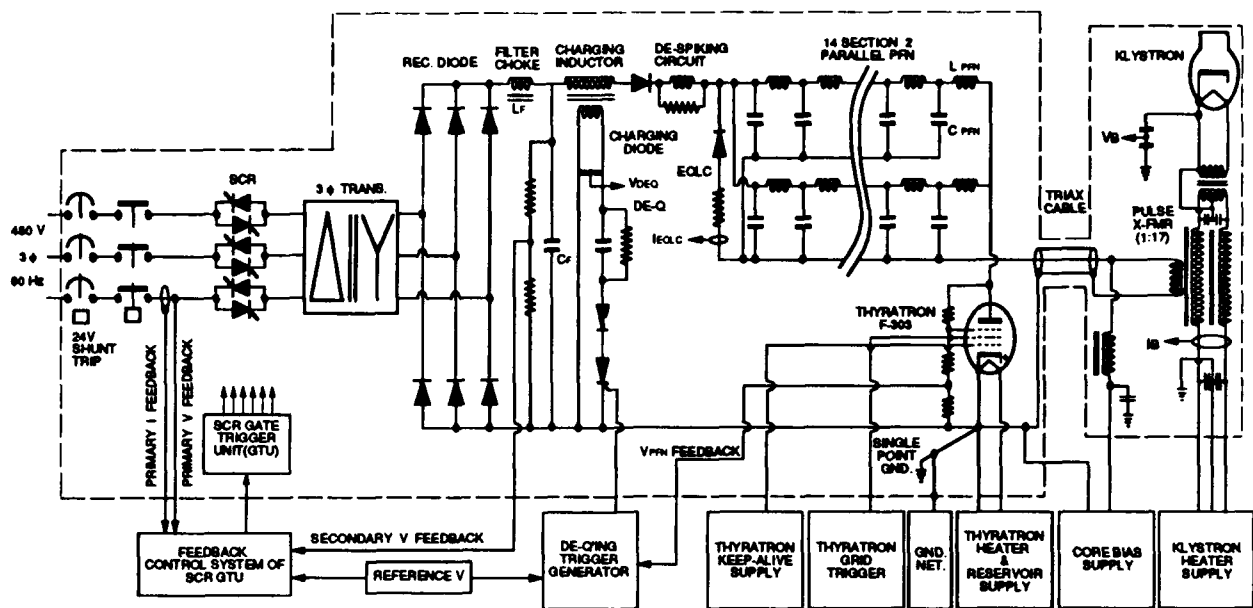


Fig. 2 : Simplified circuit diagram of 200-MW modulator.

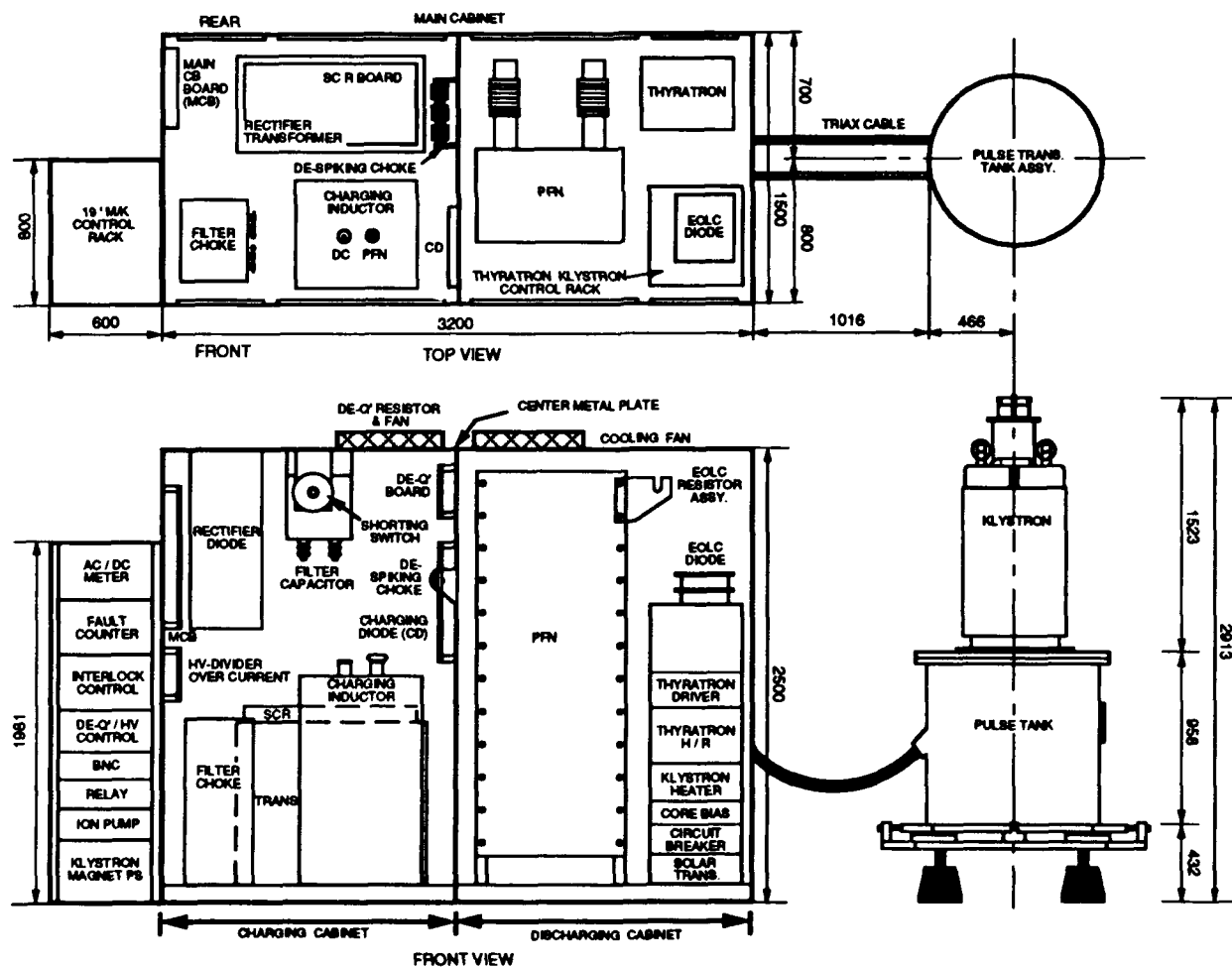


Fig. 3 : Configuration of main components in 200-MW modulator cabinet (units are in mm).

Pulse Modulator Developments in Support of Klystron Testing at SLAC

R. F. Koontz, R. Cassel, J. de Lamare, D. Ficklin, S. Gold, K. Harris
Stanford Linear Accelerator Center
Stanford, CA 94309 USA

Abstract

Several families of high power klystrons in S- and X-Band are being developed in the Klystron Laboratory at SLAC. To support these developments, a number of new pulse modulators are being designed from scratch, or upgraded from existing laboratory test modulators. This paper outlines the modulator parameters available in the SLAC Klystron Laboratory, and discusses two new modulators that are under construction.

I. BACKGROUND

Thirty years ago, the first building constructed at the new site of the Stanford accelerator was the Klystron Test Lab. The sources of the microwave power needed to drive this massive accelerator were very much in doubt. The Test Lab was equipped with twelve line type modulators built by Ling for the purpose of testing new developmental klystrons and other components needing high power S-Band rf. Over the years, these test positions have been upgraded and radically changed to meet the needs of ongoing rf development projects. Currently, the lab is supporting the continuing production of the 65 MW pulsed klystrons that power the Stanford Linear Collider (SLC), and has developmental programs underway on both S- and X-band pulsed power sources. The Test Lab now has sixteen test positions of which five are dedicated to R&D

of new klystrons. The photograph in Fig. 1 shows the floor layout of the laboratory. Test Stand capabilities are listed below, and details of the new modulator developments are outlined in the paragraphs following.

A. Production Test Stands

Test Stands 1, 5, 7, 9, & 11 are dedicated to 65 MW production klystron testing. These test stands are conventional line type modulators with thyatron switching. Primary power supplies are variable transformer programmed 25 kV DC units that resonant charge two parallel section pulse lines. DeQing, cutting off the resonant charge when a reference voltage is reached, is used for regulation. When the thyatron fires, a 23 kV pulse of 5 μ s (3 dB points) duration is supplied through a pulse cable to the klystron pulse transformer. The 15:1 transformer delivers a 350 kV pulse to the cathode of the klystron. The klystron perveance is nominally 2 μ erv, and this translates to a delivered pulse current of 414 amps. The primary current in the thyatron is in excess of 6,000 amps. An electrical layout of these modulators is shown in Fig. 2.

B. Thyatron Test Stands

In the last year there has been a major effort to secure multiple sources of reliable thyatrons for modulator service at SLAC. The SLC has 245 operating modulators that require thyatrons, and the failure rate of thyatrons in this service is about four per week. Currently, two manufacturers, ITT and EEV, are supplying thyatrons, and Litton is close to delivering a newly designed thyatron that should give long service. ITT and EEV are upgrading their thyatron designs as well. Three test stands in the Test Lab are dedicated to thyatron evaluation and qualification. Thyatron testing involves detailed monitoring of thyatron operating parameters. High Voltage Over Current faults are counted and automatically reset during processing and acceptance testing. Each test modulator oper-

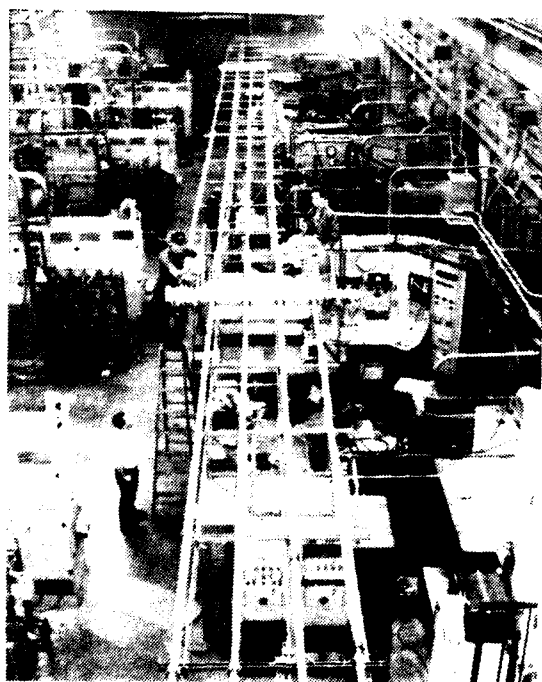
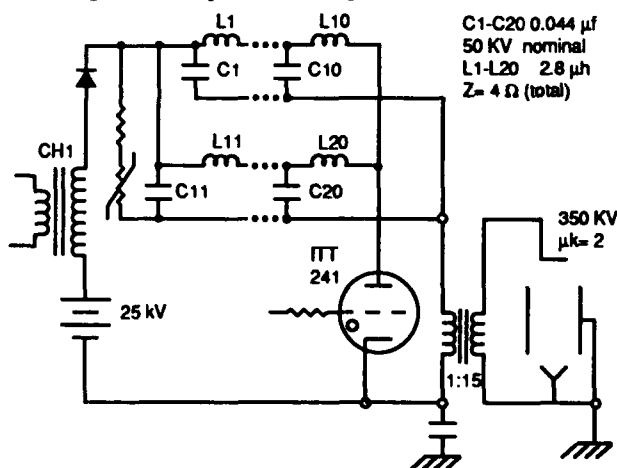


Figure 1. Klystron test lab overview.

*Supported by Department of Energy contract DE-AC03-76SF00515.



SIMPLIFIED SCHEMATIC - 350 KV MODULATOR

5-88
7428A2

Figure 2. Standard pulse modulator schematic.

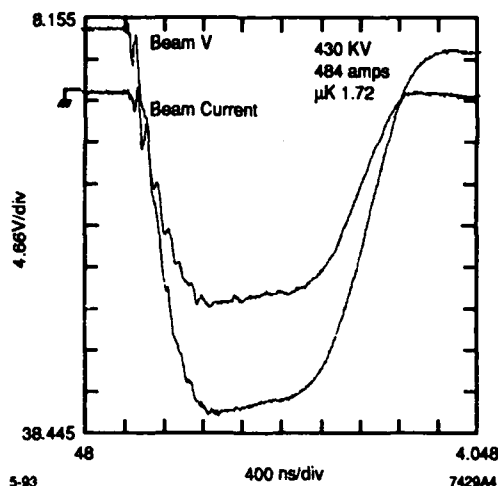


Figure 3. Test stand 8 beam pulse voltage.

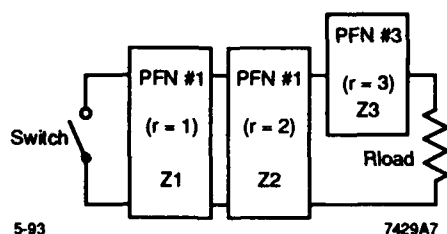


Figure 4. Test stand 3 Blumlein schematic

ates into a pulse transformer tank equipped with a glass-tube-enclosed liquid load, containing a detergent solution, in place of the actual klystron. These test stands are also used to dynamically test all pulse transformer-tank assemblies before klystrons are mated to the tanks.

C. S-Band Resonant Ring - Window Test

One test stand is dedicated to operation of an existing resonant ring which can circulate over 200 MW. The modulator in this test stand has an extended network that delivers a 6.5 μ s beam pulse. A 5045 klystron delivers up to 50 MW of rf (5 μ s) to the ring, or to a separate window test waveguide assembly. Windows were previously tested in the ring, but it has been found to be more effective to test windows with the full output of the klystron which acts as a lower impedance drive source than the high Q resonant ring. In the ring, fields collapse rapidly when a discharge occurs at a test window, and the window is not damaged. When driven directly from a klystron, the fields do not collapse, and the klystron drives energy into a window discharge, such that subsequent inspection shows it to be defective. Windows used on production klystrons go through this direct drive testing process.

D. X-Band Resonant Ring Test Stand

Two high voltage test stands have been dedicated to the development of high power X-Band klystrons. One of these test stands has been used intermittently to drive an X-Band resonant ring that can operate at over 300 MW circulating power (Ref. 1). To allow this ring to be used regularly in component testing, a new, but completely conventional modulator and test position is under construction that will provide a 3 μ s beam pulse of up to 400 kV to an experimental X-Band klystron that

will be dedicated to ring drive service. This test stand will be operational by August 1993.

E. Medium Voltage X-Band R&D Test Stands

The two test stands mentioned above, 6 and 8, have been upgraded with network modifications—ITT-303 12,000 amp thyratrons, and 20:1 ratio pulse transformer tanks close coupled to the modulators to produce 600 ns rise time beam voltage pulses up to 450 kV. The networks can be configured to produce pulses as short as 600 ns, or as long as 1.7 μ s. X-Band R&D klystrons operate at a nominal perveance of 1.8 μ perv. At full voltage, the thyatron must switch over 11,000 amps from the network. The ITT-303 large cathode thyatron has this capability.

The electrical configuration of these two modulators is similar to that of the production modulators, but the layout is optimized to reduce stray inductance and capacitance. This permits the fast rise times obtained in the beam pulse image shown in Fig. 3

F. 650 kV, 1.2 μ perv Blumlein Test Stand for X-Band Klystron R&D

The parameters of this test modulator were presented (Ref. 2) by Cassel et al. This modulator design is under construction in the Klystron Test Lab in test stand position 3. The three section network in the Blumlein configuration is charged in the conventional resonant charging mode by a programmable 45 kV DC power supply. The variable autotransformer of the original test stand is used for level control, and a new SCR switching bridge in the power supply primary is used to provide "soft start" capability. Later, this circuit will be used for direct voltage control. The three stage Darlington network that composes the pulse forming line delivers an output pulse of 1.5 times the peak charging voltage to the pulse transformer when the thyatron is fired. A block schematic of this network is shown in Fig.4. The use of this voltage multiplier network allows the thyatron to see only the PFN charging voltage of 85 kV while delivering a network output voltage of 127 kV. With a conventional pulse line the output voltage would only have been 42 kV. A serious limitation to fast rise time is leakage inductance in high ratio pulse transformers. Using this Blumlein multiplier technique, a fast rise time pulse transformer of only 6:1 ratio can be employed in the system, and still produce klystron cathode beam pulses of over 650 kV. All components for this modulator are now in house including the pulse transformer, and low level network testing is underway. We expect this modulator to be assembled and ready for high power testing in the Fall of 1993.

G. 550 kV, 1.8 μ perv Test Stand for 150 MW S-Band klystron Development

Test Stand 13 is being modified to operate a 150 MW S-Band klystron, with microperveance 1.8, at a beam voltage of 550 kV maximum. The most expeditious and cost effective method of modification is to build a standard line-type modulator using as many of the existing modulator components as possible. The existing set up has a 25 kV power supply and charging choke system, and 50 kV thyratrons are available. A pulse transformer ratio of 1:23 and a Pulse Forming Network

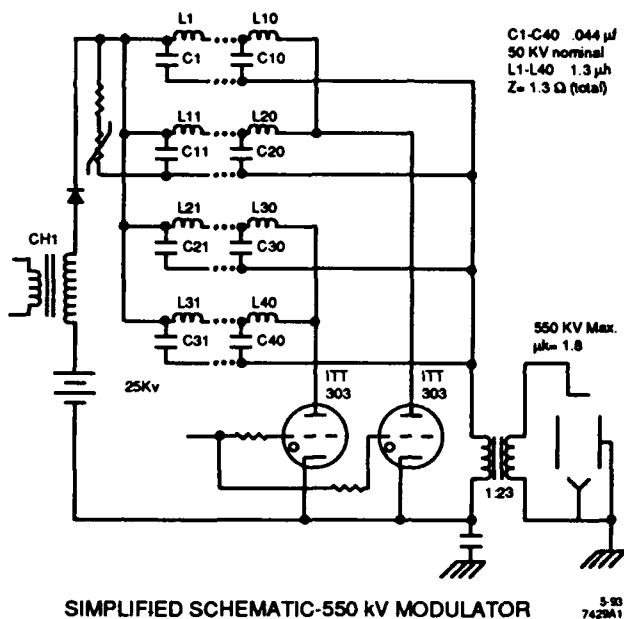


Figure 5. Test stand 3 (550 kV) modulator schematic.

impedance of 1.3 ohms was chosen to obtain the slight positive mismatch. Based on the PFN impedance, the reflected klystron impedance, and the required output voltage, the thyatron voltage (PFN voltage) will be 46 kV which is a comfortable operating point for a 50 kV thyatron. The total thyatron discharge current is 17,000 amperes. Two ITT Model 303 Thyratrons will be used to discharge the PFN.

Stangenes Industries of Palo Alto, California is designing a pulse transformer with a 600 ns rise time (10% to 90%) and 3.5 μ s flat top for this application. The required PFN pulse width is 4.5 μ s.

The rise time of the output pulse to the klystron is dominated by the rise time of the pulse transformer. However, a 10-section PFN is needed so that the beam pulse width can be shortened, by removing sections, during initial turn on and processing of the klystron yet still maintain a usable pulse shape. The impedances are very low and the peak currents high in this type of conventional design. Wiring and component inductances can significantly effect the output pulse and system noise. These potential problems are addressed by:

- a) using four parallel, ten-section PFNs and discharging each pair with a thyatron.
- b) mechanically designing the PFNs, thyratrons, etc. in a symmetrical configuration with short leads to the pulse transformer that can be copper bus.

The four parallel PFN's, as shown in Fig. 6 enable each inductor to be four times larger than an equivalent single PFN structure. The calculated value for each inductor is 1.16 μ Henrys. The inductors are designed for 1.3 μ Henrys and can be tapped and fine tuned with a slug. Each of the inductors is in series with one of the forty capacitors. The capacitance of each section is nominally 0.045 μ Farads, which is similar to the capacitors already in use. The plastic case capacitors manufactured today are significantly smaller than those in use at SLAC and can be made with much lower internal inductance (35 nHy). Using 4" \times 6" capacitors approximately 13" long, the

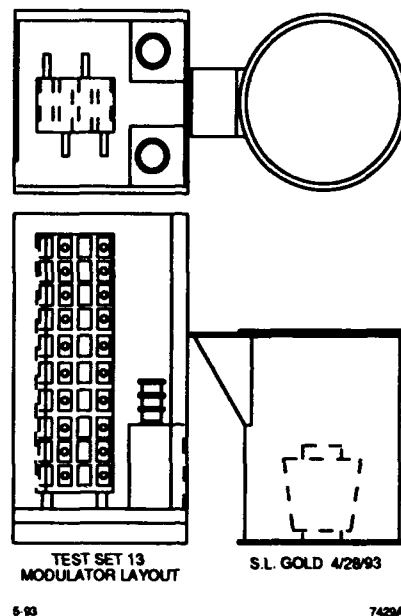


Figure 6. Test stand 13 modulator layout.

four Parallel PFN's can be packaged in the same space as the present systems.

To make room for all the inductors, the capacitors are alternated such that two PFN's face one direction and two face the opposite direction. This layout is shown in Fig. 7. Also shown is the placement of the thyratrons and the pulse transformer tank. Each thyatron discharges two PFN's. Because of the symmetry and close proximity of the components, the inductances can be minimized and somewhat equalized.

The pulse transformer and cathode end of the klystron are housed in a round tank. This tank will also be used on the 650 kV modulator.

2. Other Test Lab Support Facilities

The Test Lab is also home to two major testing facilities, the 70 kV, half-Megawatt CW rf test stand that is used for processing and qualifying PEP klystrons, and the X-Band accelerator Test Facility where X-Band power from experimental klystrons is used to power accelerator structures (Ref. 3). This facility is equipped with an electron gun and a spectrometer. A new 1.2 MW CW rf test stand is being planned for testing a B factory klystron.

References

- [1] Component Development for X-Band Above 100 MW W. R. Fowkes, et al 1991 IEEE Particle Accelerator Conf. SLAC-PUB-5544.
- [2] 600 kV Modulator Design for the SLAC Next Linear Collider Test Accelerator R. Cassel et al 20th Power Modulator Symposium, Myrtle Beach, SC SLAC-PUB-5851.
- [3] Accelerator and RF System Developments for NLC A. E. Vlieks, et al This Conference SLAC-PUB-7415.

A Blumlein type modulator for 100MW-class X-band klystron

H.MIZUNO

KEK(National Laboratory for High Energy Physics)
1-1 Oho,Tsukuba-shi, Ibaraki-ken, 305 Japan

T.MAJIMA, S.SAKAMOTO and Y.KOBAYASHI

IHI(Ishikawajima-Harima Heavy Industries Co., Ltd.)
Toyosu 3-1-15, Koto-ku, Tokyo, 135 Japan

Abstract

To achieve the high efficiency in the X-band pulsed klystron modulator for the main linac in Japan Linear Collider, a new modulator with the Blumlein type PFN was designed and fabricated. Two identical 12-stage PFN's of the 23 ohm characteristic impedance are set on the both sides of the 1 to 7 step-up pulse transformer. Simulations showed that with this pulse transformer, 500 ns 560 kV pulse of 200 ns rise time could be obtained with the droop of 2%. The design and some test results of the Blumlein type modulator and the pulse transformer are presented.

Introduction

At the present status of the design studies and the R&D works dedicated to the next generation of the electron- positron colliders, the necessary output power of the RF power sources in the X-band range is still under discussions(REF-1)(REF-2). As X-band main linac's in JLC(Japan Linear collider), the accelerating structure with the filling time less than 100 nsec is considered. Therefore, considering the multi bunch operation of this linac's, the RF power duration is around 100-200nsec is required in the accelerating structures. This means that the RF power source should produce the 100MW class RF peak power with the duration of 400-800nsec, even with the RF pulse compression system of the factor 4. This RF pulse is much shorter than that of the present S-band linac's which is typically a few micro-sec. In KEK, we have utilized conventional modulator with the 1 to 15 pulse transformer to drive the present 100MW class X-band

klystrons(REF-3)(REF-4). This conventional modulator has revealed sufficient performance as for the test of the X-band klystron named XB-72K, but as the possible driver for the future linear collider pulse shape especially it's rise time was not sufficiently fast to assure the efficiency necessary for the future linear collider. A new Blumlein type modulator and new 1 to 7 step up pulse transformer was designed and fabricated.

Design and parameters

Table-1a) and 1b) show the circuit design and the parameters of the Blumlein type PFN and 1 to 7 pulse transformer parameters, respectively. The output voltage was decided same as the present modulator, thus the same charging system and the thyatron switching tube is utilized. One specific feature of this circuit different from an ordinary Blumlein circuit, is that the primary winding of the pulse transformer is kept at the charging voltage of 80 kV. As shown in the Table-1a), the inductance and the capacitance of the PFN are much smaller than those of the ordinary PFN's of S-band modulators. By setting the primary winding at the charging voltage as shown in Fig-1), the ground lines can be always kept at the ground potential, and this can minimize the undesirable effects of the stray inductance and capacitance of the PFN circuits those are not so small compared with the circuit constants themselves. The configuration of PFN's can be achieved symmetrically as shown in Fig-2a and 2b). This symmetric configuration is expected to keep the stray capacitance and

TABLE-1a) PFN Specifications	
Impedance	23 Ohms
Charging Voltage(Max.)	86 kV
Pulse Width(Total)	700 nsec
No. of stages	12 stages (x2sets)
Inductance/one stage	340 nH
Capacitance/stage	2.9 nF

Table-1b) Pulse transformer	
Step-up ratio	1/7
Leakage L.	830 nH
Stray capacitance	4 nF
Loss at 200pps(Hysteresis)	100W
(Eddy Current)	1000W
Rise time(Trans. only)	~100ns
Fall Time(Trans. only)	~200ns
Sagging(500ns width)	2.8 %
Core material	Si-Fe 25microns

Fig-2a,b) PFN and discharge circuit

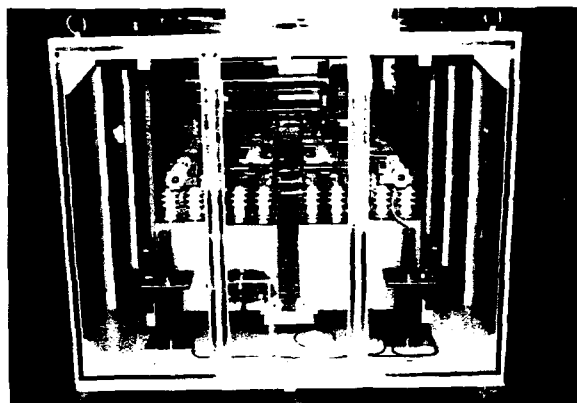


Fig-3a) Equivalent circuit for "SPICE" simulation

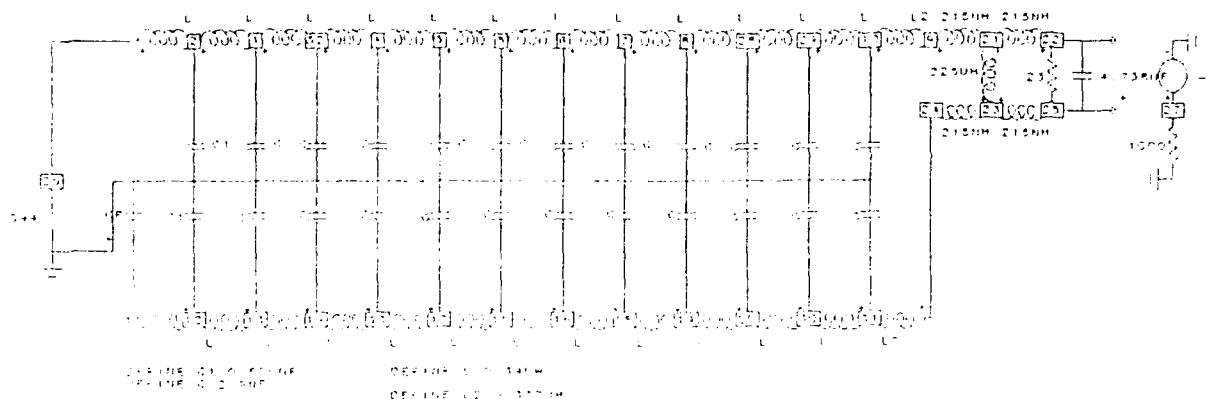
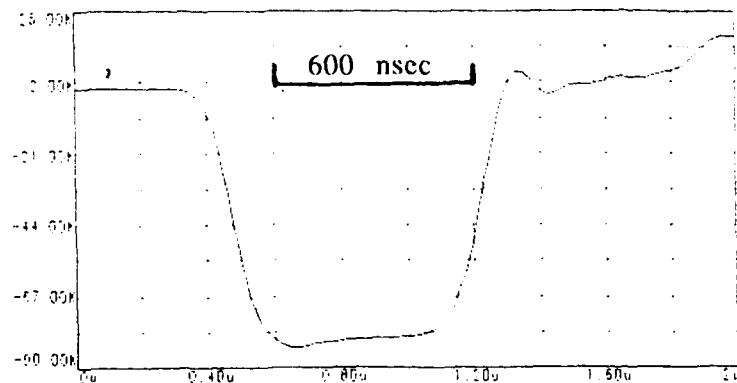


Fig-3b) Pulse shape by "SPICE"



inductance practically equal in each two PFN's of the Blumlein structure.

As the pulse transformer design, as shown in Table-1b), ordinary core material such as Si-Fe of thickness of 25 microns which is currently available in the market has sufficient performance concerning the hysteresis and eddy current losses. One specific feature of this pulse transformer mentioned above is that the primary winding is always kept at the charging voltage (80 kV), and this could be achieved by setting the insulation distance between the core and the secondary winding respectively, without sacrificing other performances such as stray capacitance or leakage inductance those affect to the output pulse shape. This transformer is used in the insulation oil tank as usual for this kind of high voltage pulse transformers.

The circuit simulation was carried out by the use of "SPICE" code. The equivalent circuit for the simulation including the pulse transformer is shown in FIG-3a), and this equivalent circuit includes the stray inductance and capacitance of the pulse transformer, but the stray inductance of the capacitance are neglected. The calculated pulse shape is also shown in the FIG-3b), and the rise time around or less than 200 nsec was achieved.

Fabrication of the Blumlein type PFN

The fabrication of this PFN was carried out in Ishikawajima-Harima Heavy Industries Co., Ltd.. As shown in Fig-2), the PFN's and their casing have been completed, and the first high voltage test with the dummy load is scheduled to the end of May.

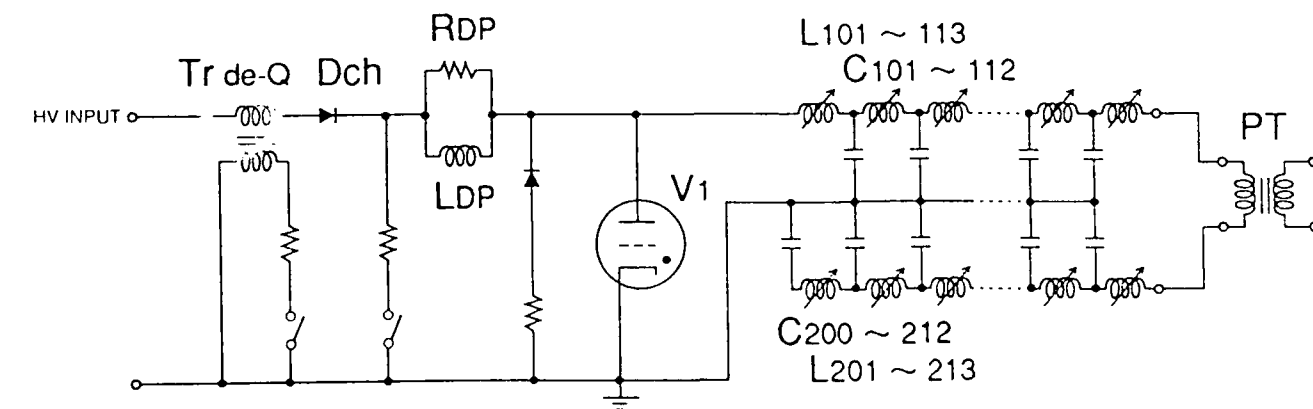
Discussions

The stray inductance of the capacitors may limit the rise and fall time of this PFN system. The main source of this stray inductance is the lead wire which is located in the insulation ceramics of the capacitor. To avoid this problem, PFN circuit should be placed in the insulation oil tank and wirings in the PFN should be made as short as possible to decrease The primitive design work on this subject are under progress.

References

- 1)"JLC-1", ed. by JLC group, KEK Report 92-16(1992)
- 2)K.Takata. " Proc. of HEACC92", Hamburg(1992)p.811.
- 3)H.Mizuno et al.,KEK Preprint 92-122(1992)
- 4)M.Akemoto et al., "Proc. of the 1991 IEEE particle Accelerator Conference", San Francisco, p.1040(1991)

Fig-1) Blumlein PFN



L101-103=340nH. C101-112=2.9nF
L201-213=340nH. C201-212=2.9nF

V1 Thyatron(CX1937A; EEV)

Noise Reduction Techniques Used on the High Power Klystron Modulators at Argonne National Laboratory*

Thomas J. Russell

Argonne National Laboratory, 9700 S. Cass Avenue, Argonne, IL 60439

Abstract

The modulators used in the Advanced Photon Source at Argonne National Laboratory have been redesigned with an emphasis on electrical noise reduction. Since the modulators are 100 MW modulators with <700 ns rise time, electrical noise can be coupled very easily to other electronic equipment in the area. This paper will detail the efforts made to reduce noise coupled to surrounding equipment. Shielding and sound grounding techniques accomplished the goal of drastically reducing the noise induced in surrounding equipment. The approach used in grounding and shielding will be discussed, and data will be presented comparing earlier designs to the improved design.

I. MODULATOR PARAMETERS AND SYSTEM CONFIGURATION

There are five high power modulators used on the Advanced Photon Source injection linac at Argonne National Laboratory. The modulators are line type modulators incorporating command charge for regulation and control. The modulators consist of a monitor and control rack, high voltage power supply cabinet, charging choke cabinet, pulse forming network cabinet, klystron control rack, and pulse transformer tank. The configuration of these cabinets and racks is shown in Figure 1.

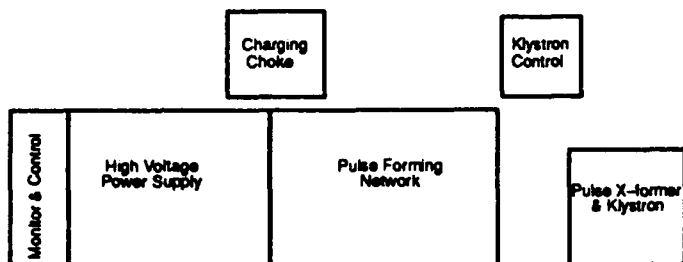


Figure 1. Basic layout of the modulator for the ANL APS linac.

The monitor and control cabinet contains the main control chassis, an interface to the main system computer, and an oscilloscope to locally monitor various wave shapes. All connections made from the monitor and control cabinet to other portions of the modulator are accomplished through fiber optic links. A limited number of connections are hard-wired to other portions of the linac system. These connections are limited to AC power and connection to the system safety system.

* Work supported by U.S. Department of Energy, Office of Basic Energy Sciences, under Contract No. W-31-109-ENG-38.

The submitted manuscript has been authored by a contractor of the U. S. Government under contract No. W-31-109-ENG-38. Accordingly, the U. S. Government retains a nonexclusive, irrevocable, and exclusive license to publish and/or to reproduce and distribute reprints for government purposes, not withstanding any copyright notation that may appear hereon.

The high voltage power supply cabinet houses a 25 kV, 2 A DC power supply. The design incorporates a 480 V 3 ϕ variac driving a Δ -Y and a Δ - Δ stepup transformer. This configuration results in a 12-pole system and reduces the filter capacitor requirements. The filter capacitor is 14 μ F at 30 kV. The high voltage power supply cabinet also houses the command charge deck. The command charge is accomplished through the use of an EIMAC 4CX15,000 tetrode, specially processed to behave as a series switch. The high voltage power supply cabinet also houses all the electronics for the pulse forming network.

The charging choke cabinet contains a 22 H charging choke, some dampening circuits, and the regulation diode with its associated load resistor. These components are contained in a 7-foot-high heavy-duty equipment rack which is connected to the high voltage power supply cabinet and the pulse forming network cabinet with RG-220 cable. Also contained in the pulse forming network (PFN) cabinet is a dump switch for the PFN and a voltage divider to monitor the PFN. Output from the PFN cabinet travels to a step-up transformer feeding the klystron through two RG-220 cables modified into a triaxial configuration.

The basic operating parameters of the klystron (Thomson CSF 2128) are given in Table 1. The design of the modulators was based on these requirements, and they were tested into a dummy load meant to represent these parameters.

Table 1
Klystron Parametric Requirements

Parameter	Required
Beam Voltage	315 kV
Beam Current	315 A
Perveance	1.78 μ
Efficiency	35 %
Frequency	2856 MHz
Output Power	35 MW

The modulators were built and tested; Table 2 presents the data measured.

II. SPECIAL NOISE REQUIREMENTS

Because of the close proximity to other electronic equipment, special emphasis was placed on minimizing the electrical noise generated by the modulator. One modulator built by a commercial vendor was installed and tested in our linac test stand, but the level of radiated noise was unacceptable. In addition to anecdotal evidence (e.g. modulator control electronics

Table 2
Modulator Parametric Requirements and Achievements

Parameter	Required	Achieved
Peak Output Voltage	20.5 kV	22 kV
Peak Output Current	4,820 A	4,990 A
Peak Output Power	100 MW	110 MW
Output Impedance	*4.25 Ω	**4.42 Ω
Transformer Step-up Ratio	1:15.3	1:15.3
Pulse Width	5 μ s	5 μ s
Repetition Rate	60 pps	60 pps
Modulator Rise Time	<700 ns	<150 ns

*Measured at low voltage **Calculated by Ohm's Law

operating incorrectly, sparks between mating cabinet doors), several measurements were made. It was found that the behavior of much of the electronic equipment not associated with the modulators deteriorated when the vendor-supplied modulator was operating.

Measurements of radiated noise were made on the original design using a loop antenna input to an oscilloscope. The antenna and oscilloscope were terminated into 10 k Ω . The locations of the measurements are shown in Figure 2.

Our modulator design was engineered based entirely on coaxial principles. At any point where pulse currents flow, the return current path is coaxial about the conductor. This eliminates any magnetic loop antenna configuration which might radiate an interference signal. In order to assure that all the return current flowed through the coaxial configuration, it was necessary for the current path to be separated from ground.

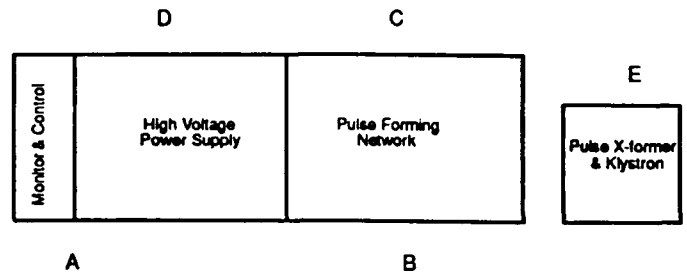


Figure 2. Locations of radiated noise measurements.

Therefore, all components were floating above ground by several 10's of volts. Figure 3 is an abbreviated schematic design for the improved shielding configuration.

III. TEST RESULTS

Tests were conducted on the improved modulator to compare the radiated noise to the original modulator design. Similar data was collected using the original design. The results of both measurements are shown in Table 3. The data is presented in power for simpler comparison to other data. It should be noted that while efforts were made to make the measurements as similar as possible, some differences in the testing exists.

IV. CONCLUSIONS

There has been a vast improvement in radiated noise on the high powered klystron pulsed modulators at the Advanced Photon Source. These efforts were made to improve operation of nearby sensitive equipment in the equipment gallery. Data clearly shows the improvement is on the order of 40 to 50 dB. Additionally, a simple test was made by the author using an inexpensive AM radio. With the modulator operating at full pow-

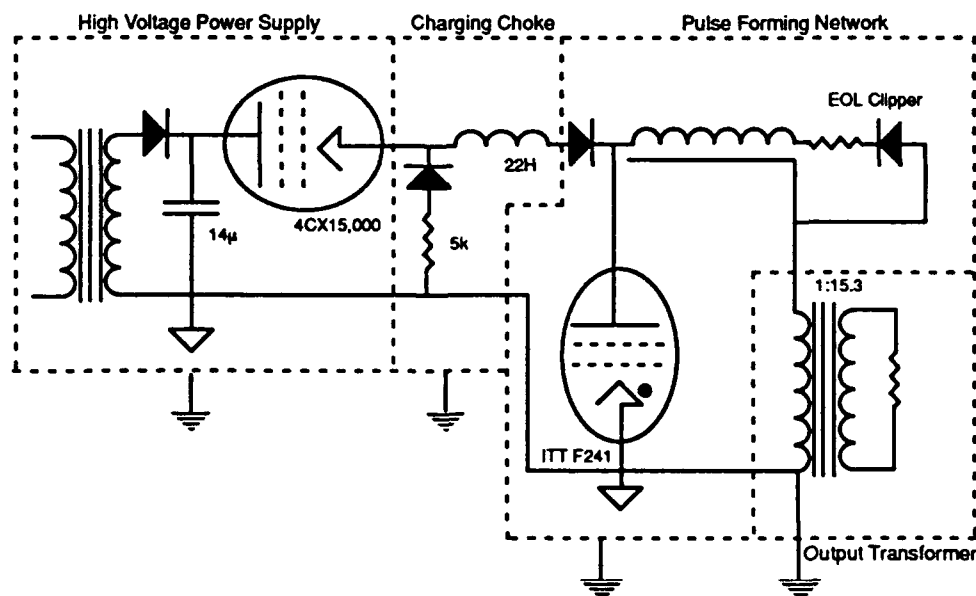


Figure 3. Abbreviated circuit design with grounds and shields.

er and full rep rate, noise was barely noticeable on the radio located three feet from the modulator.

V. ACKNOWLEDGMENTS

The author would like to thank many people in the design and construction of the modulator: Ray Fuja, for offering assistance and experience on numerous occasions; Matt Lagessie, Kevin Dunne, Rob Wright, and Mike Phelan and many others who, under a great deal of pressure, built five modulators in nine months; and Quentin Kerns of FNL for explaining the idea of a coaxial modulator.

Table 3
Measurements of radiated noise for
both the original and improved design

Location	Original Design		Improved Design	
A	2.4	mW	0.12	μ W
B	3.2	mW	0.02	μ W
C	9.8	mW	0.16	μ W *
D	0.8	mW	—	
E	20	mW	22	mW **

Notes:

*The test on the improved design was performed with the cabinet doors open while tests on the original design were made with the cabinet doors closed; therefore, actual results should be even better.

**Location E is directly next to the dummy load which was the same for both tests. No effort was made in shielding the dummy load; therefore, results should be similar.

Novel Gigawatt Power Modulator for RF Sources*

I. Yampolsky, G. Kirkman, N. Reinhardt, J. Hur and B. Jiang

Integrated Applied Physics, Inc.

50 Thayer Road, Waltham, MA 02154 USA

Tel. (617) 489-1818

Abstract

A novel method for producing high voltage rectangular pulses for driving RF sources is described. The approach uses two advances in pulsed power technology: 1) The BLT switch and 2) Novel transmission line transformer techniques using switches between lines. Experimentally demonstrated is a modulator producing 80kV, 800A output pulse requiring only 22kV switch voltage. The output pulse is ~120nsec long with <40nsec rise and fall times. A modulator designed to produce 1MV, 1kA output pulse using 50kV switches is described and simulated by computer. The application of this modulator to drive RF sources for advanced accelerators is discussed.

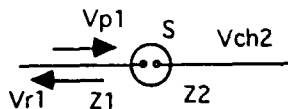
I. INTRODUCTION

There have been many attempts to use the Marx generator to get short rectangular pulses in nanosecond region of time. The stray capacitances of the lines spoiled the shape of the pulse. In this work, we describe a novel approach to obtaining a rectangular output pulse from a multistage Marx like generator. We started the investigation with a transmission line transformer scheme what was proposed by Smith¹. In a standard transmission line transformer a single switch is used at the input and the step up ratio is typically limited to about 5 or 6 thus a 1MV output requires an input switch of ~200kV. Switching at this level at high rep rates and currents is extremely difficult. In our design we use several lower voltage switches at the transition points of the transmission line transformer. This approach allows us to obtain an output of 1MV using 50kV switches.

II. SWITCHED TRANSMISSION LINE TRANSFORMER

The main idea of our approach is to locate switches between lines. In this case, the capacitance of isolation transformers and triggering transformers can be included to the capacity of lines and the switch inductance can be included to the inductivity of the lines. This means that the influence of the parasitic parameters of the switch on the output pulse can be eliminated. The charge voltage of the lines can be tripled between switches uniformly by means of charging transformer or with help of some dividers.

If we have two transmission lines and an ideal switch between them,



the reflected wave in the first line is:

$$Vr1 = (Vch2 - Vp1(1 - Z2/Z1)) / (1 + Z2/Z1) \quad (1)$$

*This work was supported by the U. S. DOE through the SBIR program.

The main problem in design of TLT (Transmission line transformer) to bring to 0 each reflected wave. By different law of increasing charging voltage it is very hard to get entire formula, about how the resistance of the line has to respond to this increasing. But it is very easy to write a computer program for optimization purposes.

When designing the actual device, we can use several active sections and several passive ones. Some examples at such approach are shown in Fig 2. From this figure, one can see that the closer to the beginning are pulsed the switches, the higher is the gain at the output voltage. The upper limit can be achieved when all switches are put in the very beginning of the lines. But in such case, they need to work in series which is not easy to accomplish.

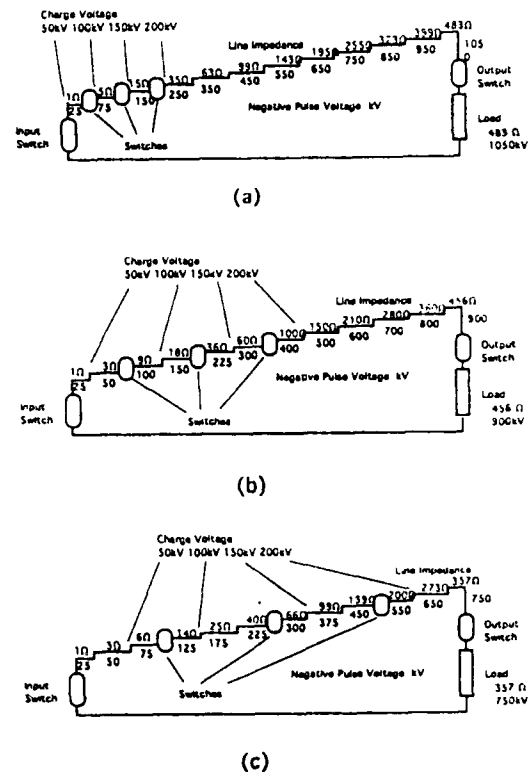


Figure 3. Three possible schemes for the switched TLT. Charge voltage is with respect to ground such that each switch is required to holdoff 50kV. a) Scheme using 3 switched sections and 9 passive sections to give 1050 kV output. b) Scheme using one impedance step between switches for 6 sections followed by 6 passive sections to give 900kV output. c) Scheme using two impedance steps between switches for 9 sections followed by 3 passive sections. For design purposes the total number of switches was limited to 4 and number of sections to 12, for computational purposes an output switch is used which will be replaced by an isolating line in the final design.

III. EXPERIMENT

An experiment to demonstrate the switched TLT was undertaken using two BLT switches capable of operating at up to 50kV in a configuration to give an output which is four times the switch voltage. The circuit design is that of scheme b in figure 2 using a total of four sections plus an output isolating line. The block diagram of the pulse generating system is shown in figure 3.

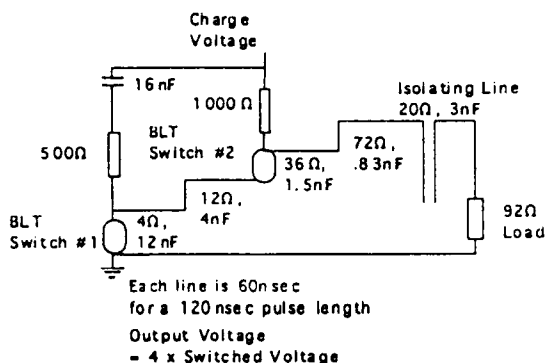


Figure 4. Experimental circuit for demonstrating the feasibility of the switched transmission line transformer using multiple BLT switches.

The test circuit was fabricated using discrete components to produce five transmission lines of different impedances. The first two lines, 4 and 12- Ω impedance, consist of ceramic capacitors and inductance formed by a rectangular coaxial housing. The third and fourth lines, 36 and 72- Ω impedance, are formed from custom capacitors fabricated by IAP using a cylindrical geometry and mylar film dielectric. Each line is twelve sections of equal capacitance the length of each line is 60nsec. The fifth line 20 Ω isolates the charging voltage from the load.

The switches used in this system are the BLT-250-T which is an electrically triggered single gap BLT switch. Performance of the switch is described in another paper at this conference². The switch is capable of operation at 1 Ω circuit impedances at up to 50kV when pulse charged in $\sim 10\mu\text{sec}$. The switch uses a cold cathode to conduct the main discharge current therefore requires very low heater power. The small amount of heater power allows the switch to operate at floating voltages without large isolation transformers for the heater power.

In optimized operation using two switches an output pulse of 80kv with a 40nsec voltage risetime (10 to 90%) has been obtained at a 22kV switch voltage and is shown in the figure 4. The optimized output pulse occurs when the second switch closes precisely at the time the pulse from the first switch arrives. This is 120nsec after the first switch closes.

The BLT switch has been demonstrated to operate with timing jitter on the order of 1nsec when operating at high power. In this system two BLT switches have been synchronized to produce an output pulse with timing jitter of $<1.5\text{nsec}$. The jitter of the load voltage is measured statistically taking a sample of 2000pulses while operating continuously at 5Hz for 25minutes. The resulting data is presented in figure 5.

This data shows the statistical jitter of the BLT and indicates the long term stability of the system. When operating at higher power some drift of delay may occur due to thermal variations in the system however these can be compensated for with computer control. We have developed a microprocessor based system to control the drift of the BLT. The BLT uses a quickly responding gas reservoir which when combined with a computer controlled power supply the drift can be eliminated. Drift can further be reduced by varying the trigger delay time to the BLT switch.

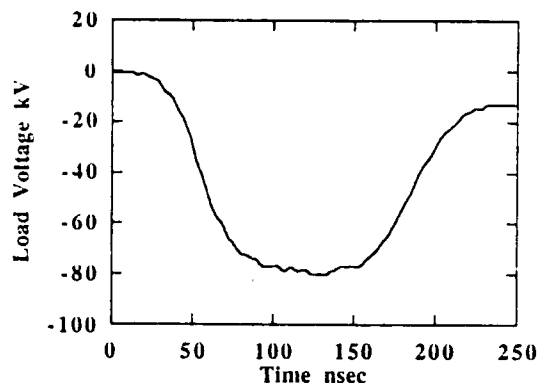


Figure 4. Output voltage obtained in experimental circuit using two BLT switches. Switch voltage was 22kV and repetition rate 5Hz, load current is 800A.

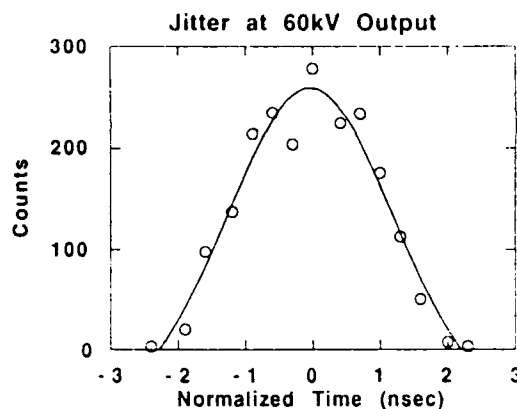


Figure 5 Statistical measurement of the jitter. Data consists of a 2000 pulse sample taken while continuously operating at 5Hz for 25 minutes. No pulses occurred outside of the data range shown.

IV. MODULATOR DESIGN FOR 1 MV

A key element in the development of higher energy and higher luminosity linear colliders is the availability and cost of the RF power required to drive the accelerator. In present designs RF power is required at 11.4GHz in 100 to 200nsec long pulses with peak powers of 1GW³. The present approach to obtain this output is to drive the RF source at $\sim 100\text{MW}$ for $\sim 1.4\mu\text{sec}$ then use RF pulse compression to shorten the pulse and increase the peak power. The pulse compression is inefficient therefore requires that the pulse modulator be very efficient. The pulse modulator in this approach can be a transformer based system provided that the step up ratio is not too high, however this puts severe demands on the high voltage input switch and special

techniques must be used to reduce the required switch voltage⁴.

Our pulse modulator techniques can be applied to directly drive an RF source at the 1GW power level with 200nsec pulse length. This approach eliminates the need for RF compression increasing the system efficiency. Additionally the modulator design operates at a maximum switch voltage of 50kV, greatly reducing the cost while improving the reliability and system lifetime.

Fig. 6 shows the system which uses twelve pulse forming lines in our novel switched transmission line modulator configuration. Each line is 1.5m long and 20cm diameter. Each BLT switch operates at 50kV holdoff voltage with the total charge voltage being 200kV. A Darlington section is used to isolate the load from the charging voltage canceling any prepulse. A passive tuning line is transformer coupled to the output for adjusting the pulse shape. The tuning line operates at ~10% of the load voltage reducing fabrication complexity.

One of the problem consists of very different wave resistances required for different lines. They start from 2 Ω for the first line and finish with 1 k Ω for the last line. The size of the lines is kept reasonable by using water dielectric for the low impedance lines, oil for the higher impedance lines and a delay structure within the lines to minimize the length.

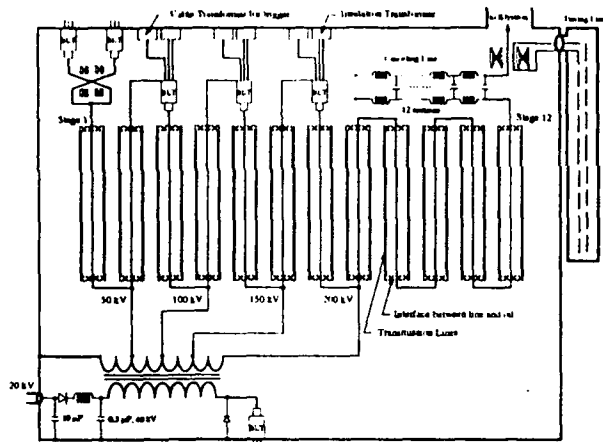


Figure 6. Modulator design to produce 1MV using 50kV switches.

Design Simulation

Computer simulation of the modulator design has been undertaken for two configurations of the pulse forming lines. Figure 7. shows the output voltage for a twelve section modulator for two cases. 1) each pulse forming line uses 12 sections, and 2) each pulse forming line uses 24 sections. In each case an optimization procedure was used to determine the inductance between lines and precise time of switching. One can see that in the case of 24 cells the rise and fall time of the pulse are shorter and the flat top longer. Since only the flat portion of the pulse is useful to RF generation the efficiency

of the 24 cell system is higher. In the final design conclusion economical details must be considered.

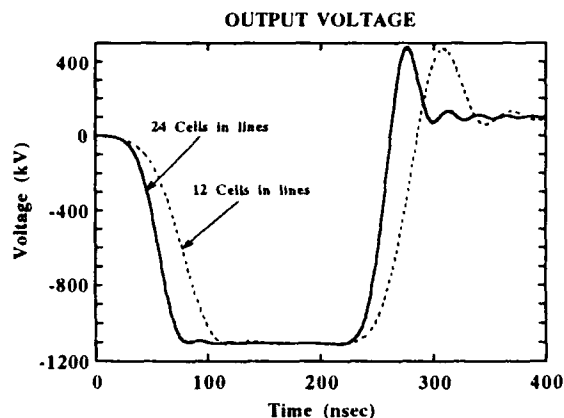


Figure 7. Computer simulated output of modulator using four 50kV switches to produce 1MV. Dashed line is for pulse forming lines consisting of 12 cells and the solid line is for lines with 24 cells.

V. CONCLUSION

In this work we have demonstrated the feasibility of producing high voltage output pulses using a transmission line transformer incorporating BLT switches between line sections. We have successfully demonstrated synchronization of two BLT switches and an output that is four times the switch voltage. Based on these results a system for producing 1MV, 1kA, 200nsec pulses has been designed and modeled by computer.

The key result is the demonstration of an innovative modulator system that could be scaled up to drive RF sources at the gigawatt power level for future accelerators. The modulator would produce high peak power with 200nsec pulse length eliminating the need for RF pulse compression. This would greatly enhance the efficiency and reduce the overall cost of RF power.

REFERENCES

- ¹I. Smith "A novel voltage multiplication scheme using transmission lines," 15th Power Modulator Symposium, page 223, 1982, I. Smith "Principles of the design of lossless tapered transmission line transformers," 1989 Pulsed Power Conference, page 103, 1989.
- ²G. Kirkman, N Reinhardt, B. Jiang, J. Hur and I. Yampolsky, "High voltage switches for accelerator applications," 1993 Particle Accelerator Conference, paper #Sb89.
- ³G. Caryotakis, "Multimegawatt RF power sources for linear colliders," 1991 Particle Accelerator Conference, page 2928.
- ⁴K. Harris, J. de Lamare, V. Nesterov and R. Cassel, "600kV modulator design for the SLAC next linear collider," 20th Power Modulator Symposium, page 139, 1992.

Optimization of Speed-Up Network Component Values for the 30 Ω Resistively Terminated Prototype Kicker Magnet

M. J. Barnes, G. D. Wait,
TRIUMF, 4004 Wesbrook Mall, Vancouver, B.C., Canada V6T 2A3

Abstract

Kicker magnets are required for all ring-to-ring transfers in the 5 rings of the proposed KAON factory synchrotron. The kick must rise from 1% to 99% of full strength during the time interval of gaps created in the beam (80 ns to 160 ns) so that the beam can be extracted with minimum losses. In order to achieve the specified rise-time and 'flatness' for the kick it is necessary to utilize speed-up networks, comprising a capacitor and a resistor, in the electrical circuit. Speed-up networks may be connected electrically on both the input and output of the kicker magnet. In addition it is advantageous to connect a 'speed-up' network on the input of the resistive terminator(s). A sequence which may minimize the number of mathematical simulations required to optimize the values of the 8 possible speed-up components is presented. PE2D has been utilized to determine inductance and capacitance values for the resistive terminator; this data has been used in PSpice transient analyses. Results of the PE2D predictions are also presented. The research has culminated in a predicted kick rise time (1% to 99%) of less than 50 ns for a TRIUMF 10 cell prototype kicker magnet. The proposed improvements are currently being implemented on our prototype kicker system.

I. INTRODUCTION

The magnetic field rise time of a transmission kicker magnet results from a superposition of the rise time of the pulse from the pulse generator and the propagation time of the pulse through the magnet (fill time) [1]. Many of the kicker magnets for the proposed KAON factory synchrotron require 1% to 99% kick rise/fall times of less than 82ns [2,3].

In order to compensate for unavoidable impedance mismatches it is necessary to include several 'speed-up' networks in the design of the pulse generator. In the case of a kicker magnet which is terminated in a short-circuit on its output, for example the booster extraction kicker magnet for the KAON factory [1], only one or two speed-up networks are required [4].

The collector injection kicker magnet for the KAON factory requires both a 1% to 99% rise and fall time of 82ns [2]. In order to achieve both the specified rise and fall time, a kicker magnet which is terminated resistively may require four speed-up networks, which results in eight components whose values are to be optimized. A methodology has been developed which permits optimum values to be determined for these eight components, with a minimum number of mathematical simulations.

As part of the KAON Factory project definition study a prototype transmission line type kicker magnet has been built at TRIUMF [2]. This kicker magnet is based on the design of those of CERN PS division [3,5]. The prototype kicker is a 10 cell magnet with a design value of 30 Ω for the characteristic impedance [1]. The prototype magnet has been simulated for the PSpice studies reported in this paper.

II. EQUIVALENT CIRCUIT

Fig. 1 shows a block diagram of the equivalent circuit for the kicker magnet and pulse generator; connections, cable plugs and sockets, as well as losses in the ferrite and mutual coupling between adjacent cells of the kicker magnet

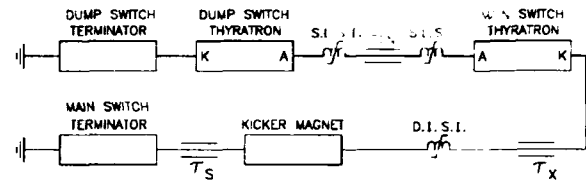


Figure 1: Block diagram of pulse generator and magnet

are simulated [6] but not shown in Fig. 1. The equivalent circuit of the main switch and dump switch thyatron allows for both anode and cathode displacement current [1,7]. The D.I.S.I. (Displacement Current Saturating Inductor) shown in Fig. 1 reduces the magnitude of pre-pulse cathode displacement current which flows through the kicker magnet to an acceptable level [1], therefore significantly decreasing the 1% to 99% field rise-time in the kicker magnet [1,8].

As mentioned above four speed-up networks are required in order to achieve the specified rise and fall times for the collector injection kicker magnet. Speed-up networks connected on the output and input of the kicker magnet mainly effect the leading and trailing edge, respectively, of the kick [9].

During the post-pulse period the D.I.S.I. is unsaturated (relatively high impedance); in order to obtain a satisfactory post-pulse kick, any reflections from the non-ideal main-switch resistive terminator must be suppressed. Hence it is advantageous to connect a speed-up network on the input to the kicker magnet, between the magnet and the D.I.S.I. In addition, connecting the speed-up network between the magnet and the D.I.S.I. helps to suppress impedance resonances which the beam might otherwise 'see' [10].

In order to be able to select optimum component values for the speed-up networks, Figures of Merit (FOM) are calculated for the kick [11]. The integral with respect to time of the deviation of the kick from the ideal levels (0% and 100% of full kick strength) and outside of specified levels ($\pm 1\%$ deviation of full kick strength from the ideal levels) is used to determine two FOM's for each of the pre-pulse, 'flat-top' and post-pulse periods: these FOM's also take into consideration the predicted and specified rise-times.

The resulting complex equivalent circuit has been analysed in the time domain by utilizing the transient analysis capabilities of PSpice [12]. The Analogue Behavioral Modelling capability of PSpice has been utilized to calculate the time integral of the deviation of the predicted kick from the ideal and specified levels. The powerful Goal Function capabilities of the Probe [12] post-processor are then utilized to determine the FOM's. The Goal Function capability of Probe has been used in conjunction with the Parametric Analysis capability of PSpice to rapidly determine the value of a component which results in a minimum FOM.

III. PROPOSED DESIGN METHODOLOGY

The D.I.S.I. may significantly effect the optimum values of the speed-up network components connected on the input to the kicker magnet, hence it is necessary to simulate the D.I.S.I. throughout the optimization process. The following design methodology has been developed for identifying

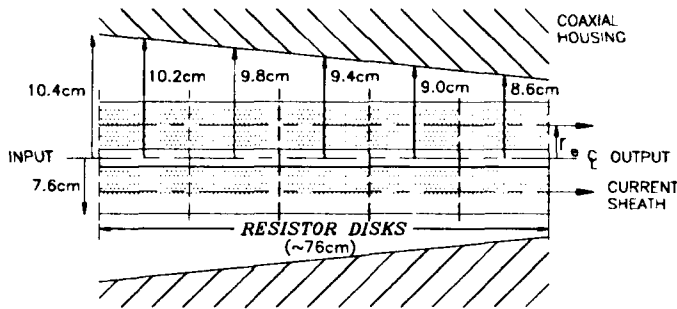


Figure 2: CERN PS Division Resistive Terminator

'optimum' values for speed-up network components, for a resistively terminated kicker magnet, with a minimum number of mathematical simulations [9]:

1. Simulate the main switch and dump switch resistive terminator as being ideal. The ideal main-switch resistive terminator must be simulated as being directly connected on the output of ideal transmission line τ_s (Fig. 1). Simulate a speed-up network on the output of the kicker magnet only:
 - this speed-up network is modelled as having a resistor whose value is equal to the characteristic impedance of the Pulse Forming Network (PFN). The value of the speed-up capacitor is swept through a range of values to identify an optimum;
 - subsequently simulate this speed-up network as having a capacitor whose value is equal to the optimum value identified above. The value of the speed-up resistor is swept through a range of values to identify an optimum value.
2. A speed-up network with optimized values for the capacitor and resistor is simulated on the output of the kicker magnet. A speed-up network is simulated on the input of the magnet too:
 - this input speed-up network is modelled as having a resistor whose value is equal to the characteristic impedance of the PFN. The value of the speed-up capacitor is swept through a range of values to identify an optimum;
 - subsequently simulate the input speed-up network as having a capacitor whose value is equal to the optimum value identified above. The value of the speed-up resistor is swept through a range of values to identify an optimum.
3. A realistic mathematical model of the main-switch resistive terminator is simulated, and speed-up networks with optimized values for the capacitor and resistor, as identified above, are simulated on both the output and input of the kicker magnet. A 'speed-up' network is simulated on the input of the main-switch resistive terminator:
 - the 'speed-up' network on the input to the main-switch terminator is modelled as having a resistor whose value is equal to the characteristic impedance of the PFN. The value of the capacitor is swept through a range of values to identify an optimum.
 - the 'speed-up' network on the input to the main-switch terminator is modelled as having a capacitor whose value is equal to the optimum value identified above. The value of the 'speed-up' resistor is swept through a range of values to identify an optimum.

A S.L.S.I. (Switching Loss Saturating Inductor) may be connected adjacent to the anode of the main switch thyratrons [1,7]. The S.L.S.I. has several beneficial effects such as reducing switching-losses in the thyatron, improving current rise-time, and reducing the effect of anode displacement current [1,7]. If a S.L.S.I. is to be incorporated,

experience has shown that the S.L.S.I. should be simulated prior to optimizing the values of the components associated with the 'speed-up' network connected in parallel with the dump-switch resistive terminator. This 'speed-up' network mainly compensates for the tail which the S.L.S.I. may otherwise introduce: as the S.L.S.I. comes out of saturation magnetically stored energy is released into the system. When optimizing these component values, the optimum values for the other three speed-up networks, as identified above, are modelled.

Experience has shown that it is not necessary to re-optimize the values of the speed-up capacitors after the resistor values have been optimized.

The predicted results for the kick are relatively insensitive to the exact value of the parasitic inductance associated with the speed-up networks.

IV. RESISTIVE TERMINATOR

The inner diameter (D) of the coaxial housing of the CERN resistive terminator is tapered (see Fig. 2). This design permits the resistive terminator to withstand the pulse voltage while minimizing the parasitic inductance of the terminator. PE2D [13] has been utilized to calculate the inductance of the CERN PS Division resistive terminator [9]. Since PE2D is a two dimensional electromagnetic analysis package, it cannot simulate a tapered terminator. Hence the PE2D analysis is repeated for several diameters, between the minimum and maximum inner diameters, of the tapered housing.

The overall inductance per metre length (L_{pm}) of the resistive terminator is calculated by using the stored energy/unit length (integral $B \cdot H / 2 \, ds$), as determined using PE2D. The effective radius (r_e) of current flow in the resistor disks is calculated from this inductance:

$$r_e = \left(\frac{D}{2 \times e^{\left(\frac{L_{pm}}{2 \times 10^{-7}} \right)}} \right) \quad (1)$$

Analysis of the results of PE2D simulations, for a given driving frequency, shows that r_e is independent of the inner diameter of the coaxial housing. Thus, for a given driving frequency and resistivity of resistor disks, the PE2D analysis need only be carried out for one diameter of a tapered housing: from a knowledge of r_e the inductance per metre length can then be calculated for any inner diameter along the length of the tapered housing.

The inside diameter of the resistor disks is 34.2mm. Approximately 30 disks, with a resistance of 1Ω each, may be used for a 30Ω terminator. For a disk of resistivity $0.68\Omega \cdot m$ (as per the CERN PS Division resistive terminator) the effective radius of the current sheath is approximately 6.1cm, and only increases by about 1% as frequency is increased from 1MHz to 60MHz. At 60MHz the current density in the disk increases linearly, by about 16%, from the inside to the outside diameter of the resistor disks. As a result of proximity effect image current flows on the inside diameter of the coaxial housing. Assuming a dissipation of 60W per resistor disk, cooling of $0.02W \cdot K^{-1} \cdot cm^{-2}$ on all surfaces of a disk, thermal conductivity of the resistor material of $0.0334W \cdot K^{-1} \cdot cm^{-2}$ [14], and a disk thickness of 25.4mm, the maximum predicted temperature, which is $10^\circ K$ above bulk fluid temperature, occurs at a radius of 45mm and halfway through the thickness of the disk [15]. For a disk of resistivity $0.34\Omega \cdot m$ the effective radius of the current sheath increases by about 4% as frequency is increased from 1MHz to 60MHz.

The capacitance per metre length of a coaxial structure is given by:

$$C = \left(\frac{2 \times \pi \times \epsilon_0 \times \epsilon_r}{Ln \left(\frac{D}{2 \times r_e} \right)} \right) \quad (2)$$

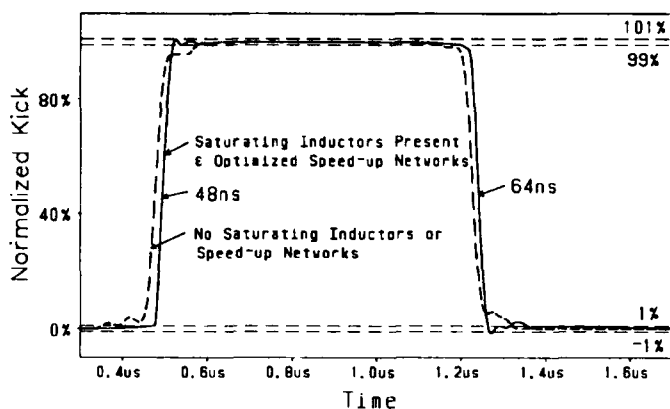


Figure 3: Predicted normalized kick for the 10 cell prototype kicker magnet

In order to calculate capacitance per metre, for use in PSpice simulations, ϵ_r for the resistor disks has been assumed to be unity.

The resistive terminator is simulated, in the PSpice analyses, as five equal length sections connected in series [9] (see Fig. 2).

V. GENERAL RESULTS

The presence of resistors in the speed-up networks, connected on the input and output of the kicker magnet, do not have a significant effect upon the predicted field in the flat-top or post-pulse period. However the presence of a resistor, whose value is equal to the characteristic impedance of the PFN, in the speed-up network on the input to the kicker magnet, damps some of the impedance resonances which the beam may 'see' [10]. The resistor associated with the 'speed-up' network, connected on the input of the main-switch resistive terminator, does help to damp oscillations during the flat-top and post-pulse period.

A 'speed-up' network on the input of the resistive terminator is effective at dealing with the non-ideal characteristics of the terminator. In addition the 'speed-up' network can be optimized to permit the use of a cylindrical housing, rather than the tapered coaxial housing associated with the CERN PS division resistive terminator; the diameter of the housing would be as per the input of the tapered housing, so as to maintain voltage withstand. With a suitably optimized 'speed-up' network, a cylindrical coaxial housing results in virtually identical FOM's as a tapered housing.

Fig. 3 shows two predicted time-responses for the 30 Ω prototype kicker magnet connected in a representative electric circuit. The 'dashed' pulse in Fig. 3 is predicted when there are no D.I.S.I., S.L.S.I. or speed-up networks. The 'continuous' pulse in Fig. 3 is the prediction obtained when the D.I.S.I. and S.L.S.I. inductors, and the optimized speed-up network values are utilized: the predicted rise-time (1% to 99%) is less than 50ns, as opposed to 164ns without saturating inductors or speed-up networks.

VI. CONCLUSION

A sequence which may minimize the number of mathematical simulations required to optimize the values of the speed-up network components has been developed. Initially the main-switch and dump-switch resistive terminators are modelled as being ideal and the speed-up networks on the output and input of the magnet are optimized, respectively. It is necessary to simulate the D.I.S.I. while optimizing these speed-up networks. Subsequently a realistic main-switch resistive terminator is simulated and the 'speed-up' network on the input to the main-switch terminator is optimized independent of the other speed-up networks. In order to properly optimize values of the

resistor and capacitor associated with the 'speed-up' network connected on the input to the dump-switch resistive terminator it is necessary to simulate the S.L.S.I.'s.

PE2D has been utilized to determine inductance and capacitance data for the resistive terminators. A 'speed-up' network on the input of each resistive terminator is effective at dealing with the terminators non-ideal characteristics. In addition the 'speed-up' network can be optimized to permit the tapered coaxial housing, associated with the CERN PS division resistive terminator, to be manufactured as a coaxial cylinder instead.

VII. REFERENCES

- [1] M.J. Barnes, G.D. Wait, "Kickers for the Kaon Factory" Proceedings of XVth International Conference of High Energy Accelerators (HEACC'92), Hamburg, July 1992.
- [2] M.J. Barnes, G.D. Wait, "Improving the Performance of Kicker Magnet Systems" Proceedings of XVth International Conference of High Energy Accelerators (HEACC'92), Hamburg, July 1992.
- [3] "TRIUMF KAON FACTORY STUDY," *Accelerator Design Report*, May 1990.
- [4] M.J. Barnes, G.D. Wait, "Optimization of Speed-Up Network Component values for the Short-Circuit 30 Ω Prototype Kicker Magnet". TRI-DN-91-K195.
- [5] D. Fiander, K. Metzmacher and P. Pearce, "Kickers and Septa at the PS Complex, CERN". *Proceedings of the KAON PDS Magnet Design Workshop*, October 1988, pp 71-79.
- [6] M.J. Barnes, G.D. Wait, "Suppression of the Effect of Thyatron Displacement Current upon the Field in the 30 Ω Prototype Kicker Magnet". TRI-DN-91-K170.
- [7] M.J. Barnes, G.D. Wait, "A Mathematical Model of a Three-Gap Thyatron Simulating Turn-On", to be published in the proceedings of the Ninth IEEE Pulse Power Conference, June 1993. Albuquerque.
- [8] T. Mattison, R. Cassel, A. Donaldson, H. Fischer, D. Gough, "Pulse Shape Adjustment for the SLC Damping Ring Kickers". *IEEE Conference Record of the 1991 Particle Accelerator Conference*, May 6-9, 1991, pp3156-3158.
- [9] M.J. Barnes, G.D. Wait, "Optimization of Speed-Up Network Component Values for the Resistively Terminated 30 Ω Prototype Kicker Magnet". TRI-DN-91-K187.
- [10] M.J. Barnes, H. Tran, G.D. Wait, Y. Yin, "Longitudinal Impedance of a Prototype Kicker Magnet", Proceedings of this Conference.
- [11] M.J. Barnes, G.D. Wait, "Analysis of the Transient Response of Magnetic Kickers for the KAON Factory". TRI-DN-89-K75.
- [12] Microsim Corporation, 20 Fairbanks, Irvine, California. U.S.A. Tel. (714) 770 3022.
- [13] Vector Fields Ltd, 24 Bankside, Kidlington, Oxford. OX5 1JE. U.K. Tel. (08675) 70151.
- [14] A-B Publication 4901, May 1986, General Hybrid, Jarrow, Tyne & Wear, U.K. Tel (091) 489 7771
- [15] Private Communication with T. Hodges, University of Victoria, Victoria, B.C., Canada.

Test results of the 8.35 kA, 15 kV, 10 pps pulser for the Elettra Kickers

R.Fabris, P.Tosolini

Sincrotrone Trieste, Padriciano 99, 34012 Trieste, Italy

Abstract

With reference to the Conceptual Design of ELETTRA [1], the kicker magnets to be used for the injection into the 2 GeV storage ring Elettra require to be supplied by a high peak pulsed current whose characteristics must be strictly controlled over a long period of operation. A thyatron friendly circuit configuration, based on a capacitor discharge type power pulser with a resistive recovery, has been designed and tested at 8800 A peak current, 10 pps, showing the ability to operate for more than 2 million pulses without any fault firing and with no significant degradation of the thyatron.

I. INTRODUCTION

After a long and accurate analysis of the problem the following parameters for each Kicker have been defined, as it is shown in table 1.

Table 1. Kicker Magnet main parameters.

Electron beam energy	2 GeV
Deflection angle	22 mrad
Magnetic core length	600 mm
Free aperture	90 H x 48 V mm
Peak magnetic field	0.22 T
Magnet inductance	1.5 μ H
Total inductance	2 μ H
Peak current	8350 A
Charging voltage	15 kV
Pulse duration	5 μ s
Pulse repetition rate	10 pps

It should be pointed out that the mandatory characteristics are:

- 1 - the intensity and the shape of each pulse;
- 2 - the perfect synchronism between the four Kickers;
- 3 - the absolute identity of the pulses even during long periods of time.

The power pulser is based on a capacitor discharge circuit: a capacitor is charged up to the full voltage, then it is discharged by means of a thyatron switch, which is triggered when the pulse is required.

Because of the intensity of the current pulse the use of thyatrons connected in parallel could be adopted as well, but the required compact design of the injection section, the problem of sharing the current in a correct way without increasing the jitter and moreover the needed reliability of the

whole system forced us to investigate the possibility of using a single thyatron solution.

The configuration of a circuit able to operate in safe conditions even for such high peak currents is presented and the results of the most relevant tests at 8800 A peak current, at 10 pps repetition rate are reported and discussed.

II. THE POWER PULSE CIRCUIT

A. General considerations

The capacitor discharge power circuit with the magnet inductance L and the resistive recovery path (diode D and resistor R) is shown in fig. 1.

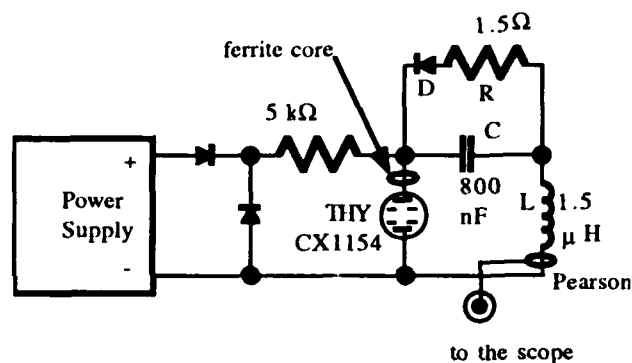


fig. 1 Simplified scheme of the power pulse circuit.

The capacitor C is charged up to the full voltage, then when the thyatron THY is fired the anode voltage falls down to its conduction value. If the time constant of the recovery path is high compared to the pulse duration, at the moment when the anode current reaches the zero crossing point, i. e. when the thyatron switches off, the anode rapidly jumps to a reverse voltage which is comparable to the full voltage.

The tube manufacturer usually recommends to stay within a specified negative voltage value (10 kV) within the first 25 μ s after the zero crossing; if this prescription is violated then the thyatron, which is still highly ionized, could arc back and, if the current or voltage values exceed the thyatron maximum ratings, could cause the circuit to oscillate.

Moreover the reverse arcing causes an evaporation of the cathode emissive coating and a severe damage to the electrodes surface [2], thus shortening the lifetime of the tube.

The reverse conduction also produces a short negative current pulse, which is strongly dependent from the characteristics of the thyatron; these ones cannot be exactly

(the same for the four Kickers of the injection section, thus lowering the efficiency of the injection process.

In order to obtain a safe long term operation with such a high current, friendly circuit conditions for the thyatron are to be found.

An effective solution has been reached lowering the recovery stray inductance to a minimum practical value, then trimming the recovery resistance to an optimum value (in the range of 1.5Ω) and adding a saturable inductance in series with the thyatron's anode. It is possible to show that, in these conditions the anode current reaches the zero value with low derivative, thus reducing the negative anode voltage to a safe value (below 1kV).

B. The thyatron

The thyatron used in this application is a EEV CX1154, a deuterium filled tetrode ceramic thyatron with separate reservoir; the absolute maximum ratings are summarized in table 2.

Table 2. CX1154 maximum ratings.

Anode:		
peak forward voltage		35 kV
peak inverse voltage		35 kV
peak forward current (high ppr)		3 kA
peak forward current (ppr < 60 pps)		4 kA
peak forward current (ppr < 0.1 pps)		15 kA
average current		3 A
current rise rate	(high ppr)	5 kA/ μ s
current rise rate	(low ppr)	100 kA/ μ s

Even if the 8350 A peak current of the Kickers is high with respect to the nominal current ratings, the following consideration suggested us to investigate the possibility of using a EEV CX1154 in this application:

- the maximum anode peak current capability rapidly increases as the pulse repetition rate is reduced, starting from 3 kA at high ppr, to 15 kA in single shot-crowbar operation, provided that the pulse has a $i \cdot t$ less than $0.1 \text{ A} \cdot \text{s}$ and a ppr less than 0.1 pps; similarly the anode current rise rate increases from 5 kA/ μ s at high repetition rate to 100 kA/ μ s in single shot-crowbar operation;

- the average current of the system is about 0.3 A which is a factor 10 smaller than the 3 A maximum rating;

- the operating voltage is less than a half of the tube maximum rating, so there is a wide range of possibility in adjusting the reservoir voltage to obtain a good compromise among voltage hold-off, recovery time and current rise rate during the tube life;

- a suitable rechoke network allows to control the anode inverse voltage keeping it within a small amount, which is useful to quickly turn off the thyatron; in this way the accidental refiring of the tube can be avoided even at such high current levels.

- the heaters, grid bias and drive requirements, as the relative cooling and mechanics, remain for this tube quite contained with respect to what is needed for bigger devices, allowing efficient and relatively simple circuitry and compact overall size of the system with increased reliability.

C. The bias circuit

Taking into account the required tube performances, special care has been taken in the design of the thyatron bias circuit. The chosen configuration is characterized by the grid1 DC primed and by the grid2 pulsed.

The cathode and reservoir filaments have been independently supplied stabilizing the AC mains and then using shielded adjustable step-down transformers, with a NTC protection against inrush currents and with local decoupling capacitors. This allows to minimize the intrinsic jitter of the tube.

The grid1 and grid2 bias circuit has been connected to the same stabilized AC mains; after a rectification and a smoothing, the grid1 has been primed with 140 V open circuit, 130 mA DC, while grid2 has been biased with -130 V DC voltage. This circuit include also the grid2 fast pulse driver that converts a logic level trigger signal into a positive slope pulse with a peak voltage of about 800 V, a rise time of 20 ns and a duration of 2.5 μ s.

In this way the requirements for a correct tube operation are fully satisfied.

III. TEST RESULTS

The power pulse circuit is characterized by the following components:

- Kicker Magnet (inductance 1.5 μ H)
- Thyatron EEV CX1154
- Low inductance oil filled capacitor 800 nF, 25 kV, made by NWL
- Ferrite core Thomson T22
- Resistive recovery system made up by a parallel of 5 connections, each connection made by a high voltage diode SEMIKRON HSK E 100000/4500-1,2 and a home made low inductance power resistor.

The anode voltage has been monitored with a high voltage probe TEKTRONIX P6015, the current with a pulse current transformer PEARSON 110A (0.1 V/A) and the trigger signal has been sent directly to a digital oscilloscope. Typical waveforms of the anode voltage and of the current pulse are shown in fig. 2.

The digital oscilloscope has been connected to a PC computer by means of a GPIB board in order to monitor the three signals; the status of the thyatron, i.e. filaments, grids voltage and current, has been monitored as well by means of a I/O board.

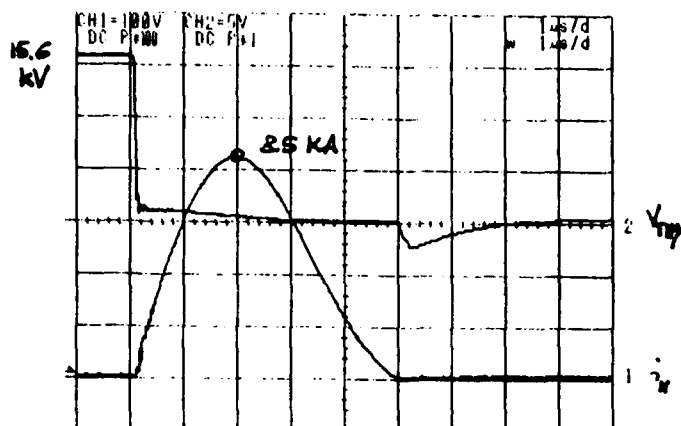


fig. 2 Anode voltage and current pulse waveforms.
chan. 2: anode voltage 5 kV/div
chan. 1: current pulse 2kA/div

The delay from the trigger pulse and 1/3 of the peak current value has been evaluated and the general status of the working system has been output on the computer display as it can be seen in fig 3.

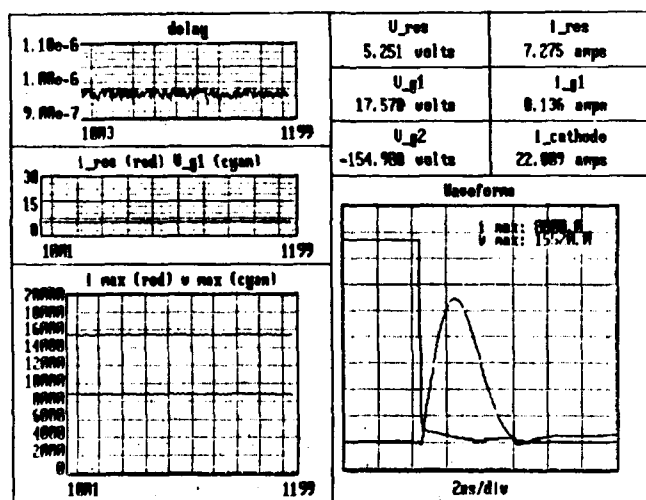


fig. 3 Waveforms and signals during the test.

More than 2 million pulses at the nominal repetition rate and at a current value 5% higher than the nominal one required at 2 GeV have been shot and some point can be remarked:

- keeping constant the charging voltage, the peak current value always remained the same within the PEARSON + oscilloscope accuracy;
- the delay between the trigger pulse and 1/3 of the current pulse peak value showed a total jitter which is less than the corresponding sampling interval of the oscilloscope;
- all the monitored parameters of the thyatron did not show significant variation during the test; in particular no drift toward dangerous values has been noticed suggesting a safe

long term operation of the thyatron with respect to electrodes degradation;

- the number of power and trigger pulses have been monitored as well showing a total absence of fault fires, i.e. the number of trigger and power pulses have been exactly the same during the whole test; this is very important for the Kicker Magnets which are installed directly in the storage ring, because an unmatched kick would kill the whole electron beam.

IV. CONCLUSIONS

The test results achieved until now allow the following conclusions:

- the EEV CX1154 is an adequate device for this application even if the peak current levels are high; a correct biasing and triggering is essential to have optimum performances and a good reproducibility of the current pulse;
- the efforts to arrange the circuit in order to keep the inverse voltage drop across the thyatron have been one of the principal goals in designing this system because this parameter is directly connected with the thyatron ageing; the higher is the inverse voltage drop, the lower is the lifetime of the tube;
- no significant degradation in the parameters of the thyatron has been noticed showing the ability of the system to operate in safe conditions during a long period of time.

V. REFERENCES

- [1] The ELETTRA conceptual design report", April 1989.
- [2] G. Mc Duff, K. Rust, "Life extension of thyatrons in short pulse circuits with the use of saturable magnetic sharpeners", IEEE 19th Power Modulator Symposium, S. Diego, CA, June 26 - 28, 1990.

Preliminary Testing of the LEB to MEB Transfer Kicker Modulator Prototype*

G.C. Pappas, D.R. Askew
Superconducting Super Collider Laboratory
2550 Beckleymeade Avenue, Dallas, TX 75237-3997 USA

Abstract

The extraction kicker for the Low Energy Booster (LEB) is used to deflect a 12 GeV/c proton beam from the synchrotron into a transfer line. A kicker system of similar design is used to inject the beam from the transfer line into the Medium Energy Booster (MEB). The modulator requirements for these kicker systems are to deliver a pulse train of seven 1.6 kA, 2.5 μ s pulses at a pulse repetition frequency of 10 pps, every seven seconds for one hour. The impedance of the modulator is 12.5 Ω , resulting in a charge voltage of 40 kV. The 10-90% rise time of the pulses is 20 ns, and the 1-99% fall time is 2 μ s. The allowable pulse ripple is $\pm 1\%$ of the peak current during the pulse, and $\pm 0.3\%$ from pulse to pulse. The shot-to-shot timing jitter requirement is less than 2 ns. This paper describes the design and performance of the prototype modulator which was fabricated to meet these specifications.

I. INTRODUCTION

A LEB extraction kicker prototype power system has been fabricated at the SSC. This system consists of a command, resonant charging system, a coaxial cable pulse forming line, and a thyatron switch tube, which delivers a 1.6 kA, 2.5 μ s pulse to two parallel-connected magnet loads terminated by matching resistors [1], [2]. A photograph of the power system is shown in Figure 1.



Figure 1. LEB Extraction Kicker Power System Prototype (The PFL is shown in foreground, with the charging tank on the left and modulator to the right)

II. THE CHARGING SYSTEM

A prototype of the charging power supply designed to charge four 254 m, parallel connected spools of RG-220 cable,

* This work supported by the United States Department of Energy under contract DE-AC35-89ER40486.

to 40 kV in 1.8 ms, has been fabricated. A schematic of the charging supply and test circuit is shown in Figure 2. The DC power source is a commercially available 300 V, 8 A supply. The capacitor bank consists of fifteen parallel 680 μ F, 350 WVDC, electrolytic capacitors. The SCR is a S15CG12AO, stud mounted type. Low voltage testing of the charger showed that all components performed as designed.

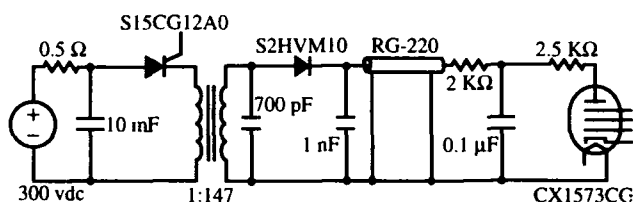


Figure 2. Charging Supply Test Circuit

The circuit was tested by gradually increasing the voltage, at repetition rates of less than one Hertz. At a charge voltage of approximately 30 kV, and a PRF of 0.9 Hz, a "double current pulse" was observed. This double pulse could also be seen at lower voltages as the PRF was increased. An oscillograph of this pulse is shown in Figure 3.

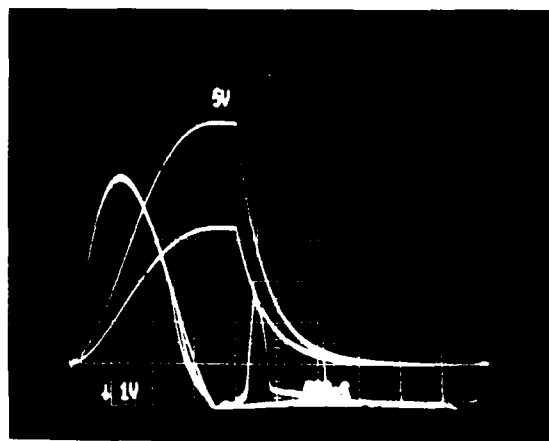


Figure 3. "Double Current" Charging Pulse (Primary current is 100 A/div, secondary voltage is 5 kV/div, time base is 500 μ s/div)

One possible explanation for this phenomenon is that the open circuit inductance of the transformer is below that specified. A low open circuit inductance would allow enough magnetizing current to flow in the transformer at the end of the pulse to latch the SCR. Several hundred microseconds later the trans-

former saturates, and the double pulse is seen.

The open circuit inductance, leakage inductance, and the winding capacitance of the transformer were measured with an HP 4284A LCR meter. The open circuit inductance was highly dependant upon frequency, and the transformer resonates at approximately 380 Hz. The measured values at 300 Hz were 100 mH for the open circuit inductance, 104 μ H for the leakage inductance, and 374 pF for the winding capacitance. The specified values were >450 mH, <145 μ H, and <10.8 μ F respectively. All of these values are referred to the primary. SPICE analysis of the charging circuit was run with the measured transformer parameters. The results of this analysis is shown in Figure 4, and verify that the SCR does not commutate at the end of the pulse.

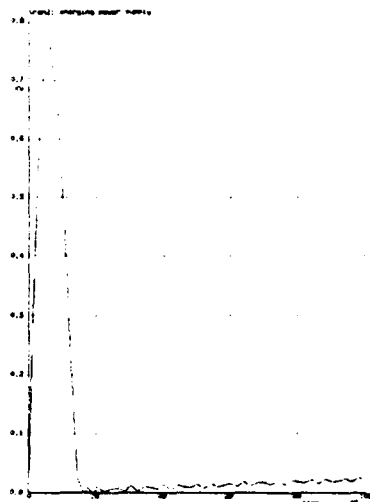


Figure 4. SPICE Analysis Showing the SCR Latching (Primary current is shown at 100 A/div, time base is 2 ms/div)

Another transformer with twice the core area and twice the open circuit inductance has been ordered. In order to continue testing while waiting on the new transformer, force commutation of the SCR was investigated. However, a suitable commutating circuit could not be found because of the very low impedance of the primary circuit. It was estimated that the open circuit inductance could be doubled with core reset, so a tertiary winding was wound around the secondary to carry a DC reset current. The tertiary winding had sixteen turns, one fifth the number of the primary, and carries 15 A to reset the core. This approach did not work because the impedance of the tertiary circuit was the output stage of a power supply, or essentially a short circuit. Isolating the tertiary circuit with an inductor was investigated, but the required inductance was approximately 20 H which is not feasible for an air core inductor. Further SPICE analysis showed that adding a small capacitor directly across the secondary could provide enough reverse current through the SCR for circuit commutation. A 700 pF capacitor was placed across the secondary, and the SCR now commutated. Figure 5 shows an oscillograph of the charging waveforms with the secondary charging to 35 kV at a PRF of 10 Hz. The charging system was tested to 40 kV secondary voltage at 10 Hz. The storage capacitor finally began arcing, as the capacitor was only rated for single shot duty. Further testing was postponed to fabricate the modulator.

It has been proposed to charge two PFLs with one charger in the final system. This topology would limit the number of reflections caused by a load arc to one, and should not require a hollow anode tube. SPICE analysis of this topology has been run and show that the ordered transformer should be adequate. Pulsed core reset will probably be required. The present charger and modulator design will allow testing of this topology.

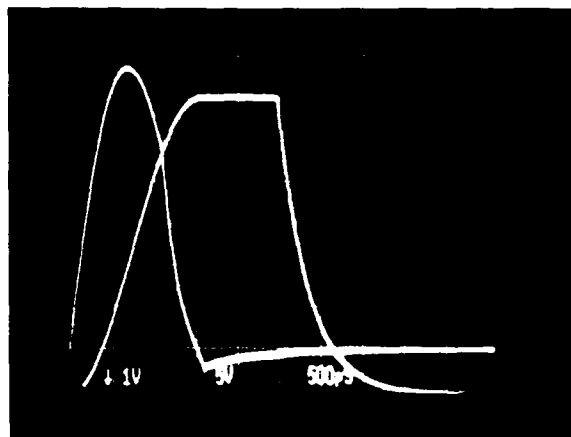


Figure 5. Charging Waveforms (Primary current at 100 A/div, secondary voltage at 5 kV/div, and time base at 500 μ s/div)

III. THE MODULATOR

A photograph of the modulator section of the kicker power system is shown in Figure 6. A tail biter tube has been added to the modulator to provide pulse width control, to protect against load arcing, and to test different topologies of the pulse forming line. EEV CX 1573CG hollow anode tubes are used in the prototype to guard against current reversals in the event of a load arc. Cathode heater, reservoir, and bias power supplies are located on a floating deck inside the modulator tank. Grid drivers are grounded, with the grid pulses coupled through one-to-one pulse transformers also in the tank. All grid drivers, and low voltage electronics have been tested, and perform to the design requirements. Custom high voltage connectors for the RG-220 cable have also been tested and meet design specifications.

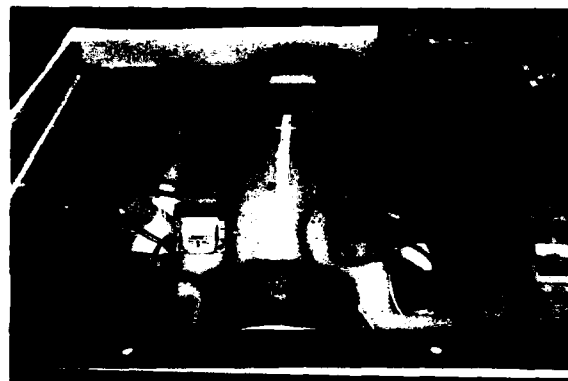


Figure 6. The Prototype Modulator.

The fabrication of the modulator section was finished only a few weeks before the writing of this paper, so only very preliminary data is available. Figures 7 and 8 show the load current rise time and flat top respectively. Figure 9 shows the entire load current pulse. The poor rise time current, and flat top may be explained by several different hypotheses. Calibration of the probes has not been completed. The resistive load designed for the system has not been delivered at the time of writing. A temporary load was fabricated using four 50 Ω Carborundum type 1028 resistors mounted in individual coaxial housings. The measured resistance of this array is approximately 16 Ω . Reflections from this load are clearly visible at the end of the pulse, but deleterious effects on rise time and flat top are not known. The coaxial housing for the switch tube could not be built to be 12.5 Ω because this would require placing the inner diameter of the housing inside of the switch tube grid flanges. The actual impedance of the housing is probably between 30 to 60 Ω , with an electrical length of approximately 10 ns. Again there has not been time to characterize the housing, but this mismatch could explain the steps seen on the rising edge of the current pulse. If the tube housing is found to be the problem, an easy fix could be to add discrete capacitors axially along the tube housing.

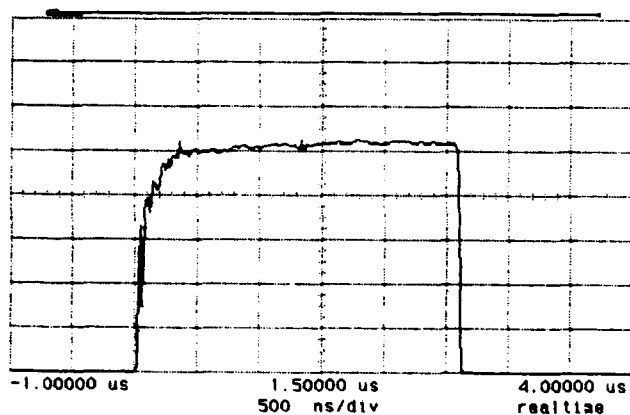


Figure 7. Load Current at 16 A/div, Peak Current is 1468 A (Time base is 500 ns/div)

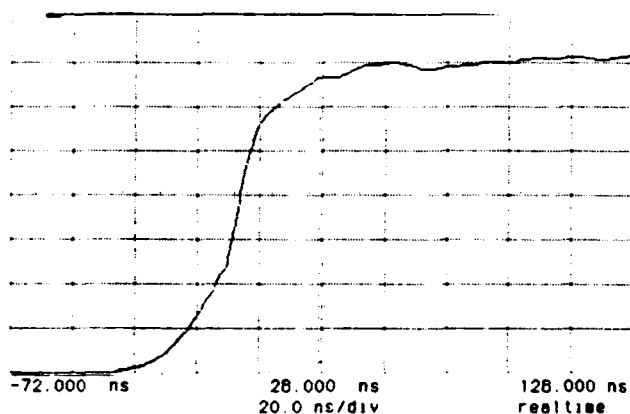


Figure 8. Load Current at 200 A/div (Time base is 20 ns/div)

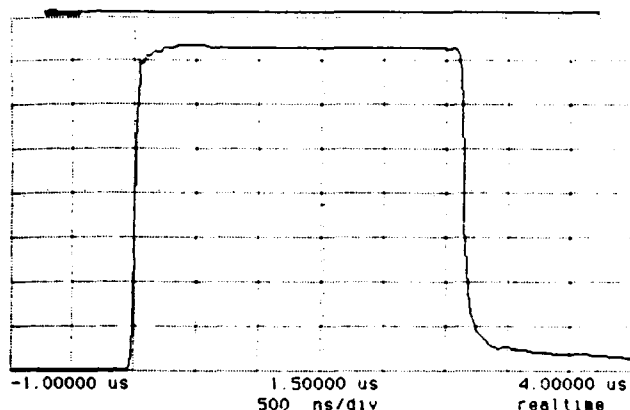


Figure 9. Load Current Pulse at 200 A/div (Time base is 500 ns/div)

The last possible cause for the poor pulse fidelity may be attributed to not properly setting the reservoir heater voltage. Testing the effects of cathode heater, reservoir, grid bias and grid drive voltages, as well as grid triggering delays will be explored. Future testing will include timing jitter measurements, pulse-to-pulse ripple, and prefire and misfire rates.

IV. CONCLUSIONS

The charging system has been fully tested for functionality. The system meets or exceeds all design specifications, however much more testing needs to be done to get reliability data. The initial testing of the modulator is encouraging. Pulse fidelity does not seem to be within the requirements of the kicker specifications, but testing has just begun, and several easily corrected problems have been identified. The modulator has been run at charge voltages of approximately 35 kV, at a PRF of several Hertz. No arcing, prefire or misfire problems have been identified. Full characterization, and tuning of the charger and modulator, is scheduled for completion by the late summer of 1993, when high voltage testing of the kicker magnet will begin.

V. REFERENCES

- [1] C. Pappas, et al, "Low Energy Booster Extraction Kicker Prototype Modulator", *Twentieth Power Modulator Symposium*.
- [2] D Anderson, "Design and Preliminary Testing of the LEB Extraction Kicker Magnet at the SSC", presented at this conference.

A Novel Technique for Pulsing Magnet Strings with a Single Switch*

R. J. Sachtschale, C. Dickey, P. Morcombe
Duke University, Free Electron Laser Laboratory
Box 90319 Durham, NC 27708-0319

Abstract

A new approach to switching a succession of kicker magnets using a single switch will be described. This technique can be used when different timing delay and power inputs are needed for each kicker. The approach is straight forward and is limited only by the pulse length. Timing jitter between kickers becomes a function of the switch diodes and the transmission lines, rather than the accumulated jitter of individual switches. It is likely that this approach can be used whenever a repeatable pulse train, with arbitrary individual pulse amplitudes, needs to be generated from a single switch and trigger.

1 Introduction

At the Duke University Free Electron Laser Laboratory electron bunches will be injected to a storage ring from a 1.2 GeV linac. In order to achieve the design goal of 1 ampere, *average* e-beam current, the bunches circulating in the storage ring must be augmented by injections from the linac. This is done by making a stored bunch execute a chicane pattern in the injection area as shown schematically in Figure 1.

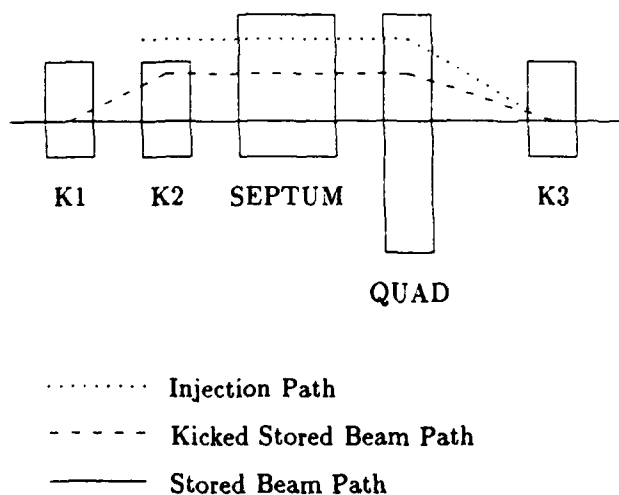


Figure 1: Schematic of Injection Section

There are three beam paths represented in figure 1. They are; the Injection Path, the Kicked Stored Beam Path and

*Supported by the United States Air Force Office of Scientific Research, contract AFOSR-90-0112.

the Stored Beam Path. Kickers K1 and K2 kick a stored bunch as shown. This action places the stored bunch closer to the injected bunch. Upon leaving the Septum the kicked stored bunch and the injected bunch are off axis of the Quad. The Quad bends the off axis bunches back toward the stored beam path. Kicker K3 then straightens the bunches into the stored beam path.

For this approach to work, all three kickers must have the same general pulse shape, but with differing amplitudes. Also they must be rigidly phased with each other. In our case it is also important to keep the expense of the system within a very modest budget. To achieve these requirements a circuit using a single switch was developed to switch all three kicker magnets.

2 Switching Circuit

2.1 Overview

The switch circuit is shown in Figure 2. The kicker magnets, K1-K3, are essentially lumped inductances. The kicker Pulse Forming Networks and Delay Lines are made from four lengths of RG-213 in parallel. All of the PFNs are the same length. The delay lengths are varied to provide the appropriate timing skew between the kickers.

Each kicker has three diodes associated with it. They are labeled in figure 2 as; Isolation, Clamp and Termination. The termination diode keeps the PFN voltage from going negative. The magnet and PFN are switched into a shorted load ($Z_L \approx 0\Omega$). For the PFN, $Z_o = 12.5\Omega$. Since $Z_o \gg Z_L$, the voltage at the termination end of the PFN will try to reverse polarity. The termination diode and resistor prevent this.

PS 1 through PS 4 are programmable high voltage power supplies with high impedance outputs. The first three charge the PFNs to a level that will supply the required magnet current when switched. The fourth supply is set higher than the others so that the isolation diodes are reverse biased. The isolation diode, when reverse biased, isolates the PFNs from each other so they can be charged to different levels.

When the switch is closed, the delay lines discharge. The voltage on the delay line will try to reverse when it reaches the diodes. This will cause the isolation and clamping diodes to become forward biased. The clamping diode clamps the magnet to ground. This is important because reflections will occur in the delay line and degrade the magnet circuit if the magnet is not clamped to ground.

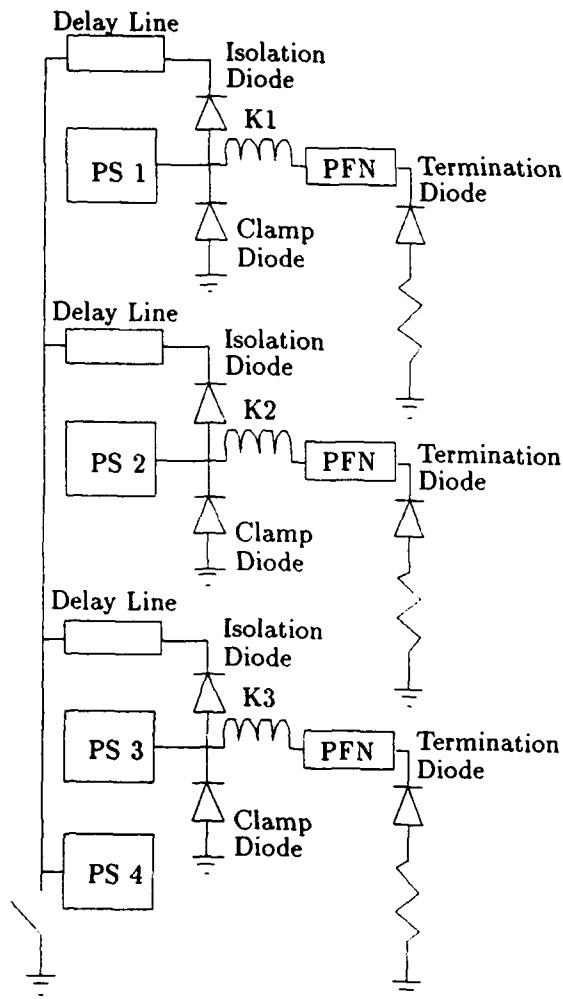


Figure 2: Schematic of Switch Circuit

2.2 Initial Development

The circuit was modeled with PSPICE. The modeled magnet current is shown in Figure 3. It was tested at low level using an avalanche transistor as a switch and 1N4004 diodes. The circuit performed as the PSPICE model predicted. The circuit then had to be scaled up to operational levels.

The diodes used must withstand 2.5 kiloamps surge and 30 kilovolts. At the suggestion of W.M. Portnoy at Sandia Labs, uncased diodes were selected. These are raw diodes from standard stud mounted cases. Diodes can be found that are rated for 1800 volts and 2850 amperes surge. When stacked, a compact package can be designed for a wide range of standoff voltages.

A holder was designed to stack the diodes. Between each diode is a 25 mil aluminum disc. The holder compresses the stack for proper contact between each element. The holder fits into a copper microwave guide. The wave guide is filled with transformer oil to improve voltage standoff and heat dissipation from the large surge currents.

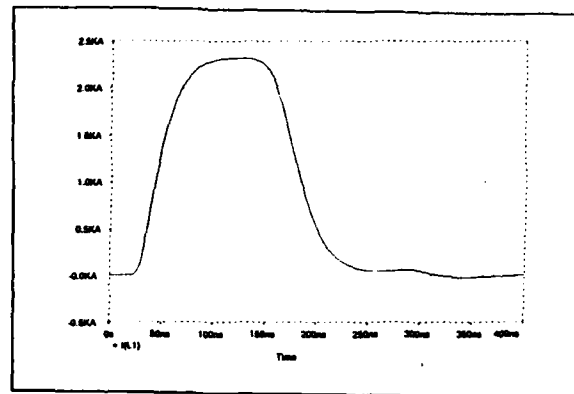


Figure 3: PSPICE Modeled Magnet Current

During the initial phase the kicker circuit consisted of only the magnet and PFN with a diode/resistor terminator. The magnet and PFN were charged to 30 kilovolts and discharged through a hydrogen thyatron switch, once a second. (The pulse repetition rate for injection from the linac to the storage ring is 1 pps). The circuit was life tested for 1.25 million pulses. The only degradation observed in the diodes was an increase in leakage current.

The outer insulation was removed from the PFN cables and they were wound around a 12 inch diameter by 18 inch long copper tube. This was done to keep the outer conductor resistance as low as possible. The assembly is placed in transformer oil. The cable has been in service for over a year, with more than 2 million shots at 30 kilovolts, without a failure.

2.3 Present Development

To improve switch performance the hydrogen thyatron was replaced by a Maxwell Labs 40184 spark gap. This spark gap is rated for 15-35 kilovolts with less than 1 nanosecond of jitter when used with a Maxwell Labs 40168 Trigger Generator.

We are testing a single branch of the circuit shown in figure 2 (i.e. just one kicker magnet). The overall pulse shape in the magnet is good but contains small oscillations from reflections in the delay line of the trigger circuit. If the clamping diode turns on properly and clamps the magnet to ground, the oscillations from the trigger leg should not be present.

To test this, the clamping diode was removed from the circuit. The circuit performed identically with or without the clamping diode. The waveform is shown in Figure 4. Various techniques are being discussed and tested to make the diode turn on and clamp the magnet to ground.

To turn the clamping diode on, the delay line must be able to sink more current than the magnet can initially source. Since the magnet is a lumped inductance, it cannot source current instantaneously. The magnet inductance is estimated to be 400 nH. Recalling that the delay line is

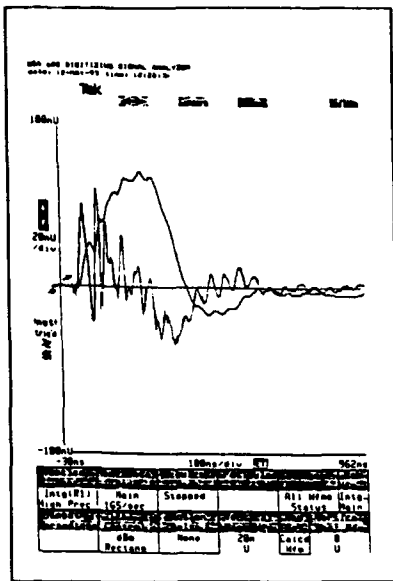


Figure 4: Normally Triggered \dot{B} and $\int \dot{B}$

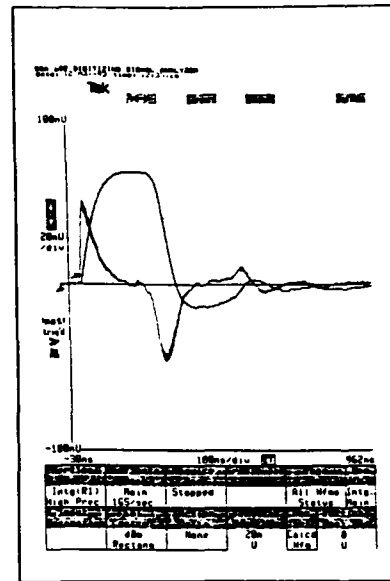


Figure 5: Self Triggered \dot{B} and $\int \dot{B}$

made of four lengths of 50Ω cable, the inductance is less than 20 nH/ft. The cable used for these tests is only three feet long.

We have realized that four cables in parallel aren't necessary for the delay line. That choice was made to keep symmetry with the PFN. The PFN uses four cables to keep Z_0 low. Also, lower Z_0 requires less PFN voltage for a given magnet current. If there is only a single 50Ω delay cable, the inductance will be 75 nH/ft but a larger voltage will be required to flow the same current. The same current flowing through a larger inductance will sink more current from the kicker circuit. Using a single length of RG-220 will raise the delay line inductance and the voltage can be increased to maintain current levels through the higher impedance. The salient point being, delay line current flowing in a larger inductance will sink more current from the circuit and turn on the clamping diode before the magnet can begin to source current.

3 Unexpected Observations

While working with the diode disks some unexpected, but explainable observations were made. Each disk was tested for leakage at rated reverse voltage. The leakage current rose and fell regularly at approximately three second intervals. Our high voltage lab has a red rotating warning beacon. It was determined that the light from the beacon increased leakage in the diode due to the photo-electric effect.

During testing the circuit self triggered. The B and $\int B$ waveforms were nearly ideal. Figure 5 shows the waveforms and the magnet's potential as a kicker. We have not acquired such clean waveforms via normal triggering.

While switching the magnet with and without the clamping diode in place, air bubbles or some other foreign debris may have gotten inside the clamping diode assembly. There may have been an arc to ground or possibly the clamping diode avalanched. Recalling our observations during leakage testing, photons from an arc may have triggered an avalanche of the diode. If this is possible and reproducible, a very fast, high power, optically triggered switch could be made. A common feature of some diodes is controlled avalanche breakdown and we are investigating the availability of such diodes.

4 Results

Although a simple circuit at low levels, making it operate at the high levels required has been difficult. During development, much has been learned about all the components in the circuit. The biggest difficulty has been in turning on the clamping diode. Future experiments will involve using a single length of RG-220 for the delay line part of the circuit. Another area we look forward to investigating is the possibility of developing a high power, optically triggered avalanche switch.

5 Acknowledgements

We are grateful for the advice provided by W.M. Portnoy of Sandia Laboratories in making compact pulse power diodes from stacked diode disks. Also the mechanical designs by Chris Ware and the technical efforts of Richard Taylor and Rob Cataldo were indispensable.

Batavia, IL 60510

1342

LC filter. The transformer secondary is capable of 1130 Vrms line to line. Final operation allowed us to connect up to the 90% tap (1017). The LC filter has a pole of 4 Hz to minimize noise generated and AC line disturbance.

Choosing the 1/2 wave pulse width of 2 ms, a L1 of 1mh, and the magnet inductance of 1.8 mh are the first decisions in the pulser design.

$$\omega_0 = 2\pi f = 1.57 \times 10^3 \text{ Rad / Sec} \quad (1)$$

The energy storage cap is chosen by:

$$C = \frac{1}{(2\pi f)^2 (L1 + L_{mag})} = 144 \mu f \quad (2)$$

The impedance to discharge current is:

$$Z_0 = \sqrt{L/C} = \sqrt{2.8 \text{ mh} / 144 \text{ mf}} = 4.4 \text{ W} \quad (3)$$

For the 3rd harmonic circuit:

$$3\omega_0 = 4.71 \times 10^3 \text{ Rad / Sec} \quad (4)$$

Solving for the amplitude of the 3rd harmonic by taking the 2nd derivative of the following equation and setting the function equal to 0.

$$f(t) = \sin \omega t + A \sin 3\omega t \quad (5)$$

$$A = 1/9$$

The 3rd harmonic reduces the peak current by 1/9 therefore the charge voltage on the main cap (C1) will

need to be a factor of about 1.1 higher.

$$V_c \approx 1.1 \times I_{\text{peak}} \times (Z_0 + R_{\text{cable}} + R_{\text{mag}}) \quad (6)$$

$$\approx 1.1 \times 200 \times (4.4 + 0.2 + 0.5) = 1122 \text{ volts}$$

The equivalent circuit that the 3rd harmonic circuit capacitor has to match is shown in figure #2

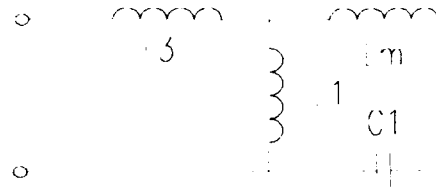


Figure #2

$$X_{eq} = X_{L3} + \frac{X_{L1}(X_{LM} + X_{C1})}{X_{L1} + X_{LM} + X_{C1}} \quad (7)$$

The equivalent circuit impedance at the 3rd harmonic is 7.116 ohms therefore the reactance of C3 must be equal to this value.

$$C_3 = \frac{1}{3\omega_0 X_{eq}} = 30 \mu f \quad (8)$$

The actual magnet current needed is 175 amps. The third harmonic current will be about 1/9 of this current or 19.4 amps.

Circuit analysis plots were done using spice with various component changes. The circuit could be

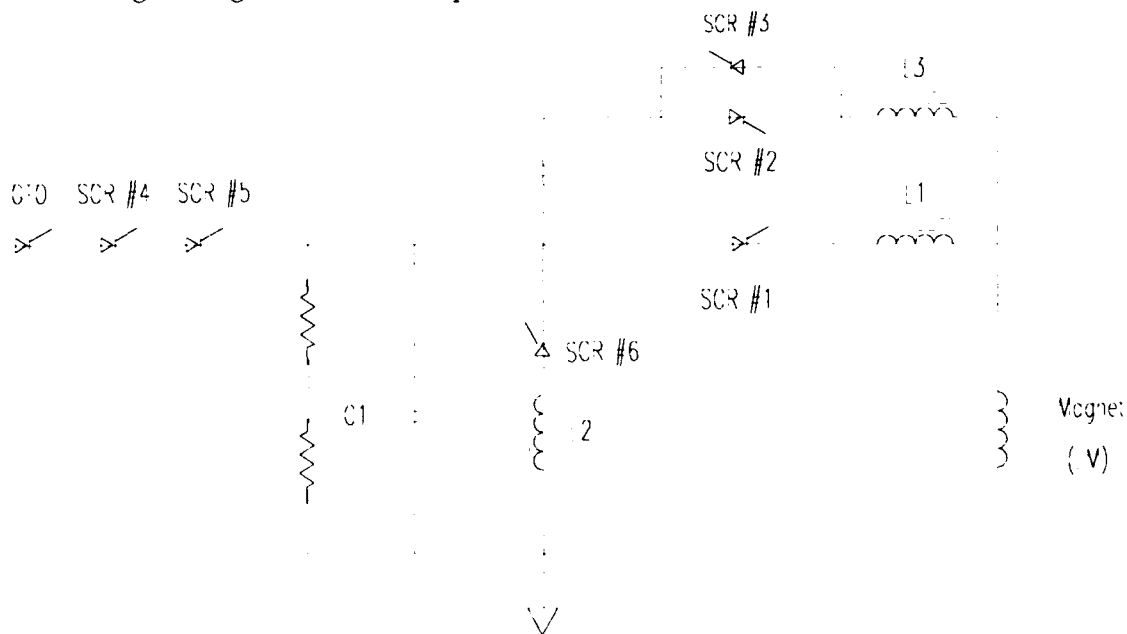


Figure #3

configured without L3 if one put an initial charge on C3. This change would mean a floating supply is needed to charge this cap. Due to simplicity and reliability L3 was left in the circuit and C3 starts the cycle with a 0 volt charge. Changing the gap in L3 allows one final method to adjust the flattop width.

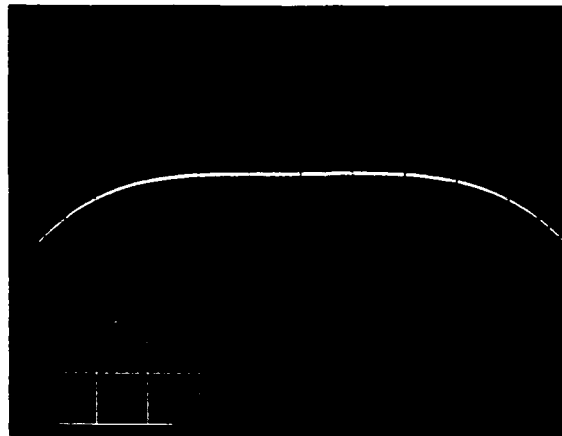
The energy discharge cap (C1) is charged by turning on SCR #4, #5, and the GTO as shown in figure #3. After the loop comparator is satisfied a stop charge is applied to the GTO to end the charge cycle. The discharge cycle generates magnet current and is started by turning on SCR #1. After a small delay SCR #2 is gated on, this generates a faster rise in the magnet current and produces the charge needed on C3 for flattop. When the current in SCR #2 drops to 0, then SCR #3 is turned on which generates the current needed to produce a flattop current wave form in the magnet. Adjusting the turn on time also adjusts the tilt during flattop. SCR #2 is turned back on after SCR #3 shuts off to discharge C3. Charge recovery is initiated by gating SCR #6 on which allows the current to flow through L2 which resonates with C1 and flips the charge on this cap.

IMPLEMENTATION

Minimum noise would be transmitted if one had a true bipolar source. Therefore the pulser common was made to float so that both leads of the cable could bounce with the signal producing a smaller noise signal in the shield of the cable. Due to the capacitance to ground of the large components a true bipolar source was not achievable. However there is a significant noise signal difference in the shield if one grounds the common lead going to the magnet.

A control crate contains 4 timing modules, 4 regulator modules, 1 control module, and 1 power supply module. The system will operate with this crate in the stand alone mode or in a computer controlled mode. Monitor signals are available at the front panel to aid in system checkouts.

Operation of 8 pulsers have been running for 1 year with very good results. The waveform shown was taken from a unit operating at a flattop current of 175 amps.



Magnet current showing flattop current
200 ma/div @ 50 μ s/cm

Acknowledgments

The author would like to thank J. Dinkel and C. Jensen for their original ideas on the 3rd harmonic implementation.

The AGS New Fast Extracted Beam System Orbit Bump Pulser*

J.S.Chang and A.V.Soukas
Brookhaven National Laboratory
Associated Universities, Inc.
Upton, Long Island, New York 11973

Abstract

The AGS New Fast Extracted Beam System (New FEB) is designed for RHIC injection and the g-2 experiment, performing single bunch multiple extraction at the prf of 20 to 100 Hz up to 12 times per AGS cycle. Capacitor-discharge pulsers are required to produce local orbit bumps at the fast kicker and ejector magnet locations. These pulsers have to deliver half-sine current pulses at 1 KA peak with a base width of 5 msec. The discharge voltage will require approximately 800V with a $\pm 0.1\%$ accuracy. Direct charging will require a charger too costly and difficult to build because of the high prf. An alternative charging system is being developed to take advantage of the 1.5 sec idle time between each group of pulses. The charger power supply ratings and regulation requirements are thus greatly reduced. The system analysis and results from a prototype will be presented.

I. INTRODUCTION

In previous fast extraction systems of the AGS, either a single bunch was kicked out per cycle, or all 12 bunches were extracted in one revolution. In the AGS's New Fast Extracted Beam system (NewFEB) the requirements are for single bunch multiple extraction which normally extracts 3 bunches in a row, but with a capability of up to 12 consecutive bunch extractions. This would normally not present a severe problem but for the fact that it has to be accomplished at a pulse repetition frequency of 50 Hz. This requirement is set by both major users, the g-2 muon anomalous magnetic moment measurement[1], which is statistics dominated and hence requires very high average beam intensity, and RHIC injection[2] which should be accomplished as quickly as possible to prevent beam quality deterioration in its beam stacking mode. DC supplies either cause beam orbit problems in the AGS or equipment heating problems that are difficult or unreliable to overcome. Due to the amount of stored energy in the orbit deformation bumps and the ejection septum, large capacitor banks must be used. To charge these banks in less than 15 msec, the charging power supplies would be complex and expensive to construct. A quick approximation shows that a 800V/300A/0.1% charging power supply is needed for the task. Charging supplies of this category can only be found in high frequency switching technology. The charging power supply also suffers from low efficiency because between the 12th pulse and the beginning of the next AGS cycle, there is a 1.5 sec idle time which the

charging supply is doing nothing. This is why we looked for a new, more reasonable method to recharge the capacitors.

II. SYSTEM PARAMETERS

Each pulser has 4 AGS Main Magnet Back-Leg Windings connected in series as the load. The system parameters are summarized as the following.[3]

Beam deflection	:	2 mrad per pair of magnets
Peak Field	:	500 Gauss
Peak Current	:	1000 A
Pulse Rep. Rate	:	50 Hz, 1-12 times/AGS cycle
Wave Form	:	Half-sine with 5 msec basewidth
Inductance	:	1.2 mHy
Discharge Voltage	:	750 V
Discharge Cap.	:	2110 uF
Discharge energy	:	593 J
Reproducibility	:	$\pm 0.1\%$
No. required	:	4 pulsers

III. DESIGN AND ANALYSIS

A. Design and Circuit Realization

Our design shown in fig. III.1 has many advantages. The charging supply does not directly charge up the discharge capacitor C2. Instead, it supplies current into a large capacitor bank C1 whose capacitance is 1 to 2 orders larger than C2. A large C1 is necessary to prevent excessive voltage drop in each successive charging of C2. C2 is charged up very accurately through the switch G1 which is controlled by the feedback loop. When C2 voltage reaches the reference level, G1 opens and stops charging. C1 is replenished to 850V, which is 100V higher than the discharge voltage requirement of C2, from the charging power supply during the 1.5 secs idle time and is ready for the next AGS cycle. The first immediate consequence is that the power supply current rating is greatly reduced due to the long charging time. Secondly, the burden of accuracy is shifted from the charging supply to the feedback loop and the switch G1. An ordinary 3 phase off-the-shelf SCR power supply will satisfy the design requirement.

All circuit elements are readily achievable. Fig. III.2 shows the system implementation in component level. G1 has to withstand at least twice the supply voltage ($2 \times 850 = 1700$ V) due to fly-back voltage of C2. Transistors are

*Work done under the auspices of the US Department of Energy.

ruled out because the voltage is too high. A GTO appears to be a good choice in implementing the switch G1 for its excellent voltage blocking, fast operating, and current interrupting capabilities. An asymmetrical GTO will suffice because the voltage of C1 is always higher than that of C2. Further, the gate drives of GTOs are commercially available. Although C2 have to be quality discharge capacitors due to voltage reversal, C1 can be implemented with inexpensive and high capacitance-per-volume aluminum electrolytic capacitors. These aluminum can capacitors have a maximum voltage rating of 450V DC; therefore, two stacks in series are needed in our application. Alternatively, resonant LC charging can be used provided the accuracy requirement is not too stringent.

B. Analysis

The objective of this section is to calculate the charger power supply rating requirement and to discuss the source of pulse to pulse error.

1. Power Supply Rating

The power supply rating is calculated using the law of conservation of charge. In each charging process, the charge loss from C1 must equal to the charge gain by C2. Therefore,

$$C1 \Delta V1 = C2 \Delta V2 \quad (1)$$

where $\Delta V1$ = Voltage drop of C1 per recharge
 $\Delta V2$ = Voltage gain by C2 per recharge

Assuming the fly-back choke is able to recover 50% of the initial C2 voltage, $\Delta V2 = (0.5)(750) = 375$ V. Since C1 is chosen to be 100 times larger than C2, $\Delta V1$ can be determined. The total voltage drop of C1 for 12 pulses is 45 volts. C1 has an initial overhead of 100V more than the discharge voltage of C2, therefore the 45 volts drop is well covered. C1 is recharged during the 1.5 sec idle time. The current rating can be calculated.

$$12 (C1) (\Delta V1) / 1.5 = 6.33 \text{ amp} \quad (2)$$

The minimum charging power supply rating is 850V and 6.33A.

2. Source of Pulse to Pulse error

The source of pulse to pulse error comes from the GTO turn-off delay which is approximately 25 us. Fig. III.3 shows the RC charging current wave form through the GTO. The initial charging current at the GTO turn-on for each pulse is successively lower for each extraction pulse, but the charging time is longer. C2 is overcharged for 25us at a different current interrupting level. The difference in overcharge

constitutes the pulse to pulse error.

The current interrupting level can be obtained as follows:

$$I_{cut_n} = (V_n - 750) / R \quad (3)$$

$$V_n = 850 - (n) (\Delta V1)$$

where $n = 1..12$

I_{cut_n} = current interrupting level at nth recharge

V_n = voltage of C1 at the end of nth recharge.

The largest pulse to pulse discharge voltage variation is

$$V_{err} = (I_{cut_1} - I_{cut_{12}}) (25) (10^{-6}) / C_2 \quad (4)$$

and the percentage error is

$$\%err = (V_{err} / 750) (100\%) \quad (5)$$

We also want to check the charging time t_n for each pulse to make sure that it does not exceed the available time frame of 10ms (Recall that there is a 20ms period between each pulse. 5 ms is used for discharge and 5 ms is used for energy recycling). Assuming $C1 \gg C2$, the following charge relationship can be approximated.

$$\int_0^{t_n} \frac{(V_{n-1} - V2)}{R} e^{-\frac{t}{RC2}} dt = (C2) (\Delta V2) \quad (6)$$

where $V2$ = voltage recovered on C2.

Solving for t_n ,

$$t_n = -RC_2 \ln(1 - \Delta V2 / (V_{n-1} - V2)) \quad (7)$$

We conveniently chose $R = 1$ ohm and again assume 50% C2 voltage recovery. The calculated results are $\%err = 0.07\%$ and $t_{12} = 4.2$ msec. Both values are certainly within the specification of the system requirement.

IV. PROTOTYPE RESULTS

A scaled down prototype was built to confirm the capability of the system. In reference to fig.III.2,

C1	=	50,000	uf
C2	=	2,000	uf
Lo	=	1	mHy
Lf	=	1.8	mHy
R	=	1	ohm

C1 was charged up to about 210 V initially and the reference for the C2 discharge voltage was set to 150 V. Six pulses were fired at the rep. rate of 20 msec per AGS cycle. The peak current was measured to be 200 A. The current was measured at point A in fig.III.2. Fig.IV.1 shows the voltage(upper trace, 50V/div) and current(lower trace, 100A/div) of the discharge bank C2 for the first 2 pulses. The positive half-sine current pulse is the discharge current going to the load. The negative half-sine current recycles the energy back to C2 and recovers 73% of the discharge voltage. The negative trapezoidal current charges C2 from 110 V to the target 150 V.

The discharge voltage of C2 was measured using a triggered 16-bit digital voltmeter over 10 AGS cycles. The deviation of all the discharge voltages falls within $\pm 0.1\%$. To achieve $\pm 0.1\%$ for 12 pulses, C1 will have to be larger. C1 is only 25 times larger than C2 in the prototype.

V. Conclusion

Both our analysis and prototype have demonstrated encouraging results. Our design greatly reduced the current rating of the charger. The control and accuracy of recharge is shifted from the power supply to the feedback control loop which can be modified easily for different applications. We have planned modifications to the reference and the feedback control to achieve pulse to pulse modulation operating mode.

Figure Captions

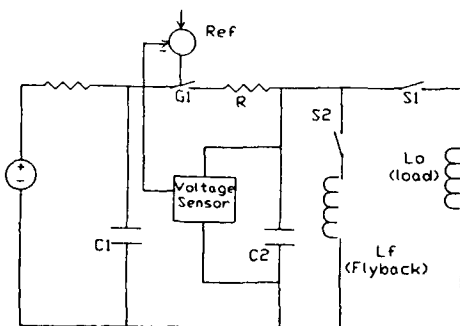


Fig. III.1 Design Configuration

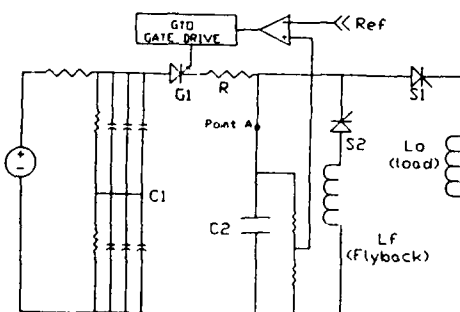


Fig. III.2 System Implementation

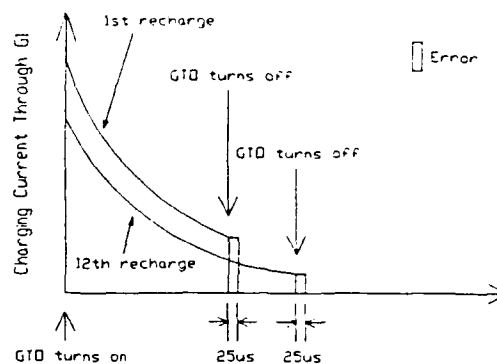


Fig. III.3 Source of Recharge Error

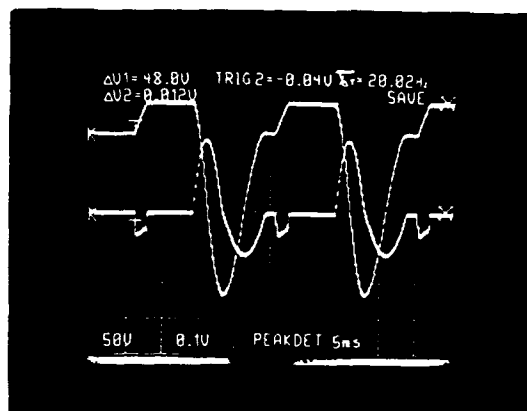


Fig IV.1 Discharge Voltage and Current Measured at Point A in Fig. III.2
(Upper Trace 50V/div)
(Lower Trace 100A/div)
(Time Base 5ms/div)

Acknowledgement

The authors would like to thank Carl Eld, Fred Schaefer, David Warburton, and John Addressi for excellent technical support on the prototype.

References

- [1] Experiment 821, A New Precision Measurement of the Muon g-2 Value at the Level of 0.35 ppm.
- [2] M. Tanaka and Y.Y. Lee, "The AGS New Fast Extraction System for the g-2 Experiment and RHIC Injection", Proc. 1991 PAC, San Francisco, Calif.
- [3] M. Tanaka, private conversation.

Experimental Investigation Of High Voltage Nanosecond Generators Of Injection System For SIBERIA-2 Storage Ring

Andrey Kadnikov

Russian Research Center - Kurchatov Institute, 123182 Moscow, Russia

Yury Matveev

Budker Institute of Nuclear Physics, 630090 Novosibirsk, Russia

Abstract

The injection system for SIBERIA-2 storage ring (Kurchatov Institute, Moscow) has been put into commissioning. The high voltage impulse generators with double coaxial forming lines and three electrode nitrogen filled spark gaps are intended for linac electron gun and fast full-aperture kickers supply. The output impulses are up to 60 kV in amplitude, 15 - 20 ns in duration with front about 3 ns. A root-mean-square dispersion of time delay of gaps is 0.7-0.8 ns. The experimental results of operation of the generators are presented.

I. INTRODUCTION

The dedicated SR source SIBERIA-2 [1] consists of linac (80 - 100 MeV), booster (450 MeV)

and main ring (1.5 - 2.5 GeV). The one turn injection system [2] uses full-aperture kickers for injection into booster and from booster to main ring. This scheme requires impulses for kickers with 7 -- 60 kV amplitude, 15 --20 ns time length and very short edges. For high efficiency an essential time stability is needed (about 1--2 ns). Linac electron gun needs 40 kV impulse.

II. HIGH VOLTAGE GENERATORS

The high voltage nanosecond generators were developed for kickers and electron gun supply. Figure 1 presents a simplified scheme of the generator.

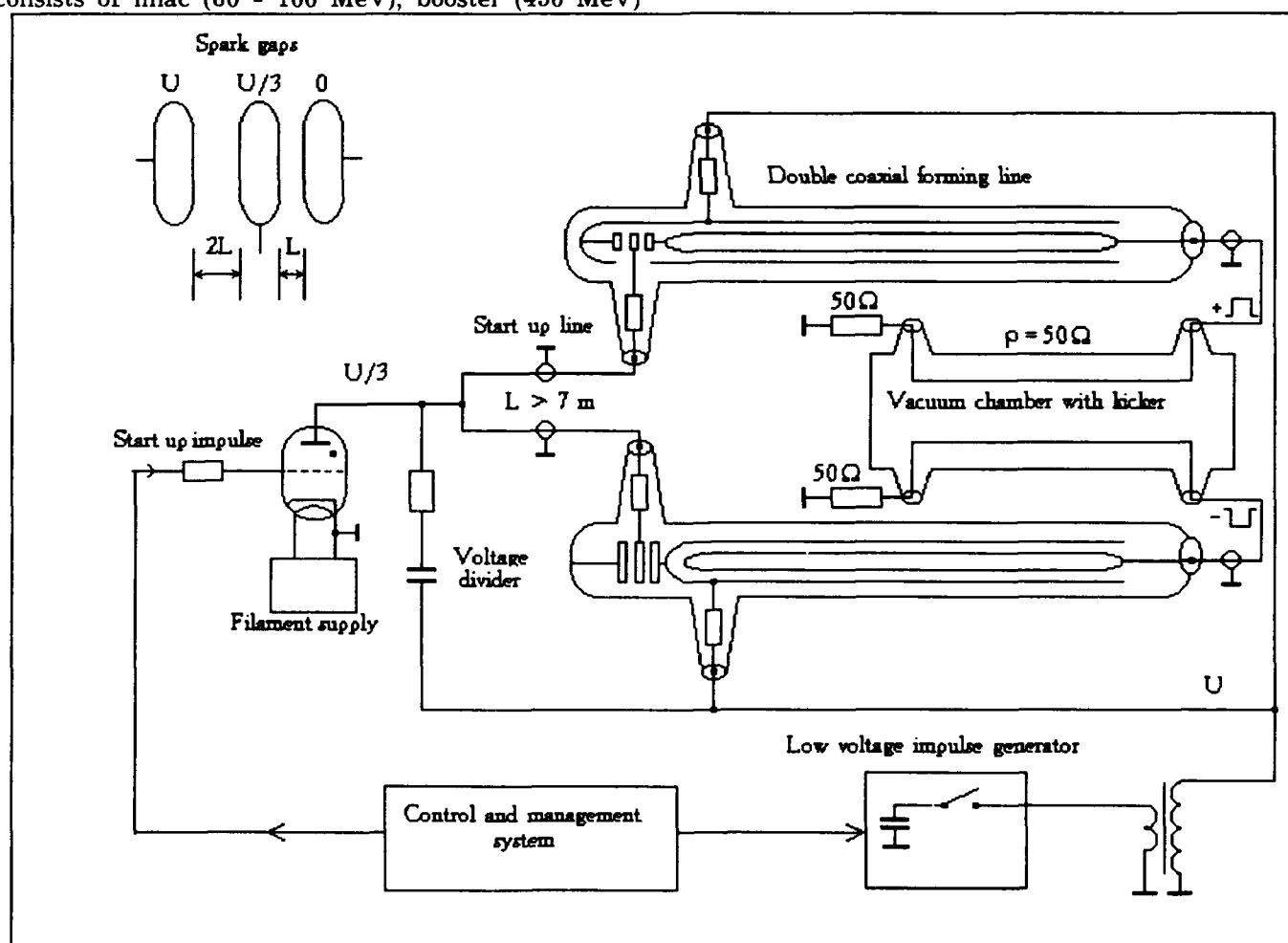


Figure 1: The simplified scheme of high voltage generator.

Double coaxial lines produce output impulses of electrical power with time interval equaling double passing time of electromagnetic wave through line. In each double forming line, two spark's gaps with three electrodes are used for fast commutation of electrical power. Polarity of output impulses depends on how gaps are connected up between lines. The electrodes are made of duralumin, because it is just this material that provides necessary time stability. We can tune electrical characteristics of the spark by changing pressure of nitrogen (5 - 20 atmospheres) in the gap.

An impulse hydrogen thyatron is used to start up spark gaps. All elements of generator, transport lines and kickers have wave resistance 50 ohms. An impulse transformer with coefficient of transformation about 100 charges forming lines to output voltage. Start up circuit is charged to one third output voltage due to capacity divider.

A low voltage (800 V) impulse generator supplies a primary winding of the transformer. SF_6 gas fills cables and lead-ins at a pressure 5 atmospheres to increase electrical strength.

Resistance's and capacity's dividers (not shown in picture 1) allow us measure voltage and examine shape of impulses.

A control system uses electronics in CAMAC standard: microcomputer, ADC unit, etc. For time measurements we use time-digit converter unit with 0.6 ns per bit resolution. Software can measure average time delay, root-mean-square dispersion and changes of these values during long time.

III. EXPERIMENTAL RESULTS

An oscillogram of output positive impulse with amplitude 60 kV is shown in figure 2. The spark gaps provide enough abrupt impulse's edges. The leading edge is about 3 ns, an impulse's plate is 13 ns, and trailing edge is 5 ns.

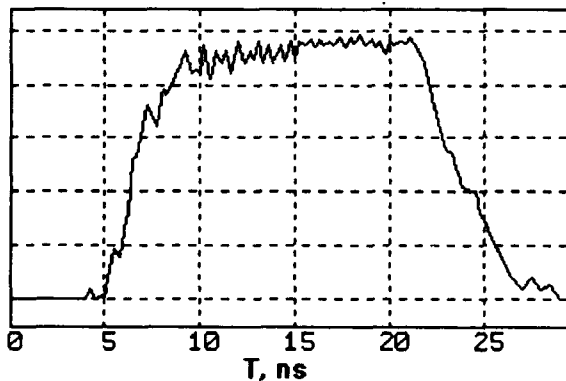


Figure 2: Oscillogram of output impulse 60 kV in amplitude.

A negative impulse has roughly the same characteristics. We have gotten 0.7--0.8 ns root-

mean-square dispersion of time delay of the output impulses after careful tuning and training of the spark gaps. The results of examining of time stability of the thyatron, the spark gaps and whole generator during working day are shown in figures 3, 4.

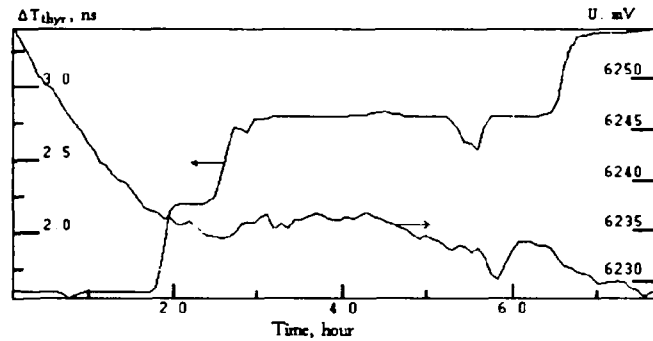


Figure 3: Changes of filament voltage and time delay of thyatron during working time.

The permanent thyatron's time delay needs stabilization of filament voltage not worse then 0.1%. After training during 2 hours, spark gaps show sufficient time stability.

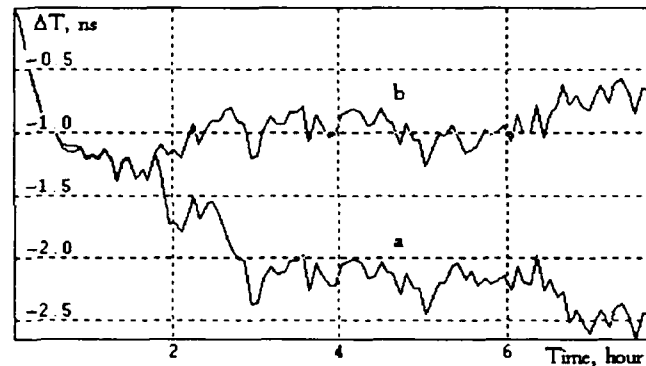


Figure 4: Changes of time delay of spark gaps (a) and whole generator (b).

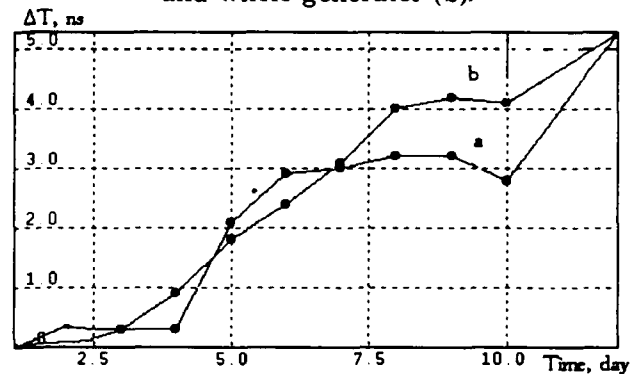


Figure 5: Time delay's increasing of positive (a) and negative (b) spark gaps due to wear and tear of electrodes during 12 days. Total number of impulses about 700,000.

With long operation time, erosion of electrodes occurs that leads to increase of gaps. First it results

in increase time of gaps and then leads to decrease of operation's stability of generator.

Figure 5 shows increasing of time delay of spark gaps due to wear and tear of electrodes during 12 days. Total number of impulses about 700,000.

The obtained results let us make a conclusion that these high voltage generators suit for power supply of injection system for SIBERIA-2 storage ring.

For more detailed information on the subject, please contact us by the addresses given under the headline, or use e-mail kuzn@ksrs.msk.su.

IV. REFERENCES

- [1] V.Anashin, A.Valentinov et al, "The dedicated SR source SIBERIA-2", The Proceedings of the 11-th Russian Particle Conference, Dubna 1989, p.277-280 (in Russian)
- [2] G.Erg et al. "Injection system for the SIBERIA-2 storage ring", these proceedings.

Design and Preliminary Results for a Fast Bipolar Resonant Discharge Pulser Using SCR Switches for Driving the Injection Bump Magnets at the ALS*

Greg Stover and Lou Reginato
Lawrence Berkeley Laboratory, University of California
1 Cyclotron Road, Berkeley, CA 94720 USA

Abstract

A fast (4.0 μ s half period) resonant discharge pulser using SCRs has been designed and constructed to drive the injection bump magnet system at the Advanced Light Source (ALS). The pulser employs a series-parallel arrangement of Silicon Controlled Rectifiers (SCRs) that creates a bipolar high voltage (± 10 KV), high peak current (6600 amps.) and a high di/dt (6000 amp/ μ s) switch network that discharges a capacitor bank into the magnet load. Fast recovery diodes in series with the SCRs significantly reduces the SCR turn-off time during the negative current cycle of the magnet. The SCR switch provides a very reliable and stable alternative to the gas filled Thyatron. A very low impedance transmission system allows the pulser system to reside completely outside the storage ring shielding wall.

I. INTRODUCTION

Injection into the storage ring (SR) employs a well proven technique of stacking in radial phase space. Prior to injection, the SR closed orbit is deflected (15 mm max.) in a sinusoidal manner towards the injection septum by two pairs of bump magnets. At the peak of the sinusoid wave form a packet (1 to 10 bunches) of 1.5 MeV electrons is extracted from the booster synchrotron, transported through the extraction septa, the transfer line, the injection septa, and into the storage ring. This paper will discuss the design of the electrical system that drives the SR bump magnets.

II. SYSTEM DESIGN

A. Magnet Specifications

Each bump magnet is constructed in a window-frame geometry with a nickel-zinc ferrite core and is energized by a single-turn copper conductor. For ease of maintenance and cost all the magnets were designed to fit outside the vacuum chamber. The chamber is made of a high-alumina ceramic and has a Titanium Molybdenum semiconductive coating that has been thermally evaporated on the inner surface of the tube. The coating provides a consistent and predictable electrical impedance to the electron beam with enough resistive loss to minimize the magnetic field cancellation effects.

The purpose of the SR bump magnets driver is to produce the temporary (4 μ s) desired beam deflection to accept the electron packet while minimizing induced coherent betatron motion and simultaneously avoiding a fourth turn collision with the injection septum.

*This work was supported by the Director, Office of Energy Research, Office of Basic Energy Sciences, Materials Sciences Division of the U.S. Department of Energy, under Contract No. DE-AC03-76SF00098.

B. Electrical Specifications

The physics of the injection process produced the following electrical driving parameters for each magnet; a half sinusoidal current wave form with a period of 4.0 μ s, a peak current of 3300 amperes, a reactive voltage of 6000 volts, and a maximum reverse recovery amplitude of <1.0% of the peak forward current in the magnets.

C. Overall System Layout

The sinusoidal current wave form is generated by the resonant discharge of a capacitor bank through an electronic switch into the predominantly inductive magnet load. The hydrogen thyatron is the switching device usually specified to handle the voltage and current levels required for this system. Unfortunately, thyatrons have reliability problems and lifetimes that are limited to a few thousand hours or less[1]. In the face of this situation, we decided to develop a solid-state switch using off-the-shelf, very reliable, high voltage, high di/dt, Silicon Controlled Rectifiers (SCRs).

The basic topology for the pulse system is shown in Figure 1. The bump magnets are connected by a very low inductance transmission network to four parallel bipolar SCR-capacitor discharge modules that are shown in Figure 2. The modules are charged by two opposite polarity high voltage power supplies.

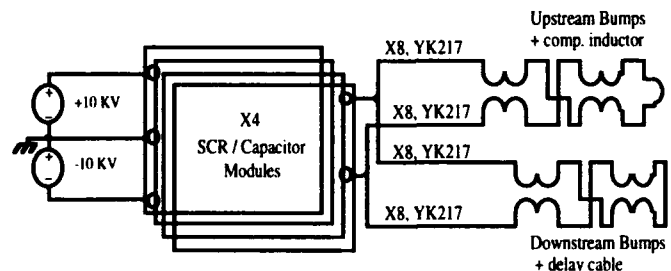


Figure 1. Bump pulser system.

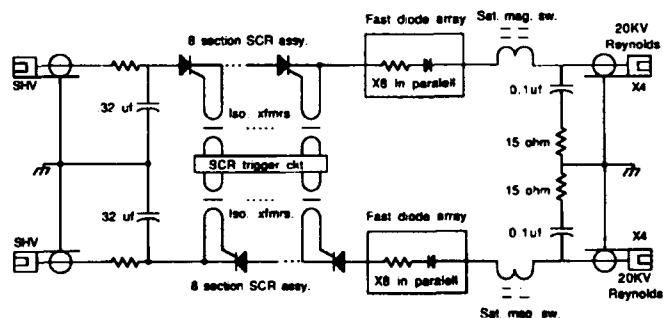


Figure 2. One of four bipolar SCR-capacitor discharge modules.

D. The Load Configuration

Great care was taken to minimize any potential offsets in the beam closed orbit during the injection cycle. Precise magnetic field correspondence between the two magnet groups was accomplished through the exacting construction of each magnet and the series-parallel connection of the magnets to the discharge modules. Furthermore, the "downstream" magnets have an additional 5.3 ft. of cable to make up for the electron "time of flight" between the two magnet groups. A small balancing inductor was added to the "upstream" group to compensate for the inductance of the extra "downstream" cable.

E. Low Inductance Transmission System

For ease of maintenance and accessibility we chose to locate all the active components of the pulse system outside of the SR shielding wall. The average cable run length is approximately 60 feet from the magnet load to the driver. In an effort to minimize the inductive voltage drop and the overall cost of all the high voltage charging components a very low inductance transmission system was constructed. As shown in Figure 1, each of the magnet terminals is connected to the discharge modules by 8 parallel low inductance cables. A total of 32 cables are cross connected from the four magnet terminals to the four modules to further enhance the current distribution. The coax cable, YK217 [2], has linear inductance 33 NH/ft and cable impedance of approximately 15 ohms.

F. The SCR-Capacitor Discharge Modules

The series/parallel connection of the load sets the nominal peak load current at 6600 amperes. For a sinusoidal wave form this generates a maximum di/dt value of 5.2 Kilo amps./sec at the beginning of the discharge cycle. This di/dt rating is much higher than any single commercial SCR can physically support. As shown in Figure 1 problem was solved by dividing the load current equally between four parallel pulsers.

The SCR used is a WESTCODE, R200CH18F2K0 [3] that has a 34 mm die diameter and employs a interdigitated amplified gate structure. The 1800 volt blocking voltage keeps the number of stacked devices to a manageable number of 8 and the di/dt spec. of 1500 amps/ μ s limits the number of required parallel modules to four. Recent articles[4] and our operating results indicate that the vendor specified di/dt value is quite conservative.

The long recovery time, $T_q = 40 \mu$ s, of the R200 is shortened to 300 ns by the insertion of a parallel array of high voltage fast recovery diodes in series with the SCR string. See Figure. 2. In reality, the system reverse recovery time is effectively forced to zero by the in-series addition of low inductance saturable magnetic reactors. Any remaining reverse recovery transients are snubbed by the shunt RC network connected to the outputs.

Moreover, these reactors improve the SCR turn-on and di/dt capabilities. During the first 300 ns of the turn-on cycle the majority of the applied voltage is dropped across the as yet unsaturated reactors allowing time for extra charge injection into the gate structure of the SCRs. This condition avoids initial current crowding effects during turn-on that can destroy these devices. When the reactors saturate the SCRs are effectively ON and ready to conduct current.

The SCR strings are mounted in a compression clamp holds all eight devices. The voltage across the stack is graded by a string of 20 megohm resistors. Each SCR has an RC

snubber in shunt from anode to cathode. High frequency toroidal 3E2A ferrite transformers isolate the individual SCR gates from the low level trigger circuitry. The peak trigger current into the each gate of each SCR is approximately 20 amperes.

Monitoring of the discharge module current and voltage is accomplished through in-house designed Rogowski belts and high frequency dividers. The field of each bump magnet is measured by individual B dot loops and passive integrators.

III. OPERATIONAL RESULTS

The photo in Figure 3 is the exact overlay of two oscilloscope wave forms of the magnet currents measured simultaneously in the "upstream" and "downstream" bump magnets. The current was measured with two separate Pearson current transformers matched to better than 0.1%. The identical nature of the wave forms confirms the validity of the current sharing schemes employed by this system. The reverse recovery wave form is smooth but larger than the 1.0% specified. IsSPICE [5] circuit simulations indicate that the load snubber impedance can be reduced to minimize the amplitude of the recovery.

The upper trace in Figure 4 is the magnetic field measured by a 3 turn B dot loop and a passive integrator. The discrepancy in shape between the magnet current and the field wave forms is do to the bandwidth limit of the field measuring electronics. The lower trace is the output current from one of the four SCR switch units. The current wave forms of the other three units are very closely matched to the form shown. The high frequency ringing superimposed on the discharge pulse has a nominal period of 800 ns. Due to the ringing peak di/dt has been measured as high as 3300 amps/ μ s or twice the specified maximum listed by the manufacturer. A SPICE analysis has confirmed the suspected parasitic components of this ringing to be a C,L,C resonance excited by the initial turn-on transient. The lumped components are the distributed series inductance of the SCR switch interacting with the series inductance and shunt capacity of the transmission cable.

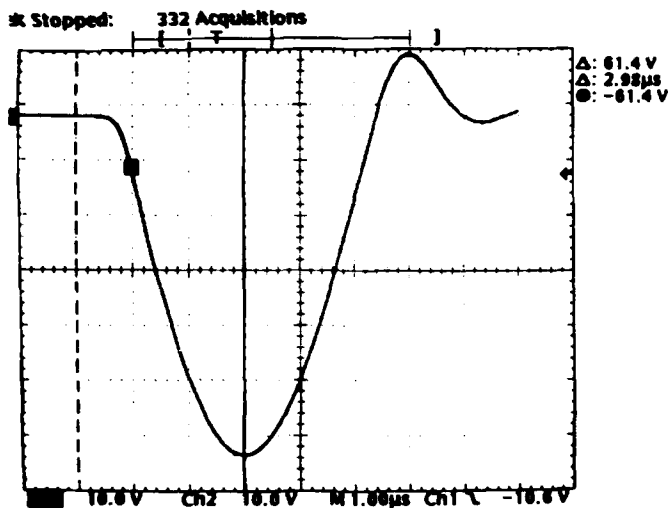


Figure 3. Magnet current wave forms (overlaid) in "upstream" and "downstream" bump magnets (100 amps./div.).

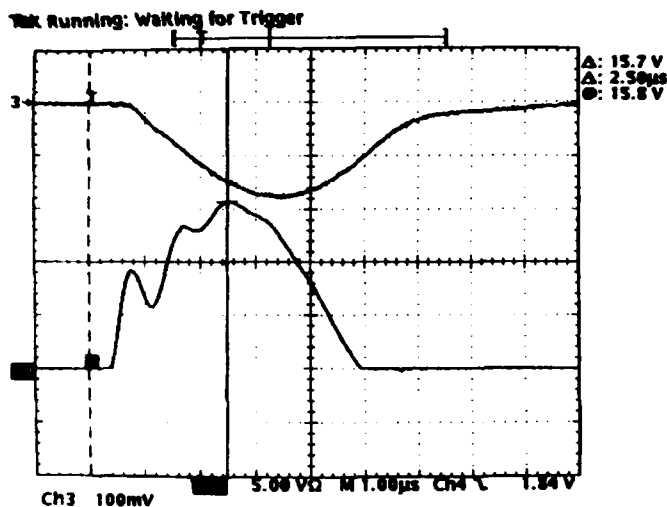


Figure 4. Magnetic field (upper trace, 666 gauss/div.) and pulser output current (lower trace, 500 amps./div.)

The SPICE model wave forms of the pulser output current (upper trace) and magnet load current (lower trace) are shown in Figure 5. The model has been empirically adjusted to give reasonably good agreement with the actual wave forms shown in Figures 3 and 4. The noticeable discrepancy is in the amplitude and duration of the reverse recovery cycle. This difference is in part due to the absence of an equivalent saturable reactor in the SPICE model. The reactor will be included in future models.

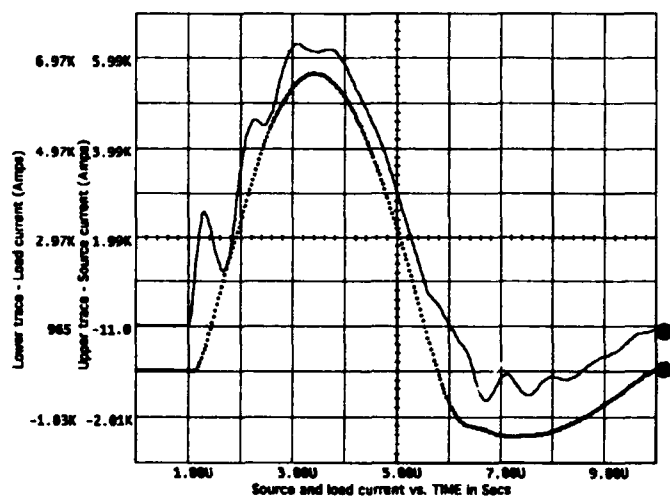


Figure 5. SPICE model output wave forms: Pulser output current (upper trace, 1000 amps./div.) and magnet load current (lower trace, 1000 amps./div.)

One solution to the resonance problem is shown in Figure 6. The ringing is almost eliminated and the reverse recovery wave form is greatly improved. In this case the number of transmission cables was halved from 32 to 16 and the snubber shunt capacitance was increased by a factor of 10. At present we still considering at the most optimal solution.

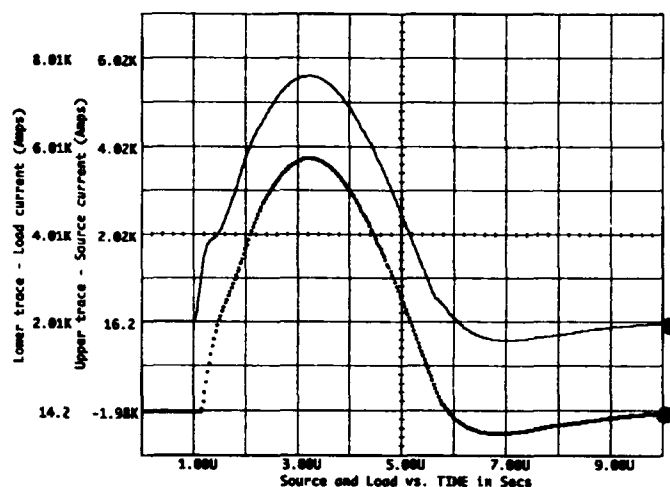


Figure 6. SPICE model output wave forms: Pulser output current (upper trace, 1000 amps./div.) and magnet load current (lower trace, 1000 amps./div.)

IV. CONCLUSION

The bump pulser system has been operating at the peak current of 6600 amps since the initial commissioning phases of the ALS in January. Despite the excessive di/dt stresses placed on the SCR's, the system has operated without fault up to shutdown date of May 1.

VI. REFERENCES

- [1] B.T. Merritt, F. R. Dreifuerst, "A New, High-Power, Solid State Switch Outperforms Thyatron Tubes" E&TR Sept.-Oct. 1991.
- [2] Manufactured by Belden Wire and Cable (special order).
- [3] Manufactured by WESTCODE Semiconductors Limited of England.
- [4] J.L. Hudgins, V.A. Sandaran, W.M. Portnoy, and K.M. Marks "High di/dt Switching with Thyristors" Dept. of Electrical and Computer Engineering, University of South Carolina, Columbia, SC 29208.
- [5] Trademark of Intusoft, P.O. Box 710 San Pedro, CA. 90733-0710 (310) 833-0710.

Design and Preliminary Testing of the LEB Extraction Kicker Magnet at the SSC

D. E. Anderson and L. X. Schneider
Superconducting Super Collider Laboratory*
2550 Beckleymeade Ave., Dallas, TX 75237 USA

Abstract

The kicker magnet for extracting beam out of the Low Energy Booster is required to generate an integrated field of 0.06 T-m for 2 μ s, rising from 1% to 99% of peak in ≤ 80 ns. Technologies for pulsed magnets of this variety, along with the engineering trade-offs of each, will be presented. Details of the electrical design of a vacuum-insulated 25- Ω travelling-wave (TW) kicker magnet, with a 5 \times 7 cm ferrite aperture, will be discussed. The results of low-voltage tests of the prototype TW magnet and a solid-core design will also be presented. Application of experimental data and design theory to the final magnet design will be mentioned.

I. INTRODUCTION

The Low Energy Booster (LEB) at the Superconducting Super Collider (SSC) is designed to accelerate protons to momentum of 12 GeV/c. In order to steer the beam upon extraction into the septum magnets, a vertical angular deflection of 1.5 mrad is required. Table 1 summarizes the LEB Extraction kicker magnet requirements.

Table 1
LEBE Kicker Magnet Requirements Extraction

Nominal $\int B \cdot dl$	0.06 T-m
$\Delta B/B$ Temporal	$\leq \pm 1\%$
$\int B \cdot dl$ Risetime	≤ 80 ns (1-99%)
$\int B \cdot dl$ Pulsewidth	2 μ s
$\int B \cdot dl$ Faltime	≤ 50 ms (99-1%)
Aperture	5 H \times 7 V cm
Good Field Region (GFR)	2 H \times 4 V cm
GFR "Kick" Uniformity	$\leq 5\%$

Kicker magnet design has historically taken two approaches, depending on the magnets' performance requirements. The more common approach utilizes a lumped section of C-shaped ferrite or magnetic steel cores, energized by a conductor passing through the cores' aperture. The other technique, used for faster risetime requirements, divides the C-cores into discrete sections to form a uniform impedance transmission line. The sections are capacitively coupled to the return conductor through a series of capacitive plates or discrete capacitors.

*Operated by the Universities Research Association, Inc., for the U.S. Department of Energy under Contract No. DE-AC35-89ER40486.

Prototype magnets of the two varieties discussed above were built and tested at the SSC Laboratory. A 25- Ω "travelling wave" TW magnet utilizing 28 or 25 cells was designed [1] with 25.1-mm cell lengths. Figure 1 shows a cutaway view of this magnet. A "solid core" (SC) magnet was also built to compare against the TW variety and to establish a database for future systems.



Figure 1. Cutaway view of the 28-Cell LEB extraction TW kicker magnet.

II. TW MAGNET DESIGN

A. Inductance Calculations

A first-order approximation of the inductance can be made from the following simple formula, which assumes that all of the magnetic energy is contained in the airgap and that the field is uniform throughout the gap:

$$\frac{L}{l} = \mu_0 \frac{W}{g},$$

where W is the width of the airgap and g is the gap length. For a 5 \times 7-cm gap, this becomes 1760 nH/m. The magnet geometry was simulated using Maxwell2D (Ansoft Corporation) to account for fringe magnetic and electric field effects. The $\mathbf{B} \cdot \mathbf{H}$ product was integrated over the magnetic region to determine the magnet's inductance per unit length. The result was 2123.2 nH/m, giving a resultant cell inductance of 2123.2 nH/m \times 0.0251 m/cell = 53.3 nH. The formula yields a low value since it does not account for fringing fields and energy contained in the ferrite. Figure 2 shows the Maxwell2D plot of the equal magnetic vector potential lines with $\mu_r = 300$, the approximate value at the frequencies present in the risetime of the pulse. Electric field vectors, which also produce undesirable $q\mathbf{E}$ forces on the beam, are also shown.



Figure 2. Maxwell2D Plot of LEBE extraction prototype magnet flux lines and electric field vectors.

B. Capacitance Calculations

Knowing the cell inductance and the desired magnet impedance, the cell capacitance can be calculated from the formula $C_{\text{cell}} = L_{\text{cell}} / Z_0^2 = 85.3 \text{ pF}$. Capacitance is developed by interleaving aluminum plates that connect to the busbar and return conductor to produce an overlap area A . The capacitance of this geometry is given by:

$$C_{\text{cell}} = 2 \frac{A\epsilon_0}{d} + 2C_{fr}$$

where d is the plate spacing and C_{fr} is the fringing effect from the edges of the plates. The fringing term can be approximated as 10 pF per linear meter of plate edge [2]. From this equation, an estimated overlap area of 204 cm² was indicated to achieve the desired capacitance and magnet impedance.

C. Electrical Length

It can be shown that for a first order approximation, the risetime of the integrated field is the sum of the electrical length of the magnet and the current risetime of the input pulse. A pulse generator has been built at the SSC that is designed to produce a voltage pulse risetime into 12.5 Ω of 20 ns (10–90%)[3]. This sets the maximum electrical length of the magnet to approximately 60 ns.

The electrical length of a TW magnet cell can be approximated as $(L_{\text{cell}}C_{\text{cell}})^{1/2}$, or 2.13 ns for this design. Dividing this into the maximum electrical length, the maximum number of cells is found to be 28. The prototype magnet was designed to accommodate fewer cells in the event actual cell parameters varied significantly from design calculations.

D. Other Magnetic Calculations

Three other important parameters were derived from the Maxwell2D simulations. The magnetic “g.l.n,” which defines the flux density achievable per unit of current, was found to be 22.6 $\mu\text{T/A}$ in the center of the airgap. At 580 A, a flux density of 0.0131 T is achievable, allowing 110% of the $\int B \cdot dl$ specification to be met with 8 TW magnets 25 cells long. The variation of the flux density over the area enclosed within the “good field region” was found to be within $\pm 0.95\%$ of nominal. The total variation for a magnet operating at 580 A and 14.5 kV, including electric field contributions, is $+1.2\text{--}0.3\%$ of nominal

in the same region. Finally, the maximum flux density in the ferrite was found to be $2.62 \times 10^{-4} \text{ T/A}$, giving a maximum flux density in the ferrite of 0.151 T at the expected operating current of 580 A. For the CMD5005 ferrite used in this application, the saturation flux density is 0.33 T at 25°C.

E. SPICE Simulations of Magnet Performance

The cells of the TW kicker magnet were modelled using an equivalent T-section circuit model [1]. The L_1 term, arising from mutual coupling between cells and self-inductance of the capacitor plates, was calculated to be about 70 nH from Grover’s formula [4] scaled to the CERN FAK magnet data [2]. A 25-cell TW magnet was then simulated using SPICE, with the results shown in Figure 3. From this, an $\int B \cdot dl$ signal 1–99% risetime of 73.8 ns is predicted, and $\Delta B/B$ varies by $\pm 0.55\%$.

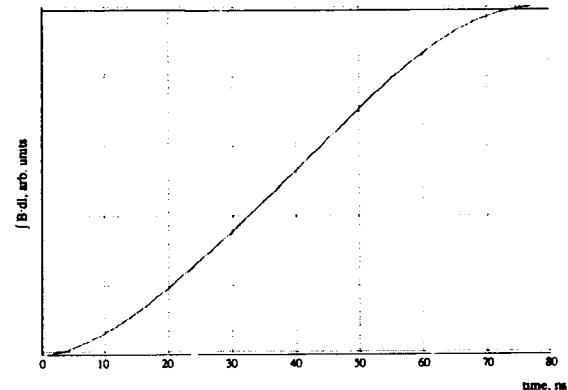


Figure 3. SPICE simulation of magnet performance.

III. EXPERIMENTAL RESULTS

A. Experimental Setup and Probes

An HP 8082A variable rise and falltime 5-V, 50- Ω pulser, with a 50-to-25- Ω impedance-matching network, was used to pulse the magnet in the majority of the experiments. Where greater signal levels were required, a Spi-Pulse 25-reed switch pulser with 115 ns of charged cable was used to drive the magnet up to 40 A. Digitizers included a Tektronix 11403 with a 11A34 amplifier for repetitive signals and an HP 54510A for single-shot signals.

B-dot probes were fabricated using printed circuit board technology. Spot probes consisted of a circular “wire” trace with an area of 9.57 mm², coupled to the scope via RG-405 semirigid coaxial cable. $\int B \cdot dl$ probes were designed using an exponentially tapered strip mounted on a G-10 substrate. The taper should provide a high-bandwidth match at both the scope input end and the shorted end. Due to the significant capacitive coupling between the $\int B \cdot dl$ probe and the magnet, the signal produced when the probe was right-side-up was subtracted from the signal produced when the probe was inverted. Furthermore, to minimize errors resulting from the direction of wave propagation in the probe relative to the magnet, responses from the two probe orientations were averaged [2], [5].

B. Travelling Wave Magnet Results

A 25- and 28-cell TW magnet were constructed and compared. When pulsed with a 10–90% voltage risetime of 20 ns (1–99% ~55 ns), the $\int B \cdot dl$ 1–99% risetimes were 78.4 and

84.0 ns, respectively. The difference between the measured and simulated risetime was primarily due to subtle differences in the simulated and actual input waveforms.

The 28-cell magnet's total inductance and capacitance were measured using an HP 4284A Precision LCR Meter. At 1 MHz, an inductance of 1927.6 nH and a capacitance of 3315.1 pF were measured. Dividing by the number of cells and correcting for end effects, these numbers scale to $L_{\text{cell}} = 66.4$ nH and $C_{\text{cell}} = 92.7$ pF. The cell inductance is about 25% higher than that predicted by Maxwell2D, probably attributable to cell-to-cell mutual coupling. The capacitance is very close to that predicted by simple formulas, and can be corrected for fringe field effects by using $C_{\text{fr}} = 11$ pF/(linear m).

Another technique was used to determine cell inductance by measuring the propagating cell voltages. From this, the cell inductance can be calculated as τ^2/C_{cell} , where τ is the propagation delay through a given cell. For an average cell propagation time of 2.38 ns, a cell inductance of 61 nH is calculated. Figure 4 shows the measured voltages for the first 8 cells.

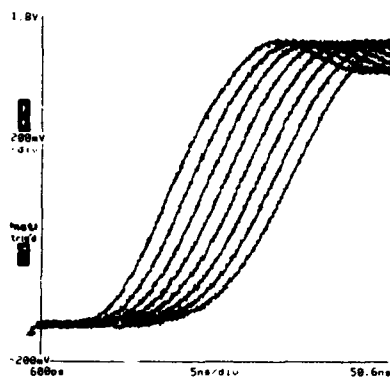


Figure 4. Measured cell voltages for the first 8 cells.

Using an HP 8751A Network Analyzer, the cutoff frequency was measured to be approximately 50 MHz. From this and the L_{cell} and C_{cell} values measured, an L_1 term for the T-section model of 100 nH can be calculated.

C. Solid-Core Magnet Results

A solid-core magnet was constructed by placing a variable number of 20-mm-long ferrite cores in an aluminum enclosure designed to fit tightly around the cores. A busbar of dimensions identical to the TW magnet was then routed through the ferrite pieces. Inductances and other magnetic parameters were therefore similar to those in the TW magnet. Varying voltage risetimes from a 25- Ω system were pulsed into the magnet, for various numbers of ferrite cores, and the integrated flux density risetime was measured. Figure 5 graphs the results of this experiment.

To improve risetime performance, the solid-core magnet was compensated with discrete capacitors at various locations along its length. By introducing gaps between ferrite units and inserting discrete capacitors, a lumped N-section transmission line was produced. Values for $N = 1, 2$, and 3 were tested. A 25-ferrite core magnet, grouped into sections of 9, 8, and 8 20-mm ferrite cores, with corresponding compensation

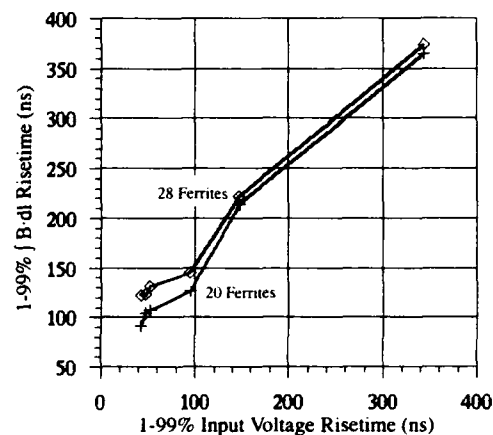


Figure 5. Solid-core magnet response.

capacitance values of 100, 200, and 440 pF, was constructed and tuned empirically. When pulsed with a voltage with a 10–90% risetime of 20 ns, the 1–99% [B-dl] risetime was found to be ~70 ns, while $\Delta B/B$ remained within the $\pm 1\%$ flat-top tolerance. This risetime is better than that measured for a TW magnet of an identical number of ferrite cores, probably due to the lack of inter-ferrite fringing fields, lower overall capacitance and inductance, and lower stray inductance of the discrete capacitors. However, the applicability of these results to a higher-current, high-voltage version of this magnet is questionable. Higher field magnitudes may lead to additional dispersion and/or other effects, thereby further degrading the magnet's performance.

IV. CONCLUSION

Although a complex structure, the TW magnet can be accurately modelled using a few simple formulas and simulation tools, with prediction of pertinent parameters to within ~10% or better. Experimental results confirm the TW magnet design, and indicate the need for further investigations into the behavior of capacitively-compensated solid core magnets. The encouraging solid-core magnet results, if applicable under high-voltage conditions, will substantially reduce the complexity and cost of kicker magnets requiring risetimes under 100 ns.

V. REFERENCES

- [1] D. Fiander, "A Review of the Kicker Magnet Systems of the PS Complex," *Conference Record of the 12th National Particle Accelerator Conference* (Moscow, 1990).
- [2] Private conversation with D. Fiander, 12/91.
- [3] G. Pappas & D. Askew, "Preliminary Testing of the LEB to MEB Transfer Kicker Modulator Prototype," presented at this conference.
- [4] Grover, *Inductance Calculations*, p. 35 (Dover, NY, 1946).
- [5] G. Nassibian, "Travelling Wave Kicker Magnet with Sharp Rise and Less Overshoot," *IEEE Trans. on Nuc. Sci.*, Vol. NS-26, June 1979, pp. 4018–20.

Development of a High Quality Kicker Magnet System

J. Dinkel, B. Hanna, C. Jensen, D. Qunell, R. Reilly

Fermilab

P.O. Box 500

Batavia IL 60510

Abstract

As part of the Fermilab Tevatron upgrade, a 6.25Ω ferrite loaded traveling wave kicker magnet has been designed. The critical parameters are the field rise time and flatness during and after the pulse. A picture frame pole piece configuration was chosen which requires two pulses of equal amplitude but opposite polarity. Low inductance, high voltage capacitors placed between each of the pole pieces provide the shunt reactance necessary to achieve the 6.25Ω impedance. Cross coupling adjacent cells is used to improve the transient response of the magnet. The compensated termination resistors are built into the magnet to minimize reflections. Two spark gap pulsers provide the two 4800A fast rise time current pulses necessary to drive this magnet. The field in this 2.4 m long magnet rises to 1055G in less than 400ns. This paper describes the design choices involved with this system and preliminary test results.

Introduction

Presently, there are 6 proton and 6 antiproton bunches used for collider operation in the Fermilab Tevatron. As the number of particles in these bunches increases, experimenter's detectors begin to saturate. To alleviate this situation, protons and antiprotons will be redistributed in 36 bunches instead of 6. In order to carry this out, the rise and fall times of the Tevatron antiproton injection kicker which deflects the antiprotons into their equilibrium orbit must be reduced to accommodate the increased number of bunches circulating in the machine.

To function in its new capacity, the kicker magnet system must meet the requirements in Table I:

Table I
System Design Parameters

$ Bdl $	0.508 T m
Space available	5.8 m
Horizontal aperture	50.8 mm
Vertical aperture	40.6 mm
Good field ($\pm 0.1\%$) width	35 mm
Field rise/fall times	395 ns
Flattop	1260 ns
Flattop stability	$\pm 1\%$
Post flattop stability	$\pm 1\%$ of full field

For a magnet to meet these criteria, its inductance per unit length as seen by the source must be minimized. For a given aperture, this can be done by using a picture frame

magnet powered by two pulses of opposite polarity. Two magnets are required, each with a magnetic length of 2.41 m. The relevant parameters for the magnet are in Table II:

Table II
Magnet Design Parameters

Magnetic length	2.41 m
Gap height	5.72 cm
Gap width	6.50 cm
Peak field	1055 G
Peak current	4800 A
Characteristic impedance	6.25Ω
Field propagation time	275 ns
Number of cells	68
Inductance per half cell	25.3 nH
Capacitance per half cell	645 pF

Magnet Design

Of the 5.8 m available in the tunnel for this magnet system, only 4.82 m remain for the production of field. Assuming negligible reluctance drop in the ferrite, the peak current can be determined from gap dimensions. We will consider the picture frame magnet design as two "C" magnets sharing a common gap as shown in Figure 1. The inductance per half cell is determined by the aperture volume of each "C" magnet.

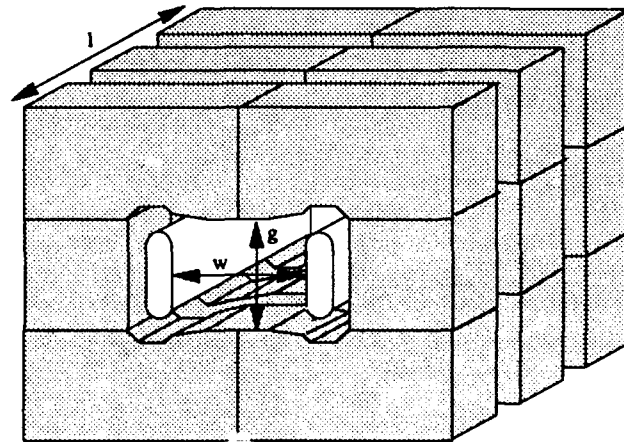


Figure 1 "Picture Frame" magnet showing ferrite and bus bars

Work supported by the U. S. Department of Energy under contract no. DE-AC02-76CHO3000.

For the sake of reliability, the pulse forming line cables are operated around 60 kV, therefore, the magnet impedance must be such that the design current can be achieved. This impedance is also required to be a submultiple of 50Ω. A magnet impedance of 6.25Ω meets these two requirements. A shunt capacitor is required to compensate the inductance of each ferrite pole piece to achieve this impedance in a traveling wave magnet according to $Z_0 = \sqrt{L_c/C_c}$.

The function of the ferrite is to efficiently guide stored magnetic energy into the gap. In order to do this, the magnetization must increase to the required value as rapidly as possible for a given drive level and source impedance. To select the ferrite which best meets this criteria, samples of a standard size were obtained from four manufacturers. These samples were subject to pulsed tests where the B and H fields were measured at high drive levels, ~6 kV, into a 50Ω load. The selection of the ferrite was based on these criteria:

1. high saturation magnetization
2. low remnant induction
3. fast time to a given induction level

Three of the samples; CMD5005 by Ceramic Magnetics, Inc. ; 8C11 by Phillips Components; and PE12C by TDK performed similarly in the testing having roughly the same magnetic flux density rise time. The CMD5005 has a slightly higher saturation flux density than the other two samples. The operation of the test system was verified by replacing the ferrite with a dielectric sample of the same dimensions.

It should also be noted that magnetic properties for ferrites can vary by as much as ± 20 % from batch to batch for the same material so that differences much less than this have little relevance.

The amount of energy required to drive the ferrite can be approximated by multiplying B(t) and H(t) to get the energy density. The larger the volume of ferrite, the more total energy is required to reach the desired induction level. The peak power required to reach this level will be determined by the source impedance. For the sample cores approximately 5 mJ were required to reach an induction level of 1400 Gauss in ~25 nsec. The volume of ferrite in the magnetic circuit of a half cell is 5 times greater than the test core, therefore we can conclude that ~25mJ would be required for the ferrite in a half cell or 3.3J for the whole magnet. This is about 0. 2% of the total stored energy.

The program POISSON was used to generate a pole tip profile which would meet the required field flatness over the desired horizontal aperture. The field at the mid plane of the gap is flat to within ± 0.05%. For a 3.8 mm offset from the mid plane, the field is flat to within ± 0.1%.

In previous designs, it was found that 2.5 cm wide ferrite pole pieces could be spaced up to 1 cm apart to accept the shunt capacitor without significant effect on the field at the mid plane. This spacing does, however, increase the flux in the ferrite by 40%.

A 29-cell low voltage test magnet has been built to measure the inductance and impedance characteristics of the

final design. A copper Faraday shield 0.062 in. thick was placed vertically down the centerline of the test magnet to enable us to perform realistic measurements on a C- shaped half-cell magnet. Average inductance measurements at 1 MHz of a half cell are 25.8 ±0.3 nH. Repositioning the ferrite from adjacent to distant cells also permits us to measure the mutual coupling between cells directly. In both cases it was found to be 7.0 nH. Although the measured cell inductance calls for a shunt capacitance of 660 pF, the best pulse response was found with 640 ±5 pF of shunt capacitance per half cell and the flattest frequency response was found with 650 ±5 pF.

The displacement current through the shunt capacitor must pass between the backlegs of two adjacent ferrite pole pieces. This increases the inductance in series with the capacitor. To minimize this effect, these two backlegs can be cross-coupled to effectively cancel this flux. This effect was measured to be 12.9 nH less than with the two ferrites separated. Cross-coupling, from an equivalent circuit viewpoint, puts a negative inductance in series with the capacitor. The peak current in a typical cross coupling winding was measured and scales to 240A peak. Resistances of 10 Ω were introduced in these circuits to provide damping of the ringing of the displacement current.

The capacitor located at the input side of the first cell has a value of 320 pF and has a series resistor equal to Z_0 to terminate frequency components of the input pulse which are above the magnet cutoff frequency.

The shunt capacitors used in this magnet are a parallel plate design. They are required to operate at voltages of 35 kV peak and maintain a stable capacitance over their operating lifetime. Physically, each must fit within the 1 cm space between adjacent ferrite pole pieces. Such a design offers the lowest practical inductance. These capacitors are essentially six layer printed circuit boards which use a glass reinforced polyimide dielectric. Each conducting surface is made from double sided C-stage material which is 0.012" thick with 2oz. of copper cladding. Between these 3 conducting surfaces, which are externally connected as two capacitors in parallel, are layers of B and C stage material which form the working dielectric. The thickness of this dielectric is 0.090" which stresses it to 25% of its rated breakdown voltage of 1600v/mil. Twelve of these capacitors were pulsed to full voltage for 5x10⁶ shots with minor degradation of the corona extinction level.

Another unique feature of this magnet system is the fact that the load resistors are an integral part of the magnet structure. This has the advantage of eliminating reflections from the cables and their associated connectors normally used with external resistors. With external resistors, it becomes necessary to match the magnet, the cables, and the load. Since the impedance of the cables is fixed, both the load and the magnet must be trimmed to match the cables.

Ideally, the load is matched to the impedance of the magnet for frequencies within its pass band of 40 MHz. The best results were obtained with 8 parallel 50 Ω resistors each

of which is placed in a cylindrical tube to minimize inductance. A ninth resistor will be run in parallel to allow precise matching and trimming if necessary. The load resistors are Carborundum 'rod' type resistors with no-arc corona terminals. Pulses in this system are actually applied about eighteen times a day, spaced several minutes apart, resulting in a negligible average power dissipation in the load resistors.

A current viewing resistor (CVR) is used to monitor the current in the termination. The CVRs selected offer a 1 nsec rise time and a 3 J rating at 0.005 Ω .

Pulser Design

A triggered spark gap was chosen for this design instead of a thyratron for a variety of reasons. Most importantly, spark gap systems are much smaller than thyratron systems. Next, spark gaps can transfer more energy at higher levels of voltage and current than thyratrons. Also, spark gaps are lighter and cheaper than thyratrons. There is also no filament or reservoir power, and thus no warm up time. Finally, spark gaps are more robust and can withstand larger inverse currents typical in tail-biter circuits. Disadvantages of spark gaps include low repetition rates, lower lifetime, necessity of a pressurized gas system, and finally the need for a high voltage trigger system.

The nominal PFL design voltage of 60 kV is also the voltage which must be held off by the spark gap. The Maxwell gap chosen for this application is rated for operation from 25 kV to 100 kV, at a maximum of 100 kA. The minimum length of the PFL cables is determined by the pulse length. The actual length will be somewhat longer than this minimum length to insure proper operation of the tail-biter spark gap.

An energy of 228 J stored in the PFL is also the energy transferred by the spark gap on each pulse. The charge stored by the cable determines the estimated lifetime of the spark gap. This is 400,000 shots of 7.6 mC for the Maxwell gap.

The rise time of the pulse is determined by the electrical properties of the pulser, specifically, the inductance related to the geometry of the tank. The pulser is constructed in a coaxial geometry to minimize the inductance while giving adequate clearance for high voltage constraints. Inductance as calculated from the physical geometry is 120 nH which agrees well with measurements. With a time constant of $L/2Z_0 = 9.6$ nsec, it takes approximately 50 nsec (5 time constants), to get to within 1% of the maximum value, neglecting any mismatches in the load.

The PFLs are charged through a series resistance which provides satisfactory isolation of the power supply during the pulse.

It is necessary to incorporate a high voltage pulse transformer to isolate the trigger generator from the main switch since it is in series with the PFL and the load. The trigger pulse transformer is a coaxial 3:1 step down design with the primary as the center conductor. The primary

consists of 3 turns of 60kV silicon rubber insulated wire strung thru three single helical loops of refrigeration tubing connected in parallel to form the secondary. Current limiting resistors are placed on both sides of this transformer to maintain a high common mode impedance for the trigger circuit. We have been able to achieve a jitter of 7.4 nsec for 32 shots, and flattop ripple within 1% peak-to-peak.

High voltage requirements necessitate the use of a dielectric with adequate breakdown strength. In this system, the pulser is pressurized with sulfur hexafluoride to about 12 psig. At this pressure, sulfur hexafluoride has a breakdown strength greater than that of transformer mineral oil.

The exponential like 'tail' at the end of the pulse due to the $1/\sqrt{f}$ skin effect losses in the cables requires the use of a second 'tail biter' switch to short the output of the pulser to ground at the end of the pulse. This will reduce the fall time of the output pulse to the order of the rise time, about 50 nsec. Due to the inductance of the pulser, some energy is reflected into the PFL upon closure of the main switch. This energy can reflect back into the load one PFL length later. Fortunately, the recovery time of spark gaps is relatively long so reflections from any source will effectively be terminated by the tail biter and resistor/diode termination at the far end of the PFL.

The tail biter will also use a spark gap switch similar to that used for the main switch but with a capacitive divider network to provide the necessary mid plane biasing.

No discussion of a delay line pulser would be complete without addressing the dispersion effects caused by the skin effect losses in the PFL and interconnecting cables. The step response of a coaxial cable in which the skin-effect losses produce an attenuation whose magnitude in dB varies as the square-root of frequency have been approximated by:

$$(1) E_o = E_i \left[1 - \operatorname{erf} \left(\frac{1.018 \times 10^{-8} \times A \times l}{\sqrt{t}} \right) \right]$$

where A is the cable attenuation in dB/100 ft. at 1000 MHz, l is the cable length in ft., t is the time in sec., and erf is the error function. The step response of a coaxial cable used as a PFL can then be derived to be:

$$(2) E_o = E_{PFL} \left[1 - \operatorname{erf} (1.018 \times 10^{-8} \times V_p \times A \sqrt{t}) \right] \\ 0 \leq t \leq T_{PFL}$$

We can, therefore, combine these to approximate the transient performance of this system by the expression:

$$(3) E_o = E_{PFL} \left[1 - \operatorname{erf} (1.018 \times 10^{-8} \times V_p \times A \sqrt{t}) \right] \\ \times \left[1 - \operatorname{erf} \left(\frac{1.018 \times 10^{-8} \times A \times l}{\sqrt{t}} \right) \right] \\ 0 \leq t \leq T_{PFL}$$

where l is the length of the cable between the magnet and the pulser. At the end of the pulse, the response is described by equation (3) with l equal to twice the physical length of the PFL plus the cable length between pulser and magnet.

Consequences of Kicker Failure During HEB to Collider Injection and Possible Mitigation

R. Soundranayagam, A. I. Drozhdin, N. V. Mokhov, B. Parker, R. Schailey and F. Wang
Superconducting Super Collider Laboratory*
2550 Beckleymeade Avenue, Dallas, Texas 75237 USA

I. INTRODUCTION

In the injector chain for the Superconducting Super Collider (SSC) [1], the High Energy Booster (HEB) is the final stage injector. HEB is a bipolar machine located 14 m above the Collider bottom ring. A schematic representation of the transfer lines from HEB to Collider rings is shown in Figure 1.

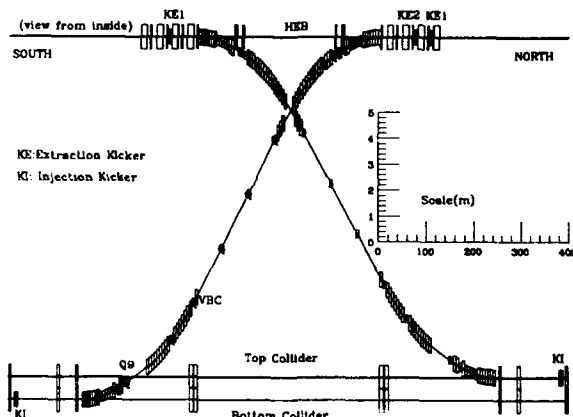


Figure 1. Schematic representation of the transfer lines.

The HEB beam extraction involves introducing a closed orbit bump at the extraction Lambertson magnets and deflecting the beam by kicker magnets. The HEB magnets guide this beam into the field region of the extraction Lambertson magnets. Rolling the first Lambertson provides a horizontal bend in addition to the vertical bend needed to direct the beam down the vertical transfer line. The extraction system for the clockwise beam is shown in Figure 2. Counter clockwise extraction system is similar in principle but differs in detail. The extraction kicker rise time is $\sim 1.7 \mu\text{s}$ and the flat top is $\sim 36 \mu\text{s}$.

At the collider level, the beam from the transfer line travels through the field region of the collider injection Lambertson magnets and levels horizontally with the Collider closed orbit. Rolling the last injection Lambertson initiates a horizontal bend. The off-centered beam is bent further by the Collider quadrupoles. Finally, the injection kickers guide the beam back towards ring center and onto the closed orbit of the Collider.

From experience, it is known that there is a finite probability that a kicker may fail, that is, either prefire without triggering or misfire when required to fire. The probability of one kicker failure is high enough that it can occur about once a month [2]. The probability of simultaneous failure of two extraction kickers or two injection kickers is very low. Clean beam transfer depends also on the correct timing between the HEB extraction and Collider injection kickers.

* Operated by Universities Research Association, Inc., for the U. S. Department of Energy under contract No. DE-AC35-89ER40486

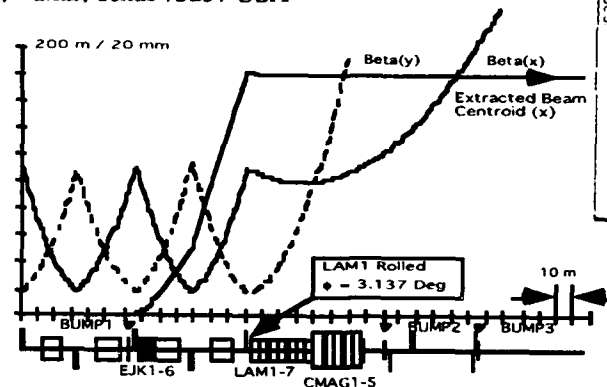


Figure 2. The HEB extraction system for the clockwise beam.

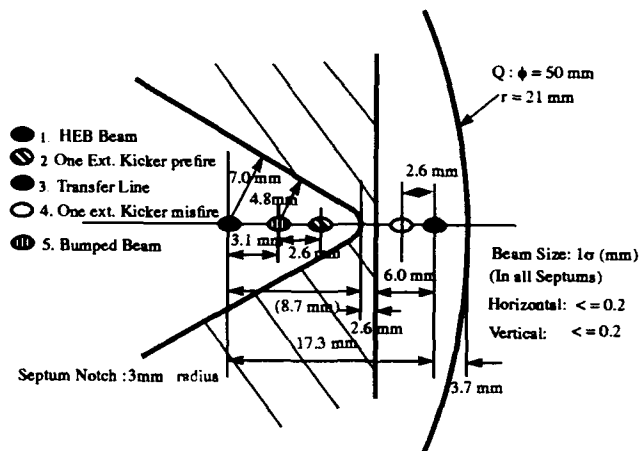


Figure 3. The interface cross section of HEB extraction Lambertson magnet and quadrupole Q1.

The limiting aperture of the HEB at 2 TeV is $\sim 40 \sigma$. The transfer line aperture is limited by the extraction and injection Lambertsons and the neighboring quadrupole magnet. The interface cross section of the HEB extraction Lambertson and quadrupole Q1 is shown schematically in Figure 3. A corresponding schematics for the injection Lambertson and quadrupole QU3B is given in Figure 5 of Ref. [3]. The arc represents part of the vacuum chamber through the quadrupole. The iron of the Lambertson magnet is shaded. The septum notch has a curvature of 3 mm radius instead of sharp edge. This enables the straight edge to move towards the field free region and increases the field region by few σ . Note that the circulating beam in each ring passes through the field free region of the Lambertson magnets. The Collider aperture at injection energy is limited by the abort Lambertson to $\sim 16 \sigma$.

In the following sections we discuss the three failure modes, namely, single kicker failure, two kickers failure and timing error between the extraction and injection kickers. We propose possible means of protecting the accelerator components.

The submitted manuscript has been authored by a contractor of the U.S. Government under Contract No. DE-AC35-89ER40486. Accordingly, the U.S. Government retains a nonexclusive, royalty-free license to publish or reproduce the published form of this contribution, or allow others to do so, for U.S. Government purposes.

II. SINGLE KICKER FAILURE

The extraction and injection kickers are segmented to reduce the kick per module so that beam from a single kicker prefire circulates with little or no beam loss before being aborted.

If a single extraction kicker misfires, the extracted beam is in the field region ~ 3.4 mm ($\sim 17\sigma$, $\sigma = 0.2$ mm) from the edge of the HEB septum. In the injection Lambertson it is ~ 2.7 mm ($\sim 10\sigma$, $\sigma = 0.25$ mm) from the edge of the septum. In tracking this beam around the Collider ring for the maximum three turns abort, we find that less than 0.01% of the beam is intercepted by the collimators in the interaction regions, and poses no problem to any components.

A single injection kicker misfire produces the same effect as that of prefire and the beam from a kicker misfire will be aborted safely.

III. TWO KICKERS FAILURE

Even though the probability of two extraction kickers failure (prefire or misfire) is very small, it is not insignificant to be ignored. At the HEB extraction Lambertson, the beam resulting from two kickers prefire is in the field free region ~ 0.6 mm ($\sim 3\sigma$) from the edge of the septum. As for the misfire, the beam is in the field region ~ 1 mm ($\sim 5\sigma$) from the septum. Thus we expect the extraction Lambertson to intercept less than 1% of the HEB beam in the event of two kickers failure. Energy deposition simulation with the MARS12 code [4] reveals that a 1% loss in the septum would produce a maximum temperature rise of ~ 420 °C, which is within the tolerable region. Thus there is no cause for concern at the HEB level as the HEB ring has large enough aperture to accommodate the beam from two kickers prefire with small loss before abort.

In the case of misfire, however, the beam will hit the Collider injection Lambertson directly. Energy density deposited by 2 TeV HEB beam in steel (high Z and high density material) septum is high enough to melt a long section of the septum and to even vaporize part of it. Thus it is necessary to intercept the beam before it reaches the septum using a low Z, low density material like pyrolytic graphite or carbon-carbon composite (C-C). For the purpose of energy deposition they are identical as they have the same density and Z.

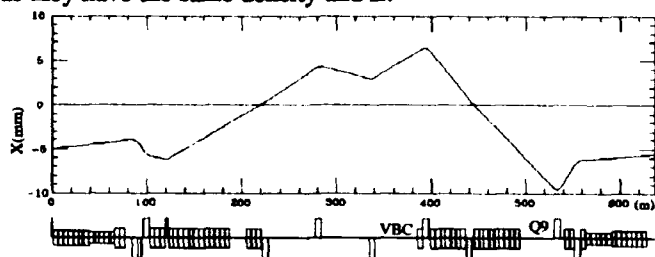


Figure 4. A stretched out transfer line and the beam displacement from two kicker misfire relative to nominal trajectory.

In the transfer line there are only two possible locations with both a large beam excursion from the nominal beam orbit and long free space (see Figure 4) for collimation. The first

location is upstream of the first upward bending magnet VBC. The second location is upstream of the quadrupole Q9. Beam sizes and two kicker misfire positions near these two locations are given in Table 1. The last column gives the separation between the beam positions due to two and one misfire in unit of beam size.

Table 1
Beam Sizes and Excursions at the Chosen Locations

Location	σ_x (mm)	σ_y (mm)	x_2 (mm)	$x_2 - x_1$ (σ)
VBC	0.227	0.120	5.50	12.2
Q9	0.394	0.124	8.07	10.2

The first location has three advantages: 1) at this location the collimator will intercept much less beam if a single kicker misfire occurs (last column in the Table 1); 2) this is farther away from the superconducting components and thus the secondaries will have minimum effect; 3) no interference with other beam lines. But it is highly disadvantageous since the interior of a graphite collimator can reach up to 4500 °C (assuming no sublimation) compared to 1750 °C, if placed at the second location (see Figure 5).

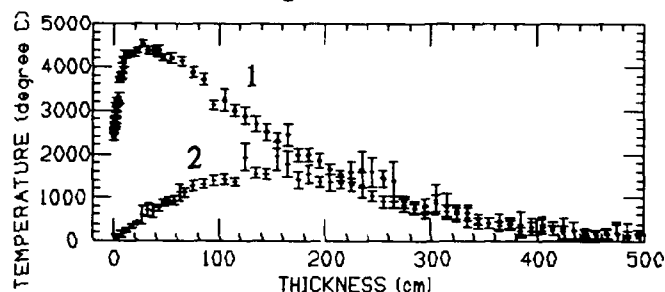


Figure 5. Temperature distribution along a 1σ cross section of a graphite collimator at location 1 (diamonds) and location 2 (cross).

Graphite in vacuum begins to sublime at ~ 1750 °C [5]. Since a surface can cool radiatively and the energy deposition peaks in the interior, sublimation will occur in the interior before anywhere else. We estimate the instantaneous pressure to be ~ 20000 atm, using ideal gas laws and the fact that the instantaneous vapor density is equal to the solid density. Laminating the collimator can minimize the effect of such a high instantaneous pressure or even eliminate the possibility of vaporization. The separation between laminations should be few σ (beam size) to allow radiative cooling and the thickness of the laminations should be as small as practically possible considering that the effective length of graphite required is ~ 5 m.

Hence, barring other technical difficulties, the second location, upstream of Q9, is the best place for the collimator to intercept the beam. Considering the fact that the MARS12 simulation can have $\sim 20\%$ uncertainty, and that there is some uncertainty in the assumptions such as beam profile and size, we would like to have at least a 50% safety margin; which means that the maximum temperature reached in the simulation should be kept below 750 °C.

Reduction of temperature in the collimator can be achieved by placing a short piece of graphite or C-C at the first location as a beam spoiler. As shown in Figure 6, a 30 cm graphite beam spoiler will reduce the maximum temperature in the collimator well below 750 °C.

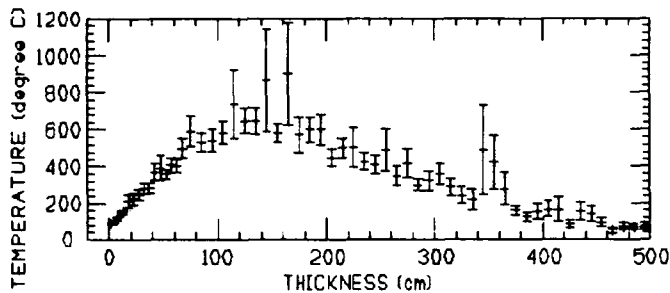


Figure 6. Temperature distribution along the 1σ cross section of a graphite collimator at location 2 with a 30 cm beam C-C spoiler at the location 1.

The beam spoiler will itself be spoiled by the beam. However, if it is only a short piece in an isolated region, it can be regarded as a sacrificial piece with a special vacuum chamber to be replaced if and when such a failure occurs.

An alternative approach is to rotate the beam spoiler fast enough to spread the beam and keep the maximum temperature in the spoiler below the 750 °C. This means that the maximum energy deposited in a $1\sigma \times 5$ cm volume of C should not exceed 10 J. From the MARS12 simulation the maximum energy deposited in that volume per proton is 5×10^{-12} J. Thus the maximum number of protons in 1σ cross section should not exceed 2×10^{12} protons, which is $1/8$ or $4.5 \mu\text{s}$ of HEB beam. Hence the spoiler should be rotated by full with half maximum ($2.345\sigma_y$) of the beam in $4.5 \mu\text{s}$. This corresponds to the rim speed of 70 ms^{-1} . The required minimum rotation speed for a 35 cm radius spoiler is then 2000 rpm.

Mechanically tolerable rim speed depends on the tensile strength and the density of the material. For graphite, the tensile strength is $\sim 25 \text{ MPa}$ allowing maximum rim speed of $\sim 54 \text{ ms}^{-1}$ that is well below our requirement. C-C material has ~ 11 times higher tensile strength and tolerable rim speed is then $\sim 180 \text{ ms}^{-1}$. Thus a 30 cm thick C-C composite cylinder of 35 cm radius rotating at ~ 5000 rpm can survive two kickers failure and spoil the beam enough to protect the downstream collimator also. It should be noted that a 35 cm radius C-C system rotating at 40000 rpm is currently in operation[6].

Two injection kickers failure, also a serious problem for the collider, is currently under investigation.

IV. TIMING ERROR

The most serious failure related to the HEB extraction and Collider injection kickers is that the injection kickers may fire either before the HEB beam arrives at the kickers or after it has passed the kickers. Should this failure occur, the HEB beam continues into the Collider ring in the trajectory as shown in Figure 7. Further, an equivalent HEB length of circulating beam will be kicked off the closed orbit in the opposite direction giving rise to a mirror image trajectory about the vertical

plane through the closed orbit. Tracking and energy deposition simulations indicate that the two superconducting dipoles in the dispersion suppressor region will be melted with yet unknown consequences related to the cryogenic systems.

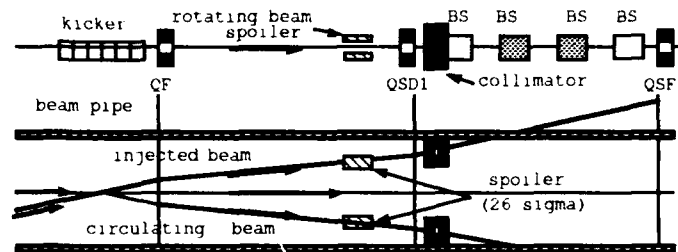


Figure 7. Collider components in the vicinity of injection kickers and the trajectories of the injected and circulating beam due to timing failure.

A logical choice of location for intercepting both the beam is upstream of the dispersion suppressor quadrupole QSD1. The beam sizes near this region are $\sigma_x = 0.18 \text{ mm}$ and $\sigma_y = 0.34 \text{ mm}$, similar to that at the collimator in the transfer line. Maximum temperature in a graphite collimator will reach up to $\sim 1750 \text{ °C}$. A system of a rotating beam spoiler upstream and a long fixed aperture collimator downstream of the quadrupole is a feasible option and is under investigation.

During the rise ($\sim 1.7 \mu\text{s}$) and fall time ($\sim 4 \mu\text{s}$) of the injection kickers an additional $\sim 16\%$ of HEB length equivalent circulating beam will be sprayed off the closed orbit. Only $\sim 12\%$ will be lost around the Collider ring, and most of it in the collimators. Few dipole magnets in the dispersion suppressor may quench due to excessive beam loss in them from the spray.

V. CONCLUSION

Failure of a single HEB extraction or Collider injection kicker poses no problem to the components in the two rings or in the transfer line. Consequences of two HEB extraction kickers failure or of timing error between the Collider injection and HEB extraction kickers can be minimized if not eliminated by use of a rotating C-C beam spoiler and graphite collimator.

VI. REFERENCES

- [1] SSC Design Report SSCL-SR-1056, SSC Lab, July 1990.
- [2] Statistics on Tevatron kicker failures. Fermilab accelerator division "Early Bird Reports."
- [3] F. Wang, et al., "Lattice Design and Injection Issues for the 2 TeV SSCL High Energy Booster to Collider Injection Lines," IEEE Particle Accelerator Conference (1993).
- [4] N. V. Mokhov, The MARS12 Code System, In Proc. SARE Workshop, Santa Fe (1993).
- [5] "Recent Carbon Technology including Carbon & SiC fibers," edited by T. Ishikawa & T. Nagaoki, English editor: I.C.Lewis, JEC Press Inc. (1983).
- [6] David L. Hunn, P.E., Loral Vought Systems, private communication.

High efficiency beam deflection by planar channeling in bent silicon crystals

K. Elsener, M. Clément, N. Doble, L. Gagnon, P. Grafström
CERN, SL-Division, CH-1211 Geneva 23, Switzerland

S.P. Møller, E. Uggerhøj, T. Worm
ISA, University of Aarhus, DK-8000 Aarhus C, Denmark

M. Hage-Ali and P. Siffert
Centre de Recherches Nucléaires,
F-67037 Strasbourg, France

Abstract

Experimental results on the deflection of a 450 GeV proton beam by means of (111) planar channeling in a bent silicon crystal are presented. The H8 microbeam in the CERN SPS North Area was tuned to be highly parallel in the horizontal plane, i.e. to a divergence smaller than the critical angle for planar channeling at this proton energy, and focussed to less than 1 mm in the vertical plane. The Si crystal was bent to deflect the beam horizontally in a classical 3-point bender. Unprecedented deflection efficiencies of up to 50 % have been observed. Since channeling of positive particles is a well-understood phenomenon over many orders of magnitude in particle energy, the present data can be extrapolated to the TeV range. This opens exciting possibilities for the application of bent crystals, e.g. as small and tunable beam splitters or as extraction devices, in the future multi-TeV proton accelerators.

I. INTRODUCTION

Deflection of high energy protons using the channeling effect in bent silicon crystals has been studied since several years [1,2]. While the attractive features of bent crystals as beam splitters to produce low intensity test beams was of prime interest in the earlier studies at FERMILAB [3], the possible application for a new CP-violation experiment [4] lead to more detailed studies with 450 GeV protons at CERN [5-7]. Recently, the ultimate limitations of deflecting high energy protons in bent crystals have been much debated in the context of proposals to extract protons from the beam halo in the future multi-TeV hadron colliders SSC and LHC for fixed target experiments [8,9]. The expected flux of such a multi-TeV proton beam depends on simulations of the expected proton distribution in the halo of the collider [10] and on the theoretical estimates on the deflection efficiency for protons in bent crystals [11].

II. CHANNELING and BENDING

Channeling of high energy particles in single crystals is now a well-established phenomenon. Positively charged particles entering a silicon crystal at small angles to a major plane or axis are channeled, i.e. reflected from the planes or strings of nuclei, and thus experience less energy loss, multiple scattering, nuclear interactions etc. than particles incident far away from such directions, i.e. at so-called "random directions". Usually, for a quantitative description of channeling the transverse energy of particles in the crystal is considered: if

this energy E_{\perp} is low enough, particles are "trapped" in the channeling potential Y_{\perp} , the electric potential obtained from smearing the charges of all atoms in a crystal plane - the Lindhard "continuum approximation" (see [2] and references therein). For the planar case,

$$Y_{\perp}(y) = Nd_p \int_0^{\infty} 2\pi p dp V(\sqrt{y^2 + \rho^2})$$

where y is the distance from the plane, Nd_p represents the number of atoms per unit area of the plane, d_p being the distance between planes. $V(R)$ is the ion-atom potential and ρ the polar coordinate inside the plane. For example, one finds that 450 GeV protons inside a critical angle of $\pm 9 \mu\text{rad}$ to the (111) planar direction in silicon have an energy $E_{\perp} < Y_{\perp, \text{max}}$ and can be channeled.

Nevertheless, even for a perfectly parallel beam, the probability for channeling is not unity. The surface transmission, or in other words the "crystal acceptance", has to be considered. Assuming a uniform beam distribution in space, aligned with the crystal, the surface transmission at high energies is found to be typically 80% or less for planar orientation of the crystal.

In long straight crystals, the protons once channeled are lost only by multiple scattering - they are dechanneled. In a bent crystal, however, additional dechanneling may occur: due to the curvature of the crystal the potential Y_{\perp} is asymmetrically lowered by a centrifugal term (κ is the crystal curvature, p and v are momentum and velocity of the beam particle, respectively),

$$Y_{\text{eff}}(x) = Y_{\perp}(x) - pv\kappa x$$

such that only particles with lower transverse energies may remain trapped and be channeled for the full length of the crystal. The bending dechanneling losses occur at the point of largest curvature of the crystal. At a given beam momentum, the efficiency of deflection in a bent crystal is therefore determined by the length of the crystal and by the maximal curvature [2, 12].

III. EXPERIMENT

The present experiment aims at testing the current understanding of channeling and dechanneling in bent crystals and offers a quantitative comparison of measured deflection efficiencies with theoretical estimates for different crystal

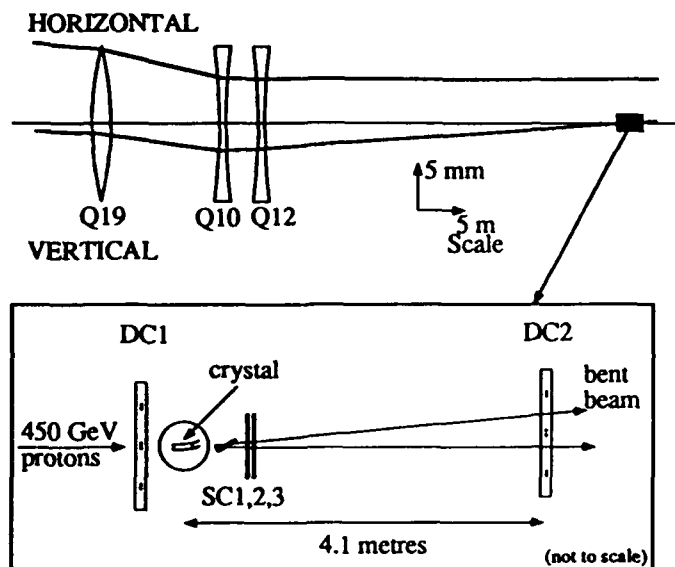


Figure 1: Schematic view of a section of the SPS H8 beam (beam optics) and the experimental set-up for the bent crystal experiment. Two drift chambers (DC) are used to track the protons. The scintillation counters (SC1,2,3) serve as trigger counters.

curvatures. The measurements were performed in continuation of our earlier tests [5,6] in the H8 beam in the North Area of the CERN SPS. The experimental arrangement is schematically shown in Fig. 1. The 450 GeV proton beam was set up to be highly parallel in the horizontal (deflection) plane and focused in the vertical plane (for further details, see [5]). The bent silicon crystal is mounted on a goniometer turntable with $1.7 \mu\text{rad}$ step-size. The incident and exiting proton positions are measured in two drift-chambers, one 20 cm upstream, the other 4.1 metres downstream of the crystal. Scintillation counters are used to trigger on protons passing through or near the crystal.

The silicon crystal, 50 mm long in the beam direction, 10 mm wide and 0.9 mm thick, was cut parallel to one of the (111) planes. It was mounted in a classical 3-point bender for deflection in the horizontal plane (see Fig. 2). The bending

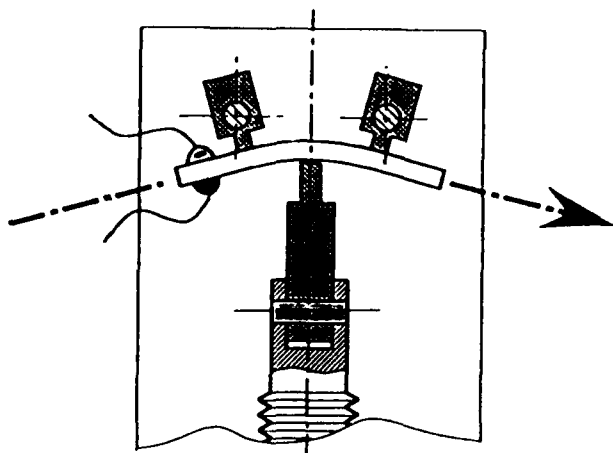


Figure 2: Detail of the 3-point bending device used to curve the crystal to variable radii. The dE/dx detector at the entrance side of the crystal is indicated.

was varied by a thumbscrew. A surface barrier detector was implanted on the entrance part of the crystal, allowing to measure the dE/dx of protons hitting the crystal. Channeled protons have about 60% of the energy loss of unchanneled ones - therefore, the variation of the dE/dx spectrum of this detector can be used to align the crystal with respect to the proton beam. Moreover, by maximizing the fraction of channeled protons in the dE/dx spectrum on the aligned silicon crystal, the beam was blown up horizontally (using Q19) in order to achieve the smallest possible angular spread for the fraction of protons hitting the crystal. Using the dE/dx information allows to tune the beam to an angular spread of a few microradians, beyond the accuracy reached with the standard beam instrumentation.

IV. MEASUREMENTS

Measurements were performed at different deflection angles, i.e. different bendings of the silicon crystals. In order to avoid sensitivity to surface imperfections, only protons hitting within the central 0.3 mm on the crystal entrance were considered in the analysis (i.e. cut in DC1). Horizontal beam profiles as measured in drift-chamber DC2 are shown in Fig. 3. For relatively modest deflection angles (e.g. 2.4 mrad), the intensity of the deflected beam is almost 50% of the total beam hitting the crystal, with about 35% of protons being undeflected and 15% being lost due to dechanneling in the bent crystal. For comparison, the dotted line in Fig. 3 shows the beam profile for an equal number of protons incident on a non-aligned crystal (random orientation), i.e. all particles are in the straight beam peak.

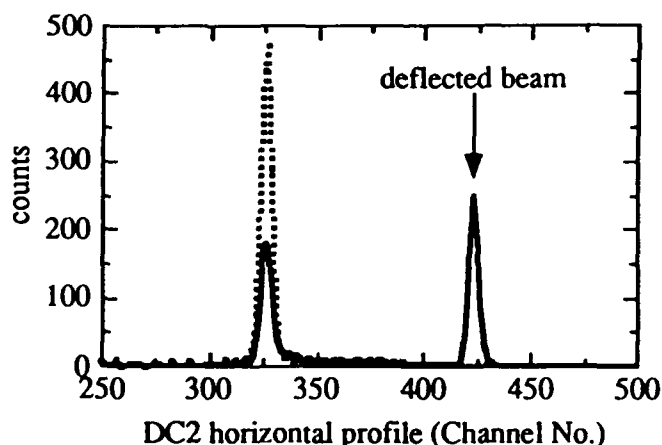


Figure 3: Horizontal beam profile as seen in the downstream drift-chamber DC2 for a deflection angle of 2.4 mrad . The dotted line indicates the beam profile as measured for a non-aligned crystal, when the full beam is undeflected.

The results of the present experiment are summarized and compared to theoretical estimates in Fig. 4. Measured deflection efficiencies for various deflection angles from 1.5 to 11.5 mrad show values up to 50 %. The error bars indicate statistical errors only. Systematic errors due to mechanical or

other instabilities may be deduced from the scattering of the data points - note that the experiment is sensitive to angular changes in the order of one microradian!

V. THEORETICAL ESTIMATES

The experimental results in Fig. 4 are compared to the expected efficiency for an ideally bent crystal (uniform curvature) - this is difficult to achieve in practice and was not attempted in the present experiment. The theoretical estimate involves the following factors:

a) The surface transmission was calculated for a perfectly parallel 450 GeV beam incident on a (111) silicon crystal and was found to be 0.75. This is the **ultimate** efficiency theoretically possible for bending a 450 GeV beam in a (111) silicon crystal.

b) The multiple scattering dechanneling in the straight parts of the crystal was included - this is an effect of a few percent at the present energies.

c) Bending dechanneling and multiple scattering dechanneling were considered in the bent part of the crystal - these effects determine the reduced efficiencies at the larger deflection angles.

In fact, in the present experiment, the crystal was bent in a 3-point bender, which was chosen for its simplicity (Fig. 2). Estimates of the expected deflection efficiency for an "ideal" 3-point bender (maximum curvature in the centre equals twice the average curvature) are also shown in Fig. 4. The calculation includes the same terms as described above for uniform curvature, with the change of the bending dechanneling term due to the larger maximum curvature. The data are seen to be bounded by the two theoretical estimates.

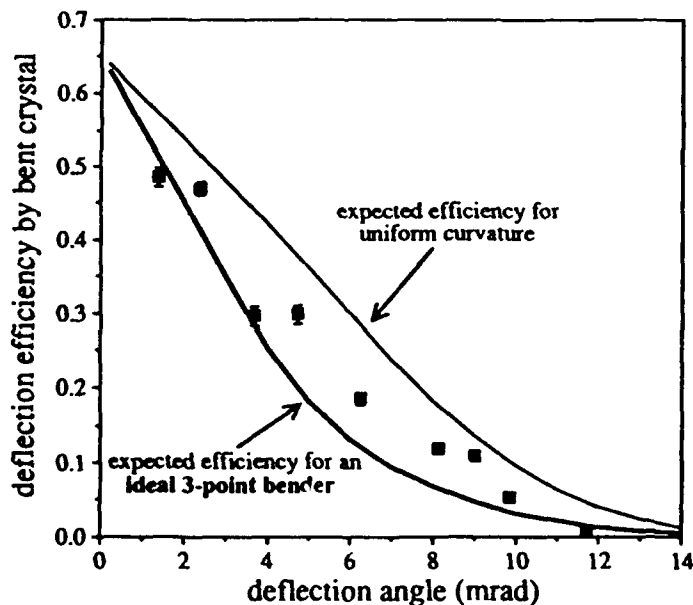


Figure 4: Comparison of experimental results (dots with bars indicating the statistical errors) with theoretical estimates for uniform curvature and an ideal 3-point bender. Details are explained in the text.

VI. CONCLUSION and PERSPECTIVES

In conclusion, the experiments on deflection of a 450 GeV proton beam in a bent silicon crystal show that by choosing the appropriate crystal curvature, efficiencies as high as 50% can be obtained in a parallel beam, in agreement with the expected values. The present results confirm the validity of the channeling and de-channeling models also at the highest energies available today. While an application of the silicon crystal as a beam splitter is already well advanced at CERN, the results presented here also give confidence in extrapolations to the higher energies available in future proton colliders. For example, a 7 TeV proton beam in a uniformly bent silicon crystal of 20 cm length could be deflected with an efficiency of 50% through an angle of 1 milliradian. Most crystal extraction schemes for LHC and SSC rely on a perfect crystalline surface. This represents a considerable technical challenge both for cutting and polishing the silicon crystals. Nevertheless, the present results show that if the surface layer can be made to resemble the bulk of the crystal, then high extraction efficiencies are not excluded for a beam, the divergence of which is matched to the critical angle for channeling (about one microradian for protons at 10 TeV energy).

VII. REFERENCES

- [1] A.F. Elishev et al., *Phys. Lett.* **88B** (1979) 387.
- [2] J.F. Bak et al., *Phys. Lett.* **93B** (1980) 505, and *Nucl. Phys.* **B242** (1984) 1.
- [3] S.I. Baker et al., *Nucl. Instr. Meth.* **A234** (1985) 602.
- [4] G.D. Barr et al., "Proposal for a precision measurement of ϵ'/ϵ in CP violating $K^0 \rightarrow 2\pi$ decays", CERN/SPSC/90-22, SPSC/P253 (experiment NA48).
- [5] S.P. Møller et al., *Phys. Lett.* **B256** (1991) 91.
- [6] B.N. Jensen et al., *Nucl. Instr. Meth.* **B71** (1992) 155.
- [7] M. Clément et al., "Tests of proton channeling in bent crystals with a view to a future beam line application", CERN/SL/92-21, 1992.
- [8] The SFT collaboration, "An Expression of Interest in a Super Fixed Target Beauty Facility (SFT) at the Superconducting Super Collider", 25 May 1990.
- [9] S. Weisz et al., these proceedings, and B.N. Jensen et al., "A proposal to test the beam extraction by crystal channeling at the SPS: a first step towards a LHC extracted beam", CERN/DRDC 91-25, DRDC/P29 (experiment RD22).
- [10] B.S. Newberger et al., *A325* (1993) 9. The LHC Study Group, "Design Study of the Large Hadron Collider. A multiparticle collider in the LEP tunnel", CERN 91-03.
- [11] J.A. Ellison, *Nucl. Phys.* **B206** (1982) 205, M.D. Bavizhev et al., IHEP pre-print 89-222, Serpukhov, 1989.
- [12] J.S. Forster et al., *Nucl. Phys.* **B318** (1989) 301.

Extraction from the Fermilab Tevatron using Channeling with a Bent Crystal

G. Jackson
(for the Experiment 853 Collaboration[†])
Fermi National Accelerator Laboratory*
P.O. Box 500 MS 341
Batavia, IL 60510

Abstract

Experiment 853 at Fermilab is approved to test the possibility of extracting very low intensity beams from the Tevatron using channeling in a bent crystal as the extraction device and RF modulations to move halo beam onto the crystal. The purpose of the experiment is to prove that the extraction technique is feasible, and that it does not create backgrounds for collider experiments which are unacceptable. In the first phase of the experiment, an unbent crystal has been inserted close to the beam at the site of the future bent crystal. In this paper we discuss the technological challenges of the bent crystal and measurements planned with both the unbent and bent crystals.

I. INTRODUCTION

In order to extract beam from the SSC Collider for B-meson high energy physics experiments while the major Collider experiments are taking data, it is necessary to design a system which extracts protons at an acceptable rate while not unduly impacting the luminosity or backgrounds. The replacement of a traditional septum magnet with a crystal in the SSC was first proposed in 1984 [1]. After a considerable amount of refinement [2,3] it was determined [4] that the east campus straight section of the SSC collider would be the optimum location for a crystal extraction system. Based on these studies, a proposal for an experiment which would use the extracted beam for B-meson physics was submitted to the SSC Laboratory [5].

Based in part on suggestions from the SSC laboratory, a test of crystal extraction of protons from a superconducting collider was proposed for the Tevatron. Partially funded by SSCL, this approved experiment E853 was approved for 72 hours of dedicated accelerator beam time during the Fermilab Collider Run Ib. While waiting for the fabrication of the bent crystal and positioning hardware, some preliminary experiments were completed parasitically during both proton

only and Collider operations in the Tevatron. The results of those experiments are reported in a separate paper [6].

II. TEVATRON SYSTEM DESIGN

A. Beamline

A sketch of the beamline geometry of the Tevatron Collider crystal extraction system is shown in figure 1. Protons in the halo of the beam distribution which intercept the bent crystal with the correct angle are deflected. These particles oscillate about the design orbit until they enter the Lambertson. Since the Lambertson magnet and the crystal are separated by an odd multiple of 90° , the angle generated by the bent crystal is exhibited as a position offset into the Lambertson field free region (figure 2). The circulating protons see the deflecting field of the Lambertson, which acts as one of the normal Tevatron dipoles. Protons in the field free region travel straight into the Tevatron C0 abort line toward the extracted beam detectors.

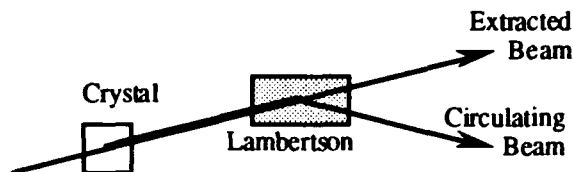


Figure 1: Sketch of the beamline geometry in the Tevatron Collider at the crystal extraction region.

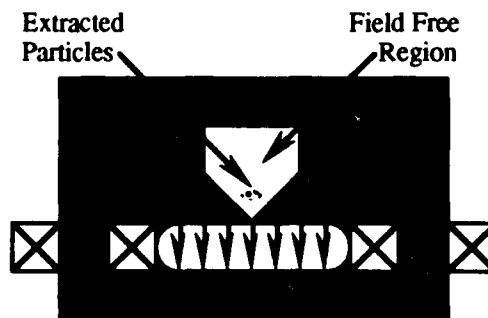


Figure 2: Sketch of a lambertson magnet, showing a portion of the magnetic flux lines generated by the bus bars pictured as crossed boxes.

[†] Fermilab, SSC Laboratory, U. Virginia, UCLA, U. Texas at Austin, U. New Mexico, U. Wisconsin, CEBAF, SUNY at Albany, JINR at Dubna, IHEP at Serpukhov, and PNPI at Gatchina.

*Operated by the Universities Research Association under contract with the U.S. Department of Energy.

B. Crystal

The crystal is positioned in the B48 straight section, replacing one of 4 proton abort kickers normally occupying that region. The monocrystal, aligned so that the protons will travel down the (1,1,0) planes, has the dimensions 30 mm long, 10 mm wide, and 3 mm thick. This alignment is produced by remotely controlled optical table positioners with a required precision of 0.24 mrad, which is the acceptance angle of the channels. The crystal is bent to create a 0.64 mrad deflection, requiring a sagitta of 1.6 microns. This sagitta is measured by means of optical interferometry. The crystal geometry and bender are shown in figure 3.

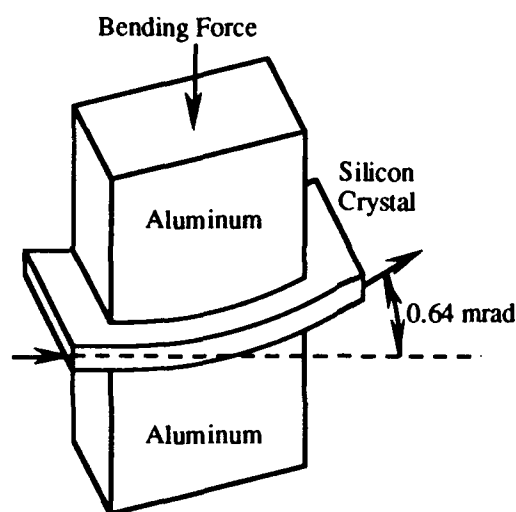


Figure 3: Drawing of the crystal in the holder which is designed to bend it without distorting the lattice structure.

A comprehensive analysis of the effect of the holder on the crystal lattice was recently completed [7]. The research used the materials program ANSYS to simulate the stresses and deformation in the crystal while being squeezed in the holder. It was found that due to the finite stiffness of the aluminum benders and the flap-back of the bent crystal, a design bend of 0.96 mrad was required to get an actual full bending angle of 0.64 mrad. Along the surface of the crystal facing the beam, the variation of this bend angle was negligible at the entrance and exit of the crystal due to the silicon overhang beyond the lengths of the aluminum pieces. The force required to accomplish this bend is less than 11 lbs, with a maximum stress in the crystal of less than 1500 psi.

This same study shows that at the crystal entrance at the top edge of the surface of the crystal facing the beam is closer to the beam than the bottom edge by 40 microns. Because this distortion is relatively constant from the entrance face up to the point where the holders start, this effect is not expected to affect the channeling efficiency. Of greater importance to

channeling is the alignment and polishing of that surface. A particle must strike deep enough into the crystal that it sees an uninterrupted lattice structure.

C. Abort Line Instrumentation

The Tevatron abort line was designed to maximum the angular acceptance of the aperture at the point of the kickers (and now of the crystal). Therefore, the beam in the abort line itself has very little divergence. To detect the particles sent into this channel, a pair of air gaps near the downstream end of the line have been inserted for instrumentation purposes. The heart of this equipment is a pair of active, segmented silicon counters, one in each air gap (which are separated by 40 m). Each channel of these detectors is read out by a FastBus crate of electronics physically located in the tunnel. The data acquisition trigger is derived from a set of plastic scintillators. A secondary diagnostic is a CCD camera imaging a fluorescent flag. The camera signal is digitized and stored by a computer as well as broadcast realtime over the Fermilab video distribution system.

In the Tevatron itself at B48 there are two monitors whose purpose it is to measure the interaction of the circulating protons with the crystal. The first is a loss monitor identical to those used in the Fermilab flying wire profile monitor systems [8], and is used to measure the turn-by-turn showers caused by inelastic collisions of circulating protons with the atoms in the crystal. The interaction rate measured by this counter will give crystal to beam halo proximity information. It may also act as a crystal angle diagnostic, where the inelastic scattering rate drops when the crystal is properly aligned and the majority of particles are being cleanly extracted. The second monitor is a phototube aimed at the crystal surface along the beam. By measuring the photon flux from the crystal caused by fluorescence, it is hoped that a direct measure of incident protons on the crystal is possible.

The C0 abort line is used for disposing of 150 GeV protons. Therefore, the detectors in the line must retract when the Tevatron is not in a 900 GeV store. This is accomplished with horizontal motion stages driven by standard stepping motors.

D. Diffusion

Probably the biggest challenge of the crystal extraction system is the diffusion of particles from the core of the beam into the halo. It is found in the Tevatron (and expected in the SSC storage ring) that there is an insufficient population of protons in the transverse or longitudinal halos of the beam available for extraction. Therefore, transverse or longitudinal external stimulation of beam diffusion are required. In the case of longitudinal excitation, the crystal must be placed at a high dispersion point of the magnet lattice.

This stimulation must not cause excessive background counting rates in the collider high energy physics detectors. Since detector backgrounds are extremely sensitive to tune, coupling, and chromaticity, changes in these parameters for

such processes as resonant extraction are disallowed. In addition, the extraction process must be very efficient in order to provide the greatest flux possible to a future fixed target experiment while simultaneously maximizing the proton intensity and luminosity lifetimes during each store. Finally, because the fixed target experiment in the SSC will be rate limited to no more than one incident proton passage per RF bucket, a slow and steady method of extraction is necessary. Therefore, we and others at CERN [9,10] have come to the conclusion that the most promising technique of populating the halo is by generating amplitude dependent diffusion rates in either the longitudinal (SSC and Tevatron) or transverse (LHC and SPS) planes. By generating a signal which has a small effect at low amplitudes but generates large particle diffusion rates at greater oscillation amplitudes, luminosity lifetime can be preserved while creating a steady state population of particles which strike deep (greater than approximately 1 micron) into the crystal (hence avoiding surface irregularities and maximizing the extraction efficiency). This diffusion rate profile is generated by taking advantage of phase space nonlinearity which create amplitude dependent particle tunes. Since each particle only reacts to signals at their local resonant frequencies, frequency dependent signal power densities cause amplitude dependent diffusion rates. Though in most cases shaped random noise is utilized, it has been proposed to use more complicated waveforms [11] to improve the mean penetration depth into the crystal.

III. EXPERIMENTAL GOALS

The goal of the Tevatron and SSC crystal extraction systems is to remove 10^{-6} of the circulating protons in the accelerator each second. In the Tevatron this amounts to 10^6 protons/sec being extracted. The present Tevatron luminosity lifetime is approximately 18 hours. The above extraction rate corresponds to a proton beam intensity lifetime of 278 hours. Therefore, the luminosity lifetime during these extraction experiments should be roughly 17 hours, which is barely noticeable and falls within the normal range of luminosity lifetimes (observed variations during and between stores).

The main goal of the Tevatron experiment is to prove the feasibility of efficient and nondisruptive proton extraction from colliding beams. The Tevatron is perfect for such a study since, like the SSC Collider ring, it is superconducting, a collider, and has high energy physics experiments. The latter is a distinct advantage over the other crystal extraction experiment at CERN in that the presently active detectors have background monitor systems. Therefore, the luminosity lifetime and detector background rates measured in the Tevatron are directly applicable to estimates of SSC Collider effects.

Given our experience with applying RF noise and collimation to the beam during normal collider operations, it is anticipated that experiment setup work such as diffusion calibration, crystal alignment, and detector commissioning can occur parasitically. In this way the study time allocated to the experiment can be dedicated toward direct observation and manipulation of extracted beam.

IV. PRESENT STATUS

With financial support from the SSC Laboratory, mechanical support from the Fermilab Accelerator Division, and approval for 72 hours of dedicated accelerator study time, experiment 853 is in the process of building all of the required hardware and fabricating the crystals. The micropositioning stages have been purchased and the required stands and vacuum chamber are under construction. The crystal holder design has not yet been finalized, nor has the method for measuring the total crystal deflection angle been tested. The detectors and associated electronics in the abort line are under construction.

V. REFERENCES

1. C.R. Sun and D. Neuffer, *Proc. Summer Study on the Design and Utiliation of the SSC* (Snowmass) eds. R. Donaldson and J. Marx (APS, New York, 1986), p. 483.
2. M. Harrison and T. Toohig, *Proc. Summer Study on the Physics of the SSC* (Snowmass), eds. R. Donaldson and J. Marx (APS, New York, 1986), p. 534.
3. B. Cox, et al., *Proc. Summer Study on High Energy Physics in the 1990's* (Snowmass), ed. S. Jenson (World Scientific, New Jersey, 1988), p. 538.
4. C.T. Murphy and R. Stefanski, SSCL Note 428 (1989).
5. The SFT Collaboration, "An Expression of Interest in a Super Fixed Target B-Physics Facility at the SSC", EOI-14, submitted to the SSC Laboratory (1990).
6. G. Jackson, "Results from Beam Diffusion and Collimation Measurements in Preparation for Fermilab Tevatron Crystal Extraction", Proc. 1993 Part. Acc. Conf., Washington D.C. (1993).
7. Z. Tang, "Silicon Crystal Under Bending", Internal Fermilab Memo TM-1827 (1993).
8. J. Zagel, et al., "Upgrades to the Fermilab Flying Wire Systems", Proc. 1991 Part. Acc. Conf., San Francisco (1993) 1174.
9. The RD22 Collaboration, "Status Report on RD22: Crystal Extraction at the SPS", CERN Report CERN/DRDC 92-51 (1992).
10. S. Weisz, et al., "Proton Extraction from the CERN-SPS by a Bent Crystal", Proc. 1993 Part. Acc. Conf., Washington D.C. (1993).
11. W. Gabella, J. Rosenzweig, R. Kick, and S. Peggs, "RF Voltage Modulation at Discrete Frequencies, with Applications to Crystal Channeling Extraction", Proc. 1993 Part. Acc. Conf., Washington D.C. (1993).

2 TeV HEB Beam Abort at the SSCL

R. Schailey, J. Bull, T. Clayton, P. Kocur, N. V. Mokhov
Superconducting Super Collider Laboratory*
2550 Beckleymeade Avenue, Dallas Texas 75237 USA

Abstract

The High Energy Booster (HEB) of the Superconducting Super Collider Laboratory (SSCL) will require a full aperture beam abort over a dynamic energy range of 200 GeV to 2 TeV. Since the HEB is a bi-polar machine, both clockwise (CW) and counter-clockwise (CCW) beam aborts are required. Also, the stored beam energy of 6.55 MJ in the superconducting HEB imposes the full aperture requirement. In this report, we describe the abort channels in the HEB utility straight sections, aperture restrictions, mechanical interferences and solutions, kicker misfires, and a 2 TeV beam absorber.

I. INTRODUCTION

The description of the HEB Abort consists of two major parts: 1.) the abort channel, common to the HEB ring, and 2.) the absorber, which lies in a gallery on a line of tangency (Fig. 1) from the HEB ring. Each part challenges the design of the 2 TeV beam abort. We shall describe the "top level" requirements first, and then show how the major parts, and their components, meet these requirements.

II. TOP LEVEL REQUIREMENTS

Table 1. lists the conditions, or requirements, which are imposed on the abort system. These requirements drive what the abort hardware will look like. The most difficult requirements to satisfy are those relating to beam energy and power. This is true, since any HEB ring component could be melted if the aborted beam were to strike a limiting aperture in the machine, before being aborted, within three turns, to the graphite absorber.

III. ABORT CHANNEL

The HEB beam may need to be aborted because of either high beam loss, large (> 3 mm) "free" β oscillations due to kicker misfires, large transverse injection errors, or other technical reasons, such as vacuum leaks, refrigeration plant failure, quench detection, etc. When such adverse conditions are detected, then the abort kicker magnets are triggered and fire, with a risetime of 1.7 μ s, synchronously at the beginning of the abort gap. The kickers move the aborted beam vertically into the field region of the Lambertson magnets. The field of the Lambertson's is such that the beam is bent horizontally "out of" the HEB ring. The kicker magnet waveform has a $\pm 10\%$ droop, such that vertical "painting" of ± 25 mm is seen at the face of the

* Operated by Universities Research Association, Inc., for the U. S. Department of Energy under contract No. DE-AC35--89ER40486.

Parameter	Requirement
Beam Power: Collider Injection Test Beam(future upgrade)	192 GW @ 10^{10} /bunch 960 GW @ 5×10^{10} /bunch
Beam Stored Energy: Collider Injection Test Beam(future upgrade)	6.55 MJ 32.75 MJ @ 5×10^{10} /bunch
Proton Energy Range	0.2 to 2.0 TeV
Number of Protons	1×10^{14} @ 5×10^{10} /bunch Max
Number of protons per year	1.8×10^{19} Max @ 5×10^{10} /bunch
Abort Kicker Risetime	Current Rise to Maximum within abort Gap time = 1.7 μ s
Abort Kicker Flat Top	One full Ring Circumference to abort all beam= 36.1 μ s
Abort Control	Automatic & Manual
Delay Time	Beam removed within three turns from when any of the permits is removed or from when an abort condition is detected
Kicker Prefire/Misfire	The abort system shall successfully abort beam within a 10 mm offset from the closed orbit with any one kicker misfiring or prefiring.
Muon Vector	The Muon vector after the backstop shall fall within the stratified fee site boundaries

Table 1. HEB Abort System Top Level Requirements

graphite beam absorber = 400 m from the utility straight section. This $\pm 10\%$ droop is consistent with Lambertson apertures (Figs. 3,4) and allows the HEB beam absorber to be placed "close" to the HEB ring, and therefore, far from site boundaries where " μ vectors" are a concern. We will visit this concept in another section. The Lambertson magnets will be placed in series on the main power bus along with the dipoles and quadrupoles of the HEB ring. This is done to take advantage of the large inductance, and therefore, time constant, $\tau = L/R = 30$ sec. This allows the aborted beam to be extracted from the HEB ring in a "fail-safe" way, even with a shorted, or "ground faulted" bus, since the orbit will only decay by ≈ 4 mm in the nominal three turns before beam abort is completed.

It should be noted that the criterion of a "full aperture" abort is satisfied in the following way. The

dynamic aperture has a radius of $\approx 7\text{-}8\text{ mm}$, and the beam abort provides a radius of 10 mm , thus allowing for all the accelerated beam, that normally survives field and alignment errors, to be aborted cleanly to the absorber, even with a single kicker misfire.

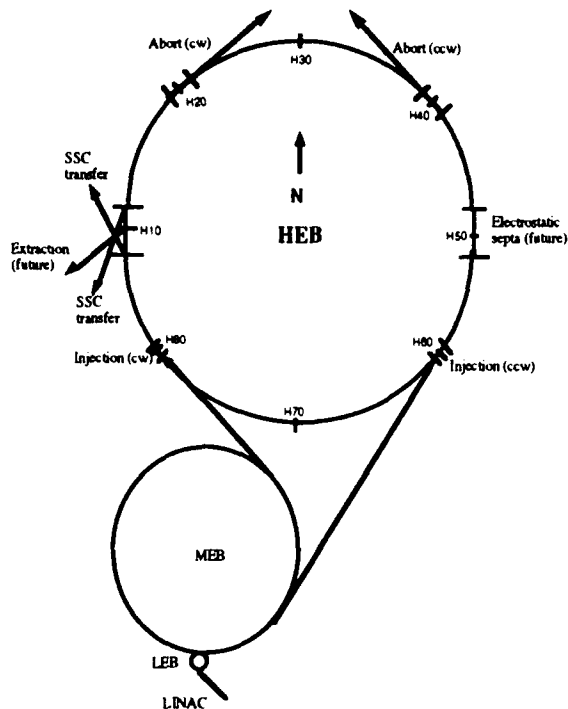


Figure 1. HEB Ring Plan View

It should also be noted that the present abort scheme has a beam trajectory which offers a mechanical design challenge for the two superconducting quadrupoles, QS3 and QS2 (Fig. 2), and associated spool pieces which are directly downstream of abort Lambertson magnets. This is true since the present design minimizes the number of abort kickers and Lambertson magnets by passing aborted beam through the

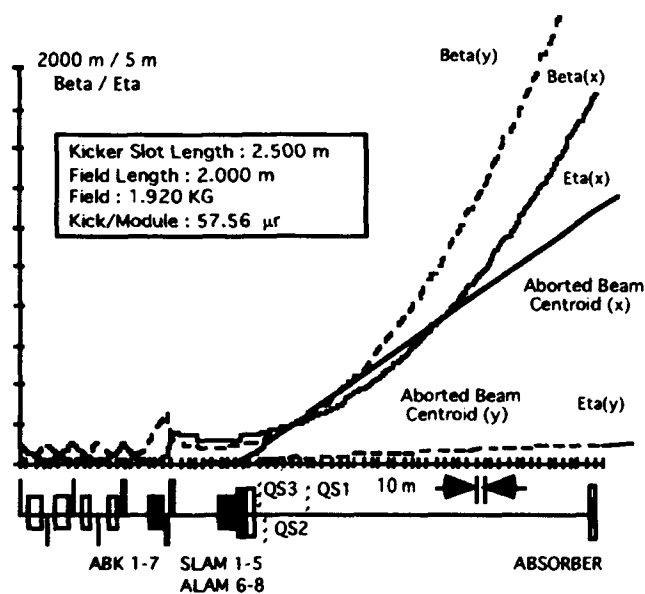


Figure 2. HEB Abort Channel

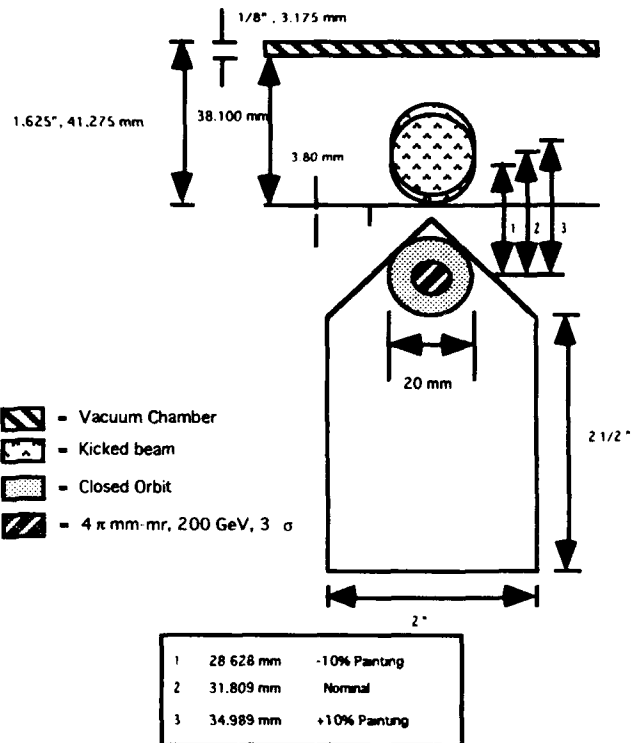


Figure 3. First Symmetric Lambertson Aperture of Abort Channel, Upstream End

side of cryostats for the two superconducting quadrupoles, and spool pieces. Conceptual design for these special cryostats presently exists.

IV. BEAM ABSORBER

The location of the HEB absorber relative to the ring is constrained by two boundary conditions. First, the " μ vector" at the site boundary, and second, the ΔT , or instantaneous temperature rise of the graphite core of the beam absorber. The first constraint would allow for a design that would place the absorber far from site boundary, or close

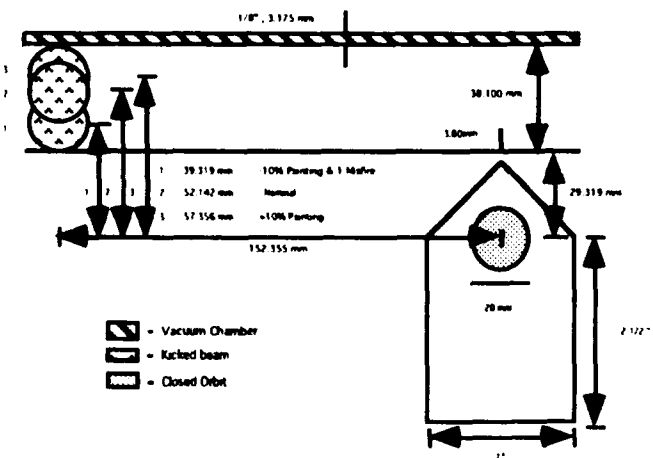





Figure 4. Last Asymmetric Lambertson Aperture of Abort Channel, Downstream End

-  Fe / Collider Injection (0.75E18 p/yr Accelerated & 20% Max Aborted)
-  Fe / Test Beam (1.5E19 p/yr Accelerated & 20% Max Aborted)
-  Graphite

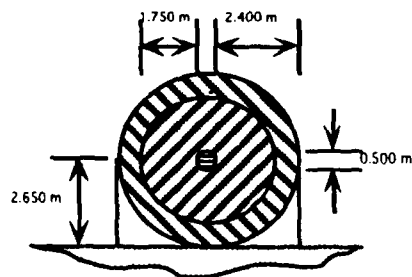





Figure 5. HEB Absorber / Cross Section

to HEB ring. A 2 TeV μ vector is defined as a 10 mrem/year isodose contour, assuming that aborted beam is attenuated only through natural earth shield (ie. Austin Chalk). The aborted beam is absorbed in a graphite and steel absorber, and the resultant μ vector, as calculated by N. Mokhov, is found to be 1625 m [1]. The HEB absorber is tentatively placed some 1900 m from the site boundary. The second constraint, of ΔT , would allow for a design that would place the absorber far from the HEB ring, in order to allow natural beam spot to become larger, and energy deposition and ΔT , to become smaller. These two constraints are clearly in conflict. The resolution is to force the "natural droop" of the kicker flat top to be as large as 20% (ie. $\pm 10\%$) and still fit through Lambertson magnets, in order to "paint" a 50 mm vertical stripe on the face of the graphite absorber core. This allows the core to reach a maximum temperature of $\approx 900^\circ\text{C}$, and $\approx 1,100^\circ\text{C}$ [1] with a single kicker misfire. The choice of graphite as core material is such that the ionization shower is spread out over a large volume and minimizes growth of instantaneous temperatures.

The absorber, as well as absorbing 6.55 MJ of beam energy, must also protect the environment from ground water activation. This is, in large part, the role of the iron shield surrounding the graphite core. J. Bull has calculated [2] the required amount of iron shielding assuming a maximum of 20% of all accelerated beam is aborted per year.

-  Fe / Collider Injection (0.75E18 p/yr Accelerated & 20% Max Aborted)
-  Fe / Test Beam (1.5E19 p/yr Accelerated & 20% Max Aborted)
-  Graphite

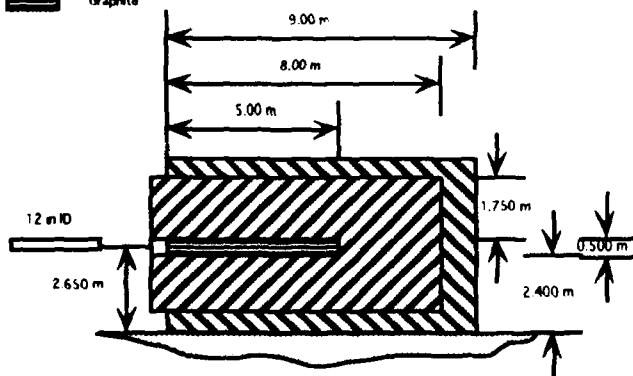


Figure 6. HEB Absorber / Lengthwise Section

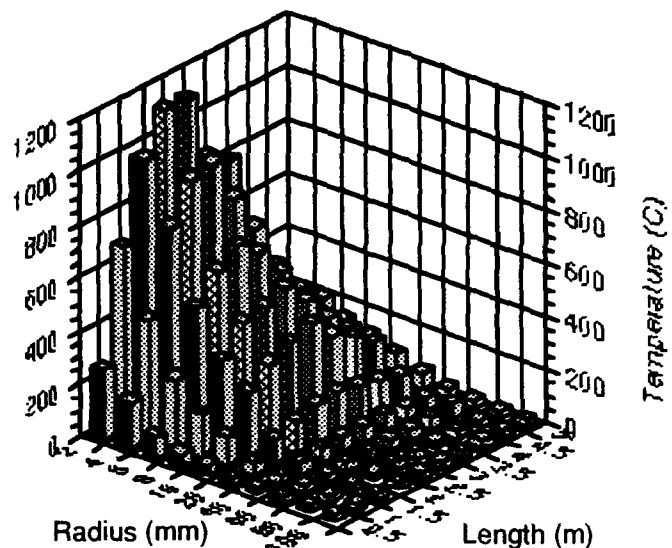


Figure 7. HEB Absorber Core Temperatures / Single Misfire

It should be noted that between the abort channel and the absorber there is only a vacuum beam pipe which telescopes to 12 in. I.D. to accommodate magnification of 10 mm "off axis" aborted beam, and single kicker misfire.

V. SUMMARY

In conclusion, a conceptual design exists for a full aperture HEB abort and absorber which addresses all top level requirements and related safety issues.

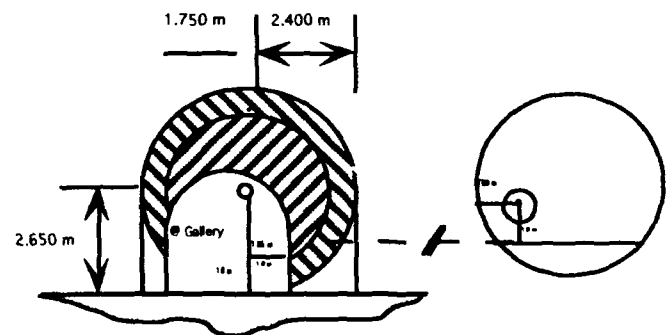


Figure 8. HEB Ring / Absorber Tunnel Relative Orientation

VI. ACKNOWLEDGMENTS

The authors would like to thank M. Harrison, D. E. Johnson, E. Kindler, K. Rust, D. Strube, S. Sheynin, G. Shuy, B. Smellie, M. Wilson, and V. Yarba for their continued support on this design effort.

VII. REFERENCES

- [1] N. V. Mokhov, The MARS12 Code System, Proc. SARE Workshop, Sante Fe, (1993).
- [2] A. Van Ginneken, CASIM "Program to Simulate Transport of Hadronic Cascades in Bulk Matter", FN-272, Fermilab, 1975.

Electrostatic Septa Design and Performance for Injection and Extraction to and from the MIT-Bates South Hall Ring(SHR)*

S. Sobczynski, R. Averill, M. Farkhondeh, W. Sapp, C. Sibley
MIT-Bates Linear Accelerator Center
P.O. Box 846, Middleton, MA 01949-2846

Abstract

The MIT-Bates South Hall Ring (SHR) is an electron storage ring undergoing commissioning. Electrostatic septa are used to inject electrons into and resonantly extract electrons from the ring. This report describes the engineering design and performance achieved for 2 electrostatic septa constructed with 270, 50 micron thick, 5 mm wide molybdenum foils stretched over a long precision machined, C-shaped carrier. The septa gaps are 2 cm and are designed to operate at 50 kV/cm over their 1.5 m effective lengths to produce a 7.5 mr horizontal bend for 1.0 GeV electrons.

I. ELECTROSTATICS

The septum gap is 2.0 cm and the anode will be excited to +100 kV maximum to produce the desired gradient of 50 kV/cm. The deflection of an electron traveling transverse to the electric field is determined by the following formula:

$$a = (e/m) * E * L / [c * \exp(2)] \text{ radians}$$

$$c = 3 * 10 \exp(8) \text{ m/s}$$

$$L = \text{length (m)}$$

$$E = \text{electric field (V/m)}$$

$$e/m \text{ at } 1.0 \text{ GeV} = 9.0030 * 10 * \exp(7)$$

The field quality in the mid-plane of the septa is very good based on POISSON^[1], and calculations of the geometry^[2], which was varied in the height of the foils above and below the mid-plane and the spacing between foils to obtain the design selected. The ratio of the maximum field gradient to the average field gradient is called the field enhancement factor^[3] and for the foil septa design this factor is minimized, consistent with reasonable spacing needed for assembly.

II. MECHANICAL AND VACUUM

There are 270 active foils and 3 guard foils made out of molybdenum, produced by Metalwerk Plansee GmbH of Austria, and procured from SAL. Other materials, such as tungsten, had been considered, but molybdenum was chosen based on its optimum combination of

parameters, which include atomic weight, tensile strength at elevated temperature, and emissivity. The raw foil stock was produced by a continuous shearing process and exhibited a typical sharp edge roll-up as a result. For this reason, all foil edges were carefully burnished and inspected under a microscope (as shown in Figure 1) to make sure they were properly rounded off and smooth.



Figure 1. Foil burnishing to eliminate sharp edge roll-up.

The foils were mounted along a carefully machined foil carrier, which was fabricated from Type 316 SS and annealed 3 times during various phases of manufacture in order to produce a stable, stress-free structure, which would be immune to thermally-induced warpage.

A creative foil tensioning/extraction mechanism (shown in Figures 2 and 3) was developed, to maintain a constant 3.9 kg tensile force per foil, in order to prevent both excessive and non-uniform deflection in the electrostatic field, as well as to allow rapid spring-activated removal of a failed foil from the active gap area. This action averts a high-voltage short and enables continued operation of the septum, but at a somewhat lower (-0.35%/foil) deflection angle.

* This work is supported in part by the Department of Energy under contract #DE-AC02-76ER03069.

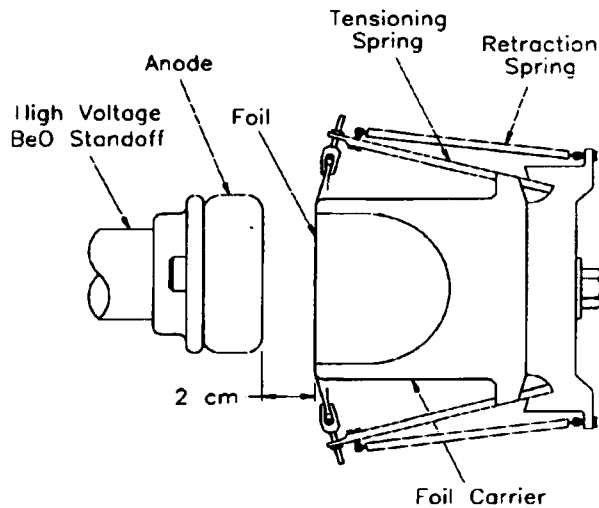


Figure 2. Foil carrier cross-section. Shown: foil tensioning/retraction mechanism.

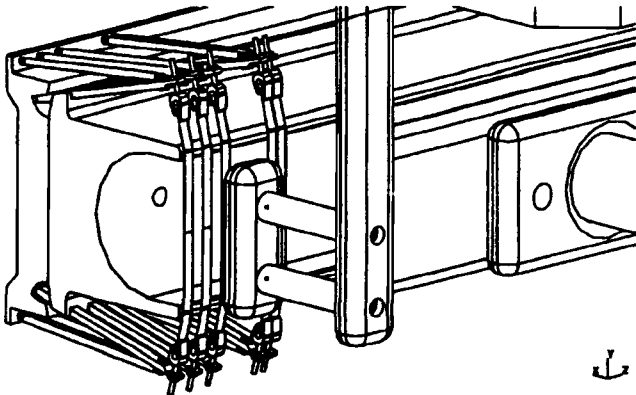


Figure 3. Leading edge of the foil carrier with 3 guard foils and first 2 out of 270 active foils shown.

All internal components of a septum, such as: the foil carrier assembly, the anode assembly, the high voltage feedthrough, the guard electrode, the signal feedthrough, and the viewing ports, were mounted/suspended from the top cover of the cylindrically shaped vacuum vessel as shown in Figure 4. This configuration allows easy access to all internal components during the various phases of the assembly, alignment, as well as for future maintenance or repairs.

The vacuum vessel was fabricated from Type 304 SS following all prescribed UHV practices^[4]. A 230 1/s ion pump attached under the vessel to a large diameter pumpout port is the only septum component not attached to the top cover.

A six-strut septum support stand shown in Figure 5 was designed to support and allow remotely controlled horizontal motion of each end of the septum by ± 1 cm. Two of the horizontal struts were motorized using stepper motors, and the remaining struts, 3 vertical and 1 axial, were made over 60 cm long to control their "cosine errors" in those struts for the intended horizontal motion.

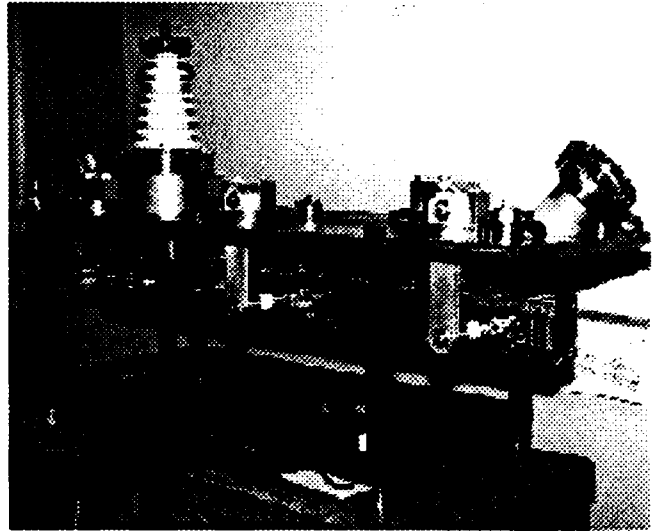


Figure 4. Internal components suspended from the top cover. The anode is shown supported by temporary AL203 insulators.

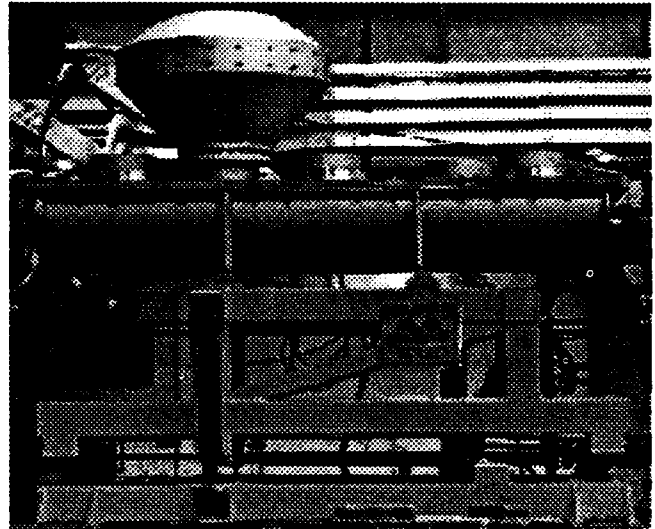


Figure 5. Injection electrostatic septum installed in ring lattice.

III. ELECTRICAL

The stainless steel anode is burnished to reduce asperities, which helps suppress arcing and pitting of the surface. The electrical standoff insulators were made of BeO to provide a high voltage standoff and a high thermal conductance path to the tank for any heat input to the anode.

The high voltage feedthrough is per a commercial design obtained from Ceramaseal. The high voltage power supply, cable connectors and series/resistor box were purchased from Glassman, Inc. The series resistor absorbs the energy in the cable if the septum arcs, reducing the potential damage to the anode surface.

The foil carrier is grounded to the tank through 50 ohms to allow monitoring of any collected current if the beam should hit the septa. The guard electrode can be biased up to -3kV below ground by a separate connector

and power supply. The intent is to use this circuit to reduce the flow of secondary electrons to the anode, when the guard foils are struck by the beam, as they must during the resonant extraction process.

During the assembly of the injection septa, the BeO insulators were not delivered in time, so a temporary fix was made by using stock Al₂O₃ insulators and modifying the supports to allow testing of the septum but not at full voltage. The modified anode circuit withstood 50 kV easily. The septum windows were a source of X-rays when the high voltage processing was performed and bluish light was seen near the modified insulator ends. The rating of the modified unit was reduced by 1/2 from the design. This allowed the injection septum to be installed and inject electrons (5 mr bend) at about 300 MeV operating at 20 kV. The present plan is, at some convenient time, to install the now delivered BeO insulators.

IV. FIDUCIALIZATION

The foil carrier was set up and fiducialized to verify that the edges of the C-shaped foil carrier were flat and parallel. The 2 cm gap spacing between the foils and the anode was surveyed in and verified and the whole assembly was fiducialized to allow placing the septum on the designed beam orbits for injection and circulating beams. An important measurement made at final assembly was the effective thickness of the 270 foils when mounted on the foil carrier. For the injection septum this was found to be 145 microns versus the 70 microns expected thickness. When the extraction septum is constructed, a number of different assembly steps are planned, which are expected to reduce the effective septum thickness to the design value.

V. TESTING

The injection unit was installed in ring lattice and tested to the 50 kV level consistent with the shorter Al₂O₃ temporary standoff insulators after high vacuum was obtained. The electron beam used to test the deflection of the beam into the ring was 300 MeV so that the operating voltage required was about 20 kV. The electron beam was deflected smoothly by computer control of the power supply.

VI. ACKNOWLEDGEMENTS

The assistance of the following is gratefully noted; Saskatoon Accelerator Laboratory staff, Miguel Olivo of Paul Scherrer Institute, Jim Walton of Fermi Laboratory, R. Winje and R. Prechter of SAIC for conceptual and detail design efforts, E. Ihloff of our staff for his valuable vacuum engineering input. Special thanks to D. Fitch for his hard work and dedication over the past many months in assembling the septum.

VII. REFERENCES

- [1] Reference Manual for the POISSON/SUPERFISH Group of Codes, Los Alamos National Lab, LA-UR-87-126 (1987).
- [2] G. Parzen, BNL 50536, CH 7 Jan. 1976.
- [3] M. Olivio, et al., "An Electrostatic Beam Splitter for the SIN 590 MeV Proton Beam" IEEE Trans Nuc. Sci. Vol. NS-28 No.3, June 1981.
- [4] J.T. Walton, Technical Specifications for Electrostatic Separator Vacuum Vessel 2214-ES-261549.

Injection into the Elettra Storage Ring

D. Tommasini

Sincrotrone Trieste, Padriciano 99, 34012 Trieste, Italy

Abstract

The Elettra storage ring will be filled with a 2 GeV electron beam from its full energy linear accelerator. Two pulsed septum magnets will be housed in a vacuum tank and four identical fast kicker magnets in air, with an internal ceramic vacuum chamber, will be symmetrically placed around the mid-point of a single straight section. The layout of the injection section, the design of the main individual components, their manufacture and the results of the relevant test are presented and discussed.

I. INTRODUCTION

The design of the layout of Storage Ring Injection has been already described and discussed in a previous paper [1]. All the injection components are now constructed, tested and installed in the storage ring. The injection elements (Figure 1) consist in:

- a vacuum tank housing two septum magnets;
- four kicker magnets symmetrically placed around the mid-point of a single straight section
- four ceramic tubes as vacuum chamber for the kickers;
- the power pulsers for the kickers and the septa.

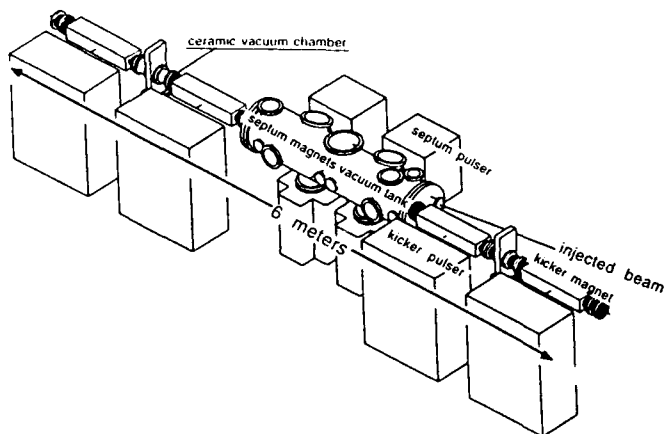


Figure 1. Layout of Storage Ring Injection.

II. KICKERS

A. Magnet

The kickers (Table 1) are window frame magnets, with a free window 90 mm wide and 48 mm high (Figure 2). The magnetic core is made by 0.1 mm thick laminations, which are able to provide the required 0.22T peak, 5 μ s duration, half

sine wave pulsed magnetic field with a repetition rate of 10 pps.

TABLE 1. Main parameters of the kicker magnets.

Energy of the electron beam	2 GeV
Deflection	22 mrad
Peak magnetic field	600 mm
Magnet inductance	1.5 μ H
Peak current	8.5 kA
Peak voltage	15 kV
Pulse duration	5 μ s

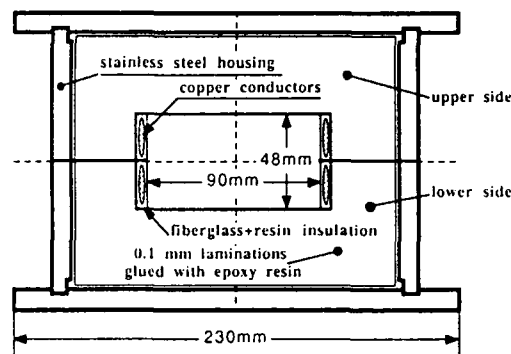


Figure 2. Kicker magnet cross section.

The magnet is splittable into two parts to allow the insertion of the ceramic vacuum chamber. The coil is made by two half coils connected in parallel, the insulation is a fiber glass tape impregnated under vacuum with a standard epoxy resin type bisphenol A (Araldit F) with anhydride hardener and amine-substituted phenol-type accelerator.

The kicker support (Figure 3) is made to position and fix two adjacent magnets, with the possibility of lowering the bottom side of the support for the ceramic vacuum chamber bake out.



Figure 3. Half kicker magnets on the support.

B. The pulse power circuit.

The pulse circuit [Figure 4] is of the capacitor discharge type, with a resistive recovery path. The capacitor is charged to the peak voltage, then the thyatron is fired when the pulse is required and the anode voltage falls to its conduction value. In order to keep the negative anode voltage after the forward conduction at the lowest possible value the recovery resistance has been carefully chosen. The reverse arcing, in the thyatron which is still highly ionized due to the very high peak current pulse, causes circuit ringing [2] and, due to the evaporation of the cathode emissive coating, causes severe damage to the electrodes surface [3], thus shortening the lifetime of the tube.

The use of a low value recovery resistor resulted in a smoothing of the current pulse (Figure 5), limiting the negative anode voltage after conduction below 1000 V.

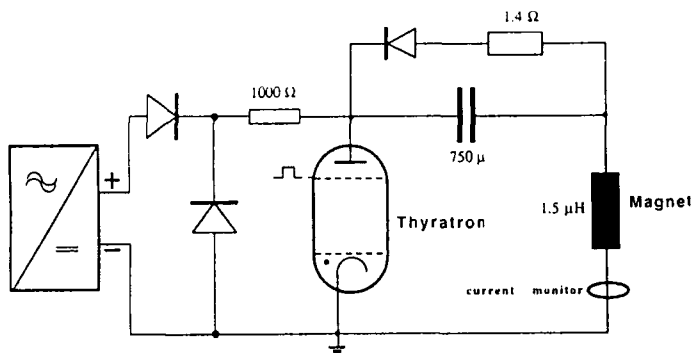


Figure 4. Kicker magnet power pulse circuit.

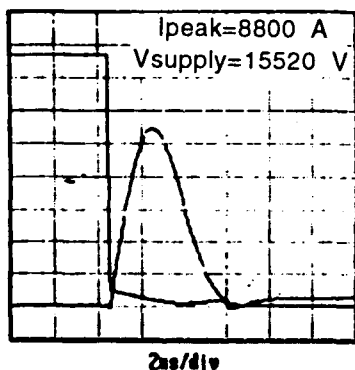


Figure 5. Anode voltage-current waveforms.

The pulsers are placed close to the magnets to minimize the total discharge circuit inductance. The thyatron filaments are supplied by two step-down transformers housed in a metallic box which acts also as a support and a forced air cooling system for the thyatron itself (Figure 6). All the main control and monitoring electronics are placed in the service area, behind the concrete shielding blocks where people is allowed to access for maintenance during the operation of the machine. The trigger grid signals are then transmitted with a coaxial cable from the service area directly to the thyatron.

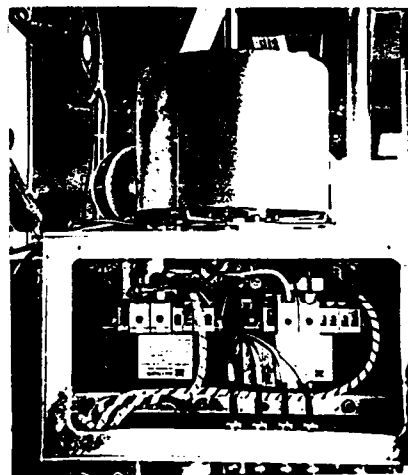


Figure 6. The thyatron box.

C. Test results.

Extensive tests have been made on the pulser [4], to verify the ability to operate at 10 pps without fault fires and with an acceptable lifetime. More than 2 million pulses have been fired up to now in a well monitored prototype pulser with excellent results and without any significant degradation of the thyatron.

The behaviour of the laminated magnetic core of the kickers was also first verified with a 200 mm long prototype, supplied by a 3 μ s duration half sine-wave pulse; then all the four series magnets have been tested to measure the magnetic field inside the magnets and the linearity current-magnetic field. The behaviour of the magnetic field along the longitudinal axis is shown in Figure 6.

The residual magnetic field was also measured along the magnetic axis, an integrated value of 9.6 Gauss-meter was obtained after having supplied the magnet at the maximum peak current for several pulses. The same integral was obtained for the four different magnets, resulting in a negligible total integrated magnetic field for the four magnets when operating in the straight section.

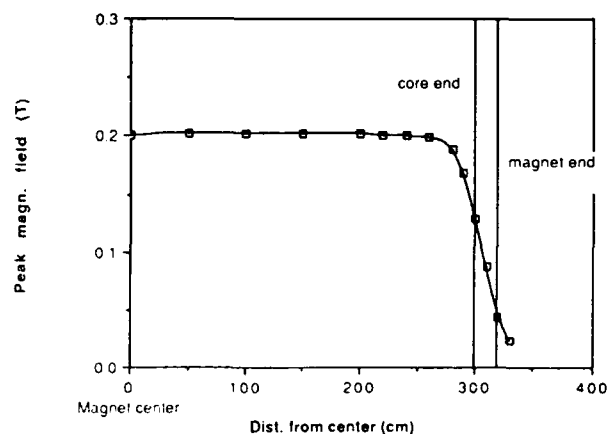


Figure 6. Behaviour of the magnetic field along the longitudinal magnet axis.

D. Ceramic Vacuum chamber

The vacuum chamber inside the kicker magnets (Figure 7) is made of ceramic in order to let the pulsed magnetic field pass through the wall of the chamber. The inside of the chamber is coated with a 3 μm thick titanium layer to provide a conducting path for the image charges [5]. As most of the image currents flow close to the beam in the centre of the chamber, it was possible to decrease up to 1.5 μm the thickness of the coating in the curved parts of the vacuum tube. Titanium was chosen for its very good reactivity and adhesion with ceramic, due to chemical bounds to the silicon phase of the alumina [6]. The vacuum chamber is a monolithic tube 710 mm long with a minimum thickness of 3.5 mm, maximum 5.0 mm, 72 mm wide and 34 mm high. To achieve the highest mechanical strength the chamber was isostatically pressed. The external surface was grinded and the inside was fired at the final roughness of 0.8 μm . The ceramic tube was braised to a covar ring, then welded to a stainless steel bellow and to a CF flange. The continuity of the vacuum chamber shape between the ceramic side and the stainless steel side through the bellow was obtained by inserting RF contacts (Figure 8).

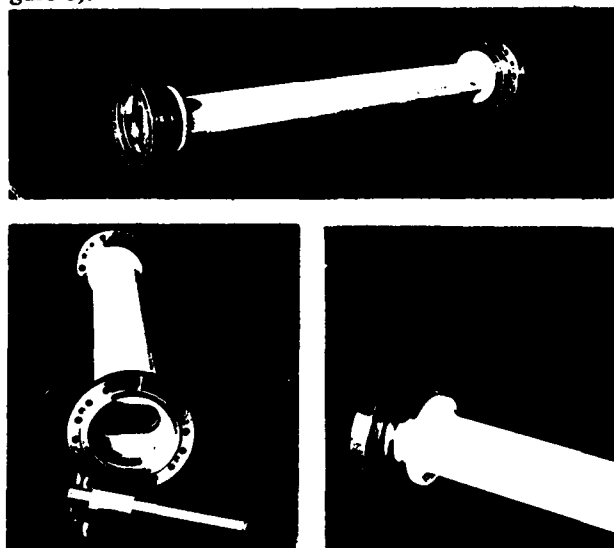


Figure 7. The ceramic vacuum chamber.

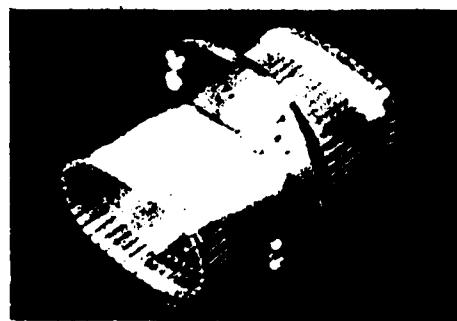


Figure 8. The RF contacts.

III. SEPTA AND VACUUM TANK

A detailed description of the injection vacuum chamber (Figure 9) and of the two septum magnets can be found elsewhere [7].

The chamber allows the primary storage ring pressure of 10^{-9} torr to be maintained and the septum magnets to be individually displaced to optimize the injection process.

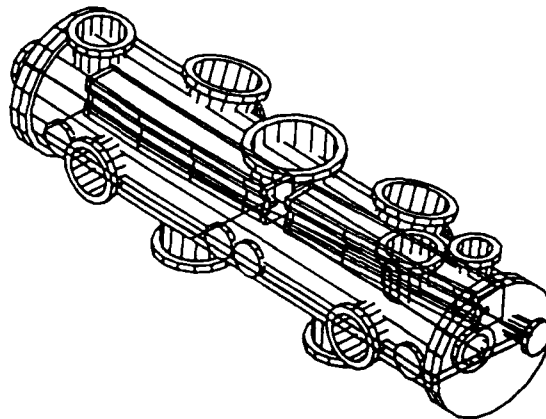


Figure 9. Septum magnets vacuum chamber.

The septa are two laminated 760 mm long magnets with a curved shape to keep the inductance at acceptable values.

The magnets are of the eddy current type, i.e. the septum screen acts against the magnetic field leakage thanks to the rapid variation of the pulsed magnetic field which is produced by discharging a capacitor into the magnet coil. The magnets are cooled by copper straps connected to the vacuum tank, then externally water cooled.

IV. REFERENCES

- [1] D.Tommasini, "The Elettra Fast Magnets", Proc. of the 3rd EPAC, Berlin 24-28 March, 1992.
- [2] D.Tommasini, "High current, high voltage pulser for the Elettra kicker magnets", Proc. of the 3rd EPAC, Berlin 24-28 March, 1992.
- [3] G. Mc Duff and K.Rust, "Life extension of thyratrons in short pulse circuits with the use of saturable magnetic sharpeners", IEEE 19th Power Modulator Symposium, San Diego, CA, June 26-28, 1990.
- [4] R.Fabris, D.Tommasini and P.Tosolini, "Test Results of the 8.5 kA, 15 kV, 10 pps Pulser Prototype for the Elettra Kickers", Sincrotrone Trieste Internal Note ST/M-92/12.
- [5] E.Karantzoulis, "On the resistive coating of the Kicker ceramic chamber", S.T. Internal Note 91-1.
- [6] M.Mayer et al., "Metallized ceramic vacuum chambers for the LEP injection kicker magnets.", CERN SPS/88-19.
- [7] R.Fabris, M.Giannini, D.Tommasini, P.Tosolini, These Proceedings.

The Septum Magnets System of Elettra

R.Fabris, F.Daclon, M.Giannini, D.Tommasini, P.Tosolini
Sincrotrone Trieste,Padriciano 99,34012 Trieste,Italy

Abstract

Two septum magnets are used to deflect the 2 GeV electron beam coming from the transfer line into a trajectory which is parallel to that of the beam circulating in the storage ring Elettra. The septum magnets will be housed in a UHV vacuum tank, thus avoiding a physical separation between the transfer line and the storage ring vacuum systems. In order to obtain a high injection efficiency, the two magnets will be individually supplied with a high peak pulsed current and their positions can be individually adjusted with an external mechanical system. The design of the whole system, the manufacture and the results of the relevant tests are presented and discussed.

I. THE SEPTUM MAGNETS

The septum magnets main requirements are shown in Table 1. The pulsed high peak magnetic field is produced with a magnetic core made of thin silicon iron laminations. Commercially available 0.18 mm thick laminations have been chosen in order to keep the magnetic field value inside each lamination below saturation.

TABLE 1. Main parameters of the septum magnets

Energy of the electron beam	2 GeV
Deflection	80 mrad
Magnetic length	720 mm
Physical length	760 mm
Peak magnetic field	0.76 T
Free aperture	30Hx15V mm
Nominal distance septum-closed orbit	25 mm
Minimum thickness of the septum sheet	2.1 mm
Magnet inductance	2.5 μ H
Peak current	9.0 kA
Peak voltage	1.8 kV
Pulse duration	60 μ s

To shield the stored beam against the magnetic field produced inside the magnet, a tapered thick copper plate makes the separation between the septum magnet environment and the storage ring vacuum chamber (Figure 1). Eddy currents flowing in the screen are able to reduce the integrated magnetic field below the maximum allowed value of 15 Gauss-m.

Due to the vacuum environment, no glue was used for the laminations: therefore oxide isolated laminations have been assembled in a stainless steel housing. All the components have been designed with UHV criteria to avoid any trapped air and to allow the gas between the laminations to be extracted from the magnet. The coil is made by a parallel of three

OFHC copper conductors with ceramic spacers. The magnet has a curved shape with a total length of 760 mm (Figure 2) to keep the inductance at the lowest value.

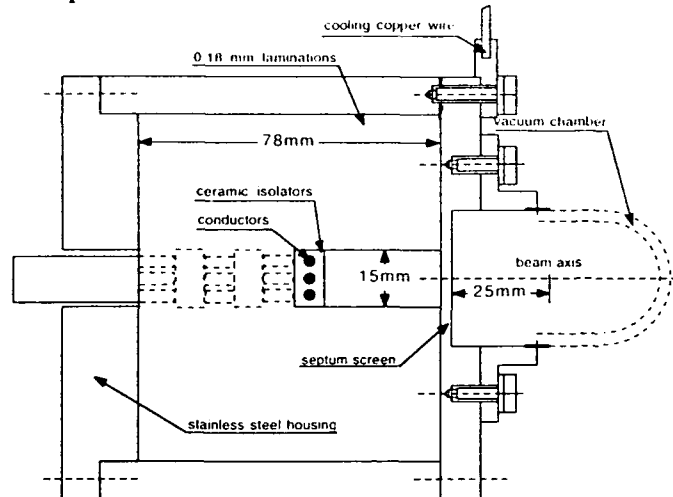


Figure 1. Septum magnet cross section.

The specific degassing rate was measured with a 100 mm long prototype according to PNEUROP specifications. The tests result was:

$$q=6 \cdot 10 \text{ mbar} \cdot \text{l/sec} \cdot \text{cm}^2$$

The following assembling procedure has been adopted for the magnets:

- US cleaning of all the components and the assembling tools.
- Assembly in clean room, with a grinded tool.
- 300 °C bake out in a vacuum oven.
- Dry N₂ protection in an envelope.

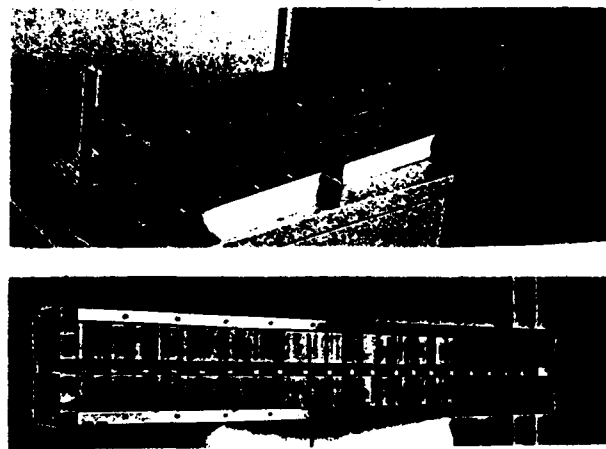


Figure 2. The septum magnet with and without the copper shield.

II. POWER CIRCUIT.

The septum magnets are powered by two independent pulsed circuits, providing a high peak half sine wave current. The circuits (Figure 3) are of the capacitor discharge type, the capacitor bank is made of 20 metallized polypropylene capacitors, 5 μF capacitance each, rated for 2400 VDC. The switch is a fast turn off power thyristor. A recovery of energy is provided by an inductance ten times higher than that of the magnet. The recovery diode and the thyristor have been snubbed, in order to limit the reverse voltage which appears during the turn off (Figure 4). This configuration was tested for several million pulses at a repetition rate of 10 pps with a supply voltage of 1800V and a corresponding peak current of 9000 A.

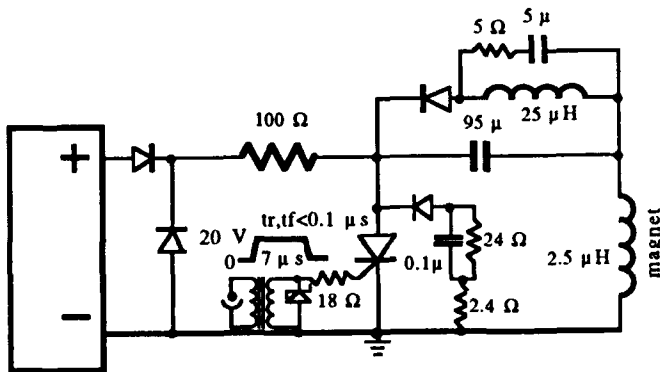


Figure 3. Power pulse circuit

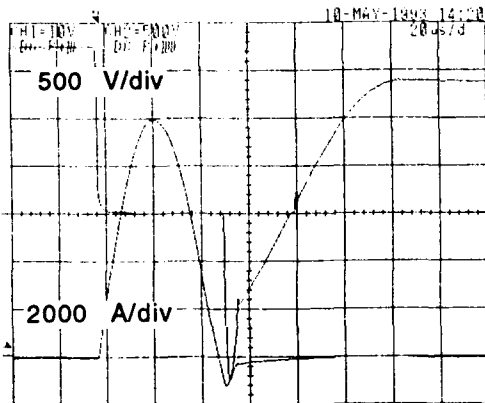


Figure 4. Thyristor voltage and current waveforms.

III. THE VACUUM TANK

The main tasks of the vacuum tank (Figure 6) are:

- to maintain the primary pressure of the Storage Ring;
- to keep the electrical continuity of the vacuum chamber of the Storage Ring: an internal chamber is connected to the side bellows through electrical contacts avoiding sharp variations for beam impedance reasons.
- to allow independent radial adjustment (15 mm) of the two septa (Figure 5);
- to cool the magnets;
- to supply the magnets.

The total amount of losses can strongly be related to the injection efficiency, therefore the magnets are cooled from the copper screen to the upper flange of the vacuum tank through short copper straps. A hollow tube for water cooling from the external side of the vacuum tank (Figure 7) is then fixed to the flange.

The vacuum system is made by:

- one prevacuum turbomolecular oil free pump (500 l/sec);
- two SIP 960 l/sec each;
- two NEG modules 1000 l/sec each;

The "in situ" vacuum procedure will be the following:

- prevacuum
- 200°C bake out
- SIP activation
- NEG activation.

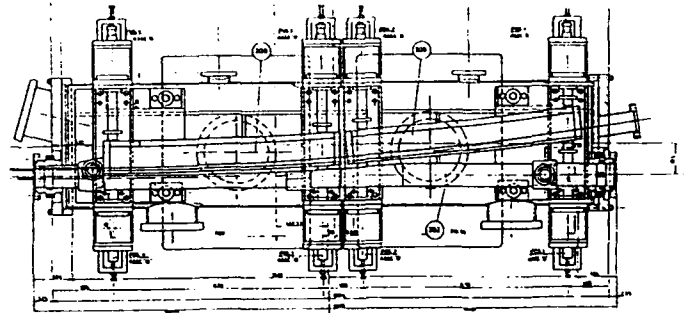


Figure 5. Layout of the septa inside the vacuum tank



Figure 6. The septum magnets vacuum tank.

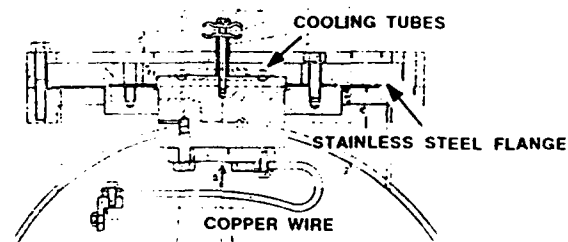


Figure 7. The septum magnets cooling system.

IV. MAGNETIC TEST RESULTS

The linearity of the peak magnetic field versus the peak supply current has been measured by integrating the signal from a coil probe. The results show a perfect linearity within the accuracy of the measurement system (a digital oscilloscope + some electronics) up to the highest field values (Figure 8).

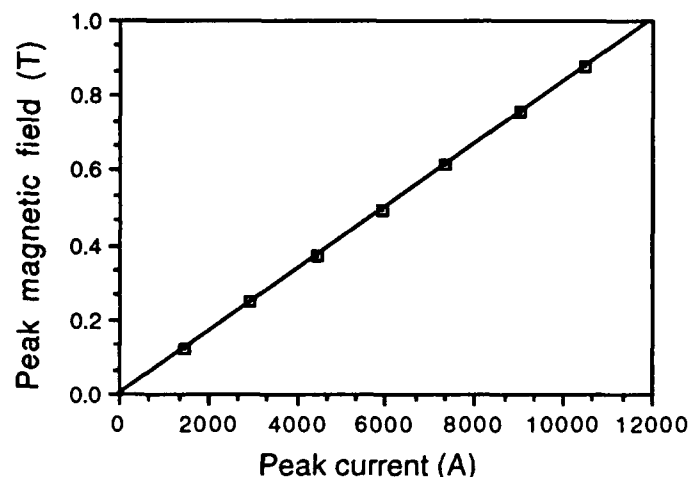


Figure 8. Peak magnetic field vs. peak current.

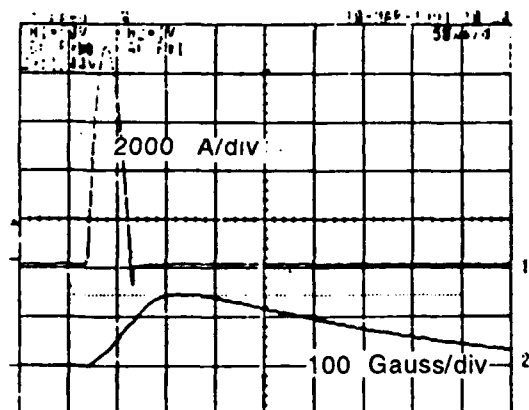


Figure 9. Magnetic field 2 mm far from the septum screen.

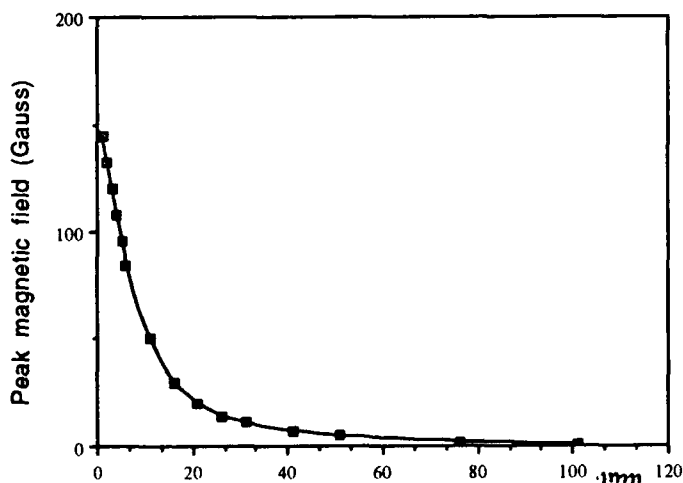


Figure 10. Peak magnetic field vs. distance from the septum.

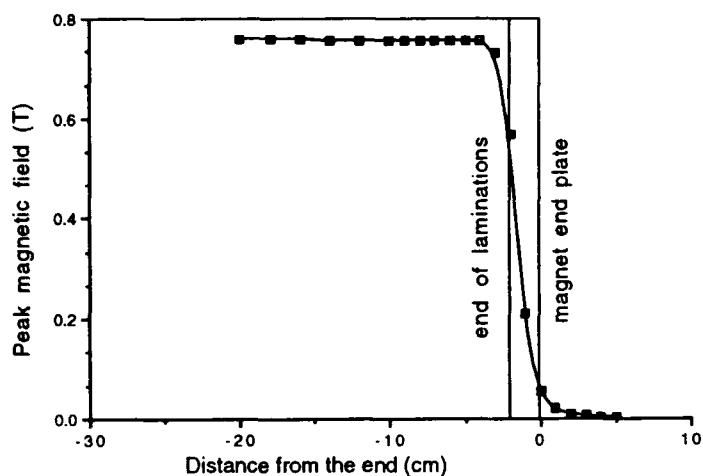


Figure 11. Peak magnetic field along the longitudinal axis.

The behaviour of the magnetic field outside the septum screen at the 2.1 mm thickness location has also been measured (Figure 9 and Figure 10). The longitudinal scan of the peak magnetic field is shown in Figure 11.

V. CONCLUSIONS

The septum magnets that have been installed in the 1.5-2.0 GeV Light Source Elettra presently under construction in Trieste have been described. The magnets will operate in vacuum without direct water cooling, the magnetic field leakage is kept below 15 Gauss-m by using an eddy current screen. The vacuum system has been designed to maintain inside the septa vacuum tank the primary pressure of the Storage Ring, in the range 10^{-9} - 10^{-10} torr.

The magnets have been completely constructed and assembled in house, the vacuum chamber was delivered by RIAL (Parma, Italy).

High Voltage Vacuum Insulation in Crossed Magnetic and Electric Fields

W.T. Diamond
AECL Research, Chalk River Laboratories
Chalk River, Ontario, Canada, K0J 1J0

Abstract

Research on high-voltage vacuum insulation has been conducted using several test stands to support development of an improved electrostatic deflector for the Chalk River superconducting cyclotron. One test stand uses a magnetic field of 0.5 T normal to the electric field. It is instrumented with isolated electrodes above and below the negative high-voltage electrode, an isolated anode and monitors of X-rays, light emission and residual gas analysis. This test stand has been used to study high-voltage conditioning and microdischarge phenomena for gaps from 1 to 3 mm. Copper and stainless steel with a variety of surface treatments have been used during these experiments. Results from this research have led to improved understanding of high-voltage conditioning in "practical" vacuum systems that reach about 2×10^{-7} torr with no bakeout capability. DC electric fields as high as 67 kV/mm (100 kV across a 1.5 mm gap) have been obtained with vacuum degassed and electropolished copper electrodes. Other surface preparation have been tested and results are compared in this paper.

I. INTRODUCTION

The electrostatic deflector of the Chalk River superconducting cyclotron operates in a magnetic field of 2.5 to 5 T. It has been observed [1] that operation of electrostatic deflectors in a strong magnetic field can reduce the peak electric field compared to operation without magnetic field.

A test stand has been built [2] that permits high-voltage tests with a 0.5 T magnetic field normal to the electric field. Tests have been made with stainless steel and copper electrodes with and without magnetic field. No significant differences have been found attributable to the magnetic field. However, the well-instrumented test stand has been used to obtain valuable insight into vacuum high-voltage insulation.

II. TEST STAND

Figure 1 shows details of the test stand that was used for these measurements. Negative high voltage is provided by a 100 kV supply that is fed through one of the insulators developed for the Chalk River superconducting cyclotron [2]. The anode is mounted on a moveable solid rod that is isolated from ground with 1 k Ω resistor and a protective spark gap. The electrodes were made from 1.9 cm diameter by 1 cm long cylinders with a 2 mm radius on

the outer edge. Isolated sparking plates are positioned above and below the electrodes and the magnetic field has the orientation shown in Figure 1. A glass window is mounted on the side of the chamber for visual or X-ray measurements. For some measurements, a second insulator and positive 100 kV power supply was used to obtain nearly 200 kV between the electrodes. The chamber was pumped with a turbomolecular pump and maintained a vacuum of about 10^{-7} torr. A Residual Gas Analyzer (RGA) was used to measure the outgassing produced by high electric fields.

III. HIGH-VOLTAGE TESTS

The test stand was used for a number of high-voltage tests. Electrodes made from 304 stainless steel and Oxygen-Free, High-Conductivity (OFHC) copper were subjected to different surface treatments and then tested to the maximum electric field that could be sustained. Two types of 304 stainless steel were used. One was commercial grade 304 and the second was vacuum re-melted.

Typical testing procedures were to set a wide gap (from 1 to 2 cm) and condition the chamber for about one hour to the maximum power supply voltage. Considerable outgassing often occurred during this process. The high voltage was then turned off and the gap re-set to values such as 1 or 1.5 mm for a given test. The voltage was increased

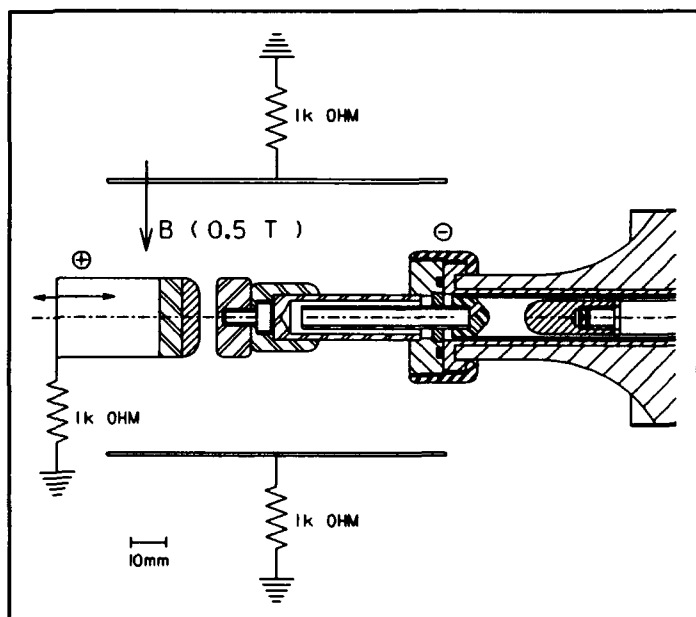


Figure 1 Details of the test stand.

to about 30 kV in 10 minutes and then in 5 kV increments with 10 to 30 minutes of conditioning between increments. Observations were made of the electrical activity to the sparking plates and anode, X-ray production and the composition of outgassing that occurred as the voltage was slowly increased.

IV. ELECTRODE PREPARATION

Surface preparation for these tests included as-machined, polishing with an abrasive pad, electropolishing and heat treatment in a vacuum oven. Samples that were heat treated were either electropolished and heat treated or heat treated and electropolished. The heat treatment was to about 850°C in a vacuum that was measured as 2×10^{-6} torr in a cool region of the oven. Samples were heated for several hours at this temperature followed by a cooldown of about 12 hours. The electropolished samples were rinsed in running tap water followed by a rinse with ethyl alcohol. After these procedures the samples were transferred in air and installed in the test stand.

V. PROCESSES AT INCREASING ELECTRIC FIELD

The processes that occur at electrode surfaces are complex and still poorly understood. Electrical breakdown may be initiated by Field Emitted Electrons (FEE) especially for gaps of less than a few millimetres. The electrons are produced from sites on the cathode and impinge on the anode producing heat and an intense source of X-rays. The intensity of field-emitted electrons increases exponentially with electric field. This can result in electrical breakdown from two sources: the field emitter can explode (explosive emission) producing a cathode plasma or anode heating can cause a plasma to form near the anode. The former is more likely to occur during fast high-voltage pulses while the latter is common for dc high voltage.

Microdischarges are another common phenomenon that occurs between electrodes for gaps from one to many millimetres. These are partial discharges that extinguish without a full breakdown between the electrodes. Figure 2 shows a typical microdischarge between two stainless-steel electrodes at a gap of 2.5 mm and 60 kV. The upper trace shows X-ray production measured with a 1 cm^3 cesium iodide crystal mounted on a photomultiplier. The pulse is caused by pile-up of X-rays during the microdischarge. The lower trace is the signal measured on a sparking plate (the magnet was on). The slow rise time and long pulse width suggests that the microdischarge is caused by the motion of gas atoms or ions. Some of these must travel from the anode to the cathode, releasing secondary electrons upon impact because there is always X-rays and visible light produced during each microdischarge. Secondary electrons released from the anode would not produce X-rays. Figure 2 shows no X-ray production after the microdischarge. There is usually no

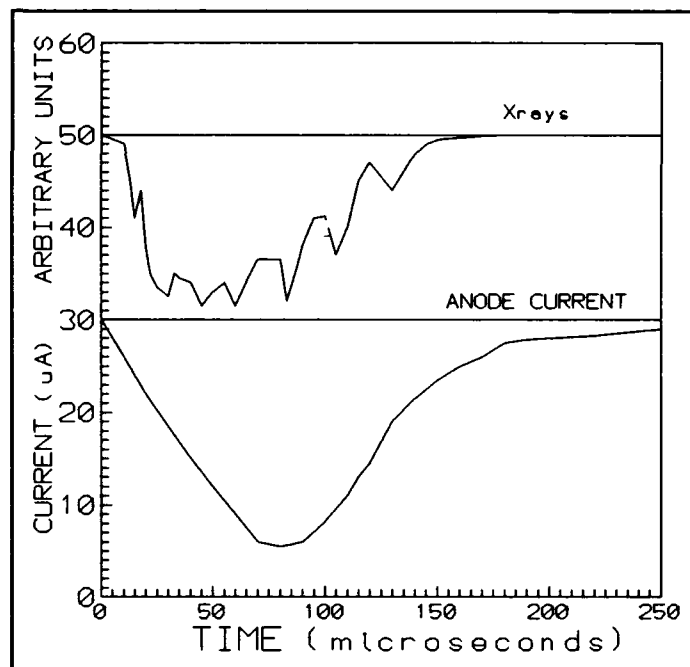


Figure 2 Microdischarge activity between two electrodes at 2.5 mm gap. The top trace shows x-ray activity. The lower trace shows electrons collected on a sparking plate.

X-ray production before a microdischarge, indicating that FEE production is not a precursor to the process. The magnetic field does not change the shape or the approximate electrical charge collected. Electron collection changes from the anode to the sparking plate and the X-ray yield changes because of geometric considerations.

Residual gas analysis shows that a single microdischarge produces a measurable gas release, mostly of hydrogen (50 to 80 percent) and light hydrocarbons. The gas release per microdischarge has been estimated to be about 5×10^{13} molecules per burst. Visual observations with a "night vision" camera show that the microdischarges are typically from a few discreet locations. Depending on the details of gas evolution, it may be that this is sufficient gas to support a Townsend type of discharge. The gas density then becomes too small to support the discharge and it extinguishes.

VI. RESULTS

Microdischarge production occurs for some surface preparations but not all. As-machined surfaces and surfaces polished with abrasive pads usually produce field emission and sparking at low fields and do not produce microdischarges. Electropolished surfaces generally produce microdischarges at moderate fields. Field emission and sparking are then suppressed until significantly higher fields. This is shown by the data in Figure 3. The surface that was electropolished and heat treated produced no observable activity until microdischarges at about 50 kV. When these electrodes were conditioned slowly (3 kV increments every 20 minutes), fields

as high as 65 kV/mm were reached before a spark changed the activity from microdischarges to field emission. After the spark, the field was increased slowly until about 77 kV/mm before a destructive spark occurred.

Table 1 shows a summary of some results obtained with copper and stainless-steel electrodes. The table shows the onset of microdischarges (μ dis), field emission (FEE) and the maximum field (max).

TABLE 1

Grade	Process	Gap mm	Electric Field (kV/mm)	FEE μ dis	max
COPPER					
ETP	EP+HT	1	66	50	78
OFHC	HT+EP	1.5	>66	37	>66
OFHC	AP	1.5	33	--	43
OFHC	AM	1	27	--	45
OFHC	EP+HT	2.2	40	30	65
OFHC	HT+EP	3	47	33	57
STAINLESS STEEL					
304	EP	1	55	36	73
304	HT+EP	1.5	30	--	63
VRM	EP	1.5	43	26	55
VRM	HT+EP	1	30	--	75

ETP	Electrolytic Tough Pitch
VRM	Vacuum re-melted 304 SS
EP	Electropolished
HT	Vacuum degas at about 850°C
AP	Abrasive pad
AM	As machined

Several items are noteworthy from this data. The copper electrodes that have been heat treated and electropolished hold higher electric fields than stainless-steel electrodes. The stainless-steel electrodes also reach field emission at lower fields than the copper electrodes. A tedious conditioning process was required to eventually reach the maximum field shown in this table for stainless-steel electrodes.

The two measurements at 2.2 and 3 mm are the first using two high-voltage supplies.

VII. SUMMARY

A test stand with a 0.5 T magnetic field orthogonal to the electric field has been used for high-voltage tests of copper and stainless-steel electrodes at gaps of 1 to 3 mm. The magnetic field did not produce significant differences in the maximum fields attained but was a useful diagnostic tool in the study of microdischarges.

Surface treatments such as vacuum heat treatment to temperatures of greater than 850°C followed by electropolishing have been used to obtain very high dc fields

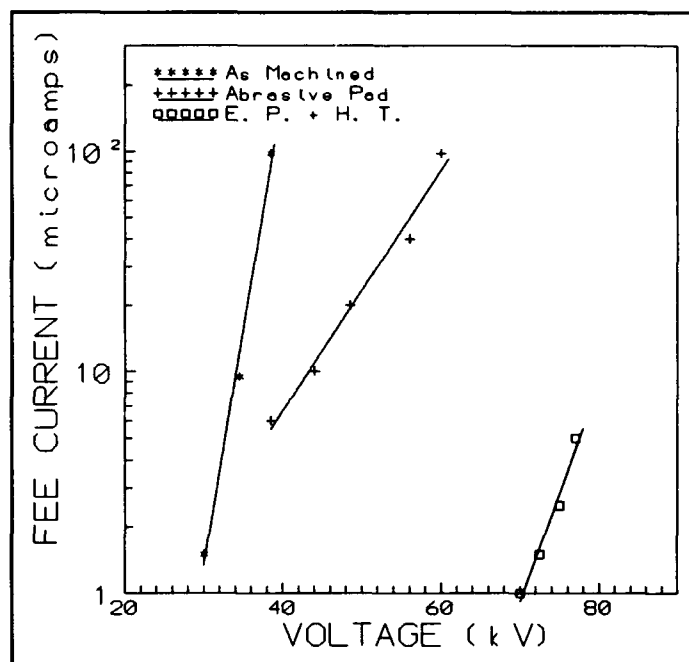


Figure 3 The maximum voltage sustained by two OFHC copper electrodes for three surface treatments. Repeated sparking occurred at the highest voltage shown for each curve.

with copper electrodes. Copper treated in this manner had superior high-voltage performance compared to stainless steel with any surface treatment tested to date. Tests with two high-voltage power supplies have reached breakdown fields as high as 57 kV/mm over a 3 mm gap with heat treated copper.

VIII. ACKNOWLEDGEMENTS

The author would like to acknowledge the valuable technical help of J.F. Mouris, D.R. Proulx and J.S. Wills.

IX. REFERENCES

- [1] W.T. Diamond, C.R. Hoffmann, G.R. Mitchel and H. Schmeing, "Performance of the Electrostatic Deflector of the Chalk River Superconducting Cyclotron", XIV International Symposium on Discharges and Electrical Insulation in Vacuum, Santa Fe, New Mexico, (1990), p. 630.
- [2] C.R. Hoffmann and J.F. Mouris, "Model Study of an Electrostatic Deflector Configuration with an Intermediate Electrode", Proceedings of the 13th International Conference on Cyclotrons and their Applications, Vancouver, (1992) p. 577.

Injection system for the SIBERIA-2 storage ring

G.Erg, A.Evstigneev, V.Korchuganov, G.Kulipanov, E.Levichev,
Yu.Matveev, A.Philipchenko, L.Schegolev and V.Ushakov
Institute of Nuclear Physics 630090 Novosibirsk, Russia

Abstract

A single-turn injection scheme with two kickers and one septum was proposed to be used for injection into SIBERIA-2. The incoming 450 MeV electron beam from the SIBERIA-1 storage ring is injected with 20 degrees horizontally. The fast kickers generate electromagnetic pulses with rise and down time of 3 ns and a flat top of 15 ns duration. The septum magnet provides a pulse of magnetic field about 100 μ s duration with 20 kG amplitude. This report shows the injection scheme, the design of 450 MeV transfer line and injection equipment. The results of the relevant tests of septum and kickers are discussed.

I. INTRODUCTION

The injection part of the SIBERIA-2 consists of a 80 MeV electron linear accelerator, a 450 MeV booster storage ring SIBERIA-1 and two electron transfer lines - TL-1 and TL-2 [1]. In November-December of 1992 the linac and SIBERIA-1 were commissioned and now the work is continued with the 450 MeV electron beam in SIBERIA-1. SIBERIA-1 operates in single-bunch mode and the stored current is supposed to be 100 mA. The ejected 450 MeV beam has the energy spread $\sigma_E/E = 3.9 \times 10^{-4}$, the bunch length is $\sigma_s = 30$ cm and its horizontal emittance is $\epsilon = 8.6 \times 10^{-5}$ cm-rad.

The ejected electrons are transferred from the midplane of SIBERIA-1 to the midplane of SIBERIA-2 by means of the 20° vertical bending magnet of TL-2. Then after two 20° horizontal bends the electron beam comes to the SIBERIA-2 septum magnet. To match the optics of SIBERIA-1 and SIBERIA-2 eight quadrupole lenses are used. There are also four vertical and two horizontal correctors to control the trajectory in TL-2. To prevent the SIBERIA-2 vacuum deterioration the Be-foil of the 100 μ m thickness is installed at the end of TL-2. Fig. 1 shows the electron beam sizes along the transfer line TL-2.

SIBERIA-2 is designed to be capable of operating both in the 100 mA single-bunch mode and in the 300 mA multi-bunch mode. A maximum possible bunch number is equal

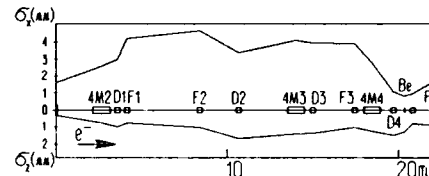


Figure 1: The electron beam sizes in TL-2.

to 30. The injection procedure is repeated with a frequency given by the booster, the storage ring SIBERIA-1. The expected rate of current storage for a circulation of about 100 mA is roughly equal to 10-20 min. Table 1 shows the injection parameters of the stored beam for the septum azimuth.

Table 1
SIBERIA-2 (450 MeV and 100 mA single bunch mode)

Revolution frequency f_0 , MHz	2.465
Harmonic number q	75
RF wavelength λ_0 , m	1.655
Damping times τ_x, τ_z, τ_s , sec	0.52, 0.54, 0.26
Emittances ϵ_x, ϵ_z , cm-rad	$34 \times 10^{-6}, 3.4 \times 10^{-6}$
Beam sizes $\sigma_x, \sigma_z, \sigma_s$, cm	0.25, 0.05, 2.7
Beam life time (Touschek), hr	0.7

II. INJECTION

For the SIBERIA-2 storage ring the injection scheme was chosen to be horizontal with one prekick of the stored beam and one kick of the injected and stored beams, Fig.2. The SIBERIA-2 lattice comprises six mirror-symmetrical su-

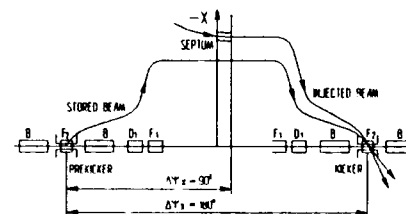


Figure 2: The layout of storage ring injection scheme.

perperiods with achromatic bends. All injection devices are located inside the achromatic bend. Due to the achromatic bend the horizontal betatron phase

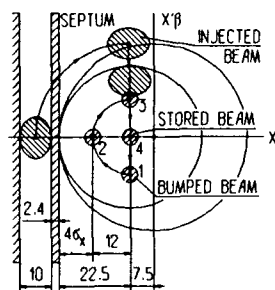


Figure 3: The injection horizontal phase space.

advance from the center of a superperiod to the center of the quadrupole F2 does not depend on the betatron tune and is always equal to $\pi/2$. A prekicker and a kicker are housed inside the vacuum chamber of lenses F2 with the π -phase advance between them.

Prior to the injection the prekicker deflects the stored beam (the maximum angle is equal to 5 mrad) in parallel to the equilibrium orbit at 1.25 cm towards the septum knife. The kicker dumps the deviation of the stored and injected beams. The kickers location permits us to use more effectively the ring horizontal acceptance and to dump the deviation of the stored beam rather precisely, that is important for the storing in the single-bunch mode.

Fig. 3 shows the injection scheme in normalized horizontal phase space. In the case, when the kick is equal to the prekick, the needed horizontal aperture is

$$X = (A_x \beta_{x0})^{1/2} = 4\sigma_x + t + 2a_x = 22.5 \text{ mm},$$

where $4\sigma_x = 10.1$ mm is a distance between the deflected orbit and the septum, $t = 2.4$ mm is the total septum knife thickness, $2a_x = 10$ mm is the septum aperture, A_x is the required acceptance and $\beta_{x0} = 17$ m is the amplitude function at the septum azimuth.

Really we have $X = 30$ mm that satisfies both the injection condition and good lifetime requirement of a 100 mA single-bunch mode at 2.5 GeV. At the injection we need a lower aperture, therefore to reduce the kickers voltage we will switch on two horizontal steering magnets combined with quadrupoles F2. The steering magnets will shift equilibrium orbit towards the septum at a distance of 7.5 mm. The expression for X is independent of the injected beam emittance ($\epsilon_x = 8.6 \times 10^{-5} \text{ cm-rad}$), because it is expected to be considerably less than the storage ring acceptance ($A_x = 3.0 \times 10^{-3} \text{ cm-rad}$).

III. SEPTUM MAGNET

The septum bends the 450 MeV electrons at an angle of 20° in horizontal plane and injects them into the storage ring chamber at the azimuth of quadrupole focusing lens F1. The main septum parameters are as follows: the field

amplitude 2 T, the horizontal aperture 10 mm, the vertical aperture 14 mm, the total azimuth length 0.294 m and the bending radius 0.75 m.

The compact pulse septum has been designed and manufactured according to the initial requirements:

- to operate in the high vacuum conditions at the pressure as low as $1 \div 0.1$ nTorr and to be heated in situ up to 400°C ,
- to have a low leakage magnetic flux to avoid the distortion of the circulating beam,
- to have high mechanical strength and high stability of the pulse field amplitude.

The septum has been made of copper. The septum electrical scheme is system of the three conductors shorted out at one of the ends, Fig.4. Another end is connected to the 300 V voltage output of a pulse transformer, fed by a 7

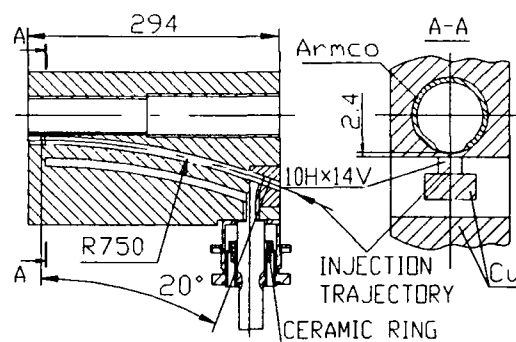


Figure 4: The cross sections of the septum.

kV pulse generator. The available pulse repetition rate is 0.1 Hz. The parallel skin currents induce a magnetic field on the injected beam trajectory being passed between the central and external conductors.

The magnetic forces of about 1.5 t act on the central bus in the opposite directions. The good dynamical balance of the central bus was attained by its symmetrical position relative to lateral buses.

The septum is housed in the vacuum tank. The outward metal surfaces of the septum are welded to the vacuum tank steel wall. To separate the vacuum volume from the outside atmosphere a ceramic ring was installed between the inner and outer cylindrical surfaces of the septum electrical input.

The septum inductance is $0.053 \mu\text{H}$. The half-sine current pulse in the central bus has an amplitude of 180 kA. The pulse duration is chosen to be equal to $100 \mu\text{s}$. The corresponding skin thickness in copper is 0.93 mm, that is less than the 2 mm thickness of the copper part of the knife. According to our estimation, in this case the magnetic field penetrating through the metal in the stored beam direction falls off to $2 \div 5\%$ of its maximum value.

To screen very reliably the storage ring aperture from the remaining long-lived leakage field a 3 mm ARMCO tube was inserted into the vacuum chamber and joined with the copper surface by means of diffusion welding. The lowest magnetic screen thickness is equal to 0.4 mm at the

knife, so the total knife thickness is 2.4 mm. The fringing field existing close to the opened septum exit is nearly suppressed by the 20 mm long exit hole.

According to the measurements the reproducibility of the septum magnetic field from pulse to pulse is $\leq 2 \times 10^{-4}$. During the tests there was no any vacuum deterioration because of the ceramic ring failure. Fig.5. shows the measured longitudinal distribution of the septum magnetic field. The measured effective length is equal to 252.6 mm

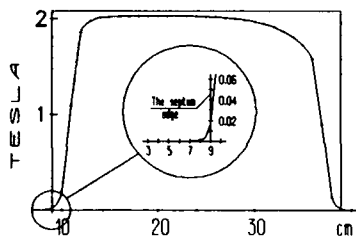


Figure 5: The measured longitudinal distribution of the septum magnetic field

instead of the calculated 261.8 mm. This difference is quite permissible. The sharply reduced fringing field is no more than 0.1 % of the maximum value at a distance of 2 mm from the septum exit. So the measured leakage magnetic field integral in the storage ring aperture is much less than the 200 Gs-cm tolerance.

IV. NANOSECOND KICKERS AND GENERATORS

The requirements to be satisfied when designing the kicker were the following:

- high voltage amplitude is no more than 60 kV,
- wave impedance 50 Ohm,
- the relative deviation of the electric field inside the aperture is as low as 5%,
- the gap equals 25 mm and the kicker length is 500 mm,
- each kicker plate has a longitudinal slit of 8 mm height to avoid its heating by synchrotron radiation and to reach the field symmetry.

The kicker layout is shown in Fig.6. The 5% field homo-

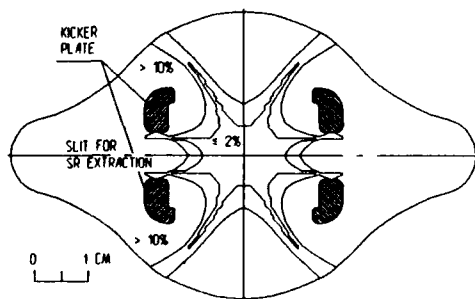


Figure 6: The calculated transverse field distribution of the kicker.

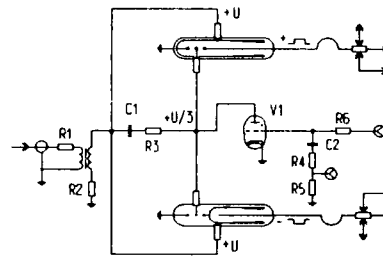


Figure 7: The scheme of the bipolar nanosecond generator.

geneity corresponds to the apertures $2X = 12$ mm and $2Z = 14$ mm. It is quite sufficient for injection.

The kickers are fed by the bipolar high voltage nanosecond generators and operate in the travelling wave mode. The scheme of the bipolar generator is shown in Fig.7. The generator operates on the basis of the fast discharge of double forming lines which are connected to the kickers by nitrogen filled coaxial cables. The discharge is realized by a gaseous spark gap (the so-called 3-electrode discharger). The discharge is initiated by a thyatron connected to the central electrodes of the dischargers. The discharge moment is tuned by varying the pressure of nitrogen inside the electrode volume. The pulse duration is equal to doubled propagation time of electromagnetic wave travelling along the forming line.

In the case of high amplitude nanosecond pulse, the double forming line has the following advantages in comparison with the single forming line: it enables one to reduce twice the charging voltage and to simplify the scheme of the generator, because this makes it possible to give up the inverters for producing the pulses of opposite polarities. The nanosecond generators were manufactured and tested.

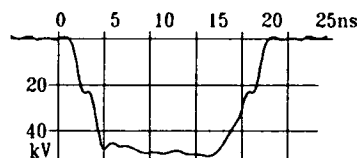


Figure 8: The typical kicker pulse oscillogram.

Fig.8 shows the typical oscillogram of the high voltage pulse at the kicker plate. The pulse parameters are: the duration is equal to 20 ns with the edges as sharp as 5 ns and voltage amplitude up to 50 kV. The rms time spread of the moments when the signal comes to the kicker plates is about 1 ns.

REFERENCES

- [1] V.V.Anashin et al., Nucl. Instr. and Meth. A282 (1989) 369-374

FIXED TARGET TO COLLIDER CHANGEOVER AT A0

Katharine J. Weber
Fermi National Accelerator Laboratory
P.O. Box 500, Batavia, Ill. 60510 USA

Abstract

The A0 sector of the Main Accelerator at Fermilab serves a dual function. During a collider run this sector is used as an abort. The same area is used to divert beam to the switchyard during a fixed target run. The area is subject to high residual radiation, therefore making it important that personnel working to change the equipment do so with a minimal amount of radiation exposure. A system has been designed to reduce the time a technician must spend in this area.

I. INTRODUCTION

The method of changing from fixed target physics to collider physics at Fermilab requires that equipment be moved in or out of the beam line. At the A0 sector of the ring, the residual radiation is high, necessitating either a larger number of technicians required to do this work, or allowing the technicians to accumulate larger amounts of radiation exposure.

The addition of ten kickers and two abort dumps in this area for collider physics meant that there would need to be some major changes made, even if equipment was simply swapped out. Because of these major changes this project became a good candidate for a new approach.

A method for changing this equipment was devised to not only decrease the amount of radiation exposure, but to also reduce the number of technicians required to change the equipment. This was the first attempt to design a system with minimal radiation exposure as the primary concern.

The project was divided into two phases. The first phase included the collider devices and their associated hardware. The second phase includes all the fixed target devices and their associated hardware. Phase two also includes some construction work.

Phase one was completed in January 1992. Phase two design and fabrication work has been completed. The construction work and final installation will take place during the summer of 1994.

II. PHASE ONE

A. Kicker Magnets

There are two groups of five kickers magnets. The purpose of these magnets is to steer the beam into one of two abort dumps. The proton kickers are at approximately F49, the anti-proton kicker magnets are at approximately A11.

B. Abort Dumps

There are two abort dumps, one for protons and one for anti-protons. The abort dumps were fabricated from the steel of a Tevatron dipole. The abort dumps are shielded by two inches of steel on all four sides. This minimizes the amount of radiation to the ground water, as

well as the surrounding equipment in the main ring tunnel.

C. Support System

The stands for the kicker magnets were left with same degree of adjustment that they would normally have at any other location in the tunnel. The abort dumps use the Tevatron stands. Minor changes, such as the addition of a bracket to attach the stand to the transfer system were made. This left both the device and the stand interchangeable with other like types both around the ring and in spare storage. (Figure 1)

D. Transfer Mechanism

The method used to transfer magnets in or out of the beam line is a system of plates. Plates are tied together to form banks of like components. Each set of five kickers comprises one bank, the abort dumps comprise another bank. Stands mount directly to the plates. Once the magnets are mounted, each bank becomes an integral unit. This is a permanent arrangement, with a magnet change being the only exception. The plates have ball transfers on the floor side. This makes maneuvering in all directions possible for rough alignment. Final alignment is done in the usual way, using the adjusters on the stands. Steel plates are grouted and fastened to the concrete floor for the ball transfers to ride on.

During a collider run, the proton kickers occupy the same space the Lambertsons occupy during a fixed target run. Up to one inch of concrete had been chiseled out of the floor under the Lambertsons to allow for downward adjustment of the magnet. This area was too rough to allow placement of kicker stands on the floor. Since the amount of concrete removed was not consistent over the entire length, this left the area too uneven to allow placement of steel plates. The depressions were filled with epoxy grout and leveled before the steel floor plates were installed.

The steel floor plates were installed in two segments, which allows the removal of one segment for phase two and does not disturb the other segment.

E. Vacuum System

Each bank of components has a beam valve at each end. These valves are closed before moving equipment out of the beam line. The kickers especially need to be protected from atmosphere as much as possible, since they have ceramic beam tubes. Beam valves are installed at the extreme upstream and downstream ends to protect equipment not affected by this project.

All cabling was done in such a manner that they do not need to be disconnected when the equipment is moved from one mode to the other.

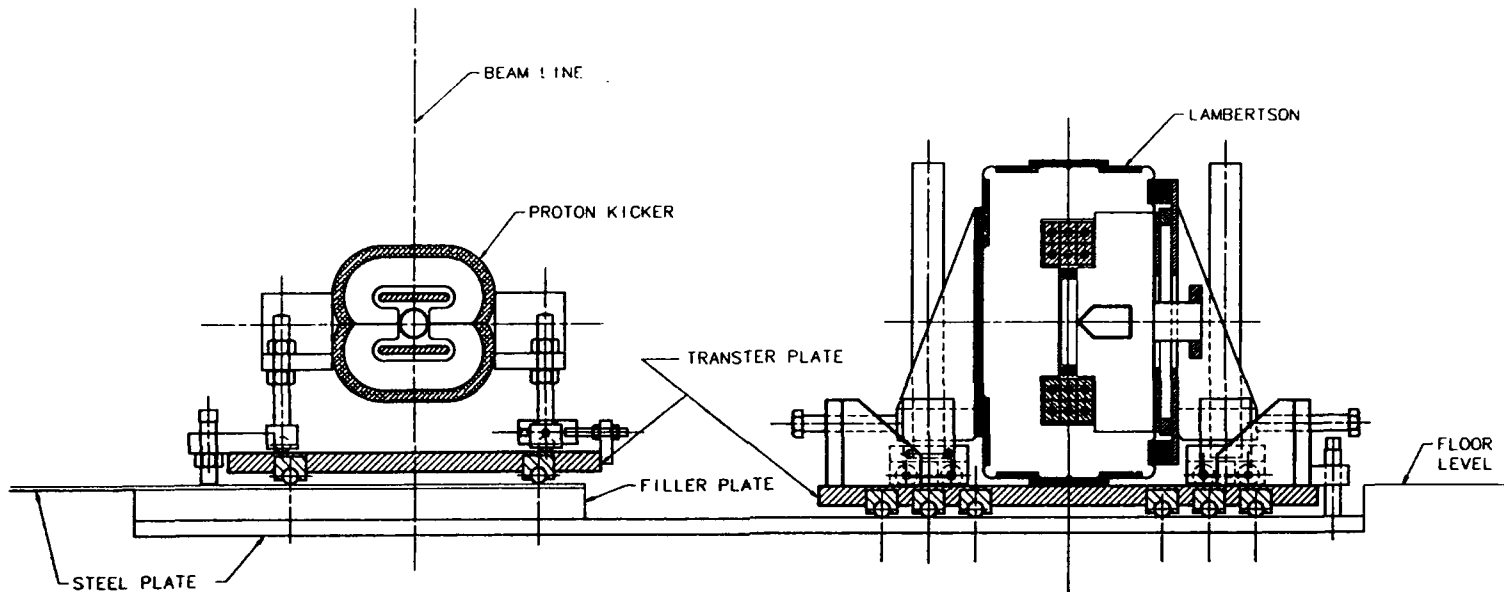


Figure 1

another bank. The three skew dipoles comprise the third fixed target bank.

III. PHASE TWO

A. Skew Dipoles

Three skew dipoles are installed for fixed target physics. The skew dipoles take the proton beam out of the circular orbit and direct it to the switchyard. Skew dipoles are located at A11.

B. Lambertsons

Starting at F49, there are three six inch symmetric Lambertsons followed by two A0 downstream Lambertsons. The purpose of the Lambertsons is to prepare the beam for extraction to switchyard. This function causes them to become highly radioactive. It is not uncommon for these magnet to be class 4 (>100Mr @ 1ft.)

C. Support System

New skew dipole stands were made to allow them to be attached to transfer plates. The new stands are shorter than the previous stands to allow for the thickness of the transfer plates, but otherwise are identical to the old stands. (Figure 2)

The Lambertson stands were not changed in any way, except to allow them to be mounted to transfer plates. They retain the same degree of adjustment and any Lambertson of a like type can replace those at A0. (Figure 1)

D. Transfer Mechanism

The same system of plates was used for the fixed target devices as for the collider devices. Plate thickness' were increased to carry the additional loads. In the same manner, transfer balls are mounted on the underside of the plates. The number of transfer balls per plate was increased for the increased loading.

The three six inch symmetric Lambertson comprise one bank, the two A0 downstream Lambertsons comprise

E. Installation

Placing the Lambertsons on the transfer plates raises the center of these magnets. Complicating the matter was the fact that some of these magnets were already sitting below the floor level in the chiseled out area. A trench will be carved out of the concrete floor in order to be able to install these magnets at the proper height for the beam line as well as allow for some downward adjust. There was no downward adjustment previously. The trench will be approximately 6' wide by 100' long. The depth of the trench will vary from 1.25" to 3.5" depending on the distance from the present floor level to the beam line. Varying the depth of the concrete removal allows the minimum amount of concrete to be removed. Steel plates will be grouted and fastened in the trench for the transfer plates to ride on. The areas where there are no plates will be removed just deep enough to clear the equipment. A magnetic survey of the floor has been made to determine the depth and location of the concrete rebar. This survey indicates that, at most, one or two pieces of rebar will need to be cut or bent out of the way.

Since the concrete floor may be radioactive, in preparation for the removal of the concrete, the area will be sealed off. Ventilating equipment will be used to keep this enclosure dust free and provide a negative pressure. All dust will be vented through hepa filters. In addition, all personnel will wear the appropriate respirator while working in this enclosure.

One of the methods being considered to remove the concrete is a dry method. This method uses steel shot to break up the concrete. The shot is recycled and the waste is passed through two filters, making this operation virtually dust free. One filter box collects gravel and other large particles, the other collects the fine particles and dust. The air that is exhausted passed through a hepa filter.

The dry removal method also provides the option to re-use the concrete removed. The coarse and fines can be

combined with an additive during the removal process. Later, water can be added and the mixture poured into forms to make concrete blocks. These blocks can later be used for shielding.

F. Vacuum System

Like the collider devices, each bank of equipment has a beam valve at each end. This valve is closed before moving the equipment. All cabling for ion pumps and electrical as well as water connections need not be disconnect before moving equipment.

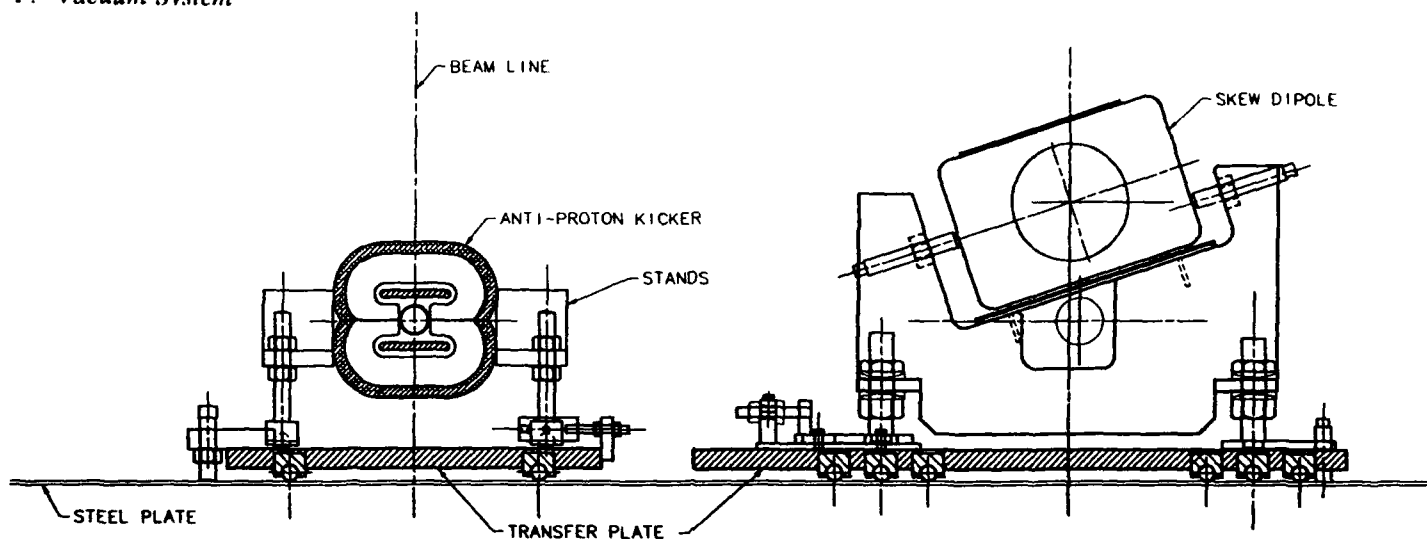


Figure 2

IV. CHANGEOVER

A. Off Line Collider Devices

When the accelerator is in the fixed target mode, the kicker magnets and abort dumps must be removed from the beam line. The kicker magnets are stored along the outside wall, in order to minimize any damage to the epoxy from radiation. The abort dumps are moved just enough to the radial outside to allow the fixed target equipment to be installed.

B. Off Line Fixed Target Devices

The Lambertsons and skew dipoles are stored just to the radial inside of the beam line during a collider run.

C. Switching From Fixed Target to Collider Physics

In order to change from fixed target physics to collider physics, large screw mechanisms are used. One end of the mechanism is attached to a bracket on the transfer plate, while the other end is attached to a bracket mounted on the floor near the inside wall.

The beam valves are closed, the water is shut off and any necessary electrical shut off before moving any devices. No connections need to be broken except beam tube. Spool pieces are also removed.

Once the screw mechanism is attached, two technicians are able to slowly turn the screws, moving the bank of devices towards the inside of the beam line. When the bank of devices is out of the beam line, pins are used to lock the plates to the floor. The screw mechanism is removed and the next bank is moved. Once all three fixed target banks are moved out of the way, the collider banks can be moved into place.

Filler plates are placed in the trench where the kicker magnets will be located. The purpose of these plates is to

elevate the rolling surface for the transfer plates from the Lamberton height to the kicker height.

The screw mechanisms are again used to move the three collider banks into the beam line. Because the kicker magnets are stored against the outside wall, they must be moved in two steps. First the bank is pulled towards the beam line, then the mechanism is mounted on the other side of the transfer plate and the bank is pushed the rest of the way into the beam line. Abort dumps, which are stored next to the beam line are simply pushed several feet into the beam line. Because of the length and placement of the screw devices, while this transfer is taking place, the technicians are not working in close proximity with the radioactive devices.

The kicker magnets and abort dumps are connected to the beam line, the beam valves are opened and the electrical devices turned on.

The switch from collider to fixed target physics is achieved by reversing the steps described above.

V. CONCLUSION

Using the methods described above, the changeover from fixed target to collider physics at Fermilab can be accomplished safely and easily. The steps involved in this switch keep the technicians as far from radioactive devices as possible. The entire process can be accomplished by two technicians in a fraction of the time it would take using the traditional method. It has been estimated that the use of the screw mechanism and having only beam pipe connections to break, the time these technicians will take to accomplish this changeover can be reduced by a factor of ten.

Surface Resistivity Tailoring of Ceramic Accelerator Components*

S. Anders¹, A. Anders¹ and I. Brown

Lawrence Berkeley Laboratory, University of California, Berkeley, CA 94720

¹on leave from Max-Planck-Institut für Plasmaphysik, Bereich Berlin, Germany

Abstract

Metal plasma deposition and metal ion implantation techniques have been developed that could provide a good tool for the surface modification of insulating materials for accelerator applications such as ceramics and that could provide a method for tailoring the surface resistivity over a range of many orders of magnitude. The methods make use of the metal plasma that is produced by the cathodic arc discharge; the plasma itself can be deposited onto the surface at an energy of order 100 eV so as to form an adherent thin film, or an energetic metal ion beam can be formed for deep implantation of the metal species below the surface so as to incorporate a controllable amount of metallic composition into the ceramic.

I. INTRODUCTION

High voltage insulators for accelerator application need to be of very high resistance for good voltage hold-off and the resistivity needs to be uniform so that the electric field is uniformly distributed along the insulator length. The insulator bulk material normally has a higher voltage holdoff capability than a vacuum gap of the same size; the weak point of the insulator is its surface and in particular the triple junction (the interface of insulator, vacuum and electrode). It has been found that surface coatings which are more conductive than the bulk material are useful, and surface treatments which penetrate into the outer layers of the insulator are particularly resistant to surface damage caused by surface flashover (for an excellent review see [1]).

In other applications, for example for beam deflectors, it would be advantageous to be able to form a conducting coating on an insulating component to define an electric potential and also allow rapid penetration of a magnetic field.

Metal plasma deposition and implantation techniques provide a means to modify the surface and the first few hundred angstroms of many materials, including ceramics and other insulators. The surface conductivity can be changed continuously from a value typical for ceramics to a value typical for metals by depositing metal films of various thickness.

*This work was supported by the U. S. Department of Energy, Advanced Energy Projects, under DE-AC03-76SF00098, by the Army Research Office under Proposal No. 25833, and two of the authors (S. A. and A. A.) were supported by the Deutsche Forschungsgemeinschaft.

Essential for this purpose is a very good adhesion of the metal films. By implanting the metal ions deep into the material, the modification of the conductivity can be extended to a layer of several hundred angstroms. Here we outline the plasma and ion beam tools that we've developed and describe their applications for this function.

II. VACUUM ARC PLASMA DEPOSITION

A. The Vacuum Arc Plasma Sources

Plasma sources based on vacuum arc discharges have been used for the production of the metal plasmas. The plasma source consists of a rod cathode and a cylindrical anode (Fig. 1); the arc discharge is triggered by a high voltage spark. The arc current is typically 50-300 A, and the arc duration and repetition rate can be varied in the range of 10 μ s - 10 ms and from single shot to 10 Hz, respectively.

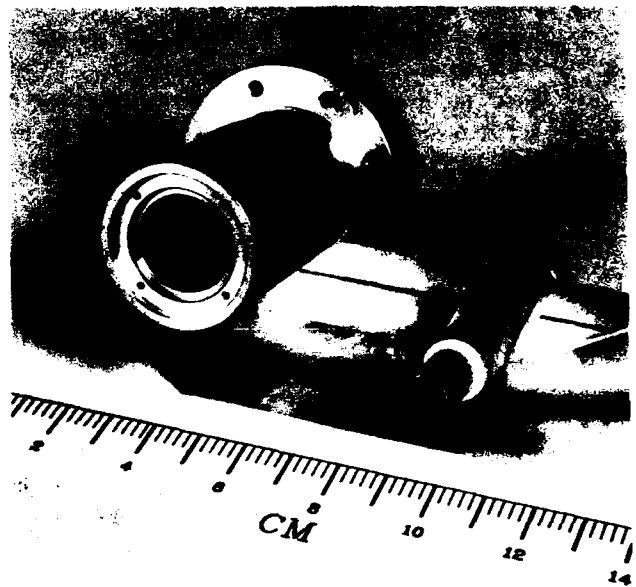


Figure 1: Plasma gun (dismantled) of the type used for the deposition of metal on the inside of ceramics tubes. Left - anode, right - cathode holder with cathode.

Fully ionized metal plasma with mean ion charge states between 1 and 3 [2] for the different metals is produced and streams away from the plasma source with a directed kinetic energy of the ions of typically 100 eV [3]. The plasma stream can be focused by an axial magnetic field around the electrodes, providing a dense directed plasma stream with a density of order 10^{18} m^{-3} . By adjusting the arc current, pulse length and the distance between plasma source and substrate, films of thickness between a monolayer and many micrometers can be produced. Due to the possible small dimensions of the plasma sources (we have developed a micro-version with a length of 7 cm and a diameter of 2 cm [4]) the application is very flexible, e.g. the plasma sources can be moved inside of tubes or around samples with complex shapes. Vacuum arc plasma sources can also be scaled up to large facilities [5] with kiloamperes of arc current and very high deposition rates, up to hundreds of micrometers per second.

B. Experiments and Results

A number of experiments have been done to show the relevance of this method. A gold film was deposited on an alumina surface with a thickness of about 1 μm and a resistivity of 0.5 Ω/sq . The adhesion of the film was tested by the usual "scotch tape test" and found to be very good. This is a consequence of the high ion energy.

The insides of several alumina tubes of 4 cm diameter were covered by titanium and gold films of various thicknesses, showing surface resistivities of 1 - 10 Ω/sq depending on the film thickness and material. The adhesion was also very good.

These preliminary experiments show that the metal vapor arc deposition technique is well suited to form adhesive films of various metals of the desired thickness and conductivity on ceramic materials.

III. METAL ION IMPLANTATION

A. The Vacuum Arc Ion Source

The ions of a vacuum arc plasma can be extracted and accelerated to form an ion beam of high energy. In the multicathode, broad beam ion source version that we have developed [6], a three grid accel-decel system is used to accelerate ions to energies up to 300 keV. Any conducting, solid material (metals, alloys, highly doped semiconductors, carbon) can be used as vacuum arc cathode material, and an ion beam of up to several amperes during the arc pulse and up to several tens of mA time-averaged is produced. The substrates can be mounted on a fixed or rotating water-cooled sample holder. The beam diameter (FWHM) can be as large as 33 cm [7] thus allowing metal ion implantation on an almost industrial scale.

B. Experiments and Results

We have used our vacuum arc ion implantation facility to implant Ti ions with an energy of 100 keV and a dose of 10^{16} cm^{-2} into alumina ceramic pieces. The ceramic pieces had a cylindrical shape, a diameter of 40 mm and a height of 5 mm; they were polished to a micro-roughness of about 20 μm . During the implantation, the samples were continuously rotated to ensure a uniform implantation. After implantation the end faces were covered with a 1 μm thick gold film using the vacuum arc plasma sources described in section II in order to provide contacts for subsequent resistance measurements and breakdown tests. These tests showed that the relatively low dose implantation decreases the resistance of our samples to about 10 G Ω , which is rather low for electric field control purposes. Further experiments are planned with lower implantation doses.

To compare the results of metal ion implantation into ceramics with calculations, and to predict the implanted depth profile and retained doses, we have measured the implanted depth profiles for an Ti implantation into Al_2O_3 with an ion energy of 100 keV and a dose of $6 \times 10^{16} \text{ cm}^{-2}$ by Rutherford Backscattering Spectrometry (RBS). Fig. 2 shows the implantation depth profile calculated with the T-DYN 4.0 computer code [8] in comparison with the measured data.

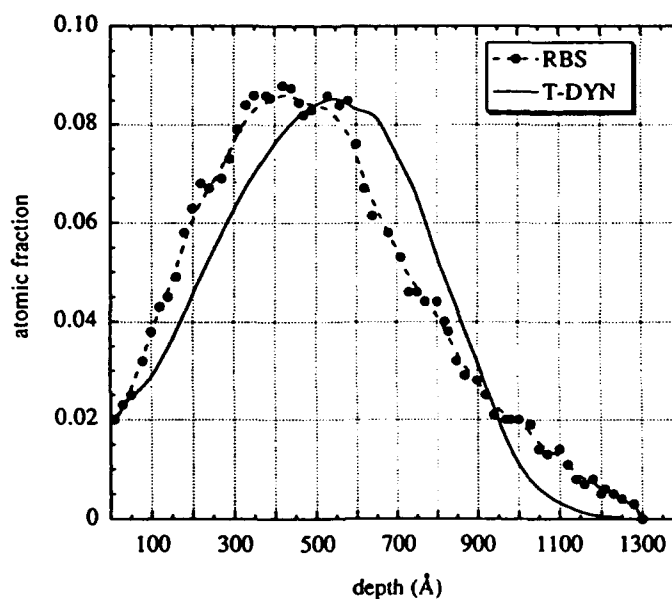


Fig. 2: Implantation depth profile for a Ti implantation into Al_2O_3 with an ion energy of 100 keV and a dose of $6 \times 10^{16} \text{ cm}^{-2}$. Comparison between experiment (RBS profile) and calculation using the T-DYN 4.0 code [8].

The maximum fraction of Ti was 9 % at a depth of about 500 Å; the substrate was modified by the implantation up to a depth of almost 1500 Å. The agreement between calculation and experiment is good.

IV. CONCLUSIONS

It has been shown that vacuum arc deposition techniques provide a useful means for the formation of well-bonded conducting metal films to ceramics. The method is very flexible with respect to deposited material, film thickness and substrate shape.

Ion implantation based on plasma formation by vacuum arcs is a further tool for modification not only of the ceramic surface but to a depth below the surface of a few thousand angstroms. By implanting metal ions with a defined dose and energy, the conductivity of the insulator surface can be tailored as desired, either homogeneous or with gradients over the insulator surface. A combination of both techniques widens further the possible fields of applications.

V. ACKNOWLEDGMENTS

We are grateful to Dr. Kin Man Yu (LBL, Berkeley) for performing the RBS investigation, and to Dr. Jos Wetzer (TU Eindhoven, The Netherlands) for the resistance measurements. We also acknowledge the technical support of Robert A. MacGill and Michael R. Dickinson.

VI. REFERENCES

- [1] H. C. Miller, "Flashover of insulators in vacuum: Techniques to improve the holdoff voltage," *XVth Int. Symp. Disch. and Electr. Insul. in Vacuum*, Darmstadt 1992, p. 165.
- [2] I. G. Brown and X. Godechot, "Vacuum arc ion charge-state distributions," *IEEE Trans. Plasma Sci.* **19**, 713 (1991).
- [3] J. Kutzner and H. C. Miller, "Ion flux from the cathode region of a vacuum arc," *IEEE Trans. Plasma Sci.* **17**, 688 (1989).
- [4] X. Godechot, M. B. Salmeron, D. F. Ogletree, J. E. Galvin, R. A. MacGill, M. R. Dickinson, K. M. Yu and I. G. Brown, "Thin film synthesis using miniature pulsed metal vapor arc plasma guns," *Mat. Res. Soc. Symp.* **190**, 95 (1991).
- [5] R.L. Boxman and S. Goldsmith, "Principles and application of vacuum arc coatings," *IEEE Trans. Plasma Sci.* **17**, 705 (1991).
- [6] I. G. Brown, J. E. Galvin, R. A. MacGill and F J. Paoloni, "Broad-beam multi-ampere metal ion source," *Rev. Sci. Instrum.* **61**, 577 (1990).
- [7] I. G. Brown, M. R. Dickinson, J. E. Galvin and R. A. MacGill, "Development of a dc, broad beam, MeV ion source," *Rev. Sci. Instr.* **63**, 2417 (1992).
- [8] J. P. Biersack, S. Berg and C. Nender, "T-DYN Monte Carlo simulations applied to ion assisted thin film processes," *Nucl. Instrum. & Meth. in Phys. Res.* **B59/60**, 21 (1991).

Compensation of Field Shaking due to the Magnet Vibration

Yao, Cheng and Ching-Shiang Hwang
Synchrotron Radiation Research Center

No. 1 R&D Road VI, Hsinchu Science-based Industrial Park, Hsinchu 30077, Taiwan R.O.C.

Abstract

Recently, The global feedback scene of the beam stabilization is broadly discussed for the third generation light source. Since the low frequency disturbance of the orbit is mainly coming from the quadrupole magnet vibration of a certain dominate mode, a feedforward sense is developed to cancel the filed shaking without the BPM feedback. We applied the seismic accelerometer to detect the magnet vibration and drove the compensation current into the trim coil of the quadrupole. Better than 99% canceling of the filed shaking due to $10\mu\text{m}$ magnet vibration was observed in the laboratory. This method is superior to the feedback system in many aspects, such as locality, simplicity and economy.

I. Introduction

The global feedback system for the transverse beam positioning has become a standard subsystem of the third generation synchrotron light source [1]. In this paper, the general idea of the feedback system will be described first. Then, a primitive model is used to estimate the performance of this feedback system in the SRRC case. The result shows that there are limitations for this feedback system.

A low cost feedforward method is proposed to suppress the effect from the vibration source. Hence, the beam jitters can be reduced and the accuracy of the beam orbit estimation can be enhanced.

II. General Description of a Beam Feedback System

Figure 1 is a general block diagram of the linear beam feedback system.

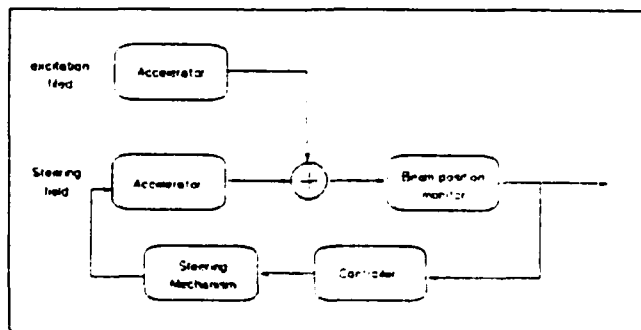


Figure 1. Linear model of beam feedback system.

The transfer function of the accelerator is discussed in another paper of the main author [2]. We will not go into details in this paper. Roughly speaking, the transfer function contains a pair of conjugate poles caused by the damping effect and the betatron oscillation. The beam position monitor, like a radio receiver, contains a pole, which is interested by us. In a digital system, this pole is very important, since it can avoid the aliasing error. The correction signal coming out from the controller is used to control the steering field which is affected by the bandwidth of the power supply, correction magnet, and vacuum chamber. The poles of these components are listed in following two groups.

A. High Frequency Poles

1. Accelerator ~ 300 KHz
2. Beam Position Monitor ~ 1 KHz.

B. Low Frequency Poles

1. Vacuum Chamber (4 mm-thick Aluminum)
vertical ~ 40 Hz
horizontal ~ 15 Hz
2. Correction Magnet + Power Supply ~ 200 Hz

Except the bandwidth of the accelerator, the numbers given above have been measured in the laboratory [3].

III. Limitation of the Open loop Gain

To avoid instability and increase the open loop gain in the control system, one pole in the low frequency range has to be compensated. It doesn't make sense to remove poles at high frequency range. Hence, the closed loop unity-gain bandwidth is limited to $200\text{ Hz} \sim 500\text{ Hz}$.

Assumed that the magnet field shaking is mainly caused by the quadrupole vibration. Our measurement on the quadrupole vibration shows that there is a main peak at 20 Hz . With a slope of 20 dB/decade of the open loop gain, there is a 20 dB drop from 20 Hz to 200 Hz . Thus for the unity gain at 200 Hz , the gain at 20 Hz is only ten. It will take too much effort to increase this gain at 20 Hz but with only a poor factor.

IV. Resolution of Beam Observation

Let's say, the resolution of each beam position monitor is $10\mu\text{m}$ at 20 Hz . The closed orbit correction in the least

square sense can increase the resolution by a factor of \sqrt{n} . The "n" is the number of the position monitor. Thus, a factor of seven can be achieved for total 48 BPMs (Beam Position Monitor) in the SRRC storage ring. However, if the quadrupole vibration disturbs the observation, this factor will go down.

V. Reduction of the Field Shaking

In order to get a more stable beam, the effect from the excitation source should be suppressed. If the magnet field is trimmed against the vibration, it is possible to have a large magnet vibration but a stable field. Usually the vibration of the quadrupole is much less than 10 μm . The bore radius of the ring quadrupole in SRRC is 38 mm. The current in the trim coil with the same winding number of the main coil is less than one part in four thousand. With the maximum main-coil current of 250 A, the current in the trim coil will be less than 60 mA (the power supply ripple current is about 5 mA). Thus, the power needed to drive trim coil is less than one millionth of the power in main coil.

A modern piezo type vibration sensor provides a resolution of 0.01 μm at 20 Hz. It is possible to get a higher resolution, if a higher frequency carrier, such as 10 K Hz, is used to reduce low frequency noise.

The other important character is the vibration mode of the magnet. From the three points support, there is no degeneration of vibration at resonant frequency. It means only one sensor located on the magnet is able to detect the three dimensional motion of the resonant vibration.

The field strength of the quadrupole is depend on the main current, which may be changed from time to time for the third generation synchrotron light source. Hence, an adaptive current amplifier with self calibration is considered to optimize the gain.

VI. Dipole Field Compensation Model for Quadrupole Magnet Vibration

For an ideal quadrupole magnet, the higher multi-pole field is very weak, so the scalar potential can be expressed as

$$\phi(x, y) = G \cdot x \cdot y \quad \text{---(1)}$$

Where G is the gradient field strength. Therefore, the transverse midplane, the magnetic flux density, by definition

$\vec{B} = -\vec{\nabla}\phi(x, y)$, can be reduced as Eq. 2

$$\vec{B}(x, y) = G(x \hat{j} + y \hat{i}) \quad \text{---(2)}$$

If the vibration happens on the transverse plane of the quadrupole magnet, there will be an extra dipole field exists on the quadrupole magnet. Thus, the flux equation becomes

$$\vec{B}(x, y) = G[(x + x_0 \cos(w_x t))\hat{j} + (y + y_0 \cos(w_y t))\hat{i}] \quad \text{---(3)}$$

Where w_x, w_y are the vibration frequency and x_0, y_0 are the vibration amplitude on the transverse plane of the quadrupole magnet. Hence Eq. 3 can be changed to

$$\vec{B}(x, y) = G[(x_0 \cos(w_x t))\hat{j} + (y_0 \cos(w_y t))\hat{i}] + [G(x \hat{j} + y \hat{i})] \quad \text{---(4)}$$

This extra dipole field $G[x_0 \cos(w_x t)\hat{j} + y_0 \cos(w_y t)\hat{i}]$ will induce a kick angle for the electron beam. In order to compensate this dipole field, the dipole trim current on the quadrupole magnet can be used to produce another dipole field whose frequency is the same as the vibration frequency. The strength of the field induced by the trim current is shown below

$$\vec{B} = [-B_y \cos(w_x t)\hat{j} - B_x \cos(w_y t)\hat{i}] \quad \text{---(5)}$$

To create the fields B_y and B_x , a model similar to the Beam Position Monitor model is used. In this model, there are two kinds of dipole trim current to create B_y and B_x fields. The location of the trim coil and the poles on the quadrupole magnet is shown in Figure 2. In this figure, the A, B, C, and D, are the four poles, and the trim current combination for each pole is

$$\begin{aligned} A &= I_x + I_y \\ B &= I_x - I_y \\ C &= -I_x - I_y \\ D &= -I_x + I_y \end{aligned} \quad \text{---(6)}$$

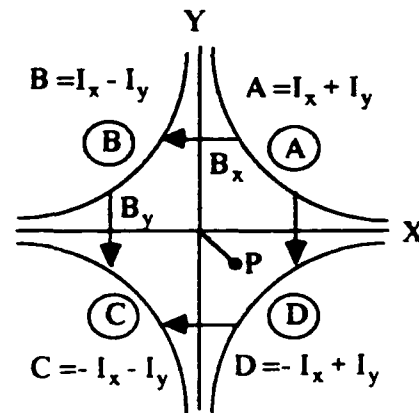


Figure 2. Arrangement of the trim coils and the magnetic poles on the quadrupole.

Combining these pole current equations, the horizontal and vertical current can be expressed as below

$$\begin{aligned} I_x &= (A + B - C - D) / 4 \\ I_y &= (A + D - B - C) / 4 \end{aligned} \quad \text{----(7)}$$

Hence, the relationship between the field strength (B_y, B_x) and the current (I_y, I_x) can be expressed as

$$\begin{aligned} B_y &= f(I_y, I_x) - B_{y0} \\ B_x &= g(I_y, I_x) - B_{x0} \end{aligned} \quad \text{----(8)}$$

Where f, g are functions of trim current (I_y, I_x), and can be calibrated by the magnetic field transfer function. The B_{y0} and B_{x0} are the magnetic field center offset which are obtained from the magnetic field measurement.

Similar to the BPM using four electrode to detect beam position, this model uses four poles (A,B,C,D) to create dipole field. From this model and Eqs. 4 and 5, the required field strength to cancel the dipole field caused by the vibration can be derived by using following equations.

$$B_y = -G \cdot x_0 \quad \text{and} \quad B_x = -G \cdot y_0 \quad \text{----(9)}$$

The trim current (I_y, I_x) can then be obtained through the transfer functions f and g in Eq. 8. Thus from the well known gradient field G and the vibration amplitude x_0 and y_0 , the required trim current can be obtained. By feeding this trim current into the trim coil, the dipole field induced from the vibration can be cancelled.

VII. Experiment Result

In the laboratory of SRRC, a stepping motor was used to generate a 4 Hz vibration with a level of 10 μm . A hall probe is fixed on the center of the quadrupole and the vibration sensor is mounted directly on the quadrupole. The vibration signal is fed into the trim coil with a dipole winding. Figure 3. is the result of this experiment. It shows the trim current brings the field shaking down to 0.1 μm , when the feed-forward is turned on.

VIII. Conclusion

The field stabilization circuit is able to reduce beam jitters to ultra high quality. It also avoid the impact of ground vibration on the stored beam. Since the low power and low frequency electronics are applied, the cost is rather low

comparing with a feedback system. On the other hand, the control system is very compact. The sensor is mounted directly on quadrupole. It turns out this system is a very cost effective solution for the field shaking due to magnet vibration.

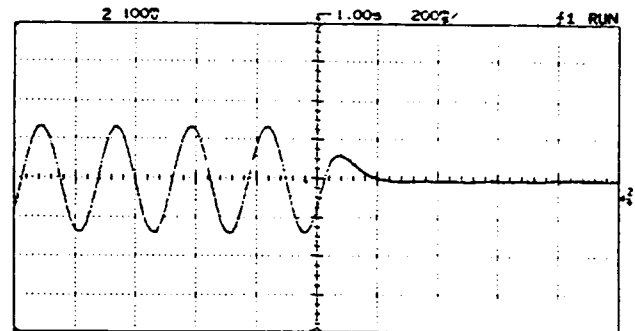


Figure 3. Field shaking killed by the onset of trim correction.

IX. References

- [1] ELECTRA Conceptual Design Report, (SINCROTRONE TRIESTE, April 1989), SPring-8 Project Part 1: Facility Design, (JAERI-RIKEN SPring-8 Project Team 1990), Pohang Light Source Design Report, (Pohang Accelerator Laboratory, January 1991).
- [2] Yao Cheng, "Dynamic Closed orbit Correction", this conference.
- [3] SRRC Status Report, (SRRC, April 1993).

Superconducting Cavity Tuner Performance at CEBAF*

J. Marshall, J. Preble, and W. Schneider
Continuous Electron Beam Accelerator Facility
12000 Jefferson Avenue, Newport News, VA 23606-1909 USA

Abstract

At the Continuous Electron Beam Accelerator Facility (CEBAF), a 4 GeV multipass CW electron beam is to be accelerated by 338 SRF, 5-cell niobium cavities operating at a resonant frequency of 1497 MHz. Eight cavities arranged as four pairs comprise a cryomodule, a cryogenically isolated linac subdivision. The frequency is controlled by a mechanical tuner attached to the first and fifth cell of the cavity which elastically deforms the cavity and thereby alters its resonant frequency. The tuner is driven by a stepper motor mounted external to the cryomodule that transfers torque through two rotary feedthroughs. A linear variable differential transducer (LVDT) mounted on the tuner monitors the displacement, and two limit switches interlock the movement beyond a 400 kHz bandwidth. Since the cavity has a loaded Q of $6.6 \cdot 10^6$, the control system must maintain the frequency of the cavity to within ± 50 Hz of the drive frequency for efficient coupling. This requirement is somewhat difficult to achieve since the difference in thermal contractions of the cavity and the tuner creates a frequency hysteresis of approximately 10 kHz. The cavity is also subject to frequency shifts due to pressure fluctuations of the helium bath as well as radiation pressure. This requires that each cavity be characterized in terms of frequency change as a function of applied motor steps to allow proper tuning operations. This paper describes the electrical and mechanical performance of the cavity tuner during the commissioning and operation of the cryomodules manufactured to date.

I. INTRODUCTION

CEBAF's accelerating structure is a 5-cell niobium cavity of the Cornell type manufactured by Siemens. The operating specifications are as follows:

E_{acc}	> 5 MV/m	
Q_0	$> 2.4 \cdot 10^9$	
Frequency	1.497 GHz	
$Q_{ext, fpc}$	$6.6 \cdot 10^6$	(fundamental power coupler)
$Q_{ext, fp}$	$1.3 \cdot 10^{11}$	(field probe)

Prior to cavity-pair assembly, inelastic tuning is performed on the cells of the cavity to ensure a flat field profile to within $\pm 2.5\%$ cell to cell [1]. The tuning corrections required for each cell are determined by bead-pull and are made by axially

deforming the cells. The cavities are chemically processed, assembled into pairs and tested in a vertical dewar at 2.0 K. After verification of the cavity performance, the pairs are built up into a cryomodule. The module is then delivered to the tunnel to await cooldown and subsequent commissioning to verify the cavity specifications as well as operational criteria such as cryostat static and dynamic heat loads, helium pressure sensitivity and cavity tuner performance.

II. ELASTIC CAVITY TUNING

As previously indicated, each cavity is inelastically tuned to ~ 1494.7 MHz so that, after cooldown, will shift to the operating frequency of 1497 MHz, ± 100 kHz. This frequency is maintained by *elastically* tuning the cavity by compressing it with the mechanical tuner (see figure 1). The tuner is attached to the first cell with a fixed cell holder, and to the fifth with a swivel cell holder. A rigid titanium rod connects the two holders at one end and a drive shaft assembly connects the two at the other end. Tuning is accomplished by translating rotational motion of the worm/wheel gear assembly into axial movement of the swivel cell holder.

The tuning range of the cavity is specified to be ± 200 kHz from the initial frequency after cooldown, which corresponds to an operating range of ± 0.125 in. This travel is bounded by limit switches located at ± 0.125 in. and by solid stops limiting movement to ± 0.187 in., the latter to obviate travel into the inelastic region and over stressing the interconnecting bellows. During operations, the feedback control system measures the phase difference between the forward and transmitted power, calculates the tuning angle, and drives the tuner stepper motor. A resonant phase shift of 20° corresponds to a frequency shift of 41 Hz.

$$\Phi = \tan^{-1} \left[2Q_L \left(\frac{\Delta f}{f_{drive}} \right) \right]$$

where $\Delta f = f_{drive} - f_{resonance}$

A change in tuning angle will result from fluctuations in the cryomodule helium bath pressure where ± 1 Torr results in a cavity frequency shift of 100 Hz. At the design accelerating gradient of 5 MV/m, the frequency shifts ~ 75 Hz due to radiation pressure.

* This work was supported by DOE contract DE-AC05-84ER40150

During cryomodule commissioning, each cavity is characterized in terms of its sensitivity to each of these conditions as well as the relationship to the tuner assembly attached to it.

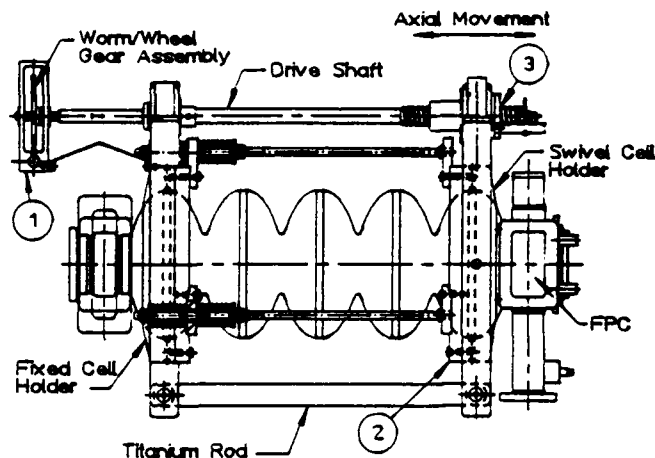


Figure 1. A cavity-tuner assembly depicting three sources of error (see text for explanation of each).

III. TUNER PROBLEMS AND SOLUTIONS

Ten tuners were delivered in early May 1990 to maintain a production schedule to supply 2 1/4 cryomodules for the injector section of the accelerator and the subsequent Front End Test. These tuners provided the initial evaluation of the design in an operational environment. The first and most serious problem was that some tuners would seize after cooldown. The problem was corrected by modifying a press-fit thrust bearing on the fixed cell holder to a slip-fit to mitigate binding due to thermal contractions. To allow operation of these tuners, a local stepper motor controller was connected that would "exercise" the assembly through the transitional temperatures. This method proved to be successful, but after two or three cooldowns it invariably fatigued the rotary feedthroughs causing catastrophic vacuum degradation, so it was quickly abandoned. A second concern was that the position of the limit switch, referenced to the cavity's axial movement of ± 0.050 in., corresponded to less than half of the expected tuning range of ± 200 kHz. This was corrected by increasing the distance between the switch to more than twice that value, or ± 0.125 in. The hard stops were also increased ± 62 mils beyond the control switch after it was verified that the new cold tuning range was still in the elastic region. The third concern was that the frequency after cooldown did not shift to the expected 1497 MHz, ± 100 kHz. In fact, results indicated that most were as much as 200 kHz lower than resonance which caused the LVDT to be out of range and useless. This problem was corrected by adjusting the warm frequency position from 1494.6 MHz to 1494.7 MHz. Recent performance data indicates that these were all successful design modifications.

IV. TUNER PERFORMANCE

The performance of the production-type cavity tuner is measured by phase-locking a self-excited loop oscillator to the cavity, tuning it to 1497 MHz and looping through a ± 50 kHz span. Figure 2 is a typical hysteresis loop of the early production tuner.

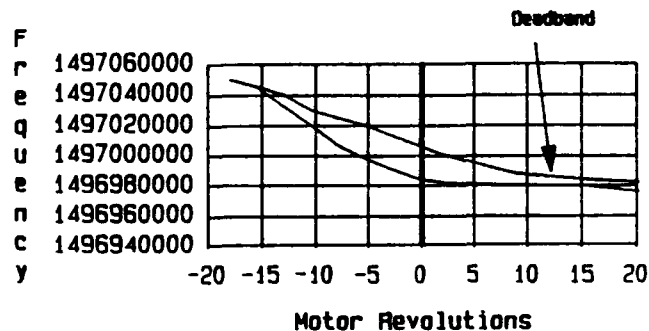


Figure 2. Typical hysteresis loop of CEBAF's early production tuner.

This curve depicts problems resulting from design flaws of three types (see Figure 1): 1) The backlash of stepper-motor-to-tuner gear slop. 2) The cell/cell holder mismatch due to inadequate allowances for thermal contractions. 3) The "deadband" caused by the failure to ensure that the cavity and tuner were adequately pre-stressed. The primary concern was the amount of hysteresis at resonance (mostly resulting from the cell/cell holder gap) of ± 10 kHz related to about 10 motor revolutions. As stated previously, the control system is required to maintain the frequency to within ± 50 Hz of resonance and operates the tuner only when it falls outside this window to prevent excessive tuning. On the average, cavities were in need of adjustment about twice a day[2], indicating a worst-case motor operation of 20 revolutions. If the operational lifetime of the rotary feedthroughs meets the specified 50,000 revolutions[3], one might expect to repair a feedthrough every 7 years. This is less than the 10-year cryomodule removal/maintenance period. Obviously, the cell/cell holder fit was a critical issue to resolve.

Since the cavity and tuner assembly are subject to thermal contraction and the expansion coefficient of the aluminum cell holder is ~ 3 times that of the niobium cell, an unrealizable zero clearance leaves an inherent gap. Therefore, a region of hysteresis will always exist. For this reason the cell holders are manufactured as two half-cells matching the contours of the production cavity cells resulting in a very repeatable fit. In addition, a final shim adjustment is made during assembly. On average, only 10 mils or so has been the amount of shim required. The need for clearances in bearing and sub-assemblies has made it difficult to eliminate the "deadband" region, but if it is far enough away from the nominal required tuning range, it poses no problem. This was considered when the inelastic tuning frequency was increased by 100 kHz.

Figure 3 is a ± 50 kHz hysteresis loop of a cavity-tuner assembly tested in the fall of 1992. The location of the deadband is approximately 30 kHz lower than resonance, which is the frequency after cooldown, and is largely narrowed. This is typical of the tuners presently installed after the aforementioned design and assembly modifications were incorporated.

Figure 4 depicts a ± 5 kHz hysteresis loop performed on the same tuner. Notice that the hysteresis region has been reduced to ± 1 kHz, corresponding to about a half of a motor revolution. This indicates a daily use of about one revolution which would increase the mean time between repairs to more than the 10-year cryomodule maintenance schedule.

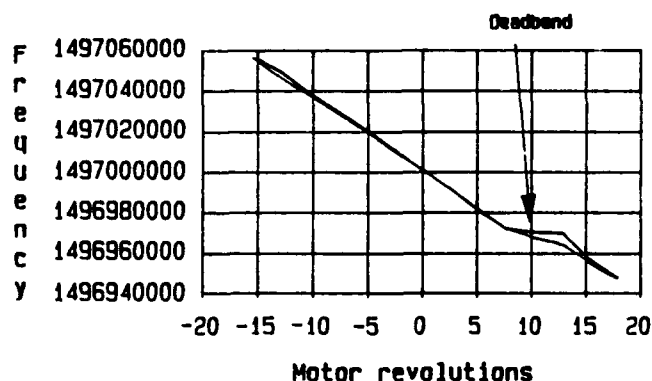


Figure 3. ± 50 kHz hysteresis loop of a cavity-tuner assembly tested in the fall of 1992.

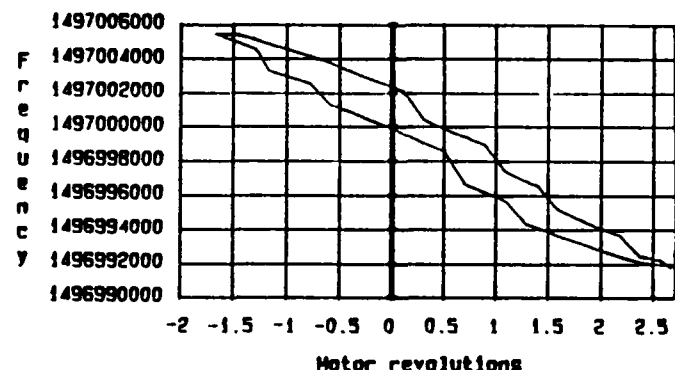


Figure 4. ± 5 kHz hysteresis loop performed on the same tuner as in Figure 3.

V. CONCLUSION

The mechanical tuner used at CEBAF to maintain the resonant frequency of the SRF cavity has undergone a variety of design changes and assembly procedural modifications. These are the result of an ongoing initiative to improve the control capability as well as the lifetime expectations of this critical accelerator component.

VI. REFERENCES

- [1] J. Mammosser, *et al.*, Analysis of Mechanical Fabrication Experience with CEBAF's Production SRF Cavities, *Proceedings of the 1993 Particle Accelerator Conference*, Washington DC.
- [2] C. Hovater *et al.*, CEBAF Technical Note, TN#92-013, February 1992.
- [3] A. Guerra, Jr., CEBAF internal document "Specification for Cryogenic Rotary Feedthroughs," 7/31/90.

Test Results and Design Considerations for a 500 MHz, 500 kWatt Vacuum Window for CESR-B*

D. METZGER, P. BARNES, A. HELSER, J. KIRCHGESSNER, H. PADAMSEE
Laboratory of Nuclear Studies, Cornell University, Ithaca, NY 14853 USA

SUMMARY

A previous paper [1] described the design of a vacuum window proposed for use in WR-1800 waveguide. This work details the results of a high power test of the completed prototype window. The window passed all design goals when operated into a short-circuited load. For the case of a matched load, the travelling wave power reached a maximum of 260 kWatts CW with vacuum bursts as a limiting factor. In addition to the results from the high power tests, some results from low power tests using a network analyzer are given. Some general conclusions are drawn concerning the design of vacuum windows in rectangular waveguide.

INTRODUCTION

The Laboratory of Nuclear Studies is proposing an upgrade to the existing CESR electron positron storage ring to make possible the study of CP violation of B meson decays. This "B-Factory", because of the required luminosity and the resultant high beam current, will require very high RF power levels to replace the synchrotron radiation and the higher order mode energy losses of the beam. The proposed design requires vacuum windows in WR-1800 waveguide which can handle 500 kWatts at 500 MHz.

There are two different operating scenarios for the window. The first is the case of total reflection from the cavity. During beam injection or after the beam has been lost, nearly all the power incident on the cavity will be reflected due to the low wall losses of the superconducting cavity (approx. 100 Watts). This scenario may exist up to a maximum of 125 kWatts incident (and reflected). Thus the window must be designed to operate in a standing wave resulting from an incident and reflected wave of 125 kWatts. This standing wave may shift in position according to the phase characteristics of the load. The second scenario is the case of no reflection from the cavity. This corresponds to maximal delivery of power to the beam. For this case there is almost no reflected power from the cavity. To survive in this scenario the window must be designed to operate in a travelling wave of 500 kWatts.

Two identical prototype windows were constructed. Fig. 1 shows the basic design of each. The waveguide from the klystron is standard WR-1800 (9 in. by 18 in.).

*Supported by the National Science Foundation, with supplementary support under the U. S. -Japan Agreement.

It was reduced in height by means of an aluminum taper to 5.5 in. by 18 in. Three beryllium oxide disks were brazed into a water cooled copper frame which was welded on the end of a copper plated stainless steel waveguide 5.5 in. by 18 in. The beryllium oxide was chosen for its high thermal conductivity. A matching post was placed approximately 18 in. from the disks in the waveguide on both sides of the disks.

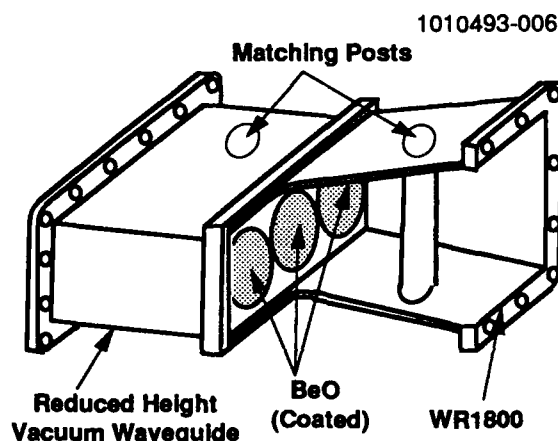


Fig. 1 500 kWatt, WR-1800 waveguide window for use at 500 MHz

II. LOW POWER TESTS

Each of the windows was measured using a vector network analyzer. The analyzer was calibrated in WR-1800 waveguide using the Thru-Reflect-Line method. A waveguide section two wavelengths long tapering from the reduced 5.5 in. height to the full 9 in. height was added to the window. The window and added taper were then measured together. The resulting VSWR is shown in Fig. 2. The system responds like a three element filter (post, windows, post). Fig. 3 shows the voltage transmission coefficient of the system.

III. HIGH POWER TESTS

A full power test was performed on the proposed window design. The test setup used two windows back-to-back with a vacuum region between as shown in Fig. 4. The input VSWR of this configuration is shown in Fig. 5.

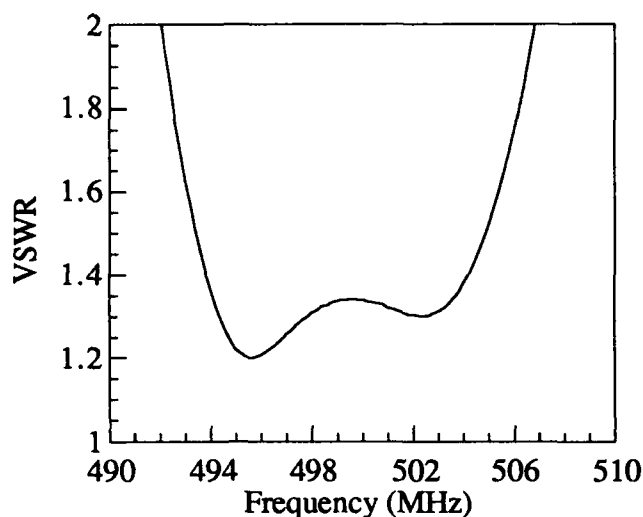


Fig. 2 Input VSWR of the waveguide window.

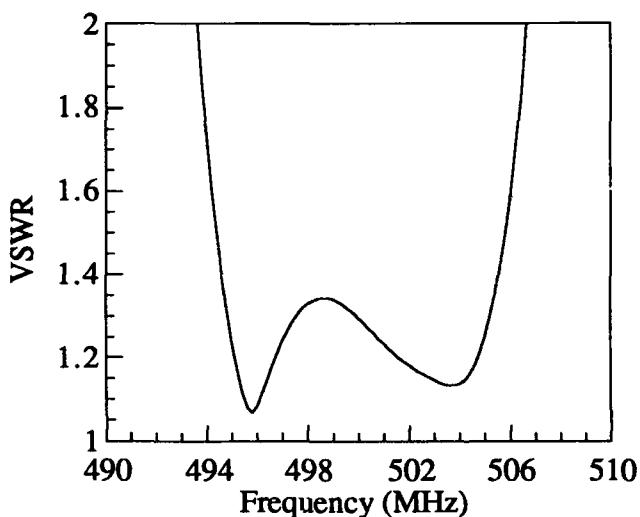


Fig. 5 Input VSWR of the test setup in Fig. 4.

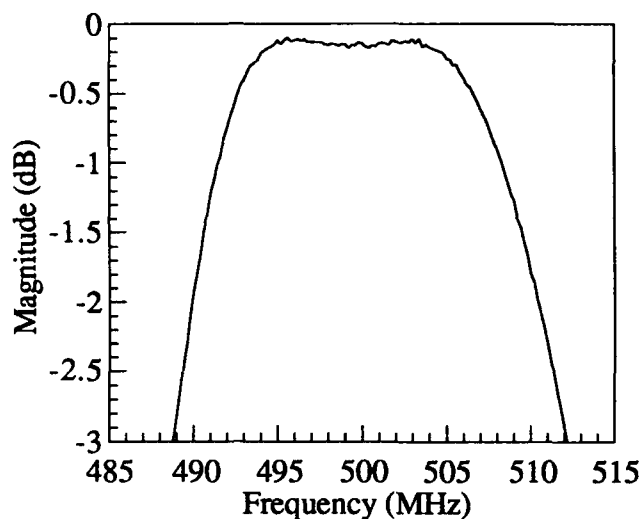


Fig. 3 Voltage transmission coefficient of the waveguide window.

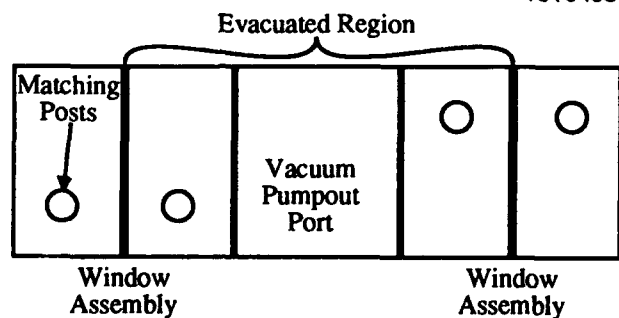


Fig. 4 High power test setup

The output side was first terminated with a high power matched load. A maximum CW power of 260 kWatts was achieved at a vacuum level of 1.5×10^{-8} Torr. The walls of the vacuum section between the post and the window frame rose to about 60 °C at this power level. Increasing RF power resulted in degraded vacuum due to the heating of the waveguide walls. The temperature of the beryllium oxide windows rose less than 5 °C at the full 260 kWatts power level.

A second set of tests was performed with varying distances between the windows and a short circuit as a load. Because nearly all of the incident power was reflected back to the klystron, the ultimate power was limited by the circulator protecting the klystron. In all cases a power of 100 kWatts CW was achieved. For some positions of the short the circulator allowed testing up to 125 kWatts.

Further high power tests will be carried out after completion of the beam test of the superconducting cavity.

IV. GENERAL DESIGN CONSIDERATIONS

Several conclusions can be drawn from our experience with this design for a window in large rectangular waveguide.

First, because the frame holding the beryllium oxide windows was such a poor match to the waveguide, the posts were necessary in order to achieve a good overall VSWR. However, this matching causes the storing of energy in standing waves between the windows and the matching posts. If the walls of the waveguide were perfectly conducting, this standing wave would not pose a problem. However, because the walls are not perfect conductors (copper plated stainless steel) the standing wave from the matching elements deposits a non-insignificant amount of heat into the walls. There is no substitute for a window geometry which is inherently well-matched to the waveguide. The use of matching elements increases the storage of energy and thus heating. A possible

candidate for a window geometry is a single round disc of beryllium oxide or aluminum oxide about 10 in. in diameter. Scale models have been fabricated which show excellent VSWR characteristics.

If it is necessary to have matching elements then it is best, from a wall heating standpoint, to maintain the largest waveguide size possible. This is illustrated by the data given in Table 1. This table shows the power dissipated in the finitely conducting walls of standard height (9 in.) and reduced height (5.5 in.) WR-1800 waveguide as a percent of the power flowing in a TE₁₀ mode at 500 MHz. (One wavelength of waveguide was used to calculate the power dissipated.) Note that using reduced height waveguide results in about 1.5 times as much power dissipation. The reduction in height reduces the cross-sectional area of the guide which carries the power more quickly than it reduces the perimeter of the cross-section which determines the power dissipation. This results in increased wall losses for the same amount of power flowing in the guide.

Table 1 Percent of the power flowing in a WR-1800 waveguide at 500 MHz which is dissipated in the walls for different heights and wall materials.

Wall Material	Height (inches)	P _{diss} / P _{flow}
Stainless Steel	5.5	0.21%
Stainless Steel	9	0.15%
Copper	5.5	0.030%
Copper	9	0.021%

V. CONCLUSIONS

A window has been designed and fabricated which is close to meeting the design goals of the B-Factor requirements. Both high and low power tests of the window have been performed. Several areas have been identified which should aid in achieving an acceptable window in the next design sequence.

VI. REFERENCES

- [1] J. Kirchgessner, et al., "Prototype 500 MHz Planar RF Input Window for a B-Factor Accelerating Cavity," Conference Record of the 1991 Particle Accelerator Conference, Vol. 2, pp. 678-680

An Experimental and Analytical Study of a Buoyancy Driven Cooling System for a Particle Accelerator*

B. Campbell and R. Ranganathan
Superconducting Super Collider Laboratory
2550 Beckleymeade Avenue, Dallas, TX 75237 USA

Abstract

A buoyancy driven closed-loop cooling system that transports the heat generated in a particle accelerator to the ambient has been evaluated both through experiments performed earlier [1] and analysis techniques developed elsewhere [2, 3]. Excellent comparisons between measurements and calculations have been obtained. The model illustrates the feasibility (from a heat transfer viewpoint) of such a cooling system for a particle accelerator.

I. INTRODUCTION

The primary purpose of this study was to establish the feasibility of cooling a typical particle accelerator by a *purely* natural convection, closed-loop, cooling system without the need for pumps, blowers etc. However, the use of fins and blowers were also evaluated as a secondary objective.

Consideration was given to a low energy booster (LEB), radio-frequency (RF) cavity, tuner concept at the Superconducting Super Collider (SSC) (Figure 1). During operation the heat generated in the tuner has to be removed in order to maintain the ferrites at a safe temperature. While studies of forced flow [4] and solid conduction [5] cooled tuners are available, a study of a natural convection cooled tuner has not been reported.

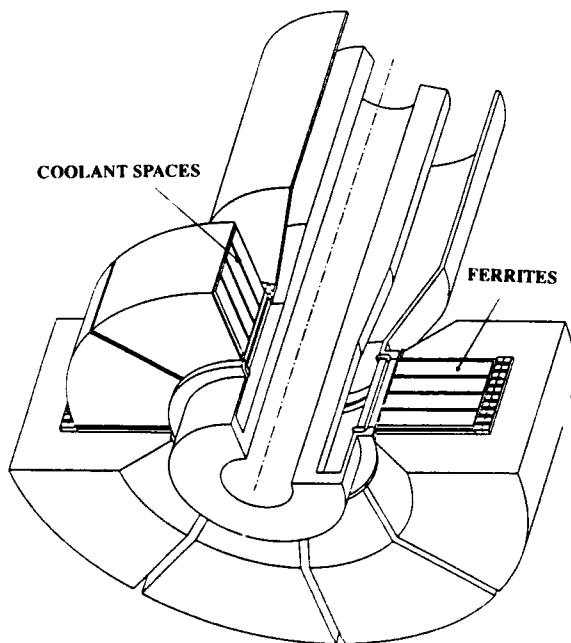


Figure 1. SSC, LEB, RF-cavity concept.

The cooling system involved the use of a coolant storage tank. The bottom of the tank and the tuner as well as their tops were assumed to be connected by tubes. Due to heat generation, the coolant in the tuner will rise and exit through the tubes at the top and flow to the tank. To conserve mass, coolant from the bottom of the tank will flow to the tuner, creating a closed-loop flow of the coolant. Since the flow will occur automatically in response to the magnitude of the heat input rate, the system is self-controlling. The general features of such a cooling system should be the same for any particle accelerator. Only the parameter values may be different.

II. EXPERIMENTS

The experiments consisted of submerging heated plates (that simulate the ferrites) vertically in a tank of water, and measuring the transient water and plate temperatures (Figures 2 and 3) [1]. Heat was generated in the plates by embedded resistive heaters (to simulate tuner operation). The plate temperature vs time at different locations are given in Figure 4.

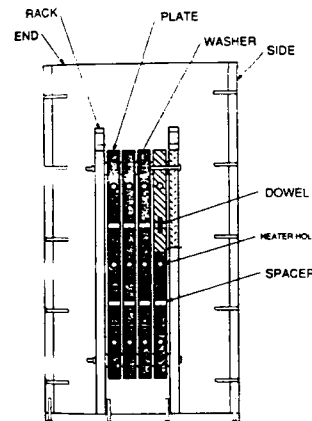


Figure 2. Experimental apparatus (front view).

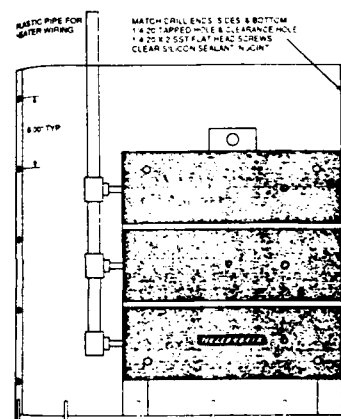


Figure 3. Experimental apparatus (side view).

*Operated by the Universities Research Association, Inc., for the U.S. Department of Energy under Contract No. DE-AC35-89ER40486.

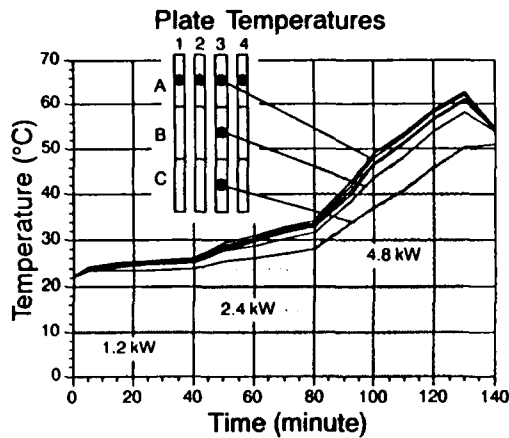


Figure 4. Plate temperatures.

III. ANALYSIS

The heat transfer and flow were assumed to be transient and one dimensional with temperature dependent properties. The Boussinesq approximation was invoked. Conduction in the water was neglected [2, 3]. The momentum balance giving the coolant velocity between the ferrites was derived as:

$$f_e = Gr / Re^2$$

where f_e is an equivalent coefficient of friction; the length scale is the ferrite spacing; Gr is the time-dependent Grashoff number based on the tuner and tank temperatures; and Re is the time-dependent Reynolds number. The above expression is coupled to the governing conservation equations of mass and energy and the set of partial differential equations was integrated in a lagrangian fashion using the predictor-corrector technique [2].

IV. VALIDATION

Figure 5 shows the comparison between measurements and analysis of the water temperature with time. The corresponding water flow rate (between the plates) indicates a spike each time the heat load is increased (according to the schedule shown in Figure 4). The model is "non-empirical," in the sense that there are no constants in the input to "adjust" the results. In this context, the close comparisons obtained are noteworthy. Note also that the present model has given good comparisons with measurements in an earlier application [2].

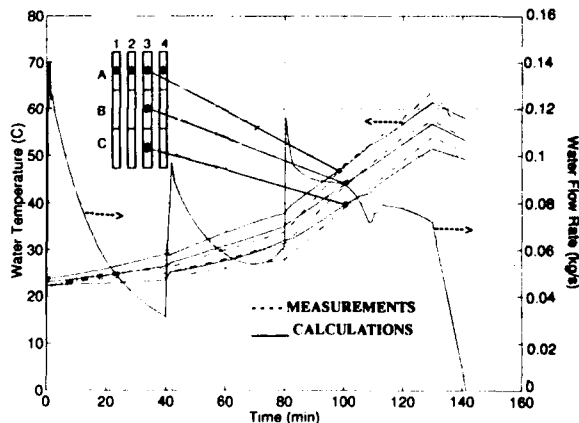


Figure 5. Comparison of measurements and calculations.

V. RESULTS

A. Baseline Designs

Two baseline configurations were considered, one for a copper plated tuner housing and the other without copper plating. Though different coolants were considered, only results for water are given here. The parameters for a tuner with a copper plated housing were: datum = tuner bottom, tank volume = 0.5 m³, tank height = 0.5 m, elevation of tank bottom = 0 m, heat transfer coefficient on the tank surface = 1 W/m²°C, tube inside diameter = 50 mm, number of tubes at the bottom (top) = 3 (3), initial temperature = 20°C, maximum tuner operation time = 3 hours, housing heat load = 2.5 kW.

For a tuner housing without copper plating, the baseline parameters were the same (as the above baseline) with the following exceptions: tank volume = 2.5 m³, tank height = 1 m, the number of tubes at the bottom (top) = 12 (12) and housing heat load = 25 kW. For this case a coolant jacket was assumed to be used due to the high heat load on the housing.

Figure 6 shows the temperature distribution in the tank, tuner water and ferrites at hourly intervals, for the baseline case with no copper plating. After three hours of operation of the tuner, the peak ferrite temperature of 77°C is less than the boiling point of water and the curie temperature of ferrite (200°C). The thermal stratification in the tank is due to the poor (zero) conductivity of water and this has been observed in other experiments [2, 3].

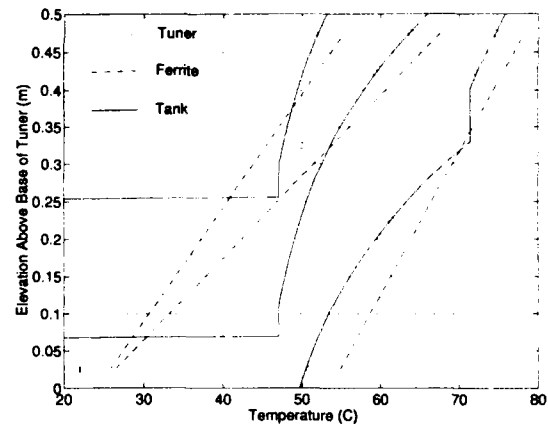


Figure 6. Water cooled tuner: housing = 25 kW.

B. Sensitivity Studies

The sensitivity of the baseline designs to the height, the elevation and the volume of the tank, the heat transfer rate from the tank, the number and diameter of the tubes are shown in Figures 7 through 9 (after 3 hrs of operation). The baseline cases are denoted by the letters B. The spikes in the curves are caused by the thermal stratification in the tank, which results in a sudden elevation of the tuner temperatures at intervals. Heat transfer coefficients (in W/m²°C) on the tank varying from 1-10 (free convection of air), 100 (blowing of air), 1000 (finned tank with free convection), and 10000 (finned tank with blowing air) were considered. An optimum cooling system can be chosen based on these results.

VI. SUMMARY

A closed-loop, buoyancy driven, cooling system for a particle accelerator has been experimentally and analytically evaluated. Sensitivity studies indicate the feasibility of such a cooling system for an SSC, LEB, RF cavity tuner concept from a heat transfer viewpoint. The present model can be used to thermally optimize such cooling systems for particle accelerators.

VII. REFERENCES

- [1] B. Campbell, "SSC LEB cavity mechanical design considerations," presented at the RF Workshop, TRIUMPF, Vancouver, B.C., Oct 25-26, (1990).
- [2] R. Ranganathan, Z. Vafa, R. J. Schoenhals, and F. W. Gilleland "An experimental and analytical study of a thermosiphon-type thermal energy storage system," presented at the VIIth International Heat Transfer Conf., Munich, Germany, 1982, *Heat Transfer-1982*, Hemisphere, vol. 6, pp. 479-484, (1982).
- [3] R. Ranganathan, and R. J. Schoenhals, "Analysis, design and testing of a thermal energy storage system," Purdue University report HL 82-44 submitted to Owens Corning Fiberglas Corp., Toledo, Ohio, December, (1982).
- [4] R. Ranganathan, A. D. Propp, B. Campbell, and B. Dao, "Three-dimensional model of a liquid-cooled, low energy booster, radio-frequency cavity tuner at the Superconducting Super Collider," May 6-8, IISSC-5, (1993).
- [5] R. Ranganathan, A. D. Propp, B. Dao, and B. Campbell, "Structural and thermal analysis of a solid-cooled, low energy booster, radio-frequency cavity tuner at the Superconducting Super Collider," May 6-8, IISSC-5, (1993).

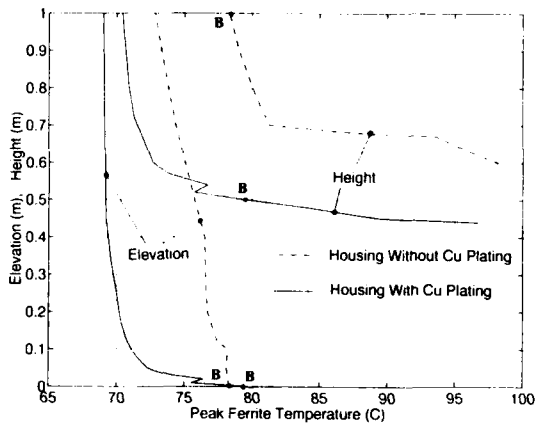


Figure 7. Effect of the height of the water within the tank and the elevation of the tank bottom above the datum.

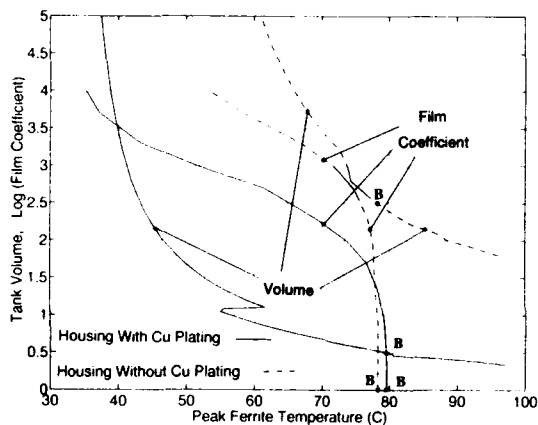


Figure 8. Effect of the tank volume (m^3) and the \log^{10} of the film coefficient ($W/cm^2\text{ }^\circ C$) on the tank outside surface.

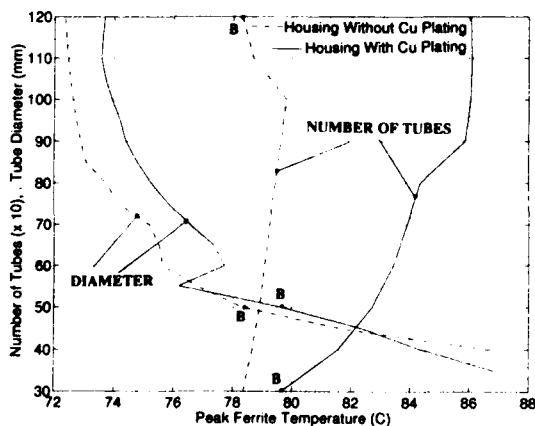


Figure 9. Effect of the number of tubes and the tube diameter.

Collider Bypass Diode Thermal Simulations and Measurements for the SSCL*

Cyrus Rostamzadeh and Gerry Tool
Superconducting Super Collider Laboratory
2550 Beckleymeade Avenue, Dallas, TX 75237-3997 USA

Abstract

Warm bypass diodes will be used as a component of a quench protection system to bypass an exponentially decaying current of 36 sec. time constant and peak current of 7000 A. Temperature excursions due to approximately 252 Kilo Ampere Sec. are studied using ANSYS, a finite element analysis program. A parabolic current waveform of similar energy but higher MITTs (1058 MITT) was applied to the bypass circuit and temperature excursion was measured at various locations. The procedure of current waveform generation and thermal measurements is illustrated in this paper. A comparison of simulation technique with actual measurements confirms the accuracy of the bypass diode assembly model. This assembly is installed at the SSC half-cell string test facility and results are extremely encouraging.

I. Introduction

A design has been created, and thermal analyses of the assembly performance have been conducted to predict the temperature rise in the assemblies during the current bypass function. The purpose of these tests is to verify with physical measurements that the assembly design is adequate, and to gauge the accuracy of the thermal analysis procedures for future use.

Figure 1 shows the electrical circuit of Accelerator System String Test (June 1992) in which these assemblies are connected. The nominal bypass current waveform to be conducted by the bypass assembly during quench is shown in Figure 2. The test setup used was not easily configured to provide an exponential decay from an initial value, so a power supply was programmed to provide a fast rising current to I_0 followed by a parabolic decay as shown in Figure 3. The waveform was configured to provide the same $\int Idt$ as that to be exercised during the operational scenario. The nominal peak operating current for the collider is 6500 A, but a special "conditioning" scenario possibly requires operation at 7000 A. Therefore, our tests exercised the devices to this level.

II. Test Setup Description

Each bypass diode assembly consists of two independent (thermal and electrical) diode circuits which can be configured as one, two, or three diodes in series. Each of these independent circuits can be used to protect one or more magnets which together make up a "quench bypass unit". Figure 4 shows a total assembly loaded with 3 diodes in each section. These tests were conducted using a three-diode and a two-diode stack.

Each circuit is composed of a stack of International Rectifier type R77R6A diodes alternating with copper disks acting as heat sinks and clamped under a force of 10000 lb. Disks next to the anode side of the first diode and the cathode side of the last diode are connected externally through copper bus bars (3/4" x 1/2") brazed to the copper disks. A pair of MCM500 bypass

cables is connected to each of the bus bars using two-hole MCM500 lugs.

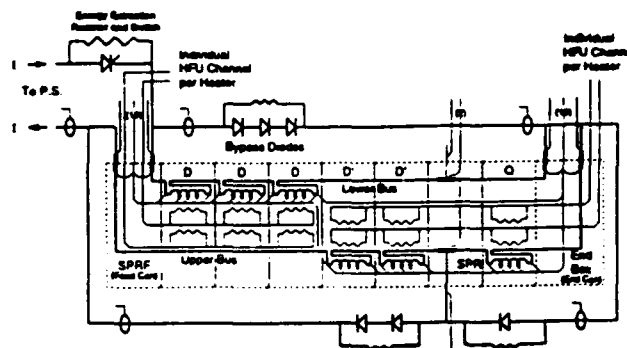


Figure 1 - ASST Phase I Electrical Circuit

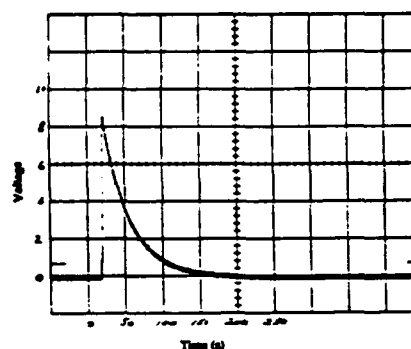


Figure 2 - Nominal 7 kA Program to power supply (10V = 8000A)

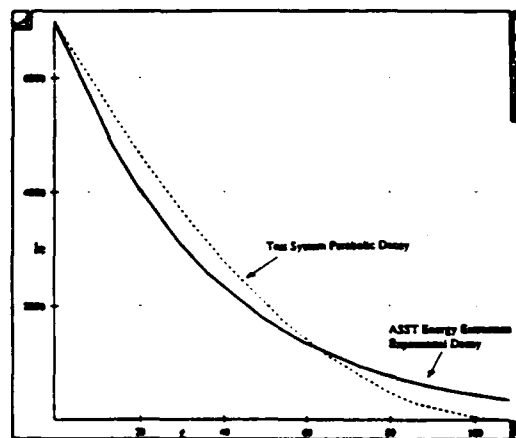


Figure 3 - Parabolic Approximation to Nominal Current Waveform

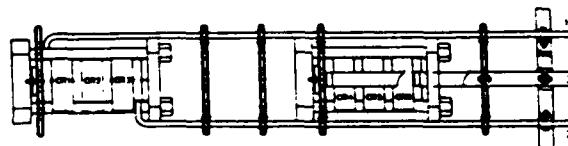


Figure 4 - Assembly with 3 diodes in Series

* This work supported by the United States Department of Energy under contract DE-AC35-89ER40486.

Thermal sensors (RTD - Resistor Temperature Detectors) were inserted into the sides of the copper disks between the diodes and in the connecting bus bars to monitor temperature excursions during current pulsing. Instrumentation cables were used to interface the RTD signals to signal conditioning amplifiers (OMEGA OM3-600). Signals were digitized and stored in two Lecroy data loggers for analysis. Sampling rates of 1 Hz and 10 Hz were used to record slow and fast processes. Table 1 lists the signals measured and the data logger channels for the first series of tests using one 3-diode section

Table 1: Data Logger Signal Definitions

Description	Calibration	Lecroy 1 Signal Name	Lecroy 2 Signal Name
Anode 1 Bus	200°C/10 V	V8	V4
Anode 1	600°C/10 V	V10	V5
Cathode 1	600°C/10 V	V11	V6
Anode 2	600°C/10 V	V12	V7
Cathode 2	600°C/10 V	V13	V8
Cathode 3 Bus 2 (3/4")	200°C/10 V	V6	V2
Cathode 3 Bus 1 (18")	200°C/10 V	V5	V1
LEM Transducer	10 kA/5 V	V9	V14

The bypass diode assembly was inserted in a 4 ft long G10 sleeve for 3.5 kV dc electrical isolation from ground. The total assembly was then inserted into a 4 ft long stainless steel tube similar to the enclosure that will be used for mounting the assemblies in the eventual Collider tunnel.

A 0.1% LEM transducer was used to monitor the bypass current waveform. The actual accuracy of this device was less than specification due to use of an uncalibrated burden resistor in this setup, therefore, a comparison was made with the IRING current transducer measurement in the power supply. The comparison indicates approximately 1% difference between the two signals in the $\int I dt$ for the current pulses used. The signal from the LEM transducer was instrumented by an Analog Devices amplifier (3B41) before connection to the data logger for digitization and storage. The String Test power supply control microprocessor (SECAR) was used to generate a parabolic waveform that is comparable to the real waveform as discussed earlier. This waveform provides the current reference for a Dynapower power supply capable of delivering 0 - 8000 A at 0 - 40 V.

The diode assembly was connected across the power supply in various configurations:

1. three diodes in series,
2. two diodes in series,
3. five diodes in series.

We also added additional copper mass (disks) to the three diode configuration for later runs.

III. Test Process Description

The power source was easily programmed to provide parabolic and linear ramp segments. For a parabolic decay waveform to

provide the same heating effect as the exponential decay, one wants to match the $\int I dt$ in the two waveforms since the voltage drop across diode devices is approximately constant in the current range of interest. (For a resistive system, such as the bypass cabling, the heating is proportional to the $\int I^2 dt$. Analysis of the exponential and parabolic waveforms then leads to the condition that $I_0 \tau = \frac{1}{3} I_0 t_f$, where $\tau = 36$ s for the exponential decay and t_f is the final time at the end of the parabolic decay. This condition results in $t_f = 108$ s for the case where $\int I dt = 252$ kA-s. Since the resistive parts of the system will be heated proportional to $\int I^2 dt$, we calculate that result for the maximum stress waveform and find that for the parabolic decay, $\int I^2 dt = 1058$ MIITs as compared with 882 MIITs for the reference exponential decay. This additional heating in the cables and connecting busbars is in a safe range and assures that we have data from a case which is more pessimistic than actual Collider operation.

A variety of electrical tests were performed and temperatures at the points listed in Table 1 were recorded. The power supply was quickly ramped up at 1.4 kA/sec starting from an initial current of 50 A and was then parabolically ramped down. On the first run with the three diode configuration, the peak current was limited to 3500 A, and the temperature profile was recorded. Six more runs were performed by increasing the peak current in 700 A steps. The waveform generation algorithm used easily scales the peak current with fixed rates of change, so the waveforms at different currents do not have areas which scale with the peak current value. Hence, data must be analyzed with respect to the actual waveform area, not with respect to peak current.

Tests were also performed on the two-diode section and on the two sections in series by strapping the two independent sets together. In order to establish that damage had not occurred during the high current testing, reverse bias measurements were made on all 5 diodes before and after electrical and thermal stress.

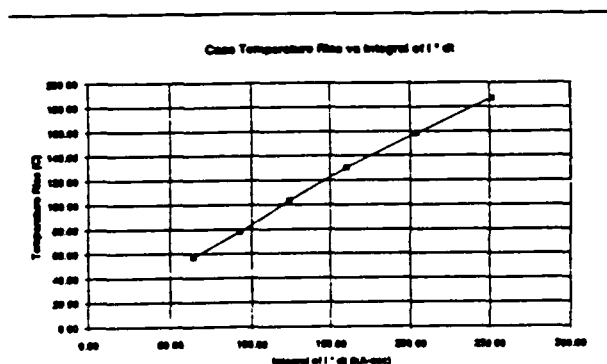


Figure 5 - Temperature Rise at Hottest Spot in Assembly

IV. Data Analysis

Data was extracted from the Lecroy data logger files on computer system, reconfigured to a convenient format, and plotted using the SPICE circuit analysis postprocessor tools.

Table 2 and Figure 5 indicate the temperature rise measured at the hottest spot in the assembly as a function of the area under the I vs t curve during these tests.

The current waveform and temperature profile vs time at four points along the assembly are shown for the 7000 A run in Figure 6 and Figure 7.

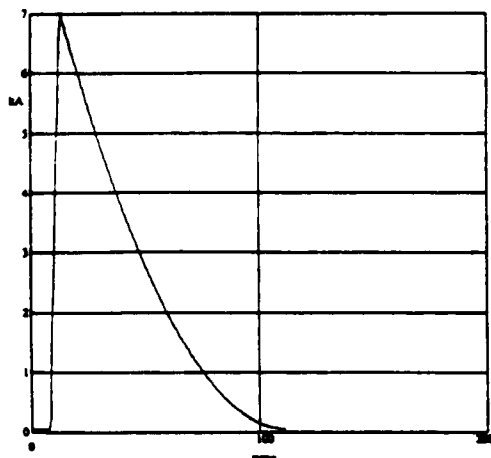


Figure 6 - Current Waveform for Test at 7 kA

Table 2: Temperature Rise during Experimental Rise

Run	Peak Current (A)	T initial (°C)	T Final (°C)	∫ Idt (kA-s)	ΔT (°C)
1	3,500	20	76.8	64.3	56.8
2	4,200	24	102.2	93	78.2
3	4,900	23.1	126.3	124	103.2
4	5,600	24.7	155.1	160.6	130.4
5	6,300	26	184.2	203.8	158.2
6	7,000	36.7	223.7	251.7	187

V. Comparison With Thermal Analysis

As indicated above, prior to the testing, a finite element model was constructed to perform a thermal transient analysis of the diode assembly using ANSYS. The purpose of the study was to predict the maximum temperature of the silicon wafers of the diodes and to provide a basis for comparisons of temperatures that could be measured and hence extrapolated to the silicon wafer.

The model placed three diodes in series as described in the test setup description. Details of the two-dimensional axisymmetric thermal solid modeling included the mechanical dimensions and thermal properties of the many different layers such as the copper cathode and anode, molybdenum buffer, silicon wafer, aluminum junction and silver disk. Details of the construction of the diode were provided by Art Felix of International Rectifier. The material properties were obtained from the CRC handbook.

The heat generation function applied to the silicon wafer layers was

$$P_d = 693.4 e^{-t/36} \ln(1 + 7 \times 10^{14} e^{-t/36}).$$

Natural convection was assumed to occur to the bypass cables. The simulation results predicted a maximum temperature of about 233°C at the outside edge of the silicon wafer, with the peak occurring about 60 s after the heat generation started as shown in figure 8. The simulation results indicate a temperature profile very close to that measured in the tests.

VI. Thermal Recovery

During the test runs, the recovery to ambient temperature takes about 2 hours. In the operation of the Collider, this presents no problem since data analysis from the quench and recovery of the refrigeration system to operating conditions require a similar length of time.

VII. Conclusions

The tests have shown that the current design will work satisfactorily for the Collider with three or less diodes per bypass unit (number of diodes is dependent on bypass unit inductance and ramp rate). From separate measurements made in the laboratory, the forward conduction threshold of the three diodes is 0.95 V at 35°C, allowing a maximum ramp rate of 4.2 kA/s with magnet inductance of (3 x 75 mH = 225 mH) and for a leakage current of 1.5 mA established as the system requirement.

The peak temperature rise of the assembly is much higher than good design practice would allow for steady state operation such as in power converter applications. However, the transient, low rate of occurrence nature of this application coupled with the absence of reverse bias voltage for the device to block after the current pulse permits reliable operation of these diodes at temperatures above 250°C according to the manufacturer.

VIII. Acknowledgments

The tests described above were conducted with the cooperation and assistance of Al McInturff and Bob Flora of Fermilab, Milan Kuret, Roger Nehring, Gerry Sorensen and Nghia Tran of SSCL, and Art Felix of International Rectifier.

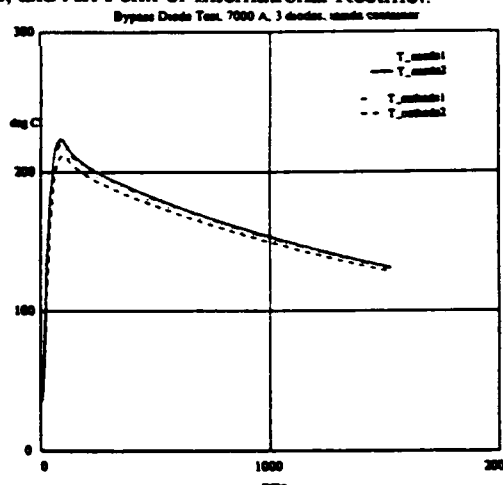


Figure 7 - Temperature Profile vs Time for 3-Diode Assembly at 7 kA

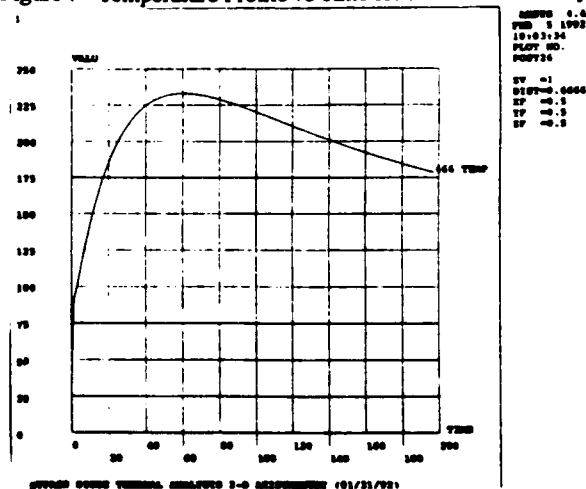


Figure 8 - Thermal Analysis Temperature Profile

Frequency-feedback Tuning for Single-cell Cavity Under RF Heating*

Jeffrey D. Stepp, James F. Bridges
Argonne National Laboratory
9700 S. Cass Avenue, Argonne, IL 60439 USA

Abstract

A tuning system is described that is being used to match the source frequency of a high-power klystron on the resonant frequency of the prototype single-cell cavity for the 7-GeV Advance Photon Source (APS) storage ring. Typically a water-cooled piston tuner is required to adjust the reactive component of the cavity's impedance to minimize reflected power back to the RF drive source. As the cavity walls expand due to RF heating, the resonant frequency decreases. Adjusting the source frequency to follow the cavity resonant frequency is a convenient method used to condition the cavity (for vacuum) at high power levels, in this case, 1 MV gap voltage at 100 kW power level. The tuning system consists of two coupling ports, a phase detector, a digitizing I/O system, and a DC coupled FM-modulated RF source. Proportional Integral Derivative (PID) loop parameters for the Experimental Physics and Industrial Control System (EPICS) software are calculated, and data is presented showing the damped response to perturbations on the loop.

The tuning system presented here does not need water-cooling, has no moving parts to wear out, and has an inherently faster response time. Its one limitation is the digitizing sampling rate. The only limitation in tuning range is the bandwidth of the RF source.

I. INTRODUCTION

A block diagram of the RF system is shown in Figure 1. That portion of the RF test stand controlling the amplitude and phase of the RF in the single-cell cavity being tested is described below. Also included is a description of the phase regulation that maintains the cavity's resonance point. Both pulse and continuous wave (CW) operation are supported to allow connection and testing of various high-power components.

The single-cell cavities being designed for the APS storage ring will require RF input power of 57 kW and 800 kV gap voltage each at a nominal frequency of 352 MHz to maintain a 200 mA, 7.5 GeV stored beam [1]. The engineering design is 1 MV.

A cavity resonance-control loop is used to match the source frequency of a high-power klystron with the cavity's resonance frequency. The loop modulates the RF frequency to track the resonant frequency of the RF cavity load under RF heating if a tuner is not used. In operating accelerators, a control loop adjusts a water-cooled mechanical tuner slug through a stepper motor to match the cavity's resonant frequency with the RF source frequency to satisfy any beam loading requirements, as well as minimize reflected power back to the high-power RF source. Temperature regulation of the cavity structure has been used for the purpose of thermal detuning correction [2].

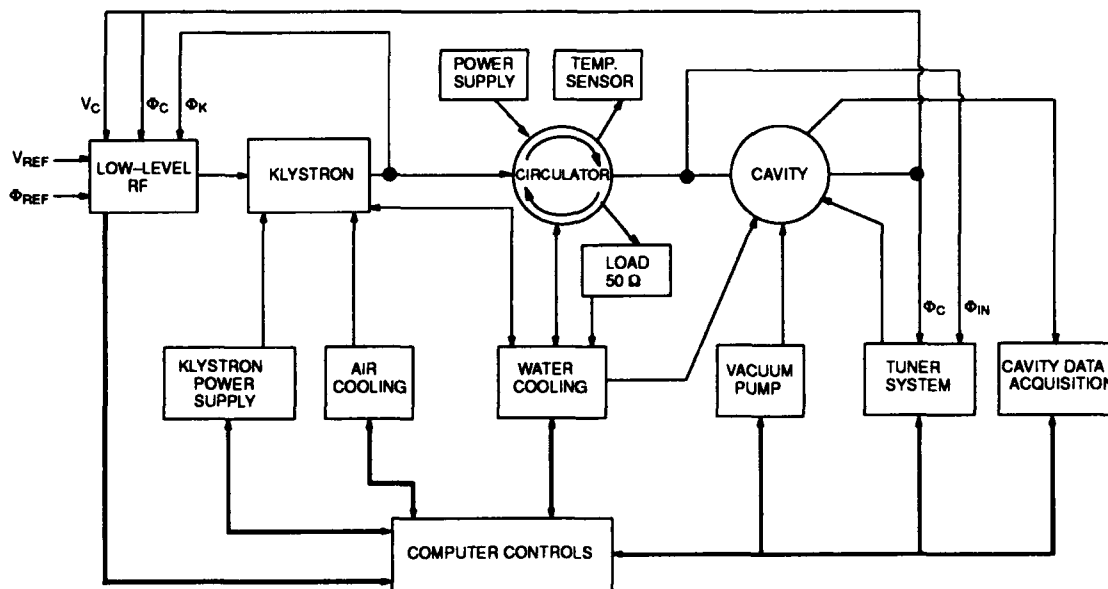


Figure 1. Resonance control setup of the RF test stand.

*Work supported by the U.S. Department of Energy, Office of Basic Sciences, under Contract W-31-109-ENG-38.

The submitted manuscript has been authored by a contractor of the U. S. Government under contract No. W-31-109-ENG-38. Accordingly, the U. S. Government retains a nonexclusive, royalty-free license to publish or reproduce the published form of this contribution, or allow others to do so, for U. S. Government purposes.

Under CW operation the cavity will heat up causing the resonant frequency to shift. If a tuner is not installed, then the RF source frequency can be modulated to follow the cavity's resonant frequency. The frequency will track until the maximum frequency deviation is reached. Past this point, the cavity will begin to detune. When a preset value of VSWR is reached, the reverse power will trip off the RF drive. This can be prevented by changing the RF source frequency by an amount equal to the maximum deviation. The inherent fast response of this method is a convenient way to vacuum condition the cavity at high power levels.

II. DESCRIPTION

For cavity tuning control, a feedback system is used to compare the cavity phase with the input phase, from a waveguide coupling port, and adjust the tuner system to keep the cavity at the resonant frequency within $\pm 1^\circ$. The two signals are compared with a digital phase meter to produce an error signal. A phase shifter is inserted in the cavity input power signal to set the cavity phase at the resonance frequency near zero. The digital phase information is read by a microprocessor located in the slot 0 controller card of a VME crate, which then adds the required phase offsets, producing an error signal to control the frequency of the RF source.

The digitizing I/O system modulates the synthesizer with a frequency offset to follow the cavity's resonant frequency changes under RF heating, without the need for a water-cooled mechanical tuner system. The bandwidth of this system is limited by the modulation bandwidth (50 kHz) and the maximum FM deviation (in this set-up, ± 100 kHz) of the RF source.

The loop corrects only the reactive element of cavity input impedance by keeping the phase difference between the RF input and field probe at a constant value.

For this instance where the cavity does not have a mechanical tuner, the frequency of the RF source will be modulated by a DC-coupled voltage under computer control to track the resonance point of the cavity as it drifts due to RF heating.

III. RESONANCE LOOP PARAMETERS

The cavity's phase sensitivity is

$$\frac{90^\circ}{3 \text{ dBBW}} = \frac{90^\circ}{17 \text{ kHz}} = 5.3 \frac{\text{mDeg.}}{\text{Hz}}.$$

The A/D and D/A converters used were 12-bit VME modules in the controller crate. The A/D resolution over its input voltage range of ± 10 V limits the phase error of the cavity to

$$\frac{\pm 10 \text{ V}}{12 \text{ bits}} = 4.8 \frac{\text{mV}}{\text{bit}} \times \frac{0.1^\circ}{\text{mV}} = \frac{0.48^\circ}{\text{bit}}.$$

The modulation sensitivity is defined by the modulation index of the RF source and was set to ± 10 kHz/V for initial loop tuning and then the full ± 100 kHz/V deviation for operation.

A proportional integral controller (PI) sets the feedback function of the resonance tracking loop. Its easy tuning and offset adjusting allowed quick closed-loop operation. The feedback system is shown graphically in Figure 2.

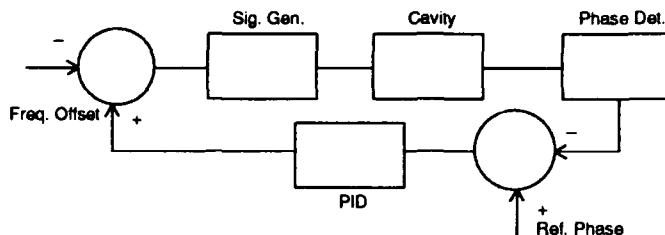


Figure 2. Gain line-up.

The transfer function of the feedback loop is calculated, from the frequency deviation voltage to the phase detector voltage, to be

$$\beta = \frac{+100 \text{ mV}}{+100 \text{ kHz}} \times \frac{1 \text{ Hz}}{5.3 \text{ mDeg}} \times \frac{+1^\circ}{+10 \text{ mV}} = 0.189.$$

The FM bandwidth of the RF source is 50 kHz at 1 dB. The scan rate of the A/D and D/A is set by the program to be a maximum of 10 readings/sec. The phase detector's output has a 3rd-order elliptic filter with a 3-dB bandwidth of 800 Hz and a rise time of 334 μ s.

IV. PID PARAMETERS

The Ultimate tuning method [3] was used to set the PI parameters in the EPICS software. The ultimate gain (S_u) is the value of K_P needed to sustain oscillations about the set point value. The ultimate period (P_u) is the period of sustained oscillation. A rule of thumb for controllers of the form $K_c(1 + 1/T_i + T_d p)$ using proportional plus reset control is $K_c=0.45 S_u$, and $T_i=P_u/1.2$. In the EPICS software PID control algorithm, the change in error function (or velocity algorithm) has the form

$$DM = K_P x(de) + exdt \times \frac{K_I}{60} * K_P + \left(\frac{de}{dt} - \frac{dep}{dtp} \right) * \frac{K_D}{60} * K_P.$$

Therefore, the program values for proportional plus reset control are $K_P=K_c=0.45 S_u$, $K_I=60/T_i=72/P_u$.

A proportional integral derivative controller (PID) could have been used to offset the dead time caused by the 10-Hz scan rate of the A/D and D/A and provide a faster response. However, the initial tuning would be much more difficult and was not pursued. A procedure is given in Ref. [4].

V. OPERATION

Before the loop is run in a closed loop, the phase offset of the cavity must be adjusted to compensate for cable differences. This value then becomes the reference for the loop. The procedure used is the following:

- Set klystron output power to below 1 kW to minimize RF heating.
- Turn off signal generator modulation.
- Adjust signal generator frequency until reflected power is a minimum (< -15 dB).
- Read phase value on vector voltmeter.
- Record as phase offset value.

With $K_I=K_D=0$, K_P was set to sustained oscillation of phase difference after a step input of 1 kHz in frequency in a

closed loop mode with the RF source modulation index set initially for 10 kHz deviation. This was done to keep the reflected power small.

The ultimate gain and period were found to be $S_u=1.47$ and $P_u=0.625$ seconds. Once the loop was optimized, the RF source deviation was set to a maximum to allow increased tuning for higher RF power. Scaling the PID parameters for maximum source frequency deviation, KP only was changed to 0.2.

Figure 3 shows the response of the resonance tracking loop due to perturbation of 1 kHz in the PID setpoint. This data was taken for $K_P=0.1$, $K_I=10000$, $SCAN=0.2$, and the RF source deviation set to 10 KHz.

VI. ACKNOWLEDGMENTS

The authors wish to thank Donald Voss and Terry Smith for their part in integrating the system. We also wish to thank Frederick Vong for providing the application code, writing the PID database, and designing the interface control panel.

VII. REFERENCES

1. 7 GeV Advanced Photon Source Conceptual Design Report, Argonne National Laboratory, ANL-87-15, 1987.
2. L. M. Young, R. S. Biddle, "Resonance Control for a CW Accelerator," *Proceedings of the 1987 PAC*, Washington, D.C., March 16-19, pp. 634-636, 1987.
3. Murtil, Paul W., *Automatic Control of Processes*, International Textbook Co., Scranton, PA, pp. 348-350, 1967.
4. Puglisi, Mario, *New Techniques for Future Accelerators II*, Plenum Press, Vol. 36, 1989.

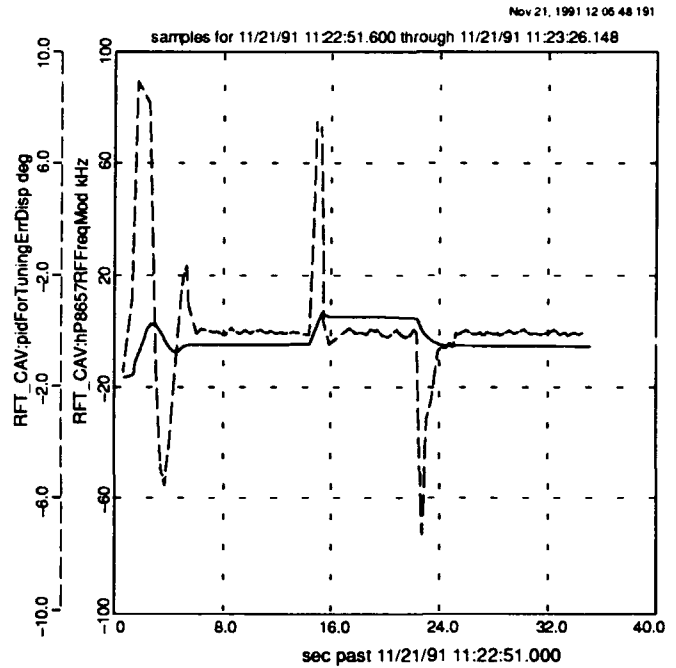


Figure 3. Closed-loop response for $K_P=0.1$, $K_I=1000$.

A DEVICE OF AMPLITUDE AND PHASE STABILIZATION FOR THE FEL INJECTOR IN THE L-BAND

Zhang Qinghai, Wang Xiulong, Sun Yuzhen, Bu Sunfu
Zhang Meifang, Su Guoping
China Institute of Atomic Energy, Linac Laboratory
P.O.Box 275(17), Beijing 102413, P.R. China

Abstract

A device of amplitude and phase stabilization for the FEL injector in the L-Band is developed in CIAE. without the distortion of the pulsed envelopes, the stabilities of amplitude and phase of the closed circuits in the device can be better than $\pm 1\%$ and $\pm 1^\circ$ respectively. The device is used in the FEL injector in the CIAE Linac Laboratory.

1. CONSTRUCTION OF THE DEVICE

There are two component parts in the device, i.e. Amplitude and phase stabilization part. The amplitude stabilization part mainly consists of a source (S), electronic attenuator (EA), power amplifier (PA), level amplifier (LEVEL), detector (DT) and load(L) or buncher cavity(B), as shown in Figure 1.

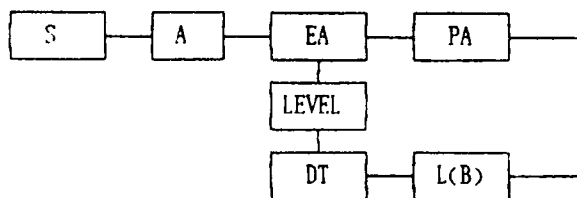


Fig 1. Schematic of amplitude stabilization part

In the amplitude stabilization part of the device, a sampling signal from the load or the buncher cavity, through the DT and the LEVEL, is back fed into the EA. The rf amplitude in the EA will be adjusted negatively. And also the amplitude of the rf field in the load or the buncher cavity will be balanced and stabilized at once.

The Phase stabilization part mainly

consists of a source (S), electronic phase shifter (EPS), power amplifier (PA), double balanced mixer (DBM), level amplifier (LEVEL) and load (L) or buncher cavity (B), as shown Figure 2.

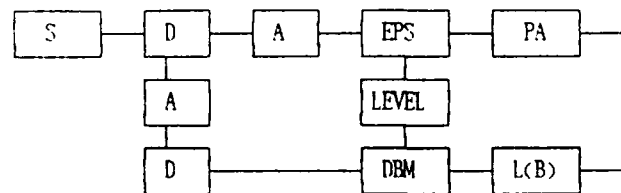


Fig 2. Schematic of phase stabilization part

In the phase stabilization part, the phase of the rf field in the load or the buncher cavity may be changed by some disturbances, and a sampling signal of the rf field phase from the load will be compared with the conference signal from the S in the DBM. The amplitude of the output signal voltage from the DBM will be made to be proportion to the phase difference between them. Then the voltage signal is back bed into the EPS through the LEVEL, the phase of the rf field in the load or the buncher cavity will be adjusted negatively and stabilized at once [1].

2. PERFORMANCES OF THE DEVICE

In order to secure the device and get the best performances of the device, the rf power level through it must be limited below 50mW. But the device in the rf system (as shown Fig 1 and 2) can control and stabilize with the rf power of Mws in the system.

The operating frequency of the rf power signal in the device is 1300MHz ± 10 MHz in the L-band. The device can be used in the continuous wave model or the pulsed wave model. The pulse duration

for the FEL injector can be from one μs to tens μs . The response time of the closed circuits in the device is about 2 μs .

The capture range of the amplitude stabilization can be about $\pm 50\%$ of the relative amplitude. The stability of the closed circuit in the device can get better than $\pm 1\%$ of the relative amplitude, if the amplitude of the open circuit is changed within $\pm 10\%$ of it.

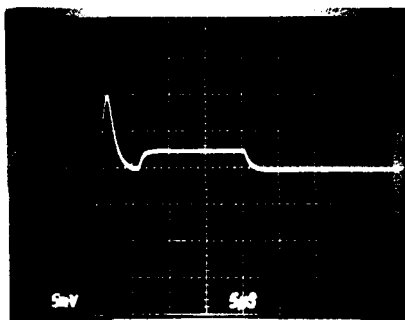
The capture range of the phase stabilization can be about $\pm 30^\circ$ of the phase in the device. The stability of the closed circuit can get better than $\pm 1^\circ$ of the phase, if the phase of $\pm 10^\circ$ of the open circuit is changed.

The pulsed envelopes of the rf signal must be kept to be approaching rectangles and can not be distorted in the adjustment and the test. The oscilloscopic envelopes of the closed circuits in the device, as shown Figure 3.

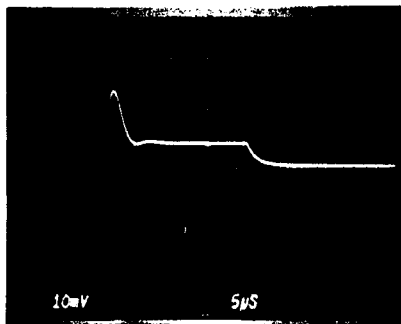
The device has been used and operated normally in the injector; but the regulation of the injector has not been completed yet and there are still a lot of works to do.

3. REFERENCE

- [1] M.T.Lynch, P.J.Tallerico and E.F.Higgins. "Phase and Amplitude Feedback control system for the Los Alamos FEL", IEEE Trans, on Nuclear Science, Vol. NS-32, No.5. October 1985.



(a) The Amplitude envelop



(b) The phase envelop

Figure 3. The oscilloscopic envelopes of the control signal in the closed circuits.

A Jet Neutralizer Concept

T.E. Horton

School of Engineering, University of Mississippi
209 St. Andrews Cr., Oxford, MS 38655

Abstract

When gas cell neutralizers are inadequate for large aperture ion beams, one must turn to supersonic jets to achieve a neutralizer. A transverse supersonic jet concept for neutralizing ion beams is presented. The concept eliminates the problems posed by boundary layer development in a low density nozzle flow. Operating conditions are presented for optimum neutralizers using several gases.

I. INTRODUCTION

A. Gas Cells

In using a gas stripper for a negative ion beam there are two neutralizer concepts: the gas cell and the transverse supersonic jet. For either, a controlling parameter is the "target thickness parameter", the integral of gas density along the ion beam path. Data on this parameter have been presented in Reference [1] and are used as the data base for this work. For optimum neutral yield these data can be translated into the pressure for a one meter thick neutralizer. The optimum pressures are

Neutralizer Gas	P (torr)
HELIUM	4.8
ARGON	0.22
XENON	0.058

Considering beamline pressures of 10^{-5} to 10^{-9} torr, the escape of gas from the neutralizer into the beamline represents a significant problem. In addition to the gas load on the beamline pumps, other concerns are the complexity of the system, the total gas consumption, and the beam length required.

B. Gas Jets

In terms of both concept and implementation, supersonic jets are complex. Conceptually, one is utilizing the limited lateral expansion available to a high Mach number flow. The flow is directed transverse to the beam to create a wedge of neutralizer gas. Above a Mach number of 6 the flow velocity approaches a constant value, thus the conservation of mass assures a constant target thickness parameter over the beam

aperture. The total mass flow rate through the jet scales as the product of the beam aperture and the neutralizer length along the beam. Of this flow only a fraction, less than 5%, enters the beamline.

The concerns with supersonic transverse jet neutralizers are: the mass of gas required, viscous effects, and rarefied gas effects. As a measure of the importance of each of these, the following data are presented for our nominal 1 meter beam aperture:

Gas	Mass Flow (gm/s)	Reynolds No.	Knudsen No.
HELIUM	180	11000	0.0005
ARGON	26	1400	0.004
XENON	13	660	0.009

The above were based upon the optimum target thickness parameter for each gas with a gas supply temperature of 300K. The Reynolds number, which is a measure of the importance of viscous effects, is the minimum value evaluated at the Mach 1 condition in the jet. These values are low, indicating a significant viscous problem. The Knudsen number, the ratio of mean free path to neutralizer length, was evaluated in the high Mach number flow of the neutralizer volume. These values indicate the continuum assumption remains valid for purposes of analysis.

From the above one can conclude that the primary concern in the choice of a jet neutralizer concept must be with the viscous effects. It is imperative to increase the minimum Reynolds number to prevent a viscous distortion of the jet. Equally important is the reduction or elimination of the significant thickness of boundary layer which develops on the walls of conventional nozzles.

In the following, a concept is presented for achieving a well confined wedge of supersonic flow in which viscous effects can be minimized by controlling the Reynolds number at Mach 1 and eliminating boundary layers.

C. The Corner-expansion

Corner-expansion flows are common to under-expanded supersonic flows as they escape the confines of a nozzle. They are characterized by the abrupt turning

of the streamline at the lip of the nozzle. A classic illustration of the phenomena is reproduced in Figure 1.

Here an initially uniform sonic flow has been depicted as series of streamlines emanating from the Mach 1 source cross-section and as a series of dashed constant Mach number lines radiating from the lip. The lip will be referred to as the "source lip" below.

The constant Mach lines also represent lines of constant properties and in this figure they represent order of magnitude reductions of pressure.

II. THE DOUBLE CORNER-EXPANSION JET

The concept presented in this paper, which has been termed the "double corner-expansion", can be most easily introduced by referring back to the Mach 1 source corner-expansion of Figure 1. Consider a second lip placed on a streamline, pointing in opposition to the flow, and rotated through a slight positive acute angle to the streamline. This lip will "scrape off" those streamlines above the lip streamline. These will experience compression by an oblique shock just above the scraper lip. Those streamlines below the lip will expand via a high Mach number corner-expansion originating at the scraper lip.

The streamlines above the scraper lip are referred to as the "primary flow" and those passing between the source and scraper lips compromise the "secondary flow". One can conceive of the primary flow as being that of a

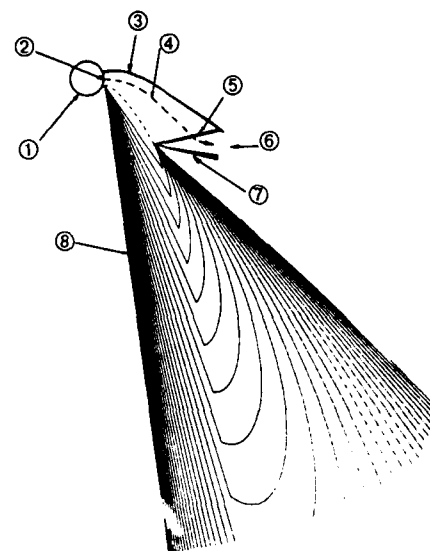


Figure 2. Possible configuration of the Primary Flow Circuit to achieve a double corner-expansion jet for a neutralizer. With: 1—gas supply plenum, 2—sonic throat, 3—upper wall of primary flow circuit, 4—a primary flow streamline, 5—oblique shock in primary flow, 6—exhaust from diffuser, 7—scraper lip, 8—secondary flow jet directed transverse to beamline.

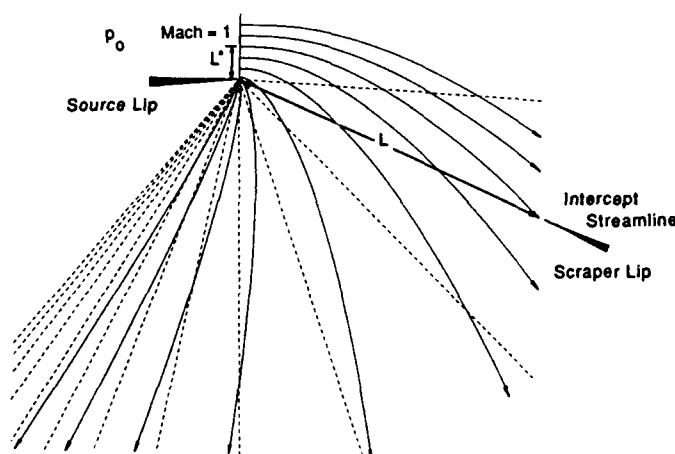


Figure 1. Corner-expansion of an initially uniform Mach 1 flow. Mach lines are dashed and shown for multiples of 10 in pressure. Streamlines are plotted with solid lines. Positioning of Scraper Lip for double expansion is shown with parameters: L —lip spacing, L^* —the source layer thickness, and P_0 the supply stagnation pressure.

slightly bent wind tunnel, depicted in Figure 2, with the gas supplied by a plenum to the Mach 1 throat, which is followed by the supersonic nozzle (formed by the upper bound streamline and the lip streamline), and exiting by the diffuser (formed by the continuation of the upper-bound streamline and the scraper lip plate). The use of an appropriate dimension for the primary flow throat eliminates the throat Reynolds number problem. If we think of the primary flow path as that of a wind tunnel then the secondary flow can be thought of as a leak through a slit in the tunnel wall. The secondary flow is utilized as the jet neutralizer.

Focusing on the secondary flow jet, consider the factors influencing the positioning of the scraper lip relative to the source lip. Clearly, high values of the intercept Mach numbers are advantageous in achieving compact jets. Recall from Figure 1 that the radial dashed lines represent constant values of Mach number and that Mach numbers increase in the clockwise direction. The intercept Mach number position also results in the skewness of the secondary flow jet to the primary flow. Increasing the radial position of the scraper lip relative to the source lip increases the mass flow in the jet and consequently the target thickness parameter.

Intercept Mach numbers below 3 result in extreme spreading of the jet. Mach numbers above 12 represent increasingly improved wedge angles but are considered to be unattainable because of condensation at the

extremely low temperatures achieved in the flow. The contoured field shown in Figure 2 represents 97% of the mass flow in the jet and is for a Mach 6 intercept. The contours of the jet are unit increments of the Mach number and may be converted into pressure or density contours by the usual gasdynamic relations.

III. OPERATING PARAMETERS

The target thickness parameter determines the scale and operating pressure. Using the optimum target thickness data with results for the double corner-expansion computations, operating parameters have been computed for comparisons of helium and argon. These data, which are a function of intercept Mach number, are presented in Figures 3a and 3b, and supplement data presented earlier in this paper.

With the elimination of Reynolds number as a primary design parameter the decisive parameter would appear to be the mass flow rate of the jet. Contrasting the 1 meter beam requirements of 180 gm/s for helium with the 26 gm/s for argon, argon would seem the better choice. However, this conclusion is based only on the mass rate of the secondary flow. A mass rate of 20 times the argon number might be circulating in the primary flow to eliminate the throat Reynolds number problem. For helium only 2.5 times the secondary flow rate is required to achieve the same throat Reynolds number. This translates into primary flow rates for argon which are over 10% greater than that of helium. Furthermore, this would translate into an argon primary flow tunnel which is 8 times the scale of that for helium.

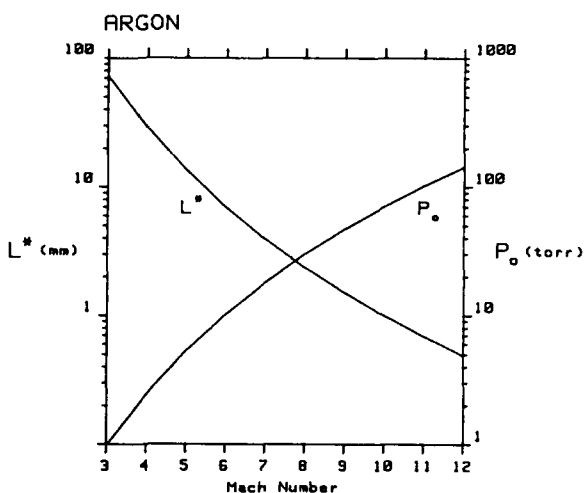
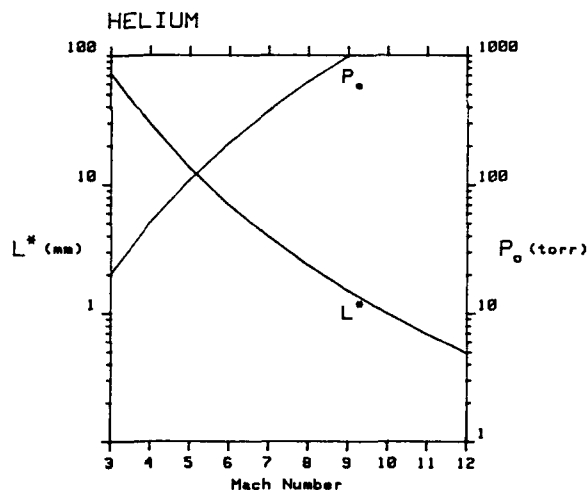
Several questions have not been treated in this study. One concerns the asymmetry of the flow--will this create problems in designing a supersonic diffuser to recover the jet flow? Will it be allowed to escape or recovered by condensation? A metal vapor jet is considered in Reference [2].

We can conclude that the double corner-expansion concept is a viable collisional neutralizer concept for large beams. It involves the complexity of a primary flow circuit to eliminate viscous effects; however, this is more reliable and effective than a more complex system of boundary layer control on conventional nozzles at high Mach numbers.

IV. REFERENCES

- [1] R. Fuehrer, *Tabulation of Electron Stripping Parameters for Various Gas and Solid Neutralizer Targets Interacting with 50 MeV H-Ion Beams*, Memorandum LANL Q-13:86:443, (1986).
- [2] J.J. Guy Durocher, C.S. Bohun, and G.R. Smith, "Production of 20 to 50 MeV Neutral Hydrogen Beams", *IEEE Particle Accelerator Conference*, CH2387, 1869 (1987).

Figures 3a and 3b. Data for a lip spacing, L , of one meter. The quantity P_0 is the stagnation pressure in the gas supply plenum. The quantity L^* is the thickness of the layer of gas at sonic flow which forms the jet. As the actual parameters are $P_0 L$ and L^*/L , these data can be scaled to systems of any size.



Modulator Upgrade of the KEK 2.5-GeV Linac

Tetsuo Shidara, Hiroyuki Honma, Shozo Anami, and Isamu Sato
KEK, National Laboratory for High Energy Physics
Oho, Tsukuba, Ibaraki, 305 Japan

Abstract

There is a plan to upgrade the energy of the KEK 2.5-GeV linac to 8.5 GeV relevant to the B-factory project. The increase from the present 2.5 GeV requires reinforcing the existing microwave source. In order to realize this reinforcement with a limited budget, the upgraded modulator was designed so as to utilize those components of the old modulator as much as possible, expect for a necessary change in the main line components. This article describes the upgraded modulator specifications and its performance tests.

I. INTRODUCTION

Reinforcement of the KEK 2.5-GeV linac from the present 2.5 to 8.5 GeV is presently under consideration as a future project relevant to the KEK B-factory [1]. This energy upgrade necessitates replacing the existing 30-MW klystrons with new units [2], together with a certain microwave power multiplying scheme, such as a traveling-wave resonant ring or a SLED (SLAC energy doubler) [3]. Although the details concerning this energy upgrade have not yet been decided, we have started to modify one of the existing modulators at the klystron gallery (No. 4-6) in order to confirm the feasibility and long-term stability of this modification.

II. MODULATOR SPECIFICATIONS

There are two limitations concerning our modulator upgrade: the maximum available space at the klystron gallery and the budget for the modulator modification. Taking these limitations into account, the average power of the upgraded modulator was designed so as to be twice that of the existing modulator. This amount of reinforcement is the limit for us to utilize those components of the existing modulator as much as possible. The specifications of the original [4] and two types of modified modulators (SLED and a traveling-wave resonant ring, respectively) are shown in Table 1. A simplified diagram of the upgraded modulator is also shown in Figure 1. The rectifier transformer and charging transformer assemblies are water cooled in order to maintain the present volume. The inductance of the charging transformer was reduced to half that of the original modulator in order to realize the same charging time (10 msec). A new pulse-forming network (PFN) which reuses the existing capacitors is being fabricated with two identical networks in parallel. This scheme lessens the effect of any residual inductance of the PFN capacitors, since the characteristic impedance of each network is twice that of the modulator.

Table 1
Comparison of the original and modified modulator specifications

	Original	Modified (SLED)	Modified (recirculation)
Maximum peak power (MW)	84	117	153
Maximum average power (kW)	14.7	30	30
Transformer step-up ratio	1:12	1:13.5	1:15
Output pulse voltage (kV)	23.5	23.5	23.5
Output pulse current (A)	3600	5000	6530
PFN impedance (Ω)	6.0	4.7	3.6
PFN total capacitance (μ F)	0.3	0.6	0.6
Pulse width (μ s)	3.5	5.6	4.3
Rise time (μ s)	0.7	0.8	0.8
Fall time (μ s)	1.2	1.3	1.5
Pulse repetition rate (pps)	50	50	50
Maximum pulse height deviation from flatness (%)	0.3 (peak to peak)	0.3	0.3
Maximum pulse amplitude drift (%/hour)	0.3	0.3	0.3
Thyratron anode voltage (kV)	47	47	47

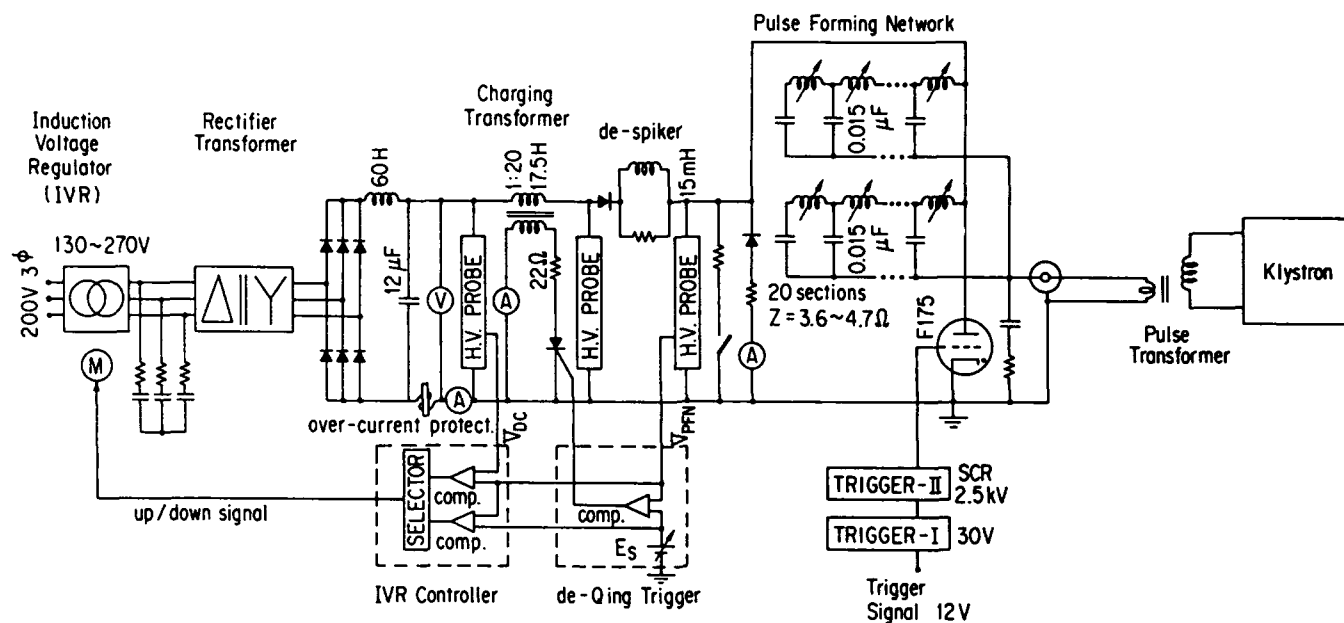


Figure 1. Simplified diagram of the upgraded klystron modulator.

III. PERFORMANCE TESTS

The No. 4-6 klystron modulator was reinforced in order to confirm the above-mentioned modification (see Figure 2).

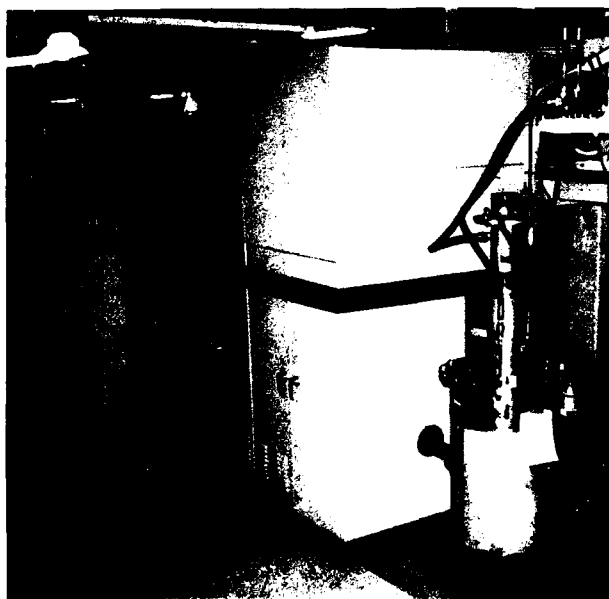


Figure 2. Modified klystron modulator in the klystron gallery.

Figure 3 shows the output pulse voltage (peak ~260 kV) and power output (peak ~32MW) waveforms. As an expanded trace of the pulse top shows in Figure 4, the pulse top was flat within 0.3% after adjusting the PFN inductances. The short-term pulse voltage stability was satisfactory and was less than 0.1%.

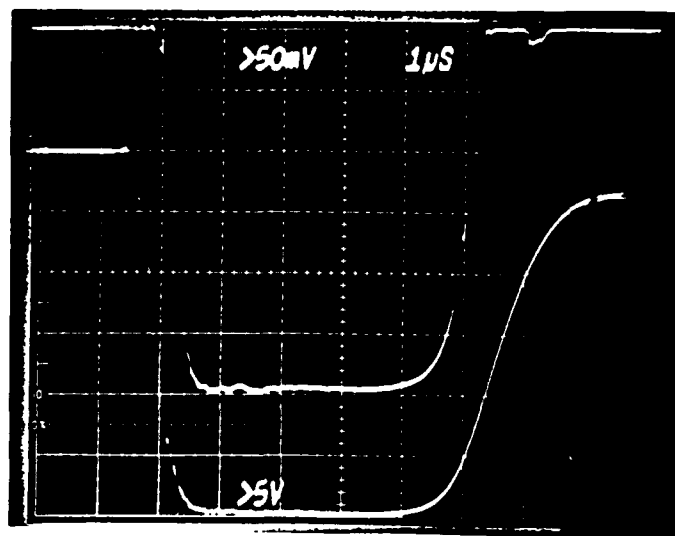


Figure 3. Power output (upper: peak ~32 MW, hor. 1μs/div.) and output pulse voltage waveforms (lower: peak ~260 kV).

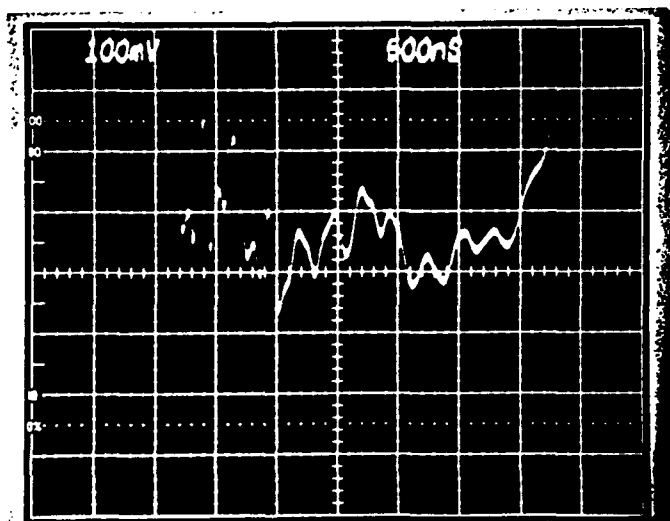


Figure 4. Expanded pulse top trace of the output pulse voltage (peak ~ 260 kV) at the klystron (vert. 0.2%/div., hor. 500 ns/div.).

IV. PRESENT STATUS AND FUTURE WORK

After completing the modification in October, 1992, the No. 4-6 klystron modulator has been successfully operated for about 3000 hours for the use of practical tests utilizing a SLED-type cavity [5]. We are therefore planning to modify another eight klystron modulators in the gallery during FY1993 as the first step to reinforce the KEK injector linac relevant to the KEK B-factory project.

V. REFERENCES

- [1] B Physics Task Force, "Progress report on physics and detector at KEK asymmetric B factory," KEK report 92-3 (1992).
A. Enomoto, et al., "Linac upgrade plan for the KEK B-factory," these proceedings.
- [2] S. Anami, et al., "The rf system of the Photon Factory injector linac," *Proc. 1981 Linear Accelerator Conference*, pp. 177-179.
S. Fukuda, et al., "Upgrade of an RF source of the KEK linac for B factory project," these proceedings.
- [3] Z. D. Farkas, et al., "Recent progress on SLED, the SLAC energy doubler," *IEEE Trans. Nucl. Sci.* NS22, No. 3 1299 (1975).
- [4] T. Shidara, et al., "Klystron modulator for the KEK 2.5 GeV linac," *Nucl. Instr. Meth.* A279, 423 (1989).
- [5] H. Matsumoto, et al., "High power test of a SLED system with dual side wall coupling irises for linear colliders," to be published in *Nucl. Instr. Meth.*: KEK preprint 92-179 Jan. (1993).

NSLS X-RAY SYSTEM RF SYSTEM UPGRADE *

M.G. Thomas, R. Biscardi, W. Broome, S. Buda, R.D'Alsace, S. Hanna, J. Keane, P. Mortazavi, G. Ramirez, J.M. Wang
National Synchrotron Light Source, Brookhaven National Laboratory, Upton NY 11973

Abstract

Presently (Dec. 1992) three RF systems power the electron beam at the NSLS X-Ray storage ring to 250 mA at 2.58 GeV. A fourth RF cavity and system is being installed to increase the machine reliability over pre-shutdown operational conditions (3 cavities). It also permits new levels of beam intensity and energy to be achieved in the X-Ray ring. Intensities of 500 mA at 2.5 GeV as well as 250 mA at 2.8 GeV are anticipated. A description of the hardware, the installation and the modes of operation will be outlined in this paper. X-Ray ring operations are scheduled to resume January 1993. Injection performance and high energy reliability will also be discussed.

INTRODUCTION

The National Synchrotron Light Source (NSLS) is a national user facility in which proprietary research may be done by groups within and outside of Brookhaven National Laboratory. Two electron storage rings are currently operating: a 750 MeV VUV ring with 16 ports for VUV and IR research, and an X-Ray ring with 28 ports for X-Ray research.

The NSLS X-Ray ring is dedicated to the production of high brightness, synchrotron radiation that normally operates at 2.58 GeV at 250 mA. Power to return the energy lost to synchrotron radiation is supplied by 125 kW transmitters driving 52.88 MHz resonators.

Present operation with three RF systems is at 2.584 GeV and 250 mA with an average lifetime that exceeds 20 hours. The radiation loss per turn is 574 keV, thus the beam power is $0.25 \text{ amp} \times 574 \text{ kV} = 143.5 \text{ kW}$ or 48 kW per cavity. The beam power to cavity copper loss ratio, $P_b/P_c = 48 \text{ kW}/31 \text{ kW} = 1.55$, and the total power per system is 79 kW; as shown in Table 1a. With the addition of a fourth RF system, reliability can be improved in either of two modes of operation. If the excitation power of each cavity is left at 31 kW, the beam loading is reduced to 36 kW each. Note, that a fault in one system still allows enough remaining power to retain circulating stored beam. However, if the power/cavity is reduced to 17.5 kW (same O.V.F. as 3 systems), the total power requirement is only 53.5 kW as shown in 1b.

Each RF system is capable of producing 100 kW of power reliably, so there is ample power for higher beam currents or higher energy operation, as mentioned above. Operation at 500 mA is summarized in Table 1c. The beam power to cavity power ratio is rather high for the second mode, but presently the VUV cavities are run at P_b/P_c ratios greater than 7:1. This mode requires additional study.

Higher energy parameters are shown in Table 1d.

* Work performed under the auspices of the U.S. Department of Energy under contract DE-AC02-76CH00016.

2.584 GeV with 3 CAVITIES								
V _{rad}	V _{gap} / CAV	x O.V.F.	V _{gap} / CAV	P / CAV	I _b	P _b	P _{tot}	P _b / P _{cav}
574 kV	191.3 kV	1.3	250 kV	31 kW	0.25 A	48 kW	79 kW	1.55

1a.

2.584 GeV with 4 CAVITIES								
V _{rad}	V _{gap} / CAV	x O.V.F.	V _{gap} / CAV	P / CAV	I _b	P _b	P _{tot}	P _b / P _{cav}
574 kV	144 kV	1.7	250 kV	31 kW	0.25 A	36 kW	67 kW	1.2
574 kV	144 kV	1.3	187 kV	17.5 kW	0.25 A	36 kW	53.5 kW	2.1

1b.

2.5 GeV with 4 CAVITIES								
V _{rad}	V _{gap} / CAV	x O.V.F.	V _{gap} / CAV	P / CAV	I _b	P _b	P _{tot}	P _b / P _{cav}
503 kV	126 kV	2.0	250 kV	31 kW	0.5 A	63 kW	94 kW	2.0
*503 kV	126 kV	1.5	187 kV	17.5 kW	0.5 A	63 kW	80.5 kW	* 3.6

1c.

2.8 GeV with 4 CAVITIES								
V _{rad}	V _{gap} / CAV	x O.V.F.	V _{gap} / CAV	P / CAV	I _b	P _b	P _{tot}	P _b / P _{cav}
791 kV	198 kV	1.3	257 kV	33 kW	0.25 A	50 kW	83 kW	1.5

1d.

Table 1

CAVITY HARDWARE AND INSTALLATION

A Varian Y-567B (4CW100,000E) tube was chosen as the final amplifier to power the new installation. This tube has functioned reliably to above 90 kW in a Varian-built transmitter since 1986 (>50000 hours) in daily operations, without replacement. A new printed circuit RF processor was installed which includes all the low level processing, such as the phase and amplitude loops, signal detection and monitors, and tuning control. A frequency control loop drives the tuner to compensate for reactive beam loading. Linking to the computer is done via a newly designed VME crate, for level-setting, monitoring, and communications with control-room operators.

The resonator is a capacitively loaded, copper-clad steel cavity, with loop coupling and a shorted loop, motor-driven tuner. 80% of the total power is dissipated in the water cooled electrode which is made of OFHC copper. Due to the relatively large surface area, each cavity has a 440 lit./sec. ion pump, a 45 lit./sec. Star cell ion pump and a titanium sublimation pump. Water cooled apertures were placed upstream of each RF cavity in order to intercept unwanted synchrotron radiation before impinging onto the accelerating gap surfaces. Cavity 4 installation in the beam line, paired with cavity 3, is shown in Fig. 1.

Inner surfaces of the cavity have been coated with a 300-400 angstrom layer of titanium/titanium nitride. It was concluded during initial testing that the coating was sufficient to prevent multipactoring, but after installation, a persistent,

low level, 2 kW multipactoring level still exists. Future testing of the loop window and cavity should determine the exact source of this problem.

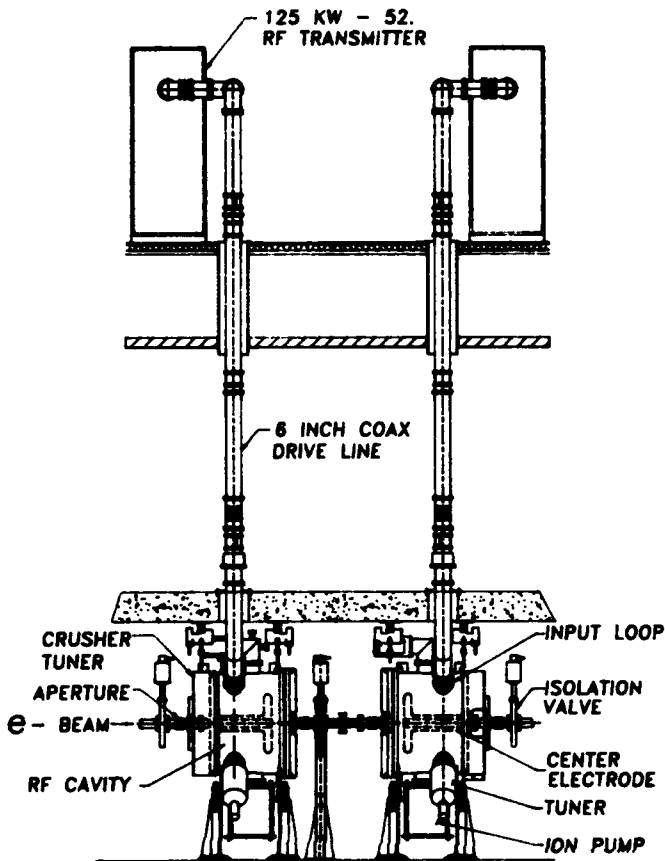


Fig. 1. System 3 and 4 RF Cavities

HIGHER ORDER MODE SUPPRESSION

Higher order modes (HOMS) are damped using five electric field probes inserted into the cavity. The probe locations provide coupling to the HOMS while minimizing their effect on the accelerating mode. Each probe is terminated with a water cooled, 50 Ohm load. The approximate shunt impedances of the HOMS were measured using on-axis E and H field¹ probes to obtain the undamped (Q_0) and damped (Q_D) quality factor of the mode. The approximate damped shunt impedance of the mode can be found by scaling the value of the shunt impedance as calculated by URMEL. This assumes that the value of R/Q does not change with damping.

Another impedance measurement technique^{2,3} was implemented using a central wire to simulate the electron beam. This method was used to characterize the cavity modes up to 1 GHz and confirmed the effectiveness of the damping antennae. Scattering parameters were measured using a network analyzer (HP 8510B) with a PC as a controller. System analysis based on S and T parameters was used to solve for the cavity impedance, $Z(\omega)$, as a function of the measured transmission response, $S_{12}(\omega)$. Search techniques were used to find the shunt resistance, R_{sh} , and Q from the calculated $Z(\omega)$ different modes. Results for R/Q showed good agreement with URMEL simulations. The values of Q

for undamped and damped modes for the 52 MHz cavity were compared with the above probe technique and were in good agreement. Results of both methods for the monopole modes are summarized in Table 2. Similar results were achieved for the dipole modes using the probe technique.

Impedance Measurement			Probe Q-Measurement		
f (MHz)	Q	Qd	f (MHz)	Q	Qd
53.235	10,471	7,598	52.948	16,100	13,800
275.101	36,122	145.0	273.673	33,050	160
338.092	26,663	--	338.002	26,500	30
387.249	32,385	45.5	396.859	26,800	30
511.212	23,342	--	506.514	26,450	200
534.308	17,366	722.6	--	--	--
546.576	35,337	1,474	--	--	--
567.980	33,142	567.9	578.808	34,150	400
586.102	29,447	333.7	--	--	--
663.574	37,092	1,697	663.403	37,500	1900
713.817	44,822	--	713.534	44,000	180
756.819	35,746	3,355	756.709	37,100	3,600
792.287	14,806	1,737	788.966	10,750	1,900
878.156	22,260	817.7	861.651	22,680	420
954.737	30,329	2,729	954.783	48,900	200
975.377	6,471	1,493	972.216	6,080	340

Table 2.

CONCLUSIONS

X-Ray operations have resumed with 4 systems since early January with good results. Injection at 745 MeV and 502 mA has been achieved during limited study periods. A beam current of 410 mA has been accelerated to 2.528 GeV with 12 hour lifetime. The lifetime will improve as the ring vacuum conditions at the new higher current. Presently, beam-line shutters and insertion devices (undulators and wigglers) are disabled during these studies because of possible heating due to increased photon power. Calculations are being made to determine operational limits. X-Ray energy has also been ramped to 2.8 GeV with a 20 mA test current for a radiation survey. Plans for the future are to optimize injection and to determine the RF parameters necessary to reach 500 mA at 2.5 GeV and 250 mA at 2.8 GeV.

REFERENCES

- [1] NSLS Tech Note #482 - Higher Order Mode Damping in X-Ray Ring Accelerating Cavity, W. Broome, R. Biscardi - 1993.
- [2] S.M. Hanna and P. Stefan, "Application of Impedance Measurement Techniques to Accelerating Cavity Mode Characterization", submitted to Nucl. Instr. and Meth. in Physics Research, 1993.
- [3] S.M. Hanna and P. Stefan, "Characterization of NSLS Accelerating Cavities Using Impedance Measurement Techniques," to be published in the Proc. of the 1993 IEEE Particle Accelerator Conf., 1993.

A Wide Tuning Range Rf Cavity with External Ferrite Biasing*

X. Pei

Brookhaven National Laboratory, Upton, NY 11973, USA

S. Anderson, D. Jenner, D. McCammon, T. Sloan

Indiana University Cyclotron Facility, Bloomington, IN 47405, USA

Abstract

A wide tuning range rf cavity with external quadrupole ferrite biasing was successfully built and has been in operation in the Indiana University Cooler Synchrotron Ring. The new biasing scheme was proposed by S. Papureanu and allows a large number of turns on the biasing coils. Large ampere-turns achieving strong biasing B field can therefore be achieved by a power source of much smaller current rating. The external biasing also makes the rf cavity design straightforward, eliminating biasing structure related parasitic effects, such as hard to predict high order modes.

I. INTRODUCTION

The electron-cooled Indiana University Cooler Synchrotron has a circumference of 86.8 m and a maximum rigidity of 3.6 T-m. It was designed with long straight sections free of beam optical elements to suit the internal target nuclear physics experiments. When its longitudinal emittance is reduced by electron cooling, the beam forms a tight bunch in the center of an rf bucket. Operation of the rf system at the fundamental beam revolution frequency makes the beam of the entire ring congregate as a macro particle. This allows certain operations of the ring that are inevitably lossy, such as transverse kickers for multi-turn stacking injection, to avoid the beam azimuth position to minimize beam loss. An rf system capable of $h=1$ operation is therefore introduced in addition to the existing rf system. It was also hoped that the new rf system has a wider tunable frequency swing to accommodate acceleration of heavier-than-proton particles. The frequency swing of the existing rf system is limited to an approximate 2:1 ratio with a bulky power supply rated at 4000 Amperes.

II. CAVITY DESIGN

Based on the revolution frequency of 45 MeV protons in the 86.8 m ring, the lower frequency limit of the cavity was chosen at 0.5 MHz. Fast tuning of the cavity is accomplished by utilizing the non-linear permeability characteristics of ferrite materials. At a higher magnetic field, the permeability of ferrites decreases and eventually approaches zero due to field saturation. Thus a biasing DC field can be used to tune the cavity. Although the art of ferrite biasing has been tried for

decades, a scheme proposed by S. Papureanu and first adopted at Max Planck Institute appeared to suit our application especially well. Because of the origin, the cavity was named the MPI cavity. Fig.1 shows the principle of this biasing scheme.

The rf cavity is loaded with ferrite rings for tuning and for shortening the length required for a quarter wave coaxial resonant structure at 0.5 MHz. The outer conductor of the coaxial cavity is made of copper which is non-ferromagnetic. The entire cavity then is placed within a quadrupole magnet cut to fit the cavity. 40 turns of windings are put on each tip of the quadrupole. The biasing magnetic field path is shown in Fig.1. The center of the ferrite ring where the beam pipe is located is well protected from the biasing field due to a), the cancellation of field due to quadrupole field symmetry and b), the shielding and shunting of high permeability ferrite rings. Because the biasing structure is totally outside the rf cavity, it is not seen by the rf field. The rf design of the cavity is therefore clean and does not suffer from the parasitic effects brought in by the biasing structure. In addition, the entirely external biasing structure has sufficient space to allow a large number of bias winding turns. This is crucial to the use of a much smaller power supply rated at 20 Amperes as the biasing magnetic field strength depends on the total ampere turns of the bias windings.

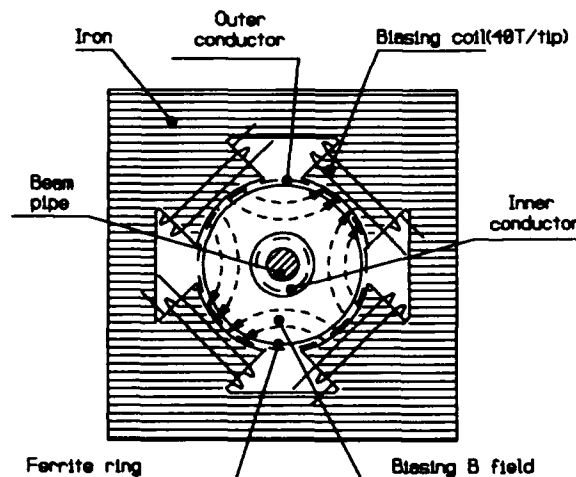


Fig.1 Principle of external quadrupole magnet ferrite biasing.

An additional variable capacitor (4100 pf maximum capacitance) is added across the gap to reach a resonant frequency of 0.5 MHz and to make the cavity capable of covering an even wider tuning range. The heavy capacitive

* Work supported in part by NSF PHY9015957.

loading of the cavity also makes the cavity store predominantly magnetic energy (short transmission line approximation). Therefore it has the additional advantage of making the driving port of the cavity, which consists of a magnetic loop connected to the center conductor of the cavity, have a relatively constant impedance to match the 50 Ohm feeding transmission lines. Cooling of the cavity is via forced air. The ferrite rings have spaces between them. The center conductor of the cavity is perforated. And the outer conductor of the cavity is made of copper straps with spaces in between rather than solid copper. A fan forces air through all these air passages and keeps the ferrite and the cavity cool. Fig.2 is a cutaway illustration of the cavity design. The diameter of the cavity is about 0.55 meters and the length 0.6 meters. A total of 10 Philips accelerator ferrite rings, material: 8C12; dimensions: $\phi 498 \times \phi 270 \times 25$ mm, were used.

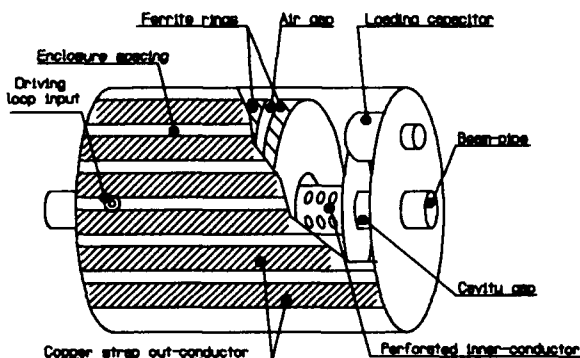


Fig.2. Cutaway illustration of the MPI cavity showing its internal structure.

The bottom outer conductor was partially removed to allow support of the cavity. The loading capacitor across the cavity gap is placed above the beam pipe. The driving loop is a simple side-insertion type. All these severely break the symmetry of the cavity so the small rf leakage inherent with coaxial structures no longer holds true. The cavity has to be shielded against rf radiation and aluminum lids were placed on both the front and back sides of the biasing quadrupole as shown in Fig.3. The quadrupole itself serves as rf shield in the center.

III. PERFORMANCE MEASUREMENTS

In the vicinity of resonance, the cavity can be modeled with a lossy shunt L - C - R circuit. The LC part determines the resonant frequency. Accurate to the first order in our case, the L value is variable by the ferrite biasing field and the C value is determined by the mechanical tuning of the variable capacitor. For our application, we are also very concerned with the field strength developed across the gap at a given driving power.

Because power dissipation only occurs on the resistor, we call the shunt resistor "gap resistance" and is defined as R_g as follows:

$$R_g = \frac{V_g^2}{2P}$$

where V_g is the total voltage developed across the gap of the cavity and P the total power absorbed by the cavity. It is obvious that for higher R_g 's, less power is needed to drive the cavity to desired voltage.

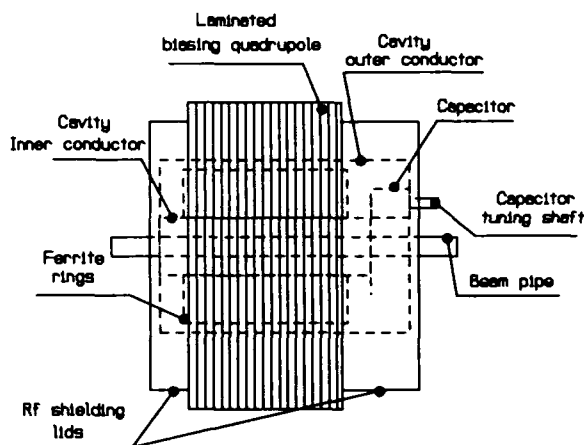


Fig.3 Sideview of the cavity with rf shielding lids.

Fig.4 through Fig.7 are measured frequency versus bias supply current plots and frequency versus gap resistance plots at four different loading capacitor settings. Note that the effective ampere-turn is 40 times of the bias supply current as the quadrupole magnet has 40 turns of windings on each of its tip.

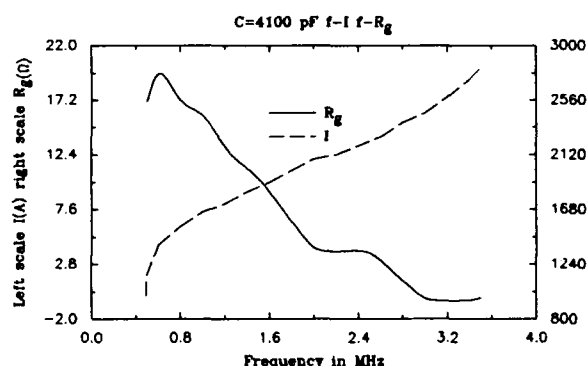


Fig.4 Frequency versus bias supply current and frequency versus gap resistance at $C=4100$ pf.

IV. ACKNOWLEDGEMENTS

This work was supported by the U.S. National Science Foundation under grant NSF PHY9015957 and was partially funded by Indiana University and the State of Indiana. The authors wish to thank R. E. Pollock for suggesting the MPI cavity design and calculating key specifications. This work was made possible by the concerted efforts of all the staff of the Indiana University Cyclotron Facility.

V. REFERENCES

- [1] Pei, X., "Cooled Rf Stacking Injection in the IUCF Cooler," Ph.D. Dissertation, Indiana University, 1991.
- [2] Pei, X. et. al., "Low Frequency Rf System for the Indiana University Cooler Ring", 13th International Conference on Cyclotrons, Vancouver, Canada, 1992.
- [3] Pollock, R. E., "Cooler Design Notes," IUCF, 1988.

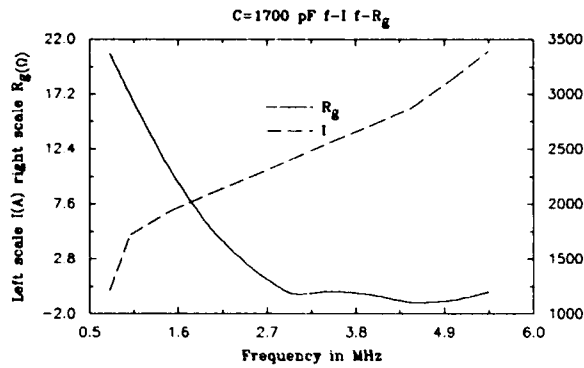


Fig.5 Frequency versus bias supply current and frequency versus gap resistance at $C=1700$ pf.

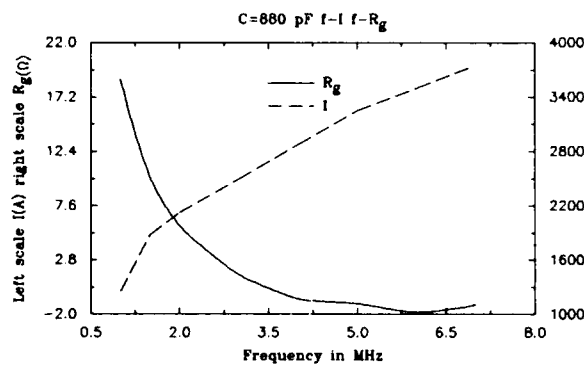


Fig.6 Frequency versus bias supply current and frequency versus gap resistance at $C=880$ pf.

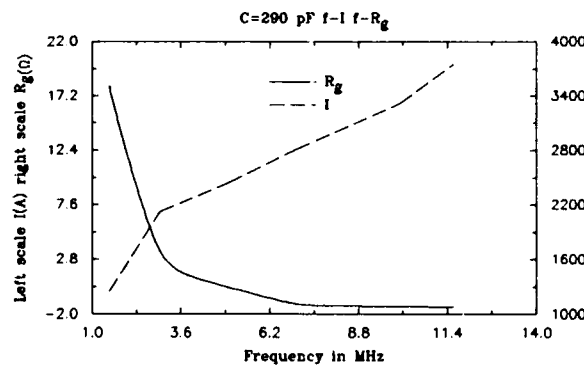


Fig.7 Frequency versus bias supply current and frequency versus gap resistance at $C=290$ pf.

Longitudinal Rf Matching during AGS-RHIC Beam Transfer*

X. Pei

Brookhaven National Laboratory, Upton, NY 11973, USA

Abstract

The Relativistic Heavy Ion Collider is a 2.5 mile long superconducting colliding synchrotron currently under construction in the Brookhaven National Laboratory. It is capable of accelerating heavy ions such as gold to energies as high as 100 GeV/u. The collision of such high energy heavy ion beams is expected to demonstrate important statistical quark and gluon plasma phenomena. The RHIC will be injected with the existing Alternate Gradient Synchrotron (AGS) and the rf systems of both the Collider and the AGS must be matched to accomplish bucket to bucket beam transfer.

I. INTRODUCTION

The designed RHIC circumference is 19/4 that of the AGS^[1]. At this ratio, if we have 12 bunches in the AGS synchrotron and 57 bunches in the RHIC collider, we have, assuming isochronous bunch distribution:

$$57/19 = 12/4$$

which means that both rings have the same bunch spacing.

After the initial commissioning, it is hoped that the RHIC have twice as many bunches. So its bunch number will be increased to 114^[1]. In this case the RHIC bunch spacing is half that of the AGS. In both the 57 and 114 RHIC bunch cases, the RHIC rf system will operate at the 342nd harmonic of the beam revolution frequency and the AGS rf system will operate at the 12th harmonic of the beam revolution frequency.

II. KICKER CONTROL

It is always possible to change the rf phase of the injecting ring to inject the m th bucket from the injecting ring into the n th bucket of the receiving ring. A phase shift equivalent to an effective delay is introduced after the phase locking of the first rf bunch of both rings:

$$\tau_d = ms_{inj} - ns_{rec} - lT_{inj} \quad (1)$$

$$m, n, l = 1, 2, 3, \dots$$

where s_{inj} and s_{rec} are the bunch spacings of the injecting and the receiving rings and T_{inj} is the period of the injecting ring. l is an integer to keep the delay within one revolution period of the injecting ring.

In reality, it is advantageous to minimize rf phase shift operations as the adiabatic phase change requirement slows

down the injection operation and complicates operation as well as hardware and software designs.

We therefore take advantage of the simpler bunch spacing relation in the AGS and the RHIC and divide the longitudinal matching into the kicker control part (called "cogging") and the rf phase match part (called "synchronization")^[2]. In this scheme, rf phase locking needs only to be done once every AGS acceleration cycle.

Fig.1 is a block diagram showing the principle of such a scheme and the description is as follows:

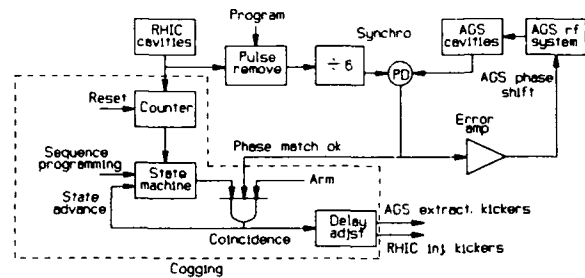


Fig.1 Block diagram of cogging (enclosed by the dotted box) and synchronization between the RHIC and the AGS during beam transfer.

The rf cavity signals are obtained by vector-summing all the cavities in each ring. Since the RHIC has to be filled by the AGS in many acceleration cycles, the RHIC rf buckets are numbered by a counter. There is no need to number the AGS buckets as the simple bunch spacing relation will automatically align each AGS bucket to the RHIC bucket as if two gears are cogged. The counter has the modulus of the RHIC harmonic number and a reset starts counting. The cogging circuit controls the AGS extraction and the RHIC injection kicker triggers according to the RHIC rf pulses. The rf phase is assumed to be matched by the synchronization circuit. In the case of equal bunch spacing in both rings, the RHIC buckets are injected sequentially. At present, the plan is for the kickers to transfer one bunch of beam at a time. Because not every RHIC rf bunch is to be filled with beam, a digital state machine circuit will delay, in the case of 57 bunches, 6 rf pulses after each kick, so that the kicker trigger sequence will be at the 1st, 7th, 13th... etc. of the RHIC rf pulses. In the case that the RHIC bunch number is 114, its bunch spacing is half that of the AGS. Only every other RHIC rf bucket will be cogged to the AGS bucket. To minimize phase shift operations, the odd numbered RHIC beam buckets will be filled first. The injection kickers in this scheme can only kick one bucket into the RHIC --- otherwise the already injected beam in the RHIC can be kicked out. The kicker trigger sequence controlled by

*This work was funded by the U.S. Department of Energy.

the state machine will therefore be the 1st, 7th,...13th, etc. of the RHIC rf pulses --- corresponding to the 1st, 3rd, and 113th RHIC beam bunches. The AGS rf phase is then changed to match the even numbered RHIC beam bunches and the kickers will be triggered at the sequence of the 2nd, 4th,... and 114th RHIC bunches.

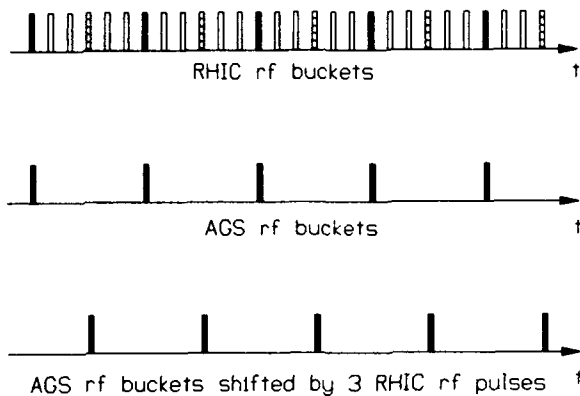


Fig.2 Rf bucket relation between the RHIC and the AGS. Each pulse is an rf bucket. In the RHIC, beam is injected into every 6th bucket (solid fill) during the 57 bunch operation and into both the solid filled and the stripe filled buckets in the 114 bunch operation. To inject the stripe-filled RHIC bucket, the AGS is phase shifted three RHIC rf pulses.

Note that triggering the kickers according to the RHIC rf pulses is only a necessary condition. A sufficient condition must also include the AGS rf phase being matched to the RHIC rf phase and the AGS beam being ready for extraction. Thus the signal from the state machine, the phase lock ok signal and the AGS beam ready signal (labeled as the "arm" input in Fig.1) should be coincided to trigger the kickers. Once a trigger to the kickers is sent, the state machine advances to the state corresponding to the next RHIC bunch. Finally, some delay adjustment is needed to take the beam TOF and signal transmission time into account.

III. RF PHASE MATCH

The RHIC rf frequency is 6 times that of the AGS frequency so a divide-by-6 circuit is used to bring the RHIC rf frequency down to be phase compared to the AGS rf frequency. The error signal is integrated and drives a phase shifter to change the AGS rf phase.

In the case of 114 RHIC bunches, the difference in bunch spacings in two rings makes it necessary to switch from even-numbered RHIC bunch injection to odd-numbered bunch injection. A pulse removing circuit removes three RHIC rf pulses to insure the phase lock as shown in Fig.2 to flip between the states.

A question of concern is how fast the phase locking process can take place. Accompanying rf phase shifting, there always is a frequency shift which causes a bucket energy error.

The following is the basic longitudinal equations describing particle motions:

$$\begin{aligned} \frac{dp}{dt} &= \frac{QeV}{C} \sin \phi \\ \frac{d\phi}{dt} &= 2\pi(hf - f_r) \\ \frac{df}{f} &= \left(\frac{1}{\gamma^2} - \frac{1}{\gamma_r^2} \right) \frac{dp}{p} = \eta \frac{dp}{p} \end{aligned} \quad (2)$$

where C is the ring circumference, f the beam revolution frequency, h the harmonic number of the ring, f_r the rf frequency, ϕ the vectored rf phase the beam sees and V the vectored rf peak voltages of the ring. Q and p are the charge and momentum of the beam at the velocity of γ and γ_r is the transition γ of the ring.

From the above we can map the traditional longitudinal phase space into a space where the energy axis is replaced by the fundamental revolution frequency f in a ring and the horizontal axis consists of the rf phase the beam sees. In this coordinate system, we have, for a stationary bucket^[3]:

$$h\Delta f_{max} = 2f_s \quad (3)$$

where Δf_{max} is the half height of an rf bucket in terms of beam revolution frequency and f_s the beam synchrotron oscillation frequency at the harmonic h .

The above result shows that, in terms of beam frequency, the half height of a stationary bucket is just twice the synchrotron oscillation frequency!

Thus a linear phase shift in T , which corresponds to a shift of rf frequency by $\delta f = (1/2\pi)\Delta\phi/T$, will move a synchronous particle in the bucket by:

$$\frac{\delta f}{2f_s} = \frac{1}{2\pi} \frac{T}{2f_s} \quad (4)$$

So for a phase shift of 2π , the percentage error caused by a linear phase shift is simply $(1/2)(T_s/T)$ of the total bucket, where $T_s = 1/f_s$. To control the energy error within 5 percent of the bucket height, for example, the linear phase shift needs to last 10 synchrotron oscillation periods.

Once the beam is shaken out of the center of the bucket, it starts undamped synchrotron oscillation. Should the oscillation be fairly linear, when the phase shift is stopped after an integer number of oscillations, the energy error will disappear and so will the oscillation. Particular care should be taken to avoid a phase shift that lasts half integer synchrotron periods, such as 0.5, 1.5, 2.5 times T_s , as this will double the oscillation amplitude and the oscillation will persist when the phase shift is over.

The longitudinal oscillation problem can be effectively treated with beam feedback. The feed back loop effectively

introduces a damping term for the oscillation and automatically shifts the rf phase adiabatically.

Fig.3 is a beam phase feedback loop that is nested in a larger radial feedback loop to be implemented for the RHIC. The reference signal actually comes from the beam radial sensor. For simplicity we won't go into details about its behavior in this paper.

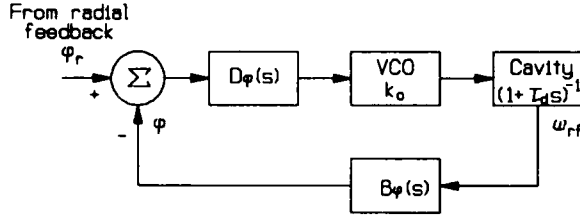


Fig.3 The beam feedback loop nested in the beam radial feedback system. In this loop, ϕ_r is obtained from the beam radial feedback and serves as a reference signal. ϕ is the beam phase. D_ϕ is the transfer function of an error amplifier that converts the phase error to the VCO control voltage. k_o is the gain of the VCO. The cavity's delay constant is τ_c . The beam's phase change in response to a frequency change of the cavity is B_ϕ .

We let the products of all the parts determined by electronics be K and the response of the system in s domain is just:

$$\phi = \frac{KB_\phi}{1 + KB_\phi} \phi_r \quad (5)$$

Since B_ϕ is simply the particles' undamped small phase motion in response to a sudden frequency or energy change of the bucket:

$$\ddot{\phi} + \omega_s^2 \phi = \omega_{rf} \quad (6)$$

Its Laplace transform is just:

$$B_\phi(s) = \frac{s}{s^2 + \omega_s^2} \omega_{rf}(s) \quad (7)$$

Substituting the above into Eq.5, we get:

$$\phi(s) = \frac{Ks}{s^2 + Ks + \omega_s^2} \phi_r(s) \quad (8)$$

The first power s term in the denominator shows that there could be damping. By adjusting the constant K we can change the beam response as desired.

An important concern is the deviation of the RHIC

ring from the designed 19/4 circumference ratio with respect to the AGS due to construction tolerances. Let's estimate the effect of such errors on the injection process. Denote 4/19 of the RHIC circumference to be C , which is the supposed AGS circumference, and f the beam revolution frequency in the AGS. We have:

$$C = \frac{\beta}{f}, \quad \frac{\partial C}{\partial f} = -\frac{\beta}{f^2} \quad (9)$$

which leads to:

$$\frac{\Delta C}{C} = -\frac{\Delta f}{f} \quad (10)$$

The circumference error thus results in a reduction of the AGS momentum acceptance:

$$\frac{\Delta p}{p} = \frac{1}{\eta} \frac{\Delta f}{f} = -\frac{1}{\eta} \frac{\Delta C}{C} \quad (11)$$

We hope that the deviation of the designed circumference ratio is small so that the AGS will have as large a momentum aperture as possible. If the deviation results in unacceptable momentum aperture loss, the bending field of the AGS can be varied. This, however, will change the particle revolution frequency in the AGS. The rf frequency ratio will be more complicated between the two rings. Modern frequency synthesis technologies, fortunately, are able to lock two frequencies with any rational ratios steadily. The additional concern will be only to choose the appropriate time periods to make the beam transfer as the phase difference between the two rings is a function of time.

IV. ACKNOWLEDGEMENTS

This work was funded by the U.S. Department of Energy. The author would like to thank Dr. M. Brennan, Dr. D. Deng and Dr. M. Harrison for their patient review of the evolving design and for their helpful suggestions and criticisms.

V. REFERENCES

- [1] RHIC Dept., Brookhaven National Laboratory, "RHIC Design Manual," 1992.
- [2] Brennan, M., "Rf Beam Control for the AGS Booster," Brookhaven National Laboratory, 1992.
- [3] Pei, X., "Cooled Rf Stacking Injection in the IUFC Cooler," Ph.D. Dissertation, Indiana University, 1991.

Commissioning and Performance of the ESRF

Project Team,
European Synchrotron Radiation Facility, Grenoble, France
Presented by J.L. Laclare

Abstract

The ESRF (European Synchrotron Radiation Facility) is a fundamental research institute based in Grenoble, France. Construction of the ESRF source [1], [2], [3] started in 1988 as a joint project of 12 European countries (Belgium, Denmark, Finland, France, Germany, Italy, Netherlands, Norway, Spain, Sweden, Switzerland, United Kingdom). The facility consists of a 200 MeV electron linear accelerator, a 6 GeV fast cycling booster synchrotron and a 6 GeV low emittance storage ring optimized to produce high brilliance X-rays from insertion devices. The project is now well advanced. The electron linac delivered its first beam in May 1991 and reached design performance in the 1 μ s pulse operation during the following one month commissioning period. Commissioning of the booster started in September 1991, with the operational energy of 6 GeV being reached in November 1991. Storage Ring commissioning began in February 1992, and progress was extremely fast and promising since, less than 4 months later, the target intensity of 100 mA in the multibunch mode was reached. In July 1992 the first undulator was operated without any effect on the beam and the machine diagnostics beamline was run at the full nominal current with a record brilliance in the 10^{17} range. The focusing of X-rays using a bent crystal has also been carried out to a record-breaking level for the spot size (22.7 μ m). Components of three user beamlines have already been tested with beam and several more beamlines will be built and commissioned in 1993. The first external users for routine operation are expected for the beginning of 1994.

I. INTRODUCTION

The ESRF was created as a private company under French law following the signature of an international convention on December 16th 1988 by 12 European countries (France, Germany, Italy, United Kingdom, Spain, Denmark, Finland, Norway, Sweden, Belgium, Netherlands, Switzerland).

The main objectives were set as follows : To design, construct, operate and develop a synchrotron radiation source and associated instruments for the use of the scientific community of the contracting parties. These objectives had to be met within a certain time schedule. The international convention covers a period of 11 years split into 2 phases :

- ◊ Phase 1 or construction phase covers the first 6 1/2 years, ending with the completion of the commissioning of the first set of at least 7 beamlines in June 1994. An important intermediate milestone was to be the reaching of the source design goal performances by July 1993.

- ◊ Phase 2 is to cover the remaining 4 1/2 years with the completion of the experimental facility, 30 beamlines in total, by December 98.

The means provided to meet these objectives were as follows :

- ◊ 2,2 GFF in Phase 1
- ◊ 1,6 GFF in Phase 2
- ◊ and a total staff of 450 people.

This paper reflects the status of the ESRF in May 1993.

II. REVIEW OF THE SPECIFICATIONS AND ASSOCIATED TECHNICAL OPTIONS

The institute is built around a synchrotron radiation source. It consists of :

- ◊ an 850 m long Storage Ring for 6 GeV electrons or positrons
- ◊ a 300 m long 6 GeV booster synchrotron functioning at 10 Hz
- ◊ a linac preinjector.

The source had to fulfill a series of detailed target specifications.

- I Priority was given to insertion devices.
- II High flexibility of the lattice at the ID location.
- III Brilliance from undulators in the range of 10^{18} to 10^{19} photons/sec/mm²/mrad²/0.1% bandwidth.
- IV In particular brilliance larger than $1 \cdot 10^{18}$ in the fundamental of an undulator at 14.4 keV.
- V Bending magnet sources at 10 and 20 keV
- VI Stability of the X-ray beam greater than one tenth of the rms dimensions.
- VII Beam lifetime longer than 8 hours.

These could only be satisfied by adopting a storage ring lattice with a high periodicity, 32 periods, with a 6 m long straight section in every period. We opted for an expended Chasman-Green lattice.

In Figure 1, the optical functions are shown. The straight sections which accommodate the Insertion Devices are equipped with triplets at both ends.

Figure 1
Optical Functions



The essential target specification is expressed in terms of brilliance of undulator beams in the fundamental of the photon energy spectrum. To obtain such performances, one has to combine in an optimal way:

- ◊ the energy of the stored beam,
- ◊ its intensity,
- ◊ the smallest achievable emittance,
- ◊ the gap, the field and the period of the Insertion Devices.

The resulting main accelerator parameters adopted for the ESRF are summarized in Figure 2

Figure 2

A. Preinjector 200 MeV e⁻ / 400 MeV e⁺

Repetition rate	10 Hz
Pulse Length	1000 - 2 ns
Electron Current	25 - 2500 mA
Positron Current	0.12 - 12 mA

B. Synchrotron injector

Repetition rate	10 Hz
Energy	6 GeV
Circumference	300 m
Emittance at 6 GeV	$1.2 \cdot 10^{-7} \pi \text{ m} \times \text{rad}$

C. Storage Ring

Energy	6 GeV
Current (Multi Bunch Mode)	$\geq 100 \text{ mA}$
Current (Single Bunch Mode)	$\geq 5 \text{ mA}$
Filling time (e ⁻ /e ⁺ Multi Bunch Mode)	0.2 / 6 min
Filling time (e ⁻ /e ⁺ Single Bunch Mode)	0.9 / 20 min
Circumference	844 m
Radio Frequency	352 MHz
Horizontal beam emittance	$6.2 \cdot 10^{-9} \pi \text{ m} \times \text{rad}$
Vertical beam emittance	$< 6.2 \cdot 10^{-10} \pi \text{ m} \times \text{rad}$
Natural rms Bunch Length	6 mm
Maximum number of Insertion Devices	29
Free length of straight sections	6 m
N° of Bending Magnet Ports	26 at 10 - 20 keV

We have adopted an energy of 6 GeV, a current of 100 mA, a lattice which can be tuned to obtain emittances in the few nanometer range : $6.2 \cdot 10^{-9} \pi \text{ m rad}$ horizontally, a small fraction of that, 10% for instance, in the vertical plane; a minimum Insertion device gap of 20 mm.

Our choice could appear a little conservative when compared to our competitors, the APS and Spring 8. Both of them have based their project on higher energy, higher current and smaller gap.

A few of the target specifications required the adoption of unconventional techniques. This is the case for beam position stability and reproducibility.

Table 1

Beam sizes at source points

	Bending Magnet Source	High Beta	Low Beta
$\beta_x \text{ (m)}$	2.2	26.6	0.8
$\beta_z \text{ (m)}$	26.8	11.3	3.5
$\sigma_x \text{ (mm)}$	0.16	0.41	0.069
$\sigma_z \text{ (mm)}$	0.129	0.084	0.047
$\sigma_{x'} \text{ (mrad)}$	0.137	0.015	0.089
$\sigma_{z'} \text{ (mrad)}$	0.005	0.007	0.013

Combined with beta values ranging between 0.8 and 27, the target emittances lead to rms beam sizes at source points significantly smaller than $100 \mu\text{m}$ vertically, a few hundreds μm horizontally. The unit for angles is the μrad .

The storage ring optics is hypersensitive to orbit distortion and therefore to magnetic errors and alignment. To work well, the closed orbit has to be perfect within the 0.1 mm range in rms.

Obviously we had to implement a series of unusual measures to combat this machine's hypersensitivity to imperfections and limit beam center of mass displacements to the specified 1/10 of the beam size, that is to say a few μm . Long term settlement is treated by means of the Hydrostatic Leveling System (HLS) detectors sensitive to variations of altitude in the μm range. The HLS [4] is a series of pots filled with liquid and interconnected by pipes. On the top of each pot a capacitive sensor detects the level of the liquid in the pot. These detectors constitute the input to a system of remotely controlled jacks equipping every girder of the quadrupoles and sextupoles. The horizontality of the machine can be restored within a couple of hours.

For periods of about one day, the machine and the experimental equipment are very sensitive to temperature variations. A temperature change of 1°C over 1 m of steel, which is the typical height of a support, gives an expansion of $10\ \mu\text{m}$. The $300\ 000\ \text{m}^3$ of the Experimental Hall are stabilized to within $\pm 1^\circ$, and the interior of the storage ring tunnel to better than $\pm 0.5^\circ$. We permanently record the temperature of the interior of the tunnel with one probe every 5 meters. There is no rigid connection of pipes or cables to the ground or to the magnet supports. Needless to say that ramping the SR magnetic field with the constraint, after the refill, of having to get back to the original position within a μm is excluded. Therefore we have a full energy injector which has to be turned off during photon beam service to avoid any vibration at 10 Hz.

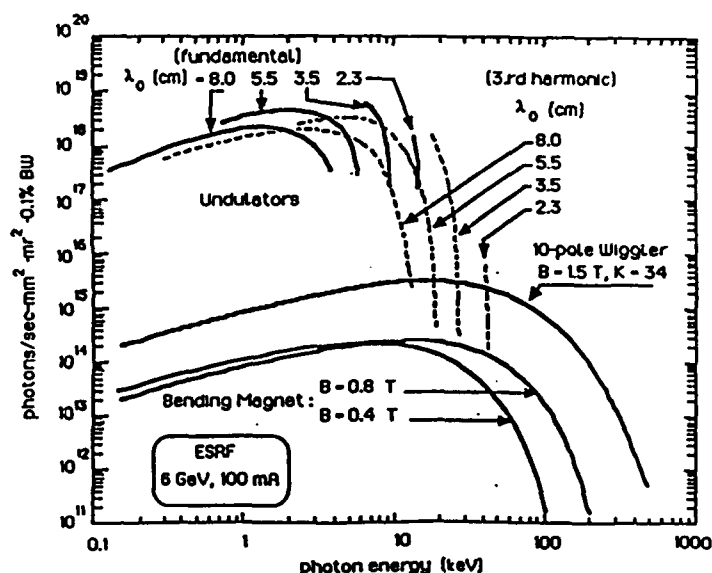
Over short periods of time, vibrations from magnets transmitted via their supports and the ground constitute the main source of instabilities. We are also permanently recording and fighting these vibrations. Every insertion device is surrounded by feedback systems which use X-ray beam position monitors to feed correctors which act locally on the stored particle beam position.

Our undulators are made of permanent magnets with longitudinal periods ranging between 8 and 2.3 cm. The full range between 0.1 and 15 keV can be covered on the fundamental with a minimum gap of 2 cm. The brilliance reaches the several 10^{18} (see Figure 3).

The power density from Insertion Devices is extremely high. It can reach about $1.5\ \text{kW per mm}^2$ for the most powerful undulators at 10m from the source point. In case of beam missteering, the storage ring can behave like a welding machine that would take 20 ms to drill a hole in the vacuum vessel. The power density from a standard wiggler is about one third of that of an undulator, although the total power in the 10 kW range is higher. However, the spectrum is white and therefore the brilliance is 3 to 4 orders of magnitude below that of undulators.

To make our unavoidable dipole sources attractive, at the request of our potential users we have designed the magnet in such a way so that the fringing field has a flat intermediate step at 0.4T, half of the full field value, 0.8T.

Figure 3
Brilliance from ESRF light source



With the third generation of synchrotron radiation machines like the ESRF, the brilliance has been increased by 11 orders of magnitude when compared to the X-ray tube sources available in the 60s.

III. STATUS OF PROGRESS OF THE SOURCE

Hereafter the status of progress of the source as per May 1993 is given. The construction phase started in January 1988 and the construction of the first technical buildings started in January 1990.

III.1 Pre-Injector

Fourteen months later, in February 91, the pre-injector building was placed at our disposal. The installation of the linac took a couple of months. This linac is based on a conventional (non-Sled) gradient of 17 MV/m. The buncher tank is followed by two 6 m long cavities, each of them producing a 100 MV acceleration. In June 91, the linac had achieved its target performances in the long pulse mode.

Table 2
June 1991

Commissioning of the Linac in the long pulse mode

Energy	200 MeV
Repetition Frequency	10 Hz
Current	25 mA
Pulse Length	1 μs
Momentum spread	$\pm 1\%$
Transverse emittances	$0.5 \cdot 10^{-6} \pi$

III.2 Booster Injector

The installation of the booster started in March 91. The 300m long machine was completely installed by the end of July, that is to say less than 5 months after. After 4 months of commissioning from September to December 1991, the booster reached its nominal performances.

Table 3
September-December 1991
Commissioning of the Booster

Energy	6 GeV
Repetition Frequency	10 Hz
Accelerated current peak performance	5 mA
Routine Operation	3 mA accelerated / 2.5 mA extracted

III.3 The X-ray Source

The month of January and a part of February 1992 were used to commission the large sub-systems of the infrastructure : ventilation of the experimental hall and storage ring tunnel, electricity substations, large deionized water cooling units etc..., necessary to provide utilities to the Storage Ring. The front end parts of the photon beam lines inside the tunnel had already been installed with the view to avoiding repeated slack periods linked with the re-opening and closing of the roof.

With regards to our target specifications, progress accomplished on the Storage Ring commissioning has been extremely fast [5]. Several working points have been explored but for injection efficiency reasons, there is a strong tendency to prefer tunes just below the coupling resonance and the half integer. In general the closed orbit is extremely well corrected. The corresponding rms closed orbit amplitude is 0.15 mm in both the horizontal and vertical planes.

Concerning the horizontal and vertical emittances, which are two key parameters entering into the definition of the brilliance, we use several methods based on the light emitted by the beam, either the X-ray light from an undulator or the visible light from a bending magnet.

We also use the more simple scraper method which consists in reducing step by step the physical aperture left to the beam, while we measure the lifetime of the beam. The fit of the measured curve leads to the value of the rms local beam size. In the horizontal plane we measured values between $8.2 \cdot 10^{-9}$ and $1.3 \cdot 10^{-8}$ to be compared with $6.2 \cdot 10^{-9}$ mrad for the perfect machine. In the vertical plane, error bars are larger and the result depends on coupling. Experimental results range between $5.0 \cdot 10^{-10}$ and $3.4 \cdot 10^{-9}$ to be compared with $6.2 \cdot 10^{-10}$. We have therefore obtained the small target emittances in the nanometer range.

The second essential parameter entering into the formula for brilliance is the stored current. In the multibunch mode, we had reached our 100 mA target already in June. Since then, we have slowly but steadily increased the current up to 135 mA. To

go any further, we need to replace our X-ray beam absorbers made of standard OFHC copper by the more heatload resistant glidcop absorbers. This work will be completed by the end of the year and will allow a current of up to 200 mA.

In the uniform multibunch mode of filling, strong coupled bunch instabilities can develop. Transversally, we have to face a resistive wall instability that can be damped by increasing the chromaticity. However, the more Insertion Device narrow gap chambers we install, the more we increase the impedance and the stronger the required chromaticity to damp the beam, with the consequence that the unwanted non linear effects eat up the remaining dynamic aperture more and more. The uniform multibunch mode can also excite longitudinal Higher Order Modes in the RF cavities. However, at the present current level these HOMs are not systematically excited. They can be detuned by careful control of the temperature in the cavities. Neither transverse nor longitudinal coupled bunch instabilities show when only one third of the circumference is filled with beam.

A long lifetime is essential for the quality of service offered to users. We have now accumulated some 150 A*hours. As of today, we reach a lifetime of 17 hours at 100 mA, which is already significantly above our 8 hours target. Our objective is to reach 24 hours by the end of the year.

In the single bunch mode, the goal had been set rather low at 5 mA. We now routinely achieve 10 mA by pushing the chromaticity to high positive values. We can also apply some feedback. In that case we can go beyond 15 mA with a temporary best performance at 20 mA. Single bunch purity is essential for time of flight experiments and Mossbauer ones, for example. By means of an RFKO technique using a shaker and a scraper, we are able to clean up all lowly populated bunches and reach purities in the 10^{-6} range.

For high current needs, we anticipated several advantages in running the machine with a few (8 or 16) equally spaced and filled bunches. The long space between bunches makes it much more difficult for cross-talk to occur between them. Therefore it leaves less potential for coupled bunch instabilities and in any case the required feedback system to damp instabilities would be of moderate bandwidth. Unfortunately, we systematically found an unexpectedly high dynamic pressure and correspondingly a short lifetime (3 to 5 hours at 100 mA). The mechanism is not fully understood. However, the gap to be bridged to make the few bunch mode as attractive as the multi-bunch mode in terms of lifetime is very challenging.

In June 1992 we tested the first 1.6 m long undulator segment with a 2 cm minimum gap in one of the straight sections. The undulator was shooting in the direction of the Machine diagnostic beam line which had been thoroughly equipped to perform full tests of the emitted X-ray beam. In particular, we installed a diamond monochromator which has been submitted to the full 100 mA current and which proved to have excellent characteristics over the full intensity range.

The high quality of the undulator magnetic field resulted in a meagre 3 μm vertical displacement of the beam in one of the nearby dipoles equipped with a visible light output when the gap was opened and closed. Since then 5 IDs are routinely operated in the Storage Ring. All of them can be manipulated at will with no significant displacement of the X-ray beam in other beamlines. To check the overall stability of the beam in actual experimental conditions, at low current, the photon beam was focused vertically down to a 20 μm FWHH spot. The stability of the spot measured with slits centered at the edge of the spot where the slope is maximum was found to be 1 μm rms. In other words, the natural stability of the photon beam is better than the target, ie 10 % of the beam size.

As already mentioned, all IDs will be equipped with dynamic correctors to feed back the position and angle of the X-ray beam by acting on the electron beam. The feedback loop was closed during the experiment and we saw an appreciable difference between feedback on and feedback off. The gain was a factor of 4 reduction of the beam center of mass amplitude. Therefore, at the ESRF, the brilliance of the beam will not be spoilt by the instability in position of the beam center of mass. We hope to minimize the displacement to a few percent of the beam size.

Up till now, four shutters have been opened to allow X-rays through for the commissioning of beam lines. Another ten shutters will be opened before the end of the year. A few prototype experiments have already started. The goal is to place the beamlines, once commissioned, at the service of the European user community in less than one year from now. First results are extremely encouraging.

During the design period, it was anticipated that at design current and emittances, only ions of mass higher than 50 could be trapped due to the over-focusing of the electron beam. This did not exclude problems at lower current during ramping or with very heavy particles such as dust particles according to experience from CERN, the Photon factory at KEK, or super Aco in Orsay. We therefore started the machine with electrons and kept the option for the positron part of the preinjector open up till now. Given the results obtained, we conclude that it is obviously unnecessary to implement the e+ option in order to achieve our target performances in current lifetime, emittances and stability.

The trapping of macro particles is not presently observed. Should this be the case one day (after accidental venting for instance), we would still have resources such as leaving a gap in the bunch train in reserve.

To leave nothing to chance, we have prepared a full e+ preinjector project ready to be started. We will continue our observations and if one day the advantage of positrons becomes apparent, we will reconsider this option.

IV. OPERATION

Since the beginning of the year, we are operating the machine 50% of the time (in periods of 2 weeks on followed by 2 weeks of shutdown) to serve the commissioning of beam lines. Excellence in operation with the target performances is our primary objective and results are very promising. From January to April, we were able to really serve 91.7% of the scheduled 1000 hours of operation time. During the periods of real service, the beam was made available to beam lines for 92% of the time, the rest being used for refilling and other beam preparation.

We will operate the source 3000 hours in 1993 for X-ray production, with a plan to go to 4500 hours in 1994 and 6000 hours in 1995.

V. CONCLUSION

For several years, we considered the objectives of a 3rd generation machine to be very challenging and were anxious as to the outcome of the commissioning of the first machine of its type. The rapid success of the ESRF will now enable speculation to be accelerated as to the next generation of diffraction limited machines. In this sense the ESRF has shown that at least one order of magnitude more can be gained in the foreseeable future.

VI. REFERENCES

- [1] J.L. Laclare, "Synchrotron light sources", *Proceedings of the 1988 European Particle Accelerator Conference*.
- [2] J.L. Laclare, "Synchrotron radiation light sources", *Proceedings of the 1990 European Particle Accelerator Conference*.
- [3] A. Ropert, "The Status of the ESRF", *Proceedings of the 1992 European Particle Accelerator conference*.
- [4] D. Roux, "The Hydrostatic Levelling System (HLS) / Servo-controlled precision jacks : a new generation altimetric alignment and control system", these proceedings.
- [5] A. Ropert, "Challenging issues during the ESRF storage ring commissioning", these proceedings.

Commissioning and Performance of the Advanced Light Source

Alan Jackson

Lawrence Berkeley Laboratory, University of California, Berkeley, California 94720

Abstract

The Advanced Light Source (ALS) at the Lawrence Berkeley Laboratory is the first of the lower energy (1- to 2-GeV) third-generation synchrotron radiation facilities to come into operation. Designed with very small electron beam emittances, to operate with long insertion devices to produce very high brightness beams of synchrotron radiation in the VUV and soft x-ray regions of the spectrum, these facilities are complementary to the higher energy (6- to 9-GeV) facilities [1] designed for harder x-radiation. From the earliest periods of their design it was recognized that the performance of the required low-emittance lattices would be dominated by nonlinear particle dynamics caused by the strong lattice sextupoles required for chromatic correction, the effects of undulators and wigglers, and the requirement for very narrow-gap vacuum vessels. Commissioning of the ALS storage ring began early in 1993. In this paper we will briefly review the main characteristics of the storage ring design, describe our commissioning experiences, and review the present performance and performance limitations of the facility.

I. INTRODUCTION

The Advanced Light Source at the Lawrence Berkeley Laboratory is the first of the lower energy (1- to 2-GeV) third-generation synchrotron radiation facilities to come into operation. Designed with very small electron beam emittances, to operate with long insertion devices to produce very high brightness beams of synchrotron radiation in the VUV and soft x-ray regions of the spectrum, these facilities are complementary to the higher energy (6- to 9-GeV) facilities designed for harder x-radiation. From the earliest periods of their design it was recognized that the performance of the required low-emittance lattices, which utilize relatively strong focusing quadrupoles, would be dominated by nonlinear particle dynamics caused by the powerful lattice sextupoles required for chromatic correction. The dynamics are also modified by the fields of the undulator and wiggler magnets (collectively known as insertion devices, or IDs), and their requirement for very narrow-gap vacuum vessels. However, neither the IDs, nor their narrow-gap chambers, were installed during the commissioning period reported here.

The ALS storage ring commissioning was divided into two phases: January 13 to March 15, 1993, when beam could be injected but not accelerated, and March 16 on, after the RF system was brought into operation. Commissioning activities were curtailed on April 30 in order to install two IDs and their beamlines, three bend-magnet beamlines, and a diagnostic beamline. Other shutdown activities include an in-situ bake and realignment of half of the storage ring girders.

In this paper we will briefly review the main characteristics of the storage ring design, outline the chronology of the commissioning period, review the

performance and performance limitations of the facility, and describe our commissioning experiences, concentrating on the second phase when RF was available.

II. LATTICE DESIGN

The ALS storage ring lattice is based on a triple-bend achromat configuration with twelve-fold symmetry. A compact structure is achieved by including vertical focusing gradients in the bend magnets, using a single quadrupole family (QFA) to control the dispersion function, a quadrupole doublet family (QF and QD) to match the betatron tunes, and two families of sextupoles (SF and SD) to correct the chromaticity, in the arrangement shown in Figure 1. Small natural emittance (3.5 nm at the nominal energy of 1.5 GeV) is ensured through the juxtaposition of low values of dispersion and horizontal beta-function (and their derivatives) in the bend magnets. The major lattice parameters are shown in Table 1.

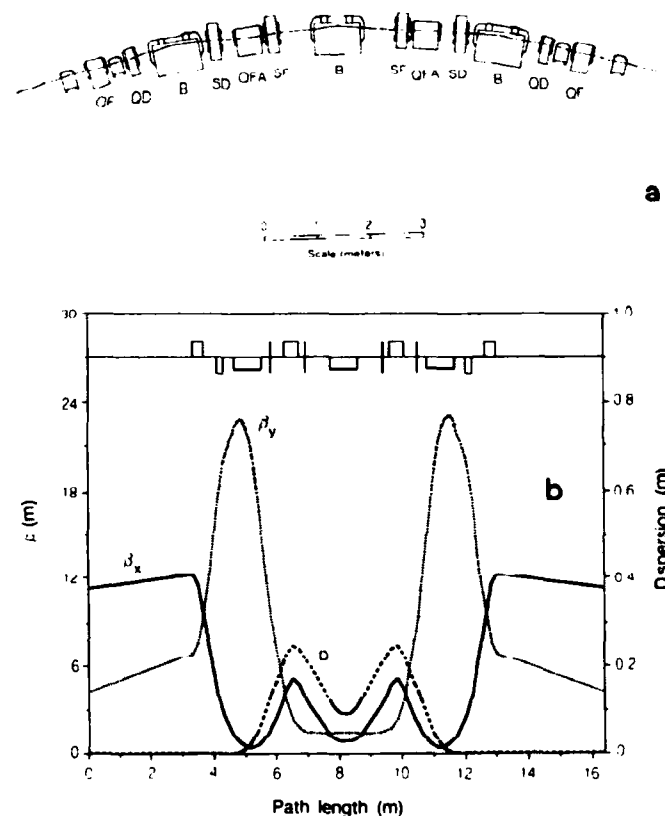


Figure 1.

- (a) One superperiod of the ALS triple-bend achromat lattice.
(b) Horizontal and vertical β functions and dispersion for one superperiod of the storage ring lattice.

Table 1
Main Parameters of the ALS Storage Ring

Energy (nominal)	1.5 GeV
(minimum)	1.0 GeV
(maximum)	1.9 GeV
Current (multibunch)	400 mA
(single bunch)	8 mA
Beam parameters at 1.5 GeV	
Natural emittance	3.5 nm
Bunch length	3.5 mm
Energy spread	6.5×10^{-4}
Radiation Loss/turn	91.5 keV

III. CHRONOLOGY OF STORAGE RING COMMISSIONING

Three significant dates paced the progress of commissioning the storage ring: January 13, when the personnel protection system was brought into operation, defining the time when we could first bring beam into the storage ring; March 16, when the storage ring RF system was fully activated; and April 30, when commissioning was suspended in order to install IDs and beamlines. Major events and achievements during these periods are shown in Table 2.

Table 2
Chronology of Storage Ring Commissioning

Date	Event
Phase I	
Jan. 13	Personnel Safety System commissioned
Jan. 15	Beam through 2/3 of circumference
Jan. 19	1-1/3 turns established
Feb. 2	Discovered vertical scraper obscuring beam aperture
Feb. 4	Found and fixed shorted coil on quadrupole magnet, immediately achieving 60 turns with NO steering
Feb. 8	DCCT commissioned, observed 1.5 mA injected beam
Main problems during this period: booster dipole power supply failure; continuing failure of SR quad power supplies due to low water flow (all flow restrictors eventually removed); fast kicker magnet failures; SR bend magnet power supply failures (two); BPM system fault, requiring replacement of 200 PLA's.	
Phase II	
Mar. 16	RF system commissioned, 6 mA accumulated in 4 bunches
Mar. 24	65 mA accumulated in 240 bunches (DOE Project Plan Technical Baseline)
Apr. 9	407 mA in multibunch mode (c.f. 400 mA project goal)
Apr. 15	27 mA in a single bunch (c.f. 8 mA project goal)
Apr. 30	Beam lifetime 92 minutes (from 100 mA to 37 mA)

IV. PERFORMANCE, LIMITATIONS, AND MISCELLANEOUS OBSERVATIONS

The primary performance indicators for the ALS are stored beam current (in single-bunch and multibunch modes), emittance, and beam lifetime. By the end of the commissioning period 460 mA had been accumulated in a filling pattern where 240 consecutive bunches, out of 328, were filled — there did not appear to be any fundamental limit at this current. In single-bunch mode, a current of 27 mA was achieved, apparently limited by a large coherent vertical oscillation. No optimization was attempted in this mode (by tuning the higher-order modes in the RF cavities, for example), since this current is already far in excess of the nominal single-bunch current of 8 mA.

As described below, we were not instrumented to directly observe the beam emittance. However, those lattice parameters that determine the natural emittance were measured, and found to be consistent with the model. For some time at the beginning of the run, we were unwittingly operating with QFA set about 5% low, leading to a natural emittance about a factor of two greater than nominal. This is the so-called "relaxed lattice" described in reference [2]. In the vertical plane the betatron coupling was measured to be much smaller than expected (a few tenths of 1%); however, we observed vertical dispersion of around 2 cm, which will lead to a vertical emittance between 1% and 10% of the natural horizontal emittance. This analysis is continuing.

Beam lifetime is consistent with elastic gas scattering lifetime of 30 hours at 1 ntorr, with an aperture of 18 mm. Note that the vacuum pressure was typically 10 ntorr at current levels of 30 mA, the ring was not baked, the powerful titanium sublimation pumps were not commissioned, and beam lifetime was improving at a rate of 2 to 3 minutes per day due to beam conditioning! No differences were observed between high currents in a few bunches and the same current in 240 bunches, indicating that the Touschek effect is not significant at lifetimes of 2 to 3 hours. No effects on lifetime due to ion trapping were observed: there were no significant differences in lifetime for different filling patterns, and there were no sudden losses of current after the beam was stored.

Accumulation rate is a secondary performance indicator. The injection efficiency was optimized at 65% (1.5 mA per shot in the storage ring from a circulating current of 6 mA in the booster). We expect to improve on the efficiency after the shutdown, with a better corrected horizontal orbit. Also, the injection rate will increase with improved booster current (to 15 mA), expected as a result of implementing the beam-loading-compensation scheme in the linac.

V. INSTRUMENTATION

The full complement of storage ring instrumentation was not available during this commissioning period. In particular, the synchrotron light monitor, transverse kickers, and remotely adjustable scrapers were not installed, somewhat limiting the scope of measurements that could be made. These capabilities will be added during the current shutdown.

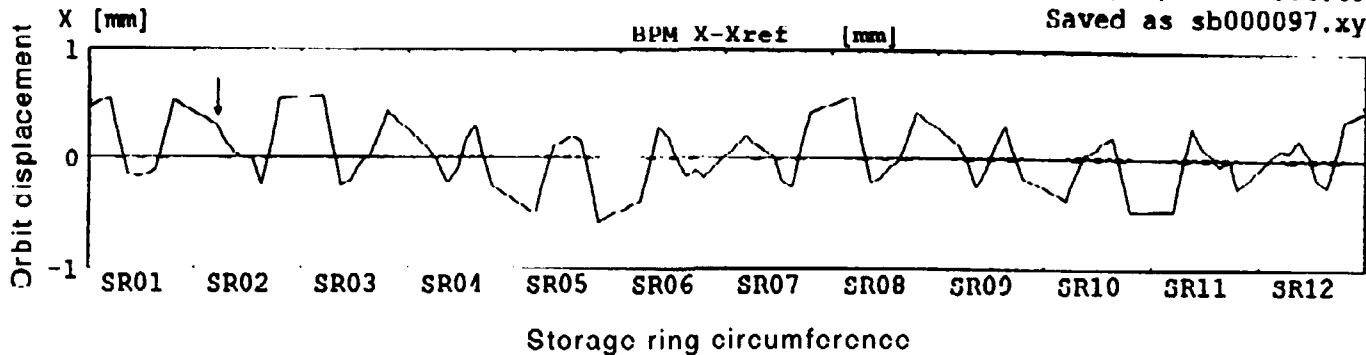


Figure 2. Change in horizontal closed orbit resulting from one corrector. Arrow marks the position of the corrector.

What were operational were the 96 beam position monitors (BPMs), each capable of providing turn-by-turn intensity and position signals, or more accurate time-averaged data, and three sets of higher fidelity button monitors (the LEP buttons), used with spectrum analyzers for fractional longitudinal and transverse tune measurements. The data from the BPMs could be analyzed on line with the ALS control system, or stored for further off-line analysis. Example are shown below.

VI. MEASUREMENT TECHNIQUES AND RESULTS

Between March 16 and April 30, we accumulated a large amount of data. Some of this data, particularly that used to compare the real machine to our model, was analyzed in real time. However, a significant amount of analysis remains to be done, especially of data on instabilities and nonlinear dynamics. In this section we outline the scope of the studies undertaken, and present a summary of the results of our analyses to date.

A. Closed-Orbit Distortions

Closed orbits were measured by taking BPM data in the more accurate averaging mode. Absolute measurements of the orbits were used in conjunction with a local-bump, closed-orbit-correction algorithm to successfully adjust the vertical orbit. An uncorrected orbit with peak-to-peak variations of 12 mm was reduced to one with an RMS displacement of less than 0.5 mm (see also reference [3]). This same technique was not as successful in the horizontal plane for reasons not yet understood. By taking difference orbits it was possible to construct the full sensitivity matrix for the storage ring, i.e., the effect of each corrector magnet on the beam position all around the machine. An example of one such difference orbit is shown in Figure 2. By analyzing the data from homologous magnets in each sector we could quickly establish the excellent periodicity of the lattice (<10% variation, corresponding to the accuracy of the measurement).

The same technique was also applied to empirically construct localized distortions across a straight section in order (eventually) to steer ID radiation down user beamlines.

"Leakage" from the local bump was measured at less than 10%, again limited by the accuracy of the measurement. By taking difference orbits as a function of RF frequency, it was possible to measure the dispersion function. Figure 3 shows a typical result. The first analysis of such data suggested that the QFA family of magnets were miscalibrated by a factor of 5%. The power supply calibration was checked and indeed found to be in error by 5.5%! Dispersion was also "driven" by frequency modulating the RF, which permitted real-time tuning to minimize dispersion in the straight sections.

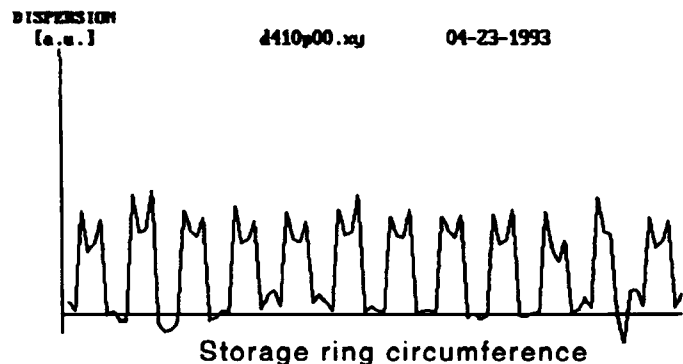


Figure 3. Dispersion function created by taking difference orbits at different RF frequencies.

B. Tune Measurements

Betatron tunes could only be measured because of the residual oscillations arising from the imbalance of the injection bump magnets (amounting to about 1 mm, in the horizontal plane only), or from the small oscillations set up by transverse instabilities. An attempt was made to drive oscillations through powering the LEP buttons with an amplified tracking generator signal. This was partially successful in the horizontal plane (where good data already exists!), but not successful in the vertical plane. Tunes were measured through either the spectrum analyzers, or more often by Fourier analysis of the turn-by-turn data from the 96 BPMs. Despite this inconvenience, a huge amount of data was taken. Variation of

tunes as a function of quadrupole and bend magnet settings has been used to calibrate the storage ring model, to measure transverse coupling, and to measure and correct the chromaticity. After chromatic correction the data is good enough to show the nonlinear chromaticity, which agrees well with our model predictions. A typical set of data, showing the variation of betatron tunes through a coupling resonance, is shown in Figure 4, the data indicate an emittance coupling ratio of less than 1%. Also, nonlinear tune shifts were measured by exciting different betatron oscillation amplitudes at injection.

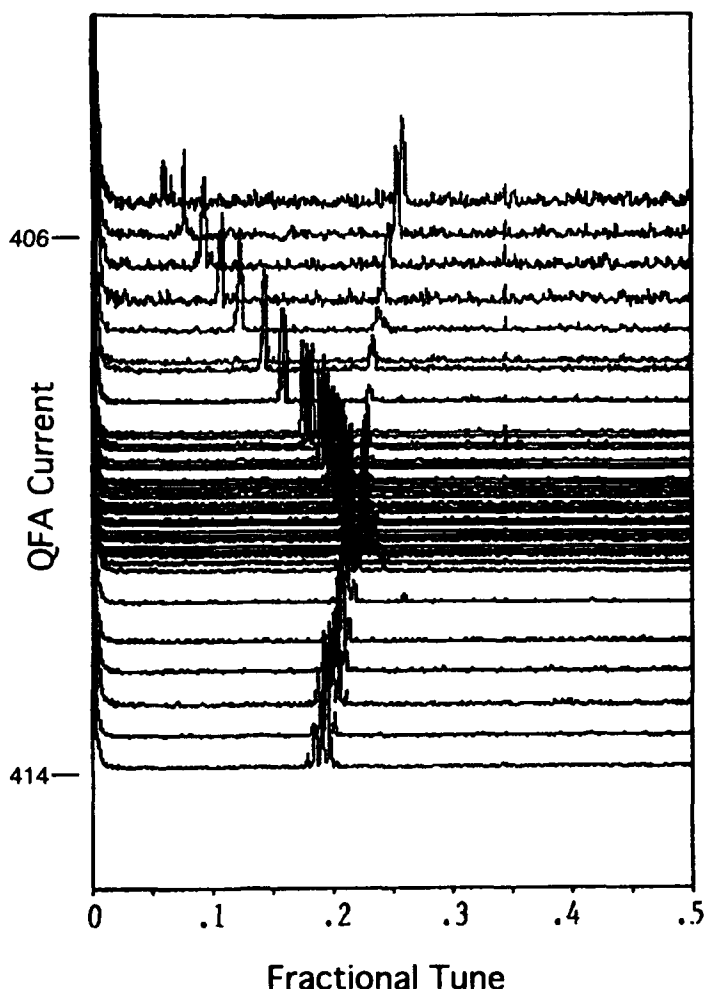


Figure 4. Tune scans as a function of QFA current, constructed from Fourier transforms of turn-by-turn orbit data.

Synchrotron tunes were always easy to measure, even at low beam current. Their variation as a function of RF voltage (from a nominal value of 10 kHz, where $f_s = 0.007$) was used to estimate RF cavity voltage and power.

C. Instability studies

Phase oscillations arising from multibunch instabilities, limiting at about 10° , were observed in a filling pattern where 82 equidistant bunches were filled; however, this instability did not appear to limit the amount of current that could be accumulated. The spectrum of synchrotron side-bands around

the orbit harmonics were in good correspondence to the aliased longitudinal higher-order modes in the accelerating cavities (see reference [4]). In single-bunch mode, the longitudinal damping system, being developed jointly with SLAC, was tested and successfully damped a deliberately driven oscillation to less than 1° . Measurements of the width of the synchrotron side-bands gave an upper limit to the bunch length of 8 mm, or 27 ps FWHM. Single-bunch currents up to 27 mA were accumulated.

Measurements were also taken on the effects of the newly injected beam (with large betatron oscillations), on the already stored beam, to compare with models recently developed in collaboration with SLAC . . . analysis is in progress.

VII. SUMMARY

Commissioning the ALS storage ring was undertaken in two periods. The first, with no RF acceleration available, was extremely useful in debugging the instrumentation and controls, making the hardware reliable, checking the efficacy of the environmental shielding, and making preliminary measurements on injection and the computer model. The second phase lasted less than seven weeks, in which time all the project goals at 1.5 GeV were met, and a huge amount of data was taken towards understanding the parameters of the storage ring. During the months through July 1993, the IDs and beamlines will be installed in preparation for establishing the ALS as a full user facility.

VIII. ACKNOWLEDGMENTS

The work presented here was carried out by the ALS Accelerator Physics Section and Operations Section. The sheer volume of work could not have been accomplished without the help of our visitors, particularly Peter Kuske and Bettina Kuske from BESSY, and from members of the LBL Center for Beam Physics. Instrumentation and controls naturally played a major role in the success of the commissioning activities and it is a pleasure to acknowledge the response to requests for "urgent" changes provided by Jim Hinkson and Chris Timossi.

This work was supported by the director, Office of Energy Research, Office of Basic Energy Sciences, Material Sciences Division of the U.S. Department of Energy, under Contract No. DE-AC03-76SF00098.

IX. REFERENCES

- [1] See for example A. Ropert, "The Status of the ESRF," in *Proceedings of the Third European Particle Accelerator Conference, Berlin '92*, pp. 35-39.
- [2] Lawrence Berkeley Laboratory PUB-5172, "1-2 GeV Synchrotron Radiation Source, Conceptual Design Report," 1986.
- [3] L. Schachinger and V. Paxson, "A Software System for Modeling and Controlling Accelerator Physics Parameters at the ALS," these proceedings.
- [4] J. Byrd, J. Corlett, "Coupled-bunch Stability at the ALS," these proceedings.

STATUS of BESSY II *

a High Brilliance Synchrotron Light Source in the VUV to XUV Range

D.Krämer for the BESSY II design team**
BESSY mbH, Lentzeallee 100, D-1000 Berlin 33, Germany

Abstract

The approval of the BESSY II project marked the start of the construction of the first third generation synchrotron light source in Germany. BESSY II, designed for low emittance ($\epsilon = 6 \cdot 10^{-6} \text{ radm}$) and the incorporation of a large number of insertion devices (IDs) is expected to deliver VUV to XUV radiation with a brilliance in excess of $10^{18} \text{ photons}/(\text{sec} \cdot \text{mm}^2 \cdot \text{mrad}^2 \cdot 0.1\% \text{ bandwidth})$, the photon energies ranging from 10 to 2000 eV from undulators and wigglers. Photon spectra with a critical energy of 11.5 keV will be generated in the 6 T field of a superconducting wavelength shifter (WLS) which is planned to be installed in one of the 14 straight sections available for insertion devices. The decision to build BESSY II at a new site at Berlin Adlershof gave the challenge for a complete redesign of the storage ring without the severe boundaries compared to earlier proposals [1], with respect to requirements and practicabilities of constructing an accelerator complex mid in the center of West-Berlin.

1. Introduction

On July 7th 1992 a new third generation synchrotron light source was approved by the German Ministry of Research and Technology. This date marked the start for construction of the high brilliance synchrotron light source BESSY II to be located at the area of the former Academy of Science of the GDR at Berlin-Adlershof. BESSY II is optimised to accommodate up to 14 insertion devices providing radiation in the VUV to soft X-ray range using undulators and wigglers as well as standard bending magnets. A large number of user groups from physics and astrophysics, life science, chemistry, material science and catalytics, surface science and radiation metrology will use the new facility. Industrial applications especially deep X-ray lithography for micromechanics will benefit considerably from the new radiation source thus demonstrating the wide potential of synchrotron radiation in fundamental and applied research.

*Funded by BMFT and Land Berlin

**W. Anders, J. Bahrdt, B. Bauda, T. Becker, K. Bürkmann, W. Braun, W. Dörhage, V. Dürr, G.v. Egan-Krieger, W. Gericke, A. Gaupp, W. Gudat, Ch. Geyer, M.v. Hartrott, E. Jaeschke, S. Khan, D. Krämer, B. Kuske, P. Kuske, M. Martin, R. Müller, K. Ott, W. Peatman, H. Prange, J. Rahn, D. Richter, M. Scheer, F. Senf, T. Schneegans, U. Strönisch, L. Schula, E. Weihreter, G. Wüstefeld, Th. Westphal

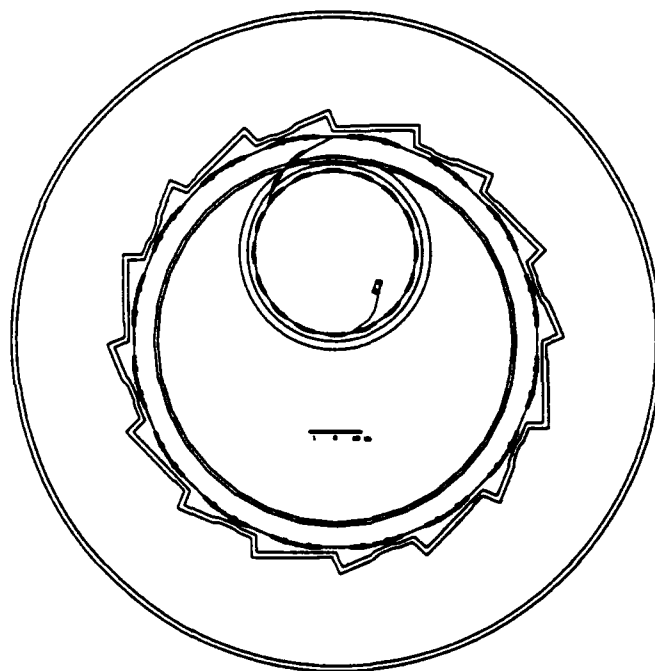


Figure 1: Layout of the BESSY II synchrotron and storage ring. The diameter of the experimental hall will be 120 m.

2. The accelerator

The accelerator complex BESSY II consists of three major components:

- a 50 MeV racetrack microtron as pre-injector,
- a full energy 10 Hz booster synchrotron and
- a storage ring capable to run at energies from 0.9 to 1.9 GeV.

Figure 1 gives a plan view on the 120 m diameter experimental hall with the storage ring and the injectors in the center. In table 1 the basic parameters of the injectors are listed.

As the new site for BESSY II offers significant advantages compared to former proposals with respect to spacial and technical boundaries a complete redesign for the storage ring has been done [2]. The result is a 2 times 8-fold Double Bend Achromat (DBA) structure with good emittance and large dynamic aperture. A quadrupole doublet at every second straight section enables high beta values in this straight whereas triplet focussing allows for a small horizontal beta function of less than 1 m. The DBA structure is very compact with a large flexibility of its 9 families of quadrupoles and 6 families of sextupoles. In table 2 the

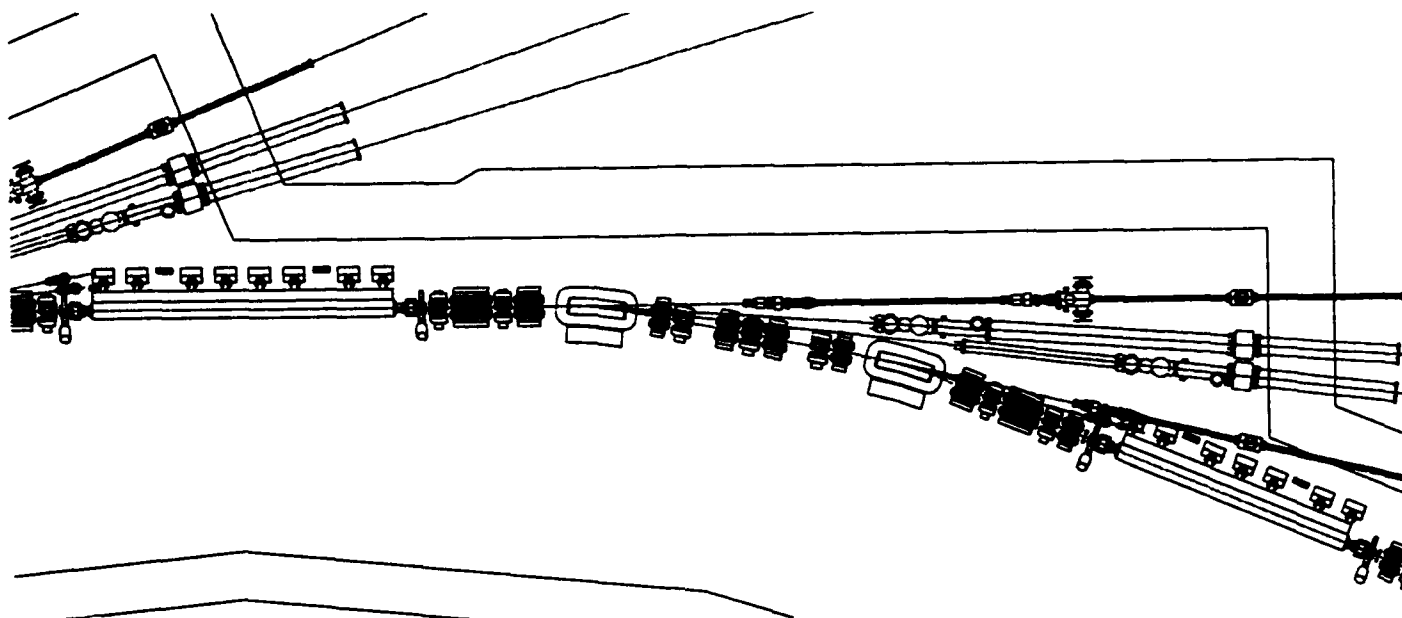


Figure 2: Section of the storage ring. The straight sections on both sides of the achromat will accommodate Undulators and Wigglers. Synchrotron Radiation beamlines are indicated.

main parameters of the storage ring are summarized. Figure 2 gives a view on the achromat with the long straights.

Table 1: Basic Parameters of the BESSY Injectors

Racetrack Mikrotron	
Nominal energy	50 MeV
Energy spread	$\pm 2 \cdot 10^{-3}$
Max. current	25 mA
Emittance	$2 \cdot 10^{-7} \text{ radm}$
Repetition frequency	10 Hz
Max. pulse duration	1 μs
Synchrotron	
Injection energy	50 MeV
Extraction energy	1.9 GeV
Extracted current	3 mA
Emittance at extraction	$1.4 \cdot 10^{-7} \text{ radm}$
Natural energy spread	$\pm 5.5 \cdot 10^{-4}$
Lattice structure	FODO
Number of cells	16
Circumference	96 m
Harmonic number	160
Repetition frequency	10 Hz

The storage ring will have 16 long straight sections of which 14 are used for insertion devices. Half of the straight sections will have a useable length of 4.708 m while the others are of 3.888 m length. 'High' beta functions are foreseen in the long straights: $\beta_x = 16.2 \text{ m}$, $\beta_z = 3.1 \text{ m}$ to accommodate undulators whereas the short straights with 'low' beta functions of $\beta_x = 0.93 \text{ m}$ and $\beta_z = 2.1 \text{ m}$ are reserved for high field wigglers and superconducting wavelength shifters to minimise their impact on the beam.

3. The insertion devices

The IDs planned for BESSY II are ranging from permanent magnet undulators U140 - U30 to a 6 T wavelength shifter. There are 32 bending magnets generating synchrotron radiation of characteristic photon energy of 2.5 keV at nominal beam energy. Beam lines emerging from the dipoles can be set up with a max. length of 42.5 m. Space is available on the site to install super long beam lines (more than hundred meters). Table 3 gives a list of the IDs planned for operation in BESSY II.

Table 2: General Parameters of the Storage Ring

Energy range	0.9 - 1.9 GeV
Circumference	240 m
Number of cells	16
Natural emittance	$6.1 \cdot 10^{-9} \text{ radm}$
Momentum compaction	$7.5 \cdot 10^{-4}$
Structure	$8 \cdot (S1, -S1)$
S1 = FDBDFFDBDFD	
Max. hor. beta function	17.2 m
Min. hor. beta function	0.384 m
Max. vert. beta function	20.5 m
Min. vert. beta function	2.44 m
Max. dispersion function	0.415 m
Nom. current multi bunch operation	100 mA
Rf frequency	500 MHz
Beam lifetime	10 h
Usable length of straight sections:	
'high' beta section	4.708 m
'low' beta section	3.888 m

Table 3: List of Insertion Devices of BESSY II

ID name	U-140	U-100	U-52	U-30	W-100	WLS
Period λ_0 (mm)	140	100	52	30	100	
Number of periods	32	40	80	110	40	
Length (m)	4.48	4.0	4.16	3.3	4.0	1.0
Magnetic gap (mm)	24	24	24	12	24	
Vacuum gap (mm)	20	20	20	10	20	
K_{max} (NeFeB)	6.5	4.7	2.5	1.6	9.7	
1 st Harmonic (eV)	9 - 174	23 - 244	128 - 469	401 - 813		
K Region	6.5 - 0.5	4.7 - 0.5	2.5 - 0.5	1.6 - 0.5		
2 nd Harmonic (eV)	130 - 261	183 - 366	352 - 704	802 - 1220		
K Region	2.0 - 1.0	2.0 - 1.0	2.0 - 1.0	1.6 - 1.0		
3 rd Harmonic (eV)	143 - 392	200 - 549	384 - 1056	1204 - 1830		
K Region	2.5 - 1.0	2.5 - 1.0	2.5 - 1.0	1.6 - 1.0		
B_0 (T)	0.5	0.5	0.461	0.594	1.04	6
ρ_0 (m)	11.3	11.3	12.3	9.5	5.4	
Charact. Energy (eV)	961	961	886	1142	1995	11532
Radiated power (W)	203	185	202	197	789	
$\frac{dP}{d\Omega} \frac{W}{\text{mrad}^2}$	144	182	368	554	376	
Lin. tune shift ($\frac{1}{m}$)	$1.39 \cdot 10^{-3}$	$1.24 \cdot 10^{-3}$	$1.09 \cdot 10^{-3}$	$1.44 \cdot 10^{-3}$	$5.36 \cdot 10^{-3}$	
$\frac{\Delta Q_x}{\beta_y} = \frac{L}{8\pi\rho^2}$						
Nonlin. tune shift ($\frac{1}{m^2}$)	1.40	2.44	7.99	31.6	10.6	
$\frac{\Delta Q_x}{\beta_x \gamma^3} = \frac{\pi L}{4(\lambda_g \rho)^2}$						

For the first phase of operation 6 undulators and wigglers and at least one wavelength shifter will be available. 6 beamlines will be prepared for experiments. Furthermore 8 dipole beamlines will be setup equipped with monochromators. Figure 3 gives the brilliance for the insertion devices under construction in comparison to the present 0.8 GeV BESSY I synchrotron radiation source.

4. Status of the project

After approval by the Federal Ministry of Research and Technology and the Senate of Berlin preparations for civil engineering are under way to start with the building in march 1994. According to the time schedule prototyping is in preparation to fit to the comissioning of the booster planned for June 1996 and start the storage ring commissioning in summer 1997 in order to deliver first synchrotron radiation from an undulator before 1998.

References

- [1] BESSY II - Eine optimierte Undulator/Wiggler Speicherring Lichtquelle für den VUV- und XUV Spektralbereich, Technische Studie, Berlin 1989
- [2] E. Jaeschke, D. Krämer, B. Kuske, P. Kuske, M. Scheer E. Weihreter, G. Wüstefeld Lattice Design for the 1.7 GeV Light Source BESSY II, contribution to these proceedings

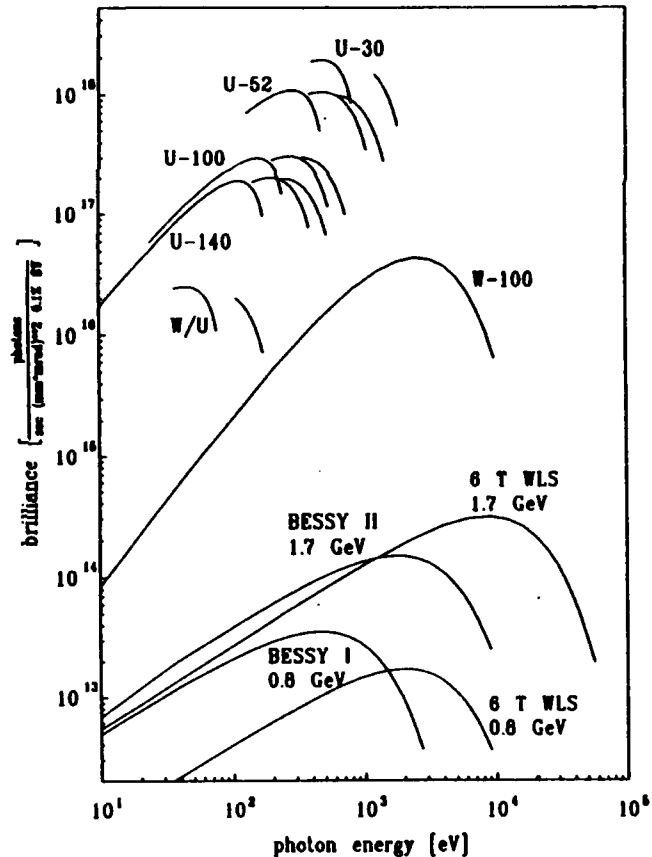


Figure 3: Brilliance of radiation from insertion devices at BESSY II compared with radiation from dipoles and with the 0.8 GeV BESSY I synchrotron radiation source.

A Superconducting Short Period Undulator for a Harmonic Generation FEL Experiment*

G. Ingold, L. Solomon, I. Ben-Zvi, S. Krinsky, D. Li, D. Lynch,
J. Sheehan, M. Woodle, X.Z. Qiu, L.H. Yu and X. Zhang

National Synchrotron Light Source
Brookhaven National Laboratory, Upton, NY 11973

W. Sampson, M. Gardner and K. Robins
RHIC Magnet Division
Brookhaven National Laboratory, Upton, NY 11973

I. Lehrman, R. Heuer, J. Sheehan and D. Weissenburger
Grumman Corporation
4 Independence Way, Princeton, NJ 08540

Abstract

A three stage superconducting (SC) undulator for a high gain harmonic generation (HGE) FEL experiment in the infrared is under construction at the NSLS in collaboration with Grumman Corporation. A novel undulator technology suitable for short period (6-40mm) undulators will be employed for all three stages, the modulator, the dispersive section and the radiator. The undulator triples the frequency of a $10.4\mu\text{m}$ CO_2 seed laser. So far a 27 period (one third of the final radiator) prototype radiator has been designed, built and tested.

0.3-1.2T). Finally, energy is extracted from the coherently bunched beam in the radiator (84 periods, 1.80cm, 0.54T), where radiation will be amplified exponentially. The last part of the radiator will be tapered. A schematic diagram of the harmonic generation experiment is shown in Fig.1.

The undulator design allows implementation of several features which are essential for single pass high power FEL amplifiers at shorter wavelengths such as 1) high magnetic field on axis at short periods, 2) convenient K-tuning, 3) adjustable dispersion, 4) adjustable field taper, 5) two-plane focusing and 5) field amplitude errors at or below the state of the art 0.2 – 0.3% rms as machined which is needed to minimize electron beam trajectory walk-off.

1 Introduction

Short period undulators for Free Electron Laser (FEL) applications offer the advantage of producing shorter wavelength radiation with a given electron energy. The design and theory of the seeded single pass harmonic generation UV-FEL has been described elsewhere [1]. As a proof-of-principle a harmonic generation FEL experiment in the infrared has been designed [2] to be carried out at the accelerator test facility (ATF) at BNL. The fully constructed undulator for this experiment consists of three stages, the modulator, the dispersive section and the radiator, all superconducting. The radiator is tuned to the third harmonic of the modulator. We plan to amplify the third harmonic of a $10\mu\text{m}$ CO_2 laser with a 30MeV high brightness electron beam from a laser-photocathode rf gun injected into a 50-100MeV S-band linac. The modulator (12 periods, 2.60cm, 0.81T) causes an energy modulation in the electron beam. This energy modulated beam gets spatially bunched in the tunable dispersive section (12cm long,

2 Basic Undulator Design

The basic design of an undulator section magnet has been discussed elsewhere for a 0.88cm period planar undulator [3]. Here we use the same approach. It is based on precision machining a sequence of poles and grooves on a bar of low carbon steel. A field uniformity of $\Delta B/B \simeq 0.1\%$ as manufactured, without trimming or shimming of individual undulator elements requires machining tolerances within $10\mu\text{m}$ for the periodicity and the gap spacing. The design can easily be modified for different undulator geometries, namely the periodicity and the pole shape geometry. Basically the same design is used for the modulator, the dispersive section and the radiator. The coils are continuously wound in several layers with multifilamentary NbTi conductor on the machined form of an undulator section magnet. Two 25.2cm long section magnets for the HGE radiator are shown in Fig.2. The poles are parabolically shaped to provide focusing in the wiggles plane [4]. The full gap in the center is 8.0mm and the curved pole geometry is truncated into a flat pole at $x = \pm 3.0\text{mm}$ and

*Work performed under the auspices of the U.S. Department of Energy

a 6.0mm full gap to accommodate microstriplines later on.

The full length undulator is made up of discrete magnet sections shown in Fig.2. The magnet sections are assembled end-to-end but otherwise continuous over the entire length both for the modulator (2 sections, each 15.60cm long) and the radiator (6 sections, each 25.20cm long). There are no axial drift spaces other than those between the dispersive section and the modulator and the radiator respectively. This situation avoids the tuning of drift spaces to match the phase angle. Electron beam steering coils (providing a field integral of 300G-cm and 100G-cm for horizontal and vertical steering respectively) are mounted outside the beam pipe and are spaced with an even number of poles in regular intervals to control the electron beam walk-off to within $\pm 40\mu\text{m}$ (2/10 th of the beam radius).

The magnetic field of the radiator is quadratically tapered. The taper can be approximated in six flat steps without a compromise in the FEL power performance. The taper profile will be adjustable through 'bleed-off' currents in the six tapered sections using the power supplies $PS_D - PS_H$ shown in Fig.3. The entrance and exit of each undulator stage as well as the five field taper transitions have a binomial current excitation pattern, which satisfies the nonsteering condition [5]. Field clamps at the undulator ends are used to control the fringe fields.

A non-magnetic steel (nitronic 40) fixture provides sufficient clamping of the section magnets shown against a gap defining precision "spacer". After the full-length assembly of the cold mass it will be inserted into a 2.50m long hori-

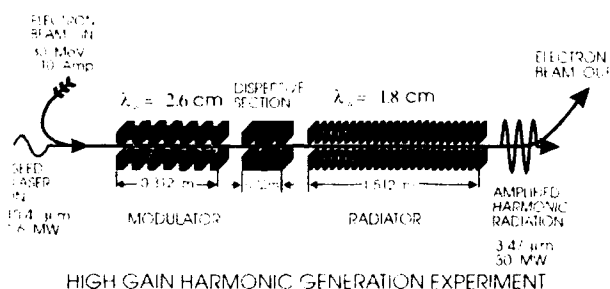


Figure 1: Schematic diagram of the HGE experiment.

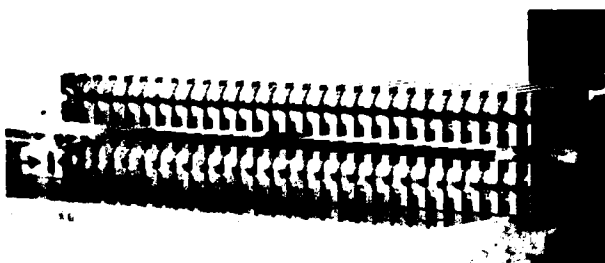


Figure 2: Two 25.2cm long SC undulator magnets for the HGE radiator. The period is 1.80cm.

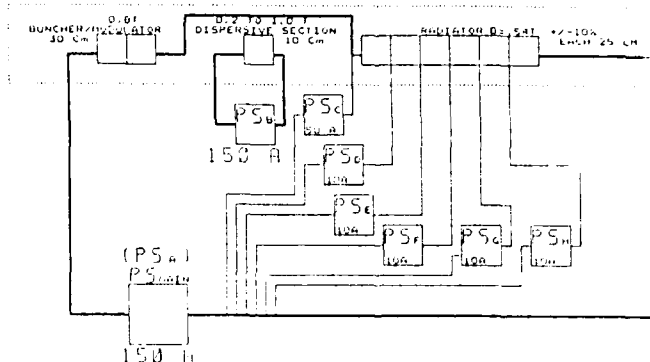


Figure 3: Magnet power for the three undulator stages. The field taper in the radiator is done with the power supplies $PS_D - PS_H$.

zontal cryostat. The magnet structure is of the cold bore, cold yoke type and is cooled by pool boiling helium at 4.4K. The position of the undulator magnet relative to a straight line reference can be controlled with an adjustable suspension system after cooldown. Electron beam diagnostics from stripline monitors is available at the entrance and exit of the cold mass assembly.

3 Experimental Results

So far our work has concentrated on the performance of a 0.5m long prototype radiator undulator (27 periods). Proven features include a suitable conductor, the field level on axis, the field profile, the field quality and the related machining tolerances. The magnetic measurements and additional results are discussed in [6].

FIELD ON AXIS: Quench stability limits the highest possible current in a SC magnet. We tested radiator sections with two different conductors (conductor I: Cu/SC=1.3:1, conductor II: Cu/SC=2.4:1). The quench current for the HGE radiator sections shown in Fig.2 was $I_q = 200 \pm 5\text{A}$ and $I_q = 170 \pm 3\text{A}$ for conductor I and II respectively. Both results agree within 5% with predictions from the load curve analysis which uses measured "short sample" critical data. The field on axis (full gap $g(x=0)=8.0\text{mm}$, $\lambda_w=18.0\text{mm}$) as a function of current (for conductor II) is shown in Fig.4. The HGE design field is 0.54T. At 150A (10% below I_q) the field on axis is 0.72T. For comparison, the field for a Nd-Fe-B hybrid undulator would be 0.46T (Halbach formula). In Fig.4 the excitation data for parabolic shaped poles are compared to 2D POISSON calculations where a flat pole approximation at a 8.0mm full gap has been used.

FIELD PROFILE For the proper matching of the magnetic field at the undulators ends the non-steering current excitation pattern 1:3:4 is used [5]. The same pattern is used for the mixing of the currents I_n and I_{n+1} at the taper transitions $n=1-5$. The taper currents $I_D - I_H$ will be

adjusted for a 10% quadratic field taper.

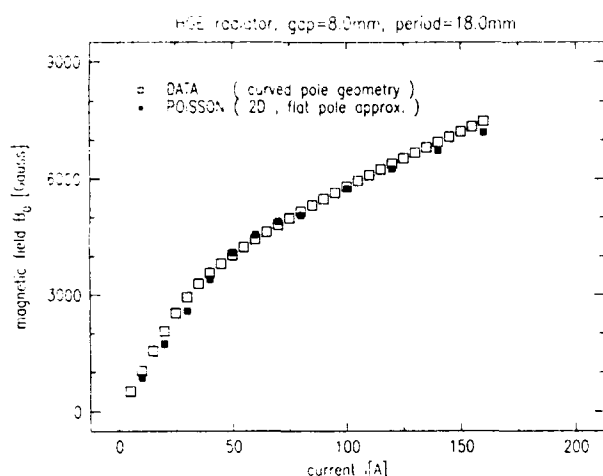


Figure 4: Excitation curve for the HGE radiator. The operating field is 0.54T. The quench current is 170A (conductor I) and 200A (conductor II).

For horizontal focusing the iron poles are parabolically shaped. The half gap dependence is $y(x) = 4.0\text{mm} \cdot (1 - ax^2)$ with $a=0.028$ for $-3\text{mm} \leq x \leq 3\text{mm}$ and $y=3.0\text{mm}$ elsewhere (z is the beam axis, y is normal to the x - z wiggle plane). The measured transverse field profile is $B_y(x) = B_0 \cdot (1 + bx^2)$ where $b=0.021$ at low currents (Fig.5). This value decreases by about 17% at the operating current ($I=90\text{A}$). This change with saturation is in agreement with 3D TOSCA calculations. The truncation of the pole curvature to a 6mm full gap in the flat pole region limits the transverse field increase. TOSCA predicts that for equal natural x and y undulator focusing the pole curvature should be $a=0.033$. The cold measurements are done using a multiple Hall-probe setup which is calibrated in-situ with a pair of Helmholtz coils [6].

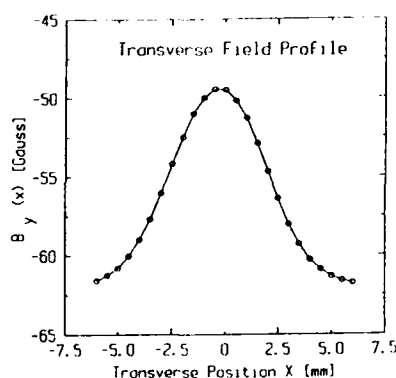


Figure 5: Room temperature measurement ($I=0.5\text{A}$) of the transverse field profile. The data agree with 3D TOSCA calculations.

FIELD QUALITY In a first step we analyze the beam trajectory (second field integral) for individual undulator sections (Fig.2). Independent of the field on axis (i.e. of

saturation, Fig.4), the trajectory remains within $\pm 20\mu\text{m}$ [6]. No trimming fields or shimming corrections have been applied. This result is obtained although 10% of the iron poles have been identified with machining errors in the pole width a factor 6-7 beyond the required mechanical tolerance of $10\mu\text{m}$. These large errors are understood and have been removed in the machining of new sections.

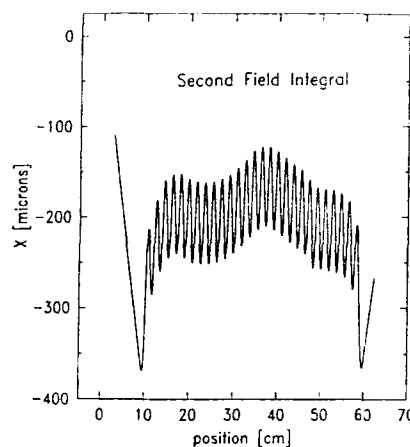


Figure 6: Beam trajectory from magnetic measurements ($I=50\text{A}$) of a 27 period radiator undulator.

In a second step a 27 period prototype radiator (two sections) has been tested. Now the trajectory for a 30MeV beam wanders $\pm 35\mu\text{m}$ (Fig.6). The deflection in the center is probably due to the identified machining error of the half poles at the joint combined with a clamping error between both sections beyond the $10\mu\text{m}$ gap tolerance. The rms peak field variations for the first (second) section was 0.22% (0.29%) (poles with large identified machining errors not included). The steering coils to control the electron beam to within $\pm 40\mu\text{m}$ are conservatively designed.

The basic magnetic unit for the HGE undulator has been developed. As machined this SC undulator technology provides the field performance needed for high power single pass FEL applications. It allows complex multi-stage undulators with cw operation. Important parameters can conveniently be changed during operation.

References

- [1] L.H. Yu, Phys. Rev. A99 (1991) 5178.
- [2] I. Ben-Zvi et al., NIM A318 (1992) 208.
- [3] I. Ben-Zvi et al., NIM A318 (1992) 781.
- [4] E.T. Scharlemann, J. Appl. Phys. 58,6 (1985) 2154.
- [5] K. Halbach, NIM A250 (1986) 95.
- [6] L. Solomon et al., these proceedings.

UV-VUV FEL Program at DUKE storage ring with OK-4 optical klystron

V.N.Litvinenko, J.M.J.Madey

Duke University Free Electron Laser Laboratory*
Box 90319 Duke University, Durham, NC 27708-0319

N.A.Vinokurov

Budker Institute of Nuclear Physics
630090 Novosibirsk, Lavrentyev av. 11, Russia

Abstract

A 1 GeV electron storage ring dedicated for UV-VUV FEL operation is under construction at the Duke University Free Electron Laser Laboratory. The UV-VUV FEL project, based on the collaboration of the Duke FEL Laboratory and Budker Institute for Nuclear Physics is described.

The main parameters of the DFELL storage ring, of the OK-4 optical klystron, and the experimental set-up are presented. The parameters of UV-VUV FEL are given and the possible future upgrades to this system are discussed.

I. INTRODUCTION

In April 1992, Duke University Free Electron Laser Laboratory and Budker Institute of Nuclear Physics signed a Memorandum of Understanding on collaborative efforts in FEL research. As the first step in this collaboration, the OK-4 optical klystron system, including the magnetic system and its power supplies, vacuum system, optical cavity system and diagnostic system will be transferred to Duke FEL for UV-VUV FEL experiments on the Duke storage ring.

The layout of the Duke/OK-4 UV-VUV FEL is shown in Figure 1.

diagnostic systems and NIST undulator (soft X-ray source).

Construction of the storage ring and linac-injector started in 1992. Magnetic measurements (excitation curves and 2-D maps) of all magnets in their real environment was performed before installation using an eleven element Hall probe array [2]. The overall accuracy of these measurements was better than 0.01%.

At present, all storage ring magnets and 80% of the vacuum chambers and other hardware have been installed. A vacuum of $(0.6-6) \times 10^{-10}$ torr was achieved in the ring. The 178 MHz RF cavity [3] (64th harmonic of revolution frequency), manufactured in Novosibirsk, passed high power tests and has been installed on the Duke storage in a shielded cave. The RF system, including RF cavity, circulator and transmitter should be commissioned by Fall 1993.

The 280 MeV injector comprising a microwave electron gun [4], eleven SLAC accelerator sections fed by three S-band klystrons, and low and high energy spectrometers is now under construction. The commissioning of the linac and linac-to-ring transport channel is scheduled for the end of 1993. The energy of the linac will be extended to 1 GeV in 1994 by increasing the number of accelerator sections to 28 and number of

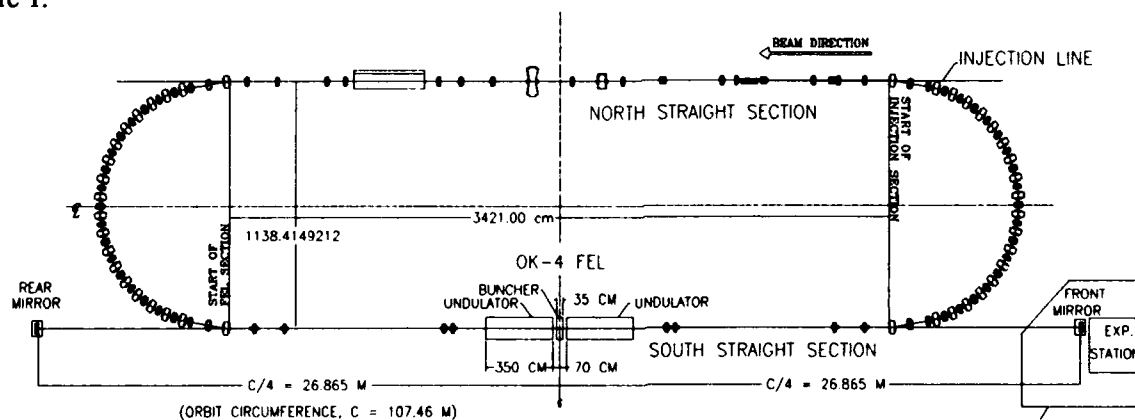


Figure 1. Layout of the Duke/OK-4 UV-VUV storage ring FEL.

A. Status of the Duke storage ring.

The Duke FEL electron storage ring is designed to drive UV and soft X-ray FELs. One of the two 34-meter straight sections is dedicated for FEL installation. The other straight section is used for injection, installation of the RF cavity,

klystrons to eight. A fast chopper installed after the microwave gun will form short (~5 nsec) electron bunch trains to fill individual (from a possible 64) electron buckets in the ring. Electrons from the linac will be injected into the storage ring through a vertical chicane and 9-degree septum magnet [5]. Three 200 nsec ferrite kickers [6] will be used for storing the beam.

The initial performance of the ring will be limited by the

* Work supported by AFOSR grant #90-0112.

temporary crotch vacuum chambers installed at the ends of the arcs. These crotches will be replaced in 1994 by permanent "RF-smooth" vacuum chambers with ports for FEL, NIST undulator and synchrotron radiation equipped with absorbers capable of operation with (1-2)A average beam current.

The description of the Duke storage ring with combined quadrupole and sextupole magnets in the arcs, modified second order achromat lattice of the arc canceling second order geometrical aberration, etc., can be found elsewhere [5,7,8].

Extensive studies of the Duke storage ring dynamic aperture [7] have shown that the dynamic aperture of low emittance FODO lattice exceeds the physical aperture of the ring. A $\pm 5\%$ energy acceptance, extraordinarily large for strong-focusing storage rings, has been verified. The main parameters of the Duke storage ring are summarized in Table I.

Table I. Main Parameters of Duke Storage Ring

Operation energy [GeV]	0.25 - 1.0
Ring circumference [m]	107.46
Arc and straight section length [m]	19.52; 34.21
Revolution frequency [MHz]	2.7898
RF frequency [MHz]	178.547
Number of dipoles and quadrupoles	40; 64
Betatron tunes, Qx and Qy	9.111, 4.180
Orbit compaction factor, α	0.0086
Natural chromaticities, Cx and Cy	-10.0, -9.78
Compensated values, Cx and Cy	+0.1; +0.1
Acceptances [mm mrad], Ax and Ay	56., 16.
Energy acceptance, $\Delta E/E$, the ring limited by existing RF	$> \pm 5.0\%$ $\pm 2.8\%$
Maximum β -functions [m], x and y	13.6, 21.3
Maximum η -function [m]	0.245

Commissioning of the storage ring is scheduled to begin in early 1994. The commissioning lattice [8] is optimized for the OK-4 FEL magnetic system to facilitate the start of the first FEL experiments.

B. Status of the OK-4 optical klystron.

The OK-4 was the first operational UV FEL [10,11] demonstrating lasing down to 240 nm. It still holds the short wavelength record for FELs.

The OK-4 magnetic system is comprised of two 3.5 meter electromagnetic undulators [9] and a buncher (3-pole compensated wiggler) located between them. The use of a buncher distinguishes optical klystrons from conventional FELs and permits the optimization of longitudinal dispersion for higher gain and, as a result, the enhancement of the gain by a factor 5-20.

The OK-4 magnetic system has very high performance. The direct magnetic measurements and experimental results achieved with the OK-4 in Novosibirsk have shown the practically perfect performance of this system. The main parameters of the OK-4 magnetic system are listed in Table II.

The OK-4 optical klystron has been employed for a number of recent FEL experiments on the Novosibirsk VEPP-

3 storage ring bypass. This scientific program will be finished in 1993.

Table II. Main Parameters of OK-4 magnetic system

Total length [m]	7.8
Undulator	
Length [m]	3.40
Period [m]	0.10
Peak magnetic field [kGs]	(0.0-5.8)
Undulator parameter, K	(0.0-5.42)
Tuning range ($\lambda_{\max}/\lambda_{\min}$)	15.67
Buncher	
Length [m]	0.34
Magnetic field [kGs]	(0-12)

Following these experiments, the magnetic and optical systems of the OK-4 optical klystron will be moved to Duke for the first FEL experiments using the DFELL storage ring.

II. DUKE/OK-4 UV-VUV FEL

The tuning range (K vs wavelength) of the fundamental harmonic wavelength of the OK-4 FEL is shown in Figure 2. The parameters of the electron beam are very critical for performance of a short wavelength FEL. The most important Duke storage ring electron beam parameters are given below:

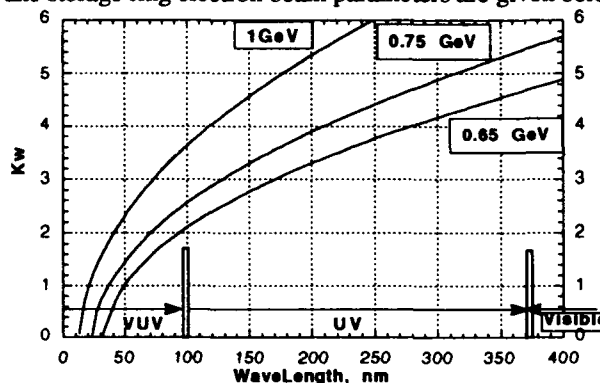


Figure 2. OK-4 tuning range for 0.65, 0.75 and 1 GeV.

Table III. Parameters of electron beam at 1 GeV energy

Average beam current, A	0.1 (1.0*)
Peak current, A	80-130 (350*)
Emittances [mm mrad], ϵ_x and ϵ_y	0.018; <0.0018 (0.009; .0045*)
Relative energy spread (low current)	0.0005
at peak current of 130 A	0.0016
Bunch length, cm, (low current)	1.15
at peak current of 130 A	3.7
Beam size in OK-4 [mm], σ_x and σ_y	0.27; 0.085

* final specification of the ring.

At 1 GeV energy, the beam emittance will be practically natural. Intrabeam scattering will affect only the electron beam lifetime (down to 30-45 minutes with 350 A peak current). Maximum achievable peak current will be limited by the

impedance of the vacuum chambers, which have RF-smooth connections and transitions.

The 3-D OK-4 gain curve at the modest average current of 100 mA in the Duke ring is shown in Figure 3. Finite electron beam emittance and energy spread are taken into account. The finite emittance is responsible for gain drop in the short wavelength range.

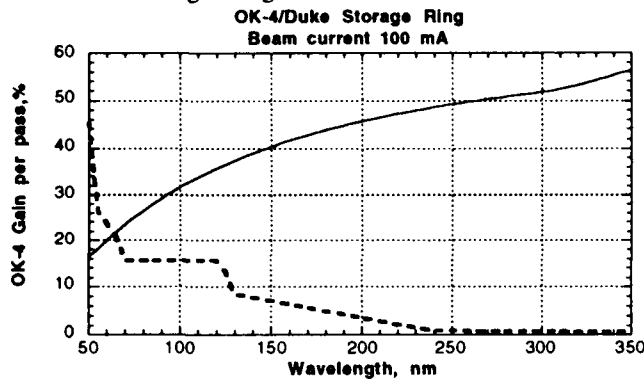


Figure 3. OK-4 gain vs wavelength - solid curve. Dashed curve - lasing threshold gain (adopted from [12]).

The expected OK-4 average CW lasing power for 100mA and 1A average current are plotted in Figure 4. The high energy acceptance of the ring is very essential, because under these conditions the energy spread (excited by lasing) can reach 1%. The energy acceptance of $\pm 5\%$ will provide an acceptable lifetime. These conditions can occur in the UV range where low loss mirrors are available.

In the VUV range average lasing power will be limited by gain degradation due to electron beam heating (even with the multifacet mirrors [13] we intend to use in this range).

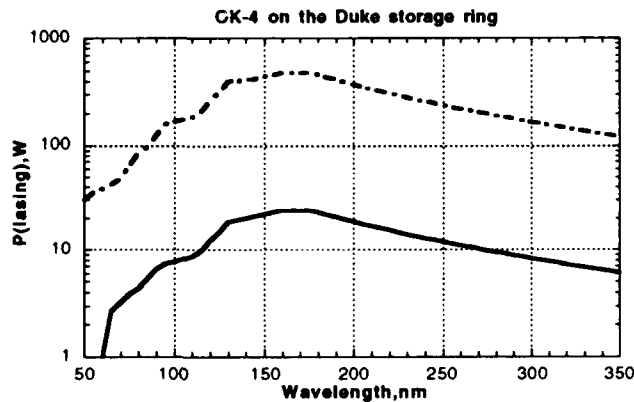


Figure 4. OK-4 FEL lasing power: solid line for 100 mA and dashed curve for 1 A average current.

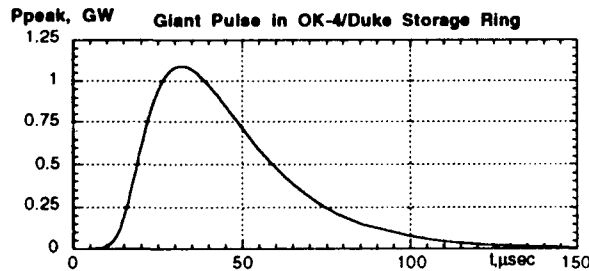


Figure 5. Giant Pulse Envelope (computer simulations).

In a storage ring driven FEL only the average lasing power is limited. Thus, we can redistribute the lasing power using gain modulation [10] to produce giant pulses with gigawatt levels of peak power and 50-100 Hz repetition rate. These techniques were tested both in Novosibirsk [11] and Orsay and results are accurately predictable. A typical giant pulse simulation result for OK-4/DUKE FEL at 200 nm is shown in Figure 5.

The other parameter of OK-4/DUKE UV-VUV FEL are presented in Table IV.

Table IV. Parameters OK-4/DUKE UV-VUV FEL

Tuning range, nm	50-400
Linewidth, $\delta\lambda/\lambda$: natural	(1-3) 10^{-4}
with linewidth narrowing [14]	(5-30) 10^{-7}
Micropulse duration, psec	5-30
Micropulse separation, nsec	358.45
Spatial distribution	TEM ₀₀

III. FUTURE UP-GRADES

Possible future up-upgrades of the Duke storage ring will include:

- full scale (27 meter long) high gain soft X-ray FEL;
- advanced 3 cavity RF-system (64 and 256 harmonics);
- lower impedance vacuum chambers;
- lower emittance optics.

The lattice for a 27 meter long FEL has been designed [8]. First results with a 26 meter undulator have shown good dynamic aperture.

The distributed optical klystron and phase-shift amplifier with 20-40 dB gain are under study as candidates for future up-upgrades. The lasing range with these devices can be extended down to 10-20 nm.

Lower emittance lattices (from 9 to 3 nm-rad) as well as electron beam conditioning are under consideration for further wavelength shortening down to the "water window".

IV. REFERENCES

- V.Litvinenko et al, SPIE Vol.1552 (1991) 2.
- B.Burnham, DFELL internal report, August 1992
- V.Arbutov et al., "RF system of the CW race-track microtron recuperator", these proceedings.
- G.A.Wetenskov et al, HEPL Tech. Note TN-86-1, 1986.
- B.Burnham et al., "Specific features of magnetic design for the Duke FEL storage ring", these proceedings.
- R.Sachtschale et al., "A novel technique for pulsing magnet strings with a single switch", these proceedings.
- Y.Wu et al., "Dynamic aperture study for the Duke FEL storage ring", Proc. of Fourteenth Int. FEL Conference, Kobe, Japan, August 23-28, 1992, Nucl.Instr. and Meth.
- Y.Wu et al., "Lattice and Dynamic aperture of the Duke FEL storage ring", these proceedings.
- N.G.Gavrilov et al, Nucl.Inst.and Meth.A282 (1989) 422
- V.N.Litvinenko, PhD, Novosibirsk, 1989.
- I.B.Drobyazko et al., SPIE v.1133 (1989) 2
- J.B.Kortright, FEL Handbook, 1988
- B.E.Newnam, SPIE v.1227 (1990) 116
- V.Litvinenko et al., IEEE J. of QE 27 (1991) 2560

A 2-4 nm Linac Coherent Light Source (LCLS) Using the SLAC Linac*

H. Winick, K. Bane, R. Boyce, G. Loew, P. Morton, H.-D. Nuhn, J. Paterson, P. Pianetta
T. Raubenheimer, J. Seeman, R. Tatchyn, V. Vylet

Stanford Linear Accelerator Center, Stanford University, Stanford, CA 94309-0210, USA

C. Pellegrini, J. Rosenzweig, G. Travish

Department of Physics, UCLA, Los Angeles, CA 90024-1447, USA

D. Prosnitz, E.T. Scharleman

Lawrence Livermore National Laboratory, Livermore, CA 94550, USA

K. Halbach, K.-J. Kim, M. Xie

Lawrence Berkeley Laboratory, University of California, Berkeley, CA 94720, USA

Abstract

We describe the use of the SLAC linac to drive a unique, powerful, short wavelength Linac Coherent Light Source (LCLS). Operating as an FEL, lasing would be achieved in a single pass of a high peak current electron beam through a long undulator by self-amplified spontaneous emission (SASE). The main components are a high-brightness rf photocathode electron gun; pulse compressors; about 1/5 of the SLAC linac; and a long undulator with a FODO quadrupole focussing system. Using electrons below 8 GeV, the system would operate at wavelengths down to about 3 nm, producing ≥ 10 GW peak power in sub-ps pulses. At a 120 Hz rate the average power is ≈ 1 W.

I. INTRODUCTION

Two recent developments have opened the possibility to construct linac-based x-ray lasers operating at short wavelengths, down to 2 nm and eventually as low as 0.1 nm. The first is the development, at Los Alamos and elsewhere, of rf photocathode electron guns which can now deliver low emittance (3-4 mm-mrad normalized emittance), high charge (>1 nC) electron beams. The second is the development at SLAC, as part of the SLC project, of the tools and understanding associated with the transport, acceleration and compression of electron bunches without dilution of phase space density. These developments make it possible to deliver electron beams with the required phase space density to drive short wavelength lasers.

The main components of the short wavelength LCLS we have studied are (1) a high brightness, rf photocathode electron gun, (2) 7 sectors of linac, (3) beam transport and compressor systems, (4) beam diagnostics and controls, (5) a long undulator (50-75 m), (6) an enclosure to house the undulator, (7) electron beam dump, (8) mirror station, (9) a photon beam line and two diagnostic/experimental stations and (10) a building to house these stations.

In addition to the existing linac, an enclosure to house the undulator exists at the end of the SLAC linac. This is the Final Focus Test Beam (FFTB) housing completed in early 1993 for r&d associated with final focus systems for future linear colliders. There is ample room in this enclosure for the LCLS undulator. After a slight upgrade, the FFTB enclosure would provide adequate shielding for

alternating operation of both facilities.

We propose an r&d facility aimed at the development of linac-driven, short wavelength x-ray lasers, and their scientific and technological utilization. The first laser would start operation at a wavelength around 10 nm or longer and then reach the 3 nm region. With more extensive r&d, along with the use of higher energy electrons and additional undulators, and with improvement in the performance of certain components such as the rf photocathode gun, it is expected that the facility could achieve (with additional funding) a laser functioning at even shorter wavelengths, possibly in the 0.1 nm region.

The LCLS photon beams emerge into the SLAC research yard, about 125 m from SSRL beam lines on SPEAR. Thus, once the LCLS facility is operational, it is possible to bring a beam from it and SPEAR to the same sample chamber, for pump/probe experiments for example.

The proposed LCLS operates on the principle of the FEL, but does not require an optical cavity which is difficult or impossible to make at such short wavelengths. Instead, x-ray laser operation is achieved by Self-Amplified-Spontaneous-Emission (SASE) in a single pass of an electron beam through a 50-60 m long undulator.

Although SASE theory is well developed, there is, to date, little experimental data with which to compare it since most FELs have used oscillator cavities. It is therefore important to make detailed comparisons between experiment and theory, for example to verify the accuracy and wavelength dependence of simulation codes and assumptions about startup from noise. We plan to do this initially at wavelengths around 10 nm or longer. At these wavelengths certain tolerances are more manageable. As experience is gained and tighter tolerances met, operation down to about 3 nm can be expected, still using electrons below the 10 GeV that will be available in the proposed facility. The characteristics of the light produced by the LCLS at 4 nm are projected to be:

Peak Coherent Power (GW)	≥ 10
Pulse Repetition Rate (Hz)	120
Pulse Width (1 sigma - fs)	<160
Photons/pulse	$\geq 10^{14}$
Energy/pulse (mJ)	3
Bandwidth (1 sigma)	0.1-0.2%
Peak Brightness *	$\geq 10^{31}$
Average Brightness *	$\geq 10^{21}$

* photons/(s,mm²,mrad²) within 0.1% bandwidth

*Supported in part by the Department of Energy, Office of Basic Energy Sciences and High Energy and Nuclear Physics and Department of Energy Contract DE-AC03-76SF0015.

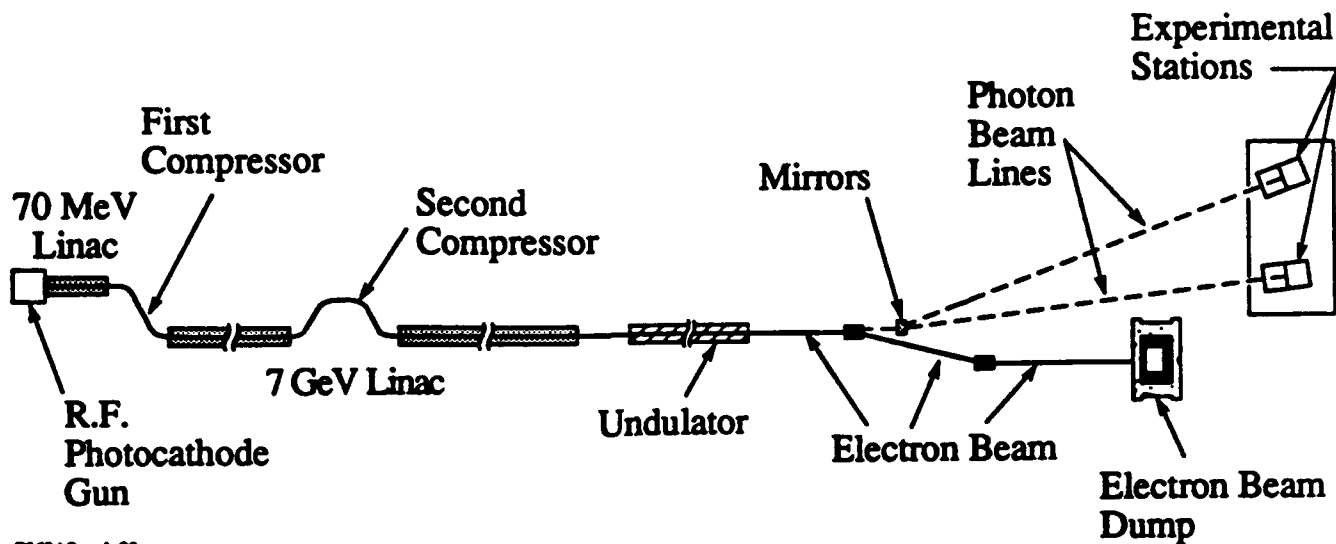


Figure 1
LCLS Schematic Overview

The average values of brightness and coherent power are about 3 orders of magnitude greater than projected for 3rd generation light sources such as the ALS and the peak values are about 9 orders of magnitude higher. Photon beams with this extraordinarily high brightness, coherence and peak power will make possible a wide range of experimental studies in many scientific and technical fields including x-ray imaging of biological specimens in and around the "water window" (including producing x-ray holograms of live biological specimens in a single sub-picosecond pulse); time resolved studies of condensed matter systems and chemical reaction dynamics; and non-linear processes. Because the properties of this light source go many orders of magnitude beyond that available from any other source in operation or construction, it is likely that entirely new scientific applications will be opened up. Exploratory experiments will be carried out on two diagnostic/experimental stations. With two experiments able to receive pulses, techniques will be developed for the rapid switching of the beam, as well as rapid changing of beam parameters such as wavelength and intensity to meet different experimental needs. An FY 1996 Short Form Construction Project Data Sheet has been submitted to DOE for this project. The total estimated cost is \$29.45M.

II. SIMULATIONS

Extensive numerical studies have been performed using (primarily) the FRED3D and TDA3D codes. In agreement with simple models, the simulations predict that the LCLS can provide in excess of 10 GW of peak power in a sub-picosecond pulse. The saturation length is about 60 m with strong focusing provided throughout the undulator. The system gain, its optimization and tolerance to beam parameter changes, wiggler errors and misalignments have been studied.[1]

The operating parameters chosen provide relative insensitivity to beam current and emittance fluctuations. By running to saturation, variations in the output radiation due to changes in the beam parameters are minimized. The requirements on the uncorrelated energy spread of the beam are tight ($<0.04\%$ rms) and are determined primarily by the desire to maintain a narrow bandwidth and maximum gain. Energy spreads twice as large as specified do not seriously degrade the (single frequency) performance. This, along with the high power (brightness) of the optical pulse, suggests that filtering could be used to narrow the line width.

According to the simulations (using a random walk), the wiggler field errors required are small ($<0.2\%$ rms) but within state of the art. Steering and alignment requirements are also tight ($30\text{ }\mu\text{m}$ rms), yet less stringent than required for many future linear collider designs.

III. TECHNICAL COMPONENTS

A. RF Photocathode Gun

We have studied the design of an rf photocathode gun which can produce the beam characteristics required for reliable operation of the LCLS. The dynamics of the photoelectron beam have been modelled using both PARMELA, and an axisymmetric particle-in-cell code, ITACA. These simulations show that a one nC, 10 MeV electron beam can be produced in a $3+1/2$ cell, 2.856 GHz structure, which has a pulse length of 2 psec and a normalized rms emittance of 3 mm-mrad. The major challenge in designing this source concerns reproducibility of the beam properties. In particular, due to wake-fields in the transport, it is critical that the jitter in the total charge per pulse and the injection timing be minimized [2]. We believe that a solution to these problems exists based on choice of a rugged cathode material and a commercial diode-pumped laser system

with timing stabilization [3].

B. Transport, Acceleration & Compression

The bunch produced by the LCLS photo-injector must be accelerated and length compressed before injection into the undulator. In the present scheme the bunch is accelerated from 10 MeV to about 7 GeV using three linear accelerators separated by two compressors[2]. The final bunch length is about 0.05 mm (FWHM) (over a factor of 10 smaller than that produced by the photocathode gun) yielding a peak current of 2500 to 3500 A. The final energy spread is less than 0.2 % (rms).

The choices of energies at which to compress are influenced by the need to 1) control longitudinal wakefields for energy spread minimization, 2) minimize emittance growth from transverse forces, and 3) reduce the effects of time-phase jitter as well as beam intensity jitter from the injector and in the compression process.

The first compression is performed at 70 MeV where the bunch length is reduced from 0.5 mm to 0.2 mm (rms). The second compression is near 2 GeV and reduces the length to about 0.05 mm (FWHM). To study the development of longitudinal phase space in this process, a computer program is used which considers the effects of longitudinal wakefields, curvature of the RF wave, and phase and intensity jitter. The second compression is made to deliberately over-compress the bunch length beyond the 0.003 mm (rms) minimum. This over-compression and acceleration from 2 to 7 GeV allows approximate cancellation of upstream errors with downstream errors, thus providing significantly relaxed timing and intensity jitter tolerances of the injector and accelerator RF. Bunch intensity fluctuations up to ± 2 % and injection phase jitter of roughly ± 0.5 degree can be tolerated[2]. After the first compression the bunch length is still nearly gaussian, but after the second compression the beam distribution is more sharply spiked and has long tails.

A second set of parameters for this length compression scheme is being studied which would provide a distribution that is more flat topped. Both distributions produce the peak current and energy spread needed to satisfy the FEL requirements.

The emittance dilution effects due to transverse wakefields, RF deflections, and dispersive effects have been modeled in the SLAC linac for this configuration assuming 150 μm random misalignments of the quadrupoles and BPMs, 300 μm rms random misalignments of the accelerating structures, and a random transverse-longitudinal coupling of $g_{\text{rms}} = 2 \times 10^{-4}$ for the RF deflections. A transverse beam jitter equal to the rms beam size was also assumed. At a bunch length of 200 μm (rms), we find 25 % emittance growth along the linac. Emittance growth after the second compression is negligible due to the short bunch length and small energy spread.

An experimental test of the second bunch compressor including longitudinal and transverse effects has been designed and is under consideration. [4]

C. Undulator [5]

Based on 3D simulations of a continuous single-pass field structure, the following parameter set has been established

for the LCLS (water window) insertion device: 1) period = 8 cm; 2) peak field amplitude = 0.8 T; 3) $K = 6$; 4) total length = 60 m; 5) focussing betatron wavelength = 60 m. Design work has concentrated on a pure permanent magnet undulator structure with a superimposed focussing (FODO) field lattice generated by 40 cm long 15 T/m quadrupoles placed at 80cm intervals. To facilitate orbit and phase correction, beam position monitors are spaced at 1.6 m intervals, with corrector coils located every 3.2 m. Work on a short prototype section is in progress to help resolve selected engineering, magnet tolerance, and field measurement issues.

D. Beam Lines & Experimental Stations [6]

Due to the extreme brevity and peak intensity of the LCLS output radiation, special emphasis has been placed on the design of the beam line system. To minimize the likelihood of sustaining damage at the expected 10^{12} W/cm² normal-incidence power densities, a deflection scheme utilizing solid-state mirrors at grazing incidence has been developed [6]. Furthermore, the necessity of maintaining high reflectivity to avoid peak-power damage leads to the need for an ultra-high vacuum environment with provisions for in situ cleaning of all the reflecting surfaces. To exploit the diffraction-limited source size of the LCLS, the use of a simple monochromator configuration utilizing a single grating in a conical diffraction geometry, with the source as the effective entrance slit, is under consideration.

IV. ACKNOWLEDGEMENTS

This project benefitted greatly from a technical review in November, 1992. We thank the members of this review committee: Ilan Ben-Zvi (Chairman), Joseph Bisognano, Luis Elias, John Goldstein, Brian Newnam, Kem Robinson, Ross Schlueter, Andrew Sessler and Richard Sheffield.

V. REFERENCES

- [1] K.-J. Kim, M. Xie, E.T. Scharlemann, C. Pellegrini, and G. Travish, "Performance Characteristics, Optimization, and Error Tolerances of a 4nm FEL Based on the SLAC Linac." This conference - Mb26, 1993.
- [2] K. Bane, T. Raubenheimer, and J. Seeman, "Electron Transport of a Linac Coherent Light Source (LCLS) using the SLAC Linac." This conference - Jb19, 1993.
- [3] J. Rosenzweig, J. Smolin, G. Jackson, and T. Nicol, "Design of a High Duty Cycle, Asymmetric Emittance RF Photocathode Injector for Linear Collider Applications.." This conference - Ma9, 1993.
- [4] R. Holtzapple and J. Seeman, "Short Bunch Length and Low Emittance Test Area Using the SLAC Linac." This conference - Jb36, 1993.
- [5] R. Tatchyn, T. Boyce, K. Halbach, H.-D. Nuhn, J. Seeman, H. Winick, and C. Pellegrini, "Design Considerations for a 60 Meter Pure Permanent Magnet Undulator for the SLAC Linac Coherent Light Source (LCLS)." This conference - Mb52, 1993.
- [6] R. Tatchyn and P. Pianetta, "X-Ray Beam Lines and Beam Line Components for the SLAC Linac Coherent Light Source (LCLS)." This conference - Mb29, 1993.

The Vanderbilt University Compton Scattering X-Ray Experiment*

Perry A. Tompkins, Charles A. Brau, Wei Wei Dong and James W. Waters
Department of Physics and Astronomy, Vanderbilt University, Nashville, TN 37235

Frank E. Carroll, David R. Pickens and Ronald R. Price
Department of Radiology and Radiological Sciences, Vanderbilt University Medical Center, Nashville, TN 37232

Abstract

The Vanderbilt University Free-Electron Laser Program is developing the capability to create near-monochromatic X-rays for medical purposes. For this experiment we feed-back the normal infrared FEL light to collide with the electron beam. This causes Compton backscattering of the incident photons which creates X-rays. These X-rays cannot feed a X-ray laser, but they have a collimated intensity and tunability which will make them highly suitable for medical imaging and therapy. This paper reviews the present design of the experiment and focuses on the X-ray beam transport to be used. This transport must re-direct the X-ray beam to match a beam chase located in the vault ceiling at an angle of 40 degrees with respect to the electron beam axis. A description of the creation mechanism, X-Ray and electron beam properties are included.

I. INTRODUCTION

Tunable near-monochromatic X-ray beams will be produced by the Vanderbilt Free Electron Laser (FEL) in the near future. A team of physicians and scientists has been formed to complete this project for imaging and treatment of breast cancer. Near-monochromatic X-rays between 14 and 18 keV offer the greatest potential for lowering radiation dose to the breast, while boosting the signal-to-noise in the beam that passes through. As the project progresses, additional research directions will be added. This could include other types of medical imaging and treatment along with various topics presently associated with synchrotron radiation research.

A test stand has been created using a conventional mammography X-ray unit to investigate the various transport components during the development and assembly stages of the project. Initially this stand is being used to measure reflectance of the mosaic crystals discussed later in this paper.

The Vanderbilt University FEL, built by Sierra Laser Systems, is fairly compact and lases in the mid-infrared from ~2 to 8 μm [1]. The operator computer is a Apple Macintosh II-ci running National Instruments LabVIEW 2 software. The electron beam is produced by an ~43 MeV, 2.856 GHz rf traveling-wave linac. This beam is created in an rf electron gun with a LaB6 cathode. The wiggler is a 2.3 cm period, Halbach type, hybrid design, using permanent magnets with steel pole pieces. There are 208 SmCo permanent magnets used in the wiggler. Further details of the accelerator, wiggler, and laser performance have been published elsewhere[2].

II. THE COMPTON X-RAY PROJECT

A. X-ray Creation

When a photon collides with a free electron, its energy and direction change to conserve energy and momentum. When the electron is relativistic, and the photon has a low energy, or $\lambda_L \gg \lambda_C = h/mc = 2.42 \times 10^{-12} \text{ m}$, where λ_C is the Compton wavelength and λ_L the wavelength of the incident photon, the wavelength of the scattered photon (λ_S) is given by the formula:

$$\lambda_S = \lambda_L(1 + \gamma^2 \phi^2) / 4\gamma^2, \quad (1)$$

where ϕ is the angle through which the electron is scattered and γ is the Lorentz factor. For an infrared photon with a 2 μm wavelength scattered in the backward direction ($\phi = 0$) by a 43 MeV electron, the wavelength of the scattered photon is 0.7 \AA . This corresponds to an X-ray with an energy of 17.6 keV. The intense monochromatic FEL infrared beam will be the light source for this experiment. Since this beam is very monochromatic, when combined with the monoenergetic FEL electron beam, the X-rays produced by Compton scattering are quite monochromatic, especially when compared with conventional X-ray sources.

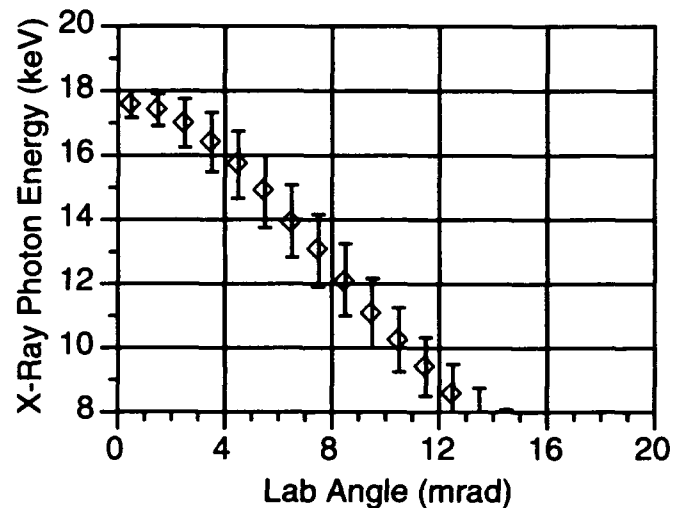


Figure 1. X-Ray Photon Energy Distribution as a Function of Angle.

The electron and the infrared beams will both be focused to create a 40 μm diameter interaction zone. The created X-ray beam will have a specific topology and bandwidth due to the electron beam's energy spread and emittance, and the photon beam's divergence (Figure 1). The central ray and off-axis rays will have a finite bandwidth. The off-axis rays will have decreasing average energy with increasing angle. Bandwidth considerations along with transport restrictions will define a

* Supported by the ONR, contract no. N 00014-91-C-0109.

"usable" containment angle of the beam. Interaction calculations, with a beam emittance of $4\pi \text{ mm} \cdot \text{mrad}$ and an energy spread of 0.5% indicate that the Compton scattering should yield $\sim 3.0 \times 10^8$ photons/sec in a 10 mrad full angle cone. The bandwidth for this X-ray beam is approximately 20% with a central maximum energy of 17.6 keV. By changing the photon wavelength and/or electron beam energy the central maximum can be tuned down to 14.5 keV. Enhancements of the FEL could bring the central maximum energy above 20 keV.

Additionally, Vanderbilt is developing a "Cerenkov-light" pumped free-electron laser resonator using our existing electron accelerator operating at reduced energy[3]. It will be continuously tunable between 200 and 50 microns in the far-infrared. If this beam is used to create another Compton source it could operate in the range from 100-400Å. This type of source could have many applications for additional research.

B. Applications

The creation of a powerful, tunable, near-monochromatic source of medium energy X-rays will herald a new and exceptionally diverse generation of diagnostic medical imaging techniques, as well as creating new therapeutic possibilities. In diagnostic radiology, higher keV radiation is associated with the production of unusable and objectionable scattered radiation. Photons of lower energy may add little to the diagnostic information obtained, but contribute heavily to the radiation dose to the patient. If it is possible to select radiation of optimal energy for the specific procedure, while eliminating those X-rays of higher and lower energy, radiologists and other scientists can significantly enhance their ability to perform very high contrast/low dose imaging. This could also assist in accomplishing *in vivo* trace element analysis and achieve 3-D X-ray imaging. An optimized system for breast imaging using monochromatic radiation such as that described here may reduce entrance exposure to the breast by a factor of 9 to 46[4].

III. THE X-RAY TRANSPORT

The use of the Compton X-ray facility at the Vanderbilt FEL is complicated by the design of the FEL building. The FEL is located in an accelerator vault beneath the laboratory level. In order to make near line-of-sight access between the two levels, a 12" PVC pipe was included within the 6 feet of concrete shielding. This pipe is oriented at an angle of $\sim 40^\circ$ Degrees in both θ and ϕ directions of a spherical coordinate system with z being the electron beam axis and x being beam left. Provision must be made to aim the X-rays up the pipe and into the laboratory.

A. Redirecting the Electron Beam

The original design for bringing the X-rays into the laboratory was to re-direct the electron beam along an alternate beamline and aim the electrons up the pipe[5]. The infrared beam would then be aimed in the down-pipe direction from within the vault. After the interaction, the electrons would be re-deflected before reaching the pipe and transported to the beam dump at the end of the vault. This design was abandoned due to the extreme complexity of the alternate beamline along with safety considerations. The design being

presently implemented incorporates broad-band mosaic crystals to deflect the X-ray beam after creation.

B. Mosaic Crystals

Crystals with a relatively large mosaic spread can reflect a range of different X-ray energies. This broadening of the crystal bandwidth includes a reduction in the maximum reflection efficiency. When compared to a conventional X-ray source our system is very monochromatic, but compared to an X-ray spectroscopist's needs, it is very broad band. Using the Bragg condition for X-ray reflection from a crystal, we identified a few potential crystals to transport the X-ray beam through the 40° bend. Of the possible choices, LiF and graphite seemed the best candidates. Sparks[6] gives the relative efficiencies of these reflections.

From his data it can be concluded that while the LiF may be very efficient in its near perfect crystalline form, it suffers greatly when modified to allow for a large mosaic spread. The $\sim 0.4^\circ$ mosaic graphite however should accept most of the 10 mrad divergence cone along with ~ 1 keV in energy spread ($\sim 6\%$ bandwidth which is more than 40% of the photon number shown in Figure 1) and reflect it with 25-50% efficiency. For our present experiments photon quantity is more important than a narrow bandwidth. The graphite mosaic crystals indicate a greater total photon flux delivered at $\sim 6\%$ energy bandwidth. Four crystals in first order can bend X-rays with energies up to 20.5 keV to the laboratory.

C. Four Crystals in First Order

Sequential reflections from four mosaic graphite crystals can be used to transport the X-ray beam to the laboratory. With a single reflection efficiency of 0.25-0.5 the total efficiency within the bandwidth and divergence acceptance should be between 0.004-0.063. By moving the crystals out of the plane defined by the electron beam axis and the PVC pipe axis, lower energy X-rays can be deflected through the same angles allowing the beam to have a parallel, energy independent, fixed transverse position in the PVC pipe. The beam vectors and crystal normal vectors are easily defined for each energy. This was done with Mathematica and the parameter space of the various crystal positions was explored. For each position and energy a different set of orientation vectors and coordinate positions and z positions was generated.

D. The X-Ray Interaction Zone And Transport

The X-ray experimental setup is shown in Figure 2. This figure is from the mechanical assembly drawings of the modified electron beam-line. Shown in Figure 2 is the electron chicane, the IR transport and the crystals of the X-ray transport. The IR beam is brought within anti-coincidence with the pre-chicane electron beam using a thin beryllium mirror. The IR and electron beams are focussed to a small spot at the interaction zone. The created X-rays pass through the beryllium mirror and a beryllium vacuum window with $>80\%$ transmission and onto the mosaic crystal beam transport. The electron beam is deflected before reaching the mirror. Each of the four crystals has its orientation and position controlled by a goniometric stage as shown in figure 3. These stages allow orientation of a normal vector from a point on the front surface of the crystal through a solid angle of 40° by 60° . Coupled with a 25 mm linear stage, each crystal can be placed to allow transport through the 40° bend.

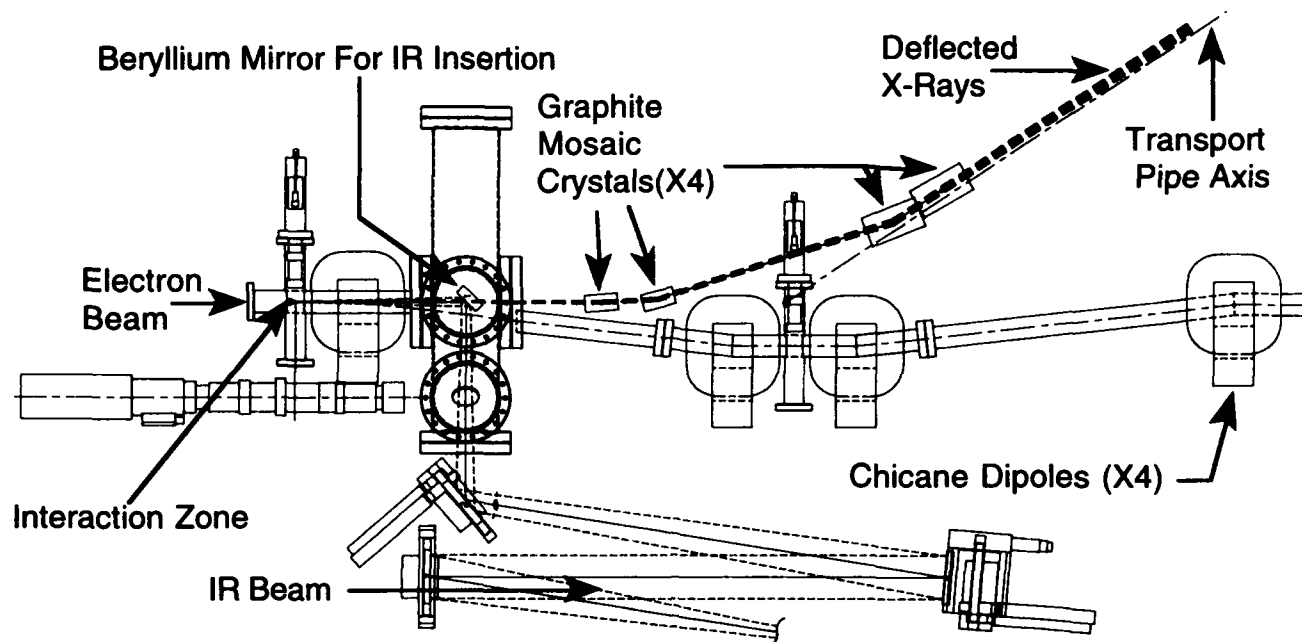


Figure 2. The Compton experiment assembly. This interaction zone and electron Chicane will be inserted into the present electron beamline. The system includes transports for the infrared, X-ray and electron beams.

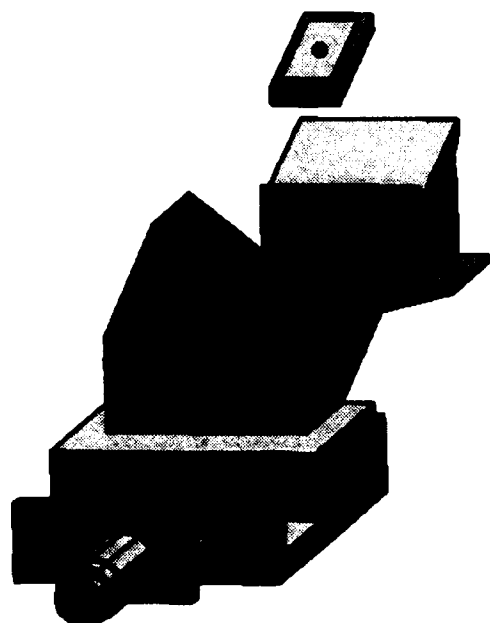


Figure 3. Each crystal will be controlled by a motion control goniometer combining a 25mm linear stage, an angular shim, two angular stages and a crystal holder. The system is set to allow orthogonal orientation of the crystal.

IV. CONCLUSIONS

Tunable near-monochromatic X-ray beams will be produced by the Vanderbilt FEL in 1993. Interaction calculations, with an electron beam emittance of $4\pi \text{ mm} \cdot \text{mrad}$ and an energy spread of 0.5% indicate that the Compton scattering should yield $\sim 3.0 \times 10^8$ photons/sec

in a 10 mrad full angle cone. The bandwidth for this X-ray beam is approximately 20% and should be initially tunable between 14.5-17.6 keV.

The four crystal transport system will accommodate X-rays from 14.5 keV to 20.5 keV with approximately 6% energy bandwidth. With reflectivities between 0.25-0.5 in first order, 4 crystals would transmit 0.004-0.063. Characterization of individual and paired crystals will be accomplished on the test-stand. This beam transport is being readied for insertion into the accelerator vault.

An optimized system for breast imaging using monochromatic radiation such as that described here may reduce entrance exposure to the breast by a factor of 9 to 46 times. Funding searches have been initiated to form this experiment into a compact hospital-sized instrument.

V. REFERENCES

- [1] P. A. Tompkins, *et.al.*, "Initial Operation of the Vanderbilt Free Electron Laser," Proc of the 1991 IEEE Particle Accelerator Conf., Apr 91, 1115.
- [2] Perry. A. Tompkins, *et.al.*, "The Vanderbilt University Free-Electron Laser X-Ray Facility," SPIE Proceedings 1736, 72, 1992.
- [3] J. E. Walsh and J. B. Murphy, J. Quant. Electron. QE-18, 1259 (1982).
- [4] Carroll F.E., *et.al.*, "Near-Monochromatic X-ray Beams Produced by the Free Electron Laser and Compton Backscatter," Invest Radiol, 25, 1990, 465.
- [5] W. D. Andrews, *et.al.*, "Development of the Vanderbilt Compton X-Ray Facility," NIM, Section A, A318, 189-196, 1992.
- [6] Cullie J. Sparks, Jr., "Mosaic Crystals for Obtaining Larger Energy Bands and High Intensities from Synchrotron Radiation Sources," SSRL Report No. 78/04, May 1978.

Observations of Effects of Ion Accumulation in the Maxwell Model 1.2-400 Synchrotron Light Source

R. P. Johnson *, D. Y. Wang, Maxwell Laboratories, Inc.

H. Bluem, Louisiana State University

*Now at CEBAF, Newport News, Virginia

Abstract

The commissioning phase of the Maxwell model 1.2-400 synchrotron light source was successfully completed at the end of August, 1992, with more than 200 mA accelerated to 1.3 GeV. This is the first synchrotron light source built by a commercial firm in the U.S. The injector is a 200 MeV linac. Ions trapped in the beam have played a major role in beam accumulation during injection, despite ion clearing electrodes which cover 70% of the circumference. The dependence of the maximum stacked current on the location of ion clearing electrodes and on the applied voltages is discussed. Other observed effects due to ions include the vertical blow-up of the beam at injection as seen on an optical monitor, and beam stability at negative chromaticity. These effects are discussed in relation to some prevailing theories.

Introduction

Ion trapping is a well known phenomena at various electron synchrotron facilities, including Aladdin at Wisconsin[1] and the SXLS at Brookhaven National Laboratory[2]. As a result of consultation with these facilities the Maxwell model 1.2-400 synchrotron [3] was designed with ion clearing electrodes (ICE) covering some 70% of the circumference of the ring. Electrodes were divided into six groups. All electrodes in a given group were placed at homologous positions in the lattice and were powered by the same power supply. The voltages applied to each group could thus be independently varied.

Ions can cause undesired tune spreads and chromaticities which limit the accumulated current when resonances are encountered. The

conditioning of the vacuum chamber by synchrotron radiation is thus delayed. However, the commissioning of the Maxwell model 1.2-400 synchrotron light source proceeded rapidly in the presence of ions. Figure 1 shows the stored current at 1.3 GeV versus the number of days spent in commissioning. Judicious control of ions in the beam with ICE's may actually aid the commissioning process.

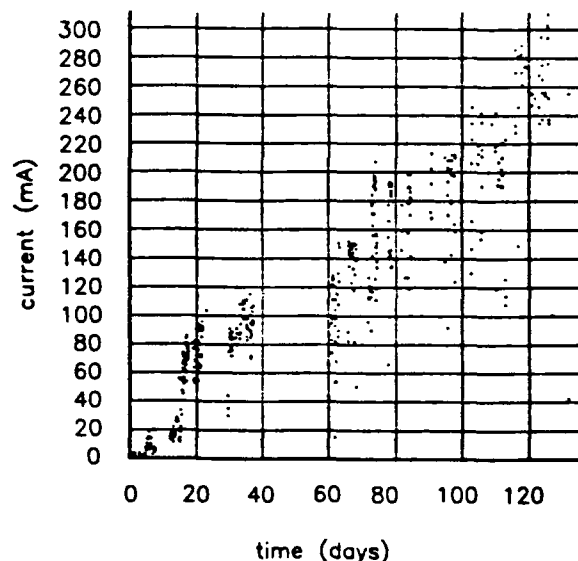


Fig. 1 Initial Current at 1.3 GeV vs. time
Since start of commissioning

Ions may stabilize the beam against instabilities to enable a greater stored current at injection. It was observed experimentally that for a given current and pressure, there was always an optimum ICE voltage. A larger voltage would clear ions more effectively, but this actually resulted in less current accumulated. At the same time, the vertical blow-up of the beam was a definite indication that ions are still trapped in the beam even at the optimum ICE voltage.

The main section of this paper will describe this and other ion effects more fully in relation to prevailing theories. Due to incomplete data, it is not possible to make detailed quantitative comparisons. But the observations are consistent with general understanding.

1. Observed Ion effects

a. Required ICE voltage as a function of stored current at injection

The required ICE voltage must increase linearly with stored current [2] in order to overcome the beam's self-potential. The exact voltage depends on beam dimensions and the geometry of ICE's within the vacuum chamber. For ICE's located within the dipoles (which were the most effective), it was estimated that for every mA of stored electron current, 6 volts would be necessary. In practice, during initial commissioning about 100 volts were needed just to store 2-10 mA's, and at 200 mA, about 300 volts were needed.

During initial commissioning, the vacuum chamber outgassing is significant. Probably a higher voltage is needed to clear ions rapidly, beyond the necessity of overcoming the beam's self-potential. At higher beam currents, which occurred after about 24 amp-hours of accumulated stored beam time, the fact that less voltage was needed could indicate substantial neutralization.

The experimental observations confirm that the figure of 6 volts/mA is a good rough estimate of the required ICE voltage.

For any given store, an optimum ICE setting is found. The effect of varying the ICE voltage by about 10-20 volts about the optimum on the accumulated current can be illustrated with the strip chart recording of one store as shown in figure 2. The trace shows the reading from a DCCT (Direct Current Current Transformer) in the synchrotron versus time. Current is continuously injected from the Linac at a repetition rate of 0.5 Hz. (The damping time is 1.5 seconds)

With a constant ICE voltage applied, the stored current rises linearly with time

initially and then "saturates". Subsequent changes in the "saturation" level are caused by changes in the ICE voltage of about 10-20 volts out of 200-400 volts. This shows how sensitive the stacked current is to the ICE voltage. Such small voltage changes cannot clear the beam of ions. Rather, this suggests fine adjustments in the ion density within the beam.

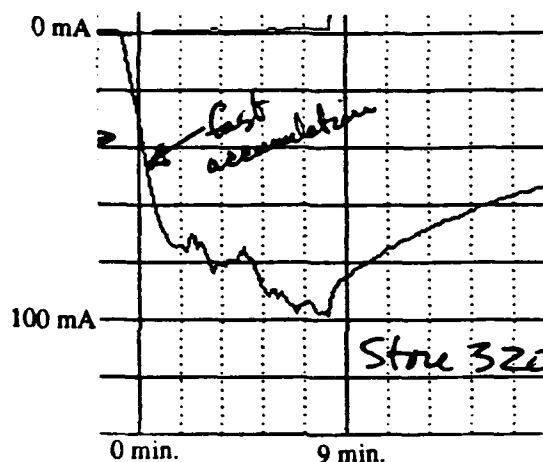


Fig. 2 Effect of ICE voltage adjustment on stacking

b. Location of most effective ICE

According to theory, ions tend to be trapped at sites along the circumference where there is an abrupt change in vacuum pipe geometry since a potential well is formed. For the Maxwell model 1.2-400, the dipole chamber to short straight section transition meets this criterion. The dipole chamber is rectangular in cross-section, with a vertical aperture of 50 mm, while the straight section is a round pipe with an inner diameter of 65 mm. Moreover, this location is where the beam size is minimum so that the beam potential is maximum.

It was found that the dipole ICE's were indeed the most effective in terms of controlling ions. Varying the dipole ICE voltage had the most significant effect on the amount of accumulated current, whereas most other ICE's had little effect. The dipole ICE's consisted of single flat plates located near the chamber bottoms. A negative voltage with respect to the vacuum chamber was applied.

During the initial period of commissioning, some of the dipole ICE's were shorted out. Their subsequent repair led to further increases in the current stacked. This

suggested that ions were present and had to be controlled throughout the entire ring.

c. Gaps in bunch train

It has been shown [4] that a gap in the bunch train can significantly improve the performance of a synchrotron by reducing the ion density. In this theory, the nearly stationary ions are periodically focussed by the electron bunches encountered. Whether ions are captured or not depends on whether their motion in this periodic lattice is stable or not.

For a given bunch fill pattern, one can calculate the critical mass of an ion which would be captured. Ions with lighter mass are not trapped. For the Maxwell model 1.2-400, a completely filled ring has 92 bunches. At a beam current of 100 mA and if only 50 buckets are filled, the critical mass was calculated to be about 0.01 (atomic weight). Typical ions are H_2 , CO or CO_2 which all have much larger masses. Therefore all such ions are predicted to be trapped.

Since ions should be captured even with a gap in the bunch train present, the ring was run with 50 as well as 92 bunches. As expected, the accumulated current was the same in both cases.

d. Vertical and horizontal coupling

Significant horizontal to vertical coupling was caused by ions. This was most easily observed at 1.3 GeV. At this beam energy, the ICE voltage could be set to zero with no reduction in stored beam lifetime. The beam spot within a dipole chamber was imaged by a TV vidicon through optics arranged such that only the visible portion of synchrotron radiation was detected. What is observed is that the vertical beam size more than doubles to become equal to the horizontal beam size.

At injection energy, the observation was less direct since the ICE voltage could not be turned off without losing beam. However, it is seen that as the current increases, the beam spot gradually evolves from a horizontal ellipse to nearly a round spot. By inference from the observations at 1.3 GeV, more ions are being trapped as the beam current increases.

e. Chromaticity correction

It was found that the sextupole strength needed to attain zero chromaticity was about half of that predicted. This was not directly verified to be caused by ions. However, given that ions are trapped in the beam and that they form a non-linear lens, this is the most likely explanation.

Summary:

In the MLI model 1.2-400, various ion effects have been observed. The locations of ions pockets and the necessary ICE voltages can be estimated by theory. At any time, there exists an optimal ICE voltage for the most accumulated current at injection. At this optimal ICE voltage, some ions are still trapped in the beam. This suggests that ions may be beneficially stabilizing the beam. This is consistent with the experience at SXLS [2]. It has been conjectured that the tune spread caused by ions and consequent Landau damping may be the reason for this stabilization. Further analytical work is needed.

References

- [1] E.M Rowe, AIP Conference Proceedings No. 199, 93 (1989)
- [2] H. Halama, E. Bozoki, Proceedings of PAC, San Francisco, 2313 (1991)
- [3] M.A. Green et al., NIM A291, 464 (1990)
B.C. Craft et al., NIM B40/41, 379 (1989)
R.C. Sah, NIM B56/57, 379 (1991)
D.Y. Wang et al., San Francisco: PAC, 2727, (1991)
R.P. Johnson et al., Berlin: EPAC, 197 (1992)
P. Letellier et al., Berlin: EPAC, 575 (1992)
- [4] M. Barton, Nuc. Inst. & Meth. A243, p.278 (1983)

A Progress Report on the Laboratório Nacional de Luz Síncrotron (Brazil)

A. R. D. Rodrigues^(a), C.E.T. Gonçalves da Silva^(b), and D. Wisnivesky^(b)

Laboratório Nacional de Luz Síncrotron

Cx. P. 6192 Campinas 13083 SP BRAZIL

Abstract

We present a progress report on the design and construction of the Brazilian synchrotron light source facility, which is based on a 1.15 GeV (nominal energy) electron storage ring. To date, the first part of the LINAC injector (50 MeV) has been completed and is in operation. Prototypes for all the ring main components - magnets, vacuum chambers, kickers and septa, power supplies, control system, beam position monitors, RF cavity - have been developed in-house and characterized. An update of the production of these components, which is already under way, is presented here. A report will be given on the experience acquired with laser cutting technique for the production of laminated magnets, pioneered by LNLS.

INTRODUCTION

The Brazilian synchrotron light source is based on an electron storage ring, the main parameters of which are listed in Table I.

Energy	1.15 GeV
Injection energy	0.1 GeV
Nominal current	100 mA
Circumference	88.804 m
RF frequency	476 MHz
Natural emittance	65.3(34.1) nm·rad
Horizontal betatron tune	5.27(5.72)
Vertical betatron tune	2.17(1.85)
Synchrotron tune	9.420 1/1000
Momentum compaction	$8.72 \cdot 10^{-3}$
Energy spread	0.059 %
Horizontal chromaticity	-8.17(-18.71)
Vertical chromaticity	-9.70(-9.23)

TABLE I - Main parameters of the UVX ring normal mode of operation (low emittance mode in parentheses).

Thus far five different modes of operation have been studied. In three of these modes the six-fold symmetry is preserved, but, by using different quadrupole and sextupole excitations, the natural emittance can be varied (130, 60 - shown above - and 30 nm·rad). In a two-fold symmetric mode, a very small vertical betatron function value is obtained in the middle of a straight section. The minimum physical aperture at this point can reach 6.8 mm. The operation of a small gap insertion device is envisaged in this mode. Finally, the fifth mode is three-fold symmetric and allows the operation of the ring in a quasi-isochronous mode, with a momentum compaction factor two orders of magnitude smaller than in the normal mode¹.

MAGNETS

The dipoles are curved C-type laminated magnets, with the staggered laminations held together by tie-rods, not welded. The laminations are laser cut from low carbon steel sheets of 1.5 mm thickness. By the end of the process 11,112 laminations will have been cut with the required tolerances and reproducibility. The last laminations are to be cut on June 4, 1993. Six core are already assembled and the remaining six will be assembled by the end of June, 1993. Fully assembled cores show measured standard deviation from the design gap smaller than ± 25 microns.

Figure 1 shows the results for the transverse field measured at the central longitudinal point of the dipole, for various excitation currents.

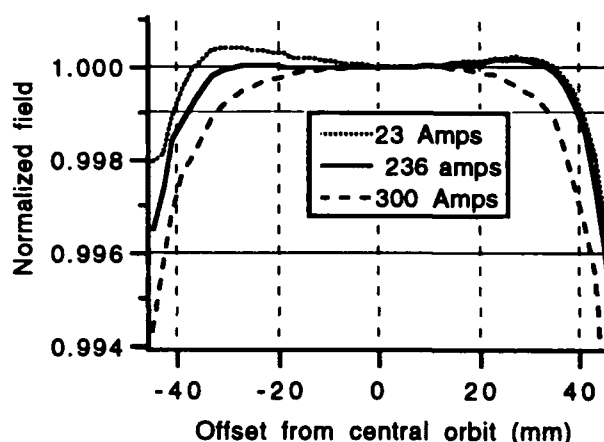


FIGURE 1 - Transverse profile of the field (dipole center).

Figure 2 shows the results for the longitudinally integrated field as a function of the transverse position (0 is the ideal orbit).

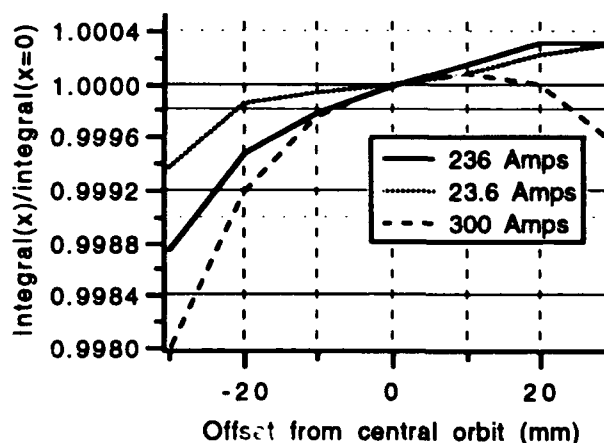


FIGURE 2 - Integrated longitudinal field at different transverse positions.

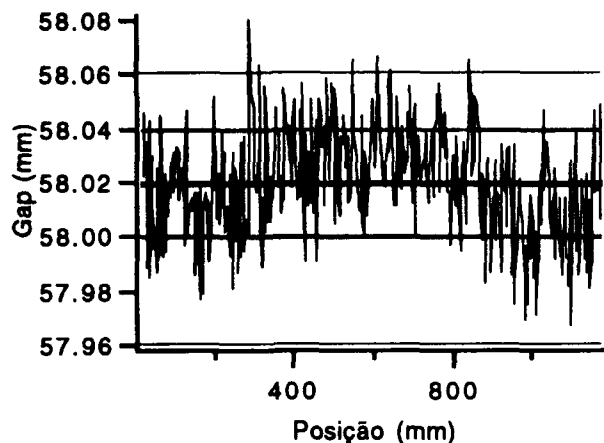


FIGURE 3 - Gap measurements for dipole #2. The average value is 58.0194 mm (middle thick straight line), with a standard deviation of 19.7 μm (the upper and lower thick lines indicate the average plus and minus one standard deviation, respectively).

Figure 3 shows the results of the dipole gap measurements for dipole #2.

Although the magnets were designed to operate at 1.4 T, it turns out that they can be run at higher fields, pushing the ring energy up to about 1.35 GeV. This is very desirable for the X-ray community, which can make use of radiation from the bending magnets, without waiting for the installation of the planned wiggler insertion.

Prototype work has already been done for quadrupoles and sextupoles, with production scheduled to begin immediately after the dipole laminations have been cut. The prototypes were characterized by the standard rotating coil set-up. A second measurement system, based on an integrator, is being developed.

VACUUM CHAMBERS

The standard bending magnet vacuum chambers are produced from 316 L steel and have light ports at 4 and 15 degrees. The parts are laser cut and TIG welded. The chamber has the following characteristics: (i) a copper water cooled absorber on the outer (radiation) side, with slits for extraction of synchrotron light; (ii) a permanent NEG strip on the inner side and a removable NEG cartridge on the outer side (placed in between the copper absorber and the chamber outer wall); (iii) metal-coated ceramic (vertical) clearing electrodes on the inner side. Thus far, LNLS has closed, baked and pumped-down six of the twelve vacuum chambers. The NEG strips have not been activated yet. They are all under vacuum better than 10^{-9} mbar.

There will also be non-standard vacuum chambers with ports at 0 and 15 degrees for insertion devices and bending magnet radiation, respectively, and one chamber with a backport for studies of X-ray scattering at $\pi/2$ Bragg angle. They are under construction.

Figure 4 shows the pump-down and bake-out curves for the bending magnet chamber #6.

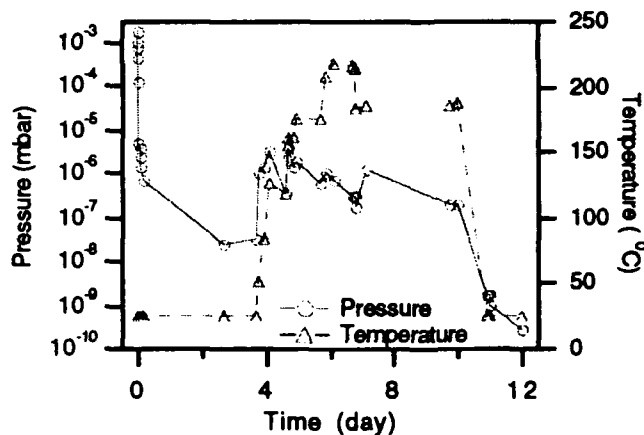


FIGURE 4 - Pump-down and bake-out curves (pressure and temperature) for bending magnet chamber #6.

RF CAVITY

The RF system is designed to supply 56 kW CW to the cavity, sufficient to supply the required 5.6 kW per 100 mA of stored current at 1.15 GeV. The RF power is produced by a 62 kW CW klystron. The 160 kW transmitter, including the main power supply and all auxiliary controls and power supplies, have been completed. The transmitter has been tested with a resistive load. The high power klystron is specified and in the process of being procured. The klystron pre-amplifier, as well as the cavity control system, are completed and tested.

LNLS is developing a single cell RF cavity for use in its storage ring. All the cavity designs were evaluated using the code URMEL-T². A scaled down version (1.2 GHz) in Al has been fully characterized. In this Conference, preliminary results for the Al prototype of the 476 MHz cavity are being reported for the 476 MHz cavity which is under development³. A first prototype was built, based on the proposed design for the PEP II B factory. It uses wave guide suppressors, which couple to HOM. Measurements indicate that there is a very strong reduction of the Q value and shunt impedance of the HOM which could cause multibunch instabilities. The cavity which will be effectively used in the ring will be made of Cu and the first full scale prototype will be built in the second Semester of 1993.

OTHER COMPONENTS

The transport line from the LINAC to the ring consists of a quadrupole doublet immediately after the LINAC at underground level, a vertical achromatic system to transfer the beam to the hall level and a horizontal achromatic arc leading to the injection point. The whole line uses 11 quadrupoles and 3 dipoles. No hardware development has as yet taken place.

The injection will be performed by thick and thin septa, in the transport line, and three kickers in the ring. The kicker developed and built to date have ferrite core inside the vacuum chamber and provides pulses with 150 ns of rise-time, 200 ns duration and 200 ns fall-time. A prototype for the thin

septum has been built and operated with 30 μ s sinusoidal pulses peaking at nominal field.

The 24 beam position monitors will be of the stripline type and their acquisition electronics, still under development, will allow both circulating beam and single shot readouts. The ring current is to be measured by a commercial DCCT monitor.

The control system consists of a few serial networks of local controllers, at the level of the ring equipments, connected to a parallel (SCSI) network of commercial desktop computers via a concentrator. The hardware and software library have been developed and tested.

The high precision power supplies for the storage ring magnets have been developed at LNLS using high power switching IGBTs⁴. Extensive performance tests of this new type of power supply have been made with excellent results on stability (8 ppm/K), ripple (5 ppm on the magnetic field), and reproducibility of the current (0.01 %). The power supply has a dynamic range of 1 - 100 and can be ramped, without tracking error, to the maximum current. A single power supply, 300 A, 1000 V, is used for the 12 dipoles. The 36 quadrupoles are arranged in three families. Nevertheless, to gain flexibility, every 2 quadrupoles belonging to the non-dispersive straight sections have a separate power supply, while the 12 remaining quads have a single power supply. Thus a total of thirteen power supplies are required for the quadrupoles. In-house production is under way and is scheduled to be completed by the end of 1993. Power supplies for the sextupoles, steering coils and transport line magnets have been prototyped and production is scheduled to start in the second Semester of 1993. In all, 75 different power supplies, with power ranging from 350 W to 300 kW, are being produced and expected to be finished in the first Semester of 1994.

INSTRUMENTATION

In parallel with the construction of the storage ring, LNLS has developed instrumentation for the beamlines.

A toroidal grating monochromator beamline, covering the spectral range from 12 to 300 eV photon energy has been designed, built and tested in Campinas. It is now installed on the storage ring of the Center for Advanced Microstructures and Devices (CAMD) of Louisiana State University. It will return to LNLS upon completion of the UVX ring⁵. A spherical element monochromator beamline is under development.

Two- and 4-crystal X-ray monochromators of original design⁶ have been built and successfully tested at DCI (LURE, France)⁷. The 4-crystal monochromator has performed exceptionally well, with an energy resolution of $8 \cdot 10^{-6}$ at 10 keV.

Two beamlines for X-rays, one for small angle scattering (SAXS) and another for EXAFS, are in advanced stages of construction. The former uses a one-bent-crystal monochromator, the third type of X-ray monochromator

developed by LNLS. Additional beamlines are being designed.

In total, six beam lines will be operational at LNLS when the storage ring is completed: two for VUV radiation and four for X rays.

CONCLUSION

Construction of the storage ring building has started, early in 1993, with the LINAC tunnel. The tunnel will be completed in June 1993, when construction of the main storage ring and experimental hall is scheduled to begin.

In spite of severe financial constraints over the past three years, specially in the last eighteen months, the LNLS project has moved ahead, in the construction of the light source, scientific instrumentation, and buildings. There are indications that financial constraints will be alleviated in the near future, allowing the speedy conclusion of the storage ring.

Innovative designs and developments for storage ring components and beam lines have been pursued with success. The relative isolation of LNLS, imposed by both geography and finances, has been a spur to try new designs and concepts, ranging from magnet production to power supplies to scientific instruments, which emphasize low cost, high quality and superior performance. Commissioning of the storage ring, expected to start in late 1994, will be the crucial test of these new developments.

ACKNOWLEDGEMENTS

The authors would like to acknowledge all their collaborators in the technical and scientific divisions of LNLS, who have contributed, directly and indirectly, to the preparation of this progress report.

REFERENCES

- (a) On leave from the University of São Paulo (USP).
- (b) Also at State University of Campinas (UNICAMP).
- ¹ For details, see the paper by Liu Lin and Gonçalves da Silva in these Proceedings (poster Ga 84).
- ² U. Laströer, U. van Rienen, T. Weiland, "URMEL and URMEL-T User Guide", DESY M-17 03 (1987).
- ³ For details, see the paper by Wisnivesky *et al.* (poster Sa 118).
- ⁴ J. A. Pomilio, D. Wisnivesky, and A.C. Lira, IEEE Trans. on Nuclear Science, **39**, 1506 (1992).
- ⁵ A. Rubens B. de Castro, P.T. Fonseca, J.G. Pacheco, J.E. Verdugo, M.S.Z. Graeff, and G.B. Fraguas, Brazilian J. of Phys. **23**, 53 (1993); P.T. Fonseca *et al.*, Rev. Sci. Instrum. **63**, 1256 (1992).
- ⁶ LNLS patents.
- ⁷ H. Tolentino, A.R.D. Rodrigues, C. Cusatis, and I. Mazzaro, Synchrotron Rad. News, **6**, No.2, p.28 (1993).

An Overview of the PLS Project*

Tong-Nyong Lee

Pohang Accelerator Laboratory, POSTECH
P. O. Box 125, Pohang, Korea 790-600

Abstract

PLS (Pohang Light Source) is a synchrotron radiation facility currently under construction in Pohang, Korea. It consists of a 2-GeV full energy injector linac, a storage ring, and three initial beam lines. The PLS belongs to a third generation machine with an expected beam emittance of 12 nm rad. The commissioning of the PLS is scheduled to take place toward the late fall of 1994. The facility will be opened to users by mid-1995 and will eventually provide high brightness source of radiation in the wide spectral region from bending magnets and insertion devices.

I. INTRODUCTION

Construction of the Pohang Light Source (PLS) in Pohang, Korea is well in under progress since the ground-breaking of the site in April of 1991. The main part of the accelerator facility consists of a full energy injector linac and a storage ring optimized at 2-GeV of electron energy [1]. The PLS belongs to a third generation light source with an expected emittance of 12 nm rad. Ten 6.8-m long straight sections are available for installation of insertion devices. Two initial bending magnet beamlines and a superconducting wiggler are under construction. The PLS conventional facility which includes the linear accelerator buildings with a total floor space of 38,678 m² have been completed 87% of its total schedule as of April, 1993. Figure 1 shows a general layout of the PLS facility. The machine installations for both the injector linac and the storage ring are under progress. The commissioning of the injector linac and storage ring will be taken place respectively by beginning and fall of 1994.

II. INJECTOR LINAC

The electron linac consists of 60-MeV preinjector and 2-GeV main linac which are located 6 meters below the ground level. Total of 42 SLAC-type accelerating columns are powered by 11 klystrons and 10 pulse compressors. A nominal beam energy is 2-GeV and total length of the linac is 150 m. The linac will be operated at 10 Hz when the beam is injected into the storage ring injection system via 98 m long beam transfer line which will bring the beam above the ground level. A detailed description of the PLS injector linac can be found in this proceedings [2].

III. STORAGE RING

A. Lattice and Magnets

The storage ring lattice has a Triple Bend Achromat structure with 12 superperiods and total circumference of the ring is

280.56 m. Table 1 summarizes major storage ring parameters. There are 3 flat dipole magnets, 12 quadrupoles, and 4 sextupoles in each superperiod. Figure 2 shows the PLS magnetic lattice of one superperiod. A large number of quadrupoles provides flexibility and diversity. Two pairs of sextupoles, one focusing and one defocusing are used for chromaticity correction. The required strengths of these sextupoles are considerably smaller than those for other third generation light sources, resulting in smaller nonlinear effects and somewhat larger dynamic aperture. The sextupoles have additional horizontal and vertical trim windings to correct the closed orbit distortions and to control the skew quadrupole components. The closed orbit is monitored by total of 108 beam position monitors. Correction of the orbit is accomplished by 82 horizontal and 82 vertical dipoles distributed around the ring.

Table 1: Major storage ring parameters

Nominal energy	2 GeV
Circumference	280.56 m
Harmonic number	468
Radio Frequency	500.082 MHz
Critical photon energy	2.8 keV
Maximum current	
Single bunch mode	7.0 mA
Multi bunch mode	100 mA
Natural emittance	12 x 10 ⁻⁹ m rad
Available straight section for insertion device	10
Time structure	20 ~ 50 psec
Beam lifetime	> 5 hours
RMS beam size at insertion device center	
σ_x	330 μ m
σ_y	70 μ m
Energy loss per turn from bending magnet	225 keV

The injection system of the storage ring consists of four bump magnets and one Lambertson septum magnet. The beam from the linac is vertically bent 8° by means of Lambertson magnet in order to make the beam level the same as the storage ring orbit.

Prototype magnets for the storage ring dipole, quadrupole, sextupole, and correction dipoles (all supplied by Hyundai Electrical Engineering Co.) have been examined and the field measurements have been performed. The magnetic field error multipole components are found to be within allowable tolerances. All 36 bending magnets have now been delivered and the field measurements have been performed. The delivery of the remaining quadrupoles, sextupoles, and correction dipoles will

* Work supported by Pohang Iron & Steel Co. and Ministry of Science and Technology, Korea.

be completed by the beginning of 1994. Prototype power supplies for the magnets have been designed and tested successfully. The main products are now being delivered by POSCON Co. and Daewoo Heavy Industries Co.

B. Vacuum Chamber

The storage ring vacuum chamber is made of aluminum alloy 5083-H 321. Each superperiod has two sector chambers (7-m and 10-m long) and one straight section. Each sector chamber consists of a top and a bottom pieces and these are machined separately and welded together. Three beam line ports per superperiod are provided, one from insertion device and two from a middle bending magnet. The vacuum chamber is divided into two regions, a beam channel and an antechamber in order to reduce vacuum problem in the beam channel caused by photon induced desorption. A number of water-cooled photon stops are positioned to prevent the synchrotron radiation striking the chamber wall directly, except the beamline ports. The storage ring vacuum system is pumped by sputter ion pumps (SIP) and combination pumps consisting of lumped non-evaporable getter pump (NEG) and SIP. The combination pumps are located directly below each photon stops. So far, three main sector chambers which are mounted on supporting girders have been evacuated to the order of 10^{-10} torr and installed into the storage ring tunnel.

C. Survey and Alignment

Since the PLS is a third generation machine, its components should be placed as accurately as possible within the respective allowable tolerances. In order to control the absolute position of the PLS components, a global reference network is formed based on the PLS coordinate system. There are total of ten global reference points: four on the surrounding hill tops, two on the linac and four on the storage ring tunnel floor. These ten geodetic points are to be sighted directly each other to form a surface network. This is done by penetration hole right above the geodetic points and the platform built at the roof top of the storage ring building. Based on the 10 geodetic points, the

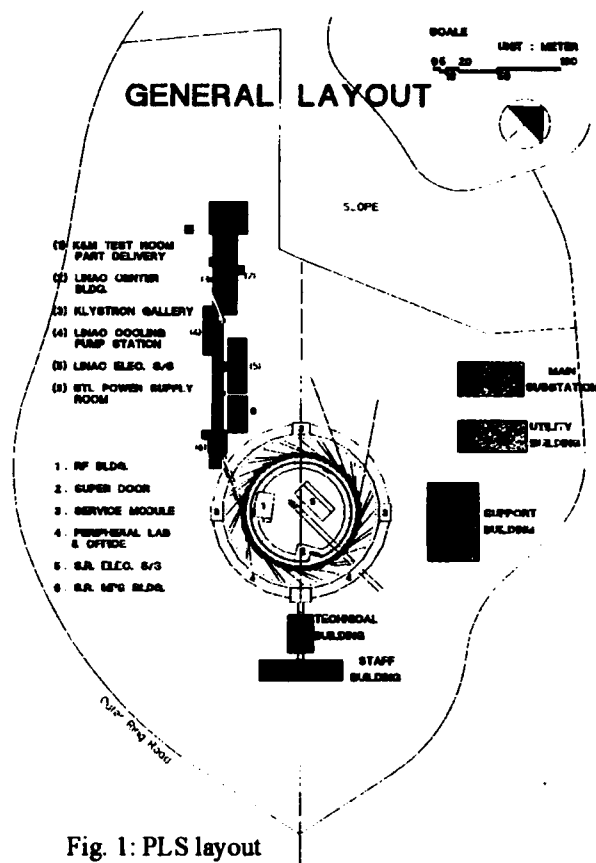


Fig. 1: PLS layout

storage ring control network is formed, which consists of 48 monuments fixed at inner wall brackets of the tunnel.

D. Storage Ring RF Cavity

The storage ring RF cavity system will have four single cell cavities all installed in the dispersion free straight section just before the injection straight. The storage ring RF system has a provision to increase the stored beam current to 400 mA at electron energy of 2-GeV. For the initial phase of commissioning however, only two cavities will be used. Accelerating fre-

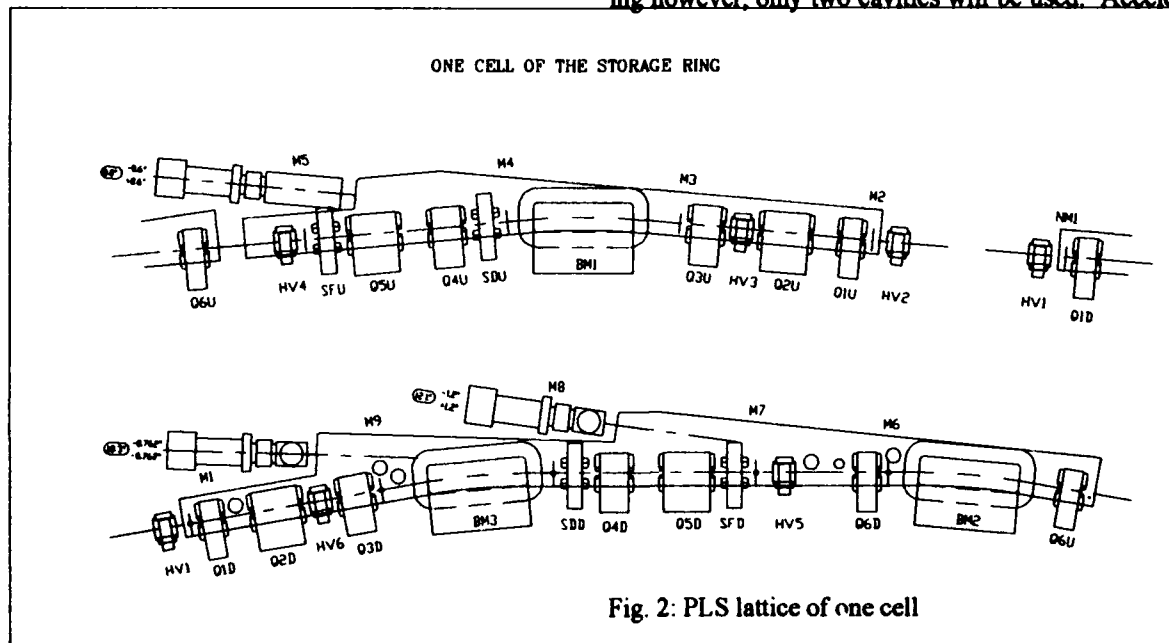


Fig. 2: PLS lattice of one cell

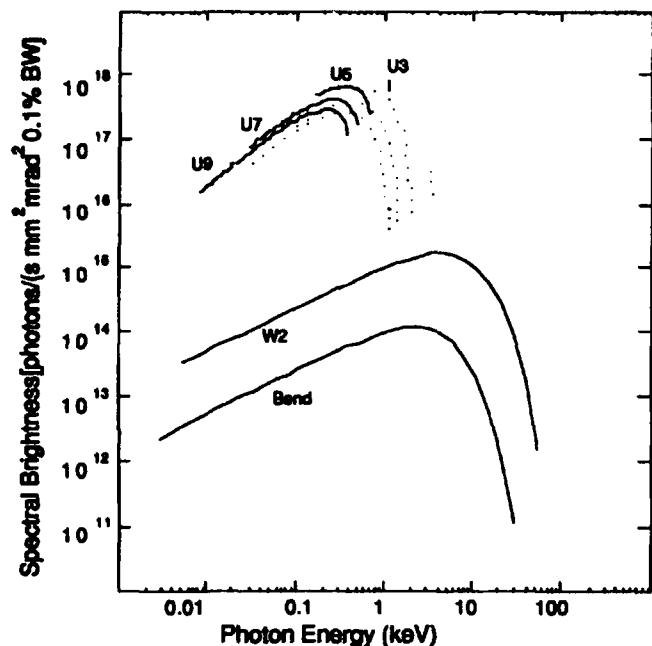


Fig. 3: Spectral brightness of the PLS photon beam

quency of the storage ring is chosen to be 500.082 MHz. High power test of the prototype cavity (fabricated by Toshiba Co., Japan) powered by a 60-kW klystron (Harris TVT Co., England) has been made successfully and the second cavity will be delivered by the end of 1993.

E. Instrument and Control

The PLS control system consists of a host computer, an expandable set of console computers, and VME-bus based Data Acquisition and Control Systems (DACS). The DACS consists of Subsystem Control Computers (SCC), Machine Interface Units (MIU), and low level communication networks. It performs many control and monitor functions, such as reading and setting parameter values of machine components, feedback control, alarm handling, and raw data processing, etc. A number of beam diagnostic monitors are used in the storage ring in order to obtain essential beam parameters, such as beam position, beam current, beam intensity profiles, betatron tune, etc. These includes 108 beam position monitors, a DC current transformer, two photon beam position monitors, two striplines, six screen monitors, and a scraper.

IV. BEAMLINES

PLS bending magnets with a field strength of 1.058 T and a beam energy of 2-GeV operation, the critical photon energy is 2.8 keV. Figure 3 shows spectral brightness as a function of photon energy and Table 2 indicates some parameters for possible PLS insertion devices. There will be two experimental beamlines from the bending magnets, in the initial phase, each for vacuum ultraviolet (VUV) and X-ray, respectively. For the VUV beamline, a spherical grating monochromator which accepts 10 mrad of the radiation are being constructed with a set

of five gratings. It will deliver photon energies between 13 and 1,250 eV mainly for photoemission studies. This beamline is also designed to accommodate another branch for Seya-Namioka optics for lower energy photons.

Table 2: PLS insertion device (ID) parameters

ID*	Period (cm)	No. of period	Field (T)
U3	3.0	140	0.22
U5	5.0	80	0.56
U7	7.0	60	0.90
U9	9.0	48	1.18
W2	15	20	2.0
W6	110	1	6.0

* U for undulator, W for wiggler.

For the x-ray beamline, a mirror will accept 4 mrad of radiation and a double crystal monochromator with a fixed exit beam position is used to give focused photon beam at photon energies between 3 and 12 keV. This beamline will be mainly used for X-ray diffraction and XAFS experiments. In addition to the two bending magnet beamlines, a 7.5 Tesla, 3 poles superconducting wiggler is also under construction in collaboration with the Budker Institute of Nuclear Physics, Russia. This beamline will provide hard X-ray region by general broad band radiation up to 30 keV of photon energy. In the normal operation mode, the time structure of the synchrotron radiation will comprise pulses with a FWHM of 20 ~ 50 ps with a minimum separation of 2 ns between pulses.

V. SUMMARY

The PLS project officially started in April of 1988. The PLS conventional facility is near completion, and the machine installation for the injector linac and the storage ring is at its peak. The commissioning will start toward the end of 1994. The project is funded jointly by Pohang Iron and Steel Company and the Ministry of Science and Technology of the Korean government. The PLS will be the national user's facility and will eventually provide high brightness radiation up to 30 keV of photon energy.

VI. REFERENCES

- [1]. *Design Report of Pohang Light Source*, Revised ed. (Pohang Accelerator Laboratory, POSTECH, January 1992).
- [2]. W. Namkung, et al., "Progress of PLS 2-GeV Linac," these proceedings.

PRESENT STATUS OF SRRC

Edward Yen
Synchrotron Radiation Research Center
No. 1 R&D Road VI, Hsinchu Science-Based Industrial Park
Hsinchu, Taiwan, Republic of China

ABSTRACT

The Synchrotron Radiation Research Center (SRRC) has been established to construct and operate a 1.3 GeV third generation synchrotron radiation facility at Hsinchu, Taiwan, Republic of China. Following is a brief report on its present status.

I. INTRODUCTION

A. Site

Hsinchu is about 75 kilometer south of Taipei. SRRC is located at the northwest bound of the Hsinchu Science-Based Industrial Park in the vicinity of two leading technical universities, namely, the National Tsing Hua University and the National Chiao Tung University, and the leading Industrial and Technological Research Institutes of Taiwan. The SRRC site is triangular in shape with an area of 15 hectares.

B. General Characteristics of SRRC

The SRRC synchrotron layout is shown in Figure 1. The

Booster and the Storage Ring Buildings are in a lower and upper level with a height difference of 4 m between them. The Booster and the Storage Ring are connected by a 70 m BTS (Booster-to-Storage Ring) transport line. The injection system consists of an electron gun, a 50 MeV linac and a 1.3 GeV booster synchrotron. The storage ring is characterized by a circumference of 120 m, a 6-fold symmetry, and 6 straight sections, with each 6 m long.

The major parameters of the injector and the storage ring are given in Table 1 and Table 2 respectively.

Table 1 Design Parameters of the Injector

Linac energy	50 MeV
Linac current	30 mA
(multi-bunch mode, average current)	
Booster energy	1.3 GeV
Booster current	5 mA
Booster pulse rate	10 Hz
	(for positron option)

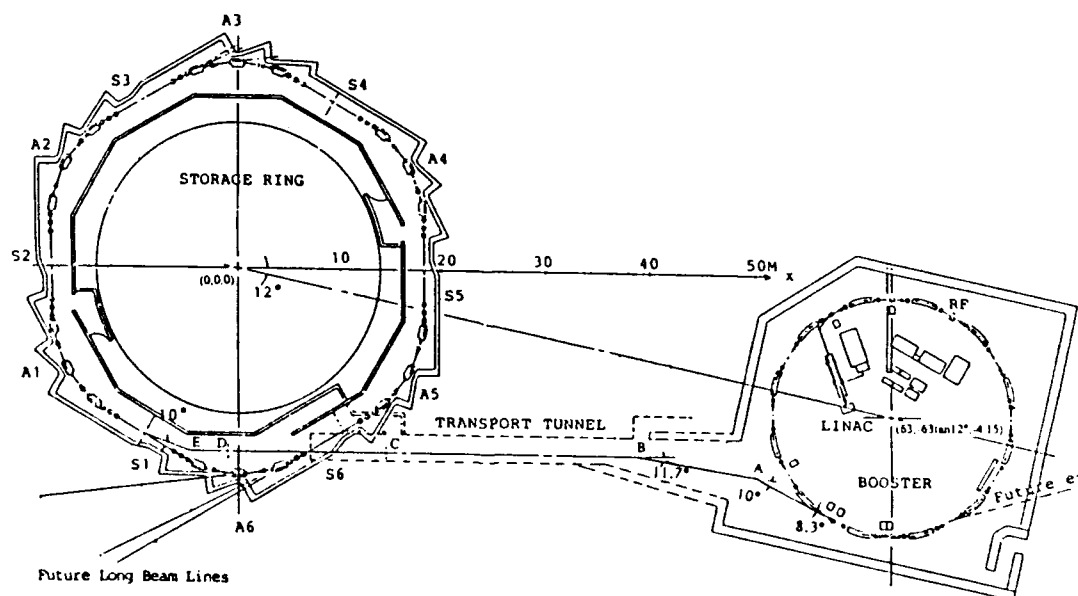


Figure 1. SRRC Synchrotron Layout

Table 2. Major Parameters of the Storage Ring

Lattice structure	TBA (combined function bending magnets)		Orbital period	400.3	ns
Nominal energy	1.3	GeV	Radio frequency	499.654	MHz
Nominal circulating current, multibunch	200	mA	Harmonic number	200	
Number of stored electron, multibunch	$5 \cdot 10^{11}$		Nominal peak rf voltage	0.8	MV
Nominal circulating current, single bunch	5	mA	Number of superperiods	6	
Number of stored electron, single bunch	$1.25 \cdot 10^{10}$		Insertion straight section length	6	m
Natural emittance	$1.92 \cdot 10^{-8}$	m*rad	Bending field	1.24	T
Natural energy spread, rms	$6.6 \cdot 10^{-4}$		Bending radius	3.495	m
Relative energy spread, rms			Injection energy	1.3	GeV
Multibunch	$6.6 \cdot 10^{-4}$		Number of dipoles	18	
Single bunch	$6.6 \cdot 10^{-4}$		Number of quadrupoles	48	
Bunch length, rms (1σ), natural	7.4	mm	Number of sextupoles	24	
Bunch length, (2σ), natural	49	ps	Momentum compaction factor	$6.78 \cdot 10^{-3}$	
Bunch length, (2σ), nominal current			Betatron tunes		
Multibunch	49	ps	Horizontal	7.18	
Single bunch	49	ps	Vertical	4.13	
Beam lifetime, half-life			Synchrotron tune	$1.15 \cdot 10^{-2}$	
Gas scattering lifetime at 1 n Torr			Natural chromaticities		
20 mm vertical gap	39	hr	Horizontal	-15.261	
Touschek lifetime at nominal current			Vertical	-7.885	
Multibunch	19	hr	Damping time		
Single bunch	5.5	hr	Horizontal	10.691	ms
Filling time			Vertical	14.397	ms
Multibunch	10	sec	Longitudinal	8.708	ms
Few bunch	5	sec/bunch	Envelope function beta x at insertion	10.52	m
Circumference	120	m	Envelope function beta y at insertion	2.94	m
			Beam size (1σ) at insertion middle		
			Horizontal	0.428	mm
			Vertical (10% emittance ratio)	0.428	mm
			Critical photon energy (dipole)	1.39	keV

Optical Functions

TBA, Tune (7.18, 4.13)

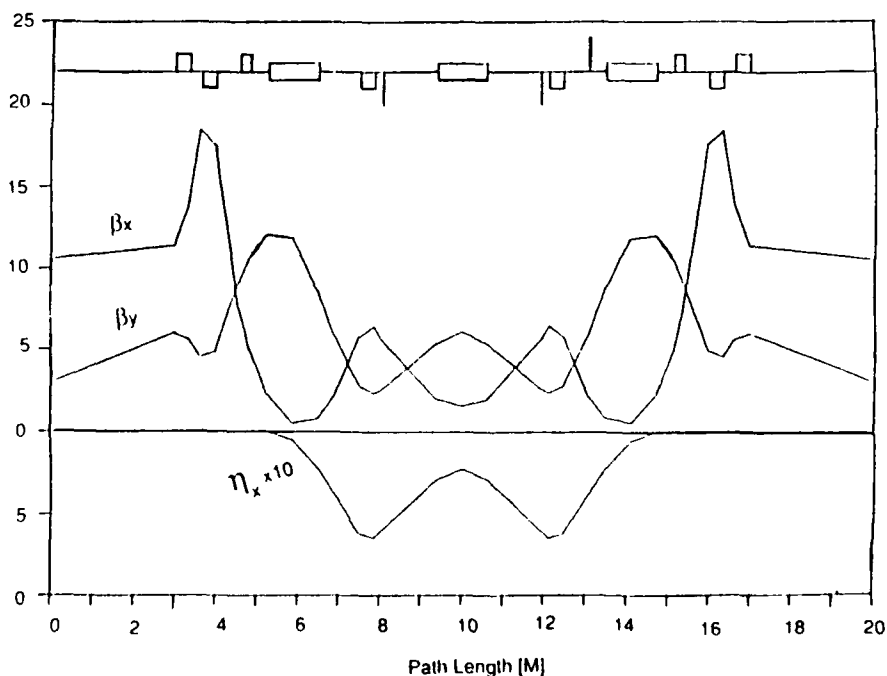


Figure 2. The Optical Functions of the Lattice for One Superperiod

The TBA lattice with horizontal emittance of 1.92×10^{-8} mrad was chosen for the ring. There are six superperiods. The optical functions of the lattice for one superperiod are shown in Figure 2.

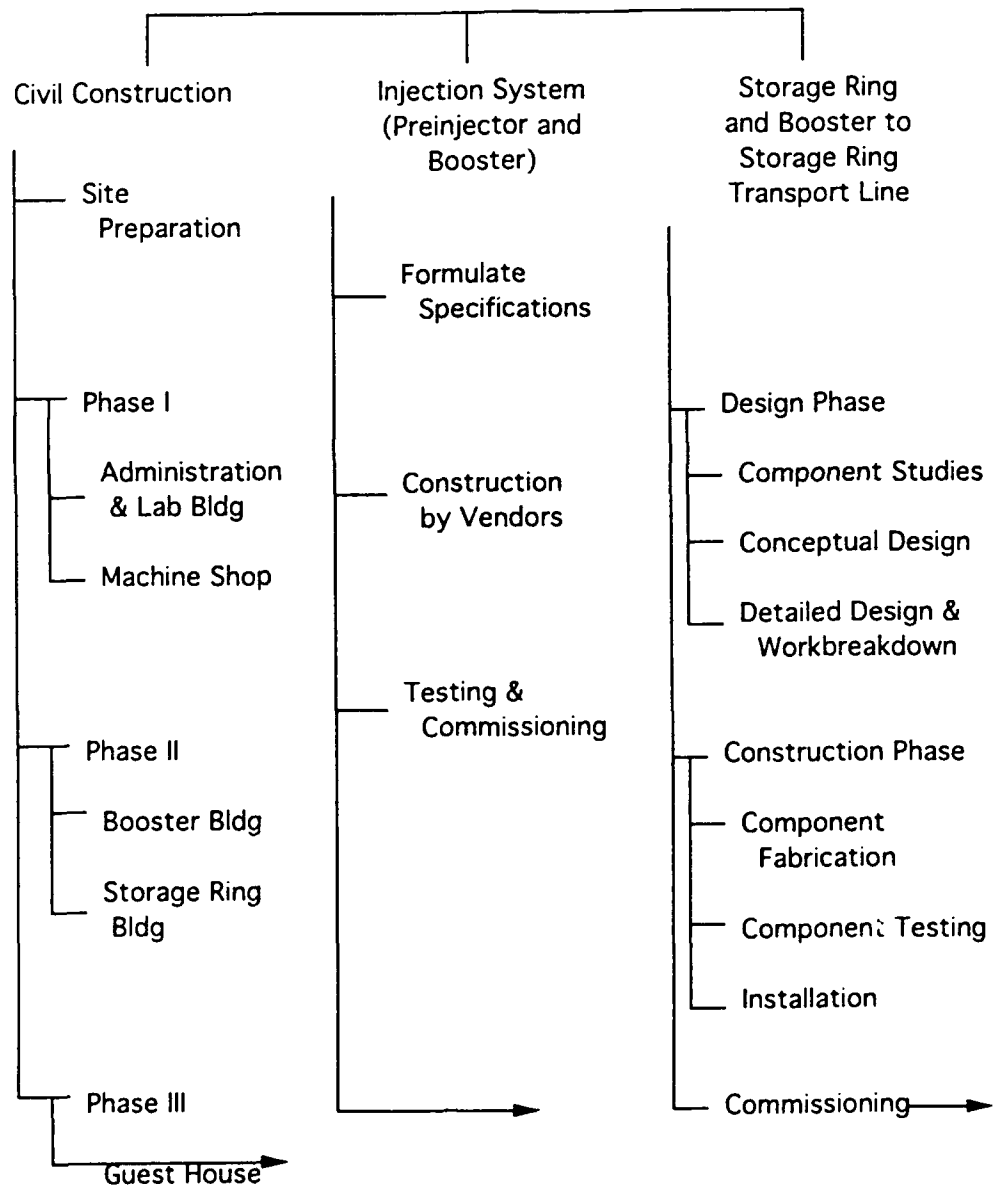
II. SRRC CONSTRUCTION OVERVIEW

An overview of the SRRC construction is shown in Table 3.

A. Civil Construction

The Phase I construction including the Administration and Lab Building and the Machine Shop was completed in May 1990. The entire staff move into the Hsinchu site in June 1990. The Phase II construction took about one and a half year. The Booster Building was completed in February 1991 just in time for the delivery of the injector components. The Storage Ring Building was completed in December 1991.

Table 3. SRRC Construction Overview



B. Injection System

The injection system was contracted out to Scanditronix AB, Sweden in August 1988. However, SRRC is fully responsible for the RF system of the booster synchrotron.

The SRRC staff has been operating the injection system since July 1992 with very satisfactory performance. Machine studies have been performed. Parameters of the booster are measured at the injection energy of 50 MeV. The results are in good agreement with the design values.

C. Component Fabrication and Testing for the Storage Ring

A general account on this subject will be given here. A more detailed report can be found in another paper in these Proceedings entitled "Construction and Commissioning of the SRRC Storage Ring".

Most of the vacuum chambers were made of aluminum. All the chambers are already fabricated and installed. One sextant section has been baked, tested and maintained at 4×10^{-11} Torr for more than six months. At present, without turning on the ion pumps, the vacuum pressure is about 10^{-8} Torr without beam, and about 10^{-7} Torr with a few mA stored beam current. Bakeout of the vacuum chamber will be carried out in June 1993. With the ion pumps turned on, the vacuum should improve greatly. Further improvement is also expected from synchrotron radiation cleaning.

There are three identical RF systems at SRRC. One for the booster and two for the storage ring. Six 500 MHz cavities were bought from DESY. The low level electronics and transmitters were constructed by SLAC and Mountain Technology, USA, respectively. SRRC is responsible for assembling the RF systems. The booster RF system became operative in December 1991. It is highly reliable. In more than 3300 accumulated operating hours, only four days were needed for checkup and maintenance. One of the RF system for the storage ring became operative in March 16, 1993.

There are 18 bending magnets, 48 quadrupoles, 24 sextupoles, 24 horizontal and 30 vertical correctors around the ring. The bending magnets are curved, combined function types. In addition, there are pulsed magnets, 4 kickers and 1 septum. All these magnets were designed, constructed and measured locally. All the magnets installed in the ring are within acceptable tolerances in terms of multipole errors.

We would like to refer the reader to another paper entitled "Diagnostic Instrumentation System for the SRRC 1.3 GeV Synchrotron Radiation Light Source" in these Proceedings which has the details of the control and diagnostic system of SRRC.

Installation and subsystem testing of the storage ring were completed March 1993. Major efforts were put in the survey

and alignment. Accuracy of ± 0.2 mm at the quadrupole location has been achieved.

III. STORAGE RING COMMISSIONING

A brief summary of the commissioning of the SRRC storage ring as to date is given in Table 4.

Table 4. Commissioning Milestone

Feb 23, '93	First turn (On axis injection at 1.3 GeV)
RF installation:	
Feb 22, '93	Transmitter arrived
Mar 16, '93	The first rf system worked
All four kickers installed	
Apr 2, '93	First few turns
Apr 13, '93	First beam stored
Apr 26, '93	BPMs became operative
	Machine parameters study started

At present, beam can be routinely stored with a current of a few mA with lifetime of ~ 30 minutes. Machine studies are carried out. Current and lifetime are presently limited by the vacuum. The vacuum is expected to greatly improve when the bakeout is carried out and the ion pumps are turned on.

Starting this May, the beam energy can be measured to an accuracy of $\pm 10^{-3}$. Synchrotron radiation from the stored beam has been observed. The bunch length of the beam was measured to be $\sigma \sim 42$ psec. Closed orbit distortions in both vertical and horizontal directions are measured by the BPMs. Application programs are used to make corrections. This indicates that both the hardware and software are working properly.

The dispersion function $\eta(s)$ and the momentum compaction factor α are measured showing results in good agreement with the design values. It has also been demonstrated that chromaticity can be corrected to $\xi \sim 0$ using the sextupole at the nominal strength.

In order to study the transverse dynamic features of the lattice, we have measured $\nu_x = 7.14$, $\nu_y = 4.17$ to compare with the design values (7.18, 4.13). The β_x , β_y function are also measured. The results are in very good agreement with the designed values.

With the measurement of the machine parameters, the first part of the commissioning phase has been completed. There will be a two-month shutdown for (i) bakeout of the chamber, (ii) installation of the three VUV photon beamlines, and (iii) continuing survey and alignment work. Further commissioning of the storage ring will start in July 1993. With the completion of commissioning and installation of the beamlines, the SRRC facility is expected to become operative in September 1993.

IV. ACKNOWLEDGEMENT

The success of the early stage commissioning of this rather complicated accelerating system is due to the excellent performance of the essential components and subsystems. However, without the hardwork and full commitment of the entire SRRC staff, this achievement could not have been possible. Our deepest gratitude and thankfulness also to all

our friends abroad who have given us their invaluable advices and support which are essential for the project.

V. REFERENCES

- [1] "SRRC Design Handbook", SRRC, April 28, 1989.
- [2] "SRRC Status Report", SRRC, January 1993 Edition.
- [3] "SRRC Status Report", SRRC, April 1993 Edition.

SOLEIL, a New Synchrotron Radiation Source for LURE¹

M.P. Level, P. Brunelle, P. Marin, A. Nadji, M. Sommer, H. Zyngier

LURE

Centre Universitaire de Paris-Sud, Bât. 209 A, 91405 Orsay Cedex, FRANCE

J. Faure, J. Payet, A. Tkatchenko

LNS

CE Saclay, 91191 Gif sur Yvette Cedex, FRANCE

Abstract

LURE is designing a new storage ring of energy 2.15 GeV which will provide radiation in the intermediate energy range, 20 eV-1.5 keV, from undulators and 5 keV critical energy photons from dipole bends. On the basis of what was learned from Super-ACO experience, a number of criteria were retained for the new machine: large number of insertion sections (13), 3 and 5 m long, for a comparatively short circumference (216 m), moderate emittance ($3.7 \cdot 10^{-8}$ m.rad) to secure good Touschek lifetime for the operation with a few intense bunches and for a realistic energy acceptance. Particular attention is paid to all aspects leading to the stability of the photon beam. A decision is looked for 1993-94. The construction time should be 4 years.

I. INTRODUCTION

A new storage ring, named SOLEIL, is being designed at LURE with in mind to ultimately replace both DCI and Super-ACO, while retaining the potentialities of these two machines for the users.

The experience gained from Super-ACO in the last 5 years shows that an energy well above 1.5 GeV is necessary to reach a compromise between low emittance, good lifetime at high intensity, good lifetime with a small number of intense equidistant bunches, operation with a large variety of insertions. In consequence the choice was made to build a polyvalent radiation source with an energy of 2.15 GeV which will provide photons in the energy range 20 eV-1.5 keV from undulators, 5 keV critical energy photons from dipole bends and 10 to 30 keV X-rays from a wiggler magnet.

A number of specifications were defined by the users. These concern, for the multibunch operation, a beam current of 300 mA and a 15 hours lifetime and for the 6 bunch operation (temporal structure studies) a bunch current of 60 mA and a beam lifetime larger than 10 hours. These figures have to be reached as a compromise to low emittance. It ended up with the choice of an horizontal beam emittance of $35 \cdot 10^{-9}$ m.rad.

From the past experience on Super-ACO, the following choices were made: implementation of insertions both in zero and non-zero dispersion straights and sextupolar coils inside the quadrupoles. Furthermore great emphasis was put by the users on the photon beam stability in all its aspects. This concerns positron filling to avoid ion and macroparticle trapping in all circumstances, transverse and longitudinal stability of the bunches and the overall stability of the photon beam with respect to experimental set-ups.

II. LATTICE PARAMETERS

For the required critical length 2.5 \AA ($\epsilon_c = 5 \text{ keV}$) and for a 1.6 T magnetic field, the machine energy is 2.15 GeV. The structure is a Double Bend Achromat (modified Chasman-Green lattice) with parallel face magnets and zero field index. The doublet located in zero dispersion sections in Super-ACO has been replaced by a triplet. The chosen emittance leads to 8 periods.

The optical functions are presented on Figure 1. The main optical parameters are: $\epsilon_x = 37 \text{ nm.rad}$, $Q_x = 9.70$, $Q_z = 8.70$, $\alpha = 3.42 \cdot 10^{-3}$ and $\sigma_E/E = 8.53 \cdot 10^{-4}$.

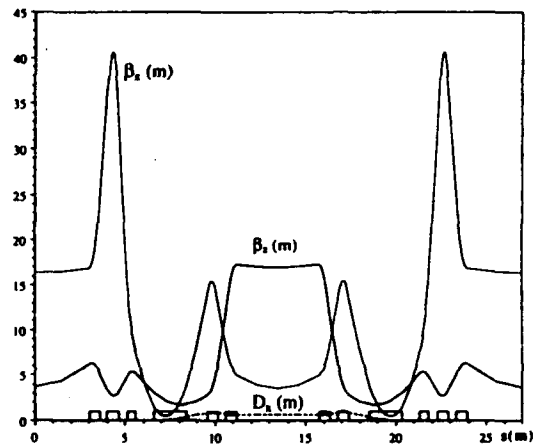


Figure 1.

The chromaticity correction is achieved using 2 sextupole families located in the non-zero dispersion sections and the dynamic aperture is optimized using 3 other families in the zero dispersion sections (Figure 2). A 25 T.m^{-2} sextupolar strength allows one to increase the chromaticity up to 3 units in order to combat the transverse mode coupling instability.

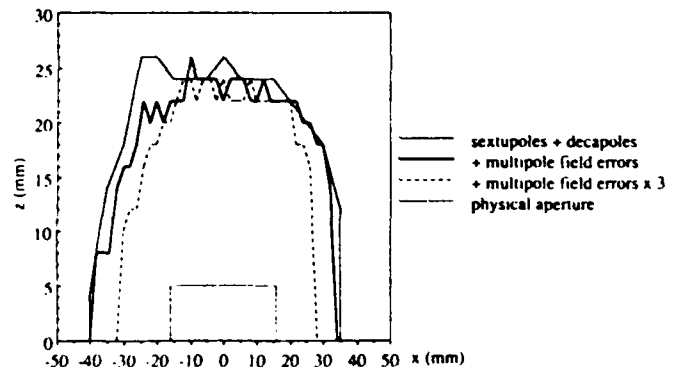


Figure 2.

¹ Work supported by CNRS-CEA-MEN.

Figure 3 shows a schematic diagram of the location of beam position monitors (BPM) and correction dipoles in a typical cell of SOLEIL. There are per half cell, 3 BPM, 3 horizontal correctors and 3 vertical correctors. Both global and local correction will be provided. The global one, using all monitors and correctors, leads to zero on each BPM in both planes and a residual orbit distortion with a maximum value of 0.2 mm elsewhere. An adjustment in the straight sections can be made independently (angle and position) using photon BPM in beam line.

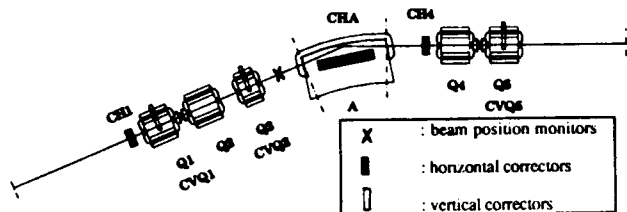


Figure 3.

III. PHOTON SOURCES

Figure 4 shows a general lay out of the storage ring together with the insertion and bending magnet beamlines.

The distribution of the beamlines and the transverse source sizes are :

- 24 bending magnet beamlines :
 - . 2 beamlines per odd numbered bending :
 $\sigma_x = 130 \mu\text{m}$ $\sigma_z = 90 \mu\text{m}$
 - . 1 beamline per even numbered bending :
 $\sigma_x = 260 \mu\text{m}$ $\sigma_z = 80 \mu\text{m}$
- 13 straight sections for insertion devices :
 - . odd straight $\sigma_x = 780 \mu\text{m}$ $\sigma_z = 110 \mu\text{m}$
 - . even straight $\sigma_x = 560 \mu\text{m}$ $\sigma_z = 250 \mu\text{m}$

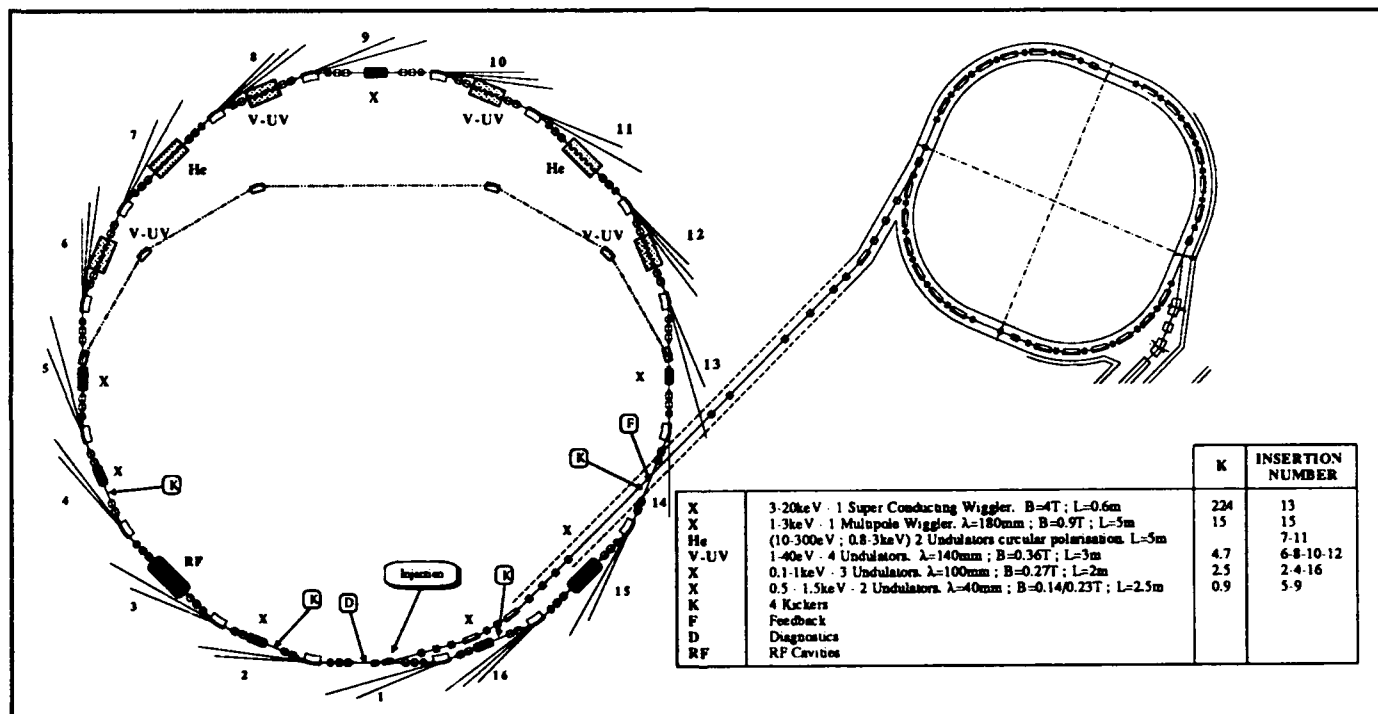


Figure 4.

The linear effects due to the insertions (Δv_z ; $\Delta \beta_z/\beta_z$) are compensated by a local correction for the SC wiggler and the multipole wiggler, and a global correction for the undulators. The residual β -beat is less than 5 % everywhere except at the location of the SC wiggler where it reaches 20 %. The non linear effects (proportional to $(\beta_z^2 B_0^2 L / \lambda^2)$) act on the dynamic aperture which remains much larger than the physical aperture (Figure 5).

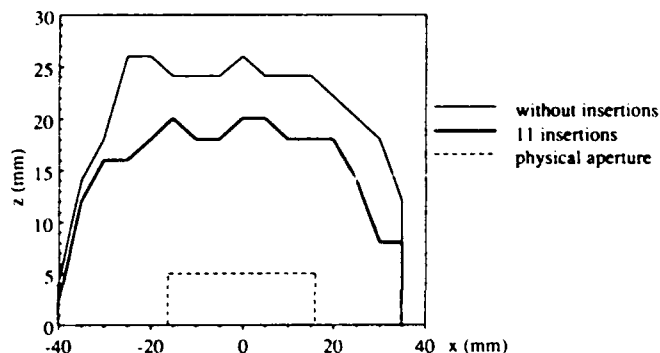


Figure 5.

IV. HIGH INTENSITY

A. Coherent instabilities

Monomode RF cavity is invaluable in order to ensure longitudinal and transverse stability for multibunch operation. It is especially important for SOLEIL since there will be insertions in non zero dispersion sections.

A 500 MHz superconducting cavity of the type which is being developed by CORNELL would suit the requirements. One aims at an accelerating voltage of 3 MV in order to reach an energy acceptance of 2.4 % and a beam power of 225 kW to cope for a maximum current of 0.5 A.

A five meter long straight section could house two cavities of this type.

B. Beam lifetime

Table 2 summarises the values of beam gas lifetime (τ_g) and Touschek lifetime (τ_T) for different situations, assuming 10 % coupling and a 10^{-9} Torr pressure nitrogen.

Table 2

I (mA)	300	6 x 10
τ_g (h)	24	82
$\epsilon_E = \epsilon_{RF}$ V_{RF} (MV)	2.4 %	3
σ_E (mm)	6.6	
τ_T (h)	405	33.7
τ_{total} (h)	23.5	24
ϵ_E V_{RF} (MV)	1.8 %	2
σ_E (mm)	7.2	
τ_T (h)	239	20
τ_{total} (h)	22	16

Remark : The computation of Touschek lifetime has been made with the nominal RF energy acceptance (2.4 %) and also in a most pessimistic case (1.8 %) taking into account the possible limitation due to the insertion non linearities.

Table 3 summarises the main machine parameters.

Table 3

Energy	E = 2.15 GeV
Maximum current	$I_m = 300$ mA
Maximum current per bunch	$I_b = 10$ mA
Emittance	$\epsilon_x = 37$ nm rad
Orbit length	L = 215.96 m
Revolution frequency	$f_0 = 1.388$ MHz
Number of periods	8
Number of straight sections	8 x 6 m + 8 x 4.5 m
Magnets :	
Dipoles : number, length, gap, B_{max} :	16, 1.81 m, 0.06 m, 1.6 T
Quadrupoles : number, length : bore radius, G_{max} :	80, 0.65/0.45 m 0.0575 m, 13 T.m ⁻¹
Sextupolar coils : number, length : strength :	80, 0.65/0.45 m 25 T.m ⁻²
RF system :	
Frequency	$f_{RF} = 500$ MHz
Harmonic number	$h = f_{RF}/f_0 = 360$
Maximum voltage	$V_{RF} = 3$ MV
Energy acceptance	$\epsilon_{RF} = 2.4$ %
Energy loss per turn (with insertions)	$\delta E \approx 450$ keV

V. INJECTOR

A. Positron source

Depending on the filling mode of the machine, the gun will provide a 5 ns, 15 A pulse or alternatively 300 ns, 1.4 A pulse at a repetition rate of 10 Hz. A high current Linac with an energy of 200 MeV is followed by a quarter wave length converter and a 400 MeV positron Linac.

B. Booster

A Booster increases the beam energy to 2.15 GeV. It is a FODO structure with 4 periods and 108 m in circumference.

The main characteristics are shown in Table 4.

Table 4

Number of dipoles :	24
Number of quadrupoles :	32
Dipoles length :	$L = \rho \times \pi/12 = 1.877$ m
Quadrupoles length :	$L = 0.4$ m
Dipole maximum induction (E = 2.15 GeV) :	1 T
Quadrupole maximum gradient (E = 2.15 GeV) :	10 T/m
Tune ν_x, ν_z :	5.65, 2.65
$\beta_{xmax}, \beta_{zmax}$:	17 m, 17 m
Maximal dispersion, D_{max} :	≈ 2 m
Emittance at 2.15 GeV :	$\epsilon_x/\pi = 3.84 \cdot 10^{-7}$ mrad
Energy spread at 2.15 GeV :	$6.8 \cdot 10^{-4}$

The Booster RF frequency is 100 MHz in order to match the 5 ns Linac pulse to the 500 MHz RF storage ring acceptance. Injection time is 5 mn for both operation modes.

VI. MISCELLANEOUS

A study of a By-pass option has been made aiming at a high gain Free Electron Laser tunable between 350 and 100 nm. It is schematically shown on Figure 4. It would allow a 12 m long straight section for the implementation of a set of optical klystrons.

The main characteristics are :

Energy	E = 1.5 GeV
Emittance	$\epsilon_x \approx 20$ nm rad
ℓ_{cavity}	25 m
Maximum current	40 mA in 4 bunches
Amplification	25 %
Beam lifetime	$\tau = 4$ h

ACKNOWLEDGEMENTS

It is a pleasure to acknowledge major contributions of the technical staff from both LURE and LNS Laboratories.

Many thanks to Phi Nghiem who calculated the By-pass lattice.

CONCEPTUAL DESIGN OF A COMPACT ELECTRON STORAGE RING SYSTEM DEDICATED TO CORONARY ANGIOGRAPHY

Y. Oku, K. Aizawa, S. Nakagawa

Akashi Technical Institute, Kawasaki Heavy Industries, Ltd.

1-1, Kawasaki-cho, Akashi, Hyogo 673, Japan

M. Ando, K. Hyodo, S. Kamada

Photon Factory, National Laboratory for High Energy Physics

1-1, Oho, Tsukuba, Ibaraki 305, Japan

H. Shiwa

SR Facility Project, Japan Atomic Energy Research Institute

2-4, Shirane, Shirakata, Tokai, Naka, Ibaraki 319-11, Japan

Abstract

We designed a compact electron storage ring system which gives a X-ray photons density of 10^{10} photons/mm²/sec at 33keV for the K-edge subtraction method using a two-dimensional imaging system. We adopted a beam energy of 1.75GeV, the maximum field of superconducting wigglers of 8.3 Tesla, a stored current higher than 800mA and a low energy injection system. The ring system with a circumference of about 60m is feasible.

1. Introduction

The K-edge subtraction method is effective for coronary angiography by peripheral venous injection [1][2][3]. This method demands intense monochromatic X-rays whose energy is 33keV, if we select iodine as a contrast material. Synchrotron radiation is very intense and it allows selection of monochromatic X-rays. Recently, the number of patients suffering from ischemic heart disease is increasing. Coronary angiography is a standard method for diagnosis of coronary artery diseases. Since it is an invasive method using a catheter inside a peripheral artery, it has a little peril, although it gives excellent images. If a sufficient image quality for coronary angiography could be obtained by intravenous injection of the contrast material, the patients would be examined safely and painlessly.

Development of K-edge subtraction systems was initiated by E. Rubenstein etc. in U.S.A. [2]; in Japan, a two-dimensional imaging system is being developed [1][3]. So, we designed a compact storage ring system dedicated to coronary angiography using a two-dimensional imaging system.

2. Requirements for SR

A. Photon flux

High intensity of monochromatic X-rays at 33keV is required for K-edge subtraction method using iodine as the contrast material. The photon flux density of X-rays at 33keV should be 10^{10} photons/mm²/sec on the front surface of the patient's body with the conditions as follows: patient's body thickness (water equivalent) of 150mm, pixel size of a digital image of 0.3×0.3 mm² and exposure time per one image of 2msec.

If the 33keV photon flux density is 10^{10} photons/mm²/sec in front of the patient's body, it decreases to 5.5×10^7

photons/mm²/sec after passing through the patient's body. The photon flux to one pixel in a digital image, I_p is 10^4 photons/pixel/exp.time. So, the signal-to-noise ratio S/N is $I_p/\sqrt{I_p} = 100$.

B. Exposure area

The X-ray exposure area should be larger than 150×150 mm² in order to cover the whole images of coronary arteries using a two-dimensional imaging system.

Therefore, total photon flux in front of the patient's body should be more than 2.25×10^{14} photons/sec. Supposing the monochromator diffraction efficiency of 60% [5], the total photon flux in front of the monochromator should be more than 3.8×10^{14} photons/sec.

C. The third higher harmonics

On the other hand, the third higher harmonics (99keV X-ray) diffracted by a Si crystal monochromator also comes into the imaging system [3]. So, the photon flux density due to that should be less than 3% of the photon density at 33keV in order to avoid deterioration of the image contrast.

3. Radiation source

Wiggler magnets are suitable for meeting these three requirements. The spectral photon flux from a wiggler magnet is given by the next equation [4]:

$$N(\epsilon) = C_n E \theta I N_w \Delta\epsilon/\epsilon S(X) \quad (1)$$

where the coefficient, $C_n = 4 \times 10^{11}$ GeV⁻¹ mrad⁻¹ mA⁻¹ sec⁻¹ (1%BW)⁻¹, E the beam energy in GeV, θ the angle of the radiation cone in mrad, I the beam current in mA, N_w the pole number of the wiggler magnet, $\Delta\epsilon/\epsilon$ the spectral band width in % and $S(X)$ a mathematical function defined by:

$$S(X) = \frac{9\sqrt{8}}{8\pi} \cdot X \cdot \int_X^\infty K_{5/3}(z) dz \quad (2)$$

with $K_{5/3}$ being a modified Bessel Function. The radiation spectrum given by $S(X)$ with $X = \epsilon/\epsilon_{crit}$ is characterized by the critical photon energy given by:

$$\epsilon_{crit} = C_c E^2 B \quad (3)$$

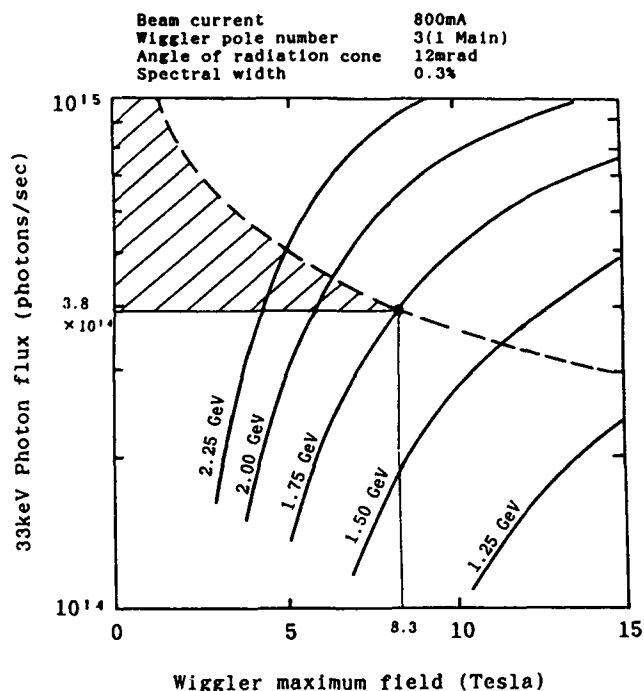


Fig.1 33keV photon flux from a wiggler as a function of the maximum field strength of the wiggler
(The shaded portion is the acceptable area)

where the coefficient, $C_c = 6.64 \times 10^{-7} \text{ GeV}^{-1} \text{ Tesla}^{-1}$, and B the field strength of the wiggler magnet in Tesla. In order to obtain a horizontal photon beam width of 150mm at a distance of 12.5m from the radiation source, the horizontal angle of the radiation cone should be greater than 12mrad. A spectral band width of 0.3% at 33keV is produced using a lapped silicon monochromator [5]. A wiggler magnet whose pole number is 3 (1 Main, 2 Sub) is easy to make because it's the simplest form. The supposed beam current is 800mA; this seems feasible with little development of the storage ring.

In Fig. 1 the available 33keV photon flux from a wiggler as derived from Eq.(1) is shown, for a parameter of different electron beam energies, as a function of the maximum wiggler magnetic field. On the broken line, the rate of the third higher harmonics photon flux relative to 33keV flux is 3% [4]. In the upper region of the broken line, the ratio of the third higher harmonics is more than 3%. As the photon flux of the third higher harmonics must be less than 3% when compared to that at 33keV and the 33keV flux of 3.8×10^{14} photons/sec is desired, the acceptable area is in the shaded portion of Fig. 1. Thus as a best choice of a beam energy of 1.75GeV and a maximum wiggler magnetic field of 8.3Tesla have been adopted, because the lower the electron beam energy, the shorter the diameter of an electron storage ring.

4. Storage Ring

The lattice of our storage ring is the Chasman-Green type in order to avoid an excess increase of emittance; it was chosen due to its ability to control the dispersion function at the insertion point of the wigglers.

The machine design parameters are shown in Table 1. The

Table 1 Machine design parameters

Beam energy, E	1.75 GeV
Operating	250 MeV
Injection	800 mA
Beam current, I	Chasman-Green
Lattice structure	2
Number of superperiods	101
Harmonic number, h	60.6 m
Circumference	RF system parameters
RF system parameters	Frequency 500 MHz
Frequency	Voltage, V 1.5 MV
Voltage, V	Momentum compaction factor 0.040567
Momentum compaction factor	Betatron tunes
Betatron tunes	Horizontal 3.24
Horizontal	Vertical 2.32
Vertical	Natural emittance
Natural emittance	at 1.75 GeV 4.5×10^{-7} m.rad
at 1.75 GeV	at 250 MeV 9.2×10^{-9} m.rad
at 250 MeV	SR energy loss per turn at 1.75 GeV 339.4 keV
SR energy loss per turn at 1.75 GeV	Wiggler parameters
Wiggler parameters	Peak field 8.3 Tesla
Peak field	Pole number 3 (1 Main, 2 Sub)
Pole number	SR critical energy
SR critical energy	Bending magnet 3.0 keV
Bending magnet	Wiggler 17.0 keV
Wiggler	

low energy injection is adopted so that an injector (linac) can be compact. At the time of injection, the wigglers are excited proportional to the magnetic field strength of the bending magnets, because there is much difference in the betatron tunes between when wigglers are excited and when not excited. The design code MAGIC [6] has been used to calculate machine parameters and lattice functions, and the design code ZAP [7] also has been used to study the intrabeam scattering in order to estimate the emittance at the time of the low energy injection.

5. Layout plan of facility

A layout plan of a SR facility dedicated to coronary angiography using the storage ring described above is shown in Fig. 2. A linac is placed on the underground level, in order to accommodate three other experiment rooms. SR angiography rooms, X-ray control rooms, medical treatment rooms etc. are 50cm higher than the ground floor level, because the diffracted X-rays by a Si(311) single crystal monochromator go upward at an angle of about 13 degree. Radiation shields and pillars in the underground level are placed at the same location relative to the ones on the ground level in order to support the structure on the ground.

6. Conclusions

An electron storage ring system dedicated to coronary angiography using a two-dimensional imaging system was designed. The system is feasible, needing little development to store a high electron beam current of more than 800mA and to give a high magnetic field of more than 8Tesla. The photon flux density of $10^{10} \sim 10^{11}$ photons/mm²/sec on the front surface of the patient's body after expansion of the photon beam to $150 \times 150 \text{ mm}^2$ is possible. The electron beam energy of 1.5~2.0GeV and the magnetic field of the wiggler magnet of 5~10Tesla are suitable for coronary angiography, because of the limitation of the third higher harmonics. Therefore, if much more photon flux density is desired, development of storage of a high beam current of more than 1A or a multipole wiggler whose pole number is more than 15 is needed.

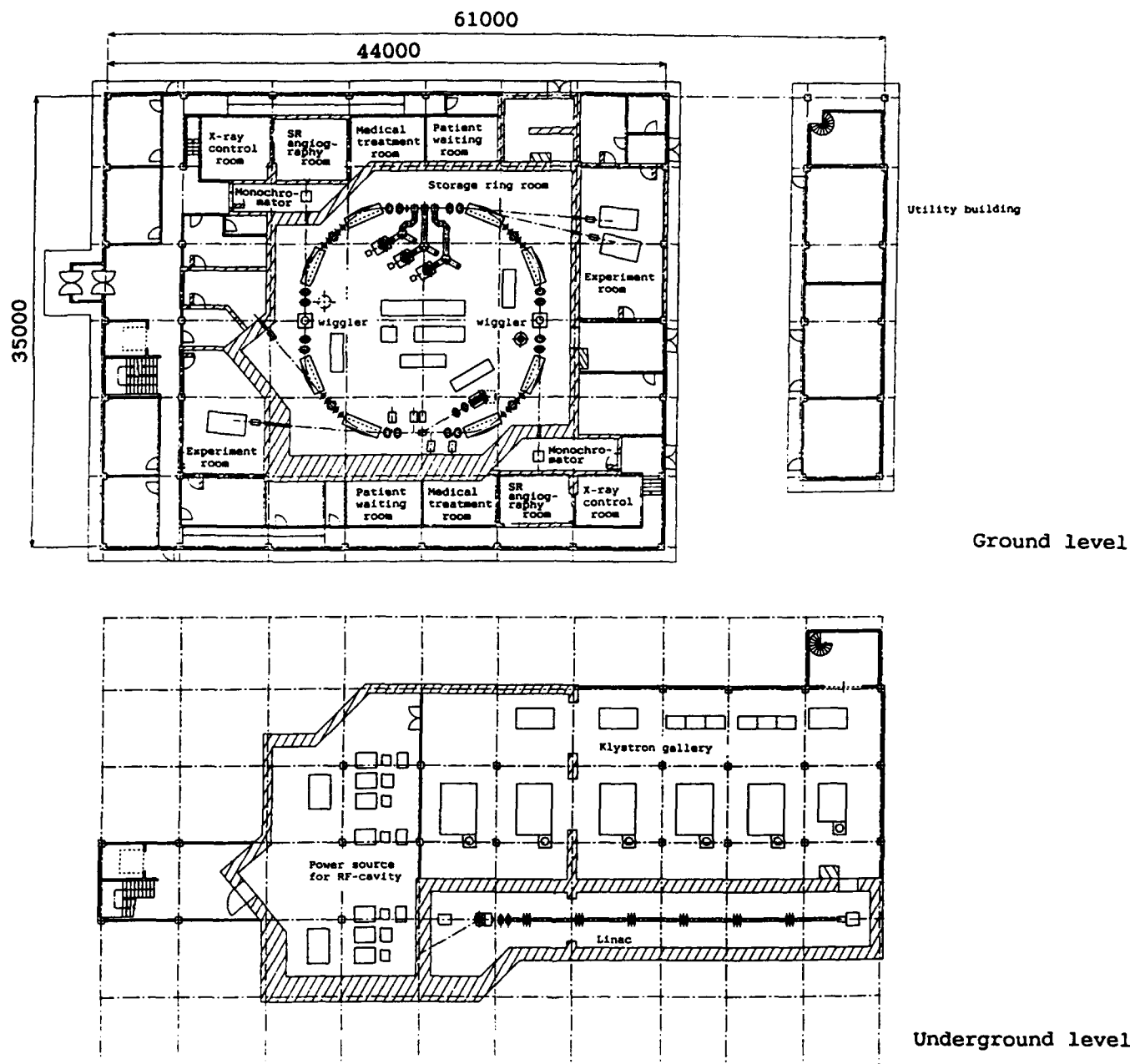


Fig.2 Layout plan of SR facility dedicated to coronary angiography

Acknowledgments

The authors would like to thank Dr. M. Kato, Dr. Y. Kobayashi and Dr. M. Izawa of the Photon Factory, KEK, for their help and support. Also, they wish to thank Dr. A. Iwata of Akashi Technical Institute, Kawasaki Heavy Industries, Ltd. for his support and encouragement.

References

- [1] K. Hyodo, K. Nishimura and M. Ando: Handbook on Synchrotron Radiation, Vol. 4; 55 (1991)
- [2] E. Rubenstein, R. Hofstadter, H. D. Zeman, A. C. Thompson, J. N. Otis, G. S. Brown, J. C. Giacomini, H. J. Gordon, R. S. Kernoff, D. C. Harrison and W. Thomlinson: Proc. Natl. Acad. Sci. USA 83; 9724 (1986)
- [3] A. Akisada, M. Ando, K. Hyodo, S. Hasegawa, K. Konishi, K. Nishimura, A. Maruhashi, F. Toyofuku, A. Suwa and K. Kohra: Nucl. Instr. and Meth. A246; 713 (1986)
- [4] H. Wiedemann: Italian Physical Society Conference Proceedings, Vol. 10; 299 (1988)
- [5] H. Shiwaku, K. Hyodo and M. Ando: Japanese Journal of Applied Physics, Vol. 30, No. 12A; L2065 (Dec. 1991)
- [6] A. S. King, M. J. Lee and W. W. Lee: SLAC Report No. 183 (Aug. 1975)
- [7] M. S. Zisman, S. Chattopadhyay and J. J. Bisognano: ZAP User's Manual LBL-21270 (1986)

Report on DELTA, One Year Before Routine Operation

Niels Marquardt

DELTA Group, Institute of Physics, University of Dortmund
4600 Dortmund 50, Germany

Abstract

A status report of the Dortmund ELection Test Accelerator DELTA [1] in its final phase of construction is presented. DELTA is a 1.5 GeV 3rd generation synchrotron light source designed for low emittance (10^{-8} m rad), high currents (500 mA for ≥ 12 bunches) and beam life times of ≥ 10 hours, which is dedicated to free-electron-laser (FEL) and accelerator-physics research and development. With the first FEL experiment [2], already funded and to be installed in one of the two long straight sections of the racetrack-shaped storage ring, DELTA represents a new Storage-Ring-FEL facility. After first oscillator operation in the visible (planned for end of 1994), FEL experiments in the VUV clearly below 100 nm are foreseen. In the second long straight section an asymmetric superconducting wiggler, providing 1 Angström radiation, will be installed in the future and used as wave-length shifter. A predesign study of this second insertion device has been performed already. Details of the construction of DELTA and present status of most hardware components of 100 MeV LINAC, booster synchrotron, storage ring, vacuum system, beam lines and first FEL experiment will be discussed.

1 INTRODUCTION

The high-brilliance 1.5 GeV synchrotron light source DELTA dedicated to FEL and accelerator-physics research has been described previously in a technical status report and several publications [1]. In contrast to most other synchrotron-radiation sources, DELTA will not be a user machine. Instead of being available for long-term research experiments and industrial applications, the purpose of DELTA is different. It represents a test facility for research in radiation and accelerator physics, for preparing and testing of experimental setups and for performing measurements with very special beam characteristics.

When designing the machine, it was noticed that a triplet focussing cell with strong bending fields (max. 1.5 T), as the reflection symmetric version of the FODO cell, represents optically the most flexible separated-function structure. Besides this triplet focussing, the DELTA lattice provides two long dispersion-free straight sections with

nearly constant beta functions for magnetic insertions. Accordingly, the DELTA storage ring in conjunction with its FEL undulator devices [2] has been optimized to provide radiation of unprecedented beam quality, concerning high intensity (0.1-0.5 A for 1 to 12 bunches), low emittance (10 nm rad), large coherence and short time structure. Other characteristics of this third-generation light source are its short damping time (about 4 msec) and bunch length (2 cm) and large energy spread ($< 10^{-3}$), qualities which are indispensable to obtain a large FEL gain. Moreover, the flexible optics with variable emittance and energy, the high beam stability due to its low impedance and the long lifetime (about 10-20 hours) due to optimum vacuum conditions, make DELTA an ideal test machine. Machine experiments are planned for investigating beam stability, machine-parameter dependencies and for developing all kinds of accelerator components and diagnostic tools. Accordingly, one aim is to develop a fully automatic diagnostic and computer-control system. A predesign study has been undertaken for constructing also an asymmetric superconducting wiggler, producing short-wavelength radiation with a high degree of polarization, suitable for a large variety of research applications [3]. As a university institute, the DELTA facility with its relatively small storage ring of 115 m circumference will serve as an ideal instrument for the education of students, technicians and physicists in accelerator technology.

2 STATUS OF THE PROJECT

-Building and Infrastructure-

After funding of the DELTA project has been approved end of 1989, work on the final design of the three machines, 100 MeV LINAC, booster synchrotron and storage ring, continued in 1990. Besides these design activities parts of an old LINAC from the University of Mainz were shipped to Dortmund and rebuilding of this machine has started for its use as preinjector. End of 1990 ground breaking of the laboratory site happened and from May 1991 till June 1992 construction of the laboratory building with its 40 m by 74 m large accelerator hall and its offices and laboratories was performed. Since moving into the new building trafo station, power-supply circuits, cabling and many other parts

of infrastructure have been installed, the concrete wall for radiation protection erected and the electronical and mechanical workshops and the vacuum lab equiped and put into operation. Radiation safety and interlock system is under design. Most parts of the cooling-water and heat-exchange system with cooling tower and tube circuits are mounted.

-Accelerator Components-

The components of the old Mainz LINAC are under test, in particular klystrons and accelerating structures (with 40 MeV/section particle energy at 20 MW pulsed RF-power and 2.9985 GHz operating frequency). A new design of the LINAC focussing system is completed, the buncher section, built by LAL in Orsay, was delivered, the 3 GHz RF-system is ready, PFN and klystron tanks are under construction, a new design of the LINAC modulator has been developed in cooperation with the University of Bonn and its construction has been ordered. A new pulsed triode gun with integrated pre-buncher cavity is under test.

The status concerning booster and storage ring is the following. Design work for beam transfer between the accelerators and the injection and ejection systems are finished. The corresponding beam lines, focussing elements and the various kicker magnets and septum tanks are under construction. A simple, new kicker design of very low impedance has been invented by DELTA (see fig. 1). Whereas the magnetic elements of LINAC and transfer channels are being built at Dortmund, the kicker and septa tanks will be built by the KFA-Jülich. Prototypes are expected to be ready in late summer of this year. The girders to support the magnets for all machines and transfer channels are installed. The series production of quadrupole and dipole magnets is in progress. More than one half of all magnets, which are identical for booster and storage ring, is already in house and has been mounted on the magnet girders. Field measurements were found to be well within the tolerances. Whereas the yokes of the sextupole magnets will be manufactured by the lab workshop, the coils will soon be ordered from a company. The correction coils will also be made by industry. Manufacturing of quadrupoles and dipoles of the transfer lines has started in house. Ion-clearing electrodes are designed and foreseen for the booster only. The main power supplies for the two dipole circuits and the two klystron amplifiers arrived early this year. The chopper power supplies for the quadrupoles and the power supplies for steering coils, LINAC beam transport etc. are ready.

The topology of the DELTA control system consists of the display level (HP graphic workstations), the control level (risc workstation as databases) and the process level (VME CPU's with VX-Works). For the field level an object oriented fieldbus system (CAN bus), nowadays widely spread as industrial standard, is foreseen because of its high functionality, data security, flexibility and easy programming and timing.

-UHV System-

The DELTA ultra-high-vacuum (UHV) system has to

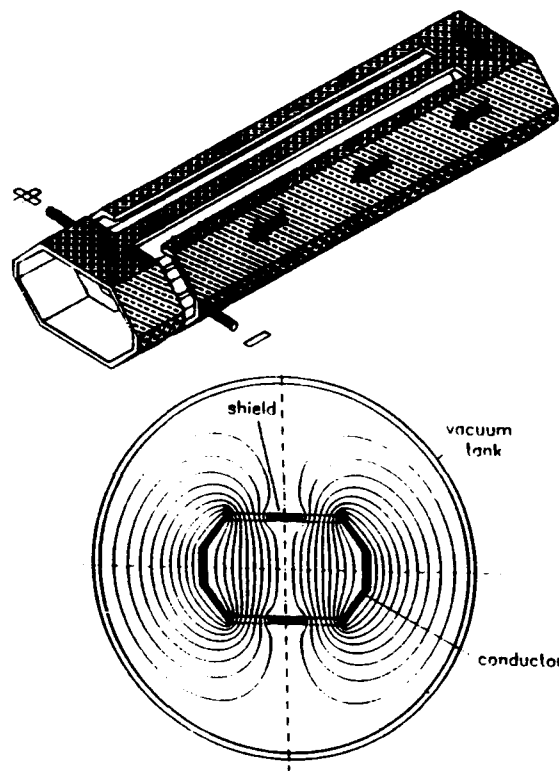


Figure 1: Sketch of the new kicker design showing the particular geometry of the 12 mm wide slit cut into the beam-chamber and the field distribution inside the vacuum tank of the kicker (below).

fulfill the following three basic requirements : (i) stored-beam lifetime of the order of 10 to 20 hours; (ii) smooth and uniform beam chambers along the circumference of the storage ring; (iii) short vacuum-conditioning times, which is indispensable for a test accelerator. In order to realize these particular features for a machine with closely arranged magnets of small apertures (50 mm) and vacuum vessels of low longitudinal conductance, a number of technical novelties were introduced at DELTA. For the first time a vacuum vessel of keyhole cross section, totally made of stainless steel (316 LN), with an antechamber all along the inner side of the ring circumference has been constructed and successfully manufactured. Inside of this chamber both types of distributed UHV pumps are mounted at some locations side by side, namely ion-getter pumps of the diode-noble-gas type and non-evaporable-getter pumps (St 707). External lumped ion-getter pumps (IP's) and titanium-sublimation pumps (TSP's) are additionally installed. The type of flanges and gaskets (VAT-SEAL) with their very particular keyhole aperture used at DELTA are other novel features. All these design criteria were described elsewhere [1]. The prototype hardware was tested in detail. The series production of UHV chambers and integrated pumps is well on the road and all chambers with these pumps will be ready before the end of this year.

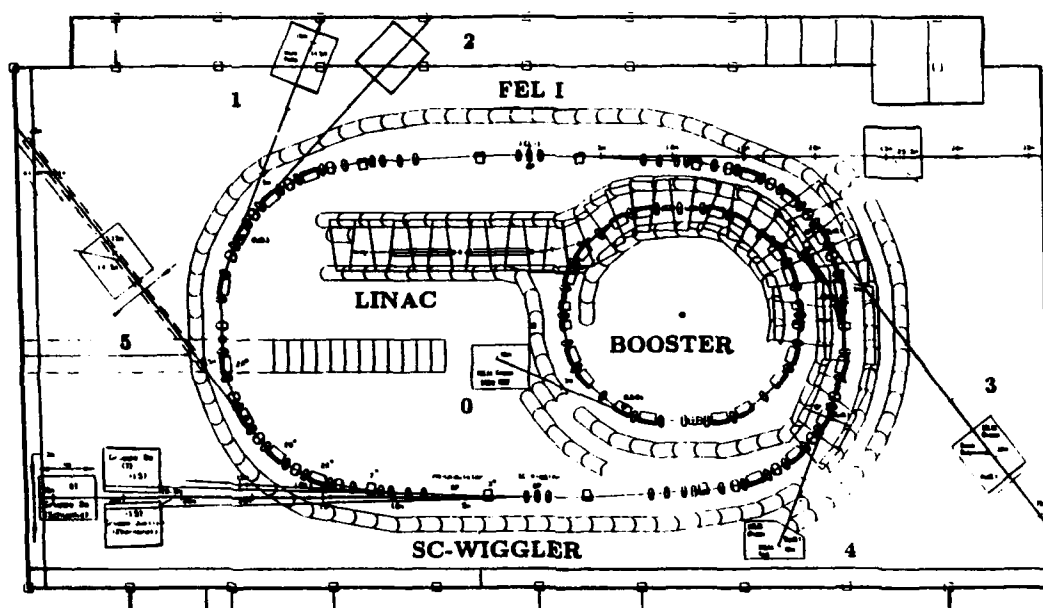


Figure 2: Floor plan of the accelerator hall with LINAC, booster and storage ring, together with radiation-protection wall and the various beam lines.

A new design of a very flexible compensator, made of a double-membrane bellow and a two-sided RF shield, has been developed to interconnect the vacuum vessels. All external pumps, IP's and TSP's, mounted in a common housing, were delivered already.

-SR Sources, Beamlines and Experiments-

Although DELTA will not be a user machine, a number of synchrotron-radiation (SR) beam lines will be provided for a variety of user experiments. Three sources of very different radiation characteristics will be available at DELTA, namely the photon flux from bending magnets ($E_c = 2.26\text{keV}$; $2.5 \cdot 10^{10}$ photons) and that from two different insertion devices, from the undulator [2] of the first FEL experiment (FELICITA I with $E_1 = 27\text{eV}$; $2.5 \cdot 10^{12}$ photons) and from the superconducting asymmetric multipole wiggler [3] or wavelength shifter ($E_c = 8.23\text{keV}$; $1.2 \cdot 10^{11}$ photons; circularly polarized X-rays). In total, 5 beam lines for radiation from the 1.5 T dipole magnets of the storage ring will be installed and one line from a dipole of the booster. Besides these conventional sources, the FEL undulator and the superconducting wiggler, mounted in the two long straights of the storage ring, will both produce radiation fans of quite different characteristics, which can be used by up to three experiments independently. Whereas till now only a predesign study of the superconducting wiggler has been carried out [3] and a feasibility study is ordered from industry, the electromagnetic undulator of the first FEL is already under construction. FEL undulator and optical cavity with its control units will be ready for experiments soon after routine operation of DELTA will start. In fig.2 a floor plan of the accelerator hall is exhibited, with the accelerators, the concrete

wall for radiation protection and the various beam lines from bending magnets, FEL undulator and superconducting wiggler, respectively.

3 SUMMARY

A status report of the construction work at DELTA has been given. The project is on time. The first stored beam is expected to circulate in early summer of 1994.

References

- [1] N. Marquardt et al., DELTA, a Low-Emittance Storage Ring as Free-Electron-Laser Radiation Source, Proc. 1989 IEEE PAC, Vol.2 of 3 (1989) 780; N. Marquardt, *The Dortmund Electron Test Accelerator "DELTA", a New Low-Emittance Storage Ring of 1.5 GeV*, Part. Accel. Vol.33 (1990) 27; N. Marquardt, *Status of DELTA and Design of its Vacuum System*, Proc. 1991 IEEE PAC, Vol.5 of 5 (1991) 2862; DELTA Group, *DELTA Status Report 1990*, University of Dortmund, unpublished.
- [2] D. Nölle et al, DELTA, a new Storage-Ring-FEL Facility at the University of Dortmund, Nucl. Instr. and Meth. A296 (1990) 263.
- [3] D. Schirmer, DELTA Int. Report (1992), unpublished; D. Schirmer, Proc. XV. Intern. Conf. on High En. Accel., HEACC 92, (1992), Hamburg, Germany.

Lattice Design for the 1.7-GeV Light Source BESSY II *

E.Jaeschke, D.Krämer, B.Kuske, P.Kuske, M.Scheer,
E.Weihreter, G.Wüstefeld

BESSY mbH, Berlin, Germany

1. Introduction

BESSY II is a third generation synchrotron radiation light source presently under construction at Berlin-Adlershof /1/. BESSY II will go into operation at the end of 1997. In this paper, the main lattice features of the low emittance storage ring are presented. Special aspects of the design are a compact and flexible double bend achromat (DBA) lattice, which offers 16 straight sections at a circumference of 240 m. About 3 superconducting wave length shifters (WLS) are foreseen for operation.

2. General Design Goals

The user requirements for the BESSY II storage ring are discussed in the design study /2/. The main design goals are a low natural emittance of the order of $5 \cdot 10^{-9}$ rad m and a large number of long, straight sections for insertion devices (IDs). Recently, there was a further demand for about 3 superconducting WLSs, compatible with the low emittance operation of the ring.

The WLSs will be used for micro mechanics application and for radiation-metrology. A detailed study of the effects of these WLSs on the beam emittance and beam stability was done in /3/. It was found that for the operation of the WLSs at low emittance conditions, a horizontal beta function of ≈ 0.80 m and a vanishing dispersion at the WLS location are required.

The early plan was to build the BESSY II ring close to the present BESSY I site at Berlin-Wilmersdorf. Because of space limitations there, a 10-fold triple bend achromat (TBA) was the favoured solution /4/. After the reunification of Germany, a new site for BESSY II was chosen on the former site of the East German "Akademie der Wissenschaften" at Berlin-Adlershof which offers a larger area. With a circumference enlarged by 25% a compact double bend solution is possible, which offers 16 straight sections, 14 could be used for IDs. For further information on the general scheme of BESSY II see /1/.

3. The Storage Ring Lattice

Several achromats were studied for the storage ring lattice, such as FODO types, triple bends (TBA) /4/ and double bends (DBA). We found that the DBA was superior to other solutions with respect to the compactness of the achromat and the number of magnets required.

* Funded by the Bundesministerium für Forschung und Technologie and by the Land Berlin.

Table 1: General Ring Parameters

nominal energy	1.7 GeV
energy range	0.9 - 1.9 GeV
circumference	240 m
number of cells	16
natural emittance ϵ_n	$6.1 \cdot 10^{-9}$ mrad
natural energy width $\Delta E/E$	$7.0 \cdot 10^{-4}$
damping times $\tau_x \approx \tau_y/\tau_z$	16.2 / 8.0 ms
hor. and ver. tune $Q_x; Q_y$	17.84 ; 6.82
natural chromaticity $\xi_x; \xi_y$	-45 ; -24
momentum compaction factor α	$7.5 \cdot 10^{-4}$
number of dipoles	32
bending radius	4.361 m
critical energy	2.5 keV
max./min. hor. beta function	17.2/0.384 m
max./min. ver. beta function	20.5/2.44 m
max. dispersion function	0.415 m

For the DBA type we obtained good results for the emittance and the dynamic aperture. Since the BESSY II ring is designed for an effective use of IDs, the number of 14 usable straight sections further supports the DBA solution. The main parameters of the DBA are summarized in the Tab. 1, and Fig. 1 shows the lattice functions of half a unit cell.

In order to tune the DBA lattice to the theoretical minimum emittance, a long achromat with a minimum of the horizontal beta function is necessary. We did apply a different approach by choosing a very compact achromat to obtain space for more unit cells around the planed circumference. We are away from the minimum emittance by a factor of 3 but we obtain the required emittance through the larger number of unit cells ($\epsilon_n \propto 1/(\text{number of cells})^3$).

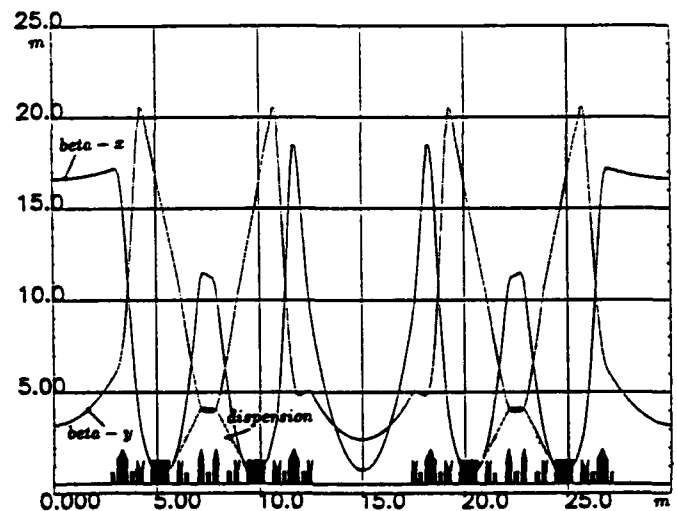


Fig.1 Lattice functions of the BESSY II DBA cell.

Table 2: Parameter List For Typical Insertion Devices

ID name, ring dipoles	WLS1	WLS2	U11	U33	U25	dipole	ID sum	dipole sum
number of IDs, dipoles	1	2	4	3	4	32	14	32
length ID, dipoles [m]	0.60	0.70	4.00	3.30	4.16	0.856	44.5	27.4
field strength B_0 [T]	7.5	5.6	1.1	0.58	0.46	1.3	-	-
period length [m]	-	-	0.10	0.03	0.052	-	-	-
lin. tune shift ΔQ_y ^{a)}	0.044	0.026	0.018	0.0038	0.0031	-	0.190	-
non.lin. tune shift ΔQ_y ^{b)}	-	-	0.0035	0.0083	0.0022	-	0.047	-
radiated power [kW] at 1.7 GeV and 100 mA	2.30	1.38	0.92	0.20	0.16	0.53	10.0	17.0

^{a)}= calculated at $\beta_y = 2.8m$; ^{b)}= octupole-like tune shift; calculated at $\beta_y = 2.8m$ and $y = 1cm$;

To obtain horizontally parallel synchrotron radiation out of the undulators and for injection, a large beta function in the straight section is optimal, whereas for the WLSs operation a low beta function is required. To satisfy these contradicting demands we use a structure where the vertical beta function is ≈ 2.8 m in all straight sections, but the horizontal beta function is alternating between 16.6 m and 0.75 m from one straight section to the next.

In this way we arrive at an 8-fold periodicity with 16 straight sections. The focussing in the high beta straights is done by using a quadrupole doublet and in the low beta straights by using a triplet. The length of the low beta straight is shorter than the length of the high beta straight by the length required for the third quadrupole family. Thus there are two types of straight sections, leaving free space for IDs up to 4.71 m and 3.89 m in length. With the third quadrupole family switched off, the lattice can be tuned to a 16-fold symmetry.

There are 6 sextupole families required to correct higher order effects in the optics. The beta and dispersion functions inside the achromat show nearly a 16-fold symmetry; therefore two chromatic sextupole families are sufficient to adjust the chromaticity. For the harmonic correction the two groups of straight sections require two different families of sextupoles. The harmonic sextupoles are only differently powered but at equal locations in the straight sections to preserve the option for a 16-fold symmetry.

The 16-fold symmetric lattice solution shows excellent properties with respect to linear and non-linear beam dynamics but is not further discussed here.

4. Nonlinear Lattice Effects

While the work on the linear lattice was done using the code LATTICE /5/, the nonlinear behaviour of the optics was mainly studied using the codes BETA /6/ and RACE-TRACK /7/. For all tracking calculations, the setting of the chromatic sextupoles was adjusted to obtain a non-normalized chromaticity of +1 in both planes, required to suppress head-tail effects.

The higher order chromatic tune shift is reduced by the setting of the harmonic sextupoles, because the DBA does produce some small second order dispersion ($\approx 3m$) outside

of the achromatic bends.

Harmonic sextupoles are required to reduce the amplitude dependent tune shift by a factor of ≈ 3 to a value of ≈ 0.1 for particles at the limit of the dynamic aperture.

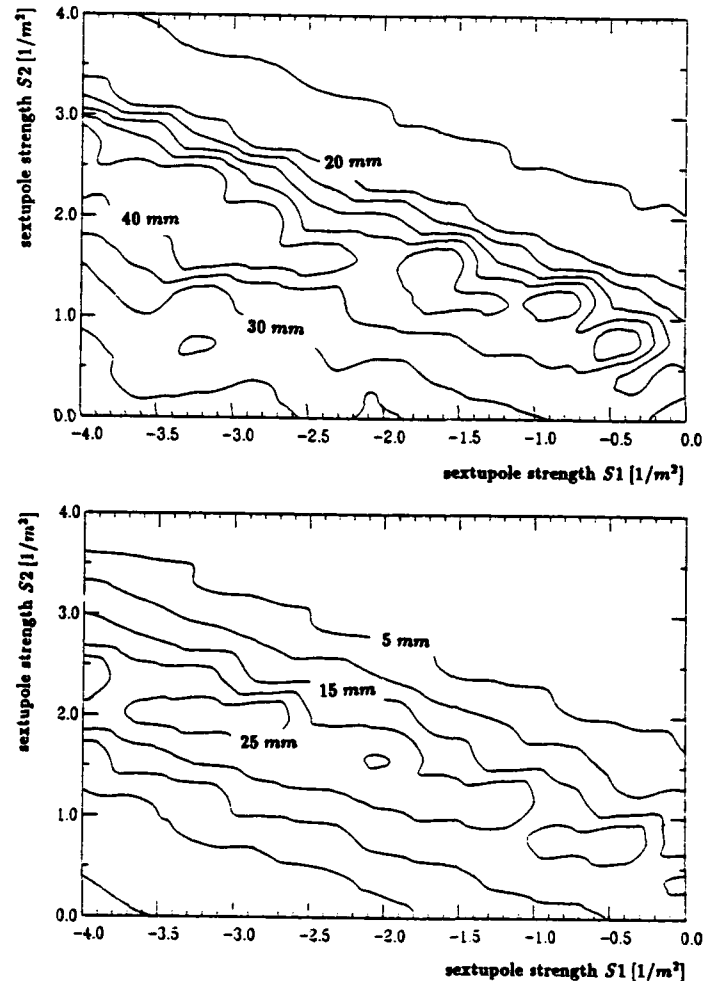


Fig.2 A contour-plot of the dynamic aperture as a function of the strength of the two harmonic sextupoles in the low beta section. The aperture is measured at the high beta section with $\beta_x = 16.6m$ (upper picture) and $\beta_y = 3.2m$ (lower picture), the tracking results are given for 400 stable turns.

The optimum sextupole strength is found by comparing the dynamic apertures at different sextupole settings. In Fig. 2 the dependence of the dynamic aperture on the strength of the two harmonic sextupoles in the low beta section is shown. Both transverse planes are optimized simultaneously, and the result has a broad maximum. In this calculation the second group of harmonic sextupoles in the high beta section is kept at a fixed, optimized value. The results are observed at the the high beta section.

5. Effects on the Beam Due to Insertion Devices

In the final version, 14 IDs will be installed in the BESSY II ring. These IDs will cover 44.5m or 18 % of the ring circumference. Beam dynamical effects of the IDs are simulated with 3-dimensional, highly periodic magnetic fields derived from the scalar potential of the type:

$$V = -(B_0/k_y) \cos k_x x \sinh k_y y \cos k_s s, \quad k^2 = k_y^2 - k_x^2$$

and $k_y = 5k_x$ to simulate a small transverse gradient. The period length λ of the ID in longitudinal direction s is related to the wave number k by the expression $\lambda = 2\pi/k$.

This field expansion is probably good for IDs with many periods and negligible entrance field effects. For the tracking simulation of these types of IDs a fast and precise tracking routine was developed [8]. The WLS with only one main pole and a strong linear term was studied by tailoring a tracking routine to the explicit magnetic field shape [3]. However, for our low beta section a simplified approach based on the above field expansion was possible as well.

A parameter listing of typical IDs used in the tracking simulation is given in Tab. 2. Furthermore, a linear and nonlinear tune shift can be estimated due to quadrupole- and octupole- like fields acting mainly in the vertical plane.

In the tracking simulation, the linear effects of the IDs are corrected by simply readjusting the global tune with the doublets in the high beta sections. For the WLSs we did apply in addition a local quadrupole (triplet) correction to cancel the beta beat. Since the beta beat is not always explicitly canceled in the present method, there remains a beating of up to $\approx 30\%$. We still could apply a full correction of the beta beat introduced by an ID with the adjacent doublet.

The effects of the IDs on the transverse beam dynamics was simulated by the tracking codes BETA and RACETRACK. Results of the tracking simulation with and without 14 IDs are presented in Fig. 3. All tracking calculations are done with small position and strength errors of the magnetic elements. These errors generate closed orbit oscillations with an rms value up to 5mm. The presented results are not corrected with respect to these errors in order to simulate a symmetry break of the optics. Further tracking studies, based on realistic errors and their correction and also including some skew quadrupoles at the IDs location have been done but are not presented here.

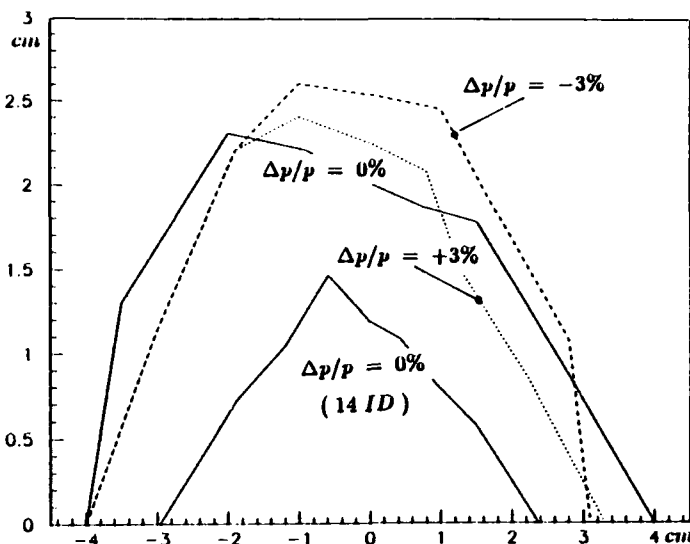


Fig.3 Dynamic aperture results for 1000 stable turns with small errors activated to break the ring symmetry. The calculation for the bare lattice was done at a momentum deviation of -3%, 0% and +3%. The beta function at the observation point are $\beta_x = 16.6m$ and $\beta_y = 3.2m$. For the nominal momentum a tracking example is shown for a filling of the ring with 14 IDs leaving the other parameters are unchanged.

6. Acknowledgments

The authors would like to thank our colleagues from the laboratories DESY(Hamburg), ELETTRA(Trieste), GSI(Darmstadt), INP(Novosibirsk), MPI(Heidelberg) for fruitful and helpful discussions.

References

- /1/ D.Krämer, Status of BESSY II, the High-Brightness Synchrotron Radiation Source in the VUV to XUV Range, contribution to this conference.
- /2/ BESSY II-Eine optimierte Undulator/Wiggler-Speicherring Lichtquelle für den VUV-und XUV-Spektralbereich, Teil 1, 1986 und Teil 2 Technische Studie, 1989.
- /3/ M. Scheer, G. Wüstefeld, "Impact of a Wavelength Shifter on the Performance of the Synchrotron Light Source BESSY II", Proceedings of the 3rd European Particle Accelerator Conference, Berlin, 1992.
- /4/ B.Kuske, G.Isoyama, H.Lehr, G.Wüstefeld, "Layout of the BESSY II Lattice", Proceedings of the 2nd European Particle Accelerator Conference, Nice, 1990.
- /5/ Philip F. Meads, Jr., Oakland, CA, USA, Private Communication
- /6/ L.Farvaque, J.L.Laclare, A.Roport, BETA, ESRF-SR/LAT-88-08
- /7/ A.Wrulich, RACETRACK A Computer Code for the Simulation of Nonlinear Motion in an Accelerator, DESY 84-026 (1984)
- /8/ J.Bahrdt, G.Wüstefeld, Canonical Particle Tracking in Undulator Fields, Proceedings of the 1991 IEEE particle accelerator conference, San Francisco, USA.

The Synchrotron Light Source ROSY

D.Einfeld, H.Büttig, S.Dienel, W.Gläser, Th.Goetz*), H.Guratzsch, B.Hartmann, D.Janssen, H.Krug, J.Linnemann, W.Matz, J.B.Murphy*), W.Neumann, W.Oehme, M.Picard*), M.Plesko~), D.Pröhl, R.Rossmannith#), R.Schlenk, D.Tomassini~), H.Tyrroff

Research Center Rossendorf Inc., Box 51 01 19, D-01314 Dresden, Germany

*) University of Bonn, Germany, *) NSLS Brookhaven, Upton NY, USA

~): Sincrotrone Trieste, Italy, #): CEBAF, Newport News, VA, USA

Abstract:

ROSY, a 3rd generation synchrotron radiation source, has been proposed to be built at the Research Center Rossendorf in the region Dresden of the country Saxony in Germany. ROSY will be dedicated to material research and industrial application. The critical wavelength of the synchrotron radiation spectrum has to be 0.15 nm corresponding to a critical photon energy of 8.4 keV. Electrons with an energy of 3 GeV deflected in a 1.4 T bending magnet provide this spectrum. It is proposed to use a "Modified Multiple Bend Achromat (MBA)" lattice in order to get a compact machine as well as a low emittance. For 3 GeV an emittance smaller than 30 nm rad can be obtained. With a fourfold symmetry and two larger straight sections within the achromatic arcs the circumference is 148.1 m. 23% of the circumference can be used for installing insertion devices. The natural chromaticities and the compensating sextupole strengths are moderate, the dynamic aperture as well as the momentum acceptance are sufficient.

I. INTRODUCTION

In the region Dresden of Germany exists a concentration of institutes and universities working in the field of material research, solid state- and surface physics. All these institutes require a synchrotron radiation source for analytical purposes. The Research Center Rossendorf as the biggest of these institutes will use the synchrotron radiation source in material research related to ion beam techniques as well as in radiochemistry, nuclear physics, biomedical- and radiopharmaceutical research [1]. The Institute of Solid State and Material Research as well as the Institute of Polymer Research, both located in Dresden, cover a wide field of applications too. The Fraunhofer Society runs establishments with active among others in the fields of layer technology, ceramics, sintered materials powder metallurgy, electron beam- and plasma technology. Beside all this activities in Saxony research institutes in Poland and Czechia are also interested in using the light source ROSY [2]. According to the demands of the research fields mentioned above ROSY should emit synchrotron light in the energy region between 5 and 18 keV with a high brilliance. The emittance should be small and the design of the source must have enough space for installing insertion devices. In short, ROSY has to be a 3rd generation light source.

II. LATTICE

As lattices for SR-sources the FODO-, DBA- and TBA- structures are well known and discussed in many papers [3 - 7]. Substantially different is the behaviour of a modified QBA-structure [8]. One gets with this lattice a low emittance as well as a smaller circumference. The idea of the *Modified QBA-Optics* has been adopted for ROSY.

The achromat (Figure 1) contains three bending magnets named B_2 and B_M , respectively with a deflection angle of 20 degrees as well as two bending magnets (B_1) with 15 degrees. The bending magnets are also vertically focusing in order to built a compact machine and to obtain a minimum of the β_x and η_x functions within the magnets. This minimum of both twiss functions results in an optimized emittance. Due to the gradient in the bending magnets the emittance will be further reduced, because the partition function J_x is larger than one. With this lattice one gets for a 3 GeV machine and a circumference of 148 m an emittance of less than 30π nm rad. The cross section of the beam in the middle of the bending magnets is roughly a circle with a radius of 200 μ m.

ROSY has a fourfold symmetrie (Figure 1) with 4.1 m long straight sections. The dispersion function in this four regions is zero in order to obtain a high brilliance from the insertion devices. To reduce the influence of wigglers and undulators on the behaviour of the lattice the β_y functions have been fitted to small values. Within the arc of the achromat there are two more straight sections with a length of 3.5 m. Four of the eight straight sections are used for the injection, the rf-cavities and the beam diagnostics. The four other sections within the arc can be used for insertion devices. Because of their non-vanishing dispersion function the brilliance is here smaller than in the 4.1 m long straight sections. They are useful for many experiments wherever the photon flux is important. The β_y function has a minimum in this region and reduces the influence of the wigglers. The main parameters of the storage ring ROSY are given in Table 1.

III. DYNAMICAL APERTURE

With respect to the dynamical aperture a lot of working points have been investigated. It is possible to run ROSY in the region $7.5 \leq Q_x \leq 9.2$ and $3.0 \leq Q_y \leq 5.5$.

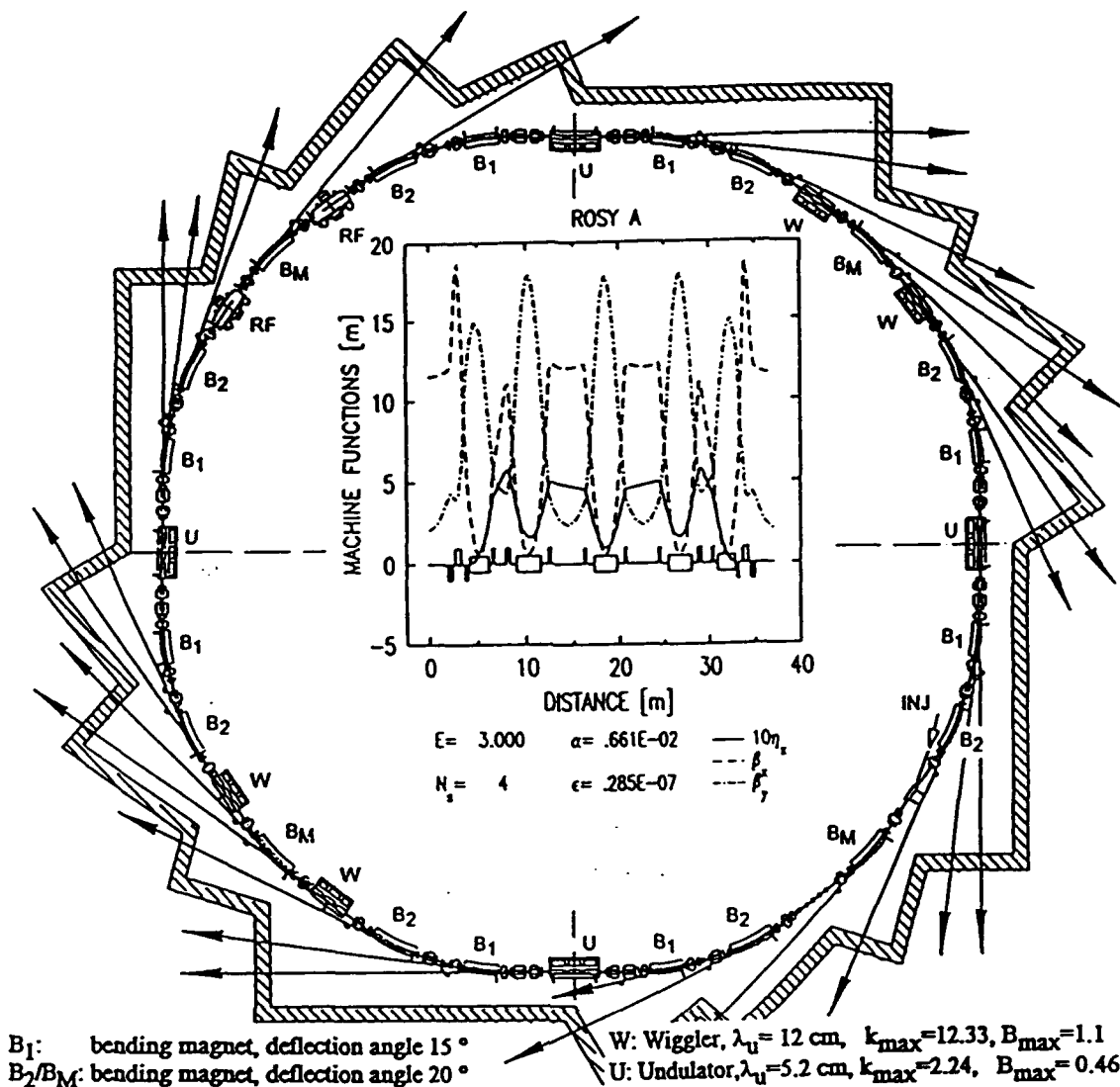


Fig.1: Layout of the 3rd Generation Synchrotron Light Source ROSY including the Lattice and Twiss Functions within one Achromat

Tab. 1: Main Parameters of the Light Source ROSY

Critical Energy of S.R.	E_C	8.4 keV	Number of Quadrupoles (QP)		
Critical Wavelength	λ_C	0.15 nm	0.28/0.4/0.6 m		24/24/8
Energy of Electrons	E_0	3.0 GeV	Max. Gradient in QP		20 T/m
Electron Current	I_0	0.1 (0.25)* A	QP-Strength	K	2 m ⁻²
Nat. Emittance	ϵ_{nat}	28.6 π mm mrad	Number of Sextupoles (SP)	0.1m	56
Beam Life Time	τ_b	≥ 6 hrs.	Diff. Gradient	G'	262 T/m ²
Lattice Structure	Modified MBA		SP-Strength	M	35 m ⁻³
Circumference	U	148.1 m	Injector		LINAC
Periodicity of the Lattice		4	Injection Energy	E_{inj}	800 MeV
Natural Energy Width		0.1 %	Pulse Current	$I_{inj(p)}$	10 mA
Momentum Compaction	α	7.2 10^{-3}	Pulse Repetition Rate		10 Hz
Radio Frequency	f	352 MHz	Places for Insertion Devices		8
Working Points	Q_x/Q_y	8.84/4.75	(23 % of the total Circumference)		
Nat. Chromaticity	ξ_x/ξ_y	-18.5/-11.1	Length of Straight Sections		4.1/3.6
Number of Dipoles 15°/20°		8 / 12			
Radius of Curvature on Orbit	ρ_0	7.148 m			
Magnetic Field on Orbit	B_{max}	1.4 T			
Gradient in the Dipoles		2.018 T/m			

(*in a future phase of ROSY is planned, to store 250 mA electrons)

The favorite working points are $Q_x=5.13 / Q_y=8.72$ and $Q_x=8.84 / Q_y=4.75$. The dynamic aperture for the tune $Q_x=8.84$ and $Q_y=4.75$ are given in figure 2. These calculations have been done with four wigglers in the straight sections and four undulators in the arcs. The code used was RACETRACK [9]. The dynamical aperture with $X \geq 60$ mm ($\geq 120 \sigma_x$) and $Y \geq 15$ mm ($\geq 190 \sigma_y$) gives enough space for the injection and a long beam life time.

IV. COMPONENTS OF ROSY

For the time being a lot of 3rd generation light sources have been built. ROSY takes advantage of this fact and most of the components for ROSY will be copied or modified using the experiences and cooperations of other laboratories.

The basic design of the bending magnets and the quadrupoles is that one of ELETTRA, only the pole shape will be redesigned in order to obtain the gradient desired. For the sextupoles we intent to use the ESRF design because of its additional steerer function.

A comparison between well established rf-systems (ALS, LEP/ESRF, ELETTRA, DORIS, PETRA) led to the choice of two LEP cavities [10] because of the lowest power consumption at the required parameters (cavity peak voltage of 3450 kV, quantum lifetime 10 hrs., beam power 118 kW / 295 kW respectively at $I_e=0.1A/0.25A$).

As the basic concept for the control system is to be proposed a distributed control system with four network layers. Further details can be seen in [11]. The vacuum system is designed in a close cooperation with DESY. We intent to use the HERA profile for the vacuum chambers.

V. ACKNOWLEDGEMENTS

It is a pleasure to acknowledge the contributions and fruitful discussions we had with the machine groups of BESSY, BONN, CERN / LEP, DESY, DELTA, ESRF, ELETTRA and NSLS.

VI. REFERENCES

- [1] D.Einfeld and W.Matz, "ROSY-Rossendorfer Synchrotronstrahlungsquelle", FZR 92-10, Rossendorf (June 1992).
- [2] W. Matz, "Nutzung einer zukünftigen Synchrotronstrahlungsquelle", (Report on the 1st Users Meeting, Dresden), FZR 93-03, Rossendorf (Jan.1993).
- [3] R.Chasman and K. Green, "Preliminary Design of a Dedicated Synchrotron Radiation Facility", IEEE Trans. Nucl. Sci., NS-22, 1965 (1975).
- [4] D.Einfeld and G. Mülhaupt, "Choice of the Principal Parameters and Lattice of BESSY", Nucl. Inst. Meth. 172 (1980).

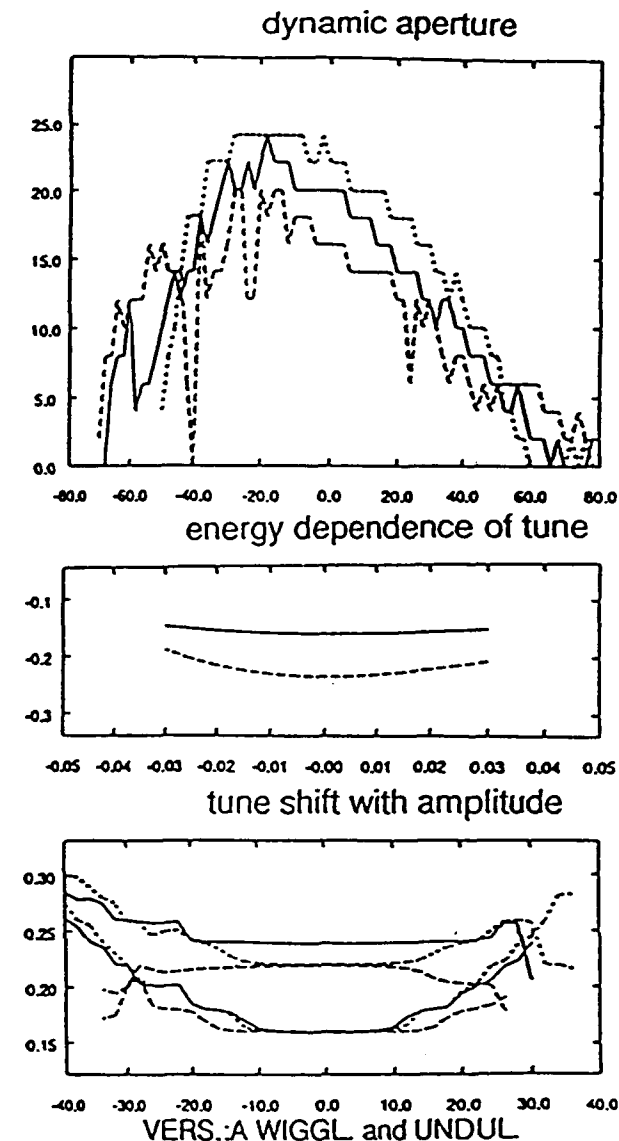


Fig 2: Dynamic Aperture and Tune Shift with Momentum as well as Amplitude for ROSY. Solid line: $\Delta p/p: 0$, Dotted line: $\Delta p/p: +2\%$, Dashed line: $\Delta p/p: -2\%$

- [5] A.Jackson, "A Comparison of Chasman-Green and Triple Bend Achromat Lattices", Particle Accelerators, Vol.22, 111 (1987).
- [6] R.Maier, "High Brilliance Lattices", CERN 89-01, 89 (1989).
- [7] A.Roper, "High Brilliance Lattices and the Effects of Insertion Devices", CERN 90-03, 158 (1990).
- [8] D.Einfeld and M.Plesko, "The QBA Optics for the 3.2 GeV Synchrotron Light Source ROSY II", these proceedings.
- [9] F.Iazzourene, C.J.Bocchetta, R.Nagaoka, L.Tosi, A.Wulich, "RACETRACK Users Guide", Sincrotrone Trieste, STM-91/11, (July 1991).
- [10] I.Wilson and H.Henke, "The LEP Main Accelerator Structure", CERN 89-09, (1989).
- [11] T.Goetz, M.Picard and M.Plesko, "The ROSY Control System", these proceedings.

A SOURCE OF SYNCHROTRON RADIATION FOR RESEARCH AND TECHNOLOGY APPLICATIONS

V. Bar'yakhtar*, E. Bulyak, V. Chechetenko, A. Dovbnya, S. Efimov, A. Gevchuk, P. Gladkikh, I. Karnaukhov, V. Kozin, S. Kononenko, V. Likhachev, V. Lyashchenko, V. Markov, N. Mocheshnikov, V. Molodkin*, V. Moskalenko, A. Mytsykov, V. Nemoshkalenko*, Yu. Popkov, A. Shcherbakov, A. Shpak*, M. Strelkov, A. Tarasenko, Yu. Telegin, V. Trotsenko, A. Zelinsky

Kharkov Institute of Physics and Technology, 310108 Kharkov, Ukraine;

*Metallophysics Institute of the Ukrainian Academy of Sciences, 252142 Kiev, Ukraine

Abstract

The synchrotron ring for the scientific and industrial applications is designed at Kharkov Institute of Physics and Technology. The ring is dedicated for Ukrainian Synchrotron Radiation Center in Kiev. The synchrotron light generating by the 800 MeV electron beam with current up to 200 mA and the radiation emittance of $2.5 \cdot 10^{-8}$ m*rad will be utilized by 24 beam lines. Two wigglers and an undulator will be inserted into the magnet lattice. The ring lattice is to provide large enough dynamic aperture and to decrease sensitivity to the collective effects.

I. INTRODUCTION

The report is concerned with a source of synchrotron radiation (SSR) which is to be the base facility in the Ukrainian Research Center of Synchrotron Radiation in Kiev for fundamental and applied research. A beam of 800 MeV electrons at a current of 200 mA and a radiation emittance of $2.5 \cdot 10^{-8}$ m must ensure investigations in X-ray lithography, photoelectron spectroscopy, EXAFS, etc. It is anticipated that the SSR will have up to 24 SR channels, including three channels formed by special insertion devices, viz., wigglers and undulators. On designing the facility, special attention has been given to the dynamic aperture and collective effects.

Many physical methods of research in the fields of fundamental (in particular, atomic and molecular physics, biology) and applied sciences (materials science, microelemental analysis, medical diagnostics, etc.) involve the employment of synchrotron radiation. This report describes the proposals for the choice of the storage ring structure and gives a brief outline of the principal systems of the complex. The storage ring under consideration is expected to be the base research tool of the Synchrotron Radiation Center of the Ukraine [1].

In the SSR-800 design, two main requirements were taken into consideration. These are the provision of high spectral brightness of the source in the wavelength band needed, and the possibility of extending the spectral range employed.

To generate SR of the necessary spectral range, we have chosen the beam energy in the storage ring to be 800 MeV and the field in bending magnets to be 1.34 Tesla. After careful tests and comparison between two types of the magnet lattice (Chessman-Green and TBA), comprising a four-superperiod racetrack with long dispersion-free straight

sections, we have preference to the TBA-type lattice as providing higher photon beam parameters even though being more complicated in the structure. The main physical parameters of the storage ring are presented in Table 1.

Table 1.

Electron beam energies, MeV	
injected	120
nominal	800
top	1000
Stored current, mA	200
Perimeter, m	46.729
Number of dipole magnets	12
Magnet curvature radius, m	2.005
Magnet length, m	1.05
Magnetic field, T (800 MeV)	1.34
Field index	3.0
Vertical gap, mm	36.0
Number of quadrupole lenses	24
Lens length, m	0.2
Highest gradient, T/m ²	300
Betatron tunes	
horizontal Q_x /vertical Q_y	4.26 / 3.20
Momentum compaction factor, α	0.0247
Natural chromaticity, ξ_x/ξ_y	-7.27/-7.24
Damping times, μs $\tau_x/\tau_y/\tau_z$	8.77/13.87/9.76
Emittance, nm rad ϵ_x/ϵ_y	27.6/1.38
Energy spread, %	$5.8 \cdot 10^{-2}$
Energy losses per turn, keV	18.0
RF, MHz	699.3
Number of bunches	109
Accelerating voltage amplitude, kV	200
RF Power, kW	10
Critical photon energy, keV	0.6
Flux, phot/(A*sec*mrad*0.1%BW)	$1.25 \cdot 10^{12}$

The storage ring lattice is a combined system comprising four superperiods (Fig.1). Table 2 lists the lattice parameters for one superperiod. The curved-ray trajectory part includes three rectangular magnets with a bending angle of 30° , a curvature radius $R=2.0053$ m and the field index $n=3$, as well as two horizontally focusing quadrupole magnets providing achromaticity of the long straight part of the trajectory.

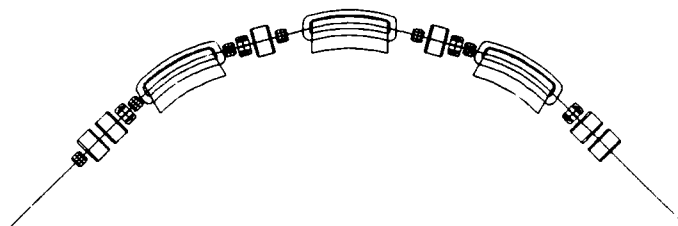


Figure 1. Layout of the storage ring superperiod.

Table 2.

Element	Length, m	Strength
D0(1/2)	1.6162	
Q1	0.2	4.4765 m ⁻²
D1	0.15	
Q2	0.2	-2.6920 m ⁻²
D2	0.7	
RB	1.05	30°, -0.7453 m ⁻²
D3	0.6	
Q3	0.2	7.520 m ⁻²
D4	0.6	
RB(1/2)	0.525	15°, -0.7453 m ⁻²

The straight part of the trajectory comprises four quadrupole magnets, which, being used in combination with two quadrupole magnets of the curved ray part and the vertical-correcting dipole magnets, ensure the stability of radial and vertical motion. Fig. 2 shows the lattice focusing functions for a superperiod (calculations were performed by the DeCA program [2]). The mode of the SSR-800 operation is characterized by a low radiation emittance, which is due to a greater rigidity of the lattice. This leads to the increase in the natural chromaticity which can be compensated by sextupole lenses mounted in the sections with a nonzero dispersion. The dispersion-free section incorporates the second family of sextupole lenses to correct the dynamic aperture. Fig.3 depicts the computer-simulated dynamic aperture in the center of the long straight section. It is seen that with the sextupole compensation lenses turned on, the dynamic aperture is greater than the geometrical one.

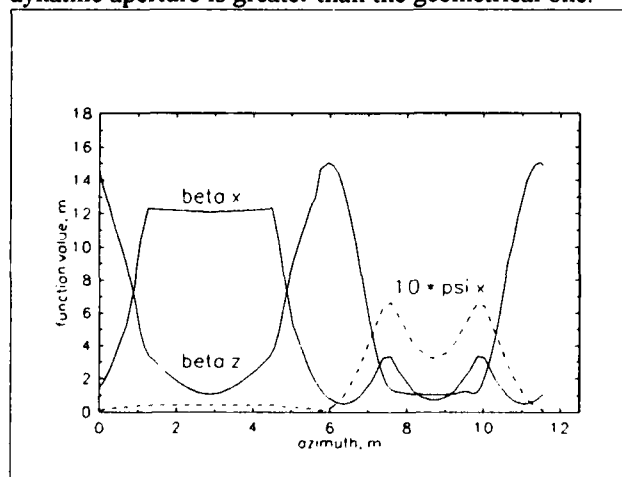


Figure 2. Structure functions of the storage ring.

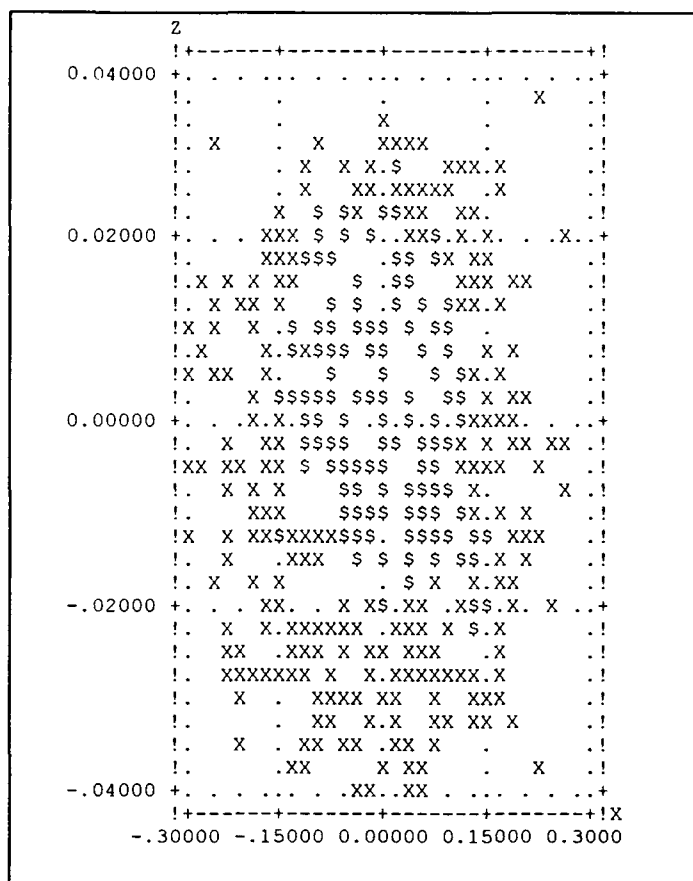


Figure 3. Dynamic aperture. x: lost particles; \$: stable particles.

We have considered the effect of a three-pole wiggler with a field amplitude of 10 T on the beam dynamics in the storage ring, which results in the tune shift (mainly, vertical), $\Delta Q_z = 0.2$, and the decrease in the dynamic aperture size. As a result, the system of wiggler focusing was chosen. The added doublets of quadrupole lenses placed at the wiggler ends provide a complete coincidence of the transport matrix of the insert section with that of a standard long straight section. As a consequence, the dynamic aperture has decreased by less than 5%, and the linear optics of the lattice has been restored.

Residual gas molecules in the vacuum chamber of the storage ring cause the scattering of circulating beam particles. This involves an increase in the transverse dimensions and the divergence of the beam, and also increases its losses. To attain the acceptable beam lifetime value (about 6 h), which is determined in the storage ring mainly by the Touschek effect and residual gas scattering, it is necessary to ensure a pressure of about 10^{-9} Torr and to mount ion clearing electrodes.

As an injector, we intend to employ the 120 MeV electron linac, designed at the Kharkov Institute, with a pulsed beam current of 100 mA and a transverse emittance of 2×10^{-7} m. The injection to the storage ring is accomplished in the horizontal plane by means of three kicker magnets and a magnet septum.

Beam energy losses by synchrotron radiation and parasitic losses in the vacuum chamber walls are compensated with the help of a 10 kW RF (699.3 MHz) system. The accelerating voltage of 200 kV chosen in view of the Touschek lifetime, is provided by a single half-wave cavity, whose shape has been optimized against the shunt resistance at the main (operating) mode (Ω -cavity). As calculations and measurements [3] indicate, this cavity has lower coupling impedances at higher-order modes than the cylindrical cavity has and, therefore, is less sensitive to the excitation of coupled oscillations of bunches.

Sixteen pickup stations and a current transformer are used to monitoring the beam in the storage ring.

We expect that the construction of the building for the SSR-800 will be started in 1993, the fabrication and installation of the equipment are scheduled for 1994, and in 1995 initial experiments using the SR will be started (four SR dedicated channels at the first stage).

V. REFERENCES

- [1] E. Bulyak et al, "Synchrotron radiation source," *HEPACC-92 Proceedings, Hamburg, 1992*.
- [2] A. Zelinsky et al, "New version 3.3 of the DeCA code," *Proc. of the III EPAC, Berlin, 1992, pp. 685-687*.
- [3] Yu. Popkov et al, "A study of electrodynamic characteristics of the dummy accelerating cavity of an optimized shape," (in Russian), *Prepr KhFTI 90-17, Kharkov, 1990*.

Optimum Steering of Photon Beam Lines in SPEAR*

W. J. Corbett, B. Fong, M. Lee, V. Ziemann
Stanford Linear Accelerator Center
Stanford, CA 94309 USA

Abstract

A common operational requirement for many synchrotron light sources is to maintain steered photon beamlines with minimum corrector strength values. To solve this problem for SPEAR, we employed the Singular Value Decomposition (SVD) matrix-inversion technique to minimize corrector strengths while constraining the photon beamlines to remain on target. The result was a reduction in corrector strengths, yielding increased overhead for the photon-beam position feedback systems.

I. INTRODUCTION

The SPEAR storage ring is a 234-m-circumference device operating with 3 GeV electrons. It is presently equipped with nine photon beam ports to serve a range of synchrotron radiation user needs in the uv and x-ray regions. As with all synchrotron radiation devices, there is a premium on maintaining the photon beams on target.

Using closed three-magnet bumps, Hettel [1] pioneered the first feedback-stabilized servo loops to reduce photon-beam motion at detectors located about 10 m from the radiation source point. These systems proved to be reliable and are still in use today. The only problem with the servo loops, however, was the occasional tendency for the feedback circuit to drive corrector currents to the power supply limits. Painstaking manual efforts were therefore made to reduce the initial corrector strengths so that the feedback loops had maximum operational overhead.

To further complicate the problem, the SPEAR BPM system contains large DC readback errors, making it difficult to steer the beams on target following realignment of the magnets. In addition, the corrector to photon-beam position response can be non-linear because the photo-ionization chambers are non-linear. As a result, attempts to reduce the corrector strengths while maintaining steered photon beams via measured response-matrix techniques proved futile. A solution was then found which utilizes the unique mathematical properties of singular-value matrix decomposition [2] which was applied successfully on SPEAR.

II. SINGULAR VALUE DECOMPOSITION

In the course of studying modeling techniques for SPEAR, we found that we could adapt a 'corrector ironing' algorithm, originally developed by one of the

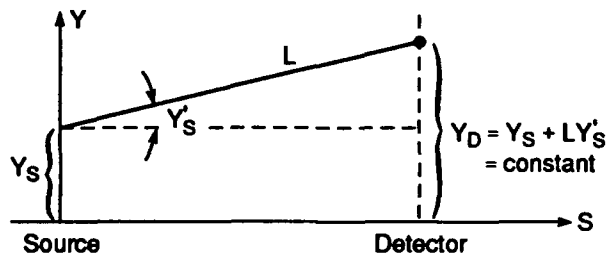


Figure 1. Photon beam positioning at detector requires $y_S + Lx_S = \text{constant}$.

authors for the SLC final focus [3], to SPEAR. In the SLC application, the RMS excitation of correctors was reduced subject to the constraint that the beam position remained constant in the sextupoles, and the beam trajectory remained constant at the collision point. Since there were typically more correctors than constraints, the technique of Singular Value Decomposition (SVD) was used to solve the under-determined linear system, exploiting the advantageous property of SVD to minimize the RMS of the solution vector which contains the corrector excitations.

In SPEAR, the problem translated into reducing corrector strengths across regions of the storage ring with four or five consecutive photon beamlines while keeping the photon beams fixed on target. Geometrically, the constraint of constant photon-beam position required the electron-beam coordinates (y, y') at the photon beam source point to satisfy $\Delta(y + Ly') = 0$, where L is the distance from source point to detector as shown in Figure 1. The Δ -operator indicates the change after the steering correction.

For the SVD calculations, typically, five target photon-beam positions and two bump closure constraints were used, with about twelve (variable) corrector strengths to be minimized. To optimize performance of the system, the accelerator-optics model used for the corrector-response calculation was derived using numerical fitting techniques to match the measured data [4]. For this application, the virtues of the SVD solution were two-fold: (1) the solution satisfied the constraints exactly (beams fixed on target), and (2) RMS reduction of the corrector-strength vector caused the

* Work supported by Department of Energy contract DE-AC03-76SF00515.

largest current decrease in the initially strongest correctors. The new corrector configuration therefore exhibits optimum steering of the photon beams, leaving maximum overhead for the feedback systems to operate.

III. EXPERIMENTAL RESULTS

Initial tests of the algorithm produced a 60% RMS reduction in the vertical-corrector strengths relative to the nominal steered configuration. More important, after a three-month shutdown with magnet realignment and the decision to operate SPEAR with a new high-brightness lattice [5], a new corrector configuration had to be found in which all photon-beam lines were steered properly. Using the corrector-ironing program, the steering procedure was simplified to a series of closed-bump corrector adjustments to position the photon beams, followed by ironing the correctors to gain overhead for the next iteration. In addition to producing an optimally steered orbit, it was estimated that the corrector ironing program saved about one week of accelerator commissioning time.

One of the most dramatic demonstrations of corrector strength reduction came about after rough vertical beam steering was completed. In the first iteration for the horizontal correctors, the RMS excitation of the horizontal correctors in SPEAR was reduced from 1 mrad to 35 μ rad, and still the beams remained on target.

IV. FURTHER APPLICATIONS

Possible applications for the SVD-based, corrector-ironing program used at SPEAR range from generating closed bumps to modern orbit feedback systems [6]. Here, we list a few:

Commissioning Tool: A terminal-interactive (X-Windows) system is planned for SPEAR which will allow the operator to adjust the electron-beam orbit at selected photon-beam detectors using a subset of corrector magnets with strengths computed via SVD. This tool will allow the operator to quickly steer photon beams on target with optimum corrector settings. In general, local beam bumps can be constructed for injection, photon-beam steering, or coupling control, for example. The corrector-strength weighting feature allows the user to depress individual correctors.

Photon Beamline Alignment: By assigning variables to the positions of photon beam monitors, low-strength solutions can be determined for the corrector pattern which would require realignment of the photon beamlines. Conversely, with accurate knowledge of the photon beam-position monitor elevations relative to the plane of the storage ring, SVD (or direct computation) can be used to estimate magnet misalignments.

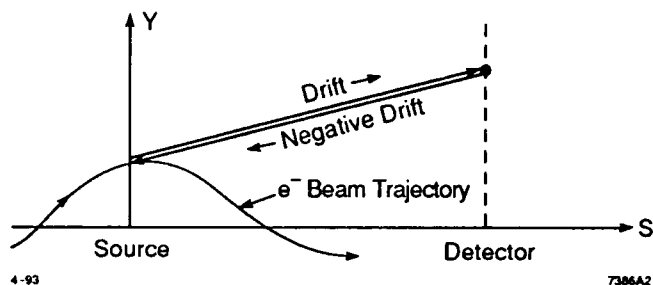


Fig. 2. Drift/Negative Drift modeling technique allows photon-beam detector to be treated similar to nominal BPM.

Closed Orbit Control: The original closed-bump SVD program for corrector ironing in SPEAR has been modified for closed-orbit operation. In addition, the photon-beam position constraint, $\Delta(y+Ly')=0$, was replaced with a new drift/negative-drift model whereby the photon beam is propagated along a drift of length L from the source point to the detector, followed by a negative-drift back to the source point. The electron-beam motion is then simulated farther downstream (see Fig. 2). Effective response-matrix coefficients can be computed at the photon BPMs.

Orbit Feedback: Many third-generation light sources are considering SVD algorithms as drivers for fast-orbit feedback systems.

Acknowledgments

The authors would like to thank Max Cornacchia for supporting and encouraging this work.

V. REFERENCES

- [1] R. O. Hettel, *IEEE Trans. Nucl. Sci.* NS-30 2228 (1983).
- [2] W. Press et al., *Numerical Recipes*, Section 2.9, Cambridge University Press, Cambridge, 1986.
- [3] V. Ziemann, "Corrector Ironing for the SLC," these proceedings.
- [4] W. J. Corbett et al., *Proc. 3rd EPACS, Berlin*, 24-28 March, 1992, p. 753; and W. J. Corbett et al., "A Fast-Model Calibration Procedure for Storage Rings," these proceedings.
- [5] J. Safranek, Ph. D. Thesis, Stanford University, 1991.
- [6] Y. J. Chung, "Closed-Orbit Correction Using Singular-Value Decomposition of the Response Matrix," these proceedings.

Establishment of a Tolerance Budget for the Advanced Photon Source Storage Ring*

H. Bizek, E. Crosbie, E. Lessner, L. Teng
Argonne National Laboratory, 9700 So. Cass Avenue, Argonne, IL 60439

Abstract

The limitations on the dynamic aperture of the Advanced Photon Source storage ring due to magnet misalignments and fabrication errors are presented. The reduction of the dynamic aperture is analyzed first for each error considered *individually*, and then for *combined* error multipole fields in dipole, quadrupole, and sextupole magnets, excluding and including magnet misalignments. Since misalignments of the strong quadrupoles in the ring induce large orbit distortions, the effects on the dynamic aperture are investigated before and after orbit correction. Effects of off-momentum particles and the tune dependence with momentum are also presented. This extensive analysis leads to the establishment of a tolerance budget. With all the errors set at the tolerance level, and with the orbit distortions corrected, the dynamic aperture reduction is no greater than 50% of that of the ideal machine.

I. INTRODUCTION

The Advanced Photon Source is a 7-GeV synchrotron radiation source designed for high brilliance. Its storage ring has a Chasman-Green lattice, with strong quadrupoles and chromaticity-correcting sextupoles. The sensitivity of the lattice to *individual* magnet errors was studied extensively, both analytically [1] and by numerical simulation [2], [3]. In this paper we present the results of studies of *combined* random magnet fabrication and alignment errors and the establishment of error limits based on the extent of reduction of the dynamic aperture.

When alignment and fabrication errors are combined, the dynamic aperture reduction is expected to be large. Due to the strong focusing required by the low emittance, orbit distortions caused by quadrupole displacements can be considerable—the APS storage ring has a large orbit-to-quadrupole displacement ratio¹, of the order of 50 [4]. Since orbit distortions are mainly caused by dipole strength errors, dipole roll, and quadrupole misalignments, we have analyzed first, the effects of combined errors that do not affect the closed orbit to first order, and then, of all errors together. For the latter group, we determined the dynamic aperture reduction both *before* and *after* orbit correction.

II. MULTIPOLE FIELD ERRORS

We define multipole field errors as those which do not cause closed orbit distortions. Analysis of the lattice responses to variations of a single error strength is straight-forward; not

so, when several errors are present. In order to understand the dynamic aperture behavior in the latter case, we studied several levels of error values, starting with *every* error at its individual tolerance limit² and the subsequent levels with strengths reduced proportionately. The resulting **tolerance budget**, shown in Table I, represents those values for which, when construction and alignment errors are combined, the extent of dynamic aperture reduction, *after correction of closed orbit distortions*, is no greater than 50%. In general, combined multipole error tolerance budget limits are smaller than individual tolerance limits by a factor of five to ten. We note that in Table I the multipole coefficients refer to values at a radius of 1.0 cm, and are normalized such that, for a $2n$ -pole magnet, $b_{n-1} = 1.0 \text{ cm}^{-n+1}$, with the magnetic field parametrized by:

$$B = B_0 \sum_{n=0} (b_n + ia_n)(x + iy)^n$$

We also studied the combined normal and the combined skew multipole errors separately. The combined *normal* multipole errors alone, set at the budget tolerance limits, produce an average dynamic aperture reduction of about 43%. The corresponding combined *skew* multipole errors produce an average reduction of about 35%. Both *normal* and *skew* errors together yield a reduction of some 50%, as mentioned. The dynamic aperture in the presence of multipole errors is shown in Figure 1, where the ideal dynamic aperture is also shown for comparison.

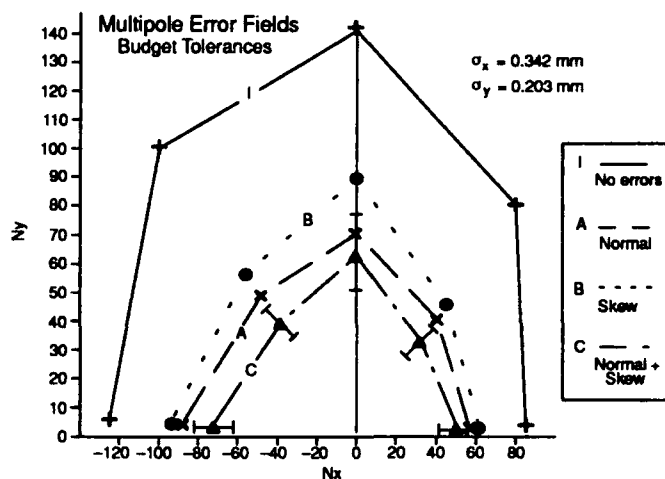


Figure 1

Comparison of the dynamic aperture in presence of random normal multipole errors fields (A); random skew multipole error fields (B); and random normal and skew errors combined (C). Error field components are at the budget tolerances. Axes are in units of the rms beam sizes at the center of the straight section (σ_x and σ_y). The bars represent the error spread over ten machines

* Work supported by U.S. Department of Energy, Office of Basic Energy Sciences under Contract No. W-31-109-ENG-38.

¹ Defined as the ratio of the rms quadrupole displacements and the rms orbit distortions.

² Defined as the error strength which reduces the ideal dynamic aperture by 50%.

The submitted manuscript has been authored by a contractor of the U. S. Government under contract No. W-31-109-ENG-38. Accordingly, the U. S. Government retains a nonexclusive, royalty-free license to publish or reproduce the published form of this contribution, or allow others to do so, for U. S. Government purposes.

Table 1 Error Tolerance Budget

Error Type	Individual Tol.	Budget Tol.	
Roll angle misalignments of dipole magnets	1.0	0.5	mrad
Horizontal or vertical displacements of quadrupole magnets	0.1	0.2	mm
Error dipole fields in dipole magnets	2×10^{-3}	1×10^{-3}	
Horizontal or vertical displacements of sextupole magnets	0.2	0.2	mm
Normal quadrupole field errors in dipole magnets	4×10^{-4}	1×10^{-4}	cm^{-1}
Normal sextupole field errors in dipole magnets	3×10^{-4}	1×10^{-4}	cm^{-2}
Normal octupole field errors in dipole magnets	3×10^{-4}	1×10^{-4}	cm^{-3}
Error field gradients in quadrupole magnets	4×10^{-3}	1×10^{-3}	cm^{-1}
Normal sextupole field errors in quadrupole magnets	1×10^{-3}	2×10^{-4}	cm^{-2}
Normal octupole field errors in quadrupole magnets	3×10^{-4}	2×10^{-4}	cm^{-3}
Error sextupole field gradients in sextupole magnets	2×10^{-2}	4×10^{-3}	cm^{-2}
Normal octupole field errors in sextupole magnets	1×10^{-2}	5×10^{-3}	cm^{-3}
Skew quadrupole field errors in dipole magnets	7×10^{-4}	1×10^{-4}	cm^{-1}
Skew sextupole field errors in dipole magnets	2×10^{-4}	3×10^{-5}	cm^{-2}
Skew octupole field errors in dipole magnets	1×10^{-4}	5×10^{-5}	cm^{-3}
Skew quadrupole field errors in quadrupole magnets	3×10^{-3}	5×10^{-4}	cm^{-1}
Skew sextupole field errors in quadrupole magnets	7×10^{-4}	1×10^{-4}	cm^{-2}
Skew octupole field errors in quadrupole magnets	2×10^{-4}	1×10^{-4}	cm^{-3}
Skew sextupole field errors in sextupole magnets	2×10^{-2}	2×10^{-3}	cm^{-2}
Skew octupole field errors in sextupole magnets	2×10^{-2}	2×10^{-3}	cm^{-3}

When momentum errors of 2% are added to multipole errors, the average reduction is 57%, 5% more than for on-momentum particles. The horizontal tune shifts by 4×10^{-2} and the vertical tune by -5×10^{-3} with respect to the on-momentum particles. The horizontal and vertical tune shifts due to the combined multipole error fields alone are -1×10^{-3} and -7×10^{-4} , respectively. The tune variation due to the combined field and momentum errors can be seen in Figure 2.

III. CONSTRUCTION AND ALIGNMENT ERRORS

As expected, the dynamic aperture reduces drastically when orbit distortions are added to construction errors. Multipole errors at the budget tolerances combined with orbit distortions resulting from estimated precision obtainable even with the best survey and alignment techniques produced zero dynamic aperture for eight of the ten seeds considered. Since closed orbit errors are the main cause of optics distortions, an effective orbit correction mechanism is necessary.

Our simulations of combined errors with orbit distortion correction were performed with the program "RACETRACK with Orbit Corrections" [5] using the 3-magnet bump method. Nine beam position monitors and eight horizontal and six vertical correction dipole magnets are provided in each cell, with the monitors positioned as close as possible to the sextupole mag-

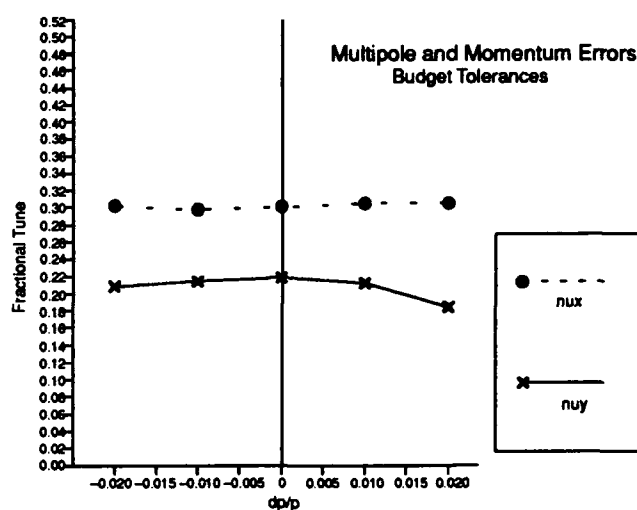


Figure 2

Tune variation with momentum errors in the presence of multipole error fields at the budget tolerances. Only the fractional part of the tunes are depicted.

nets. We employed a total of seven beam position monitors, four horizontal and four vertical corrector magnets per cell.

Random quadrupole displacements of 0.2 mm rms, dipole field strength errors of 1×10^{-3} rms and dipole roll angle misalignments of 5×10^{-4} were added to normal and skew random multipoles up to octupole error fields. We also set the resolu-

tion of the beam position monitors (BPM) to 0.2 mm rms. However, at this level the BPM inaccuracies do not affect the dynamic aperture: if we define the average recovery ratio of the dynamic aperture as the ratio of the dynamic aperture obtained with 0.2 mm rms beam monitor accuracy to that obtained with perfect monitor accuracy, the recovery ratio for the storage ring is as high as 96%.

After correction, 50% of the ideal dynamic aperture is recovered, as can be seen in Figure 3. For comparison, we included the reduction for the corresponding errors at the individual tolerance limits. The maximum residual closed orbit distortion is on the order of 0.15 mm in both planes. The maximum corrector strength distribution has a mean of 0.4 mrad, well within the corrector magnet specifications. The corrected orbit functions are also within acceptable values. Figure 4 shows the horizontal closed orbit distortions for a typical seed, before and after correction.

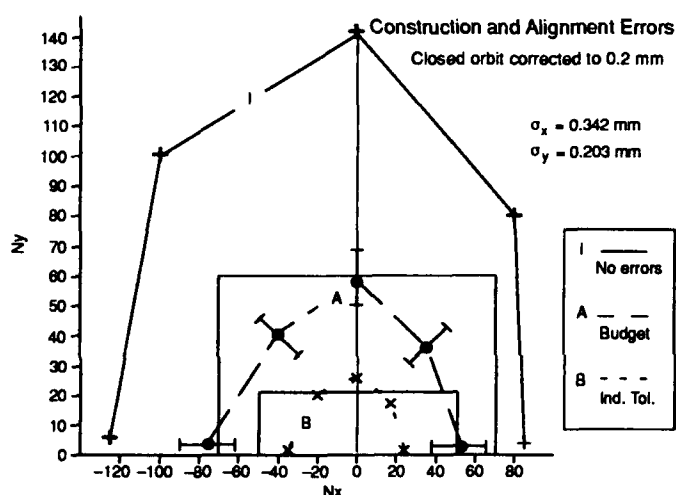


Figure 3

Dynamic aperture in the presence of magnet construction and alignment errors, *after* orbit corrections to 0.2 mm rms, for errors at the budget tolerances and at the individual tolerance limits. The physical aperture at the insertion device and elsewhere in the ring are also shown.

IV. CONCLUSION

With the criterion that a minimum of half of the ideal dynamic aperture be available after orbit corrections, an error tolerance budget for the APS storage ring is established. These tolerances are conservative for all magnets: the most recent set of multipole coefficients measured on the prototype dipole,

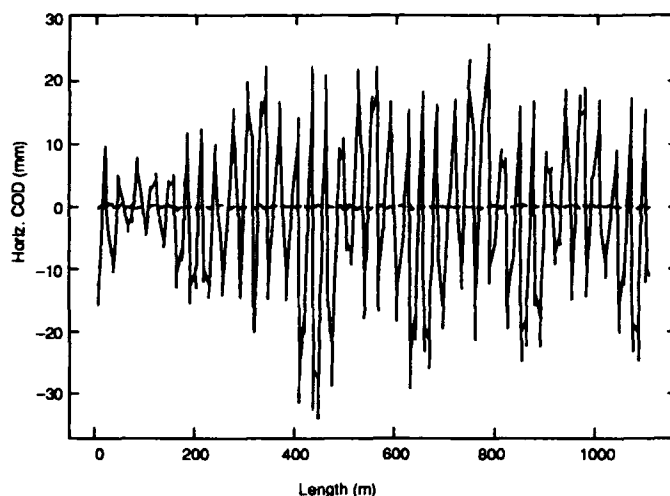


Figure 4

Horizontal closed orbit distortions for a typical seed *before* and *after* corrections to 0.2 mm rms. Magnet field and alignment errors at budget tolerances.

quadrupole, and sextupole magnets are lower than those adopted for the budget by at least a factor of two. Within the budget requirements and with orbit corrections obtained with the corrector system as designed, the dynamic aperture at the insertion devices is still larger than the physical aperture.

The most severe reduction effects on the dynamic aperture of the storage ring come from quadrupole displacements, as expected. However, in the worst case scenario, when all errors are included *at the specified tolerance levels* and when closed orbit distortions are corrected, the orbit functions and the dynamic aperture are entirely acceptable.

V. REFERENCES

- [1] L. C. Teng, Argonne National Laboratory, *unpublished report* (1992).
- [2] H. Bizek, E. Crosbie, E. Lessner, L. C. Teng, J. Wirzbinski, "Effects of Errors on the Dynamic Aperture of the Advanced Photon Source Storage Ring," *1991 Particle Accelerator Conference Record*, 210-212 (1991).
- [3] H. Bizek, E. Crosbie, E. Lessner, L. C. Teng, J. Wirzbinski, "Effects of Construction and Alignment Errors on the Orbit Functions of the APS Storage Ring," *1991 Particle Accelerator Conference Record*, 2778-2780 (1991).
- [4] E. Crosbie, Argonne National Laboratory, *unpublished report* (1991).
- [5] H. Nishimura, A. Wulrich, "RACETRACK with Orbit Corrections" (1987).

Study of Transverse Coupled Bunch Instabilities by Using Non-Linear Taylor Maps for the Advanced Light Source (ALS)*

M. Meddahi and J. Bengtsson
Lawrence Berkeley Laboratory, University of California
1 Cyclotron Road, Berkeley, CA 94720 USA

Abstract

To study coherent bunch instabilities for the third generation light source, ALS, it is insufficient to rely on a linear map with radiation damping for the lattice to obtain the correct dynamics. We have implemented a code for transverse bunch instabilities, using a 4-dimensional map for the lattice and wake field expansions for cavities and resistive wall effects. This model has been used to study the injection process and to determine the needed performance of the proposed feedback system for the storage ring.

I. INTRODUCTION

The effects of the cavity HOMs and the resistive wall on the beam dynamics have been studied for the ALS. A tracking code used at SLAC [1, 2] was generalized to the 4-dimensional transverse case. The model is based on a map for the ring and localized kicks in both planes due to cavities and resistive wall wake fields [3]. The dynamics of the beam at injection has also been studied.

II. CALCULATIONS ON TRANSVERSE COHERENT BEAM INSTABILITIES.

The linearized equation of motion perturbed by transverse dipole wake fields is [3, 4] (see the references for definition of the parameters) :

$$x_i'' + \left(\frac{\omega_{\beta 0}}{c}\right)^2 x_i = \frac{Q e}{E_0 C} \sum_{j=1}^{N_b} \sum_{n=0}^{N_t} W_{\perp} (L_{ij} + n C) x_j (s - L_{ij} - n C)$$

Using the following ansatz we get the corresponding dispersion relation

$$x_i(s) = x_{0i} \exp\left(-i \frac{\omega_{\beta}}{c} s\right),$$

$$\Delta \omega = \omega_{\beta} - \omega_{\beta 0} = \frac{1}{2 \omega_{\beta 0} x_{0i}} \sum_{j=1}^{N_b} \chi_{ij}^{\perp} x_{0j},$$

$$\chi_{ij}^{\perp} = \frac{c^2 Q e}{E_0 C} \exp\left(i L_{ij} \frac{\omega_{\beta 0}}{c}\right) \sum_{n=0}^{\infty} W_{\perp} (L_{ij} + n C) \exp\left(i n \frac{\omega_{\beta 0}}{c} C\right)$$

It follows that

$$\frac{1}{\tau} = \text{Im}(\omega_{\beta}), \quad \Delta \omega = \text{Re}(\omega_{\beta}) - \omega_{\beta 0}$$

where τ is the time constant. The eigenmodes are therefore determined by the linear eigenvalue problem

$$M \bar{x}_0 = \omega_{\beta} \bar{x}_0, \quad M_{ij} = \omega_{\beta 0} \delta_{ij} - \frac{1}{2 \omega_{\beta 0}} \chi_{ij}^{\perp}$$

*This work was supported by the Director, Office of Energy Research, Office of High Energy and Nuclear Physics, High Energy Physics Division, of the U.S. Department of Energy under Contract No. DE-AC-76SF00098.

For a given eigenmode the relative amplitude and phase of the initial conditions for each bunch are given by the corresponding (complex) eigenvector. In this case, all the bunches are oscillating coherently with the same frequency. Comparison of analytical results with numerical simulation (tracking) for this case can be found in section 4. For the general case, however, we have a superposition of eigenmodes.

For the non-displaced bunches (i.e. stored beam) we use the following ansatz and dispersion relation

$$x_i(s) = \frac{T_i}{c} s \exp\left(-i \frac{\omega_{\beta 0}}{c} s\right)$$

$$T_i = \left| \frac{1}{2 \omega_{\beta 0}} \sum_{j=1}^{N_b} \chi_{ij}^{\perp} x_{0j} \right|$$

where T_i is the linear growth rate.

III. OVERVIEW OF THE ALS

The ALS is a 1.5 GeV Synchrotron Radiation Source based on a triple bend achromat lattice [5]. The injection system consists of a high intensity electron gun, a 50 MeV traveling wave linac, and a 1 Hz, 1.5 GeV booster synchrotron. The injection scenario requires the storage ring closed orbit to be deflected close to the end of the injection septum using four bump magnets capable of displacing the orbit up to 15 mm. A pulse of electrons is ejected from the booster and transported through the injection septa into the storage ring.

Assuming that the HOMs of both RF cavities (iris radius 0.035 m, length 0.28 m, frequency 499.764 MHz, harmonic number 328) has been damped by a factor of 30 giving an average transverse shunt impedance of 2 M Ω /m, we investigate the HOMs with a shunt impedance greater than this value to study the effect on the beam dynamics. Table 1 shows the HOMs used [6].

f (MHz)	Polarization	Q	Rsh (k Ω /m)
810.08	H	48000	14800
1121.77	V	7000	3700
1122.72	H	17000	9000
1189.85	H	18000	92
1529	H	1800	200
1801.61	V	2000	1100

Table 1.

The effect of the resistive wall is also addressed using a total impedance (at the first sideband of the DC component) of 355.013 k Ω /m in the horizontal and 883.259 k Ω /m in the vertical plane.

IV. ANALYSIS

In the following analysis 10 bunches were used: 4 bunches (1 to 4) displaced by $x=5\text{mm}$ and $y=1\text{mm}$ and 6 bunches in the storage ring (5 to 10) assumed to be damped down to zero amplitude. The study was limited to 5 mm due to the use of a Taylor series map, proven accurate up to this amplitude using a symplectic integrator. Amplitudes up to 13 mm can be expected in reality. Tracking was done for 4096 turns and the final amplitudes are shown for bunch number 1 and 5.

A- Linear map

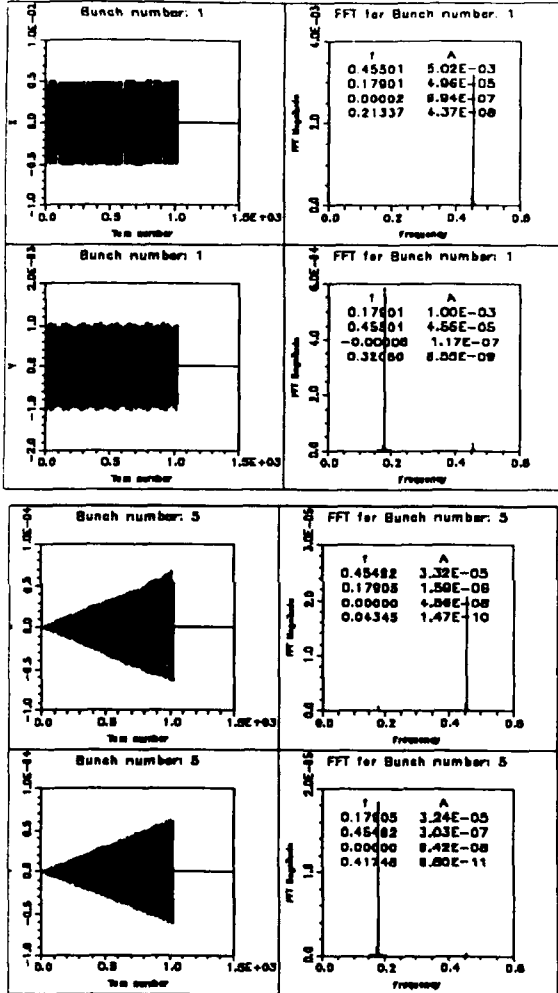


Figure 1: x and y amplitudes for bunch 1 and 5 .

In table 2a we present the effect on the final amplitudes of one cavity, of the resistive wall , and of both, respectively. For the resistive wall (R.W.) the wake field was stored for one turn in Table 2a and 500 turns in Table 2b.

	R.W. and CAV.		R.W. (1 wake)		CAVITY	
bunch #	x [mm]	y [mm]	x [mm]	y [mm]	x [mm]	y [mm]
1	5.0387	1.0156	5.026	1.015	5.012	1.0002
5	0.0237	0.0243	0.0342	0.0242	0.0107	0.0001

Table 2a.

bunch #	R.W. (500 wakes)	
	x [mm]	y [mm]
1	5.0387	1.0156
5	0.0237	0.0243

Table 2b.

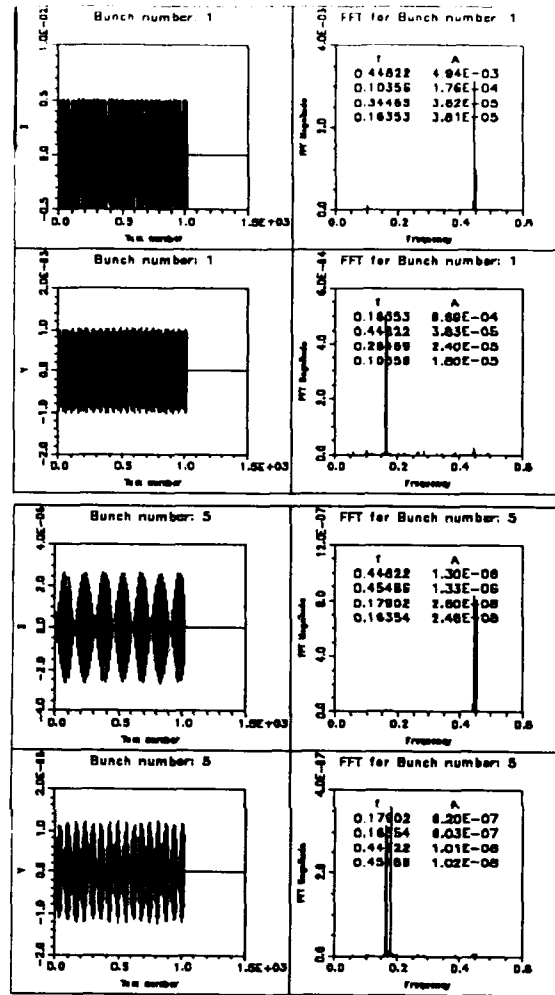


Figure 2: x and y amplitude for bunch 1 and 5 .

The amplitude of bunch 1 slowly increases to 5.038 mm in x-plane and 1.015 mm in y-plane. For bunch 5, the amplitude reaches 0.0237 mm in x and 0.0243 mm in y (Table 2a). Figure 1 shows the linear growth for the stored bunches. The use of one wake instead of five hundred wakes for the resistive wall is a good approximation and will be used for the following tracking studies (Table 2b).

B- Growth rates

H-Growth rate (s)		V-Growth rate (s)	
tracking	calculated	tracking	calculated
0.128	0.122	0.0902	0.0881
0.103	0.0979	0.0727	0.0706
0.0892	0.0848	0.0631	0.0611
0.0800	0.0761	0.0566	0.0548
0.0732	0.0696	0.0517	0.0502
0.0678	0.0646	0.0479	0.0466

Table 3.

Growth rates from tracking and estimates using the theory of section 2 were compared for the two cases of zero or non zero initial amplitude. In table 3 the results are shown for the stored bunches (5 to 10) with zero initial amplitude. We find very good agreement between tracking and calculation. Table 4 shows the results for the displaced bunches (1 to 4). The agreement is good.

H-Growth rate (s)		V-Growth rate (s)	
calculated	tracking	calculated	tracking
0.0208	0.0164	0.00569	0.00495
0.0208	0.0247	0.00569	0.00582
0.0208	0.0279	0.00569	0.00633
0.0208	0.0281	0.00569	0.00656

Table 4.

C- Nonlinear map

Table 5 shows the difference on the final amplitudes for bunch 1 and 5 when using a non-linear map

map	x1	y1	x5	y5
Linear	5.1048	1.0561	0.0602	0.0621
Non-linear	5.1006	1.0487	0.0027	0.0012

Table 5.

The non-linear map introduces a modulation of the amplitude for the stored bunches which leads to limited final amplitude (Figure 2). For the selected initial amplitudes, the change of the final amplitudes, after 4096 turns, are very small. The FFT on the bunches 5 to 10 shows a double peak around the tunes. An explanation was found by numerical simulation of a driven anharmonic oscillator leading to the same double peak when Fourier analyzed (Figure 3).

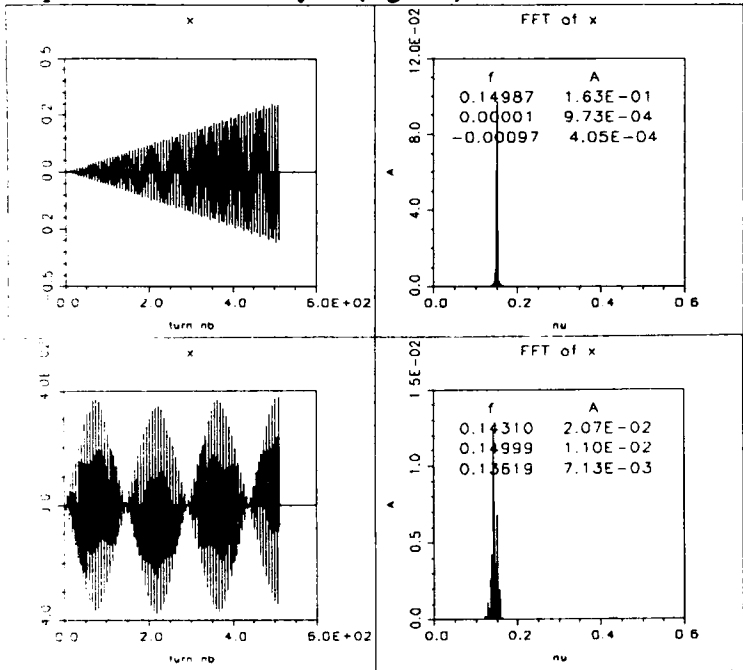


Figure 3. Driven harmonic and driven anharmonic oscillator.

V. INJECTION DYNAMICS

The bunches are injected from the booster to the storage ring with an amplitude of approximately 13 mm in the

horizontal and 1 mm in the vertical plane. We have studied the behavior of the beam just after the injection, for 15,000 turns (the damping time is approx. 15 ms), neglecting wake fields but simulating the full 6-dimensional dynamics [7].

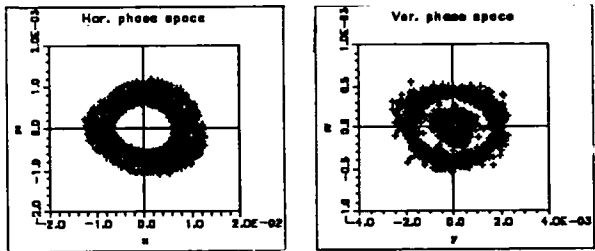


Figure 4. Phase space at injection.

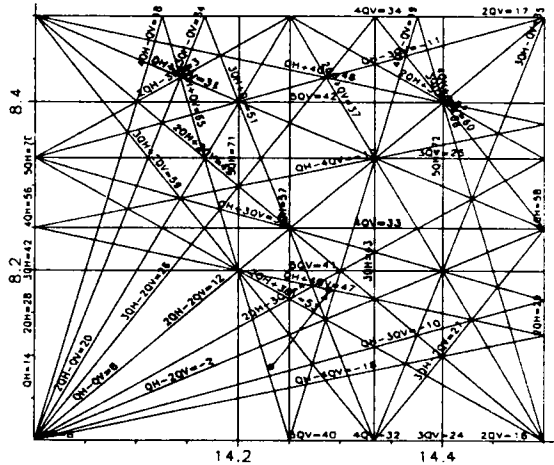


Figure 5. Tune diagram at injection.

Damping is observed in the horizontal plane together with beating in the vertical plane leading to large amplitudes. The large horizontal amplitude drives the vertical plane due to coupling. The change of amplitude due to radiation damping leads to a change of tune and crossing of resonances due to large amplitude dependent tune shifts.

VI. CONCLUSION

The tracking shows the importance of correct modeling of the lattice in the estimate of growth rates. Using a non-linear map for the lattice led to modulation of the amplitude, instead of linear growth, for an initially non-displaced bunch. However, the growth rates obtained in both planes are small. Study of the injection dynamics shows beating in the vertical, driven by the horizontal plane, leading to crossing of resonances.

VII. REFERENCES

- [1] K. Bane.et al, AIP Conf. Proc. No 127, chap.2, 1983.
- [2] K. A. Thompson and R. D. Ruth, SLAC-PUB 4962.
- [3] K.A. Thompson, Asym. B-factory collider note ABC-57.
- [4] M. Meddahi and J. Bengtsson, LBL-CBP Note/017.
- [5] LBL-Pub-5172 Rev.
- [6] J. Byrd and J. Corlett, ESG Tech Note-220.
- [7] E. Forest, to appear in Part. Accel.

Plans to Increase Source Brightness of NSLS X-Ray Ring*

J. Safranek and S. Krinsky
National Synchrotron Light Source
Brookhaven National Laboratory
Upton, NY 11973

Abstract

We discuss plans to increase the NSLS X-Ray ring source brightness by an order of magnitude. Proposed improvements include doubling current from 250 mA to 500 mA, reducing vertical emittance by a factor of 6 and reducing insertion device gaps and periods by up to a factor of two. Experimental results are reported which indicate we have succeeded in reducing the vertical emittance below 2 Å.

1 Introduction

The NSLS X-Ray ring provides a high brightness source of x-rays from bending magnets and insertion devices. In this note we discuss plans to increase the source brightness by an order of magnitude. The recent installation of a fourth 52 MHz RF cavity provides sufficient RF power to allow the stored current to be increased from 250 mA to 500 mA [1]. At present, 500 mA has been stored at injection energy (750 MeV) and 410 mA at 2.5 GeV. However, before running operations at 500 mA, it will be necessary to provide increased cooling downstream of the high power wigglers. A further increase in brightness can be achieved by replacing the existing wigglers by new devices operating with shorter periods and smaller gaps. An experiment [2] is in preparation using the X13 straight section to elucidate the operational limit of the vertical electron beam aperture. Finally, we have embarked on a study aimed at reducing the vertical emittance of the ring, and we have succeeded in reducing the emittance coupling from 1% to below 0.2%. The remainder of this paper will be devoted to a discussion of our approach to reducing the vertical emittance.

2 Method of Reducing Vertical Beam Size

Betatron oscillations in the vertical plane of an electron storage ring can be excited in two ways - horizontal oscillations can be coupled into the vertical plane, or vertical

oscillations can be excited directly when a photon is radiated where there is nonzero vertical dispersion, η_y . In order to reduce the vertical beam size, σ_y , one must correct both coupling and vertical dispersion. Measurements in the NSLS X-Ray ring indicate that η_y and coupling give approximately equal contributions to σ_y .

When we started our work to reduce σ_y , the X-Ray ring had eight skew quadrupoles grouped in two families with a single power supply powering the four skews in each family. There was no method for correcting η_y . Now each of the eight original skew quadrupoles have individual power supplies, and nine additional skew quadrupoles have been added. Four of the new skews are located in positions of high η_x , so they can be used to correct η_y efficiently without exciting much coupling.

COUPLING: In the past the coupling on the X-Ray ring was minimized by adjusting the two families of skew quadrupoles to minimize the split between the transverse tunes at the difference resonance. With 17 individually powered skew quadrupoles, we needed a better method for measuring coupling than the tune split at the difference resonance. One such method has been developed at Cornell [3] in which the two transverse normal modes are excited on resonance, and the ellipse traced out by the betatron oscillations is measured at the beam position monitors. This method requires turn-by-turn beam position measurement capability which is not available with the present X-Ray ring hardware, so we developed another coupling correction algorithm that takes advantage of the high accuracy closed orbit monitors [4] in the X-Ray ring.

We sample the coupling by measuring the shifts in the vertical orbit, Δy , produced by varying the strengths, individually, of a set of horizontal steering magnets. Then we correct the coupling by determining the skew quadrupole strengths that minimize the vertical orbit shifts. We chose to simultaneously minimize 16 different vertical orbit shifts created by 16 different horizontal steering magnets distributed about the X-Ray ring. The vertical orbit distortion from a single steerer does not have all the coupling information. Skew quadrupoles located at positions of zero orbit distortion for that steering magnet do not create any vertical orbit distortion. Two horizontal steering magnets separated by close to an odd integer multiple of 90° in hor-

*Work performed under the auspices of the U.S. Department of Energy

horizontal betatron phase sample all the skew quadrupoles. We chose to use more than two steerers, because there is some vertical orbit shift that is simply due to imperfect rotational alignment of the steering magnets. This shift is not due to coupling and should not be corrected with the skew quadrupoles. We found that the most effective way to solve this problem is to look at the vertical orbit distortions from many horizontal steering magnets. The vertical distortions really caused by rotated quadrupoles are well corrected with the same skew quadrupole distribution for all the steerers, while the vertical orbit distortions from rotated steerers are randomly distributed and cannot be simultaneously corrected with the skews. We added horizontal steering magnets until we found that adding more no longer changed the skew quadrupole distribution derived to best correct the vertical orbit shifts.

Simulations with PATPET [5] confirmed that there is a strong correlation between the vertical orbit shift and the vertical emittance, and that reducing the vertical shift is an effective way to reduce the vertical emittance (figure 1). Both before and after the skew quadrupoles were adjusted to reduce the vertical orbit shifts, the calculated vertical emittance was found to exhibit the approximate dependence

$$\epsilon_y(\text{\AA}) \approx .002 < \frac{\Delta y^2(\mu\text{m})}{\beta_y(\text{m})} > \quad (1)$$

where the shift in the vertical closed orbit, Δy , results from changing a horizontal steering magnet to give a 3 mm rms horizontal orbit distortion.

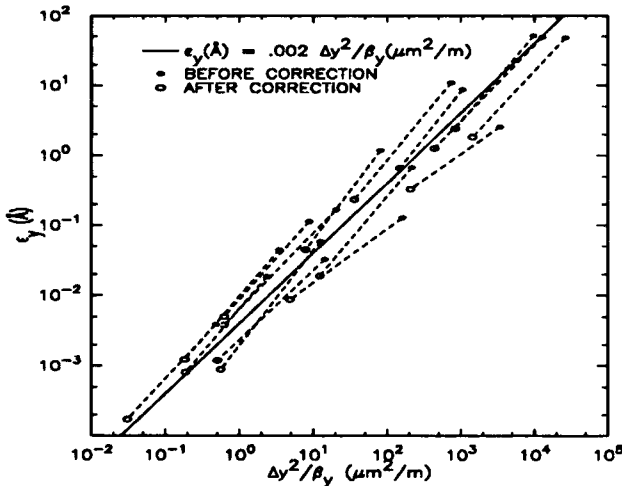


Figure 1: Simulation results from PATPET. Only coupling errors (no η_y) were introduced in the lattice. The dotted lines connect points for the same set of quadrupole rotation errors before and after correction.

VERTICAL DISPERSION: In order to minimize quantum excitation and thus minimize the vertical beam size, η_y should be minimized in the bending magnets where the photons are radiated. In reference [6], the author shows that the emittance from dispersion is given by $\epsilon_y = \frac{C_x \gamma^2}{\rho} <$

$\mathcal{H}_y >$, where $< \mathcal{H}_y >$ is the average value of the Courant-Snyder invariant in the bending magnets. In reference [7] the author shows that $< \mathcal{H}_y >$ is approximately equal to $2 < \frac{\eta_y^2}{\beta_y} >$, so for the X-Ray ring ($\rho = 6.9\text{m}$ and $\gamma = 5057$) the vertical emittance from dispersion is given by

$$\epsilon_y(\text{\AA}) \approx .03 < \frac{\eta_y^2(\text{mm})}{\beta_y(\text{m})} > \quad (2)$$

Vertical dispersion can be excited by vertical bending or by skew quadrupoles at locations of nonzero η_x . We did not want to change the vertical closed orbit from the standard operational orbit in which the beamlines are steered, so we used skew quadrupoles at locations of large η_x to correct the vertical dispersion.

CORRECTION ALGORITHM: The coupling and vertical dispersion correction was done simultaneously by solving a system of linear equations

$$\mathbf{MK} = \mathbf{V}$$

using singular value decomposition [8]. Here the vector \mathbf{V} has $48 \times 16 + 48$ elements. The first 48×16 elements are the measured vertical orbit shifts, $\Delta y / \sqrt{\beta_y}$, at the 48 beam position monitors for each of 16 horizontal steering magnets. The last 48 elements are the measured, $\eta_y / \sqrt{\beta_y}$, at the 48 BPMs. The $48 \times 16 + 48$ by 17 matrix \mathbf{M} is the measured change in \mathbf{V} with changes in the 17 skew quadrupoles. The linear equations are solved for \mathbf{K} , the 17 skew strengths that minimize the rms of $\Delta y / \sqrt{\beta_y}$ and $\eta_y / \sqrt{\beta_y}$. The relative weight for correcting $\Delta y / \sqrt{\beta_y}$ versus $\eta_y / \sqrt{\beta_y}$ can be adjusted to give more or less correction of coupling versus vertical dispersion.

3 Experimental Results

The correction algorithm was very successful in reducing the vertical dispersion and vertical orbit shifts. We were able to reduce $< \frac{\Delta y^2}{\beta_y} >$ by a factor of nine compared to the value ($5500 \mu\text{m}^2/\text{m}$) achieved with the previous coupling correction algorithm using only two families of skew quadrupoles. Figure 2 shows the reduction of $\Delta y / \sqrt{\beta_y}$ for a typical one of the sixteen horizontal orbit steering magnets. We were simultaneously able to reduce $< \frac{\eta_y^2}{\beta_y} >$ by a factor of seven (figure 3) from a starting value of $300 \text{ mm}^2/\text{m}$.

According to equations 1 and 2, we expect the reduction in $< \frac{\Delta y^2}{\beta_y} >$ and $< \frac{\eta_y^2}{\beta_y} >$ to give a reduction in the vertical emittance of about eight. We measured the emittance reduction in two ways - by measuring the decrease in Touschek lifetime [9] with approximately 80 mA stored in a single bunch, and by directly measuring the vertical beam size reduction using x-ray pinhole cameras. We saw nearly a factor of 2.5 decrease in the Touschek lifetime which indicates about a factor of 6 reduction in the vertical emittance.

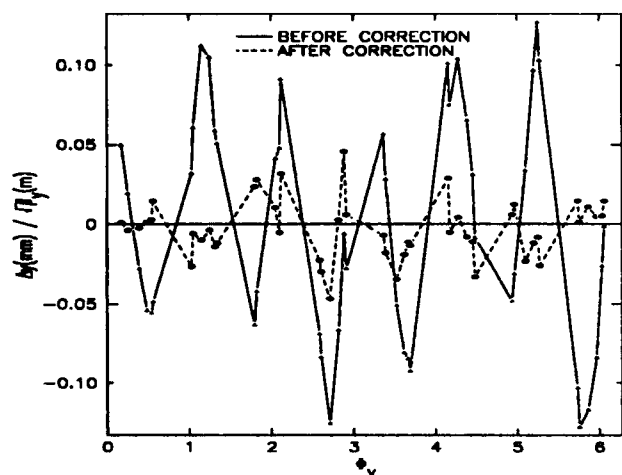


Figure 2: Measured vertical orbit shift resulting from a 3 mm rms horizontal orbit shift from a single steerer.

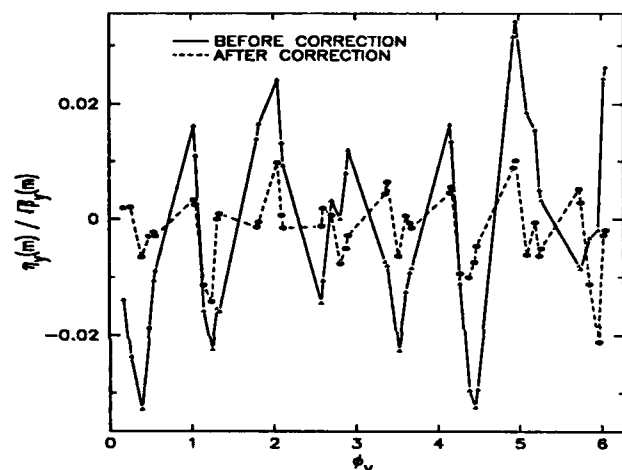


Figure 3: Measured vertical dispersion.

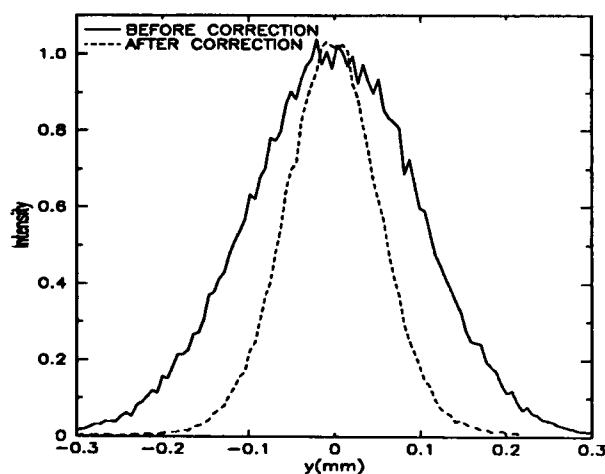


Figure 4: Vertical beam size at X26 ($\beta_y=15\text{m}$).

We measured the beam size reduction with x-ray pin-

hole cameras on beamlines X10 and X26. The results with beamline X26 appeared to give the best resolution. Figure 4 shows the profile measured at X26 with the old skew quadrupole correction and the smaller profile with the new correction. Subtracting a small resolution factor in quadrature, these measurements indicate a reduction in electron beam size of 2 which gives a reduction in vertical emittance of 4.

The measurements on X26 indicate that the vertical emittance is 6 Å with the old skew quadrupole settings compared to a horizontal emittance of 110 nm. With the new skew correction the X26 measurements indicate a vertical emittance of 1.5 Å. The fact that a greater reduction in Touschek lifetime was seen than the reduction in electron beam profile may indicate that we are running into a resolution limit with the X26 pinhole camera. If we assume this is the case and take the true reduction in vertical emittance to be a factor of six as measured with the Touschek lifetime, this would indicate that the vertical emittance with the new skew quadrupole correction is 1 Å. Work is continuing to better understand the resolution and absolute calibration of the pinhole cameras.

4 Acknowledgements

We would like to express our sincere appreciation for the help we received measuring the beam size from M. Sansone, S. Sutton, and M. Rivers. Discussions with R. Gluckstern were helpful when we were working to derive a correction algorithm.

References

- [1] M.G. Thomas, R. Biscardi, W. Broome, S. Buda, R. D'Alsace, S. Hanna, J. Keane, P. Mortazavi, G. Ramirez, J.M. Wang, these proceedings.
- [2] P.M. Stefan, L. Solomon, S. Krinsky, G. Rakowsky, Proceedings 1991 Part. Accel. Conf. San Francisco, CA, p. 1096.
- [3] P. Bagley, D. Rubin, Proceedings 1989 IEEE Part. Accel. Conf. Chicago, IL, p. 874.
- [4] R. Biscardi, J.W. Bittner, Proceedings 1989 IEEE Part. Accel. Conf. Chicago, IL, p. 15.
- [5] L. Emery, H. Wiedemann, J. Safranek, SSRL/ACD note 36 revised, June, 1988.
- [6] M. Sands, SLAC-121, November, 1970.
- [7] T. Raubenheimer, SLAC-PUB-4937, February, 1990.
- [8] W. Press, B. Flannery, S. Teukolsky, W. Vetterling, Numerical Recipes, Cambridge, 1990.
- [9] H. Bruck, Circular Particle Accelerators, Los Alamos report LA-TR-72-10 rev.

A Design Concept for the Inclusion of Superconducting Dipoles within a Synchrotron Light Source Lattice

M. W. Poole, J. A. Clarke, N. A. Mezentsev *, S.L. Smith, V. P. Suller, L. A. Welbourne

SERC Daresbury Laboratory, Daresbury, Warrington, WA4 4AD, UK

* BINP, Academy of Science Russia, Novosibirsk, Russia

Abstract

The advantage of using high field superconducting dipoles to provide hard radiation in a synchrotron light source is that, in contrast to using high field wigglers, scarce insertion device straights are not used up. A strategy is proposed for replacing selected conventional dipoles within a lattice with superconducting devices where and when required. The potential of both double and triple bend achromats is compared and contrasted. The properties of the superconducting dipoles as radiation source points are considered as also is their overall impact on the lattice behaviour. In a feasibility study for the advanced x-ray source DIAMOND, which is briefly described, it is concluded that a triple bend achromat is the best choice for a 3 GeV structure with 16 cells that meets the defined specification.

I. BACKGROUND

The SRS at Daresbury was the world's first high energy, dedicated (second generation) light source and its effective exploitation continues to be of high priority to the UK synchrotron radiation community. Recently a major review of existing and future requirements has been underway and a series of design options has been considered, initially concentrating on a single source called DAPS [1]. Finally a proposal has been made for a new VUV source (SINBAD) and for the eventual replacement of the SRS by an advanced facility called DIAMOND, that is designed to cover the intermediate spectral range between SINBAD and the ESRF. The lattice design of SINBAD is similar to DAPS but a different concept is considered here for DIAMOND.

II. GENERAL DESCRIPTION

The choice of 3.0 GeV for the storage ring energy has been dictated by the simultaneous requirements for high brightness soft x-ray beams from 150 eV to 3 keV and high flux x-rays in the 3 - 30 keV photon range. To match the anticipated experimental programme DIAMOND would require space for at least twelve insertion devices. To provide the necessary space for injection and RF systems a 16 cell lattice was chosen. The approximate circumference would be 300 m and either DBA or TBA designs could provide the required dispersion free straights for insertion devices. An important consideration in the design was that it should flexibly allow for the progressive replacement of conventional dipoles within the lattice by superconducting dipoles. These superconducting dipoles would satisfy the national requirement for harder x-rays without using up the limited supply of straight sections. The main parameters for the storage ring are shown in Table 1.

Table 1
Main Design Parameters

Energy	3.0 GeV
Circumference	~300 m
Number of cells	16
Normal conducting dipole	1.3 T
Superconducting dipole	4.5 T
Emittance	10-50 nm-rad
Beam current	300 mA
Insertion straight length	3.0 m

III. CHOICE OF LATTICE

Double Bend Achromat

In the case of a DBA structure two possibilities were considered:

1. Two dipoles per cell in a conventional design
2. Four dipoles per cell, installed in pairs

In the first case, the length of the normal conducting magnet is 1.3 m and the corresponding length of a replacement superconducting magnet is 0.45 m. The bend angle is large enough to permit full extraction and utilisation of the synchrotron radiation. In the second case, the length of the normal and superconducting magnets are 0.65 m and 0.2 m respectively. Here the superconducting magnets are too short, not only to create good field quality in an acceptable vertical aperture but also to provide adequate length of uniform field through the magnet. It is also clear that replacement of only one dipole in a cell is undesirable from the point of view of beam dynamics as it breaks the symmetry of the lattice.

Triple Bend Achromat

In the TBA lattice the cells contain three dipoles with equal bending angles. The central normal conducting dipole could be replaced by a superconducting one while still maintaining the symmetry of the cell structure. The magnetic length for normal and superconducting magnets is 1.0 m and 0.3 m respectively. The shorter length of the superconducting magnet in the TBA case is still acceptable in terms of providing synchrotron radiation. The design which produces acceptable beam performance and the best access to the superconducting magnet radiation with minimal impact on the insertion device beam lines is the TBA. For these reasons, early in the studies this was chosen as the best solution, although a limited amount of work has been carried out in parallel on the two magnet DBA lattice to allow the comparison of some basic parameters.

Optimisation of the linear properties of the TBA structure was carried out using the in-house computer program ORBIT [2]. Various options were considered for the quadrupole type and order within the achromatic bend. Figure 1 illustrates the structure of the final optimised TBA lattice that was chosen.

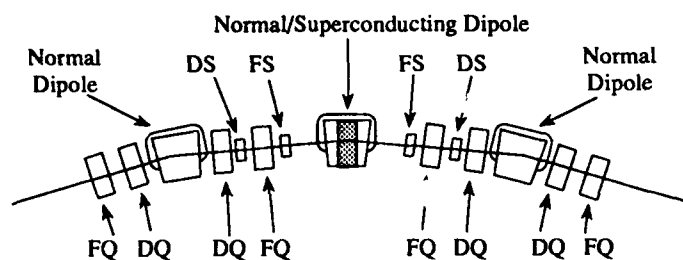


Figure 1. Sketch of TBA unit cell

With both sets of quadrupoles in the achromatic arc at approximately equal values this lattice with 16 superconducting magnets has a reasonable emittance of around 30-50 nm-rad and relatively low chromaticity. Some basic parameters of the lattice with all conventional dipoles, at a representative tune point, are summarised in Table 2. Reducing the level of the D-quadrupole in the achromat produces a very low emittance lattice: at the extreme an emittance of around 5 nm-rad can be achieved, even with 16 superconducting magnets installed, but at the expense of high beta values and chromaticity. The existence of this low emittance mode could provide a possible, but probably very challenging, additional upgrade path for the future development of DIAMOND.

Table 2
Lattice Parameters of the TBA

Radial, vertical tune	16.74, 7.53
Emittance (nm-rad)	19.16
Energy loss per turn (MeV)	0.94
Momentum compaction	0.00158
Radial, vertical chromaticity	-20.5, -31.5

IV. DESIGN OF SUPERCONDUCTING DIPOLES

A superconducting dipole has been designed with a field of 4.36 T and the required bending angle of 7.5°. A diagram of the proposed superconducting magnet is shown in Figure 2. It uses a steel yoke to improve the field quality and minimise the stray fields at the superconducting windings and to give excellent field uniformity. The predicted performance of this type of magnet is very good and a prototype [3] including several of its features has been built at Novosibirsk and tested to 6 T.

The change in photon output when replacing the normal conducting 1.3 T magnet with the high field superconducting 4.36 T magnet is shown in Figure 3 together with the expected output from representative insertion devices. The calculations were carried out using the Daresbury program SPECTRA [4]. These curves illustrate the resulting

enhancement in photon output at the higher energies. It has also been shown that the small radius of curvature of the superconducting dipole would allow very short beam lines which would provide very high flux at the sample.

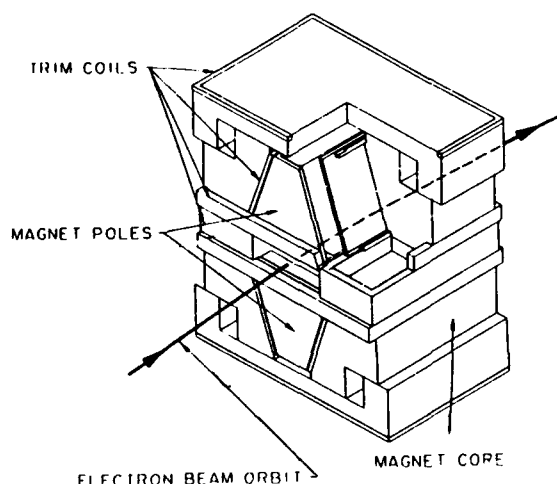


Figure 2. Proposed superconducting dipole magnet.

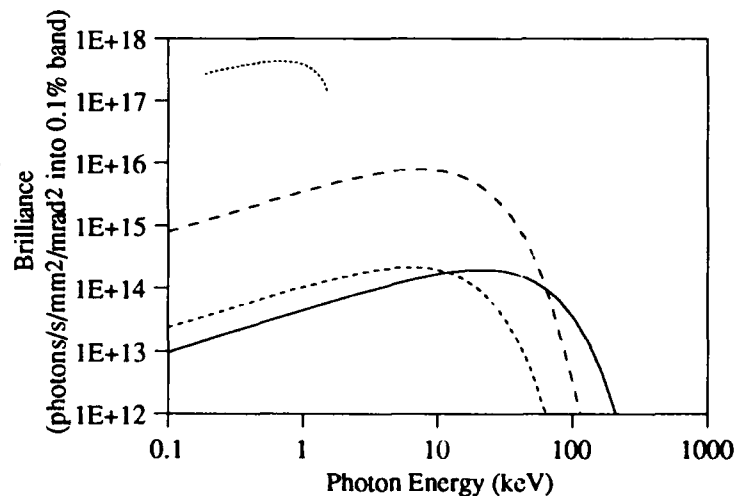
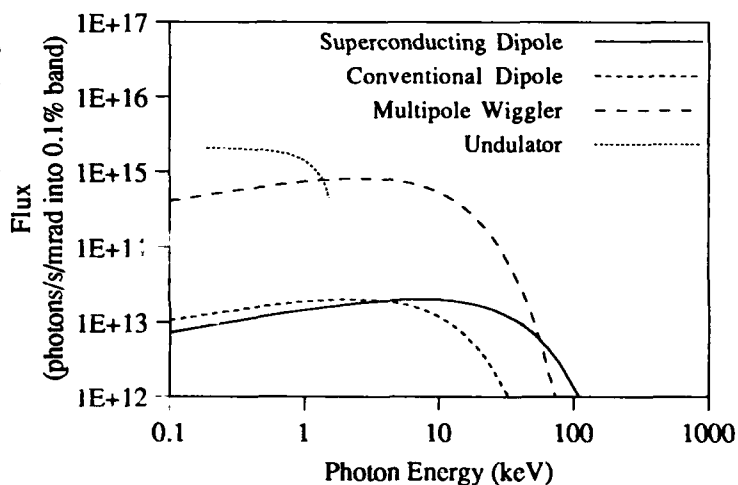


Figure 3. Flux and brilliance of sources in DIAMOND including output from representative insertion devices.

V. EFFECT OF SUPERCONDUCTING DIPOLES

To minimise the disruption to the beam dynamics as the ring is upgraded with additional superconducting magnets, it is planned to install in the first stage two magnets diametrically opposite. The next two would then also be installed diametrically opposite, but at 90° to the first pair and so on. The conversion to a superconducting magnet must be carried out with minimal effect to the other source points in the lattice. To this end, the linear lattice functions of the cell with superconducting magnets have been matched to those of the all-conventional magnet cells. This matching process was carried out using the program LATTICE [5]. The lattice functions at an illustrative tune point for two matched unit cells, one with a normal conducting dipole and one with a superconducting dipole, are shown in Figure 4.

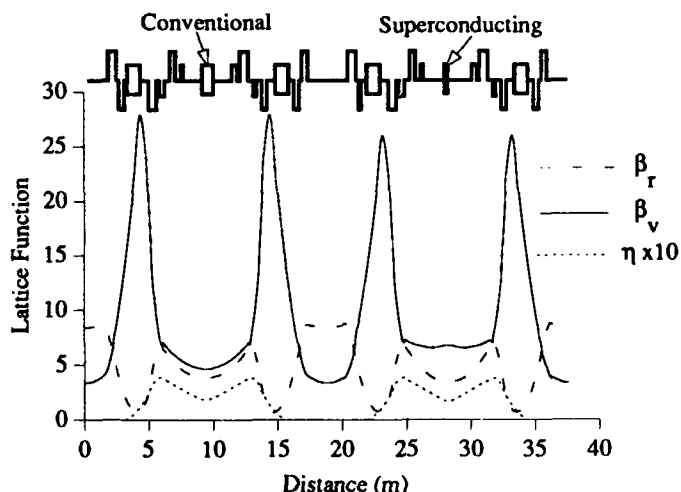


Figure 4. Matched lattice functions in DIAMOND

The central superconducting dipole inevitably has a larger contribution to the storage ring emittance than the replaced normal conducting one. This will lead to an increase in emittance as the source is developed and the number of installed superconducting magnets increases. Figure 5 shows the calculated increase in emittance as a function of the number of superconducting dipoles inserted in the lattice. This level of emittance increase is an acceptable compromise given the requirements of the experiments envisaged on DIAMOND. The introduction of the superconducting dipoles also increases the energy loss per turn and the design of the RF system has included an assessment of the requirements to allow an expansion to a possible 16 superconducting magnets and 10 multipole wigglers, although this would require two straight sections to be reserved for the accelerating cavities.

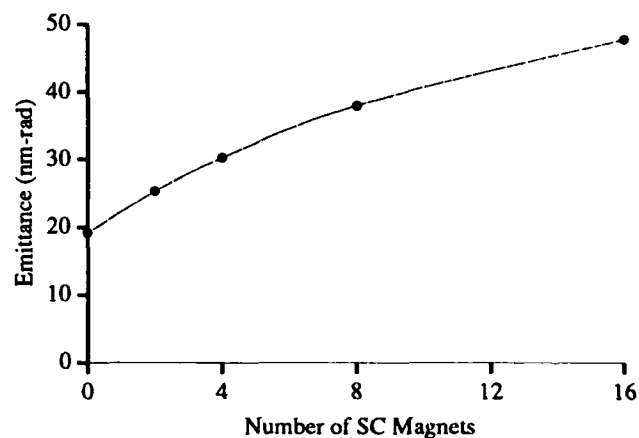


Figure 5. Emittance increase with number of superconducting dipoles.

VI. CONCLUSION

The studies carried out so far have enabled the feasibility to be assessed of a source which has the potential for progressive upgrade by the replacement of normal conducting dipoles with superconducting magnets. This has allowed reasonable estimates to be made of the costs and performance of such a source as a possible replacement for the Daresbury SRS. Such an assessment was required in order that the future strategy for the provision of synchrotron radiation to UK scientists could be developed. Clearly if this concept is approved further work would be required to optimise the nonlinear aspects of the design.

VII. ACKNOWLEDGEMENTS

We would like thank P. N. Vobly for his contribution in the design of a suitable superconducting dipole.

VIII. REFERENCES

- [1] J. A. Clarke et al, "Accelerator Physics Aspects of the Daresbury Advanced Photon Source", *Daresbury report DL/SCI/R31*, 1992.
- [2] S. L. Smith, "ORBIT User guide", *Daresbury internal report*.
- [3] G. N. Kulipanov, "Development of superconducting compact storage rings for technical purposes in the USSR", *Rev. Sci. Instrum.* 63 (1), January 1992.
- [4] J. A. Clarke, "SPECTRA Version 1.2 User Guide", *Daresbury Internal Report*, October 1992.
- [5] J. Staples, "LATTICE ... a beam transport program.", *LBL*, Revised August 1989.

A Conceptual Design and Thermal Analysis of High Heat Load Crotch Absorber*

I. C. Sheng, S. Sharma, E. Rotela, J. Howell
Advanced Photon Source, Argonne National Laboratory
9700 South Cass Avenue, Argonne, IL 60439

Abstract

A high heat load crotch absorber has been designed for the Advanced Photon Source (APS) storage ring curved chambers. The absorber, which uses a beryllium diffuser brazed to oxygen free high-conductivity copper (OFHC) plates, has been optimized to spread the beam power in order to reduce its temperature rise and thermal stresses. Circular copper tubes are brazed to the absorber for water cooling. The absorber design and analytical results from a three-dimensional finite element model are presented in this paper.

I. INTRODUCTION

Crotch absorbers in the curved chambers of the APS storage ring are subjected to extremely high power densities. For instance, at 300 mA beam current the crotch absorbers will intercept 750 watts/mm² at normal incidence. Such high power density with Be-Cu composite absorber design was also presented by Dennis Mills and his coworkers [1]. The vertical opening angle ($1/\gamma$) of the x-ray beam is only 0.07 mrad, which corresponds to a beam height of approximately 0.2 mm at the absorber. There are two important constraints in designing a crotch absorber for a curved chamber with an exit port: (1) it is not possible to completely avoid a normal incidence (horizontally) on the surface of the absorber, and (2) since the vertical beam size is very small, inclining the absorber surface vertically to reduce the power density does not reduce the temperature rise significantly. Because of these severe limitations the previous absorber designs [2] did not have a sufficient margin of safety at 300 mA. A new absorber design has, therefore, been developed which is able to sustain the required high heat load.

II. BASIC DESIGN

The main feature of the present absorber design is a beryllium diffuser which is placed at a vertically shallow angle in the central zone (zone A in Fig. 1a) of normal incidence. The absorber is inclined with respect to the fan of the radiations such that the vertical angle of incidence is 7 degrees. In a 3-mm-thick inclined beryllium diffuser plate, harder x-rays will traverse up to 25 mm inside the diffuser. For the APS bending magnet radiations, the power deposited in the diffuser plate is estimated to be 40 percent of the total beam power. The remaining power is deposited at the beryllium copper interface.

The beryllium diffuser is brazed to an OFHC copper assembly made of upper and lower absorber plates. The plates in-

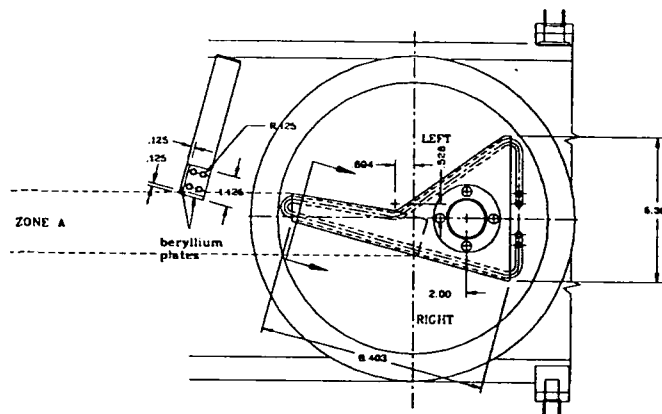


Figure 1a. Top View of the Crotch Absorber.

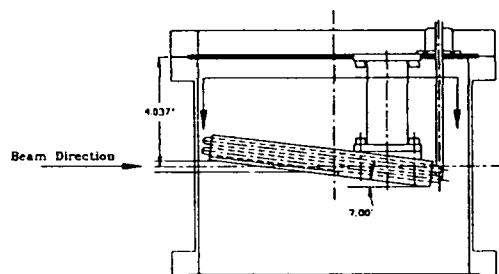


Figure 1b. Elevation of the Crotch Absorber.

tercept x-ray radiations at small incidence angles (16 degrees to 32 degrees horizontally) outside the central zone. The temperature rise and thermal stresses in these plates are, therefore, reduced significantly. Circular grooves are machined in absorber plates for brazing two 3-mm inner diameter copper tubes for convective water cooling. These copper tubes eliminate the need for a water-to-vacuum joint.

III. POWER IMPLEMENTATION

A generalized preprocessing program is used to implement the bending magnet power. For a given chamber geometry, the program calculates the distance from the source l and incident angle δ on the surface being exposed. The power is applied according to the well-known photon spectrum equation:

*Work supported by U.S. Department of Energy, Office of Basic Energy Sciences under Contract No. W-31-109-ENG-38.

The submitted manuscript has been authored by a contractor of the U.S. Government under contract No. W-31-109-ENG-38. Accordingly, the U.S. Government retains a nonexclusive, royalty-free license to publish or reproduce the published form of this contribution, or allow others to do so, for U.S. Government purposes.

$$q \left[\frac{\text{kW}}{\text{mm}^3} \right] = \frac{1.4107 \times 10^3 B [T] E^4 [\text{GeV}] I [A] \sin(\delta)}{\ell^2 [\text{mm}]} \times \int_0^\infty \alpha_i \left(\frac{e}{e_c} \right)^2 F \exp(-\alpha_i \xi) d \left(\frac{e}{e_c} \right) \quad \text{in Be}$$

$$q \left[\frac{\text{kW}}{\text{m}^2} \right] = \frac{1.4107 \times 10^3 B [T] E^4 [\text{GeV}] I [A] \sin(\delta)}{\ell^2 [\text{mm}]} \times \int_0^\infty \left(\frac{e}{e_c} \right)^2 F \exp(-\alpha_i \xi) d \left(\frac{e}{e_c} \right) \quad \text{on Cu-Be interface}$$

where e is the photon energy, e_c is the critical photon energy (19,500 eV), ξ is the distance the photon travels inside the beryllium, and F is function of photon energy and the azimuthal angle, ψ . A detailed expression for F can be found in text books, e.g., Jackson [3]. The absorption coefficient α_i (1/mm) is function of photon energy and can be obtained by utilizing the program TRANSMIT.

There are three areas which will be subjected to x-ray heating. One is on the leading edge of the absorber where the L-shaped beryllium diffusers are brazed, and the other two are on the sides of the absorber. Therefore, the entire problem can be discretized into two parts: the analysis on the leading edge, and along the two sides of the absorber.

IV. TEMPERATURE RISE IN THE BERYLLIUM DIFFUSER

Figure 2a shows the temperature contours in the L-shaped beryllium diffuser brazed to OFHC copper plates. The contours show that as the x-ray power is transmitted into the beryllium

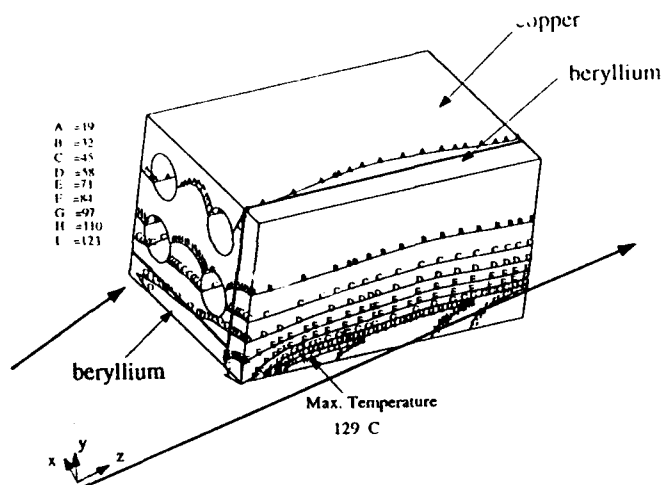


Figure 2a. Temperature Contour in the Leading Edge Crotch Absorber

diffuser, it is distributed in the material and efficiently dissipated by the two nearest water channels. As shown in Fig. 2a, the temperature contours are almost parallel to the water channels, which indicates that the highly concentrated power has been uniformly distributed throughout the beryllium material before reaching the water channels.

The maximum temperature rise, 129 °C, occurs in the right angle corner of the beryllium diffuser. This corner is farthest away from the water channels and is subjected to both bottom and side heating. A sectional contour plot is shown in Fig. 2b, in which the top surface represents the horizontal plane coplanar to the photon fan. Since 60 percent of the beam power is incident on the beryllium-copper interface, secondary high temperature contours appear in this region. The maximum temperature rise at the interface is 112 °C.

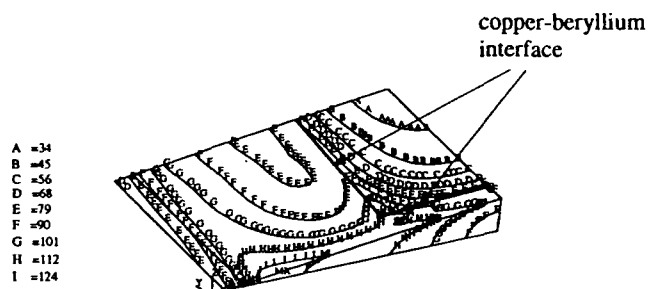


Figure 2b. Sectional Temperature Contour Plot in the Leading Edge Crotch Absorber

V. TEMPERATURE RISE ON THE ABSORBER PLATES

Outside the central zone, the x-ray beam strikes the left and right sides of the absorber plates. On the left side the source distance and the incident angles are 3 meters and 32 °, respectively. The corresponding values on the right side are 1.78 meters and 16 °. These design values were chosen to minimize the temperature rise on both sides of the absorber. Fig. 3 shows temperature contours in the tail region of the right side. At 300 mA beam current, the maximum temperature rise is about 186 °C and drops down to 100 °C at the surface of the water tube. While electron beam experiments [2] have shown OFHC to survive

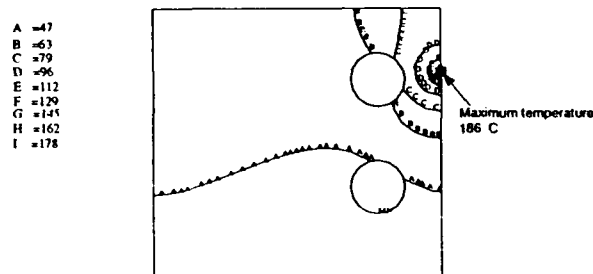


Figure 3. Temperature Contour on the Right Side of the Crotch Absorber Plates

60,000 cycles at a temperature amplitude of 300 °C, significant microcracking can be observed in the test piece.

VI. CONCLUSIONS

A high heat load crotch absorber based on inclined beryllium diffusers has been designed and analyzed. Analytical results show a maximum temperature rise of less than 200 °C for the APS storage ring bending magnet radiation at 300 mA.

VII. ACKNOWLEDGEMENTS

The authors would like to thank Ms. Catherine Eyberger for editing this paper.

VIII. REFERENCES

- [1] Dennis M. Mills, Donald H. Bilderback, and Boris W. Batterman, "Thermal Design of Synchrotron Radiation Exit Ports at CESR," *IEEE Transactions on Nuclear Science*, Vol. NS-26, pp. 3854-3856, June 1979.
- [2] I. C. Sheng and J. Howell, "Thermal Analysis of the Crotch Absorber in APS," *Proceedings of SPIE-The International Society for Optical Engineering, High Heat Flux Engineering*, Ali M. Khounsary, Editor, Volume 1739, pp. 200-213, 1992.
- [3] J. D. Jackson, *Classical Electrodynamics*, Jon Wiley & Sons, 1975.

Thermal Analysis of the Beam Missteering in APS Storage Ring*

I. C. Sheng, J. Howell, S. Sharma
Advanced Photon Source, Argonne National Laboratory
9700 South Cass Avenue, Argonne, IL 60439

Abstract

Several bending magnet beam missteering cases have been investigated for the 7-GeV storage ring of the Advanced Photon Source (APS). One of the critical missteering events is presented in this paper. Finite element analyses are performed to solve for both temperature and stress fields. Thermally induced deflections are determined by utilizing beam bending theory. A safe current limit is established for the storage ring chambers.

I. INTRODUCTION

As shown in Fig. 1, a typical sector of the APS storage ring contains three straight sections (sections 1, 3, 5 and 6) and two curved sections (sections 2 and 4). The cross-section geometry of the aluminum storage ring extrusion is shown in Fig. 2. The x-rays are generated in the bending magnet chamber as positrons travel along the curved chamber. A significant missteering of the x-ray fan will subject the curved chamber to local heating which may result in an unacceptably large temperature rise, thermal deflections, and stresses.

As shown in Fig. 2, the chamber extrusion contains three 0.5 inch water channels for both chamber bakeout and cooling. During normal operation, water flows 2 ~ 3 GPM at 25 °C through the three channels. The corresponding Reynolds number is 16,500. By employing the Colburn equation

$$h \left[\frac{W}{m^2 \cdot ^\circ C} \right] = (2.26 + 0.028 T_\infty) \frac{\dot{Q}^{0.8} \left[\frac{m^3}{hr} \right]}{D^{1.3} [m]}$$

the equilibrium water convection coefficient is found to be $0.4 \frac{W}{cm^2 \cdot ^\circ C}$; where T_∞ , \dot{Q} and D are water temperature, flow rate, and channel diameter, respectively.

For most missteering cases the bending magnet fan hits the chamber at a shallow grazing angle. The power is, therefore, widely spread out along the beam direction. A two-dimension-

al analysis is then sufficient to predict the temperature gradients. The stress induced by thermal gradients can be decomposed into two parts: (1) stress generated by the two-dimensional inhomogeneous temperature field under plane strain conditions, and (2) bending stresses due to thermally induced chamber deflections. Chamber deflections are calculated by imposing the averaged temperature and bending moment changes due to temperature gradients. Details of this analysis procedure can be found in text books, e.g., Boley and Weiner [1].

II. BENDING MAGNET MISSTEERINGS

Ideally the bending magnet x-ray fan will be in the middle of the 10 mm vertical aperture of the photon channel (see Fig. 2). Because of the accidental beam missteerings, however, the x-ray fan can hit the positron beam chamber or the photon channel. Several possible cases of beam missteerings are identified in Table 1. The most critical case is when the positron beam is vertically offset by 5 mm, and the x-ray fan hits its own positron chamber in a region just before the entrance to the photon channel. From the geometry of the curved chamber, a source distance of 1.8 meters and an incident angle of 47 mrad are obtained for this case. A beam power of $2.24 \frac{W}{mm}$ is deposited on the surface along the z direction.

Assuming the upper and bottom halves of the positron chamber are composed of flat plates of same thicknesses, this heat transfer problem can be solved by a simplified one-dimensional analysis. Let L_1 and L_2 represent the distances of the two water channels from the beam interception point, and q represent the linear power density of the intercepted beam. The maximum temperature rise is then given by

$$\Delta T_{max} = T_{max} - T_\infty = \frac{q'}{\frac{1}{L_1} + \frac{1}{L_2} + \frac{1}{Kt}}$$

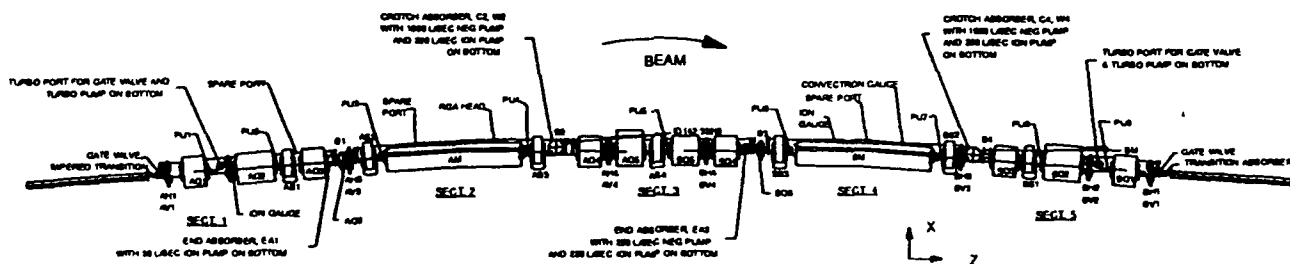


Figure 1. Storage Ring Sector

*Work supported by U.S. Department of Energy, Office of Basic Energy Sciences under Contract No. W-31-109-ENG-38.

The submitted manuscript has been authored by a contractor of the U.S. Government under contract No. W-31-109-ENG-38. Accordingly, the U.S. Government retains a nonexclusive, royalty free license to publish or reproduce the published form of this contribution, or allow others to do so, for U.S. Government purposes.

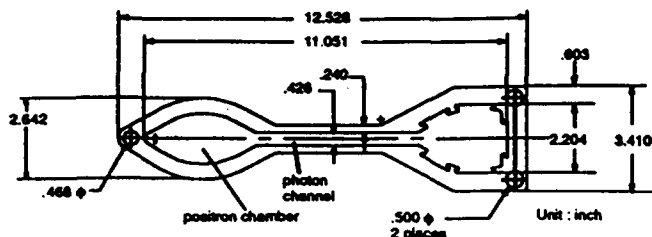


Figure 2. Storage Ring Extrusion

where K and t represent conductivity and thickness of the chamber, respectively. Substituting $L_1 (= 96.5 \text{ mm})$, $L_2 (= 229 \text{ mm})$, $K (= 0.16 \frac{\text{W}}{\text{mm} \cdot ^\circ\text{C}})$, $h (= 0.4 \frac{\text{W}}{\text{cm}^2 \cdot ^\circ\text{C}})$, $t (= 12.7 \text{ mm})$ and $q' (= 2.24 \frac{\text{W}}{\text{mm}})$, the maximum temperature rise $T_{\text{max}} - T_\infty$ is found to be 100°C , which is in fair agreement with the maximum temperature rise (110°C) obtained by a detailed two-dimensional finite element analysis shown in Fig. 3.

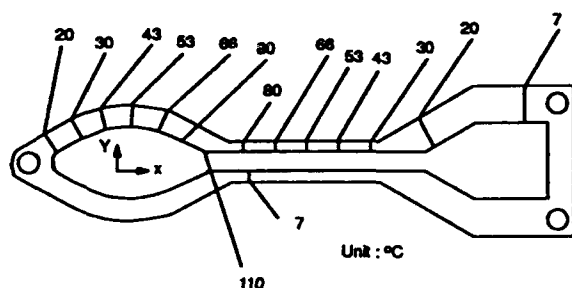


Figure 3. Temperature Rise due to Beam Missteering (Case 2)

When the Gaussian beam size is relatively small, a closed form stress analysis developed by Sheng and Howell [2] can be used. This analysis shows that the maximum stress is practically equal to the off-plane stress (σ_{zz}), and can be obtained by the simple formula:

$$\sigma_{zz} = -\alpha E \Delta T_{\text{max}}$$

where α and E represent thermal expansion and Young's modulus, respectively. For 6063-T5 aluminum, they are $2.25 \times 10^{-5} \frac{1}{^\circ\text{C}}$ and $1.1 \times 10^7 \text{ Psi}$, respectively, and the maximum off-plane stress becomes -27 Ksi . Figure 4 shows off-plane compressive

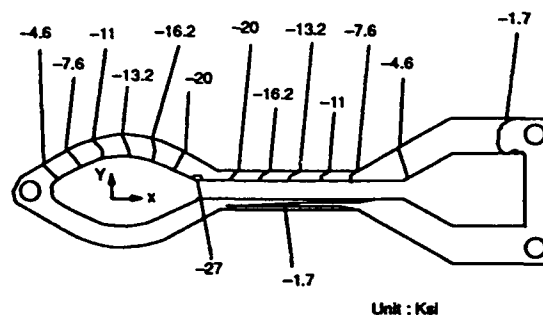


Figure 4. Plane Strain Off-Plane Stress due to Temperature Rise

stress contours. The maximum stress agrees closely with the calculation shown above. Since the entire section behaves like a beam subjected to line heating, the actual maximum stress along the chamber will be lower than that calculated in the two-dimensional model. This is because the chamber at both ends is flexible in the longitudinal direction and releases thermal stresses as it deforms. The procedure for calculating the actual

Table 1
Case Studies of Beam Missteering

No.	Vacuum System Location Being Heated	Source	Distance to Source	Missteering Angle/offset	Current (mA)	Results (maximum)			
						Temperature (0°C ambient)	Stress*	Displacements	
								X Direction	Y Direction
1	Photon Channel, S2	M2 Bending Magnet (Upstream Sector)	18.6 m (731 in)	.54 mR/5 mm .27 mR/O	300	5°C	1,231 Psi		
2	Positron Chamber S2 or S4	M1 or M2 Bending Magnet	1.8 m (70.87 in)	0/5 mm+	100	110°C (1.1°C/mA)	20,000 Psi (200 Psi/mA)	0.066 in (6.6e-04 in/mA)	0.145 in (1.45e-03 in/mA)
3	Photon Channel S2 or S4	M1 or M2 Bending Magnet	3.6 m (141.73 in)	4.0 mR/9 mm	300	1.4°C (0.05°C/mA)			
4	Back Wall of S4 No additional cooling	M1 Bending Magnet	10.0 m (393.70 in)	None	300	76°C (0.25°C/mA)	18,688 Psi (62.3 Psi/mA)	0.0037 in (1.23e-05 in/mA)	0.0018 in (6.0e-06 in/mA)
5	Positron Chamber S2	M2 Bending Magnet (Upstream Sector)	15.9 m (627.24 in)	.6 mR/5 mm	300	47°C (0.16°C/mA)	5,200 Psi (17.3 Psi/mA)	0.056 in (1.9e-04 in/mA)	0.038 in (1.3e-04 in/mA)
6	Commissioning S6	M2 Bending Magnet	5.3 m (207.3 in)	0/5 mm	300	20°C (0.1°C/mA)	3,566 Psi (16.32 Psi/mA)	0.0183 in (6.1e-05 in/mA)	0.0185 in (6.2e-05 in/mA)

* Resultant bending stress.

maximum chamber stresses and deformations is summarized as follows :

(1) By using the temperature field shown in Fig. 4, across the chamber extrusion one can determine the averaged axial force P and in-plane bending moments M_x , M_y due to temperature gradients,

$$\begin{aligned} P &= \int_A \alpha E T(x^*, y^*) dA, \\ M_x &= \int_A \alpha E T(x^*, y^*) y^* dA, \\ M_y &= \int_A \alpha E T(x^*, y^*) x^* dA, \end{aligned}$$

where A is the cross sectional area, and x^* , y^* are the plane coordinates with respect to the centroid point of the extrusion.

(2) Generate a three-dimensional finite element beam model and place P , M_x , and M_y on the starting and ending points of the beam heating area. The opposite signs are chosen such that the resultant forces and moments are self balanced. Calculate the chamber deflections and axial force P' and bending moments M'_x , M'_y .

(3) Determine the moments of inertia I_{xx} and I_{yy} , the resulting bending stresses obtained by reducing the off-plane compressive stress σ_{zz} with axial stresses generated by $\frac{P'}{A}$, $\frac{M'_x y^*}{I_{xx}}$, and $\frac{M'_y x^*}{I_{yy}}$. (Note that $A = 12.97 \text{ in}^2$, $I_{xx} = 11.6 \text{ in}^4$, and $I_{yy} = 220 \text{ in}^4$ for the current chamber design.)

The maximum thermal stress in this case is calculated to be 20 Ksi, which is almost 7 Ksi lower than the value obtained un-

der plane strain assumptions. Since this stress is compressive and lower than the yield stress (25 Ksi at 150 °C), as well as confined in a localized region, it is considered to be within the allowable stress limits.

III. CONCLUSIONS

Several beam missteering cases for the APS storage ring chamber were modeled to determine the temperature, deformations, and stress fields. Analysis results indicate that the chambers are passively safe (i.e., they require no active interlock for protection) for beam currents up to 100 mA.

IV. ACKNOWLEDGEMENTS

The authors would like to thank J. Noonan, G. Decker, and G. Goepfner for many helpful technical discussions. Editing of this paper by C. Eyberger is also sincerely appreciated.

V. REFERENCES

- [1] B. A. Boley and J. H. Weiner. *Theory of Thermal Stresses*, Krieger Publishing Company, 1984.
- [2] I. C. Sheng and I. Howell, "Quasi-static Thermoelastic Analysis for a Semi-infinite Plane Subjected to a Gaussian Heat Source - Beam Missteering of the Storage Ring in the APS", Argonne National Laboratory Light Source Note, LS-199, 1992.

Dynamic Response Analysis of The LBL Advanced Light Source Synchrotron Radiation Storage Ring*

K. K. Leung

Superconducting Super Collider Laboratory
2550 Beckleymeade Ave., Dallas, TX 75237 USA

Abstract

This paper presents the dynamic response analysis of the photon source synchrotron radiation storage ring (Figure 1) excited by ground motion measured at the Lawrence Berkeley Laboratory advanced light source building site [1, 2]. The high spectral brilliance requirement the photon beams of the advanced light source storage ring specified displacement of the quadrupole focusing magnets in the order of 1 micron in vertical motion [2]. There are 19 magnets supported by a 430-inch steel box beam girder. The girder and all magnets are supported by the kinematic mount system normally used in optical equipment. The kinematic mount called a six-strut magnet support system is now considered as an alternative system for supporting SSC magnets in the Super Collider. The effectively designed and effectively operated six-strut support system is now successfully operated for the Advanced Light Source (ALS) accelerator at the Lawrence Berkeley Laboratory. This paper will present the method of analysis [3, 4, 5, 6] and results of the dynamic motion study at the center of the magnets under the most critical excitation source as recorded at the LBL site.

I. INTRODUCTION

Ground motion at the ALS site was measured from 4 to 100 Hz. The measured noise based upon 2% damping is about 0.1 microns. The significant mode of frequency for the storage ring is about 3 Hz and the damping coefficient is below 1%. Dynamic motion of the quadrupole focusing magnet (QF) is designed for a maximum 1 micron vertical motion limit to obtain photon beams with high spectral brilliance. This analysis predicts that the vertical motion of the quadrupole magnet should be below 0.8 microns based on an assumption that 0.5% damping composite is designed for the ALS storage ring system.

II. METHOD OF ANALYSIS AND MODELLING

The response spectra method [5], see Figure 2, is used as the computation technique in the present analysis [7,8,9,10]. Finite element method [6] is employed for the storage ring modeling. The actual spring constant for the six-strut system is experimentally determined. The strut spring constant has significant effect on the dynamic behavior of the storage ring structural system. An integrated finite model includes the steel girder, magnets, vacuum chamber and the six-strut supporting system. The ground motion is expressed as spectra [5] that is the envelope of all the individual responses from 0.5 Hz to 100 Hz. The spectra is applied at the floor slab level. The soil-structural interaction is included in the spectra as long as the location of the measurement of the ground motion is representative of strut's anchoring points and no major building is erected to influence the soil-structure interaction.

ALS STORAGE RING GIRDER FINITE ELEMENT MODEL FOR GROUND MOTION RESPONSE STUDY

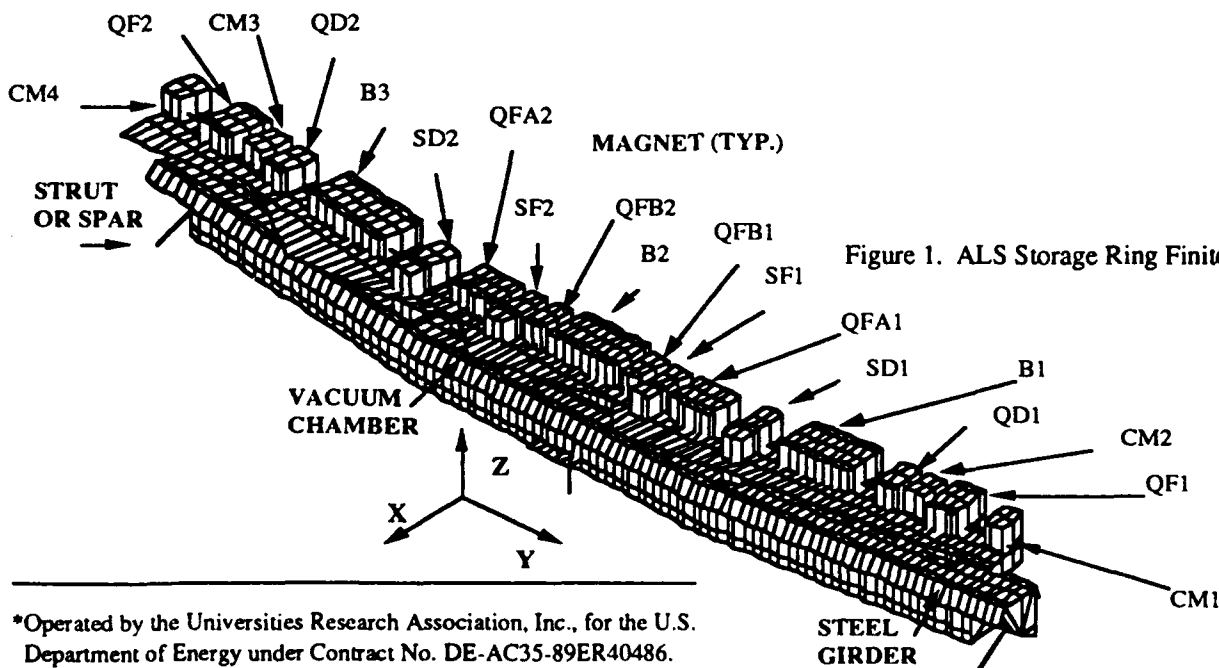


Figure 1. ALS Storage Ring Finite Element Model.

*Operated by the Universities Research Association, Inc., for the U.S. Department of Energy under Contract No. DE-AC35-89ER40486.

The eigenvector and eigenvalue of the normal mode are first calculated. The modal spectra displacement, participation factors and effective mass are then evaluated for each mode. The modal dynamic motion is combined to give the maximum displacement response at the interested point. The method of modal sum [7, 8, 9,10] combination is based on the method of square root of the sum of the square for the non-closed spaced modes. For closed spaced modes, the algebraic sum method is used. The response spectrum is applied[10] at three directions, x, y, and z, independently.

III. GROUND AND SEISMIC MOTION

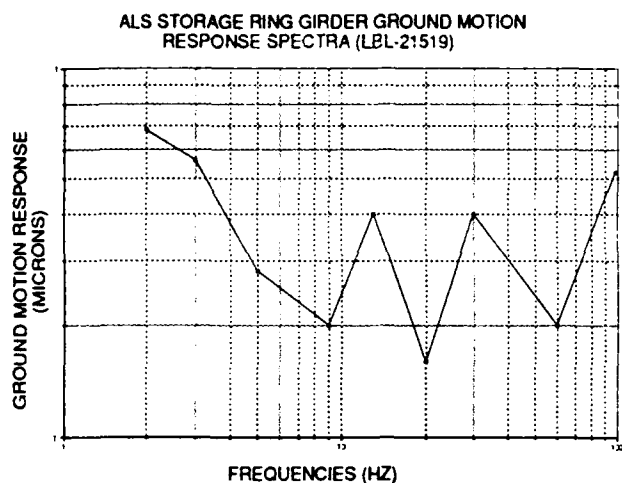


Figure 2. ALS Ground Motion Spectra.

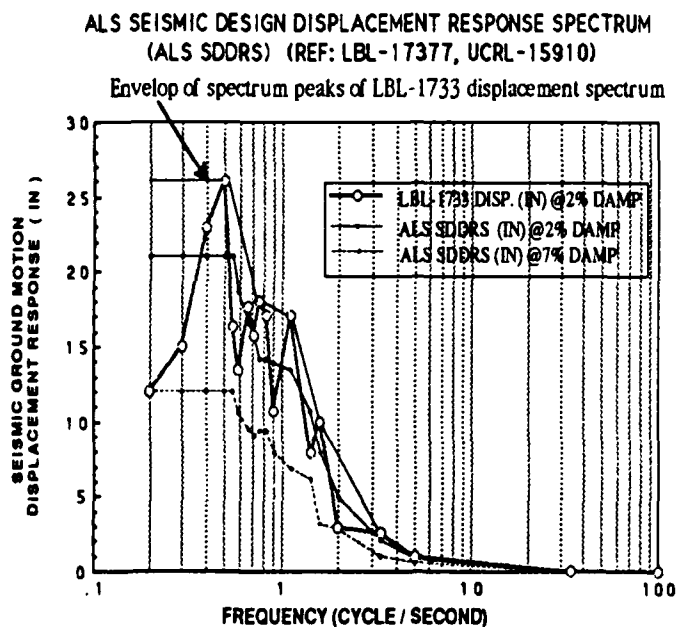


Figure 3. ALS Store Ring Magnet Vertical Displacement.

IV. RESULT OF DYNAMIC ANALYSIS

A three-dimensional model dynamic analysis is used to predict the actual response of the girder system from specified ground and earthquake motion as shown in Figures 2 and 3. The dynamic model includes correct mass point selection in each magnet to represent all significant modes. Coupled equipment masses and compliance are incorporated in the system mathematical model. The results of the finite element analysis are shown in Figure 4 for the maximum vertical deflection of each magnet in the ALS storage ring. The maximum vertical deflection for the focusing magnet is specified as 1.0 microns. The vertical deflection for the quadrupole magnet QF2 is 0.7 microns as shown in Figure 4. The ALS storage ring structural dynamic design appears to be successful. The design for controlling the ground motion response is based on selection of the boxed beam for maximum torsional rigidity for the steel girder, and arranging the six struts in the most effective position to limit the vertical response to the focusing magnets. The seismic dynamic design involves many structural components design including the welding, connection bolts, six strut system for each magnet, the plate, web, girder, and six- strut system for the storage ring.

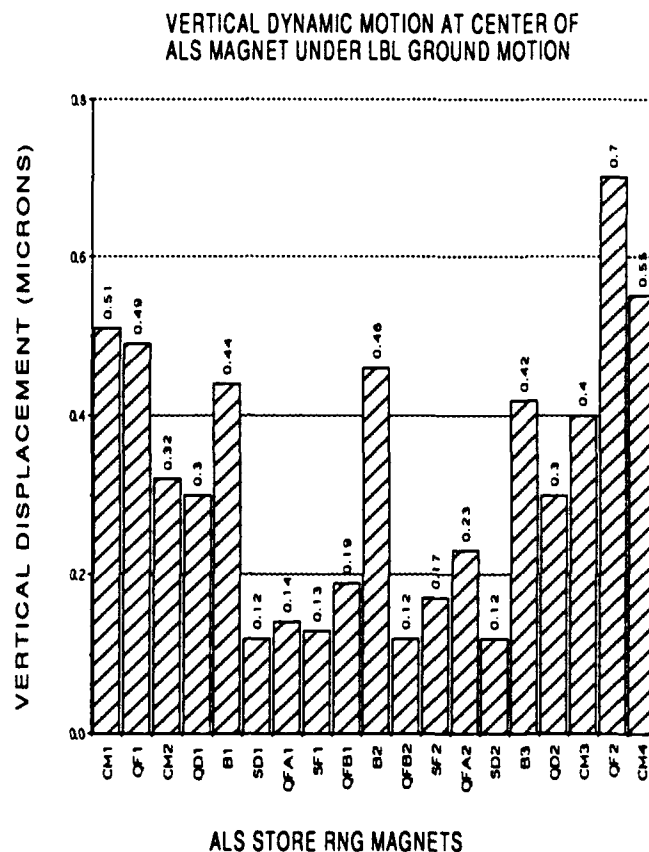


Figure 4. Vertical deflection of at Center of Magnet Subjected to Ground Motion Excitation.

The most critical structural component of the supporting system for the storage ring is the six strut that supporting the girder (Figure 5) because there are no redundant supports for the storage ring. The buckling loading capacity (Figure 6) for the strut is about three times larger than the seismic load and the seismic design of the ALS storage ring is therefore acceptable. An earthquake of 7.1 magnitude occurred at 100 miles from the ALS site in 1989 before the ALS storage ring structure is completed.

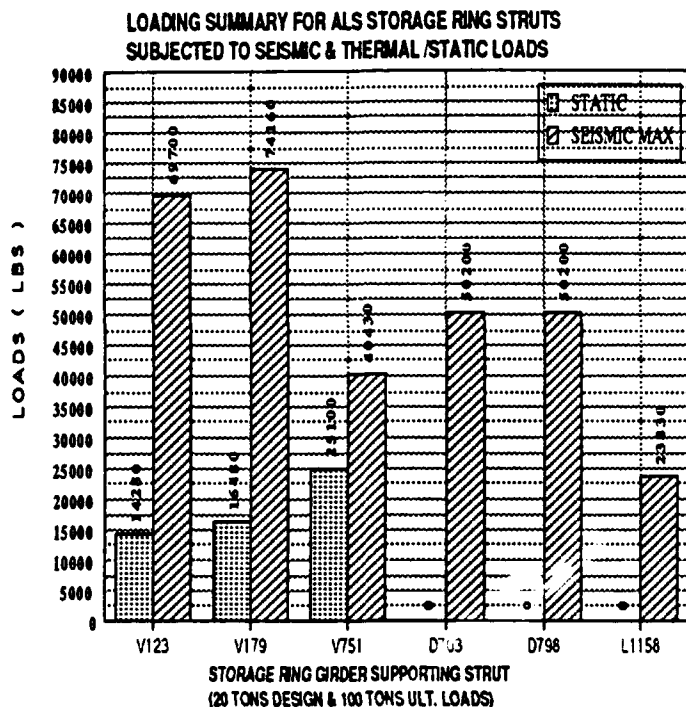


Figure 5. Total axial load for each of the six struts.

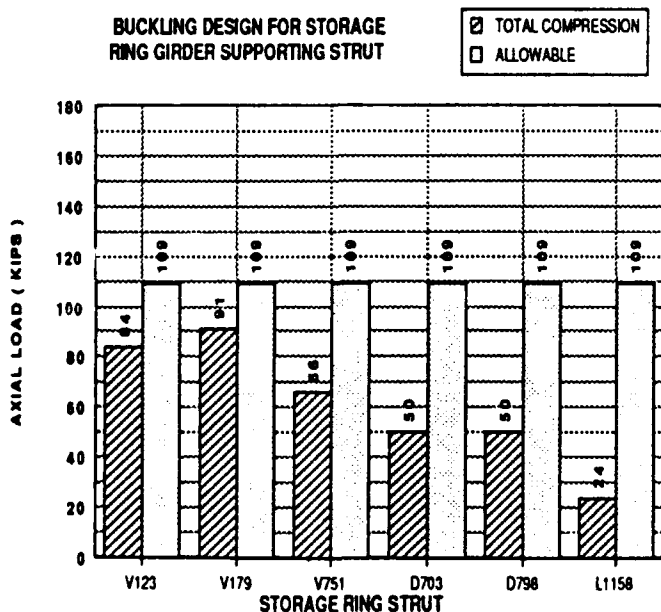


Figure 6. Comparison of seismic load and allowable buckling load on the six strut.

V. REFERENCES

- [1] B. A. Bolt, "Strong Seismic Ground Motion for Design Purpose at the Lawrence Berkeley Laboratory," Report LBL-17377, July 1979, DOE Contract Number DE-AC03-76SF00098.
- [2] M. A. Green et al., "Ground Motion Measurements at the LBL Light Source Site, the Bevatron and the SLAC," LBL Report-21519, 1086.
- [3] K. K. Leung, M. S. Lin, et al., "Fast Flux Test Facility of Atomic Energy Commission Final Seismic Analysis Report," 1974.
- [4] K. K. Leung, "Seismic Stresses of Piping Systems and Equipment on Heat Exchanger Supporting Structures," Section K-7/6, *Transactions of the 3rd International Conference*, 1975.
- [5] N. C. Tsai, "Spectrum-Compatible Motions for Design Purposes," *Journal of Engineering Mechanics Division*, ASCE, Vol. 98, No. EM2 proceedings 8807, 1972.
- [6] G. J. DeSalvo "ANSYS Engineering Analysis System," Swanson Analysis Systems Inc., Penn., U.S.A
- [7] "Combination of Modes and Spatial Components in Seismic Response Analysis," USAEC Directorate of Regulatory Standards Regulatory Guide 1.92, 1974.
- [8] F. C. Nelson. "The Role of Closely Spaced Modes in the Seismic Response of Equipment and Structures," *Proceedings of the U.S. National Conference on Earthquakes Engineering* 1975, Ann Arbor.
- [9] N. M. Newmark et al., "Earthquake Spectra and Design," *Earthquake Engineering Research Institute*, 1982.
- [10] E. H. VanMark, "Structural Response to Earthquakes," *Seismic Risk and Engineering Decision*, Elsevier Scientific Publishing Co, Amsterdam Oxford, New York, 1976 (edited by C. Lomitz and E. Rosenblueth), pp. 287-337.

VI. ACKNOWLEDGMENTS

The author wishes to thank A. Jackson, A. Paterson, T. Lauritzen of the Lawrence Berkeley National Laboratory for their support and recommendation in the ground motion and seismic design of the Advanced Light Source Storage Ring. The author also thank the SSCL Magnet System Division Analysis Group for encouragement in publishing this paper.

The Study of Seismic Vibration of SR Source "Zelenograd"

S.Kuznetsov,

Kurchatov Institute, Moscow 123182, Russia

E.Levichev,

Budker Institute of Nuclear Physics, Novosibirsk 630090, Russia

Abstract

The measurement results of ground displacement in the frequency range from 0.1 to 100 Hz on the site of the SR source "Zelenograd" (Moscow) are presented. The data acquisition system and digital signal processing software are described. The computed amplitude spectra and correlation functions of vibrations are analyzed. Some models: uncorrelated ground motion and plane waves are investigated. The experimental results allow to estimate the effects of the ground motion on SR beam stability.

I. INTRODUCTION

The successful performance of experiments using high brilliant SR from a low-emittance light source calls for tough tolerances to the orbit stability. Among many sources of time dependent closed orbit distortion (power supplies ripple, temperature gradient, etc.) the mechanical vibration of the magnetic elements has an essential effect on beam stability because of the strong optics and rather large amplification factor of the low-emittance lattice. Consequently, in the designing of high brilliant light rings, it becomes of great importance to analyze the effect of ground motion and find a way for effective elimination or control of the vibration to restrict orbit instabilities to an acceptable level. The dedicated SR source "Zelenograd" is a low-emittance 1.5-1.9 GeV storage ring intended for industrial application [1]. It has six-fold symmetry lattice with 115.7 m circumference. The horizontal emittance of the electron beam at 1.5 GeV is as small as 2.7×10^{-8} m-rad. Ten 3-m-long straight sections are optimized for insertion devices (including undulators and high field superconducting wigglers).

II. DISTORTION TOLERANCES

Due to the vibration of quadrupole lenses the error fields deflect the particle orbit. As the vibration frequencies (0.1-100 Hz) are much less than the revolution frequency,

we can consider the orbit distortion caused by the constant displacement of magnetic elements. But the observer, who performs experiments using SR beam will see a time-dependent angular and positional displacement of the light source. If the duration of experiment is much more than the vibration period, the source displacement will lead to the growth of an "effective" emittance and to the reduction of the brightness [2]. If the vibration period is about the same as the experiment duration, there will be slow change in experiment conditions (radiation wavelength, flux, polarization, etc.) with time. In our case, the SR users requirement can be written as: $\langle z' \rangle / \psi \leq 5\%$, where $\langle z' \rangle$ is an effective angular deviation of the source point (rms) and ψ is the natural SR angular divergency. The above requirement corresponds to a 10 % emittance growth. For the case of the radiation from undulator (poles number $N = 24$) at 1.7 GeV energy $\psi = 1/\gamma\sqrt{N} = 60\mu\text{rad}$ and $\langle z' \rangle = 3\mu\text{rad}$. With the beta-function at the radiation point $\beta = 8$ m, the effective orbit disturbance can be estimated as $\langle z \rangle \simeq 20\mu\text{m}$.

III. INSTRUMENTATION AND SOFTWARE

The industrial seismometer SM3-KV [3] is used to measure the ground vibration amplitudes. The ratio of the signal voltage to the displacement within the frequency range $f = 0.1-100$ Hz obeys the dependence $U/X = 5.2 \times 10^5 f$ [V/m]. CAMAC standard was chosen for the control electronics: a microcomputer, an ADC unit, a timer, etc. The measured data are treated by a set of codes running on IBM PC/AT under the MS-Windows. The features of the treatment are: Fourier analysis, signal correlation functions calculation, quadrupole displacement magnification factor calculation, etc.

IV. MEASUREMENTS

The vibration spectrum was measured in the 0.5-250 Hz range, with a frequency resolution equal to 0.5 Hz (the measurement frequency is 500 Hz, points number is 1024

and the total measurement time is 2 s). The ring foundation is a solid concrete mat which has no connection with the building walls. The seismometers were placed on the ring foundation. The data were averaged over 16 measurements. First, the correlation of vertical vibration was studied for two detectors at a distance of 0, 10 and 30 m between them. For adjacent detectors, the correlation function is close to unity within the 1-70 Hz range. As the distance increases, the frequency range where correlation is observed reduces. The vibration spectra were taken in different periods of the day. In particular, the effects of several local sources were under investigation. For example, Figure 1 demonstrates the growth of the amplitude of vertical vibration if a 10 t crane is in service in the storage ring building.

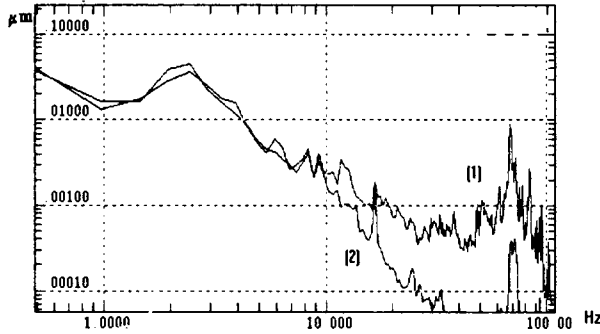


Figure 1: The vibration amplitude spectrum in the vertical plane, with the crane being run (1) and when it is idle (2).

V. MAGNETS DISPLACEMENT MODELS

For a strong focusing lattice of low emittance rings a major source of orbit distortion is the transverse shift of quadrupoles δz . The vertical closed orbit displacement (COD) at position s where $\beta(s)$ and $\phi(s)$ are the betatron function and the betatron phase respectively is given by:

$$z(s) = \sqrt{\beta(s)} / 2 \sin(\pi\nu) \sum_i (\sqrt{\beta_i} k_i l_i \delta z_i \cos(|\phi(s) - \phi_i| - \pi\nu)) \quad (1)$$

Here β_i and ϕ_i are the betatron amplitudes and phase for the i -th lens with the strength k_i and length l_i ; ν is the vertical betatron tune.

Two models were under studies:

i) the lenses are randomly displaced, with the rms deviation, $\langle \delta z \rangle$. For this case, the rms COD $\langle z(s) \rangle$ is determined by:

$$\langle z(s) \rangle = P \langle \delta z \rangle, \quad (2)$$

where P is the COD magnification factor:

$$P = \sqrt{\beta(s)} / (2\sqrt{2} \sin(\pi\nu)) \sqrt{\sum_i \beta_i k_i^2 l_i^2}.$$

For the middle of the straight intended for undulator

$$P = 35.$$

ii) The displacement of quadrupole lenses is caused by the plane wave propagating in the ground. This is true for a vibration source being far apart from the object to be examined. Of significance is to analyse the dependence of the magnification factor on the vibration frequency and to calculate the COD for a particular spectrum of vibrations. In the case of plane waves, the i -th lens is displaced depending on the the direction of wave propagation, the wavelength and the position of the lens over the azimuth of the storage ring:

$$\delta z_i = A \cos(\omega t + (1 - \cos\vartheta_i) 2\pi R / \lambda), \quad (3)$$

where A , ω , and λ are the amplitude, frequency and length of the wave, ϑ_i is the angle between the wave propagation direction and the azimuth of the i -th lens (the lenses are assumed to be positioned over a circle with radius R).

According to (1) and (3), the displacement and the angular deviation of the closed orbit at point s are:

$$z(s) = A P(\omega, \vartheta) \quad (4)$$

$$z'(s) = A P(\omega, \vartheta) \sqrt{1 + \alpha^2(s)} / \beta(s) \quad (5)$$

where $P(\omega, \vartheta)$ is the plane wave magnification factor. Figure 2 shows the results of calculation of the magnification factor P in the case of random displacements of quadrupole lenses and the plane wave magnification factor $P(\omega, \vartheta)$ as a function of the wave frequency at a wave velocity of 1000 m/s.

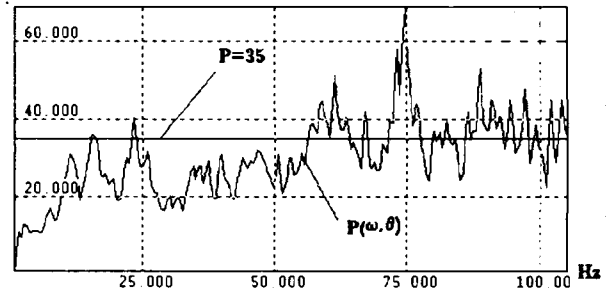


Figure 2: The error magnification factors.

Figure 3 gives the ϑ -averaged amplitude spectrum of ground vibration which was measured on the ring site and the vertical COD at the observation point in the middle of the undulator straight section.

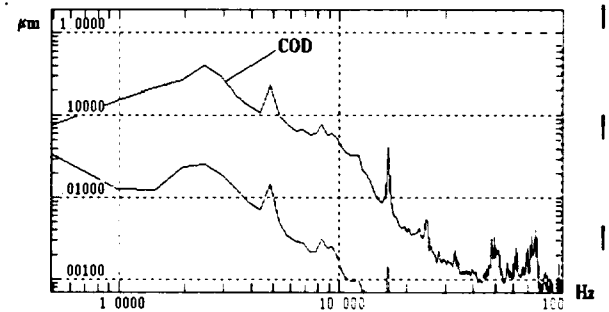


Figure 3: The spectrum of vibrations and COD.

The maximum displacement and angular deviations of the closed orbit in the vertical plane occurred at the frequency 2.5 Hz: $z = 0.6\mu\text{m}$ and $z' = 0.3\mu\text{rad}$.

VI. CONCLUSIONS

The developed instrumentation and software make it possible to measure the spectrum of the microseismic vibrations and calculate COD due to the transverse shift of quadrupoles. In our case, the measured results are quite good and they meet the requirements for the beam stability. But when the machine equipment (vacuum pumps, ventilation, compressors, etc.) will be put into operation, it may effects drastically the magnet components displacement. The local noise sources and the influence of the magnets supports is planning to be investigated in the near future.

For more detailed information on the subject, please contact us by the address given under the headline or use e-mail: kuzn@ksrs.msk.su

REFERENCES

- [1] A.G.Valentinov, V.N.Korchuganov, et al. "Parameters of TNK - the dedicated SR source", *INP Preprint 90-129*, Novosibirsk 1990.
- [2] "7 GeV Advanced Photon Source (Conceptual Design Report)", *ANL-87-15*, April 1987.
- [3] B.A.Baklakov et al."Vibration measurements in UNK tunnel", *INP Preprint 90-88*, Novosibirsk 1990.

Measurement of the Orbit Parameters at SOR-RING

Hirofumi KUDO, Kenji SHINOE, Hiroyuki TAKAKI, Tadashi KOSEKI, Haruo OHKUMA and Yukihide KAMIYA
The Institute for Solid State Physics, The University of Tokyo, JAPAN

Abstract

In the 1992 summer shutdown, beam position monitors (BPM's)[1] [2] have been installed in SOR-RING as one of the R&D's for the future plan of a VUV high-brilliant source. They have been also aimed at measuring the closed orbit of the ring and correcting it by beam steerings that have been also installed at the same time as the BPM's. With these systems, we measured the closed orbit distortion (C.O.D.) at the first time since the ring had been constructed. Horizontal and vertical C.O.D.'s were then corrected within 1 mm by exciting the steerings and changing the RF frequency. We also measured the other orbit parameters such as betatron and dispersion functions, chromaticity and RF-cavity parameters. Moreover, it was proved in a recent machine study that SOR-RING is capable of accelerating the electrons up to 450 MeV or more from the present energy of 380 MeV.

I. Operational Status of SOR-RING

A. General

SOR-RING [3] is the oldest among the storage rings that have been constructed as rings dedicated to synchrotron radiation experiments from the start. Its construction was completed in 1974. The ring is located in the site of the Institute for Nuclear Study (INS), the University of Tokyo, but the facility of SOR-RING belongs to the Synchrotron Radiation Laboratory (SRL), the Institute for Solid State Physics (ISSP) of the same university. Electrons with an energy of 308 MeV are injected into SOR-RING at a repetition rate of 1 Hz from ES, Electron Synchrotron of the INS, which is a 21-Hz rapid-cycle machine with a maximum energy of 1.3 GeV and provides the electrons to their own users.

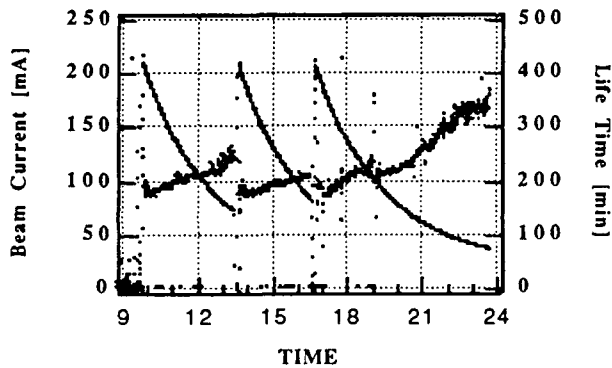


Fig. 1 Typical daily operation of SOR-RING (beam current and lifetime versus time)

Electrons injected into the ring are accelerated up to 380 MeV and then stored until the next injection. The ring is usually operated from morning to night with the beam injection three times per day, and the weekly schedule is from Tuesday to Friday in accordance with the schedule of ES. In 1992, initially stored beam current was around 220 mA and the beam lifetime about 200 minutes at 200 mA (recently the lifetime has been much improved). A typical daily operation of the ring is shown in Fig.1. Total operation time in the 1992 fiscal year was about 2100 hours including injection and machine study.

B. Ring parameters

Figure 2 shows the plan view of SOR-RING. The ring is 17.4 m in circumference and consists of eight bending magnets and four quadrupole triplets. At 380 MeV the beam emittance is about 320 nm·rad and the critical energy of photons from bending magnet is 110 eV. The ring parameters are listed in Table I.

C. Accelerator problems

There are accelerator problems in SOR-RING yet to be solved; (1) ion-trapping that gives rise to growth and fluctuation of the vertical beam size (see Sec. VI), (2) vacuum pressure growth around the RF-

Table I. Principal parameters of SOR-RING[†]

Injection energy	308 MeV
Storage energy	380 MeV
Circumference	17.4 m
Bending radius	1.1 m
Bending field	1.15 T
RF frequency	120.83 MHz (at present)
Harmonic number	7
Revolution frequency	17.3 MHz
Horizontal tune	1.28 (typical)
Vertical tune	1.22 (typical)
Momentum compaction	0.636
Natural emittance	~320 nm·rad
Horizontal beam size	~0.9 mm (at bending magnets)
Vertical beam size	~0.2 - 0.3 mm (at bending magnets)
Horizontal damping time	31 msec
Vertical damping time	26 msec
Longitudinal damping time	12 msec
Critical photon energy	110 eV
Energy loss per turn	1.7 keV
Energy spread	3.8×10^{-4}
Bunch length	~10 cm
Synchrotron frequency	110 kHz (typical)
RF Voltage	22 kV (typical)

[†]The parameters dependent on the beam energy are the values at 380 MeV.

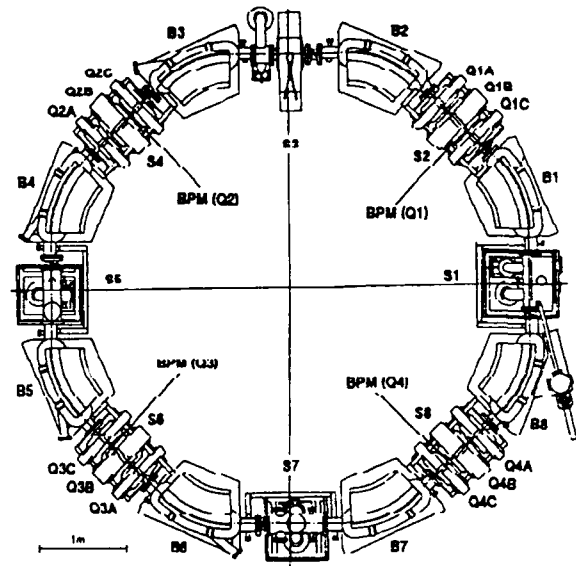


Fig. 2 Schematic of SOR-RING

cavity, which might be caused by outgassing from the elastic vacuum seal of the cavity or by heating of the upstream glass window due to direct irradiation of synchrotron light and (3) a longitudinal instability caused by a higher-order-mode of the RF-cavity; for multi-bunch mode the threshold currents of longitudinal instability are about 3 mA at 380 MeV and 1 mA at 308 MeV.

II. BPM and Steering Systems

A. General

In last summer shutdown, four vacuum chambers for quadrupoles were replaced by new ones in order to install BPM's and ion-clearing electrodes. The purposes of the BPM system that is one of R&D's for a high-brilliant light source are to test the whole system with a real beam and to measure and correct the C.O.D. of SOR-RING. In addition, an auxiliary coil was wound on every pole of all quadrupole magnets in order to produce steering fields for correcting C.O.D. and to change quadrupole fields for measuring betatron function. Furthermore we replaced manually controlled shunt resistances for changing bending fields with computer-controlled electric loads. As the BPM system is reported elsewhere [2] and [3], we will describe the auxiliary coils here.

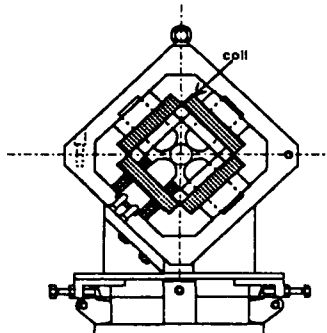


Fig. 3 Auxiliary coils in a quadrupole magnet

B. Auxiliary coils

The coils wound around quadrupoles (Fig. 3) are capable of producing both horizontal and vertical dipole fields by exciting appropriate pairs of coils or of changing the quadrupole strength, though the dipole fields produced by them are not so uniform as in a case of sextupoles. However, beam steering by these coils does work well for SOR-RING. The conductor of coils is 1.8 mm in diameter and the number of turn is 196 per coil. The power supplies ($35 \text{ V} \times 5 \text{ A}$) are controlled by the same computer as the BPM system. At present auxiliary coils of two quadrupoles in a triplet are used for steering and those of the remaining one for changing its quadrupole field.

III. C.O.D. and Its Correction

A. Uncorrected C.O.D.

It was found with the BPM system that maximum values of horizontal and vertical C.O.D.'s were about 3 mm and 4 mm at 380 MeV, as shown in Fig. 4 (a). It was also found that RF frequency did not conform to the ring circumference since the average of horizontal C.O.D. along the ring was about 2 mm. At the injection energy, the maximum horizontal C.O.D. is about 9 mm. In SOR-RING, however, it seems that the large orbit distortion at the septum helps the injection.

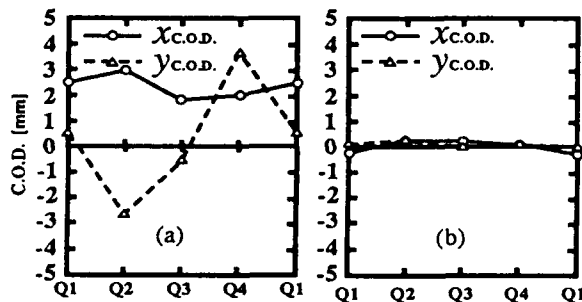


Fig. 4 (a) uncorrected C.O.D. and (b) corrected C.O.D.

B. Correction of C.O.D.

To correct both horizontal and vertical C.O.D.'s, we excited the beam steering (auxiliary coils). In addition, we changed RF frequency by 100 kHz to correct the horizontal C.O.D. As a result, both horizontal and vertical C.O.D.'s were corrected less than 1 mm as shown in Fig. 4 (b).

IV. $\Delta\beta/\beta$, η and Chromaticity

A. Measured $\Delta\beta/\beta$ and η

Betatron function β at a quadrupole magnet can be obtained by changing its quadrupole strength and measuring the tune shift. Figure 5 (a) shows $\Delta\beta/\beta$, the fractional variation in betatron function. Dispersion function can also be obtained by measuring horizontal C.O.D. at different RF frequencies. The measured η is shown in Fig. 6 (b).

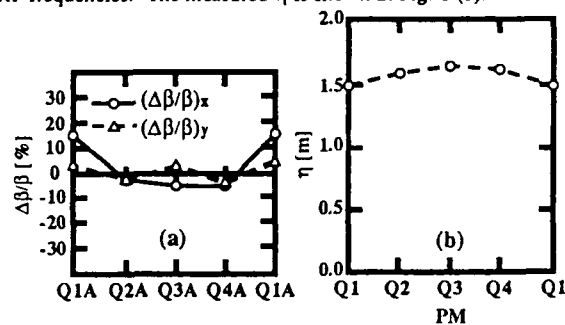


Fig. 5 (a) measured $\Delta\beta/\beta$ and (b) η

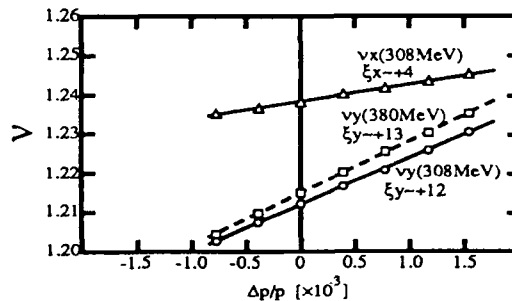


Fig. 6 Measured chromaticity

B. Measured chromaticity ξ

Figure 7 shows the measured chromaticity. At 380 MeV the horizontal chromaticity was not accurately measured. The figure shows that the measured chromaticities in both directions are relatively large in spite of a small ring and even positive, whereas their theoretical values are horizontally -2 and vertically 0.2. This discrepancy has not been settled yet.

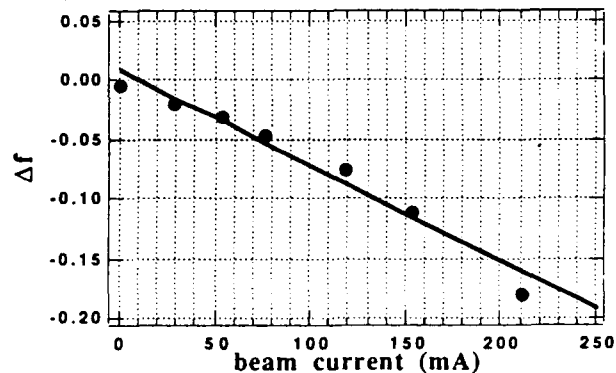


Fig. 7 Measured beam loading
The solid line is the theoretical calculation.

V. RF-Cavity Parameters

A. Measurement of the RF cavity parameters

We newly measured RF power and transmission/reflection coefficients of the RF-cavity. The measured parameters of RF-cavity are listed in Table II. The value of V_a in the table is a theoretical one and the V_c is deduced from V_a and the measured synchrotron frequency. Resonance frequencies and Q-values of the higher-order-modes (HOM's) were also measured and their changes due to the cavity tuners (called flappers) were

examined. Since the changes are very complicated, however, the data of HOM's have not been fully analyzed yet.

Table II. Parameters of RF cavity

RF frequency f_{RF}	120.83 MHz
Generator power P_g	5 kW (typical)
Cavity power P_c	0.4 kW (typical)
Cavity voltage V_c	22 kV (typical)
Accelerating voltage V_a	1.68 kV at 380 MeV
Shunt impedance R_s	1.1 M Ω
Unloaded Q-value Q_0	6.4×10^3
Loaded Q-value Q_L	2.9×10^3
Coupling coefficient β	1.22
Tuning range of flappers	500 kHz

B. Beam loading

Beam loading may be expressed by;

$$(V_c + V_{br} \sin \phi)^2 + (V_c + V_{br} \cos \phi)^2 = V_{gr}^2,$$

where $V_{br} = I_0 R_s / (1 + \beta)$, $V_{gr}^2 = 4\beta \cdot P_g \cdot R_s / (1 + \beta)^2$, ϕ =synchrotron phase and $t = -2Q_L \Delta f / f$, f being the resonance frequency of cavity. In a case of SOR-RING where the RF cavity is largely detuned and V_a is relatively small, the Δf is approximated by (the exact expression for the optimum tuning),

$$\Delta f = \frac{-f_{RF} R_s \sin \phi}{2Q_L V_c (1 + \beta)} \Delta I.$$

We can therefore observe an effect of beam loading by measuring Δf in a function of beam current. We first measured the Δf in a function of the position of one flapper at low RF level; the other flapper was fixed. We then measured the flapper position at several beam currents by keeping the cavity voltage constant; the constant cavity voltage would guarantee no frequency shift due to thermal effect. Figure 7 shows the measured result, which well agreed with the theoretical prediction.

VI. Topics in Recent Machine Study

A. Lifetime improvement

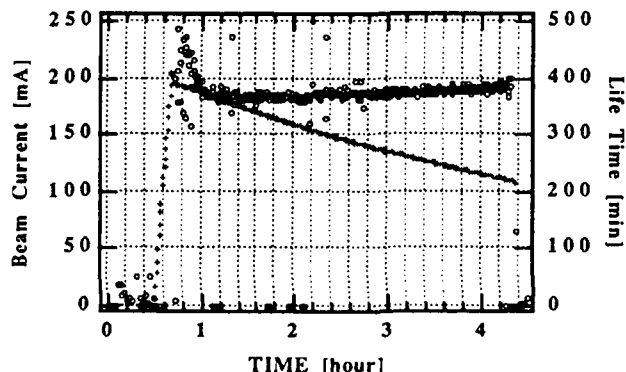


Fig. 8 Improved lifetime

Until recently, the operating point was near a sum resonance and the growth of beam size due to the resonance helped to decrease the Touschek effect at a high current. However, the beam sometimes fluctuated in size, probably due to a combined effect of the sum resonance and the ion trapping. Therefore, we changed the operation point to a new one, near the difference resonance of $v_x - v_y = 0$. As a result, the beam lifetime was increased by a factor of two at a low current. In addition, about 2-KV DC voltage was applied to ion-clearing electrodes. Then the lifetime was improved even at a high current as shown in Fig. 8.

B. Beam position spectra

In a recent machine study, one of the BPMs was connected to a hybrid circuit that can produce RF signals directly proportional to the beam

positions. The RF signals were then fed into the BPM system through PIN diode switches. Almost DC signals from the BPM system were in turn fed into a FFT analyzer to find how the beam positions were fluctuating in a low frequency region. Figure 9 shows the Fourier-analyzed signals of vertical beam position within a frequency span of 50 Hz. Figure 9 (a) is the case where the synchrotron, ES, is operating with a repetition rate of 21.25 Hz, while Figure 9 (b) is the case where ES is turned off. Clearly, almost low-frequency fluctuations have their sources in ES, but presently we are not sure which source causes the fluctuations, magnetic field, AC line noise or mechanical vibration of ES. On the other hand, the frequency spectra around 10 Hz seen in both figures are probably generated from SOR-RING itself; suspicious are air-conditioner, cooling water system, vacuum pumps or cooling fans of RF power supply. With ES operational, the amplitudes of fluctuation were horizontally 3.6 μ m and vertically 0.8 μ m at 21 Hz.

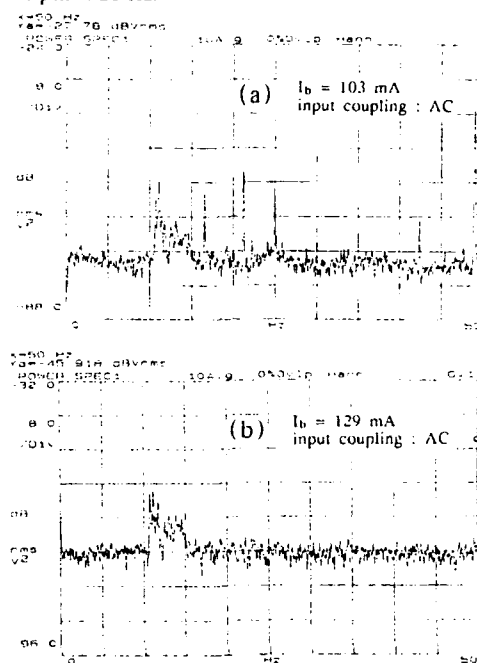


Fig. 9 Frequency spectra of vertical beam position (a): with ES operational, (b): with ES turned off.

C. To a higher energy

It was proved that SOR-RING has a capability of accelerating the beam up to 450 MeV or more with minor modification; the critical photon energy then becomes about 200 eV. Indeed, a low-current beam of a few tens of mA was successfully accelerated to 450 MeV without any appreciable beam loss. And it is possible to accelerate the beam further, probably up to 470 MeV, since the ring magnets and their power supplies as well as RF power source still have a sufficient capacity. To accelerate a high-current beam as much as in the present user run, however, we need to replace the glass window for a synchrotron light monitor with a new one; the temperature of the window directly irradiated by synchrotron light is more than 100 $^{\circ}$ C at present.

VII. Acknowledgements

We would like to thank Prof. T. Ishii, Director of Synchrotron Radiation Laboratory of ISSP, and the other staff members for their continuous encouragement and full support. We also thank Prof. T. Katsura and Drs. T. Ieiri and N. Nakamura of KEK for their cooperation of developing the BPM system.

VIII. References

- [1] K. Shinoe et al.: *Design and Calibration of Pickup-Electrodes for Beam Position Monitoring at SOR-RING*, in these proceedings.
- [2] K. Shinoe et al.: *Beam Position Monitoring System using PIN Diode Switches*, in these proceedings.
- [3] T. Miyahara et al.: *SOR-RING An Electron Storage Ring Dedicated to Spectroscopy*, Part. Accel., Vol. 7, pp. 163-175, 1976.

Challenging Issues during ESRF Storage Ring Commissioning

Annick Ropert for the ESRF Team
European Synchrotron Radiation Facility
BP 220, F - 38043 Grenoble Cedex

Abstract

Third-generation synchrotron light sources raise numerous challenges associated with the low emittance requirement. The 6 GeV ESRF storage ring is among the first of these new sources to successfully meet these challenges. This paper will emphasize some of the most significant outcomes achieved during the ten month commissioning. The experimental approach to obtain the large dynamic aperture needed to allow the injection-accumulation process and a long lifetime will be presented. The upgrading of the predicted current thresholds set by multibunch instabilities and transverse mode coupling will be discussed. We will as well report on photon beam stability which is one of the most stringent requirements for the high brilliance light sources.

1. INTRODUCTION

The ESRF storage ring is a 6 GeV low emittance ring based on a Chasman-Green type lattice. The low emittance is being achieved by low β_x in a large number of dipoles, thus implying a very strong focusing and a large natural chromaticity. The need for strong sextupoles makes the machine highly sensitive to errors. A perfect correction of the orbit is a prerequisite for the obtention of a large dynamic aperture. The first injection trials into the storage ring started on February 17th, 1992. Progress was very successful since all target performances were achieved and even exceeded before the end of the ten months of scheduled commissioning [1], [2]. The issues of adequate dynamic aperture, beam instabilities, X-ray beam stability associated with the running-in of this third generation light source are discussed.

2. OBTENTION OF A LARGE DYNAMIC APERTURE

The primary challenge in the early stage of commissioning arose directly from the extreme sensitivity of the lattice to imperfections due to the requirement for low emittance. Magnet positioning errors are greatly magnified by the beam in such a high focusing lattice, with amplification factors of 50 (horizontal) and 100 (vertical). Although the tolerance on quadrupole and sextupole alignment had been set to 1/10 mm, the probability of getting the beam transmitted over the entire circumference from the outset was very small.

2.1 First turns

It was decided to immediately test the low emittance optics of the storage ring, and not a detuned version, since we believed that running a detuned version in order to reduce the sensitivity to errors would not bring any valuable information. The strategy used during the turn-on process was to inject the beam on-axis, with no sextupoles and no RF. The achievement of the first turns circulating in the ring as soon as the injection parameters were set proves that this strategy was very effective. The maximum amplitudes of the beam trajectory measured by the Beam Position Monitor (BPM) system operated in the first turn mode was 15 mm

horizontally and 5 mm vertically, prior to any correction.

Since we had foreseen these large initial orbit distortions, the first turn correction strategy had been carefully studied. The correction which is based on a step by step transport of the incoming beam makes use of the 96 horizontal steerers and 64 vertical steerers whilst the orbit is sampled at 224 beam position monitors around the circumference. Each corrector strength is computed so as to minimize the orbit deviations on the next position monitors. By means of this step by step correction followed by a careful closing of the first turn trajectory, the maximum excursion of the orbit was significantly reduced in the horizontal plane, thus enabling a circulation of the beam for 15 turns to be obtained.

2.2 First stored beam

After having switched on the RF, we obtained the first stored beam. The lifetime was very short: 100 ms, but long enough to get a fully damped beam (14 transverse and 25 longitudinal damping times). There were good reasons for this short lifetime. Without sextupoles, the uncorrected chromaticity is very large. The beam is widely spread in tune:

$\sigma_{u_x} = -115 \sigma_{\Delta E/E} = -0.12$, $\sigma_{u_z} = -33 \sigma_{\Delta E/E} = -0.04$, with $\sigma_{\Delta E/E} = 1.06 \cdot 10^{-3}$. Large energy excursions push the tunes to the nearby integer and half integer resonance and thus limit the lifetime. A one hour lifetime was immediately obtained once the chromaticity sextupoles were set to their nominal values. Finally, before accumulating beam, we had to switch to the normal off-axis injection mode and then to power the harmonic sextupoles, the primary role of which is to enlarge the dynamic acceptance spoilt by the chromaticity sextupoles and to accommodate the 8 to 10 mm betatron amplitude which enables the freshly injected beam from the booster to be accumulated.

2.3 Achieved performance

It was essential to correct the closed orbit at best in order to obtain correct performance. Otherwise, puzzling distorted β -functions and non-periodic dispersion could show-up. Measured transverse and longitudinal acceptances are in agreement with estimations. Present lifetime (17 hours at 100 mA, i.e. twice the design value) is vacuum dominated.

Since the first beam was accumulated, the storage ring has been operated on a working point $\nu_x = 36.43$, $\nu_z = 11.39$ which is understandably close to a coupling resonance. For reasons of injection efficiency, we have always been forced to work near the half-integer horizontally and just below the coupling. We still have to quantify the benefits of this coupling for the dynamic aperture. The resulting vertical emittance ($3.2 \cdot 10^{-9}$ m.rad) is not as small as the one measured with the fully decoupled optics ($6.0 \cdot 10^{-10}$ mrad).

3. BEAM STABILITY

3.1 Target specifications

The quality of the closed orbit correction is essential for obtaining intrinsic performances (small spurious dispersion to avoid spoiling the low emittance, large dynamic aperture for injection and lifetime,...) and ensuring the reproducibility of the X-ray beam alignment. Beam position stability requirements have been expressed in terms of a maximum value of 10 % of the beam size in each plane. Assuming that the beam is stabilized at high frequency, these values should be satisfied in a very large frequency range: higher frequency of the order of 100 Hz, longest periods in terms of days. A feedback system using special fast steerers is implemented in each straight section to compensate for the high frequency fluctuations whilst slow fluctuations are corrected with the standard orbit steerers.

3.2 Influence of the environment

Environmental stability is of prime importance to achieve stabilities of a few microns. In the long-term this performance can be affected by movements of the tunnel resulting from ground settlements. Permanent monitoring of the relative girder vertical position is performed by means of a Hydrostatic Levelling System. A peak to peak evolution of 3 mm over the circumference following the removal of a large amount of earth was recorded during commissioning. This global movement did not affect storage ring performance since the wavelengths were long compared to the betatron wavelengths. However, the zero of the HLS system was moved outside its operational range, thus imposing a realignment of the ring. Thanks to the use of remote-controlled jacks that equip the girders, this operation took only a couple of hours in January 1993. Following the realignment, the machine performance in terms of residual closed orbit was easily re-established.

Medium-term stability of the closed orbit can be deteriorated by temperature variations along the tunnel. A variation of 0.2° C over one week is currently recorded at a given location around the circumference. Low frequency vibrations induced by cultural noise could also affect the closed orbit. Components at 7 Hz induced by the eigenmodes of the girders and at 10 Hz from the pulsed magnets of the booster have been identified. Their contribution is below the 10 % target.

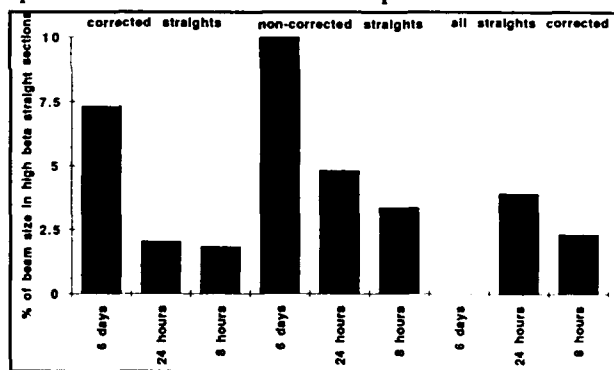
From the outset of commissioning, we had a strong concern about any misalignment of the photon beam impacting the vacuum vessel, since power densities from insertion devices are equivalent to that of a welding machine and a fault on a single steerer can generate an intolerable orbit distortion. The protection of the vacuum chamber is therefore ensured by a low frequency interlock relying on a set of dedicated beam monitor positions triggering a fast beam abort system (<2 ms) based on RF switch-off. In the early stage of commissioning, we ran by accident and for several hours a 20 mA beam which was coherently unstable in the vertical plane and thereby damaged a few vacuum vessels. This instability, occurring at betatron frequencies (140 kHz), was not detectable on the interlock system. We have now installed a dedicated

interlock.

3.3 Present closed orbit correction strategy and results

The closed orbit procedures consist in a combination of local bumps and harmonic compensation. They routinely bring the orbit distortions within 120 μm rms horizontally and 140 μm rms vertically. These figures are as expected. This does not ensure the reproducibility of the beam position within the specifications because the orbit drifts with time, more specially in the horizontal plane, so that a new orbit correction is necessary after a few hours.

Therefore a permanent closed orbit correction had to be implemented. This periodic correction must ensure that the drift between two corrections does not exceed the stability specification and that the beam displacement induced during the correction itself is acceptable. This is presently achieved with a correction automatically triggered every 15 minutes. A global correction is first applied by means of an harmonic compensation of a few harmonics around the tune. It has the advantage that all the existing BPMs are not necessary to compute the correction; we therefore exclude the straight sections which might be influenced by the local feedback. Also this method provides a correction at all source points. The ultimate stability in straight sections is achieved by two local bumps (to provide both position and angle) which are powered as a function of the readings on 2 BPMs. Each straight section can be corrected independently of its neighbours. The resulting long-term stability presented in the graph hereunder is below the 10 % specifications.



3.4 Local feedback

This already excellent performance can be improved by means of a feedback. For that purpose, each insertion device front-end is equipped with two photon beam position monitors. The signals from these sensors are used to feed four fast steerers located at both ends of the straight section which act on the position and angle of the electron beam in both planes. The first feedback was installed and commissioned on the machine diagnostics beamline. The typical performance is the following: a factor of 10 gained at 7 Hz and a factor of 2 at 50 Hz. Since then, three more feedbacks are operational and enable to obtain peak to peak displacements of a few microns when the loop is closed.

Effects of insertion devices were expected to be very small since the focusing effect scales inversely as the square of the

energy. Due to the high field quality achieved after shimming, no significant orbit distortions are observed with the 4 insertion devices presently operated.

4. INTENSITY LIMITATIONS

4.1 Multibunch case

The ESRF has been designed to run mainly in the multibunch mode (992 bunches) at target current of 100 mA. Transverse coupled bunch instabilities appeared at rather low intensities and led to damaging a few vacuum vessels before the problem was clearly identified and cured. The manifestation of the instability corresponds to about 10 betatron lines, each of them associated with a coupled bunch coherent motion with decreasing amplitudes on both sides of every harmonic of the revolution frequency. The source of the instability is the long range wake of the resistive wall instability. To stabilize these modes, we applied the standard over compensation of the chromaticity which enables the spectrum of the mode to be pushed towards the positive frequency region associated with the damping effect of broad-band positive resistance. As soon as this remedy was applied, we were immediately able to raise the intensity to 100 mA.

Our present vertical chromaticity stands at 0.4. In the long-term, a large number of flat insertion device vessels will be installed and the resistive wall impedance will increase. Increasing the chromaticity to provide more and more damping cannot be pursued to infinity since it would induce detrimental non-linear pollution of the dynamic aperture and consequently of the injection speed and lifetime. With a view to lowering the strength of the instability, we tried to decrease the vertical tune just above the integer, down to 11.1. In these conditions, the coupled bunch mode with a frequency line at $-0.9 f_0$ interacts with a lower resistance. However the much lower injection efficiency and the much higher sensitivity of the beam centre of mass to vibrations which spoils the brilliance led us to abandon this solution.

One is more used to coupled bunch modes excited by Higher Order Modes in cavities. Our multicell LEP type cavities with a high shunt impedance at the accelerating 352.2 MHz frequency were predicted to induce longitudinal and transverse coupled bunch instabilities. Threshold currents of the order of 60 mA were anticipated from computations. In the longitudinal plane, we are confronted with strong coupled bunch modes driven by HOMs around 500 MHz and 900 MHz when the machine is filled uniformly. Most of the time, these non-destructive instabilities occur between 90 and 100 mA in a non-systematic way and this leads to a saturation of the filling process or lifetime accidents. Extensive investigations are being made to avoid their excitation; in particular a temperature control of the cavities to keep the HOM frequency away from the beam frequency looks attractive. The present solution consists in adopting a different filling pattern. The beam is clearly very stable (both longitudinally and transversally) with respect to HOMs and the resistive wall, when filling the machine with a gap. Apparently, the 2 μ s gap between the passage of the tail and the head renders the coupling impossible. We have already succeeded in storing a 125 mA beam with these conditions. HOM driven transverse instabilities were supposed to severely limit the current. Until now, we did not suffer from them.

4.2 Single bunch

Some experiments of the time of flight type require single short bunch (5 mm) operation. The instabilities are driven by the short term wake resulting from bunch interaction with the vacuum chamber broad-band impedance. On the basis of our model of impedance, no strong bunch lengthening was expected. The transverse instability threshold resulting from the classical fast head-tail scenario of coupling between modes 0 and -1 was expected at a current of about 7.5 mA.

A threshold at 2.5 mA, i.e. 2 times less than the 5 mA target was measured at zero chromaticity. Fortunately, by increasing the chromaticity to a large positive value ($\xi_z = 0.7$), we have been able to push the threshold up to 10 mA. The follow-up of vertical betatron frequency shift as a function of bunch current indicates that the mechanism of the instability is more complex than mode 0, -1 coupling and that the total frequency shift could be much larger than the nominal synchrotron frequency.

4.3 Few bunch mode

This mode of operation (8 or 16 bunches equally spaced) looks very attractive since it can serve simultaneously a large community of users, those requiring a high current and those running time of flight experiments. In addition coupled bunch instabilities would be much less severe and easier to feedback. For the moment, we have not pushed this mode of filling further because of a surprisingly bad lifetime (only a few hours at 100 mA) associated with a very high pressure. There are however encouraging signs that the bad vacuum conditions are due to the poor electrical contacts from the springs maintaining the RF fingers all around the ring and damaged during bakeout.

4.4 Electrons or positrons

Beam stability and lifetime could be strongly affected by ion trapping. It had been decided at the beginning of the project to start the facility with electrons and to review the need for positrons according to the experience gained worldwide in the mean time. After one year of commissioning and operation, design performance in terms of current, lifetime, emittances have been reached and even exceeded without any evidence of detrimental ion-related effect. Of course, trapping of dust or macro particles cannot be excluded in the future. For the time being however, the positron option will not be implemented.

5. CONCLUSIONS

The innovative solutions developed during the ESRF design phase to face the challenging problems raised by third-generation synchrotron light sources have been successfully applied during commissioning and beginning of routine operation. We are now ready to take up the challenges that will be raised by the next generation of sources.

The author would like to gratefully acknowledge the major contribution of many colleagues to these results.

6. REFERENCES

- [1] J. I. Laclare, "Commissioning and Performance of the ESRF", These proceedings
- [2] A. Ropert, SR Commissioning Notes 1-21, Internal Reports

Upgrading to 500mA of the Stored Beam Current at SORTEC 1-GeV Source Facility

M.Kodaira*, N.Awaji**, T.Kishimoto, K.Mukugi and M.Watanabe
SORTEC Corporation
16-1 Wadai Tsukuba-shi Ibaraki300-42, Japan

T.Iida and H.Tsuchida
Mitsubishi Electric Corporation
3-1-1 Marunouchi, Chiyoda-ku, Tokyo 100, Japan

Abstract

At the SORTEC 1-GeV SR source facility for the study of X-ray lithography, the upgrade of the stored beam current to over 500 mA was performed. The RF cavity power supply was increased from 14 kW to 28 kW together with modification of the RF coupler. In addition, the pumping system and the cooling capacity of the storage ring were also reinforced. Reconstruction work and beam tests for upgrade were carried out for 3 months beginning April '92. A stored beam current of 500 mA was successfully achieved within only 2 weeks after the beam operation was restarted. At present the lifetime has reached 25 h. These results are discussed from the aspects of the key issues for upgrading of the stored current and the SR beam aging effects on the time-evolution of the lifetime.

I. INTRODUCTION

The SORTEC SR facility is the dedicated machine which was constructed mainly for x-ray lithography development and has been successfully operating since October 1989 without serious failures. In order to use this system for SR lithography, the exposure time by SR will be required to be as under as that by conventional optical lithography in high throughput requirements.

To reduce the losses of the beamline at the mirror and the Be window and develop a high sensitive resist and so, a maximum stored beam current of 500mA with lifetime of 20h will be required for SR ring [1]. To achieve this requirement, upgrading of the SR ring to 500 mA was scheduled to begin in April 1992. The preliminary machine studies to solve technical problems had been carried out within the capacity limits of existing SR ring in parallel with the regular operations since November 1990 [2].

II. MAIN ITEMS OF THE UPGRADE [3]

For the upgrade of the stored beam current to 500 mA, the nominal capacity of power supply for RF cavity was

increased from 14 kW to 28 kW by replacing the main power tube RS2012CJ with RS2058CJ. The RF coupler was also replaced to accommodate the increase of nominal capacity of the RF power supply. Figure 1 is a photograph of the upgraded RF power coupler and RF power supply.

In addition, the vacuum system of the storage ring was reinforced by increasing the pumping speed against the higher photo desorption gas under increased beam current. The ultrahigh vacuum pump using NEG modules (SAES WP-1250, ST707) (NEG pump) was newly added to remove H_2 at downstream from of the each straight section where the pressure is relatively higher than that in the each bending section.

The ion clearing voltage to cancel out the beam self field was needed to minimize the reduction of beam lifetime and the increase of beam instability due to extension of beam current. The nominal voltage of power source applied by the existing disk-type ion clearing electrode, installed at seven out of eight straight sections, was increased to 1.5 kV from 500 V. A clearing electrode was newly installed at the one straight section previously not equipped with an electrode. The stripe-type ion clearing electrode, instead of the existing disk-type, was newly installed in each chamber of the NEG pump. The diagram of the vacuum system of the ring is shown in Fig. 2.

The temperature rise due to the increase of beam

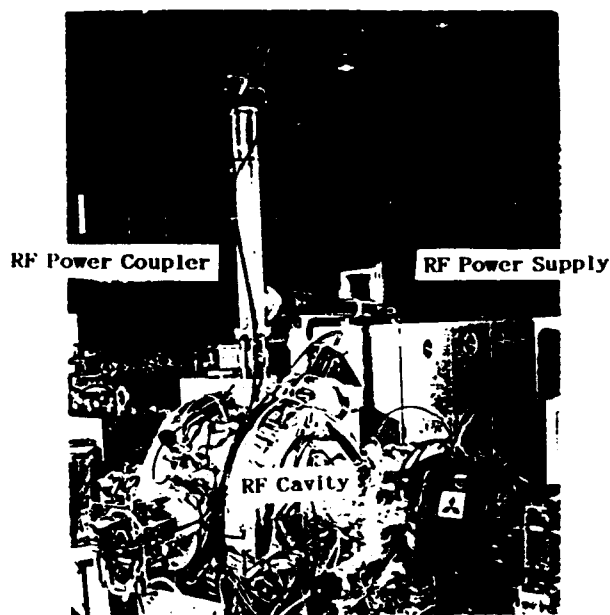


Fig. 1 Photograph of RF coupler and RF power supply.

- * Present Address: Kelhin Product Operations, Toshiba Corporation, 2-4 Suehiro-cho, Turumiku, Yokohama 230, Japan
- ** Present Address: Technology Development Div. FUJITSU LIMITED, 1015, Kamikodanaka Nakahara-ku Kawasaki 211, Japan

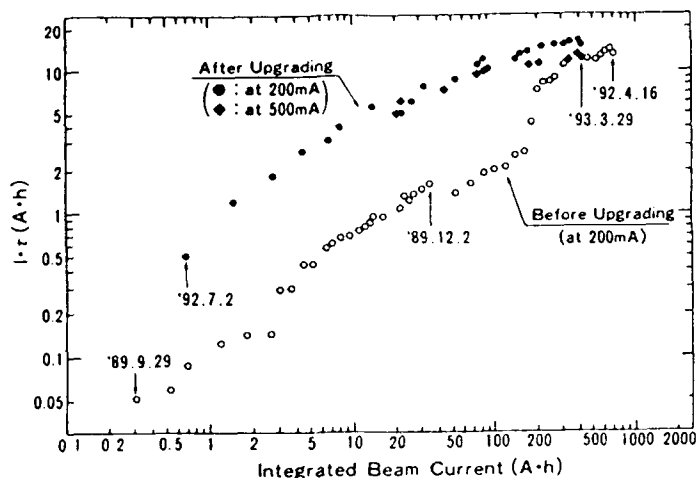


Fig. 6 Improvement of beam lifetime as function of integrated beam current.

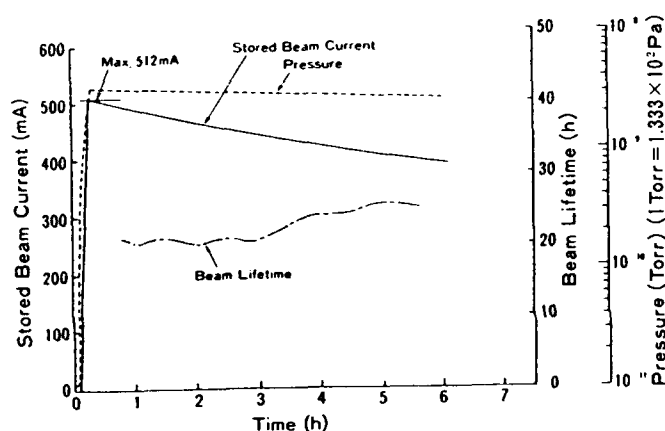


Fig. 7 Typical operation of the facility

Table 1 Main parameters of SR facility at SORTEC.

		Designed	Achieved
Storage Ring			
Energy	GeV	1	1
Dipole Field	T	1.2	1.2
Critical Wavelength	nm	1.55	—
X-Ray Power	kW	15.9	15.9
Beam Current	mA	500	500*
Beam Lifetime	h	>4	>22**
Natural Emittance	mm·mrad	0.51	—
Circumference	m	45.7	—
Synchrotron (Injector)			
Injection Energy	MeV	40	40
Maximum Energy	GeV	1	1
Beam Current	mA	30	50
Circumference	m	43.2	—
Linac (Pre-Injector)			
Energy	MeV	40	40
Beam Current	mA	>30	60~80
Energy Spread	%	<±1.5	±0.67
Emittance	mm·mrad	<3.8	0.7

* max. 512 mA

** max. 25 h (80 h at 200 mA)

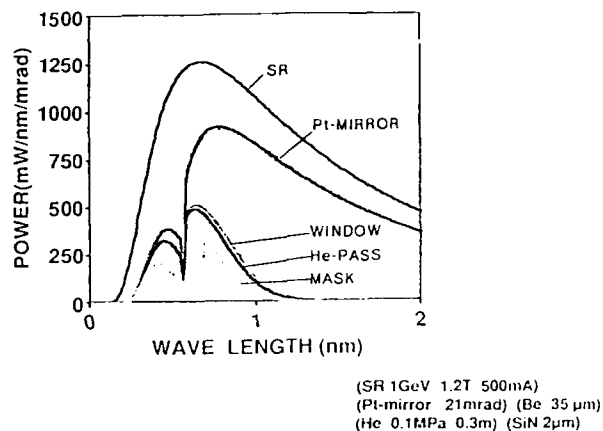


Fig. 8 SR spectrum at 1GeV-500mA SORTEC ring.

vacuum and replacement of the components. This remarkable extension of the lifetime after upgrading mainly depends upon the memory effects of beam duct cleaned by beam dose over a long period. The highest stored beam recorded so far at 1 GeV is 512mA on Oct. 22, 1992, as shown in Fig. 7. The SR ring is filled to 500mA within 10 min. The beam lifetime at 500 mA is 21 h. At present, the maximum beam lifetime reached 25 h in February.

Table 1 summarizes the designed and achieved performance. As a result of the upgrade of the stored beam current to 500 mA from 200 mA, synchronous radiation power was increased by two and a half times. The power density per horizontal angle of 1 mrad ranging from 0 to 2 nm was 1470 mW /mrad. Figure 8 shows the spectrum of synchrotron radiation for the upgraded 1-GeV 500 mA ring.

V. CONCLUSIONS

The works for upgrading has been completed successfully as scheduled with high performance beyond our expectations. As a result of the success of upgrading to 500 mA with over 20 h, the SORTEC 1-GeV SR source has attained top levels all for beam current, beam lifetime and X-ray power as a dedicated SR source for industrial use.

VI. ACKNOWLEDGEMENT

The authors wish to thank all of their colleagues at SORTEC Corporation and Mitsubishi Electric Corporation. The success of the upgrade to 500 mA was the result of their efforts through preliminary studies and reconstruction work. Also, the authors wish to express deep thanks to the many people who provided useful suggestions.

VII. REFERENCE

- [1] T.Hosokawa and T.Kitayama,Oyo Buturi(In Japanese) Vol..60,703(1991).
- [2] N.Awaji,M.Kodaira,T.kishimoto,T.Iida,Y.Kijima and H.Tsuchidate, EPAC92,Vol.1,pp.304-306(1992).
- [3] M.Kodaira,N.Awaji,T.Kishimoto,O.Asai and M.Haraguchi, EPAC92,Vol.1,pp.203-205(1992).

Performance of Upgraded SORTEC 1-GeV 500 mA SR Source Facility

T.Kishimoto, M.Kodaira*, N.Awaji**, K.Mukugi and M.Araki
SORTEC Corporation
16-1 Wadal, Tsukuba-shi, Ibaraki 300-42, Japan

Y.Kijima and M.Haraguchi
Mitsubishi Electric Corporation
3-1-1 Marunouchi, Chiyoda-ku, Tokyo 100, Japan

Abstract

At SORTEC, the 1GeV SR source facility has been successfully upgraded. The ultrahigh vacuum of the storage ring was completely recovered. At present, the maximum beam lifetime reached 25 h at 500mA and 80 h at 200 mA. Machine studies are continuing for investigation of the beam behavior at various stored beam currents of up to 500mA, by using the merit of the full energy injection scheme. In this paper, the performance of RF accelerating system, ion clearing effects and vacuum characteristics are described. As a result, It is shown that the lifetime predicted from the theoretical considerations has been almost attained.

1. INTRODUCTION

The reconstruction work for the upgrade, which was performed by shutting down the facility from April 20 through July 20, 1992., has been completed successfully as scheduled with high performance beyond our expectations. As a result of the success of upgrading to 500 mA with over 20 h which will be requested in order to use for SR lithography, the SORTEC 1-GeV SR source has attained top levels all for beam current, beam lifetime and X-ray power as a dedicated SR source for industrial use. The beam lifetime at 200mA extended 70 h at the before upgrade and the ultrahigh vacuum of the storage ring was completely recovered[1]. At present, the maximum beam lifetime reached 25 h at 500mA and 80 h at 200 mA. Machine studies are continuing for investigation of the beam behavior at various stored beam currents of up to 500 mA, by using the merit of the full energy injection scheme.

II. UPDATE BEAM OPERATION

Figure 1 represents a typical daily operation. The beam lifetime of the ring is 24 h at 1GeV, 500mA of the storage current. After an initial warm-up of 1 h in the morning, a nominal beam current of 500 mA is stored within 10 min. New beams are refilled in one or two minutes only once or

twice a day to recover the beam reduction of about 15 % because of long beam lifetime. Table 1 shows main parameters of the storage ring.

Table 1 Main parameters of the storage ring.

Operation mode		"Flat"	"Round"
E (GeV)	beam energy	1	
I (mA)	beam current	500	
t (h)	beam lifetime	20 (25)	60 (80)
f (Hz)	injection cycle	0.31	
v_x/v_y	betatron tune	2.20/2.23	2.143/2.149
β_x/β_y (m)	avg. beta function	4.36/6.55	4.41/5.93
κ	coupling of beta func.	0.1	1
ϵ_x/ϵ_y (μm rad)	emittance	0.622/0.062	0.35/0.35
ξ_x/ξ_y	natural chromaticity	-2.99/-0.20	
ξ_x/ξ_y	chromaticity	2.26/-1.83	
α	momentum compaction	0.185	0.184
$\Delta p/p$ ($\times 10^{-3}$)	momentum spread	0.462	
L (m)	ring circumference	45.73	
f _{RF} (MHz)	RF frequency	118	
f _{rev} (MHz)	revolution frequency	6.5556	
h/B	harmonics/bunch no.	18/18	
R _{sh} (Mohm)	shunt impedance	1.35	
β (0)	coupling factor	4.0	
U ₀ (keV)	radiation loss	31.83	
U _c (kV)	cavity gap voltage	100	
f _s (kHz)	synchrotron frequency	46.3	46.1
P (kW)	RF power (Max 28kW)	22	

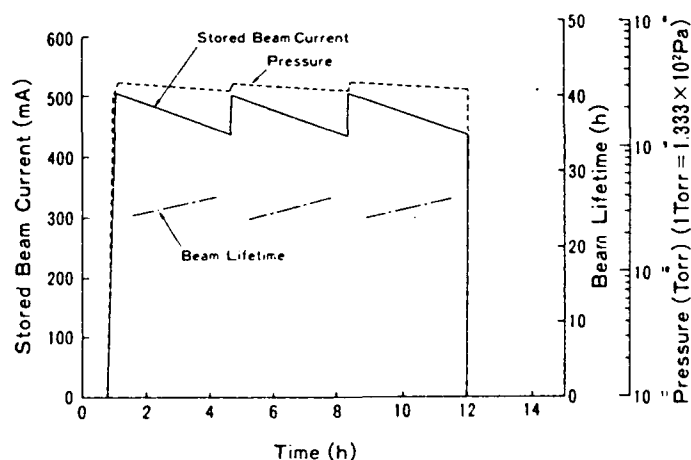


Fig. 1 Typical daily operation.

* Present Address: Keihin Product Operations, Toshiba Corporation, 2-4 Suehiro-cho, Turumiku, Yokohama 230, Japan

**Present Address: Technology Development Div. FUJITSU LIMITED, 1015, Kamikodanaka Nakahara-ku Kawasaki 211, Japan

A. Optimization of RF Acceleration System

The output power and reflection power were optimized by taking into account the stability of the system. Figure 2 shows the vector diagram and indicates that the peak cavity voltage V_c is a vector summation of the beam loading voltage V_b and generator produced voltage V_g . The cavity voltage V_c was increased from 90 kV to 100 kV by improving the Touschek terms effecting on lifetime [2] and stability of the beam. The condition for phase stability is theoretically given by using the stability factor s [3] as

$$S = V_c \cdot \sin \phi + V_b \cdot \sin \psi > 0$$

The relationship between output power and reflection power were investigated by taking into account a margin of 10 kV (namely $s > 10$ kV). Under this condition, it was also found that coupling constant β would be required 4 and detune angle α for phase stability would be needed $10 \sim 20^\circ$ for attaining 500 mA and set up for regular operation.

As a result it was found that the output power of 28 kW was attained and the reflection power of 10 kW was absorbed by the circulator of the RF power supply as a result of the RF system test.

Figure 3 shows calculated RF generator produced power P_g , reflected power P_r and stability factor S as a function of beam current at $\alpha = 20^\circ$. The measured values of up to 500 mA were compared and agreed well with the calculated values. According to these results, P_g is 22 kW at 500 mA and up to 600 mA can be stored at 28 kW (an upper limit of P_g).

B. Vacuum characteristics and beam lifetime

Figure 4 shows the dependence of normalized pressure rise $\Delta P/I$ for the straight section and bending section on integrated beam dose since the beginning of operation in 1989. $\Delta P/I$ was almost flat before the upgrade, and however again begins to decrease sharply after the upgrade. The ultrahigh vacuum of the storage ring was completely recovered when the beam lifetime exceeded 70 h, which was the maximum value before the upgrade at 200 mA. It reached 80 h only after 8 months as shown in Fig. 5. These effect may have been caused by installation of a new NEG pump, although closer observation will be needed.

C. Effect due to a trapped ion

To clear an ion, the existing disk-type ion clearing electrode, installed at seven out of eight straight sections. To all electrodes including already installed before the upgrade, applied voltage was increased to 1.5 kV from 500 V. One ion clearing electrode was newly installed at the one straight section previously not equipped with an electrode. A stripe-type ion clearing electrode, was newly installed in each chamber of the NEG pump. When the clearing voltage is decreased from 0V after storing beam current, the beam lifetime is clearly improved at less than some fixed voltage. These threshold voltages are almost proportional to stored beam currents and are higher than those when voltage is

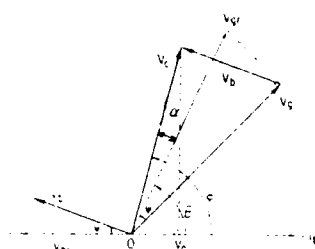


Fig. 2 Vector diagram of an RF accelerating system.

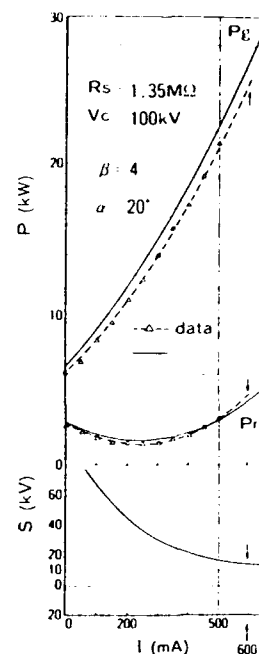


Fig. 3 P_g , P_r and S as a function of beam current.

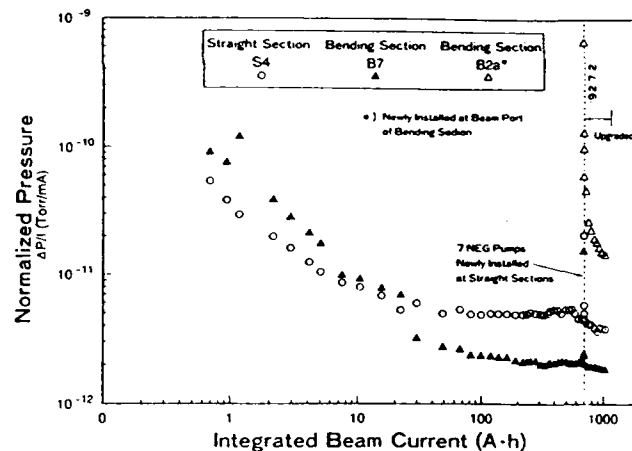


Fig. 4 Change of normlized pressure rise $\Delta P/I$

increased from lower voltage, for example -1100V or less. Figure 6 shows the clearing voltages showing hysteresis as a function of stored beam currents in three zones: A, B and C. The clearing voltage is required for set up in zone A. Figure 7 shows the beam lifetime as a function of clearing voltage at different beam modes of round beam (No. 2R) and flat beam (No. 2F) as shown in Table 1 and stored beam currents of 200 mA and 500 mA. For No. 2R the beam lifetime was improved to 75 h from 20 h at 200 mA and 22 h from 9 h at 500 mA by applying $V_{ic} = -1100V$ previously been used in

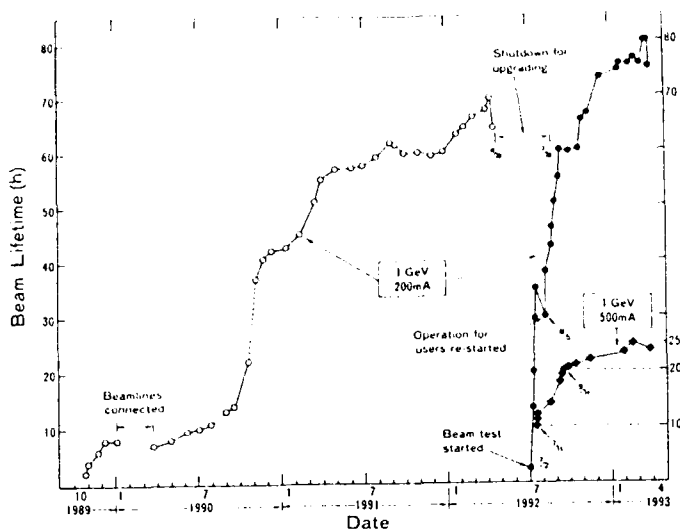


Fig. 5 Improvement of beam lifetime.

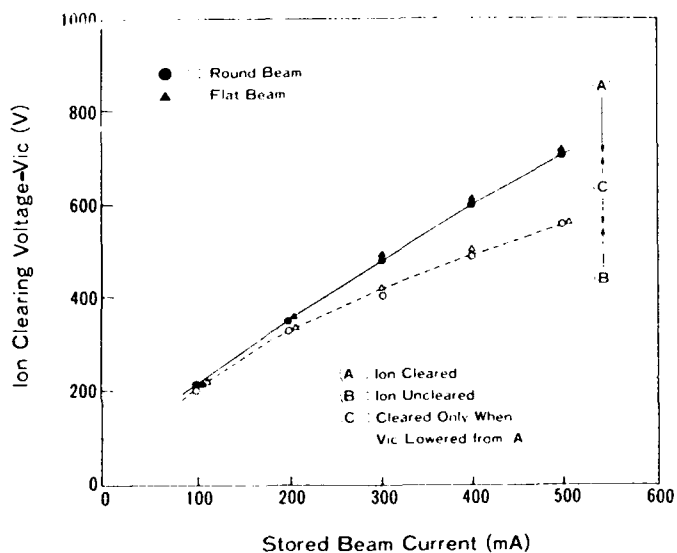


Fig. 6 Clearing voltage as a function of beam current

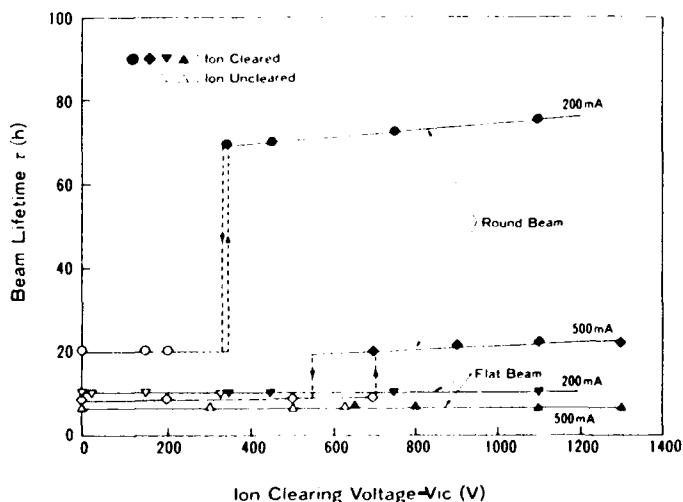


Fig. 7 Beam lifetime as a function of clearing voltage at different beam modes

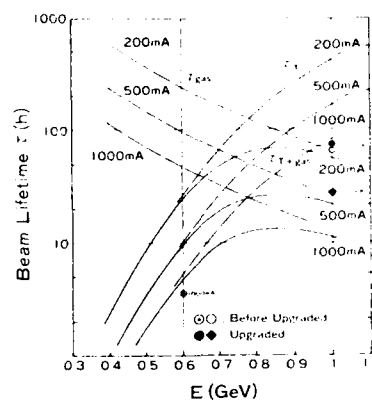


Fig. 8 Comparison of measured beam lifetime and calculated one.

regular operation. When ions are cleared, average pressures in the vacuum duct of the ring being increased. However for No.2F, the beam lifetime was not clearly confirmed to have been changed. It was nearly 10 h at 200 mA and 6 h at 500 mA at either $V_{ic}=0$ or -1100 V in spite of average pressures in the ring being increased when $V_{ic}=-1100$ V.

D. Beam lifetime

Figure 8 shows the beam lifetime calculated for the round beam based on the Touscheck lifetime and beam-gas lifetime for different beam energy and current. In the figure, the measured beam lifetime at 1GeV-200 mA and 1GeV-500mA are compared and agreed well with the calculated values. The lifetime at 600MeV-1000mA tested before the upgrade are also shown.

IV. CONCLUSION

The performance of the upgraded 1-GeV 500 mA SR ring is presented. The performance of RF accelerating system, ion clearing effects and vacuum characteristics was presented. The measured beam lifetimes are compared and agreed well with the calculated values predicted by preliminary R&D and machine studies. As a result, the SR source facility has attained top levels all in beam current, beam lifetime and x-ray power as a dedicated SR source for industrial use.

V. ACKNOWLEDGEMENT

The authors wish to express deep thanks to all of their colleagues to many people who offered useful suggestion and helpful discussions.

VI. REFERENCE

- [1] M.Kodaira, N.Awaji, T.Kishimoto et al., In this Conference.
- [2] M.Kodaira, N.Awaji, T.Kishimoto, O.Asai and M.Haraguchi, EPAC92, Vol.1, pp.203-205(1992).
- [3] S.Sakanaka, KEK Report 91-7, August, 91A.
- [4] N.Awaji, M.Kodaira, T.Kishimoto et al., Review of Sci.Inst., Vol.63, pp745-748.
- [5] N.Awaji, M.Kodaira, H.Usami and T.Kishimoto, Journal of the Vacuum Society Japan, Vol.34, No.10(1991)752.

DESIGN OF TEST LINAC FOR FREE ELECTRON LASER*

H. Kang, I. Ko, M. Cho, and W. Namkung
Pohang Accelerator Laboratory, POSTECH
P. O. Box 125, Pohang 790-600, Korea

Abstract

Pohang Accelerator Laboratory (PAL) is constructing the 2-GeV Pohang Light Source (PLS), a dedicated synchrotron radiation source. The injector of the storage ring is a 2-GeV linear accelerator. The construction of the linac will be completed by the end of 1993. We plan to construct a test linac using some spare components after the linac construction. The design of the test linac is based on two accelerating columns and a matching girder, a klystron, and a modulator after upgrading current 60-MeV preinjector. The energy of the test linac will be 50-MeV, and the peak current be 30 A. The radiation wavelength is expected to be from 3 to 30 microns. A thermionic RF-gun is considered as an electron beam source. The whole test linac can be installed by sharing present 2-GeV linac tunnel and the gallery.

I. INTRODUCTION

Pohang Accelerator Laboratory is constructing a 2-GeV linear accelerator as a full energy injector to the storage ring, a dedicated synchrotron radiation source. The 60-MeV preinjector was completed by February 1992 under the international collaboration with Institute of High Energy Physics, Beijing, China. At present, nearly half of the 2-GeV linac is completed, and by December this year, the whole linac will be installed and will be ready for its commissioning [1]. The 2-GeV linac will be controlled under VME-based control system during commissioning and normal operation that is expected from July 1994.

However, the preinjector control system which is based on INTEL Bitbus system is different from the rest of the 2-GeV linac. Thus, a modulator and a klystron of the preinjector along with its control system will be replaced by VME-based ones later this year.

There are also spare parts from the preinjector and the main linac. Two accelerating columns and an aluminum girder are left from the preinjector program. Some of waveguide components will be available if they are not completely used during the installation. The design of the test linac for a free electron laser (FEL) is based on these left-over components.

II. LINAC DESIGN

A. General Layout

Figure 1 shows a general layout of the test linac assigned at the corridor of the E-gun room in the tunnel. This space is approximately 30-m long and 4-m wide. The linac consists of a thermionic cathode RF gun as an electron source, an alpha

magnet for bunch compression and energy selection, and two standard accelerating columns.

A 30-MW klystron will provide RF power to the gun cavity and two accelerating columns. Two undulators will be set up at the end of each column. A circulator and an integrated phase shifter/attenuator will be used for RF gun system. The klystron and its modulator will be located at the corner between the klystron gallery and the test lab. One penetration hole to the tunnel has been prepared at this corner for the waveguide.

B. Design Parameters

For the SLAC type accelerating column, the peak value of the beam induced voltage is about $0.15 \text{ MV/m}/10^{10} e^-$ due to the longitudinal wakefield effect [2]. It gives a peak voltage of 45 kV/m for a bunch of 0.5 nC charges. Throughout the total 6-m long accelerating sections, the peak induced voltage will be about 270 kV. This is about 0.5 % of final beam energy which is 50 MeV. To compensate this effect, a phase shifter will be inserted to the waveguide line in the second accelerating column.

The phase change of the RF field from the klystron creates an energy spread. The tolerance of the phase change should be less than 2.5 degrees in order to minimize the energy spread. An adaptive RF feed-forward control of the klystron is currently studied [3]. Major parameters for the test linac is summarized in Table 1.

Table 1. Major parameters for test linac.

Beam Energy Range	20 ~ 50 MeV
RF Frequency	2,856 MHz
Electron Beam Source	Thermionic RF gun
Beam Energy after RF-gun	0.9 MeV
Klystron Output	30 MW
Pulse Length	8 μ s (flat top)
Tolerance of Phase Change	< 2.5 deg.
Energy Spread	< 0.5 %
Micropulse Peak Current	30 A
Normalized Emittance	< 95 π mm-mrad for $\lambda = 3 \mu\text{m}$ at 50 MeV
Repetition Rate	10 Hz

III. RF-GUN DESIGN

A. Type of RF-Gun

There are usually three different electron sources dedicated to FEL research. One is a conventional type thermionic gun with a subharmonic buncher and a buncher. Others are a photocathode RF-gun which uses short laser pulses, and a thermionic RF-gun. The conventional type is a reliable one, but it is limited

* Work supported by Pohang Iron & Steel Co. and Ministry of Science and Technology, Korea.

in reducing the emittance. The photocathode type is very expensive and complicated, although it has many good features. We have, thus, chosen the thermionic RF-gun for the test linac. Although this has some disadvantages such as back bombardment, it is quite compact and relatively inexpensive. In order to reduce the back bombardment, several methods have been proposed such as an 1-1/2 cell with different field amplitude, a ring cathode, and a magnetic deflection [4].

B. RF_GUN code

A code called RF_GUN is used to simulate the RF-gun cavity. This code integrates the longitudinal equation of motion under

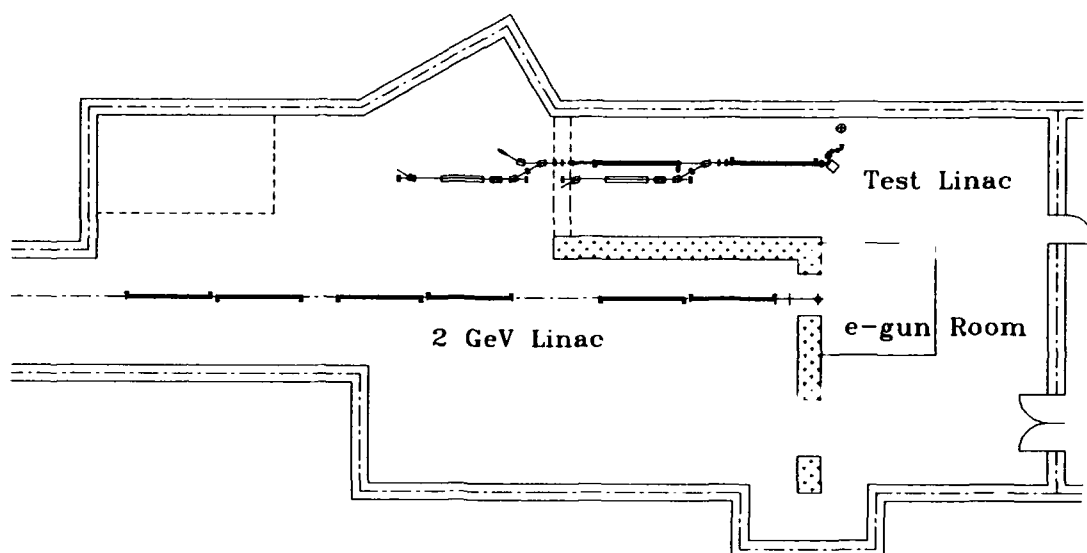


Fig. 1: Layout of test linac with present 2-GeV linac tunnel.

external electric field. The field profile is calculated by the SUPERFISH program in the absence of space charge, and the RF_GUN code uses it as an input data. The RF_GUN code includes a power balance equation in the cavity. With a given input power, the RF_GUN runs until the sum of beam loading power and power loss at the wall equals the input power.

Figure 2 shows changes of maximum beam power and average current in terms of the input power and cathode temperature, respectively. The average current is a sum of electrons with their momenta within the range of $\pm 40\%$ with respect to the peak momentum of the bunch. The bunch length of useful electrons is about 20 ps. Normalized rms emittance calculated by PAR-MELA is 35π mm-mrad.

C. RF-Gun Design

The RF-gun is a standing wave type one-cell cavity. Optimization of the cavity shape was done by using the SUPERFISH and the RF_GUN codes. The ratio of the peak axis field to the peak surface field is about 0.5, and the ratio of the field at the cathode to the field on the axis is about 0.64. The cold coupling coefficient $\beta (= 1 + P_{\text{beam}}/P_{\text{cavity}})$ calculated by the RF_GUN is about 2.5. It is chosen, however, as 3.5 in order to allow higher beam loading. The iris hole size of coupling structure is determined by MAFIA code.

Figure 3 shows a cross-sectional view of the RF-gun cavity. The cathode assembly can be demountable, and an RF choke joint around the cathode stem is adopted. Cathode material is LaB₆ and its diameter is 3 mm.

D. Gun-to-Linac Design

The Gun-to-Linac (GTL) transport line is shown in Figure 4. An alpha magnet is used to match the longitudinal acceptance of the linac. The good field region of the alpha magnet is about 13 cm. A momentum filter is introduced inside the alpha magnet vacuum chamber. A pair of electric plates (30mm x 30mm, 2 cm gap) is placed inside the alpha magnet vacuum chamber in order to deflect undesirable electrons which are generated during the RF-filling time ($\sim 0.83 \mu\text{s}$) of the accelerating column. Required voltage is larger than 4 kV.

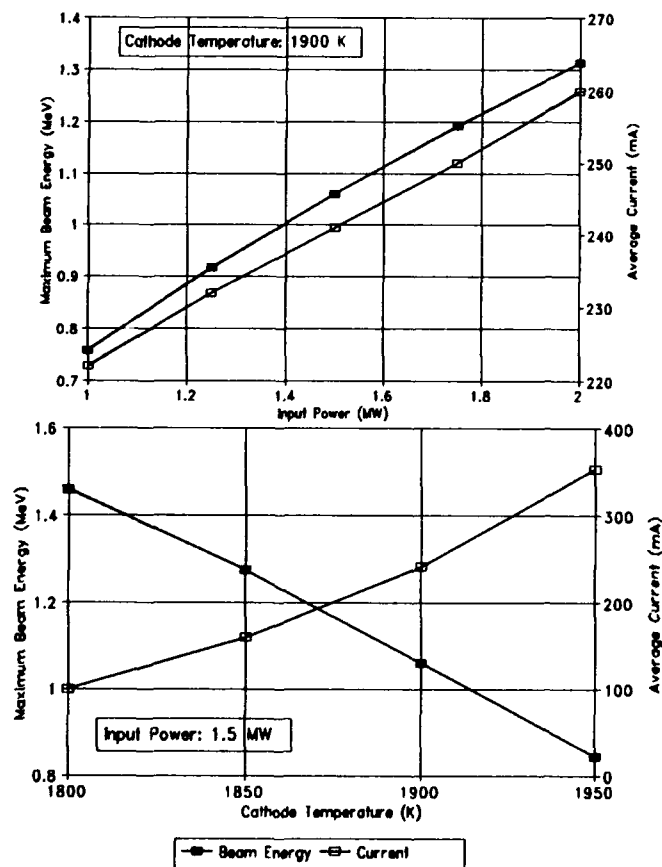


Fig. 2: Beam energy and current changes in terms of input power (top) and cathode temperature (bottom).

IV. FEL DESIGN

A. FEL Parameters

Parameters for undulators and optical radiation are summarized in Table 2 and 3, respectively. The wavelength of resonant radiation is given by

$$\lambda = \lambda_w (1 + K^2) / 2 \gamma^2 \quad (1)$$

where λ_w is the undulator period, γ is the relativistic factor, and K is the undulator parameter.

Table 2: Undulator parameters

Period Length (λ_w)	3.0 cm
No. of Period	50
Gap	10 ~ 15 mm
Undulator Parameter (K)	0.5 ~ 1.5
Structure	Tapered
Type of Magnet	NdFeB

B. Electron Beam Transport

There are two electron beam exits in the test linac as shown in Figure 1. Main considerations in the design of beam transport lines were that the beam waist be located at the center of the undulator, and that the size of the beam waist be less than 0.8 mm for 3 μ m radiation. The effective length and the bending angle of bending magnets in the achromatic section are 27 cm and 30°, respectively. A quadrupole triplet is used to match the electron beam waist to that of the optical beam at the center of the optical cavity.

Table 3: Design parameters for optical radiation

Spectral Range	3 ~ 30 μ m
Cavity Length	4.5 m
Reyleigh Length	0.75 m
Mirror Curvature	2.5 m
Beam Waist (min.)	0.85 mm for $\lambda = 3 \mu$ m 2.68 mm for $\lambda = 30 \mu$ m
Spot Size (radius) on Mirrors	2.53 mm at $\lambda = 3 \mu$ m 8 mm at $\lambda = 30 \mu$ m
Macropulse Length	5 μ s (flat top)
Micropulse Length	5 ps (FWHM)
Small Signal Gain for $I = 30$ A	73 % at $\lambda = 10 \mu$ m
Operation Mode	- Oscillator - Amplifier - Harmonic Generator

The layout of optical resonator beamline is shown in Figure 5. There are three beam profile monitors (BPRM) in the beamline. The first one is located to find the center of the electron beam. Second and third BPRMs will be used to measure the energy spread.

V. REFERENCES

[1]. W. Namkung, et al., "Progress of PLS 2-GeV Linac," these proceedings.

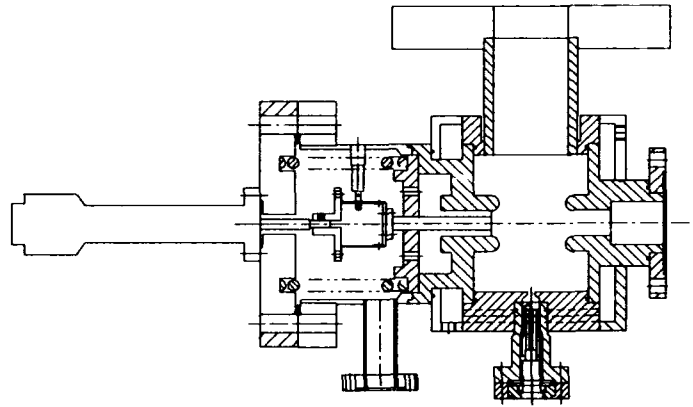


Fig 3: Cross-sectional view of RF-gun cavity.

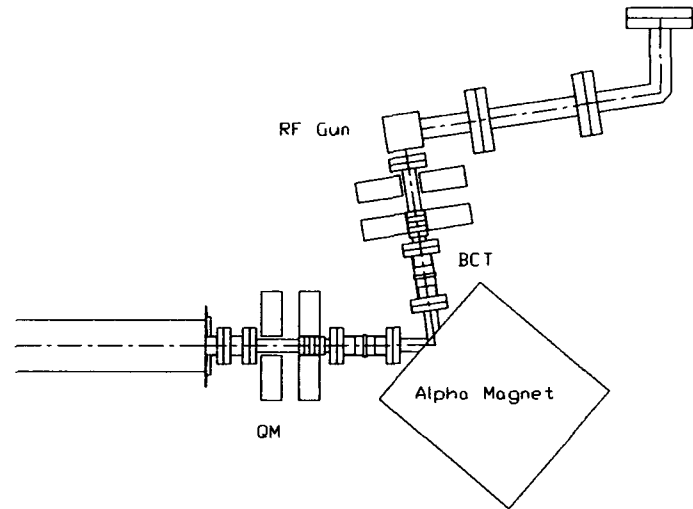


Fig. 4: Gun-to-Linac transport line.

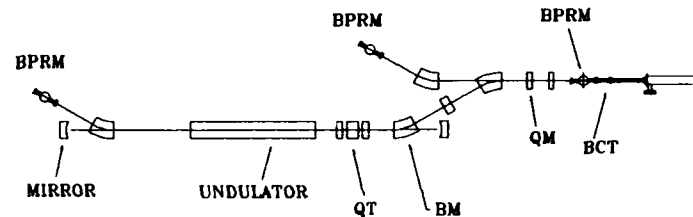


Fig. 5: Layout of optical resonator beamline.

- [2]. P. B. Wilson, et al., "Application of Storage Ring RF systems and Linear Colliders," *AIP Conf. Proc. Series*, Vol. 87, p. 450 (1982).
- [3]. J. Xie, "An Adaptive RF Feed Forward Control System for ATF," CAP-ATF-Tech. Note 12 (1991).
- [4]. C. B. McKee, J. M. J. Madey, "Optimization of a Thermionic Microwave Electron Gun," *Nucl. Inst. and Methods*, A304, pp. 386-391 (1991).

The Revised ELFA Project

E. Acerbi¹, F. Alessandria¹, P. Arcioni², G. Baccaglioni¹, W. A. Barletta³, G. Bellomo¹, C. Birattari¹, R. Bonifacio¹, I. Boscolo¹, A. Bosotti¹, F. Broggi¹, M. Bressan², G. Conciauro², R. Corsini¹, L. De Salvo¹, G. Gemme⁴, D. Giove¹, C. Maroli¹, R. Parodi⁴, P. Pierini¹, N. Piovella¹, M. Pullia¹, G. Rivoltella¹, L. Rossi¹, V. Stagno⁵, V. Variale⁵, G. Varisco¹

¹INFN and Università degli Studi, Milano, Italy; ²INFN and Università degli Studi, Pavia, Italy

³Lawrence Berkeley Laboratory, USA; ⁴INFN Genova, Italy; ⁵INFN and Università degli Studi, Bari, Italy

II. Status of the Project

Abstract

The goal of the revised ELFA project (Electron Laser Facility for Acceleration) is to operate with short bunches a high-gain free electron laser (FEL). The paper describes the main components of the experiment and discusses the choice of the parameters for the linac, the electromagnetic wiggler, the microwave generator, the waveguide and the beam and radiation diagnostics.

I. Introduction

ELFA is a high gain free electron laser designed to operate in the microwave region with the waveguide control of the group velocity of the radiation[1].

At the level of fundamental physics the goals of ELFA are to verify and characterize quantitatively:

- the self-bunching of the electron beam;
- the production of high power radiation by coherent spontaneous emission on higher harmonics in a two wiggler scheme;
- the FEL lethargy starting from noise.

The first goal includes the experimental demonstration of the existence of three different regimes of FEL operation: the steady state regime (zero slippage), the strong superradiance regime (strong slippage) and the weak superradiant regime (very strong slippage)[2]. With respect to the production of radiation the performances of a high gain FEL amplifier in the steady state regime were first measured several years ago at Livermore[3,4] using long electron pulses from a linear induction accelerator. The physics in the two superradiant regimes, however, has never been investigated experimentally. ELFA intends to study these regimes with short electron pulses by controlling the slippage with a properly designed waveguide[5].

The first two researches have also significant applications in the accelerator technology. In fact the bunching of the electrons in the picosecond or sub-picosecond domain should be able to produce electron pulses with tens of kiloamperes of peak current useful as a drive beam in a two beam accelerator[6]. Similarly, the second research can allow the production of high power coherent ultraviolet radiation in absence of a stimulating source and without starting from noise (very long wiggler).

The general layout of the ELFA project has undergone an extensive review since its first presentation[7]. The fundamental physics goals, which are at the heart of the proposal, have gained a primary role over the technological development. The main components of the original proposal (semiconductor photocathode injector, superconducting cavities and hybrid wiggler) would require a research and development effort that would not be compatible with the time scale and economical planning of the overall experiment. In this sense our new approach has been to seek a design that could produce beams with minimum characteristics necessary to demonstrate all the physics of ELFA eliminating all non-essential technical risks and minimizing both the delivery time and the cost of the main subsystems. A general layout of the revised apparatus is shown in Fig. 1 and the main parameters are summarized in Table 1.

Table 1. Main ELFA parameters

Electron Beam	
Beam Energy	$E_k = 6 \text{ MeV}$
Normalized emittance (hard edge)	$\epsilon_n = 200 \pi \text{ mm mrad}$
Energy spread	$\Delta\gamma/\gamma = \pm 1\%$
Peak current	$I > 50 \text{ A}$
Microbunch length	$\tau > 35 \text{ ps}$
Microbunch number	3
Repetition rate	10 Hz
Wiggler	
Wiggler period	$\lambda_w = 10 \text{ cm}$
Peak wiggler field	$B_w = 1.0\text{-}3.6 \text{ kG}$
Wiggler parameter	$a_w = 0.66 - 2.4$
Overall length	$L_w = 8 \text{ m}$
Betatron wavelengths (m)	$\lambda_{\beta x} = 2.2 \quad \lambda_{\beta y} = 0.8$
rms field errors	0.1 %
Groove waveguide	
Width	5 cm
Height (center)	10.04 mm
Microwave radiation	
Wavelength	$\lambda_r = 3 \text{ mm}$
Input power	$P_{in} = 1 \text{ kW}$
Expected peak output power	$P_{out} \approx 10 \text{ MW}$
FEL parameters	
Fundamental FEL parameter	$\rho \approx 2 \times 10^{-2}$
Saturation length	$L_{sat} \approx 5 \text{ m}$
Gain length	$L_g \approx 0.5 \text{ m}$

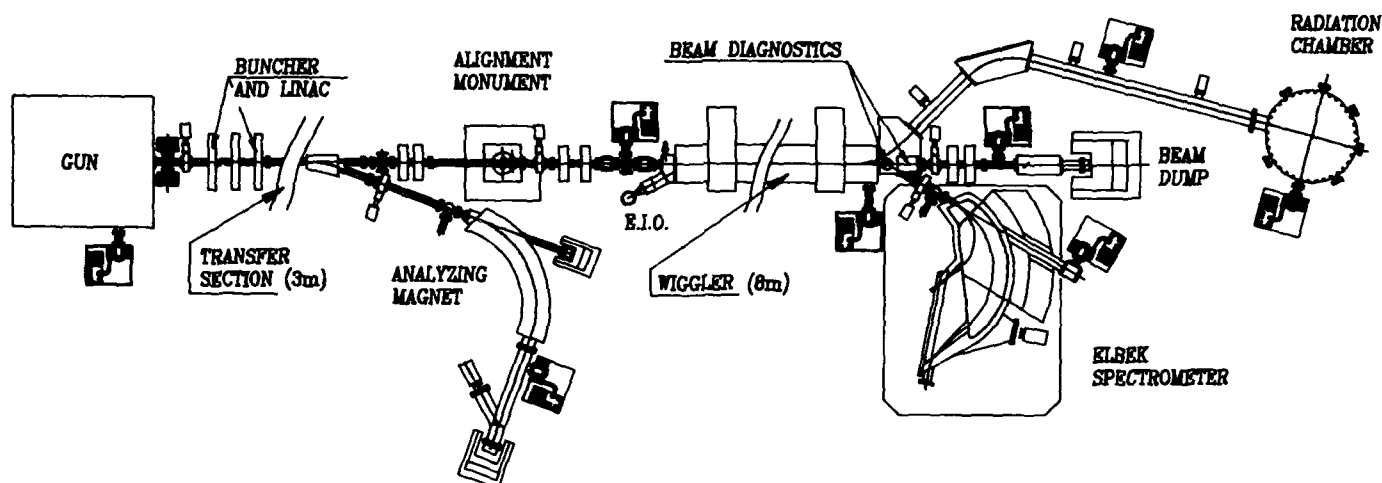


Fig.1 General layout of the experiment

The basic components of the ELFA project are:

- a RF linac delivering a 6 MeV electron beam with a peak current of 50 A;
- an electromagnetic wiggler of period 10 cm with a maximum peak dipole field on axis of about 3.6 kG;
- a microwave source (100 GHz) and a waveguide inserted in the wiggler gap in order to control slippage effects in the FEL;
- beam and radiation diagnostics to measure the energy spectrum and time structure of the electron and FEL radiation.

III. The Accelerator System

The linac consists of a gridded triode electron gun, a prebunching standing wave cavity at 1.3 GHz and a linac operating at 1.3 GHz to produce a 6 MeV electron beam. Details on the linac design are reported in other papers [8,9] presented at this Conference.

The beam line has been designed in a modular way to provide flexibility and it consists of three sections:

- the transport section to obtain electron beam waists in both the transverse planes;
- a matching section to adapt the beam to the wiggler;
- an analysing section to control on line the stability of the beam energy and energy spread.

IV. The Wiggler

Some additional parameters of the wiggler are listed in Table 2.

The wiggler period and gap have been chosen in such a way to satisfy the FEL resonance condition in all the different experimental setups, without achieving prohibitive working

conditions for the power consumption and the saturation level in the iron.

Table 2. Main wiggler parameters

Type	DC iron core electromagnet
On axis gap	$g = 4.0$ cm
Harmonics content	< 1 %
Pole length	22.5 mm
Pole profile	Cylindrical ($R = 160$ mm)
Maximum current	300 A
Magnetomotive force/coil	3600 At
Total maximum power	$P = 250$ kW
Excitation pattern	1-2-2-2-1

The wiggler has been designed in order to produce an horizontal focusing of the electron beam in addition to the intrinsic vertical focusing. A transverse profiling of the pole surfaces[10] has been preferred with respect to external quadrupole focusing or pole canting techniques[11] because it is less disturbing for the FEL process. Finally, the global harmonics content has been reduced, by optimizing the pole length, to be lower than 1% of the fundamental, in order to maintain a high coupling between the field and the electron beam. A full scale, one λ_w , model (at $\lambda_w = 12$ cm instead of 10) has been built to test the theoretical predictions, based on analytical models and numerical 2D simulations, for the field strength and quality, the harmonics content and the transverse field distribution needed for focusing.

Fig. 2 shows the peak on axis field as a function of the current with and without PM assisting, compared with the 2D POISSON simulation results.

At the maximum nominal current ($I = 300$ A), where the pole iron begins to saturate, a peak field about 6% lower than the one obtained with the 2D POISSON code has been found. For this reason transverse pole tapering, in order to further reduce the power consumption and the saturation effects, will be carried out in the wiggler prototype. More details on this work can be found in Ref.[12].

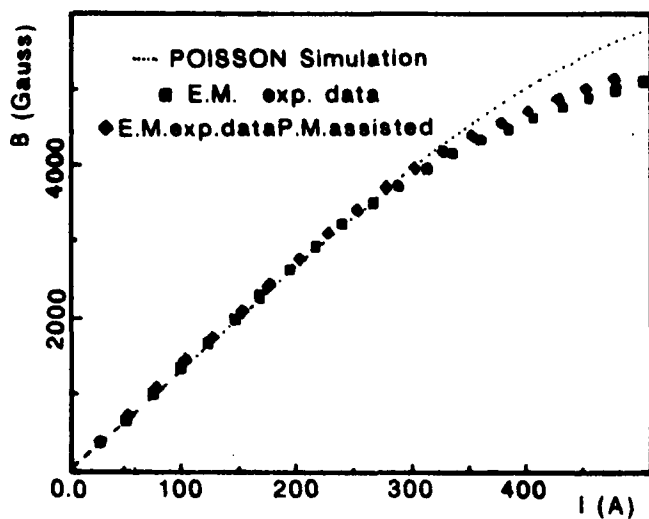


Fig. 2 Measured peak on-axis field as a function of current, compared to POISSON simulations.

V. Microwave generator and waveguide

The high gain FEL amplifier needs a 100 GHz master oscillator with enough power to trigger the FEL process and to maintain the saturation length shorter than the wiggler length. A commercial Extended Interaction Oscillator (EIO) at 100 GHz with a peak power of 1 kW, a mechanical tuning of ± 1 GHz and a maximum duty cycle about 1%, seems the most suitable solution.

The interaction structure, inserted in the gap of the wiggler, is a waveguide, whose large cross section is necessary in order to accommodate the transverse motion of the electron beam. An oversized rectangular waveguide can be used in the experiment also if this guiding system leads to some problems related to the control of unwanted high order modes, that are excited by the beam itself and by any waveguide discontinuity. For this reason another guiding system has been considered, the so-called groove guide, which is a typical low loss transmission structure in the 3 mm band. It consists of two parallel conducting planes, where two longitudinal grooves permit to trap a guided electromagnetic wave. The characteristics and properties of the groove guide are described in more details in a paper presented at this Conference[13].

VI. Electron and Radiation Diagnostics

Electron beam diagnostic would rely on the use of electromagnetic detectors, like strip-lines, which provide resolutions in position measurements up to tens of microns, and of image based systems. A lot of information about beam characteristics (profile, position with respect to pipe axis, transverse emittance, time structure) may be obtained placing on the beam path a material that gives a linear optical emission in response to the interaction of the beam and to look at the image through a camera. We started investigating

fluorescent screen characteristics using a very low energy electron beam and developing a complete station for image acquisition and analysis. Horizontal and vertical profiles, transverse emittances (using the pepper pot technique) are automatically measured after an image of the beam has been taken. Real time display of the intensity distribution over the spatial coordinates of the beam may be displayed on a dedicated color monitor, to help the beam transport up to the wiggler.

The longitudinal profile of the beam would be studied using Cerenkov radiation analyzed using a streak camera which will give us resolutions up to 2 ps. Such a limit is well within the requirements before the beam experience FEL interaction. The energy distribution and the energy spread at the exit of the wiggler contain a quantitative description of the FEL interaction mechanism. To measure these quantities with a suitable resolution (0.1-0.2%) it is necessary to use a magnetic spectrometer with a large dispersion. A complete design of such a component has been carried out.

Microwave radiation average power would be measured using He cooled bolometers. Radiation pulse duration and time structure would be investigated by means of interferometric techniques.

VI. Conclusion

The ELFA project has been submitted to an international referee committee which gave a positive evaluation at the end of 1992. We are now waiting for the final approval and funding from INFN.

References

- [1] R.Bonifacio et al., *Nucl. Instrum. and Methods*, **A289** (1990), 1;
- [2] R.Bonifacio, L.DeSalvo, P.Pierini, N.Piovella, *Nucl. Instrum. and Methods*, **A296** (1990), 358;
- [3] T.J.Orzechowsky et al., *Nucl. Instrum. and Methods*, **A250** (1986), 144;
- [4] T.J.Orzechowsky et al., *Phys. Review Lett.*, **57** (1986), 2172;
- [5] R.Bonifacio, L.DeSalvo, *Nucl. Instrum. and Methods*, **A276** (1989), 394;
- [6] W.Schnell, *CERN-LEP-RF/88-59* (1988);
- [7] E.Acerbi et al., *Proceedings of the 2nd European Particle Accelerator Conference*, Nice, June 1990;
- [8] W.A.Barletta et al., "Design study for the ELFA linac", these Proceedings;
- [9] G.Bellomo et al. "Design and test of prototype cavities for the ELFA linac", these Proceedings;
- [10] E.T.Scharlemann, *J.Appl. Phys.*, **58** (1985), 2154
- [11] K.E. Robinson, D.C. Quimby and J.L. Slater, *IEEE Journ. Quantum Electr.*, **QE-23** (1987), 1497
- [12] E. Acerbi et al., *Proceedings of the 3rd European Particle Accelerator Conference*, Berlin, March 1992;
- [13] P.Arcioni et al., "The groove guide: a non-conventional interaction structure for microwave FEL experiments", these Proceedings.

Design and Construction of a Compact Infra Red Free Electron Laser CIRFEL

J. KRISHNASWAMY, I.S. LEHRMAN, J. SHEEHAN, R.L. HEUER, M.F. REUSCH, and R. HARTLEY
Grumman Aerospace Corporation
4 Independence Way
Princeton, N. J. 08540-6620

Abstract

The 5-15 micron Grumman Compact Infra Red Free Electron Laser CIRFEL which will produce extremely short pulses of tunable radiation under construction is described. Electron pulses are produced at a repetition rate of up to 10 Hz by the illumination of a single crystal <001> LaB6 photo cathode with a photon injector, a 6-10 psec, 349 nm (frequency tripled Nd-YLF) laser mode locked to the 20th subharmonic of 2856 MHz. Photoelectrons are further accelerated and guided to the superconducting microwiggler by a robust beam transport system through an achromatic bend. The ~ 10 MeV electrons interact with the optical radiation inside of a near symmetric laser cavity. The FEL output will be coupled out through a hole in one of the cavity mirrors. The CIRFEL system is expected to be delivered in 1994.

I. INTRODUCTION

The compact IR Free Electron Laser under construction by Grumman will be assembled at the Princeton University's Physics Department under a Joint Research Agreement and will serve as a platform for advanced research in Physics and Engineering. The facility will be used initially by groups working in the area of multi-photon dissociation for pollution control and biophysics. The CIRFEL system is described, summarizing the progress made with each system component.

II. SYSTEM DESCRIPTION

The CIRFEL system comprises of the following system components, (1) High brightness photocathode electron gun, (2) Photo-injector laser, (3) 30 MW S-Band RF source, (4) the beam transport system, (5) the FEL microwiggler, (6) the FEL optical cavity, and (7) associated support hardware sub-systems. Figure 1 shows the layout of the CIRFEL which occupies two levels with the photoinjector and the high power RF system on one level, and the rest of the system on the ground floor.

A. High Brightness Photocathode Electron Gun

The high brightness photocathode gun designed for CIRFEL is an extremely bright source of electron beams and is specified by the parameters shown in Table 1. The Photoelectron source comprises of a 6 mm diameter LaB6 cathode illuminated by a photon injector and is situated in a

3.5 cell, Pi mode RF cavity, which produces a very high gradient (60 to 80 MeV/meter) on its surface. The "electrodeless emission" of electrons is controlled by the laser and allows extremely smooth control of the spatial and temporal profiles, and the electron current. The cathode is also heated from the rear to a temperature below the

Table 1
Electron Beam Specifications

Beam Energy	< 7 - 13 MeV
Total Charge	1 - 2 nC
Pulse Width(FWHM)	5 - 7 psec
Normalized Emittance	< 6 Π mm-mrad
Slice Emittance	~ 1 - 3 Π mm-mrad
Peak Current	> 150 A
Energy Spread	0.2 - 1.5% Selectable

thermionic emission level so as to present an extremely clean surface to obtain a high degree of repeatability with the lowest possible emittance. A cold model of the gun cavity has been tested and the the final version of the gun is being fabricated.

B. Photoinjector Laser

In order to optimize the efficiency of photo-emission and to have control over the characteristics of the emitted electrons, a photo injector laser which meets exacting specifications and repeatable performance is required. The electron gun is in the process of being fabricated. The photo-injector consists of an oscillator, an isolator, a pulse slicer and two stages of amplification. A schematic of the photon seed laser system is shown in Figure 2. The mode locked, diode pumped oscillator operates in the TEM00 mode with 1% energy stability and less than 1psec RMS phase jitter over 10-20,000 Hz. The >200 mW output from this laser is produced at a frequency of 142.8 MHz and single pulse pulse widths of 10 psec or less at 1047 nm. The oscillator feeds into the amplifiers separated by a passive Faraday isoator. Before being fed into the amplifiers the light pulses go through a pulse slicer which will select a variable range of 200 to 1400 pulses for amplification. The two stage amplifier system amplifies the 10 Hz pulse train to >0.13mJ per pulse at 1047 nm after 5 passes. The beam will then be down collimated and frequency tripled for an expected 20 microjoules in 5 - 7 psecs at 349 nm. The near collimated beam produced by this system is transported to the CIRFEL system at ground level by turning and steering mirros with reflectivities optimized for 45 degree incidence and p-polarization. The beam is then expanded in a telescope and then focussed with a long focal length refractive optics

followed by a half wave plate so as to optimize incidence angle of the polarized light on the cathode. Optical elements to correct the unequal pathlengths reaching the cathode illuminated at shallow angle to the normal at the cathode surface are being studied.

The oscillator has been completed and has met all the specifications for being integrated into the amplifier, frequency multiplier system. The beam delivery optics from the photo-injector to the cathode has been worked out except for the details of the optical element to correct path length.

C 30 MW S-Band RF source

The RF power feed to the gun and booster cavities is based on a ITT 2960 Klystron. Variable attenuation and variable phase features are incorporated into the design. The RF source is presently under construction. The master oscillator has been fabricated and tested.

D. The Beam Transport System

The beam transport system is shown in Figure 1. A zero current achromat is designed for the chosen achromat bend radius. A beam size is chosen at the entrance of achromat and with TRACE 3D the beam is symmetrized so that it has an $\alpha=0$ at the center. Enough drift spaces are left on either side of the magnets for their corners. The bends are not sectors and the entrance angle is 22.5 degrees. The source beam is guided into the achromat via telescope, a pair of lenses and drift spaces and the post achromat focussing system guides the beam to the wiggler. The system is still in the process of being refined to take into consideration the conditions at the slit and tune the system for space charge effects. The system design has been confirmed with PARMELA. The quadrupoles and the steering magnets have been acquired and the dipoles are being fabricated. Automation of the magnetic measurements and preliminary measurements on the quadrupoles have been completed.

E. The Microwiggler

Initial experiments will be carried out with a permanent magnet wiggler. The mechanical design has taken into consideration the incorporation of a superconducting wiggler in the final design whose parameters are as shown in Table 2. An alternative pulsed microwiggler with normal conductors is also under investigation.

F. The FEL Optical Cavity

The preliminary design under study consists of a near concentric, near symmetric stable cavity, a choice near universal in FEL optical cavities. This design superposes the optical field on the electron beam as effectively as possible for as large a distance along the electron trajectory in the wiggler. The cavity will consist of totally reflecting mirrors which can be used over a wide wavelength range, especially in the 5 to 12 micron range. The method of coupling light will be by a

intercavity Brewster plate or a hole coupling through one of the mirrors. A preliminary set of optical elements,

Table 2
FEL Microundulator

Undulator Period	7 - 8 mm
Number of Periods	50 (tapering possible)
Yoke Material	1066 Iron
Conductor	Superconducting Wire or Copper Sheet
Peak Field	4 kGauss
Field Error	~ 0.3 % RMS
Number of Passes to saturation	~ 30
Energy extraction	1% (untapered)

and optical parameters have been determined using the lowest order Gaussian optical mode. The FEL wiggler cavity vacuum is sealed using ZnSe windows set at Brewster angle for the initial working wavelength.

G. Support Sub-systems

The support subsystems comprises of (1) The vacuum system, (2)The power supply for magnet control, (3) the master control system, (4) the photo injector laser and electron beam diagnostic system, (5) the cryogenic system, and (6) the FEL optical cavity control hardware/software system. The CIRFEL control system software is written using National Instruments' LabView software package, running on a Macintosh Quadra 950 with a GPIB (IEEE-488) interface card and a GPIB bus extender. The design is still in very preliminary stages. In the normal mode of operation, the software checks the operator input for any changes to settings for power supplies or other devices. If such changes are detected, the appropriate device is reset. The devices are cycled through the control strategy and after each control cycle the output levels are read for all devices and the display updated. If appropriate, the level of each is checked against its setting and a tolerance specification and a warning is issued if necessary. All devices will be controlled through the operator console via the virtual representation of the system .

III. CONCLUSIONS

The CIRFEL when it becomes operational will provide Fourier transform limited pulses in the TEM00 mode, infra red radiation with the characteristics shown in Table 3.

IV. ACKNOWLEDGMENT

This work is supported by the Grumman Aerospace Corporation.

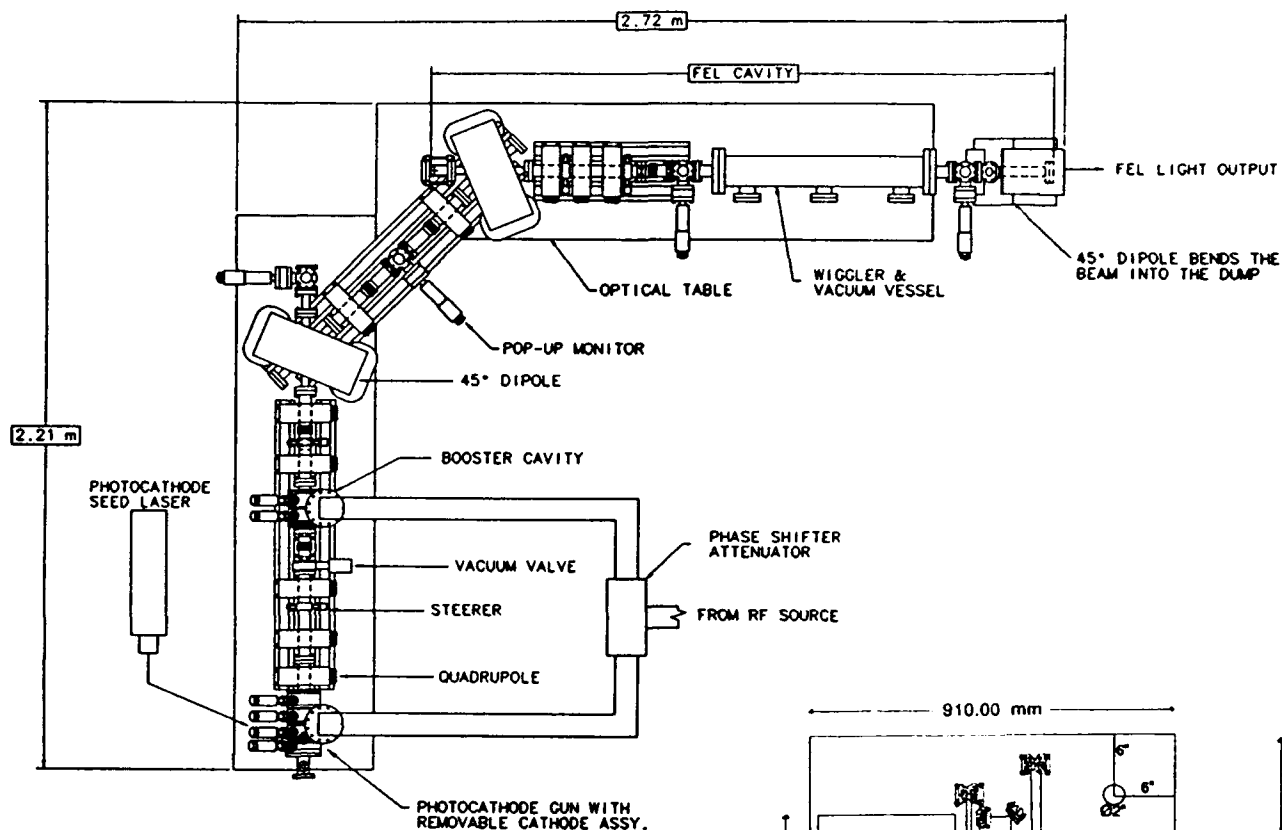


Figure 1. CIRFEL System Layout

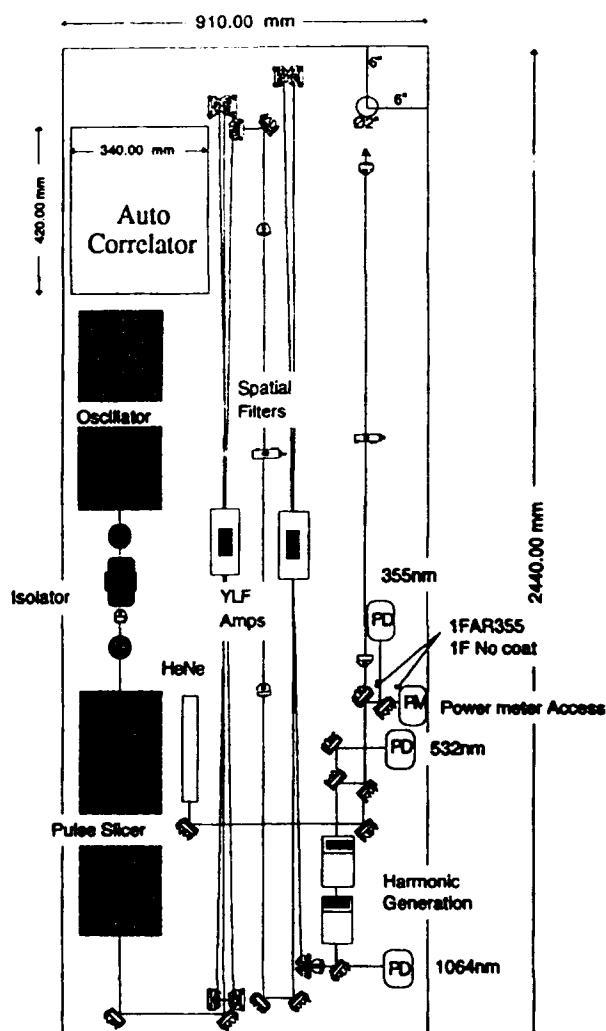


Figure 2. Photocathode Drive Laser

Table 3
FEL Laser Pulse *Specifications

Radiation Wavelength	5.3 - 14 μ m
Pulse Width (FWHM)	5 - 10 psec
Energy / pulse	> 100 μ J
Pulse Separation	7 nsec
Peak Field	4 kGauss
Pulses / macropulse	200 - 1400
Repetition Rate	1 - 10 Hz
Maximum Average Power	~ 1.5 W

* Fourier transform limited pulses in TEM 00 mode

Coherence and Linewidth Studies of a 4-nm High Power FEL*

W.M. Fawley and A.M. Sessler

Lawrence Berkeley Laboratory, University of California
Berkeley, CA 94720 USA

E.T. Scharlemann

Lawrence Livermore National Laboratory, University of California
Livermore, CA 94550 USA

Abstract

Recently the SSRL/SLAC and its collaborators elsewhere have considered[1] the merits of a 2 to 4-nm high power FEL utilizing the SLAC linac electron beam. The FEL would be a single pass amplifier excited by spontaneous emission rather than an oscillator, in order to eliminate the need for a soft X-ray resonant cavity. We have used GINGER, a multifrequency 2D FEL simulation code, to study the expected linewidth and coherence properties of the FEL, in both the exponential and saturated gain regimes. We present results concerning the effective shot noise input power and mode shape, the expected sub-percent output line widths, photon flux, and the field temporal and spatial correlation functions. We also discuss the effects of tapering the wiggler upon the output power and line width.

I. Introduction

The free-electron laser (FEL) has an attractive feature of being tunable over a fairly extensive operating range in wavelength. For the VUV and soft x-ray regions of the spectrum, FEL's may offer brightnesses many orders of magnitude larger than existing lasers and synchrotron light sources, presuming that GeV-energy beams of relatively high currents (≥ 1 kA) and low emittance ($\epsilon_n \leq 10$ mm-mrad) are available. Recently workers at SSRL/SLAC and collaborators elsewhere have suggested using the SLAC linac electron beam in a single-pass FEL amplifier excited by spontaneous emission to make an extremely high brightness laser (~ 10 GW peak power, 10^{18} photons/micropulse-mm²-mrad² peak brightness) in the 4-nm wavelength regime. For many applications, the output linewidth and mode shape are primary concerns since the spontaneous emission input "seed" is incoherent both temporally and spatially. In this work, we present results from a multifrequency 2D FEL simulation code that bear on these concerns. First, however, we review theoretical predictions by others for the predicted effective input power, gain lengths, saturated power, and linewidths for a

high gain, single pass amplifier relying upon self-amplified, spontaneous emission (SASE).

Many features of an FEL single-pass amplifier depend on the dimensionless FEL parameter[2][3][4] ρ given by

$$\rho^3 \equiv \frac{eZ_o J_o a_w^2 f_B^2}{16\gamma^3 k_w^2 m_e c^2} = \frac{\omega_p^2 a_w^2 f_B^2}{16\gamma^3 k_w^2 c^2} \quad (1)$$

where k_w is the wiggler wavenumber, a_w is the dimensionless wiggler vector potential, J_o is the current density, $Z_o \approx 377$ ohms, and f_B denotes the Bessel function coupling term for a linearly polarized wiggler. For most FEL's of interest, $\rho \sim 10^{-4} - 10^{-2}$ and is thus a small parameter; the proposed 4-nm SLAC FEL has $\rho \approx 1.5 \times 10^{-3}$. For cases where the diffraction length is much greater than the gain length, the peak growth rate for the power is $\Gamma_{max} \approx 4k_w \rho x_m$ where $x_m = \sqrt{3}/2$ for the limiting case of no energy spread, and approximately $\sqrt{\rho/(\Delta\gamma_{eff}/\gamma)}$ when $\Delta\gamma \geq 2\rho\gamma$. Here $\Delta\gamma_{eff}$ is the total "effective" energy spread (i.e. true spread plus the equivalent spread introduced due by non-zero transverse emittance and external focusing effects). Saturation (due to the energy spread exceeding $\rho\gamma$) occurs at a total power[2]

$$P_{sat} \approx \rho P_{beam} \quad (2)$$

For the particular case of a SASE FEL, Kim[5] predicts that after the necessary 2-3 gain lengths for exponentially growing modes to dominate over decaying and oscillatory modes, the spectral intensity has an rms width

$$\Delta\omega/\omega_o \approx (9\rho/2\pi\sqrt{3}N)^{1/2} \quad (3)$$

where N is the number of wiggler periods, $k_w z/2\pi$. The effective input power produced by shot noise is

$$P_{in} \approx \rho^2 \gamma m_e c^2 \frac{\omega_o}{2\pi} \quad (4)$$

Ref. [5] also predicts domination by a single transverse mode with full transverse coherence for most cases of interest and that the spectral bandwidth at saturation is

$$\Delta\omega/\omega_o \approx 1/N_{sat} \approx \rho \quad (5)$$

Beyond saturation one can extract, in theory at least, additional power by tapering the wiggler (e.g. reducing a_w). To the best of our knowledge, there are no quantitative predictions as to the behavior of the spectral bandwidth in a SASE-dominated FEL beyond saturation; i.e. in the non-linear regime.

*This work was supported at LBL by the Director, Office of Energy Research, Office of Fusion Energy and Office of High Energy and Nuclear Physics, U.S. Department of Energy, under Contract No. DE-AC03-76SF00098 and at LLNL under contract W-7405-ENG-48.

Table 1. Parameters and Simulation Results

Standard parameters: $\gamma = 1.37 \times 10^4$ $\Delta\gamma = 5.48$ $\varepsilon_n(\text{rms}) = 3.0 \text{ mm-mrad}$ $a_w = 4.13$ $\lambda_w = 83 \text{ mm}$										
Input & Predicted					Simulation Results					
I_{beam}	ρ	$1/\rho$	P_{in}	ρP_{beam}	dim.	N_{sat}	P_{in}	P_{sat}	$\tau_{1/2}$	$\Delta\omega/\omega_0$
0.5 kA	9.83×10^{-4}	1015	81 W	3.4 GW	1D	1000	110 W	4.8 GW	3.3 fs	7.6×10^{-4}
0.75 kA	1.13×10^{-3}	885	110 W	5.9 GW	1D	850	140 W	6.2 GW	2.4 fs	1.1×10^{-3}
1.0 kA	1.24×10^{-3}	806	130 W	8.7 GW	1D	745	200 W	8.8 GW	2.5 fs	1.0×10^{-3}
2.5 kA	1.68×10^{-3}	595	240 W	29 GW	1D	565	300 W	32 GW	1.6 fs	1.6×10^{-3}
					2D	865	160 W	17 GW	2.7 fs	9.3×10^{-4}

II. Simulation Code Description

GINGER [6] is a 2D, time-dependent particle simulation code directly descended from the LLNL FEL-simulation code, FRED [6]. Like FRED, it models single-pass amplifiers and follows electron motion in all three dimensions. The electromagnetic field is presumed to be axisymmetric and, as is generally done, to be composed of a "slow" temporal modulation of the "fast" time behavior of the fundamental mode [$\propto \exp(-i\omega_0 t)$]. Within GINGER itself, all quantities are followed in the time domain - decomposition into frequency components is done only as a diagnostic by a postprocessor code. Both the electron beam and EM field are divided into longitudinal slices in time (generally 128 in number for this investigation). As the electron-beam slices move through the wiggler, they "slip" behind the optical-field slices due to their slightly lower longitudinal velocity. For these runs, both the beam and field were assumed to be periodic in time, with a period more than twice that of the total slippage time over the full wiggler length of 83 m. Since the expected correlation time is less than one-quarter the slippage time ($= 13 \text{ fs}$), we do not believe that the adoption of periodic boundary conditions has led to significant, unphysical effects.

The initial "seed" for the SASE runs presented here was shot noise, which is modeled by adding the appropriate random $\delta\psi$ and δx to the particles's initial uniform longitudinal phase and transverse coordinates respectively.

In order to minimize CPU time, most runs were done in an "1D" mode where both the EM field and beam current are modeled by their on-axis densities. These runs are useful in checking the theoretical results summarized in the Introduction, but neglect effects such as diffraction, emittance, and betatron motion which may play an important role in restricting $\Delta\omega/\omega_0$.

III. Results

We did a series of 1D GINGER simulations, varying the current from 2.5 kA to 0.5 kA keeping all other parameters constant (see Table 1). We adopt, as a "standard case", the parameters of Ref. [1]; namely, $I_b = 2.5 \text{ kA}$ and

$\varepsilon_n(\text{rms}) = 3.0 \text{ mm-mrad}$. The rms beam radius of $66 \mu\text{m}$ corresponds to that expected from external quadrupole focusing with $\beta = 10 \text{ m}$. Note that this focusing is much greater than the "natural" wiggler focusing. Save for the lowest current density run, saturation occurred well within the chosen wiggler length of 83 m. Plots of the spectral power density show a Gaussian distribution with a width decreasing with increasing z until saturation, as predicted by [5] and others. To measure quantitatively the narrowing of the spectrum, we have computed the temporal autocorrelation function $C(\tau)$. Defining $\tau_{1/2}$ as the point at which $C(\tau)$ falls to a value of 0.5, a Gaussian spectrum distribution of width $\Delta\omega$ will follow

$$\Delta\omega/\omega_0 \approx 1.18/\omega_0\tau_{1/2} \quad (6)$$

When the autocorrelation decreases exponentially[7] [i.e. $C(\tau) \propto \exp(-\tau/\tau_c)$], the numerical factor increases to ≈ 1.39 . Table 1 presents values for $\tau_{1/2}$ and $\Delta\omega/\omega_0$ for the various 1D runs, together with the predicted [c.f. Eq.(4)-(5)] and measured values of the effective input power, saturated power and N_{sat} . In general, there is very good agreement between the measured and predicted values, and, furthermore, the growth of $\tau_{1/2}$ with z , as shown in Fig. 1, also confirms the predictions of Eq. (3).

A limited number of 2D GINGER simulations, which include both diffraction and the increased effective energy spread from beam emittance and external focusing, were done for the standard case. The results (see the last row of Table 1) showed larger required distance for saturation, lower saturated power, and reduced spectral bandwidth. The 2D runs shows transverse coherence being established rapidly (e.g. within a couple of gain lengths) and excellent optical beam quality at saturation (Strehl ratios of 0.98 or greater). Diffraction (the Rayleigh range is only $\approx 2 \text{ m}$) plays a key role in narrowing the gain curve and thus determining the output spectrum. Fig. 2 shows the spectrum at saturation; since this corresponds to only $\approx 25 \text{ fs}$ of a 150-fs micropulse, one should do a mental "ensemble" average of $P(\lambda)$ to obtain a more realistic estimate of the spectral profile. A second 2D run increased the external focusing by a factor of two (i.e. $\beta = 5 \text{ m}$), thereby decreasing the electron beam area and Rayleigh range by the same factor. The saturated power increased to 27 GW, nearly the

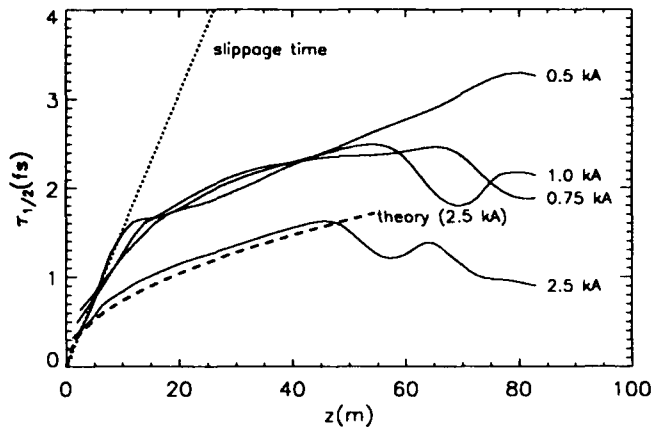


Figure 1: The autocorrelation time $\tau_{1/2}$ versus z for different beam current values; the data are from 1D simulations. The region to the upper left of the dotted line label "slippage time" is forbidden due to causality. The dashed line labeled "theory" corresponds to Eq. (3) and (6).

same as the standard case 1D run, but $\tau_{1/2}$ decreased (to 1.8 fs). Reducing β further to 3 m led to no further power gain but, beginning near the saturation point of $z = 50$ m, the transverse mode quality began to decrease rapidly. As a side note, *monochromatic* 2D runs initiated with 160 W of field power produced saturated powers of 15 GW for the standard case for $\beta = 5$ and 10 m.

We also ran a few 1D simulations with tapered wigglers, in which a_w was appropriately reduced with z to keep a design particle ($\psi_r \equiv 0.35$) at a constant longitudinal phase. Although the output power at $z = 83$ m increased significantly (300 GW for $I_{beam} = 2.5$ kA, 40 GW for 1.0 kA), the output spectral bandwidth increased by 30% or greater compared with the values at power saturation to the untapered wiggler cases. Some of this increase may be due to the peak of the gain curve shifting in wavelength from the nominal value of 4 nm in the untapered regime; this shift might be prevented by a "better" tapering strategy. On the other hand, we have seen no evidence from these 1D simulations that the bandwidth *decreases* from its minimum value at saturation.

IV. Discussion

The results from our simulations confirm the previous theoretical predictions concerning required saturation length, saturated power, and spectral bandwidth for a single-pass FEL amplifier initiated by SASE. Although the predicted power at saturation for a full 2D run is $\approx 40\%$ less than that from 1D theory, this bad news is partially ameliorated by a simultaneous 40% decrease in output spectral bandwidth. If it is desirable for particular applications to reduce ω/ω_o further, it may be necessary to reduce I_b since $\omega/\omega_o \sim \rho \sim I_b^{1/3}$. This would have the consequence of reducing P_{sat} which scales as $I_b^{4/3}$ for an

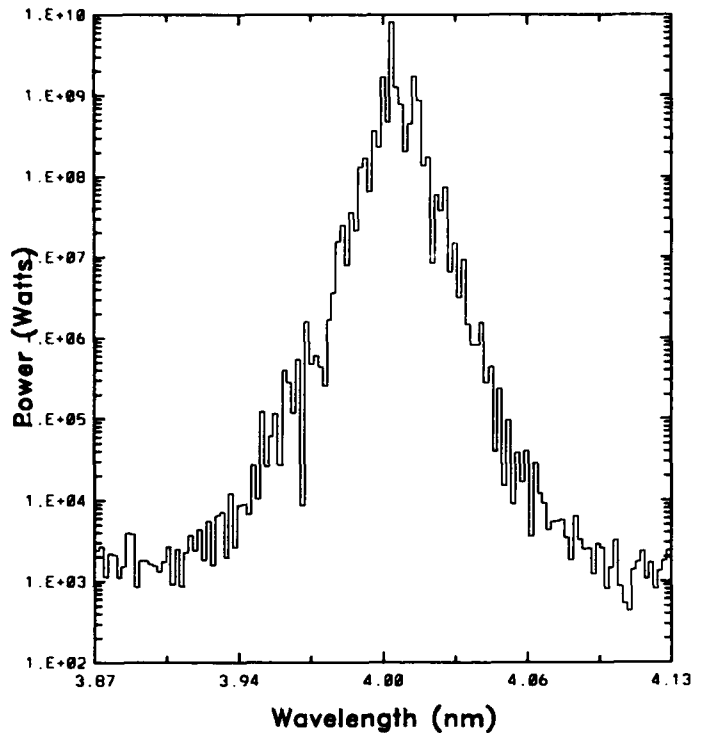


Figure 2: The spectrum at saturation from a 2D GINGER simulation for the "standard case". The power is binned into wavelength intervals of .002 nm.

untapered wiggler. Tapering may restore much or all of this lost power while keeping the bandwidth small, but we caution that the output power and electric field is expected to be "spiky" in time (rather than in optical phase which is more common for many chemical lasers). This spikiness might preclude certain applications. Both these changes (lower I_b , tapering) will, of course, require a longer wiggler.

References

- [1] C. Pellegrini *et al.*, "A 2- to 4-nm High Power FEL on the SLAC Linac", *Proceedings of the 14th International FEL Conference*, to be published 1993.
- [2] B. Bonifacio, N. Narducci, and C. Pellegrini, *Opt. Commun.*, **50**, 373 (1984).
- [3] L.H. Yu, Krinsky, S., Gluckstern, R.L., *Phys. Rev. Lett.*, **64**, 3014 (1990).
- [4] Chen, Y-H., Kim, K-J., Xie, M., *Nucl. Inst. & Meth. Phys. Res.*, **A318**, 481 (1992).
- [5] K. Kim, *Phys. Rev. Lett.*, **57**, 1871 (1986).
- [6] R.A. Jong, W.M. Fawley, E.T. Scharlemann, "Modeling and Simulation of Laser Systems", *SPIE 1045*, 18 (1989).
- [7] Yariv, A, *Optical Electronics*, 3rd ed. (Holt-Rinehart, New York, 1985), pp. 327ff.

Performance Characteristics, Optimization, and Error Tolerances of a 4nm FEL Based on the SLAC Linac

K.-J. Kim, M. Xie

Lawrence Berkeley Laboratory, University of California, Berkeley, CA 94720

E. T. Scharlemann

Lawrence Livermore National Laboratory, Livermore, CA, 94550

C. Pellegrini and G. Travish

Department of Physics, University of California, Los Angeles, CA 90024

Abstract

A 4nm free electron laser (FEL) operating in Self Amplified Spontaneous Emission (SASE), and using the SLAC linac as a driver has been extensively studied using the FRED3D[1] and TDA3D[2] codes. Using a 7 GeV beam with a normalized rms emittance of 3 mm-mrad and a peak current of 2500 A, obtained by longitudinal bunch compression, the FEL can provide about 20 GWatt of peak power, in a subpicosecond pulse. The FEL saturation length is about 60 m. Strong focusing in both planes is provided throughout the undulator by a FODO quadrupole system. We have studied the system gain, its optimization and FEL tolerance to beam parameter changes, wiggler errors and misalignments.

Introduction

The promise of producing bright, coherent, short wavelength XUV and X-ray radiation has yet to be fulfilled. Free electron lasers have long been touted as the right tool for this task. Yet, in the nearly twenty years since the first operation of the FEL, the short wavelength challenge has not been met because of the limitations on beam brightness. Now it seems possible to produce copious amounts of short wavelength radiation using technology developed in the last few years [3,4,5]. The primary distinguishing feature of this device is the electron beam. A high current, low emittance (high brightness) beam produced by an RF photocathode gun is accelerated to high energy (multi GeV) using a portion of the SLAC linac. This beam is what distinguishes this design from other potential x-ray FEL schemes [6].

A large parameter space was explored in order to optimize the FEL. The constraints were to maximize the output peak power while restricting beam and undulator parameters to state of the art. A three dimensional analytic model [7] was used to initially explore the parameter space while particle simulations were used to refine the choices. Table 1 lists a set of base parameters. Subsequent sections of this paper present FEL performance as functions of beam and undulator parameters. The main objective here is to establish the FEL tolerances with respect to changes in beam and undulator parameters and alignment errors.

Table 1: The base set of parameters for the SLAC based x-ray FEL.

γ	Energy (mc ²)	14000
ϵ_n	Emittance normalized (mm-mrad)	3×10^{-6}
	Peak Current (A)	2500
	Pulse Length (fs)	160
σ_E	Uncorrelated energy spread	4×10^{-4}
a_u	Undulator parameter	6
λ_u	Undulator period (cm)	8.3
λ_r	Optical wavelength (nm)	4
ρ	FEL parameter	1.7×10^{-3}

Beam Parameter Studies

The sensitivity of the FEL output to input beam parameters is paramount. The results presented below are given in terms of the power gain length, L_g .

$$P(z) = P_0 e^{z/L_g} \quad (1)$$

where P is the power as a function of the distance down the FEL, z , and P_0 is the input power. The effects of electron beam and undulator parameters on the FEL performance have been described by a 1-D model [3] and by a full 3-D analysis (reviewed in Ref. [5]).

Emittance

The usual constraint on the (unnormalized) beam emittance is that it be smaller than the wavelength of radiation divided by four pi ($\epsilon < \lambda/4\pi$). Typically, the gain length of a device starts to increase dramatically when this limit is violated. Conversely, when the emittance is reduced, the gain length shortens. The total output power at saturation is not dependent on the emittance until the limit is strongly violated. This last statement is true for a fixed strength (beta function) focusing channel. It is possible to optimize the focusing strength for a given emittance.

For the 4nm case of interest here, a normalized beam emittance of 4.5×10^{-6} mm-mrad is required by the limit. As Figure 1 shows, the power gain length increases rapidly after the limit is exceeded.

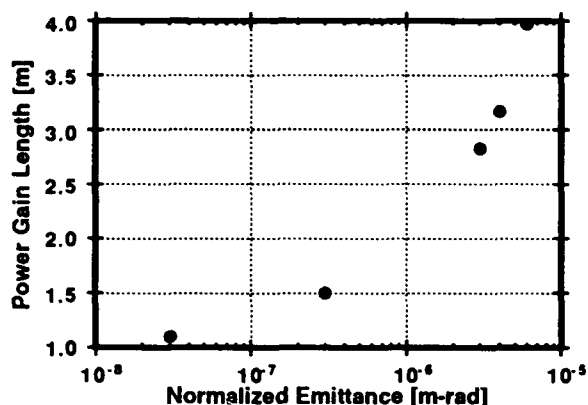


Figure 1: The power gain length for various emittances. Note that the emittance is a log scale.

Energy Spread

The energy spread is characterized in two ways: the correlated and the uncorrelated energy spread. FEL performance (gain length) is affected by the uncorrelated energy spread which is primarily determined by the electron source. The theoretical limit is that $\sigma_E < \rho$. The transport line and bunch compressors must preserve the minimum uncorrelated energy spread. The correlated energy spread is determined by the bunch compressor system and wakefields in the linac [8]. The correlated energy spread affects the radiation bandwidth but not the gain length. Users and experiments have varying requirements on the output radiation line width. Some of these requirements can best be met by using optical methods such as monochromators near the experiment. Effects of the uncorrelated energy spread have been investigated in the range where $\sigma_E < \rho$.

As Figure 2 shows, the saturation levels are nearly equal for a wide range of energy spreads. However, the gain length is adversely affected by an energy spread much larger than specified by the base parameters.

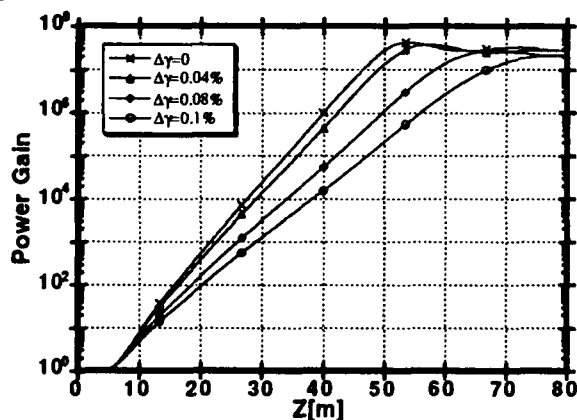


Figure 2: The power gain curves are shown as a function of the distance along the undulator for various uncorrelated energy spreads.

Beam Peak Current

Fluctuations in the electron beam peak current depend strongly on the pulse length and charge

variations. Not only does the source have to be stable, but so does the compression scheme. Hence, it is important that the FEL not be strongly sensitive to variations about the design current. Simulations reveal that, again at saturation, the output level is nearly identical for a wide range of currents (see Figure 3). Of course, the gain length varies with the current, but not so much as to pose a problem.

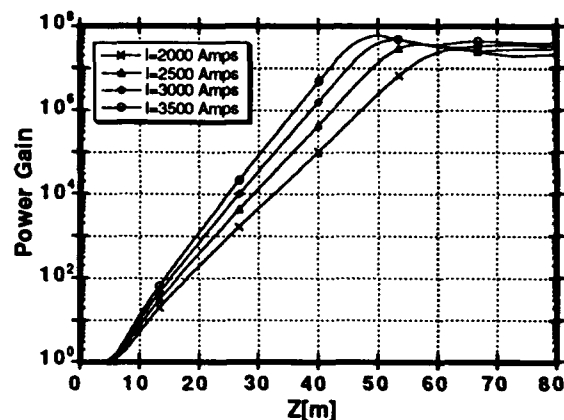


Figure 3: Power gain along the undulator for various peak beam currents.

Focusing

The SLAC X-ray FEL design calls for an undulator approximately 60 meters in length. The natural beta function of the undulator is 56 meters (and this is only in one plane) which gives a very large gain length. Additional focusing is required. Simulations show that there is substantial improvement for a beta function, β , ~ 10 meters and optimum performance for $\beta \sim 5$ meters [9]. This is in agreement with the theoretical limit that $\beta > L_g$. External quadrupole FODO lattice can provide beta functions of ~ 10 meters with conventional magnets. Performance for various drift and focusing lengths have been done. A period of 60 cm drifts and 60 cm quads seems close to optimal in terms of gain length and number of quads required. Numerous ideas have been reviewed in the course of this study. Extensive simulations have been performed on the various concepts [8]. Alternative schemes which might offer much higher field gradients (~ 50 - 100 T/m) are being investigated [10]. Such gradients would allow for beta functions of ~ 5 meters, closer to the optimal.

Undulator Tolerances

Propagation of an electron beam through a long undulator has already been proven [11]. The beam alignment required is proportional to the beam radius. As beam energy goes up, radius decreases. At ~ 7 GeV and 4 nm the beam radius is $\sim 50 \mu\text{m}$ and the required mechanical tolerances are $\sim 25 \mu\text{m}$, similar to those for the next linear collider [12]. The undulator must also satisfy tight magnetic tolerances.

Field Errors

Simulations have been performed using random walk models of undulator rms field errors. Errors in excess of 0.4% seriously degrade the output power (see Figure 4). The specified 0.2% tolerance is considered presently achievable. In fact, undulators meeting this requirement have already been constructed [13]. The question still remains whether rms errors are a figure of merit for free electron lasers. It is possible to construct undulators with large field errors and still achieve good lasing [14]. A more detailed study of field errors needs to be performed.

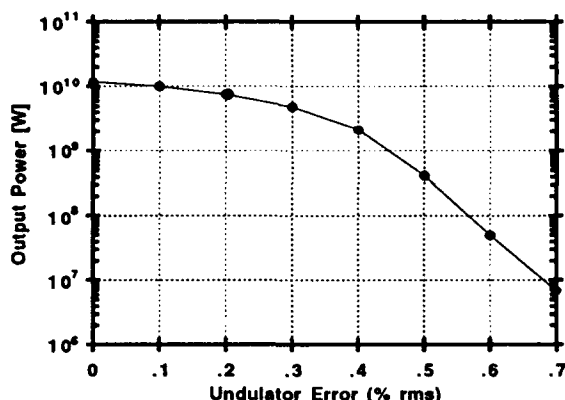


Figure 4: The output power as a function of the undulator field errors is plotted. A total (rms) steering accuracy of 30 μ m is assumed.

Steering Errors

Whereas field errors are a dubious measure of the quality of the undulator, the second integral of the field is generally considered a good measure. Steering errors can be corrected by judicious undulator construction as well as a combination of beam position monitors and coils.

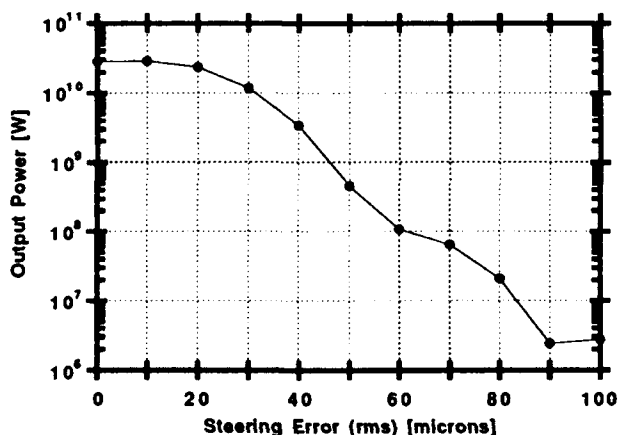


Figure 5: FEL output power as a function of the beam misalignment.

Simulations have shown that steering errors ~ 30 μ m can be tolerated. Figure 5 shown the FEL output for various steering and alignment errors when correctors are placed every 2 meters and a perfect undulator (no errors) is assumed.

Conclusions

The numerous simulations performed for the proposed SLAC based X-ray FEL have shown that the parameters chosen are stable to fluctuations in beam parameters and achievable with present state of the art accelerator, mechanical and magnetic technology. Further theoretical work needs to be performed to extend the 1-D theory of the start up and saturation regimes (see Ref. [5] for a review). Simulations of these regimes will require codes which include pulse length (time) effects.

Acknowledgments

We Thank Mark Hogan for his help in performing some of the simulation used for this paper. This work was supported by the US Department of Energy.

References

- [1] E. T. Scharlemann, et al., Jour. Appl. Phys **58** (1985) p. 2154.
- [2] T. M. Tran and J. S. Wurtele, Comput. Phys. Commun., **54** 263 (1989).
- [3] C. Pellegrini, "A 4 to 0.1 nm FEL Based on the SLAC Linac," Proceedings of the Workshop on Fourth Generation Light Sources (1992).
- [4] W. Barletta, A. M. Sessler and L.-H. Yu, "Using the SLAC Two-Mile Accelerator For Powering An FEL," Proceedings of the Workshop on Fourth Generation Light Sources (1992).
- [5] K.-J. Kim and M. Xie, Proceedings of 14 FEL Conference, Kobe, Japan (1992).
- [6] H. Winick, et al., "A 2-4 nm Linac Coherent Light Source (LCLS) Using the SLAC Linac," Proceedings this conference.
- [7] Y. H. Chin, K.-J. Kim and M. Xie, Phys. Rev. **A46**, 6662 (1992).
- [8] J. Seeman, K. Bane and T. Raubenheimer, "Electron Transport of a Linac Coherent Light Source (LCLS) Using the SLAC Linac," Proceedings of this conference.
- [9] See G. Travish and J. Rosenzweig, "Numerical Studies of Strong Focusing in Planar Undulators," Proceedings of this conference.
- [10] R. Tachyn, "Permanent Magnet Edge-Field Quadrupoles As Compact Focussing Elements For Single-Pass Particle Accelerators," SLAC-PUB-6058.
- [11] The Advanced Test Accelerator at LLNL operated the 25 m Paladin FEL.
- [12] R. B. Plamer, SLAC-PUB 4295 (1987).
- [13] The UCLA-Kurchatov Hybrid undulator has a period of 1.5 cm a peak field ~ 7.25 kG and a peak field error of <0.25%. Third generation light sources have similar tolerances for their insertion devices.
- [14] Private communication, Cliff Fortgang (Los Alamos National Laboratory).

X-Ray Beam Lines and Beam Line Components for the SLAC Linac Coherent Light Source (LCLS)*

R. Tatchyn and P. Pianetta

Stanford Linear Accelerator Center, Stanford, CA 94305, USA

Abstract

The LCLS is a novel high-brightness x-ray source designed to operate in the 300-400 eV range. In contrast to conventional synchrotron radiation sources, its output pulses will be characterized by unprecedented levels of brevity and peak power. In this paper we present recently-developed beam line layouts and design features intended to optimize the delivery of the LCLS photons to various experimental stations.

I. INTRODUCTION

The LCLS, a Free-Electron Laser (FEL) operating in the Self-Amplified Spontaneous Emission (SASE) regime [1], is an intense novel x-ray source whose high-brightness, sub-picosecond pulses are expected to provide new research opportunities in a number of diverse areas of x-ray science and technology [2]. A brief list of selected output parameters is tabulated below.

Table 1
Nominal LCLS Output Parameters

1st Harmonic Wavelength (λ)	40Å-30Å
Peak Power (P_{peak})	10 GW
Beam Diam. (D_w) at Optics Locations	1mm-2mm
Full Pulse Duration ($\sqrt{2\pi}\sigma_\tau$)	0.5ps
Full Pulse Length	150 μ
Pulse Repetition Rate	120Hz
Energy per Pulse	$\approx 5\text{mJ}-10\text{mJ}$
Peak Power Density (Norm. Incidence)	$\approx 10^{16} \text{ W/m}^2$
Source Emittance (Diffraction Limited)	< 20Å-rad

Evidently, a number of these parameters represent extensions of conventional x-ray source characteristics (e.g., peak power and pulse length in 3rd Generation synchrotron storage rings [3]) by several orders of magnitude. The purpose of this paper is to describe design aspects of selected optical components and beam line systems that have been recently studied for delivering the LCLS output radiation to experimental users.

II. PEAK POWER DAMAGE LIMITATIONS

From Table 1 it is evident that a photon pulse at normal incidence can deposit of the order of 1eV per atom for

absorptivities [4] and penetration depths typical of solid state materials in the soft x-ray range. Since this level of energy loading can be shown to lead to the enhanced probability of lattice damage [5], an important stratagem for reducing it involves decreasing the angle of incidence, θ_i , on the optical surface in question. As shown in Fig. 1, this leads to the notion of employing multiple reflections at grazing incidence to deflect the LCLS beam into a desired angle θ_T . For

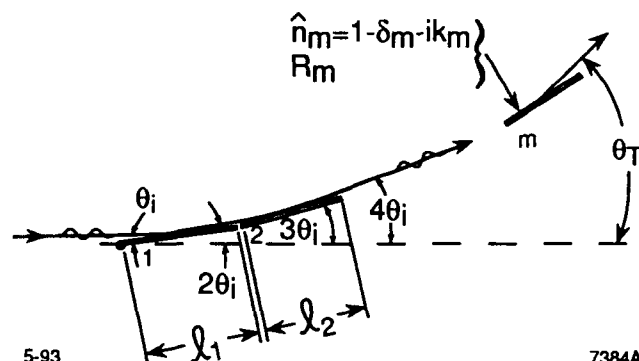


Figure 1. Parameters for multiple grazing-incidence reflection.

reflectors all with equal surface reflectivities R , indices of refraction $n=1-\delta+ik$, atomic densities [$\#/cm^{-3}$], and approximate (vertical) penetration depths δ_p ($\delta_p \approx \lambda/4\pi\sqrt{k}$), a useful figure of merit, η_A [eV/atom], can be defined [5] from which practical design parameters can be established:

$$\eta_A = \frac{P_{peak} \sqrt{2\pi}\sigma_\tau}{q} \left[\frac{\theta_i}{D_w^2} \right] \left[\frac{1-R}{\delta_p \#} \right] \ll 1. \quad (1)$$

Selecting $\eta_A \leq 0.01$, a criterion established by earlier experimental work at SSRL [6], acceptable grazing-incidence angles for Au (or Pt) reflecting surfaces of $\leq 34\text{mr}$ were arrived at. For future FEL sources with significantly greater levels of peak output power (e.g., tapered-wiggler FELs), the correspondingly smaller angles of incidence predicted by eq. (1) could imply impractically long optical surfaces and alternative methods of beam deflection and processing may need to be considered [7]. The second important peak power damage limitation of importance to the present study is associated with the intense electrostatic stresses that will be generated by photoemission from the LCLS optical surfaces. Preliminary assessments indicate that this will necessitate the use of metal substrates for both mirrors and gratings, (to minimize charge-neutralization intervals) and the elimination

* Supported by DOE Offices of Basic Energy Sciences and High Energy and Nuclear Physics and Department of Energy Contract DE-AC03-76SF0015.

of sharp-featured grooves or profiles on diffraction grating surfaces (to reduce the generation of high edge- field stresses).

II. BEAM LINE LAYOUT

As reported elsewhere, the presently proposed location for the LCLS undulator, electron beam dump, and beam lines is at the end of the Final Focus Test Beam (FFTB) enclosure at SLAC [1]. A 1st phase layout of the beam lines and experimental station locations is shown in Fig. 2. The 4° line

LCLS Beam Lines (Phase 1)

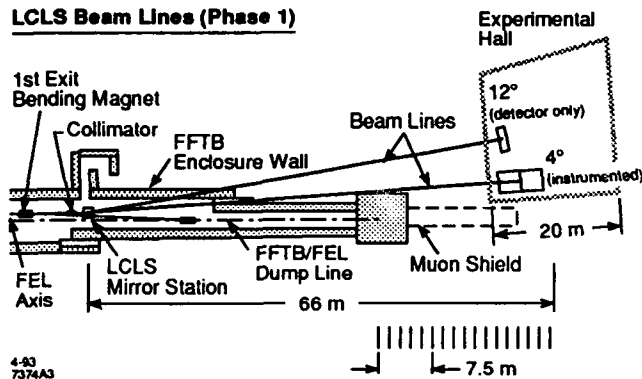


Figure 2. LCLS initial-phase beam lines.

line is planned as a flexible, fully-instrumented research and development facility capable of supporting a variety of initial or demonstration experiments. These will emphasize both basic science and technological applications [2], including the further development of optical instrumentation. The basic purpose of the 12° line will be to investigate beam-switching techniques and strategies that may be utilized in the future to accommodate larger numbers of user end stations. This line will be minimally instrumented, serving primarily to characterize the position and stability of the switched photons.

A more detailed layout indicating essential beam-transport, vacuum, mechanical stabilization, and optical components is shown in Fig. 3.

III. MECHANICAL AND OPTICAL DESIGN FEATURES

In view of the long distances involved, small mechanical perturbations of the mirrors will introduce appreciable deflections at the experimental locations. Active suppression of such deviations can be accomplished by detection followed by feedback and correction of the mirror chamber coordinates. Stabilization with respect to both low and high frequency motion (into the kHz regime) will be provided.

A major problem experienced by mirror surfaces in synchrotron radiation (SR) installations with vacuums in the $<10^{-9}$ Torr range is the gradual accumulation of carbon [8]. This problem will be compounded in the LCLS due to the fact that its operating energy lies near the carbon K-edge, and even marginal increases in absorptivity (as represented by the 1-R factor ineq. (1)), could lead to serious damage. In

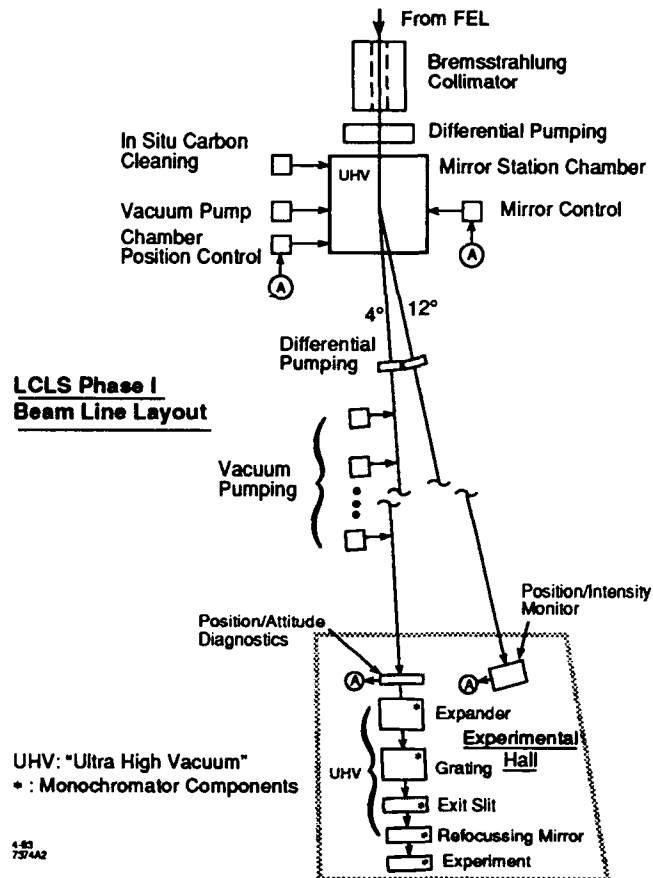


Figure 3. Beam line component layout in block form.

consequence, all of the LCLS sections containing optical surfaces will need to be maintained as Ultra High Vacuum (UHV) environments. Highly effective differential pumping sections will need to be used to help isolate UHV sections from higher-pressure transport ducts, and provisions for periodic in situ cleaning of mirror (Fig. 4) and grating

LCLS Beam Lines Mirror Station

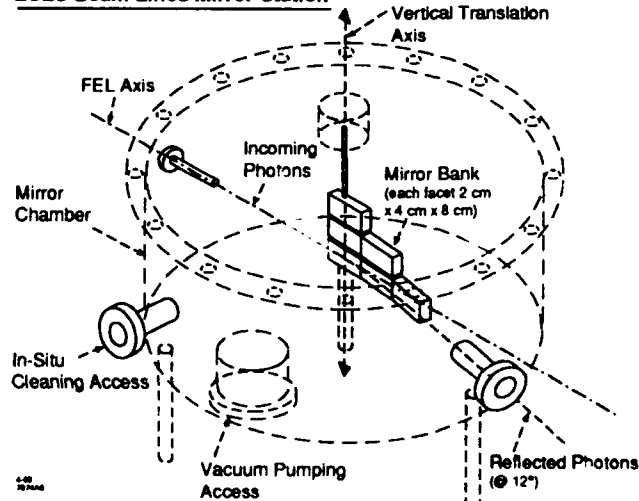


Figure 4. LCLS mirror station tank.

surfaces will need to be provided. Due to existing lack of experience with the effects of bremsstrahlung on the carbon contamination of surfaces, the installation of a special collimating aperture upstream of the mirror chamber has been proposed.

The mirror station, shown in Fig. 4, features multiple reflectors, vertically arranged to provide switching among different beam lines with a single vertical motion. The mirror facets have been made 4cm high to allow several successive vertical translations to unused portions of their surfaces in the event that the rate of surface damage is found to be severe. As may be deduced from Table 1, the time-averaged power impinging on each of the mirror surfaces is less than 1 Watt, and the expected absorbed power should ideally remain at 1-2 orders of magnitude below this. As a consequence, apart from providing adequate thermal conduction paths to the outside, no specialized heat-removal technology will need to be implemented. Regarding the mirrors, presently available polishing techniques can attain surface smoothness down to the 1-2Å level, which is significantly smaller than the LCLS operating wavelength. Apart from special surface contamination or damage effects, the mirror reflectivity should consequently be insensitive to surface-roughness scattering and should display its approximately ideal value.

The monochromator, in view of the unique spectral properties of the LCLS, allows for a number of novel approaches to its design. The most important simplifying advantage of the LCLS is that the emittance of its source point is, by definition, diffraction limited. This eliminates the need for initial optical processing of the radiation upstream of the monochromator entrance: the source point itself serves as the best possible entrance aperture. This type of design, in principle, allows the use of a single grating with an exit slit followed by a refocussing mirror, a configuration of minimal complexity. Due to the extremely small divergence angle of the LCLS beam, however, provisions have been allowed for expanding the beam prior to diffraction, in order to maximize the attainable resolution. A further refinement necessitated by the peak intensity of the radiation is the mandatory avoidance of diffraction gratings with sharp-featured groove profiles. Furthermore, diffraction with the grooves placed perpendicularly to the axis of the incoming light constrains the saliency of the (smoothed) grooves even further, since the incidence angle over the entire grating surface should be kept small enough to prevent all but negligible levels of absorption. These constraints have led to the consideration of a sinusoidally-profiled diffraction grating operating in a conical dispersion geometry [9] as perhaps the best candidate solution.

Apart from conventional design issues, further development work on the monochromator is anticipated due to fundamental performance limits stemming from the brevity of the LCLS pulses. In the limit where the photon pulse length begins approaching the coherence length of the monochromatized light, the resolving power of the monochromator becomes attenuated by the effective acceptance of its dispersion aperture [5,7]. This problem can

be mitigated by attempting to lengthen the photon pulses prior to diffraction, either by lengthening the electron bunch in the linac, or by optical means.

IV. ACKNOWLEDGMENTS

Valuable technical support and contributions to this project have been provided by David Lunt (Photon Sciences, Inc.) and Chris Sheppard and Kent Pflibson (Kaman Aerospace Corporation). Continuing support by the members of the LCLS research group is gratefully acknowledged.

V. REFERENCES

- [1] H. Winick, K. Bane, R. Boyce, K. Halbach, K.-J. Kim, G. Loew, P. Morton, H.-D. Nuhn, J. Paterson, C. Pellegrini, P. Pianetta, D. Prosnitz, J. Rosenzweig, J. Seeman, T. Raubenheimer, T. Scharlemann, R. Tatchyn, G. Travish, V. Vylet, M. Xie, "A 2-4 nm Linac Coherent Light Source (LCLS) Using the SLAC Linac," this conference - F7, 1993.
- [2] W. Spicer, J. Arthur, H. Winick, eds., Proceedings of the Workshop on Scientific Applications of Short Wavelength Coherent Light Sources, Stanford, CA, October 21, 1992, SLAC-Report-414, February 1993.
- [3] M. Cornacchia and H. Winick, eds., Proceedings of the Workshop on Fourth Generation Light Sources, SSRL, Feb. 24-27, 1992, SSRL Pub. 92/02, p. 86.
- [4] B. L. Henke, P. Lee, T. J. Tanaka, R. L. Shimabukuro, and B. K. Fujikawa, "The Atomic Scattering Factor, $f_1 + if_2$, for 94 Elements and for the 100 to 2000eV Photon Energy Region," AIP Conference proceedings No. 75, 340(1982).
- [5] R. Tatchyn, "LCLS Optics: Selected Technological Issues and Scientific Opportunities," Proceedings of the Workshop on Scientific Applications of Short Wavelength Coherent Light Sources, W. Spicer, J. Arthur, H. Winick, eds., Stanford, CA, October 21, 1992, SLAC-Report-414, February 1993, p. 93.
- [6] R. Tatchyn, P. Csonka, H. Kilic, H. Watanabe, A. Fuller, M. Beck, A. Toor, J. Underwood, and R. Catura, "Focusing of undulator light at SPEAR with a lacquer-coated mirror to power densities of 10^9 Watts/cm²," SPIE Proceedings No. 733, 368(1987).
- [7] R. Tatchyn, "Photon Pulse Filtering and Modulation Based on the Extreme Temporal Compression and Correlated Energy Spread of the Electron Bunches in the SLAC Linac Coherent Light Source (LCLS)," this conference - Mb28, 1993.
- [8] T. Koide, M. Yanagihara, Y. Aiura, S. Sato, T. Shidara, A. Fujimori, H. Fukutani, M. Niwano, H. Kato, "Resuscitation of carbon-contaminated mirrors and gratings by oxygen-discharge cleaning. 1: Efficiency recovery in the 4-40-eV range," Applied Optics 26(18), 3883(1987).
- [9] M. C. Hettrick and S. Bowyer, "Variable line-space gratings: new designs for use in grazing incidence spectrometers," Applied Optics 22, 3921(1983)

Photon Pulse Filtering and Modulation Based on the Extreme Temporal Compression and Correlated Energy Spread of the Electron Bunches in the SLAC Linac Coherent Light Source (LCLS)*

R. Tatchyn

Stanford Linear Accelerator Center, Stanford, CA 94305, USA

Abstract

The LCLS photon pulses are expected to attain unprecedented levels of brightness and brevity in the 300-400eV range. Nominally, the photon pulse length will be dominated by the electron bunch length, while the performance of conventional x-ray reflecting and band-shaping optics will be limited by: 1) peak power damage, and 2) transform-limited monochromatization. In this paper we describe how: 1) the correlated energy spread in the electron bunch can be used to selectably compress the LCLS photon pulses to below their nominal length; 2) gas optics can be used to mitigate peak damage problems; 3) the LCLS pulse structure can, in principle, accommodate schemes based on "disposable" optics; and 4) pulse lengthening schemes can be used to extend the attainable degree of monochromatization.

I. INTRODUCTION

A list of parameter values characterizing the coherent output photon pulses of the LCLS operated at $E=7\text{GeV}$ is given in Table 1 [1,2]. Based on current 3-dimensional models and analyses of the Self Amplified Spontaneous Emission (SASE) process [3] in a Free-Electron Laser, the photon bunch length is associated with the physical length

Table 1
LCLS Photon Output Parameters

1st Harmonic Wavelength (λ)	40Å-30Å
Peak Power (P_{peak})	10 GW
Beam Diam. (D_w) at Optics Locations	1mm-2mm
Full Pulse Duration ($\sqrt{2\pi}\sigma_\tau$)	0.5ps
Full Pulse Length	150 μ
Pulse Repetition Rate	120Hz
Energy per Pulse	$\approx 5\text{mJ}$
Peak Power Density (Norm. Incidence)	$\approx 10^{16} \text{ W/m}^2$

of an ultrashort electron bunch containing $0.5 \times 10^{10} - 10^{11}$ electrons (1-2nC). Due to the sensitivity of the FEL gain process to the local particle density in the bunch, however, it should be noted that further refinements in SASE models (or actual experimental measurements) may demonstrate a narrowing of the photon pulses to values significantly

smaller than those listed in the table.

An important property of the electron bunch accelerated through the linac is the development of an energy gradient (or "correlated energy spread") in the forward direction due to electrons in the front of the bunch loading the accelerating fields addressed by the trailing particles [4]. This energy spread is superimposed on the "uncorrelated" energy spread of the bunch characterized by its (stochastic) emittance parameters. For our purposes, we note that these energy spreads show up as, respectively, "inhomogeneous" and "homogeneous" line broadenings in the FEL photon pulse. Due to the γ^2 (or E^2) dependence of the FEL's output photon energy, these broadenings can be shown to appear with roughly twice the relative size in the photon spectrum as in the electron bunch energy.

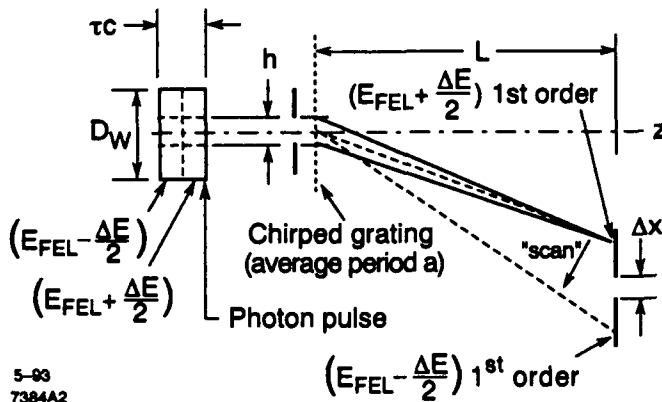
In a recent workshop [5] on selected scientific applications of the LCLS, attention was focussed on the unprecedented spectral and temporal parameter ranges of the LCLS for opening up new experimental possibilities. In this paper we review selected approaches for utilizing the cited and tabulated properties of the LCLS in conjunction with specialized techniques and instrumentation [6] to further extend the output parameter ranges and potential uses of this novel x-ray source.

II. LCLS PULSE COMPRESSION TECHNIQUES

Perhaps the most direct and effective approach to photon pulse compression would be to reduce the length of the linac electron bunches even further. As described elsewhere [7], electron bunch compression in the SLAC linac is already necessary for attaining the pulse lengths given in Table 1. Preliminary technical assessments of further applications of this technique indicate that another factor of 10 (viz., down to 50 fs) could perhaps be feasible [8]. This method, while non-trivial to implement, would evidently be the most attractive, since increasing the particle density will tend to amplify the FEL gain, leading to increased numbers of in-band photons. A less efficient, alternative method, based on utilizing the inhomogeneous energy gradient of the photon beam in the forward direction, could also be used to extract x-ray pulses from the LCLS with durations down to 50 fs and beyond. The procedure for accomplishing this, based on normal-incidence dispersion by a transmission grating with a chirped period a , is schematized at the top of Fig. 1. If we assume that the inhomogeneous energy spread in the photon pulse can be resolved into two levels, each associated with a distinct longitudinal region, it is apparent that the photons from the

* Supported by DOE Offices of Basic Energy Sciences and High Energy and Nuclear Physics and Department of Energy Contract DE-AC03-76SF0015.

lower-energy region will be dispersed into a larger angle than the ones from the forward region. As the dispersed photons "scan" away from the z axis, a suitably-sized aperture will segregate out a temporally -resolved subinterval of the initial pulse. Since the photons are extracted in a volume which is significantly truncated in both the x and z directions, and since the indicated diffraction will incur a 90%-95% loss into 1st order, it is evident that significant loss factors will be associated with the implementation of this technique. In Table



5-93
7384A2

Figure 1. Temporal pulse compression based on chirped photon energy in the source pulse.

2 we show some of the attainable pulse lengths (τ'), correlated and inhomogeneous energy spreads ΔE_{inh} and ΔE_{corr} , grating line densities (l/m), exposed lines N , and expected loss factors associated with compressing an 0.5ps LCLS pulse.

Table 2
 $D_W=0.001m$; $L=2m$; $\Delta E_{FEL}/E_{FEL}=0.001$

τ ps.	$h[m]$ $\times 10^{-5}$	N	l/m $\times 10^5$	$\frac{\Delta E_{inh}}{\Delta E_{FEL}}$	$\frac{\Delta E_{corr}}{E_{LINAC}}$	$\tau'[fs]$ $\times 10^1$	loss factor $\times 10^{-3}$
0.5	25	10	0.4	2	0.001	25	125
0.5	10	25	2.5	5	0.0025	10	20
0.5	5	50	10	10	0.005	5	5
0.5	2.5	100	40	20	0.01	2.5	1.25
0.5	1.25	200	160	40	0.02	1.25	0.31

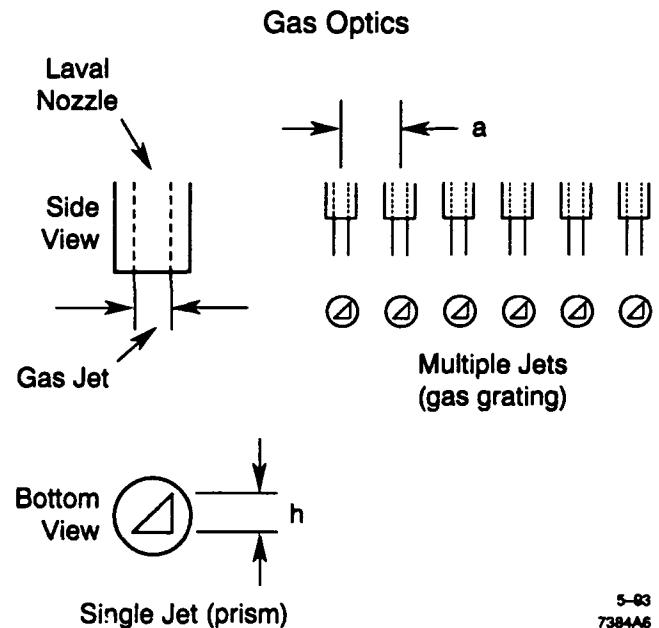
III. PEAK INTENSITY AND MATERIALS DAMAGE ISSUES

At normal incidence, it is easy to estimate from typical attenuation coefficients in the soft x-ray range [9] and Table 1 that 1 eV or more of energy can be deposited per atom in 0.5 ps. Keeping in mind that typical atomic or molecular lattice binding energies are of the order of 1 eV and considering the relative time constants and efficiencies of primary energy-removal channels, it can be argued [6] that

the probability of fragmentation must start becoming appreciable under the cited conditions. We can consequently expect enhanced probability of damage in solid state materials by the LCLS photons from two primary effects: 1) lattice disruption/ablation, and 2) photoemissively-generated field stresses.

An intuitively evident way to mitigate peak intensity damage is to dilute the energy deposited per unit area (and thereby per atom) by the artifice of grazing incidence. As described in a related paper [2], this approach has been used to generate a practical design for a mirror station for the LCLS. Nevertheless, future x-ray FEL configurations can be posited (e.g., the tapered wiggler) whose peak outputs may be too high to be adequately handled by solid-state specular reflection even at extreme grazing incidence. To this end, we consider two alternative options: 1) gas optics, and 2) disposable normal-incidence optics.

Two possible schemes utilizing gas optics are shown in Fig. 2. The first, a single-jet "gas prism" deflects the



5-93
7384A6

Figure 2. Gas jet configurations for x-ray deflection.

LCLS output beam by inducing a phase gradient in its wavefront, similarly to an ordinary optical prism. The major difference lies in the rather large differential attenuation accompanying the phase gradient, which can incur an appreciable intensity-loss penalty per degree of deflection. The second configuration is a multi-jet "gas grating" with period a , enabling a minimum deflection angle of λ/a to be attained. Here, however, the relative efficiency of the diffracted orders will be determined by the density contrast attained in the gas and the absolute efficiency by the average gas thickness, and it will be a difficult task to generate thin gas sheets with significant density or particle-number contrasts for grating periods extending down to 10μ and beyond. In either configuration, numerical studies indicate

relatively lossy and weak steering using low-Z neutral gases, including H₂. Although fully or partially ionized plasmas could offer more advantageous optical constants for effective beam steering, the preparation of sufficiently small and dense jets would in general be expected to be more difficult than with non-ionized gases.

Given these observations, we note that the relatively sparse pulse structure (120 Hz) of the LCLS can easily allow mechanical motion of optical surfaces and shutters over distances significantly greater than the beam waist to occur between pulses. This makes feasible the notion of using "disposable" optics at normal or near-normal incidence to deflect or otherwise process the LCLS beam. For example, with a beam spot size of 1 mm, we can estimate that if the 1 mm area of impact is totally obliterated by one pulse, we would require a renewal rate of the optical surface of about 1 m²/hour. For ultra-thin optics (e.g., zone plates or transmission gratings), suitably-placed rotating shutters could be used to effectively trap and collect the debris, and recovery and re-fabrication schemes could perhaps be developed to sustain economic feasibility.

IV. PULSE-LENGTH LIMITATIONS ON COHERENCE

Under the condition that the correlated and uncorrelated energy spreads in the electron bunch are equal, the FEL radiation spectrum will be broadened to more than twice its natural relative width. For larger correlated energy spreads the inhomogeneous broadening will be correspondingly greater. The present lack of detailed knowledge of the actual spread in the width of the LCLS pulses underscores the desirability of being able to monochromatize the emitted FEL photon pulses, and a number of important scientific applications such as, e.g., high-precision absorption or photoemission spectroscopy, will demand it.

Referring to Fig. 3, we note that conventional soft x-ray

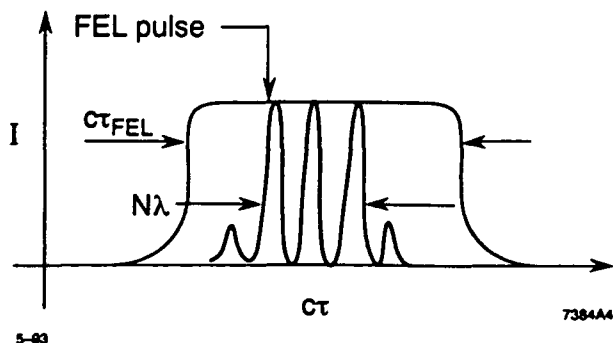


Figure 3. Total vs. coherence length of LCLS pulse.

monochromators usually process temporal pulses whose physical length (τc) is considerably longer than the coherence length ($N\lambda$) of the wave trains corresponding to their resolving power. For the LCLS, however, the pulse length could approach or even become smaller than this coherence length. For a monochromator with maximum

resolving power R_M , operating at normal incidence dispersion, the actual pulse-length-limited resolving power R can be expressed as

$$R = \left[\left(\frac{1}{R_M} \right)^2 + \left(\frac{\lambda'}{\pi} \right)^2 \right]^{-0.5}, \quad (1)$$

where $\lambda' = \lambda + (D_W a / 2L)$, D_W is the beam diameter, a is the grating period, and L is the dispersion length. Since variation of the monochromator parameters can at best be used to reduce λ' to λ , it is evident that the most effective way to maintain $R \rightarrow R_M$ is to lengthen the LCLS pulse. One way to accomplish this is to utilize the diffraction process itself, which lengthens the pulse diffracted into any order. By selecting a small fraction of the dilated pulse with suitable spatial and angular filtering, one can obtain an attenuated and dilated pulse suitable for further monochromatization. An alternative approach, which would also reduce the number of in-band photons (by reducing gain), would be to underutilize the compression stages in the linac to produce longer electron bunch lengths with smaller peak currents.

V. REFERENCES

- [1] H. Winick, K. Bane, R. Boyce, K. Halbach, K.-J. Kim, G. Loew, P. Morton, H.-D. Nuhn, J. Paterson, C. Pellegrini, P. Pianetta, D. Prosnitz, J. Rosenzweig, J. Seeman, T. Raubenheimer, T. Scharlemann, R. Tatchyn, G. Travish, V. Vylet, M. Xie, "A 2-4 nm Linac Coherent Light Source (LCLS) Using the SLAC Linac," this conference - F7, 1993.
- [2] R. Tatchyn and P. Pianetta, "X-Ray Beam Lines and Beam Line Components for the SLAC Linac Coherent Light Source (LCLS)," this conference - Mb29, 1993.
- [3] K. Kim, M. Xie, E. Scharlemann, C. Pellegrini, G. Travish, "Performance Characteristics, Optimization, and Error Tolerances of a 4-nm FEL Based on the SLAC Linac," this conference - Mb26, 1993.
- [4] R. B. Palmer, "Prospects for High Energy e+e- Linear Colliders," *Annu. Rev. Nucl. Part. Sci.* 1990.40:529-92.
- [5] W. Spicer, J. Arthur, H. Winick, eds., *Proceedings of the Workshop on Scientific Applications of Short Wavelength Coherent Light Sources*, Stanford, CA, October 21, 1992, SLAC-Report-414, February 1993.
- [6] R. Tatchyn, "LCLS Optics: Selected Technological Issues and Scientific Opportunities," *ibid.*, pp. 93-119.
- [7] J. Seeman, K. Bane, T. Raubenheimer, "Electron Transport of a Linac Coherent Light Source (LCLS) Using the SLAC Linac," this conference - Jb19, 1993.
- [8] T. Raubenheimer and K. Bane, private communication.
- [9] B. L. Henke, P. Lee, T. J. Tanaka, R. L. Shimabukuro, and B. K. Fujikawa, "The Atomic Scattering Factor, f1 + if2, for 94 Elements and for the 100 to 2000 eV Photon Energy Region," *AIP Conference Proceedings No. 75*, 340(1982).

Infrared (IR) vs. X-Ray Power Generation in the SLAC Linac Coherent Light Source (LCLS)*

R. Tatchyn

Stanford Linear Accelerator Center, Stanford, CA 94305, USA

Abstract

The LCLS, a Free-Electron Laser (FEL) designed for operation at a first harmonic energy of 300 eV ($\lambda = 40\text{\AA}$) in the Self-Amplified Spontaneous Emission (SASE) regime, will utilize electron bunches compressed down to durations of $<0.5\text{ps}$, or lengths of $<150\text{ }\mu$. It is natural to inquire whether coherent radiation of this (and longer) wavelength will constitute a significant component of the total coherent output of the FEL. In this paper a determination of a simple upper bound on the IR that can be generated by the compressed bunches is outlined. Under the assumed operating parameters of the LCLS undulator, it is shown that the IR component of the coherent output should be strongly dominated by the x-ray component.

I. INTRODUCTION

We are interested in estimating upper bounds on the coherent IR emission generated by the LCLS bunches as they pass through the LCLS undulator [1]. In preface, attempting to associate copious quantities of coherent radiation at wavelengths equal to or exceeding the bunch length might appear, *prima facie*, warranted. After all, there is a naive tendency to infer that if the emitted wavelength is longer than the entire bunch, the emission should be enhanced in proportion to the square of the number of particles in the bunch. In fact, as will be shown, for short-to-medium period insertion devices this inference can be justified only for suitably low values of the particle bunch energy; at ultrarelativistic energies relativistic effects serve to suppress the necessary coherent superposition to relatively small or even negligible values.

In addressing this problem we will employ: 1) the result that the total number of photons emitted by a physical system is a relativistic invariant, and 2) the relativistic Doppler shift relations, expressed in reference to Fig. 1 as

$$f = f' \gamma (1 + \beta \cos \theta') \quad (1)$$

and

$$\cos \theta = \frac{\cos \theta' + \beta}{1 + \beta \cos \theta'} \quad (2)$$

where $\beta \cdot c$ ($(\beta = 1 - (1 + K^2/2)/2\gamma^2)$, with K the undulator deflection parameter) represents the average speed of the electron bunch in the forward direction.

* Supported by DOE Offices of Basic Energy Sciences and High Energy and Nuclear Physics and Department of Energy Contract DE-AC03-76SF0015.

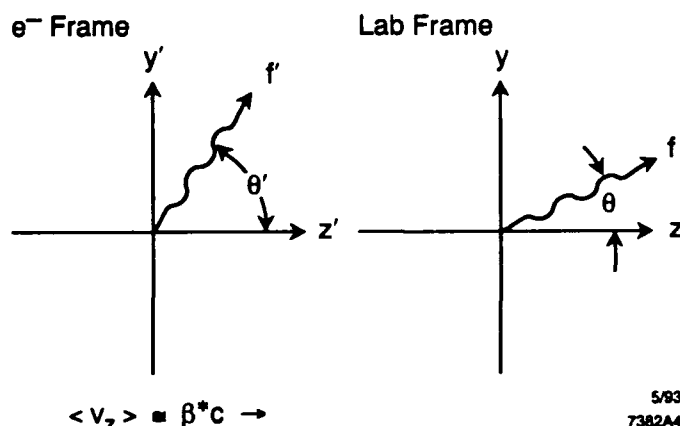


Figure 1. Monochromatic emission observed in electron and lab frames.

In Table 1, we list the physical parameters of the LCLS required for our analysis.

Table 1
Basic LCLS parameters for 40Å operation.

$(2\pi)^{0.5} \sigma_B$ (bunch length)	150 μ
N_C (total number of particles in bunch)	10^{10}
B (undulator field amplitude)	0.8T
λ_u (undulator period)	8cm
$K (=0.934B \lambda_u)$	6
L_u (undulator length)	60m
N_u (number of undulator periods)	750
E (electron energy)	7GeV
N_{SP} (total number of spontaneously emitted photons in 40Å equivalents per pulse)	3×10^{13}
N_{COH} (number of coherent x-ray photons per pulse)	10^{14}

II. ANALYSIS

Our basic approach to the problem will be to analyze the emission in question in the average rest frame (e-frame) of the electron bunch [2]. For low-to-moderate values of K , the dominant radiation component in the e-frame is a dipole pattern, as depicted in Fig. 2. We note that at the tabulated value of K the periodic electron motion in the e-frame will be relativistic. As a consequence, in addition to higher discrete multipole components stemming from K , there will also be a set of continuous spectral components arising from synchrotron radiation (SR) emitted by the circulatory motion of the electron in the e-frame [3]. However, the lowest spectral component will be the fundamental determined by the period of the undulator as observed in the e-frame, and it is this component that will dominate contributions to the IR

emissions in the lab frame.

Dipole Radiation Pattern ($K \ll 1$) vs Isotropic Intensity Distribution

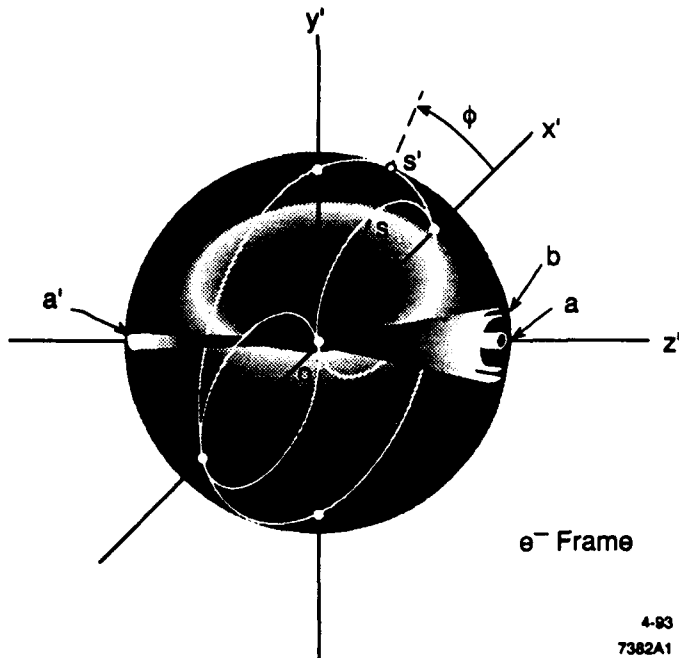


Figure 2. Dipole radiation pattern in the electron frame.

In the electron frame the undulator appears contracted by the factor $E/m_e c^2 (= \gamma)$, while the bunch is dilated by the same factor (see Fig. 3). The frequency of the fundamental in

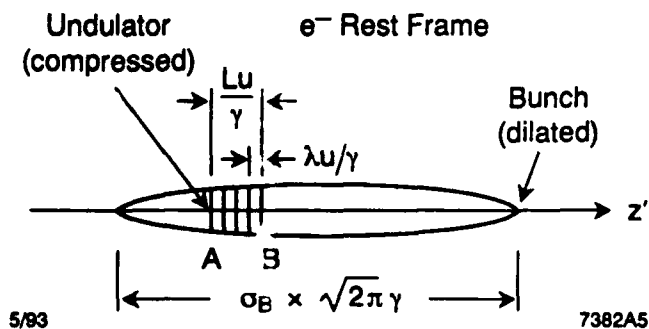


Figure 3. Relativistic scaling in the electron frame.

the e-frame is consequently given by $f = c \gamma / \lambda_u$. Assuming an approximately isotropic distribution in this frame, we use the Doppler relation (1) to identify the angle θ' at which f gets converted into the desired IR component in the lab frame. Specifically, we have

$$\frac{c}{\sqrt{2\pi}\sigma_B} = \left(\frac{c\gamma}{\lambda_u} \right) \gamma (1 + \beta \cos \theta'). \quad (3)$$

This transformation is depicted in Fig. 4. Using the parameter

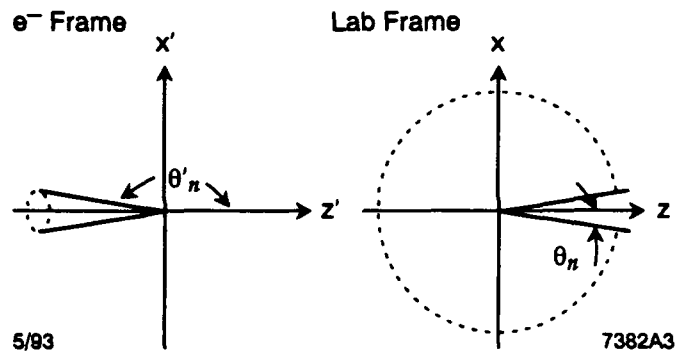


Figure 4. Transformation of the backward fundamental emission angle ($\pi - \theta'_n$) in the e-frame into the IR emission angle ($\pi - \theta_n$) in the lab frame. Radiation cones are defined by the dotted contours

values in Table 1, we find $\pi - \theta'_n = 2.34 \text{ mr}$ and, using eq. (2), $\theta_n = 0.264 \text{ r}$. As anticipated, the radiation that appears as IR of the desired frequency in the lab frame originates from a very small solid angle in the e-frame.

We next define the total number of spontaneously emitted photons per electron per each period of the undulator in the lab frame by the quantity $(N_{SP}/N_U N_C)$. Clearly, this number will be the same for each electron in the e-frame. Referring to Fig. 3 and assuming, for simplicity, a uniform density vs. z' , the total number of spontaneously emitted photons by the electron group traversed by one undulator period can be approximated by

$$f_1 = (N_C/f_2)(N_{SP}/N_U N_C), \quad (4)$$

with

$$f_2 = (2\pi)^{0.5} \sigma_B \gamma^2 / \lambda_u. \quad (5)$$

Next, the same group of electrons will emit the same number of photons N_U times, for a total number of $N_U f_1$ photons. Clearly, there are f_2 such groups in the entire bunch, and we consequently have $N_U f_1 f_2 = N_{SP}$, as expected.

Next, we define the fraction f_3 of these photons that are converted into the desired IR photons in the lab frame by referring to Figs. 2 and 4. Taking into account the geometry of the dipole pattern, we obtain

$$f_3 = (\pi - \theta'_n)^2 / 2. \quad (5)$$

We can now consider the effects of the FEL bunching process in enhancing the number of radiated photons in the e-frame. In Fig. 5 we depict the relative bunching (or phase coherence) of the electrons within each period of the undulator. Although it is evident that any group of electrons of the order of size of an undulator period doesn't attain full bunching until almost the entire undulator has passed over it, for our purpose of estimating upper bounds, we will assume that each such group is actually fully bunched, but that the radiation from the N_U individual groups is uncorrelated. This leads to the enhancement of the number of photons emitted by each group

by the factor N_C/f_2 , i.e., the number of photons becomes proportional to the square of the number of electrons in each group. Denoting the number of IR photons in the lab frame by

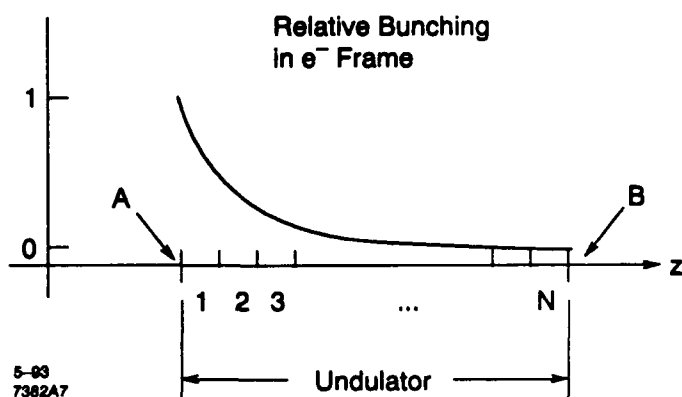


Figure 5. FEL bunching along undulator in electron frame.

N_{IR} , the resulting upper bound may be expressed as

$$\frac{N_{IR}}{N_{COH}} < \frac{N_C f_3}{f_2} \left\{ \frac{N_{SP}}{N_{COH}} \right\} = \frac{N_C (\pi - \theta_n)^2 \lambda_u}{2 \sqrt{2} \pi \sigma_B \gamma^2} \left\{ \frac{N_{SP}}{N_{COH}} \right\}. \quad (6)$$

Inserting the previously derived numbers for θ_n and the values from Table 1 yields $(N_{IR}/N_{COH}) < 0.022$.

III. DISCUSSION

We have derived an upper bound on IR emission from the LCLS for lab frame wavelengths equal to or greater than $(2\pi)^{0.5} \sigma_B (=150 \mu)$. This can be considered a weak upper bound, viable in the present case due to the strong suppression (by the relativistic f_3 (or $(\pi - \theta_n)^2/2$) factor) of the greatly overestimated coherent emission in the e-frame. While it is noteworthy that this upper limit is inversely proportional to σ_B , which indicates that IR emissions from the LCLS should remain perturbative on the coherent x-ray emission even for bunches down to 30μ long, we point out that for significantly smaller energies and/or bunches more than 10 times shorter our upper bound estimate should start being replaced with more comprehensive analytical calculations of the spontaneous and coherent radiation distributions.

It is of interest to inquire whether significant IR emission of the wavelength in question could in fact be induced by the LCLS, and under what conditions. The general criterion is straightforward, namely that the standard resonance condition, viz.,

$$\frac{\lambda_u}{2\gamma^2} \left(1 + K^2/2 \right) = \lambda \geq (2\pi)^{0.5} \sigma_B \Rightarrow \lambda_u \geq \frac{2(2\pi)^{0.5} \gamma^2 \sigma_B}{1 + (K^2/2)}, \quad (7)$$

be fulfilled. We can examine this criterion quantitatively by contrasting λ_u at the LCLS beam energy of 7GeV with bunch and energy parameters appropriate to a 40MeV short-bunch generation experiment planned at SSRL [4]. Table 2 shows

the relevant parameters.

Table 2

Undulator periods required for resonant IR emission @ $K=6$.

40MeV	7GeV
$(2\pi)^{0.5} \sigma_B = 12 \mu$	$(2\pi)^{0.5} \sigma_B = 150 \mu$
$\gamma = 80$	$\gamma = 13700$
$\gamma^2 = 6400$	$\gamma^2 = 1.9 \times 10^8$
$\lambda_u \geq 8 \text{ mm}$	$\lambda_u \geq 1185 \text{ m}$

This comparison dramatically illustrates the extent to which ultrarelativistic energies tend to suppress IR emission. At 7GeV, the LCLS undulator field structure, with its 8cm period, would need to contain significantly strong Fourier components of $>1\text{km}$ period to resonantly induce IR emission from the 150μ bunch (see Fig. 6). With reasonably careful design and alignment, such aberrations (represented in the figure by an impulsive offset associated with a non-zero 1st field integral) should not be overly difficult to suppress.

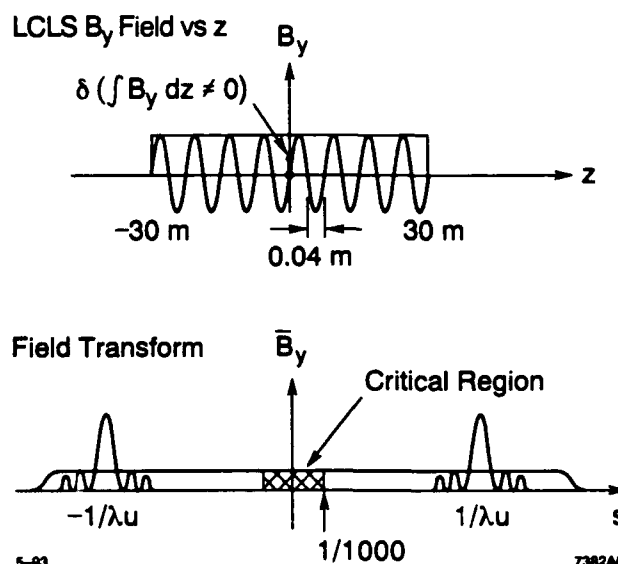


Figure 6. Fourier decomposition of undulator field along z .

VI. REFERENCES

- [1] H. Winick, K. Bane, R. Boyce, K. Halbach, K.-J. Kim, G. Loew, P. Morton, H.-D. Nuhn, J. Paterson, C. Pellegrini, P. Pianetta, D. Prosnitz, J. Rosenzweig, J. Seeman, T. Raubenheimer, T. Scharlemann, R. Tatchyn, G. Travish, V. Vylet, M. Xie, "A 2-4 nm Linac Coherent Light Source (LCLS) Using the SLAC Linac," this conference - F7, 1993.
- [2] R. Tatchyn and I. Lindau, "Off-axis radial properties of undulator light," SPIE Proceedings 733, 115(1987).
- [3] J. D. Jackson, *Classical Electrodynamics*, John Wiley & Sons, New York, 1975, Chapter 14.
- [4] H. Wiedemann, P. Kung, and H. C. Lin, "Ultra Short Electron and Photon Pulses," SSRL ACD-Note No. 116, November 11, 1991.

Saturation of a High Gain FEL*

R.L. Gluckstern[†], S. Krinsky[‡] and H. Okamoto[§]

Abstract

We study the saturated state of an untapered free electron laser in the Compton regime, arising after exponential amplification of an initial low level of radiation by an initially monoenergetic, unbunched electron beam. The saturated state of the FEL is described by oscillations about an equilibrium state. Using the two invariants of the motion, and certain assumptions motivated by computer simulations, we provide approximate analytic descriptions of the radiation field and electron distribution in the saturation regime. We first consider a one-dimensional approximation, and later extend our approach to treat an electron beam of finite radial extent. Of note is a result on the radiated power in the case of an electron beam with small radius.

I. INTRODUCTION

In this paper we study the saturated state of an untapered FEL in the Compton regime. Guided by the results of simulations starting with a monoenergetic unbunched electron beam and a low initial level of radiation, we make assumptions which prove to give an accurate picture of what happens in the saturation regime. The solutions in the saturation regime are related to the initial conditions by using the two invariants of the motion. Finally we extend our one-dimensional model to treat an electron beam of finite radial extent, including the effects of the diffraction of the radiation and the radiation focussing properties of the electron beam bunched by the FEL interaction. This work will be presented in greater detail[1].

The starting point of the analysis is the scaled equations for the evolution of the one dimensional electron distribution and for the monochromatic radiation field. The notation is that of Bonifacio et. al.[2] and the equations are

$$\frac{d\sigma_j}{d\tau} = p_j, \quad (1)$$

$$\frac{dp_j}{d\tau} = -Ae^{i\sigma_j} - A^*e^{-i\sigma_j}, \quad (2)$$

$$\frac{dA}{d\tau} = \langle e^{-i\sigma_j} \rangle + iA\delta, \quad (3)$$

where σ_j and p_j are the phase of the j^{th} electron relative to the radiation and its (scaled) momentum deviation, A is the (scaled) radiation amplitude at the (scaled) longitudinal position $\tau = 2\rho k_w z$, where $2\pi/k_w$ is the wiggler period and ρ is the Pierce parameter, δ is the detuning of the laser, and $\langle \rangle$ is an average over the electron distribution.

It is easy to show from Eqs. (1)-(3) that

$$\langle p_j \rangle + |A|^2 = C_1 \quad (4)$$

and

$$\frac{\langle p_j^2 \rangle}{2} + 2\text{Im}[A\langle e^{i\sigma_j} \rangle] - \delta|A|^2 = C_2 \quad (5)$$

are constants of the motion. For an initially monoenergetic unbunched electron beam and a low initial level of radiation, the constants C_1, C_2 are taken to be zero.

II. EQUILIBRIUM DISTRIBUTION

In Fig. 1 we show a typical evolution of the radiation with τ . The field builds up exponentially as the electrons bunch. After the bunched electrons are captured in buckets, the radiation oscillates with modest amplitude about an equilibrium distribution. The approximations in our model are to consider only up to linear terms in the amplitude of these oscillations, and to consider only the lowest harmonic frequency of these oscillations.

In Fig. 2 we show the phase of the radiation, which appears to be very nearly linear with τ . We therefore write

$$A = (P + iQ)e^{i\nu(\tau - \tau_0)} \quad (6)$$

and introduce the equilibrium displaced electron phase $\phi_j(\tau)$

$$\phi_j(\tau) \equiv \sigma_j + \nu(\tau - \tau_0) + \pi/2, \quad (7)$$

requiring ν to be chosen such that $\langle \phi_j' \rangle = 0$, where the prime stands for $d/d\tau$. For zero detuning $\delta = 0$, we find in the saturation regime that all quantities oscillate about an equilibrium state for which

$$P = P_0, \quad Q = 0, \quad \nu = P_0^2, \quad (8)$$

*Work supported by the Department of Energy

[†]University of Maryland, College Park, MD 20742

[‡]Brookhaven National Laboratory, Upton, NY 11973

[§]University of Maryland, College Park, MD 20742; on leave from: Institute for Chemical Research, Kyoto University, Japan

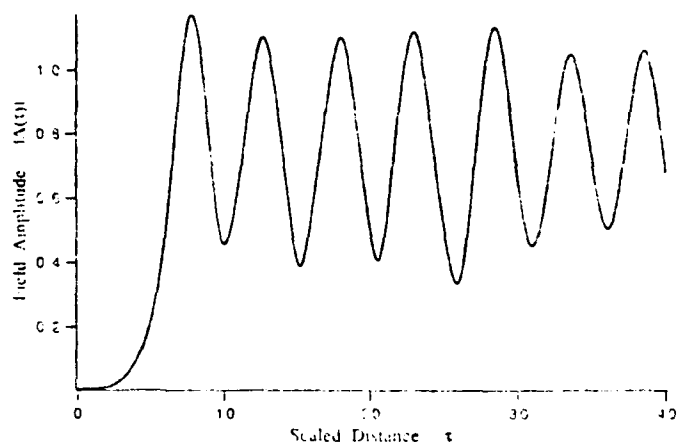


Figure 1: Evolution of radiation field amplitude $|A|$ with τ .

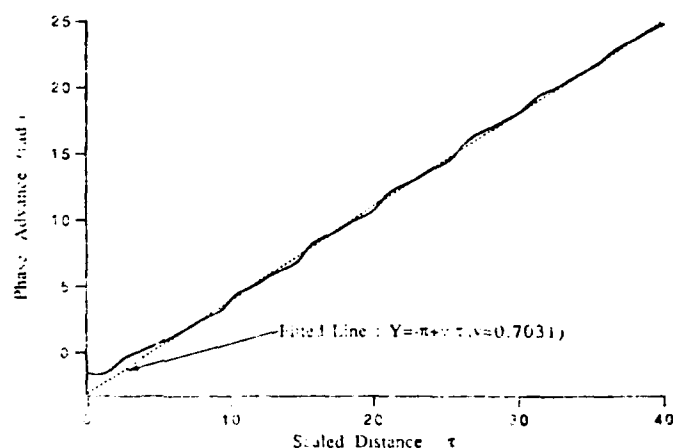


Figure 2: Phase of the radiation field as a function of τ .

$$\langle \cos \phi_j \rangle = P_0^3, \quad \langle \sin \phi_j \rangle = 0, \quad \langle \phi_j'^2 \rangle = 3P_0^4. \quad (9)$$

Equilibrium distributions satisfying the conditions in Eqs. (8) and (9) can be constructed as $f(\phi, \phi') = F(H)$, where

$$H = \phi'^2/2 - 2P_0 \cos \phi. \quad (10)$$

We have considered three widely different distributions

$$f_{KV} = N_{KV} \delta(H - H_0) \quad (KV)[3] \quad (11)$$

$$f_{-1/2} = N_{-1/2} (H - H_0)^{-1/2} \quad (12)$$

$$f_B = N_B \exp(-\alpha H) \quad (\text{Boltzmann}) \quad (13)$$

and find in all cases that $P_0 = 0.81$, in good agreement with Fig. 1. In Fig. 3 we show the three different distributions plotted as a function of H . And in Fig. 4 we show the electron distributions obtained from the simulations for $\tau = 20, 40$. The background from the electrons which are not trapped is seen to be more or less independent of H , and the distributions of the trapped electrons seems to most resemble the Boltzmann distribution.

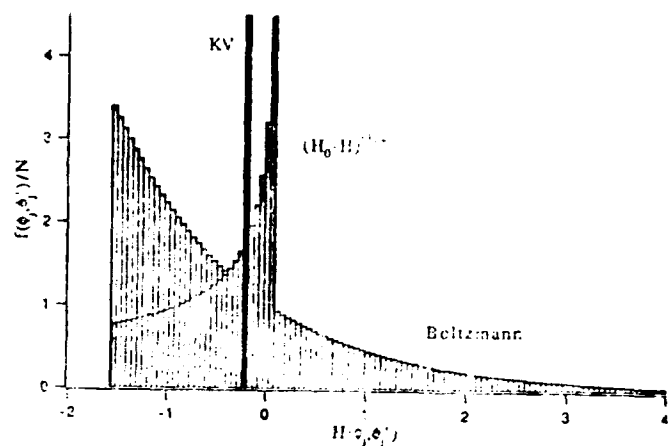


Figure 3: The three distributions, KV, $(H_0 - H)^{1/2}$ and Boltzmann plotted as functions of H defined in Eq. (10).

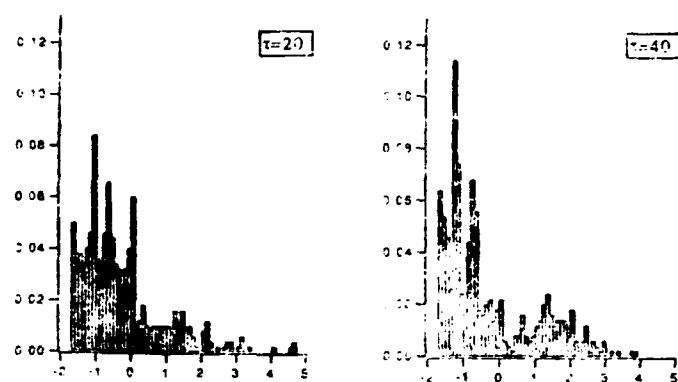


Figure 4: Electron distributions obtained from simulation for $\tau = 20, 40$ plotted as functions of H .

III. EXPONENTIAL GROWTH REGIME

If we take two derivatives of Eq. (3) and consider only those terms linear in p_j and A , we find, for $\delta = 0$

$$\frac{d^3 A}{d\tau^3} = iA. \quad (14)$$

The exponential growth regime then corresponds to the solution

$$A(\tau) \simeq A_0 \exp[(\sqrt{3} + i)\tau/2]. \quad (15)$$

When $|A(\tau)|$ is of order 1, non-linear terms in A, p_j must be included, and some sort of saturation will take place.

IV. SATURATION REGIME

The saturated state of the FEL is described by oscillations about an equilibrium state[4, 5, 6]. This equilibrium state corresponds to a steady state solution of Eqs. (1)-(3). The proper choice of the equilibrium solution is significantly restricted[4] by the two invariants of Eqs. (4) and (5), relating properties of the saturated state back to the initial conditions at the start-up of the FEL.

We now consider oscillations about the equilibrium distribution, defining the displaced electron phase as

$$\beta_j(\tau) = \sigma_j(\tau) + \nu(\tau - \tau_0) + \pi/2. \quad (16)$$

Using Eqs. (6) and (16), we now write, with $\delta = 0$,

$$\beta_j''(\tau) = -2P \sin \beta_j - 2Q \cos \beta_j \quad (17)$$

$$Q' + \nu P = \langle \cos \beta_j \rangle \quad (18)$$

$$P' - \nu Q = \langle \sin \beta_j \rangle \quad (19)$$

together with the two invariants

$$\langle \beta_j' \rangle + P^2 + Q^2 = \nu, \quad (20)$$

$$\langle \beta_j'^2 \rangle - 2\nu \langle \beta_j' \rangle + \nu^2 = 4P \langle \cos \beta_j \rangle - 4Q \langle \sin \beta_j \rangle. \quad (21)$$

We now consider oscillations about the equilibrium distribution of the form

$$P(\tau) = P_0 + P_1 \cos \Omega \tau, \quad Q(\tau) = Q_1 \sin \Omega \tau \quad (22)$$

$$\beta_j(\tau) = \phi_j(\tau) + a \sin \Omega \tau, \quad (23)$$

where the oscillation of the electrons is assumed to be coherent. Keeping only terms linear in P_1, Q_1 and a , we can show[1] that $\Omega = \sqrt{3}P_0^2 = 1.14$, slightly smaller than the value $\Omega = 1.25$ seen in the simulation in Fig. 1.

V. TRANSITION FROM THE EXPONENTIAL TO THE SATURATION REGIME

A plot of $dP/d\tau$ vs. $P(\tau)$ from the simulation shows a straight line starting at $(0,0)$, corresponding to the exponential regime, approximately tangent to a repeated elliptical orbit centered at $(0.8,0)$, corresponding to the oscillation in the saturation regime. Postulating this model of approximate tangency for the transition from the exponential to the saturation regime leads to the prediction of $P_1 \simeq 0.49, Q_1 \simeq 0.28$, somewhat larger than the values $P_1 \simeq .40, Q_1 \simeq .20$ seen in the simulations. Considering the crude nature of the transition model, this agreement is quite good.

VI. ELECTRON BEAM WITH FINITE RADIAL EXTENT

We now extend the single harmonic model considered above to the two-dimensional case of an electron beam with finite radial extent. We ignore betatron oscillations, assuming the electron beam has no angular spread, but include the diffraction of the radiation and the radiation focusing properties of the electron beam bunched by the FEL interaction.

The equations for the electron motion are still those in Eqs. (1) and (2). But Eq. (3) for the evolution of the radiation is now changed to

$$A' - i\nabla^2 A = u(r) \langle e^{-i\sigma_j} \rangle \quad (24)$$

where $u(r)$ is the fixed electron beam density profile. We also take $\delta = 0$. The form of the two invariants is also changed somewhat. The scaled transverse coordinate is $\mathbf{r} = \sqrt{4\rho k_w k_s} \mathbf{r}_d$ where k_s is the resonant radiation wave number and \mathbf{r}_d is the unscaled transverse coordinate vector.

The equilibrium state is now governed by the solution of the differential equation

$$\nu P_0 - \nabla^2 P_0(r) = u(r) \langle \cos \phi_j \rangle, \quad \langle \sin \phi_j \rangle = 0 \quad (25)$$

and the modified invariants lead to

$$\nu = \frac{\int_0^\infty r dr P_0^2(r)}{\int_0^\infty r dr u(r)},$$

$$\nu^2 = \frac{\int_0^\infty r dr u(r) \langle \phi_j'^2 - 2P_0 \cos \phi_j \rangle}{\int_0^\infty r dr u(r)}. \quad (26)$$

Explicit relations can now be obtained for these parameters with the specific phase space distributions $f_a(H), b_b(H), f_c(H)$, and for a given beam profile $u(r)$.

As a result of this analysis, we obtain an equilibrium guided solution and oscillations about this solution. There are two types of oscillation modes, one guided and one corresponding to radiation propagating to $r = \infty$. The escape of the radiation from the electron beam leads to a damping of the oscillations. Also, explicit results have been obtained[1] in the limits of large and small electron-beam radius. In particular, we find that, for small beam radius, the radiated power is proportion to $I_0^{3/2}$ where I_0 is the current. This result is intermediate between the incoherent (I_0) and fully coherent (I_0^2) limits.

References

- [1] R.L. Gluckstern, S. Krinsky and H. Okamoto, to be published in Phys. Rev. E, June 1993.
- [2] B. Lane and R.C. Davidson, Phys. Rev. A **27**, 2008 (1983).
- [3] Kapchinsky and Vladimirskiy first introduced the δ -function distribution in H for use in two-dimensional transverse beam dynamics with space charge. See, for example, I.M. Kapchinskiy, *Theory of Resonance Linear Accelerators* (Harwood Academic, New York, 1985), p. 247ff (translated from the Russian).
- [4] B. Lane and R.C. Davidson, Phys. Rev. A **27**, 2008 (1983).
- [5] R.C. Davidson and J.S. Wurtele, Phys. Fluids **30**, 557 (1987).
- [6] W.M. Sharp and S.S. Yu, Nucl. Instrum. Meth. A **272**, 397 (1988); Phys. Fluids B **2**, 581 (1990).

Numerical Studies of Strong Focusing in Planar Undulators

G. Travish and J. Rosenzweig
Department of Physics,
University of California, Los Angeles, CA 90024

Abstract

The present trend towards short wavelength operation with long undulators places tight requirements on the electron beam quality and hence the need to maintain a well focused beam. This paper examines the performance of alternating gradient (AG) sextupole focusing in planar undulators [1]. Numerical simulation results of Free Electron Laser (FEL) performance using AG sextupole focusing are compared to results using only natural focusing and to those using quadrupole focusing.

Introduction

Free Electron Laser performance is affected by the overlap (in six dimensional phase space) between the electron beam and the optical beam. The extent of overlap (assuming perfect alignment) is dependent on electron beam size, emittance and energy spread and optical beam size and Rayleigh range. In general, the brighter the electron beam, the better the FEL performance. The electron and optical beam overlap is maintained by the well known optical guiding phenomenon. However, without focusing the electron beam diverges. When the electron beam density is reduced, FEL performance is degraded. Hence, maintaining a focused electron beam over the distance of the FEL undulator is paramount to high FEL performance. Obviously, for a given beam, the longer the undulator the more significant focusing becomes. Recent proposals for short wavelength devices have called for long undulators from 25 to over 60 meters long.

It is possible to make some simple quantitative statements about how electron beam focusing affects FEL performance. For a high gain (exponential regime) amplifier, the power output can be written as

$$P(z) = P_0 e^{z/L_g} \quad (1)$$

where P_0 is the input power, z is the distance along the device and L_g is the power gain (e-folding) length. The gain length can be characterized by the fundamental FEL parameter, ρ . [2]

$$L_g = \frac{\lambda_u}{4\sqrt{3}\pi\rho} \quad (2)$$

where λ_u is the undulator period. The fundamental FEL parameter scales with the third power of peak beam current density, $J^{1/3}$.

A general feature of free electron lasers is that if variations occur on a scales shorter than a gain length, performance is affected. For focusing, this rule of thumb implies a limit on the beta function, $\beta > L_g$. A limit on the focusing strength as a function of the emittance is given by

$$\beta \geq \frac{2\gamma\epsilon_n}{\rho(1+a_u^2/2)} \quad (3)$$

where γ is the beam Lorentz factor, ϵ_n is the normalized rms emittance and a_u is the usual normalized (unitless) undulator parameter. This limit is derived in the one dimensional limit assuming no energy spread. It is useful for setting an approximate limit on how strong a given FEL's focusing channel can be. As is discussed in the following sections, it is not merely the strength but also the type of focusing that affects FEL performance.

Sextupole Focusing

Free electron lasers provide weak natural focusing; in both planes for helical devices, but only in one plane for planar undulators. Fortunately, this problem can be solved by using Scharlemann's curved pole faces [3]. Constant gradient sextupole focusing (via curved pole faces or any other means), like natural focusing, has a constant transverse velocity for each electron. For a distribution of electrons there is a corresponding distribution of velocities. Natural focusing does not perturb the transverse phase space; however, it can not provide sufficient focusing for longer devices.

A relation between the focusing betatron wavenumbers is required by the Maxwell equations:

$$k_{\beta_x}^2 + k_{\beta_y}^2 = \frac{e^2}{2E_b^2} B_u \quad (4)$$

where x and y are the two transverse directions, B_u is the undulator magnetic field, e is the electron charge and E_b is the beam energy. For a planar undulator $k_{\beta_x}=0$ or $k_{\beta_y}=0$; typically for a helical undulator or curved pole faces, $k_{\beta_x}=k_{\beta_y}$. Relation (4) sets a limit on the weak (constant gradient)

focusing strength. A large $k\beta^2$, and hence a strong focus in one direction implies a negative $k\beta^2$, and hence a defocus in the other direction. Consequently, strong focusing implies alternating gradients.

External quadrupoles have been proposed and used [4] to produce AG focusing in an FEL. An external FODO lattice can provide strong focusing for undulators. Unfortunately, only iron free undulators can be used with conventional schemes. Various novel schemes have been devised in an attempt to overcome this limit: canted poles, Panofsky quads, edge field permanent magnet arrays [5], etc.. Regardless, it has long been stated that quadrupole focusing can degrade FEL performance because it modulates the transverse velocity of the electrons.

Recently the idea of alternating gradient sextupole focusing in an FEL was studied. The original scheme called for alternating the curvature of the undulator poles, thus producing a strong focusing lattice. Other methods to achieve this type of lattice have also been considered: external sextupoles, side mounted magnet arrays, etc.. The beam dynamics and hence the FEL action are the same (in the limit of averaging over an undulator period) and so the exact form of the sextupole focusing is unimportant. Here the wavenumbers are allowed to be imaginary so that relation (4) does not limit the focusing strength. This is analogous to quadrupole strong focusing and to the feed down effect in circular machines.

The transverse electron velocity is, in general, different in a focusing section from that in a defocusing section. Of course a given electron can be matched between the two sections, but a distribution of velocities precludes matching.

This leads to the central question: Is the continuous periodic oscillation of the transverse beam velocity caused by a quadrupole lattice better or worse than the discrete changes caused by sextupoles? The answer is that quadrupoles are better. Upon reflection this seems to be intuitively correct. Abrupt disruptions of the beam phase space will tend to degrade the FEL action [6]. Smooth changes which occur on scales greater than a gain length are less deleterious. It is perhaps easiest to show this by performing a complete 3D simulation.

Simulations

The code TDA3D [7] was modified to allow for sextupole focusing. This code solves the averaged FEL equations in 3D and takes into account known phenomenon for the regime

studied here. The sextupole focusing is accounted for in the simulation by modifying the vector potential of the undulator (a_u). Quadrupole focusing is simulated by adding a term to the particle equations of motion.

The example parameter set discussed here is the SLAC based X ray FEL [8,9]. The parameters are given in Table 1. It serves as a good test case due to the long length of the undulator and low beam emittance. Notice that applying equation (3) yields a beta function of 5 meter for peak FEL performance.

Table 1: SLAC X ray FEL parameters used in the simulations for this paper.

γ	Energy (mc ²)	14000
ϵ_n	Emittance normalized (mm-mrad)	3×10^{-6}
	Peak Current (A)	2500
	Pulse Length (fs)	160
a_u	Undulator parameter	6
λ_u	Undulator period (cm)	8.3
λ_r	Optical wavelength (nm)	4
ρ	FEL parameter	1.7×10^{-3}

In order to reliably compare sextupole and quadrupole focusing, identical lattices were calculated (same period, beta function and phase advance per cell). Monoenergetic beams were used (no energy spread), in a focus/ defocus (FD) lattice (no drifts). A study of the effect of the phase advance per cell was first done. Typically, a phase advance per cell of 90 degrees is used to minimize the average beam envelope. However, this creates large fluctuations in the beam size. As expected, simulations confirm that when the phase advance is large and hence the beam is modulated a great deal, then the FEL action is degraded. To avoid this added effect, subsequent comparisons were performed with a phase advance per cell of about ten degrees.

Figure 1 shows the results of a series of simulations. Three sets of data points are plotted: quadrupole lattice, sextupole lattice and 3D semi-analytic calculations¹⁰. The quadrupole set is clearly the best. As expected, there is an optimal focusing strength. Peak quadrupole performance occurs close to, but not precisely at the theoretically predicted 5 meter beta function. A figure of merit for the effect of focusing on an FEL is given by the variation of the phase over a betatron period. This is related to the extent of detrapping of electrons from the pondermotive well. For quadrupole cases, this effect is small. For the sextupoles used in this example, detrapping becomes significant for a beta function ≤ 5 meters.

Conclusions

Strong (alternating gradient) sextupole focusing does not work as well as comparable quadrupole focusing. Strong quadrupole focusing performs very well in an FEL. Simulations indicate that the 1D emittance limit on focusing can even be exceeded provided that a small phase advance per cell is used. This implies a need for a high field gradient focusing systems. Such systems would allow for the construction of shorter, higher gain free electron lasers.

There may be occasions when sextupole focusing is advantageous, but this is unknown at this time. An independent numerical confirmation of this work would be a useful endeavor.

Acknowledgments

The authors thank Claudio Pellegrini for his many useful comments. A great deal of this work is based on the work of Ted Scharlemann. This work was supported by the US Department of Energy under Grant DE-FG03-92ER-40493.

References

[1] For a detailed discussion of AG sextupole focusing see G. Travish and J. Rosenzweig, Strong

focusing for Planar Undulators, Proceedings of the Third Workshop on Advanced Accelerator Concepts (1992).

[2] R. Bonifacio, C. Pellegrini, and L. M. Narducci, Opt. Commun. **50**, p373 (1984).

[3] E. T. Scharlemann, *Wiggle plane focusing in linear wigglers*, J. Appl. Phys. **58** 6, p. 2154 (1985).

[4] T. J. Orzechowski, et al., *High Efficiency Extraction of Microwave Radiation from a Tapered Wiggler Free Electron Laser*, UCRL-94841 (1986).

[5] R. Tachyn, "Permanent Magnet Edge-Field Quadrupoles As Compact Focusing Elements For Single-Pass Particle Accelerators," SLAC-PUB-6058. Also, see the Proceedings this conference.

[6] C. Pellegrini, Nucl. Instr. and Meth. **A272** p364 (1988).

[7] T. M. Tran and J. S. Wurtele, Comput. Phys. Commun., **54** 263 (1989).

[8] H. Winick, et al., "A 2-4 nm Linac Coherent Light Source (LCLS) Using the SLAC Linac," Proceedings this conference.

[9] SLAC X-ray FEL simulations are presented in, *Performance Characteristics, Optimization, and Error Tolerances of a 4nm FEL Based on the SLAC Linac*, Proceedings of this conference.

[10] Y. H. Chin, K.-J. Kim and M. Xie, Phys. Rev. **A46**, 6662 (1992).

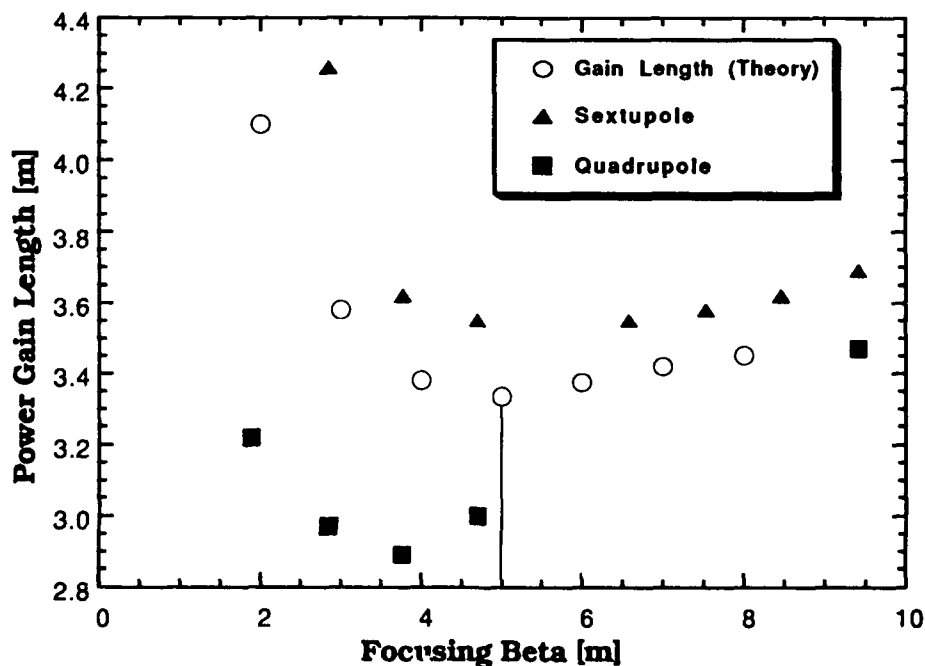


Figure 1: A comparison of quadrupole and sextupole focusing in an FEL. Analytic results are also plotted for comparison. The emittance limited optimal focusing is indicated by the vertical line (at 5 meters).

Generation of High Power 140 GHz Microwaves

with an FEL for the MTX Experiment*

S.L. Allen, C.J. Lasnier, B. Felker, M. Fenstermacher, S.W. Ferguson, S. Fields, E.B. Hooper, S. Hulsey, M. Makowski, J. Moller, W. Meyer, D. Petersen, E.T. Scharlemann, B. Stallard, R. Wood
Lawrence Livermore National Laboratory, Livermore CA 94551

ABSTRACT

We have used the improved ETA-II linear induction accelerator (ETA-III) and the IMP steady-state wiggler to generate high power (1-2 GW) microwaves at 140 GHz. The FEL was used in an amplifier configuration with a gyrotron driver. Improved control of energy sweep and computerized magnetic alignment in ETA-III resulted in small beam corkscrew motion (< 1.5 mm) at 6 Mev, 2.5 kA. Reduction of wiggler errors ($< 0.2\%$), improved electron beam matching, and tapered wiggler operation resulted in peak microwave power (single-pulse) of up to 2 GW. These pulses were transported to the MTX tokamak for microwave absorption experiments. In addition, the FEL was run in a burst mode, generating 50-pulse bursts of microwaves; these results are discussed elsewhere [1].

I. INTRODUCTION

Generation of high power microwaves with an FEL is advantageous for fusion experiments for several reasons: 1) the output is a simple TE₀₁ mode which couples directly to the plasma, 2) there is no output window which could fail at high power, and 3) frequency sweeping is possible by varying a low power source. The FEL for the MTX experiment is made up of four major parts: the ETA-II linear induction accelerator, the electron beamline, the IMP wiggler, and a quasi-optical microwave transport system connected to the MTX tokamak. FEL performance in 1989 was limited to short (5-10 ns) 0.2 GW pulses at 140 GHz because of a substantial corkscrew motion (~ 1 cm) of the beam and the nonreproducibility of the electron beam pulse (making empirical wiggler tapering difficult). The corkscrew motion is caused by the energy sweep of the beam during the pulse, coupled with misalignments of the solenoidal transport system of the accelerator [2].

The 2-D FEL simulation code FRED [3] was used to estimate the beam parameters required for high-power FEL operation. At a beam energy of 7.35 Mev, 2 kA of beam current, and 50 W of drive power, calculated output power is approximately 5 GW [4]. This estimate requires a ± 0.1 cm beam displacement, a $\pm 1\%$ energy sweep, and a 0.1% error in the wiggler magnetic fields. The sensitivity of the output power to these quantities is shown in Table 1, along with achieved parameters.

Table 1
FRED Predictions of FEL Output Power

Parameter	Variation	% Out	Achieved
Beam Energy	7.5 to 6 Mev	50	6.3 Mev
Beam Current	2.5 to 2 kA	60	2.5 kA
	2.0 to 2 kA	17	
Brightness	1 to 0.2×10^8 $A m^{-2} r^{-2}$	60	$> 10^8$
Beam Motion			± 1 mm (40ns)
Energy Sweep	$\pm 1\%$ to $\pm 2\%$	80	$\pm 1\%$ (35 ns)
Wiggler Error			0.2% RMS

Several hardware and operational improvements were first tested on a 20-cell version of the whole (60 cell) ETA-III system, resulting in reduction of the corkscrew motion and improved energy regulation [2,5-6]. These improvements were then implemented on a 60-cell version called ETA-III, and a steady-state wiggler was installed. Note from Table 1 that the required electron beam parameters have been achieved. Tapered FEL operation resulted in the generation of single pulse microwaves up to 2 GW which were transported to the MTX tokamak with a quasi-optical microwave transport system. Further optimization of the output power was not performed because of extremely limited experimental time. Electron Cyclotron Resonance Heating (ECRH) experiments on MTX with the FEL demonstrated nonlinear absorption of the high power microwaves, in agreement with theory [7]. Extrapolation of this theory shows good absorption for reactor conditions, indicating that FELs are useful for future fusion machines.

II. DESCRIPTION OF THE FEL

A. The ETA-II 60-Cell Accelerator

The ETA-II accelerator consists of an electron beam injector and 60 accelerator cells. The injector consists of a thermionic, osmium-coated (12.7-cm-diameter) dispenser cathode operated in a diode configuration to generate about 2500 A at 1 Mev in the space-charge limited regime. Several

*Work performed under the auspices of USDOE by LLNL under contract W-7405-ENG-48.

improvements tested on the 20-cell prototype were implemented on the 60-cell version of ETA-II for these experiments: 1) a multicable pulse distribution system[8], 2) arc and overvoltage protection, 3) feedback control of pulse timing, 4) an improved cell design to minimize arcing and the Beam Break-Up Instability, 5) in-situ magnetic alignment[9], and 6) a computerized tuning algorithm to minimize corkscrew directly[10]. The computer processing was substantially improved compared to the 20 cell case so that the whole accelerator could be tuned in about 1 day. Improvements (1) and (3) resulted in much better energy regulation, as shown in Table 1, $\Delta T/T$ of $\pm 1\%$ for 35 ns was achieved. The feedback system enabled pulse-to-pulse corrections in the timing of each magnetic compressor (MAG-1D) to be maintained within ~ 1 -2 ns; daily variations of over 20 ns were continuously corrected. Energy flatness was also improved by optimization of the operating point of the MAG-1D; a slightly rising waveform was used on the first 20 cells to compensate for a falling waveform from the injector. The corkscrew amplitude was found to depend weakly on the operating point (± 10 kV from 90 kV per cell gap).

were measured with current return monitors and processed into a corkscrew amplitude A by the MAESTRO system. The MAESTRO system also controls the 60 pairs of power supplies for the sin and cos correction coils in each cell block used to minimize A . The computer system has been optimized so that A is calculated and the currents are changed between pulses at 1 Hz. MAESTRO can automatically process all 60 cells in a few hours.

B. The IMP Wiggler and Microwave System

Shown in Fig. 1 is the FEL system; a series of magnetic lenses are used to transport and match the electron beam into the input of the wiggler. The 140 GHz gyrotron is the master oscillator (MO); a mirror in the sidecoupler focuses the microwave beam into the wiggler; a 4-cm diameter central hole is provided to pass the electron beam. The IMP wiggler[11] is a tuneable 5.5 m hybrid (both permanent and electromagnets) steady-state wiggler with a 10 cm period. The field is adjustable from 2.7-5.5 kG in the first half, and 0.6-4.1 kG in the second half of the wiggler. After careful

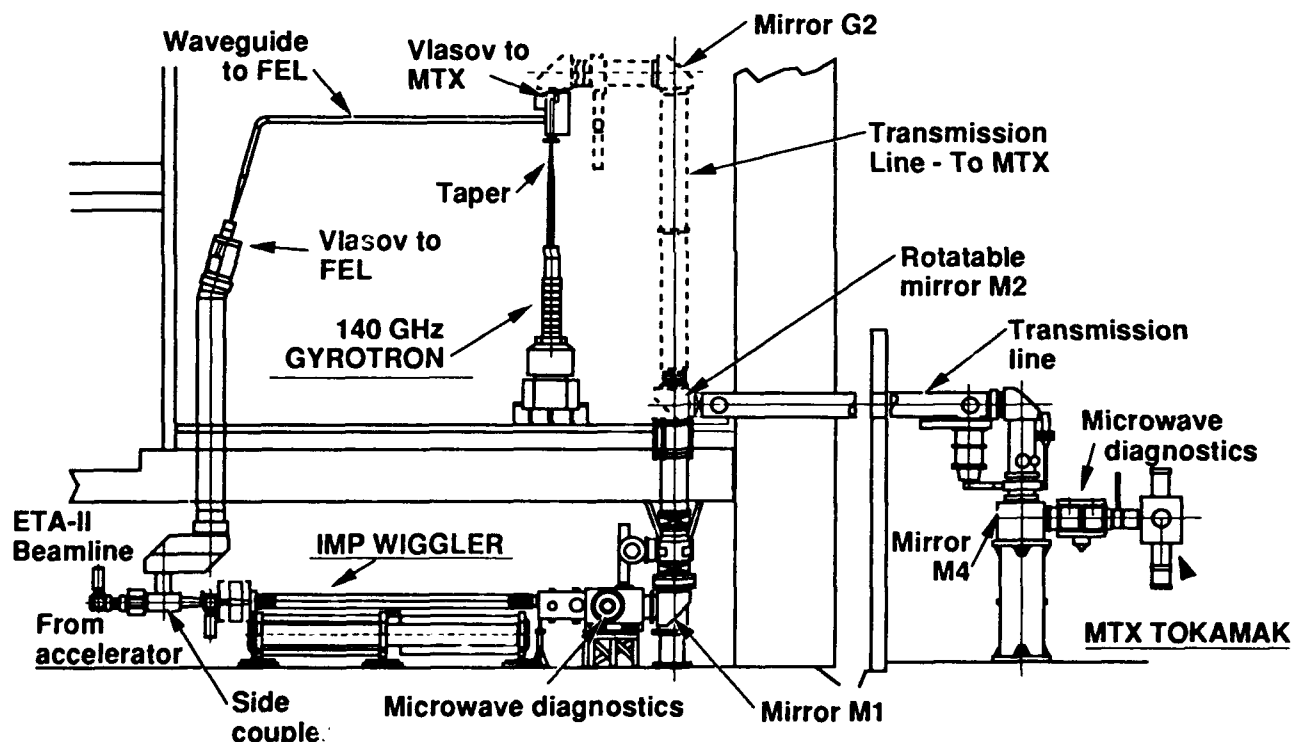


Fig. 1 The FEL is composed of the ETA-II accelerator (at left), the electron beamline, the master oscillator (gyrotron), and the quasi-optical microwave transport system to MTX.

Reduction of magnetic errors with (5) and (6) resulted in transverse beam motion nearly comparable to that obtained for the 20-cell experiment[5], i.e., ± 1 mm for 40 ns. A Stretched Wire Alignment Technique (SWAT) was used for alignment before operation. During electron beam operation, the MAESTRO[10] computerized control system minimized the corkscrew directly. The x and y components of the beam motion (referenced either to the beam or apparatus centroid)

construction, hall probe measurements indicated that the RMS wiggler errors were reduced to 0.1% for electromagnets alone, and 0.2% for the whole wiggler. We have verified the electron beam matching in the wiggler with a moveable optical target; no strong evidence of beam steering or abnormal growth in beam size was observed.

III. EXPERIMENTAL RESULTS

A. FEL Output Power at 140 GHz

The FEL system was operated at 1 Hz, and scans of the wiggler magnetic field were used to determine the IMP operating point. The wiggler was then tapered to optimize the output power, again using the MAESTRO system for control. We started with a theoretically-derived taper, and then empirically optimized the output power. The output power waveform was measured with both a calibrated diode and a receiver. A more precise calibration of the time-integral of this signal was provided by a precision calorimeter. An example of a pulse is shown in Fig. 2; we measured peak powers up to about 2 GW.

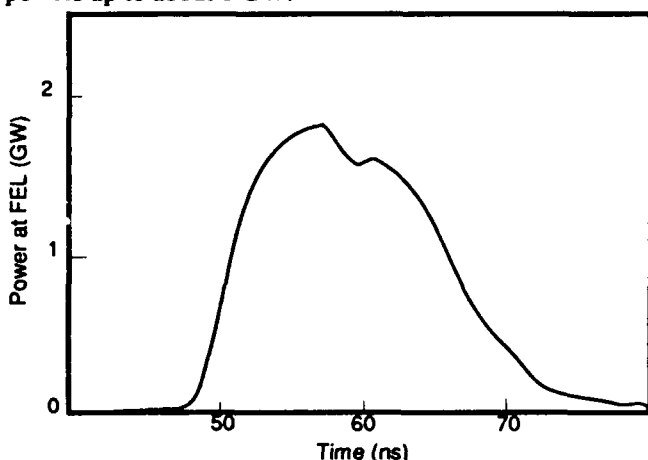


Fig. 2 A sample trace showing the output power versus time measured at the output of the FEL.

At this point, even though the theoretical models indicated that powers of 2-3 times greater were possible, we concentrated on MTX plasma experiments rather than FEL optimization. (In addition, one IMP coil was damaged, limiting the tuning range and therefore the usable tapers). The FEL output power was transmitted to the MTX tokamak with a quasi-optical transmission system consisting of several mirrors. This system is very efficient, transmitting nearly 90% of the power. FEL operation in the single-pulse mode was fairly reproducible; routine operation for several days with only minor tuning was achieved. An example of the peak power measured at MTX for one experimental day is shown in Fig. 3 (the FEL runs at 1 Hz, MTX shots are 5 minutes apart.)

IV. DISCUSSION

Improved energy regulation and reduced corkscrew motion of the electron beam from the ETA-III accelerator have made possible high power FEL operation. Peak powers of ~2 GW at 140 GHz has been generated in single pulses. Further optimization of the FEL power was not possible due to limited experimental time. These high-power pulses were

used in microwave transmission experiments in the MTX tokamak; nonlinear ECRH behavior was observed, in semi-quantitative agreement with theory. Burst mode operation of the FEL was also demonstrated, and is described in Ref. 1.

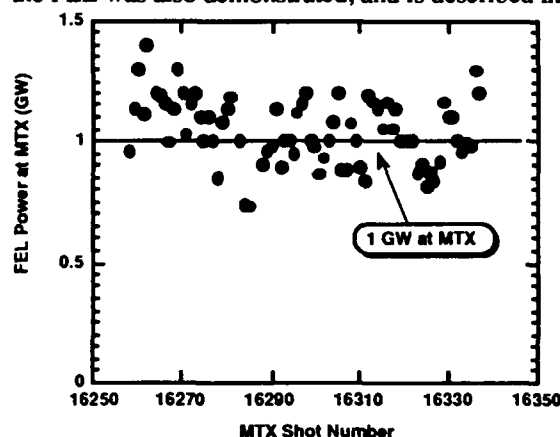


Fig. 3. The peak microwave power (measured at MTX) varies from 0.75-1.4 GW during a day of experiments

We would like to acknowledge the fundamental accelerator and FEL work done by the Beam Research Group at LLNL that made these FEL experiments on the MTX tokamak possible.

REFERENCES

- [1] C. J. Lasnier et al., "Burst Mode FEL with ETA-III Induction Linac," these proceedings.
- [2] W.C. Turner, "Control of Energy Sweep and Transverse Beam Motion in Induction Linacs," in Proc. 1991 Part. Accel. Conf. (San Francisco, 1991) 3094.
- [3] E.T. Scharlemann, Laser Handbook, Vol 6, (North Holland, New York, 1990) 291.
- [4] R.A. Jong et al., Nucl. Instrum. Meth. Phys. Res. A285 (1989) 379, also private communications April, 1992.
- [5] S.L. Allen, et al., "Measurement of Reduced Corkscrew Motion on the ETA-II Linear Induction Accelerator," Proc. 1991 Part. Accel. Conf. (San Francisco, 1991) 3094.
- [6] W.E. Nexsen et al., "Reduction of Energy Sweep of the ETA-II Beam," Proc. 1991 Part. Accel. Conf. (San Francisco, 1991) 3103.
- [7] S. L. Allen et al., "Nonlinear Absorption of High Power FEL-Generated Microwaves at ECRH Frequencies in the MTX Tokamak," submitted to Phys. Rev. Lett.
- [8] S.E. Sampayan et al., "Energy Sweep Compensation of Induction Accelerators," in Proc. 1990 LINAC Conf. (Albuquerque, 1990).
- [9] L. Griffith and F. Deadrick, "Progress in ETA-II Magnetic Field Alignment Using Stretched Wire and Low Energy Electron Beam Techniques," in Proc. 1990 Linac Conference, Albuquerque, NM, September 10-14, 1990.
- [10] Darrel L. Lager et al., "Artificial Intelligence Techniques for Tuning Linear Accelerators," Proc. 1991 Part. Accel. Conf. (San Francisco, 1991) 3082.
- [11] R. Schlueter and G. Deis, "Tuneability Enhanced Electromagnetic Wiggler," US Patent 5099175 March 24, 1992.

Burst Mode FEL with the ETA-III Induction Linac*

C.J. Lasnier, S.L. Allen, B. Felker, M.E. Fenstermacher, S.W. Ferguson, S.D. Hulsey, E.B. Hooper, M.C. Jackson, M.A. Makowski, W.H. Meyer, J.M. Moller, D.E. Petersen, S.E. Sampayan, B.W. Stallard, W.F. Fields

Lawrence Livermore National Laboratory, Livermore CA 94551

K. Oasa

Japan Atomic Energy Research Institute, Tokai, Japan

Abstract

Pulses of 140 GHz microwaves have been produced at a 2 kHz rate using the ETA-III induction linac and IMP wiggler. The accelerator was run in bursts of up to 50 pulses at 6 MeV and greater than 2 kA peak current. A feedback timing control system was used to synchronize acceleration voltage pulses with the electron beam, resulting in sufficient reduction of the corkscrew and energy sweep for efficient FEL operation. Peak microwave power for short bursts was in the range 0.5-1.1 GW, which is comparable to the single-pulse peak power of 0.75-2 GW [1]. FEL bursts of more than 25 pulses were obtained.

I. INTRODUCTION

Pulses of high-power microwaves were generated using the ETA-III (an upgrade of ETA-II), a linear induction accelerator at the Lawrence Livermore National Laboratory, and the IMP (Intense Microwave Prototype) wiggler. The microwaves were produced as part of the MTX fusion energy project. To progress from single pulse operation to bursts of pulses at multi-kilohertz rates, modifications were made in the pulsed-power systems, and a new timing compensation scheme was implemented for synchronizing the acceleration voltage pulses with the electron beam.

The timing system was especially critical [4]. The electron beam provided most of the loading for the high-voltage pulse at the induction gaps. If the high voltage pulse did not arrive at the gap within ± 10 ns of the electron beam pulse, the unloaded voltage would have been too high, causing an arc and damaging insulators. To achieve the best acceleration of the beam, the high voltage pulse timing needed to be controlled to within ± 2 ns for each pulse of a burst. This was shown to be within the capability of the feedback timing compensation system. Note that it is not the standard deviation of timing measurements which is critical in preventing arc damage, it is the largest excursion of timing from the target value.

ETA-III was run in 2 kHz bursts of up to 50 pulses. The electron beam reached peak currents of over 2 kA at 6 MeV. An example of a long burst is shown in Fig 3. For FEL operation, the beam used in IMP wiggler with 7 kW of master oscillator power at 140 GHz generated by a gyrotron.

*Work performed under the auspices of U.S.DOE by LLNL under contract W-7405-ENG-48

The FEL peak output power exceeded 1 GW during many bursts. This is not as great as the highest power (≈ 2 GW) measured during single-pulse operation [1]. Corkscrew and energy sweep of the beam during a burst remained within the acceptable range during short bursts, as evidenced by consistent FEL output (Fig 4). The experimental time to optimize operation was limited, so the longest recorded burst of microwaves contained slightly more than 25 pulses (Fig. 5).

II. DESCRIPTION OF THE EXPERIMENT

A. The ETA-III Accelerator

The accelerator was configured in nearly the same way as for the previous 20-cell experiment [1,2,3], except that 60 accelerator cells were in place to provide 6 MeV beam energy. The high voltage pulses to drive the induction gaps were provided by four pulsed power systems, each consisting of a MAG-1D magnetic pulse compressor fed by a Pulsed Power Unit (PPU) (Fig 1). The PPU's were energized by DC power supplies typically run at 10-14 kV. A capacitor bank for each DC supply helped maintain voltage during bursts.

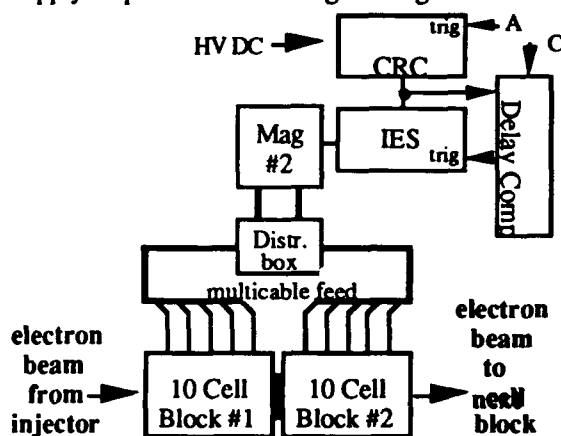


Fig. 1 A typical Pulsed Power system drove 20 cells.

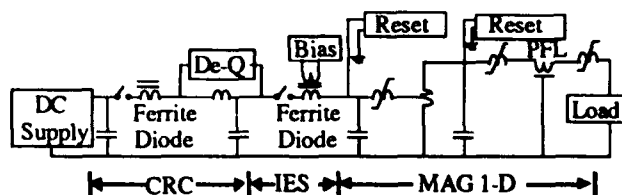


Fig. 2 Pulsed Power Schematic (from Ref. 3).

The first stage of each PPU was the Charge Resonant Command (CRC) circuit, which regulated the voltage. The

second stage was the Intermediate Energy Storage (IES) which was triggered to fire the accumulated charge into the MAG-1D.

Thyratron tubes were used as switches in the PPU's. The PPU's, the MAG-1D's, and the accelerator cells all contained ferrite material to act as magnetic switches. The ferrites were reset to the bottom of their hysteresis loops by currents in field windings.

The PPU typically generated a voltage pulse of 20-22 kV peak value. This pulse was compressed by the MAG-1D units, which were able to step up the peak voltage to over 130 kV. The output pulse had a full width at half maximum of 70 nS.

The injector was run by a dedicated PPU and MAG-1D unit, ordinarily at 100-120 kV peak voltage. Three other PPU's each ran a MAG-1D, which each in turn drove 20 accelerator cells in parallel at 80-100 kV peak. A distribution box split the output of each MAG-1D into 10 cables, each of which drove two cells. The cable length provided transit time isolation during the pulse, protecting cells from reflected voltage originating at cells attached to other cables.

Changes made to the pulsed power system for burst mode included an additional high voltage DC power supply and capacitor banks for the PPU's. Thyratron tubes were replaced with high repetition rate units, new ferrite diodes were installed in the PPU's, and new bias circuits were made for the IES reset. MAG-1D pre-compression reset inductors were installed, thyratron trigger chassis were modified, and the DC power supply for the trigger chassis was upgraded. The high voltage trigger distribution units were improved, and circulation pumps were added for the fluid in the cell resistors [4].

B. IMP Wiggler

The IMP wiggler [6] is a steady-state hybrid laced wiggler with a period of 10 cm and an active magnetic length of 545 cm. This replaced the pulsed ELF wiggler to maintain resonance during long bursts. The wiggler field in the upstream resonance region, tunable from 2700 G to 5500 G, was ordinarily near 3 kG. The downstream part had a linear range of 600-4100 G. Each electromagnet was cooled by separately instrumented and interlocked water lines. Independently computer-controlled power supplies were used to drive the electromagnets. A copper circular wave guide of 3.25 cm inner dimension was used between the wiggler magnet poles. The wiggler field errors were measured during assembly at 0.2% RMS.

The computer control of the wiggler allowed repeatable remote-controlled tapering of the wiggler field without physically moving magnets. Different magnet configurations were stored and re-loaded easily. The computer was also helpful in performing scans of the wiggler field, raising and lowering whole sets of magnet poles together.

Because of the permanent magnets, when lower field was selected on any pole, the computer ran an hysteresis loop of the whole wiggler to repeatably arrive at the requested field.

C. Timing Compensation System

The feedback timing compensation system for the high-voltage pulses was expanded to handle four MAG-1D pulse compression units independently. The previous single-correction LabVIEW® control system [5] was modified by using a LeCroy 2228A Time-to-Digital Converter to measure the firing time of each MAG-1D, from capacitive probe samples of the output. The computer adjusted the delay generator triggering each of the PPU's to cause firing at the target time.

For burst mode, a Kinetics List Sequencing Crate Controller was used to record the delay values for each of the 50 pulses of a burst. Timing corrections were written to a Digital-to-Analog converter. The analog voltages, one for each pulse of a burst, went to a delay compensation chassis for each PPU, which converted the voltage into a trigger delay [7].

The timing system was able to time-align the pulses to within 2-4 nS of the target value when the jitter in the MAGs and PPU's was low (normal operation).

To achieve operation at normal voltage (80 kV) on the accelerator gaps and 2300 Amps injector current (FEL parameters), the accelerator was started at low voltage and raised slowly. This was because the voltage pulses had to be precisely timed with the beam load to avoid over-voltage and gap arcs. Changing voltage caused large timing changes in the PPU's.

For burst mode at full current, it was necessary to start with 2- or 3-pulse bursts at low voltage and slowly raise voltage. The operators found that a sodium thiosulfate solution giving a resistance of 150 Ohms in the cell load resistors prevented arcing and allowed easier startup than de-ionized water, and did not place an unreasonable load on the MAG-1D units. This was due to the resistors providing some load even if beam loading was poor. Ideal beam load was 40 Ohms.

III. EXPERIMENTAL RESULTS

The injector was operated independently at up to 3 kHz, in bursts of 50 pulses. The entire accelerator was run at 2 kHz because some trigger chassis required reduced inductance in ferrite diodes to run at higher rates. This was not done due to time constraints. Repeatable operation of up to 50 pulse bursts of electron beam at over 2 kHz and over 6 MeV was achieved. A 45-pulse burst is shown in Fig. 3.

Short bursts of FEL pulses were repeatedly obtained with peak power near 1 GW (Fig 4). For longer bursts, the microwave output was less repeatable but still produced many good pulses (Fig 5).

The reduced effectiveness of long bursts is at least partially attributed to the beam falling out of resonance in the wiggler, due to the pulsed power capacitor banks being drained during the burst. Power supplies connected to the banks were able to recharge capacitors between bursts, but not maintain voltage during a burst. For long bursts, the capacitor bank supplying the injector was drained so that less beam current was produced (Fig. 6). Due to reduced load on the induction gaps, this most likely increased the beam energy unless gap voltage dropped at the corresponding rate.

In some cases, FEL microwave output power dropped off during a burst due to a mode shift in the gyrotron master oscillator, seen as a change in gyrotron microwave monitors.

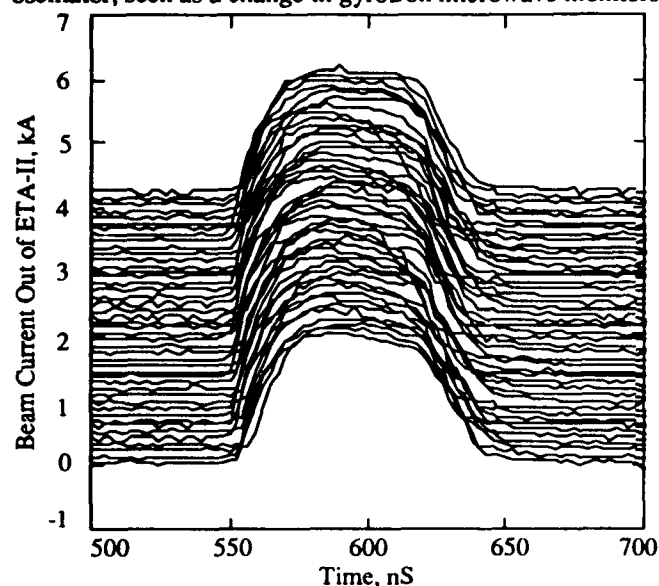


Fig. 3 Electron Beam Current vs. Time for a Burst of 45 Pulses of Electron Beam at 6 MeV.

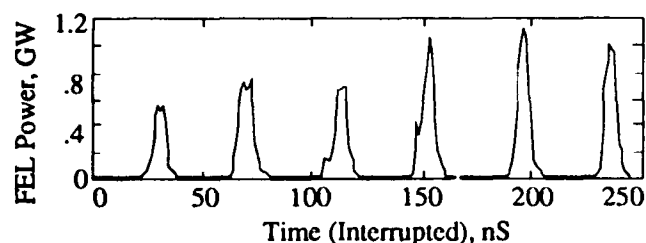


Fig. 4 Microwave Power vs. Time for a Short FEL Burst. The time axis is interrupted: the dead time between pulses recurring at a 2 kHz rate has been removed.

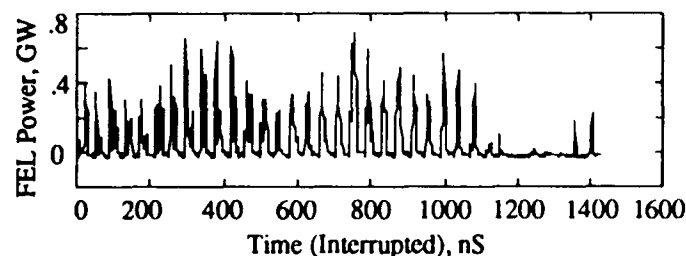


Fig. 5 Microwave Power vs. Time for a Long FEL Burst.

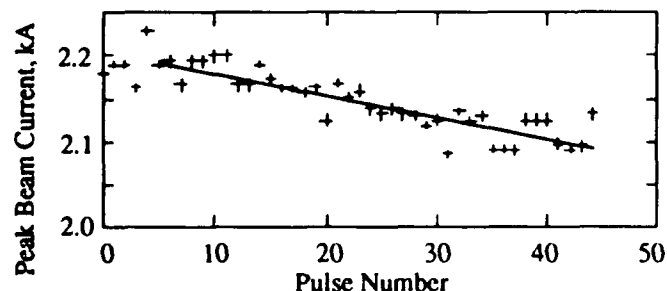


Fig. 6 Peak Current vs. Pulse Number in a 45-Pulse Burst. Peak current falls off slightly during the burst as capacitor banks are drained. The line is a least-squares fit to the points.

The FEL microwave power was measured by a diode which detected a sample of the wiggler output power, by means of a small coupling hole in the center of the first mirror of an evacuated quasi-optical transport system. The diode was calibrated by calorimetry at the end the transport section [8].

IV. DISCUSSION

Burst Mode Free Electron Laser operation using an induction linear accelerator has been demonstrated for the first time, and was used to produce bursts of high power (~ 1 GW) pulsed microwaves. The accelerator hardware was upgraded for high repetition rate, and the timing compensation system was expanded to control burst mode timing synchronization.

There is potential for improvement. Using a much larger power supply (5 MW compared to 695 kW total for ETA-III), the High Average Power Test Stand at LLNL was able to consistently demonstrate operation of a PPU and MAG-1D pulse compressor into a dummy load for 800-pulse bursts (a result of the work described in ref [4]). Burst length could also be extended by using larger capacitor banks.

REFERENCES

- [1] S.L. Allen et al., "Generation of High Power 140 GHz Microwaves with an FEL for the MTX Experiment," these proceedings
- [2] S.L. Allen et al. "Measurement of Reduced Corkscrew Motion on the ETA-II Linear Induction Accelerator", Proceedings of the 1991 Part. Accel. Conf. (San Francisco, 1991) 3094
- [3] W.C. Turner, "Control of Energy Sweep and Transverse Beam Motion in Induction Linacs," Proc. 1991 Part. Accel. Conf. (San Francisco, 1991) 3097.
- [4] S.E. Sampayan, et al., "Performance Characteristics of an Induction Linac Magnetic Pulse Compression Modulator at Multi-Kilohertz Pulse Repetition Frequency," Proc. 1991 Part. Accel. Conf. (San Francisco, 1991) 3097
- [5] Previous Single-pulse timing system by F.E. Coffield
- [6] B. Felker and S.W. Ferguson, "The Intense Microwave Prototype (IMP) Free Electron Laser, 140 Gigahertz Microwave System for the Microwave Tokamak Experiment (MTX)", Proc. 14th IEEE Symposium on Fusion Engineering (San Diego, 1991)
- [7] M.A. Newton and J.A. Watson, "Timing and Voltage Control for Magnetic Modulators on ETA-II," Proc. 7th IEEE Pulsed Power Conf. (Monterey, CA 1989)
- [8] B.W. Stallard et al., "ECH by FEL and Gyrotron Sources on the MTX Tokamak," in Proceedings of the 16th Symp. on Fus. Tech., London, Sept. 1990.

INTRODUCTION

SG-1 FEL is a raman region free electron laser amplifier, with wavelength of 8-9 mm, based on induction LINAC. The SG-1 FEL contains a 3.5 MeV accelerator, electron beam transport system, tapered electro-magnetic wiggler, microwave source and computer controlled system.

The design parameters of SG-1 FEL is as follows¹

$$E = 3-3.5 \text{ MeV}, \quad \Delta E/E = 3\%, \quad I = 450 \text{ A},$$

$$\epsilon_n = 0.47 \pi \text{ CM RAD}, \quad \tau = 60 \text{ ns}, \quad B_w = 3.1 \text{ kGs}$$

$$\lambda_w = 11 \text{ cm}, \quad N = 36, \quad \lambda_s = 8-9 \text{ mm}$$

$$P_{in} = 10-20 \text{ kW}, \quad P_{out} = 10^7 \text{ W (with constant wiggler)} P_{out} > 10^8 \text{ W (with tapered wiggler)}$$

The layout of SG-1 FEL is illustrated in Fig. 1

DESIGN OF SG-1 FEL

The induction LINAC² consists of a 1 MeV injector and 8 accelerating cells. Each cell can give the electron an energy increment of 300 keV. It is well known, an electron beam must have high brightness to appropriate for FEL requirement and FEL gain is strongly dependent on quality of electron

beam. So the cathode of diode is finely designed to provide electron beam with small emittance and strong current. The diode has planer configuration and its emitter is made of velvet.

For improvement the stability and reliability of accelerator, the switch system of Marx generators are carefully adjusted and the total jitter time of switches are $< 5 \text{ ns}$. So the synchronism deviation between acc. and RF source is very small. The cross section of injector is shown in Fig. 2.

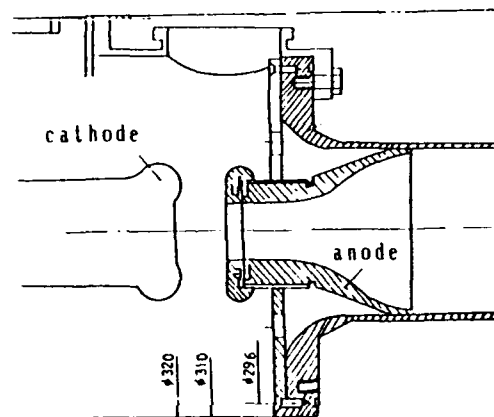
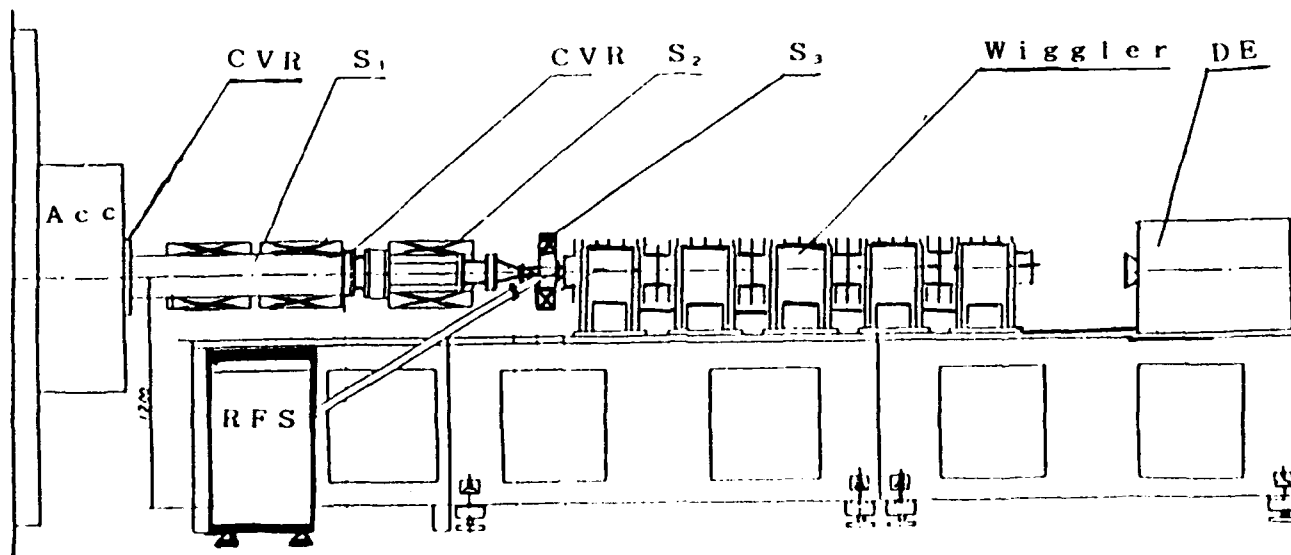


Fig 2 The cross section of injector



S_1, S_2 : Beam transport solenoid coil, RFS: Radio Frequency Source,
 S_3 : Thin focussing coil, DE: Diagnostic Equipment

Fig 1 Layout of SG-1 FEL

In order to decrease the loss of electron beam, the beam transport system is designed simply and shortened. It consists of two beam transport coils and one thin focusing coil and is easy to turning its parameters. The electron beam parameters at the input of wiggler is measured as follow:

$$E = 3.3 \pm 1.5 \text{ MeV}, \Delta E/E = 3\%, I = 600 \text{ } 700 \text{ A},$$

$$\epsilon_n = 0.43 \pi \text{ cm rad } \tau = 40 \text{ ns}, r_w = 1 \text{ cm}$$

A new shield-pulse tapered electromagnet wiggler² with parabolic pole surface has been designed. This wiggler has some special features. It is very easy to adjust the magnetic field, it can provide horizontal focus of electron beam and small electric power is needed. Each two periods of the wiggler magnet is energized by its own independently controlled power supply. Thus the profile of the wiggler magnetic field along the beam axis can be tailored to almost any desired shape. The power supply is consisted by thyristors, capacitor and wiggler coils. The half period time of the excitation current through the wiggler coils is 1ms. To ensure that the wiggler axis of the beam coincides with the mechanical axis of the wiggler, the first and second period of the wiggler is energized to $(0.3 B_w - 0.8 B_w)$, and the last period is energized to $(0.8 B_w - 0.3 B_w)$, where B_w is the peak wiggler field inside the uniform wiggler. The magnetic field of the wiggler is given by

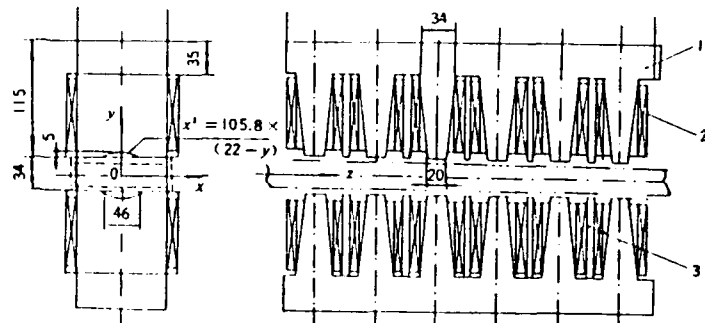
$$\vec{B}_w = B_0 \left\{ \cosh k_x X \cosh k_y Y \cos k_z Z \hat{Y} + \left(k_x/k_y \right) \sinh k_x X \sinh k_y Y \cos k_z Z \hat{X} + \left(k_w/k_y \right) \cosh k_x X \sinh k_y Y \sin k_z Z \hat{Z} \right\} \quad (1)$$

with $k_x^2 + k_y^2 + k_z^2 = k_w^2$, k_w -- wave number of wiggler

More importantly, this field ensures that the longitudinal velocity of an electron remains constant over a betatron period. Without this property the electrons could detrapp from the ponderomotive well with serious consequences for the FEL performance.

The focussing property is dependent by coefficient $\propto k_y/k_x$. For our case the optimum value of is (1.4-2). The shield plate is used for enha-

ncing the field strength. It has been found that the field strength can increase by a factor of 15-20%. The layout of the shield-pulse electromagnet wiggler and its photograph are shown by Fig.3,4



1. Magnetic pole, 2. Coil, 3. Shield plate.

Fig. 3 The layout of the shield-pulse electromagnet wiggler

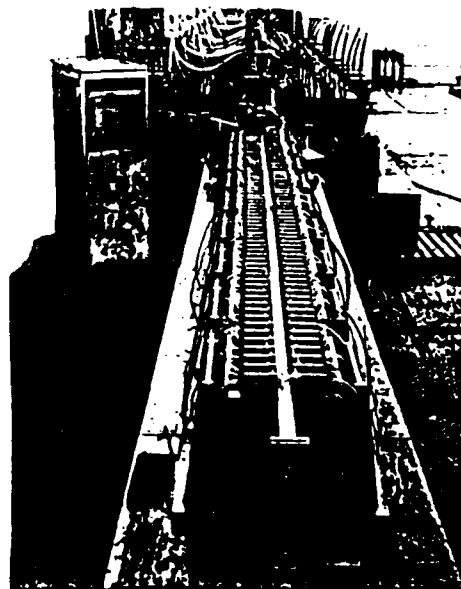


Fig. 4

NUMERICAL SIMULATION AND EXPERIMENTAL RESULTS

We have developed a 3-D numerical code (WAGFEL) incorporating standard FEL equations, modified by off-axis effects in the particle dynamics and the field equations. WAGFEL can model propagation and interaction electron beam with microwave in a rectangular waveguide. In order to obtain good agreement between experimental results and numerical

simulations, it is necessary to include the effect of longitudinal space charge forces and the effect of relativistic factor of electron in the KMR equations⁶. In simulation, the wave number k includes the waveguide corrections for the TE₀₁ mode

$$k^2 = \omega^2/c^2 - \pi^2/b^2 \quad (2)$$

where b is the waveguide width. To study the FEL dependence on wiggler length, we started with the uniform wiggler and measured the amplifier output as a function of wiggler magnetic field. The detuning curve for uniform wiggler is shown in Fig. 5

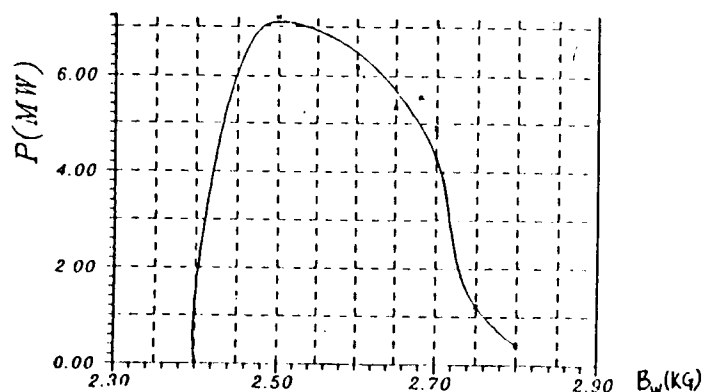


Fig. 5 Detuning curve for a uniform wiggler

Using the magnetic field corresponding to the peak at the detuning curve from experiment, we examined the FEL output power as function of wiggler length, illustrated in Fig. 6

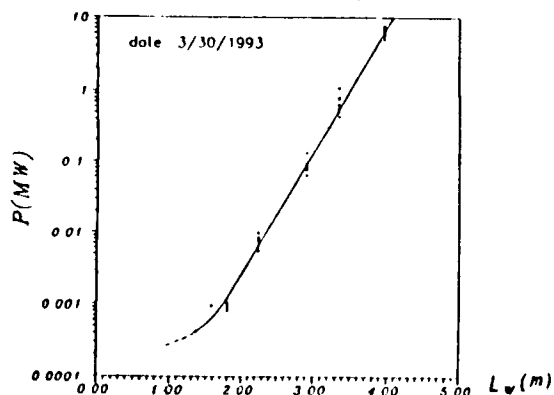


Fig. 6 Power output as a function of wiggler length

The maximum amplifier gain 20 dB/m is obtained. The output power is 10 MW, and frequency is 34 GHz at input beam $E=3.1$ MeV, $I=600$ A. But the saturation output power does not obtained yet. At the next stage we wish to obtain saturation point and continue experiment with tapered wiggler.

SUMMARY

We have successfully designed a SG-1 FEL amplifier, that is a microwave FEL with no axial guide field and has demonstrated high gain, efficiency and output power. We also have developed a 3-D numerical code WAGFEL, which can model propagation and interaction electron beam with microwave in a rectangular waveguide. In order to obtain agreement between experiment and theory we have found, it is necessary to include the effects of longitudinal space charge forces and the effect of relativistic factor of electron in the particle dynamics and field equations. The agreement between experimental results and numerical simulations is quite good. We have obtained a detuning curve and have studied the output power of SG-1 FEL with uniform wiggler as a function of wiggler length. The maximum output power 10 MW has been achieved.

ACKNOWLEDGEMENT

I am happy to acknowledge prof. Yang Zhenhua, Ding Bainan, Deng Jianjun, Zhou Chuanming, Hu Kesong, Toun Longzhou, Wu Ruian, Tao Zucong for their valuable contributions.

REFERENCES

- (1) Hui Zhongxi, High power laser and particle beams, Vol. 2, No. 3, (1991) 1.
- (2) Ding Bainan, et al. High power laser and particle beams, Vol. 1, No. 1, (1989), 92.
- (3) E. T. Scharlemann, W. M. Fawley, B. R. Anderson and J. J. Orzechowski, Nucl. Instr. and Meth. A 250 (1986) 150.
- (4) J. J. Orzechowski, et al. Phys. Rev. Lett. 53 (1984) 1728.
- (5) J. J. Orzechowski, E. T. Scharlemann, V. K. Neil and et al., IEEE J. Quantum Electron. QE-21 (1985), 831.
- (6) Yang Zhenhua et al. High power laser and particle beams, Vol. 1, No. 1, (1989), 60.
- (7) Zhou Chuanming, Wang Mingli, High power laser and particle beams, Vol. 1, No. 2, (1989), 157.
- (8) N. M. Kroll, P. E. M. R. Rosenbluth, IEEE Quantum Electron. QE-17, (1981), 1436.

Phillip Sprangle^{a)}, B. Hafizi^{b)}, Glenn Joyce^{a)} and Philip Serafim^{c)}

a) Plasma Physics Division, Naval Research Laboratory, Wash., DC 20375-5346

b) Icarus Research, 7113 Exfair Road, Bethesda, MD 20814

c) Northeastern University, Boston, MA 02115

Abstract

The operation of free electron lasers can be severely limited by the axial velocity spread of the beam electrons. We propose a method for reducing the axial velocity spread in electron beams by redistributing the electron energy via interaction with an axially symmetric, slow, TM waveguide mode. In this method, the energy redistribution is correlated with the electrons' betatron amplitude. Reductions of more than a factor of 40 in the rms axial velocity spread have been obtained in simulations.

Many coherent radiation generation mechanisms are based on the longitudinal bunching of electron beams. These sources include traveling wave tubes and free electron lasers (FELs) [1]. The degree to which an electron beam can be bunched is a strong function of the beam quality. The two independent contributions to the electron beam quality are the intrinsic energy spread and emittance, both of which lead to a spread in the axial electron velocity and limit the operating wavelength, gain and efficiency of the device [1]. A method for conditioning, i.e., reducing the axial beam velocity spread, was recently proposed in which the beam was propagated through a periodic array of focusing, drift, defocusing, drift channels and microwave cavities [2].

Here, we propose an alternative conditioning method which redistributes the electrons' energy according to their betatron amplitude by using the electric field of an axially symmetric, slow, TM waveguide mode [3].

In the FEL mechanism, the resonance condition is $\omega - v_z (k + k_w) \approx 0$, where $\omega = ck$ is the frequency, v_z is the axial electron velocity, $k_w = 2\pi/\lambda_w$ and λ_w is the wiggler wavelength. This condition

implies that the beam's axial velocity spread, δv_z , should satisfy $\delta \beta_z \ll \lambda/2L$ where $\delta \beta_z = \delta v_z/c$, λ is the radiation wavelength and L is the interaction length (e-folding length) of the radiation field in the low gain (high gain) regime. The axial velocity spread can be written as

$$\delta \beta_z = \left((1 + a_w^2/2) \delta \gamma / \gamma - \epsilon_n^2 / (2r_b^2) \right) / \gamma^2$$

where $\gamma = 1 + E/m_0 c^2$ is the relativistic factor, E is the beam energy, $\delta \gamma / \gamma$ is the fractional intrinsic beam energy spread, ϵ_n is the normalized emittance, $a_w = |e| B_w / (k_w m_0 c^2)$ is the wiggler strength parameter, B_w is the wiggler field amplitude and r_b is the radius of the matched electron beam. In many cases, electron beam quality is limited by the emittance contribution and not the energy spread term, i.e., $\delta \gamma / \gamma \ll (1/2)(\epsilon_n/r_b)^2$. In any case, it is clear that electron beam quality, in particular, $\delta \beta_z$, limits the operation of FELs.

To analyze our conditioning method we consider the electron trajectories in a planar wiggler with parabolic pole faces. These orbits consist of rapidly varying (wiggler period scale length) and slowly varying (betatron period scale length) terms [4].

In the highly relativistic limit, the axial particle velocity normalized to the speed of light is given by $\beta_z \approx 1 - 1/2\gamma^2 - (\beta_x^2 + \beta_y^2)/2$, where $\beta_{x,y} = v_{x,y}/c$ is the ratio of the transverse velocity components to the speed of light. The square of the perpendicular velocity, averaged over the wiggler period, is independent of z . Substituting the fast and slow orbits into the expression for β_z and setting $\gamma = \gamma_0 + \delta \gamma$, where $\delta \gamma$ is the electron's energy deviation term, we find that $\beta_z = \beta_{0z} + \delta \beta_z$, with $\beta_{0z} = 1 - (1 + a_w^2/2)/(2\gamma_0^2)$, and

$$\delta \beta_z = \left(1 + a_w^2/2 \right) \delta \gamma / \gamma_0^3 - k_\beta^2 r_0^2 / 2. \quad (1)$$

* Work supported by ONR

Here γ_0 is the gamma associated with the reference electron, traveling along the z-axis without a betatron oscillation, $r_0^2 = x_0^2 + y_0^2$, where x_0, y_0 are the amplitudes of the slow components of the displacement from the axis and terms varying on the wiggler wavelength scale have been neglected. The normalized beam emittance, for a matched beam in the focusing fields of the wiggler, is $\epsilon_n = \gamma_0 k_\beta r_0^2$, where $k_\beta = a_w k_w / 2\gamma$ is the betatron wavenumber. Note that the emittance contribution to the velocity spread in (1), i.e., $k_\beta^2 r_0^2 / 2$ is independent of propagation distance. It will be assumed that the axial velocity spread due to emittance initially dominates the velocity spread caused by the intrinsic energy spread.

The proposed conditioning field is an axially symmetric, slow, TM waveguide mode with axial electric field

$$E_z = -E_0 I_0(k_\perp r) \cos \psi,$$

together with the associated transverse electric and magnetic fields, where E_0 is the maximum electric field amplitude on axis, k_\perp is the transverse wavenumber, k is the axial wavenumber, $\omega = c(k^2 - k_\perp^2)^{1/2}$ is the frequency, $\psi = kz - \omega t$ is the phase and I_n is the modified Bessel function of order n . The axial phase velocity of the traveling wave is matched to the axial beam velocity, $\beta_{ph} = \omega / ck = \beta_0$, where $\beta_0 = (1 - 1/\gamma_0^2)^{1/2}$ is the normalized axial velocity of the reference electron. To maintain synchronism between the conditioning field and the electrons, the axial and transverse wavenumbers must satisfy $k = (\omega/c)\gamma_0(\gamma_0^2 - 1)^{-1/2} = (\omega/c)/\beta_0$ and $k_\perp = (\omega/c)(\gamma_0^2 - 1)^{-1/2} = (\omega/c)/(\gamma_0\beta_0)$, respectively.

In our conditioning method the beam electrons are given an energy increment which cancels out the emittance contribution to the axial velocity spread. To reduce the velocity spread to zero, the conditioning field must give all the individual electrons a different fractional energy increment, $\delta\gamma_c/\gamma_0$, given by

$$\frac{\delta\gamma_c}{\gamma_0} = \frac{\gamma_0^2 k_\perp^2 r_0^2}{2(1 + a_w^2/2)} = \frac{\epsilon_n^2 r_0^2}{2(1 + a_w^2/2)r_b^4}.$$

The energy increment is proportional to the square of the betatron amplitude and the electron pulse length remains approximately constant. Our results show that the degree of beam conditioning can be significantly improved by removing the accelerating component of the TM field. It can be shown that complete conditioning of the beam is achieved at $k_\beta z = n\pi$, ($n = 1, 2, 3, \dots$) provided the normalized strength of the waveguide field, $a_0 = |e|E_0/(m_0 c \omega)$, is given by

$$a_0 = \frac{4\gamma_0^5 (k_\beta/k)^3}{n\pi(1 + a_w^2/2)} = \frac{\gamma_0^2}{2\pi n} \frac{a_w^3}{(1 + a_w^2/2)} \left(\frac{\lambda}{\lambda_w}\right)^2. \quad (2)$$

The conditioning method is illustrated with full scale particle simulation of two examples, a 10 MeV and a 1 MeV electron beam, see Table I. For the 10 MeV example, the axial velocity spread of the beam in the conditioning fields will reach a minimum at $z \approx \pi/k_\beta = 375$ cm, beyond which it increases to its original value. To maintain the minimum spread the conditioning field is adiabatically removed at $z \lesssim \pi/k_\beta$. Figure 1 shows the evolution of the fractional axial energy spread for 100 randomly selected electrons as a function of distance along the waveguide. The convergence of the trajectories in Fig. 1 with propagation distance indicates that the spread in axial velocity of the electrons is significantly reduced by the conditioning field. Figure 2 shows the root mean square (rms) beam axial energy spread, $\gamma_0^2(\delta\beta_z)_{rms}$, as a function of distance. In this illustration the spread is reduced by a factor of ~ 40 . For the 1 MeV example, the rms spread in the axial velocity is observed to be reduced by a factor of approximately 30. In both examples, the required value of the conditioning field is in excellent agreement with the analytical prediction in Eq. (2). For a waveguide diameter of 1 cm the power in the conditioning field is ~ 10 MW and ~ 4 kW for examples 1 and 2, respectively.

In conclusion, in this paper a method is proposed for dramatically reducing the electron axial velocity spread in FELs. The beam conditioning

field is that of an axially symmetric, slow, TM waveguide mode. A reduction in the velocity spread by a factor of 40 was obtained.

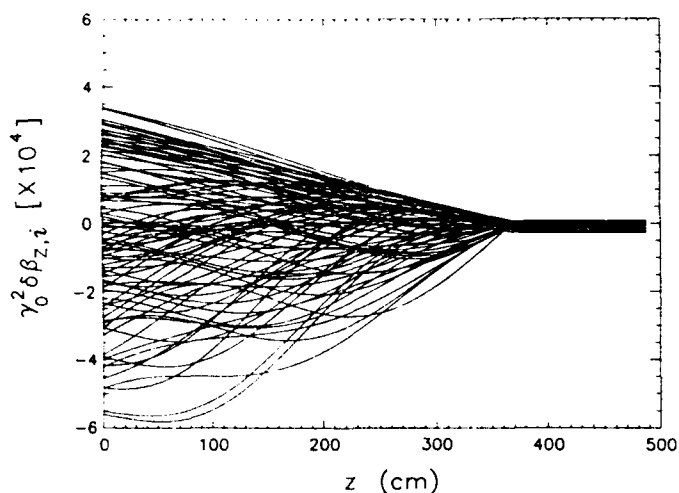


Fig. 1. Fractional axial energy spread, $\gamma_0^2 \delta \beta_{z,i}$, where $i = 1, 100$, versus distance along the conditioning waveguide. The curves represent 100 particles chosen randomly from a distribution of 10^3 particles. In this figure, the conditioning field is adiabatically turned off at ≈ 375 cm.

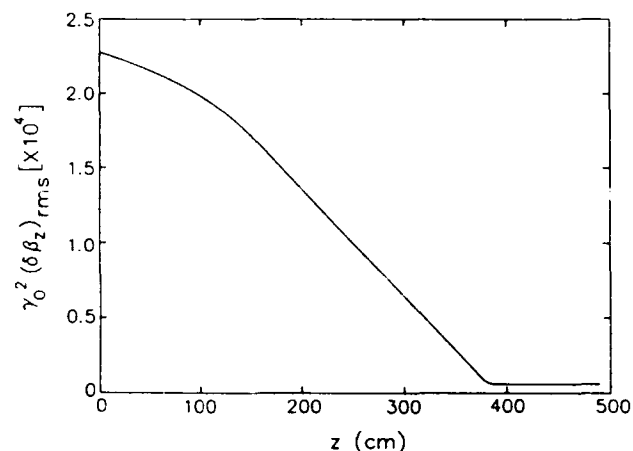


Fig. 2 Root mean square (rms) fractional axial energy spread versus distance. The spread is reduced by a factor of ~ 40 .

REFERENCES

- [1] C. W. Roberson and P. Sprangle, Phys. Fluids B1, 3 (1989).
- [2] A. M. Sessler, D. H. Whittum and L. H. Yu, Phys. Rev. Lett. 68, 309 (1992).
- [3] P. Sprangle, B. Hafizi, G. Joyce and P. Serafim, Phys. Rev. Lett. 70, 2896 (1992).
- [4] E. T. Scharlemann, J. Appl. Phys. 58, 2154 (1985).

Table I

Electron Beam	Example #1	Example #2
Energy, E	10 MeV	1 MeV
Emittance, ϵ_n	3.5×10^{-3} cm-rad	3.5×10^{-3} cm-rad
RMS Radius, r_b	0.14 cm	0.14 cm
Initial Axial Energy Spread	2.3×10^{-4}	2.4×10^{-4}
Final (Min.) Axial Energy Spread	5.8×10^{-6}	7.9×10^{-6}
Wiggler		
Strength Parameter, a_w	0.175	0.175
Period, λ_w	3.14 cm	3.14 cm
Betatron Period, λ_β	754 cm	104 cm
Conditioning Field		
Wavelength, λ	2 cm	2 cm
Strength Parameter, a_0	0.1	2×10^{-3}
Electric Field, E_0	160 kV/cm	3.2 kV/cm
Interaction Length, $\sim \lambda_\beta/2$	375 cm	53 cm

Table I. Simulation parameters for conditioning a 10 MeV (Example #1) and 1 MeV (Example #2) electron beam.

An Optical Approach to Emittance Compensation in FELs*

George R. Neil and Hongxiu Liu

Continuous Electron Beam Accelerator Facility

12000 Jefferson Avenue, Newport News, VA 23606-1909 USA

Abstract

We present a new approach to compensating for the emittance in very short wavelength Free Electron Lasers (FELs). The idea is based on the realization that the impact of finite emittance is to "wash out" the phase coherence of the electrons after passing some distance through the wiggler. This occurs because the electrons undergo betatron oscillations and those electrons with the largest transverse motion must travel a longer path. The new approach is to compensate for this by introducing an intense optical beam colinear with the electrons. If the beam has a transverse Gaussian profile in the field then the core electrons see on the average a higher field strength and undergo larger oscillations can retard the core electrons sufficiently to allow them to stay in phase with the electrons with large betatron excursions. This paper presents the derivation of this effect, details of the physical interaction and simulation results for sample cases. Limitations as to the practicality of the approach are also discussed.

I. INTRODUCTION

The sensitivity of FEL gain to the electron beam energy spread and emittance is a major limitation especially when wavelengths in the DUV to soft X-ray region are considered. At such short wavelengths the beam emittance and/or energy spread becomes a limiting factor in the performance of most practical devices. Many designs have resorted to very long wigglers or very high peak currents in a MOPA configuration to achieve the required gain since mirrors have limited reflectivity in this region. Early proposals to improve the FEL acceptance for such situations worked with dispersed electrons and involved wiggler modifications to introduce a gradient in the wiggler resonant field. Recent work¹ involves modifications of the electron beam momentum distribution by means of a FODO channel and accelerator cavities operating on the TM₂₁₀ mode to establish a correlation between energy and amplitude of transverse oscillations. These ideas have shown the potential to reduce demands on the accelerator energy and on wiggler length with concomitant cost savings. Presented below is a different idea to accomplish a similar goal, that is to reduce the negative impact of transverse motion of electrons in a wiggler.

The idea of reducing emittance sensitivity is based on the realization that phase coherence is lost because electrons which spend the most time nearest the core are ahead of others after passing some length of the wiggler. (See Figure 1.) The idea of Ref. 1 is to have the electrons on the outside have higher energy so as to better maintain coherence. Our suggestion is the opposite: slow down γ_z for the core e's. This would be accomplished by co-propagating with the e's a

non-resonant optical beam of high intensity. (See Figure 2.) Assuming a radial profile to the optical beam, the core electrons wobble more strongly than those on the outer edges of the distribution the central electrons, take a longer path, are slightly retarded in phase, and therefore remain in resonance longer in terms of the parallel gamma. This increases gain and effectively decreases the influence of emittance.

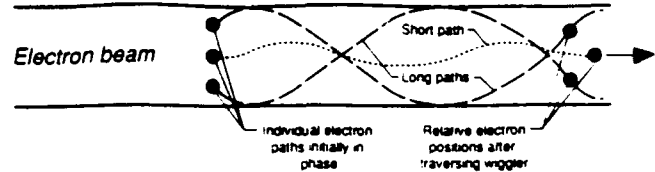


Figure 1. Matched electron beam in wiggler

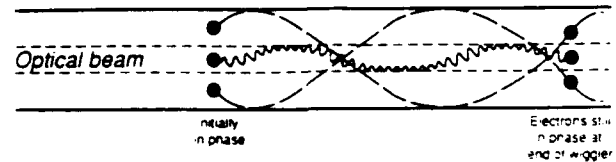


Figure 2. As Figure 1 but with addition of intense optical beam at core

The matching can be calculated in terms of $\gamma_{||}$

$$\lambda_s = \frac{\lambda_w}{2\gamma_z^2} \text{ where } \gamma_z^2 = \gamma_0^2 / (1 + K^2 + \dots)$$

and where λ_s is the FEL wavelength, λ_w is the wiggler wavelength, and γ_z is the standard relativistic factor but projected onto the z (propagation) axis. Typically terms other than K^2 are ignored. K is a function of offset from the axis; finite emittance requires a radial profile to the electron density. For a linear wiggler with infinite planes oriented with the field in the \hat{y} direction

$$\gamma_z^2 = \gamma_0^2 / \left(1 + \frac{K^2}{2} \left(1 + \frac{k_w^2 y^2}{2} \right) \right).$$

The result of the finite emittance of the electron beam is a variation on the order of 0.1% to 1% in the effective K^2 over the beam radius leading eventually to a phase mismatch across the beam. The phase slip is

$$\frac{dv}{dz} = k_w - \frac{k_s}{2\gamma_z^2} (1 + K^2 - 2\alpha_w \alpha_s \cos \Psi + \gamma_z^2 \beta_z^2 + a_{s1}^2)$$

where the new term a_{s1}^2 represents the addition of a new

optical wave $a_{s1}^2 = \frac{eE_{s1}}{mc^2 k_{s1}}$. As an engineering formula for

Gaussian beams at focus $a_{s1}^2 = 1.4 \times 10^{-15} \lambda_{s1} P_{s1} / R_{L1}$, where

* Supported by U.S. DOE contract #DE-AC05-84ER40150

P_{s1} is the power of the additional laser and R_{L1} its Rayleigh range. We will attempt to decrease a_{s1}^2 off axis to compensate K^2 increase. It is important to note at this point that this effect is occurring in a non-resonant way, i.e., there is no particular restriction on the frequency relationship between the lasing wavelength and the new wave. In practice we will want $\omega_s \approx \omega_{s1}$, but such that many oscillators occur in a betatron period.

For resonant electrons at $\Psi = 0$ (a constant wiggler),

$$\Delta v = 2\pi N \left[2 \frac{\Delta \gamma}{\gamma} - \frac{K^2 k_w^2 \gamma^2 \bar{\theta}^2 + a_{s1}^2}{1 + K^2} \right] \quad (1)$$

$$f(r) = \frac{e^{-r^2/2\bar{r}^2}}{2\pi\bar{r}^2} \quad f(\Theta) = \frac{e^{-\Theta^2/2\bar{\theta}^2}}{2\pi\bar{\theta}^2}$$

$$\Delta v_{\text{beam}} = 2\pi N \left[2 \frac{\Delta \gamma}{\gamma} - \frac{K^2 k_w^2 \bar{r}^2 + 2\gamma^2 \bar{\theta}^2 + a_{s1}^2}{1 + K^2} \right] \quad (2)$$

For a matched beam, the first two terms in the numerator of the second term are equal and

$$r_m = \left[\frac{\sqrt{2}\epsilon}{k_\beta} \right]^{\frac{1}{2}}$$

In this case the phase slip refers to an average over the beam profile. Imagine now the effect of a_{s1} in Eq. (1) remembering that both K and a_{s1} are functions of r . K increases off-axis and a_{s1} decreases off-axis. With a proper choice of radial profile the laser beam can tend to compensate for the increase of wiggler field off-axis so that the resonant field is maintained over a larger volume. It is helpful at this point to consider an example: the proposed CEBAF IR FEL where $r_m = 0.34$ mm, $\lambda = 6$ cm, and $K = 1.76$. The emittance-driven two terms are 4×10^{-3} total. They represent an equivalent energy spread of 10^{-3} . If we introduce a 10^{13} W, $1 \mu\text{m}$ laser on axis with $R_{L1} = 1$ m, then $a_{s1}^2 = 1.4 \times 10^{-3}$ on axis and could therefore have a significant canceling effect.

II. MODELING

1. Original 1-D Model

The following is a brief introduction about the 1-D model for FEL modeling when the external laser is not applied.

First, we assume that the wiggler field B_w and the laser field (E_s , B_s) have the following forms

$$B_w = B_0 \cos(k_w z) \hat{y}, \quad (3)$$

$$E_s = E_{s0} \cos \Psi_s \hat{x}, \quad (4.1)$$

$$B_s = B_{s0} \cos \Psi_s \hat{y}, \quad (4.2)$$

where $k_w = 2\pi/\lambda_w$ is the wiggler wavenumber, B_0 the peak on-axis wiggler magnetic field, $\Psi_s = (k_s z - \omega_s t + \phi)$ the phase of the optical field, and ω_s and k_s are the angular frequency and wavenumber of the laser field, respectively.

Then the one-dimensional equations describing the interaction between the electrons and the optical fields with a

linearly polarized wiggler configuration can be written in mks units as

$$\frac{d\gamma_i}{dz} = -k_s a_s a_w F_\xi \frac{\sin \Psi_i}{\gamma_i}, \quad (5.1)$$

$$\frac{d\Psi_i}{dz} = k_w - \frac{k_s}{2\gamma_i^2} (1 + a_w^2 + a_s^2 - 2a_s a_w \cos \Psi_i) + \frac{d\phi}{dz}, \quad (5.2)$$

$$\frac{d\phi}{dz} = \frac{\omega_p^2}{2c^2 k_s} \frac{a_w F_\xi}{a_s} \left\langle \frac{\cos \Psi}{\gamma} \right\rangle, \quad (5.3)$$

$$\frac{da_s}{dz} = \frac{\omega_p^2}{2c^2 k_s} a_w F_\xi \left\langle \frac{\sin \Psi}{\gamma} \right\rangle - \alpha a_s, \quad (5.4)$$

where

$a_w = eB_0 / \sqrt{2} m_0 c k_w$ is the rms wiggler parameter;
 $a_s = eE_s / \sqrt{2} m_0 c^2 k_s$ the normalized optical electrical field strength;
 $\omega_p^2 = (e/m_0) Z_0 |J|$ the electron plasma angular frequency;
 e the electron charge amount;
 c the speed of light;
 m_0 the rest mass of an electron;
 Z_0 the wave impedance of free space;
 $J = I_p / \Sigma_0$ the electron current density;
 I_p the electron micropulse current;
 Σ_0 the average optical mode area;
 α the attenuation coefficient of the optical field in the sense $a_s(z) = a_{s0} e^{-\alpha z}$;
 $\langle \dots \rangle$ averaging over sample electrons;
 γ_i the relativistic factor of the i th electron;
 $\Psi_i = (k_w + k_s)z - \omega_s t + \phi$ the phase of the i th electron in the ponderomotive potential well;
 ϕ the slowly varying phase of the laser field; and
 $F_\xi = J_0(\xi) - J_1(\xi)$ the coupling constant resulting from the linear wiggler configuration with $\xi = 0.5 a_w^2 / (1 + a_w^2)$.

2. Modified 1-D Model

When the external laser is added, the original 1-D FEL model is modified as follows

$$\frac{d\gamma_i}{dz} = -k_s a_s a_w(y) F_\xi \frac{\sin \Psi_i}{\gamma_i}, \quad (6.1)$$

$$\frac{d\gamma_i}{dz} = k_w - \frac{k_s}{2\gamma_i^2} (1 + a_w^2(0) + (a_w(0)k_w y)^2 + a_{s1}^2(y) + a_s^2 - 2a_s a_w(y) \cos \Psi_i) + \frac{d\phi}{dz}, \quad (6.2)$$

$$\frac{d\phi}{dz} = \frac{\omega_p^2}{2c^2 k_s} \frac{a_w(y) F_\xi}{a_s} \left\langle \frac{\cos \Psi}{\gamma} \right\rangle, \quad (6.3)$$

$$\frac{da_s}{dz} = \frac{\omega_p^2}{2c^2 k_s} a_w(y) F_\xi \left\langle \frac{\sin \Psi}{\gamma} \right\rangle - \alpha a_s, \quad (6.4)$$

where $a_{s1} = eE_{s1} / \sqrt{2}m_0c^2k_{s1}$ is the normalized strength parameter of the external laser.

It is noted that the main difference between eqs. (5.1)–(5.4) and eqs. (6.1)–(6.4) is that two terms, $(a_w(0)k_w y)^2$ and $a_{s1}^2(y)$, are added in eq. (6.2). In addition, all the fast-varying terms resulting from the external laser are neglected.

4. Canceling Effect or Compensation?

Let's look at the term

$$(a_w(0)k_w y)^2 + a_{s1}^2(y), \quad (7)$$

in eq. (6.2).

If we expand

$$a_{s1}^2(y) = a_{s1}^2(0)(1 - (y/\sigma_{s1})^2), \quad (8)$$

and write expression (7) into

$$(a_w(0)k_w y)^2 + a_{s1}^2(0) - a_{s1}^2(0)(y/\sigma_{s1})^2, \quad (9)$$

and then if we consider

$$(a_w(0)k_w y)^2 - a_{s1}^2(0)(y/\sigma_{s1})^2 = 0, \quad (10)$$

or

$$a_{s1}(0)/\sigma_{s1} = a_w(0)k_w, \quad (11)$$

this is a canceling effect.

If we consider

$$a_{s1}^2(0) \gg (a_w(0)k_w y)^2, \quad (12)$$

it is a compensation, since the term $a_{s1}^2(0)$ predominates in the phase evolution.

We may probably have the compensation effect only, since eq. (11) sets $a_{s1}(0)$ to a very high value that cannot be easily accomplished by using an E-M wave (the magnetostatic wiggler is the only way to get a field strength parameter like $a_w \geq 1$, and this is why few E-M wave wigglers or electrostatic wigglers are used for FELs). In addition, one principle should be that when the external laser is added, the resonance wavelength should not change too much.

III. SIMULATION RESULTS

Figure 3 shows the impact of applying the additional laser field. As an example, we are applying this idea to the CEBAF IR FEL. The parameters for the additional laser are: λ_{s1} (wavelength) = 1 μm , σ_{s1} (spot size) = 0.4 mm, R_L (Rayleigh range) = 1 m. The different field strength parameters are chosen for the additional laser, where $a_{s1} = 0.0$ and 0.02, respectively, for the curves #1 and #2, $a_{s1} = 0.088$ for curve #3, and $a_{s1} = 0.2$ for curve #4. The FEL power gain is calculated versus the position of the electrons in the y -direction. Note that when there is no additional laser, the gain drops to -8% at $y_0 = 1.5$ mm. But if the additional laser is

applied with the parameters chosen in the calculation, we still can have a gain of 18% at $y_0 = 1.5$ mm.

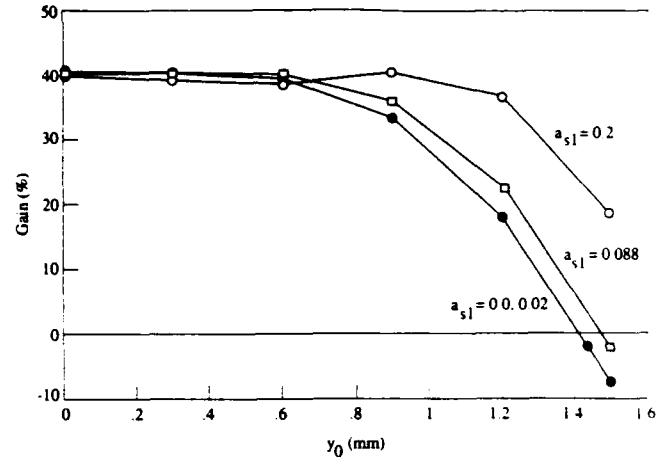


Figure 3. FEL gain for four different optical field strengths

It is pointed out that the above results were obtained with the 1-D model. Although we believe some of the most important aspects of this idea can be reflected with the 1-D model, as for FELs with no additional laser, the real 3-D calculations are necessary to confirm our estimations. Some further calculations will be presented in the near future.

III. REFERENCES

- [1] A. M. Sessler, D. H. Whittum, and Li-Hua Yu, *Phys. Rev. Lett.* **68**, 309 (1992).

Ultrahigh-Brightness Microbeams: Considerations for Their Generation and Relevance to FEL

H. Ishizuka, Y. Nakahara

Fukuoka Institute of Technology, Higashi-ku, Fukuoka 811-02, Japan

S. Kawasaki

Faculty of Science, Saitama University, Urawa, Saitama 388, Japan

K. Sakamoto, A. Watanabe, N. Ogiwara and M. Shiho

Japan Atomic Energy Research Institute, Naka, Ibaraki 311-02, Japan

Abstract

Field-emission tips have ever been the brightest electron source, but the current of focused beams from them has been very low. A substantial improvement in beam intensity and brightness is expected with the use of a microfabricated gated-emitter which produces a parallel beam near the emitter. A high-gradient accelerating field suppresses large displacement of electrons from the beam axis and thus reduces the emittance growth due to aberration. The emission is typically 100 μ A per tip, while higher currents are generated by tightly-packed arrays of the gated-emitters. The attainable normalized brightness is estimated to exceed 10^{13} A/m²rad², and such beams have unique uses for extending the laser wavelength to the X-ray region at moderate beam energies.

INTRODUCTION

The free-electron laser (FEL) performance is remarkably affected by the characteristics of driving beams. The radiation wavelength is fundamentally limited by the beam emittance by the relationship $\lambda \geq \pi \epsilon$, and the growth rate is an increasing function of the beam brightness. The requirements for good beam quality are especially stringent with compact FELs, that employ low-energy electron beams and short-period wigglers [1,2]. The beam quality deteriorates with propagation, and therefore the high source brightness is one of the key issues in obtaining a bright beam. So far the major effort has been directed to the development of photocathode combined with RF linac, and brightness of 8×10^{11} A/m²rad² has been reached [3].

With regard to current density, field emission is superior to the photoemission by orders of magnitude. Due to their high brightness, field emission tips have been commonly used in electron microscopy and electron-beam lithography. On the other hand the microfabrication technology has been applied to produce a gated field-emitter tip structure with submicrometer dimensions. Techniques for fabricating arrays of such emitters have also been established. Emission current densities of up to 1 kA/cm² have been demonstrated on small area arrays.

Those microemitters have been developed to meet the requirements of vacuum microelectronics: cold emission, low voltage operation, high current density, small size, high-frequency response and uniformity of emission. Application of microemitters to FEL has recently been proposed [5,6] in the light of their advantages.

FIELD-EMISSION SOURCES

The electron emission from a tip is characterized by a high current density, small emitting area and large divergence angle (≈ 0.3 rad). The current density given by the Fowler-Nordheim equation well exceeds 10^7 A/cm² for an electric field of 10^8 V/cm at the surface and a work function of 4 eV. The average thermal energy of emitted electrons is calculated to be 0.6 eV for the same parameters. The emitting area is of the order of 10 nm in radius when drawing 10 - 100 μ A. The normalized intrinsic emittance and source brightness are then of the order of 10^{-11} m rad and 10^{14-15} A/m²rad², respectively, though the details of the emission from a fine tip has not been clarified yet [7]. For conventional microbeams, up to 1 mA can be emitted from a single tip but the current at a focal spot is typically of the order of 10 nA. The reasons for this reduction are: 1) the beam spreads out quickly due to the initial angle, 2) the diversion is enhanced by the space-charge and 3) the beam is scraped by apertures placed in the lens system. The aperture system is designed to minimize the focal spot size, discarding electrons with high angular divergence or electrons with high displacement. In order to increase the current of a focused beam, therefore, one must keep the beam paraxial all through the system that includes the source and accelerator. The strategy is discussed in the next section.

ACCELERATION OF A MICROBEAM FROM A GATED FIELD-EMISSION TIP

High-Gradient Acceleration

The basic features of beam behavior are described by a paraxial envelope equation for the K-V distribution [8]

$$a'' + \frac{\gamma' a'}{\beta^2 \gamma} + \left(\frac{\gamma''}{2\beta^2 \gamma} + \frac{\Omega_L^2}{\beta^2 c^2} \right) a - \frac{K}{a} - \frac{\epsilon_n^2}{\beta^2 \gamma^2} \frac{1}{a^3} = 0 \quad (1)$$

where a is the beam radius, ' indicates the derivative with respect to axial position z , β and γ are conventional relativistic notations, c is the speed of light, Ω_L the relativistic Larmor frequency, ϵ_n the normalized emittance, and $K = 2I / \beta^3 \gamma^3 I_0$ represents the space-charge of the beam current I in terms of $I_0 = 17$ kA. Equation (1) shows that the acceleration γ' has a focusing effect on a diverging beam. This effect is specially important at the early stage of acceleration where β is small and the space-charge causes the main problem. With conventional field-emitters the electric field is strong only on

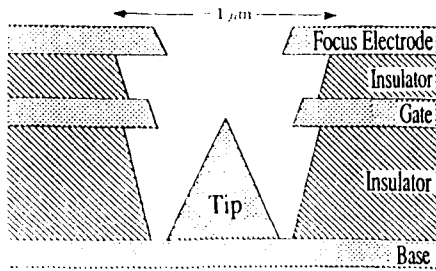


Fig. 1. Microemitter with a focusing electrode.

and around the tip. In gated microemitters as shown in Fig. 1, a gate (grid) is located close to the tip and provides a boundary beyond which an intense electric field can be present. In the following we assume a uniform accelerating field ($\gamma'' = 0$) of up to 4 MV/m, which is practical even in dc mode.

Electrostatic Pre-Focusing at the Source

As proposed by Spindt [7], addition of a focusing electrode to the emitter enables the formation of a parallel beam near the tip. Computer simulation has demonstrated that the radius and divergence angle at 1 keV energy can be as small as 3 μm and 5 mrad, respectively, in the presence of an accelerating field of 4 MV/m [9]. The phase plot is distorted due to the spherical aberration of the lens, but the effective normalized emittance is evaluated to be a few times 10^{-10} m rad for a 10 μA beam.

After leaving the source the beam radius increases with axial distance. Solving eq. (1) numerically for $\gamma'' = \Omega_L = 0$, we plot in Fig. 2 the beam radius at 10 keV vs the beam current. The initial values (at 1 keV) of a and a' are 3 μm and 5 mrad, respectively, and the axial electric field and normalized emittance are the parameters. The focusing effect of the axial electric field is clearly seen. The six curves in each group are, from the bottom to the top, for $\epsilon_n = 0$ to 10^{-9} m rad at an interval of 2×10^{-10} m rad. Note that the beam radius is insensitive to both the emittance and the beam current when E_z is high; $a \leq 10 \mu\text{m}$ for $I_b \leq 100 \mu\text{A}$ and $E_z \geq 4$ MV/m.

Magnetic Pre-Focusing near the Source

A magnetic field can be utilized, instead of the electrostatic lens, to suppress the divergence of microbeams. An immersed

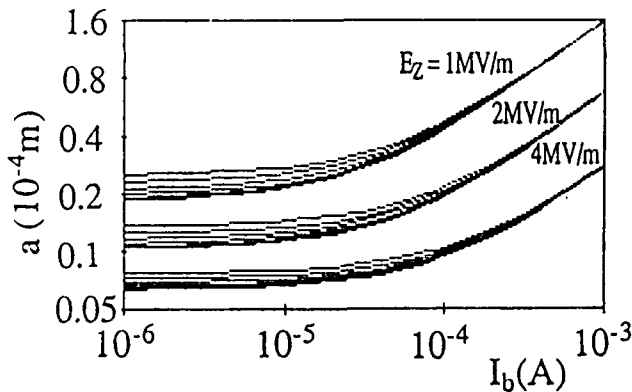


Fig. 2. Beam radius at 10 keV vs current. Beams from emitters with a focusing electrode and accelerated in uniform electric field E_z . $\epsilon_n = 0, 2, 4, 6, 8, 10 \times 10^{-10}$ m rad.

cathode has already been a practical option for enhancing the brightness of microbeams in the submicroampere range [10]. In the presence of a strong accelerating field, much higher currents can be confined by the axial magnetic field.

A field-emission tip is assumed to be located at $z = 0$ in a magnetic field given by a vector potential

$$A_\theta = \frac{r}{2} B_0 \left(1 - \frac{1}{8} \frac{r^2}{z_0^2} \right) \exp(-z/z_0) - \frac{r}{2} B_1 \quad (2)$$

where r is the radial variable. In Fig. 3a is shown the on-axis field B_z for $B_0 = 3$ kG, $B_1 = 1$ kG and $z_0 = 4$ cm. The equations of motion, including the self-field term of uniform beam, were solved for electrons leaving the tip of 10 nm radius under the following conditions at 100 eV energy: beam radius 500 nm, divergence 0.3 rad, and the spread in transverse energy 0.6 eV. Formation of a nearly parallel beam is shown in Fig. 3b for a 10 μA beam and $E_z = 4$ MV/m (the electron energy is 400 keV at $z = 10$ cm). When increasing the current to 100 μA , the maximum radius becomes slightly larger than 0.1 mm.

The initial value of the canonical angular momentum is small because of smallness of the source. If the magnetic field is not reversed as in Fig. 3a, the beam converges to a spot and crossover appears. The magnetic cusp was introduced to avoid this and produce a Brillouin-like flow. The emittance diagram computed at different axial positions did not show significant distortions due to the spherical aberration.

Emittance Preservation during acceleration

The pre-focused beams are accelerated to higher energies by a uniform electric field. In Fig. 4 are plotted the radius and divergence angle as functions of axial position z . Here 10 μA and 100 μA beams from the emitter with a focusing electrode are accelerated to 10 MeV. No lens is assumed outside the emitter, and so γ'' and Ω_L are put to 0 in eq. (1). The effect of emittance on the beam dynamics is negligibly small. In the accelerator the emittance is preserved because the space

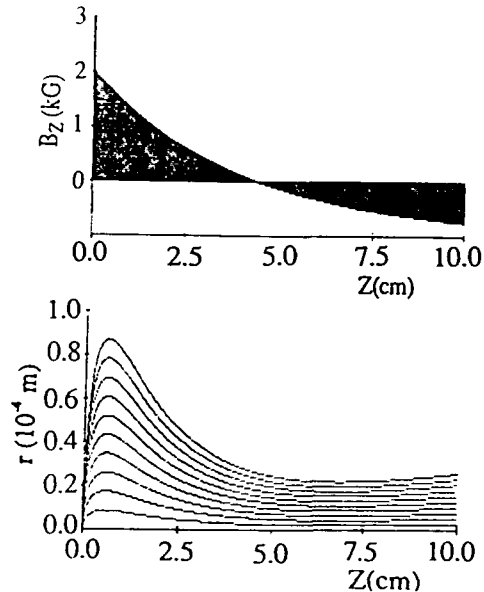


Fig. 3. Magnetic pre-focusing. (a) Magnetic field vs z . (b) Radial position vs z in a 10 μA beam. $E_z = 4$ MV/m.

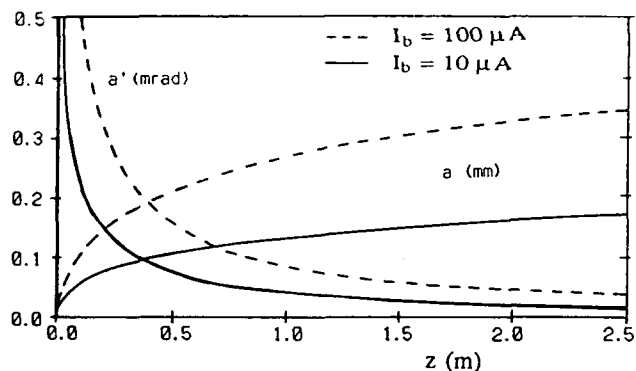


Fig. 4. Beam radius and divergence vs axial position in the accelerator. The beam energy is 10 MeV at $z = 2.5$ m.

charge is insignificant, the beam is very paraxial, and there exists no lens to cause aberration. The beam is finally focused to a spot whose size is limited by the emittance [6, 8].

APPLICATION OF MICROBEAMS TO FEL

The beam parameters crucial to the FEL operation are peak current and energy spread. Electron beams from microemitters have low current and will be used for FELs in the Compton regime, where the space-charge force is negligible. A single-pass and short-wavelength FEL should be the most suitable target in view of the small beam emittance. In the high-gain Compton regime, the velocity spread $\Delta \gamma_z$ directly affects the interaction between the beam and the co-moving radiation through the trapping of electrons into the pondermotive potential well; the acceptable velocity spread is expressed as $\Delta \gamma_z / \gamma_z \ll 1/2N$, where N is the number of wiggler periods.

Finite transverse emittance of the beam causes an axial electron velocity spread $\Delta \gamma_z / \gamma_z \approx (\epsilon_n / r_b)^2 / 2 (1 + K^2)$, where ϵ_n is the normalized emittance, r_b the radius of the electron beam and K is the normalized rms undulator vector potential amplitude. Axial velocity spread is also introduced by many other factors including the space-charge, wiggler field error, wiggler focusing field and the axial magnetic field in the beam source and/or the wiggler [11, 12]. (The presence of axial magnetic field at the source induces effective emittance due to the canonical angular momentum. In that case it is desirable to extend the axial field over the whole system to the wiggler section.) However, the contribution of emittance to the total effective axial energy spread is the most important limiting factor in the application of the beam to the generation of short-wavelength radiation.

Another effect of the beam emittance ϵ on FEL is related to geometrical overlap of the beam and the radiation. Though the laser efficiency peaks at a nonzero value of ϵ [13], the beam emittance must be smaller than, or at least nearly equal to, λ / π for good overlap to be achieved. This requirement sets an upper bound to the radiation wavelength λ and suggests that the beam from microemitters would take advantage of its small emittance to lase at λ 's smaller than a few μm .

Thin beams from microemitters fit into different kinds of microwigglers. Tunable millimeter and submillimeter waves

have been generated by ledatron [14] using a Fabry-Perot resonator as wiggler; an electron beam propagating through a closely arranged pair of a metallic diffraction grating and a reflector gives rise to stimulated emission. Generation of visible light has also been studied with this device. Another FEL has been proposed based on the Cherenkov emission of light by a beam passing through a waveguide loaded with a dielectric pipe, whose inner radius is of the order of $1 \mu\text{m}$ [15].

Generation of coherent X-rays due to crystal channeling of electrons is also an attractive subject. It has been shown theoretically that the necessary current density is $\sim 10^5 \text{ A/cm}^2$, when multiple Bragg reflections are effectively utilized for radiation guiding [16]. A 10 MeV, $10 \mu\text{A}$ pulsed beam with normalized brightness $\sim 10^{13} \text{ A/m}^2 \text{ rad}^2$ is supposed to yield X-ray emission which is intense enough for practical use.

In this paper we have shown that diversion of a microbeam is greatly reduced by applying a strong accelerating field in the region directly connected to the source. The beam quality may be significantly improved by increasing the (peak) electric field to $\sim 100 \text{ MV/m}$ as in RF linacs, and the microbeam will find wide application to FEL owing to their unique characteristics.

REFERENCES

- [1] C.W. Roberson and B. Fafizi, IEEE J. Quantum Electron. **27**, 2508 (1991).
- [2] C.M. Tang, B. Fafizi, E. Esarey, A. Ting, W. Marable and P. Sprangle, "Key Physics Issues Affecting the Performance of Free-Electron Lasers," AIP Conference Proceedings No. 249, Physics of Particle Accelerators, ed. M. Month and M. Dienes (1992).
- [3] J. Fraser and R. L. Sheffield, IEEE J. Quantum Electron. **23**, 1489 (1987).
- [4] C.A. Spindt, C.E. Holland, A. Rosengreen and I. Brodie, IEEE Trans. Electron Devices **38**, 2355 (1991).
- [5] C.M. Tang, A.C. Ting and T. Swyden, Nucl. Instr. and Meth. **A318**, 353 (1992).
- [6] H. Ishizuka, Y. Nakahara, S. Kawasaki, N. Ogiwara, K. Sakamoto, A. Watanabe and M. Shiho, 14th Intern. Conf. FEL, 1992, to be published in Nucl. Instr. Meth.
- [7] W.B. Herrmannsfeldt, R. Becker, I. Brodie, A. Rosengreen and C.A. Spindt, "High-Resolution Simulation of Field Emission," SLAC-PUB-5217 (1990).
- [8] J.D. Lawson, "The Physics of Charged-Particle Beams," Second Edition (Clarendon Press, Oxford, 1988).
- [9] R. M. Mobley and J. E. Boers, IEEE Trans. Electron Devices **38**, 2383 (1991).
- [10] J.R.A. Cleaver, Optik **52**, 293 (1978/79).
- [11] L.H. Yu, S. Krinsky and R.L. Gluckstern, Phys. Rev. Lett. **64**, 3011 (1990).
- [12] H.P. Freund and R.H. Jackson, Phys. Rev. **A45** (10) 7488 (1992).
- [13] B. Fafizi and C.W. Roberson, Phys. Rev. Lett. **68**, 3539 (1992).
- [14] K. Mizuno and J. Bae, JAERI-M 91-141, p. 94 (1991).
- [15] T. Taguchi and K. Mima, 14th Intern. Conf. FEL., 1992, to be published in Nucl. Instr. Meth.
- [16] M. Strauss and N. Rostoker, Phys. **A40**, 7097 (1989).

THE GROOVE GUIDE: A NON-CONVENTIONAL INTERACTION STRUCTURE FOR MICROWAVE FEL EXPERIMENTS

P. ARCIONI*, M. BRESSAN*, F. BROGGI*, G. CONCIAURO,* P. PIERINI*

* Dept. of Electronics, University of Pavia
Via Abbiategrasso 209, 27100 Pavia, ITALY

* LASA - INFN Sezione di Milano
Via Fratelli Cervi 201, 20090 Segrate (Milano), ITALY

Abstract

We discuss the use of a groove guide as the FEL interaction structure for the ELFA experiment: the groove guide confines the 100 GHz radiation and controls the slippage, permitting to investigate different FEL regimes. The groove guide is a laterally open structure: it supports a *single* guided mode even if its dimensions are large compared with the wavelength, as required in the experiment to accommodate the beam. Thus, differently from conventional oversized rectangular waveguides, the groove guide allows the beam to interact with a single mode, simplifying the design of the structure. The lateral openings ease the beam diagnostics as well, and overcome pumping problems.

1. INTRODUCTION

ELFA [1] is a high gain FEL designed to operate in the millimeter wavelength range ($\lambda = 3$ mm). One of the main goal of ELFA is to study the different regimes of the FEL interaction, i.e. the steady-state (SS) and the superradiance (SR) [2]. This is accomplished by controlling the slippage due to the different propagation velocities of the radiation and of the electron beam. Thus the structure that guides the radiation along the beam path is one of the critical component of the experiment. A rectangular waveguide operating in the TE_{01} mode is the solution considered in previous FEL experiments [3,4,5]. The rectangular waveguide that could be used for the ELFA experiment would have a width of 50 mm and a height of 8.7 mm (SS regime) or 9 mm (SR regime). The width of 50 mm depends on the amplitude of the transverse motion of the bunches and on the necessity of providing a suitable clearance for alignment purposes. These dimensions are very large compared to λ , and about 300 modes, many of them having

potential interaction with the beam, could propagate at the operating frequency of ELFA (100 GHz). Thus the use of such an oversized waveguide would lead to many problems related to the control of unwanted modes excited by the beam itself and by any waveguide discontinuity. Moreover, the high operating frequency and the huge number of high order modes would preclude the use of standard waveguide components (e.g. directional couplers, detectors, attenuators, loads, transitions and so on) in the design of the microwave circuitry connecting the FEL waveguide to the generator and to the output diagnostics.

To overcome these problems we considered a different guiding system, the so called "groove-guide" (GG), which is a typical low-loss transmission structure in the 3 mm band [6,7,8]. It is an open waveguide, consisting of two parallel conducting planes (see Fig. 1), where two longitudinal grooves permit to trap the electromagnetic energy. In general, the field inside the GG can be considered as the sum of some trapped modes, plus a continuous eigenfunction spectrum [9]. When the GG is suitably designed, only one mode remains trapped in proximity of the grooves: this mode is suitable for FEL interaction, since it has a field distribution that resembles the TE_{01} pattern in a rectangular waveguide (see Fig. 2). Differently from a rectangular waveguide, however, in a GG the beam interacts only locally with the fields associated with the continuous eigenfunction spectrum, that in any case are excited by the waveguide discontinuities and by the beam itself. In fact, the electromagnetic energy associated with these fields is radiated laterally, and thus it is effectively removed from the beam region. For this reason, when dealing with the electron/radiation interaction in a GG, only the trapped mode can be considered, since its field is the only one which gives rise to a continuous interaction along the whole structure.

The use of a GG in FEL experiments appears very attractive also because the lateral openings make feasible a number of sensing devices to be placed along the beam path to monitor the beam/radiation interaction.

2. THE GROOVE GUIDE

Fig. 2 shows the geometry of a GG and the electric field pattern of its dominant mode. The GG offers single-mode propagation up to a spacing b of the order of some wavelengths, provided the depth d of the grooves is about $b/4$ and their width a is of the order of b [10]. Since the fields of the dominant mode decay exponentially in the transverse direc-

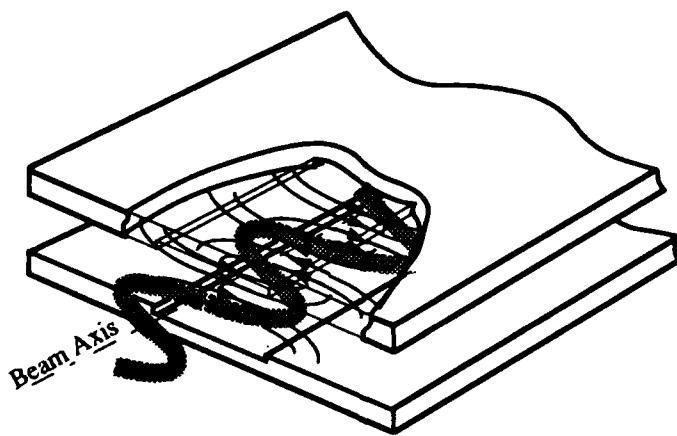


Fig. 1

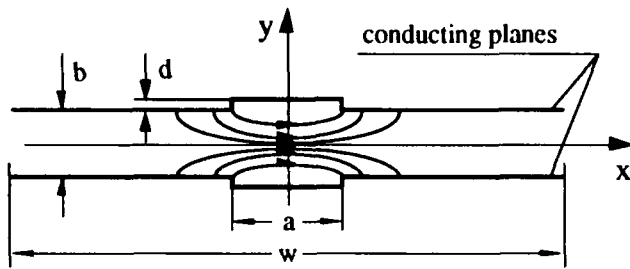


Fig. 2

tion, the propagation properties of the GG do not depend on the overall width w , provided it is sufficiently large. Thus the dimension w of the structure is not critical, and a value of about 6 times b is adequate [10].

The group velocity can be adjusted by a suitable choice of the dimensions a , b and d of the GG. In particular, for given dimensions a and d of the grooves, the spacing b affects mainly the group velocity. This fact suggests that it is possible to use the same structure to experiment both SS and SR regimes, provided the mechanical design allows one to trim the spacing b . Moreover, the dimensions of the groove affect the amount of the confinement of the electromagnetic energy. We can take advantage of this feature to increase the density of the electromagnetic energy in the region spanned by the beam and, consequently, the efficiency of the FEL interaction.

3. DIMENSIONING OF THE STRUCTURE

The actual dimensioning of the GG is performed with the aim of increasing as much as possible the coupling between the beam and the field, keeping the spacing b adequate to allow the beam alignment. To this end we carried out many numerical tests on different structures, considering different values of the dimensions a and b , and adjusting the groove depth d to obtain the group velocity suitable for SS regime. The resulting values of d are plotted in Fig. 3 as a function of the groove width a for values of the plane spacing b ranging from 5 mm to 7 mm (larger values of b result in poor confinement of the field, whereas 5 mm was considered to be the minimum allowable plane separation). The calculations

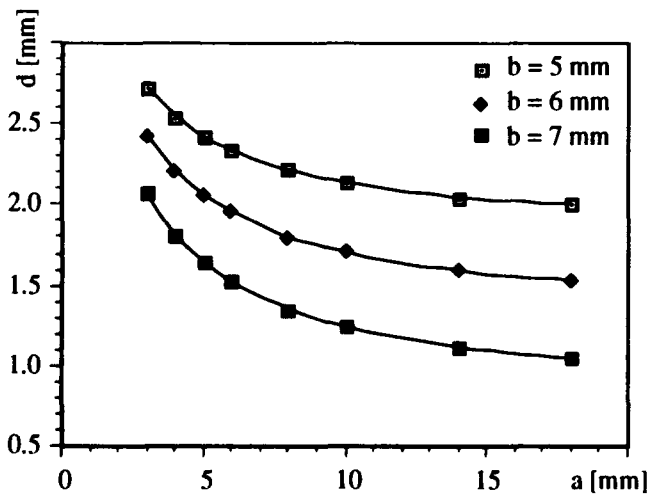


Fig. 3

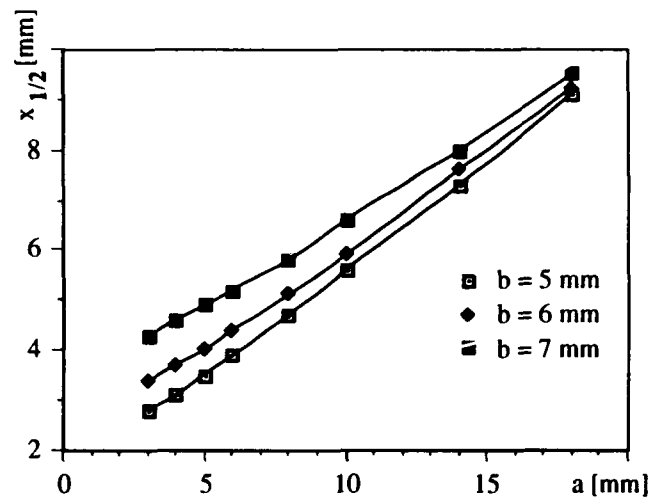


Fig. 4

were performed using the code PAGODA [11] that gives propagation constants and modal field of arbitrarily shaped waveguides.

From the modal field we calculated the coupling C of the wiggling electrons with the propagating electric field, normalized to the coupling in a reference rectangular waveguide:

$$C = \frac{\langle E^{GG} \cdot v \rangle_{\lambda_w}}{\langle E^{RW} \cdot v \rangle_{\lambda_w}} = \frac{\langle E_x^{GG} v_x \rangle_{\lambda_w}}{\langle E_x^{RW} v_x \rangle_{\lambda_w}} \quad (1)$$

where E^{GG} and E^{RW} are the (normalized) modal electric field of the groove guide and of the rectangular waveguide respectively, v is the velocity of the electrons and the average is performed on the wiggler period λ_w ($\lambda_w = 10$ cm for ELFA). When evaluating (1) it is possible to expand the electric field around the beam axis ($x=0$, $y=0$, see Fig. 2), and to truncate the expansion at the second order. It has been verified that this approximation is very accurate up to a distance $x/2$ from the beam axis where the field is 1/2 of its maximum value. The distance $x/2$ is of the order of $a/2$ and increases for increasing b , as shown in Fig. 4; in any case it is comparable or larger than the amplitude Γ of the wiggling motion of the electrons ($\Gamma = 3.18$ mm for ELFA). From (1) it is obtained:

$$C = \left[E_x(0,0) + \frac{\partial^2 E_x}{\partial x^2} \frac{\Gamma^2}{4} \right] \sqrt{\frac{a^{RW} b^{RW}}{2}} \quad (2)$$

where the derivative is evaluated at the beam axis and $a^{RW} = 50$ mm, $b^{RW} = 8.7$ mm are the dimensions of the reference rectangular waveguide (see the Introduction). Fig. 5 reports the values of C as a function of the groove width a for different values of the plane spacing b : in all the considered cases C is greater than 1, i.e. the coupling in the GG is larger than in the reference rectangular waveguide. Moreover, it is noted that for each value of the spacing, it is possible to maximize the coupling by choosing a suitable value of a . Since the maximum values of C are only slightly different for the

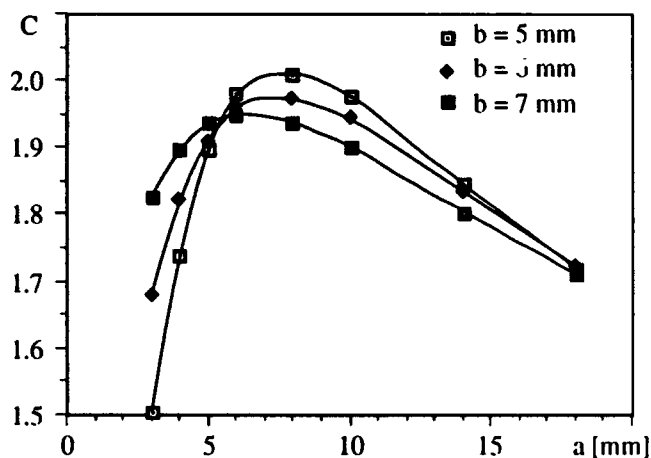


Fig. 5

three curves, the largest spacing, more convenient to accommodate the beam, can be used. For these reason the dimensions of the GG best suited for ELFA are: $a = 6 \text{ mm}$, $b = 7 \text{ mm}$, $d = 1.52 \text{ mm}$.

In order to verify the sensitivity of the slippage to the dimensional tolerances, some numerical evaluations have been carried out, considering small variations of the above mentioned values. Defining the normalized slippage parameter l_s/L_w as

$$\frac{l_s}{L_w} = \frac{v_g - v_{\parallel}}{v_{\parallel}}$$

where l_s is the "slippage length", L_w the length of the wiggler, v_g the group velocity and v_{\parallel} the longitudinal velocity of the electrons, the following sensitivity values were found:

$$\begin{aligned} \partial(l_s/L_w)/\partial a &= 1.2 \cdot 10^{-3} \text{ [mm}^{-1}\text{]} \\ \partial(l_s/L_w)/\partial d &= 5.6 \cdot 10^{-3} \text{ [mm}^{-1}\text{]} \\ \partial(l_s/L_w)/\partial b &= 5.5 \cdot 10^{-3} \text{ [mm}^{-1}\text{]} \end{aligned}$$

Since the length of the ELFA wiggler is 8 m, and assuming that the slippage length must be controlled with an accuracy of the order of 1 mm, the obtained sensitivities show that the dimensional tolerances required in the manufacturing of the GG are not very critical, and precision milling of metal blocks appears to be adequate. Moreover, the last sensitivity value shows that it is possible to change the slippage length from 0 (SS regime) to 15 mm (SR regime) by increasing the plane spacing b from 7 mm to 7.34 mm.

4. INFLUENCE ON THE FEL GAIN AND ON THE OUTPUT POWER

According to the 1-D FEL model [12], the enhanced coupling between the guided mode and the electron beam gives rise to an increase of the FEL gain parameter ρ , which determines all the relevant scaling laws and operating constraints for a FEL [12]. Introducing the coefficient C , defined in the previous section, in the FEL universal scaling of Ref. [13], it can be seen that the FEL gain parameter ρ is multiplied by a factor $C^{2/3}$. Considering a value of $C = 1.95$ for the preferred GG (see Fig. 5), the gain parameter ρ increases approximately by a factor of 50%. All the quantities related to ρ changes ac-

cordingly. In particular, the gain length, i.e. the e-folding length of the exponential growth of the radiation power along the wiggler, is given by:

$$L_{\text{gain}} = \frac{\lambda_w}{4\pi\rho}$$

Thus, the increase in the gain parameter ρ leads to a reduction of the gain length by a rough factor of 30%, allowing for a significantly shorter wiggler length required to saturate the emitted radiation. Moreover, the emitted FEL power at saturation is given by

$$P_{\text{out}} \approx \rho P_{\text{beam}}$$

where P_{beam} is the electron beam power. Again, the increase in ρ due to the coupling enhancement predicts an increase of the emitted FEL power of nearly 50%.

Also considering these 1-D scaling laws, the groove guide appears to be a very promising interaction structure, having superior characteristics with respect to the standard rectangular waveguide used for previous FEL microwave experiments. A more careful 3-D analysis of the FEL interaction in the groove guide is under way in order to verify these attractive features of the use of this structure for microwave FEL experiments.

REFERENCES

- [1] E. Acerbi et al., "The Revised ELFA Project", these Proceedings.
- [2] R. Bonifacio et al., Nucl. Instrum. and Meth., A 296 (1990), pp. 359-367.
- [3] T.J.Orzechowsky et. al., "Microwave Radiation from a High Gain Free-Electron Laser Amplifier," Phys. Rev. Lett. 54, 889 (1985).
- [4] A.L Throop et. al., "Experimental Results of a High Gain Microwave FEL at 140 GHz", Nucl. Instrum. and Meth., A 272, (1988), pp.15-21.
- [5] R. Bartolini et al., "Theoretical and Experimental Aspects of a Waveguide FEL", Nucl. Instrum. and Meth., A 304, (1991), pp. 417-420.
- [6] D. J. Harris, K. W. Lee, and R. J. Batt, "Low-Loss Single-Mode Waveguide for Submillimetre and Millimetre Wavelengths", J. Infrared Physics, Vol. 19, pp.741-747, 1878.
- [7] D. J. Harris, K. W. Lee, and J. M. Reeves, "Groove and H-Waveguide Design and Characteristics at Short Millimetric Wavelength", IEEE Trans. Microwave Theory and Tech., Vol. MTT-26, pp. 998-1001, Dec. 1978.
- [8] D. J. Harris, K. W. Lee, "Groove-Guide as a Low-Loss Transmission System for Short Millimetric Waves", Electron. Lett., Vol 13, n. 25, 8 Dec. 1977, pp. 775-776.
- [9] R. E. Collin, "Field Theory of Guided Waves" - 2nd ed. Chapter 11, IEEE Press, New York, 1990.
- [10] D. J. Harris, K. W. Lee, "Groove-Guide Propagation Characteristics at 3mm Wavelength", Electron. Lett., Vol. 14, n. 4, 16 Feb. 1978, pp. 101-102.
- [11] P. Arcioni, M. Bressan, G. Conciauro: "PAGODA: a Computer Code for the Analysis of Waveguides - Operating Manual", Technical Report 03/90, Dept. of Electronics of Pavia, Jan. 1990.
- [12] R.Bonifacio et al, "Physics of the High Gain FEL and Superradiance", La Rivista del Nuovo Cimento, vol 9, 1990.
- [13] R.Bonifacio, C. Pellegrini and L.Narducci, "Collective Instabilities and High Gain Regime in a Free Electron Laser", Opt. Commun. 50 (1984), 313.

First Undulators For The Advanced Light Source

E. Hoyer, J. Akre, J. Chin, B. Gath, D. Humphries, B. Kincaid, S. Marks, P. Pipersky, D. Plate, G. Portmann, and R. Schlueter
Lawrence Berkeley Laboratory, University of California, Berkeley, California 94720

W. V. Hassenzahl

Lawrence Livermore National Laboratory, University of California, Livermore, California 94551

Abstract

The first three undulators, each 4.6 m in length, for the Advanced Light Source (ALS) at Lawrence Berkeley Laboratory (LBL), are near completion and are undergoing qualification tests before installation into the storage ring. Two devices have 5.0-cm period lengths, 89 periods, and achieve an effective field of 0.85 T at the 14 mm minimum magnetic gap. The other device has a period length of 8.0 cm, 55 periods, and an effective field of 1.2 T at the minimum 14 mm gap. Measurements on the first 5 cm period device show the uncorrelated field errors to be 0.23%, which is less than the required 0.25%. Measurements of gap control show reproducibility of ± 5 microns or better. The first vacuum chamber, 5.0 m long, is flat to within 0.53 mm over the 4.6 m magnetic structure section and a 4×10^{-11} Torr pressure was achieved during vacuum tests. Device description, fabrication, and measurements are presented.

I. INTRODUCTION

The ALS, a third-generation synchrotron radiation source is currently being commissioned at LBL. Concurrently, the first ALS undulators are nearing completion, undergoing qualification testing, and are to be installed soon in the low-emittance 1.5 GeV storage ring to produce high brightness beams in the UV to soft x-ray range. Two devices have 5.0-cm period lengths (IDA-U5.0 and IDB-U5.0), and the third device has an 8.0-cm period length (IDC-U8.0), which will produce high brightness in the 50 to 1500 eV and 6 to 1000 eV ranges respectively. The undulator specifications and design have been reported elsewhere [1, 2, and 3]; the first U5.0 Undulator near completion is shown in Figure 1.

II. MAGNETIC STRUCTURE

As seen in Figure 1, the magnetic structure includes two large backing beams, each has five assembly sections and two end pole structures attached. Six low-reluctance flux shunts connect the two backing beams magnetically. A U5.0 assembly section, Figure 2, consists of 35 half-period pole assemblies, each bolted to a pole mount.

The basic building block of the magnetic structure is the half period pole assembly which consists of an aluminum keeper, a Vanadium Permendur pole and six Nd-Fe-B magnetized blocks. Manufacture of these assemblies is as follows:

- Nd-Fe-B blocks are ordered with stringent specifications which include $H_c \geq 10400$ Oe [4].

- Blocks are inspected for defects, mechanical dimensions, magnetic imperfections and measured using an automated Helmholtz coil system [5]. Results show that the 4,582 U5.0 blocks have average easy axis magnetization of 1.1137 T ($\sigma = 0.0110$ T) and average minor axis magnetization components of 0.0031 T ($\sigma = 0.0044$ T) and 0.0011 T ($\sigma = 0.0043$ T) [6].



Figure 1. U5.0 Undulator

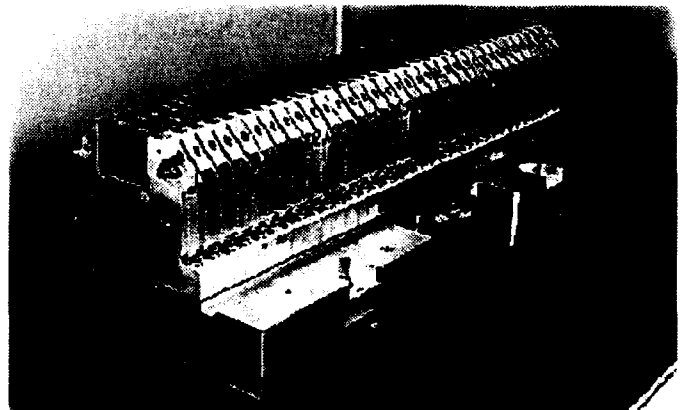


Figure 2. U5.0 Undulator Assembly Section

- Blocks are sorted into the six-block arrays. The sorting algorithm, code INSORT, minimizes pole excitation errors, reduces direct field effects at the electron beam, and generates assembly diagrams showing where each block goes in each half-period pole assembly.
- The Vanadium Permendur poles are machined, heat treated in a hydrogen furnace at 875 degrees C for four hours and then finish machined. Each pole is pinned to its keeper with four stainless pins.
- The Nd-Fe-B blocks are positioned with a bonding fixture and bonded into the pole-keeper assembly with a room temperature curing epoxy (Technicol 8260/8261) [7].

Assembly section fabrication utilizes a milling machine and a pole assembly holding fixture to place and bolt the half-period pole assemblies to the pole mount. To achieve the 25 μm vertical and 50 μm longitudinal pole tip positional tolerances, the half-period pole assemblies are aligned using an automated coordinate measurement machine, statistically-based error reference planes, and shimming techniques.

The aligned assembly sections are installed on the backing beams and aligned relative to each other using optical tooling and laser interferometric techniques [8]. The longitudinal positions of the assembly sections are measured using a simple linear interferometer and associated optics. Because of the differential expansion coefficient between the aluminum assembly section and the steel backing beam, a bi-linear temperature compensation function is applied to the position data to predict periodicity errors at a pre-determined operating temperature which in general differs from measurement temperatures.

The vertical alignment of the assembly section reference planes, to within a 12 μm tolerance, is obtained by using an angular interferometer, and performing an integrated angle calculation on the data. Repeatability error for these measurements is typically less than 3 μm .

The magnetic structure is terminated with end structures that contain Nd-Fe-B rotor assemblies to null the undulator dipole field. These rotors are driven through linkages from the backing beams and can be positioned to within 2 degree [9 and 10].

Each end structure is outfitted with a multiple trim magnet cartridge that corrects higher order magnetic field errors in the undulator. A cartridge contains up to nine transversely located permanent magnets (Nd-Fe-B) that are vertically oriented and adjustable to correct for both vertical and horizontal undulator field integral errors [11].

The backing beams are of low carbon steel construction and stress-relieved at 600–700 degrees C for four hours. The Ni-Fe flux shunts connecting the upper and lower backing beams reduce the effect of environmental magnetic fields on the undulator magnetic field [12].

III. SUPPORT/DRIVE /CONTROL SYSTEMS

A generic support/drive/control system is used for the ALS undulators. The support and drive systems, shown in

Figure 1, include the support structure that provides the framework for holding the magnetic structure and the drive system that opens and closes the magnetic gap. Gap motion is achieved with a stepper-motor/gear box/roller chain drive with coupled left-hand & right-hand 2 mm pitch Transrol roller screws attached to the upper and lower backing beams [13]. Adjustment of the magnetic gap can be as fine as 5 μm through the use of offset keys in the roller screw shaft couplings. Compensating springs match the gap dependent magnetic load to within 20%. Magnetic field taper can be provided manually by stepping one of the main roller chain sprocket's teeth with respect to the chain in increments of 87 μm /sprocket tooth ($\Delta E/E = 0.96\%$ at 1.4 cm gap).

A Compumotor system, Indexer Model No. 500—Driver Model PK130M—Absolute Rotary Encoder Model ARC, is used to drive and control the magnetic gap. This stepper motor and absolute rotary encoder system is designed such that each motor step and encoder step corresponds to 0.067 μm and 0.106 μm motion of the gap respectively. The motor control system also allows for velocity profiling during a move. Results of support, drive, and control system tests are given in Table 1.

Table 1.
Support/drive/control system test results

Test	Performance
Magnetic structure alignment (upper-to-lower structure)	Gap parallelism within 5 μm ; transverse within 250 μm ; longitudinal within 150 μm
Gap range	14 mm to 210 mm
Gap opening-closing time	1 minute
Reproducibility	$\leq \pm 5 \mu\text{m}$; $\pm 20\%$ for 1 μm steps
Backlash (encoder to gap)	$\leq 10 \mu\text{m}$
Scan rate	3.33 mm/sec max.

A gage block and a laser interferometer is used to calibrate the absolute encoder to the gap position. Figure 3 shows the deviation from linearity with and without compensating springs (three hysteresis loops each). The backlash of the system has gap dependence, and the character of the upper hysteresis curve is due to the compensating springs not exactly canceling the force of the magnetic field. Nonlinearities are removed with calibration.

Each undulator is outfitted with a transparent enclosure for safety, and for maintaining uniform temperature throughout the insertion device. Tests show that the gap sensitivity coefficient, due to a vertical temperature gradient in a backing beam, is 6 $\mu\text{m}/0.1$ degree C and that the temperature gradient is eliminated when fans circulate air within the enclosure.

IV. VACUUM SYSTEM

The 5.1 m long IDA-U5.0 commissioning vacuum chamber, shown in Figure 1, is machined from two 5083-H321 aluminum plates and welded together [14]. Pockets machined

into the chamber accommodate the poles of the magnetic structure for small magnetic gap operation. Mechanical measurements taken at the completion of final assembly, after UHV conditioning and under vacuum, are given in Table 2.

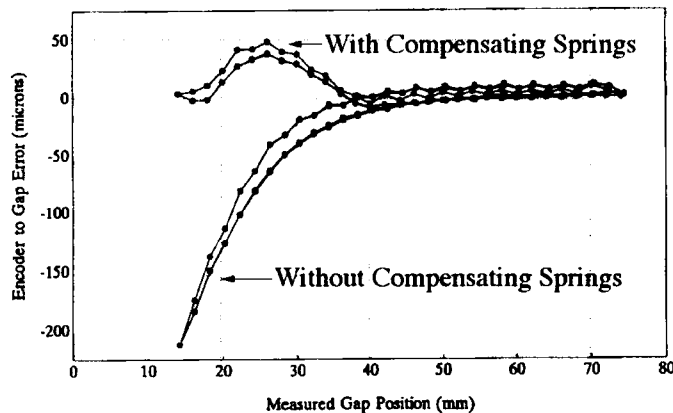


Figure 3. Hysteresis Loops with and without compensating springs for IDB-U5.0.

Table 2.

ALS Commissioning Vacuum Chambers Measurements			
Measurement	IDA-U5.0	IDB-U5.0	IDC-U8.0
Vertical aperture	18.97 mm	18.83 mm	In progress
Min. v.c. gap	21.64. mm	21.77 mm	In progress
V.C. flatness	0.53 mm	0.74 mm	In progress
Hor. straightness	0.08 mm	0.05 mm	In progress

The pumping system of each vacuum chamber includes three combination 60 l/s ion-600 l/s titanium sublimation pumps, a 2400 l/s ALS absorber tsp pump, and 4800 l/s of non-evaporable getter (Saes-type ST707/CTAM/30D strip).

Chamber ultra-high vacuum conditioning is at 140 degrees C, for a minimum of 48 hours [15]. The base pressure achieved after conditioning is 3.7×10^{-11} Torr for the IDA-U5.0 chamber and 7.0×10^{-11} Torr for the IDB-U5.0 chamber.

V. MAGNETIC MEASUREMENTS

A high speed, precision magnetic measurement system has been designed and built for detailed magnetic characterization of ALS insertion devices [16]. Primary magnetic field information, integral and local data, are derived from Hall probe measurements. A 5.5 m long integral coil is also used to measure field integrals.

The rms harmonic residual, defined as the rms value of the deviation of the measured field on axis from the ideal field, provides an indication of spectral performance [17]. For IDA - U5.0, the specified rms harmonic residual is 0.25%; magnetic measurements show a value of 0.23%.

Field integrals through IDA are close to specified tolerances and very acceptable for ALS operations.

VI. ACKNOWLEDGMENT

*This work was supported by the Director, Office of Energy Research, Office of Basic Energy Sciences, Materials Sciences Division, of the U. S. Department of Energy, under Contract No. DE-AC03-76SF00098.

VII. REFERENCES

- [1] "U5.0 Undulator Conceptual Design Report," LBL PUB-5256 (Nov. 1989).
- [2] "U8.0 Undulator Conceptual Design Report," LBL PUB-5276 (May 1990).
- [3] E. Hoyer, et. al., "The U5.0 Undulator for the ALS, 4th International Conf. on Sync. Rad. Inst.," [LBL-30459], Rev., Sci. Instrum. 63 (1), 359 (January 1992).
- [4] E. Hoyer, "U5.0 Magnetic Structure Magnetized Nd-Fe-B Blocks," LBL Spec. M734D (Apr. 1989)
- [5] S. Marks, et. al., "ALS Insertion Device Block Measurement and Inspection," [LBL-29955], IEEE PAC. 91CH3038-7, 2739 (May 1991).
- [6] S. Marks, "Measurement & Characterization of U5.0 Permanent Magnet Blocks," LBL Eng. Note M7225 (Oct. 1991).
- [7] D. Humphries, "Block Bonding Procedure for IDA/IDB/IDC," LBL Eng. Note M7121 (Feb. 1991)
- [8] B. Gath, "Magnetic Structure Installation and Alignment into Backing Beam," LBL Eng. Note M7265 (Mar. 1992).
- [9] D. Humphries, et al, "Modeling and Measurement of the ALS U5.0 Undulator End Magnetic Structure," IEEE PAC (May 1993).
- [10] P. Pipersky, "U5.0 End Module Assembly & Installation," LBL Eng. Note M7277A (April 1992).
- [11] E. Hoyer, "Multiple Trim Magnets," LBL Eng. Note M7354 (May 1993).
- [12] E. Hoyer, et. al, "Flux Shunts for Undulators," IEEE PAC (May 1993).
- [13] J. Chin, "IDA, IDB, IDC Support & Drive System Assembly and Alignment Notes," LBL Eng. Note M7349 (July 1992).
- [14] D. Plate, "Fabrication Procedure & Production Inspection Record for Vacuum Chambers," LBL Eng. Note M7292A (Aug. 1992).
- [15] D. Plate, "Insertion Device Vacuum Chamber Bakeout Procedure," LBL Eng. Note M7304 (Sept. 92).
- [16] S. Marks, et al, "ALS Insertion Device Magnetic Measurements," IEEE PAC (May 1993).
- [17] C. Wang, et. al, "Calculated Radiation Spectrum of ALS U5.0 Undulator Based Upon Magnetic Measurements," IEEE PAC (May 1993).

Insertion Device Magnet Measurements for the Advanced Light Source*

S. Marks, C. Cork, E. Hoyer, D. Humphries, B. Kincaid, D. Plate, A. Robb, R. Schlueter, C. Wang,
Lawrence Berkeley Laboratory, University of California,
1 Cyclotron Road, Berkeley, CA 94720 USA

W. Hassenzahl

Lawrence Livermore National Laboratory, University of California, Livermore, CA 94550 USA

A. Abstract

Allowable magnetic field errors for the 4.6 m long insertion devices for the Advanced Light Source (ALS) are extremely small and are driven by electron beam and radiation requirements. Detailed measurements and adjustments of each insertion device are performed to qualify them for installation in the ALS. To accomplish this, a high speed, precision magnetic measurement facility has been designed and built. Hall probe mapping equipment, capable of completing a 2500 sample, 6 m scan with precision axial position monitoring using a laser interferometer in under one minute, is used to obtain both local and integrated field information. A 5.5 m long, 1 cm wide coil is used to measure the field integral through an entire insertion device. This paper describes magnetic measurement equipment, and results of measurements on IDA, the first of the ALS insertion devices.

I. INTRODUCTION

The ALS is a third generation synchrotron light source designed to produce XUV radiation of unprecedented brightness. To meet the high brightness goal, the storage ring has been designed for very small electron beam emittance, and the insertion devices (IDs) must be built to a high degree of precision. The allowable magnetic field errors are driven by both electron beam and radiation requirements. Detailed magnetic measurements and mechanical adjustments of each ID are performed to qualify it for installation in the ALS. The paper by E. Hoyer [1] et al., describes the first three ALS IDs.

The influence of an ID's magnetic field errors on ALS performance is separated into those that affect spectral brightness of the radiation and those that affect dynamics and life-time of the electron beam. Magnetic field data, consisting of both local field and integral field information, is analyzed to assess these affects. Degradation in spectral brightness is influenced both by systematic and random variations from an ideal periodic field. C. Wang, et al.[2] examines the relationship between magnetic errors and spectral performance. The primary influence on the electron beam is due to errors in the integrated magnetic field.

Primary magnetic field data is derived from Hall probe measurements. This data allows examination of both local and integral field characteristics. In addition, a field integral can be separated into the contribution due to errors in the periodic

middle section, and the contributions from each end. These data provide a prescription for nulling the first and second field integrals, which affect electron beam steering. A system of dual permanent magnet rotors is included in the end structure for this purpose [3]. In addition to Hall probe measurements, full field integrals are also measured with a 5.5 m long integral coil, which confirms integrated Hall probe data.

II. MAGNET MEASUREMENT FACILITY

B. Hall Probe Measurement System — Mechanical

Figure 1 is a photograph of the "Luge", a custom built stage which translates axially (z) through the gap of an ID. Probes are mounted to a light weight plastic platform on the Luge. Horizontal (x) and vertical (y) probe position can be varied, via micro-stepping motors which move the support platform. Support for the Luge is provided by a rail on the one side of the gap and a pneumatic cylinder on the other. The cylinder and rail are mounted directly to the ID support structure. The pneumatic cylinder provides the mechanism for axial translation.



Figure 1. Photograph of "Luge."

Accurate axial position monitoring of the Luge is accomplished with a resolution of 1 μ m using a dual beam laser interferometer system. Two retro-reflectors mounted to the Luge provide interferometer beam targets. They are mounted over the pneumatic cylinder and over the track and correspond to interferometer channels 1 and 2, respectively.

C. Electronics

Design of the instrumentation system is based upon use of a dedicated subsystem for real-time instrument control along

*This work was supported by the Director, Office of Energy Research, Office of Basic Energy Sciences, Material Sciences Division of the U.S. Department of Energy under Contract No. DE-AC03-76SF00098.

The diagram illustrates the VME-based control system architecture, showing the interconnections between various hardware components. The components are organized into three main vertical sections: the top section for digital I/O and motor control, the middle section for motion control and timing, and the bottom section for operator interaction and real-time processing.

- Top Section:**
 - Pneumatic Drive** is connected to the **I/O Opto-Isolator**.
 - Luge** is connected to the **X & Y Axis Motor Drivers**.
 - The **I/O Opto-Isolator** is connected to the **Digital I/O** module.
 - The **X & Y Axis Motor Drivers** are connected to the **Motor Indexer**.
- Middle Section:**
 - A **GPB Bus** connects the **DTMs** (Digital Timing Modules) and **DVMs** (Digital Voltage Modules).
 - The **DTMs** are connected to the **Laser Interferometer**.
 - The **DVMs** are connected to the **Laser Interface**.
 - The **Laser Interferometer** is connected to the **Laser Interface**.
- Bottom Section:**
 - The **Operator Workstation** is connected to the **Real-Time CPU** via an **Ethernet** connection.
 - The **Real-Time CPU** is connected to the **GPB Controller**.
 - The **GPB Controller** is connected to the **Timer/Counter**.

The **GPB Bus** and **Ethernet** connections represent the primary data and control pathways for the system.

The electronics rack contains various instruments and a real-time subsystem for fast data collection and instrument control. The equipment includes a VME crate, two Hewlett Packard 3458A digital voltmeters (DVMs), two Compumotor LN-Series micro-stepper motor drivers, an LBL-designed optoisolator interface chassis, a ZYGO Axiom 2/20 laser interferometer system, and two Group 3 DTM-141-DG digital tesla meters (DTMs). The VME crate includes a Motorola-147S real time central processing unit (CPU), a Burr Brown MPV991 timer/counter module, a Motorola MVME-300 GPIB instrument bus controller, an Oregon Microsystems VME-44 four channel stepper motor indexer, and a VMIC VMIVME-2534 digital input/output module. An LBL-designed electronics chassis interfaces the timer/counter module with the laser interferometer and DVMs.

The operator workstation includes a Sun IPC workstation and an non-interruptible power supply. The workstation pro-

The DVMS, laser interferometer, and Hall probes are controlled via GPIB. Communication between the MVME-147S and the Sun IPC occurs via an Ethernet interface.

Coordination between the real-time subsystem and the workstation is based upon a client/server model. Software running on the workstation provides basic coordination of measurements; this software acts as a client which requests service from the real-time instrument control software running on the VME crate. Communication between the subsystems is provided by the Sun remote procedure call (RPC) mechanism.

Scan_svc is the top level server task on the real-time sub-system, providing remote procedure call service to client tasks. *Scan_svc* is spawned during system initialization and listens to the network for service requests. *Scan_clnt* is the client interface module. It resides on the operator workstation as a sub-routine library that coordinates network connections, RPC access, and disconnection to the server module. *ID_scan* runs on the operator workstation and provides basic coordination of a field scan. A set of additional utility routines also exist for single value DVM read (*readDVM*), single value DTM read (*readDTM*), Luge motion control (*homeXY*, *moveX*, *moveY*, and *launchZ*), and ID gap control (*initGap* and *moveGap*). Each utility routine calls *Scan_clnt* for access to the device control subroutines. A Unix script routine, *multiScans*, is a user interface which provides a mechanism for the definition and automated control of a set of field scans.

A raw data file consists of a header including measurement parameter settings and the following values for each data sample: Hall probe voltage, interferometer channel 1 counts, interferometer channel 2 counts, and time interval between samples. Program *Convert* creates a first level reduced data file consisting of (z, B_y) pairs for each data sample. Input for *Convert* consists of a Hall probe conversion table file and a raw data file. A Hall probe conversion table consists of corre-

sponding values of output voltage and magnetic field. The B_y value is calculated by linear interpolation of the conversion table. Note that the conversion table is preprocessed using a spline routine to create a dense mesh of voltage-magnetic field pairs; this allows an efficient and accurate conversion.

The axial position z is calculated from interferometer count and timer information according to the following equation

$$z = \frac{n_1(X_1 - x) + n_2(X_2 - x)}{X_1 + X_2} + v\tau/2$$

where n_1 and n_2 are counts from interferometer channels 1 and 2, respectively, x is the horizontal probe position relative to a horizontal datum, X_1 and X_2 are the horizontal distances between retro-reflectors 1 and 2, respectively, and the horizontal datum, v is the probe velocity, and τ is the DVM integration time.

Higher level data reduction is performed on the converted file using a set of utilities included in program *analyze* [4]. This program includes utilities for spline fit of a data set, calculation of deviation from an ideal periodic field, Fourier transform of data, and calculation of the optical phase and radiation spectrum.

IV. RESULTS

Figure 3 shows a Fourier transform of a magnetic field scan from IDA. The large spectral peaks at odd harmonic numbers is characteristic of the periodic magnetic field of an insertion device. This figure also illustrates the signal to noise level achieved in the measurement system. The background spectrum at the right side of the graph indicates the level of random measurement noise. Note that this is at a level of less than 1×10^{-5} relative to the first harmonic. In other words, the measured value of peak fields is 1×10^5 times larger than the noise level.

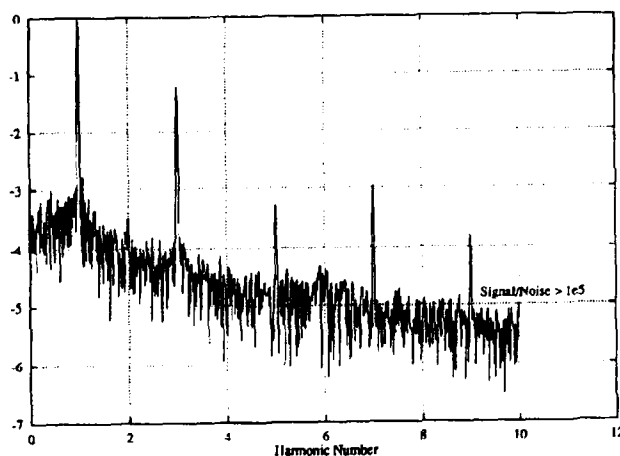


Figure 3. Fourier transform of B_y scan.

Figure 4 shows the results of a series of measurements of $\int B_y dz$ at different x locations within the range ± 30 mm and at 14 mm and 23 mm ID gaps. Integrals are shown both for integrated Hall probe scans and integral coil measurements.

Note that the agreement between the two methods of integral measurement is quite good. The graph also illustrates the level of uniformity that was achieved in $\int B_y dz$ as a function of x ; nonuniformity in this function affects electron beam dynamics.

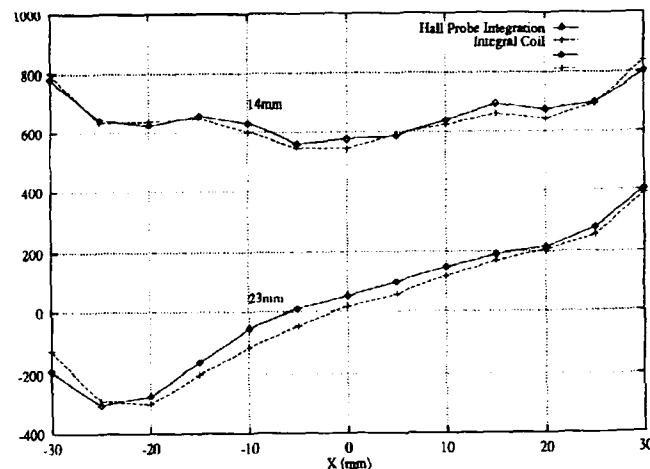


Figure 4. $\int B_y dz$ as a function of x .

V. CONCLUSIONS

The insertion device magnetic measurement system described in this paper has proven to be very efficient and reliable. The mechanisms for rapid compilation and analysis of data has allowed for an extensive characterization of ALS insertion devices. To date, over 2 GB of magnetic scan data have been collected, and the luge has logged over 25 km of travel.

VI. REFERENCES

- [1] E. Hoyer, J. Akre, J. Chin, B. Gath, D. Humphries, B. Kincaid, S. Marks, P. Pipersky, D. Plate, G. Portmann, R. Schlueter, W.V. Hassenzahl, "First Undulators for the Advanced Light Source," IEEE PAC (May 1993)
- [2] C. Wang, S. Marks, B. Kincaid, "Spectral Quality of ALS U5.0 Undulator and Field Error Effects," IEEE PAC (May 1993)
- [3] D. Humphries, K. Halbach, E. Hoyer, B. Kincaid, S. Marks, R. Schlueter, "Modeling and Measurement of the ALS Undulator End Magnetic Structures," IEEE PAC (May 1993)
- [4] J. Bahrdt, B. Kincaid, W. Hassenzahl, "ANALYZE, A Program for the Analysis of Magnetic Field Data."

Spectral Quality of ALS U5.0 Undulator and Field Error Effects

C. Wang, S. Marks and B. Kincaid

Lawrence Berkeley Laboratory, University of California, Berkeley, California 94720

Abstract

The first insertion device of the Advanced Light Source (ALS), a U5.0 undulator, has been carefully adjusted and qualified with a specially designed magnetic measurement system. The magnetic field of the undulator has been fully mapped at a series of gaps with very high accuracy. Based upon these measured field data, we evaluate the radiation spectral quality of this device in terms of an ideal sinusoidal device and examine the field error effects. Moreover, the statistical correlation between the field errors and radiation degradation is examined by using the large quantity of magnetic field data sets accumulated in the process of adjusting and qualifying the U5.0 undulator.

I. INTRODUCTION

In order to obtain high brightness photon sources, a low emittance storage ring and long insertion devices have been implemented at the ALS. However, it is well known that the magnet field errors tend to degrade the performance of an insertion device. To achieve the high performance required, state of the art technology is employed to build the insertion devices and the magnetic measurement system. The first insertion device being installed at ALS is the U5.0 undulator [1]. Before installation, it was carefully adjusted and qualified based upon magnetic measurements [2] as well as radiation calculations using the measured field data. In this report, we present some results that demonstrate the quality of the U5.0 radiation spectrum. Instead of showing the general performance of U5.0, which is available in earlier publications [3], we pick up a few representative cases and present a detailed spectral comparison between an ideal sinusoidal field and the measured real device.

In the process of adjusting and qualifying the U5.0 undulator, a large number of magnetic field data sets have been accumulated. This collection of data consists of a statistical assembly that represents real devices with different field errors. It is interesting to examine the correlation between spectral quality and field errors. This is the first time that such a real measured data set assembly is available. We will show the statistical correlation between the field errors and radiation degradation and compare it with earlier computer simulation studies. [4]

To examine the magnetic field error effects on spectral quality, all spectrum properties are calculated using the measured field data, and then normalized by the values calculated using the ideal field, which consists of a sinusoidal field and one half peak pole at each end. The radiation spectral calculations are done with program RADID, whose undulator radiation calculation algorithm is based on Ref. 5. The

magnetic field analysis are done with a program ANALYZE [6].

II. SPECTRAL QUALITY OF U5.0 UNDULATOR

The U5.0 undulator has 89 periods of 5 cm each. It is designed to produce high brightness radiation from 50 eV to 1.9 keV [3] by using up to the 5th harmonic. From B. Kincaid's theory [7] about random field error effects in undulators we know that, in the small error limit, for an N period undulator with relative rms random field error σ , the nth harmonic peak flux density is degraded by a factor of e^{-30q} , where

$$q = n^2 \sigma^2 N \left[\frac{\frac{K^2}{2}}{1 + \frac{K^2}{2}} \right]^2 \quad (1)$$

Since the factor decreases exponentially with $n^2 N$ for a given σ , it applies a stringent requirement on the magnetic field errors in order to keep the peak flux density decrease within 30% at the 5th harmonic for such a long undulator. The field errors specification for U5.0 is $\sigma < 0.25\%$.

To accomplish this, special effort was put into design and construction of the device [1]. A specially designed magnetic measurement system was used to adjust and qualify the device after its assembly. Full maps of the magnetic field at a series of gaps and off-axis positions were obtained with measurement accuracy of 0.5 Gauss [2]. Such field measurement allows us to examine the quality of the device in terms of spectral performance and storage ring requirements. Here we show the spectral quality of U5.0 by calculating the on-axis flux density, central brightness and flux accepted within a certain solid angle using real measured field data and comparing results with those from an ideal sinusoidal field.

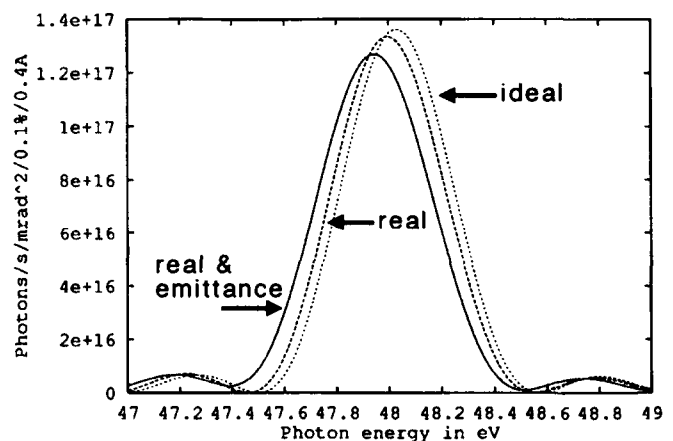


Figure 1. On-axis flux density at 14 mm gap, 1st harmonic.

Figure 1 shows the on-axis flux density of the first harmonic at the minimum vertical magnet gap, 14 mm. The three curves corresponding respectively to the ideal field, measured field and measured field with ALS emittance included. The well known red-shift of peak position and the reduction of peak value are clearly seen, but their effects on spectral quality are negligible. In this case, $\sigma=0.25\%$. The real spectra are calculated at $69 \mu\text{rad}$ off axis. A linear least square fit of the trajectory is used to obtain the off-axis angle. The trajectory angle is due to a dipole kick at the end of the device and random electron trajectory walks.

Figure 2 is similar to Figure 1 but shows the 5th harmonic at a medium gap, 23 mm. The off-axis angle is $18.8 \mu\text{rad}$ in this case. The field error and emittance effects on flux density are significant. Though the relative rms field errors is slightly larger (0.33%) than the above, the decrease in peak value is much larger due to the higher harmonic number. The emittance effect is also much bigger due to the higher photon energy. However, the peak shape is still quite good and the peak value satisfies the 70% requirement.

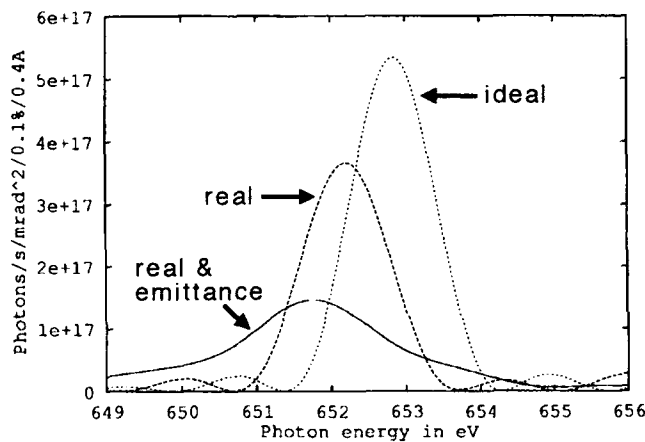


Figure 2. On-axis flux density at 23 mm gap, 5th harmonic.

To get a more general picture of the field error effects on the spectral quality, in Table 1, we list the ratios of the real peak flux density to the ideal one for a series of gaps and different harmonics. For reference, the relative rms field errors and the deflection parameter K at each gap are also listed.

Table 1. Normalized peak flux densities.

	14 mm	18 mm	23 mm	35 mm	47 mm
1st	98%	95%	93%	92%	93%
3rd	90%	87%	85%	84%	87%
5th	76%	70%	69%	69%	71%
σ	0.25%	0.30%	0.33%	0.41%	0.63%
K	3.974	3.008	2.132	0.973	0.453

This table confirms that the spectral quality of this device is quite good at all gaps and meets the design specification. No satisfactory method is available to estimate this table from device parameters and field error characteristics, although

such a method is very important in practical design of insertion devices.

It is well known that one figure of merit for a synchrotron radiation source is its central brightness. The field errors may affect brightness in two ways. One is through the degradation of the angular distribution (shape as well as peak value) of single electron flux density. The other is through enlargement of the source size due to random trajectory walks. However, the second one is negligible because the electron beam size is much larger than the amplitude of the single electron orbit, even with the random walks. When considering brightness, electron beam emittance must be taken into account. To evaluate the field error influence on brightness, we calculate the ALS emittance averaged flux densities using the measured field and ideal field. The ratios of corresponding peaks indicate the field error effect on source brightness because the electron beam size effects on both cases are the same. In Table 2, we list the peak ratios for two typical gaps, 14 mm and 23 mm.

Table 2. Normalized peak brightness.

	1st	3rd	5th
14 mm	98%	88%	75%
23 mm	91%	83%	70%

A Monte Carlo simulation is used to take into account the beam emittance. The accuracy of these calculations is about 5%. Comparing Tables 1 and 2 we see that the field error effects on the on-axis flux density and brightness are nearly the same. This is an expected result because the field errors do not change the distribution pattern very much, although the peak value is decreased.

Another figure of merit of a photon source is the flux obtainable in a certain solid angle. Usually, the solid angle for an undulator is the central radiation cone. In Table 3, we show the total flux in a $90 \times 90 \text{ mrad}^2$ and $180 \times 180 \text{ mrad}^2$ acceptance angle for the 23 mm gap case. 90 mrad is about the angular width of the central cone at first harmonic. Because the main effect of field errors is to destroy the constructive interference in an undulator, it has much less effect on the angular integrated flux. The larger the acceptance aperture, the less the field error effect.

Table 3. Normalized flux in different solid angle.

	1st	3rd	5th
$90 \mu\text{rad}$	89%	79%	76%
$180 \mu\text{rad}$	96%	99%	93%

III. CORRELATION OF FIELD ERRORS AND SPECTRAL QUALITY

In the above section, we have evaluated the spectral quality of the U5 undulator for several on-axis cases which represent the operating regime of the U5. Besides these on-axis cases, many off-axis field scans were also measured in

order to characterize the integrated field error distributions. All of these field sets can be viewed as an assembly of real devices with different field errors. These errors are dominated by random errors due to magnetic blocks and manufacturing tolerance. However, there may also be significant systematic errors, especially for off-axis scans.

Because of the random distribution feature of field errors, only statistical characteristics such as rms value can be used to specify the random field errors. For a specific realization of an error distribution, we can examine its effect on the spectrum as above. However, the general effect of errors on the spectrum can be described only by statistical correlation, which has been studied analytically by B. Kincaid [5] and with a computer simulation by B. L. Bobbs, et al. [4]. Here we use the measured data set assembly to examine the correlation between field errors and spectral peak flux densities normalized by corresponding ideal values.

Usually, two characteristic values are used to specify field errors. One is the relative rms field error; the other is the rms optical phase error. As pointed out by Bobbs et al. [4], the rms phase error is a better indicator of the device radiation performance.

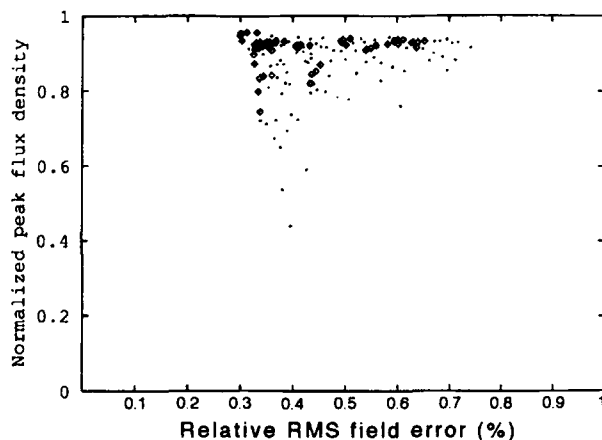


Figure 3. Correlation with relative RMS field errors.

In Figure 3 and 4, we show the correlation between normalized peak flux densities of the first harmonic and the field error characteristic values. Figure 3 uses the relative rms field errors while Figure 4 uses rms phase errors. Each point represents the result for a different field data set. We see that the correlation is not very good for either case. The correlation with phase errors is stronger but surely not as good as the computer simulation result shown in Ref. 4. In this case, the radiation performance tends to be better than the results from purely random errors. These are probably due to dependency between some data sets and some non random field errors in each set. In fact, if we get rid of the far off-axis cases, we obtain a better correlation as represented by the boxes.

IV. CONCLUSIONS

The spectral quality of the ALS U5.0 undulator is quite good and satisfies the design requirements of achieving better than 70% brightness at the 5th harmonic. The correlations

between the field error characteristics and the spectral performance obtained from different field data sets of U5.0 are not as good as former computer simulation results, which assume random errors only.

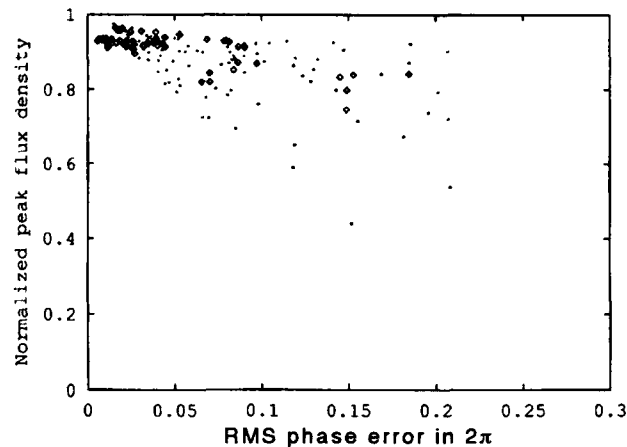


Figure 4. Correlation with RMS phase errors.

V. ACKNOWLEDGMENT

This work was supported by the Director, office of Energy Research, Office of Basic Energy Science, Materials Science Division of the U.S. Department of Energy, under contract No. DE-AC03-76SF00098.

VI. REFERENCES

- [1] E. Hoyer, J. Akre, J. Chin, B. Gath, D. Humphries, B. Kincaid, S. Marks, P. Pipersky, D. Plate, G. Portmann, R. Schlueter, W. V. Hassenzahl, "First Undulators for the Advanced Light Source," IEEE PAC (May 1993).
- [2] S. Marks, C. Cork, E. Hoyer, D. Humphries, B. Kincaid, D. Plate, A. Robb, R. Schlueter, C. Wang, "Insertion Device Magnet Measurements for the Advanced Light Source," IEEE PAC (May 1993).
- [3] "ALS Handbook," Lawrence Berkeley Laboratory Report PUB-643, Rev. 2 (1989).
- [4] B. L. Bobbs, G. Rakowsky, P. Kennedy, R. A. Cover, and D. Slater, "In Search of a Meaningful Field-error Specification for Wiggler," Nucl. Instrum. Methods A296 (1990).
- [5] C. Wang, "Concise expression of a classical radiation spectrum," Phys. Rev. E, (June 1993).
- [6] J. Bahrtdt, B. Kincaid, W. V. Hassenzahl, "ANALYZE—a Program for the Analysis of Magnetic Field Data."
- [7] B. Kincaid, "Random Errors in Undulators and Their Effects on the Radiation Spectrum," J. Opt. Soc. Am. B/Vol. 2, No. 8 (1985).

Modeling and Measurement of the ALS U5 Undulator End Magnetic Structures*

D. Humphries, K. Halbach, E. Hoyer, B. Kincaid, S. Marks, and R. Schlueter
Lawrence Berkeley Laboratory, University of California
1 Cyclotron Road, Berkeley, CA 94720 USA

Abstract

The end structures for the ALS U5.0 undulators utilize a system of dual permanent magnet rotors intended to establish gap independent field performance. They may also be used for tuning of the first and second magnetic field integrals of these devices. The behavior of these structures has been studied by means of two dimensional modeling with the POISSON Group of computer codes. A parametric study of the magnetic field distribution and first and second integrals of the fields has been conducted. In parallel, magnetic measurements of the final completed structures have been performed using an automated Hall probe measurement system. Results of the modeling and measurements are compared. Implications for tuning of the ends of the devices within the context of the electron beam parameters of the ALS are discussed.

I. INTRODUCTION

The first two U5.0 undulators for the Advanced Light Source (ALS) [1] are hybrid permanent magnet structures which have mirror symmetric end structures. The engineering design of these end structures was based upon a truncation theory [2] which indicated a means of compact termination of the structure and minimization of 1st and 2nd field integral effects on the electron beam of the ALS.

II. 2-D NUMERICAL MODEL

To model the U5.0 end structures, a 2-D numerical non-linear magnetostatic problem was constructed. Figure 1 illustrates the geometry of the model and the vector potential solution (field lines) for a particular case. The upper half of the last three periods of the magnetic structure are included in the model. The left boundary condition is Dirichlet ($\vec{A} = 0$)

while the remaining three are Neumann ($\nabla \vec{A} \cdot \hat{n} = 0$). The upper and right boundaries are remote and not shown in the figure. A magnetic shunt is shown attached to pole 0 at the far right. This shunt is connected to the upper Neumann boundary and provides a flux return path through an implied infinite permeability region formed by the upper and right Neumann boundaries.

The eight regions with orientation arrows represent the Nd-Fe-B permanent magnet material which energizes the structure. The six rectangular regions are fixed material while the two octagonal regions represent elements that can be rotated. Seven pole regions are shown with the far left pole split at the Dirichlet boundary symmetry plane.

*This work was supported by the Director, Office of Energy Research, Office of Basic Energy Sciences, Materials Sciences Division of the U.S. Department of Energy, under Contract No. DE-AC03-76SF00098.

The geometry shown, in conjunction with the described boundary conditions, gives calculated fields which are equivalent to those of a complete upper and lower, 26 pole, 2-D device.

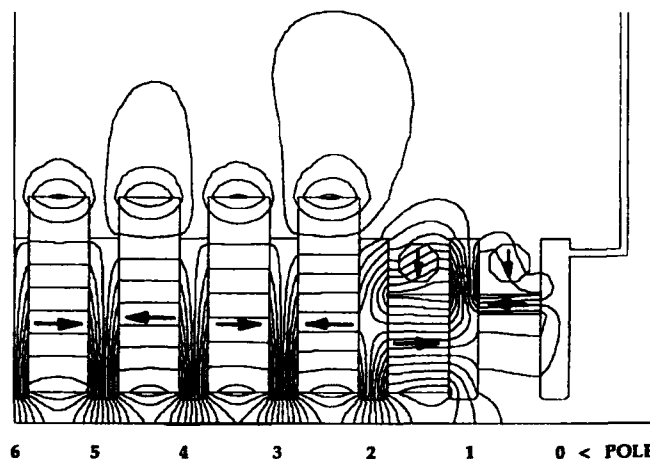


Figure 1: 2-D PANDIRA Model

III. CALCULATED FIELDS

PANDIRA a member of the POISSON Group [3] of computer codes, was used to solve this model. PANDIRA is able to model 'analytic' anisotropic material with arbitrary orientations via simple B-H intercepts and easy axis orientation angles. This is particularly helpful in this application since it allows rotor orientation to be varied by changing a single number in the input parameter list.

The permanent magnet material used for these devices is Nd-Fe-B. This material was modeled using a linear B-H curve with intercepts of $B_r = 11000$ G and $H_c = -10700$ Oe. The pole material is vanadium permendur and was modeled using a non-linear B-H curve.

PANDIRA solves Poisson's equation directly for the vector potential (\vec{A}) on an irregular triangular mesh. The mesh for this model contains approximately 15000 intersection points with high density in the regions of interest, e.g. the gap. The code then applies a differentiated interpolating polynomial to the nodes of the problem to calculate the \vec{B} fields. Thus we have \vec{B} and $\int \vec{B} dz$ immediately from PANDIRA.

To further extract information from the model, the calculated B_y and vector potential information was transferred to a graphical spreadsheet. The 2nd integral of B_y on the mid plane was then calculated and a 'progressive integral signature' was generated which is shown in figure 2.

On this graph, $z=0$ cm is the left Dirichlet boundary of the PANDIRA model. The seventh and last pole (pole 0) is at $z=15$ cm. The solid line on the graph is B_y calculated on the mid

plane of the device. The line shown in long dashes is the first integral of B_y i.e. the vector potential.

The line shown in short dashes is the second integral of B_y which defines a path proportional to the trajectory (rotated 90 deg) of a particle traveling through the mid plane field. The portion of this path from $z=0$ to $z=2.5$ cm of this trajectory indicates the relative amplitude of the transverse particle oscillation through the periodic section of the device. The deviation of the remaining part of the trajectory can thus be compared to this oscillation amplitude to see the significance of tuning effects in the model.

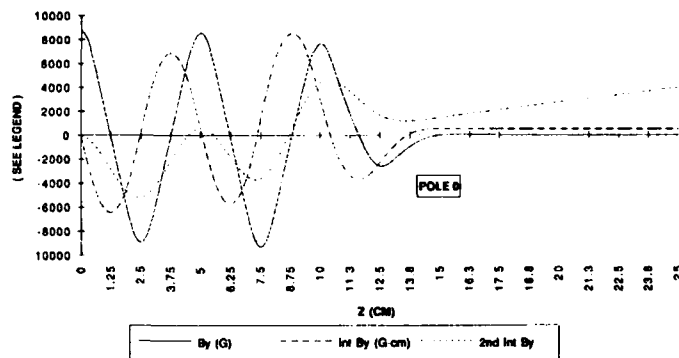


Figure 2: Progressive Integral Signature

If we examine the first integral curve in this graph we see that it takes on a positive constant value for $z > 15$ cm (where $B_y = 0$). This implies a net integrated steering field produced within this end configuration. Correspondingly, we see the effect on the trajectory curve as it diverges linearly from the $z=15$ cm point on the graph.

IV. COMPARISION TO MEASUREMENTS

In parallel with the construction of the U5.0 undulators, a state-of-the-art automated magnetic measurement system [4] was developed to measure and characterize the devices. This system is able to perform high precision field mapping using Hall probes. The measurement data are processed using spline interpolation to generate a smooth function which is evaluated at 6000 points.

To compare the model results with the measured results, the ends of the data sets were extracted and re-interpolated to produce field values at the exact locations of the calculated values for the 2-D PANDIRA model.

Figure 3 shows a comparison of the calculated B_y fields from the 2-D model and those measured in the actual device. The 2-D model was originally scaled to produce a B_0 value of .87 tesla. For this comparison the 2-D fields were scaled to give exact equivalence to the measured B_0 (.9 tesla) at $z=0$ cm. This gives a picture of the divergence of the two results moving through the end region of the magnetic structure. As shown in the graph, the agreement between the two results is good with a discrepancy of only a few percent near the last two poles of the end structure.

The most significant disagreement between the model and the real device occurs in the gap dependency of the integrated dipole from the ends. Figure 4 shows measured results for the integrated dipole as a function of gap. A large increase of

approximately 900 G-cm occurs in the integral of B_y as the gap approaches 14 mm.

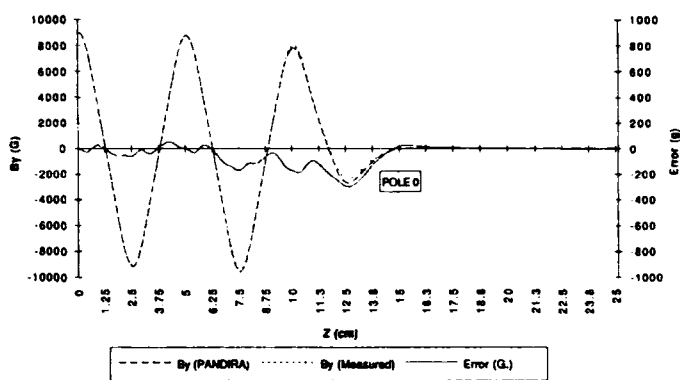


Figure 3: Calculated vs Measured B_y

The 2-D model manifests no such increase, even when the gap of the model is closed to 10 mm. The model shows a maximum variation over this gap range of only 100 G-cm. This behavior was not predicted by the original theory and initial conjecture is that it is likely to be related to a 3-dimensional effect which occurs at small gaps.

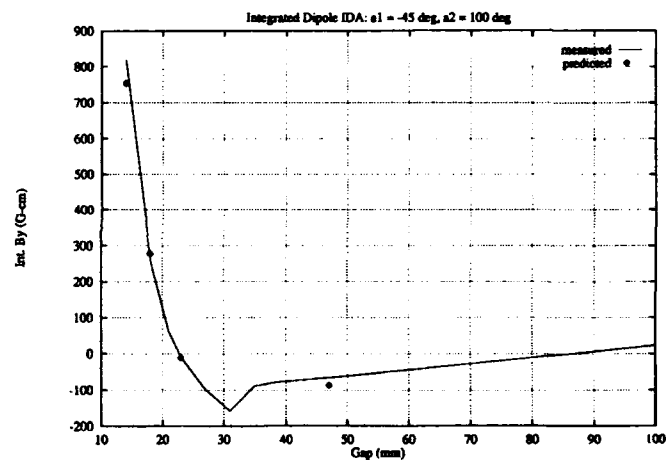


Figure 4: Measured Integrated Dipole

V. ROTOR EFFECTS

The primary effect of the rotors is to vary the scalar potential of the adjacent poles and thus to effect a change in the field distribution at the mid plane. Maximum effect is obtained for rotors oriented horizontally at approximately 0 or 180 degrees. The field integral at the mid plane is non-zero for rotor orientation combinations which cause unequal pole potential sums above and below the midplane.

The undulator magnetic structures for these devices are surrounded on three sides by steel backing beams which act to shield the overall structure from ambient fields. Flux shunts connect the last pole at each end of each magnetic structure to the backing beam ends. The upper and lower backing beams are magnetically connected via hinged yokes which allow a low reluctance path to be maintained during opening and closing of the magnet gap. In the 2-D model, these backing

beams and return yokes are represented by the upper and right hand Neumann boundary. A complete flux return path is thus established from the upper magnetic structure to the lower magnetic structure to carry any unbalanced error flux or induced flux from the rotors which crosses the air gap between the poles.

In addition to the primary rotor induced flux carried through the shunts, there is a secondary induced flux effect from direct magnetic linkage of the poles to the backing beam through the air. This effect is maximum for approximately vertical (90 and 270 degree) rotor orientations.

This combination of primary and secondary effects leads to an analytic characterization of the rotors in terms of their orientation angles and the resulting net end steering effect or integral of B_y at the mid plane.

Letting α_1 be the orientation of the inner or left rotor as shown in figure 1 and α_2 be the orientation of the outer or right rotor then I_S where $I_S = \int B_y dz$ can be expressed as follows:

$$I_S = c_0 + c_1 \cos(\alpha_1) + c_2 \sin(\alpha_1) + c_3 \cos(\alpha_2) + c_4 \sin(\alpha_2) \quad (1)$$

The c_n are obtained in each case by calculating or measuring the integral of B_y for multiple rotor orientations and performing a simple matrix calculation.

Figure 5 is a graphical representation of this function evaluated for the 2-D model case. This graph shows that the outer rotor has approximately twice the effect of the inner rotor. Also shown is a slight asymmetry along both the α_1 and α_2 axes resulting from the sine terms in equation (1) above.

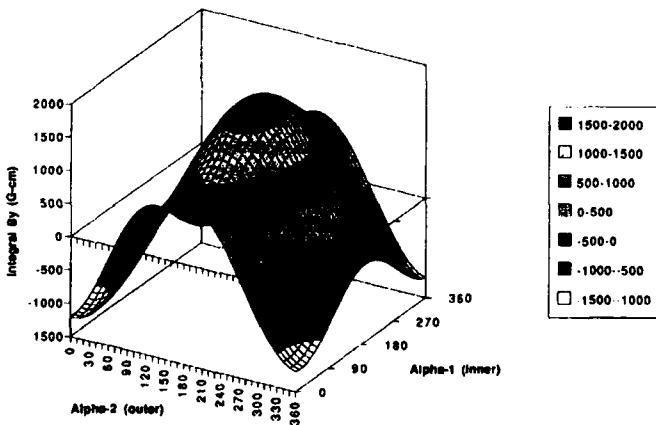


Figure 5: Rotor Effect on $\int B_y dz$ for 2-D Case

The corresponding function was calculated for the measured case which yielded a similar contour but with an amplitude approximately .6 times that of the 2-D model. This discrepancy is attributable to some combination of inaccurate modeling of the flux return path through the backing beam and, to a lesser degree, errors in the 2-D equivalent rotor volume in the PANDIRA model.

To make a meaningful comparison of the two functions, they were both zero shifted by averaging. The 2-D contour was then normalized to peak amplitude of the measured contour

and a difference contour was obtained. This is shown in Figure 6 and indicates relatively good qualitative agreement between the two cases with a standard deviation of the error of approximately 44 G-cm or less than 5% of the peak measured rotor effect on $\int B_y dz$.

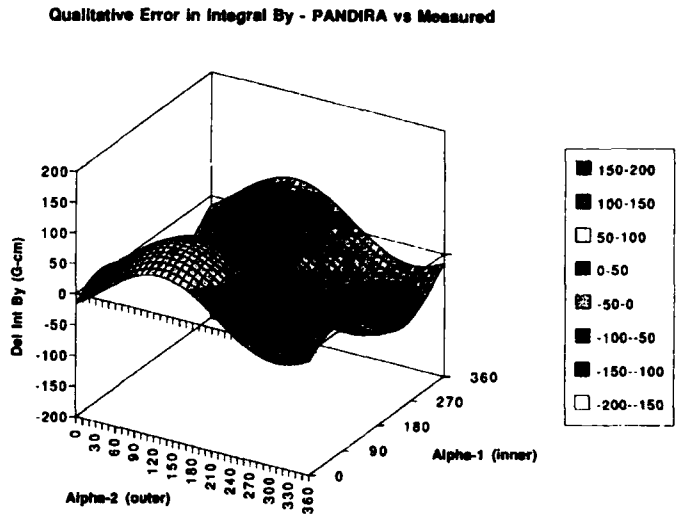


Figure 6: Rotor Effect Difference Contour, 2-D vs Measured

VI. CONCLUSIONS

In spite of certain areas of disagreement, 2-D modeling has proven to be a useful and cost effective tool for the understanding and design of the complex end structures of the U5.0 undulators. It has yielded good qualitative agreement with the actual measured devices in most areas. It has also pointed to subtle behaviors which were not predicted by the original theory. We plan to utilize this modeling technique to refine the end designs of future insertion devices for the ALS.

VII. REFERENCES

- [1] E. Hoyer, et al, "First Undulators for the Advanced Light Source", IEEE PAC (May 1993).
- [2] "U5.0 Undulator Conceptual Design Report", LBL PUB-5256, Sect 5.2.2, (Nov. 1989).
- [3] "POISSON/SUPERFISH Reference Manual", LANL LA-UR-87-126, (Jan. 1987).
- [4] S. Marks, et al, "ALS Insertion Device Magnetic Measurements", IEEE PAC (May 1993).

FLUX SHUNTS FOR UNDULATORS

E. Hoyer, J. Chin

Lawrence Berkeley Laboratory, University of California, Berkeley, Ca 94720

W. V. Hassenzahl

Lawrence Livermore National Laboratory, University of California, Livermore, Ca 94551

Abstract

Undulators for high-performance applications in synchrotron-radiation sources and periodic magnetic structures for free-electron lasers have stringent requirements on the curvature of the electron's average trajectory. Undulators using the permanent magnet hybrid configuration often have fields in their central region that produce a curved trajectory caused by local, ambient magnetic fields such as those of the earth. The 4.6 m long Advanced Light Source (ALS) undulators use flux shunts to reduce this effect. These flux shunts are magnetic linkages of very high permeability material connecting the two steel beams that support the magnetic structures. The shunts reduce the scalar potential difference between the supporting beams and carry substantial flux that would normally appear in the undulator gap. Magnetic design, mechanical configuration of the flux shunts and magnetic measurements of their effect on the ALS undulators are described.

I. INTRODUCTION

Periodic magnetic structures for undulators and free electron lasers have stringent requirements on the average magnetic field. The average dc field should be very small so that the long-range deflection of a beam is insignificant compared to the amplitude of the oscillatory motion caused by the periodic magnetic field. If a larger dc field is present over the central region, the curved trajectory may become greater than the amplitude of the oscillations associated with the periodic magnetic structure; this may be unacceptable in many applications. Possible sources of the dc field component are the earth's magnetic field, other environmental fields, and improper device design. Methods available to reduce this dc component include active coils that buck the dc field, external ferromagnetic shielding and flux shunts.

Active coils mounted around, or adjacent to, the magnetic structure must be powered by an external power supply, and energized with a current that depends on the magnetic gap of the insertion device and its physical orientation and location in the local environmental magnetic field. Significant temperature variations may result from coil heating. Excessive heat can cause mechanical distortions, variation of the magnetization of the permanent magnet materials, and, if an excessive temperature excursion occurs, permanent damage to permanent magnet material. Cooling is probably necessary for active coils.

Providing external magnetic shielding for the entire device is rather complicated because of its physical size and ap-

pendages, and because of the low-field levels. Reducing field levels to sub-gauss levels requires special magnetic materials with low coercivity and very high permeability at low field, e.g., high nickel alloys.

In this paper we describe a new method, the Flux Shunt, for reducing the dc component of magnetic fields in undulators and other types of magnetic structures that use support members made of a soft magnetic material. The approach is straightforward, a magnetic coupling is made between the top and bottom support structures. This connection reduces the scalar potential difference between the two structures. The flux shunt forming this coupling must be made of a material with a very high permeability at low fields, have a low coercivity, and a low residual field in the operational state. The advantages of this technique are that it can be passive, with no need for a power supply, and the method is effectively independent of the source of external field. The application of flux shunts to the 4.6 m long ALS undulators, Figure 1, is described below.

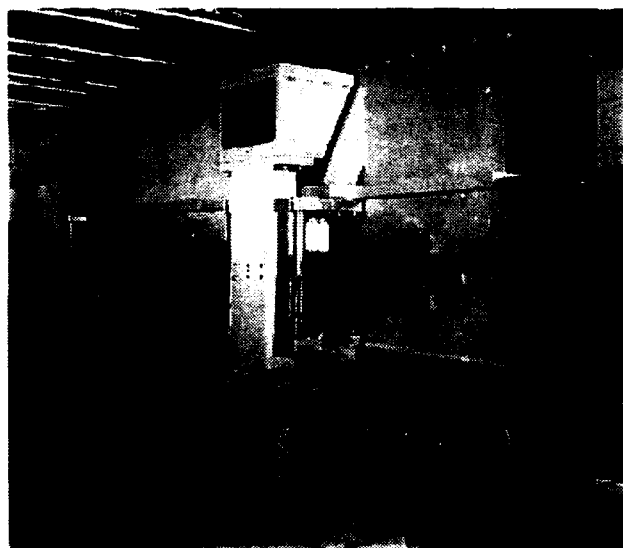


Figure 1. U5.0 Undulator support structure with flux shunts.

II. FLUX SHUNT MAGNETIC DESIGN

One objective in undulator design is to achieve as low an average dc magnetic field as possible in the region of the electron beam. Maintaining the upper and lower structures at the same scalar potentials requires that they be magnetically shorted together by a low reluctance material, a flux shunt.

However, assembly tolerances and finite permeabilities limit the minimum achievable scalar potential difference. Requirements for the flux shunt design and performance are based on the allowable vertical magnetic field integral, which is 100 G cm in the 4.6 m long ALS undulators [1]. Half of this tolerance is budgeted to environmental field effects that can be controlled by the flux shunt. An average dc field of 0.11 G is thus allowed. Because the fields are roughly sinusoidal, the maxima under the poles is about 0.17 G. This field corresponds to a pole scalar potential of 0.121 G cm with respect to the midplane.

The structure of the undulator distorts the external magnetic field, as shown in Figure 2 (note that only the vertical component of the external magnetic field need be considered), and it is concentrated by a factor of 1.36 at the electron beam position [2]. Thus, the 0.3 G external vertical field at the ALS will produce an integrated field of 187 G cm ($0.3 \text{ G} \times 1.36 \times 4.6 \text{ m}$). In addition, the ALS undulator geometry (1.4 cm gap) is such that the scalar potential of the structure is 10.3 times that of the poles, a factor 3.7 too high. To reduce this minimum gap undulator field to 0.11 G, the structure scalar potential from the midplane must not exceed $0.121 \text{ G cm} \times 10.3 = 1.25 \text{ G cm}$.

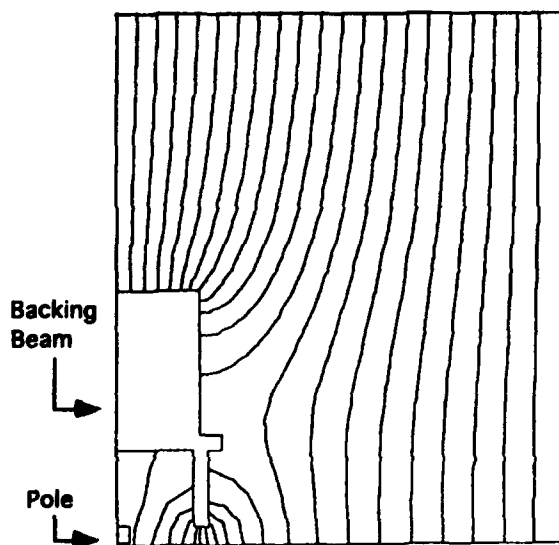


Figure 2. Field distribution around the undulator structure due to a background field.

The maximum flux that can enter the structure, again the Figure 2 configuration, occurs when the support structure is shorted to the midplane and for a 0.3G background field is $4.30 \times 10^4 \text{ G cm}^2$.

Maximum total flux and allowable scalar potential difference determines the mechanical configuration of the flux shunt. For the ALS undulators, 6 flux shunts per device were selected, each flux shunt is a linkage because the undulator gap opens and closes to change field. The material selected for the linkage is 50% Ni-Fe because of its very high permeability at low field and its low coercive force. Using a 5 cm x 7.5 cm cross-section for the Ni-Fe shunt members, the computed

scalar potential drop is 0.65 G cm for the Ni-Fe and 0.30 G cm for the air gaps for a total of 0.95 G cm, which is less than the allowable 1.25 G cm limit.

III. DESIGN AND CONSTRUCTION

The design requirements for the flux shunts include an undulator gap change of 20.2 cm, no effect on the precision motion of the magnetic structures and meet the reluctance goal of the design. The linkage design shown in Figure 3 was selected. There are five members and six spring-loaded, rotary hinge joints in this design allowing six degrees of freedom.

Hot rolled, 50% Ni-Fe was used for the linkage members annealed at 1200 degrees C for four hours after part fabrication to achieve the high permeability. The annealed state makes the material soft and gummy, resulting in galling at the joints. To ameliorate this problem, parts were plated with 15 μm thick electroless nickel and molykote grease was applied on all mating surfaces. To achieve the maximum surface contact, the faces were ground to 16 micro inch and hand lapped to a mirror finish before plating. To hold the adjoining faces together and allow motion, spring washers were installed on the ends of a hinge pin. A complete array of six flux shunts installed on the IDB U5.0 Undulator is shown in Figure 1.

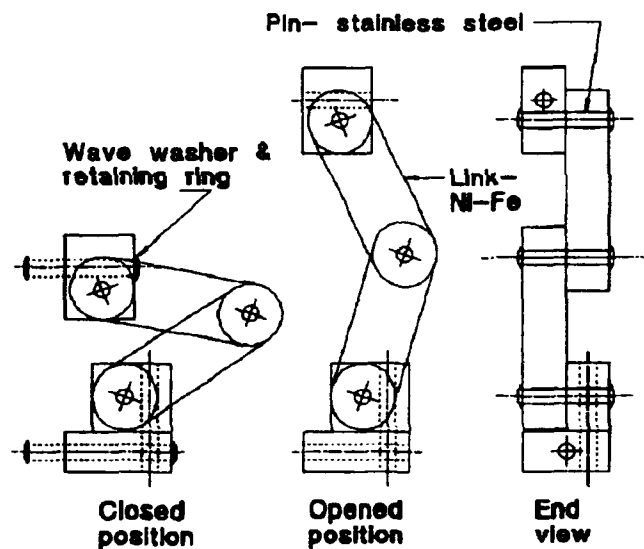


Figure 3. Flux shunt linkage.

IV. MAGNETIC MEASUREMENTS

The first measurements were carried out with a single flux shunt attached to two 80 cm square by 5 cm thick 1010 steel plates, Figure 4, to simulate 1/6 of an ALS undulator [3]. With a 22.5 cm plate spacing and the flux shunt disconnected from the plates, the average central field above the top plate was 0.36 G and between the plates 0.42 G for a field enhancement of 1.17. With the flux shunt connected, the field at the top increased to 0.49 G and the internal field dropped to 0.11 G, a reduction of a factor 3.82, which verified that the concept works. The shunt carried 3750 G cm^2 flux. Qualitatively,

when the gap is increased, the field above the plate increases, the internal field decreases but the field integral between the plates increases. A 31,500 cycle life test of the flux shunt decreased the magnetic performance by 6.6%.



Figure 4. ALS prototype flux shunt in test configuration.

Tests were carried out with the assembled undulator support structure/drive system and the magnetic structure backing beams, but without the periodic structure installed, as shown in Figure 1 [4]. Results show that the near midplane vertical field integral, due to the environmental fields, is 115–150 G cm over the undulator operating range without the flux shunts. Calculations of this configuration using the Figure 2 model, without the pole, yields field integrals of 160–200 G cm, which suggests that approximately 25% of the flux is shunted through the large vertical members of the support structure. With the six flux shunts attached to the backing beams, the field integral is reduced to 70 G cm for all gaps or an average gap field of 0.15 G. Based on calculations, with and without the pole installed in the magnetic structure, at 1.4 cm gap, field integral with poles would be 80 G cm for an average field reduction factor of 2.57. This field integral is greater than the predicted 50 G cm and is probably due to saturation in the backing beams (annealed 1005 steel). As the shunts were added, the amount of flux carried by the shunts increased, though the flux carried in each individual shunt decreased with the distribution of flux among these shunts being fairly uniform.

Magnetic measurements on the completed IDB-U5.0 Undulator showed that the six flux shunts reduced the magnetic field integral by 110 G cm over the range of magnetic structure gaps from 1.4 cm to 21 cm. However, the measured field integrals are dominated by magnetic structure errors and the ends of the undulator so the environmental fields only make a partial contribution to the field integral in this case.

Energizing the flux shunts was explored to cancel the field integral at any gap. Because the coil excitation is outside the magnetic structure, the effects of coil heating will not affect the magnetic field.

A coil was put on each flux shunt to change the undulator vertical magnetic field integral. Measurements carried out with individual shunts, energized at a given current, show that the undulator centerline vertical field integrals generated by the shunts on the ends of the undulator are about 20 % higher than those generated by the shunts located in the center of the

undulator. This is believed to be due to the end configuration of the magnetic structure, in particular the shorting of the outermost poles to the backing beams.

With all six flux shunts energized in series, the change in the undulator vertical magnetic field integral is only 87% of the change that is obtained when the field integral changes of the individual shunts are added together when excited with the same current.

Data was obtained for the six flux shunts energized that gives the changes in the centerline vertical magnetic field integral as a function of ampere-turns for several gaps. The results show, for a given excitation, that the field integral change increases with gap closing until the permanent magnet structure begins to saturate at about 2.2 cm, after which it decreases. The ampere turns required to null the vertical magnetic field integral as a function of undulator gap are determined.

V. SUMMARY

Tests demonstrate that the flux-shunt concept effectively reduces the average dc magnetic field in the undulator. For the IDB-U5.0 support structure alone, the vertical support members shunt approximately 25% of the flux between the backing beams and the flux shunts carry 35% more resulting in a 70 G cm field integral and an average field of 0.15 G. Flux shunts reduced the field integral for the completed device to 110 G cm, but the environmental field effects are a fraction of the periodic structure field errors. In this case, the field integral can be canceled by energizing coils on the flux shunts.

VI. ACKNOWLEDGMENT

This work was supported by the Director, Office of Energy Research, Office of Basic Energy Sciences, Materials Sciences Division of the U.S. Department of Energy under Contract No. DE-AC03-76SF00098.

VII. REFERENCES

- [1] "U5.0 Undulator Conceptual Design Report," LBL PUB-5256, (Nov. 1989).
- [2] E. Hoyer, "Flexible Yoke Design," LBL Engr. Note M7039B (July 1990).
- [3] E. Hoyer, "Flexible Yoke and Prototype ALS Flux Shunt Tests," LBL Engr. Note M7229 (Oct. 1991).
- [4] E. Hoyer and K. McCabe, "Flux Shunt Magnetic Measurements on the SDS," LBL Engr. Note M7285 (July 1992).
- [5] E. Hoyer, "Flux Shunt Magnetic Measurements on IDB," LBL Engr. Note M7350 (April 1993).

Design, Construction and Testing of Insertion Devices for ELETTRA

R. P. Walker, A. Codutti*, R. Bracco, B. Diviacco, D. Millo, C. Poloni† and D. Zangrando
Sincrotrone Trieste, Padriciano 99, 34012 Trieste, Italy, (* student) † Department of Energetics, University of Trieste, Italy

Abstract

The design, construction and testing of the first two undulators that will be installed in ELETTRA is described. Some details are given also of the future program of Insertion Device development.

I. INTRODUCTION

The ELETTRA storage ring will accommodate 11 insertion devices, each up to 4.8 m long. At present five devices have been approved for construction, serving a total of 8 beamlines, as detailed in Table 1. Undulators (U) will have a pure permanent magnet configuration, while the multipole wiggler (W) will be of the hybrid type. Each device consists of up to 3 separate sections based on a standard 1.5 m support structure. Previous work on the construction of prototypes was reported in ref. [1].

Table 1. Main parameters of the initial ELETTRA Insertion Devices, in order of construction; N = number of periods.

Beamlines	ID	N	Gap (mm)	Bo (T)	K
ID3A,B	U12.5	36	25.0	0.486	5.67
ID2A,B	U5.6	81	25.0	0.445	2.33
			20.0	0.590	3.09
ID5A,B	W14.0	30	25.0	1.15	15.0
			20.0	1.55	20.3
ID4	U8.0	19	25.0	0.713	5.33
			20.0	0.866	6.47
ID6	U12.5	36	25.0	0.486	5.67

The first device (U12.5) has been constructed and tested, and the second (U5.6) is presently being assembled. Both devices will be installed in the ring this Summer, before beam commissioning. At this time the standard vacuum chamber will permit a minimum gap of 60 mm. Early next year one section of the wiggler and the undulator U8.0 will be installed, together with the 25 mm narrow gap vacuum vessels. The remaining two sections of the wiggler W14.0 and a second U12.5 will subsequently be installed. Beyond this first phase there are plans for other undulators, including a device for circularly polarized radiation. Initial operation will be at 1.5 GeV. Future developments will include operation at 2 GeV, and reduction of selected ID gaps to 20 mm.

II. UNDULATOR U12.5

The first undulator is required to operate over a total range 10-800 eV, for ring energies of 1.5-2 GeV. To obtain the minimum energy various period lengths could have been chosen. The value selected, 12.5 cm, is a compromise between minimizing the power density (long period, small K) and maximizing the flux at high energy (small period, high

K). The resulting field strength, 0.486 T, is sufficiently small that a space of 5.25 mm can be left between the blocks (4 blocks per period), and a block height of only 21.5 can be used. In addition a simple clamping scheme can be used, increasing the gap between magnets to 29 mm. A block width of 100 mm was chosen in order to limit the systematic quadratic field variation, $\cos(k_x x)$, to $k_x/k < 0.2$ ($k=2\pi/\lambda_0$). The correct periodicity is maintained by means of an accurately machined 'comb', making use of the spaces between the blocks. The resulting structure, shown in fig. 1, is thus very simple and cost effective.

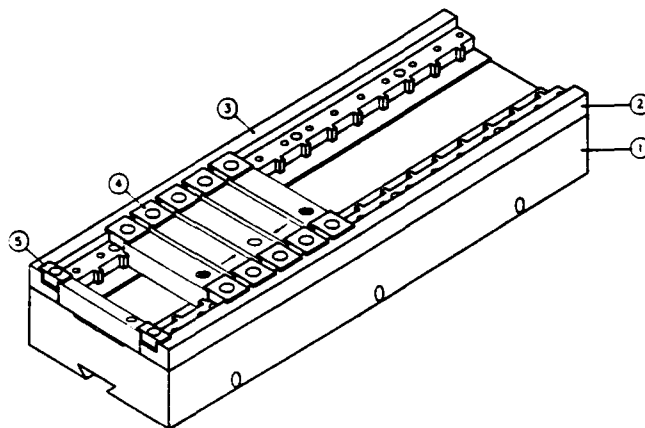


Figure 1. Structure of the magnetic arrays of undulator U12.5.

NdFeB permanent magnet blocks of NEOREM 30 H were obtained from Outokumpu magnets, with Nickel coating. Each block was measured in detail using a Hall plate system [2] in the two possible orientations that were allowed for assembly. Both transverse field components were measured at a grid of points, 81 points in z over ± 2 period lengths and 13 points in x over ± 60 mm; the vertical height (y) corresponded to the minimum gap of 29 mm. About 15 minutes were required in total for each block.

Data from the measurements were used in a "simulated annealing" program to optimize the block configuration, based on linear superposition of the fields of different blocks. The optimization was performed for all 3 sections at the same time, but including some parameters based on the individual sections. The cost function to be minimized included the following terms: first and second field integrals of both field components at all x positions within ± 60 mm, for each section separately and for all 3 sections; r.m.s. phase error for the complete device and separately for the top and bottom arrays. Further details may be found in a separate report [3]. The second field integral is defined in such a way that it corresponds to the displacement of the electron beam referred to the centre of the device.

Each of the 3 sections has been assembled using the

Table 2.
Magnetic measurement results for the 3 sections of U12.5
before and after shimming. Units: gap (mm), σ_B (%),
 σ_ϕ (deg.), $\Delta I_{1,x,y}$ (Gm), $\Delta I_{2,x,y}$ (Gm²)

	Section 1			Section 2			Section 3		
gap	29	50	100	29	50	100	29	50	100
<i>before shimming:</i>									
σ_B	1.1	0.8	0.8	1.3	0.8	0.6	1.4	1.0	1.0
σ_ϕ	4.5	4.7	4.1	2.9	3.2	3.6	5.4	4.9	3.7
$\Delta I_{1,x,y}$	1.4	0.7	0.5	0.9	0.6	0.3	1.5	0.7	0.3
$\Delta I_{2,x,y}$	1.5	0.8	0.3	1.0	0.5	0.2	1.0	0.5	0.2
R_1	1.0	1.0	0.99	1.0	1.0	0.99	0.97	0.97	1.0
R_3	0.96	0.94	0.95	0.99	0.98	0.98	0.89	0.96	0.96
R_5	0.85	0.86	0.84	0.93	0.92	0.91	0.85	0.81	0.88
<i>after shimming:</i>									
σ_B	0.8	0.6	0.7	1.1	0.8	0.6	0.9	0.6	0.7
σ_ϕ	3.2	3.5	3.8	3.0	3.2	3.6	2.8	3.0	3.4
$\Delta I_{1,x,y}$	0.5	0.3	0.3	0.3	0.3	0.2	0.4	0.3	0.2
$\Delta I_{2,x,y}$	1.3	0.8	0.3	1.0	0.5	0.2	1.3	0.7	0.3
R_1	1.0	1.0	0.99	1.0	1.0	0.99	0.98	0.98	1.0
R_3	0.97	0.96	0.95	0.98	0.98	0.95	0.94	1.0	0.97
R_5	0.92	0.90	0.88	0.96	0.91	0.90	0.95	0.90	0.92

defined configuration and measured using the same system as for the block measurements. The results for all sections are summarized in Table 2, which includes the r.m.s. field amplitude and r.m.s. phase, the maximum range of variation of the first and second field integrals over the "good field region" of ± 25 mm, and intensities of the first, third and fifth harmonics relative to an ideal undulator (R_1 , R_3 , R_5). The results are generally in very good agreement with the predictions based on the superposition of the field from individual blocks [3]. However, although the field integrals are similar in magnitude to the predictions the actual distribution is different, being very sensitive to the errors in the block measurements. The field integrals are close to or within the specified limits of ± 1 Gm and ± 2.5 Gm² at all gaps. The r.m.s. phase error is less than 5.4° for all sections, with the result that the 5th harmonic has at least 80% of its ideal intensity for each section. The r.m.s. field error is shown only for interest since it bears little relationship to the resulting performance.

Further improvements have been made to the field quality by means of shimming [3]. A simulated annealing algorithm has been developed to position the shims in order to correct both field integrals and phase error simultaneously, at 3 different gaps. The program uses "shim signatures" calculated using a model for the shim effect. In all 3 sections it has proved possible to both improve spectral performance and reduce field integral variation, using between 21 and 35 shims. Table 2 includes the final results obtained after shimming and fig. 2 shows a typical distribution of field integrals for one section.

The superposition of the measured field for the three sections produces the trajectory shown in fig. 3. The phase values at the position of the poles is also shown. Table 3 summarizes the performance of the combined undulator at three different gaps. The field amplitude and K values are also

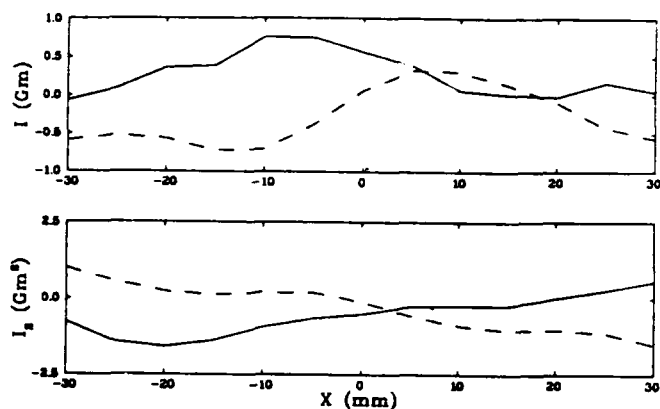


Figure 2. First and second field integrals for a typical section of U12.5.

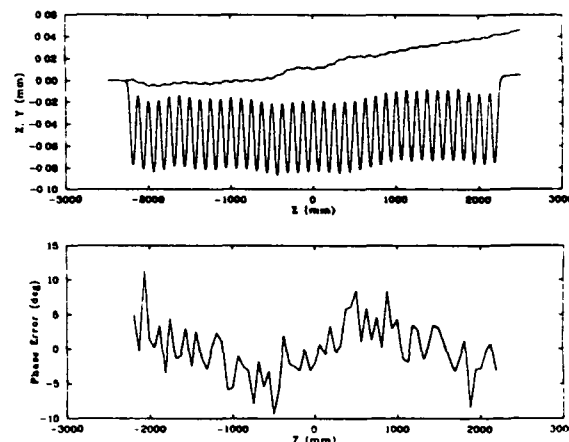


Figure 3. Calculated trajectory and radiation phase in the complete U12.5 undulator at minimum gap.

Table 3.
Results of the superposition of the measured field of the three U12.5 sections.

Gap (mm)	29.0	50.0	100.0
B_0 (T)	0.545	0.315	0.083
K	6.4	3.7	1.0
σ_B (%)	1.0	0.6	0.6
σ_ϕ (deg.)	4.1	3.8	3.7
R_1	0.99	0.99	0.99
R_3	0.94	0.96	0.92
R_5	0.88	0.87	0.81

shown, and it can be seen that they meet the required performance given in Table 1. The phase error is sufficiently small to produce good output up to at least the 9th harmonic, as shown in fig. 4.

Placing the sections together introduces additional effects that need to be considered in order to achieve the performance indicated above. The finite separation introduces a phase difference of the radiation emitted in each section. In the present case this will be minimized by positioning the devices with less than 1 mm separation. Secondly, the non-unit permeability of the NdFeB material introduces a small vertical field component that will be compensated using small

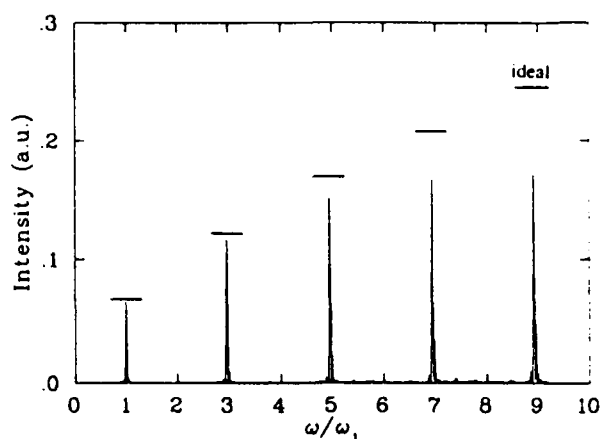


Figure 4. Calculated on-axis spectrum for the complete U12.5 device at minimum gap. The intensities of an ideal undulator are as indicated.

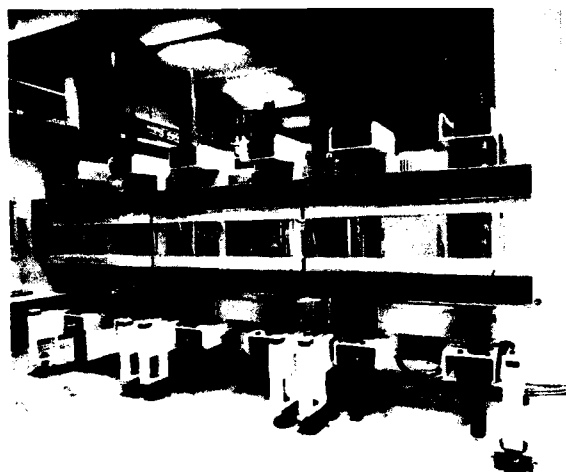


Figure 5. Photo showing the completed U12.5 device.

correction coils. Further details may be found in ref [4].

The undulator U12.5 is now ready for installation in ELETTRA. Figure 5 shows how the three sections will appear when assembled together to form a complete 4.5 m device.

III. UNDULATOR U5.6

The second undulator is designed to cover the range 250 eV - 1 keV at 1.5 GeV, with higher photon energies at 2 GeV. A period length of 5.6 cm was selected in order to give a sufficiently high K value (2.3) to provide a reasonable overlap between the first and third harmonics with a minimum gap of 25 mm. A standard arrangement of 4 blocks per period will be used, with 28 mm block height. A block width of 85 mm was chosen to obtain $k_x/k < 0.1$. A similar construction scheme to that used for the prototype has been used: blocks are clamped into individual holders, which are then assembled onto a baseplate.

NdFeB permanent magnet blocks were obtained from Outokumpu magnets (NEOREM 440i). To prevent corrosion the blocks have been passivated and oiled, a cheaper option than metal coating and sufficiently effective for the ambient conditions in ELETTRA. Each block has been measured in an

identical way to those of U12.5, but using a new bench dedicated to block measurements. This allowed measurements of completed sections to be continued during the 2 months that were necessary to measure the 740 blocks. A reference block was measured each day in order to guarantee that there were no changes in conditions during the measurement period.

The simulated annealing algorithm used for these blocks was similar to that used for U12.5, with the exception that additional terms were included to guarantee a linear electron trajectory. Some difficulties were experienced in optimizing the structure, possibly due to the increased number of periods, or possibly because of the actual set of measurement data. The optimization was also hindered by the significant increase in the required computer time compared to U12.5 [3]. For the configuration chosen the predicted performance was very similar to that of U12.5, including also the phase errors, but with the exception of the first integral field errors, which showed maximum values up to 4 Gm in all sections. This was accepted however on the basis that shimming is more effective in correcting field integral errors than phase errors.

The first section of U5.6 has been completed recently and measurements will start soon.

IV. WIGGLER W14.0

Construction of a 0.5 m prototype device which successfully reached the required 1.6 T field level was described in ref. [1]. Since then the mechanical design of each cell has been modified. Previously each permanent magnet block was a single piece 14.0 x 11.5 x 2.38 cm, composed of 6 smaller blocks glued together. Problems arose however due to failure of the bonding, and so the new scheme uses only two blocks which are clamped into position. All components for the wiggler are presently on order, with the exception of the end-terminations, pending completion of tests using a rotating block for field integral correction.

V. UNDULATOR U8.0

This device is required to operate over a very wide range of photon energy, from 250 eV to 1.5-2.0 keV in an undulator mode, and from 2-8 keV as a wiggler. The period chosen was a compromise between increasing the flux at low photon energy (short period and therefore small K value) or high energy (long period, high field and therefore high critical energy). Permanent magnet blocks have been ordered with a height of 40 mm, selected to give close to the maximum possible field, and with a width of 100 mm, to satisfy the requirement $k_x/k \sim 0.1$. A similar block holding structure to that of U5.6 will be used.

VI. REFERENCES

- [1] R.P. Walker et. al., "Status of Development of Insertion Devices for ELETTRA", Proc. 3rd European Particle Accelerator Conference, Berlin, March 1992, p. 1656.
- [2] D. Zangrando and R.P. Walker, "Magnetic Measurement Facility for the ELETTRA Insertion Devices", *ibid*, p.1355.
- [3] B. Diviacco, these proceedings.
- [4] B. Diviacco and R.P. Walker, these proceedings.

Performance Optimization of Pure Permanent Magnet Undulators

Bruno Diviacco
Sincrotrone Trieste
Padriciano 99, 34012 Trieste ITALY

Abstract

An application of the Simulated Annealing technique to the problem of optimizing the performance of Pure Permanent Magnet Undulators is described. This method has been applied to the optimization of the first two undulators for Elettra. Predictions are shown to be in good agreement with the actual measurements of undulator sections which have been performed so far.

I. INTRODUCTION

The problem of optimizing the field quality of Pure Permanent Magnet Undulators (PPMU) has been discussed by several authors [1]. All of the proposed solutions are based on a more or less accurate ability to predict the field resulting from the superposition of a large number of permanent magnet blocks. Therefore, the first step for any optimization process usually consists in a precise characterization of the individual blocks.

Another important issue is to define suitable quantities to be used as 'quality parameters' of the undulator field. For devices which have to be installed in low emittance storage rings for the production of high brilliance synchrotron radiation, attention must be paid not only to the spectral purity of the emitted light, but also to the possible disturbing effect on the stored electron (positron) beam.

To actually perform optimization, an appropriate method has then to be found for sorting the available blocks, in order to increase as much as possible the undulator field quality.

Recently an additional technique has been developed which consists in placing thin ferromagnetic shims on the surface of the magnet, thus introducing small localized field perturbations. The problem in this case is to find the optimum configuration of shim positions and thicknesses, subject to some practical constraints such as the maximum number of shims to be used and the maximum shim thickness.

Both sorting and shimming can be successfully managed by stochastic search techniques such as Simulated Annealing [3]; this method has been applied to the optimization of the first two undulators for Elettra.

II. BLOCK SORTING

A. Individual Blocks Measurements

The method adopted consists in a Hall Plate scanning performed above and below the magnets over a range of longitudinal and transverse positions. Two components of the magnetic field are measured, giving enough information for predicting (by linear superposition of the individual fields) the on-axis and off-axis transverse field distributions for any configuration of blocks. Although this approach is complicated due to the large quantity of information which has to be handled, it gives the possibility of making accurate

predictions both of the main electron trajectory and of the integrated multipole contents of the undulator field.

Taking measurements on two sides of each block is of particular importance because of the high dishomogeneity of magnetization often present in commercially available high field materials such as NdFeB. As an example, fig.1 shows the statistical distributions of the total intensity of the blocks which have been used for the U12.5 undulator. Also shown is the distribution of the difference in field integrals above and below the blocks. It is clear that the effect of non-uniform magnetization can be even larger than that produced by the spread of average intensity values.

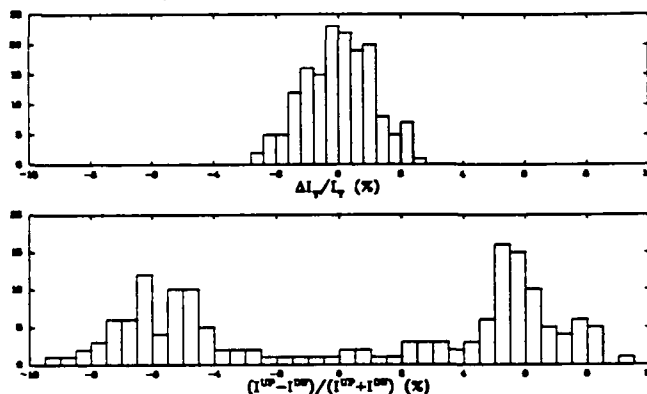


Figure 1. Statistics of intensity and dishomogeneity parameters for the U12.5 magnets.

B. Field Quality Parameters (Cost Function Definition)

The traditional way of assessing the field quality of an undulator is the rms on-axis peak field variation. As recently pointed out by some authors [2] this parameter is not very well correlated to the spectral intensity produced by a particular device. In ref. 2, the requirements that an alternative parameter should satisfy are clearly stated:

- i. It must be well correlated to the undulator performance
- ii. It must be simple to calculate
- iii. It must be general, i.e. independent of the particular device one is considering
- iv. It must be sensitive to small adjustments of the field distribution.

A good candidate to fulfill these requirements is the phase error (or 'phase shake'). This is the difference in phase of photons emitted by an electron moving along the real trajectory with respect to the ideal case where no field errors are present. The good correlation between the rms phase error (σ_ϕ) and the on-axis spontaneous emission intensity has been demonstrated by computer simulations [2,3]. As for point ii. above, the evaluation of σ_ϕ for any measured or computed field is straightforward. Points iii. and iv. are also easy to verify.

As mentioned before, there is another class of effects that we want to minimize, namely those which affect the circulating beam. Integrated multipoles are responsible for angular deflection of the particles passing through the device. Also the second integrals of the field, describing the final trajectory displacement, should be taken into account if the minimum disturbance condition has to be obtained.

All these considerations lead to the definition of the Cost Function. In the language of stochastic optimization, this is the combination of the various error terms that have to be minimized. In the present work the cost function is simply a weighted sum of three terms, corresponding to

- rms phase error
- maximum value of the first field integrals at any transverse position
- as in point b) for the second field integrals.

The optimization for the Elettra undulators is in reality complicated by the fact that they are segmented, i.e. build in up to three sections which could be operated individually if necessary. The cost function in this case has also terms corresponding to the single sections, but the general philosophy remains the same.

Having defined a unique cost associated with each possible configuration of blocks, a simulated annealing algorithm is used to find an optimum solution. The algorithm, starting from an arbitrary configuration, works by swapping pairs of randomly chosen blocks. Good and bad swaps are allowed with equal probability at the beginning, but, as the computation proceeds, bad swaps are less and less likely to be accepted. Eventually, when no more bad swaps are allowed, the process terminates. This method has the advantage of being able to approach the global minimum of the cost function without being trapped in a local one (see ref. 4 for details). A complication arises from the fact that the weighting coefficients of the various terms in the cost function must be adjusted empirically in order to achieve an overall satisfactory solution.

C. Results

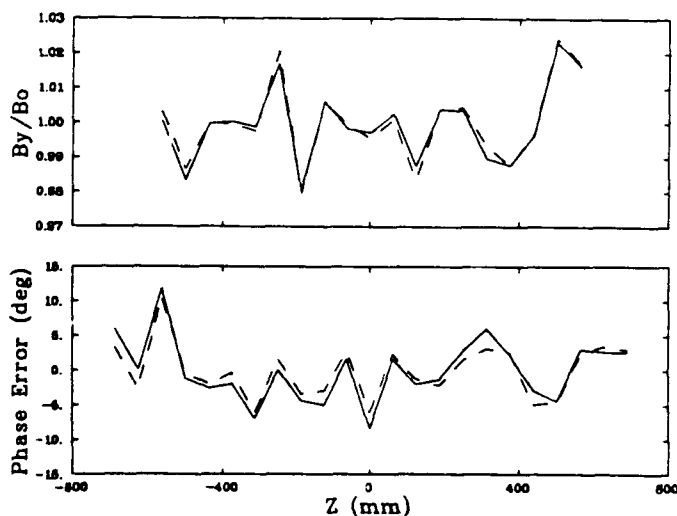


Figure 2. Measured (solid line) and predicted (dotted) field variation and phase error under each pole for U12.5, section 1.

The results obtained for the optimized U12.5 undulator are in good agreement with the predictions. As an example fig. 2 shows this comparison for the on-axis field and the phase error in the case of one of the three 12 period sub-sections.

During the process of simulated annealing, a large number of configurations are considered; for each of them the cost function is evaluated, giving all the important field quality parameters. It is therefore possible, with a simple modification of the program, to compute also the corresponding radiated spectrum. In this way it is easy to compare various parameters with the on-axis peak intensity. In fig. 3 the intensities for the first, third and fifth harmonic of the spectrum are plotted as a function of the rms phase error σ_ϕ . This calculation refers to the complete 36 period undulator (three sections). The point mentioned before about the good correlation between σ_ϕ and spectral intensity is confirmed in this case. It is worth noting that no particular model for the field errors is used in this simulation, suggesting the general validity of this correlation.

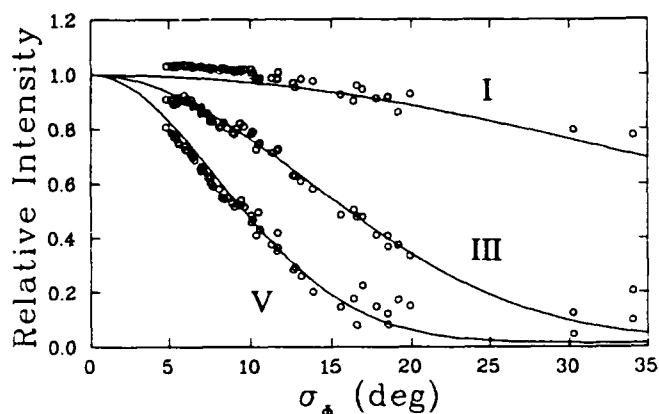


Figure 3. Correlation between spectral intensity and rms phase error. Also shown (continuous line) is the result of a model for the effect of random phase errors taken from ref. 3.

Finally, Table 1 and 2 compare predictions and measurements for the three individual sections. The overall agreements is very good, with the exception of the first integral variation which appears to be the most difficult parameter to control.

Table 1. Predicted (measured) rms field error, phase error and relative intensity for the U12.5 undulator. R1, R3 and R5 are expressed in percentage of the ideal case.

	σ_B (%)	σ_ϕ (deg)	R1 (%)	R3 (%)	R5 (%)
section 1	1.0 (1.1)	3.8 (4.5)	98 (99)	95 (95)	88 (85)
section 2	1.2 (1.3)	2.8 (2.9)	98 (99)	96 (98)	93 (93)
section 3	1.4 (1.4)	6.9 (5.4)	97 (97)	84 (89)	71 (85)

Table 2. Predicted (measured) first and second integral variation for the U12.5 undulator over ± 60 mm in x.

	ΔI_1 (G m)	ΔI_2 (G m ²)
section 1	± 0.9 (2.0)	± 1.3 (1.9)
section 2	± 0.8 (1.0)	± 1.0 (1.0)
section 3	± 0.8 (1.3)	± 1.0 (1.3)

III. SHIMMING

The shimming technique has been first proposed as a method to reduce the on-axis peak field variation based on the measured effect of shims placed between the poles of a hybrid undulator [5]. It has then been extended to the correction of the transverse field integral in a PPMU [6]. This correction is based on a model of the magnetizing effect of the external undulator field on a thin ferromagnetic shim sticking on its surface [7]. This model allows one to compute a set of 'field integral signatures' describing the effect of a shim placed at a given position in the undulator. The appropriate distribution of thicknesses required to correct the measured integral error is then found by determining the appropriate coefficients in a linear combination of these signature functions.

Combining the two methods, it is simple to extend the calculation of the shim effect in order to include also the perturbation to the longitudinal field distribution. As an example fig. 4 shows the computed and measured 'longitudinal signature' for a 0.4 mm thick shim positioned at the centre of the U12.5 undulator.

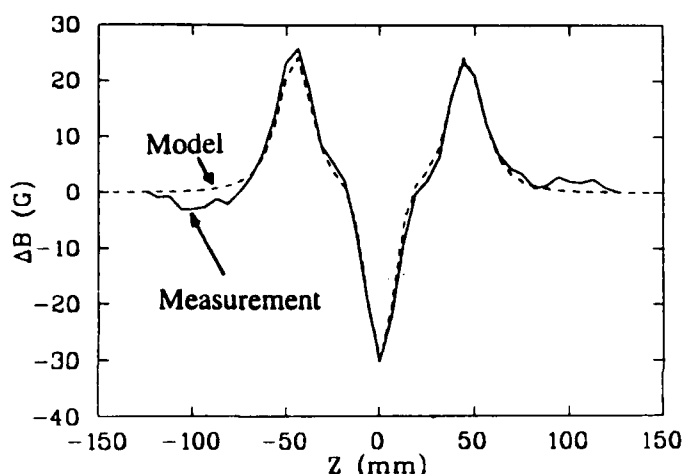


Figure 4. Measured and computed effect of one shim ($88 \times 13 \times 0.4$ mm) on the on-axis field of the U12.5 undulator at 29 mm gap.

With a suitable set of transverse and longitudinal signatures, it is therefore possible to predict the effect that any combination of shims will have on the measured undulator field. This effect includes first and second integrals, on-axis field, trajectory, phase error and spectral intensity.

Similarly to the case of block sorting, a cost function can be evaluated which gives the desired quality parameters for each shim configuration. The simulated annealing algorithm can then be used to find the optimum shim placement in order to improve the field quality of an existing undulator structure. This approach has the advantage that correction of the field integrals and phase optimization can be performed simultaneously. The correction can also be extended to several magnetic gap values, if the appropriate signatures are computed.

This method has been applied to the three U12.5 sections; the purpose was to correct the first and second field integral error to within the specified limits of ± 1 Gm and

± 2.5 Gm² over a transverse range of ± 25 mm at all gaps. At the same time we tried to reduce the rms phase error of sections 1 and 3 which showed a larger value compared to the central section 2. This attempt has been successful, using between 21 and 35 shims of thickness 0.2 to 0.5 mm. Table 3 shows that the measured values of the phase error for the three sections at three different gaps are in very good agreement with prediction. The required field integral correction has also been achieved. More details about the final results can be found in ref. 8.

Table 3. Predicted (measured) rms phase and peak field errors in the three sections of U12.5. σ_B is listed only to show the good agreement with the predictions, but is not used at all in the optimization.

	gap	σ_ϕ (deg)	σ_B (%)
section 1	29	3.0 (3.1)	0.9 (0.8)
	50	3.5 (3.5)	0.6 (0.6)
	100	3.7 (3.8)	0.6 (0.7)
section 2	29	2.8 (2.9)	1.2 (1.2)
	50	3.2 (3.2)	0.8 (0.8)
	100	3.5 (3.6)	0.6 (0.6)
section 3	29	2.6 (2.8)	0.9 (0.9)
	50	2.9 (3.0)	0.6 (0.6)
	100	3.4 (3.4)	0.7 (0.7)

IV. CONCLUSION

The simulated annealing method has been successfully applied to the optimization of the U12.5 undulator, both for block sorting and shimming. The same approach is therefore being used for the shorter period device U5.6, presently under construction.

V. REFERENCES

- [1] For recent reports on this topic see for example: A.Bhowmik et al., Nucl. Instr. Meth. A281 (1989) 224; M.E Couprie et al., Nucl. Instr. Meth. A304 (1991) 710; G. Rakowsky et al., Proc. 1991 IEEE Particle Accelerator Conference, pag. 2773.
- [2] B.L. Bobbs et al., Nucl. Instr. Meth. A296 (1990) 574; P.Kennedy et al., Nucl. Instr. Meth. A296 (1990) 607.
- [3] R.P.Walker, to be published in Nucl. Instr. Meth.
- [4] A.D.Cox and B.P.Youngman, Proc. International Conference on Insertion Devices for Synchrotron Sources, SPIE Proceedings vol. 582 (1986) 91; W.H.Press et al., 'Numerical Recipes', Cambridge University Press (1990), cap.10.9.
- [5] D.C.Quimby et al., Nucl. Instr. Meth. A285 (1989) 281; S.C.Gottshalk et al., Nucl. Instr. Meth. A296 (1990) 579.
- [6] J.Chavanne, E.Chinchio, P.Ellaume, ESRF Internal Report SR/ID-89-27, September 1989.
- [7] J.Chavanne, P.Ellaume, F.Revol, ESRF Internal Report SR/ID-89-32, November 1989.
- [8] B.Diviacco and R.P.Walker, these proceedings.

Magnetic Interaction Effects in ELETTRA Segmented Pure Permanent Magnet Undulators

B. Diviacco and R. P. Walker
Sincrotrone Trieste, Padriciano 99, 34012 Trieste, Italy

Abstract

The effects of finite separation and non-linear superposition between pure permanent magnet sections are considered. Measurements of finite permeability effects are compared to the results of calculations with a program, PMU3Dμ.

I. INTRODUCTION

The standard undulators for the ELETTRA synchrotron radiation facility will be 4.5 m long, and will be composed of three independent sections, for flexibility in use, greater mechanical stability and ease of construction, testing and handling [1]. A general problem of segmentation is that the correct phase relationship must be maintained between the radiation emitted in the different sections, in order to preserve the high radiation brightness. In the present case it was decided to adopt a pure-permanent magnet configuration so that phase errors could be minimized, while still permitting independent operation of the sections [1,2].

A second problem is that the fields of two adjacent sections do not superimpose exactly, due to the effects of non-unit permeability of the permanent magnet material. This is one aspect of a general problem that arises when individually measured blocks or sections are put together [3]. The situation is worse for NdFeB material compared to SmCo₅, since although the permeability in the direction of magnetization is similar, 1.03-1.08, that in the perpendicular direction is significantly larger: 1.15-1.18, compared to 1.02-1.08.

In this report we consider these two effects for the first two undulators that will be installed in ELETTRA, with period lengths of 5.6 cm and 12.5 cm [4]. Measurements of non-linear superposition effects are compared with the results of a computer program, PMU3Dμ, which is based on an earlier program for ideal, unit-permeability, permanent magnet undulators [5].

II. PHASE DIFFERENCE

Figure 1 shows the result of calculating the phase difference between the radiation emitted in two ideal pure permanent magnet undulators as a function of their separation, at three different gaps. The examples correspond to the first two devices that will be installed in ELETTRA [4]. It can be seen that for small separation the phase difference increases linearly with separation, and varies inversely with the period length. The variation with gap is however quite complicated since it depends on the exact form of the fringe field. The effect of the phase difference $\Delta\phi$ is to introduce an additional factor into the expression for the spectrum for one section (N periods):

$(2 + 2\cos(2\pi N\Delta\omega/\omega_1 + \Delta\phi))$ for 2 sections,
 $(3 + 4\cos(2\pi N\Delta\omega/\omega_1 + \Delta\phi) + 2\cos(4\pi N\Delta\omega/\omega_1 + 2\Delta\phi))$,
 for 3 sections. Figure 2 shows the calculated reduction in peak on-axis angular flux density (zero emittance).

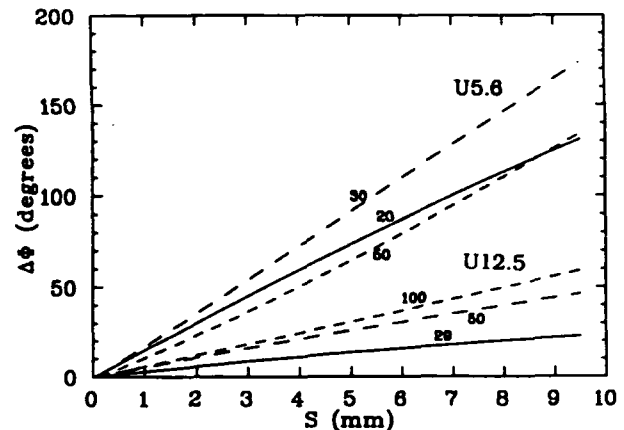


Figure 1. Phase difference as a function of separation in two undulators, with various gaps.

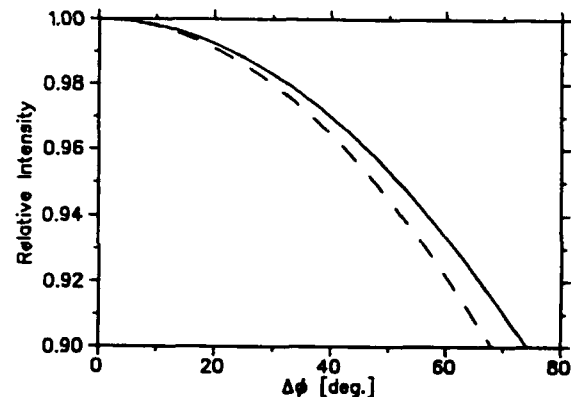


Figure 2. Relative intensity as a function of phase difference; upper curve - 2 sections, lower - 3 sections.

It can be seen that the intensity is not very sensitive to $\Delta\phi$, at least for the fundamental. However, the phase is calculated at the fundamental wavelength in each case, and is therefore 3 times larger for the third harmonic, and so on. A small separation is therefore needed in order to have negligible effect on the higher harmonics. In ELETTRA the IDs will be separated by 0.5-1 mm to give a phase difference of less than 10° , and hence a reduction of less than 5 % for the 5th harmonic.

III. NON-SUPERPOSITION EFFECTS

A. Calculation of Non-Unit Permeability Effects with PMU3Dμ

To a good approximation the field inside the permanent magnet material can be expressed in the following way [6]:

$\mathbf{B} = \mu_0 (\mu \cdot \mathbf{H} + \mathbf{B}_r)$, where \mathbf{B}_r is the remanent field and $\mu = (\mu_{||}, \mu_{\perp})$ the permeability in the direction of magnetization and perpendicular to it respectively. The magnetization can therefore be written as: $\mathbf{M} = \mathbf{B}_r + \mu_0 (\chi \cdot \mathbf{H})$, where $\chi_{||} = \mu_{||} - 1$, $\chi_{\perp} = \mu_{\perp} - 1$. The equivalent current density is given by $\mathbf{J}_m = \text{curl } \mathbf{M}$. The additional field that arises from non-unit permeability can therefore be calculated from a current density $\mathbf{J}_m = \mu_0 \text{curl } (\chi \cdot \mathbf{H})$. It can be seen that the additional current density contains both a volume term, due to changing \mathbf{H} , and surface terms, arising from discontinuities in χ and \mathbf{H} .

The program PMU3D μ uses the fact that the additional effect is a small perturbation. It first calculates the field due to a set of ideal $\mu=1$ blocks in the standard way [5] at regularly spaced points in each block, takes the appropriate derivatives to obtain the current density, and then calculates the additional field. To be more efficient the program can divide the blocks into groups whose fields are to be superimposed. The non-linear effect within each group is not calculated since this does not appear as an additional effect when the groups are put together.

B. Magnet Blocks

We first consider the interaction effects between two or more individual permanent magnet blocks. In ref. [7] measurements and calculations using POISSON were shown to be in good agreement for the non-superposition effect of two blocks with perpendicular magnetization. Here we examine the more complex case of an array of 4 periods, 17 blocks, of undulator U5.6.

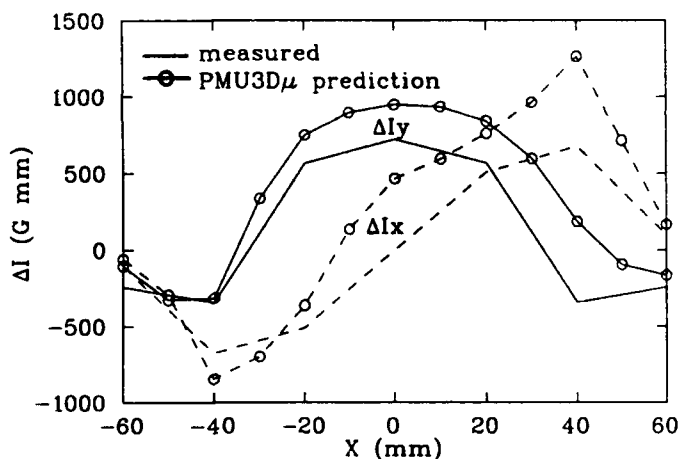


Figure 3. Measured and calculated field integrals arising from the superposition of blocks in a 4 period array.

Figure 3 shows the difference between the measured transverse variation of the field integrals and the values expected from a linear superposition of the fields of the individual blocks. The values calculated with PMU3D μ are also shown, and it can be seen that there is good agreement, given the small magnitude of the effect. The permeability assumed in these and the following calculations are $\mu = (1.0, 1.15)$. The effects are generally much less influenced by $\mu_{||}$. The value of μ_{\perp} corresponds to that measured by the block manufacturer, Outokumpu Magnets.

C. Magnet Arrays

When individually measured linear arrays are put together above and below the electron beam there is another non-superposition effect, but only on the vertical field integral. This top/bottom effect has been measured using two 0.5 m long arrays of the undulator U5.6. Figure 4 shows the difference between the field integrals measured for the two arrays together and the sum of the integrals for the two arrays measured separately. Again there is good agreement of the vertical field integrals with the values calculated with PMU3D μ , and the horizontal integrals are close to zero as expected.

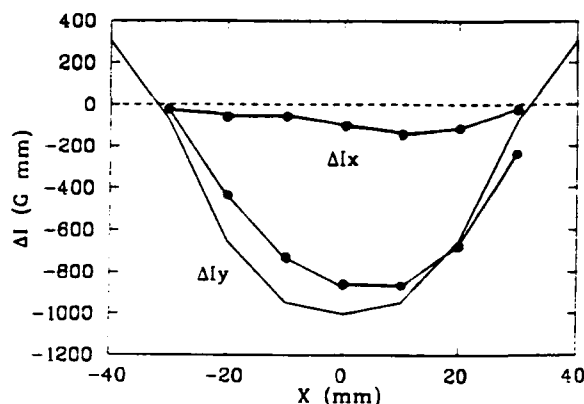


Figure 4. Measured (points) and calculated field integrals arising from the superposition of two magnet arrays.

The difference between the complete undulator, with top and bottom arrays, and the result expected from a linear superposition of the field of the individual blocks is - for the vertical field integral - twice the result shown in fig. 3 plus the top/bottom effect, as shown in fig. 5. The effect on the horizontal field integral is zero, due to cancellation of the distribution shown in fig. 3. In practise however the field integrals of a complete device are not dominated by this effect, but by sum of the errors of the many individual block measurements.

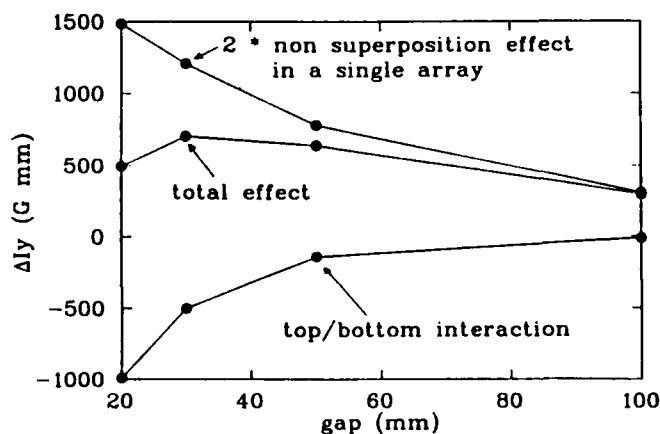


Figure 5. Calculated non-superposition effects for blocks in single and double arrays, and the top/bottom effect.

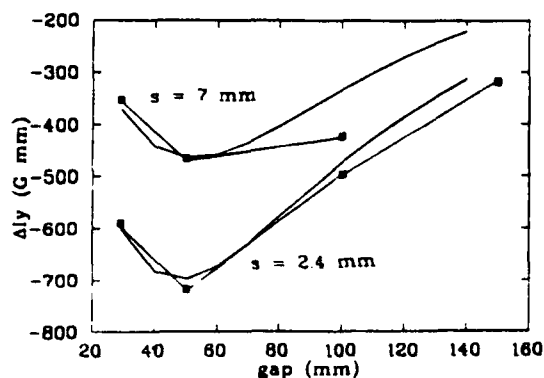


Figure 6. Measured (points) and calculated variation in field integral with gap for two sections of U12.5.

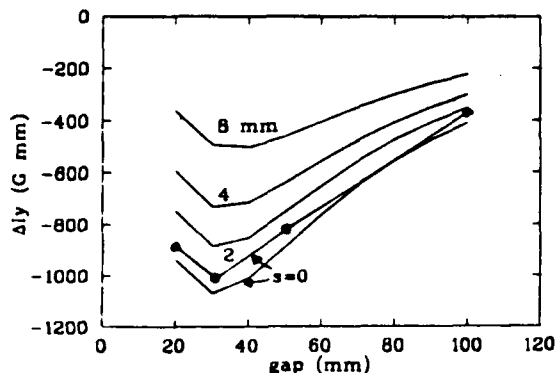


Figure 7. Measured (points) and calculated variation in field integral with gap for two sections of U5.6.

D. Undulator Sections

The most important effect in the present case is the non-superposition between two undulator sections, which gives rise only to a vertical field component. Figures 6 and 7 show the integral of this component at $x=0$ as a function gap, for various separations (s) between the sections. It can be seen that the effect decreases with increasing separation and that there is a complex variation with gap. Good agreement is again shown between measurements and calculation. Figure 8 shows the transverse variation of the field integrals, indicating a small integrated sextupole field of 0.1 T/m. The measured horizontal integral is close to zero, as expected.

Figure 9 shows the calculated longitudinal variation in the vertical field component. It can be seen that the major part of the effect of non-unit permeability occurs within the central half period.

The effect of the field integral would be to cause a variation in the storage ring closed orbit with gap. This could be corrected externally, however it also leads to a difference in the angle of radiation emission in each section. In the present case at 1.5 GeV a field integral of 1 Gm is equivalent to an angular deflection of 20 μ rad. Calculations show that this results in a significant reduction in brightness at the seventh harmonic and above. For high harmonic operation therefore it will be important to correct the field integral locally. This will be done using simple air cooled correction coils that will be located on each side of the interface, each with a correction capacity of about 1 Gm.

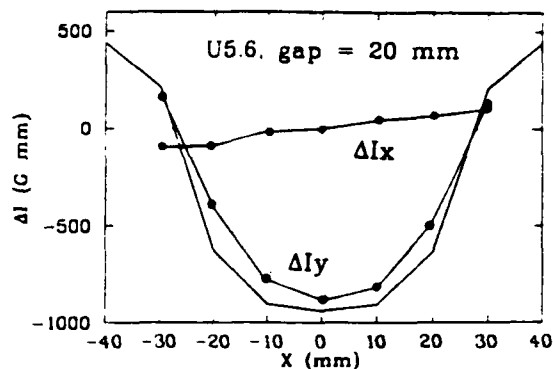


Figure 8. Measured (points) and calculated transverse variation in the field integral for two sections of U5.6.

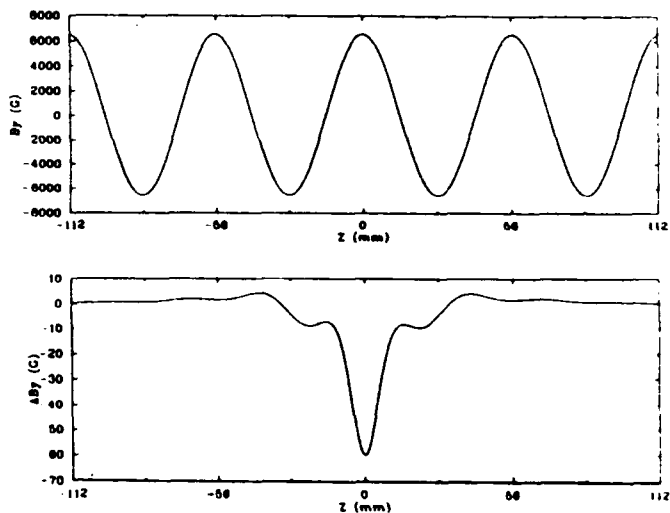


Figure 9. Calculated vertical field component for two sections of U5.6; upper-total field, lower-effect of non-unit permeability.

IV. ACKNOWLEDGEMENTS

It is a pleasure to acknowledge J. Chavanne and P. Elleaume for fruitful discussions about non-unit permeability effects, and K. Aittoniemi of Outokumpu Magnets for carrying out the perpendicular permeability measurements.

V. REFERENCES

- [1] ELETTRA Conceptual Design Report, Sincrotrone Trieste, April 1989.
- [2] B. Diviacco and R.P. Walker, "Phase Variations in a Segmented Undulator", Sincrotrone Trieste Internal Report ST/M-88/9, May 1988.
- [3] M.E. Couprie, C. Bazin and M. Billardon, Nucl. Instr. Meth. Phys. Res. A278 (1989) 788.
- [4] R.P. Walker et al., these proceedings.
- [5] R.P. Walker, Daresbury Laboratory Technical Memorandum, DL/SCI/TM54A, November 1987.
- [6] K. Halbach, Nucl. Instr. Meth. 169 (1980) 1.
- [7] D. Zangrando and R.P. Walker, Proc. 2nd European Particle Accelerator Conference, Nice, June 1990, p. 1365.

Planar Helical Undulator Sources of Circularly Polarized X-rays*

Roger Carr
Stanford Synchrotron Radiation Laboratory
P.O. Box 4349, bin 69
Stanford, CA 94309 USA

Abstract

The planar helical undulator is a charged particle accelerator insertion device that produces a helical magnetic field using only planar magnet arrays. The helical field causes the particles to execute helical trajectories, and to emit x-rays with a degree of circular polarization. To switch the x-ray helicity, some designs require a mechanical shift of the magnet arrays. Other designs use a chicane, a separate undulator to produce each polarization, and a chopper to switch between them. We present an analysis of the different magnetic designs that have been proposed, with emphasis on a device for the 500-1000 eV x-ray range on the SPEAR storage ring.

I. INTRODUCTION

There is an increasing demand for circularly polarized soft x-rays in the study of magnetic materials, biological molecules, and other systems that exhibit circular dichroism. At present, most experiments have been done with bending magnet radiation, which is elliptically polarized above and below the horizontal midplane of the storage ring. Insertion devices such as undulators and wigglers have been used to date mostly as sources of linearly polarized radiation. They yield much more intense radiation than bending magnets, so there is an apparent need for insertion device sources of elliptically polarized x-rays.

A number of insertion devices generate elliptically polarized x-rays, such as bifilar solenoids, elliptical and asymmetric wigglers, crossed undulators, and planar helical undulators. [1] We have chosen to study the pure permanent magnet planar helical undulator, which was pioneered by Elleaume at ESRF where he has installed a device of this type called 'Helios'. [2] Diviacco and Walker [3] and Sasaki [4] have developed alternative planar helical undulators; our study is an attempt to compare the different designs.

One class of planar helical undulators involves a chicane and a pair of in-line undulators as in the Helios design. One undulator creates left circularly polarized (LCP) light and one creates right circularly polarized (RCP) light. The chicane strategy creates two beams simultaneously, which both pass through the monochromator. They may be chopped alternately, to give the user only RCP or LCP light at any time. Each undulator is shorter than half of the available insertion region, because of the need to leave space for chicane magnets.

The other class of sources is the single undulator

* This work supported by the U.S. Dep't of Energy, Office of Basic Energy Sciences, Division of Materials Science.

without chicane. Some designs of this type of source can be shifted from RCP to LCP, and it has only one beam through the monochromator. The alternation of polarization would be lower than with a chopper, and might interact with the electron beam, but it would use the center, and not the two horizontal edges of the monochromator optics. This strategy would have more than twice the flux of the corresponding chicane design, both because more periods are used, and because the peak width is inversely proportional to the number of periods.

II. PLANAR HELICAL UNDULATOR DESIGNS

All of the devices discussed here have four rows of magnets, one in each quadrant surrounding the beam axis. Some of the magnets are used to generate horizontal fields, and some generate vertical fields. Critical parameters include flux, polarization rate, switching convenience between RCP and LCP, and mechanical complexity.

The Helios device of Elleaume is one which employs a standard Halbach jaw (both bottom rows the same) and another jaw that consists of two standard Halbach rows phased longitudinally apart by 1/2 period. [5] The Helios device is mechanically complicated, because its jaw motions are not symmetrical. It creates horizontal fields with one jaw, and vertical fields with the other; in order to generate a circular helix, the half gaps between axis and jaw must be changed separately. The jaws may also be moved longitudinally with respect to each other to change helicity or they could be fixed in phase in a chicane design with two undulators. This device is shown in figure 1:

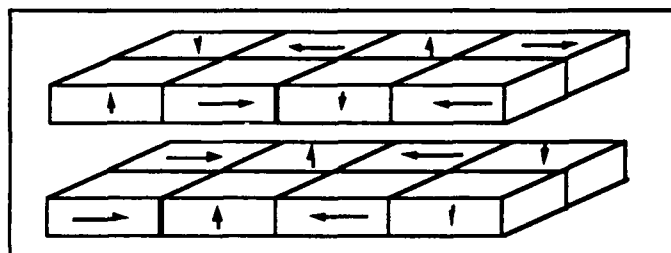


Figure 1: The Helios device, with arrows showing the direction of the easy axis of magnetization in each block.

The design of Walker and Diviacco is like four standard Halbach rows, but instead of blocks with magnetization parallel to the beam axis, those blocks have transverse magnetization. The horizontal and vertical fields are equal in strength at any value of gap, so it does not require any phase adjustment. This device cannot be phase shifted to

reverse the helicity, so it would not be usable as a single device to generate both RCP and LCP x-rays. To generate x-rays of the opposite helicity to those created by the device in figure 2, one would have to reverse the direction of magnetization of the vertically or the transversely oriented blocks.

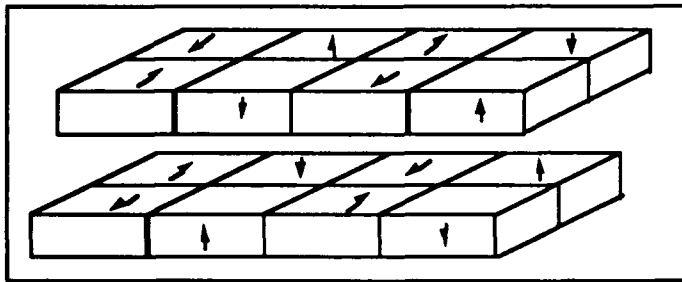


Figure 2: The device of Walker and Diviacco; blocks with vertical arrows create horizontal transverse fields; blocks with horizontal arrows create vertical fields.

The Sasaki device consists of four standard Halbach rows, but two of the rows must be phase adjustable in order to maintain a circular helix. Two rows, (say upper left and lower right) are moved together with respect to the fixed rows, but by a rather small amount (.13 to .18 period) to maintain a circular helix. By switching the phase through zero, the opposite sense of polarization is obtained. This geometry is shown in figure 3:

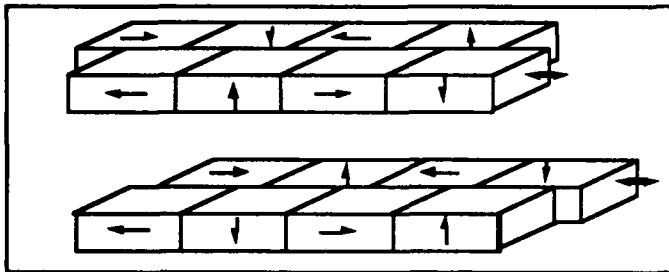


Figure 3: The Sasaki design; the lower front, and upper back rows are fixed and aligned; the lower back row and the upper front row are shifted to the right.

We are currently building a device starting with the Sasaki concept, but with the further extension that all four of the cassettes are moveable longitudinally. This will allow us to create vertically, circularly, and horizontally polarized radiation. In addition, we will be able to change the characteristic energy of the radiation by moving the top jaw longitudinally with respect to the bottom jaw or by moving the rear pair of cassettes with respect to the front pair. Such motions maintain ellipticity according to the way the original Sasaki phase is set, but they change the magnitudes of the magnetic fields, with no need to change the gap, as with the linearly polarizing adjustable phase undulator [6]

III COMPARISON OF DESIGNS

We modeled these devices using a program based on finite element decomposition of magnet blocks. For a circular helix, the field strengths must be equal, and the fields must be 90° apart in phase. We consider only pure permanent magnet devices where the magnet blocks have square cross section; this generates almost all the field strength that could be obtained from blocks of greater height. We consider the blocks to be 'wide' in the transverse direction, so that we do not suffer from finite width effects.

In designing an undulator for a given energy range, it is useful to study the following plots of B field versus period length, which are derived from the equations: [7]

$$E_f = \frac{950 E_e^2 (\text{GeV})}{\lambda (1 + K^2/2 + \theta^2 \gamma^2)} \quad [1a]$$

$$K = .934 B(T) \lambda (\text{cm}), \quad B = \sqrt{B_x^2 + B_y^2} \quad [1b]$$

For circular polarization, $B_x = B_y$, so that $B = \sqrt{2} B_{x,y}$.

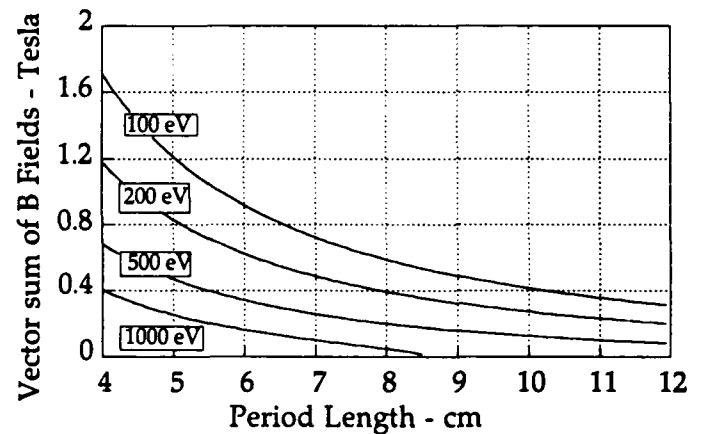


Figure 4: B field as a function of period to create x-rays of various fundamental energies with a 3 GeV electron beam.

The table below shows the calculated characteristics of various undulator designs, based on a minimum energy of 500 eV.

Undulator Type	Period Length	K Parameter	Number of Periods	P1 Flux Watts/100mA
Halbach Single	6.9	1.72	27	7.95
Elleaupe Single	7.6	1.57	24	5.32
Elleaupe Chicane	7.6	1.57	10	2.22
Walker Chicane	7.4	1.67	10	2.58
Sasaki Single	6.5	1.79	28	9.49
Sasaki Chicane	6.5	1.79	11	3.73

Table 1: The values were based on computations of B fields from the modeling program, and period lengths from Figure 6.

The undulator calculations assumed $B_f = 1.2 T$ NdFeB magnets of square cross section and 60 mm width, with a gap of 30 mm. The total length of 'single' devices is

1.9 m. and for the 'chicane' geometries, we use 1.5 m as the length available for the undulators. The Halbach linearly polarizing device is included for comparison. Flux was calculated for the power in the first harmonic: [7]

$$P_1 = \frac{\pi c I e N Z_0 g^2 K^2}{3 \lambda_u \left(1 + \frac{(K_x^2 + K_y^2)}{2} \right)^2} \quad [2]$$

N is the number of periods, and I is the electron current. Note that the single Sasaki device produces 19% more flux than a single Halbach device. This may be thought of as a consequence of the fact that the electrons are being accelerated continuously in a helical path, but only sinusoidally in a planar oscillating trajectory. The plot below shows the flux integrated over the undulators' central cones: [8]

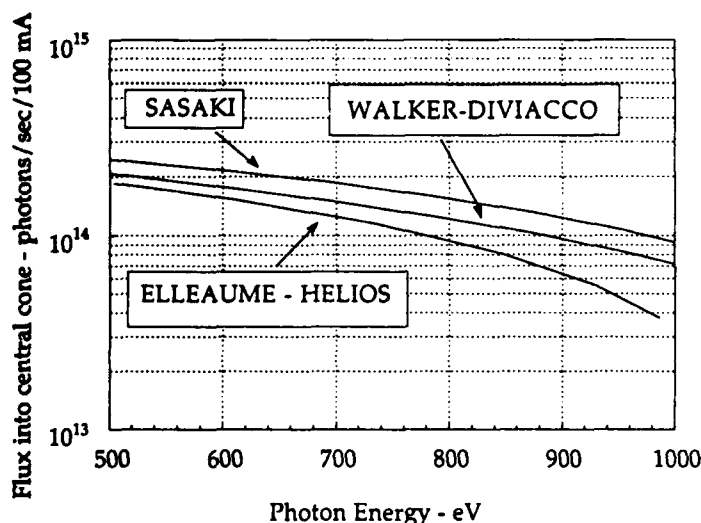


Figure 5: Central cone flux compared for 2 meter devices on SPEAR, with 100 mA electron beams.

IV: DISCUSSION

For an ideal electron beam, the flux from all of the planar helical undulators with circular helical orbits is 100% circularly polarized. A bending magnet or wiggler does not yield appreciable flux with more than about 90% circular polarization.

From flux considerations, it would appear that a single Sasaki type device would be preferred. Not only is the flux in the fundamental peak higher even than the comparable Halbach device, but the peak is narrower than all the other circularly polarizing devices because of the greater number of periods. From our experience on the adjustable phase undulator [6] it appears that the phase of an undulator may be changed with negligible disruption of the electron beam, so both directions of polarization would be available, with a slewing time of a few seconds between directions.

In the Walker-Diviacco design, the helicity of the electron trajectory remains exactly circular, independent of gap. This is convenient in that it does not require phase motion, but it does not allow the user to generate elliptical polarization, which may be useful. Elliptical polarization may be needed to overcome ellipticity in the optics, or to overcome ellipticity which occurs when the electron beam is off axis. Also, since its helicity cannot be changed by phase shifting, its use would be limited to a chicane geometry if both directions of circular polarization were desired.

The Elleaume design is more complicated mechanically, and has less flux than the other two designs. Also, with separate half gap adjustments for each jaw, one would have to move the undulator magnets separately from the chicane magnets. The Sasaki device can be phase shifted so that it produces linearly polarized light in the horizontal (phase = 0) or vertical direction (phase = 1/2 period). The Elleaume device can also be phase adjusted to produce linearly polarized light, but in the ± 45° directions.

The first choice is between the chicane and single undulator strategies. The single undulator uses the monochromator optics in a simple way, gives much more flux, and requires no chicane magnets, but is limited with regard to helicity switching. The chicane strategy would allow rapid switching with no disturbance to the electron beam, but makes more demands on monochromator optics, has much less flux, and requires effort in the design of the chicane. If a chicane strategy is adopted, the Walker strategy allows phase to be fixed for all gap settings; if the Sasaki phase is fixed, the polarization would be somewhat elliptical.

A problem common to all of the 4 cassette planar helical undulators is that their horizontal fields have a narrow horizontal profile. The vertical field can have a broad profile, proportional to the transverse width of the magnets. But the narrow horizontal field profile is a consequence of the sharp discontinuity between the parallel cassettes. This creates the requirement that the electron beam be steered accurately down the axis of the undulator. The x-ray spectrum will be blue shifted if the beam is horizontally off-axis.

V: REFERENCES

- [1] K-J. Kim, SPIE Proceedings, 1345, (1990), p. 116
- [2] P. Elleaume, Nucl. Inst. & Methods A291, (1990) p. 371
- [3] B. DiViacco and R. P. Walker, Nucl. Inst. & Methods, A292 (1990), p. 517
- [4] S. Sasaki, K. Miyata & T. Tanaka, Jpn. J. Appl. Phys 31 (1992) p. L1794
- [5] K. Halbach, Nucl. Inst. & Methods 187, (1981), p. 109
- [6] R. Carr, Nucl. Inst. & Methods A306, p. 391 (1991)
- [7] ALS Handbook, LBL-PUB 643 (1989)
- [8] The author thanks Steve Lidia of LBL for this data.

Polarized Wiggler for NSLS X-ray Ring*

A. Friedman, X. Zhang, S. Krinsky, E.B. Blum and K. Halbach†

National Synchrotron Light Source Brookhaven National Laboratory Upton, NY 11973

Abstract

We examine the properties of an elliptically polarized wiggler that will generate circularly polarized photons with energy spectrum of 3–12 KeV. The vertical wiggler magnetic field is produced by permanent magnets while the horizontal wiggler field is generated by electric coils capable of AC excitation. The radiation parameters of the wiggler are presented. Numerical values are calculated for radiation from the wiggler. A conceptual design for such a wiggler is discussed. We consider AC excitation of the wiggler to produce the time modulation of the elliptic polarization. The power dissipated in the vacuum chamber due to the eddy current is considered.

1 Introduction

By using circularly polarized X-rays, magnetic properties can be detected much more effectively than with linearly polarized or unpolarized photons. Some effects can only be detected with circularly polarized photons. A typical experiment using circularly polarized light involves measuring the absorption or scattering of the photons by a target. Measurements are taken for right and left circular polarization. The results are then subtracted from each other in order to yield the net polarization. In the example of a magnetic Compton scattering experiment involving a soft magnetic material [1], an axial magnetic field is applied to the target and the scattered photon intensity I^+ is measured, the magnetic field is then reversed and the scattered photon intensity I^- is measured at the same angle. The net spin of the material can be calculated from:

$$\frac{I^+ - I^-}{I^+ + I^-} = \frac{f^+ - f^-}{f^+ + f^-} \frac{n_1 - n_l}{n_1 + n_l} \frac{\Phi_{spin}}{\Phi_0} \quad (1)$$

where f^+ , f^- are the fluxes of the right polarized and the left polarized incoming photons respectively. Φ_0 is the spin independent scattering cross section, and Φ_{spin} is the spin dependent component of the scattering cross section. $f^+ + f^-$ is the total photon flux, $n_1 + n_l$ is known, Φ_0 and Φ_{spin} are calculated theoretically. Thus, either the net spin $n_1 - n_l$ or the circular polarization parameter ($P_c \equiv (f^+ - f^-)/(f^+ + f^-)$) can be determined from Eq. 1.

Hard ferromagnetic materials do not yield the same net spin when the DC magnetic field is reversed. It is, thus, beneficial to be able to reverse, instead, the helicity of

the photon beam. Such reversal is also described by the relations of Eq. 1.

In most cases $\Phi_{spin}/\Phi_0 \ll 1$. Hence, there is a serious detection problem. This problem may be alleviated by using an incoming photon beam in which the polarization is modulated sinusoidally in time. The signal detected in this case (Eq. 1) has a fundamental harmonic oscillating with the polarization. The measurement of the intensities I^\pm is a small AC signal (spin effect) modulating a large DC offset (charge effect). This AC signal can be readily detected using such techniques as lock-in amplifiers and high-pass filters. Fig. 1 describes an elliptically polarized wiggler [2, 3] constructed from a vertical permanent magnet wiggler and a horizontal wiggler which may be constructed either of a permanent magnet [2, 3] or an electromagnetic magnet [4]. In the case of an electromagnetic wiggler, the oscillation of P_c is achieved by exciting the horizontal wiggler with AC current.

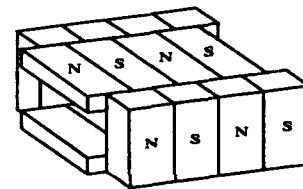


Figure 1

Schematic of an elliptically polarized wiggler

2 Elliptically polarized wiggler

Consider a wiggler magnet constructed from a vertical wiggler and a horizontal wiggler superimposed with a $\pi/2$ phase difference between them [2, 3] (Fig. 1). The magnetic field on axis is:

$$B_y = -\frac{2\pi mc K_y}{e \lambda_w} \sin k_w z, \quad B_x = -\frac{2\pi mc K_x}{e \lambda_w} \cos k_w z \quad (2)$$

where λ_w is the wiggler period, $k_w \equiv 2\pi/\lambda_w$ and K_x , K_y are the horizontal and vertical wiggler strength parameters. The horizontal wiggler field is weaker than the vertical wiggler field ($K_x/K_y < 1$).

In order to get a rough estimate of the properties of the radiation, we utilize the "Bend Source" approximation [2]. The radius of curvature of an electron in an elliptical wiggler is:

$$\rho = \lambda_w (1 + \xi^2)^{3/2} \frac{\gamma}{2\pi \sqrt{K_y^2 - \gamma^2 \xi^2}} \quad (3)$$

*Work performed under the auspices of the US Department of Energy under contract no. DE-AC02-76CH00016.

†Lawrence Berkeley Laboratory, Berkeley CA 95720

where ξ is the projection of the angle between the wiggler axis and the target of the radiation into the x - z plane. The vertical angles between the viewer and the arcs are:

$$\psi_+ = \psi + \frac{K_x}{\gamma}, \quad \psi_- = \psi - \frac{K_x}{\gamma}. \quad (4)$$

where $\psi = \pi/2 - \xi$. Figs. 2 show the photon flux and polarization that can be produced by elliptical wigglers in NSLS X-ray ring straight sections ($\epsilon_y = 2 \times 10^{-9}$ m, $\beta_y = 30$ cm, $\sigma_y = 80 \mu$ rad). The fluxes are computed per wiggler period and should be multiplied by the total number of periods in the wiggler. There is a trade off between the polarization and the flux on axis. A higher K_x value will yield a higher degree of circular polarization, but will decrease the photon flux on axis significantly. This is due to the fact that for large K_x the angle between the two bends in a period becomes larger, thus producing less radiation on axis. Fig. 2c shows the circular polarization as a function of the electron beam vertical angular spread. Note that a vertical emittance of $\epsilon_y = 0.2 \times 10^{-9}$ m has recently been achieved [5] in the ring, corresponding to an angular spread of 25 μ radians, which for $K_x = 1$ will yield $P_c > 85\%$.

3 Conceptual designs for elliptical wigglers

We consider the vertical wiggler to be built from permanent magnets. Its realization is straightforward since the vertical gap is small and the desired value of $K_y = 13$ is easily achieved in a configuration with static horizontal field. An electromagnetic horizontal wiggler is of interest, so that the polarization can be modulated. In addition, if it is possible to move the horizontal wiggler relative to the vertical wiggler, we could also provide a configuration yielding a time-dependent linear polarization.

With an AC horizontal wiggler there may be eddy currents in the permanent magnet material. To solve this problem, one could use a high resistivity permanent magnet, such as epoxy bound materials. Alternatively it could be possible to build the permanent magnet blocks from laminations. At present, we favor laminated NdFeB because of its higher remnant field.

The problem of eddy currents may be alleviated by using 0.5 mm thick iron laminations. The use of transformer iron which contains silicon, would further reduce the generation of eddy currents. A typical configuration of an iron core electromagnetic wiggler is shown in Fig. 3. In reference [6] Halbach developed an algorithm for optimizing such a configuration. Table 1 shows calculation of the various parameters for a wiggler with $\lambda_w = 16$ cm, and $D_1/\lambda_w = 0.2875$. We limited the field in the iron to $B \leq 1$ Tesla in order to use transformer iron, and the current density to 200 Amp/cm² in order to use air cooled coils. Two gap sizes are examined. The first row in Table 1 represents the field on axis with $J = 200$ Amp/cm². The second row represents the current density required for $K_x = 1$.

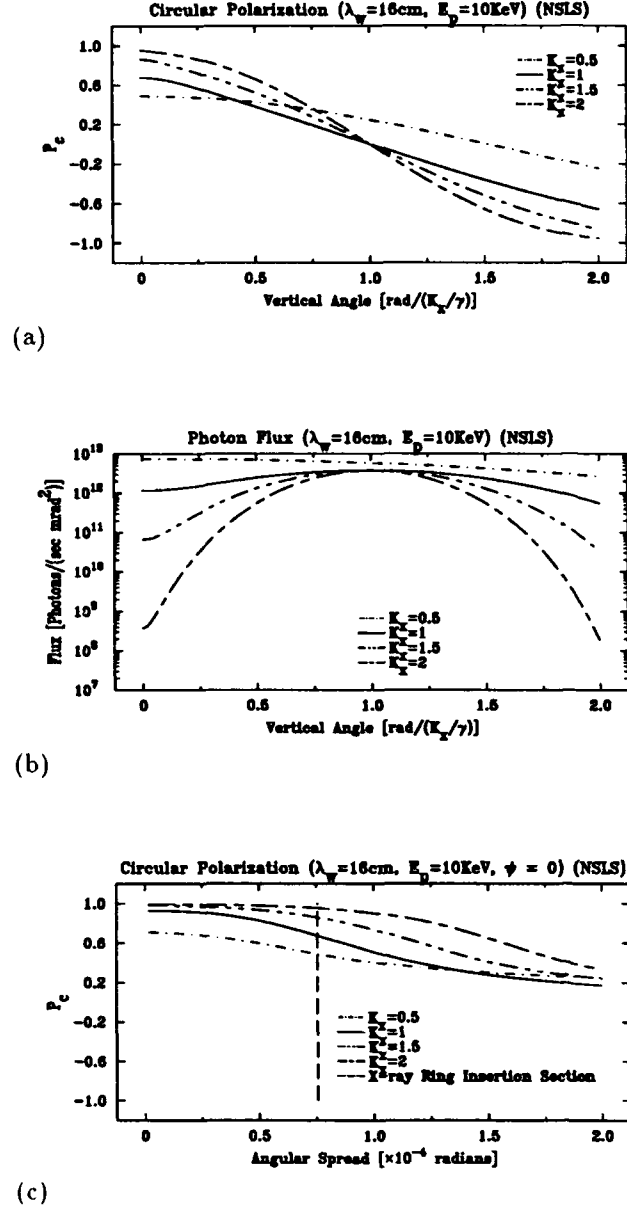


Figure 2

Elliptical wiggler radiation parameters (a) Circular polarization, (b) photon flux, (c) circular polarization as a function of electron beam vertical angular spread. [$K_y = 13$, $I = 200$ mA, $\Delta\lambda/\lambda = 10^{-3}$].

Table 1: Iron Core Electromagnetic Wiggler Parameters ($\lambda_w = 16$ cm, $D_1 = 4.6$ cm, $D_2 = 9.8$ cm)

	$g = 6$ cm	$g = 8$ cm
$B_{0_{max}}$ [Tesla]		
($J = 200$ Amp/cm ²)	0.1532	0.1214
J [Amp/cm ²]	87.32	110.2

The design with $g = 8$ cm requires a current density of 110 Amp/cm² which is well under the limit for air cooled coil.

4 Eddy currents in the vacuum chamber

The time variation of the horizontal magnetic field B_x gives rise to eddy currents flowing along the vacuum chamber in the axial z - direction. Approximating the wiggler magnetic field by a spatially constant dipole field, the eddy current density becomes

$$J_z = -\sigma \dot{B}_x y, \quad (5)$$

where σ is the chamber conductivity. The power dissipated is

$$P = \frac{1}{2\sigma} \int dv J_z^2, \quad (6)$$

where the integral is over the chamber wall. Assuming a stainless steel chamber with $\sigma = 10^6 \Omega^{-1}m^{-1}$, of thickness $t = 1$ mm and length L , having elliptical cross-section with half-width $a = 1$ cm in the (vertical) y - direction and $b = 3.5$ cm in the (horizontal) x - direction, we find, mks units,

$$P = \frac{\pi \sigma t L a^2 b \dot{B}_x^2}{2} F\left(\frac{1}{2}, -\frac{1}{2}; 2; \frac{b^2 - a^2}{b^2}\right). \quad (7)$$

The hypergeometric function has the values $F = 1$ for $a = b$ and $F = 8/3\pi$ for $a^2 \ll b^2$. Taking $\dot{B}_x = 2\pi(100 \text{ Hz})(0.07 \text{ T})/\sqrt{2}$ (the $\sqrt{2}$ factor is due to the sinusoidal behavior of B_x in the z direction) we find $P/L = 4.5$ watts/m. A more accurate calculation taking into account the actual field with period $\lambda_w = 16$ cm yields a power dissipation of 1 watt/period (i.e. 6.4 watts/m). The larger value is due to the increase in the wiggler field as $\cosh k_w x$ away from the $y - z$ plane.

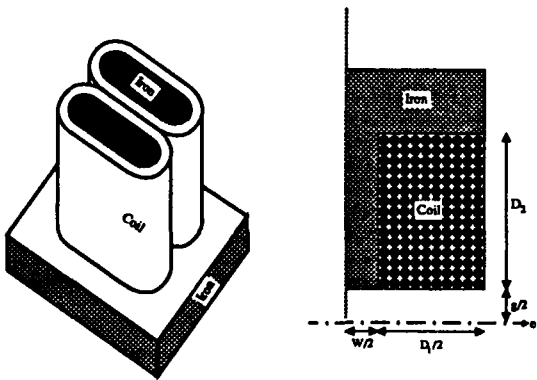


Figure 3
Iron core magnet configuration.

5 Concluding remarks

From the results presented, use of an elliptically polarized wiggler looks like a viable way to achieve 3–12 KeV circularly polarized X-rays from the NSLS X-ray ring. Other concepts, such as cross field undulator [7] or a bending magnet will either not yield the high photon energy required or will not produce enough photon flux. These approaches are more sensitive to the electron beam angular spread and hence they are not appropriate for the NSLS ring, which has low vertical β in its straight section. In order to increase the sensitivity of detection, AC modulation of the polarization is recommended. This can be done in an elliptical wiggler by constructing one of the wigglers from electromagnets and operating it with AC current.

A major challenge will be to maintain stability of the orbit with AC excitation of the horizontal wiggler. Time varying correction coils at the entrance and exit of the wiggler will be required, operating at 100 Hz both in phase and 90° out of phase with the main wiggler current. Nonlinear effects in the iron can result in time harmonics which might also require correction. Two beam position monitors outside the wiggler separated by 90° in betatron phase, could be used to determine the needed corrector strengths. The ends of the wiggler magnet should be designed to maintain satisfactory orbit stability inside the wiggler [8].

A more detailed discussion of some of the issues in this paper can be found in ref [9].

6 Acknowledgment

We wish to thank M. Blume, D. Gibbs, J. Hastings, K.J. Kim, D. McWhan and P. Siddons for helpful discussion.

I. REFERENCES

- [1] N. Sakai, O. Terashime and H. Sekizawa, Nucl. Instrum. and Methods, Phys. Res. Sect. B **221**, 419 (1984).
- [2] S. Yamamoto, T. Shioga, S. Sasaki and H. Kitamora, Rev. Sci. Instrum. **60** (7), 1834 (1989).
- [3] S. Yamamoto, H. Kawata, H. Kitamora and M. Ando, PRL **62** (23), 2672 (1989).
- [4] C. Poloni, R. Brocco, B. Diviacco, R.P. Walker and D. Zangrando, Proc. of the 1991 PAC.
- [5] J. Safranek and S. Krinsky, in this proceedings.
- [6] K. Halbach, NIM **A250**, 115 (1986).
- [7] K.J. Kim, AIP conference proceedings **185**, 565 (1987).
- [8] K. Halbach, NIM **A250**, 95 (1986).
- [9] A. Friedman, S. Krinsky and E. Blum, BNL report No. 47317, March 1992.

Magnetic Field Measurements of A Superconducting Undulator for a Harmonic Generation FEL Experiment at the NSLS

L.Solomon, G. Ingold, I. Ben-Zvi, S. Krinsky, and L.H. Yu
National Synchrotron Light Source
Brookhaven National Laboratory, Upton, NY 11973, USA

W. Sampson and K. Robins
RHIC Magnet Division
Brookhaven National Laboratory, Upton, NY 11973, USA

Abstract-

An 18mm period, 0.54 Tesla, 8mm gap superconducting undulator with both horizontal and vertical focusing has been built and tested. This magnet, which is fabricated in 25 cm length sections, is being tested for use in the radiator section (total magnet length of 1.5m) of the Harmonic Generation Free Electron Laser experiment at the National Synchrotron Light Source - Accelerator Test Facility at Brookhaven National Lab, in collaboration with Grumman Corp. The measurement system is outlined, sources and estimates of errors are described, and some magnetic field data are presented and discussed.

Introduction

A three stage superconducting undulator (modulator, dispersive section, and radiator) is under construction at the NSLS at Brookhaven for use in a high gain, harmonic generation experiment.¹ The three stage undulator triples the frequency of a 10.4 micron CO₂ seed laser using a 30MeV electron beam. The superconducting magnet yokes are iron core with a pole face shaped for transverse focusing. The magnets are machined in physical sections which are 25cm long and are wound independently of each other. The full length magnet is made up of several of these yoke sections, which are assembled end to end. There are no axial drift spaces other than those between each of the three stages of the undulator. Additional design details and considerations are provided in Ref.1. Prototype radiator undulator sections have been built and tested. The test setup allows measurement of up to two sections (for a total magnet length of 50 cm, with 27 periods) at a time. The testing results can be used for sorting of the magnet yoke sections so that errors from adjacent sections tend to cancel, analogous to the sorting and annealing techniques often used in permanent magnet and hybrid wigglers.

The magnet pole faces are shaped to establish transverse focusing, which is accomplished with a 1mm depth and +/-3mm width parabolic cut in the pole faces. The flat pole region of the magnet has a 6mm gap. The transverse focusing necessitates measurements with multiple probes in order to map the transverse field profile. For testing of the magnet sections before assembly of the full mag-

net, the sections are supported in a vertical cryostat with a magnet holder which permits measurement of 2 sections, or 50 cm of magnet, at a time (Figure 1-left).

Measurement System

For testing, the magnets are assembled into a aluminum box for clamping, with a precision ground spacer setting the gap. A slot machined into the spacer serves as a guide for a G10 slider which holds an array of five hall probes for measurements. This probe array is required for characterization of the field focusing due to the pole shaping. Taking z as the long axis of the magnet, y as the main direction of the undulator field, and x as the direction orthogonal to both of these, the hall probes are mounted so that one is nominally along the magnet centerline ($x=y=0$), and the others are displaced by 1.5 mm in the +y,-y,+x, or -x direction. The slider is attached to an actuator, and is driven with a stepping motor. The probe voltages are read through either a HP data acquisition switching system, or through independent voltmeters. The control and acquisition software is PC based.

Hall Probes

The hall probes used for testing are Siemens SBV604. The probes are powered in series with an excitation current of 50 mA, which gives a probe output voltage of about 27 microvolts/gauss. The power supply stability is ≈ 50 ppm, corresponding to $\approx 0.3G$. A third order fit to the probe voltage as a function of field is adequate to the level of +/-0.75 Gauss, which is also the level of the repeatability of the probe, at room temperature, as referenced against an NMR probe. Upon thermal cycling of the probe, the subsequent dependence of voltage on field is unpredictable. Both cool-downs which made little difference in the probe calibration, and cooldowns which significantly changed the calibration were observed. For this reason a Helmholtz coil was incorporated into the test setup, permitting in-situ calibration and cross calibration of the probes. The Helmholtz coil has a 16mm radius, and although a larger coil gives a larger uniform field volume, the difference in the coil field at the central probe as compared to the offset probes of the array is about 10 Gauss in a field of 5500G, so cross calibration errors are minimal. Figure 1 (right) shows the output of the

*Work performed under the auspices of the U.S.Department of Energy

5 probes of the array with the data for each probe shifted by the physical distance between each of the probes along z. This data was taken at an excitation current of 75 amps in the Helmholtz coil, which corresponds to about 8600 Gauss. The different probe voltages are due to the different calibrations for each probe, and the fact that the probes are displaced in x or in y from the center of the Helmholtz coil.

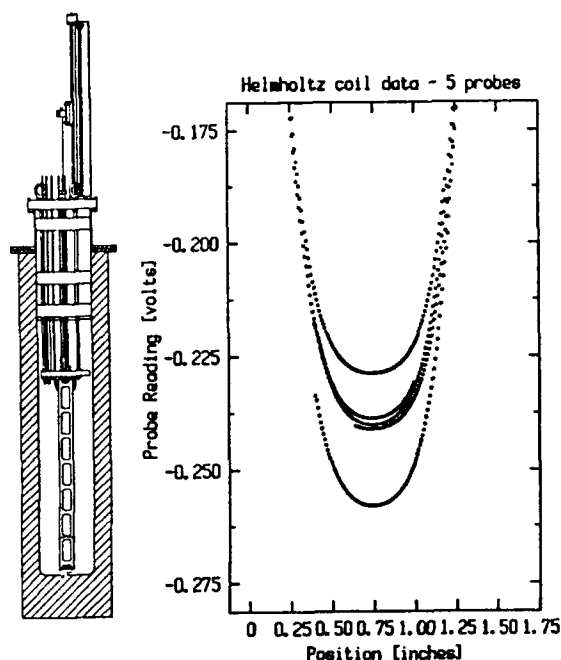


Figure 1:

Left:

A schematic of the magnet box supported within the vertical cryostat for measurement of the magnet sections.

Right:

Helmholtz Coil data of the five probe of the array at a field of 8600 Gauss.

Determination of the field profile requires both relative probe calibrations, and knowledge of the relative positions of the probes on the slider. A dual setup consisting of a needle magnet (an iron needle held and magnetized by a permanent magnet block) and a quadrupole magnet has been used for this. The needle magnet provides a high spatial gradient field, in which the position of maximum probe output voltage is searched for. The transverse (x) and axial (z) positions of the probes with respect to each other are determined. The magnetic center of the quadrupole provides a field point which can also be used to determine the relative probe positions, taking into account the probe offset voltage in zero field. If there is no angle "error" of the probe on the slider, i.e. if the probe is in the x-z plane, and therefore senses only the y field, then the null readings of the field are independent of y. The dependence of the null readings on y yields the probe angle with respect to the coordinate system of the quadrupole magnet. The data obtained indicate that

the probes had angle errors below 4 degrees, with repeatabilities of ± 0.3 degrees. Application of pressure to maintain a desired orientation while the probes are being mounted is not possible due to the mechanical fragility of the hall element.

The position of the active areas on the probes is repeatable and consistent between these two methods to $\pm .002$ ". The axial position of the probes along the length of the slider is redetermined in the superconducting undulator magnet itself, both with the zero crossings of the magnetic fields which serve as extremely sensitive position markers, and with the data from the Helmholtz coil. The data obtained from the undulator magnet in this way agreed with the data taken in the lab on the slider to within 0.001".

Measurement Errors

The errors associated with the relative position determination of the hall probes directly affects the level to which the absolute transverse field profile of the magnets can be determined. As the spatial dependence of the field increases, the sensitivity to the position information about the probes also increases. Taking the probe location error as $\pm .002$ ", and a field reading error of ± 10 Gauss (i.e. assume probe linearity is $\pm 1\%$ between calibration points spaced 1000G apart), then the absolute value of the curvature of the magnetic field can be determined to $\approx \pm 10\%$, and the centerline of the magnet can be determined to $\approx \pm 70$ microns. This absolute focusing determination error is within specification in terms of FEL performance.

Optical survey measurements have been made of the slider in the magnet assembly, indicating horizontal and vertical motions of the slider below ± 0.001 " along the magnet length. Field reading changes due to these mechanical translations and possible rotations are negligible (e.g. the change in peak field readings are below 0.03%).

Results

Measurements were made on two magnet yokes assembled end to end, and on a single magnet yoke. Magnetic field measurements were made at several fields (see Table 1). The quench current for these magnets is 170 Amps. The peak field data highlights four magnet poles whose fields differ by more than 1% from the average. Mechanical inspection revealed large pole width machining errors for three of these poles (≈ 75 microns). All the other poles were within 10 microns of an average value, indicating that the stringent tolerances can be achieved. There is one remaining significant field error which has not yet been linked to a machining error. The yoke was rewound and all the four larger errors were present in the rewound yoke data, indicating that all four are due to the iron, and not the details of the winding. These four poles have been left out of the calculation of the RMS field errors, since we consider them errors which can be eliminated with improved machining procedures. When this is done, rms field error levels at 15amps, where saturation effects in the

iron are at a minimum (see ref.1 for an excitation curve for this magnet), give a rms peak field error of 0.1%. This is consistent with the measured machining tolerances of 10 microns. As the current is increased, the field errors increase but level off, as seen in Table 1. This error increase with excitation is possibly due to inhomogeneities in the iron which is reflected in a difference in the slope of the permeability as a function of field for various parts of the yokes. As the iron saturates and its μ value decreases, the contribution of coil placement errors to the peak field errors will increase.

Field	1550 G	4030 G	5800 G	6675 G	7220 G
I(amps)	15	50	100	130	150
RMS Error	0.1%	0.29%	0.35%	0.34%	0.33%

Table 1 : Field (in Gauss), and RMS Variation in the Peak Field Values of a Magnet Section as a Function of Excitation Current. A different undulator section showed 0.22% RMS errors at 50Amps.

The 150 amp, 50 amp, and the 15 amp data is shown in Figure 2, integrated twice to give the electron trajectory for a 30 MeV electron beam. These integrals contain the four bad poles of the magnet which result from machining errors, discussed above. Though the rms field error changes by more than a factor of 3 as the current is increased from 15 to 150 amps, the wander in the electron trajectory is within ± 20 microns for all currents (1/10th of the electron beam radius, as required). This may be due to the fact that as the iron saturates and μ decreases, the effects of the errors is increasingly localized, leading to compensating effects in the trajectory.² New magnet pieces without the large machining errors are being tested, and should show improved performance.

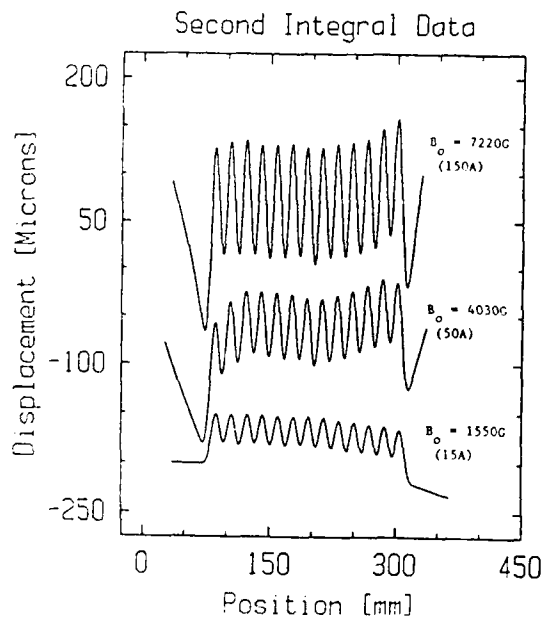


Figure 2 : The electron trajectories at 150, 50, and 15 amp excitation (top to bottom plots) corresponding to a 7220, 4030, and 1550 Gauss central field in the magnet. The plots are displaced vertically for clarity.

Figure 3 shows the results of the transverse field measurements for the magnet at 0.5amps, 15, 50, and 100 amps. The 0.5A measurements are made with a single probe on a precision translation stage. The cryogenic measurements (15, 50, and 100 Amps) are made with the multiple hall probe setup, i.e. there are three probes along the $y=0$ plane, which are cross calibrated in the helmholtz coil. As the field increases from 1550 Gauss to 5800 Gauss, a decrease in curvature of about 15% is measured, due to saturation effects in the iron. This change is consistent with Tosca predictions.³ The agreement between the 15A (multiple probe data) and the 0.5A (single probe data) results is consistent with the error estimates due to relative position and cross calibration errors.

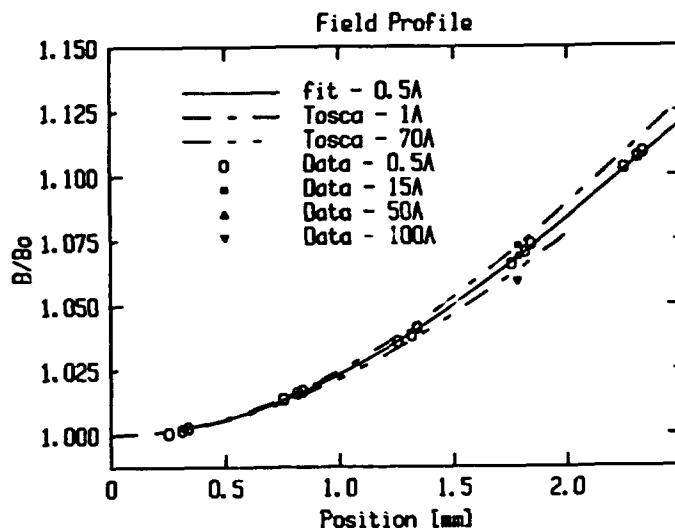


Figure 3 Transverse Field Profile Measurements at 0.5A, 15A, 50A, and 100A compared to Tosca calculations at 1A and 70A.

References

1. G.Ingold et al, *IEEE PAC Conference Proceedings*, 1993.
2. K.Halbach, *Private communication*, 1993.
3. Tosca results provided by D.Weisenburger, Grumman Corp, Princeton, N.J., 1992.

Magnetic Performance of the NSLS Prototype Small-Gap Undulator*

George Rakowsky and Ralph Cover
Rockwell International, Rocketdyne Division
P.O.Box 7922, Canoga Park, CA 91309-7922

and
Lorraine Solomon
National Synchrotron Light Source
Brookhaven National Laboratory, Upton, NY 11973

Abstract

The magnetic design of the pure-permanent magnet Prototype Small-Gap Undulator for the NSLS X-ray Ring is reviewed. Measurements of individual magnets, half-period modules and the complete undulator are described. Results of performance optimization, including minimization of optical phase error, trajectory wander and integrated multipoles by means of simulated annealing are presented.*

I. INTRODUCTION

The NSLS Prototype Small-Gap Undulator [1] (PSGU) is a very compact insertion device, with magnetic length of only 320 mm, 16 mm period, and a variable gap as small as 4 mm. Its purpose is to study the effects of reduced vertical aperture in the NSLS X-ray Ring, as well as to generate undulator radiation at the first and third harmonics in the bands from 1.8 to 3.8 and 5.4 to 11 keV. The project is a collaboration between NSLS and Rocketdyne, with NSLS responsible for the vacuum chamber, mechanical structure and the dual gap (magnetic and vacuum chamber) drive system, and Rocketdyne building the PSGU magnetic assembly. The objectives of the magnetic design were to attain maximum brightness in the desired energy bands and to meet the limits on integrated multipoles dictated by X-ray Ring beam dynamics. The magnetic assembly has been completed and delivered to NSLS. In the following sections we review the magnetic design, the optimization procedures and the measured magnetic performance.

II. MAGNETIC DESIGN

The PSGU is to be installed in the X13 straight section at NSLS and its total length cannot exceed 320 mm. For a fundamental resonant optical wavelength $\lambda_0=5\text{\AA}$, with e-beam energy $E=2.5\text{ GeV}$ ($\gamma=4892$), and a desired value of deflection parameter $K=1$, we chose the undulator period to be $\lambda_u=16\text{ mm}$, nominal gap $g=6\text{ mm}$ and a peak field $B_0=0.67\text{ Tesla}$. Depending on the type of termination, 18 or 19 full periods can be accommodated in the available length. The desired field can be attained with either pure permanent magnet (PPM) or hybrid technology, using available NdFeB magnets. We have

chosen the high-performance 6 block/period version of the Halbach PPM design [2], and employed multi-stage, multi-parameter performance optimization using simulated annealing (SA) [3], as described in Section IV.

The design calls for magnets with remanent field $B_r \geq 1.2\text{ Tesla}$, a linear B-H characteristic extending well into the third quadrant, and tolerances of $\pm 2\%$ on variation of total magnetic moment and $\pm 2^\circ$ on magnetization angle. Suitable NdFeB materials are available. We chose ¹ a local magnet fabricator ² to supply Sumitomo NEOMAX 35H³ material, to cut, machine, magnetize and certify the magnets, and to assemble the half-period triplet modules. Prior to magnetization, the finished magnets were coated with aluminum chromate by Sumitomo. Helmholtz coil characterization of the magnets was done by the Magnetics Group at Lawrence Berkeley Laboratory (LBL).

In the 6 block/period design, magnets are grouped into half-period triplet modules, consisting of a vertically magnetized (Type A) magnet flanked by two 60° (Type B) magnets. "Up" and "down" modules alternate in the array. The three magnets forming each triplet were brought into alignment in a special fixture and bonded under pressure with an anaerobic, fast-curing, radiation resistant adhesive.⁴ The triplets are positioned on the trays by stainless steel dowel pins and are held down by nonmagnetic clips. The magnets are thus constrained even if the adhesive should fail.

Since the PSGU magnet gap drive system was unavailable during magnet assembly, a fixed-gap test stand was built to allow repeatable positioning for bench measurements of magnets, triplets, of the top or bottom half individually or the complete magnet assembly, at a fixed gap of 6 mm. The completed PSGU magnetic assembly has been shipped to NSLS, where it will be mounted to the gap drive system while still in its test fixture, so the initial magnet alignment will be preserved. Only then will the test fixture be removed.

III. MAGNETIC MEASUREMENTS

- ¹ Product and source data provided for information only.
- ² Magnet Sales & Manufacturing Co. Inc., 11248 Playa Ct., Culver City, CA 90230
- ³ Sumitomo Special Metals, 23326 Hawthorne Blvd., Suite 360, Skypark 10, Torrance, CA 90505
- ⁴ Loctite #325 with Activator #707. Loctite Corp., Newington, MA (213)390-4357

* Work performed under Brookhaven Contract No. 535600 and U.S. Department of Energy Contract No. DE-AC02-76CH00016

A. Homogeneity of Stock Blocks

To help reduce field errors due to magnetic inhomogeneity, a 50x40x25 mm stock NEOMAX 35H block was cut into 15 PSGU-sized test magnets, which were then magnetized and characterized by Helmholtz coil measurement at LBL. The magnetic moment data indicated that only the samples from the interior 2/3 of the volume had angle errors of $<2^\circ$. The fabricator agreed to supply the PSGU magnets solely from this core region of the large stock blocks.

B. Helmholtz Coil Measurements

The cut, coated and magnetized magnets were sent to LBL for measurement of magnetic moments. The Helmholtz coil data showed that for all 340 magnets the total magnetic moment variation was well under 1%, ($\sigma=0.35\%$). Transverse angle errors were $<1^\circ$ for Type A and $<2^\circ$ for Type B magnets. Inclination angle in the vast majority of A-magnets was within $0^\circ\pm 2^\circ$, as specified. However, in the B-magnets the average inclination angle turned out to be 59° (rather than 60°), with variations as large as $\pm 5^\circ$. We accepted the 1° systematic error, since its effect on the field would be minimal. However, nearly 19% of the B-magnets were excluded due to excessive angle error.

C. Integrating Coil Design

To predict the e-beam trajectory in a PPM undulator it is necessary to measure the vertical (y) and transverse (x) field components of each magnet or module along the undulator axis. In the past we have done this with Hall probes. The scans were integrated numerically to give total dipole kicks, which were then entered into a point-kick trajectory model. However, Hall probe measurements of 3D fields are subject to "planar-Hall effect" distortion [4] which contributes an apparent DC offset and results in systematic trajectory errors.

Planar-Hall errors can be avoided by integrating the on-axis field of single magnets or modules directly with a long integrating coil, as was done by Goodman *et al.* [5] and Poloni *et al.* [6]. For precise control of coil geometry, a 2-axis, 160-turn, 480 mm long coil was designed and fabricated using multilayer printed circuit technology. The effective width of the y and x-field coils is 7.0 and 3.7 mm respectively. The coil was long enough to measure the entire PSGU, as shown in the photograph in Figure 1. It was mounted on a high-speed translation stage, its midplane at a height of 3 mm (half the nominal gap) above the test magnet, parallel to the nominal undulator axis. The stage moved the coil from a field-free region to the axis and back. The induced voltages were measured with an integrating voltmeter (fluxmeter).⁵ Integrated quadrupole and sextupole components were obtained by stepping the coil $\pm\Delta x$ about the axis (3-point characterization). In addition, detailed dipole profiles could be measured by stepping the coil in small steps along the midplane. To reduce noise due

to integrator drift to $<0.1\%$ we typically averaged 10 scans per measurement. Each scan took about 15 seconds.



Figure 1. PSGU magnetic assembly set up on its test stand for measurements using the printed circuit integrating coil.

D. Multipole Measurements

From the Helmholtz coil measurements it was evident that the dominant contributor to y-field error would be the variation of the inclination angle in the B-magnets. For this reason the y-field dipole kicks of the B-magnets were measured in each of four possible orientations, using the integrating coil method. As expected, "up" and "down" kicks differed in magnitude by up to $\pm 1.5\%$ (0.8% RMS). This data was input to the SA code. However, the A-magnets, as well as the x-field components of the B-magnets showed much less inhomogeneity, and therefore for these components the Helmholtz coil data was input to the SA code.

The half-period triplet modules were characterized in more detail, with measurement of both normal and skew dipoles, quadrupoles and sextupoles, in each of two possible orientations, for use in trajectory optimization and multipole minimization by SA. Some 40 spare single magnets were characterized in the same way, in each of 4 orientations, to provide a selection of magnets for the terminations. The coil was also used to measure the integrated multipoles at all stages of assembly, as well as of the complete undulator.

E. Integrated Dipole Profiles

Initially, dipole profiles of representative single magnets and triplets were mapped, from which $\Delta x=4$ mm was found to give a good 3-point fit to the actual field profile in the vicinity of the magnetic axis. Dipole profiles were also mapped for each unterminated and terminated tray, as well as for the complete PSGU. These measurements revealed a skew octupole component, which suggests the need for 5-point, rather than 3-point characterization of magnets and the assembled structure. This could achieve flatter field profiles.

⁵ Model MF-5D Fluxmeter, Walker Scientific, Inc. Rockdale St., Worcester, MA 01606

IV. MULTI-STAGE OPTIMIZATION

The PSGU performance was optimized by a three-stage process. First, magnets were selected from the pool of 284 accepted magnets to form 40 "up" and 40 "down"-oriented half-period triplet modules. A Stage 1 SA code was used to minimize the total x-field dipole kicks and the variation in total y-kicks. Table 1 compares standard deviations σ_y and σ_x for triplets with constituent magnets selected (a) at random; (b) by Stage 1 SA code; (c) with uncertainties in input data taken into account; (d) measured triplet kick errors; and (e) peak y-field variation and RMS x-field from field maps of the PSGU.

Table 1. Predicted and measured triplet kick and field errors

Std.dev.	(a)	(b)	(c)	(d)	(e)
σ_y	1.13%	0.15%	0.27%	0.38%	0.52%
σ_x	1.24%	0.13%	0.29%	0.48%	0.18%

The Stage 2 SA code then selected 36 "up" and 36 "down" triplets and their placement sequence to minimize RMS phase shake [7], RMS walkoff in x and y, and the normal and skew integrated dipoles, quadrupoles and sextupoles.

After measuring the residual multipoles in the unterminated upper and lower trays, we used the Stage 3 SA code to select 12 magnets for the displacement-free terminations.[8] The results are summarized in Table 2. The final values are well within design goals.

Table 2. PSGU integrated multipoles.

Multipole	Goals	Unterm	Termin	Units
Dipole	100	-7	7	G•cm
Skew Dipole	100	58	-20	G•cm
Quadrupole	10	-12	-5	gauss
Skew Quadrupole	100	-5	-18‡	gauss
Sextupole	50	-6	-37	G/cm
Skew Sextupole	50	15	-30‡	G/cm

‡Values determined using $\Delta x = \pm 2$ mm. All others: ± 4 mm.

V. PERFORMANCE ANALYSIS

The y and x-fields in the completed PSGU were mapped at a fixed gap of 6 mm using a pair of Hall probes⁶ on a granite-rail mapper. After correction for a slight gap taper, $B_y(z)$ was fitted with a sinusoid with amplitude $B_{y0} = 0.623$ Tesla, which is 6.5% lower than expected. The integrated RMS field error was 1.18%, while peak field variation was only 0.52% RMS. Most of the error appears near zero crossings, indicating the presence of longitudinal position errors.

$B_x(z)$ was corrected for planar-Hall distortion by subtracting $\beta B_y^2(z)$, with β determined from the slope of the first integral of $B_x(z)$. The corrected fields were then integrated twice to obtain the trajectory plots in Figure 2. The goal was to reduce RMS walkoff to less than one wiggle amplitude a . We achieved $x_\sigma = 0.1a$ and $y_\sigma = 0.04a$.

⁶ Models HTJ-0608 and SAK-1808; F.W. Bell Co., 6120 Hanging Moss Rd., Orlando, FL 32807

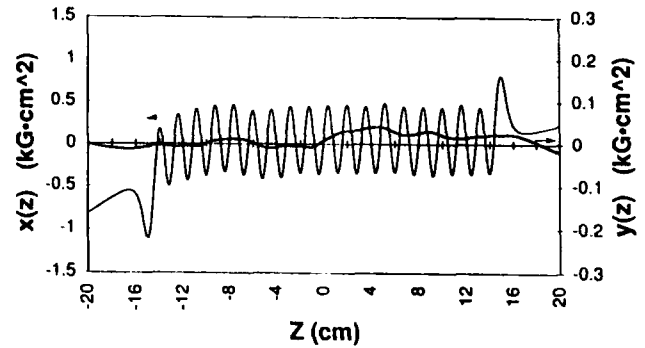


Figure 2. X and y trajectories in the PSGU. The x -scale is on the left, the y -scale is on the right (in $\text{kG}\cdot\text{cm}^2$).

The optical phase error was obtained by computing the cumulative path length error, relative to a best-fit sinusoid, converted to optical degrees at the fundamental resonant wavelength. The phase error is plotted in Figure 3. Statistical studies for a 24-period device [9] showed that to assure third harmonic spectral brightness >90% of the ideal, error-free case (single-electron, on-axis calculation) requires that RMS "phase shake" $\phi_\sigma \leq 2^\circ$. Our results indicate that $\phi_\sigma < 1.4^\circ$.

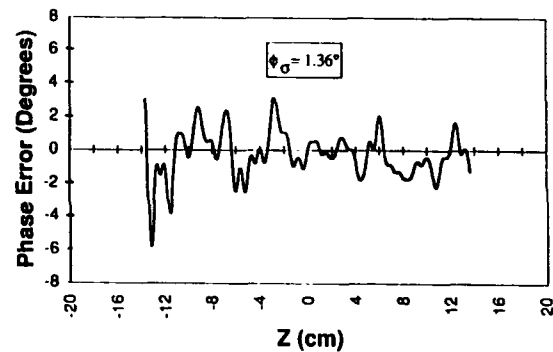


Figure 3. Cumulative optical phase error

VI. ACKNOWLEDGEMENTS

The authors thank P. Stefan and J. Bohanek (BNL), D. Nelson (LBL), R. Burke, K. Carillo, M. Curtin, R. Dinius, Y. Kohanzadeh, M. Lampel, H. Schlanger, R. Shah, M. Stormo and G. Swoyer, (Rocketdyne) for assistance and support.

VII. REFERENCES

- [1] P.M. Stefan *et al.*, *Proc. Part. Accel. Conf.*, 1096 (1991).
- [2] G. Rakowsky *et al.*, *Proc. XI FEL Conf.*, 597 (1989).
- [3] A. Cox and B. Youngman, *Proc. SPIE*, 582, 91 (1986).
- [4] M.W. Poole and R.P. Walker, *IEEE Trans. Magn.*, MAG-17, No.5, 2129 (1981).
- [5] D.L. Goodman *et al.*, *Proc. XIII FEL Conf.*, 825 (1991).
- [6] C. Poloni *et al.*, *Proc. Part. Accel. Conf.*, 2712 (1991).
- [7] B.L. Bobbs *et al.*, *Proc. XI FEL Conf.*, 574 (1989).
- [8] G. Rakowsky *et al.*, *Proc. Part. Accel. Conf.*, 2733 (1991).
- [9] G. Rakowsky, *Small Gap Undulator*, Conceptual Design Report, BNL Contract No. 406593, Nov. 30, 1989.

Design Considerations for a 60 Meter Pure Permanent Magnet Undulator for the SLAC Linac Coherent Light Source (LCLS)*

R. Tatchyn, R. Boyce, K. Halbach, H.-D. Nuhn, J. Seeman, H. Winick
Stanford Linear Accelerator Center, Stanford, CA 94305, USA
C. Pellegrini

Department of Physics, UCLA, Los Angeles, CA 90024-1547, USA

Abstract

In this paper we describe design, fabrication, and measurement aspects of a pure permanent magnet (PM) insertion device designed to operate as an FEL at a 1st harmonic energy of 300 eV and an electron energy of 7 GeV in the Self-Amplified Spontaneous Emission (SASE) regime.

I. INTRODUCTION

In recent years, progress in the development of short-pulse, low emittance, laser-driven RF photocathode guns [1], and in the modulation and control of high energy particle beams [2], has made possible the consideration of linac-driven Free Electron Lasers (FELs) designed for SASE [3] operation at 1st harmonic energies extending well into the soft x-ray range. In this paper selected design considerations for an undulator optimized for operation in the water window (300-400eV) on a subsection of the Stanford Linear Accelerator Center (SLAC) 3km linac are described. Using three-dimensional SASE simulation codes reported on elsewhere [4,5], the basic undulator parameters were derived from optimization studies incorporating: 1) the effects of the undulator period λ_u , 2) the field amplitude B_0 , and 3) a strong external focussing β on both the undulator's effective gain parameter, ρ_{eff} , and gain length, $L_G (= \lambda_u / 4\pi\sqrt{3\rho_{eff}})$. Using the optimization goals of increasing the gain and simultaneously reducing the gain length (to avoid overly long undulator structures [6]) the following set of basic operating parameters was derived:

E (electron energy) = 7GeV $\gamma\epsilon$ (emittance) = 3×10^{-6} r-m
 λ (1st harmonic) = 40Å I (peak current) = 2500A
 λ_u (und. period) = 8 cm β (focussing) = 8.2m
 B_0 (field amplitude) = 0.8T L_G (gain length) = 2.37m

Further simulation studies investigating the effects of field errors on the SASE gain were also conducted [7], and the results were used to help assess the minimal required mechanical and field tolerances of the undulator components.

II. GENERAL DESIGN FEATURES

Given the broad base of experience acquired by the

* Supported by DOE Offices of Basic Energy Sciences and High Energy and Nuclear Physics and Department of Energy Contract DE-AC03-76SF0015.

scientific community in the area of PM undulators [8], the continuing improvement of commercially available PM materials, and the advantage of relatively straightforward analytical investigations, the LCLS group decided to base its initial undulator studies on a pure PM design. Upon consideration of a number of alternatives, the focussing lattice was chosen to consist of current-driven iron quadrupoles in a FODO configuration. As shown in Fig. 1, the configuration selected for the PM undulator lattice is of the standard type [9], with 8 magnets per period.

Standard PM Structure

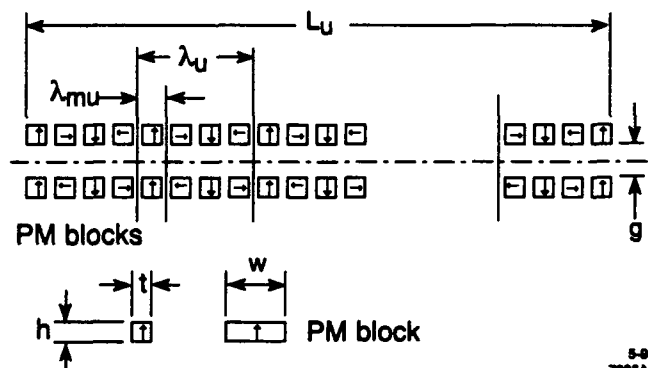


Figure 1. Standard PM configuration of the LCLS.

The PM blocks' dimensional and field parameters were arrived at by both analytical [9] and numerical field calculations. The quadrupole design follows from the computer-study identification of an optimal betatron wavelength of 51.4m, which determined the necessary focal length of the individual quads to be approximately 4.1m. The individual quad dimensions were arrived at by: 1) utilizing 50% of the longitudinal free space along the undulator to help reduce the required quad gradients, and 2) specifying a minimum quad aperture radius of 6cm to inhibit the perturbation of the PM undulator fields by the quad yoke material. The resulting basic parameters are given below.

PM Lattice parameters

λ_u = 8cm
 λ_{mu} = 2cm
 h = 1.9cm
 t = 1.9cm
 w = 4cm
 g = 1.5cm
 B_r = 1.08T

FODO lattice parameters

Quad aperture radius = 6cm
Quad outside diameter = 20cm
Quad length = 40cm
Quad gradient = 15T/m
FODO period = 1.6m
Phase advance per cell = 11.5°
Total Pwr. Budget ~ 300kW

III. MECHANICAL DESIGN

As depicted in Fig. 2, the basic approach to the mechanical design of the LCLS undulator is modular. Two basic reasons for this are: 1) simplification and statistical control of the fabrication and field measurement processes; and 2) facilitation of the installation and alignment of the undulator in the SLAC FFTB tunnel [10] prior to operation.

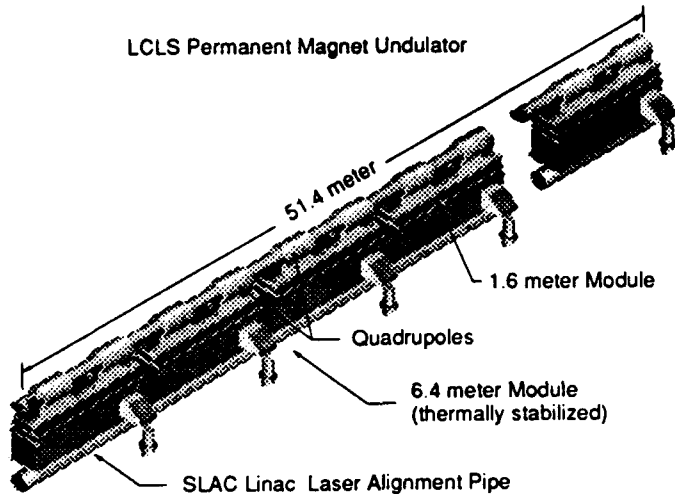


Figure 2. LCLS undulator layout showing modular sections.

Given the possibility of tuning the 1st FEL harmonic by varying E , the conventional use of undulator jaw motion was determined to be dispensable, making possible the design of a relatively simple support system for the PM and quadrupole lattices. At the same time, the small gap necessary for the attainment of the required B_0 introduced troublesome design obstacles to the incorporation of the necessary system components. In Fig. 3, the basic modular unit of the LCLS, a 1.6 meter PM lattice section integrated with one period of the

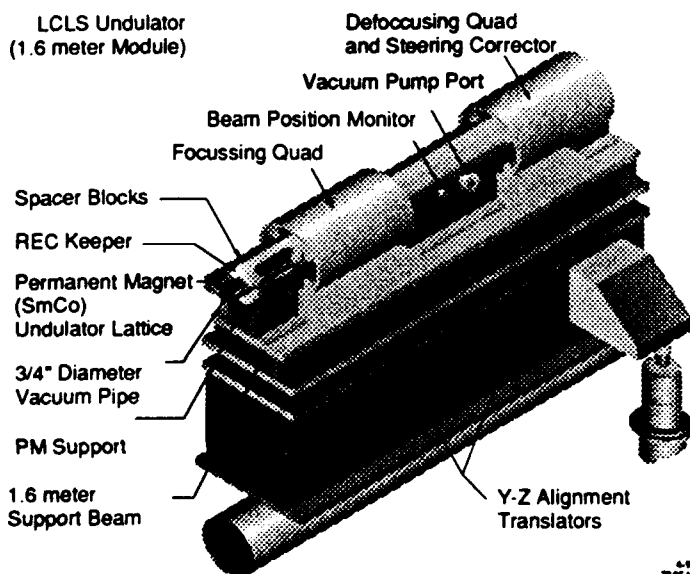


Figure 3. Selected mechanical and electrical details of a 1.6m LCLS module.

FODO lattice, is shown with a minimal repeating set of system components. For clarity, a schematized and enlarged cross section of the LCLS undulator is shown in Fig. 4.

LCLS Cross Section

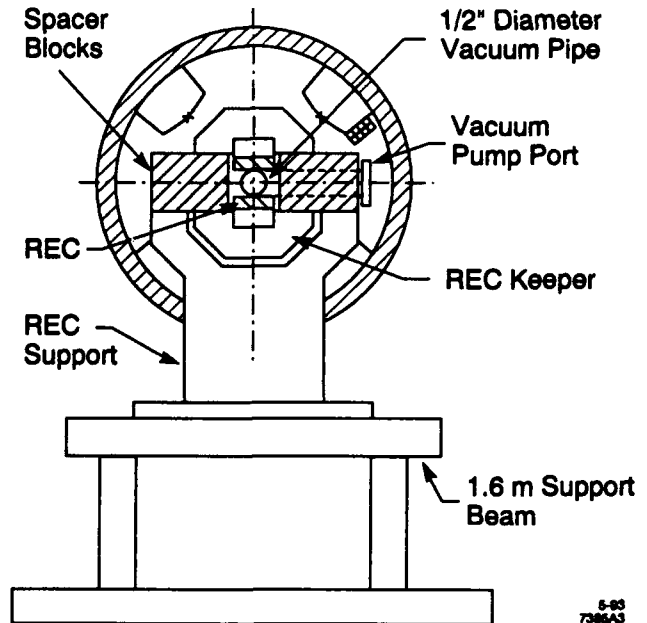


Figure 4. Selected component details of the LCLS insertion device in cross section.

The field gap is set by spacer blocks with optional provisions for limited PM adjustment designed into the keepers. The computed force/period on each linear PM array for the given parameters is approximately 90lbs, necessitating careful attention to the mechanical and compositional details of the keeper assemblies. To allow for longitudinal phasing control and attitude alignment, precision translators are indicated for y-z alignment of each 1.6 meter module. Not explicitly shown are: 1) short magnet block assemblies for continuing the PM lattice in proper phase from one module to the next, 2) coarse y-adjustment provisions for each 6.4m module, 3) a water-based thermal stabilization system for suppressing temperature deviations in excess of $\pm 0.5^\circ\text{C}$ along the entire length of the LCLS insertion device, and 4) in-vacuum Beam Position Monitors (BPMs).

IV. TOLERANCES

The assessment of the effects of random field errors and their correction on the SASE gain process was based primarily on comprehensive 3-D simulations [7]. These simulations, which yield the expected degradation of SASE in the LCLS as a function of random magnetic errors and the precision of compensating orbit corrections, indicate a reduced sensitivity of the FEL gain to field errors, especially in the high gain

regime. The results of these studies suggest that dimensional and field tolerances typical of the best currently available "3rd generation [8]" magnets should result in passable performance of the LCLS provided: 1) the magnets are optimally sorted; 2) sufficiently precise orbit detection is achieved; and 3) equally precise orbit correction is implemented every 3m or less. In practical terms, typical magnet field strength tolerances of 0.1%-0.2% and easy axis orientation errors of < 5 mr would be required. Typical positional tolerance on the, say, vertically oriented magnets in Fig. 1 lie in the <15 μ range. Using these figures, typical field vs. temperature coefficients (e.g., -0.03%/°K for Sm₂Co₅) lead to the above-cited requirement of a $\pm 0.5^\circ\text{C}$ temperature variation along the undulator's PM lattice. A number of closely related tolerance parameters, such as, e.g., the accuracy of the BPMs, are expected to be difficult to attain under the design constraints of the LCLS, and directed development is likely to be required to attain the design goals.

V. FIELD MEASUREMENT ISSUES

An important procedure for attaining an undulator field of the requisite quality consists of accurately measuring and sorting the magnets to reduce the field irregularities that adversely influence gain [11,12]. An important advantage of the modular configuration of the LCLS undulator is that this procedure can be applied to sections whose length is typical of 1st-3rd generation insertion devices, and can consequently be expected to attain the necessary field quality without unexpected difficulties. However, the total length of the LCLS insertion device represents an order of magnitude increase over conventional structures, and the problem of measuring its entire field following assembly appears difficult to resolve. Evidently, this raises the issue of the final alignment of the device prior to operation. If no suitable method of alignment based on the full field measurement is developed, it may prove necessary to turn the FEL on and attempt to align it by using the emitted radiation and suitable detector arrays. To this end, it will be important for the field quality over a single gain length to be high enough to produce the required (i.e., observable) gain. A backup strategy that has been considered is to further reduce the field and fabrication tolerances by a factor of 2-3 beyond the above-cited minimums to minimize the number of controls required for successful operation. In either case, the complete fields of at least the (16) 3.2m subsections of the 6.4m modules will evidently need to be characterized with exceptional accuracy. To this end, the development of existing or novel techniques capable of rapid and accurate field measurement [13] is expected to play an important role in the successful implementation of the LCLS.

At present, we are continuing our research activities in a number of the directions described in this note. A short prototype section is in the process of being prepared to help

resolve selected tolerance and field measurement issues raised by our analytical and numerical studies.

VI. REFERENCES

- [1] J. Rosenzweig, J. Smolin, and L. Serafini, "Design of a High Brightness Photoinjector for the SLAC X-Ray Linear Coherent Light Source," this conference - Ma10, 1993.
- [2] K. Bane, T. Raubenheimer, J. Seeman, "Electron Transport of a Linac Coherent Light Source (LCLS) Using the SLAC Linac," this conference - Jb19, 1993.
- [3] B. Bonifacio, N. Narducci, and C. Pellegrini, "Collective instabilities and high-gain regime in a free electron laser," *Opt. Commun.* 50(6), 373(1984).
- [4] K.-J. Kim, "Three Dimensional Analysis of Coherent Amplification and Self-Amplified Spontaneous Emission in Free-Electron Lasers," *Phys. Rev. Lett.* 57(15), 1871(1986).
- [5] C. Pellegrini, "A 4 to 0.1 nm FEL Based on the SLAC Linac," *Proceedings of the Workshop on Fourth Generation Light Sources*, M. Cornacchia and H. Winick, eds., SSRL, Feb. 24-27, 1992, SSRL Pub. 92/02, p. 364.
- [6] R. Tatchyn, "Optimal Insertion Device Parameters for SASE FEL Operation," *ibid.*, p. 605.
- [7] K. Kim, M. Xie, E. Scharlemann, C. Pellegrini, G. Travish, "Performance Characteristics, Optimization, and Error Tolerances of a 4-nm FEL Based on the SLAC Linac," this conference - Mb26, 1993.
- [8] P. J. Viccaro, R. Tatchyn, and R. Coisson, "Summary of the Insertion Device Working Group Discussions at the SSRL Workshop on 4th Generation Synchrotron Light Sources," *Proceedings of the Workshop on Fourth Generation Light Sources*, M. Cornacchia and H. Winick, eds., SSRL, Feb. 24-27, 1992, SSRL Pub. 92/02, p. 86.
- [9] K. Halbach, "Physical and optical properties of rare earth cobalt magnets," *Nucl. Instrum. Meth.* 187, 109(1981).
- [10] H. Winick, K. Bane, R. Boyce, K. Halbach, K.-J. Kim, G. Loew, P. Morton, H.-D. Nuhn, J. Paterson, C. Pellegrini, P. Pianetta, D. Prosnitz, J. Rosenzweig, J. Seeman, T. Raubenheimer, T. Scharlemann, R. Tatchyn, G. Travish, V. Vylet, M. Xie, "A 2-4 nm Linac Coherent Light Source (LCLS) Using the SLAC Linac," this conference - F7, 1993.
- [11] A. D. Cox and B. P. Youngman, "Systematic selection of undulator magnets using the technique of simulated annealing," *SPIE Proceedings No. 582*, 91(1986).
- [12] G. Rakowsky, "Considerations for Optimizing the Performance of Permanent Magnet Undulators," *Proceedings of the Workshop on Fourth Generation Light Sources*, M. Cornacchia and H. Winick, eds., SSRL, Feb. 24-27, 1992, SSRL Publication 92/02, p. 86.
- [13] R. W. Warren, "Limitations on the use of the pulsed -wire field measuring technique," *Nucl. Instrum. Meth.* A272,257(1988).

ADJUSTMENT AND MEASUREMENT OF A HYBRID UNDULATOR

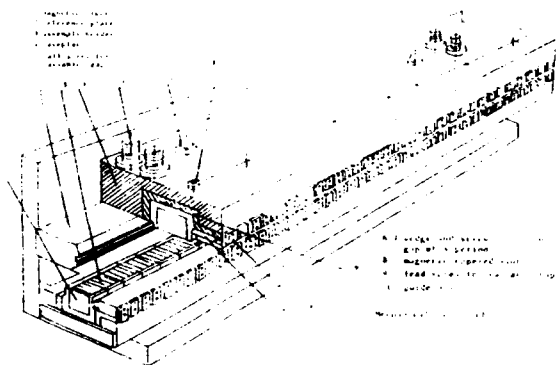
Wu Bing, Ma Youwu, Liu Bo, Zhang Zhaoming
China Institute of Atomic Energy
P.O.Box 275(17), Beijing 102413, P.R.China

Abstract

Adjustment and measurement of a hybrid undulator have been discussed. The magnetic field quality is limited by factors such as inhomogeneities of the permanent magnets, fabrications and assembly errors. Considering these factors, re-sorting of aluminum holders using Simulated Annealing method and iron shimming have been used for the adjustment of undulator. The measured rms field error was reduced from 3% to 0.3%, the electron trajectory deviation is around 0.1mm. During our magnetic measurement, small variation of magnetic period length was observed. An approach to reduce the deviation of relative phase of electrons in the ponderomotive potential, which will lead to the reduction of laser gain degradation due to magnetic field errors have also been discussed.

1. INTRODUCTION

A typical Halbach REPM-steel hybrid undulator is under construction for a free electron laser(FEL) project in CIAE. It is 1.5m long, including 50 magnetic periods, each 30mm. The magnetic field on axis is 3 KG at 1.3cm gap. Fig.1 shows its mechanical layout. Two permanent magnets (SmCo_5 , 2:17) and two steel blocks are glued in an aluminous holder which



we call as a magnetic period unit. 100 units are in turn bolted into the magnetic taper slots, three sections of the slots are fixed into the baseplate. Before its construction, possible assembly and fabrication imperfectness which would result in magnetic field errors had been analyzed [1], and necessary strict mechanical tolerance were required: the tolerance of thickness of the magnet(or pole) was limited in 0.08mm, the gap tolerance was 0.03mm. In the

meantime, magnetization strength of 400 magnet blocks(45mm×30mm×8mm) were measured, and 200 blocks were sorted and optimized using Simulated Annealing method [2]. Unfortunately, the quality of measured magnetic field after the first assembly is poor, the rms peak field error is around 3%. The poor quality results from following reasons: (1) inaccurate measurement of the permanent magnets before sorting; (2) imperfectness of fabrication and assembly, the real mechanical tolerances are much higher than what we required; (3) large deflexion(around 0.4mm) in the middle of two aluminous baseplate.

Generally, less than 0.5% of rms field errors is required for a high quality undulator. Special adjustment must be adopted to reduce the rms error from 3% to 0.5% for our undulator. In the second section of this paper, we will introduce our process of adjustment. In the third section, we will discuss the small variation of magnetic period length we found during measurement. Finally, an approach to correct the magnetic field errors for reducing the gain degradation have been presented.

2. ADJUSTMENT

At present, two effective methods of tuning an undulator to the desired field quality are tuning of magnetic gap [3] and iron shimming [4]. Tuning of magnetic gap does not work well in our undulator because of mechanical difficulties, and it is impractical to reduce field errors from 3% to 0.5% only by means of shimming. So, at first we disassemble our undulator to re-sort the aluminous holders.

(1) re-sorting of aluminous holder

After disassemble the undulator, we again use Simulated Annealing method to re-sort the magnetic period units so that the rms field error is reduced to a much lower value. As presented in section 1, field errors result from inaccurate measurement of permanent magnets and imperfection of assembly and fabrication, quantitative relationships between these errors will be useful for the calculation of cost function in Simulated Annealing calculation. Careful measurement of mechanical errors, including: deflexion of aluminous baseplate, the flatness of the magnet and steel pole surface of a magnetic period unit, are completed. these two factors

are the main reasons of magnetic gap error. Empirical formula have been developed and described elsewhere [5]. Much more accurate magnetic measurement of magnetic period units can be achieved now, because a new magnetic measurement system [6] have been completed in 1991. Measurement of single magnet is impossible because it is glued in the magnetic period unit. Fig.2 shows the sketch

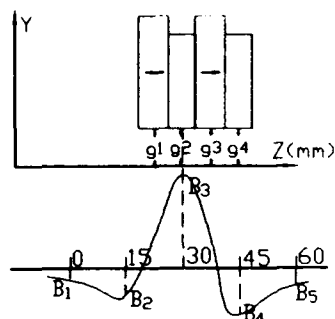


Fig.2

of measurement of magnetic field and surface flatness of a unit. 5 special points of magnetic fields B_1, B_2, B_3, B_4, B_5 , containing the information of inhomogeneity of permanent magnet and g_1, g_2, g_3, g_4 , indicating the gap errors, are all used in the evaluation of magnetic errors along the axis of undulator [5]. Considering all these mechanical errors and inhomogeneity of magnets, peak magnetic fields calculated by the empirical formula well correspond with the measured peak magnetic fields. So, in the calculation of cost function of Simulated Annealing technique, these empirical formula can be reliably used.

After the magnetic period units were re-sorted, the undulator was reassembled. The measured rms peak magnetic field error is reduced to 1.3%.

(2). Shimming

Shimming is widely adopted as an efficient technique in adjustment of undulator. Through shimming, the rms error of our undulator is easily reduced to 0.3%. Fig.3 shows the measured magnetic field. Then, little extra shimming was carried out, which reduced the deviation of electron trajectory to around 0.1-mm, as shown in Fig.4.

3. THE VARIATION OF LENGTH OF MAGNETIC PERIOD

The variation of magnetic period length λ_w have rarely been mentioned before. During measurement of our undulator, we discovered that, λ_w is not strictly equals to 30mm. As designed, there should be a zero magnetic field point every 15mm. In fact, there is small variation of distance between two zero mag-

netic field point, demonstrating the small

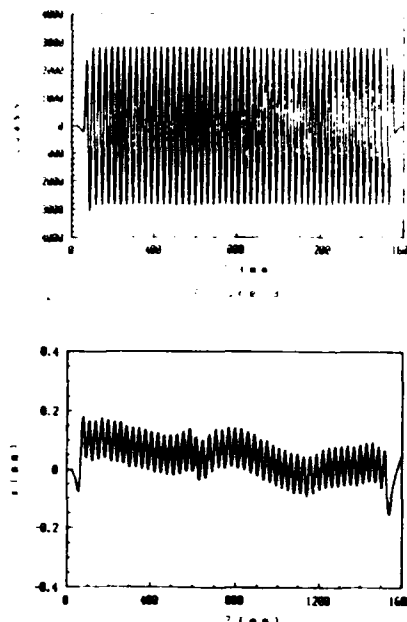


Figure 4

variation of λ_w . In our magnetic measurement system [6], a photo-electric encoder is adopted to detect the displacement of the GaAs hall probe with the precision 0.005mm. In a scan of our measurement, we acquire 1 magnetic data every 0.1mm, 300 data points per period. Some 0.1mm variation of λ_w were observed. In several periods, variation reached 0.3mm. From $a_w = eBw\lambda_w / 2\pi mc$, we can see, λ_w of 1% variation will equally change the value of a_w with the Bw of 1% variation. This should be paid attention to, it means that variation of λ_w is also an important reason for the error of a_w .

It is possibly because of insufficient measurement data points in a period so that the variation of λ_w has rarely been mentioned. For example, if $\lambda_w = 30mm$, 1 data point is acquired per 0.3mm, the variation of λ_w can not easily be observed. Though we have not scan our undulator with 0.1mm per step before shimming, we think shimming should be an important reason for the variation of λ_w .

4. AN APPROACH TO REDUCE THE GAIN DEGRADATION

The effects of random field errors on the performance of free electron laser have become a topic of recent concern. The random magnetic field errors will result in [7]: (1) Random walk of the electron beam centroid, δx ; (2) Deviations of the relative phase of the electrons in the ponderomotive potential, $\delta\psi$, both leads to the loss of radiation gain. Steering can be used to reduce the gain degradation results from δx [8]. Another method--floating wire technique has been developed

and facilitate the adjustment of undulator in reducing δx . Though adjustment of $\delta\psi$ has been suggested [7] and discussed in more detail [10], it has not been tried before and should be highlighted because reduction of δx does not indicate smaller $\delta\psi$, and $\delta\psi$ contributes a large part of gain loss due to magnetic field errors. In section 2, we have demonstrated the reduction of δx through shimming, now we want to reduce $\delta\psi$ through shimming too.

a_w , instead of B_w , is the magnetic parameter we will adjust, because it directly relates to the gain and efficiency of our free electron device, and as shown in section 3, the error of a_w included the variation of both B_w and λ_w which are both the main reasons of $\delta\psi$. The same value of rms errors but different distribution of errors of a_w may result in different $\delta\psi$. Our approach is to adjust the variation of B_w (here we use the amplitude of 1st harmonic) and λ_w , on condition that this adjustment does not result in large change of δx , so that the distribution of a_w is changed, $\delta\psi$ is reduced and loss of gain decreased.

Here, for the first step of our approach, we only consider the small signal gain G_0 . We use formula of Gain function [11] to calculate G_0 . Some parameters used in the simulation are following:

Average electron energy	24.89 MeV
Energy spread	1%
Density of beam current	300 A/cm ²
Length of undulator	1.5 m
Length of a period	30 mm
Ideal a_w	0.86
Wavelength of laser	10.6 μ m

Fig.5 shows calculated G_0 as a function of undulator length (in terms of period number). Curve 1 is the result when using ideal a_w .

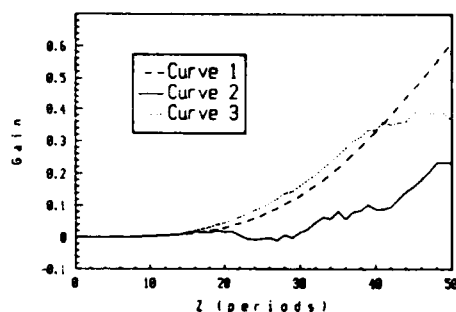


Figure 5.

Curve 2 is the result of using real magnetic data (a_w of each period). obviously the gain is reduced. Now, we simulate change of a_w within 1.5% in 10 different period, we think this can be managed in our adjustment without obviously changing the δx . Curve 3 shows the

calculated G_0 , the gain loss is obviously decreased, and G_0 is near the ideal value. Now a verifying numerical simulation code is under developing.

5. CONCLUSIONS

Our adjustment of undulator is efficiently proved, the quality of undulator is good both in rms peak magnetic field error and in amplitude of transverse trajectory wander δx . Variation of λ_w is observed, and variation of both B_w and λ_w are reasons of gain degradation. If the distribution of errors of B_w , λ_w is rearranged, the deviation of relative phase of electrons in ponderomotive potential can be reduced and loss of gain can be reduced. Here we emphasize the practicality of adjustment of $\delta\psi$, and we will try it in our next step of adjustment of our undulator.

6. REFERENCES

- [1] M.Youwu, et al., "Hybrid Undulator Design and Field Error Analysis, Proc. of 2nd EPAC, 1990, France, Vol 2, P1377
- [2] Wu Bing, et al., "Optimization of Magnets in an Hybrid Undulator", Young Men's First Professional Conference of China Laser Science and Technology. 1991, YanTai, China(in Chinese)
- [3] Varfolomeev, et al., "Large-field-strength Short-period Undulator Design". Proc. of 13th International Free Electron Laser Conference, Santa Fe, NM, USA, 1991, P813
- [4] S.C.Gottschalk, et al., "Wiggler Error Reduction Through Shim Tuning", Nucl. Instr. & Meth. A296(1990), P579
- [5] Wu Bing, et al., "Field Error Analysis During Adjustment of a Hybrid Undulator". Proc. of 5th Particle Accelerator Conference of China, 1992, Beijing, China(in chinese)
- [6] Liu Bo, et al., "A Magnetic Fields Measurement System for Undulator". to be published in China Nuclear Science & Technology Re port.
- [7] E.Esarey, et al., "The Effects of Wiggler Errors on Free Electron Laser Performance", Nucl.Instr. & Meth., A 296(1990), P423
- [8] C.J.Elliott, et al., "Detrapping from Magnetic Field Errors as a Random Walk Escape", Proc. of 14th International Free Electron Laser Conference, Kobe, Japan, 1992
- [9] L.H.Yu, et al., "Reduction of FEL Gain Due to Wiggler Errors", Proc. of 13th International Free Electron Laser Conference, Santa Fe, NM, USA, 1991, P500
- [10] Charles.A.Brau, "Free-Electron Lasers", Academic Press, 1990, P105

Coherent Radiation at Submillimeter and Millimeter Wavelengths

M. Oyamada, R. Kato, T. Nakazato, S. Urasawa, T. Yamakawa, M. Yoshioka
Laboratory of Nuclear Science, Tohoku University
Mikamine, Taihaku-ku, Sendai 982, Japan
M. Ikezawa, K. Ishi, T. Kanai, Y. Shibata and T. Takahashi
Research Institute for Scientific Measurements, Tohoku University
Katahira, Aoba-ku, Sendai 980, Japan

Abstract

The paper describes the experimental results on coherent synchrotron radiation (SR), coherent Cherenkov radiation (CR) and coherent transition radiation (TR) at submillimeter and millimeter wavelengths. Coherent radiation intensities vs. He-gas pressure are shown at $\lambda = 500$ nm and 4 m. Angular distributions of coherent CR and/or coherent TR were obtained in vacuum and at the atmospheric pressure. Coherent TR spectra at different emission lengths were obtained at $\lambda = 0.2 \sim 5$ mm.

I. INTRODUCTION

Complete spectrum of coherent synchrotron radiation, produced by the passage of mm long electron bunches through a bending magnetic field, has been obtained. [1],[2], [3] Our results on coherent SR have been supported by Blum et al. using a linear accelerator at Cornell University. [4] Ohkuma et al. observed the high-intensity coherent Cherenkov radiation emitted in air from a high current single bunch at Osaka University. [5] Happek et al. observed coherent transition radiation at Cornell. [6] We have measured the coherent CR spectrum and angular distributions at the wavelengths of 0.6 to 4.0 mm and the coherent TR ones at 0.2 to 6.0 mm using a grating-type spectrometer and a polarizing interferometer. Broad peaks of the angular distributions of coherent CR and coherent TR were observed at the angles larger than the usual Cherenkov angle, $\cos^{-1}(1/n\beta)$, and the transition radiation angle, $1/\gamma$, respectively. Bunch shapes were estimated by Fourier analysis from these spectra, and they agreed with one from coherent SR spectrum.

II. COHERENT SYNCHROTRON RADIATION

Michel pointed out that intense coherent SR could be observed from bunched electron beam. [7] The intensity of coherent SR is given as follows;

$$P_{coh}(\lambda) = p_0(\lambda)N_e[1 + (N_e - 1)f(\lambda)],$$

$$\cong p_0(\lambda)N_e[1 + N_e f(\lambda)], \quad (1)$$

$$f(\lambda) = \left| \int \exp(i2\pi x/\lambda) S(x) dx \right|^2, \quad (2)$$

where $p_0(\lambda)$ is the intensity from an electron, $f(\lambda)$ bunch form factor, $S(x)$ the density distribution of electrons and N_e the number of electrons in a bunch.

In 1989 the coherent effects in SR were observed for the first time by using Tohoku 300 MeV electron linac. [1] Careful efforts have been done to get the complete spectrum from a few tenth mm to several mm wavelengths region. [2] Figure 1 shows the observed spectrum of coherent SR. Intensity was calibrated absolutely by black body radiation of 1500 K. The accuracy of the absolute intensity of coherent SR after correction was estimated to be within a factor of 1.5. The spectrum shows a broad peak at the wave length $\lambda \cong 1.5$ mm and the peak intensity is enhanced by a factor of 5×10^6 in comparison with ordinary incoherent SR. The enhancement factor is comparable with the number of electrons in a bunch. The bunch form factor was derived from the observed spectrum normalized by the incoherent spectrum and the square of the number of electrons in a bunch. The electron distribution function in the bunch was obtained by the Fourier transform of the bunch form factor and the half width of the distribution curve is $= 0.25$ mm.

The spectrum in the region $\lambda > 2$ mm declines below the theoretical tendency of the incoherent SR spectrum which does as $\lambda^{-1/3}$. This suggests the suppression effect of coherent SR by a metallic boundary condition as predicted by Nodvick and Saxon. [8] This effect will be discussed in another paper at this conference. [9]

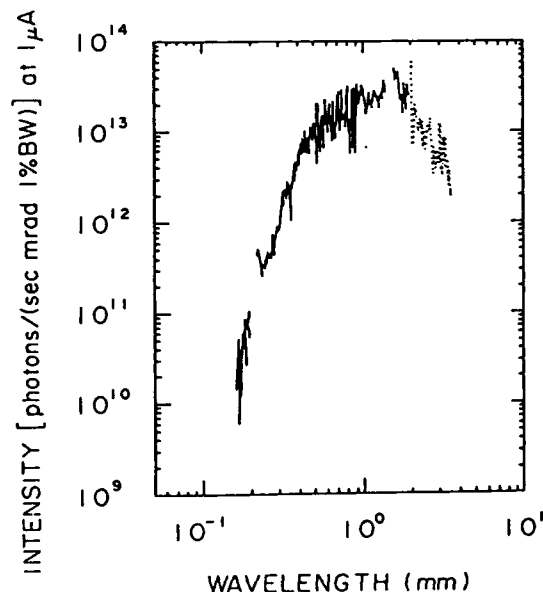


Figure 1. The Observed spectrum of CSR. The intensity is calibrated by blackbody radiation of 1500 K.

III. COHERENT CHERENKOV RADIATION

Coherent CR using travelling-wave linac has been investigated in the microwave region. [10],[11] They found that the peak in the microwave CR occurs at an angle much larger than that expected from application of the ordinary Cherenkov formula, $\theta = \cos^{-1}(1/n\beta)$.

Figure 2 shows the schematic layout of our recent experiments on coherent CR and coherent TR. Titanium beam windows (W1,W2) of 20 μm separates the vacuum between the linac and an experimental chamber, which is evacuated or filled with He-gas at various pressures. Movable aluminum foil (15 μm thick) bounds the emission length from 75 mm up to 880 mm and emitted radiation is guided to the spectrometer using plane mirrors (M1, M2, M3) and a spherical mirror (M3). The grating-type far-infrared spectrometer was used with liquid-He cooled Si-bolometer in the far-infrared region and photomultiplier tube in the visible region, respectively. The experiments were performed at 150 MeV and energy spread of electrons was 0.2% using momentum analyzer.

Figure 3 shows the relations of the coherent CR and/or coherent TR intensities vs. He-gas pressure at the emission length $L = 165$ mm. The open and solid circles show the observed intensity at $\lambda = 500$ nm and 4 mm, respectively. The dashed and broken curves show the theoretical values for each wavelengths. The intensities are normalized to those in vacuum. The pressure of the Cherenkov threshold p_{th} and the formation length Z at the atmospheric pressure are 126 mmHg and 17.1 mm at $\lambda = 500$ nm, and 127 mmHg and 138 m at $\lambda = 4$ mm, respectively. The intensity at $\lambda = 500$ nm increases rapidly above the Cherenkov threshold pressure. On the other hand, in the case of $\lambda = 4$ mm, the intensity is almost constant and independent of the pressure. This suggests that the observed radiation at $\lambda = 4$ mm should be transition radiation from an aluminum foil. The horizontal angular distributions obtained in vacuum and in atmospheric He-gas, at $\lambda = 500$ nm, 1 mm and 4 mm, are shown in figure 4. The broken lines, dotted lines and solid lines show horizontal and vertical components, and total intensities, respectively.

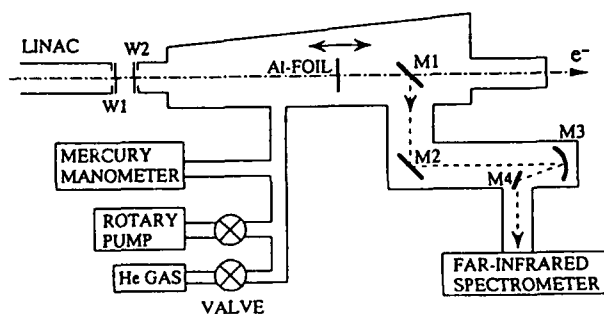


Figure 2. The schematic layout of the CCR and CTR experiments.

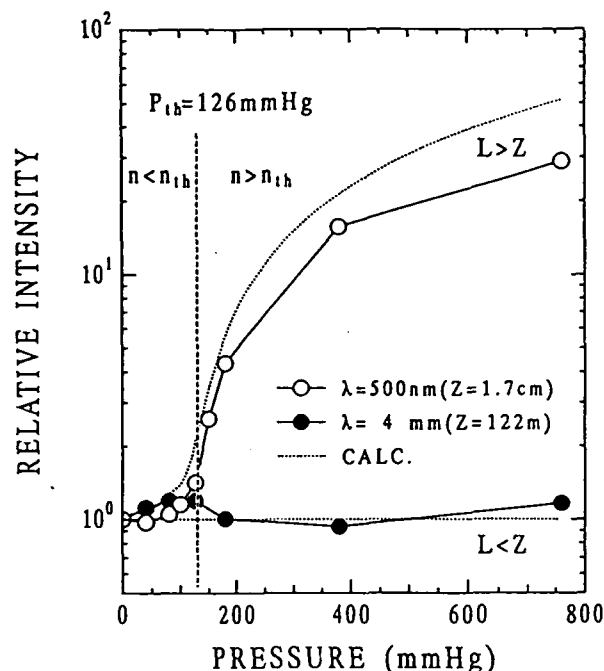


Figure 3. The relation of the intensities of CCR and/or CTR vs. He-gas pressure.

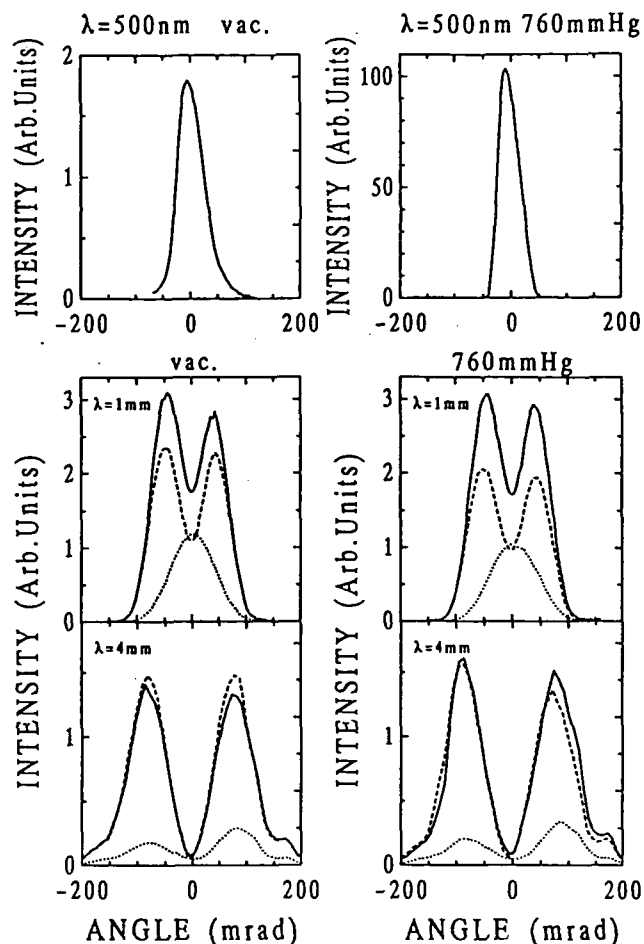


Figure 4. Angular distributions of CCR and/or CTR in vacuum and atmospheric He-gas.

IV. COHERENT TRANSITION RADIATION

The intensity of metal-vacuum TR is given as follows, [12]

$$P = 2p_f \{1 - \cos(L/Z)\} \approx p_f \left(\frac{L}{Z}\right)^2, \quad (3)$$

$$p_f \approx \frac{\alpha \beta^2 \sin^2 \theta}{4\pi^2 \lambda (1 - \beta \cos \theta)^2}, \quad (4)$$

$$Z = \frac{\beta \lambda}{2\pi(1 - \beta \cos \theta)}, \quad (5)$$

where α , β , θ , and L are the fine structure constant, the ratio of a velocity of electrons to that of light, the angle between the direction of the observing point and the trajectory of electrons, and the emission length of TR. Z defines a formation length.

A spectrum of coherent TR emitted from 150 MeV electron bunches passing through aluminum foil has been observed in the wavelength region from 0.2 mm to 5 mm. The intensity at wavelength of 1 mm is enhanced by a factor of 0.9×10^6 in comparison with that of incoherent TR. This factor is about a quarter of the number of electrons in a bunch. The intensity shows nearly quadratic dependence on the electron beam current. The electron distribution in a bunch has been derived from the observed spectrum. It has the full width at half maximum of 0.28 mm and agrees with the value derived from the coherent SR experiment. Figure 5 shows the observed spectra from the emission lengths of 156 mm (A) and of 872 mm. The intensities are given in the unit of photons per second per 1 % band width at a beam current of 1 μ A. Vertical bars show estimated observational errors. The dashed lines show the theoretical intensities of incoherent TR for the emission lengths of 156 mm (A) and 872 mm (B). The observed intensities have been confirmed to be proportional to the square of emission length at these wavelengths.

V. CONCLUSION

Complete spectra of coherent SR and coherent TR have been obtained. The bunch lengths derived from these spectra coincide each other. Bunch length monitor using coherent SR and coherent TR is useful for a short bunch accelerator operation.

Coherent CR is not so intense in the case of short emission length even though the pressure is above the Cherenkov threshold. Electron passing through a beam window emit intense coherent TR.

The intensity of the coherent TR is proportional to the square of emission length which is much shorter than formation length. Broad peaks of the angular distribution shift to the angle larger than the theoretical transition angle, $1/\gamma$.

Intense coherent SR and coherent TR are useful source for spectroscopy.

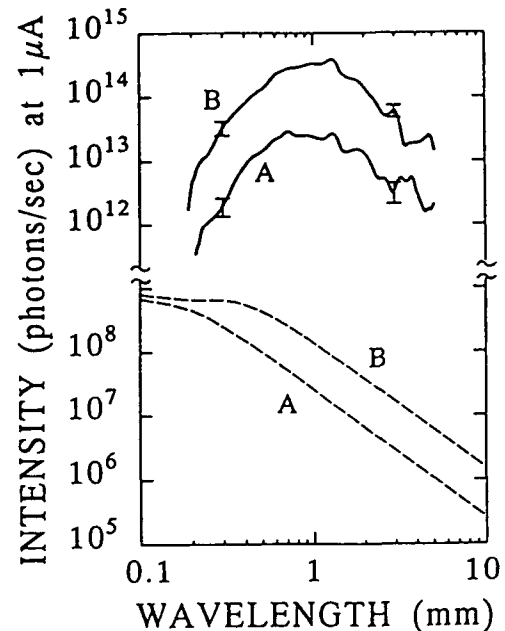


Figure 5. Coherent TR spectra at different emission lengths.

VI. REFERENCES

- [1] T. Nakazato et al., "Observation of Coherent Synchrotron Radiation," *Phys. Rev. Lett.* **63**, 1245-1248 (1989).
- [2] K. Ishi et al., "Spectrum of Coherent Synchrotron Radiation in the Far-Infrared Region," *Phys. Rev.* **A43**, 5597-5604 (1991).
- [3] T. Nakazato et al., "Spectrum of Coherent Synchrotron Radiation," *Conference Record of the 1991 IEEE Particle Accelerator Conference*, Vol. 2, pp. 1118-1120.
- [4] E. B. Blum et al., Observation of Coherent Synchrotron Radiation at the Cornell Linac," *Nucl. Instr. & Meth. in Phys. Res.* **A307**, 568-576 (1991).
- [5] J. Ohkuma et al., "Measurement of Coherent Cherenkov Radiation from an Intense Beam of a Picosecond Electron Bunch," *Phys. Rev. Lett.* **66**, 1967-1969 (1991).
- [6] U. Happek et al., "Observation of Coherent Transition Radiation," *Phys. Rev. Lett.* **67**, 2962-2965 (1991).
- [7] F. C. Michel, "Intense Coherent Submillimeter Radiation in Electron Storage Rings," *Phys. Rev. Lett.* **48**, 580-583 (1982).
- [8] J. S. Nodvick and D. S. Saxon, "Suppression of Coherent Radiation by Electrons in a Synchrotron," *Phys. Rev.* **96**, 180-184 (1991).
- [9] R. Kato et al., "Suppression of Coherent Radiation in Conducting Boundaries," in these proceedings.
- [10] F. R. Buskirk and J. R. Neighbours, "Cherenkov Radiation from periodic electron bunches," *Phys. Rev.* **A28**, 1531-1538 (1983).
- [11] J. R. Neighbours et al., "Cherenkov Radiation from a finite-length path in a gas," *Phys. Rev.* **A29**, 3246-3252 (1984).
- [12] L. Wartski et al., *Appl. Phys.* **46**, 3644 (1975).

Suppression of Coherent Synchrotron Radiation in Conducting Boundaries*

R. Kato[†], T. Nakazato, M. Oyamada, S. Urasawa, T. Yamakawa, M. Yoshioka,
Laboratory of Nuclear Science, Tohoku University
Mikamine, Taihaku-ku, Sendai, 982, JAPAN
M. Ikezawa, K. Ishi, T. Kanai, Y. Shibata and T. Takahashi
Research Institute for Scientific Measurements, Tohoku University
Katahira, Aoba-ku, Sendai, 980, JAPAN

Abstract

The intensity of coherent synchrotron radiation was measured in the presence of finite parallel plate metallic shields with a variable gap by using the Tohoku 300 MeV Linac. The results can be qualitatively explained by the theory of suppression effect obtained by Nodvick and Saxon.

I. INTRODUCTION

In early 1940's it was predicted that bunched electrons might radiate coherently at wavelengths comparable to or longer than the bunch length, and that the radiation loss from all the electrons would be proportional to the square of the number N of electrons in the bunch. According to this idea, the shorter the bunch length would be, the more serious the electron energy loss would become. However coherent radiation loss has not observed for long years.

It was considered that this reason was suppression effect due to metallic walls of the vacuum chamber. This idea was developed by Schwinger. After that Nodvick and Saxon [1] studied radiation in detail by an electron beam following a circular orbit midway between two conducting parallel plates of infinite extent. In order to examine the theory, coherent radiation loss needed to be observed.

In 1989 coherent synchrotron radiation from short electron bunches was observed by using the Tohoku 300 MeV Linac [2] [3]. Hereby, it became possible to verify the suppression theory. The intensity of coherent synchrotron radiation was measured in the presence of finite parallel plane metallic shields while the distance of those was changing. In this paper experimental results are compared with the theory obtained by Nodvick and Saxon, and features of the suppression effect are shown.

The effect seems to be applicable to electron accelerators with high current and short bunch length, such as bunch

compressors of high energy linear colliders or bending arcs of large storage rings.

II. THEORY

Here we account for the suppression theory discussed by Nodvick and Saxon for a beam circulating between two infinite parallel conducting plates. Assuming that these plates exist at $z = \pm a/2$ in three dimension (r, ϕ, z) and that an electron bunch moves in the $z = 0$ plane in a circular orbit of radius R with angular velocity ω_0 , the power P_{coh} coherently radiated by electrons can be expressed as

$$P_{coh} = N^2 \sum P_n f_n, \quad (1)$$

where N is the number of electrons in one bunch, f_n is the bunch form factor, and P_n is the power radiated in the n -th harmonic by an electron.

P_n obtained by Nodvick and Saxon, in MKSA unit, is approximated in the case of β approaching unity as

$$P_n = \frac{n\omega_0 e^2}{3\pi^2 \epsilon_0 a} \left\{ \sum_{j=1,3,\dots}^{j < na/\pi R} \left(\frac{\xi_j}{n} \right)^4 \times \left[\left\{ K_{1/3}^{(1)}(\xi_j^3/3n^2) \right\}^2 + \left\{ K_{2/3}^{(1)}(\xi_j^3/3n^2) \right\}^2 \right] \right\} \quad (2)$$

where $K_{1/3}^{(1)}$ and $K_{2/3}^{(1)}$ are the modified Bessel functions, and $\xi_j = j\pi R/a$. In order to convert P_n to $P(\omega)$ [Photons/electron/mrad/1%BW], replace the factor outside of the big braces by

$$\frac{4 \times 10^{-5} \omega R}{3\pi\omega_0 a} \alpha, \quad (3)$$

where α is the fine structure constant.

III. EXPERIMENTAL METHOD

A conceptual drawing of this experiment is shown in Figure 1. There are finite parallel shields (Aluminum, 1 mm in thick) in the field of a dipole magnet, where synchrotron radiation is produced by an electron beam. The distance

*This work was supported in part by a Grant-in-Aid for General Scientific Research, for Developmental Scientific Research and for Encouragement of Young Scientists of Ministry of Education, Science and Culture.

[†]Present address : Free Electron Laser Laboratory, Department of Reactor Engineering, Japan Atomic Energy Research Institute, Tokai-mura, Naka-gun, Ibaraki-ken 319-11, JAPAN.

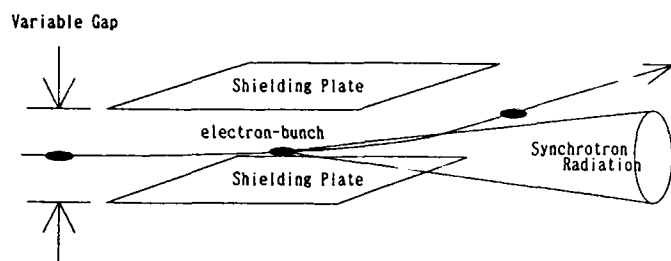


Figure 1: A conceptual drawing of the experiment. The luminous region of synchrotron radiation accepted in an optical system is covered with two parallel metallic shields. The distance between them is changed by remote control.

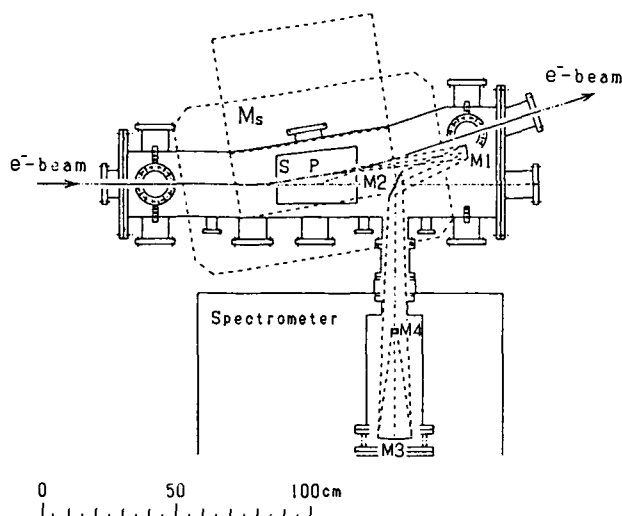


Figure 2: Schematic layout of the experimental setup. M_s : bending magnet, S: shielding plates, P: luminous point, M_1 , M_2 and M_4 : plane mirrors, M_3 : spherical mirror.

between those can be varied from 81 mm to 14 mm. The shape of shields are trapezoidal, of which the transverse size to the beam axis is 180 mm (upstream) and 200 mm (downstream), and the longitudinal size is 300 mm.

The experimental setup is shown in Figure 2. Electron beam accelerated by the linac was injected from left to bending magnet. The beam energy was 50 MeV with an energy spread of 0.2 % and the field strength of the bending magnet was 68.6 mT. A duration of the beam pulse was 2 μ sec and its repetition rate was 300 pulses/sec. One pulse was made up of about 5700 electron bunches. One bunch consisted of 3.6×10^6 electrons and its longitudinal length was about 1.65 mm which corresponded to 5.5° in the phase of 2856 MHz accelerating rf.

Synchrotron radiation was condensed by a round spherical mirror with an acceptance angle of 70 mrad and was led to spectrometers. A grating-type far-infrared spectrometer [4] was used at a fixed wavelength with scanning the distance between the shielding plates. A polarizing interferometer [5] was used at the fixed distance between those

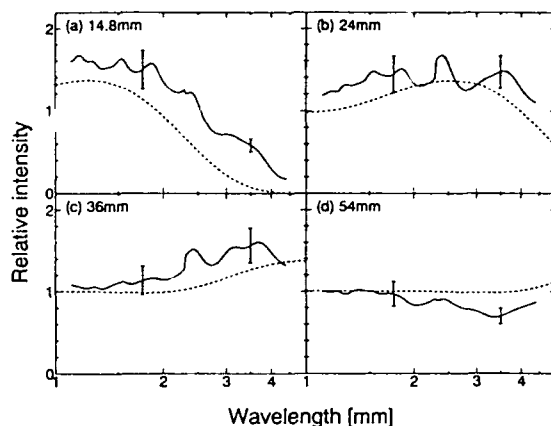


Figure 3: Relative spectra obtained by using a polarizing interferometer at fixed distance between the shielding plates. Panel (a), (b), (c) and (d) show spectra at the distance of 14.8, 24, 36 and 54 mm, respectively. Spectra were normalized by those at the distance of 81 mm. Solid lines show measured values with a slit to block stray light. Dashed lines show theoretical values calculated by formula by Nodvick and Saxon.

to measure the spectrum of synchrotron radiation.

In order to block the stray light reflected by the shielding plates, a slit was set at a focal point just at the entrance of the spectrometer.

The radiation was detected by liquid-helium-cooled silicon bolometers [6].

IV. EXPERIMENTAL RESULTS

As is shown in Figure 3, relative spectra at the distance between the shields of 14.8, 24, 36 and 54 mm were obtained by using the polarizing interferometer. Spectra in the wavelength regions of 1.1 ~ 2.3 mm and 2.3 ~ 4.4 mm were measured by using 1 mm and 2 mm low-pass filters, respectively. If suppression effect does not exist, relative spectra must be unity. The observed results show the existence of this effect.

The relation between the intensity of coherent synchrotron radiation and the distance of the shield gap, which is shown in Figure 4, was obtained by using the grating-type spectrometer at fixed wavelength 1.6, 3, 4, 4.5 and 5 mm. The results show a tendency comparable with theoretical values by the formula (2) and can be qualitatively explained by the theory by Nodvick and Saxon.

Moreover, it is obvious that the shielding effect enhances the intensity of synchrotron radiation at the wavelengths just shorter than suppression region. Furthermore, by comparing the theoretical spectrum calculated by formula by Nodvick and Saxon with that by Schwinger [7], it has been found that the suppressed power due to the shielding plates is equal to the enhanced power, and that total energy of incoherent synchrotron radiation does not change due to conducting boundaries.

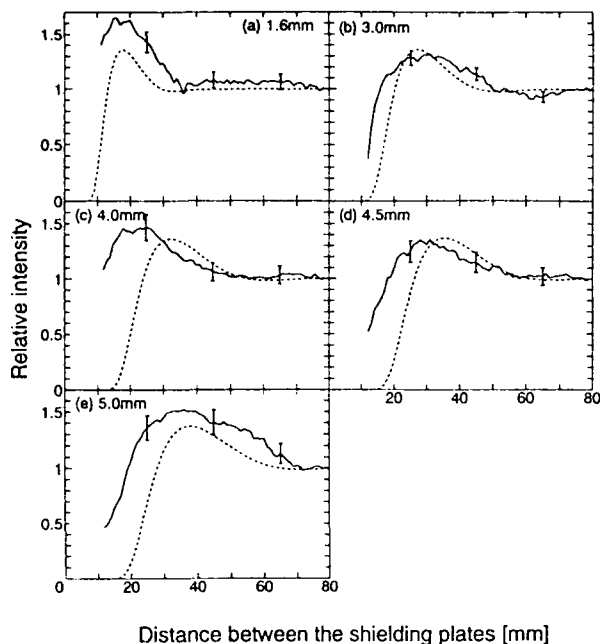


Figure 4: The relation between the intensity of coherent synchrotron radiation and the distance of the shield gap. Panel (a), (b), (c), (d) and (e) show the intensity at fixed wavelength 1.6, 3.0, 4.0, 4.5 and 5.0 mm, respectively. The intensity was normalized by those at the distance of 80 mm. Solid lines show measured values with a slit to block stray light. Dashed lines show theoretical values calculated by formula of Nodvick and Saxon.

V. CONCLUSION

The following important results were obtained by these experiments.

1. Suppression effect of coherent synchrotron radiation in conducting boundaries was observed.
2. The intensity of coherent synchrotron radiation which is suppressed by conducting boundaries can be qualitatively explained by the theory derived by Nodvick and Saxon.
3. Total energy of incoherent synchrotron radiation does not change due to conducting boundaries.

VI. ACKNOWLEDGMENTS

We thank Mr. T. Tsutaya for his technical support on optical elements, Dr. O. Konno for his technical guidance on the vacuum duct and the staff at the Laboratory of Nuclear Science, Tohoku University for their technical assistance.

VII. REFERENCES

- [1] J. S. Nodvick and D. S. Saxon, "Suppression of Coherent Radiation by Electrons in a Synchrotron," *Phys. Rev.* **96**, 180 (1954).

- [2] T. Nakazato, M. Oyamada, N. Niimura, S. Urasawa, O. Konno, A. Kagaya, R. Kato, T. Kamiyama, Y. Torizuka, T. Nanba, Y. Kondo, Y. Shibata, K. Ishi, T. Ohsaka and M. Ikezawa, "Observation of coherent synchrotron radiation," *Phys. Rev. Lett.* **63**, 1245 (1989).
- [3] T. Nakazato, M. Oyamada, N. Niimura, S. Urasawa, Y. Shibasaki, R. Kato, S. Niwano, M. Ikezawa, T. Ohsaka, Y. Shibata, K. Ishi, T. Tsutaya, T. Takahashi, H. Mishiro, F. Arai and Y. Kondo, "Spectrum of Coherent Synchrotron Radiation," *Conference Record of the 1991 IEEE Particle Accelerator Conference*, Vol.2, pp.1118-1120.
- [4] K. Ishi, Y. Shibata, T. Takahashi, H. Mishiro, T. Ohsaka, M. Ikezawa, Y. Kondo, T. Nakazato, S. Urasawa, N. Niimura, R. Kato, Y. Shibasaki and M. Oyamada, "Spectrum of coherent synchrotron radiation in the far-infrared," *Phys. Rev.* **A43**, 5597 (1991).
- [5] Y. Shibata, T. Takahashi, K. Ishi, F. Arai, H. Mishiro, T. Ohsaka, M. Ikezawa, Y. Kondo, S. Urasawa, T. Nakazato, R. Kato, S. Niwano and M. Oyamada, "Observation of interference between coherent synchrotron radiation from separate bunches," *Phys. Rev.* **A44**, R3445 (1991).
- [6] Infrared Laboratory Inc., Product Brochure (January, 1988).
- [7] J. Schwinger, "On the Classical Radiation of Accelerated Electrons," *Phys. Rev.* **75**, 1912 (1949).

A COMPACT TUNABLE X-RAY SOURCE BASED ON PARAMETRIC X-RAY GENERATION BY MODERATE ENERGY LINACS*

X.K. Maruyama, K. DiNova, D. Snyder
Naval Postgraduate School, Monterey, CA 93943

M.A. Piestrup, Qiang Li
Adelphi Technology, Palo Alto, CA 94301

R.B. Fiorito, D.W. Rule
Naval Surface Warfare Center, Silver Spring, MD 20903

Abstract

Parametric x-radiation can be described as the diffraction of virtual photons associated with the electric field of a relativistic charged particle passing through a crystal. In analogy with Bragg reflection of x-rays, these diffracted photons appear as real photons, with an energy which satisfies Bragg's law for the reflecting crystal planes. We describe the results of experiments performed on the Naval Postgraduate School linac which were designed to explore the basic properties of PXR in order to assess its potential application as a compact tunable x-ray source. Experiments using a mosaic graphite radiator show that this radiator produced multiple order, narrow bandwidth reflections from 5 - 45 keV. The measured production efficiency is found to exceed that predicted for spectral orders $n > 1$. We demonstrated the tunability of PXR by rotating the crystal in order to change the Bragg angle relative to the incident 90 MeV electron beam.

I. INTRODUCTION

Parametric x-radiation (PXR) is generated when a charged particle passes through a crystalline structure. The real x-rays produced by this mechanism are quasi-monochromatic and therefore spectrally intense¹. Through the proper selection of the crystal, Bragg angle, angular aperture and electron beam parameters, the photon energy and the bandwidth can be specified. In contrast to other mechanisms for the production of x-rays, to produce 10 keV photons, PXR requires less than a 50 MeV electron beam whereas synchrotron radiation (SR) requires 3 GeV and transition radiation (TR) 300 MeV. Furthermore, the spectral brightness exceeds that of SR, TR and channeling radiation (CR) on a per electron basis.

Experiments done in the former Soviet Union have studied the intensity, angular

distribution, bandwidth and polarization of PXR from beams with energies from 25 to 900 MeV¹.

II. THEORY

The spectral distribution over the solid angle subtended by the detector, $d\Omega = \Delta\theta_x \Delta\theta_y$, can be approximated by

$$\partial N / \partial \omega = \Psi J_2(\alpha_y, u) S(\alpha_x - |u|),$$

where the function J_2 describes the main features of each spectral line² and the step function S , which is unity when the argument is positive and is zero otherwise, describes the effect of $\Delta\theta_x$.

$$\alpha_{x,y} = \Delta\theta_{x,y} / 2\theta_p,$$

$$u = [(\omega - \omega_B) / \omega_B] \cdot \tan \theta_B / \theta_p = \theta_x / \theta_p$$

where, $\theta_p = (\gamma^{-2} + \chi_o + \theta_s^2)^{1/2}$, with γ and χ_o , respectively, the Lorentz factor and the mean dielectric susceptibility. $\theta_s^2 = \theta_d^2 + \theta_{scat}^2 + \theta_{mos}^2$ is included, ad hoc, to approximate the effects of beam divergence, multiple scattering of electrons and crystal mosaicity. The factor,

$$\Psi = \frac{e^2}{\hbar c} \frac{|\chi_{10}|^2}{(4 \sin \theta_B \cos \theta_B)} \frac{L_a (1 - e^{-L/L_a})}{\pi c \theta_p},$$

describes the roles of absorption length, L_a , the interaction length, L , θ_B and χ_{10} , the structure factor.

Fig. 1 illustrates the spectral function, $J_2(u)$, and the portion of the spectrum observed by our fixed detector when the crystal is oriented at $\theta_B = 22.5^\circ$ and $\theta_B = 23.5^\circ$. At a distance of 1 meter $\Delta\theta_{x,y} = 16$ mrad and $\Delta\theta_x$ prescribed the observed bandwidth (4%).

III. MEASUREMENTS

We have recently measured higher order spectra of parametric x-radiation from thick graphite and silicon crystals. The production is

*This work was partially supported by the Defense Nuclear Agency, the Naval Postgraduate School and USDOE SBIR Contract (No. DE-FG03-91ER81099)

determined by the interaction length, L , rather than by absorption lengths, L_a , for higher energy x-rays. For these conditions, the intensity of the higher harmonics is considerably enhanced and the $n=2$ intensity is comparable to the fundamental². The measurements presented here show that PXR is a promising compact source of spectrally bright hard x-rays, and demonstrates that PXR production is directional, quasi-monochromatic and tunable.

The absolute PXR yield (photons/electron) has been obtained by simultaneously monitoring the x-ray fluorescence from a tin foil placed directly behind the PXR target³. The crystal was a 1.39 mm thick mosaic compression annealed pyrolytic graphite (CAPG), a form of highly oriented pyrolytic graphite (HOPG), which is reported to have the highest x-ray reflectivity of any known crystal⁴. Fig. 2 illustrates the experimental arrangement. Optical transition radiation was used to align the beam and crystal^{5,6}. The $\langle 002 \rangle$ reflection planes are parallel to the face of the crystal so that the PXR is produced in the Bragg geometry. Since graphite is not a good optical reflector, a small mirror mounted coplanar to the surface was used to align the crystal.

The Bragg condition, $2d\sin\theta_B = n\lambda$, defines the resonance condition for the production of PXR. Figure 2 illustrates the experimental arrangement for silicon in a Laue geometry for which the Bragg angle, $\theta_B = 22.5^\circ$. Figure 3 shows a series of spectra for mosaic graphite in a Bragg geometry for Bragg angles varying from 19.1° to 25.6° and a fixed detector angle $\theta_D = 45^\circ$. The fall off of intensity of the high order spectra as θ_B departs from 22.5° is due to the fact that the spectral line falls off the fixed detector aperture as shown in Fig. 1.

IV. DISCUSSION

Table 1 presents the measured PXR yields for a Bragg scattering angle of 22.5° . The electron energy in this case was 90 MeV. The important observation to be made here is that the measured yields for the higher order peaks are many times larger than predicted by theory. We are theoretically investigating several possible mechanisms to explain our observations, but our present understanding of the phenomenon is incomplete². Our experiments involving PXR from the $\langle 111 \rangle$ and $\langle 022 \rangle$ planes of silicon have definitely shown that the yield for the higher

orders increases with thickness². There is also some evidence that the enhancement over theory observed in graphite may not exist for silicon. We are planning further experiments to investigate the role of the mosaic structure of the graphite target.

order n	Energy (keV)	PXR Yield (N/e) 10^{-9}	Theory Yield (N/e) 10^{-9}	Data Theory
1	4.88	1670	5230	0.3
2	9.53	1720	990	1.7
3	14.29	850	240	3.6
4	19.08	420	80	5.3
5	23.88	230	34	6.9
6	28.68	130	16	8.3
7	33.56	68	8	8.8
8	38.44	34	4	8.8

Table 1. Measured and Theoretical PXR yields in graphite.

IV. REFERENCES

1. e.g. S.A. Vorob'ev et al., Sov. Phys. JETP Lett. 41, 1 (1985); V.G. Baryshevsky et al. Phys. Lett. 110A, 477 (1985); Yu. N. Adishev et al. Nucl. Inst. and Methods A248, 48 (1987); A.V. Shchagin et al. Phys. Lett. A148, 458 (1990); V.P. Afanasenko et al., Phys. Lett. A141, 313 (1989).
2. R.B. Fiorito, D.W. Rule, X.K. Maruyama, K.L. DiNova, S.J. Everson, M.J. Osborne, D. Snyder, H. Rietdyk, M.A. Piestrup and A.H. Ho, "Observation of Higher Order Parametric X-ray Spectra in Mosaic Graphite and Single Silicon Crystals", submitted to Physical Review Letters.
3. X.K. Maruyama, T. Fasanello, H. Rietdyk, M.A. Piestrup, D.W. Rule and R.B. Fiorito, "A Method for Measuring Dark Current Electron Beams in an RF Linac", these proceedings.
4. A.W. Moore, in Chemistry and Physics of Carbon, Vol 17, pp 233-286, P. Walker and P.A. Thrower (eds.), Marcel Dekker, NY (1981).
5. D.W. Rule, R.B. Fiorito, M.A. Piestrup, C.K. Gary and X.K. Maruyama, "Production of X-rays by the Interaction of Charged Particle Beams with Periodic Structures and Crystalline Materials, SPIE 1552, 240 (1991).
6. X.K. Maruyama, M.J. Hellstern, C.B. Reid, R.B. Fiorito and D.W. Rule, "Optical Transition Radiation Interferometry and Beam Emittance Measurements", to be published in Nuc. Inst. and Meth. B, April 1993.

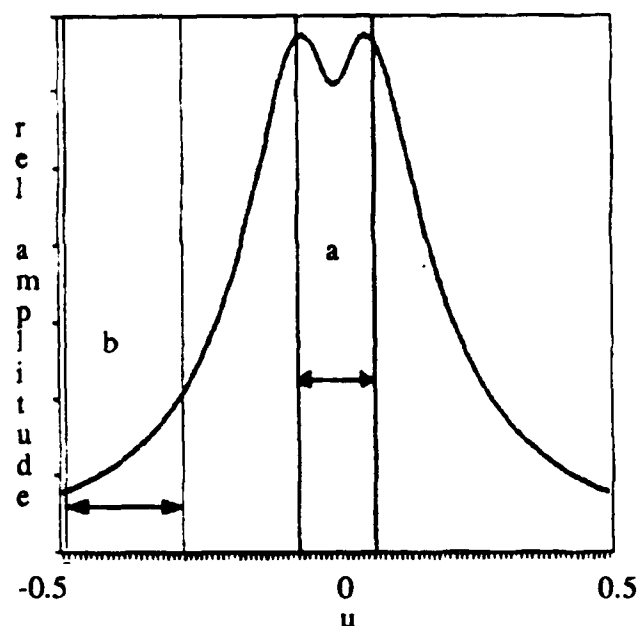


Figure 1. The spectral function $J_2(u)$. The regions between the vertical lines represent the bandwidths Δu corresponding to the detector aperture $\Delta\theta_x$ for crystal orientation a) $\theta_B = 22.5^\circ$ and b) $\theta_B = 23.5^\circ$

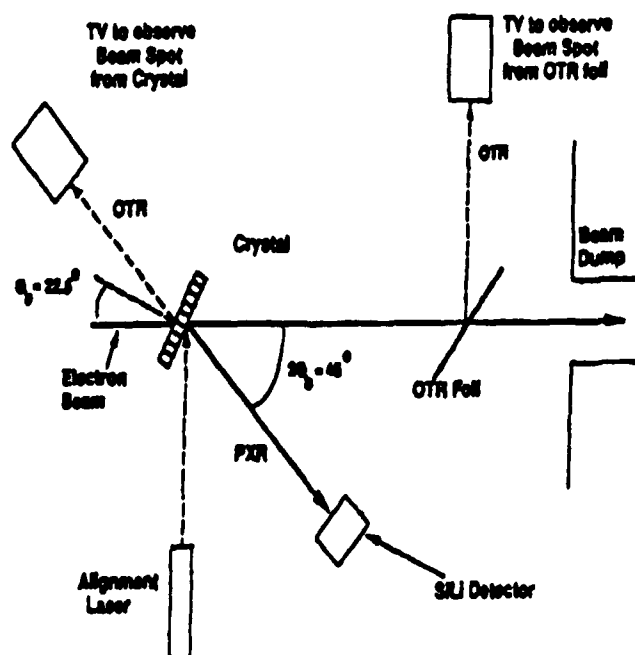


Figure 2. Experimental setup for observing parametric x-ray in the Laue geometry with $\theta_B = 22.5^\circ$. In the Bragg geometry, the photons exit from the same side as the incoming electron beam.

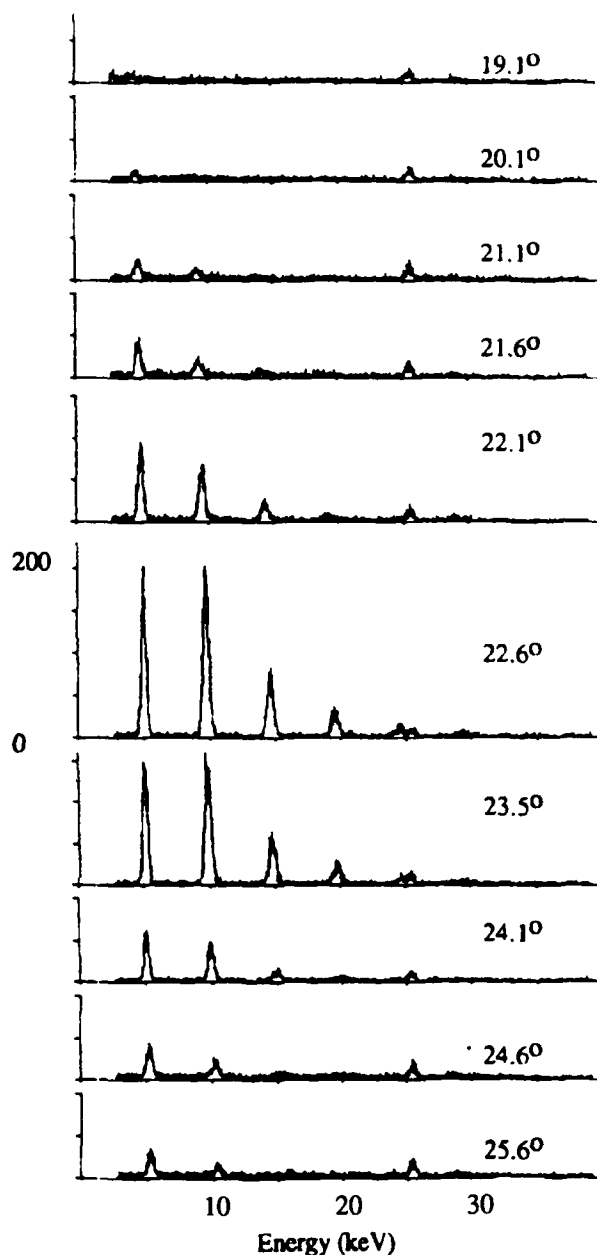


Figure 3. PXR spectra from the $\langle 002 \rangle$ plane of mosaic graphite, observed with the detector fixed at 45° and the crystal oriented at the indicated Bragg angles. The tin fluorescence line at 25.2 keV serves as an energy and beam intensity calibration peak.

Fundamental and Harmonics of Thomson Backscattered X-Rays from an Intense Laser Beam

Cha-Mei Tang¹, B. Hafizi² and Sally K. Ride³

¹ Plasma Physics Division, Naval Research Laboratory, Washington, DC 20375-5346

² Icarus Research, 7113 Exfair Rd., Bethesda, MD 20814

³ Department of Physics, University of California at San Diego, La Jolla, CA 92093-0021

Abstract

We have formulated and obtained analytical expressions for Thomson backscattered x-ray radiation for an electron beam interacting with a linearly polarized electromagnetic undulator. The analytical expressions are valid for the fundamental and harmonics with arbitrarily large laser intensities. The formulation includes the effect of small angular misalignment between the laser pulse and the electron beam. This misalignment is found to increase the spectral width and distort the symmetry of the backscattered radiation.

I. INTRODUCTION

Tunable, near monochromatic, high brightness x-rays would be an important tool in research and medical diagnostics. Synchrotron light sources produce useful x-rays for a large user community. In this paper we examine a closely related method of x-ray generation, Thomson backscattering of x-rays from intense laser beams. [1-4] The configuration, shown in Fig. 1, consists of an electron beam intercepting an incoming laser pulse propagating in the opposite direction. Radiation is backscattered at a double Doppler upshifted frequency. The laser pulse acts in the same way as the static magnetic wiggler in synchrotron light sources or free electron lasers. [5-6]

One advantage of using a laser undulator is that the electron beam energy can be much lower than the electron beam energy using static magnetic undulators to obtain the x-ray of identical energy, since the wavelength of the laser may be many orders of magnitude smaller than that of the magnetic wiggler. Thus, this method has the virtue of being extremely compact.

II. FORMULATION

The laser pulse is assumed to be linearly polarized with frequency ω_L . The vector potential of the laser pulse can be separated into fast and slow components, $A(\eta) = A(\eta)\sin(\eta)\hat{e}_x$, where $\eta = k_L z + \omega_L t$, $k_L = \omega_L/c$. The pulse shape $A(\eta)$ and the wavenumber k_L are assumed to be constants for the interaction time T and $\sin(\eta)$ is a fast oscillating component. We consider an electron with small initial transverse velocity, $\beta_{x0} \equiv v_{x0}/c$, $\beta_{y0} \equiv v_{y0}/c \ll 1$.

It is possible to separate the energy radiated per unit solid angle ($d\Omega$) per unit frequency ($d\omega$) per electron into two components

$$\frac{d^2 I}{d\omega d\Omega} = \frac{d^2 I_\theta}{d\omega d\Omega} + \frac{d^2 I_\phi}{d\omega d\Omega}. \quad (1)$$

Analytical expressions for each term on the right-hand side of Eq. (1) can be obtained.

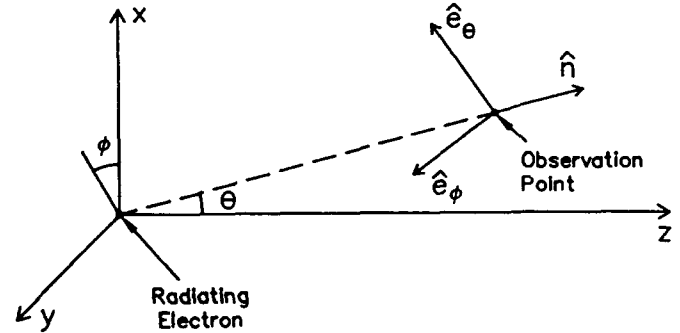


Fig. 1. Schematic of the Thomson backscatter configuration, where an electron beam intersects an incoming laser pulse.

The frequencies of the on-axis radiation associated with the peak intensity are

$$\omega_h = h4\omega_L\gamma_0^2/(1 + a^2/2), \quad (2)$$

where h is the harmonic number, γ_0 is the relativistic factor, $a = (e/m_0c^2)A$ and m_0 is the rest mass of the electron.

To obtain the analytical expression for (1), we assumed that the electron transverse motion is small, i.e., $a(\beta_{x0}^2 + \beta_{y0}^2)\gamma_0^2/2 \ll 1$, the laser intensity is not exceedingly large, i.e., $a \ll 2\gamma_0/\beta_{x0}$, and $k_\perp \Delta r \ll 1$, where Δr is the radius of the electron oscillation in the transverse direction driven by the laser and k_\perp is a measure of the transverse wavenumber of the laser field. We find

$$\frac{d^2 I_\theta}{d\omega d\Omega} \simeq \frac{e^2 \omega^2}{4\pi^2 c \omega_L^2} \left| \left[g_{0,\theta} I_0 - \frac{\bar{a}^2}{4\gamma_0^2} I_x \sin \theta - \frac{\bar{a}}{\gamma_0} I_x (\cos \theta \cos \phi + \bar{\beta}_{x0} \sin \theta) \right] \right|^2, \quad (3)$$

$$\frac{d^2 I_\phi}{d\omega d\Omega} \simeq \frac{e^2 \omega^2}{4\pi^2 c \omega_L^2} \left| \left[g_{0,\phi} I_0 + \frac{\bar{a}}{\gamma_0} I_x \sin \phi \right] \right|^2, \quad (4)$$

where

$$g_{0,\theta} = (\bar{\beta}_{x0} \cos \phi + \bar{\beta}_{y0} \sin \phi) \cos \theta - \left(\bar{\beta}_1 - \frac{\bar{a}^2}{4\gamma_0^2} \right) \sin \theta, \quad (5a)$$

$$g_{0,\phi} = \bar{\beta}_{x0} \sin \phi - \bar{\beta}_{y0} \cos \phi, \quad (5b)$$

$\beta_{x0} = (1 - \gamma_0^{-2} - \beta_{x0}^2 - \beta_{y0}^2)^{1/2}$ is the initial axial velocity, $\bar{\beta}_1 = (1 - (1 + \gamma_0^2(\beta_{x0}^2 + \beta_{y0}^2))/(\gamma_0^2(1 + \beta_{x0}^2)))/2$, $\bar{\beta}_{x0} = \beta_{x0}/(1 + \beta_{x0})$, $\bar{\beta}_{y0} = \beta_{y0}/(1 + \beta_{x0})$ and $\bar{a} = a/(1 + \beta_{x0})$. The expressions for I_0 , I_x and I_z , written in terms of the harmonic number, are

$$I_0 = 2e^{i\psi_0} \sum_{h=1}^{\infty} i^h p_h \sum_m (-1)^m J_m(d_x) J_{h+2m}(d_x) \quad (6a)$$

$$I_x = -e^{i\psi_0} \sum_{h=1}^{\infty} i^h p_h \sum_m (-1)^m J_m(d_x) [J_{h+2m-1}(d_x) + J_{h+2m+1}(d_x)], \quad (6b)$$

$$I_z = -e^{i\psi_0} \sum_{h=1}^{\infty} i^h p_h \sum_m (-1)^m J_m(d_x) [J_{h+2m-2}(d_x) + J_{h+2m+2}(d_x)], \quad (6c)$$

$$d_x = \frac{\omega}{\omega_L} [\sin \theta \cos \phi + \bar{\beta}_{x0}(1 + \cos \theta)] \frac{\bar{a}}{\gamma_0}, \quad (7a)$$

and

$$d_z = -\frac{\omega}{\omega_L} (1 + \cos \theta) \frac{\bar{a}^2}{8\gamma_0^2}. \quad (7b)$$

The form for p_h is $p_h = \pi N_o \sin \chi_h / \chi_h$ and it is peaked at $\chi_h = 0$, where $\chi_h = (d_0 - h)\pi N_o$,

$$d_0 = \frac{\omega}{\omega_L} \left\{ 1 + \left[-(\bar{\beta}_{x0} \cos \phi + \bar{\beta}_{y0} \sin \phi) \sin \theta - \left(\bar{\beta}_1 - \frac{\bar{a}^2}{4\gamma_0^2} \right) (1 + \cos \theta) \right] \right\},$$

and N_o is the number of periods in the laser pulse. See Ref. [3] for the derivation.

The analytical expression for the radiated energy per unit solid angle per unit frequency per electron, given by the sum of the expressions (3) and (4), with definitions given by (5a-b), (6a-c) and (7a-b), are valid for a wide range of values of laser amplitudes. For $a \ll 1$, only fundamental radiation will be observed. Intensity of harmonic radiation becomes important for $a > 1$.

III. NUMERICAL RESULTS

In this section we present numerical results for the energy radiated per unit solid angle per unit frequency per electron. Three examples are given: 1) no transverse beam velocity, and beam intercepting the laser at a small angle 2) $\beta_{x0} = 0.005$ and 3) $\beta_{y0} = 0.005$. In all cases, the electron beam has $\gamma_0 = 80$. The normalized laser amplitude is $a = 1.0$ and the number of periods in the laser pulse is taken to be 20. The small number of periods is not typical for a laser pulse, but it illustrates the principles, while avoiding difficulties in displaying data with very narrow line widths.

For the electron beam without initial transverse velocity, the backscattered radiation is peaked on-axis for the fundamental and the odd harmonics and is null on-axis for even harmonics. Figure 2 is a plot of $d^2I/d\omega d\Omega$ as a function of normalized frequency and angle θ (evaluated in the $\phi = 0$ plane), where ω_1 is the frequency of the fundamental based on Eq. (2). The contour plots of the intensity distribution in the x-y plane are shown in Figs. 3a-f. The intensities are normalized to the peak of the fundamental for (a) $\omega = 0.94\omega_1$ and (b) $\omega = 1.0\omega_1$. The intensities are normalized to the peak of the second harmonic for (c) $\omega = 1.94\omega_1$ and (d) $\omega = 2.0\omega_1$. The intensities are normalized to the peak of the third harmonic for (e) $\omega = 2.94\omega_1$ and (f) $\omega = 3.0\omega_1$. This shows that the fundamental is close to axially symmetric and peaked on-axis. The second harmonic has mirror symmetry with respect to the y-axis and null on-axis. The third harmonic has mirror symmetry with respect to the x-axis and peaked on-axis.

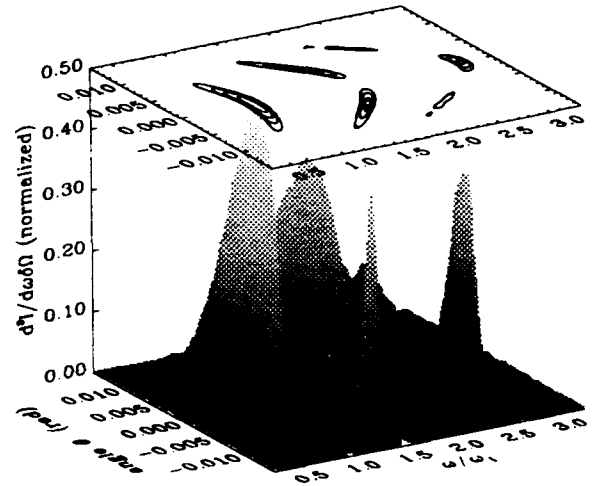


Fig. 2. Plot of normalized $d^2I/d\omega d\Omega$ per electron as a function of normalized frequency and angle θ (evaluated in the $\phi = 0$ plane) for an electron with no initial transverse velocity.

With this formulation, we can examine the effect of misalignment of the laser with respect to the beam. For $\beta_{y0} = 0.005$, all the radiation moves off-axis with the center located to $(x/R = 0.0, y/R = 0.005)$. For $\beta_{x0} = 0.005$, the radiation profiles become distorted.

Figure 4 is a plot of the energy radiated as a function of frequency and angle θ (evaluated in the $\phi = 0$ plane), for $\beta_{x0} = 0.005$. The contour plot of the intensity distribution in the x-y plane are shown in Figs. 5a-f. The intensities are normalized to the peak of the fundamental for (a) $\omega = 0.94\omega_1$ and (b) $\omega = 1.0\omega_1$. The intensities are normalized to the peak of the second harmonic for (c) $\omega = 1.94\omega_1$ and (d) $\omega = 2.0\omega_1$. The intensities are normalized to the peak of the third harmonic for (e) $\omega = 2.94\omega_1$ and (f) $\omega = 3.0\omega_1$. This figure shows that the fundamental is not symmetric and peaked off-axis at $(x/R = 0.005, y/R = 0.0)$. The second harmonic becomes almost axially symmetric peaked at the same position as the fundamental. This is completely different from the

perfectly aligned case. The third harmonic also becomes more axially symmetric and the peak is off-axis, as in the case of the fundamental.

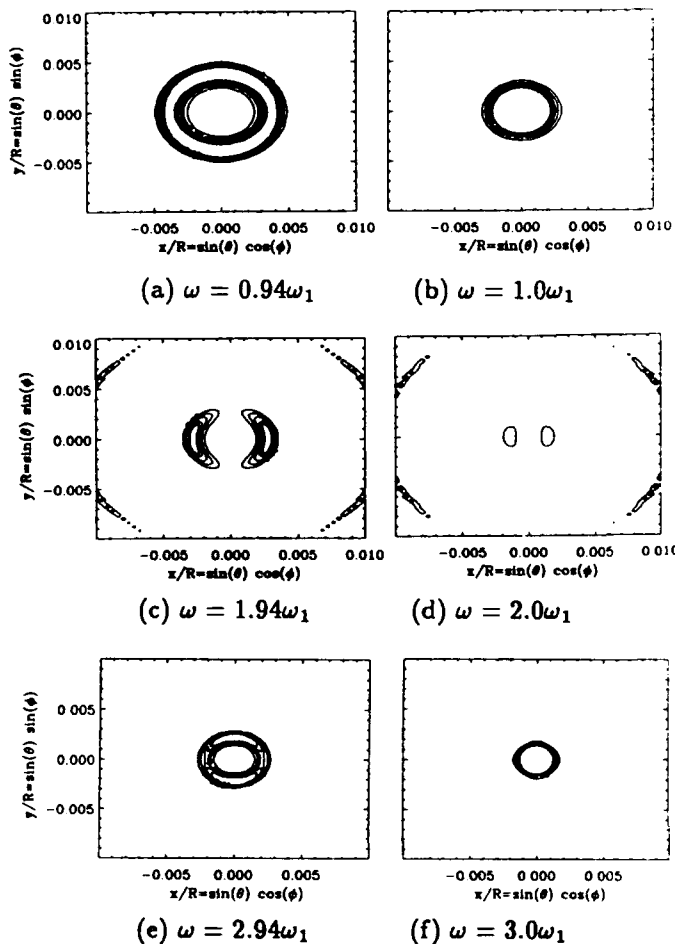


Fig. 3. Contour plots of $d^2I/d\omega d\Omega$ in the x-y plane for an electron beam with $\beta_{x0} = 0.0, \beta_{y0} = 0.0$.

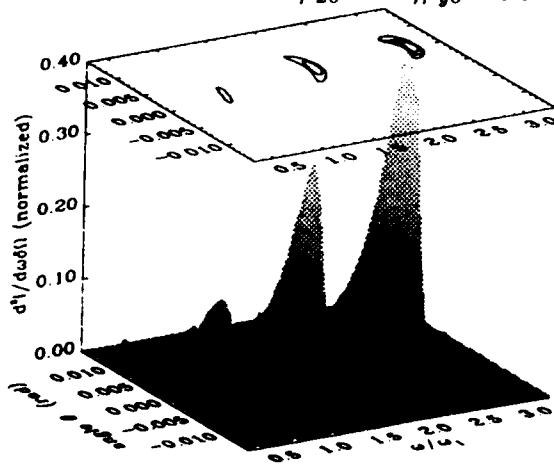


Fig. 4. Plot of normalized $d^2I/d\omega d\Omega$ per electron as a function of normalized frequency and angle θ (evaluated in the $\phi = 0$ plane) for $\beta_{x0} = 0.005$.

IV. CONCLUSION

We have derived an analytic expression for the intensity distribution of Thomson scattered radiation for the

case of a linearly polarized laser pulse incident on a counterpropagating electron beam. We have calculated the effects of small initial transverse momentum, including the distortion of the intensity distribution, the reduction in on-axis intensity, and the increase in bandwidth. We are currently extending this work to consider the effects of emittance (for a distribution of electrons) and laser pulse shape on the scattered radiation.

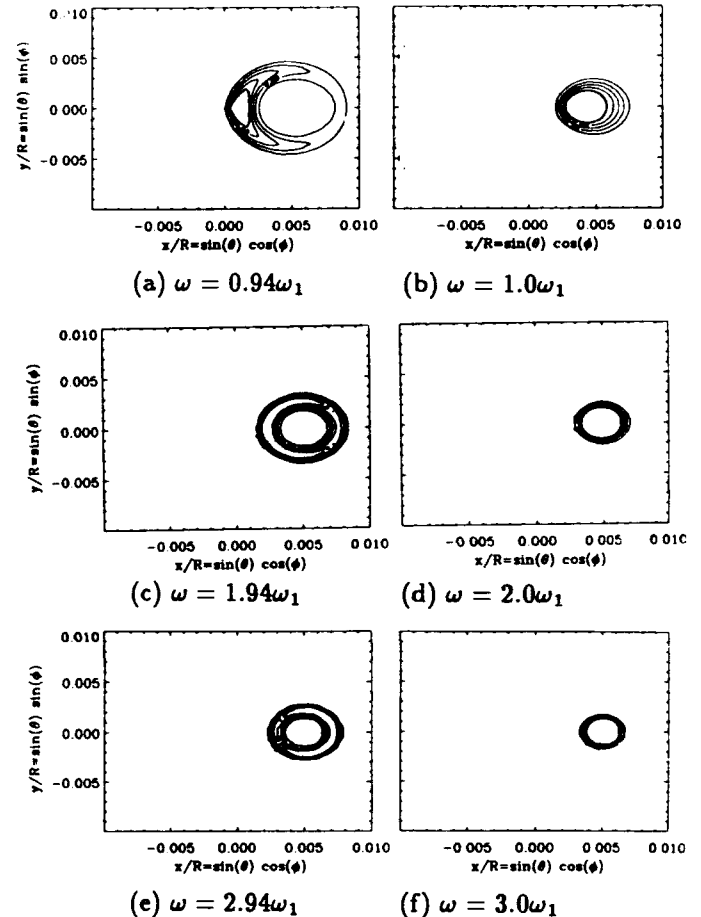


Fig. 5. Contour plots of $d^2I/d\omega d\Omega$ in the x-y plane for an electron beam with $\beta_{x0} = 0.005, \beta_{y0} = 0.0$.

Acknowledgements

This work is supported by the Medical Free Electron Laser Program of ONR.

References

- [1] M. A. Piestrup, G. E. Rothbart, R. N. Fleming and R. H. Pantell, *J. Appl. Phys.* **46**, 132 (1975).
- [2] P. Sprangle, A. Ting, E. Esarey and A. Fisher, *J. Appl. Phys.* **72**, 5032 (1992).
- [3] C. M. Tang, B. Hafizi and S. K. Ride, to be published in the *Nucl. Instr. and Methods*.
- [4] E. Esarey, P. Sprangle, A. Ting and S. K. Ride, to be published in the *Nucl. Instr. and Methods*.
- [5] W. B. Colson, "Free Electron Laser Theory", Ph.D. Thesis, Stanford University, 1977.
- [6] S. K. Ride and W. B. Colson, Stanford University High Energy Physics Lab Report 858 (1979).

Generation of Intensive Long-wavelength Edge Radiation in High-energy Electron Storage Rings

O.V.Chubar and N.V.Smolyakov, Russian Research Center - Kurchatov Institute, 123182 Moscow, Russia

Abstract

Computation results on bending magnet edge radiation (ER) in 2.5 GeV electron storage ring Siberia-2 are reported. Special features of the ER in high-energy electron storage rings are discussed. This radiation differs from standard synchrotron radiation as well as from short-wavelength ER in proton storage rings. Emission peculiarities of the long-wavelength ER in high-energy electron storage rings are considered. The ER is shown to possess certain features of long-wavelength bremsstrahlung.

I. INTRODUCTION

Electromagnetic edge radiation is generated by ultra-relativistic charged particles in the region of magnetic field change at bending magnet edge.

It was shown both theoretically and experimentally [1] - [3], that in high-energy proton synchrotrons the short-wavelength ER (at $\lambda \ll \lambda_c$, where λ_c is critical wavelength of standard synchrotron radiation from uniform field of bending magnet) is much more intensive than the standard synchrotron radiation (SR).

The ER in electron synchrotrons and storage rings was considered in [4] - [8]. The electron ER intensity exceeds corresponding SR intensity level at $\lambda \gg \lambda_c$; spectral angular characteristics of the ER are much different from those of the standard SR.

In this paper, the features of ER at $\lambda > \lambda_c$ are discussed. First the computation results of the ER characteristics for the Siberia-2 electron storage ring (under construction in Kurchatov Institute, Moscow) are presented, and thereafter the peculiarities of the ER formation are analytically considered. The calculations were made in the approximation of infinitely thin electron beam (ER computation results obtained with due regard for finite beam emittance are discussed in [9]).

II. COMPUTING THE EDGE RADIATION CHARACTERISTICS

Fourier transformation of electric field emitted by single electron in its motion along the trajectory $\vec{r}(\tau)$ may be given by the relation obtained from Fourier transformations of delayed potentials [10]

$$\vec{E}_\omega = \frac{ie\omega}{c} \int_{-\infty}^{\infty} \frac{\vec{\beta} - \vec{n}}{R} \exp[i\omega(\tau + R/c)] d\tau, \quad (1)$$

where $\vec{\beta} = (d\vec{r}/d\tau)/c$ is relative velocity of electron; $\vec{n} = \vec{R}/R$, $\vec{R} = \vec{r}^* - \vec{r}$, $R = |\vec{R}|$; \vec{r}^* denotes observation point position, ω is radiation frequency, e is charge of electron; c is the speed of light, i is unit imaginary number.

Spectral angular distribution of the radiation energy is

$$\frac{d\varepsilon}{d\Omega d\omega} = \frac{cr^2}{4\pi^2} |\vec{E}_\omega|^2, \quad (2)$$

where $r^* = |\vec{r}^*|$ [10].

It is practically more convenient to consider number of photons emitted by all the electron beam per time unit, dN/dt . If longitudinal bunch length exceeds the observed radiation wavelength, then the radiation of different electrons is known to be essentially incoherent. Therefore it is obtainable for infinitely thin electron beam,

$$\frac{dN}{dt d\Omega (d\omega/\omega)} = \frac{\alpha c^2 r^2 I}{4\pi^2 e^3} |\vec{E}_\omega|^2, \quad (3)$$

where I is electron current, α is the fine-structure constant. In line with approximation (3), spectral angular distribution of the beam radiation is defined by that of one electron.

Let the y -axis be coincident with straight section axis in the storage ring; x is horizontal axis and z is vertical one. Electromagnetic radiation of ultra-relativistic particle is directed forward for the most part [10]. Hence one can set in Eq.(1) $|\beta_x| \ll 1$, $|\beta_z| \ll 1$, $|\beta_y| \approx 1$. The electron is assumed to move in median plane, therefore $\beta_z = 0$. With regard to it, the exponent phase in (1) may be shown up as

$$\begin{cases} \omega(\tau + R/c) \approx \Phi_0 + \Phi; \\ \Phi = (\pi/\lambda) \int_0^s [\gamma^2 + n_z^2 + (n_x - \beta_x)^2] ds', \end{cases} \quad (4)$$

where the trajectory length $s = \tau\beta c$ is used as integrating variable; γ is the electron reduced energy ($\gamma \gg 1$); Φ_0 does not depend on s . Squared magnitudes of σ - and π -component of \vec{E}_ω are given by the expressions

$$\begin{cases} |(E_\omega)_\sigma|^2 = \frac{4\pi^2 e^2}{c^2 \lambda^2} \left| \int_{-\infty}^{\infty} \frac{n_x - \beta_x}{R} \exp(i\Phi) ds \right|^2; \\ |(E_\omega)_\pi|^2 = \frac{4\pi^2 e^2}{c^2 \lambda^2} \left| \int_{-\infty}^{\infty} \frac{n_z}{R} \exp(i\Phi) ds \right|^2. \end{cases} \quad (5)$$

In accordance with the definition of \vec{n} : $n_x = (x^* - x)/R$, $n_z = z^*/R$; x^* , z^* are Cartesian coordinates of observation point in the detector screen; $x(s)$ and $\beta_x(s)$ are defined from the equation of motion,

$$x(s) \approx \int_0^s \beta_x(s') ds' + x(0), \quad \beta_x(s) \approx \frac{1}{r_0} \int_0^s f(s') ds' + \beta_x(0), \quad (6)$$

where $r_0 = -mc^2\gamma/(eB_0)$; B_0 is uniform field in bending magnet; $f(s)$ is magnetic field form-factor, $f(s) = B(s)/B_0$.

In storage rings the ER measurement geometry is such that a superposition of radiation emitted at two adjacent bending magnet edges is observed (see Fig.1). Therefore in a number of papers [4] - [7] general attention was paid to the interference effect. On the other hand, the characteristics of interfering ER in many respects are defined by the

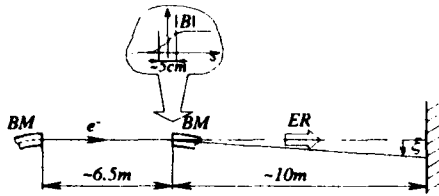


Figure 1. Edge radiation detection scheme.

peculiarities of radiation generated at single bending magnet edge. Relations (3) - (6) allow to calculate the characteristics of single bending magnet ER as well as the ER from two adjacent bending magnet edges.

The convergence of integrals in (5) is provided by the phase Φ ; therefore Eqs.(5) are not convenient for immediate computation. The integrals may be represented as

$$\int_{s_1}^{\infty} A \exp(i\Phi) ds \approx \int_{s_1}^{s_2} A \exp(i\Phi) ds + \left(\frac{A}{i\Phi'} + \frac{A'\Phi' - A\Phi''}{\Phi'^3} + \dots \right) \exp(i\Phi) \Big|_{s_2}^{s_1},$$

where A denotes pre-exponent factors; prime means differentiation with respect to s ; the series in braces is obtained through sequential integration by parts of the residuals

$$\int_{s_1}^{s_2} A \exp(i\Phi) ds \text{ and } \int_{s_2}^{\infty} A \exp(i\Phi) ds. \text{ The actual numerical}$$

integration limits ($-\infty < s_1 < s_2 < +\infty$) should be chosen to make the series effectively converge. The use of only a few terms of the series makes the computation much easier.

When computing the ER characteristics, the following parameters of the Siberia-2 storage ring were used: $\gamma = 5 \cdot 10^3$, $I = 100 \text{ mA}$, $|r_0| = 1960 \text{ cm}$. The function $B(s)$ was determined according to measurements performed in the Institute of Nuclear Physics (Novosibirsk).

In line with the results of computing the single bending

magnet ER for $\lambda > \lambda_c$, intensive peaks appear in the angular distribution of radiation. In terms of angles respective to straight section axis, the horizontal one ξ and vertical one ζ , the peaks are located at $\xi \cong \pm \gamma^{-1}$, $\zeta = 0$ for σ -component and at $\xi = 0$, $\zeta = \pm \gamma^{-1}$ for π -component (the origin of coordinates is set in the intersection of the electron trajectory and the magnet edge). This result correlates well with ER analysis at $\lambda \rightarrow \infty$ [6]. The peak intensity considerably exceeds the intensity of the standard SR at $\lambda \gg \lambda_c$. The ER peaks are symmetrical with respect to median plane at any wavelength, whereas the peak symmetry with respect to vertical plane appears only at $\lambda \gg \lambda_c$. Fig.2 shows the angular distributions of radiation at $\lambda = 400 \text{ nm}$. In this figure the standard SR corresponds to large horizontal angle ($\xi \gg \gamma^{-1}$).

There are not peaks at $\lambda < \lambda_c$ and the radiation intensity at small angles ($|\xi| < 2\gamma^{-1}$) is below the level of standard SR.

Intensity distributions of the $\lambda = 400 \text{ nm}$ radiation generated at two adjacent bending magnet edges are presented in Fig.3. Geometrical parameters used in the computation are shown in Fig.1. The combined intensity distribution comprises the system of concentric interference circles well-known in optics.

III. PECULIARITIES OF ER FORMATION IN LONG-WAVELENGTH REGION

In this chapter some approximate formulae revealing the mechanism of the ER formation at $\lambda > \lambda_c$, are given.

At large distance from the emission region transversal components of the vector \vec{n} may be treated as coincident with observation angles, $n_x \cong \xi$, $n_z \cong \zeta$. In terms of it, the relations (3) - (5) may be modified as

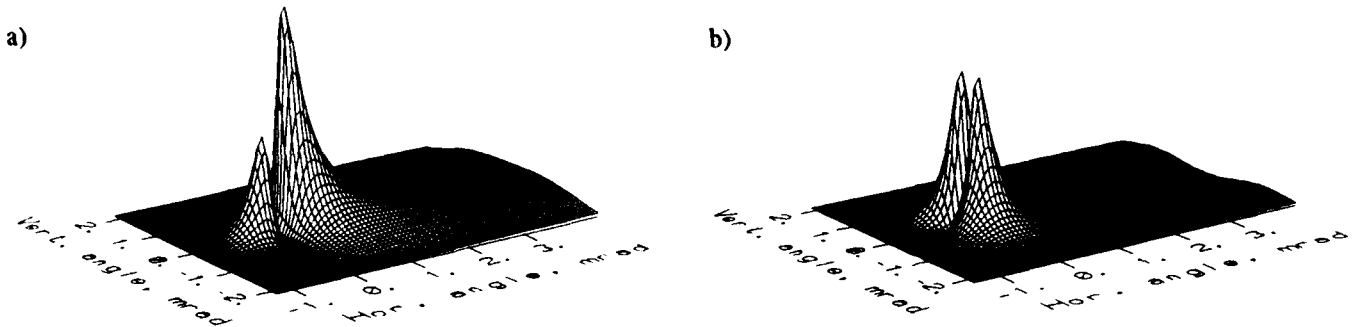


Figure 2. Angular distribution of single bending magnet edge radiation at $\lambda = 400 \text{ nm}$: a) σ -component; b) π -component.

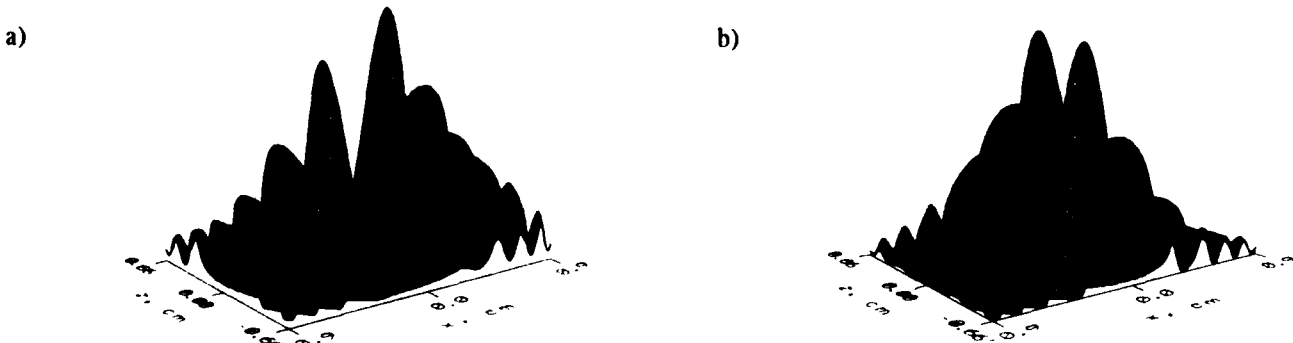


Figure 3. Intensity distribution of interfering edge radiation at $\lambda = 400 \text{ nm}$: a) σ -component; b) π -component.

$$\frac{dN}{d\lambda d\Omega(d\lambda/\lambda)} \approx \frac{\alpha \gamma^2 l}{\pi^2 e} |F_\sigma \bar{e}_\sigma + F_\pi \bar{e}_\pi|^2; \quad (7)$$

$$\begin{cases} F_\sigma = \frac{i\pi}{\lambda \gamma} \int_{-\infty}^{+\infty} (\xi - \beta_x) \exp(i\Phi) ds; \\ F_\pi = -\frac{i\pi \zeta}{\lambda \gamma} \int_{-\infty}^{+\infty} \exp(i\Phi) ds; \end{cases} \quad (8)$$

$$\Phi \approx \frac{\pi}{\lambda} [(\gamma^{-2} + \zeta^2 + \xi^2)s - 2\xi \int_0^s \beta_x ds' + \int_0^s \beta_x^2 ds']. \quad (9)$$

To analyze the convergence of integrals (8), one should consider the structure of the phase Φ . Characteristic length unit may be easily found for each term of the phase in Eq.(9) (the term's contribution to Φ value is of the order of one at this length). The length units are the following at $|\xi| \sim 1$, $|\zeta| \sim 1$: $\lambda \gamma^2$ for the first term, $(\lambda r_0 |\gamma|)^{1/2}$ and $(\lambda r_0 |\beta|^2)^{1/3}$ for the second and third terms respectively. Therewith, it is obtainable from the λ_c definition that at $\lambda > \lambda_c$: $\lambda \gamma^2 > (4\pi/3)^{1/2} (\lambda r_0 |\gamma|)^{1/2} > (4\pi/3)^{2/3} (\lambda r_0 |\beta|^2)^{1/3} > (4\pi/3) |\beta| \gamma^{-1}$; the relation signs become opposite at $\lambda < \lambda_c$.

Let the characteristic length of magnetic field dropping be Δs . Analysis of Eqs. (8), (9) reveals that if Δs is much smaller than the smallest length unit of the phase (i.e., in the trajectory region Δs the phase change is much less than one), Δs value can be ignored in (8), (9) and the magnetic field can be regarded as the step-changing one,

$$f(s) = \Theta(s), \quad (10)$$

where $\Theta(s)$ is the step function.

One can find from the outlined considerations that in the case $\Delta s \ll r_0 |\gamma|^{-1}$ Eq. (10) is reasonable approximation for $\lambda > \lambda_c$; also, it is reasonable for $\lambda < \lambda_c$ if $\Delta s \ll \lambda \gamma^2$. Otherwise, in the case $\Delta s > r_0 |\gamma|^{-1}$ Eq.(10) may be reasonable only at $\lambda > \lambda_c$, if the following relation takes place: $\Delta s \ll (\lambda r_0 |\beta|^2)^{1/3}$.

It is worth mentioning that the requirement $\Delta s \ll (\lambda r_0 |\beta|^2)^{1/3}$ is much weaker than the $\Delta s \ll r_0 |\gamma|^{-1}$ one being traditionally used [6] as the restriction on application of the approximation (10). In the case of the Siberia-2 storage ring $\Delta s > r_0 |\gamma|^{-1}$, but values Δs and $(\lambda r_0 |\beta|^2)^{1/3}$ are comparable even in VUV wavelength region.

In the $\lambda \gg \lambda_c$ limit the following asymptotic expansion of Eqs. (8) is valid in approximation (10) for $|\xi| \sim 1$, $|\zeta| \sim 1$:

$$\begin{cases} |F_\sigma|^2 \approx \frac{\gamma^2 \xi^2}{[1 + \gamma^2 \xi^2 + \gamma^2 \zeta^2]^2} + 2c_1 p^{1/3} \frac{\gamma \xi}{1 + \gamma^2 \xi^2 + \gamma^2 \zeta^2} + (c_1^2 + c_2^2) p^{2/3}; \\ |F_\pi|^2 \approx \frac{\gamma^2 \zeta^2}{[1 + \gamma^2 \xi^2 + \gamma^2 \zeta^2]^2} - 2c_3 p^{2/3} \frac{\gamma^2 \zeta^2}{1 + \gamma^2 \xi^2 + \gamma^2 \zeta^2}, \end{cases} \quad (13)$$

where $p = \pi r_0 / (\lambda \gamma^3) = 3\lambda_c / (4\lambda)$; c_1, c_2, c_3 are the constants: $c_1 = \pi / (3^{1/3} \Gamma(1/3))$, $c_2 = \pi / (3^{2/3} \Gamma(1/3))$, $c_3 = \pi / (3^{7/6} \Gamma(1/3))$; Γ is the gamma-function.

Approximate relations (13) qualitatively agree with the computation results (Fig.2). As may be seen from Eqs. (13), the angular positions and widths of the ER peaks no longer depend on λ at $\lambda \gg \lambda_c$. Moreover, it is obtainable that for ER

$$\left. \frac{dN}{d\lambda d\Omega(d\lambda/\lambda)} \right|_{\lambda \rightarrow \infty} \rightarrow \frac{\alpha \gamma^2 l}{4\pi^2 e}, \text{ while for the SR } \left. \frac{dN}{d\lambda d\Omega(d\lambda/\lambda)} \right|_{\lambda \rightarrow \infty} \rightarrow 0.$$

This makes the ER similar to the soft bremsstrahlung possessing the corresponding feature [10].

By these means, the ER peaks at $\lambda > \lambda_c$ arise in consequence of the sudden change in magnetic field, from nil to the constant value, along the electron trajectory in high energy electron storage rings. The peaks appear in the case that the effective trajectory region of forming the radiation is larger than the length of magnetic field dropping.

For the radiation emitted at two adjacent bending magnet edges, the following relations may be easily obtained from Eqs. (8), (9), (10) at $\lambda \gg \lambda_c$:

$$\begin{cases} |F_\sigma| \approx \frac{4\gamma^2 \xi^2}{(1 + \gamma^2 \xi^2 + \gamma^2 \zeta^2)^2} \sin^2 \left[\frac{\pi l}{2\lambda} (\gamma^{-2} + \xi^2 + \zeta^2) \right]; \\ |F_\pi| \approx \frac{4\gamma^2 \zeta^2}{(1 + \gamma^2 \xi^2 + \gamma^2 \zeta^2)^2} \sin^2 \left[\frac{\pi l}{2\lambda} (\gamma^{-2} + \xi^2 + \zeta^2) \right], \end{cases} \quad (14)$$

where l is inter-magnet distance. Eqs. (14) are valid for far removed detector ($r^* \gg l$) and small angles ($|\xi| \sim 1$, $|\zeta| \sim 1$). The similar relations were obtained in [6] at somewhat different modeling assumption. The qualitative agreement of Eqs. (14) and computation results (Fig. 3) is evident.

In line with Eqs. (14), the highest amplification of the ER due to the interference takes place at $l = \lambda \gamma^2 (2n-1)/2$, $n=1,2,\dots$. This amplification is unattainable at $l < \lambda \gamma^2/2$, and in the limit $l \ll \lambda \gamma^2$ the ER is suppressed.

IV. SUMMARY

The ER features at $\lambda > \lambda_c$ in high-energy electron storage rings look very attractive to SR users in spectral range extending from VUV to IR. The electron beam diagnostics seems to represent a distinct promising application of the edge radiation [9].

We would like to thank Dr. V.N.Kogchuganov (Institute of Nuclear Physics, Novosibirsk) for the results of bending magnet field measurements he kindly presented.

Contact e-mail address: chubar@ksrs.msk.su

V. REFERENCES

- [1]. R.Coisson, "Angular-spectral distribution and polarization of synchrotron radiation from a "short" magnet", *Phys.Rev.A*, Vol.20, No.2, 524(1979).
- [2]. R.Bossart, J.Bosser *et al.*, "Observation of visible synchrotron radiation emitted by a high-energy proton beam at the edge of a magnetic field", *Nucl. Instr. and Meth.*, Vol.164, No.2, 375 (1979).
- [3]. N.V.Smolyakov, "Interference accompanying radiation from protons in the field of dipole magnets in a synchrotron", *Sov. Phys. Tech. Phys.*, Vol.30, No.3, 291 (1985).
- [4]. M.M.Nikitin, A.F.Medvedev, M.B.Moiseyev, V.Ya.Epp, "Interference of synchrotron radiation", *Sov. Phys. JETP*, Vol.52, 388 (1980).
- [5]. M.M.Nikitin, A.F.Medvedev, M.B.Moiseyev, "Synchrotron radiation from ends of straight-linear interval", *IEEE Trans. Nucl. Sci.*, Vol. NS-28, No.3, 3130 (1981).
- [6]. E.G.Bessonov, "On strange and quasi-undulator radiation", *Sov. Phys. Tech. Phys.*, Vol.28, 837 (1983).
- [7]. Yu.A.Bashmakov, "Synchrotron radiation of electrons in the edge magnetic fields of storage rings", *Rev. Sci. Instrum.*, Vol.63, No.1, 343 (1992).
- [8]. O.V.Chubar, N.V.Smolyakov, "VUV range edge radiation in electron storage rings", *J. Optics (Paris)*, Vol.24, No.1 (1993).
- [9]. O.V.Chubar, E.S.Masunov, these proceedings.
- [10]. L.D.Landau, E.M.Lifshits, *The Classical Theory of Fields*, Pergamon, Oxford (1971).

THE RADIATION EMISSION BY A HIGH ENERGY ELECTRON-POSITRON PAIR AND ULTRARELATIVISTIC HYDROGEN-LIKE ATOM MOVING THROUGH THICK TARGET.

A.V.Koshelkin

Theoretical Physics Department, Moscow Engineering Physics Institute
Kashirskoye sh., 31, Moscow 115409, Russia.

1. INTRODUCTION.

We consider the radiation emission by a set of ultrarelativistic charged particles which undergo multiple elastic collisions with atoms of an amorphous scattering medium. The radiation emission by a high energy electron-positron pair and an ultrarelativistic hydrogen-like atom in the medium is investigated theoretically in detail.

2. STATEMENT OF THE PROBLEM.

We consider the system of charged ultrarelativistic ($E_\mu \gg m_\mu$) classically fast ($E_\mu \gg \omega$ is a radiation frequency) particles which do not interact with each other (E_μ , m_μ , and e_μ are the energy, the mass and the charge of the particle, $\hbar=c=1$). These particles enter a homogeneous, semi-infinite, amorphous scattering medium. In the initial period, $t=0$, particles are located in the points \vec{r}_{01} , \vec{r}_{02} , ..., \vec{r}_{0N} , and are the velocity \vec{v}_{01} , \vec{v}_{02} , ..., \vec{v}_{0N} , equal to $v_0 = [1 - (m_\mu/E_\mu)^2]^{1/2}$. They are directed under the $|\Delta_\mu| \ll$

$\ll 1$ ($\mu=1, \dots, N$ - is the number of the particles) angle to the \vec{e}_z vector (vector of the inward normal to the boundary of the medium) at $t=0$. Let the characteristic longitudinal size of the beam L_b be such that $L_b v_0^{-1} \ll T$ (the time when the particles move in the medium).

3. SOLUTION OF THE PROBLEM.

The spectral-angular distribution of the energy emitted by these particles is

$$\frac{d\mathcal{E}_{\omega\vec{k}}}{d\omega d\Omega_{\vec{k}}} = \frac{\omega^2}{2\pi^2} \operatorname{Re} \sum_{\mu, \nu=1}^N e_\mu e_\nu \int_0^\tau \int_0^\omega dt d\tau \cdot \quad (1)$$

$$[\vec{n} \times \vec{v}_\mu] \cdot [\vec{n} \times \vec{v}_\nu] \cdot \exp\{-i\omega\tau + i\vec{k} \cdot (\vec{r}_\mu - \vec{r}_\nu + \vec{r}_{0\mu} - \vec{r}_{0\nu})\},$$

\vec{k} is the wave vector of the radiation field, $d\Omega_{\vec{k}}$ is an element of solid angle in the direction $\vec{n} = \vec{k}/k = \vec{k}/\omega$, $\vec{r}_\mu = \vec{r}_\mu(t+\tau)$, $\vec{v}_\mu = \vec{v}_\mu(t+\tau)$, $\vec{r}_\nu = \vec{r}_\nu(t)$, $\vec{v}_\nu = \vec{v}_\nu(t)$ are coordinates and velocities of the particles at the time $t+\tau$ and t respectively,

τ is the time scale of the radiation formation (the coherence time), and the t is the time at which the radiation is emitted.

To calculate the observed spectral distribution of the emission energy of the particles in the medium, $dE_\omega/d\omega$, we must average expression (1) over all possible trajectories of the particles in the scattering matter [1]. To solve this problem it is necessary to find [2] two-time distribution function of the particles in a scattering medium. In the case of ultrarelativistic classically fast particles the solution of the problem is determined by the Fourier component of this function

$$F_k(\vec{v}_\mu, \vec{v}_\nu, t, \tau):$$

$$\frac{dE_\omega}{d\omega} = \frac{\omega^2}{2\pi^2} \text{Re} \sum_{\mu, \nu=1}^N e_\mu e_\nu \int d\Omega_\mu d\vec{v}_\mu d\vec{v}_\nu \int_0^\tau dt \int_0^\tau d\tau$$

$$[\vec{n}_\mu \times \vec{v}_\mu] \cdot [\vec{n}_\nu \times \vec{v}_\nu] \cdot \exp\{-i\omega\tau + i\vec{k} \cdot (\vec{r}_\mu - \vec{r}_\nu +$$

$$- \vec{r}_{0\mu} - \vec{r}_{0\nu})\} \cdot F_k(\vec{r}_\mu, \vec{v}_\nu, t, \tau)$$

The function $F_k(\vec{v}_\mu, \vec{v}_\nu, t, \tau)$ satisfies to the following equations and the initial

conditions [2]:

$$\frac{\partial F_k(t, \tau)}{\partial \tau} - i\vec{k} \cdot \vec{v}_\mu(\vec{\eta}) \cdot F_k(t, \tau) =$$

$$= \alpha_\mu^2 \frac{q}{4} \cdot \frac{\partial^2 F_k(t, \tau)}{\partial \vec{\eta}^2}$$

$$\frac{\partial F_k(t, 0)}{\partial t} - i\vec{k} \cdot (\vec{v}_\mu(\vec{\eta}) - \vec{v}_\nu(\vec{\phi})) F_k(t, 0) =$$

$$= \frac{q}{4} \cdot \left[\frac{\alpha_\mu \partial}{\partial \vec{\eta}} + \frac{\alpha_\nu \partial}{\partial \vec{\phi}} \right]^2 F_k(t, 0)$$

$$F_k(0, 0) = \delta(\vec{\eta} - \vec{\Delta}_\mu) \cdot \delta(\vec{\phi} - \vec{\Delta}_\nu) \cdot$$

$$\cdot \exp[i\vec{k} \cdot (\vec{r}_{0\mu} - \vec{r}_{0\nu})],$$

$$\alpha_\mu = U_\mu(\vec{g}) \cdot E \cdot E_\mu^{-1} \cdot U(\vec{g}),$$

where q is the average square of multiple scattering angle for a positron per unit of path [3],

$U_\mu(g)$; E_μ ; $U(g)$; E correspond to the Fourier component of the potential of interaction with the atom of a medium and the energy for the particles which number is μ and for the positron respectively; $\vec{\eta}$ and $\vec{\phi}$ the angle vectors which are connected with $\vec{v}_\mu(\vec{\eta})$ and $\vec{v}_\nu(\vec{\phi})$ by the

ordinary formulae of the theory of multiple scattering in a amorphous medium [3].

4.RESULTS.

The theory of radiation emission by the set of nonidentical particles which are scattered multiple elastic in a amorphous medium is developed. The spectral-angular distribution of the emission energy by these particles is obtained.

The emission by an ultrarelativistic electron-positron pair ($-x_{\text{positron}} = x_{\text{electron}} = -1$) in a scattering medium is researched in detail. We have shown that the interference of waves emitted by the electron and by the positron leads to the suppression of the intensity of the emission energy at long wave frequency range while at shortwave frequency region the interference effects is negligible and the value of the emission energy is proportional to the number of the irradiating particles. We show that under the certain conditions the emission spectrum of the electron-positron pair has overbending point which is situated on the frequencies in order of qE^2m^{-2} . It is shown that the angular distribution of the emission energy of the

electron-positron pair has a maximum which is on the emission angles $\theta_k \cong (qT)^{1/2}$.

We consider the radiation emission by a hydrogen-like atom in a "strong" scattering medium.

We show that under the certain conditions ($q_n \leq q$; $Z_n^2 \ll (q/q_n)^{1/2}$, where q_n and Z_n are the average square of multiple scattering angle per unit path and the charge of the core for hydrogen-like atom) the spectral distribution of the emission energy by this atom has step-like view. The width and the height of the "step" depend sufficiently on the charge and on the mass of the core of the emitting hydrogen-like atom.

REFERENCES.

- 1.A.B.Migdal, Phys.Rev., 103, 1811 (1956).
- 2.A.V.Koshelkin. Zh. Eksp.Teor.Fiz. (Sov. JETP) 100, 1724-1738 (1991).
- 3.N.P.Kalashnikov, V.S.Remizovich, M.I.Ryazanov, Collisions of Fast Charged Particles in Solids, Gordon and Breach Science Publishers, New York, 1985.

BREMSSTRAHLUNG BY THE BUNCH OF ULTRARELATIVISTIC CHARGED PARTICLES INTO A THICK TARGET.

A.V.Koshelkin

Theoretical Physics Department, Moscow Engineering Physics Institute
Moscow 115409, Russia.

1. INTRODUCTION.

Bremsstrahlung of a system of classically fast charged particles which do not interact with each other but which do undergo multiple elastic scattering by randomly positioned atoms of the medium is studied. We derived the spectrum of the bremsstrahlung of such particles through a systematic kinetic analysis of radiation process in the medium. It is shown that the spectral distribution of the emission energy of the bremsstrahlung depends significantly on both the characteristics of the scattering of the particles in the medium and the parameters characterizing the initial set of the particles.

2. STATEMENT OF THE PROBLEM.

We consider the system of charged ultrarelativistic ($E \gg m$) classically fast ($E \gg \hbar\omega$ is a radiation frequency) particles which do not interact with each other (E , m , and e are the energy, the mass and the charge of the particle, $\hbar=c=1$). These particles enter a homogeneous,

semi-infinite, amorphous scattering medium. In the initial period, $t=0$, particles are located in the points $\vec{r}_{o1}, \vec{r}_{o2}, \dots, \vec{r}_{oN}$, and are the velocity $\vec{v}_{o1}, \vec{v}_{o2}, \dots, \vec{v}_{oN}$, equal to $v_o = [1 - (m/E)^2]^{1/2}$ and they are directed under the $|\vec{\Delta}_\mu| \ll 1$ ($\mu=1, \dots, N$ - is the number of the particles) angle to the \vec{e}_z vector (vector of the inward normal to the boundary of the medium). Let the characteristic longitudinal size of the beam L_b be such that $L_b v_o^{-1} \ll T$ (the time when the particles move in the medium).

3. SOLUTION OF THE PROBLEM.

The spectral distribution of the energy emitted by these particles is

$$\frac{d\varepsilon_\omega}{d\omega} = \frac{e^2 \omega^2}{2\pi^2} \operatorname{Re} \sum_{\mu, \nu=1}^N \int d\Omega_{\vec{k}} \int_0^\tau \int_0^\omega dt \int d\tau [\vec{h}_x \vec{v}_\mu] \cdot [\vec{h}_x \vec{v}_\nu] \cdot \exp\{-i\omega\tau + i\vec{k} \cdot (\vec{r}_\mu - \vec{r}_\nu + \vec{r}_{o\mu} - \vec{r}_{o\nu})\}, \quad (1)$$

\vec{k} is the wave vector of the radiation field, $d\Omega_{\vec{k}}$ is an element of solid angle in the direction

$\vec{R} = R/k = R/\omega$, $\vec{r}_\mu = \vec{r}_\mu(t+\tau)$, $\vec{v}_\mu = \vec{v}_\mu(t+\tau)$, condition [2]:

$\vec{r}_\nu = \vec{r}_\nu(t)$, $\vec{v}_\nu = \vec{v}_\nu(t)$ are coordinates and velocities of the particles at the time $t+\tau$ and t respectively, τ is the time scale of the radiation formation (the coherence time), and the t is the time at which the radiation is emitted.

To calculate the observed spectral distribution of the emission energy of the particles in the medium, $dE_\omega/d\omega$, we must average expression (1) over all possible trajectories of the particles in the scattering matter [1]. To solve this problem it is necessary to find [2] two-time distribution function of the particles in a scattering medium. In the case of ultrarelativistic classically fast particles the solution of the problem is determined by the Fourier component of this function

$F_k(\vec{v}_\mu, \vec{v}_\nu, t, \tau)$:

$$\frac{dE_\omega}{d\omega} = \frac{e^2 \omega^2}{2\pi^2} \text{Re} \sum_{\mu, \nu=1}^N \int d\Omega_\mu d\vec{v}_\mu d\vec{v}_\nu \cdot \int dt \int d\tau$$

$$[\vec{n} \times \vec{v}_\mu] \cdot [\vec{n} \times \vec{v}_\nu] \cdot \exp\{-i\omega\tau + i\vec{k} \cdot (\vec{r}_\mu - \vec{r}_\nu + \vec{r}_{0\mu} - \vec{r}_{0\nu})\} \cdot F_k(\vec{v}_\mu, \vec{v}_\nu, t, \tau)$$

The function $F_k(\vec{v}_\mu, \vec{v}_\nu, t, \tau)$ satisfies to the following equations and the initial

$$\frac{\partial F_k(t, \tau)}{\partial \tau} - i\vec{k} \cdot \vec{v}_\mu(\vec{\eta}) \cdot F_k(t, \tau) =$$

$$= \frac{q}{4} \cdot \frac{\partial^2 F_k(t, \tau)}{\partial \vec{\eta}^2}$$

$$\frac{\partial F_k(t, 0)}{\partial t} - i\vec{k} \cdot (\vec{v}_\mu(\vec{\eta}) - \vec{v}_\nu(\vec{\phi})) F_k(t, 0) =$$

$$= \frac{q}{4} \cdot \left[\frac{\partial}{\partial \vec{\eta}} + \frac{\partial}{\partial \vec{\phi}} \right]^2 F_k(t, 0)$$

$$F_k(0, 0) = \delta(\vec{\eta} - \vec{\Delta}_\mu) \cdot \delta(\vec{\phi} - \vec{\Delta}_\nu) \cdot$$

$$\cdot \exp[i\vec{k} \cdot (\vec{r}_{0\mu} - \vec{r}_{0\nu})],$$

where q is the average square of multiple scattering angle per unit of path [3], $\vec{\eta}$ and $\vec{\phi}$ the angle vectors which are connected with $\vec{v}_\mu(\vec{\eta})$ and $\vec{v}_\nu(\vec{\phi})$ by the ordinary formulae of the theory of multiple scattering in a amorphous medium [3].

4. RESULTS

We have constructed a consistent kinetic theory for the radiation emission by a system of

classically fast noninteracting charged particles which undergo multiple elastic collisions in a scattering matter. We have found the spectral distribution of the emission energy from such particles. The obtained spectrum depends strongly both on the parameters of the scattering medium, and on the characteristics of the initial system of the particles.

We have studied in detail the emission by the beam of identical particles. It is shown in this case that the spectral distribution of the emission energy has at least one extremum in contradiction to the situation of an individual particle [1] when the emission spectrum is a monotonic function from emission frequency. If the pulse beam of identical particles takes place then the extremum is a maximum. Moreover if the width of the initial beam D is such that the condition $qD\xi^{-3} \ll \xi \cdot (qT)^{-1/2} \ll 1$ holds, the maximum of bremsstrahlung energy spectrum is a plateau with a width on the order $D^{-1}(qT)^{-1/2}$. The ratio of $(dE_\omega/d\omega)_{\max}$ to the background level $((dE_\omega/d\omega)_0 = 2e^2 qT/3\pi\xi^3)$ is approximately equal to N , the number of emitting particles. As the parameter $qD\xi^{-3}$ increases

$qD\xi^{-3} \leq \xi \cdot (qT)^{-1/2} \ll 1$ the plateau convert into "strict" maximum. As before, we have $(dE_\omega/d\omega)_{\max} \cdot (dE_\omega/d\omega)_0^{-1} \cong N$. If we have $qD\xi^{-3} \gg 1$, then the quantities $(dE_\omega/d\omega)_{\max}$ and $(dE_\omega/d\omega)_0$ become approximately equal to 1.

The bremsstrahlung by a highly anisotropic point source of ultrarelativistic particles is investigated. We show that in this case the spectral distribution of the emission energy has a maximum. The last is unique. The shape of the maximum as well as the magnitude of the emission energy depend strongly both on the value $X_0 \ll 1$ of cone vertex angle which includes the initial velocities of the particles and on the scattering properties of a scattering medium.

REFERENCES.

1. A.B. Migdal, Phys. Rev., 103, 1811 (1956).
2. A.V. Koshelkin. Zh. Eksp. Teor. Fiz. (Sov. JETP) 100, 1724-1738 (1991).
3. N.P. Kalashnikov, V.S. Remizovich, M.I. Ryazanov, Collisions of Fast Charged Particles in Solids, Gordon and Breach Science Publishers, New York, 1985.

Construction and Commissioning of the SRRC Storage Ring

Y.C. Liu^{a)}, J.R. Chen^{b)}, and C.C. Kuo

Synchrotron Radiation Research Center

No 1. R&D Rd VI, Hsinchu Science-Based Industrial Park, Hsinchu, Taiwan, R.O.C.

^{a)}Department of Physics, National Tsing-Hua University, Hsinchu, Taiwan, R.O.C.

^{b)}also Institute of Nuclear Science, National Tsing-Hua University, Hsinchu, Taiwan, R.O.C.

Abstract

A 1.3 GeV synchrotron radiation storage ring is currently under construction at SRRC. The installation activities had gone through about one year, from March 1992 to March 1993. The commissioning of the booster to storage ring (BTS) transfer line started from August 1992 soon after a 1.3 GeV synchrotron booster injector had been delivered in July 1992. The intensive activities of the storage ring beam tests began in April 1993. We had stored beam in April and some machine parameters have been measured

There are 18 dipole magnets powered in series and four families of quadrupole magnets, each with 12 magnets powered in series. The chromaticities are corrected with 2 families of 24 sextupoles. In addition, there are 24 horizontal and 30 vertical corrector for orbit correction. Several skew quadrupoles were installed. The magnets were designed, constructed, measured, and analyzed with care. All magnets installed in the ring are within acceptable tolerances in terms of the multipole errors and integrated fundamental field errors[1,6]. The pulsed magnets such as septum and kickers also meet specification.

I. INTRODUCTION

To provide continuous, tunable and bright VUV and soft x-ray light sources for the researches ranging over physics, chemistry, biology, medicine, etc., a third generation dedicated synchrotron radiation facility was established in Taiwan. The SRRC accelerating system consists of a 50 MeV e^- linac, a 1.3 GeV synchrotron booster[1,2], a 70 m long BTS transfer line[1,3], and a 1.3 GeV storage ring[1,4,5]. Up to now, the storage ring is in the commissioning stage. The stored beam was accomplished in April. We expect the designed current of 200 mA will be achieved soon after the vacuum vessels are baked in June. The design parameters and components are described in Sec. II. Installation activities are given in Sec. III, and finally the early commissioning results are shown in Sec. IV.

II. DESIGN PARAMETERS AND COMPONENT

A. Lattice

The lattice structure is a combined-function triple-bend-achromat (TBA) type with 6-fold symmetry[1,4,5]. There are six dispersionless long straight sections, each 6 m, for the accommodation of injection elements, RF cavities, undulators and wigglers. Some major parameters are listed as follows:

Energy	1.3 GeV
Circumference	120 m
Natural emittance	19 nm-rad
Tune ν_x/ν_y	7.18/4.13
Momentum compaction	0.00678

The dynamic aperture of the single particle dynamics and collective effects of the particle beam were studied in detail. The acceptable tolerances of the magnetic properties and alignment errors were given accordingly[1,3,4].

B. Magnet and Power Supplies

C. Vacuum

The most of the vacuum chambers were made of aluminum. Cares were taken as to provide ultrahigh vacuum, low impedance environments. The clearance of the material, tapering of the chamber, shielding of the bellows, the thermal load, deformation, rigidity and flexibility of the supporting frame, etc., were seriously considered to meet the requirements. Up to now, without turning on ion pumps, the vacuum pressure was about 10^{-8} Torr without beam and about 10^{-7} Torr with a few mA stored beam current. The bake-out of the vacuum chamber will be done in June. After turning on ion pumps, we expect the vacuum pressure can reach 10^{-11} Torr without beam.

D. RF system

In one of the long straight sections, two Doris I type cavities purchased from DESY were installed. Each cavity is with 60 kW maximum RF power provided by individual transmitter. The system can accelerate 1.3 GeV electron beam of more than 200 mA current in the presence of insertion devices. The nominal RF frequency is 499.654 MHz.

E. Survey and Alignment

Extremely tight requirements on the alignment of the magnet, especially quadrupole magnets in the ring in the transverse directions are necessary in order to reduced closed orbit distortions. The acceptable alignment errors in both planes are 0.15 mm rms and rotation errors are 0.5 mrad rms. The quadrupole magnets were prealigned in the girders and then moved into the tunnel. The final results of the alignments for dipoles and quadrupoles were 0.14 mm rms and 0.12 mm rms in the horizontal and vertical plane, respectively. The tilt errors was 0.2 mrad rms in dipoles and 0.06 mrad in quadrupoles. For sextupoles, the results were 0.20 mm rms and 0.15 mm rms in the horizontal and vertical plane, respectively. All were within acceptable tolerances.

The measured closed orbit distortions were consistent with the simulated results and will be described in Sec IV.

F. Beam Diagnostics

There are seven destructive screen monitors for first turn beam observations in the ring. Two were used for injection launching adjustment. The number of button type beam position monitors (BPM) are 47 in total. Two stripline electrodes are also installed. One excitation electrode station can be used for the tune measurements as well as for the transverse instability damping. The fast beam signal can also be measured using fast current transformer and precise beam current are obtained from DCCT. Some other elements such as scraper, photon light monitor, etc., are described in ref.[7].

G. Control and Operation[8]

VAX workstations running VMS operating system are used for control computer system. Between database and the sub-system devices, several intelligent local controllers (ILC) were implemented. A friendly graphical user interface (GUI) operation panel was developed. The radiation safety interlock system is a self-protected subsystem and will be linked to the central control system.

III. INSTALLATION

The installation task of such a rather complicated system in deed need well planning and full cooperation among all sub-systems. A cell of 20 m long was installed in the shop by the end of 1991. We gained a lot of practical experience. The installation of the BTS started in March 1992 and completed in September 1992 except the septum magnet. The installation of the ring began from March 1992. By May 1992, the cabling work and magnet stands installation were finished. Power supplies and all magnets except pulsed magnets were installed by October 1992. Finally, the vacuum system including diagnostics elements, RF cavities, and RF low level system were installed by the end of 1993. In February 1993, we passed the full power tests of magnet power supplies and the ring chambers were connected as a closed form by then. The installation of the RF high power transmitter and four kicker pulsers were finished in March 1993. The alignment of the magnets reached the acceptable level in March. In the meantime, the subsystem tests with control computer and developments of the control system software were under way. The subsystem tests with beam were taken whenever necessary. The storage ring commissioning started in April and we had stored beam very soon.

IV. COMMISSIONING

A. milestones

The BTS beam tests started in August 1992 when the lower level section of the transfer line was completed. By September, the beam reached septum entrance point. After the pulsed magnets had been installed, the beam passed

through septum and injected into ring in January 1993. In February 23, the first beam revolution for the first time was accomplished using one kicker for on-axis injection. The beam was observed in each screen monitor without using any corrector. It showed that many sub-systems were basically in good condition. The beam sizes in the screen were consistent with the theoretical values. The alignment errors proved to be barely acceptable in the horizontal plane and extremely good in the vertical plane. Due to the long half-sine base width of 1.6 μ s (400 ns revolution time) of the kicker pulse and only one kicker available, the second turn observation was impossible. Soon after all four kicker were available in April, we have several hundred beam revolutions using a few correctors without RF power and beam was captured on April 13 after turning on RF power with minor adjustments of the magnet settings and RF frequency. The stored beam current was a few mA and beam lifetime was a few minutes under vacuum pressure of 10^{-7} Torr.

B. Closed Orbit

We performed the closed orbit measurements soon after the BPM system was operative and the orbit was corrected down to 0.5 mm and 0.3 mm rms in the horizontal and vertical plane, respectively, using on-line application programs[9]. Further suppression of the orbit distortions will be obtained as soon as the BPM system is well calibrated. The preliminary results of the closed orbit measurements without using corrector are fairly consistent with simulation results using existing alignment data. Figure 1 show the closed orbit before and after correction, and simulated results as well.

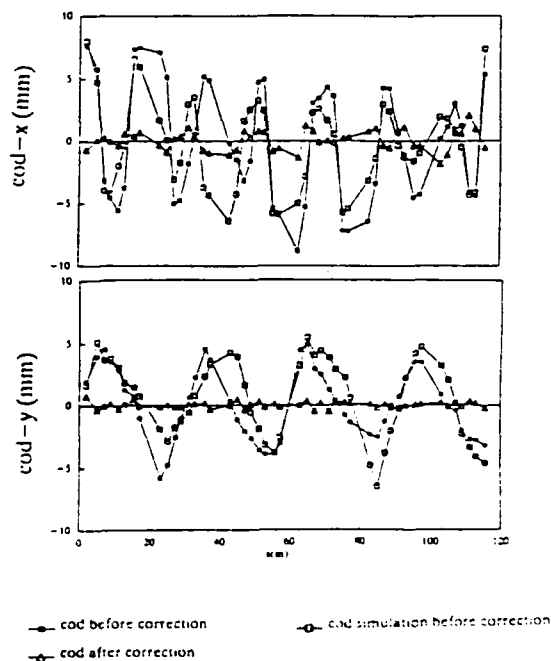


Figure 1. Closed orbit distortions before and after correction in both planes and the simulated orbit before correction are shown.

C. Synchrotron Tune and Momentum Compaction Factor

The electron beam signal was picked-up with a stripline electrode and analyzed with a spectrum analyzer. Synchrotron sideband was measured and the momentum compaction factor was extracted. The measured momentum compaction factor was 0.00663 and in good agreement with the design value of 0.00678.

D. Betatron Tune and Betatron Function

The turn-by-turn signal from one BPM electrode was FFT analyzed after electron beam was kicked using one of the kicker magnet with about 1 mrad in the horizontal plane. The betatron sidebands were observed. The measured tunes were $\nu_x=7.142$ with nominal sextupole setting and corrected orbit. The vertical tune $\nu_y=4.170$ was obtained from the orbit changes with vertical corrector setting. We will measure the tunes in both planes using the tracking generator and spectrum analyser system in the near future. Optimum working point will be searched soon. By varying the quadrupole strength and measuring the horizontal tune shift, we obtained the averaged betatron function at each family of quadrupole location. The results were in good agreement with the design value. From the orbit change with vertical corrector, it was found the vertical betatron function was in agreement with the design value[9].

E. Dispersion Function and Chromaticity

The dispersion function was deduced from the orbit difference with different RF frequency setting. In Figure 2 the measured horizontal dispersion functions as well as the design values are shown. The vertical dispersion is very small. The horizontal chromaticity was measured by observing the tune shift with the RF frequency change. It was found that the horizontal chromaticity was corrected to zero with nominal sextupole strengths.

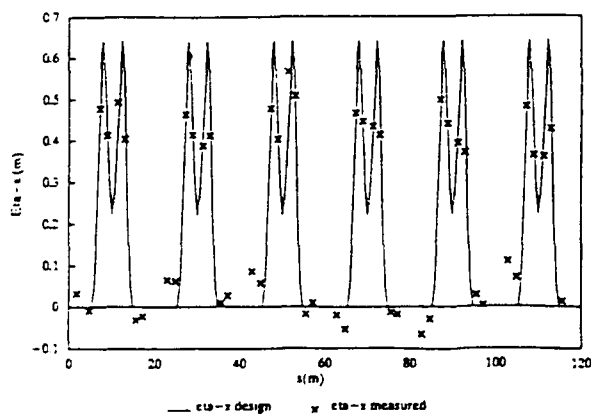


Figure 2. The measured and design dispersion function.

F. Beam Energy and Circumference

The injected beam energy was defined by varying the magnet setting and RF frequency. From the closed orbit distortions, one can obtain the energy deviation from the magnet settings. It was found that the injected beam was 1.3033 GeV. The accuracy is about 0.05 %. The circumference was less than 0.5 mm from the survey and alignment data, which was consistent with the closed orbit data.

G. Bunch Length

The electron beam signal picked-up with stripline electrode was analyzed with a fast digital sampling oscilloscope to obtain bunch length. The measured bunch length σ_t of 42 ps at 300 kV RF peak voltage was in good agreement with the theoretical value of 37 ps.

V. ACKNOWLEDGMENT

The authors would like to thank all SRRC personnel who involved in the design, construction and commissioning of such a delicate complex. Thanks are extended to outside advisers for their invaluable guidance, advice and suggestions.

VI. REFERENCES

- [1] "SRRC design handbook", SRRC, 1991
- [2] K.K. Lin, K.T. Hsu, and T.S. Ueng, "Measurement on the SRRC 1.3 GeV Electron Booster Synchrotron Operation Parameters and the Ramping Behaviour", this proceeding.
- [3] M.H. Wang, C.C. Kuo, and C.S. Hsue, "The booster to Storage Ring Transport Line for SRRC", IEEE PAC91, vol. 5, pp. 2697-2699.
- [4] C.S. Hsue, C.C. Kuo, J.C. Lee, and M.H. Wang, "Lattice Design of the SRRC 1.3 GeV Storage Ring", IEEE PAC91, Vol. 4, pp. 2670-2672.
- [5] C.C. Kuo, C.S. Hsue, J.C. Lee, M.H. Wang, and H.P. Chang, "Beam Dynamics of the SRRC 1.3 GeV Storage Ring", IEEE PAC91, vol. 4, pp. 2667-2669.
- [6] C.H. Chang, H.C. Liu, G.J. Hwang, "Design and Performance of the dipole magnet for SRRC Storage Ring", this proceeding.
- [7] G. Jan, K.T. Hsu, "Diagnostic Instrumentation System for the SRRC 1.3 GeV Synchrotron Radiation Light Source", this proceeding.
- [8] J.S. Chen, C.J. Wang, S.J. Chen, and G.J. Jan, "A Graphical User-Interface Control System at SRRC", this proceeding.
- [9] P. Chang, C.H. Chang, C.C. Kuo, M.H. Wang, J.C. Lee, J.Y. Fan, H.J. Tasi, and C.S. Hsue, "Machine Physics Application Program for Control, Commissioning and Error Findings for Storage Rings", this proceeding.

Commissioning a Second Superconducting Wiggler in the Daresbury SRS

M W Poole, J A Clarke, P D Quinn, S L Smith, V P Suller and L A Welbourne

SERC Daresbury Laboratory, Daresbury, Warrington, WA4 4AD, UK.

Abstract

A second superconducting wiggler magnet has now been installed on the SRS at Daresbury. This three pole device generates a field of 6 T on the beam axis and greatly extends the range of useful synchrotron radiation on the light source. The magnet properties are briefly reviewed, together with the necessary and major modifications that have had to be made to the SRS to accommodate this powerful addition to the lattice. Initial commissioning trials in the Spring of 1993 are described and a comparison made with expected influence on the beam behaviour. Successful operation has been demonstrated, including simultaneous excitation with the earlier 5 T wiggler.

I. INTRODUCTION

Since 1982 a 5 T superconducting wavelength shifter (W1) has been an important operating feature on the 2 GeV electron storage ring at Daresbury. Because the SRS has a simple FODO lattice such an insertion device has an inevitable effect on the beam emittance in addition to a significant vertical tune shift. Predicted and measured effects were compared in an earlier paper [1] and a method of focussing compensation using an active current shunt on an adjacent quadrupole has also been described [2].

Following this success in extending the available range of photon energies a second wiggler project was initiated and the outline design has been presented [3]. The magnet (W2) was specified to have a field strength of 6 T and to provide a usable radiation fan of 50 mrad to five experimental stations on a new beam line. Extrapolation of the 5 T design to the higher field suggested an unacceptable increase in source dimensions and so a new design was pursued in order to minimise the emittance blow up, particularly since the two superconducting devices were required to operate simultaneously.

II. SRS MODIFICATIONS

The SRS has been operated for users since 1981 and a large number of its sixteen bending magnets are now being exploited for beam lines. Few straight sections of the FODO lattice remain empty and the experimental area around the ring is also very congested. This has forced the selection of a straight immediately upstream of the injection area and the resultant beam line from the new wiggler must therefore cross the transfer line from the booster synchrotron injector. The septum magnet power supply has had to be relocated to avoid the emerging radiation beam and the opportunity has also been taken to redesign the septum itself.

In order to provide sufficient space for a realistic wiggler design it has been necessary to remove components from the

straight and the most important is one of the four D-sextupoles used for chromaticity correction. Unfortunately both numerical simulations and subsequent experiments have confirmed that a breach of the present four-fold symmetry cannot be permitted since the dynamic aperture collapses [4]. This behaviour is due to the influence of resonance lines up to at least fifth order.

All four sextupoles have therefore been moved by one straight and this has only been made possible by a complete redesign of the injection kickers to make room in their straight sections. Together with a series of other major changes this necessitated a long shutdown of several months duration and the SRS did not return to full operational status until the second half of 1992. Following cryogenic commissioning the first tests of the new wiggler with beam became possible in the early part of this year.

III. WIGGLER MAGNET DETAILS

A contract for the detailed design and construction [5] of the superconducting magnet was placed with Oxford Instruments. The specification was based on a conservative design philosophy that would guarantee performance, with a warm bore avoiding unnecessary complications at the interface with adjoining UHV vessels. Use of magnetic steel poles generates additional field and also assists in reacting against the large forces arising from the central pole coils. These main coils are a racetrack geometry wound from rectangular Nb-Ti conductor and have a graded current density over three sections to exploit the varying field across them. The chosen coil design ensures that a comfortable calculated temperature margin of about 2 K exists. The main coil power supply needs to be rated to 700 A but an 80 A supply is more than sufficient for trim purposes on the small coils around the end poles.

The magnet has a relatively short central pole, sufficient only to provide the required field level over about 70 mm of beam orbit, but in contrast the end poles have been stretched to the maximum permitted by the available overall length in the straight of just over 1 m. The reason for this geometry is to reduce the cubic field integral, a requirement explained in the next section.

The cryogenic design is quite conventional and includes a nitrogen screen. There is provision for *in situ* bakeout of the beam pipe to 150 °C. The normal mode of operation is to provide liquid helium from a closed cycle refrigerator that also drives the first wiggler, but it is also possible to bulk fill if this supply is interrupted. The current leads are a major source of heat leakage, but despite this the helium usage is less than 5 liquid litres per hour even at 6 T and the magnet endurance exceeds 20 hours.

The magnetic field specification is an onerous one. The quadratic field integral must not exceed $5.5 \text{ T}^2\text{-m}$ and the (modular) cubic one must be less than $22 \text{ T}^3\text{-m}$. A first integral of 0.04 mT-m ensures an acceptably small closed orbit ripple but this can only be achieved by feeding a small trim coil on the end poles from a separate supply. Because the SRS is injected at a lower energy of 600 MeV the residual integral with the magnet switched off must be even smaller and the anticipated remanent level of over 1 mT-m will need to be corrected or removed.

Even the measurement of such small terms is a considerable challenge: for example the dipole field integral at full excitation is less than 3×10^{-5} of the modular one. An accurate rotating coil system was developed by the manufacturer and this could also be scanned laterally to monitor the transverse harmonics. These measurements confirmed that the magnet did meet its design specification at all field levels, although the resultant trim currents unexpectedly demanded a bipolar power supply. Supplementary data from a Hall plate gave measured second and third integrals of $4.8 \text{ T}^2\text{-m}$ and $20 \text{ T}^3\text{-m}$.

IV. BEAM STUDIES

The initial trials before delivery had demonstrated excellent training with a first quench at 4.8 T and only three more to reach full field; high ramp rate tests thereafter only induced one further quench (at 6.1 T). After its delivery to Daresbury the magnet was set up in a temporary position outside the ring tunnel and briefly energised to full field to confirm there had been no transit damage. No quenches have been experienced in the ring and beam tests were able to commence once power supply checks had been completed.

A first trial at 600 MeV with the coil excitations set to values established during the magnet measurements showed beam loss due to horizontal orbit movements even at fields below 0.5 T and the trim was therefore adjusted empirically. At higher field levels there was good agreement and it seems that this minor discrepancy might have been associated with remanent field behaviour. With optimised trim settings resultant rms orbit displacements below 0.2 mm could easily be achieved up to the full 6 T . However with the magnet switched off orbit variations of up to 1 mm were in evidence, but these remanence effects have been readily compensated by small changes to the injection orbit steers. An alternative is to remove the unwanted field and suitable techniques have been established, employing either a proven degaussing cycle or a bucking current in the trim coils.

Initially the tune shift was corrected by a global change to the D-quadrupole family and routine 6 T operation was then established. It has previously been confirmed that for lattice calculations a three pole wiggler can be accurately simulated by a hard edge model [1] if the appropriate field integrals are used, with measured and predicted tune shifts on the first 5 T wiggler in excellent agreement [2]. Table 1 summarises the more important parameter changes caused by both the old and the new wigglers and it can be seen that the tune shifts are almost equal despite the increase of field to 6 T . All of the data

is for the present SRS working point ($Q_r = 6.15$, $Q_v = 3.35$) and the W1 shift is therefore somewhat greater than reported in reference [1].

Table 1
Calculated SRS Parameters at 2 GeV

	W1/W2 Off	W1 On	W2 On	W1/W2 On
Vertical tune shift		0.06	0.062	
Max. vert. beta (m)	11.7	12.5	12.7	13.8
Hor. damp. time (ms)	5.3	4.9	4.8	4.5
Energy spread (10^{-4})	7.2	7.6	7.9	8.2
Hor. emittance (nm-rad)	105	134	155	186
Overvoltage ($T_q = 100 \text{ h}$)	2.73	2.80	2.88	2.90

With global correction there remains a very strong beta beating with increases up to 40% but the data in Table 1 assumes the use of the local quadrupole shunt correction scheme which leaves only a small ripple. Identical active shunt designs can be used for each wiggler and these are rated well above the predicted requirement of about 55 A . The measured vertical tune shift is presented in Figure 1 and does exhibit the expected quadratic dependence on wiggler field level. However the best fit to this data has a coefficient about 20% below the computed value so that clearly the model is inaccurate, a surprising result in view of the success of a similar model with the first wiggler.

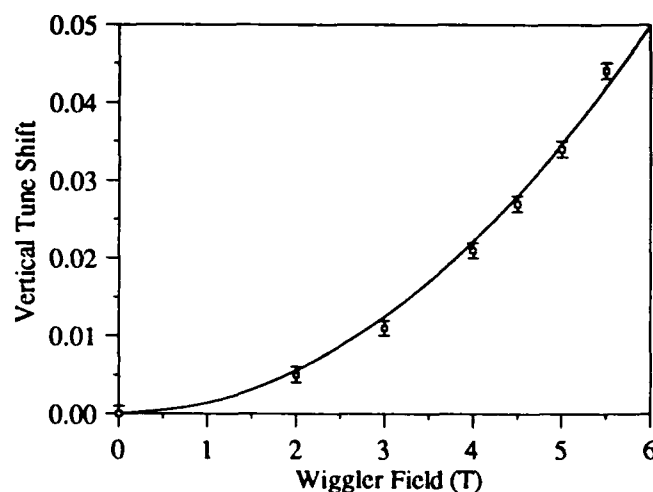


Figure 1. Measured variation of vertical tune with wiggler excitation, with best quadratic fit.

Preliminary checks of the beta modulation confirm that the residual ripple after compensation is less than 10% but it is known that the SRS does have unexpected beta variations

from cell to cell that might explain the discrepancy. A secondary check is to examine the experimental values of quadrupole shunt current and these are plotted in Figure 2.

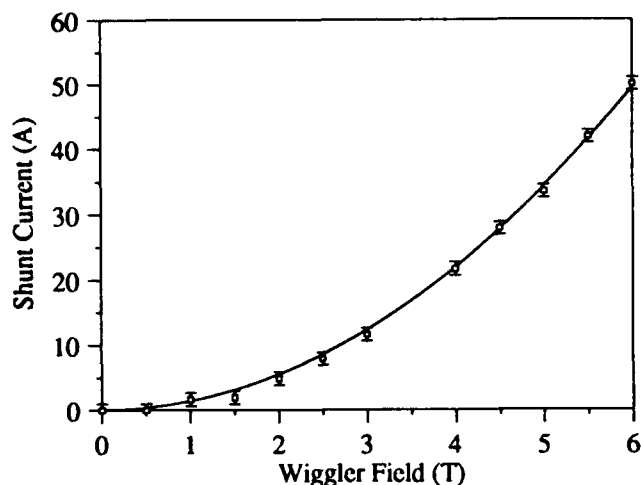


Figure 2. Best quadratic fit to values of D-quadrupole shunt current for fixed vertical tune with wiggler excitation.

These shunt values hold the tune steady to better than 0.002 and exhibit the correct functional dependence. Moreover the figure of 50 A at 6 T is to be compared with a prediction of 56 A, a difference of about 10 % in the demanded 1.36 T/m gradient reduction of the D-quadrupole in the wiggler straight. This suggests that at least half of the difference between the actual tune shift of 0.050 and the computed value of 0.062 is due to an overall reduction of the beta at the locations of both the wiggler and the quadrupole, with the remainder perhaps arising from a difference in their relative betas.

The finite dispersion of the SRS lattice at the location of the wiggler implies that there will be an inevitable emittance increase when the magnet is energised, to first order proportional to the cubic field integral [3]. As shown in Table 1 the horizontal emittance is expected to grow by almost 50 % for the measured $\int |B'|^3 dl$ of 20 T³-m. This would produce a noticeable increase of the source dimensions and in the vertical plane the beta variation is also important. Such effects, but with a smaller emittance change, have previously been encountered on the first wiggler [6] and that magnet also appeared to induce a reduced overall coupling between the planes. For the new wiggler few measurements have yet been taken but there does seem to be negligible change of vertical source dimensions. The magnitude of the horizontal blowup (10 %) is similar but more linear with field than on the first device.

The additional radiation loss of 24 keV per turn from the second wiggler, together with the need for a higher overvoltage factor, demands a 25 % enhancement of the rf power delivered to the accelerating cavities but this is well within the capacity of the installed system. Other implications, such as reduced damping times and bunch length, are too small to be noteworthy. Finally it can be reported that during the last

period of tests both wigglers were energised simultaneously and their tune shifts fully compensated. As anticipated from Table 1 the horizontal source dimensions then increased significantly, but no unexpected beam effects were encountered.

V. CONCLUSIONS

A 6 T superconducting wiggler magnet has been successfully designed, constructed and installed in the SRS. Its field properties have been carefully measured to high accuracy and lattice simulations have been compared with recent operating experience.

This second wiggler can now be used routinely with high current beams and few commissioning tasks remain. The only significant anomaly so far discovered is a vertical betatron tune shift much smaller than expected, probably due to a non-ideal beta function distribution around the storage ring. Following planned commissioning of the port and beam line scheduled user beams will commence in August 1993 when the SRS will become the first light source with two such insertion devices.

VI. REFERENCES

- [1] V P Suller et al, "SRS Behaviour with a Superconducting 5 Tesla Wiggler Insertion," *IEEE Trans. Nucl. Sci.* NS-30, 3127 (1983).
- [2] M W Poole et al, "Wiggler Tune Shift Compensation on the Daresbury SRS," *Conference Record of the 1989 IEEE Particle Accelerator Conference*, Vol. 1, pp. 208-210.
- [3] M W Poole et al, "A Second Superconducting Wiggler Magnet for the Daresbury SRS," *Conference Record of the 1989 IEEE Particle Accelerator Conference*, Vol. 2, pp. 1250-1252.
- [4] M W Poole et al, "Dynamic Aperture, Tune Space Characteristics and Sextupole Distribution in the Daresbury SRS," *Proc. 2nd Euro. Part. Accel. Conf.*, Vol. 2, pp. 1533-1535 (1990).
- [5] J S H Ross and K D Smith, "Design and Manufacture of a 6 T Wiggler Magnet for the Daresbury SRS," *Rev. Sci. Instr.* Vol. 63, No 1 (Part IIA), pp. 309-312 (1992).
- [6] J A Clarke et al, these proceedings.

Conference Author Index

A

Aas, T. 2967
 Abbott, S. 3748
 Abe, I. 3087
 Abrahamsson, K. 1735
 Acerbi, E. 1524
 Ackerman, G. D. 3169
 Adam, S. R. 3639
 Adams, F. P. 829, 832, 835, 1039
 Adamski, J. 2967
 Adler, R. J. 1306
 Adney, J. 3745
 Adolphsen, C. 414, 417, 543, 2019, 3342
 af Ugglas, M. 1735
 Ahrens, L. 3633
 Ahrens, L. A. 3763
 Aiello, G. R. 2322, 2367
 Aiello, R. 2118
 Aizawa, K. 1468
 Akai, K. 769, 992, 3450
 Akbari, H. 2492
 Akchurin, N. 32
 Akemoto, M. 1309
 Akre, J. 1572
 Alberti, S. 2656, 2690
 Aleksandrov, A. 3243
 Alessandria, F. 1524
 Alexandrov, V. 2042
 Alimov, A. S. 2059
 Allen, C. K. 3145, 3648
 Allen, L. J. 1689, 1691
 Allen, S. L. 1551, 1554
 Alley, R. 3045, 3047
 Alley, R. K. 2978, 3027, 3036
 Allison, P. 3172
 Allison, S. 1884, 2106
 Alton, G. D. 2979
 Amidei, D. 2199
 Amiranoff, F. 2450
 Amiry, A. 173
 Anami, S. 590, 1163, 1193, 1416, 3087
 Anamkath, H. 608, 611
 Anashin, V. 3876
 Anashin, V. V. 2022
 Anders, A. 1390
 Anders, S. 1390
 Anderson, D. 3745
 Anderson, D. E. 1354
 Anderson, K. 3096, 3163
 Anderson, R. R. 2919
 Anderson, S. 1421
 Anderson, T. 2835
 Andler, G. 1735
 Ando, M. 1468
 Andreev, V. A. 3121, 3124
 Andreev, V. G. 980
 Andreev, V. V. 297
 Anerella, M. 2744, 2766, 2790
 Annala, G. 3808
 Annala, J. 354
 Anne, R. 1789, 1792

Anthouard, P. 670, 697
 Antoine, C. 798
 Antropov, V. 2042
 Aoki, T. 2039
 Aoyagi, H. 2978, 3036
 Arai, S. 1780, 1783, 1786
 Arakaki, Y. 41
 Araki, M. 1518
 Arbique, G. 827, 3127
 Arbique, G. M. 2124, 2426, 2986
 Arbuzov, V. 1226
 Archie, C. N. 480
 Arcioni, P. 772, 1524, 1569
 Arinaga, M. 2292, 3552
 Arkhipov, O. 2042
 Arnaudon, L. 44
 Arnold, D. E. 989
 Arnold, N. D. 1957, 1960
 Artiomov, A. S. 2166, 2169
 Artru, X. 3093
 Asami, A. 3087
 Askew, D. R. 1336
 Assang, A. 2187
 Asseev, A. A. 315, 318, 320, 322, 324
 Assmann, R. 44
 Åström, J. 2068
 Atkins, W. H. 1669
 Aurerbach, E. H. 1872
 Ausset, P. 858
 Austin, R. H. 2970
 Averbukh, J. 824
 Averill, R. 1372, 2054, 2331, 2868, 2871, 2874, 3851
 Awaji, N. 1515, 1518
 Ayvazian, H. 1750
 Azuma, O. 1202

B

Baartman, R. 3330
 Baba, H. 959
 Babenko, E. 2423
 Baccaglioni, G. 1524
 Bachman, D. A. 3190
 Bachmor, R. 1178
 Badano, L. 32
 Bagge, L. 1735
 Baglin, V. 2720
 Bai, X. 3237
 Baier, T. 3093
 Baier, V. N. 3093
 Baik, K. H. 679
 Bailey, J. 3757
 Bailey, R. 1937, 2001, 2013
 Baiod, R. 2826
 Baishev, I. S. 3109, 3772
 Bak, J. 581
 Bak, J. S. 593
 Balabin, A. I. 3675
 Balandin, V. 441, 444, 477
 Ball, M. 29, 224, 227, 420, 2289, 3745

Ball, M. S. 2243, 3536
 Balleyguier, P. 1136
 Baltrusaitis, R. M. 2400
 Band, A. 2240
 Bane, K. 543, 1445, 3240, 3375
 Bane, K. L. 596
 Bane, K. L. F. 3339, 3342, 3432
 Baptiste, K. 1238
 Baranovsky, A. E. 682
 Barbier, M. M. 3102
 Bardy, J. 670, 697
 Barklow, T. 2019
 Barletta, B. 2638
 Barletta, W. 2010, 3836
 Barletta, W. A. 775, 1524, 1988, 3817
 Barlow, D. 1703
 Barlow, D. B. 2480
 Barnard, J. 703, 706
 Barnard, J. J. 712, 715, 733, 3612
 Barnes, M. J. 1148, 1181, 1330, 3402
 Barnes, P. 763, 886, 889, 892, 918, 921, 977, 995, 1399
 Barov, N. 561, 2617, 2623, 3216
 Barr, D. S. 2163
 Barranco-Luque, M. 2956
 Barry, W. 2109
 Barsotti, E., Jr. 3294
 Barsotti, E. L. 2531
 Bartalucci, S. 778
 Bartelson, L. 918, 1342
 Barth, W. 3142
 Barts, T. 3444
 Bar'yakhtar, V. 1480
 Bassetti, M. 2048
 Batchelor, K. 2486, 3000, 3012
 Batishchev, O. V. 2620
 Batskikh, G. 2717
 Batskikh, G. I. 980
 Batygin, Y. K. 50
 Bazzani, A. 273
 Be, S. H. 3845
 Bearzatto, C. 1184
 Beaufait, J. 3103
 Beckert, K. 1645, 1738
 Beebe, E. 1735
 Beechy, D. 2118
 Behrsing, G. 83
 Belk, A. 1937
 Belkacem, A. 3751
 Bell, R. A. 1039, 2010
 Bellomo, G. 775, 1001, 1524
 Belloni, F. 3839
 Belomestnykh, S. 1226
 Belomestnykh, S. A. 3669
 Belomestnykh, S. E. 2022
 Beloshitsky, P. 2042
 Belov, V. 2042
 Belov, V. P. 3820, 3822
 Belova, N. G. 664, 3546
 Bemes, M. 2967
 Benaroya, R. 3857
 Benes, S. J. 1957
 Benesch, J. 1016

- Benesch, J. F. 748, 781, 947
 Bengtsson, J. 567, 1488, 2272, 3312
 Benke, T. 1706
 Bennett, G. 2070
 Bennett, L. F. 667
 Bennett, M. 3748
 Bennett, P. 1916
 Benson, S. 3663
 Benvenuti, C. 806
 Ben-Zvi, I. 849, 1439, 1602, 2486, 2962, 3000, 3012
 Berg, J. S. 291
 Berg, W. 605
 Bergher, M. 3708
 Bergmann, U. 2145
 Bernard, D. 2450
 Bernard, M. 694
 Bernard, P. 806
 Bernardini, M. 3842
 Beroud, Y. 784
 Bertrand, P. 1789
 Bertsche, K. J. 1727
 Berz, M. 155, 164
 Bethel, S. 2967
 Bethke, S. 2172
 Betto, A. 1220
 Bhandari, R. 381
 Bharadwaj, V. 2228, 3806
 Bhat, C. M. 405, 787, 1223
 Biagini, M. E. 2048
 Bickley, M. 1835, 1895
 Bieniosek, F. 3096
 Bieniosek, F. M. 3163
 Bieri, R. L. 742
 Bieth, C. 1789
 Bijleveld, J. 2343
 Billan, J. 68
 Billen, J. 1712
 Billen, J. H. 790, 793
 Billquist, P. 1694
 Birattari, C. 1524
 Birnbaum, I. 2420
 Birnbaum, I. A. 3012
 Biscardi, R. 1419
 Biscari, C. 2048
 Bishop, D. 1148, 1181
 Bisoffi, G. 1747
 Bisognano, J. 512, 3663
 Bisognano, J. J. 179, 2364, 2929, 3246, 3473, 3515
 Bixio, A. 1063
 Bizek, H. 1485
 Blaker, G. 1300
 Blasche, K. 357, 3736
 Blaskiewicz, M. 3321, 3324
 Blell, U. 357
 Bleser, E. 3766
 Bleser, E. J. 3763
 Blewett, J. P. 2546
 Blind, B. 56
 Blockus, D. 2172
 Bloess, D. 806
 Blokland, W. 2528
 Blondel, A. 44
 Bloom, E. 3084
 Bluem, H. 1451
 Blum, E. 3579
 Blum, E. B. 1599, 2246, 2307
 Blumberg, L. N. 3579
 Bobin, J. L. 3202
 Bobyleva, L. 2042
 Boden, A. 2051
 Boers, J. E. 327
 Boeuf, J. P. 3039
 Bogacz, S. A. 74, 77, 2587
 Bogatov, N. 2769
 Bogaty, J. M. 1694
 Böge, M. 460
 Bogert, D. 3793
 Bohl, T. 2001
 Bohn, C. L. 838, 1715, 3666
 Boiteux, J. P. 2358
 Bollinger, L. M. 1694
 Bolme, G. O. 1669, 3118
 Bondarev, B. I. 980
 Boni, R. 611, 778
 Bonifacio, R. 1524
 Bonin, B. 798
 Bonnafond, C. 670, 697, 2115
 Bordoley, M. 1867, 2313
 Bordry, F. 44, 2001
 Bordua, M. 3748
 Borer, J. 2103, 2492
 Borisov, O. N. 518
 Borland, M. 285, 2028, 3015
 Bosch, F. 1645
 Bosch, R. A. 3369
 Boscolo, I. 1524
 Bosotti, A. 1524
 Bossert, R. 2769
 Bossingham, R. 3751
 Botlo, M. 128
 Botman, J. I. M. 1072, 1820, 2062, 2065, 2892, 2927, 3423, 3645
 Bourg, F. 2997
 Bourgarel, M. P. 1789
 Bourianoff, G. 128, 203, 515
 Boussard, D. 2376, 2379
 Bovet, C. 2492
 Bowling, B. A. 1895, 2298, 2477
 Bowling, S. 1669
 Boyce, R. 1445, 1608
 Boyce, R. F. 543
 Boyd, J. K. 463
 Boyes, J. 667
 Bozoki, E. 105, 2284, 3636
 Brabson, B. 29, 224, 227, 420
 Bracco, R. 1587
 Bradley, S. 2054
 Brandeberry, F. 824, 880
 Brandt, D. 3429
 Branson, B. H. 1220
 Brau, C. A. 1448
 Brauer, S. O. 1217
 Braun, A. 354
 Bravar, A. 32
 Brennan, J. M. 1241, 3763
 Brennan, M. 2286
 Bres, M. 1184
 Bressan, M. 772, 1524, 1569
 Bressler, V. E. 2736, 2950
 Briand, P. 2997
 Brianti, G. 3917
 Bridges, J. 285, 1013
 Bridges, J. F. 766, 910, 913, 1157, 1408, 1906
 Briegel, C. 1914
 Briggs, R. J. 3922
 Brindza, P. 3103
 Brinkgreve, P. 2892
 Brinkmann, R. 3742
 Brittain, D. L. 1169
 Broggi, F. 1524, 1569
 Brooks, T. 1154
 Broome, W. 1419
 Brouk, V. 2382
 Browman, A. 1683
 Browman, M. J. 3267
 Brown, B. 3757
 Brown, B. C. 351, 2829
 Brown, D. 2181
 Brown, D. J. 2664
 Brown, G. 2760
 Brown, I. 1390
 Brown, K. 384
 Brown, K. L. 333, 378
 Brown, N. 62
 Brown, P. 2358
 Brown, R. 2507, 3184
 Browne, M. 3045, 3047
 Brownman, M. J. 800
 Bru, B. 1789, 1792
 Brütsch, E. 2748
 Bruhwiler, D. L. 59, 3624
 Brumwell, F. 3757
 Brunelle, P. 1465
 Bruns, W. 904, 1133, 3714
 Bryant, H. 369
 Bu, S. 1411
 Buchanan, E. 3533
 Buda, S. 1419
 Budlong, J. 3533
 Budnick, J. 29, 224, 227, 420, 2865
 Budzko, A. 3642
 Budzko, A. V. 3784
 Builta, L. 3055
 Bull, J. 1369
 Buller, T. L. 1075
 Bulos, F. 3084
 Bultman, N. 1712
 Bulyak, E. 300, 1480
 Bulyak, E. V. 3512
 Buon, J. 469, 2513
 Burgett, W. 2731, 2757, 2763
 Burke, D. 2019
 Burke, D. L. 543
 Burkhardt, H. 2001
 Burnham, B. 2889
 Burns, A. 2103, 2301
 Burns, M. 3055
 Burns, M. J. 2944
 Burtin, G. 2495
 Burton, R. J. 829, 832
 Busch, G. 2967
 Bushuyev, A. 1226
 Butterworth, A. 1903
 Büttig, H. 1477
 Byrd, J. 2349, 3315
 Byrd, J. M. 2109, 3318, 3408
 Byrne, T. 567

C

- Cai, S. Y. 3075
 Cai, Y. 203, 2781
 Calabrese, R. 3243
 Calame, J. P. 2667, 2670
 Calderon, M. 3836
 Callahan, D. A. 730, 733, 3660
 Callin, R. 543, 620, 1106
 Calloway, D. 2172
 Calo, A. 3127
 Calvert, J. 1160, 3748
 Camas, J. 2498
 Cameron, P. 1166
 Cameron, P. R. 2328
 Campbell, B. 1402
 Campisi, I. E. 1115, 1220
 Capista, D. 2252
 Caporaso, G. 703
 Caporaso, G. J. 712, 715
 Cappi, R. 3570
 Cardito, M. 2154
 Cardman, L. S. 3246
 Carey, D. C. 47
 Carlé, P. 1735
 Carlini, R. 2136, 3103
 Carlisle, L. 1718
 Carlson, R. L. 661
 Carlsten, B. 2675
 Carlsten, B. E. 2537, 2664
 Carmel, Y. 2714
 Carpenter, J. 3757
 Carr, R. 1596
 Carroll, F. E. 1448
 Carron, G. 1066, 3426
 Carson, J. 2769
 Carter, A. 2054
 Carwardine, J. 1709
 Carwardine, J. A. 3210
 Caryotakis, G. 543, 1106, 1259
 Casella, R. 1277
 Caspers, F. 2157, 3381
 Cassel, R. 543, 1318
 Castellano, M. 573
 Castro, P. 2103
 Catani, L. 573
 Caussyn, D. 3745
 Caussyn, D. D. 29, 224, 227, 420, 3536
 Cavallari, G. 806
 Celata, C. M. 724, 3748
 Cerniglia, P. 2310
 Chabert, A. 1789
 Chae, Y. 282
 Chae, Y. C. 182
 Chamberlain, O. 2172
 Champion, M. 809, 918, 1127
 Champion, M. S. 989
 Chan, C. F. 3157, 3160
 Chan, K. D. C. 2970
 Chanel, M. 2157
 Chang, C. H. 1943, 2886
 Chang, C. R. 122, 812, 3585
 Chang, H. P. 1943
 Chang, J. S. 1345
 Channell, P. J. 38
 Chao, A. 3781
 Chao, A. W. 29, 224, 227, 420, 3345, 3348
 Chao, Y. 587
 Chapman, L. 1914, 2249
 Chappelier, J. 158, 161
 Charruau, G. 858
 Chase, B. E. 2355
 Chattopadhyay, S. 83, 2638, 3042
 Chautard, F. 267, 2720
 Chechetenko, V. 1480
 Chehab, R. 3093
 Chel, S. 855
 Chen, B. 3345, 3348
 Chen, C. 2656
 Chen, H. 2151
 Chen, J. 1095
 Chen, J. R. 1635
 Chen, J. S. 1878
 Chen, P. 617, 2638
 Chen, S. 200, 3255
 Chen, S. C. 2575, 2696, 2699
 Chen, S. J. 1878
 Chen, T. 3479
 Chen, Y. 303, 718, 2841
 Chen, Y. J. 703, 706
 Cheng, J. 2659, 2667
 Cheng, W. 221
 Cheng, Y. 1262, 1393, 2269
 Chepurinov, A. S. 2059
 Chesnokov, Y. A. 454
 Chester, N. 2826
 Chester, N. S. 2823
 Chevallier, M. 3093
 Chiaveri, E. 806, 849
 Chida, K. 41
 Chimenti, V. 3906
 Chin, J. 1572, 1584
 Chin, Y. H. 3347, 3414
 Ching, C. H. 3351
 Chiou, T. C. 2635
 Chirkov, P. 2769
 Chmielewski, A. G. 1890
 Cho, C. 2151
 Cho, M. 581, 1521
 Cho, M. H. 593, 1315
 Cho, Y. 399, 3757
 Cho, Y. S. 679
 Choi, B. H. 679, 3196
 Choi, J. 2516, 3273
 Choi, J.-Y. 3087, 3705
 Chojnacki, E. 815, 1844, 2596, 3061
 Chou, P. J. 3363
 Chou, W. 818, 2281, 3444, 3609, 3781, 3888
 Christensen, K. 1712, 2947
 Christiansen, C. F. 1098, 2139
 Christianson, M. 2757
 Chu, C. 306, 2841
 Chubar, O. V. 1626, 2474, 2510
 Chubarov, O. V. 2059
 Chugun, T. 2205
 Chung, K. H. 679, 3196
 Chung, Y. 188, 1814, 2112, 2263, 2266, 2275, 2304
 Chupp, W. W. 703, 3199
 Church, M. 330
 Chuvilo, I. V. 1675
 Ciapala, E. 1903, 2358
 Ciardullo, D. J. 1241
 Ciarlette, D. 285
 Ciarlette, D. J. 1814
 Cifarelli, F. 3099
 Ciullo, G. 3243
 Claborn, G. 2222
 Clark, D. 369, 3888
 Clark, D. J. 1724, 1727
 Clark, S. L. 543
 Clarke, J. A. 1494, 1638, 3594, 3672
 Claudet, S. 2956
 Claus, J. 2895
 Clay, W. 3888, 3891
 Clayton, C. 2976, 3003
 Clayton, C. E. 558, 2551, 3543
 Clayton, T. 1369, 2781
 Clément, M. 1363
 Clendenin, J. 3033
 Clendenin, J. E. 2978, 3027, 3036
 Clerc, G. 1184
 CLIC Study Group 540
 Clifft, B. E. 1694
 Cline, D. 2051, 2638
 Clout, P. 1801
 Clozza, A. 3906
 Coacolo, J. C. 3567
 Coadou, B. 798
 Cobb, J. K. 2838
 Codutti, A. 1587
 Cohen, S. 369
 Colby, E. 3021
 Colchester, R. J. 2495
 Cole, B. 128, 203
 Cole, M. 821, 3012
 Cole, R. 1669
 Coleman, P. 824
 Coleman, P. D. 1033, 1256, 3252
 Colestock, P. 3294
 Colestock, P. L. 3303, 3306, 3384, 3540
 Collet, G. J. 3030
 Collet, P. 1187
 Collier, P. 1937, 2001
 Collins, J. 29, 224, 227, 420
 Collins, J. P. 2823
 Colton, E. 3297
 Combs, C. 1703
 Combs, C. M. 846
 Conciauro, G. 1524, 1569
 Conde, M. E. 3042
 Condé, H. 1771
 Connolly, R. 1669
 Conte, M. 32, 438
 Conway, P. 2388
 Coombes, R. 2769
 Cooper, R. 3297
 Cooper, R. G. 2400
 Cooper, R. K. 3267
 Cooper, W. S. 3169
 Coosemans, W. 44
 Corbett, J. 173
 Corbett, W. J. 108, 114, 1483, 2275
 Cork, C. 1575
 Corlett, J. N. 2109, 3318, 3408, 3411
 Cornacchia, M. 173
 Cornelis, K. 2001, 3429

Cornelius, W. D. 2994
 Corredoura, P. 2370, 3240
 Corsini, R. 626, 1524
 Cottingame, W. B. 3118
 Courant, E. 3778
 Courant, E. D. 137
 Cover, R. 1605
 Craddock, W. 2638
 Crandall, K. R. 1042, 3585, 3657
 Crane, M. 1922, 1966
 Cravey, W. R. 739
 Crawford, A. 1223
 Crawford, C. 886, 918
 Crawford, C. A. 3540
 Crawford, J. F. 1771
 Crawford, K. 1925, 3757
 Crist, C. 2121
 Crist, C. E. 2124, 2130, 2426, 2456, 2501
 Crockford, G. 2504
 Crofford, M. 587
 Crofford, M. T. 2364
 Crosbie, E. 285, 1485
 Crosbie, E. A. 282, 506
 Crouch, R. 2199
 Cuevas, C. 1838, 3127
 Culwick, B. 1277
 Cuneo, M. E. 694
 Curbow, J. 941
 Curry, B. P. 375
 Curtin, M. 1154, 1244
 Cutler, R. 3509
 Cutler, R. I. 827, 1250

D

Dabrowski, J. 1274, 1855, 1858, 1861
 Daclon, F. 1378, 3842, 3873
 Dalesio, L. R. 1806
 D'Alsace, R. 1419
 Daly, R. 1960, 2142
 Damjanovich, R. 3175
 Damm, R. 1166
 Danared, H. 1735
 Danby, G. T. 2883
 Danilov, V. 3429, 3711
 Danly, B. G. 2575, 2656, 2690
 Dasbach, D. 1080
 Datte, P. 1703, 2118, 2483, 3127
 D'Auria, G. 953, 956, 1145
 D'Auria, J. M. 1641
 Dauvergne, J.-P. 2739
 Davidson, A. D. 1175
 Davis, K. 2967
 Davis, P. 561, 2976, 3003, 3216, 3543
 Davis, T. J. 2653, 2687
 Dawson, J. 2462
 Dawson, R. 1733
 Deadrick, F. 703
 Debiak, T. 821
 Debiak, T. W. 2420, 3193
 Decker, C. 2635
 Decker, F. 3582
 Decker, F.-J. 414, 2019, 2278, 2435, 2507, 3234, 3240, 3576

Decker, G. 188, 2196, 2263, 2275, 2304
 Decker, G. A. 1814
 Deckers, R. 1820
 DeFord, J. 3450
 Degen, C. M. 2310
 DeHaven, R. 1021, 1683
 Dehen, J. 3142
 Dehning, B. 44
 Deitinghoff, H. 3139, 3142
 de Jong, M. S. 829, 832, 835, 1039
 Dekkers, E. 2892
 de Lamare, J. 1318
 Delaunay, M. 2997
 Delayen, J. R. 288, 838, 1715, 3666
 Delchamps, S. W. 2769
 Delcourt, B. 2513
 Delhez, J. L. 1820, 2062, 2065, 3423
 Delikaris, D. 2739
 Dell, G. F. 171
 Delmere, C. 2492
 Delsart, P. 670, 697
 de Mascureau, J. 670, 697, 2115
 de Menezes, D. 858
 Demmel, E. 1178
 Demos, P. T. 829, 832
 Demroff, H. 2711
 Demroff, H. P. 2705, 2708
 Demsky, M. I. 682
 Deng, D. P. 1172
 Denney, P. 1154, 1669
 Denney, P. M. 1232, 2391
 Depaola, F. 1013
 Derenchuk, V. 29, 224, 227, 420, 3184
 de Rijk, G. 1937, 2001
 Deruyter, H. 543, 620, 907, 986, 1121
 Derwent, P. F. 2199
 De Salvo, L. 1524
 Desforges, B. 2001
 Despe, O. D. 1864
 Destler, W. W. 685
 Devin, A. 670, 697, 2115
 Devred, A. 2769
 deVries, G. J. 3169
 Dewa, H. 1697
 Dey, J. 405, 1223
 Diamond, W. T. 1381
 Dickey, C. 1339
 Didelez, J. P. 3093
 Didenko, A. A. 2022
 Dienel, S. 1477
 Dikansky, N. 3243
 Dikansky, N. S. 2022, 3684
 DiMarco, J. 2769
 DiMarco, J. N. 1021
 Di Massa, G. 2154
 Dinkel, J. 1357
 Dinova, K. 1620
 Diviaco, B. 1587, 1590, 1593
 Dmitrieva, I. 2769
 Do, S. H. 3196
 Dobeck, N. 587
 Doble, N. 1363
 Doi, M. 1783, 1786

Dolinsky, A. V. 3822
 Dolique, J.-M. 3567
 Dombeck, T. 2731, 2757, 2763
 Dombrowski, R. 2459
 Donahue, J. 369
 Donald, M. 131
 Dong, W. W. 1448
 Dooling, J. 1709
 Doolittle, L. R. 748
 Doose, C. 2802, 2805
 Doose, C. L. 2799
 Dorfman, J. M. 2010
 Dortwegt, R. 3857
 Douglas, D. 587, 1895
 Douglas, D. R. 584, 2929
 Dovbnya, A. 1480
 Dow, K. 2054, 2868
 Dow, K. A. 2935, 2938, 2941
 Dowell, D. 2967
 Dreher, K. 2748
 Drew, M. M. 2705
 Drobot, A. 3267
 Drozhdin, A. I. 1360, 3109, 3772
 Drury, M. 841
 Ducar, R. 2199
 Dugan, G. F. 3717
 Dunbar, A. 1166
 Dunn, A. 2199
 Dunnam, C. R. 578, 2394
 Dutt, S. 29, 224, 227, 267, 420, 3609
 Dutto, G. 2991
 Duval, M. 1789
 Dvornikov, V. A. 844
 Dwinell, R. 3748
 Dwyer, S. 2760
 D'Yachkov, M. 3330
 Dykes, D. M. 3594, 3672
 Dylla, H. F. 748, 3867
 Dymnikov, A. 206, 3618
 Dyshkant, A. 454

E

Early, R. 620, 2025
 Early, R. A. 2880
 East, G. 29, 224, 227, 420
 Eaton, L. 1154
 Eaton, L. E. 2391
 Ebihara, K. 673
 Eden, J. R. 3485
 Edwards, D. A. 134
 Edwards, H. 918
 Edwards, H. T. 537
 Efimov, S. 300, 1480, 2057
 Egan-Krieger, G. V. 1887
 Ehrlich, R. 995
 Ehrnstén, K. 1735
 Eickhoff, H. 357, 1645, 1738
 Eidelman, Y. 450
 Einfeld, D. 149, 152, 1477
 Eisen, N. 2076, 2352
 Ekdahl, C. A. 2400
 Elayi, A. 3093
 Elia, R. 2172
 Elkins, J. 1160
 Elkonin, B. V. 849

Elliot, T. S. 2705
 Elliott, T. S. 2708, 2711
 Ellis, S. 1718
 Ellison, J. 423
 Ellison, J. A. 387, 3588
 Ellison, M. 29, 224, 227, 420
 Ellison, M. J. 3536
 Ellison, T. 29, 224, 420, 3745
 Ellison, T. J. P. 2243, 2289, 3536
 Elmgren, K. 1771
 Elsener, K. 1363
 Emery, L. 2266, 3360
 Emma, P. 116, 429, 635, 2019, 2160
 Emma, P. J. 98, 100
 Emoto, T. 546
 Endo, K. 1291
 Enegren, T. 846, 877, 941, 1703
 Enge, H. 2868
 Engels, O. 3139
 Engström, A. 1735
 Enomoto, A. 546, 590, 2516, 3087, 3705
 Eppley, K. 1106
 Eppley, K. R. 1190
 Erdman, K. 1733
 Erdt, W. K. 2956
 Erg, G. 1384
 Erickson, J. 1669
 Esarey, E. 2626, 2629, 2632
 Esin, S. 2426
 ESRF Project Team 1427
 Evans, D. 3127
 Evans, K., Jr. 188, 2263, 2275
 Evans, L. R. 1983
 Everett, M. 2551, 3003
 Evstigneev, A. 1384
 Eyharts, P. 670, 697
 Eyl, P. 670, 697
 Eylon, S. 703, 706, 709, 712, 3199

F

Fabbricatore, P. 1001
 Fabris, A. 953, 956, 1145
 Fabris, R. 1333, 1378
 Facco, A. 849
 Faehl, R. 2675
 Faehl, R. J. 2664
 Fahmie, M. 1869
 Faillon, G. 1184
 Fainberg, Y. B. 2620
 Faltens, A. 703, 721, 724
 Fan, J. Y. 1943
 Fan, M. 306, 1721, 2841
 Fang, J. 2578
 Fant, K. 543, 1106
 Fant, K. S. 620
 Farias, R. H. A. 1089
 Farkas, Z. D. 620, 1121, 1196, 1208
 Farkhondeh, M. 1372, 2054, 2868, 2935, 2938, 2941
 Fasanello, T. 2397
 Fathizadeh, M. 1288
 Faugier, A. 2001

Faure, J. 1465
 Faus-Golfe, A. 2045
 Fawley, W. M. 724, 1530
 Fazio, M. 2675
 Fazio, M. V. 2664
 Fedele, R. 209, 212
 Fedorov, V. 2769
 Fedotov, Y. S. 315, 318
 Feinberg, B. 2187, 3748, 3751
 Felker, B. 1551, 1554
 Fenstermacher, M. 1551
 Fenstermacher, M. E. 1554
 Ferguson, M. 1294
 Ferguson, S. W. 1551, 1554
 Ferioli, G. 2498, 2504
 Fero, M. 2172
 Ferrario, M. 573, 968, 3279
 Ferry, J. 3745
 Feschenko, A. 2426
 Fessenden, T. 703
 Ficklin, D. 1318
 Fieguth, T. 3084
 Fields, S. 1551
 Fields, W. F. 1554
 Filimonov, M. Z. 2208
 Filtz, M. 901, 1036
 Fink, C. L. 375
 Finley, D. A. 3721, 3806
 Fiorito, R. B. 1620, 2397, 2453
 Firebaugh, J. 1817, 1912
 Firjahn-Andersch, A. 3139
 Fischer, C. 2504, 3597
 Fischer, G. E. 44
 Fischer, J. 2929
 Fischer, R. 2632
 Fischer, W. 246, 2301
 Fisher, A. 2632
 Fisher, A. S. 2578
 Fishler, Y. 1297
 Fitzgerald, D. 366, 369, 2216, 2219, 3297
 Fitzgerald, D. H. 3739
 Flannigan, J. 1852
 Flanz, J. 2868, 2871, 2874, 3851
 Flanz, J. B. 1875, 2054, 2331
 Fleck, R. 1080
 Flora, R. 1914
 Flynn, T. 889
 Foelsche, H. W. 2895
 Foerster, C. 3836, 3876
 Foley, M. 852, 3294
 Fomin, M. 1226
 Fong, B. 1483
 Fong, K. 1139
 Fontana, J. R. 2614
 Force, R. 3748
 Forest, E. 131, 291
 Fortgang, C. M. 2480, 3118
 Fouaidy, M. 855
 Fougeron, C. 858
 Fowkes, R. 1106
 Fowkes, W. R. 620, 1259
 Fowler, W. 3793, 3796
 Fowler, W. B. 2823
 Fox, J. 2352
 Fox, J. D. 2076, 2109
 Fox, W. 995, 1712
 Fraivillig, J. 2790
 Franck, A. 2249, 2835

Franczak, B. 1645, 3736
 Frandsen, P. 2956
 Frandsen, P. K. 2739
 Frankle, S. 366, 369, 2216, 2219, 3297
 Franzke, B. 357, 1645, 1738
 Frias, R. 3748
 Friddell, K. 2967
 Friedman, A. 105, 703, 727, 730, 1599, 2284
 Friedrichs, C. 803, 824
 Friesel, D. 29, 224, 227, 420, 3184
 Frisch, J. 3045, 3047
 Frisch, J. C. 2978, 3027, 3036
 Frischholz, H. 1247, 2358
 Fritsche, C. T. 2501
 Fu, S. 1686
 Fugitt, J. 939, 1109
 Fuja, R. 605
 Fujita, H. 1697
 Fujita, Y. 2260
 Fukuda, S. 1193
 Fuller, R. 543
 Fullett, K. D. 3309
 Funakoshi, Y. 3497
 Funk, L. W. 812, 1700, 1706, 2130
 Funk, W. 1703, 1765, 3585
 Furman, M. A. 3485
 Furukawa, K. 2516, 3087, 3705
 Fuzesy, R. 2172

G

Gabella, W. 420, 2051, 2638
 Gabella, W. E. 233
 Gagliardi, P. 1063
 Gai, W. 2596, 3050
 Gallardo, J. C. 2578, 3012, 3081, 3615
 Gallo, A. 778
 Galloway, C. 620
 Galluccio, F. 209, 2154
 Galyaev, N. A. 454
 Gammel, G. 3193
 Ganetis, G. 2744, 2766
 Gannon, J. 1898, 2731, 2757, 3870
 Gao, J. 862, 865, 868
 Gao, S. 745, 3521, 3696
 Garavaglia, T. 3591, 3609, 3769
 Garber, M. 2744, 2766
 Gardelle, J. 626
 Garden, C. 3033
 Garden, C. L. 2978, 3027, 3036, 3039
 Gardner, C. 3633, 3763
 Gardner, M. 1439
 Gareyte, J. 246
 Garnett, R. 1712
 Garoby, R. 3570
 Garren, A. 2051, 3778
 Garren, A. A. 137
 Gath, B. 1572
 Gatignon, L. 1363
 Gattu, R. 2760

Gavrilov, N. 1226
 Gayet, P. 2956
 Geisik, C. 3172
 Gelbart, W. Z. 3099
 Gelfand, N. 2835
 Gelfand, N. M. 3790
 Geller, J. 1277
 Gemme, G. 775, 1001, 1524
 Genesio, F. 806
 Genin, R. D. 3018
 George, M. J. 661
 Georges, P. 3053
 Gerasimov, A. 3276, 3291
 Gerig, R. 267, 3558
 Gerig, R. E. 333
 Geschonke, G. 2358
 Gevchuk, A. 1480
 Ghosh, A. 2744, 2766
 Ghosh, A. K. 2742, 2790
 Giacuzzo, F. 3842
 Giannini, M. 1378
 Giardino, G. 3202
 Gierman, S. M. 2970
 Giguët, E. 2656
 Gilgenbach, R. M. 2693, 3351, 3354
 Gillespie, G. H. 86
 Gillier, R. 3900
 Gilpatrick, J. D. 1669, 2163, 2316, 2334, 2480
 Giovannozzi, M. 246, 273, 500
 Giove, D. 1524
 Girard, M. 2997
 Gjaja, I. 3387
 Gladkikh, P. 1480, 2057
 Gladkikh, P. I. 194
 Gläser, W. 1477
 Glass, H. D. 351, 2829, 2856, 2859
 Glenn, J. W. 3633, 3763
 Glock, H.-W. 614, 623
 Gluckstern, R. L. 221, 1545, 3219, 3387, 3390
 Godden, D. 1709
 Goderre, G. 354, 3482
 Godfrey, G. 3084
 Godwin, R. P. 3090
 Goetz, T. 1477, 2534
 Golceff, P. 3018
 Gold, S. 1318
 Gold, S. H. 2644, 2647
 Goldberg, D. A. 871, 874
 Goldin, L. 1771
 Goldman, M. 1166
 Goldman, M. A. 2916, 2919
 Goldstein, J. C. 3090
 Golubeva, N. 441, 444
 Gonçalves da Silva, C. E. T. 252, 390, 1454
 Gonczy, I. 2769
 Gonichon, J. 2575, 2696, 2699
 Gonzalez, R. E. 2322
 Goodwin, J. E. 2835
 Goren, Y. 824, 846, 877, 880, 883, 1703, 3405, 3888
 Gormley, M. 1127
 Gorniker, E. 1226
 Gould, H. 3751
 Gourber, J.-P. 68

Gourlay, S. 2769
 Govil, I. M. 1753
 Gower, E. 1244
 Graber, J. 886, 889, 892, 918
 Grafström, P. 1363
 Granatstein, V. I. 2572
 Granatstein, V. L. 2667, 2670, 2673
 Gras, J. J. 2495, 2504
 Grau, M. C. 2328
 Gray, E. 1021
 Green, K. 998
 Greene, A. 2744, 2766
 Greenwald, Z. 3690
 Gregory, W. 3055
 Greiner, P. 798
 Greiser, M. 1747
 Grellick, A. 605, 2412
 Grenier, J. 626
 Gribov, I. V. 2059
 Griffin, J. 405
 Griffin, J. E. 408
 Grigor'ev, Y. 2057
 Grimm, T. 824, 1083
 Grimm, T. L. 3252
 Grippe, J. 827, 1250, 3213
 Grippe, J. M. 1169
 Grishanov, B. I. 2022
 Grossberg, P. 2106
 Grote, D. 703, 709
 Grote, D. P. 727
 Groupe d'Etudes des Cavités Supraconductrices 796
 Groves, T. 2249
 Grüneberg, H. 2748
 Grua, P. 670, 697
 Gruber, A. 1645
 Grudzien, D. M. 2213
 Grun, J. 2632
 Grusell, E. 1771
 Guharay, S. K. 3145, 3648
 Guidee, P. 1184, 1187
 Guidi, V. 3243
 Guigli, J. 1238
 Guignard, G. 3336, 3426, 3600
 Guirlet, R. 2450
 Guk, I. 2057
 Gulley, M. 369
 Gundersen, M. 3039, 3072, 3537
 Gundersen, M. A. 3066
 Günther, C. 3381
 Guo, Z. Y. 3237
 Gupta, R. 258, 2744, 2766
 Gupta, R. C. 2754, 2778
 Guratzsch, H. 1477
 Gurd, D. P. 1916
 Güsewell, D. 2956
 Gutscher, W. D. 1154
 Guy, F. 1703, 2986, 3585
 Guy, F. W. 122, 2124, 2127, 2426, 2483, 3130

H

Haas, A. 2222
 Haber, C. 2199

Haber, I. 724, 727, 730, 3612, 3627, 3660
 Haberichter, W. 2462
 Habs, D. 1747
 Haebel, E. 806, 898
 Haenni, D. 2757
 Hafizi, B. 1560, 1623, 2584, 2644, 2647
 Hage-Ali, M. 1363
 Hagedoorn, H. L. 1072, 2062, 2065, 2892, 2927, 3423, 3645
 Hahn, A. 2193
 Hahn, K. 3285
 Hahn, R. v. 1747
 Hairapetian, G. 561, 2976, 3003, 3216, 3543
 Halbach, K. 1445, 1581, 1599, 1608, 1727
 Halbleib, J. A. 691
 Halka, M. 369
 Hall, J. 32, 1244
 Hall, T. 2865
 Halling, A. M. 472, 474, 2193
 Halling, H. 1253
 Halling, M. 3814
 Halliwell, J. 3748
 Hamilton, B. 29, 224, 227, 420, 3745
 Hamilton, B. J. 2243, 2289, 3536
 Hamm, C. 962
 Han, H. S. 2796
 Hanaki, H. 590, 1163, 3087
 Hancock, S. 3570
 Hanft, R. 2769
 Hanna, B. 354, 1357
 Hanna, S. 1419
 Hanna, S. M. 895, 1118
 Hansberry, E. 1154
 Hansen, S. 1229
 Hanson, D. L. 694
 Haraguchi, M. 1518
 Hardek, T. 2319, 3297
 Hardek, T. W. 2240
 Hardekopf, R. A. 3760
 Harding, D. J. 2823, 2826, 2829
 Harfoush, F. A. 342, 345, 348, 351, 2829
 Harkay, K. 3258
 Harkay, K. C. 3306
 Harkewicz, R. 1694
 Harmer, P. 1916
 Harms, E. 3533
 Harms, E., Jr. 3803
 Harris, K. 1318
 Hart, R. 1901
 Hartley, R. 1527
 Hartman, S. 575, 2976, 3003, 3357, 3543
 Hartman, S. C. 561, 3216
 Hartmann, B. 1477
 Hartog, P. D. 1709
 Hartung, W. 898, 921, 3450
 Haseroth, H. 2720
 Hashimoto, Y. 1780, 1783
 Hassenzahl, W. 1572
 Hassenzahl, W. V. 1575, 1584
 Hatton, V. 2001
 Hattori, T. 1783, 1786, 3115
 Haug, F. 2739

Hauviller, C. 3854
 Hawkins, S. A. 739
 Haworth, M. 1703, 2124, 2986
 Hayashi, S. 2039
 Hayes, T. 1241
 Haynes, W. 2675
 Hays, T. 3450
 Hayward, T. D. 1075
 Hayworth, M. D. 846
 He, A. 2775
 Hebert, J. 2986, 3151
 Hébert, J. E. 2483
 Heefner, J. 1838
 Heese, R. 608
 Heifets, S. 543, 3456, 3459
 Heifets, S. A. 3462
 Heinrichs, H. 995
 Hellborg, R. 206, 3618
 Heller, H. 2892
 Helm, R. 92, 131, 185
 Helser, A. 1399
 Hemmer, F. M. 2919
 Hendrickson, L. 1972, 2106
 Hendry, G. O. 1730
 Henestroza, E. 703, 709, 3199
 Henke, H. 549, 901, 904, 1133, 2593, 3288
 Henrichsen, K. 44
 Henriot, C. 798
 Herr, S. 2187
 Herrlander, C. J. 1735
 Herrup, D. 2199
 Herrup, D. A. 2249
 Herz, P. R. 3190
 Hettel, R. 2275
 Heuer, R. 1439, 2420
 Heuer, R. L. 1527, 3012
 Hewett, D. 703
 Hewett, D. W. 706, 718
 Heydari, H. 411
 Hicks, J. 3184
 Higgins, C. S. 2298
 Higo, T. 1027, 3503
 Hildreth, M. 2019
 Hilke, J. 1735
 Hill, B. W. 86, 1762
 Hill, J. 1154
 Hill, N. 3050
 Hill, S. F. 3594, 3672
 Hiller, M. 921
 Hilleret, N. 806
 Himel, T. 1972, 1975, 2019, 2106, 2373
 Himeno, Y. 546
 Hindi, H. 2076, 2352
 Hinkson, J. 2097, 2109
 Hipple, R. 703
 Hiramatsu, S. 673
 Hiramoto, K. 309
 Hirano, K. 546
 Hirao, Y. 1291, 1686
 Hirata, K. 466, 3491
 Hirota, J. 309
 Hirshfield, J. L. 2584
 Hitz, D. 2997
 Ho, C. 1844, 2596, 3050
 Hoag, H. 543, 1106
 Hoag, H. A. 620, 907, 1121
 Hochadel, B. 1747

Hodgson, J. A. 1039
 Hoeberling, R. F. 2664
 Hoehn, M. 3739
 Hoffberg, M. G. 1957
 Hoffstätter, G. H. 164
 Hofler, A. 587, 1895
 Hofler, A. S. 2298
 Hofman, J. M. A. 3423
 Hofmann, A. 44, 173, 3429
 Hogan, B. 2667, 2670
 Hogan, M. 3494
 Hogrefe, R. 2799, 2802, 2805
 Holdener, F. 3836
 Holmes, S. 3793
 Holt, J. A. 80, 3806
 Holtzapple, R. 638
 Holtzapple, R. L. 3234, 3564
 Honaberger, D. 3055
 Honaberger, D. J. 2944
 Honma, H. 1416
 Hooper, E. B. 1551, 1554
 Horan, D. 1294, 3757
 Hori, T. 602
 Hori, Y. 3903
 Horton, T. E. 1413
 Hou, Y. 2841
 Houck, T. L. 2590, 2611
 Hourany, E. 3093
 Hovater, C. 587, 3515
 Hovater, J. C. 2364
 Howard, D. 1160, 3748
 Howell, J. 1497, 1500
 Hower, N. 2889
 Hoyer, E. 1572, 1575, 1581, 1584, 2850
 Hoyt, E. 3033
 Hoyt, E. W. 2978, 3036, 3039
 Hs, I. C. 2465
 Hseuh, H. C. 3897
 Hsieh, H. 611, 3906
 Hsu, I. 2151, 2638
 Hsu, K. T. 2031, 2091
 Hsu, T. 3066, 3072
 Hsue, C. S. 1943, 3369
 Hu, K. H. 2091
 Hu, Y. 2841
 Huang, H. 29, 224, 227, 420, 432
 Huang, T. H. 2465
 Huang, Y. 3558
 Hughes, E. 2172
 Hughes, E. A. 3594, 3672
 Hughes, T. 3055
 Hughes, T. P. 661
 Hui, M. 1160
 Hui, Z. 1557
 Hulsey, G. 803, 824, 877, 1083
 Hulsey, S. 1551
 Hulsey, S. D. 1554
 Hülsmann, P. 614, 623
 Humphrey, R. 543
 Humphries, D. 1572, 1575, 1581
 Humphries, S. J., Jr. 1199
 Hunt, D. 3748
 Hunt, S. 128, 1823, 1826, 1829, 1838
 Hunter, T. 393
 Hur, J. 1327
 Hurd, J. 1703, 2986, 3127, 3509

Hurd, J. W. 122, 2124, 2127, 2130, 2426, 2444, 3130, 3585
 Hurh, P. 2148, 2459, 3533
 Husmann, D. 152
 Hutcheon, R. M. 829, 832
 Hutson, R. 363, 366, 369, 2216, 2219, 3297
 Hutton, A. 527
 Hwang, C. 1393
 Hwang, G. J. 2886
 Hyodo, K. 1468

I

Ieiri, T. 2292, 2295, 3333
 Igarashi, Z. 1163
 Ihloff, E. 2054, 2331, 2868, 2871, 2874, 3851
 Iida, T. 1515
 Ikegami, M. 1697
 Ikezawa, M. 1614, 1617
 Iliev, A. 3784
 Imanishi, A. 1783
 Ingalls, W. 3118
 Ingalls, W. B. 1669
 Ingold, G. 1439, 1602
 Inoue, M. 1697
 Irwin, J. 92, 95, 116, 119, 131, 185
 Ishi, K. 1614, 1617
 Ishida, T. 2540
 Ishimaru, H. 3885
 Ishizuka, H. 676, 1566
 Ishkhanov, B. S. 2059
 Itano, A. 1291, 1686
 Ivanov, A. S. 555
 Ivanov, P. M. 2022
 Ivanov, S. 3561
 Ivers, J. D. 1312, 2687
 Iwashita, Y. 1697, 3154
 Izawa, M. 930

J

Jach, C. 1297
 Jachim, S. P. 1154, 1232, 2391
 Jackson, A. 1432
 Jackson, G. 402, 1366, 2148, 2418, 2525, 3021, 3363, 3366, 3533
 Jackson, G. P. 3799
 Jackson, J. W. 2883
 Jackson, L. T. 1265
 Jackson, M. C. 1554
 Jacobs, K. 3851
 Jacobs, K. D. 1875, 2054, 2331
 Jacobsen, R. 44
 Jacquet, F. 2450
 Jaenker, P. 1019
 Jaeschke, E. 1474, 1747
 Jaffery, T. S. 2769
 Jahnelt, L. 390
 Jain, A. 2744, 2766
 Jain, A. K. 2754, 2778
 Jakob, H. 2301

Jameson, R. 1683
 Jameson, R. A. 3926
 Jamieson, G. 1703, 2118, 2127
 Jan, G. J. 1878, 2091
 Janssen, D. 1477
 Jason, A. 1683
 Jason, A. J. 56, 3760
 Jean, P. 3093
 Jeanjean, J. 2513
 Jeansson, J. 1735
 Jecic, A. 3093
 Jenner, D. 1421
 Jensen, C. 1357
 Jensen, D. R. 2838
 Jensen, K. 1300
 Jerng, D. 3757
 Jia, H. 2841
 Jiang, B. 1327, 3078
 Jiang, S. 3390
 Jiao, C. 2841
 Jiao, J. 2841
 Jin, J. T. 3196
 Jobe, R. K. 2234, 2423
 Joh, K. 71, 89
 Johnson, A. 939
 Johnson, A. M. 1220
 Johnson, C. D. 626
 Johnson, D. 236, 378
 Johnson, J. 2109
 Johnson, K. F. 1669, 3118
 Johnson, P. 2967
 Johnson, R. P. 1451, 1949
 Johnson, R. R. 3099
 Johnstone, C. 1912
 Johnstone, J. 342
 Jones, A. 2118
 Jones, C. M. 1660
 Jones, R. M. 936
 Jones, T. A. 3063
 Jones, W. P. 29, 224, 227, 420
 Jonker, M. 2001
 Joshi, C. 561, 2551, 2976, 3003,
 3216, 3543
 Jost, W. 998
 Jostlein, H. 2835
 Joubert, A. 1789, 1792
 Jowett, J. M. 2013
 Joyce, G. 1560, 2626
 Judd, D. 703
 Judkins, J. 3240
 Judkins, J. G. 1039
 Juillard, C. 3429
 Juillard, J. C. 2358
 Julian, J. 1238
 Junck, K. 3540
 Jung, J. 3654
 Jung, K.-S. 3196
 Jung, R. 2202, 2495, 2498, 2504
 Junk, T. 2172
 Junquera, T. 855
 Juras, R. C. 1660
 Jurgens, T. 852

K

Kadnikov, A. 564, 1348
 Kadokura, E. 2540

Kahana, E. 1814, 2112, 2237,
 2304
 Kahn, S. 2744
 Kahn, S. A. 2754, 2766
 Kaiser, H. 944
 Kakigi, S. 1697
 Kakihara, K. 3087
 Kako, E. 992, 1024
 Kalbfleisch, C. 1823, 1826, 1829
 Kalbreier, W. 2013
 Källberg, A. 1735
 Kalnins, J. 3748
 Kaltchev, D. 2042
 Kamada, S. 1468
 Kamikubota, N. 3087
 Kamitani, T. 590, 2516, 3087,
 3705
 Kamiya, Y. 930, 1509, 2260,
 2295, 2337
 Kanai, T. 1614, 1617
 Kanazawa, K. 3860
 Kanazawa, M. 1291, 1686
 Kang, B. K. 2751, 2796
 Kang, H. 1521
 Kang, Y. G. 1268
 Kang, Y. W. 549, 766, 910, 913,
 1057
 Kapchinskiy, I. M. 1675
 Kapustin, A. A. 3822
 Karabekov, I. P. 457
 Karas', V. I. 664, 2620, 3546
 Karl, F. X. 2919
 Karliner, M. 824
 Karnaukhov, I. 1480, 2057
 Kasha, D. 1166
 Kashihi, V. S. 3822
 Kasproicz, T. B. 2708
 Kasuga, T. 2409
 Katalev, V. 916
 Katayama, T. 41, 1783, 1786
 Katkov, V. M. 3093
 Kato, R. 1614, 1617
 Kato, S. 3518
 Kato, T. 1291
 Kato, Y. 2556
 Katsouleas, T. 2635, 2638, 3543
 Katsura, T. 2257, 2260, 2295,
 2337, 2409
 Kauffman, S. 267
 Kauffmann, K. 3609
 Kauffmann, S. 2489
 Kauffmann, S. K. 137, 197
 Kauppila, T. 3055
 Kawakubo, T. 2540, 2556, 3552
 Kawamura, M. 1163
 Kawamura, Y. 3006
 Kawasaki, S. 676, 1566
 Kawazu, S. 3115
 Kazacha, V. 2042
 Kazarezov, I. 2650
 Kazarinov, N. 2042
 Kazimi, R. 599, 939, 1109
 Kazmark, D., Jr. 2919
 Keane, J. 608, 1118, 1419, 1852
 Keating, P. 369
 Keeney, D. S. 706
 Kehne, D. 62, 65, 3282, 3627
 Keller, F. 2811
 Keller, R. 2910

Kelley, E. 2790
 Kellogg, N. 1160
 Kelly, E. 2744
 Kennedy, W. L. 838, 1042
 Kerns, C. 1214
 Kerns, Q. 1127, 1214
 Kersevan, R. 3842, 3848, 3888
 Kerslick, G. S. 1312, 2687
 Kersteins, D. 1669
 Kewisch, J. 1835, 1895
 Kheifets, S. 543, 635
 Kheifets, S. A. 3462
 Kick, R. 233
 Kiehlmann, D. 1080
 Kijima, Y. 1518
 Killian, E. 2744
 Kim, C. H. 2036
 Kim, D. E. 2751, 2796
 Kim, G. H. 2564
 Kim, J. 2593
 Kim, J. M. S. 1112
 Kim, J. S. 3288
 Kim, K. 2799, 2802, 2805, 2808,
 2814
 Kim, K.-J. 83, 1445, 1533, 3042
 Kim, S. H. 2799, 2802, 2805,
 2808, 2814
 Kim, W. 3196
 Kimura, T. 2690
 Kimura, W. D. 2564, 2581, 2614
 Kimura, Y. 673
 Kincaid, B. 1572, 1575, 1578,
 1581
 King, R. 2172
 Kinross-Wright, J. 2664
 Kinross-Wright, J. M. 2970
 Kinsho, M. 3181
 Kipper, A. 3139
 Kirbie, H. C. 739
 Kirby, R. E. 2978, 3030, 3036
 Kirchgessner, J. 763, 769, 886,
 889, 892, 918, 921, 977, 995,
 1399, 2953, 3450
 Kirchman, J. 2266
 Kirk, H. G. 3012, 3615
 Kirkman, G. 1327, 3066, 3072,
 3078
 Kirsch, R. 3093
 Kiselev, V. A. 2022
 Kishimoto, T. 1515, 1518
 Kishiro, J. 673
 Kitagawa, A. 1291
 Kitagawa, S. 1686
 Kitagawa, Y. 2556
 Klaisner, L. 3033
 Klaisner, L. A. 2978, 3027, 3036
 Klamp, L. 3384
 Kleb, R. 3757
 Kleeven, W. J. G. M. 1072, 2065,
 3423
 Kleffner, C. M. 1747
 Klein, H. 614, 623
 Kleman, K. J. 924, 1235
 Klepper, O. 1645
 Kloeppel, P. K. 2298
 Kneisel, P. 927, 947, 1010, 1016,
 1060, 3867
 Knobloch, J. 889
 Knott, J. 2720

Knott, M. 1960
 Knowles, H. B. 1762
 Knox, A. 3757
 Knox-Seith, J. F. 255
 Ko, I. 581, 1521, 3654
 Ko, I. S. 593
 Ko, K. 936, 986, 1039, 1121
 Kobari, T. 3903
 Kobayashi, H. 3087
 Kobayashi, M. 3903
 Kobayashi, T. 3552
 Kobayashi, Y. 215, 1321
 Kobliska, G. R. 2823
 Kocur, P. 236, 1369
 Kodaira, M. 1515, 1518
 Kodama, R. 2556
 Koechlin, F. 798
 Koepke, K. 918, 1127
 Kohno, T. 1291, 1686
 Koiso, H. 3497
 Kokorin, A. M. 3822
 Kolomiets, A. A. 1675
 Kondakov, A. 1226
 Konecny, R. 815, 2596
 Kong, S. H. 2970
 Kononenko, S. 1480, 2057
 Koo, Y. M. 2751, 2796
 Koontz, R. 543, 620
 Koontz, R. F. 1318
 Koop, I. 3711
 Koopman, J. 2504
 Korchuganov, V. 230, 564, 1384, 2793
 Korenev, I. L. 2543
 Koscielniak, S. R. 3506, 3639
 Koseki, S. 1291
 Koseki, T. 930, 1509, 2295
 Koshelkin, A. V. 1629, 1632
 Kostas, C. 3267, 3270
 Kosyakin, M. 2769
 Kot, N. C. 3243
 Kotov, V. I. 454
 Koujbida, R. P. 2853
 Koul, R. 2922
 Koul, R. K. 2924
 Kourbanis, I. 35, 405, 3630, 3799
 Koutchouk, J. P. 44, 68
 Kovachev, V. 3888
 Kowalski, S. 2054
 Kowitt, M. 2172
 Kozchekin, M. A. 2853
 Kozin, V. 1480, 2057
 Kozub, S. 2769
 Kozyrev, E. 2650
 Krafft, G. A. 426, 587, 599, 1895, 2298, 2364, 3246, 3515
 Krammer, M. 1960
 Krall, J. 2626, 2629, 2632
 Krämer, D. 1436, 1474
 Krasnopolsky, V. 2717
 Krasnopolsky, V. A. 933
 Krasnykh, A. 552, 2042
 Kraus, R. 1669, 1703
 Kraushaar, P. 2731, 2757, 2763, 3888
 Krauter, K. 1922
 Krawczyk, F. 1712
 Krebs, G. 2187
 Kreiser, H. 32

Krejcik, P. 2019, 2370, 2373, 3240
 Kreutz, R. 2748
 Krinsky, S. 492, 1439, 1491, 1545, 1599, 1602, 1852, 3375
 Krishnaswamy, J. 1527
 Kroc, T. K. 1689
 Kroes, F. 1998, 2343
 Krogh, M. 2124, 2130
 Krogh, M. L. 2501
 Kroll, N. 620, 936, 1039, 1121, 2559
 Kroll, N. M. 543, 983, 1196, 3453
 Kropachev, G. N. 3675
 Krueger, W. 1004, 3267
 Krug, H. 1477
 Krupnick, J. 83, 2850
 Krycuk, A. 939, 1109
 Krylov, Y. 564
 Kryshkin, V. I. 454
 Kuang, E. 2687
 Kubo, H. 1291
 Kubo, K. 992, 1027, 2364, 3503, 3515
 Kubo, T. 1163
 Kubota, C. 1163
 Kuchnir, M. 918
 Kudelainen, V. 3243
 Kudelainen, V. I. 2022
 Kudo, H. 1509
 Kudo, K. 1163
 Kudryavtsev, V. 916
 Kukhtin, V. P. 3205
 Kulikov, A. V. 2978, 3027, 3036
 Kulinski, S. 336, 573, 611, 968
 Kulipanov, G. 564, 1384
 Kulipanov, G. N. 2751
 Kumada, M. 1291, 1686
 Kumazawa, R. 2205
 Kunkel, W. B. 1727
 Kuo, C. C. 1635, 1943
 Kuo, C. H. 2091
 Kuo, T. 372
 Kuo, T. T. Y. 1730
 Kuprianov, A. P. 682
 Kuptsov, I. 1226
 Kuramoto, R. 1300
 Kurennoy, S. S. 3417, 3420
 Kurkin, G. 1226
 Kurochkin, I. A. 2190
 Kuroda, S. 2340
 Kurokawa, S. 294, 2004, 2073
 Kurz, M. 614, 623
 Kusche, K. P. 2564
 Kushin, V. V. 1798
 Kushnick, P. 1016
 Kuske, B. 1474
 Kuske, P. 1474
 Kustom, R. 285, 549, 1013, 1057, 1294, 3757
 Kustom, R. L. 766, 910, 913, 1217, 2213, 3393, 3396
 Kuzmin, I. A. 844
 Kuznetsov, G. 2650
 Kuznetsov, N. A. 2022
 Kuznetsov, S. 564, 1506, 1955
 Kvashonkin, I. 2042
 Kwan, C. M. 2385
 Kwan, J. W. 3169

Kwan, T. 2675
 Kwiatkowski, S. 824, 941
 Kwok, P. 2638
 Kwon, S. 1832
 Kwon, S.-I. 3042

L

Labrousche, J. 670, 697
 Lackey, J. 2228
 Lackey, S. 1912, 1914
 Laclare, J. L. 1427
 Lahey, T. 1969
 Lai, P. 2638
 Laird, R. J. 1814
 Lal, A. 2551
 Lamanna, G. 3243
 Lambert, G. 2376
 Lambertson, G. 1039
 Lambertson, G. R. 2109
 Lamm, M. J. 2769
 Lamont, M. 1937, 2001
 Lampel, M. 3009
 Lamzin, E. A. 3205
 Lancaster, C. 2967
 Landis, R. 2222
 Langdon, A. B. 730, 733, 3660
 Lange, F. 3864
 Langenbeck, B. 3736
 Langenbrunner, J. 1021
 Lanni, C. 3876
 Lanz, P. 1151
 Lapitsky, S. N. 2190
 Lapostolle, P. 3606
 Larsen, R. 2070
 Larsson, B. 1771
 Laslett, L. J. 724
 Lasnier, C. J. 1551, 1554
 Lath, A. 2172
 Latham, P. E. 2659, 2661, 2670, 2673
 Latushkin, S. T. 1795
 Lau, Y. Y. 3351, 3354
 Launspach, J. 670
 Launspauch, J. 697
 Laverty, M. 1139
 Lavine, T. 543
 Lavine, T. L. 620, 1121, 1196, 1208
 Lawson, W. 2667, 2670
 Lawson-Chroco, L. 44
 Laxdal, R. E. 372
 Lazarev, N. V. 1675
 Lebedev, V. A. 2022, 3243
 Leblond, B. 3053
 Le Diberder, F. 2513
 Le Duff, J. 2045
 Lee, B. 2705, 2708, 2711
 Lee, E. P. 3678
 Lee, H. 581
 Lee, H. K. 2796
 Lee, H. S. 593
 Lee, J. C. 1943
 Lee, M. 173, 1483
 Lee, M. J. 108
 Lee, M. K. E. 2667, 2670

Lee, S. Y. 6, 29, 102, 224, 227, 420, 432, 435, 2865, 3291
 Lee, T. 841, 1106, 1457, 3273
 Lee, T. G. 1259
 Lee, Y. Y. 360, 3633
 Leemans, W. 83, 567, 2638
 Lefrancois, M. 3900
 Legg, R. 587
 Lehrman, I. 1439
 Lehrman, I. S. 1527, 3012
 Leibfritz, J. 3864
 Leifeste, G. T. 2124, 2130, 2426
 Lemaitre, E. 798
 Lenisa, P. 3243
 Lenkszus, F. 1960, 2304
 Lenkszus, F. R. 1814
 Lennox, A. J. 1666, 1756
 Lenz, J. 2986, 3133
 Lenz, J. W. 3151
 Leonhardt, W. J. 3882
 Leonov, V. V. 1795
 Leontin, S. 1735
 Lepeltier, V. 2513
 Leroy, R. 1789, 1792
 Lessner, E. 1485, 3757
 Lessner, E. S. 399
 Le Taillandier, P. 670, 697
 Leung, K. 3888
 Leung, K. K. 1503, 2787
 Leung, K. N. 1727, 3169, 3190
 Leung, K.-N. 3042, 3160
 Level, M. P. 1465
 Levichev, E. 230, 564, 1384, 1506, 2793
 Levin, M. 2757
 Levitt, S. 1969
 Levy, C. D. P. 2991
 Lewis, S. 3748
 Lewitowicz, M. 1792
 LHC Machine Group 3917
 Li, C. Y. 1727
 Li, D. 29, 224, 227, 420, 1439, 2865, 3006
 Li, G. X. 3237
 Li, M. 38, 236
 Li, N. 2862
 Li, Q. 1620
 Li, R. 1909, 3473
 Li, T. 2841
 Li, X. 3527
 Li, Z. 179, 1721
 Liang, C. 2841
 Liang, C. F. 1792
 Liang, D. 3696
 Lidbjörk, P. 2068
 Liebmman, J. 1747
 Lien, E. 1106
 Liger, P. 3663
 Likhachev, V. 1480, 2057
 Liljeby, L. 1735
 Lima, S. 1892
 Limberg, T. 429, 2019, 2025, 2435, 3240
 Lin, K. K. 2031
 Lin, L. 252
 Lin, L. C.-L. 2575, 2696, 2699
 Lin, X. 3453
 Lindner, A. 1160
 Lindner, A. F. 2210

Linnekar, T. P. R. 2376
 Linnemann, J. 1477
 Linscott, I. 2076, 2352
 Liou, R. 2638, 3039, 3066, 3072, 3537
 Lipkin, I. M. 1675
 Lipnicky, M. 1151
 Lippmann, G. 944
 Lipsett, M. G. 1039
 Liska, D. 1718
 Littmann, B. 1133
 Litvinenko, V. N. 218, 1442, 2889
 Liu, B. 1611
 Liu, C. J. 688
 Liu, H. 279, 512, 1563, 3663
 Liu, H. C. 2886
 Liu, J. 182, 285, 2841
 Liu, K. 1262
 Liu, Y. 2151
 Liu, Y. C. 1635
 Liu, Z. 2070
 Lo, C. C. 1142, 1238, 3058
 Lobanov, N. R. 3187
 Lockner, T. R. 667
 Loew, G. 1445, 3084
 Loew, G. A. 543, 620, 644
 Logachov, P. 3243
 Loiselet, M. 1672
 Lom, C. 821, 2133
 Lombardi, A. 3121, 3606
 Lopez, F. 2922, 2924
 López, G. 200, 2784, 3255, 3467
 Lorello, M. 1709
 Lorenz, R. 1133, 2325
 Losito, R. 2154
 Low, K. 1823, 1826, 1829
 Lu, J. 2711
 Lu, J. J. 1303
 Lu, X. 3366, 3799
 Lu, X. P. 472
 Lublinsky, B. 1817, 2249
 Luccio, A. 438, 1872, 2175
 Luchini, K. 1265
 Ludewigt, B. A. 1759
 Ludmirsky, E. A. 315
 Ludwig, P. 2997
 Ludwig, T. 3139
 Luginsland, J. W. 3354
 Luijckx, G. 1998
 Lujan, R. 2947
 Lukasiewicz, J. 1890
 Lulevich, V. I. 2853
 Lumpkin, A. 2304
 Lumpkin, A. H. 2086, 2112
 Luo, G. 1211
 Lütkehaus, H. 2748
 Lutz, I. 1265
 Lyashchenko, V. 1480
 Lynch, D. 1439, 3000
 Lynch, M. T. 1683, 2391
 Lyons, S. 608, 611
 Lysenko, A. 3711
 Lysenko, W. P. 1669

M

Ma, Y. 1611

Maas, R. 1901, 1998
 Macek, R. 363, 366, 369, 2216, 2219, 2319, 3297
 Macek, R. J. 3739
 Macek, R. W. 3760
 Macha, K. 2929
 Machida, S. 176, 255, 3224, 3558
 Maciga, B. 3243
 Maciszewski, W. 1890
 Mackenzie, G. H. 372
 Mackenzie, R. 1966
 MacKenzie, R. 1969
 Mackerrow, E. 369
 MacLachlan, J. 405
 Maddocks, J. 3879, 3888, 3891
 Madduri, V. B. 2711
 Madey, J. M. J. 218, 1442, 2889
 Madlung, J. 3139
 Maeda, H. 676
 Magyaray, S. 1811
 Mahale, N. 423, 3769
 Mahale, N. K. 877
 Mahoney, K. L. 2298
 Maier, K. 3093
 Maillard, J. 3093
 Main, W. 2714
 Maisheev, V. A. 315, 322
 Majima, T. 1321
 Makarov, A. A. 3822
 Makarov, I. 2650
 Mako, F. M. 2702
 Makowski, M. 1551
 Makowski, M. A. 1554
 Makulkin, A. V. 3702
 Malitsky, N. 128
 Malone, R. 2486
 Malyshev, O. 3876
 Mammosser, J. 781, 947, 1016, 2929
 Manarin, A. 2492
 Manca, J. 608, 611, 1244
 Mane, V. 3435, 3438
 Mangino, J. 2382
 Manheimer, W. M. 2644, 2647
 Manini, P. 3839
 Mankofsky, A. 3267
 Mann, J. 2498, 2504
 Mao, N. 333
 Mapes, M. 3882, 3897
 Mariam, F. G. 384
 Marin, M. 1063
 Marin, P. 1465
 Marino, M. 3839
 Markov, V. 1480, 2057
 Marks, N. 2898
 Marks, S. 1572, 1575, 1578, 1581
 Marneris, I. 1277
 Maroli, C. 1524
 Marquardt, J. 3118
 Marquardt, N. 1471
 Marrufo, O. 827, 1169, 3213
 Marsden, E. 3127, 3213
 Marsden, S. 827
 Marsh, K. A. 558, 2551
 Marsh, W. 1912
 Marshall, J. 841, 1396
 Martens, M. 405
 Martens, M. A. 1963, 3300
 Martin, D. 1703, 2118, 3888

- Martin, K. 1914
 Martin, P. 3793
 Martin, R. 2913
 Martini, M. 3570, 3699
 Maruyama, T. 2172
 Maruyama, X. K. 1620, 2397
 Marziali, A. 950
 Mashiko, K. 602
 Maslennikov, I. 3876
 Massarotti, A. 953, 956, 1145
 Masuda, H. 1780, 1783
 Masullo, M. R. 2154
 Masunov, E. S. 1681, 2474
 Mathae, J. C. 2432
 Matheisen, A. 918
 Mathewson, A. G. 3828
 Mathieson, D. 1823, 1826, 1829
 Matsumoto, H. 959, 1124
 Matsumoto, S. 1291, 3491
 Matsuoka, M. 1024
 Matthews, H. W. 2667
 Matuk, C. 83
 Matumoto, M. 3903
 Matveev, Y. 1348, 1384
 Matz, W. 1477
 Mavrogenes, G. 549, 605
 May, R. 2184
 Mayoud, M. 44
 Mazarakis, M. G. 667
 Mazumdar, T. K. 2705, 2708, 2711
 Mazur, P. 2769
 Mazur, P. O. 2856
 McAllister, B. 2054
 McAllister, B. G. 1875
 McAshan, M. 2757
 McCammon, D. 1421
 McCauley, G. 1718
 McCormack, F. 2187
 McCormick, D. 1975, 2160, 2423
 McCrory, E. S. 1691, 1952
 McDonald, D. S. 3190
 McDowell, C. 2477
 McDowell, W. 1960
 McGhee, D. 1864, 3757
 McGhee, D. G. 1271, 2817
 McGill, J. 378, 381, 384
 McGill, J. A. 333
 McGinnis, D. 35, 2100, 2228, 2231, 2361, 3533, 3787
 McGinnis, K. 2124, 2130
 McInturff, A. 2731, 2763
 McInturff, A. D. 2757
 McIntyre, P. M. 2705, 2708, 2711
 McKenzie-Wilson, R. 1172
 McMahan, M. A. 2187
 McMichael, G. E. 1175
 McMurry, D. 1669
 McNerney, A. 1166
 McNerney, A. J. 1241
 McPherson, J. 32
 Meads, P. F., Jr. 3825
 Meddahi, M. 1488, 3312
 Medvedko, A. 1297
 Meigs, M. J. 1660
 Meinke, R. 203, 2468, 2489
 Meisner, K. 405, 2519, 2522, 2525
 Meitzler, C. R. 3148
 Melin, G. 2997
 Meller, R. E. 578
 Mellors, W. 1039
 Melnychuk, S. 3193
 Melton, J. G. 2944
 Mendelsohn, S. L. 1774
 Menegat, A. 543, 620, 1121, 1196, 1208
 Meng, W. 2883, 2904, 2907
 Menge, P. R. 2693, 3351
 Menninger, W. L. 2656
 Men'schikov, L. 552
 Mercier, E. 3202
 Merl, R. 2799, 2802, 2805
 Merle, E. 670, 697, 2115
 Merminga, L. 599, 2184, 2364, 3515
 Merz, W. 1841, 1898
 Meshcherov, R. 2717
 Mestha, L. K. 2382, 2385
 Meth, M. 1166, 1241, 2286
 Metty, P. 1244
 Metzger, D. 918, 995, 1399, 3450
 Meuth, H. 962, 1253, 3381
 Meyer, D. 3888
 Meyer, F. 1841, 1898
 Meyer, R. 1703
 Meyer, R. E. 2334, 2480
 Meyer, W. 1551
 Meyer, W. H. 1554
 Meyerhof, W. E. 3751
 Meyerhofer, D. D. 2638
 Mezentssev, N. A. 1494, 2751
 Michelotti, L. 80, 495
 Michizono, S. 1193
 Micklich, B. J. 1715
 Miele, G. 209, 212
 Miertusova, J. 3842, 3873
 Migdal, W. 1890
 Mihelic, R. 3888
 Milburn, J. E. 2796
 Miles, J. 44, 2001
 Militin, B. L. 2022
 Milityn, B. 3711
 Miller, E. 1972
 Miller, J. 3612
 Miller, R. 608, 608, 611, 611, 3084
 Miller, R. H. 543, 620, 3027, 3063
 Miller, W. 369
 Millich, A. 965, 3426
 Milliman, L. 2967
 Millo, D. 1587
 Mills, F. 285, 549, 3757
 Mills, F. E. 2817, 2922, 2924
 Mills, M. R. 2322
 Mills, R. S. 3657
 Millsom, D. 1966
 Milstead, I. 2301
 Milton, B. 1733
 Mimashi, T. 2340
 Miné, P. 2450
 Ministrini, M. 573, 968
 Minty, M. 224, 227, 447, 2019, 2370, 2373, 2435, 3240
 Minty, M. G. 29, 420
 Miram, G. 1106
 Mironov, V. 2042
 Mirzozan, A. 2426
 Mishin, A. V. 971
 Mishnev, S. I. 2022
 Mishra, C. S. 342, 345, 348, 351, 2829
 Mitchel, G. R. 2415
 Mitra, A. K. 974, 1303
 Mitsuhashi, T. 215
 Mitsui, H. 2205
 Miura, A. 959, 1124
 Miura, I. 1650
 Miwa, H. 1024
 Miyahara, Y. 653
 Mizuno, A. 602
 Mizuno, H. 1202, 1321
 Mocheshnikov, N. 1480, 2057
 Mock, R. C. 691
 Modéer, J. 2034
 Moe, H. 3757
 Moe, H. J. 2213
 Moerel, J. 2892
 Moffat, D. 763, 769, 886, 889, 892, 918, 921, 977, 995, 3450
 Moffeit, K. 2172
 Moiseev, V. A. 3249
 Mokhov, N. V. 1360, 1369, 3090, 3109, 3772
 Moller, J. 1551
 Moller, J. M. 1554
 Møller, S. P. 1363, 1741
 Molodkin, V. 1480
 Momose, T. 3885
 Mondelli, A. 1004, 3267, 3270
 Montès, B. 2450
 Montuclard, J. 3900
 Morales, G. 3888, 3891
 Morales, H. 3018
 Morano, R. 2450
 Moravec, K. 3864
 Morcombe, P. 1339
 Morduev, A. 1672
 Moretti, A. 1127, 1214
 Morgan, G. 2744, 2766
 Morgan, G. H. 2754
 Morgillo, A. 2744, 2766
 Mori, W. B. 2635
 Mori, Y. 2991, 3181, 3754
 Morillo, J. 2450
 Morishita, O. 1686
 Moritz, G. 3736
 Morpurgo, G. 2103
 Morse, W. 2070
 Mortazavi, P. 1419
 Morton, P. 1445
 Moshhammer, H. 131, 2025
 Moskalenko, V. 1480, 2057
 Mosnier, A. 629, 855
 Mottershead, C. T. 1669
 Mourou, G. 2632
 Moz, S. 1063
 Mroczkowski, T. T. 2919
 Mudiugin, B. 2042
 Mud'jugin, B. G. 3822
 Mukugi, K. 1515, 1518
 Mulholland, G. 2757
 Muller, H. 889, 918, 995, 2953
 Müller, R. 1887
 Munson, F. H. 1694
 Murakami, T. 1291, 1686

Muratore, J. 2744, 2766
 Murin, B. P. 980
 Murphy, J. B. 1477
 Murphy, K. 2967
 Murray, D. 1838, 2757
 Murray, J. 1274, 1855, 1858, 1861
 Musenich, R. 1001
 Mustaine, R. E. 1033
 Myae, E. A. 318, 322
 Mynk, J. 1250
 Mytsykov, A. 1480, 2057
 Myznikov, K. 2769

N

Nadji, A. 1465
 Nagaenko, M. 2057
 Nagafuchi, T. 2039
 Nagaitsev, S. 29, 224, 227, 420, 3524, 3745
 Nagaitsev, S. S. 3536
 Nah, Y. G. 2796
 Nakagawa, S. 1468
 Nakahara, Y. 1566
 Nakajima, K. 2556, 2638, 3552
 Nakajima, S. 676
 Nakamura, H. 2260
 Nakamura, K. 3537
 Nakamura, N. 2257, 2295, 2337
 Nakamura, T. 3464
 Nakanishi, H. 2556, 2638, 3552
 Nakao, K. 1193
 Nakayama, H. 2340
 Nakazato, T. 1614, 1617
 Nam, S. 581
 Nam, S. H. 593, 1315
 Namkung, W. 581, 593, 1315, 1521
 Nantista, C. 543, 620, 983, 1196
 Napoly, O. 632, 3347
 Nassiri, A. 605, 2142, 2412
 Nation, J. A. 1312, 2653, 2684, 2687
 Natter, E. F. 1154, 2391
 Nawrocki, G. J. 1957
 Nawrocky, R. 2246
 Nawrocky, R. J. 2145
 Nazmov, V. 3876
 Neil, G. 279, 3663
 Neil, G. R. 1563
 Nelson, E. M. 983, 1086
 Nelson, J. 1916
 Nelson, W. R. 185
 Nemoshkalenko, V. 1480
 Neri, F. 56
 Nesterenko, I. 3711
 Nesterov, N. A. 1798
 Nett, D. 611
 Neuffer, D. 2136, 3297, 3663
 Neumann, W. 1477
 Neuschaefer, G. 1683
 Newberger, B. S. 387, 3588
 Newman, W. 2133
 Newton, M. A. 739
 Nexsen, W. 2468, 2489
 Nezhevenko, O. 564, 2650
 Ng, C. K. 986, 1039, 2638, 3432

Ng, K. Y. 29, 35, 102, 224, 227, 405, 420, 3300, 3630
 Ng, L. S. B. 1949
 Ng, Y. 2133
 Nguyen, D. C. 2970
 Nguyen, T. K. 2997
 Nguyen-Tuong, V. 1007
 Nick, W. 2748
 Nicol, T. 3021
 Nicol, T. H. 989
 Nielsen, R. 3757
 Nightingale, M. P. S. 1777
 Niki, K. 1780, 1783, 1786
 Nikiforov, A. 2650
 Nilsson, A. 1735
 Nilsson, B. 1771
 Ninan, L. 599
 Nishi, M. 309
 Nishida, Y. 2556, 2638, 3552
 Nishimura, H. 111
 Noda, A. 41, 1291, 1697
 Noda, K. 1291, 1686
 Nodarse, F. F. 1892
 Noguchi, S. 992, 1024
 Nolden, F. 1645, 1738
 Nolen, J. A. 71, 89, 1694
 Nomura, M. 546
 Noomen, J. 1998
 Noomen, J. G. 2343
 Nordberg, E. 995
 Norem, J. 2462, 2638
 Nortier, F. 3099
 Nosochkov, Y. 125, 143, 239, 3778
 Novak, J. 1021
 Novak, W. 2462
 Nuhn, H.-D. 173, 1445, 1608
 Nurushev, S. B. 315
 Nusinovich, G. S. 2572, 2659, 2661, 2673
 Nyman, M. 3748

O

Oasa, K. 1554
 Obert, J. 1792
 Obina, T. 2409
 Ochsner, J. 2790
 O'Connell, J. S. 3657
 O'Day, S. 330, 2459, 3096
 Oeftiger, U. 2157
 Oehme, W. 1477
 Oganessian, R. 1672
 Ogata, A. 2556, 2638, 3552
 Ogawa, H. 1291, 1686
 Ogawa, Y. 2516, 3087, 3705
 Ogitsu, T. 2769
 Ogiwara, N. 1566
 Ogloblin, A. A. 1795
 Ogren, H. 2172
 Ogura, K. 2714
 Oguri, Y. 3115
 Oh, J. S. 593, 1315
 Ohkuma, H. 1509
 Ohmori, C. 3297
 Ohnuma, S. 3148, 3603
 Ohsawa, S. 2516, 3087, 3705

Ohsawa, Y. 2205
 Oide, K. 466, 2340, 3339
 Oikawa, Y. 3845
 Okamoto, H. 221, 1545, 1697, 3390
 Okamura, M. 3115
 Okay, N. 2986, 3151
 Okay, N. C. 2483, 3133
 Oku, Y. 1468
 Okuda, S. 650
 Olchowski, F. 32
 Oldfather, D. E. 2210
 Oliphant, V. 1706
 Olivier, R. 44
 Olivo, M. 3190
 Ollis, C. W. 739
 Olsen, D. K. 1660
 Olsen, R. 44, 1274, 1855, 1858, 1861
 Olson, R. E. 667
 Onel, Y. 32
 Onillon, E. 2379
 Onischenko, L. 2042
 Onischenko, L. M. 518
 Ono, M. 546, 1024, 1163
 Oogoe, T. 3087
 Oothoudt, M. A. 3106
 Oren, W. 2929
 Orlov, Y. 3488
 Orr, N. 1792
 Orris, D. 2769
 Orthel, J. L. 1762
 Orzechowski, J. 3099
 Oshita, H. 546
 Osipov, V. 3876
 Ostiguy, J. 2901
 Ostiguy, J.-F. 2829
 Ostreiko, G. 564
 O'Sullivan, M. 1925
 Otis, A. 1241
 Otter, A. J. 2898
 Ovchinnikov, V. P. 555
 Owens, T. L. 1689, 1691
 Oxoby, G. 2076, 2352
 Oyamada, M. 1614, 1617
 Ozaki, T. 673, 2205

P

Paál, A. 1735
 Padamsee, H. 763, 769, 886, 889, 892, 918, 921, 977, 995, 998, 1399, 3450
 Page, T. 2459
 Page, W. 2222
 Palkovic, J. A. 21, 3261
 Palmer, D. 620
 Palumbo, L. 212, 778
 Pan, C. 44
 Pang, Y. 2705, 2708, 2711
 Papash, A. 372
 Papash, A. I. 3822
 Pappas, G. C. 1336
 Papureanu, S. 962, 1747
 Pardo, R. C. 1694
 Paris, P. 1792
 Parish, D. J. 2790

Parisi, G. 3121, 3124
 Park, K. H. 2796
 Park, S. 561, 570, 2976, 3003, 3216
 Park, S. S. 593, 1315
 Parker, B. 1360, 3772, 3775
 Parkhomchuk, V. V. 2022, 2959
 Parodi, R. 775, 778, 1001, 1524
 Parry, R. 2222
 Parry, R. R. 2225
 Parsa, Z. 509, 2723
 Parshin, I. O. 1798, 3675
 Parzen, G. 483, 486, 489
 Pasotti, C. 953, 956, 1145
 Pasquinelli, R. 3533
 Pasquinelli, R. J. 2081, 2355, 2361
 Passardi, G. 2739
 Paterson, A. 2850
 Paterson, J. 1445
 Paterson, J. M. 543
 Patteri, P. 573
 Patterson, D. 2112
 Paulson, C. C. 1774
 Pauluhn, A. 270
 Pavlov, S. N. 3822
 Pawlak, T. 3793
 Paxson, V. 1940
 Payet, J. 1465
 Payne, A. N. 736
 Payne, J. 3870
 Pearce, W. J. 1949
 Pearson, C. 543, 907, 1106, 1259
 Pearson, C. C. 620
 Pedersen, F. 2370, 3240
 Peggs, S. 35, 168, 233, 258, 261, 351
 Peggs, S. G. 74
 Pei, X. 29, 224, 227, 420, 1421, 1424
 Peiniger, M. 1080
 Pekeler, M. 918
 Pellegrini, C. 173, 561, 570, 575, 1445, 1533, 1608, 2617, 2976, 3003, 3216
 Pelligrini, C. 3543
 Pendleton, R. P. 1039
 Penner, S. 381
 Penzo, A. 32
 Perelstein, E. 2042
 Perevedentsev, E. 3429, 3711
 Perkins, L. T. 3190
 Perregrini, L. 772
 Perret, R. 2202
 Perry, J. 587, 1925, 2184
 Persov, B. 2650
 Peschardt, E. 1903, 2358, 3429
 Peschel, H. 2748
 Pestrikov, D. 294
 Pestrikov, D. V. 3681, 3684, 3687
 Peter, W. 2702
 Peters, C. 703
 Petersen, D. 1551, 3836
 Petersen, D. E. 1554
 Peterson, D. 809, 3533
 Peterson, D. W. 3573
 Peterson, E. 2400
 Peterson, J. 203, 2281, 3769, 3781
 Peterson, T. 809

Petillo, J. 1004, 3267
 Petradza, M. 2172
 Petrov, E. 2042
 Petrov, S. 1297
 Petrov, V. 824, 1226
 Petrov, V. M. 877, 941
 Petrucci, G. 2820
 Pettersson, O. 1771
 Pewitt, E. G. 2823
 Peyromaure, J. 858
 Pfeffer, H. 918
 Philipchenko, A. 564, 1384, 2793
 Phillips, H. L. 1007
 Phillips, R. 543, 1106
 Phinney, N. 116, 2019
 Pianetta, P. 1445, 1536
 Picard, M. 1477, 2534
 Pickens, D. R. 1448
 Pierini, P. 1524, 1569
 Piestrup, M. A. 1620, 2397
 Pikin, A. 1735
 Pilat, F. 143, 203, 239, 515
 Pile, G. 1709, 3210
 Pimiskern, K. 944
 Pindyurin, V. 3876
 Pinkow, J. 357
 Piovella, N. 1524
 Pipersky, P. 1572
 Pirkel, W. 1172, 1241
 Pirozhenko, V. M. 3112
 Pisent, A. 32
 Pistoresi, D. 2967
 Pitchford, L. 3039
 Pivarc, J. 3894
 Placidi, M. 44
 Plate, D. 1572, 1575
 Platt, R. C. 2456
 Plesea, L. 3133
 Plesko, M. 149, 152, 1477, 2534
 Plink, O. V. 3112
 Plotnikov, S. V. 1798
 Plotnikov, V. K. 1675
 Plouffe, D. 2736
 Ployard, G. 2115
 Plum, M. 366, 2181, 2319, 3297
 Pogorelsky, I. 2564, 2614
 Poilleux, P. 2450
 Poirier, R. L. 753
 Poizat, J. C. 3093
 Poliakova, R. V. 1892
 Poll, D. 3533
 Pollock, D. 2760
 Poloni, C. 1587
 Pontonnier, M. 2997
 Poole, M. W. 1494, 1638, 3594, 3672
 Popkov, Y. 1480, 2057
 Popov, A. 2042
 Popov, Y. 552
 Popovic, M. B. 1214, 1689, 1691
 Porro, M. 3839
 Porter, J. 2133, 2420
 Portmann, G. 1572, 2272
 Postiau, N. 1672
 Potter, J. 1004
 Potts, C. 3757
 Potukuchi, P. N. 1045
 Poukey, J. W. 667, 691, 694
 Power, J. 1669, 1844, 2596, 3061

Power, J. F. 2334
 Powers, T. 1007, 1010, 1016
 Pozdeev, E. 3711
 Pradal, F. 3842
 Preble, J. 841, 1396, 2929
 Preger, M. A. 2048
 Preist, D. H. 1103
 Prescott, C. 3033
 Prescott, C. Y. 2978, 3027, 3036
 Price, E. 587
 Price, R. R. 1448
 Primdahl, K. 766, 1013, 1294
 Pripstein, D. 2172
 Proch, D. 758
 Prodell, A. 2744, 2766
 Pröhl, D. 1477
 Propp, A. 824, 941
 Prosnitz, D. 1445
 Prusakov, V. 552
 Pruss, S. 2252
 Pruss, S. M. 3802
 Ptitsin, V. 3711
 Puech, V. 3039
 Pullia, M. 1524
 Pusterla, M. 32
 Putaux, J. C. 1792
 Puzo, P. 2513

Q

Qian, G. 745, 3521, 3696
 Qian, Q. 2670
 Qin, J. 3237
 Qin, Q. 3237
 Qiu, X. Z. 1439
 Quinn, P. D. 1638, 3594, 3672
 Qunell, D. 1357

R

Raabe, P. 1645
 Raffone, G. 2048, 3906
 Rahn, J. 1887
 Raimondi, P. 98, 100, 116, 2019
 Rajagopalan, S. 2638, 3555
 Rakowsky, G. 1605
 Ramamoorthy, S. 1849, 1852
 Ramaswamy, K. 685
 Rambaldi, S. 273
 Ramirez, G. 1419
 Ramseier, G. 44
 Ranganathan, R. 1402
 Rao, M. G. 927, 3867
 Raparia, D. 122, 1765, 2127, 2426, 2986, 3130, 3151, 3509, 3585
 Rathke, J. 1709
 Ratner, L. 432
 Ratti, A. 1166, 1172
 Raubenheimer, T. 417, 1445, 2019
 Raubenheimer, T. O. 11, 596, 635, 2025, 2880
 Rauchas, A. 3757
 Rawlins, A. 1727
 RD22 Collaboration 26

Reece, C. 1007, 1016
 Reece, R. K. 1277, 3763
 Reed, L. 2462
 Rees, D. 3213
 Rees, D. E. 1169, 1199, 1205
 Rees, G. 3297
 Rees, G. H. 3731
 Reeve, P. A. 2898
 Reeves, S. 2817
 Regan, A. 1683, 3213
 Regan, A. H. 1154, 2391
 Reginato, L. 703, 1351
 Reginato, L. L. 656
 Rehak, M. 2744, 2766
 Reich, H. 1645
 Reid, C. 809
 Reilly, R. 1357
 Reimund, J. A. 1280
 Reinhardt, N. 1327, 3078
 Reiniger, K. W. 1112, 1283
 Reiser, M. 62, 65, 685, 2667,
 2670, 3145, 3282, 3627, 3648,
 3660
 Reist, H. 1771
 Reistad, D. 1744, 3745
 Remelius, D. 2967
 Remillieux, J. 3093
 Remondino, V. 68
 Remy, M. A. 1089
 Rendon, A. M. 2480
 Renou, G. 3093
 Rensfelt, K.-G. 1735
 Repnow, R. 1747
 Reusch, M. F. 59, 1527, 3624
 Rhee, M. J. 688
 Ricaud, C. 1789
 Rice, D. 1978, 3479
 Rice, D. H. 2007
 Richardson, R. D. 2456, 3772
 Richter, R. 1160
 Richter-Sand, R. J. 1306
 Ride, S. K. 1623
 Riedel, C. 3736
 Rietdyk, H. 2397
 Rieubland, J.-M. 2739
 Rifkin, J. 543
 Rimmer, R. 1039
 Rimmer, R. A. 871, 874, 3411
 Rinckel, T. 32
 Ringwall, A. 1703
 Ringwall, A. D. 846
 Riordon, J. 2118
 Risselada, T. 246
 Ritchie, A. L. 2210
 Ritson, D. M. 125, 143, 3778
 Riunaud, J. P. 3570
 Rivkin, L. 3429
 Rivoltella, G. 1524
 Rizzi, V. 1145
 Robb, A. 1575
 Robb, J. 2929
 Robertson, S. 2641
 Robin, D. 131, 173
 Robins, K. 1439, 1602
 Robins, K. E. 2742
 Robinson, W. 2731, 2757, 2763
 Roche, C. T. 1715
 Ródenas, J. 647
 Rodenburg, R. 2967

Rodenz, G. 2664, 3267
 Rodger, E. 2895
 Rodgers, J. 685
 Rodrigues, A. R. D. 1454
 Rodriguez, J. P. 798
 Rodriguez, R. 827, 1250
 Roecklein, J. C. 2919
 Rogdestvensky, B. V. 3822
 Rogers, J. D. 1033, 1256
 Romero, A. 128
 Rondeau, G. 420
 Rönnqvist, T. 1771
 Root, L. 372
 Ropert, A. 1512
 Roques, A. 670, 697
 Rose, C. 1669
 Rose, C. R. 2334
 Rose, J. 1172
 Rosengård, U. 1735
 Rosenthal, S. E. 694
 Rosenzweig, J. 233, 561, 1445,
 1548, 2623, 2638, 2976, 3024,
 3216, 3357, 3494
 Rosenzweig, J. B. 3021
 Roser, T. 2286, 3207, 3633, 3763
 Rosier, L. 3093
 Rosing, M. 815, 2596
 Ross, M. 522, 1975, 2019, 2234,
 2435
 Ross, M. C. 1972, 2160, 3564
 Rossa, E. 2432, 2492, 3429
 Rossi, C. 953, 956, 1145
 Rossi, L. 1524
 Rossmanith, R. 32, 429, 457, 1477
 Rostamzadeh, C. 1405
 Rotela, E. 1497
 Roth, G. 3072
 Rothman, J. L. 2307
 Rouaud, C. 3900
 Roux, D. 2932
 Rowson, P. 2172
 Roy, A. 1045
 Rubin, D. 921, 3450, 3479
 Rubingh, M. J. A. 1072
 Rudchik, A. T. 3822
 Rudd, H. 65
 Rudenko, V. 552
 Rudolph, K. 1019
 Ruggiero, A. G. 700, 3530
 Ruggiero, F. 503
 Ruiz, E. 3405
 Ruland, R. E. 2736, 2950
 Rule, D. W. 1620, 2397, 2453
 Rullier, J. L. 2656
 Ruschman, M. 809
 Rusnak, B. 1021
 Russell, S. J. 2537, 2970
 Russell, T. 605
 Russell, T. J. 1324
 Russo, D. 2286
 Rusthoi, D. P. 1669, 3118
 Ruth, R. D. 291, 543, 620, 907,
 1196, 3693
 Rutkowski, H. 703
 Rutkowski, H. L. 706
 Ryan, W. A. 2310, 2328
 Rybakov, E. 2769
 Rybalko, V. 2717
 Rychagov, A. 2769

Ryckewaert, G. 1672
 Ryder, R. 3739
 Ryne, R. 3267
 Ryne, R. D. 3229
 Ryu, C. 581
 Rzaev, R. A. 454
 Rzezonka, B. 2748

S

Saadatmand, K. 2124, 2127,
 2426, 2483, 2986, 3127, 3130,
 3133, 3145, 3151
 Sacepe, B. 697
 Sachtschale, R. J. 1339
 Saeki, H. 3885
 Sáez, P. 3033
 Sáez, P. J. 2978, 3027, 3036
 Safranek, J. 1491, 2275
 Sagalovsky, L. 288, 838, 1715
 Sagan, D. 53, 3470, 3479
 Sage, J. 1838, 2444, 2483, 3127
 Saint Laurent, M. G. 1792
 Saito, K. 673, 1024
 Saito, Y. 1193
 Sajaev, V. 230
 Sakamoto, K. 1566
 Sakamoto, S. 676, 1321
 Sakanaka, S. 1027, 3503
 Sakaue, H. A. 3845
 Sakawa, Y. 2556
 Saladin, V. 2763
 Sale, K. E. 1663
 Salimov, A. 3876
 Sampayan, S. E. 1554
 Sampson, W. 1439, 1602, 2744,
 2766
 Sampson, W. B. 2742, 2904
 Sandberg, J. 1277
 Sander, O. R. 1669, 3118
 Sanders, R. 1241
 Sanders, R. T. 1166
 Sandoval, D. P. 1669
 Sandweiss, J. 2578, 2617
 Sanford, T. W. L. 691
 Sannibale, F. 611
 Sapozhnikov, L. 2076, 2352
 Sapp, W. 1372, 2054
 Sapp, W. W. 2832, 2935, 2938,
 2941
 Saraniti, D. 921
 Saritepe, S. 354
 Sarkar, S. 1841, 1898, 1916, 1919
 Sasaki, Y. 2039
 Sass, R. 2106
 Sass, R. C. 1946
 Sathe, S. 1846, 1852
 Sato, H. 1291
 Sato, I. 546, 590, 1193, 1416,
 2516, 3087, 3705
 Sato, K. 1291, 1686
 Sato, Y. 1291, 1686
 Satogata, T. 261
 Satoh, K. 3115
 Sauer, L. 3863, 3864
 Saulter, Q. 841
 Saunders, C. 1864

- Saversky, A. J. 1030
 Savord, T. 1914, 2731, 2757
 Sawada, K. 1686
 Sawyer, D. 2838
 Sazhin, V. 2717
 Scala, R. G. 2519
 Scandale, W. 16, 246
 Schachinger, L. 1940
 Schachter, L. 1312
 Schächter, L. 2567, 2653, 2684, 2687
 Schaefer, J. 907
 Schäfer, P. 2748
 Schaffer, G. 1033, 1256
 Schailey, R. 236, 378, 1360, 1369
 Scharlemann, E. T. 1530, 1533, 1551
 Scharlemann, T. 1445
 Scheer, M. 1474
 Schegolev, L. 1384
 Schellekens, P. H. J. 2927
 Schempp, A. 3139, 3142
 Schimmel, F. 1901
 Schlenk, R. 1477
 Schlueter, R. 1572, 1575, 1581
 Schlueter, R. D. 1727
 Schmalzle, J. 2790
 Schmickler, H. 2001
 Schmid, J. 2739, 2956
 Schmidt, C. W. 1655, 1689, 1691
 Schmidt, F. 246, 500, 2301
 Schmidt, R. 44, 2103, 2133
 Schmitt, D. R. 3172
 Schmor, P. W. 2991
 Schmüser, P. 886, 918
 Schnase, A. 962, 1253, 2381
 Schneider, J. D. 1669, 3166, 3172
 Schneider, L. X. 1354
 Schneider, W. 841, 1396
 Schneider, W. J. 2929
 Schoessow, P. 1844, 2596, 3050
 Scholz, T. 1036
 Schriber, S. O. 3760
 Schukeilo, L. A. 3822
 Schultz, D. 3033
 Schultz, D. C. 2978, 3027, 3036, 3039
 Schultz, S. 2559
 Schumm, B. 2172
 Schürmann, M. 264
 Schwalm, D. 1747
 Schwandt, P. 3184, 3745
 Schwarz, H. D. 1039
 Schweppe, E.-G. 1178
 Schwettman, H. A. 950
 Schwitter, R. 3781
 Sciutto, W. 1063
 Sears, J. 763, 769, 886, 889, 892, 918, 921, 977, 995
 Sebek, J. 3018
 Sedlacek, M. 3745
 Sedlyarov, I. 1226
 Seeman, J. 1445, 1608, 2019
 Seeman, J. T. 414, 596, 638, 2423, 2507, 3234, 3564
 Segalov, Z. 685
 Seidl, P. 721
 Seifrid, P. 3533
 Seleznev, V. S. 2190
 Selin, A. V. 2853
 Sellyey, W. 2112, 2237, 2304
 Selph, F. 83
 Semertzidis, Y. 2070
 Sen, T. 134, 137, 140, 143, 146, 239, 3778
 Senichev, Y. 3509, 3642
 Seo, H. S. 2751
 Serafim, P. 1560
 Serafini, L. 3024, 3279
 Serdobintsev, G. 564, 2650
 Serebrennikov, D. 2042
 Sereno, N. S. 3246
 Sergeeva, O. S. 2853
 Serio, M. 778, 2076, 2352
 Servranckx, R. 236, 255
 Servranckx, R. V. 167, 3784
 Sessler, A. 2638
 Sessler, A. M. 1530, 2593, 2608, 3288, 3527
 Sethi, R. 1703
 Settles, M. 2172
 Severgin, Y. 2057, 2769
 Severgin, Y. P. 2208, 3205, 3820, 3822
 Shafer, B. E. 1285
 Shafer, R. E. 2316
 Shaimerdenov, E. 564
 Shako, V. V. 2406
 Shalz, L. 3748
 Shan, J. 405
 Shan, J. P. 35, 74, 3787
 Shan'gin, V. 2769
 Shankland, L. W. 1175
 Shapiro, G. 2172
 Sharma, S. 1497, 1500
 Sharp, W. M. 733, 2593
 Shatunov, Y. 3711
 Shchedrin, I. S. 1030
 Shcherbakov, A. 1480, 2057
 She, K. 995
 Shea, T. 3438
 Shea, T. J. 2310, 2328, 2916
 Sheedy, E. 3012
 Sheehan, J. 1439, 1439, 1527, 3000
 Sheffield, R. L. 2970
 Sheikh, J. Y. 1175
 Shen, J. 2178, 2438
 Sheng, I. C. 1497, 1500
 Shepard, K. W. 1042, 1045, 1694
 Shephard, W. 821
 Sherman, J. D. 3166
 Sherwin, G. 1881
 Sheynin, S. 393
 Shi, J. 242, 243, 3603
 Shibata, H. 3552
 Shibata, Y. 1614, 1617
 Shidara, T. 590, 1416
 Shih, H.-J. 387, 3588
 Shiho, M. 676, 1566
 Shiltsev, V. D. 2959
 Shinoe, K. 1509, 2295, 2337
 Shintake, T. 1048, 1051
 Shiraga, H. 2556
 Shirai, T. 1697
 Shishido, T. 992, 1024
 Shiwaku, H. 1468
 Shoace, H. 1946, 2106
 Shofstall, D. 2967
 Shoji, T. 2556
 Shoji, Y. 3633, 3763
 Shpak, A. 1480
 Shrader, M. B. 1103
 Shtirbu, S. 1934
 Shu, Q. S. 921, 2787
 Shu, Q.-S. 3888, 3891
 Shutt, R. 2744
 Shvedunov, V. I. 1069, 2059
 Shvets, G. 2635
 Sibley, C. 1372, 2054, 2868
 Siddons, D. P. 2145
 Siemann, R. 2019, 2370
 Siemann, R. H. 532, 2373, 3240
 Siergiej, D. 3482
 Sievers, W. 1916
 Siffert, P. 1363
 Sigov, Y. S. 2620
 Sikora, R. E. 2328, 2916
 Sillanoli, M. 2492
 Silva, J. 3093
 Sim, J. W. 2856
 Simmons, J. 3888
 Simpson, J. 815, 2596, 3050, 3061
 Simrock, S. 1925, 2184
 Simrock, S. N. 599, 1909, 2364, 3515
 Sims, R. E. 2769
 Sinclair, C. 3663
 Sinclair, C. K. 1109, 3246
 Singh, O. 2254, 2284
 Sissakian, A. 2042
 Skachkov, D. G. 3675
 Skachkov, V. S. 2853
 Skarpaas, K. 1039, 3030
 Sladen, J. P. H. 2346
 Sloan, T. 29, 224, 227, 420, 1421
 Sluijk, T. 2343
 Smellie, R. 2757, 2781
 Smirnov, Y. 2042
 Smith, B. H. 1175
 Smith, D. D. 2705, 2708, 2711
 Smith, D. L. 667
 Smith, D. R. 1075, 2559
 Smith, H. V., Jr. 3172
 Smith, J. 1852, 2222, 2284
 Smith, J. D. 1846, 1849
 Smith, J. R. 694
 Smith, K. S. 3178
 Smith, L. 3678
 Smith, M. 1669, 3118
 Smith, P. 1718, 2953
 Smith, S. L. 1494, 1638, 3594, 3672
 Smolucha, J. 1817, 1912
 Smolyakov, N. V. 1626
 Smythe, W. R. 1054
 Snee, D. 1013
 Snitchler, G. 3888
 Snyder, D. 1620
 Snydstrup, L. 3897
 So, I. 2275
 Sobczynski, S. 1372, 3851
 Sohn, Y. U. 2751
 Sokolov, S. V. 318, 320
 Sokolowski, J. S. 849
 Solensten, L. 2133

Solheim, N. 2956
 Solomon, L. 1439, 1602, 1605
 Solomons, R. 3748
 Sommer, F. 2748
 Sommer, M. 1465
 Somov, L. 552
 Song, J. 1057, 2142
 Song, J. J. 2213, 3393, 3396
 Song, T. 2199
 Sortais, P. 1789, 1792
 Soukas, A. 1277, 3633
 Soukas, A. V. 1345
 Soundranayagam, R. 1360
 Spädtkle, P. 1645, 1738
 Spalek, G. 1021
 Spanggaard, J. 2492
 Spata, M. 841
 Spataro, B. 611, 778
 Spataro, C. 2883
 Spayd, N. 880, 3405
 Specht, J. E. 1694
 Specht, V. 2670
 Specka, A. 2450
 Spence, W. 2019
 Spence, W. L. 3234, 3576
 Spencer, J. 543, 2025, 2638
 Spencer, J. E. 396
 Spencer, N. 1884, 1969, 1975
 Spencer, T. A. 2693
 Spinos, F. 2757
 Spitz, R. 1166, 1241
 Sprangle, P. 1560, 2584, 2629, 2632, 2647
 Sredniawski, J. 821, 2133, 3193
 Srinivasan-Rao, T. 3012
 Stagno, V. 775, 1524
 Stallard, B. 1551
 Stallard, B. W. 1554
 Stampke, S. 203, 2781
 Staples, J. W. 1759
 Stapleton, G. 2184
 Starker, J. 1735
 Starkovich, V. S. 1075
 Steck, M. 1645, 1738
 Steckmeyer, J. C. 1792
 Stefan, P. M. 895
 Stege, R. E., Jr. 2234
 Steimel, J. M., Jr. 2100, 2231
 Steinbach, C. 339
 Steiner, H. 2172
 Steinhauer, L. C. 2564, 2581, 2614
 Stelzer, J. E. 3172
 Stepanov, A. 2426
 Stepp, J. D. 1157, 1408, 1906
 Steski, D. B. 3178
 Stevens, J. 3357
 Stevens, R. R., Jr. 3166
 Stevenson, N. 1733
 Stevenson, N. R. 3099
 Stiening, R. 143, 239, 3778
 Stillman, A. 2471
 Stittsworth, D. 2124, 2130
 Stoker, J. 703
 Stover, G. 1351
 Strait, J. 2769
 Strakhovenko, V. M. 3093
 Strelkov, M. 1480, 2057
 Strelkov, M. A. 194

Striffler, C. D. 2667, 2670, 3075
 Stringfield, R. 2675
 Stringfield, R. M. 2664
 Struckmeier, J. 1645
 Stuart, M. E. 1727
 Stucki, H. 339
 Stupakov, G. V. 197
 Su, G. 1411
 Su, J. J. 2638
 Subbotin, S. 552
 Sudou, M. 1291, 1686
 Suemine, S. 650
 Suenaga, M. 2904
 Sueno, T. 1291
 Suetsugu, Y. 3860
 Sugahara, R. 2340
 Suhring, S. 587
 Sulgin, I. 916
 Suller, V. P. 1494, 1638, 3594, 3672
 Sullivan, C. A. 2644
 Sullivan, M. 131
 Sulyaev, R. M. 454
 Summers, L. K. 1220
 Sun, D. 1127
 Sun, H. 3696
 Sun, N. 515
 Sun, T. 1411
 Sundelin, R. M. 1092
 Sundquist, M. 3745
 Surma, I. V. 2059
 Susta, J. 1060
 Suwada, T. 2516, 3087, 3705
 Suzuki, H. 2039
 Suzuki, K. 2556
 Suzuki, S. 602
 Suzuki, T. 1024
 Svandrlik, M. 953, 956, 1145
 Svinin, M. P. 555
 Swartz, M. 2172
 Swenson, D. 1703
 Swenson, D. A. 812, 846, 2426
 Swenson, D. R. 3175
 Sychev, V. 2769
 Symon, K. 285
 Syphers, M. 29, 203, 224, 227
 Syphers, M. J. 38, 134, 137, 140, 146, 420, 3588
 Sytchevsky, S. E. 3205
 Sytnikov, V. 2769

T

Tacconi, E. J. 1098, 2139
 Tadokoro, M. 309
 Tagawa, S. 3552
 Tajima, T. 1024, 2556
 Takada, E. 1291, 1686
 Takada, Y. 1291
 Takahashi, N. 546
 Takahashi, S. 3845
 Takahashi, T. 1614, 1617
 Takaki, H. 1509
 Takamuku, S. 650
 Takasaki, E. 1163
 Takayama, K. 673, 2205
 Takeda, O. 3115

Takeda, S. 1309
 Takeda, Y. 1783
 Takenaka, T. 1163
 Takeo, T. 2409
 Tallerico, P. 1683
 Tallerico, P. J. 1199
 Talman, R. 203, 236
 Tamezane, K. 602
 Tamura, K. 2409
 Tanabe, J. 2850
 Tanabe, T. 1291, 3006
 Tanabe, Y. 3115
 Tanaka, M. 360, 2907
 Tang, C. 1623
 Tang, H. 2978, 3027, 3033, 3036, 3039
 Tang, Y. 1852, 2275
 Tang, Y. N. 492, 1846
 Tanii, T. 2205
 Tantawi, S. 543, 936, 1106
 Tantawi, S. G. 620, 1121, 1130, 1196
 Tao, Q. 2841
 Taran, A. 2769
 Tarasenko, A. 1480, 2057
 Taratin, A. 2489
 Tarovik, M. N. 3822
 Tarrant, M. 1937
 Tatchyn, R. 1445, 1536, 1539, 1542, 1608, 2429
 Taylor, B. 1142, 1238
 Taylor, L. 824
 Tazzari, S. 573, 968
 Tazzioli, F. 573, 3279
 Tecchio, L. 3243
 Tecker, F. 2432, 3429
 Tekawa, M. 3748
 Tegin, Y. 1480, 2057
 Temkin, R. J. 2575, 2656, 2690, 2696
 Temnykh, A. B. 2007, 3476
 Tenenbaum, P. 2838
 Teng, L. 224, 285, 420, 1485
 Teng, L. C. 182
 Tepikian, S. 168, 420
 Terrien, J. C. 1187
 Terzi, F. 1063
 TESLA Collaboration 537
 Thern, R. E. 2471
 Thevenot, M. 670, 697
 Thiagarajan, V. 3372
 Thieberger, P. 3178
 Thielheim, K. O. 276
 Thiessen, H. 3297
 Thiessen, H. A. 1021, 3760
 Thivent, M. 339
 Thomas, M. G. 1419
 Thomas, P. 3053
 Thompson, K. 3757
 Thompson, K. A. 543, 3342, 3693
 Thompson, K. M. 2808, 2814
 Thompson, P. 2744, 2766
 Thompson, P. A. 2754
 Thorndahl, L. 1066, 3426
 Thuot, M. E. 1806
 Tidwell, S. C. 2564
 Tiefenback, M. 587
 Tiefenback, M. G. 426
 Tieger, D. 2054, 2871, 2874

Tieger, D. R. 2832, 2938
 Tighe, R. 2370, 2373
 Tigner, M. 769, 918, 921, 977,
 995, 3450, 3479, 3690, 3931
 Timmer, C. A. 2970
 Timmermans, C. J. 1072, 1820,
 2892, 2927, 3645
 Ting, A. 2629, 2632
 Titcomb, C. 2956
 Tiunov, A. V. 1069, 2059
 Tiunov, M. 2650
 Tkatchenko, A. 1465
 Tobiyama, M. 2409
 Todd, A. M. M. 1774, 1777
 Toge, N. 98, 100, 116, 3912
 Tojyo, E. 1783
 Tokuchi, A. 676
 Tokuda, N. 1783
 Tokumoto, S. 1202
 Toldo, F. 1241
 Tolstun, N. G. 555
 Tomassini, D. 1477
 Tomizawa, M. 41, 1780, 1783,
 1786
 Tomkins, J. C. 2769
 Tomlin, R. 2228, 3787
 Tommasini, D. 1375, 1378, 2820
 Tompkins, P. A. 1448
 Tooker, T. F. 1706
 Tool, G. 1405, 2731, 2757
 Tornoe, R. N. 1103
 Tosolini, P. 1333, 1378
 Towne, N. A. 2415
 Toyama, S. 546
 Toyoda, K. 3006
 Tran, H. J. 3402
 Tran, P. 173
 Tran-Ngoc, T. 829, 832, 1039
 Travier, S. 3053
 Travish, G. 561, 1445, 1533,
 1548, 3216
 Trbojevic, D. 102, 168
 Treas, P. 608, 611
 Tribendis, A. 977, 3450
 Tribouillard, C. 1792
 Trifonov, D. E. 682
 Tron, A. M. 2403, 2406
 Tronc, D. 1768
 Trost, H.-J. 2705, 2708, 2711
 Trotsenko, V. 1480
 Trotz, S. 2575, 2699
 Trzeciak, W. 285
 Tsai, H. J. 1943
 Tsang, K. T. 3270
 Tsarik, S. V. 454
 Tschalaer, C. 2054
 Tsiang, E. Y. 3621
 Tsoupas, N. 2895
 Tsuchidate, H. 1515
 Tsuchiya, M. 3845
 Tsumori, K. 650
 Tsyganov, E. 2468, 2489
 Tuckmantel, J. 806
 Tuli, M. 3888
 Tupa, D. 3175
 Turchetti, G. 273
 Turlington, L. 939, 1109
 Turner, J. L. 2978, 3027, 3036

Turner, L. R. 2799, 2808, 2814,
 2817
 Turner, W. 3876, 3888
 Turner, W. C. 3833
 Tyrroff, H. 1477
 Tyson, E. 2967

U

Ueda, A. 215
 Ueda, S. 3903
 Ueda, T. 3552
 Ueng, T. S. 2031
 Ueyama, Y. 2039
 Uggerhøj, E. 1363
 Uher, T. 2382
 Uhm, H. S. 2599, 2602, 2605,
 2678
 Ulc, S. 2578
 Umezawa, H. 1024
 Umstadter, D. 2632
 Underwood, K. 1884, 1969
 Unser, K. B. 2394
 Urano, T. 2516, 3705
 Urasawa, S. 1614, 1617
 Ushakov, V. 564, 1384
 Ushkov, V. 564
 Utino, K. 1291
 Utterback, J. 1928, 1931

V

Vaccarezza, C. 3906
 Vaccaro, V. 2154
 Vaidya, M. 1010
 Vakhrushin, Y. P. 682
 Valbuena, R. 2202
 Valicenti, R. A. 3133
 Val'kov, A. E. 3822
 van Asselt, W. 3633, 3763
 van den Berk, F. 1820
 van der Heide, J. A. 1072
 van der Laan, J. 1901, 1998
 van der Stok, P. D. V. 1820
 Vandeusen, A. 2124, 2130
 Van Deusen, A. L. 2121
 van de Vijver, Y. 1820
 van Dyck, O. 369
 Vanecek, D. 703
 van Garderen, G. 1901
 van Laar, J. 3645
 van Oers, W. T. H. 2991
 VanOlst, D. 1884
 van Steenbergen, A. 2578
 Van Straagen, P. K. 86
 Van Westrum, D. C. 1054
 van Zeijts, J. 587
 Variale, V. 775, 1524
 Varisco, G. 1524
 Vasil'ev, A. N. 315
 Vasiliev, A. 2717
 Vasserman, I. 3711
 Vaughn, G. 1669
 Vejck, S. 2199
 Vella, M. C. 3157

Verdier, A. 158, 161, 249
 Verdú, G. 647
 Vergamini, A. 1205
 Vescovi, W. C. 611
 Veshcherevich, V. 977, 1226,
 3450
 Vetter, A. M. 1075
 Vignola, G. 611, 1993, 2048
 Villate, D. 670, 697, 2115
 Vinnik, V. 1297
 Vinokurov, N. A. 1442
 Viola, R. 2913
 Vishnevsky, I. N. 3822
 Visnjic, V. 3811, 3814
 Vlieks, A. 543, 1106
 Vlieks, A. E. 620, 1121, 1196,
 1208
 Vobly, P. D. 2751
 Vodopianov, F. A. 1078
 Vogel, H. 1080
 Volk, K. 3139
 Volzhev, A. A. 682
 Vong, F. C. 1906
 Vormann, H. 3139
 Vorobjov, I. A. 1675
 Voroshilov, A. N. 2022, 3669
 Vos, L. 2301
 Voss, D. 285
 Votaw, A. 2112
 Votaw, A. J. 1814
 Vouillot, J. M. 2495
 Vretenar, M. 3121
 Vulcan, W. 3103
 Vylet, V. 543, 1445

W

Wadlinger, E. A. 1669
 Wagner, W. 2838
 Wait, G. D. 1148, 1181, 1330,
 3402
 Wake, M. 2769
 Walend, D. 2953
 Walker, N. 2019
 Walker, N. J. 92, 95, 98, 100,
 116, 119
 Walker, R. P. 1587, 1593, 2844,
 2847
 Wallace, J. D. 1033, 1256
 Walling, L. 824, 877, 880, 1083,
 3405, 3888
 Walstrom, P. 1021
 Walter, M. 3351
 Walter, M. T. 2693
 Walz, D. 185
 Walz, H. V. 2838
 Wan, W. 155
 Wanderer, P. 2726, 2744, 2766
 Wang, C. 1575, 1578, 2608
 Wang, C. J. 1878
 Wang, D. 2013, 2331, 3429, 3851
 Wang, D. X. 62, 3282, 3627, 3660
 Wang, D. Y. 1451, 1949
 Wang, F. 378, 381, 1360
 Wang, J. G. 62, 3282, 3627, 3660
 Wang, J. M. 1419

Wang, J. W. 543, 620, 907, 1086, 1208
Wang, K. 3148
Wang, M. H. 1943
Wang, S. 1411
Wang, T. 3297
Wang, T. F. 883, 3500
Wang, T.-S. 2319
Wang, X. 2051, 2112, 2237
Wang, X. J. 2486, 3000
Wang, X. Q. 1033, 1256
Wang, Y. 29, 224, 227, 420, 3845
Wang, Y. L. 546
Wangler, T. P. 1712, 3606, 3657
Warn, C. E. 2400
Warner, D. 2760
Warnock, R. L. 291, 3378
Warren, D. S. 2480
Watanabe, A. 1566
Watanabe, K. 3845
Watanabe, M. 1515
Watanabe, S. 41, 1291, 2714
Watanabe, T. 41
Waters, G. 1148, 1181
Waters, J. W. 1448
Watson, S. 3055
Watson, S. A. 2447
Weaver, H. J. 2959
Weaver, J. 2714
Weaver, J. N. 3018
Webber, R. 2118
Webber, R. C. 2094, 2382
Weber, K. J. 1387, 2877
Webers, G. A. 2062, 2065, 2927, 3423
Wedekind, M. 3184
Wei, J. 258, 3527, 3651
Wei, K. 312
Weihreter, E. 1474
Weingarten, W. 806
Weisend, J., II 2757
Weiss, R. 1669
Weissenburger, D. 1439
Weisz, S. 26
Welbourne, L. A. 1494, 1638, 3594, 3672
Welch, D. R. 661, 3549
Welch, J. J. 2007, 3476
Wells, F. D. 2316
Wells, R. P. 1727, 3169
Weng, W. T. 3264, 3633, 3726, 3763
Wenninger, J. 44
Werkema, S. J. 3303, 3309, 3573
Wesolowski, W. 605
Westenskow, G. 2638
Westenskow, G. A. 2611
Wetherholt, D. M. 2483
Wetzels, S. F. C. L. 2927
Wheat, R. M. 2664
Whelen, C. 2967
White, G. R. 1881
White, M. 605
Whitham, K. 608, 611, 1244
Whittenberg, W. A. 2483, 3130
Whittum, D. 2638, 3552
Whittum, D. H. 673, 3288, 3399
Wienands, U. 255, 393
Wiik, B. H. 1

Wildman, D. 405, 1223, 3258
Wilke, M. D. 2480
Wilkinson, C. 366, 369, 2216, 2219, 3297
Willeke, F. 3742
Willen, E. 2744, 2766, 2790
Williams, R. 2638
Williams, S. H. 2838
Wilson, D. C. 3090
Wilson, I. 641
Wilson, P. 2681
Wilson, P. B. 543, 620, 1208
Winans, J. R. 1957
Wines, R. 3103
Wingate, C. A. 3090
Winick, H. 173, 1445, 1608
Winkler, G. 2956
Wiseman, M. 841, 1060, 2929
Wisnivesky, D. 1089, 1454
Witherspoon, S. 599
Witherspoon, S. D. 2364
Won, S. C. 1832
Wood, F. 2118
Wood, R. 1551, 1712
Woodbury, K. 1912
Woodle, M. 1439, 2578, 3000
Woodley, M. 92, 95, 119, 2019
Woodley, M. D. 3576
Woods, M. 2172, 2978, 3036, 3045, 3047
Woods, M. B. 3027
Woods, R. 3760
Woodworth, E. 2184
Worm, T. 1363
Worth, G. T. 3118
Wright, B. 998
Wright, E. 1106
Wright, E. L. 1259
Wright, S. 2124, 2130
Wu, B. 1611
Wu, D. 173
Wu, G. 2228, 2252
Wu, X. 255, 393
Wu, Y. 218, 1901, 1998, 2889
Wuensch, W. 641, 2346
Wuppertal, U. 995
Wurtele, J. 2638
Wurtele, J. S. 2575, 2635, 2699, 3327, 3399
Wüstefeld, G. 1474
Wyss, C. 2016

X

Xi, B. 2892, 3645
Xie, M. 1445, 1533
Xiu, L. 3148
Xu, C. Y. 3845
Xu, G. 3237
Xu, Y. 3148

Y

Yakimenko, V. 450
Yakovlev, S. 824

Yakovlev, V. 2650
Yakovlev, V. P. 877, 941
Yamada, S. 1291, 1686
Yamada, T. 1291, 1686
Yamaguchi, S. 959
Yamakawa, T. 215, 1614, 1617
Yamamoto, N. 466, 2340
Yamamoto, T. 650
Yamashita, Y. 676
Yamazaki, Y. 3087
Yampolsky, I. 1327
Yan, C. 2136, 3103
Yan, Y. 236, 3402
Yan, Y. T. 29, 38, 224, 227, 242, 243, 420, 423, 515
Yanagi, Y. 3845
Yanagida, K. 602
Yandon, J. C. 1916
Yang, B. 3243
Yang, X.-F. 2462
Yao, C. G. 812
Yao, C. Y. 122, 2444
Yarba, V. 236
Yarosh, V. E. 1795
Yartsev, D. I. 1795
Yelk, J. 2070
Yen, E. 1460
Yeremian, A. 543
Yeremian, A. D. 2978, 3027, 3063
Yeung, K. S. 2385
Yin, Y. 2441
Yokomizo, H. 602, 2039
Yokota, M. 3087
Yokouchi, S. 3845
Yokoya, K. 3441
Yoneda, C. 620
Yonehara, H. 2039
Yoneyama, S. 2039
Yoon, J. R. 2796
Yoon, M. 3273
York, R. 236, 255, 393, 3739
York, R. L. 3175
Yoshida, K. 1780, 1783
Yoshida, Y. 3552
Yoshikawa, H. 602
Yoshioka, M. 1614, 1617
Yoshizawa, J. 1291, 1686
Yoshizawa, M. 41, 1783, 1786
Young, A. 1205, 1285
Young, A. T. 1727, 3042
Young, L. M. 790, 3136
Youngman, B. 543
Yu, D. 2388, 2681
Yu, D. U. L. 936
Yu, J. X. 1727
Yu, K. 2787, 3888, 3891
Yu, L. H. 1439, 1602
Yu, S. 703, 709, 3199
Yu, S. S. 712
Yu, X. T. 3327, 3399
Yuan, V. 1669
Yücel, A. 3879
Yudin, I. P. 191, 297, 1892
Yudin, L. A. 2543
Yudin, L. I. 1795
Yugami, N. 2556, 3552
Yule, T. 1709
Yule, T. J. 1777
Yunn, B. 3663

Yunn, B. C. 179, 1092, 1909
Yupinov, Y. 564
Yvlov, T. 2042

Z

Zach, M. 1151
Zagel, J. R. 2193
Zakhavatkin, M. N. 2022
Zaltsman, A. 1241
Zangrando, D. 1587, 2844, 2847
Zante, T. 608, 611
Zapalac, G. 2172
Zapolsky, V. N. 454
Zapryagaev, I. 2650
Zarcone, M. J. 3178
Zarucheisky, V. G. 454
Zatopek, J. 2757
Zbasnik, J. 2787, 3888, 3891
Zelanzy, M. 1884
Zelazny, M. 1966
Zelenski, A. N. 2991

Zelinsky, A. Y. 194, 1480
Zelynsky, A. 2057
Zenkevich, P. 2073
Zhabitsky, V. M. 2543
Zhang, B. 1001
Zhang, C. 312, 3237
Zhang, H. 2841
Zhang, M. 1411
Zhang, P. 176
Zhang, P. L. 29, 224, 227, 420
Zhang, Q. 1411
Zhang, R. 561, 575, 3009, 3216
Zhang, S. Y. 1277, 3264
Zhang, T. 306, 2556, 2841
Zhang, W. 2841
Zhang, X. 312, 1439, 1599, 1721, 2841, 3081
Zhang, X. L. 3237
Zhang, Z. 303, 1611
Zhao, Y. 1033, 1256
Zhao, Z. 2841
Zhao, Z. T. 3237
Zhmendak, A. V. 3822
Zholents, A. 131

Zhou, C. 2841
Zhou, J. 3396, 3772
Zhou, P. 3303, 3309, 3540, 3573
Ziemann, V. 98, 100, 108, 114, 116, 498, 1483, 3909
Zinchenko, A. 2468, 2489
Zinkann, G. P. 1694
Zinneman, T. 1709
Zinneman, T. E. 3210
Ziomek, C. 1154, 3213
Ziomek, C. D. 2391
Zisman, M. S. 2010
Zolfaghari, A. 829, 832, 2331, 3851
Zolfaghari, Z. 2054
Zolotorev, M. 2172, 3027, 3045
Zolotorev, M. S. 2978, 3036
Zoni, G. 1063
Zotter, B. 3347, 3429
Zu, D. 1095
Zumbro, J. 1021
Zumbro, J. D. 2832, 2941
Zyngier, H. 1465